NIST Special Publication 1018-3
Sixth Edition

Fire Dynamics Simulator Technical Reference Guide Volume 3: Validation

Kevin McGrattan
Simo Hostikka
Jason Floyd
Randall McDermott
Marcos Vanella

http://dx.doi.org/10.6028/NIST.SP.1018

VTT Technical Research Centre of Finland

National Institute of Standards and Technology
U.S. Department of Commerce

NIST Special Publication 1018-3
Sixth Edition

Fire Dynamics Simulator Technical Reference Guide Volume 3: Validation

Kevin McGrattan
Randall McDermott
Marcos Vanella
Fire Research Division, Engineering Laboratory, Gaithersburg, Maryland

Simo Hostikka
Aalto University, Espoo, Finland

Jason Floyd
UL Fire Safety Research Institute, Columbia, Maryland

http://dx.doi.org/10.6028/NIST.SP.1018

June 28, 2022
Revision: FDS6.7.9-0-gec52dee42

U.S. Department of Commerce
Gina M. Raimondo, Secretary

National Institute of Standards and Technology
Laurie E. Locascio, NIST Director and Undersecretary of Commerce for Standards and Technology

National Institute of Standards and Technology Special Publication 1018-3
Natl. Inst. Stand. Technol. Spec. Publ. 1018-3, 1084 pages (October 2013)
CODEN: NSPUE2

FDS Developers

The Fire Dynamics Simulator and Smokeview are the products of an international collaborative effort led by the National Institute of Standards and Technology (NIST) and VTT Technical Research Centre of Finland. Its developers and contributors are listed below.

Principal Developers of FDS

Kevin McGrattan, NIST, Gaithersburg, Maryland
Simo Hostikka, Aalto University, Espoo, Finland
Jason Floyd, UL Fire Safety Research Institute, Columbia, Maryland
Randall McDermott, NIST, Gaithersburg, Maryland
Marcos Vanella, NIST, Gaithersburg, Maryland

Principal Developer of Smokeview

Glenn Forney, NIST, Gaithersburg, Maryland

Principal Developer of FDS+Evac

Timo Korhonen, VTT, Finland

Contributors

Salah Benkorichi, BB7, UK
Daniel Haarhoff, Jülich Supercomputing Centre, Germany
Susan Kilian, hhpberlin, Germany
Vivien Lecoustre, University of Maryland, College Park, Maryland
Anna Matala, VTT, Finland
William Mell, U.S. Forest Service, Seattle, Washington
Kristopher Overholt, RStudio, Austin, Texas
Benjamin Ralph, University of Edinburgh, UK
Topi Sikanen, VTT, Finland
Julio Cesar Silva, Brazilian Navy, Brazil
Ben Trettel, The University of Texas at Austin
Craig Weinschenk, UL Fire Safety Research Institute, Columbia, Maryland

About the Developers

Kevin McGrattan is a mathematician in the Fire Research Division of NIST. He received a bachelor of science degree from the School of Engineering and Applied Science of Columbia University in 1987 and a doctorate at the Courant Institute of New York University in 1991. He joined the NIST staff in 1992 and has since worked on the development of fire models, most notably the Fire Dynamics Simulator.

Simo Hostikka is an associate professor of fire safety engineering at Aalto University School of Engineering, since January 2014. Before joining Aalto, he worked as a Principal Scientist and Team Leader at VTT Technical Research Centre of Finland. He received a master of science (technology) degree in 1997 and a doctorate in 2008 from the Department of Engineering Physics and Mathematics of the Helsinki University of Technology. He is the principal developer of the radiation and solid phase sub-models within FDS.

Jason Floyd is a Lead Research Engineer at the Underwriters Laboratories Fire Safety Research Institute in Columbia, Maryland. He received a B.S. (1993), M.S (1995), and a Ph.D. (2000) from the Nuclear Engineering Program of the University of Maryland. After graduating, he was awarded a National Research Council Post-Doctoral Fellowship at the Building and Fire Research Laboratory of NIST. He is a principal developer of the combustion, control logic, aerosol, droplet evaporation, and HVAC sub-models within FDS.

Randall McDermott joined the Fire Research Division at NIST in 2008. He received a B.S. from the University of Tulsa in Chemical Engineering in 1994 and a Ph.D. from the University of Utah in 2005. His research interests include subgrid-scale models and numerical methods for large-eddy simulation, turbulent combustion, immersed boundary methods, and Lagrangian particle methods.

Marcos Vanella joined the Fire Research Division at NIST in 2019. He received diplomas in Mechanical and Aeronautical Engineering from the National University of Cordoba, Argentina, and M.S. and Ph.D. degrees in Mechanical Engineering from the University of Maryland, College Park. His research interests include computer simulation and scientific software development applied to engineering systems, mainly in the areas of fluid flow and multiphysics interaction problems.

Glenn Forney is a computer scientist in the Fire Research Division of NIST. He received a bachelor of science degree in mathematics from Salisbury State College and a master of science and a doctorate in mathematics from Clemson University. He joined NIST in 1986 (then the National Bureau of Standards) and has since worked on developing tools that provide a better understanding of fire phenomena, most notably Smokeview, an advanced scientific software tool for visualizing Fire Dynamics Simulation data.

Timo Korhonen is a Senior Scientist at VTT Technical Research Centre of Finland. He received a master of science (technology) degree in 1992 and a doctorate in 1996 from the Department of Engineering Physics and Mathematics of the Helsinki University of Technology. He is the principal developer of the evacuation sub-model within FDS.

Daniel Haarhoff did his masters work at the Jülich Supercomputing Centre in Germany, graduating in 2015. His thesis is on providing and analyzing a hybrid parallelization of FDS. For this, he implemented OpenMP into FDS 6.

Susan Kilian is a mathematician with numerics and scientific computing expertise. She received her diploma from the University of Heidelberg and received her doctorate from the Technical University of Dortmund in 2002. Since 2007 she has been a research scientist for hhpberlin, a fire safety engineering firm located in Berlin, Germany. Her research interests include high performance computing and the development of efficient parallel solvers for the pressure Poisson equation.

Vivien Lecoustre is a Research Associate at the University of Maryland. He received a master of science in Aerospace Engineering from ENSMA (France) in 2005 and a doctorate in Mechanical Engineering from the University of Maryland in 2009. His research interests include radiation properties of fuels and numerical turbulent combustion.

Anna Matala worked as a research scientist at VTT Technical Research Centre of Finland 2008-2019. She received her PhD from Aalto University School of Science in 2013 and MSc in Systems and Operations Research from Helsinki University of Technology in 2008. She works as a fire safety engineering and research consultant. Her research concentrates on pyrolysis modelling and parameter estimation in fire simulations.

William (Ruddy) Mell is an applied mathematician currently at the U.S. Forest Service in Seattle, Washington. He holds a B.S. degree from the University of Minnesota (1981) and doctorate from the University of Washington (1994). His research interests include the development of large-eddy simulation methods and sub-models applicable to the physics of large fires in buildings, vegetation, and the wildland-urban interface.

Kristopher Overholt is a solutions engineer at RStudio. He received a B.S. in Fire Protection Engineering Technology from the University of Houston-Downtown in 2008, an M.S. in Fire Protection Engineering from Worcester Polytechnic Institute in 2010, and a Ph.D. in Civil Engineering from The University of Texas at Austin in 2013. He worked in the Fire Research Division at NIST from 2013 to 2015, where he was central to the development of the FDS continuous integration framework, Firebot. He also worked on aspects of FDS related to verification and validation and quality metrics. His research interests include inverse fire modeling problems, soot deposition in fires, and the use of fire models in forensic applications.

Topi Sikanen is a Research Scientist at VTT Technical Research Centre of Finland and a graduate student at Aalto University School of Science. He received his M.Sc. degree in Systems and Operations Research from Helsinki University of Technology in 2008. He works on the Lagrangian particle and liquid evaporation models.

Ben Trettel is a graduate student at The University of Texas at Austin. He received a B.S. in Mechanical Engineering in 2011 and an M.S. in Fire Protection Engineering in 2013, both from the University of Maryland. He develops models for the transport of Lagrangian particles for the Fire Dynamics Simulator.

Julio Cesar Silva is a Lieutenant in the Naval Engineers Corps of the Brazilian Navy. He worked in the Fire Research Division of NIST as a Guest Researcher from National Council for Scientific and Technological Development, Brazil. He received a M.Sc. in 2010 and a doctorate in 2014 from Federal University of Rio de Janeiro in Civil Engineering. His research interests include fire-structure interaction and he develops coupling strategies between FDS and finite-element codes.

Benjamin Ralph is a fire safety engineer and Ph.D. student at the BRE Centre for Fire Safety Engineering at University of Edinburgh, UK. He received his M.Eng. in Civil Engineering from the University of Southampton, UK in 2008 and his P.G.Dip. in Fire Safety Engineering from the University of Ulster, UK in 2014. He was a Guest Researcher in the Engineered Fire Safety Group at NIST in 2016. His research interests include coupled hybrid modeling and performance-based design in fire safety engineering. He is a developer of the HVAC sub-model - specifically the transient mass and energy transport solver.

Salah Benkorichi is a researcher and a Fire Engineer at the BB7, in Manchester, UK. He received his M.Sc. in 2016 from the University of Poitiers. His research activities focus on flame spread and pyrolysis modeling using multi-scale methods.

Craig Weinschenk is a Lead Research Engineer at the Underwriters Laboratories Fire Safety Research Institute, in Columbia, Maryland. He worked in the Fire Research Division at NIST as a National Research Council Postdoctoral Research Associate in 2011. He received a B.S. from Rowan University in 2006 in Mechanical Engineering. He received an M.S. in 2007 and a doctorate in 2011 from The University of Texas at Austin in Mechanical Engineering. His research interests include numerical combustion, fire-structure interaction, and human factors research of fire-fighting tactics.

Preface

This is Volume 3 of the FDS Technical Reference Guide. Volume 1 describes the mathematical model and numerical method. Volume 2 documents past and present model verification work. Instructions for using FDS are contained in a separate User's Guide [1].

The FDS Technical Reference Guide is based in part on the "Standard Guide for Evaluating the Predictive Capability of Deterministic Fire Models," ASTM E 1355 [2]. ASTM E 1355 defines *model evaluation* as "the process of quantifying the accuracy of chosen results from a model when applied for a specific use." The model evaluation process consists of two main components: verification and validation. *Verification* is a process to check the correctness of the solution of the governing equations. Verification does not imply that the governing equations are appropriate; only that the equations are being solved correctly. *Validation* is a process to determine the appropriateness of the governing equations as a mathematical model of the physical phenomena of interest. Typically, validation involves comparing model results with experimental measurement. Differences that cannot be explained in terms of numerical errors in the model or uncertainty in the measurements are attributed to the assumptions and simplifications of the physical model.

Evaluation is critical to establishing both the acceptable uses and limitations of a model. Throughout its development, FDS has undergone various forms of evaluation, both at NIST and beyond. This volume provides a survey of validation work conducted to date to evaluate FDS.

Disclaimer

The US Department of Commerce makes no warranty, expressed or implied, to users of the Fire Dynamics Simulator (FDS), and accepts no responsibility for its use. Users of FDS assume sole responsibility under Federal law for determining the appropriateness of its use in any particular application; for any conclusions drawn from the results of its use; and for any actions taken or not taken as a result of analysis performed using these tools.

Users are warned that FDS is intended for use only by those competent in the fields of fluid dynamics, thermodynamics, heat transfer, combustion, and fire science, and is intended only to supplement the informed judgment of the qualified user. The software package is a computer model that may or may not have predictive capability when applied to a specific set of factual circumstances. Lack of accurate predictions by the model could lead to erroneous conclusions with regard to fire safety. All results should be evaluated by an informed user.

Throughout this document, the mention of computer hardware or commercial software does not constitute endorsement by NIST, nor does it indicate that the products are necessarily those best suited for the intended purpose.

Acknowledgments

The following individuals and organizations played a role in the validation process of FDS.

- The US Nuclear Regulatory Commission Office of Research has funded key validation experiments, the preparation of the FDS manuals, and the development of various sub-models that are of importance in the area of nuclear power plant safety. Special thanks to Mark Salley, David Stroup, and Jason Dreisbach for their efforts and support.

- Anthony Hamins of NIST directed the NIST/NRC and WTC experiments, conducted smaller methane burner measurements, and quantified the experimental uncertainty of these and other experiments used in this study. Alex Maranghides was the Director of the Large Fire Laboratory at NIST at the time these tests were conducted, and he helped to design the experiments. Therese McAllister oversaw the instrumentation of the structural steel during the WTC experiments.

- Anthony Hamins of NIST developed the technique of evaluating experimental uncertainty that is used throughout this Guide. Blaza Toman of the Statistical Engineering Division of NIST developed the method of quantifying the model uncertainty.

- Rick Peacock of NIST assisted in the interpretation of results from the "NBS Multi-Room Test Series," a set of three room fire experiments conducted at the National Bureau of Standards (now NIST) in the mid-1980's.

- Bryan Klein, currently employed at Thunderhead Engineering, Inc., assisted in the development of techniques to automatically generate the plots that are found throughout this Guide.

- Bill Pitts, Nelson Bryner, and Erik Johnsson of NIST contributed and interpreted test data for the "NIST Reduced Scale Enclosure Experiments." Matthew Bundy, Erik Johnsson, Paul Fuss, David Lenhart, Sung Chan Kim, and Andrew Lock of NIST contributed similar data collected within a full-scale standard compartment in 2010.

- Rodney Bryant of NIST contributed velocity profile data for the "Bryant Doorway" series.

- Anthony Putorti and Scott Bareham of NIST contributed temperature measurements from plate thermometer experiments in a cone calorimeter.

- David Sheppard, currently of the Bureau of Alcohol, Tobacco and Firearms (ATF), conducted the experiments referred to as the "UL/NFPRF Test Series" on behalf of the Fire Protection Research Foundation (then known as the National Fire Protection Research Foundation) while working at Underwriters Labs in Northbrook, Illinois. Sheppard, along with Bryan Klein, currently employed at Thunderhead Engineering, Inc., conducted the experiments referred to as the "ATF Corridors" series in 2008.

- Jerry Back, Craig Beyler and Phil DiNenno of Hughes Associates and Pat Tatem of the Naval Research Laboratory contributed experimental data for the "HAI/NRL Wall Fire" series. Thanks also to Craig Beyler for assistance with the data for the "Beyler Hood Experiments."
- Ken Steckler provided details about the "Steckler Compartment Experiments" of 1979.
- Jianping Zhang at the University of Ulster contributed heat flux measurements from the SBI apparatus.
- At the University of Maryland, Professor Fred Mowrer and Phil Friday were the first to apply FDS to the NRC-sponsored experiments referred to in this document as the "FM/SNL Test Series" (Factory Mutual and Sandia National Laboratories conducted these experiments).
- Jukka Vaari of VTT, Finland, contributed the Cup Burner test cases.
- Steve Nowlen of Sandia National Laboratory provided valuable information about the FM/SNL series, and he also conducted the CAROLFIRE experiments.
- Ulf Wickström of SP, Sweden, contributed experimental data from a series of experiments (SP AST) that were designed to evaluate the feasibility of using plate thermometer measurements as boundary conditions for a heat conduction calculation within several types of steel beams. The adiabatic surface temperature concept was tested in both the experiments and model.
- Jeremy Thornock at the University of Utah provided data on the Sandia helium plume.
- Sheldon Teiszen at Sandia National Laboratories, Albuquerque, provided detailed statistics for the helium plume and pool fire experiments conducted in the Sandia FLAME facility.
- Taylor Myers, a student at the University of Maryland and a Summer Undergraduate Research Fellow (SURF) at NIST, analyzed the Vettori Flat and Sloped Ceiling sprinkler experiments. Thanks also to Bob Vettori of the U.S. Nuclear Regulatory Commission and formerly of NIST for his help in locating the original test data and laboratory notebooks.
- Hans la Cour-Harbo, a masters degree student at the Technical University of Denmark, provided guidance and insight on the NRCC Facade experiments. Scott Bareham of NIST provided the technical drawing of the test enclosure.
- Prof. Stanislav Stoliarov and graduate students Mark McKinnon and Jing Li of the University of Maryland provided the properties of several polymers for the FAA Polymers example.
- Michael Spearpoint and masters degree students Roger Harrison and Rob Fleury of the University of Canterbury, New Zealand, supplied measurements of mass entrainment rates into spill plumes (Harrison Spill Plumes) and heat flux measurements from propane burner fires (Fleury Heat Flux).
- Ezti Oztekin of the Federal Aviation Administration (FAA) developed the FAA Cargo Compartments cases based on experiments sponsored by the FAA.
- Topi Sikanen of VTT, Finland, and Jonathan Wahlqvist of Lund University, Sweden, contributed FDS input files for the PRISME DOOR series.
- Paul Tyson, a student at the University of Ulster, Northern Ireland, contributed the input files and supporting documents for the NRCC Smoke Tower experiments.
- James White, a student at the University of Maryland, provided documentation and input files for the UMD Line Burner cases.

- Charlie Hopkin and Michael Spearpoint of Olsson Fire & Risk provided the data and FDS input files for experiments conducted by Adam Bittern at the University of Christchurch, New Zealand.
- The simulations of liquefied natural gas (LNG) dispersion experiments that are described in this report were originally designed by Jeffrey Engerer and Anay Luketa of Sandia National Laboratories on behalf of the Pipeline and Hazardous Materials Safety Administration of the U.S. Department of Transportation.

Contents

FDS Developers i

About the Developers iii

Preface vii

Disclaimer ix

Acknowledgments xi

Contents xv

List of Figures xxv

List of Tables xliii

List of Acronyms xlv

1 What is Model Validation? 1
- 1.1 Blind, Specified, and Open Validation Experiments . . . 1
- 1.2 How to Use this Guide . . . 2

2 Survey of Past Validation Work 5
- 2.1 Validation Work with Pre-Release Versions of FDS . . . 6
- 2.2 Validation of FDS since 2000 . . . 7
  - 2.2.1 Fire Plumes . . . 7
  - 2.2.2 Pool Fires . . . 8
  - 2.2.3 Air and Gas Movement in the Absence of Fire . . . 8
  - 2.2.4 Wind Engineering . . . 9
  - 2.2.5 Atmospheric Dispersion . . . 9
  - 2.2.6 Growing Fires . . . 10
  - 2.2.7 Flame Spread . . . 10
  - 2.2.8 Compartment Fires . . . 11
  - 2.2.9 Sprinklers, Mist System, and Suppression by Water . . . 12
  - 2.2.10 Airflows in Fire Compartments . . . 13
  - 2.2.11 Tunnel Fires . . . 13
  - 2.2.12 Smoke Detection . . . 14
  - 2.2.13 Combustion Model . . . 14
  - 2.2.14 Soot Deposition . . . 14
- 2.3 Reconstructions of Actual Fires . . . 15

3 Description of Experiments **17**
3.1 ArupFire Tunnel Fire Experiments . . . 17
3.2 ATF Corridors Experiments . . . 17
3.3 Atmospheric Dispersion Correlations . . . 19
3.4 Backward Facing Step . . . 19
3.5 Beyler Hood Experiments . . . 19
3.6 BGC/GRI LNG Fire Experiments . . . 21
3.7 Bittern Sprinkler Experiments . . . 22
3.8 Bouchair Solar Chimney . . . 24
3.9 BRE Spray Test for Radiation Attenuation . . . 25
3.10 Bryant Doorway Velocity Measurements . . . 26
3.11 BST/FRS Wood Crib Fire Experiments . . . 27
3.12 Cable Response to Live Fire – CAROLFIRE . . . 28
3.13 Crown Fires . . . 29
3.14 CSIRO Grassland Fires . . . 29
3.15 CSTB Tunnel Experiments . . . 32
3.16 Cup Burner Experiments . . . 33
3.17 DelCo Trainer Experiments . . . 35
3.18 DoJ/HAI Pool Fire Experiments . . . 37
3.19 Droplet Evaporation . . . 38
3.20 Edinburgh Vegetation Drag . . . 38
3.21 FAA Cargo Compartments . . . 39
3.22 FAA Polymers . . . 39
3.23 Fleury Heat Flux Measurements . . . 40
3.24 FM Burner Experiments . . . 40
3.25 FM/FPRF Data Center Experiments . . . 41
3.26 FM Parallel Panel Experiments . . . 41
3.27 FM/SNL Experiments . . . 42
3.28 FM Vertical Wall Flame Experiments . . . 45
3.29 Frankman Vegetation Experiments . . . 45
3.30 Hamins Gas Burner Experiments . . . 46
3.31 Harrison Spill Plumes . . . 46
3.32 Heskestad Flame Height Correlation . . . 48
3.33 Insulation Material Fire Resistance Tests . . . 48
3.34 LEMTA Spray Test for Radiation Attenuation . . . 48
3.35 LLNL Enclosure Experiments . . . 49
3.36 LNG Dispersion Experiments . . . 52
3.37 Loughborough Jet Fire Experiments . . . 54
3.38 McCaffrey Plume Experiments . . . 55
3.39 Montoir LNG Fires . . . 58
3.40 NBS Multi-Room Experiments . . . 59
3.41 NIST Composite Beam Experiments . . . 61
3.42 NIST E119 Compartment Experiments . . . 65
3.43 NIST Douglas Firs . . . 69
3.44 NIST Enclosure Experiments . . . 70
3.44.1 NIST Reduced Scale Enclosure Experiments, 1994 . . . 70
3.44.2 NIST Reduced Scale Enclosure Experiments, 2007 . . . 70
3.44.3 NIST Full-Scale Enclosure Experiments, 2008 . . . 70

3.44.4 Modeling Notes . . . 71
3.45 NIST Helium Experiments . . . 73
3.46 NIST/NRC Compartment Experiments . . . 74
3.47 NIST/NRC Corner, Wall, and Cabinet Experiments . . . 76
3.47.1 Wall and Corner Effects . . . 76
3.47.2 Cabinet Effects . . . 78
3.48 NIST/NRC OLIVE-Fire Experiments . . . 81
3.49 NIST/NRC Parallel Panel Experiments . . . 84
3.50 NIST/NRC Transient Combustibles Experiments . . . 84
3.51 NIST Pool Fire Experiments . . . 86
3.52 NIST Smoke Alarm Experiments . . . 87
3.53 NIST Soot Deposition Gauge . . . 90
3.54 NIST Vent Study . . . 91
3.55 NRCC Facade Heat Flux Measurements . . . 93
3.56 NRCC Smoke Tower Experiments . . . 96
3.57 NRL/HAI Wall Heat Flux Measurements . . . 98
3.58 Phoenix LNG Fires . . . 98
3.59 Pool Fires . . . 100
3.60 PRISME Project . . . 101
3.61 Purdue Flames . . . 101
3.62 Ranz Marshall Droplet Experiments . . . 102
3.63 Restivo Compartment Air Flow Experiment . . . 103
3.64 Sandia Methane Burner . . . 104
3.65 Sandia Plume Experiments . . . 105
3.66 SETCOM Wall Condensation Experiments . . . 106
3.67 Shell LNG Fireball Experiments . . . 106
3.68 Sippola Aerosol Deposition Experiments . . . 108
3.69 Smyth Slot Burner Experiment . . . 110
3.70 SP Adiabatic Surface Temperature Experiments . . . 110
3.71 SP Wood Crib Experiments . . . 112
3.72 Steckler Compartment Experiments . . . 113
3.73 SWJTU Tunnel Experiments . . . 116
3.74 Wu Bakar Tunnel Experiments . . . 116
3.75 UL/NIST Vent Experiments . . . 116
3.76 UL/NFPRF Sprinkler, Vent, and Draft Curtain Study . . . 118
3.77 UL/NIJ House Experiments . . . 124
3.78 Ulster SBI Corner Heat Flux Measurements . . . 129
3.79 UMD Polymers . . . 129
3.80 UMD Line Burner . . . 129
3.81 USCG/HAI Water Mist Suppression Tests . . . 132
3.82 USFS/Catchpole Experiments . . . 132
3.83 USFS/Corsica Experiments . . . 132
3.84 USN High Bay Hangar Experiments . . . 133
3.85 UWO Wind Tunnel Experiments . . . 133
3.86 Vettori Flat Ceiling Experiments . . . 134
3.87 Vettori Sloped Ceiling Experiments . . . 137
3.88 VTT Large Hall Tests . . . 137
3.89 VTT Water Spray Experiments . . . 140

3.90 Waterloo Methanol Pool Fire Experiment . . . 140
3.91 WTC Spray Burner Experiments . . . 141
3.92 Summary of Experiments . . . 143

4 Quantifying Model Uncertainty 149
4.1 Introduction . . . 149
4.2 Sources of Model Uncertainty . . . 151
4.3 Experimental Uncertainty . . . 152
4.3.1 Uncertainty of Common Fire Measurements . . . 153
4.3.2 Propagation of Input Parameter Uncertainty . . . 155
4.3.3 Summary of Experimental Uncertainty Estimates . . . 159
4.4 Calculating Model Uncertainty . . . 159
4.5 Example . . . 162
4.6 Additional Considerations . . . 163

5 HGL Temperature and Depth 165
5.1 HGL Reduction Method . . . 165
5.2 ATF Corridors . . . 166
5.3 CSTB Tunnel . . . 170
5.4 DelCo Trainers . . . 173
5.5 FM/SNL Test Series . . . 181
5.6 LLNL Enclosure Series . . . 186
5.7 NBS Multi-Room Test Series . . . 195
5.8 NIST Composite Beam . . . 199
5.9 NIST E119 Compartment . . . 202
5.10 NIST Full-Scale Enclosure (FSE), 2008 . . . 206
5.11 NIST/NRC Test Series . . . 213
5.12 NIST/NRC Corner Effects Experiments . . . 218
5.13 NIST Vent Study . . . 224
5.14 NRCC Smoke Tower . . . 231
5.15 PRISME DOOR Experiments . . . 233
5.16 PRISME SOURCE Experiments . . . 237
5.17 Steckler Compartment Experiments . . . 240
5.18 UL/NIST Vent Experiments . . . 248
5.19 UL/NIJ House Experiments . . . 250
5.20 VTT Test Series . . . 253
5.21 WTC Test Series . . . 254
5.22 Summary of Hot Gas Layer Temperature and Height . . . 257

6 Fire Plumes 259
6.1 Plume Temperatures . . . 259
6.1.1 FM Burner Experiments . . . 260
6.1.2 FM/SNL Experiments . . . 263
6.1.3 McCaffrey's Plume Correlation . . . 266
6.1.4 NIST/NRC Corner/Wall/Cabinet Effects Experiments . . . 268
6.1.5 NIST Pool Fires . . . 270
6.1.6 NRCC Smoke Tower Experiments, Stairwell Plumes . . . 276
6.1.7 Sandia Methane Burner Experiments . . . 278

6.1.8 SP Adiabatic Surface Temperature Experiments . . . 282
6.1.9 UMD Line Burner . . . 285
6.1.10 USN High Bay Hangar Experiments . . . 287
6.1.11 VTT Large Hall Experiments . . . 291
6.1.12 Waterloo Methanol Pool Fire Experiment . . . 292
6.1.13 Summary of Plume Temperature Predictions . . . 300
6.2 Flame Height . . . 301
6.2.1 Heskestad's Flame Height Correlation . . . 301
6.2.2 UMD Line Burner . . . 305
6.2.3 Flame Height Summary . . . 306
6.3 Flame Tilt . . . 307
6.4 Harrison Spill Plumes/Entrainment Experiments . . . 308
6.5 Sandia Plume Experiments . . . 309
6.5.1 Sandia 1 m Helium Plume . . . 309
6.5.2 Sandia 1 m Methane Pool Fire . . . 314
6.5.3 Sandia 1 m Hydrogen Pool Fire . . . 320
6.6 Purdue 7.1 cm Methane Flame . . . 323
6.7 FM Vertical Wall Flame Experiments . . . 327

7 Ceiling Jets and Device Activation **331**
7.1 Ceiling Jet Temperatures . . . 331
7.1.1 ATF Corridors Experiment . . . 332
7.1.2 Arup Tunnel Experiments . . . 338
7.1.3 DelCo Trainers . . . 339
7.1.4 FAA Cargo Compartments . . . 342
7.1.5 FM/SNL Experiments . . . 347
7.1.6 NIST Composite Beam . . . 350
7.1.7 NIST Smoke Alarm Experiments . . . 352
7.1.8 NIST/NRC Experiments . . . 354
7.1.9 NIST/NRC Corner Effects Experiments . . . 357
7.1.10 NIST Vent Study . . . 361
7.1.11 NRCC Smoke Tower . . . 363
7.1.12 PRISME DOOR Experiments . . . 365
7.1.13 PRISME SOURCE Experiments . . . 367
7.1.14 SP Adiabatic Surface Temperature Experiments . . . 369
7.1.15 UL/NFPRF Series I Experiments . . . 371
7.1.16 UL/NIJ House Experiments . . . 374
7.1.17 UL/NIST Vent Experiments . . . 375
7.1.18 Vettori Flat Ceiling Experiments . . . 377
7.1.19 Vettori Sloped Ceiling Experiments . . . 384
7.1.20 WTC Experiments . . . 394
7.1.21 Summary of Ceiling Jet Temperature Predictions . . . 395
7.2 Sprinkler Activation Times . . . 396
7.2.1 Time to First Sprinkler Activation . . . 396
7.2.2 Number of Sprinkler Activations . . . 397
7.3 Smoke Detector Activation Times . . . 405

8 Gas Velocity **407**

8.1 ATF Corridor Experiments . . . 407
8.2 Backward Facing Step . . . 412
8.3 Bryant Doorway Experiments . . . 415
8.4 Edinburgh Vegetation Drag . . . 417
8.5 FM/FPRF Datacenter Experiments . . . 420
8.6 McCaffrey's Plume Correlation . . . 422
8.7 NIST Pool Fires . . . 424
8.8 PRISME DOOR Experiments . . . 425
8.9 Restivo Experiment . . . 426
8.10 Steckler Compartment Experiments . . . 427
8.11 UL/NIJ House Experiments . . . 435
8.12 Waterloo Methanol Pool Fire Experiment . . . 440
8.13 WTC Experiments . . . 449
8.14 Summary of Velocity Predictions . . . 454
8.15 Wu Bakar Tunnel Experiments . . . 455

9 Gas Species and Smoke **457**
9.1 Major Combustion Products, O_2 and CO_2 . . . 457
9.1.1 DelCo Trainers . . . 458
9.1.2 FAA Cargo Compartments . . . 461
9.1.3 LLNL Enclosure . . . 462
9.1.4 NIST/NRC Experiments . . . 479
9.1.5 NRCC Smoke Tower . . . 483
9.1.6 PRISME DOOR Experiments . . . 485
9.1.7 PRISME SOURCE Experiments . . . 489
9.1.8 WTC Experiments . . . 492
9.1.9 UMD Line Burner . . . 494
9.1.10 Summary of Major Combustion Products Predictions . . . 495
9.2 Smoke . . . 496
9.2.1 FM Burner Experiments . . . 496
9.2.2 FM/FPRF Data Center Experiments . . . 505
9.2.3 NIST/NRC Experiments . . . 506
9.2.4 FAA Cargo Compartments . . . 510
9.3 Aerosols . . . 512
9.3.1 Sippola Aerosol Deposition Experiments . . . 512
9.3.2 NIST Soot Deposition Gauge Experiments . . . 513
9.4 Droplet Evaporation . . . 516
9.4.1 Ranz and Marshall . . . 516
9.4.2 Fujita et al. . . . 516
9.4.3 Gavin . . . 521
9.4.4 Kolaitis and Founti . . . 522
9.4.5 Maqua et al. . . . 524
9.4.6 Taflin Experiments . . . 525
9.5 Products of Incomplete Combustion . . . 526
9.5.1 Smyth Slot Burner Experiment . . . 526
9.5.2 Beyler Hood Experiments . . . 530
9.5.3 NIST Reduced Scale Enclosure (RSE) Experiments, 1994 . . . 532
9.5.4 NIST Reduced-Scale Enclosure (RSE) Experiments, 2007 . . . 534

9.5.5 NIST Full-Scale Enclosure (FSE) Experiments, 2008 . . . 546
9.5.6 NIST Pool Fires . . . 573
9.5.7 Summary, Products of Incomplete Combustion . . . 580
9.6 Helium Release in a Reduced Scale Garage Geometry . . . 581

10 Pressure **587**
10.1 FM/FPRF Datacenter Experiments . . . 587
10.2 NIST/NRC Experiments . . . 589
10.3 LLNL Enclosure Experiments . . . 592
10.4 PRISME DOOR Experiments . . . 601
10.5 PRISME SOURCE Experiments . . . 606
10.6 UL/NIJ House Experiments . . . 609
10.7 Summary of Pressure Predictions . . . 616

11 Surface Temperature **617**
11.1 Wall, Ceiling and Floor Temperatures . . . 618
11.1.1 FAA Cargo Compartments . . . 618
11.1.2 NIST Composite Beam . . . 619
11.1.3 NIST Full-Scale Enclosure (FSE), 2008 . . . 626
11.1.4 NIST/NRC Experiments . . . 634
11.1.5 PRISME DOOR Experiments . . . 647
11.1.6 PRISME SOURCE Experiments . . . 651
11.1.7 WTC Experiments . . . 654
11.1.8 Insulation Materials Fire Resistance Tests . . . 668
11.1.9 Summary of Wall, Ceiling, and Floor Temperature Predictions . . . 673
11.2 Target Temperature . . . 674
11.2.1 NIST Composite Beam . . . 674
11.2.2 NIST E119 Compartment . . . 676
11.2.3 NIST/NRC Experiments . . . 677
11.2.4 NIST/NRC Corner Effects Experiments . . . 692
11.2.5 SP Adiabatic Surface Temperature Experiments . . . 705
11.2.6 WTC Experiments . . . 733
11.2.7 CAROLFIRE Experiments . . . 745
11.2.8 Frankman Vegetation Experiments . . . 751
11.2.9 PRISME Experiments . . . 752
11.2.10 Summary of Target Temperature Predictions . . . 760
11.2.11 Time to Failure . . . 761
11.3 Liquid Pool Surface Temperature . . . 762
11.3.1 Pool Fires . . . 762
11.3.2 NIST Pool Fires and Waterloo Methanol . . . 764
11.3.3 Summary of Liquid Pool Surface Temperature Predictions . . . 764

12 Heat Flux **767**
12.1 Heat Flux to Walls, Ceiling, and Floor . . . 768
12.1.1 FAA Cargo Compartments . . . 768
12.1.2 FM Parallel Panel Experiments . . . 769
12.1.3 FM Vertical Wall Flame Experiments . . . 770
12.1.4 NIST E119 Compartment . . . 772

12.1.5 NIST/NRC Experiments . . . 773
12.1.6 NRCC Facade Experiments . . . 786
12.1.7 NRL/HAI Experiments . . . 790
12.1.8 PRISME DOOR Experiments . . . 793
12.1.9 PRISME SOURCE Experiments . . . 799
12.1.10 Ulster SBI Experiments . . . 803
12.1.11 WTC Experiments . . . 804
12.1.12 Summary of Wall, Ceiling and Floor Heat Flux Predictions . . . 808
12.2 Heat Flux to Targets . . . 809
12.2.1 Fleury Experiments . . . 809
12.2.2 Hamins Gas Burner Experiments . . . 815
12.2.3 BGC/GRI LNG Fires . . . 840
12.2.4 Loughborough Jet Fire Experiments . . . 843
12.2.5 Montoir LNG Fires . . . 848
12.2.6 NIST Douglas Firs . . . 852
12.2.7 NIST/NRC Experiments . . . 853
12.2.8 NIST Pool Fires . . . 862
12.2.9 Phoenix LNG Fires . . . 865
12.2.10 Sandia Methane Burner Experiments . . . 867
12.2.11 Shell LNG Fireballs . . . 875
12.2.12 WTC Experiments . . . 876
12.2.13 UMD Line Burner . . . 880
12.2.14 Summary of Target Heat Flux Predictions . . . 882
12.3 Attenuation of Thermal Radiation in Water Spray . . . 883
12.3.1 BRE Spray Experiments . . . 883
12.3.2 LEMTA Spray Experiments . . . 883
12.4 Convective Heat Flux . . . 885
12.4.1 Bouchair Solar Chimney . . . 885
12.5 Radiation Source Term . . . 892
12.5.1 FM Burner Experiments . . . 892
12.6 Condensation Heat Flux . . . 895
12.6.1 SETCOM Experiments . . . 895

13 Suppression **897**
13.1 Minimum Agent Concentration Experiments . . . 897
13.1.1 Cup Burner Experiments . . . 897
13.1.2 FM Burner Experiments . . . 899
13.1.3 UMD Line Burner . . . 900
13.2 Compartment Fire Extinction . . . 901
13.2.1 LLNL Enclosure Experiments . . . 901
13.2.2 NIST/NRC OLIVE-Fire Experiments . . . 906
13.2.3 SWJTU Tunnel Experiments . . . 910
13.2.4 USCG/HAI Water Mist Suppression Tests . . . 911
13.2.5 Summary, Flame Extinction Time . . . 917
13.3 VTT Water Spray Experiments . . . 918

14 Burning Rate and Fire Spread **921**
14.1 FAA Polymers . . . 921

14.1.1 Glossary of Terms . . . 921
14.1.2 Non-Charring Polymers, HDPE, HIPS, and PMMA . . . 923
14.1.3 Complex Non-Charring Polymers: PP, PA66, POM, and PET . . . 925
14.1.4 Polycarbonate (PC) . . . 927
14.1.5 Poly(vinyl chloride) (PVC) . . . 929
14.1.6 Poly(aryl ether ether ketone)) (PEEK) . . . 931
14.1.7 Poly(butylene terephtalate) (PBT) . . . 934
14.1.8 PBT with Glass Fibers (PBT-GF) . . . 936
14.2 UMD Polymers . . . 938
14.2.1 One-Step Degradation: ABS, HIPS, and PMMA . . . 938
14.2.2 Two-Step Degradation: Kydex . . . 941
14.2.3 Three-Step Degradation: PEI, PET, and POM . . . 943
14.3 Corrugated Cardboard . . . 946
14.4 Wood Cribs and Similar Wood/Paper Combustibles . . . 950
14.4.1 BST/FRS Wood Crib Experiments . . . 951
14.4.2 NIST/NRC Transient Combustibles . . . 954
14.4.3 SP Wood Crib Experiments . . . 957
14.5 Liquid Pool Fires . . . 959
14.5.1 DoJ/HAI Pool Fires . . . 959
14.5.2 Pool Fire Measurements . . . 967
14.5.3 NIST Pool Fires . . . 969
14.5.4 Waterloo Methanol Pool Fire . . . 969
14.6 Vertical Flame Spread . . . 970
14.6.1 NIST/NRC Parallel Panel Experiments . . . 970
14.7 Wildland Fire Burning and Spread Rates . . . 971
14.7.1 Crown Fires . . . 971
14.7.2 CSIRO Grassland Fires . . . 972
14.7.3 USFS/Catchpole Experiments . . . 974
14.7.4 USFS/Corsica Fire Spread Experiments . . . 1021
14.7.5 Burning Trees (NIST Douglas Firs) . . . 1023
14.8 Summary of Burning and Spread Rates . . . 1025

15 Wind Engineering and Atmospheric Dispersion **1027**
15.1 UWO Wind Tunnel Experiments . . . 1027
15.2 LNG Dispersion Experiments . . . 1037
15.3 Stack Emission Plume Rise . . . 1045

16 Conclusion **1049**
16.1 Summary of FDS Model Uncertainty Statistics . . . 1049
16.2 Normality Tests . . . 1050
16.3 Summary of FDS Validation Git Statistics . . . 1055

Bibliography **1059**

List of Figures

3.1 Geometry of the ATF Corridors Experiments. . . . 18
3.2 Geometry of the Backward Facing Step experiments . . . 19
3.3 Sketch of Beyler Hood cross section . . . 20
3.4 Plan view of the Bittern Sprinkler Experiments . . . 23
3.5 Geometry of the Bouchair Solar Chimney experiment . . . 25
3.6 Geometry of Bryant's compartment . . . 27
3.7 Snapshots of the simulation of CSIRO Grassland Fire F19 . . . 31
3.8 Instrumentation of the single level DelCo training structure . . . 35
3.9 Instrumentation of the two level DelCo training structure . . . 36
3.10 Geometry of the Edinburgh Vegetation Drag experiments . . . 39
3.11 Sketch of the FM parallel panel apparatus . . . 42
3.12 Geometry of the FM/SNL Experiments . . . 44
3.13 Geometry of the Harrison Spill Plumes Experiments. . . . 47
3.14 Geometry of the LLNL Enclosure Experiments . . . 51
3.15 Photograph of a jet fire experiment at the Spadeadam Test Site . . . 54
3.16 McCaffrey Plume Centerline Temperature and Velocity Correlations . . . 56
3.17 McCaffrey Plume Burner Surface Temperatures . . . 57
3.18 Geometry of the NBS Multi-Room Experiments . . . 60
3.19 Elevation view of NIST Composite Beam experiments . . . 62
3.20 Plan view of NIST Composite Beam experiments . . . 63
3.21 Side view of NIST Composite Beam experiments . . . 64
3.22 Plan view of NIST E119 Compartment experiment . . . 66
3.23 Elevation view of NIST E119 Compartment experiment . . . 67
3.24 Elevation view of NIST E119 Compartment experiment . . . 68
3.25 Geometry of the compartment used in the NIST Full-Scale Enclosure experiments . . . 72
3.26 Geometry of the NIST/NRC Experiments . . . 75
3.27 Diagram of thermocouple layout for NIST/NRC Corner Effects experiments . . . 77
3.28 Large cabinet drawing, NIST/NRC Corner Effects Experiments . . . 79
3.29 Medium-sized cabinet drawing, NIST/NRC Corner Effects Experiments . . . 80
3.30 Cabinet grill, NIST/NRC Corner Effects Experiments . . . 81
3.31 NIST/NRC OLIVE-Fire enclosure photographs . . . 83
3.32 Description of test items . . . 85
3.33 Geometry of the manufactured home from the NIST Smoke Alarm Experiments . . . 89
3.34 Geometry of the compartment from the NIST Vent Study . . . 92
3.35 Geometry of the NRCC Facade Experiments . . . 95
3.36 Geometry of the NRCC Smoke Tower Experiments . . . 97
3.37 Photograph of Phoenix LNG Fire Test 2 . . . 99
3.38 Geometry of Restivo's compartment . . . 104
3.39 Cutaway view of the Sandia FLAME test cell . . . 105

3.40 Photographs of the Shell LNG Fireball experiments . . . 107
3.41 Geometry of the SP/AST compartment for Test 2 . . . 111
3.42 Geometry of the Steckler Compartment Experiments . . . 115
3.43 Geometry of the UL/NIST Experiments. . . . 117
3.44 Plan view of the UL/NFPRF heptane spray experiments, Series I . . . 119
3.45 Plan view of the UL/NFPRF heptane spray experiments, Series II . . . 120
3.46 Plan view of the UL/NFPRF plastic commodity Test P-3 . . . 121
3.47 Layout of the one story ranch-style house in the UL/NIJ experiments . . . 125
3.48 Geometry of UL NIJ Colonial-style House . . . 126
3.49 UMD Line Burner isometric view of burner and oxidizer assembly . . . 131
3.50 Geometry of the Vettori Flat Ceiling compartment . . . 135
3.51 Geometry of the VTT Large Fire Test Hall . . . 139
3.52 Geometry of the WTC Experiments . . . 142

4.1 Demonstration of model uncertainty . . . 150
4.2 Sample scatter plot . . . 152
4.3 Sample time history plots . . . 160

5.1 ATF Corridors, HGL temperature and height, first floor, 50 kW, 100 kW, 240 kW . . . 166
5.2 ATF Corridors, HGL temperature and height, first floor, 250 kW, 500 kW, mixed . . . 167
5.3 ATF Corridors, HGL temperature and height, second floor, 50 kW, 100 kW, 240 kW . . . 168
5.4 ATF Corridors, HGL temperature and height, second floor, 250 kW, 500 kW, mixed . . . 169
5.5 CSTB Tunnel, Test 2, temperatures at 4, 8, 12 and 24 m downstream of fire . . . 171
5.6 CSTB Tunnel, Test 27, temperatures at 4, 8, 12 and 24 m downstream of fire . . . 172
5.7 DelCo Trainers, HGL Temperature and Height, Test 2 . . . 174
5.8 DelCo Trainers, HGL Temperature and Height, Test 3 . . . 175
5.9 DelCo Trainers, HGL Temperature and Height, Test 4 . . . 176
5.10 DelCo Trainers, HGL Temperature and Height, Test 5 . . . 177
5.11 DelCo Trainers, HGL Temperature and Height, Test 6 . . . 178
5.12 DelCo Trainers, HGL Temperature, Tests 22-23 . . . 179
5.13 DelCo Trainers, HGL Temperature, Tests 24-25 . . . 180
5.14 FM/SNL experiments, HGL temperature and height, Tests 1, 2, 3 . . . 181
5.15 FM/SNL experiments, HGL temperature and height, Tests 4, 5, 6, 7 . . . 182
5.16 FM/SNL experiments, HGL temperature and height, Tests 8, 9, 10, 11 . . . 183
5.17 FM/SNL experiments, HGL temperature and height, Tests 12, 13, 14, 15 . . . 184
5.18 FM/SNL experiments, HGL temperature and height, Tests 16, 17, 21, 22 . . . 185
5.19 LLNL Enclosure experiments, HGL temperature, Tests 1-8 . . . 187
5.20 LLNL Enclosure experiments, HGL temperature, Tests 9-16 . . . 188
5.21 LLNL Enclosure experiments, HGL temperature, Tests 17-24 . . . 189
5.22 LLNL Enclosure experiments, HGL temperature, Tests 25-32 . . . 190
5.23 LLNL Enclosure experiments, HGL temperature, Tests 33-40 . . . 191
5.24 LLNL Enclosure experiments, HGL temperature, Tests 41-48 . . . 192
5.25 LLNL Enclosure experiments, HGL temperature, Tests 49-56 . . . 193
5.26 LLNL Enclosure experiments, HGL temperature, Tests 57-64 . . . 194
5.27 NBS Multi-Room experiments, HGL temperature and height, Test 100A . . . 196
5.28 NBS Multi-Room experiments, HGL temperature and height, Test 100O . . . 197
5.29 NBS Multi-Room experiments, HGL temperature and height, Test 100Z . . . 198
5.30 NIST Composite Beam, mid-compartment HGL temperatures . . . 200

5.31 NIST Composite Beam, end-compartment HGL temperatures . . . 201
5.32 NIST E119 Compartment Test 1, upper layer gas temperatures temperatures . . . 203
5.33 NIST E119 Compartment Test 2, upper layer gas temperatures temperatures . . . 204
5.34 NIST E119 Compartment Test 3, upper layer gas temperatures temperatures . . . 205
5.35 NIST FSE, HGL temperature and height, Tests 8-11 . . . 207
5.36 NIST FSE, HGL temperature and height, Tests 12-15 . . . 208
5.37 NIST FSE, HGL temperature and height, Tests 16-19 . . . 209
5.38 NIST FSE, HGL temperature and height, Tests 20-23 . . . 210
5.39 NIST FSE, HGL temperature and height, Tests 24-27 . . . 211
5.40 NIST FSE, HGL temperature and height, Tests 28-30, 32 . . . 212
5.41 NIST/NRC experiments, HGL temperature and height, Tests 1-2, 7-8 . . . 214
5.42 NIST/NRC experiments, HGL temperature and height, Tests 4, 10, 13, 16 . . . 215
5.43 NIST/NRC experiments, HGL temperature and height, Tests 3, 9, 17 . . . 216
5.44 NIST/NRC experiments, HGL temperature and height, Tests 5, 14, 15, 18 . . . 217
5.45 NIST/NRC Corner Effects, HGL temperature and height, corner experiments . . . 219
5.46 NIST/NRC Corner Effects, HGL temperature and height, wall experiments . . . 220
5.47 NIST/NRC Corner Effects, HGL temperature and height, cabinet experiments 1-4 . . . 221
5.48 NIST/NRC Corner Effects, HGL temperature and height, cabinet experiments 5-8 . . . 222
5.49 NIST/NRC Corner Effects, HGL temperature and height, cabinet experiments 9-12 . . . 223
5.50 NIST Vent Study, HGL temperature and height, Tests 1 and 2 . . . 225
5.51 NIST Vent Study, HGL temperature and height, Tests 3 and 4 . . . 226
5.52 NIST Vent Study, HGL temperature and height, Tests 5 and 6 . . . 227
5.53 NIST Vent Study, HGL temperature and height, Tests 7 and 8 . . . 228
5.54 NIST Vent Study, HGL temperature and height, Tests 9 and 13 . . . 229
5.55 NIST Vent Study, HGL temperature and height, Tests 14 and 15 . . . 230
5.56 NRCC Smoke Tower experiments, HGL temperature in the fire room and stair vestibule . . . 232
5.57 PRISME DOOR experiments, HGL temperature and height, Room 1, Tests 1-3 . . . 233
5.58 PRISME DOOR experiments, HGL temperature and height, Room 1, Tests 4-6 . . . 234
5.59 PRISME DOOR experiments, HGL temperature and height, Room 2, Tests 1-3 . . . 235
5.60 PRISME DOOR experiments, HGL temperature and height, Room 2, Tests 4-6 . . . 236
5.61 PRISME SOURCE experiments, HGL temperature and height, Room 2, Tests 1-4 . . . 238
5.62 PRISME SOURCE experiments, HGL temperature and height, Room 2, Tests 5-6 . . . 239
5.63 Steckler experiments, HGL temperature, Tests 10, 11, 12, 13, 14, 18, 612, 710 . . . 241
5.64 Steckler experiments, HGL temperature, Tests 16, 17, 19, 22, 23, 30, 41, 810 . . . 242
5.65 Steckler experiments, HGL temperature, Tests 20, 21, 114, 144, 210, 212, 242, 410 . . . 243
5.66 Steckler experiments, HGL temperature, Tests 116, 122, 220, 221, 224, 240,310, 324 . . . 244
5.67 Steckler experiments, HGL temperature, Tests 510, 512, 514, 517, 540, 542, 544, 610 . . . 245
5.68 Steckler experiments, HGL temperature, Tests 160, 513, 520, 521, 522, 524, 541, 622 . . . 246
5.69 Steckler experiments, HGL temperature, Tests 161, 162, 163, 164, 165, 166, 167 . . . 247
5.70 UL/NIST experiments, HGL temperature and height, Tests 1-4 . . . 249
5.71 UL/NIJ Experiments, HGL temperature and height, Tests 1, 2, and 5 . . . 251
5.72 UL/NIJ Experiments, HGL temperature and height, Tests 1, 4, and 6 . . . 252
5.73 VTT experiments, HGL temperature and height, Tests 1-3 . . . 253
5.74 WTC experiments, HGL temperature and height, Tests 1-3 . . . 254
5.75 WTC experiments, HGL temperature and height, Tests 4-6 . . . 255
5.76 Summary, HGL temperature, natural and forced ventilation . . . 257
5.77 Summary, HGL temperature, unventilated compartments; HGL depth . . . 258

6.1 FM Burner experiments, plume mean and rms temperatures . . . 260
6.2 FM Burner experiments, plume mean and rms temperatures . . . 261
6.3 FM Burner experiments, temperature PDFs . . . 262
6.4 FM/SNL experiments, plume temperature, Tests 1-4 . . . 263
6.5 FM/SNL experiments, plume temperature, Tests 5-12 . . . 264
6.6 FM/SNL experiments, plume temperature, Tests 13-17, 21-22 . . . 265
6.7 McCaffrey experiments, plume temperature . . . 266
6.8 McCaffrey experiments, plume temperature, Froude scaling . . . 267
6.9 NIST/NRC Corner Effects experiments, plume temperature . . . 269
6.10 NIST Pool Fires, centerline temperature, acetone, ethanol, methane . . . 271
6.11 NIST Pool Fires, centerline temperature, methanol and propane . . . 272
6.12 NIST Pool Fires, 30 cm methanol, radial profiles of mean and rms temperature . . . 273
6.13 NIST Pool Fires, 100 cm methanol, plume mean and rms temperatures . . . 274
6.14 NIST Pool Fires, 100 cm methanol fire, radial profiles of mean and rms temperature . . . 275
6.15 NRCC Smoke Tower, stairwell temperatures . . . 277
6.16 Sandia Methane Burner, plume temperature, Tests 1-4 . . . 278
6.17 Sandia Methane Burner, plume temperature, Tests 5-12 . . . 279
6.18 Sandia Methane Burner, plume temperature, Tests 13-20 . . . 280
6.19 Sandia Methane Burner, plume temperature, Tests 21-28 . . . 281
6.20 SP AST experiments, plume temperature, 1.1 m diesel fire . . . 283
6.21 SP AST experiments, plume temperature, 1.9 m diesel and 1.1 m heptane fires . . . 284
6.22 UMD_Line_Burner temperature profiles . . . 285
6.23 UMD_Line_Burner temperature contours . . . 286
6.24 USN Hangar experiments, Iceland, plume temperature, Tests 1-6 . . . 287
6.25 USN Hangar experiments, Iceland, plume temperature, Tests 7, 9-13 . . . 288
6.26 USN Hangar experiments, Iceland, plume temperature, Tests 14-15, 17-20 . . . 289
6.27 USN Hangar experiments, Hawaii, plume temperature, Tests 1-7, 11 . . . 290
6.28 VTT experiments, plume temperature . . . 291
6.29 Waterloo Methanol, centerline profile, mean temperature, 2 cm to 60 cm above burner . . . 292
6.30 Waterloo Methanol, radial mean and rms temperature, 2 cm to 8 cm above burner . . . 293
6.31 Waterloo Methanol, radial mean and rms temperature, 10 cm to 16 cm above burner . . . 294
6.32 Waterloo Methanol, radial mean and rms temperature, 18 cm to 40 cm above burner . . . 295
6.33 Waterloo Methanol, radial mean and rms temperature, 50 cm to 60 cm above burner . . . 296
6.34 Waterloo Methanol, radial profiles of $\overline{T'w'}$ and $\overline{T'u'}$, 2 cm to 8 cm above the burner . . . 297
6.35 Waterloo Methanol, radial profiles of $\overline{T'w'}$ and $\overline{T'u'}$, 10 cm to 16 cm above the burner . . . 298
6.36 Waterloo Methanol, radial profiles of $\overline{T'w'}$ and $\overline{T'u'}$, 18 cm to 30 cm above the burner . . . 299
6.37 Summary of plume temperature predictions . . . 300
6.38 Verification of the heat release rate for Heskestad Flame Height cases . . . 302
6.39 Summary of flame height predictions, Heskestad correlation . . . 303
6.40 Flame height uncertainty, multiple correlations and flame height definitions . . . 303
6.41 Predicted HRR as a function of height above the burner . . . 304
6.42 UMD_Line_Burner flame height . . . 305
6.43 Summary of flame height predictions . . . 306
6.44 Summary of flame tilt angle predictions . . . 307
6.45 Summary of plume entrainment predictions . . . 308
6.46 Sandia 1 m helium plume image . . . 310
6.47 Sandia 1 m helium plume vertical velocity profiles . . . 311
6.48 Sandia 1 m helium plume radial velocity profiles . . . 312

6.49 Sandia 1 m helium plume mean and RMS mass fraction profiles . . . 313
6.50 Sandia 1 m methane pool fire instantaneous temperature contours . . . 314
6.51 Sandia 1 m methane pool fire (Test 14) mean velocity profiles . . . 315
6.52 Sandia 1 m methane pool fire (Test 24) mean velocity profiles . . . 316
6.53 Sandia 1 m methane pool fire (Test 24) turbulent kinetic energy . . . 317
6.54 Sandia 1 m methane pool fire (Test 17) mean velocity profiles . . . 318
6.55 Sandia 1 m methane pool fire velocity signal and power spectrum . . . 319
6.56 Sandia 1 m hydrogen pool fire instantaneous temperature contours . . . 320
6.57 Sandia 1 m hydrogen pool fire (Test 35) mean velocity profiles . . . 321
6.58 Sandia 1 m hydrogen pool fire (Test 25) turbulent kinetic energy . . . 322
6.59 Purdue 7.1 cm methane flame mean mixture fraction profiles . . . 323
6.60 Purdue 7.1 cm methane flame mean temperature profiles . . . 324
6.61 Purdue 7.1 cm methane flame mean velocity profiles . . . 325
6.62 Purdue 7.1 cm methane flame rms velocity profiles . . . 326
6.63 FM Vertical Wall Flame mean temperature profiles . . . 328
6.64 FM Vertical Wall Flame soot depth measurements . . . 329

7.1 ATF Corridors experiments, ceiling jet, 50 kW . . . 333
7.2 ATF Corridors experiments, ceiling jet, 100 kW . . . 334
7.3 ATF Corridors experiments, ceiling jet, 250 kW . . . 335
7.4 ATF Corridors experiments, ceiling jet, 500 kW . . . 336
7.5 ATF Corridors experiments, ceiling jet, mixed HRR . . . 337
7.6 Arup Tunnel experiments, ceiling jet . . . 338
7.7 DelCo Trainers, ceiling jet temperature, Tests 2-4 . . . 339
7.8 DelCo Trainers, ceiling jet temperature, Tests 5 and 6 . . . 340
7.9 DelCo Trainers, ceiling jet temperature, Tests 22-25 . . . 341
7.10 Layout of ceiling TCs, FAA Cargo Compartments . . . 342
7.11 FAA Cargo Compartment experiments, ceiling jet, Test 1 . . . 343
7.12 FAA Cargo Compartment experiments, ceiling jet, Test 1 and 2 . . . 344
7.13 FAA Cargo Compartment experiments, ceiling jet, Test 2 and 3 . . . 345
7.14 FAA Cargo Compartment experiments, ceiling jet, Test 3 . . . 346
7.15 FM/SNL experiments, ceiling jet, Tests 1-6 . . . 347
7.16 FM/SNL experiments, ceiling jet, Tests 7-14 . . . 348
7.17 FM/SNL experiments, ceiling jet, Tests 15-17, 21-22 . . . 349
7.18 NIST Composite Beam, ceiling jet temperatures . . . 351
7.19 NIST Smoke Alarm experiments, ceiling jet . . . 353
7.20 NIST/NRC experiments, ceiling jet, Tests 1, 2, 4, 7, 8, 10, 13, 16 . . . 355
7.21 NIST/NRC experiments, ceiling jet, Tests 3, 5, 9, 14, 15, 17, 18 . . . 356
7.22 NIST/NRC Corner Effects experiments, ceiling jet temperature . . . 358
7.23 NIST/NRC Corner Effects experiments, ceiling jet temperature, large cabinet . . . 359
7.24 NIST/NRC Corner Effects experiments, ceiling jet temperature, medium-sized cabinet . . . 360
7.25 NIST Vent Study, ceiling jet temperature, Tests 1-6 . . . 361
7.26 NIST Vent Study, ceiling jet temperature, Tests 7-9, 13-15 . . . 362
7.27 NRCC Smoke Tower experiments, ceiling jet . . . 363
7.28 NRCC Smoke Tower, upper floor temperatures . . . 364
7.29 PRISME DOOR experiments, ceiling jet, Room 1 . . . 365
7.30 PRISME DOOR experiments, ceiling jet, Room 2 . . . 366
7.31 PRISME SOURCE experiments, ceiling jet, Room 2 . . . 368

7.32 SP AST experiments, ceiling jet, Test 1 . . . 369
7.33 SP AST experiments, ceiling jet, Tests 2 and 3 . . . 370
7.34 UL/NFPPRF experiments, ceiling jet, Series I, Tests 1-6 . . . 371
7.35 UL/NFPPRF experiments, ceiling jet, Series I, Tests 7-14 . . . 372
7.36 UL/NFPPRF experiments, ceiling jet, Series I, Tests 15-22 . . . 373
7.37 UL/NIJ Experiments, ceiling jet temperature . . . 374
7.38 UL/NIST Vents experiments, ceiling jet . . . 376
7.39 Vettori Flat Ceiling experiments, ceiling jet, Tests 1-8 . . . 378
7.40 Vettori Flat Ceiling experiments, ceiling jet, Tests 9-16 . . . 379
7.41 Vettori Flat Ceiling experiments, ceiling jet, Tests 17-24 . . . 380
7.42 Vettori Flat Ceiling experiments, ceiling jet, Tests 25-32 . . . 381
7.43 Vettori Flat Ceiling experiments, ceiling jet, Tests 33-40 . . . 382
7.44 Vettori Flat Ceiling experiments, ceiling jet, Tests 41-45 . . . 383
7.45 Vettori Sloped Ceiling experiments, ceiling jet, Tests 1-8 . . . 385
7.46 Vettori Sloped Ceiling experiments, ceiling jet, Tests 9-16 . . . 386
7.47 Vettori Sloped Ceiling experiments, ceiling jet, Tests 17-24 . . . 387
7.48 Vettori Sloped Ceiling experiments, ceiling jet, Tests 25-32 . . . 388
7.49 Vettori Sloped Ceiling experiments, ceiling jet, Tests 33-40 . . . 389
7.50 Vettori Sloped Ceiling experiments, ceiling jet, Tests 41-48 . . . 390
7.51 Vettori Sloped Ceiling experiments, ceiling jet, Tests 49-56 . . . 391
7.52 Vettori Sloped Ceiling experiments, ceiling jet, Tests 57-64 . . . 392
7.53 Vettori Sloped Ceiling experiments, ceiling jet, Tests 65-72 . . . 393
7.54 WTC experiments, ceiling jet, Tests 1-6 . . . 394
7.55 Summary of ceiling jet temperature predictions . . . 395
7.56 Comparison of measured and predicted sprinkler actuation times . . . 396
7.57 UL/NFPRF experiments, number of sprinkler activations, Series I, Tests 1-8 . . . 398
7.58 UL/NFPRF experiments, number of sprinkler activations, Series I, Tests 9-16 . . . 399
7.59 UL/NFPRF experiments, number of sprinkler activations, Series I, Tests 17-22 . . . 400
7.60 UL/NFPRF experiments, number of sprinkler activations, Series II, Tests 1-6 . . . 401
7.61 UL/NFPRF experiments, number of sprinkler activations, Series II, Tests 7-12 . . . 402
7.62 UL/NFPRF experiments, no. of sprinkler activations, Group A Commodity, Tests 1-5 . . . 403
7.63 Comparison of the number of predicted and measured sprinkler activations . . . 404
7.64 Summary of smoke detector activation times (temperature rise), NIST Smoke Alarms . . . 405
7.65 Summary of activation times, smoke detector model, NIST Smoke Alarms . . . 406

8.1 ATF Corridors, gas velocity, first level, Location H . . . 408
8.2 ATF Corridors, gas velocity, first level, Location I . . . 409
8.3 ATF Corridors, gas velocity, second level, Location J . . . 410
8.4 ATF Corridors, gas velocity, second level, Location K . . . 411
8.5 Instantaneous contours of velocity magnitude . . . 412
8.6 Friction coefficient and pressure coefficient . . . 413
8.7 Backward facing step flow profiles . . . 414
8.8 Bryant Doorway experiments, gas velocity profiles . . . 416
8.9 Edinburgh Vegetation Drag, gas velocity profiles, low bulk density . . . 417
8.10 Edinburgh Vegetation Drag, gas velocity profiles, medium bulk density . . . 418
8.11 Edinburgh Vegetation Drag, gas velocity profiles, high bulk density . . . 419
8.12 FM/FPRF experiments, gas velocity, low fan rate . . . 420
8.13 FM/FPRF experiments, gas velocity, high fan rate . . . 421

8.14 McCaffrey Plumes, centerline plume velocity . . . 422
8.15 McCaffrey Plumes, centerline plume velocity, Froude scaling . . . 423
8.16 NIST Pool Fires, centerline velocity . . . 424
8.17 PRISME DOOR experiments, gas velocity . . . 425
8.18 Restivo experiment, gas velocity . . . 426
8.19 Steckler experiments, velocity profiles, Tests 10, 11, 12, 13, 14, 18, 612, 710 . . . 428
8.20 Steckler experiments, velocity profiles, Tests 16, 17, 19, 22, 23, 30, 41, 810 . . . 429
8.21 Steckler experiments, velocity profiles, Tests 20, 21, 114, 144, 210, 212, 242, 410 . . . 430
8.22 Steckler experiments, velocity profiles, Tests 116, 122, 220, 221, 224, 240, 310, 324 . . . 431
8.23 Steckler experiments, velocity profiles, Tests 510, 512, 514, 517, 540, 542, 544, 610 . . . 432
8.24 Steckler experiments, velocity profiles, Tests 160, 513, 520, 521, 522, 524, 541, 622 . . . 433
8.25 Steckler experiments, velocity profiles, Tests 161, 162, 163, 164, 165, 166, 167 . . . 434
8.26 UL/NIJ Experiments, Velocity, single story house, Tests 1, 2, and 5 . . . 436
8.27 UL/NIJ Experiments, Velocity, two-story house, Test 1 . . . 437
8.28 UL/NIJ Experiments, Velocity, two-story house, Test 4 . . . 438
8.29 UL/NIJ Experiments, Velocity, two-story house, Test 6 . . . 439
8.30 Waterloo Methanol, radial mean and rms vert. vel., 2 cm to 8 cm above burner . . . 441
8.31 Waterloo Methanol, radial mean and rms vert. vel., 10 cm to 16 cm above burner . . . 442
8.32 Waterloo Methanol, radial mean and rms vert. vel., 18 cm to 30 cm above burner . . . 443
8.33 Waterloo Methanol, radial mean and rms horz. vel., 2 cm to 8 cm above burner . . . 444
8.34 Waterloo Methanol, radial mean and rms horz. vel., 10 cm to 16 cm above burner . . . 445
8.35 Waterloo Methanol, radial mean and rms horz. vel., 18 cm to 30 cm above burner . . . 446
8.36 Waterloo Methanol, radial profiles of $\overline{u'w'}$, 2 cm to 12 cm above the burner . . . 447
8.37 Waterloo Methanol, radial profiles of $\overline{u'w'}$, 14 cm to 30 cm above the burner . . . 448
8.38 Layout of velocity probes, WTC Experiments . . . 449
8.39 WTC experiments, inlet velocity, Points 1-3 . . . 450
8.40 WTC experiments, inlet velocity, Points 6-8 . . . 451
8.41 WTC experiments, outlet velocity, Points 1-5 . . . 452
8.42 WTC experiments, outlet velocity, Points 6-10 . . . 453
8.43 Summary of velocity predictions . . . 454
8.44 Wu and Bakar critical velocity correlation with FDS results added . . . 455

9.1 DelCo Trainers, CO_2 and O_2 concentration, Tests 2-4 . . . 458
9.2 DelCo Trainers, CO_2 and O_2 concentration, Tests 5-6 . . . 459
9.3 DelCo Trainers, CO_2 and O_2 concentration, Tests 22-25 . . . 460
9.4 FAA Cargo Compartment experiments, CO_2 and O_2 concentration . . . 461
9.5 LLNL Enclosure, O_2 and CO_2 concentration, Tests 1-4 . . . 463
9.6 LLNL Enclosure, O_2 and CO_2 concentration, Tests 5-8 . . . 464
9.7 LLNL Enclosure, O_2 and CO_2 concentration, Tests 9-12 . . . 465
9.8 LLNL Enclosure, O_2 and CO_2 concentration, Tests 13-16 . . . 466
9.9 LLNL Enclosure, O_2 and CO_2 concentration, Tests 17-20 . . . 467
9.10 LLNL Enclosure, O_2 and CO_2 concentration, Tests 21-24 . . . 468
9.11 LLNL Enclosure, O_2 and CO_2 concentration, Tests 25-28 . . . 469
9.12 LLNL Enclosure, O_2 and CO_2 concentration, Tests 29-32 . . . 470
9.13 LLNL Enclosure, O_2 and CO_2 concentration, Tests 33-36 . . . 471
9.14 LLNL Enclosure, O_2 and CO_2 concentration, Tests 37-40 . . . 472
9.15 LLNL Enclosure, O_2 and CO_2 concentration, Tests 41-44 . . . 473
9.16 LLNL Enclosure, O_2 and CO_2 concentration, Tests 45-48 . . . 474

9.17 LLNL Enclosure, O_2 and CO_2 concentration, Tests 49-52 . . . 475
9.18 LLNL Enclosure, O_2 and CO_2 concentration, Tests 53-56 . . . 476
9.19 LLNL Enclosure, O_2 and CO_2 concentration, Tests 57-60 . . . 477
9.20 LLNL Enclosure, O_2 and CO_2 concentration, Tests 61-64 . . . 478
9.21 NIST/NRC experiments, CO_2 and O_2 concentration, Tests 3, 9, 17 . . . 479
9.22 NIST/NRC experiments, CO_2 and O_2 concentration, Tests 5, 14, 15, 18 . . . 480
9.23 NIST/NRC experiments, CO_2 and O_2 concentration, Tests 1, 2, 7, 8 . . . 481
9.24 NIST/NRC experiments, CO_2 and O_2 concentration, Tests 4, 10, 13, 16 . . . 482
9.25 NRCC Smoke Tower, CO_2 and O_2 concentration, Tests BK-R and COMP-R . . . 483
9.26 NRCC Smoke Tower, CO_2 and O_2 concentration, Tests CLC-I-R and CLC-II-R . . . 484
9.27 PRISME DOOR experiments, CO_2 and O_2 concentration, Room 1, Tests 1-3 . . . 485
9.28 PRISME DOOR experiments, CO_2 and O_2 concentration, Room 1, Tests 4-6 . . . 486
9.29 PRISME DOOR experiments, CO_2 and O_2 concentration, Room 2, Tests 1-3 . . . 487
9.30 PRISME DOOR experiments, CO_2 and O_2 concentration, Room 2, Tests 4-6 . . . 488
9.31 PRISME SOURCE experiments, CO_2 and O_2 concentration, Room 2, Tests 1-4 . . . 490
9.32 PRISME SOURCE experiments, CO_2 and O_2 concentration, Room 2, Tests 5-6 . . . 491
9.33 WTC experiments, CO_2 and O_2 concentration, Tests 1-3 . . . 492
9.34 WTC experiments, CO_2 and O_2 concentration, Tests 4-6 . . . 493
9.35 UMD_Line_Burner oxygen concentration profiles . . . 494
9.36 Summary of major gas species predictions . . . 495
9.37 FM Burner experiments, plume mean and rms soot volume fraction, 20.9 % O_2 . . . 496
9.38 FM Burner experiments, plume mean and rms soot voiume fraction, 20.9 % O_2 . . . 497
9.39 FM Burner experiments, plume mean and rms soot volume fraction, 16.8 % O_2 . . . 498
9.40 FM Burner experiments, plume mean and rms soot voiume fraction, 16.8 % O_2 . . . 499
9.41 FM Burner experiments, plume mean and rms soot volume fraction, 15.2 % O_2 . . . 500
9.42 FM Burner experiments, plume mean and rms soot voiume fraction, 15.2 % O_2 . . . 501
9.43 FM Burner experiments, soot volume fraction PDFs, 20.9 % O_2 . . . 502
9.44 FM Burner experiments, soot volume fraction PDFs, 16.8 % O_2 . . . 503
9.45 FM Burner experiments, soot volume fraction PDFs, 15.2 % O_2 . . . 504
9.46 FM/FPRF Data Center, smoke concentration, propylene and cable sources . . . 505
9.47 NIST/NRC experiments, smoke concentration, Tests 1, 2, 4, 7, 8, 10, 13, 16 . . . 507
9.48 NIST/NRC experiments, smoke concentration, Tests 3, 5, 9, 14, 15, 17, 18 . . . 508
9.49 Summary of smoke concentration predictions . . . 509
9.50 FAA Cargo Compartments experiments, smoke obscuration . . . 510
9.51 Summary of smoke obscuration predictions . . . 511
9.52 Predicted and measured aerosol deposition velocities, Sippola experiments . . . 512
9.53 Summary of aerosol deposition velocity predictions . . . 513
9.54 Predicted and measured aerosol deposited mass, NIST Soot Deposition Gauge exp . . . 514
9.55 Summary of aerosol deposited mass predictions . . . 515
9.56 Droplet diameter for the Ranz and Marshall experiment . . . 516
9.57 Evaporation rates for the Ranz and Marshall experiments . . . 517
9.58 Summary of evaporation rates for the Ranz and Marshall experiments . . . 518
9.59 Normalized droplet area for the Fujita experiments . . . 519
9.60 Droplet temperature change, Fujita et al. experiments . . . 520
9.61 Droplet terminal velocity for the Gavin experiments . . . 521
9.62 Square of the droplet diameter, Kolaitis and Founti . . . 522
9.63 Droplet surface temperature, Kolaitis and Founti . . . 523
9.64 Droplet surface temperature for the Maqua et al. experiments . . . 524

9.65 Droplet diameter for the Taflin experiments . . . 525
9.66 Temperature predictions at 7 mm, 9 mm, and 11 mm above burner, Smyth experiment . . . 526
9.67 CH_4 and O_2 volume fractions at 11 mm, 9 mm, and 7 mm above burner, Smyth burner . . . 527
9.68 CO_2 and CO volume fractions at 11 mm, 9 mm, and 7 mm above burner, Smyth burner . . . 528
9.69 H_2O and H_2 volume fractions at 11 mm, 9 mm, and 7 mm above burner, Smyth burner . . . 529
9.70 Summary of gas species predictions, Beyler hood experiments . . . 531
9.71 Comparison of measured and predicted CO concentration, NIST RSE experiments . . . 532
9.72 Comparison of measured and predicted CO_2 concentration, NIST RSE experiments . . . 532
9.73 Comparison of measured and predicted O_2 concentration, NIST RSE experiments . . . 533
9.74 Comparison of measured and predicted H_2O concentration, NIST RSE experiments . . . 533
9.75 Comparison of measured and predicted temperature, NIST RSE experiments . . . 533
9.76 Summary of Test 1, NIST RSE 2007 . . . 534
9.77 Summary of Test 2, NIST RSE 2007 . . . 535
9.78 Summary of Test 3, NIST RSE 2007 . . . 536
9.79 Summary of Test 4, NIST RSE 2007 . . . 537
9.80 Summary of Test 5, NIST RSE 2007 . . . 538
9.81 Summary of Test 6, NIST RSE 2007 . . . 539
9.82 Summary of Test 7, NIST RSE 2007 . . . 540
9.83 Summary of Test 10, NIST RSE 2007 . . . 541
9.84 Summary of Test 11, NIST RSE 2007 . . . 542
9.85 Summary of Test 12, NIST RSE 2007 . . . 543
9.86 Summary of Test 15, NIST RSE 2007 . . . 544
9.87 Summary of Test 16, NIST RSE 2007 . . . 545
9.88 Summary of ISONG3, NIST FSE 2008 . . . 546
9.89 Summary of ISOHept4, NIST FSE 2008 . . . 547
9.90 Summary of ISOHept5, NIST FSE 2008 . . . 548
9.91 Summary of ISOHept8, NIST FSE 2008 . . . 549
9.92 Summary of ISOHept9, NIST FSE 2008 . . . 550
9.93 Summary of ISONylon10, NIST FSE 2008 . . . 551
9.94 Summary of ISOPP11, NIST FSE 2008 . . . 552
9.95 Summary of ISOHeptD12, NIST FSE 2008 . . . 553
9.96 Summary of ISOHeptD13, NIST FSE 2008 . . . 554
9.97 Summary of ISOPropD14, NIST FSE 2008 . . . 555
9.98 Summary of ISOProp15, NIST FSE 2008 . . . 556
9.99 Summary of ISOStyrene16, NIST FSE 2008 . . . 557
9.100 Summary of ISOStyrene17, NIST FSE 2008 . . . 558
9.101 Summary of ISOPP18, NIST FSE 2008 . . . 559
9.102 Summary of ISOHept19, NIST FSE 2008 . . . 560
9.103 Summary of ISOToluene20, NIST FSE 2008 . . . 561
9.104 Summary of ISOStyrene21, NIST FSE 2008 . . . 562
9.105 Summary of ISOHept22, NIST FSE 2008 . . . 563
9.106 Summary of ISOHept23, NIST FSE 2008 . . . 564
9.107 Summary of ISOHept24, NIST FSE 2008 . . . 565
9.108 Summary of ISOHept25, NIST FSE 2008 . . . 566
9.109 Summary of ISOHept26, NIST FSE 2008 . . . 567
9.110 Summary of ISOHept27, NIST FSE 2008 . . . 568
9.111 Summary of ISOHept28, NIST FSE 2008 . . . 569
9.112 Summary of ISOToluene29, NIST FSE 2008 . . . 570

9.113 Summary of ISOPropanol30, NIST FSE 2008 . . . 571
9.114 Summary of ISONG32, NIST FSE 2008 . . . 572
9.115 NIST Pool Fires, centerline product species, acetone . . . 574
9.116 NIST Pool Fires, centerline product species, ethanol . . . 575
9.117 NIST Pool Fires, centerline product species, methanol . . . 576
9.118 NIST Pool Fires, centerline product species, methane . . . 577
9.119 NIST Pool Fires, centerline product species, propane, 20 kW . . . 578
9.120 NIST Pool Fires, centerline product species, propane, 34 kW . . . 579
9.121 Summary of carbon monoxide predictions . . . 580
9.122 Results of the NIST_He_2009 experiments . . . 582
9.123 Results of the NIST_He_2009 experiments . . . 583
9.124 Results of the NIST_He_2009 experiments . . . 584
9.125 Summary of species concentration predictions . . . 585

10.1 FM/FPRF Data Center, differential pressure . . . 588
10.2 NIST/NRC experiments, compartment pressure, Tests 1, 2, 4, 7, 8, 10, 13, 16 . . . 590
10.3 NIST/NRC experiments, compartment pressure, Tests 3, 5, 9, 14, 15, 17, 18 . . . 591
10.4 LLNL Enclosure experiments, compartment pressure, Tests 1-8 . . . 593
10.5 LLNL Enclosure experiments, compartment pressure, Tests 9-16 . . . 594
10.6 LLNL Enclosure experiments, compartment pressure, Tests 17-24 . . . 595
10.7 LLNL Enclosure experiments, compartment pressure, Tests 25-32 . . . 596
10.8 LLNL Enclosure experiments, compartment pressure, Tests 33-40 . . . 597
10.9 LLNL Enclosure experiments, compartment pressure, Tests 41-48 . . . 598
10.10 LLNL Enclosure experiments, compartment pressure, Tests 49-56 . . . 599
10.11 LLNL Enclosure experiments, compartment pressure, Tests 57-64 . . . 600
10.12 PRISME DOOR, compartment pressure and supply/exhaust, Room 1, Tests 1-3 . . . 602
10.13 PRISME DOOR, compartment pressure and supply/exhaust, Room 1, Tests 4-6 . . . 603
10.14 PRISME DOOR, compartment pressure and supply/exhaust, Room 2, Tests 1-3 . . . 604
10.15 PRISME DOOR, compartment pressure and supply/exhaust, Room 2, Tests 4-6 . . . 605
10.16 PRISME SOURCE, pressure and supply/exhaust flow rates, Tests 1, 2, 3 and 4 . . . 607
10.17 PRISME SOURCE, pressure and supply/exhaust flow rates, Tests 5, 5a, 6 and 6a . . . 608
10.18 UL/NIJ Experiments, Pressure, Single-Story (Ranch) House, Test 1 . . . 610
10.19 UL/NIJ Experiments, Pressure, Single-Story (Ranch) House, Test 2 . . . 611
10.20 UL/NIJ Experiments, Pressure, Single-Story (Ranch) House, Test 5 . . . 612
10.21 UL/NIJ Experiments, Pressure, Two-Story (Colonial) House, Test 1 . . . 613
10.22 UL/NIJ Experiments, Pressure, Two-Story (Colonial) House, Test 4 . . . 614
10.23 UL/NIJ Experiments, Pressure, Two-Story (Colonial) House, Test 6 . . . 615
10.24 Summary of pressure predictions . . . 616

11.1 FAA Cargo Compartment experiments, ceiling surface temperatures . . . 618
11.2 NIST Composite Beam, under-deck temperatures, Sections 3 and 4 . . . 620
11.3 NIST Composite Beam, under-deck temperatures, Sections 5 and 6 . . . 621
11.4 NIST Composite Beam, inside-deck temperatures, Sections 1 and 2 . . . 622
11.5 NIST Composite Beam, inside-deck temperatures, Sections 3 and 4 . . . 623
11.6 NIST Composite Beam, inside-deck temperatures, Sections 5 and 6 . . . 624
11.7 NIST Composite Beam, inside-deck temperatures, Sections 7 and 8 . . . 625
11.8 NIST FSE experiments, floor and ceiling temperatures, Tests 3-4, 8 . . . 627
11.9 NIST FSE experiments, floor and ceiling temperatures, Tests 9-12 . . . 628

11.10 NIST FSE experiments, floor and ceiling temperatures, Tests 13-16 . . . 629
11.11 NIST FSE experiments, floor and ceiling temperatures, Tests 17-20 . . . 630
11.12 NIST FSE experiments, floor and ceiling temperatures, Tests 21-24 . . . 631
11.13 NIST FSE experiments, floor and ceiling temperatures, Tests 25-28 . . . 632
11.14 NIST FSE experiments, floor and ceiling temperatures, Tests 29, 30, 32 . . . 633
11.15 NIST/NRC experiments, north wall temperatures, Tests 1, 2, 4, 7, 8, 10, 13, 16 . . . 635
11.16 NIST/NRC experiments, north wall temperatures, Tests 3, 5, 9, 14, 15, 18 . . . 636
11.17 NIST/NRC experiments, south wall temperatures, Tests 1, 2, 4, 7, 8, 10, 13, 16 . . . 637
11.18 NIST/NRC experiments, south wall temperatures, Tests 3, 5, 9, 14, 15, 18 . . . 638
11.19 NIST/NRC experiments, east wall temperatures, Tests 1, 2, 4, 7, 8, 10, 13, 16 . . . 639
11.20 NIST/NRC experiments, east wall temperatures, Tests 3, 5, 9, 14, 15, 18 . . . 640
11.21 NIST/NRC experiments, west wall temperatures, Tests 1, 2, 4, 7, 8, 10, 13, 16 . . . 641
11.22 NIST/NRC experiments, west wall temperatures, Tests 3, 5, 9, 14, 15, 18 . . . 642
11.23 NIST/NRC experiments, ceiling temperatures, Tests 1, 2, 4, 7, 8, 10, 13, 16 . . . 643
11.24 NIST/NRC experiments, ceiling temperatures, Tests 3, 5, 9, 14, 15, 18 . . . 644
11.25 NIST/NRC experiments, floor wall temperatures, Tests 1, 2, 4, 7, 8, 10, 13, 16 . . . 645
11.26 NIST/NRC experiments, floor temperatures, Tests 3, 5, 9, 14, 15, 18 . . . 646
11.27 PRISME DOOR experiments, wall temperatures, vertical array, Room 1 . . . 647
11.28 PRISME DOOR experiments, wall temperatures, four sides, Room 1 . . . 648
11.29 PRISME DOOR experiments, wall temperatures, vertical array, Room 2 . . . 649
11.30 PRISME DOOR experiments, wall temperatures, four sides, Room 2 . . . 650
11.31 PRISME SOURCE experiments, wall temperatures, vertical array, Room 2 . . . 652
11.32 PRISME SOURCE experiments, wall temperatures, four sides, Room 2 . . . 653
11.33 WTC experiments, ceiling temperatures, north array . . . 655
11.34 WTC experiments, ceiling temperatures, south array . . . 656
11.35 WTC experiments, ceiling temperatures, east array, Points 1-4 . . . 657
11.36 WTC experiments, ceiling temperatures, east array, Points 5-7 . . . 658
11.37 WTC experiments, ceiling temperatures, west array, Points 1-4 . . . 659
11.38 WTC experiments, ceiling temperatures, west array, Points 5-8 . . . 660
11.39 WTC experiments, ceiling temperatures, diagonal array . . . 661
11.40 WTC experiments, wall temperatures, Points 98, 100, 102 . . . 662
11.41 WTC experiments, wall temperatures, Points 103, 105, 106 . . . 663
11.42 WTC experiments, wall temperatures, Points 107, 109, 110 . . . 664
11.43 WTC experiments, inner ceiling temperatures, north-south axis . . . 665
11.44 WTC experiments, inner ceiling temperatures, east-west axis . . . 666
11.45 WTC experiments, inner wall temperatures . . . 667
11.46 Insulation material cold side temperatures, Tests 1-6 . . . 669
11.47 Insulation material cold side temperatures, Tests 7-14 . . . 670
11.48 Insulation material cold side temperatures, Tests 15-22 . . . 671
11.49 Insulation material cold side temperatures, Tests 23-30 . . . 672
11.50 Summary of compartment surface temperature predictions . . . 673
11.51 NIST Composite Beam, beam temperatures . . . 674
11.52 NIST Composite Beam, beam temperatures . . . 675
11.53 NIST E119 Compartment, Plate temperatures . . . 676
11.54 NIST/NRC experiments, Cable A temperatures, Tests 1, 2, 4, 7, 8, 10, 13, 16 . . . 678
11.55 NIST/NRC experiments, Cable A temperatures, Tests 3, 5, 9, 14, 15, 18 . . . 679
11.56 NIST/NRC experiments, Cable B temperatures, Tests 1, 2, 4, 7, 8, 10, 13, 16 . . . 680
11.57 NIST/NRC experiments, Cable B temperatures, Tests 3, 5, 9, 14, 15, 18 . . . 681

11.58 NIST/NRC experiments, Cable Ca temperatures, Tests 1, 2, 4, 7, 8, 10, 13, 16 682
11.59 NIST/NRC experiments, Cable Ca temperatures, Tests 3, 5, 9, 14, 15, 18 683
11.60 NIST/NRC experiments, Cable Cb temperatures, Tests 1, 2, 4, 7, 8, 10, 13, 16 684
11.61 NIST/NRC experiments, Cable Cb temperatures, Tests 3, 5, 9, 14, 15, 18 685
11.62 NIST/NRC experiments, Cable D temperatures, Tests 1, 2, 4, 7, 8, 10, 13, 16 686
11.63 NIST/NRC experiments, Cable D temperatures, Tests 3, 5, 9, 14, 15, 18 687
11.64 NIST/NRC experiments, Cable F temperatures, Tests 1, 2, 4, 7, 8, 10, 13, 16 688
11.65 NIST/NRC experiments, Cable F temperatures, Tests 3, 5, 9, 14, 15, 18 689
11.66 NIST/NRC experiments, Cable G temperatures, Tests 1, 2, 4, 7, 8, 10, 13, 16 690
11.67 NIST/NRC experiments, Cable G temperatures, Tests 3, 5, 9, 14, 15, 18 691
11.68 NIST/NRC Corner Effects, plate and cabinet temperatures, Test 1 693
11.69 NIST/NRC Corner Effects, plate and cabinet temperatures, Test 2 694
11.70 NIST/NRC Corner Effects, plate and cabinet temperatures, Test 3 695
11.71 NIST/NRC Corner Effects, plate and cabinet temperatures, Test 4 696
11.72 NIST/NRC Corner Effects, plate and cabinet temperatures, Test 5 697
11.73 NIST/NRC Corner Effects, plate and cabinet temperatures, Test 6 698
11.74 NIST/NRC Corner Effects, plate and cabinet temperatures, Test 7 699
11.75 NIST/NRC Corner Effects, plate and cabinet temperatures, Test 8 700
11.76 NIST/NRC Corner Effects, plate and cabinet temperatures, Test 9 701
11.77 NIST/NRC Corner Effects, plate and cabinet temperatures, Test 10 702
11.78 NIST/NRC Corner Effects, plate and cabinet temperatures, Test 11 703
11.79 NIST/NRC Corner Effects, plate and cabinet temperatures, Test 12 704
11.80 SP AST experiments, Station A plate, adiabatic surface, and steel temperatures, Test 1 . . . 706
11.81 SP AST experiments, Station B plate, adiabatic surface, and steel temperatures, Test 1 . . . 707
11.82 SP AST experiments, Station C plate, adiabatic surface, and steel temperatures, Test 1 . . . 708
11.83 SP AST experiments, Station A plate, adiabatic surface, and steel temperatures, Test 2 . . . 709
11.84 SP AST experiments, Station B plate, adiabatic surface, and steel temperatures, Test 2 . . . 710
11.85 SP AST experiments, Station C plate, adiabatic surface, and steel temperatures, Test 2 . . . 711
11.86 SP AST experiments, Station A plate, adiabatic surface, and steel temperatures, Test 3 . . . 712
11.87 SP AST experiments, Station B plate, adiabatic surface, and steel temperatures, Test 3 . . . 713
11.88 SP AST experiments, Station C plate, adiabatic surface, and steel temperatures, Test 3 . . . 714
11.89 SP AST experiments, steel temperatures, 1.1 m diesel fire 716
11.90 SP AST experiments, steel temperatures, 1.1 m and 1.9 m diesel, 1.1 m heptane fires . . . 717
11.91 SP AST experiments, steel temperatures, 1.1 m heptane fire 718
11.92 SP AST experiments, Insulated Room, Test A1 720
11.93 SP AST experiments, Insulated Room, Test A2 721
11.94 SP AST experiments, Insulated Room, Test A3 722
11.95 SP AST experiments, Insulated Room, Test A4 723
11.96 SP AST experiments, Insulated Room, Test A5 724
11.97 SP AST experiments, Insulated Room, Test B1 725
11.98 SP AST experiments, Insulated Room, Test B2 726
11.99 SP AST experiments, Insulated Room, Test C1 727
11.100 SP AST experiments, Insulated Room, Test C2 728
11.101 SP AST experiments, Insulated Room, Test C3 729
11.102 SP AST experiments, Insulated Room, Test D1 730
11.103 SP AST experiments, Insulated Room, Test D2 731
11.104 Drawing of a plate thermometer 732
11.105 Predictions of plate thermometer temperatures in a cone calorimeter 732

11.106 WTC experiments, steel temperatures, upper column . . . 734
11.107 WTC experiments, steel temperatures, middle column . . . 735
11.108 WTC experiments, steel temperatures, lower column . . . 736
11.109 WTC experiments, steel temperatures, upper Truss A . . . 737
11.110 WTC experiments, steel temperatures, middle Truss A . . . 738
11.111 WTC experiments, steel temperatures, lower Truss A . . . 739
11.112 WTC experiments, steel temperatures, upper Truss B . . . 740
11.113 WTC experiments, steel temperatures, middle Truss B . . . 741
11.114 WTC experiments, steel temperatures, lower Truss B . . . 742
11.115 WTC experiments, steel temperatures, Bar 1 . . . 743
11.116 WTC experiments, slug temperatures . . . 744
11.117 CAROLFIRE, electrical cable temperatures, Penlight Tests 1, 2, 3, 7, 9, 11-13 . . . 746
11.118 CAROLFIRE, electrical cable temperatures, Penlight Tests 17, 19-20, 22-24, 27-28 . . . 747
11.119 CAROLFIRE, electrical cable temperatures, Penlight Tests 4-6, 8, 10, 14-16 . . . 748
11.120 CAROLFIRE, electrical cable temperatures, Penlight Tests 21, 25-26, 29-30, 63, 65 . . . 749
11.121 CAROLFIRE, electrical cable temperatures, Penlight Tests 18, 31, 62, 64 . . . 750
11.122 Frankman vegetation experiments, fuel temperatures . . . 751
11.123 PRISME LEAK experiments, cable temperature, Tests 1 and 2 . . . 753
11.124 PRISME LEAK experiments, cable temperature, Tests 3 and 4 . . . 754
11.125 PRISME DOOR experiments, cable temperature, Room 1, Cable BW . . . 755
11.126 PRISME DOOR experiments, cable temperature, Room 1, Cable HW . . . 756
11.127 PRISME DOOR experiments, cable temperature, Room 2, Cable BE . . . 757
11.128 PRISME DOOR experiments, cable temperature, Room 2, Cable HE . . . 758
11.129 PRISME DOOR experiments, cable temperature, Room 2, Cable HW . . . 759
11.130 Summary of target temperature predictions . . . 760
11.131 Summary of time to failure predictions for electrical cables . . . 761
11.132 ASTM E2058 water evaporation 50 kW/m^2, surface temperature . . . 762
11.133 VTT heptane pool fire surface temperatures . . . 762
11.134 Pool fire experiments, surface temperatures . . . 763
11.135 NIST 1 m and Waterloo 30 cm methanol pool fires, surface temperature . . . 764
11.136 Summary of liquid pool surface temperature predictions . . . 765

12.1 FAA Cargo Compartment experiments, heat flux to ceiling . . . 768
12.2 FM Parallel Panel experiments, side wall heat flux . . . 769
12.3 FM Vertical Wall Flame experiments, flame radiance . . . 770
12.4 FM Vertical Wall Flame experiments, centerline heat flux . . . 771
12.5 NIST E119 Compartment, wall heat fluxes . . . 772
12.6 NIST/NRC experiments, heat flux to north wall, Tests 1, 2, 4, 7, 8, 10 . . . 774
12.7 NIST/NRC experiments, heat flux to north wall, Tests 3, 5, 9, 14, 15, 18 . . . 775
12.8 NIST/NRC experiments, heat flux to south wall, Tests 1, 2, 4, 7, 8, 10 . . . 776
12.9 NIST/NRC experiments, heat flux to south wall, Tests 3, 5, 9, 14, 15, 18 . . . 777
12.10 NIST/NRC experiments, heat flux to east wall, Tests 1, 2, 4, 7, 8, 10 . . . 778
12.11 NIST/NRC experiments, heat flux to east wall, Tests 3, 5, 9, 14, 15, 18 . . . 779
12.12 NIST/NRC experiments, heat flux to west wall, Tests 1, 2, 4, 7, 8, 10 . . . 780
12.13 NIST/NRC experiments, heat flux to west wall, Tests 3, 5, 9, 14, 15, 18 . . . 781
12.14 NIST/NRC experiments, heat flux to the floor, Tests 1, 2, 4, 7, 8, 10 . . . 782
12.15 NIST/NRC experiments, heat flux to the floor, Tests 3, 5, 9, 14, 15, 18 . . . 783
12.16 NIST/NRC experiments, heat flux to the ceiling, Tests 1, 2, 4, 7, 8, 10 . . . 784

12.17 NIST/NRC experiments, heat flux to the ceiling, Tests 3, 5, 9, 14, 15, 18 . . . 785
12.18 Smokeview rendering of NRCC Facade experiment . . . 786
12.19 NRCC Facade experiments, heat flux, window configuration 1 and 2 . . . 787
12.20 NRCC Facade experiments, heat flux, window configuration 3 and 4 . . . 788
12.21 NRCC Facade experiments, heat flux, window configuration 5 . . . 789
12.22 NRL/HAI experiments, heat flux to the wall, Tests 1-5 . . . 791
12.23 NRL/HAI experiments, heat flux to the wall, Tests 6-9 . . . 792
12.24 PRISME DOOR experiments, total heat flux, vertical array, Room 1 . . . 793
12.25 PRISME DOOR experiments, radiative heat flux, vertical array, Room 1 . . . 794
12.26 PRISME DOOR experiments, total heat flux, four walls, Room 1 . . . 795
12.27 PRISME DOOR experiments, total heat flux, vertical array, Room 2 . . . 796
12.28 PRISME DOOR experiments, radiative heat flux, vertical array, Room 2 . . . 797
12.29 PRISME DOOR experiments, total heat flux, four walls, Room 2 . . . 798
12.30 PRISME SOURCE experiments, total heat flux, vertical array, Room 2 . . . 800
12.31 PRISME SOURCE experiments, radiative heat flux, vertical array, Room 2 . . . 801
12.32 PRISME SOURCE experiments, total heat flux, four walls, Room 2 . . . 802
12.33 Ulster SBI experiments, corner fire heat flux . . . 803
12.34 WTC experiments, heat flux to the floor . . . 805
12.35 WTC experiments, heat flux to the ceiling . . . 806
12.36 WTC experiments, heat flux to the ceiling . . . 807
12.37 Summary of compartment surface heat flux predictions . . . 808
12.38 Fleury Heat Flux, 100 kW fires . . . 810
12.39 Fleury Heat Flux, 150 kW fires . . . 811
12.40 Fleury Heat Flux, 200 kW fires . . . 812
12.41 Fleury Heat Flux, 250 kW fires . . . 813
12.42 Fleury Heat Flux, 300 kW fires . . . 814
12.43 Heat flux predictions, Hamins methane burner Tests 1-4 . . . 817
12.44 Heat flux predictions, Hamins methane burner Tests 5-8 . . . 818
12.45 Heat flux predictions, Hamins methane burner Tests 9-12 . . . 819
12.46 Heat flux predictions, Hamins methane burner Tests 13-16 . . . 820
12.47 Heat flux predictions, Hamins methane burner Tests 17-20 . . . 821
12.48 Heat flux predictions, Hamins methane burner Tests 21-24 . . . 822
12.49 Heat flux predictions, Hamins methane burner Tests 25-28 . . . 823
12.50 Heat flux predictions, Hamins methane burner Tests 29-30 . . . 824
12.51 Heat flux predictions, Hamins propane burner Tests 1-4 . . . 826
12.52 Heat flux predictions, Hamins propane burner Tests 5-8 . . . 827
12.53 Heat flux predictions, Hamins propane burner Tests 9-12 . . . 828
12.54 Heat flux predictions, Hamins propane burner Tests 13-16 . . . 829
12.55 Heat flux predictions, Hamins propane burner Tests 17-20 . . . 830
12.56 Heat flux predictions, Hamins propane burner Tests 21-24 . . . 831
12.57 Heat flux predictions, Hamins propane burner Tests 25-28 . . . 832
12.58 Heat flux predictions, Hamins propane burner Tests 29-32 . . . 833
12.59 Heat flux predictions, Hamins propane burner Tests 33-34 . . . 834
12.60 Heat flux predictions, Hamins acetylene burner Tests 1-4 . . . 836
12.61 Heat flux predictions, Hamins acetylene burner Tests 5-8 . . . 837
12.62 Heat flux predictions, Hamins acetylene burner Tests 9-12 . . . 838
12.63 Heat flux predictions, Hamins acetylene burner Tests 13-16 . . . 839
12.64 Schematic diagram of BGC/GRI test facility . . . 840

12.65 BGC/GRI LNG Fires, heat flux profiles for Tests 1-8 . . . 841
12.66 BGC/GRI LNG Fires, heat flux profiles for Tests 9-13 . . . 842
12.67 Location of heat flux gauges, Loughborough Jet Fires . . . 843
12.68 Loughborough Jet Fires, heat flux to pipe, Test 1 . . . 844
12.69 Loughborough Jet Fires, heat flux to pipe, Test 2 . . . 845
12.70 Loughborough Jet Fires, heat flux to pipe, Test 3 . . . 846
12.71 Loughborough Jet Fires, far-field radiometers . . . 847
12.72 Layout of the Montoir LNG Fires . . . 848
12.73 Montoir LNG Fires, far-field radiometers, Test 1 . . . 849
12.74 Montoir LNG Fires, far-field radiometers, Test 2 . . . 850
12.75 Montoir LNG Fires, far-field radiometers, Test 3 . . . 851
12.76 NIST Douglas Firs, heat flux . . . 852
12.77 NIST/NRC experiments, heat flux to Cable B, Tests 1, 2, 4, 7, 8, 10, 13, 16 . . . 854
12.78 NIST/NRC experiments, heat flux to Cable B, Tests 3, 5, 9, 14, 15, 18 . . . 855
12.79 NIST/NRC experiments, heat flux to Cable D, Tests 1, 2, 4, 7, 8, 10, 13, 16 . . . 856
12.80 NIST/NRC experiments, heat flux to Cable D, Tests 5, 9, 14 . . . 857
12.81 NIST/NRC experiments, heat flux to Cable F, Tests 1, 2, 4, 7, 8, 10, 13, 16 . . . 858
12.82 NIST/NRC experiments, heat flux to Cable F, Tests 3, 5, 9, 14, 15, 18 . . . 859
12.83 NIST/NRC experiments, heat flux to Cable G, Tests 1, 2, 4, 7, 8, 10, 13, 16 . . . 860
12.84 NIST/NRC experiments, heat flux to Cable G, Tests 3, 5, 9, 14, 15, 18 . . . 861
12.85 NIST Pool Fires, 30 cm methanol, radial profiles heat flux near surface . . . 862
12.86 NIST Pool Fires, 30 cm methanol, radial and vertical profiles of total heat flux . . . 863
12.87 NIST Pool Fires, 100 cm methanol, radial and vertical profiles of heat flux . . . 863
12.88 NIST Pool Fires, 100 cm methanol, radial profiles of heat flux . . . 864
12.89 Layout of the Phoenix LNG Fires . . . 865
12.90 Phoenix LNG Fires, radial profiles of wide-angle heat flux . . . 866
12.91 Phoenix LNG Fires, vertical profiles of narrow-angle heat flux . . . 866
12.92 Sandia Methane Burner, heat flux, Tests 1-4 . . . 868
12.93 Sandia Methane Burner, heat flux, Tests 5-8 . . . 869
12.94 Sandia Methane Burner, heat flux, Tests 9-12 . . . 870
12.95 Sandia Methane Burner, heat flux, Tests 13-16 . . . 871
12.96 Sandia Methane Burner, heat flux, Tests 17-20 . . . 872
12.97 Sandia Methane Burner, heat flux, Tests 21-24 . . . 873
12.98 Sandia Methane Burner, heat flux, Tests 25-28 . . . 874
12.99 Shell LNG Fireballs, heat flux . . . 875
12.100 WTC experiments, heat flux at Station 2, high position . . . 876
12.101 WTC experiments, heat flux at Station 2, low position . . . 877
12.102 WTC experiments, heat flux to upper column . . . 878
12.103 WTC experiments, heat flux to lower column . . . 879
12.104 UMD Line Burner contour of integrated radiation intensity. . . . 880
12.105 UMD Line Burner radiative fraction and radiative heat flux . . . 881
12.106 Summary of target heat flux predictions . . . 882
12.107 Droplet speeds and mean diameters for the three nozzles . . . 883
12.108 Comparison of radiation attenuation, BRE and LEMTA Spray experiments . . . 884
12.109 Bouchair Solar Chimney, 0.1 m thermal cavity . . . 886
12.110 Bouchair Solar Chimney, 0.2 m thermal cavity . . . 887
12.111 Bouchair Solar Chimney, 0.3 m thermal cavity . . . 888
12.112 Bouchair Solar Chimney, 0.5 m thermal cavity . . . 889

12.113 Bouchair Solar Chimney, 1.0 m thermal cavity . . . 890
12.114 Summary of Bouchair Solar Chimney results . . . 891
12.115 FM Burner experiments, mean and rms vertical heat flux profiles . . . 893
12.116 FM Burner experiments, radiant fraction . . . 894
12.117 Summary of SETCOM results . . . 895

13.1 Results of Cup Burner experiments . . . 898
13.2 FM Burner combustion efficiency . . . 899
13.3 UMD Line Burner combustion efficiency . . . 900
13.4 LLNL Extinction Time, Tests 1-8 . . . 902
13.5 LLNL Extinction Time, Tests 22, 24, 25, 27, 28, 29, 32, 37 . . . 903
13.6 LLNL Extinction Time, Tests 39, 41, 43-48 . . . 904
13.7 LLNL Extinction Time, Test 49 . . . 905
13.8 NIST/NRC OLIVE-Fire maximum HRR, Tests 3, 4, 8, 9, 12, 13 . . . 907
13.9 NIST/NRC OLIVE-Fire maximum HRR, Tests 15, 16, 17, 19, 22, 23 . . . 908
13.10 NIST/NRC OLIVE-Fire maximum HRR, Tests 24, 26, 27, 29, 30, 31 . . . 909
13.11 SWJTU Tunnel experiments, extinction time . . . 910
13.12 USCG/HAI experiments, extinction time . . . 912
13.13 USCG/HAI experiments, extinction time . . . 913
13.14 USCG/HAI experiments, extinction time . . . 914
13.15 USCG/HAI experiments, extinction time . . . 915
13.16 USCG/HAI experiments, extinction time . . . 916
13.17 Extinguishment times for the USCG/HAI water mist suppression tests . . . 917
13.18 Droplet speed, flux, and mean diameter profiles of the LN-2 nozzle . . . 919

14.1 Results of FAA Polymers, non-charring, comparison . . . 924
14.2 Results of FAA Polymers, complex, non-charring, comparison . . . 926
14.3 Heat release rate of polycarbonate (PC) . . . 928
14.4 Heat release rate of poly(vinyl chloride) (PVC) . . . 930
14.5 Heat release rate of poly(aryl ether ether ketone) (PEEK) . . . 933
14.6 Mass loss rate of poly(butylene terephtalate) (PBT) . . . 935
14.7 Mass loss rate of poly(butylene terephtalate) with glass fibers (PBT-GF) . . . 937
14.8 Mass loss rate of ABS and HIPS . . . 939
14.9 Mass loss rate of PMMA . . . 940
14.10 Mass loss rate of Kydex . . . 942
14.11 Mass loss rate of PEI and PET . . . 944
14.12 Mass loss rate of POM . . . 945
14.13 Mass loss rate of corrugated cardboard . . . 949
14.14 BST/FRS Wood Cribs temperatures, Tests 1 and 2 . . . 951
14.15 BST/FRS Wood Cribs temperatures, Tests 3 and 4 . . . 952
14.16 BST/FRS Wood Cribs temperatures, Tests 5 and 6 . . . 953
14.17 NIST/NRC Transient Combustibles: wood cribs . . . 954
14.18 NIST/NRC Transient Combustibles: boxes . . . 955
14.19 NIST/NRC Transient Combustibles: pallets . . . 956
14.20 SP Wood Cribs heat release rates, Tests 1-6 . . . 957
14.21 SP Wood Cribs heat release rates, Tests 7-12 . . . 958
14.22 DoJ/HAI Pool Fires, Tests 1-8 . . . 961
14.23 DoJ/HAI Pool Fires, Tests 9-16 . . . 962

14.24 DoJ/HAI Pool Fires, Tests 17-22 . . . 963
14.25 DoJ/HAI Pool Fires, Tests 25-32 . . . 964
14.26 DoJ/HAI Pool Fires, Tests 33-40 . . . 965
14.27 DoJ/HAI Pool Fires, Tests 41-46 . . . 966
14.28 ASTM E2058 fire propagation apparatus water evaporation at 50 kW/m^2 heat flux . . . 967
14.29 VTT Large Hall Test burning rate . . . 967
14.30 Comparison of burning rates for various liquid pool fires . . . 968
14.31 NIST 1 m methanol burning rate . . . 969
14.32 Waterloo Methanol mass loss rate . . . 969
14.33 NIST/NRC Parallel Panels experiments . . . 970
14.34 Comparison observed and predicted rates of spread for a variety of crown fires . . . 971
14.35 Measured and predicted fire front position for the CSIRO Grassland Fires . . . 973
14.36 Flame front, USFS/Catchpole experiments . . . 975
14.37 Flame front, USFS/Catchpole experiments . . . 976
14.38 Flame front, USFS/Catchpole experiments . . . 977
14.39 Flame front, USFS/Catchpole experiments . . . 978
14.40 Flame front, USFS/Catchpole experiments . . . 979
14.41 Flame front, USFS/Catchpole experiments . . . 980
14.42 Flame front, USFS/Catchpole experiments . . . 981
14.43 Flame front, USFS/Catchpole experiments . . . 982
14.44 Flame front, USFS/Catchpole experiments . . . 983
14.45 Flame front, USFS/Catchpole experiments . . . 984
14.46 Flame front, USFS/Catchpole experiments . . . 985
14.47 Flame front, USFS/Catchpole experiments . . . 986
14.48 Flame front, USFS/Catchpole experiments . . . 987
14.49 Flame front, USFS/Catchpole experiments . . . 988
14.50 Flame front, USFS/Catchpole experiments . . . 989
14.51 Flame front, USFS/Catchpole experiments . . . 990
14.52 Flame front, USFS/Catchpole experiments . . . 991
14.53 Flame front, USFS/Catchpole experiments . . . 992
14.54 Flame front, USFS/Catchpole experiments . . . 993
14.55 Flame front, USFS/Catchpole experiments . . . 994
14.56 Flame front, USFS/Catchpole experiments . . . 995
14.57 Flame front, USFS/Catchpole experiments . . . 996
14.58 Flame front, USFS/Catchpole experiments . . . 997
14.59 Flame front, USFS/Catchpole experiments . . . 998
14.60 Flame front, USFS/Catchpole experiments . . . 999
14.61 Flame front, USFS/Catchpole experiments . . . 1000
14.62 Flame front, USFS/Catchpole experiments . . . 1001
14.63 Flame front, USFS/Catchpole experiments . . . 1003
14.64 Flame front, USFS/Catchpole experiments . . . 1004
14.65 Flame front, USFS/Catchpole experiments . . . 1005
14.66 Flame front, USFS/Catchpole experiments . . . 1006
14.67 Flame front, USFS/Catchpole experiments . . . 1007
14.68 Flame front, USFS/Catchpole experiments . . . 1008
14.69 Flame front, USFS/Catchpole experiments . . . 1009
14.70 Flame front, USFS/Catchpole experiments . . . 1010
14.71 Flame front, USFS/Catchpole experiments . . . 1011

14.72 Flame front, USFS/Catchpole experiments 1012
14.73 Flame front, USFS/Catchpole experiments 1013
14.74 Flame front, USFS/Catchpole experiments 1014
14.75 Flame front, USFS/Catchpole experiments 1015
14.76 Flame front, USFS/Catchpole experiments 1016
14.77 Flame front, USFS/Catchpole experiments 1017
14.78 Flame front, USFS/Catchpole experiments 1018
14.79 Flame front, USFS/Catchpole experiments 1019
14.80 Flame front, USFS/Catchpole experiments 1020
14.81 HRR, USFS/Corsica experiments 1021
14.82 Rate of Spread, USFS/Corsica experiments 1022
14.83 Snapshots of a 2 m Douglas fir fire simulation 1023
14.84 Comparison measured and predicted mass loss rate for the Douglas fir tree experiments . .1024
14.85 Summary of heat release rate predictions 1025
14.86 Summary of burning rate predictions 1025
14.87 Summary of liquid pool burning rate predictions 1026
14.88 Summary, Wildfire Rate of Spread 1026

15.1 UWO Wind Tunnel schematic drawings 1028
15.2 UWO Wind Tunnel, SS20-Test 7 pressure coefficients, 180° 1029
15.3 UWO Wind Tunnel, SS20-Test 7 pressure coefficients, 180° 1030
15.4 UWO Wind Tunnel, SS20-Test 7 pressure coefficients, 270° 1031
15.5 UWO Wind Tunnel, SS20-Test 7 pressure coefficients, 270° 1032
15.6 UWO Wind Tunnel, SS21-Test 6 pressure coefficients, 0° 1033
15.7 UWO Wind Tunnel, SS21-Test 6 pressure coefficients, 0° 1034
15.8 UWO Wind Tunnel, SS21-Test 6 pressure coefficients, 45° 1035
15.9 UWO Wind Tunnel, SS21-Test 6 pressure coefficients, 45° 1036
15.10 LNG Dispersion experiments, Burro velocity and temperature profiles 1038
15.11 LNG Dispersion experiments, Coyote velocity and temperature profiles 1039
15.12 LNG Dispersion experiments, Falcon velocity and temperature profiles 1040
15.13 LNG Dispersion experiments, Maplin Sands velocity and temperature profiles 1041
15.14 LNG Dispersion experiments, Burro and Coyote 1042
15.15 LNG Dispersion experiments, Falson and Maplin Sands 1043
15.16 Summary of LNG Dispersion predictions 1044
15.17 Images of Plume Height simulations 1046
15.18 Atmospheric Dispersion, Plume Height results 1047

List of Tables

3.1 Summary of simulated Beyler Hood experiments . . . 21
3.2 BGC/GRI LNG Fires test parameters . . . 22
3.3 Summary of results, Bittern experiments . . . 24
3.4 Properties of sprinklers used in Bittern Experiments . . . 24
3.5 BST/FRS test cases . . . 28
3.6 Measured properties for the CSIRO Grassland Fire cases . . . 30
3.7 Assumed properties for dry grass and soil . . . 32
3.8 Summary of Cup Burner Data . . . 34
3.9 Gasoline and kerosene components . . . 37
3.10 Summary of FM/SNL Experiments . . . 45
3.11 Summary of LLNL Enclosure Experiments . . . 50
3.12 Summary of LNG Dispersion Experiments . . . 53
3.13 Summary of the Loughborough Jet Fire Experiments . . . 55
3.14 Summary of McCaffrey Plume Experiments . . . 56
3.15 Summary of the Montoir LNG Fire Experiments . . . 58
3.16 Measured properties for the NIST Douglas Fir Experiments . . . 69
3.17 Assumed properties for the NIST Douglas Fir Experiments . . . 70
3.18 Summary of NIST Reduced-Scale Experiments, 2007. . . . 71
3.19 Summary of NIST FSE Experiments selected for model validation . . . 73
3.20 Summary of NIST/NRC Cabinet Experiments. . . . 81
3.21 Average heat and product yields of the various test items . . . 84
3.22 Summary of NIST Smoke Alarm Experiments selected for model validation . . . 88
3.23 Experiment Details for Gravimetric Measurements of Soot Deposition . . . 90
3.24 Heights of the thermocouples above the floor of each level of the enclosure . . . 93
3.25 Vent State by Experiment: Time Opened . . . 93
3.26 Liquid fuel properties . . . 101
3.27 Summary of Ranz and Marshall droplet evaporation experiments . . . 102
3.28 Summary of SETCOM condensation experiments selected for model validation . . . 106
3.29 Summary of Sippola aerosol deposition experiments selected for model validation . . . 109
3.30 Parameters for SP Wood Cribs simulations . . . 113
3.31 Summary of Steckler compartment experiments . . . 114
3.32 Summary of UL/NIST Vent experiments . . . 118
3.33 Results of the UL/NFPRF heptane spray experiments, Series I . . . 122
3.34 Results of the UL/NFPRF heptane spray experiments, Series II . . . 123
3.35 Locations of measurement devices in the UL/NIJ ranch-style house . . . 127
3.36 Locations of measurement devices in the UL/NIJ colonial-style house . . . 127
3.37 Sequence of events for the one story ranch-style house in the UL/NIJ experiments . . . 127
3.38 Sequence of events for the two story colonial-style house in the UL/NIJ experiments . . . 128
3.39 Test matrix for the USFS/Corsica Experiments . . . 133

3.40 Heat release rate profiles for the Vettori experiments . . . 136
3.41 Summary of important experimental parameters . . . 144
3.42 Summary of important numerical parameters . . . 147

4.1 Summary of uncertainty estimates . . . 159

6.1 Summary of parameters for the flame height predictions . . . 302

9.1 Test parameters of the NIST_He_2009 experiments . . . 581

11.1 Wall measurement positions for the NIST/NRC series . . . 634
11.2 Ceiling surface measurement locations for the WTC series . . . 654
11.3 Property of Insulation Materials . . . 668

12.1 Summary of the NRL/HAI Wall Heat Flux Measurements . . . 790
12.2 Heat flux gauge positions relative to the center of the fire pan in the WTC series . . . 804
12.3 Parameters of the Hamins methane burner experiments . . . 816
12.4 Parameters of the Hamins propane burner experiments . . . 825
12.5 Parameters of the Hamins acetylene burner experiments . . . 835
12.6 Radiometer positions, Loughborough Jet Fires . . . 843

13.1 Summary of NIST/NRC OLIVE-Fire Experiments . . . 906
13.2 USCG/HAI water mist suppression extinguishment times . . . 911

14.1 FAA non-charring polymer properties . . . 923
14.2 FAA complex non-charring polymer properties . . . 925
14.3 Properties of polycarbonate (PC) . . . 927
14.4 Properties of poly(vinyl chloride) (PVC) . . . 929
14.5 Properties of poly(aryl ether ether ketone) (PEEK) . . . 932
14.6 Properties of poly(butylene terephtalate) (PBT) . . . 934
14.7 Properties of poly(butylene terephtalate) with glass fibers (PBT-GF) . . . 936
14.8 Properties of ABS, HIPS, and PMMA . . . 938
14.9 Properties of Kydex . . . 941
14.10 Properties of PEI, PET, and POM . . . 943
14.11 Properties of corrugated cardboard . . . 946
14.12 Cardboard composition and dimensions . . . 948
14.13 Summary of DoJ/HAI Diked Fire Tests . . . 960

16.1 Summary statistics . . . 1049
16.2 Validation Git Statistics . . . 1055

List of Acronyms

ALOFT	A Large Outdoor Fire plume Trajectory model
AST	Adiabatic Surface Temperature
ASTM	American Society for Testing and Materials
ATF	Bureau of Alcohol, Tobacco, Firearms, and Explosives
BRE	British Research Establishment
CAROLFIRE	Cable Response to Live Fire Test Program
CFAST	Consolidated Model of Fire Growth and Smoke Transport
CFT	Critical Flame Temperature
DNS	Direct Numerical Simulation
FAA	Federal Aviation Administration
FDS	Fire Dynamics Simulator
FLAME	Fire Laboratory for Accreditation of Models by Experimentation
FM	Factory Mutual Global
FSE	Full-Scale Enclosure
HAI	Hughes Associates, Inc.
HDPE	high density polyethylene
HGL	Hot Gas Layer
HIPS	high-impact polystyrene
HRR	Heat Release Rate
ISO	International Standards Organization
LEMTA	Laboratoire d'Energétique et de Méchanique Théorique et Appliquée
LES	Large Eddy Simulation
LLNL	Lawrence Livermore National Laboratory
LNG	Liquified Natural Gas
MEC	Minimum Extinguishing Concentration
NBS	National Bureau of Standards (former name of NIST)
NFPRF	National Fire Protection Research Foundation
NIST	National Institute of Standards and Technology
NRC	Nuclear Regulatory Commission
NRCC	National Research Council of Canada
NRL	Naval Research Laboratory
PDPA	Phase Doppler Particle Analyzer
PIV	Particle Image Velocimetry
PMMA	poly(methyl methacrylate)
PRISME	Propagation d'un incendie pour des scénarios multi-locaux élémentaires
PVC	Polyvinyl chloride
RANS	Reynolds Averaged Navier-Stokes

RSE	Reduced-Scale Enclosure
SBI	Single Burning Item
SNL	Sandia National Laboratory
SP	Statens Provningsanstalt (Technical Research Institute of Sweden)
TGA	Thermal Gravimetric Analysis
THIEF	Thermally-Induced Electrical Failure
UL	Underwriters Laboratories
USN	United States Navy
VTFRL	Virginia Tech Fire Research Laboratory
VTT	Valtion Teknillinen Tutkimuskeskus (Technical Research Centre of Finland)
WTC	World Trade Center

Chapter 1

What is Model Validation?

Although there are various definitions of model validation, for example the one contained in ASTM E 1355 [2], most define it as the process of determining how well the mathematical model predicts the actual physical phenomena of interest. Validation typically involves (1) comparing model predictions with experimental measurements, (2) quantifying the differences in light of uncertainties in both the measurements and the model inputs, and (3) deciding if the model is appropriate for the given application. This guide only does (1) and (2). Number (3) is the responsibility of the end user. To say that FDS is "validated" means that the end user has quantified the model uncertainty for a given application and decided that the model is appropriate. Although the FDS developers spend a considerable amount of time comparing model predictions with experimental measurements, it is ultimately the end user who decides if the model is adequate for the job at hand.

This Guide is merely a collection of calculation results. As FDS develops, it will expand to include new experimental measurements of newly modeled physical phenomena. With each minor release of FDS (version 5.2 to 5.3, for example), the plots and graphs are all regenerated to ensure that changes to the model have not decreased the accuracy of a previous version.

The following sections discuss key issues that must be considered when deciding whether or not FDS is appropriate for a given application. It depends on (a) the scenarios of interest, (b) the predicted quantities, and (c) the desired level of accuracy. FDS can be used to model most any fire scenario and predict almost any quantity of interest, but the prediction may not be accurate because of limitations in the description of the fire physics, and also because of limited information about the fuels, geometry, and so on.

1.1 Blind, Specified, and Open Validation Experiments

ASTM E 1355 [2] describes three basic types of validation calculations – *Blind*, *Specified*, and *Open*.

Blind Calculation: The model user is provided with a basic description of the scenario to be modeled. For this application, the problem description is not exact; the model user is responsible for developing appropriate model inputs from the problem description, including additional details of the geometry, material properties, and fire description, as appropriate. Additional details necessary to simulate the scenario with a specific model are left to the judgment of the model user. In addition to illustrating the comparability of models in actual end-use conditions, this will test the ability of those who use the model to develop appropriate input data for the models.

Specified Calculation: The model user is provided with a complete detailed description of model inputs, including geometry, material properties, and fire description. As a follow-on to the blind calculation, this

test provides a more careful comparison of the underlying physics in the models with a more completely specified scenario.

Open Calculation: The model user is provided with the most complete information about the scenario, including geometry, material properties, fire description, and the results of experimental tests or benchmark model runs which were used in the evaluation of the blind or specified calculations of the scenario. Deficiencies in available input (used for the blind calculation) should become most apparent with comparison of the open and blind calculation.

The calculations presented in this Guide all fall into the *Open* category. There are several reasons for this, the first being the most practical:

- All of the calculations presented in this Guide are re-run with each minor release of FDS (i.e., 5.3 to 5.4). The fact that the experiments have already been performed and the results are known qualify these calculations as *Open*.
- Some of the calculations described in this Guide did originally fall into the *Specified* category because they were first performed before the experiments were conducted. However, in almost every case, the experiment was not conducted exactly as specified, and the pre-calculated results were not particularly useful in determining the accuracy of the model.
- None of the calculations were truly *Blind*, even those performed prior to the experiments. The purpose of a *Blind* calculation is to assess the degree to which the choice of input parameters affects the outcome. However, in such cases it is impossible to discern the uncertainty associated from the choice of input parameters from that associated with the model itself. The primary purpose of this Guide is to quantify the uncertainty of the model itself, in which case *Blind* calculations are of little value.

1.2 How to Use this Guide

When considering whether to use FDS for a given application, do the following:

1. Survey Chapter 2 to learn about past efforts by others to validate the model for similar applications. Keep in mind that most of the referenced validation exercises have been performed with older versions of FDS, and you may want to obtain the experimental data and the old FDS input files and redo the simulations with the version of FDS that you plan to use.
2. Identify in Chapter 3 the experimental data sets appropriate for your application. In particular, the summary of the experiments found in Section 3.92 contains a table listing various non-dimensional quantities that characterize the parameters of the experiments. For example, the equivalence ratio of a compartment fire experiment indicates the degree to which the fire was over or under-ventilated. To say that the results of a given experiment are relevant to your scenario, you need to demonstrate that its parameters "fit" within the parameter space outlined in Table 3.41.
3. Search the Table of Contents to find comparisons of FDS simulations with the relevant experiments. For a given experiment, there may be numerous measurements of quantities like the gas temperature, heat flux, and so on. It is a challenge to sort out all the plots and graphs of all the different quantities and come to some general conclusion. For this reason, this Guide is organized by output quantity, not by individual experiment or fire scenario. In this way, it is possible to assess, over a range of different experiments and scenarios, the performance of the model in predicting a given quantity. Overall trends and biases become much more clear when the data is organized this way.

4. Determine the accuracy of the model for given output quantities of interest listed in Table 16.1. An explanation of the accuracy metrics is given in Chapter 4.

The experimental data sets and FDS input/output files described in this Guide are all managed via the online project archiving system. You might want to re-run examples of interest to better understand how the calculations were designed, and how changes in the various parameters might affect the results. This is known as a *sensitivity study*, and it is difficult to document all the parameter variations of the calculations described in this report. Thus, it is a good idea to determine which of the input parameters are particularly important.

Chapter 2

Survey of Past Validation Work

In this chapter, a survey of FDS validation work is presented. Some of the work has been performed at NIST, some by its grantees and some by engineering firms using the model. Because each organization has its own reasons for validating the model, the referenced papers and reports do not follow any particular guidelines. Some of the works only provide a qualitative assessment of the model, concluding that the model agreement with a particular experiment is "good" or "reasonable." Sometimes, the conclusion is that the model works well in certain cases, not as well in others. These studies are included in the survey because the references are useful to other model users who may have a similar application and are interested in even qualitative assessment. It is important to note that some of the papers point out flaws in early releases of FDS that have been corrected or improved in more recent releases. Some of the issues raised, however, are still subjects of active research. The research agenda for FDS is greatly influenced by the feedback provided by users, often through publication of validation efforts.

It is useful to divide the various validation exercises described in this chapter into two classes – those for which the heat release rate (HRR) of the fire is *specified* as an input to the model and those for which the HRR is *predicted* by the model. The former is often the case for a design application, the latter for a forensic reconstruction.

Design applications typically involve an existing building or a building under design. A so-called "design fire" is specified either by a regulatory authority or by the engineers performing the analysis. Because the fire's heat release rate is specified, the role of the model is to predict the transport of heat and combustion products throughout the room or rooms of interest. Ventilation equipment is often included in the simulation, like fans, blowers, exhaust hoods, HVAC ducts, smoke management systems, etc. Sprinkler and heat and smoke detector activation are also of interest. The effect of the sprinkler spray on the fire is usually less of interest since the heat release rate of the fire is specified rather than predicted. Detailed descriptions of the contents of the building are usually not necessary because these items are assumed to not contribute to the fire, and even if they are, the burning rate will be specified, not predicted. Sometimes, it is necessary to predict the heat flux from the fire to a nearby "target," and even though the target may heat up to some specified ignition temperature, the subsequent spread of the fire usually goes beyond the scope of the analysis because of the uncertainty inherent in object to object fire spread.

Forensic reconstructions require the model to simulate an actual fire based on information that is collected after the event, such as eye witness accounts, unburned materials, burn signatures, etc. The purpose of the simulation is to connect a sequence of discrete observations with a continuous description of the fire dynamics. Usually, reconstructions involve more gas/solid phase interaction because virtually all objects in a given room are potentially ignitable, especially when flashover occurs. Thus, there is much more emphasis on such phenomena as heat transfer to surfaces, pyrolysis, flame spread, and suppression. In general, forensic reconstructions are more challenging simulations to perform because they require more detailed

information about the room contents, and there is much greater uncertainty in the total heat release rate as the fire spreads from object to object.

Validation studies of FDS to date have focused more on design applications than reconstructions. The reason is that design applications usually involve specified fires and demand a minimum of thermo-physical properties of real materials. Transport of smoke and heat is the primary focus, and measurements can be limited to well-placed thermocouples, a few heat flux gauges, gas samplers, etc. Phenomena of importance in forensic reconstructions, like second item ignition, flame spread, vitiation effects and extinction, are more difficult to model and more difficult to study with well-controlled experiments. Uncertainties in material properties and measurements, as well as simplifying assumptions in the model, often force the comparison between model and measurement to be qualitative at best. Nevertheless, current validation efforts are moving in the direction of these more difficult issues.

2.1 Validation Work with Pre-Release Versions of FDS

FDS was officially released in 2000. However, for two decades various CFD codes using the basic FDS hydrodynamic framework were developed at NIST for different applications and for research. In the mid 1990s, many of these different codes were consolidated into what eventually became FDS. Before FDS, the various models were referred to as LES, NIST-LES, LES3D, IFS (Industrial Fire Simulator), and ALOFT (A Large Outdoor Fire Plume Trajectory).

The NIST LES model describes the transport of smoke and hot gases during a fire in an enclosure using the Boussinesq approximation, where it is assumed that the density and temperature variations in the flow are relatively small [3, 4, 5, 6]. Such an approximation can be applied to a fire plume away from the fire itself. Much of the early work with this form of the model was devoted to the formulation of the low Mach number form of the Navier-Stokes equations and the development of the basic numerical algorithm. Early validation efforts compared the model with salt water experiments [7, 8, 9], and fire plumes [10, 11, 12, 13]. Clement validated the hydrodynamic model in FDS by measuring salt water flows using Laser Induced dye Fluorescence (LIF) [14]. An interesting finding of this work was that the transition from a laminar to a turbulent plume is very difficult to predict with any technique other than DNS.

Eventually, the Boussinesq approximation was dropped and simulations began to include more fire-specific phenomena. Simulations of enclosure fires were compared to experiments performed by Steckler [15]. Mell et al. [16] studied small helium plumes, with particular attention to the relative roles of baroclinic torque and buoyancy as sources of vorticity. Cleary et al. [17] used the LES model to simulate the environment seen by multi-sensor fire detectors and performed some simple validation work to check the model before using it. Large fire experiments were performed by NIST at the FRI test facility in Japan, and at US Naval aircraft hangars in Hawaii and Iceland [18]. Room airflow applications were considered by Emmerich and McGrattan [19, 20].

These early validation efforts were encouraging, but highlighted the need to improve the hydrodynamic model by introducing the Smagorinsky form of large eddy simulation. This addition improved the stability of the model because of the relatively simple relation between the local strain rate and the turbulent viscosity. There is both a physical and numerical benefit to the Smagorinsky model. Physically, the viscous term used in the model has the right functional form to describe sub-grid mixing processes. Numerically, local oscillations in the computed flow quantities are damped if they become large enough to threaten the stability of the entire calculation.

2.2 Validation of FDS since 2000

There is an on-going effort at NIST and elsewhere to evaluate FDS as new capabilities are added. To date, most of this work has focused on the model's ability to predict the transport of heat and exhaust products from a fire through an enclosure. In these studies, the heat release rate is usually prescribed, along with the production rates of various products of combustion. More recently, validation efforts have moved beyond just transport issues to consider fire growth, flame spread, suppression, sprinkler/detector activation, and other fire-specific phenomena.

The validation work discussed below can be organized into several categories: Comparisons with full-scale tests conducted especially for the chosen evaluation, comparisons with previously published full-scale test data, comparisons with standard tests, comparisons with documented fire experience, and comparisons with engineering correlations. There is no single method by which the predictions and measurements are compared. Formal, rigorous validation exercises are time-consuming and expensive. Most validation exercises are done simply to assess if the model can be used for a very specific purpose. While not comprehensive on their own, these studies collectively constitute a valuable assessment of the model.

2.2.1 Fire Plumes

There are several examples of fire flows that have been extensively studied, so much so that a set of engineering correlations combining the results of many experiments have been developed. These correlations are useful to modelers because of their simplicity. The most studied phenomena include fire plumes, ceiling jets, and flame heights.

Although much of the early validation work before FDS was released involved fire plumes, it remains an active area of interest. One study by Chow and Yin [21] surveys the performance of various models in predicting plume temperatures and entrainment for a 470 kW fire with a diameter of 1 m and an unbounded ceiling. They compare the FDS results with various correlations and a RANS (Reynolds-Averaged Navier-Stokes) model.

Battaglia et al. [22] used FDS to simulate fire whirls. First, the model was shown to reproduce the McCaffrey correlation of a fire plume, then it was shown to reproduce qualitatively certain features of fire whirls. At the time, FDS used Lagrangian elements to introduce heat from the fire (no longer used), and this combustion model could not replicate the extreme stretching of the core of the flame zone.

Quintiere and Ma [23, 24] compared predicted flame heights and plume centerline temperatures to empirical correlations. For plume temperature, the Heskestad correlation [25] was chosen. Favorable agreement was found in the plume region, but the results near the flame region were found to be grid-dependent, especially for low Q^* fires. At this same time, researchers at NIST were reaching similar conclusions, and it was noticed by both teams that a critical parameter for the model is $D^*/\delta x$, where D^* is the characteristic fire diameter and δx is the grid cell size. If this parameter is sufficiently large, the fire can be considered well-resolved and agreement with various flame height correlations was found. If the parameter is not large enough, the fire is not well-resolved and adjustments must be made to the combustion routine to account for it.

Gutiérrez-Montes et al. [26] simulated 1.3 MW and 2.3 MW fires in a 20 m cubic atrium using FDS version 4. Similar experiments were conducted at VTT, Finland, in a 19 m tall test hall with similar sized fires. These results are included in Section 6.1.11.

Hurley and Munguia [27, 28] compared FDS (version 4) simulations with plume and ceiling jet measurements from a series of full-scale tests conducted by Underwriters Laboratories. The tests were conducted in a 36.6 m by 36.6 m compartment with ceiling heights ranging from 3 m to 12.2 m. Heat release rates followed a modified t-squared growth profile. Thermocouples attached to brass disks were used to simulate thermal detectors.

2.2.2 Pool Fires

Xin et al. [29] used FDS to model a 1 m diameter methane pool fire. The computational domain was 2 m by 2 m by 4 m with a uniform grid size of 2.5 cm. The predicted results were compared to experimental data and found to qualitatively and quantitatively reproduce the velocity field. The same authors performed a similar study of a 7.1 cm methane burner [30] and a helium plume [31].

The 7.1 cm diameter buoyant diffusion flame has been extensively studied both experimentally and computationally. Zhou and Gore [32] reported radial profiles of mixture fraction and vertical velocity for estimation of thermal expansion for natural gas buoyant diffusion flames stabilized on a 7.1 cm diameter diffuser burner. Xin et al. [33] used a Lagrangian thermal element based combustion model to simulate this flame. The authors noted that the simulations were sensitive to the burnout time utilized by the combustion model. To gain further insight into the species distribution inside the fire, Xin et al. [30] performed fire dynamics simulations using a mixture fraction based combustion model. Xin and Gore [34] used laser-induced incandescence to determine soot distributions in vertical and horizontal planes for methane and ethane turbulent buoyant flames. Biswas et al. [35] utilized a novel time series model to simulate the scalar concentrations and temperature fields for these flames.

Hostikka et al. [36] modeled small pool fires of methane, natural gas and methanol to test the FDS radiation solver for low-sooting fires. They conclude that the predicted radiative fluxes are higher than measured values, especially at small heat release rates, due to an over-prediction of the gas temperature. These tests are also included in the Heat Flux section of this report.

Hietaniemi, Hostikka and Vaari [37] considered heptane pool fires of various diameters. Predictions of the burning rate as a function of diameter follow the trend observed in a number of experimental studies. Their results show an improvement in the model over the earlier work with methanol fires, due to improvements in the radiation routine and the fact that heptane is more sooty than methanol, simplifying the treatment of radiation. The authors point out that reliable predictions of the burning rate of liquid fuels require roughly twice as fine a grid spanning the burner than would be necessary to predict plume velocities and temperatures. The reason for this is the prediction of the heat feedback to the burning surface necessary to *predict* rather than to *specify* the burning rate.

2.2.3 Air and Gas Movement in the Absence of Fire

The low Mach number assumption in FDS is appropriate not only to fire, but to most building ventilation scenarios. An example of how the model can be used to assess indoor air quality is presented by Musser et al. [38]. The test compartment was a displacement ventilation test room that contained computers, furniture, and lighting fixtures as well as heated rectangular boxes intended to represent occupants. A detailed description of the test configuration is given by Yuan et al. [39]. The room is ventilated with cool supply air introduced via a diffuser that is mounted on a side wall near the floor. The air rises as it is warmed by heat sources and exits through a return duct located in the upper portion of the room. The flow pattern is intended to remove contaminants by sweeping them upward at the source and removing them from the room. Sulphur hexafluoride, SF_6, was introduced into the compartment during the experiment as a tracer gas near the breathing zone of the occupants. Temperature, tracer concentration, and velocity were measured during the experiments.

In another study, Musser and Tan [40] used FDS to assess the design of ventilation systems for facilities in which train locomotives operate. Although there is only a limited amount of validation, the study is useful in demonstrating a practical use of FDS for a non-fire scenario.

Mniszewski [41] used FDS to model the release of flammable gases in simple enclosures and open areas. In this work, the gases were not ignited.

Kerber and Walton [42] provided a comparison between FDS version 1 and experiments on positive

pressure ventilation in a full-scale enclosure without a fire.

2.2.4 Wind Engineering

Most applications of FDS involve fires within buildings. However, it can be used to model thermal plumes in the open and wind impinging on the exterior of a building. Rehm, McGrattan, Baum and Simiu [43] used the LES solver to estimate surface pressures on simple rectangular blocks in a crosswind, and compared these estimates to experimental measurements. In a subsequent paper [44], they considered the qualitative effects of multiple buildings and trees on a wind field.

A different approach to wind was taken by Wang and Joulain [45]. They considered a small fire in a wind tunnel 0.4 m wide and 0.7 m tall with flow speeds of 0.5 m/s to 2.5 m/s. Much of the comparison with experiment is qualitative, including flame shape, lean, length. They also use the model to determine the predominant modes of heat transfer for different operating conditions. To assess the combustion, they implemented an "eddy break-up" combustion model [46] and compared it to the mixture fraction approach used by FDS. The two models performed better or worse, depending on the operating conditions. Some of the weaknesses of the mixture fraction model as implemented in FDS version 2 were addressed in subsequent versions.

Chang and Meroney [47] compared the results of FDS with the commercial CFD package FLUENT in simulating the transport of pollutants from steady point sources in an idealized urban environment. FLUENT employs a variety of RANS (Reynolds Averaged Navier-Stokes) closure methods, whereas FDS employs large eddy simulation (LES). The results of the numerical models were compared with wind tunnel measurements within a 1:50 scale physical model of an urban street "canyon."

FDS has recently been applied to urban canopy modeling [48] and wind engineering. Le et al. [49] modeled flow over a backward facing step using DNS with a Reynolds number of 5,100. To verify the results, Jovic and Driver [50] supplemented the DNS simulation with an identically proportioned wind tunnel experiment. Together, the data sets from these two studies have provided the baseline for analysis of recent simulations of flow over a backward facing step that are documented in this guide.

Sarwar et al. [51] used FDS to compare SGS eddy viscosity models. The constant Smagorinsky model performed the best, although the dynamic Smagorinsky and Deardorff models, nearly equivalent in accuracy, were found to perform better than the Vreman model. To avoid explicit specification of inlet turbulence conditions, the authors created an extremely long inlet section to allow turbulence to develop.

2.2.5 Atmospheric Dispersion

During the 1980s and 1990s, the Building and Fire Research Laboratory at NIST studied the burning of crude oil under the sponsorship of the US Minerals Management Service. The aim of the work was to assess the feasibility of using burning as a means to remove spilled oil from the sea surface. As part of the effort, Rehm and Baum developed a special application of the LES model called ALOFT. The model was a spin-off of the two-dimensional LES enclosure model, in which a three-dimensional steady-state plume was computed as a two-dimensional evolution of the lateral wind field generated by a large fire blown in a steady wind. The ALOFT model is based on large eddy simulation in that it attempts to resolve the relevant scales of a large, bent-over plume. Validation work was performed by simulating the plumes from several large experimental burns of crude oil in which aerial and ground sampling of smoke particulate was performed [52]. Yamada [53] performed a validation of the ALOFT model for 10 m oil tank fire. The results indicate that the prediction of the plume cross section 500 m from the fire agree well with the experimental observations.

Mouilleau and Champassith [54] performed a validation study to assess the ability of FDS (version 4) to model atmospheric dispersion. They concluded that the best results were obtained for simulations done with

explicitly-modeled wind fluctuations. Specific atmospheric flow characteristics were evaluated for passive releases in open and flat fields.

2.2.6 Growing Fires

Floyd [55, 56] compared FDS predictions with measurements from fire tests at the Heiss-Dampf Reaktor (HDR) facility in Germany. The structure was originally the containment building for a nuclear power reactor. The cylindrical structure was 20 m in diameter and 50 m in height topped by a hemispherical dome 10 m in radius. The building was divided into eight levels. The total volume of the building was approximately 11,000 m^3. From 1984 to 1991, four fire test series were performed within the HDR facility. The T51 test series consisted of eleven propane gas tests and three wood crib tests.

FDS predictions of fire growth and smoke movement in large spaces were performed by Kashef [57]. The experiments were conducted at the National Research Council Canada. The tests were performed in a compartment with dimensions of 9 m by 6 m by 5.5 m with 32 exhaust inlets and a single supply fan. A burner generated fires ranging in size from 15 kW to 1000 kW.

2.2.7 Flame Spread

Although FDS simulations have been compared to actual and experimental large-scale fires, it is difficult to quantify the accuracy because of the uncertainty associated with material properties. Most quantified validation work associated with flame spread have been for small, laminar flames with length scales ranging from millimeters to a few centimeters.

For example, FDS (or its core algorithms) have been used at a grid resolution of roughly 1 mm to look at flames spreading over paper in a micro-gravity environment [58, 59, 60, 61, 62, 63], as well as "g-jitter" effects aboard spacecraft [64]. Simulations have been compared to experiments performed aboard the Space Shuttle. The flames are laminar and relatively simple in structure, and the materials are relatively well-characterized.

FDS flame spread predictions were compared to experiments over a 5 m slab of PMMA performed by Factory Mutual Research Corporation (FMRC) [23, 24].

A charring model was implemented in FDS by Hostikka and McGrattan [65]. The model was a simplification of work done at NIST by Ritchie et al. [66]. The charring model was first used to predict the burning rate of a small wooden sample in the cone calorimeter. Full-scale room tests with wood paneling were modeled, but the results were grid-dependent. This was likely a consequence of the gas phase spatial resolution, rather than the solid phase.

Kwon et al. [67] performed three simulations to evaluate the capability of FDS, version 4, in predicting upward flame spread. The FDS predictions were compared with empirical correlations and experimental data for upward flame spread on a 5 m PMMA panel. A simplified flame spread model was also applied to assess the simulation results.

An extensive amount of flame spread validation work with FDS version 4 has been performed by Hietaniemi, Hostikka, and Vaari at VTT, Finland [37]. The case studies are comprised of fire experiments ranging in scale from the cone calorimeter (ISO 5660-1, 2002) to full-scale fire tests such as the room corner test (ISO 9705, 1993). Comparisons are also made between FDS 4 results and data obtained in the SBI (Single Burning Item) Euro-classification test apparatus (EN 13823, 2002) as well as data obtained in two ad hoc experimental configurations: one is similar to the room corner test but has only partial linings and the other is a space to study fires in building cavities. In the study of upholstered furniture, the experimental configurations are the cone and furniture calorimeters, and the ISO room. For liquid pool fires, comparison is made to data obtained by numerous researchers. The burning materials include spruce timber, MDF (Medium Density Fiber) board, PVC wall carpet, upholstered furniture, cables with plastic sheathing, and

heptane. The scope of the VTT work is considerable. Assessing the accuracy of the model must be done on a case by case basis. In some cases, predictions of the burning rate of the material were based solely on its fundamental properties, as in the heptane pool fire simulations. In other cases, some properties of the material are unknown, as in the spruce timber simulations. Thus, some of the simulations are true predictions, some are calibrations. The intent of the authors was to provide guidance to engineers using the model as to appropriate grid sizes and material properties. In many cases, the numerical grid was made fairly coarse to account for the fact that in practice, FDS is used to model large spaces of which the fuel may only comprise a small fraction.

Mangs and Hostikka [68] carried out experiments and simulations (FDS 5.4.3) of the vertical flame spread on the surface of thin birch wood cylinders at different ambient temperatures. The parameters for the pyrolysis model were estimated from TGA and cone calorimeter experiments. The gas phase flow was calculated in the DNS mode with 1.0 mm grid cells in axi-symmetric geometry. The simulation model was able to predict the flame spread rates within the uncertainties associated with the experiments and postsimulation analysis of the spread rate.

2.2.8 Compartment Fires

As part of the NIST investigation of the World Trade Center fires and collapse, a series of large scale fire experiments were performed specifically to validate FDS [69]. The tests were performed in a rectangular compartment 7.2 m long by 3.6 m wide by 3.8 m tall. The fires were fueled by heptane for some tests and a heptane/toluene mixture for the others. The results of the experiments and simulations are included in detail in this Guide.

A second set of experiments to validate FDS for use in the World Trade Center investigation is documented in Ref. [70]. The experiments are not described as part of this Guide. The intent of these tests was to evaluate the ability of the model to simulate the growth of a fire burning three office workstations within a compartment of dimensions 11 m by 7 m by 4 m, open at one end to mimic the ventilation of windows similar to those in the WTC towers. Six tests were performed with various initial conditions exploring the effect of jet fuel spray and ceiling tiles covering the surface of the desks and carpet. Measurements were made of the heat release rate and compartment gas temperatures at four locations using vertical thermocouple arrays. Six different material samples were tested in the NIST cone calorimeter: desk, chair, paper, computer case, privacy panel, and carpet. Data for the carpet, desk and privacy panel were input directly into FDS, with the other three materials lumped together to form an idealized fuel type. Open burns of single workstations were used to calibrate the simplified fuel package. Details of the modeling are contained in Ref. [71].

The BRE Centre for Fire Safety Engineering at the University of Edinburgh conducted a series of large-scale fire tests in a real high rise building in Dalmarnock, Glasgow, Scotland [72, 73]. The experiments took place in July, 2006, with the close collaboration of the Strathclyde Fire Brigade and other partners. These experiments attempted to create realistic scenario in which a wide range of modern fire safety engineering tools could be put to a test. Jahn, Rein and Torero assessed the sensitivity of FDS when applied to these experiments [74]. Fire size and location, convection, radiation and combustion parameters were varied in order to determine the associated degree of sensitivity. Emphasis was put in the prediction of secondary ignition and time to flashover. In this context and while keeping the HRR constant, simulations of fire growth were significantly sensitive to location of the heat release rate, fire area, flame radiative fraction, and material thermal and ignition properties.

Students at Stord/Haugesund University College in Norway simulated full-scale experiments of temperature and smoke spread in a realistic multi-room setting using both CFAST and FDS [75]. Data from the top 0.5 m of the compartments was compared with measurements. The simulations were found to provide satisfying results in CFAST, as an alternative to FDS.

Drean et al. [76] measured the fire exposure to an exterior facade of a two-level test facility operated

by the engineering firm Efectis in Saint-Aubin, France. The objective was to evaluate the ability of FDS, version 6, to predict the gas temperatures and heat fluxes at the exterior wall.

2.2.9 Sprinklers, Mist System, and Suppression by Water

Vettori [77] modeled sprinkler activation patterns in a room with an obstructed ceiling. In a follow-up report, Vettori [78] extended his study to include sloped ceilings, with and without obstructions. Both of these experimental series are included within the current validation guide and are referred to the Vettori Flat and Sloped Ceiling Experiments.

A significant validation effort for sprinkler activation and suppression was a project entitled the International Fire Sprinkler, Smoke and Heat Vent, Draft Curtain Fire Test Project organized by the National Fire Protection Research Foundation [79]. Thirty-nine large scale fire tests were conducted at Underwriters Laboratories in Northbrook, IL. The tests were aimed at evaluating the performance of various fire protection systems in large buildings with flat ceilings, like warehouses and "big box" retail stores. All the tests were conducted under a 30 m by 30 m adjustable-height platform in a 37 m by 37 m by 15 m high test bay. At the time, FDS had not been publicly released and was referred to as the Industrial Fire Simulator (IFS), but it was essentially the same as FDS version 1. The first and second series of heptane spray burner fires are included in this guide under the heading "UL/NFPRF Sprinkler, Vent, and Draft Curtain Study." Most of the full-scale experiments performed during the project used a heptane spray burner to generate controlled fires of 1 MW to 10 MW. However, five experiments were performed with 6 m high racks containing the Factory Mutual Standard Plastic Commodity, or Group A Plastic. To model these fires, bench scale experiments were performed to characterize the burning behavior of the commodity, and larger test fires provided validation data with which to test the model predictions of the burning rate and flame spread behavior [80, 81]. Two to four tier configurations were evaluated.

High rack storage fires of pool chemicals were modeled by Olenick et al. [82] to determine the validity of sprinkler activation predictions of FDS. The model was compared to full-scale fires conducted in January, 2000 at Southwest Research Institute in San Antonio, Texas.

FDS has been used to study the behavior of a fire undergoing suppression by a water mist system. Kim and Ryou [83, 84] compared FDS predictions to results of compartment fire tests with and without the application of a water mist. The cooling and oxygen dilution were predicted to within about 10 % of the measurements, but the simulations failed to predict the complete extinguishment of a hexane pool fire. The authors suggest that this is a result of the combustion model rather than the spray or droplet model.

Another study of water mist suppression using FDS was conducted by Hume at the University of Canterbury, Christchurch, New Zealand [85]. Full-scale experiments were performed in which a fine water mist was combined with a displacement ventilation system to protect occupants and electrical equipment in the event of a fire. Simulations of these experiments with FDS showed qualitative agreement, but the version of the model used in the study (version 3) was not able to predict accurately the decrease in heat release rate of the fire.

Hostikka and McGrattan [86] evaluated the absorption of thermal radiation by water sprays. They considered two sets of experimental data and concluded that FDS has the ability to predict the attenuation of thermal radiation "when the hydrodynamic interaction between the droplets is weak." However, modeling interacting sprays would require a more costly coalescence model. They also note that the results of the model were sensitive to grid size, angular discretization, and droplet sampling.

O'Grady and Novozhilov [87] compared the predictions of FDS version 4 against full-scale fire tests performed at SP Sweden involving a 1.5 MW steady-state fire with two different sprinkler flow rates [88]. The authors reported results for gas temperatures and the tangential flow velocity in the ceiling jet. Sensitivity of the model to a range of input parameters was investigated. The model demonstrated moderate sensitivity to the spray parameters, such as spray cone configuration, initial droplet velocities, and droplet

sizes. On the other hand, the sensitivity to other parameters such as sprinkler atomization length and rms of droplet size distribution was low.

Xiao [89] compared FDS simulations with real scale compartment measurements for unsprinklered and sprinklered experiments. Numerical results for doorway mass flow rate and temperature are compared with the experimental data for three fire sizes.

2.2.10 Airflows in Fire Compartments

Friday and Mowrer [90] studied the use of FDS in large scale mechanically ventilated spaces. The ventilated enclosure was provided with air injection rates of 1 to 12 air changes per hour and a fire with heat release rates ranging from 0.5 MW to 2 MW. The test measurements and model output were compared to assess the accuracy of FDS. These simulations have been repeated with the latest version of FDS and reported in this guide under the heading "FM/SNL Test Series."

Zhang et al. [91] utilized the FDS model to predict turbulence characteristics of the flow and temperature fields due to fire in a compartment. The experimental data was acquired through tests that replicated a half-scale ISO Room Fire Test. Two cases were explored – the heat source in the center of the room and the heat source adjacent to a wall. In both cases, the heat source was a heating element with an output of 12 kW/m^2.

2.2.11 Tunnel Fires

Cochard [92] used FDS to study the ventilation within a tunnel. He compared the model results with a full-scale tunnel fire experiment conducted as part of the Massachusetts Highway Department Memorial Tunnel Fire Ventilation Test Program. The test consisted of a single point supply of fresh air through a 28 m^2 opening in a 135 m tunnel.

McGrattan and Hamins [93] also applied FDS to simulate two of the Memorial Tunnel Fire Tests as validation for the use of the model in studying an actual fire in the Howard Street Tunnel, Baltimore, Maryland, July 2001. The experiments chosen for the comparison were unventilated. One experiment was a 20 MW fire; the other a 50 MW fire.

Piergoirgio et al. [94] provided a qualitative analysis of FDS applied to a truck fire within a tunnel. The goal of their analysis was to describe the spread of the toxic gases within the tunnels, to determine the places not involved in the spreading of combustion products and to quantify the oxygen, carbon monoxide and hydrochloric acid concentrations during the fire.

Edwards et al. [95, 96] used FDS to determine the critical air velocity for smoke reversal in a tunnel as a function of the fire intensity, and his results compared favorably with experimental results. In a further study, Edwards and Hwang [97] applied FDS to study fire spread along combustibles in a ventilated mine entry. Analyses such as these are intended for planning and implementation of ventilation changes during mine fire fighting and rescue operations.

Bilson et al. [98] used FDS to evaluate the interaction of a deluge system with a tunnel ventilation and smoke exhaust system.

Harris [99] used FDS to determine the heat flux from a tunnel fire under varying water application rates. These results were qualitatively consistent with experimental results of Arvidson [100], who conducted burn tests for shielded and unshielded standard plastic commodities under a variety of spray conditions.

Trelles and Mawhinney [101, 102] simulated with FDS 4 a series of full-scale fire suppression experiments conducted at the San Pedro de Anes test tunnel near Gijon, Asturias, Spain in February, 2006. The fuel consisted of wooden and polyethylene pallets, and the suppression system consisted of different configurations of water mist nozzles.

2.2.12 Smoke Detection

The ability of version 1 of FDS to accurately predict smoke detector activation was studied by D'Souza [103]. The smoke transport model within FDS was tested and compared with UL 217 test data. The second step in this research was to further validate the model with full-scale multi-compartment fire tests. The results indicated that FDS is capable of predicting smoke detector activation when used with smoke detector lag correlations that correct for the time delay associated with smoke having to penetrate the detector housing. A follow-up report by Roby et al. [104] and paper by Zhang et al. [105] describes the implementation and validation of the smoke detector algorithm currently incorporated in FDS.

Another study of smoke detector activation was carried out by Brammer at the University of Canterbury, New Zealand [106]. Two fire tests from a series performed in a two-story residence were simulated, and smoke detector activation times were predicted using three different methods. The methods consisted of either a temperature correlation, a time-lagged function of the optical density, or a thermal device much like a heat detector. The purpose was to identify ways to reliably predict smoke detector activation using typical model output like temperature and smoke concentration. It was remarked that simulating the early stage of the fire is critical to reliable prediction.

Cleary [107] also provided a comparison between FDS computed gas velocity, temperature and concentrations at various detector locations. The research concluded that multi-room fire simulations with the FDS model can accurately predict the conditions that a sensor might experience during a real fire event.

2.2.13 Combustion Model

A few studies have been performed comparing direct numerical simulations (DNS) of a simple burner flame to laboratory experiments [108]. Another study compared DNS calculations of a counterflow diffusion flames to experimental measurements and the results of a one-dimensional multi-step kinetics model [109].

Bundy, Dillon and Hamins [110, 111] studied the use of FDS in providing data and correlations for fire investigators to support their investigations. A paraffin wax candle was placed within a small plexi-glass enclosure. The heat flux from the candle flame was modeled with FDS.

Floyd et al. [112, 56] compared the radiation model of FDS version 2 with full-scale data from the Virginia Tech Fire Research Laboratory (VTFRL). The test compartment was outfitted with equipment capable of taking temperature, air velocity, gas concentrations, unburned hydrocarbon and heat flux measurements. The test facility consisted of a single compartment geometrically similar to the ISO 9705 standard compartment with dimensions of 1.2 m by 1.8 m by 1.2 m in height. The ceiling and walls were constructed of fiberboard over a steel shell with a floor of concrete. Three baseline experiments were completed with fires ranging in size from 90 kW to 440 kW.

Xin and Gore [113] compared FDS predictions and measurements of the spectral radiation intensities of small fires. The fuel flow rates for methane and ethylene burners were selected so that the Froude numbers matched that of liquid toluene pool fires. The heat release rate was 4.2 kW for the methane flame and 3.4 kW for the ethylene flame. Line of sight spectral radiation intensities were measured at six downstream locations. The spectral radiation intensity calculations were performed by post-processing the transient scalar distributions provided by FDS.

Zhang et al. [114] compared the experimental results of a circular methane gas burner to predictions computed by FDS. The compartment was 2.8 m by 2.8 m by 2.2 m high with natural ventilation from a standard door.

2.2.14 Soot Deposition

Several studies have been conducted that indicate soot deposition is an important factor in compartment fires for the accurate prediction of smoke concentrations, smoke detector activations, and visibility. Gottuk

et al. [115] reported that smoke concentrations predicted by FDS near smoke alarms in a corridor were two to five times greater than measured smoke concentrations. Hamins et al. [116] conducted full-scale compartment fire experiments for use in validation studies of various fire models, including FDS. The results indicated that smoke concentrations predicted by FDS were up to five times greater than measured smoke concentrations. Floyd and McDermott [117] implemented thermophoretic and turbulent diffusion soot deposition mechanisms in FDS and compared predicted soot densities and concentrations to measurements from small- and large-scale experiments. Riahi [118] conducted bench-scale experiments to measure soot densities and soot deposition patterns on walls for various fuels. Riahi identified thermophoretic deposition as an important soot deposition mechanism in the hot gas layer. Cohan [119] used FDS to simulate select cases from the Gottuk [115] corridor tests, Hamins et al. [116] NRC experiments, and Riahi [118] hood experiments with thermophoretic and turbulent diffusion soot deposition mechanisms. Overholt and Ezekoye [120] implemented gravitational settling of soot in the gas-phase in FDS and quantified the effects of gravitational settling/deposition compared to thermophoretic and turbulent diffusion deposition for small- and large-scale validation cases.

2.3 Reconstructions of Actual Fires

ASTM E 1355 states that a model may be evaluated by comparing it with "Documented Fire Experience" which includes:

- eyewitness accounts of real fires,
- known behavior of materials in fires (for example, melting temperatures of materials), and
- observed post-fire conditions, such as the extent of fire spread.

Often the term "reconstruction" is applied to this type of simulation, because the model is used to reconstruct events based on evidence collected during and after the fire. Some of the more notable studies performed at NIST include:

- McGrattan, Bouldin, and Forney simulated the fires within the World Trade Center towers and Building 7 on September 11, 2001 [71].
- Grosshandler et al. investigated the fire that occurred at the Station Nightclub in Rhode Island in February, 2003 [121].
- Madrzykowski and Vettori examined a fire in a townhouse in Washington, D.C., where two fire fighters were killed and one severely injured in 1999 [122].
- Vettori, Madrzykowski, and Walton simulated a fire in a Houston restaurant that killed two fire fighters in 2000 [123].
- Madrzykowski, Forney and Walton simulated a fire that killed three children and three fire fighters in a two story duplex house in Iowa in 1999 [124].
- Madrzykowski and Walton investigated the fire in the Cook County (Chicago) Administration Building in October, 2003, that killed six people trapped in a stairwell [125].
- Bryner et al. simulated a fire in a large furniture store that occurred in June, 2007, killing nine fire fighters [126].

Outside of NIST, FDS has been used to investigate many actual fires, but very few of these studies are documented in the literature. Exceptions include:

- A large fire in a "cash & carry" warehouse in the UK was studied by Camp and Townsend using both hand calculations and FDS (version 1) [127].
- A study by Rein et al. [128] looked at several fire events using an analytical fire growth model, the NIST zone model CFAST, and FDS.
- A similar study was performed several years earlier by Spearpoint et al. [129] as a class exercise at the University of Maryland.
- During the SFPE Professional Development Week in the fall of 2001, a workshop was held in which several engineers related their experiences using FDS as a forensic tool [130].
- The role of carbon monoxide in the deaths of three fire fighters was studied by Christensen and Icove [131].

Chapter 3

Description of Experiments

This chapter contains a brief description of the experiments that were used for model validation. Only enough detail is included here to provide a general understanding of the model simulations. Anyone wishing to use the experimental measurements for validation ought to consult the cited test reports or other publications for a comprehensive description.

3.1 ArupFire Tunnel Fire Experiments

Gabriele Vigne and Jimmy Jönsson of ArupFire conducted a series of fire experiments within a tunnel with a 50 m^2 cross section. The tunnel is located in La Ribera del Folgoso, Spain. It is approximately 6.5 m high, 8 m wide and 300 m long. Five replicate tests were conducted using a 1 m by 2 m steel pan filled with heptane on water. Near-ceiling temperatures were measured 2 m, 4 m, 6 m and 8 m from the plume centerline. The peak heat release rate was approximately 5.3 MW.

3.2 ATF Corridors Experiments

A series of eighteen experiments were conducted in a two-story structure with long hallways and a connecting stairway in the large burn room of the ATF Fire Research Laboratory in Ammendale, Maryland, in 2008 [132]. The test enclosure consisted of two 17.0 m long hallways connected by a stairway consisting of two staircases and an intermediary landing. There was a door at the opposite end of the first floor hallway, which was closed during all tests. The end of the second floor hallway was open with a soffit near the ceiling.

The walls and ceilings of the test structure were constructed of 1.2 cm gypsum wallboard. The flooring throughout the structure, including the stairwell landing floor, consisted of one layer of 1.3 cm thick cement board on one layer of 1.9 cm thick plywood supported by wood joists. The first set of stairs, which had eight risers, led from the first floor up to the landing area. The second set of stairs, which had nine risers, led from the landing area up to the second floor. The stairs were constructed of 2.5 cm thick clear pine lumber. The two set of stairs were separated by an approximately 0.42 m wide gap in the middle of the stairwell. This gap was separated from the stairs by a 0.91 m tall barrier constructed of a single piece of gypsum board. The flue space was open to the first floor. The flue space was separated from the second floor by a 0.9 m tall barrier constructed of gypsum board. There was a metal exterior type door at the end of the first floor near the burner. The door was closed during all experiments.

The fire source was a natural gas diffusion burner. The burner surface was horizontal, square and 0.45 m on each side, its surface was 0.37 m above the floor, and it was filled with gravel. The burner was located near the end of the first floor away from the stairs. A diagram of the test structure is displayed in Figure 3.1.

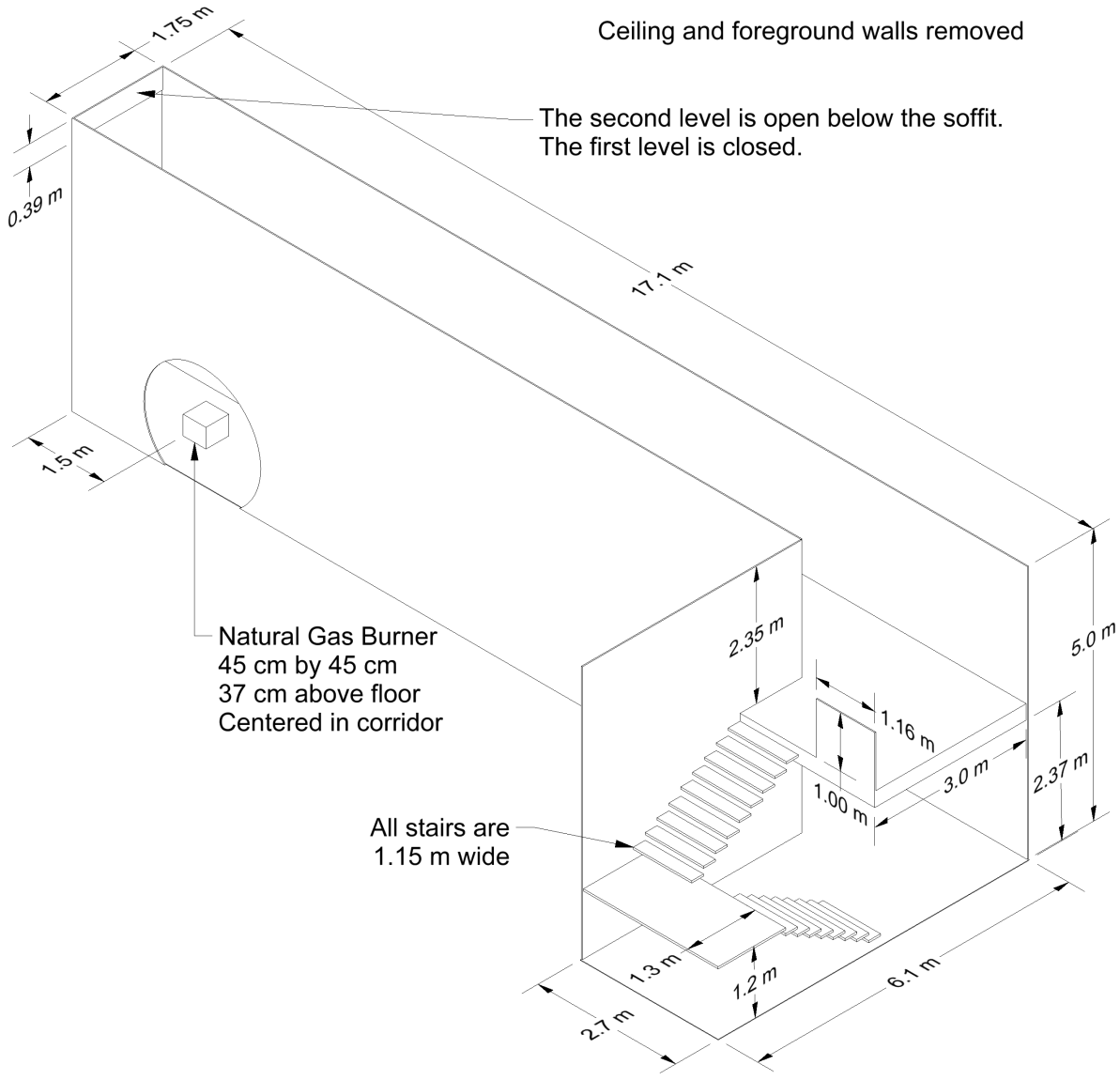

Figure 3.1: Geometry of the ATF Corridors Experiments.

3.3 Atmospheric Dispersion Correlations

A common exercise in atmospheric dispersion modeling is predicting the plume rise height of stack emissions. Stull [133] presents an empirical correlation for plume rise height from a smoke stack in a stable atmospheric boundary layer. Details of the correlation and simulation are found in Section 15.3.

3.4 Backward Facing Step

A common validation experiment for CFD codes involves flow through a channel with a backward facing step. These experiments are designed to test the influence of grid resolution, inlet turbulence, wall boundary treatments, and eddy viscosity models. One set of experiments has been conducted by Jovic and Driver [50]. A schematic view of the experiment is shown in Fig. 3.2. The dimensions of the channel are based on step height h = 0.0098 m. The length of the channel is $24h$. The width of the channel is $4h$. The height of the inlet section is $5h$, and the height of the channel downstream of the step is $6h$. The expansion ratio is thus 1.2. The inlet is split into three sub-inlets to permit localized variation of inlet turbulence. The Reynolds number of the flow is 5100, based on the free-stream velocity (7.2 m/s) and the step height.

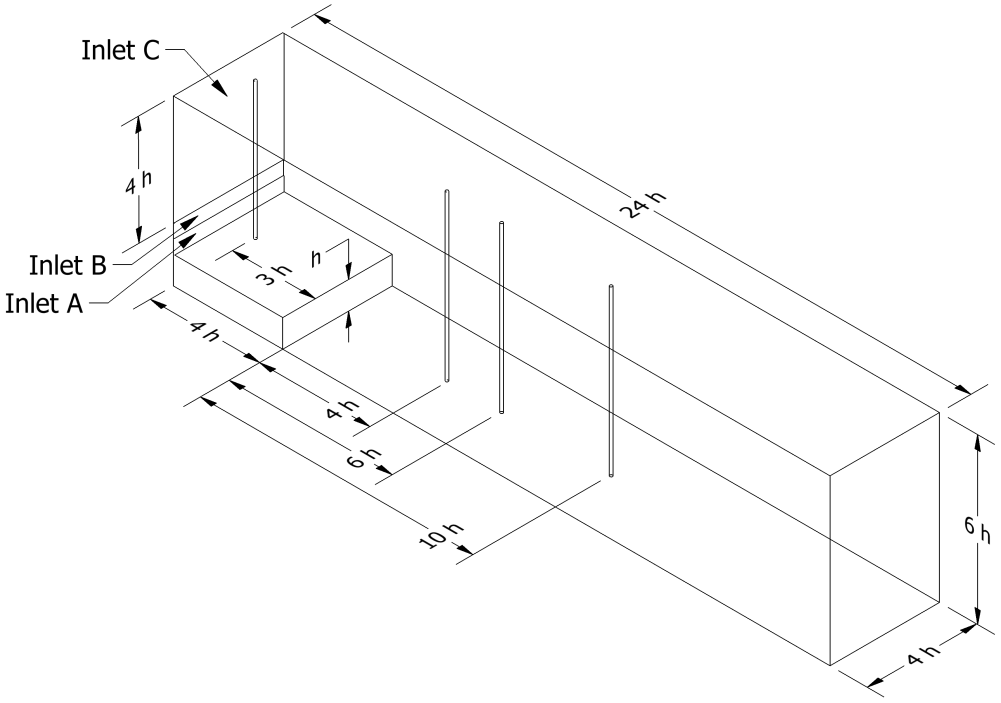

Figure 3.2: Geometry of the Backward Facing Step experiments.

3.5 Beyler Hood Experiments

Craig Beyler performed small-scale fire experiments where a variety of circular gas burners were centered at various heights underneath a closed, cylindrical hood, 100 cm in diameter and 48 cm in height [134]. The hood consisted of two concentric cylinders separated by an air gap, as shown in Fig. 3.3. The inner cylinder

was shorter than the outer and this allowed combustion products to be removed uniformly from the hood perimeter. The exhaust gases were then analyzed to determine species concentrations. The burner could be raised and lowered with respect to the bottom edge of the hood. The reported relative standard uncertainty of the measured gas species mass fractions was 6 %. The fuels consisted of acetone, ethanol, isopropanol, methanol, propane, propylene, and toluene. Hood equivalence ratios varied from 0.2 to 1.7. A subset of 47 of the original 148 experiments spanning the equivalence ratio range for each fuel were simulated for validation, see Table 3.1.

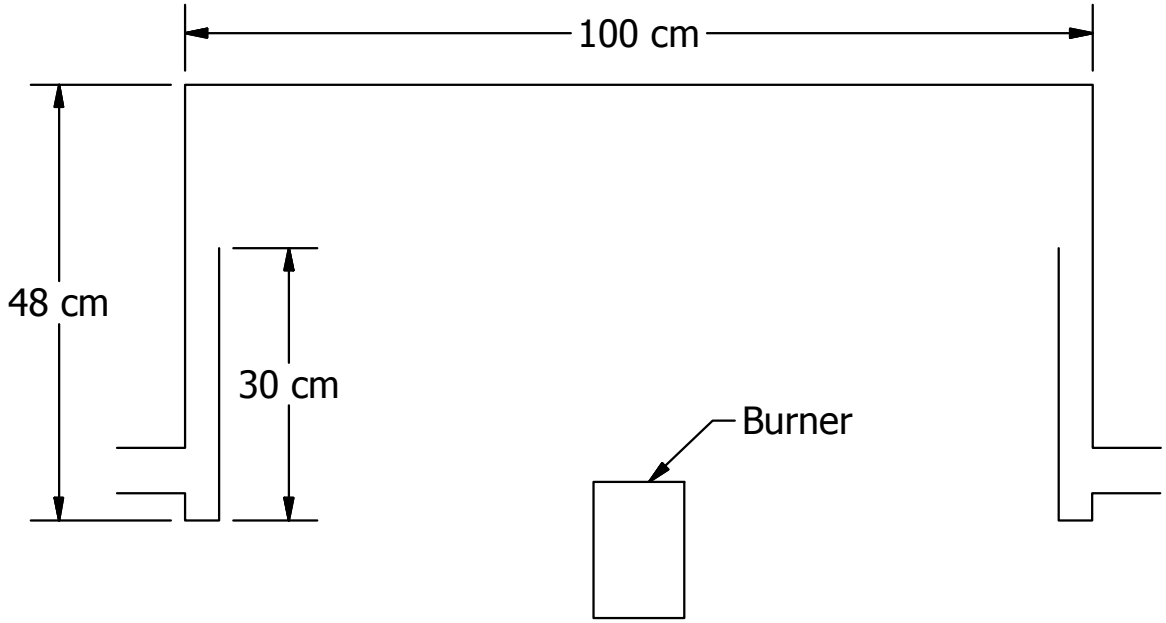

Figure 3.3: Sketch of Beyler Hood cross section.

Modeling Notes

Simulations of the Beyler Hood experiments are performed at 3 cm resolution within a fairly simple facsimile of the actual hood. The boundary conditions are set to adiabatic to allow for a relatively quick ramp up to steady-state conditions.

The two-step simple chemistry combustion scheme is applied, where an infinitely fast reaction converts the fuel to CO, soot, and water vapor, followed sequentially by a second fast reaction that converts the soot and CO to CO_2. Some of the soot and CO does not convert to CO_2, based on post-flame yields listed by Tewarson [135].

A minimum auto-ignition temperature is specified for each fuel [136] to prevent the fuel vapor from igniting at the layer interface. This restriction is relaxed in the grid cells just above the burner surface to allow for ignition without a secondary heat source. In addition, a critical flame temperature of 500 °C is applied in all cases to account for local flame extinction. The grid is too coarse to support the actual values, and the chosen value is a placeholder until a better flame extinction model is developed.

Table 3.1: Summary of simulated Beyler Hood experiments. A negative value of Separation Distance indicates the burner top is below the lower rim of the hood.

Exp. No.	Fuel Gas	HRR (kW)	Burner (cm)	Sep. Dist. (cm)	Exp. No.	Fuel Gas	HRR (kW)	Burner (cm)	Sep. Dist. (cm)
117	Acetone	18.0	22.6	-12	232	Propane	13.5	19.5	-5
119	Acetone	16.4	22.6	-1	257	Propane	8.2	19.5	-15
122	Acetone	16.4	22.6	4	287	Propane	7.9	19.5	5
142	Acetone	12.1	22.6	4	303	Propane	18.3	19.5	5
145	Acetone	12.7	22.6	4	307	Propane	21.4	19.5	5
106	Ethanol	17.3	22.6	-9	318	Propane	18.3	19.5	-20
107	Ethanol	21.3	22.6	-4	322	Propane	21.4	19.5	-20
108	Ethanol	17.3	22.6	4	334	Propane	21.4	19.5	-15
110	Ethanol	13.5	22.6	4	355	Propane	18.3	19.5	0
115	Ethanol	13.5	22.6	4	359	Propane	21.4	19.5	0
130	Isopropanol	12.4	22.6	4	371	Propane	21.4	19.5	-5
132	Isopropanol	12.4	22.6	4	389	Propane	18.3	19.5	0
133	Isopropanol	12.4	22.6	4	429	Propane	28.1	19.5	-10
136	Isopropanol	12.4	22.6	-1	433	Propane	31.5	19.5	-10
141	Isopropanol	12.4	22.6	4	445	Propane	31.5	19.5	-15
942	Methanol	11.0	22.6	0	780	Propylene	7.5	19.5	-10
943	Methanol	11.0	22.6	0	805	Propylene	7.5	19.5	-10
945	Methanol	11.0	22.6	-5	859	Propylene	31.4	19.5	-10
947	Methanol	11.0	22.6	0	870	Propylene	19.0	19.5	-2
951	Methanol	9.8	22.6	0	882	Propylene	19.1	19.5	-10
160	Toluene	11.5	22.6	-6	886	Propylene	19.1	19.5	-5
162	Toluene	11.5	22.6	-1	910	Propylene	31.4	19.5	-11
165	Toluene	11.5	22.6	4					
166	Toluene	11.5	22.6	5					
170	Toluene	11.5	22.6	4					

3.6 BGC/GRI LNG Fire Experiments

In 1982 and 1983, P.A. Croce and K.S. Mudan of Arthur D. Little, Inc., and J. Moorhouse of the British Gas Corporation (BGC) supervised 13 liquified natural gas (LNG) trench fire experiments conducted by BGC on behalf of the Gas Research Institute (GRI) [137]. Thirteen experiments were performed with nominal trench sizes ranging from 0.8 m by 4.4 m to 3.9 m by 52 m and aspect ratios ranging from approximately 5 to 30. Wind speeds varied from approximately 1 m/s to almost 10 m/s. Measurements made during the tests included flame geometry, radiative heat flux, emissive power, burning rate, LNG liquid and vapor compositions, and meteorological data. The fires were observed to exhibit substantial flame drag and flame breakup, unlike low aspect ratio pools. Steady burning was achieved in all tests.

The key parameters for each experiment are listed in Table 3.2. The Flame Tilt angle is the measured deflection of the flame from the vertical. The Flame Drag Ratio is the distance that the flame drags along the ground outside of the trench added to the trench width, and then divided by the trench width. The Avg. Flame Length denotes the time-averaged flame length, while the Max. Flame Length refers to the time-averaged extent of the fluctuating flame tips.

Table 3.2: BGC/GRI LNG Fires test parameters.

Test No.	Trench Length (m)	Trench Width (m)	Aspect Ratio	Wind Speed (m/s)	Burning Rate (kg/m^2/s)	Flame Tilt (deg)	Flame Drag Ratio	Avg. Flame Length (m)	Max. Flame Length (m)
1	23.53	1.81	13.00	3.8	0.064	56.3	2.57	4.4	8.9
2	15.52	1.81	8.57	1.5	0.069	56.1	2.30	3.8	7.3
3	9.23	1.83	5.04	1.0	0.098	45.2	1.21	7.1	11.4
4	23.50	1.83	12.84	8.36	0.054	56.8	2.96	3.4	7.3
5	9.05	1.82	4.97	9.31	0.060	60.5	2.96	4.2	8.2
6	23.45	3.94	5.95	4.98	0.082	59.6	2.62	6.9	16.8
7	23.45	0.82	28.60	3.80	0.049	48.3	3.98	2.0	4.3
8	11.82	0.82	14.41	2.05	0.058	49.8	3.77	2.1	4.6
9	9.10	0.82	11.10	5.40	0.051	47.0	3.68	1.5	3.7
10	52.05	3.89	13.38	7.05	0.060	61.3	2.83	7.9	20.3
11	4.37	0.81	5.40	5.90	0.052	49.9	4.16	1.8	3.6
12	52.15	1.82	28.65	8.60	0.046	61.3	3.70	3.3	8.1
13	23.10	0.77	30.00	3.69	0.043	55.7	4.23	2.1	5.3

Modeling Notes

The experiments are simulated using the specified fuel burning rate. The fuel is assumed to be methane. The atmosphere is assumed to be neutral with a large Obukhov length, $L = 1000000$, and the ground surface is flat with an assumed aerodynamic roughness, $z_0 = 0.1$ m. The relative humidity, ambient temperature and pressure, and wind speed at 9 m are specified in the report. The radiative fraction is assumed to 0.25 and the radiative path length is assumed to be 50 m; that is, the effective absorption coefficients of the various gas mixtures are evaluated over a distance of 50 m. The radiation source term is taken directly as 25 % of the combustion energy release rate. The soot yield is assumed to be 0.005.

Flame Height Results: Section 6.2.3

Flame Tilt Results: Section 6.3

Heat Flux Results: Section 12.2.3

3.7 Bittern Sprinkler Experiments

In 2004, a set of 22 fire experiments was conducted at the University of Canterbury, New Zealand, by Adam Bittern [138, 139]. In each experiment, a single chair was burned within an enclosure with two sprinklers installed. The sprinklers were not charged with flowing water during the experiments, but pressure gauges were installed immediately upstream of each sprinkler to indicate activation. The sprinkler actuation time, chair mass loss rate, and gas temperature profile were measured. The HRR was estimated from the measured mass loss rate and heat of combustion of the fuel.

The experiments incorporated four different types of sprinklers, two fire locations (the center and corner of the enclosure), and two ventilation conditions (open or closed door). The enclosure was timber-framed and lined with 10 mm thick gypsum plasterboard. The door was made of plywood and was 0.8 m wide by 2.1 high. The compartment layout, dimensions and experimental arrangement are shown in Figure 3.4.

The chair used as fuel for each experiment was made of flexible polyurethane foam slabs, where each slab measured approximately 0.5 m by 0.4 m by 0.1 m. The seat was ignited using a solid petroleum lighter.

Table 3.3 reports the sprinkler actuation times of each sprinkler.

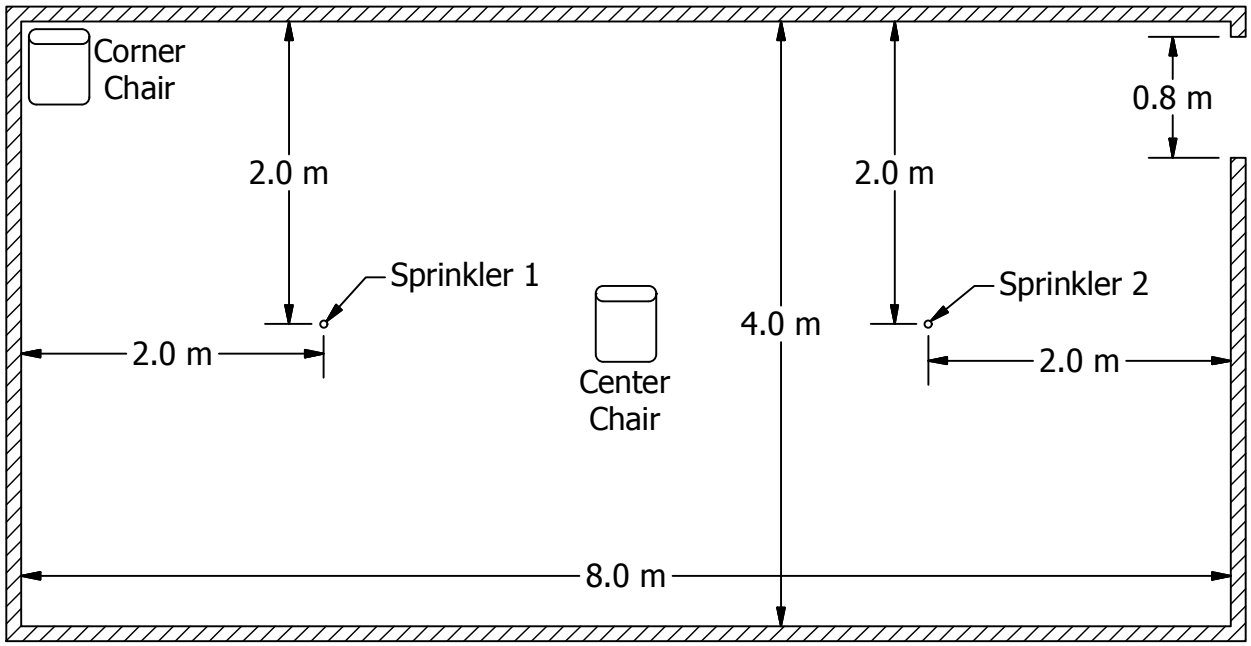

Figure 3.4: Plan view of the Bittern Sprinkler Experiments.

Modeling Notes

The assumptions given in this section were used in the original analysis of the experiments [138].

The gypsum board had a thickness of 1 cm, density of 731 kg/m^3, specific heat of 0.90 kJ/(kg·K), conductivity of 0.17 W/(m·K), and emissivity of 0.88. The concrete floor was assumed to have a thickness of 10 cm, density of 2300 kg/m^3, specific heat of 0.88 kJ/(kg·K), conductivity of 1.2 W/(m·K), and emissivity of 0.5.

The properties of the sprinklers are shown in Table 3.4. These properties are based on the manufacturer's specification where available or otherwise estimated based on measured values of comparable sprinklers. For modeling purposes, the sprinkler offset, 2 cm, was selected based on an approximate 2 cm glass bulb length, and the C-factor selected was based on a sensitivity analyses undertaken in the original study.

The average heat of combustion of the upholstery was measured in a cone calorimeter to be 21.9 MJ/kg (Exp. 1-10) and 20.4 MJ/kg (Exp. 12-22). Since the primary fuel used in the experiments was flexible polyurethane foam, the radiant loss fraction assumed in the fire model was 0.46. Other combustion parameters were as for polyurethane foam, and all parameters selected are consistent with those used in the original BRANZFIRE study [139]. For the "simple chemistry" combustion model, inputs for stoichiometric yields have been selected from literature based on GM23 foam, with an effective molecular formula of $CH_{1.8}O_{0.35}N_{0.06}$. The soot yield was assumed to be 0.227 kg/kg. The area of the fire was taken to be 0.4 m by 0.5 m. The height of the fire was assumed to be 0.65 m above the floor.

Table 3.3: Summary of results, Bittern experiments. Note that Exp. 11 has been excluded because of a failed mass loss measurement.

Exp.	Spr. 1	Time (s)	Spr. 2	Time (s)	T_0 (°C)	Door	Fire Position
1	Res A	210	Res A	250	23.7	Open	Center
2	Res A	225	Res A	211	25.5	Open	Center
3	Res B	192	Res B	192	25.5	Open	Center
4	SS68	226	SS68	226	25.7	Open	Center
5	SS68	266	SS68	272	27.5	Open	Center
6	SS68	216	SS68	211	27.7	Open	Center
7	Res A	182	Res A	186	28.2	Open	Center
8	Res B	182	Res B	187	27.9	Open	Center
9	Res B	233	Res B	230	28.9	Open	Center
10	Res A	183	Res B	184	29.4	Open	Center
12	SS68	246	Res B	228	24.0	Closed	Center
13	SS68	204	Res B	194	24.5	Closed	Center
14	SS68	203	Res B	187	24.2	Closed	Center
15	SS68	270	Res B	253	23.7	Closed	Center
16	Res B	178	Res A	224	20.6	Closed	Corner
17	Res B	181	Res A	228	23.8	Closed	Corner
18	SS68	187	Res A	221	25.0	Closed	Corner
19	SS68	189	Res A	223	26.4	Closed	Corner
20	SS68	205	Res A	DNA	25.3	Closed	Corner
21	SS93	216	SS93	330	25.2	Closed	Corner
22	SS93	205	SS93	263	25.2	Closed	Corner

Table 3.4: Properties of sprinklers used in Bittern Experiments.

Short Name	**Description**	**RTI** $(\text{m}\cdot\text{s})^{1/2}$	**C-Factor** $(\text{m/s})^{1/2}$	**Act. Temp.** °C
Res A	Residential, 3 mm glass bulb	36	0.4	68
Res B	Residential, 3 mm glass bulb	36	0.4	68
SS68	Standard Response, 5 mm glass bulb	95	0.4	68
SS93	Standard Response, 5 mm glass bulb	95	0.4	93

For experiments 11 to 22, the door to the compartment was closed. The estimated leakage area was assumed based on data for loose-fitting internal walls. An area of 0.053 m^2 was evenly distributed across the door.

3.8 Bouchair Solar Chimney

To evaluate solar-induced ventilation systems in desert climates, Bouchair [140] constructed a simple test apparatus shown in Fig. 3.5. A compartment with interior dimensions of approximately 1.6 m long, 1.8 m, and 2.0 m high had a window on one side and an air inlet slot on the other, leading into a 1.5 m wide cavity with two heating panels spanning the long dimension. The panels were heated to 10 °C, 20 °C, 30 °C, or 40 °C above ambient, drawing air through the compartment and into the thermal cavity. The mass flow rate

of air through the cavity was measured. The inlet slot was either 0.1 m or 0.4 m high, and 1.4 m wide. The thermal cavity was 1.5 m wide, and the hot panels were separated by 0.1 m, 0.2 m, 0.3 m, 0.5 m, or 1.0 m. In all, there were 40 different sets of test parameters.

In addition to the results presented in this guide, simulations of this experiment were performed by Shi and Zhang [141]. The objective of the simulations is to predict the mass flow rate by accurately modeling the convective heat transfer between the air and hot panels.

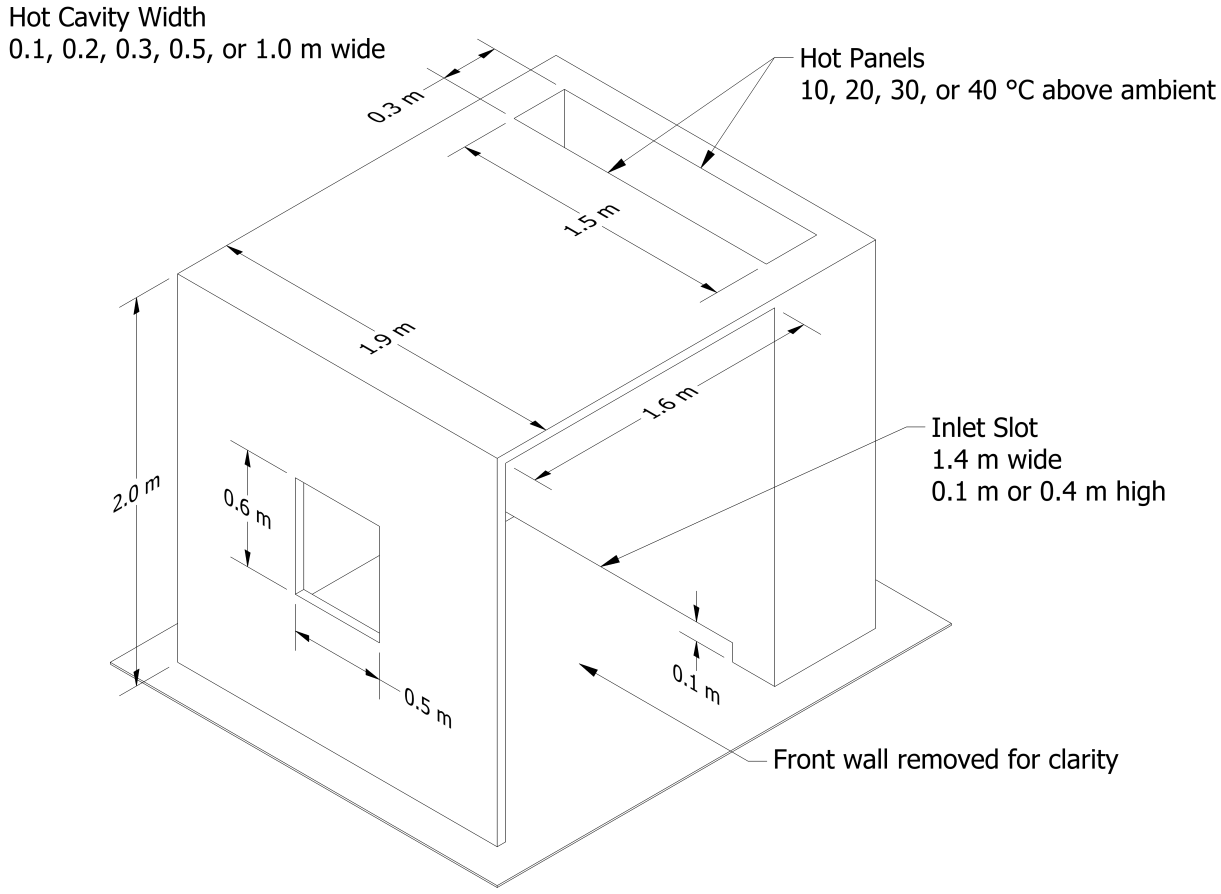

Figure 3.5: Geometry of the Bouchair Solar Chimney experiment.

3.9 BRE Spray Test for Radiation Attenuation

Murrel et al. [142] measured the attenuation of thermal radiation passing through a water spray using a heat flux gauge. The radiation was produced by a heat panel, one meter square, at 900 °C. The horizontal distance from the radiation panel to the spray nozzle was 2 m and to the measurement point 4 m. The nozzles were positioned at a height 0.24 m above the panel upper edge. The heat flux gauge was positioned at the line passing through the center of the panel. The attenuation of radiation was defined as $(q_0 - q_s)/q_0$, where q_0 is the initial radiative heat flux, measured without a spray, and q_s is the heat flux measured during the spray operation.

Experimental results are used from three full-cone type nozzles, labeled A, B and D. The opening angles of the nozzles were between 90 and 108 degrees. The purpose of the simulation is to compare the measured and simulated attenuation of radiation at different flow conditions. The nozzles were specified in terms of median droplet size and mean vertical velocity using PDPA measurement in a single position, 0.7 m below the nozzle. The droplet boundary conditions were determined by assuming $d_m \propto p^{-1/3}$ and $v \propto p^{1/2}$ type of dependencies between the droplet size, speed and pressure.

3.10 Bryant Doorway Velocity Measurements

Rodney Bryant of the Fire Research Division at NIST performed a series of velocity measurements of the gas velocity within the doorway of a standard ISO 9705 compartment for fires ranging from 34 kW to 511 kW [143, 144, 145]. A doorway served as the only vent for the enclosure. It included a jamb of 37 cm extending outward to facilitate the laser measurements. The entire compartment was elevated 0.3 m off the floor of the laboratory (see Fig. 3.6). The measurements were made using both bi-directional probes and PIV (Particle Image Velocimetry). The PIV measurements only cover the lower two-thirds of the doorway because of difficulties in seeding the hot outflow gases. The bi-directional probe measurements span the entire height of the doorway, but Bryant reports that these measurements were up to 20 % greater than the PIV measurements in certain regions of the flow. Consequently, only the PIV data was used for comparison to the model.

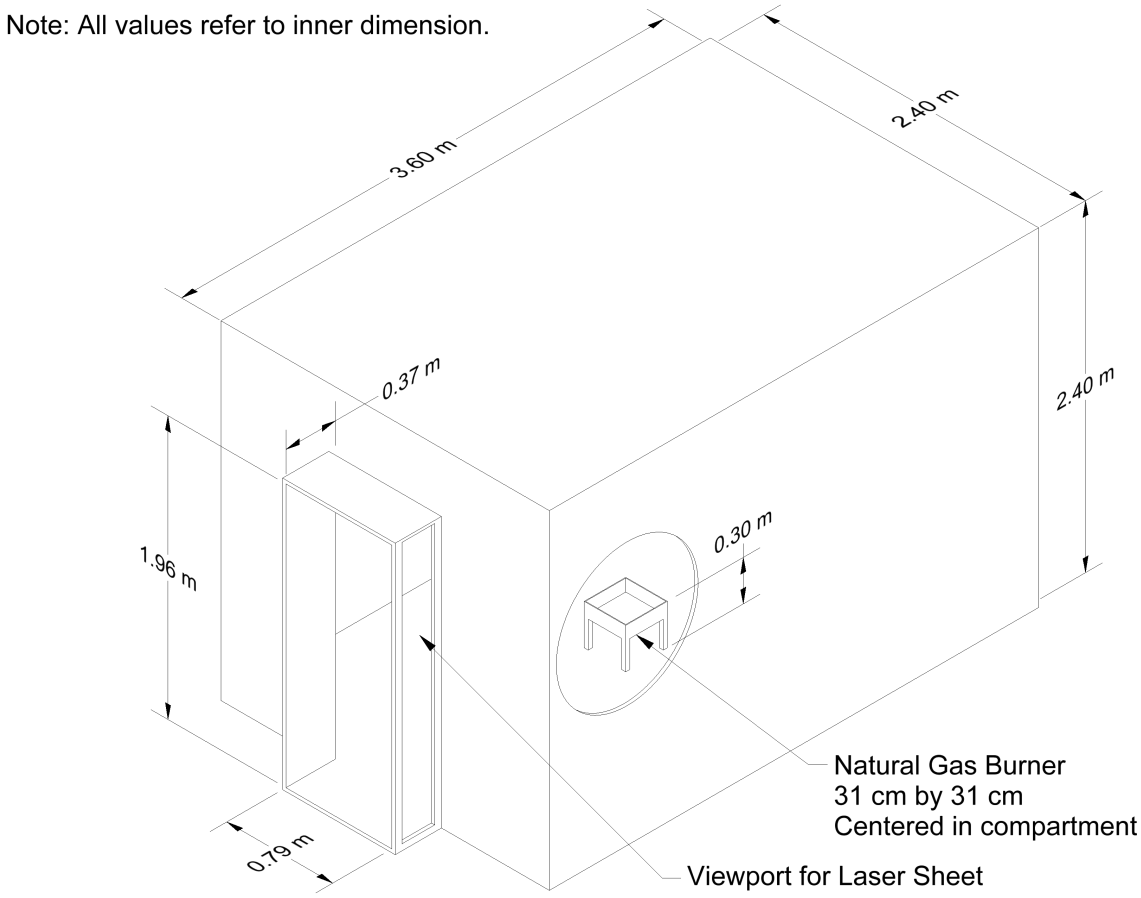

Figure 3.6: Geometry of Bryant's compartment.

3.11 BST/FRS Wood Crib Fire Experiments

In 1993, British Steel Technical, Swinden Laboratories, in collaboration with the Building Research Establishment (BRE), Fire Research Station, conducted nine fire experiments inside the BRE ex-airship hangar testing facility at Cardington, Bedfordshire, England [146]. The objective of the experiments was to examine the influence of combustible loading and ventilation on fire severity.

The roof of the test compartment was made of 20 cm thick reinforced aerated concrete slabs with a density of 450 kg/m^3. The walls were made of 215 mm thick lightweight concrete blocks with a density of 1375 kg/m^3. The floor was covered with a 125 mm deep layer of sand with a density of 1750 kg/m^3. Both the roof and walls were lined with two 25 mm thick layers of standard grade ceramic fiber blanket with a density of 128 kg/m^3. Taking into account the lining materials, the compartment was 22.9 m long, 5.6 m deep, and 2.8 m high.

Ventilation was provided at one end of the compartment through a full-width, variable height opening. Lightweight concrete blocks were used to construct temporary walls to reduce the ventilation from fully open to an eighth of the available area.

The combustibles consisted of 33 1 m square wood cribs in 11 rows. Each crib was constructed of 1 m long and 5 cm square cross section sticks of Western Hemlock softwood (density 400 kg/m^3), dried to 10 % moisture content. The sticks were stacked with 5 cm gaps. Table 3.5 lists the fire load densities

and ventilation areas. The rear-most three cribs at the back of the compartment were ignited simultaneously. Temperatures were measured along crib lines 2 (back), 6 (middle) and 10 (front), using 3 mm thermocouples placed 300 mm below the ceiling. The average of three thermocouples at the same longitudial position is used for model validation.

Table 3.5: Fire load densities and relative ventilation areas in the BST/FRS experiments [146].

Test number	1	2	3	4	5	6
Combustible load (kg/m^2)	40	20	20	40	20	20
Relative Ventilation Area	1/1	1/1	1/2	1/2	1/4	1/8

Modeling Notes

The fire spread on wood cribs is modeled as a combination of simple and complex pyrolysis models. The unresolved surface area of the wood cribs is compensated using a area multiplicator input parameter. Modeling is reported in [147].

3.12 Cable Response to Live Fire – CAROLFIRE

CAROLFIRE was a project sponsored by the U.S. Nuclear Regulatory Commission to study the thermal response and functional behavior of electrical cables [148]. The primary objective of CAROLFIRE was to characterize the various modes of electrical failure (e.g., hot shorts, shorts to ground) within bundles of power, control and instrument cables. A secondary objective of the project was to develop a simple model to predict thermally-induced electrical failure (THIEF). The measurements used for these purposes were conducted at Sandia National Laboratories and are described in Volume II of the CAROLFIRE test report. In brief, there were two series of experiments. The first were conducted within a heated cylindrical enclosure. Single and bundled cables were exposed to various heat fluxes and the electrical failure modes recorded. The second series of experiments involved cables within trays in a semi-enclosed space under which a gas-fueled burner created a hot layer to force cable failure. Only results from the first series are used here.

Petra Andersson and Patrick Van Hees of the Swedish National Testing and Research Institute (SP) proposed that a cable's thermally-induced electrical failure can be predicted via a one-dimensional heat transfer calculation, under the assumption that the cable can be treated as a homogenous cylinder [149]. Their results for PVC cables were encouraging and suggested that the simplification of the analysis is reasonable and that it should extend to other types of cables. The assumptions underlying the THIEF model are as follows:

1. The heat penetration into a cable of circular cross section is primarily in the radial direction.
2. The cable is homogeneous in composition. In reality, a cable is constructed of several different types of polymeric materials, cellulosic fillers, and a conducting metal, most often copper.
3. The thermal conductivity, specific heat, and density of the assumed homogeneous cable are independent of temperature. In reality, both the thermal conductivity and specific heat of polymers are temperature-dependent, but this information is not easily obtained from manufacturers.
4. It is assumed that no decomposition reactions occur within the cable during its heating, and ignition and burning are not considered in the model. In fact, thermoplastic cables melt, thermosets form a char layer, and both release volatile gases up to and beyond the point of electrical failure.

5. Electrical failure occurs when the temperature just inside the cable jacket reaches an experimentally determined value.

3.13 Crown Fires

The term "crown fire" refers to a wildfire that spreads from the ground surface into the tree canopy. Alexander and Cruz [150] compiled a data set of 57 crown fires that occurred in the U.S. and Canada between 1965 and 2003. For each fire, the relative humidity, ambient temperature, and dominant vegetation type are reported, along with estimated values for the vegetation moisture content, *canopy*[1] bulk density, and open 10 m wind speed. The vegetation consists mainly of coniferous trees, like pines and spruces, and dry undergrowth and ground cover, i.e. scrub brush and dry pine needles. The reported relative humidity ranges between 5 % and 50 %, the estimated moisture content ranges between 5 % and 10 %, the estimated *canopy* bulk density ranges between 0.1 kg/m^3 and 0.2 kg/m^3, the estimated wind speed ranges between 10 km/h and 50 km/h, and the observed rate of spread ranges between 10 m/min and 110 m/min.

Modeling Notes

It is not possible to compare directly the model simulations with the observed fires because of lack of information about the number, spacing, and height of the trees; and the depth, mass, and composition of the ground cover. Instead, Ziegler et al. [151, 152, 153, 154] developed tree maps based on various forests found in the western region of the U.S. The maps contain the location and rough dimensions of each tree in a 4 ha area. Eight maps were developed based on four specific locations and pre- or post-treated conditions. In addition, Ziegler et al. suggest that the moisture content of the trees is approximately 100 %, and the ground cover 5 %. The *crown* bulk density for all simulations is 1.2 kg/m^3, and the surface density is 0.72 kg/m^2 with a depth of 6 cm. The simulated fires are ignited along a strip, and the rate of spread is calculated based on the position of peak temperature.

The simulations are performed with a numerical grid that has a resolution of 1 m by 1 m by 0.5 m near the ground, and the vertical dimension increases gradually with height. Because of this relatively coarse resolution, the burning rate of the vegetation is limited to ensure that any given patch of surface vegetation or volume of canopy vegetation cannot burn completely in less than 30 s.

3.14 CSIRO Grassland Fires

In July and August of 1986, the Commonwealth Scientific and Industrial Research Organisation (CSIRO) of Australia conducted controlled grassland fire experiments near Darwin, Northern Territory [155]. July and August are in the middle of the dry season when the grasses are fully cured (dried) and the weather is warm and dry. The experiments were conducted on flat plots measuring 100 m by 100 m, 200 m by 200 m, or 200 m by 300 m. Two cases have been simulated. Case C064 was conducted on a 100 m by 100 m plot of kerosene grass (*Eriachne burkittii*); Case F19 was conducted on a 200 m by 200 m plot of kangaroo grass (*Themeda australis*).

Modeling Notes

Two of these experiments were originally simulated with FDS by Mell et al. [156]. These simulations modeled the grass as a collection of cylindrical Lagrangian particles. The pyrolysis model assigned to the

[1] Note the difference between *canopy* bulk density and *crown* bulk density, both of which are abbreviated CBD. The former is the bulk density over the entire forested area, whereas the latter refers to the bulk density within the crown of an individual tree.

particles is described in the FDS User's Guide [1], chapter "Earth, Wind and Fire," Section 19.1, "Thermal Degradation Model for Vegetation."

Now these two experiments are also simulated using the Boundary Fuel Model (BFM) [157] and the Rothermel-Albini fire spread algorithm [158, 159]. For the experiment labelled Case C064, fuel index 1 (Short Grass) is used, with a modified moisture fraction of 0.063. For F19, fuel index 3 (Tall Grass) is used, with a modified moisture fraction of 0.058.

Measured properties for the specific types of grasses burned in the two experiments are listed in Table 3.6. Properties that were not measured are listed in Table 3.7. These assumed properties are typically for wood or cellulosic fuels. The moisture is modeled as water. The grass is assumed to be composed primarily of cellulose.

Snapshots of the Lagrangian particle simulation of Case F19 is shown in Fig. 3.7. The computational domain in this case is 240 m by 240 m by 20 m. The grid cells are 0.5 m cubes. The domain is subdivided into 36 individual meshes and run in parallel. The grass is represented 1 simulated blade per grid cell. The radius of the cylinder is derived from the measured surface area to volume ratio. Each simulated blade of grass represents many more actual blades of grass. The weighting factor is determined from the measured bulk mass per unit area. The fires in the experiments were ignited by two men carrying drip torches walking in opposite directions along the upwind boundary of the plot (the red strip in Fig. 3.7). In FDS, this action was modeled using a specified spread rate along the strip.

Table 3.6: Measured properties for the CSIRO Grassland Fire cases [155].

Property	Units	Case F19	Case C064
Wind Speed	m/s	4.8	4.6
Ambient Temperature	°C	34	32
Surface Area to Volume Ratio	m^{-1}	12240	9770
Grass Height	m	0.51	0.21
Bulk Mass per Unit Area	kg/m^2	0.313	0.283
Moisture Fraction	%	5.8	6.3

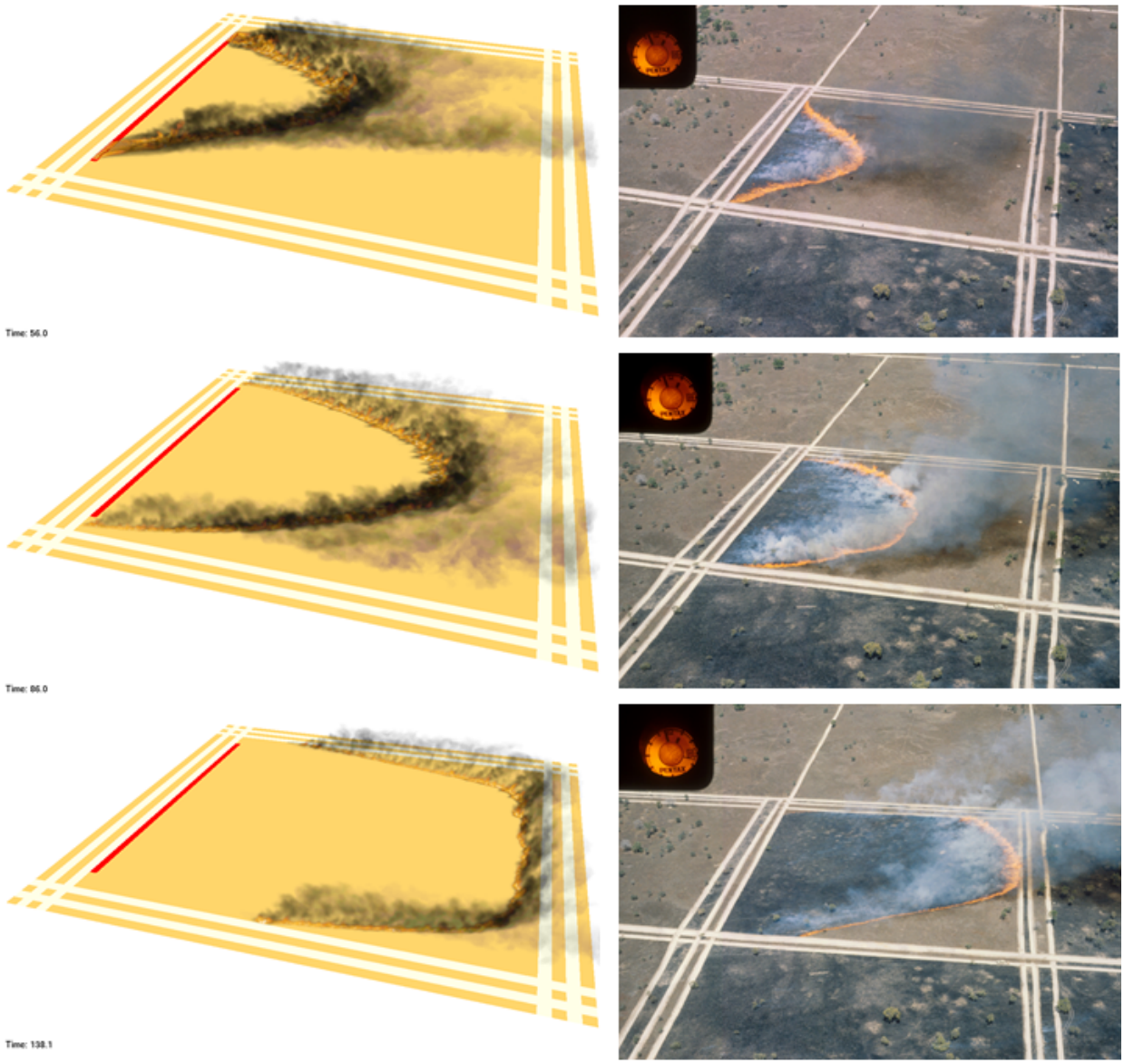

Figure 3.7: Snapshots of the simulation of CSIRO Grassland Fire F19 compared to photographs of the fire.

Table 3.7: Assumed properties for various types of dried grass and soil. Note that the Pyrolysis Temperature is taken to be the temperature at which the mass loss rate peaks in the TGA experiments of Morvan and Dupuy [160].

Property	Units	Value	Reference
Chemical Composition	–	$C_6H_{10}O_5$	Assumption
Heat of Combustion	kJ/kg	15600	[161]
Soot Yield	kg/kg	0.015	[135]
Char Yield	kg/kg	0.2	[161]
Specific Heat	kJ/(kg·K)	1.5	Various sources
Conductivity	W/(m·K)	0.1	Assumption
Density	kg/m^3	512	[158]
Heat of Pyrolysis	kJ/kg	418	[160]
Pyrolyis Temperature	°C	200	[160]
Obukhov Length	m	-500	Assumption
Aerodynamic Roughness Length	m	0.03	Assumption
Drag Coefficient	–	2.8	[162]
Soil Specific Heat	kJ/(kg·K)	2.0	[163]
Soil Conductivity	W/(m·K)	0.25	[163]
Soil Density	kg/m^3	1300	[163]

3.15 CSTB Tunnel Experiments

Between 2005 and 2008, the French building research laboratory, Centre Scientifique et Technique du Bâtiment (CSTB) cooperated with the French Tunnel Study Center (CETU), the French National Centre for Scientific Research (CNRS, Institut PPRIME) and the French Directorate for Civil Security (DSC) to conduct fire experiments in a tunnel, some of which involved a water mist system [164, 165]. The first aim was to improve the understanding of the interaction between water mist and a tunnel fire. The second was to develop a database for model validation. A one-third scale was selected with the objective of studying realistic fire phenomena in an affordable way. Twenty-eight experiments were conducted (20 with and 8 without water mist) with varying fuels (heptane pool, wood crib, and wood pallet) and longitudinal velocities (with and without back layering).

The tunnel was 43 m long, with a semi-circular cross section whose area was approximately 4 m^2. The walls were covered by a fire resistant mortar cement with well known thermal properties. The floor was made of concrete. A fan was mounted at the downstream side of the tunnel. Measurements were made of the following: fuel mass, gas temperature, air velocity, radiative heat flux and gas concentration (CO, CO_2 and O_2). Sensors were located at 11 longitudinal positions.

Tests 2 and 27 have been selected because neither exhibited back layering. The longitudinal velocity in Test 2 was approximately 2.2 m/s and in Test 27 it was 3.1 m/s. Both experiments involved a 0.5 m^2 area heptane pool. In Test 2, the HRR was deduced from the fuel mass loss rate only. In Test 27, the HRR was deduced from both the mass loss rate and from oxygen consumption calorimetry.

In Test 27, a water mist system was manually activated 300 s after ignition. The water mist system was composed of six nozzles along the centerline of the tunnel, from 4 m upstream to 3.5 m downstream of the fire, 1.5 m apart. The operating pressure was approximately 90 bar. The water flow rate injected at each nozzle was close to 5.5 L/min, corresponding to a total mist discharge rate of approximately 33 L/min. Test 27 is interesting because it involved a very low water injection rate. The main consequence is that

the HRR actually increased slightly after the nozzles were activated, and the fire did not extinguish. The experiment stopped when the fuel was exhausted. This allowed for an assessment of the model's ability to predict the gas cooling and radiation attenuation.

Modeling Notes

The simulations of these experiments are performed using 12 meshes. To prevent numerical instability due to oscillations in pressure, a common problem for tunnel fire simulations, the `VELOCITY_TOLERANCE` and `PRESSURE_TOLERANCE` are reduced to 0.01 m/s and 400 s^{-2}, respectively, and the `MAX_PRESSURE_ITERATIONS` is increased to 50. The multi-port mist nozzles are each modeled as a collection of single nozzles with varying orientations.

3.16 Cup Burner Experiments

The cup-burner is a widely used experimental apparatus for studying the effectiveness of flame extinguishing agents. Typically, these experiments feature a steady fuel-air co-flow diffusion flame that is established above the cup. The extinguishing agent is gradually introduced into the air stream to determine the minimum concentration of the agent that leads to lift off. One hundred and ten experimental data sets are examined. The data sets include sixteen fuels: acetone, acetylene, benzene, butane, dodecane, ethanol, ethylene, heptane, hexane, hydrogen, methane, methanol, octane, propanol, and toluene, and five inert gases: argon (Ar), carbon dioxide (CO_2), helium (He), and nitrogen (N_2), and sulfur hexaflouride (SF_6). A STANJAN[2] calculation has been performed to determine the equilibrium temperature using the measured minimum extinguishing concentration for each experiment. The calculation assumes constant pressure and enthalpy using a stoichiometric mixture of fuel and air plus agent. For combinations of fuel and agent with multiple experiments, the average extinguishing concentration and the average flame temperature is taken, resulting in forty-six unique combinations of fuel and agent listed in Table 3.8.

Modeling Notes

Cup burner dimensions, fuel inlet velocity, and co-flow inlet velocity vary slightly amongst the researchers; however, extinguishing concentrations have been shown to be fairly insensitive over the range of typical values. The cup burner model was implemented as a 2D, cylindrical geometry with a 1 cm radius for the burner and a 4 cm radius for the tube. A 1 mm grid resolution was used. For gaseous fuels a 1 cm/s inlet velocity was used for the burner. Liquid fuels used burning rates from the SFPE Handbook; fuels without published burning rates scaled the burning rate of a chemically similar fuel (e.g. alcohol, alkane) using the heat of vaporization for the fuel. The fuel temperature boundary condition was ambient for gaseous fuels and one-half of the boiling point for liquid fuels. The co-flow was set to 12 cm/s. The agent mass fraction was ramped from approximately 10 % below to 10 % above the values shown in Table 3.8. The `CRITICAL_FLAME_TEMPERATURE` was set to the values in Table 3.8.

[2] STANJAN is a program for chemical equilibrium calculations.

Table 3.8: Summary of Cup Burner Data

Fuel	Agent	MEC	CFT	References
Acetone	Ar	34.0	1729	[166, 167]
Acetone	CO_2	19.0	1678	[168]
Acetone	N_2	28.0	1670	[166, 168]
Acetylene	CO_2	45.0	1338	[168]
Acetylene	N_2	58.0	1312	[168]
Benzene	CO_2	20.1	1691	[168, 169]
Benzene	N_2	30.3	1683	[166, 168, 169]
Butane	N_2	31.0	1594	[168]
Butane	CO_2	19.0	1639	[168]
Dodecane	N_2	33.0	1577	[166]
Ethanol	Ar	36.5	1654	[166, 167]
Ethanol	CO_2	23.7	1542	[168, 169]
Ethanol	N_2	34.6	1529	[166, 168, 169]
Ethylene	CO_2	32.0	1471	[168]
Ethylene	N_2	45.0	1441	[168]
Heptane	Ar	39.5	1643	[166, 170, 167, 171, 172, 173, 174, 175, 176]
Heptane	N_2	31.2	1617	[166, 170, 177, 167, 178, 171, 172, 173, 168, 169, 174, 175, 176]
Heptane	CO_2	21.4	1617	[167, 178, 171, 172, 173, 168, 169]
Heptane	He	31.5	1763	[171, 172]
Heptane	SF_6	11.0	1531	[171]
Hexane	Ar	33.0	1740	[167]
Hexane	CO_2	20.0	1647	[168]
Hexane	N_2	29.0	1646	[166, 168]
Hydrogen	CO_2	60.0	913	[168]
Hydrogen	N_2	72.0	870	[168]
Methane	Ar	33.8	1659	[166, 179, 167]
Methane	N_2	24.2	1663	[179, 168, 180]
Methane	CO_2	14.4	1694	[168, 169]
Methane	He	26.7	1746	[179]
Methanol	Ar	45.0	1494	[166, 167]
Methanol	CO_2	29.2	1410	[168, 169]
Methanol	N_2	40.8	1395	[166, 168, 169]
Octane	Ar	27.0	1790	[167]
Octane	CO_2	24.0	1542	[168]
Octane	N_2	33.0	1564	[166, 168]
Propane	Ar	37.5	1652	[166, 167]
Propane	CO_2	21.0	1600	[168]
Propane	N_2	32.3	1573	[177, 168, 180]
Propanol	Ar	28.0	1781	[167]
Propanol	CO_2	22.0	1584	[168]
Propanol	He	30.0	1755	[171]
Propanol	N_2	30.0	1608	[168, 171]
Propanol	SF_6	11.0	1515	[171]
Toluene	Ar	27.0	1854	[167]
Toluene	CO_2	17.0	1744	[168, 169]
Toluene	N_2	24.4	1755	[168, 169]

MEC Minimum Extinguishing Concentration (mol/mol)
CFT Critical Flame Temperature (°C)

3.17 DelCo Trainer Experiments

The NIST Fire Fighting Technology Group conducted a series of experiments in two structures of similar design located at the Delaware County ("DelCo") Emergency Services Training Center in Sharon Hill, Pennsylvania [181]. Three propane burners were used to provide the fire source for all experiments, and various sensors were used to collect gas temperature, gas velocity, heat flux, and gas concentration measurements throughout the structure.

The single level structure was instrumented with five bare-bead thermocouple arrays and two gas sample inlet pipes at the locations shown in Fig. 3.8. Both floors of the two level structure were instrumented with three bare-bead thermocouple arrays and one gas sample inlet pipe at the locations shown in Fig. 3.9.

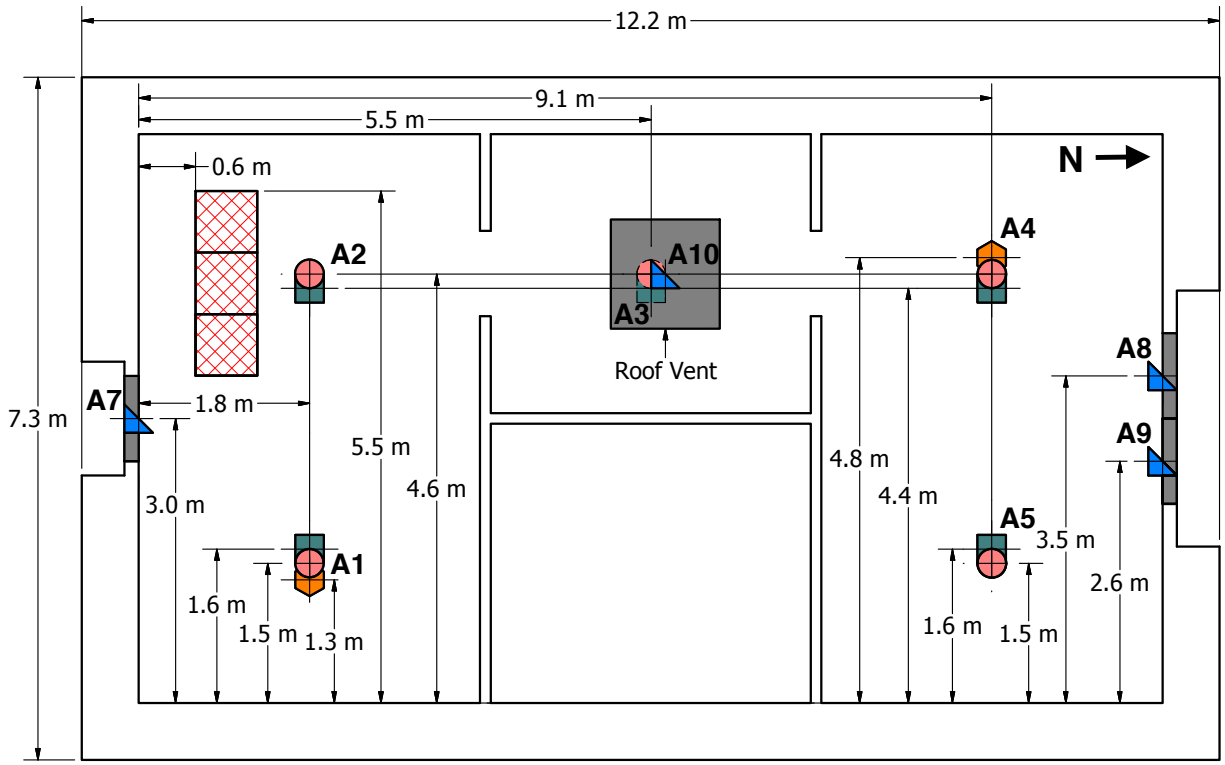

Figure 3.8: Instrumentation of the single level DelCo training structure. The thermocouple arrays are denoted by crossed circles and the gas sampling measurement locations are denoted by hexagons at locations A1 and A4. The burner is denoted by three cross-hatched squares.

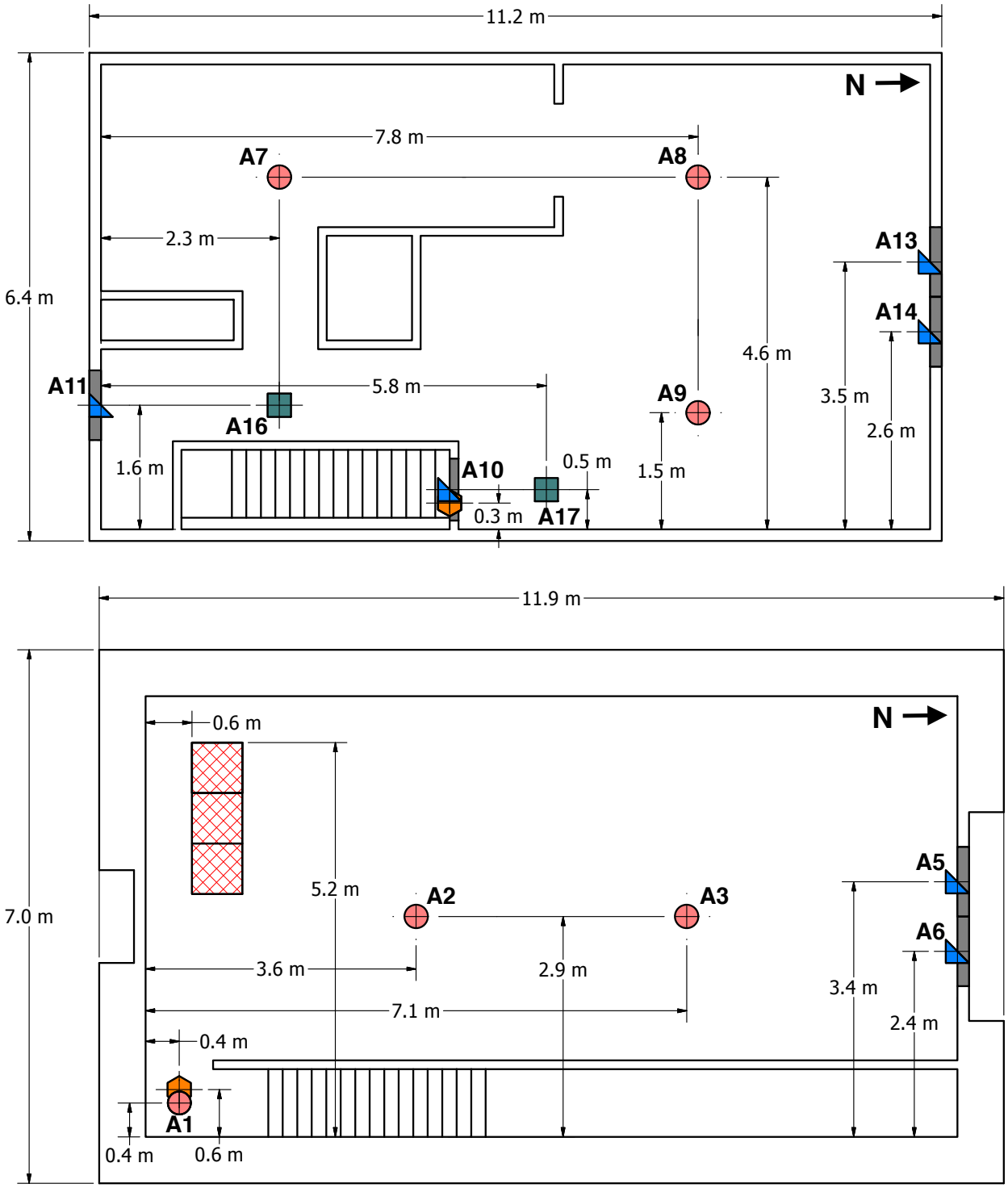

Figure 3.9: Instrumentation of the second floor (top) and first floor (bottom) of the two level DelCo training structure. The thermocouple arrays are denoted by crossed circles and the gas sampling measurement locations are denoted by hexagons at locations A1 and A10. The burner is denoted by three cross-hatched squares.

3.18 DoJ/HAI Pool Fire Experiments

The U.S. Department of Justice sponsored a series of liquid pool fire experiments performed by Hughes Associates, Inc. [182]. Hundreds of experiments were performed, involving six different liquid fuels, eight different substrates, a variety of pan sizes and pool depths. Of these, 44 experiments were chosen from the "Diked Fire Test Series," where gasoline or kerosene was burned within 0.3 m, 0.6 m, or 1.2 m square pans with liquid depths ranging from 1 mm to 20 mm. The substrate was either coated concrete or vinyl, each of which was designed to avoid liquid absorption. The vinyl flooring material had a nominal thickness of 1.2 mm applied to a 14.7 mm plywood using a vinyl adhesive. Table 14.13 provides a summary of the experimental parameters.

Modeling Notes

The test report for the experiments does not explicitly list the components of the gasoline or kerosene. Rather, distillation curves are provided showing that the initial and final boiling points for gasoline are 45 °C and 212 °C, and for kerosene 170 °C and 257 °C. The density of the gasoline is 742 kg/m^3 and the kerosene 798 kg/m^3. From various industry documents, it is postulated that the gasoline is a mixture of n-hexane (0.521 by mass), n-heptane (0.054), n-octane (0.063), n-decane (0.023), benzene (0.20), and toluene (0.139). The kerosene is assumed to be a mixture of iso-octane (0.04), n-nonane (0.19), iso-nonane (0.12), n-decane (0.15), iso-decane (0.11), n-undecane (0.09), and cis-decalin (0.30). The relavant properties of these liquids are listed in Table 3.26.

A few additional assumptions are made concerning the mixtures. First, that the absorption coefficient of all components is set to 150 m^{-1}, a value that is typical of heavy hydrocarbon liquids. Seconds, the thermal conductivity of the components is set to an artificially low value of 0.02 W/m/K to roughly account for the buoyancy that drives heated liquid upwards towards the surface. Third, all liquid components are assumed to evaporate into a single gas phase species, n-hexane. If this were not assumed, additional transport equations and combustion reactions would be needed for all liquid components.

Finally, to simulate the ignition of the liquid pools, an external flux is imposed at the surface for 10 s in the case of gasoline and 25 s for kerosene.

Table 3.9: Gasoline and kerosene components [183].

Fuel Component	Chemical Formula	W (g/mol)	ρ (kg/m^3)	c_p (kJ/(kg·K))	h_v (kJ/kg)	T_b °C
Benzene	C_6H_6	78.1	879	1.72	393	80.1
cis-Decalin	$C_{10}H_{18}$	138.3	897	1.68	297	195.8
iso-Decane	$C_{10}H_{22}$	142.3	728	2.20	269	167.0
n-Decane	$C_{10}H_{22}$	142.3	730	2.21	278	174.1
n-Heptane	C_7H_{16}	100.2	684	2.24	317	98.4
n-Hexane	C_6H_{14}	86.2	659	2.27	335	68.7
iso-Nonane	C_9H_{20}	128.3	708	2.34	350	143.0
n-Nonane	C_9H_{20}	128.3	718	2.22	290	150.8
iso-Octane	C_8H_{18}	114.2	692	2.09	270	99.2
n-Octane	C_8H_{18}	114.2	702	2.23	301	125.6
Toluene	C_7H_8	92.1	867	1.67	360	110.6
n-Undecane	$C_{11}H_{24}$	156.3	740	2.21	268	195.9

3.19 Droplet Evaporation

Five sets of experiments have been selected for validation of the evaporation of liquid droplets.

Fujita, Kurose, and Komori Experiments

Fujita, Kurose, and Komori performed a series of experiments that suspended a water drop in a heated, vertical wind tunnel [184]. Four experiments were modeled with relative humidity values of 0 % and 30 % and droplet Reynolds numbers of 60 and 150 (approximately 0.8 m/s and 2.0 m/s). Droplet size and surface temperature were recorded as functions of time.

Gavin Experiments

Gavin performed two experiments of a single water drop falling in dry air [185]. The test apparatus was a vertical wind tunnel. A drop was injected into the wind tunnel and the vertical air stream velocity was changed over time to maintain the drop at a constant elevation in the wind tunnel. The first droplet was 769 μm with an initial temperature of 23.0 °C. The second droplet was 557 μm with an initial temperature of 24.3 °C.

Kolaitis and Founti Experiments

Kolaitis and Founti measured the diameter and temperature of suspended liquid fuel droplets in a heated air stream [186]. Four experiments were chosen: a 1.26 mm droplet of ethanol at an initial temperature of 34.2 °C in 94 °C quiescent air, a 1.13 mm droplet of decane at an initial temperature of 73.8 °C in 94 °C quiescent air, a 1.15 mm droplet of heptane at an initial temperature of 49.0 °C in 94 °C quiescent air, and a 1.42 mm droplet of heptane at an initial temperature of 15.5 °C in 94 °C air at 0.146 m/s.

Maqua, Castanet, and Lemoine Experiments

Maqua, Castanet, and Lemoine measured the temperature of falling droplets of ethanol and acetone mixtures in a heated plume [187]. Because the temperature and velocity of the plume was not well-characterized, only the experiments involving a droplet falling in quiescent air were modeled. As FDS does not currently have a sub-model for the evaporation of a multi-component fuel, only the experiments for a pure ethanol droplet (140 μm) and a pure acetone droplet (140 μm) were modeled. The initial droplet temperature in both experiments was 45 °C in 20 °C air.

Taflin Experiments

Taflin measured the diameter of suspended water droplets in dry air [188]. One droplet was initially 43.9 μm and the other was 56.6 μm.

3.20 Edinburgh Vegetation Drag

Mueller et al. [189] characterized the pressure drop through beds of randomly oriented pine needles and used the results to parameterize a drag model following the form of the Forchheimer equation. They then measured the development of velocity profiles within and above these pine needle beds, using a hotwire anemometer, and compared the results to FDS predictions using the parameterized model. Fuel beds with

bulk densities of 20 kg/m^3, 40 kg/m^3, and 60 kg/m^3 were tested, with inlet velocities in the range of 0.5-2.0 m/s. A condensed version of the comparison is reproduced in this guide, which serves to test the ability of the model to represent the general features of flow in sparse multiphase media.

Modeling Notes

In the experiment, the test section extended 400 mm beyond the vegetation layer. This extent of the domain is reproduced in the simulations in order to avoid possible influence of the downstream boundary condition. The upstream boundary condition is set using the measurements located at $x = -75$ mm, which allows for the reproduction of a slight non-uniformity in the flowfield. Due to difficulties in compacting the high bulk density case, the fuel layer is set to extend to 55 mm in the 60 kg/m^3 simulations.

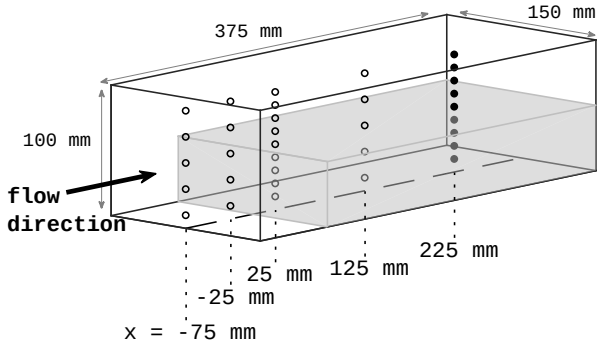

Figure 3.10: Geometry of the wind tunnel test section for the Edinburgh Vegetation Drag experiments. Vegetation filled the lower half of the 150 mm x 100 mm test section, starting from $x = 0$ mm. Circles indicate the locations of velocity measurements, with the filled circles corresponding to those used for comparison in this guide.

3.21 FAA Cargo Compartments

The U.S. Federal Aviation Administration (FAA) has sponsored experiments and modeling of smoke transport within aircraft storage compartments [190, 191]. Two types of compartments were used; one from a Boeing 707 and one from a McDonnell Douglas DC-10. The 707 compartment was 6.7 m in length, 3.2 m in width, and 1.4 m in height. The DC-10 compartment was 14 m in length, 4.4 m in width, and 1.7 m in height. The fire for all experiments was fueled by a 0.1 m by 0.1 m tray of plastic resin producing a peak HRR of 5 kW [192]. The long walls of the compartments were barrel-shaped to conform to the shape of the aircraft fuselage. The fire was placed in different locations, and measurements of gas and ceiling temperature, heat flux, gas concentration, and smoke obscuration were made at a variety of locations, mostly near the ceiling.

3.22 FAA Polymers

As part of their efforts to characterize the burning behavior of commonly used plastics, the U.S. Federal Aviation Administration (FAA) conducted measurements of the thermal properties of charring and non-charring polymers with the specific purpose of providing input data for numerical pyrolysis models [193, 194]. The study aimed to determine whether a one-dimensional conduction/reaction model could be used as

a practical tool for prediction and/or extrapolation of the results of fire calorimetry tests. The non-charring polymers included poly(methyl methacrylate) (PMMA), high-impact polystyrene (HIPS), and high density polyethylene (HDPE). The charring polymers included polycarbonate (PC) and polyvinyl chloride (PVC).

3.23 Fleury Heat Flux Measurements

Rob Fleury, a master's degree student at the University of Canterbury in Christchurch, New Zealand, measured the heat flux from a variety of propane fires [195]. The objective of the work was to evaluate a variety of empirical heat flux calculation methods. For the measurements, heat flux gauges were mounted on moveable dollies that were placed in front of, and to the side of, burners with dimensions of 0.3 m by 0.3 m (1:1 burner), 0.6 m by 0.3 m (2:1 burner), and 0.9 m by 0.3 m (3:1 burner). The heat release rates were set to 100 kW, 150 kW, 200 kW, 250 kW, and 300 kW. The gauges were mounted at heights of 0 m, 0.5 m, 1.0 m, and 1.5 m relative to the top edge of the burner.

3.24 FM Burner Experiments

A series of gas burner experiments was conducted by Zeng and Wang at FM Global in which the co-flow air stream was gradually diluted with nitrogen until flame extinction was achieved [196]. Numerical simulations were subsequently performed by Ren et al. [197]. In the experiments, a cylindrical, water-cooled steel burner (15.2 cm O.D., 13.7 cm I.D.) was placed near the floor of a 1.22 m by 1.22 m by 1.83 m tall compartment. Four fuels were used: ethylene (C_2H_4), methane (CH_4), propane (C_3H_8), and propylene (C_3H_6). The heat release rate in each experiment was 10 kW with a 1 kW ring of pilot burners to stabilize the flame. At the start of each experiment, air was pumped through the floor at a rate sufficient to supply the fire with approximately 10 times the stoichiometric requirement. Subsequently, nitrogen was slowly added to the air stream until the fire was extinguished.

In the same enclosure and using the same burner, Ren et. al [198] made high-frequency mean and rms temperature measurements along six radial profiles above a 15 kW ethylene fire. Soot measurements were made at similar locations. The co-flow air stream at the floor was set to 20.9 %, 16.8 %, and 15.2 % oxygen volume fraction. Additional experiments were performed at 19 %, 17 %, and 15 % oxygen in which global radiation measurements were made, including total radiative fraction and the vertical distribution of radiative emission.

Modeling Notes

The FDS simulations of the 10 kW ethylene, methane, propane and propylene fires are run for 65 s, in which time the oxygen concentration in the co-flow stream is ramped down linearly from 21 % to 8 %. The volume flow of the co-flow stream has been increased tenfold compared to the experiments to prevent a downwash of ambient air into the sealed compartment. The 15 kW ethylene fire simulations at the various fixed oxygen levels are performed for 20 s. For these simulations, the oxygen volume fraction is specified directly, as is the co-flow stream.

The combustion and extinction are modeled using a two-step reaction scheme. In the first step, fuel is converted to CO, soot, and water vapor, and in the second step, the CO and soot are oxidized to form CO_2. Both reactions are fast, but the oxidation step follows the first reaction in serial. That is, in a given time step, all available oxygen first converts fuel to CO and Soot, assumed to be $C_{0.9}H_{0.1}$. Any leftover oxygen is then used to oxidize existing CO and Soot. There are two assumptions. First, it is assumed that 3/5 of the carbon in the fuel molecule is converted to CO, and 2/5 to Soot in the first reaction step. Second, the post-flame

yields of Soot and CO are set to 0.043 and 0.013, respectively, based on Tewarson's measurements reported in the SFPE Handbook [135].

Under the assumption that Air contains 383 ppm CO_2 and water vapor corresponding to 40 % humidity, the full two-step reaction scheme for ethylene is written in terms of "lumped" species as follows:

$$\underbrace{(C_2H_4)}_{\text{Fuel}} + 7.60\ \underbrace{(0.208\,O_2 + 0.783\,N_2 + 0.0004\,CO_2 + 0.009\,H_2O)}_{\text{Air}} \longrightarrow 10.07\ \underbrace{(0.119\,CO + 0.201\,H_2O + 0.088\,\text{Soot} + 0.591\,N_2 + 0.0003\,CO_2)}_{\text{Products 1}} \quad (3.1)$$

$$(\text{Products 1}) + 0.63\ (\text{Air}) \longrightarrow 1.49\ \underbrace{(0.0009\,CO + 0.0073\,\text{Soot} + 0.126\,CO_2 + 0.141\,H_2O + 0.725\,N_2)}_{\text{Products 2}} \quad (3.2)$$

For each of the four fuels simulated, it has been assumed that 3/5 of the carbon in the fuel molecule is converted to CO in the first step. However, there are only detailed measurements of radiative emission and soot volume fraction for ethylene. Thus, it is not clear how the carbon is distributed between the soot and CO in the early stages. For lighter sooting fuels like methane, the fraction of carbon allocated to CO approaches unity.

The radiative fraction has been predicted rather than specified in all simulations.

3.25 FM/FPRF Data Center Experiments

The Fire Protection Research Foundation funded a series of large scale tests of smoke detection in high airflow data centers as part of a research project on behalf of the NFPA 75 and NFPA 76 Technical Committees [199]. The tests consisted of a data center mockup that was 4.9 m high, 4.9 m wide, and 7.3 m deep. The mockup was divided into a 0.9 m tall subfloor with air supplied via a natural vent opening on one short wall, a 0.9 m tall ceiling plenum with air removed via a mechanical vent opening on one short wall, two 2 m tall by 0.6 m wide by 5.3 m long enclosed cold aisles located along the outer walls, and a 3.1 m tall hot aisle. Flow from the subfloor to the cold aisles occurred through grated floor tiles, flow from the cold aisles to the hot aisle was through two rows of empty equipment cabinets with perforated metal doors, and flow from the hot aisle to the ceiling plenum was through perforated metal ceiling tiles.

Two groups of tests were performed. The first group of tests used a sonic anemometer to map the flow field in the facility for a flow of 78 air changes per hour (ACH) and 265 ACH. Additional measurements were made of the pressure drops through the floor and ceiling tiles. The second group of tests measured smoke detection response to a variety of detectors from a range of typical smoke sources plus propylene (used for its ease of characterization and repeatability).

The FDS model of the facility makes use of the screen drag model for Lagrangian particles to model the pressure losses through the various metal meshes and grates present in the mockup. The FDS model also uses the specified leakage location model to model leakage through the seams of floor and ceiling tiles. The actual leakage area was not measured during the test. Instead the area was estimated using the reduction in the FM measured pressure drop from to the manufacturer's reported pressure drop to compute a leakage flow. A description of the process used to create the FDS model and the test uncertainties can be found in a companion report documenting modeling of the tests with FDS 6.0.0 [200].

3.26 FM Parallel Panel Experiments

Patricia Beaulieu of Worcester Polytechnic Institute made heat flux measurements within a set of vertical parallel panels as part of a cooperative research program between Worcester Polytechnic Institute and FM

Global (Factory Mutual) [201]. The experimental apparatus consisted of two vertical parallel panels, 2.4 m high and 0.6 m wide, with a sand burner at the base. The objective of the project was to measure the flame spread rate over various composite wall lining materials, but there were also experiments conducted with inert walls for the purpose of measuring the heat flux from fires fueled by propane and propylene at heat release rates of 30 kW, 60 kW, and 100 kW. A sketch of the apparatus is shown in Fig. 3.11.

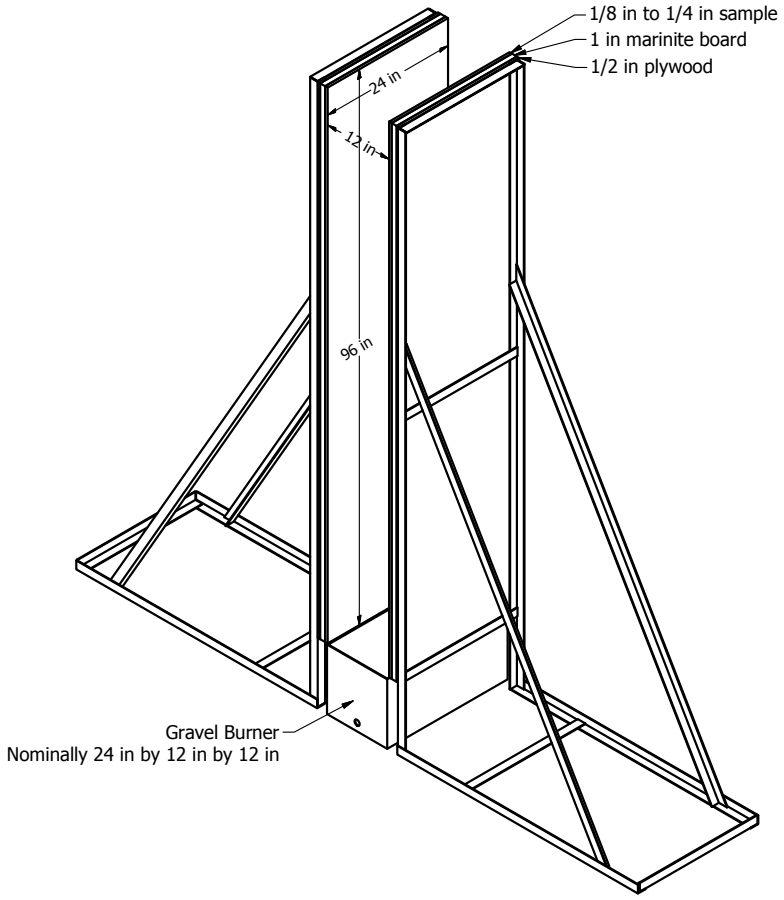

Figure 3.11: Sketch of the FM parallel panel apparatus.

3.27 FM/SNL Experiments

The Factory Mutual and Sandia National Laboratories (FM/SNL) test series consists of 25 compartment fire experiments conducted in 1985 for the U.S. Nuclear Regulatory Commission (NRC) by Factory Mutual Research Corporation (FMRC), under the direction of Sandia National Laboratories (SNL) [202, 203]. The primary purpose of these experiments was to provide data with which to validate computer models for various types of compartments typical of nuclear power plants. The experiments were conducted in an enclosure measuring approximately 18 m long by 12 m wide by 6 m high, constructed at the FMRC fire test facility in Rhode Island. A drawing is included in Fig. 3.12. All of the experiments included forced ventilation to simulate typical power plant conditions. Six of the experiments were conducted with a full-scale control room mock-up in place. Parameters varied during the experiments included fire intensity,

enclosure ventilation rate, and fire location. Only data from nineteen experiments (Tests 1-17, 21, and 22) is used in the current study. In these experiments, the fires were fueled by a propylene gas burner, and heptane and methanol liquid pools. In the experiments not selected, the heat release was not reported and could not be estimated with confidence. Table 3.10 lists the test parameters.

The following information was provided by the test director, Steve Nowlen of Sandia National Laboratory. In particular, Tests 4, 5, and 21 were given extra attention.

Heat Release Rate: The HRR was determined using oxygen consumption calorimetry in the exhaust stack with a correction applied for the carbon dioxide in the upper layer of the compartment. The uncertainty of the fuel mass flow was not documented. Several tests selected for this study had the same target peak heat release rate of 516 kW following a 4 min "t-squared" growth profile. The test report contains time histories of the measured HRR, for which the average, sustained HRR following the ramp up for Tests 4, 5, and 21 have been estimated as 510 kW, 480 kW, and 470 kW, respectively. Once reached, the peak HRR was maintained essentially constant during a steady-burn period of 6 min in Tests 4 and 5, and 16 min in Test 21. Note that in Test 21, Nowlen reports a "significant" loss of effluent from the exhaust hood that could lead to an under-estimate of the HRR towards the end of the experiment.

Radiative Fraction: The radiative fraction was not measured during the experiment, but in this study it is assumed to equal 0.35, which is typical for a smoky hydrocarbons. It was further assumed that the radiative fraction was about the same in Test 21 as the other tests, as fuel burning must have occurred outside of the electrical cabinet in which the burner was placed.

Measurements: Four types of measurements were conducted during the FM/SNL test series that are used in the current model evaluation study, including the HGL temperature and depth, and the ceiling jet and plume temperatures. Aspirated thermocouples (TCs) were used to make all of the temperature measurements. Generally, aspirated TC measurements are preferable to bare-bead TC measurements, as systematic radiative exchange measurement error is reduced.

HGL Depth and Temperature: Data from all of the vertical TC trees were used when reducing the HGL height and temperature. For the majority of the tests, Sectors 1, 2, and 3 were used, all weighted evenly. For Tests 21 and 22, Sectors 1 and 3 were used, evenly weighted. Sector 2 was partially within the fire plume.

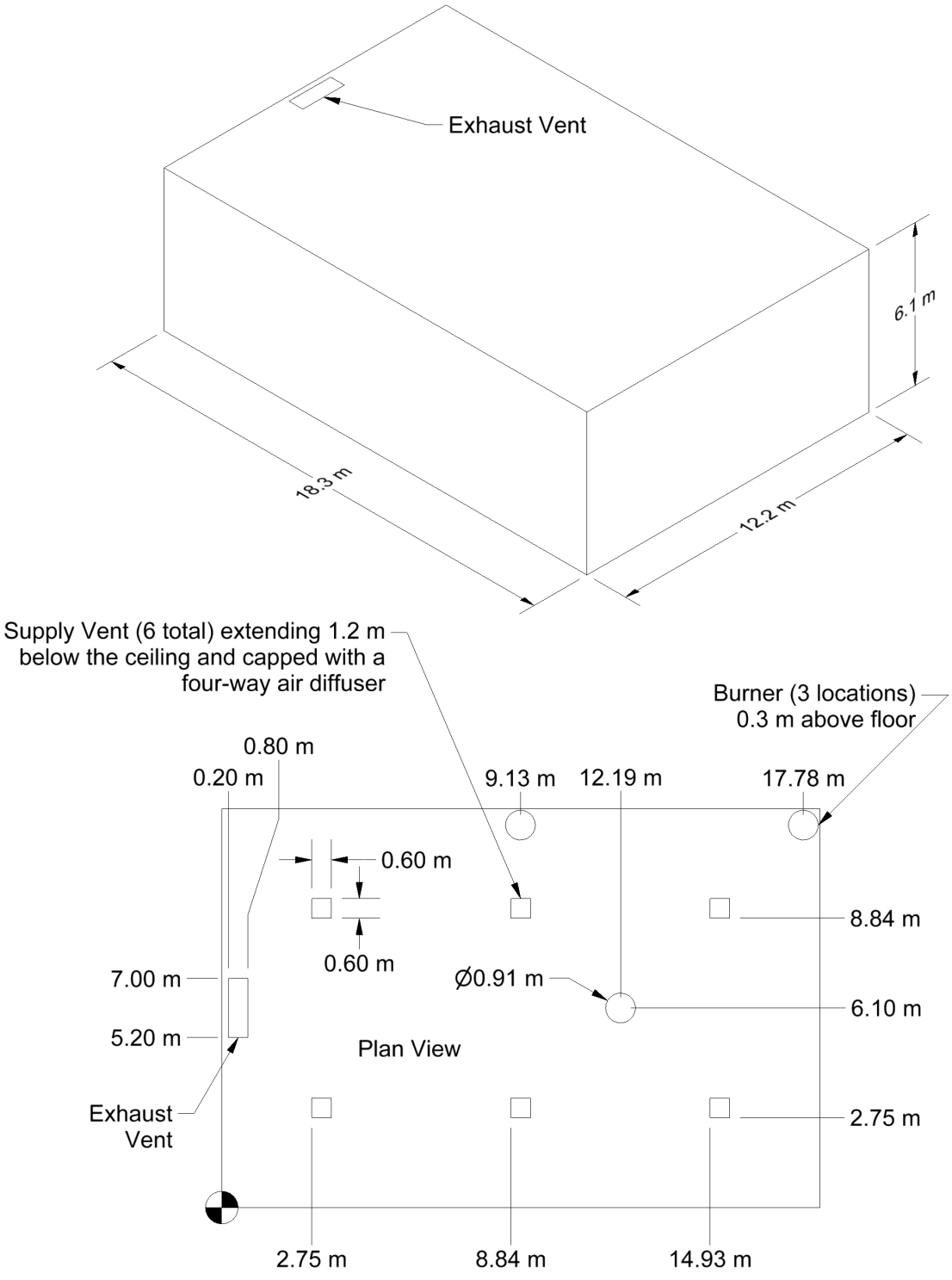

Figure 3.12: Geometry of the FM/SNL Experiments.

Table 3.10: Summary of FM/SNL Experiments. ACH stands for Air Changes per Hour.

Test No.	Fuel Type	Nominal Peak HRR (kW)	Fire Position	Ventilation Rate (ACH)	Room Configuration
1	Propylene Burner	516	Center	10	Empty
2	Propylene Burner	516	Center	10	Empty
3	Propylene Burner	2000	Center	10	Empty
4	Propylene Burner	516	Center	1	Empty
5	Propylene Burner	516	Center	10	Empty
6	Heptane Pool	500	Wall	1	Empty
7	Propylene Burner	516	Center	1	Empty
8	Propylene Burner	1000	Center	1	Empty
9	Propylene Burner	1000	Center	8	Empty
10	Heptane Pool	1000	Wall	4.4	Empty
11	Methanol Pool	500	Wall	4.4	Empty
12	Heptane Pool	2000	Wall	4.4	Empty
13	Heptane Pool	2000	Wall	8	Empty
14	Methanol Pool	500	Wall	1	Empty
15	Heptane Pool	1000	Wall	1	Empty
16	Heptane Pool	500	Corner	1	Empty
17	Heptane Pool	500	Corner	10	Empty
21	Propylene Burner	500	Cabinet	1	Furnished
22	Propylene Burner	1000	Cabinet	1	Furnished

3.28 FM Vertical Wall Flame Experiments

A series of experiments was conducted by FM Global [204] in which turbulent flames were generated by flowing various gases through a vertical, water-cooled burner, 1.32 m tall and 0.38 m wide, with 0.152 m side walls. Measurements of soot depth, temperature, radiative heat flux, and radiance were made at various heights.

3.29 Frankman Vegetation Experiments

Experiments were performed by Frankman et al. [205] at Brigham Young University in 2010 in which small wood shavings and pine needles were exposed to various levels of heat flux from a ceramic burner. Small thermocouples recorded the steady state temperatures. The fuel elements were positioned 15 cm, 25 cm, 35 cm, and 45 cm from the 23 cm by 15 cm rectangular ceramic burner with a radiative heat flux of approximately 37 kW/m^2. The fuel elements were suspended by a wire with a horizontal orientation. The hydraulic diameters of the small excelsior, large excelsior and Ponderosa pine samples were reported to be 0.44 mm, 1.29 mm, and 0.70 mm, respectively.

Modeling Notes

These calculations are performed with a relatively crude grid because typical wildland fire simulations cannot employ fine grids. A free convection correlation for horizontal cylinders is employed for the convective

heat transfer coefficient of the fuel samples. Cylindrical Lagrangian particles are used to represent the fuels with diameters equal to the reported hydraulic diameters. The burner is modeled as a hot plate with a radiative heat flux of 37 kW/m^2. Nominal values of 0.1 W/m/K, 1 kJ/kg/K, and 450 kg/m^3 are assumed for the thermal conductivity, specific heat, and density of the vegetation. The emissivity is assumed to be 1. The results are relatively insensitive to the thermal properties because the final temperatures are largely determined via the balance of radiation heat flux on to and convective heat flux off of the fuel samples. The temperature rise of all samples does not exceed 100 °C.

3.30 Hamins Gas Burner Experiments

Anthony Hamins of NIST measured the heat flux at various points around gas burner fires [36]. Three different sized circular burners were used, with diameters of 0.10 m, 0.38 m, and 1.0 m. Three different gases were used, acetylene, methane, and propane. The heat release rates ranged from 2 kW to 200 kW, and values of $\dot{Q}^*$ ranged from 0.04 to 10.6.

3.31 Harrison Spill Plumes

Roger Harrison, a student at the University of Canterbury, New Zealand, performed a series of one-tenth scale experiments to characterize thermal spill plume entrainment [206, 207, 208, 209]. The dimensions of the fire compartment were 1 m by 1 m by 0.5 m high. The height of the compartment opening was equal to the height of the compartment. The width of the opening was varied from 0.2 m to 1 m. A 0.3 m balcony was attached to the top of the compartment opening. The balcony extended 0.5 m beyond each side of the fire compartment. The heat release rate of the fire varied from 5 kW to 15 kW. The plume entrainment rate was measured at different heights by varying the exhaust rate of gases from a hood above the compartment. Two different test configurations were used to model both detached and adhered spill plumes. A diagram of the test structure is displayed in Figure 3.13.

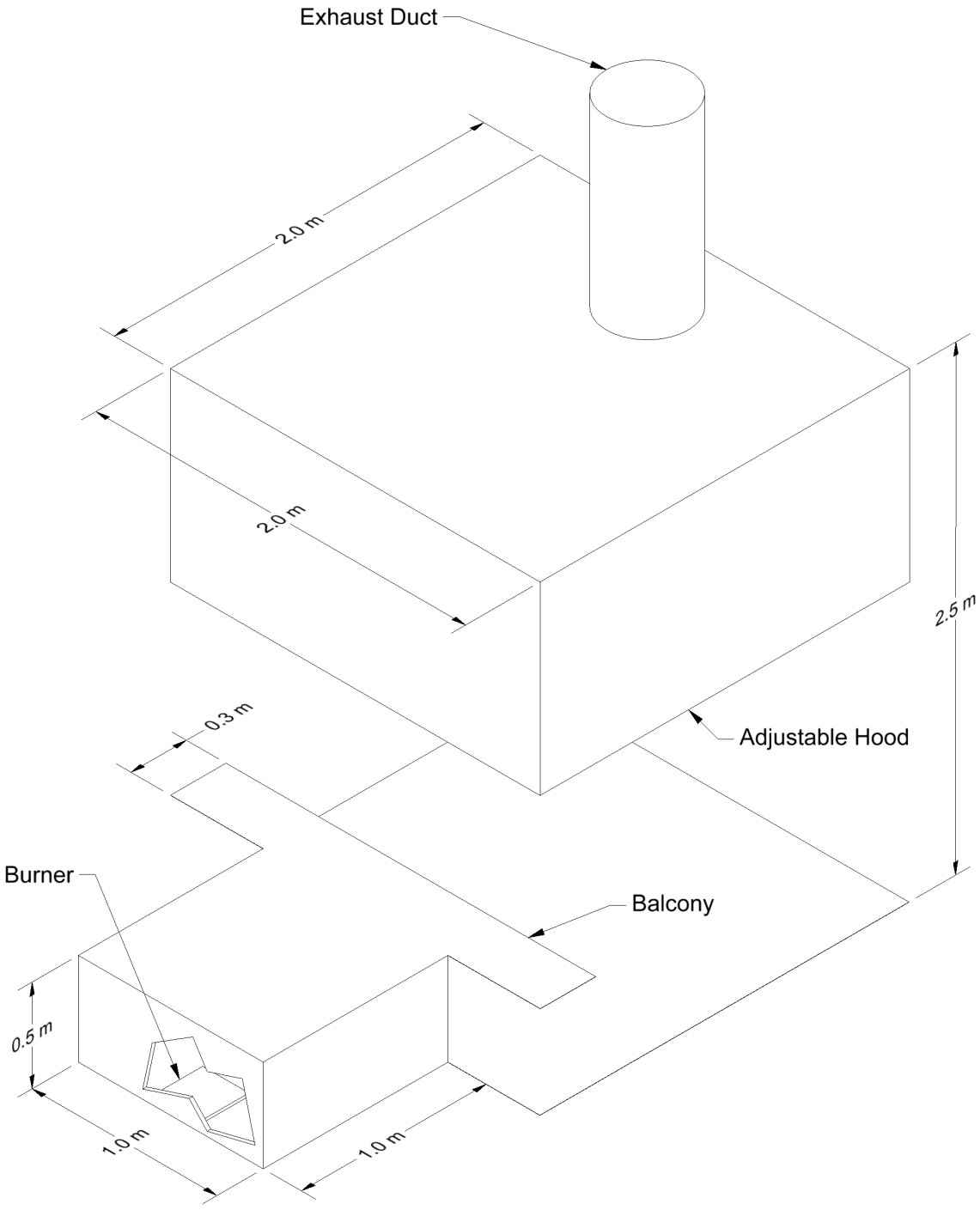

Figure 3.13: Geometry of the Harrison Spill Plumes Experiments.

3.32 Heskestad Flame Height Correlation

A widely used experimental correlation for flame height is given by the expression [210, 25]:

$$\frac{L_\mathrm{f}}{D} = 3.7\,(\dot{Q}^*)^{2/5} - 1.02 \quad ; \quad \dot{Q}^* = \frac{\dot{Q}}{\rho_\infty\, c_p\, T_\infty \sqrt{g}\, D^{5/2}} \tag{3.3}$$

where ρ_∞, c_p, and T_∞ are the ambient density, specific heat, and temperature. $\dot{Q}^*$ is a non-dimensional quantity that relates the fire's heat release rate, $\dot{Q}$, with the diameter of its base, D. The greater the value of Q^*, the higher the flame height relative to its base diameter.

3.33 Insulation Material Fire Resistance Tests

Paudel et al. [211] studied small-scale fire resistance tests for 30 different types of stone wool insulation varying in density, thickness, and organic content. During each test, a 60 cm square sample of insulation covered by a 1 mm thick steel plate was mounted to the opening of a small combustion chamber. Thus, one side of the sample was exposed to ambient (T_∞) conditions, and the other side was attached to the steel plate whose temperature followed the ISO 834 standard fire curve,

$$T_\mathrm{h}(t) = T_\infty + 345 \log_{10}(8t + 1) \tag{3.4}$$

with time, t, in minutes and exposure temperature, T_h, in °C. The temperature measurements were made using K-type thermocouples covered with 30 mm square inorganic insulating pads. The pads were attached to the back side of the sample using heat-resistant glue or pins.

Modeling Notes

The numerical simulation is explained in Ref. [211]. Because detailed kinetic properties of the material are currently not available, the chemical decomposition parameters (A, E_a and n) were optimized based on the cold-side measured temperatures. Unlike in Ref. [211], the optimized values in the simulation are constant, $A = 0.0028$ s^{-1}, $E_\mathrm{a} = 21700$ J/mol, and $n = 0.71$. The optimization used a Monte Carlo method of 1000 Latin hypercube samples, where the sampling range was 0.001 to 1000 s^{-1} for A, 1×10^4 to 1×10^5 J/mol for E_a, and 0.1 to 1 for n.

3.34 LEMTA Spray Test for Radiation Attenuation

Lechene et al. [212] measured the attenuation of thermal radiation passing through a water spray using a heat flux gauge. The radiation was produced by a 30 cm by 35 cm heat panel whose emission was close to a black body at 500 °C. The horizontal distance from the radiation panel to the spray nozzle was 1.5 m and to the measurement point 3 m. The heat flux gauge was positioned at the line passing through the center of the panel. Seven nozzles were arranged in a row, 10 cm apart. They were positioned 1.5 m high. The heat panel was translated vertically during the experiment, the distance between the panel upper edge and the nozzle row varying between 20 cm and 100 cm. The attenuation of radiation is defined as previously described for the BRE Spray experiments. The purpose of the simulations is to compare the measured and simulated attenuation of radiation at different heights. The water mist nozzle has been characterized by Lechene by measuring the spray angles and the water flow rate. The droplet size is set by using a PDPA measurement in a single position, 20 cm below the injection point.

3.35 LLNL Enclosure Experiments

Sixty-four compartment experiments were conducted at Lawrence Livermore National Laboratory (LLNL) in 1986 to study the effects of ventilation on enclosure fires [213]. These experiments are the basis of the Foote, Pagni, Alvares compartment temperature correlation [214].

The test enclosure was 6 m long, 4 m wide, and 4.5 m high (Fig. 3.14) with a methane rock burner in the center of the space positioned at various elevations. For most of the experiments the burner was placed on the floor. The fires varied in size, $\dot{Q}$, from 50 kW to 400 kW. The burner was 0.57 m in diameter and 0.23 m height. A single door was closed and sealed for most experiments, and air was pulled through the compartment at rates, $\dot{m}$, varying from 100 g/s to 500 g/s. In some tests the enclosure included a plenum space, where make-up air could be injected from above or below. The test matrix is listed in Table 3.11.

Modeling Notes

The LLNL Enclosure is modeled using a single mesh spanning the interior of the test compartment. The heat release rate of the methane burner and the thermal properties of the walls, ceiling and floor are specified based on information provided in the test report.

The test report of the LLNL Enclosure experiments lists the mass flow rate, $\dot{m}$, through the exhaust duct during the experiment. This mass flow rate is specified explicitly in the model. The make-up air into the compartment is supplied by an inlet duct and compartment leakage, both of which are modeled. The inlet duct is modeled as a 7 m long, 30 cm diameter circular duct with a loss coefficient of 25.6. The leakage area is then calculated based on the reported compartment under or over-pressures, Δp, during the experiment. The leak area is computed based on the following formulae:

$$\frac{\dot{m}}{\rho} = A_{\mathrm{L}} \sqrt{\frac{2\,|\Delta p|}{\rho}} \quad ; \quad A_{\mathrm{L}} = A_{\mathrm{L,ref}} \left(\frac{|\Delta p|}{|\Delta p_{\mathrm{ref}}|} \right)^{n-0.5} \tag{3.5}$$

The reference leakage area, $A_{\mathrm{L,ref}}$, is estimated to be 0.0033 m^2, $n = 0.6311$, $\Delta p_{\mathrm{ref}} = 50$ Pa.

In some of the experiments, the fire was reported to have self-extinguished, in which case the model employs the relatively simple Mowrer extinction model along with the one-step fast chemistry model of combustion. The Mowrer model predicts local flame extinction when the oxygen concentration within a grid cell is less than that required to raise the cell temperature to the critical flame temperature, which is 1507 °C for methane [136].

Table 3.11: Summary of LLNL Enclosure Experiments.

Test No.	Room Config.	h_0 m	$\dot{Q}$ kW	$\dot{m}$ g/s	T_∞ °C	t_{end} s	Test No.	Room Config.	h_0 m	$\dot{Q}$ kW	$\dot{m}$ g/s	T_∞ °C	t_{end} s
1	TL	0	200	0	23	560	33	PH	0	100	200	23	5100
2	TL	0	200	0	27	545	34	PH	0	100	300	34	4280
3	TL	0	400	0	27	300	35	PH	0	100	400	22	4110
4	TL	0	300	0	24	385	36	PH	0	100	500	29	4060
5	TL	0	50	0	28	2770	37	PH	0	200	100	20	520
6	TL	0	100	0	29	1295	38	PH	0	200	300	29	4100
7	TL	0	100	0	35	1240	39	PH	0	250	100	18	430
8	TL	0	200	0	35	555	40	PH	0	200	400	28	4290
9	TL	0	200	500	33	4220	41	PH	0	150	100	20	970
10	TL	0	200	100	28	6050	42	PHE	2	200	180	30	5120
11	TL	0	200	200	18	4780	43	PHE	2	200	0	32	570
12	TL	0	200	300	21	5440	44	PHE	1	200	180	19	2670
13	TL	0	200	400	28	5150	45	PHE	1	200	0	30	810
14	TL	0	200	400	28	5090	46	PHE	0.6	200	180	19	960
15	TL	0	100	300	24	4070	47	PHE	0.6	200	0	19	730
16	TL	0	200	300	21	6560+	48	PHE	0.3	200	0	21	520
17	PL	0	200	500	26	3980	49	PHE	0.3	200	180	26	970
18	PL	0	200	400	21	4840	50	PHE	1	200	180	21	4730
19	PL	0	200	300	18	5110	51	PNE	1	200	NAT	33	3360
20	PL	0	200	200	16	6570	52	PN	0	200	NAT	23	4680
21	PL	0	200	100	23	6570	53	PHGS	0	200	185	33	1540
22	PH	0	200	190	30	950	54	PHGS	0	200	215	21	4180
23	PH	0	200	215	28	4260	55	PN	0	100	NAT	31	4120
24	PH	0	200	205	26	1480	56	PHGW	0	200	190	20	1240
25	PH	0	200	205	25	2050	57	PHGW	0	200	215	29	5390
26	PH	0	200	500	24	4100	58	PHX	0	200	190	18	4090
27	PH	0	200	100	23	540	59	PHXE	1	200	190	24	4090
28	PH	0	150	150	31	1870	60	PN	0	400	NAT	22	2680
29	PH	0	250	250	28	1520	61	TN	0	200	NAT	31	2730
30	PH	0	250	300	34	4080	62	TN	0	400	NAT	22	2660
31	PH	0	250	500	36	4160	63	TN	0	50	NAT	28	3240
32	PH	0	100	100	33	4110	64	TN	0	100	NAT	17	3570

T	full compartment	N	natural ventilation (door open)
P	plenum configuration	X	3 ft extension on inlet opening
L	low inlet duct	GS	grate on inlet, north/south configuration
H	high inlet duct	GW	grate on inlet, east/west configuration
E	elevated fire, h_0		

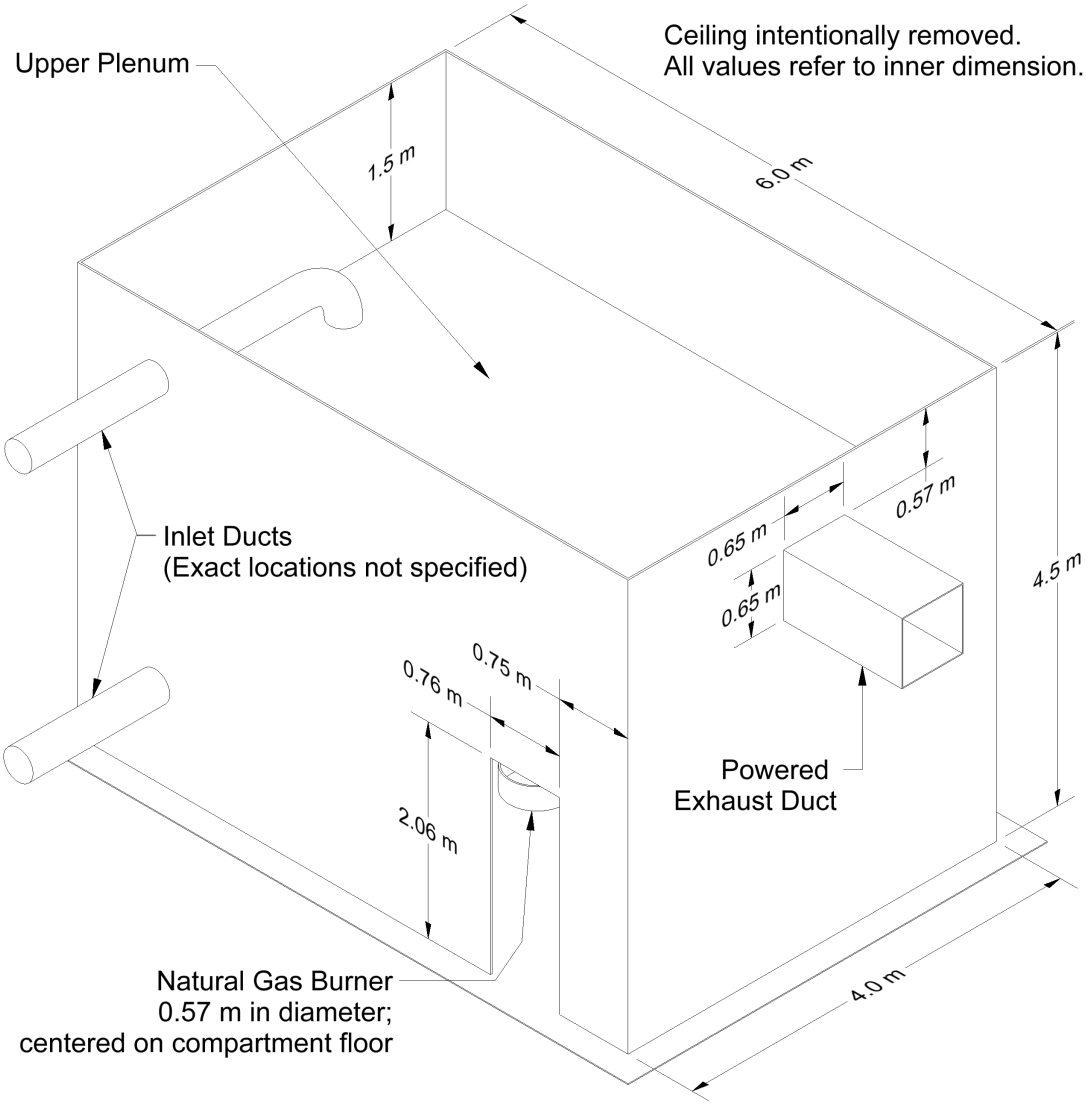

Figure 3.14: Geometry of the LLNL Enclosure Experiments.

3.36 LNG Dispersion Experiments

In 2006, the Fire Protection Research Foundation (FPRF) undertook a research project for the National Fire Protection Association (NFPA) Liquefied Natural Gas (LNG) Technical Committee to develop tools for evaluating LNG dispersion models. The work was carried out by the Health and Safety Laboratory (HSL), a directorate of the UK Health and Safety Executive (HSE). HSL developed the LNG Model Evaluation Protocol (MEP), which contained a structure for complete evaluation of LNG dispersion models [215]. The experiments are described in Ref. [216].

Modeling Notes

The simulations of liquefied natural gas (LNG) dispersion experiments that are described in this report were originally designed by Jeffrey Engerer and Anay Luketa of Sandia National Laboratories on behalf of the Pipeline and Hazardous Materials Safety Administration of the U.S. Department of Transportation.

Parameters for the LNG dispersion experiments are given in Table 3.12. In some cases, values of the Monin-Obukhov parameters are taken directly from the test reports. However, for some of the experiments, these parameters were not derived using the same similarity functions as those presented above, in which case the parameters have been recomputed to best fit the measured velocity and temperature profiles. In the table, u_* is the friction velocity, $\kappa = 0.41$ is the Von Kármán constant, z_0 is the *aerodynamic* roughness length, θ_* is the scaling potential temperature, θ_0 is the ground level potential temperature, L is the Monin-Obukhov length, and the similarity functions are those proposed by Dyer [217] and discussed in the report of the Falcon field experiments [218].

In the experiments, a fixed mass, m, of LNG was spilled onto water, forming a pool of increasing radius. For modeling purposes, it is assumed that the mass flux of natural gas from the circular pool is fixed at $\dot{m}''_{\max} = 0.167$ kg/(m^2·s), and the temperature of the gas is -162 °C, as suggested in the testing protocols. The diameter of the pool, D, is calculated using the assumed mass flux per unit area, the reported mass of LNG, m, and the spill duration, Δt.

$$D = \sqrt{\frac{4\,m}{\pi\,\dot{m}''_{\max}\,\Delta t}} \tag{3.6}$$

The values of D are given in Table 3.12.

Table 3.12: Summary of LNG Dispersion Experiments.

Series	Burro				Coyote			Falcon			Maplin Sands		
Number	3	7	8	9	3	5	6	1	3	4	27	34	35
Parameters supplied by test reports													
Fuel Mass, m (kg)	14712	17289	12453	10730	6532	12676	10139	28074	21435	18984	3714	2094	3658
Spill Duration, Δt (s)	167	174	107	79	65	98	82	131	154	301	160	95	135
p_0 (mbar)	948	940	941	940	936	939	942	908.9	900.8	906.3	—	—	—
T_0 (°C)	34.5	33.8	32.9	35.4	39.6	29.3	24.1	32.2	35.0	30.8	14.9	15.2	16.1
RH (%)	5.2	7.4	4.5	14.4	11.3	22.1	22.8	—	4.0	12.0	53	90	77
Computed parameters													
L (m)	-9.49	-111	16.2	-142	-8.56	-33.2	82.5	4.96	-422	69.4	-14.4	-75.5	-81.2
u_* (m/s)	0.255	0.372	0.074	0.252	0.310	0.480	0.210	0.061	0.305	0.369	0.190	0.280	0.315
z_0 (m)	0.0002	0.0002	0.0002	0.0002	0.0002	0.0002	0.0002	0.008	0.008	0.008	0.0003‡	0.0003‡	0.0003‡
θ_* (K)	-0.532	-0.097	0.026	-0.035	-0.890	-0.520	0.039	0.058	-0.018	0.152	-0.180	-0.075	-0.088
$\dot{q}''$ (W/m^2)	-154	-41	2	-10	-314	-284	9	4	-5	58	-39	-24	-32
D (m)	25.9	27.5	29.9	32.2	27.7	31.4	30.6	19.5†	16.0†	10.8†	13.3	12.8	14.4

‡ The roughness length was changed to 0.00002 m to better match the measured velocity and temperature profiles

† The Falcon experiments involved 4 separated spills

3.37 Loughborough Jet Fire Experiments

Researchers at Loughborough University, UK, conducted a series of six large-scale, high pressure jet fire experiments using natural gas and natural gas/hydrogen mixtures at the GL Noble Denton Spadeadam Test Site in Cumbria, UK [219]. For each fuel, the gas was released horizontally at high pressure (approximately 60 bar) through 20 mm, 35 mm and 50 mm diameter holes at the end of a 15 cm diameter pipe. The jet fires engulfed a 0.9 m diameter, 16 m long pipe section perpendicular to the flow direction. Heat flux measurements were made at various locations on the pipe and further afield. A typical jet fire experiment at the facility is shown in Fig. 3.15.

Figure 3.15: Photograph of a jet fire experiment at the Spadeadam Test Site.

Table 3.13 lists the key parameters for the natural gas experiments which have been chosen for this study. Note that the direction of the jet was nominally to the east, parallel to the prevailing wind. The wind deviated slightly in each experiment, as indicated in the table.

Modeling Notes

FDS is a low Mach number code and cannot model directly the supersonic flow at the pipe orifice. Instead, cold (-160 °C) droplets with a median volumetric diameter of 1000 μm are injected wtih an initial velocity of 1000 m/s and spray angle of 10°. These droplets evaporate readily to form methane gas. No attempt is made to model the stand-off distance because there is no mechanism in FDS to account for flame suppression due to high shear.

Table 3.13: Summary of the Loughborough Jet Fire Experiments.

Test No.	Fuel Type	Hole Diam. (mm)	Dist. to Pipe (m)	Wind Dir. (°)	Wind Speed (m/s)	Mass Flow (kg/s)	Heat Rel. Rate (MW)	Flame Length (m)	Stand-Off Distance (m)	Rad. Frac. (%)
1	Nat. Gas	20	9.45	271	6.3	2.9	140	19.8	6.0	13.7
2	Nat. Gas	35	15.45	297	6.2	9.6	462	37.8	7.5	17.9
3	Nat. Gas	50	21.61	267	3.6	19.5	939	49.9	8.7	20.2

The grid resolution is 20 cm; thus, the circular pipe is modeled as a collection of 20 cm square rods with a cross section that is 0.8 m by 0.8 m, but with the corners removed. The velocity boundary condition is assumed to be free-slip because otherwise the polygonally-shaped obstruction would exert a fictitiously high drag force on the flow. The empirical heat transfer coefficient for the pipe is calculated using parameters appropriate for a cylindrical rather than a flat plate. The Nusselt number is taken as

$$\mathrm{Nu} = 0.027\,\mathrm{Re}^{0.805}\,\mathrm{Pr}^{1/3} \quad ; \quad \mathrm{Re} = \frac{\rho D \|\mathbf{u}_t\|}{\mu} \quad ; \quad \mathrm{Pr} = 0.7 \tag{3.7}$$

This correlation is appropriate for $40,000 < \mathrm{Re} < 400,000$ [220].

The values of radiative fraction in the model are based on the measured values reported in Table 3.13. To resolve the radiation field at the far-field radiometers, 600 angles are used in solving the radiation transport equation rather than the default 100. The radiation absorption coefficients are calculated by RadCal assuming a path length of 100 m rather than the default value of 0.1 m.

The wind profile is based on measurements made 10.85 m above the relatively flat terrain. The aerodynamic roughness length, z_0, is set to 0.03 m, appropriate for relatively flat grasslands, prairies, farms, etc. The Obukhov length, L, is set to 100,000 m, typical of a neutral atmosphere. Synthetic turbulence is generated at the upstream boundary of the computational domain, with a characteristic eddy length scale of 1 m and root-mean-square velocity fluctuation of 0.1 m/s.

Flame Length Results: Section 6.2.3

Heat Flux Results: Section 12.2.4

3.38 McCaffrey Plume Experiments

In 1979, at the National Bureau of Standards (now NIST), Bernard McCaffrey measured centerline temperature and velocity profiles above a porous, refractory burner. There were five distinct heat release rates, ranging from 14 kW to 57 kW. The fuel was natural gas (35 kJ/L [45 MJ/kg assuming 19 kg/kgmol as mole weight for natural gas]). The burner was square, 0.3 m on each side. The results of the experiments are reported in Reference [221]. Along the centerline of the burner, velocity and temperature were measured using bi-directional probes and thermocouples, respectively. The centerline data collapses when scaled by the Froude number as shown in Fig. 3.16. Radiant fraction measurements for natural gas were made in [222]. For convenience, we have extracted the data from that report for the heat release rates reported in [221]. See Table 3.14. The burner surface temperatures are extrapolated to the surface location from a least squares fit of of the temperature data below $z/Q^{2/5} = 0.05$ m$\cdot$kW$^{-2/5}$. The extrapolations for each power are shown in Fig. 3.17.

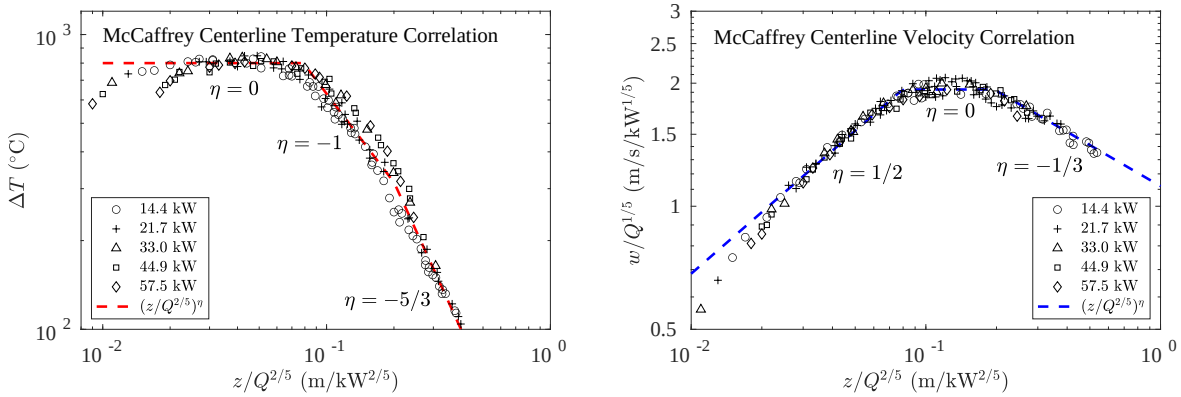

Figure 3.16: McCaffrey Plume Centerline Temperature and Velocity Correlations (dashed lines) and raw data (symbols).

Table 3.14: Summary of McCaffrey Plume Experiments, 1979.

Q (kW)	Q^*	D^* (m)	HRRPUA (kW/m^2)	χ_r	T_{surf} (°C)
14.4	0.270	0.178	160	0.17	750
21.7	0.407	0.209	241	0.21	716
33.0	0.618	0.248	367	0.25	630
44.9	0.841	0.280	499	0.27	608
57.5	1.07	0.309	639	0.27	534

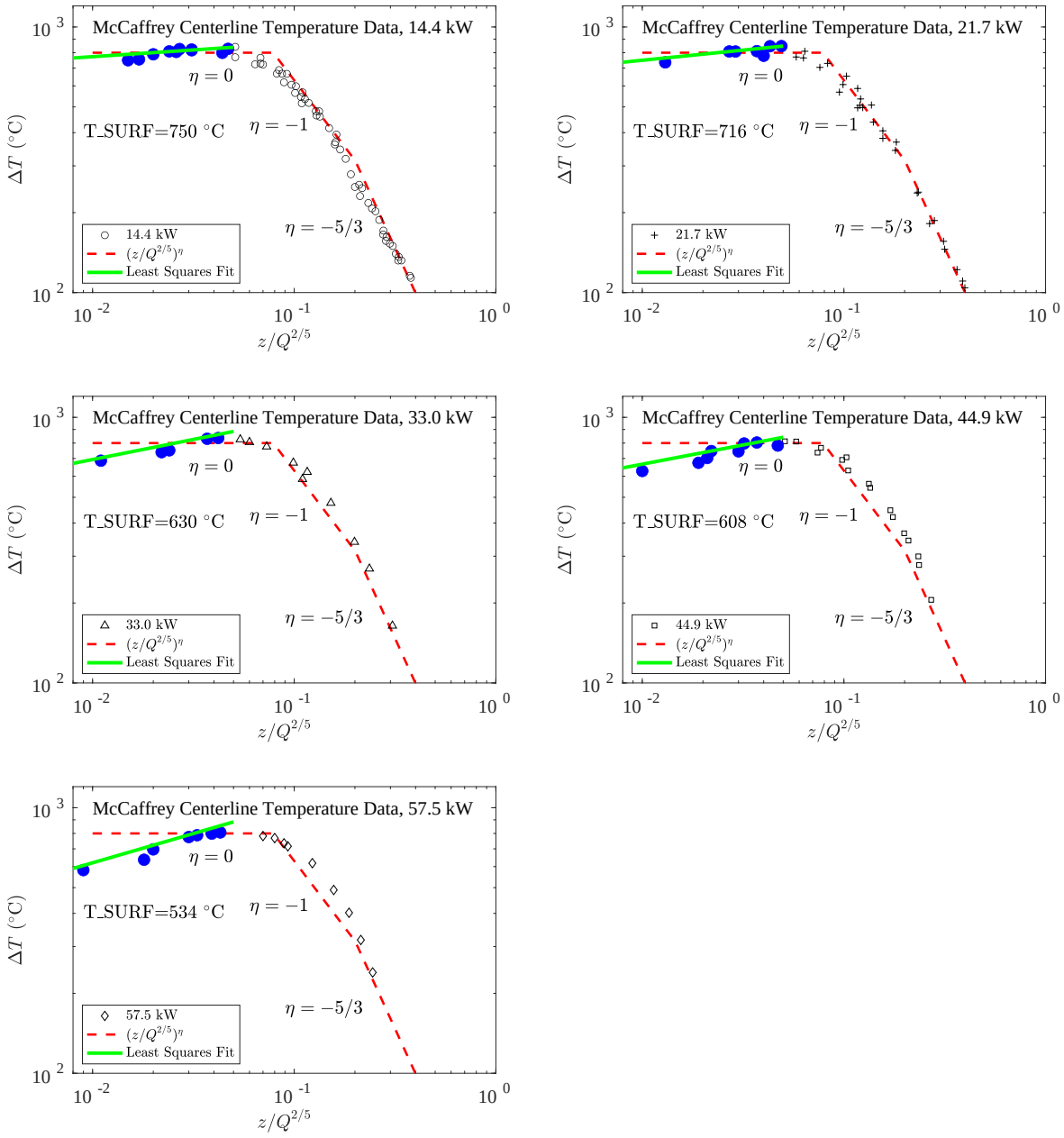

Figure 3.17: McCaffrey Plume Burner Surface Temperatures.

3.39 Montoir LNG Fires

In 1987, British Gas, British Petroleum, Shell, Elf Aquitaine, Total CFP, and Gaz de France conducted 35 m diameter LNG pool fire experiments [223]. The construction of the test facility was carried out by Gaz de France near the Montoir de Bretagne methane terminal. Three fire experiments were performed under different wind conditions. The Montoir site was selected because the ground is level and obstruction free. Wide angle radiation measurements were made at various locations around the fires, extending outwards approximately 300 m. A bund constructed of lightweight concrete and sand, approximately 1 m tall, surrounded the 35 m pool.

A summary of the key test parameters is given in Table 3.15. Note that results were compiled for specific time intervals during each experiment.

Table 3.15: Summary of the Montoir LNG Fire Experiments.

Test	Time Interval (s)	Burning Rate ($kg/m^2/s$)	Wind Direction (deg)	9 m Wind Speed (m/s)	Amb. Temp. (°C)	Rel. Hum. (%)	Atm. Pres. (mbar)
1	60-100 130-170	0.12 0.13	59 70	2.5 4.8	25	53	1022
2	35-50 65-85 100-130 165-185	0.14 0.15 0.16 0.15	268 263 260 257	6.8 9.8 10.3 9.1	21	54	1015
3	57-70 90-120 130-160	0.11 0.13 0.13	87 79 82	1.9 3.5 4.2	14	85	1009

Modeling Notes

The experiments are simulated using the specified fuel burning rates for the several time periods during each experiment. The fuel is assumed to be methane. The atmosphere is assumed to be unstable with an Obukhov length, $L = -350$, and the ground surface is roughly open with an assumed aerodynamic roughness, $z_0 = 0.1$ m. The relative humidity, ambient temperature and pressure, and wind speed at 9 m are specified in Table 3.15.

The radiative fraction is assumed to 0.14 based on field estimates and the radiative path length is assumed to be 300 m; that is, the effective absorption coefficients of the various gas mixtures are evaluated over a distance of 300 m. 600 solid angles, rather than the default 100, are used to solve the radiative transport equation. The soot yield is assumed to be 0.01.

Flame Height Results: Section 6.2.3

Flame Tilt Results: Section 6.3

Heat Flux Results: Section 12.2.5

3.40 NBS Multi-Room Experiments

The National Bureau of Standards (NBS, which is now called the National Institute of Standards and Technology, NIST) Multi-Room Experiments consisted of 45 fire tests representing 9 different sets of conditions were conducted in a three-room suite (see Fig. 3.18). The experiments were conducted in 1985 and are described in detail in Ref. [224]. The suite consisted of two relatively small rooms, connected via a relatively long corridor. The fire source, a gas burner, was located against the rear wall of one of the small compartments. Fire tests of 100 kW, 300 kW and 500 kW were conducted. For the current study, only three 100 kW fire experiments have been used, including Test 100A from Set 1, Test 100O from Set 2, and Test 100Z from Set 4. These tests were selected because they had been used in prior validation studies, and because these tests had the steadiest values of measured heat release rate during the steady-burn period.

Following is additional information provided by the test director, Richard Peacock of NIST:

Heat Release Rate: In the two tests for which the door was open, the HRR during the steady-burn period measured via oxygen consumption calorimetry was 110 kW with an uncertainty of about 15 %, consistent with the replicate measurements made during the experimental series and the uncertainty typical of oxygen consumption calorimetry. It was assumed that the closed door test (Test 100O) had the same HRR as the open door tests.

Radiative Fraction: Natural gas was used as the fuel in Test 100A. In Tests 100O and 100Z, acetylene was added to the natural gas to increase the smoke yield, and as a consequence, the radiative fraction increased. The radiative fraction of natural gas has been studied previously, whereas the radiative fraction of the acetylene/natural gas mixture has not been studied. The radiative fraction for the natural gas fire was assigned a value of 0.20, whereas a value of 0.30 was assigned for the natural gas/acetylene fires.

Measurements: Only two types of measurements conducted during the NBS test series were used in the evaluation considered here, because there was less confidence in the other measurements. The measurements considered here were the HGL temperature and depth, in which bare bead TCs were used to make these measurements. Single point measurements of temperature within the burn room were not used in the evaluation of plume or ceiling jet algorithms. This is because the geometry was not consistent in either case with the assumptions used in the model algorithms of plumes or jets. Specifically, the burner was mounted against a wall, and the room width-to-height ratio was less than that assumed by the various ceiling jet correlations.

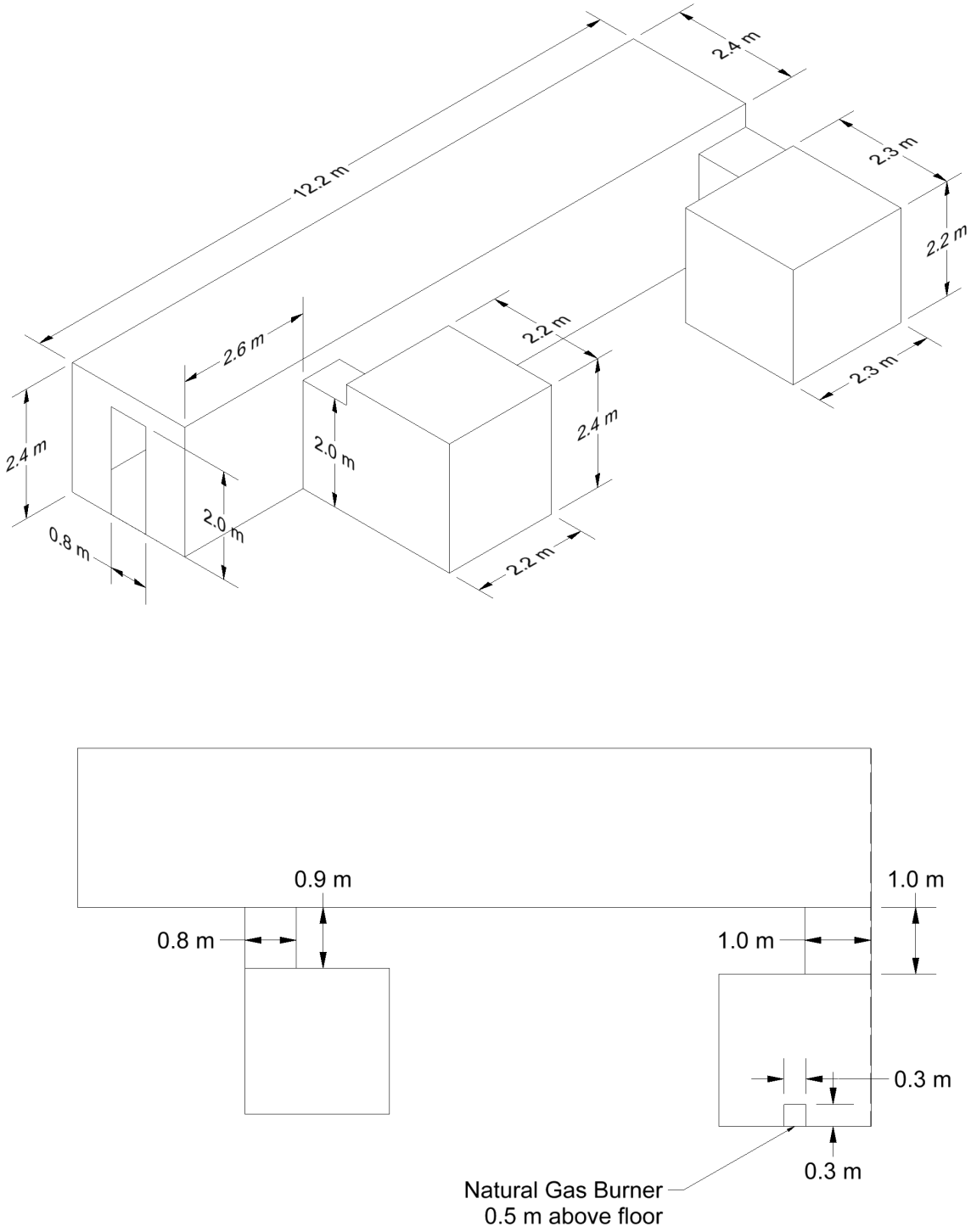

Figure 3.18: Geometry of the NBS Multi-Room Experiments.

3.41 NIST Composite Beam Experiments

A set of experiments was conducted in the Large Fire Laboratory at NIST to study the behavior of long-span steel-concrete composite floor beams designed and constructed following U.S. building codes and standards [225]. The composite beam consisted of a 12.8 m long W18×35 steel beam and an 16 cm thick lightweight concrete slab cast on top of 7.6 cm deep ribbed steel decking. Drawings of the compartment are shown in Figs. 3.19 through 3.21.

Simultaneous mechanical and fire loading was applied to the specimens. The measurements focused on evaluation of the characteristics of the fire loading, temperatures, and structural responses of the specimens to fires.

Modeling Notes

The simulations of the NIST Composite Beam experiments are performed with 5 cm grid cells and 32 meshes. The calculations are sped up by a factor of 10 using `TIME_SHRINK_FACTOR=10`, whereby a 60 min experiment is simulated in 6 min of real time because the heat release rate is held steady for most of the experiment. The specific heats of all solid materials are reduced by a factor of 10 automatically to account for the change in time scale.

Because these experiments involve a global equivalence ratio of approximately 1, the two-step simple chemistry model is used, where soot and CO are produced when the fire becomes under-ventilated.

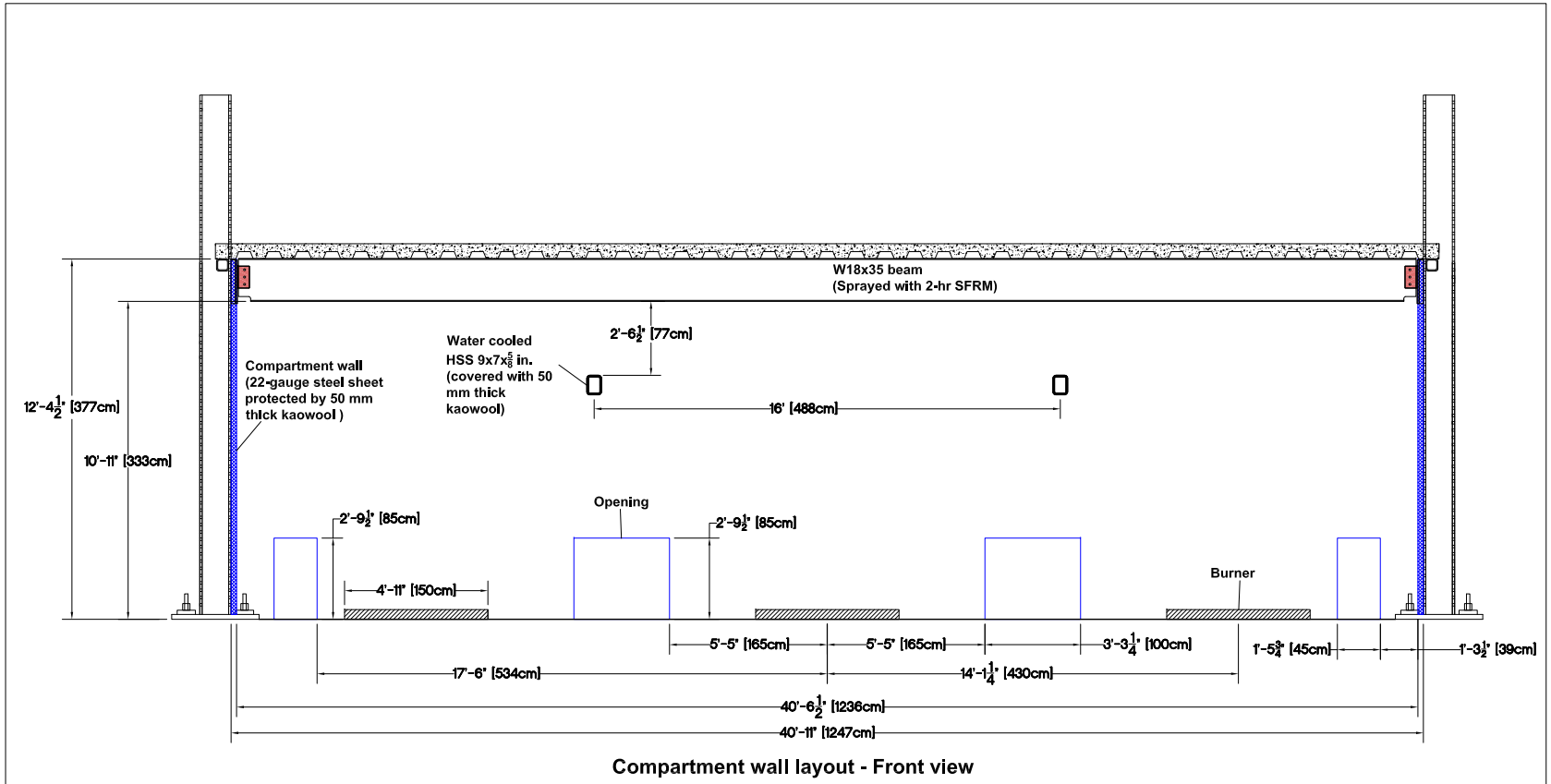

Figure 3.19: Elevation view of NIST Composite Beam experiments.

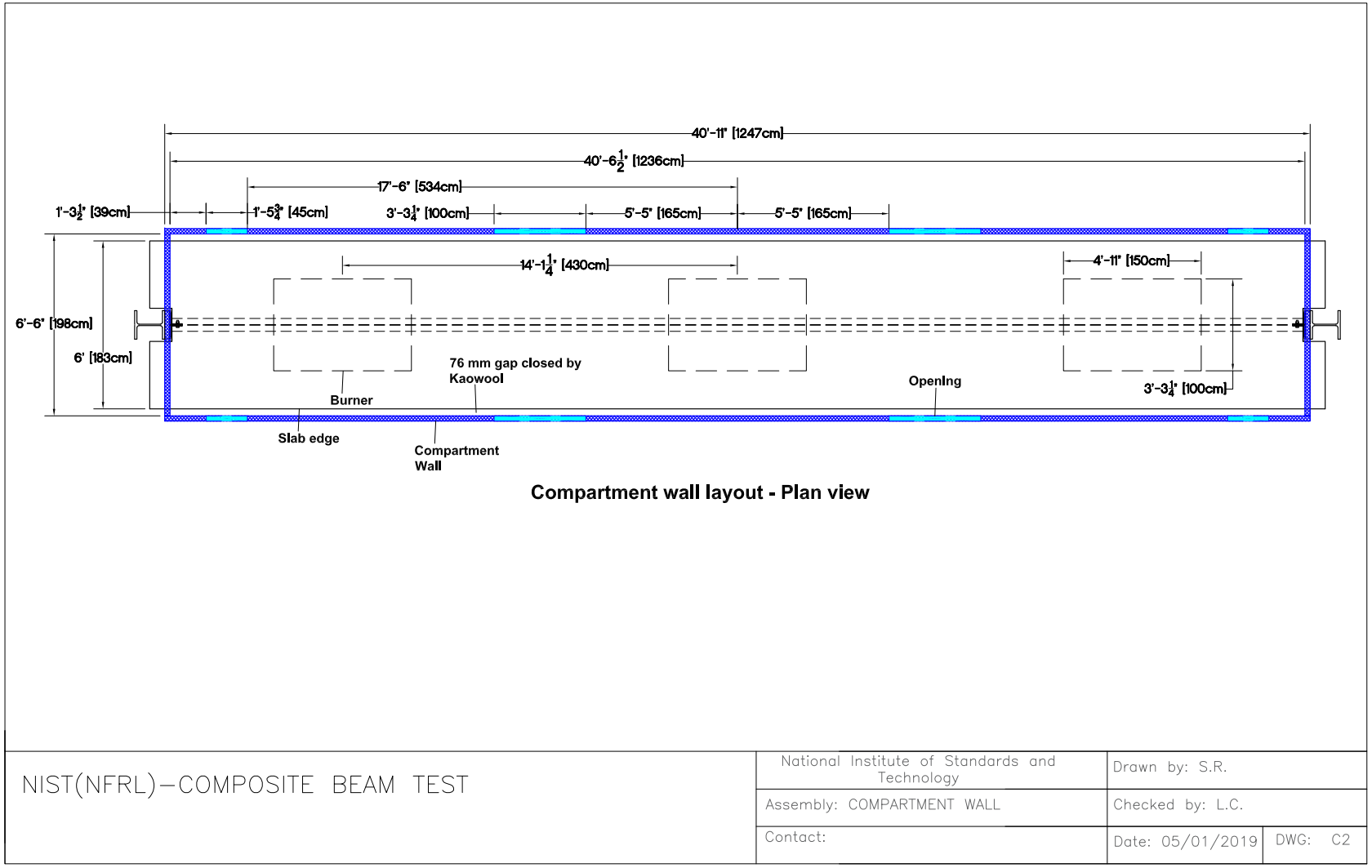

Figure 3.20: Plan view of NIST Composite Beam experiments.

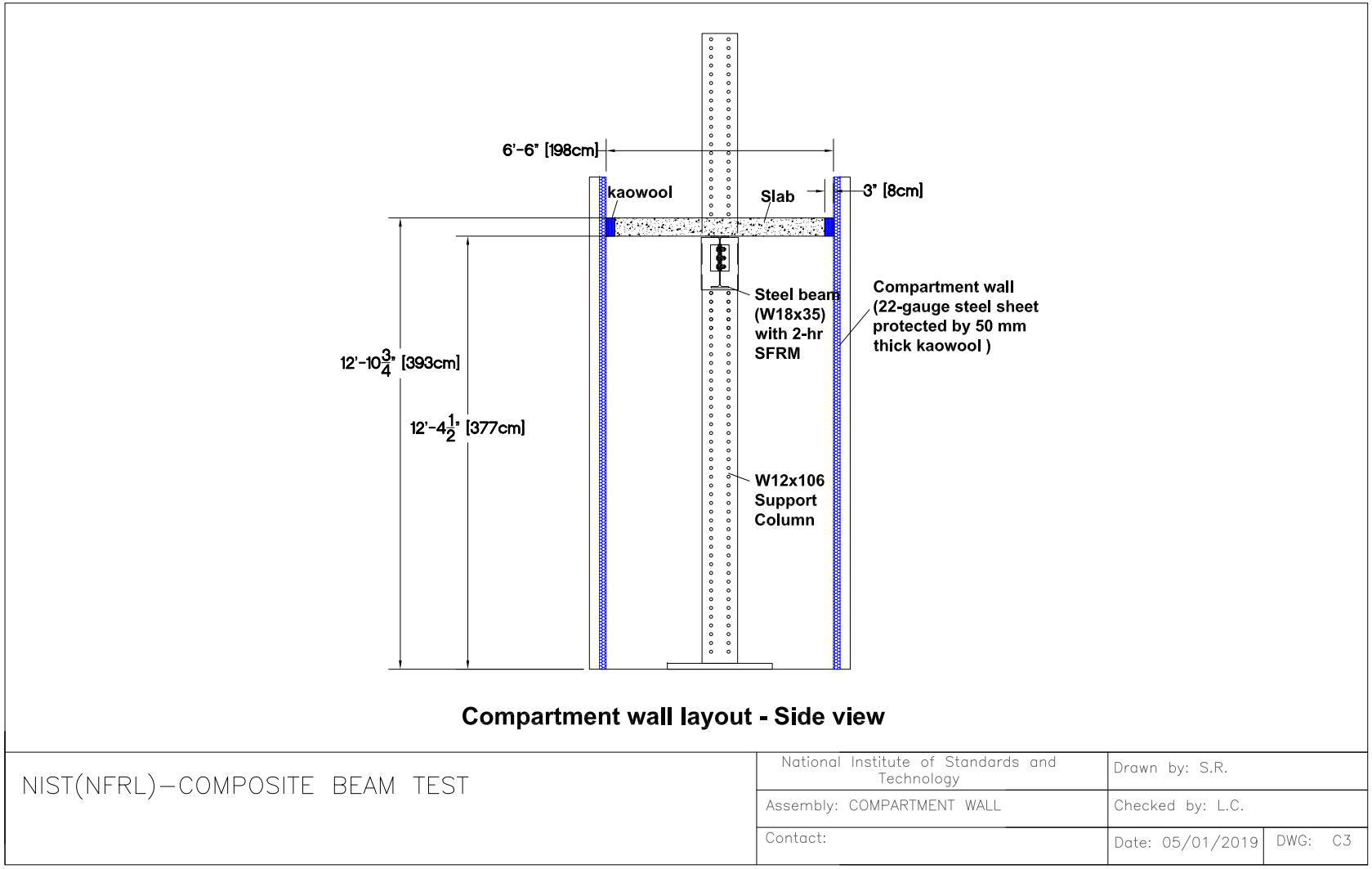

Figure 3.21: Side view of NIST Composite Beam experiments.

3.42 NIST E119 Compartment Experiments

In December 2018, three fire experiments were conducted in a compartment approximately 10.8 m wide, 7.0 m deep and 3.8 m high, constructed in the Large Fire Laboratory of NIST [226]. The experiments were designed to test different types of floor assemblies. Two experiments, designed as replicates, lasted 15 min, and the third lasted 75 min. Four natural gas burners generated a peak heat release rate of approximately 10 MW in the 75 min experiments. The measured average upper layer gas temperature was comparable with that prescribed in the ASTM E119 standard [227]. Drawings of the compartment are shown in Figs. 3.22 through 3.24.

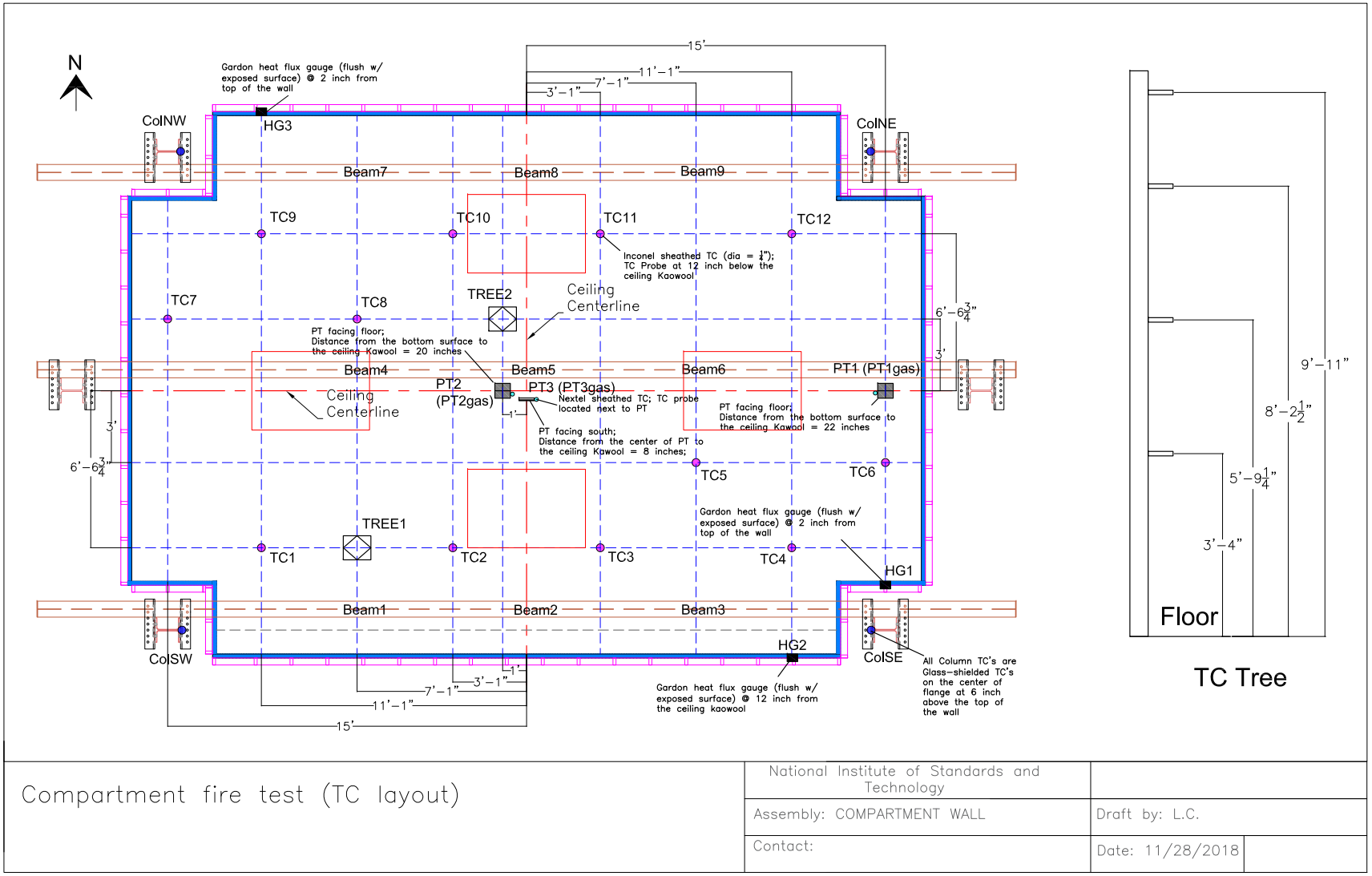

Compartment fire test (TC layout)	National Institute of Standards and Technology	
	Assembly: COMPARTMENT WALL	Draft by: L.C.
	Contact:	Date: 11/28/2018

Figure 3.22: Plan view of NIST E119 Compartment experiment.

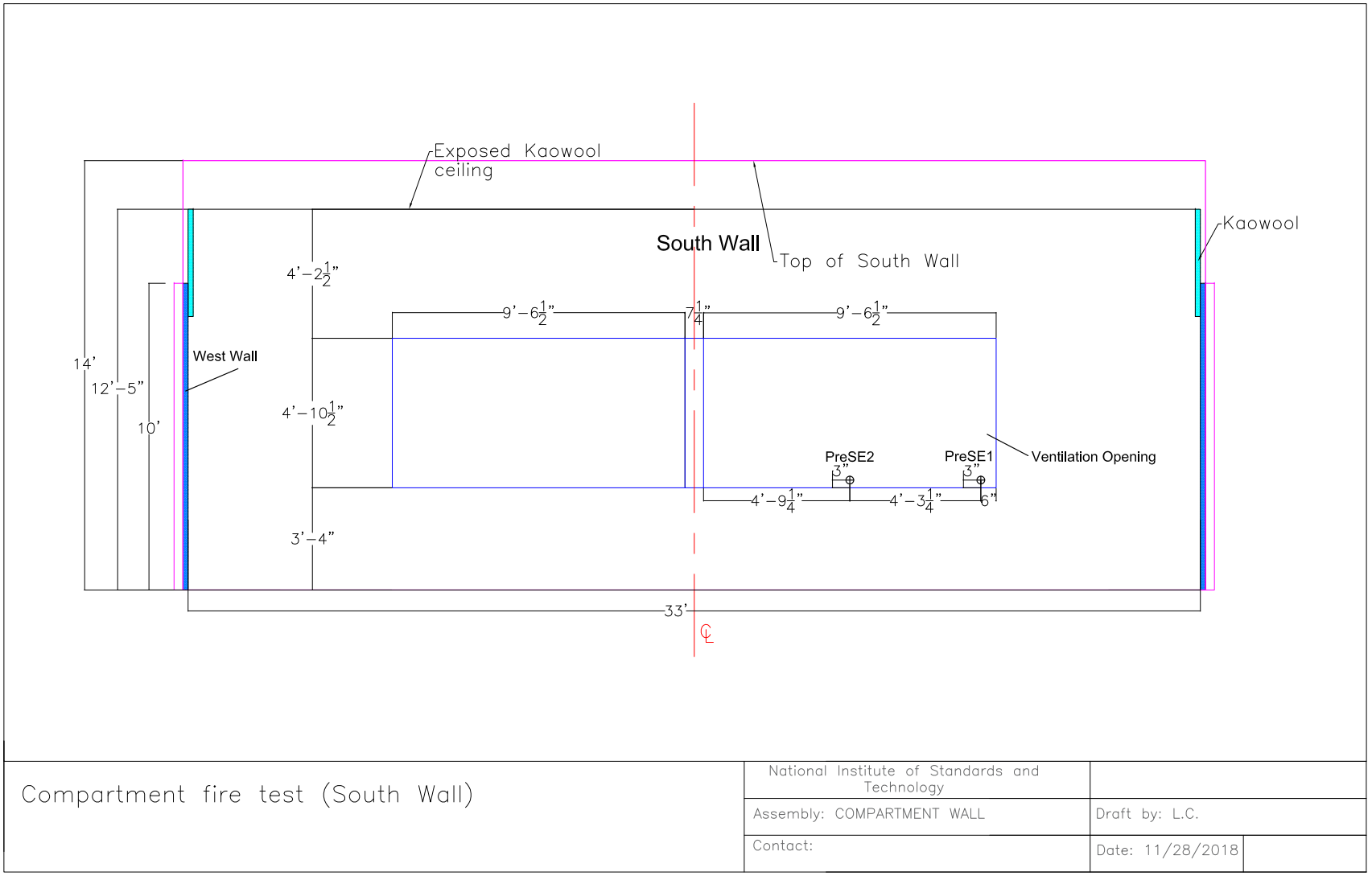

Figure 3.23: Elevation view of NIST E119 Compartment experiment.

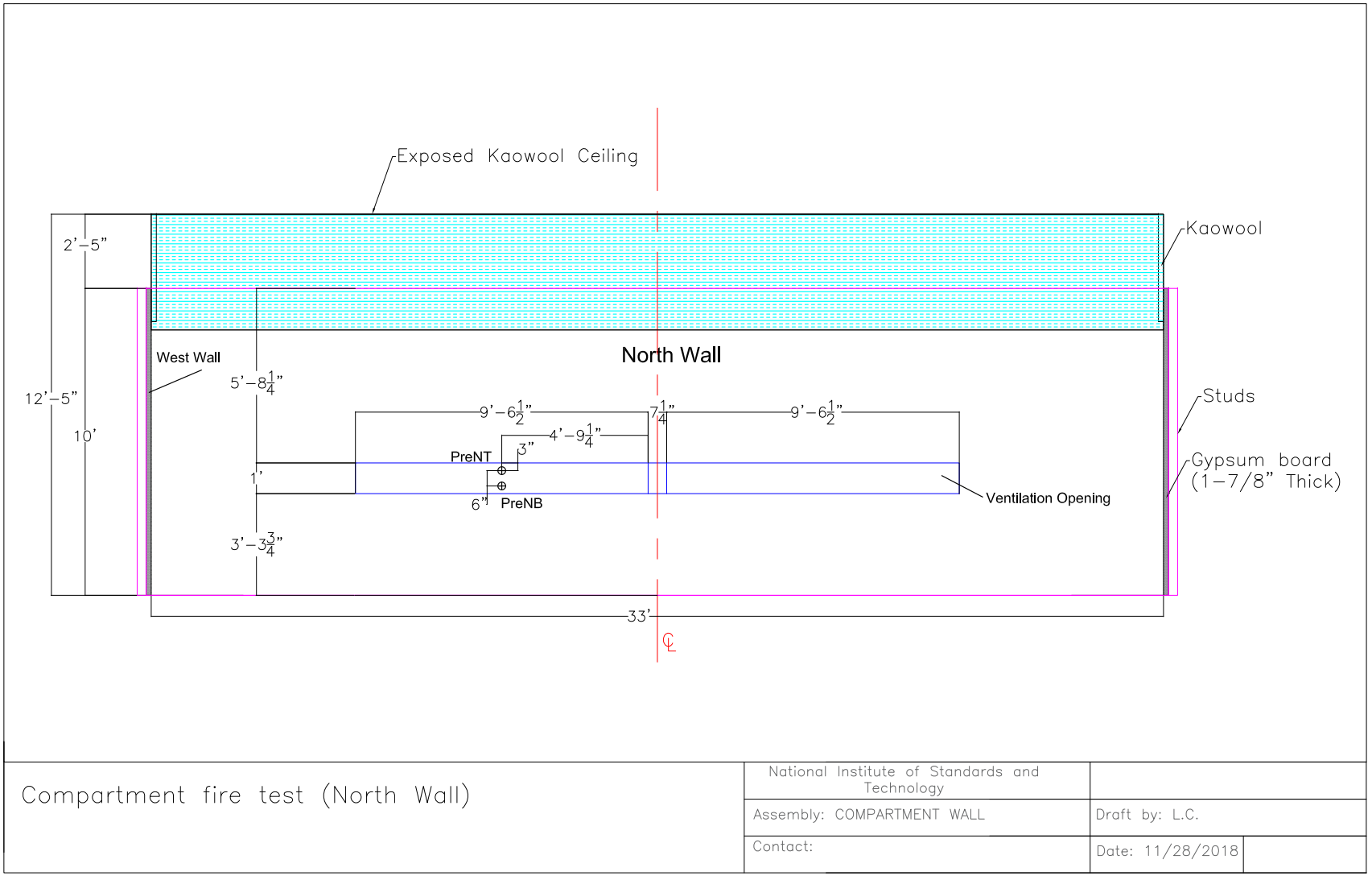

Figure 3.24: Elevation view of NIST E119 Compartment experiment.

3.43 NIST Douglas Firs

In 2009, Mell et al. measured the burning rate and heat fluxes from individual Douglas fir trees of various sizes and moisture contents [228]. Nine of the trees were approximately 2 m tall, and three were approximately 5 m tall. The results were presented as averages: the three 5 m trees had an average moisture content of 26 %, three of the 2 m trees had an average moisture content of 49 %, and the remaining six 2 m trees had a moisture content of 14 %. The 2 m trees were ignited with a natural gas ring burner with a diameter of 80 cm and a heat release rate of 30 kW. The trees with a moisture content of 14 % were exposed to the burner for 10 s and the 49 % trees were exposed for 30 s. The 5 m trees were exposed to a hexagonal burner with a span of 122 cm and HRR of 130 kW for 30 s.

Modeling Notes

The trees are modeled as a collection of cylindrical Lagrangian particles. Mell et al. [228] group the particles into three size classes. The pyrolysis model applied to the particles is based on TGA measurements of longleaf pine needles described in the FDS Verification Guide [229], chapter "Pyrolysis," Section "TGA for a Charring Sample (Needle_TGA)."

Measured properties of the trees are listed in Table 3.16, and assumed properties are listed in Table 3.17. These assumed properties are typically for wood or cellulosic fuels. The moisture is modeled as water. The vegetation is assumed to be composed primarily of cellulose. Reference [228] provides an estimate of the distribution of mass for the foliage, roundwood less than 3 mm in diameter, roundwood 3 mm to 6 mm, and roundwood 6 mm to 10 mm. For the 2 m trees, the distribution is approximately 64 %, 11 %, 10 %, and 15 %, respectively. For the 5 m trees, it is 60 %, 17 %, 12 %, and 11 %, respectively.

Table 3.16: Measured properties for the NIST Douglas Fir Experiments [228].

Property	Units	Case 1	Case 2	Case 3
Replicate Experiments	–	6	3	3
Avg. Crown Height	m	1.9	1.9	4.2
Avg. Base Height	m	0.15	0.15	0.3
Avg. Base Width	m	1.7	1.7	2.9
Foliage Surface Area to Volume Ratio	m^{-1}	3940	3940	3940
Avg. Initial Mass	kg	9.7	13.5	57.9
Avg. Moisture Fraction	%	14	49	26
Assumed Bulk Mass per Unit Volume	kg/m^3	3.2	4.6	2.7

Table 3.17: Assumed properties for the NIST Douglas Fir Experiments.

Property	Units	Value	Reference
Chemical Composition	–	$C_{3.4}H_{6.2}O_{2.5}$	[66]
Heat of Combustion	kJ/kg	17700	[161]
Soot Yield	kg/kg	0.02	[228]
Char Yield	kg/kg	0.26	[161]
Specific Heat	kJ/(kg·K)	$1.1 + 0.0037\,T$	[230]
Conductivity	W/(m·K)	0.2	Assumption
Density	kg/m^3	514	[158]
Heat of Pyrolysis	kJ/kg	416	[160]

3.44 NIST Enclosure Experiments

A variety of reduced-scale and full-scale compartment fire experiments have been performed at NIST over the past few decades. The main objective of each series is to measure the concentrations of oxygen, carbon dioxide, carbon monoxide, soot, and unburned hydrocarbons in an under-ventilated compartment. These data sets also provide extreme temperature and heat flux measurements.

3.44.1 NIST Reduced Scale Enclosure Experiments, 1994

The NIST Reduced Scale Enclosure (RSE) was a 40 % scale version of the ISO 9705 compartment [231]. It measured 0.98 m wide by 1.46 m deep by 0.98 m tall. A door, centered on the smaller wall, was 0.48 m wide by 0.81 m tall. A 15 cm diameter natural gas burner was positioned in the center of the compartment. The burner was on a stand so that its top was 15 cm above the floor. The fires ranged from 50 kW to 600 kW. Species measurements, including CO concentration, were made near the ceiling in the front and back of the compartment.

3.44.2 NIST Reduced Scale Enclosure Experiments, 2007

Another set of reduced-scale compartment experiments was conducted in 2007 at NIST [232]. The compartment was similar in dimension: 0.95 m wide by 1.42 m deep by 0.98 m tall with the exact same door dimensions. Four different burner types were used: a 13 cm square sand burner, a 25 cm square liquid fuel burner, a spray nozzle into 0.4 m diameter circular pan, and a 60 cm diameter circular pan. Six different fuels were used: natural gas; heptane, methanol, ethanol and toluene liquids; and solid polystyrene beads. The fires ranged from 15 kW to 425 kW, but only fires greater than 190 kW were used for comparison because the smaller fires produced no significant CO. Measurements of O_2, CO_2, CO, soot, and unburned hydrocarbon concentration were made near the ceiling in the front and back of the compartment.

3.44.3 NIST Full-Scale Enclosure Experiments, 2008

The NIST FSE (2008) Experiments were conducted in an ISO 9705 compartment [233]. The compartment was 2.4 m wide by 3.6 m long by 2.4 m high with a 2 m high door at one end (Fig. 3.25). The door width varied between 0.1 m and 0.8 m. The experiments were designed to study the effects of fuel type, fuel distribution, and vent size on under-ventilated compartment fires. Twenty-seven of the thirty experiments

Table 3.18: Summary of NIST Reduced-Scale Experiments, 2007.

Test No.	Fuel Type	Fuel Formula	Peak HRR (kW)	Burner Size (m^2)	Doorway Opening (cm)
1	Natural Gas	CH_4	190	0.017	48
2	Natural Gas	CH_4	395	0.017	48
3	Natural Gas	CH_4	410	0.017	48
4	Heptane	C_7H_{16}	375	0.063	48
5	Heptane	C_7H_{16}	220	0.063	24
6	Natural Gas	CH_4	420	0.063	24
7	Heptane	C_7H_{16}	340	0.063	48
10	Toluene	C_7H_8	340	0.063	48
11	Ethanol	C_2H_6O	335	0.126	48
12	Methanol	CH_4O	305	0.126	48
15	Heptane	C_7H_{16}	375	0.126	48
16	Polystyrene	C_8H_8	360	0.283	48

were simulated, which included 7 different fuels, 3 fuel sources, and 4 ventilation openings. The three experiments not simulated had several malfunctions of equipment such that the data could not be trusted.

Peak heat release rates ranged from approximately 100 kW to 2.5 MW. Table 3.19 provides a summary of the experiments. Species concentrations and temperature measurements were made at the front and rear of the compartment.

3.44.4 Modeling Notes

In the simulations of all of the NIST enclosure experiments, it is assumed that the combustion can be simplified to two fast reactions, the first converting fuel to CO and soot, and the second converting CO and soot to CO_2. By default, 2/3 of the carbon in the fuel is converted to CO in the first step, the remaining 1/3 to soot. The heats of combustion for the reactions are calculated directly from the heats of formation of the individual molecules. For cases where the fuel molecule is not pre-defined in FDS (e.g., styrene), the fuel's enthalpy of formation is specified. For cases where the fuel's enthalpy of formation is not known (e.g. nylon), the heat of combustion that is reported for complete combustion is specified in a single reaction test case, from which an effective enthalpy of formation is reported[3] and then used in the actual two-step reaction scheme.

In the experiments, the heat release rate was measured via oxygen consumption calorimetry. In the simulations, the mass loss rate of fuel was specified by taking the measured HRR and dividing by the heats of combustion listed in Ref. [135].

In all simulations, the model geometry included the compartment interior plus a comparable volume at the exterior to allow for a natural flow into and out of the compartment.

Also, in all simulations, the fire suppression algorithm has been turned off (`SUPPRESSION=.FALSE.`). The reason for this is that the suppression algorithm is not able to distinguish viability of a fire that is close

[3]The FDS diagnostic output (.out) file contains detailed information about the reaction stoichiometry, heats of combustion, and enthalpies of formation.

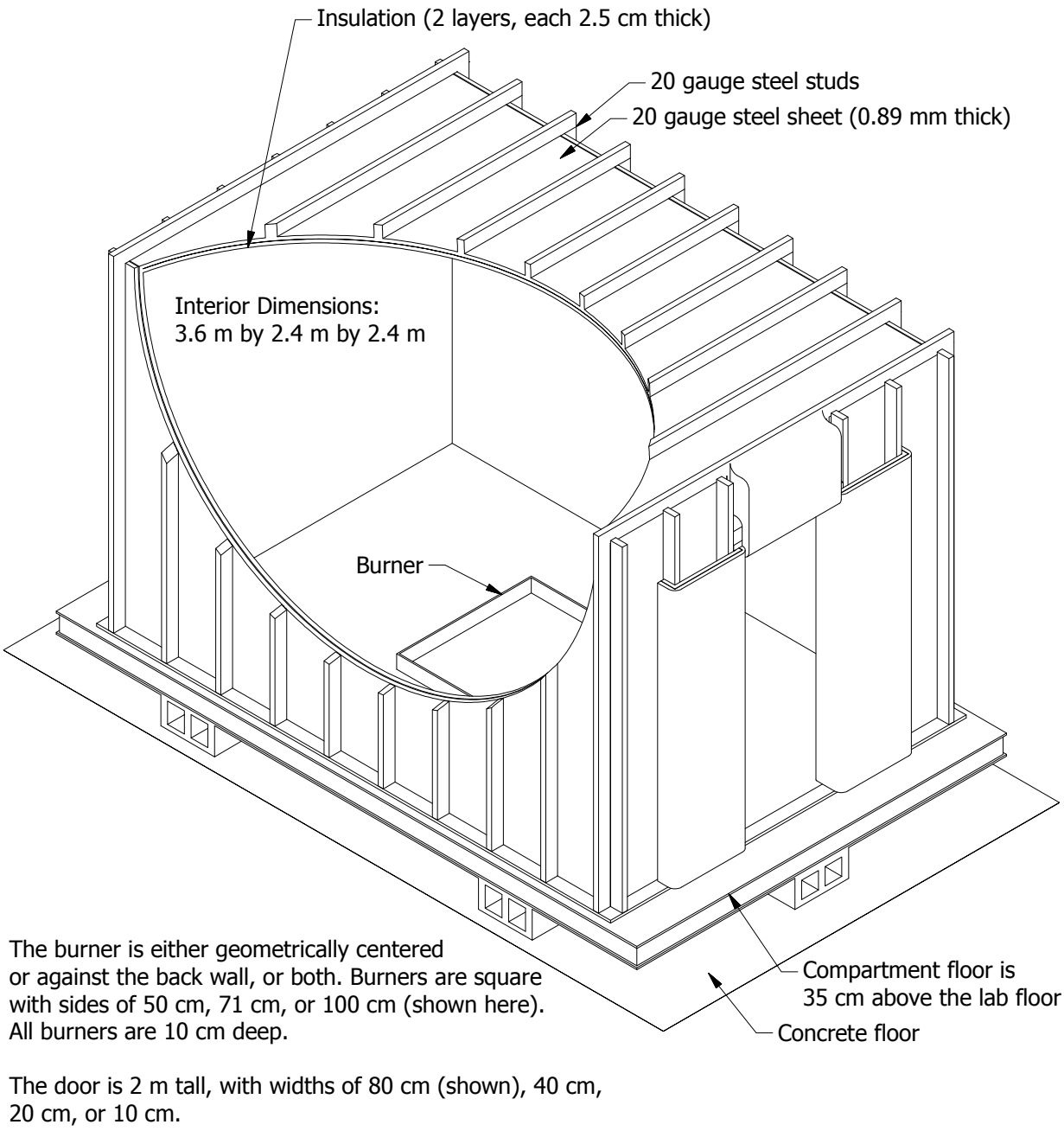

Figure 3.25: Geometry of the compartment used in the NIST Full-Scale Enclosure (FSE) experiments.

to the point of extinction. Research continues in this area.

Table 3.19: Summary of NIST FSE Experiments selected for model validation.

Test Name	Fuel Type	Fuel Formula	Fuel Mass (kg)	No. of Burners	Burner Size (m^2)	Doorway Opening (cm)
ISONG3	Natural Gas	CH_4		1	1.0	80
ISOHept4	Heptane	C_7H_{16}	Pool Fed	1	1.0	80
ISOHept5	Heptane	C_7H_{16}	Pool Fed	1	1.0	40
ISOHept8	Heptane	C_7H_{16}	10	1	0.5	20
ISOHept9	Heptane	C_7H_{16}	20	1	0.5	20
ISONylon10	Nylon	$C_6H_{11}NO$	10	1	0.5	20
ISOPP11	Propylene	C_3H_6	10	1	0.5	20
ISOHeptD12	Heptane	C_7H_{16}	20	2	0.25	20
ISOHeptD13	Heptane	C_7H_{16}	20	2	0.25	20
ISOPropD14	Propanol	C_3H_8O	24	2	0.25	20
ISOProp15	Propanol	C_3H_8O	24	1	0.5	20
ISOStyrene16	Styrene	C_8H_8	10	1	0.5	20
ISOStyrene17	Styrene	C_8H_8	30	1	1.0	20
ISOPP18	Propylene	C_3H_6	20	2	0.5	20
ISOHept19	Heptane	C_7H_{16}	20	1	0.5	20
ISOToluene20	Toluene	C_7H_8	17	1	0.5	20
ISOStyrene21	Styrene	C_8H_8	15	1	0.5	20
ISOHept22	Heptane	C_7H_{16}	Spray	1	0.5	20
ISOHept23	Heptane	C_7H_{16}	Spray	1	0.5	10
ISOHept24	Heptane	C_7H_{16}	Spray	1	0.5	10
ISOHept25	Heptane	C_7H_{16}	Spray	1	0.5	40
ISOHept26	Heptane	C_7H_{16}	Spray	1	0.5	40
ISOHept27	Heptane	C_7H_{16}	Spray	1	0.5	10
ISOHept28	Heptane	C_7H_{16}	Spray	1	0.5	20
ISOToluene29	Toluene	C_7H_8	Spray	1	0.5	20
ISOPropanol30	Propanol	C_3H_8O	Spray	1	0.5	20
ISONG32	Natural Gas	CH_4		1	0.28	20

3.45 NIST Helium Experiments

Eighteen experiments were conducted at NIST in which helium was released over a lengthy time period inside of a 1.5 m by 1.5 m by 0.75 m plexiglass box with one or two small leakage holes [234]. The experiments were intended to represent the release of hydrogen from passenger vehicle fuel cell inside of a residential garage. Test parameters included the release rate and length, the location of the release, and the size and location of the leakage. Measurements were made of the helium concentration in a rake at seven locations over the height of the compartment during the release and for a period of up to 11 hours post-release.

Test variables included all permutations of the leak rate and time (14.8 L/min over 3600 s or 3.71 L/min over 14400 s), leak location (on the floor at the center of the compartment, on the floor at the center of the rear wall, and 2.5 cm below the ceiling at the center of the compartment), and the leak area (2.4 cm by 2.4 cm at the center of the front wall, 3.05 cm by 3.05 cm at the center of the front wall, and a pair of

2.15 cm by 2.15 cm centered on the front wall 2.5 cm from the floor and ceiling).

Leakage areas were square holes under 10 cm^2 in area. Attempting to resolve flows through these holes would have required very small grid cells in the vicinity of the holes. Instead, the FDS HVAC model was used. For each leakage hole a pair of HVAC ducts was defined over a height of two grid cells (one grid cell height for each vent). Each duct was assigned one-half the leakage area and the experimentally determined orifice flow coefficient. This approach enabled bi-directional flow to occur at the leakage vent as occurred during each test following the termination of the helium release.

3.46 NIST/NRC Compartment Experiments

These experiments, sponsored by the US NRC and conducted at NIST, consisted of 15 large-scale experiments performed in June 2003. All 15 tests were included in the validation study. The experiments are documented in Ref. [116]. The fire sizes ranged from 350 kW to 2.2 MW in a compartment with dimensions 21.7 m by 7.1 m by 3.8 m high, designed to represent a compartment in a nuclear power plant containing power and control cables. A diagram of the test structure is displayed in Figure 3.26.

The walls and ceiling were covered with two layers of marinate boards, each layer 0.0125 m thick. The floor was covered with one layer of gypsum board on top of a layer of plywood. Thermo-physical and optical properties of the marinate and other materials used in the compartment are given in Ref. [116]. The room had one door and a mechanical air injection and extraction system. Ventilation conditions, the fire size, and fire location were varied. Numerous measurements (approximately 350 per test) were made including gas and surface temperatures, heat fluxes and gas velocities.

Following are some notes provided by Anthony Hamins, who conducted the experiments:

Natural Ventilation: The compartment had a 2 m by 2 m door in the middle of the west wall. Some of the tests had a closed door and no mechanical ventilation (Tests 2, 7, 8, 13, and 17), and in those tests the measured compartment leakage was an important consideration. The test report lists leakage areas based on measurements performed prior to Tests 1, 2, 7, 8, and 13. For the closed door tests, the leakage area used in the simulations was based on the last available measurement. The chronological order of the tests differed from the numerical order. For Test 4, the leakage area measured before Test 2 was used. For Tests 10 and 16, the leakage area measured before Test 7 was used.

Mechanical Ventilation: The mechanical ventilation and exhaust was used during Tests 4, 5, 10, and 16, providing about 5 air changes per hour. The door was closed during Test 4 and open during Tests 5, 10, and 16. The supply duct was positioned on the south wall, about 2 m off the floor. An exhaust duct of equal area to the supply duct was positioned on the opposite wall at a comparable location. The flow rates through the supply and exhaust ducts were measured in detail during breaks in the testing, in the absence of a fire. During the tests, the flows were monitored with single bi-directional probes during the tests themselves.

Heat Release Rate: A single nozzle was used to spray liquid hydrocarbon fuels onto a 1 m by 2 m fire pan that was about 0.1 m deep. The test plan originally called for the use of two nozzles to provide the fuel spray. Experimental observation suggested that the fire was less unsteady with the use of a single nozzle. In addition, it was observed that the actual extent of the liquid pool was well-approximated by a 1 m circle in the center of the pan. For safety reasons, the fuel flow was terminated when the lower-layer oxygen concentration dropped to approximately 15 % by volume. The fuel used in 14 of the tests was heptane, while toluene was used for one test. The HRR was determined using oxygen consumption calorimetry. The recommended uncertainty values were 17 % for all of the tests.

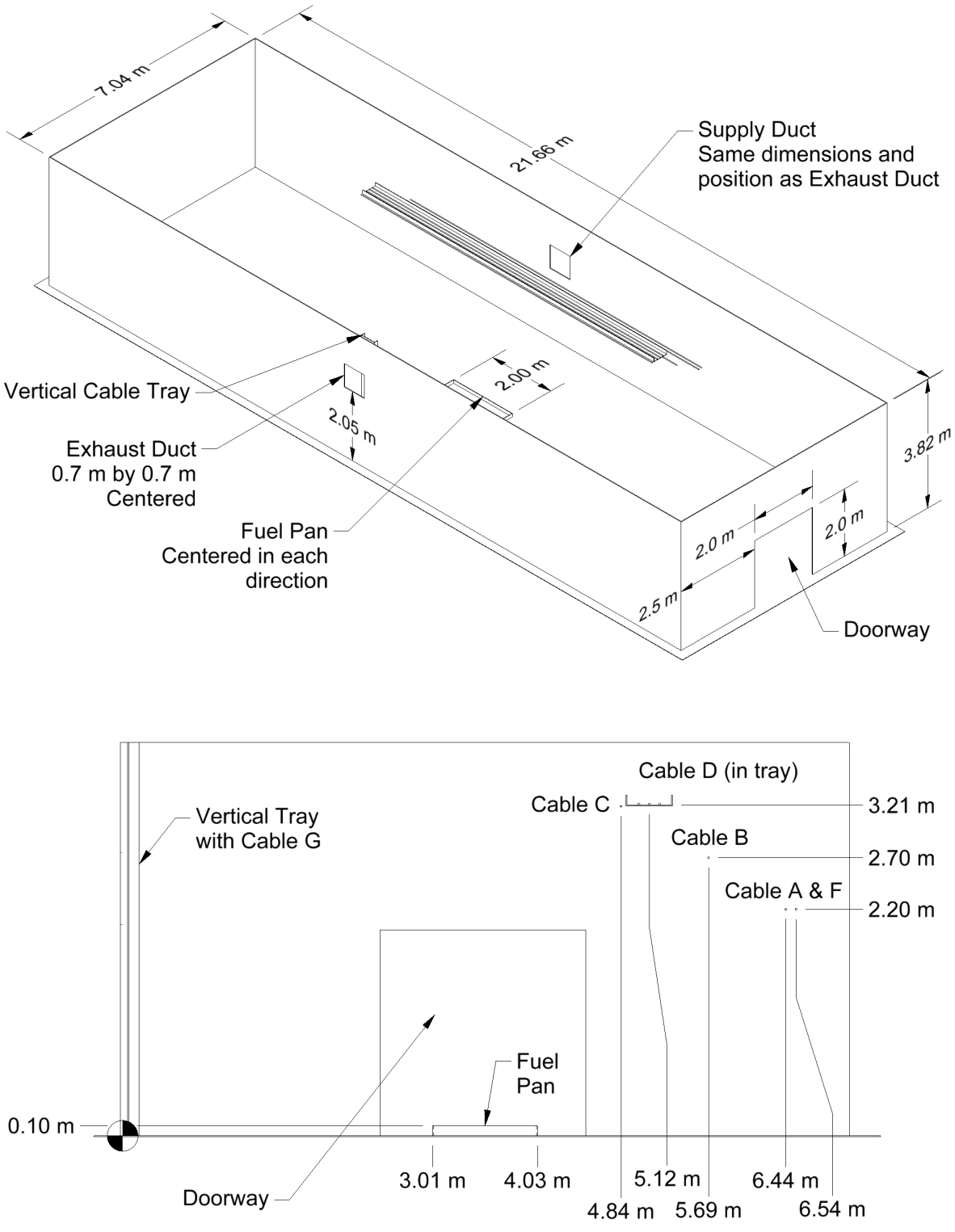

Figure 3.26: Geometry of the NIST/NRC Experiments.

Radiative Fraction: The values of radiative fraction and its uncertainty were reported as 0.44 ± 0.07 and 0.40 ± 0.09 for heptane and toluene, respectively.

Soot Yield: The values of the soot yield and its uncertainty were reported as 0.0149 kg/kg $\pm$ 0.0033 kg/kg and 0.195 kg/kg $\pm$ 0.052 kg/kg for heptane and toluene, respectively.

3.47 NIST/NRC Corner, Wall, and Cabinet Experiments

In the summer of 2017, experiments were conducted in a large compartment in the NIST large fire laboratory on behalf of the U.S. Nuclear Regulatory Commission. There were two sets of experiments. In the first set, conducted in July, 2017, a natural gas burner was positioned either in a corner or against a wall, and gradually moved outward. In the second set of experiments, conducted in September, 2017, a natural gas burner was placed inside one of two steel cabinets meant to represent typical industrial-scale electrical enclosures.

The compartment for all experiments was 11 m long, 7 m wide, and 3.8 m high. The long dimension of the compartment ran east-west. A 1.8 m wide, 2.4 m high door was centered on the east (short) wall.

All of the fires were fueled by one or more 30.5 cm (1 ft) square natural gas burners. Each burner was essentially a steel box, 30.5 cm square in plan and 15 cm deep, fueled from below. The lip of the burner was 2.5 cm (1 in) wide. A 2.5 cm thick piece of Kaowool insulation was placed under a steel mesh to form the surface of the burner.

3.47.1 Wall and Corner Effects

Six large compartment experiments [235] were conducted in July, 2017, where four natural gas burners were positioned (1) in a corner and (2) against a wall, and then moved outward in stages until the corner or wall effect became negligible. The quad burner was 60 cm by 60 cm and the burner surface was 54 cm above the floor. The corner fire was located in the southwest corner of the large compartment. The wall fire was centered on the south (long) wall.

The experiments began with the quad burner in the corner or against the wall for the first 30 min. At 30 min, the burner was moved so that its edge(s) was 10 cm away from the wall(s). It remained for 15 min, after which it was moved to 20 cm, 30 cm, 50 cm, 100 cm, and 160 cm, each time remaining 15 min for a total experiment time of 2 h.

A three-dimensional array of thermocouples was positioned on a track mounted to the ceiling above the burner. The purpose of this array was to measure maximum plume temperatures at heights of 2.1 m, 2.7 m, and 3.4 m above the floor. As the burner moved, the thermocouple array moved with it. For the corner fire experiments, when the burner was at the 0 cm, 10 cm, and 20 cm positions, the thermocouple array overhead remained at its original location in the corner. As the burner moved beyond 20 cm, the thermocouple array was moved the same amount so that the burner was always below the array in the same position. In other words, for the corner fire experiments, after the center point of the burner reached the point directly below the position 18 on the diagram below, the burner and array moved together, maintaining their relative position.

The experimental data consists primarily of thermocouple measurements. The key to the column names are as follows:

- TC-AG-01 through TC-AG-29 are the thermocouples at the top of the cage, 46 cm below the ceiling (see pattern below).
- TC-BG-01 through TC-BG-29 are the thermocouples at the mid-level of the cage, 107 cm below the ceiling (see pattern below).

- TC-CG-01 through TC-CG-29 are the thermocouples at the bottom of the cage, 168 cm below the ceiling (see pattern below).
- TC-WT-01 through TC-WT-13 are the thermocouples of the vertical array called the West Tree. The array was 2.75 m from the west (short) wall and 3.5 m from the south (long) wall. TC-WT-01 was located 2 cm below the ceiling, and the rest were spaced 30 cm apart.
- TC-ET-01 through TC-ET-13 are the thermocouples of the East Tree. The array was 2.75 m from the east (short) wall and 3.5 m from the south (long) wall. TC-ET-01 was located 2 cm below the ceiling, and the rest were spaced 30 cm apart.
- TC-C-01 through TC-C-11 are the thermocouples 2 cm from the corner above the corner fire. TC-C-01 was located 2 cm below the ceiling, and the rest were spaced 30 cm apart.
- TC-W-01 through TC-W-11 are the thermocouples 2 cm from the wall above the wall fire. TC-W-01 was located 2 cm below the ceiling, and the rest were spaced 30 cm apart.
- HRR (cal) is the heat release rate of the fire as measured using oxygen consumption calorimetry. HRR (NG) is the heat release rate determined from the mass flow rate of natural gas.

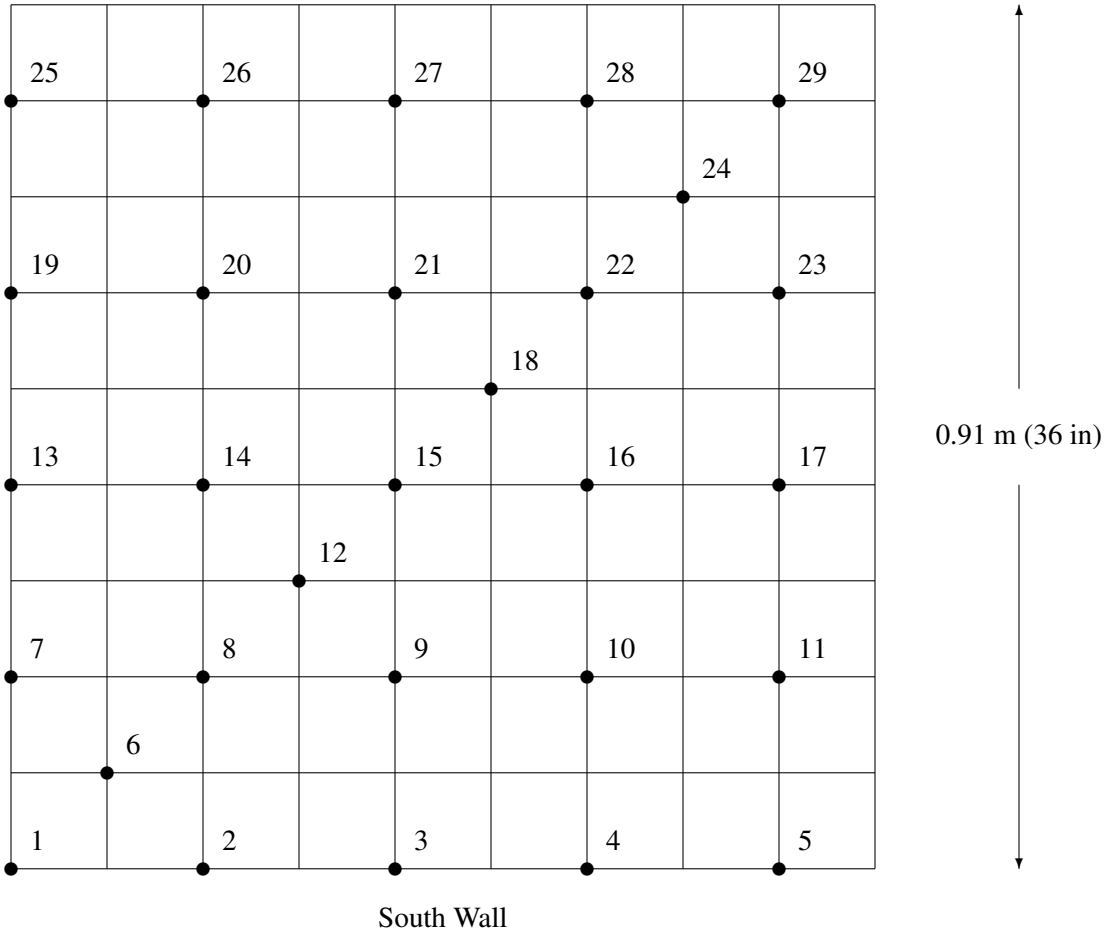

Figure 3.27: Diagram of thermocouple layout for NIST/NRC Corner Effects experiments.

The East and West Tree thermocouples were used to estimate the height of the hot gas layer (HGL), and the average temperatures of the upper and lower layers. Also, the three horizontal arrays of thermocouples above the burner were processed by first taking a 2 min running average of each TC, and then choosing the maximum value for each of the three elevations above the fire. These were taken as approximate centerline plume temperatures at each height. These experimental files are labelled with "HGL" and "Plume", respectively.

3.47.2 Cabinet Effects

In this second series of experiments, conducted in September, 2017, two different mock steel cabinets were used. Each cabinet was constructed of 12 gauge (2.8 mm or 7/64 in) steel plate with openings as shown in Figs. 3.28 and 3.29. The large cabinet was nominally 0.9 m by 0.9 m by 2.1 m and the medium size cabinet was 0.6 m by 0.6 m by 2.1 m. The openings near the top of each cabinet were sometimes covered with a steel grill, shown in Fig. 3.30.

For the first set of experiments (1-6), the large cabinet was positioned with its front opening facing eastward towards the opening of the test compartment. Its left side was 1.8 m from the south wall and its front side was 5.8 m from the east wall. Two 0.3 m by 0.3 m natural gas burners were placed side by side in the cabinet from the perspective of the cabinet front opening. The top of the burner was 50 cm above the floor of the cabinet. For Tests 1-4, the front door of the cabinet was closed, and the heat release rate was initially set to 50 kW for 30 min, then it was increased to 100 kW for 15 min, 200 kW for 15 min, and 400 kW for 15 min. For Tests 5-6, the front door was opened, and the heat release rate was set to 200 kW, 400 kW, and 700 kW for 15 min each, and then 1000 kW for 5 min, a total of 50 min.

In the second set of experiments (7-10), the medium-sized cabinet was positioned so that its front was the same distance from the east wall as the large cabinet, and its left side was 2.0 m (6.5 ft) from the south wall. A single 30 cm by 30 cm gas burner was centered within. For the closed door tests, the heat release rate was 25 kW, 50 kW, 100 kW, and 200 kW, each for 15 min. For the open door tests, the heat release rate was 40 kW, 80 kW, 200 kW, and 325 kW, each for 15 min.

In the third set of experiments (11-12), the cabinet was removed, and two 30 cm by 30 cm burners were spaced 0.9 m (3 ft) apart, side to side. One of the burners was centered under the array of thermocouples. Both burners were 2.0 m from the south wall. These experiments used the same heat release rate sequence as the open and closed door large cabinet experiments.

The data files for these experiments are labelled, `NIST_NRC_Cabinet_Test_n.csv`. These files contain the same measurement positions as the corner and wall experiments, with the following additional measurements:

- PT-1 through PT-8 are plate thermometers positioned 0.6 m (2 ft) from each side of the cabinet at heights of 0.8 m (2.5 ft) and 1.4 m (4.5 ft). PT-1 is the upper plate on the left side. PT-2 is lower left. PT-3 is upper back. PT-4 is lower back. PT-5 is upper front. PT-6 is lower front. PT-7 is upper right. PT-8 is lower right.

- STC-1 through STC-6 are sheathed thermocouples within the cabinet, 15 cm (6 in) from the left side, centered. STC-1 is 6 cm (2.5 in) from the top. STC-2 through STC-6 are 30 cm, 60 cm, 90 cm, 120 cm, and 150 cm from the top, respectively.

- TC-Cab is a single 24 gauge Type K thermocouple welded to the center of the back side on the outside of the cabinet. For Test 11, this TC was placed just under the Kaowool surface of the burner, and for Test 12, it was placed just above the surface.

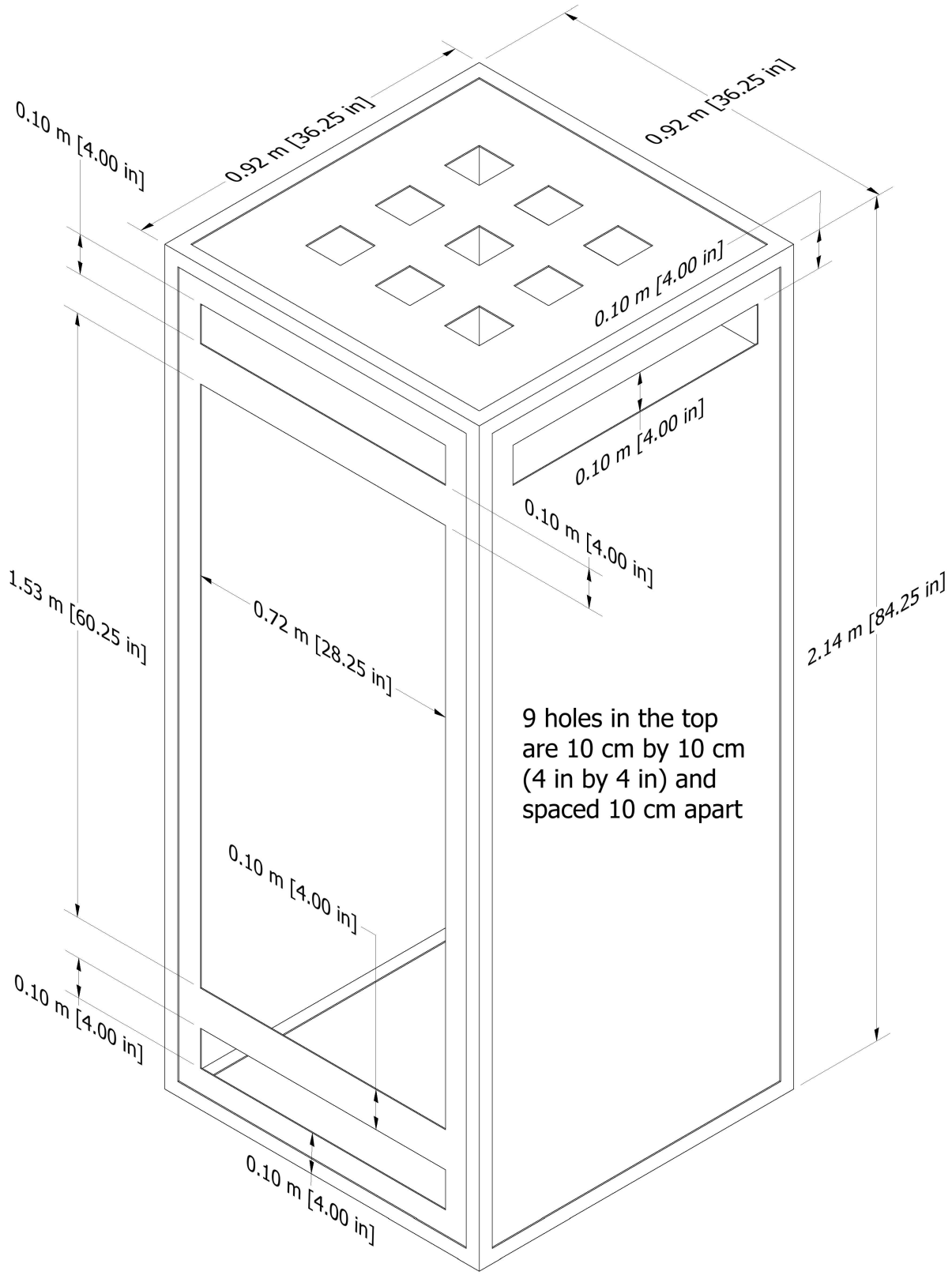

Figure 3.28: Large cabinet drawing, NIST/NRC Corner Effects Experiments.

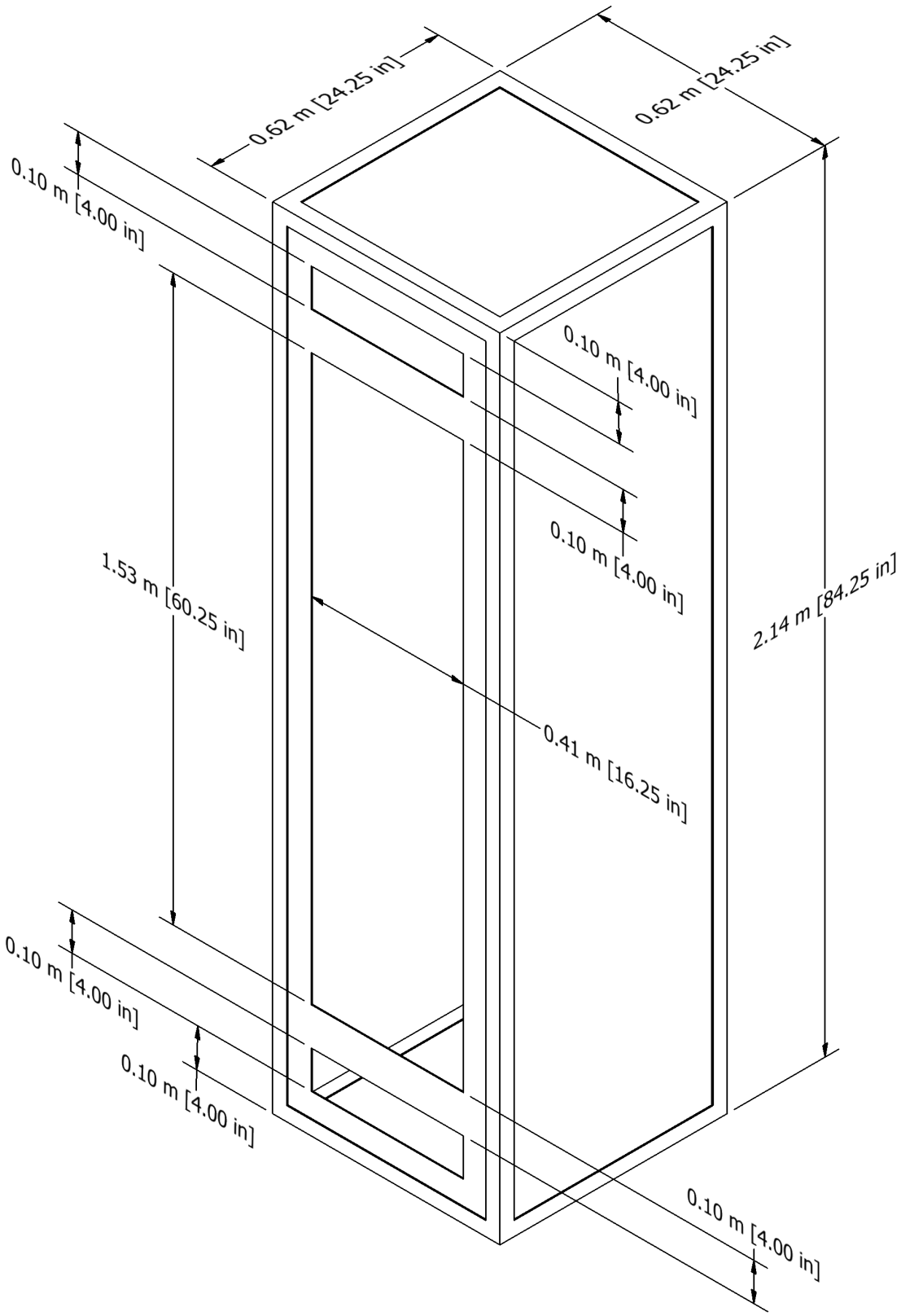

Figure 3.29: Medium-sized cabinet drawing, NIST/NRC Corner Effects Experiments.

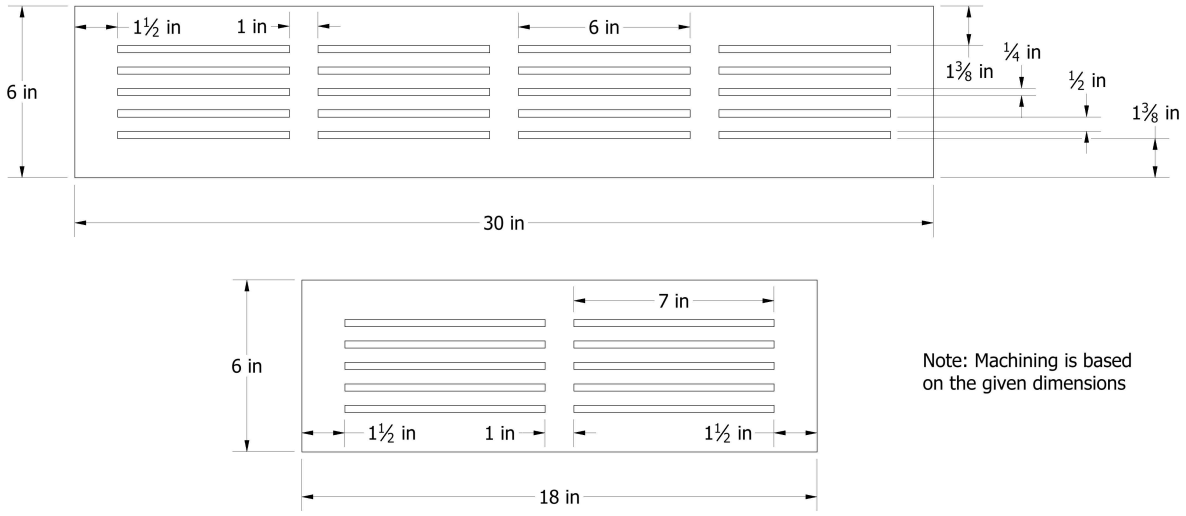

Figure 3.30: Cabinet grill, NIST/NRC Corner Effects Experiments.

The three dimensional array of thermocouples used in the wall and corner experiments was positioned over the front of the cabinet, such that TC positions 1, 7, 13, 19, and 25 in Fig. 3.27 were just above the upper front edge of the cabinet.

The test matrix is as follows:

Table 3.20: Summary of NIST/NRC Cabinet Experiments.

Test	Cabinet	Front Door	Top Vents	Upper Side Vents	HRR (kW)
1	Large	Closed	Closed	Grill	50, 100, 200, 400
2	Large	Closed	All open	Grill	50, 100, 200, 400
3	Large	Closed	Closed	Front open, all others closed	50, 100, 200, 400
4	Large	Closed	Closed	Front and back open, others closed	50, 100, 200, 400
5	Large	Open	Closed	Front and back open, others closed	200, 400, 700, 1000
6	Large	Open	Open	All open	200, 400, 700, 1000
7	Medium	Closed	Closed	Grill	25, 50, 100, 200
8	Medium	Closed	Closed	Open	25, 50, 100, 200
9	Medium	Open	Closed	Open	40, 80, 200, 325
10	Medium	Open	Closed	Closed	40, 80, 200, 325
11	None	N/A	N/A	N/A	200, 400, 700, 1000
12	None	N/A	N/A	N/A	50, 100, 200, 400

3.48 NIST/NRC OLIVE-Fire Experiments

In March, 2022, experiments were conducted at NIST to determine the maximum heat release rate that a fire can reach within steel electrical enclosures [236]. OLIVE is an acronym for Oxygen-Limited Fires Inside

Under-Ventilated Enclosures. Photographs of the enclosures are shown in Fig. 3.31. The enclosures were pressure-tested before and after the experiments to determine the leakage and vent opening areas. These opening areas are a key parameter in the numerical modeling.

Thirty-two experiments were conducted; twenty-one of which were fueled by a natural gas burner. The others involved a variety of plastics and electrical cables. Eighteen of the natural gas experiments were chosen for simulation. The natural gas cases not chosen had unexpectedly large gaps between the steel panels open up during the experiment. The leakage throught these gaps could not be measured.

Modeling Notes

The simulations are performed with a spatial resolution of 4 cm. The enclosures are modeled simply as rectangular steel boxes with no internal partitions included. Both leakage and vents are modeled in the same way by using the "localized leakage" methodology in FDS where the volume flow rate, $\dot{V}$, through a vent or a crack is a function of the pressure difference, Δp:

$$\dot{V} = CA \left(\frac{2\Delta p}{\rho_0} \right)^{0.5} \left(\frac{\Delta p}{\Delta p_{\text{ref}}} \right)^{0.1} \tag{3.8}$$

The discharge coefficient, $C = 0.61$, is recommended by the manufacturer of the calibrated fan used for determining the leakage area, A. The extra pressure term in the expression represents a weak relationship between the discharge coefficient and the pressure rise. The pressure exponent of 0.6 best fits the leakage data. The reference pressure, Δp_{ref}, is taken as 1 Pa to maintain unit consistency.

Figure 3.31: Photographs of the eight electrical enclosures used for the NIST/NRC OLIVE-Fire experiments. The enclosures are numbered 1 through 8 in sequence. Enclosure #1 and #2 (top row) have the same exterior design.

3.49 NIST/NRC Parallel Panel Experiments

As part of a Nuclear Regulatory Commission (NRC) research project to assess fire behavior in electrical enclosures, rate of spread and heat release rate measurements were made on various plastics lining a parallel panel apparatus. The panels were 0.6 m (2 ft) wide, 2.4 m (8 ft) tall, and separated by 0.3 m (1 ft). A 60 kW propane sand burner was positioned at the base of the two panels. Plastics tested to date include PMMA, PVC, and PBT, cut into 6.4 mm (0.25 in) thick panels. A sketch of the apparatus, originally developed by Factory Mutual, is shown in Fig. 3.11.

3.50 NIST/NRC Transient Combustibles Experiments

In December, 2019 and February, 2020, 40 calorimetry experiments were conducted at the National Fire Research Laboratory at NIST on behalf of the U.S. Nuclear Regulatory Commission. The experiments were conducted under a 6.1 m (20 ft) by 6.1 m hood with a nominal capacity of 3 MW. The full report on the experiments can be found in Ref. [237].

The items burned are described briefly in Fig. 3.32. These consist of commercially available materials constructed mainly of wood and paper. Each item was weighed before and after the experiment on a load cell accurate to 10 g.

The fires were all ignited using one or more 7.5 cm (3 in) segments of approximately 1 cm (0.5 in) diameter cotton rope soaked in approximately 10 mL of acetone. For some items like the wood cribs and pallets, a small amount of shredded craft or "crinkle" paper was used to sustain the ignition until steady burning was achieved.

The floor beneath the burning item was protected with a single layer of gypsum board covered by a single layer of concrete board.

The heats of combustion and product yields of the various items burned are given in Table 3.21. These values are derived from the measured initial and final mass, and an assumed value of 13.61 MJ/kg for the energy released per unit mass of oxygen consumed.

Table 3.21: Average heat and product yields of the various test items.

Item	ΔH (MJ/kg)	CO Yield	CO_2 Yield	Soot Yield	Residue Yield
Box #1	14.8 ± 0.5	0.039 ± 0.001	1.48 ± 0.05	0.0014 ± 0.0003	0.031 ± 0.016
Pallet	17.2 ± 0.5	0.031 ± 0.001	1.66 ± 0.06	0.0033 ± 0.0006	0.059 ± 0.024
Crib	16.7 ± 0.5	0.023 ± 0.001	1.63 ± 0.06	0.0020 ± 0.0003	0.053 ± 0.034

Modeling Notes

The combustible items are modeled as collections of Lagrangian particles that undergo a three-step decomposition process consisting of moisture evaporation, pyrolysis, and char oxidation. The moisture content, M, of the conditioned materials was less than the 0.05 lower limit of the moisture meter, and this value is used in the calculations.

In the model, all of the wood and paper materials are assumed to be made up of cellulose, $C_6H_{10}O_5$, with a net heat of combustion of 16.12 MJ/kg [238]. It is also assumed that the materials have a char yield of 20 %, meaning that 20 % of the dry mass is converted into char that undergoes an exothermic oxidation reaction generating 32.12 MJ/kg of char consumed. The decomposition reactions are as follows:

Box #1: Single-wall corrugated box with nominal dimensions 61 cm by 61 cm by 46 cm (24 in by 24 in by 18 in) filled with "crinkle paper," a common packing material made by shredding craft paper. The box alone had a mass of approximately 1.6 kg (3.5 lb), and the box and paper combined had a mass of 8.0 kg (18 lb). The box top flaps were closed, end over end, but not sealed with tape.

Pallet: Pine wood pallet with dimensions 122 cm by 102 cm by 12 cm (48 in by 40 in by 4.75 in). Its mass was approximately 16.0 kg (35 lb). Its moisture content was less than 5 %. Shown at right are two pallets, which were ignited with 1 kg (2.2 lb) of crinkle paper distributed evenly throughout the lower pallet.

Crib: Pine wood crib with dimensions 56 cm by 56 cm by 46 cm (22 in by 22 in by 18 in) constructed of slats with a cross-section 3.8 cm (1.5 in) square. Its mass was approximately 39 kg (86 lb). Its moisture content was less than 5 %. It was ignited with 0.75 kg (1.7 lb) of crinkle paper stuffed in the space below the first row of slats.

Figure 3.32: Description of test items.

1. Endothermic moisture evaporation

$$\text{Wet Vegetation} \rightarrow \nu_{H_2O}\,H_2O + (1-\nu_{H_2O})\,\text{Dry Vegetation} \quad ; \quad \nu_{H_2O} = \frac{M}{1+M} \tag{3.9}$$

2. Endothermic pyrolysis of dry vegetation

$$\text{Dry Vegetation} \rightarrow 0.2\,\text{Char} + 0.8\,C_{3.3}H_{10}O_5 \tag{3.10}$$

3. Exothermic char oxidation

$$\text{Char} + 1.65\,O_2 \rightarrow 2.4\,CO_2 + 0.25\,\text{Ash} \tag{3.11}$$

Note that the fuel gas is taken as cellulose with 20 % of its molecular mass decreased to account for the residual char, which is assumed to be pure carbon. The heat of combustion of this modified fuel gas is 12120 MJ/kg. The yield of residual Ash is based on the measured residual mass.

The crinkle paper is assumed to consist of 3 cm long, 4 mm wide strips with a surface area to volume ratio of 10000 m^{-1} (approximately 0.2 mm thick). The length and width are important only in defining the mass and volume of each particle. The thermal and kinetic properties of the paper are assumed to be similar to those of corrugated cardboard given in Table 14.11. The cardboard that makes up the box that holds the crinkle paper has a mass of 0.62 kg/m^2 and the box itself has a mass of 1.6 kg. The corrugated paper has an assumed dry density of 350 kg/m^3, yielding an effective thickness of 1.8 mm. In the model, the box does not undergo char oxidation but rather "burns away" to expose the crinkle paper inside.

The wood crib is made up of 104 56 cm (22 in) long, 3.8 cm (1.5 in) square interlacing pine wood strips. The particles used to model the crib are assumed to be cylindrical in shape but with a surface area to volume ratio of 69 m^{-1} based on a direct measurement of the actual crib geometry. The dry density of the wood has been measured to be 463 kg/m^3, its peak pyrolysis temperature is taken to be 320 °C [239], its char yield assumed to be 20 %, and its heat of reaction is taken to be 418 kJ/kg [240]. Other property values are based on the default vegetation pyrolysis model described in the FDS User's Guide.

The pine wood pallets are constructed of 1.6 cm (5/8 in) thick planks and modeled as a collection of flat particles with a thickness of 8 mm and the same thermal and kinetic properties as the cribs, except that the wood making up the pallets has a dry density of 414 kg/m^3.

The drag per unit volume exerted by the particles is given by

$$\mathbf{f} = \frac{\rho}{2} C_\mathrm{d}\, \kappa\, \mathbf{u}|\mathbf{u}| \quad ; \quad \kappa = C_\mathrm{s}\sigma\beta \tag{3.12}$$

where ρ is the gas density, C_d is a drag coefficient, $\mathbf{u}$ is the local velocity vector, C_s is a shape factor, σ is the surface area to volume ratio, and β is the packing ratio; that is the ratio of particle volume to cell volume. The shape factor is taken as 0.25 for all particle types. The packing ratio is determined by the measured mass of the item and the volume it occupies. The drag coefficient for the wood crib is 65, a value obtained by simulating a finely-resolved wood crib in a wind tunnel and calibrating the drag of the equivalent "crib particles" accordingly. The drag coefficient of the crinkle paper is taken as 1, and that of the pallet is taken as 3. These are only order of magnitude estimates and have not been verified.

3.51 NIST Pool Fire Experiments

The NIST Pool Fire Experiments include temperature, species concentration, velocity, and heat flux measurements of 30 cm and 100 cm diameter circular liquid fuel fires, and 37 cm gaseous burner fires.

The 30 cm burner is 15 cm deep and has a wall thickness of 1.6 mm. The burner is fitted with legs such that the burner rim is positioned 30 cm above the floor. The bottom of the burner is maintained at a constant temperature by flowing tap water (nominally 20 °C) through a 3 cm section on the bottom of the fuel pan. The dimensions of the circular burner are similar to Weckman's methanol experiment described in Section 3.90.

The 100 cm burner is also 15 cm deep, has a wall thickness of 1.6 mm, and is water-cooled.

The 37 cm burner is actually 38 cm in diameter with an effective diameter of 37 cm. It is water cooled, and the surface temperature is maintained at approximately 40 °C. The measured fuel flow rate for the methane fire was 0.69 g/s and its estimated HRR was 34.5 kW. The heat release rates of the two propane fires were 20 kW and 34 kW.

Details and references with regard to the plume temperature measurements are given in Section 6.1.5. Details on the heat flux measurements are given in Section 12.2.8. Details on the gas species measurements is given in Section 9.5.6. Details on the velocity measuremnts is given in Section 8.7.

Modeling Notes

The 30 cm pool fires are modeled at three different grid resolutions—2 cm, 1 cm, and 0.5 cm. The 100 cm pool fires are modeled at 4 cm, 2 cm, and 1 cm resolution. The mass loss rate of the fuel is specified.

A two-step reaction mechanism is implemented. In the first reaction, fuel is converted to CO, soot, H_2, and H_2O. In the second reaction, the CO, soot, and H_2 are converted to CO_2 and H_2O. Both reactions employ fast kinetics, but proceed in series, not in parallel. The relative amounts of CO, soot, and H_2 produced in the first step are still subjects of study, and for the moment have been estimated based on measured results. The fractions of carbon atoms converted to CO in the first step are as follows—0.85 for acetone; 0.95 for ethanol; 0.97 for methane; 1.0 for methanol; 0.85 for propane. For all fuels, one half of the hydrogen atoms are converted to H_2 in the first step.

The radiative fractions are specified based on measured values—0.31 for acetone; 0.26 for ethanol; 0.15 for methane; 0.21 for 1 m methanol; 0.22 for 30 cm methanol; 0.22 for propane.

3.52 NIST Smoke Alarm Experiments

A series of experiments was conducted by NIST to measure the activation time of ionization and photoelectric smoke alarms in a residential setting [241]. Tests were conducted in actual homes with representative sizes and floor plans, utilized actual furnishings and household items for fire sources, and tested actual smoke alarms sold in retail stores at that time. Thirty-six tests were conducted in two homes; 27 in a single-story manufactured home, and 8 in a two-story home. Eight experiments that were conducted in the single-story manufactured home were selected for model validation. Only tests that used a flaming ignition source with a couch or mattress fuel package were considered; the cooking oil fires and tests that used a smoldering ignition source were not considered. The flaming ignition tests used a moderate flame source to quickly ignite the fuel package.

The primary partitioning of the single-story floor plan consisted of three bedrooms, one full bathroom, one kitchen/dining area, one living room, and two hallways (see Fig. 3.33). For testing, the doors to Bedroom 3 and the bathroom were always closed. The ceiling was peaked on the long axis, reaching a height of 2.4 m. The outside walls were approximately 2.1 m in height. The slope of the ceiling was approximately 8.4°. Groups of smoke alarms were located in the room of fire origin, at least one bedroom, and in a central location. Five stations (Station A through Station E) containing smoke alarm[4] arrays were mounted parallel to the ceiling.

Although a load cell was used in the experiments to measure the mass loss rate of the fuel package, the mass loss data were not reliable enough to reconstruct the HRR curves for each test. Instead, the HRR curves were determined by approximating the fire growth using a t-squared ramp, as in Eq. (3.13). The parameters for the t-squared ramp were calibrated in FDS by using the temperature measured at the highest thermocouple in the tree (2 cm below the ceiling) in the fire room.

$$\dot{Q} = \dot{Q}_0 \left(\frac{t}{\tau}\right)^2 \tag{3.13}$$

A time offset was used to align the predicted ceiling thermocouple temperatures with the measured temperatures. This offset is reported as the time at which the t-squared ramp begins. The t-squared calibration parameters and time offsets for the HRR ramps are shown in Table 3.22. Additionally, the ignition source had a small effect on the measured ceiling thermocouple temperatures. Therefore, the size of the ignition

[4]Note that, in the FDS Guides, smoke detectors and smoke alarms are collectively referred to as smoke detectors because the same smoke detection algorithm is used to predict activation of either type of device.

source was approximated as either 3 kW or 7 kW, and the time offset of the ignition source was also calibrated by using the measured ceiling thermocouple temperatures. The resulting HRR curve was input into FDS as a fire ramp. A summary of the eight tests selected for model validation is shown in Table 3.22.

Table 3.22: Summary of NIST Smoke Alarm Experiments selected for model validation.

Test No.	Fire Source	Fire Location	$\dot{Q}_0$ (kW)	τ (s)	Time Offset (s)
SDC02	Chair	Living Room	150	180	20
SDC05	Mattress	Bedroom	200	180	20
SDC07	Mattress	Bedroom	350	180	50
SDC10	Chair	Living Room	150	180	40
SDC33	Chair	Living Room	100	180	10
SDC35	Chair	Living Room	100	180	10
SDC38	Mattress	Bedroom	120	180	25
SDC39	Mattress	Bedroom	200	180	25

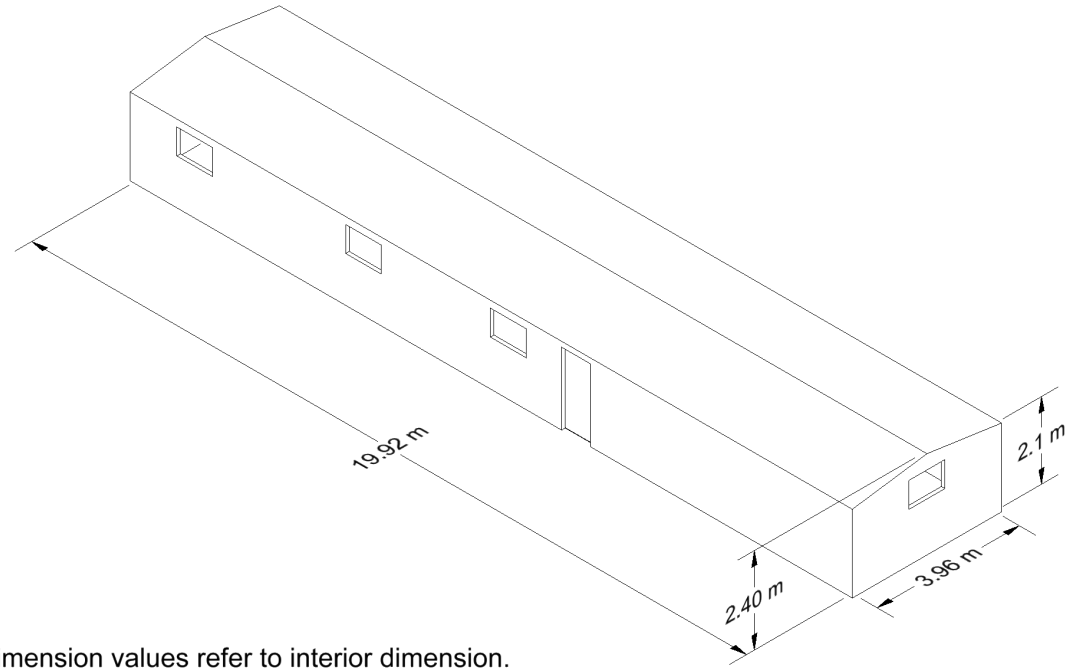

Notes:
1. All dimension values refer to interior dimension.
2. The letters A-E refer to detector locations.
3. All walls are 10 cm thick.
4. All exterior doors and windows were closed during testing.
5. Doors to Bath and Bedroom #3 closed during testing.

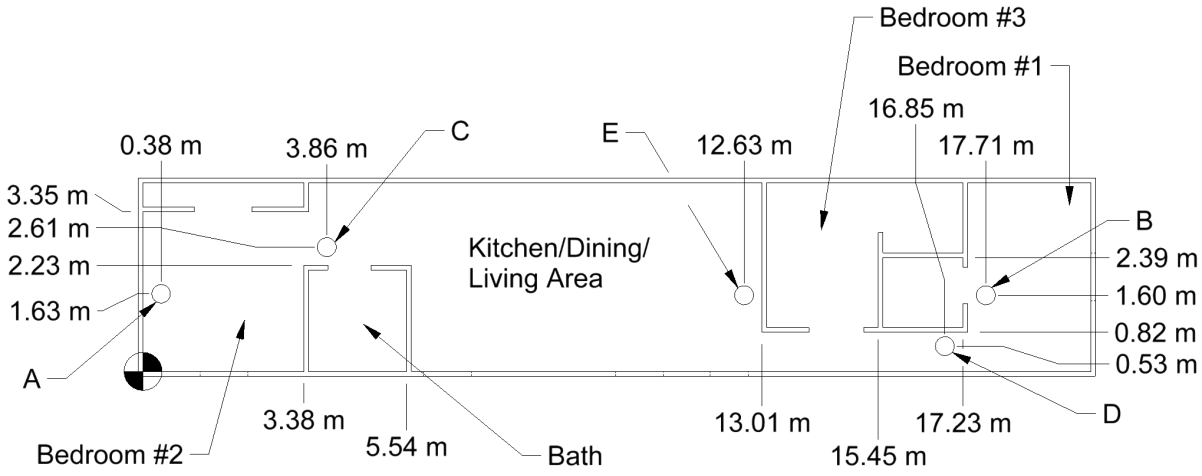

Figure 3.33: Geometry of the manufactured home from the NIST Smoke Alarm Experiments.

3.53 NIST Soot Deposition Gauge

A series of tests were performed as part of an effort to develop a gauge capable of making real time measurements of soot deposition [242]. The test apparatus consisted of a hot plate and cold plate measuring 8 cm wide by 41 cm long and separated by 1 cm. The hot plate was electrically heated and the cold plate was water cooled. A laminar diffusion flame burner using propene as the fuel was used to generate soot. A portion of the effluent from the burner was sent through the test apparatus. In addition to tests using the new gauge, a series of gravimetric tests were performed using 47 mm diameter pieces of aluminum foil attached to the cold plate in four locations. Tests with the aluminum foil used nominal flowrates of 2.5, 5.0, and 10.0 SLPM and nominal temperature differences of 100 °C and 200 °C. The test channel was mounted vertically to avoid gravitational settling and with the laminar flow speeds the device essentially creates only thermophoretic deposition. Four replicate tests were performed for the 2.5 and 5.0 SLPM flowrates and three for the 10.0 SLPM flowrate. A summary of the 22 tests modeled is given in the table below.

Table 3.23: Experiment Details for Gravimetric Measurements of Soot Deposition

Test no.	Flow Speed (SLPM)	ΔT (K)	Inlet Soot Conc. (mg/m^3)
1	2.5	94	67.6
2	2.5	94	69.2
3	2.5	96	64.2
4	2.5	96	64.2
5	5.0	96	65.5
6	5.0	95	62.7
7	5.0	92	61.9
8	5.0	94	68.4
9	10.0	97	25.9
10	10.0	98	27.4
11	10.0	99	25.5
12	2.5	187	60.2
13	2.5	190	61.5
14	2.5	189	64.2
15	2.5	187	59.1
16	5.0	188	59.7
17	5.0	186	58.5
18	5.0	187	60.7
19	5.0	187	55.5
20	10.0	191	23.5
22	10.0	188	24.4
21	10.0	189	22.6

3.54 NIST Vent Study

A series of 15 reduced-scale enclosure experiments were conducted during the summer of 2017 by Summer Undergraduate Research Fellows (SURF) Fateema Farzana and Cory Schovanec. There is no test report or paper describing these experiments; only what is included here.

Enclosure Geometry

A drawing of the enclosure is given in Fig. 3.34. The enclosure consisted of two compartments stacked one on top of the other. The interior lateral dimensions of each compartment were 119 cm by 121 cm. The height of the lower compartment was 59 cm, and the upper was 61 cm. The enclosure was located within a vented laboratory space that was approximately 3 m by 3 m by 2.8 m high. The floor of this space was tiled, but a single sheet of gypsum board served as the lower floor of the test enclosure.

The front door was open in all experiments. For some portion of some of the experiments, the second floor was completely sealed. The leakage area was approximately 18 cm^2, measured at an over-pressure of 25 Pa.

Material Properties

The walls, ceiling and floor of each compartment was 1.6 cm (5/8 in) Type X gypsum board. Wood studs formed the exterior frame. Thermo-physical properties of the gypsum board were taken from in Ref. [243] and manufacturer literature. It was assumed that the specific heat was 1.089 kJ/(kg · K), thermal conductivity 0.15 W/m/K, and density 673 kg/m^3. Additionally, a layer of kaowool, shown in Fig. 3.34 was used to seal the gap between the removable roof and the second story walls. Aluminum tape was used to seal all other seams.

Burner

For all experiments, a 10 cm square propane burner fueled at a rate of 1.65 L/min generated a 2.5 kW fire according to the following calculation:

$$1.65\frac{\mathrm{L}}{\mathrm{min}} \times \frac{1}{60}\frac{\mathrm{min}}{\mathrm{s}} \times \frac{1}{1000}\frac{\mathrm{m^3}}{\mathrm{L}} \times 1.967\,\frac{\mathrm{kg}}{\mathrm{m^3}} \times 46,300\,\frac{\mathrm{kJ}}{\mathrm{kg}} = 2.50\,\mathrm{kW} \tag{3.14}$$

Note that the mass flow controller (Sierra Instruments SmartTrak 50) assumed standard conditions to be 0 °C and 101325 Pa. For Tests 13-15, a Dwyer flow meter was used in place of the mass flow controller. The flow meter had a flow range of 4 L/min air.

Thermocouples

Eight Type-K thermocouples were inserted at each level to measure the vertical temperature profile. The thermocouples formed a vertical array at 84 cm from the left wall of the enclosure, and 17 cm from the front wall. TC-1 was defined as the uppermost thermocouple, with heights defined as the vertical distance from the compartment specific floor.

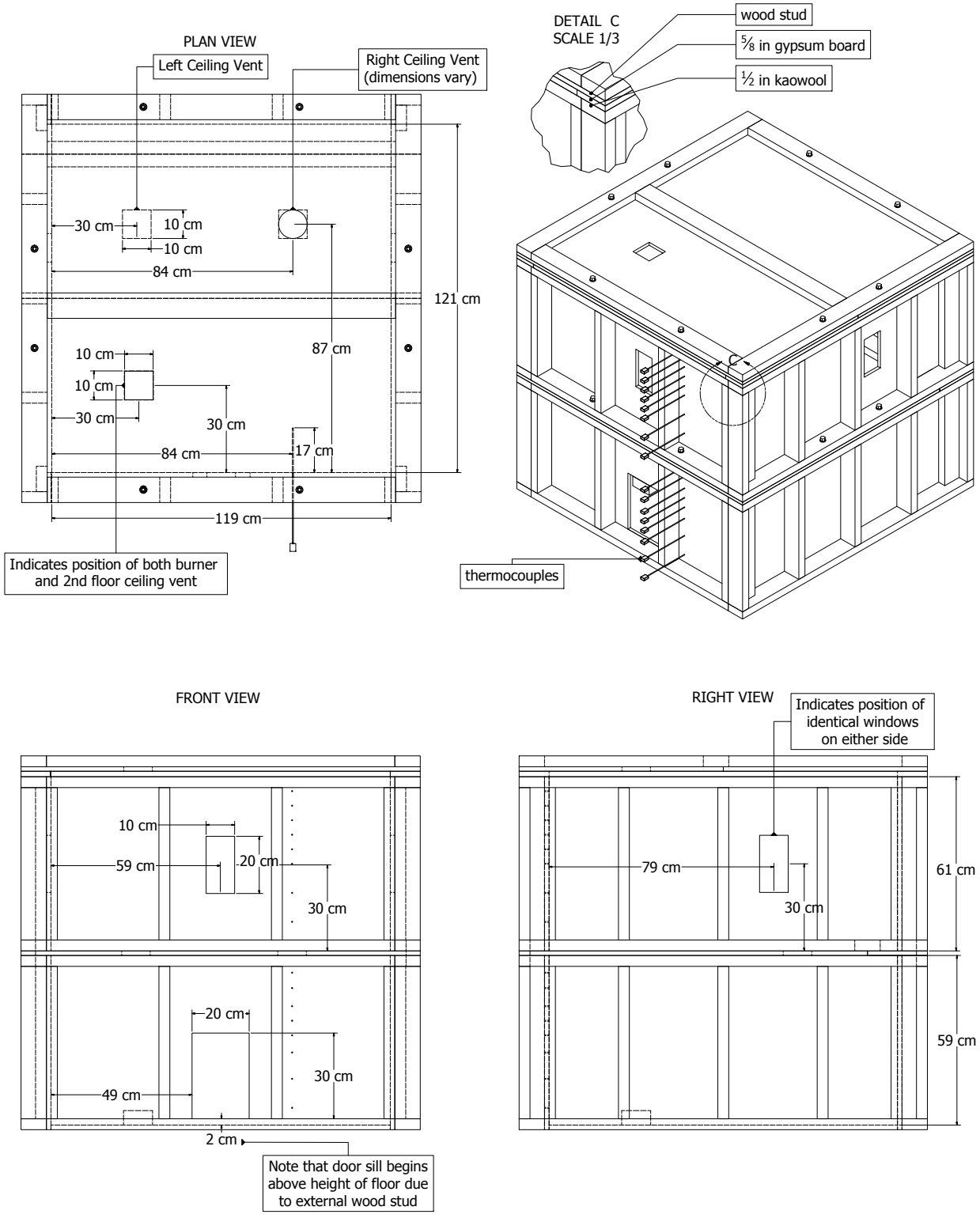

Figure 3.34: Geometry of the compartment from the NIST Vent Study

Table 3.24: Heights of the thermocouples above the floor of each level of the enclosure

Floor 2 TC's	1	2	3	4	5	6	7	8
Height (cm)	56.5	50.8	45.5	41.0	36.0	29.8	19.8	10.5
Floor 1 TC's	9	10	11	12	13	14	15	16
Height (cm)	51.8	47.0	40.64	35.6	30.48	25.7	16.5	7.0

Test Procedure

Each experiment lasted 100 min with a 5 min cool down period. Table 3.25 indicates the times when vents and windows were opened after the start of each experiment. For Test No. 1-4, two trials were performed. In each case, the difference in temperature remained within 3 percent, a difference of less than 1 °C. For this reason, no further replicates were conducted.

Table 3.25: Vent State by Experiment: Time Opened

Test No.	Front Window (min)	Left Window (min)	Right Window (min)	Left Vent (min)	Right Vent (min)	Left Vent Area (cm^2)	Right Vent Area (cm^2)	Right Vent Shape	Roof Vent (min)
1	0	0	0	Closed	0	0	100	Square	Closed
2	0	0	0	Closed	20	0	100	Square	Closed
3	60	40	Closed	Closed	20	0	100	Square	Closed
4	0	0	0	Closed	0	0	400	Square	Closed
5	0	0	0	Closed	20	0	400	Square	Closed
6	60	40	Closed	Closed	20	0	400	Square	Closed
7	0	0	0	0	0	100	400	Square	Closed
8	0	0	0	20	40	100	400	Square	Closed
9	80	60	Closed	20	40	100	400	Square	Closed
10	0	0	0	Closed	0	0	100	Circle	Closed
11	0	0	0	Closed	20	0	100	Circle	Closed
12	60	40	Closed	Closed	20	0	100	Circle	Closed
13	0	0	0	0	0	100	400	Square	0
14	0	0	0	20	40	100	400	Square	60
15	Closed	Closed	Closed	20	40	100	400	Square	60

3.55 NRCC Facade Heat Flux Measurements

A series of experiments was conducted by the Fire Research Section of the Institute for Research in Construction, National Research Council of Canada (NRCC), to measure the heat flux to a mock exterior building facade due to a fire within a compartment [244, 245]. The experiments selected for model validation were conducted using a series of propane line burners within a compartment whose interior dimensions were 5.95 m wide, 4.4 m deep, and 2.75 m high (see Fig. 3.35). There were five different door/window sizes:

1. 0.94 m by 2.00 m high
2. 0.94 m by 2.70 m high (door)
3. 2.60 m by 1.37 m high (shown in Fig. 3.35)
4. 2.60 m by 2.00 m high
5. 2.60 m by 2.70 m high (door)

There were four fire sizes: 5.5 MW, 6.9 MW, 8.6 MW, and 10.3 MW. In all, 19 experiments were conducted, with the exception of the 10.3 MW fire with Window 1. In each experiment, heat flux measurements were made 0.5 m, 1.5 m, 2.5 m, and 3.5 m above the top of the door/window.

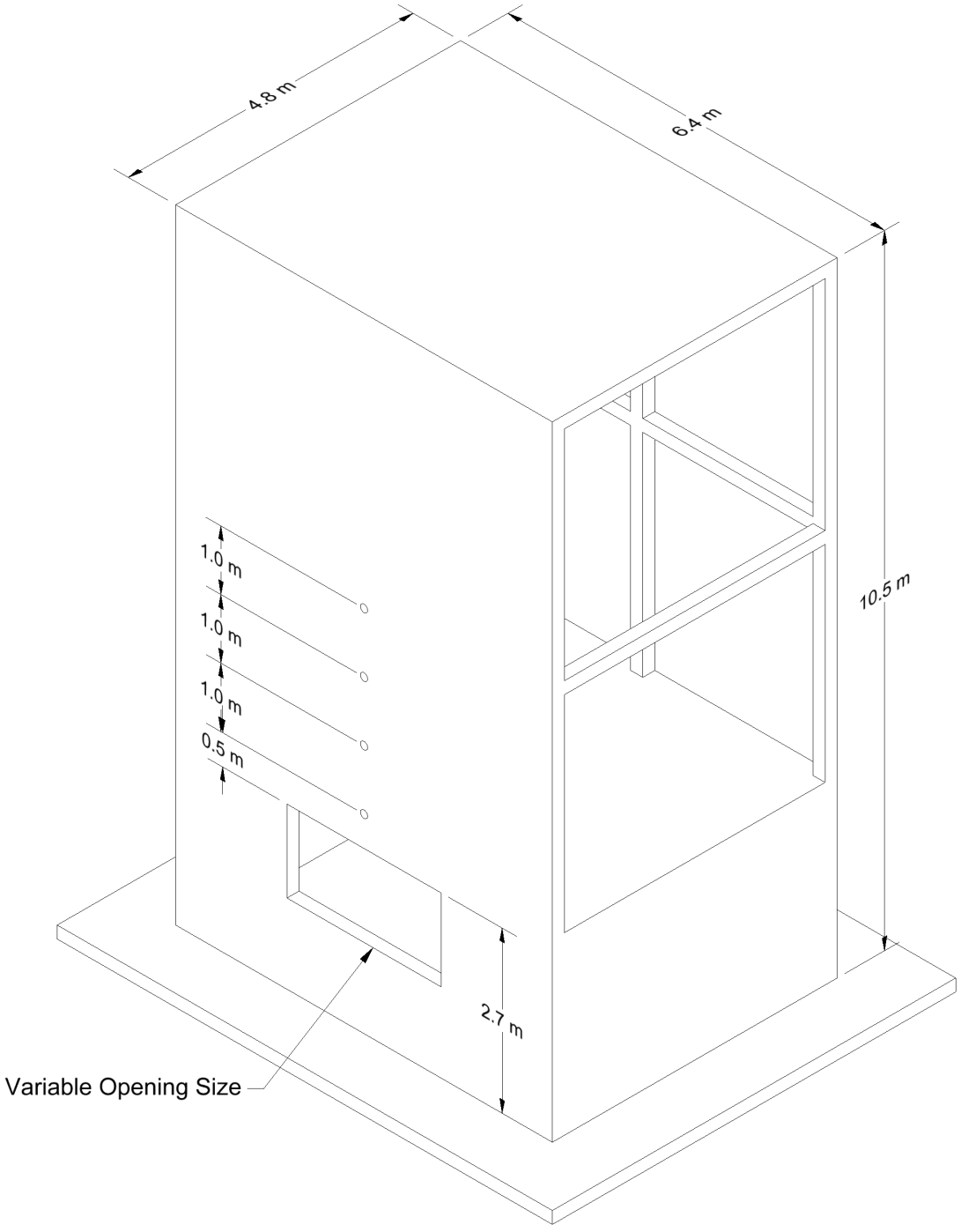

Figure 3.35: Geometry of the NRCC Facade Experiments.

3.56 NRCC Smoke Tower Experiments

In 2006 and 2007, the National Research Council of Canada (NRCC) conducted 10 fire experiments in a 10 story experimental facility in Almonte, Ontario to study smoke movement through the stair shaft to the upper floors of the building. Four of these experiments utilized actual commodities as fuel, and six utilized a propane burner. Four of the six propane fires were intended to reproduce the heat release of the commodity fires, and these experiments (BK-R, CMP-R, CLC-I-R, and CLC-II-R) have been chosen for this guide. Details of the experiments are included in a master's thesis and paper by Yan Wang [246, 247]. A description of FDS simulations of the propane experiments not included in this guide is given by Hadjisophocleous and Jia [248]. The analysis of the propane burner experiments discussed in this guide are based on the work of Paul Tyson at Ulster University as part of his master's thesis [249].

The tower was designed as a test bed for the center core of a high-rise building. It includes a compartment and corridor on each floor, a stair shaft, elevator shaft and service shafts [250]. Figure 3.36 displays the geometry of the building as modeled in FDS. All walls and floor slabs are taken to be 0.2 m thick. The first two floors are 3.4 m high, slab to slab. The upper eight floors are 2.4 m, slab to slab. The propane burner was located on the second floor and the smoke flowed through open doors to the stair vestibule and stair shaft itself. In the four experiments considered in this guide, the stair shaft was open on the fourth, sixth, eighth, and tenth floors. The other floors were closed off to the stair shaft. The ventilation system was turned off. A single door was opened on the first floor, and there were no other openings to the outside save natural building leakage. The referenced documents do not explicitly include estimates of leakage areas, but for the sake of modeling, the leakage for each floor was concentrated at a single 1.5 m by 1.5 m exterior window. The leakage area was specified based on an estimate of a "loose" building exterior in NFPA 92 [251]. This is a very important consideration in modeling because it determines the extent to which the smoke rising up the stair shaft encounters an opposing downward flow.

Thermocouples and gas analyzers were placed at various locations to measure temperature and O_2, CO_2 and CO concentrations. A vertical array of TCs was located in the fire compartment and the doorway leading into the stair shaft on the second floor. TCs were also placed at each floor in the stair shaft. The gas analyzers were located in the stair shaft at the second floor, just outside the door to the fire compartment.

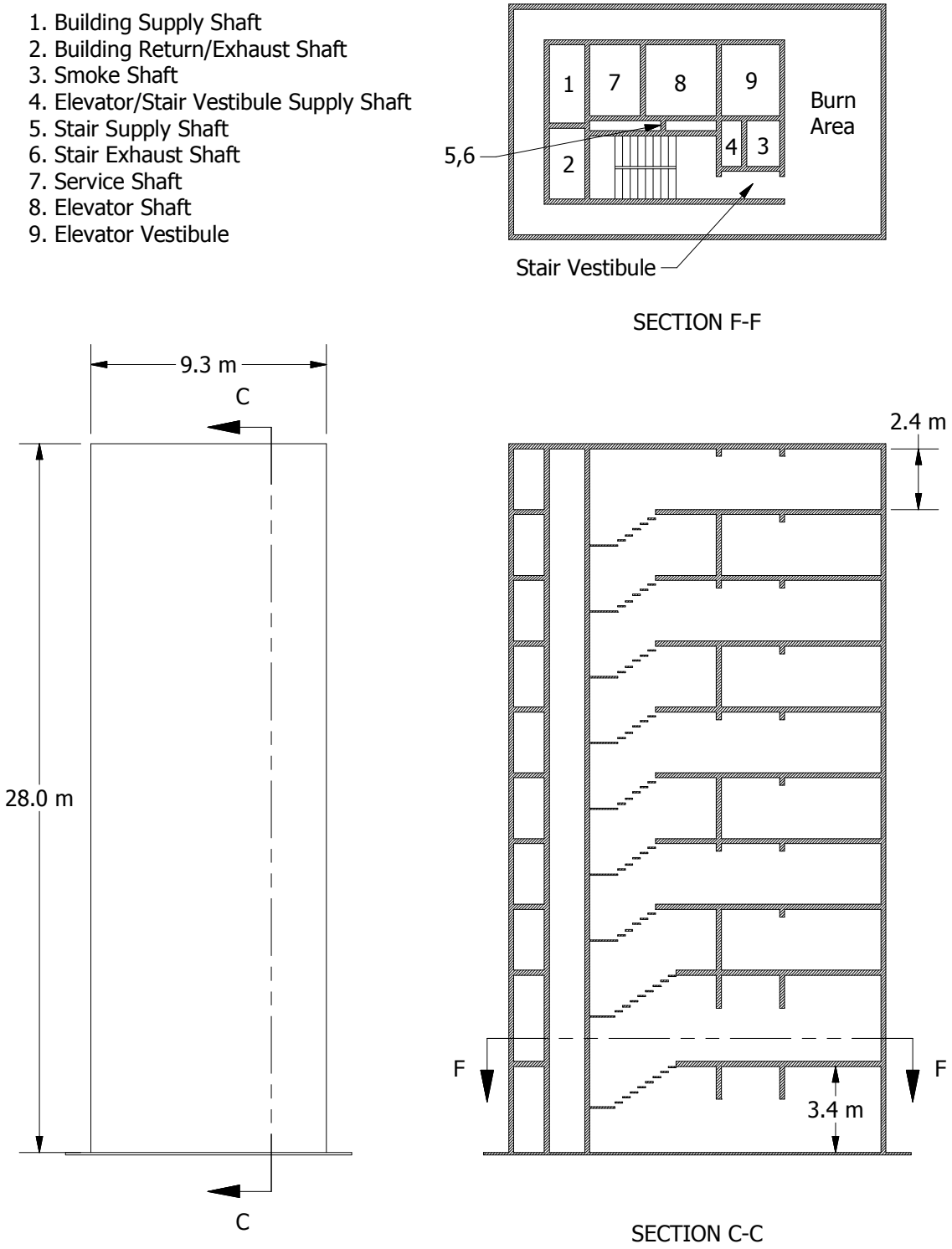

Figure 3.36: Geometry of the NRCC Smoke Tower Experiments.

3.57 NRL/HAI Wall Heat Flux Measurements

Back, Beyler, DiNenno and Tatem [252] measured the heat flux from 9 different sized propane fires set up against a wall composed of gypsum board. The experiments were sponsored by the Naval Research Laboratory and conducted by Hughes Associates, Inc., of Baltimore, Maryland. The square sand burner ranged in size from 0.28 m to 0.70 m, and the fires ranged in size from 50 kW to 520 kW.

3.58 Phoenix LNG Fires

In 2009, Sandia National Laboratories conducted two large-scale LNG pool fire experiments in a 120 m diameter pond in its Area III test complex in Albuquerque, New Mexico [253]. The fires were approximately 21 m and 83 m in diameter. Measurements of flame height, smoke production, burn rate, and heat flux were performed. A photograph of Test 2 is shown in Fig. 3.37.

Modeling Notes

The simulation of Test 1 uses 1 m grid cells, while Test 2 uses 2 m cells. The computational domain for both simulations forms the shape of a cross that includes the fire and the radiometers to the north, south, east and west. Methane is the specified fuel, with a soot yield of 0.01 and radiative fraction of 0.25. Both values are estimates.

There are 1200 solid angles, rather than the default 100, used in the radiative transport equation to uniformly distribute the fire's radiative energy outward approximately 250 m. The value of 1200 is based on an assessment of the contours of the integrated radiative intensity. Also, both wide and narrow-angle radiometer measurements were made at distances ranging from 100 m to 250 m from the pool center, with various inclination angles. For the narrow-angle measurements, FDS chooses the nearest discrete radiation angle to represent the narrow-angle heat flux. At such large distances, it is difficult to "find" an angle that emanates from the fire to the location of the device.

Flame Height Results: Section 6.2.3

Flame Tilt Results: Section 6.3

Heat Flux Results: Section 12.2.9

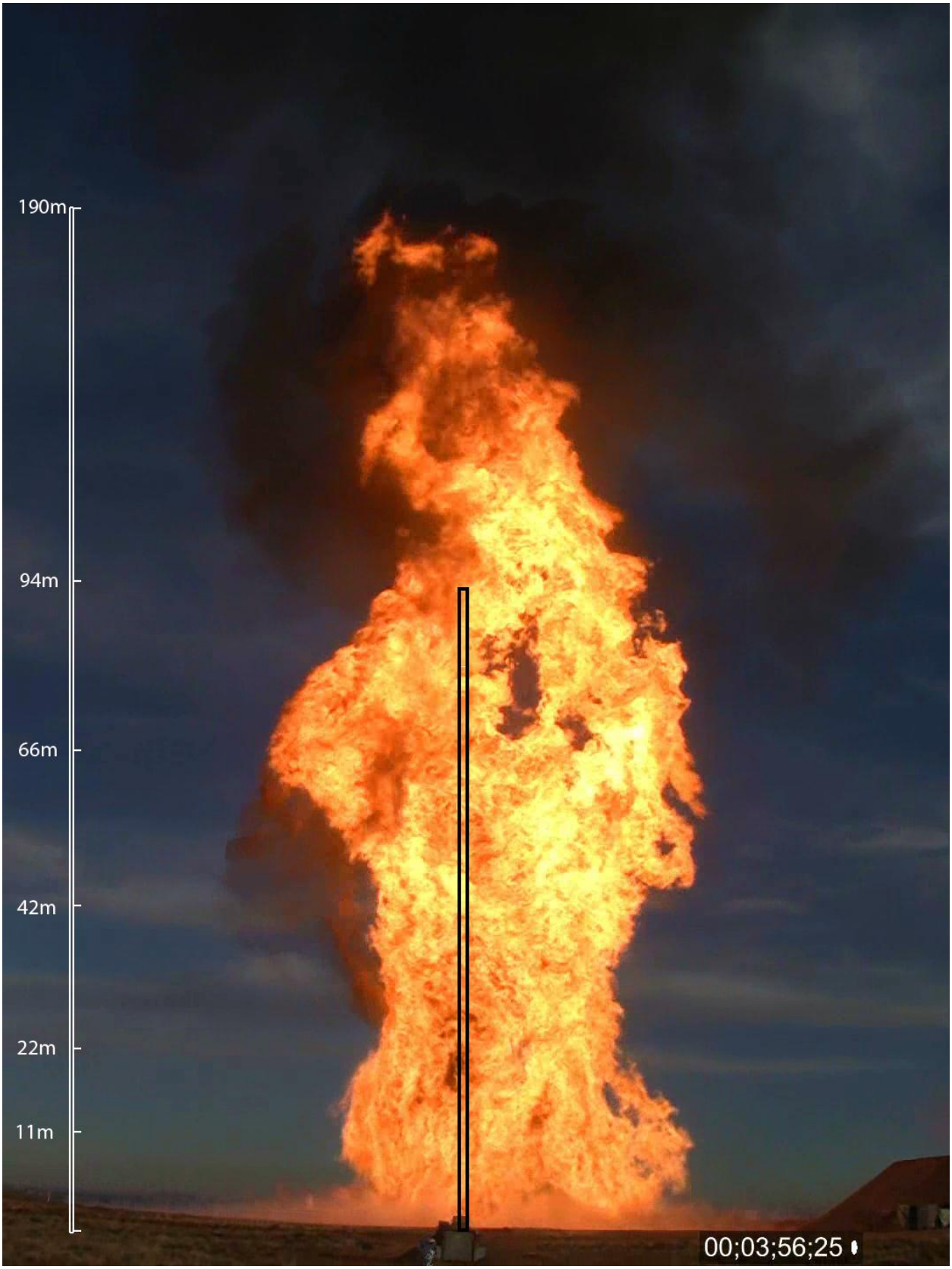

Figure 3.37: Photograph of Phoenix LNG Fire Test 2 [253].

3.59 Pool Fires

The "Pool Fires" cases include a variety of flammable and non-flammable liquid evaporation experiments:

1. A variety of pure liquid pool fires compiled by Gottuk and White [254] based on earlier compilations such as that by Mudan [255]. The liquids are listed in Table 3.26.

2. A single experiment involving the evaporation of water under a 50 kW/m^2 heat flux in the ASTM E2058 fire propagration apparatus, reported in Ref. [135].

3. Two heptane pool fire experiments described in Ref. [256].

Modeling Notes

Because there are few details concerning the burning rates cited by Gottuk and White [254], the pans for the fuels listed in Table 3.26, with the exception of water, are assumed to be 1 m square with a fuel depth of 10 cm.

The simulations of the VTT heptane pool fires are performed in a 4 m by 4 m by 6 m domain with open boundaries, and a circular pool with steel (one cell high and thick) lip. The pool surface is 1 m above the floor.

The burning rate of liquid hydrocarbon fuels has been found to correlate well with the ratio of the heat of combustion, Δh_c, and the heat of gasification, Δh_g:

$$\dot{m}'' = 0.001 \, \frac{\Delta h_c}{\Delta h_g} \quad ; \quad \Delta h_g = \Delta h_v + \int_{T_0}^{T_b} c_p \, dT \tag{3.15}$$

where Δh_v is the latent heat of vaporization, T_0 is the initial temperature, T_b is the boiling temperature, and c_p is the specific heat of the liquid fuel. The heat of gasification is the amount of energy required to raise the fuel from its initial temperature to its boiling temperature and evaporate it.

Table 3.26 lists the liquid fuel properties used in the simulations. Note that the heats of vaporization are evaluated at the liquid boiling temperature. The thermal conductivities, k, are found in Ref. [257], except for butane, which is found in Ref. [258]. The heats of combustion, Δh_c, are computed in FDS based on the heats of formation of the reactants and products listed in Ref. [259]. The heats of combustion account for the presence of products of incomplete combustion, like CO and soot.

The effective absorption coefficients. κ, for benzene and ethanol are based on curve fits to experimental data as explained in Appendix K of the FDS Technical Reference Guide. The absorption coefficient for methanol presented in Appendix K is calculated with the assumption that the incoming radiation is approximately blackbody radiation. The absorption coefficient for ethanol is calculated based on experimentally determined spectrum of an ethanol flame. Since both methanol and ethanol flames are low sooting, the blackbody radiation assumption is not correct. Instead it is assumed that the absorption coefficient for methanol should be of similar magnitude as that for ethanol. For heptane, butane and acetone the absorption coefficients are simple order of magnitude estimates.

Table 3.26: Liquid fuel properties.

Fuel	ρ kg/m^3 [260]	c_p kJ/(kg · K) [261]	k W/(m · K) [257]	Δh_v kJ/kg [258]	Δh_c kJ/kg See text	χ_r [135]	y_{CO} g/g [135]	y_s g/g [135]	T_b °C [262]	κ m^{-1} See text
Acetone	791	2.13	0.20	501	28555	0.27	0.003	0.014	56.15	100
Benzene	874	1.74	0.14	393	33823	0.60	0.067	0.181	80.15	123
Butane	573	2.28	0.12	385	44680	0.31	0.007	0.029	0	100
Ethanol	794	2.44	0.17	837	27474	0.25	0.001	0.008	78.35	1534.3
Heptane	675	2.24	0.14	317	43580	0.33	0.010	0.037	98.35	187.5
Methanol	796	2.48	0.20	1099	20934	0.16	0.001	0.001	64.65	1500
Water	1000	4.18	0.60	2260	N/A	N/A	N/A	N/A	100.0	140

3.60 PRISME Project

PRISME is the name of a fire test program conducted under the auspices of the Organization for Economic Cooperation and Development, Nuclear Energy Agency (OECD/NEA). The experiments were conducted at the French Institut de radioprotection et de sûreté nucléaire (IRSN) at Cadarache. A variety of experiments were conducted to study ventilation effects, electrical cable failure, and leakage. The test reports are not publicly available, but an entire edition of *Fire Safety Journal* documented various experimental and modeling studies [263].

The PRISME DOOR series consisted of six experiments, five of which involving two compartments connected by an open door (Tests 1-5) and one involving a third compartment (Test 6). The compartments were 5 m by 6 m by 4 m high. A well-instrumented ventilation system supplied air and exhausted combustion products at specified rates, but the thermal expansion of the gases caused these rates to change, a phenomenon that was intended to test the ventilation capabilities of the models. Wahlqvist and van Hees [264] modeled these experiments using FDS and contributed the input files for the cases documented in this guide.

The PRISME LEAK series consisted of experiments where smoke and heat flowed through various types of leaks between the test compartments. Instrumented cables were placed at various locations, and gas and solid phase temperatures were measured. FDS was used to simulate the heating up of the cables using the measured gas temperature several centimeters from the cables [265].

3.61 Purdue Flames

A turbulent buoyant diffusion flame is established on a diffuser burner with an exit diameter of 7.1 cm. The diverging angle of the burner is 7° such that the gaseous fuel (methane) is decelerated and forms a uniform velocity distribution at the burner exit [30]. The methane (CH4) mass flow rate (84.3 mg/s) The buoyant diffusion flame burns in a quiescent atmospheric pressure environment. The flame is surrounded by a screened enclosure to minimize flame disturbance. The Froude number of the flame is 0.109 and matches that of a 7.1 cm diameter liquid toluene pool fire [30, 32]. The total heat release rate of the methane flame is 4.2 kW under the assumption of complete combustion, and the visible flame height is approximately 36 cm [30]. Measured and computed vertical and horizontal velocity, mixture fraction, and temperature values for this flame have been reported by Xin et al. [30, 266] and Zhou et al. [32, 267]. The mean temperatures have been inferred from the measured species concentrations [30] by assuming an adiabatic flame. The interdependencies between species concentrations, temperature and specific heat have been ignored for determining the mean temperature.

3.62 Ranz Marshall Droplet Experiments

In 1952, Ranz and Marshall performed a set of droplet evaporation experiments that ultimately led to the development of Nusselt and Schmidt number correlations for droplets [268]. The experiments documented in Figure 8 and Tables 1-4 in the paper have been modeled with FDS. For Figure 8 of the paper, a 1043 μm water droplet was suspended in still dry air at an ambient temperature and pressure of 24.9 °C and 98792 Pa, and its diameter was measured over time. For the experiments in Tables 1-4 in the paper, droplets were suspended in a dry air stream. Experimental parameters include the fluid type (water or benzene), initial droplet diameter, ambient temperature, and velocity of the air stream. The evaporation rate in the simulations is calculated based the time required for the droplet to decrease in size to 350 μm, the minimum reported diameter. Table 3.27 summarizes the experiments.

Table 3.27: Summary of Ranz and Marshall droplet evaporation experiments.

Table No.	Test No.	Fluid	Diameter (μm)	Air Temperature (°C)	Pressure (Pa)	Velocity (m/s)
1	1	Water	954	19.9	99059	2.46
1	2	Water	954	24.6	98659	2.1
1	3	Water	954	24.9	98659	1.723
1	4	Water	954	25.3	98659	1.532
1	5	Water	954	25.4	98659	1.197
1	6	Water	954	24.3	98392	0.952
1	7	Water	954	24.4	98392	0.762
1	8	Water	954	24.5	98392	0.571
1	9	Water	954	24.5	98392	0.571
1	10	Water	954	24.6	98392	0.285
1	11	Water	954	24.7	98392	0.1513
1	12	Water	954	24.8	98392	0.1718
1	13	Water	954	24.9	98392	0.0841
1	14	Water	954	25.0	98392	0.0337
1	15	Water	954	23.2	98392	2.86
1	16	Water	954	23.6	99459	2.67
1	17	Water	954	23.7	99459	2.28
1	18	Water	954	24.0	99459	3.06
1	19	Water	954	24.9	98792	0
2	1	Water	950	90.0	98792	2.3
2	2	Water	950	77.5	98792	1.1
2	3	Water	950	78.7	98792	1.1
2	4	Water	950	78.7	98792	1.1
2	5	Water	950	84.0	98792	1.83
2	6	Water	950	82.5	98792	1.14
2	7	Water	950	83.0	98792	1.14
2	8	Water	950	66.4	98792	0.55
2	9	Water	950	71.4	98792	0.176
3	1	Water	850	115.0	98792	1.84
3	2	Water	710	115.0	98792	1.84
3	3	Water	560	85.0	98792	0.188
3	4	Water	460	85.0	98792	0.188

Table 3.27: Continued

Table No.	Test No.	Fluid	Diameter (μm)	Air Temperature (°C)	Pressure (Pa)	Velocity (m/s)
3	5	Water	960	221.0	98792	1.84
3	6	Water	580	221.0	98792	1.84
3	7	Water	880	193.0	98792	0.77
3	8	Water	600	193.0	98792	0.77
3	9	Water	1010	125.0	98792	0.21
4	1	Benzene	1100	24.4	97592	0.051
4	2	Benzene	1100	26.4	97592	0.153
4	3	Benzene	1100	27.1	98125	0.289
4	4	Benzene	1100	17.9	98525	0.748
4	5	Benzene	1100	17.5	98525	1.124
4	6	Benzene	1100	17.7	97725	1.5
4	7	Benzene	1100	20.7	97725	0.188
4	8	Benzene	1100	20.4	97725	0.283
4	9	Benzene	1100	19.9	97725	0.755
4	10	Benzene	1100	20.0	97725	1.13
4	11	Benzene	1100	20.2	97725	1.516
4	12	Benzene	1100	20.2	97725	1.9
4	13	Benzene	1100	20.4	97725	2.88

3.63 Restivo Compartment Air Flow Experiment

Velocity measurements for forced airflow within a 9 m by 3 m by 3 m high compartment (Fig. 3.38) were made by Restivo [269]. These measurements have been widely used to validate CFD models designed for indoor air quality applications. It was also used to assess early versions of FDS [19, 20, 38]. In the experiment, air was forced into the compartment through a 16.8 cm vertical slot along the ceiling running the width of the compartment with a velocity of 0.455 m/s. A passive exhaust was located near the floor on the opposite wall, with conditions specified such that there was no buildup of pressure in the enclosure. The component of velocity in the lengthwise direction was measured in four arrays: two vertical arrays located 3 m and 6 m from the inlet along the centerline of the room, and two horizontal arrays located 8.4 cm above the floor and below the ceiling, respectively. These measurements were taken using hot-wire anemometers. While data on the specific instrumentation used are not readily available, hot-wire systems tend to have limitations at low velocities, with typical thresholds of approximately 0.1 m/s.

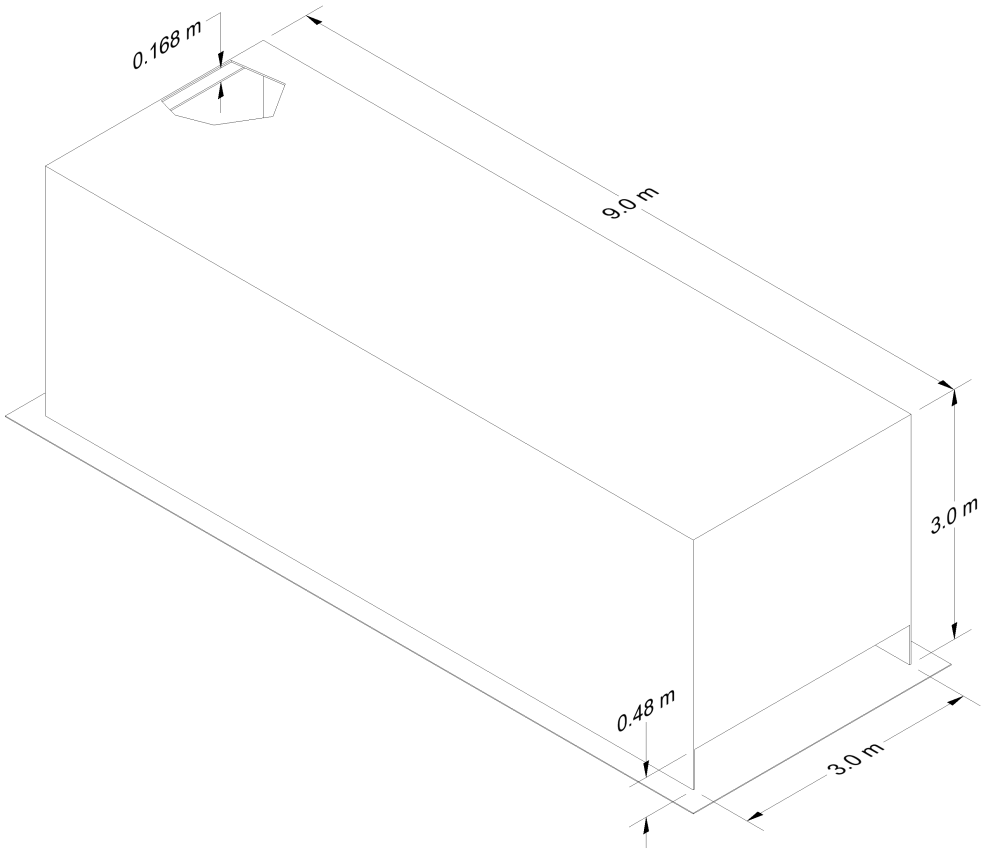

Figure 3.38: Geometry of Restivo's compartment.

3.64 Sandia Methane Burner

A series of 3 m diameter methane gas burner experiments were conducted in the Fire Laboratory for Accreditation of Models and Experiments (FLAME) facility in the Thermal Test Complex at Sandia National Laboratories [253]. The test chamber (Fig. 3.39) is cylindrical with an inner diameter of 18.3 m and a height of 13.1 m at the perimeter. The ceiling slopes upwards to a height of 15.2 m at the center. The perimeter walls are made of steel channel sections that are water-cooled. The gas burner is surrounded by a 12.7 m diameter steel spill plate. Beyond the spill plate is steel grating through which air can flow from the basement.

Modeling Notes

The simulations of the 3 m methane fires are done with 10 cm grid resolution in an open domain. That is, the walls of the cylindrical test cell are not modeled.

The radiative fraction is specified at 0.35 rather than the default 0.20 for methane because the large fire is far more sooty and luminous than a small methane flame. 600 solid angles are used to solve the radiative transport equation rather than the default 100 so as to resolve the radiative flux 9 m from the fire.

Flame Height Results: Section 6.2.3

Heat Flux Results: Section 12.2.10

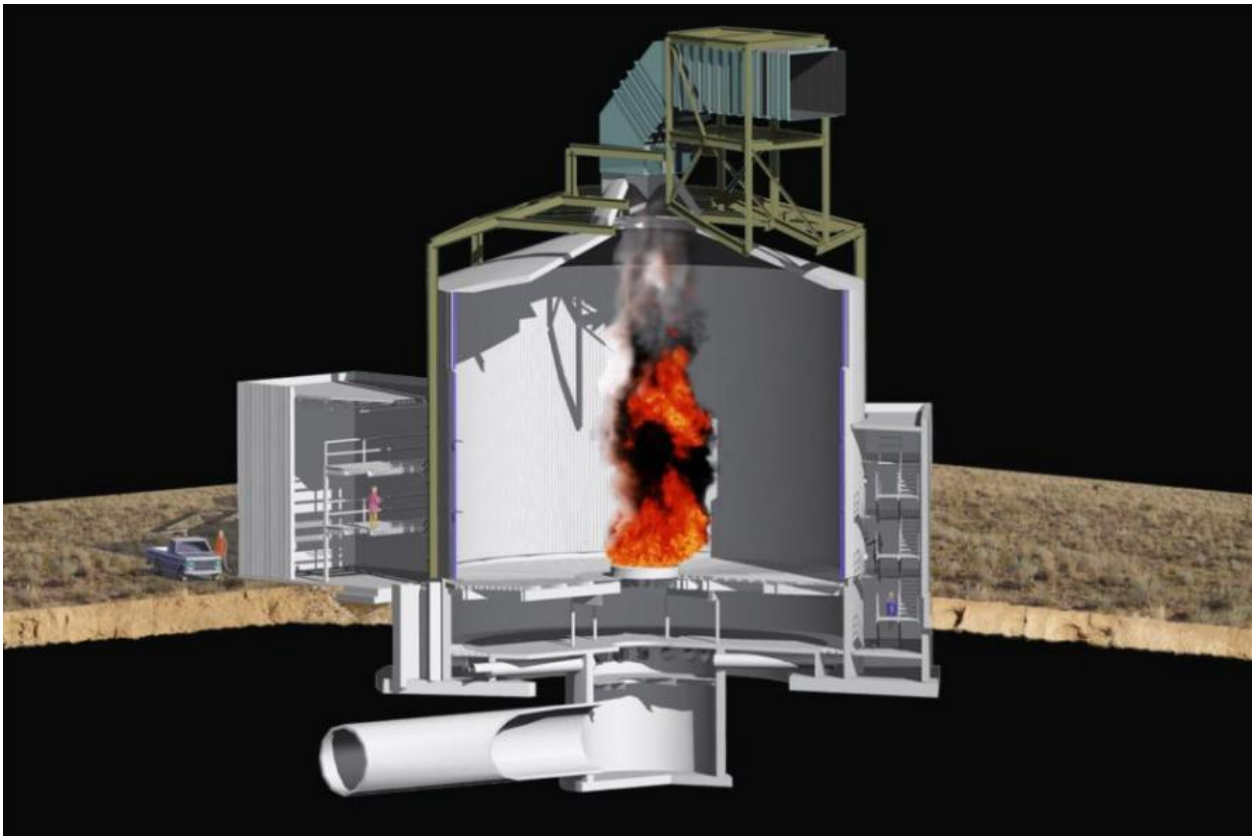

Figure 3.39: Cutaway view of the Sandia FLAME test cell.

3.65 Sandia Plume Experiments

The Fire Laboratory for Accreditation of Models by Experimentation (FLAME) facility [270, 271] at Sandia National Laboratories in Albuquerque, New Mexico, is designed specifically for validating models of buoyant fire plumes. The plume source is 1 m in diameter surrounded by a 0.5 m steel 'ground plane'. O'Hern et al. [270] studied a turbulent buoyant helium plume in the FLAME facility. PIV/PLIF techniques are used to obtain instantaneous joint scalar and velocity fields and thus obtain Favre averaged velocity fields. Earlier work to model this experiment has been performed by DesJardin et al. [272]. Tieszen et al. [273, 274] studied methane and hydrogen pool fires.

Modeling Notes

The data in the experimental repository for the helium plume is Favre averaged. The "helium" was actually a mixture of 96.4 vol % (0.7075 mass fraction) helium, 1.7 vol % (0.1809 mass fraction) acetone, and 1.9 vol % (0.1116 mass fraction) oxygen; this mixture is referred to as the "plume fluid" [270]. The data for "mass fraction" in the experimental repository is for Favre averaged plume fluid mass fraction. To account for any effect of differential diffusion, we separately transport helium, acetone, and oxygen in the simulations. Then the plume fluid mass fraction is obtained using the conversion $Y_{\text{plume fluid}} = Y_{\text{acetone}}/0.1809$.

Note that the velocity fields in the methane and hydrogen fire plumes were obtained directly from PIV and are therefore ensemble averaged [273, 274].

3.66 SETCOM Wall Condensation Experiments

The Separate Effect Test for Condensation Modeling (SETCOM) facility is located in Jülich, Germany [275]. The facility is a recirculating duct containing a flow conditioning section for establishing temperature and humidity and a test section for performing condensation experiments. The condensation section contains a 4 m or 5 m long, water-cooled, aluminum plate for its floor with the remaining walls adiabatic. The condensation section can be tilted from horizontal to vertical to investigate the effects of orientation on condensation. A set of five experiments were performed using the 4 m test section that measured the condensation heat flux from hot, high humidity air. Temperature, humidity, and flow rate were varied.

Modeling Notes

Prior to running the validation cases, a set of five scoping simulations were run with no condensation. These simulations used a short length of the test section with `PERIODIC` boundary conditions. These cases were used to determine the rms velocity as a function of the mean velocity.

The condensation simulations included a 4 m portion of duct upstream to allow for flow development, and a 1 m portion of duct downstream to avoid boundary effects on the test section. The upstream boundary condition was set with the conditions shown in the table below along with synthetic eddy method inputs using the rms velocity determine from the scoping simulations. The outlet was defined as an `OPEN` boundary. The experiments measured temperature 1.5 cm into the aluminum plate along the plate centerline. The test measured condensation heat transfer was used with the inside plate temperature to derive the plate surface temperature. The condensation plate `TMP_FRONT` was set to derived temperature as a function of length along the plate.

Table 3.28: Summary of SETCOM condensation experiments selected for model validation.

Test No.	Air Speed (m/s)	Temperature (°C)	Humidity (%)
1	0.8	86	69
2	1.8	84	57
3	3.7	79	59
4	4.2	78	71
5	5.2	75	71

3.67 Shell LNG Fireball Experiments

Shell Research Ltd. commissioned four large-scale BLEVE (Boiling Liquid Expanding Vapor Explosion) experiments using LNG (Liquified Natural Gas) at the DNV (Det Norske Veritas) GL test facility at Spadeadam, UK [276]. For Experiments 2-4, the cylindrical containment vessel (Fig. 3.40) was constructed of 6 mm stainless steel plates and had a length of approximately 6.5 m and diameter of approximately 1 m, with a total volume of 5.055 m^3. The mass of LNG for Experiments 2-4 was approximately 681 kg, 1306 kg, and 1251 kg, respectively. The LNG consisted of 96.7 % methane, 3.0 % ethane, 0.2 % nitrogen, and 0.1 % propane, by volume. The reservoir pressure for Experiments 2-4 was maintained at 13.01 bar, 6.07 bar, and 13.62 bar; and the temperatures were -115 °C, -131 °C, and -115 °C, respectively.

Figure 3.40: (Top) Pressure vessel used in the Shell LNG Fireball experiments. (Bottom) Photographs of Tests 2, 3, and 4, respectively [276].

The rupture of the vessels was initiated by an explosive cutting charge designed to rip open the vessel from end to end. Commercial fireworks were ignited just prior to the explosive charge to ensure ignition of the released gas.

Radiometers and pressure transducers were positioned at various distances from the vessel. Only a fraction of the data has been made public, including radiometer measurements at distances of 40 m, 70 m, and 100 m.

Modeling Notes

The FDS simulations of the three BLEVE experiments are performed with 1 m resolution spanning a volume that is 200 m long, 120 m wide, and 200 m high. The specified mass of LNG is injected uniformly for 0.2 s at the ground over an area 4 m long and 4 m wide. An inert obstruction that is 1 m long by 1 m wide and 1 m tall is suspended 1 m above the spill region to represent the remains of the containment vessel. No attempt is made to model the destuction of the vessel or the subsequent spill of LNG.

Approximately 600 angles are used in the radiative transport solver rather than the default 100. A radiative fraction of 30 % is used, rather than the default of 20 % for methane.

Heat Flux Results: Section 12.2.11

3.68 Sippola Aerosol Deposition Experiments

Mark Sippola, a doctoral student at the University of California, Berkeley, measured aerosol deposition velocities for various sizes of monodisperse fluorescent particles and various air velocities in a duct [277, 278]. The experimental facility consisted of a duct loop with a section for injecting fluorescent aerosol particles. The loop contained four measurement sections with two sections located after a long segment of straight duct such that fully-developed flow profiles existed. The experiments considered here include tests with measurements in the fully-developed flow test sections. Tests included 16 test for straight smooth steel duct and 15 tests in a straight duct lined with insulation. Based upon pressure drop measurements made in the duct, the roughness of the insulated duct was estimated as 1.5 mm. Both ducts had dimensions of 15 cm by 15 cm. The particle diameters were nominally 1 μm, 3 μm, 5 μm, 9 μm, and 16 μm. The air velocities in the duct were nominally 2.2 m/s, 5.3 m/s, and 9.0 m/s. In each test section, a total of twelve panels (20 cm by 10 cm) were cut from the duct section to measure the amount of particles deposited to the duct surfaces; four panels each from the duct ceiling, wall, and floor surfaces. Fluorescent measurement techniques and aerosol concentration measurements were used to calculate the deposition velocities of the particles to duct surfaces (ceiling, wall, and floor) in each of the two straight duct sections where the turbulent flow profile was fully developed. The experiments are summarized in Table 3.29.

Modeling Notes

FDS treats smoke particulate and aerosols in a similar way to other gaseous combustion products, basically a tracer gas whose production rate is a fixed fraction of the fuel consumption rate. However, there is an option in the model to allow smoke or aerosols to deposit on solid surfaces, thus reducing its concentration in the product stream. The particle deposition velocity, u_{dep}, is calculated by

$$u_{\text{dep}} = \frac{J_1 + J_2 + J_3 + J_4}{4\, C_{\text{avg}}} \tag{3.16}$$

where J_1 through J_4 are the deposition fluxes (kg/(m$^2 \cdot$ s)) for duct panels 1 through 4 given by

$$J = \frac{m_{\text{d}}}{A_{\text{d}}\, \Delta t} \tag{3.17}$$

where m_{d} is the mass of particles on the duct panel (kg), A_{d} is the area of the duct panel (m^2), and Δt is the duration over which the aerosol deposits onto the panel (s). C_{avg} is the average aerosol concentration in the duct test section (kg/m^3) and is given by

$$C_{\text{avg}} = \frac{C_{\text{upstream}} + C_{\text{downstream}}}{2} \tag{3.18}$$

Table 3.29: Summary of Sippola aerosol deposition experiments selected for model validation.

Test No.	Air Speed (m/s)	Particle Diameter (μm)	Particle Density (kg/m^3)
1	2.2	1.0	1350
2	2.2	2.8	1170
3	2.1	5.2	1210
4	2.2	9.1	1030
5	2.2	16	950
6	5.3	1.0	1350
7	5.2	1.0	1350
8	5.2	3.1	1170
9	5.4	5.2	1210
10	5.3	9.8	1030
11	5.3	16	950
12	9.0	1.0	1350
13	9.0	3.1	1170
14	8.8	5.4	1210
15	9.2	8.7	1030
16	9.1	15	950
17	2.2	1.0	1350
18	2.2	3.0	1170
19	2.2	5.3	1190
20	2.2	8.4	1090
21	2.2	13	960
22	5.3	1.0	1350
23	5.2	2.9	1170
24	5.2	4.9	1190
25	5.3	8.2	1090
26	5.3	13	960
27	8.9	1.0	1350
28	8.7	2.8	1170
29	8.8	5.0	1190
30	8.9	8.4	1090
31	8.9	13	960

3.69 Smyth Slot Burner Experiment

Kermit Smyth et al. conducted diffusion flame experiments at NIST using a methane/air Wolfhard-Parker slot burner. The experiments are described in detail in Refs. [279, 280]. The Wolfhard-Parker slot burner consists of an 8 mm wide central slot flowing fuel surrounded by two 16 mm wide slots flowing dry air with 1 mm separations between the slots. The slots are 41 mm in length. Measurements were made of all major species and a number of minor species along with temperature and velocity. Experimental uncertainties have been reported as 5 % for temperature and 10 % to 20 % for the major species.

Modeling Notes

A two-step combustion scheme (a modified version of the mechanism by Andersen et al. [281]) is used to simulate the Smyth Slot Burner Experiment. A 2D DNS calculation is run at two different grid resolutions: 0.250 mm and 0.125 mm. In the modified mechanism, the hydrocarbon/oxygen reaction to CO is assumed to be infinitely fast (mixed is burnt) to avoid complications of modeling ignition. The reversible CO to CO_2 reaction is modeled with Arrhenius kinetics. As discussed by Westbrook and Dryer [282], the kinetic constants for the reduced CO mechanism may be model dependent. Here, the Arrhenius constant for the forward CO to CO_2 reaction is tuned to match the Smyth experimental data.

A second set of simulations is run at the same two spatial resolutions, but in these cases both the first and second reactions are infinitely fast. However, the first reaction, where fuel is converted to CO and H_2O, proceeds before the second, where the CO is converted to CO_2. That is, the reactions are run serially rather than in parallel to illustrate that while both reactions are relatively fast compared to the mixing time scale, the first reaction is faster than the second. This assumption breaks down when the mixing time scale drops below approximately 3×10^{-4} s, which is on the order of δ/s_L, the flame thickness divided by the laminar flame speed. For this reason, a lower limit on the time-scale (`TAU_CHEM=3E-4`) is imposed. This same modeling strategy is used in the large eddy simulations of the NIST Reduced Scale Enclosure (RSE) experiments of 1994 (Section 3.44.1), RSE 2007 (Section 3.44.2), Full-Scale Enclosure (FSE) 2008 (Section 3.44.3), UMD Line Burner experiments 3.80, and Waterloo Methanol Experiments (Section 3.90). Note that in these LES simulations, the parameter `TAU_CHEM` is irrelevant—it is only needed when the grid resolution is on the order of 0.1 mm or less.

Comparisons of the simulations with measurements can be found in Section 9.5.1.

3.70 SP Adiabatic Surface Temperature Experiments

In 2008, three compartment experiments were performed at SP Technical Research Institute of Sweden under the sponsorship of Brandforsk, the Swedish Fire Research Board [283]. The objective of the experiments was to demonstrate how plate thermometer measurements in the vicinity of a simple steel beam can be used to supply the boundary conditions for a multi-dimensional heat conduction calculation for the beam. The adiabatic surface temperature was derived from the plate temperatures.

The experiments were performed inside a standard compartment designed for corner fire testing (ISO 9705). The compartment is 3.6 m deep, 2.4 m wide and 2.4 m high and includes a door opening 0.8 m by 2.0 m (Fig. 3.41). The room was constructed of 20 cm thick light weight concrete blocks with a density of 600 kg/m^3 $\pm$ 100 kg/m^3. The heat source was a gas burner run at a constant power of 450 kW. The top of the burner, with a square opening 30 cm by 30 cm, was placed 65 cm above the floor, 2.5 cm from the walls. A single steel beam was suspended 20 cm below the ceiling along the centerline of the compartment. There were three measurement stations along the beam at lengths of 0.9 m (Position A), 1.8 m (Position B), and 2.7 m (Position C) from the far wall where the fire was either positioned in the corner (Tests 1 and 2), or the

center (Test 3). The beam in Test 1 was a rectangular steel tube filled with an insulation material. The beam in Tests 2 and 3 was an I-beam. A diagram of the room used in Test 2 is displayed in Figure 3.41.

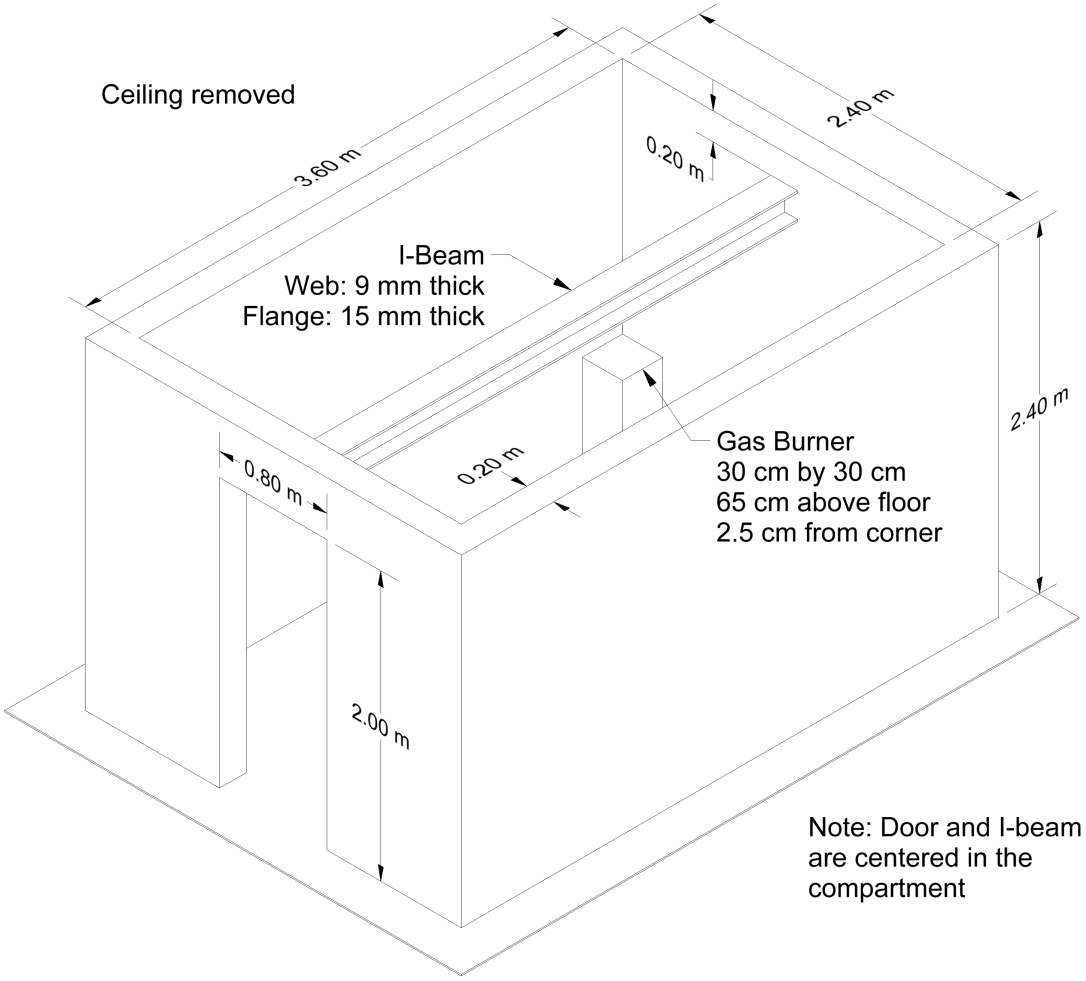

Figure 3.41: Geometry of the SP/AST compartment for Test 2.

A second series of experiments involving plate thermometers was carried out in 2011 [284]. A 6 m long, 20 cm diameter vertical steel column was positioned in the center of 1.1 m and 1.9 m diesel fuel and 1.1 m heptane pool fires. Gas, plate thermometer, and surface temperatures were measured at heights of 1 m, 2 m, 3 m, 4 m, and 5 m above the pool surface. These experiments are notable because the column is partially engulfed in flames.

A third series of experiments involving plate thermometers was conducted in 2015 [285]. A simple compartment with a single door was constructed and instrumented primarily with plate thermometers. The compartment was 2.7 m long, 1.8 m wide, and 1.8 m tall, with a 0.6 m by 1.5 m door centered on one of the short walls. The PTs were affixed to the walls. The 12 experiments were conducted with four different wall linings. In Series A, the compartment was lined with a 10 cm thick light concrete block. In Series B, the compartment was lined with a 5 cm thick layer of insulation backed by a 3 mm thick plate of steel. In Series C, the compartment was lined with an uninsulated 3 mm thick steel plate. In Series D,

the compartment was lined with a 3 mm thick steel plate backed by a 5 cm thick layer of insulation (the opposite of Series B). The fires were fueled by a 0.3 m by 0.3 m propane burner located in the center of the room except for Test A3, where it was centered on the back wall. For most of the experiments, the heat release rate was 1000 kW, except for A2 and C1, which were 500 kW, and A4 and C3, which employed linear ramp-ups to 1250 kW.

3.71 SP Wood Crib Experiments

Hansen and Ingason burned piles of reduced-scale wood pallets in a reduced-scale wind tunnel to develop a simple model that predicts the heat release rate of multiple objects separated by varying distances [286, 287]. The tunnel was 10 m long with a rectangular cross section 0.6 m wide by 0.4 m tall. Four piles of 1:4 scale pallets were placed at various positions in the tunnel. Each pile of 5 pallets was 0.3 m long, 0.2 m wide and 0.18 m tall. The fire was ignited on the windward side of the upwind pile with a 3 cm by 3 cm by 2.4 cm block of fiberboard soaked in 9 mL of heptane. The HRR was measured, along with temperature, heat flux, and oxygen concentration at various locations.

Modeling Notes

The FDS simulations of these experiments were originally performed by Janardhan and Hostikka [288, 147] using a variety of pyrolysis models in which the pallets are partially resolved. Here, however, the piles of pallets are modeled as an array of Lagrangian particles in lieu of solid obstructions so that a relatively coarse grid of 4 cm can be used. The modeling strategy is very similar to that used for vegetation in wildfire simulations. The wood planks are characterized as a homogenous collection of flat disks with a surface area to volume ratio $\sigma = 460$ m^{-1} and a packing ratio $\beta = 0.42$. The packing ratio is the bulk crib mass per unit volume divided by the density of the wood, m'''/ρ_{wood}. The average mass of a pile of pallets is 1.7 kg.

The radiation absorption coefficient is taken as $\kappa = C_{\text{s}}\sigma\beta$, where the shape factor, or ratio of plate surface area to projected area, is $C_{\text{s}} = 0.25$. The absorption coefficient, κ, also appears in the formula for wind drag, where the pressure drop, Δp, over a distance, L, is given by $\Delta p/L = 0.5\rho C_{\text{d}}\kappa u^2$. The drag coefficient, $C_{\text{d}} = 2.8$, was measured by Falkenstein-Smith et al. [162] in a study of vegetation. Its application to wood cribs has not been validated.

The wood is assumed to pyrolyze, forming $C_{3.4}H_{6.2}O_{2.5}$ [66] with a heat of combustion of 18.1 MJ/kg [286], according to the following reaction scheme [147]:

$$\text{Wet Wood} \quad \rightarrow \quad \frac{M}{1+M}\,\text{H}_2\text{O} + \frac{1}{1+M}\,\text{Dry Wood} \tag{3.19}$$

$$\text{Dry Wood} \quad \rightarrow \quad \nu_{\text{char}}\,\text{Char} + (1-\nu_{\text{char}})\,\text{Fuel Gas} \tag{3.20}$$

$$\tag{3.21}$$

The reaction rates are given by [147]:

$$r_{\text{H}_2\text{O}} = \left(\frac{\rho_{\text{s,H}_2\text{O}}}{\rho_{\text{s,0}}}\right)^{3.31} A_{\text{H}_2\text{O}} \exp\left(-\frac{E_{\text{H}_2\text{O}}}{RT}\right) \tag{3.22}$$

$$r_{\text{wood}} = \left(\frac{\rho_{\text{s,wood}}}{\rho_{\text{s,0}}}\right)^{1.69} A_{\text{wood}} \exp\left(-\frac{E_{\text{wood}}}{RT}\right) \tag{3.23}$$

The equation governing the temperature of the solid is

$$\rho_{\text{s}}\, c\, \frac{\partial T}{\partial t} = -\rho_{\text{s,0}}\left(\Delta h_{\text{H}_2\text{O}}\, r_{\text{H}_2\text{O}} + \Delta h_{\text{wood}}\, r_{\text{wood}}\right) + \nabla\cdot\dot{\mathbf{q}}''_{\text{c}} + \nabla\cdot\dot{\mathbf{q}}''_{\text{r}} \tag{3.24}$$

The parameters for the pyrolysis model are listed in Table 3.30.

Table 3.30: Parameters for SP Wood Cribs simulations [147].

Property	Units	Value
M	kg/kg	0.016
ρ_{H_2O}	kg/m^3	1000
c_{H_2O}	kJ/kg/K	4.18
k_{H_2O}	W/m/K	0.1
A_{H_2O}		9.57×10^{22}
E_{H_2O}	J/mol	136000
Δh_{H_2O}	kJ/kg	2500
ρ_{wood}	kg/m^3	393
c_{wood}	kJ/kg/K	$0.85 + 0.00241(T-20)$
k_{wood}	W/m/K	$0.07 + 0.00038(T-20)$
ε_{wood}		0.95
A_{wood}		141000
E_{wood}	J/mol	89700
Δh_{wood}	kJ/kg	250
ρ_{char}	kg/m^3	135
c_{char}	kJ/kg/K	(see Ref. [147])
k_{char}	W/m/K	$0.11 + 0.00031(T-20)$
ε_{char}		1.0
ν_{char}	g/g	0.195

3.72 Steckler Compartment Experiments

Steckler, Quintiere and Rinkinen performed a set of 55 compartment fire tests at NBS in 1979. The compartment was 2.8 m by 2.8 m by 2.13 m high[5], with a single door of various widths, or alternatively a single window with various heights. A 30 cm diameter methane burner was used to generate fires with heat release rates of 31.6 kW, 62.9 kW, 105.3 kW and 158 kW. Vertical profiles of velocity and temperature were measured in the doorway, along with a single vertical profile of temperature within the compartment. A full description and results are reported in Reference [289]. The basic test matrix is listed in Table 3.31. Note that the test report does not include a detailed description of the compartment. However, an internal report[6] by the test sponsor, Armstrong Cork Company, reports that the compartment floor was composed of 19 mm calcium silicate board on top of 12.7 mm plywood on wood joists. The walls and ceiling consisted of 12.7 mm ceramic fiber insulation board over 0.66 mm aluminum sheet attached to wood studs. A diagram of the compartment is displayed in Fig. 3.42.

[5]The test report gives the height of the compartment as 2.18 m. This is a misprint. The compartment was 2.13 m high.

[6]*Technical Research Report, Fire Induced Flows Through Room Openings - Flow Coefficients*, Project 203005-003, Armstrong Cork Company, Lancaster, Pennsylvania, May, 1981.

Table 3.31: Summary of Steckler compartment experiments.

Test	Door Width (m)	Door Height (m)	HRR $\dot{Q}$ (kW)	Burner Location	Test	Door Width (m)	Door Height (m)	HRR $\dot{Q}$ (kW)	Burner Location
10	0.24	1.83	62.9	Center	224	0.74	0.92	62.9	Back Corner
11	0.36	1.83	62.9	Center	324	0.74	0.92	62.9	Back Corner
12	0.49	1.83	62.9	Center	220	0.74	1.83	31.6	Back Corner
612	0.49	1.83	62.9	Center	221	0.74	1.83	105.3	Back Corner
13	0.62	1.83	62.9	Center	514	0.24	1.83	62.9	Back Wall
14	0.74	1.83	62.9	Center	544	0.36	1.83	62.9	Back Wall
18	0.74	1.83	62.9	Center	512	0.49	1.83	62.9	Back Wall
710	0.74	1.83	62.9	Center	542	0.62	1.83	62.9	Back Wall
810	0.74	1.83	62.9	Center	610	0.74	1.83	62.9	Back Wall
16	0.86	1.83	62.9	Center	510	0.74	1.83	62.9	Back Wall
17	0.99	1.83	62.9	Center	540	0.86	1.83	62.9	Back Wall
22	0.74	1.38	62.9	Center	517	0.99	1.83	62.9	Back Wall
23	0.74	0.92	62.9	Center	622	0.74	1.38	62.9	Back Wall
30	0.74	0.92	62.9	Center	522	0.74	1.38	62.9	Back Wall
41	0.74	0.46	62.9	Center	524	0.74	0.92	62.9	Back Wall
19	0.74	1.83	31.6	Center	541	0.74	0.46	62.9	Back Wall
20	0.74	1.83	105.3	Center	520	0.74	1.83	31.6	Back Wall
21	0.74	1.83	158.0	Center	521	0.74	1.83	105.3	Back Wall
114	0.24	1.83	62.9	Back Corner	513	0.74	1.83	158.0	Back Wall
144	0.36	1.83	62.9	Back Corner	160	0.74	1.83	62.9	Center*
212	0.49	1.83	62.9	Back Corner	163	0.74	1.83	62.9	Back Corner*
242	0.62	1.83	62.9	Back Corner	164	0.74	1.83	62.9	Back Wall*
410	0.74	1.83	62.9	Back Corner	165	0.74	1.83	62.9	Left Wall*
210	0.74	1.83	62.9	Back Corner	162	0.74	1.83	62.9	Right Wall*
310	0.74	1.83	62.9	Back Corner	167	0.74	1.83	62.9	Front Center*
240	0.86	1.83	62.9	Back Corner	161	0.74	1.83	62.9	Doorway*
116	0.99	1.83	62.9	Back Corner	166	0.74	1.83	62.9	Front Corner*
122	0.74	1.38	62.9	Back Corner					* Raised burner

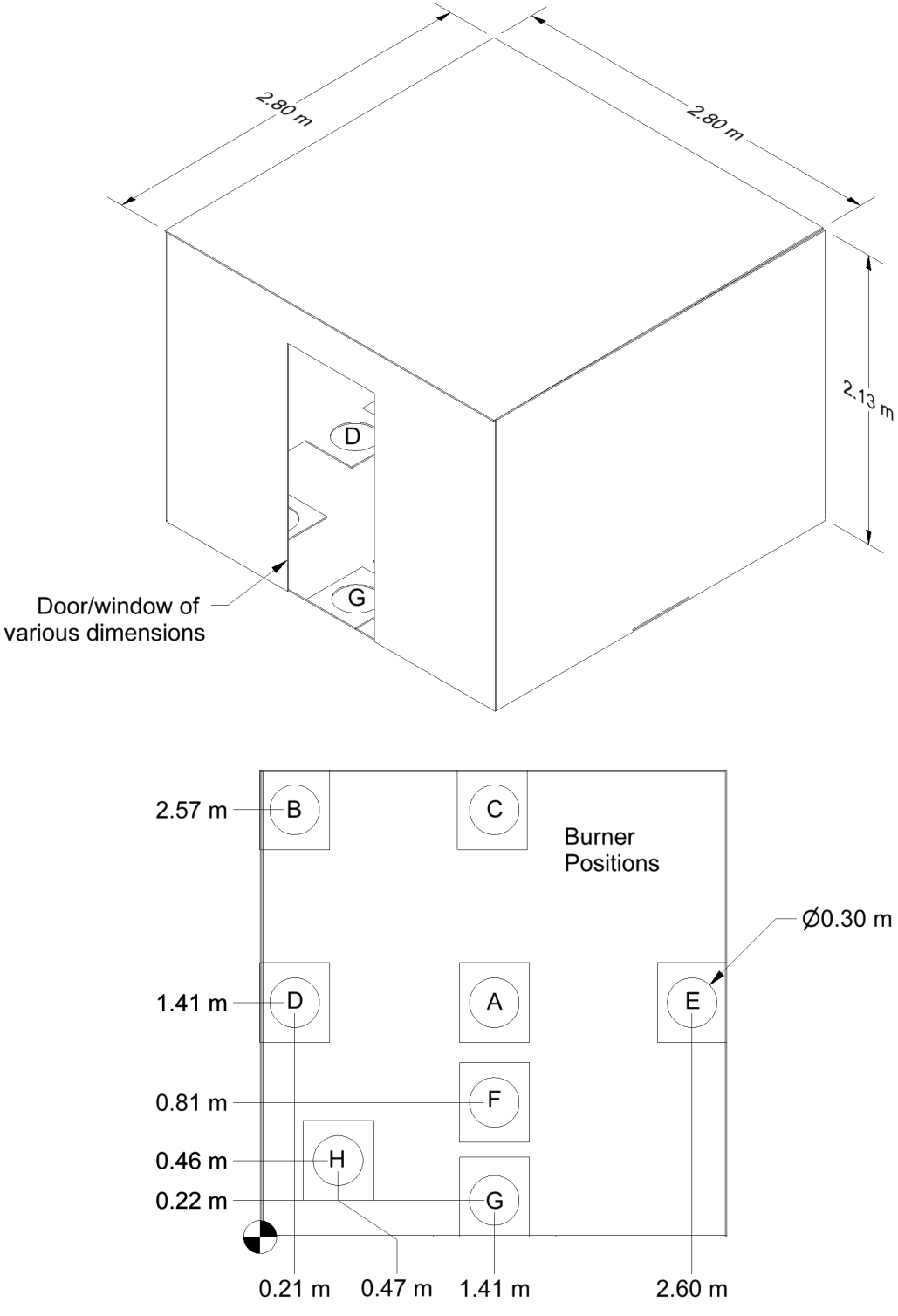

Figure 3.42: Geometry of the Steckler Compartment Experiments.

3.73 SWJTU Tunnel Experiments

Fires fueled by methanol and propane ranging from 5.6 kW to 16.8 kW were conducted in a 1:20 reduced-scale tunnel at Southwest Jiaotong University, Chengdu, China [290]. The tunnel was 0.45 m wide, 0.23 m high and 20.8 m long. The burner was located at the center of the tunnel and both ends were open. Temperatures and gas concentrations (i.e., O_2, CO and CO_2) were measured. The results showed that both methanol and propane fires self-extinguished in the 20.8 m long tunnel within approximately 10 min, except for the 5.6 kW methanol fire. The larger the heat release rate, the faster the self-extinction of the fire. The oxygen concentrations in the 20.8 m long tunnel decreased to approximately 12 % except for the 5.6 kW methanol fire, which remained well above the limiting oxygen concentration. Self-extinction was not observed for fires of the same heat release rates in a 10 m long tunnel of the same cross section. The oxygen concentrations in the 10 m long tunnel decreased to approximately 17 %. In the long tunnel with large fire sizes, the smoke layer descended to the floor, inhibiting the supply of fresh air reaching the fire.

3.74 Wu Bakar Tunnel Experiments

An important issue in road tunnel design with respect to fire safety is *back-layering*. In the event of a fire in a tunnel, a common strategy is to blow the smoke in one direction to allow occupants to escape and first responders to find the fire. The extent to which smoke from the fire spreads against imposed ventilation is known as back-layering. Experiments to quantify back-layering have been conducted at both small and full-scale. One important set of small-scale experiments was performed by Wu and Bakar [291]. The experiments were conducted in 15 m long tunnels with 5 different cross sections. Tunnels A, B, C, and D were rectangular in cross section with a height of 25 cm and widths of 13.6 cm, 25 cm, 50 cm, and 100 cm, respectively. Tunnel E was 24.4 cm high, 27.4 cm wide at the base, with walls slanted inwards 7° from the vertical leading to a circular arch ceiling.

A 12 cm diameter circular propane burner was placed flush with the floor at a distance of approximately 6 m from the upstream opening. For a range of fire sizes, the air velocity through the tunnel was ramped up until the back-layer length was reduced to zero; that is, the upstream extent of the smoke layer coincided with the upstream edge of the burner. These results were then used to develop an empirical correlation relating the *critical velocity*, tunnel cross section, and heat release rate.

Modeling Notes

Five simulations are conducted; one for each tunnel type. In each, the heat release rate is stepped over from the lowest to highest reported value in 20 s increments. During each steady period, the near-ceiling temperatures are recorded and used to infer the location of the back-layer; that is, the back-layer extent coincides with a drop in the ceiling jet temperature to within 10 °C of ambient. The surface roughness of the tunnel walls is estimated to be 1 mm. The wall material is taken as generic steel.

3.75 UL/NIST Vent Experiments

In 2012, the Fire Fighting Technology Group at NIST conducted experiments at Underwriters Laboratories (UL) in Northbrook, Illinois, to assess the change in compartment temperature due to the opening of one or two 1.2 m square ceiling vents [292]. Four experiments were conducted using a natural gas burner in a 6.1 m by 4.3 m by 2.4 m compartment with a single door opening. The fires ranged in size from 500 kW to 2 MW, and the vents were opened and closed such that during the four experiments there were 31 discrete time intervals in which model predictions could be compared to quasi-steady conditions. The

compartment contained two vertical arrays of thermocouples, and the door and vents were instrumented with thermocouples and bi-directional velocity probes. Only the thermocouple data has been used in the validation study. A diagram of the compartment is displayed in Figure 3.43. The major test parameters are listed in Table 3.32.

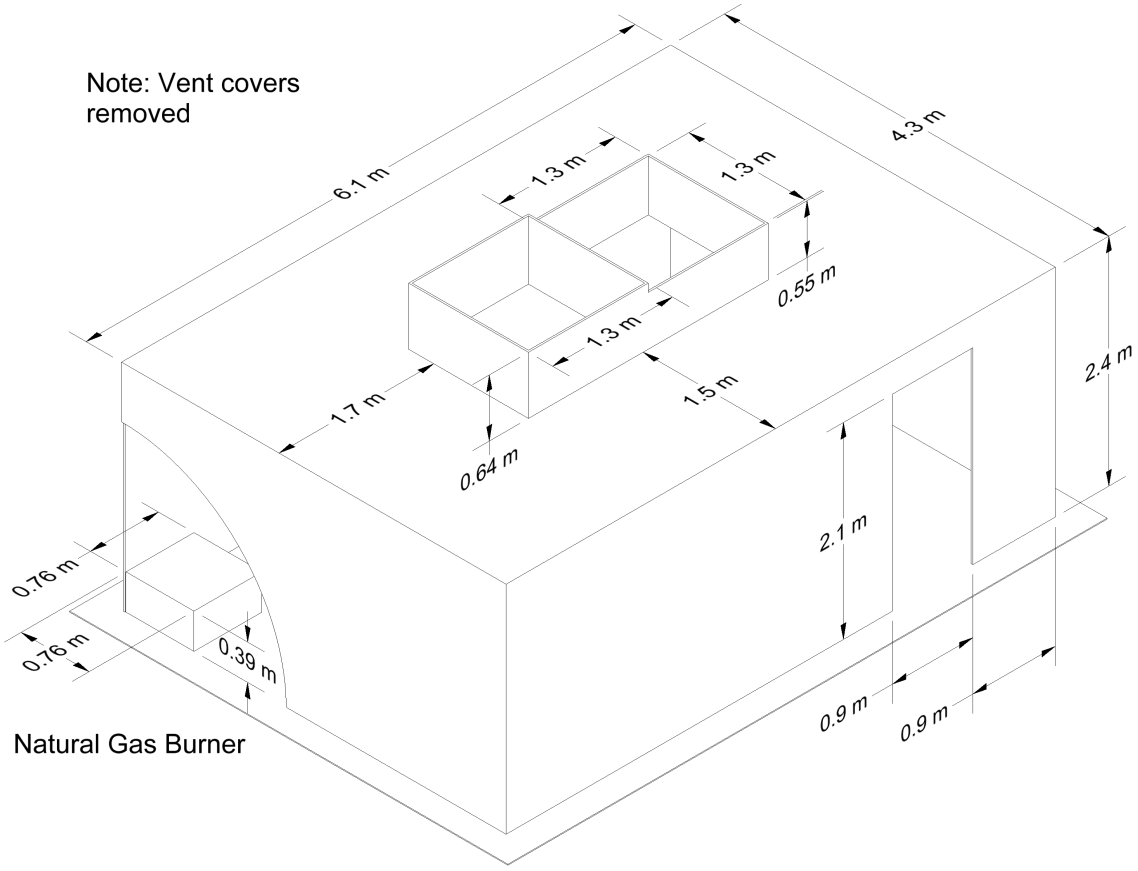

Figure 3.43: Geometry of the UL/NIST Experiments.

Table 3.32: Summary of UL/NIST Vent experiments. Note that the 31 "experiments" are actually discrete time intervals during the course of four separate fires.

Exp. No.	End Time (s)	HRR (kW)	No. of Vents	Exp. No.	End Time (s)	HRR (kW)	No. of Vents
Fire 1				Fire 3			
1	1215	430	0	14	453	476	0
2	1840	430	1	15	816	476	1
3	2168	430	2	16	1153	476	2
4	2474	430	0	17	1640	1002	0
5	2955	1011	0	18	1936	1002	1
6	3170	1011	1	19	2233	1002	2
7	3604	1011	2	Fire 4			
8	3840	1011	0	20	519	1011	0
9	4153	2188	0	21	967	1011	1
10	4284	2188	1	22	1325	1011	2
Fire 2				23	1559	470	2
11	565	2144	0	24	1653	470	1
12	833	2144	1	25	2013	470	0
13	931	2144	2	26	2411	470	1
				27	2910	470	2
				28	3399	2188	2
				29	3586	2188	0
				30	3803	2188	1
				31	4035	2188	2

3.76 UL/NFPRF Sprinkler, Vent, and Draft Curtain Study

In 1997, thirty-four heptane spray burner and five racked commodity experiments were conducted at the Large Scale Fire Test Facility at Underwriters Laboratories (UL) in Northbrook, Illinois [293, 79]. The spray burner experiments were divided into two test series. Series I consisted of 22 4.4 MW experiments. Series II consisted of 12 10 MW experiments. The objective of the spray burner experiments was to characterize the temperature and flow field for fire scenarios with a controlled heat release rate in the presence of sprinklers, draft curtains, and smoke & heat vents.

The Large Scale Fire Test Facility at UL contains a 37 m by 37 m (120 ft by 120 ft) main fire test cell, equipped with a 30.5 m by 30.5 m (100 ft by 100 ft) adjustable height ceiling. The UL/NFPRF test results (Series I) are summarized in Table 3.33. The UL/NFPRF test results (Series II) are summarized in Table 3.34. The layout of the experiments is shown in Figs. 3.44, 3.45, and 3.46.

Ceiling: The ceiling was raised to a height of 7.6 m and instrumented with thermocouples and other measurement devices. The ceiling was constructed of 0.6 m by 1.2 m by 1.6 cm UL fire-rated Armstrong

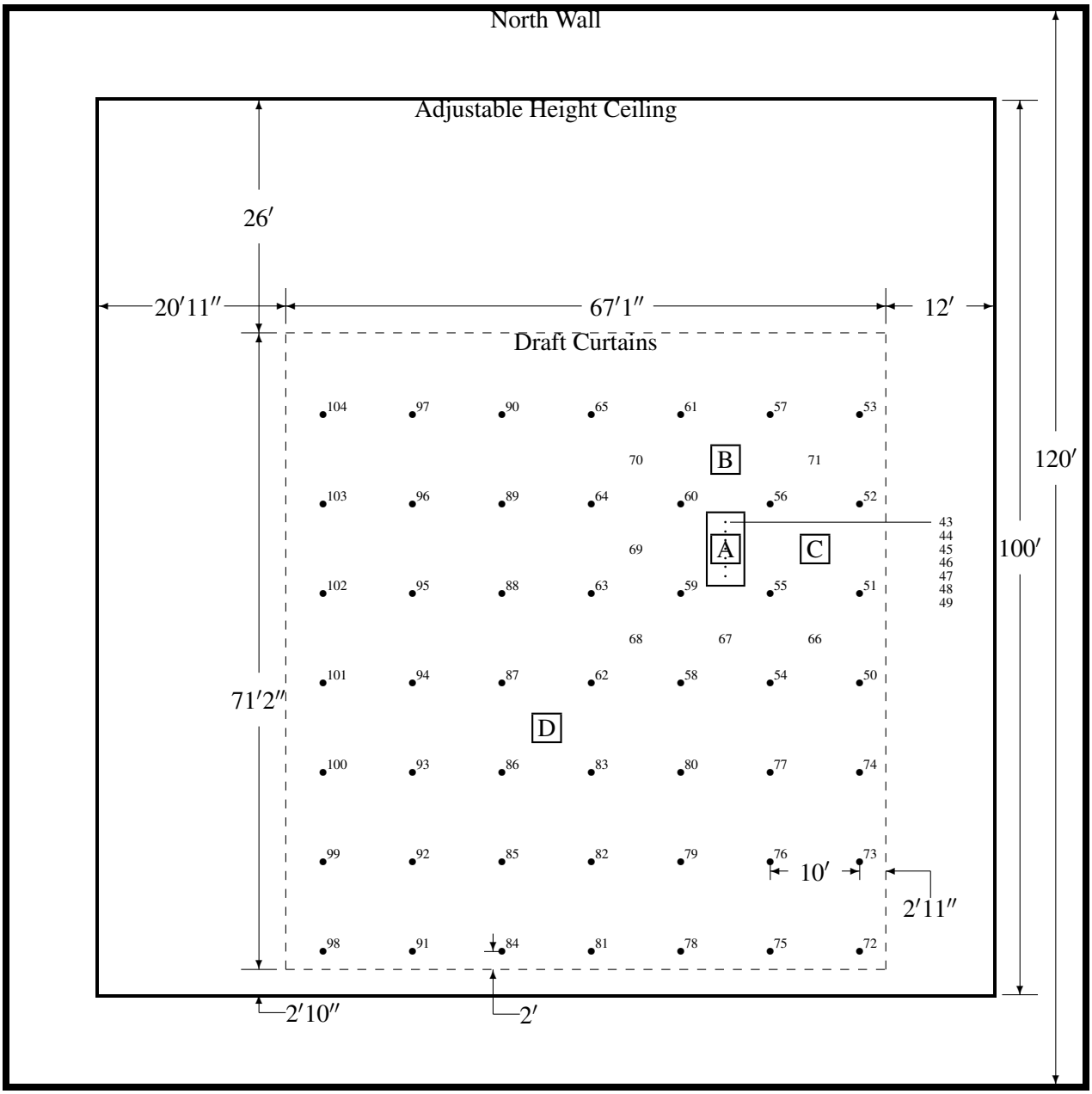

Figure 3.44: Plan view of the UL/NFPRF heptane spray experiments, Series I. The sprinklers are indicated by the solid circles and are spaced exactly 10 ft apart. The number beside each sprinkler location indicates the channel number of the nearest thermocouple. The vent dimensions are 4 ft by 8 ft. The boxed letters A, B, C and D indicate burner positions. Corresponding to each burner position is a vertical array of thermocouples. Thermocouples 1–9 hang 7, 22, 36, 50, 64, 78, 92, 106 and 120 in from the ceiling, respectively, above Position A. Thermocouples 10 and 11 are positioned above and below the ceiling tile directly above Position B, followed by 12–20 that hang at the same levels below the ceiling as 1–9. The same pattern is followed at Positions C and D, with thermocouples 21–31 at C and 32–42 at D.

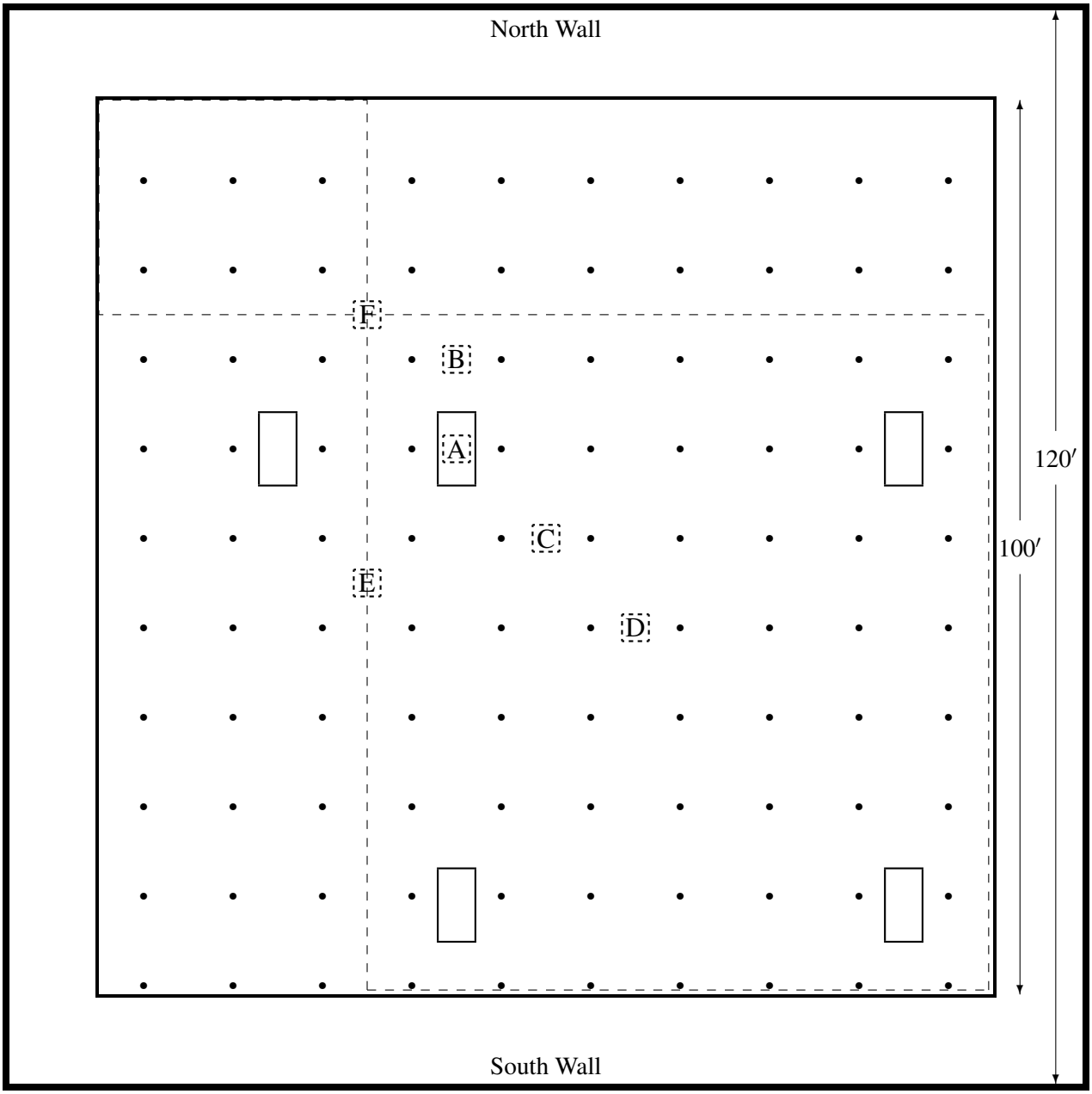

Figure 3.45: Plan view of the UL/NFPRF heptane spray experiments, Series II. The boxed letters A, B, C, D, E and F indicate burner positions. The sprinklers are indicated by the solid circles and are spaced exactly 10 ft apart. The vents are 4 ft by 8 ft.

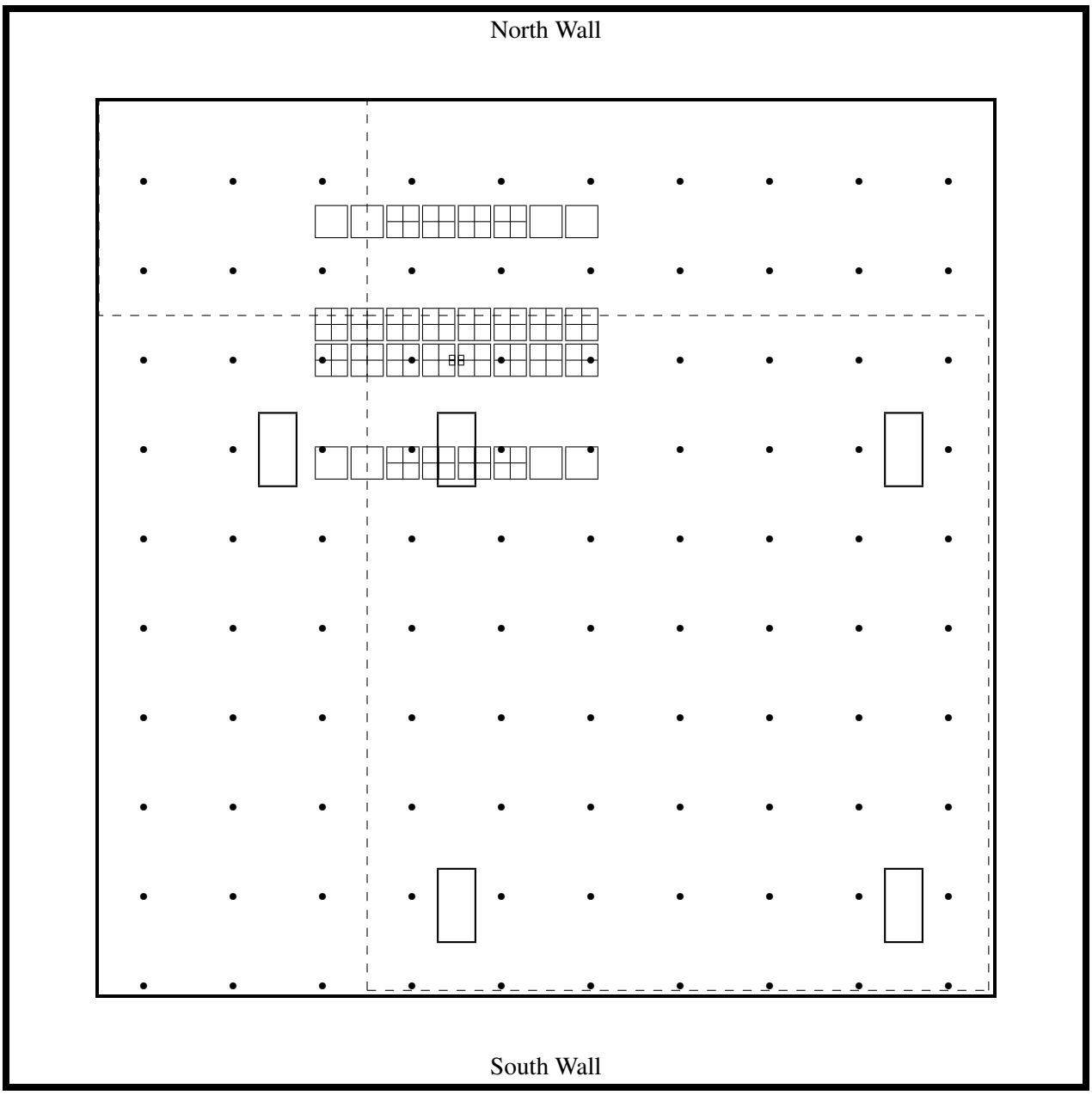

Figure 3.46: Plan view of the UL Large Scale Fire Test Facility with the layout of plastic commodity Test P-3. Tests P-1 and P-2 did not include the draft curtains (dashed lines). The sprinklers (dots) were separated by exactly 10 ft. The racks were located 30 ft south and 20 ft east of the position shown in Tests P-1, P-4, and P-5. The racks were located 10 ft south of the position shown in Test P-2. Each pallet load of boxed plastic commodity is represented by a square subdivided into four smaller squares to depict the individual boxes. Pallets containing empty boxes are represented by empty squares. Roof vents are represented by rectangles.

Heptane Spray Burner Test Series I						
Test No.	Burner Pos.	Vent Operation	First Actuation (s)	Total Actuations	Draft Curtains	Heat Release Rate MW @ s
I-1	B	Closed	65	11	Yes	4.4 @ 50
I-2	B	Manual (0:40)	66	12	Yes	4.4 @ 50
I-3	B	Manual (1:30)	64	12	Yes	4.4 @ 50
I-4	C	Closed	60	10	Yes	4.4 @ 50
I-5	C	Manual (0:40)	72	9	Yes	4.4 @ 50
I-6	C	Manual (1:30)	62	8	Yes	4.4 @ 50
I-7	C	74°C link (DNO)	70	10	Yes	4.4 @ 50
I-8	B	74°C link (9:26)	60	11	Yes	4.4 @ 50
I-9	D	74°C link (DNO)	70	12	Yes	4.4 @ 50
I-10	D	Manual (0:40)	72	13	Yes	4.4 @ 50
I-11	D	74°C link (4:48)	N/A	N/A	Yes	4.4 @ 50
I-12	A	Closed	68	14	Yes	4.4 @ 50
I-13	A	74°C link (1:04)	69	5	Yes	6.0 @ 60
I-14	A	Manual (0:40)	74	7	Yes	5.8 @ 60
I-15	A	Manual (1:30)	64	5	Yes	5.8 @ 60
I-16	A	74°C link (1:46)	106	4	Yes	5.0 @ 110
I-17	B	100°C link (DNO)	58	4	No	4.6 @ 50
I-18	C	100°C link (DNO)	58	4	No	3.7 @ 50
I-19	A	100°C link (10:00)	56	10	No	4.6 @ 50
I-20	A	74°C link (1:20)	54	4	No	4.2 @ 50
I-21	C	74°C link (7:00)	58	10	No	4.6 @ 50
I-22	D	100°C link (DNO)	60	6	No	4.6 @ 50

Table 3.33: Results of Series I of the UL/NFPRF heptane spray experiments. Note that DNO means "Did Not Open". Also note, the fires grew at a rate proportional to the square of the time until a certain flow rate of fuel was achieved at which time the flow rate was held steady. Thus, the "Heat Release Rate" was the size of the fire at the time when the fuel supply was leveled off.

Ceramaguard (Item 602B) ceiling tiles. The manufacturer reported the thermal properties of the material to be: specific heat 753 J/(kg·K), thermal conductivity 0.0611 W/(m·K), and density 313 kg/m^3.

Draft Curtains: Sheet metal, 1.2 mm thick and 1.8 m deep, was suspended from the ceiling for 16 of the 22 Series I tests, enclosing an area of about 450 m^2 and 49 sprinklers. The curtains were in place for all of the Series II tests.

Sprinklers: Central ELO-231 (Extra Large Orifice) uprights were used for all the tests. The orifice diameter of this sprinkler is reported by the manufacturer to be nominally 1.6 cm (0.64 in), the reference actuation temperature is reported by the manufacturer to be 74°C (165°F). The RTI (Response Time Index) and C-factor (Conductivity factor) were reported by UL to be 148 (m·s)$^{\frac{1}{2}}$ and 0.7 (m/s)$^{\frac{1}{2}}$, respectively [293]. When installed, the sprinkler deflector was located 8 cm below the ceiling. The thermal element of the sprinkler was located 11 cm below the ceiling. The sprinklers were installed with nominal 3 m by 3 m (exact 10 ft by 10 ft) spacing in a system designed to deliver a constant 0.34 L/(s·m^2) (0.50 gpm/ft^2) discharge density when supplied by a 131 kPa (19 psi) discharge pressure

Heptane Spray Burner Test Series II (10 MW Fires)							
Test No.	Burner Position	Vent Operation	Sprinklers Opened	First Activation	Last Activation	Avg. Peak Temp. °C	Avg. Peak Temp. °F
II-1	D	74°C link (DNO)	27	1:15	6:13	129.4	264.9
II-2	D	All Open at Start	28	1:05	5:53	128.8	263.8
II-3	A	74°C link (1:15)	12	1:08	4:00	101.8	215.2
II-4	B	74°C link (1:48)	16	1:03	5:54	108.8	227.8
II-5	D	74°C link (DNO)	28	1:10	7:07	130.0	266.0
II-6	D	All Open at Start	27	1:10	5:21	127.5	261.5
II-7	A	Closed	18	1:09	4:11	117.2	243.0
II-8	B	74°C link (1:12)	13	1:10	3:34	107.7	225.9
II-9	E	74°C link (DNO)	23	1:07	3:28	115.8	240.4
II-10	F	74°C link (3:20)	19	1:14	3:01	108.4	227.1
II-11	C	74°C link (DNO)	23	1:02	3:56	123.4	254.1
II-12	C	All Open at Start	23	0:58	4:55	119.0	246.2

Table 3.34: Results of the UL/NFPRF heptane spray experiments, Series II. Note that all fires were ramped up to 10 MW in 75 s following a t-squared curve.

Vent: UL-listed double leaf fire vents with steel covers and steel curb were installed in the adjustable height ceiling in the position shown in Figs. 3.44 and 3.45. The vent is designed to open manually or automatically. The vent doors were recessed into the ceiling about 0.3 m (1 ft).

Heptane Spray Burner: The heptane spray burner consisted of a 1 m by 1 m square of 1.3 cm pipe supported by four cement blocks 0.6 m off the floor. Four atomizing spray nozzles were used to provide a free spray of heptane that was then ignited. For all but one of the Series I tests, the total heat release rate from the fire was manually ramped up following a "t-squared" curve to a steady-state in 75 s (150 s was used in Test I-16). The fire was ramped to 10 MW in 75 s for the Series II tests. The fire growth curve was followed until a specified fire size was reached or the first sprinkler activated. After either of these events, the fire size was maintained at that level until conditions reached roughly a steady state, i.e., the temperatures recorded near the ceilings remained steady and no more sprinkler activations occurred. The heat release rate from the burner was confirmed by placing it under the large product calorimeter at UL, ramping up the flow of heptane in the same manner as in the tests, and measuring the total and convective heat release rates. It was found that the convective heat release rate was 0.65 ± 0.02 of the total.

Plastic Commodity: The Factory Mutual Research Corporation (FMRC) standard "Group A Plastic" test commodity served as the fuel for the rack storage experiments [294]. The cartoned plastic commodity consists of rigid crystalline polystyrene cups packaged in compartmented, single-wall, corrugated paper cartons. Each carton is a cube 0.53 m (21 in) on a side. Eight boxes comprise a pallet load. Two-way, slatted deck hardwood pallets support the loads. A pallet load weighs approximately 80 kg (170 lb), of which about 36 % is plastic, 35 % is wood, and 29 % is corrugated paper [294]. Each storage array consisted of a main (ignition) double-row rack at the center, flanked on two sides by single row target racks. The rows were separated by 8 ft wide aisles. Each of the two rows of the main array consisted of four 2.4 m (8 ft) long bays; a 0.15 m (6 in) flue separated the rows. Longitudinal flues of 0.2 m (7.5 in) were used to separate the pallets within a row. The overall loaded area of the double-row rack measured approximately 2.3 m (7.5 ft) wide by 10 m (33 ft) long. The racks were divided vertically into 4 tiers;

the overall loaded height was 5.8 m (19 ft). The fire was ignited with 2 standard igniters which consisted of 8 cm (3 in) long by 8 cm diameter cylinders of rolled cotton material, each soaked in 120 mL (4 oz) of gasoline and enclosed in a polyethylene bag. The rolls were placed against the carton surfaces in the first tier, just above the pallet. The igniters were lit with a flaming propane torch at the start of each test.

Instrumentation: The instrumentation for the tests consisted of thermocouples, gas analysis equipment, and pressure transducers. The locations of the instrumentation are referenced in the plan view of the facility (Fig. 3.44). Temperature measurements were recorded at 104 locations. Type K 0.0625 in diameter Inconel sheathed thermocouples were positioned to measure (i) temperatures near the ceiling, (ii) temperatures of the ceiling jet, and (iii) temperatures near the vent.

3.77 UL/NIJ House Experiments

The Firefighter Safety Research Institute (FSRI) of Underwriters Laboratory (UL), with support from the National Institute of Justice (NIJ), conducted fire experiments in a one-story ranch-style house and a two-story colonial-style house in the large fire facility at Northbrook, Illinois, in 2016 and 2017 [295]. In addition to this validation guide, modeling of the experiments is also reported in [296]. The goal of the experiments was to determine the effect of ventilation on fire patterns in fully-furnished homes. As part of the project, a natural gas burner was positioned within the unfurnished structures to evaluate changes in flow patterns as various doors and windows were opened and closed. The test structures were instrumented with thermocouple trees, pressure transducers, and bi-directional probes. The floor plan for the single story ranch-style house is included in Fig. 3.47, and plans for the two story colonial-style house in Fig. 3.48. The ceiling was 2.4 m above the floor in the ranch-style house. The colonial-style house featured an atrium with a 5.6 m ceiling height. The first story ceiling in the colonial-style house was 2.5 m above the floor, and the second story ceiling was 2.8 m above the floor.

The leakage area in the single story structure was measured to be 0.08 m^2 at 10 Pa. The leakage area in the two story structure was measured to be 0.18 m^2 at 10 Pa.

The natural gas burner in each set of experiments had dimensions of 0.6 m by 0.6 m, and the surface of the burner was approximately 0.6 m above the floor. The heat release rate for the single story ranch house was 250 kW, and 500 kW for the two story colonial. The locations of the burner in each house are indicated in the floor plans. The labels for the measurement devices in the one and two story houses are listed in Tables 3.35 and 3.36, respectively. Three experiments with unique sequences of events (e.g. opening doors and windows) were conducted in each style of house. All experiments began with all exterior doors and windows closed and the times at which each door and window was opened are listed Table 3.37 and 3.38.

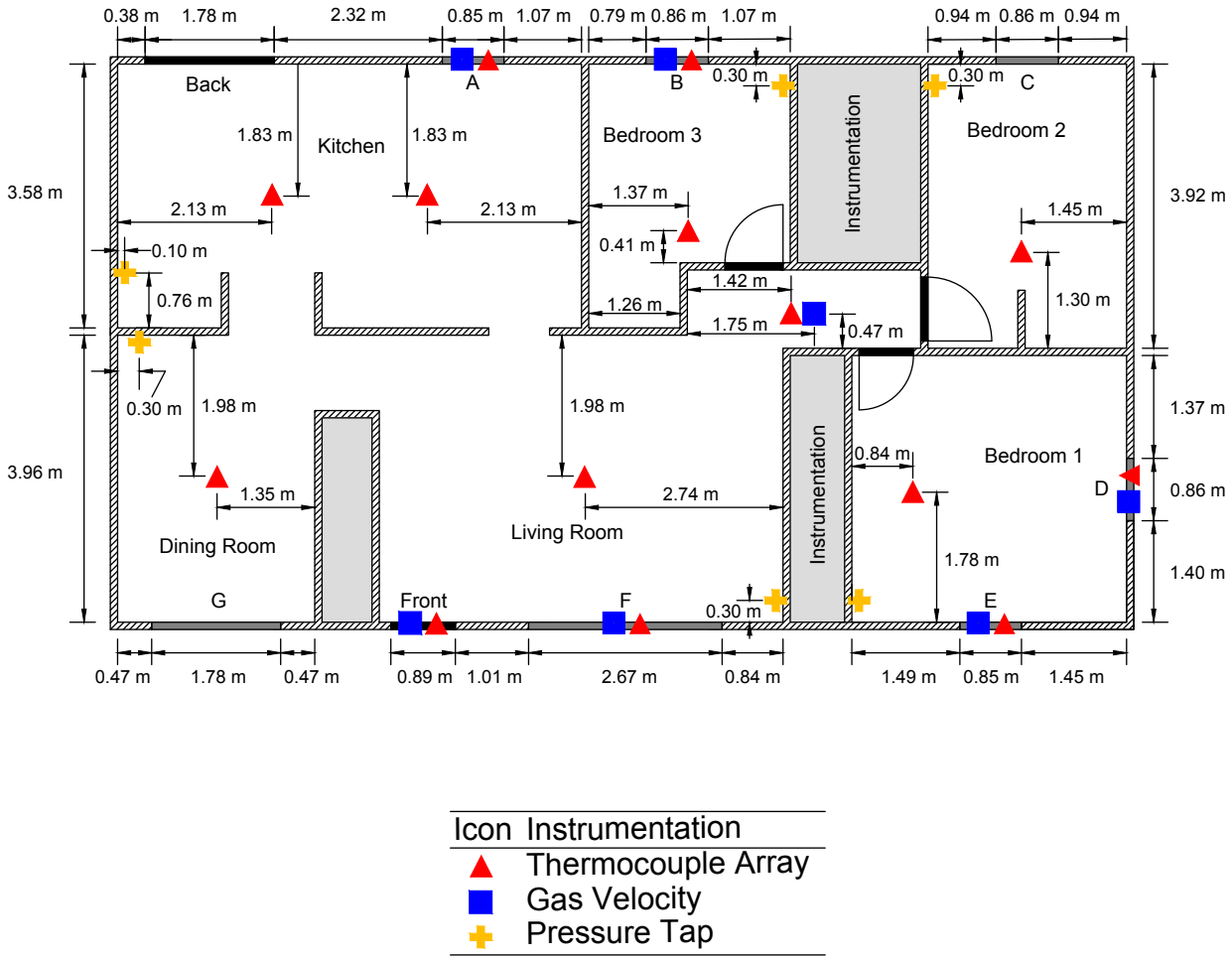

Figure 3.47: Layout of the one story ranch-style house in the UL/NIJ experiments.

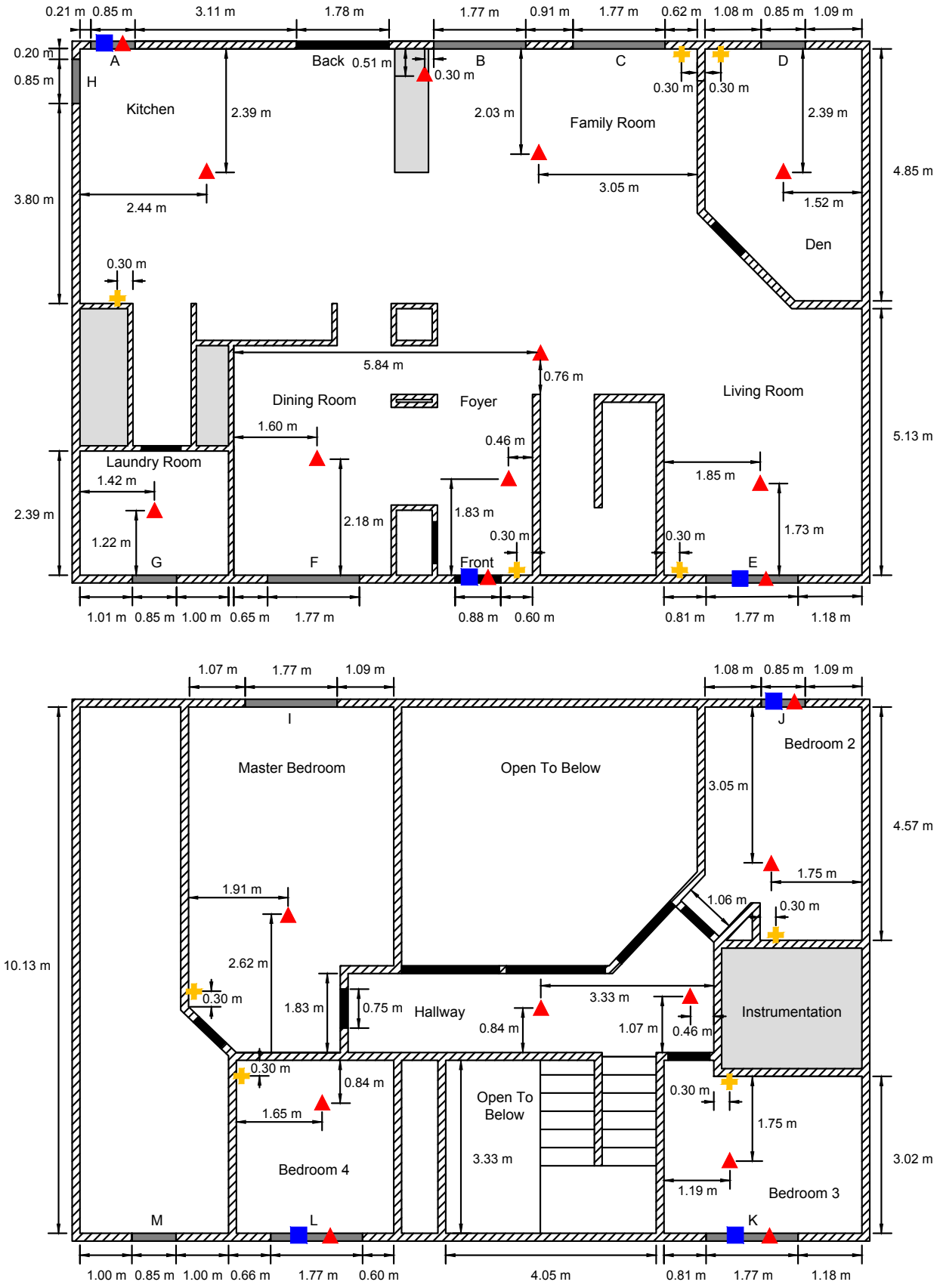

Figure 3.48: Geometry of UL NIJ Colonial-style House

Temp.	Location	Pressure	Location	Velocity	Location
1TC	Bedroom 1	1PT	Bedroom 1	1BDP	Window E
2TC	Bedroom 2	2PT	Bedroom 2	2BDP	Window D
3TC	Bedroom 3	3PT	Bedroom 3	3BDP	Window B
4TC	Hallway	4PT	Living Room	4BDP	Hallway
5TC	Living Room	5PT	Kitchen	5BDP	Window F
6TC	Dining Room	6PT	Dining Room	6BDP	Front Door
7TC	Kitchen (East)			7BDP	Window A
8TC	Kitchen (West)				

Table 3.35: Locations of measurement devices in the UL/NIJ ranch-style house.

Temp.	Location	Pressure	Location	Velocity	Location
1TC	Master Bedroom	1PT	Master Bedroom	1BDP	Front Door
2TC	Bedroom 2	2PT	Bedroom 2	2BDP	Window J
3TC	Bedroom 3	3PT	Bedroom 3	3BDP	Window K
4TC	Bedroom 4	4PT	Bedroom 4	4BDP	Window L
5TC	2nd Floor Hallway (East)	5PT	Front Corridor	5BDP	Window E
6TC	2nd Floor Hallway (Middle)	6PT	Living Room	6BDP	Window A
7TC	Family Room (West Corner)	8PT	Den		
8TC	Family Room (Center)	9PT	Family Room		
9TC	Den	10PT	Kitchen		
10TC	Living Room				
11TC	Under 2nd Floor Hallway				
12TC	Foyer				
13TC	Dining Room				
14TC	Laundry Room				
15TC	Kitchen				

Table 3.36: Locations of measurement devices in the UL/NIJ colonial-style house.

Event	Test 1	Test 2	Test 5
Front Door Open	300 s	1200 s	1290 s
Back Door Open	1275 s	1860 s	300 s
Window A Open	1260 s	1845 s	-
Window B Open	1245 s	1830 s	-
Window C Open	1230 s	900 s	-
Window D Open	1215 s	-	600 s
Window E Open	600 s	600 s	-
Window F Open	1200 s	1815 s	1200 s
Window G Open	1300 s	1875 s	-
Burner Off	900 s	1500 s	900 s

Table 3.37: Sequence of events for the one story ranch-style house in the UL/NIJ experiments.

Event	Test 1	Test 4	Test 6
Front Door Open	600 s	600 s	1200 s
Back Door Open	-	-	-
Window A Open	-	-	900 s
Window B Open	-	900 s	-
Window C Open	-	-	-
Window D Open	-	-	-
Window E Open	-	-	-
Window F Open	-	-	-
Window G Open	-	-	-
Window H Open	-	-	-
Window I Open	-	-	-
Window J Open	-	-	-
Window K Open	900 s	1260 s	600 s
Window L Open	1200 s	1320 s	-
Window M Open	-	-	-
Burner Off	1500 s	1200 s	1500 s

Table 3.38: Sequence of events for the two story colonial-style house in the UL/NIJ experiments.

3.78 Ulster SBI Corner Heat Flux Measurements

Zhang et al. [297] measured the heat flux and flame heights from fires in the single burning item (SBI) enclosure at the University of Ulster, Northern Ireland. Thin steel plate probes were used to measure the surface heat flux, and flame heights were determined by analyzing the instantaneous images extracted from the videos of the experiments by a CCD camera. Three heat release rates were used – 30 kW, 45 kW, and 60 kW.

3.79 UMD Polymers

Stoliarov et al. conducted measurements of the thermal properties of charring and non-charring polymers with the specific purpose of providing input data for numerical pyrolysis models [298, 299, 300, 301]. The study aimed to determine whether a one-dimensional conduction/reaction model could be used as a practical tool for prediction and/or extrapolation of the results of fire calorimetry tests. The non-charring polymers included poly(methyl methacrylate) (PMMA), high-impact polystyrene (HIPS), and polyoxymethylene (POM). The charring polymers included acrylonitrile butadiene styrene (ABS), polyethylene terephthalate (PET), Kydex, and polyethylenimine (PEI).

3.80 UMD Line Burner

James P. White, University of Maryland, College Park

The University of Maryland (UMD) Line Burner experimental facility provides for the study of a low-strain, buoyancy-driven, fully-turbulent diffusion flame in a canonical line-fire configuration. This facility provides well-controlled inlet and boundary conditions while introducing the complicating effects of buoyancy and turbulence characteristic of large-scale accidental fires. A variety of non-intrusive diagnostics are employed to measure local and integral flame characteristics. The facility comprises a slot burner centrally located within a surrounding, uniform co-flowing oxidizer. Controlled suppression of the flame is achieved via the introduction of either excess nitrogen gas or a fine water mist into the oxidizer stream. A detailed description of this facility is presented in White et al. [302].

A plan view illustration of the burner and oxidizer assembly is presented in Fig. 3.49. The burner features a sand-filled, stainless-steel fuel port, measuring 5 cm wide by 50 cm long, with 1.5 mm thick side walls. Methane gas (99.5 % purity) or propane gas (99.5 % purity) are the primary burner fuels. A methane flow rate of 1.00 $\pm$0.02 g/s (nominal 5.4 cm/s) or a propane flow rate of 1.08 $\pm$0.02 g/s (nominal 2.1 cm/s) is utilized, measured using a mass flow controller. Assuming complete combustion, the total heat-release rate is roughly 50 kW for either fuel.

The burner is centrally located at the mouth of a surrounding oxidizer port, measuring 50 cm wide by 75 cm long, with 10 cm thick side walls. Flow conditioning elements ensure that the oxidizer is well-mixed and exits the oxidizer port with a uniform, flat velocity profile. The co-flowing oxidizer is provided at a fixed flow rate of 75$\pm$5 g/s (total, including variable suppressant flow, nominal 22 cm/s), measured using a calibrated pitot-static probe.

Sitting on top of the oxidizer port and surrounding the fuel port is a thin, 5 mm tall, 5 cm wide annulus of ceramic fiberboard, positioned so the top of the board is 10 mm below the lip of the fuel port (and 5 mm above the oxidizer port). This board serves as a flow blockage to reduce the oxidizer velocity near the flame base, forcing the onset of buoyancy-generated turbulence upstream toward the fuel port and reducing the tendency to form laminar structures at the base of the flame.

For nitrogen-dilution suppression experiments, the flame is suppressed via the introduction of a variable flow of gaseous nitrogen into the oxidizer. Suppression potential is characterized by the oxygen mole-fraction in the oxidizer, X_{O_2}. This quantity is measured using a paramagnetic oxygen analyzer via a probe located in the oxidizer port. The analyzer provides a measurement accuracy of ± 0.125 in the volume percentage of O_2 and a response time of 5 s. An additional transport delay of approximately 20 s is compensated to provide synchronous data collection with other measurements.

Visible flame height is measured using a video camera, defined based on a 50 % intermittent flame height [302]. These image-based measurements rely on visible flame emissions, including the incandescence of soot particles, and do not strictly locate the stoichiometric flame sheet. The uncertainty in each flame height measurement is less than ± 1.5 cm.

Infrared radiative emissions are measured using a water-cooled Schmidt-Boelter heat-flux transducer. The sensor is positioned 100 cm radially outward from the burner centroid, 18 cm above the fuel port, facing perpendicular to the long axis of the burner. This device has a hemispherical absorptance of 0.94 for a spectral range between 0.6-15.0 μm, a maximum viewing angle of 90°, and a response time of 0.25 s. Measurement accuracy is ± 3 %. The convective portion of the measured heat flux is neglected and sans-flame measurements are applied to correct for background irradiation.

Heat flux data are converted to radiative loss fraction, χ_r, using a weighted multi-point radiation source model, whereby the measured heat flux is assumed to be received from an array of isotropic point sources uniformly distributed over a two-dimensional plane oriented across the visible flame surface. The uncertainty in each χ_r measurement is less than ± 4.5 %.

Mean and RMS (root mean square) temperature data are recorded using an array of R-Type thermocouple probes positioned at selected locations along the centerline of the flame. These probes are constructed using 50 um diameter wires with exposed, bead-welded junctions. Combustion products are collected in an exhaust evacuation system, wherein a gas sampling system provides measurement of the molar concentrations of oxygen (± 0.25 mol % O_2), carbon dioxide (± 1000 ppm CO_2), carbon monoxide (± 100 ppm CO), water vapor (± 3 % RH), and total hydrocarbons (± 10 ppm THC) in the exhaust stream. From these measurements, integral heat release rate and combustion efficiency measurements are derived using species-based calorimetry techniques.

Modeling Notes

The simulations of the UMD Line Burner experiments are performed for a duration of 80 s. The first 10 s allow the flame to stabilize at ambient conditions. At 10 s, nitrogen is introduced in the co-flow air stream and linearly increased so that the oxygen concentration decreases to 10 % at 80 s. When the oxygen concentration drops to 18 %, the nitrogen ramp up is delayed for 10 s in order to collect steady-state profiles of oxygen and temperature at heights of 12.5 cm and 25 cm above the burner.

The calculations are performed at three grid resolutions: 12.5 mm, 6.25 mm, and 3.125 mm, using 24, 164, and 204 meshes respectively.

The combustion and extinction are modeled using a two-step reaction scheme. In the first step, fuel is converted to CO, soot, and water vapor, and in the second step, the CO and soot are oxidized to form CO_2. Both reactions are fast, but the oxidation step follows the first reaction. That is, in a given time step, all available oxygen first forms CO and soot. Any leftover oxygen is then used to oxidize existing CO and soot. The methane reaction is written in terms of "lumped" species as follows:

$$\underbrace{(\mathrm{CH_4})}_{\text{Fuel}} + 1.333\ \underbrace{(\mathrm{O_2} + (0.79/0.21)\ \mathrm{N_2})}_{\text{Air}} \longrightarrow \underbrace{(2/3\ \mathrm{CO} + 2\ \mathrm{H_2O} + 1/3\ \mathrm{C} + 1.333(0.79/0.21)\ \mathrm{N_2})}_{\text{Products 1}} \quad (3.25)$$

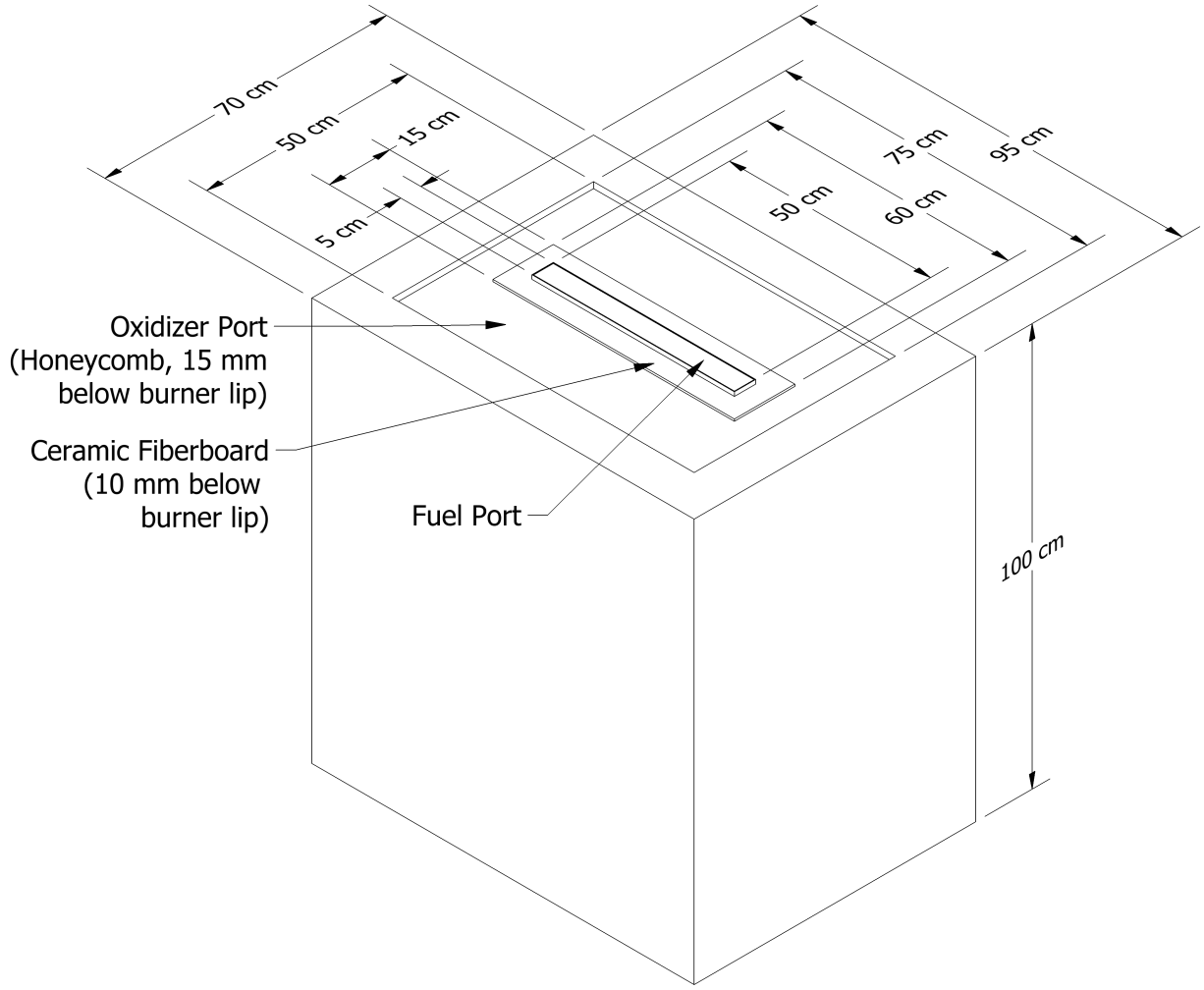

Figure 3.49: UMD Line Burner isometric view of burner and oxidizer assembly.

$$(\text{Products 1}) + 0.667\ (\text{Air}) \longrightarrow \underbrace{(\text{CO}_2 + 2\,\text{H}_2\text{O} + 2(0.79/0.21)\,\text{N}_2)}_{\text{Products 2}} \tag{3.26}$$

The propane reaction is:

$$\underbrace{(\text{C}_3\text{H}_8)}_{\text{Fuel}} + 2.2065\ \underbrace{(\text{O}_2 + (0.79/0.21)\,\text{N}_2)}_{\text{Air}} \longrightarrow \underbrace{(0.413\,\text{CO} + 4\,\text{H}_2\text{O} + 2.587\,\text{C} + 2.2065(0.79/0.21)\,\text{N}_2)}_{\text{Products 1}} \tag{3.27}$$

$$(\text{Products 1}) + 2.7935\ (\text{Air}) \longrightarrow \underbrace{(3\,\text{CO}_2 + 4\,\text{H}_2\text{O} + 5(0.79/0.21)\,\text{N}_2)}_{\text{Products 2}} \tag{3.28}$$

The stoichiometry is dictated by the composition of the fuel molecule except for the stoichiometric coefficients of CO and soot in the first step. By default, 2/3 of the carbon in the fuel molecule is converted to CO, and 1/3 to soot. No better strategy has yet emerged for determining this. For both methane and propane, soot is generated in the first step, and as the co-flow is diluted with nitrogen, the flame color changes from yellow to blue as the in-flame soot volume fraction decreases. The simple two-step reaction scheme cannot predict the distribution of soot and CO in the first step; thus, the stoichiometric coefficients for CO and soot

(C) in Eq. (3.25) are chosen somewhat arbitrarily. The choice *does* affect the predicted radiative fraction of the fire and the heat flux to the radiometer.

Extinction of the fire is achieved using the *critical flame temperature* concept, which is the default extinction model in FDS. The CFT is 1507 °C for methane and 1447 °C for propane [136]. In addition, combustion is suppressed below the auto-ignition temperatures of 540 °C and 450 °C for methane and propane, respectively, except in a small volume just above the burner where the fuel is allowed to burn on contact with oxygen. This is a simple way to simulate the effect of a spark igniter.

3.81 USCG/HAI Water Mist Suppression Tests

The U.S. Coast Guard sponsored a series of experiments to assess the fire suppression capabilities of a variety of water mist systems in a variety of ship board configurations. The experiments were conducted in 1999 by Hughes Associates, Inc., in a simulated machinery space aboard the test vessel *State of Maine* at the USCG Fire and Safety Test Detachment, Mobile, Alabama [303]. The space had nominal dimensions of 7 m by 5 m by 3 m, containing two steel engine mock-ups each measuring 3 m by 1 m by 1.5 m. The space was equipped with a door for natural ventilation and a forced ventilation system providing approximately 15 air changes per hour. Five commercially available water mist systems were evaluated. The obstructed heptane spray fires ranged in size from approximately 250 kW to 1 MW.

3.82 USFS/Catchpole Experiments

The U.S. Forest Service and collaborators from the University of New South Wales, Australia, conducted 354 fire experiments in a wind tunnel with a cross section of 3 m by 3 m [304]. The tunnel is part of the Intermountain Fire Sciences Laboratory in Missoula, Montana. The fires involved four different fuel species, a range of fuel bed depths, packing ratios, moisture contents and wind speeds. The fuels were regular and coarse excelsior (*Populus tranulos*), and pine needles and heartwood sticks (*Pinus ponderosa*). The vegetation was placed in a 1 m wide and 8 m long tray. An approximately 5 cm wide tray of ethanol liquid was positioned at one end, and the fire spread rate was measured using photocells and video analysis.

Modeling Notes

The vegetation is modeled as a collection of cylindrical Lagrangian particles. The pyrolysis model assigned to the particles is described in the FDS User's Guide [1], chapter "Earth, Wind and Fire," Section 19.1, "Thermal Degradation Model for Vegetation." The parameters for each experiment are listed in a table in Ref. [304].

3.83 USFS/Corsica Experiments

Perez-Ramirez et al. at the University of Corsica, France, and Mell at the U.S. Forest Service's Pacific Wildland Fire Science Laboratory in Seattle, Washington, simulated six bench-scale fires spreading over a 1 m wide by 2 m long bed of pine needles [157]. The heat release rates from the spreading fires were measured in a furniture calorimeter. The fuel beds were made up of *Pinus pinaster* needles, and three different fuel loadings (0.6, 0.9 and 1.2 kg/m^2) were tested under no-slope and up-slope conditions (20°).

Modeling Notes

The pine needles are modeled as a collection of cylindrical Lagrangian particles. The pyrolysis model assigned to the particles is described in the FDS User's Guide [1], chapter "Earth, Wind and Fire," Section 19.1 "Thermal Degradation Model for Vegetation."

The test parameters for these experiments are given in Table 3.39.

Exp. No.	Dry Fuel Loading (kg/m^2)	Slope (deg.)	Dry Mass per Volume (kg/m^3)	Packing Ratio	Bed Depth (cm)
1_0	0.6	0	17	0.033	3.5
2_0	0.9	0	16	0.031	5.5
3_0	1.2	0	18	0.035	6.5
1_20	0.6	20	17	0.033	3.5
2_20	0.9	20	16	0.031	5.5
3_20	1.2	20	18	0.035	7.5

Table 3.39: Test matrix for the USFS/Corsica Experiments.

3.84 USN High Bay Hangar Experiments

The U.S. Navy sponsored a series of 33 tests within two hangars examining fire detection and sprinkler activation in response to spill fires in large enclosures. Experiments were conducted using JP-5 and JP-8 fuels in two Navy high bay aircraft hangars located in Naval Air Stations in Barber's Point, Hawaii and Keflavik, Iceland [305].

The Hawaii tests were conducted in a 15 m high hangar measuring 97.8 m in length and 73.8 m in width. Of the 13 tests conducted in the facility 11 were conducted in pans ranging from .09 m^2 to 4.9 m^2 in area with heat release rates varying from 100 kW to 7.7 MW. The burner was placed in the center of the room on a scale that continuously recorded the pans weight. The facility was equipped with a number of detection devices including thermocouples, electronic smoke and spot heat detectors, projected beam smoke detectors, combination UV/IR optical flame detectors, line-type heat detectors, as well as sprinklers. Measurements were recorded at a large number of locations allowing for a thorough profile of compartment behavior.

It was suspected that fire plume behavior and response of detection devices in a cold building may not have been well replicated by the experiments held in the warm hangar in Hawaii. The Iceland tests were conducted under a 22 m barrel vaulted ceiling in a hangar measuring 45.7 m by 73.8 m. 22 tests in total were conducted. The majority of these tests fires burned JP-5 fuel with the remainder burning JP-8. The jet fuel fires ranged in size from .06 m^2 to 20.9 m^2 and in heat release rate from 100 kW to approximately 33 MW. The facility was equipped similarly to the Hawaii hangar.

3.85 UWO Wind Tunnel Experiments

Wind tunnel measurements were conducted at the University of Western Ontario (UWO) [306] on a 1:100 scale model of the Texas Tech Wind Engineering Field Research Laboratory (WERFL) building which has approximate dimensions of 9.1 m by 13.7 m by 4 m and a slightly pitched roof. In the test report, this experiment is referred to as Test 7. Pressure measurements were made for 22 wind directions for this scale model.

Modeling Notes

The 1:100 scale model of the building is approximately 14 cm long, 9 cm wide, and 4 cm tall. The simulations use 5.0 mm, 2.5 mm, and 1.25 mm cubic grid cells, uniformly spanning the computational domain of dimensions 1.12 m $\times$ 0.56 m $\times$ 0.28 m. The 4 cm height of the scale model is spanned by 8, 16, and 32 grid cells. The grid resolution was assessed by checking that the values of y^+, a non-dimensional distance, never exceed 150 for any mesh resolution. y^+ values are dependent on turbulence model wall laws and a value of 150 means that the first grid point is well within the logarithmic region.

Only two wind directions are chosen for validation, 180° and 270°, representing right angles formed with the long and short sides of the building. For each angle, 3 lines of pressure measurements running up the windward side, along the roof, and down the leeward side are used for comparison to the simulation. One line of pressure measurements along the side of the scale model is also used.

The incoming flow assigned at the inflow boundary is characterized by its mean wind speed profile and turbulent fluctuations. For consistency with the UWO experiments, the mean wind speed profile was modeled by the power law:

$$U(z) = 9.144 \left(\frac{z}{0.0396} \right)^p \tag{3.29}$$

where 9.144 m/s is the reference wind speed at the 0.0396 m roof height of the scale model and the power law exponent $p = 0.1173$ was fit to the experimental data.

Fluctuations at the inlet boundary are generated by the Synthetic Eddy Method (SEM) of Jarrin [307]. The desired value of `N_EDDY` (the number of eddies generated at the inlet) is the largest possible value that does not slow down the simulation. This value is determined by running a number of simulations for the same time while varying the `N_EDDY` input and recording the total run time. The other turbulence parameters, `L_EDDY` (characteristic eddy length) and `REYNOLDS_STRESS`, are set based on the turbulence intensity data from the UWO experiments. The Reynolds stresses are found by multiplying the turbulence intensity in each direction by the wind velocity at roof height to determine the root mean square of the velocity fluctuations, and then squaring the root mean square values.

The side walls and roof of the wind tunnel are set to free-slip. The roughness length at the ground is specified to be 0.0001 m, 1/100 the full-scale value of 0.01 m. The outlet of the wind tunnel is set to an "open" boundary condition, where pressure is set to the ambient pressure.

3.86 Vettori Flat Ceiling Experiments

Vettori [77] analyzed a series of 45 experiments conducted at NIST that were intended to compare the effects of different ceiling configurations on the activation times of quick response residential pendent sprinklers. The two ceiling configurations used consisted of an obstructed ceiling, with parallel beams 0.038 m wide by 0.24 m deep placed 0.41 m on center, and a smooth ceiling configuration, in which the beams were covered by a sheet of gypsum board. In addition to the two ceiling configurations, there were also three fire growth rates and three burner locations used – a total of 18 test configurations. The fire growth rate was provided by a computer controlled methane gas burner to mimic a standard t-squared[7] fire growth rate with either a slow, medium, or fast ramp up. The burner was placed in a corner of the room, then against an adjacent wall, and then in a location removed from any wall. Measurements were taken to record sprinkler activation time, temperatures at varying heights and locations within the room, and the ceiling jet velocities at several other locations. A diagram of the test structure is displayed in Figure 3.50.

[7] The actual heat release rate are presented in Table 3.40.

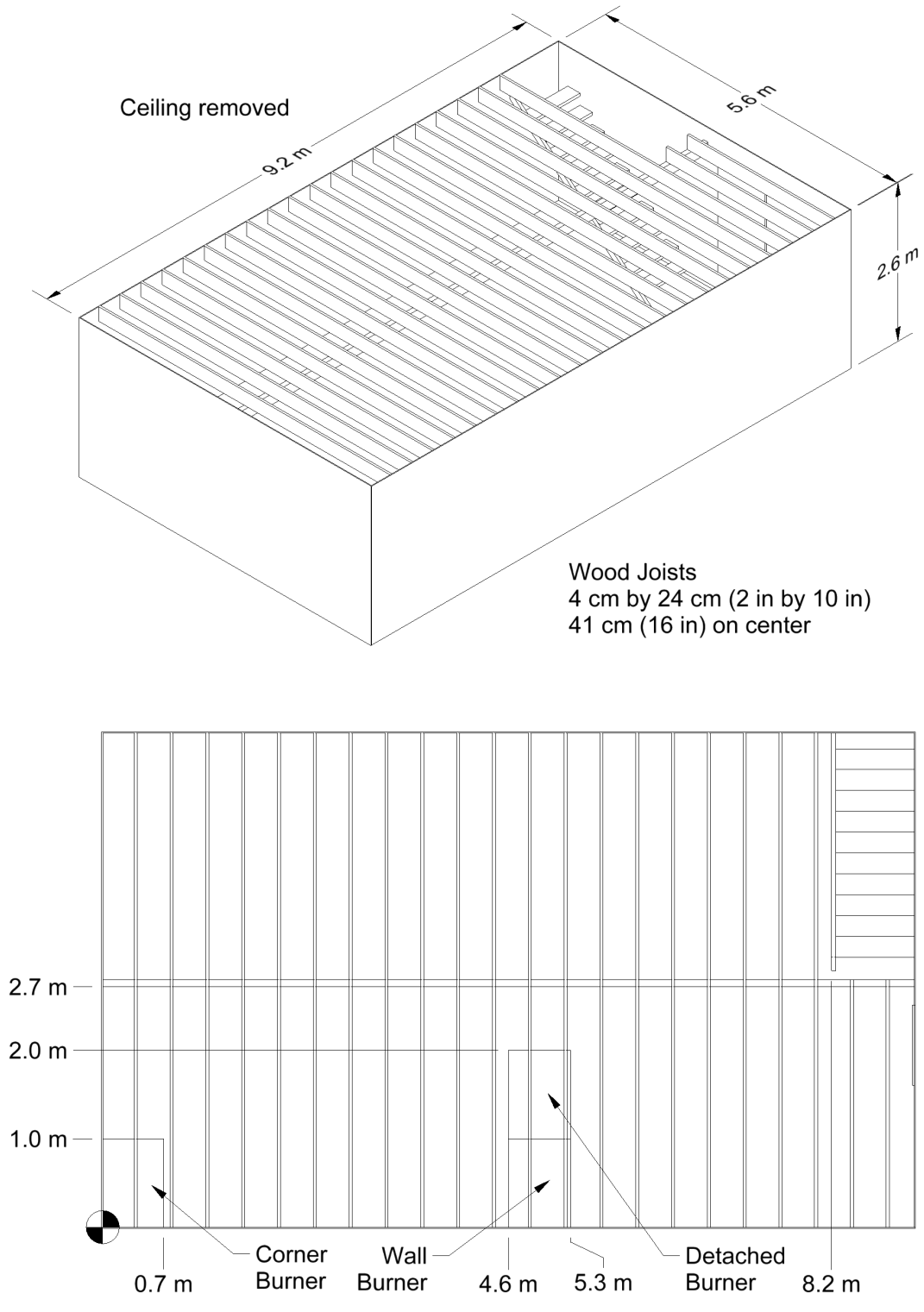

Figure 3.50: Geometry of the Vettori Flat Ceiling compartment.

Table 3.40: Heat release rate profiles for the Vettori experiments.

Time (s)	Slow (kW)	Medium (kW)	Fast (kW)
0	0	0	0
10	9	20	75
20	16	34	127
30	23	51	173
40	30	67	196
50	35	83	271
60	42	104	379
70	52	125	515
80	62	143	673
90	68	162	852
100	78	174	1053
110	85	192	
120	94	239	
130	100	279	
140	109	325	
150	115	373	
160	125	424	
170	137	479	
180	148	537	
190	163	599	
200	179	663	
210	195		
220	213		
230	231		
240	250		
250	269		
260	290		
270	311		
280	333		
290	354		
300	378		
310	402		
320	427		
330	453		
340	479		
350	506		
360	534		
370	562		

3.87 Vettori Sloped Ceiling Experiments

Vettori [78] performed a series of 72 compartment experiments to measure the activation times of quick-response residential pendent sprinklers mounted under a ceiling with an adjustable slope. There were 36 unique configurations (2 replicates of each) combining the following parameters:

- Flat, 13°, or 24° Ceiling Slope
- Smooth or Obstructed Ceiling Surface
- Fast or Slow Growth Fire
- Corner, Wall, or Detached Burner Location

Note that the Slow and Fast fire growth profiles were the same as those reported in Table 3.40.

3.88 VTT Large Hall Tests

The experiments are described in Ref. [308]. The series consisted of 8 experiments, but because of replicates only three unique fire scenarios. The experiments were undertaken to study the movement of smoke in a large hall with a sloped ceiling. The tests were conducted inside the VTT Fire Test Hall, with dimensions of 19 m high by 27 m long by 14 m wide. Each test involved a single heptane pool fire, ranging from 2 MW to 4 MW. Four types of predicted output were used in the present evaluation – the HGL temperature and depth, average flame height and the plume temperature. Three vertical arrays of thermocouples (TC), plus two thermocouples in the plume, were compared to FDS predictions. The HGL temperature and height were reduced from an average of the three TC arrays using the standard algorithm described in Chapter 5. The ceiling jet temperature was not considered, because the ceiling in the test hall is not flat, and the standard model algorithm is not appropriate for this geometry.

The VTT test report lacks some information needed to model the experiments, which is why some information was based on private communications with the principal investigator, Simo Hostikka.

Surface Materials: The walls and ceiling of the test hall consist of a 1 mm thick layer of sheet metal on top of a 5 cm layer of mineral wool. The floor was constructed of concrete. The report does not provide thermal properties of these materials.

Natural Ventilation: In Cases 1 and 2, all doors were closed, and ventilation was restricted to infiltration through the building envelope. Precise information on air infiltration during these tests is not available. The scientists who conducted the experiments recommend a leakage area of about 2 m^2, distributed uniformly throughout the enclosure. By contrast, in Case 3, the doors located in each end wall (Doors 1 and 2, respectively) were open to the external ambient environment. These doors are each 0.8 m wide by 4 m high, and are located such that their centers are 9.3 m from the south wall.

Mechanical Ventilation: The test hall has a single mechanical exhaust duct, located in the roof space, running along the center of the building. This duct had a circular section with a diameter of 1 m, and opened horizontally to the hall at a distance of 12 m from the floor and 10.5 m from the west wall. Mechanical exhaust ventilation was operational for Case 3, with a constant volume flow rate of 11 m^3/s drawn through the exhaust duct.

Heat Release Rate: Each test used a single liquid fuel pan with its center located 16 m from the west wall and 7.4 m from the south wall. For all tests, the fuel was heptane in a circular steel pan that was partially filled with water. The pan had a diameter of 1.17 m for Case 1 and 1.6 m for Cases 2 and 3. In

each case, the fuel surface was 1 m above the floor. The trays were placed on load cells, and the HRR was calculated from the mass loss rate. For the three cases, the fuel mass loss rate was averaged from individual replicate tests. In the HRR estimation, the heat of combustion (taken as 44,600 kJ/kg) and the combustion efficiency for n-heptane was used. Hostikka suggests a value of 0.8 for the combustion efficiency. Tewarson reports a value of 0.93 for a 10 cm pool fire [135]. For the calculations reported in the current study, a combustion efficiency of 0.85 is assumed. In general, an uncertainty of 15 % has been assumed for the reported HRR of most of the large scale fire experiments used.

Radiative Fraction: The radiative fraction was assumed to be 0.35, similar to many smoky hydrocarbons.

A diagram of the test structure is displayed in Figure 3.51.

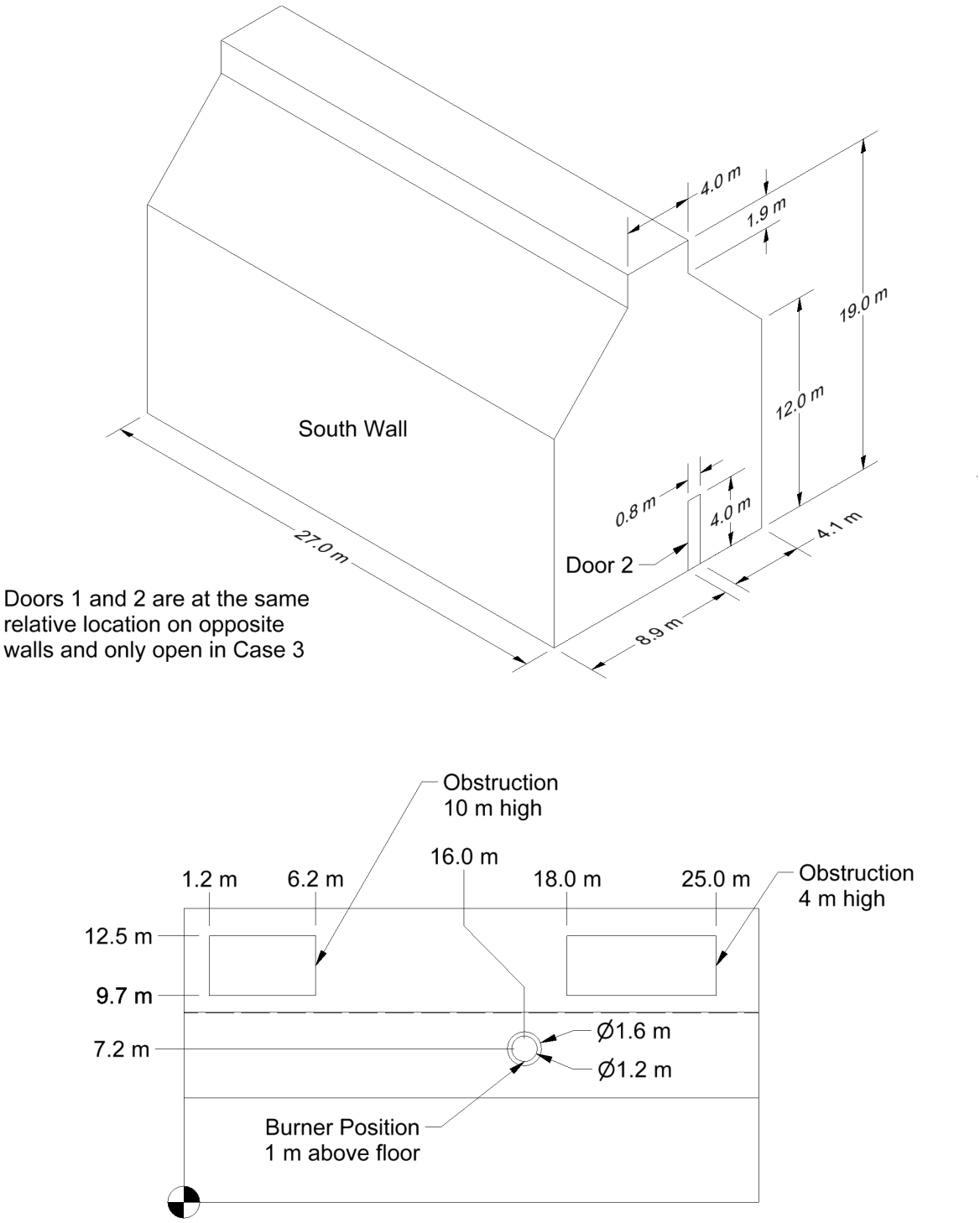

Figure 3.51: Geometry of the VTT Large Fire Test Hall.

3.89 VTT Water Spray Experiments

The spray from a single water mist nozzle was measured at Tampere University of Technology using a direct imaging technique [309]. The model number of the nozzle is LN-2, manufactured by the Spraying Systems Company. It is a fine spray hydraulic atomizing nozzle of the standard spray, small capacity type. Measurements were made 40 cm and 62 cm below the nozzle. Measured quantities include the average droplet velocity, droplet flux, and median diameter.

3.90 Waterloo Methanol Pool Fire Experiment

Beth Weckman measured near-field temperatures and velocities of a 30.5 cm diameter methanol pool fire at the University of Waterloo, Ontario, Canada [310]. The methanol fuel flow rate was maintained at 1.35 cm^3/s to maintain a burner rim height of 1 cm. Assuming complete combustion, the heat release rate was approximately 24.6 kW.

The burner was mounted on a traversing stand that allowed for radial and axial traverses of the fire flow field. The vapor core, continuous flame zone and fluctuating regions of the fire plume were characterized via profiles of axial and radial velocity and temperature taken at 2 cm intervals from the pool centerline to 16 cm from the centerline in the radial direction, and at heights from 2 cm to 20 cm above the fuel surface. A final radial profile was taken at a height of 30 cm. Measurements were made by moving the burner while the velocity and temperature transducers were held at a fixed point. To shield the fire from drafts, the entire system was enclosed by panels of wire mesh that was covered with an aluminum window screen.

Time resolved velocity measurements were performed using a two component laser doppler anemometer. Time resolved temperature data was measured using 50 μm diameter, bare-wire thermocouples (Pt vs Pt-10% Rh) with known bead diameters in the range of 75 μm to 100 μm.

Additional measurements of a 30.5 cm diameter methanol pool fire were made by Hamins et al., including the heat flux to the pool surface [311], centerline profiles of temperature and species concentrations [312], and an additional radial profile of temperature 60 cm above the pool surface [312].

Modeling Notes

The methanol pool fire is modeled at three different grid resolutions—2 cm, 1 cm, and 0.5 cm. Two sets of simulations are performed, one in which the mass loss rate of fuel is specified, and one in which it is predicted. The gas phase measurements are compared with the simulations for which the burning rate is specified.

Because measurements of CO were made within the flame envelop, a two-step reaction mechanism is implemented. In the first reaction, fuel is converted to CO and H_2O, and in the second reaction, CO is converted to CO_2. Both reactions employ fast kinetics and performed serially. It is assumed that no soot is formed in either reaction.

Physical properties of methanol are taken from a data sheet published by the Methanol Institute [313]: boiling temperature, 64.6 °C, heat of vaporization at 64.6 °C, 1098.3 kJ/kg, thermal conductivity, 0.2 W/(m·K), specific heat at 25 °C, 2.53 kJ/(kg·K), density at 20 °C, 792 kg/m^3. The heat of combustion is given as 19.9 kJ/g, but this value is not input directly, but rather calculated based on the heats of formation of the reactants and products of combustion.

The radiative fraction is *predicted* by the model, not specified by the user, for all cases. The path length used by RadCal to compute the table of effective radiative absorption coefficients for the gas mixture is set to 10 cm, the default value. The absorption coefficient of the liquid methanol is given as 1140 m^{-1}.

The modeled thermocouple has a bead diameter of 100 μm to match the experiments.

For the simulations where the burning rate is not specified, a liquid fuel evaporation model is used with a boiling temperature of 64.6 °C.

3.91 WTC Spray Burner Experiments

As part of its investigation of the World Trade Center disaster, the Building and Fire Research Laboratory at NIST conducted several series of fire experiments to both gain insight into the observed fire behavior and also to validate FDS for use in reconstructing the fires. The first series of experiments involved a relatively simple compartment with a liquid spray burner and various structural elements with varying amounts of sprayed fire-resistive materials (SFRM). A diagram of the compartment is shown in Fig. 3.52. A complete description of the experiments can be found in the NIST WTC report NCSTAR 1-5B [69]. The overall enclosure was rectangular, as were the vents and most of the obstructions. The compartment walls and ceiling were made of 2.54 cm thick marinite. The manufacturer provided the thermal properties of the material used in the calculation. The density was 737 kg/m^3, conductivity 0.12 W/m/K. The specific heat ranged from 1.17 kJ/kg/K at 93 °C to 1.42 kJ/kg/K at 425 °C. This value was assumed for higher temperatures. The steel used to construct the column and truss flanges was 0.64 cm thick. The density of the steel was assumed to be 7,860 kg/m^3; its specific heat 0.45 kJ/kg/K.

Two fuels were used in the tests. The properties of the fuels were obtained from measurements made on a series of unconfined burns that are referenced in the test report. The first fuel was a blend of heptane isomers, C_7H_{16}. Its soot yield was set at a constant 1.5 %. The second fuel was a mixture (40 % - 60 % by mass) of toluene, C_7H_8, and heptane. Because FDS only considers the burning of a single hydrocarbon fuel, the mixture was taken to be C_7H_{12} with a soot yield of 11.4 %. The radiative fraction for the heptane blend was 0.44; for the heptane/toluene mixture it was 0.39. The heat release rate of the simulated burner was set to that which was measured in the experiments. The spray burner was modeled using reported properties of the nozzle and liquid fuel droplets.

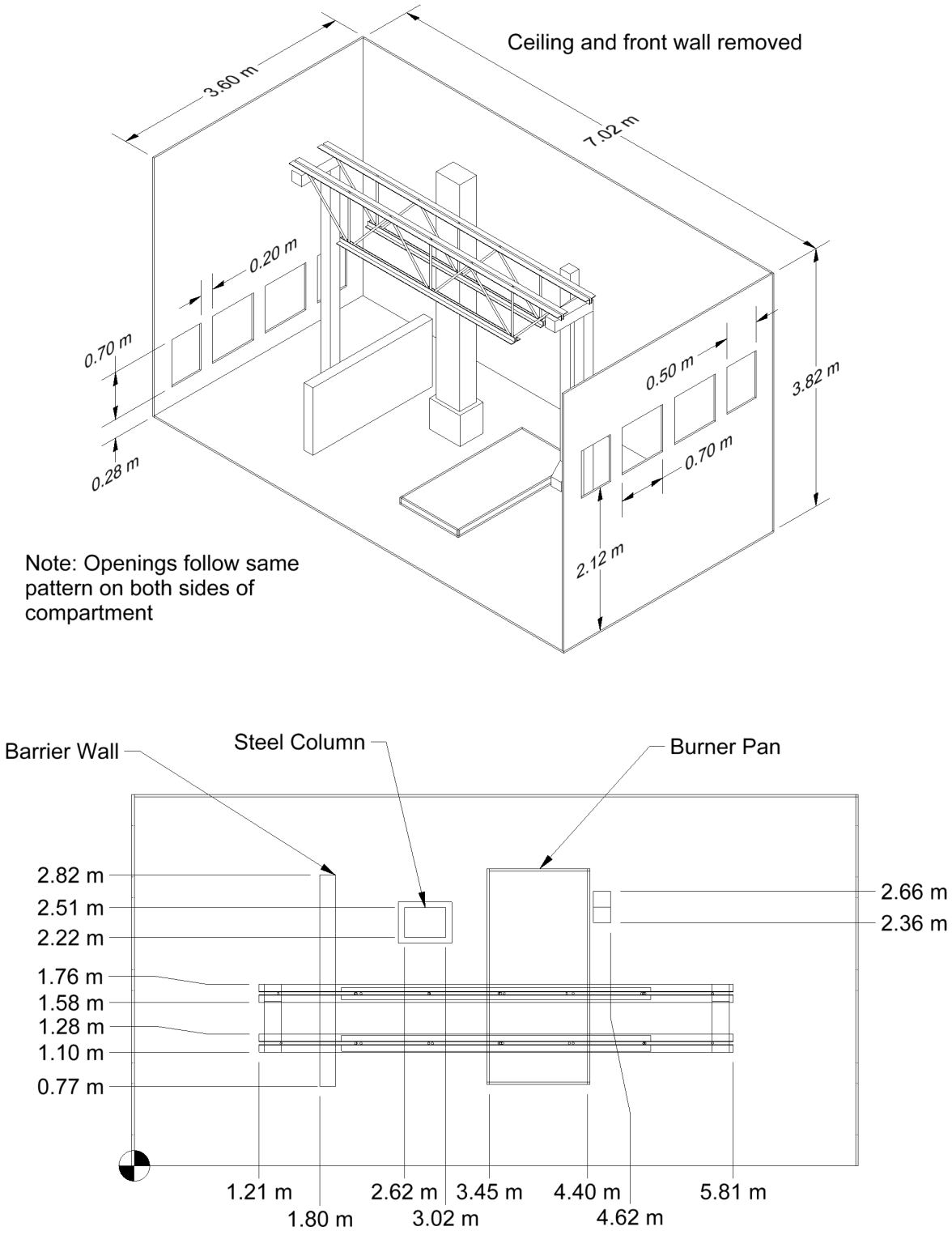

Figure 3.52: Geometry of the compartment used for the WTC Experiments.

3.92 Summary of Experiments

Table 3.41 presents a summary of all the experiments described in this chapter in terms of parameters commonly used in fire protection engineering. This "parameter space" outlines the range of applicability of the validation studies performed to date. In other words, if this guide is to be cited as justification for using FDS to simulate a given fire scenario, that scenario must be similar to these experiments in the sense of having comparable physical parameters. These parameters are explained below:

Heat Release Rate, $\dot{Q}$, is the range of peak heat release rates of the fires in the test series.

Fire Diameter, D, is the equivalent diameter of the base of the fire, calculated $D = \sqrt{4A/\pi}$, where A is the area of the base.

Ceiling Height, H, is the distance from floor to ceiling.

Fire Froude Number, $\dot{Q}^*$, is a useful non-dimensional quantity for plume correlations and flame height estimates.

$$\dot{Q}^* = \frac{\dot{Q}}{\rho_\infty c_p T_\infty \sqrt{gD}D^2} \tag{3.30}$$

It is essentially the ratio of the fuel gas exit velocity and the buoyancy-induced plume velocity. Jet fires are characterized by large Froude numbers. Typical accidental fires have a Froude number near unity.

Flame Height relative to Ceiling Height, L_f/H, is a convenient way to express the physical size of the fire relative to the size of the room. The height of the visible flame, based on Heskestad's correlation, is estimated by:

$$L_f = D\left(3.7\,(\dot{Q}^*)^{2/5} - 1.02\right) \tag{3.31}$$

Global Equivalence Ratio, ϕ, is the ratio of the mass flux of fuel to the mass flux of oxygen into the compartment, divided by the stoichiometric ratio.

$$\phi = \frac{\dot{m}_f}{r\,\dot{m}_{O_2}} \equiv \frac{\dot{Q}\,(\mathrm{kW})}{13,100\,(\mathrm{kJ/kg})\,\dot{m}_{O_2}} \quad ; \quad \dot{m}_{O_2} = \begin{cases} \frac{1}{2}\,0.23\,A_0\sqrt{H_0} & : \text{ Natural Ventilation} \\ 0.23\,\rho\,\dot{V} & : \text{ Mechanical Ventilation} \end{cases} \tag{3.32}$$

Here, r is the stoichiometric ratio, A_0 is the area of the compartment opening, H_0 is the height of the opening, ρ is the density of air, and $\dot{V}$ is the volume flow of air into the compartment. If $\phi < 1$, the compartment is considered "well-ventilated" and if $\phi > 1$, the compartment is considered "under-ventilated."

Compartment Aspect Ratios, W/H and L/H, indicate if the compartment is shaped like a hallway, typical room, or vertical shaft.

Relative Distance along the Ceiling, r_{cj}/H, indicates the distance from the fire plume of a sprinkler, smoke detector, etc., relative to the compartment height, H.

Relative Distance from the Fire, r_{rad}/D, indicates whether a "target" is near or far from the fire.

Table 3.41: Summary of important experimental parameters.

Test Series	$\dot{Q}$ (kW)	D (m)	H (m)	$\dot{Q}^*$	L_f/H	ϕ	W/H	L/H	r_{cj}/H	r_{rad}/D
Arup Tunnel	5344	1.6	7	1.5	0.8	0.0	1.1	43	0.0 – 1.1	N/A
ATF Corridors	50 – 500	0.5	2.4	0.3 – 3.3	0.3 – 0.9	0.0 – 0.1	0.8	7.1	0.8 – 6.0	N/A
Beyler Hood	8 – 30	0.2	0.5	0.5 – 1.1	0.7 – 1.3	0.2 – 1.7	2.0	2.0	N/A	N/A
Bittern Sprinklers	150	0.5	2.4	0.8	0.5	0.04	1.7	3.3	0.8	N/A
Bryant Doorway	34 – 511	0.3	2.4	0.5 – 6.9	0.2 – 1.0	0.0 – 0.2	1.0	2.1	0.6 – 0.8	N/A
DelCo Trainers	440 – 1190	0.7 – 1.2	2.4	0.7 – 1.0	0.8 – 1.1	0.1 – 0.3	1.5	2.5	0.4 – 3.8	N/A
FAA Cargo	5	0.1	1.4	1.4	0.2	0.2	2.3	4.8	0.1 – 4.8	N/A
Fleury Heat Flux	100 – 300	0.3 – 0.6	Open	0.3 – 5.5	Open	Open	Open	Open	Open	1.7 – 3.3
FM Panels	30 – 100	0.5	Open	0.2 – 0.5	Open	Open	Open	Open	Open	0
FM/SNL	470 – 516	0.9	6.1	0.6 – 2.4	0.3 – 0.6	0.0 – 0.2	2.0	3.0	0.2 – 0.3	N/A
Hamins CH_4	0.4 – 162	0.1 – 1.0	Open	0.1	Open	Open	Open	Open	N/A	0.1 – 12
Harrison Plumes	5 – 15	0.16	0.5	0.5 – 1.4	0.5 – 1.0	Open	Open	Open	N/A	N/A
Heskestad	$10^2 - 10^7$	1.1	Open	$10^{-1} - 10^4$	Open	Open	Open	Open	N/A	N/A
LLNL Enclosure	50 – 400	0.6	4.5	0.2 – 1.5	0.1 – 0.4	0.1 – 0.4	0.9	1.3	0.3 – 1.0	N/A
McCaffrey Plume	14 – 57	0.3	Open	0.2 – 0.8	Open	Open	Open	Open	N/A	N/A
NBS Multi-Room	110	0.3	2.4	1.5	0.5	0.0	1.0	5.1	N/A	N/A
NIST Composite Beam	4000	1.4	3.7	0.5	0.7	0.6	0.5	3.5	N/A	N/A
NIST FSE	100 – 2500	0.6 – 1.1	2.4	0.5 – 1.8	0.4 – 1.7	0.2 – 5.9	1.0	1.5	0.4 – 0.8	N/A
NIST/NRC	350 – 2200	1.0	3.8	0.3 – 2.0	0.3 – 1.0	0.0 – 0.3	1.9	5.7	0.3 – 2.1	2.0 – 4.0
NIST/NRC Cabinet	200 – 400	0.3 – 0.5	2.1	0.3 – 3.7	0.2 – 0.9	1.3 – 12	0.3	0.4	N/A	1.2 – 2.0
NIST/NRC Corner	200 – 400	0.7	3.8	0.4 – 0.9	0.3 – 0.5	<0.1	1.8	2.9	0.5 – 2.3	N/A
NIST RSE	50 – 600	0.15	1.0	5.2 – 63	0.9 – 2.8	0.1 – 1.1	1.0	1.5	N/A	N/A
NIST Smoke Alarms	100 – 350	1.0	2.4	0.2 – 0.3	0.2 – 0.5	N/A	1.7	8.3	1.3 – 8.3	N/A
NIST Vent Study	2.5	0.1	0.6	0.7	0.4	0.05	2.0	2.0	1.0	N/A
NRCC Facade	5000 – 10300	4.3	2.8	0.1 – 0.2	0.9 – 1.7	0.6 – 1.2	1.6	2.2	N/A	0
NRCC Smoke Tower	3000	2.2	3.4	0.4	1.0	0.7	0.1	0.2	1.2	N/A
NRL/HAI	50 – 520	0.3 – 0.7	Open	1.1 – 1.2	Open	Open	Open	Open	N/A	0
PRISME	480 – 1600	0.7 – 1.1	4.0	1.1	0.5 – 0.8	0.5	1.3	1.5	0.0 – 0.5	2.3 – 5.7
Sandia Plume	2025 – 5450	1.0	Open	1.8 – 5.0	Open	Open	Open	Open	N/A	N/A

Table 3.41: Summary of important experimental parameters (continued).

Test Series	$\dot{Q}$ (kW)	D (m)	H (m)	$\dot{Q}^*$	L_f/H	ϕ	W/H	L/H	r_{cj}/H	r_{rad}/D
SP AST	450	0.3	2.4	6.1	1.1	0.1	1.0	1.5	N/A	N/A
Steckler	31.6 – 158	0.3	2.1	0.8 – 3.8	0.3 – 0.7	0.0 – 0.6	1.3	1.3	N/A	N/A
UL/NFPRF	4400 – 10000	1.0	7.6	4.0 – 9.1	0.7 – 1.0	Open	4.9	4.9	0.6 – 3.9	N/A
UL/NIST Vents	500 – 2000	0.9	2.4	0.7 – 2.6	0.8 – 1.6	0.2 – 0.6	1.8	2.5	1.0 – 2.3	N/A
Ulster SBI	30 – 60	0.2	Open	1.5 – 3.0	Open	Open	Open	Open	N/A	0
USCG/HAI	250 – 1000	0.3	3.0	6.0 – 24	0.6 – 1.1	0.3 – 1.0	1.7	2.3	N/A	N/A
USN Hawaii	100 – 7700	0.3 – 2.5	15	0.7 – 1.3	0.1 – 0.4	Open	4.9	6.5	0 – 1.2	N/A
USN Iceland	100 – 15700	0.3 – 3.4	22	0.7 – 1.3	0.0 – 0.3	Open	2.1	3.4	0 – 1.0	N/A
Vettori Flat	1055	0.7	2.6	2.5	1.1	0.3	2.1	3.5	0.8 – 2.9	N/A
Vettori Sloped	1055	0.7	2.5	2.5	1.2	0.3	2.2	2.9	N/A	N/A
VTT Large Hall	1860 – 3640	1.4 – 1.8	19	0.7	0.2	0	1.0	1.4	0 – 0.6	N/A
WTC	1970 – 3240	1.6	3.8	0.6 – 0.9	0.8 – 1.1	0.3 – 0.5	0.9	1.8	0.0 – 0.8	0.3 – 1.3

Table 3.42 lists a few important parameters related to the numerical resolution of the calculation.

Characteristic Fire Diameter, D^*, is a useful length scale that incorporates the heat release rate of the fire.

$$D^* = \left(\frac{\dot{Q}}{\rho_\infty c_p T_\infty \sqrt{g}} \right)^{2/5} \tag{3.33}$$

Plume Resolution Index, $D^*/\delta x$, is the number of grid cells of length δx that span the characteristic diameter of the fire. The greater its value, the more "resolved" are the fire dynamics.

Ceiling Height relative to Fire Diameter, H/D^*, is the non-dimensional height of the smoke plume.

Note that the calculations performed for the various validation studies described in this Guide use a wide range of values of the Plume Resolution Index, $D^*/\delta x$. There are several reasons for this. First, typical applications of FDS often involve relatively small fires in relatively large spaces, and it is impractical to use a very fine grid that captures the detailed fire dynamics. Second, for some applications the accuracy of calculation is highly dependent on resolving the plume well, but for others, it is less important. For those citing the validation studies in this Guide, it is important that both the physical and numerical parameters are comparable to the given application.

Table 3.42: Summary of important numerical parameters.

Test Series	D^* (m)	$D^*/\delta x$	H/D^*
Arup Tunnel	1.8	9	3.8
ATF Corridors	0.3 – 0.7	3 – 7	3.4 – 8.5
Beyler Hood	0.1 – 0.2	5 – 8	2.1 – 3.5
Bryant Doorway	0.2 – 0.7	5 – 14	3.4 – 9.9
DelCo Trainers	0.7 – 1.0	6.9 – 10	2.3 – 3.5
FAA Cargo	0.1	5.6	12
Fleury Heat Flux	0.4 – 0.6	8 – 12	Open
FM Panels	0.2 – 0.4	12 – 19	Open
FM/SNL	0.7	7	8.5 – 8.8
Hamins Burner	0.04 – 0.5	6	Open
Harrison Plumes	0.1 – 0.2	5 – 7	2.8 – 4.4
Heskestad	0.4 – 44	5 – 20	Open
LLNL Enclosure	0.3 – 0.6	1 – 3	6.9 – 15.9
McCaffrey Plume	0.2 – 0.3	5 – 20	Open
NBS Multi-Room	0.4	4	6.2
NIST FSE	0.4 – 1.4	3.8 – 14	1.7 – 6.3
NIST/NRC	0.6 – 1.3	5 – 11	3.1 – 6.5
NIST/NRC Cabinets	0.2 – 0.7	2.2 – 6.7	3.1 – 9.5
NIST/NRC Corner	0.5 – 0.7	5.1 – 6.7	5.7 – 7.5
NIST RSE	0.3 – 0.8	12 – 32	1.3 – 3.5
NIST Smoke Alarms	0.4 – 0.6	3.8 – 6.3	3.8 – 6.3
NIST Vent Study	0.1	3.5	6.8
NRCC Facade	1.8 – 2.4	18 – 24	1.2 – 1.5
NRCC Smoke Tower	1.5	15	18.6
NRL/HAI	0.3 – 0.7	9 – 10	Open
PRISME	0.7 – 1.2	7 – 12	3.4 – 5.6
Sandia Plume	1.2 – 1.8	20 – 118	Open
SP AST	0.7	14	3.5
Steckler	0.2 – 0.4	5 – 9	4.8 – 9.1
UL/NFPRF	1.7 – 2.4	8 – 12	3.2 – 4.5
UL/NIST	0.7 – 1.2	7 – 12	1.9 – 3.4
Ulster SBI	0.2 – 0.3	12 – 15	Open
USCG/HAI	0.5 – 0.9	5 – 9	3.2 – 5.6
USN Hawaii	0.4 – 2.1	2 – 11	7.1 – 40.3
USN Iceland	0.4 – 2.8	2 – 14	7.8 – 59
Vettori Flat	1.0	12	2.8
Vettori Sloped	1.0	10	2.6
VTT Large Hall	1.2 – 1.6	5 – 6	12.1 – 15.8
WTC	0.9 – 1.1	9 – 11	3.5 – 4.1

Chapter 4

Quantifying Model Uncertainty

This chapter describes a method to estimate the model uncertainty using comparisons of model predictions with experimental measurements whose uncertainty has been quantified. The method is ideal for complex numerical models like FDS for which a systematic analysis of sub-components is impractical, but for which there exists a relatively large amount of experimental data with which to evaluate the accuracy of the model predictions. If the uncertainty in the experiments can be quantified, the uncertainty in the model can then be expressed in the form of a normal distribution whose mean and standard deviation are estimated from the relative difference between the predicted and measured values.

This method only addresses model uncertainty. It does not account for the uncertainty associated with the model input parameters. How the *parameter uncertainty* is treated depends greatly on the type of application. Regardless of how the parameter uncertainty is calculated, the model uncertainty needs to be addressed independently. In fact, it is incumbent on the model developers to express the uncertainty of the model in as simple a form as possible to enable the end user to assess the impact of parameter uncertainty and then combine the two forms of uncertainty into a final result.

4.1 Introduction

The most effective way of introducing the subject of uncertainty in fire modeling is by way of an example. Suppose that a fire model is used to estimate the likelihood that an electrical control cable could be damaged by a fire. It is assumed that the cable loses functionality when its surface temperature reaches 200 °C, and the model predicts that the cable temperature could reach as high as 175 °C. Does this mean that there is no chance of damage? The answer is no, because the input parameters, like the heat release rate of the fire, and the model assumptions, like the way the cables are modeled, are uncertain. The combination of the two – the *parameter uncertainty* and the *model uncertainty* – leave open the possibility that the cable temperature could exceed 200 °C.

This chapter addresses *model uncertainty* only and suggests a simple method to quantify it. While parameter uncertainty is certainly an important consideration in fire modeling, its treatment varies considerably depending on the particular application. For example, in what is often referred to as a "bounding analysis," the model input parameters are chosen so as to simulate a "maximum credible" or "worst case" fire. In other cases, mean values of the input parameters constitute a "50th percentile" design scenario. Sometimes entire statistical distributions, rather than individual values, of the input parameters are "propagated" through the model in a variety of ways, leading to a statistical distribution of the model output. Notarianni and Parry survey these techniques in the SFPE Handbook [314]. Regardless of the method that is chosen for assessing the impact of the input parameters on the model prediction, there needs to be a way of quantifying the uncertainty of the model itself. In other words, how good is the prediction for a given set of input parameters?

The issue of model uncertainty has been around as long as the models themselves. The scenario above, for example, was considered by Siu and Apostolakis in the early 1980s [315] as part of their development of risk models for nuclear power plants. The fire models at the time were relatively simple. In fact, many were engineering correlations in the form of simple formulae. This made the methods for quantifying their uncertainty reasonably tractable because each formula consisted of only a handful of physical parameters. Over the past thirty years, however, both fire modeling and the corresponding methods of uncertainty analysis have become far more complex. The current generation of computational fluid dynamics (CFD) based fire models require such a large number of physical and numerical parameters that it is considered too cumbersome to estimate model uncertainty by systematically assessing their combined effect on the final prediction. The more practical approach is to compare model predictions with actual fire experiments in a validation study, the conclusions of which typically come in the form of statements like: "The model generally over-predicts the measured temperatures by about 10 %," or "The model predictions are within about 20 % of the measured heat fluxes." This information is helpful, at the very least to demonstrate that the model is appropriate for the given application. However, even the statement that the model over-predicts measured temperatures by 10 % is useful not only to gain acceptance of the model but also to provide a better sense of the model's accuracy, and a greater level of assurance in answering the question posed above. Knowing that the model not only predicted a temperature of 175 °C, but also that the model tends to over-predict temperatures by a certain amount, increases the confidence that the postulated fire would not cause the cable to fail. The probability of cable failure could be quantified further via a statistical distribution like the one shown in Fig. 4.1. The area indicated by the shaded region is the probability that the temperature will exceed 200 °C, even though the model has predicted a peak temperature of only 175 °C.

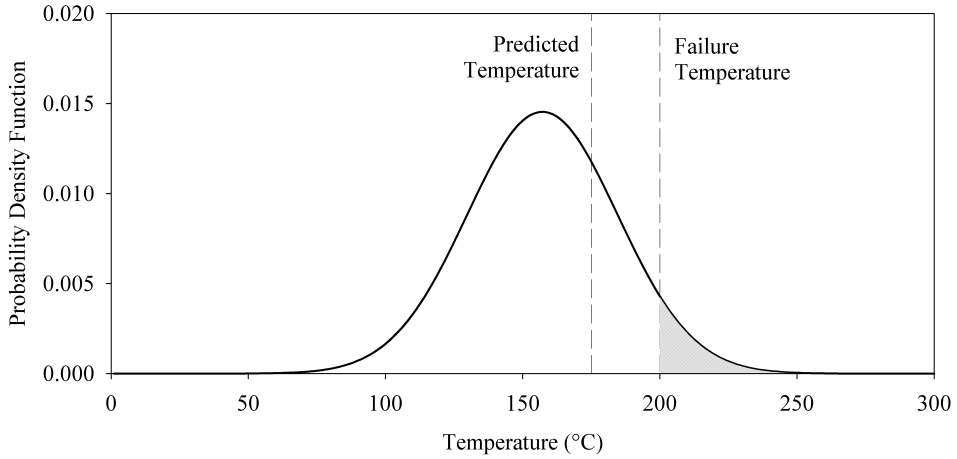

Figure 4.1: Plot showing a possible way of expressing the uncertainty of the model prediction.

This chapter describes a method for expressing *model uncertainty* by way of a distribution like the one shown in Fig. 4.1. The procedure is not a dramatic departure from the current practice of fire model validation in that it relies entirely on comparisons of model predictions and experimental measurements. The advantage of the approach is that it does not demand advanced knowledge of statistics or details of the numerical model. The parameters of the distribution shown in Fig. 4.1, namely the mean and standard deviation, are not generated by the model user. Rather, they are reported as the results of the validation study. The calculation of the probability of exceeding some critical threshold (i.e., the area under the curve) is a simple table look-up or function call in data analysis software like Microsoft Excel®.

4.2 Sources of Model Uncertainty

A deterministic fire model is based on fundamental conservation laws of mass, momentum and energy, applied either to entire compartments or smaller control volumes that make up the compartments. A CFD model may use millions of control volumes to compute the solution of the Navier-Stokes equations. However, it does not actually solve the Navier-Stokes equations, but rather an approximate form of these equations. The approximation involves simplifying physical assumptions, like the various techniques for treating subgrid-scale turbulence. One critical approximation is the discretization of the governing equations. For example, the partial derivative of the density, ρ, with respect to the spatial coordinate, x, can be written in approximate form as:

$$\frac{\partial \rho}{\partial x} = \frac{\rho_{i+1} - \rho_{i-1}}{2\,\delta x} + \mathscr{O}(\delta x^2) \tag{4.1}$$

where ρ_i is the average value of the density in the ith grid cell and δx is the spacing between cells. The second term on the right represents all of the terms of order δx^2 and higher in the Taylor series expansion and are known collectively as the *discretization error*. These extra terms are simply dropped from the equation set, the argument being that they become smaller and smaller with decreasing grid cell size, δx. The effect of these neglected terms is captured, to some extent, by the subgrid-scale turbulence model, but that is yet another approximation of the true physics. What effect do these approximations have on the predicted results? It is very difficult to determine based on an analysis of the discretized equations. One possibility for estimating the magnitude of the discretization error is to perform a detailed convergence analysis, but this still does not answer a question like, "What is the uncertainty of the model prediction of the gas temperature at a particular location in the room at a particular point in time?"

To make matters worse, there are literally dozens of subroutines that make up a CFD-based fire model, from its transport equations, radiation solver, solid phase heat transfer routines, pyrolysis model, empirical mass, momentum and energy transfer routines at the wall, and so on. It has been suggested by some that a means to quantify the model uncertainty is to combine the uncertainties of all the model components. However, such an exercise is very difficult, especially for a CFD model, for a number of reasons. First, fire involves a complicated interaction of gas and solid phase phenomena that are closely coupled. Second, grid sensitivity in a CFD model or the error associated with a two-layer assumption in a zone model are dependent on the particular fire scenario. Third, fire is an inherently transient phenomenon in which relatively small changes in events, like a door opening or sprinkler actuation, can lead to significant changes in outcome.

Rather than attempt to decompose the model into its constituent parts and assess the uncertainty of each, the strategy adopted here is to compare model predictions to as many experiments as possible. This has been the traditional approach for quantifying model uncertainty in fire protection engineering because of the relative abundance of test data. Consider, for example, the plot shown in Fig. 4.2. This is the typical outcome of a validation study, where in this case a series of heat flux measurements are compared with model predictions. The diagonal line indicates where the prediction and measurement agree. But because there is uncertainty associated with each, it cannot be said that the model is perfect if its predictions agree exactly with measurements. There needs to be a way of quantifying the uncertainties of each before any conclusions can be drawn. Such an exercise would result in the uncertainty bars[1] shown in the figure. The horizontal bar associated with each point represents the uncertainty in the measurement itself. For example, the heat flux gauge is subject to uncertainty due to its design and fabrication. Because the horizontal bar represents the experimental uncertainty, it is assumed that the vertical bar represents the model uncertainty. This is only partially true. In fact the vertical bar represents the total uncertainty of the prediction, which is a combination of the *model* and *parameter* uncertainties. The physical input parameters, like the heat release rate and material properties, are based on measurements that are reported in the documentation of

[1] The data in Fig. 4.2 was extracted from Ref. [316]. The uncertainty bars are for demonstration only.

the experiment. The total *experimental uncertainty* is represented by all of the horizontal bar and part of the vertical. If the *experimental uncertainty* can be quantified, then the *model uncertainty* can be obtained as a result.

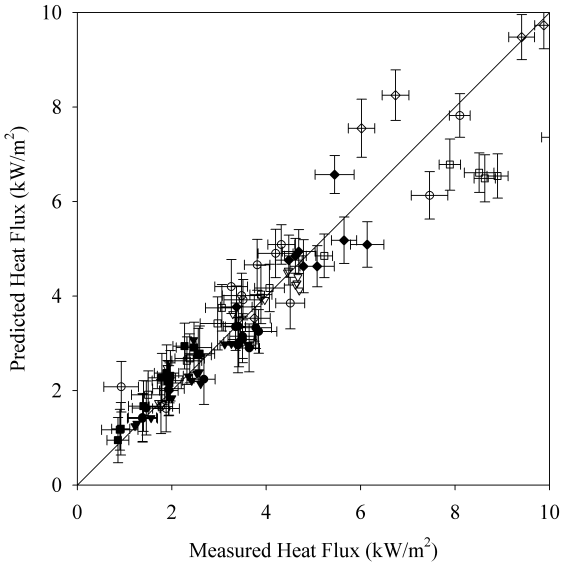

Figure 4.2: Example of a typical scatter plot of model predictions and experimental measurements.

4.3 Experimental Uncertainty

The difference between a model prediction and an experimental measurement is a combination of three components: (1) uncertainty in the measurement of the predicted quantity, (2) uncertainty in the model input parameters, and (3) uncertainty in the model physics and numerics. The first two components are related to uncertainty in the measured input and output quantities. For example, consider the hot gas layer (HGL) temperature. First, the thermocouple measurements used to calculate the HGL temperature have uncertainty. Second, the measurement of the heat release rate of the fire has uncertainty, and this uncertainty affects the predicted HGL temperature. Third, the model itself, including its physical assumptions and numerical approximations, has uncertainty. The objective of the validation study is to quantify this third component, the model uncertainty. To do this, the first two components of uncertainty related to the experimental measurements must be quantified. The combination of these two, the experimental uncertainty, is the objective of this section.

For many of the experiments considered in this guide, the uncertainty of the measurements was not documented. Instead, estimates of measurement uncertainty are made based on those few experiments that do include uncertainty estimates, and this information is supplemented by engineering judgment. In the following two subsections, each component of the experimental uncertainty is considered separately. First, the uncertainty in the measurement of the predicted quantity of interest, like the surface temperature of the compartment. Second, the uncertainties of the most important input parameters are propagated through simple models to quantify their effect on the predicted quantity. Then, the uncertainties are combined via simple quadrature to estimate the total experimental uncertainty.

Note that in this guide, all uncertainties are expressed in relative form, as a percentage. The uncertainty

of a measurement is a combination of the systematic uncertainty associated with the various underlying measurements and assumptions; and the random uncertainty associated with the conduct of the experiment. Following the recommended guidelines for evaluating and expressing the uncertainty of measurements [317], the systematic and random uncertainty values are combined via quadrature resulting in a combined relative standard uncertainty.

4.3.1 Uncertainty of Common Fire Measurements

Because most of the experiments described in this guide have little or no information about the uncertainty of the measurements, much of this section is based on the uncertainty analysis contained in the test report of the NIST/NRC Experiments[2]. The types of measurements described in this report are the ones most commonly used in large scale fire experiments. They include thermocouples for gas and surface temperature measurements, heat flux gauges, smoke and gas analyzers, and pressure sensors.

Thermocouples

Thermocouples are used to measure both gas and surface temperatures. They come in a variety of sizes and are constructed of different types of metals. Some are shielded or aspirated to limit the influence of thermal radiation from remote sources. In Ref. [116], Hamins et al. estimate the uncertainty of the various thermocouple measurements. Estimates of the combined relative standard uncertainty fall in a range between 2.5 % and 7.5 %. Because it is not possible to analyze the thousands of thermocouple measurements made in the experiments, the relative standard uncertainty applied to all thermocouple measurements is 5 %.

Heat Flux Gauges

For the NIST/NRC experiments, four types of heat flux gauges were used, some of which measured the total heat flux, and some of which measured only the radiation heat flux. The uncertainty associated with a heat flux measurement depends on many factors, including gauge characteristics, the calibration conditions and accuracy, as well as the incident flux modes (convective, radiative, conductive). Typically, the reported relative standard uncertainty of heat flux gauges varies from about 2.5 % to 5 %, with the measurement uncertainty dominated by uncertainty in the calibration and repeatability of the measurement. Repeatability of the various heat flux measurements in the NIST/NRC experiments was determined by examining measurements by the same instruments for different pairs of repeat tests. The difference between the measurements was about 3.5 %, on average, for both the radiative flux measurements and the total flux measurements. For all of the experiments described in this guide, a combined relative standard uncertainty of 5 % is suggested based on the measurement repeatability and calibration uncertainties reported for the NIST/NRC experiments.

Gas Analyzers

Gas concentrations were measured in two sets of experiments conducted at NIST, the NIST/NRC and the WTC experiments. The volume fractions of the combustion products, carbon monoxide (CO) and carbon dioxide (CO_2), were measured using gas sampling in conjunction with non-dispersive infrared analyzers, while the oxygen (O_2) volume fraction was typically measured using a paramagnetic analyzer. Gases were extracted through stainless steel or other types of lines and were pumped from the compartment and passed

[2]Note that the uncertainties in Ref. [116] are reported in the form of 95 % confidence intervals, or "2-sigma". This is referred to as the expanded uncertainty with a coverage factor of 2. To avoid confusion, in this report the uncertainty of all measurements and model predictions shall be reported in terms of a relative standard uncertainty; that is, the estimated standard deviation of the measured or predicted quantity.

through the analyzers. For several reasons, water in the sample was typically filtered, so the reported results are denoted as "dry". Analyzers were calibrated through the use of standard gas mixtures, with low relative uncertainties. Problems with the technique may involve instrument drift, analyzer response, incomplete and partial drying of sample gases, or (in the case when drying is not used) undetermined amounts of water vapor in the oxygen cell, which result in inaccurate readings.

For the NIST/NRC experiments, the species were measured in both the upper and lower layers. The relative standard uncertainty in the measured values was about 1.5 % for both the O_2 depletion and the CO_2 measurements. The largest contributors were the uncertainty in the composition of the calibration gas and the possibility of an undetermined amount of water vapor in the sample. The difference between the repeat measurements was about 1 %, on average, for both the O_2 depletion and the CO_2 measurements. Therefore, the combined relative standard uncertainty is estimated to be 2 % for measurements of both the O_2 decrease and the CO_2 increase.

Smoke Light Extinction Calculations

The smoke concentration was measured in the NIST/NRC experiments using laser transmission at 632.8 nm. The reported mass concentration of smoke, m_s''', was computed using the following expression:

$$m_s''' = \frac{\ln(I_0/I)}{\phi_s L} \tag{4.2}$$

where L is the path length, I and I_0 are the laser signal and reference signal, respectively, and ϕ_s is the specific extinction coefficient, which has a nearly universal value of 8.7 $m^2/g \pm 5$ % for hydrocarbons [318]. The systematic relative standard uncertainty of this measurement was reported to be 9 % in Ref. [116], with the dominant contribution to the uncertainty coming from drift in the laser measurement. Repeatability of the smoke measurement was investigated for the NIST/NRC experiments. The mean difference between replicate measurements was about 11 %. Therefore, a combined relative standard uncertainty of 14 % is suggested.

Pressure Gauges

The uncertainty in pressure measurements is typically small, but depends on the sensor type and calibration. In the NIST/NRC experiments, the differential pressure gauge used was temperature compensated, highly linear, and very stable. The estimated relative standard uncertainty is 0.5 %.

Bi-Directional Probes

Gas velocity is typically measured in fire experiments using bi-directional probes. These devices work like pitot tubes but have much larger openings. Bryant [143] estimates that the standard relative uncertainty of this measurement, assuming that the probe is aligned well with the flow, is approximately 7 %.

Oxygen Consumption Calorimeters

For all of the experiments described in this guide, the heat release rate (HRR) is determined either via oxygen consumption calorimetry or via the mass loss rate multiplied by the fuel heat of combustion. The accuracy of each method varies roughly between 2.5 %, where the fire is small and the fuel stoichiometry is well understood, and 13 %, where the fire is large or the smoke is not completely captured or the fuel stoichiometry is not well understood. In Ref. [116], the relative standard uncertainty of a 2 MW heptane spray fire is estimated to be 7.5 %. It is assumed that the uncertainty of the HRR for the other experiments is comparable.

Device Activation or Failure Time

Fire models are often used to predict the time to activation of devices like sprinklers and smoke detectors, and time to failure of critical equipment like electrical cables. Measuring activation or failure times in experiments is fairly precise, and, thus, the uncertainty of such measurements is essentially zero. Almost all of the uncertainty associated with these times is in the measurement or characterization of the mechanism of activation or failure. For example, the activation of a sprinkler is based on its measured RTI (Response Time Index) and activation temperature. Estimates of the uncertainty of these parameters are discussed in the next section.

4.3.2 Propagation of Input Parameter Uncertainty

Empirical correlations for basic fire phenomena provide a convenient way to assess the propagation of the uncertainty of the model input parameters. The more complex fire models may require dozens of physical and numerical input parameters for a given fire scenario. However, only a few of these parameters, when varied over their plausible range of values, significantly impact the results. For example, the thermal conductivity of the compartment walls does not significantly affect a predicted cable surface temperature, but the HRR of the fire does. The relatively simple empirical models identify the key parameters that impact the predicted quantity, and they provide the means to quantify the functional relationship between model inputs and outputs.

Gas and Surface Temperatures

According to the McCaffrey, Quintiere, and Harkleroad (MQH) correlation, the HGL temperature rise, $T - T_0$, in compartment fire is proportional to the HRR, $\dot{Q}$, raised to the two-thirds power:

$$T - T_0 = C\,\dot{Q}^{\frac{2}{3}} \tag{4.3}$$

The constant, C, involves a number of geometric and thermo-physical parameters that are unique to the given fire scenario. By way of differentials, this empirical relationship can be expressed in the form:

$$\frac{\Delta T}{T - T_0} \approx \frac{2}{3}\,\frac{\Delta \dot{Q}}{\dot{Q}} \tag{4.4}$$

This is a simple formula with which one can readily estimate the relative change in the temperature rise due to the relative change in the HRR. The uncertainty in the HRR of the validation experiments was estimated to be 7.5 %. Equation (4.4) indicates that a 7.5 % increase in the HRR should lead to a 5 % increase in the HGL temperature.

HGL Depth

Most of the experiments for which the HGL depth was predicted had at least one open door or window that effectively determined the steady-state HGL depth. Unlike all of the other predicted quantities, the HGL depth is relatively insensitive to the fire's HRR. It is largely determined by the height of the opening, and for this reason there is essentially no uncertainty associated with the model inputs that affect the layer depth.

Gas and Smoke Concentration

Most fire models assume that combustion product gases and soot, once beyond the flaming region of the fire, are passively transported throughout the compartment. The major products of combustion, like CO_2

and water vapor, plus the major reactant, O_2, are generated, or consumed, in direct proportion to the burning rate of the fuel, which is directly proportional to the HRR. The mass fraction of any species in the HGL is directly proportional to the product of its yield and the HRR.

For many of the experiments described in this guide, the yields of the major product gases like O_2 and CO_2 from pure fuels like methane gas and heptane liquid are known from the basic stoichiometry to a high level of accuracy. Thus, the relative uncertainty in the concentration of major products gases is the same as that of the HRR, 7.5 %. The uncertainty in the smoke concentration, however, is a combination of the uncertainty of the HRR and the soot yield. The relative standard uncertainty of the soot yield of heptane reported in Ref. [116] is 11 %. The uncertainties for HRR and soot yield are combined via quadrature and the resulting expanded relative uncertainty is 13 %.

Pressure

In a closed, ventilated compartment, the average pressure, p, is governed by the following equation:

$$\frac{\mathrm{dp}}{\mathrm{dt}} = \frac{\gamma - 1}{V}\left(\dot{Q} - \dot{Q}_{\mathrm{loss}}\right) + \frac{\gamma p}{V}\left(\dot{V} - \dot{V}_{\mathrm{leak}}\right) \tag{4.5}$$

where γ is the ratio of specific heats (about 1.4), V is the compartment volume, $\dot{Q}$ is the HRR, $\dot{Q}_{\mathrm{loss}}$ is the sum of all heat losses to the walls, $\dot{V}$ is the net ventilation rate into the compartment, and $\dot{V}_{\mathrm{leak}}$ is the leakage rate out of the compartment. The leakage rate is a function of the compartment over-pressure:

$$\dot{V}_{\mathrm{leak}} = A_{\mathrm{leak}}\sqrt{\frac{2(p - p_\infty)}{\rho_\infty}} \tag{4.6}$$

The maximum compartment pressure is achieved when the pressure rise term in Eq. (4.5) is set to zero. Rearranging terms yields an estimate for the maximum pressure:

$$(p - p_\infty)_{\max} \approx \frac{\rho_\infty}{2}\left(\frac{(\gamma - 1)\left(\dot{Q} - \dot{Q}_{\mathrm{loss}}\right) + \gamma p_\infty \dot{V}}{\gamma p_\infty A_{\mathrm{leak}}}\right)^2 \tag{4.7}$$

The test report for the NIST/NRC experiments contains estimates of the uncertainty in the HRR, ventilation rate and leakage area. To calculate the uncertainty in the maximum pressure rise resulting from the uncertainty in these three parameters, the pressure rise estimate in Eq. (4.7) was calculated using 1000 randomly selected sets of values of the HRR, ventilation rate, and leakage area. These parameters were assumed to be randomly distributed with mean values of 1000 kW, 1 m^3/s, and 0.06 m^2 and relative standard uncertainties of 75 kW, 0.1 m^3/s, and 0.0021 m^2. The mean values of these parameters were typical of the NIST/NRC experiments, and the uncertainties were reported in the test report. The resulting relative standard uncertainty in the pressure of a closed compartment due to the uncertainty in the HRR, ventilation rate, and leakage area is 21 %.

For an open compartment, in which the ventilation rate and leakage area have much less influence, the relative standard uncertainty in the pressure is twice that of the HRR, 15 %.

Velocity

Fire-induced velocities, as in a plume or ceiling jet, are roughly proportional to the HRR to the 1/3 power [319]. Given that the relative standard uncertainty in the HRR is 7.5 %, the uncertainty in gas velocity due to the propagated effect of the uncertainty in the HRR is 2.5 %.

Heat Flux

The heat flux to a target or wall is a combination of direct thermal radiation from the fire and convective and thermal radiation from the HGL. If the heat flux is predominantly due to the thermal radiation of the fire, it can be approximated using the point source radiation model:

$$\dot{q}'' = \frac{\chi_r \dot{Q}}{4\pi r^2} \tag{4.8}$$

where χ_r is the radiative fraction, $\dot{Q}$ is the HRR, and r is the distance from the fire. The relative standard uncertainty of the heat flux is a combination of the uncertainty in the radiative fraction and the HRR:

$$\frac{\delta \dot{q}''}{\dot{q}''} \approx \frac{\delta \dot{Q}}{\dot{Q}} + \frac{\delta \chi_r}{\chi_r} \tag{4.9}$$

Reference [116] estimates the relative standard uncertainty of the radiative fraction of a heptane pool fire to be 8 %. Combined with the 7.5 % uncertainty in the HRR (via quadrature) yields a 11 % relative standard uncertainty in the heat flux directly from a fire.

The heat flux to a cold surface due to the exposure to hot gases and not necessarily the fire itself is the sum of radiative and convective components:

$$\dot{q}'' = \varepsilon\sigma\left(T_{gas}^4 - T_\infty^4\right) + h\left(T_{gas} - T_\infty\right) \tag{4.10}$$

where ε is the surface emissivity, σ is the Stefan-Boltzmann constant, T_{gas} is the gas temperature, T_∞ is the ambient temperature, and h is the convective heat transfer coefficient. From the discussion above, the relative standard uncertainty in the gas temperature rise above ambient is 5 % resulting from an estimated uncertainty in the HRR of 7.5 %. There is also uncertainty in the convective heat transfer coefficient, but this is attributed to the model, not the experimental measurements. Thus, the uncertainty in the heat flux is largely a function of the uncertainty in the gas temperature which is largely a function of the HRR. As was done for the pressure, 1000 randomly selected values of gas temperature with a mean of 300 °C above ambient and an relative uncertainty of 5 % resulted in a corresponding uncertainty of 9 % in the heat flux.

In actual compartment fires, the heat flux to surfaces is a combination of direct thermal radiation from the fire and indirect radiation and convection from the hot gases. Given that the calculation of the former incurs a 11 % relative standard uncertainty and the latter 9 %, to simplify the analyses, a value of 10 % is used for all heat flux predictions.

Sprinkler Activation Time

The uncertainty in the reported sprinkler activation times is due mainly to uncertainties in the measured HRR, RTI (Response Time Index), and activation temperature. There is a negligible uncertainty in the measured activation time itself, which is typically determined with a pressure transducer. To determine the effect of the uncertainties in the HRR, RTI and activation temperature, consider the ordinary differential equation governing the temperature, T_{link}, of a conventional glass bulb of fusible link sprinkler:

$$\frac{dT_{link}}{dt} = \frac{\sqrt{u}}{RTI}\left(T_{gas} - T_{link}\right) \tag{4.11}$$

Here, u and T_{gas} are the velocity and the temperature of the ceiling jet, respectively. According to Alpert's ceiling jet correlation [319], the ceiling jet temperature and velocity are proportional to the HRR raised to the power of 2/3 and 1/3, respectively. Given the relative standard uncertainty in the HRR of 7.5 %, the uncertainty in the ceiling jet temperature and velocity are, thus, 5 % and 2.5 %, respectively. As for the RTI

and activation temperature, these values are measured experimentally and the uncertainties differ depending on the test procedure. Vettori [77] reports that the RTI of the sprinklers used in his experiments is 56 $(\text{m}\cdot\text{s})^{1/2}$ with a relative standard uncertainty of 11 %, and that the activation temperature is 68 °C ± 2.4 °C. This latter uncertainty estimate is assumed to represent one standard deviation. Assuming an ambient temperature of approximately 20 °C, the relative standard uncertainty in the activation temperature is assumed to be 5 %.

To determine how the uncertainties in the measured parameters affect the sprinkler activation time, Eq. (4.11) was integrated 1000 times using random selections of the ceiling jet temperature and velocity, RTI, and activation temperature. The mean ceiling jet temperature was increased linearly at rates varying from 0.5 °C/s to 2 °C/s, consistent with the variety of growth rates measured by Vettori. The mean ceiling jet velocity was assumed to be 1 m/s. This procedure yielded a relative standard uncertainty in the sprinkler activation time of 6 %.

The activation times recorded by Vettori include two or three replicates for each configuration. The standard deviation of the 45 measured activation times, normalized by the mean of each set of replicates, was 6 %, consistent with the result obtained above.

Number of Activated Sprinklers

Alpert's ceiling jet correlation [319] predicts the temperature rise, $T - T_\infty$ (°C), as a function of the HRR, $\dot{Q}$ (kW), and radial distance, r (m), from the plume centerline:

$$T - T_\infty = 5.38 \frac{\dot{Q}^{2/3}/H^{5/3}}{(r/H)^{2/3}} \quad ; \quad r/H > 0.18 \tag{4.12}$$

For a given ceiling height, H, the radial extent of the sprinkler activation temperature is directly proportional to $\dot{Q}$. The number of activated sprinklers is roughly proportional to the square of this radial distance, assuming the sprinklers are uniformly spaced on a rectangular grid. Thus, the uncertainty in the number of activated sprinklers due to the uncertainty in the HRR is 15 %.

Electrical Cable Failure Time

The uncertainty in the reported cable failure times is due mainly to uncertainties in the measured exposing temperature, cable diameter, and jacket thickness. The uncertainty in the measured mass per unit length of the cable is assumed to be negligible. To determine the uncertainty in the cable failure time, the heat conduction equation in the THIEF model was solved numerically using 10,000 random selections of the exposing temperature, cable diameter, and jacket thickness. The cable diameter was varied from 16.25 mm to 16.35 mm, and the jacket thickness was varied from 1.45 mm to 1.55 mm. The uncertainty in the exposing temperature of the cylindrical heater was assumed to be 2.5 %, the lower bound of the range of uncertainty estimates for thermocouple measurements. The mass per unit length of the cable was assumed to be 0.529 kg/m, and the ambient temperature was assumed to be 20 °C. This procedure yielded an estimated relative standard uncertainty in the cable failure time of 12 %.

Smoke Detector Activation Time

There is a single set of experiments with which to evaluate model predictions of smoke detector activation time, the NIST Home Smoke Alarm Experiments. The test report [241] does not include detailed information about the alarm mechanism within the various smoke detectors used in the experiments. Thus, from a modeling standpoint, these devices are "black boxes" and their activation can only be discerned from a variety of empirical techniques, the most popular of which is to assume that the smoke detector behaves like a sprinkler or heat detector whose activation is governed by Eq. (4.11) with a low activation temperature and

RTI. Bukowski and Averill [320] suggest an activation temperature of 5 °C to be typical of many residential smoke alarms. The propagated uncertainty of this estimate is difficult to determine because temperature rise is not particularly well-correlated with smoke concentration within the sensing chamber of the detector. Nevertheless, the relative standard deviation of the normalized activation times for the NIST Home Smoke Alarm Experiments is 34 %. Without more detailed information about the activation criteria, the models cannot predict the activation times more accurately than this value.

4.3.3 Summary of Experimental Uncertainty Estimates

Table 4.1 summarizes the estimated uncertainties of the major output quantities. The right-most column in the table represents the total experimental uncertainty, denoted as $\widetilde{\sigma}_E$, a combination of the uncertainty in the measurement of the output quantity itself, along with the propagated uncertainties of the key measured input quantities. This total experimental uncertainty is obtained by taking the square root of the sum of the squares of the measurement and propagation uncertainties that have been estimated in the previous two sections. It is assumed that the two forms of uncertainty are independent.

Table 4.1: Summary of uncertainty estimates. All values are expressed in the form of a standard relative uncertainty.

Output Quantity	Measurement Uncertainty	Propagated Input Uncertainty	Combined Uncertainty, $\widetilde{\sigma}_E$
Gas and Solid Temperatures	0.05	0.05	0.07
HGL Depth	0.05	0.00	0.05
Gas Concentrations	0.02	0.08	0.08
Smoke Concentration	0.14	0.13	0.19
Pressure, Closed Compartment	0.01	0.21	0.21
Pressure, Open Compartment	0.01	0.15	0.15
Velocity	0.07	0.03	0.08
Heat Flux	0.05	0.10	0.11
No. Activated Sprinklers	0.00	0.15	0.15
Sprinkler Activation Time	0.00	0.06	0.06
Cable Failure Time	0.00	0.12	0.12
Smoke Alarm Activation Time	0.00	0.34	0.34

4.4 Calculating Model Uncertainty

This section describes a method for calculating the *model uncertainty* [321]. Specifically, this entails developing formulae for the mean and standard deviation of a statistical distribution like the one shown in Fig. 4.1. These formulae are functions solely of the model predictions and the experimental measurements against which the model is compared. The objective is to characterize the performance of the model in predicting a given quantity of interest (e.g., the hot gas layer temperature) with two parameters; one that expresses the tendency for the model to under or over-predict the true value of the quantity and one that expresses the degree of scatter about the true value.

The predicted and measured values of the quantity of interest are obtained from one or more validation studies. Figure 4.3 is a typical example of a comparison of model and measurement. Given that usually dozens of such measurements are made during each experiment, and potentially dozens of experiments are conducted as part of a test series, hundreds of such plots can be produced for any given quantity of interest. Usually, the data is condensed into a more tractable form by way of a single metric with which to compare

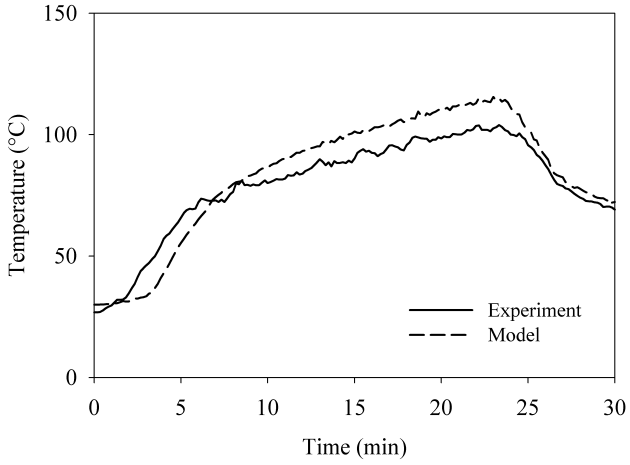

Figure 4.3: Example of a typical time history comparison of model prediction and experimental measurement.

the two curves, like the ones shown in Fig. 4.3. Peacock et al. [322] discuss various possible metrics. The metric most often used in the FDS validation process is the difference between the peak values of the time-averaged predicted and measured time histories. Thus, for each measurement point, i, there is a pair of Experimental and Modeled values, (E_i, M_i), where i ranges from 1 to n and both E_i and M_i are positive numbers expressing the greatest rise in the value of the measured/predicted quantity above its ambient. Here, n is the total number of measurement points of a particular quantity of interest from all the experiments.

As mentioned above, measurements from full-scale fire experiments often lack uncertainty estimates. In cases where the uncertainty is reported, it is usually expressed as either a standard deviation or confidence interval about the measured value. In other words, there is rarely a reported systematic bias in the measurement because if a bias can be quantified, the reported values are adjusted accordingly. For this reason, assume that a given experimental measurement, E_i, is normally distributed about the "true" value, θ_i, and there is no systematic bias:

$$E \mid \theta \sim N(\theta\ ,\ \sigma_E^2) \tag{4.13}$$

The notation[3] $E \mid \theta$ means that E is conditional on a particular value of θ. This is the usual way of defining a likelihood function. It is convenient to use the so-called delta method[4] to obtain the approximate distribution

$$\ln E \mid \theta \sim N\left(\ln\theta - \frac{\widetilde{\sigma}_E^2}{2}\,,\,\widetilde{\sigma}_E^2\right) \tag{4.14}$$

The purpose of applying the natural log to the random variable is so that its variance can be expressed in terms of the relative uncertainty, $\widetilde{\sigma}_E = \sigma_E/\theta$. This is the way that experimental uncertainties are reported.

[3] Note that the subscript, i, has been dropped merely to reduce the notational clutter.

[4] Given the random variable $X \sim N(\mu, \sigma^2)$, the delta method [323] provides a way to estimate the distribution of a function of X:

$$g(X) \sim N\left(g(\mu) + g''(\mu)\,\sigma^2/2\,,\,(g'(\mu)\,\sigma)^2\right)$$

In addition, the results of past validation exercises, when plotted as shown in Fig. 4.2, form a wedge-shaped pattern that suggests that the difference between predicted and measured values is roughly proportional to the magnitude of the measured value.

It cannot be assumed, as in the case of the experimental measurements, that the model predictions have no systematic bias. Instead, it is assumed that the model predictions are normally distributed about the true values multiplied by a bias factor, δ:

$$M \mid \theta \sim N\left(\delta\,\theta\,,\,\sigma_M^2\right) \tag{4.15}$$

The standard deviation, σ_M, and the bias factor, δ, represent the model uncertainty. Again, the delta method renders a distribution for $\ln M$ whose parameters can be expressed in terms of a relative standard deviation:

$$\ln M \mid \theta \sim N\left(\ln\delta + \ln\theta - \frac{\widetilde{\sigma}_M^2}{2}\,,\,\widetilde{\sigma}_M^2\right) \quad ; \quad \widetilde{\sigma}_M = \frac{\sigma_M}{\delta\,\theta} \tag{4.16}$$

Combining Eq. (4.14) with Eq. (4.16) yields:

$$\ln M - \ln E = \ln(M/E) \sim N\left(\ln\delta - \frac{\widetilde{\sigma}_M^2}{2} + \frac{\widetilde{\sigma}_E^2}{2}\,,\,\widetilde{\sigma}_M^2 + \widetilde{\sigma}_E^2\right) \tag{4.17}$$

To estimate the mean and standard deviation of the distribution[5], first define:

$$\overline{\ln(M/E)} = \frac{1}{n}\sum_{i=1}^{n}\ln(M_i/E_i) \tag{4.18}$$

The least squares estimate of the standard deviation of the combined distribution is defined as:

$$\widetilde{\sigma}_M^2 + \widetilde{\sigma}_E^2 \approx \frac{1}{n-1}\sum_{i=1}^{n}\left[\ln(M_i/E_i) - \overline{\ln(M/E)}\right]^2 \tag{4.19}$$

Recall that $\widetilde{\sigma}_E$ is known and the expression on the right can be evaluated using the pairs of measured and predicted values. Equation (4.19) imposes a constraint on the value of the experimental uncertainty, $\widetilde{\sigma}_E$. A further constraint is that $\widetilde{\sigma}_M$ cannot be less than $\widetilde{\sigma}_E$ because it is not possible to demonstrate that the model is more accurate than the measurements against which it is compared. Combining the two constraints leads to:

$$\widetilde{\sigma}_E^2 < \frac{1}{2}\mathrm{Var}\Big(\ln(M/E)\Big) \tag{4.20}$$

An estimate of δ can be found using the mean of the distribution:

$$\delta \approx \exp\left(\overline{\ln(M/E)} + \frac{\widetilde{\sigma}_M^2}{2} - \frac{\widetilde{\sigma}_E^2}{2}\right) \tag{4.21}$$

Taking the assumed normal distribution of the model prediction, M, in Eq. (4.15) and using a Bayesian argument[6] with a non-informative prior for θ, the posterior distribution can be expressed:

$$\delta\,\theta \mid M \sim N\left(M\,,\,\sigma_M^2\right) \tag{4.22}$$

[5]The assumption that $\ln(M/E)$ is normally distributed has been tested for each quantity of interest discussed in the chapters ahead. The results are shown in Section 16.2.

[6]The form of Bayes theorem used here states that the posterior distribution is the product of the prior distribution and the likelihood function, normalized by their integral: $f(\theta|M) = p(\theta)\,f(M|\theta)/\int p(\theta)\,f(M|\theta)\,d\theta$. A constant prior is also known as a Jeffreys prior [324].

The assumption of a non-informative prior implies that there is not sufficient information about the prior distribution (i.e., the true value) of θ to assume anything other than a uniform[7] distribution. This is equivalent to saying that the modeler has not biased the model input parameters to compensate for a known bias in the model output. For example, if a particular model has been shown to over-predict compartment temperature, and the modeler has reduced the specified heat release rate to better estimate the true temperature, then it can no longer be assumed that the prior distribution of the true temperature is uniform. Still another way to look at this is by analogy to target shooting. Suppose a particular rifle has a manufacturers defect such that, on average, it shoots 10 cm to the left of the target. It must be assumed that any given shot by a marksman without this knowledge is going to strike 10 cm to the left of the intended target. However, if the marksman knows of the defect, he or she will probably aim 10 cm to the right of the intended target to compensate for the defect. If that is the case, it can no longer be assumed that the intended target was 10 cm to the right of the bullet hole.

The final step in the derivation is to rewrite Eq. (4.22) as:

$$\theta \mid M \sim N\left(\frac{M}{\delta}\ ,\ \widetilde{\sigma}_M^2\left(\frac{M}{\delta}\right)^2\right) \tag{4.23}$$

This formula has been obtained[8] by dividing by the bias factor, δ, in Eq. (4.22). To summarize, given a model prediction, M, of a particular quantity of interest (e.g., a cable temperature), the true (but unknown) value of this quantity is normally distributed. The mean value and variance of this normal distribution are based solely on comparisons of model predictions with past experiments that are similar to the particular fire scenario being analyzed. The performance of the model is quantified by the estimators of the parameters, δ and $\widetilde{\sigma}_M$, which have been corrected to account for uncertainties associated with the experimental measurements.

When computing the relative error between measured and predicted values, an additional step is performed to ensure that the bias factor, δ, is not skewed by a large number of data points at any particular region in the scatter plot. The approach used for this procedure is called a regressogram, i.e., a bin-smoothed estimator function [325]. This approach accounts for cases in which small measured values are compared to small predicted values, which can result in a large relative error. In these cases, the calculated bias factor might not be representative of the overall model bias, especially for larger measured and predicted values. Alternatively, a regressogram treats the average values throughout the scatter plot equally by subdividing the scatter plot into bins and normalizing each bin by the number of local data points. The regressogram estimator function is implemented as follows. For each scatter plot, the x-axis is subdivided into 10 equally spaced bins. Each bin is assigned a weight that is inversely proportional to the number of points in the bin; a bin with more points is assigned a smaller weight, and a bin with fewer points is assigned a larger weight. Finally, when the relative error is calculated, each bin is multiplied by its respective bin weight.

4.5 Example

This section describes how to make use of Eq. (4.23). Referring to the sample problem given above, suppose a fire model is being used to estimate the likelihood that electrical control cables could be damaged due to a fire in a compartment. Damage is assumed to occur when the surface temperature of any cable reaches 200 °C. What is the likelihood that the cables would be damaged if the model predicts that the maximum surface temperature of the cables is 175 °C. Assuming that the input parameters are not in question, the following procedure is suggested:

[7] A uniform distribution means that for any two equally sized intervals of the real line, there is an equal likelihood that the random variable takes a value in one of them.

[8] Note that if $X \sim N(\mu, \sigma^2)$, then $cX \sim N(c\mu, (c\sigma)^2)$.

1. Assemble a collection of model predictions, M_i, and experimental measurements, E_i, from past experiments involving objects with similar thermal characteristics as the cables in question. How "similar" the experiment is to the hypothetical scenario under study can be quantified by way of various parameters, like the thermal inertia of the object, the size of the fire, the size of the compartment, and so on. Obtain estimates of the experimental uncertainty from those who conducted the experiments or follow the procedure outlined by Hamins [316]. Express the experimental uncertainty in relative terms, $\widetilde{\sigma}_E$.

2. Calculate the bias factor, δ, and relative standard deviation, $\tilde{\sigma}_M$, from Eqs. (4.21) and (4.19), respectively.

Consider the distribution, Eq. (4.23), of the "true" temperature, θ, shown graphically in Fig. 4.1. The vertical lines indicate the "critical" temperature at which damage is assumed to occur ($T_c = 200$ °C), and the temperature predicted by the model (175 °C). Given an ambient temperature of 20 °C, the predicted temperature rise, M, is 155 °C. The mean and standard deviation in Eq. (4.23) are calculated:

$$\mu = 20 + \frac{M}{\delta} = 20 + \frac{155}{1.13} = 157\ ^\circ\text{C} \quad ; \quad \sigma = \widetilde{\sigma}_M \frac{M}{\delta} = 0.20 \times \frac{155}{1.13} = 27\ ^\circ\text{C} \tag{4.24}$$

respectively. The shaded area beneath the bell curve is the probability that the "true" temperature can exceed the critical value, $T_c = 200$ °C, which can be expressed via the *complimentary error function*:

$$P(T > T_c) = \frac{1}{2}\text{erfc}\left(\frac{T_c - \mu}{\sigma\sqrt{2}}\right) = \frac{1}{2}\text{erfc}\left(\frac{200 - 157}{27\sqrt{2}}\right) \approx 0.06 \tag{4.25}$$

This means that there is a 6 % chance that the cables could become damaged, assuming that the model's input parameters are not subject to uncertainty.

4.6 Additional Considerations

Keep in mind that for any fire experiment, FDS might predict a particular quantity accurately (within the experimental uncertainty bounds, for example), but another quantity less accurately. For example, in the a series of 15 full-scale fire experiments conducted at NIST in 2003, sponsored by the U.S. Nuclear Regulatory Commission, the average hot gas layer (HGL) temperature predictions were nearly within the accuracy of the measurements themselves, yet the smoke concentration predictions differed from the measurements by as much as a factor of 3. Why? Consider the following issues associated with various types of measurements:

- Is the measurement taken at a single point, or averaged over many points? In the example above, the HGL temperature is an average of many thermocouple measurements, whereas the smoke concentration is based on the extinction of laser light over a short length span. Model error tends to be reduced by the averaging process, plus most fire models, including FDS, are based on global mass and energy conservation laws that are expressed as spatial averages.

- Is the measured quantity time-averaged or instantaneous? For example, a surface temperature prediction is less prone to error in comparison to a heat flux prediction because the former is, in some sense, a time-integral of the latter.

- In the case of a point measurement, how close to the fire is it? The terms "near-field" and "far-field" are used throughout this Guide to describe the relative distance from the fire. In general, predictions of near-field phenomena are more prone to error than far-field. There are exceptions, however. For example, a prediction of the temperature directly within the flaming region may be more accurate than that made just a fire diameter away because of the fact that temperatures tend to stabilize at about 1000 °C within the fire itself, but then rapidly decrease away from the flames. Less accurate predictions typically occur in regions of steep gradients (rapid changes, both in space and time).

Chapter 5

HGL Temperature and Depth

FDS, like any CFD-based fire model, does not perform a direct calculation of the HGL temperature or height. These are constructs unique to two-zone models. Nevertheless, FDS does make predictions of gas temperature at the same locations as the thermocouples in the experiments, and these values can be reduced in the same manner as the experimental measurements to produce an "average" HGL temperature and height. Regardless of the validity of the reduction method, the FDS predictions of the HGL temperature and height ought to be representative of the accuracy of its predictions of the individual thermocouple measurements that are used in the HGL reduction. The temperature measurements from the experiments reported in this chapter are used to compute an HGL temperature and height with which to compare to FDS. The same layer reduction method, described in the next section, is used for all the data presented in this chapter.

5.1 HGL Reduction Method

Fire protection engineers often need to estimate the location of the interface between the hot, smoke-laden upper layer and the cooler lower layer in a burning compartment. Relatively simple fire models, often referred to as *two-zone models*, compute this quantity directly, along with the average temperature of the upper and lower layers. In a CFD-based fire model like FDS, there are not two distinct zones, but rather a continuous profile of temperature. Nevertheless, there are methods that have been developed to estimate layer height and average temperatures from a continuous vertical profile of temperature. One such method [326] is as follows: Consider a continuous function $T(z)$ defining temperature T as a function of height above the floor z, where $z = 0$ is the floor and $z = H$ is the ceiling. Define T_u as the upper layer temperature, T_ℓ as the lower layer temperature, and z_int as the interface height. Compute the quantities:

$$\begin{aligned}(H - z_\mathrm{int})\, T_\mathrm{u} + z_\mathrm{int}\, T_\ell = \int_0^H T(z)\, dz &= I_1 \\ (H - z_\mathrm{int})\, \frac{1}{T_\mathrm{u}} + z_\mathrm{int}\, \frac{1}{T_\ell} = \int_0^H \frac{1}{T(z)}\, dz &= I_2\end{aligned}$$

Solve for z_int:

$$z_\mathrm{int} = \frac{T_\ell (I_1 I_2 - H^2)}{I_1 + I_2 T_\ell^2 - 2 T_\ell H} \tag{5.1}$$

Let T_ℓ be the temperature in the lowest mesh cell and, using Simpson's Rule, perform the numerical integration of I_1 and I_2. T_u is defined as the average upper layer temperature via

$$(H - z_\mathrm{int})\, T_\mathrm{u} = \int_{z_\mathrm{int}}^H T(z)\, dz \tag{5.2}$$

Further discussion of similar procedures can be found in Ref. [327].

5.2 ATF Corridors

The ATF Corridors experiments consisted of two corridors one on top of the other and connected by a stairwell. HGL temperature and depth reductions were carried out using three arrays of thermocouples in the lower corridor (Trees A, B, and C) and two arrays in the upper corridor (Trees G and H).

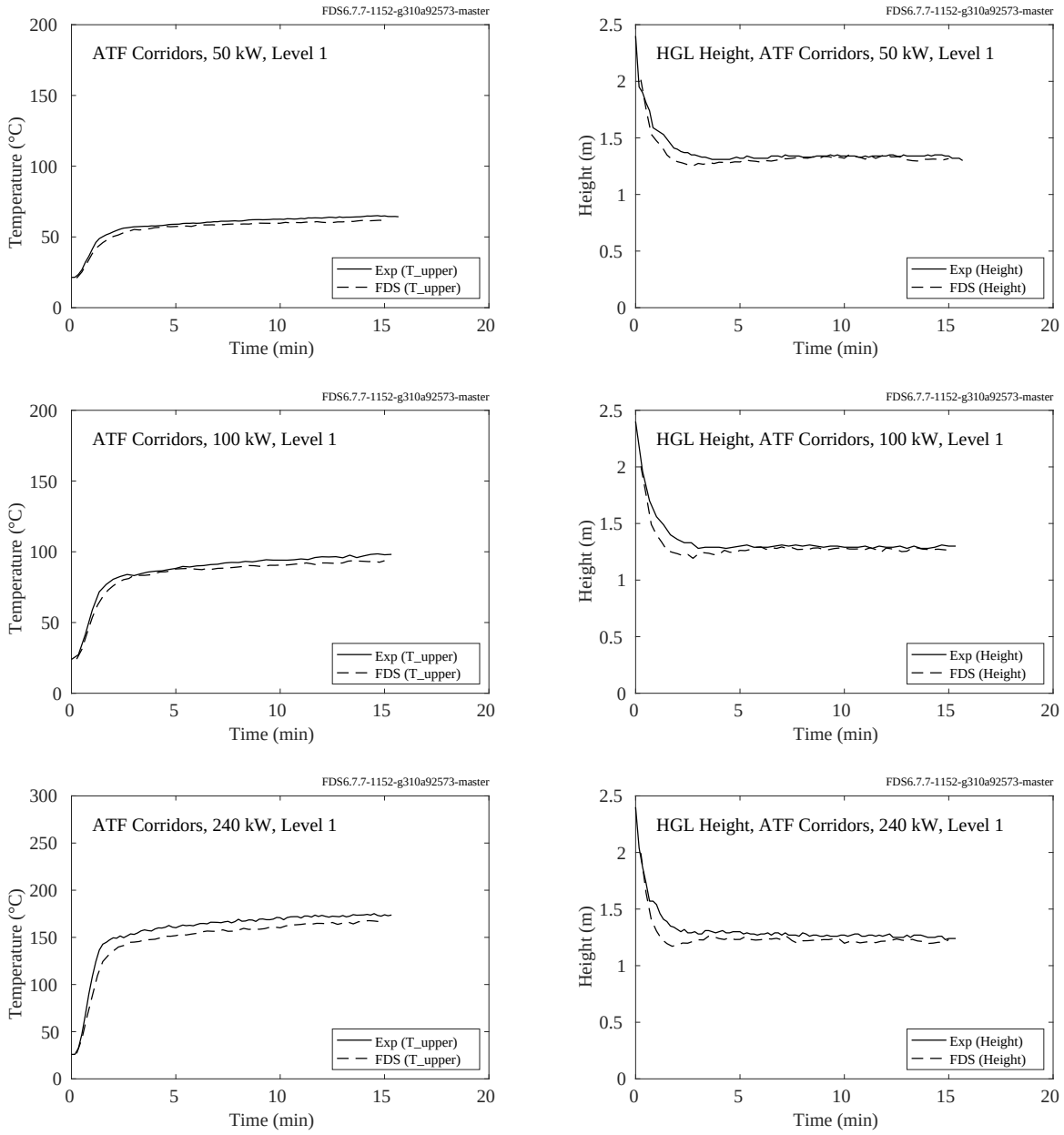

Figure 5.1: ATF Corridors, HGL temperature and height, first floor, 50 kW, 100 kW, 240 kW.

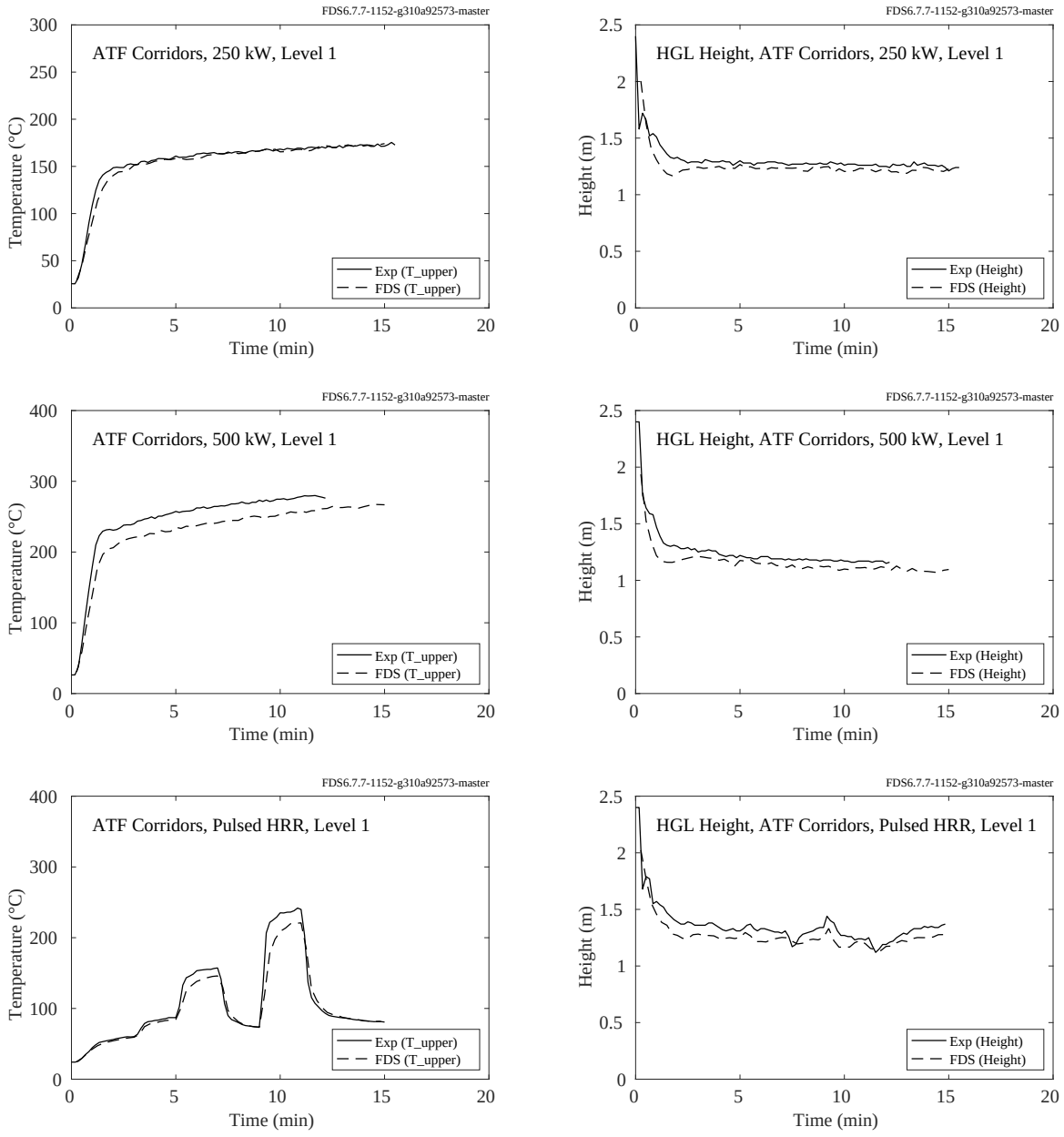

Figure 5.2: ATF Corridors, HGL temperature and height, first floor, 250 kW, 500 kW, mixed.

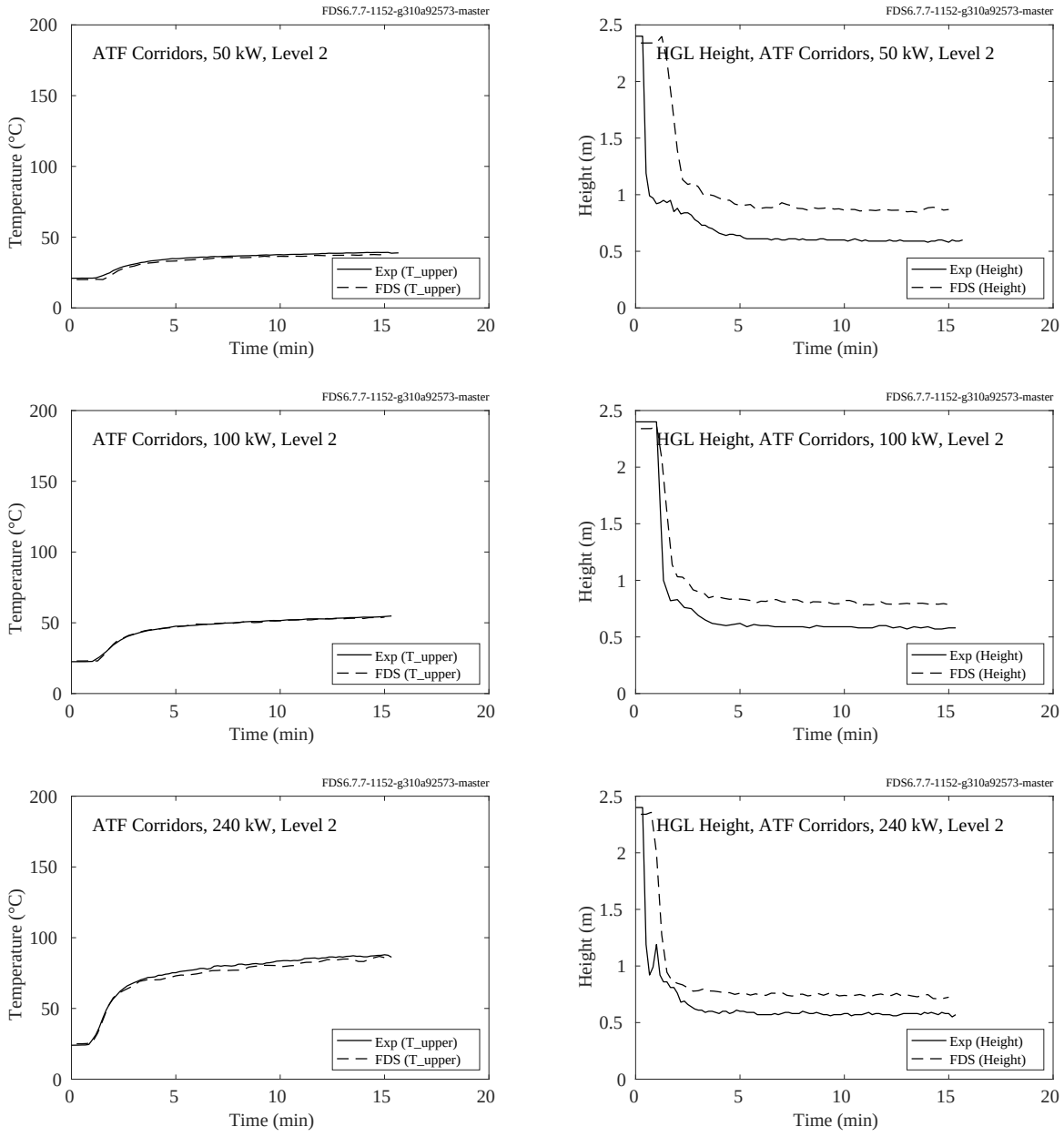

Figure 5.3: ATF Corridors, HGL temperature and height, second floor, 50 kW, 100 kW, 240 kW.

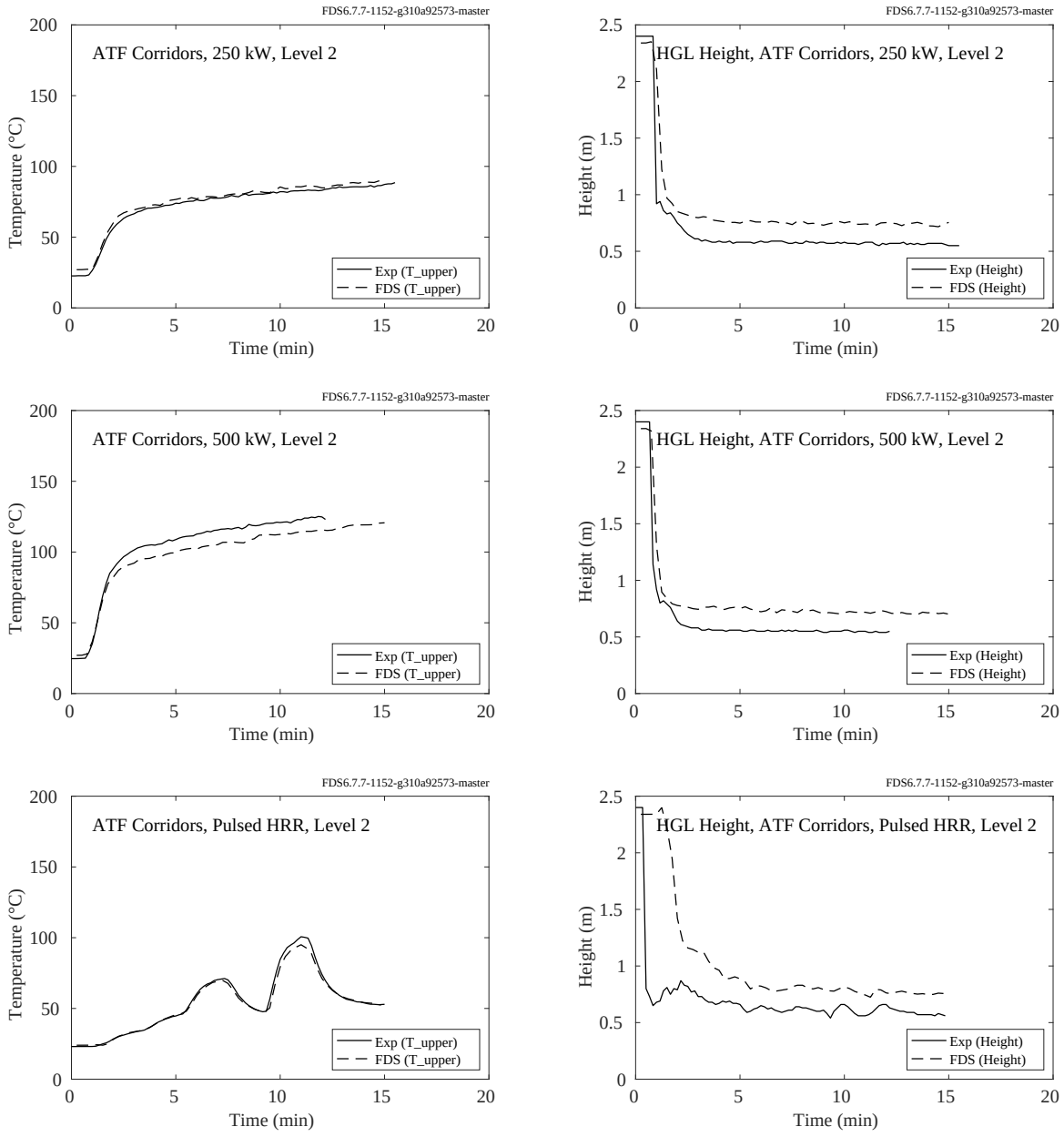

Figure 5.4: ATF Corridors, HGL temperature and height, second floor, 250 kW, 500 kW, mixed.

5.3 CSTB Tunnel

The CSTB Tunnel experiments include thermocouple measurements at various locations in a small-scale tunnel equipped with a water mist system. Two experiments (Tests 2 and 27) are simulated; the former with no mist activation and the latter with activation after 5 min. The tunnel is approximately 43 m long and the fire is located 17.5 m from the upstream opening.

On the following pages, thermocouple measurements at downwind distances of 4 m, 8 m, 12 m, and 24 m are compared to the predicted values. For a given label, say T+2411, the T denotes Temperature, the +24 means 24 m downwind of the fire, and the final two digits denote the particular thermocouple within an array at that location. The chosen TCs are located along the vertical centerline.

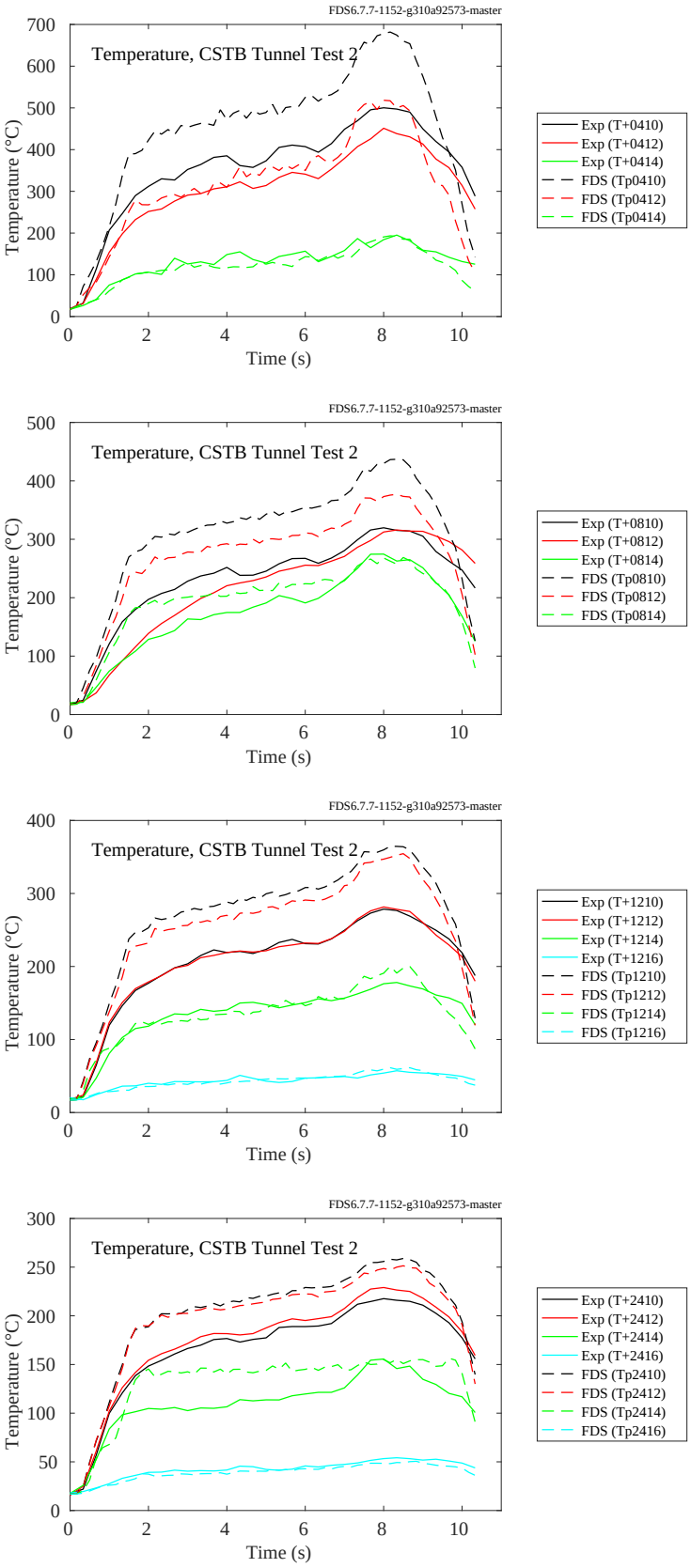

Figure 5.5: CSTB Tunnel, Test 2, temperatures at 4, 8, 12 and 24 m downstream of fire.

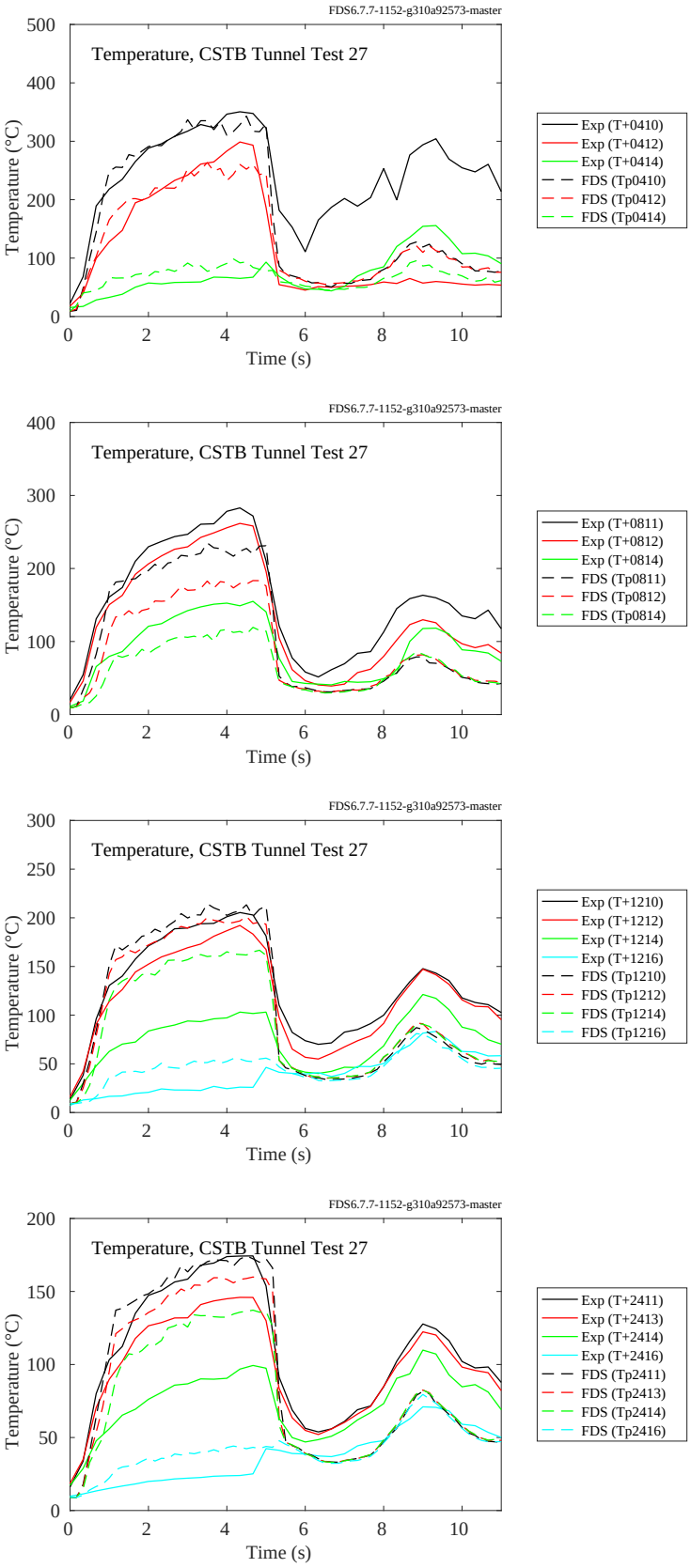

Figure 5.6: CSTB Tunnel, Test 27, temperatures at 4, 8, 12 and 24 m downstream of fire.

5.4 DelCo Trainers

The DelCo Trainer experiments were conducted in two different structures. Tests 2-6 were conducted in a single level structure consisting of three rooms. Rooms 1 and 3 had two thermocouple trees and Room 2 had one. Tests 22-25 were conducted in a two level structure. Floors 1 and 2 each had three thermocouple arrays. See Section 3.17 for their exact locations.

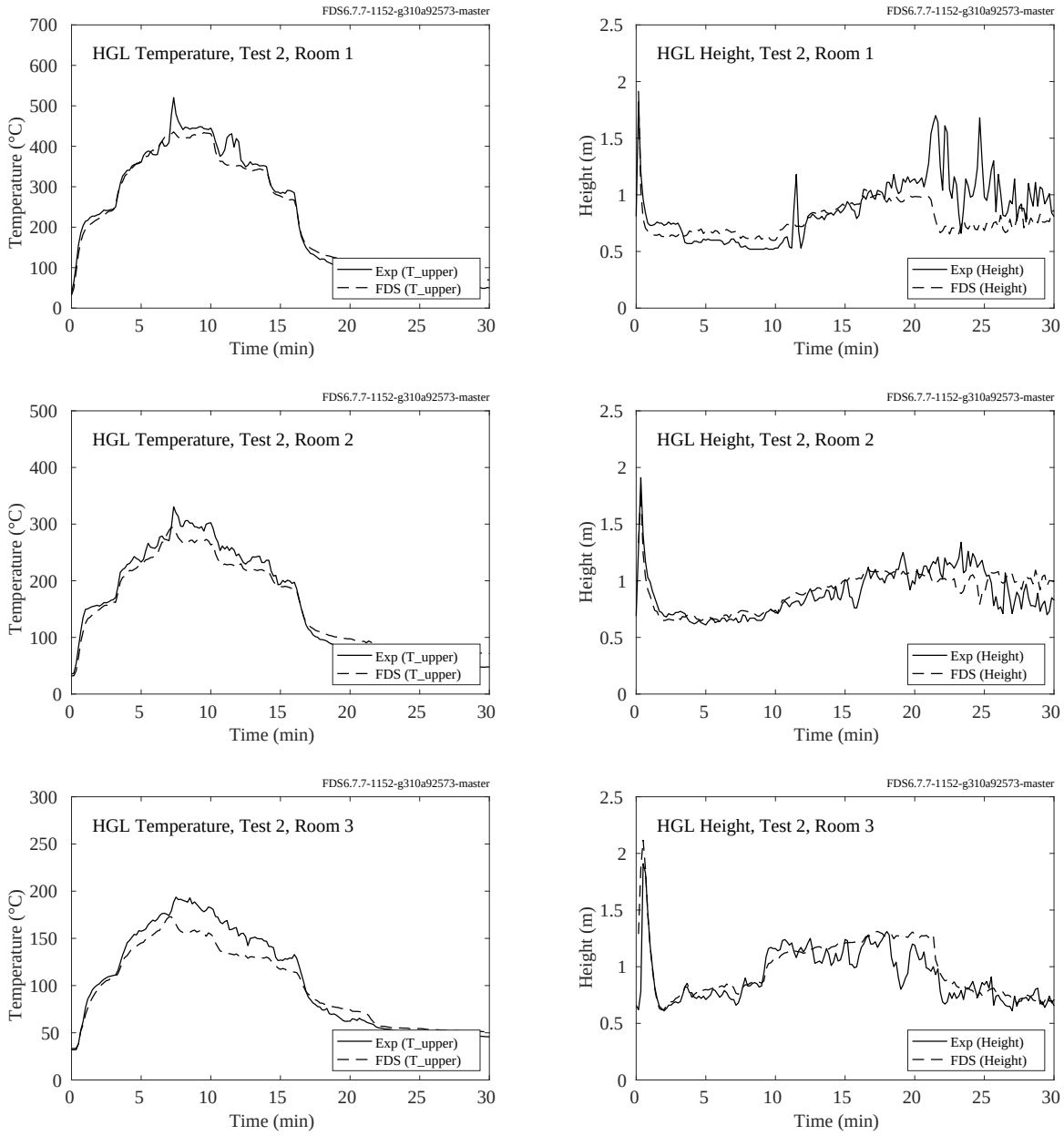

Figure 5.7: DelCo Trainers, HGL Temperature and Height, Test 2.

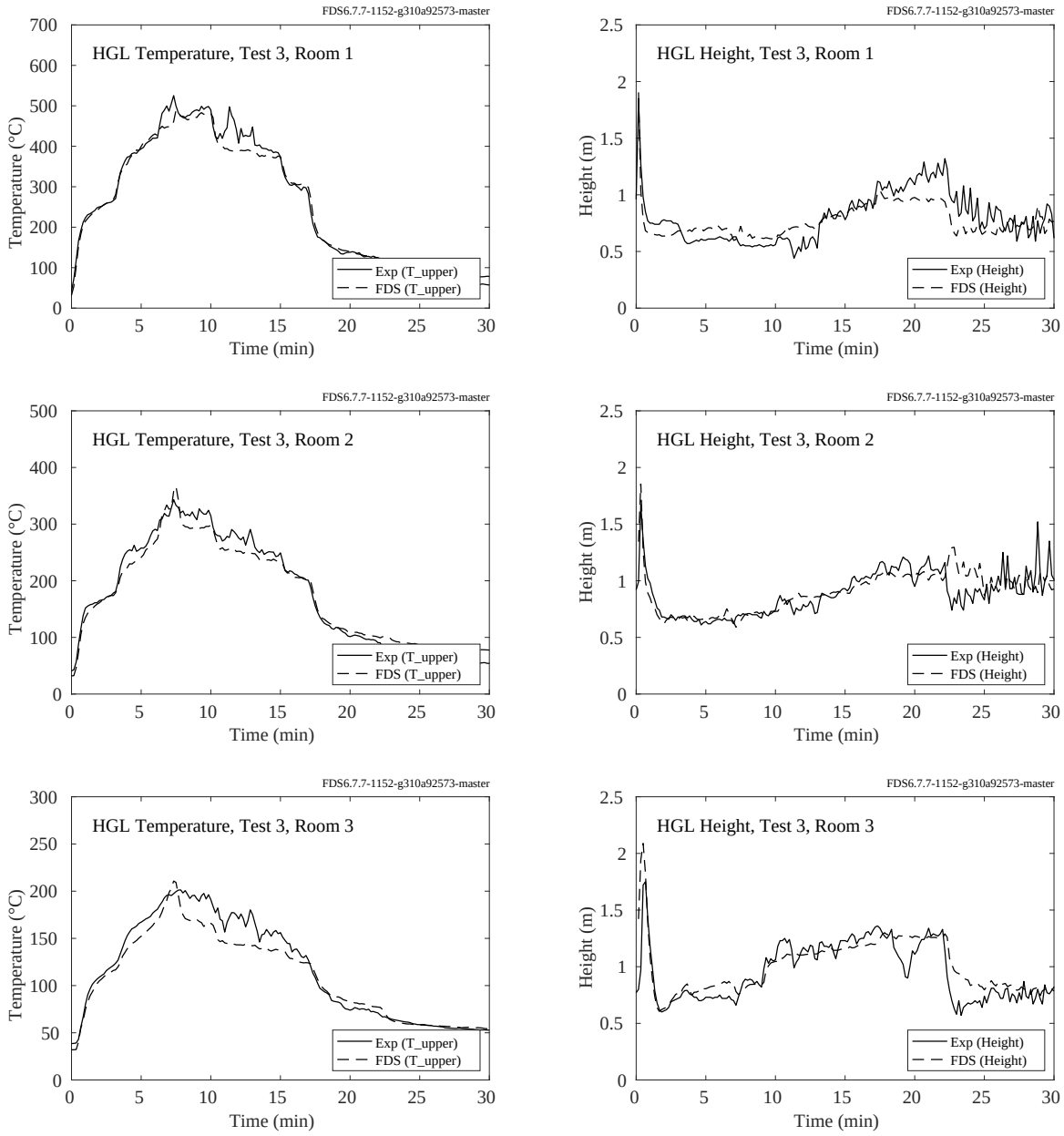

Figure 5.8: DelCo Trainers, HGL Temperature and Height, Test 3.

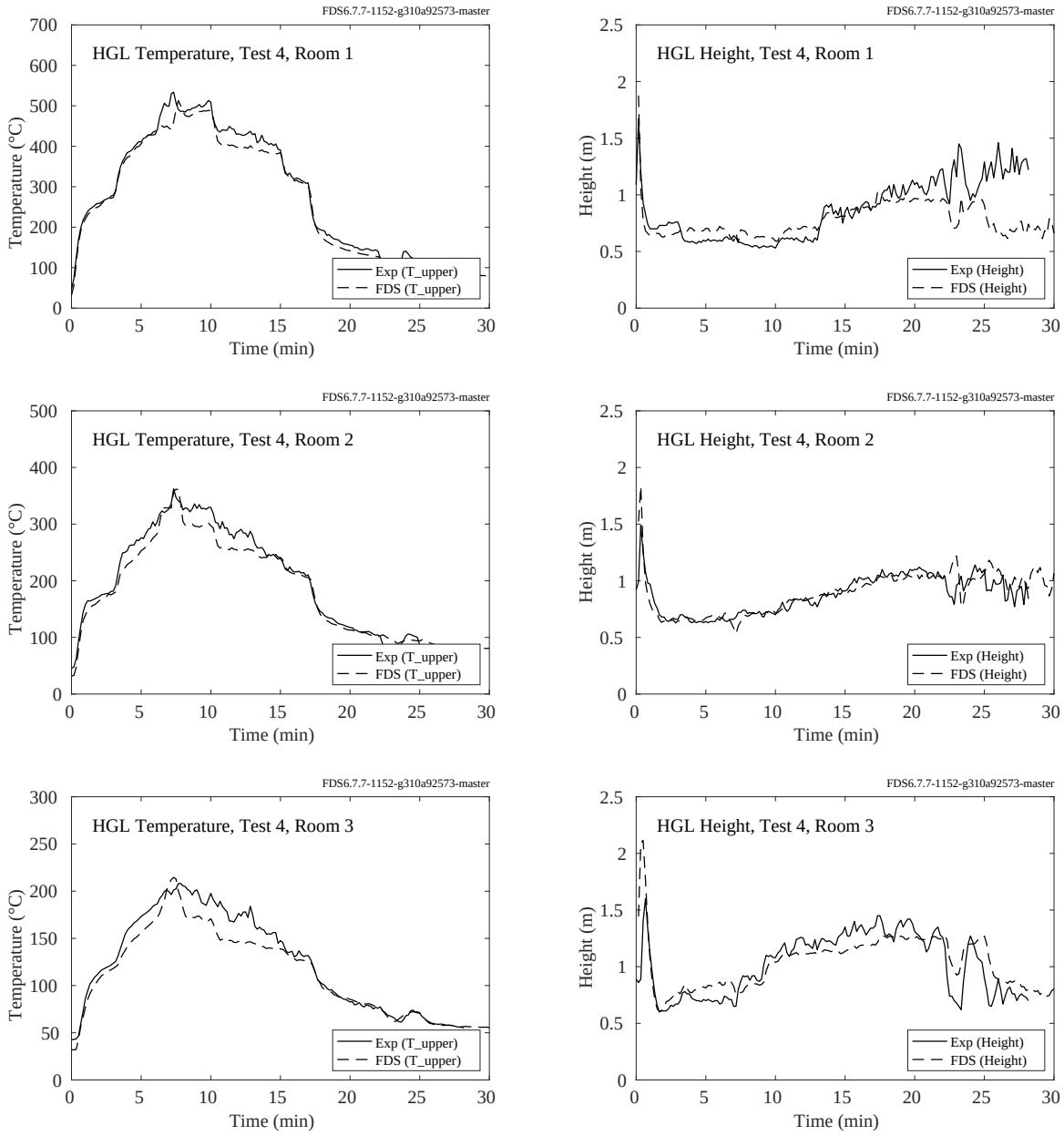

Figure 5.9: DelCo Trainers, HGL Temperature and Height, Test 4.

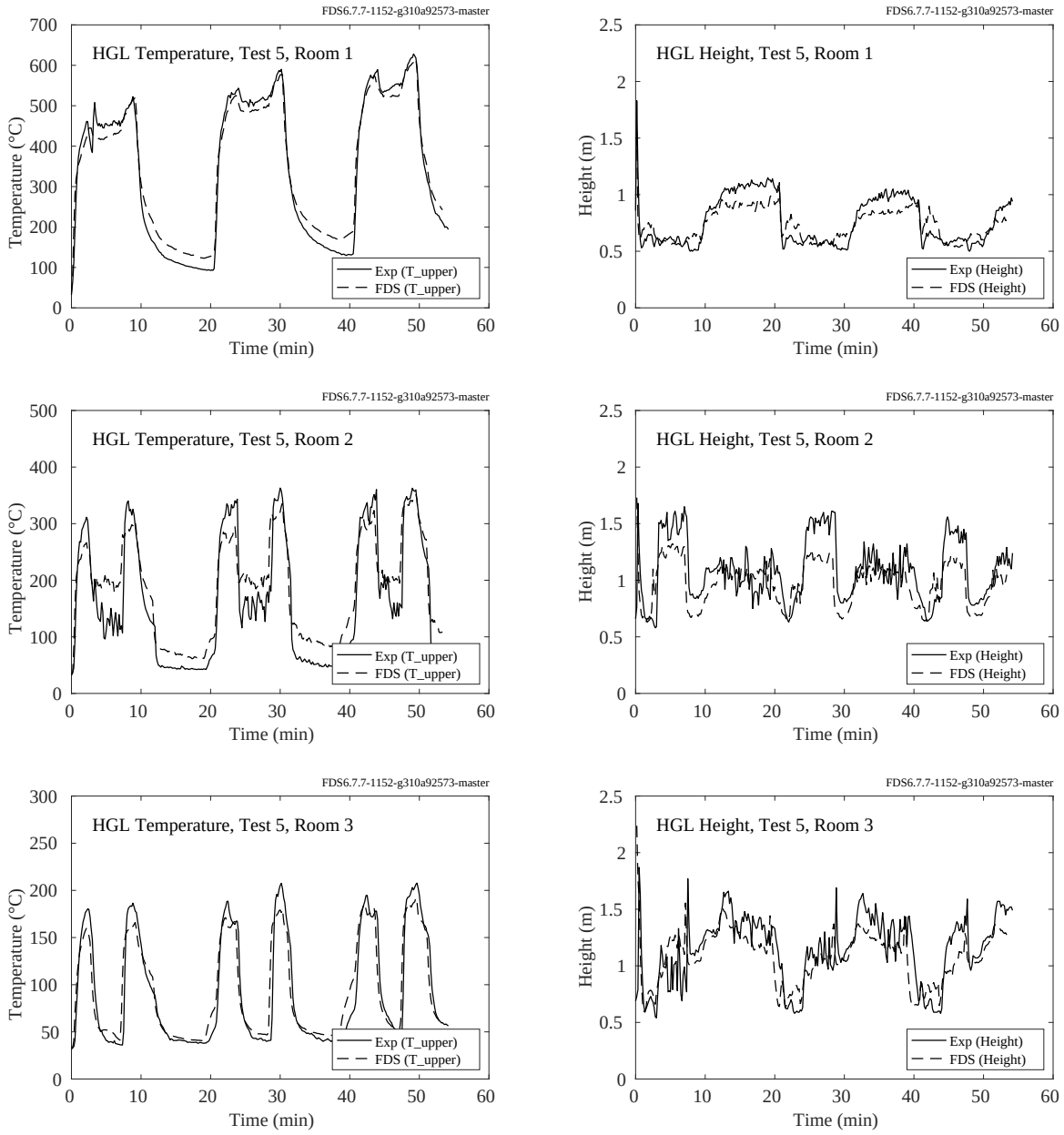

Figure 5.10: DelCo Trainers, HGL Temperature and Height, Test 5.

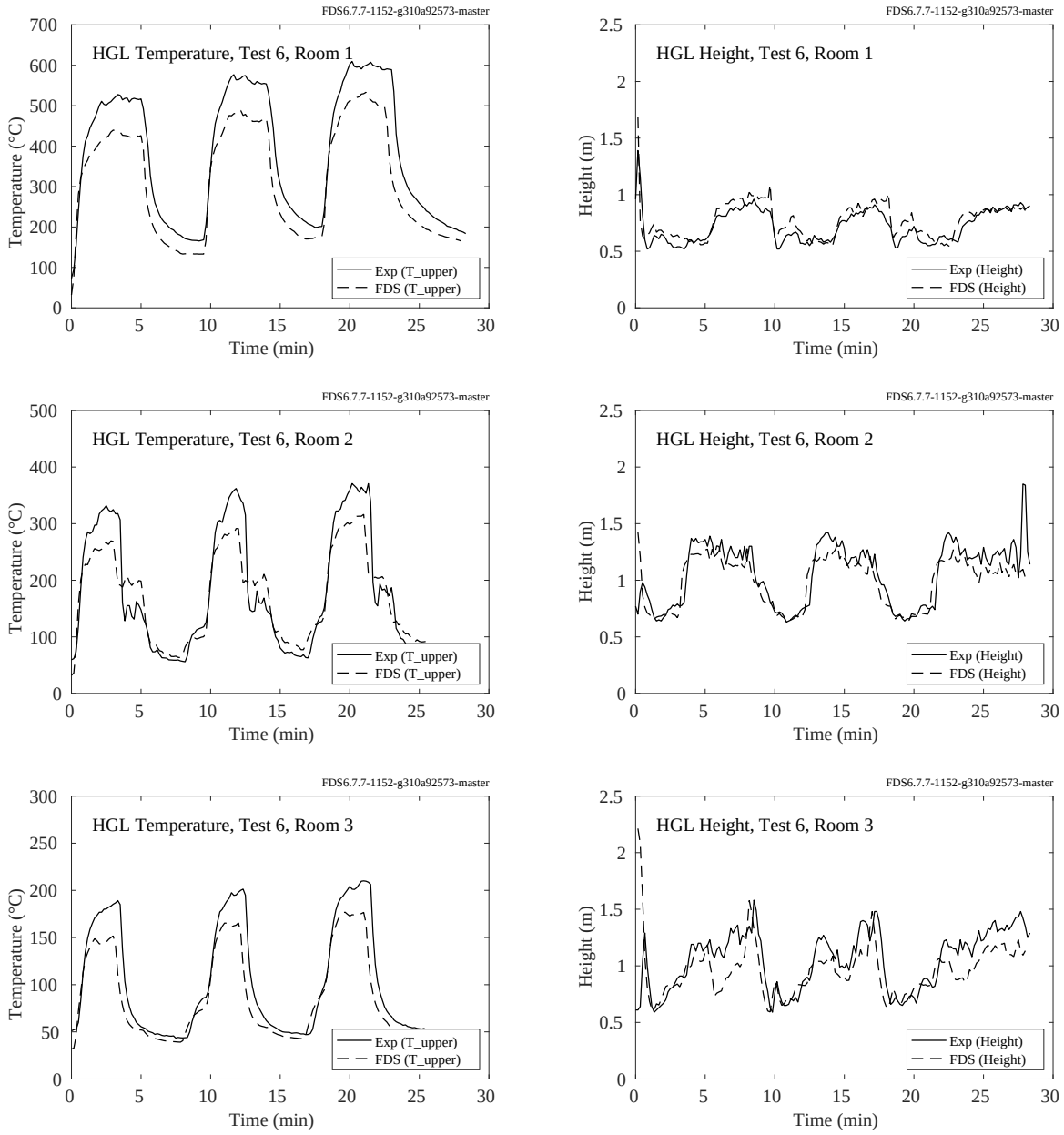

Figure 5.11: DelCo Trainers, HGL Temperature and Height, Test 6.

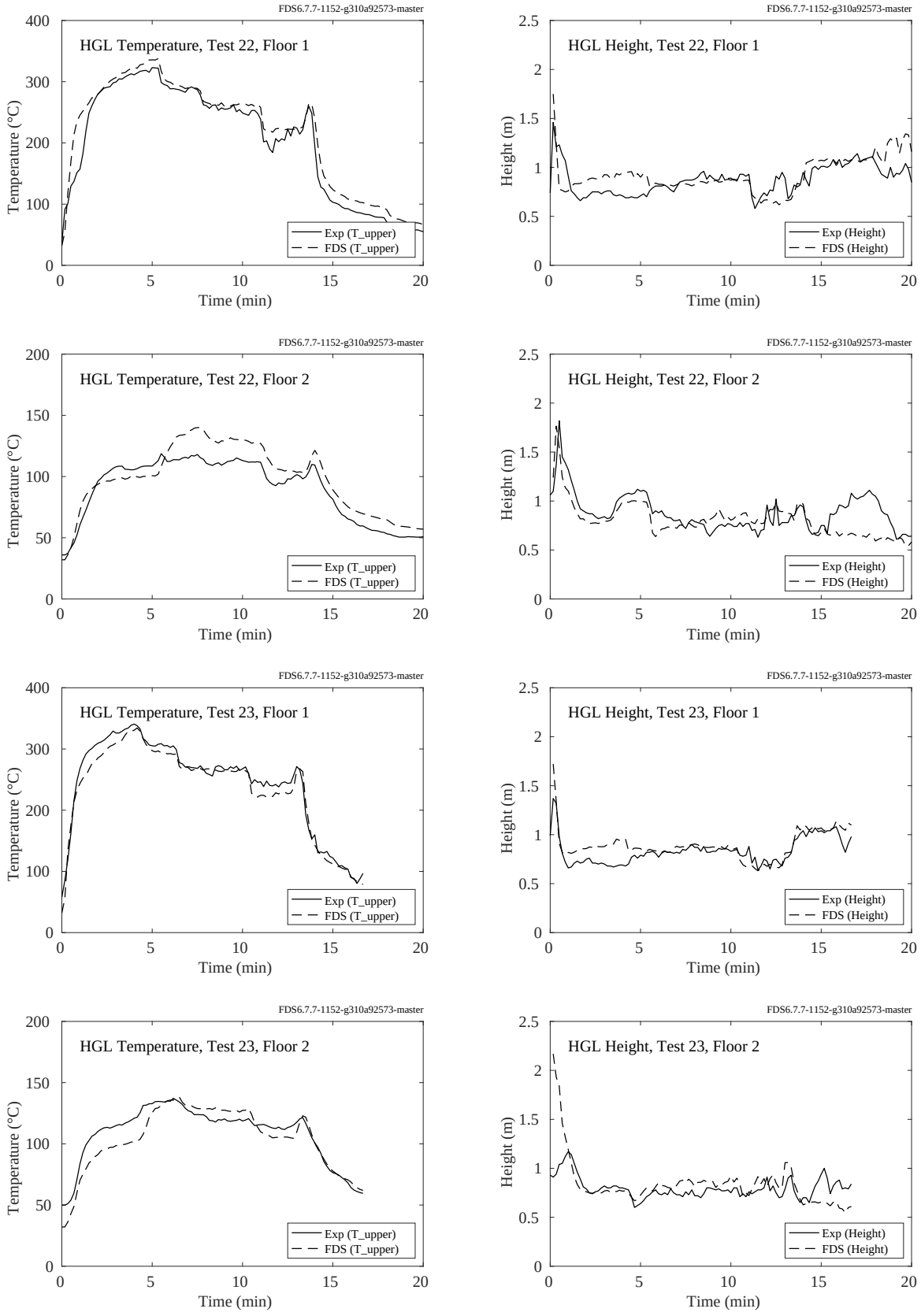

Figure 5.12: DelCo Trainers, HGL Temperature, Tests 22-23.

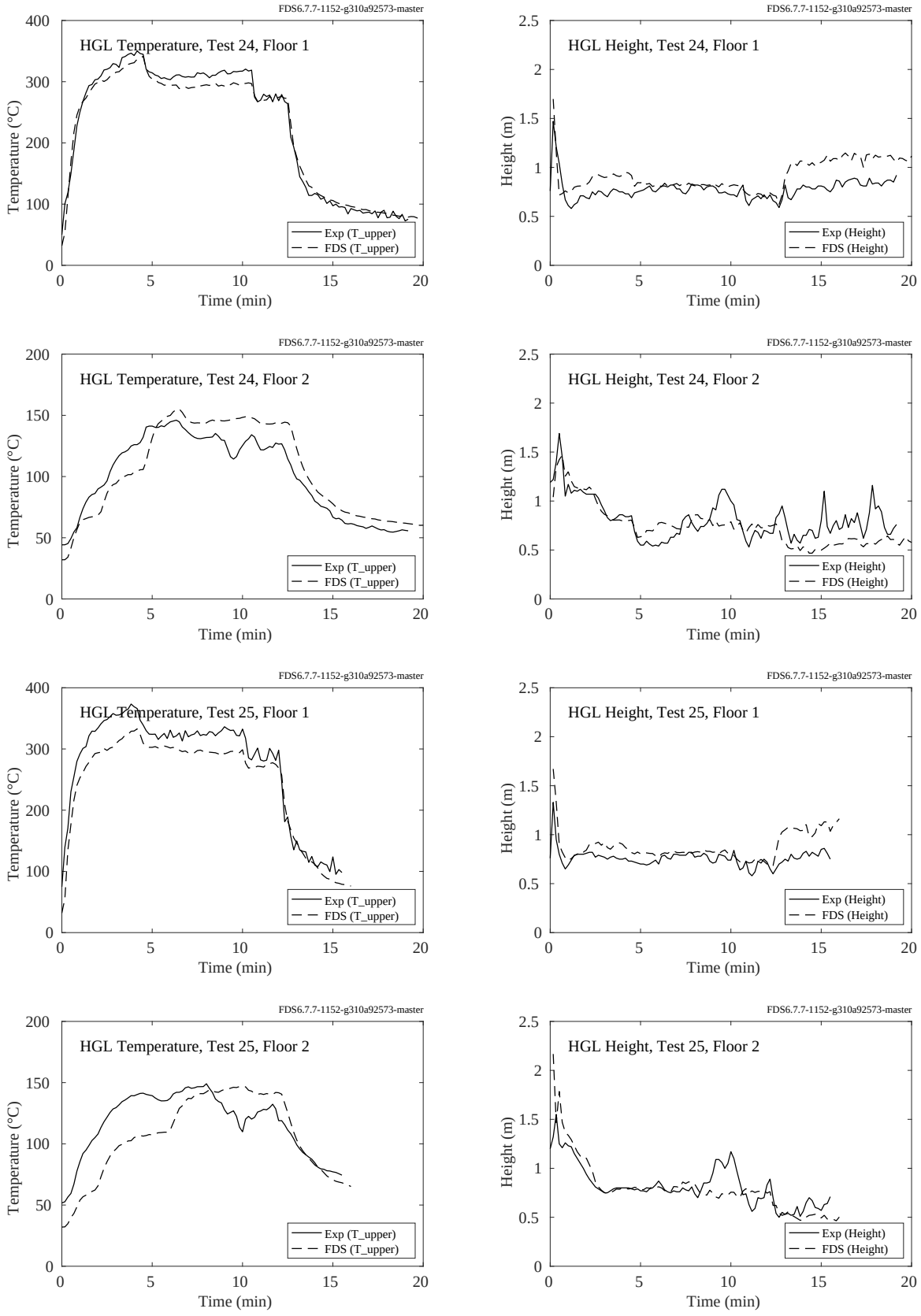

Figure 5.13: DelCo Trainers, HGL Temperature, Tests 24-25.

5.5 FM/SNL Test Series

Nineteen tests from the FM/SNL test series were selected for comparison. The HGL temperature and height are calculated using the standard method. The thermocouple arrays that were located in Sectors 1, 2 and 3 are averaged (with an equal weighting for each) for all tests except Tests 21 and 22. For these tests, only Sectors 1 and 3 are used, as Sector 2 falls within the smoke plume. Also, for all but the gas burner experiments, the time history of the HRR is estimated. Only the peak HRR is reported.

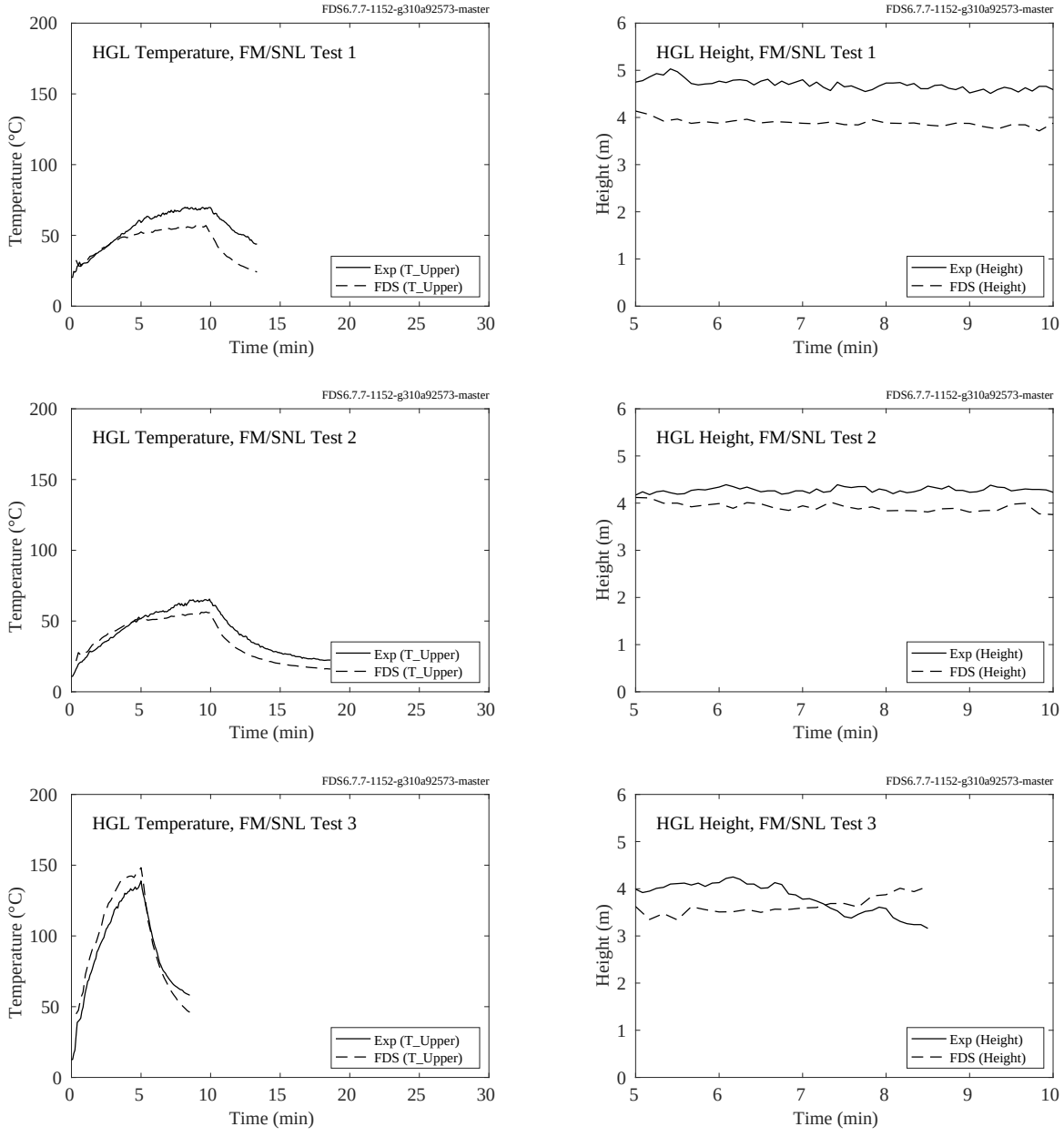

Figure 5.14: FM/SNL experiments, HGL temperature and height, Tests 1, 2, 3.

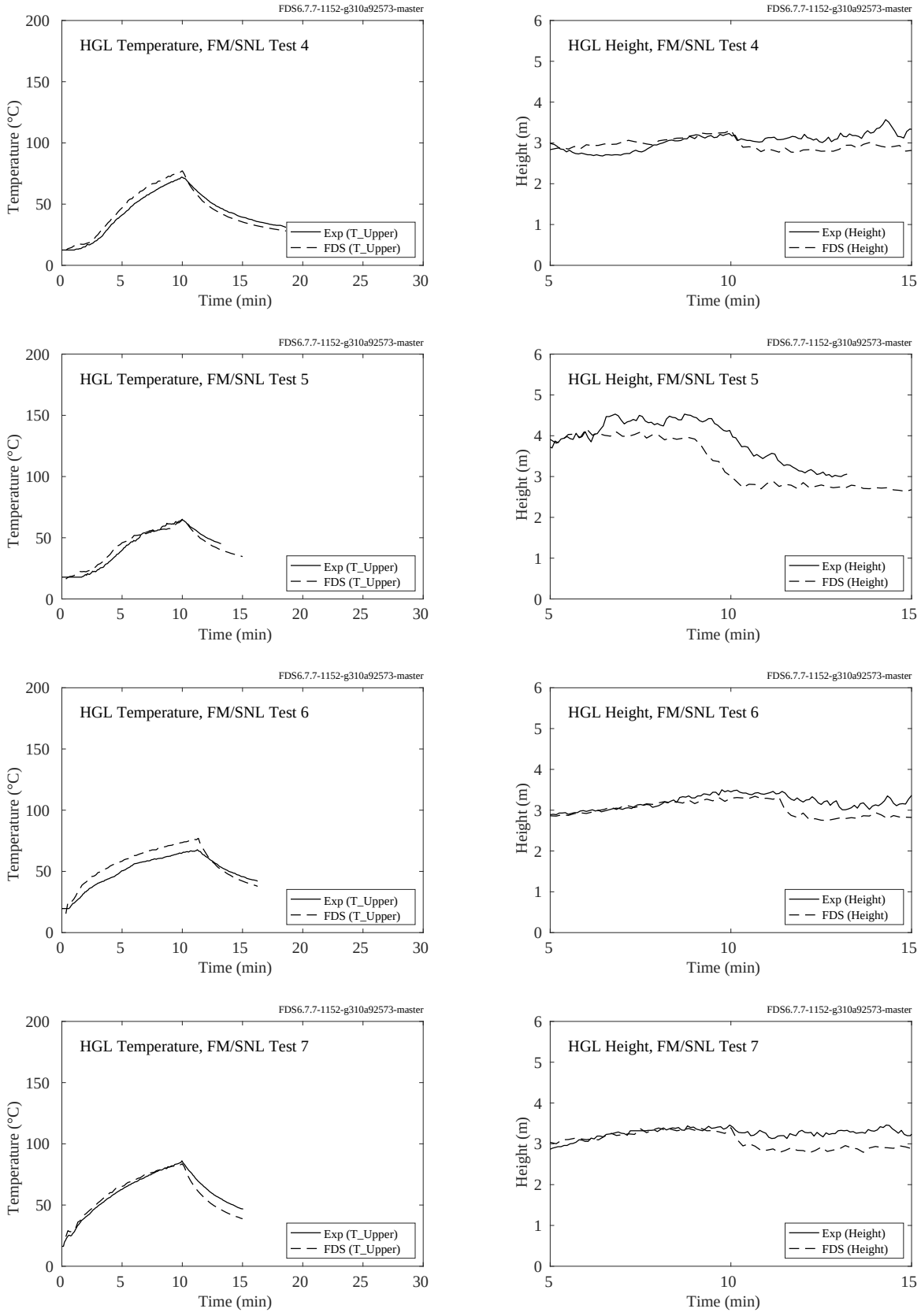

Figure 5.15: FM/SNL experiments, HGL temperature and height, Tests 4, 5, 6, 7.

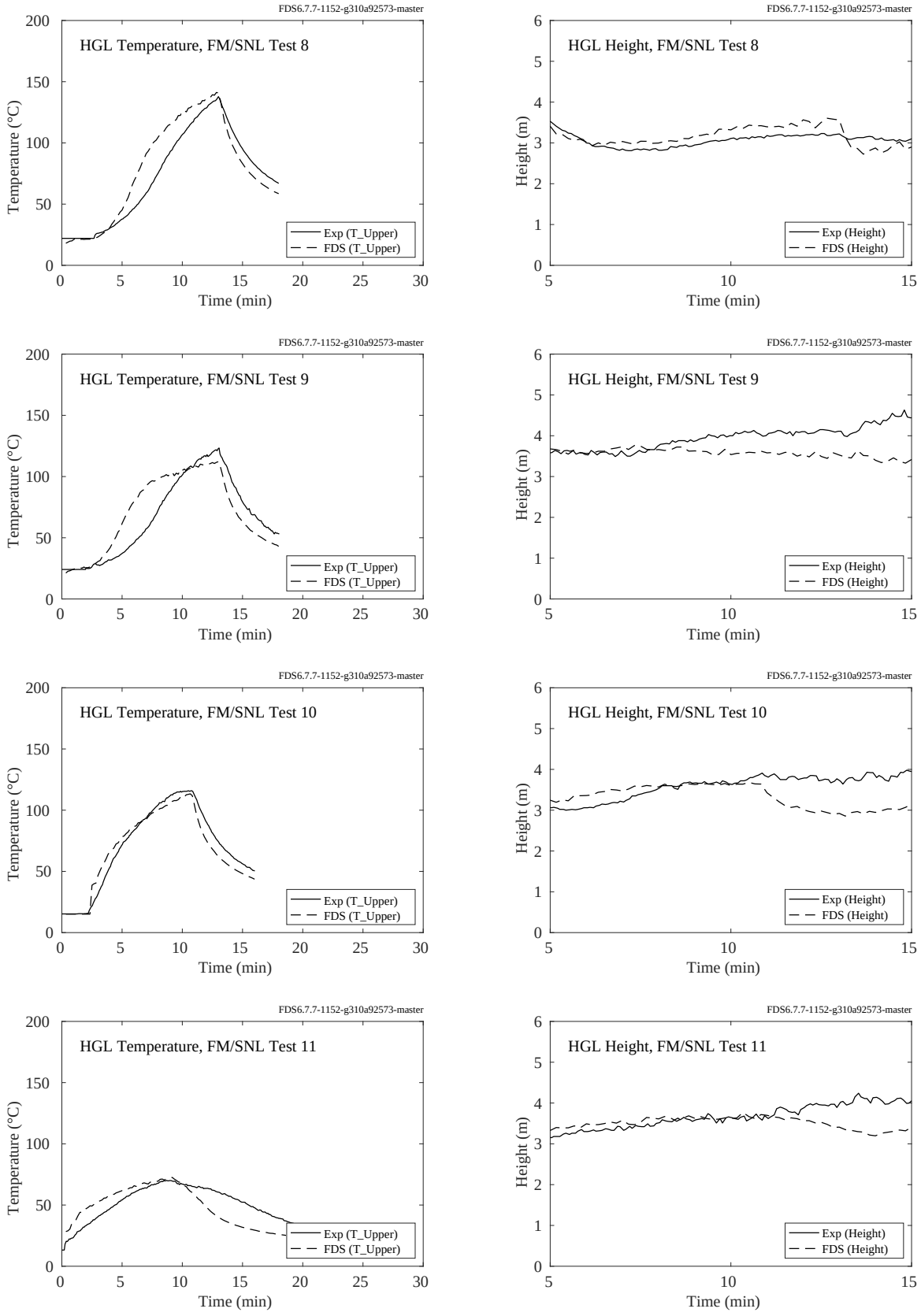

Figure 5.16: FM/SNL experiments, HGL temperature and height, Tests 8, 9, 10, 11.

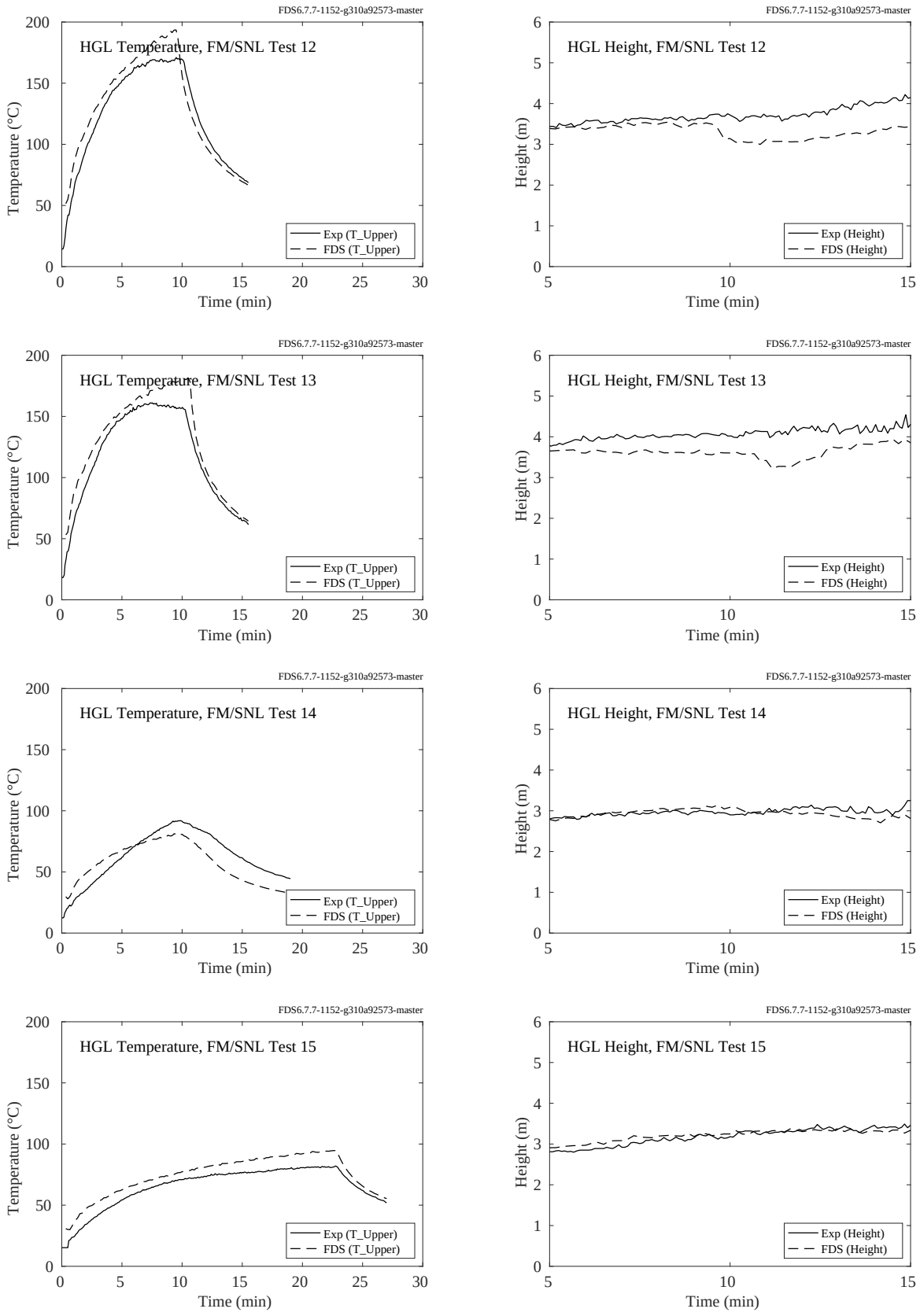

Figure 5.17: FM/SNL experiments, HGL temperature and height, Tests 12, 13, 14, 15.

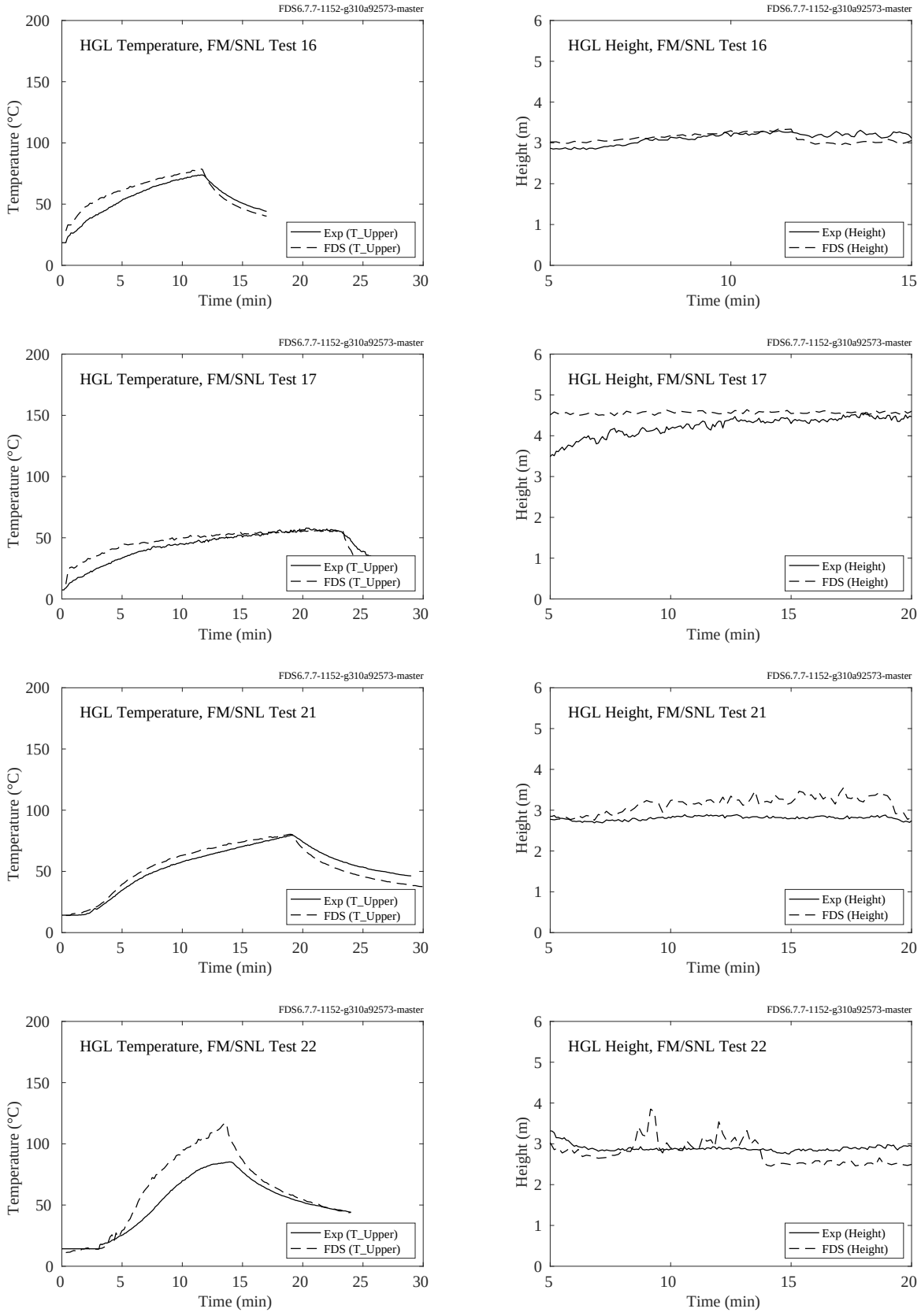

Figure 5.18: FM/SNL experiments, HGL temperature and height, Tests 16, 17, 21, 22.

5.6 LLNL Enclosure Series

The figures on the following pages compare predicted and measured hot gas layer temperatures from the LLNL Enclosure experiments. Fifteen thermocouples were evenly spaced from floor to ceiling on either side of the burner. The measured temperatures were reported as averages of the lower, middle, and upper five TCs. Some of the experiments were conducted with a separated plenum space in the top one-third of the overall compartment (Tests 17-60). In these cases, the upper five TCs are a measure of the average plenum temperature.

In the figures, the black circles represent the average of the five upper-most TC measurements. The red circles represent the average of the middle five TC measurements. The corresponding colored curves represent the simulation. For the experiments involving an upper plenum, the middle five TCs are located immediately beneath the plenum and their average temperature is typically greater than that of the upper-most TCs in the plenum. Note that in a number of experiments, the fuel flow was stopped or the fire self-extinguished. The simulations last only as long as the reported measurements.

Details on the experiments and modeling can be found in Section 3.35.

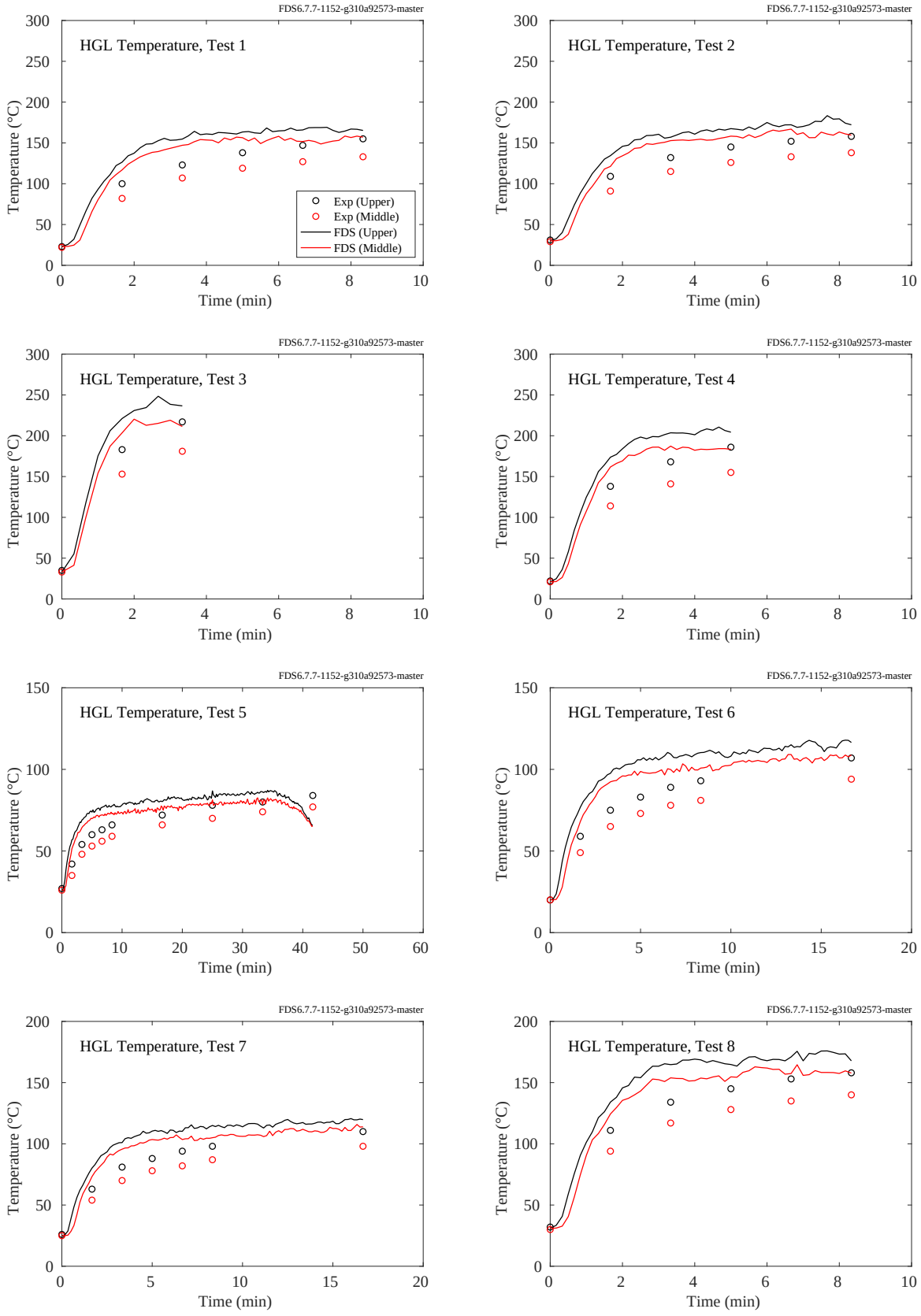

Figure 5.19: LLNL Enclosure experiments, HGL temperature, Tests 1-8.

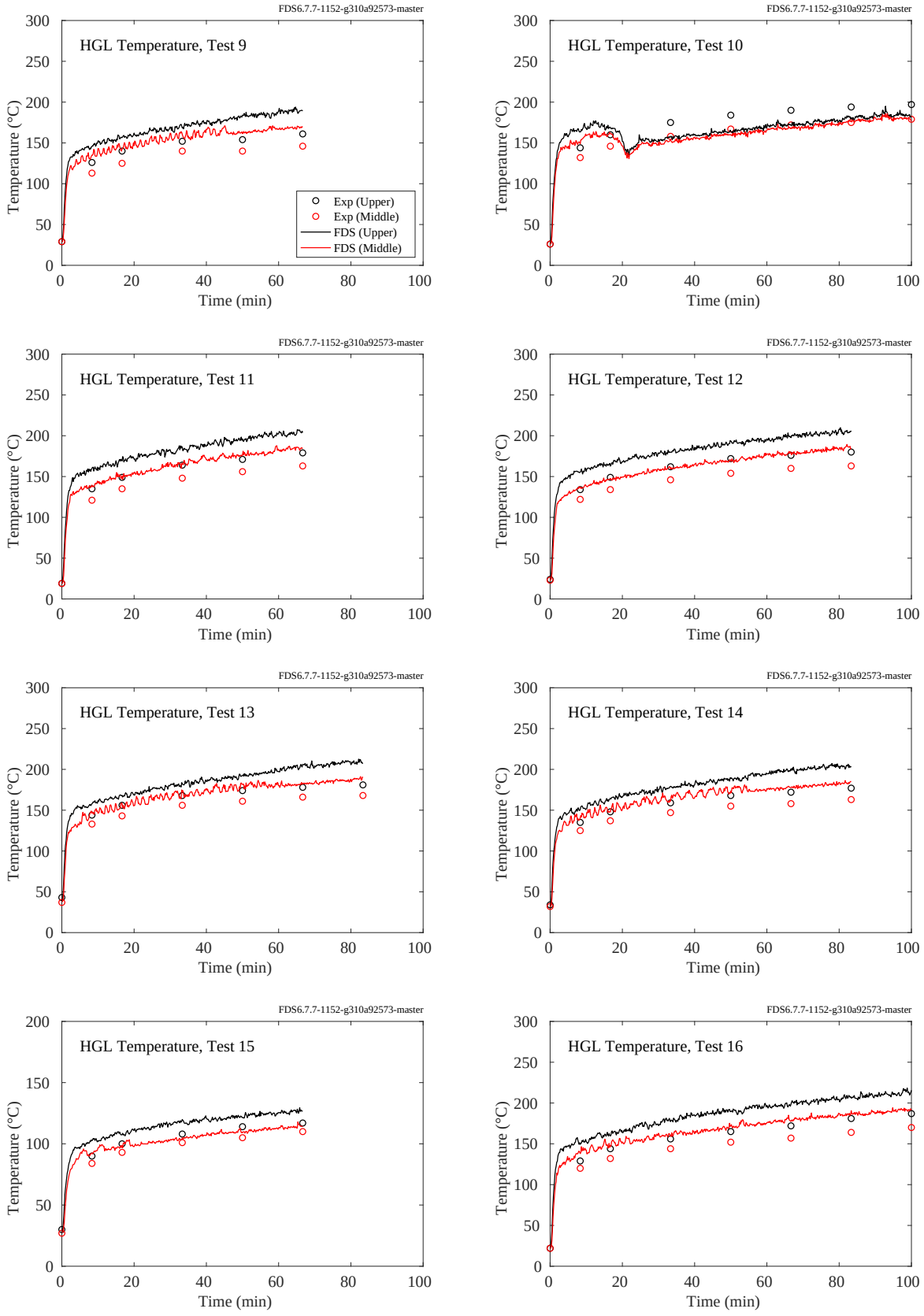

Figure 5.20: LLNL Enclosure experiments, HGL temperature, Tests 9-16.

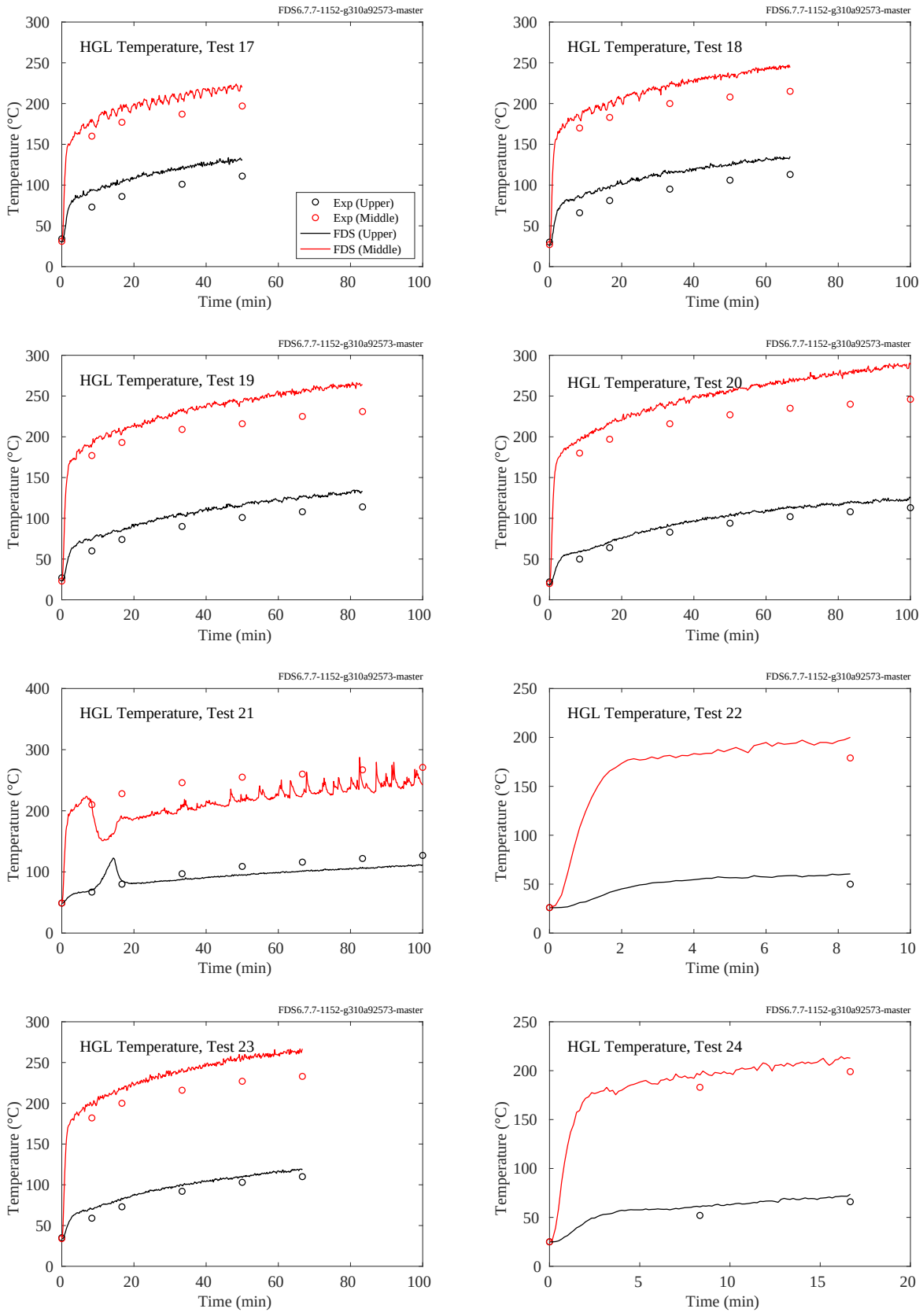

Figure 5.21: LLNL Enclosure experiments, HGL temperature, Tests 17-24.

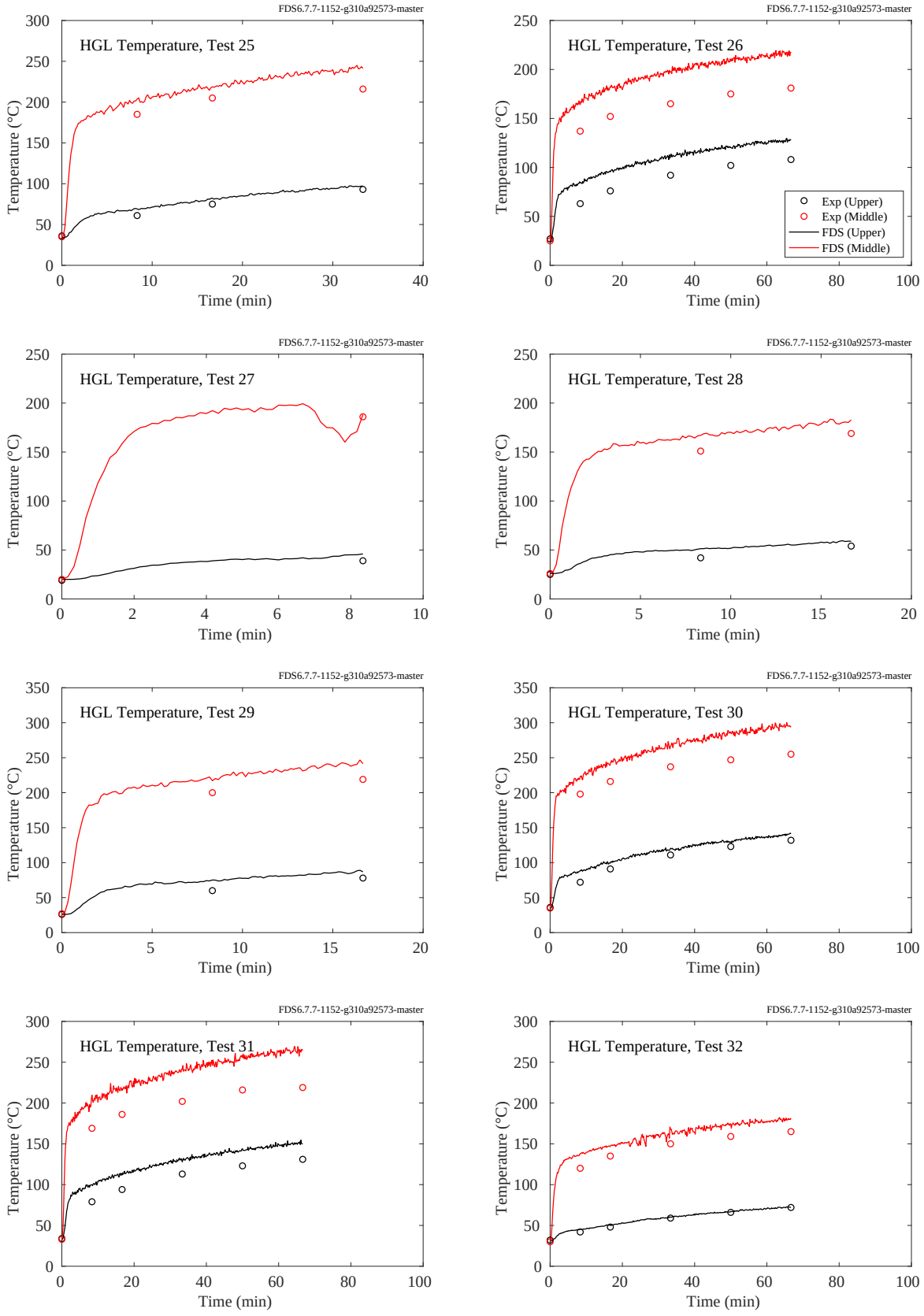

Figure 5.22: LLNL Enclosure experiments, HGL temperature, Tests 25-32.

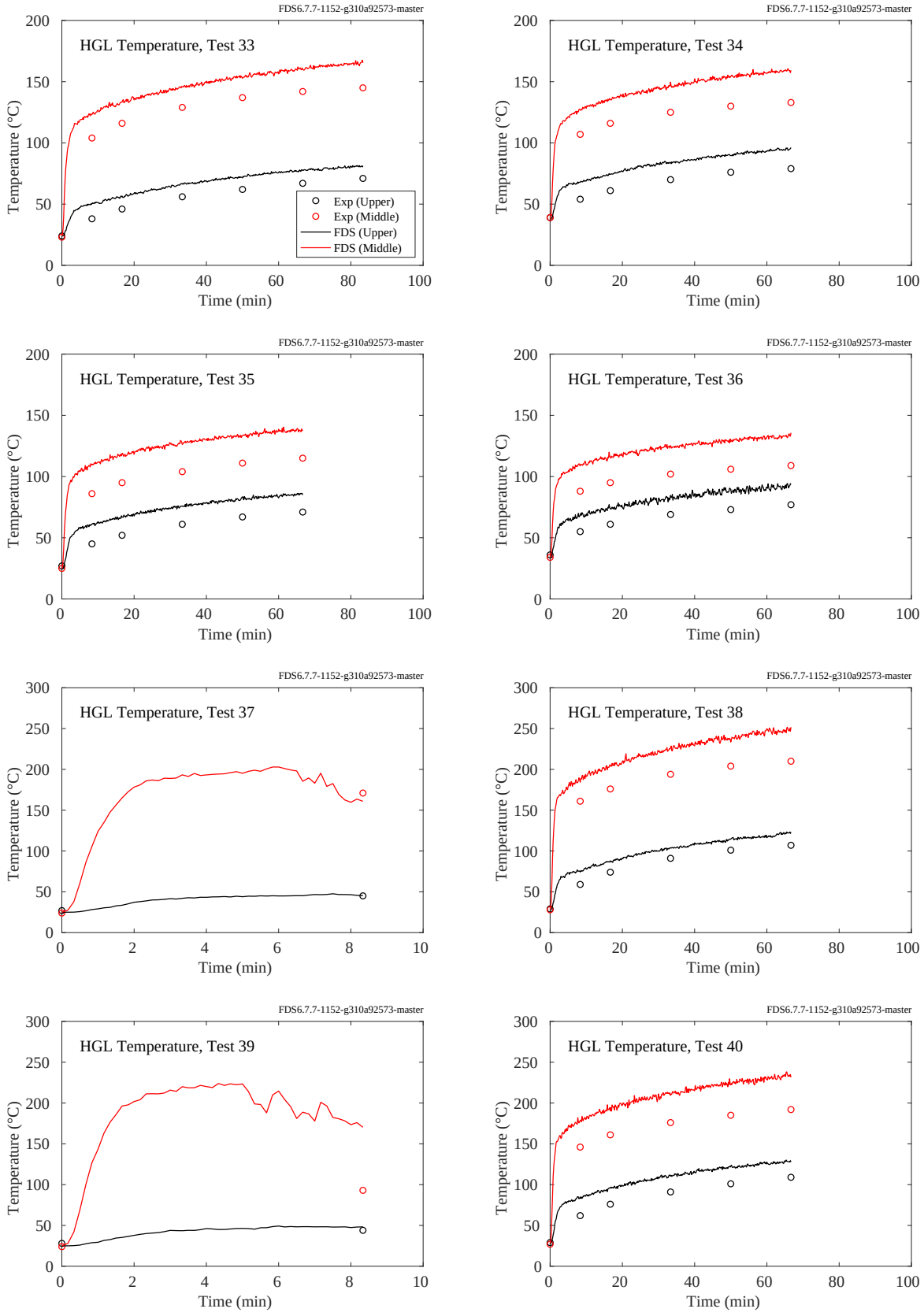

Figure 5.23: LLNL Enclosure experiments, HGL temperature, Tests 33-40.

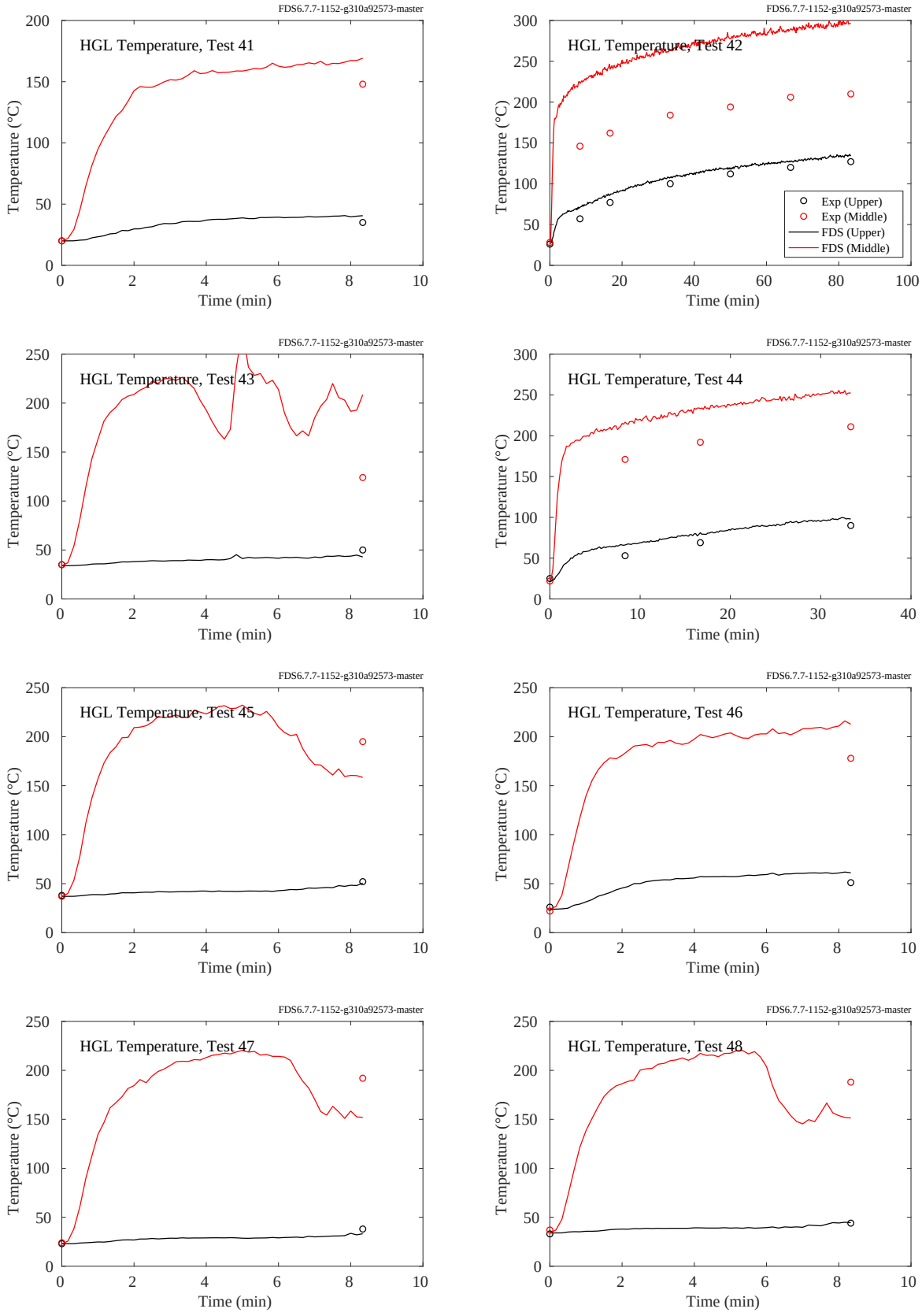

Figure 5.24: LLNL Enclosure experiments, HGL temperature, Tests 41-48.

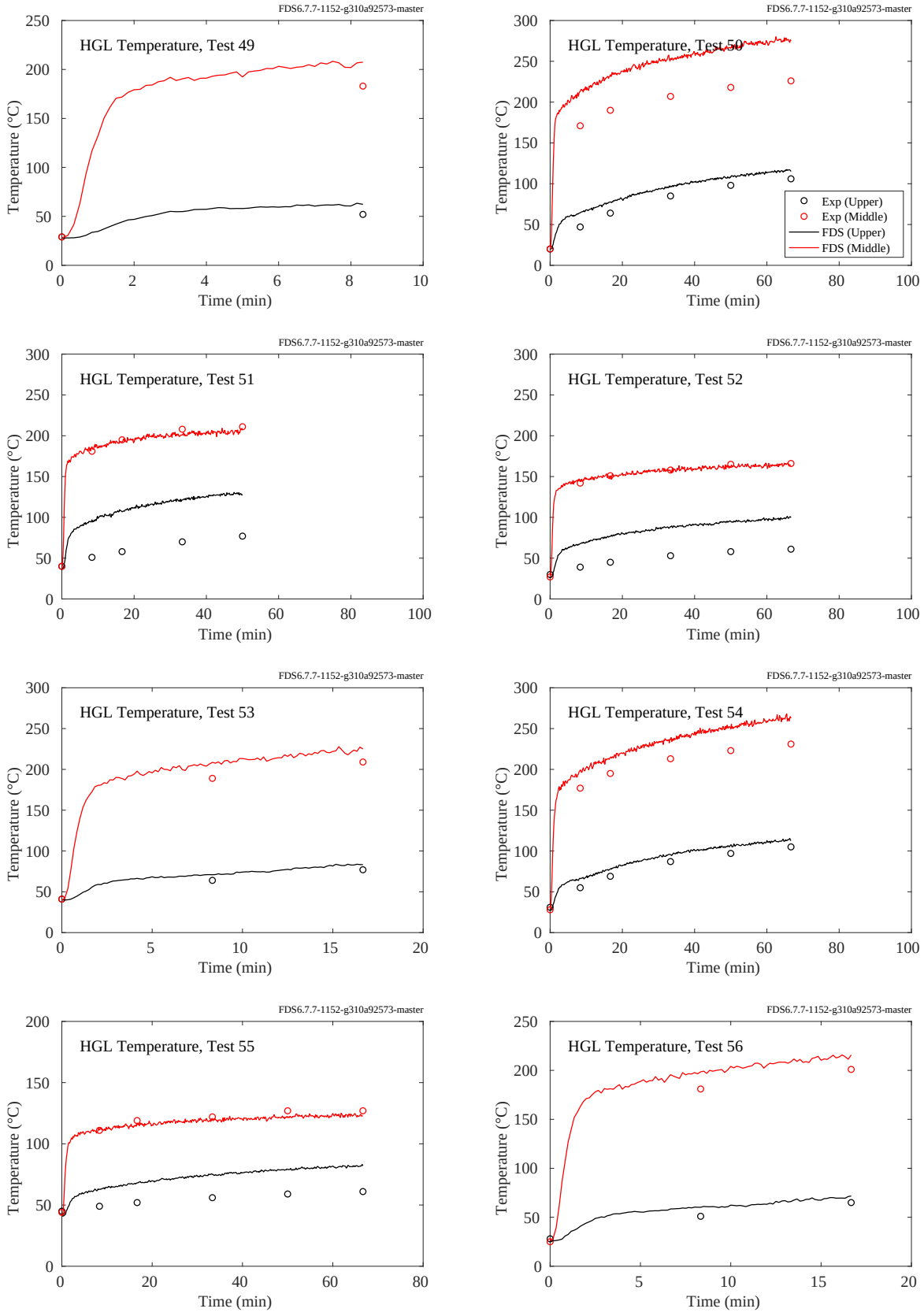

Figure 5.25: LLNL Enclosure experiments, HGL temperature, Tests 49-56.

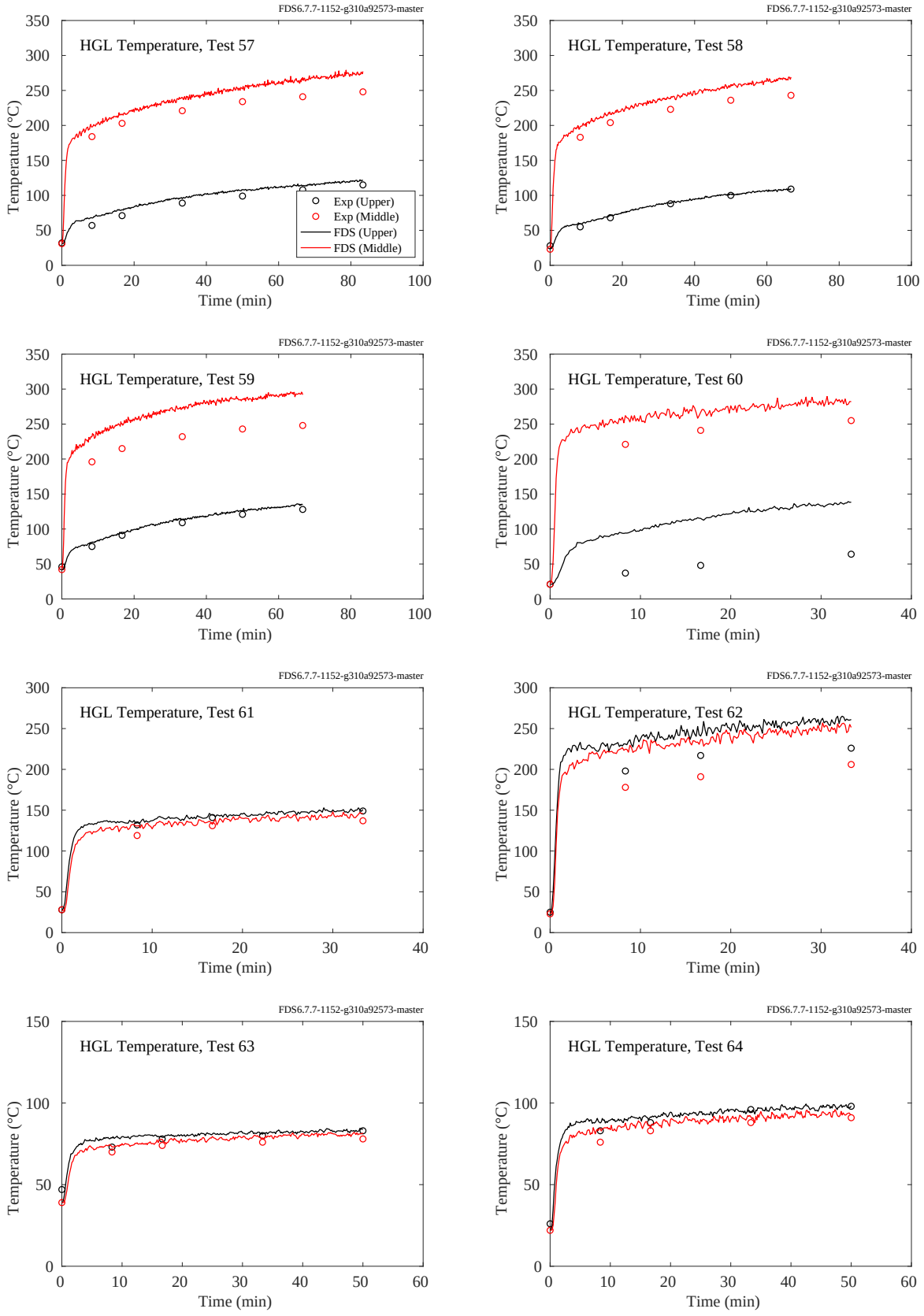

Figure 5.26: LLNL Enclosure experiments, HGL temperature, Tests 57-64.

5.7 NBS Multi-Room Test Series

This series of experiments was performed in two relatively small rooms connected by a long corridor. The fire was located in one of the rooms. Eight vertical arrays of thermocouples were positioned throughout the test space: Tree 1 in the burn room, Tree 2 in the doorway of the burn room, Trees 3, 4, and 5 in the corridor, Tree 6 in the exit doorway to the outside at the far end of the corridor, Tree 7 in the doorway of the "target" room, and Tree 8 inside the target room. Four trees have been selected for comparison with model prediction: Tree 1 in the burn room, the trees in the corridor, and Tree 8 in the target room in Test 100Z. In Tests 100A and 100O, the target room was closed. The test director reduced the layer information individually for the eight thermocouple arrays using an alternative method. These results were included in the original data sets. However, in this report the selected TC trees were reduced using the method described in Section 5.1.

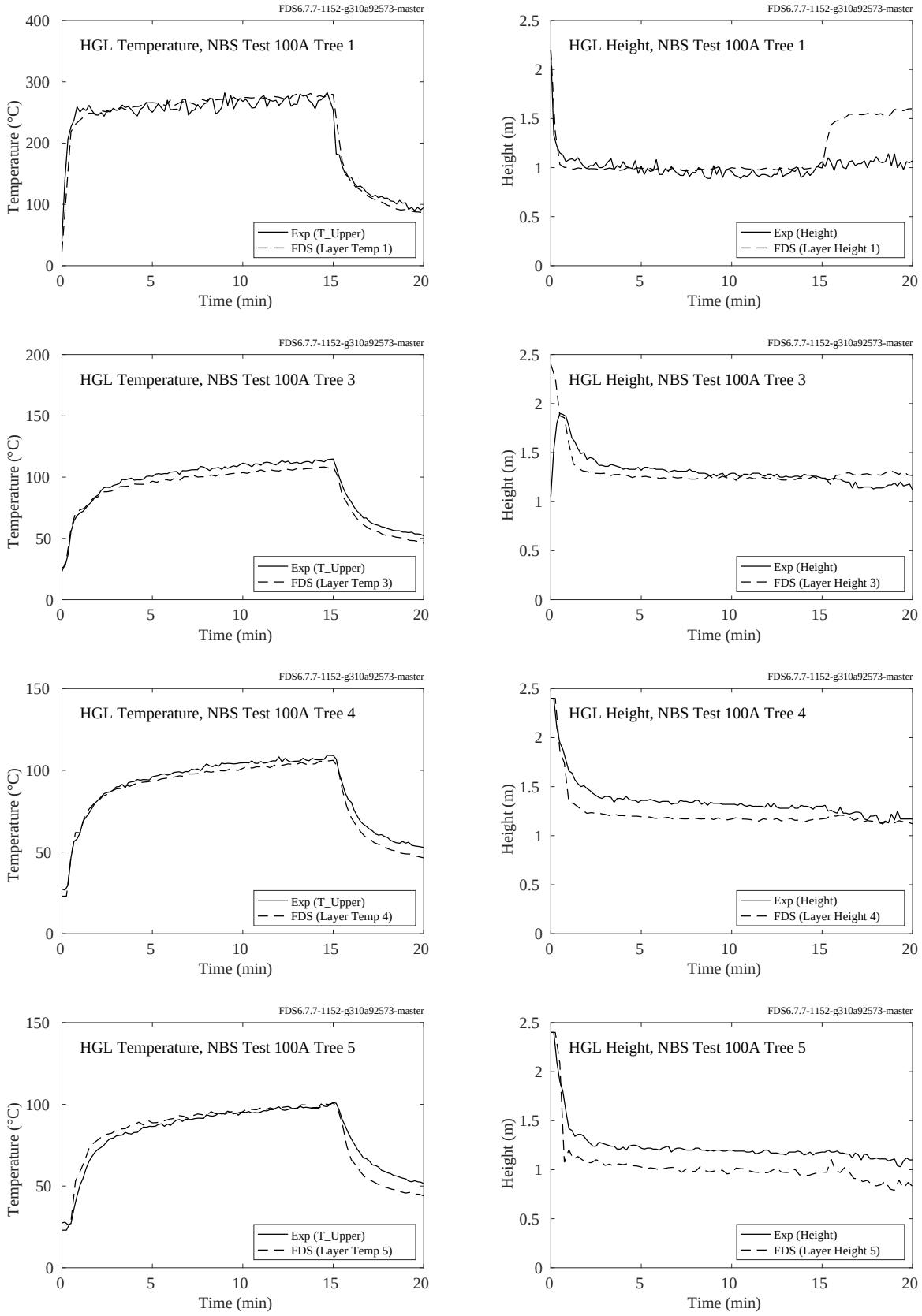

Figure 5.27: NBS Multi-Room experiments, HGL temperature and height, Test 100A.

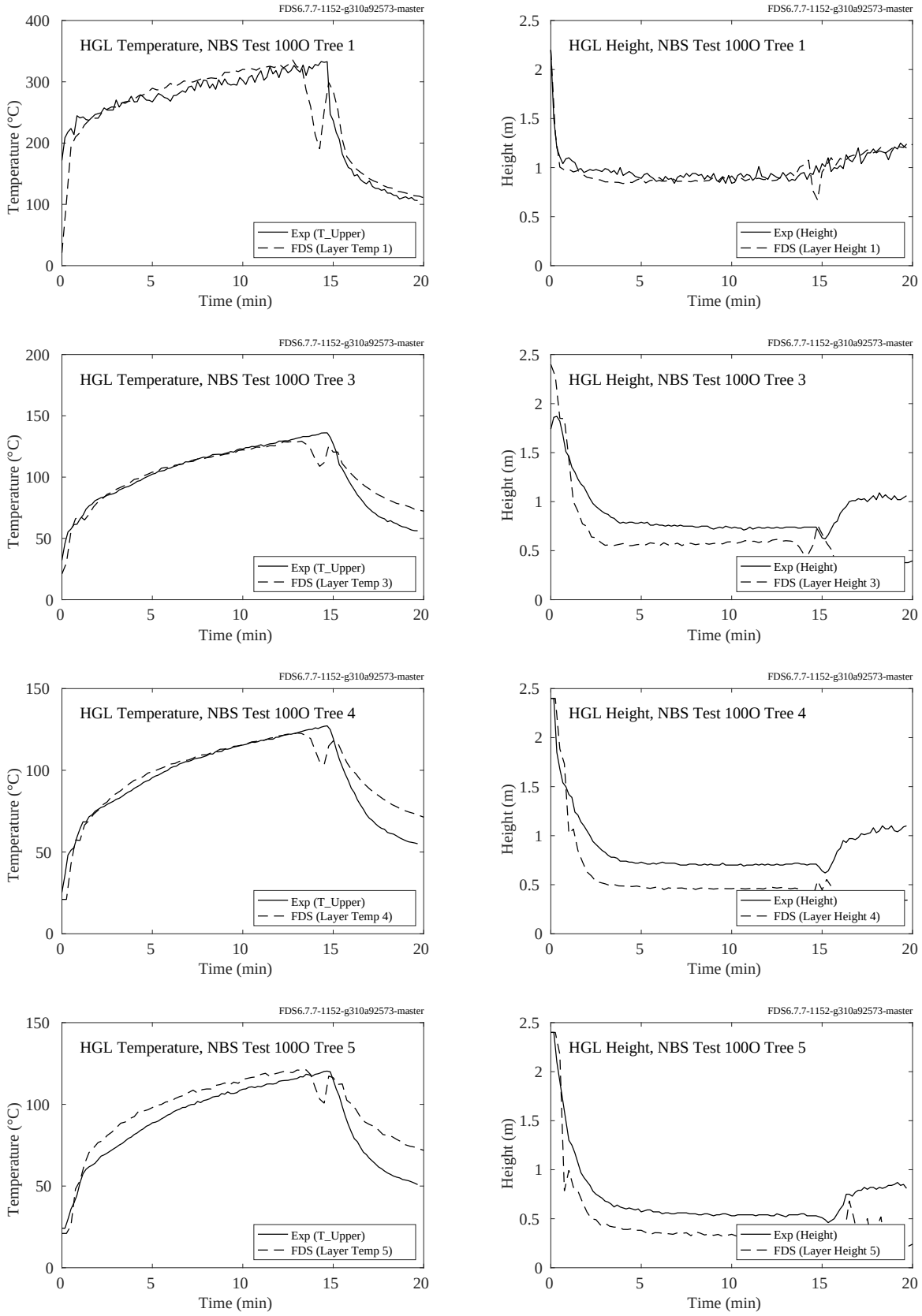

Figure 5.28: NBS Multi-Room experiments, HGL temperature and height, Test 100O.

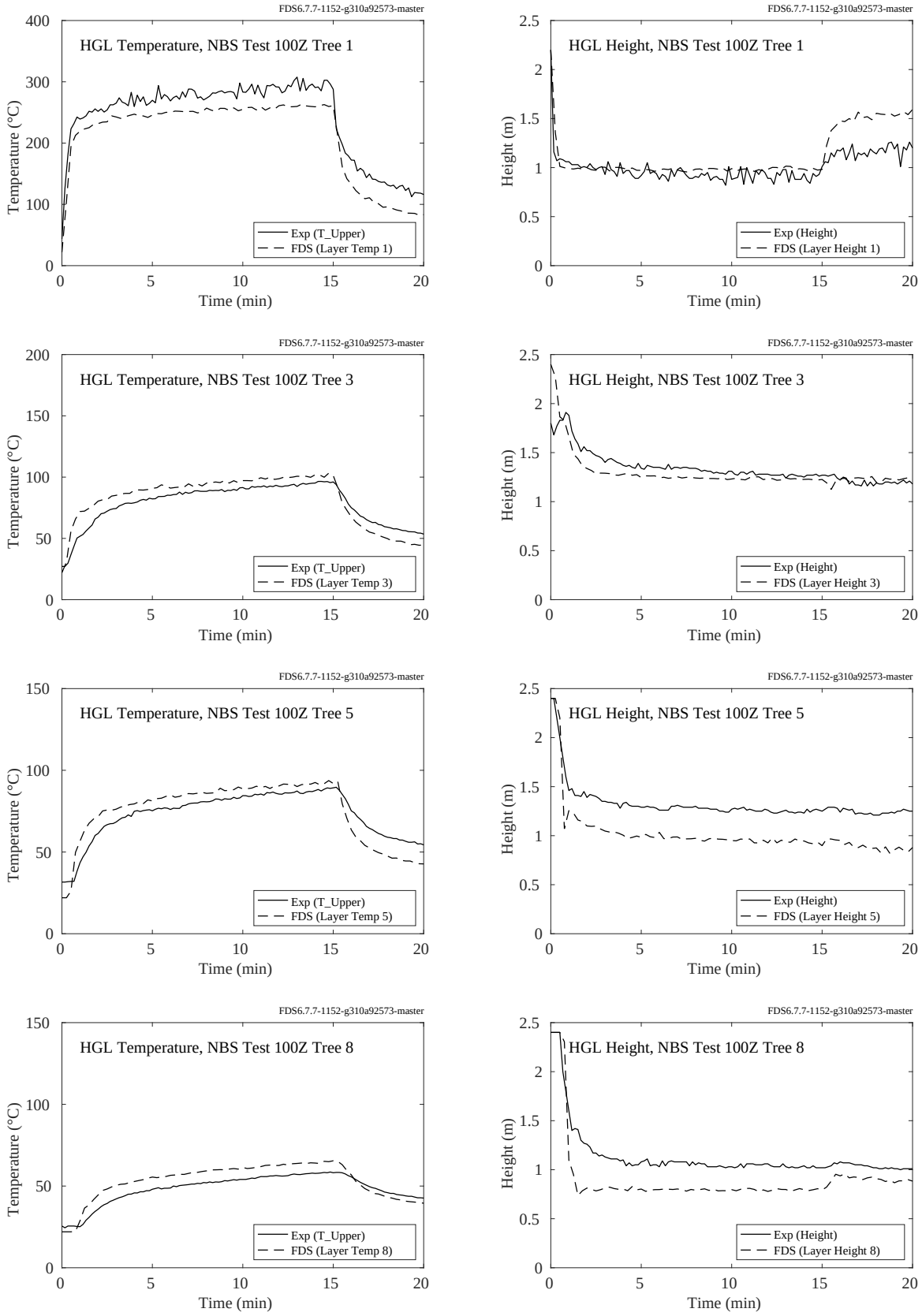

Figure 5.29: NBS Multi-Room experiments, HGL temperature and height, Test 100Z.

5.8 NIST Composite Beam

A brief description of the experiments is given in Section 3.41. The compartment interior dimensions are 12.4 m long, running east-west, 1.9 m wide, and 3.77 m high. Four experiments with fires were performed, labeled as Tests 2-5. Test 1 did not include a fire.

To measure the hot gas layer in the compartment, stainless steel sheathed thermocouples (Omega TJ36-CAXL-14U-24 and TJ36-CAXL-38U-24) were mounted 0.8 m below the concrete slab, extending out of the compartment walls. Results are shown in Figs. 5.30 and 5.31. TCC1 was mounted 30 cm from the west wall and 46 cm from the north wall. TCC5 was mounted 30 cm from the east wall and 46 cm from the south wall. TCC2, TCC3, and TCC4 were mounted 46 cm from the north wall, and at positions -4.3 m, 0 m, and 4.3 m relative to the line of east-west symmetry, respectively (east is the positive direction). TCC6, TCC7, and TCC8 were mounted 46 cm from the south wall and 4.3 m, 0 m, and -4.3 m from the east-west line of symmetry, respectively.

Because of the symmetry of the experimental configuration, TCC1 and TCC5 are duplicates, TCC3 and TCC7 are duplicates, and TCC2, TCC4, TCC6, and TCC8 are duplicates.

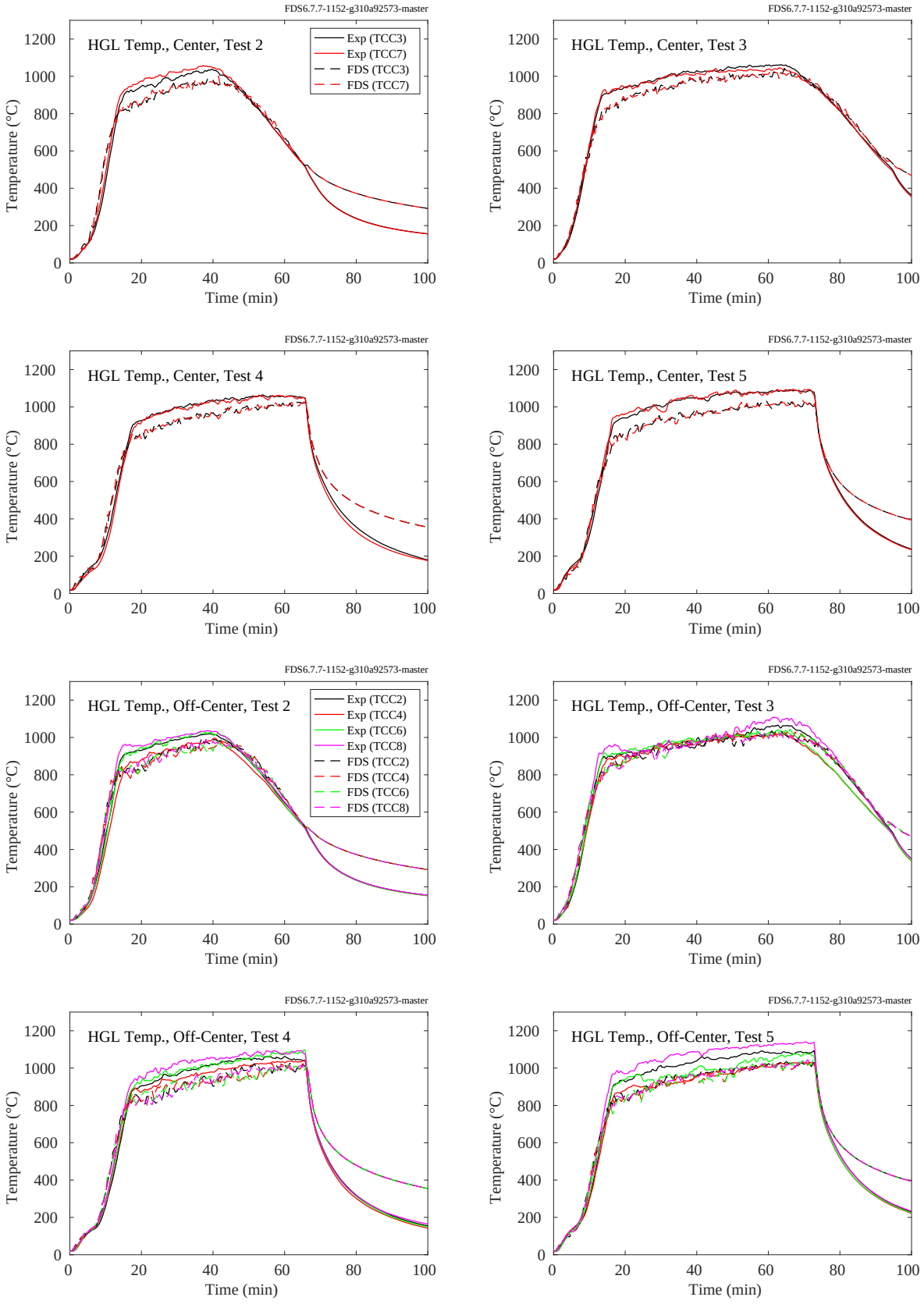

Figure 5.30: NIST Composite Beam, mid-compartment HGL temperatures.

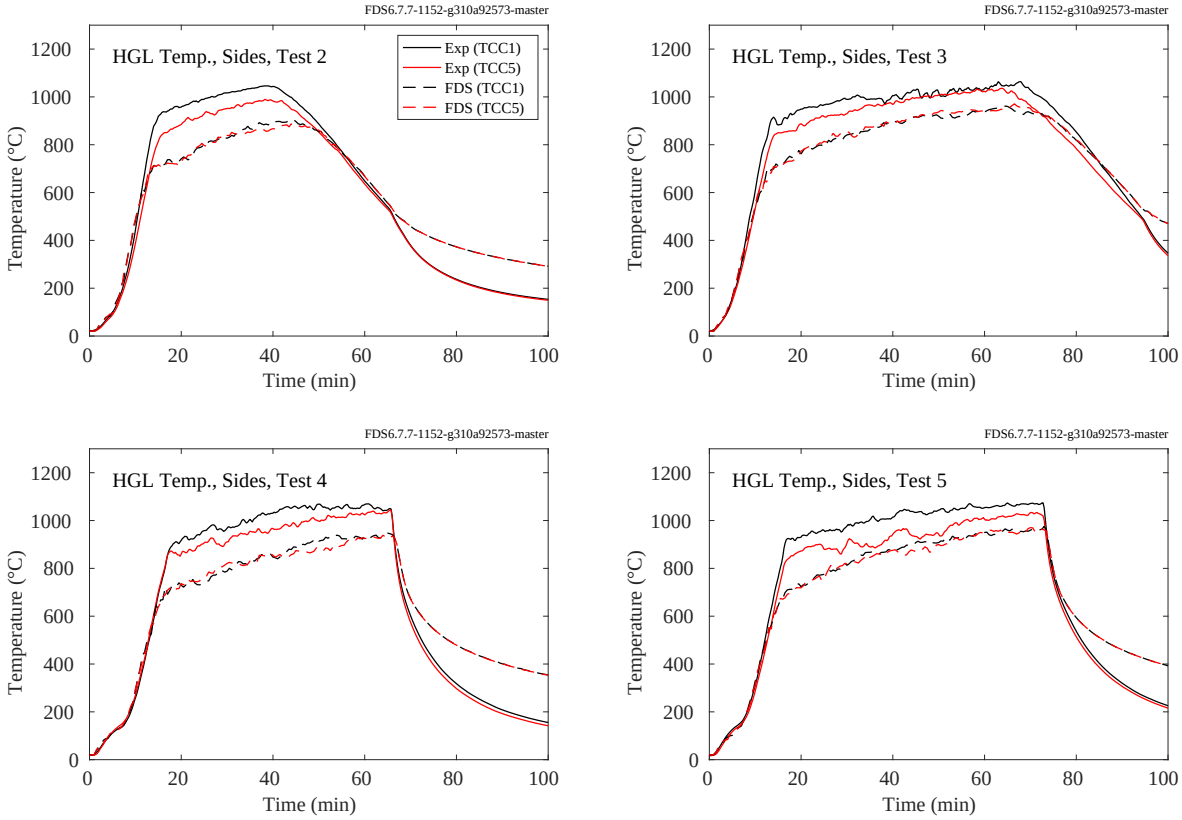

Figure 5.31: NIST Composite Beam, end-compartment HGL temperatures.

5.9 NIST E119 Compartment

A brief description of the experiments is given in Section 3.42. The compartment interior dimensions are 10.8 m long, running east-west, 7.0 m wide, and 3.8 m high. Three fire experiments were performed, labeled as Tests 1-3.

To measure the upper layer gas temperatures in the compartment, twelve stainless steel sheathed thermocouples (Omega TJ36-CAXL-14U-24) were mounted 0.305 m below the ceiling, extending out of the ceiling slab. Results are shown in Figs. 5.32 through 5.34. Locations of TC1 through TC12 were shown in Fig. 3.22. Because of the symmetry of the experimental configuration, TC1 and TC4 are duplicates, TC2 and TC3 are duplicates, TC9 and TC12 are duplicates, and TC10, TC11 are duplicates.

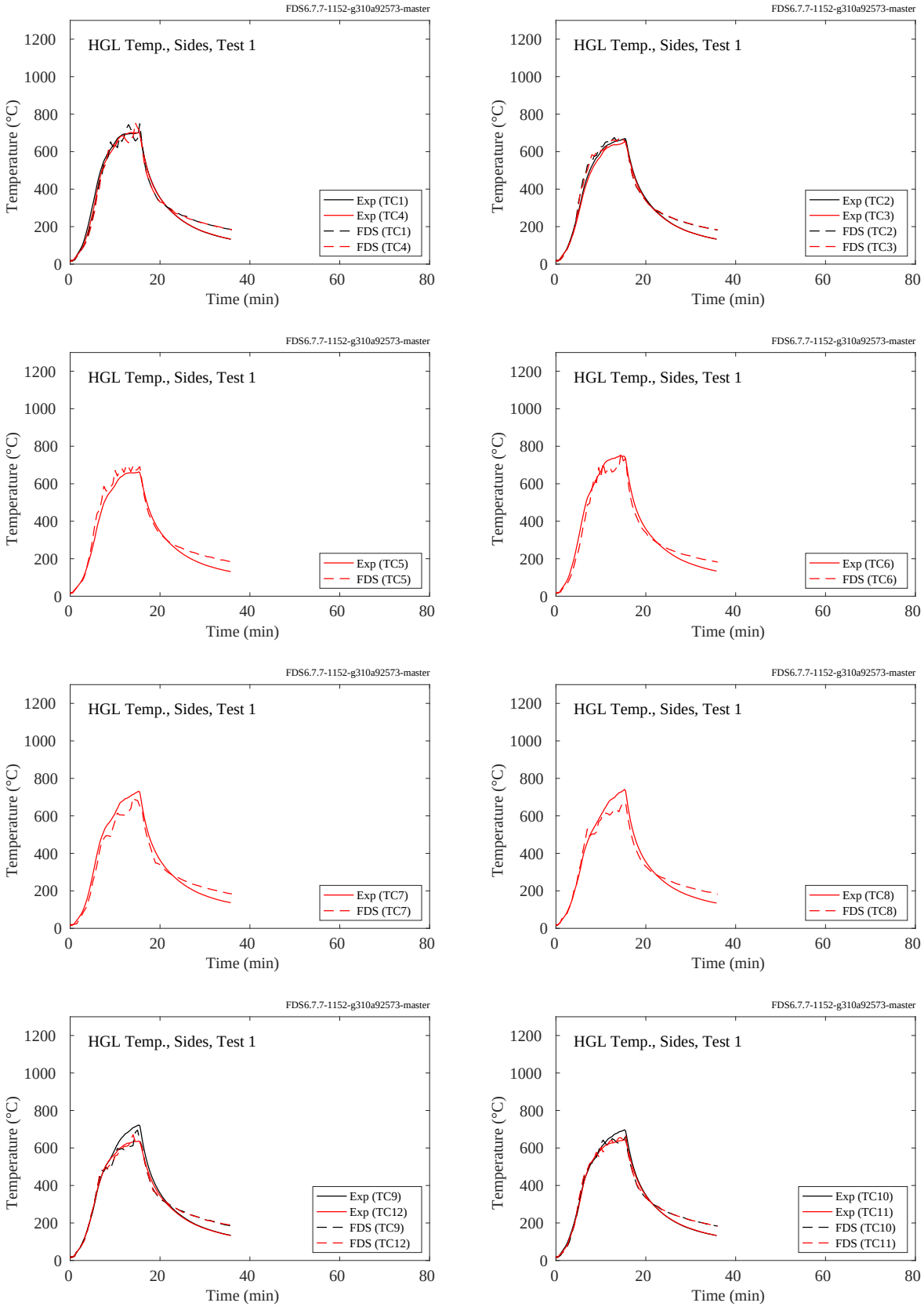

Figure 5.32: NIST E119 Compartment Test 1, upper layer gas temperatures.

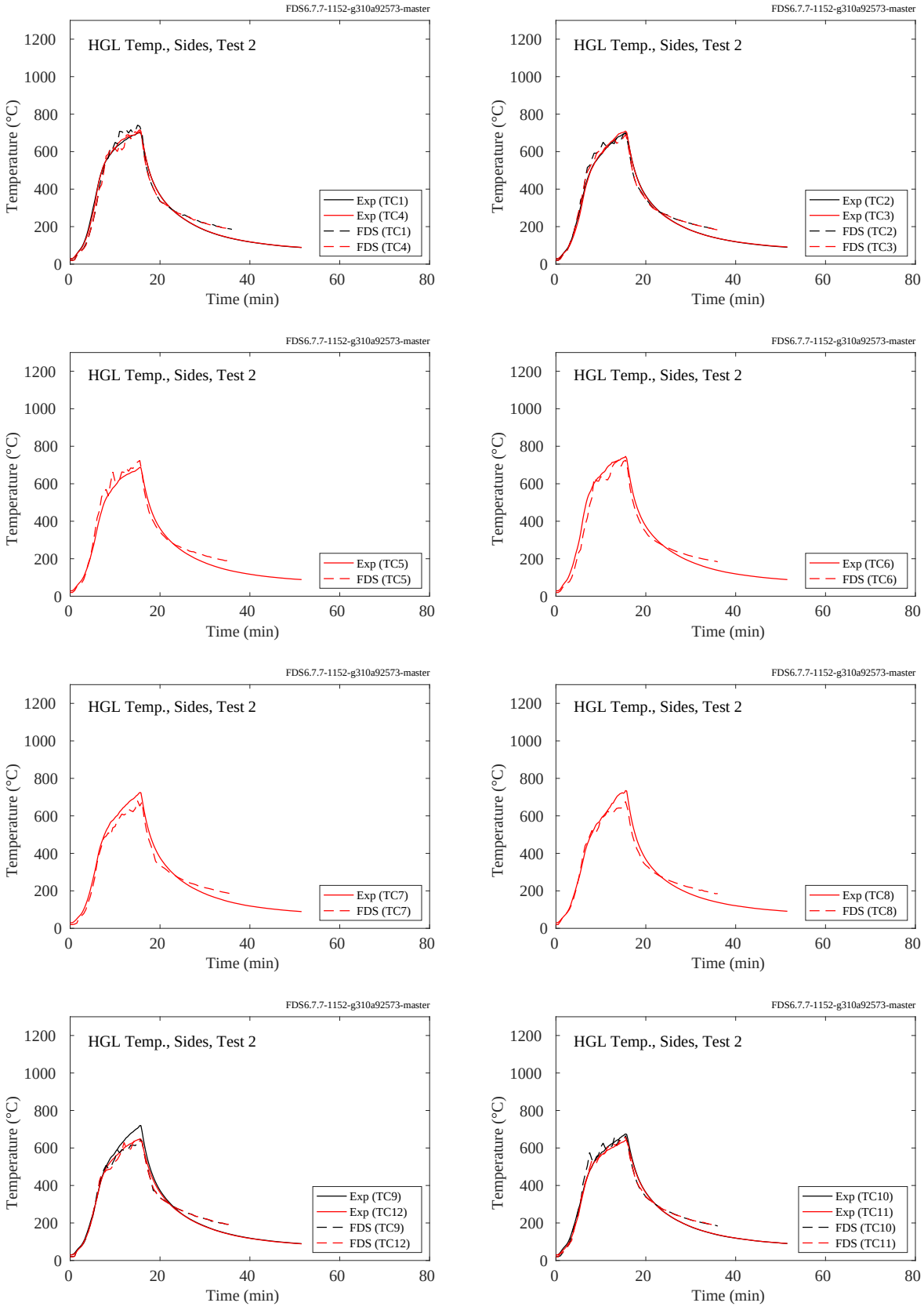

Figure 5.33: NIST E119 Compartment Test 2, upper layer gas temperatures.

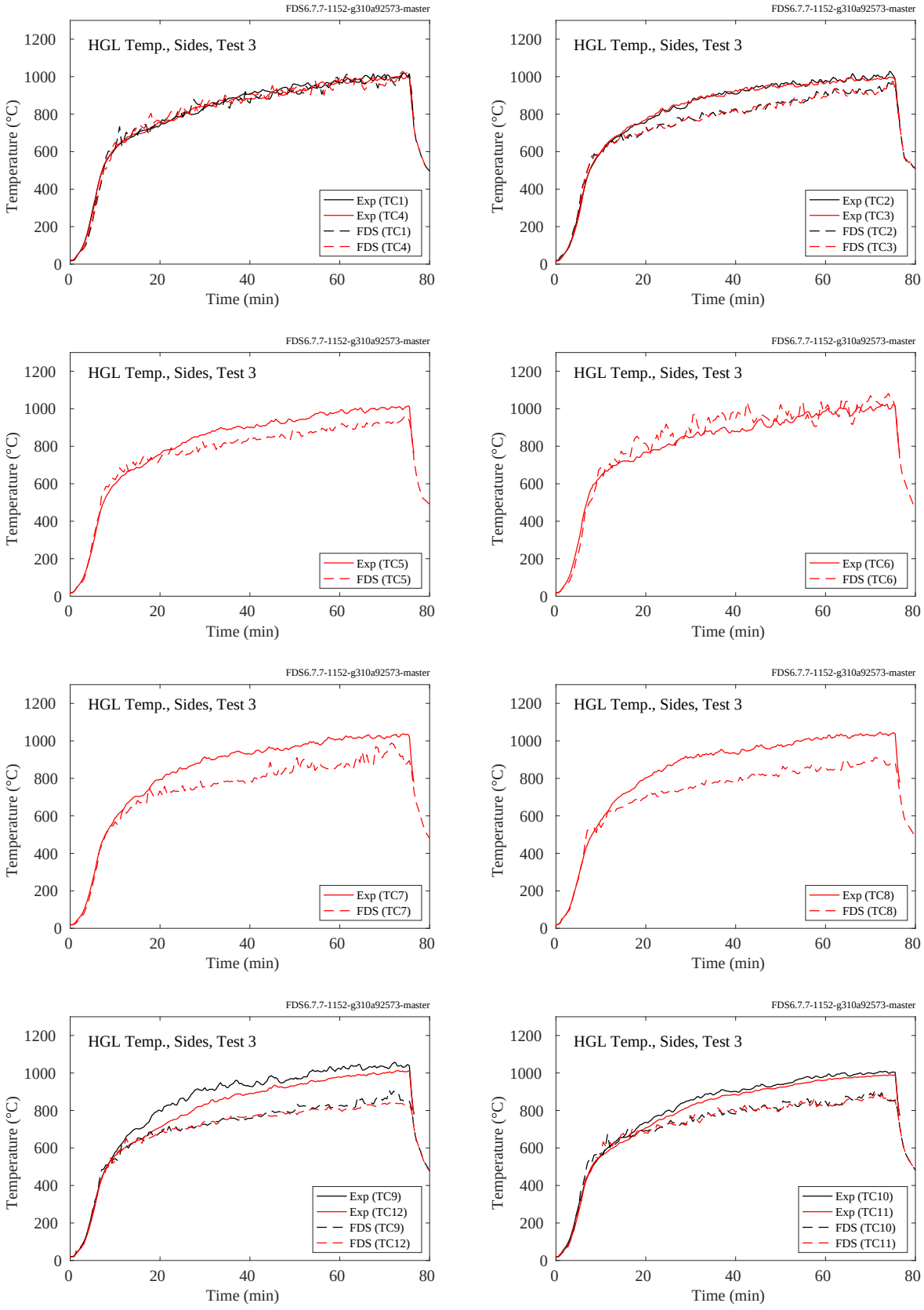

Figure 5.34: NIST E119 Compartment Test 3, upper layer gas temperatures.

5.10 NIST Full-Scale Enclosure (FSE), 2008

Thermocouple arrays were suspended from the ceiling at two points along the centerline of the ISO 9705 compartment. The array in the front of the compartment was located 72 cm inside the door, and the array in the rear was 72 cm from the back wall. Each array consisted of 11 TCs positioned at heights of 3 cm, 30 cm, 60 cm, 90 cm, 105 cm, 120 cm, 135 cm, 150 cm, 180 cm, 210 cm, and 2.38 cm. The height of the compartment was 2.4 m. In the plots on the following the pages, the average HGL temperature and layer height are shown for experiments 8 through 32. The thermocouple arrays were not installed for experiments labeled ISONG3, ISOHept4, or ISOHept5.

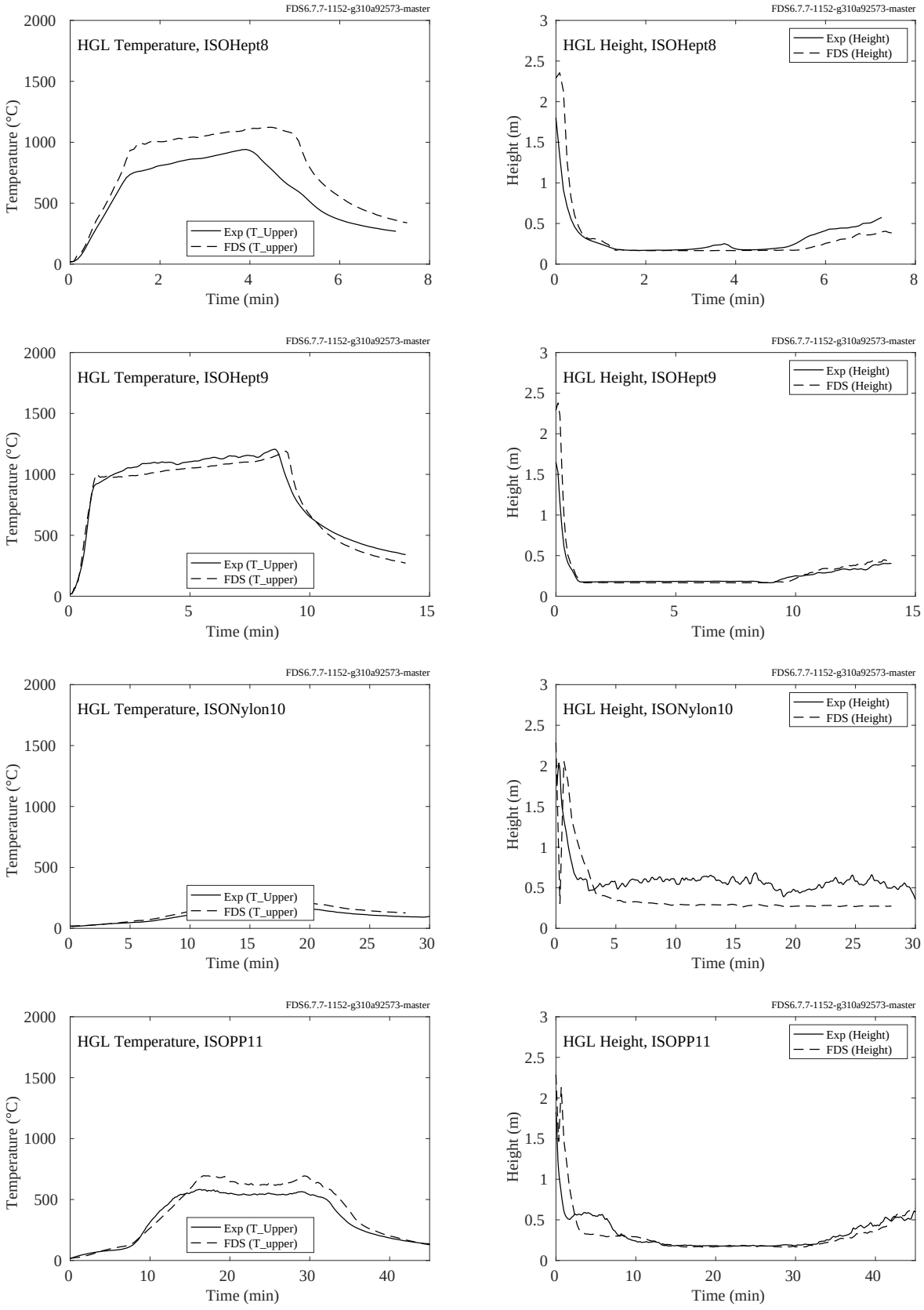

Figure 5.35: NIST FSE, HGL temperature and height, Tests 8-11.

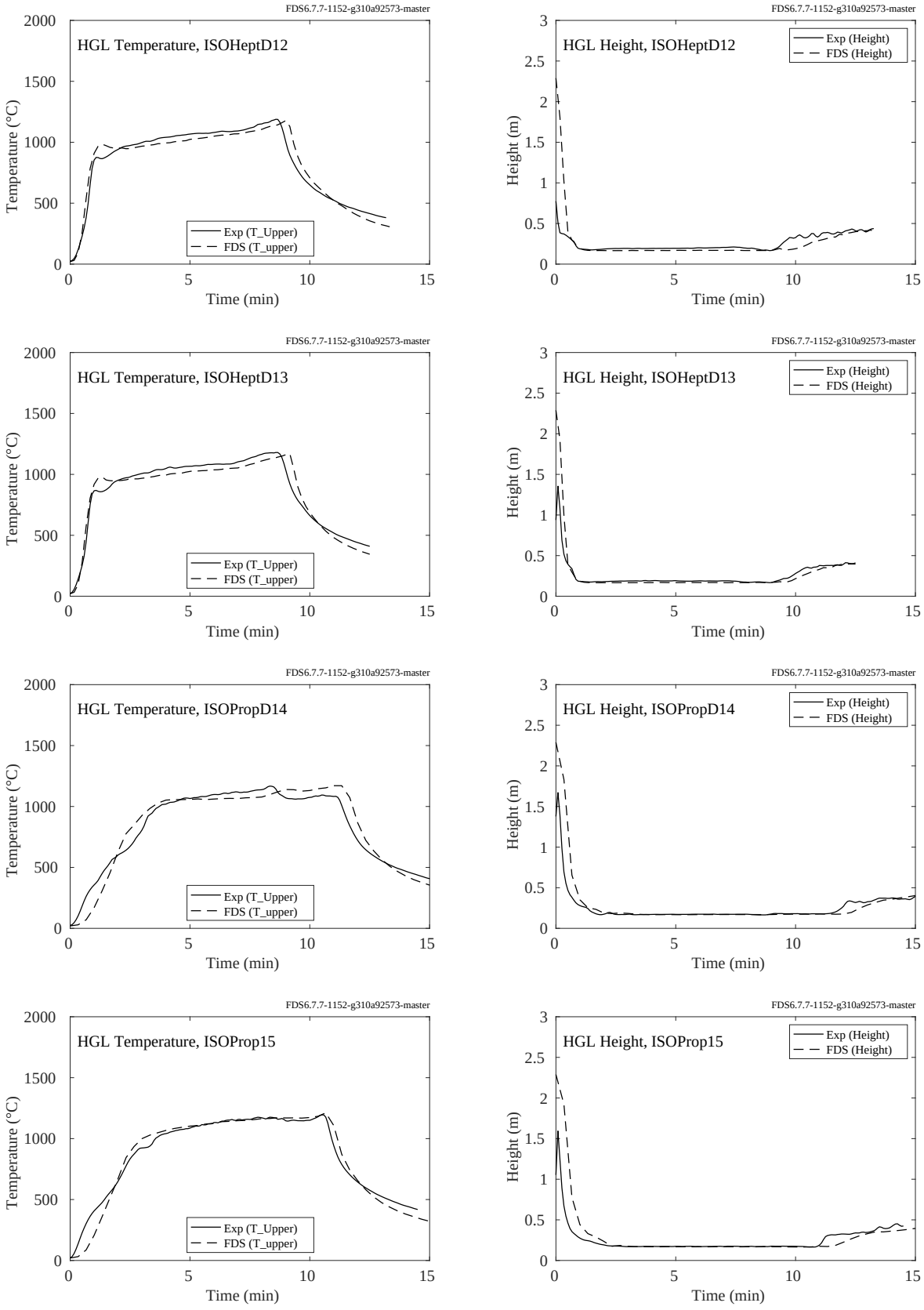

Figure 5.36: NIST FSE, HGL temperature and height, Tests 12-15.

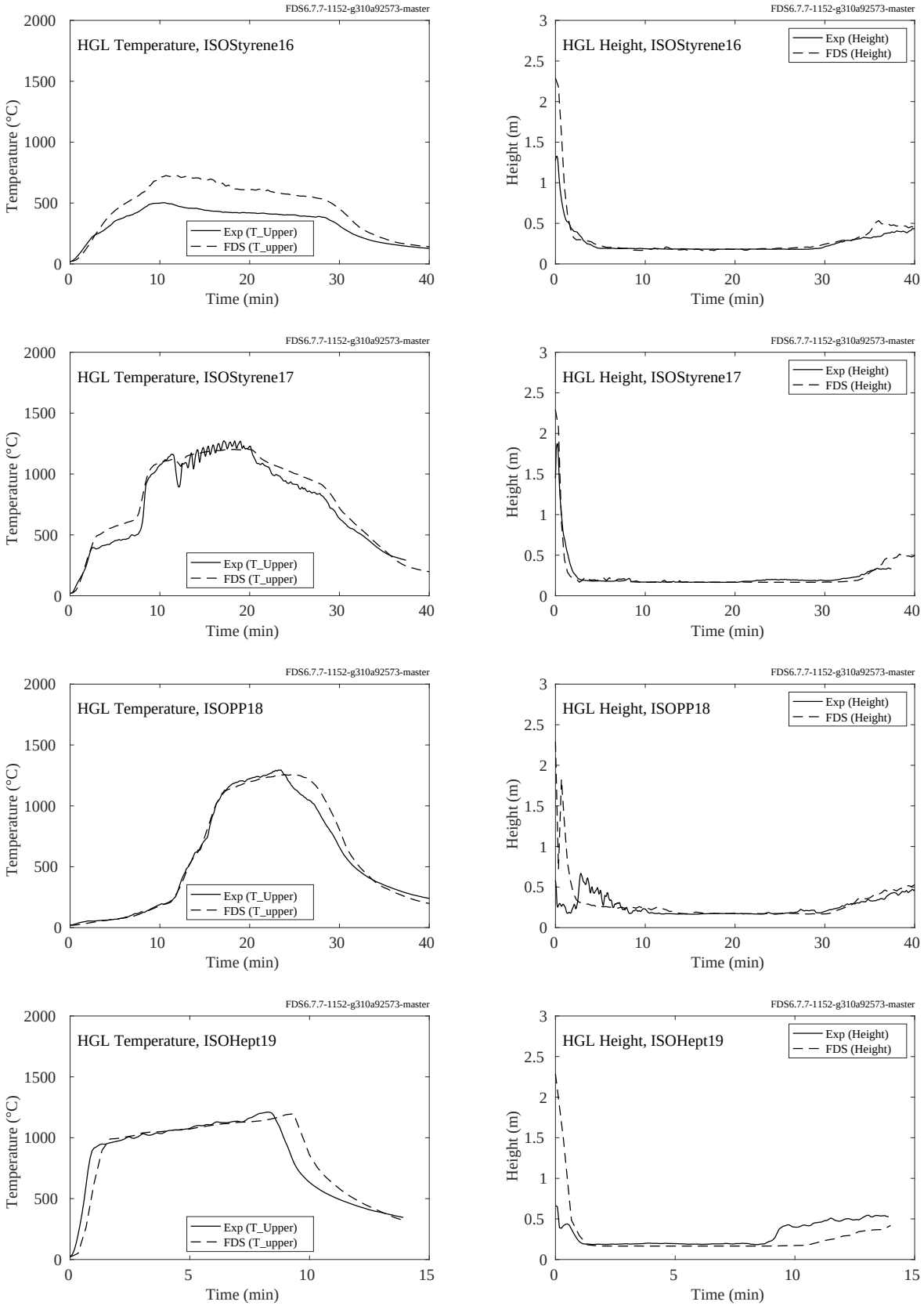

Figure 5.37: NIST FSE, HGL temperature and height, Tests 16-19.

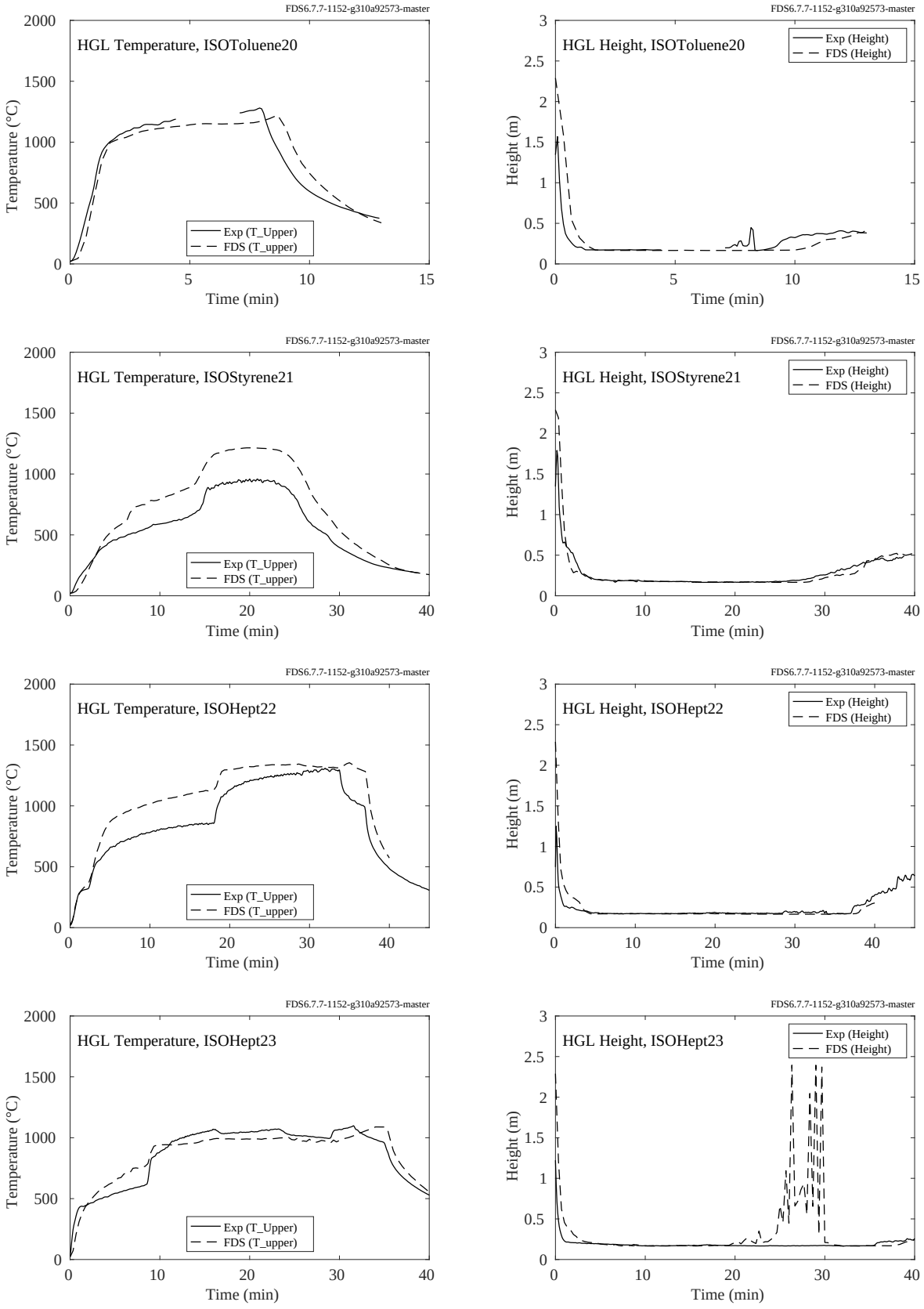

Figure 5.38: NIST FSE, HGL temperature and height, Tests 20-23.

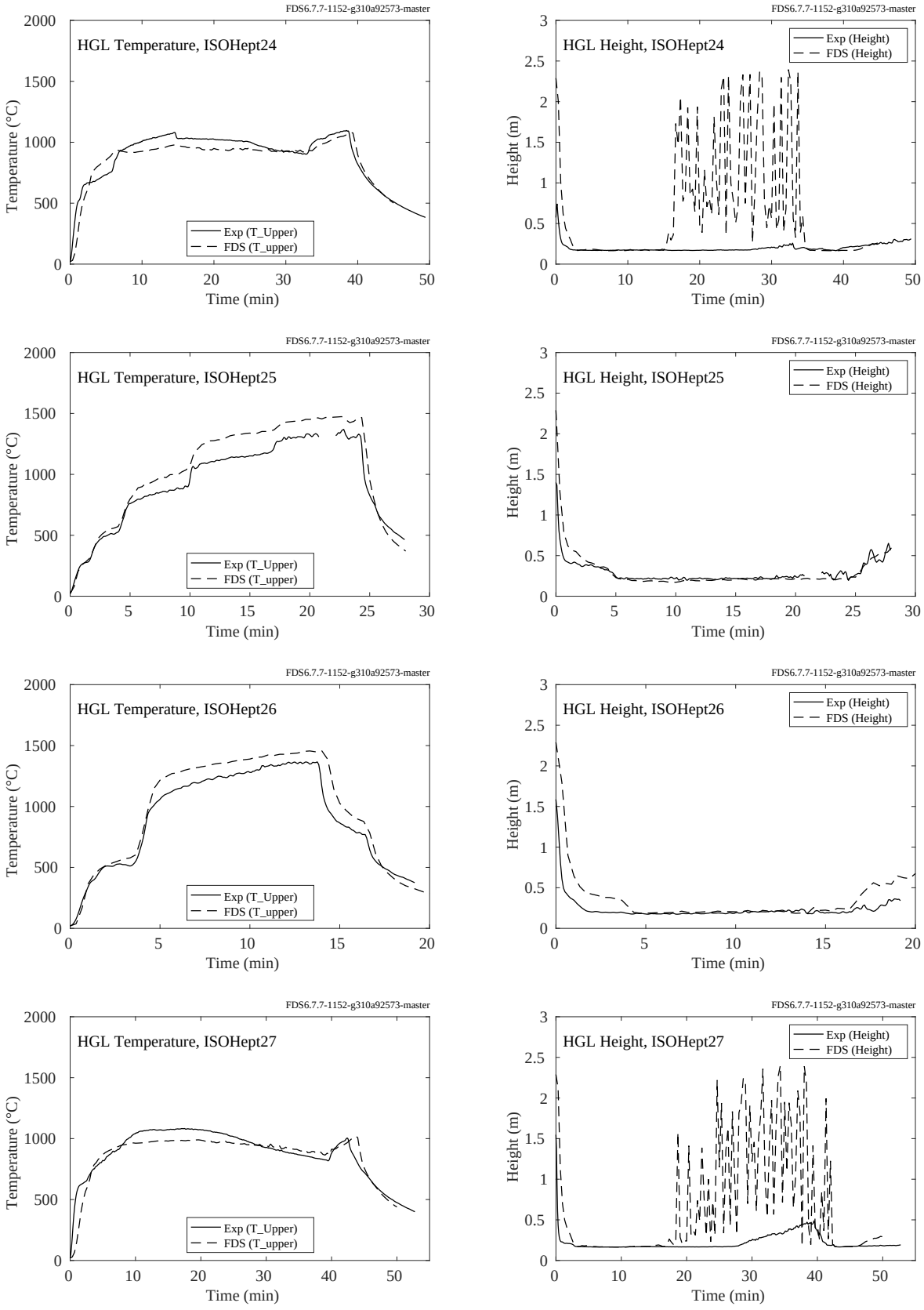

Figure 5.39: NIST FSE, HGL temperature and height, Tests 24-27.

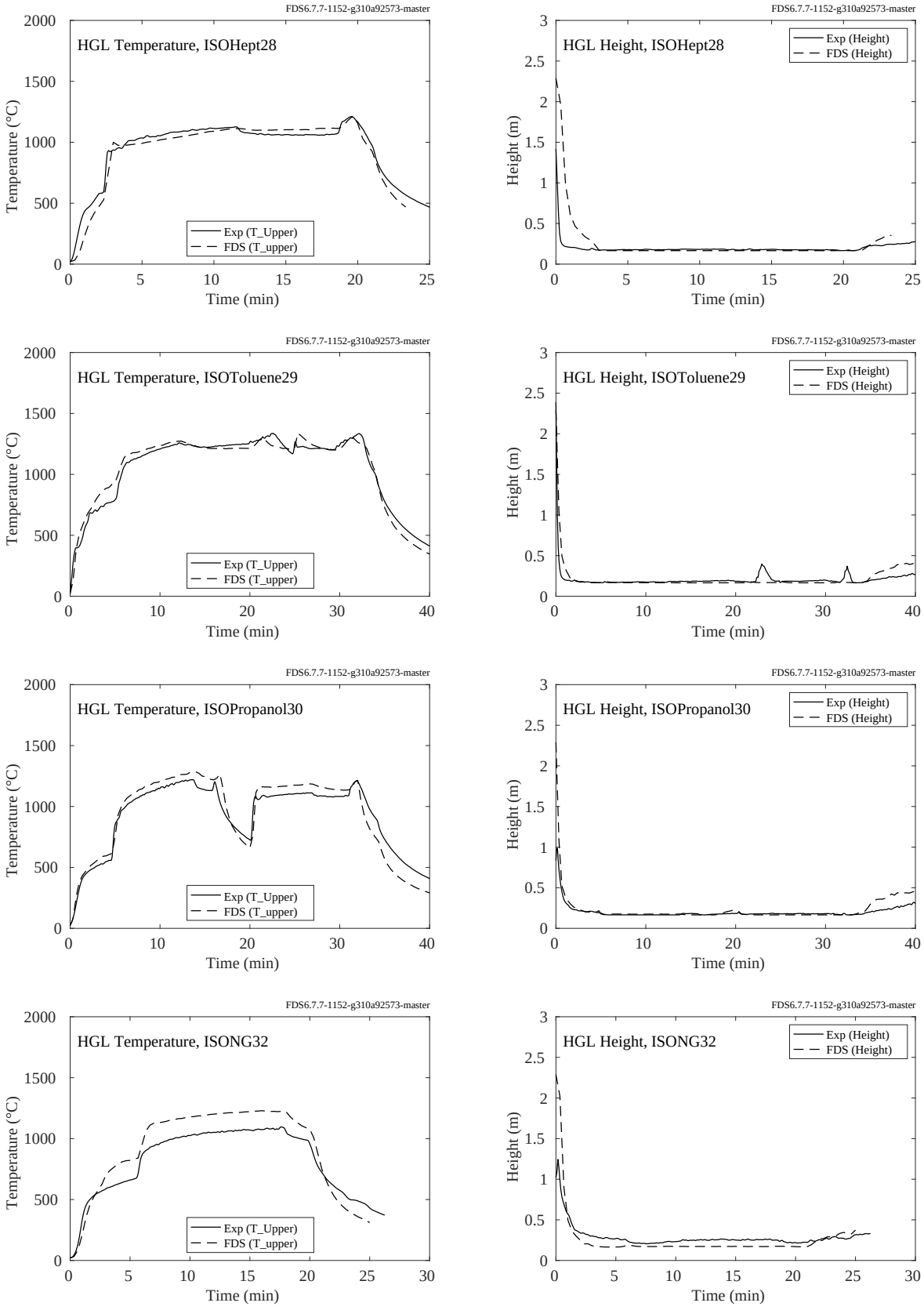

Figure 5.40: NIST FSE, HGL temperature and height, Tests 28-30,, 32.

5.11 NIST/NRC Test Series

The NIST/NRC series consisted of 15 heptane spray fire experiments with varying heat release rates, pan locations, and ventilation conditions. Gas temperatures were measured using seven floor-to-ceiling thermocouple arrays (or "trees") distributed throughout the compartment. The average hot gas layer temperature and height are calculated using thermocouple Trees 1, 2, 3, 5, 6 and 7. Tree 4 was not used because one of its thermocouples (TC 4-9) malfunctioned during most of the experiments. A few observations about the simulations:

- During Tests 4, 5, 10 and 16 a fan blew air into the compartment through a vent in the south wall. The measured velocity profile of the fan was not uniform, with the bulk of the air blowing from the lower third of the duct towards the ceiling at a roughly 45° angle. The exact flow pattern is difficult to replicate in the model, thus, the results for Tests 4, 5, 10 and 16 should be evaluated with this in mind. The effect of the fan on the hot gas layer is small, but it does have a some effect on target temperatures near the vent.
- For all of the tests involving a fan, the predicted HGL height increased after the fire was extinguished, while the measured HGL decreased. This appears to be a curious artifact of the layer reduction algorithm. It is not included in the calculation of the relative difference.
- In the closed door tests, the hot gas layer descended all the way to the floor. However, the reduction method, used on both the measured and predicted temperatures, does not account for the formation of a single layer, and therefore does not indicate that the layer drops all the way to the floor. This is neither a flaw in the measurements nor in FDS, but rather in the layer reduction method.
- The HGL reduction method produces spurious results in the first few minutes of each test because no clear layer has yet formed. These early times are not included in the relative difference calculation.

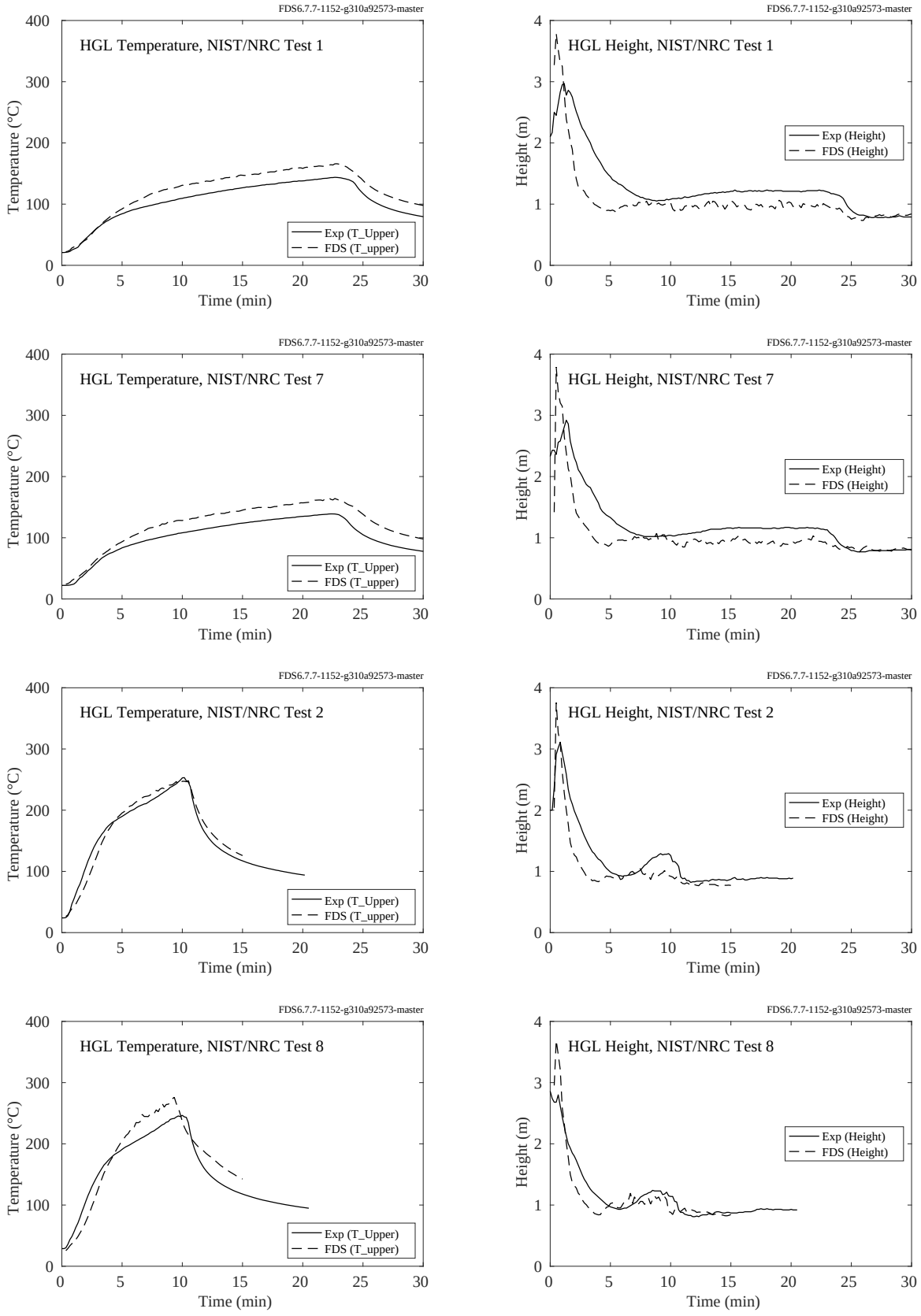

Figure 5.41: NIST/NRC experiments, HGL temperature and height, Tests 1-2, 7-8.

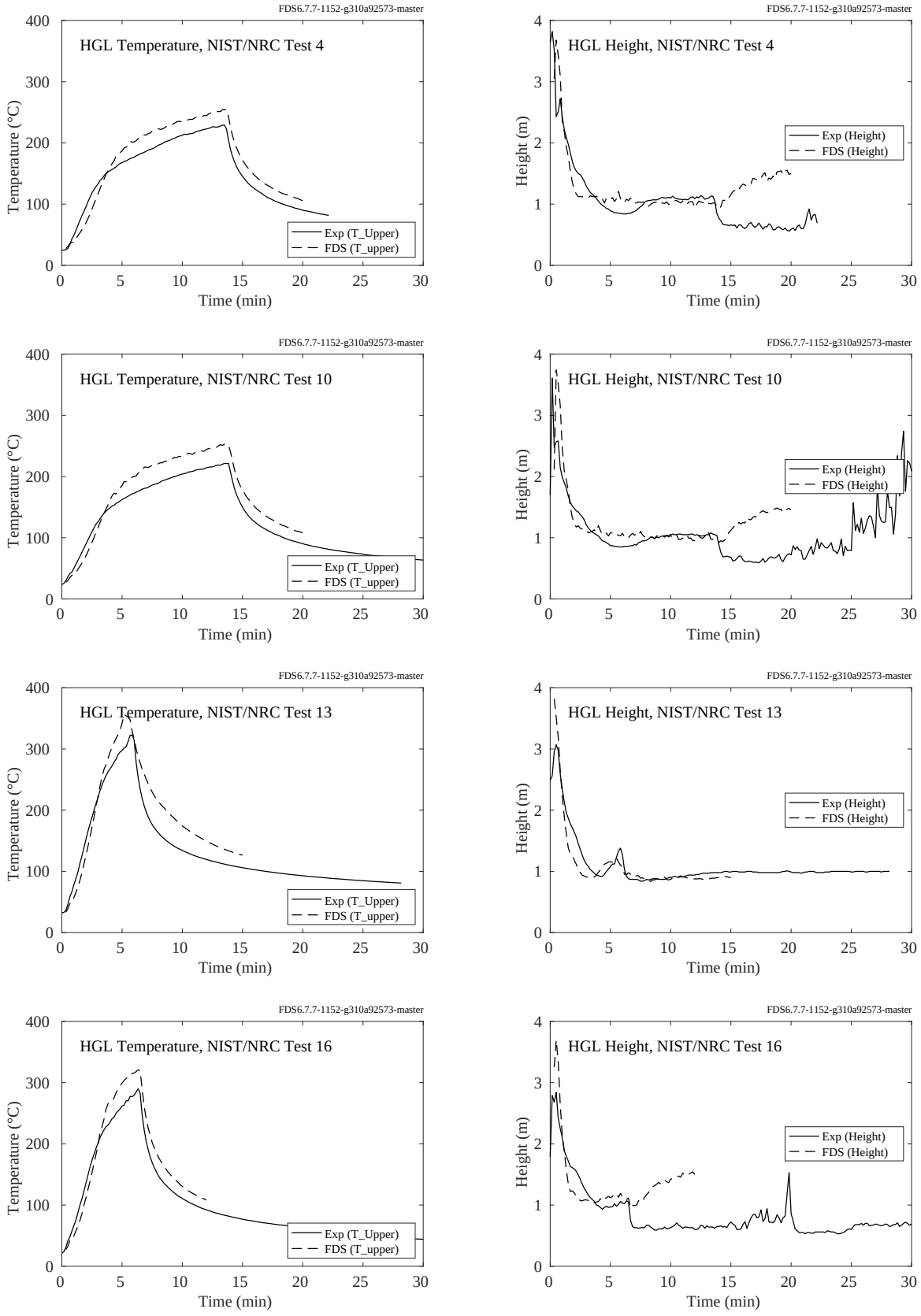

Figure 5.42: NIST/NRC experiments, HGL temperature and height, Tests 4, 10, 13, 16.

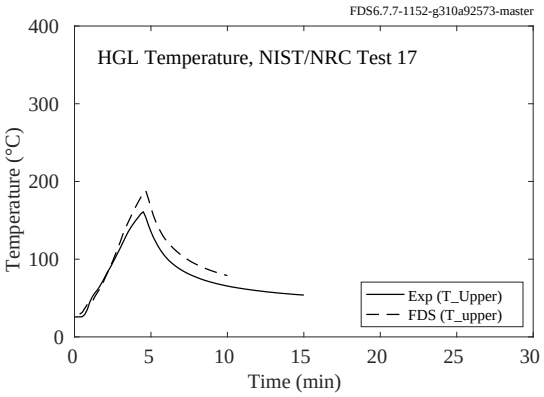

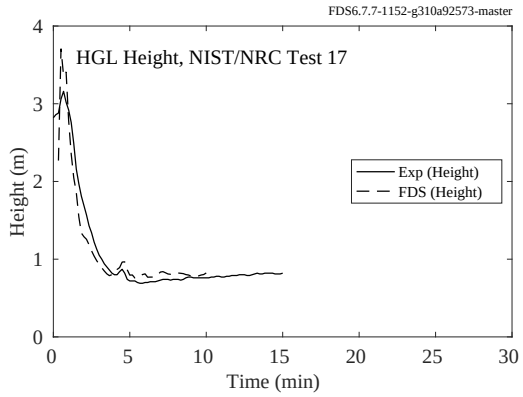

Open door tests to follow

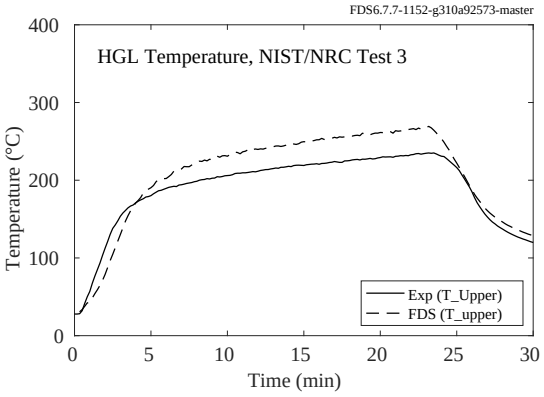

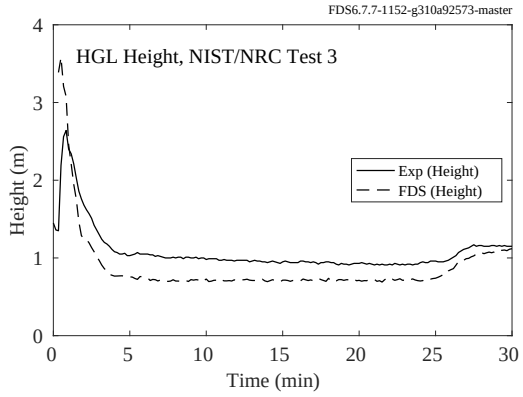

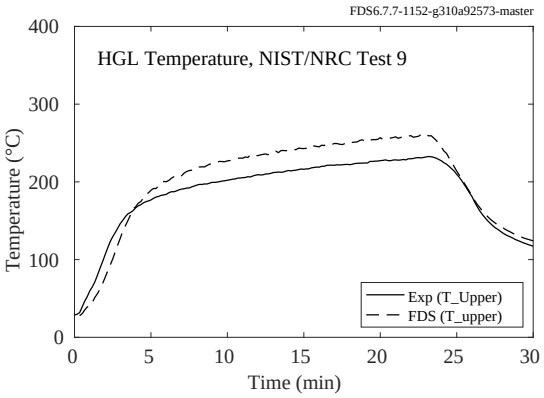

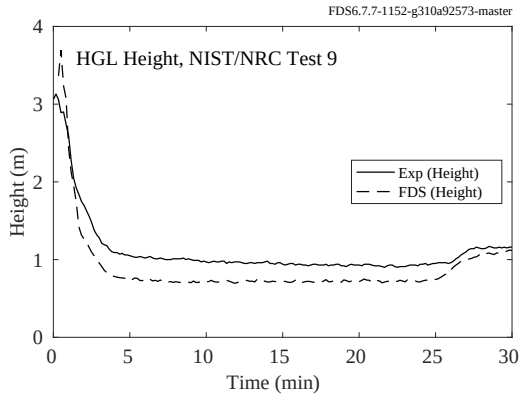

Figure 5.43: NIST/NRC experiments, HGL temperature and height, Tests 3, 9, 17.

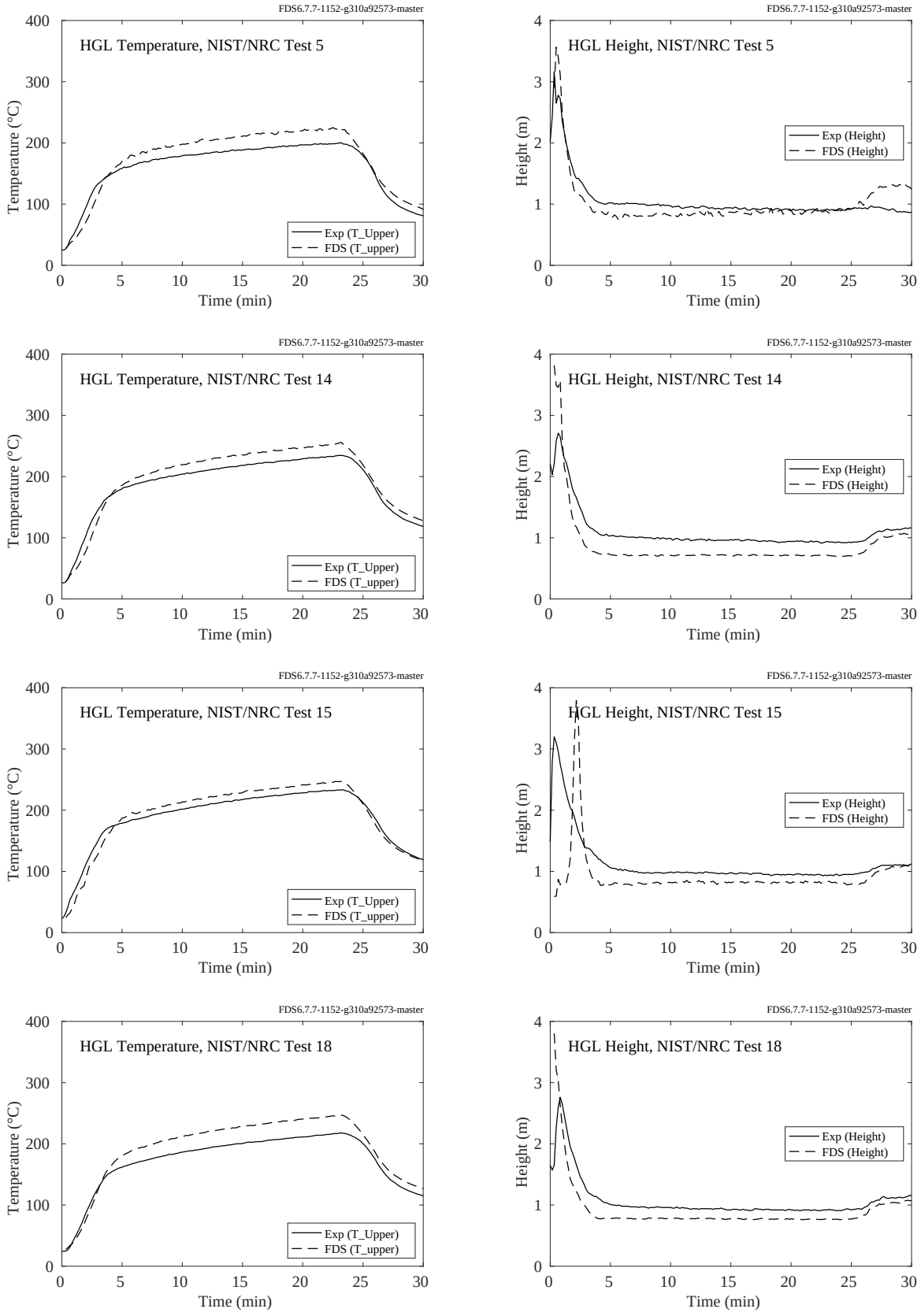

Figure 5.44: NIST/NRC experiments, HGL temperature and height, Tests 5, 14, 15, 18.

5.12 NIST/NRC Corner Effects Experiments

The plots on the following pages compare hot gas layer temperatures and heights in a large compartment where corner, wall, and cabinet effects experiments were conducted. The corner and wall experiments involved a 60 cm by 60 cm natural gas burner with heat release rates of 200 kW, 300 kW, and 400 kW. The burner was either set in a corner or against a wall. The cabinet experiments involved gas burners set in one of two mock steel cabinets, with a variety of heat release rates.

In all experiments, two vertical thermocouple arrays were placed along the centerline of the room, each one-third of the room length from each respective short wall. The arrays each had 13 bare-bead thermocouples. The first was 2 cm below the ceiling, and the rest were spaced 30 cm apart.

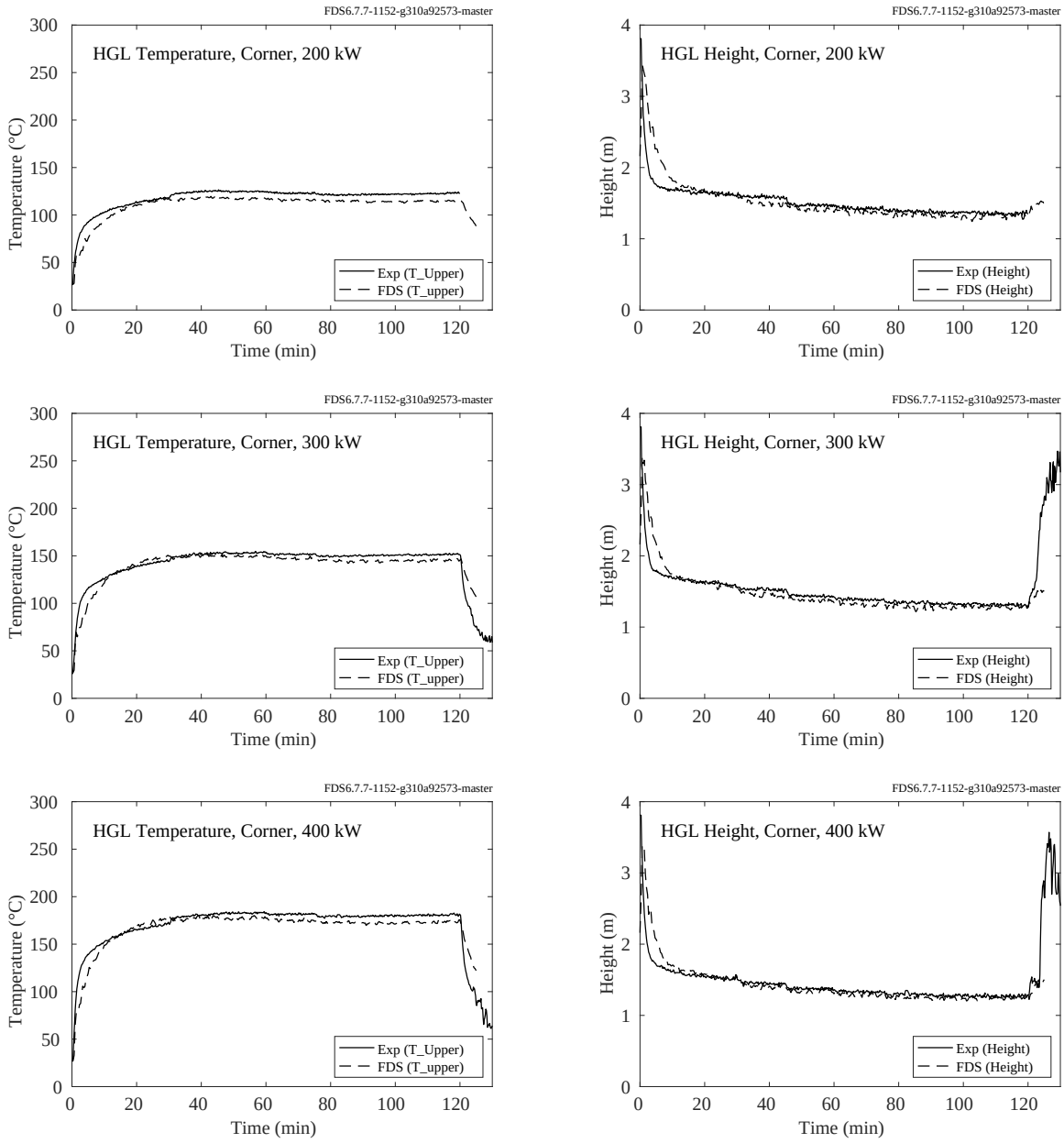

Figure 5.45: NIST/NRC Corner Effects experiments, HGL temperature and height, corner experiments.

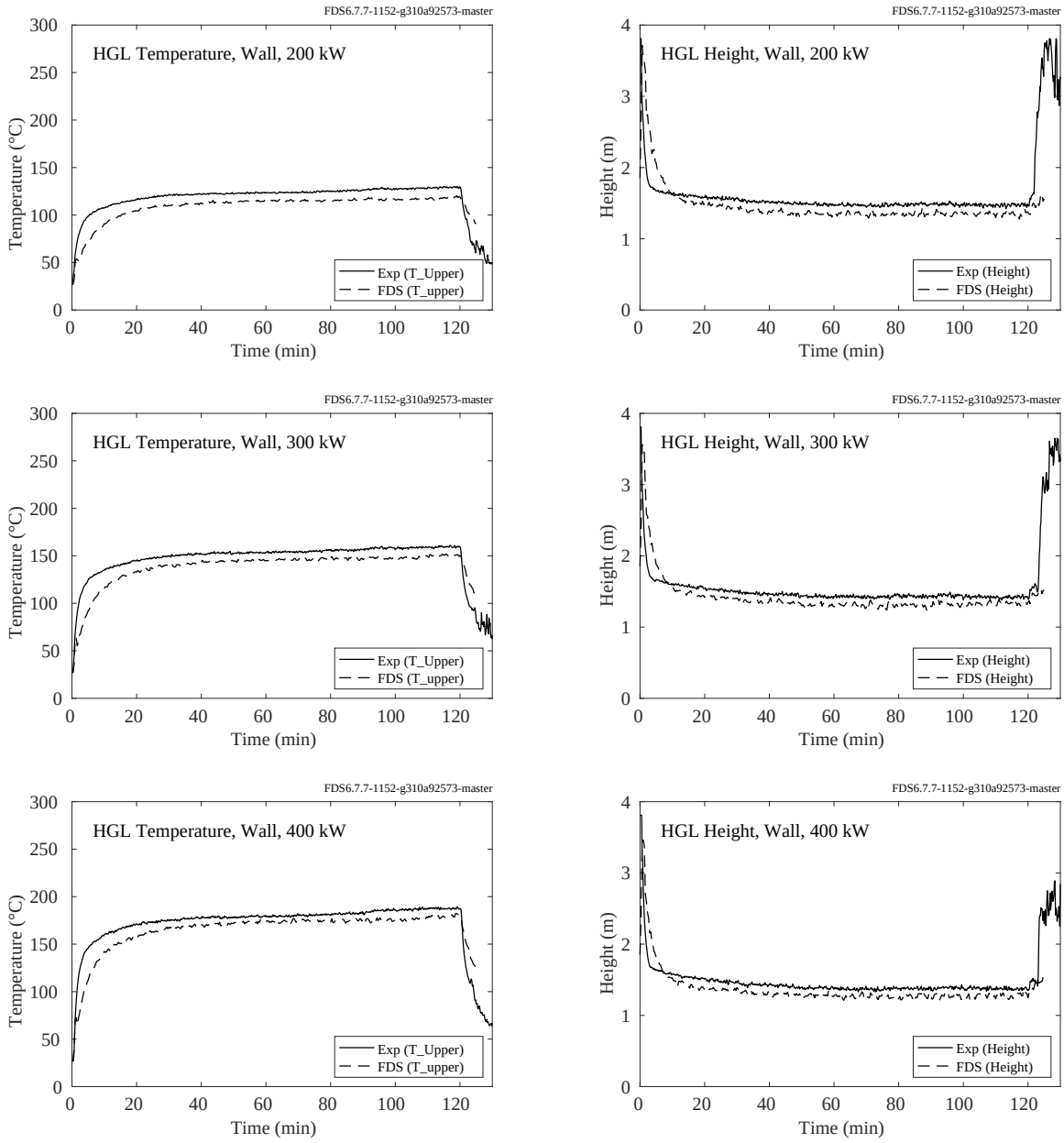

Figure 5.46: NIST/NRC Corner Effects experiments, HGL temperature and height, wall experiments.

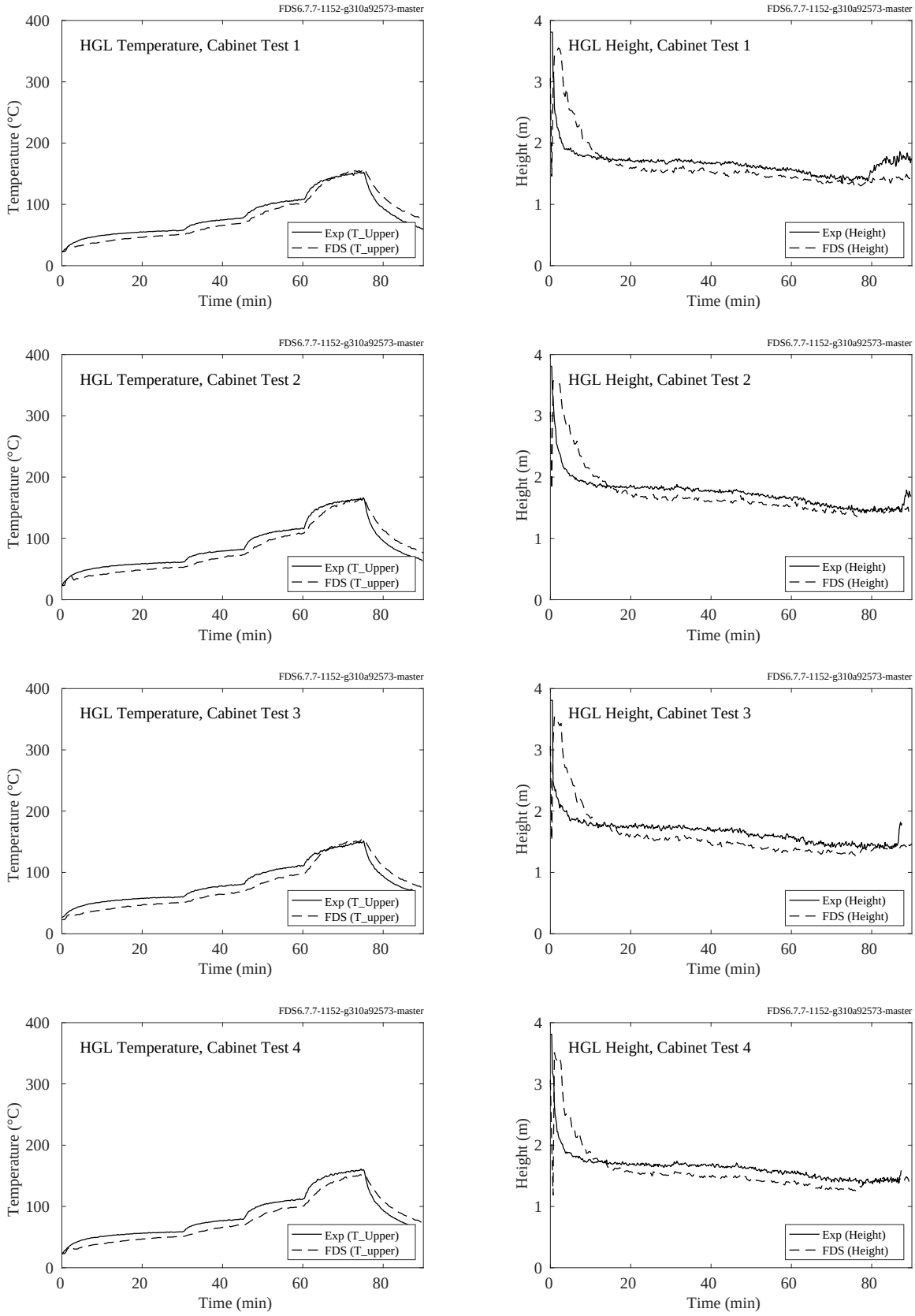

Figure 5.47: NIST/NRC Corner Effects experiments, HGL temperature and height, cabinet experiments 1-4.

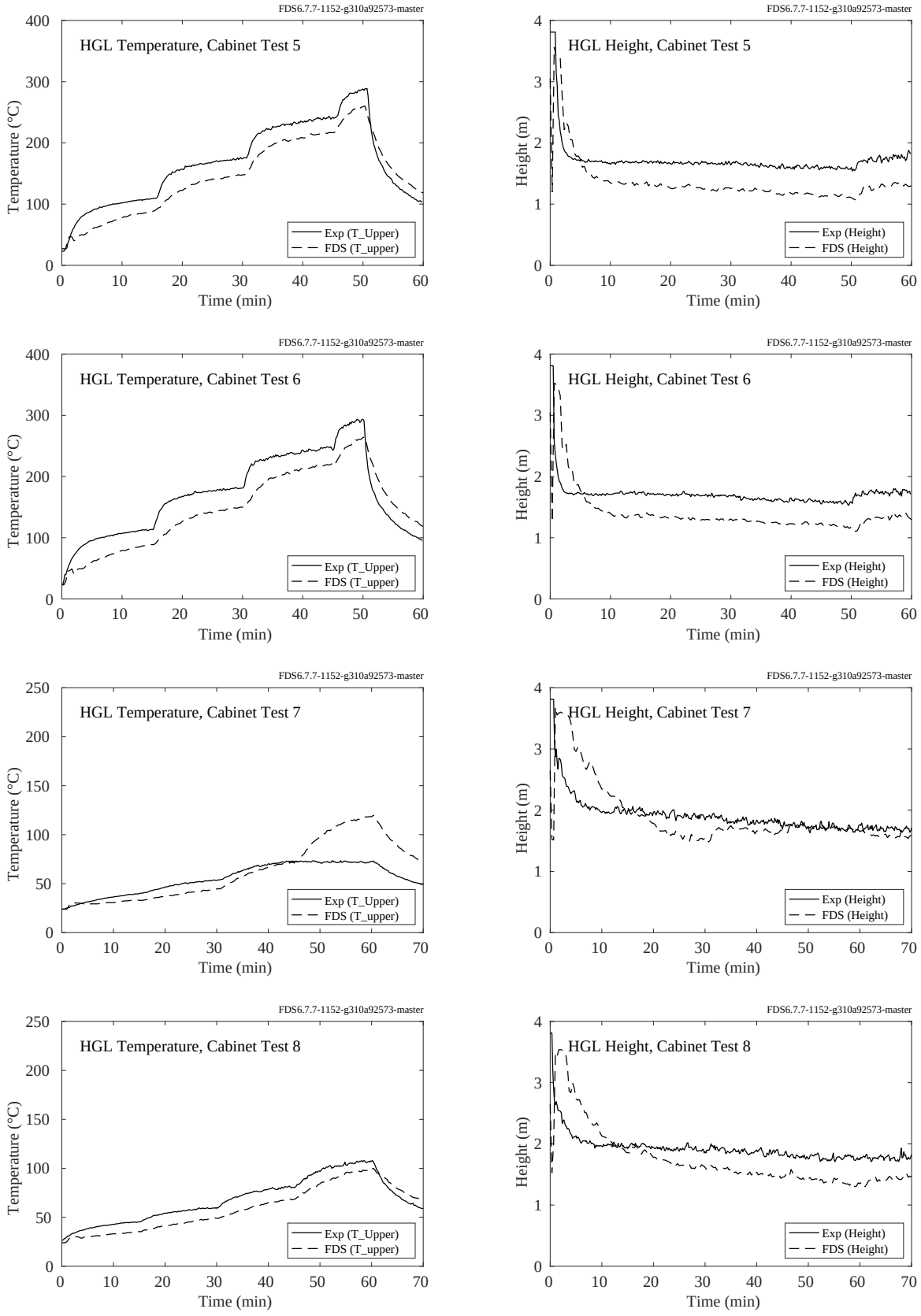

Figure 5.48: NIST/NRC Corner Effects experiments, HGL temperature and height, cabinet experiments 5-8.

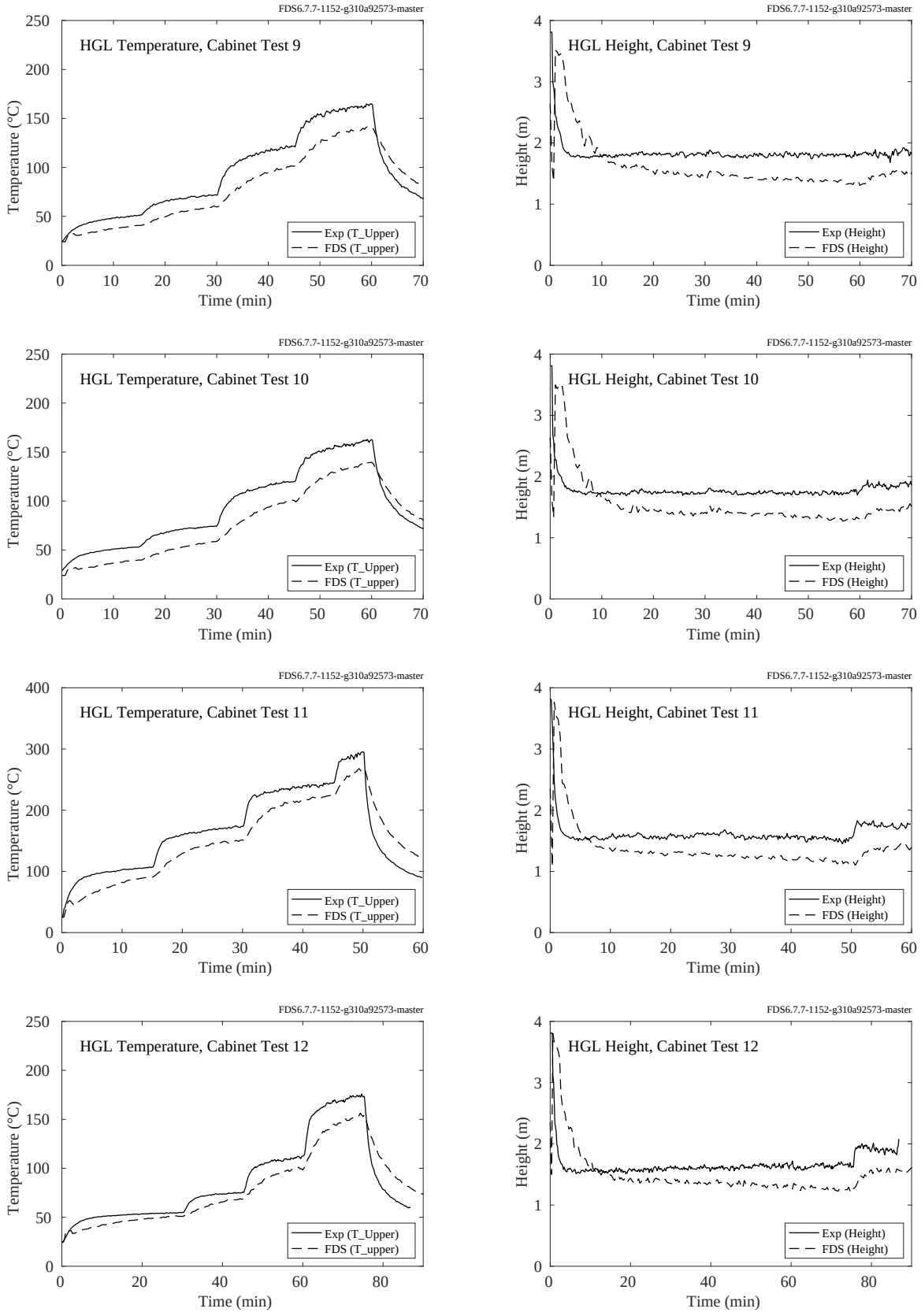

Figure 5.49: NIST/NRC Corner Effects experiments, HGL temperature and height, cabinet experiments 9-12.

5.13 NIST Vent Study

These experiments were performed in a small-scale two floor enclosure, with each floor connected by one or two ceiling vents. Each floor contained a vertical array of eight sheathed thermocouples at distances below the ceiling of 5, 10, 15, 20, 25, 30, 40, and 50 cm. Fifteen experiments were performed, but only 12 were modeled because three experiments involved a circular vent rather than square which could not be distinguished in the FDS simulations. The results of these experiments were nearly identical.

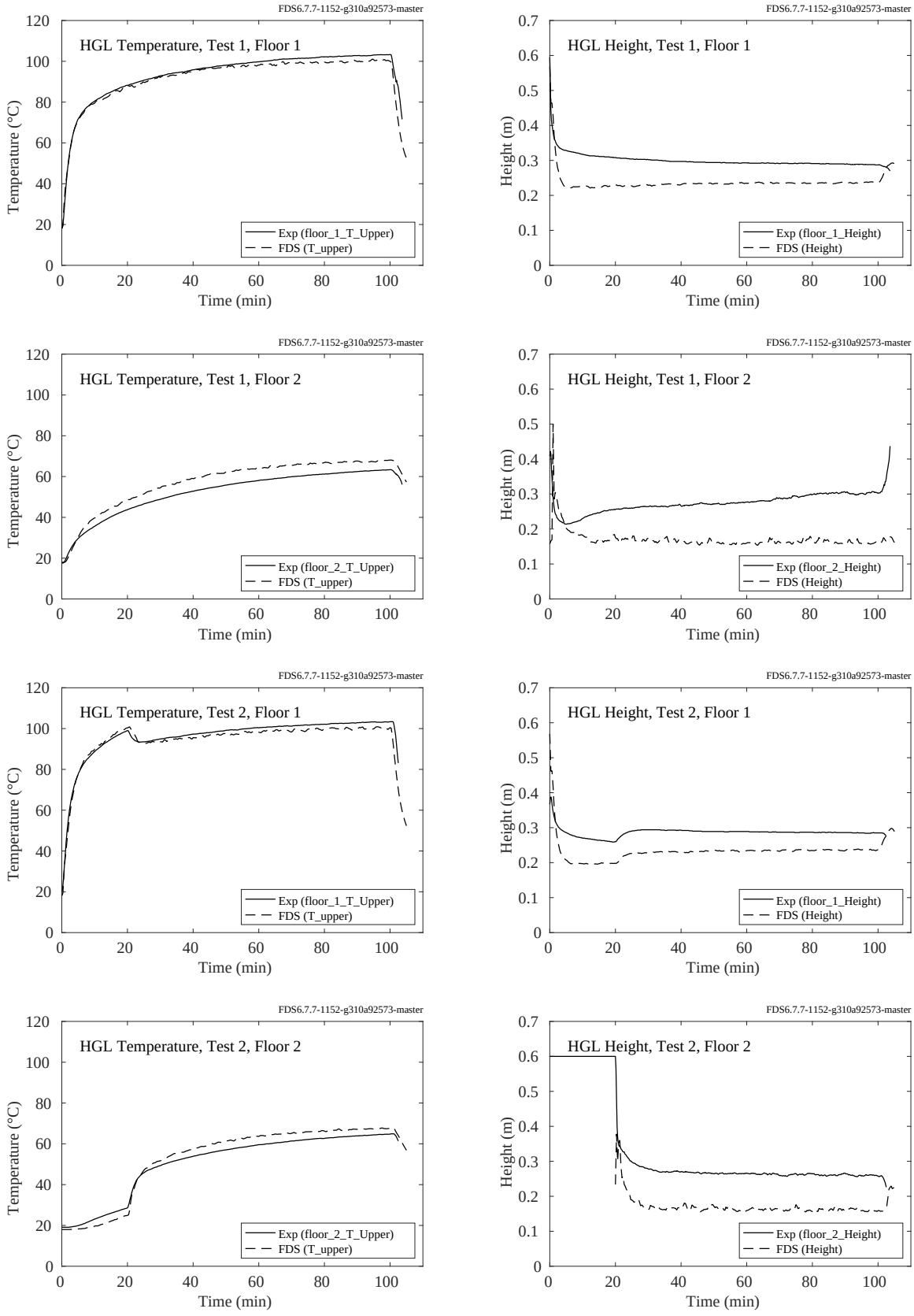

Figure 5.50: NIST Vent Study, HGL temperature and height, Tests 1 and 2.

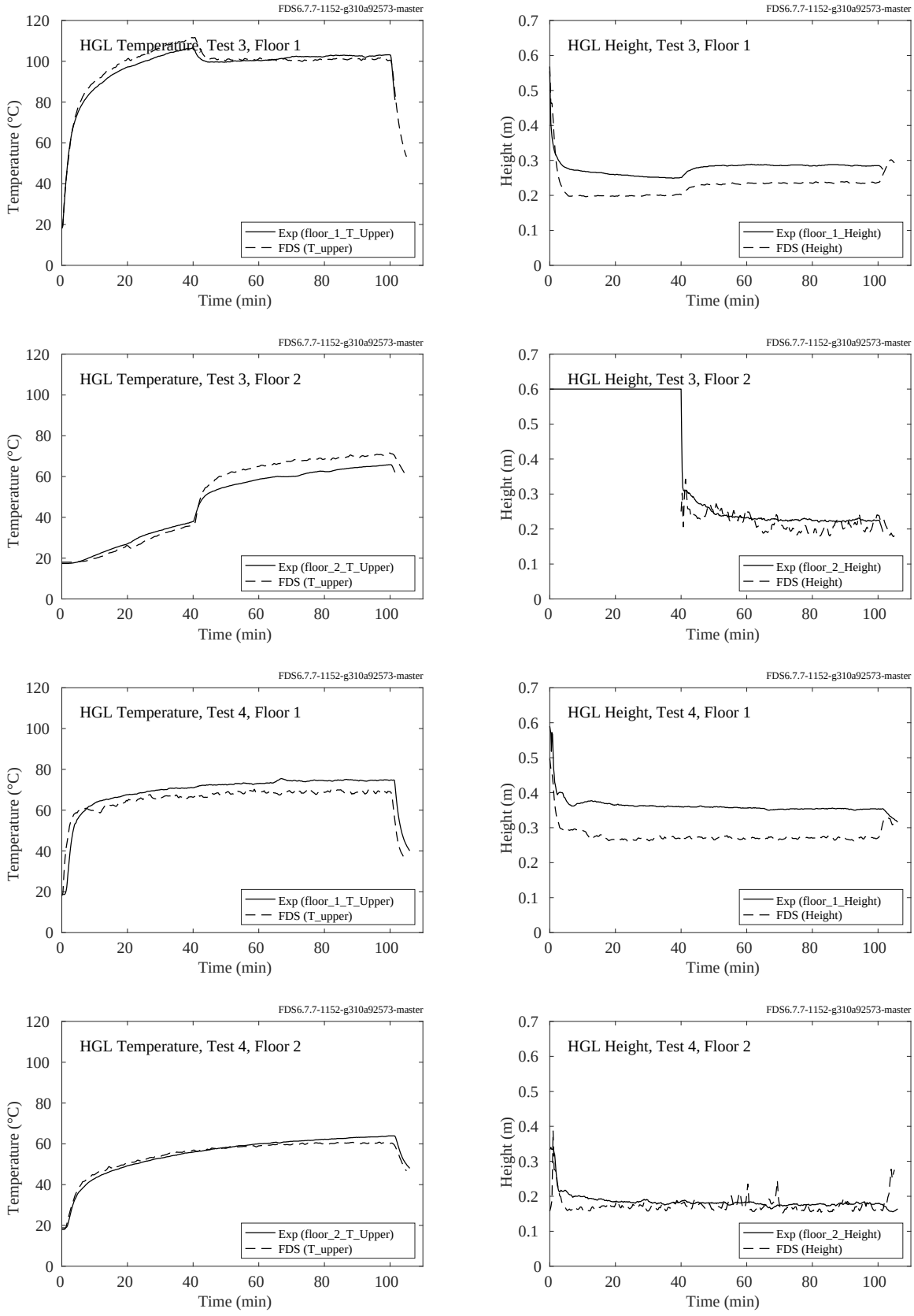

Figure 5.51: NIST Vent Study, HGL temperature and height, Tests 3 and 4.

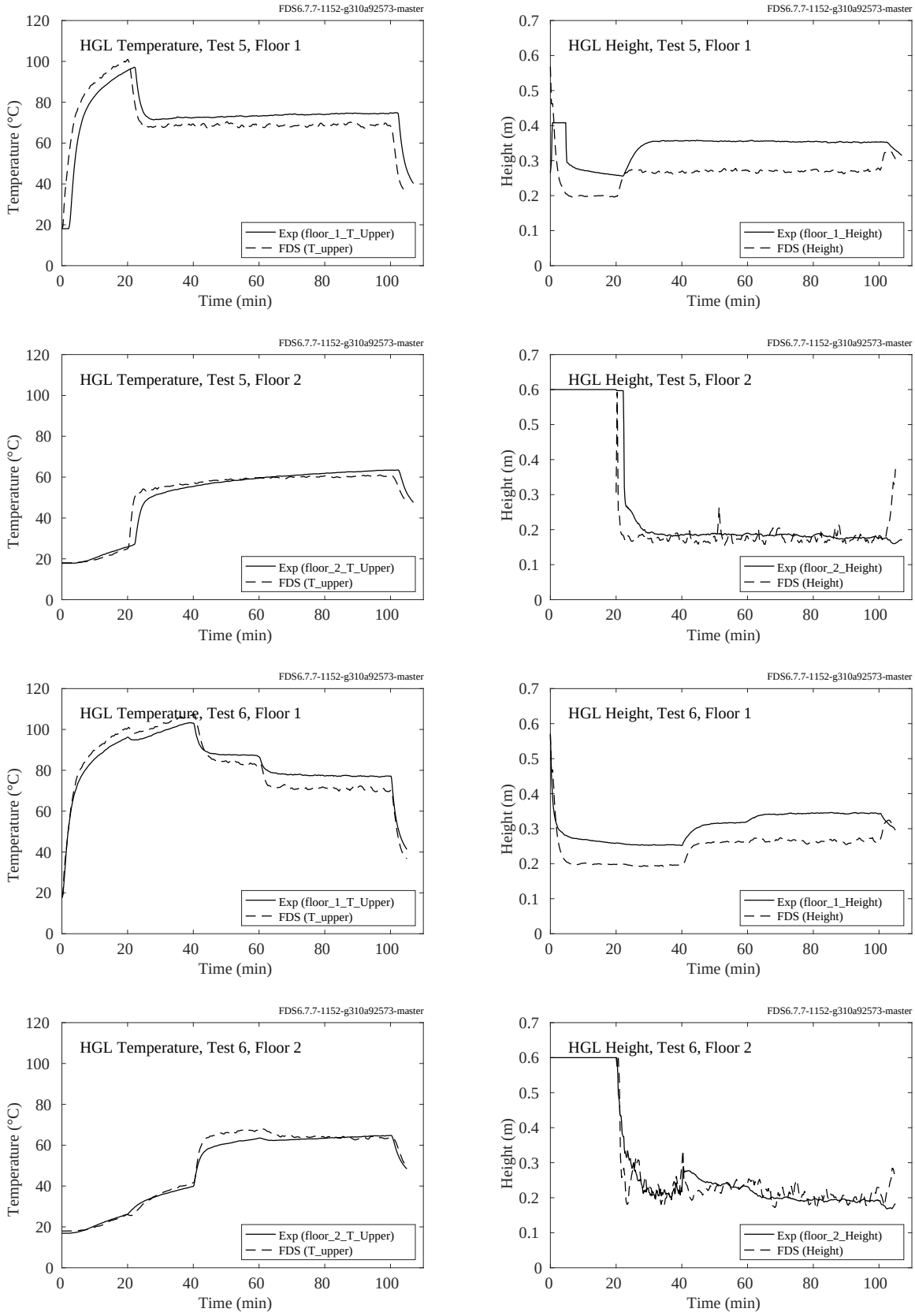

Figure 5.52: NIST Vent Study, HGL temperature and height, Tests 5 and 6.

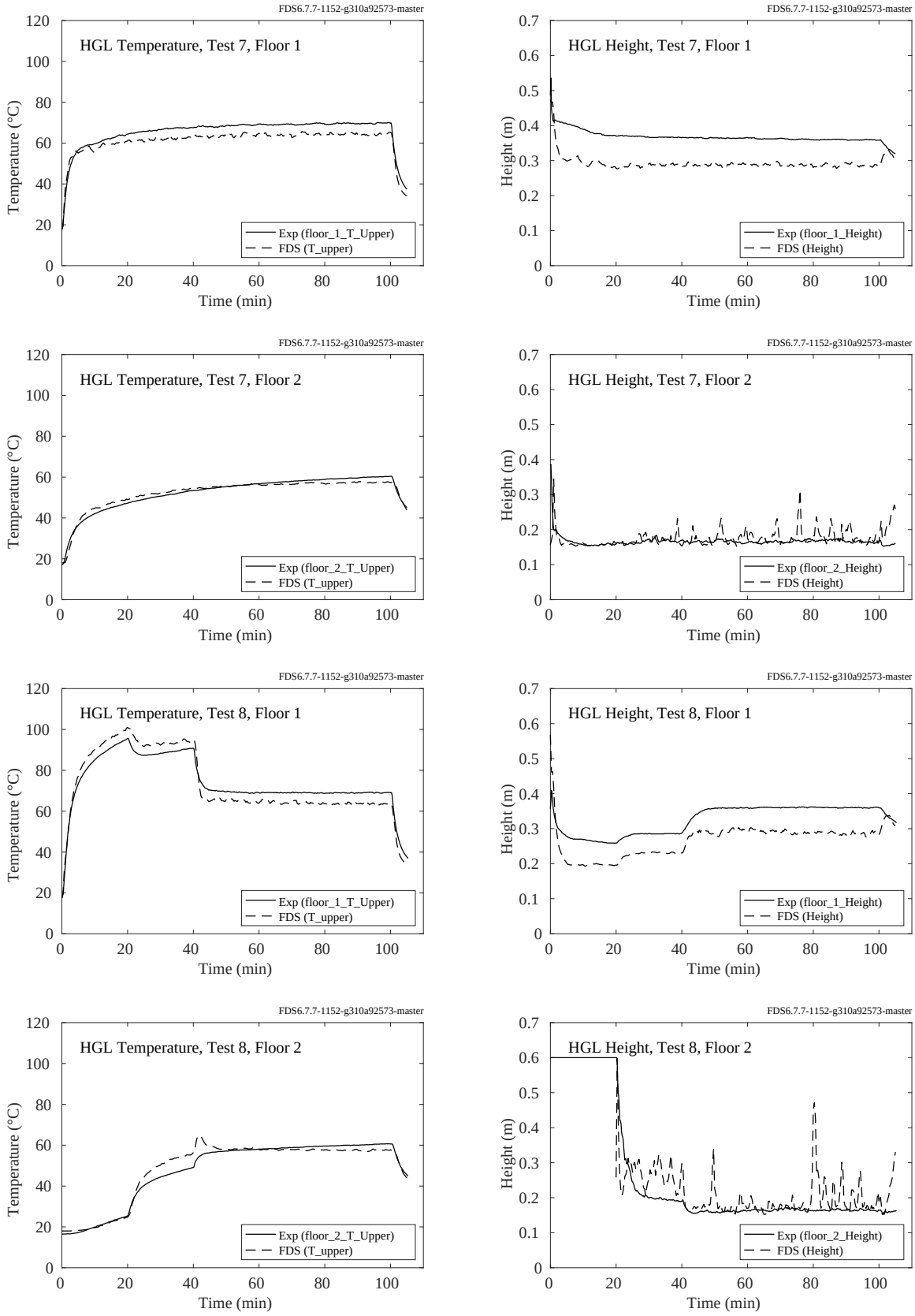

Figure 5.53: NIST Vent Study, HGL temperature and height, Tests 7 and 8.

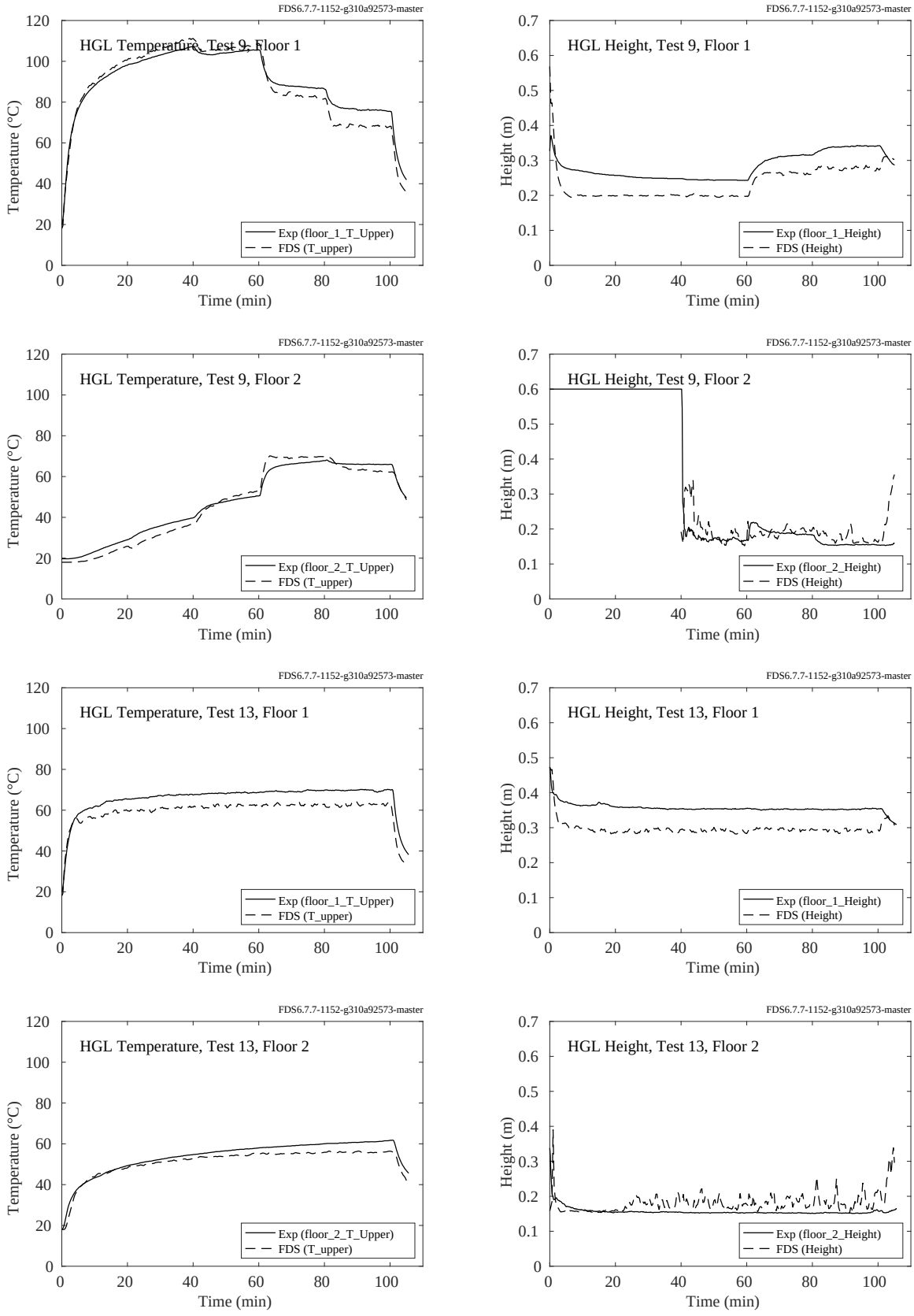

Figure 5.54: NIST Vent Study, HGL temperature and height, Tests 9 and 13.

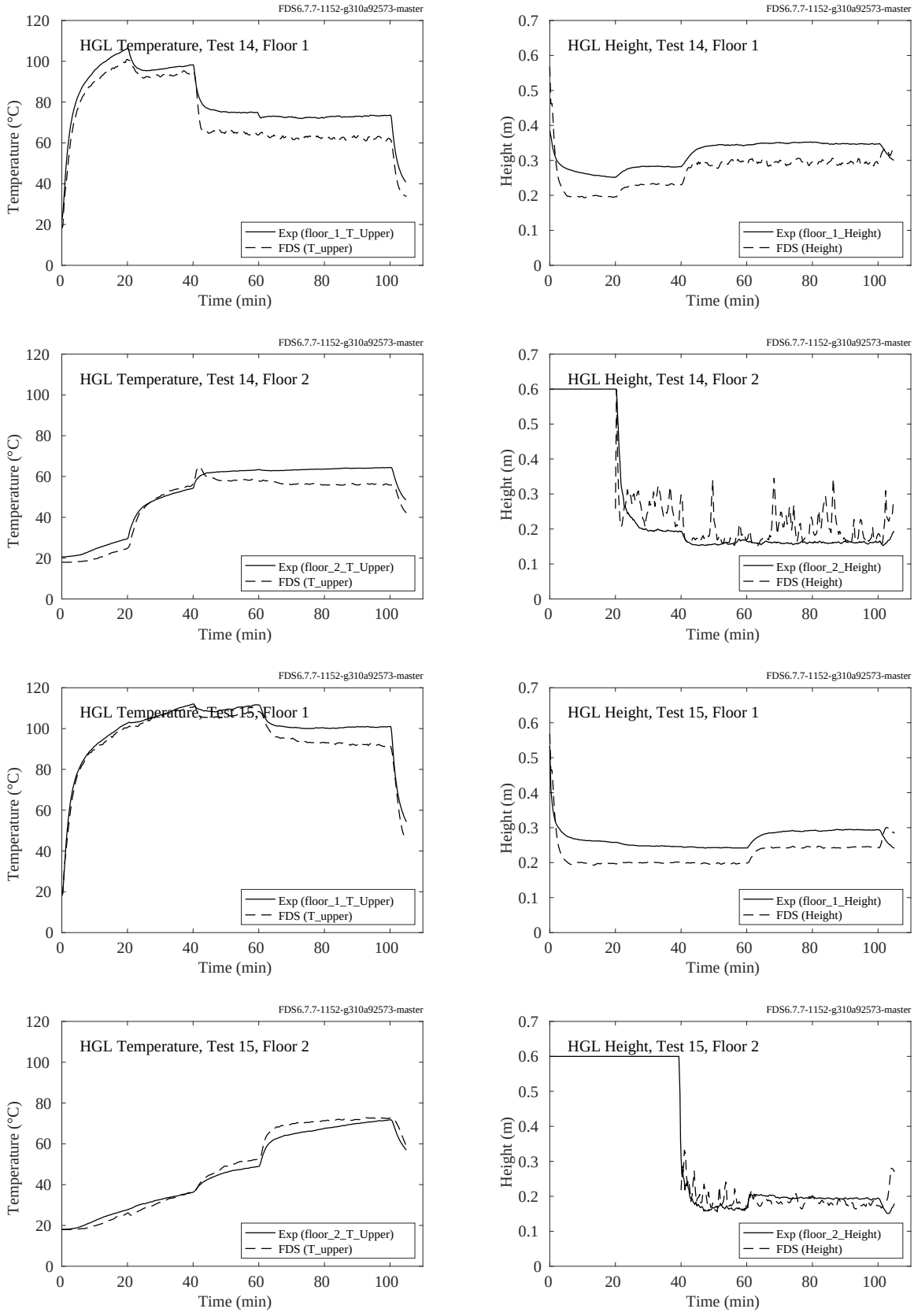

Figure 5.55: NIST Vent Study, HGL temperature and height, Tests 14 and 15.

5.14 NRCC Smoke Tower

In the NRCC Smoke Tower experiments, there was a vertical array consisting of thirteen TCs that were installed in the fire compartment on the second floor at the following heights: 0.62 m, 0.92 m, 1.22 m, 1.37 m, 1.52 m, 1.67 m, 1.82 m, 1.97 m, 2.12 m, 2.27 m, 2.42 m, 2.57 m and 2.95 m. Also, five TCs were installed in the doorway between the stair vestibule and stair shaft on the second floor. Figure 5.56 shows the predicted and measured HGL temperature for both vertical arrays.

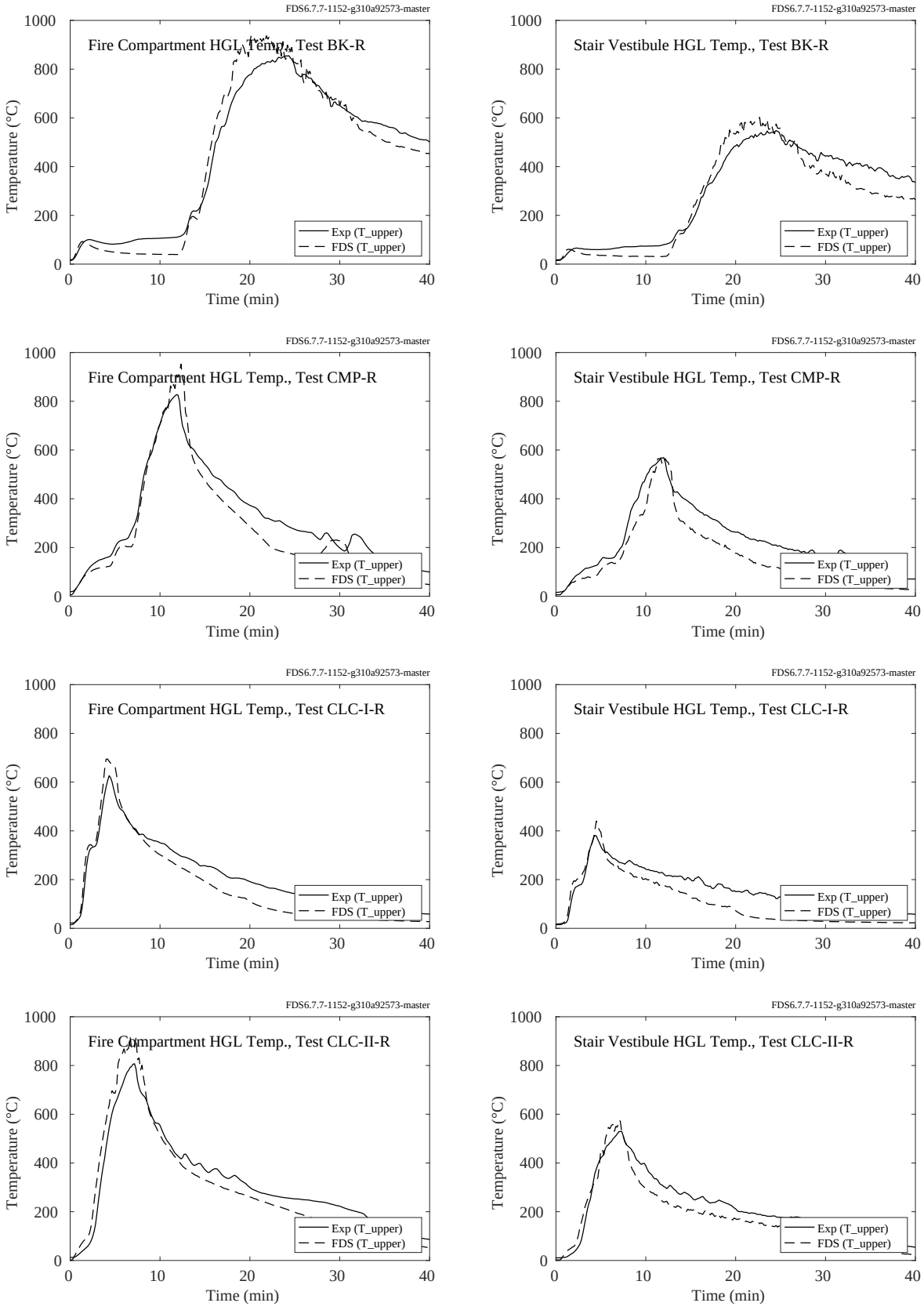

Figure 5.56: NRCC Smoke Tower experiments, HGL temperature in the fire room and stair vestibule.

5.15 PRISME DOOR Experiments

The compartments in the PRISME DOOR experiments contained vertical arrays of thermocouples to measure the HGL temperature and depth. Each array contained 18 TCs and each compartment included three arrays. The array above the fire was excluded from the calculation of the HGL temperature and depth.

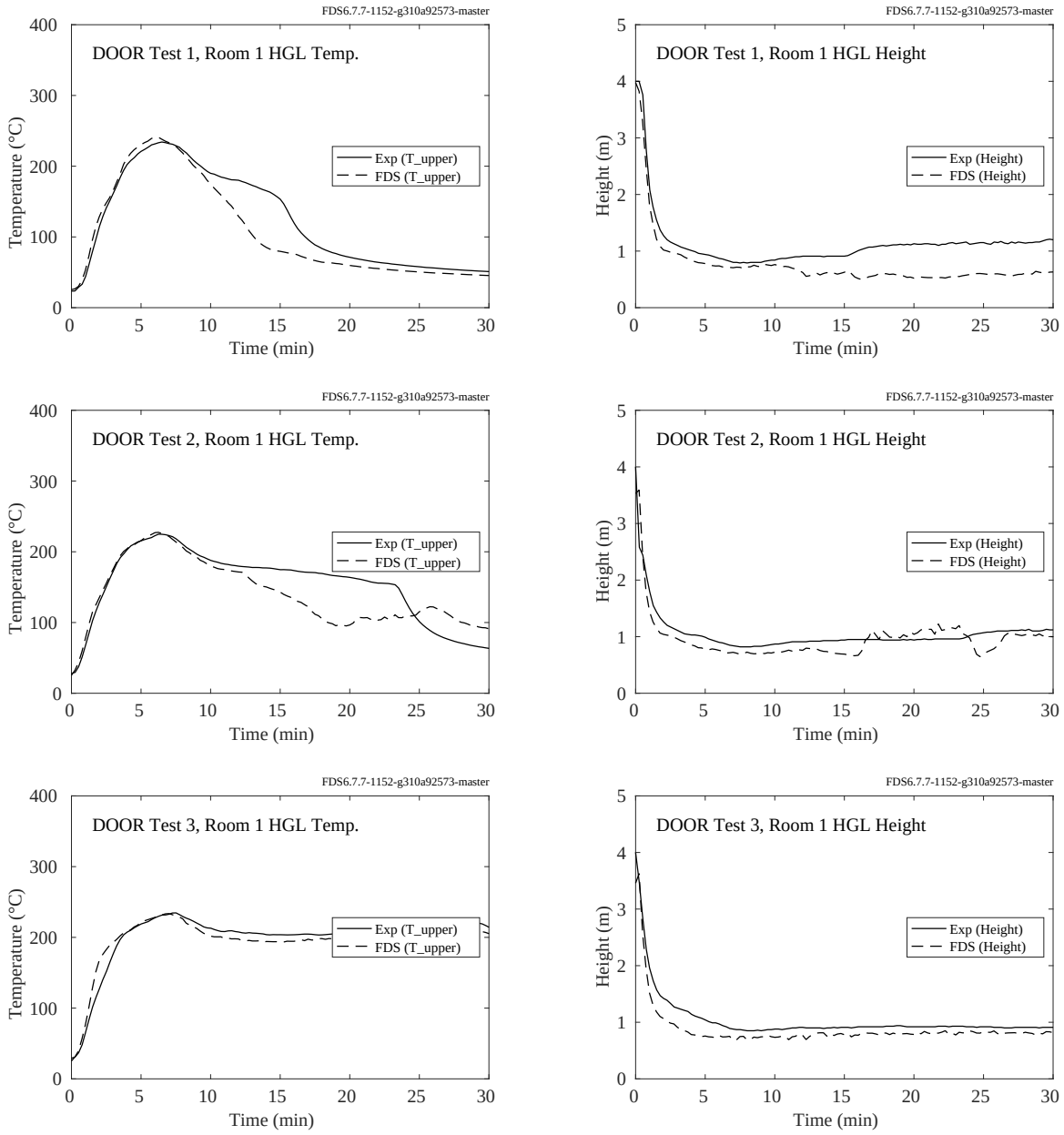

Figure 5.57: PRISME DOOR experiments, HGL temperature and height, Room 1, Tests 1-3.

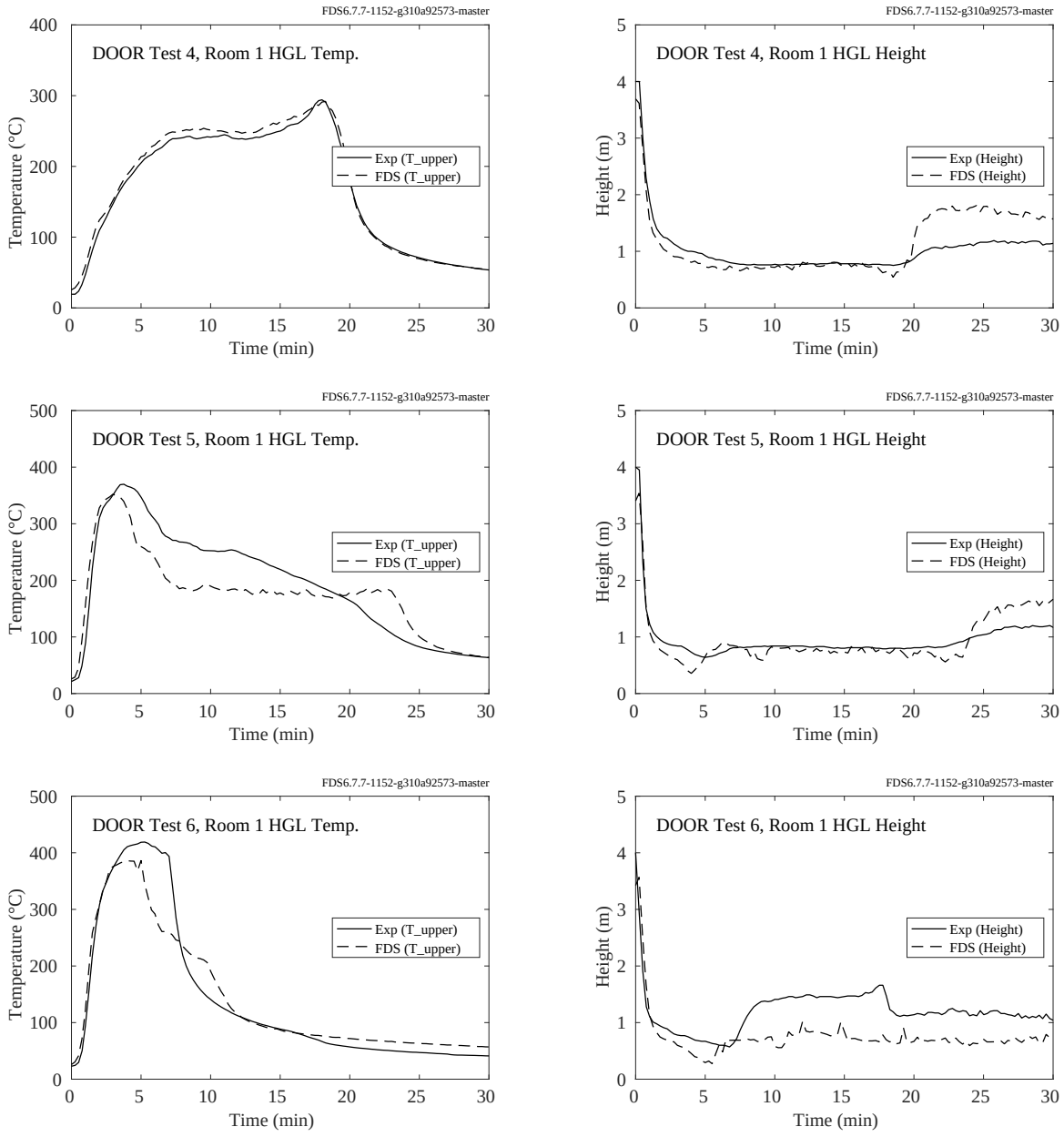

Figure 5.58: PRISME DOOR experiments, HGL temperature and height, Room 1, Tests 4-6.

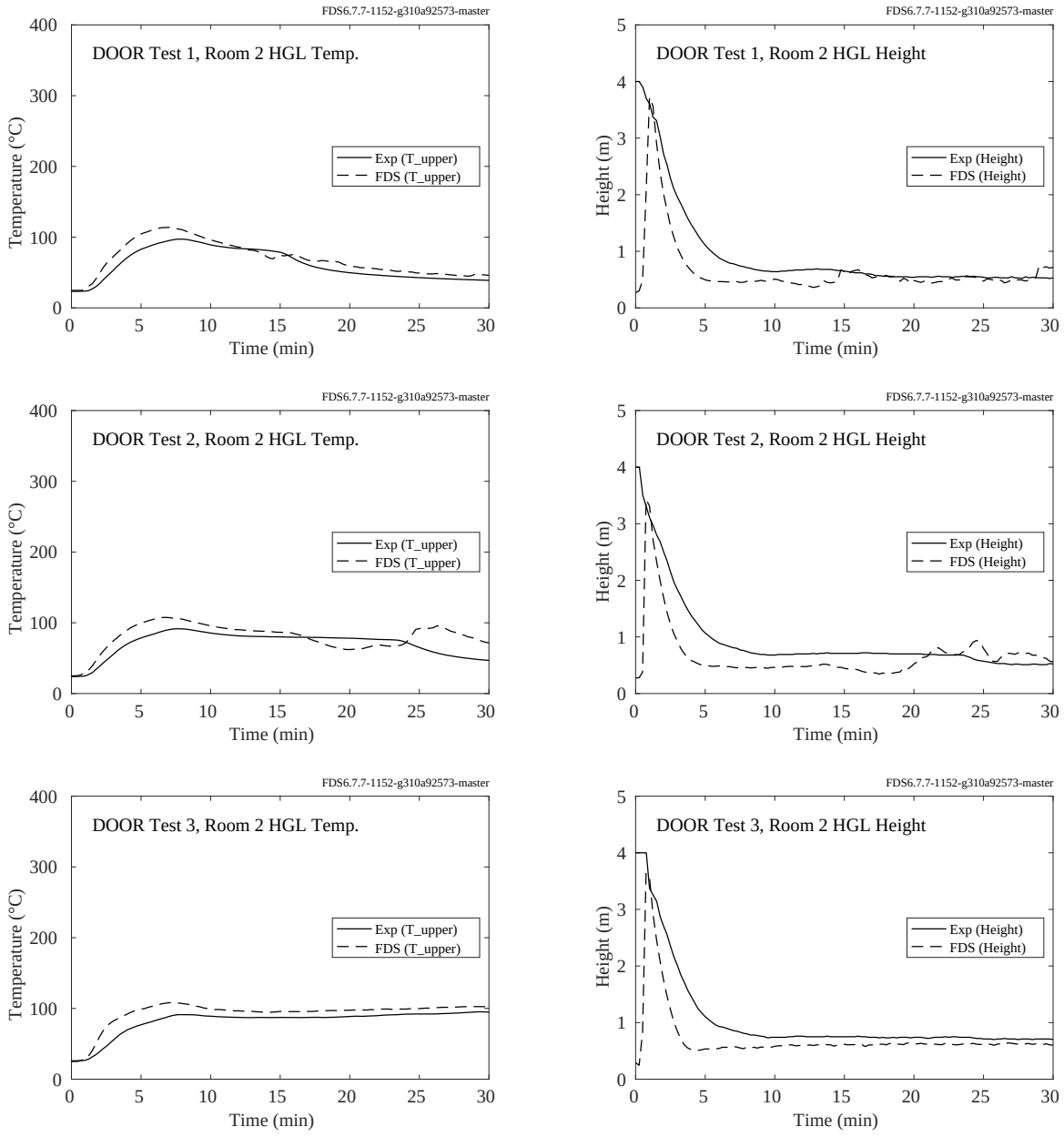

Figure 5.59: PRISME DOOR experiments, HGL temperature and height, Room 2, Tests 1-3.

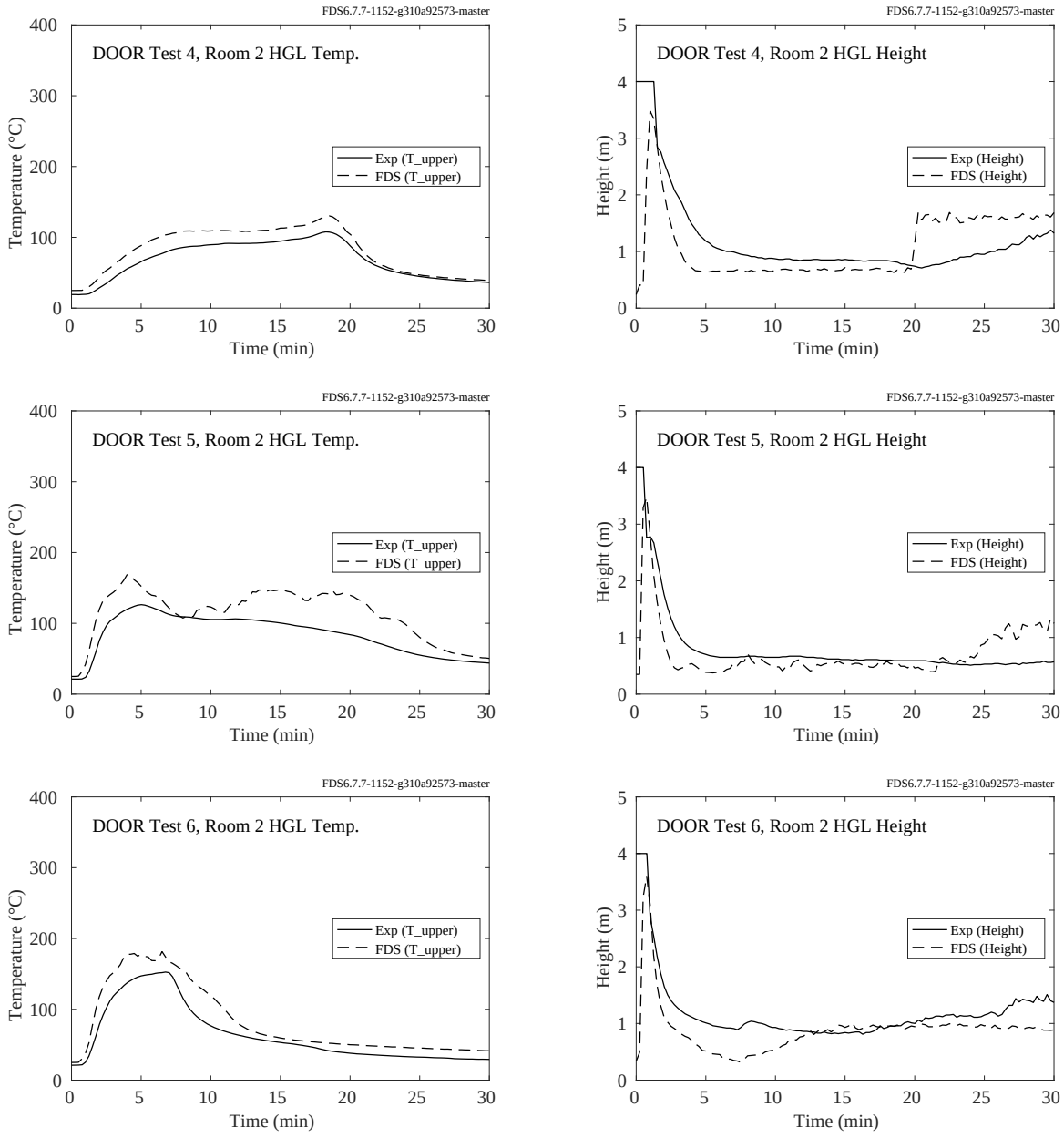

Figure 5.60: PRISME DOOR experiments, HGL temperature and height, Room 1, Tests 4-6.

5.16 PRISME SOURCE Experiments

The PRISME SOURCE experiments were conducted in a single compartment connected to an HVAC network. The compartment was 5 m by 6 m by 4 m high. The HGL temperature was computed from a single vertical thermocouple array located in the northeast quadrant of the compartment. The array contained 18 TCs; the highest one 0.1 m below the ceiling.

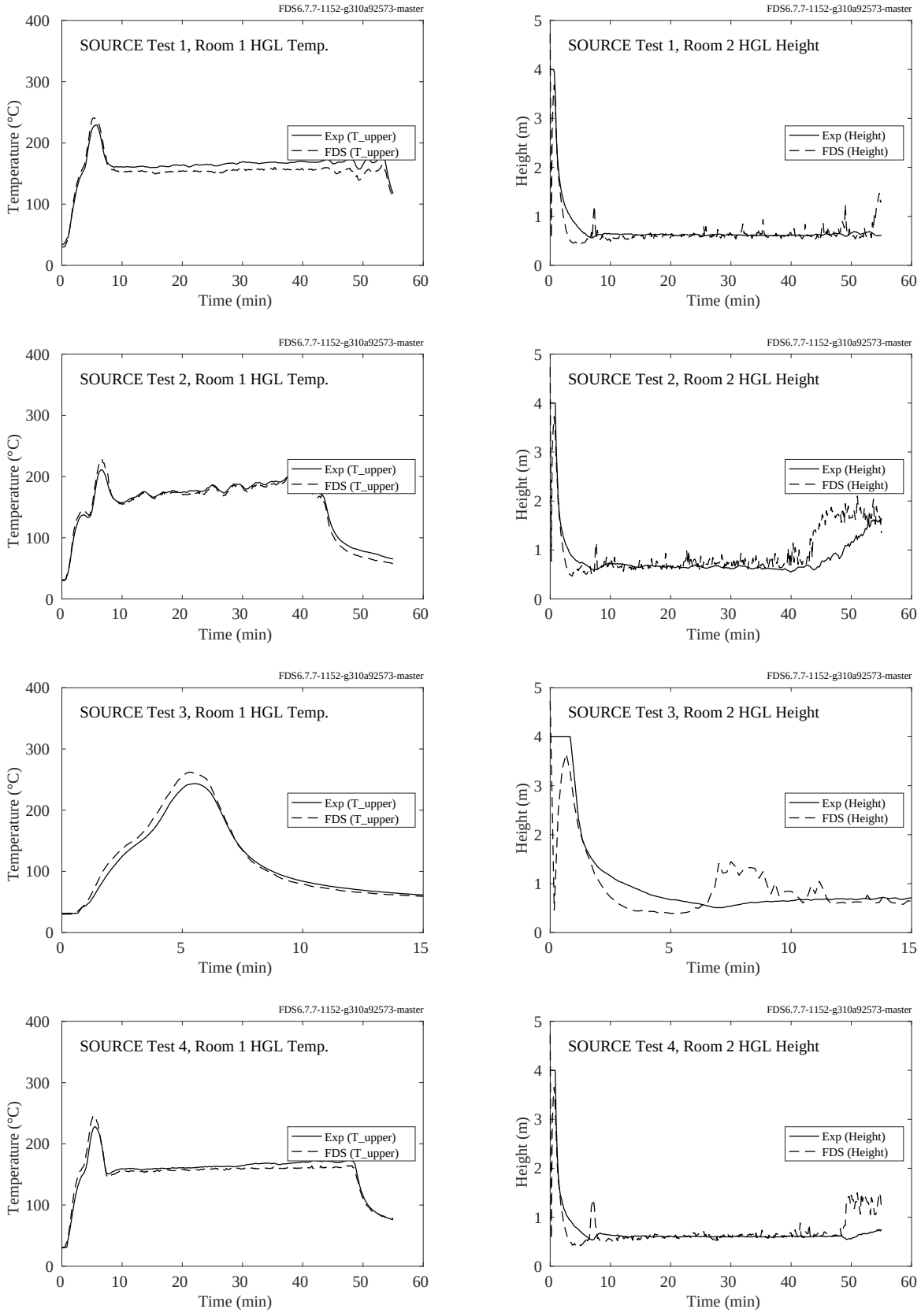

Figure 5.61: PRISME SOURCE experiments, HGL temperature and height, Room 2, Tests 1-4.

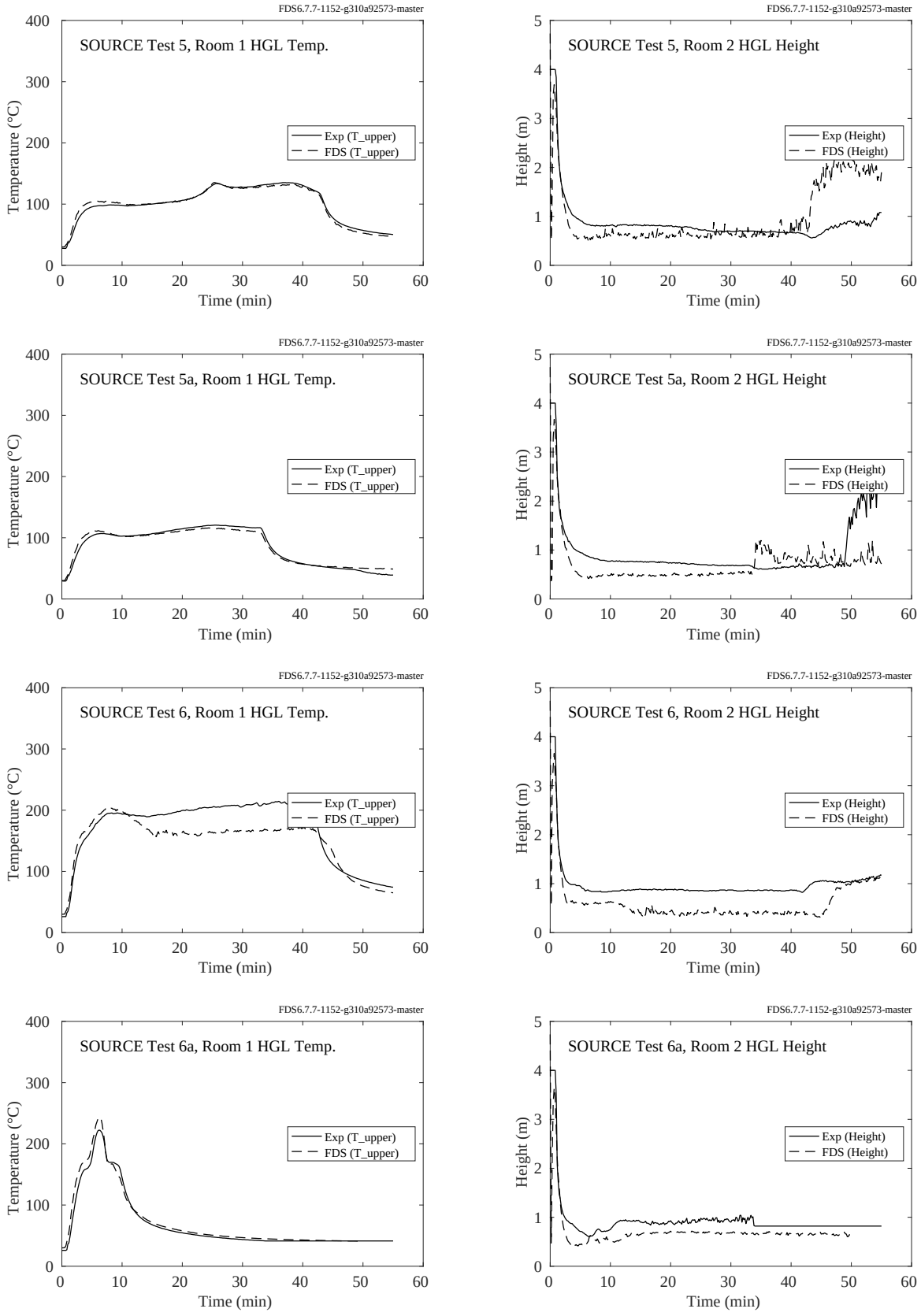

Figure 5.62: PRISME SOURCE experiments, HGL temperature and height, Room 2, Tests 5-6.

5.17 Steckler Compartment Experiments

Steckler et al. [289] mapped the doorway/window flows in 55 compartment fire experiments. The test matrix is presented in Table 3.31. Shown on the following pages are the temperature profiles inside the compartment compared with model predictions. To quantify the difference between prediction and measurement, the maximum temperatures were compared.

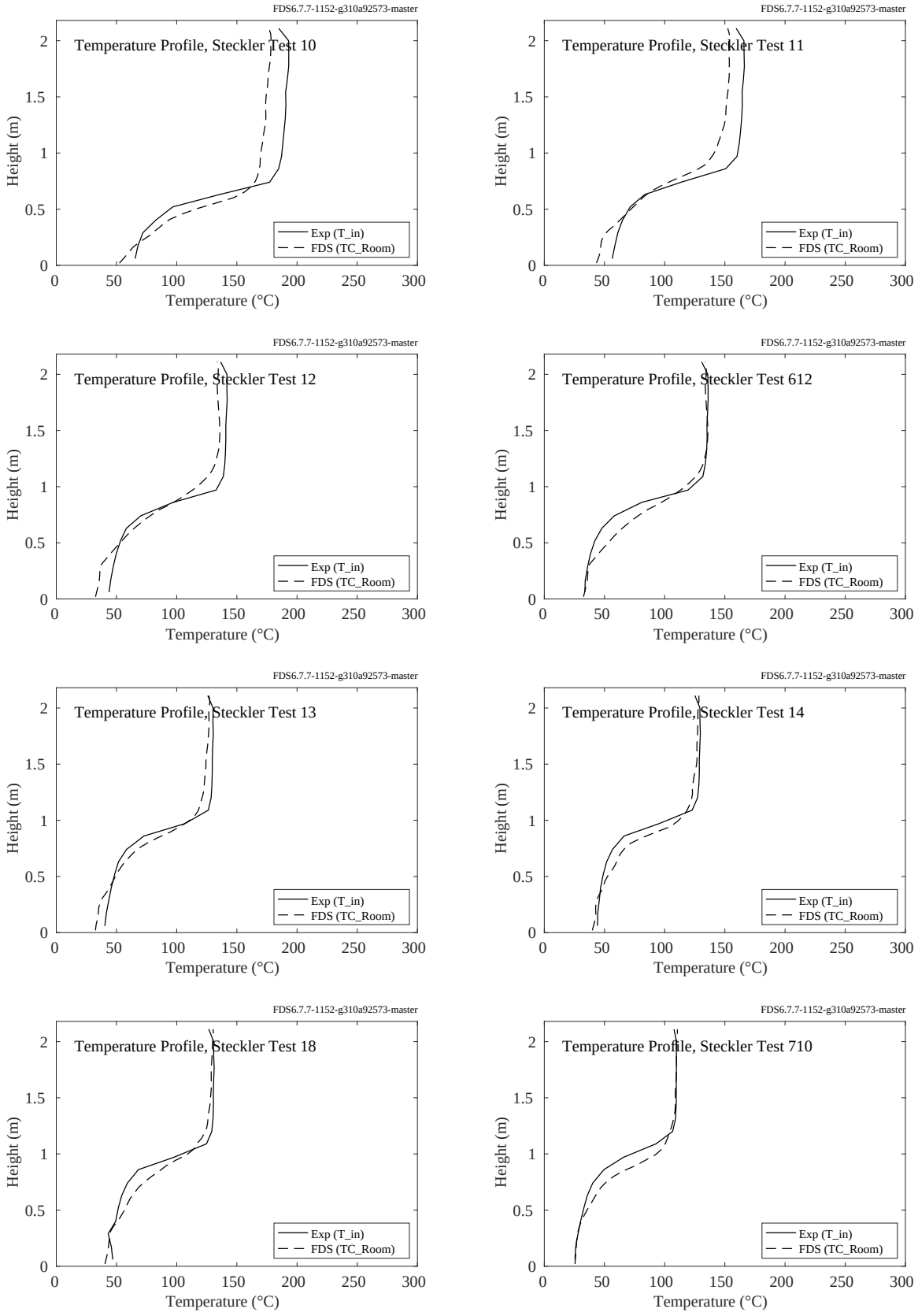

Figure 5.63: Steckler experiments, HGL temperature, Tests 10, 11, 12, 13, 14, 18, 612, 710.

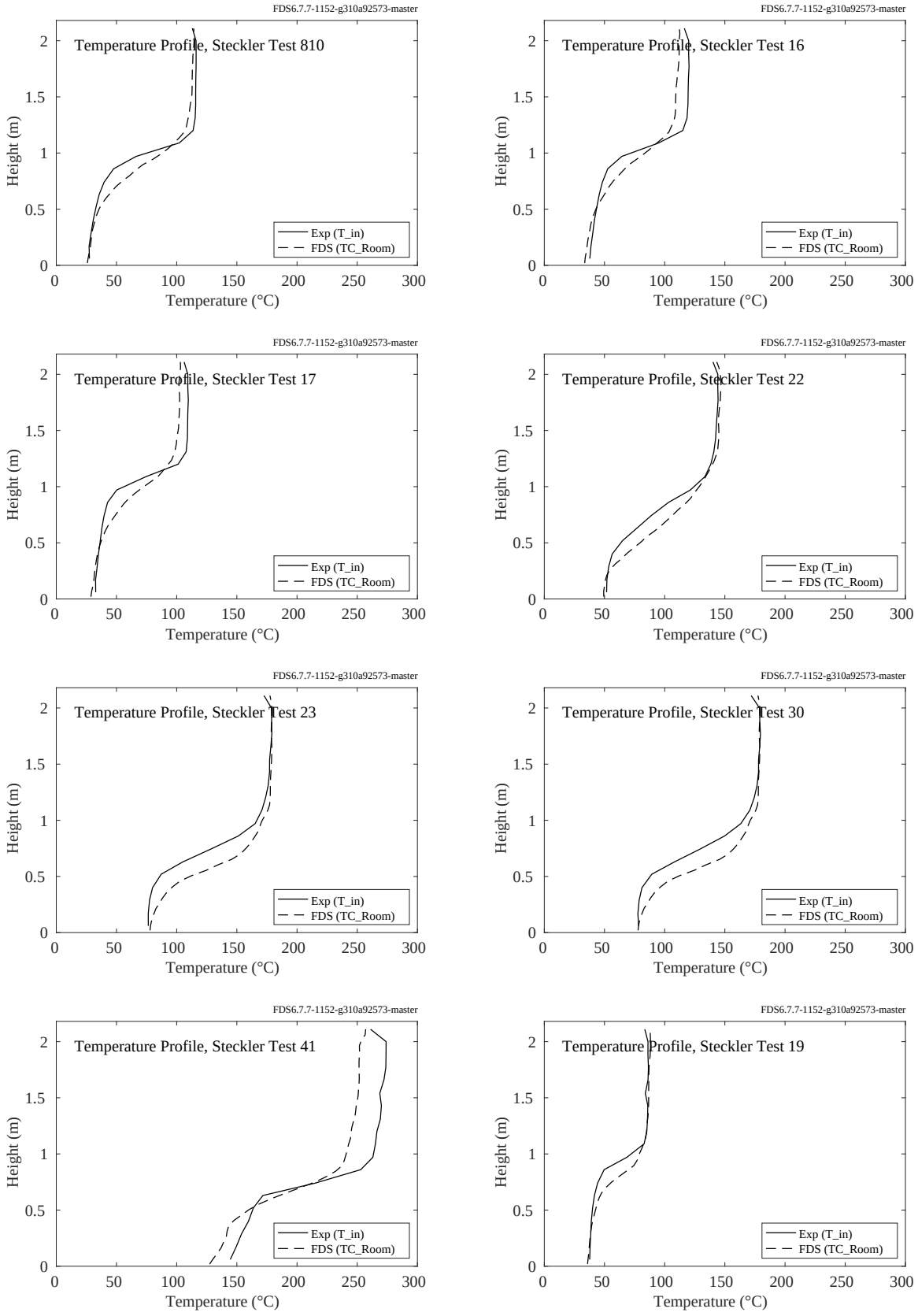

Figure 5.64: Steckler experiments, HGL temperature, Tests 16, 17, 19, 22, 23, 30, 41, 810.

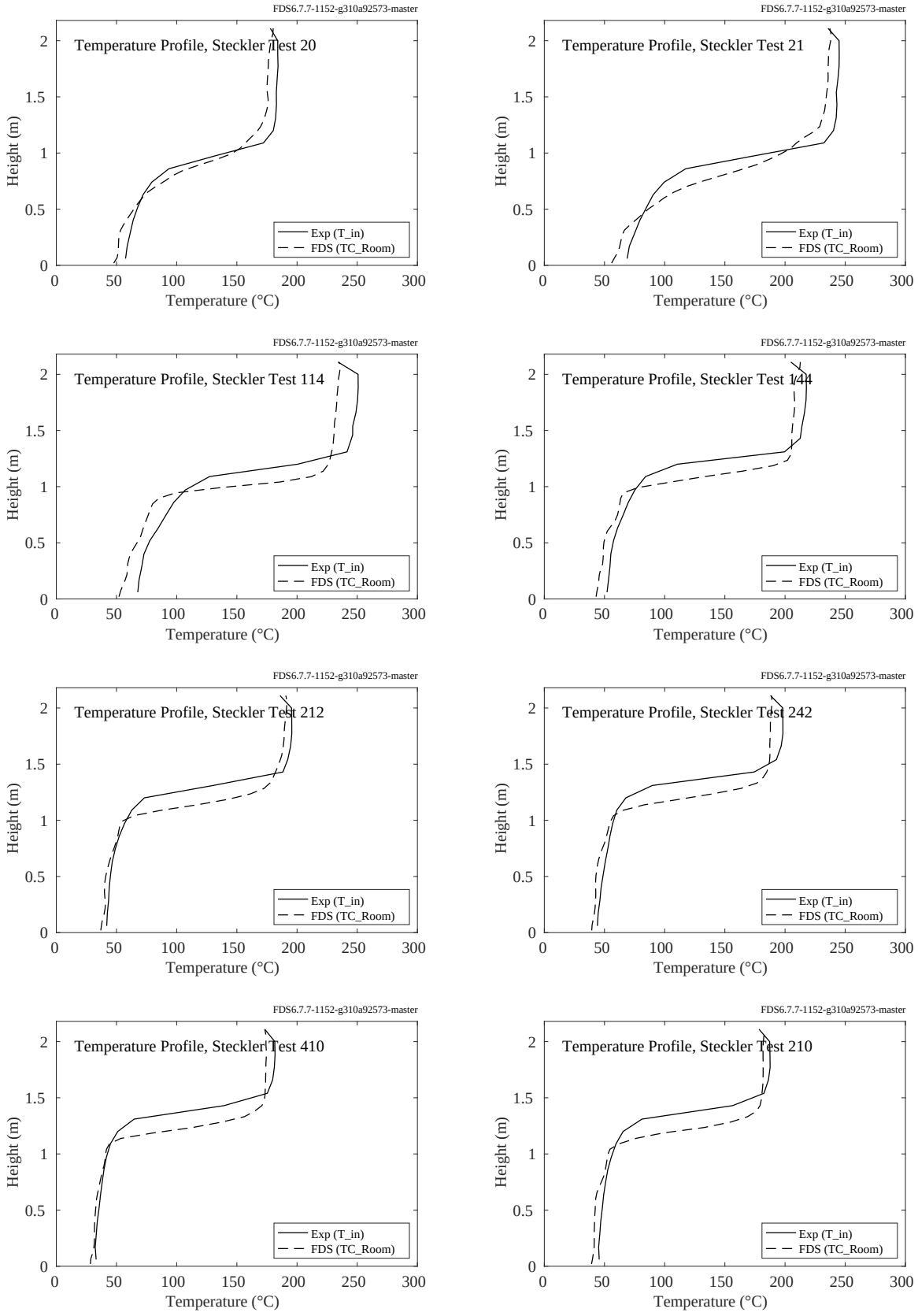

Figure 5.65: Steckler experiments, HGL temperature, Tests 20, 21, 114, 144, 210, 212, 242, 410.

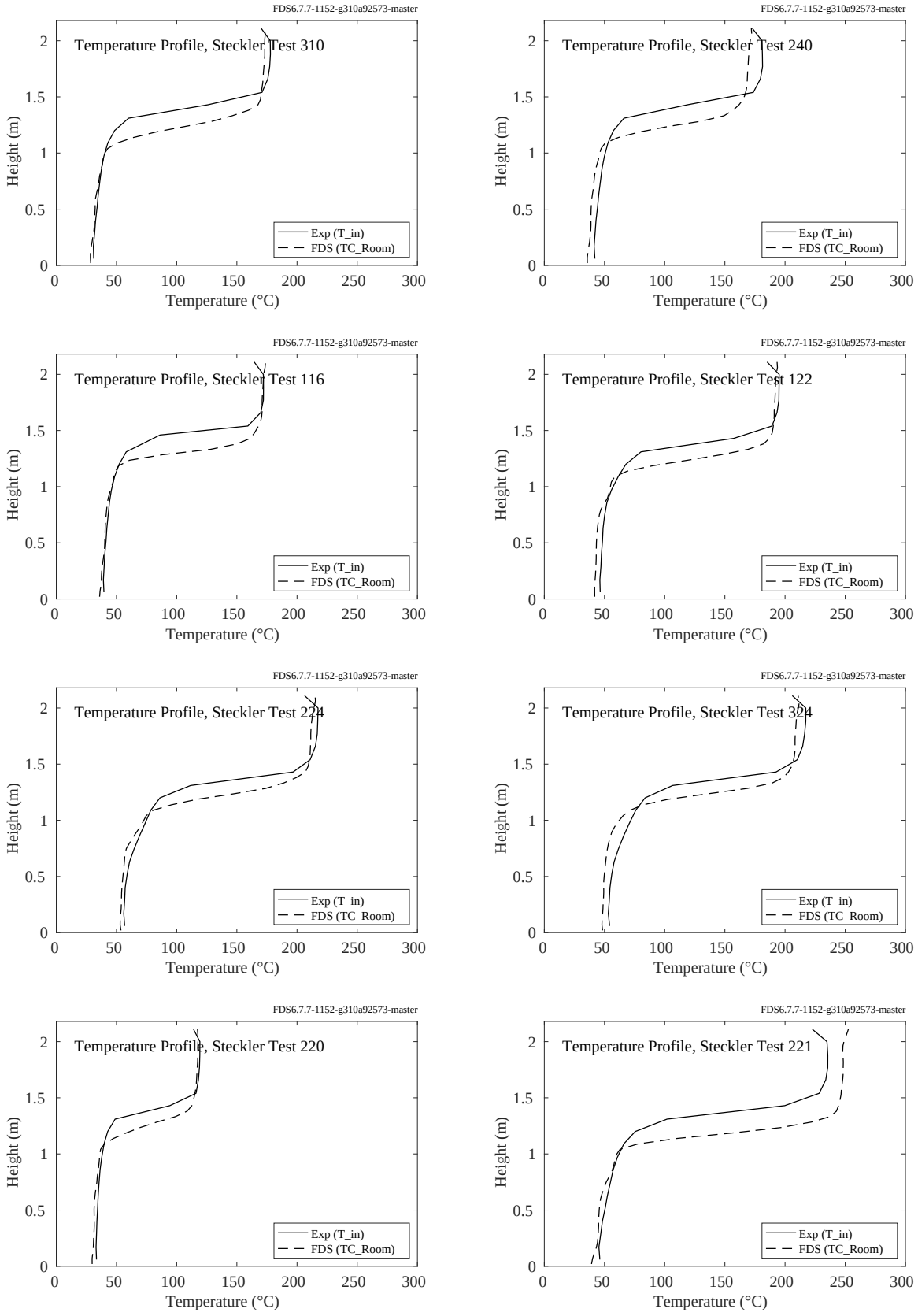

Figure 5.66: Steckler experiments, HGL temperature, Tests 116, 122, 220, 221, 224, 240,310, 324.

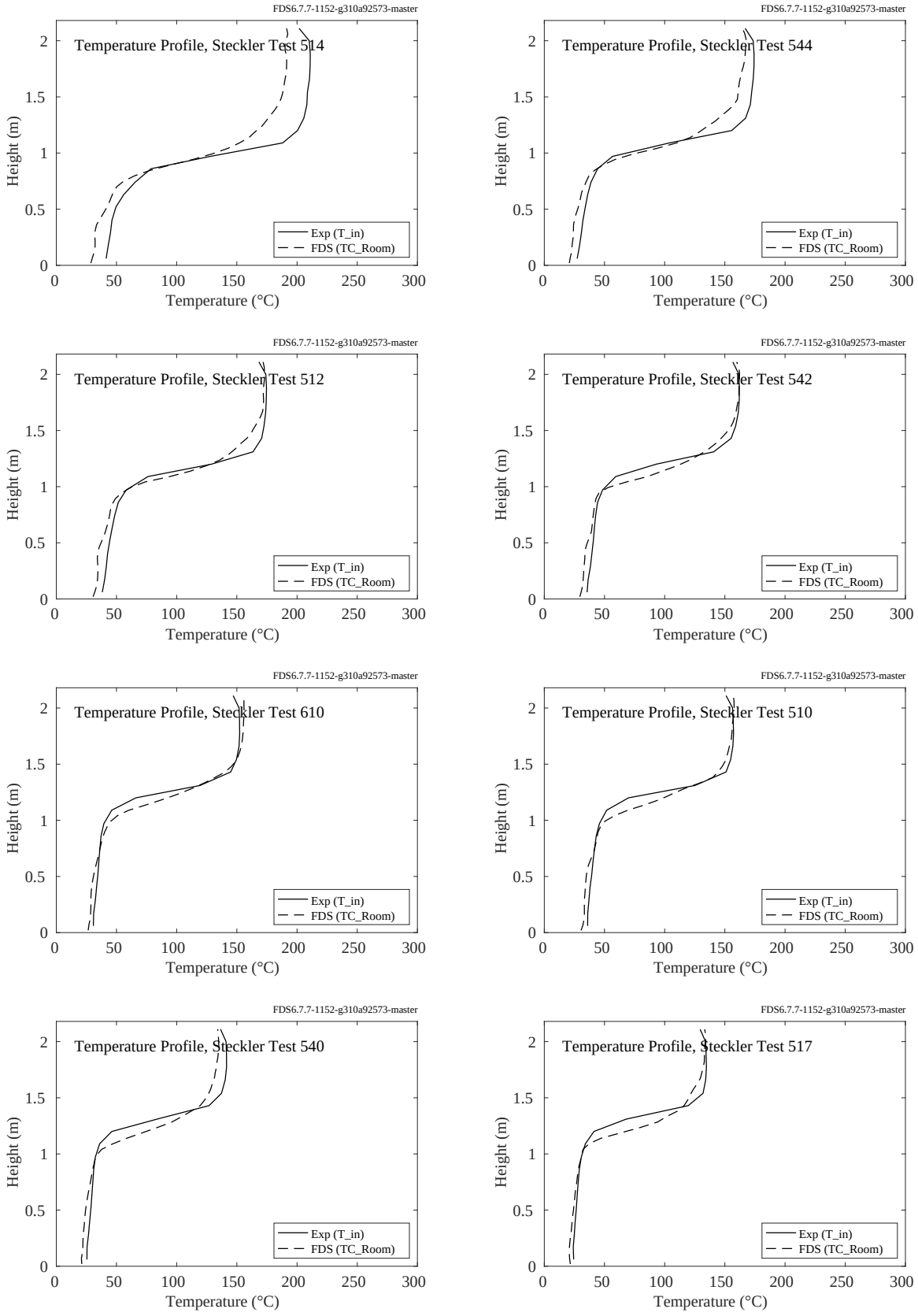

Figure 5.67: Steckler experiments, HGL temperature, Tests 510, 512, 514, 517, 540, 542, 544, 610.

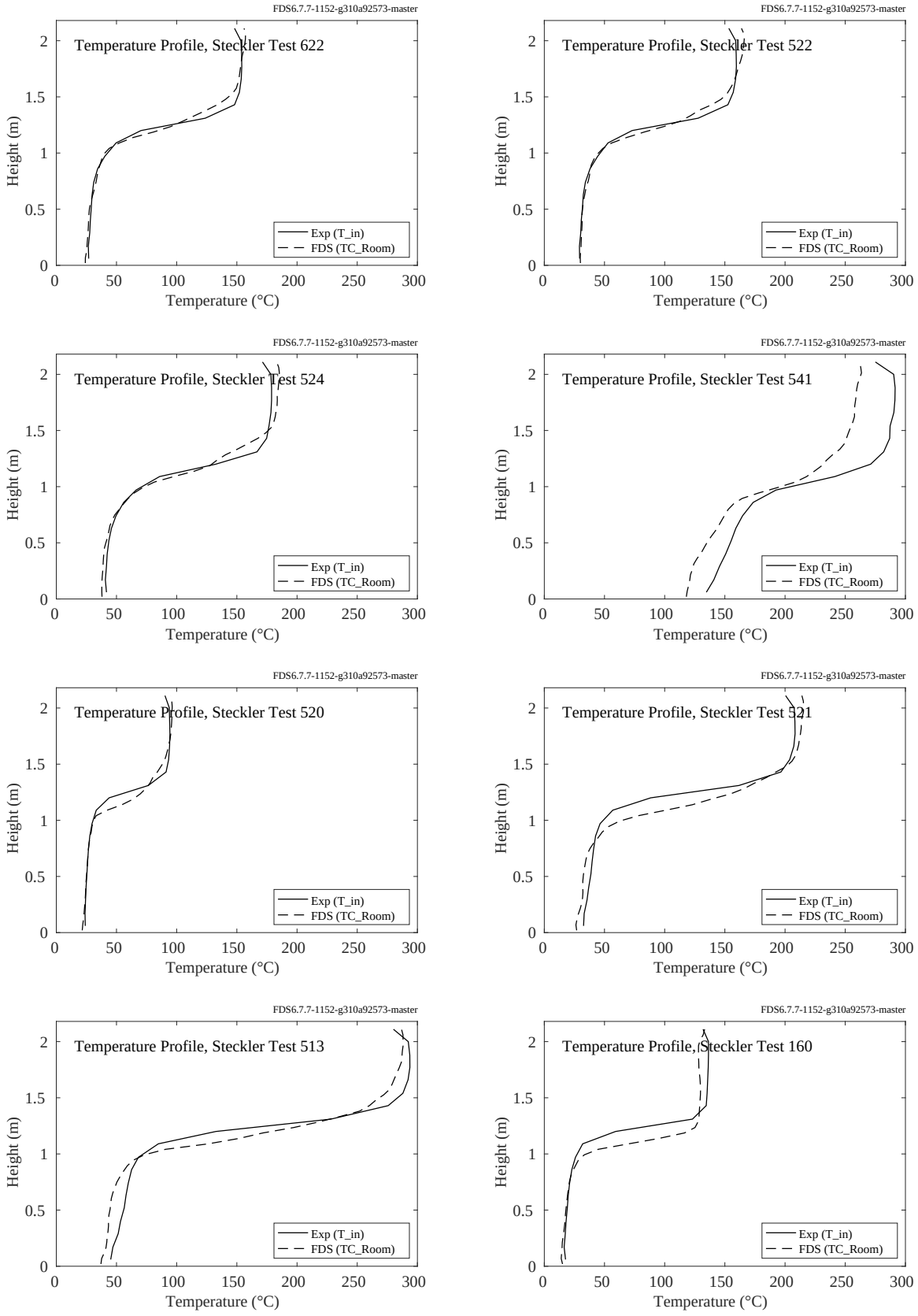

Figure 5.68: Steckler experiments, HGL temperature, Tests 160, 513, 520, 521, 522, 524, 541, 622.

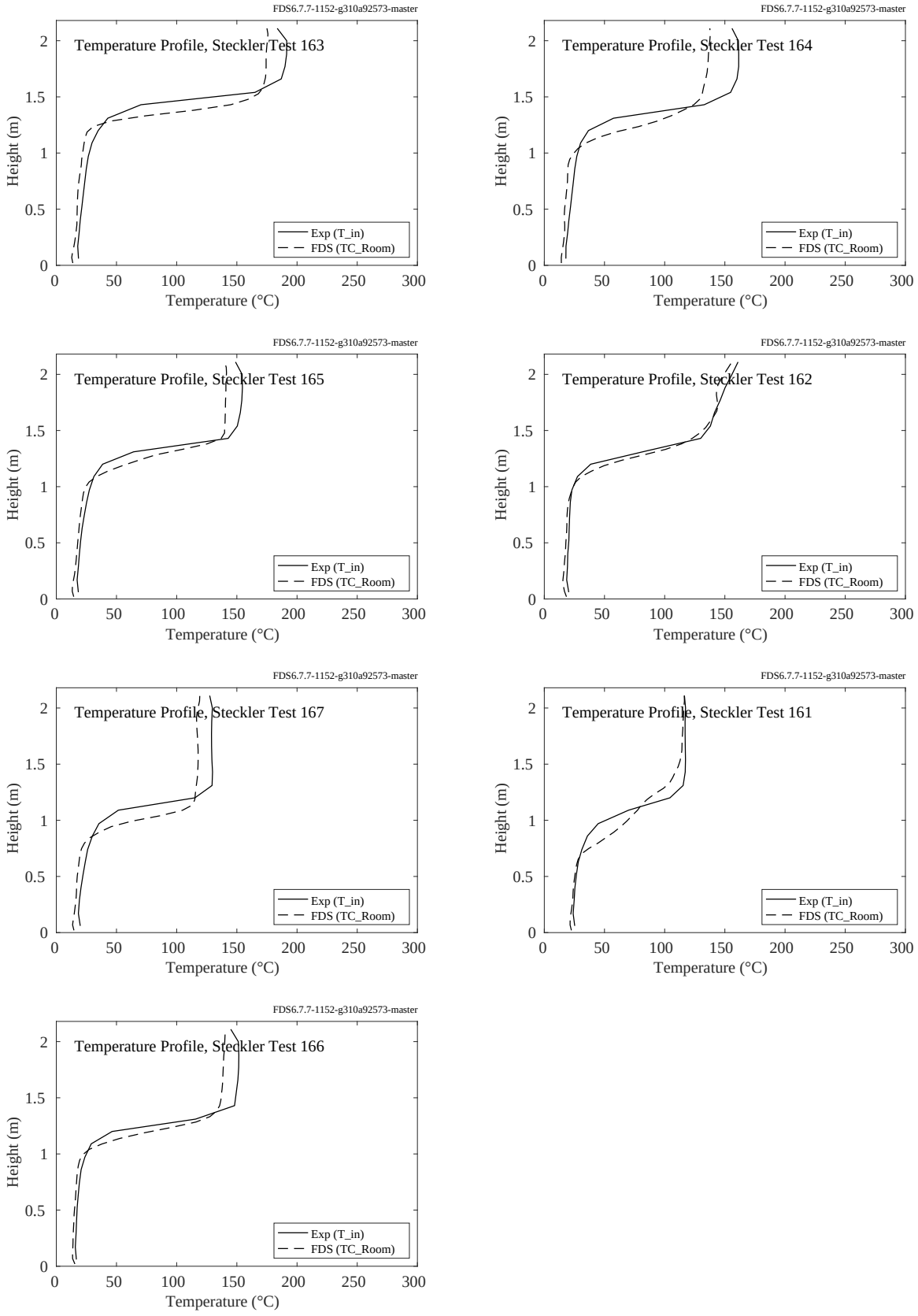

Figure 5.69: Steckler experiments, HGL temperature, Tests 161, 162, 163, 164, 165, 166, 167.

5.18 UL/NIST Vent Experiments

The HGL temperature and height for the four experiments was calculated from two vertical arrays of eight thermocouples each. The arrays were centered on the long central axis of the compartment and 90 cm from each short size wall. The 2.4 m by 1.2 m double vent was 90 cm from each array. The uppermost TC was 2.5 cm below the ceiling. The second TC was 30 cm (1 ft) below the ceiling, and the rest were spaced evenly by 1 ft.

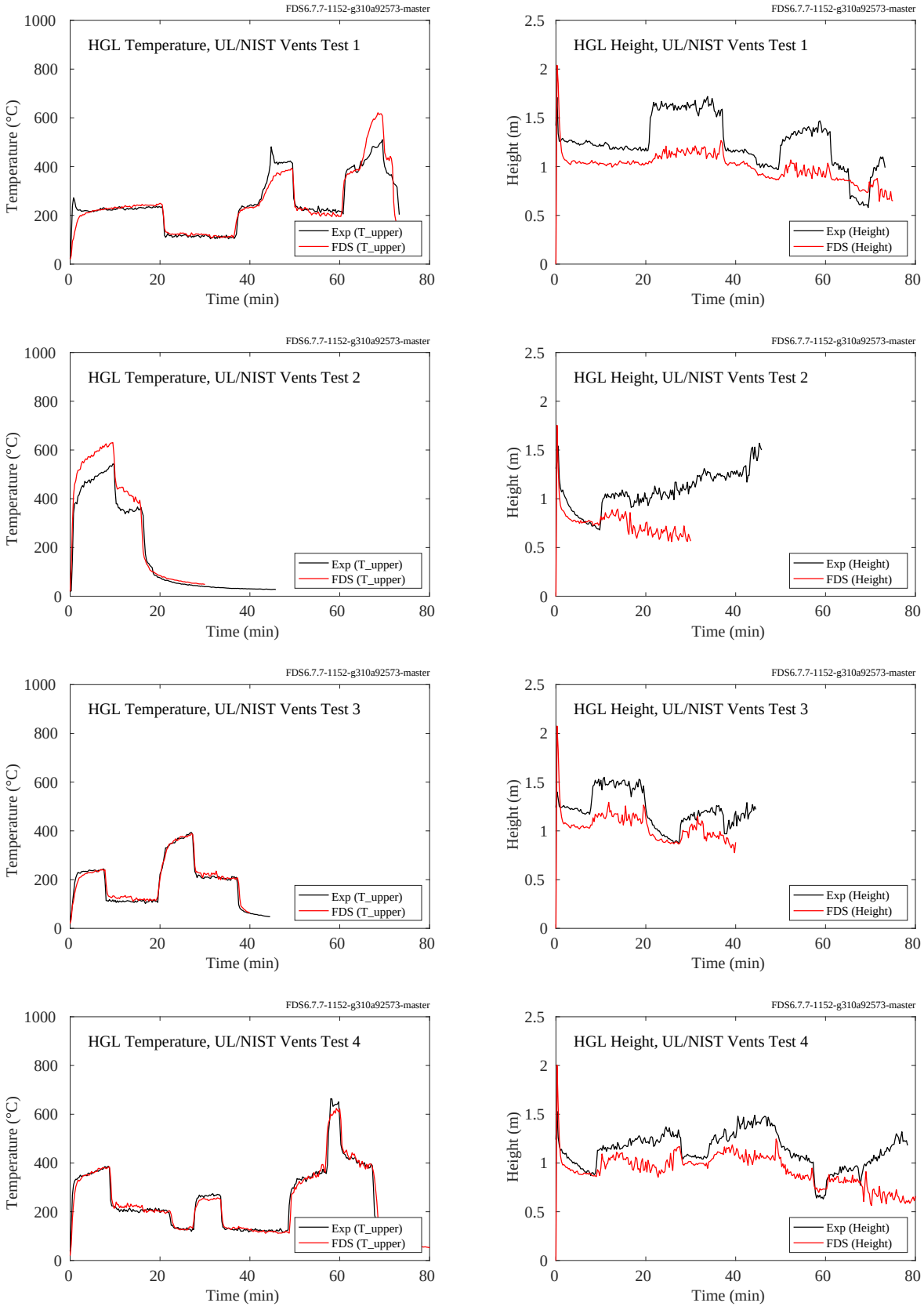

Figure 5.70: UL/NIST experiments, HGL temperature and height, Tests 1-4.

5.19 UL/NIJ House Experiments

Details of the experiments can be found in Section 3.77

The HGL temperature and height for three experiments conducted in the ranch-style house were calculated from two vertical arrays of eight thermocouples. The thermocouple arrays were located in the hallway (4TC) and in the living room (5TC).

The HGL temperature and height for three experiments conducted in the two-story colonial-style house were calculated from a vertical array of thermocouples in the center of the family room (8TC). The uppermost TC was 2.5 cm below the ceiling. The second TC was 30 cm (1 ft) below the ceiling, and the rest were spaced evenly by 30 cm (1 ft).

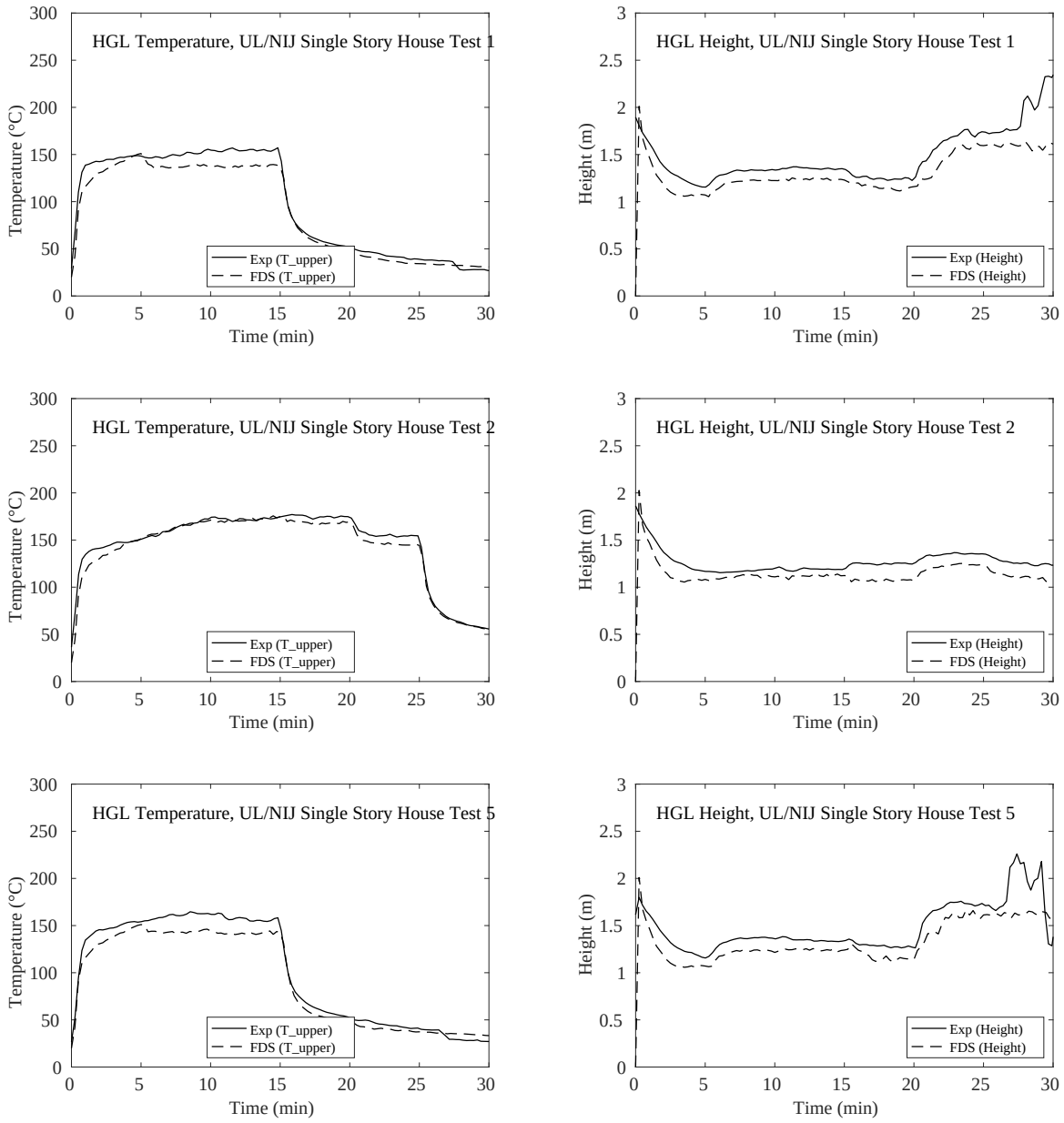

Figure 5.71: UL/NIJ Experiments, HGL temperature and height, single-story ranch-style House Tests 1, 2, and 5

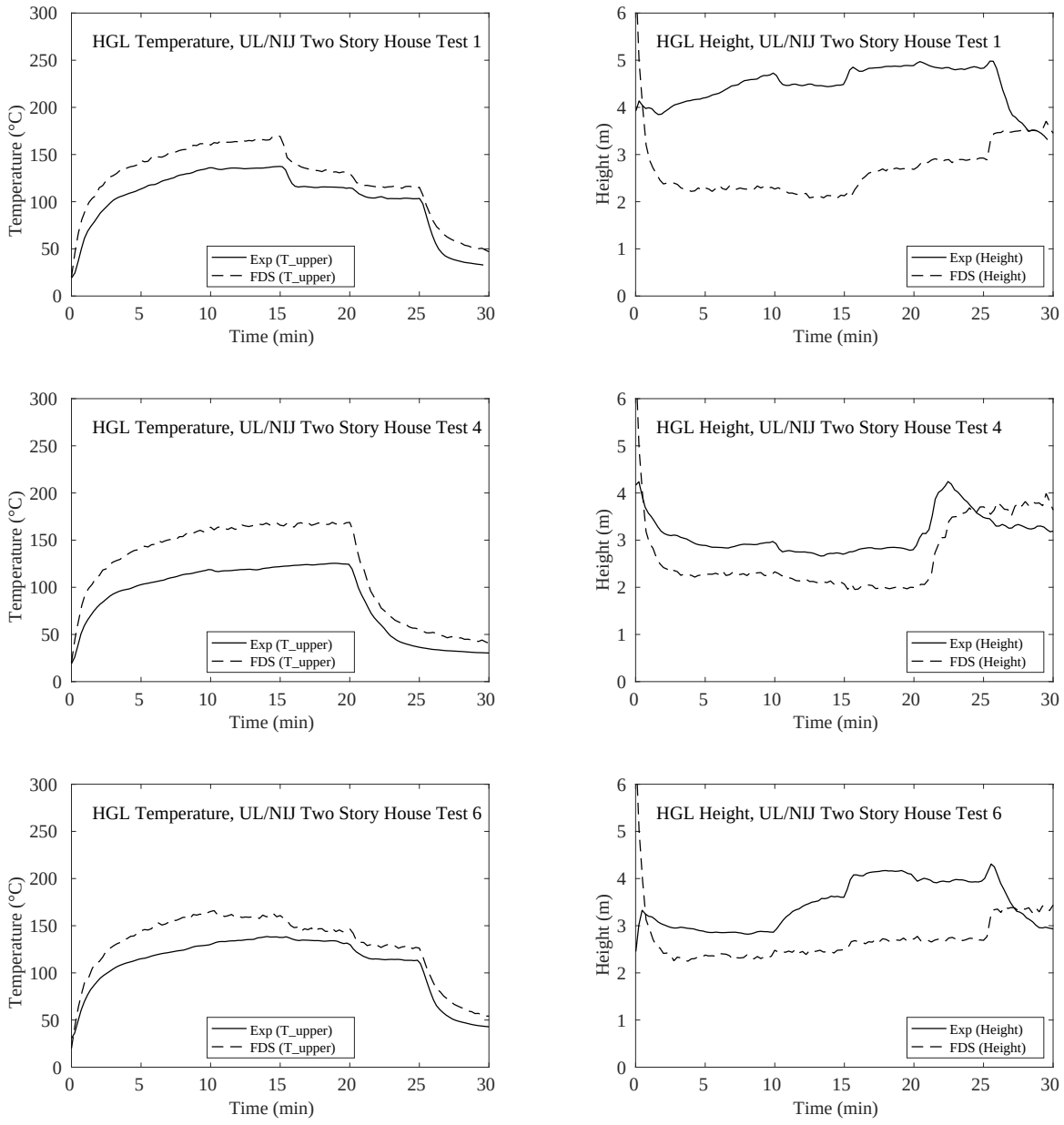

Figure 5.72: UL/NIJ Experiments, HGL temperature and height, two-story colonial-style House Tests 1, 4, and 6

5.20 VTT Test Series

The HGL temperature and height are calculated from the (1 min) averaged gas temperatures from three vertical thermocouple arrays using the standard reduction method. There are 10 thermocouples in each vertical array, spaced 2 m apart in the lower two-thirds of the hall, and 1 m apart near the ceiling.

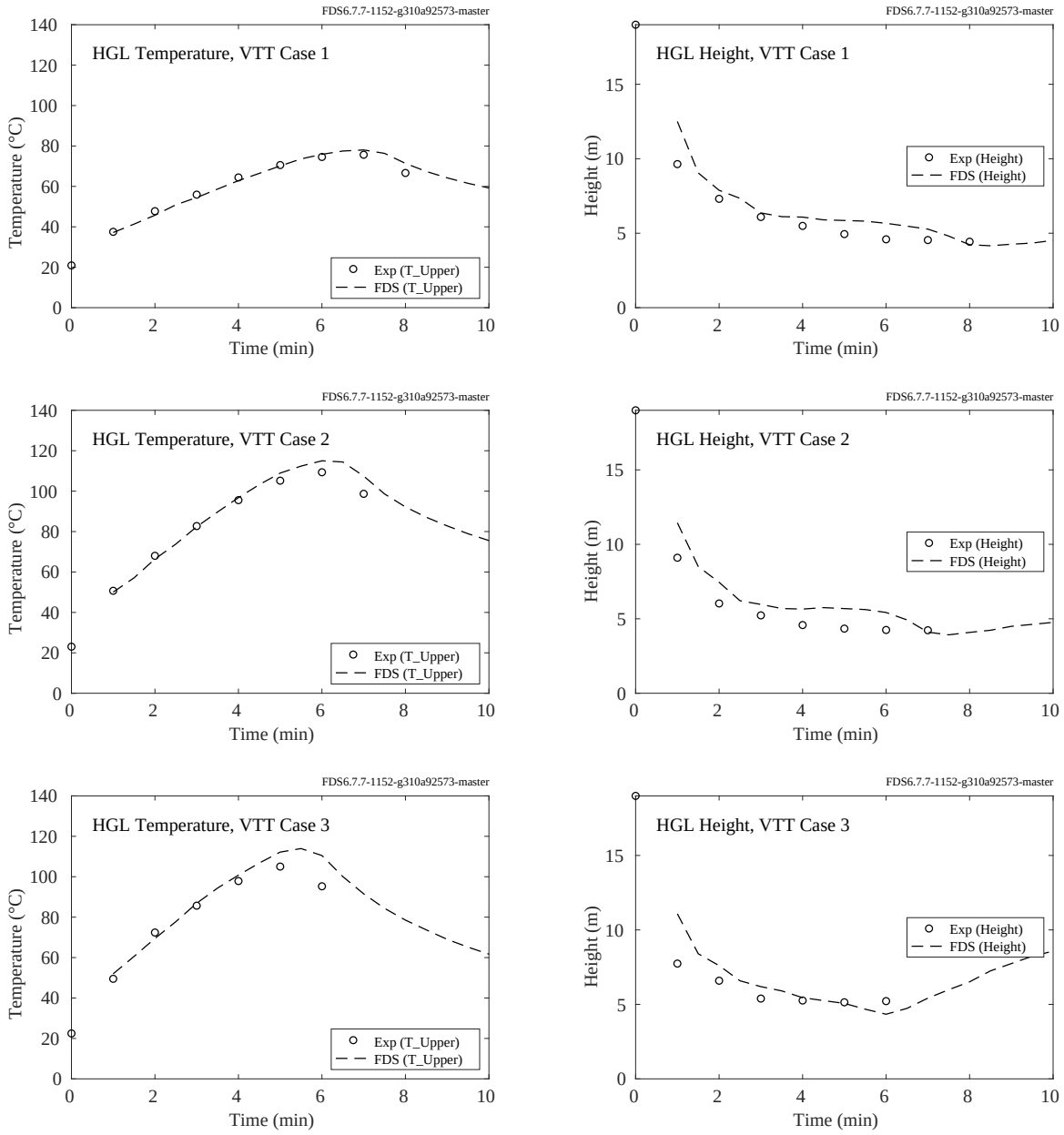

Figure 5.73: VTT experiments, HGL temperature and height, Tests 1-3.

5.21 WTC Test Series

The HGL temperature and height for the WTC experiments were calculated from two TC trees, one that was approximately 3 m to the west and one 2 m to the east of the fire pan (see Fig. 3.52). Each tree consisted of 15 thermocouples, the highest point being 5 cm below the ceiling.

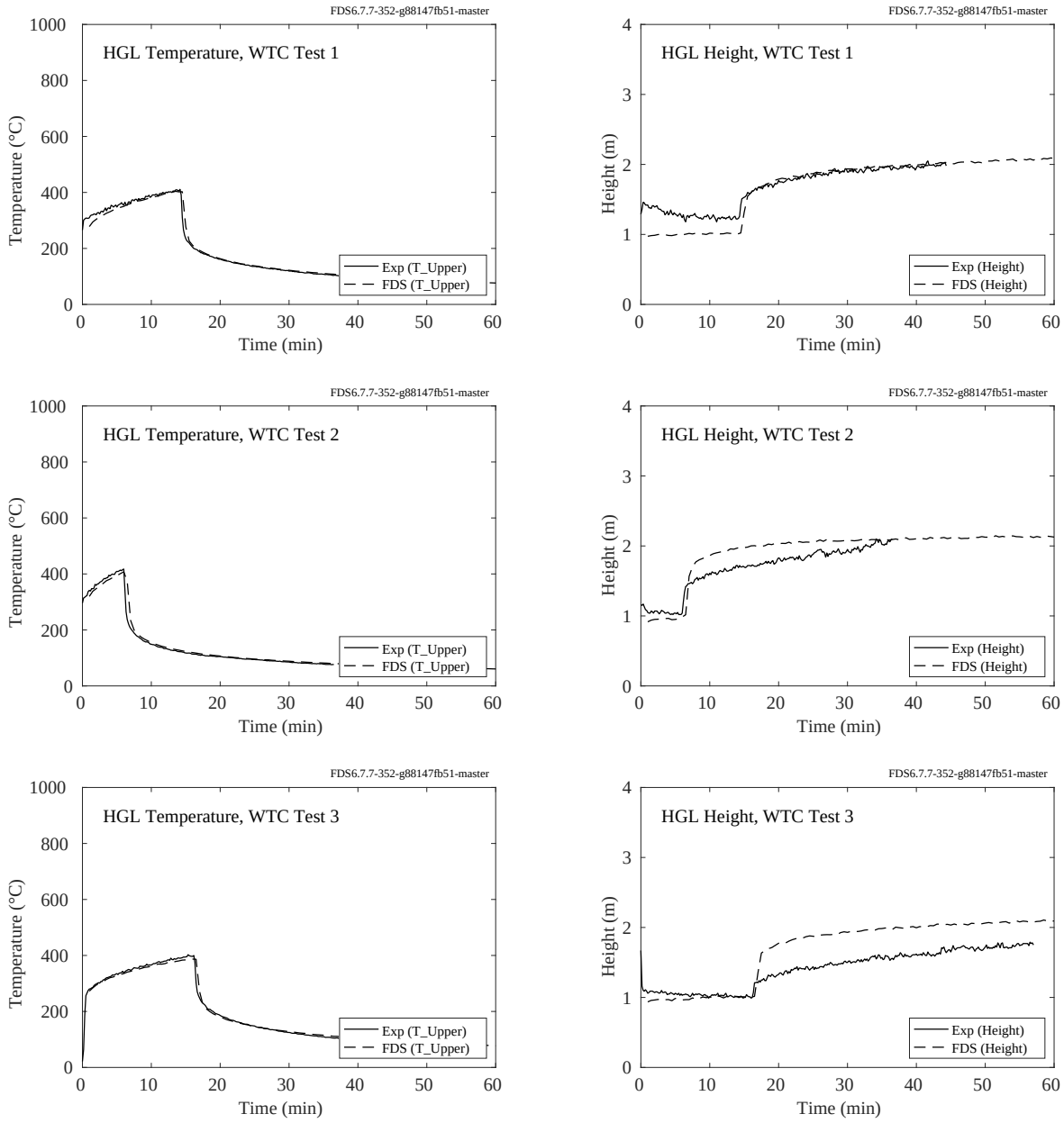

Figure 5.74: WTC experiments, HGL temperature and height, Tests 1-3.

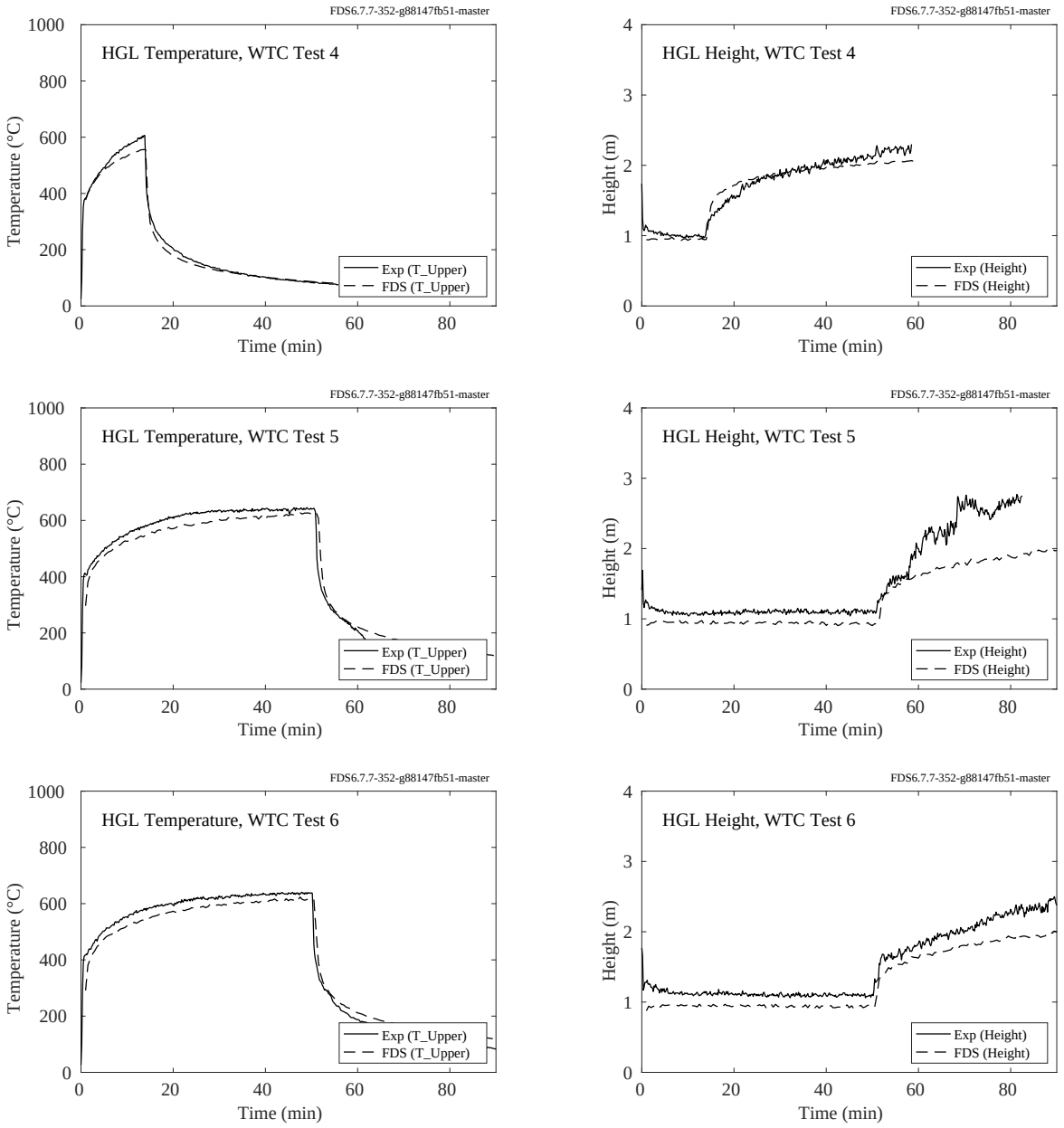

Figure 5.75: WTC experiments, HGL temperature and height, Tests 4-6.

5.22 Summary of Hot Gas Layer Temperature and Height

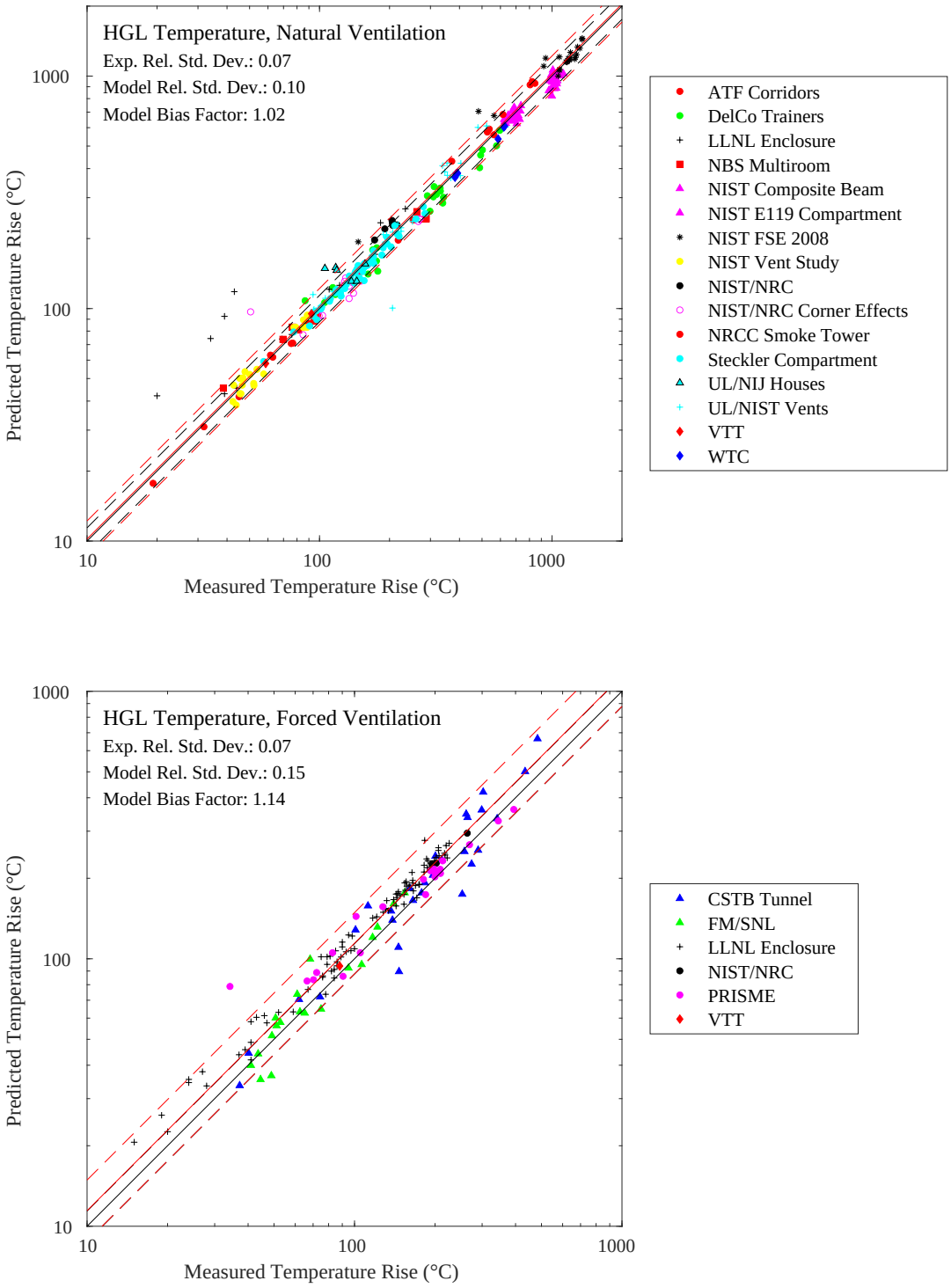

Figure 5.76: Summary, HGL temperature, natural and forced ventilation.

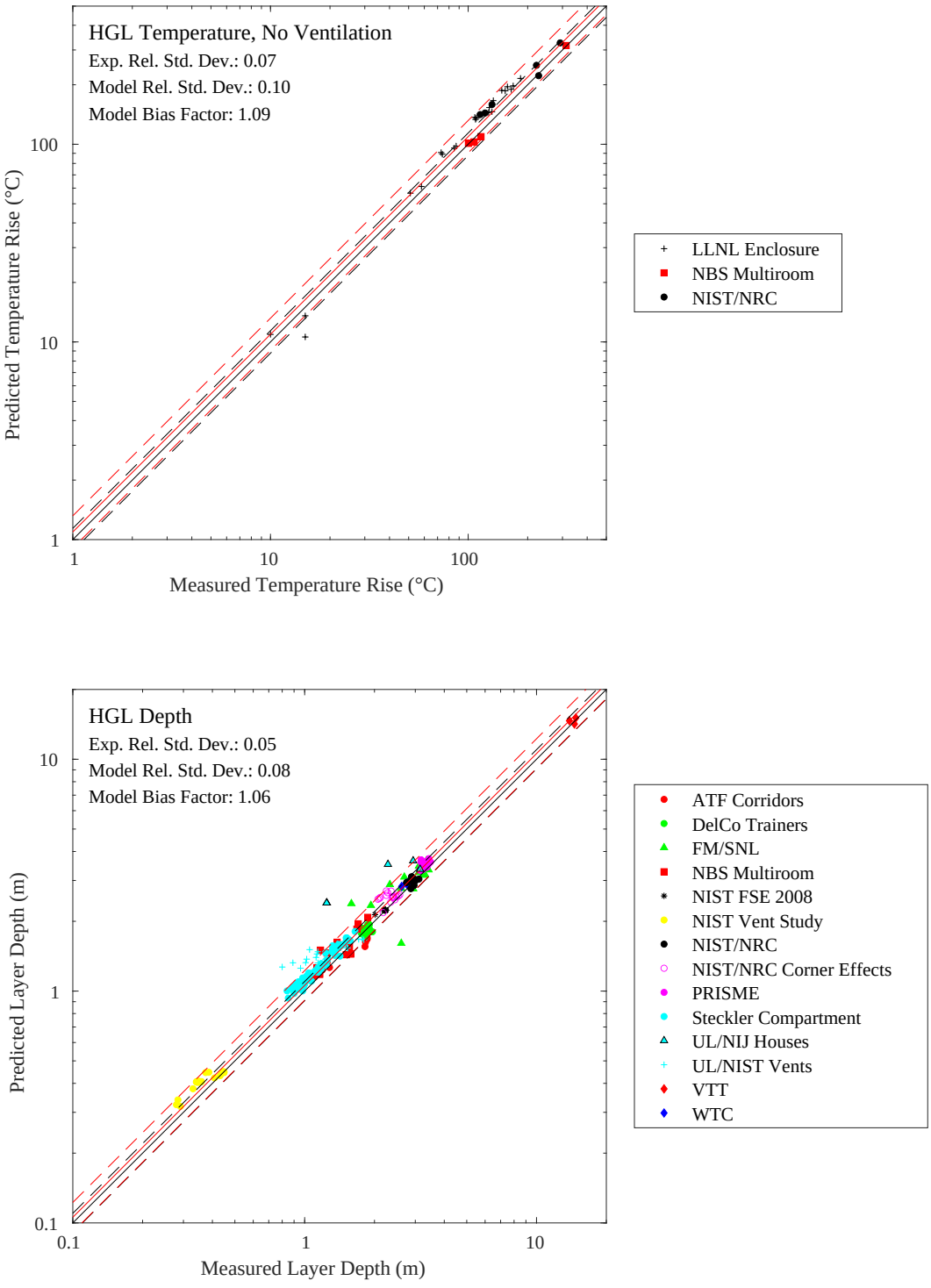

Figure 5.77: Summary, HGL temperature, unventilated compartments; HGL depth.

Chapter 6

Fire Plumes

6.1 Plume Temperatures

For fire plumes, a measure of how well the flow field is resolved is given by the non-dimensional expression $D^*/\delta x$, where D^* is a characteristic fire diameter

$$D^* = \left(\frac{\dot{Q}}{\rho_\infty c_p T_\infty \sqrt{g}} \right)^{\frac{2}{5}} \tag{6.1}$$

and δx is the nominal size of a mesh cell[1]. The quantity $D^*/\delta x$ can be thought of as the number of computational cells spanning the characteristic (not necessarily the physical) diameter of the fire. The more cells spanning the fire, the better the resolution of the calculation. It is better to assess the quality of the mesh in terms of this non-dimensional parameter, rather than an absolute mesh cell size. For example, a cell size of 10 cm may be "adequate," in some sense, for evaluating the spread of smoke and heat through a building from a sizable fire, but may not be appropriate to study a very small, smoldering source. The resolution of all the numerical simulations included in this chapter is given in Table 3.42.

[1]The characteristic fire diameter is related to the characteristic fire size via the relation $Q^* = (D^*/D)^{5/2}$, where D is the physical diameter of the fire.

6.1.1 FM Burner Experiments

A summary of these experiments can be found in Section 3.24.

Mean and rms temperature measurements were made above a 13.7 cm (inner) diameter, 15 kW ethylene burner. The radial profiles are located at heights of 1.0, 1.5, 2.0, 2.5, 3.0, and 3.5 burner diameters, D. Figure 6.3 displays the probability distributions (PDFs) at the six heights and radii of 0 cm, 1 cm, 2 cm, 3 cm, and 4 cm.

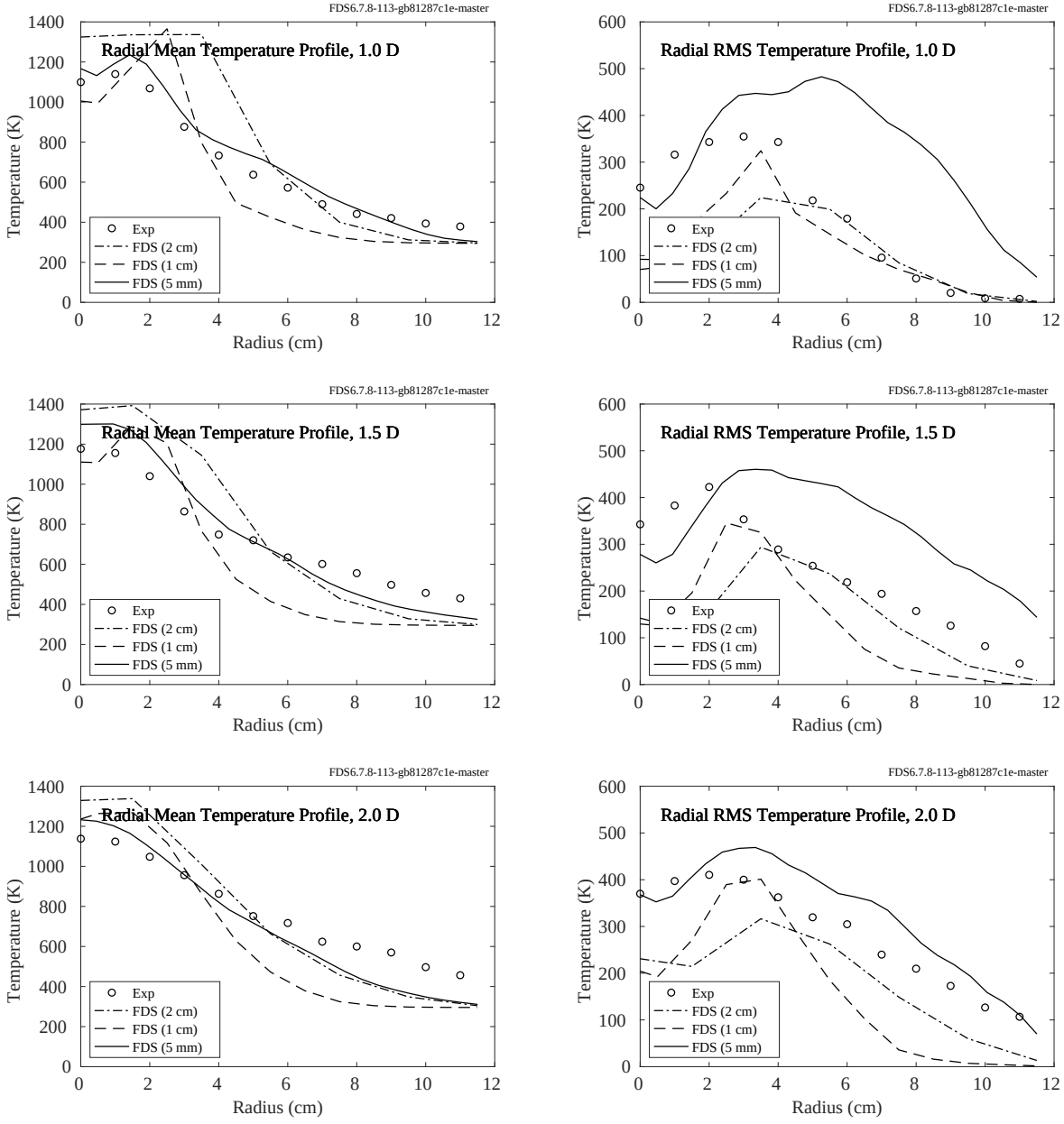

Figure 6.1: FM Burner experiments, plume mean and rms temperatures at heights of 1.0, 1.5, and 2.0 diameters.

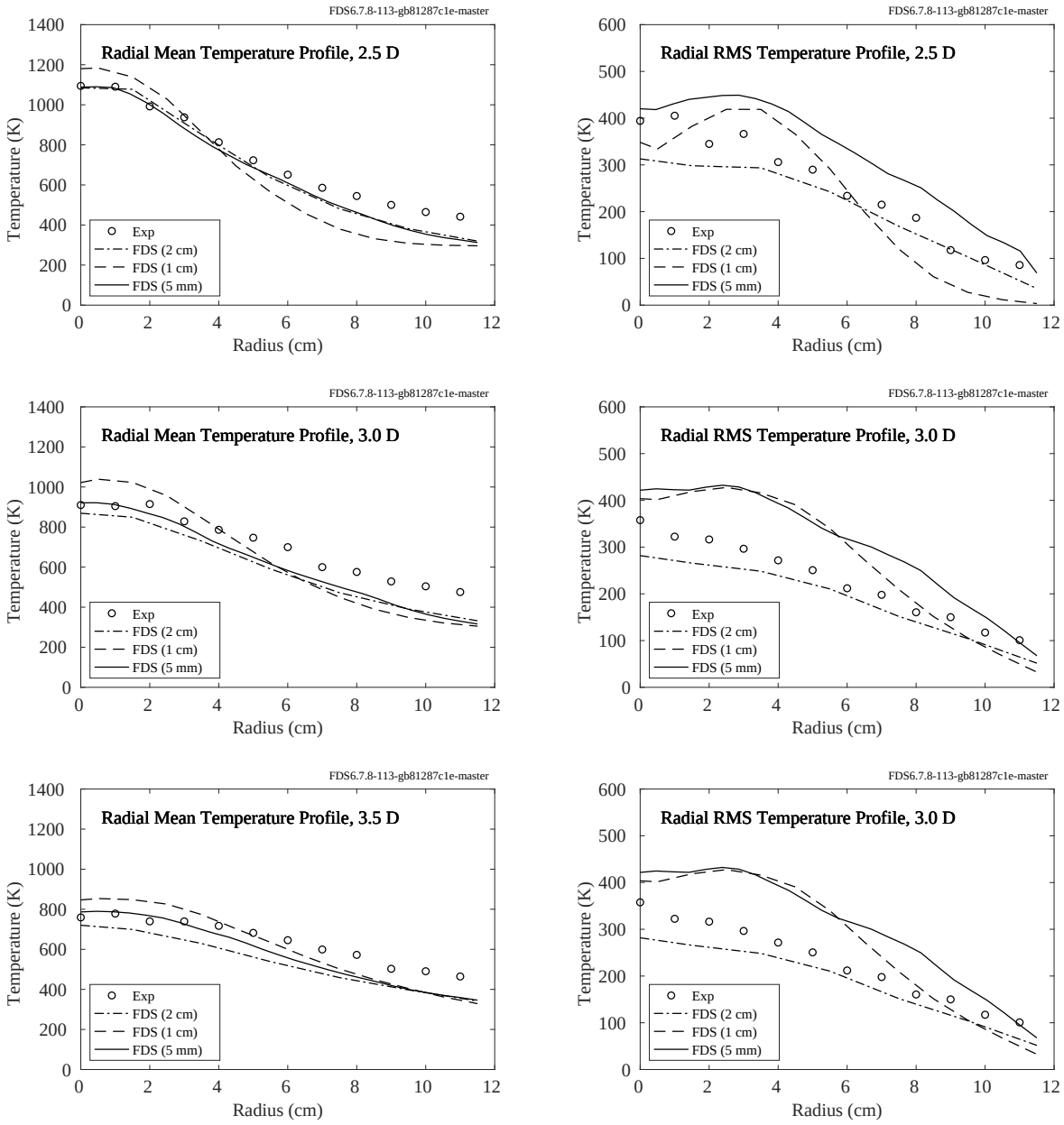

Figure 6.2: FM Burner experiments, plume mean and rms temperatures at heights of 2.5, 3.0, and 2.5 diameters.

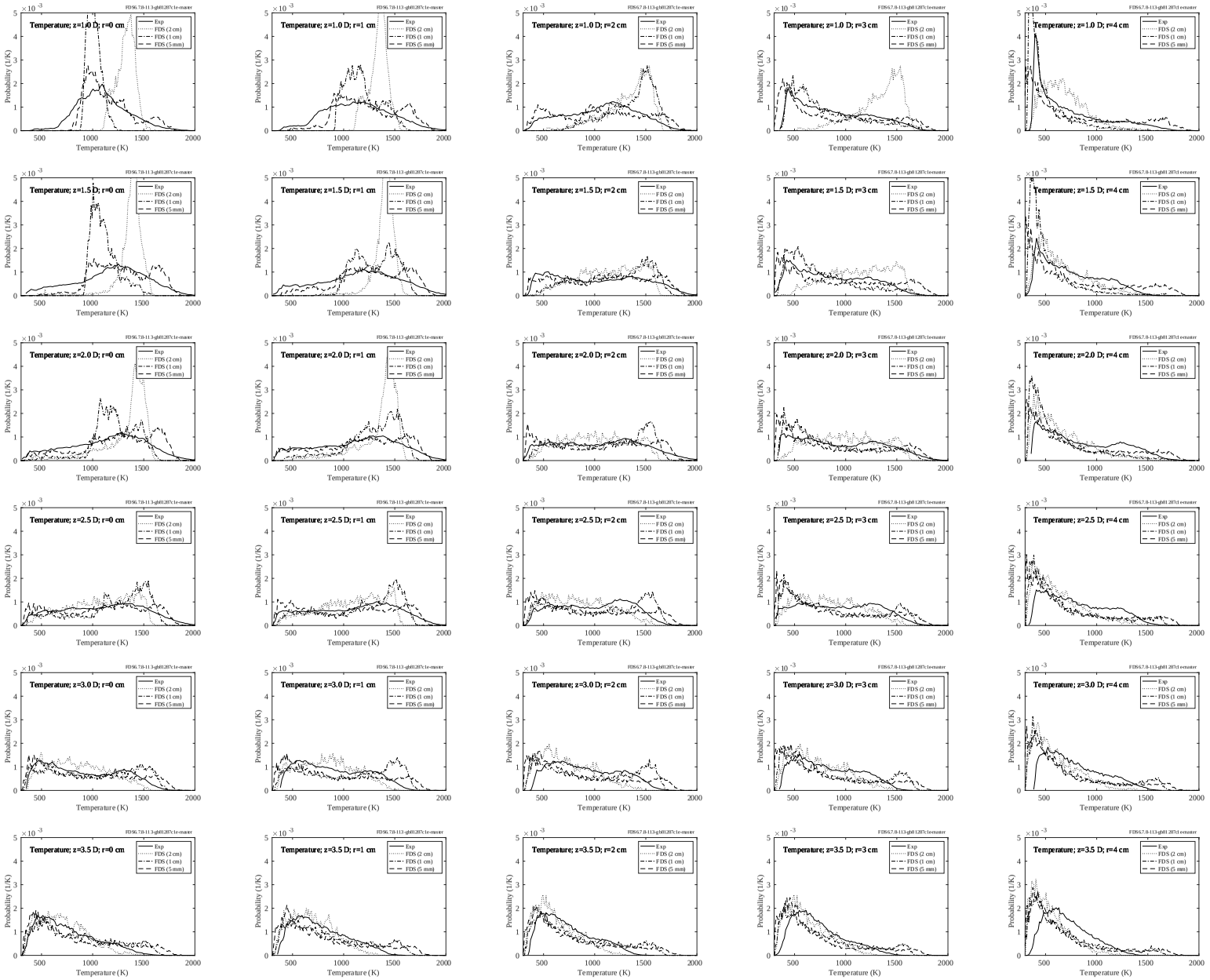

Figure 6.3: FM Burner experiments, temperature PDFs.

6.1.2 FM/SNL Experiments

A summary of these experiments can be found in Section 3.27.

The FM/SNL tests consisted of propylene gas burners, heptane pools, methanol pools, PMMA solids, as well as qualified and unqualified cables, burned in a large room which, for the first 18 tests, was free of obstructions. Plume Temperatures shown here were measured at approximately 6 m from the floor, or 0.98 times the total ceiling height. For Tests 1-5 and 7-9, the thermocouple station (Station 13) was centered above the fire pan. Tests 6 and 10-15 used an alternate fire location, centered along the south wall. Station 9 was not centered above these fires, but fell within the plume. Tests 16 and 17 had fires located in the south-west corner of the room, too remote from any stations to allow for plume measurements.

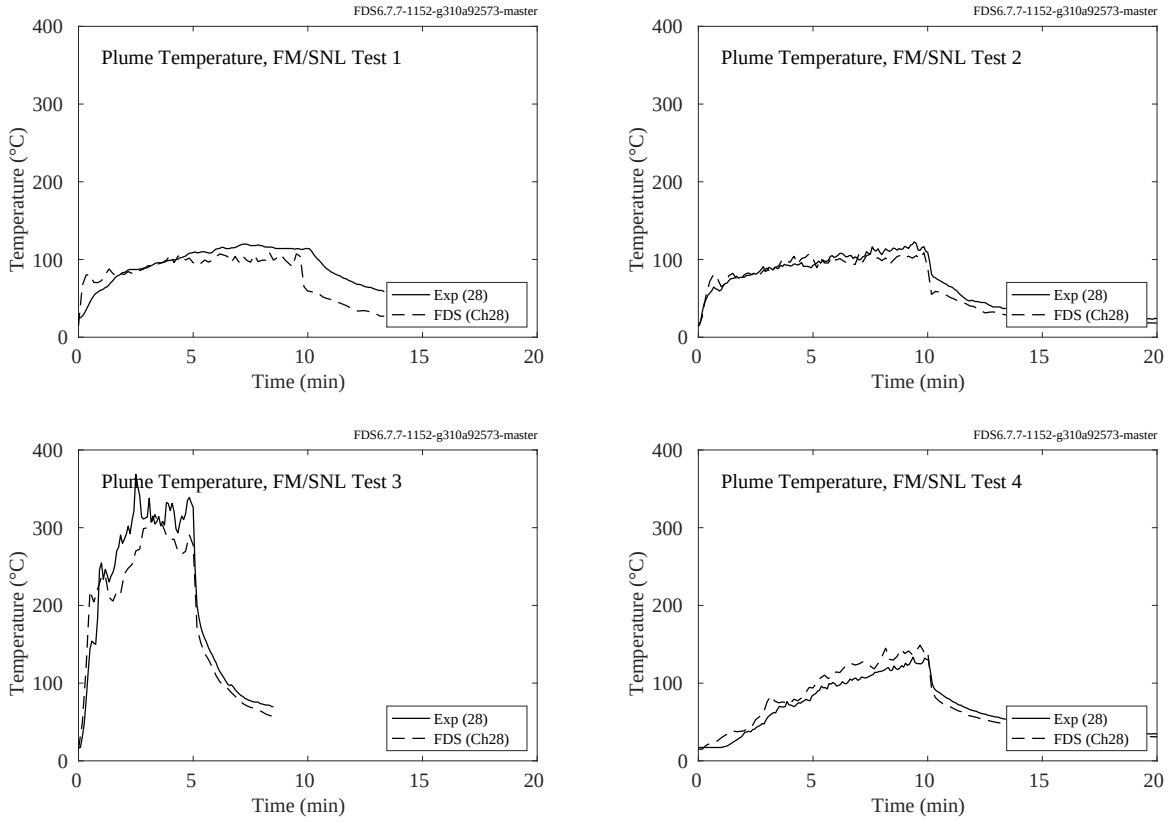

Figure 6.4: FM/SNL experiments, plume temperature, Tests 1-4.

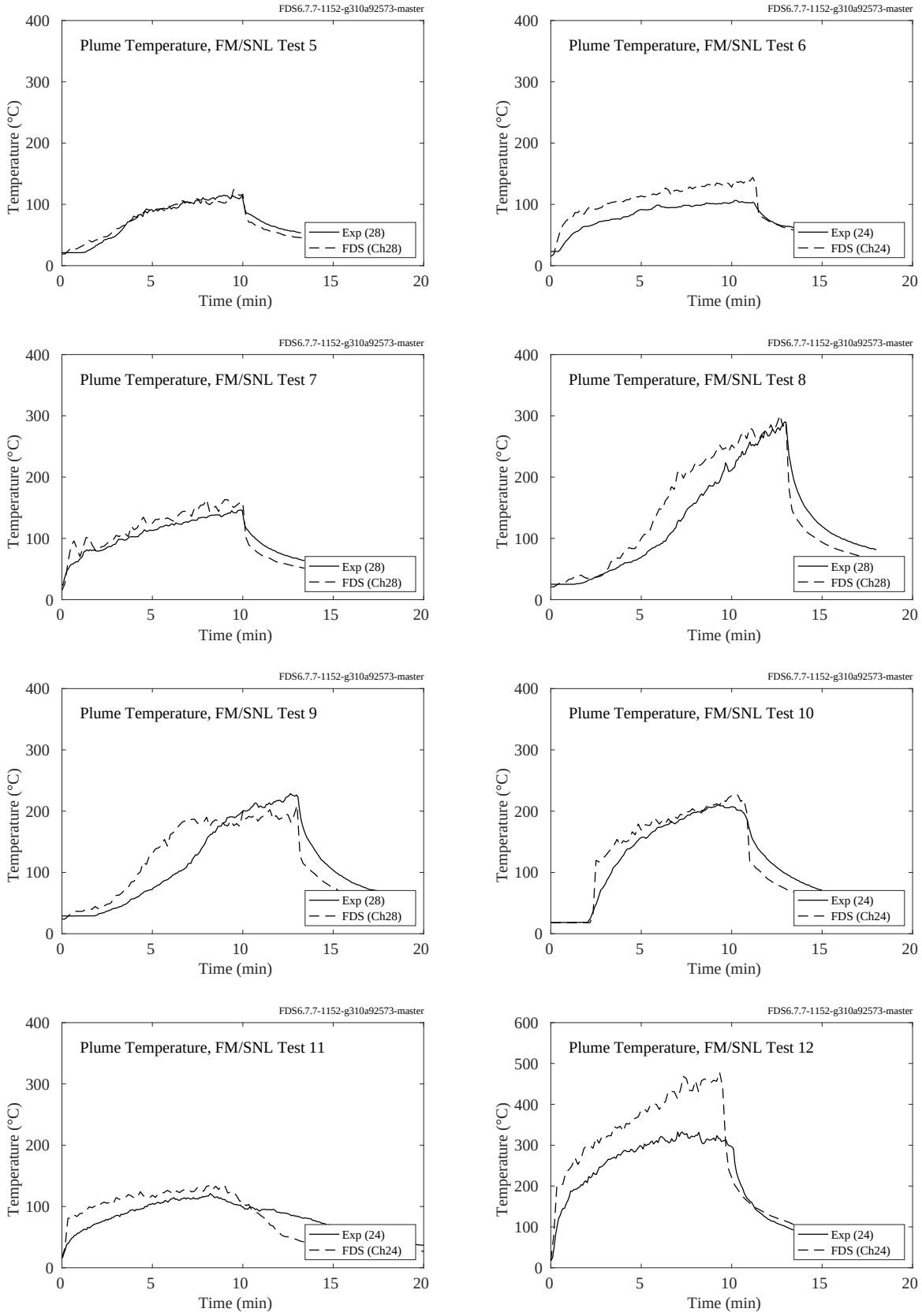

Figure 6.5: FM/SNL experiments, plume temperature, Tests 5-12.

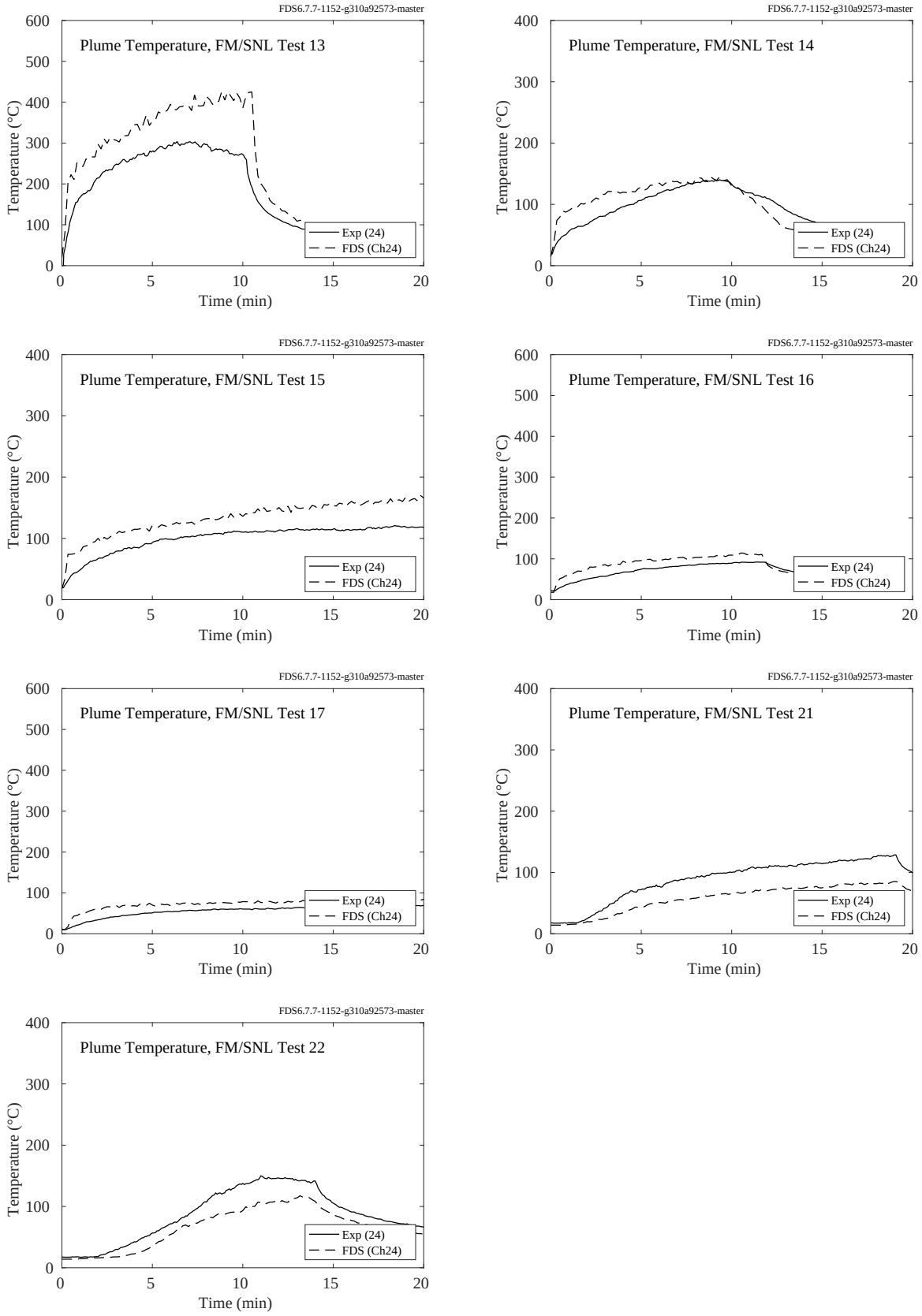

Figure 6.6: FM/SNL experiments, plume temperature, Tests 13-17, 21-22.

6.1.3 McCaffrey's Plume Correlation

A summary of these experiments can be found in Section 3.38.

The following plots show the results of simulations of McCaffrey's five fires at three grid resolutions, nominally $D^*/\delta x = [5, 10, 20]$ (respectively, coarse, medium, and fine resolution). Temperature measurements and reported simulation results are for thermocouple temperature.

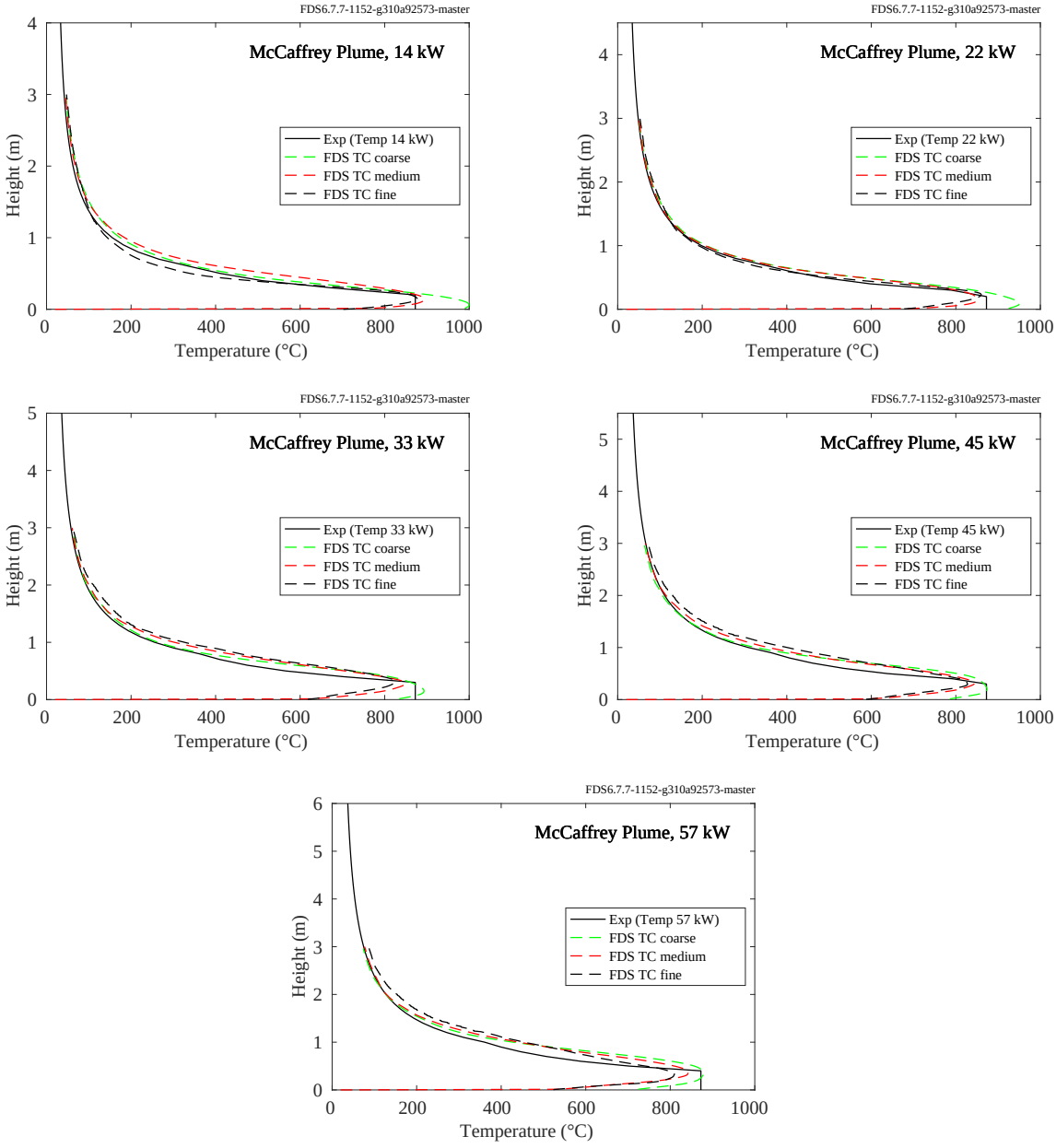

Figure 6.7: McCaffrey experiments, plume temperature.

Below we plot the same results but arranged in a different way. The height dimension is scaled by the fire Froude number and each plot represents nominally the same resolution level.

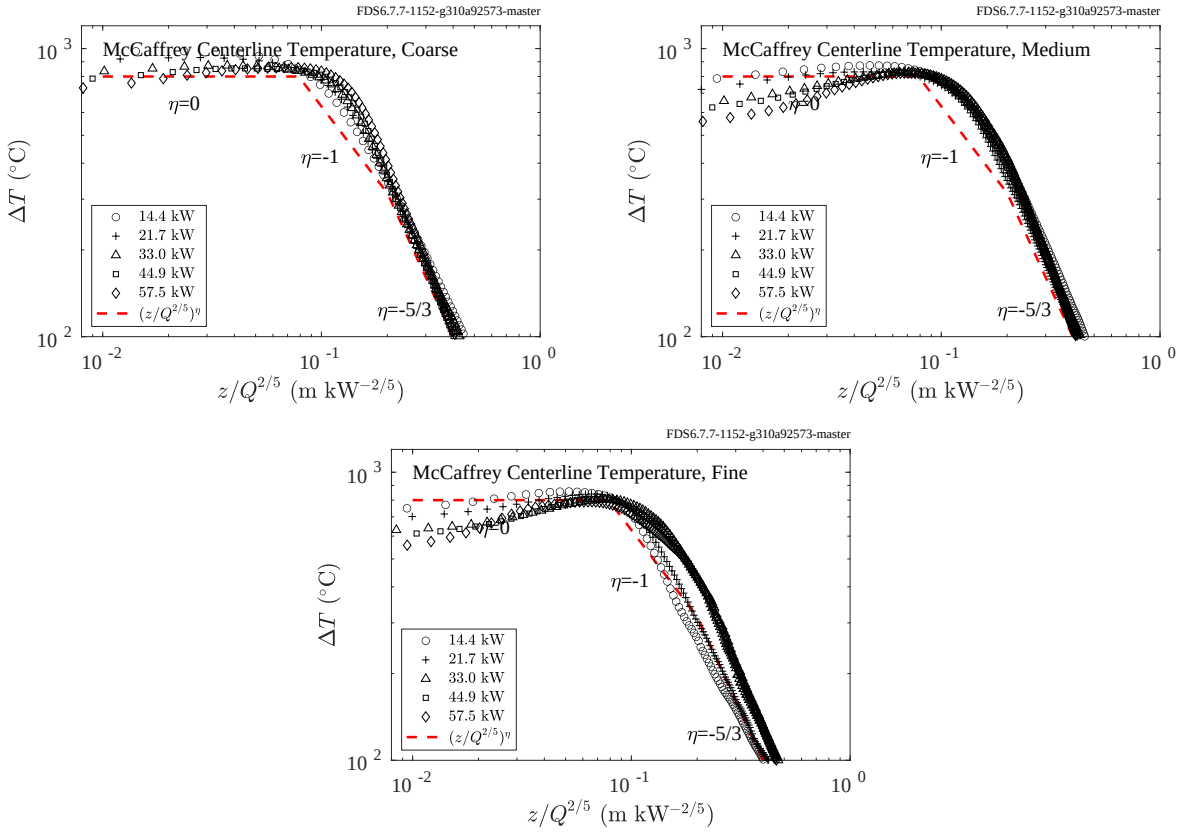

Figure 6.8: McCaffrey experiments, plume temperature, Froude scaling.

6.1.4 NIST/NRC Corner/Wall/Cabinet Effects Experiments

A summary of these experiments can be found in Section 3.47.

This set of experiments involved a 60 cm by 60 cm natural gas burner with heat release rates of 200 kW, 300 kW, and 400 kW. The burner was initially positioned in a corner or against a wall and then gradually moved away. A three-tiered array of thermocouples was positioned above the burner and moved along with it. Each tier contained 29 bare-bead thermocouples at heights of 2.13 m, 2.74 m, and 3.35 m above the floor. The plots below show the maximum temperature of the 29 thermocouples, time-averaged over 2 min, at each level. Note that FDS does not allow its devices to move; thus the time over which the model and measurement are compared is limited to that time period in the experiment when the center of the burner was underneath the fixed TC array in the corner or against the wall. In short, the last 30 min of the experiments are not considered.

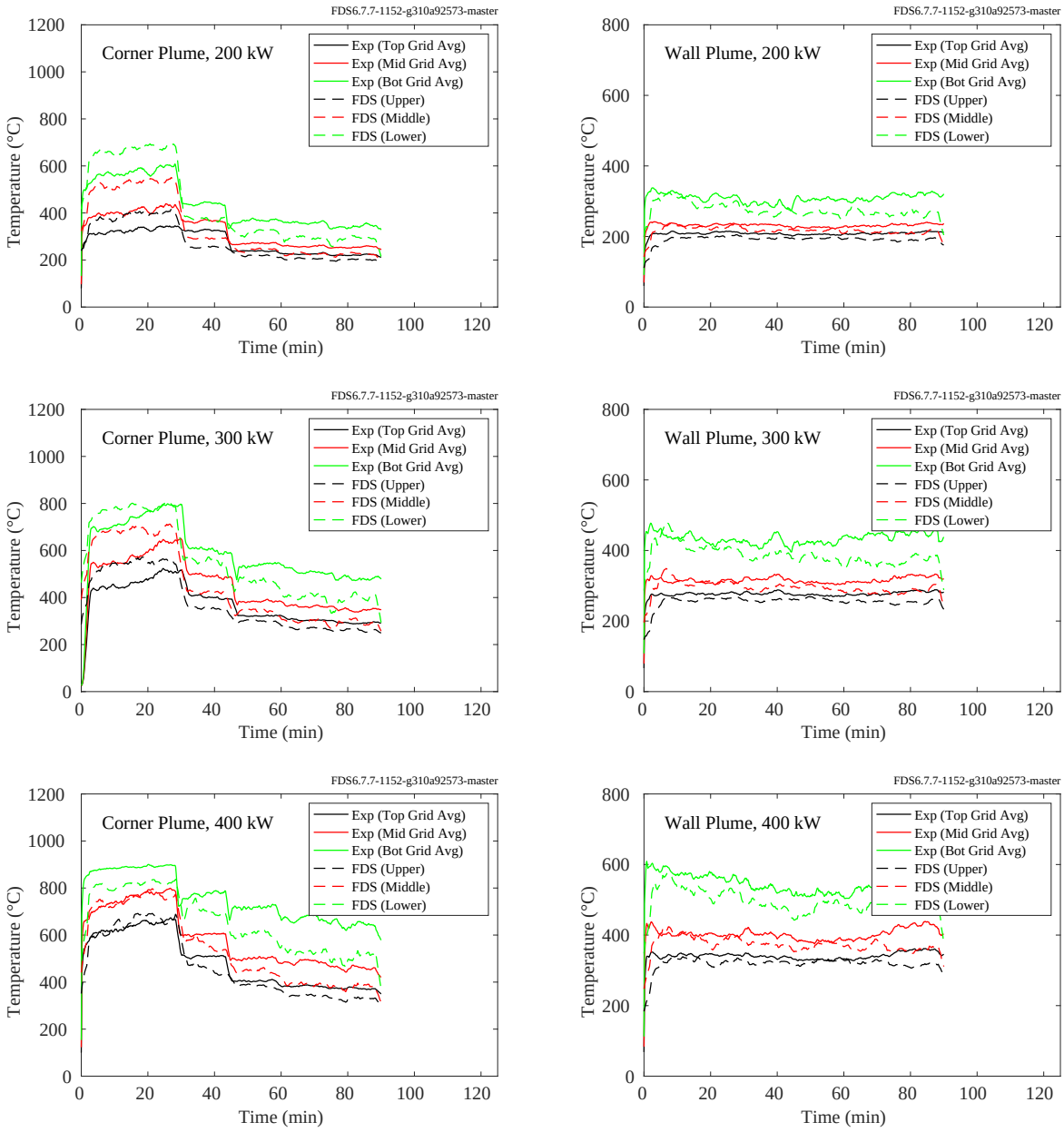

Figure 6.9: NIST/NRC Corner Effects experiments, plume temperature.

6.1.5 NIST Pool Fires

Details of the NIST Pool Fires experiments and modeling are found in Section 3.51. On the following pages are comparisons of predicted and measured temperatures at various locations in and around liquid and gaseous pool fires.

- Figures 6.10 and 6.11 display centerline profiles of mean and rms temperature for 30 cm diameter acetone, ethanol, and methanol liquid pool fires; and 37 cm methane and propane gaseous fires [328].
- Figure 6.12 displays radial profiles of mean and rms temperature for a 30 cm methanol fire at heights of $z = 3$ cm (mean only), $z = 30$ cm (mean only), $z = 41$ cm, $z = 51$ cm, and $z = 61$ cm. The profiles at 3 cm and 30 cm are from Ref. [312] and the others are from Ref. [329].
- Figures 6.13 and 6.14 display centerline and radial profiles of mean and rms temperature for a 100 cm methanol fire. The radial profiles are located at heights of $z = 20$ cm, $z = 60$ cm, $z = 100$ cm, $z = 140$ cm, and $z = 180$ cm [330].

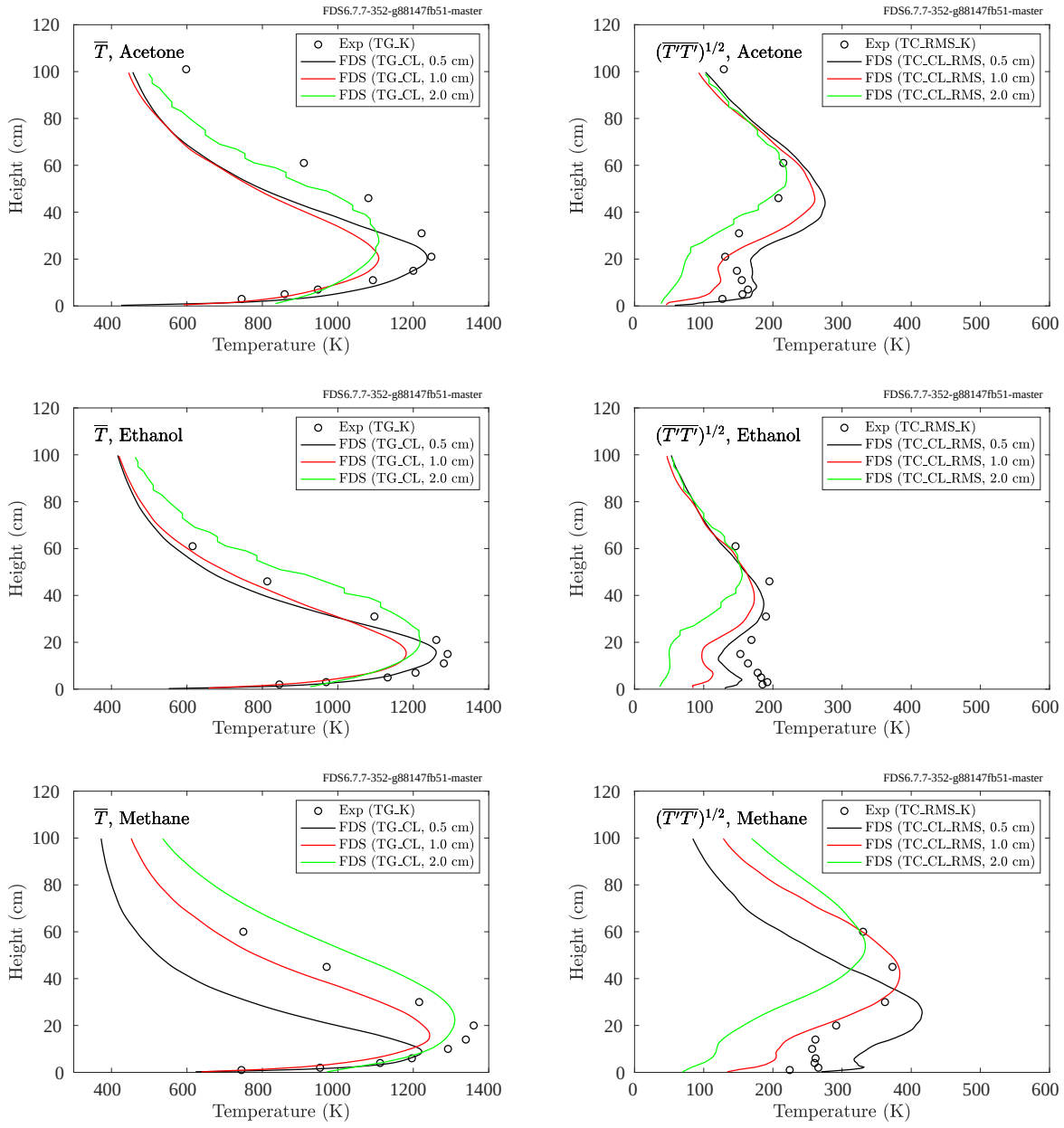

Figure 6.10: NIST Pool Fires, centerline tempertaure profiles, 30 cm acetone, 30 cm ethanol, 37 cm methane.

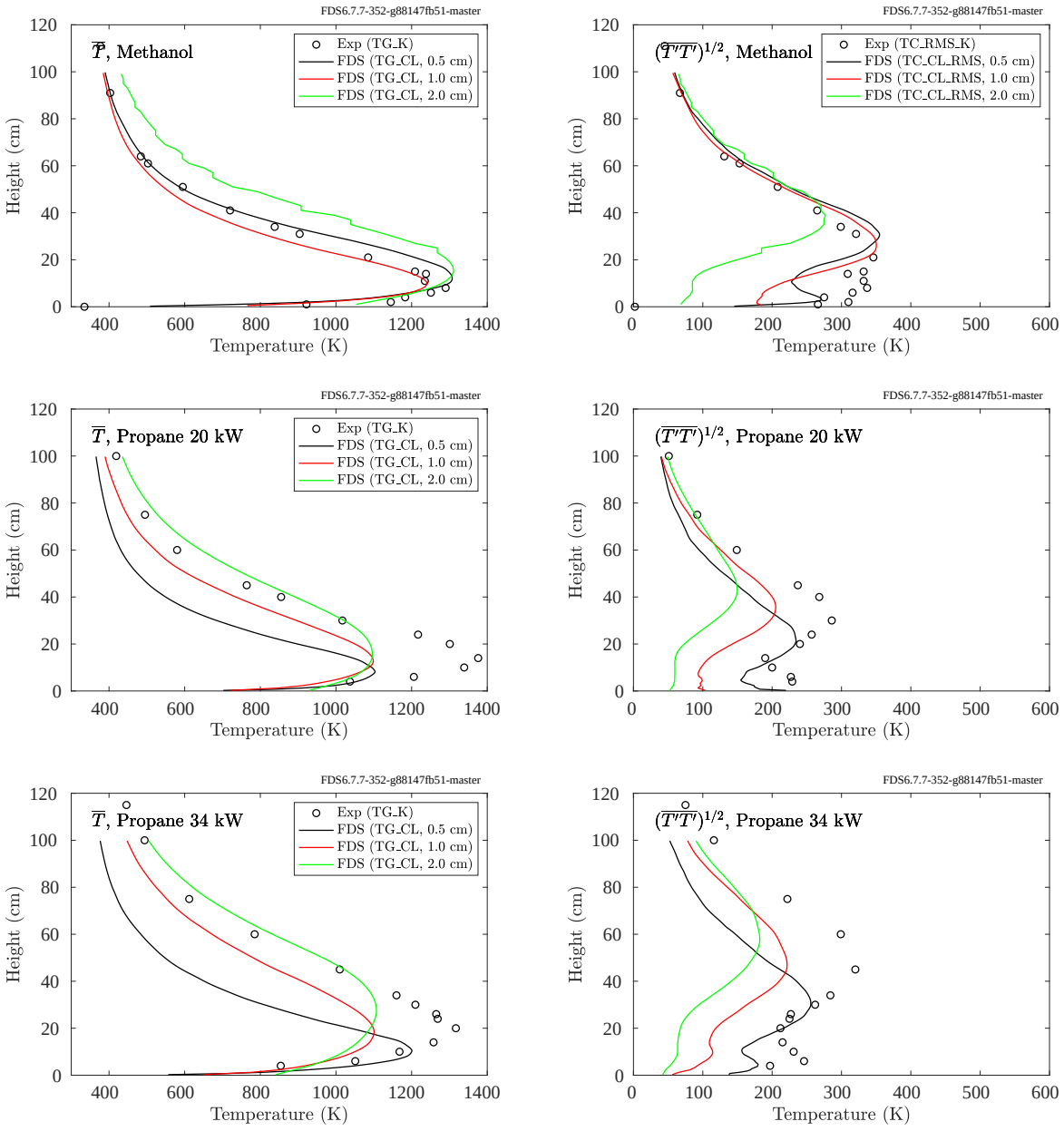

Figure 6.11: NIST Pool Fires, centerline tempertaure profiles, 30 cm methanol and 37 cm propane.

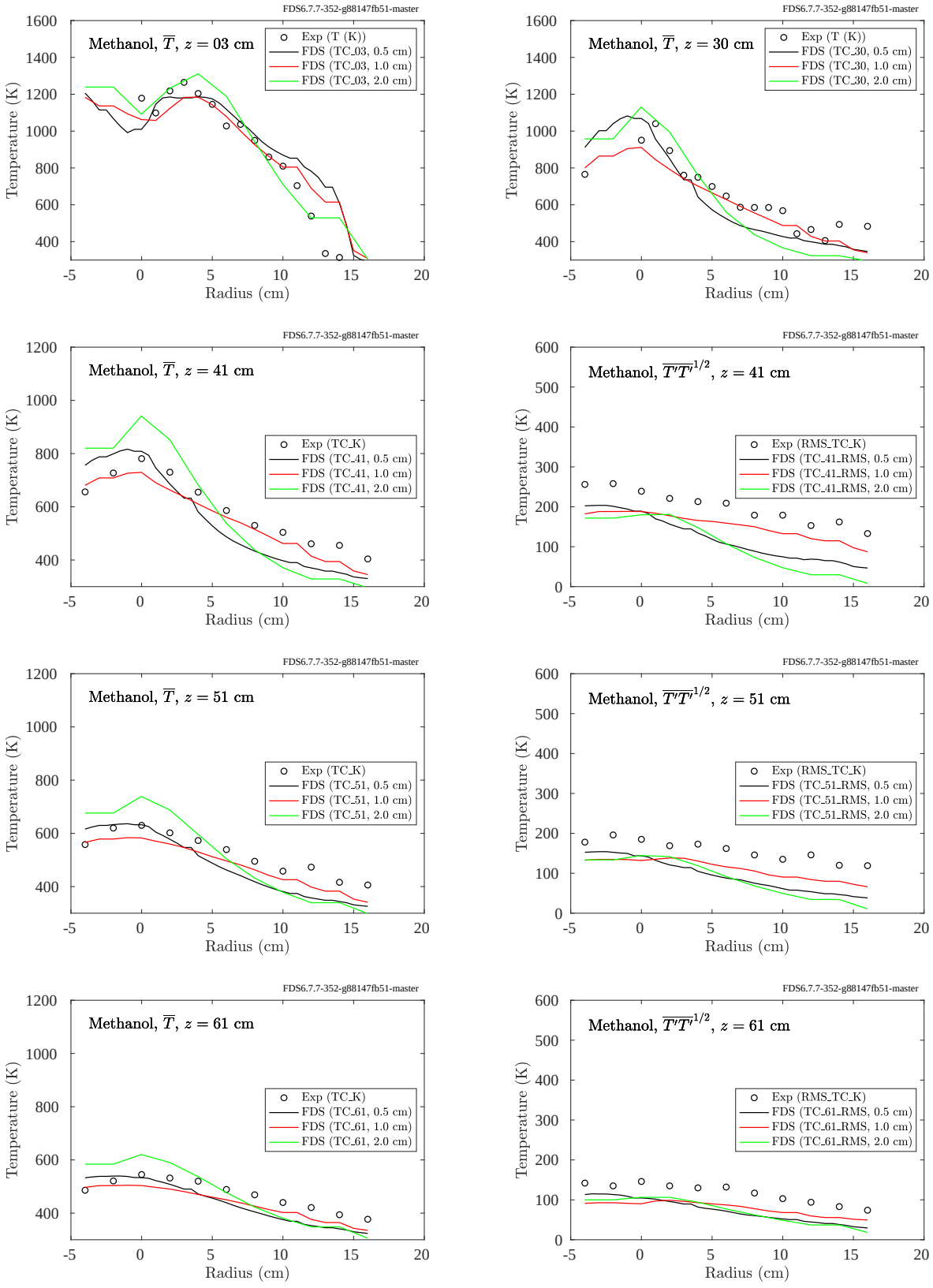

Figure 6.12: NIST Pool Fires, 30 cm methanol, radial profiles of mean and rms temperature.

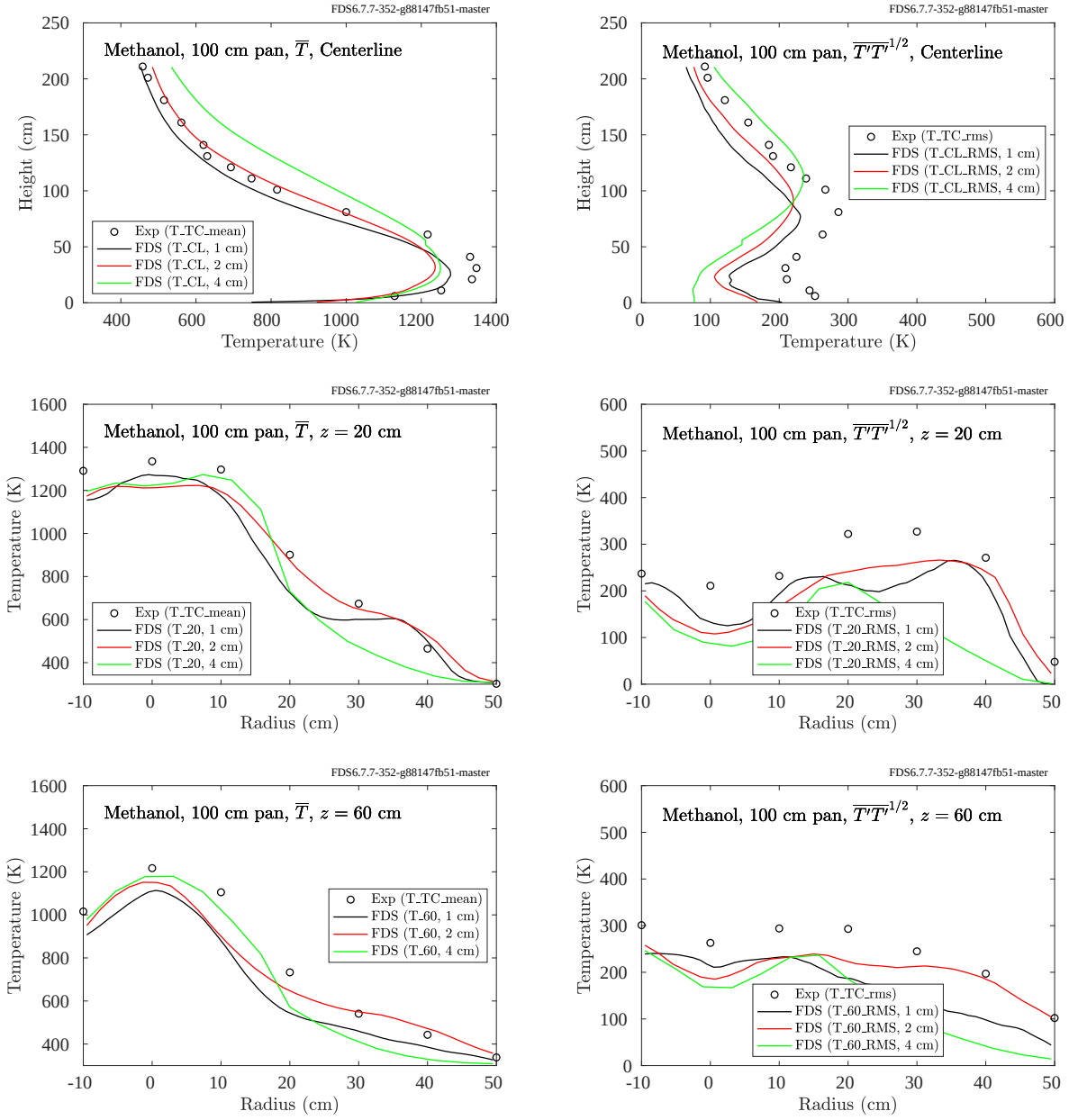

Figure 6.13: NIST Pool Fires, 100 cm methanol fire, centerline profiles of mean and rms temperature (top row), radial profiles at $z = 20$ cm (middle row) and $z = 60$ cm (bottom row).

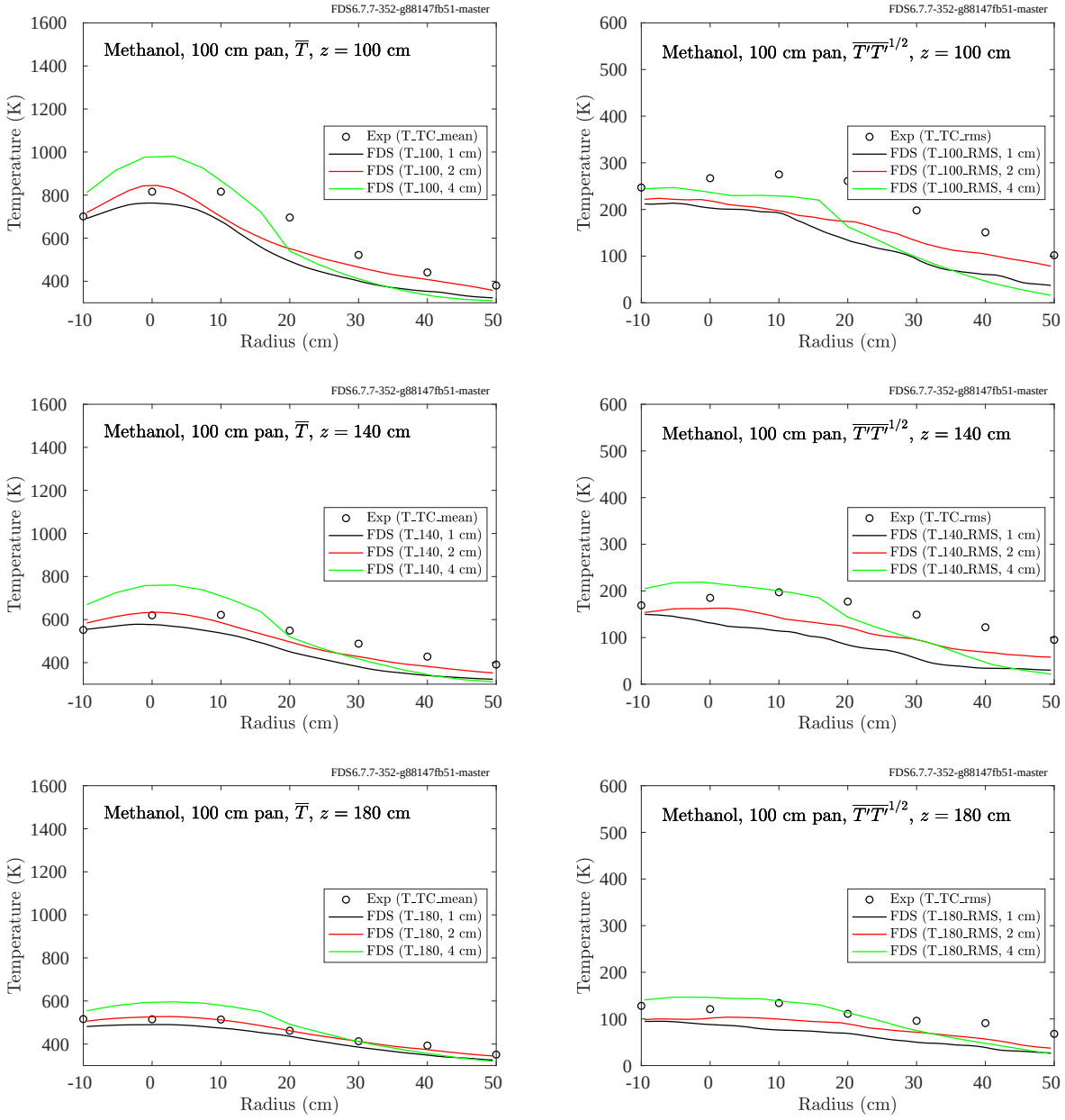

Figure 6.14: NIST Pool Fires, 100 cm methanol fire, radial profiles of mean and rms temperature at $z = 100$ cm (top row), $z = 140$ cm (middle row), $z = 180$ cm (bottom row).

6.1.6 NRCC Smoke Tower Experiments, Stairwell Plumes

A summary of these experiments can be found in Section 3.56.

The NRCC Smoke Tower experiments include measurements of the temperature of smoke ascending a 10 story stairwell. This data is included here in the chapter on Fire Plumes because smoke movement in a vertical shaft with stairs can be considered an obstructed plume. Shown in Fig. 6.15 are predictions of gas temperature measurements made in the center of the stairwell approximately 1.8 m above the slab at floors 2-10. Note that the plot labels "Slot" refer to the data acquisition system in the experiments only and have no meaning in the present context. It should be clear from the plot title how the various curves ought to be interpreted.

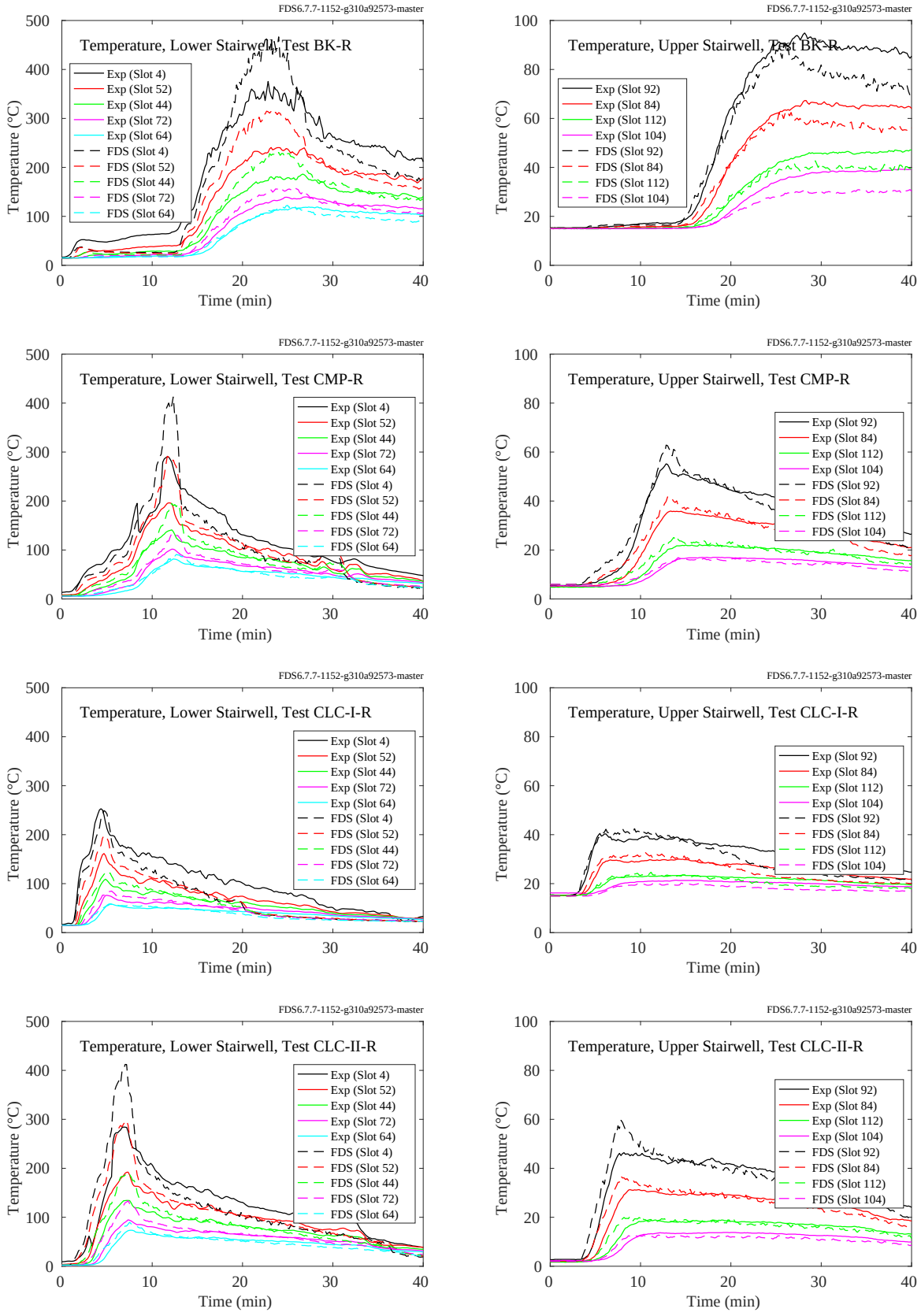

Figure 6.15: NRCC Smoke Tower, stairwell temperatures.

6.1.7 Sandia Methane Burner Experiments

A summary of these experiments can be found in Section 3.64.

Figures 6.16 through 6.19 compare measured and predicted thermocouple temperatures along the vertical centerline of 3 m methane gas burner fires.

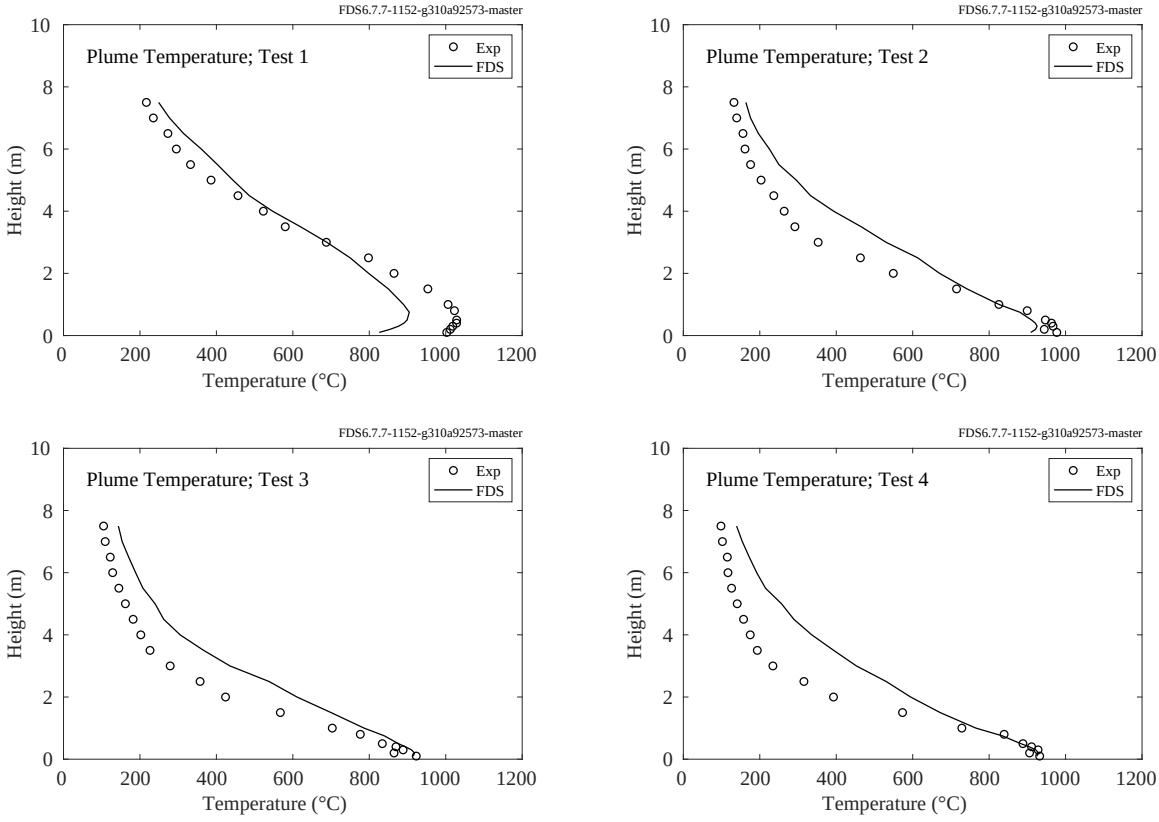

Figure 6.16: Sandia Methane Burner experiments, plume temperature, Tests 1-4.

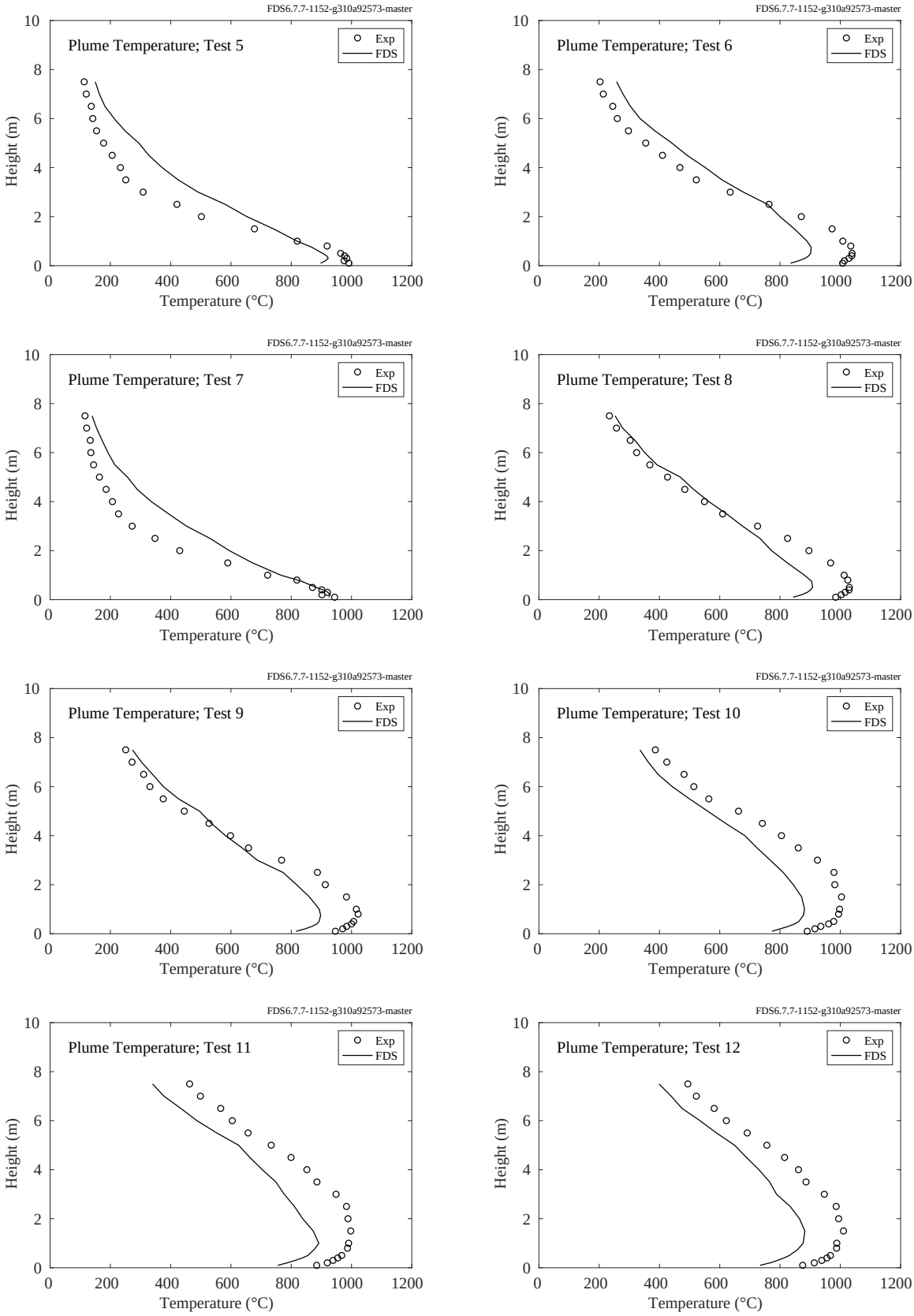

Figure 6.17: Sandia Methane Burner experiments, plume temperature, Tests 5-12.

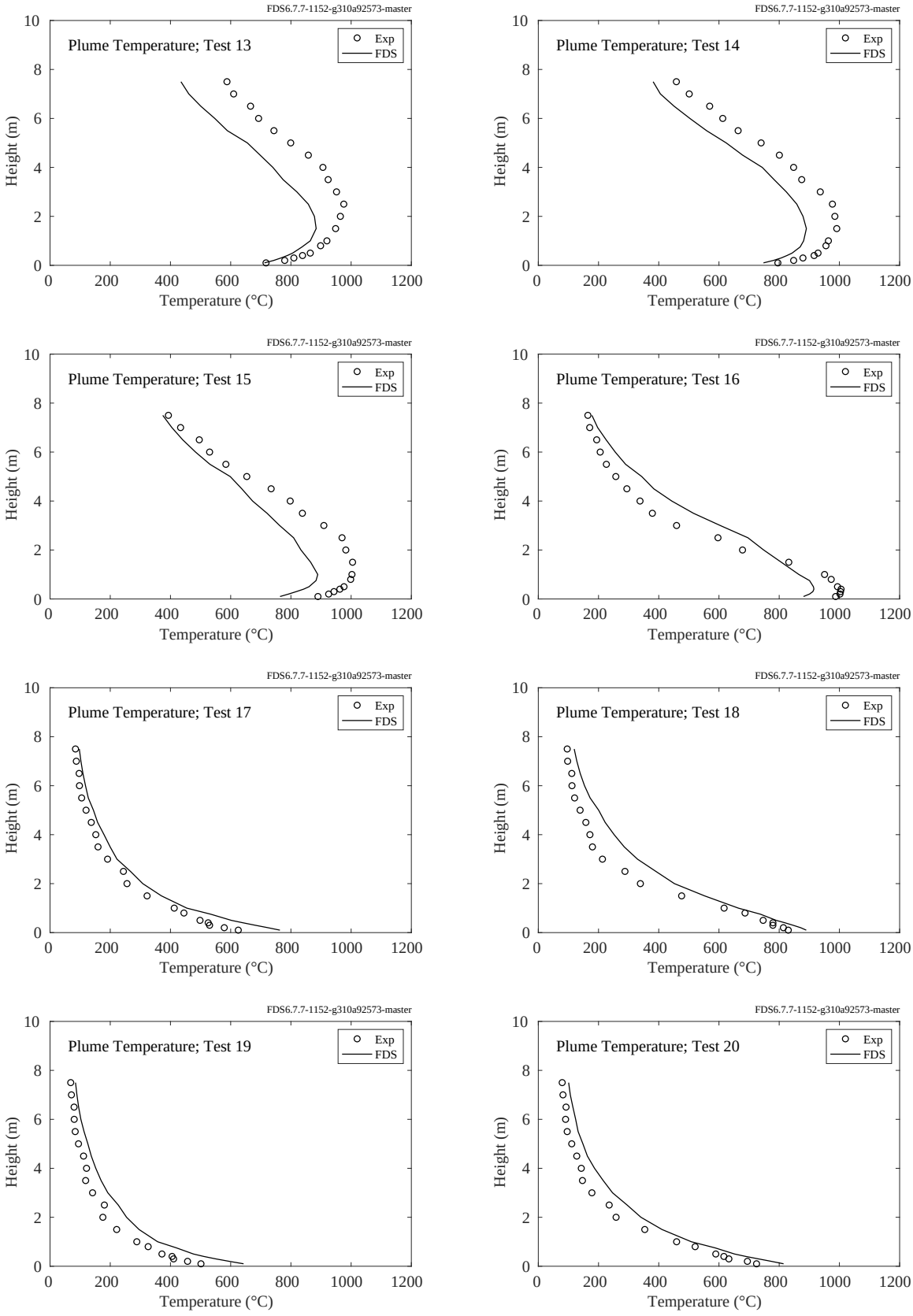

Figure 6.18: Sandia Methane Burner experiments, plume temperature, Tests 13-20.

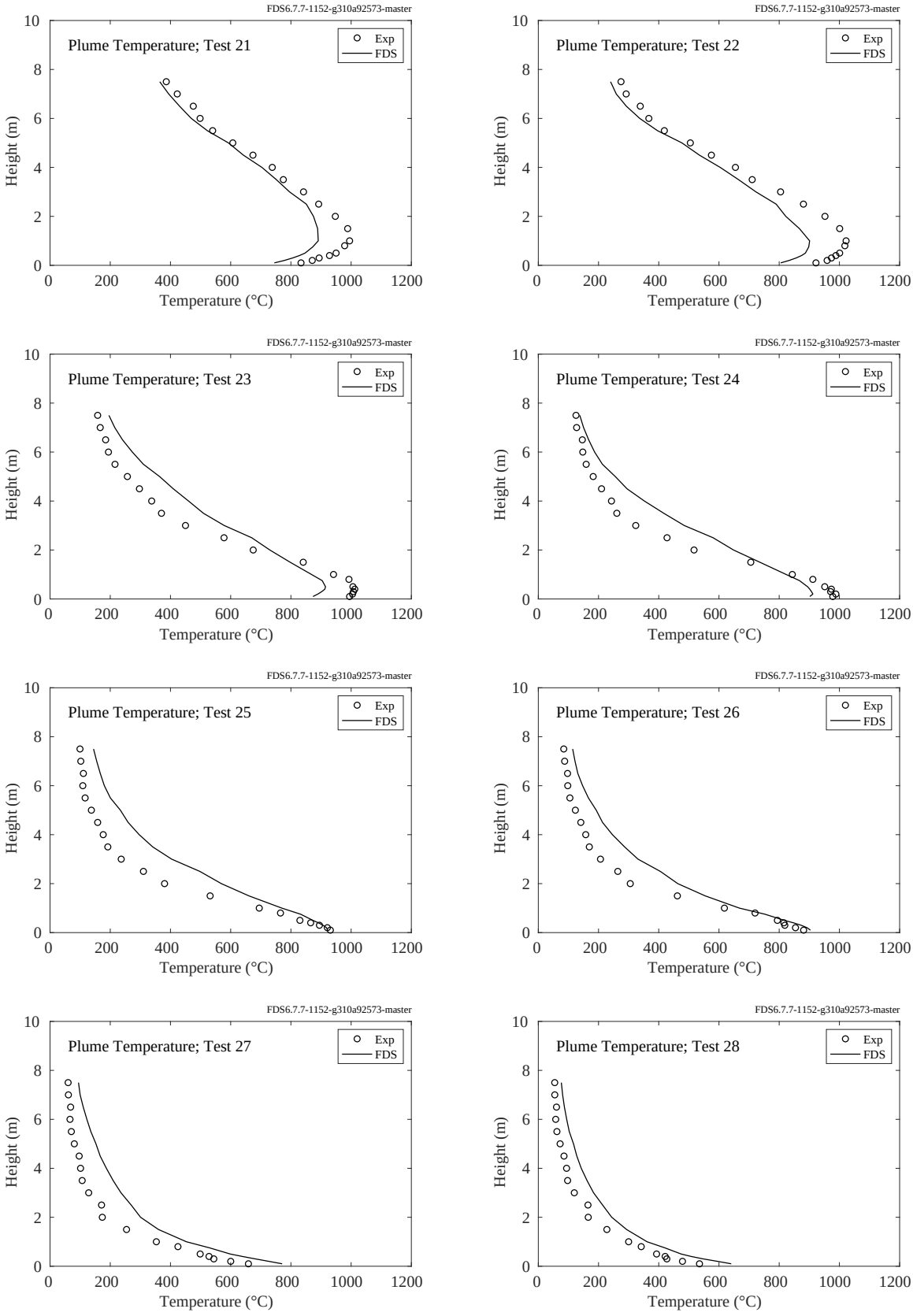

Figure 6.19: Sandia Methane Burner experiments, plume temperature, Tests 21-28.

6.1.8 SP Adiabatic Surface Temperature Experiments

A summary of these experiments can be found in Section 3.70.

Three experiments were conducted at SP, Sweden, in 2011, in which a 6 m long, 20 cm diameter vertical column was positioned in the middle of 1.1 m and 1.9 m diesel fuel and 1.1 m heptane pool fires [284]. Gas, plate, and steel surface temperature measurements were made at heights of 1 m, 2 m, 3 m, 4 m, and 5 m above the pool surface. Gas temperatures were measured with 0.25 mm and 0.50 mm bead thermocouples. The results are very similar and only the 0.25 mm values are used. In the experiments, the fire was reported to lean. The lean was significant for the 1.9 m diesel fuel fire. In that case, only data from 1 m and 2 m above the pool are used. The average temperature between 10 min and 15 min is the basic of comparison.

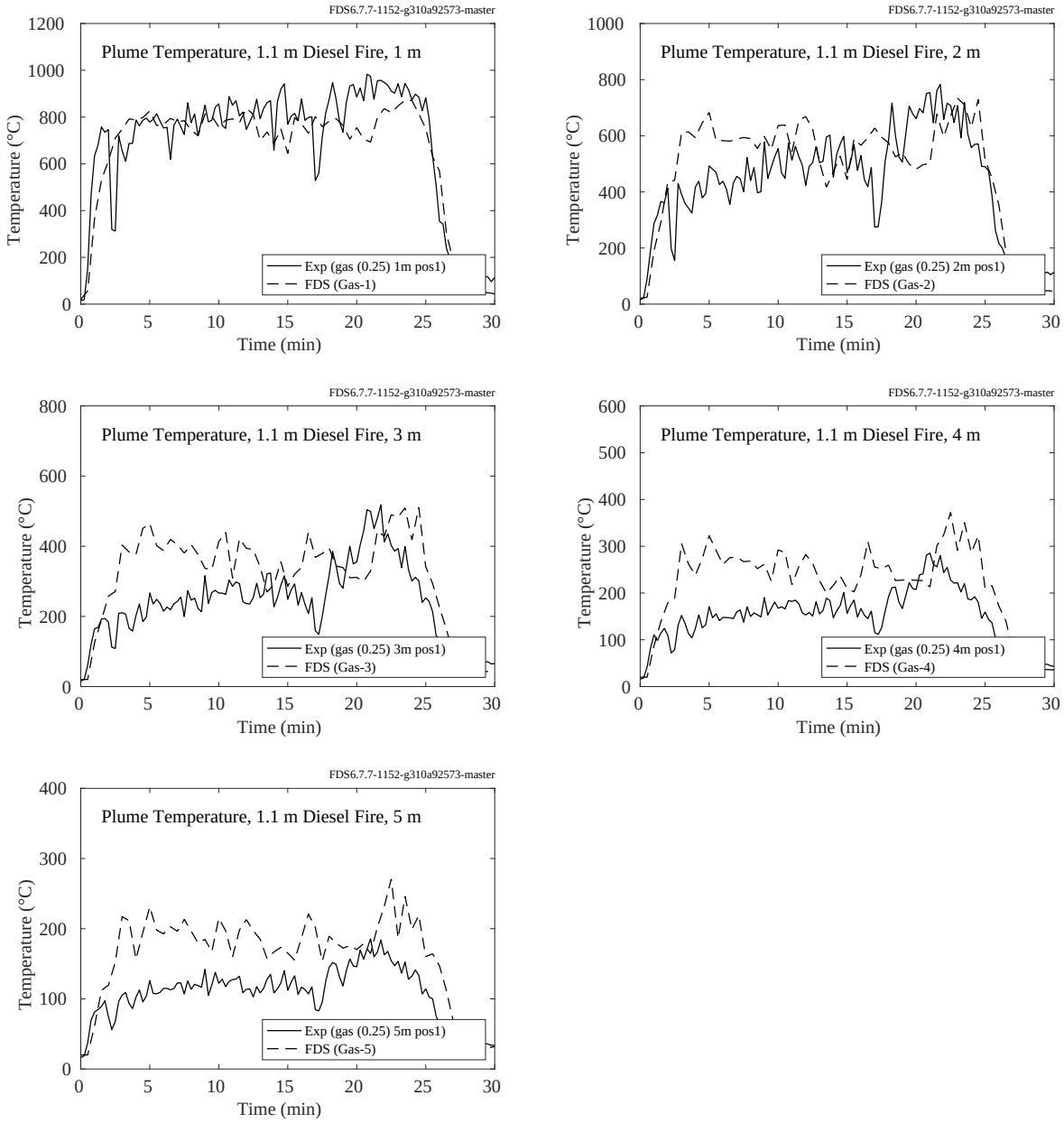

Figure 6.20: SP AST experiments, plume temperature, 1.1 m diesel fire.

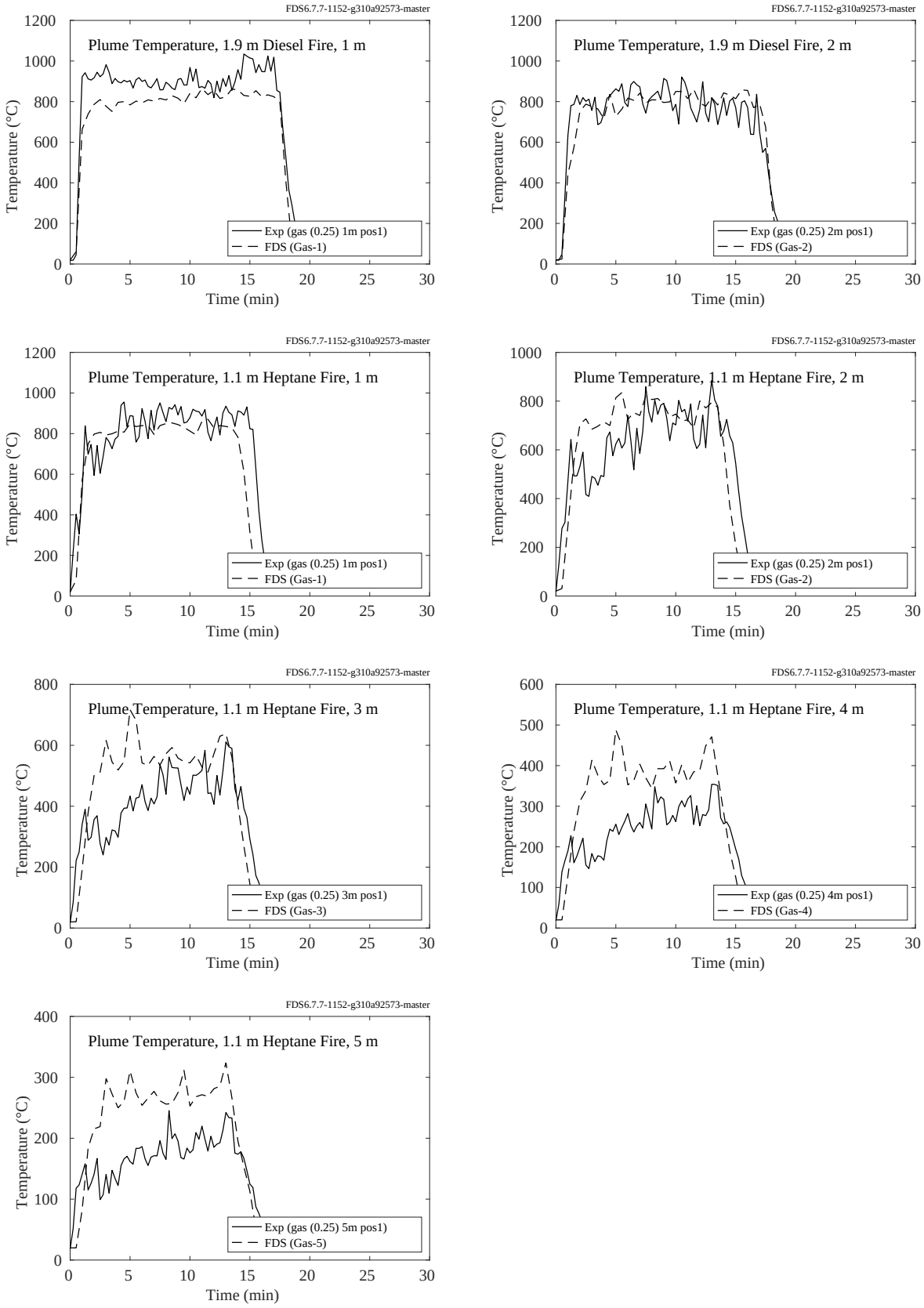

Figure 6.21: SP AST experiments, plume temperature, 1.9 m diesel and 1.9 m heptane fires.

6.1.9 UMD Line Burner

A summary of these experiments can be found in Section 3.80.

In this section, we present thermocouple temperature measurements and computational results for the UMD Line Burner. Experimental details may be found in White et al. [302]. FDS simulations are performed at three grid resolutions corresponding to $W/\delta x = 4, 8, 16$, where $W = 5$ cm is the width of the fuel slot in the line burner. Fig. 6.22 shows measured and computational results for mean thermocouple temperature across the width of the burner at two heights, z, above the burner surface. Fig. 6.23 shows a slice of gas temperature for the case with methane fuel and 18 vol. % O_2 in the coflow stream (nitrogen dilution). The purpose of the image is to provide a qualitative result for the flame.

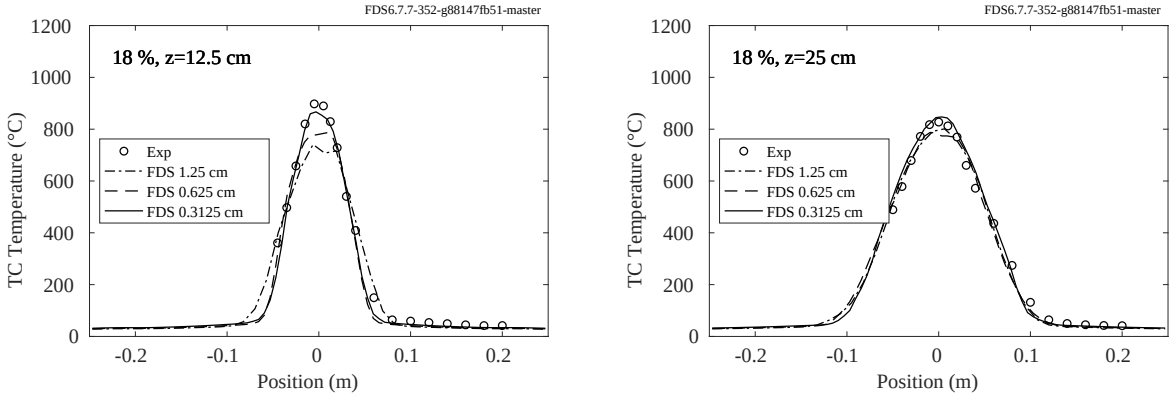

Figure 6.22: Measured and computed mean thermocouple temperature profiles at 18 vol % O_2.

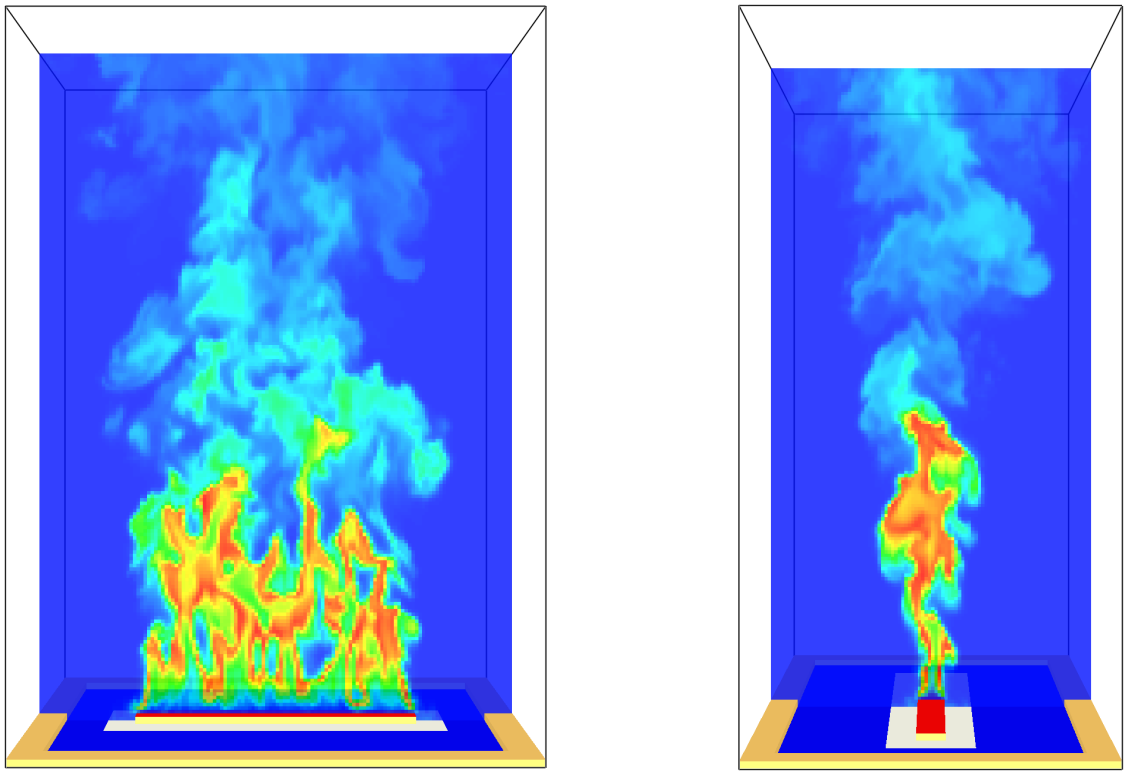

Figure 6.23: UMD Line Burner temperature contours, front (left) and side (right) views for the $\delta x = 0.625$ cm case. Fuel (natural gas in this case) enters through the red surface. The air with nitrogen dilution (to 18 vol. % O_2 in this case) enters through the blue surface. The white ceramic flame holder is seen surrounding the red burner surface. The right side view corresponds to the profiles shown in Fig. 6.22 through the center of the burner at different heights z from the red burner surface. Within the slice plane blue represents 20 °C, red 1500 °C.

6.1.10 USN High Bay Hangar Experiments

A summary of these experiments can be found in Section 3.84.

A large number of plume temperature measurements are available from the US Navy experiments conducted at Keflavik, Iceland, and Barber's Point, Hawaii. The hangars were very large in size (22 m high in Iceland and 15 m high in Hawaii) and the heat release rates varied from 100 kW to 33 MW. All experiments made use of a fuel pan filled with either JP-5 or JP-8 jet fuel, positioned in the center of the hangar.

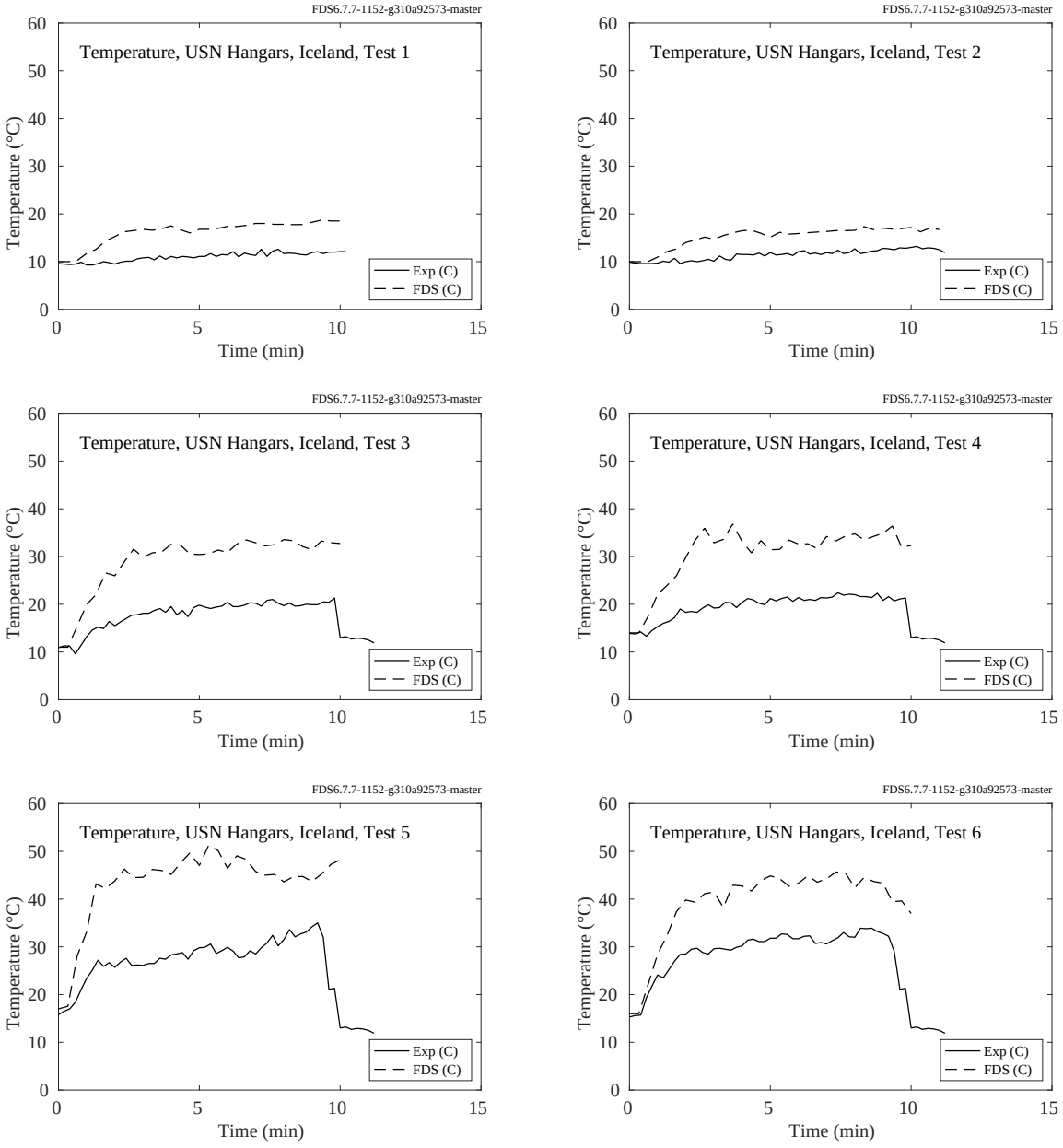

Figure 6.24: USN Hangar experiments, Iceland, plume temperature, Tests 1-6.

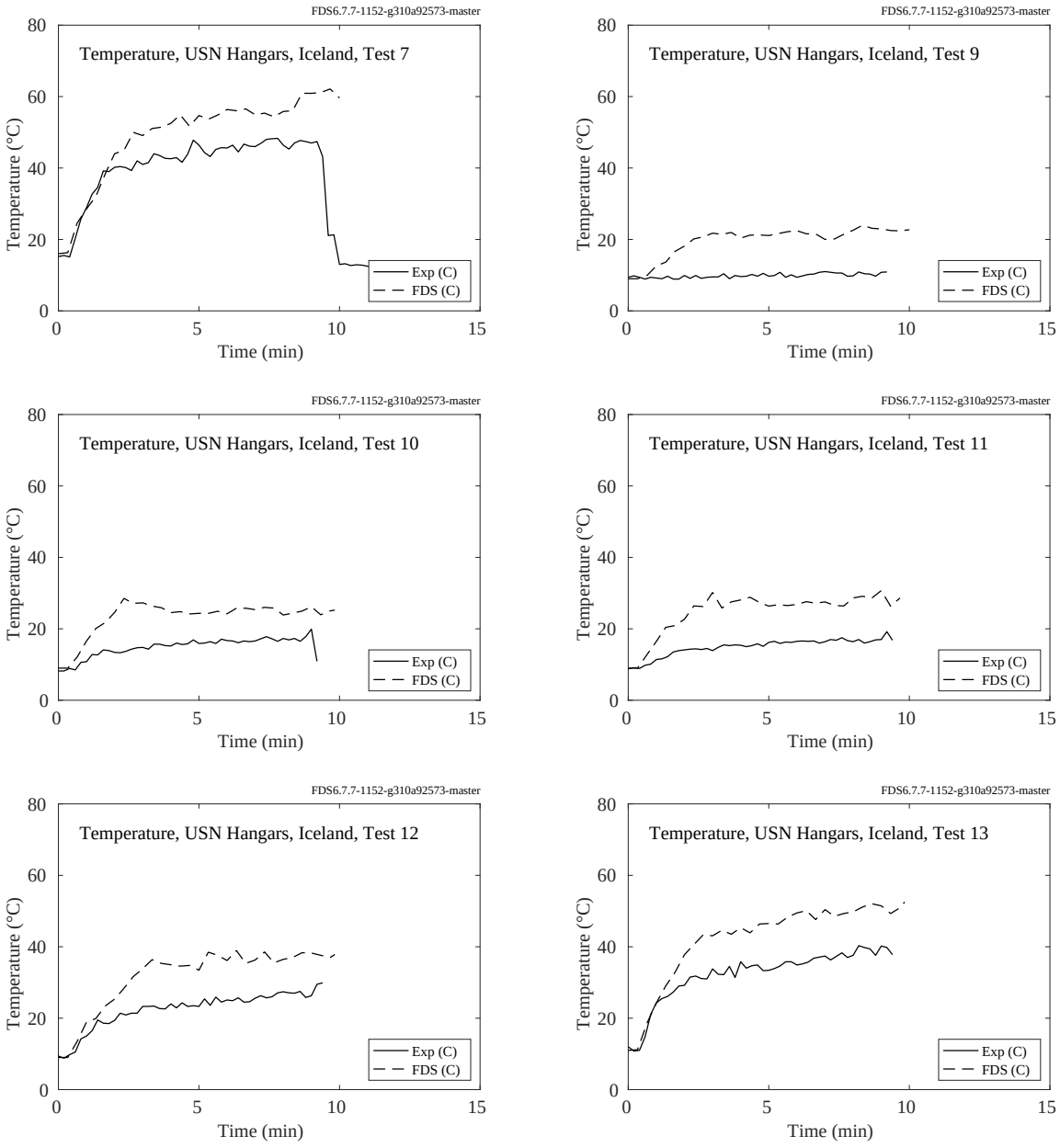

Figure 6.25: USN Hangar experiments, Iceland, plume temperature, Tests 7, 9-13.

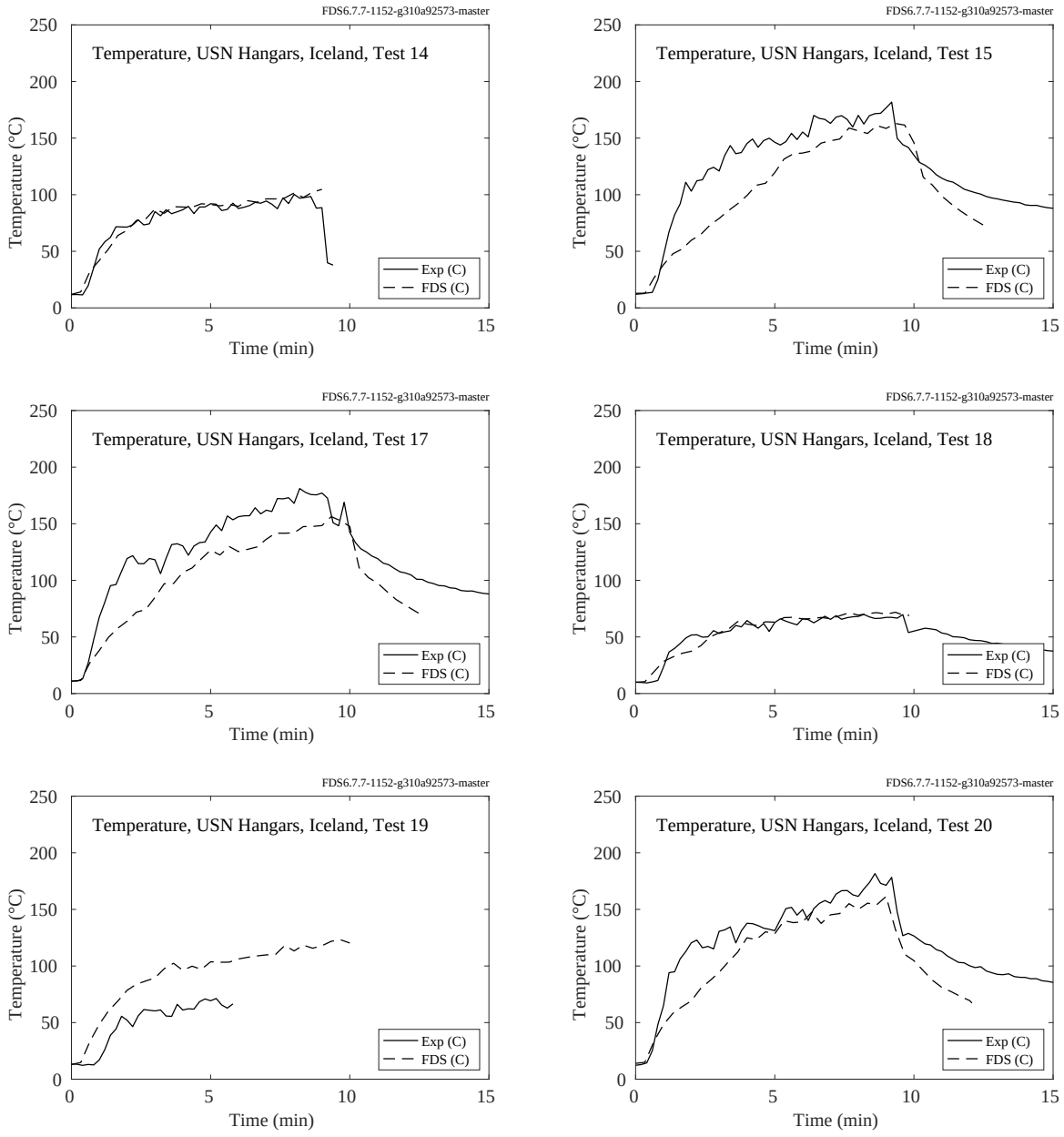

Figure 6.26: USN Hangar experiments, Iceland, plume temperature, Tests 14-15, 17-20.

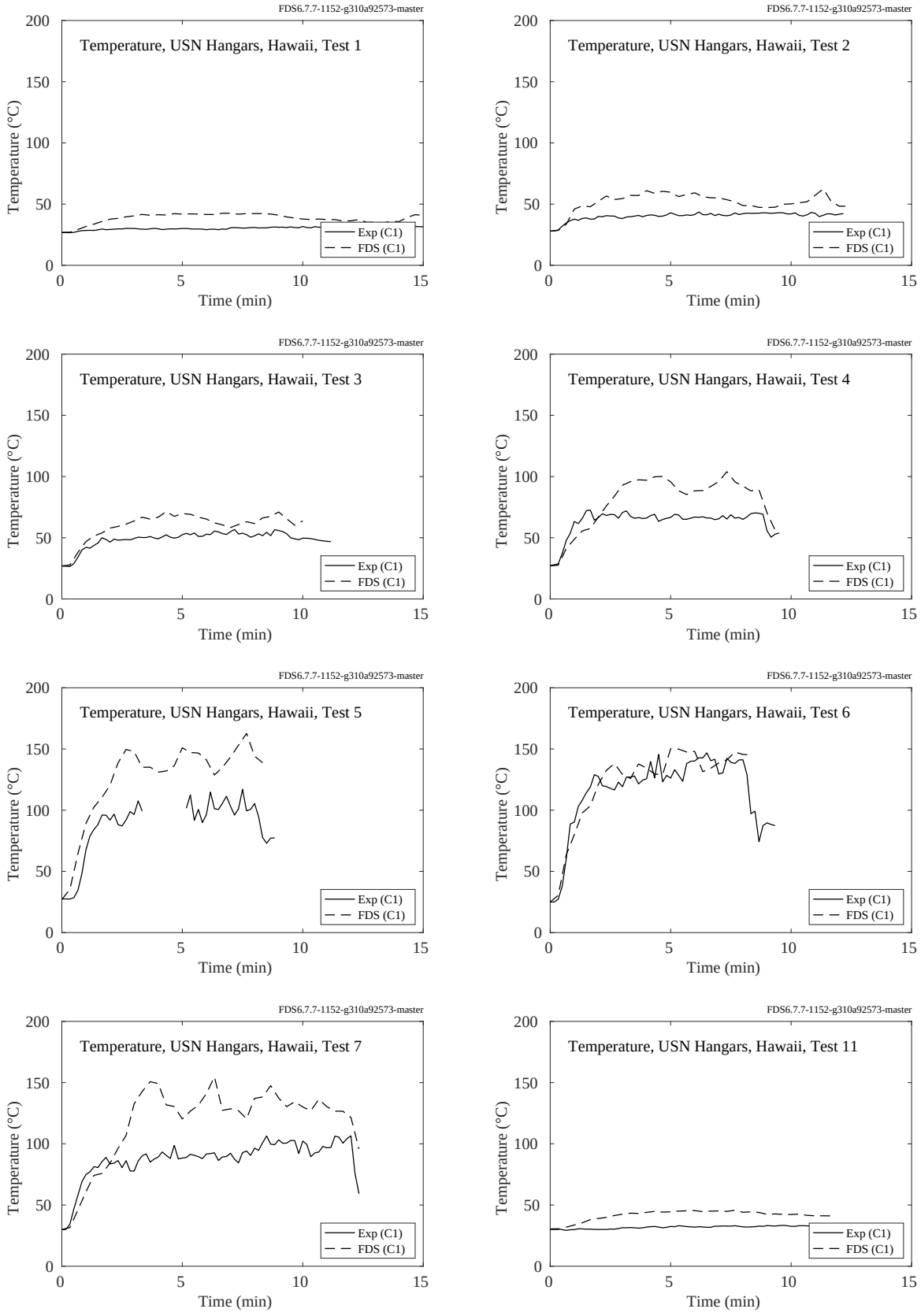

Figure 6.27: USN Hangar experiments, Hawaii, plume temperature, Tests 1-7, 11.

6.1.11 VTT Large Hall Experiments

A summary of these experiments can be found in Section 3.88.

The VTT experiments consisted of liquid fuel pan fires positioned in the middle of a large fire test hall. Plume temperatures were measured at two heights above the fire, 6 m (T G.1) and 12 m (T G.2). The flames were observed to extend to about 4 m above the fire pan.

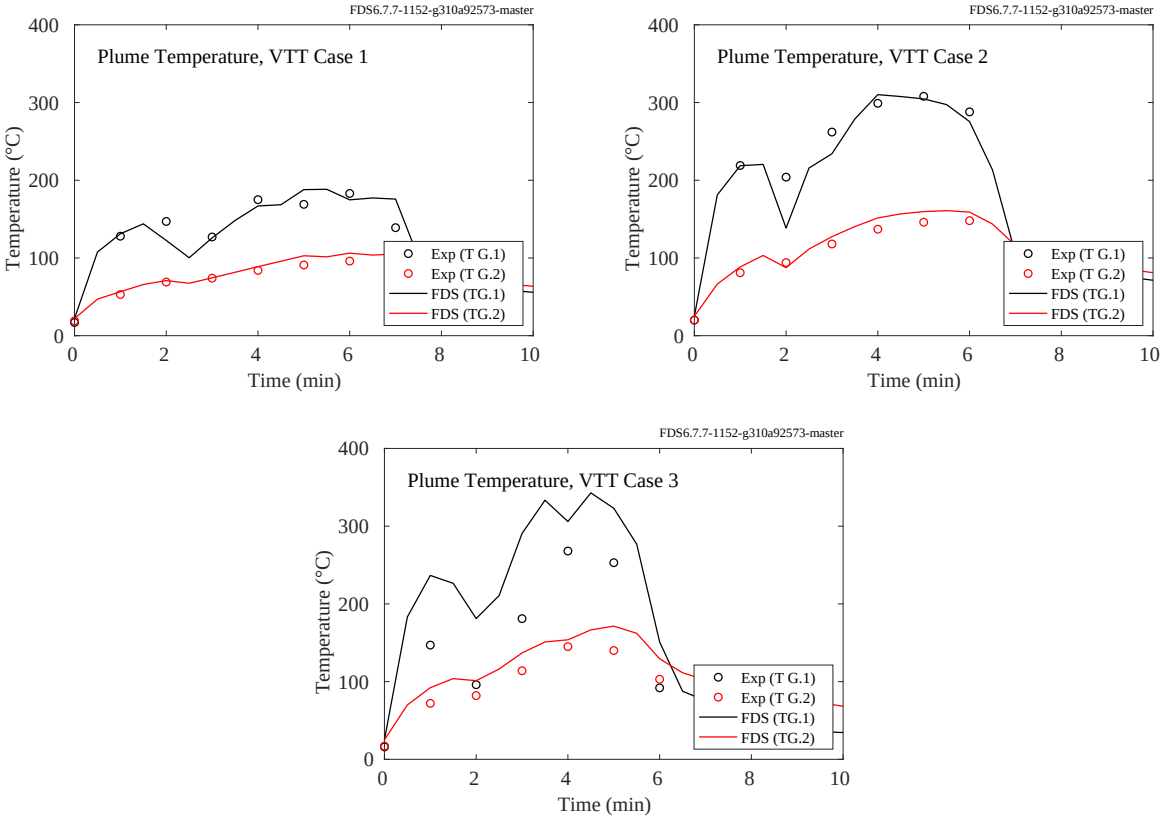

Figure 6.28: VTT experiments, plume temperature.

6.1.12 Waterloo Methanol Pool Fire Experiment

A summary of these experiments can be found in Section 3.90.

Figure 6.29 displays the centerline profile of measured and predicted mean temperatures above a 30 cm diameter methanol pool fire. These measurements were conducted by Hamins and Lock [312] at NIST, along with radial profiles at 40 cm, 50 cm, and 60 cm. All of the other measurements on the following pages were conducted by Weckman at the University of Waterloo [310].

Figures 6.30 through 6.33 display radial profiles of measured and predicted mean (left hand plots) and root mean square (right hand plots) temperatures. The root mean square of the temperature is given by

$$\left(\overline{T'T'}\right)^{1/2} = \sqrt{\frac{\sum_{i=1}^{n}(T_i - \overline{T})^2}{n-1}} \tag{6.2}$$

where T_i is the instantaneous value of temperature and $\overline{T}$ is the average value over 50 s. The profile heights range from 2 cm to 30 cm above the pool surface. Time resolved temperature data was measured using 50 μm diameter, bare-wire thermocouples (Pt vs Pt-10% Rh) with known bead diameters in the range of 75 μm to 100 μm.

Figures 6.34 through 6.36 display radial profiles of measured and predicted estimates of temperature-velocity covariances:

$$\overline{w'T'} = \frac{\sum_{i=1}^{n}(w_i - \overline{w})(T_i - \overline{T})}{n-1} \quad ; \quad \overline{u'T'} = \frac{\sum_{i=1}^{n}(u_i - \overline{w})(T_i - \overline{T})}{n-1} \tag{6.3}$$

where u_i and w_i are instantaneous values of the horizontal and vertical components of velocity and $\overline{u}$ and $\overline{w}$ are 50 s time averages.

The FDS results are shown at three grid resolutions, 0.5 cm, 1 cm, and 2 cm.

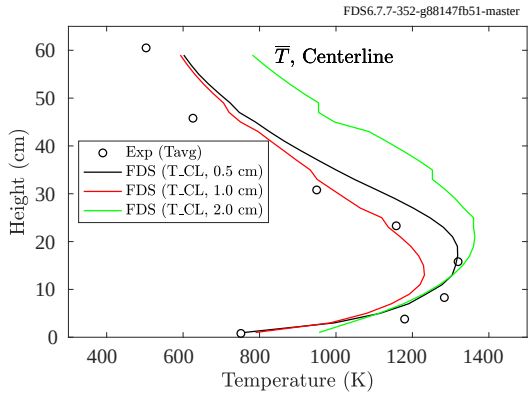

Figure 6.29: Waterloo Methanol, centerline profile of mean temperature, 2 cm to 60 cm above the burner.

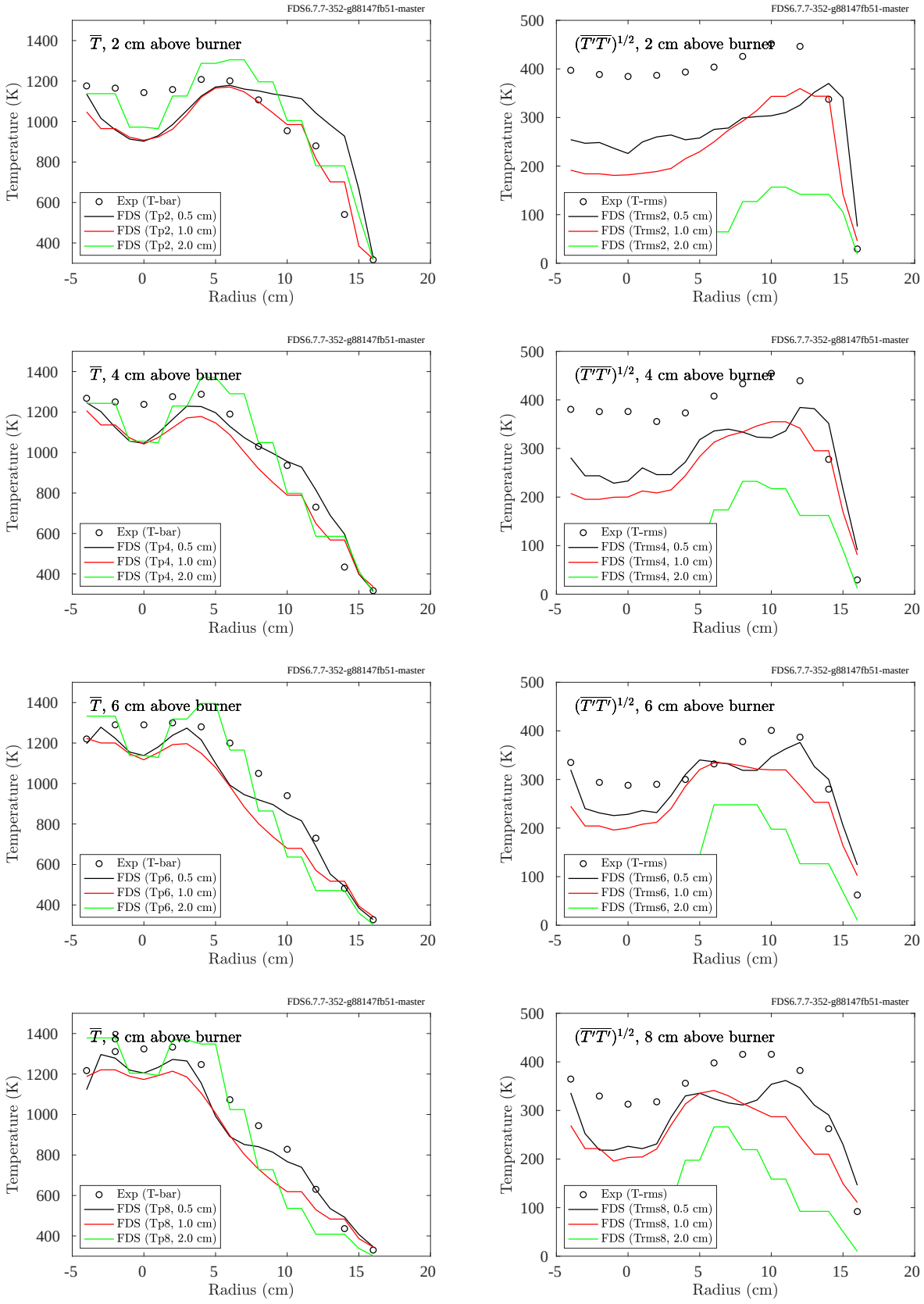

Figure 6.30: Waterloo Methanol, radial profiles of mean (left) and rms (right) temperature, 2 cm to 8 cm above the burner.

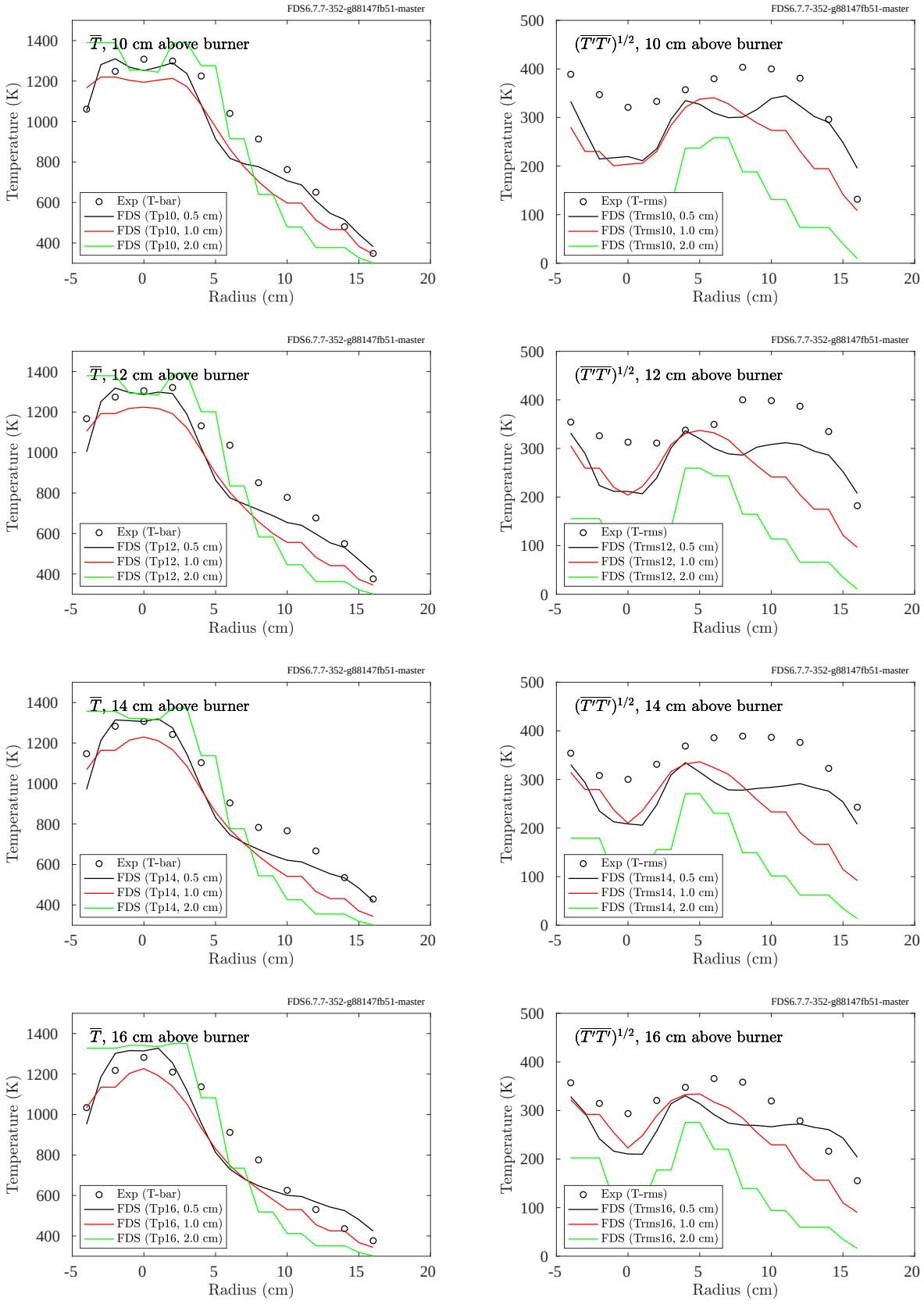

Figure 6.31: Waterloo Methanol, radial profiles of mean (left) and rms (right) temperature, 10 cm to 16 cm above the burner.

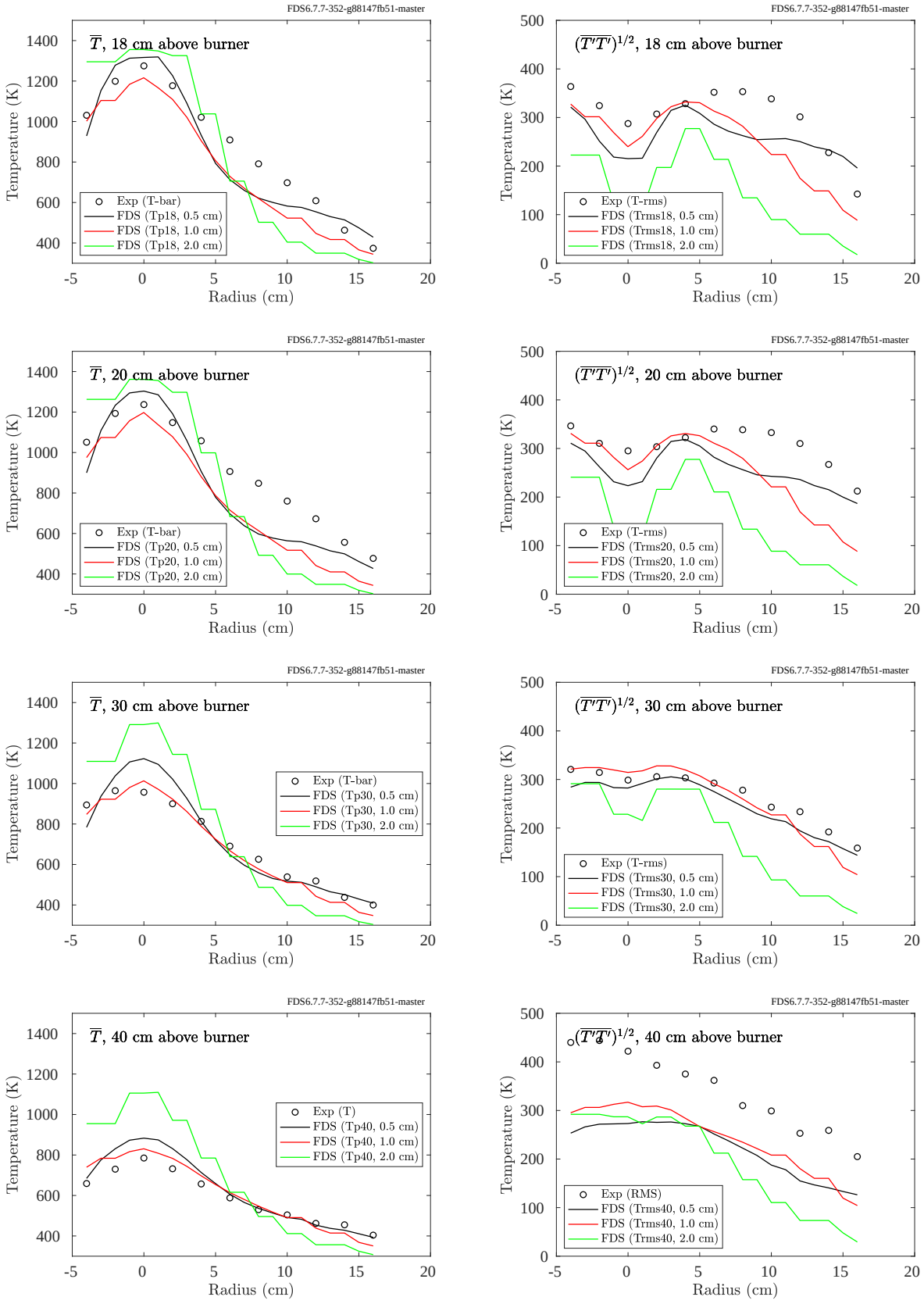

Figure 6.32: Waterloo Methanol, radial profiles of mean (left) and rms (right) temperature, 18 cm to 40 cm above the burner. The measurement at 40 cm was performed by Hamins and Lock [312].

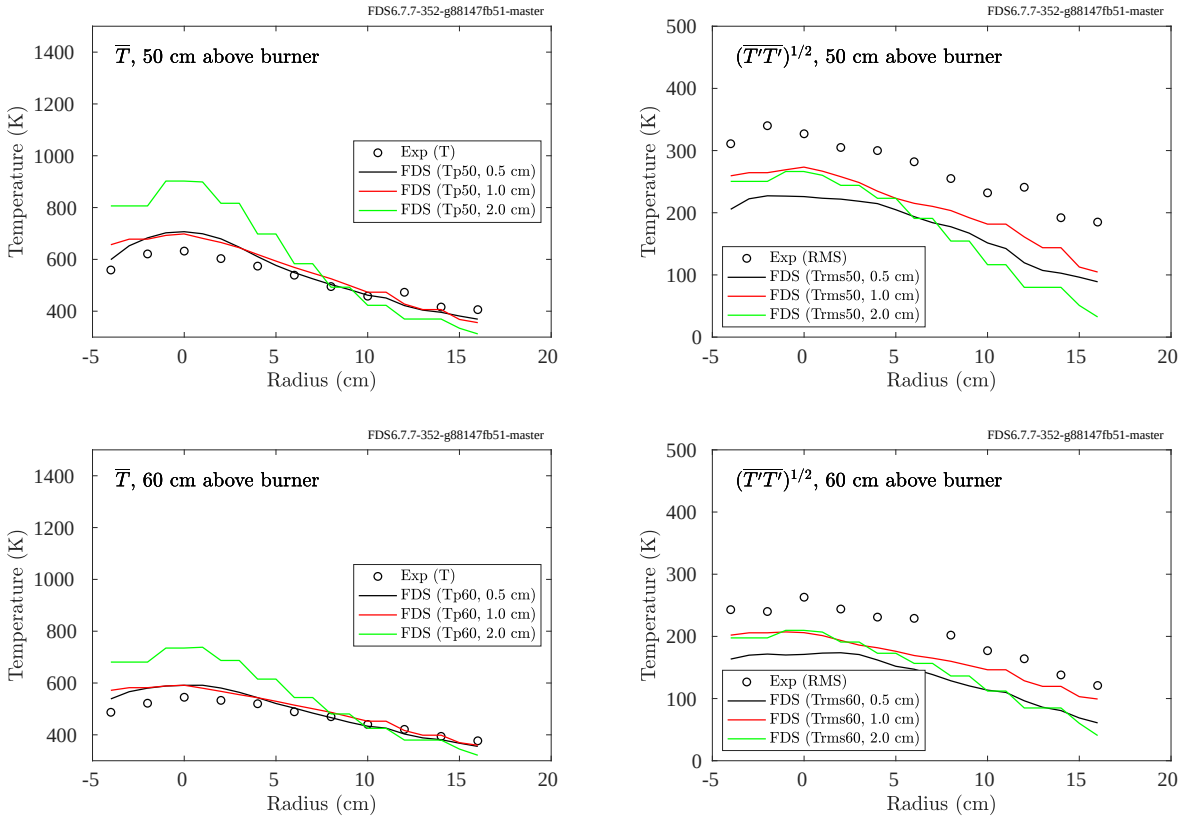

Figure 6.33: Waterloo Methanol, radial profiles of mean (left) and rms (right) temperature, 50 cm to 60 cm above the burner. The measurements were performed by Hamins and Lock [312].

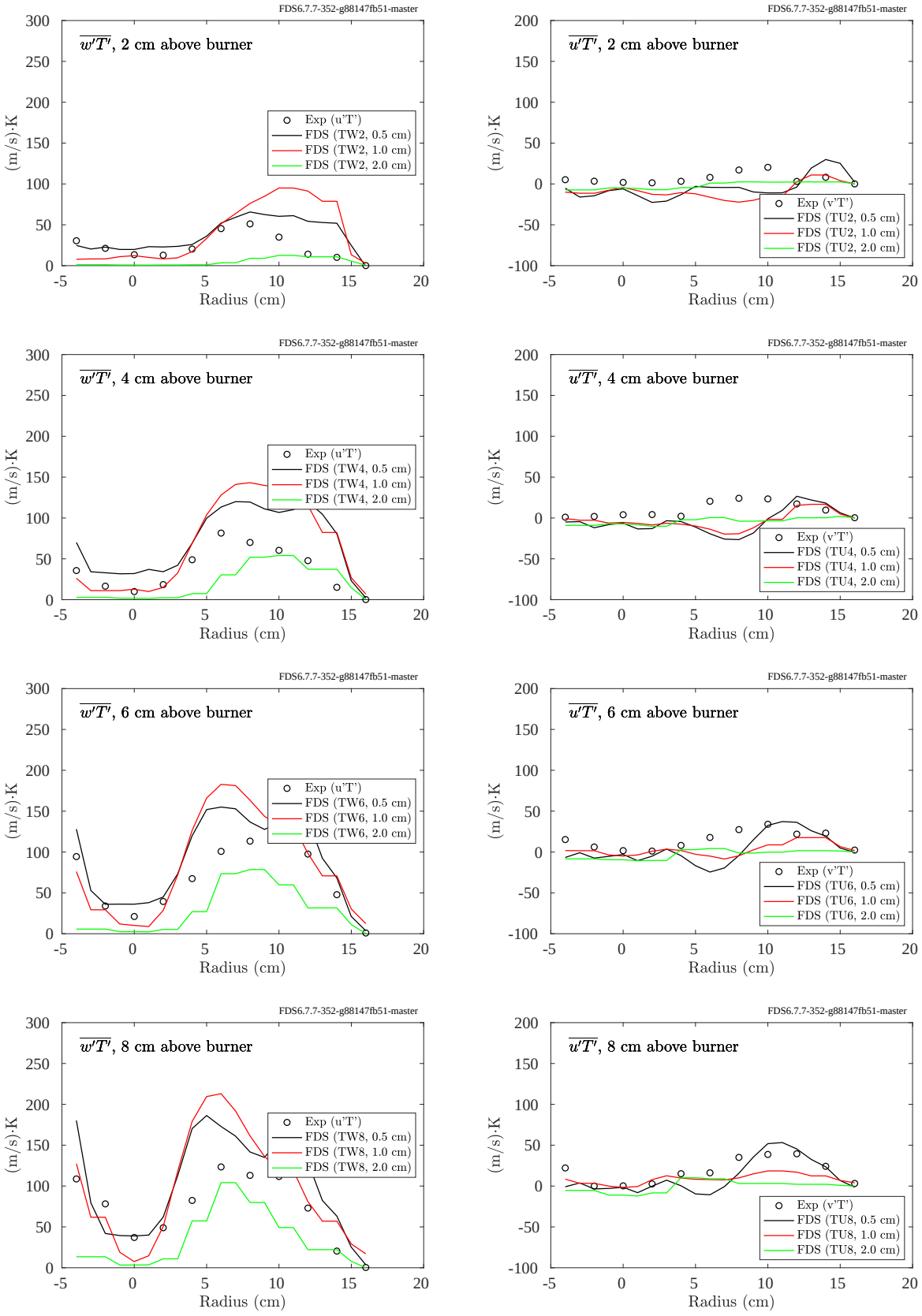

Figure 6.34: Waterloo Methanol, radial profiles of $\overline{T'w'}$ (left) and $\overline{T'u'}$ (right), 2 cm to 8 cm above the burner.

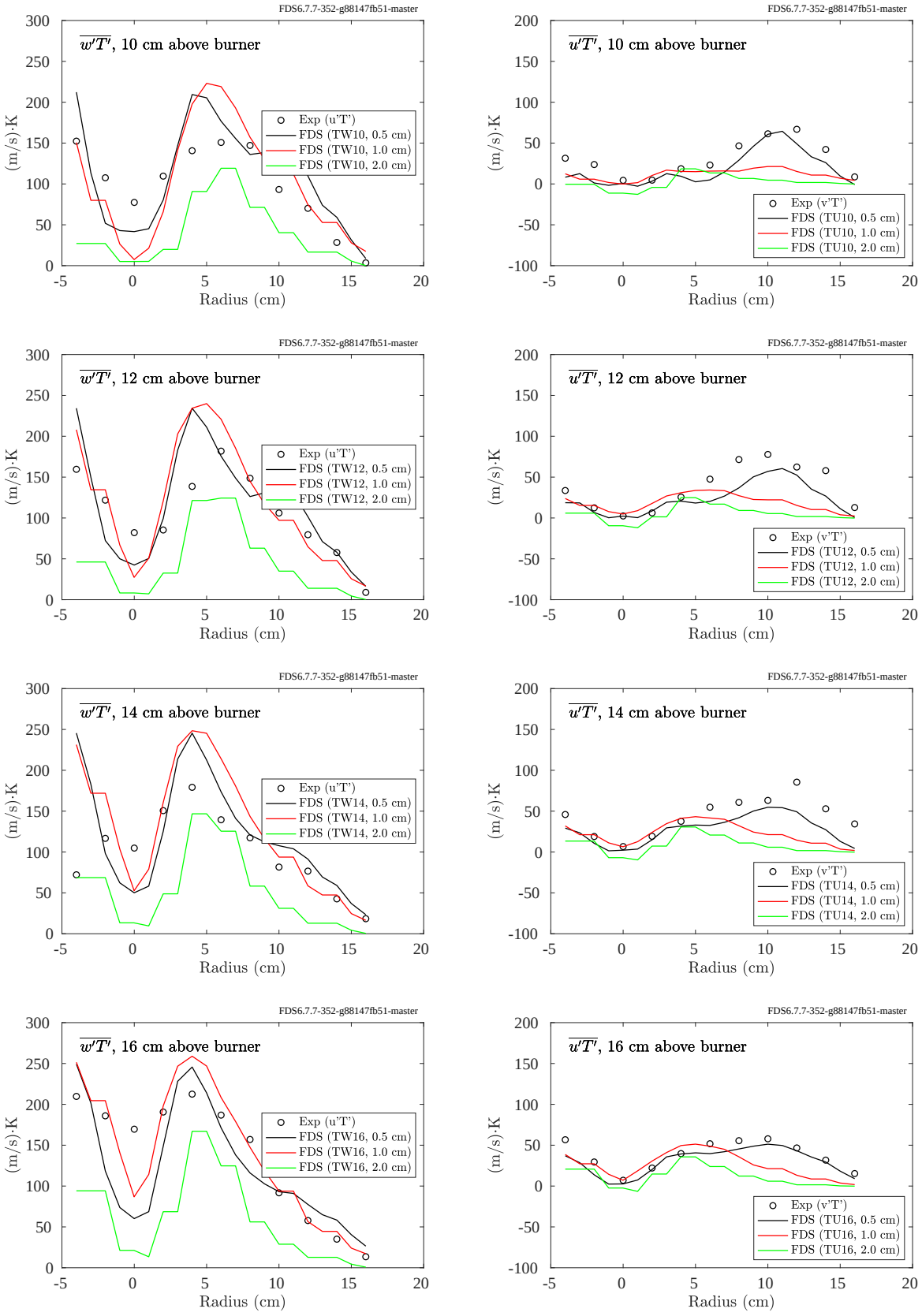

Figure 6.35: Waterloo Methanol, radial profiles of $\overline{T'w'}$ (left) and $\overline{T'u'}$ (right), 10 cm to 16 cm above the burner.

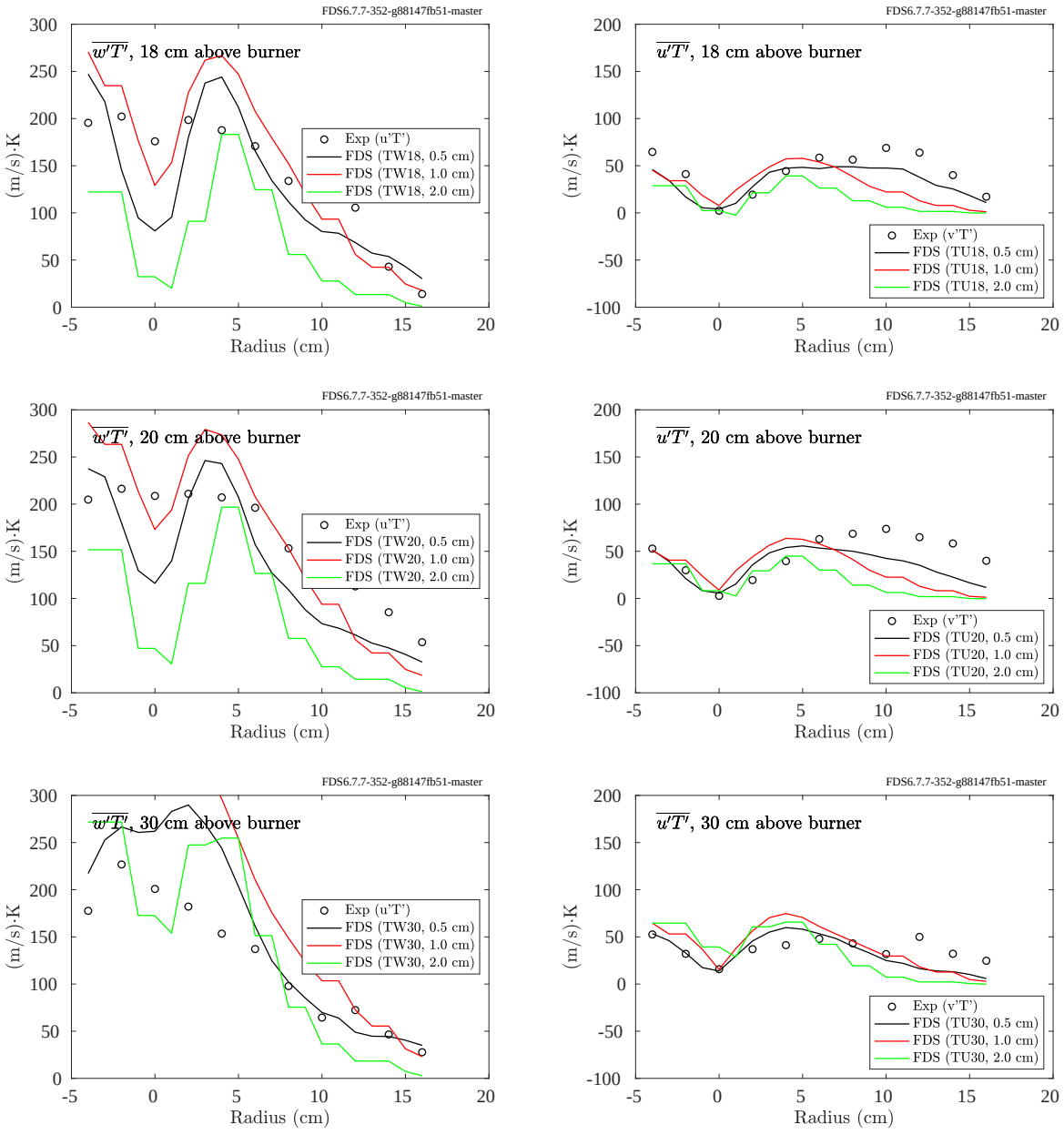

Figure 6.36: Waterloo Methanol, radial profiles of $\overline{T'w'}$ (left) and $\overline{T'u'}$ (right), 18 cm to 30 cm above the burner.

6.1.13 Summary of Plume Temperature Predictions

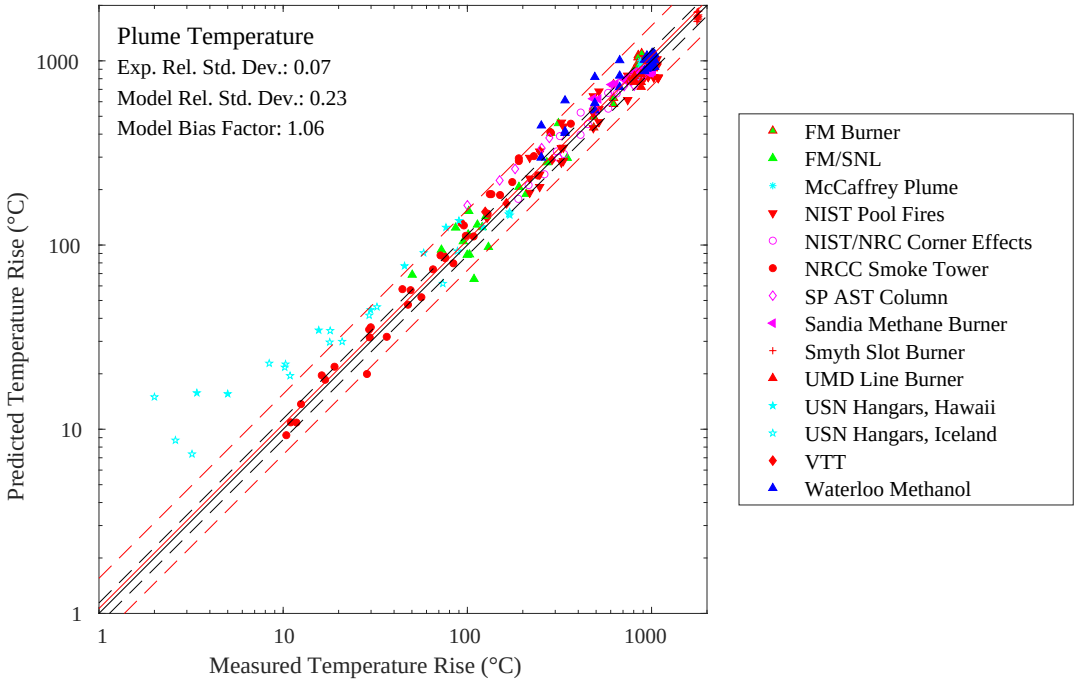

Figure 6.37: Summary of plume temperature predictions.

6.2 Flame Height

In fire experiments, the flame height is typically defined as the height at which luminous flame can be seen 50 % of the time. For simulations, the "flame height" can be defined as the height at which most of the fire's energy has been released. "Most" is taken as some fraction, f, between 0.95 and 0.99. Mathematically, this is found by considering the heat release rate per unit vertical length, z:

$$\dot{q}'(z,t) = \int_{-\infty}^{\infty}\int_{-\infty}^{\infty} \dot{q}'''(x',y',z,t)\,\mathrm{d}x'\,\mathrm{d}y' \tag{6.4}$$

where $\dot{q}'''(x,y,z,t)$ is the instantaneous heat release rate per unit volume at a specific point in the domain. The flame height of the simulated fire is given by $z_L(t)-z_0$, where $z_L(t)$ is the height at which the cumulative heat release rate reaches the fraction, f, of the total, $\dot{Q}(t)$.

$$f\,\dot{Q}(t) = \int_{z_0}^{z_L(t)} \dot{q}'(z',t)\,\mathrm{d}z' \tag{6.5}$$

z_0 is the height of the firebed or burner surface.

6.2.1 Heskestad's Flame Height Correlation

Table 6.1 lists the parameters for FDS simulations of fires in a 1 m by 1 m square pan[2]. Figure 6.38 shows a verification of the heat release rate for each case, and Fig. 6.39 compares the FDS predictions with Heskestad's empirical correlation. Note that the flame height for the FDS simulations is defined as the distance above the pan, on average, at which 99 % of the fuel has been consumed. Note also that the simulations were run at three different grid resolutions. A convenient length scale is given by

$$D^* = (Q^*)^{2/5} D \tag{6.6}$$

Given a grid cell size, δx, the three resolutions can be characterized by the non-dimensional quantity, $D^*/\delta x$, whose values in these cases are 5, 10 and 20.

The flame height definition used in Fig. 6.39 (99 % fuel consumption) is admittedly arbitrary and is often questioned when FDS predictions of flame height are compared with experimental values, which are usually based on luminosity (effectively measuring radiation emission from soot). Further, Heskestad's flame height correlation is one among many such correlations [25, 331, 332, 333, 334, 335, 336], and the reported variation is significant, especially at low values of Q^* where the details of the burner configuration (shape of the burner, etc.) become important. To illustrate the uncertainty one can expect from FDS calculations and to test the sensitivity of the reported FDS results to the flame height definition, Fig. 6.40 shows two different FDS flame height predictions, one at 99 % fuel consumption (as in Fig. 6.39)—the red curve—and one using 95 % fuel consumption—the blue curve. Three different grid resolutions were run for each flame height definition. For 99 % fuel consumption, the red dashed line is the maximum flame height from the three resolutions. For 95 % fuel consumption, the blue dashed line is the minimum flame height from the three resolutions. We also overlay several different flame height correlations (colored solid lines).

Figure 6.41 includes comparisons of the predicted HRR as a function of the height of the burner for three different values of Q^*. The experimental measurements were performed by Tamanini at Factory Mutual [337]. Both the HRR and height above the burner have been non-dimensionalized by the total HRR and the flame height, respectively. These results demonstrate that the predicted spatial distribution of the energy release improves as the numerical grid is refined.

[2]The effective diameter, D, of a 1 m square pan is 1.13 m, obtained by equating the area of a square and circle.

Table 6.1: Summary of parameters for the flame height predictions. The grid cell size, δx_{10}, refers to the case where $D^*/\delta x$=10.

Q^*	$\dot{Q}$ (kW)	D^* (m)	δx_5 (m)	δx_{10}	δx_{20}
0.1	151	0.45	0.090	0.045	0.022
0.2	303	0.59	0.119	0.059	0.030
0.5	756	0.86	0.171	0.086	0.043
1	1513	1.13	0.226	0.113	0.057
2	3025	1.49	0.298	0.149	0.075
5	7564	2.15	0.430	0.215	0.108
10	15127	2.84	0.568	0.284	0.142
20	30255	3.75	0.749	0.375	0.187
50	75636	5.40	1.081	0.540	0.270
100	151273	7.13	1.426	0.713	0.356
200	302545	9.41	1.882	0.941	0.470
500	756363	13.6	2.715	1.357	0.679
1000	1512725	17.9	3.582	1.791	0.895
2000	3025450	23.6	4.726	2.363	1.182
5000	7563625	34.1	6.819	3.409	1.705
10000	15127250	45.0	8.997	4.499	2.249

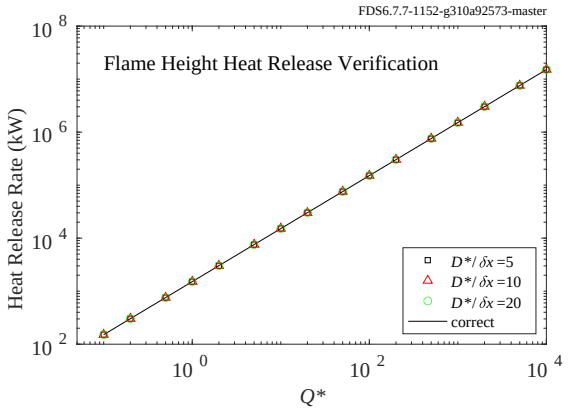

Figure 6.38: Verification of the heat release rate for Heskestad Flame Height cases.

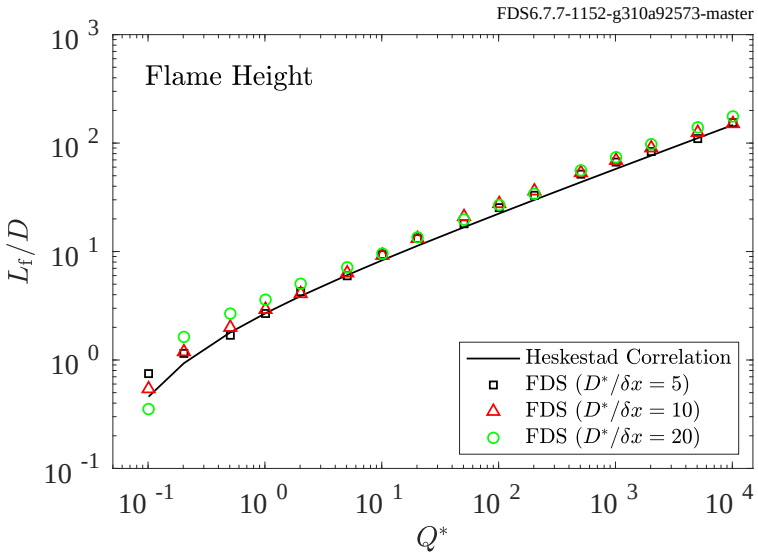

Figure 6.39: Comparison of FDS predictions of flame height from a 1 m square pan fire for Q^* values ranging from 0.1 to 10000.

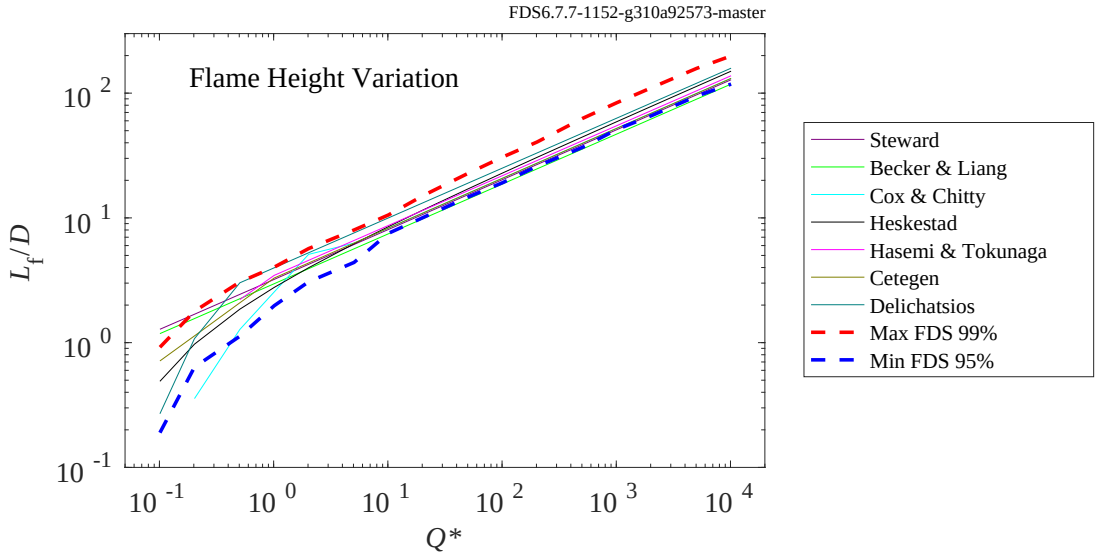

Figure 6.40: Flame height predictions from various correlations compared with FDS predictions using two different flame height definitions. Uncertainty (maximum variation) at $Q^* > 1$ is ± 15 %. At $Q^* = 0.1$, the uncertainty is approximately ± 65 %. Correlation references: Steward [331], Becker and Liang [332], Cox and Chitty [333], Heskestad [25], Hasemi and Tokunaga [334], Cetegen [335], Delichatsios [336].

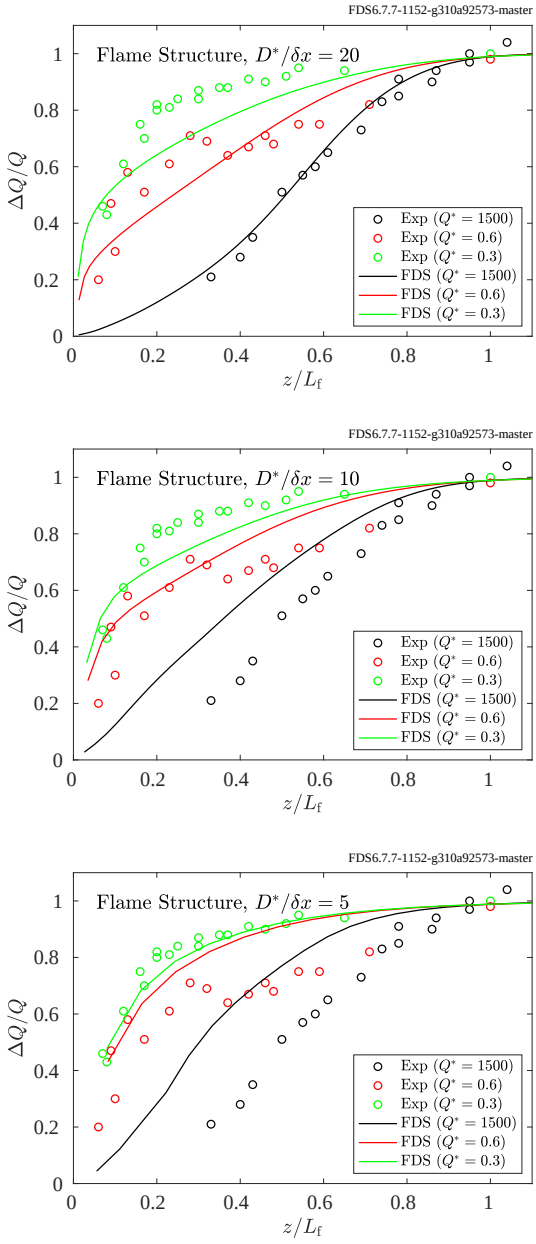

Figure 6.41: Predicted HRR as a function of height above the burner compared to measurements.

6.2.2 UMD Line Burner

A summary of these experiments can be found in Section 3.80.

FDS simulations are performed at three grid resolutions corresponding to $W/\delta x = 4, 8, 16$, where $W = 5$ cm is the width of the fuel slot in the line burner. Fig. 6.42 shows measured and predicted flame heights of the methane and propane fires as a function of oxygen concentration. For FDS, the flame height is taken as the distance above the burner where 97 % of the fuel gas is consumed, on average.

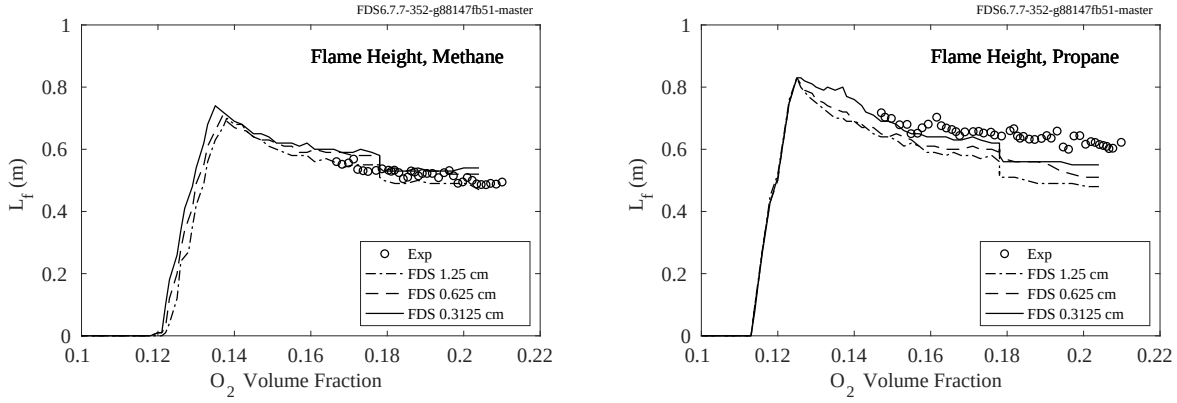

Figure 6.42: Measured and predicted mean flame heights for the methane and propane UMD Line Burner experiments.

6.2.3 Flame Height Summary

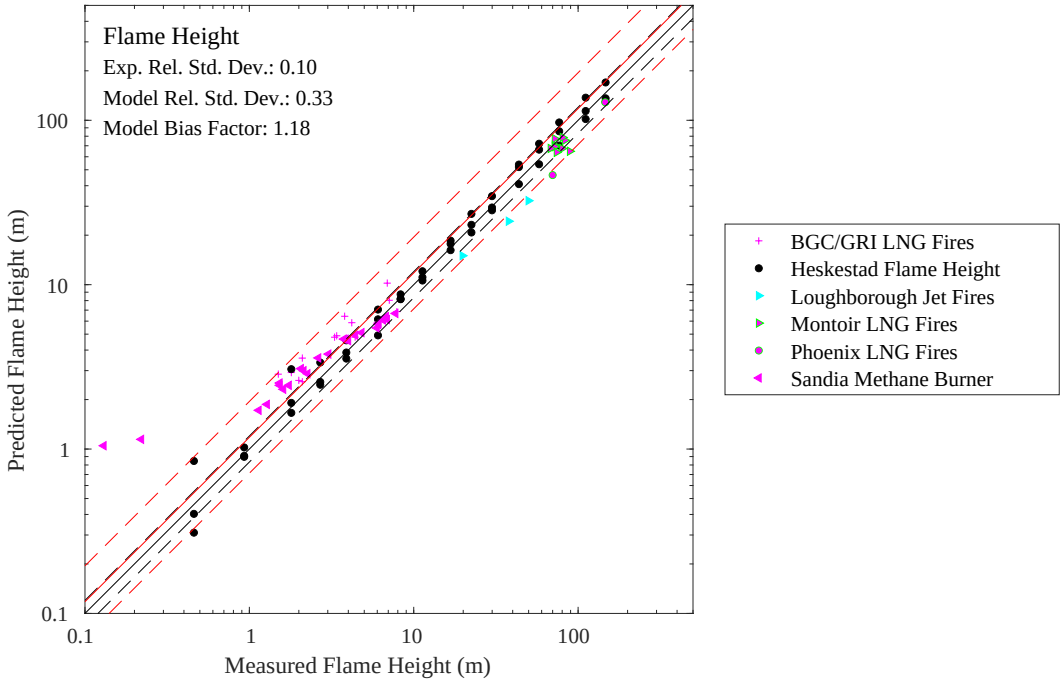

Figure 6.43: Summary of measured and predicted mean flame heights.

6.3 Flame Tilt

When assessing the hazards of a large, outdoor fire, not only is flame height a concern, but the flame tilt as well. That is, a fire in the wind tends to tilt in the windward direction. The angle from the vertical is referred to as "flame tilt." Figure 6.44 presents the results of flame tilt predictions for some large, outdoor pool fire experiments.

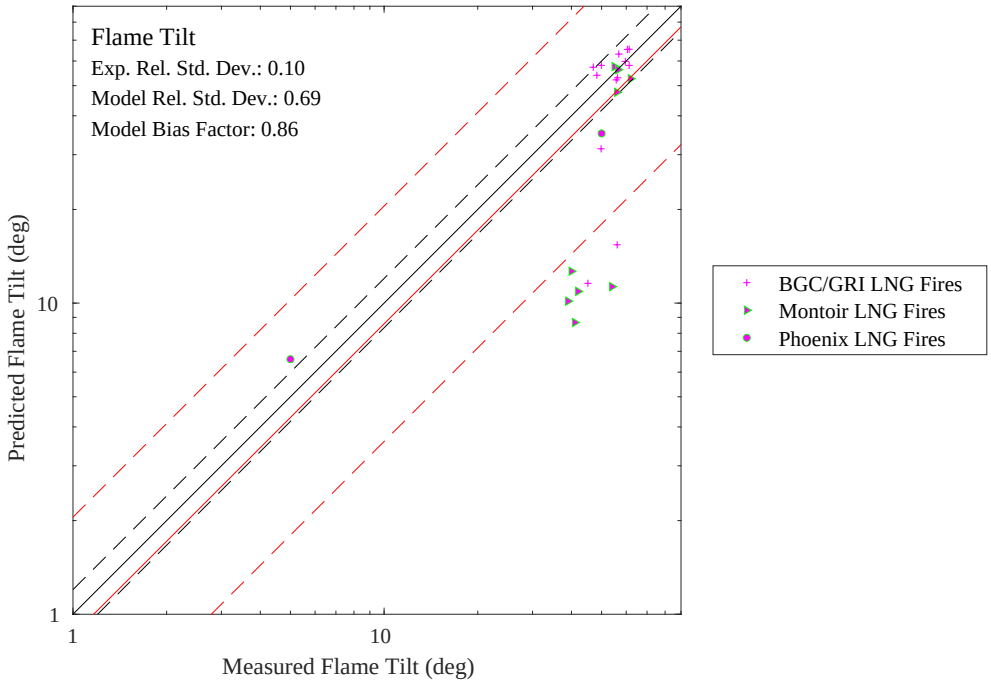

Figure 6.44: Summary of measured and predicted mean flame tilt angle.

6.4 Harrison Spill Plumes/Entrainment Experiments

Details of these experiments can be found in Section 3.31.

In each of these reduced-scale spill plume experiments, the entrained mass flow rate into the plume was measured at a series of heights by varying the flow through an exhaust hood to maintain a constant smoke layer depth. Figure 6.45 compares measured and predicted entrainment rates at five different elevations for the fire scenarios labelled SE4 through SE21 in Ref. [206]. Two general configurations are considered – one that is intended to mimic a balcony spill plume and one in which the plume adheres to a vertical wall above the compartment opening.

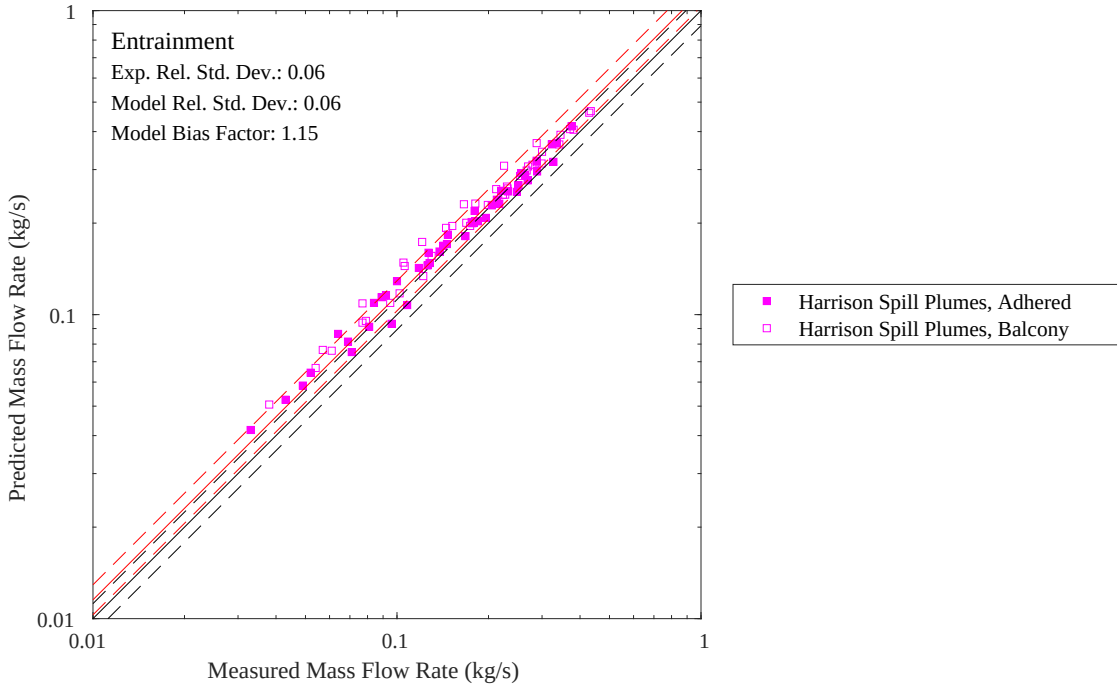

Figure 6.45: A comparison of predicted and measured mass flow rates at various heights for the Harrison Spill Plume experiments.

6.5 Sandia Plume Experiments

Details of these experiments can be found in Section 3.65.

The Fire Laboratory for Accreditation of Models by Experimentation (FLAME) facility [270, 271] at Sandia National Laboratories in Albuquerque, New Mexico, is designed specifically for validating models of buoyant fire plumes. The plume source is 1 m in diameter surrounded by a 0.5 m steel "ground plane". Particle Image Velocimetry (PIV) and Planar Laser-Induced Fluorescence (PLIF) techniques were used to obtain instantaneous joint scalar and velocity fields.

6.5.1 Sandia 1 m Helium Plume

Calculations of the Sandia 1 m helium plume are run at three grid resolutions: 6 cm, 3 cm, and 1.5 cm. To give the reader with a qualitative feel for the results, Fig. 6.46 provides a snapshot of density contours from the simulation. The calculations are run in parallel on 16 processors; the outlined blocks indicate the domain decomposition. Data for vertical velocity, radial velocity, and helium mass fraction are recorded at three levels downstream from the base of the plume, $z = [0.2, 0.4, 0.6]$ m, corresponding to the experimental measurements of O'Hern et al. [270]. Results for the mean and root mean square (RMS) profiles are given in Figs. 6.47 - 6.49. The means are taken between $t = 10$ and $t = 20$ seconds in the simulation.

The domain is 3 m by 3 m by 4 m. The boundary conditions are open on all sides with a smooth solid surface surrounding the 1 m diameter helium pool. The ambient and helium mixture temperature is set to 12 °C and the background pressure is set to 80900 Pa to correspond to the experimental conditions. The helium/acetone/oxygen mixture molecular weight is set to 5.45 kg/kmol. The turbulent Schmidt and Prandtl numbers are left at the FDS default value of 0.5. The helium mixture mass flux is specified as 0.0605 kg/s/m^2. This case was studied previously by DesJardin et al. [272].

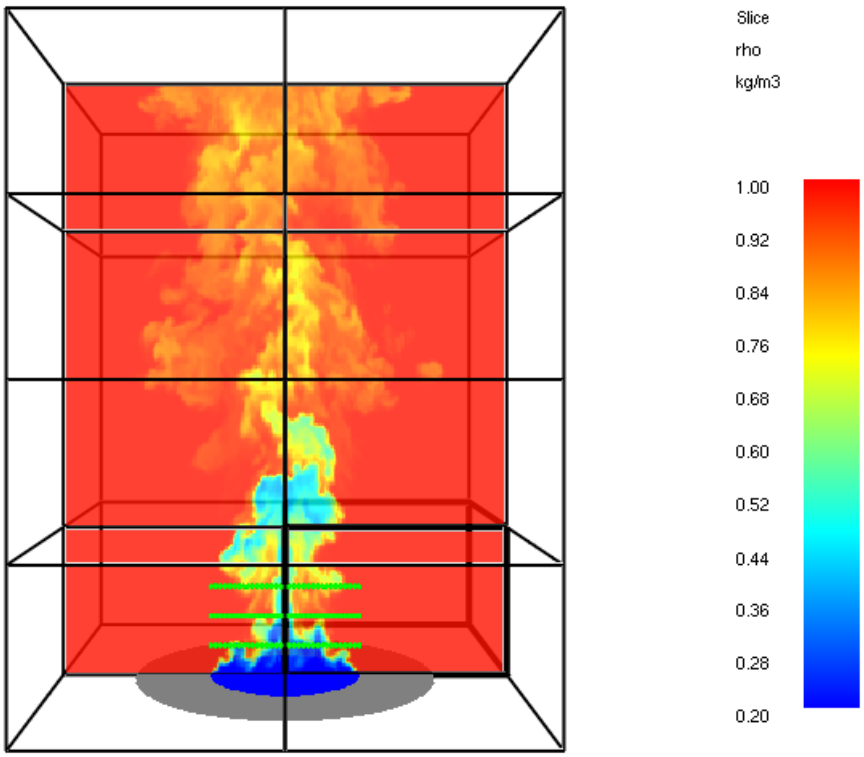

Figure 6.46: A snapshot of FDS results at 1.5 cm resolution for the Sandia 1 m helium plume showing density contours. The rows of measurement devices are visible near the base. The calculations are run in parallel on 16 processors; the outlined blocks indicate the domain decomposition.

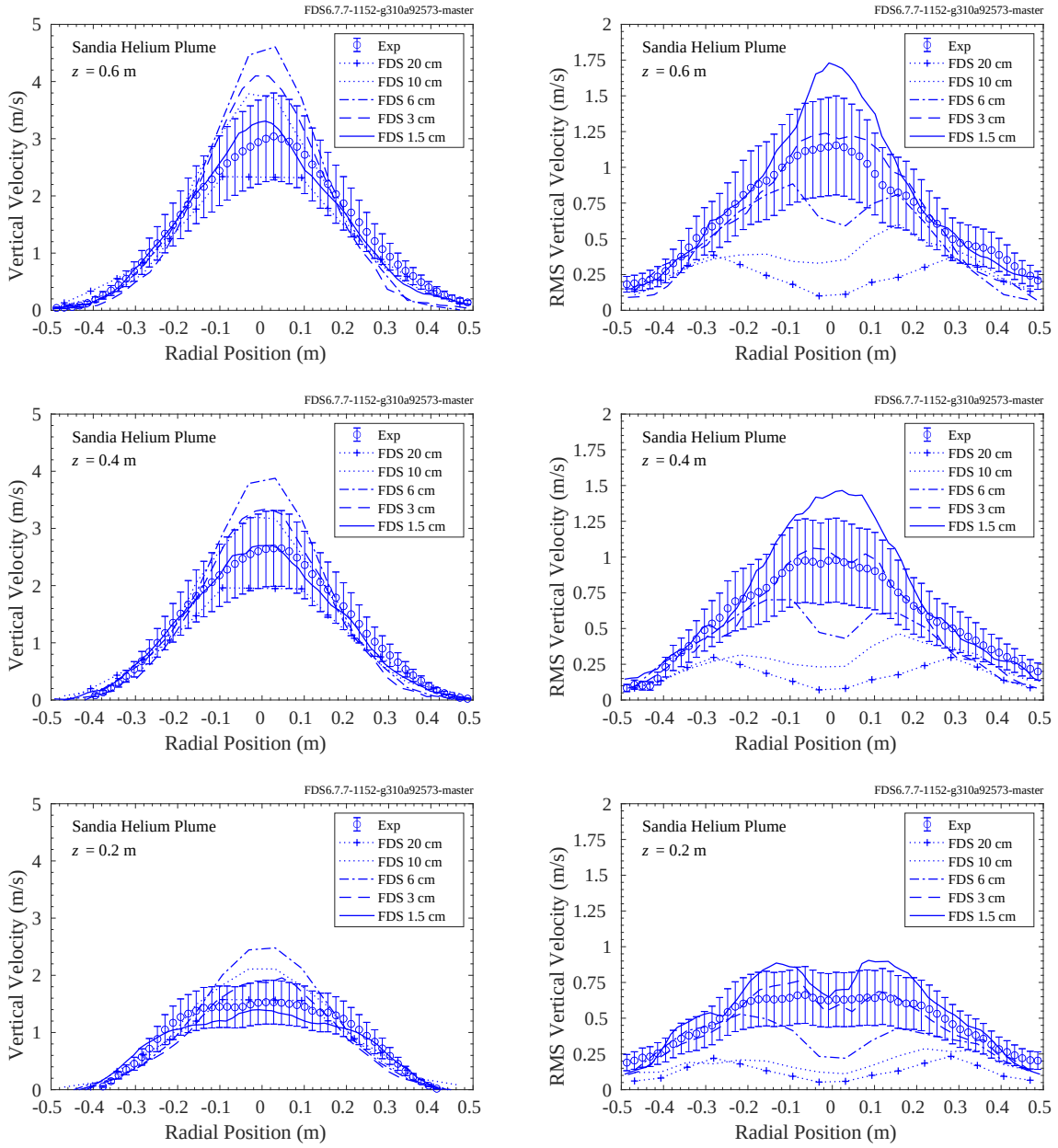

Figure 6.47: FDS predictions of mean and root mean square (RMS) vertical velocity profiles for the Sandia 1 m helium plume experiment. Results are shown for 6 cm, 3 cm, and 1.5 cm grid resolutions. With z being the streamwise coordinate, the bottom row is at $z = 0.2$ m, the middle row is at $z = 0.4$ m, and the top row is at $z = 0.6$ m.

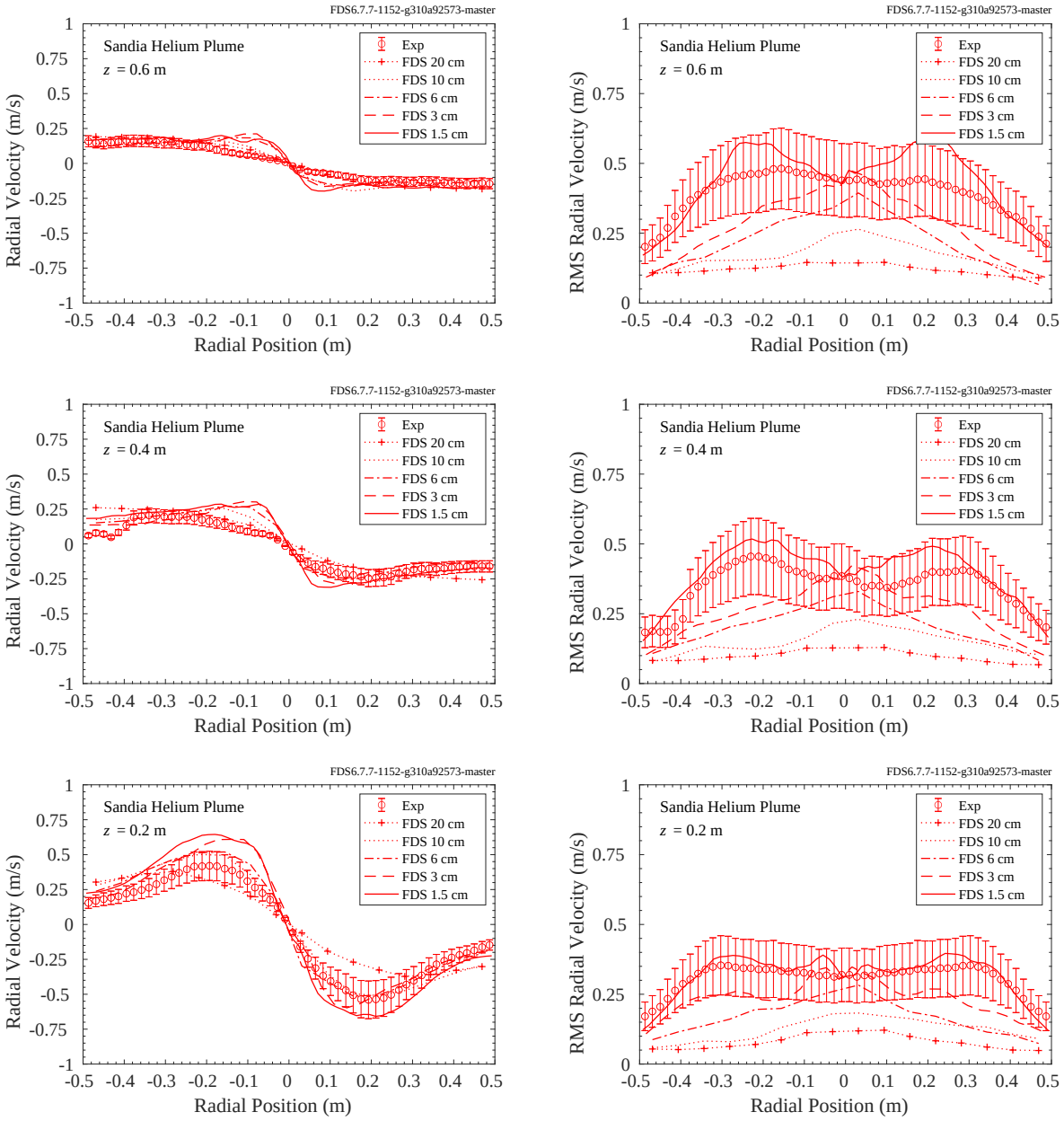

Figure 6.48: FDS predictions of mean and root mean square (RMS) radial velocity profiles for the Sandia 1 m helium plume experiment. Results are shown for 6 cm, 3 cm, and 1.5 cm grid resolutions. With z being the streamwise coordinate, the bottom row is at $z = 0.2$ m, the middle row is at $z = 0.4$ m, and the top row is at $z = 0.6$ m.

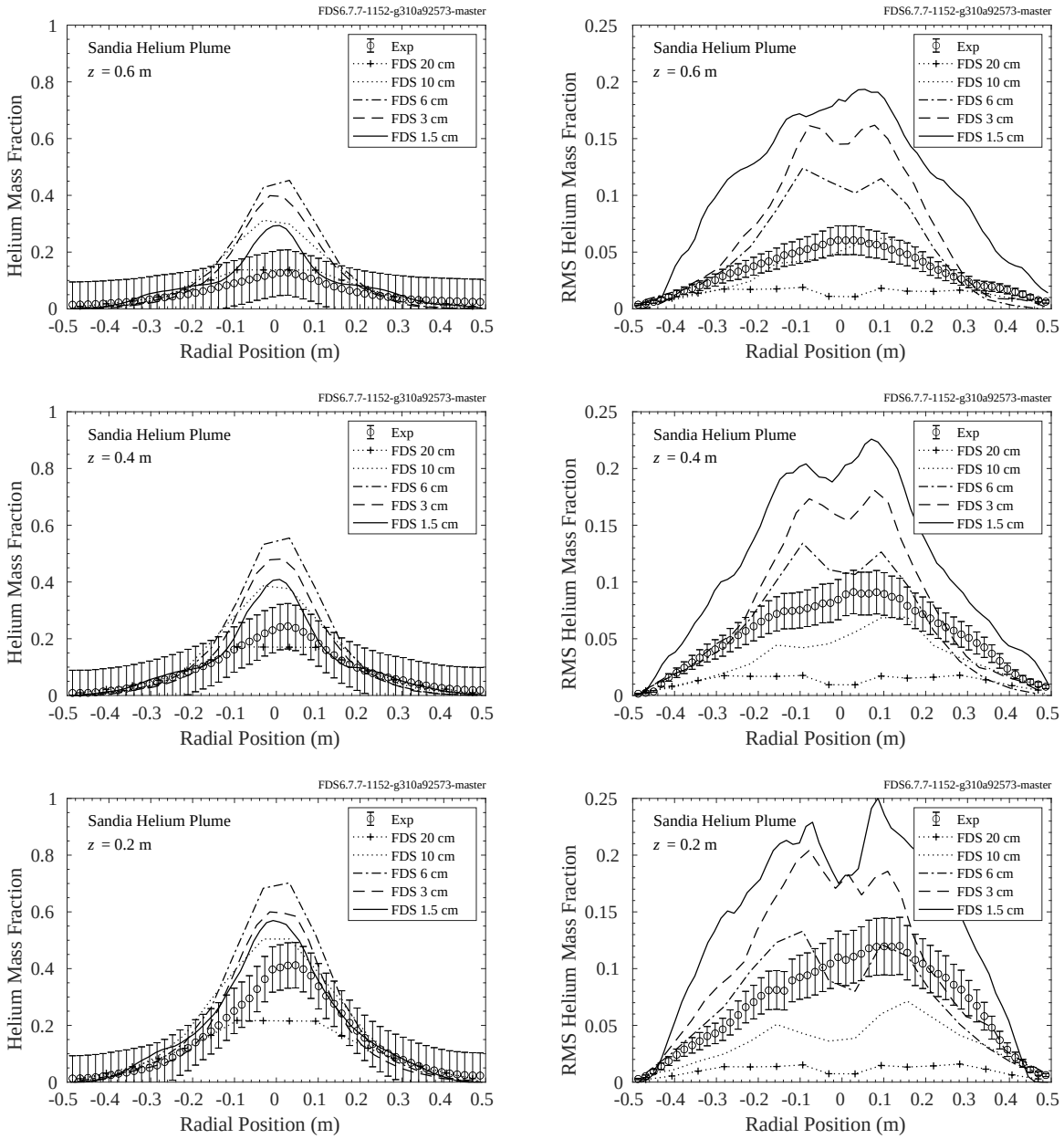

Figure 6.49: FDS predictions of mean and root mean square (RMS) helium mass fraction profiles for the Sandia 1 m helium plume experiment. Results are shown for 6 cm, 3 cm, and 1.5 cm grid resolutions. With z being the streamwise coordinate, the bottom row shows data at $z = 0.2$ m, the middle row shows data at $z = 0.4$ m, and the top row shows data at $z = 0.6$ m.

6.5.2 Sandia 1 m Methane Pool Fire

The Sandia 1 m methane pool fire series provides data for three methane flow rates: Test 14 (low flow rate), Test 24 (medium flow rate), and Test 17 (high flow rate) [273]. The experiments are simulated using three grid resolutions: 6 cm, 3 cm, and 1.5 cm. Fig. 6.50 provides a snapshot of temperature contours from the 1.5 cm Test 17 simulation. The calculations are run in parallel on 16 processors—a similar computational set up as the helium case (the experiments were run in the same facility at Sandia). Data for vertical velocity and radial velocity are recorded at three levels downstream from the base of the plume, $z = [0.3, 0.5, 0.9]$ m. Results for the mean profiles (and turbulent kinetic energy for Test 24) are given in Figs. 6.51 - 6.54. The means are taken between $t = 10$ and $t = 20$ seconds in the simulation.

For Test 17, we recorded the vertical velocity as a time series in four locations in the plume—at two positions along the centerline and at two positions on the edge. The time series from our 1.5 cm simulation at $x = 0$ m and $z = 0.5$ m, corresponding to Fig. 6 in [274], is shown in Fig. 6.55 along with the power spectrum from the average of the four time series locations. The FDS results compare well with the experimentally obtained puffing frequency of 1.65 Hz [274].

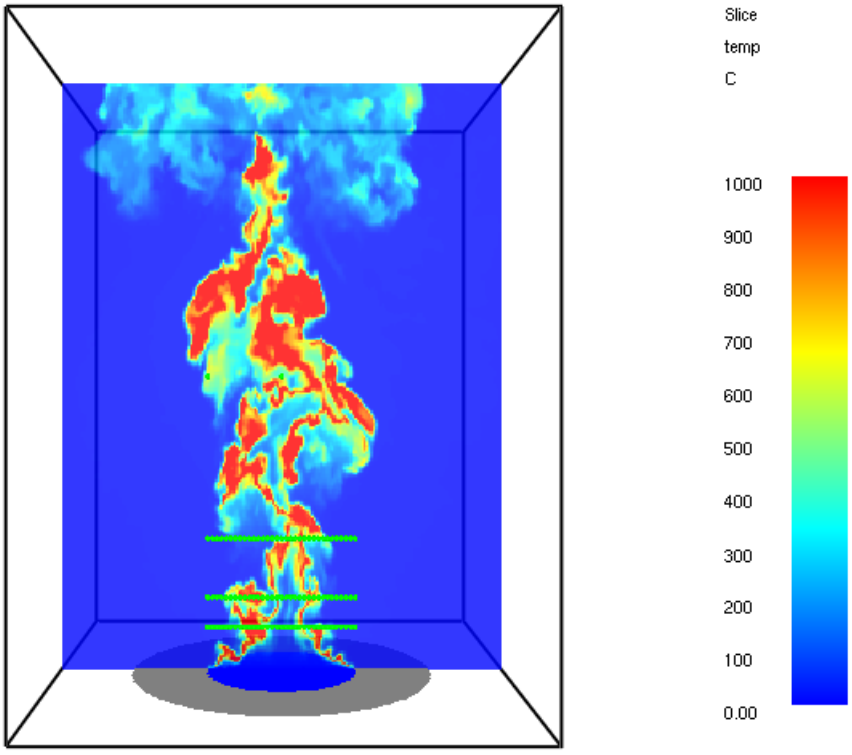

Figure 6.50: A snapshot of FDS results at 1.5 cm resolution for the Sandia 1 m methane pool fire (Test 17 – high flow rate) showing instantaneous contours of temperature. The rows of measurement devices (green) are visible near the base.

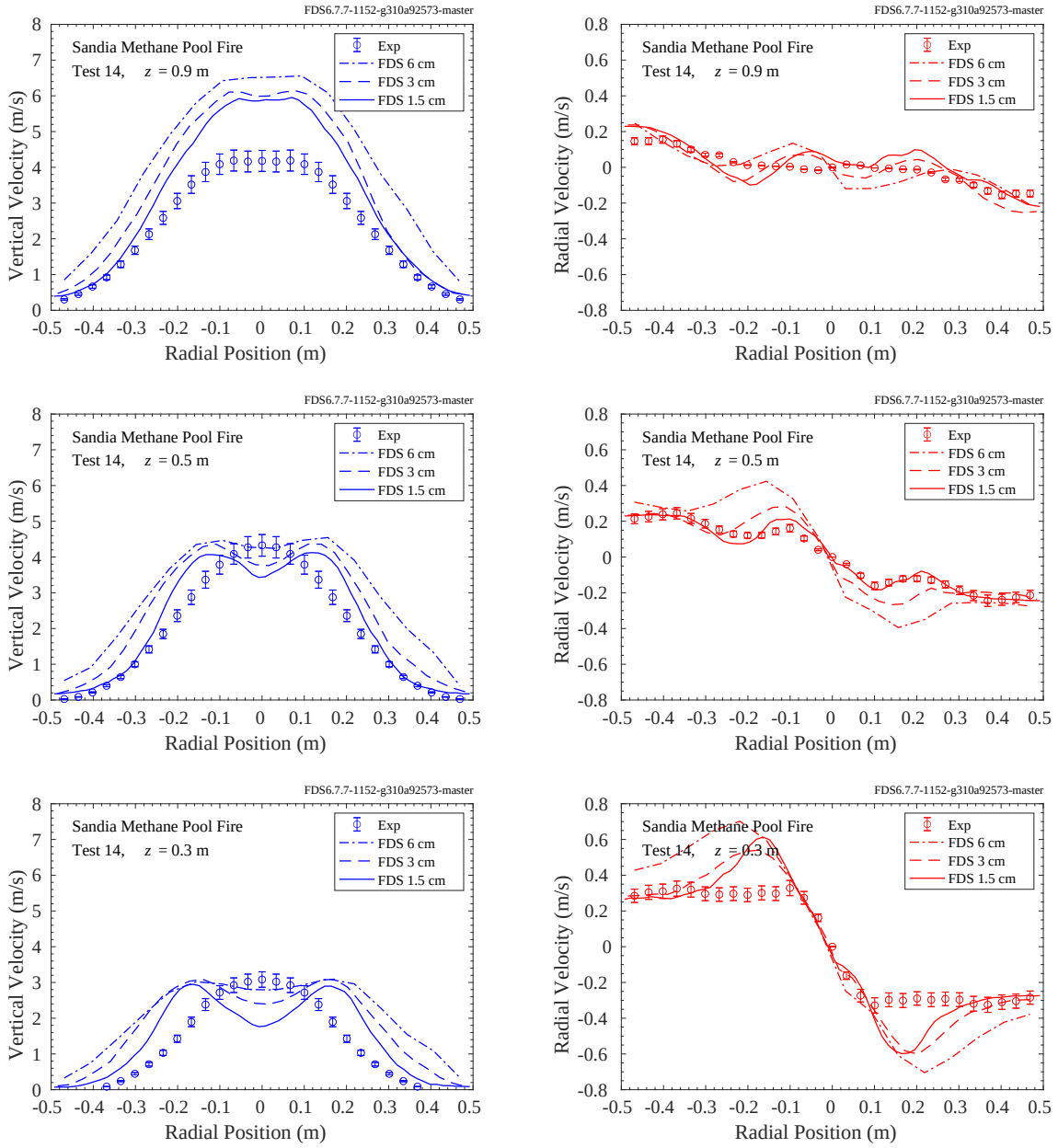

Figure 6.51: FDS predictions of mean velocity profiles for the Sandia 1 m methane pool fire experiment (Test 14 – low flow rate). Results are shown for 6 cm, 3 cm, and 1.5 cm grid resolutions. The z coordinate represents height above the methane pool; bottom row: $z = 0.3$ m, middle row: $z = 0.5$ m, and top row: $z = 0.9$ m.

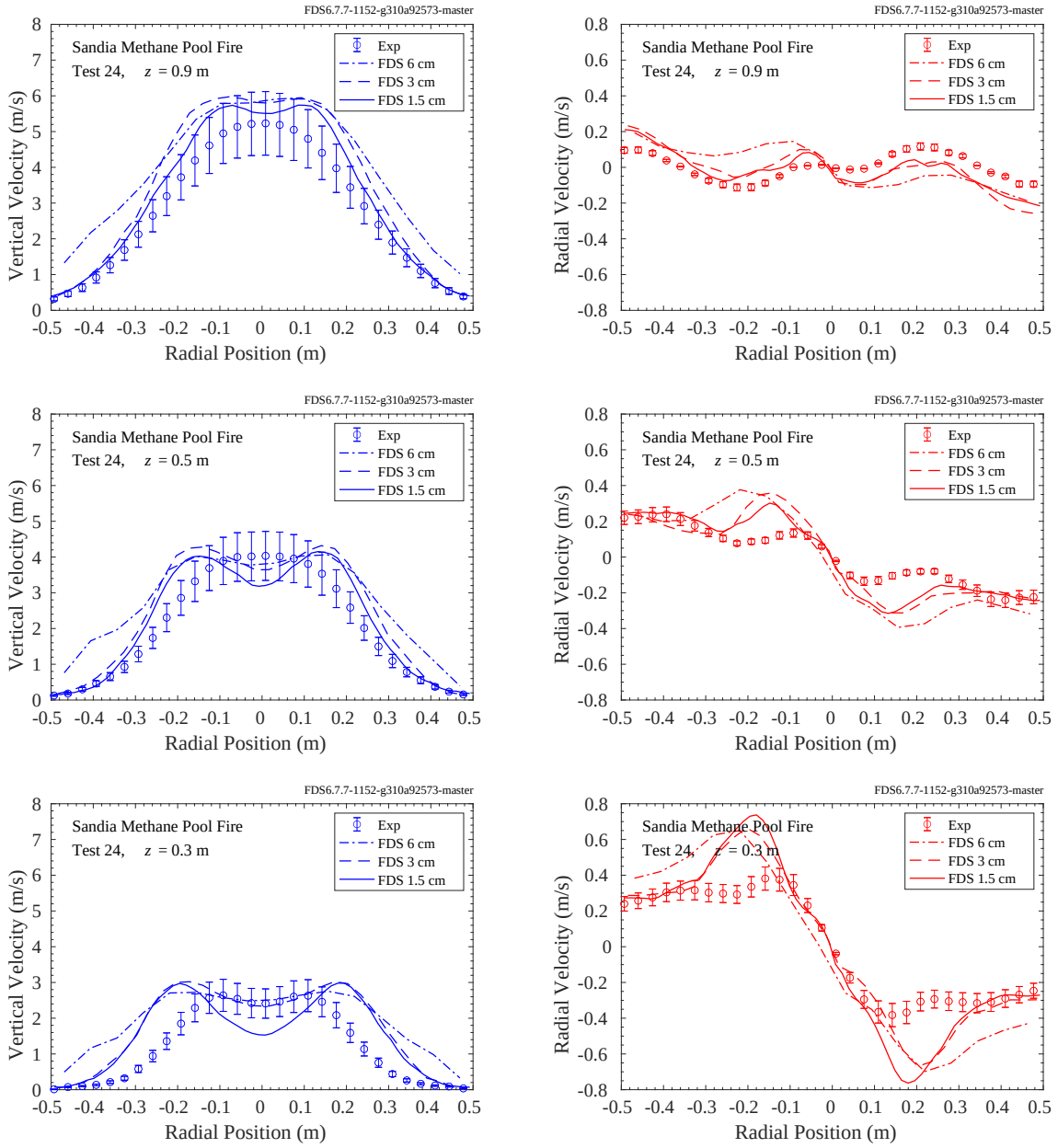

Figure 6.52: FDS predictions of mean velocity profiles for the Sandia 1 m methane pool fire experiment (Test 24 – medium flow rate). Results are shown for 6 cm, 3 cm, and 1.5 cm grid resolutions. The z coordinate represents height above the methane pool; bottom row: $z = 0.3$ m, middle row: $z = 0.5$ m, and top row: $z = 0.9$ m.

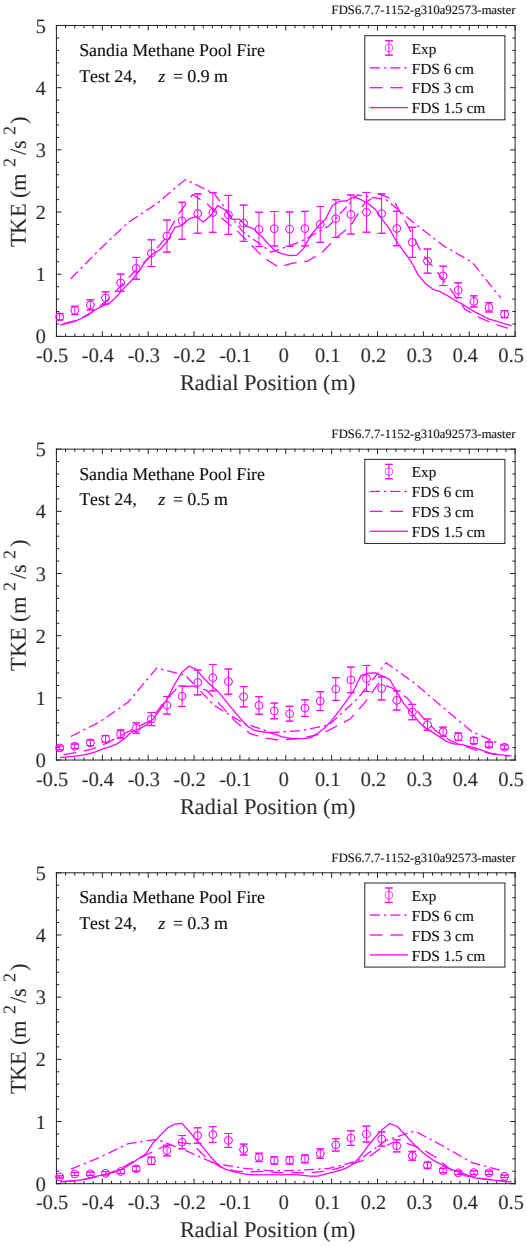

Figure 6.53: FDS predictions of turbulent kinetic energy (TKE) profiles for the Sandia 1 m methane pool fire experiment (Test 24 – medium flow rate). Results are shown for 6 cm, 3 cm, and 1.5 cm grid resolutions. The z coordinate represents height above the methane pool; bottom row: $z = 0.3$ m, middle row: $z = 0.5$ m, and top row: $z = 0.9$ m.

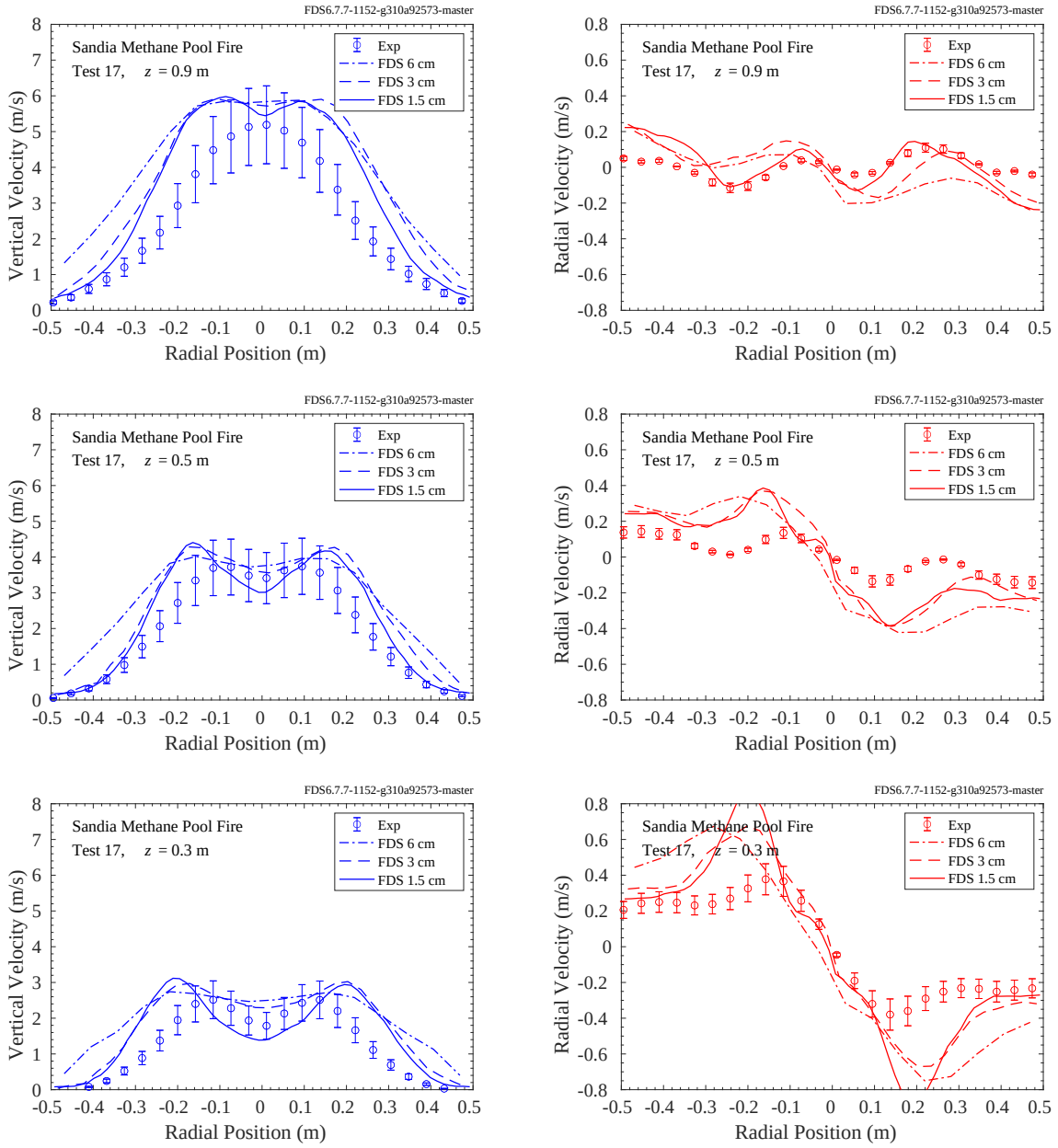

Figure 6.54: FDS predictions of mean velocity profiles for the Sandia 1 m methane pool fire experiment (Test 17). Results are shown for 3 cm and 1.5 cm grid resolutions. The z coordinate represents height above the methane pool; bottom row: $z = 0.3$ m, middle row: $z = 0.5$ m, and top row: $z = 0.9$ m.

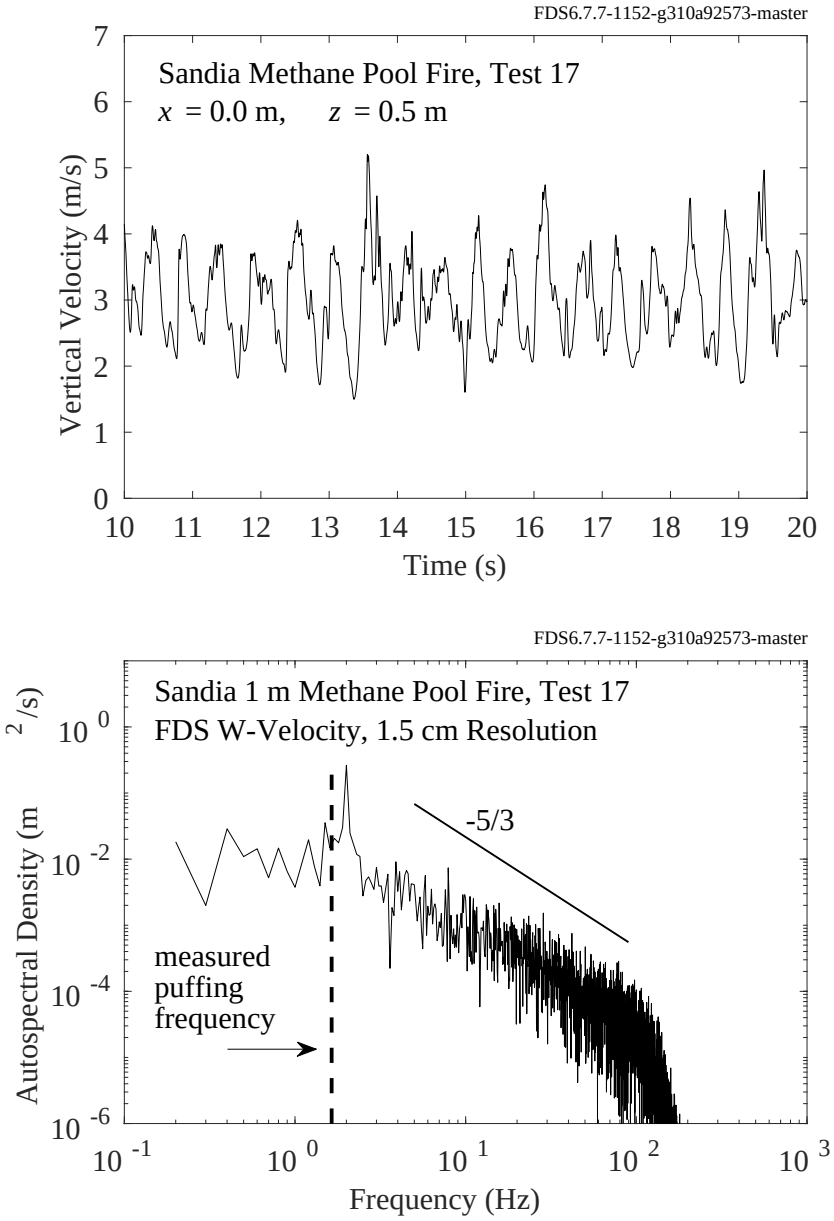

Figure 6.55: FDS velocity signal and power spectrum for the Sandia 1 m methane pool fire experiment (Test 17). The vertical velocity signal (top plot) is output from FDS on the centerline at $z = 0.5$ m downstream of the fuel source. The power spectrum of vertical velocity is measured at four locations and averaged. Two of the measurement locations are along the centerline, at $z = [0.5, 2.0]$ m, and two are along the edge of the plume, $x = 0.5$ m and $z = [0.5, 2.0]$ m. The measured puffing frequency of the plume is 1.65 Hz [274]. The temporal Nyquist limit of the simulation (the highest resolvable frequency due to the discrete time increment) is $1/(2\delta t) \approx 1000$ Hz ($\delta t \approx 0.0005$).

6.5.3 Sandia 1 m Hydrogen Pool Fire

Sandia Test 35 [273] is simulated at three grid resolutions: 6 cm, 3 cm, and 1.5 cm. The computational set up is nearly identical to the methane cases. Results for mean vertical and radial velocity are given in Figs. 6.57. Results for turbulent kinetic energy are presented in Fig. 6.58. Means are taken from a time average between $t = 10$ and $t = 20$ seconds in the simulation.

By examining movies of the simulation results we can see a qualitative difference between the methane and hydrogen cases. The dynamics of the hydrogen case tend to dominated by near total consumption events which create blowback on the pool followed by streaks of accelerating buoyant flow which increase the mean vertical velocity. An example of the consumption event is seen near the end of the case shown in Fig. 6.56. It is possible that we have not run the simulation long enough for accurate statistics and that streaking events early in the time window (between 10-20 seconds) are biasing the mean vertical velocity to be too high, as is clear from the top-left plot in Fig. 6.57.

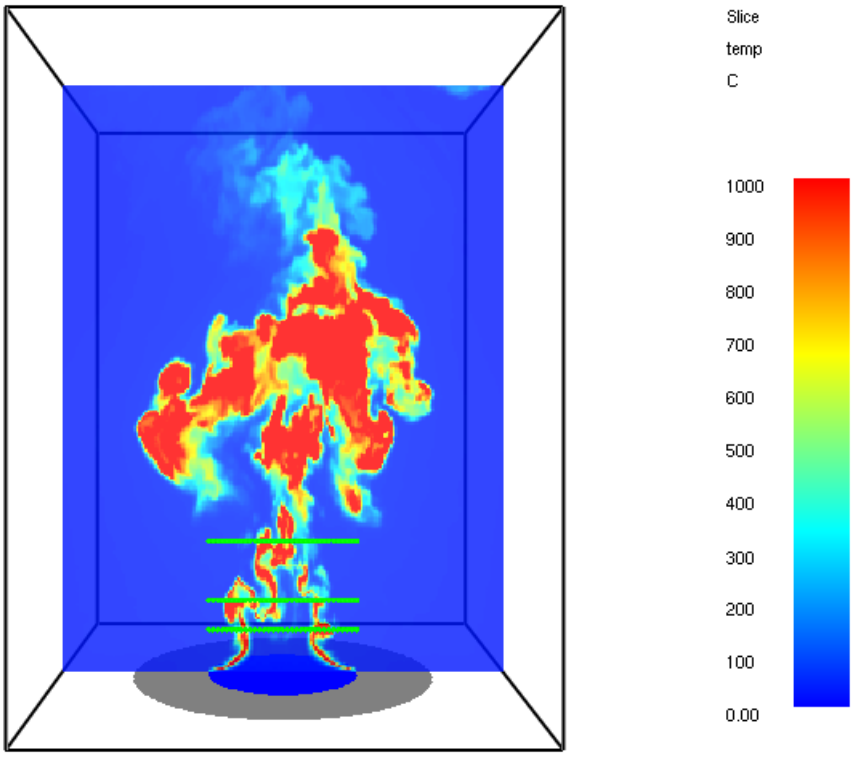

Figure 6.56: A snapshot of FDS results at 1.5 cm resolution for the Sandia 1 m hydrogen pool fire (Test 35) showing instantaneous contours of temperature. The rows of measurement devices (green) are visible near the base.

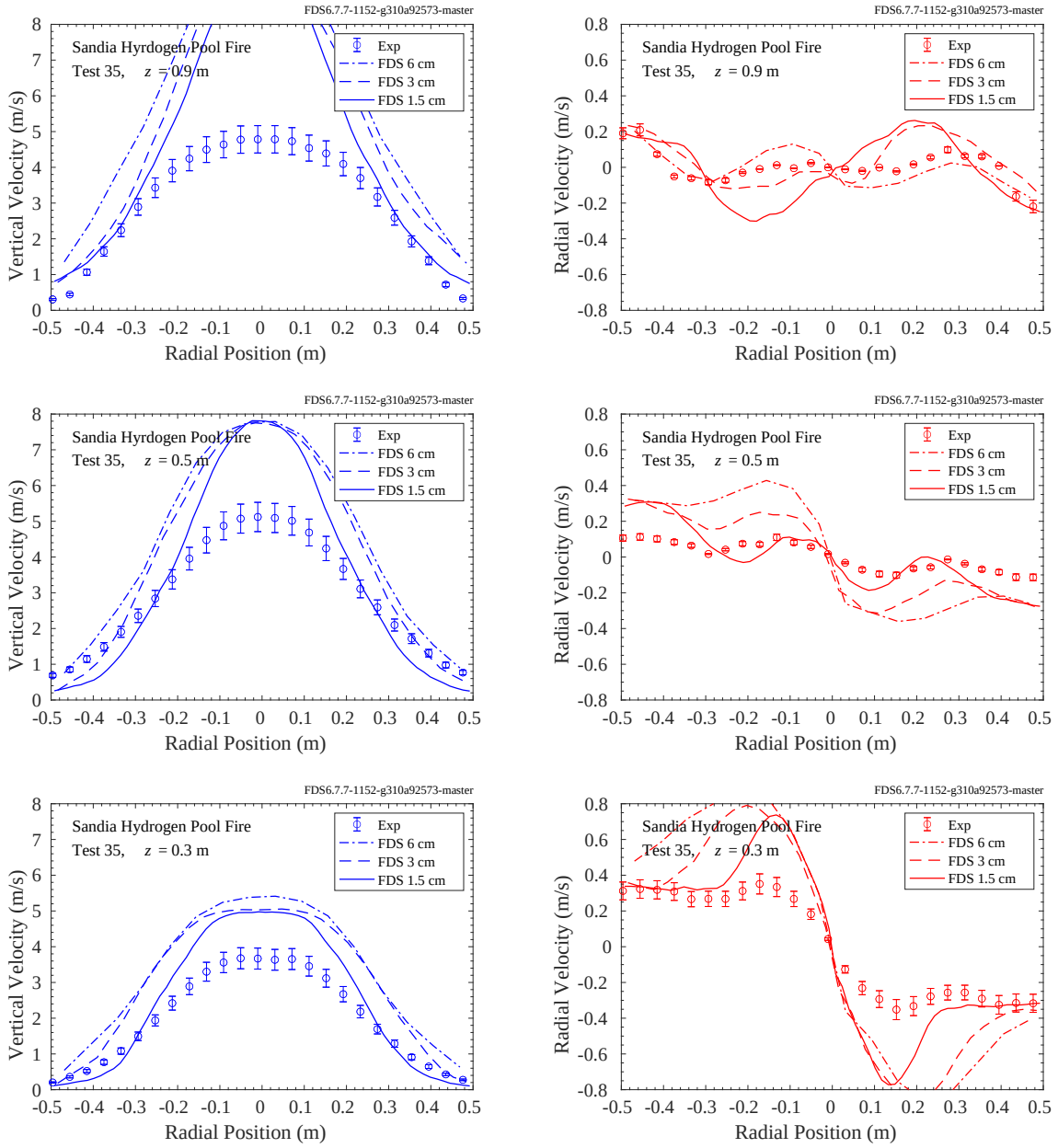

Figure 6.57: FDS predictions of mean velocity profiles for the Sandia 1 m hydrogen pool fire experiment (Test 35). Results are shown for 6 cm, 3 cm, and 1.5 cm grid resolutions. The z coordinate represents height above the pool; bottom row: $z = 0.3$ m, middle row: $z = 0.5$ m, and top row: $z = 0.9$ m.

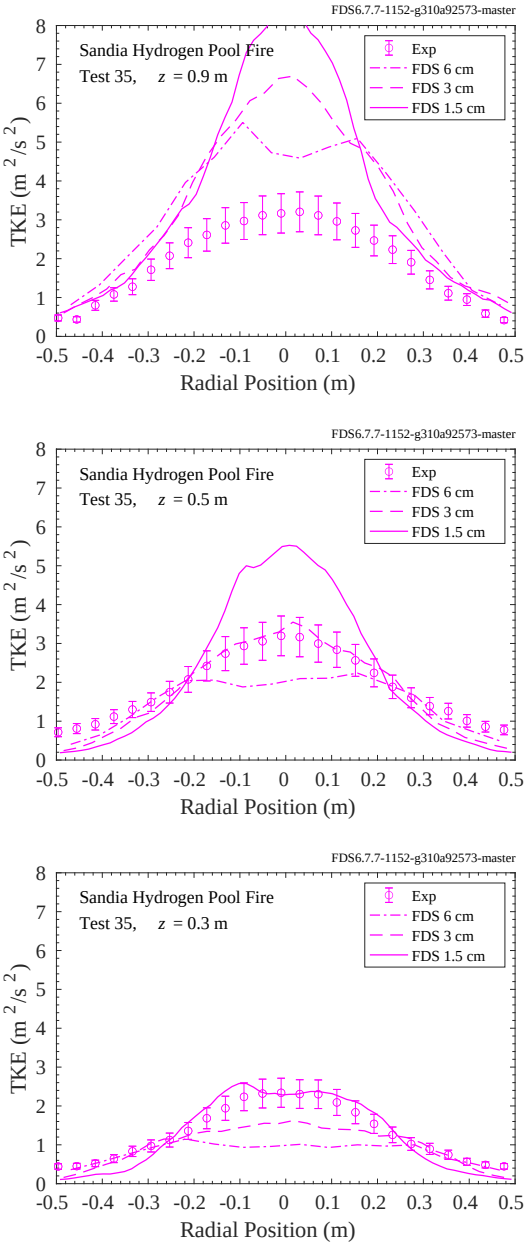

Figure 6.58: FDS predictions of turbulent kinetic energy (TKE) profiles for the Sandia 1 m hydrogen pool fire experiment (Test 35). Results are shown for 6 cm, 3 cm, and 1.5 cm grid resolutions. The z coordinate represents height above the methane pool; bottom row: $z = 0.3$ m, middle row: $z = 0.5$ m, and top row: $z = 0.9$ m.

6.6 Purdue 7.1 cm Methane Flame

Details of these experiments can be found in Section 3.61.

Figures 6.59-6.62 show results for the Purdue 7.1 cm methane flame [30]. Three sets of results are presented: two coarse (4 mm) cases and one fine (2 mm) case. The fine mesh case is run with MPI on 16 meshes. The coarse cases are run two ways: a single mesh case (dashed lines) and a 16 mesh case (dotted lines). As should be the case, the single- and multi-mesh cases yield the same results. This gives confidence in the domain decomposition strategy for open plume flows with FDS.

The discrepancy at the centerline for mixture fraction and vertical velocity may be attributed to our not accounting for (1) the slight divergence of the flow at the burner exit (7° [30]) and (2) the asymmetries and fluctuations in the burner exit and ambient environment. Examination of the FDS output shows the solution remains very symmetric, preventing large gulps of air from penetrating the centerline of the plume, which would tend to smooth out the profiles near the center reducing the bimodal vertical velocity profile and centerline mixture fraction.

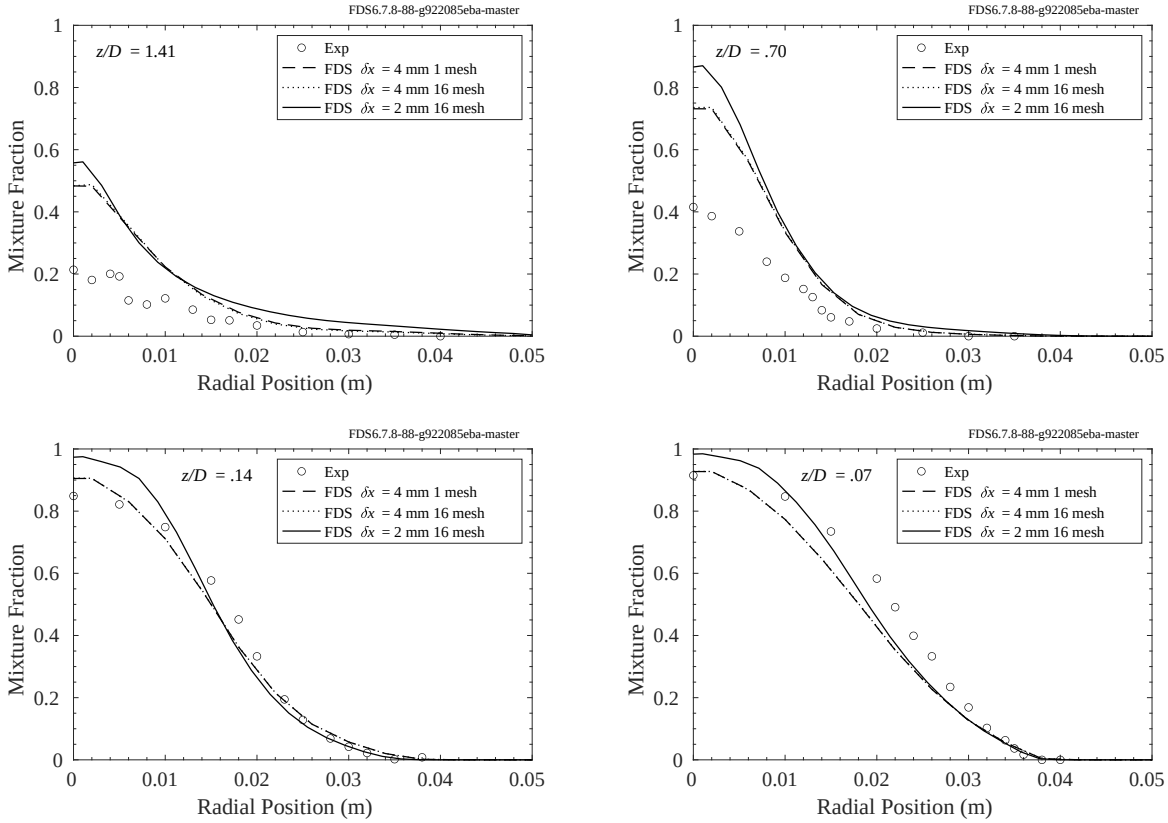

Figure 6.59: Measured [32] and computed radial profiles of the mean mixture fraction at select heights above the burner exit simulated using grids with different spatial resolutions.

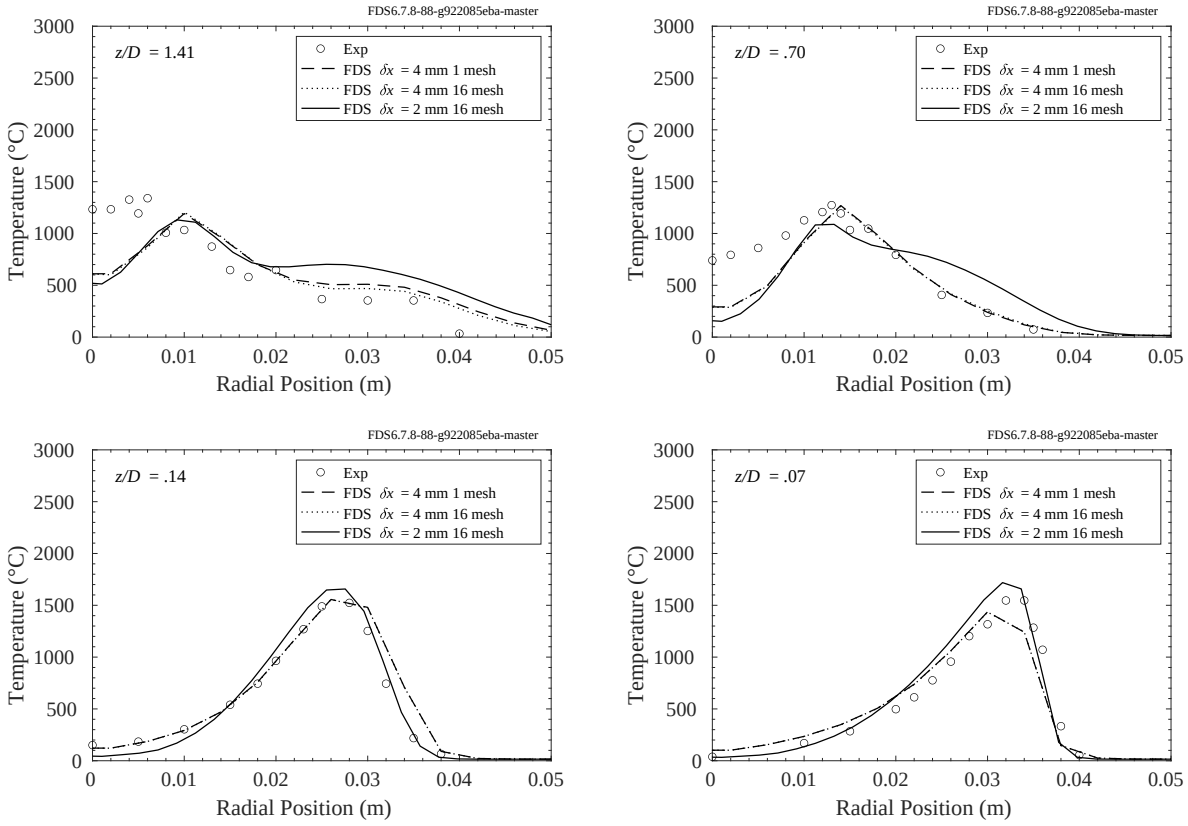

Figure 6.60: Inferred [30] and computed radial profiles of the mean temperature at select heights above the burner exit simulated using grids with different spatial resolutions.

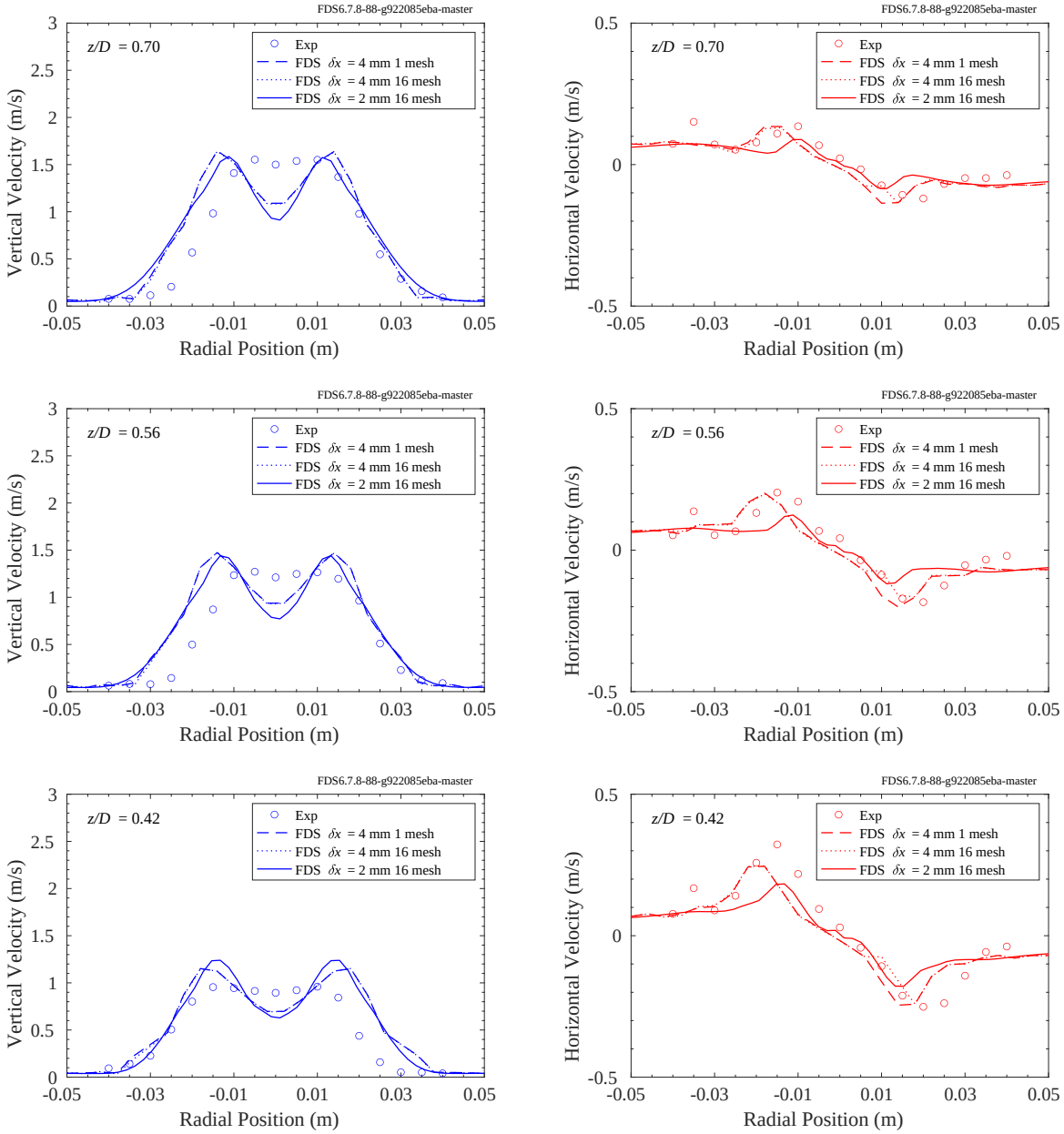

Figure 6.61: Measured [32] and computed radial profiles of the mean vertical and horizontal velocities at select heights above the burner exit simulated using grids with different spatial resolutions.

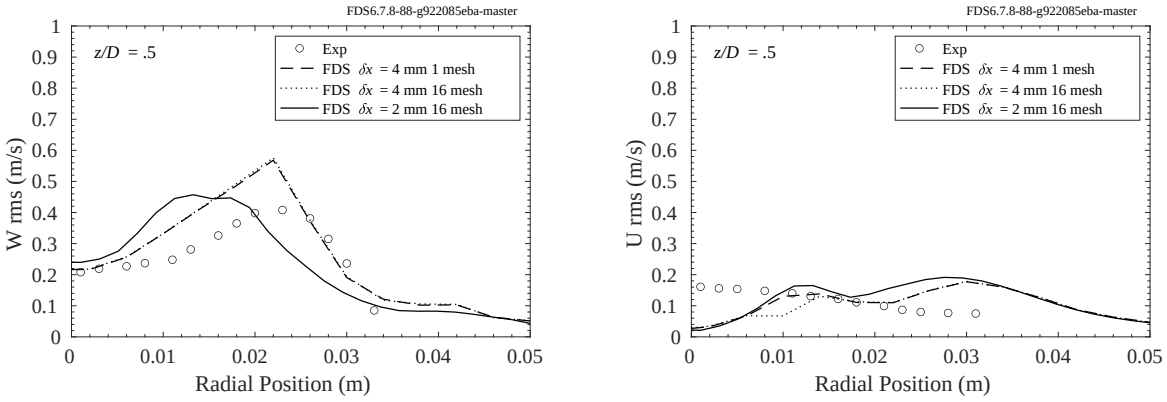

Figure 6.62: Measured and computed profiles of rms vertical (left) and radial (right) velocity profiles at $z/D = 0.5$.

6.7 FM Vertical Wall Flame Experiments

Details of these experiments can be found in Section 3.28.

Figure 6.63 displays the measured and predicted thermocouple (i.e. uncorrected) temperatures as a function of the normal distance, y, from the surface of a vertical, water-cooled burner. The measurements were made 771 mm from the base of the burner for propylene mass flow rates of 8.75, 11.85, 12.68, 17.05, 22.37, and 22.49 g/m^2/s.

Figure 6.64 displays the measured and predicted soot depth at heights of 365, 527, 771, 1022, and 1317 mm above the base of the burner for various fuel burning rates. The soot depth was measured by inserting glass rods through the flame, normal to the burner surface, for 2 s. The soot depth is the length of the blackened portion of the rod, taken to represent the average flame depth over the 2 s interval. For the FDS simulations, the soot depth was taken to be the distance from the burner surface where the soot mass fraction drops below 0.0025.

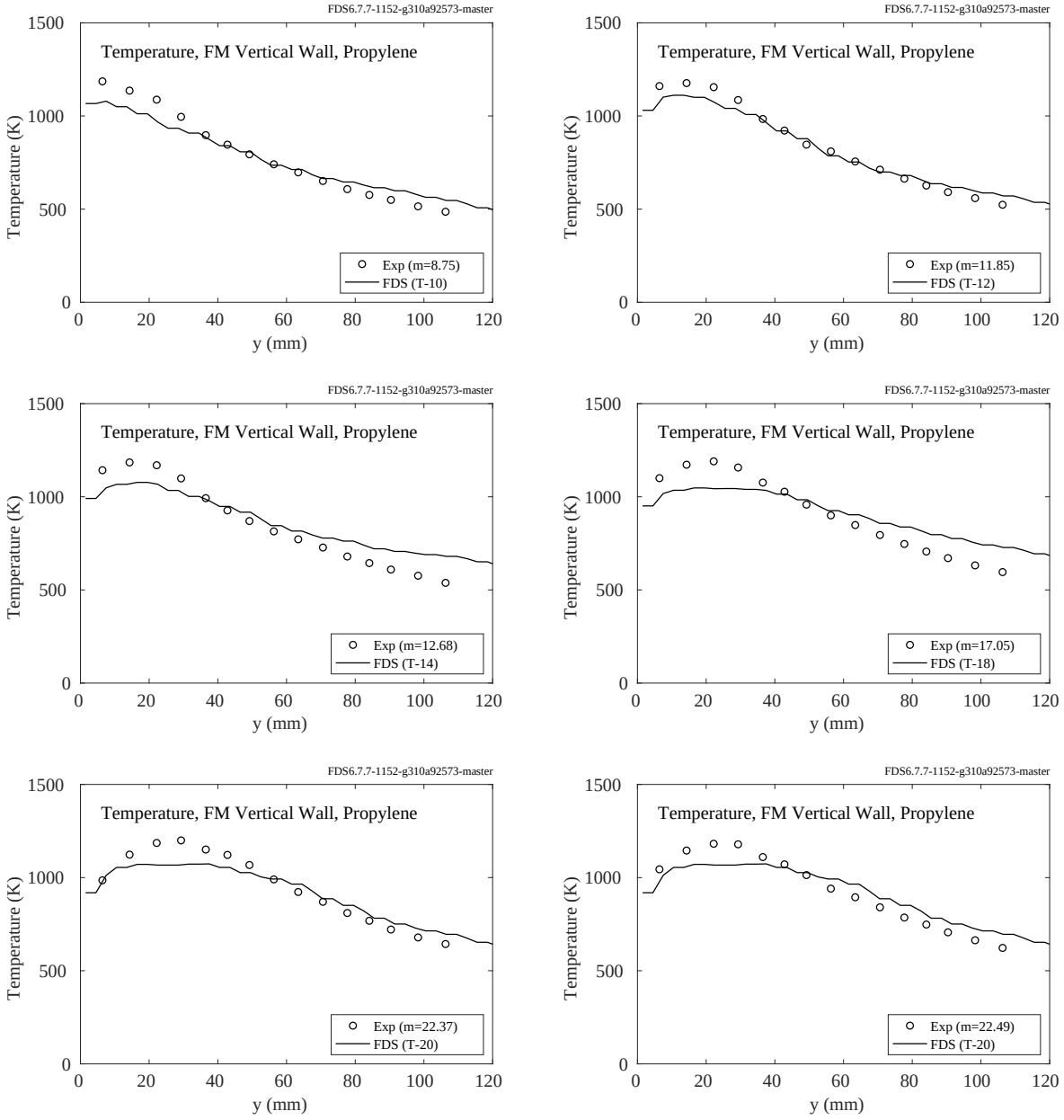

Figure 6.63: Uncorrected horizontal temperature profiles normal to the burner surface for fuel flow rates of 8.75, 11.85, 12.68, 17.05, 22.37, and 22.49 g/m^2/s.

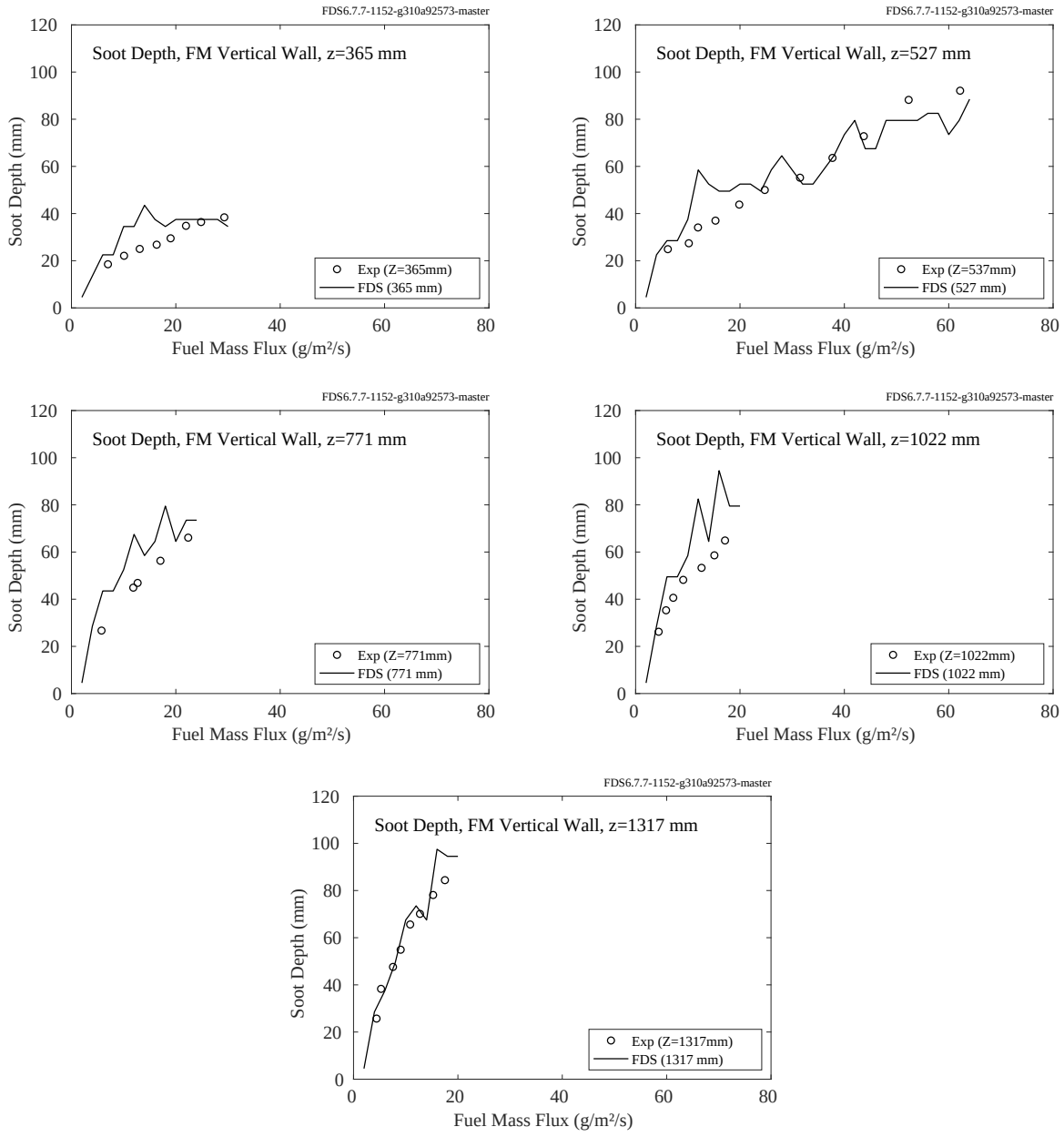

Figure 6.64: Soot depth at heights of 365, 527, 771, 1022, and 1317 mm.

Chapter 7

Ceiling Jets and Device Activation

FDS is a CFD-based fire model and has no specific ceiling jet algorithm. Rather, temperatures throughout the fire compartment are computed directly from the governing conservation equations. Nevertheless, temperature measurements near the ceiling are useful in evaluating the model's ability to predict the activation times of sprinklers, smoke detectors, and other fire protection devices. The term "ceiling jet" is used loosely here – it distinguishes a point temperature measurement near the ceiling from an average "hot gas layer" (HGL) temperature.

This chapter first presents comparisons of model predictions and temperature measurements near to the ceiling. Next, predicted sprinkler activation times and the total number of activations are compared with measurements. Finally, predicted smoke detector activation times are compared with measurements.

7.1 Ceiling Jet Temperatures

The ceiling jet temperature measurements presented in this section were made for a variety of reasons. Most often, these measurements were simply the upper most thermocouple temperature in a vertical array. Sometimes, these measurements were designed to detect the activation time of a sprinkler. In any case, these measurements are used to evaluate the model's ability to predict the gas temperature at a single point, as opposed to the hot gas layer average.

7.1.1 ATF Corridors Experiment

This series of experiments involved two fairly long corridors connected by a staircase. The fire, a natural gas sand burner, was located on the first level at the end of the corridor away from the stairwell. The corridor was closed at this end, and open at the same position on the second level. Two-way flow occurred on both levels because make-up air flowed from the opening on the second level down the stairs to the first. The only opening to the enclosure was the open end of the second-level corridor.

Temperatures were measured with seven thermocouple trees. Tree A was located fairly close to the fire on the first level. Tree B was located halfway down the first-level corridor. Tree C was close to the stairwell entrance on the first level. Tree D was located in the doorway of the stairwell on the first level. Tree E was located roughly along the vertical centerline of the stairwell. Tree F was located near the stairwell opening on the second level. Tree G was located near the exit at the other end of the second-level corridor. The graphs on the following pages show the top and bottom TC from each tree for the given fire sizes of 50 kW, 100 kW, 250 kW, 500 kW, and a mixed HRR "pulsed" fire.

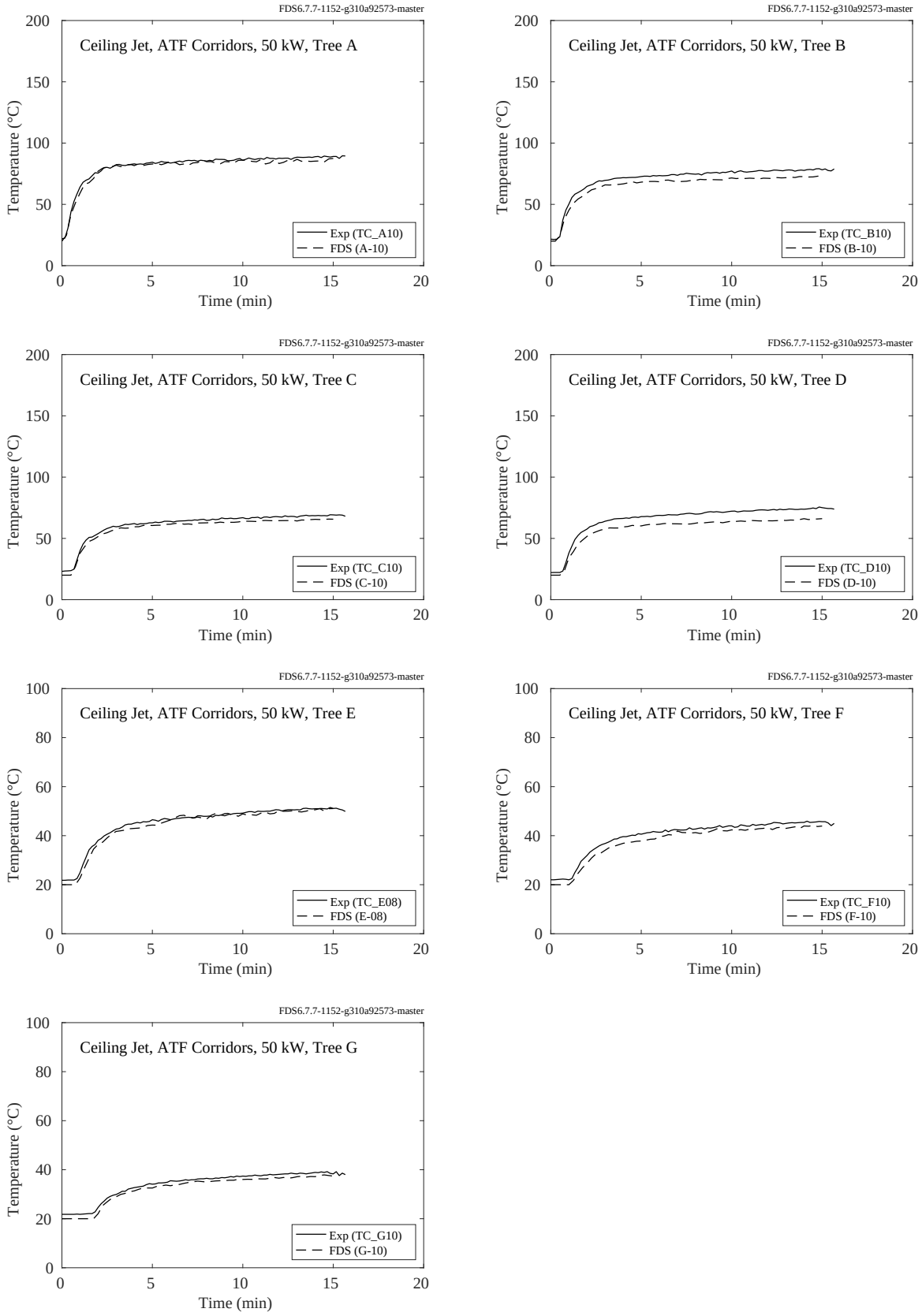

Figure 7.1: ATF Corridors experiments, ceiling jet, 50 kW.

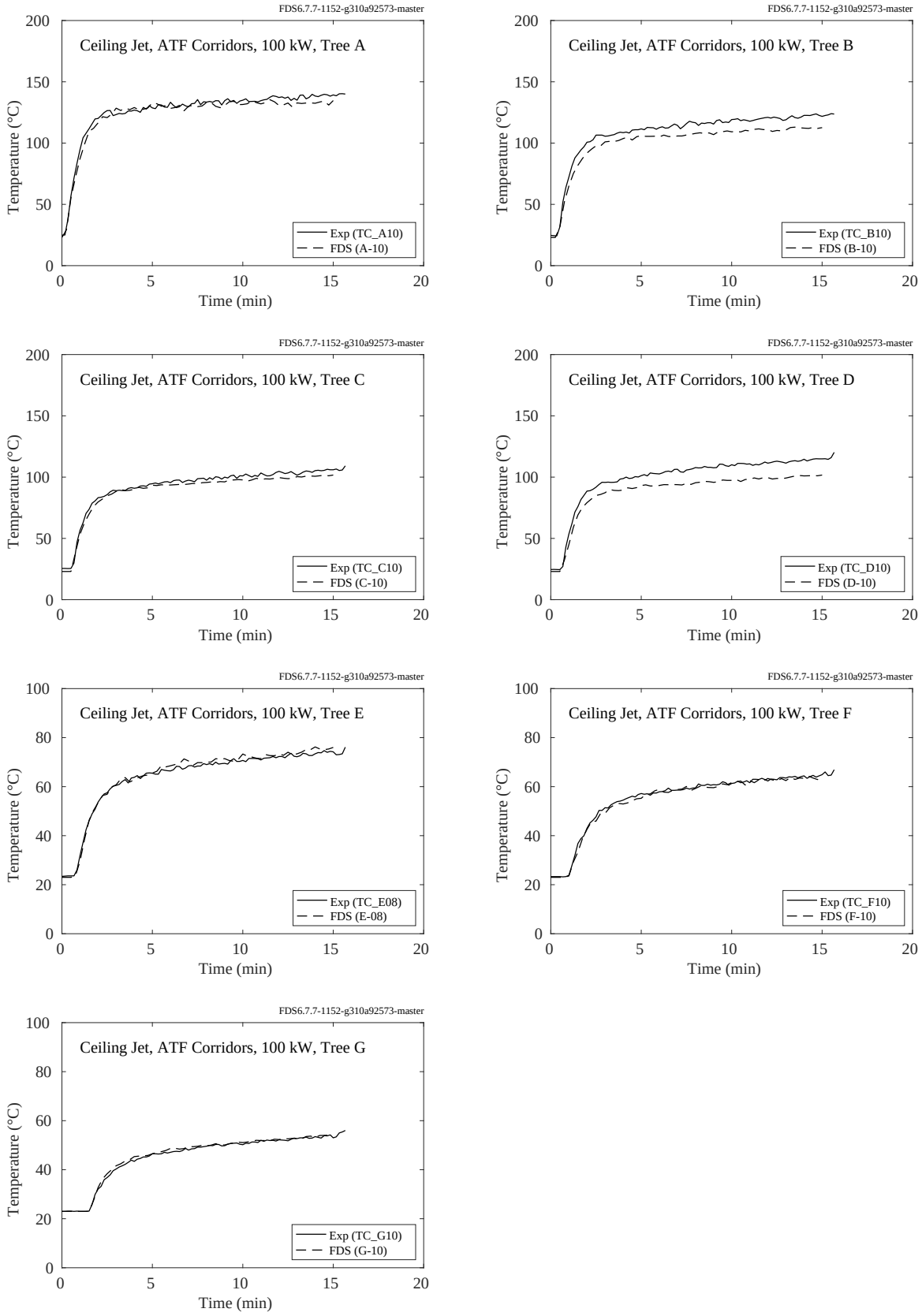

Figure 7.2: ATF Corridors experiments, ceiling jet, 100 kW.

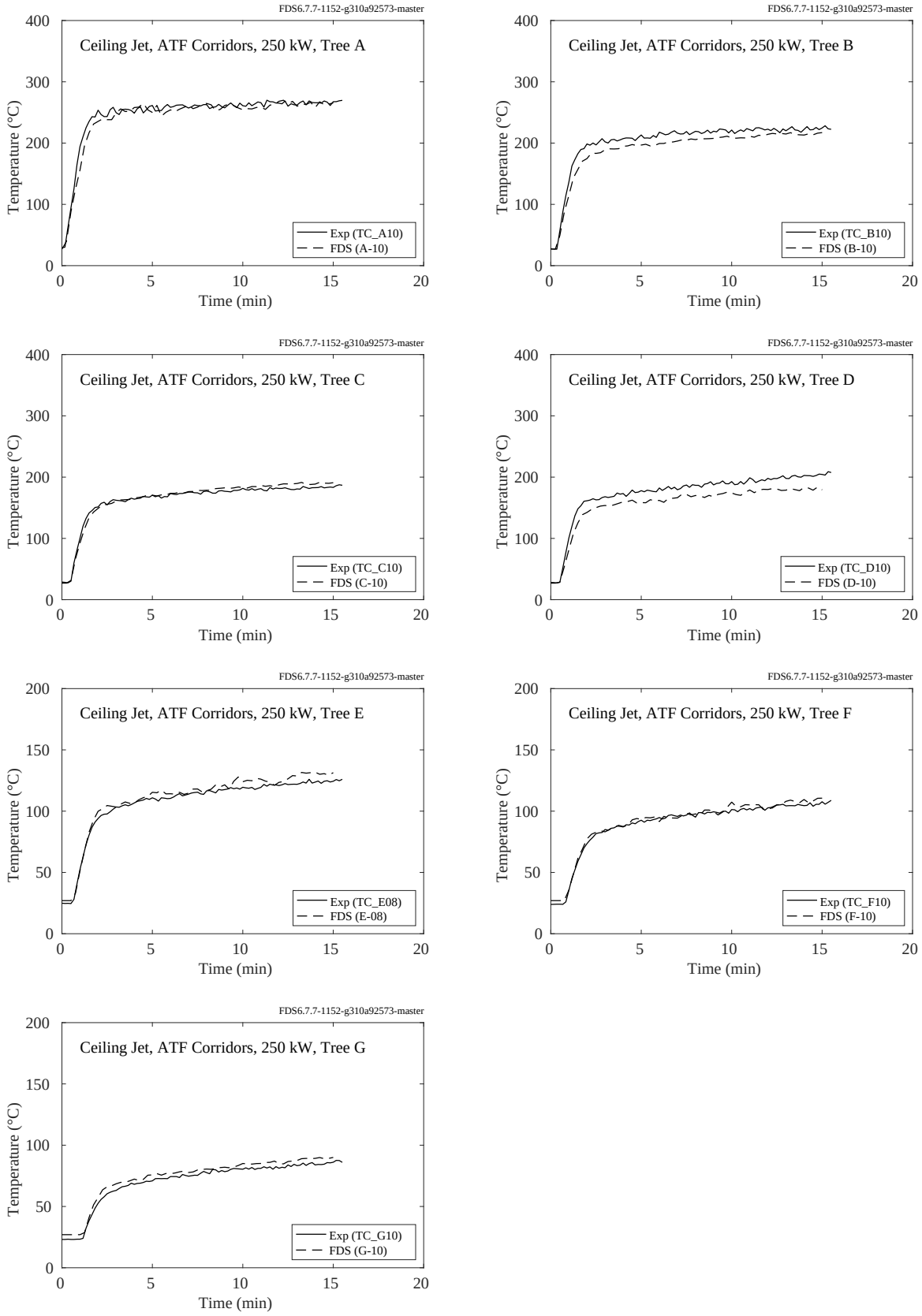

Figure 7.3: ATF Corridors experiments, ceiling jet, 250 kW.

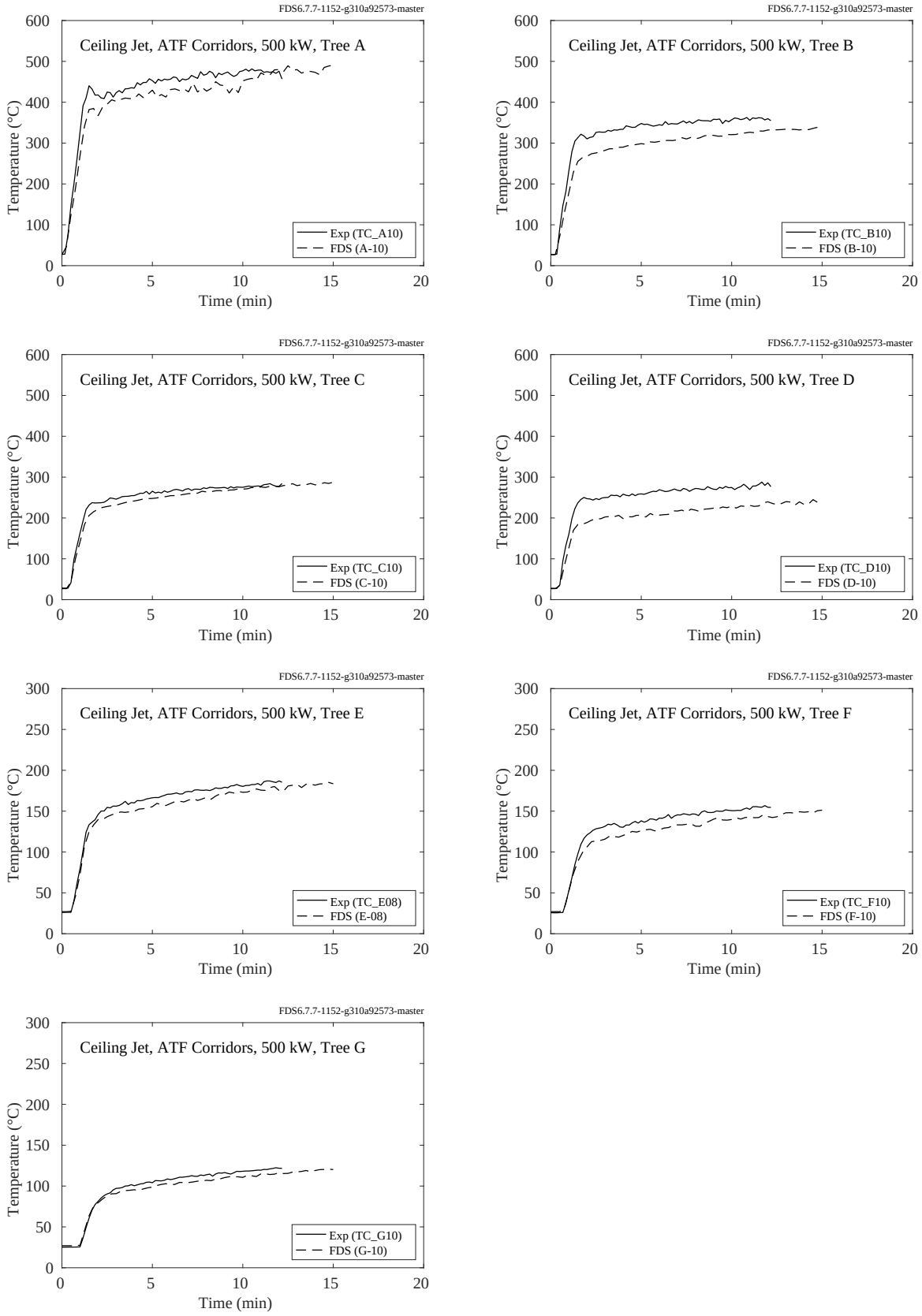

Figure 7.4: ATF Corridors experiments, ceiling jet, 500 kW.

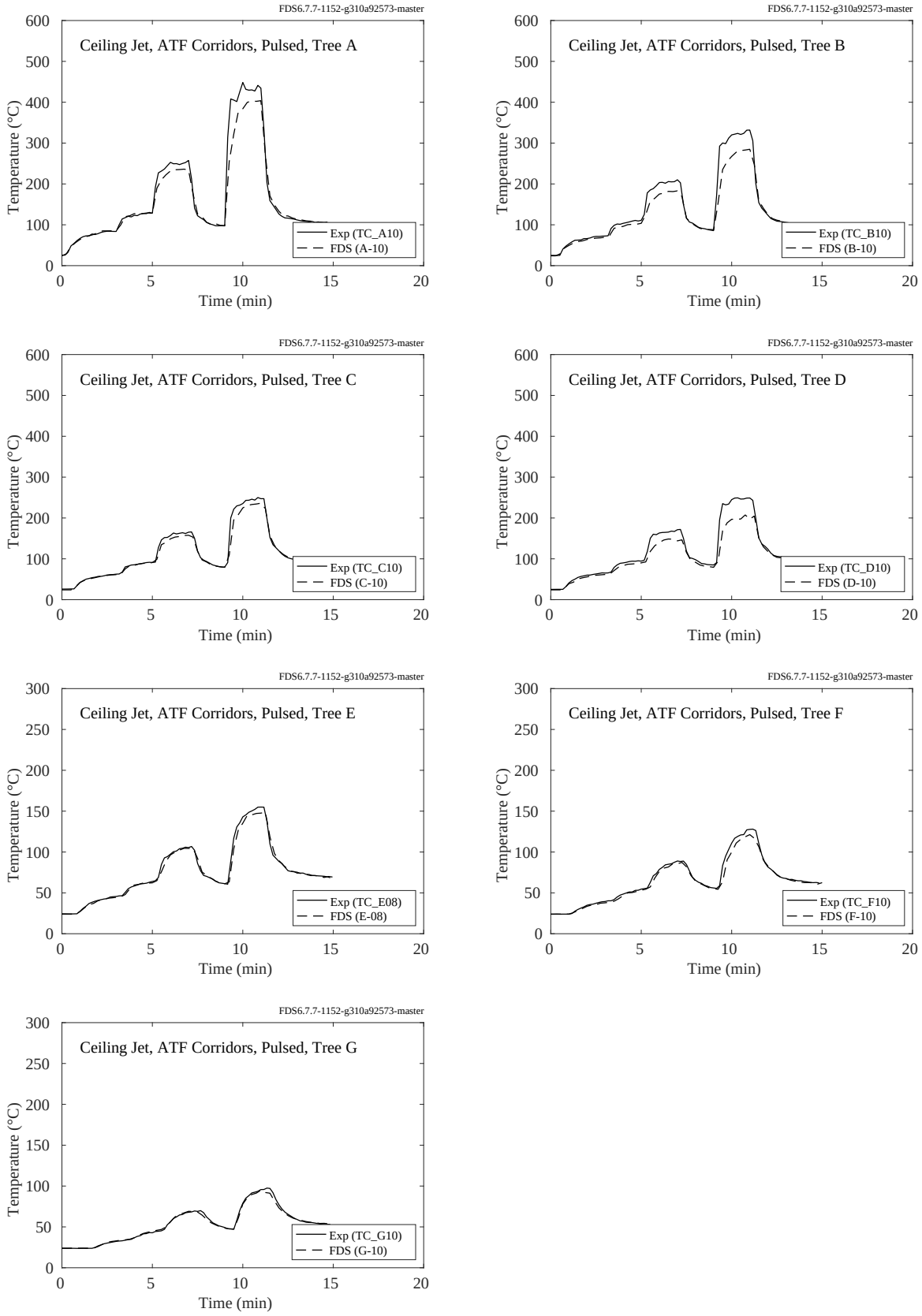

Figure 7.5: ATF Corridors experiments, ceiling jet, mixed HRR.

7.1.2 Arup Tunnel Experiments

The plots below show the predicted and measured temperatures from a fire experiment conducted in a tunnel. Near-ceiling temperatures were measured at distances of 2 m, 4 m, 6 m and 8 m from the fire along the centerline of tunnel.

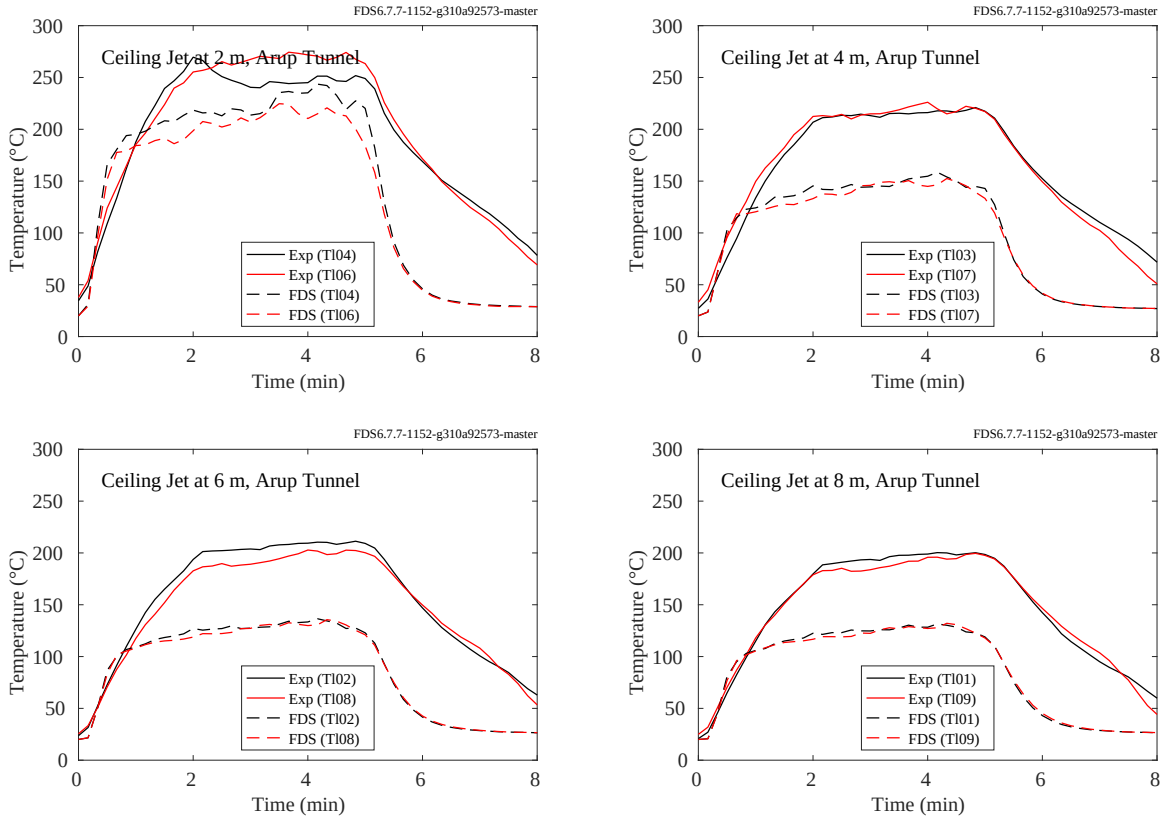

Figure 7.6: Arup Tunnel experiments, ceiling jet.

7.1.3 DelCo Trainers

The plots below and on the following pages display comparisons of ceiling jet temperatures for the DelCo Trainer experiments. Tests 2-6 were conducted in a single level house mock-up with three rooms adjacent to one another. Locations A1 and A2 were in the fire room, A3 was in an adjacent room, and A4 and A5 were in a room next to the adjacent room. Tests 22-25 were conducted in a two level house mock-up. Locations A1, A2, and A3 were 2 cm below the ceiling of the first level, and A7, A8, and A9 were 2 cm below the ceiling of the second level. See Section 3.17 for their exact locations.

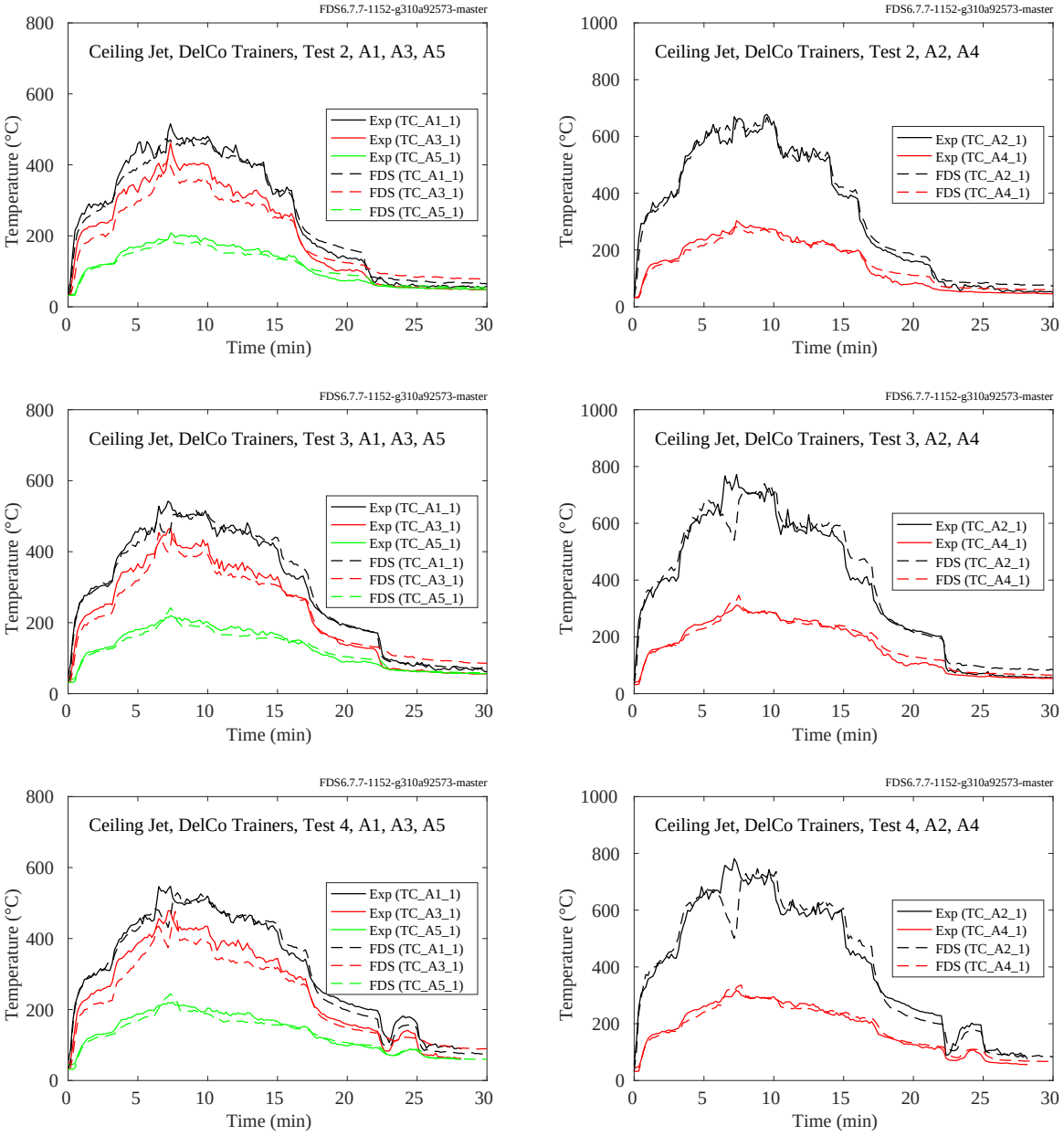

Figure 7.7: DelCo Trainers, ceiling jet temperature, Tests 2-4.

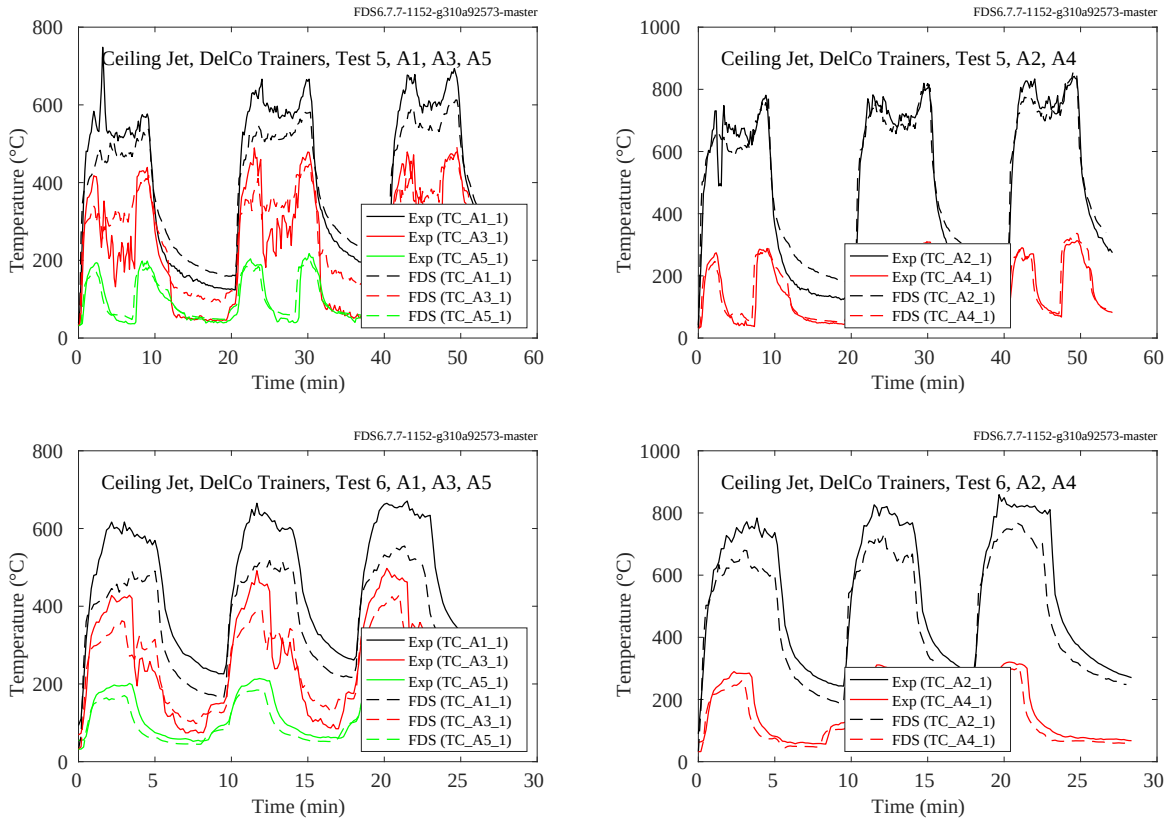

Figure 7.8: DelCo Trainers, ceiling jet temperature, Tests 5 and 6.

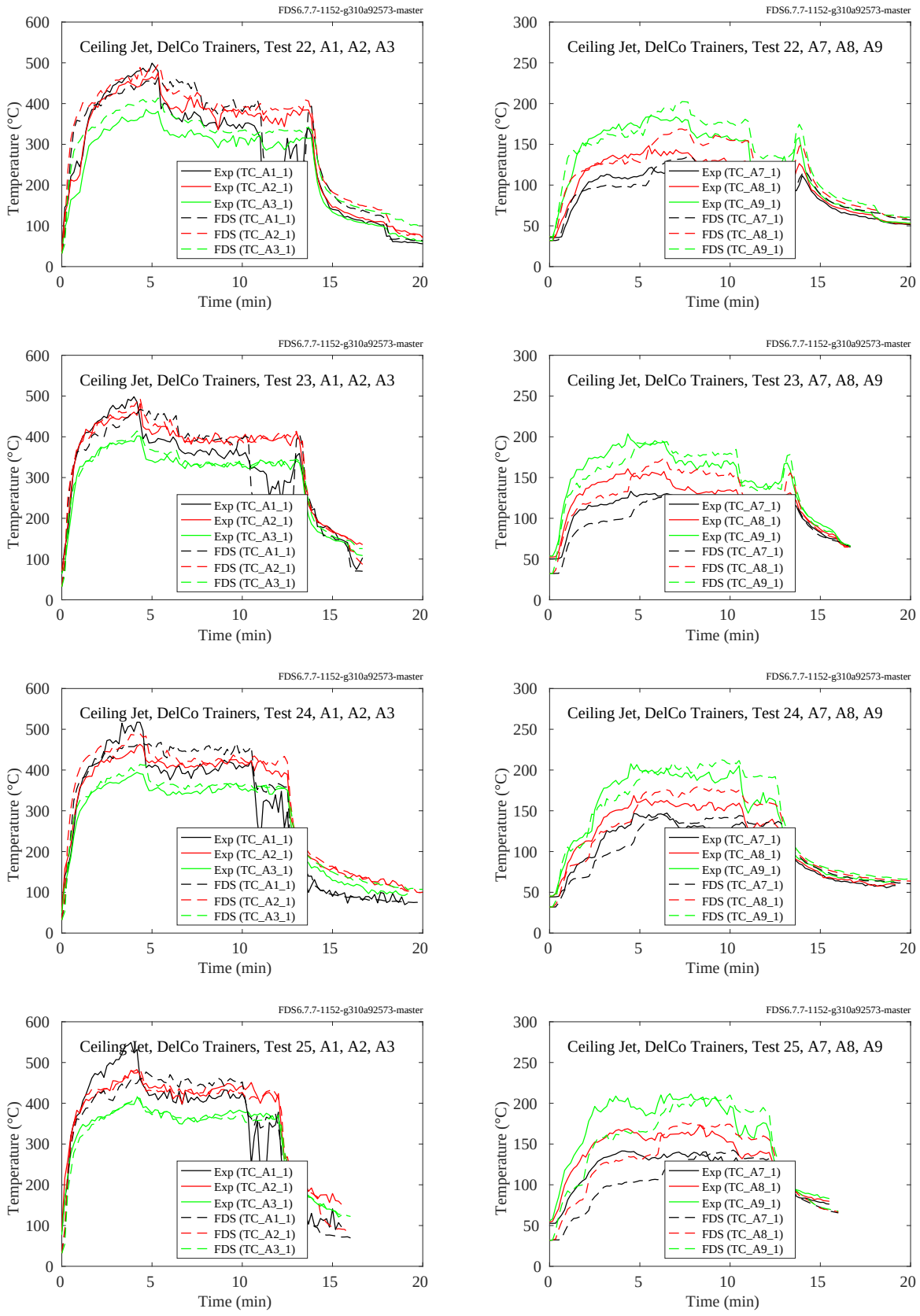

Figure 7.9: DelCo Trainers, ceiling jet temperature, Tests 22-25.

7.1.4 FAA Cargo Compartments

Figure 7.10 displays the locations of the near-ceiling thermocouples in the Boeing 707 compartment. The TCs were positioned approximately 4 cm below the ceiling. The small numbered squares indicate the fire locations for Tests 1, 2 and 3.

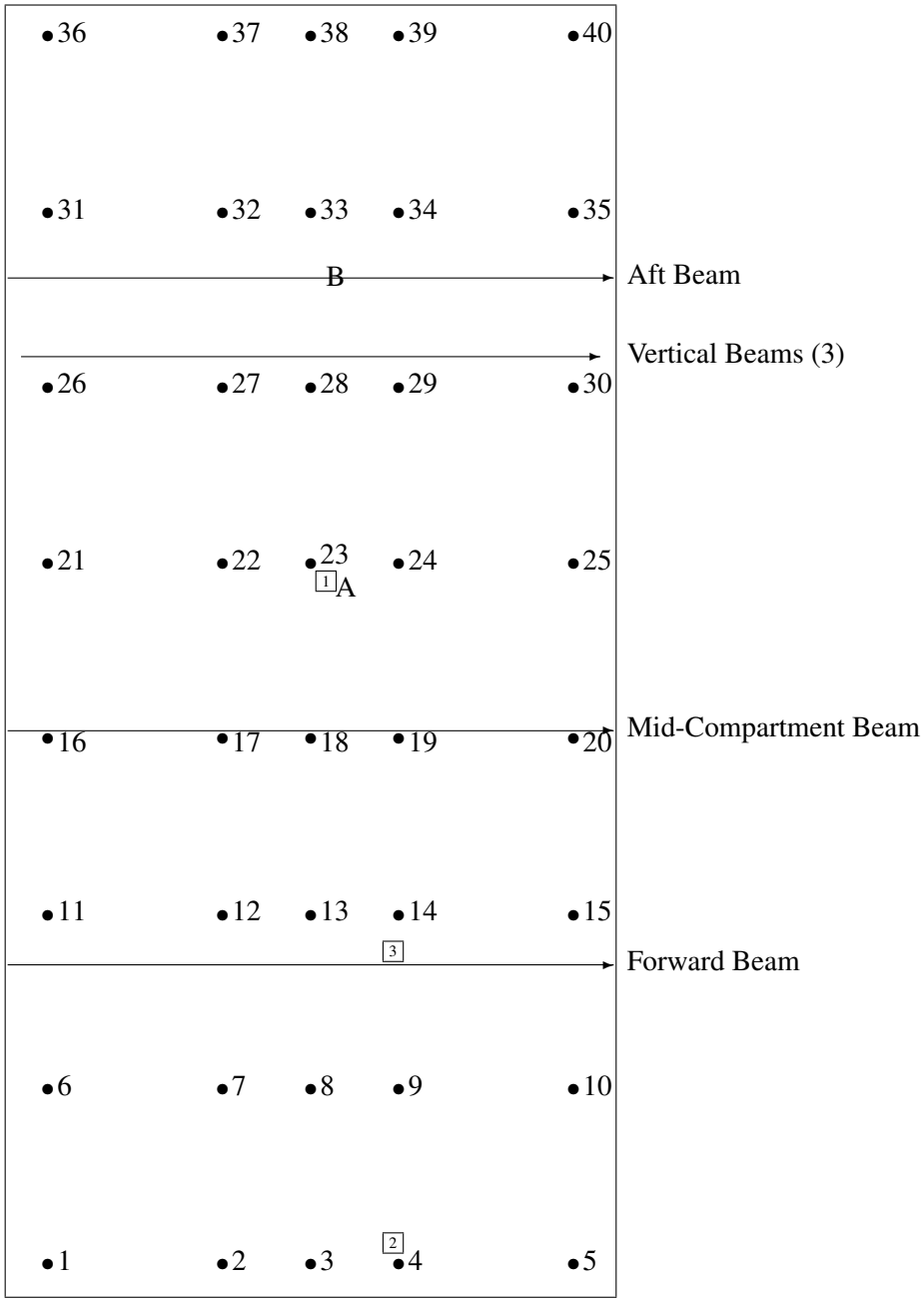

Figure 7.10: Layout of the near-ceiling thermocouples and other instruments, FAA Cargo Compartment Experiments.

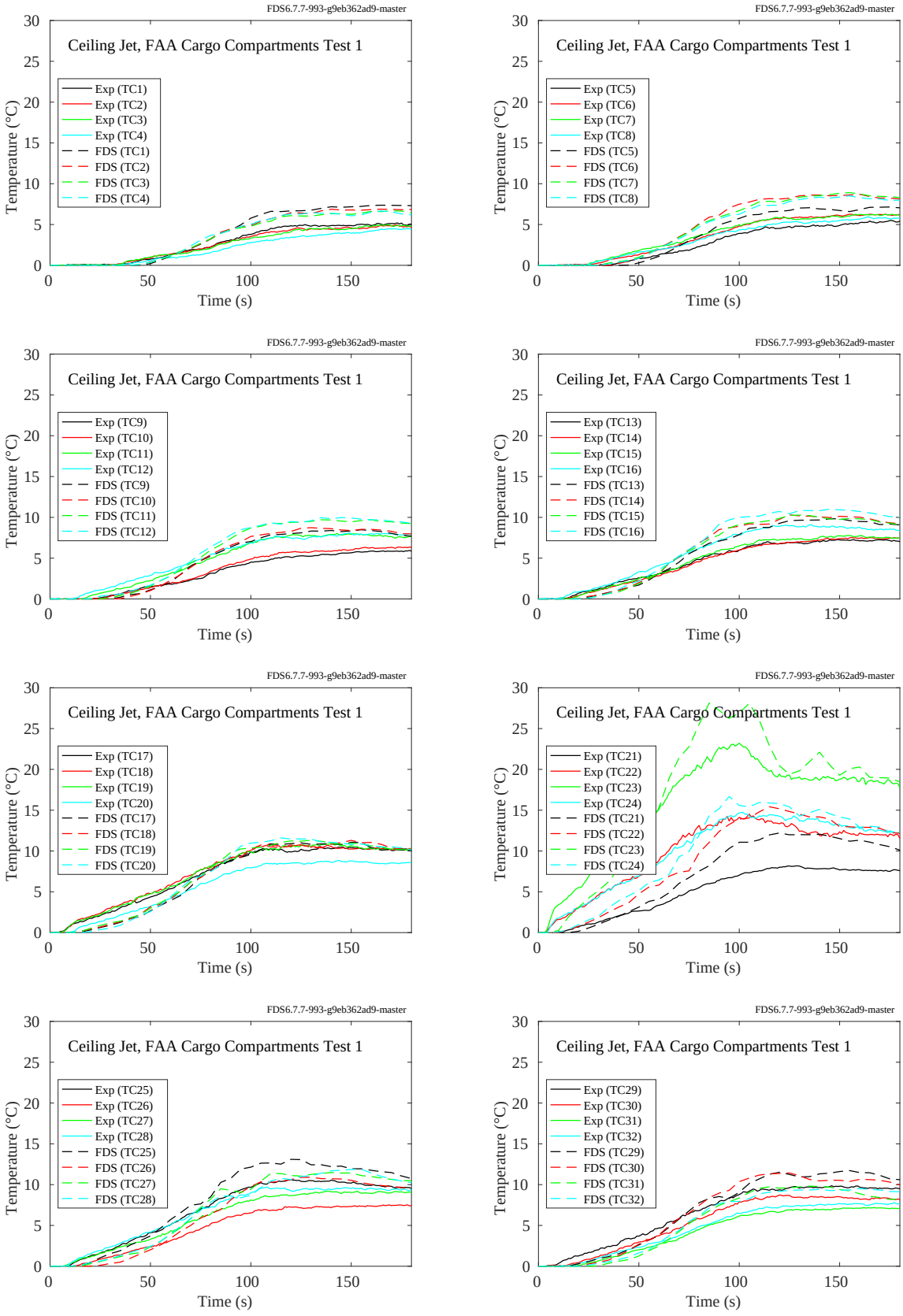

Figure 7.11: FAA Cargo Compartment experiments, ceiling jet, Test 1.

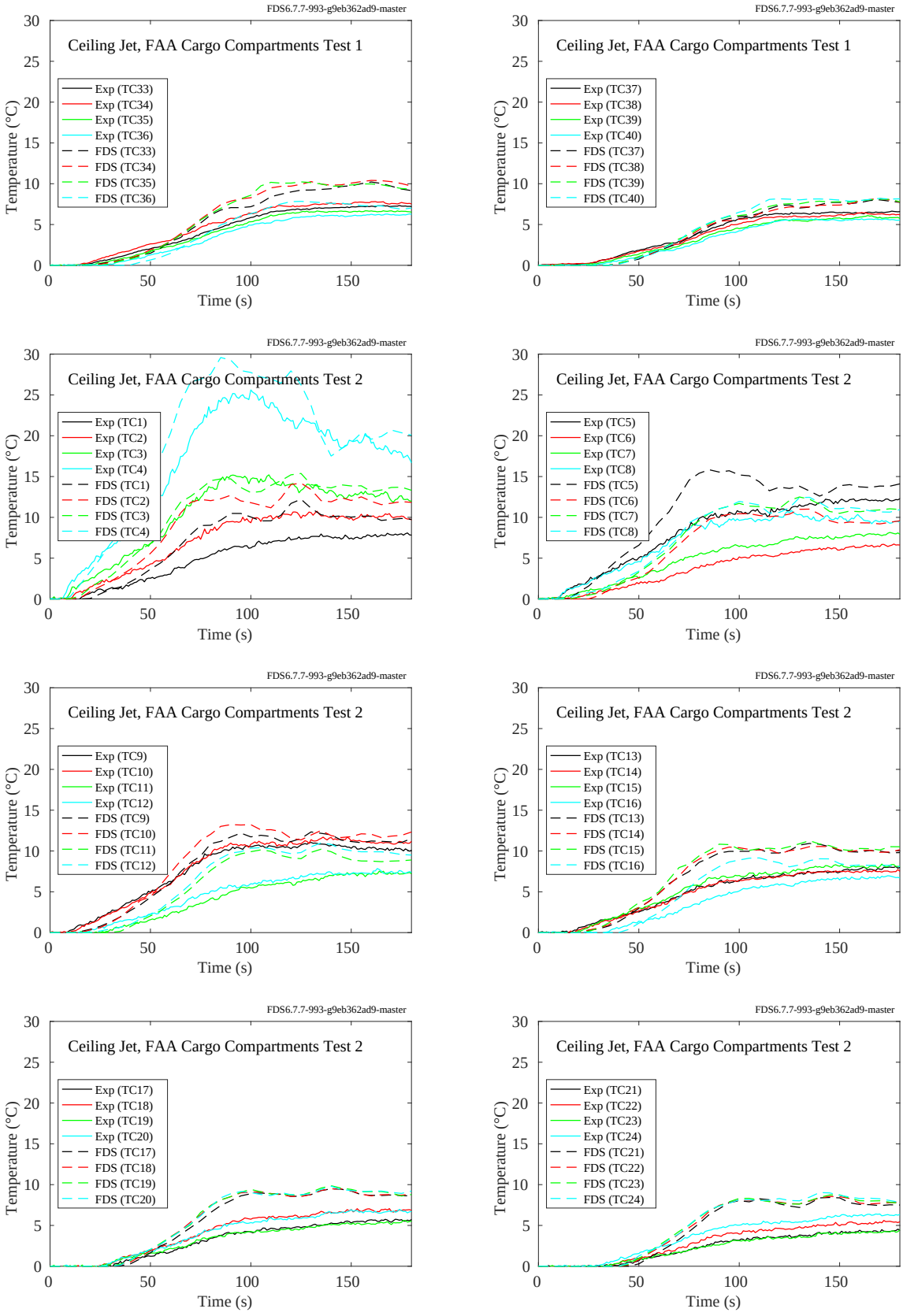

Figure 7.12: FAA Cargo Compartment experiments, ceiling jet, Test 1 and 2.

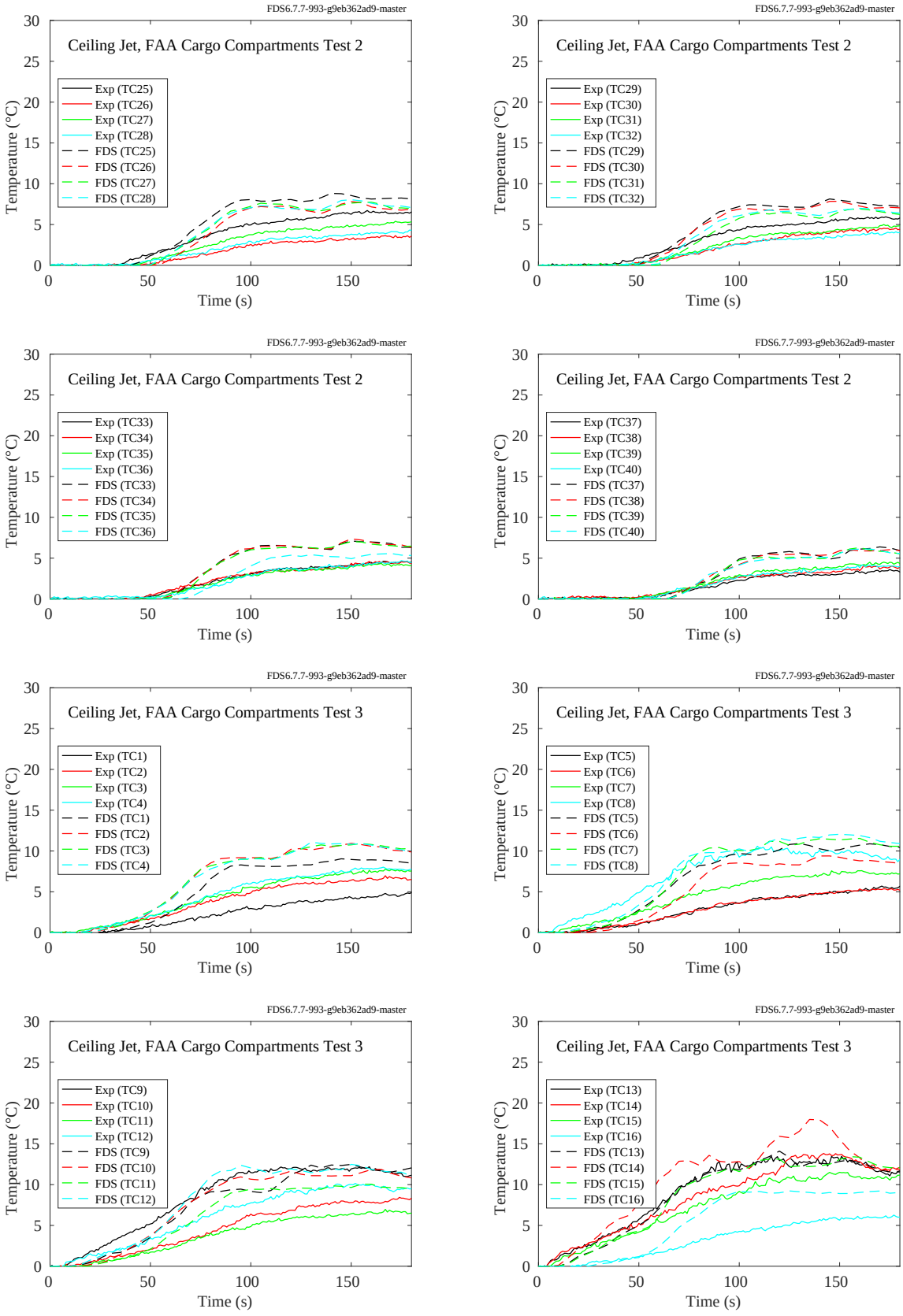

Figure 7.13: FAA Cargo Compartment experiments, ceiling jet, Test 2 and 3.

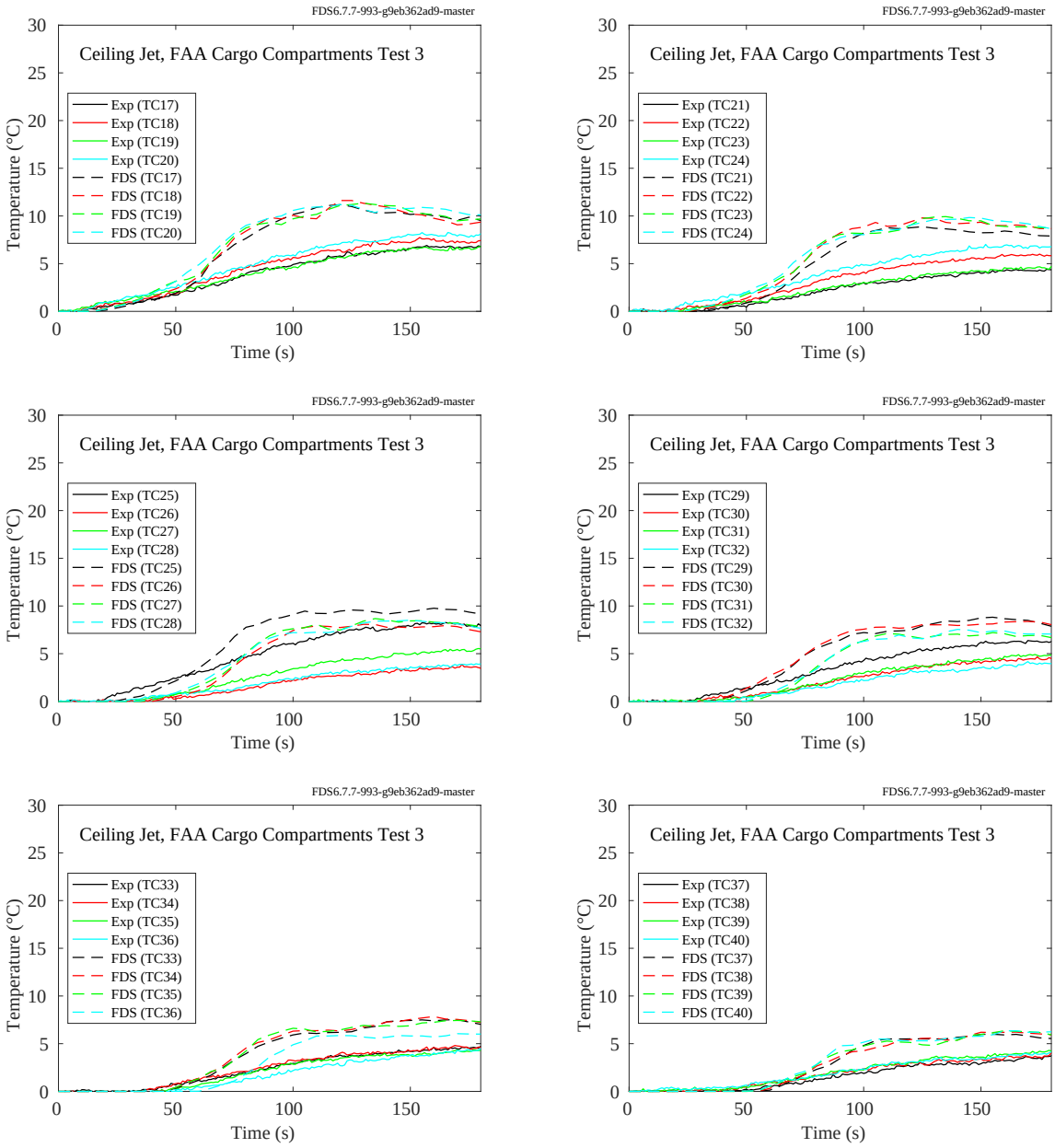

Figure 7.14: FAA Cargo Compartment experiments, ceiling jet, Test 3.

7.1.5 FM/SNL Experiments

The near-ceiling thermocouples in Sectors 1 and 3 have been chosen to evaluate the ceiling jet temperature prediction.

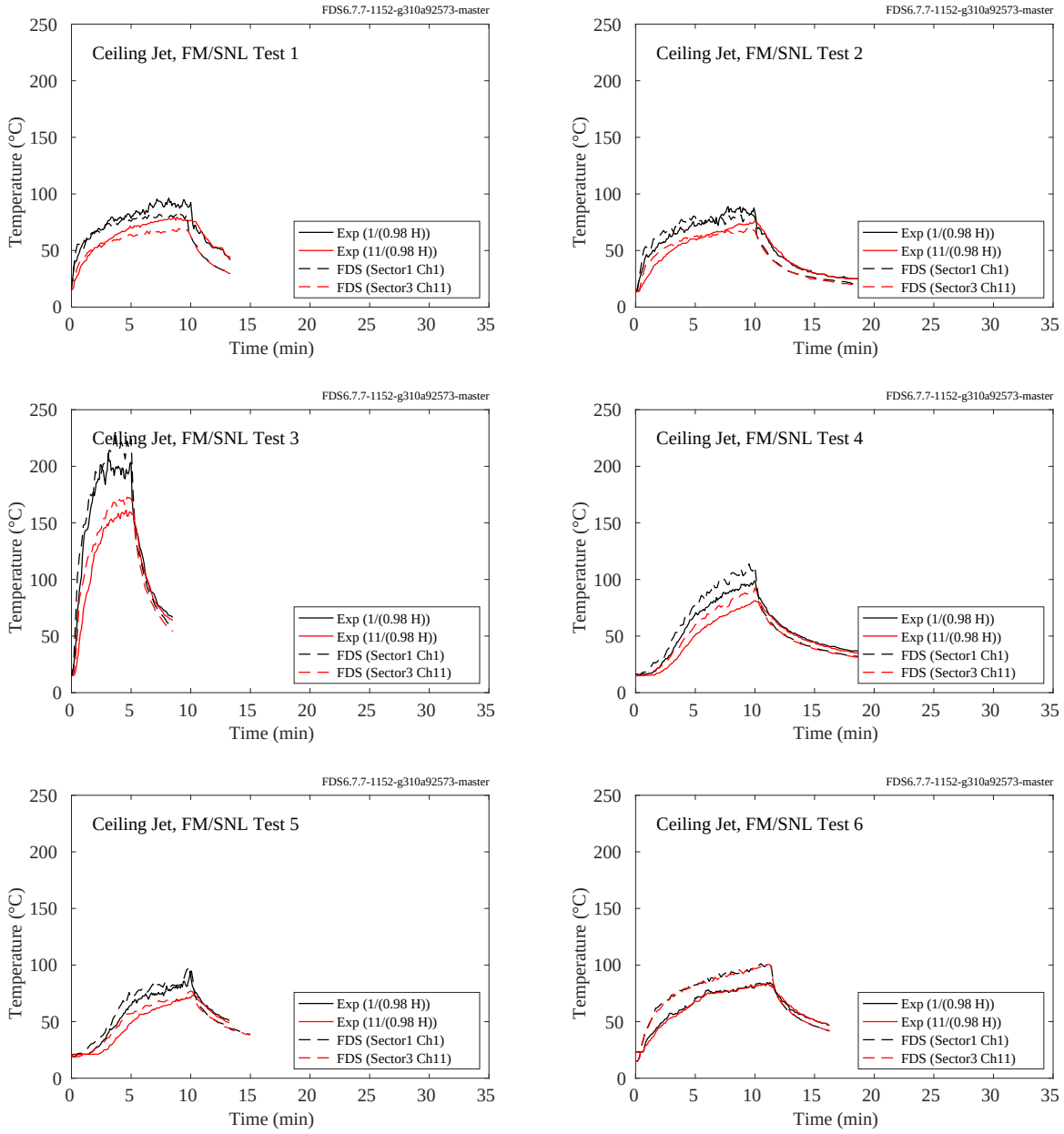

Figure 7.15: FM/SNL experiments, ceiling jet, Tests 1-6.

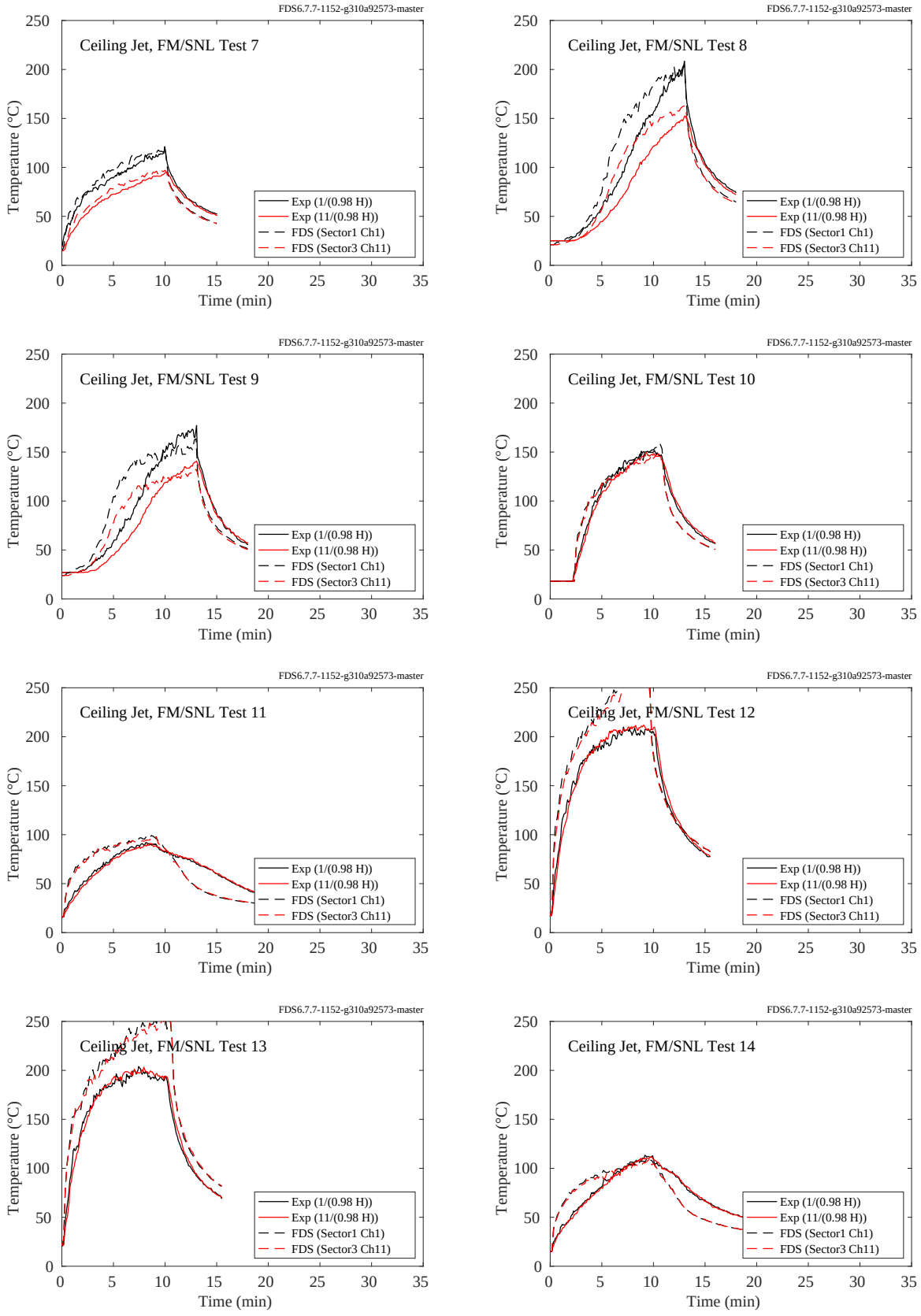

Figure 7.16: FM/SNL experiments, ceiling jet, Tests 7-14.

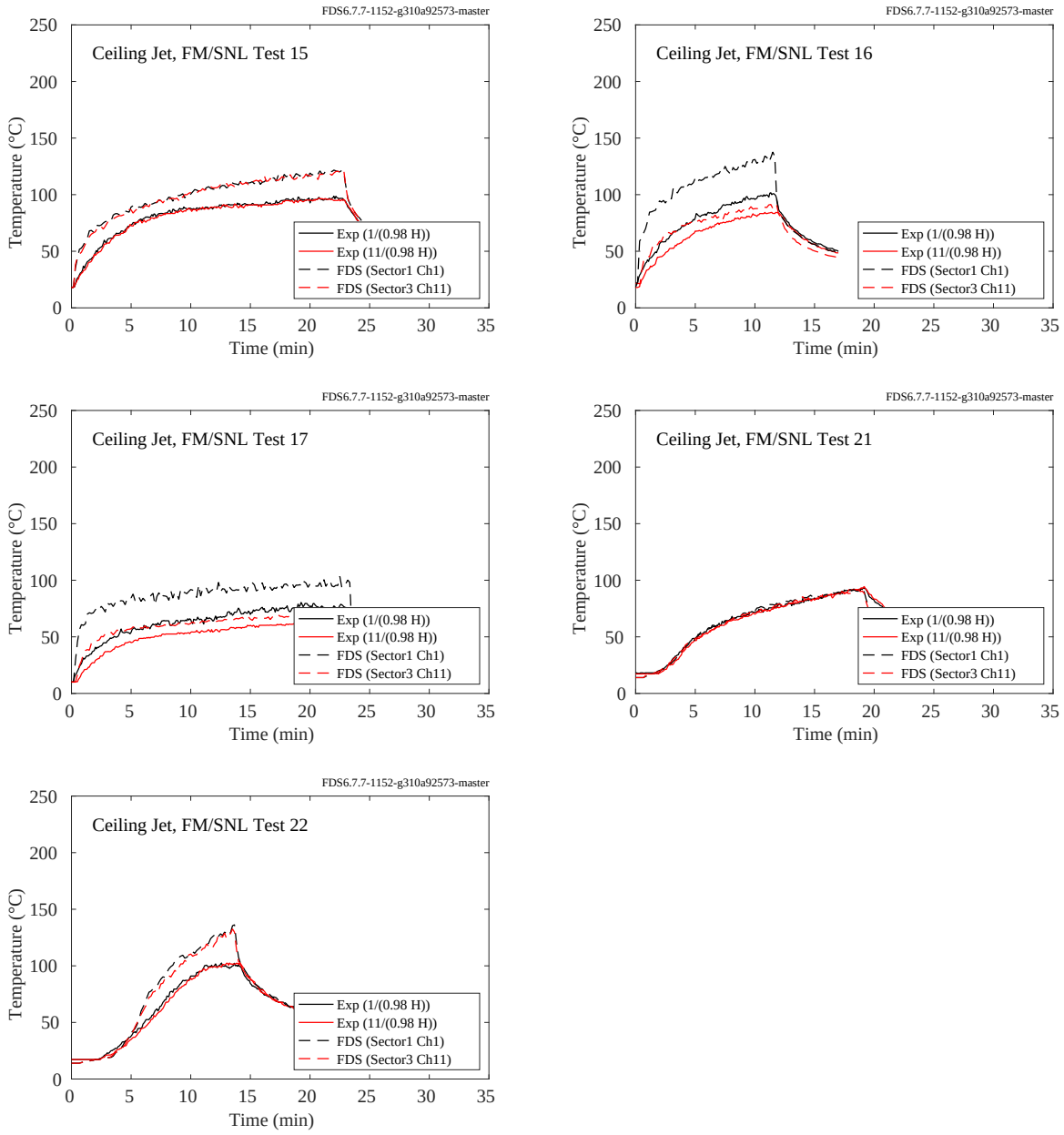

Figure 7.17: FM/SNL experiments, ceiling jet, Tests 15-17, 21-22.

7.1.6 NIST Composite Beam

A brief description of the experiments is given in Section 3.41. The compartment interior dimensions are 12.4 m long, running east-west, 1.9 m wide, and 3.77 m high. Four experiments with fires were performed, labeled as Tests 2-5. Test 1 did not include a fire.

To measure the ceiling jet temperature in the compartment, stainless steel sheathed thermocouples (Omega TJ36-CAXL-14U-24 and TJ36-CAXL-38U-24) were mounted 2.5 cm and 23 cm below the ceiling, extending through four holes drilled down through the concrete. Two TCs were located at each of the four positions. TCC9 and TCC10 were located 2.6 m west and 0.6 m north of the compartment center. TCC11 and TCC12 were located at the same location east of the center. TCC13 and TCC14 were located at the same relative location, south and east of the center. TCC15 and TCC16 were located west and south of the center.

Because of the symmetry of the experimental configuration, TCC9, TCC11, TCC13, and TCC15, all 2.5 cm below the ceiling are duplicates; as are TCC10, TCC12, TCC14, and TCC16, located 23 cm below the ceiling.

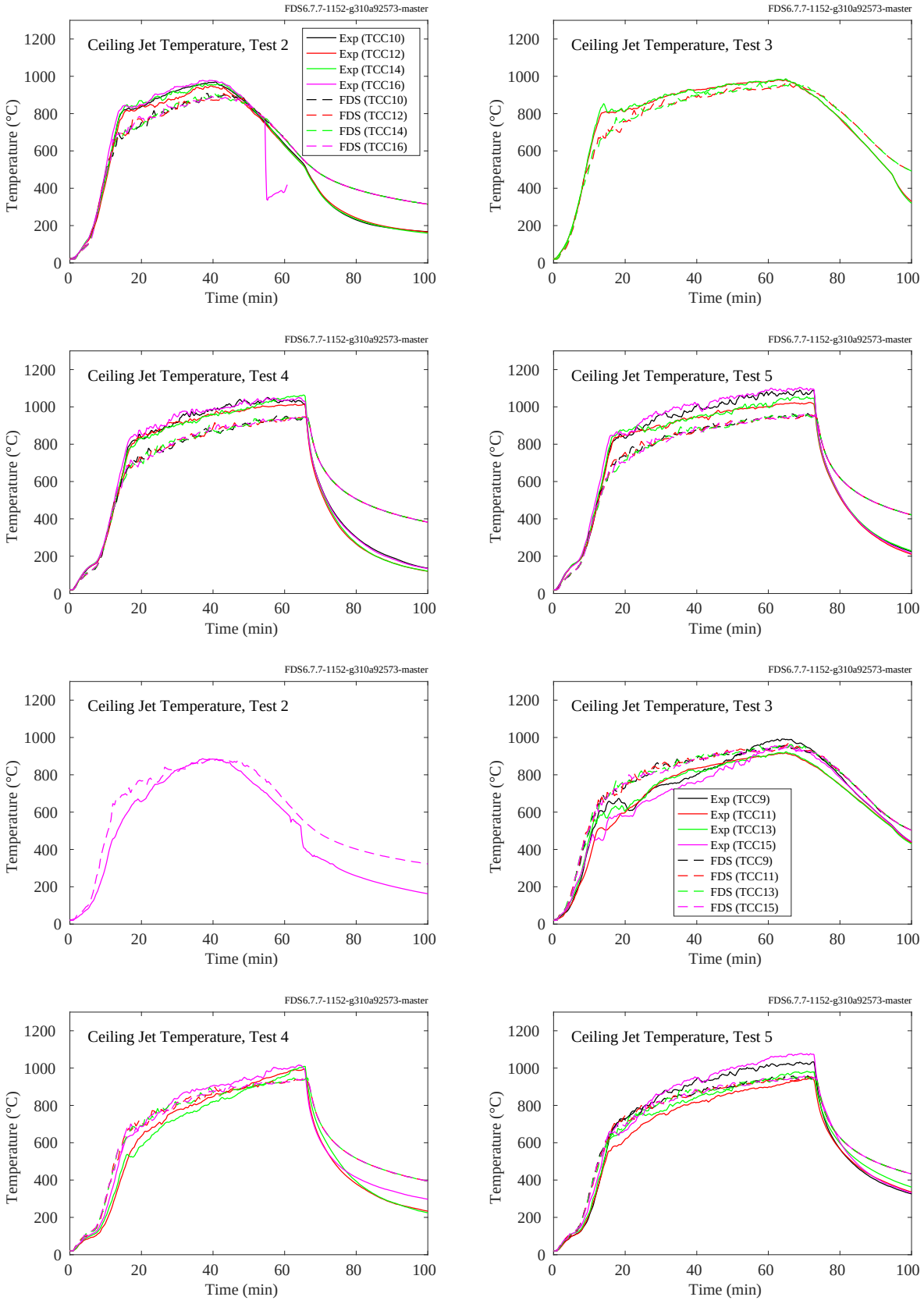

Figure 7.18: NIST Composite Beam, ceiling jet temperatures.

7.1.7 NIST Smoke Alarm Experiments

The primary purpose of the NIST Smoke Alarm Experiments was to measure smoke detector activation times in residential settings. In the single-story manufactured home tests that were selected for validation, five smoke detector measurement stations (Station A through Station E) were located in different areas of the manufactured home. Thermocouple trees were also located at each measurement station. The highest thermocouple in the tree can be compared to ceiling jet temperature predictions. The plots on the following page show the measured and predicted ceiling jet temperatures for the five measurement stations in each test.

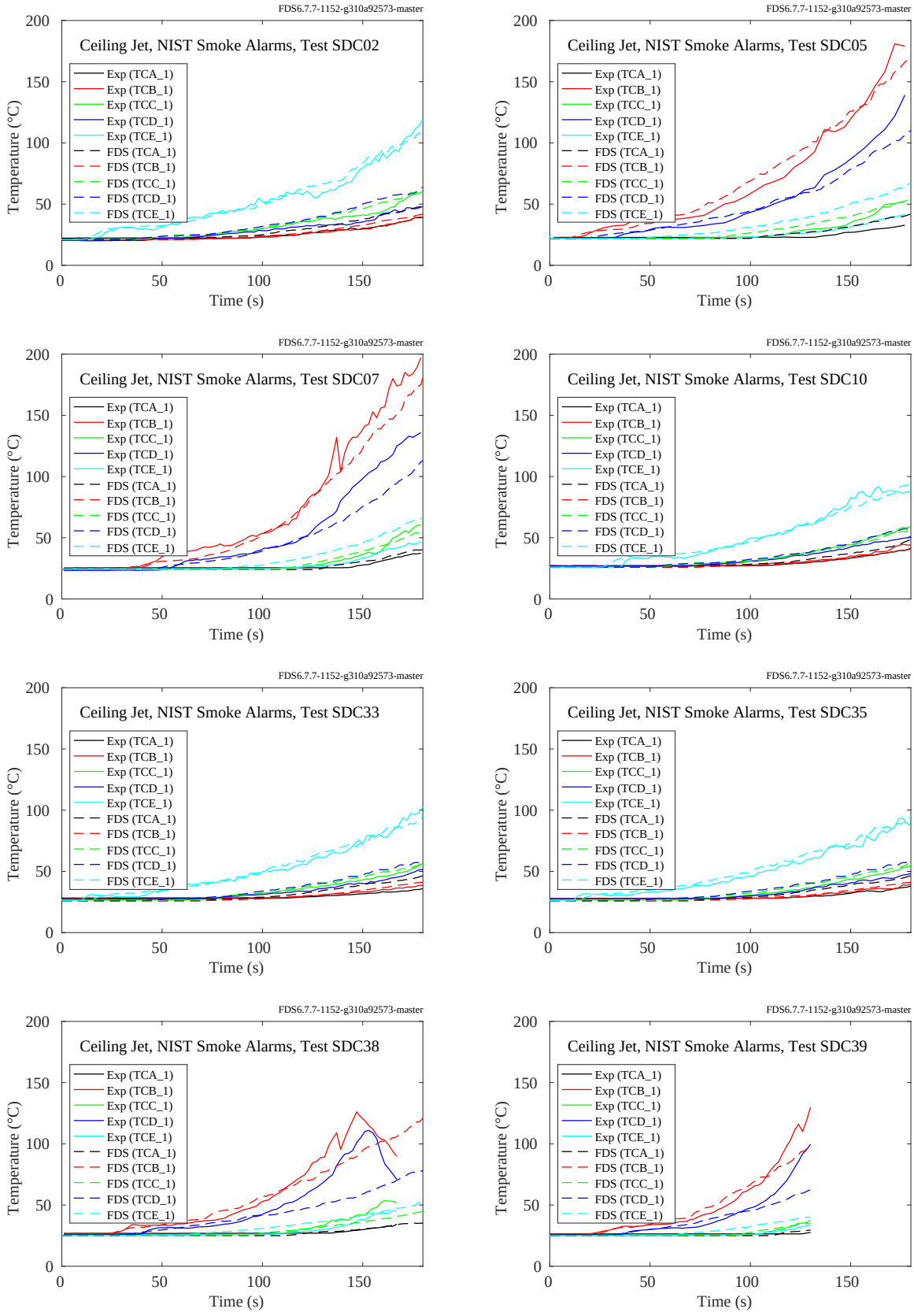

Figure 7.19: NIST Smoke Alarm experiments, ceiling jet.

7.1.8 NIST/NRC Experiments

In the NIST/NRC experiments, seven vertical arrays of thermocouples were positioned throughout the compartment. The thermocouple nearest the ceiling in Tree 7, located towards the back of the compartment away from the door, has been chosen to evaluate the ceiling jet temperature prediction.

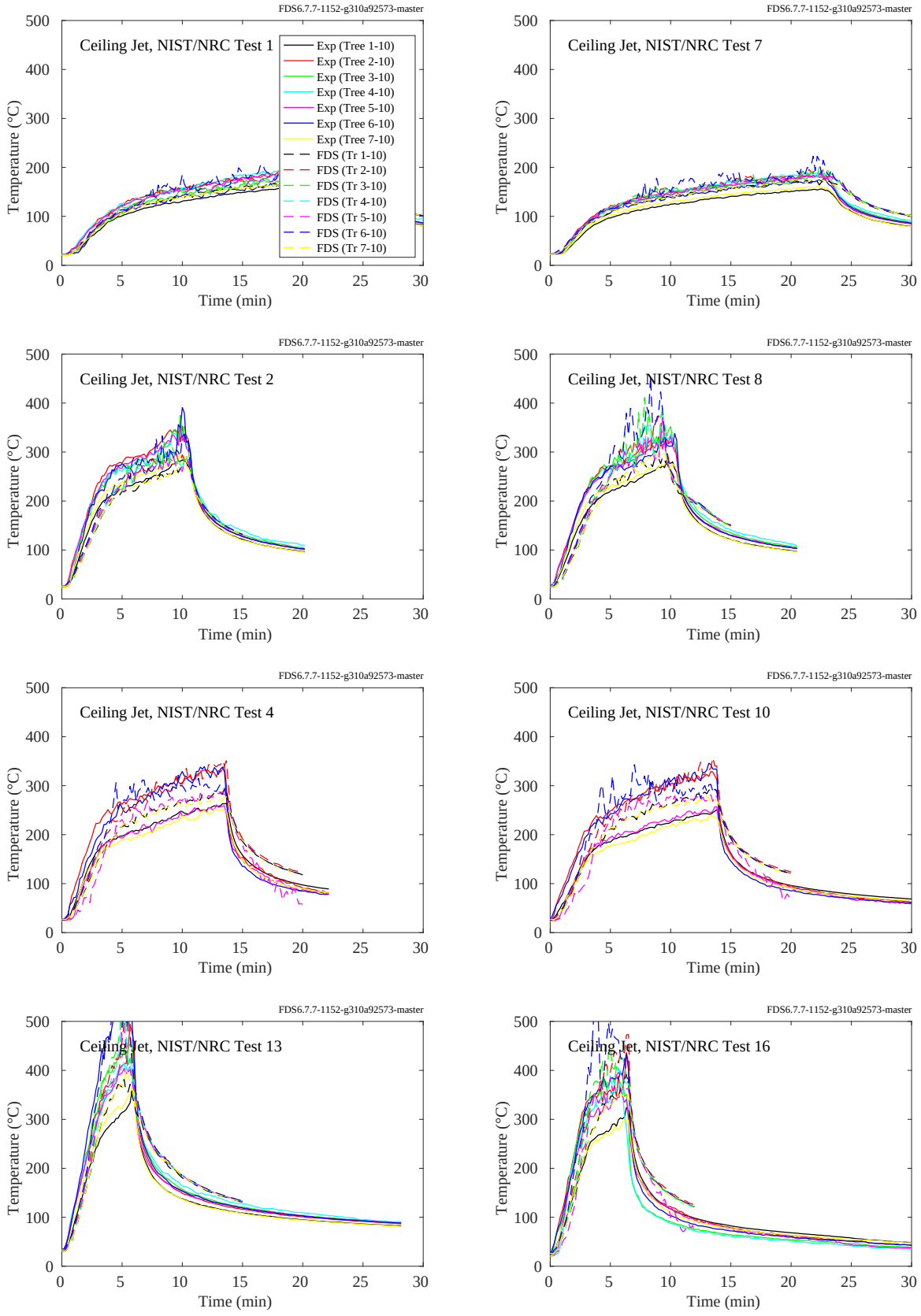

Figure 7.20: NIST/NRC experiments, ceiling jet, Tests 1, 2, 4, 7, 8, 10, 13, 16.

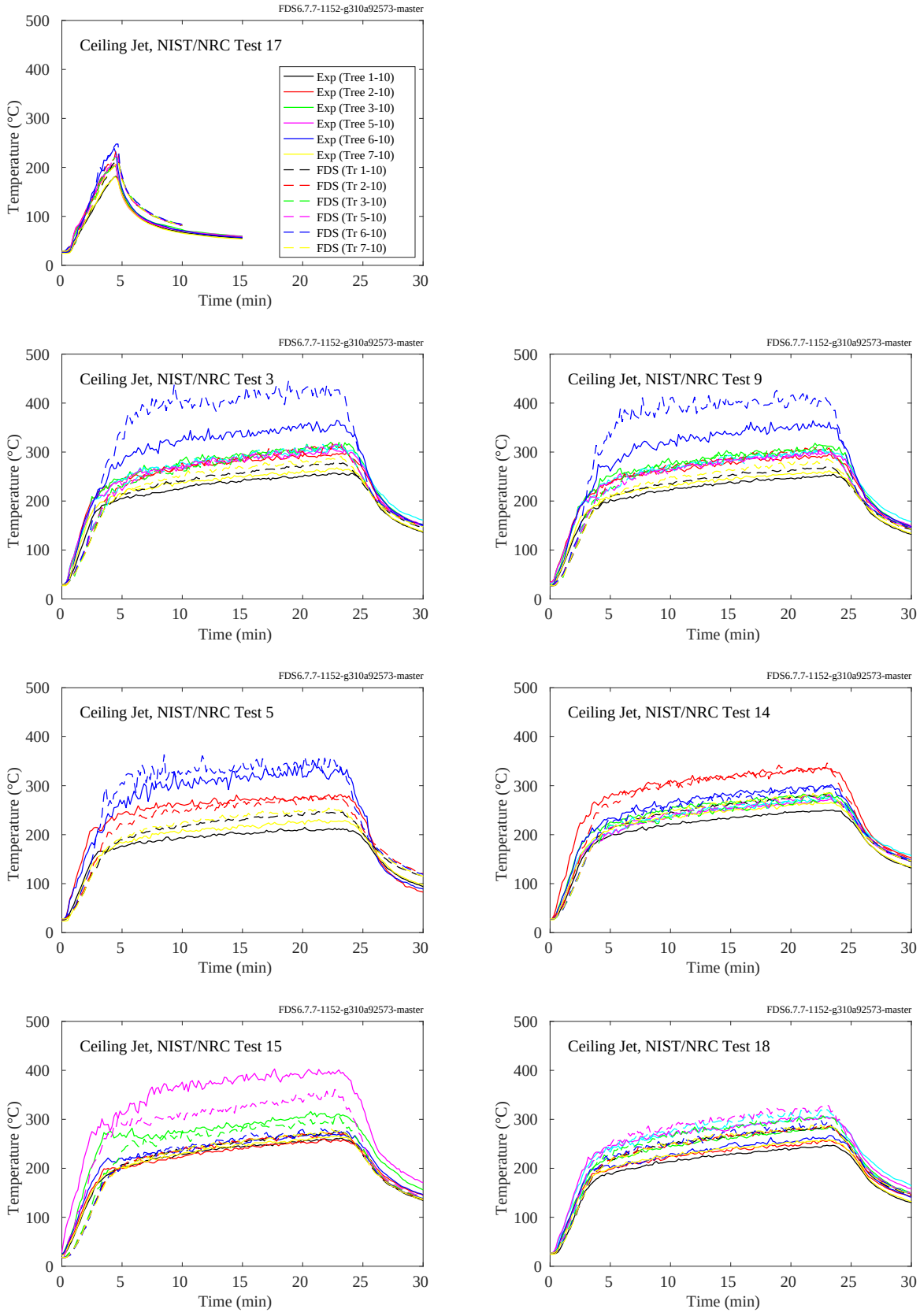

Figure 7.21: NIST/NRC experiments, ceiling jet, Tests 3, 5, 9, 14, 15, 17, 18.

7.1.9 NIST/NRC Corner Effects Experiments

The plots on the following pages compare ceiling jet temperatures at two locations in a large compartment where corner, wall, and cabinet effects experiments were conducted. The corner and wall experiments involved a 60 cm by 60 cm natural gas burner with heat release rates of 200 kW, 300 kW, and 400 kW. The burner was either set in a corner or against a wall. The cabinet experiments involved gas burners set in one of two mock steel cabinets, with a variety of heat release rates.

In all experiments, two vertical thermocouple arrays were placed along the centerline of the room, each one-third of the room length from each respective short wall. The arrays each had 13 bare-bead thermocouples. The first was 2 cm below the ceiling, used to measure the ceiling jet temperature.

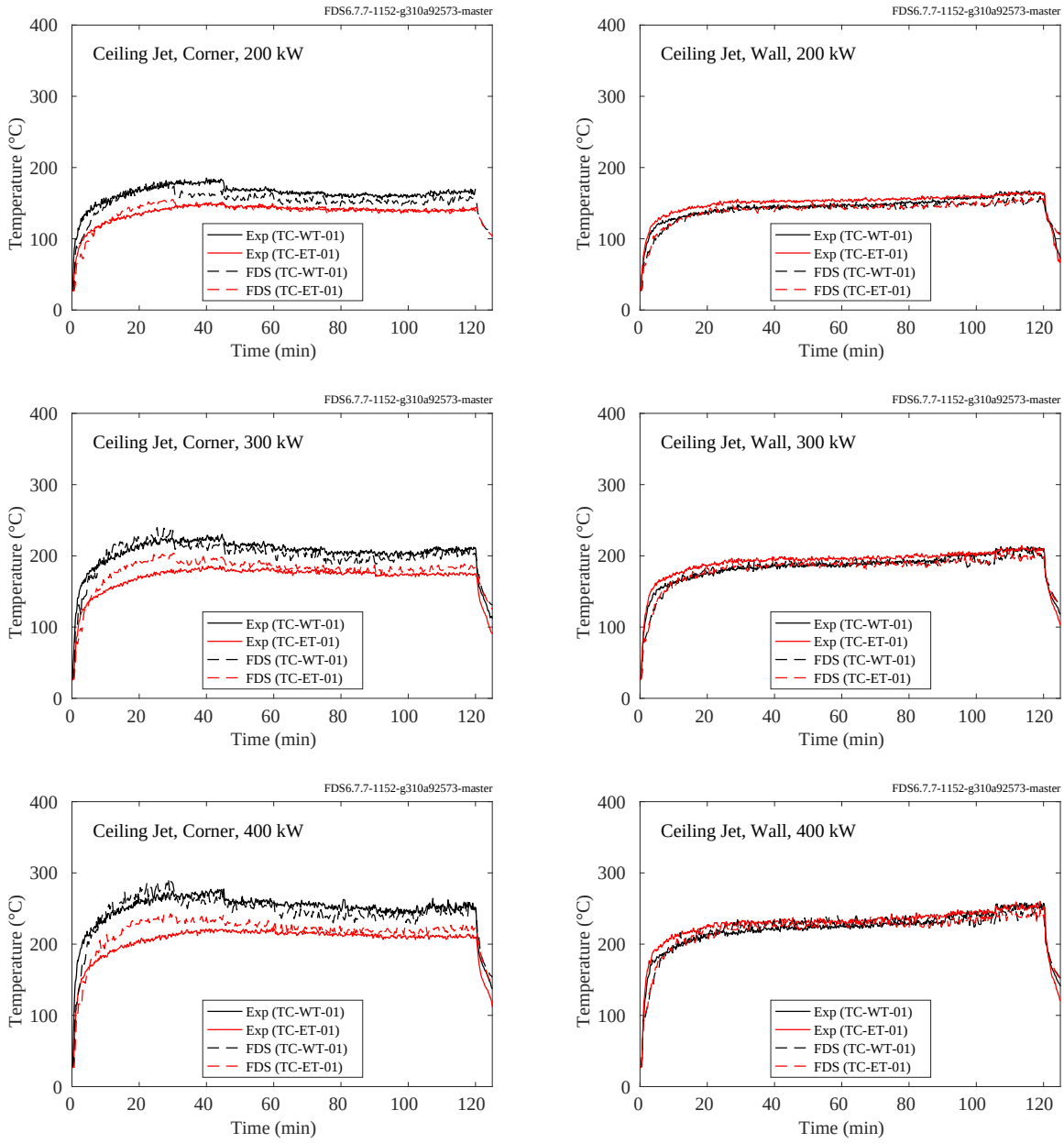

Figure 7.22: NIST/NRC Corner Effects experiments, ceiling jet temperature, wall and corner tests.

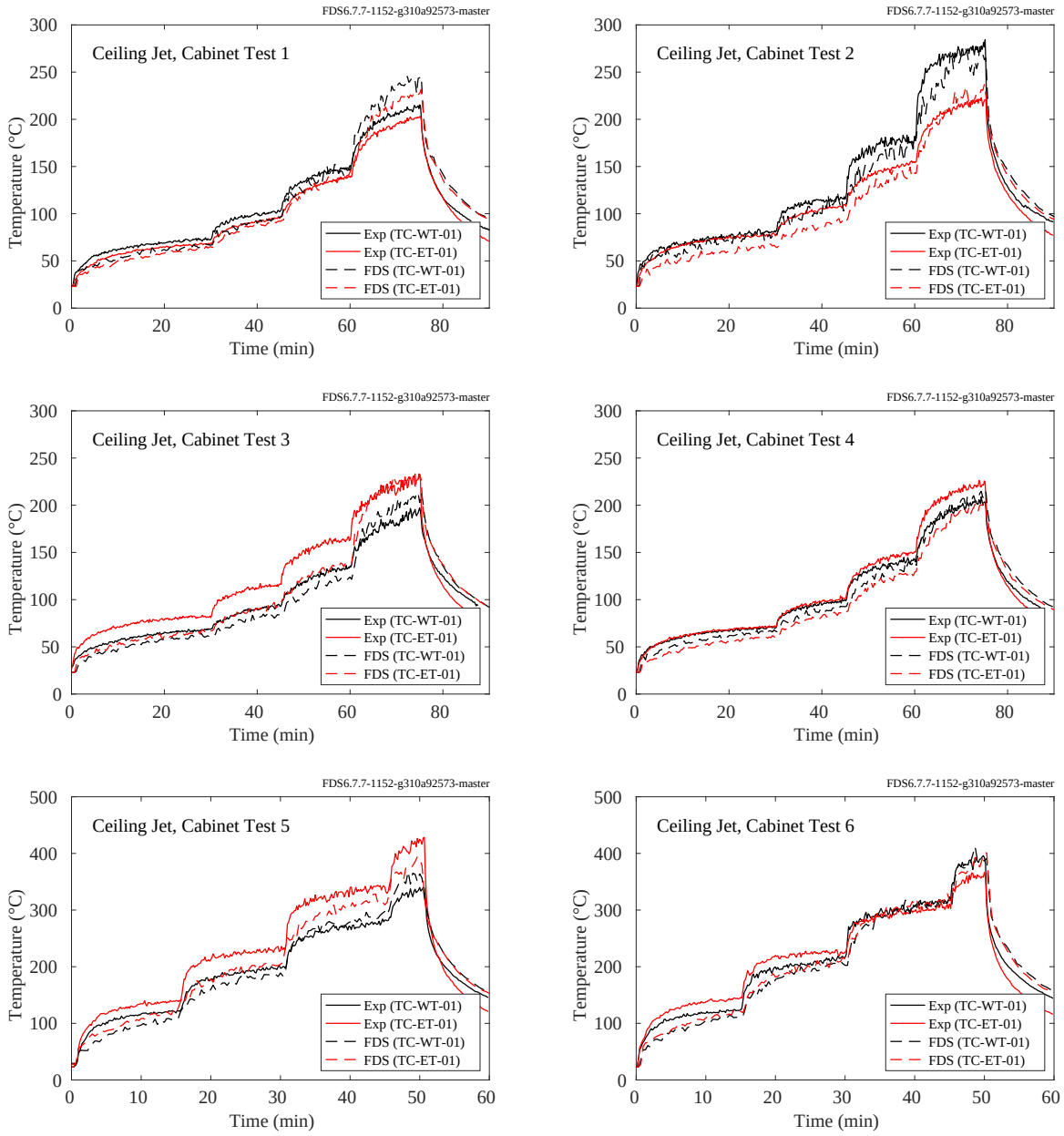

Figure 7.23: NIST/NRC Corner Effects experiments, ceiling jet temperature, large cabinet.

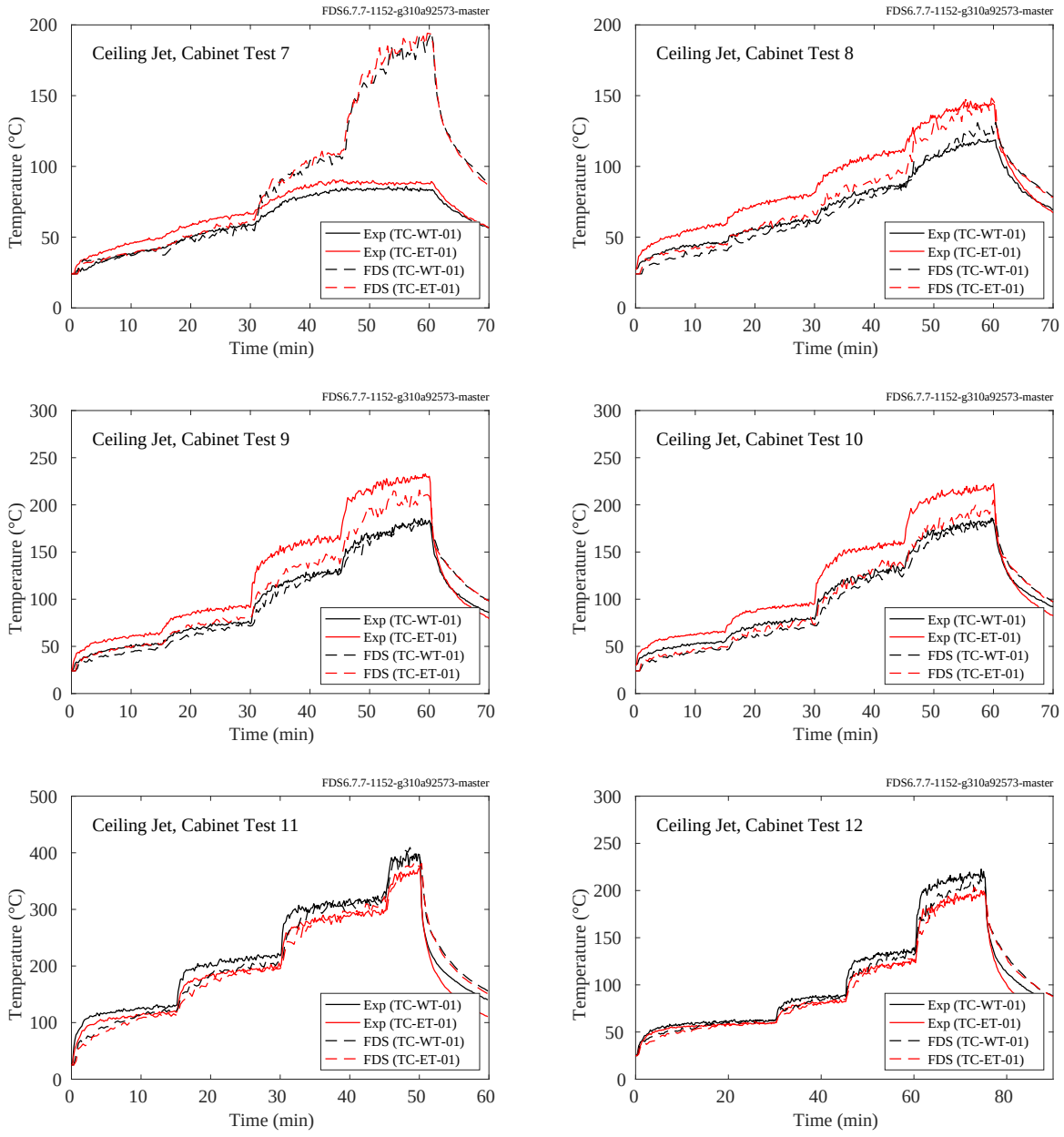

Figure 7.24: NIST/NRC Corner Effects experiments, ceiling jet temperature, medium-sized cabinet.

7.1.10 NIST Vent Study

These experiments were performed in a small-scale two floor enclosure, with each floor connected by one or two ceiling vents. Each floor contained a vertical array of eight sheathed thermocouples; the uppermost being 5 cm below the ceiling.

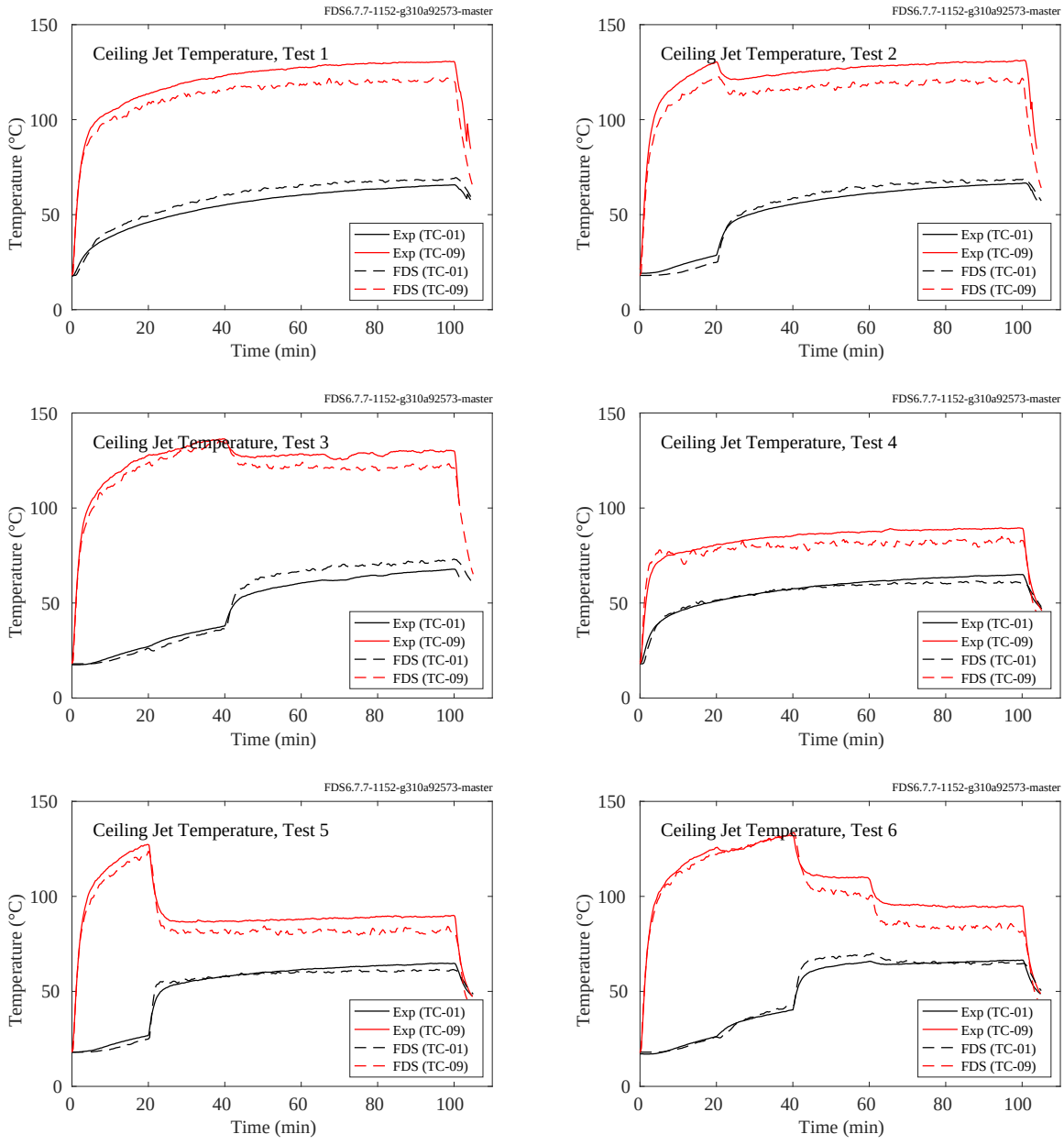

Figure 7.25: NIST Vent Study, ceiling jet temperature, Tests 1-6.

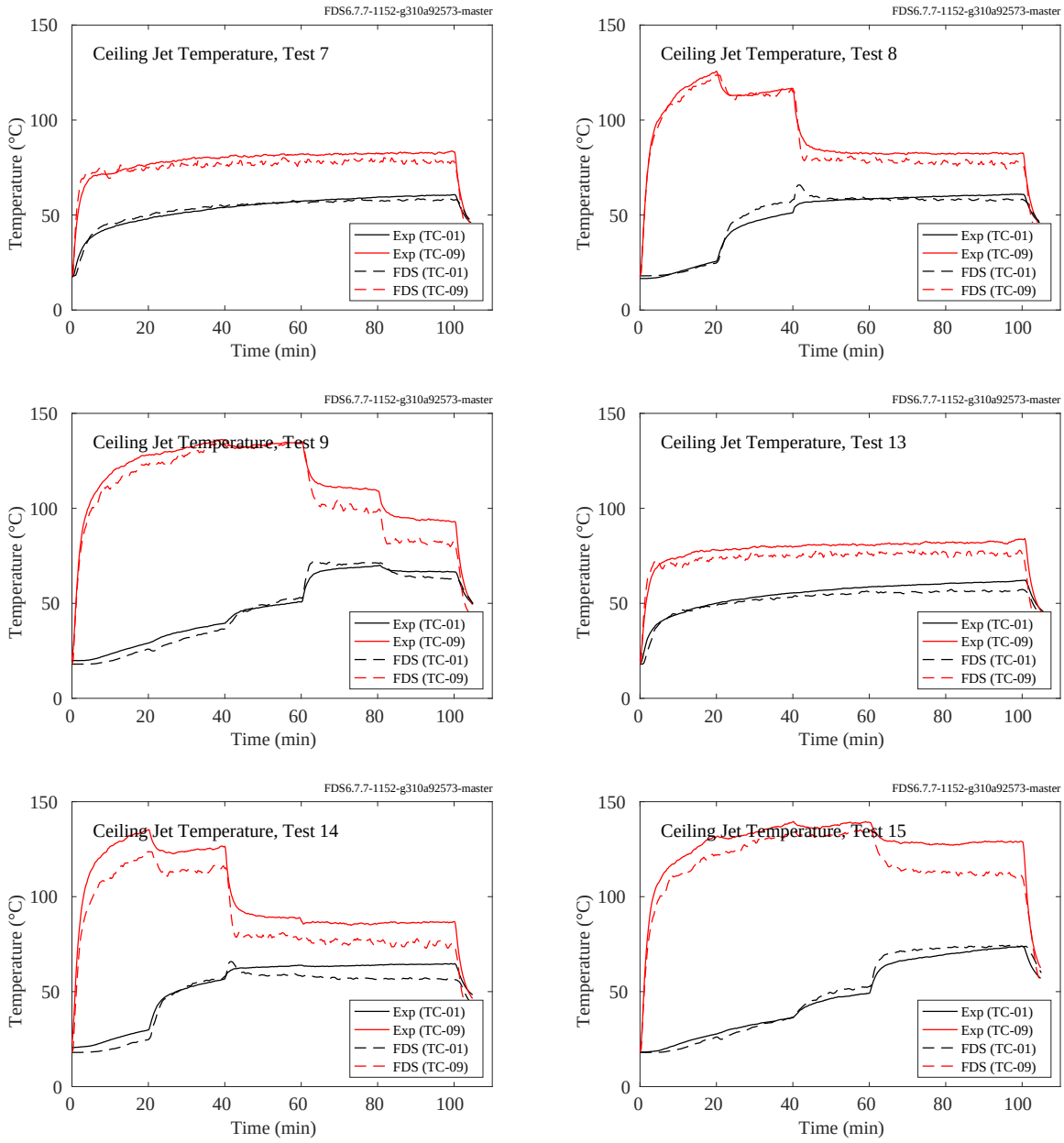

Figure 7.26: NIST Vent Study, ceiling jet temperature, Tests 7-9, 13-15.

7.1.11 NRCC Smoke Tower

In the NRCC Smoke Tower experiments, there was a vertical array of 13 TCs and a single near-ceiling TC on the opposite side of the fire compartment. Shown in Fig. 7.27 are the predicted and measured temperatures of the single TC and the uppermost TC of the vertical array in the fire compartment. Shown in Fig. 7.28 are predictions of gas temperature measurements made in the stair vestibule of floors 4, 6, 8, and 10, along with inner compartment temperature measurements made on floors 4, 8, and 10. Note that the plot labels "Slot" refer to the data acquisition system in the experiments only and have no meaning in the present context. It should be clear from the plot title how the various curves ought to be interpreted.

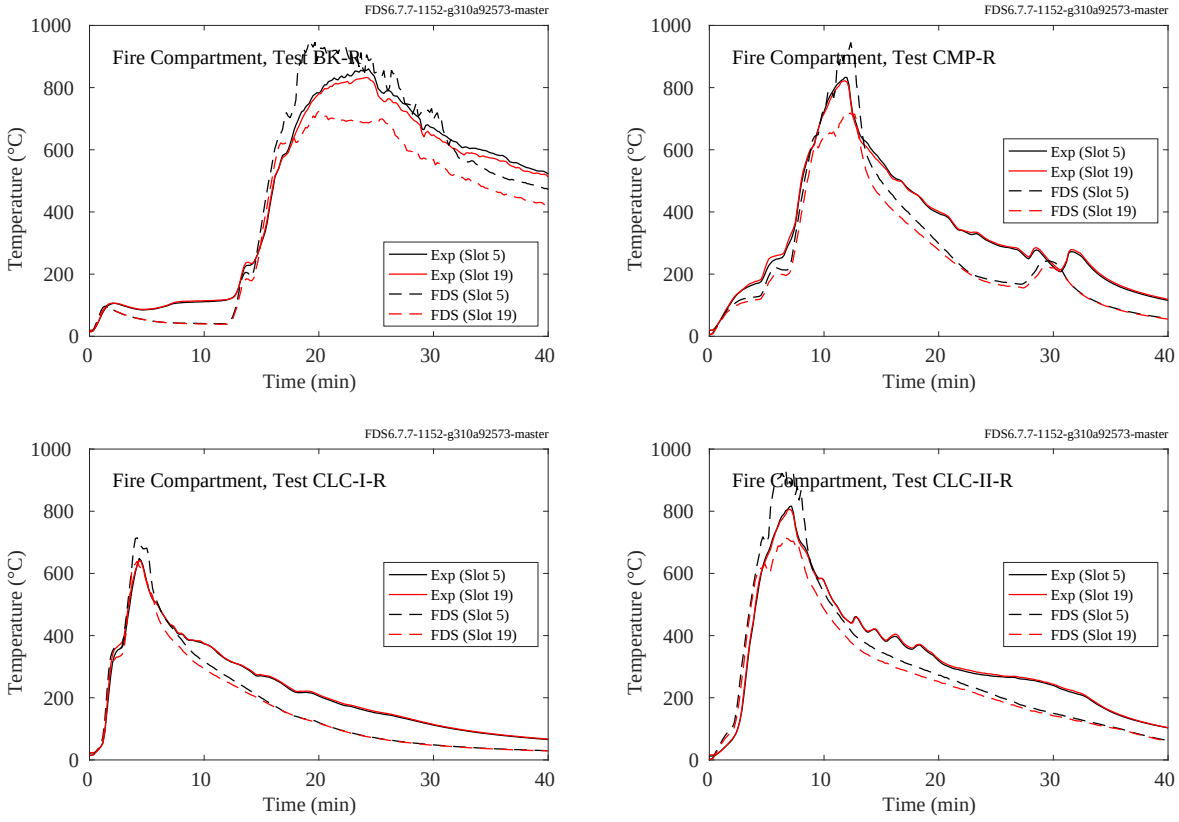

Figure 7.27: NRCC Smoke Tower experiments, ceiling jet.

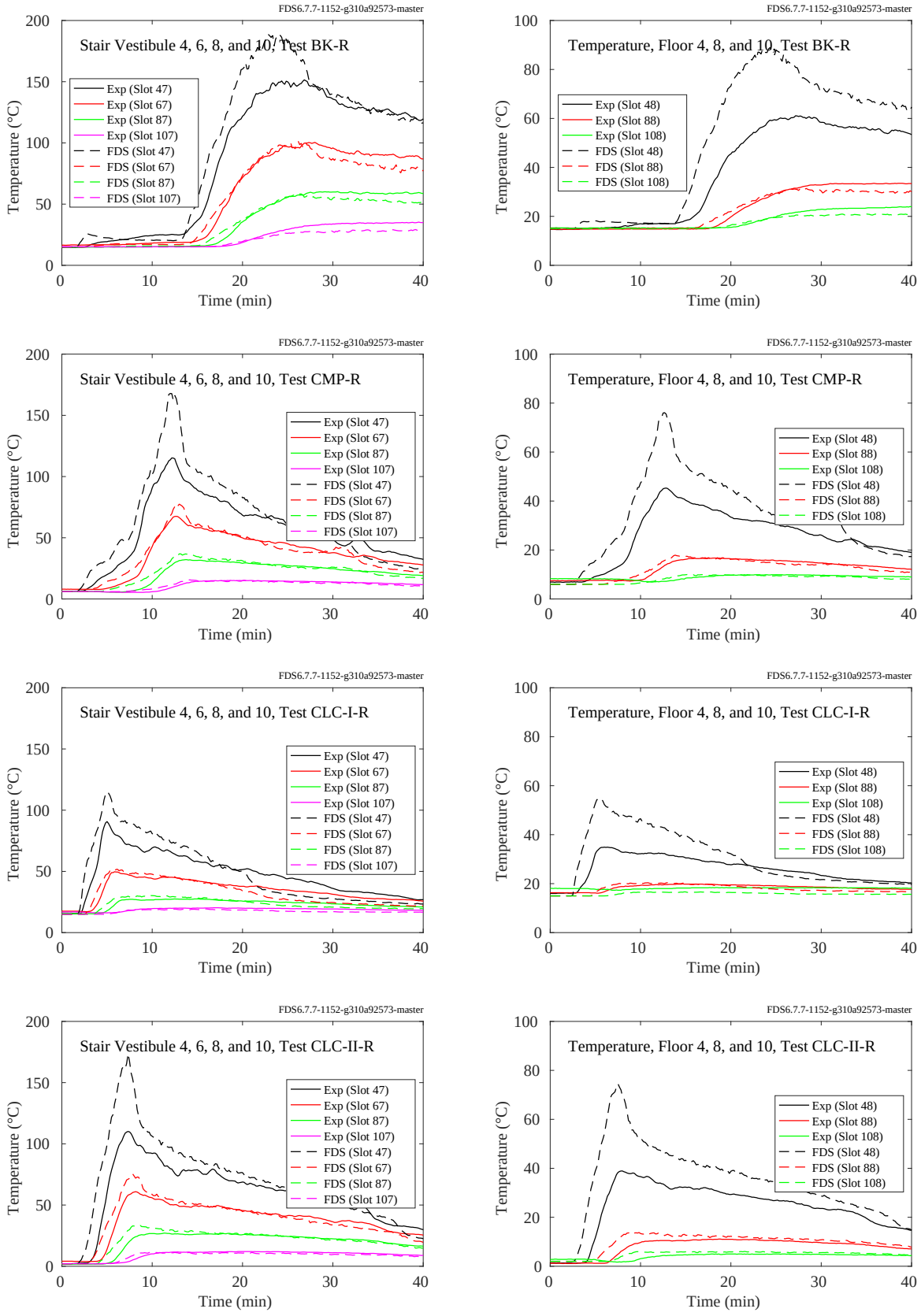

Figure 7.28: NRCC Smoke Tower, upper floor temperatures.

7.1.12 PRISME DOOR Experiments

In the PRISME DOOR experiments, the uppermost TC in the vertical arrays were used to measure the ceiling jet temperature. These TCs were approximately 10 cm below the ceiling.

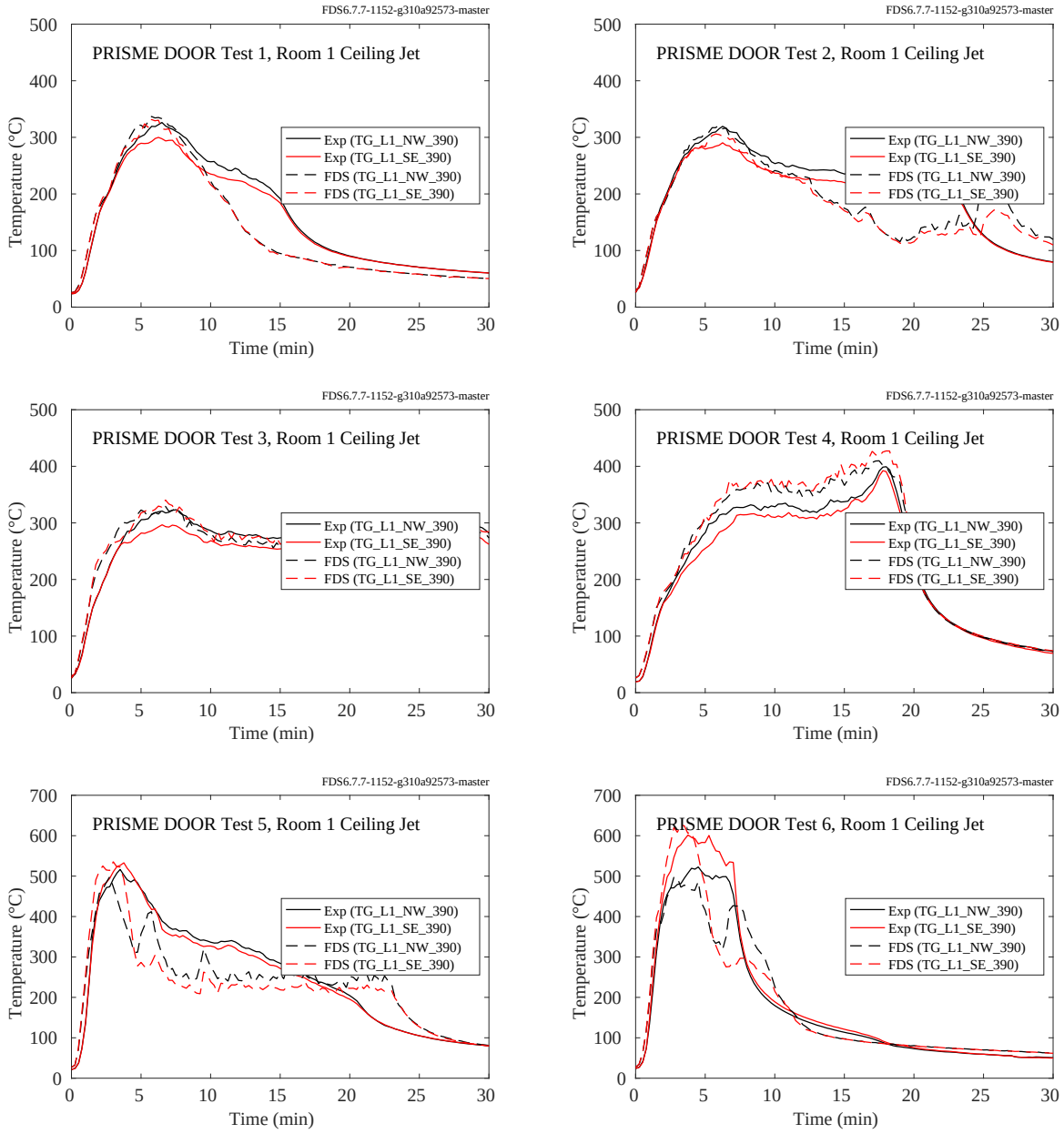

Figure 7.29: PRISME DOOR experiments, ceiling jet, Room 1.

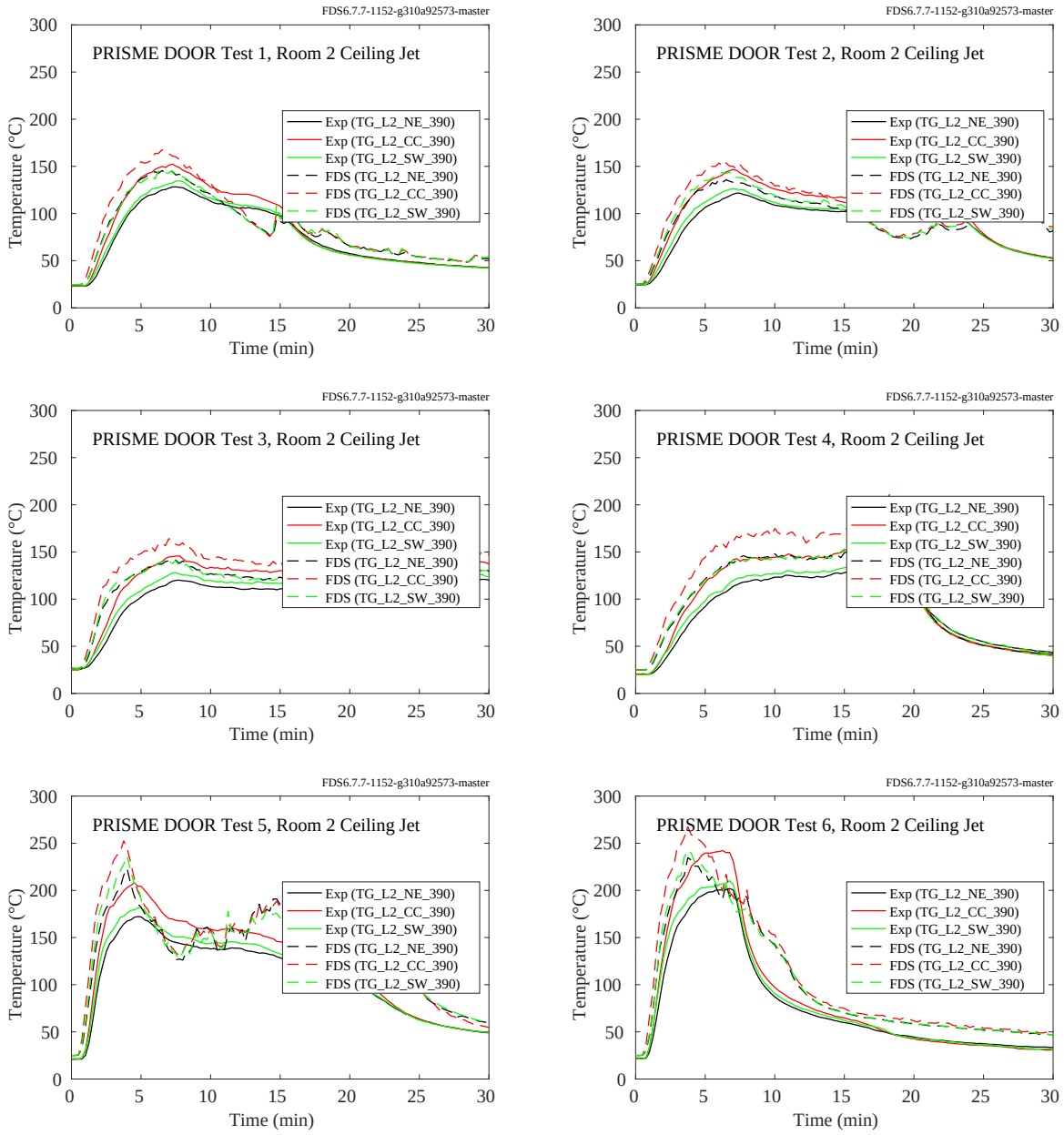

Figure 7.30: PRISME DOOR experiments, ceiling jet, Room 2.

7.1.13 PRISME SOURCE Experiments

In the PRISME SOURCE experiments, the uppermost TC in the vertical array was used to measure the ceiling jet temperature. The thermocouple array was located in the northeast corner of the room. This TC was approximately 10 cm below the ceiling.

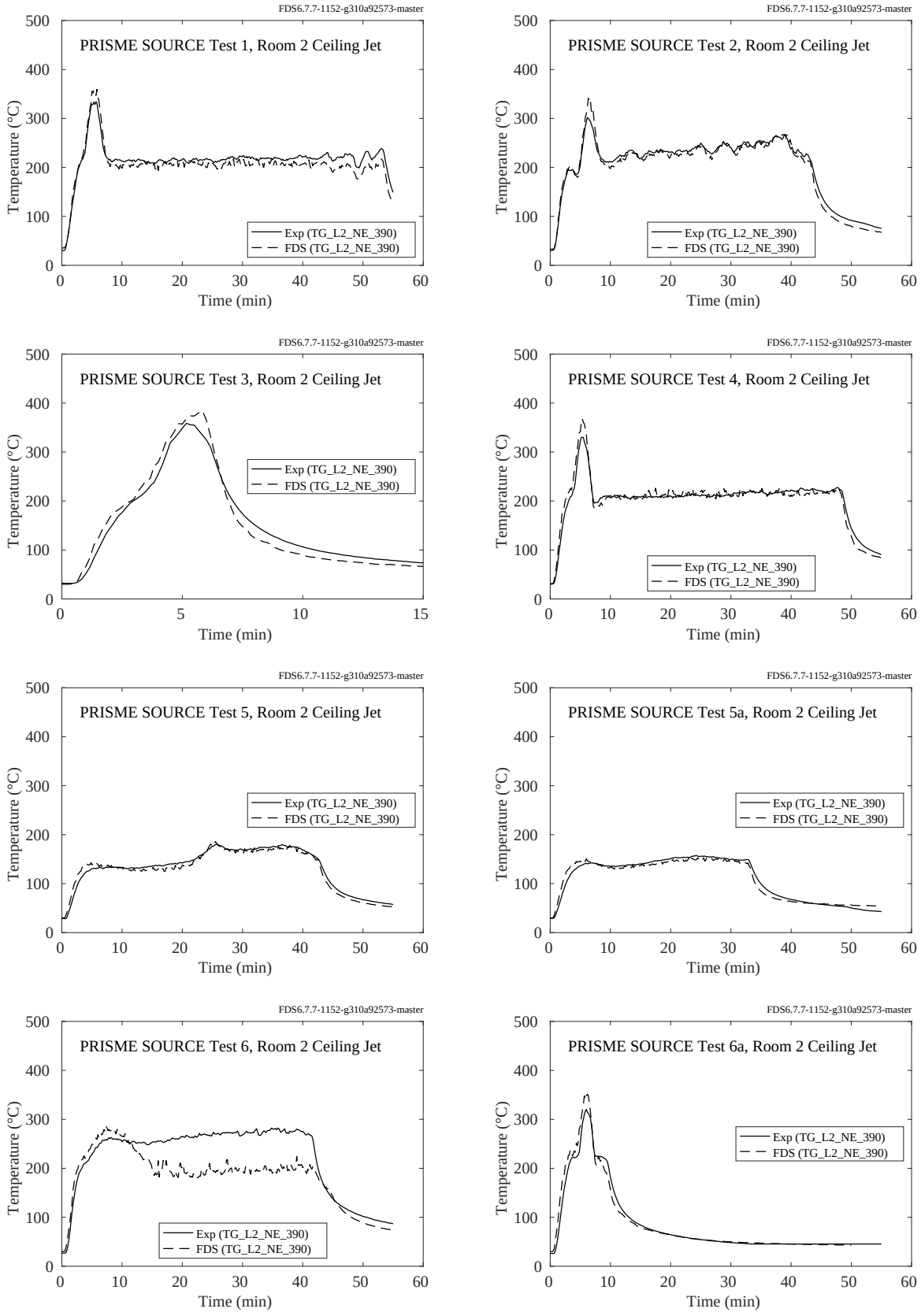

Figure 7.31: PRISME SOURCE experiments, ceiling jet, Room 2.

7.1.14 SP Adiabatic Surface Temperature Experiments

Three experiments were conducted in a standard compartment, 3.6 m long by 2.4 m wide by 2.4 m high, with a 0.8 m wide by 2.0 m high door centered on the narrow wall. A single beam was suspended 20 cm below the ceiling lengthwise along the centerline of the compartment. There were three measurement stations along the beam at distances of 0.9 m (Station A), 1.8 m (Station B), and 2.7 m (Station C) from the far wall where the fire was either positioned in the corner (Tests 1 and 2), or the center (Test 3). The gas temperatures reported here were measured 10 cm away from all four sides of the beam at Station A, and 10 cm away from the two lateral sides at Stations B and C. In the figure legends, the measurement station is denoted A, B, or C, and the position is denoted 1, 2, 3, or 4. Position 1 is 10 cm above the beam. Position 2 is 10 cm from the side of the beam facing away from the fire, Position 3 is 10 cm below the beam, and Position 4 is 10 cm away from the side of the beam facing the fire.

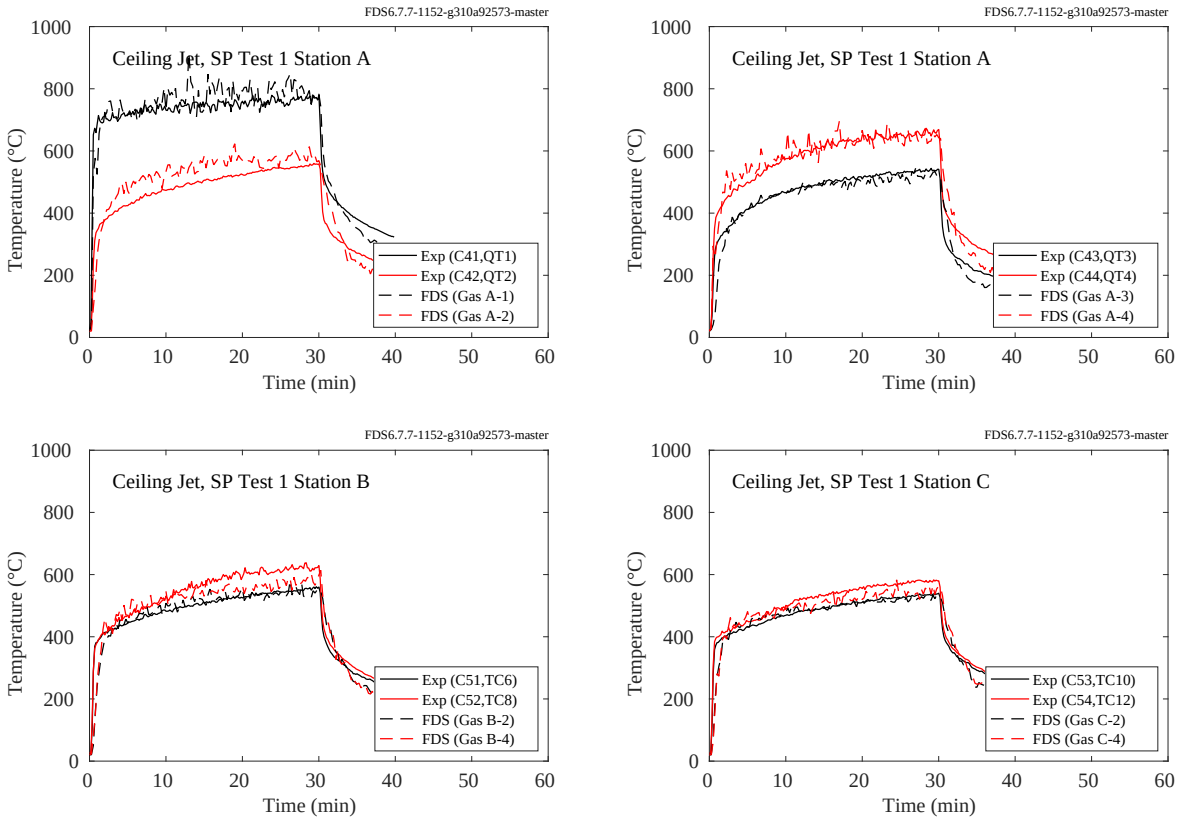

Figure 7.32: SP AST experiments, ceiling jet, Test 1.

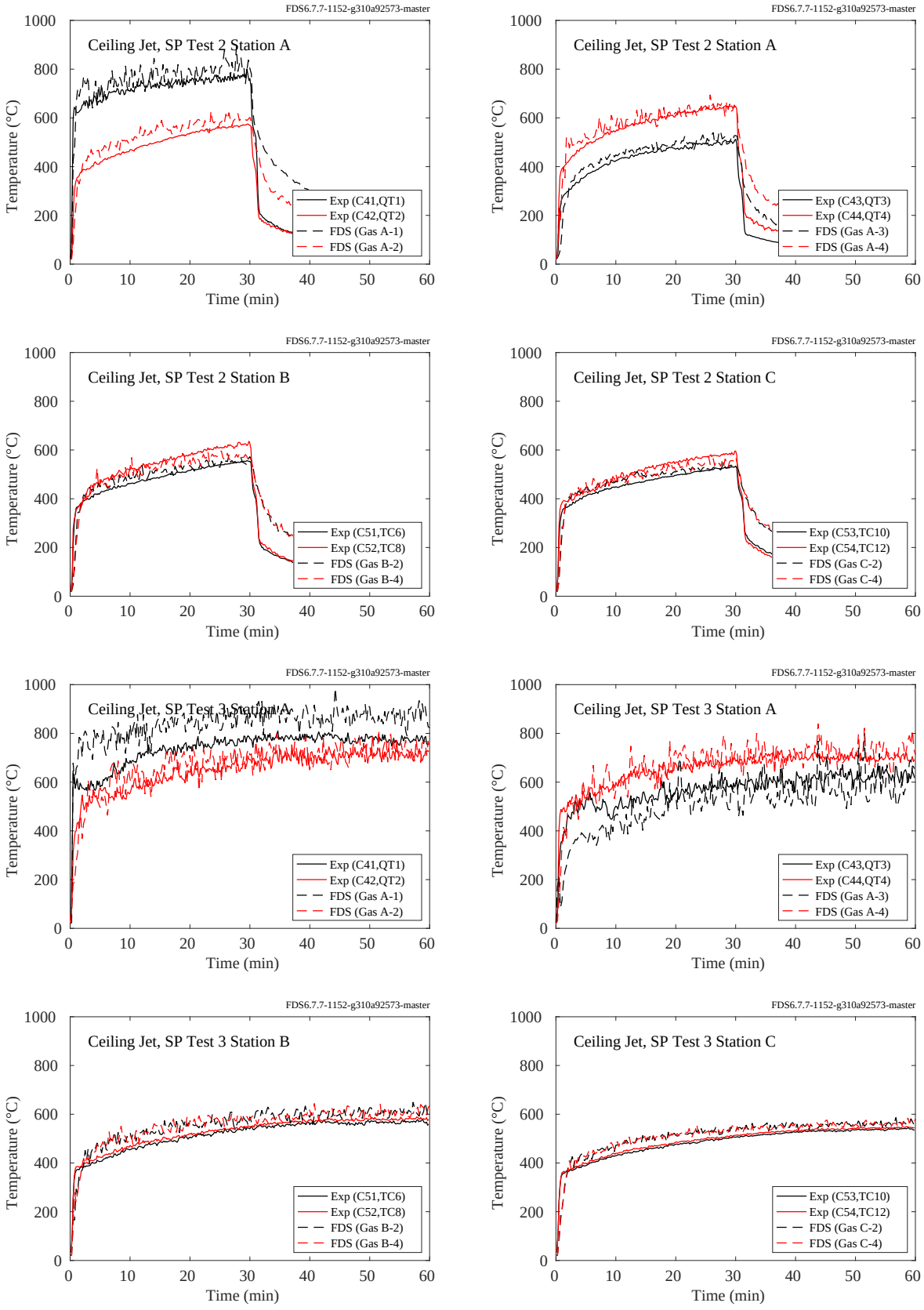

Figure 7.33: SP AST experiments, ceiling jet, Tests 2 and 3.

7.1.15 UL/NFPRF Series I Experiments

The primary purpose of the UL/NFPRF experiments was to measure sprinkler activation times for a series of heptane spray burner fires. To determine activation times, thermocouples were affixed to each sprinkler, and a sudden drop in temperature indicated activation. These same thermocouple temperatures can be compared to ceiling jet temperature predictions. Referring to Fig. 3.44, the chosen measurement locations are 56, 68, 86, and 98, providing comparisons as close to, and as far away from, the fire as possible.

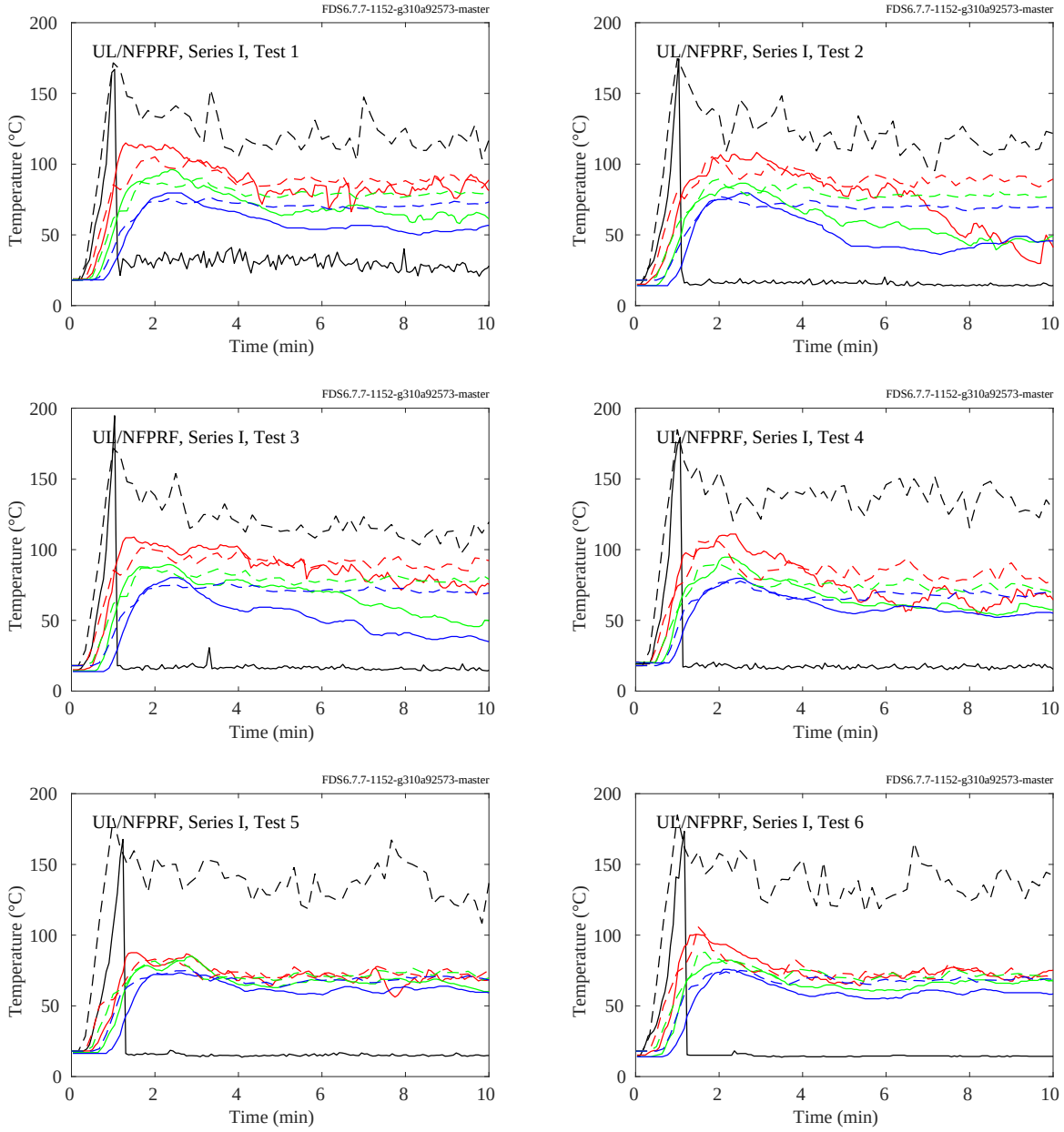

Figure 7.34: UL/NFPPRF experiments, ceiling jet, Series I, Tests 1-6.

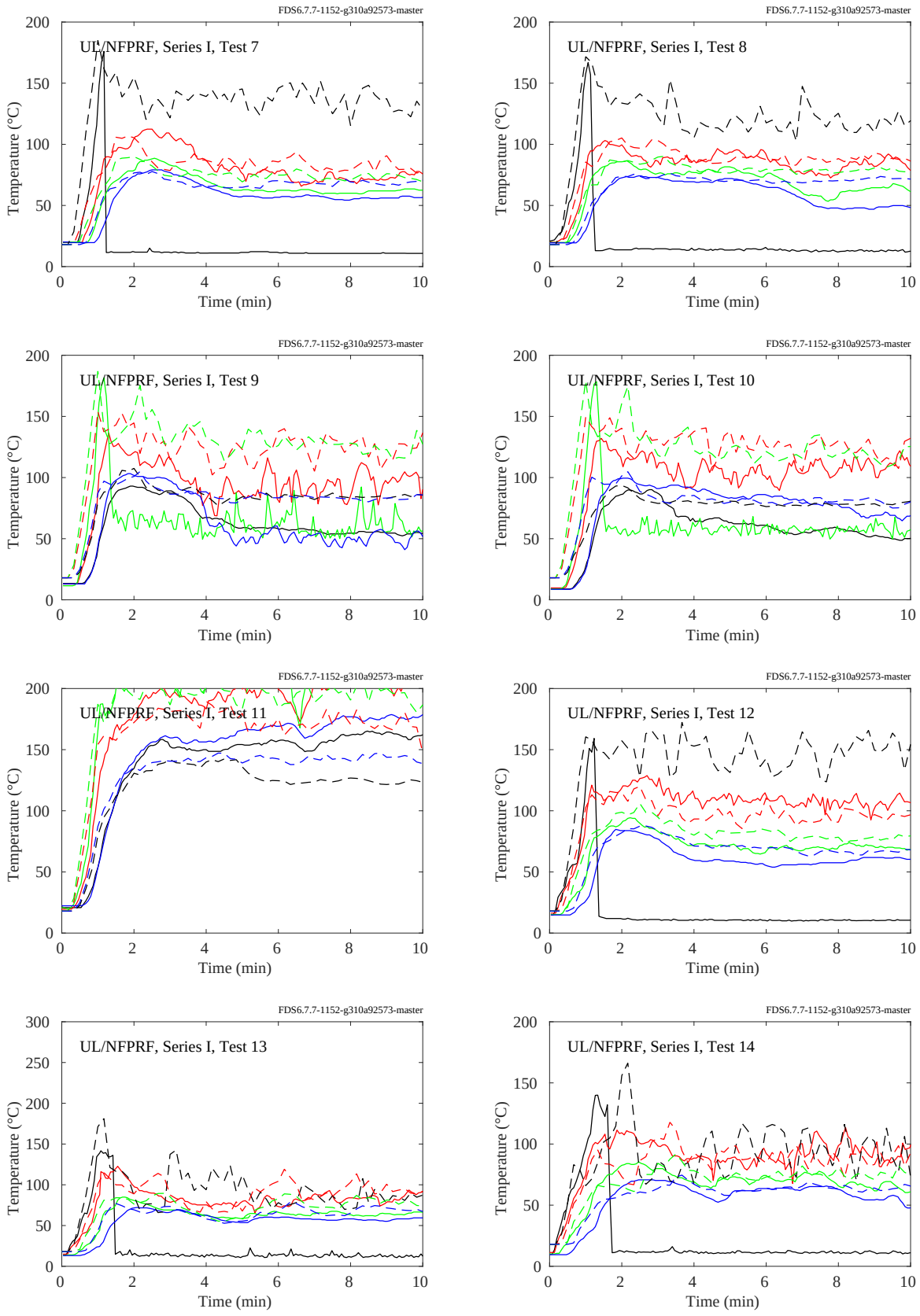

Figure 7.35: UL/NFPPRF experiments, ceiling jet, Series I, Tests 7-14.

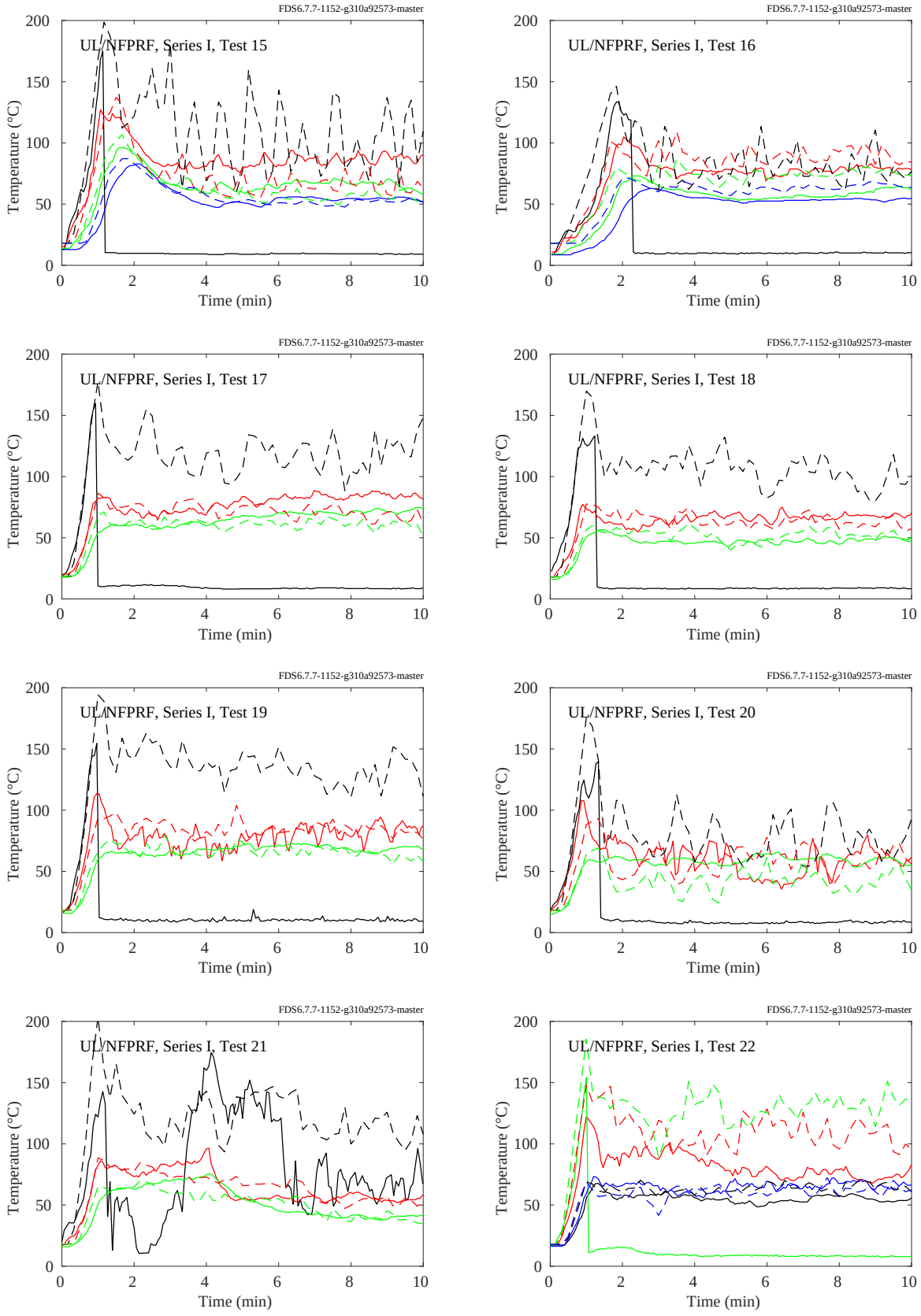

Figure 7.36: UL/NFPPRF experiments, ceiling jet, Series I, Tests 15-22.

7.1.16 UL/NIJ House Experiments

The following plots compare the uppermost thermocouple measurements with corresponding model predictions for the ranch-style and colonial-style houses.

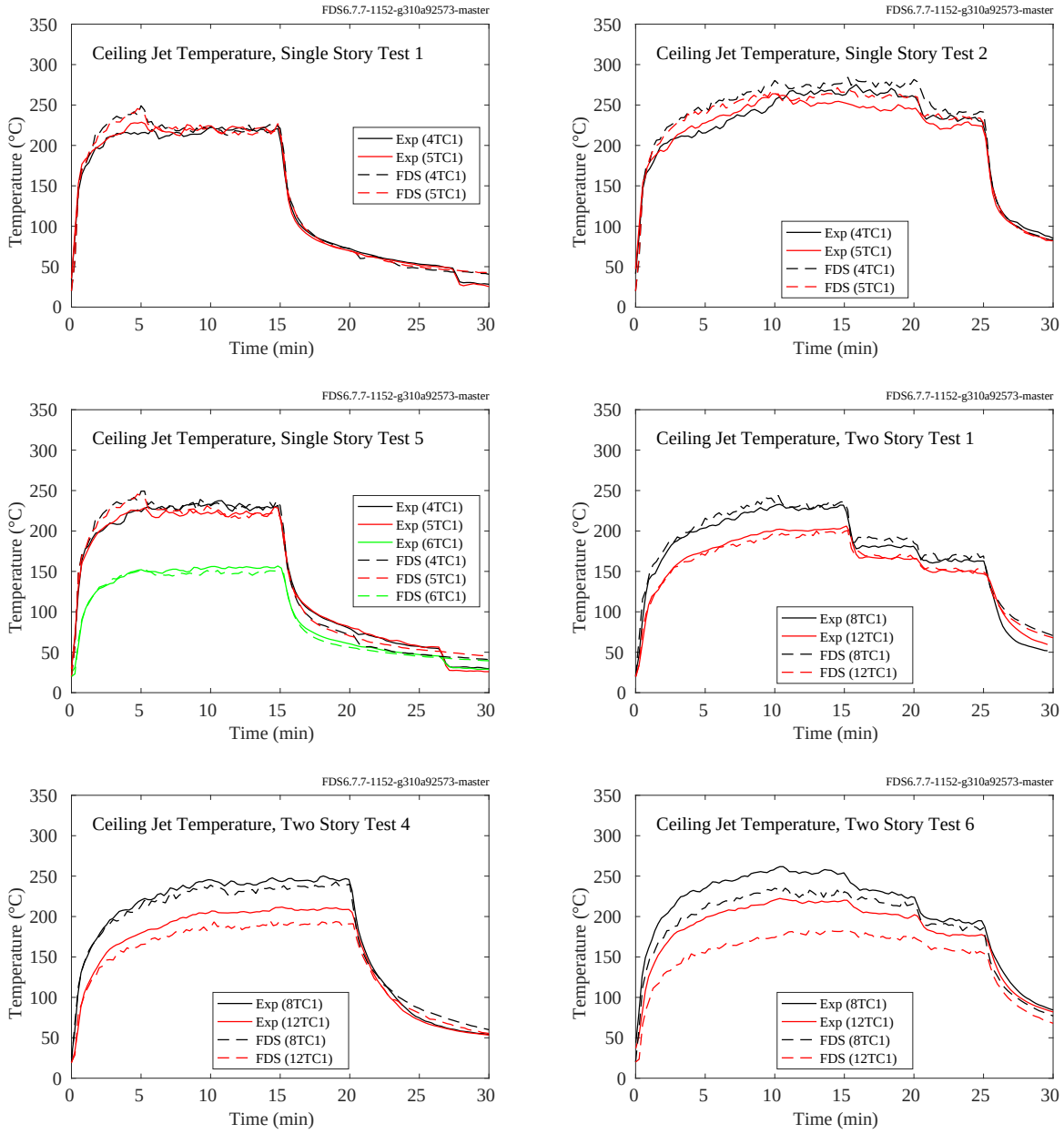

Figure 7.37: UL/NIJ Experiments, ceiling jet temperature

7.1.17 UL/NIST Vent Experiments

The ceiling jet temperatures were measured at two locations, 90 cm from the short ends of the 2.4 m by 1.2 m double vent.

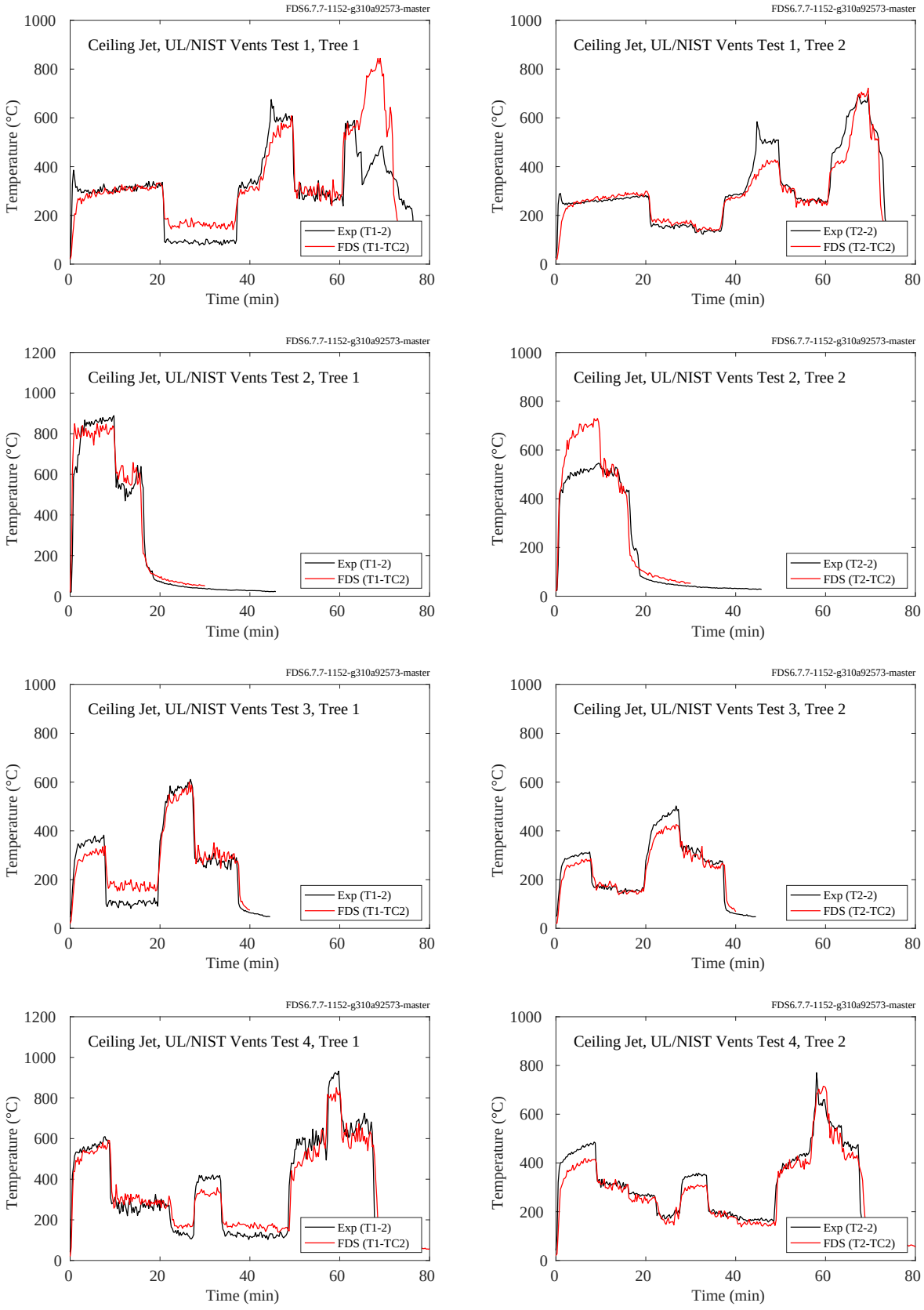

Figure 7.38: UL/NIST Vents experiments, ceiling jet.

7.1.18 Vettori Flat Ceiling Experiments

For these experiments, the measured and predicted thermocouple temperature at the location of the first two activating sprinklers are compared. The experiments consisted of either Smooth or Obstructed ceilings; Slow, Medium or Fast fires; and a burner in the Open, at the Wall, or in the Corner. The experiments included three replicates of each of the smooth ceiling configurations and two replicates of each of the obstructed ceiling configurations.

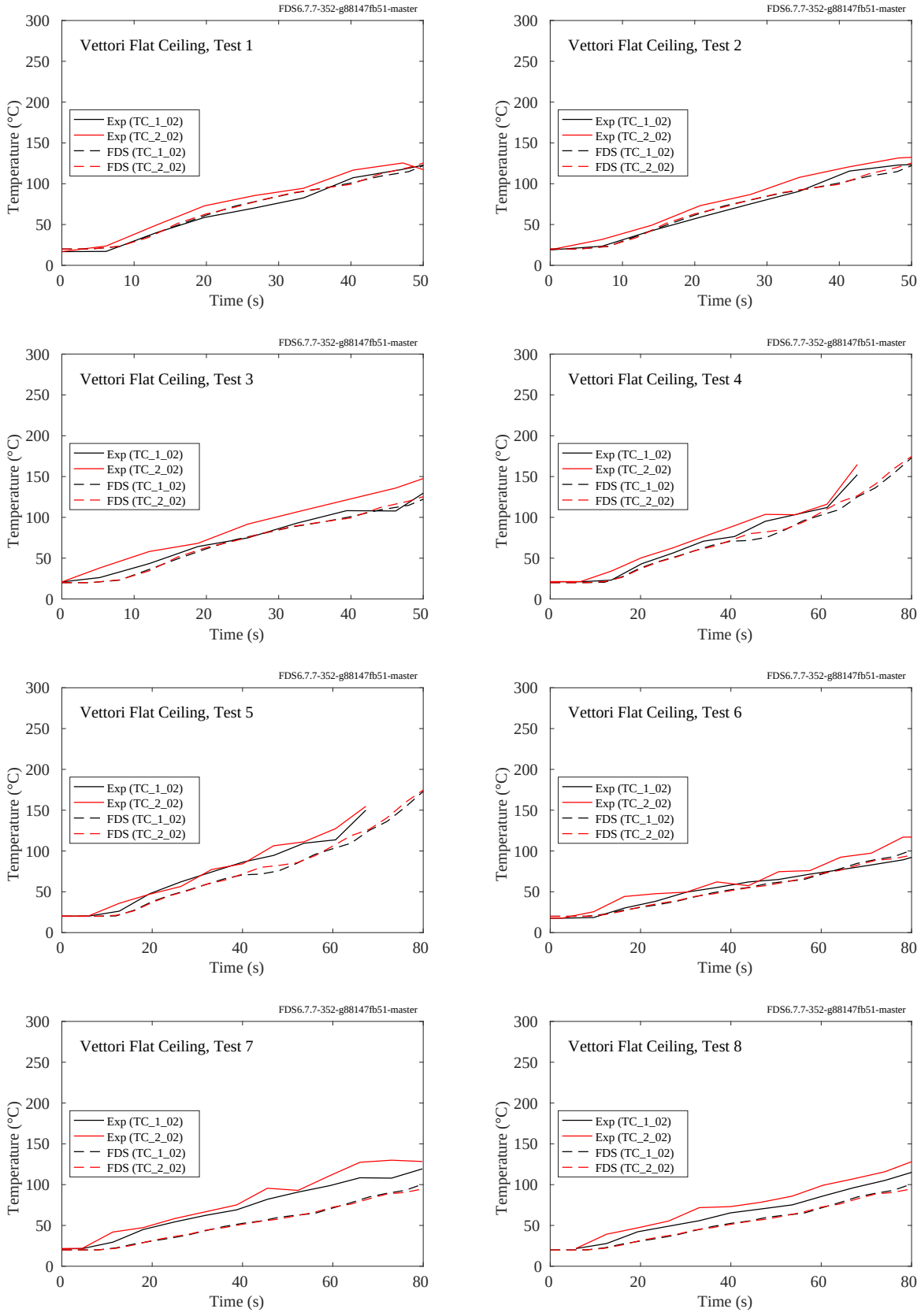

Figure 7.39: Vettori Flat Ceiling experiments, ceiling jet, Tests 1-8.

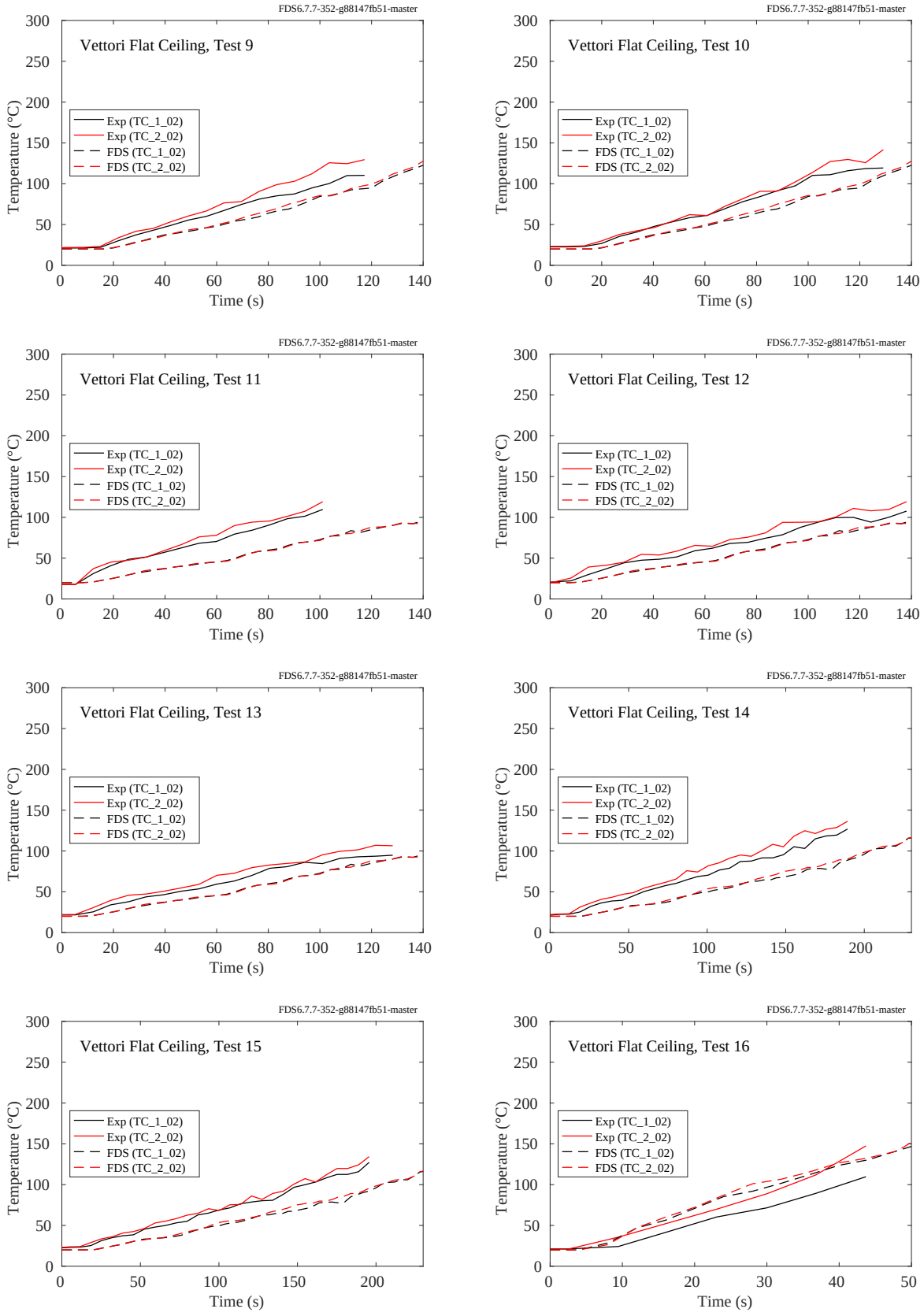

Figure 7.40: Vettori Flat Ceiling experiments, ceiling jet, Tests 9-16.

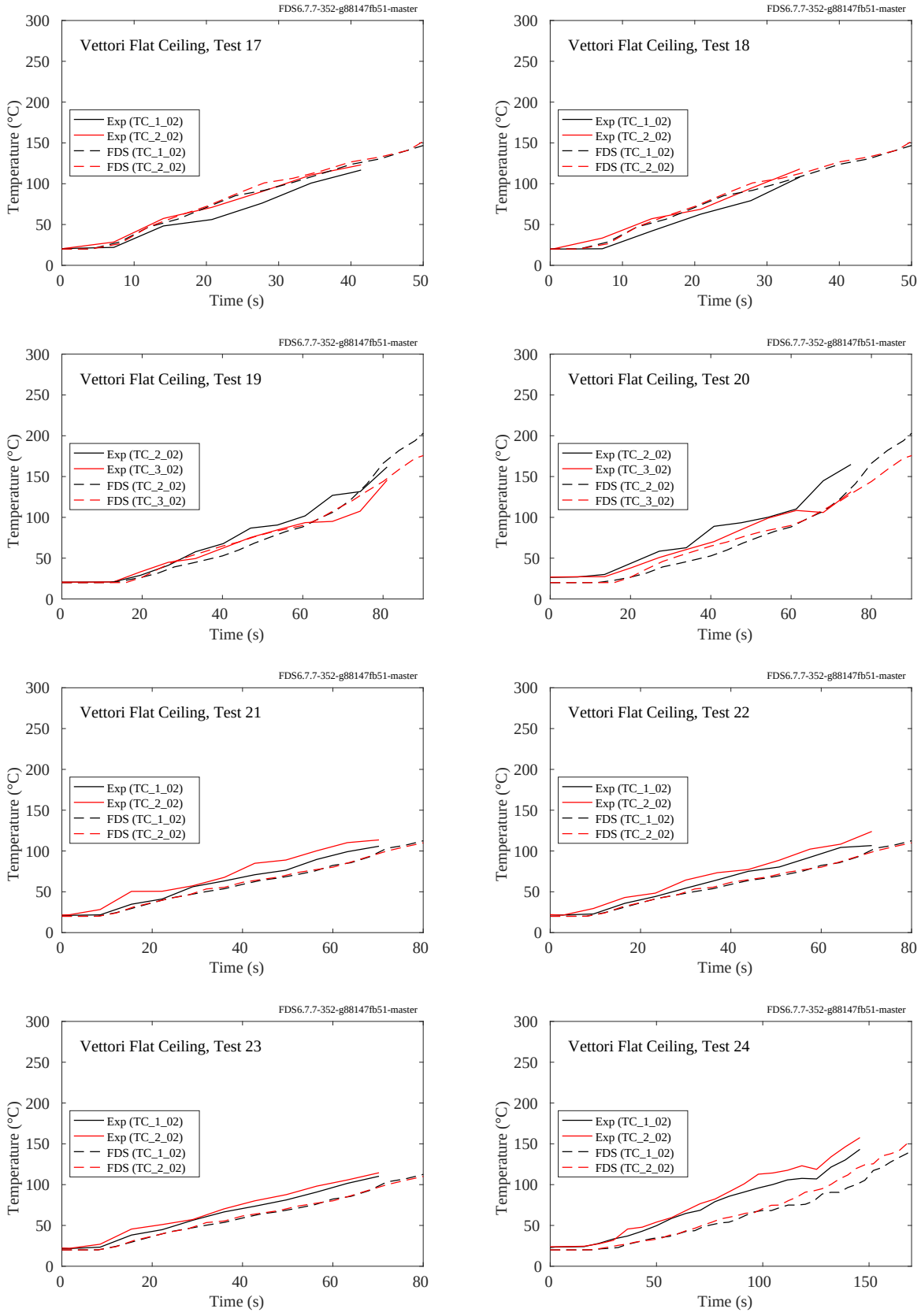

Figure 7.41: Vettori Flat Ceiling experiments, ceiling jet, Tests 17-24.

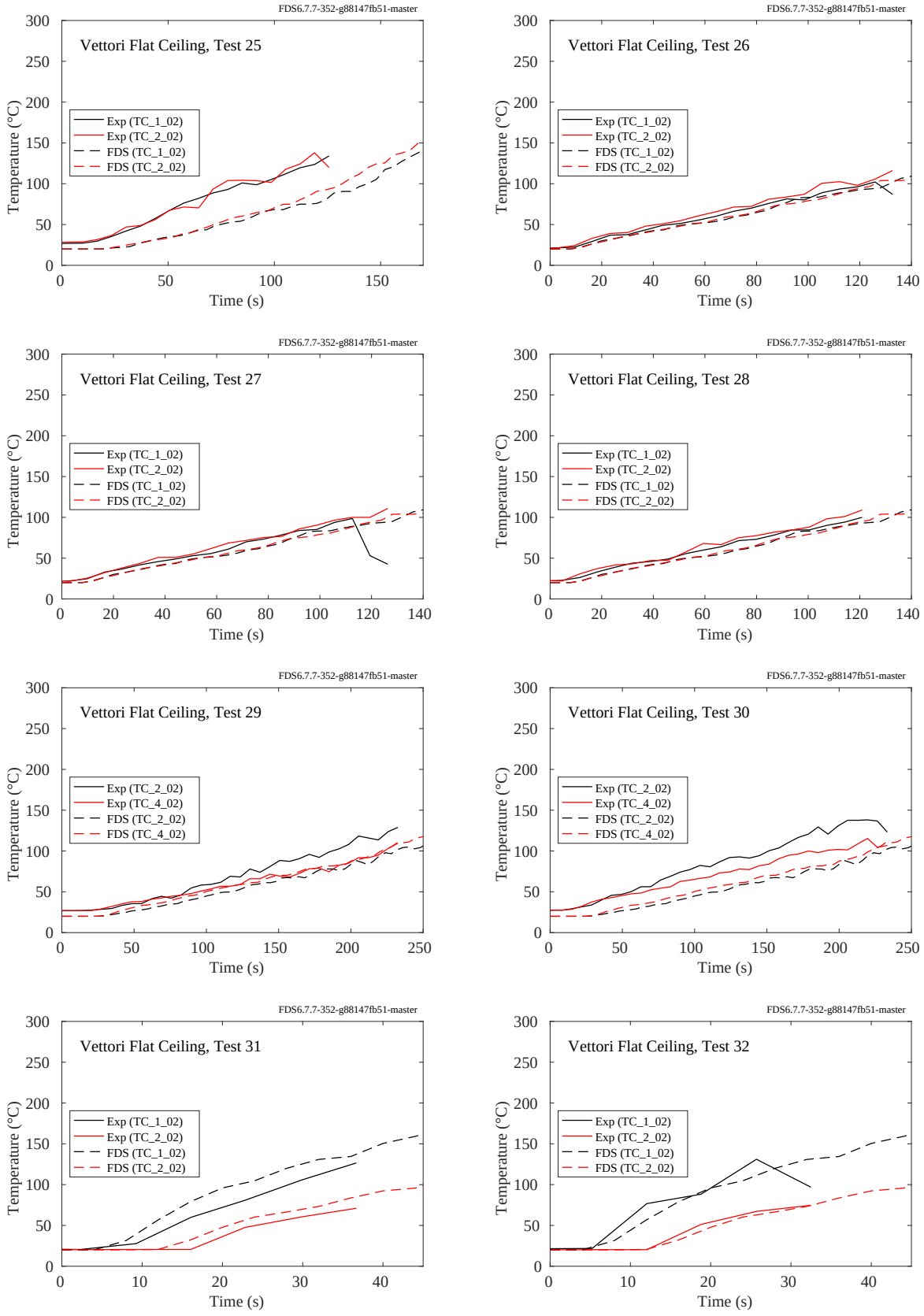

Figure 7.42: Vettori Flat Ceiling experiments, ceiling jet, Tests 25-32.

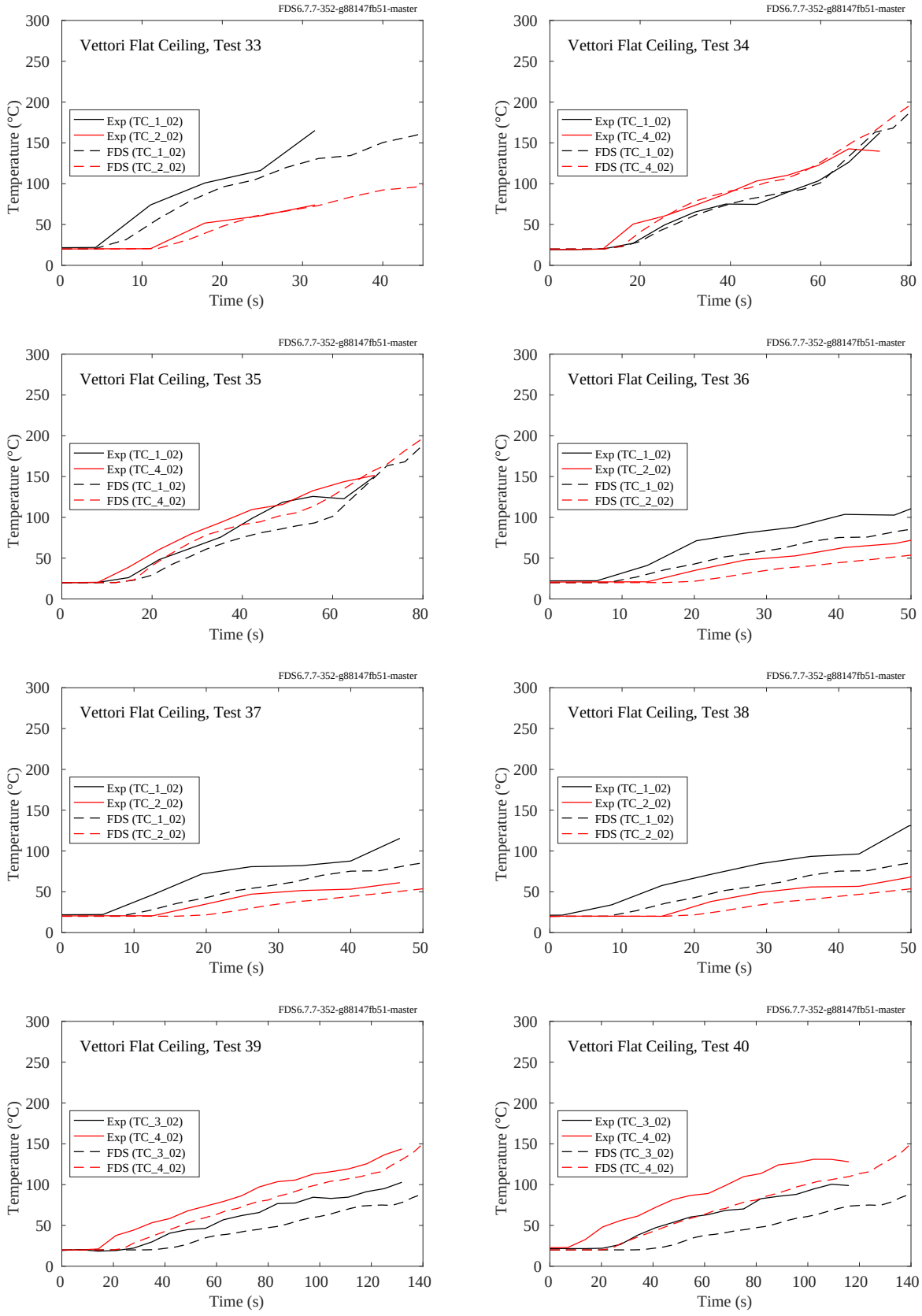

Figure 7.43: Vettori Flat Ceiling experiments, ceiling jet, Tests 33-40.

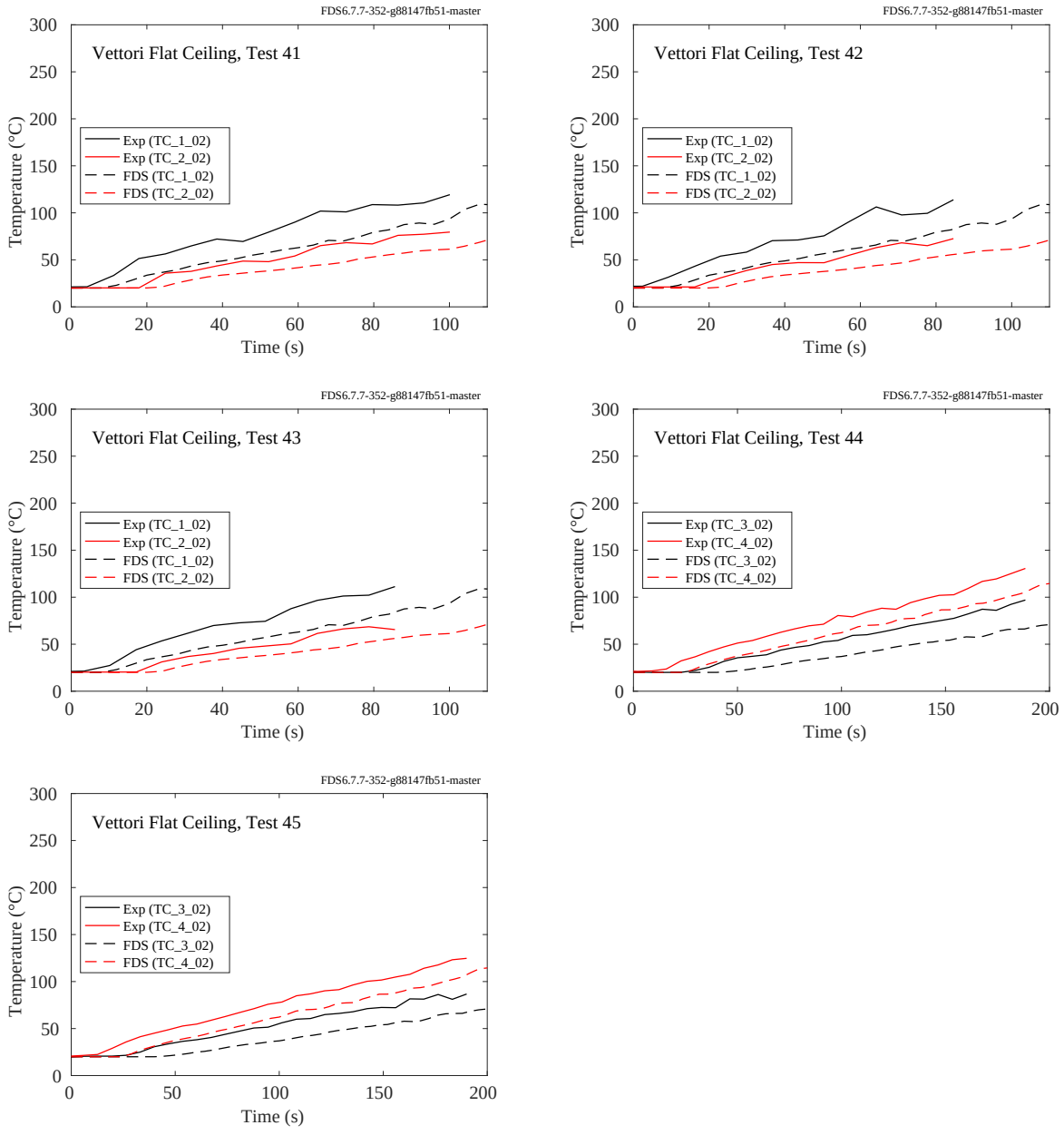

Figure 7.44: Vettori Flat Ceiling experiments, ceiling jet, Tests 41-45.

7.1.19 Vettori Sloped Ceiling Experiments

For these experiments, the measured and predicted thermocouple temperature at the locations of the first two activating sprinklers are compared. The thermocouples were located 15 cm below the ceiling. Replicate results are shown side by side, i.e. Test 2 is a replicate of Test 1; Test 4 is a replicate of Test 3, and so on. There were 36 unique configurations (2 replicates of each) combining the following parameters:

- Flat, 13°, or 24° Ceiling Slope
- Smooth or Obstructed Ceiling Surface
- Fast or Slow Growth Fire
- Corner, Wall, or Detached Burner Location

The plots are labelled using this convention. For example, "13SFC" means that the ceiling is sloped 13° from horizontal, the ceiling is Smooth (no beams), the fire growth rate is Fast, and the burner is in the Corner of the room.

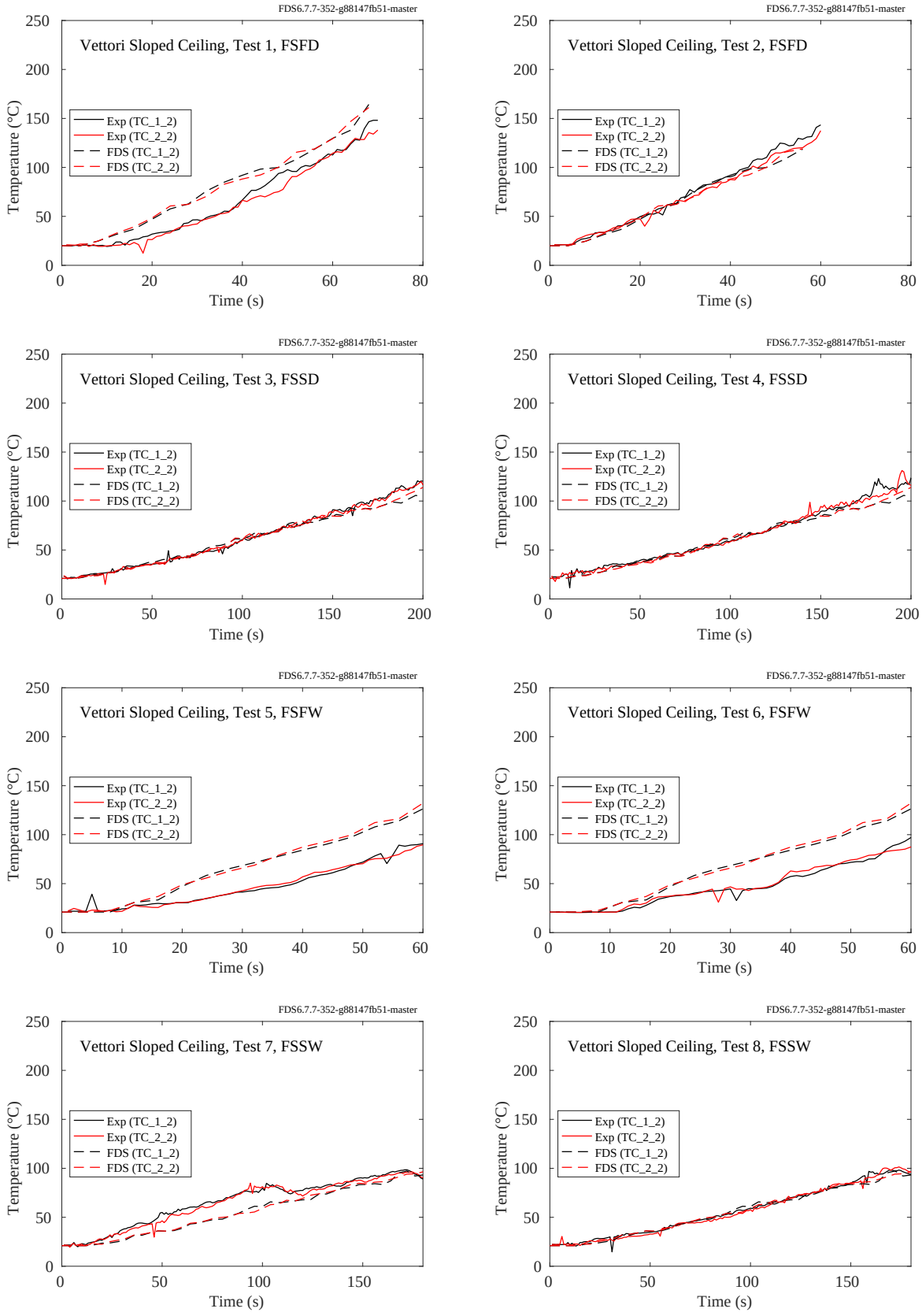

Figure 7.45: Vettori Sloped Ceiling experiments, ceiling jet, Tests 1-8.

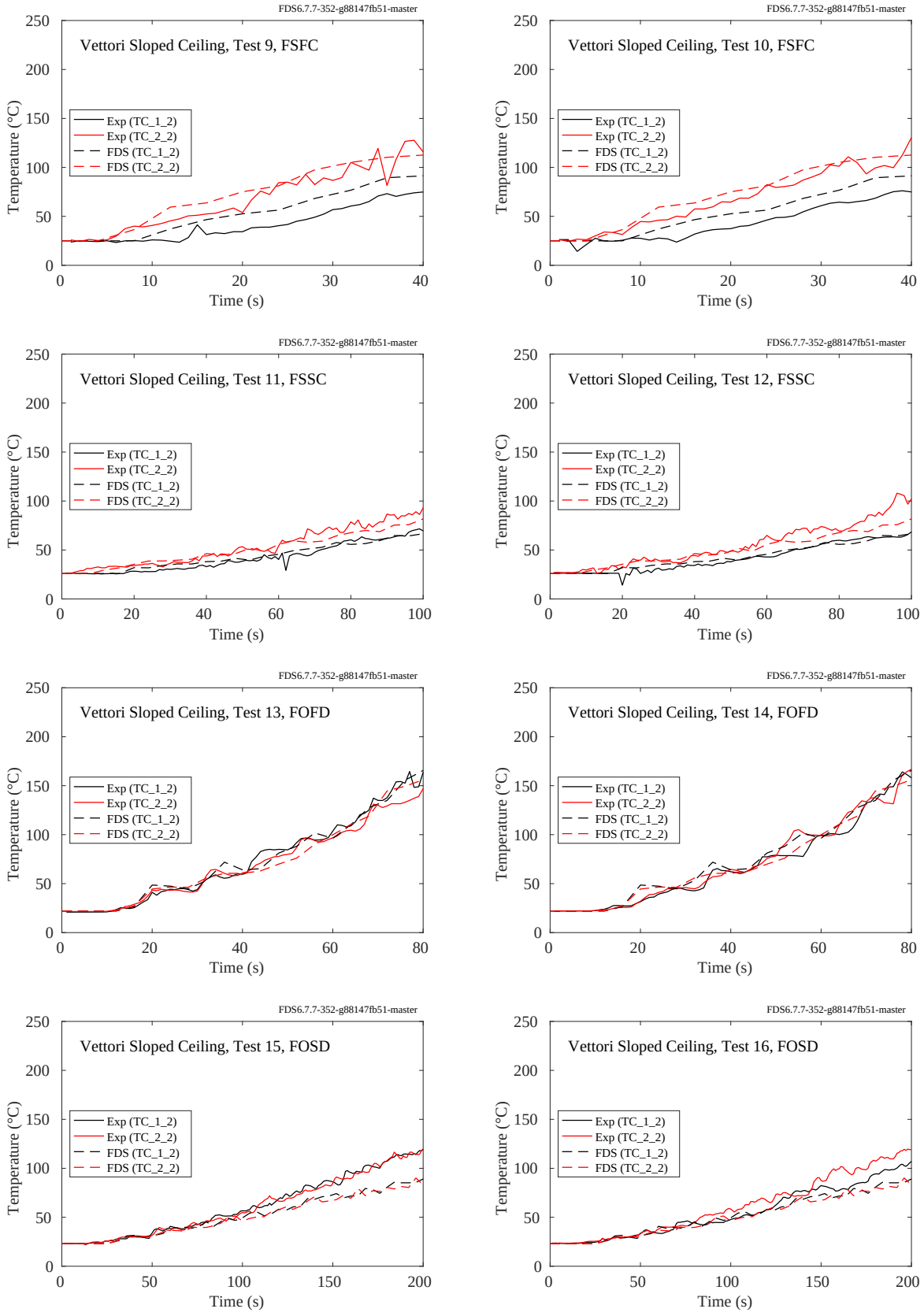

Figure 7.46: Vettori Sloped Ceiling experiments, ceiling jet, Tests 9-16.

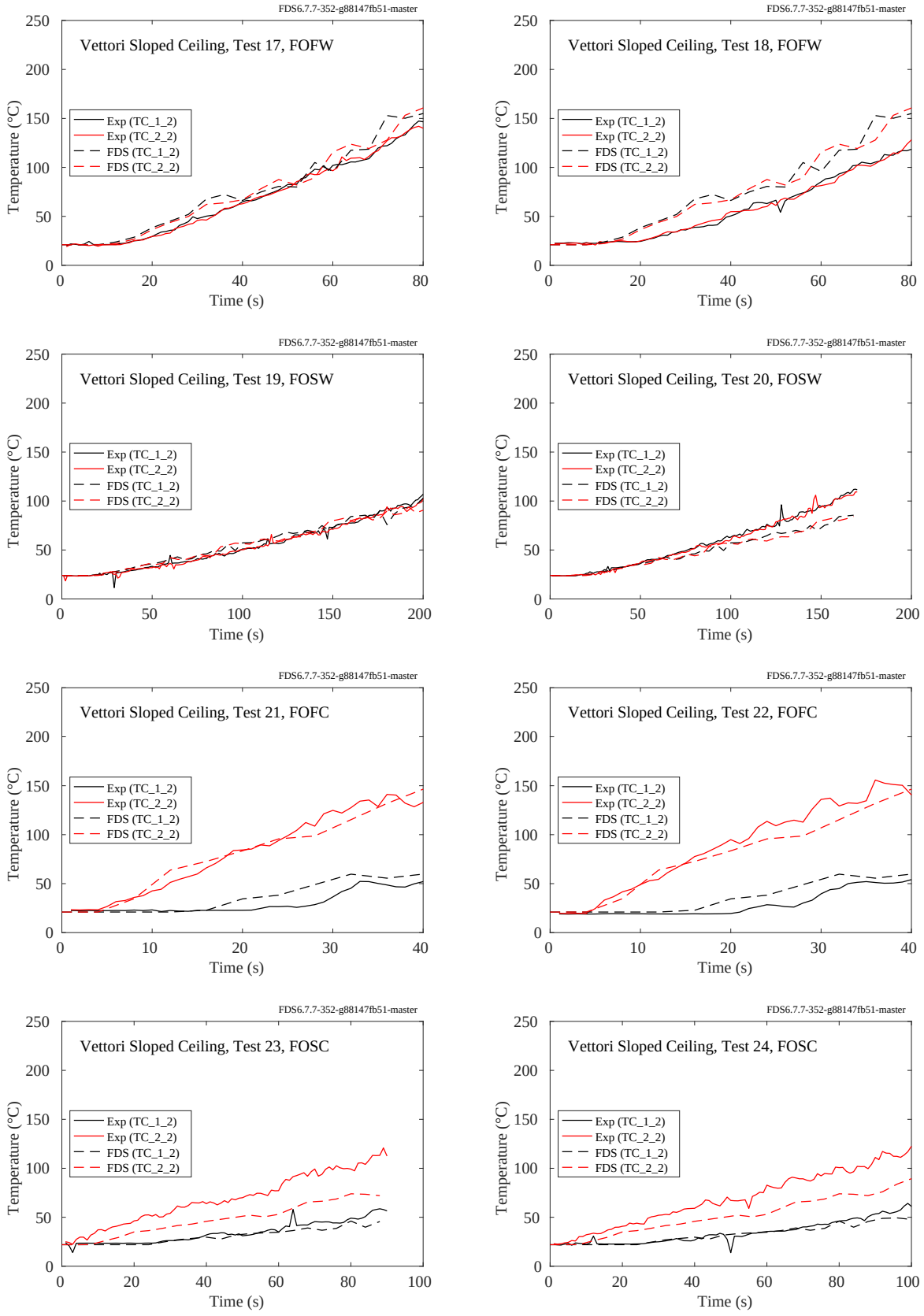

Figure 7.47: Vettori Sloped Ceiling experiments, ceiling jet, Tests 17-24.

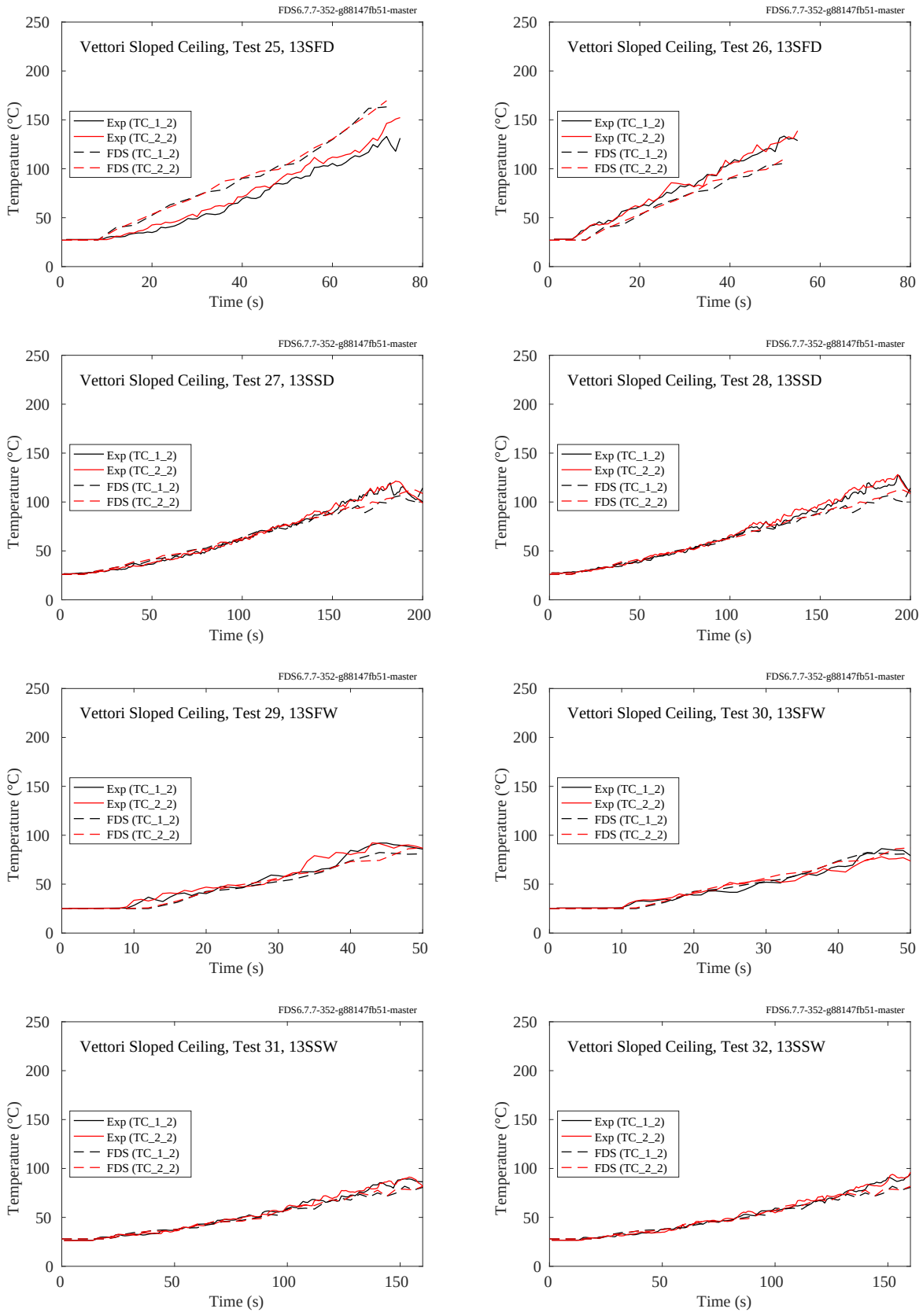

Figure 7.48: Vettori Sloped Ceiling experiments, ceiling jet, Tests 25-32.

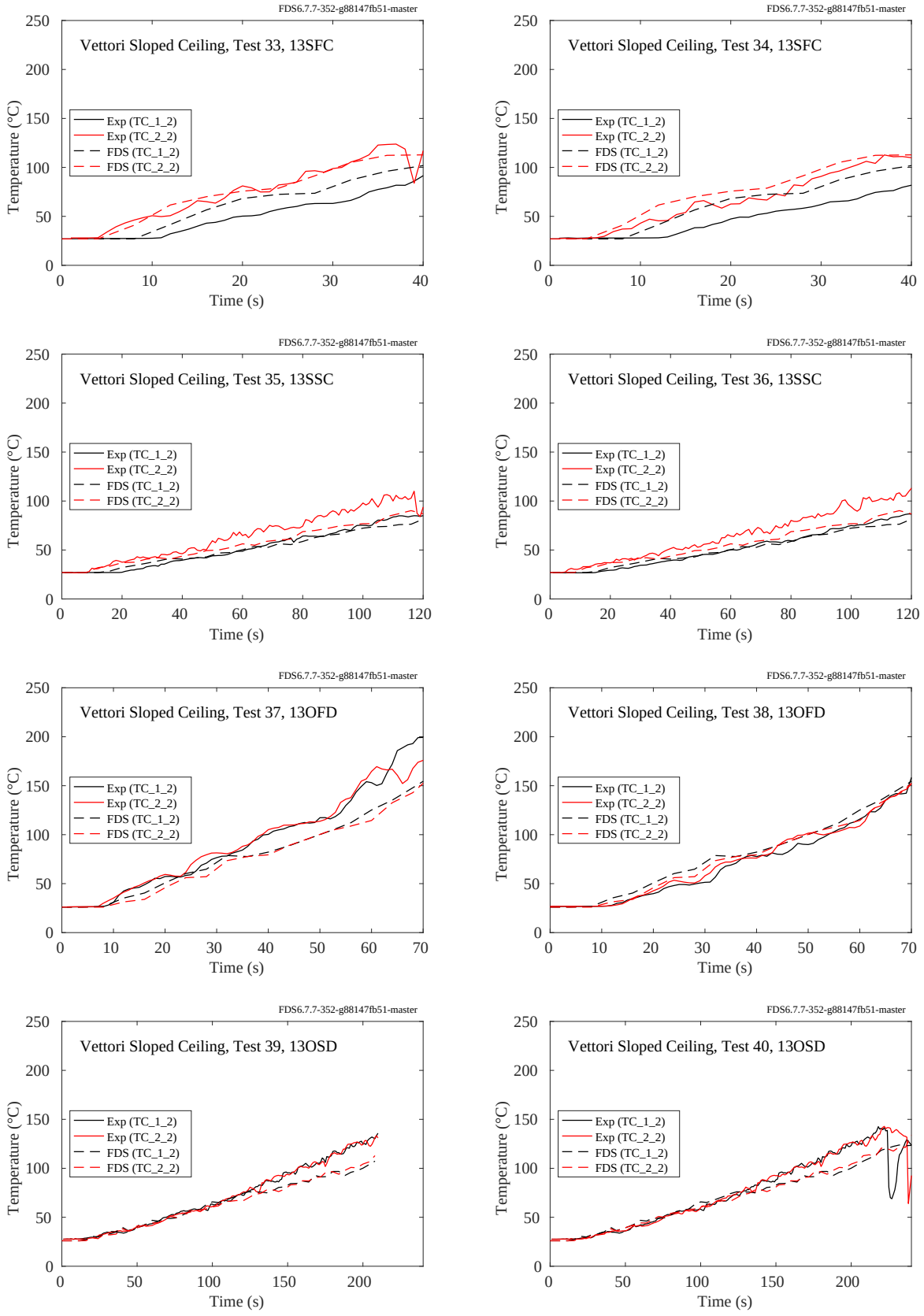

Figure 7.49: Vettori Sloped Ceiling experiments, ceiling jet, Tests 33-40.

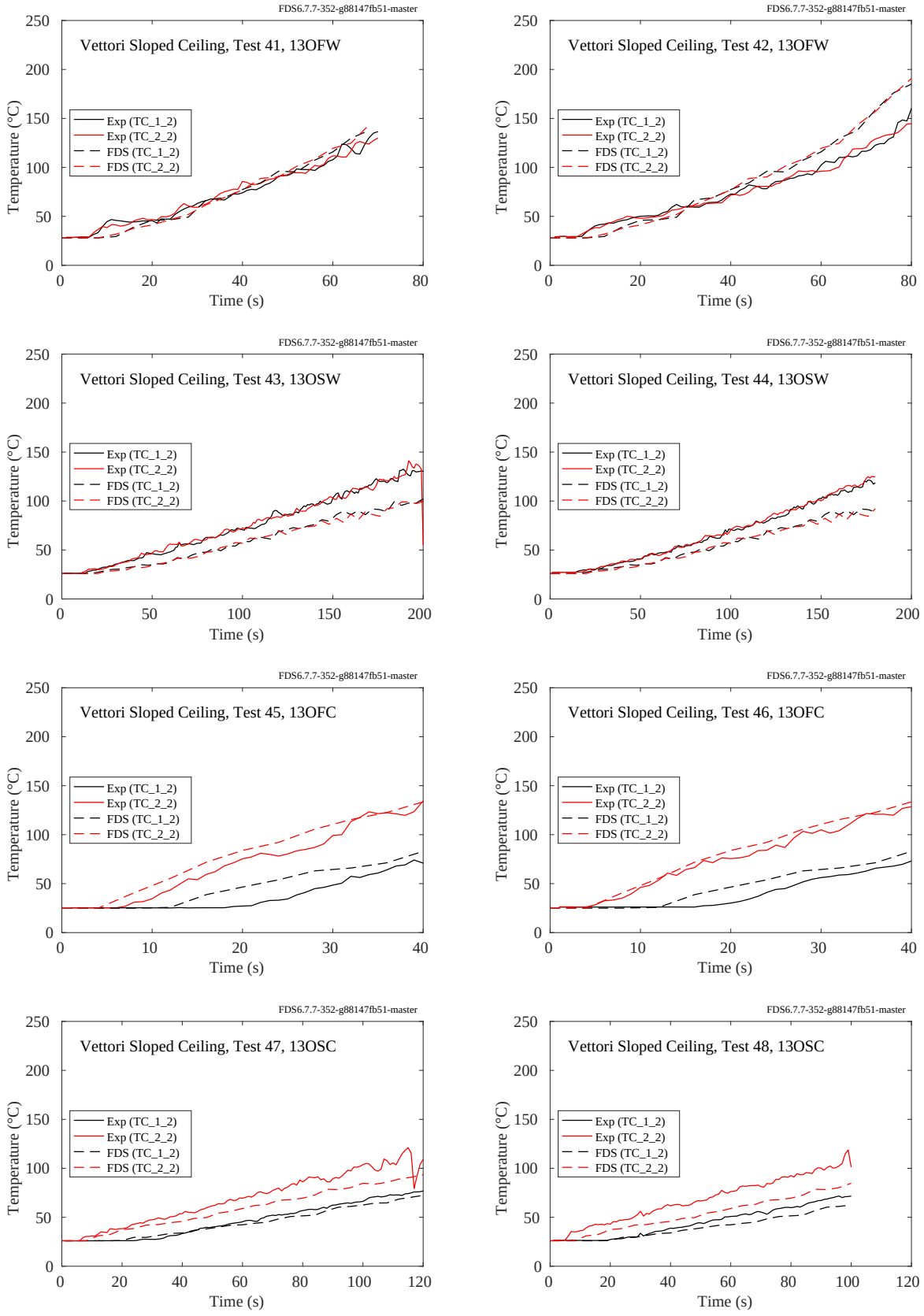

Figure 7.50: Vettori Sloped Ceiling experiments, ceiling jet, Tests 41-48.

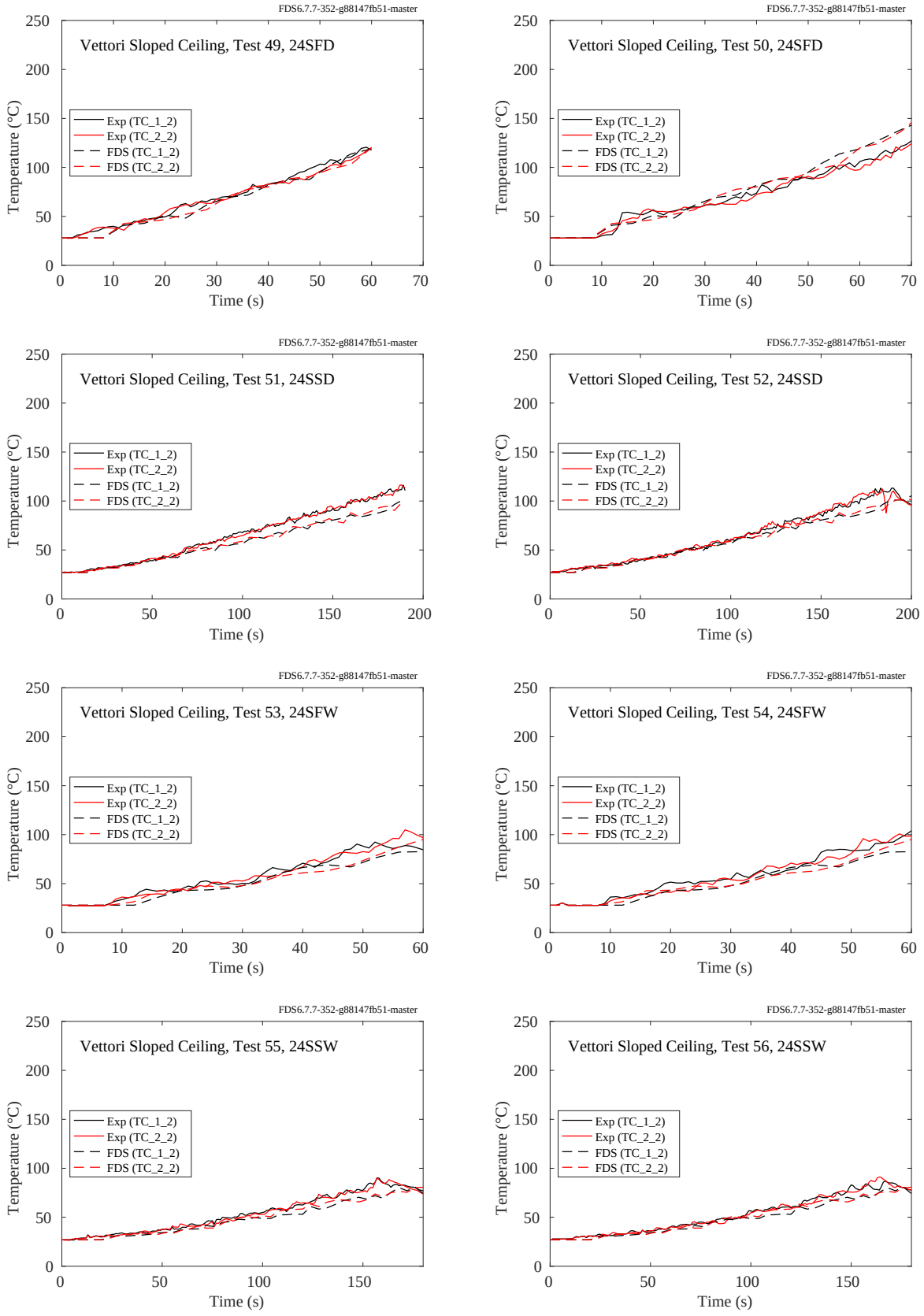

Figure 7.51: Vettori Sloped Ceiling experiments, ceiling jet, Tests 49-56.

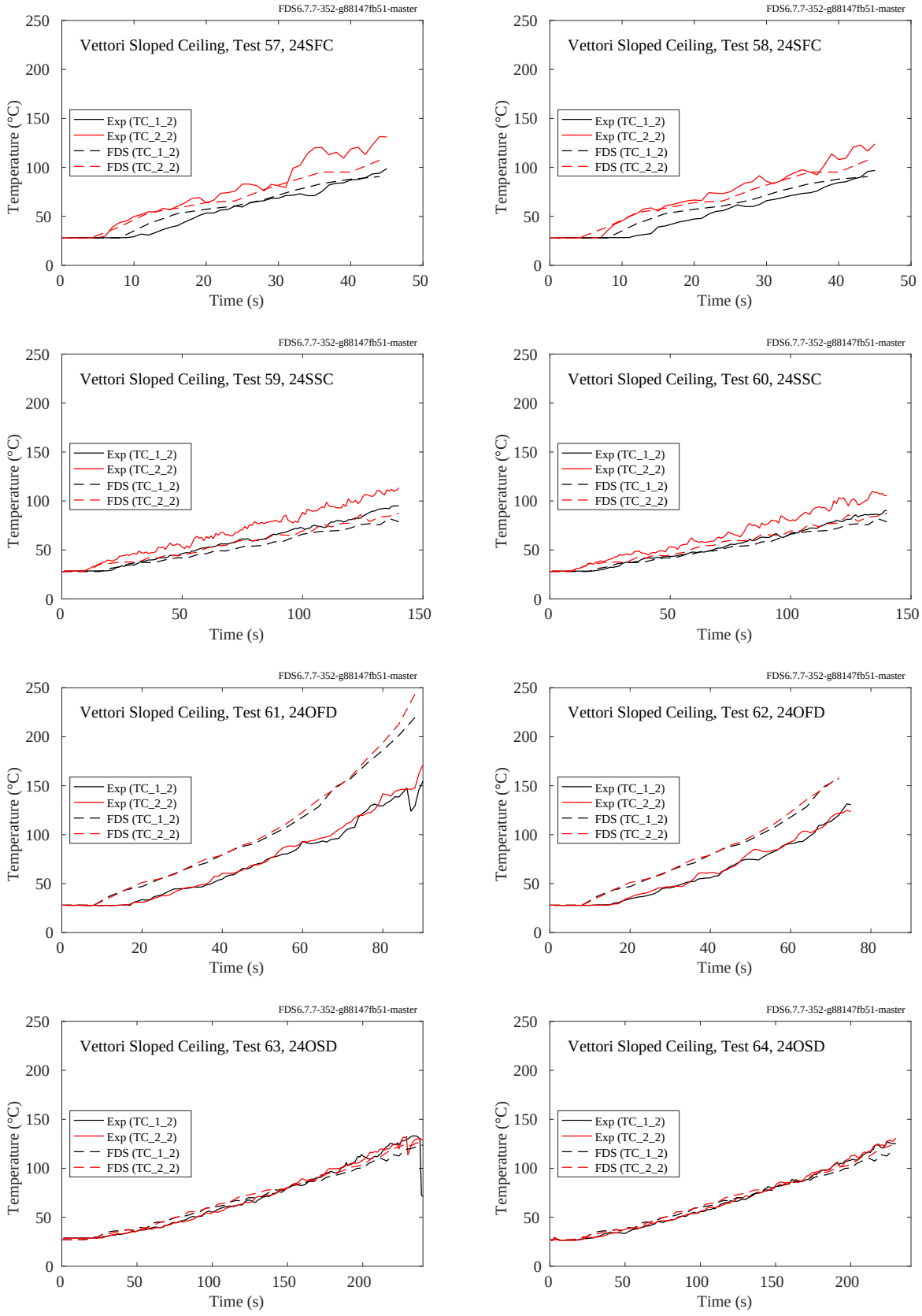

Figure 7.52: Vettori Sloped Ceiling experiments, ceiling jet, Tests 57-64.

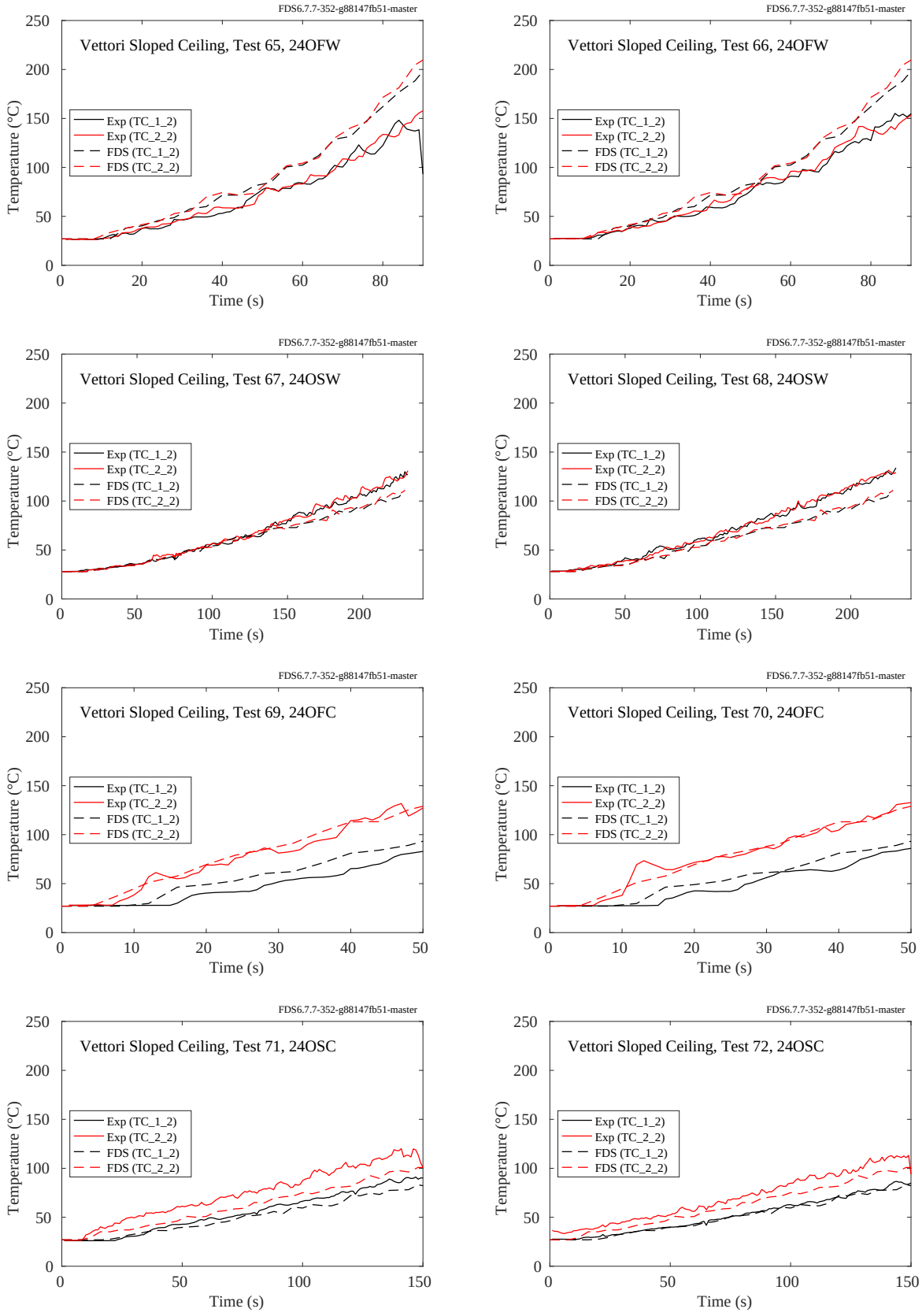

Figure 7.53: Vettori Sloped Ceiling experiments, ceiling jet, Tests 65-72.

7.1.20 WTC Experiments

In the WTC experiments, the compartment was 7 m long, 3.6 m wide and 3.8 m high. A 1 m by 2 m pan was positioned close to the center of the compartment. Aspirated thermocouples were positioned 3 m to the west (TTRW1) and 2 m to the east (TTRE1) of the fire pan, 18 cm below the ceiling.

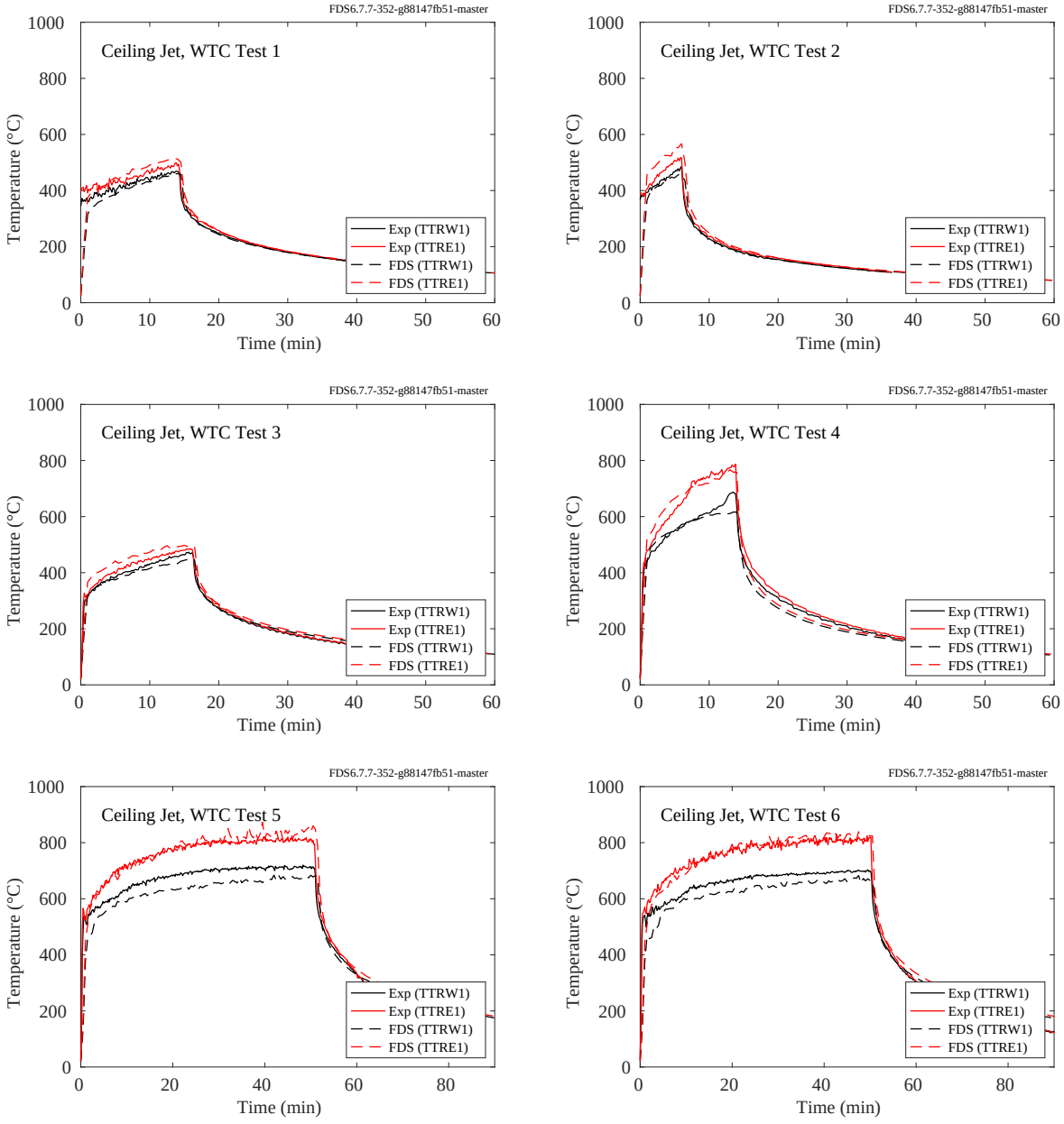

Figure 7.54: WTC experiments, ceiling jet, Tests 1-6.

7.1.21 Summary of Ceiling Jet Temperature Predictions

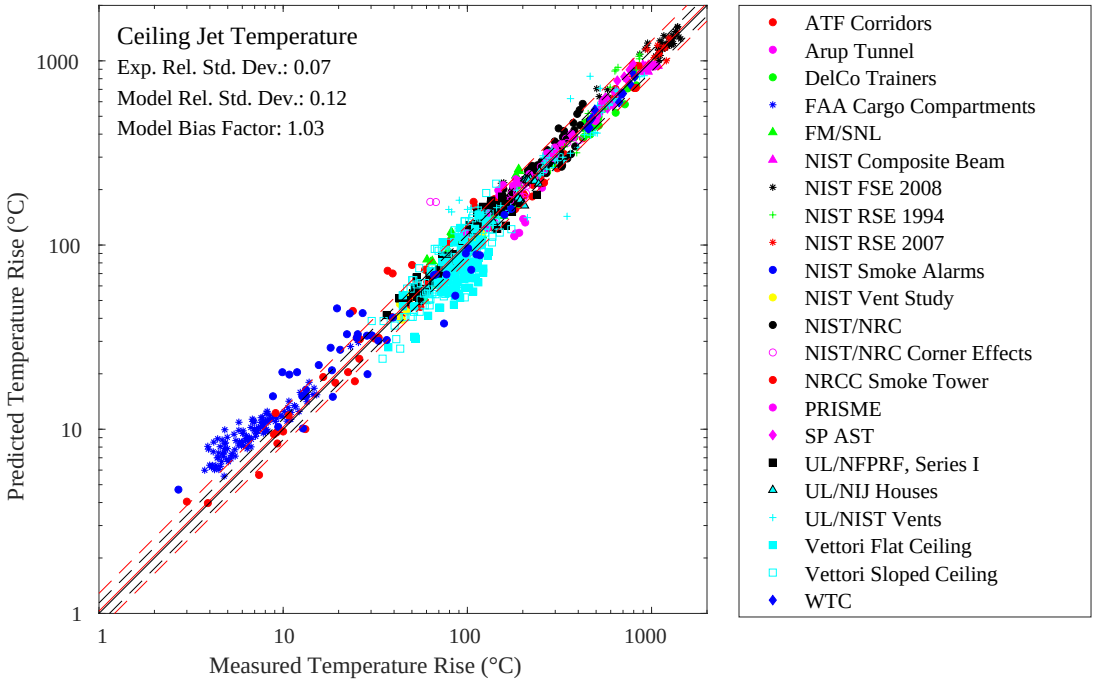

Figure 7.55: Summary of ceiling jet temperature predictions.

7.2 Sprinkler Activation Times

There are two ways to evaluate the model's ability to predict sprinkler activation. The first is to simply compare the total number of predicted versus observed activations. The second is to compare the time to first activation. Comparing the total number of activations indirectly indicates if the model accurately predicts the cooling of the hot gases by the water spray. Comparing time to first activation indirectly indicates if the model accurately predicts the velocity and temperature of the ceiling jet.

7.2.1 Time to First Sprinkler Activation

Figure 7.56 compares measured and predicted sprinkler activation times. For the UL/NFPRF experiments, only the time to first activation is compared because the resulting water spray sometimes delays the second activation substantially. While the model accounts for the cooling effect of the spray, the disruption of the activation sequence is somewhat random. A better way to check the accuracy of the model is to compare the predicted and measured total number of activation, which is discussed in the next section. For the Vettori experiments, the sprinklers did not flow water; thus, it is possible to consider the activation times of up to four sprinklers.

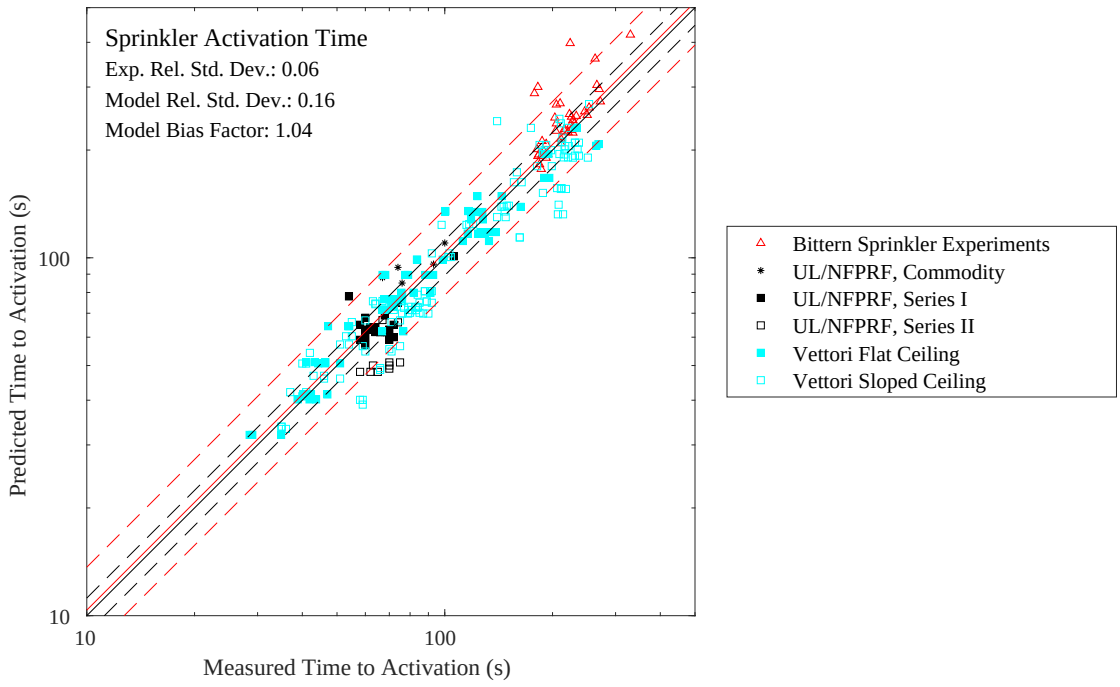

Figure 7.56: Comparison of measured and predicted sprinkler actuation times.

7.2.2 Number of Sprinkler Activations

The figures on the following pages display the number of sprinklers actuated as a function of time. The results are summarized in Fig. 7.63. The discussion of the uncertainty for this quantity can be found in Section 4.3.2.

Note that no sprinklers were installed for Test 11, Series I.

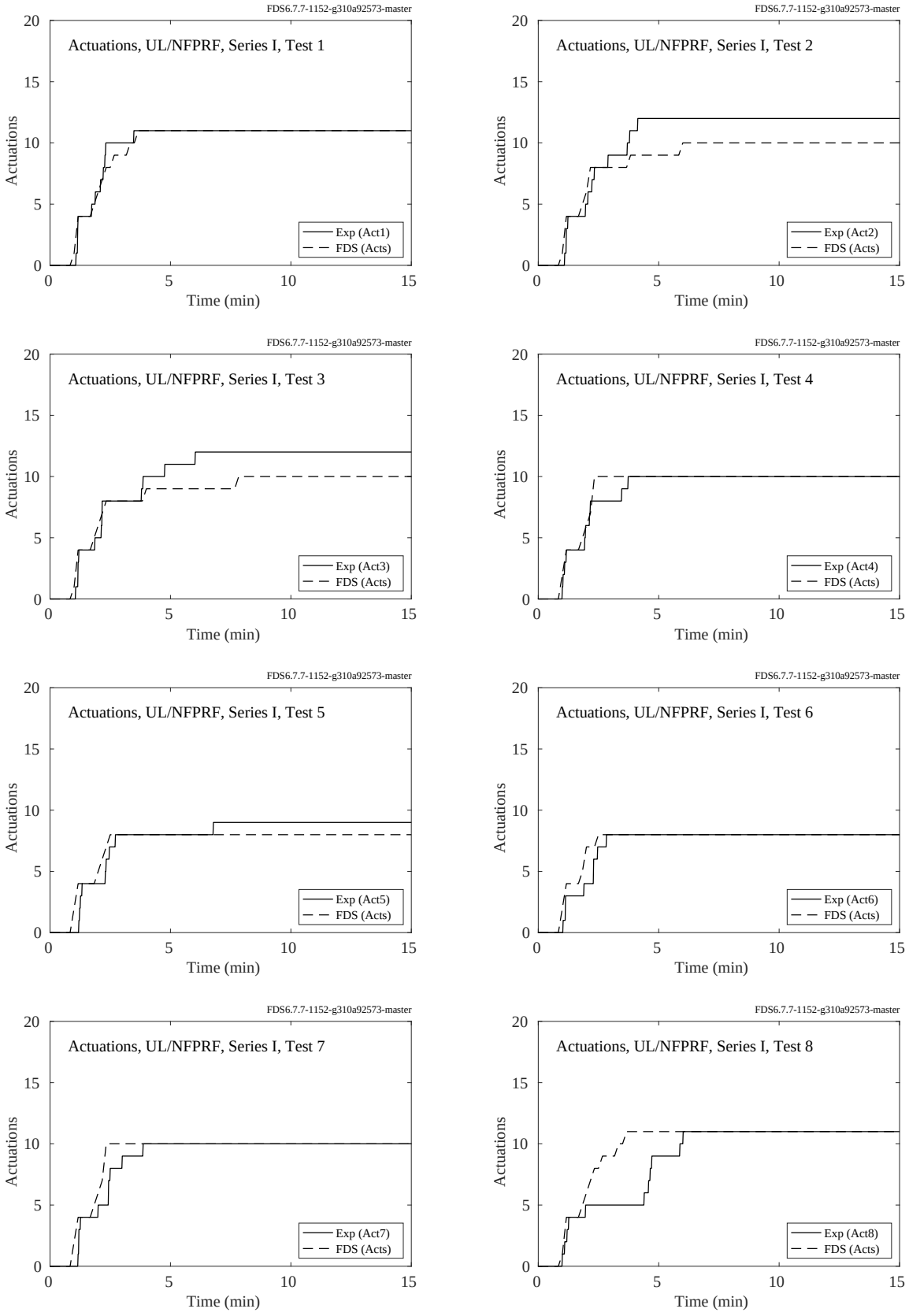

Figure 7.57: UL/NFPRF experiments, number of sprinkler activations, Series I, Tests 1-8.

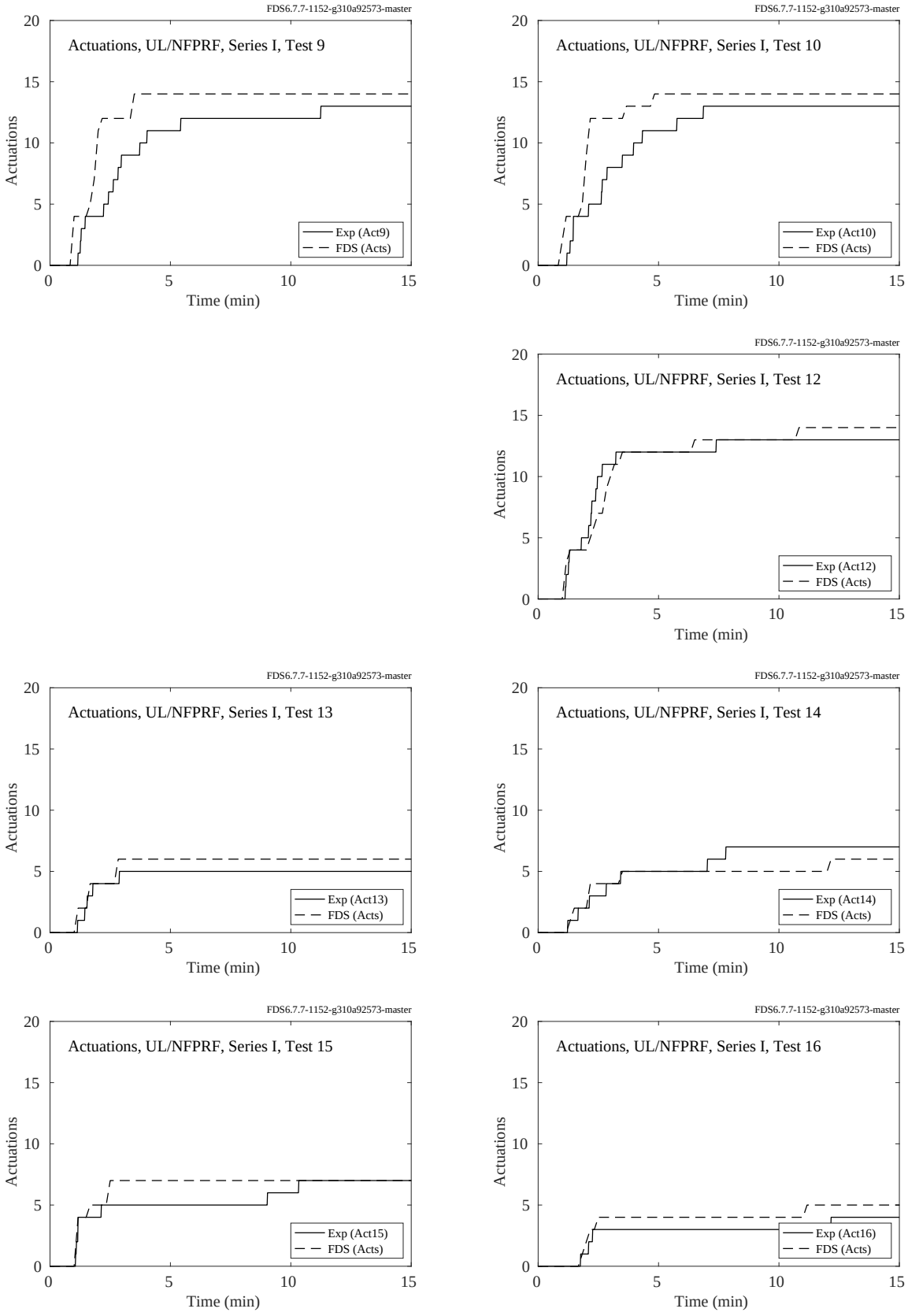

Figure 7.58: UL/NFPRF experiments, number of sprinkler activations, Series I, Tests 9-16.

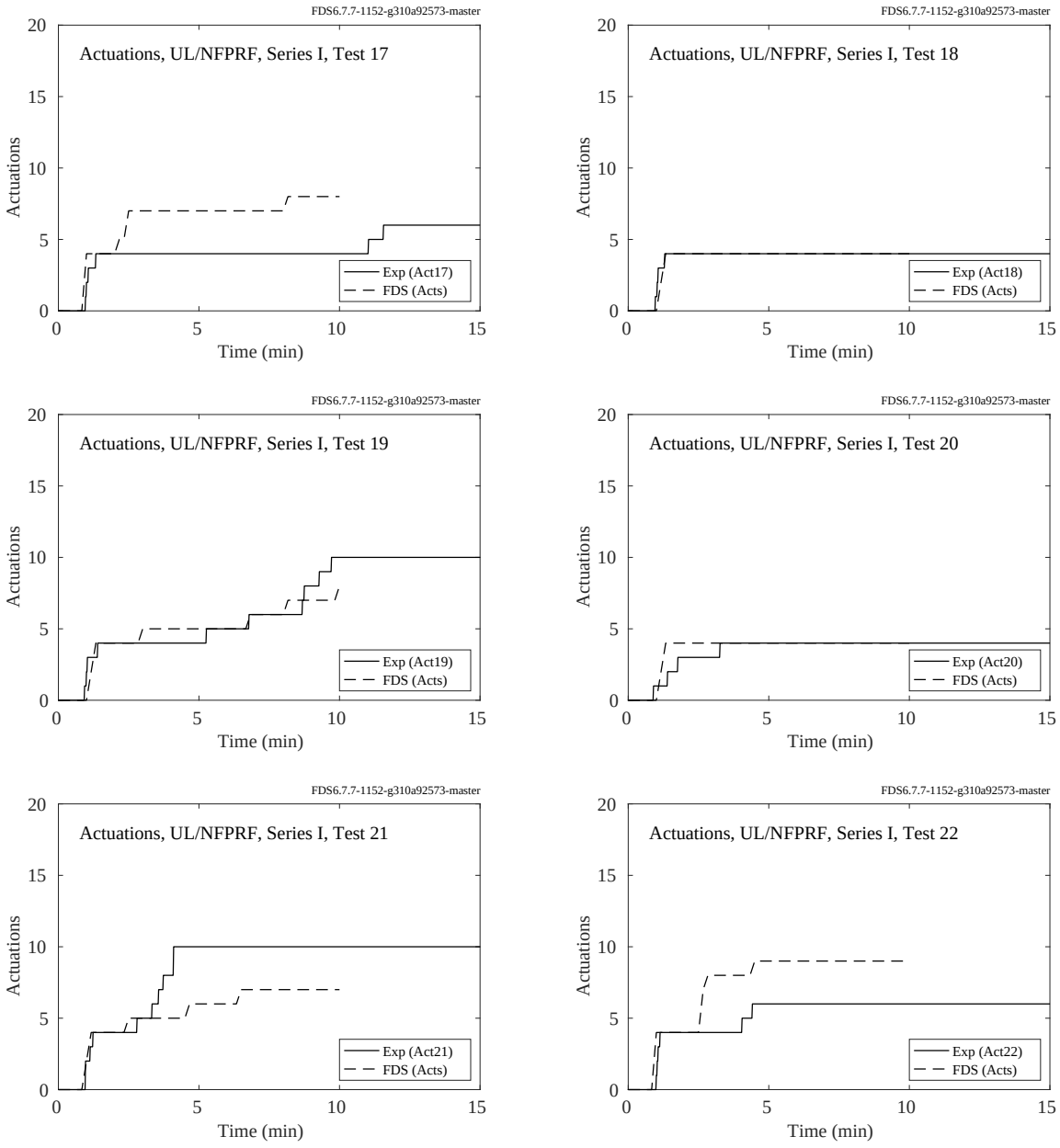

Figure 7.59: UL/NFPRF experiments, number of sprinkler activations, Series I, Tests 17-22.

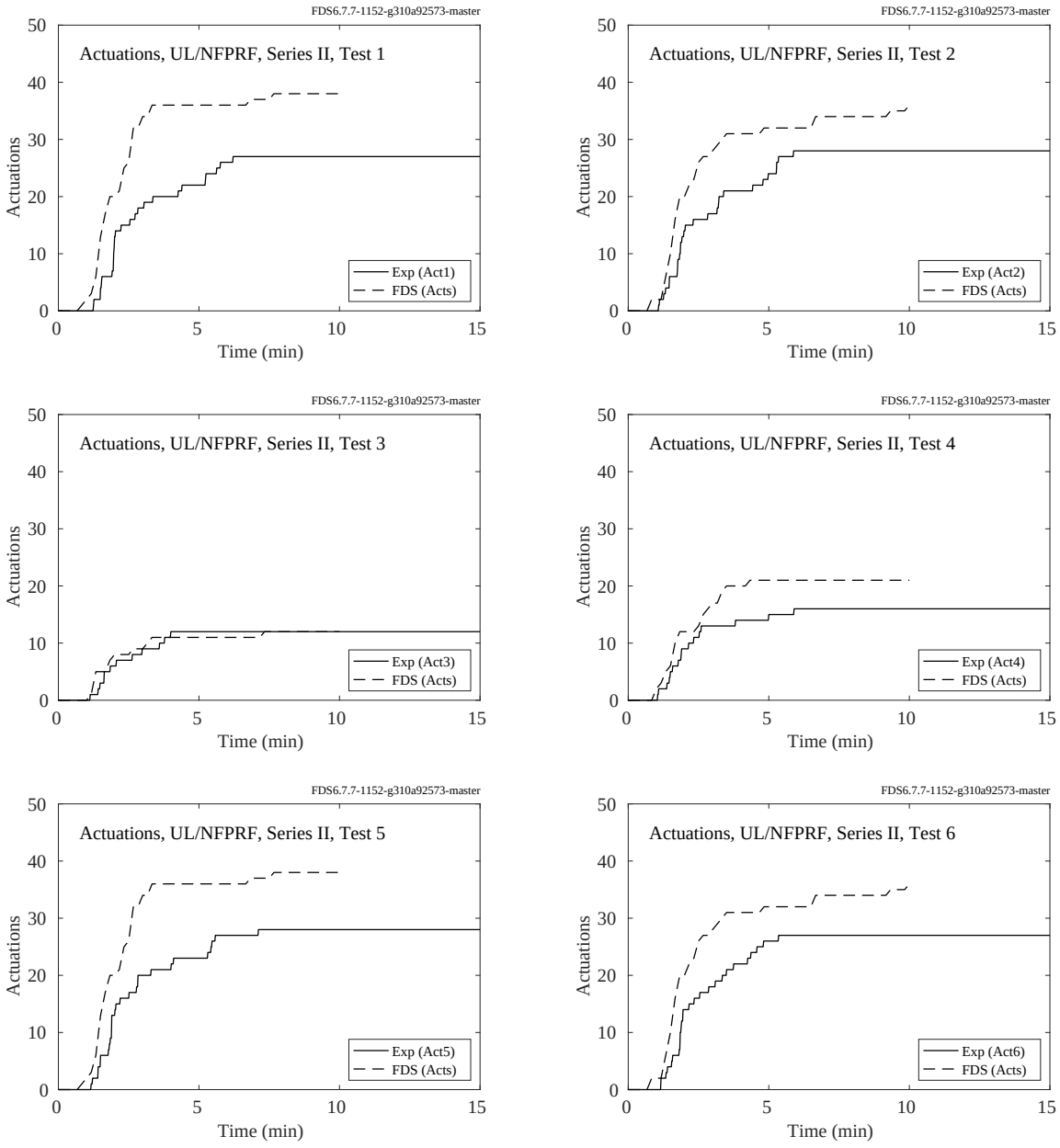

Figure 7.60: UL/NFPRF experiments, number of sprinkler activations, Series II, Tests 1-6.

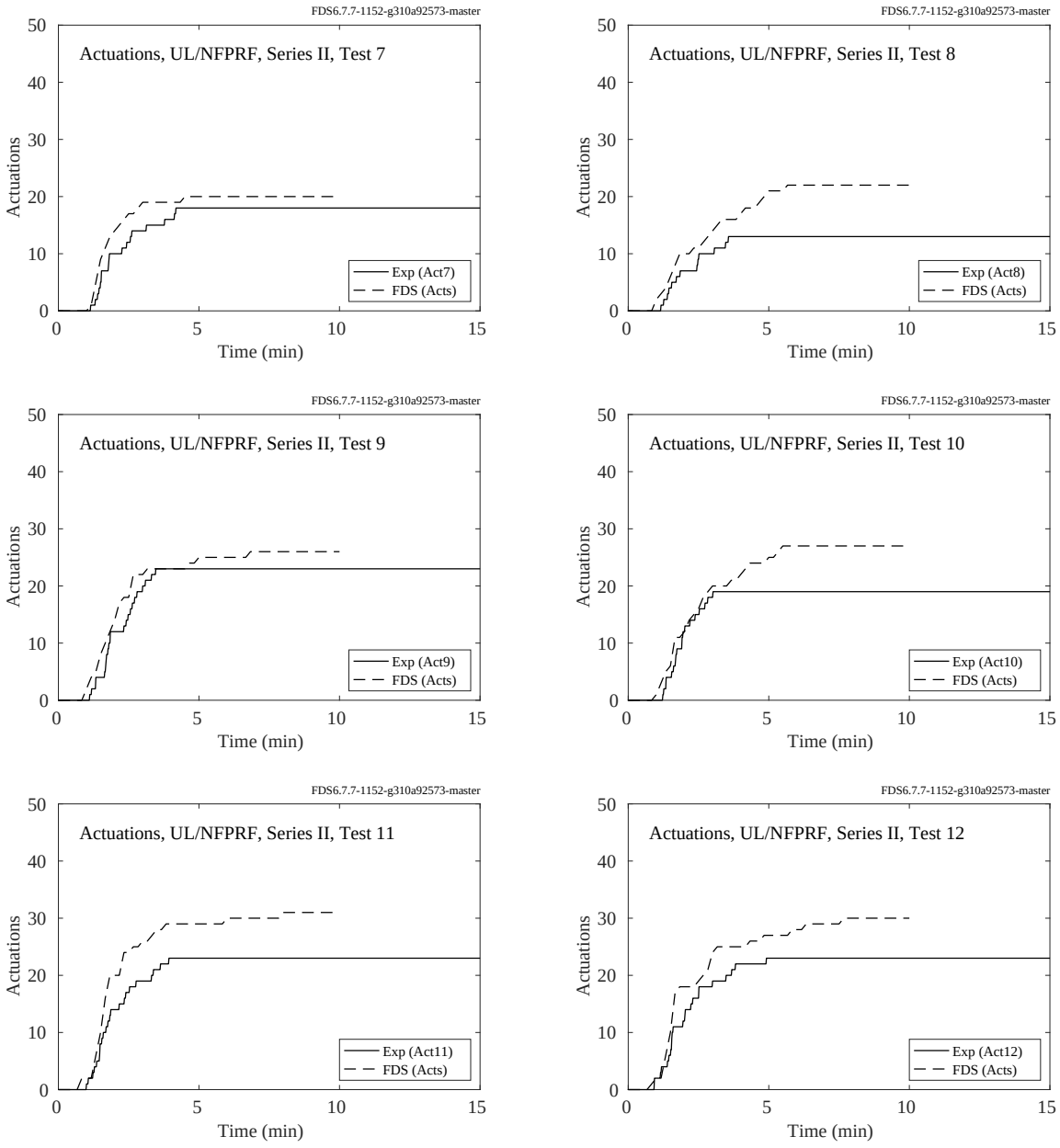

Figure 7.61: UL/NFPRF experiments, number of sprinkler activations, Series II, Tests 7-12.

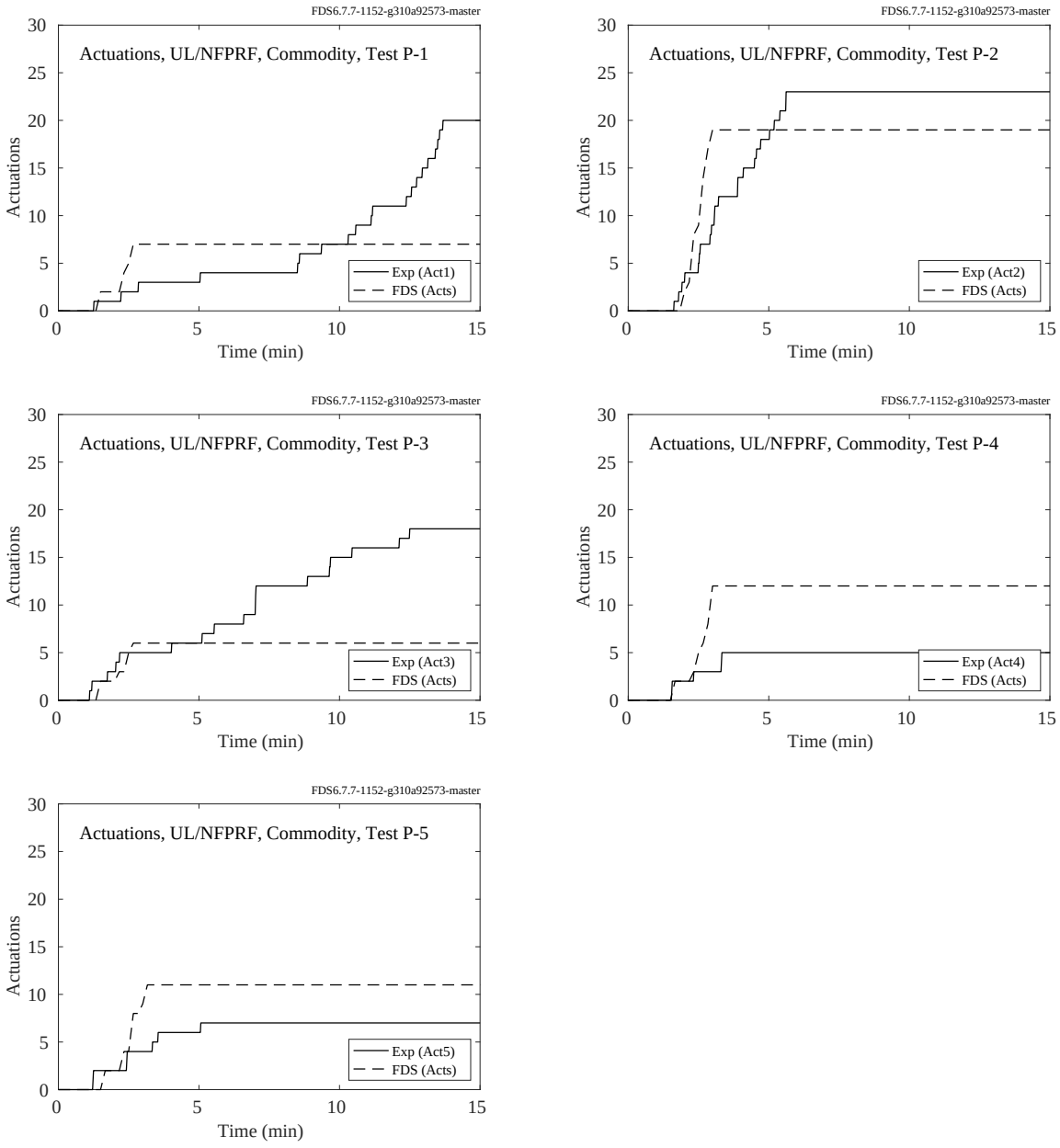

Figure 7.62: UL/NFPRF experiments, number of sprinkler activations, Group A Commodity, Tests 1-5.

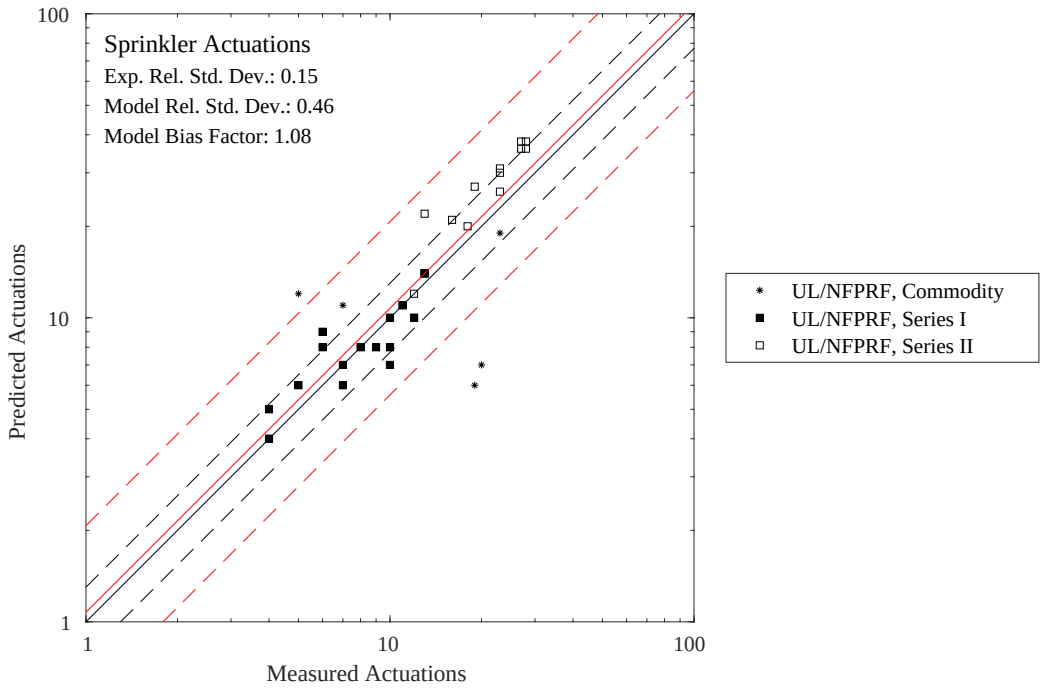

Figure 7.63: Comparison of the number of predicted and measured sprinkler activations.

7.3 Smoke Detector Activation Times

FDS can model smoke detector activation in two ways. The first method is based on the assumption that activation occurs when the gas temperature near the detector rises above a given threshold. Essentially this method treats the smoke detector exactly like a heat detector with a relatively low RTI value. Figure 7.64 compares the measured versus predicted smoke detector activation times using a heat detector/temperature rise approach. The heat detectors were set with an RTI of 5 $\sqrt{\text{m}\cdot\text{s}}$ and an activation temperature of 5 °C above ambient, based on the suggestion of Bukowski and Averill [320].

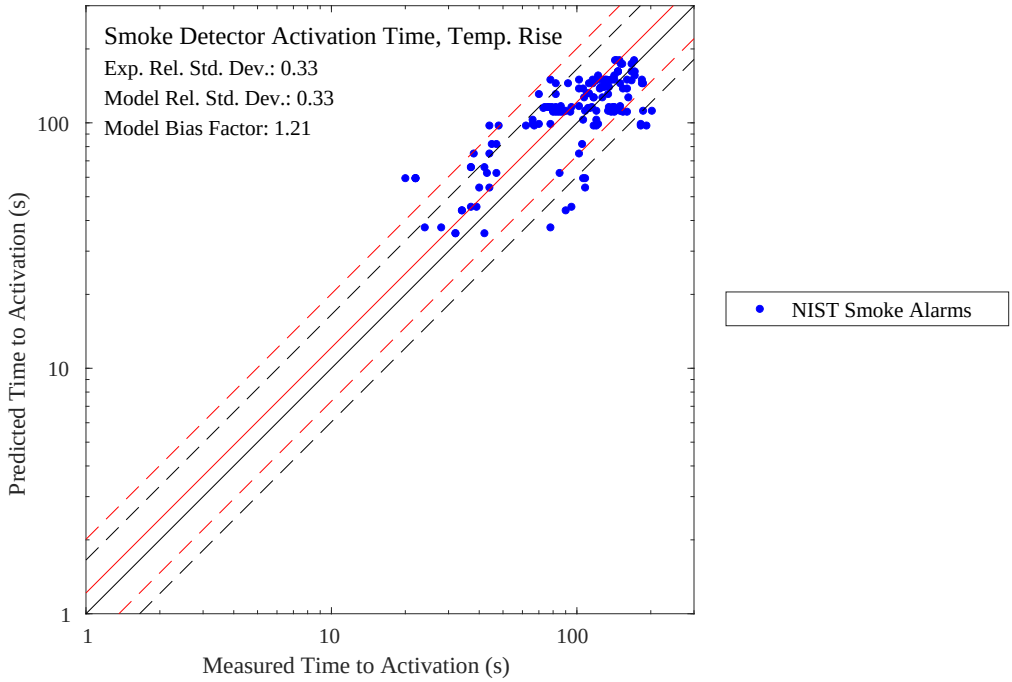

Figure 7.64: Summary of smoke detector activation times (using temperature rise), NIST Smoke Alarms.

The second method of predicting smoke detector activation is to use an empirical model of the smoke transit time within the device to estimate when the smoke concentration will rise above a particular threshold value set by the manufacturer. Figure 7.65 compares the measured versus predicted smoke detector activation times using the smoke detector model. Note that the test report [241] does not provide the parameters that characterize the smoke transit time within the detector. Instead, generic values are used.

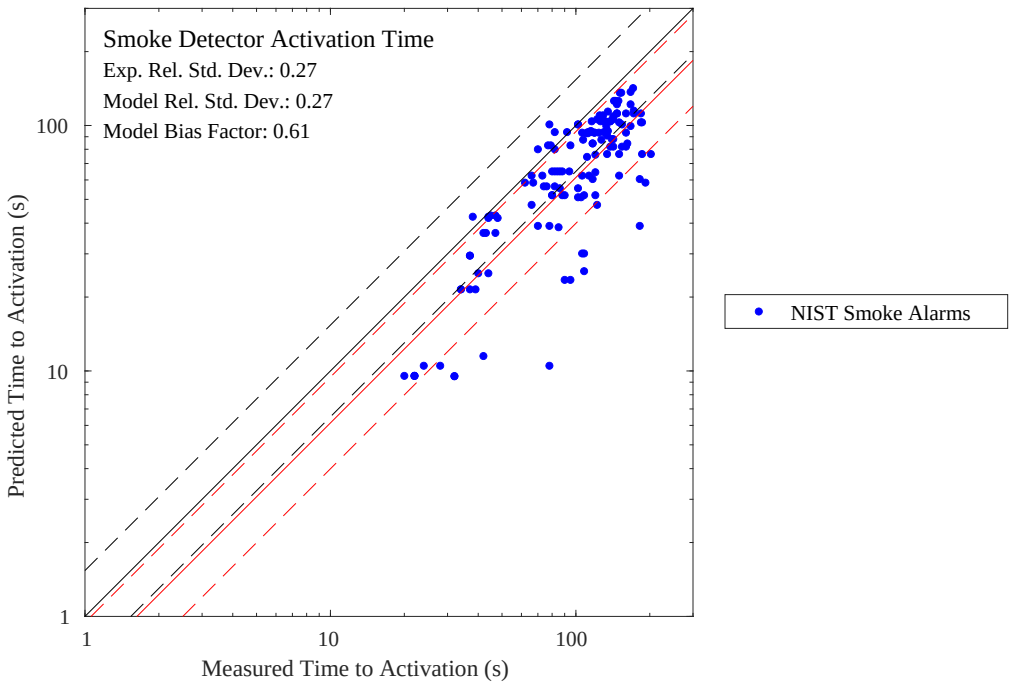

Figure 7.65: Summary of smoke detector activation times (using smoke detector model), NIST Smoke Alarms.

Chapter 8

Gas Velocity

Gas velocity is often measured at compartment inlets and outlets as part of a global assessment of mass and energy conservation. This chapter contains measurements of gas velocity and related quantities.

8.1 ATF Corridor Experiments

Comparisons of bi-directional velocity measurements with FDS predictions for the ATF Corridor experiments are presented on the following pages. Velocity measurements were made at four locations, two on the first level (Trees H and I) and two on the second level (Trees J and K). Shown are the upper-most and lower-most probe for each vertical array. Typically there were four probes per tree, with the number 1 indicating the upper-most probe.

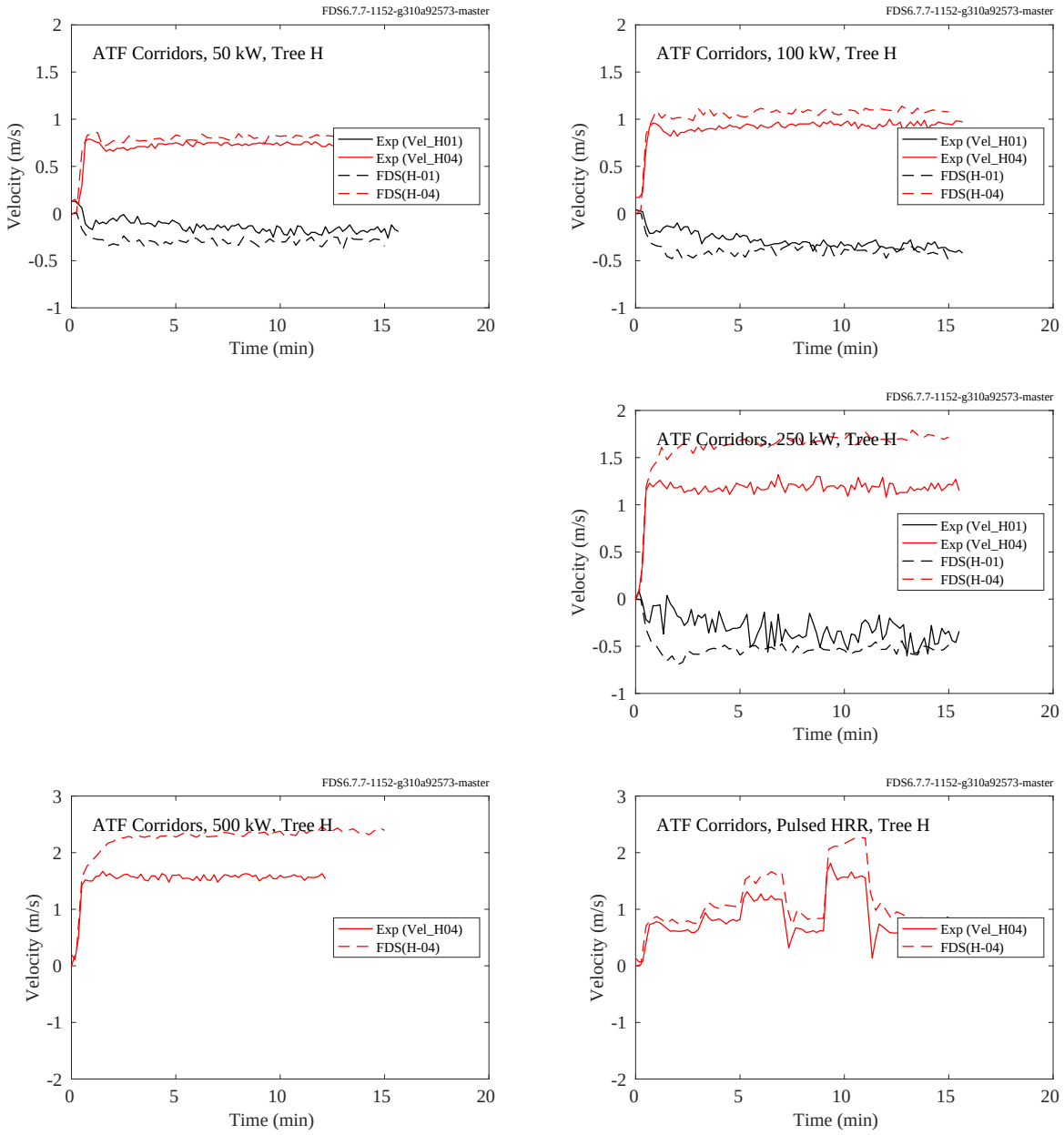

Figure 8.1: ATF Corridors, gas velocity, first level, Location H.

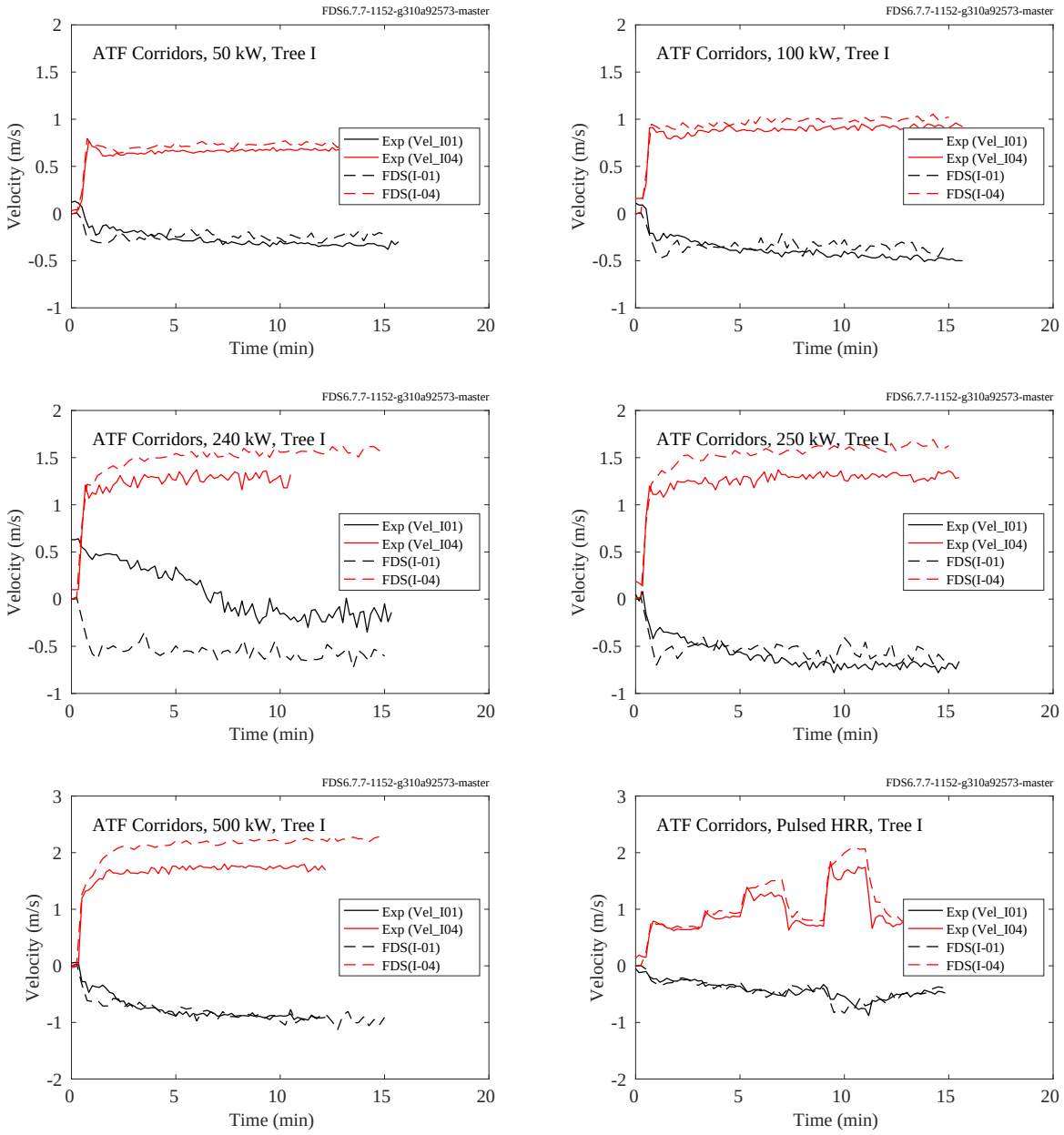

Figure 8.2: ATF Corridors, gas velocity, first level, Location I.

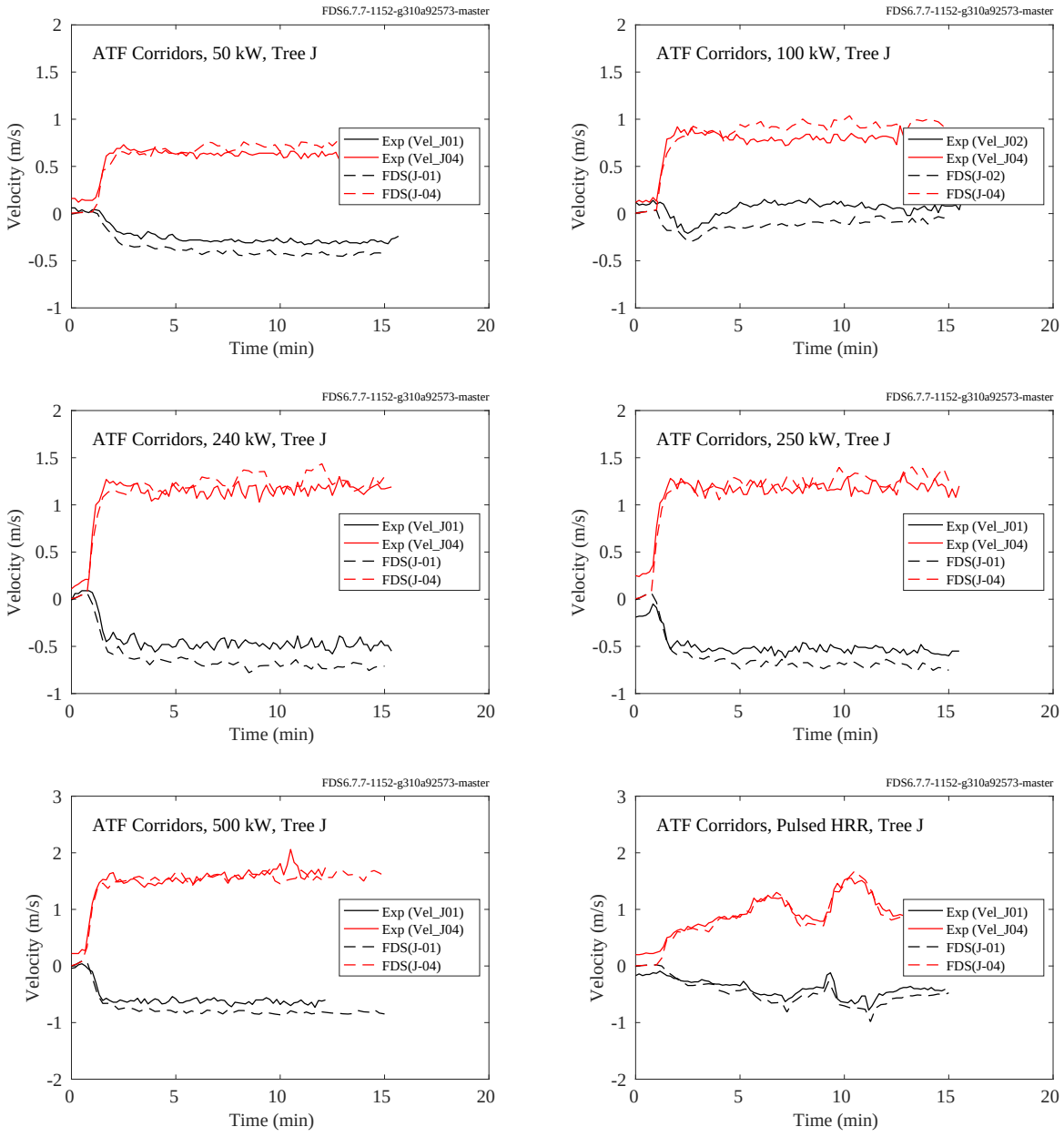

Figure 8.3: ATF Corridors, gas velocity, second level, Location J.

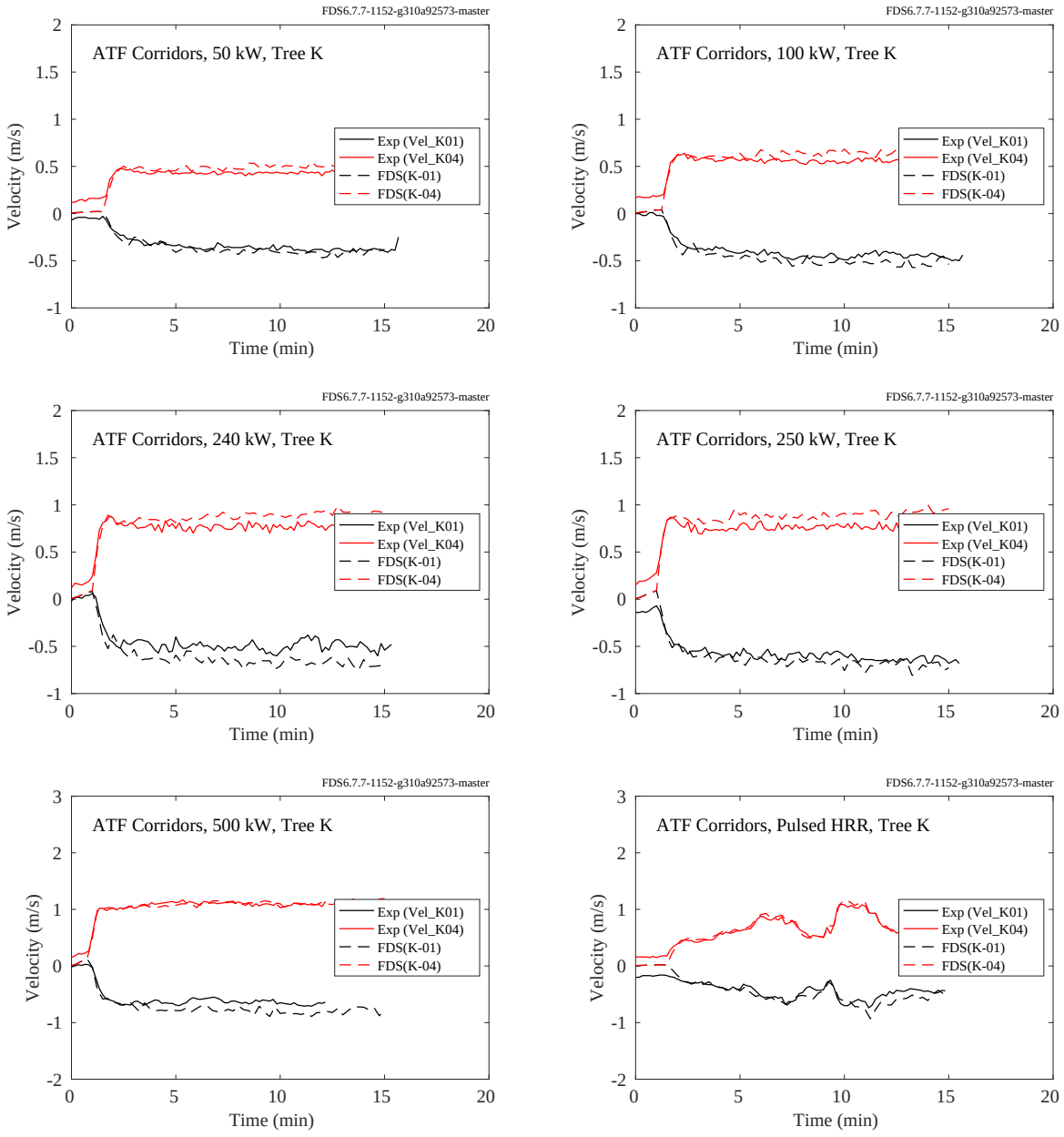

Figure 8.4: ATF Corridors, gas velocity, second level, Location K.

8.2 Backward Facing Step

A snapshot the instantaneous velocity contours of the flow over a backward facing step is shown in Fig. 8.5. The dimensions of the tunnel are given in Fig. 3.2. Virtual measurement devices are placed throughout the channel to collect data relating to flow characteristics such as velocity, turbulence RMS velocity, and friction velocity. These virtual measurement devices are placed into lines, four vertical and one horizontal, with a device in the volumetric center of each grid cell. A vertical line device is placed within the inlet region at a location of $x = -3h$, and three line devices are placed in the post-step region at locations of $4h$, $6h$, and $10h$. The post-step vertical line devices are placed accordingly to sample the recirculation, reattachment, and recovery regions. A horizontal line device is used to sample data directly adjacent to the bottom wall of the channel in the post-step region ($0h$ to $20h$).

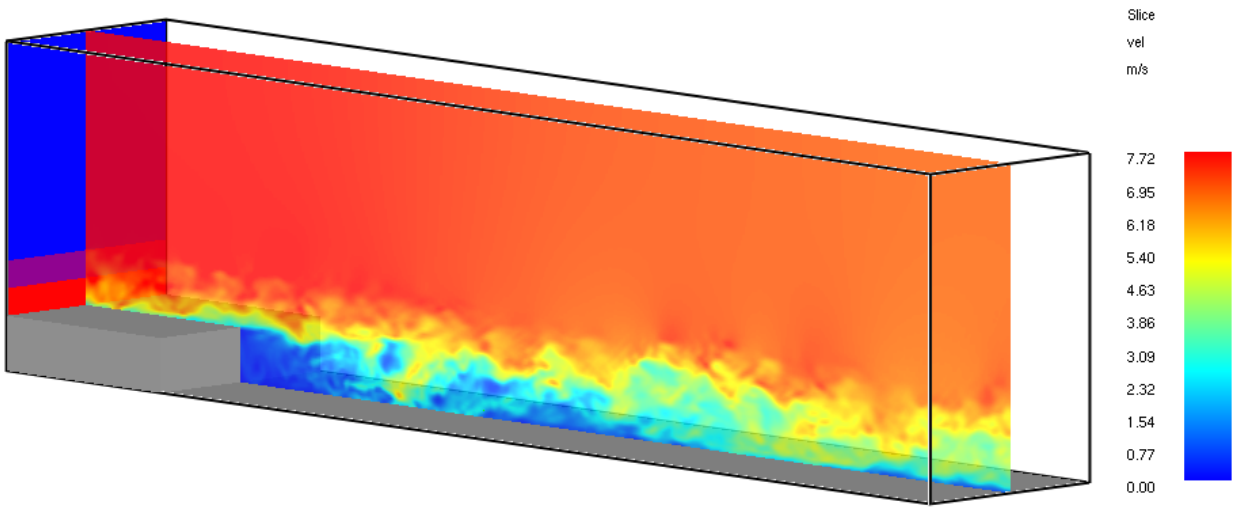

Figure 8.5: Instantaneous contours of velocity magnitude.

The profile of the inlet streamwise velocity component, $\overline{u}(z)$, is specified using experimental data provided by Jovic and Driver [50], while the transverse components, $\overline{v}(z)$ and $\overline{w}(z)$, are set to zero. Turbulent eddies are injected using the Synthetic Eddy Method of Jarrin [307]. Eddies are injected at random locations in the bottom two inlets, advected with the flow over a distance equal to the maximum eddy length scale and recycled at the inlet. The inlet maximum eddy length scale is 0.03 m, the number of eddies is 100, and the RMS velocity is set to 0.5 m/s for the middle inlet and 1.0 m/s for the bottom inlet to match the measured inlet data at $x/h = -3$ as closely as possible.

The boundary conditions for velocity and pressure on the top of the domain are "mirror", that is, zero gradient. The spanwise boundaries are periodic. The outlet boundary is "open".

Figure 8.6 shows the longitudinal profiles of the friction coefficient (left) and the pressure coefficient (right). The x/h location where C_f crosses zero is the reattachment length, a key validation metric for this flow. The measured value is approximately 6. Figure 8.7 shows the inlet ($x/h = -3$) and downstream mean and covariance profiles.

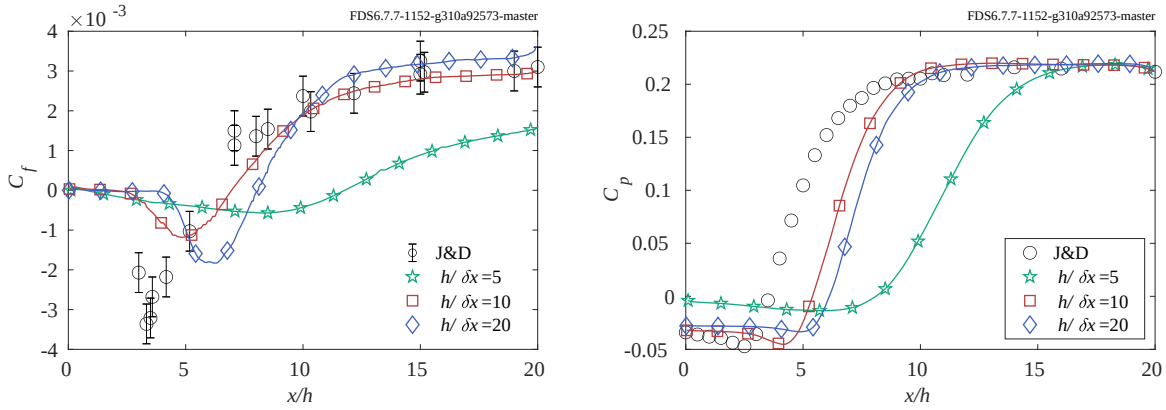

Figure 8.6: Longitudinal profiles of (left) friction coefficient and (right) pressure coefficient.

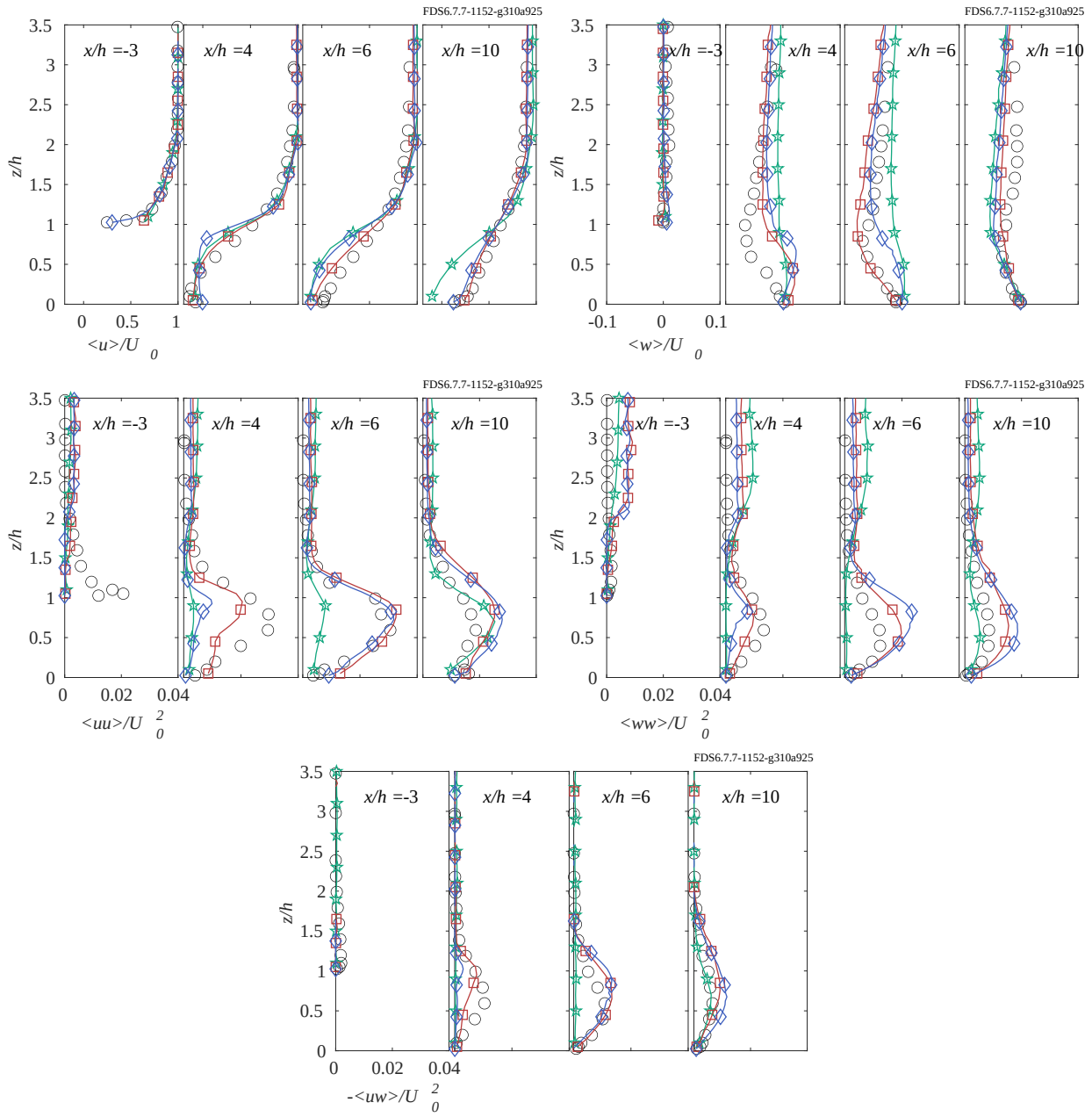

Figure 8.7: Flow profiles for various grid resolutions. Symbols: –⋆–, $h/\delta z$=5; –□–, $h/\delta z$=10; –◇–, $h/\delta z$=20; ○, J&D experimental data.

8.3 Bryant Doorway Experiments

On the following page there are seven plots comparing the predicted and measured centerline velocity[1] profiles in a doorway of a standard ISO 9705 compartment. The measurements shown are based on PIV (Particle Image Velocimetry). Note that some of the measurements do not extend to the top of the doorway (1.96 m above the compartment floor) because the heat from the fire prevented adequate laser resolution of the particles. Velocity measurements were also made using bi-directional probes [143], but these measurements were shown to be up to 20 % greater in magnitude than the comparable PIV measurement.

[1] Note that the quantity that is being compared is the total velocity multiplied by the sign of its normal component.

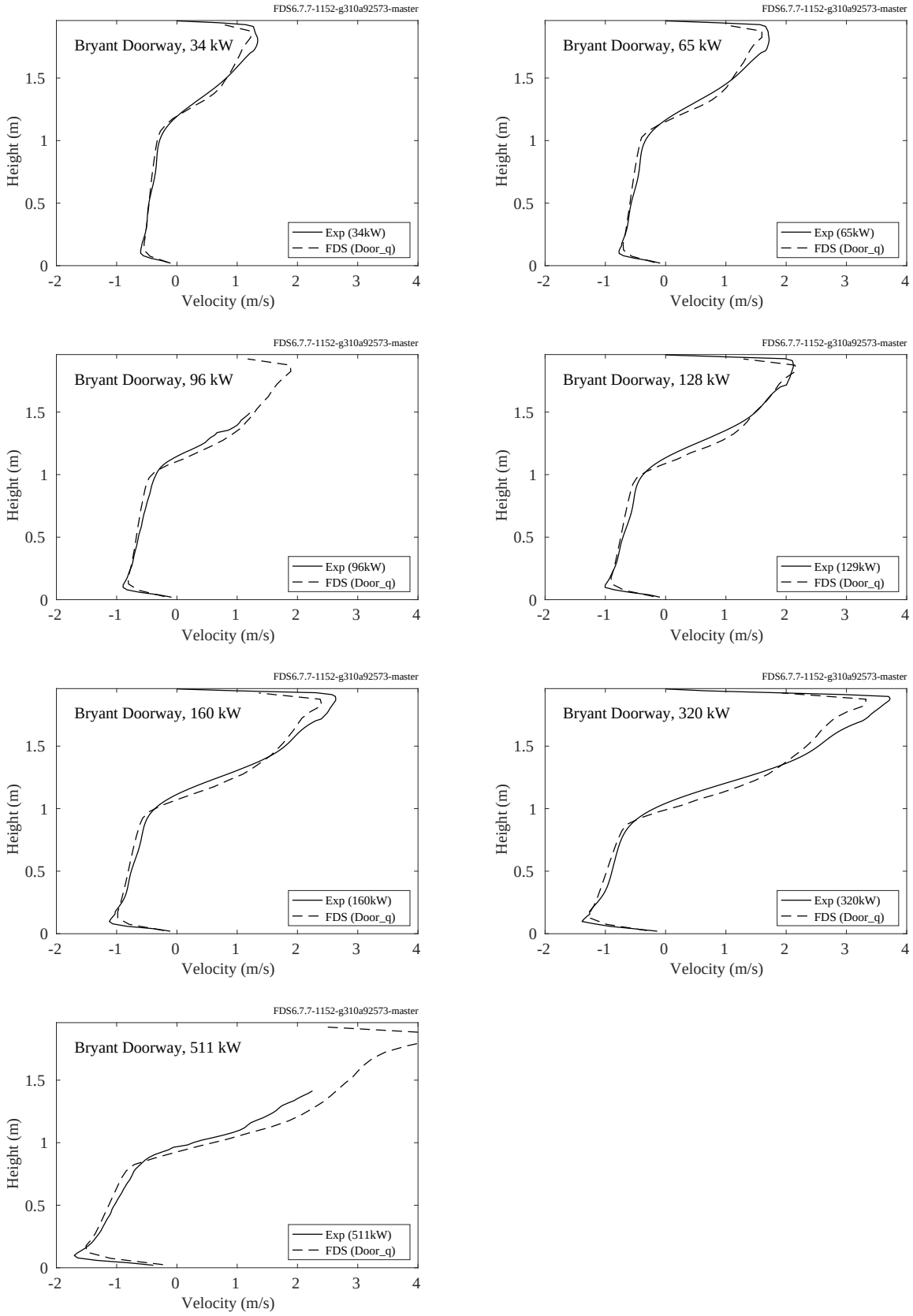

Figure 8.8: Bryant Doorway experiments, gas velocity profiles.

8.4 Edinburgh Vegetation Drag

The following figures show average velocities, taken over a 60 s period and obtained 225 mm from the leading edge of the fuel bed, as shown in Figure 3.10. In the case of the simulations, averaging starts after 20 s in order to allow quasi-steady conditions to establish. The experimental points represent an average of two repeats, involving re-packing of the fuel bed.

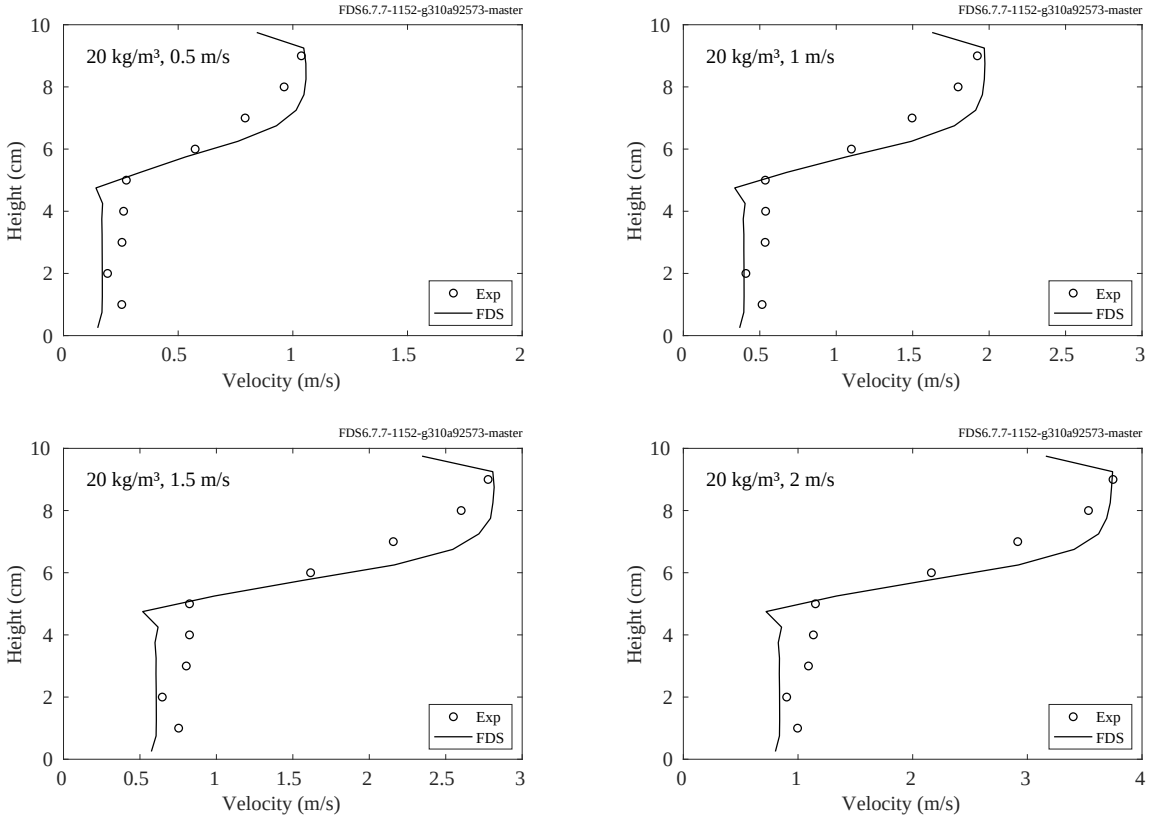

Figure 8.9: Edinburgh Vegetation Drag, gas velocity profiles, low bulk density.

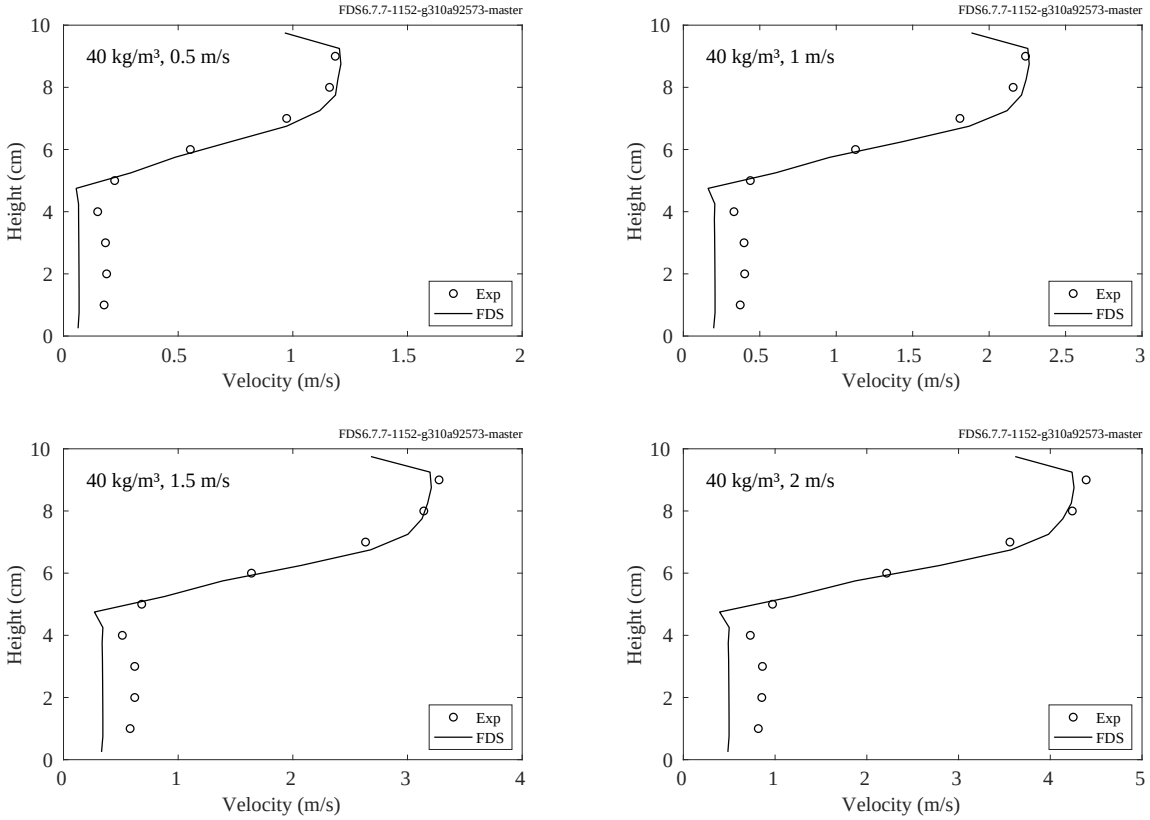

Figure 8.10: Edinburgh Vegetation Drag, gas velocity profiles, medium bulk density.

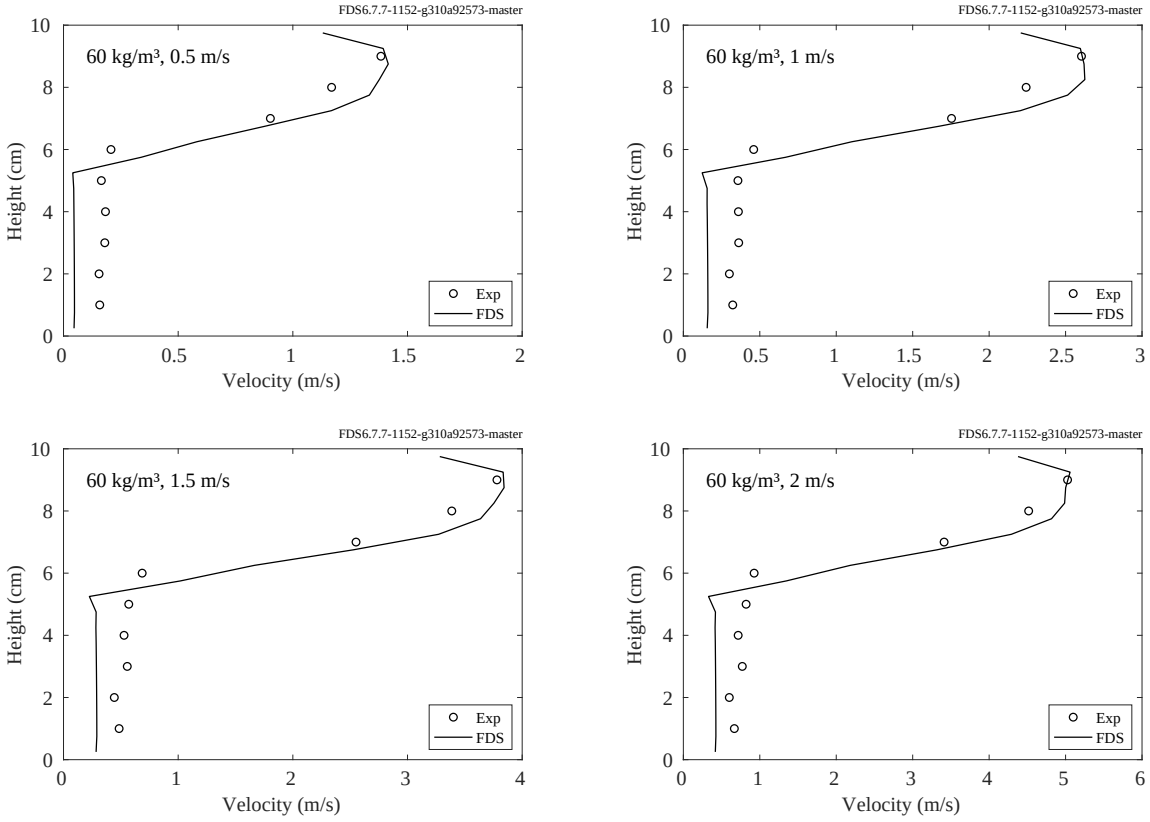

Figure 8.11: Edinburgh Vegetation Drag, gas velocity profiles, high bulk density.

8.5 FM/FPRF Datacenter Experiments

On the following page there are eight plots comparing the predicted and measured velocities for the high and low fan speed flow mapping tests in the FM/FPRF datacenter mockup. For each test there are plots for u-velocity, v-velocity, w-velocity and total velocity. Error bars are the measured and predicted RMS values. The dotted lines represent the measurement error. Measurement error was not a simple percentage of the measured value but rather was a propagation of fan flow error (the primary FDS input), sonic anemometer intrinsic error, and an estimate of the error based on the accuracy of placing the anemometer (determined from attempts to make repeat measurements after removing and replacing the probe).

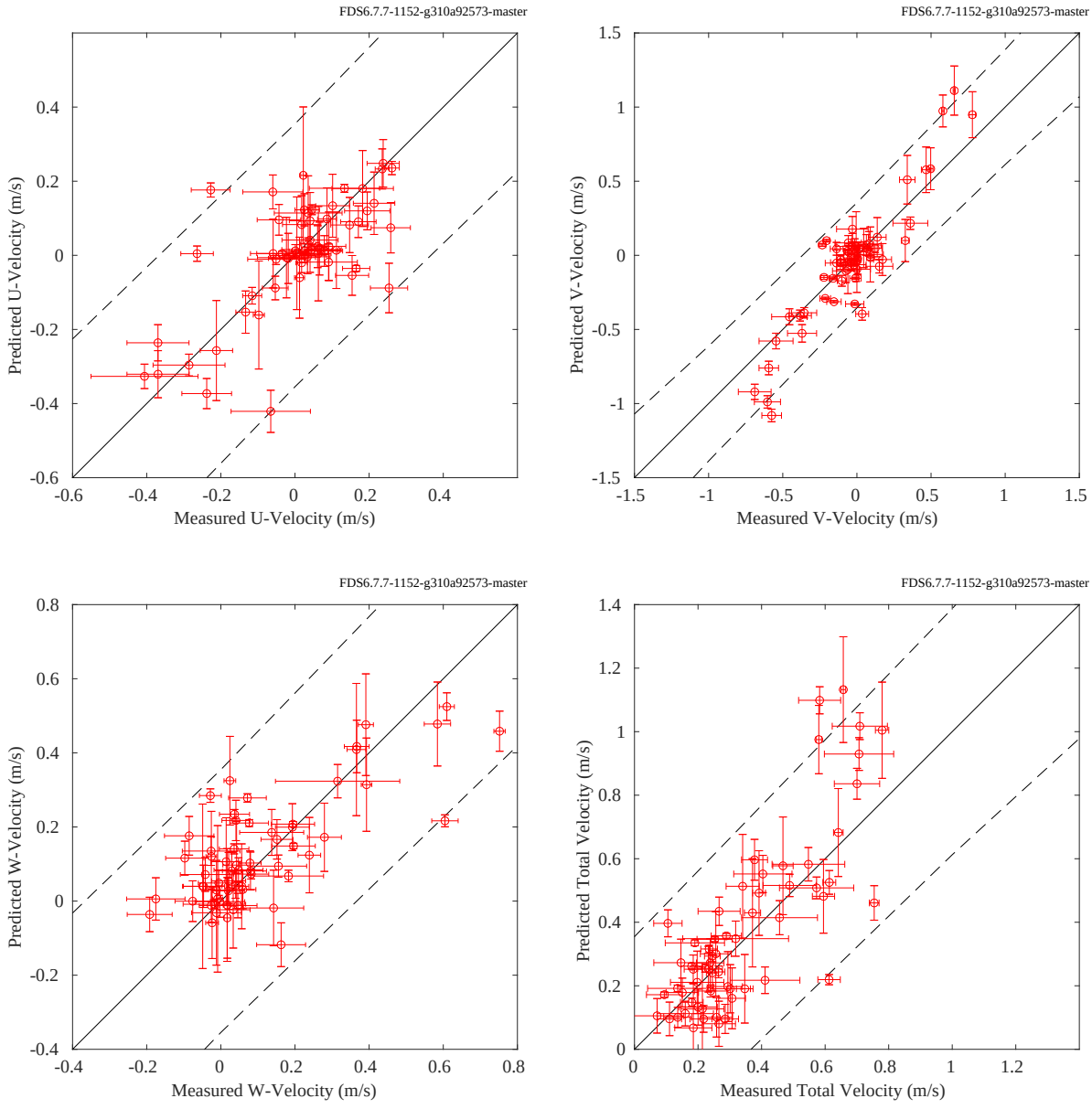

Figure 8.12: FM/FPRF experiments, gas velocity, low fan rate.

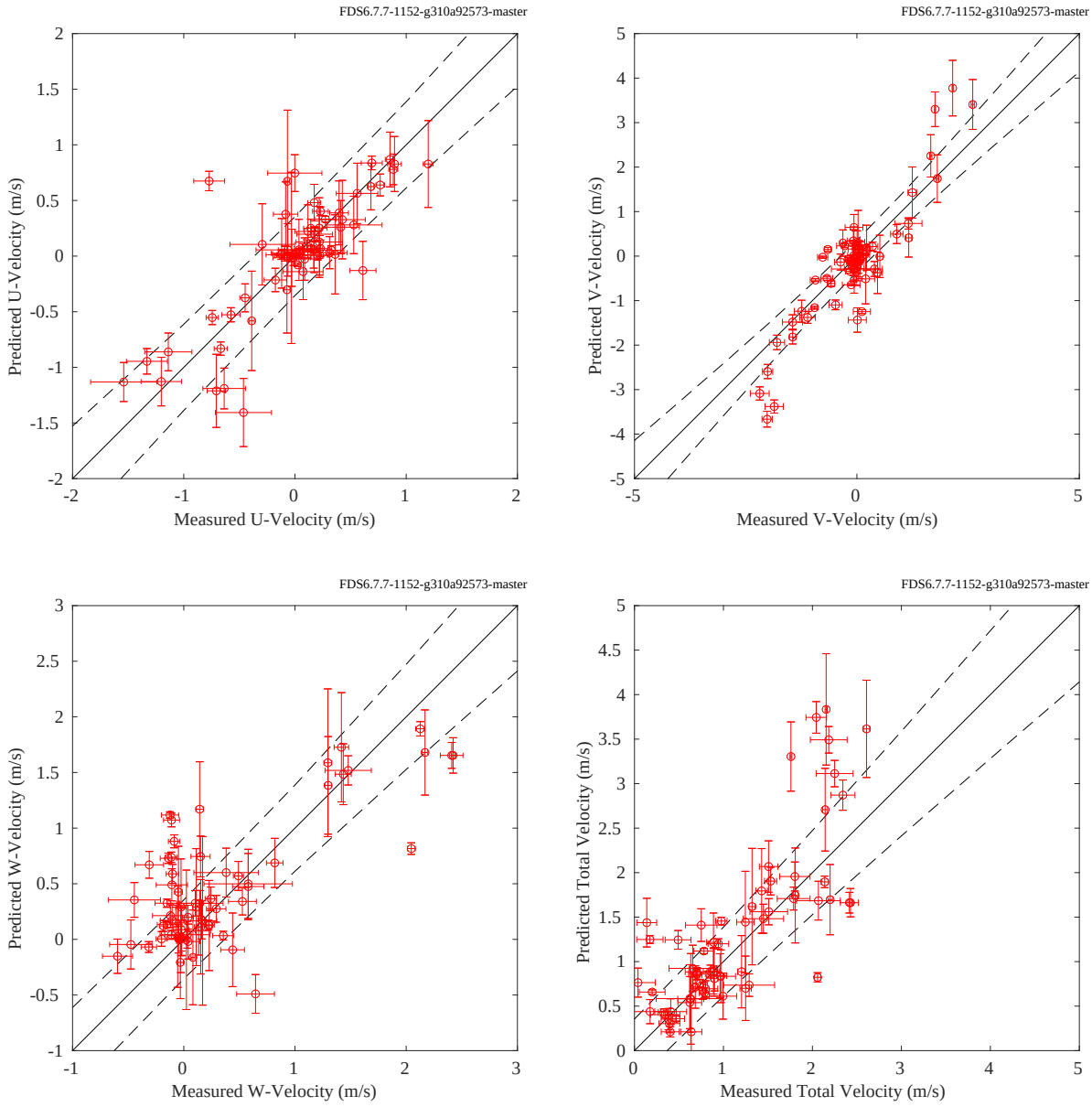

Figure 8.13: FM/FPRF experiments, gas velocity, high fan rate.

8.6 McCaffrey's Plume Correlation

The following plots show the results of simulations of McCaffrey's five fires at three grid resolutions, nominally $D^*/\delta x = [5, 10, 20]$ (respectively, coarse, medium, and fine resolution).

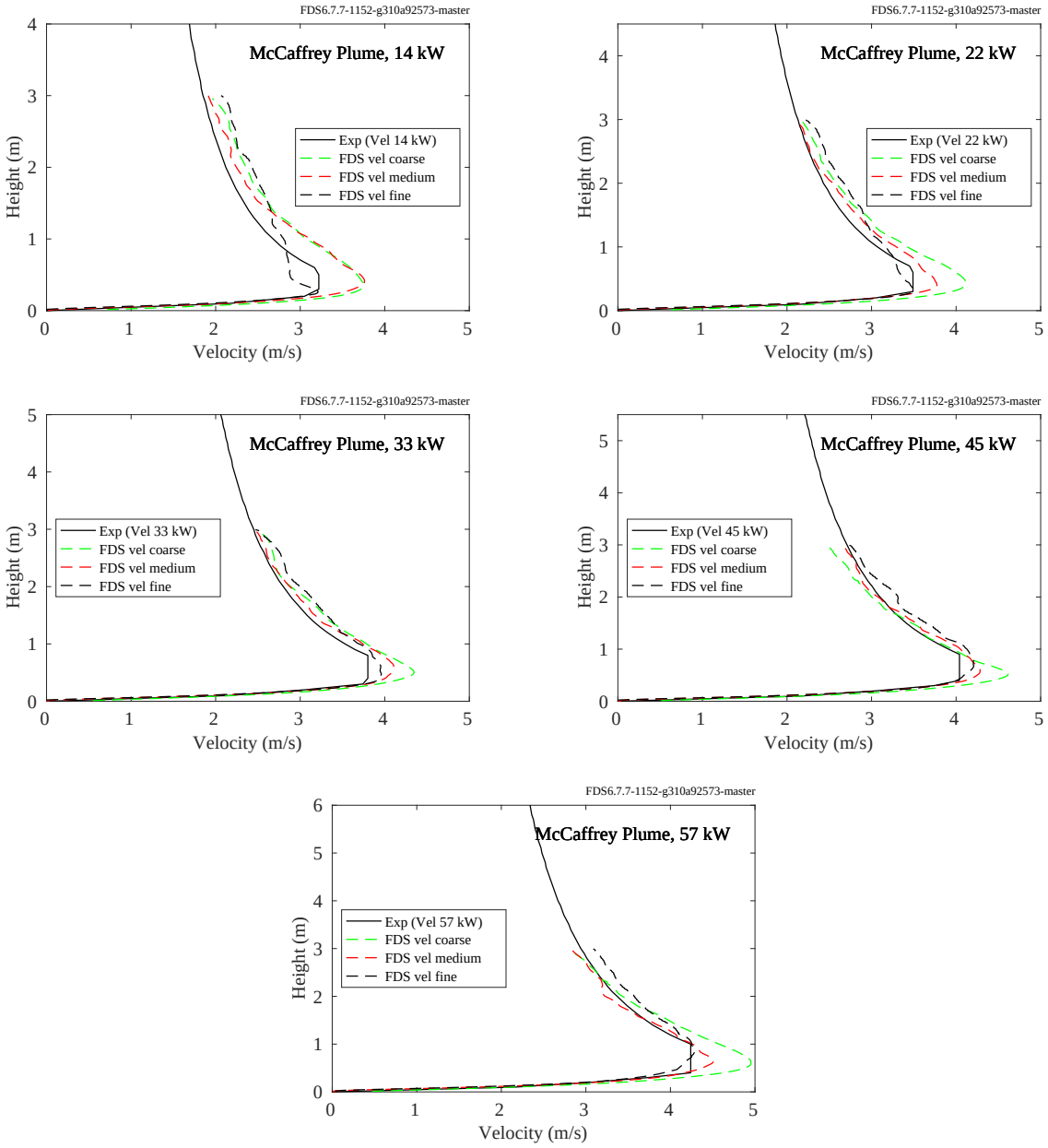

Figure 8.14: McCaffrey Plumes, centerline plume velocity.

Below we plot the same results but arranged in a different way. The height dimension is scaled by the fire Froude number and each plot represents nominally the same resolution level.

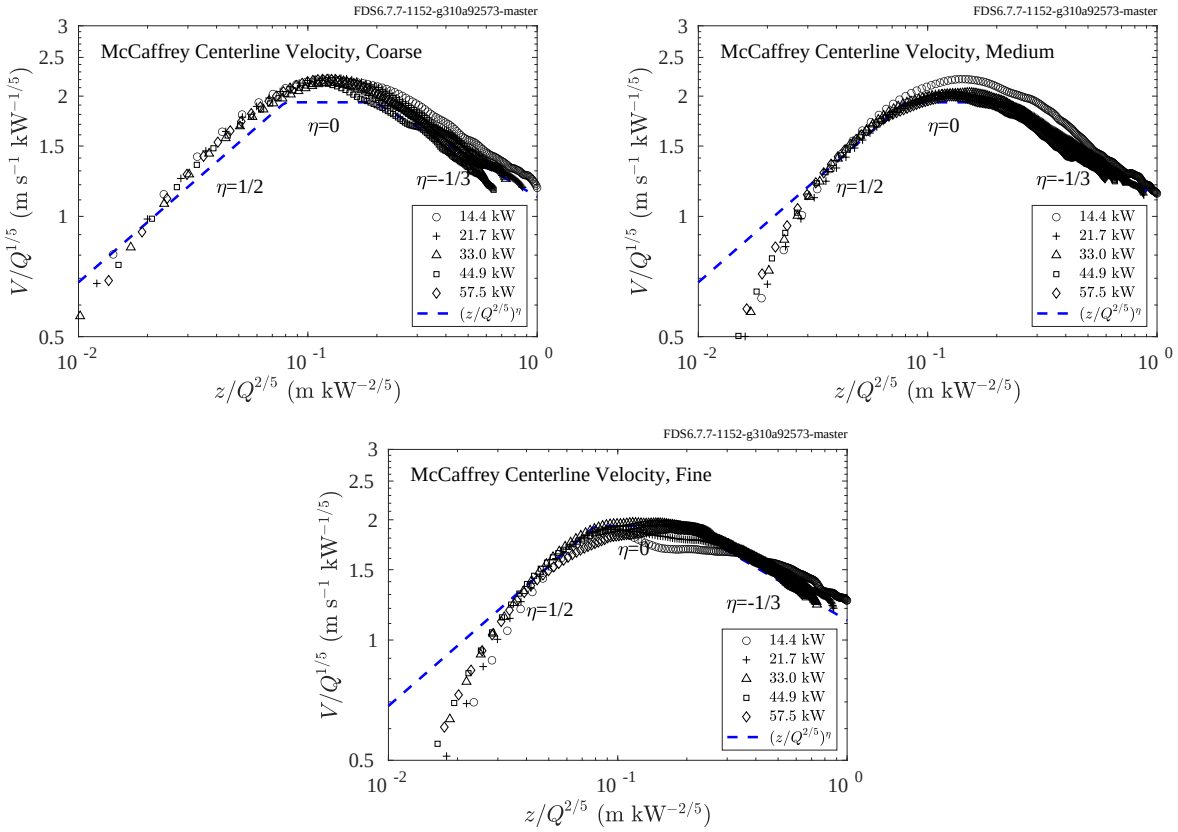

Figure 8.15: McCaffrey Plumes, centerline plume velocity, Froude scaling.

8.7 NIST Pool Fires

Figure 8.16 displays centerline profiles of mean vertical velocity for 30 cm acetone, ethanol, and methanol pool fires; and 37 cm methane and propane gas burners [329].

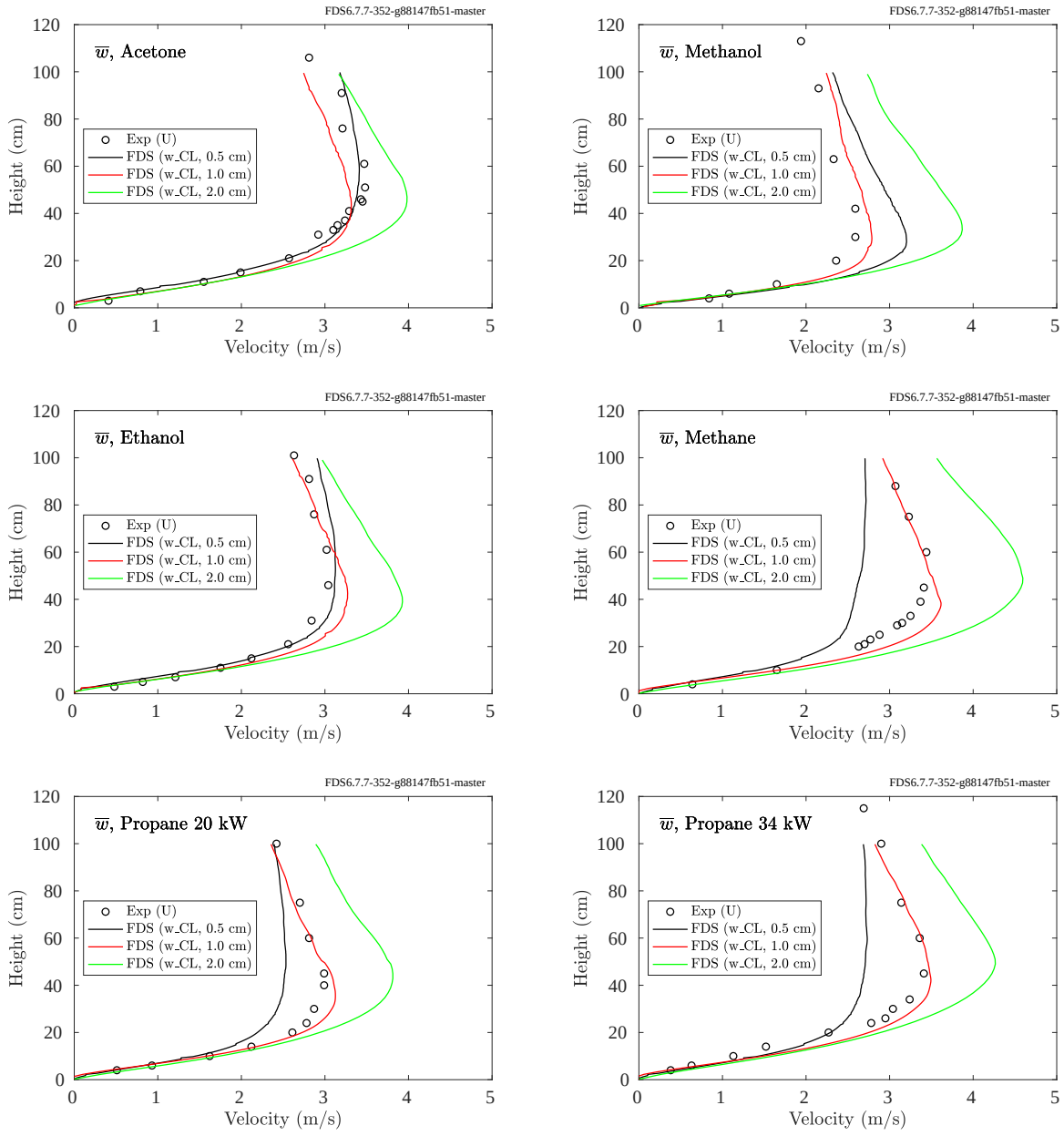

Figure 8.16: NIST Pool Fires, centerline profiles of mean vertical velocity for 30 cm acetone, methanol, and ethanol liquid pool fires, a 37 cm methane fire, and propane fires of 20 kW and 34 kW.

8.8 PRISME DOOR Experiments

Bi-directional probes were placed in the doorway separating the two compartments of the PRISME DOOR experiments. Shown on the plots below are the uppermost and lowest measurement points.

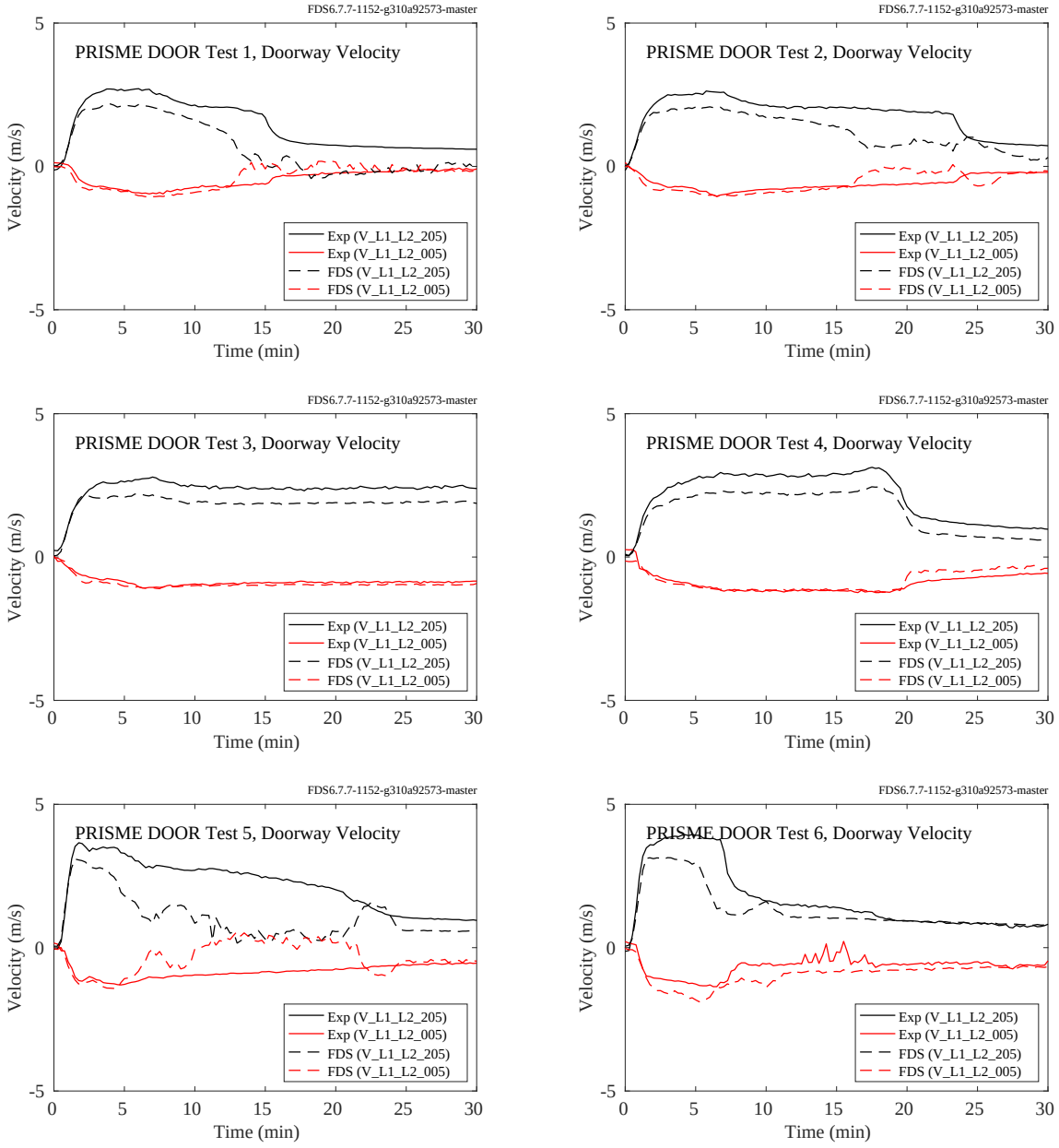

Figure 8.17: PRISME DOOR experiments, gas velocity.

8.9 Restivo Experiment

The results of a simulation of Restivo's room ventilation experiment are presented below. To capture the forced inlet flow, the volume near the supply slot needs a fairly fine grid to capture the mixing of air at the shear layer. For the results shown here, the height of the inlet was spanned with 6 grid cells, roughly 3 cm in the vertical dimension, 6 cm in the other two. Finer grids were used in the Musser study [38], but with no appreciable change in results. The component of velocity in the lengthwise direction was measured in four arrays: two vertical arrays located 3 m and 6 m from the inlet along the centerline of the room, and two horizontal arrays located 8.4 cm above the floor and below the ceiling, respectively. These measurements were taken using hot-wire anemometers. While data on the specific instrumentation used are not readily available, hot-wire systems tend to have limitations at low velocities, with typical thresholds of approximately 0.1 m/s.

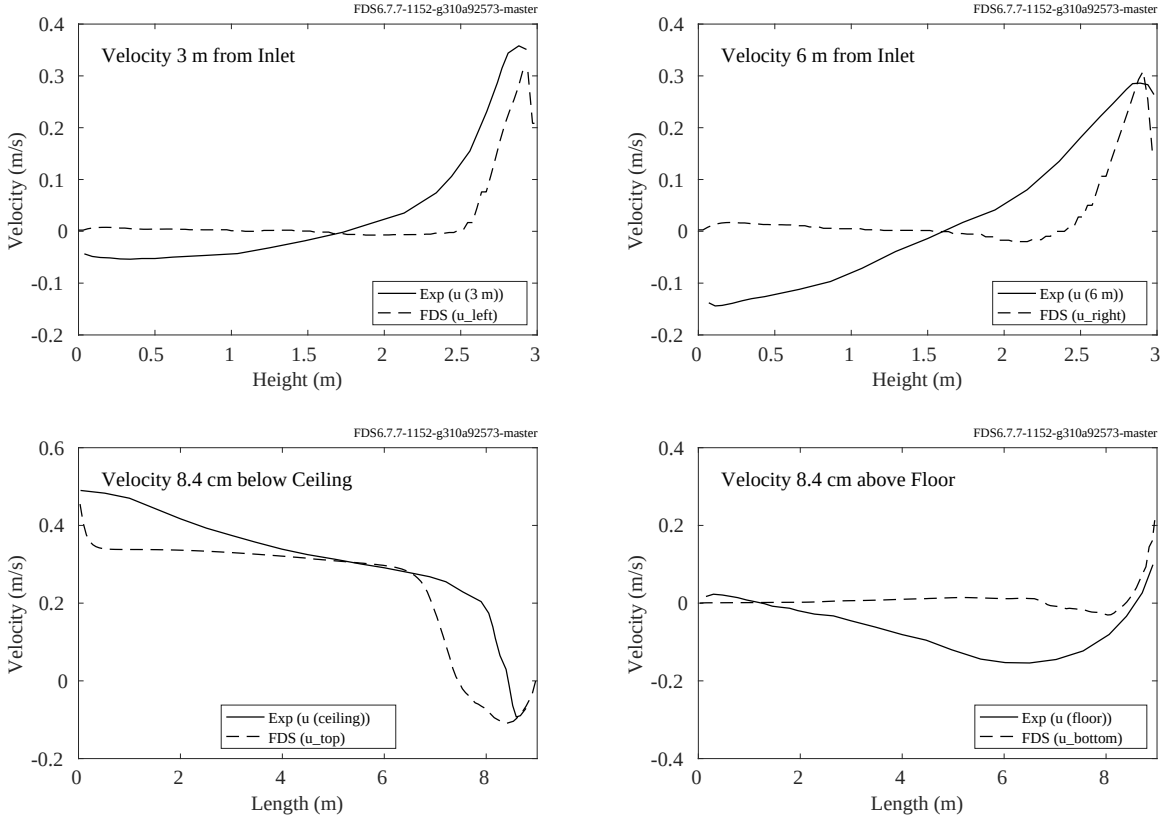

Figure 8.18: Restivo experiment, gas velocity.

8.10 Steckler Compartment Experiments

Steckler et al. [289] mapped the doorway/window flows in 55 compartment fire experiments. The test matrix is presented in Table 3.31. Shown on the following pages are the centerline velocity profiles, compared with model predictions. Off-center profiles are not considered. The vertical spacing of the measurements was approximately 11 cm, with the uppermost velocity probe centered 5.7 cm below the 10 cm thick soffit. The FDS simulations were uniformly gridded with cells of 5 cm on each side. To quantify the difference between prediction and measurement, the maximum outward velocities, which always occurred at the uppermost measurement location, were compared. It has been found that relatively minor changes in the velocity boundary conditions at the edges and bottom of the door soffit can have a noticeable impact on these results.

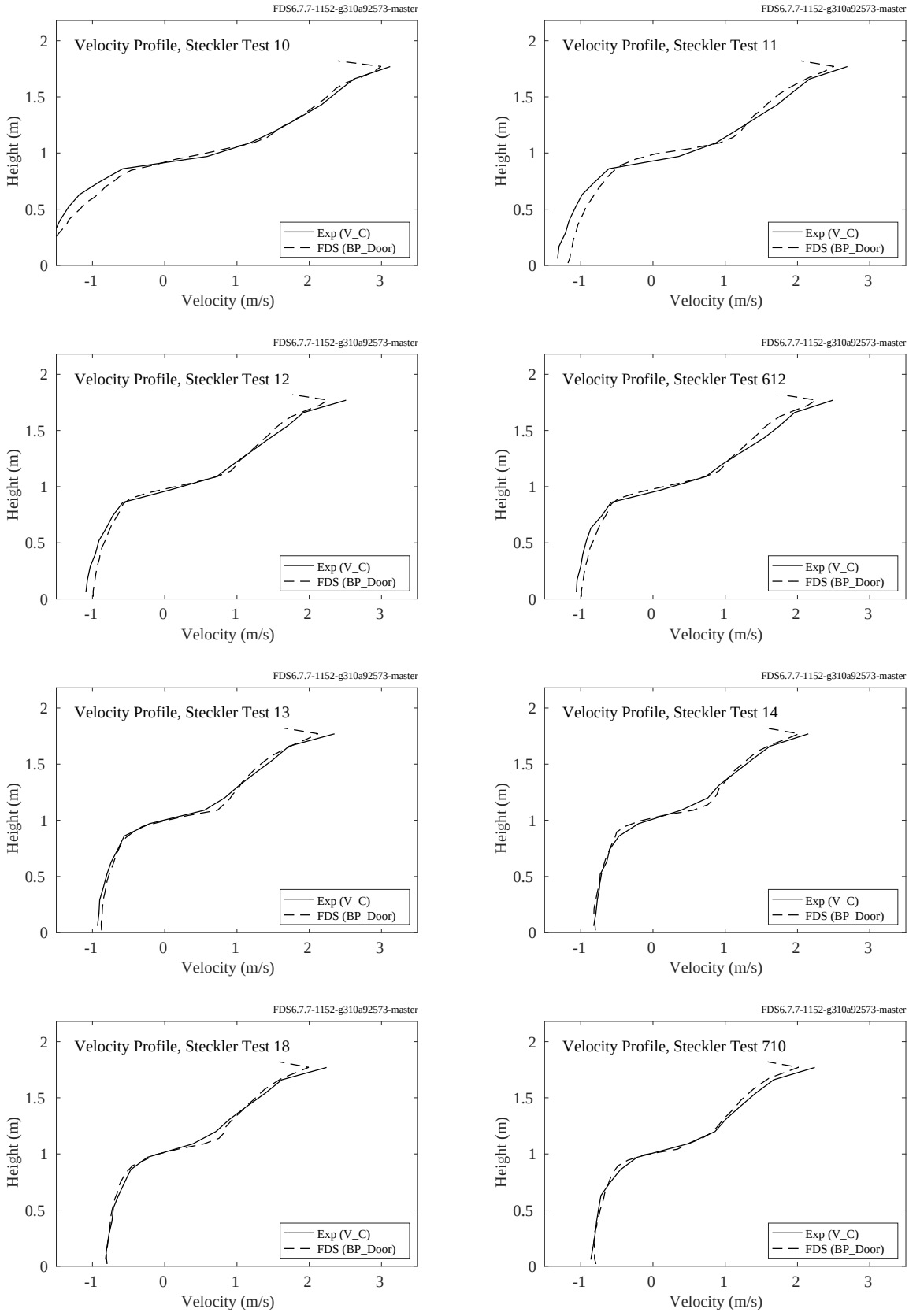

Figure 8.19: Steckler experiments, velocity profiles, Tests 10, 11, 12, 13, 14, 18, 612, 710.

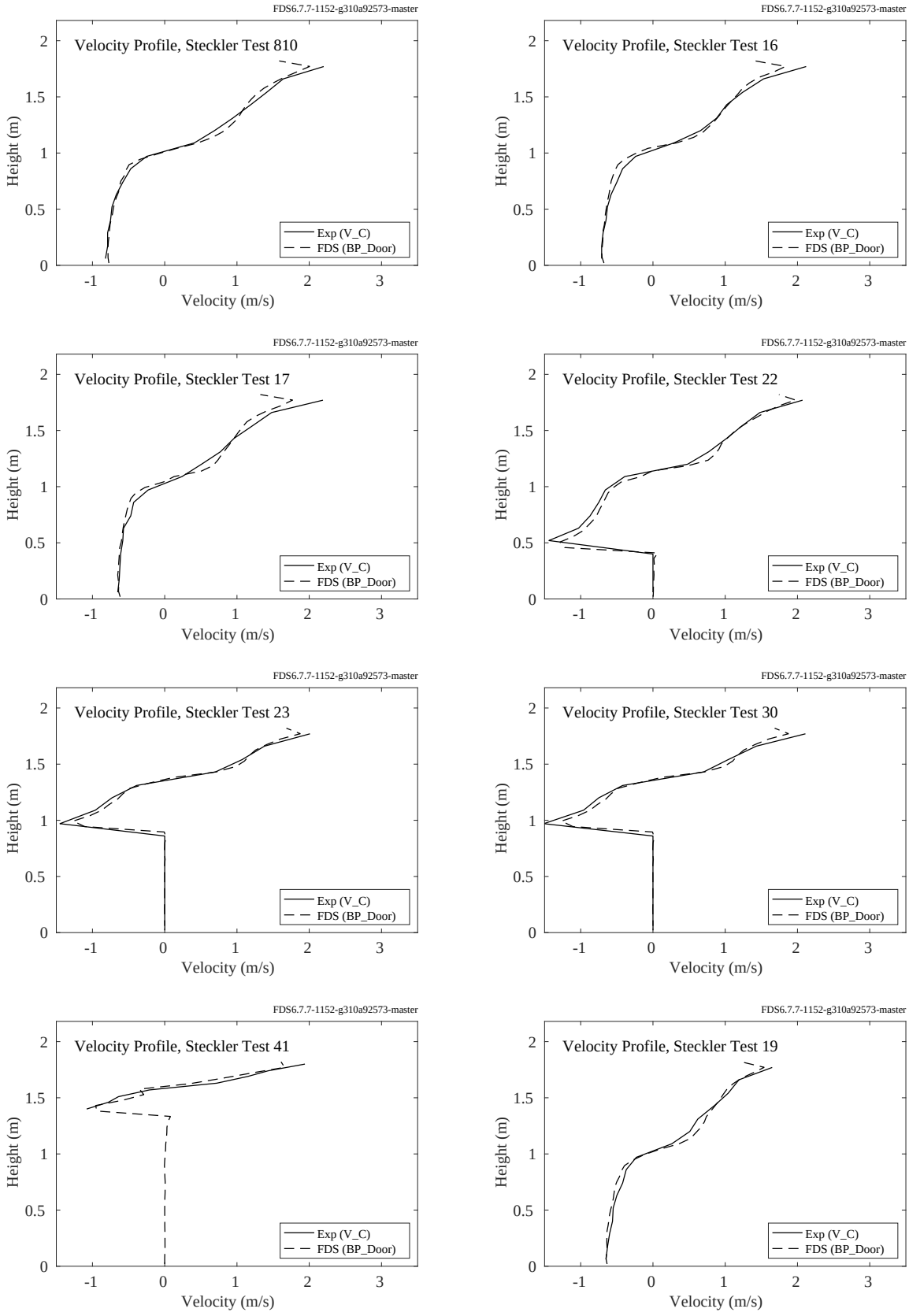

Figure 8.20: Steckler experiments, velocity profiles, Tests 16, 17, 19, 22, 23, 30, 41, 810.

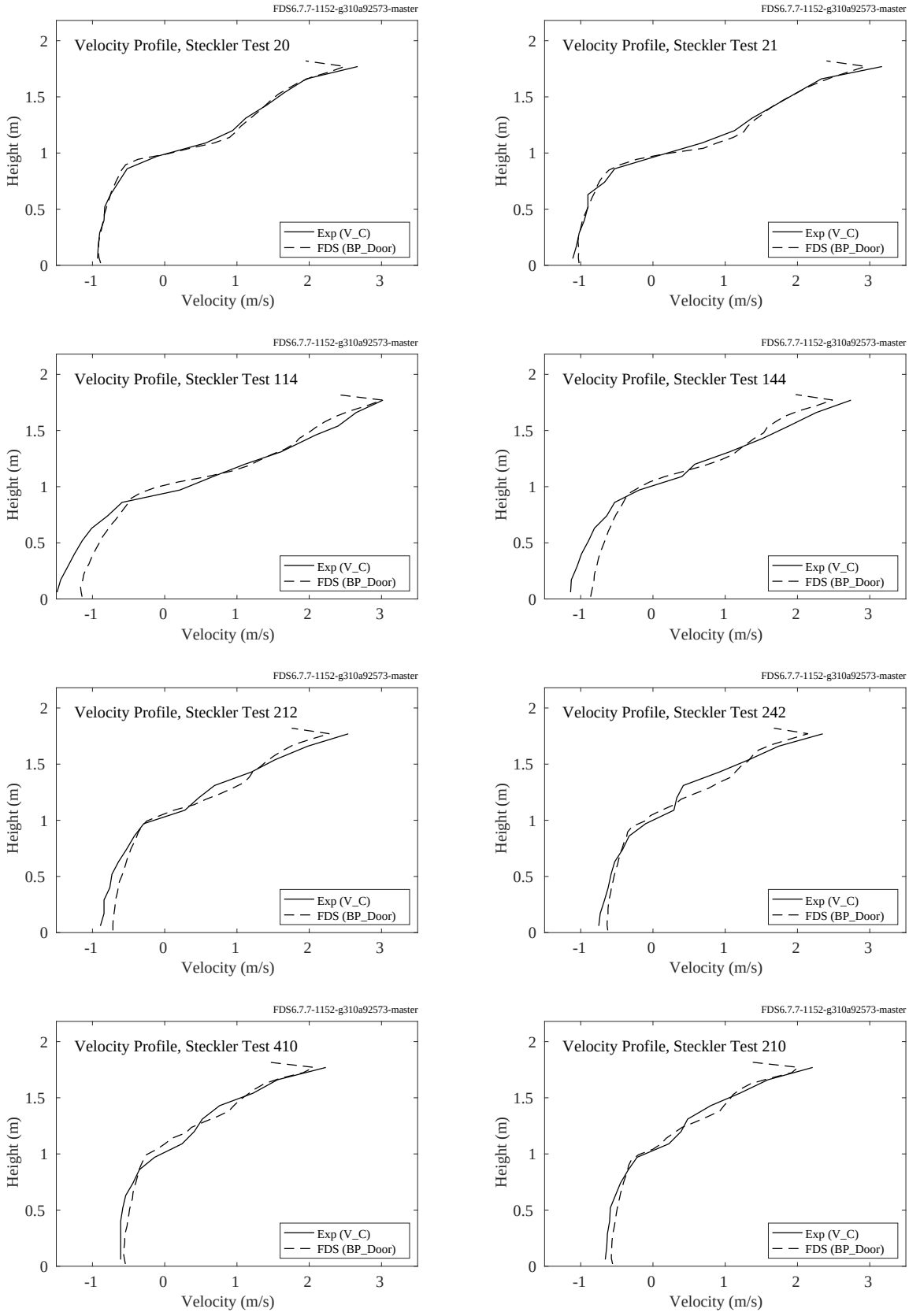

Figure 8.21: Steckler experiments, velocity profiles, Tests 20, 21, 114, 144, 210, 212, 242, 410.

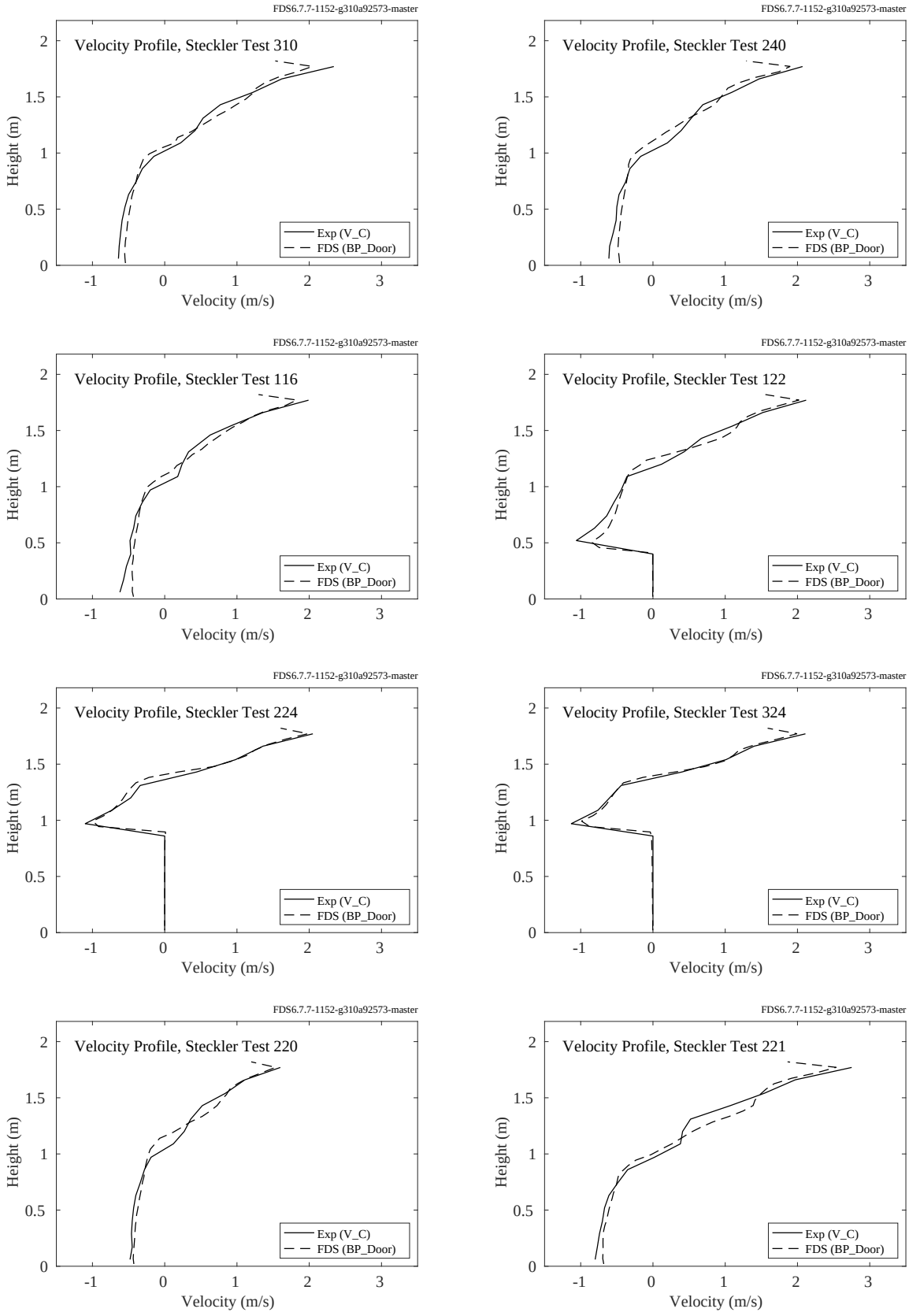

Figure 8.22: Steckler experiments, velocity profiles, Tests 116, 122, 220, 221, 224, 240, 310, 324.

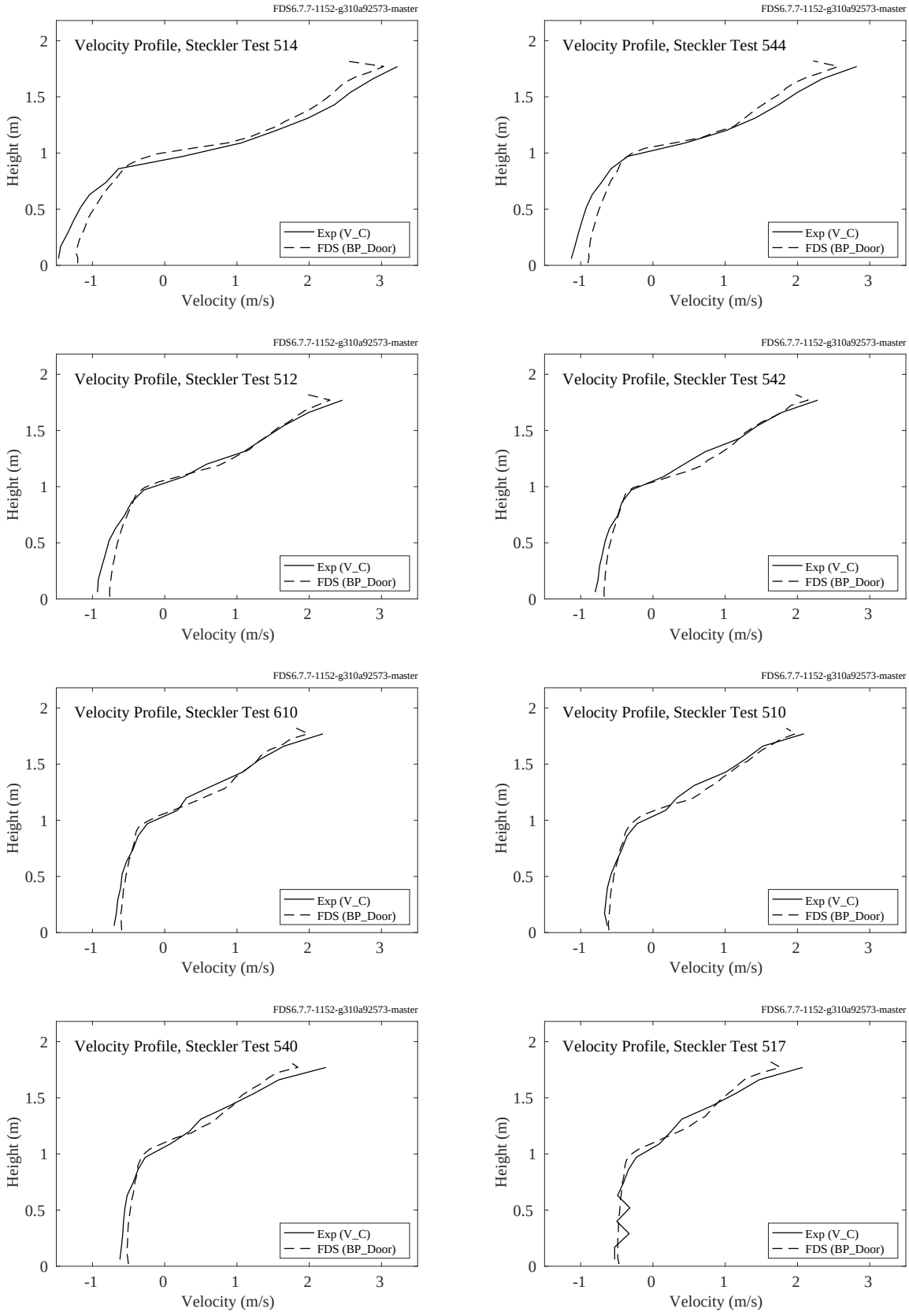

Figure 8.23: Steckler experiments, velocity profiles, Tests 510, 512, 514, 517, 540, 542, 544, 610.

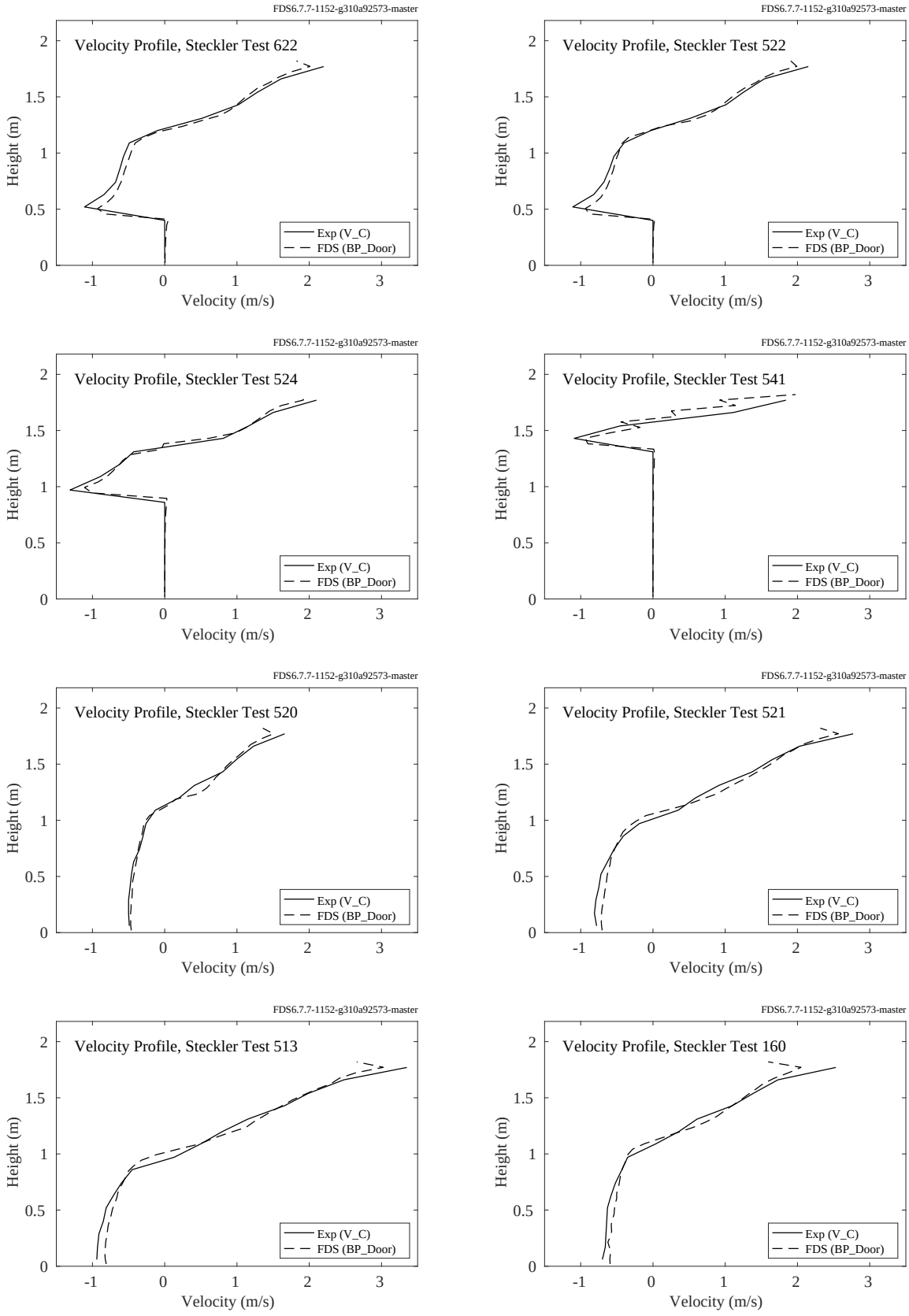

Figure 8.24: Steckler experiments, velocity profiles, Tests 160, 513, 520, 521, 522, 524, 541, 622.

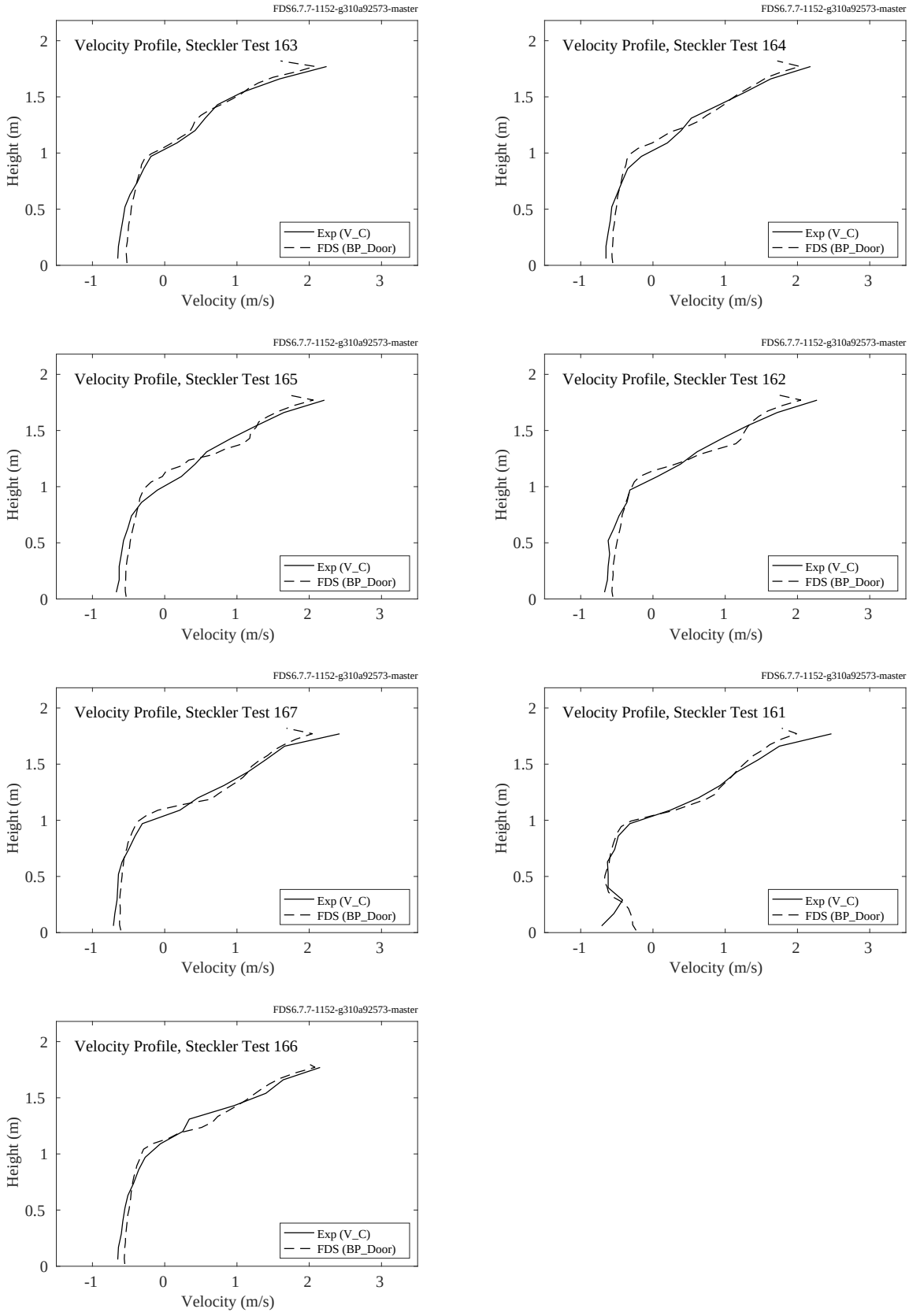

Figure 8.25: Steckler experiments, velocity profiles, Tests 161, 162, 163, 164, 165, 166, 167.

8.11 UL/NIJ House Experiments

Details of the UL/NIJ Experiments are presented in Section 3.77.

Velocity was measured at (typically) five vertical locations in the open windows and doorways of the two houses. The bi-directional probes were evenly spaced through the height of each opening.

In the single story house, the velocity profiles in the front doorway and Window E or F are used for comparison. In the two story house, the profiles in the front doorway and Windows K, L or A are used.

Note that this data has not been included in the summary scatter plot, Fig. 8.43 because it is too noisy to make precise comparisons. It is included here mainly for qualitative comparison.

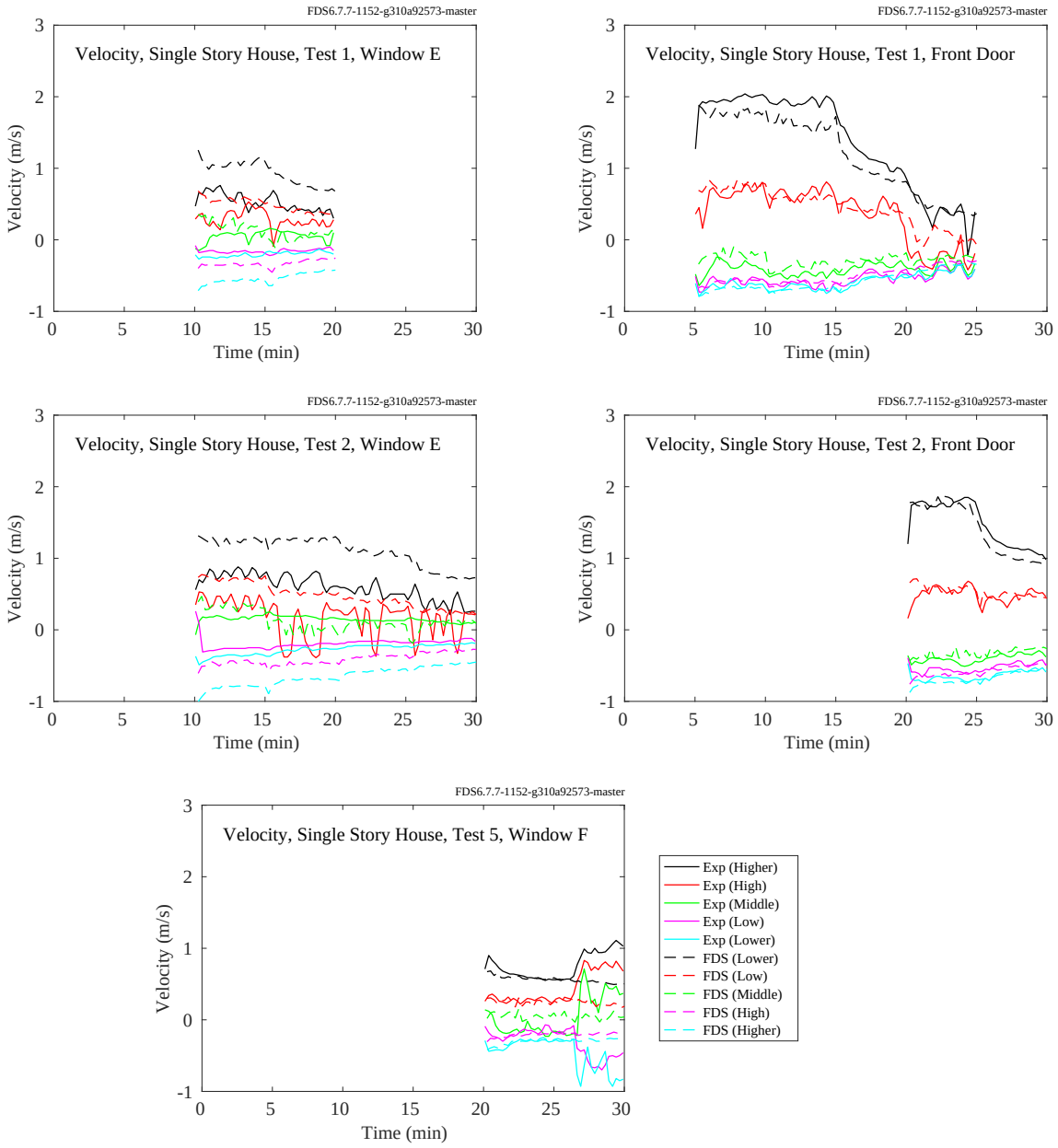

Figure 8.26: UL/NIJ Experiments, Velocity, single story house, Tests 1, 2, and 5.

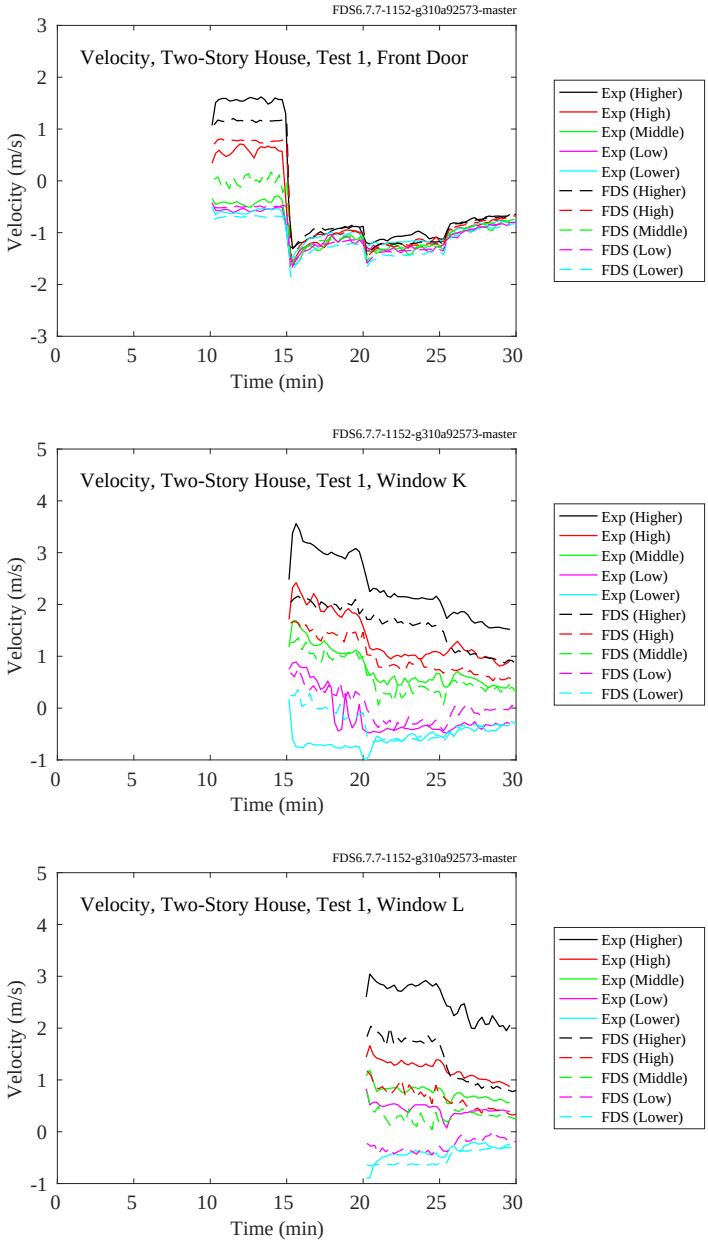

Figure 8.27: UL/NIJ Experiments, Velocity, two-story house, Test 1.

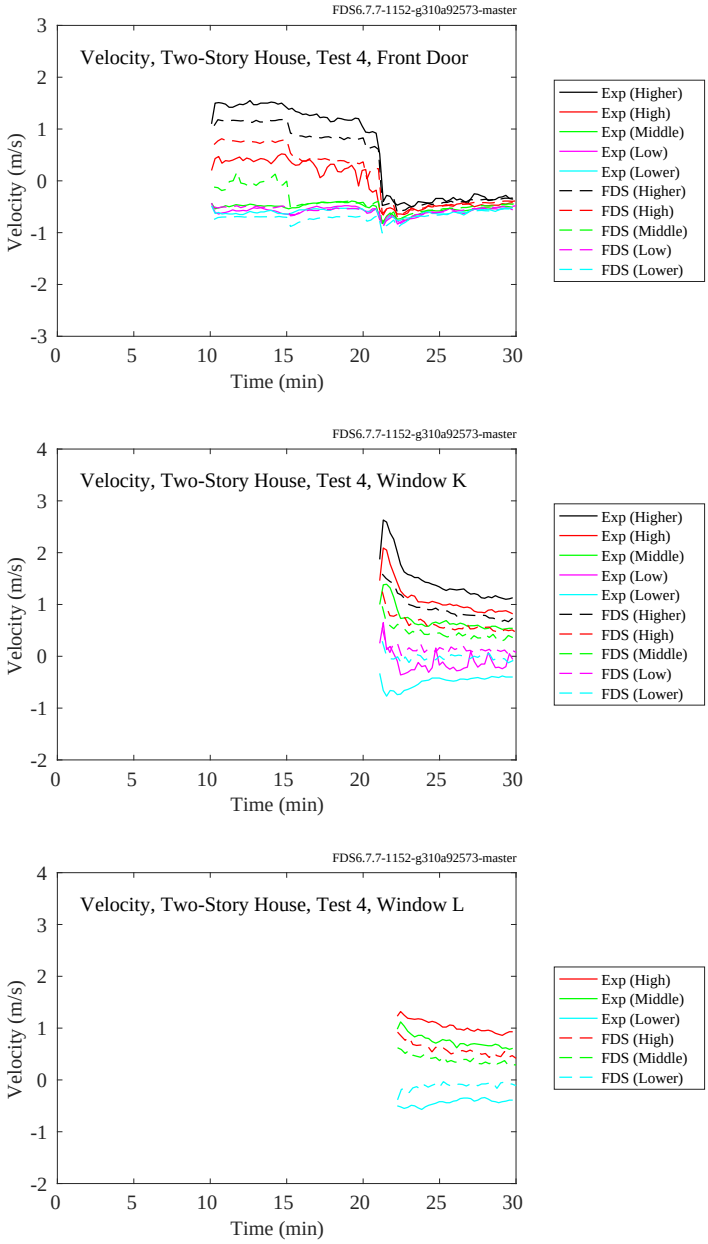

Figure 8.28: UL/NIJ Experiments, Velocity, two-story house, Test 4.

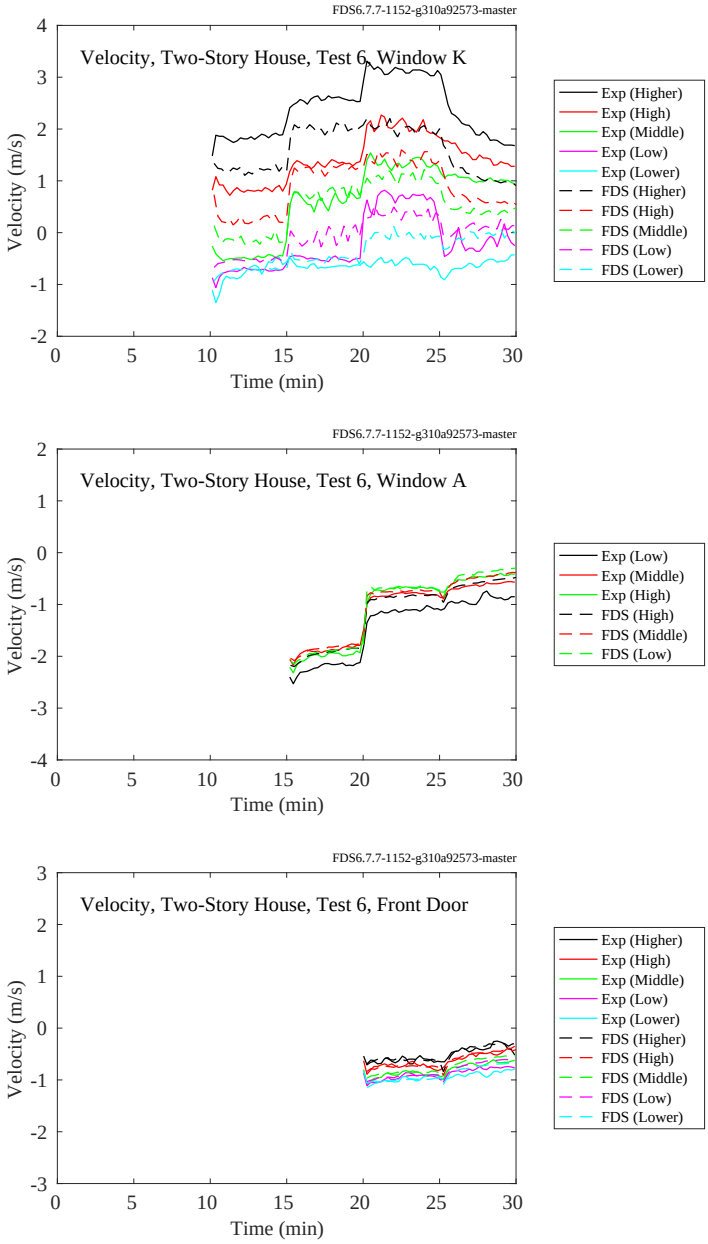

Figure 8.29: UL/NIJ Experiments, Velocity, two-story house, Test 6.

8.12 Waterloo Methanol Pool Fire Experiment

Figures 8.30 through 8.32 display radial profiles of measured and predicted mean (left hand plots) and root mean square (right hand plots) values of the vertical velocity above a 30 cm diameter methanol pool fire. The root mean square of the vertical velocity is given by:

$$\left(\overline{w'w'}\right)^{1/2} = \sqrt{\frac{\sum_{i=1}^{n}(w_i - \overline{w})^2}{n-1}} \tag{8.1}$$

where w_i is the instantaneous value of the vertical velocity and $\overline{w}$ is the average value over 50 s. The profile heights range from 2 cm to 30 cm above the pool surface. Time resolved velocity measurements were performed using a two component laser doppler anemometer.

Figures 8.33 through 8.35 display radial profiles of measured and predicted mean (left hand plots) and root mean square (right hand plots) values of the horizontal velocity.

Figures 8.36 through 8.37 display radial profiles of measured and predicted estimates of the horizontal and vertical velocity covariance:

$$\overline{u'w'} = \frac{\sum_{i=1}^{n}(u_i - \overline{u})(w_i - \overline{w})}{n-1} \tag{8.2}$$

where u_i and w_i are instantaneous values of the horizontal and vertical components of velocity and $\overline{u}$ and $\overline{w}$ are 50 s time averages.

The FDS results are shown at three grid resolutions, 0.5 cm, 1 cm, and 2 cm.

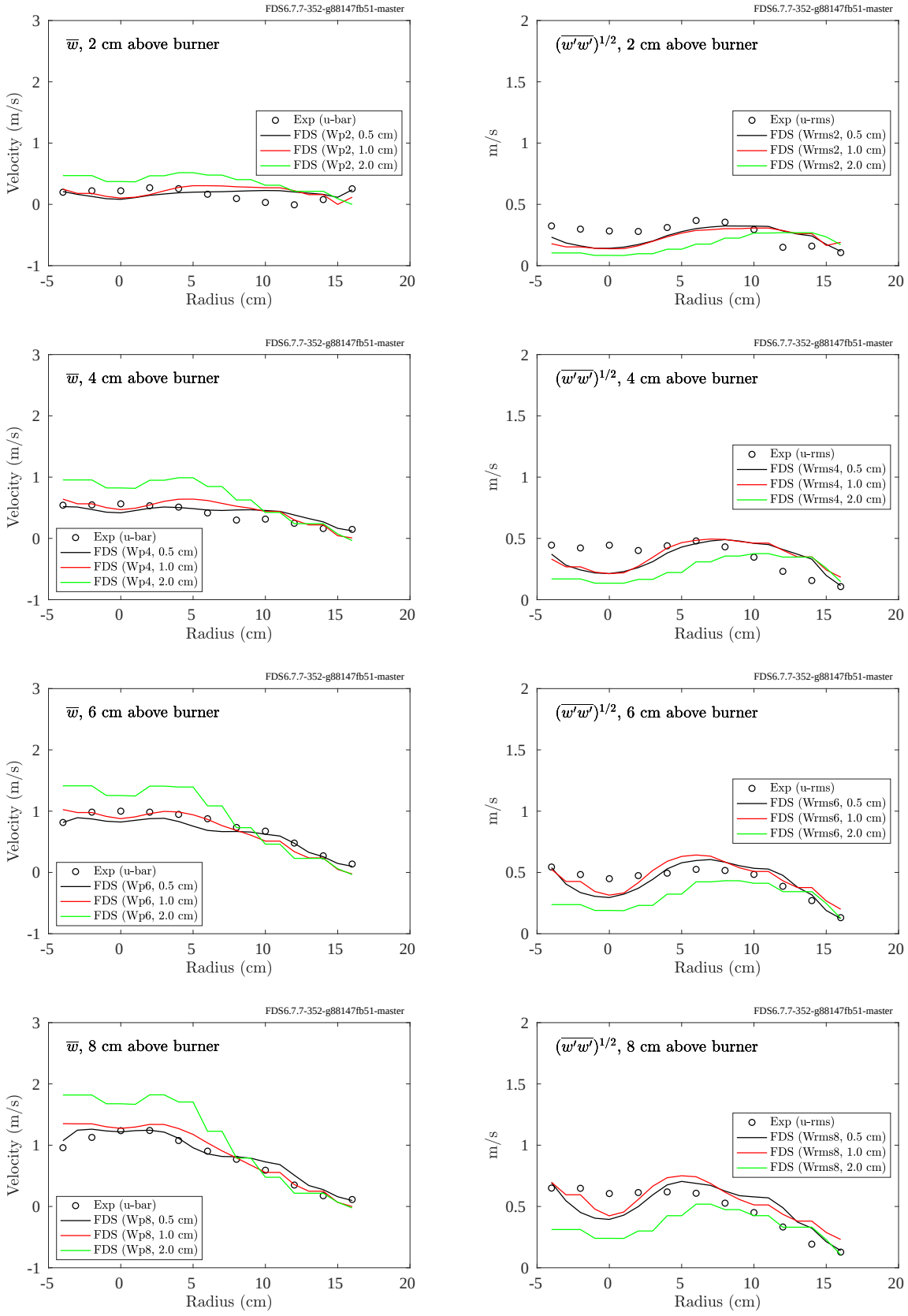

Figure 8.30: Waterloo Methanol, radial profiles of mean and rms vertical velocity, 2 cm to 8 cm above the burner.

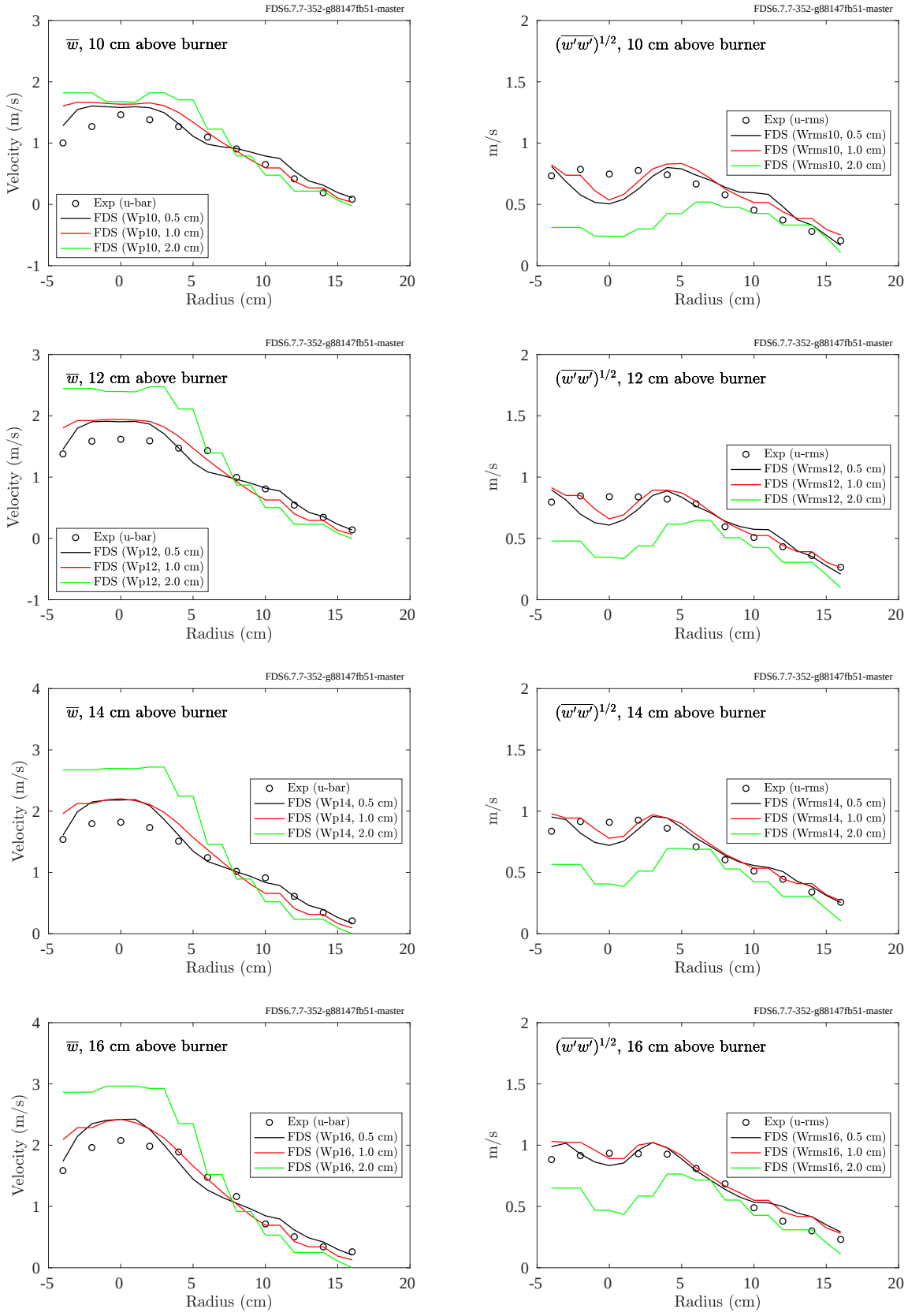

Figure 8.31: Waterloo Methanol, radial profiles of mean and rms vertical velocity, 10 cm to 16 cm above the burner.

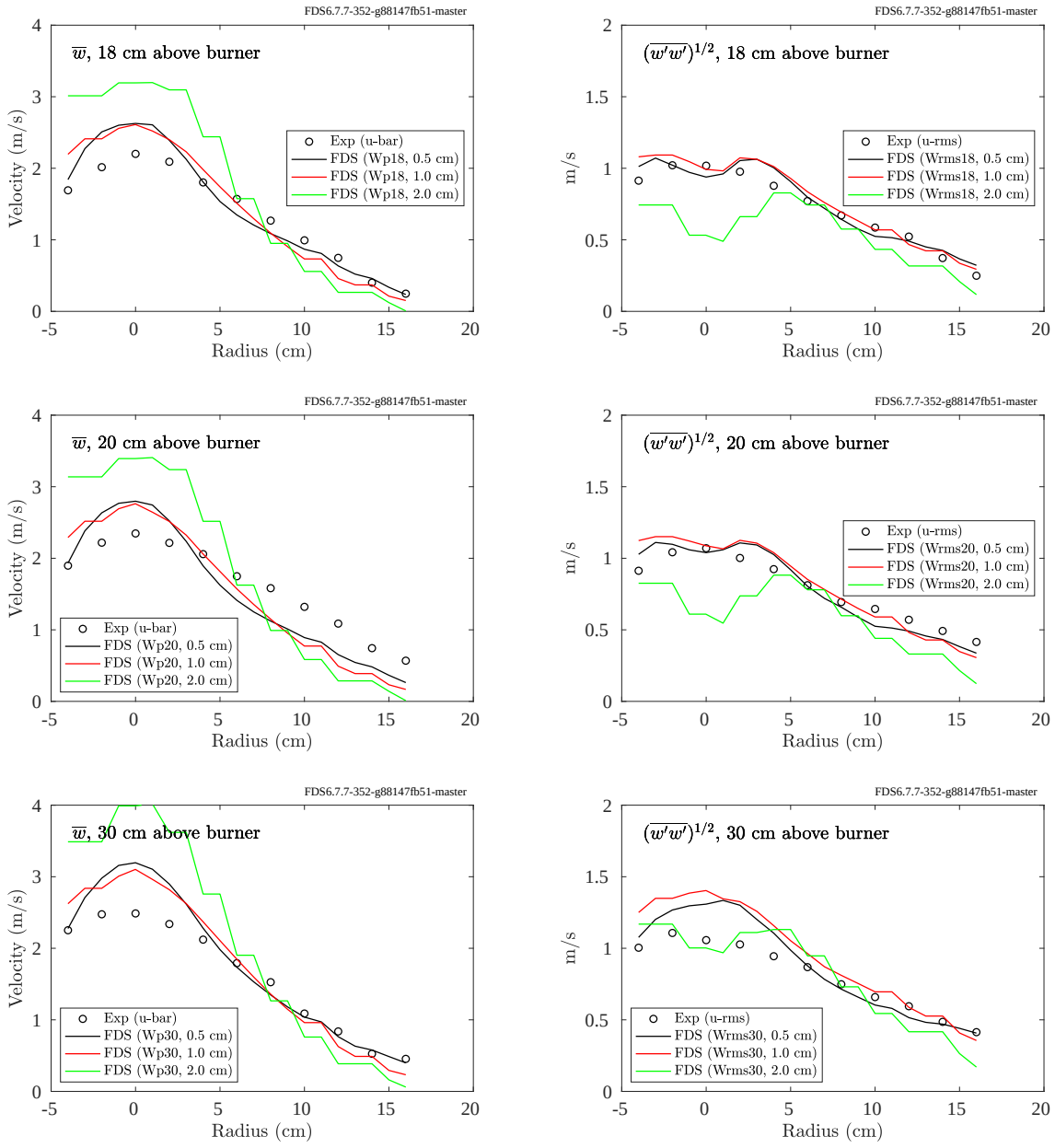

Figure 8.32: Waterloo Methanol, radial profiles of mean and rms vertical velocity, 18 cm to 30 cm above the burner.

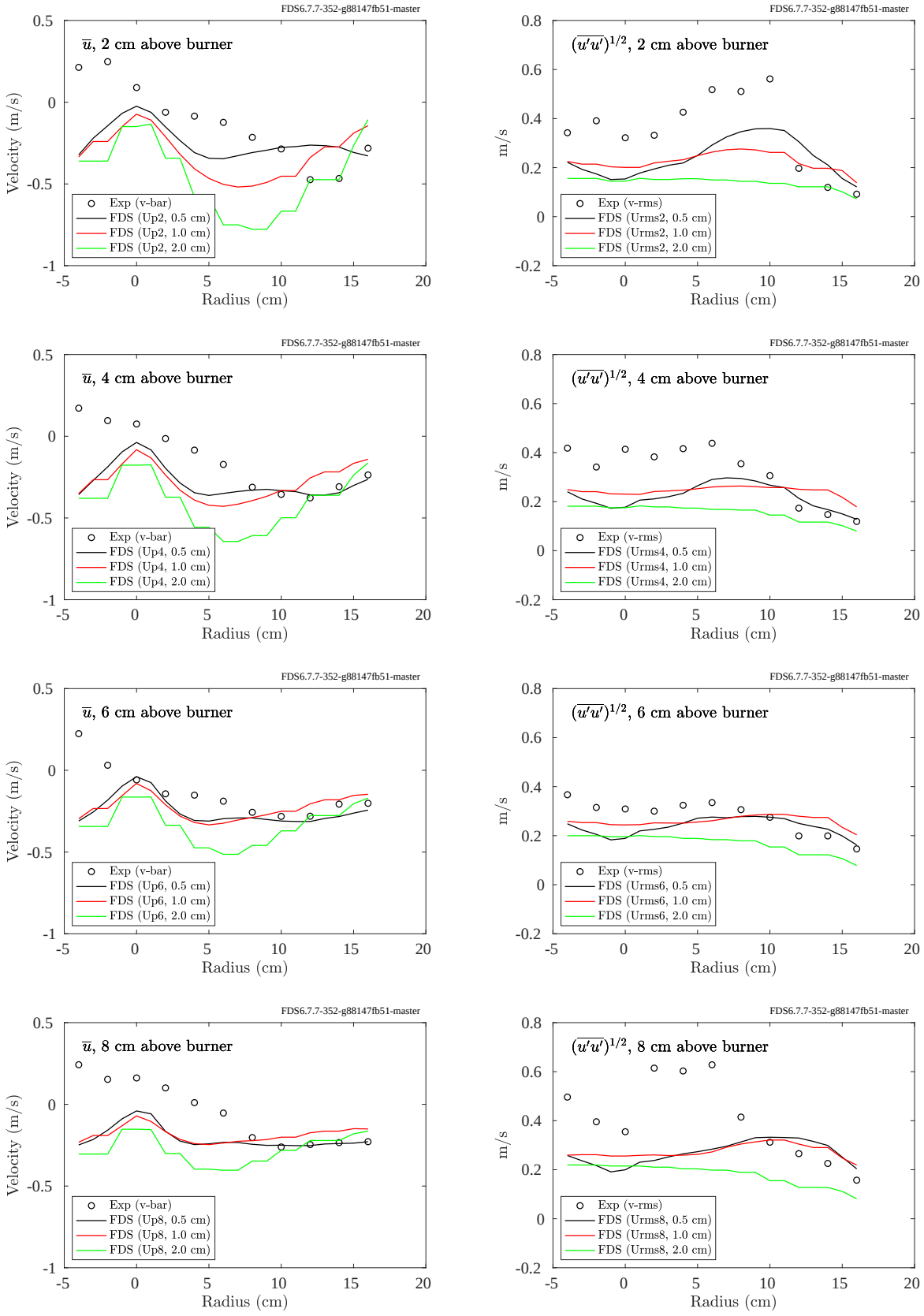

Figure 8.33: Waterloo Methanol, radial profiles of mean and rms horizontal velocity, 2 cm to 8 cm above the burner.

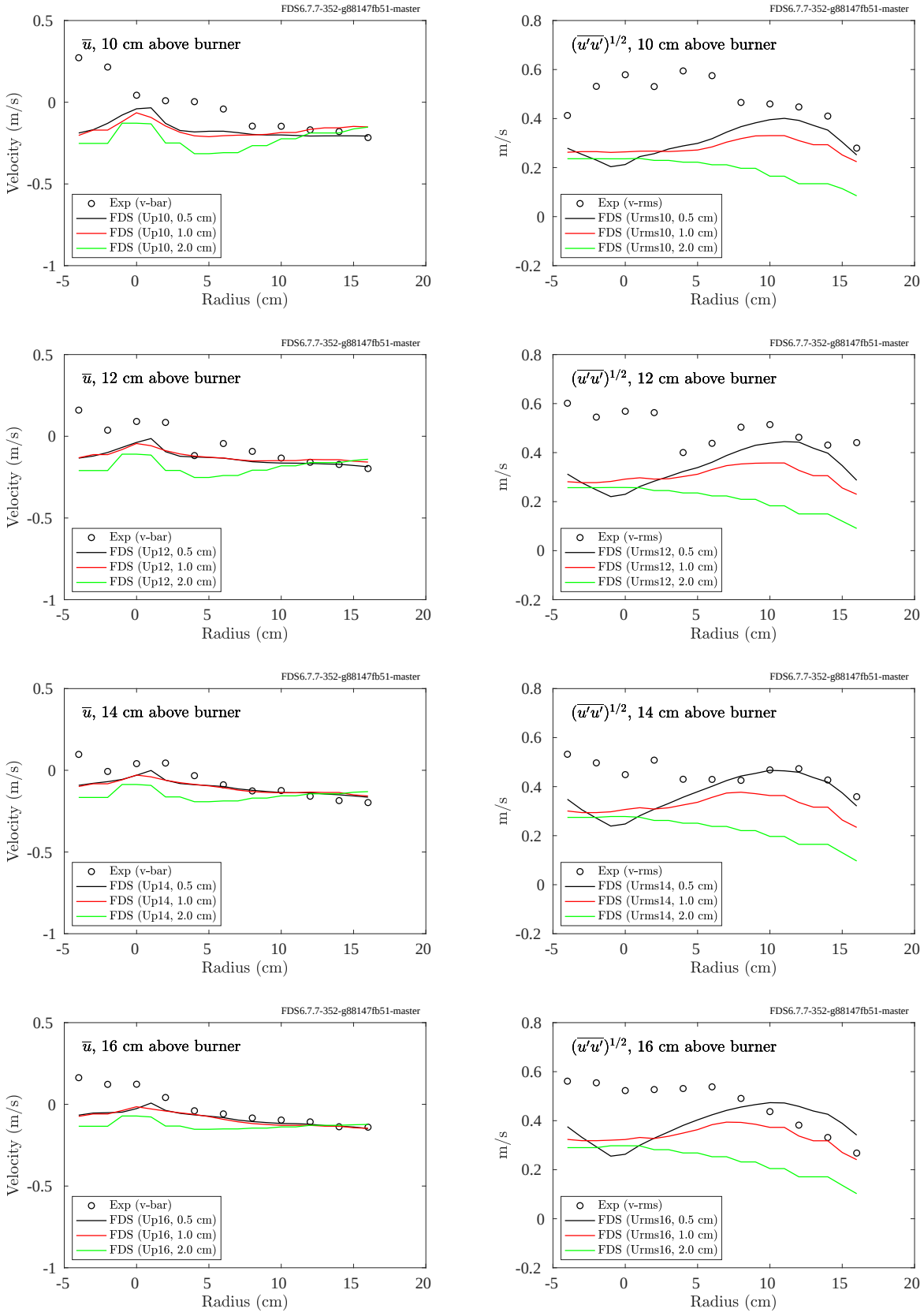

Figure 8.34: Waterloo Methanol, radial profiles of mean and rms horizontal velocity, 10 cm to 16 cm above the burner.

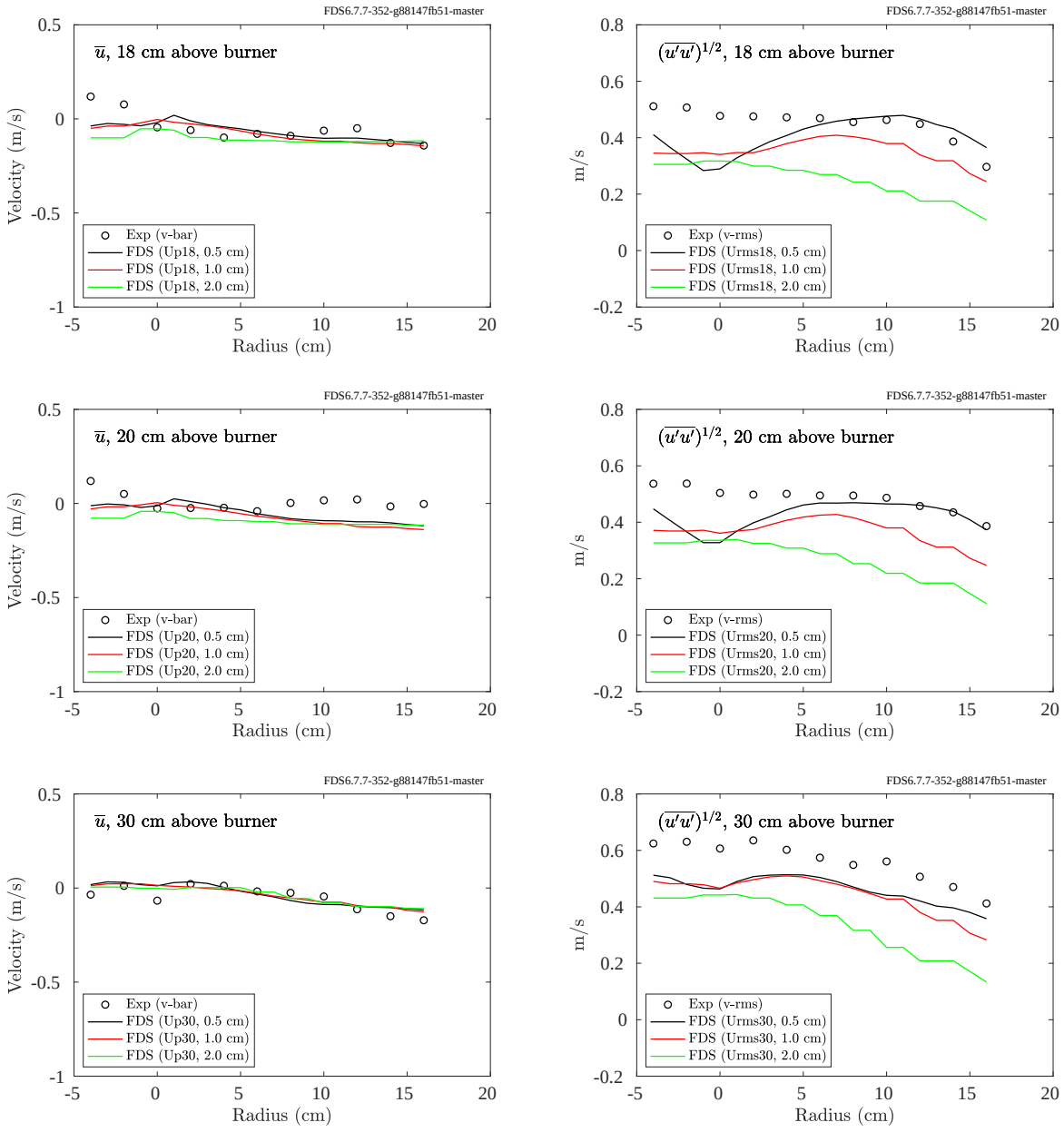

Figure 8.35: Waterloo Methanol, radial profiles of mean and rms horizontal velocity, 18 cm to 30 cm above the burner.

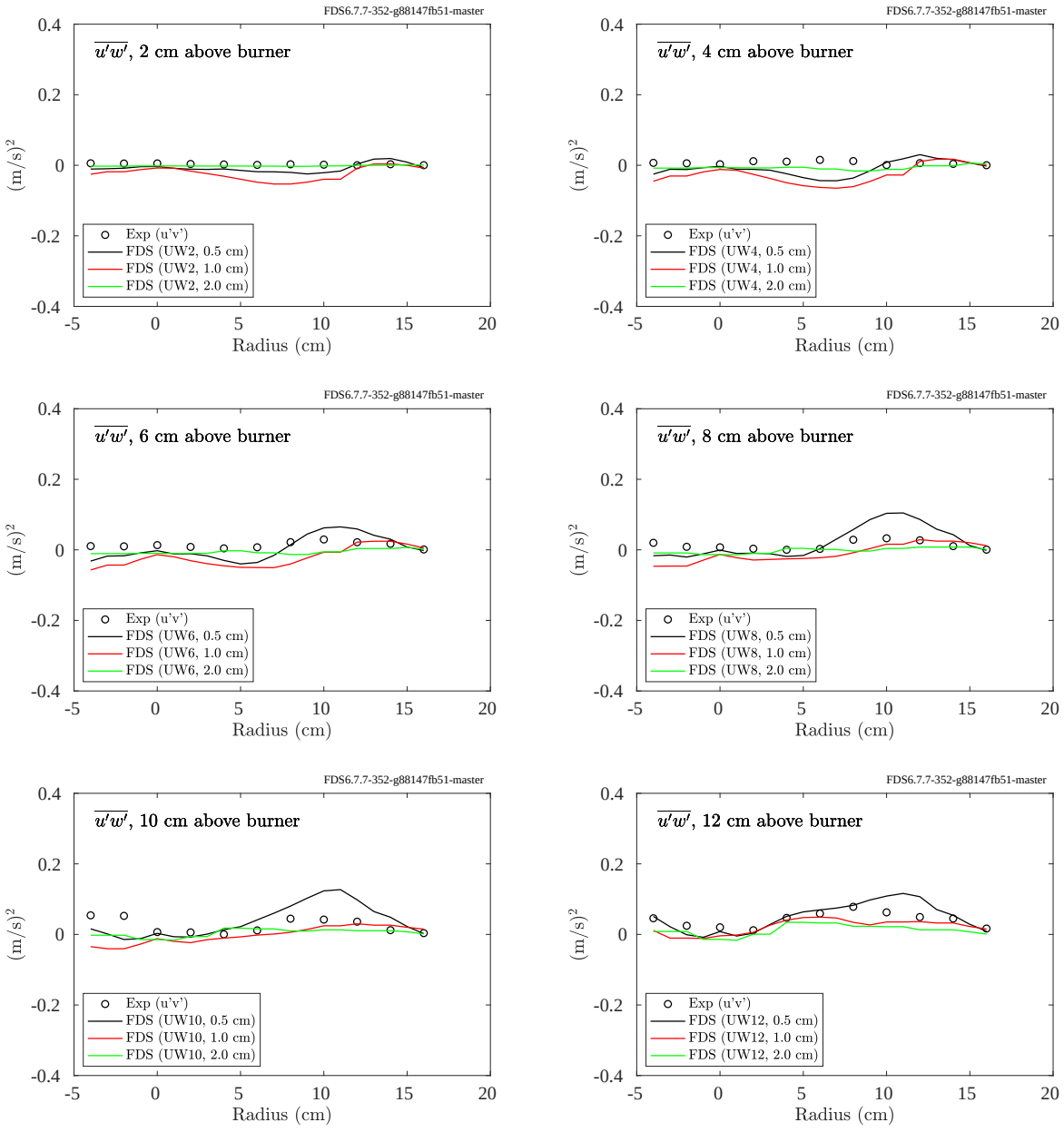

Figure 8.36: Waterloo Methanol, radial profiles of $\overline{u'w'}$, 2 cm to 12 cm above the burner.

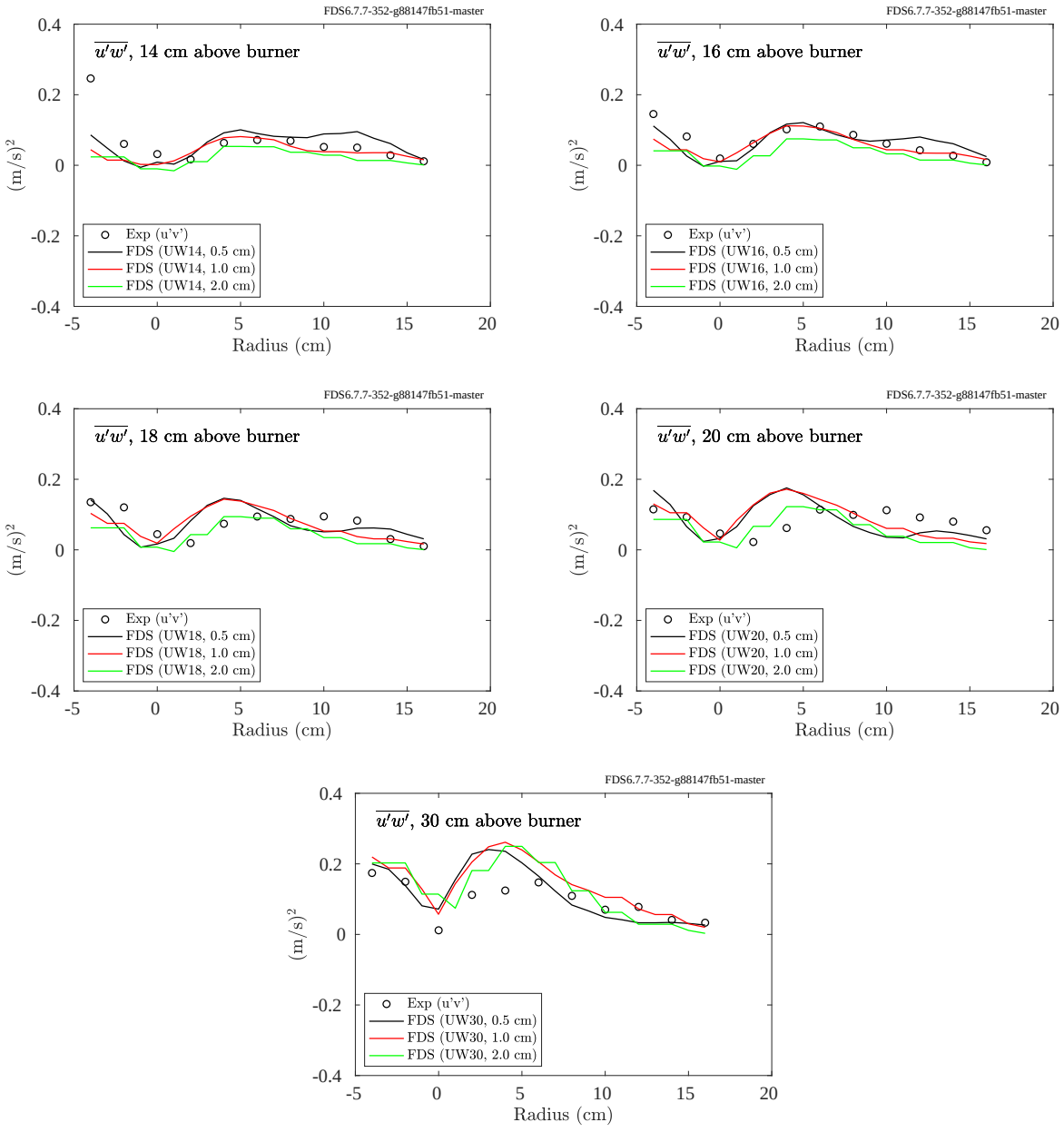

Figure 8.37: Waterloo Methanol, radial profiles of $\overline{u'w'}$, 14 cm to 30 cm above the burner.

8.13 WTC Experiments

Bi-directional probes were positioned inside two of the four inlet openings and three of the four outlet openings. The locations are shown in Fig. 8.38. Exact dimensions are given in Ref. [69].

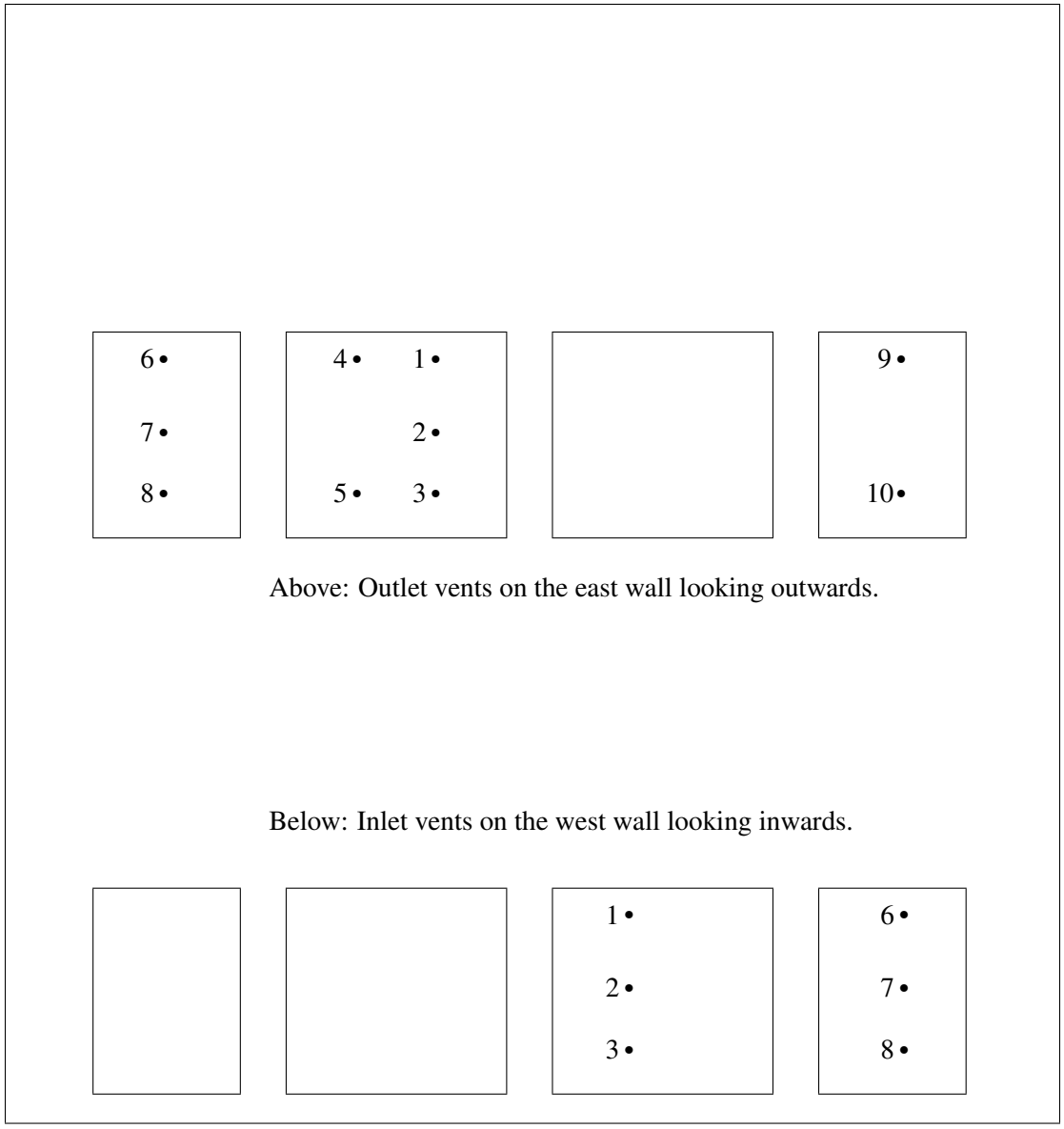

Figure 8.38: Layout of the bi-directional probes in the inlet (west wall) and outlet (east wall) vents, WTC Experiments.

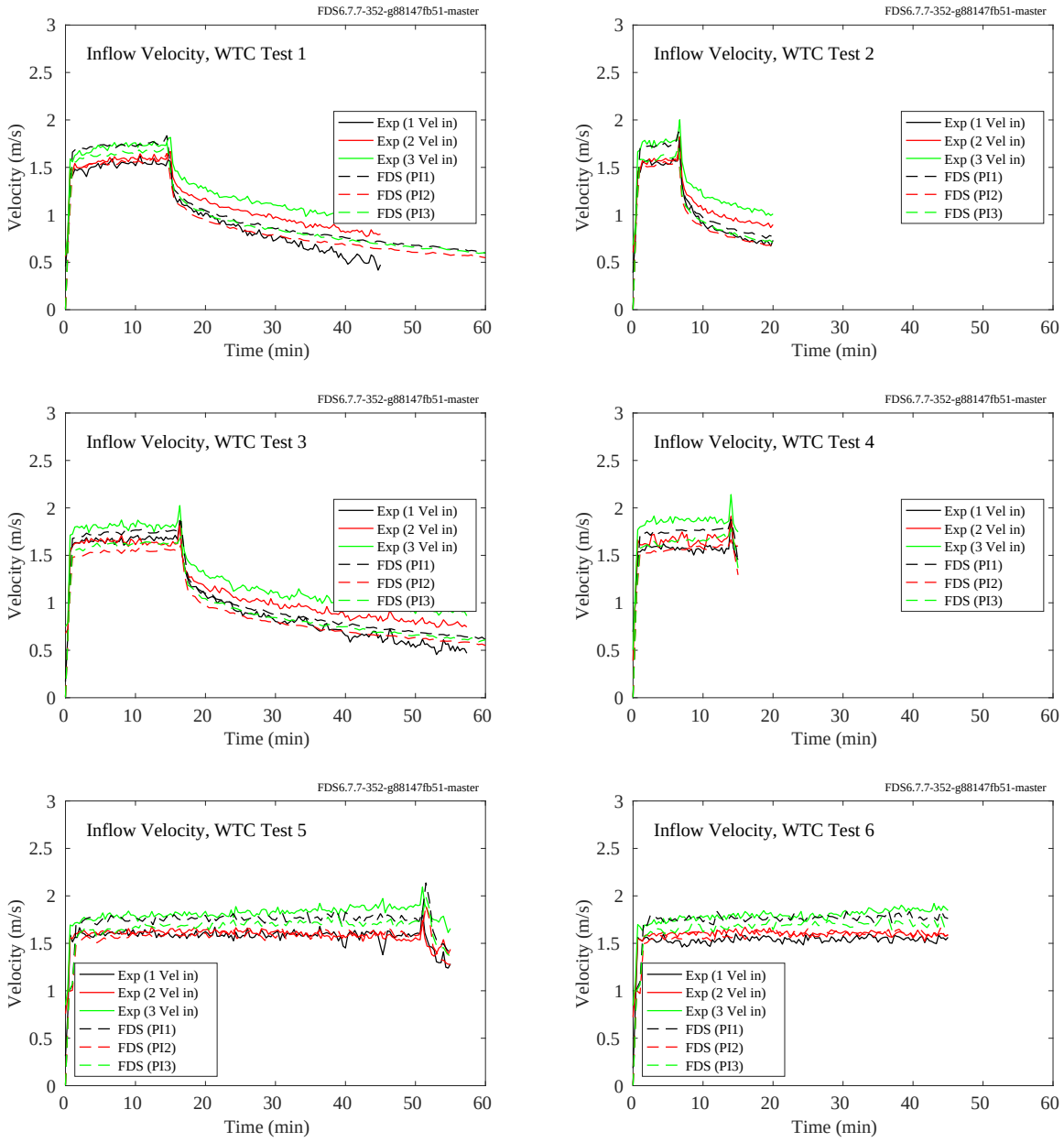

Figure 8.39: WTC experiments, inlet velocity, Points 1-3.

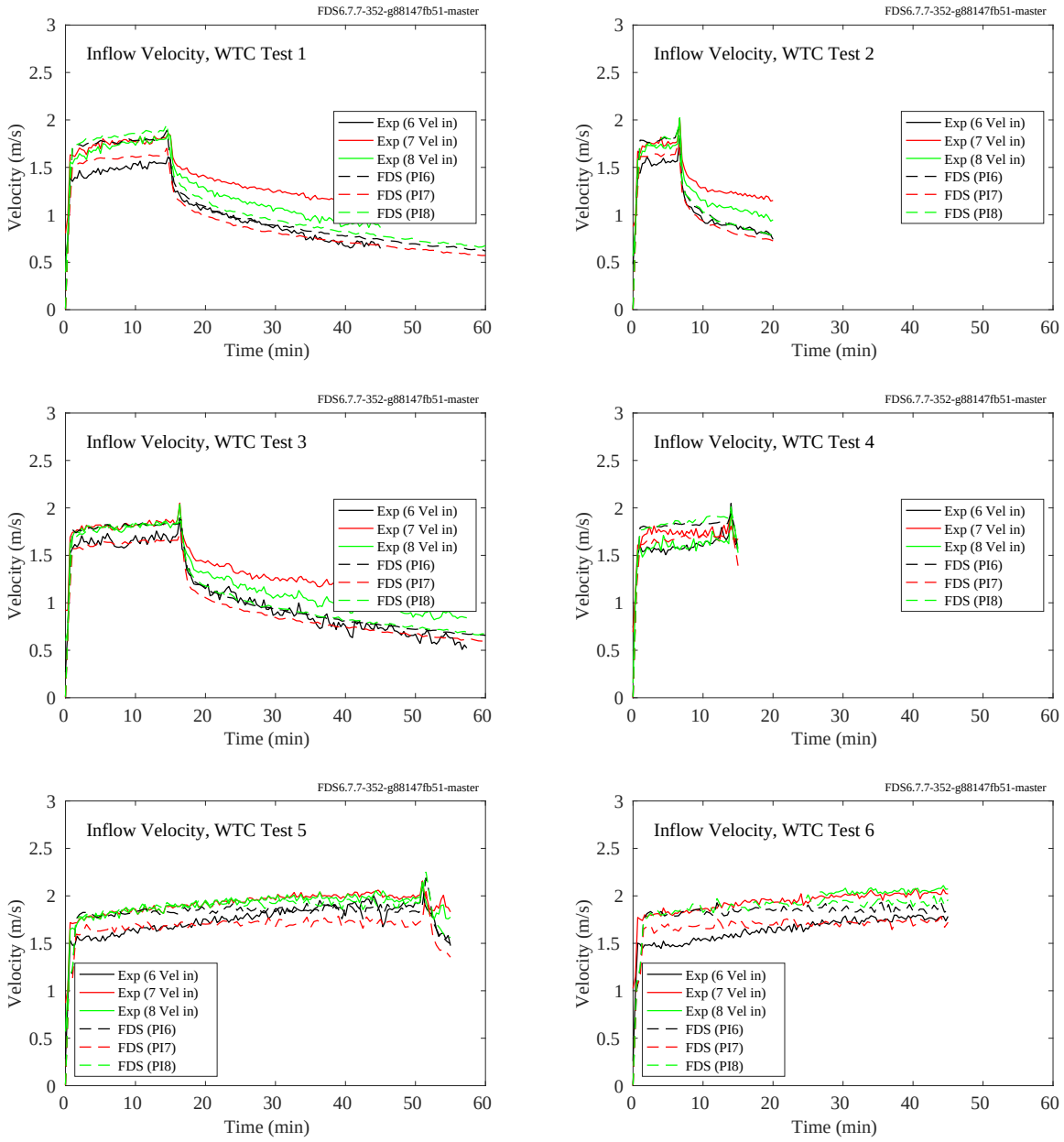

Figure 8.40: WTC experiments, inlet velocity, Points 6-8.

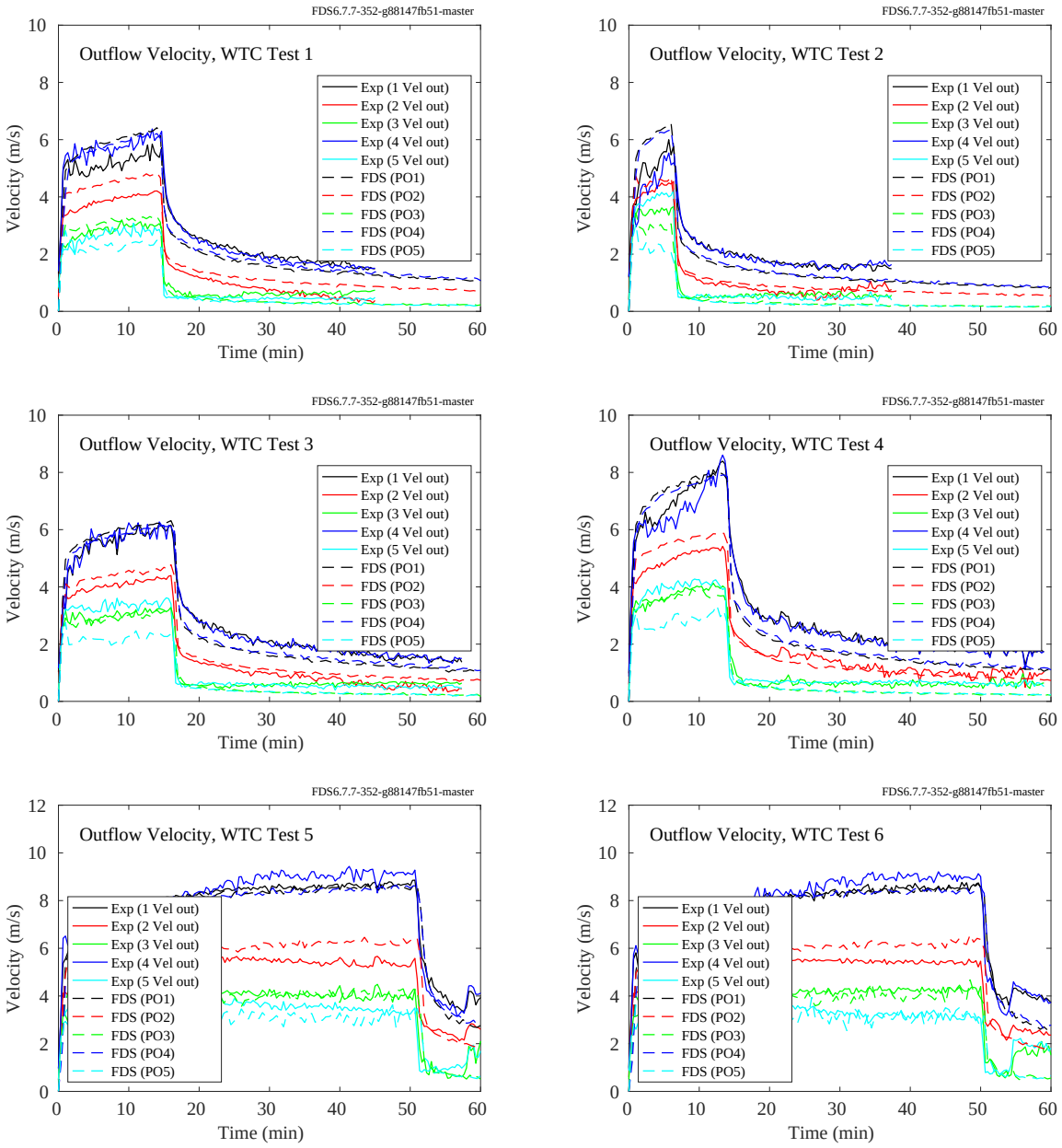

Figure 8.41: WTC experiments, outlet velocity, Points 1-5.

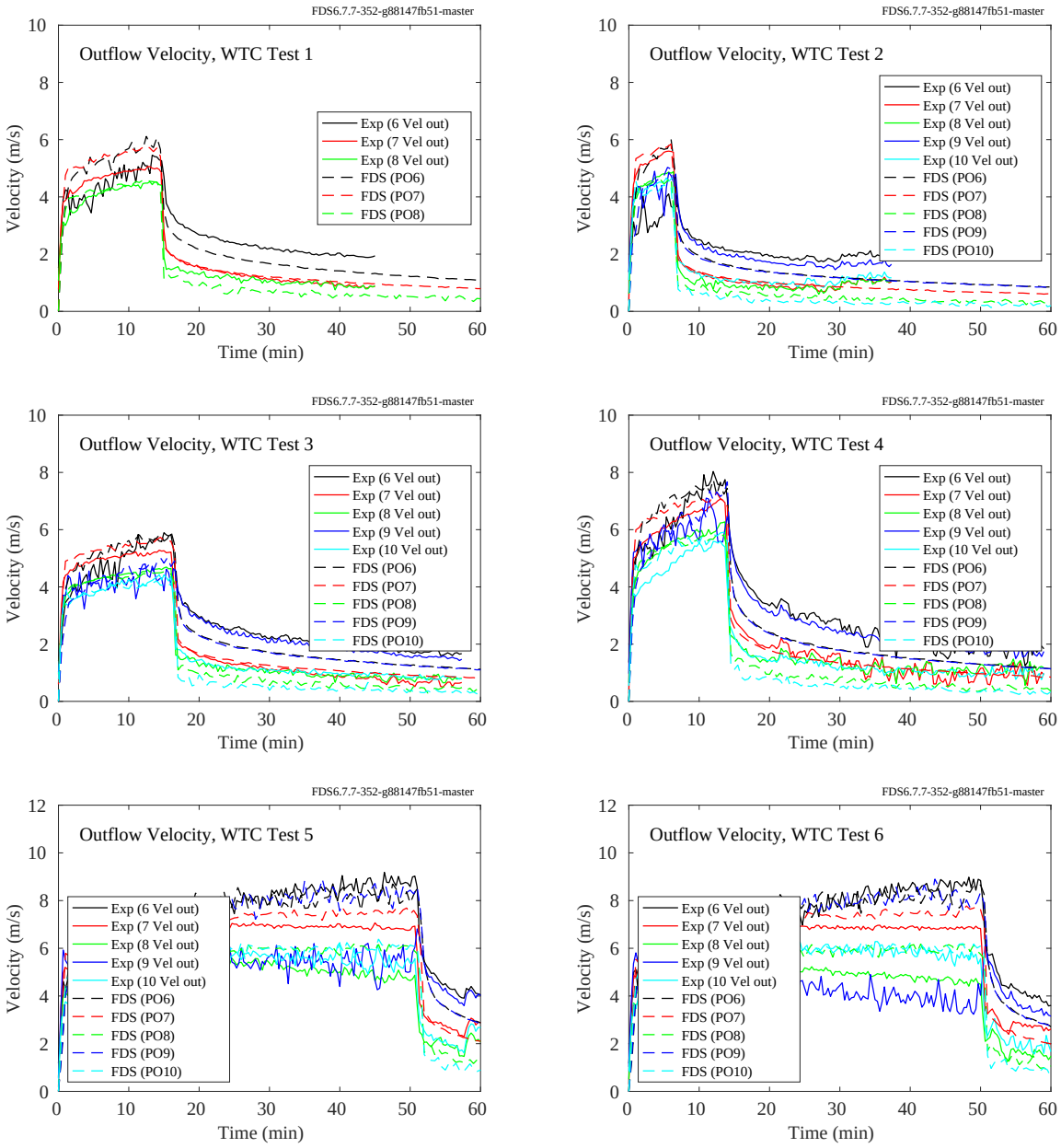

Figure 8.42: WTC experiments, outlet velocity, Points 6-10.

8.14 Summary of Velocity Predictions

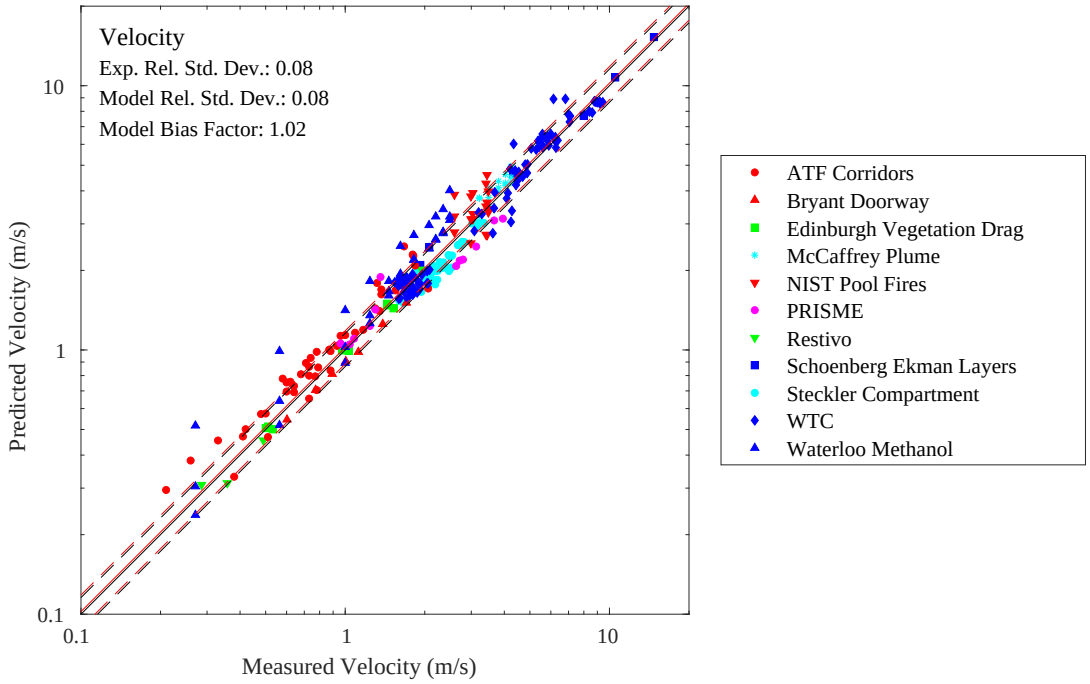

Figure 8.43: Summary of comparisons of predicted and measured maximum velocities.

8.15 Wu Bakar Tunnel Experiments

This section contains the results of the simulations of the Wu and Bakar experiments described in Section 3.74. Five simulations are conducted. In each, the heat release rate is stepped up from its lowest reported value to its highest, each step lasting 20 s. For each of the eight heat release rates, the tunnel velocity is set to the reported critical velocity. Temperature readings along the ceiling indicate where the smoke layer temperature drops below 30 °C, 10 °C above ambient. This is taken as the extent of the back-layer. Using an empirical correlation for the normalized back-layer length, L_b^*, developed by Li et al. [338]

$$L_b^* = \begin{cases} 18.5\ln(0.81\,Q^{*1/3}/V^*) & Q^* \le 0.15 \\ 18.5\ln(0.43/V^*) & Q^* > 0.15 \end{cases} \tag{8.3}$$

where

$$L_b^* = \frac{L_b}{\bar{H}} \quad ; \quad \bar{H} = \frac{4A}{P} \quad ; \quad Q^* = \frac{Q}{\rho_\infty c_p T_\infty \sqrt{g\bar{H}^5}} \quad ; \quad V^* = \frac{V}{\sqrt{g\bar{H}}} \tag{8.4}$$

the FDS-predicted critical velocity, V_{FDS}, can be estimated from the measured, V_{exp}, via

$$V_{FDS} \approx V_{exp}\left(1 + \frac{L_{b,FDS}}{18.5\bar{H}}\right) \tag{8.5}$$

Note that $\bar{H}$ is known as the *hydraulic diameter* which takes into consideration the tunnel's cross-sectional area, A, and perimeter, P. For a square cross section, the hydraulic diameter equals the tunnel height.

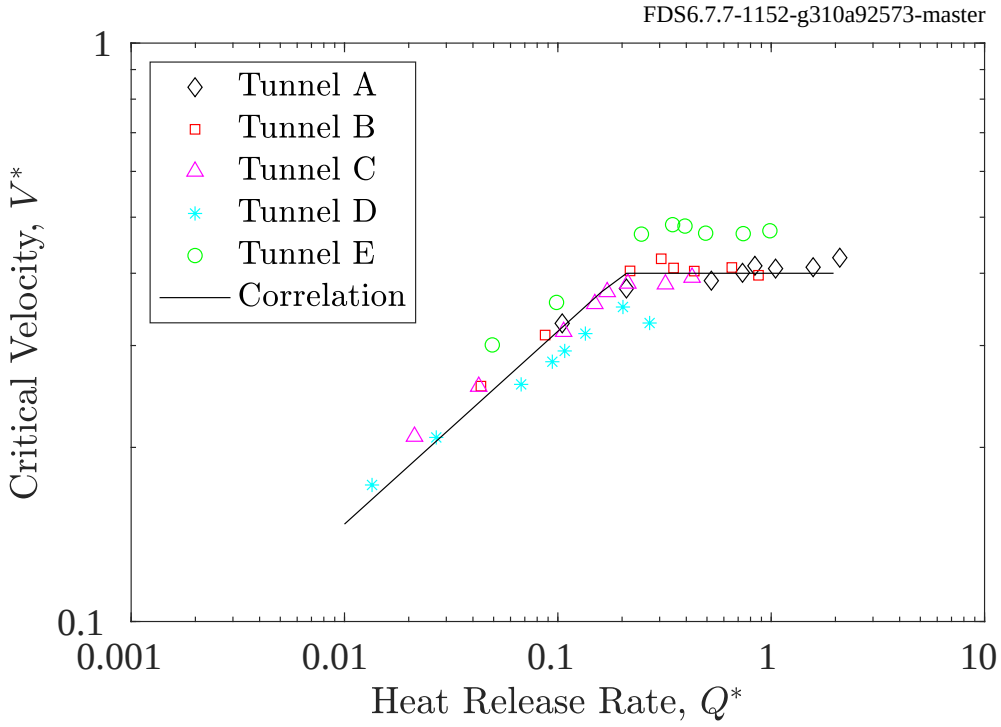

Figure 8.44: Wu and Bakar critical velocity correlation with FDS results added.

The non-dimensionalized critical velocity predictions are plotted against the non-dimensionalized HRR in Fig. 8.44. The solid line in the figure is the correlation developed by Wu and Bakar [291]:

$$V^* = \begin{cases} 0.4\,(Q^*/0.2)^{1/3} & Q^* \leq 0.2 \\ 0.4 & Q^* > 0.2 \end{cases} \tag{8.6}$$

Chapter 9

Gas Species and Smoke

For most applications, FDS uses a single step, mixing-controlled combustion model. The products of combustion are "lumped" together and tracked as a single gas mixture. These products include CO_2, H_2O, CO, and soot. However, in some cases, the combustion is incomplete due to a lack of oxygen. In others, a multiple-step reaction scheme is used to predict the production of CO.

9.1 Major Combustion Products, O_2 and CO_2

For any hydrocarbon fuel, the major combustion products are oxygen and carbon dioxide. Accurate predictions of these gases requires knowledge of the chemical composition of the fuel and an accurate transport algorithm for the combustion products.

9.1.1 DelCo Trainers

Oxygen and carbon dioxide measurements were made at several locations in the one and two level DelCo training structures. See Section 3.17 for their exact locations.

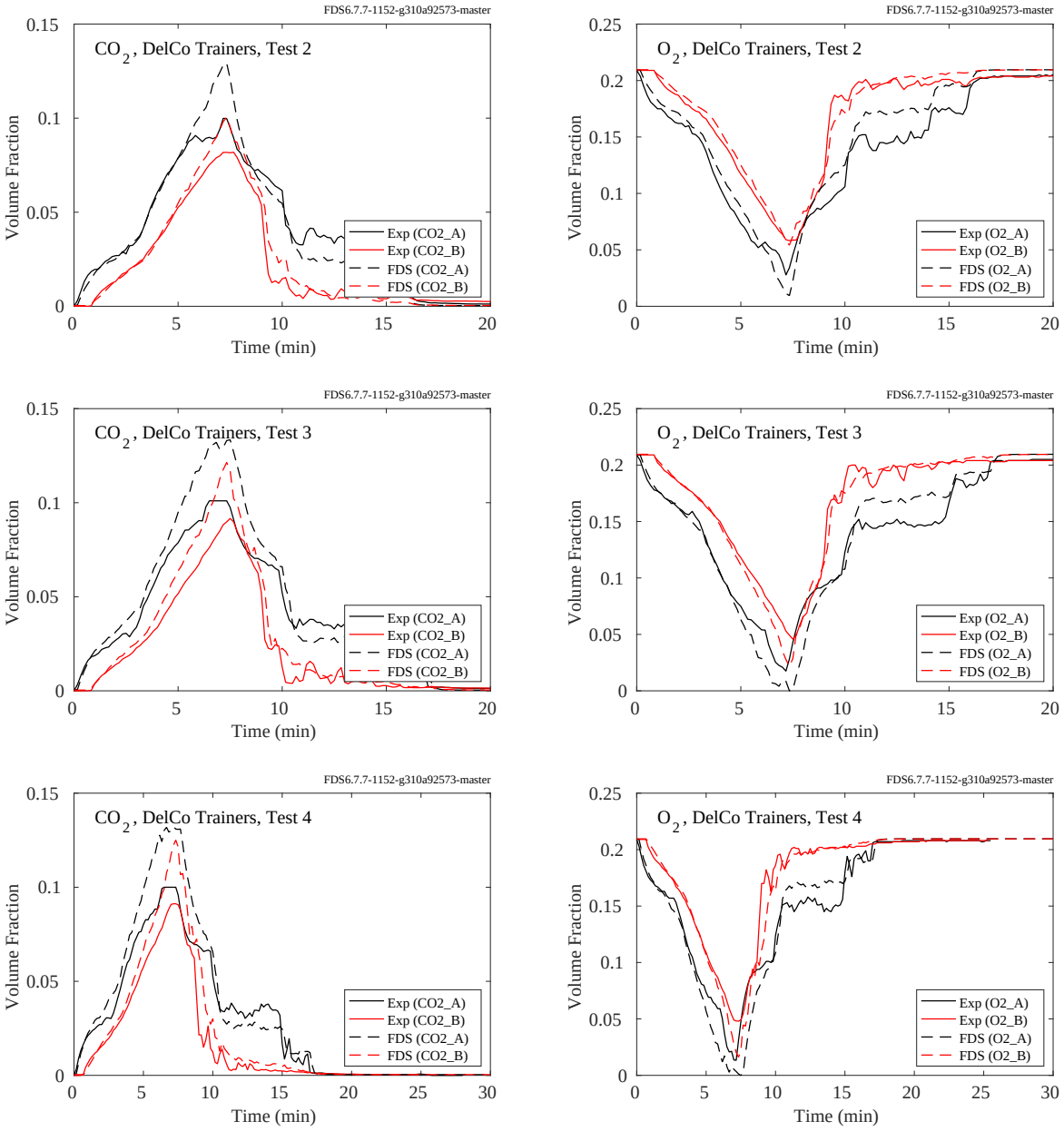

Figure 9.1: DelCo Trainers, CO_2 and O_2 concentration, Tests 2-4.

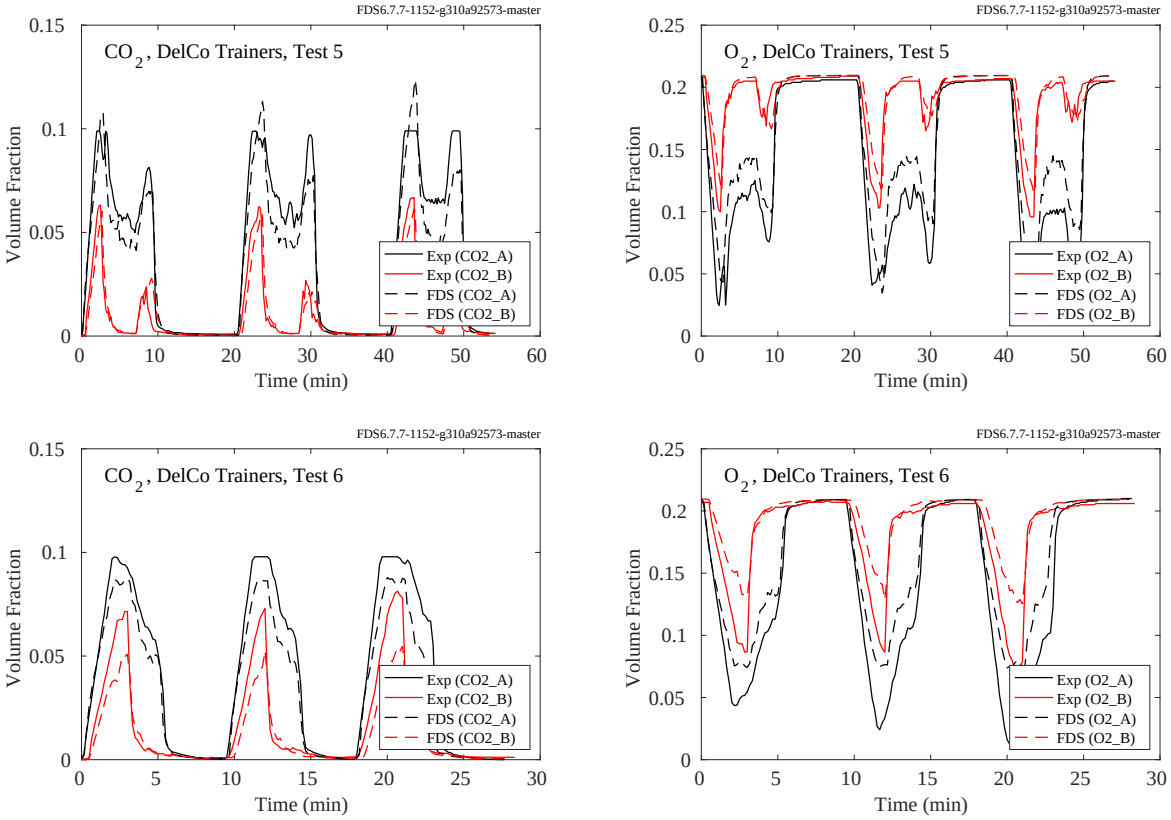

Figure 9.2: DelCo Trainers, CO_2 and O_2 concentration, Tests 5-6.

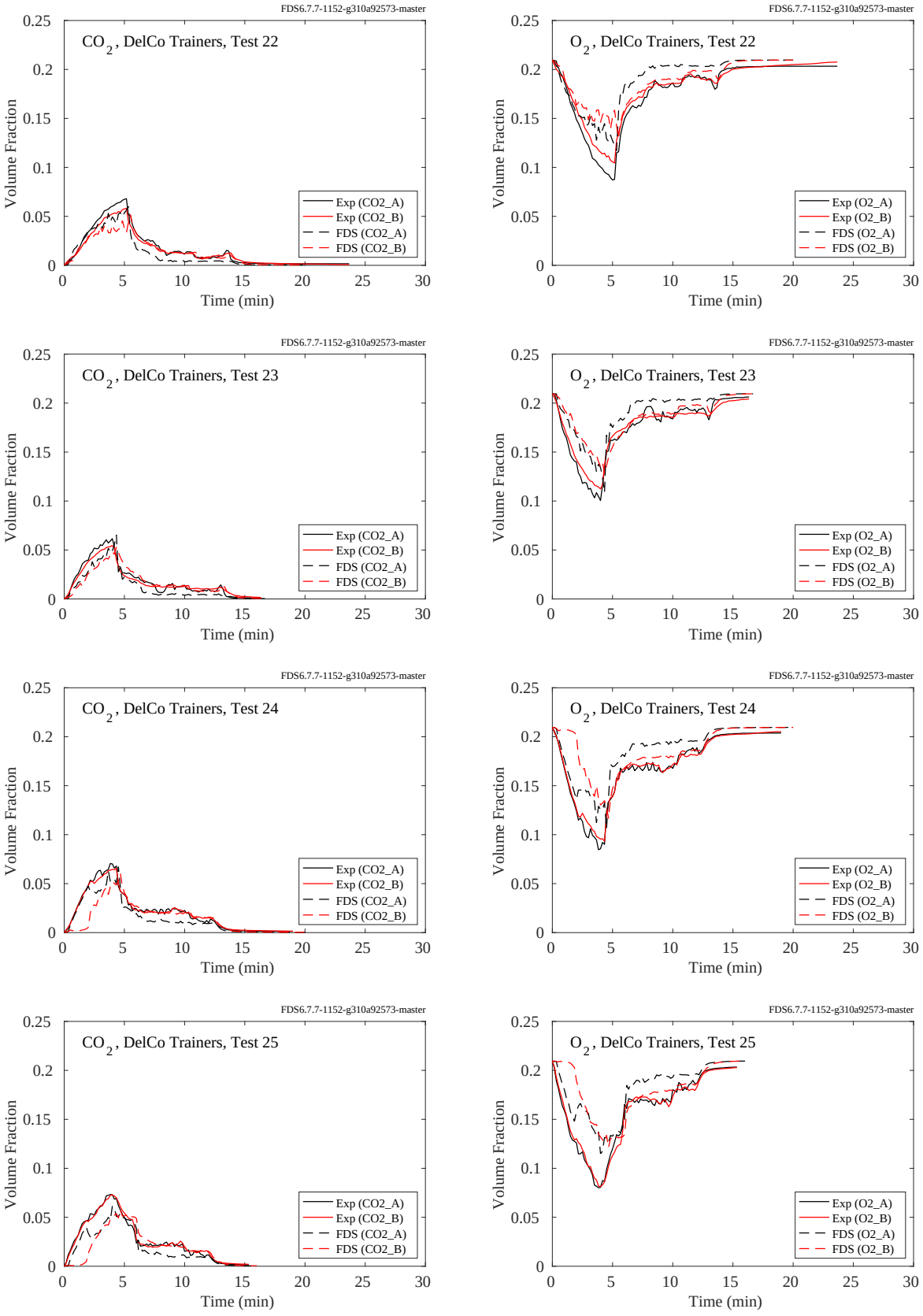

Figure 9.3: DelCo Trainers, CO_2 and O_2 concentration, Tests 22-25.

9.1.2 FAA Cargo Compartments

Carbon dioxide and carbon monoxide were measured near the ceiling in the forward, middle, and aft sections of the compartment. Note that all but the middle compartment concentrations were measured in Tests 2 and 3.

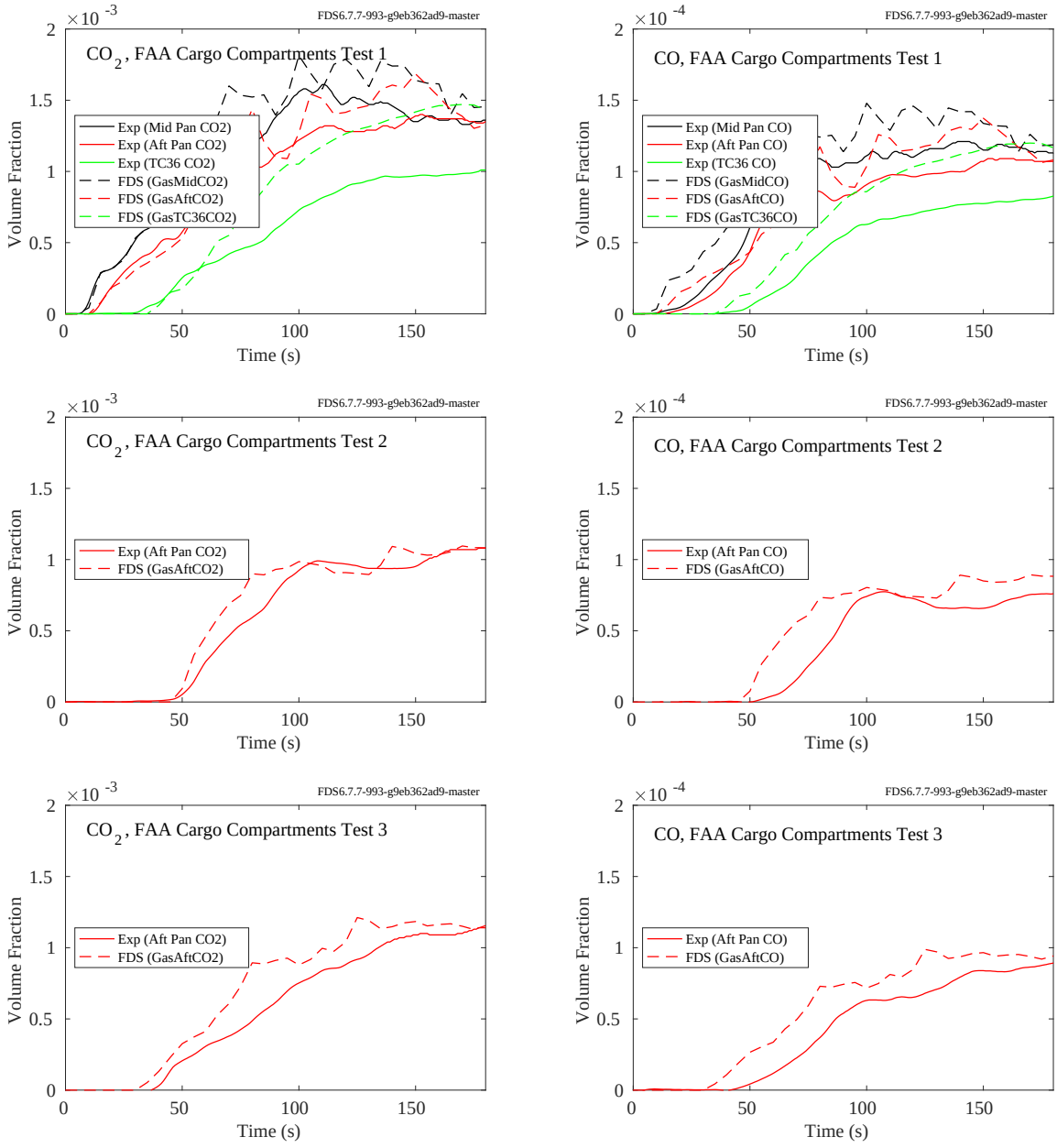

Figure 9.4: FAA Cargo Compartment experiments, CO_2 and O_2 concentration.

9.1.3 LLNL Enclosure

Oxygen and carbon dioxide concentrations were reported for a single location within the LLNL Enclosure. The test report [213] specifies the lateral location of the sensors (1.5 m from the wall opposite the exhaust duct, along the room centerline), but the reported height is only "top of room." In the model, the sensors were located 4.3 m off the floor, 0.2 m below the ceiling of the compartment.

For some experiments, only two concentrations are reported, one being the ambient value. The results of these experiments are shown for completeness, but the values are not included in the calculation of the accuracy statistics.

Also, the test report does not indicate whether the reported volume fractions were taken to be "wet" or "dry"; that is, whether the water vapor was condensed out of the sample. For the sake of comparison, the FDS results are assumed to be "dry".

Further details of the modeling can be found in Section 3.35.

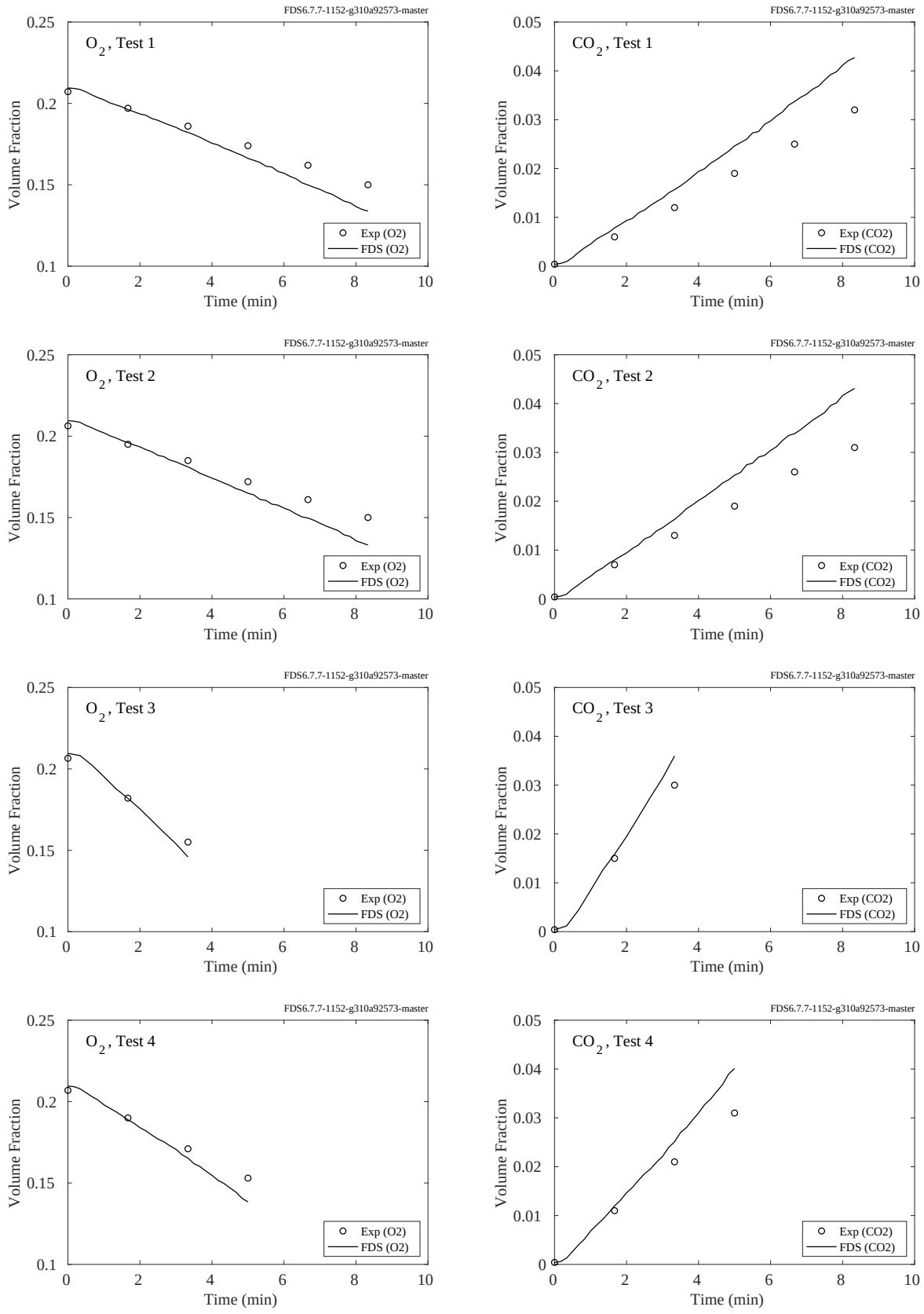

Figure 9.5: LLNL Enclosure, O_2 and CO_2 concentration, Tests 1-4.

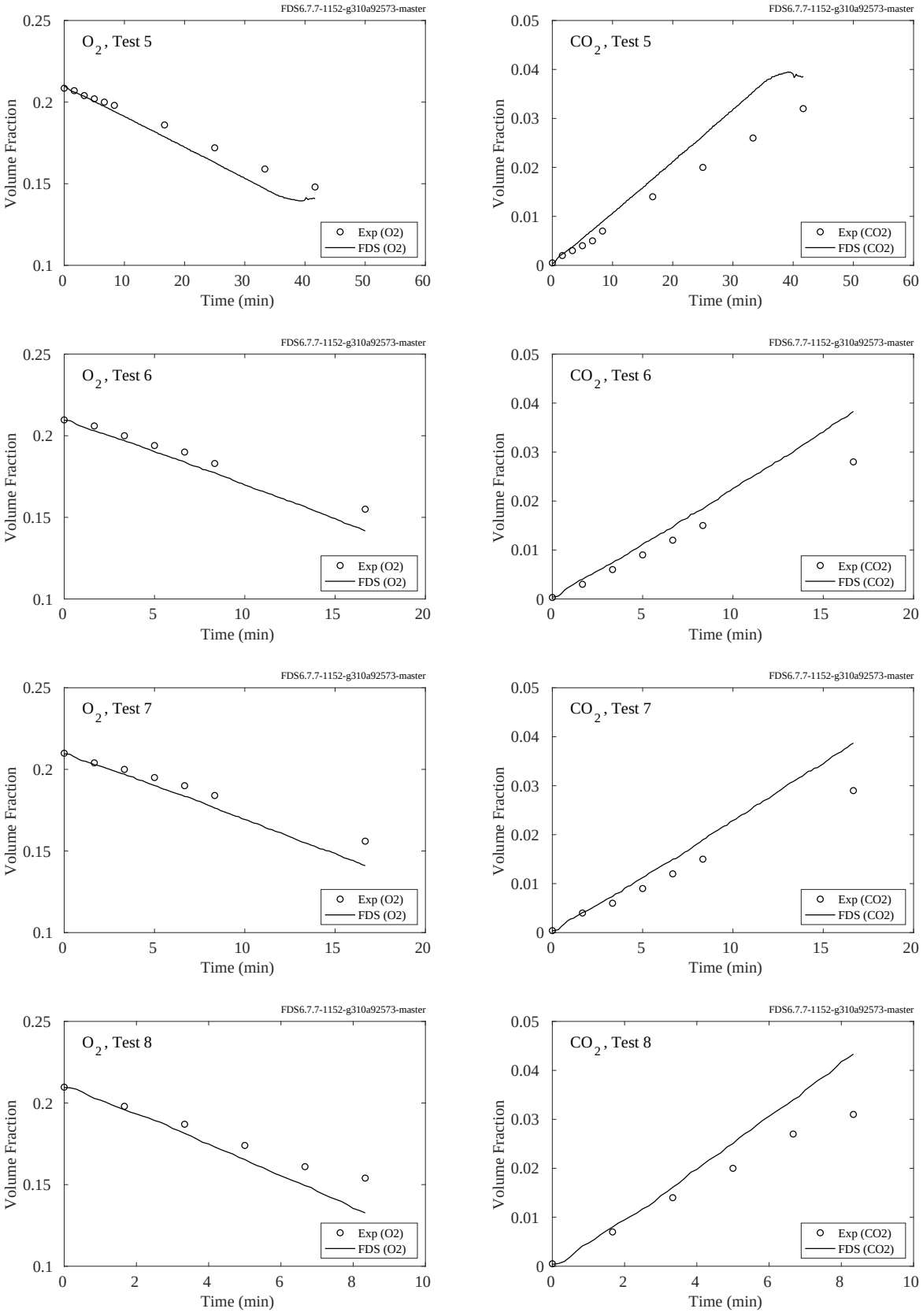

Figure 9.6: LLNL Enclosure, O_2 and CO_2 concentration, Tests 5-8.

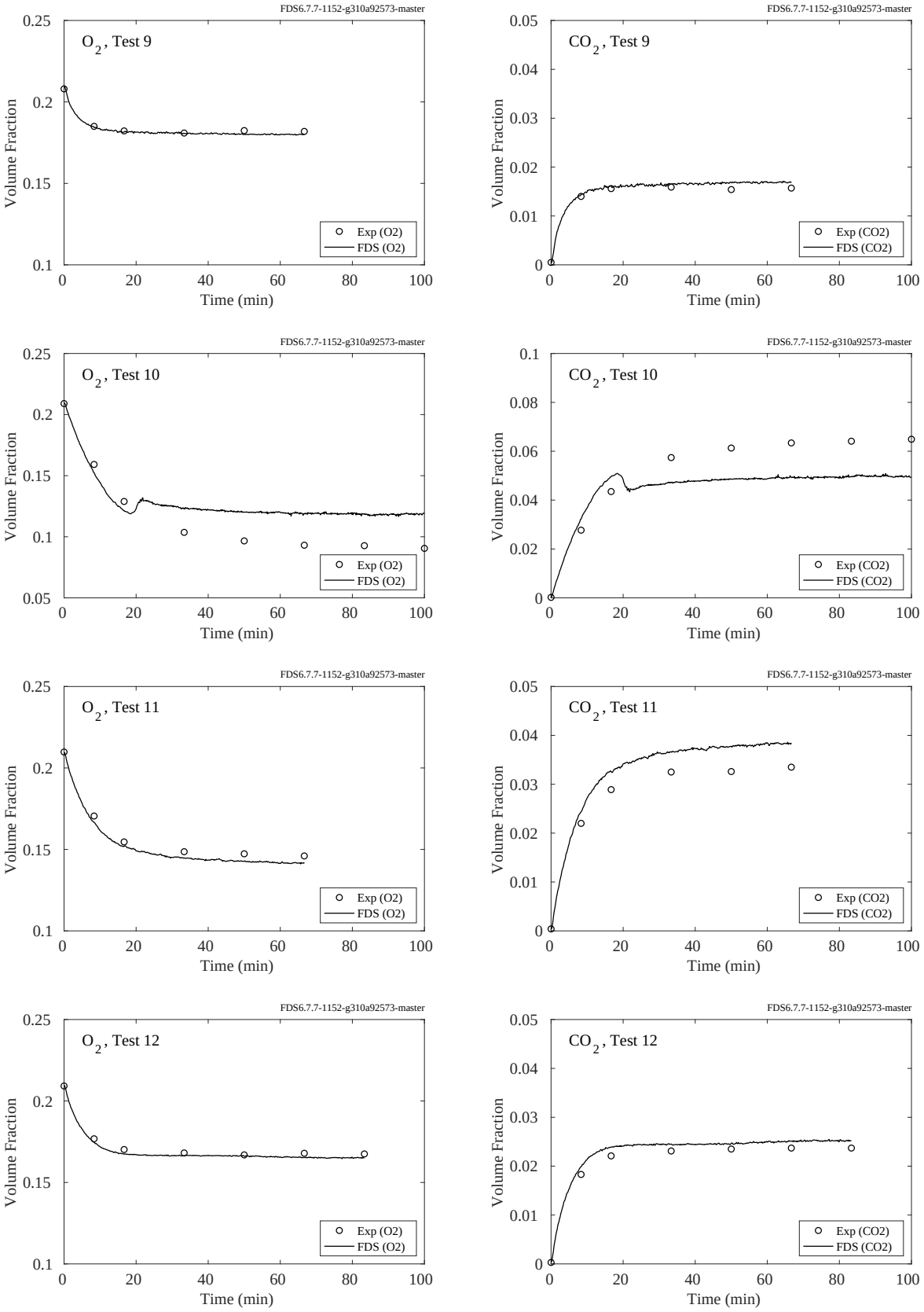

Figure 9.7: LLNL Enclosure, O_2 and CO_2 concentration, Tests 9-12.

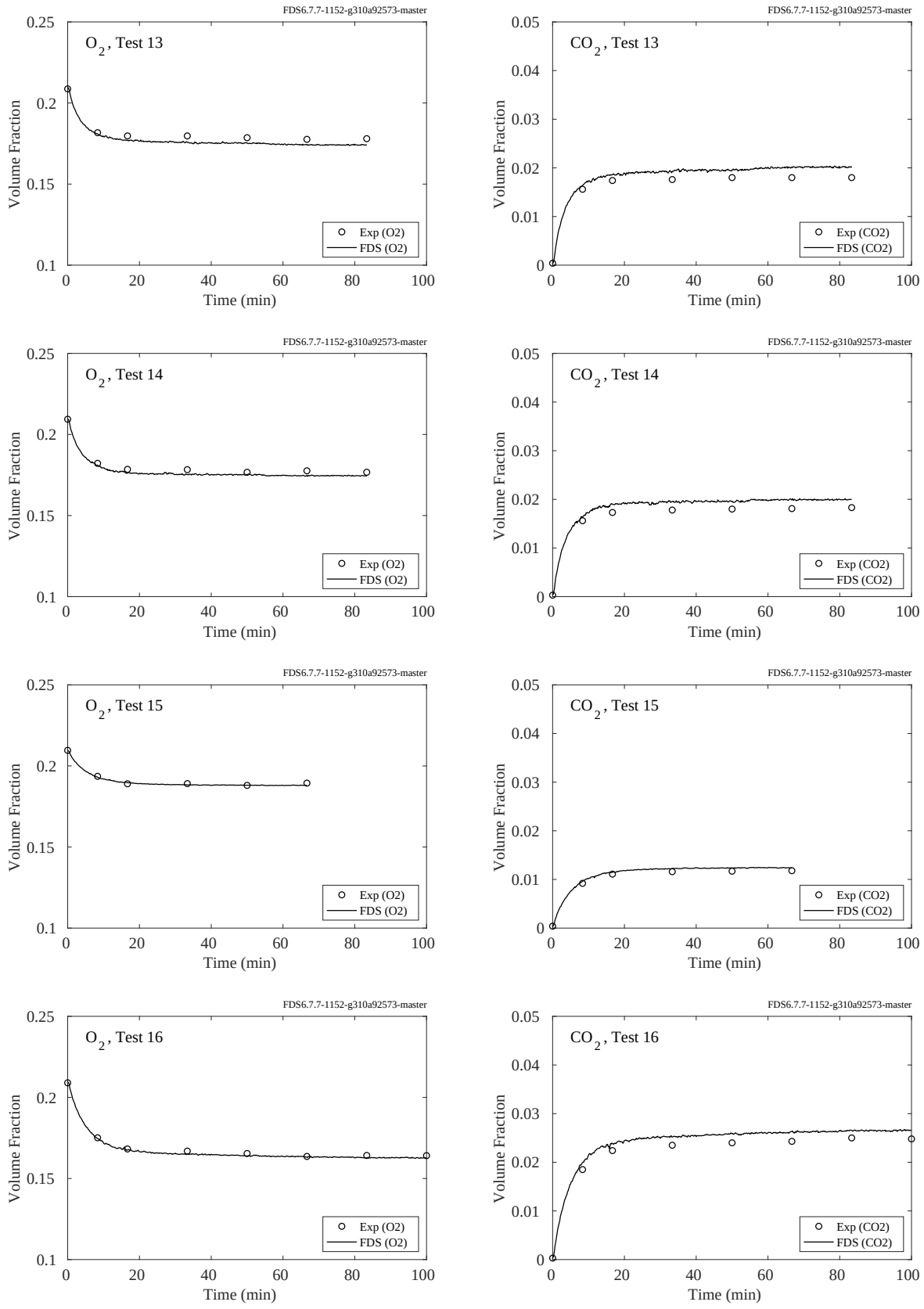

Figure 9.8: LLNL Enclosure, O_2 and CO_2 concentration, Tests 13-16.

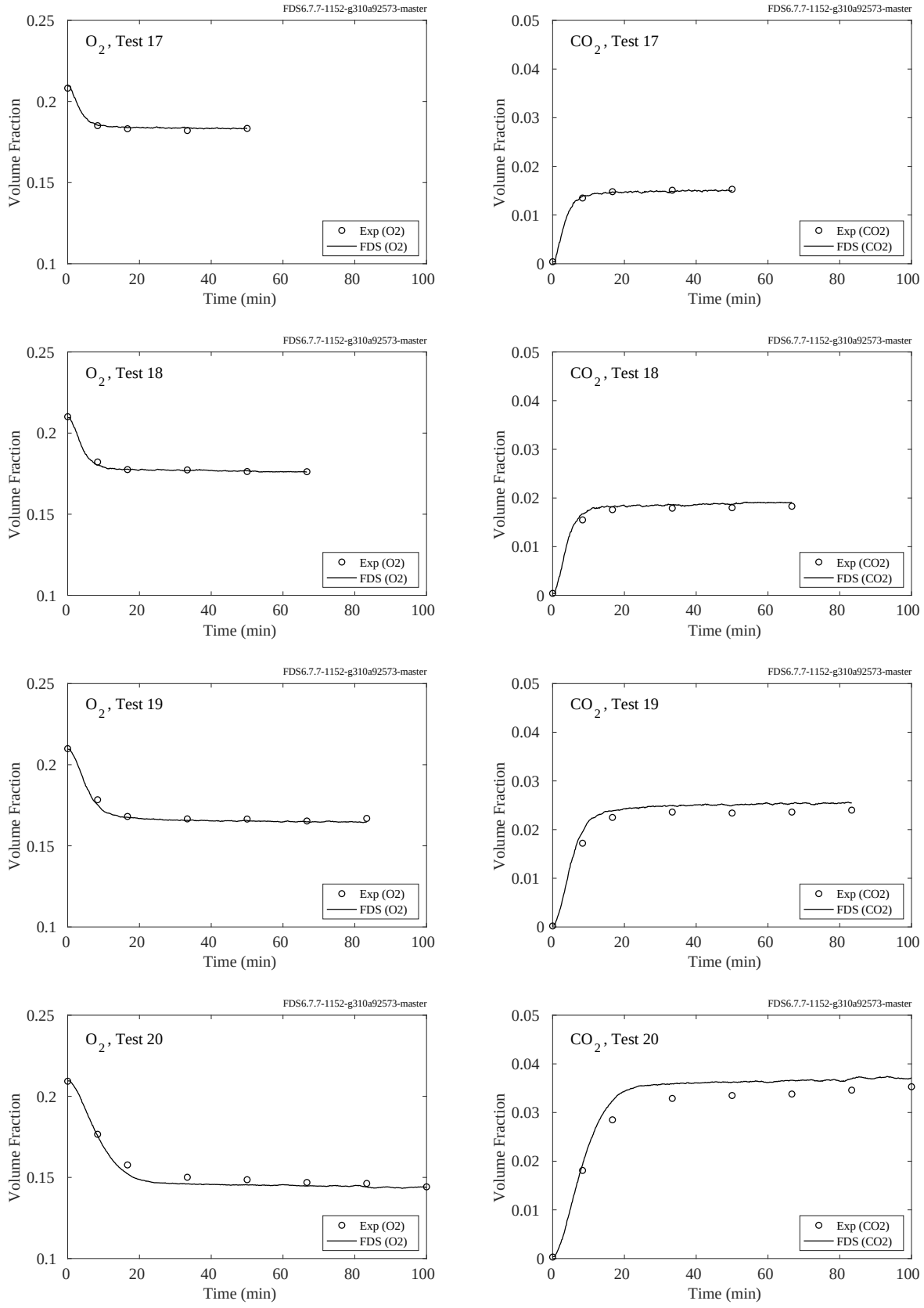

Figure 9.9: LLNL Enclosure, O_2 and CO_2 concentration, Tests 17-20.

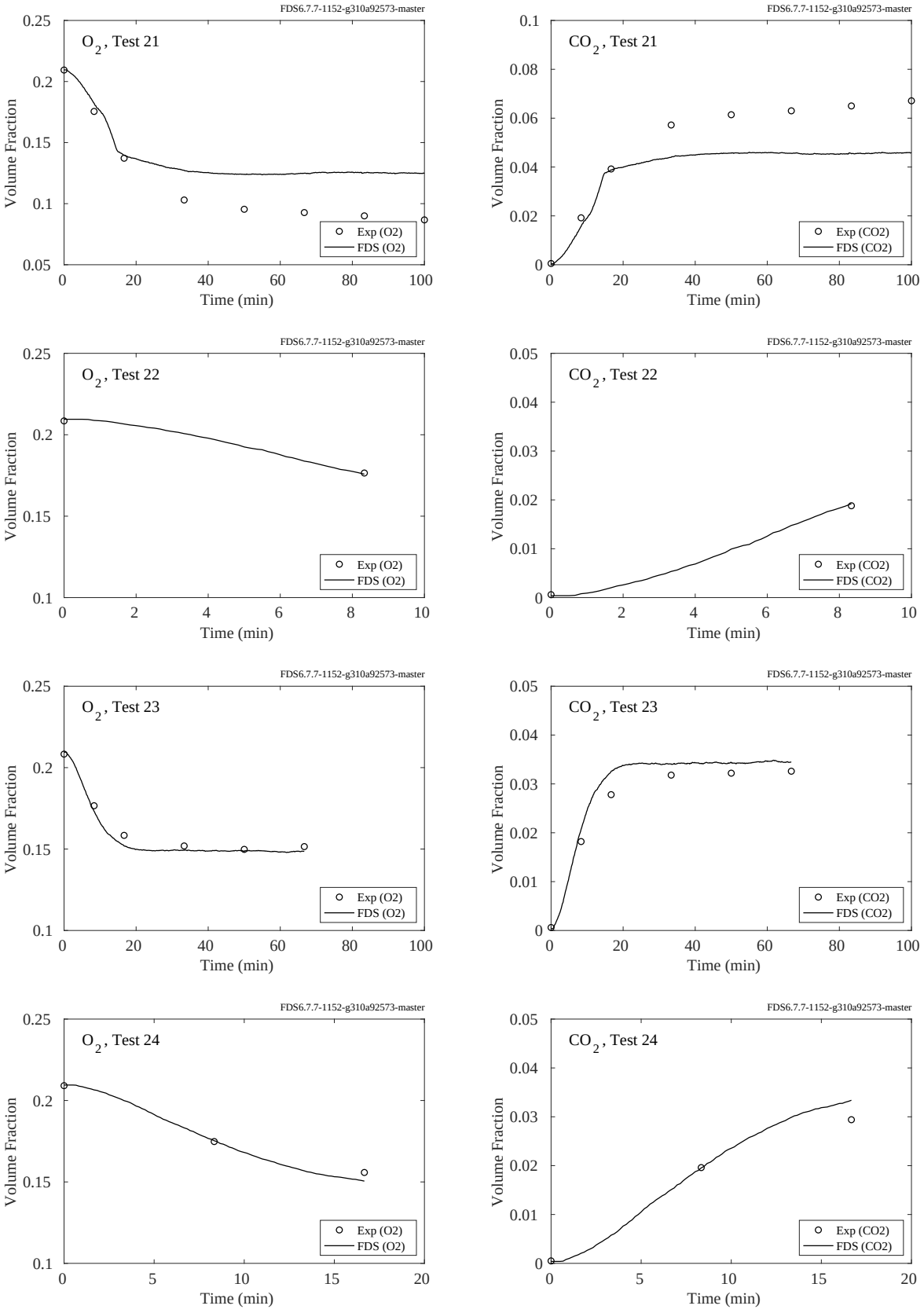

Figure 9.10: LLNL Enclosure, O_2 and CO_2 concentration, Tests 21-24.

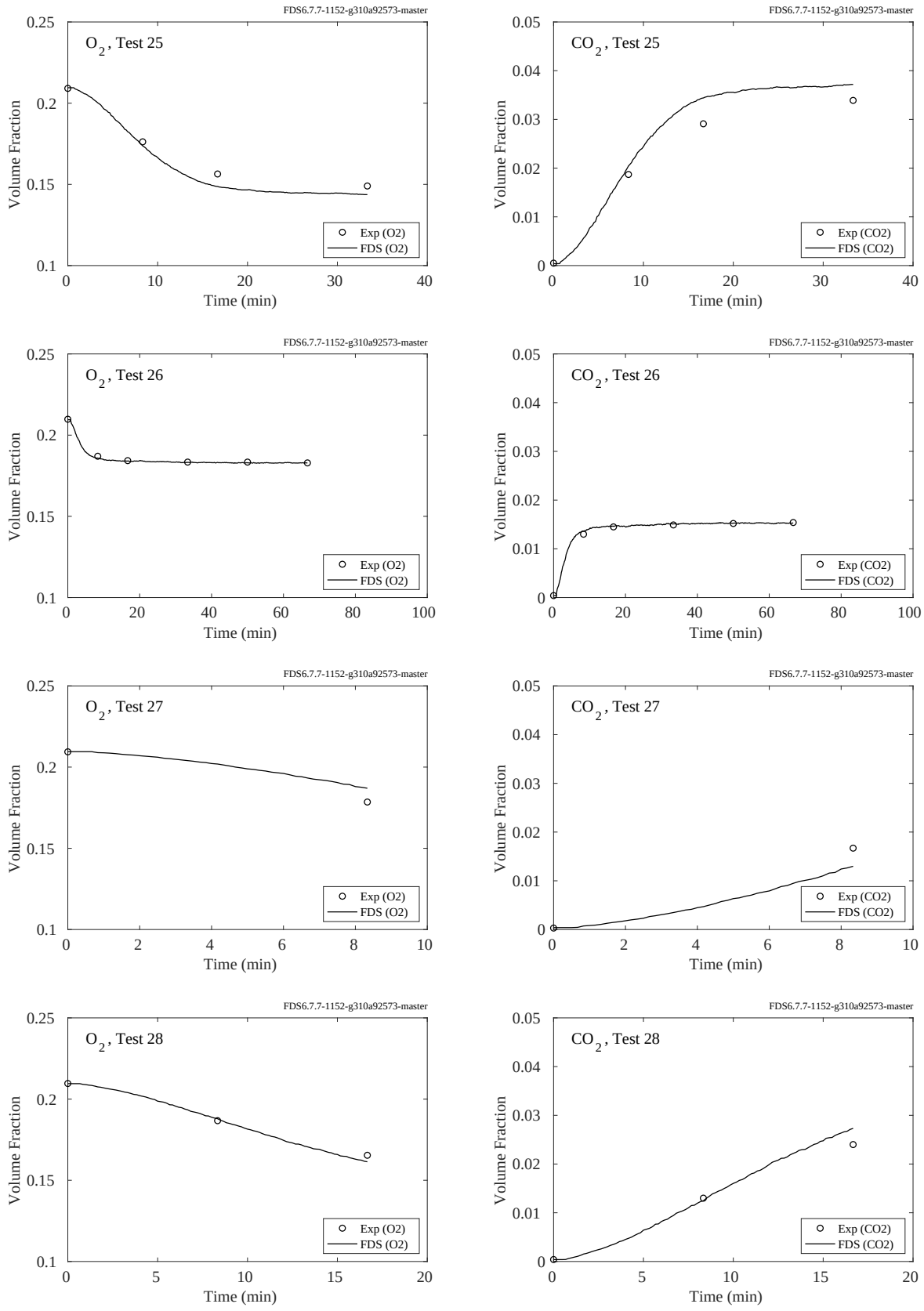

Figure 9.11: LLNL Enclosure, O_2 and CO_2 concentration, Tests 25-28.

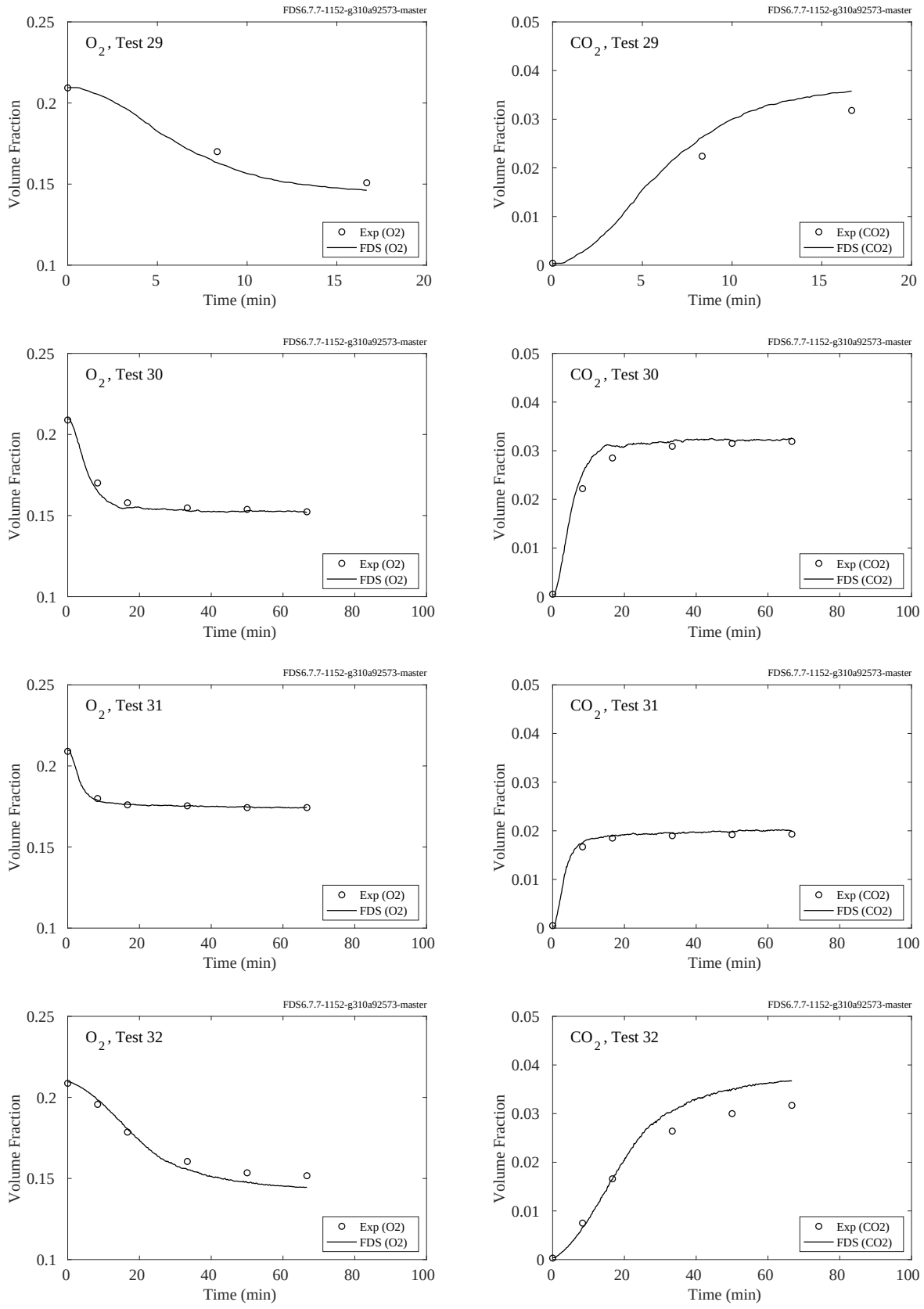

Figure 9.12: LLNL Enclosure, O_2 and CO_2 concentration, Tests 29-32.

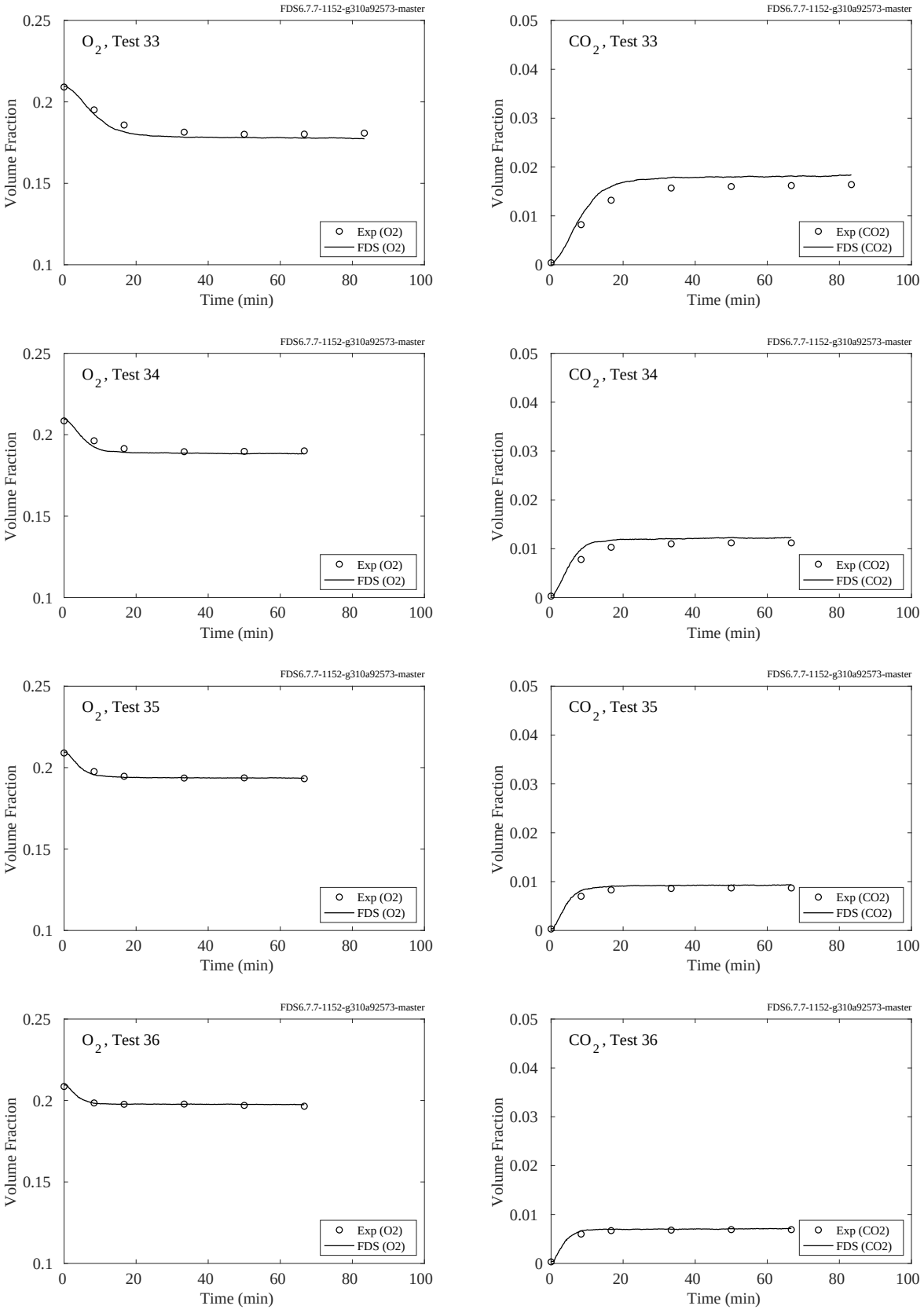

Figure 9.13: LLNL Enclosure, O_2 and CO_2 concentration, Tests 33-36.

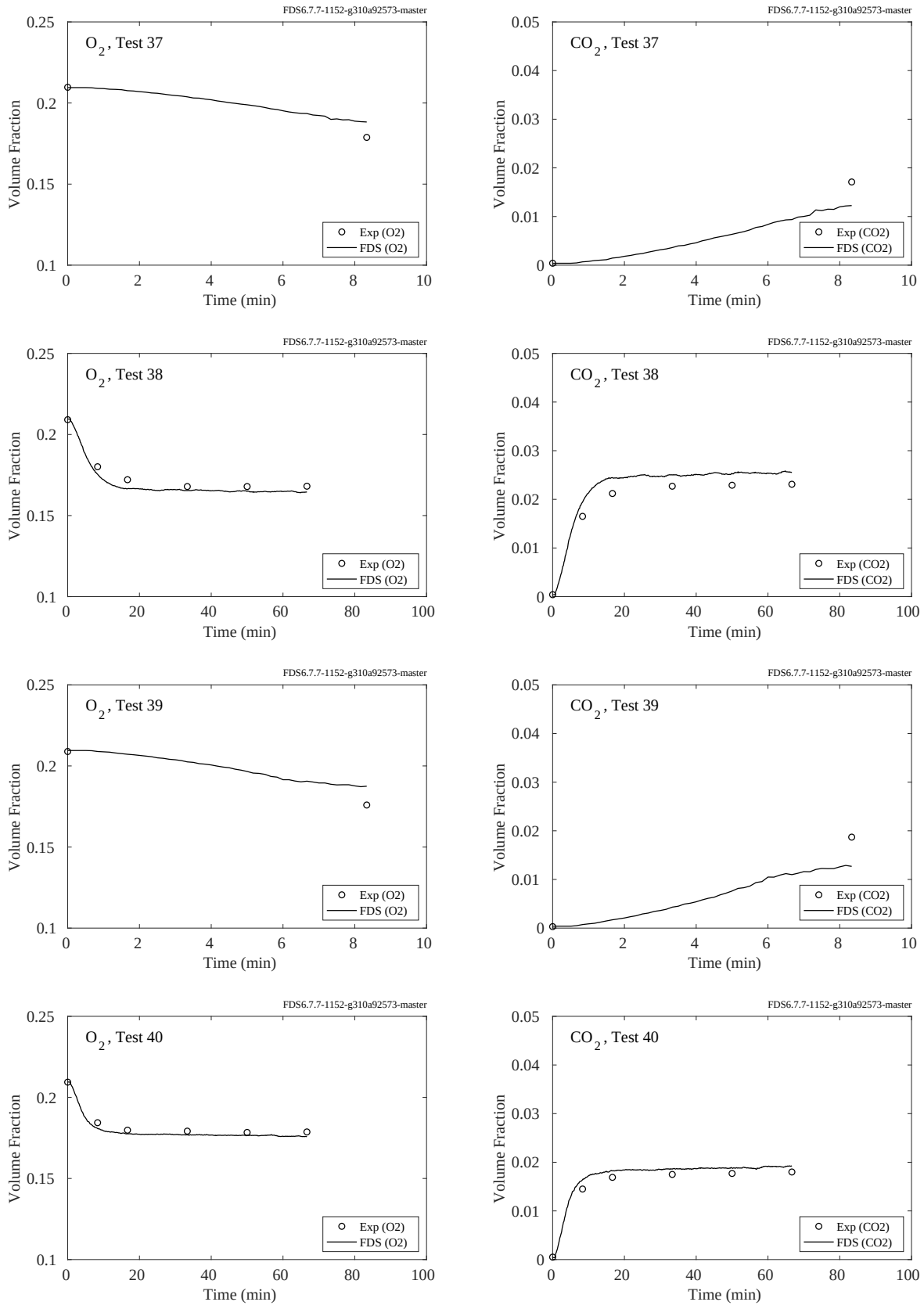

Figure 9.14: LLNL Enclosure, O_2 and CO_2 concentration, Tests 37-40.

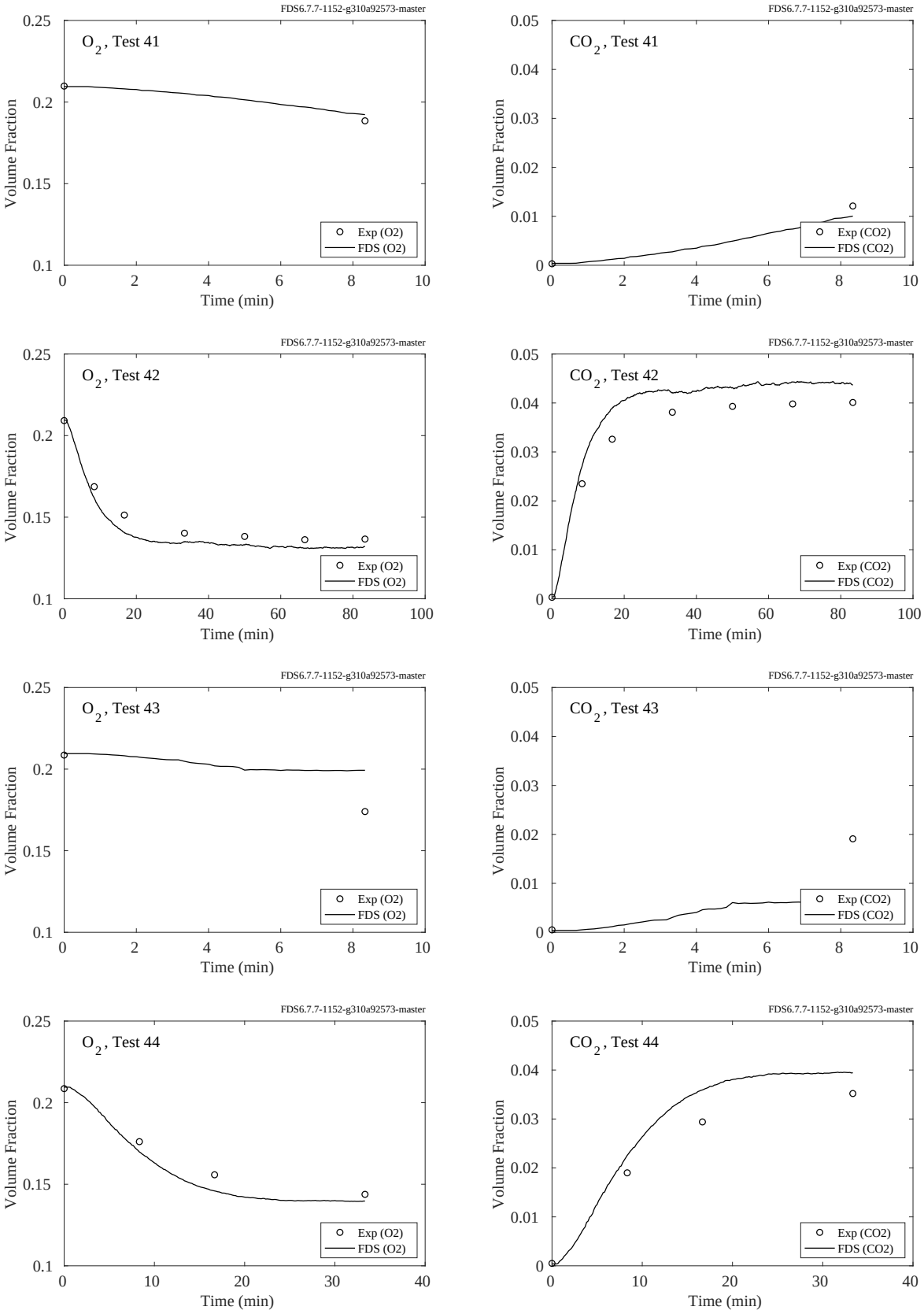

Figure 9.15: LLNL Enclosure, O_2 and CO_2 concentration, Tests 41-44.

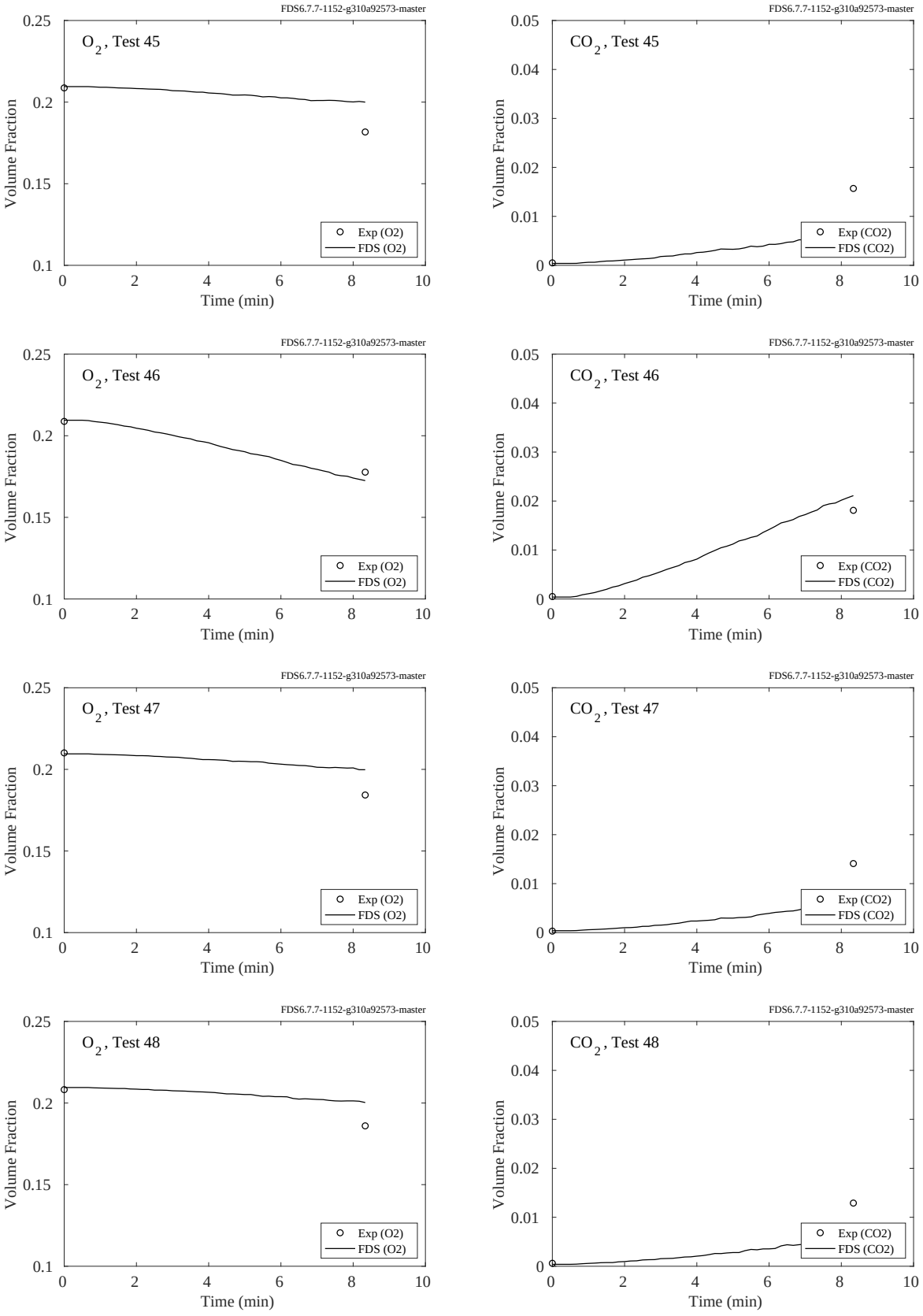

Figure 9.16: LLNL Enclosure, O_2 and CO_2 concentration, Tests 45-48.

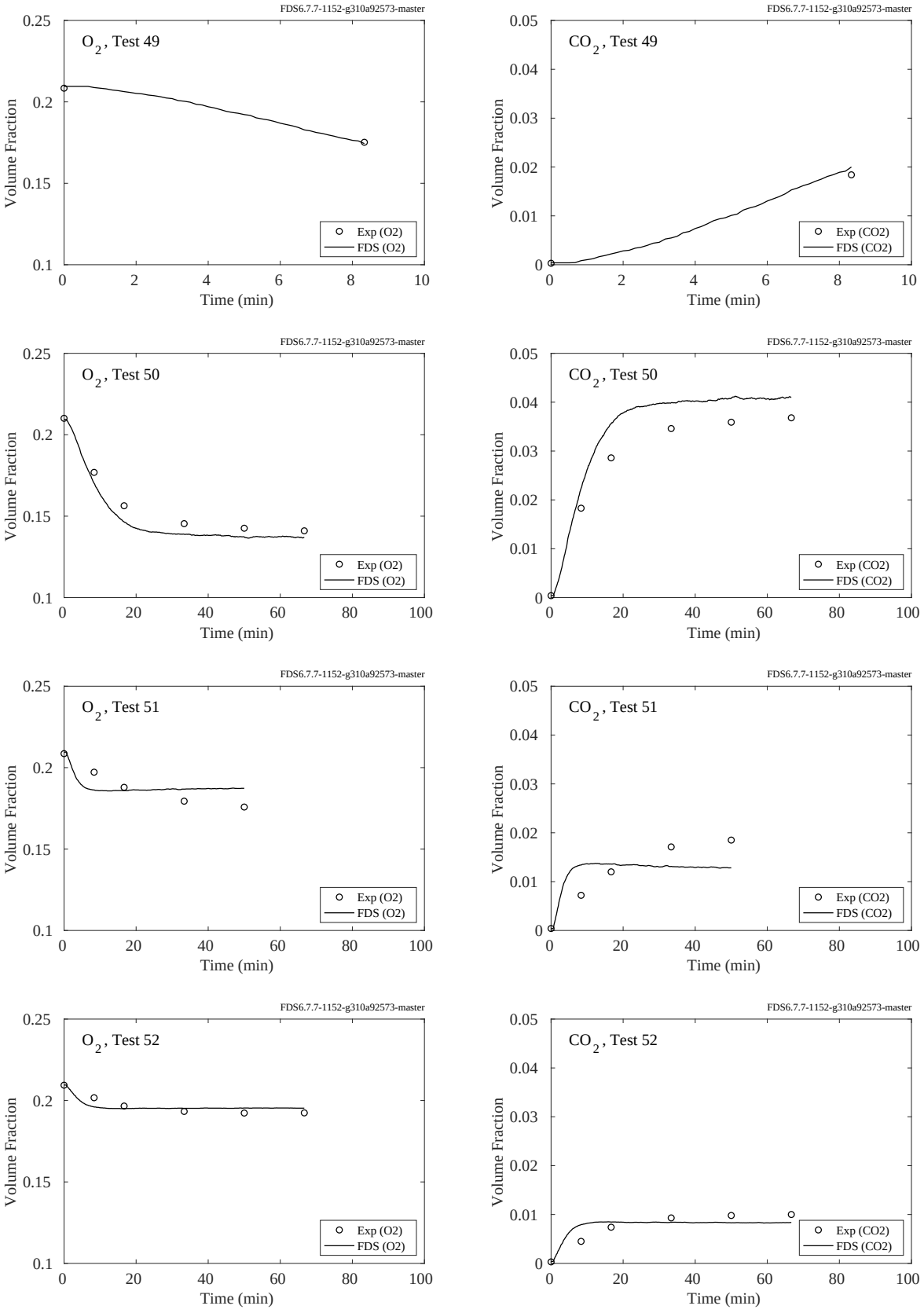

Figure 9.17: LLNL Enclosure, O_2 and CO_2 concentration, Tests 49-52.

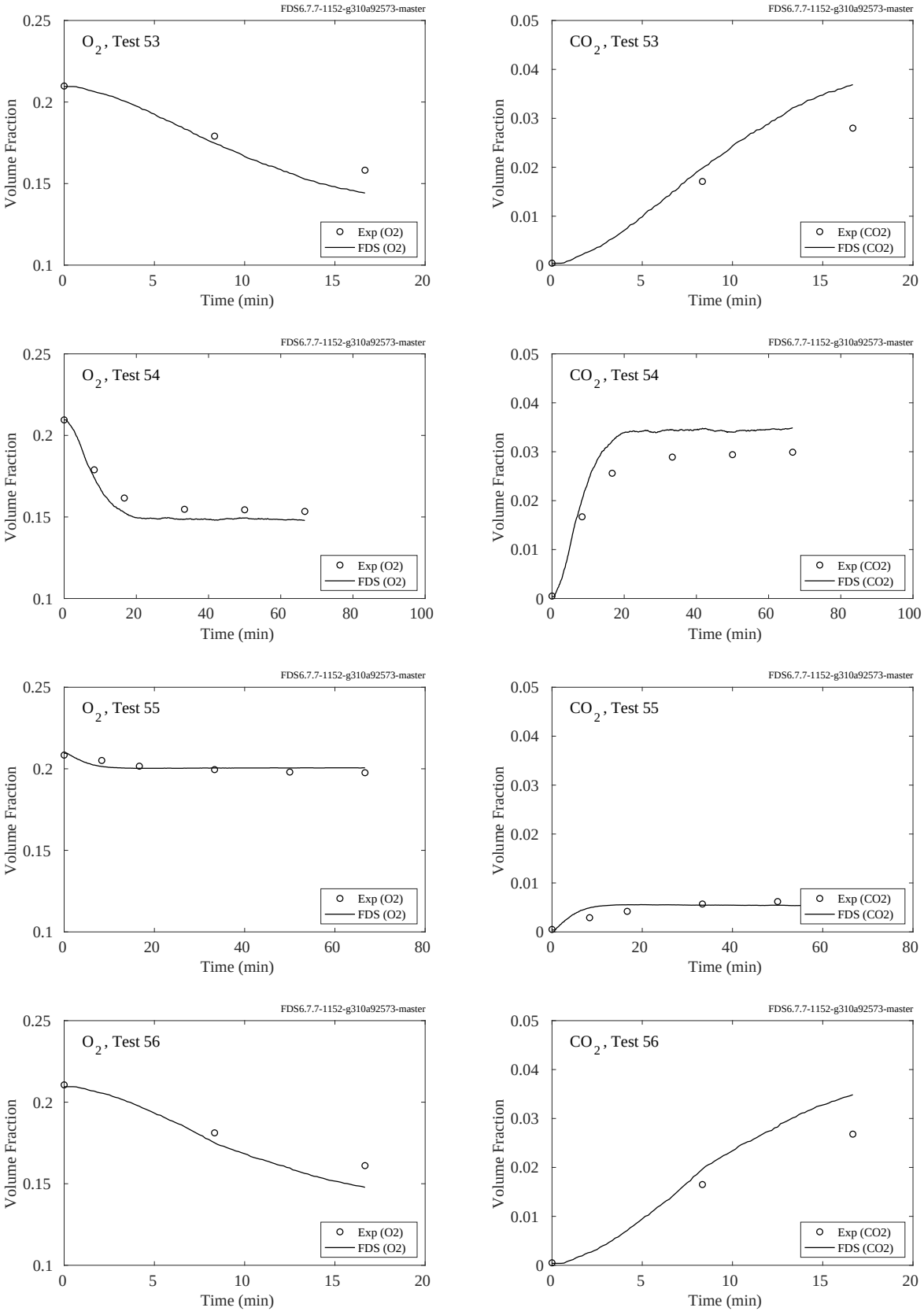

Figure 9.18: LLNL Enclosure, O_2 and CO_2 concentration, Tests 53-56.

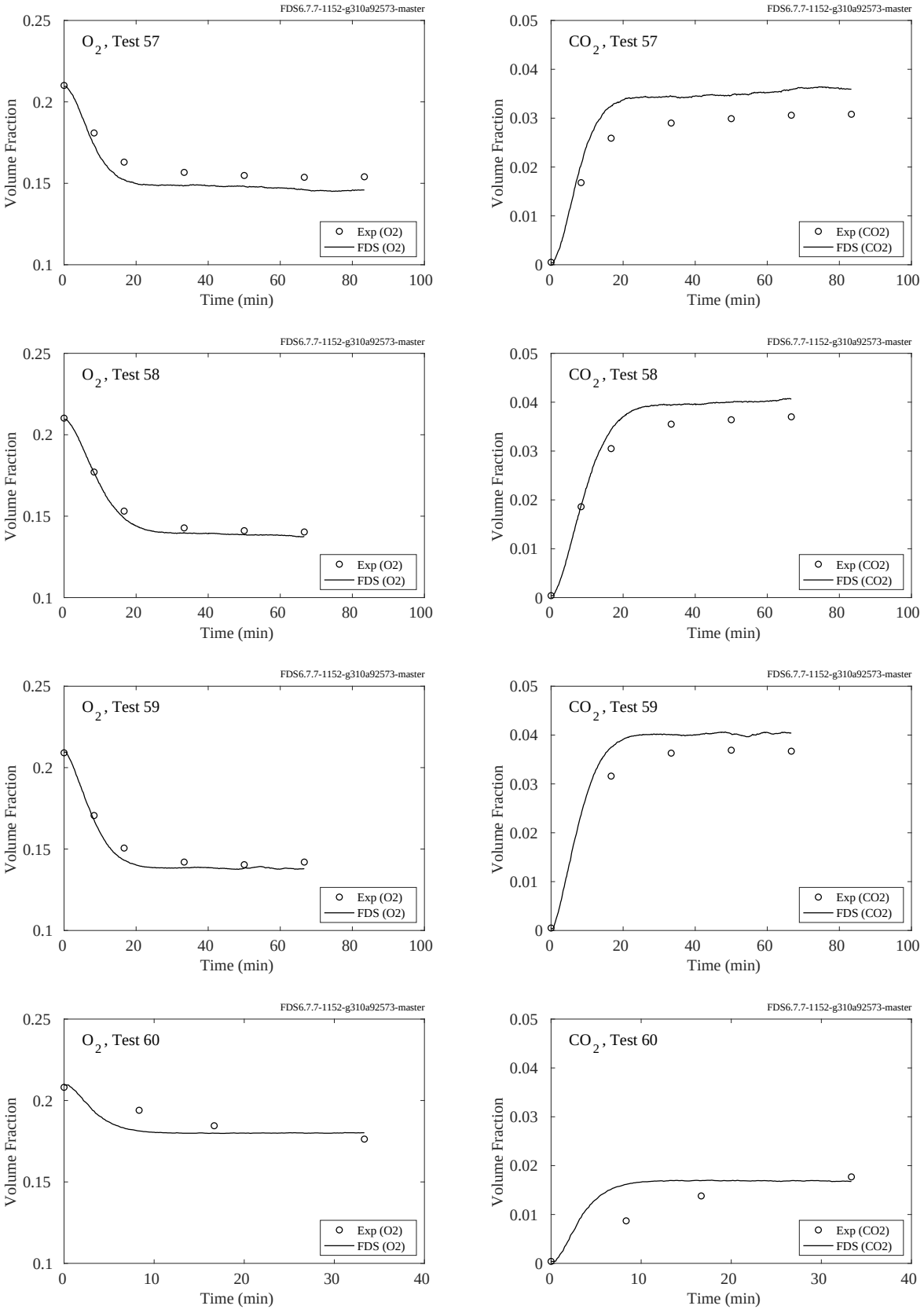

Figure 9.19: LLNL Enclosure, O_2 and CO_2 concentration, Tests 57-60.

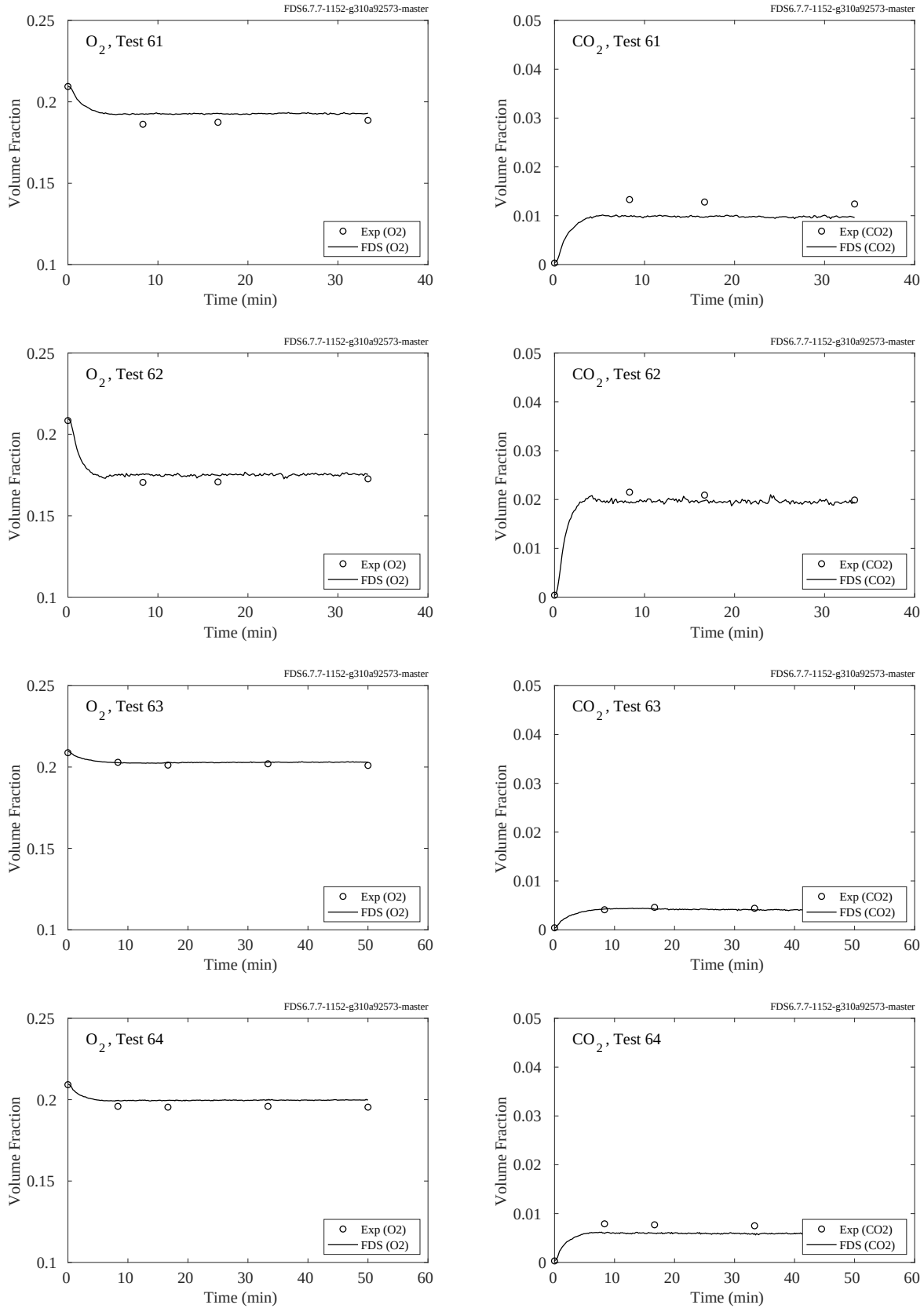

Figure 9.20: LLNL Enclosure, O_2 and CO_2 concentration, Tests 61-64.

9.1.4 NIST/NRC Experiments

The following pages present comparisons of oxygen and carbon dioxide concentration predictions and measurements for the NIST/NRC series. There were two oxygen measurements, one in the upper layer, one in the lower. There was only one carbon dioxide measurement in the upper layer.

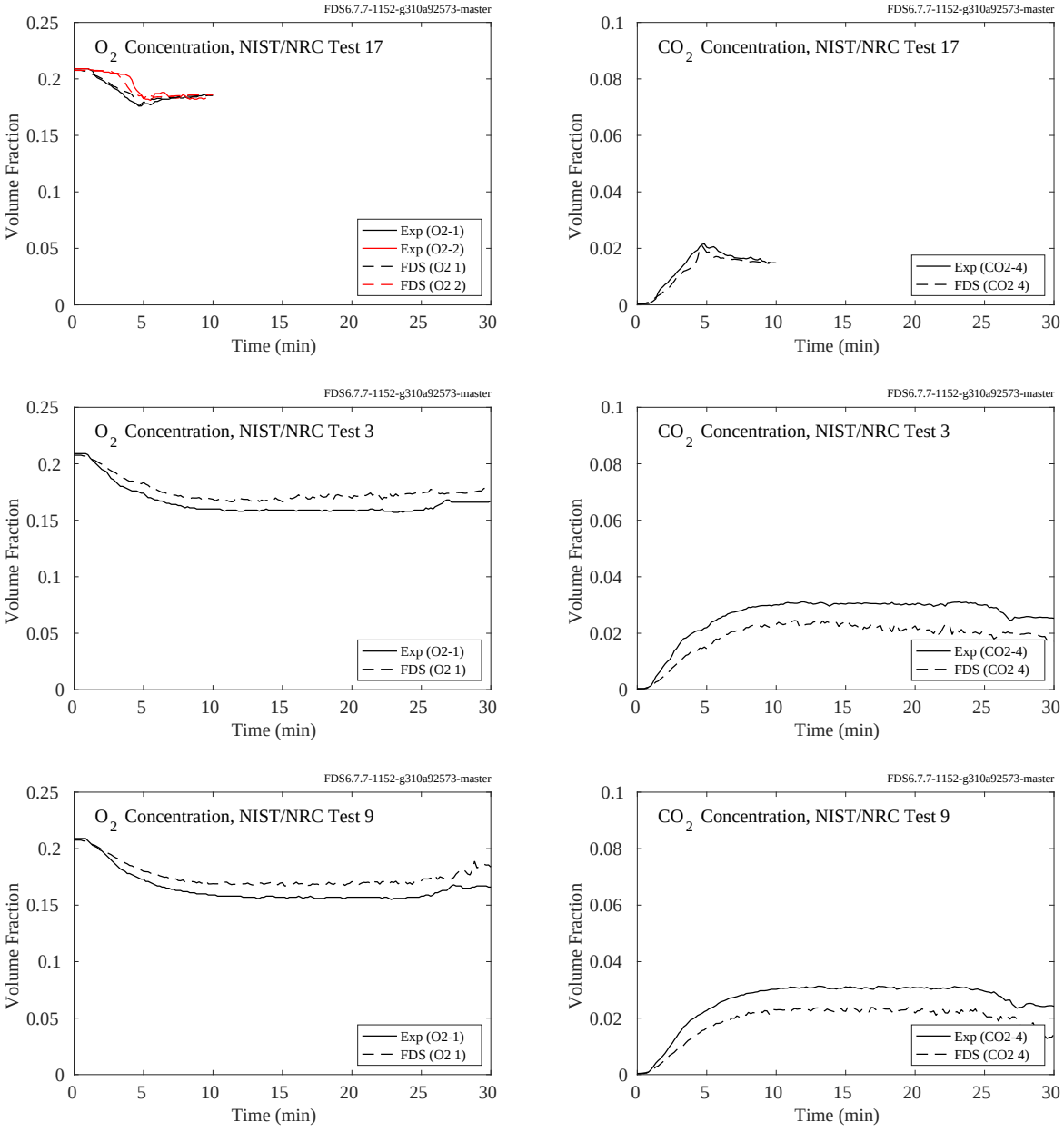

Figure 9.21: NIST/NRC experiments, CO_2 and O_2 concentration, Tests 3, 9, 17.

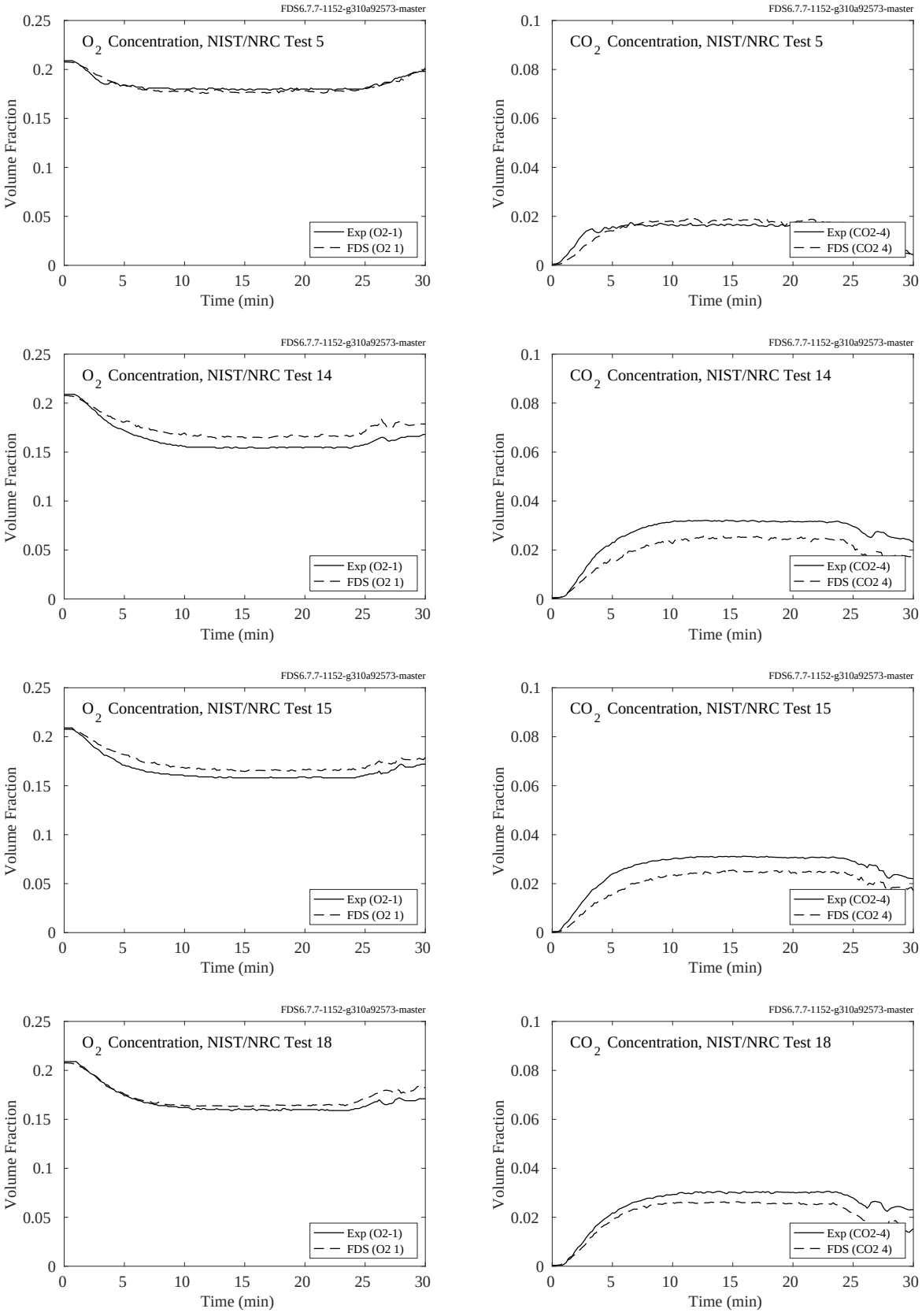

Figure 9.22: NIST/NRC experiments, CO_2 and O_2 concentration, Tests 5, 14, 15, 18.

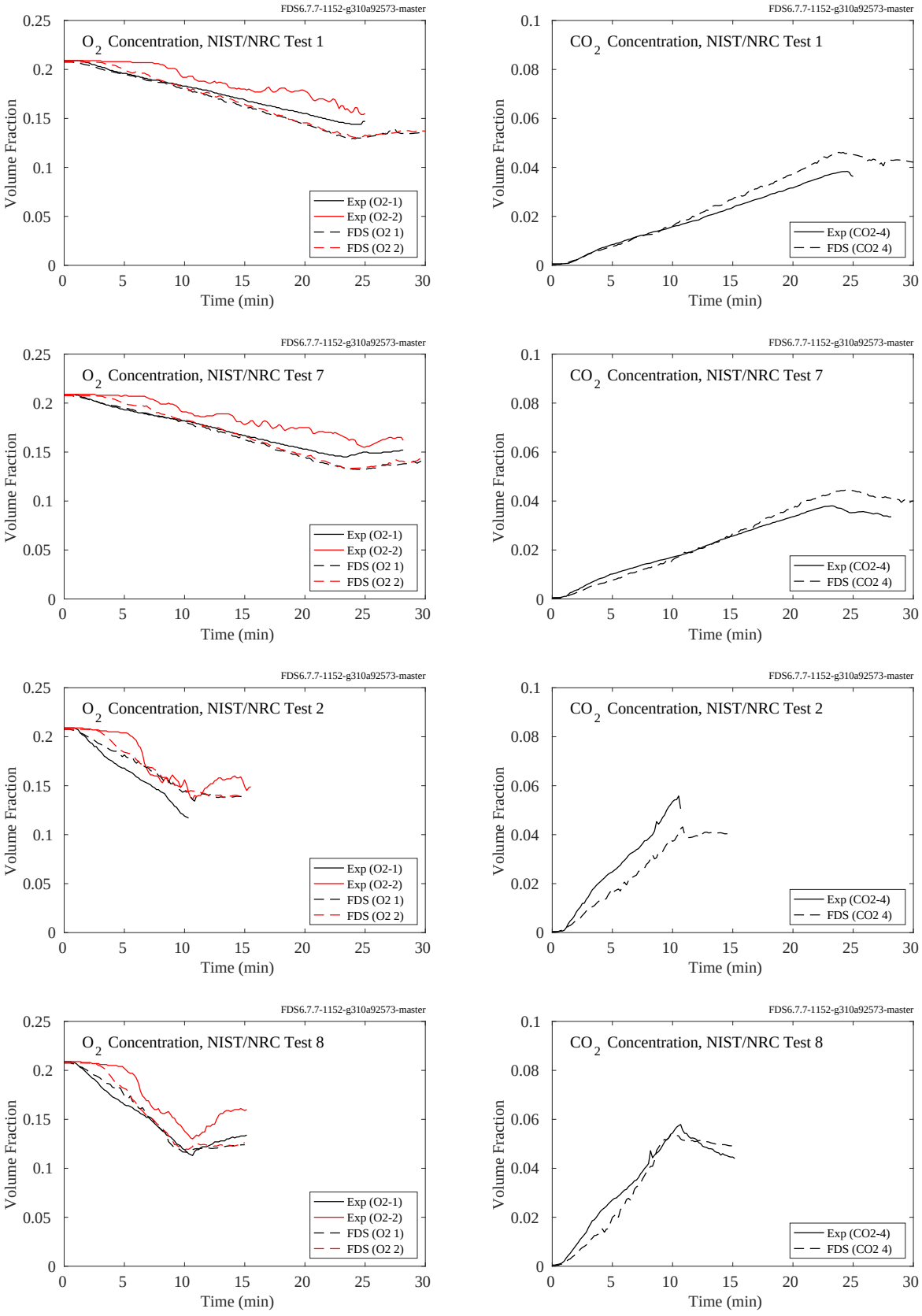

Figure 9.23: NIST/NRC experiments, CO_2 and O_2 concentration, Tests 1, 2, 7, 8.

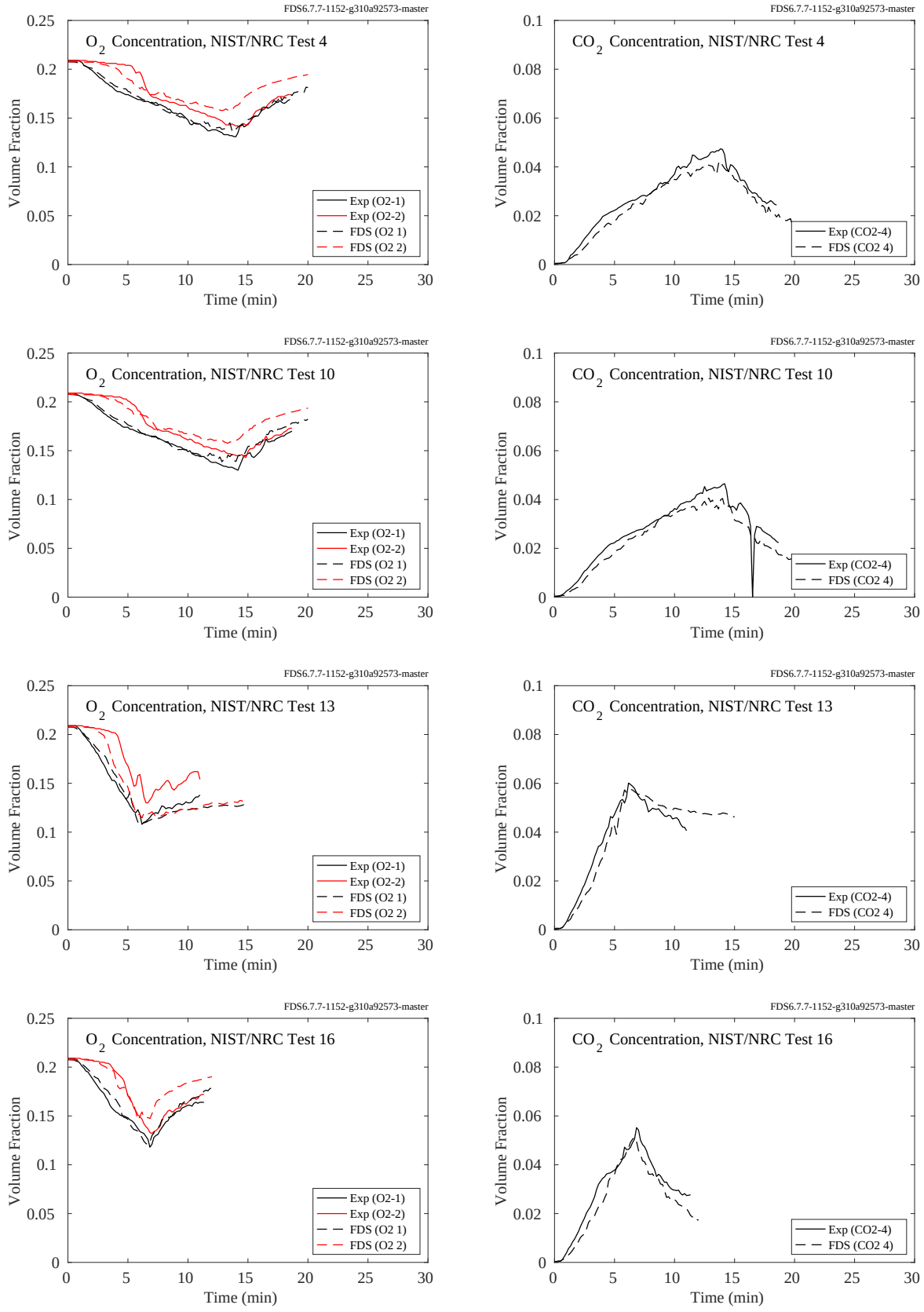

Figure 9.24: NIST/NRC experiments, CO_2 and O_2 concentration, Tests 4, 10, 13, 16.

9.1.5 NRCC Smoke Tower

In the NRCC Smoke Tower experiments, there were oxygen and carbon dioxide analyzers in the stair shaft on the second floor just outside the door of the fire compartment.

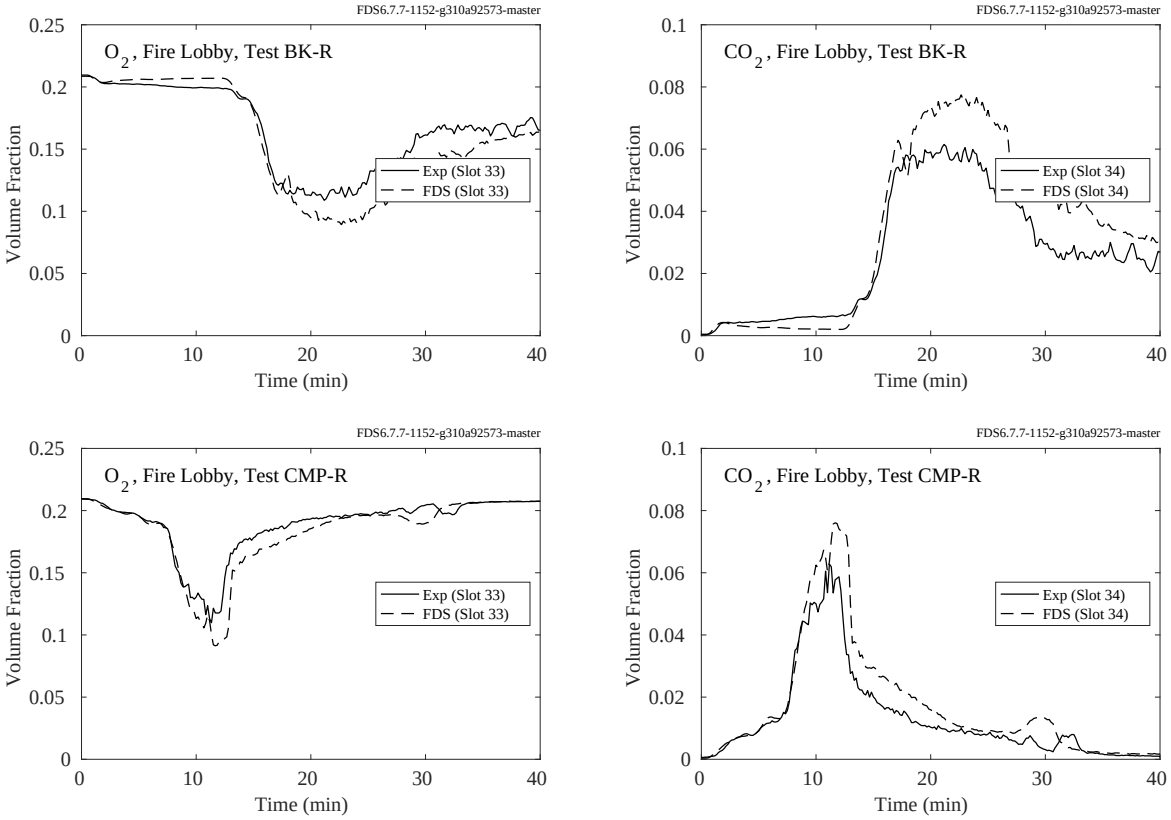

Figure 9.25: NRCC Smoke Tower, CO_2 and O_2 concentration, Tests BK-R and COMP-R.

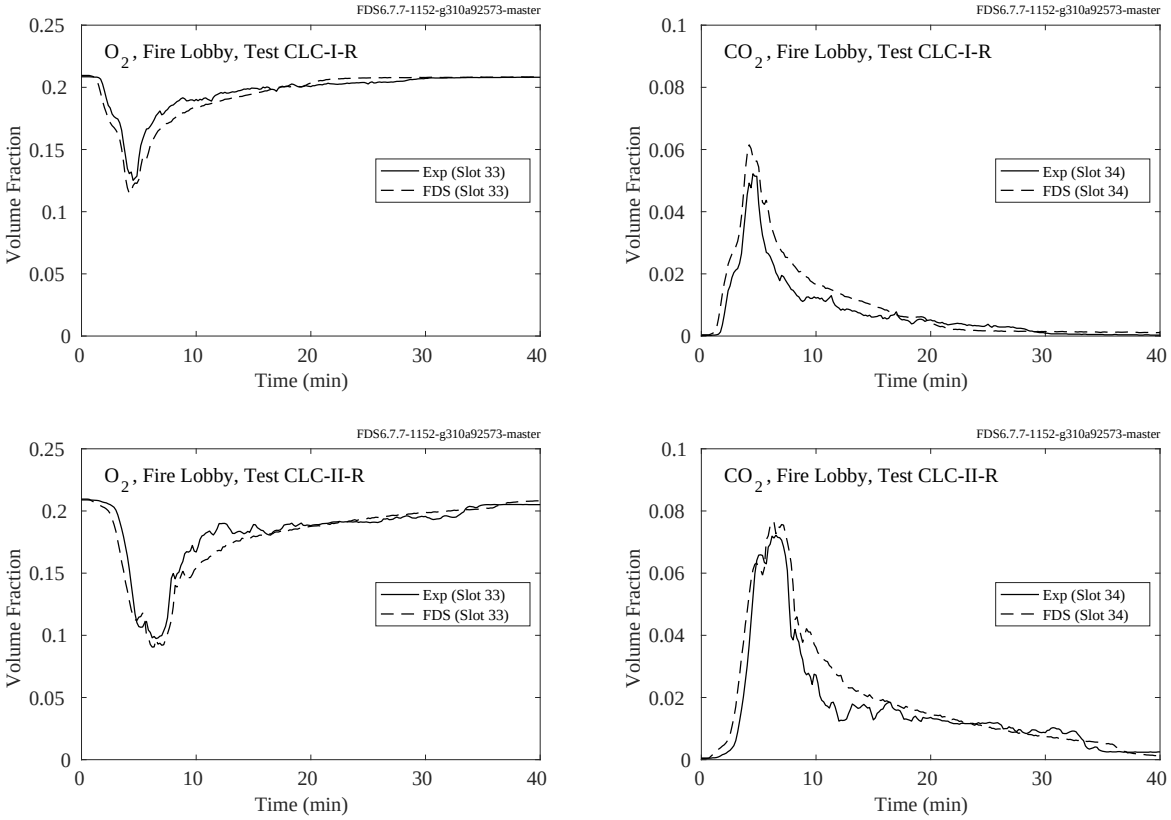

Figure 9.26: NRCC Smoke Tower, CO_2 and O_2 concentration, Tests CLC-I-R and CLC-II-R.

9.1.6 PRISME DOOR Experiments

Each compartment in the PRISME DOOR experiments contained an oxygen and carbon dioxide measurement in the upper (haut) and lower (bas) layers.

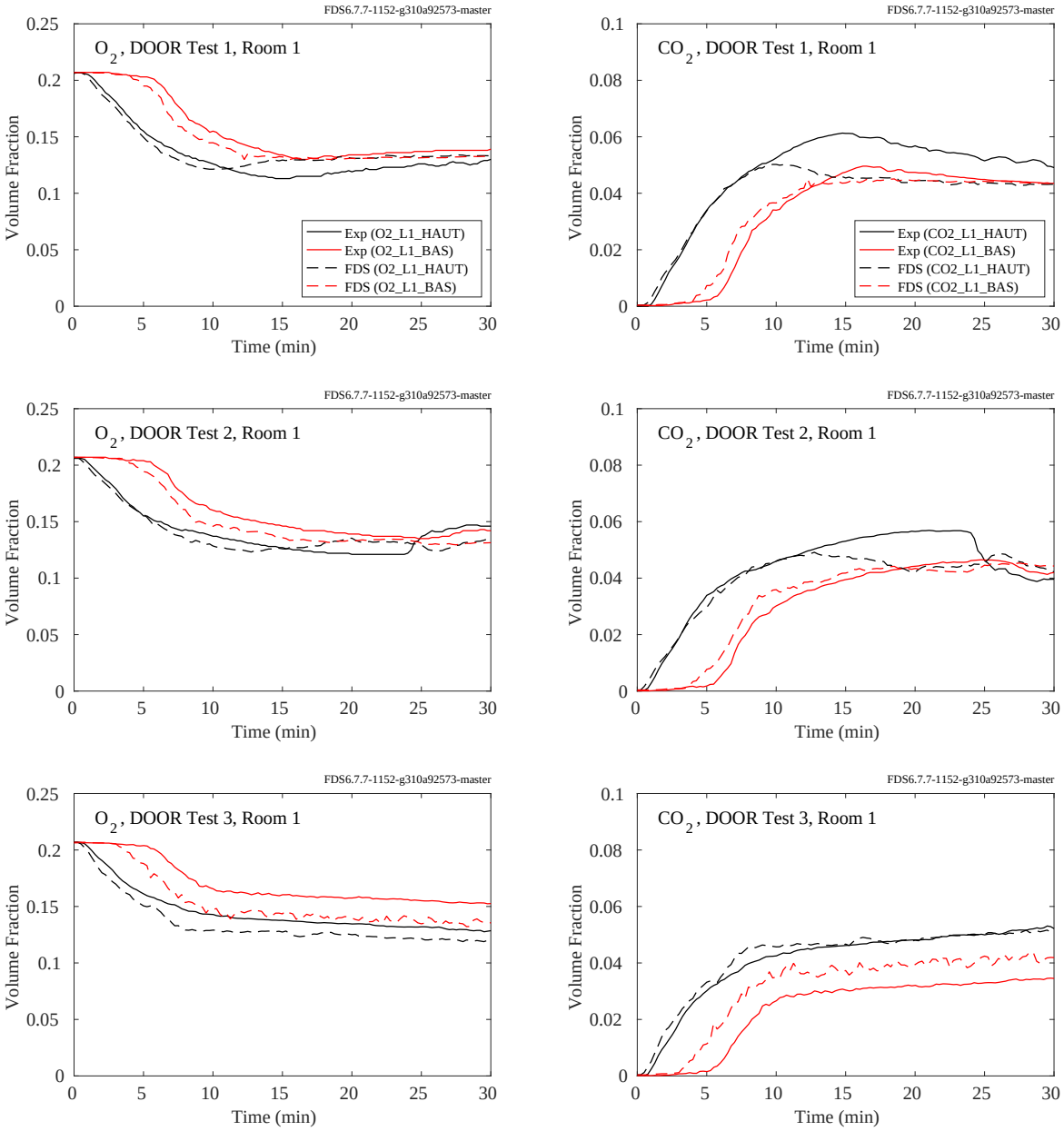

Figure 9.27: PRISME DOOR experiments, CO_2 and O_2 concentration, Room 1, Tests 1-3.

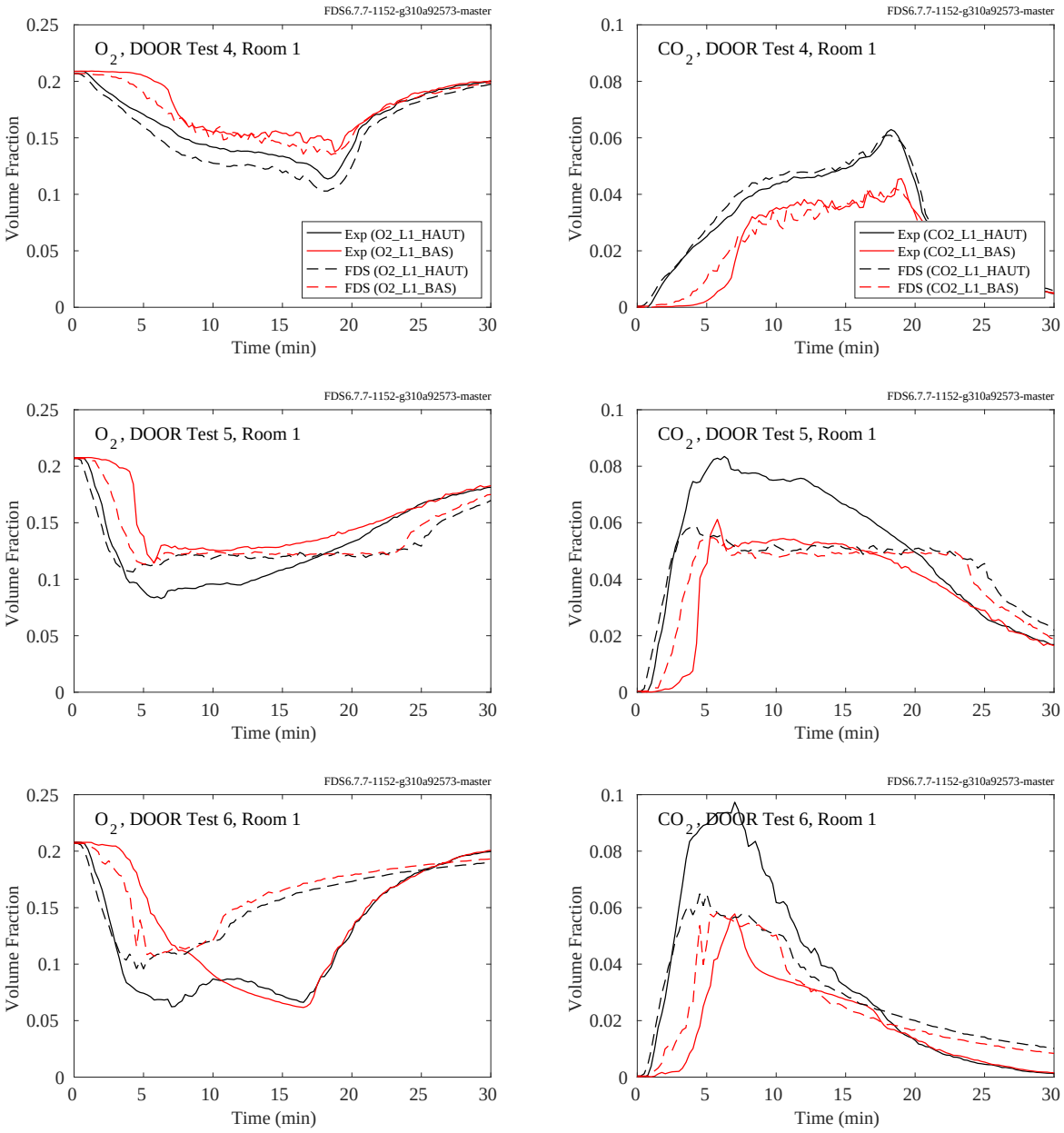

Figure 9.28: PRISME DOOR experiments, CO_2 and O_2 concentration, Room 1, Tests 4-6.

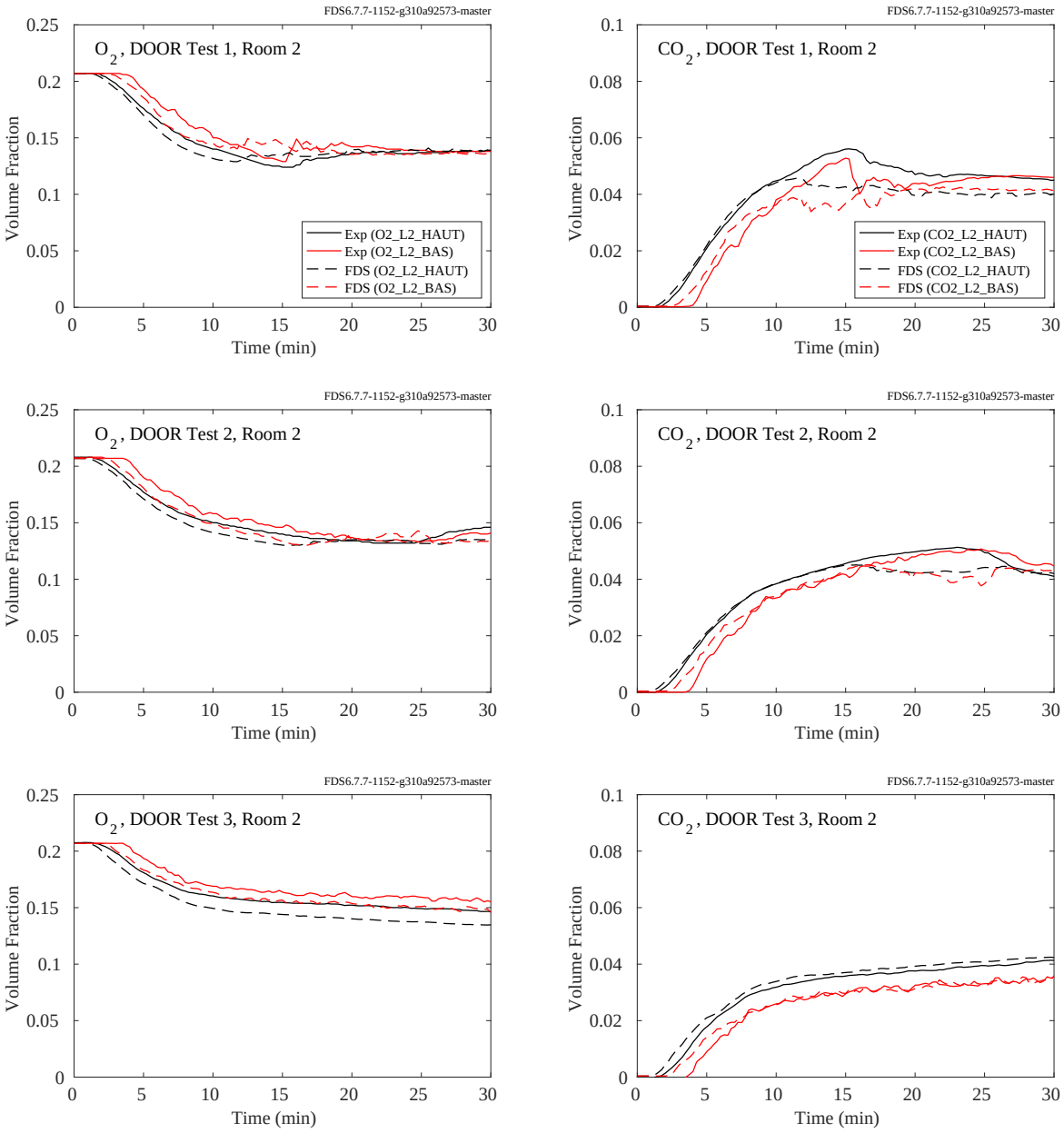

Figure 9.29: PRISME DOOR experiments, CO_2 and O_2 concentration, Room 2, Tests 1-3.

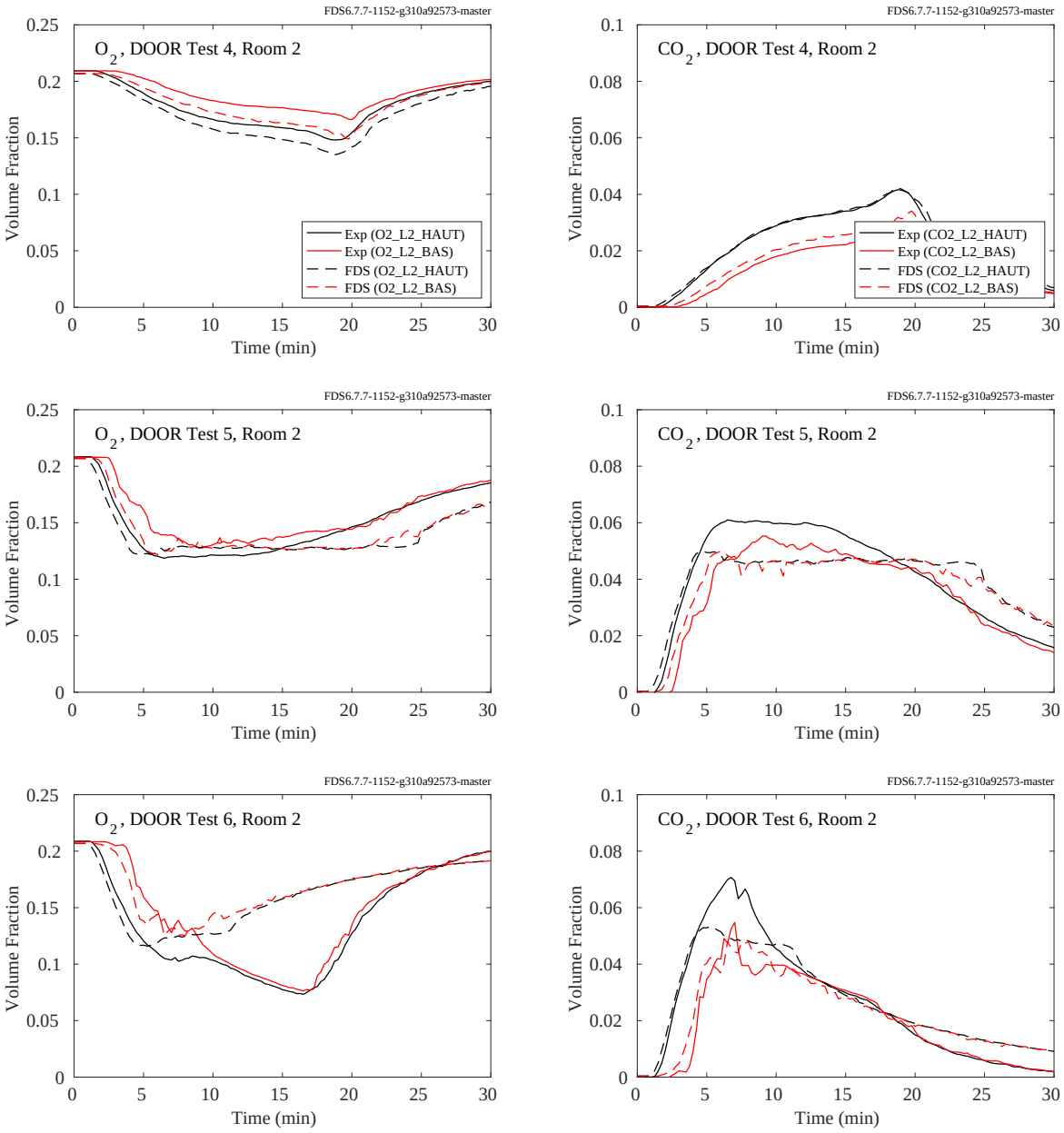

Figure 9.30: PRISME DOOR experiments, CO_2 and O_2 concentration, Room 2, Tests 4-6.

9.1.7 PRISME SOURCE Experiments

The compartment in the PRISME SOURCE experiments contained an oxygen and carbon dioxide measurement in the upper (haut) and lower (bas) layers.

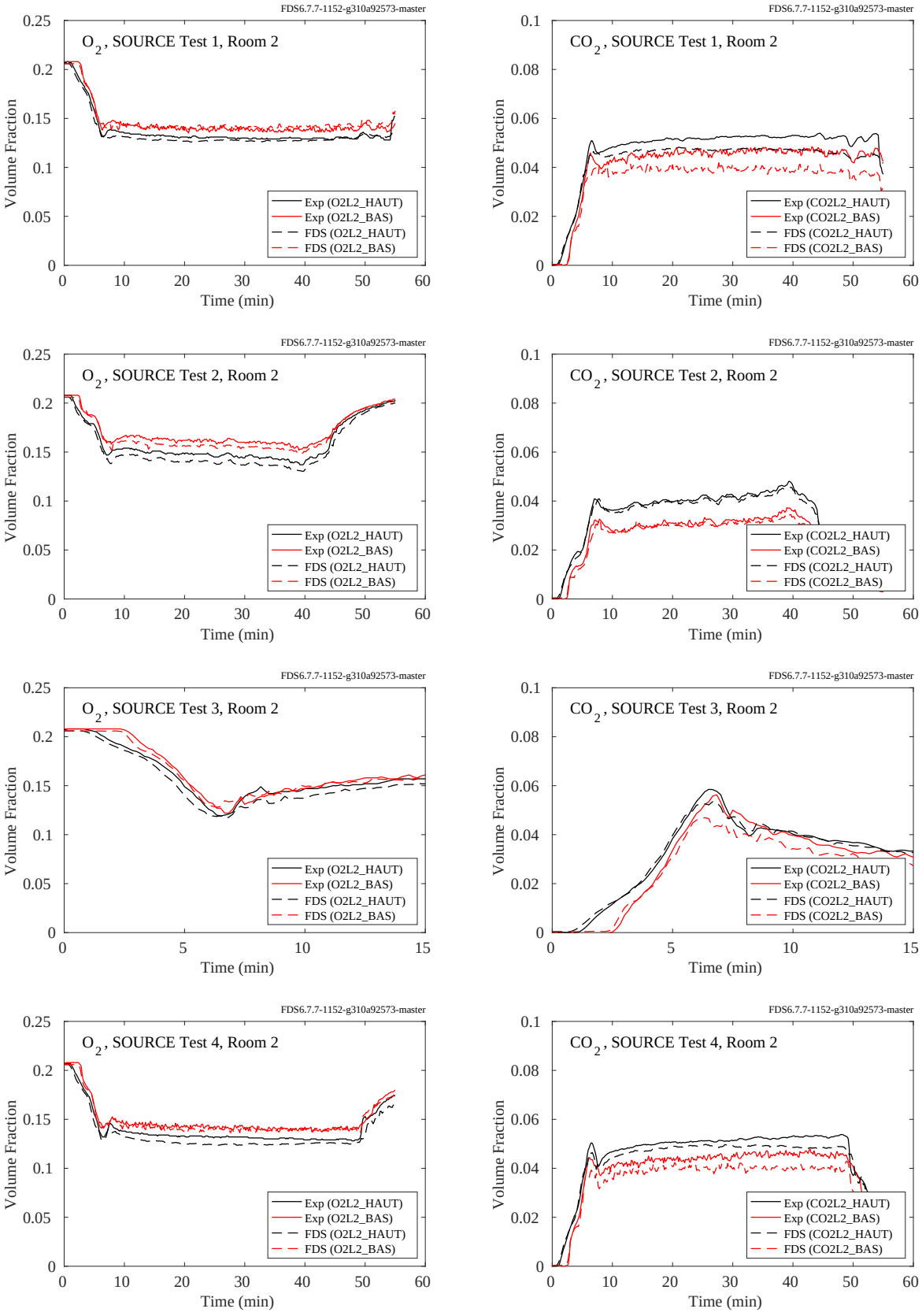

Figure 9.31: PRISME SOURCE experiments, CO_2 and O_2 concentration, Room 2, Tests 1-4.

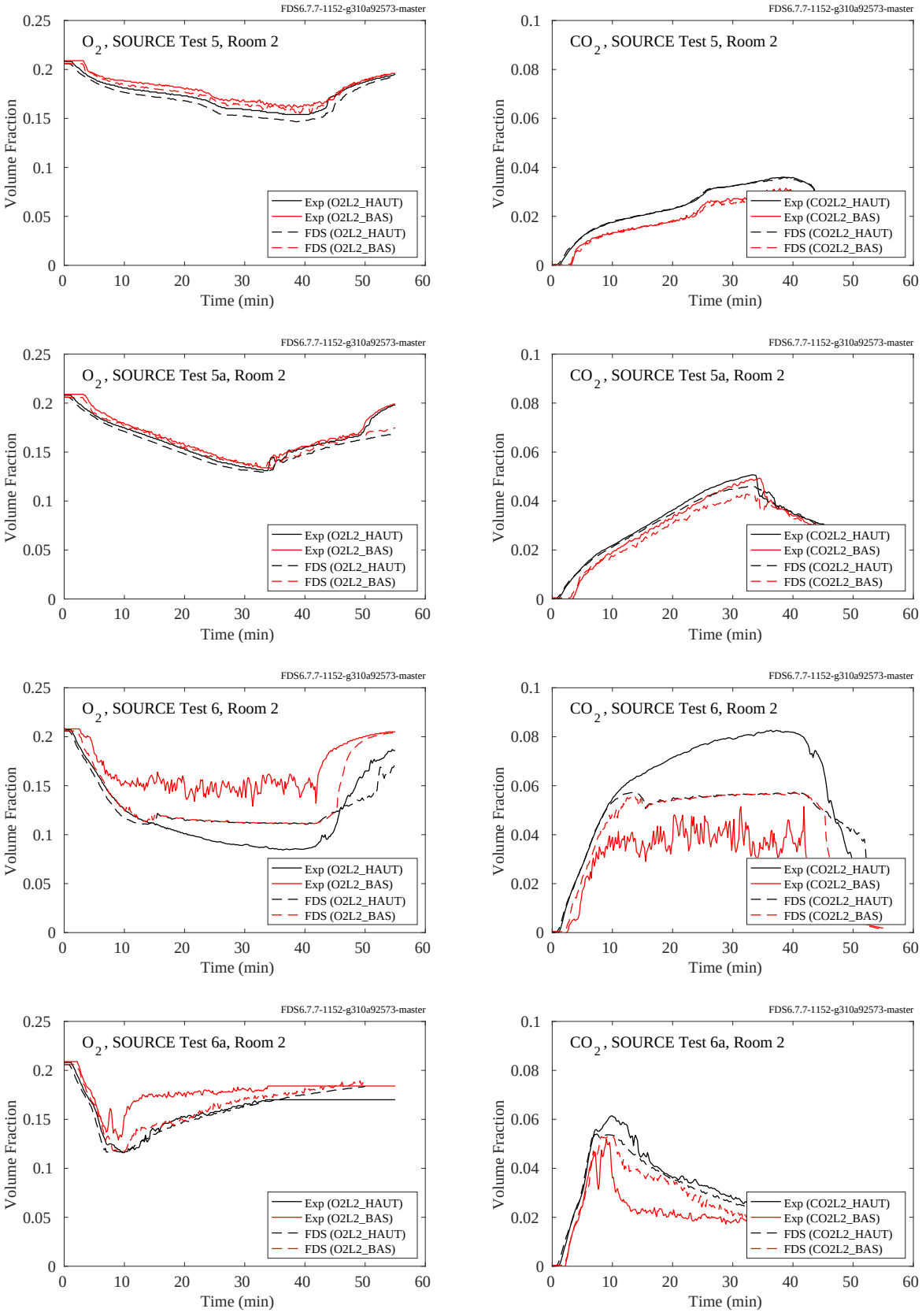

Figure 9.32: PRISME SOURCE experiments, CO_2 and O_2 concentration, Room 2, Tests 5-6.

9.1.8 WTC Experiments

The following pages present comparisons of oxygen and carbon dioxide concentration predictions and measurements for the WTC experiments. There was only one measurement of each made near the ceiling of the compartment roughly 2 m from the fire.

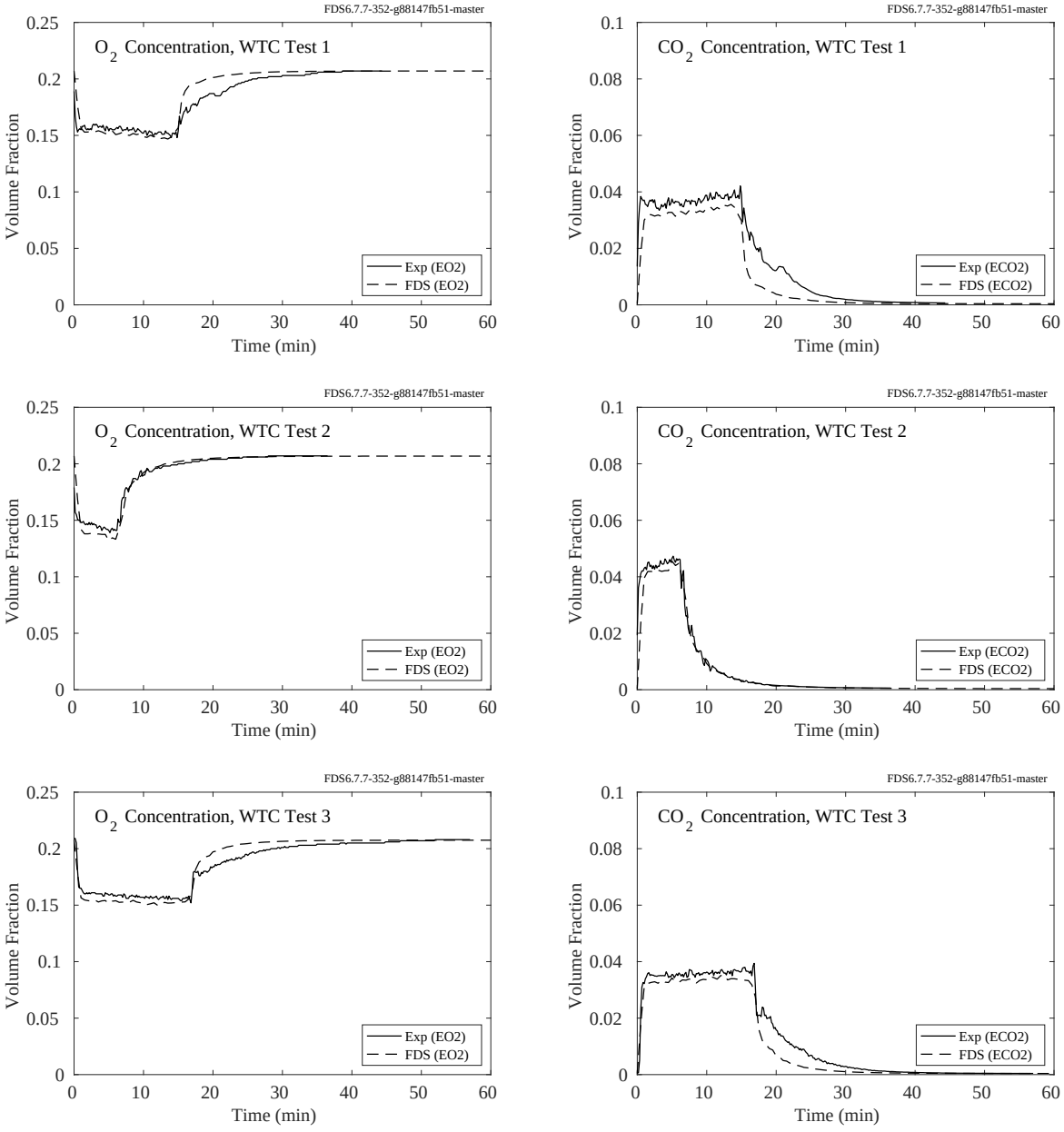

Figure 9.33: WTC experiments, CO_2 and O_2 concentration, Tests 1-3.

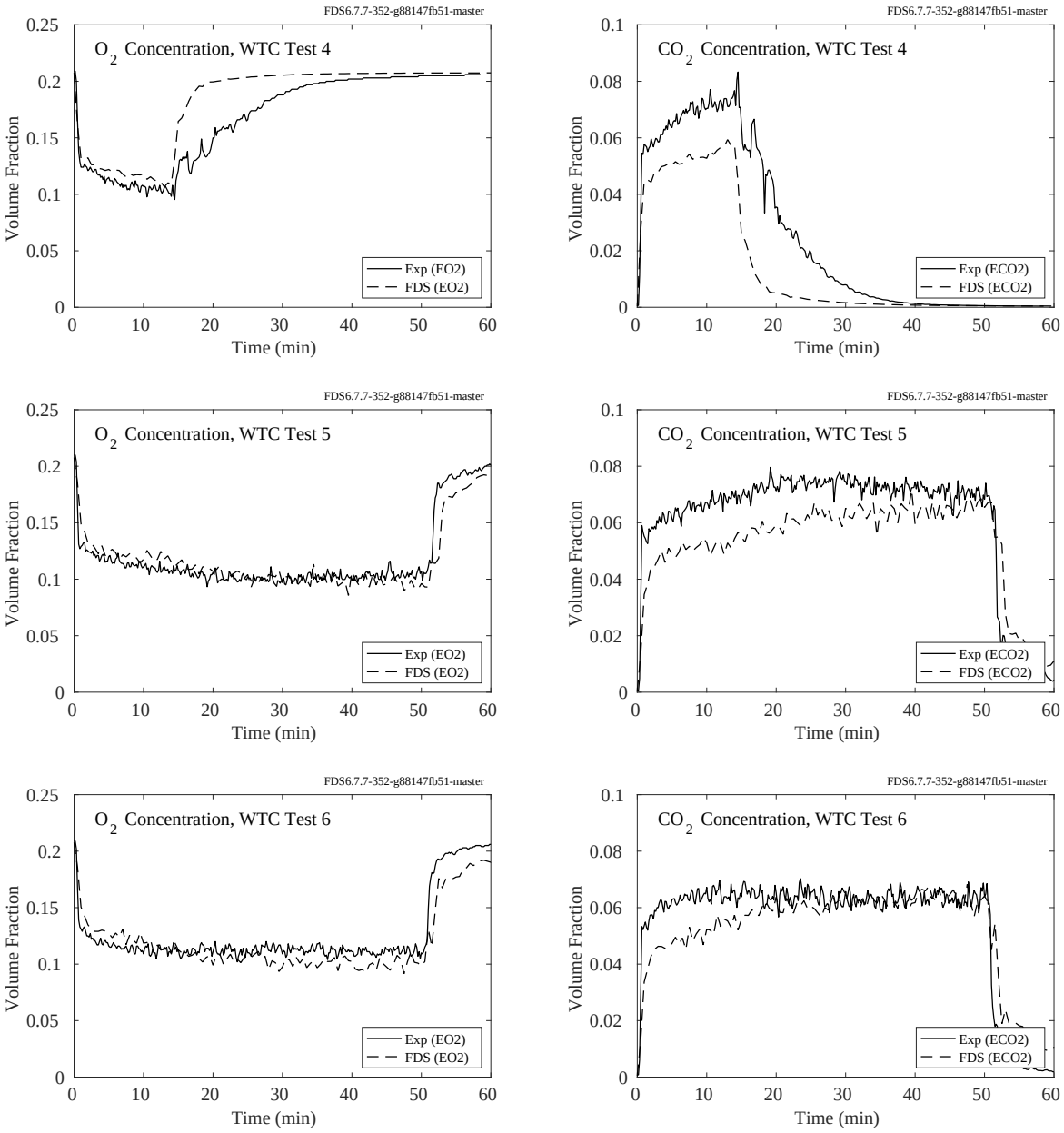

Figure 9.34: WTC experiments, CO_2 and O_2 concentration, Tests 4-6.

9.1.9 UMD Line Burner

Oxygen concentration measurements were made across the coflow section of the burner. Fig. 9.35 shows mean volume fraction O_2 profiles for two heights, z, above the burner surface for the experiment with nitrogen dilution of the coflowing air to 18 vol. % O_2 with methane as fuel. Notice that the O_2 level at the outer edge of the burner is the ambient value of 21 vol. %. Further experimental details may be found in White et al. [302]. FDS simulations are performed at three grid resolutions corresponding to $W/\delta x = 4, 8, 16$, where $W = 5$ cm is the width of the line burner (see Fig. 3.49).

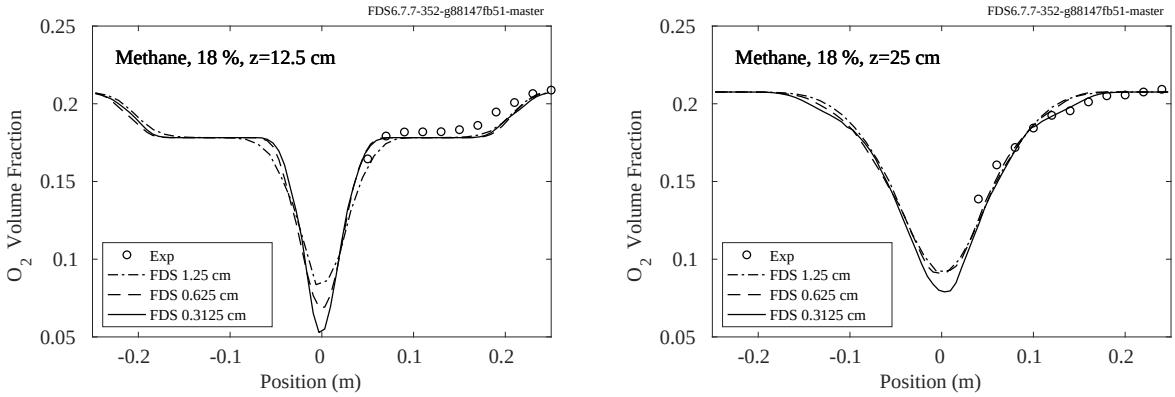

Figure 9.35: Measured and predicted mean oxygen concentration profiles at 18 vol % O_2.

9.1.10 Summary of Major Combustion Products Predictions

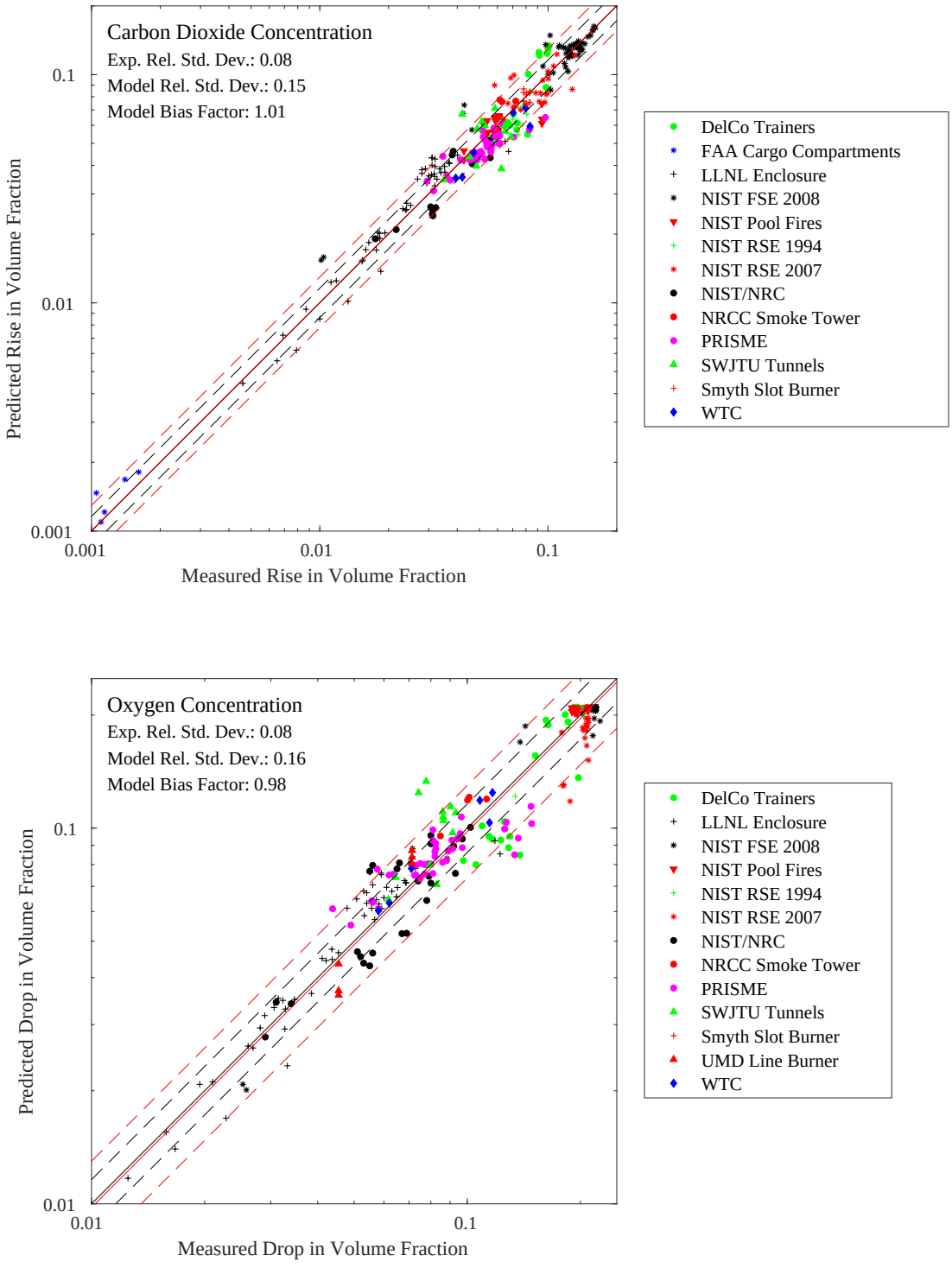

Figure 9.36: Summary of major gas species predictions.

9.2 Smoke

9.2.1 FM Burner Experiments

Mean and rms soot volume fraction measurements were made above a 13.7 cm (inner) diameter, 15 kW ethylene burner. Figures 9.37 through 9.42 display the radial profiles located at heights of 0.5, 1.0, 1.5, 2.5, and 3.5 burner diameters, D. Figures 9.43 through 9.45 display the probability distributions (PDFs) at the five heights and radii of 0 cm, 2 cm, 4 cm, 6 cm, and 8 cm.

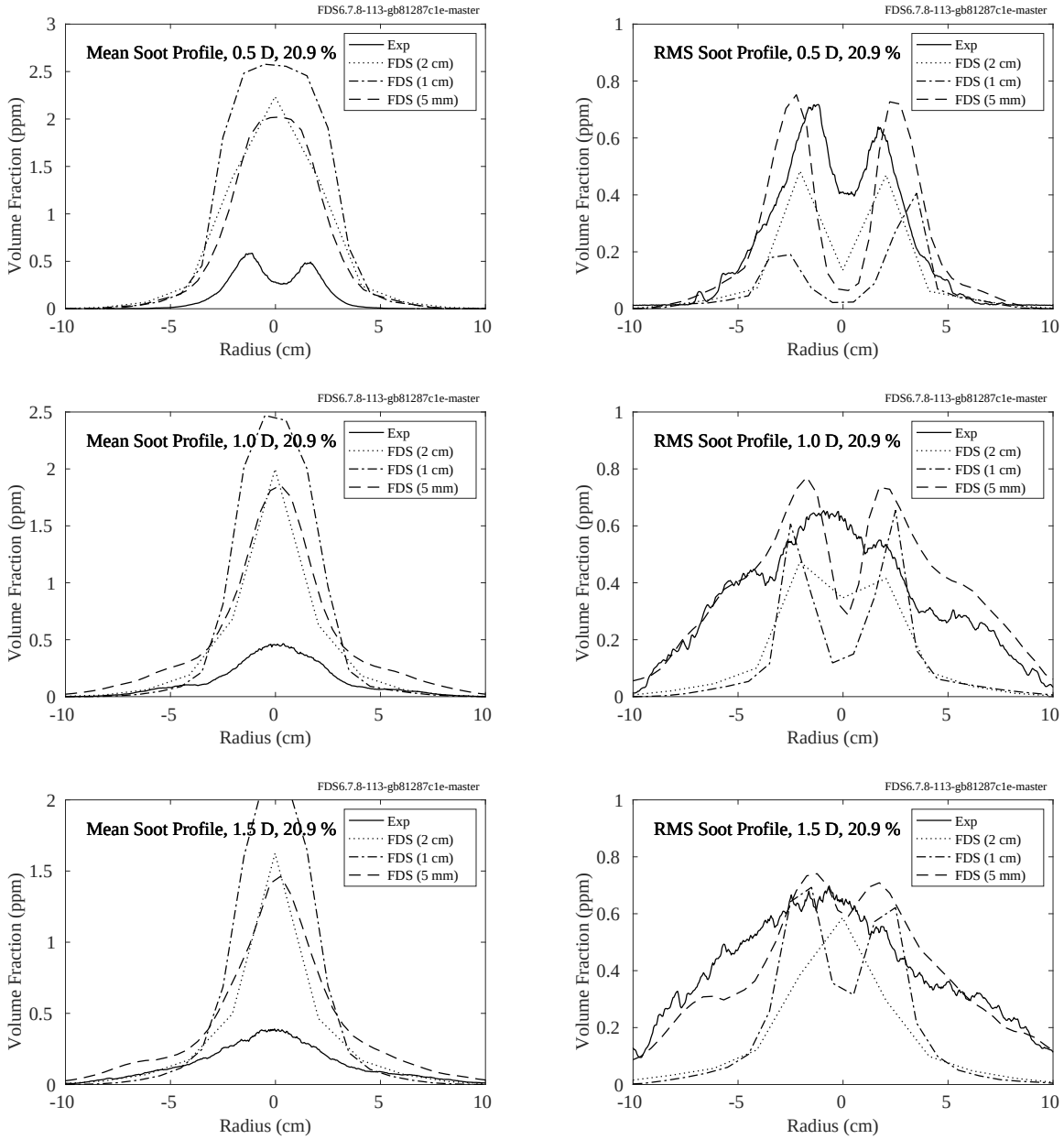

Figure 9.37: FM Burner experiments, plume mean and rms soot volume fraction at heights of 0.5, 1.0, and 1.5 burner diameters, D, 20.9 % O_2.

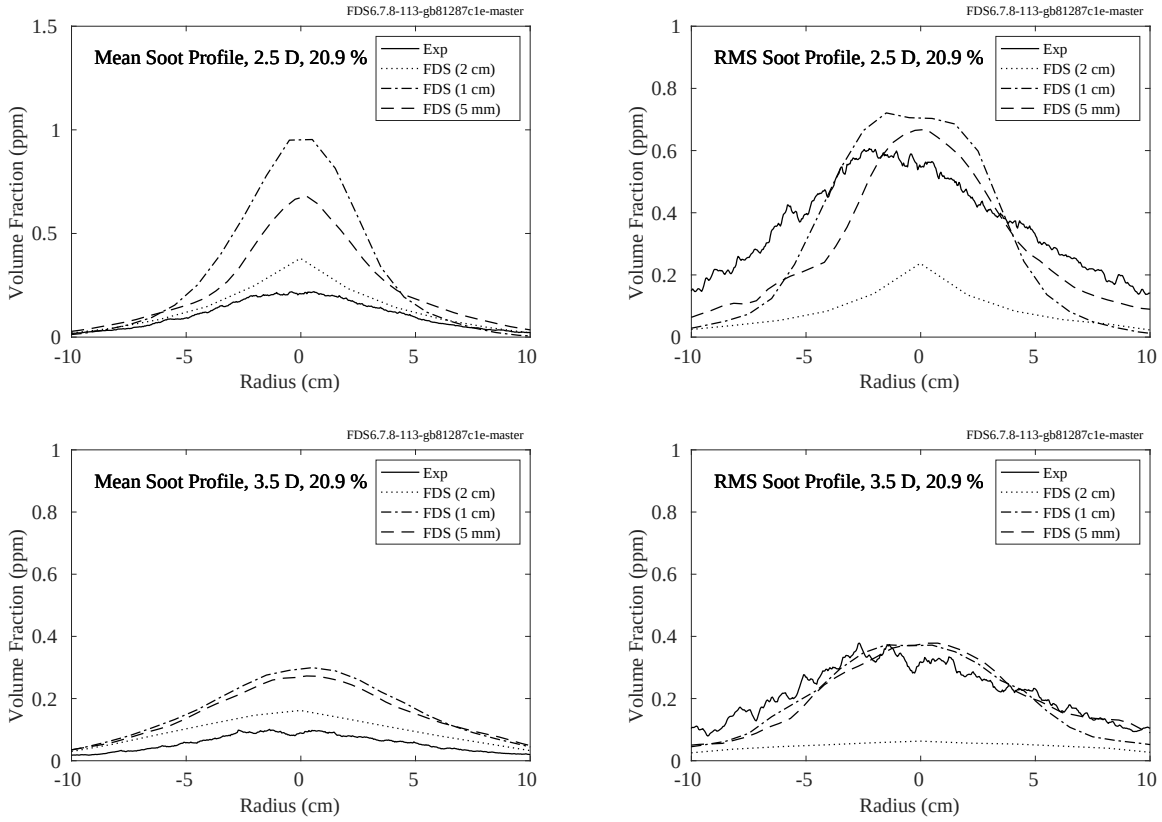

Figure 9.38: FM Burner experiments, plume mean and rms soot volume fraction at heights of 2.5 and 3.5 burner diameters, D, 20.9 % O_2.

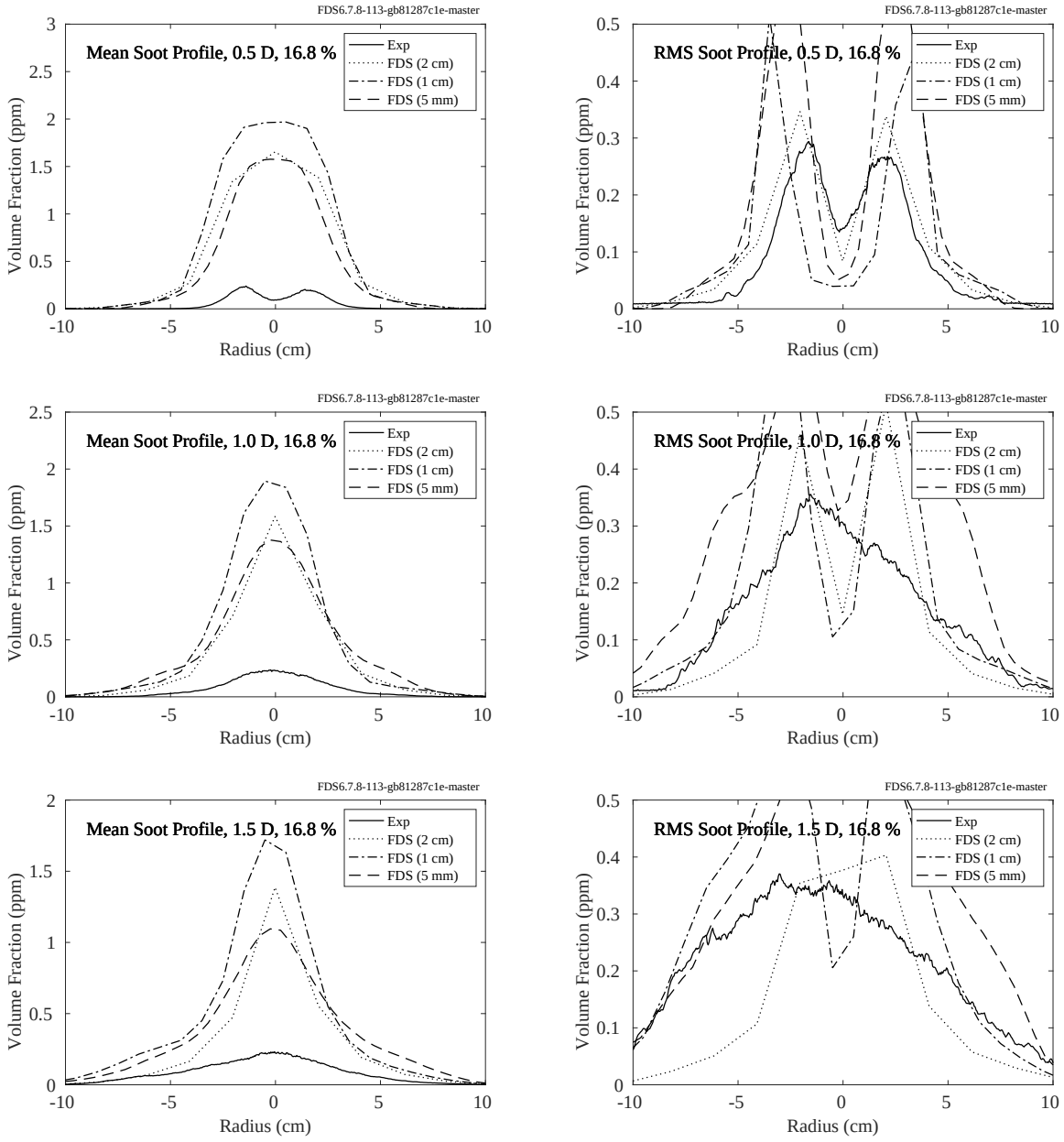

Figure 9.39: FM Burner experiments, plume mean and rms soot volume fraction at heights of 0.5, 1.0, and 1.5 burner diameters, D, 16.8 % O_2.

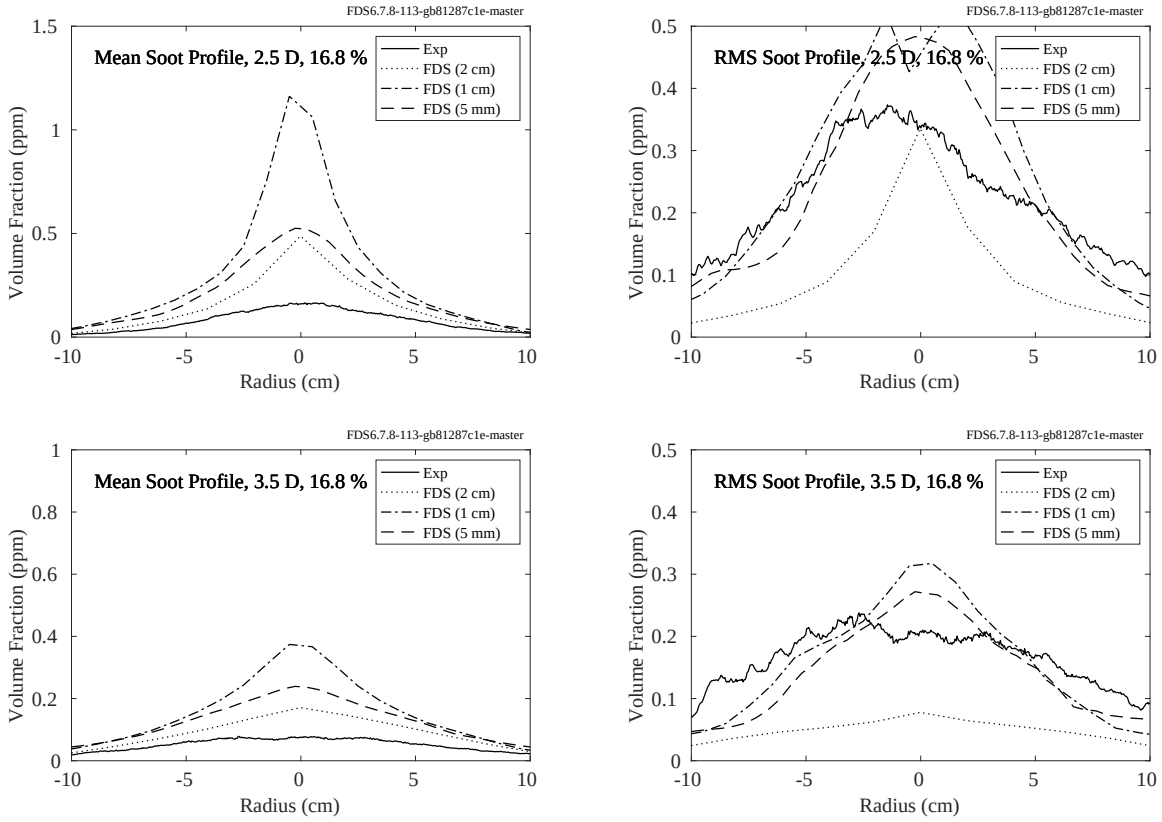

Figure 9.40: FM Burner experiments, plume mean and rms soot volume fraction at heights of 2.5 and 3.5 burner diameters, D, 16.8 % O_2.

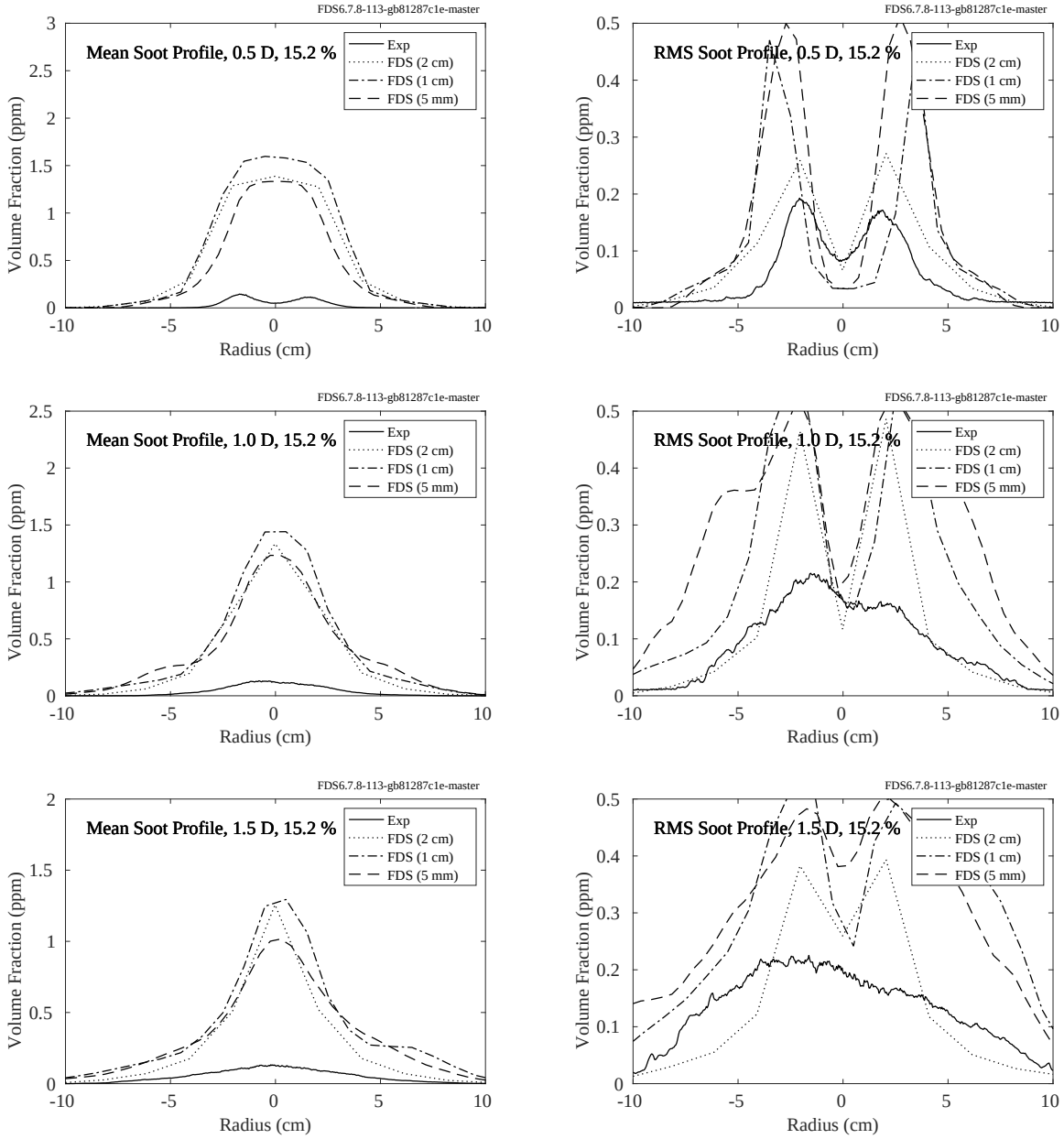

Figure 9.41: FM Burner experiments, plume mean and rms soot volume fraction at heights of 0.5, 1.0, and 1.5 burner diameters, D, 15.2 % O_2.

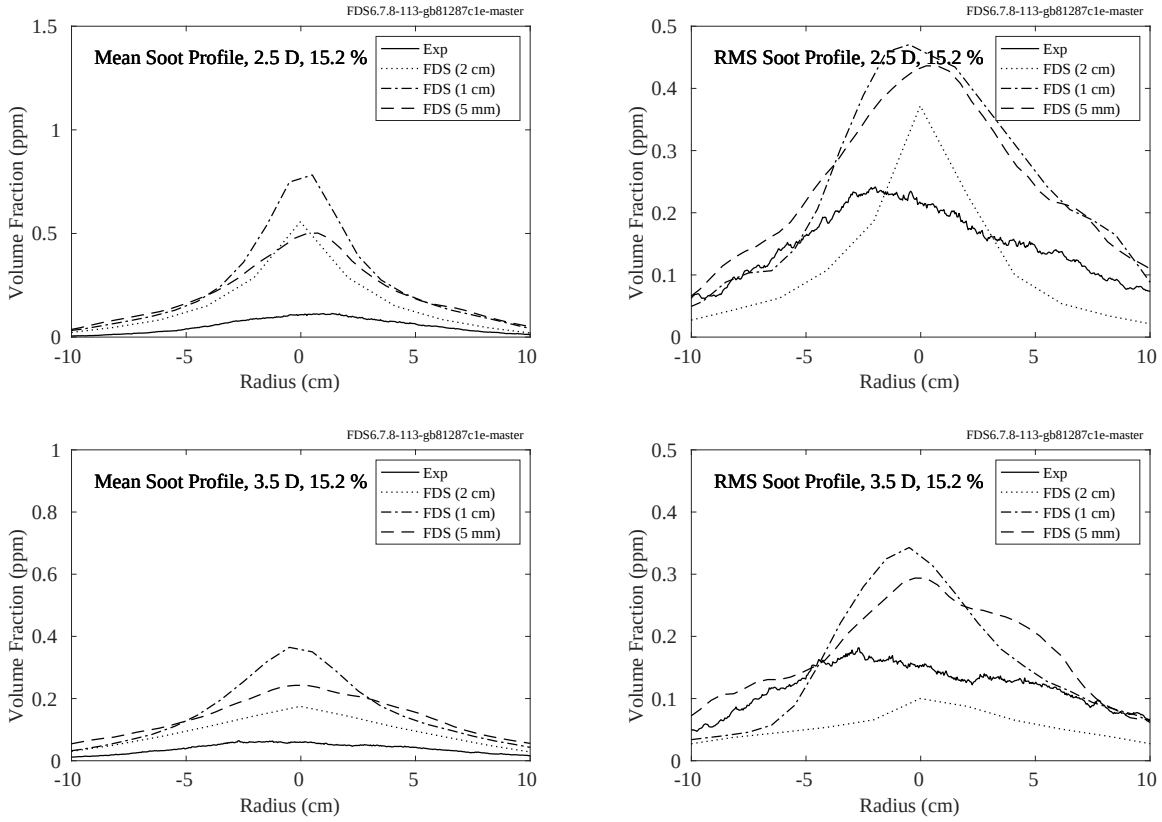

Figure 9.42: FM Burner experiments, plume mean and rms soot volume fraction at heights of 2.5 and 3.5 burner diameters, D, 15.2 % O_2.

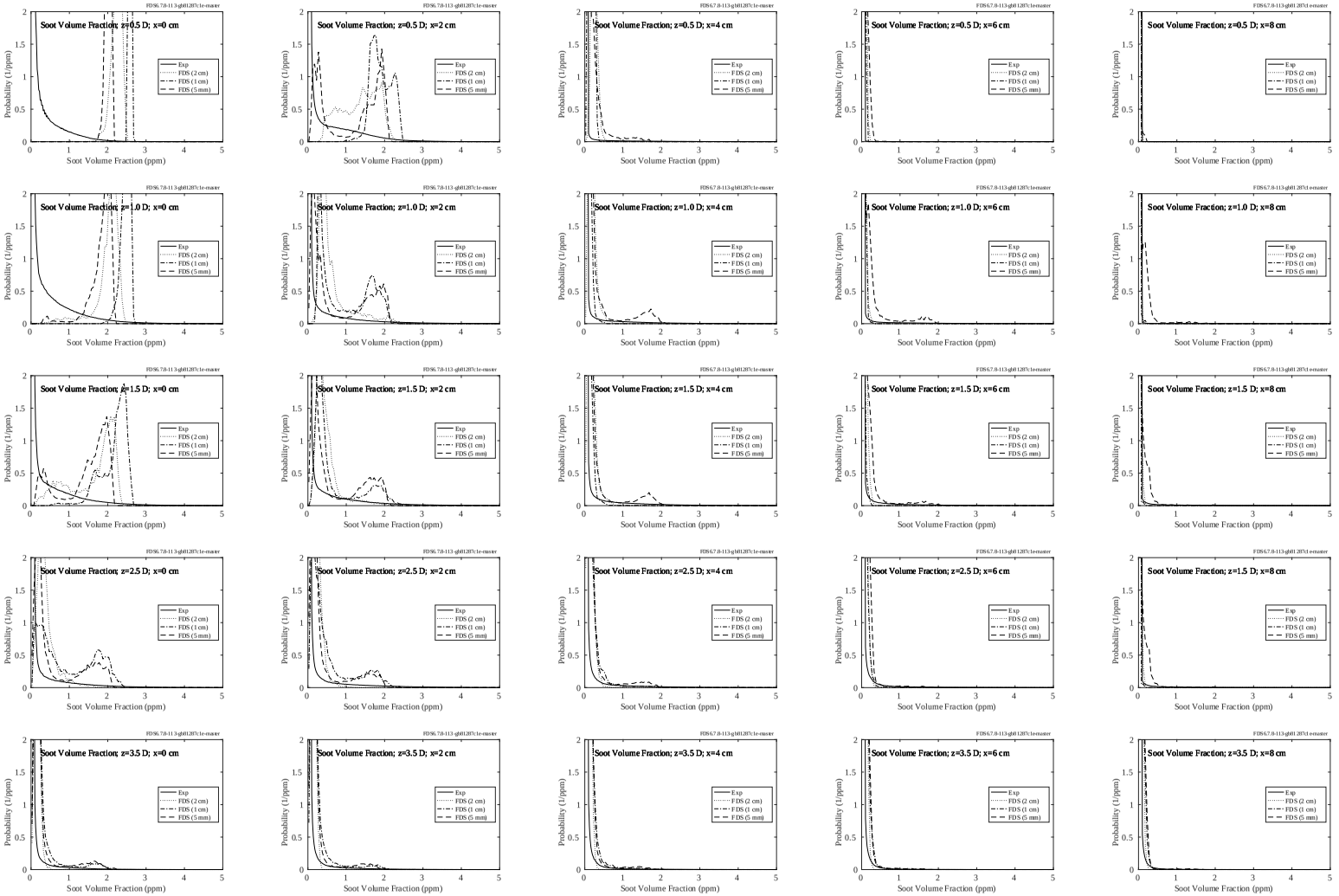

Figure 9.43: FM Burner experiments, soot volume fraction PDFs, 20.9 % O_2.

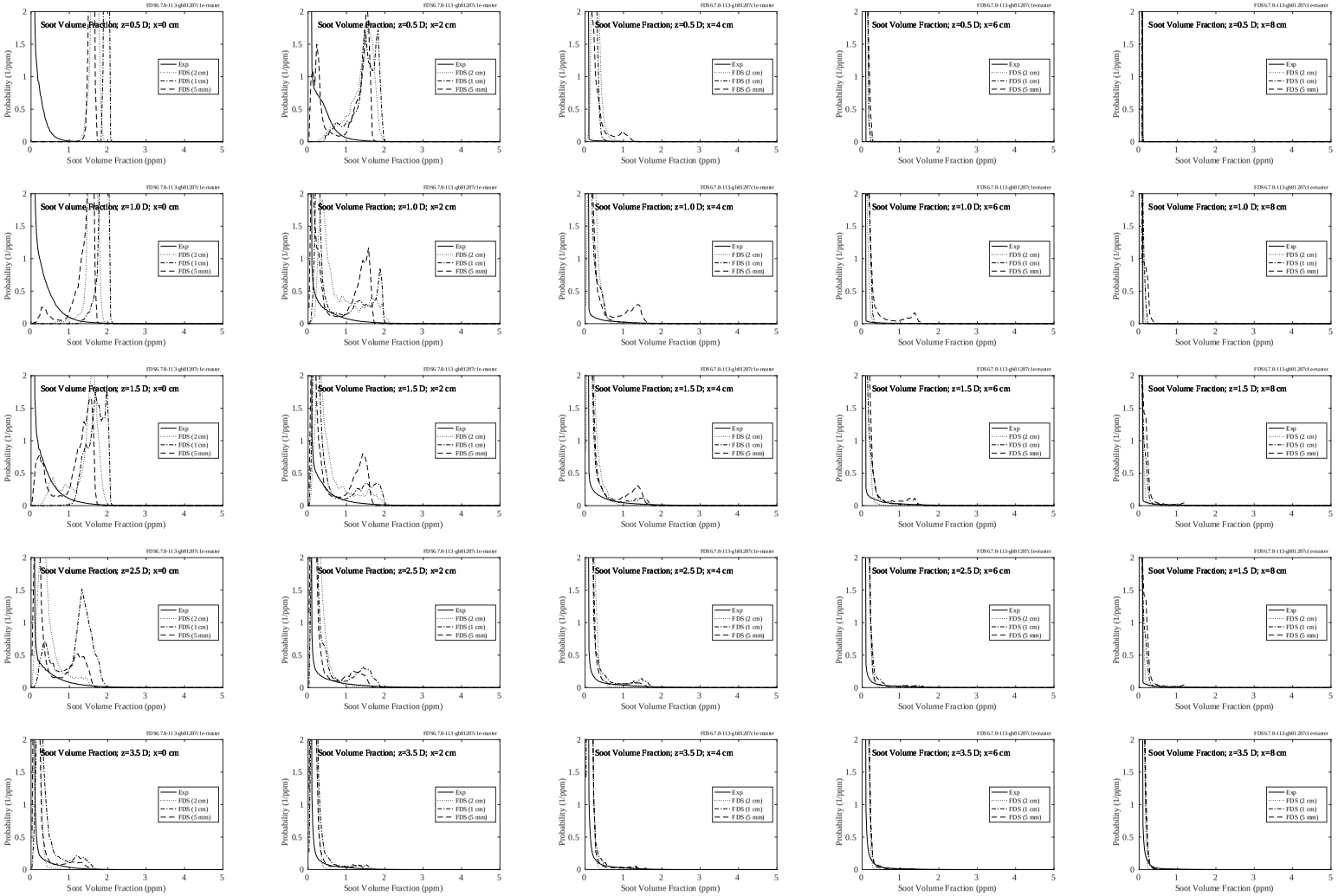

Figure 9.44: FM Burner experiments, soot volume fraction PDFs, 16.8 % O_2.

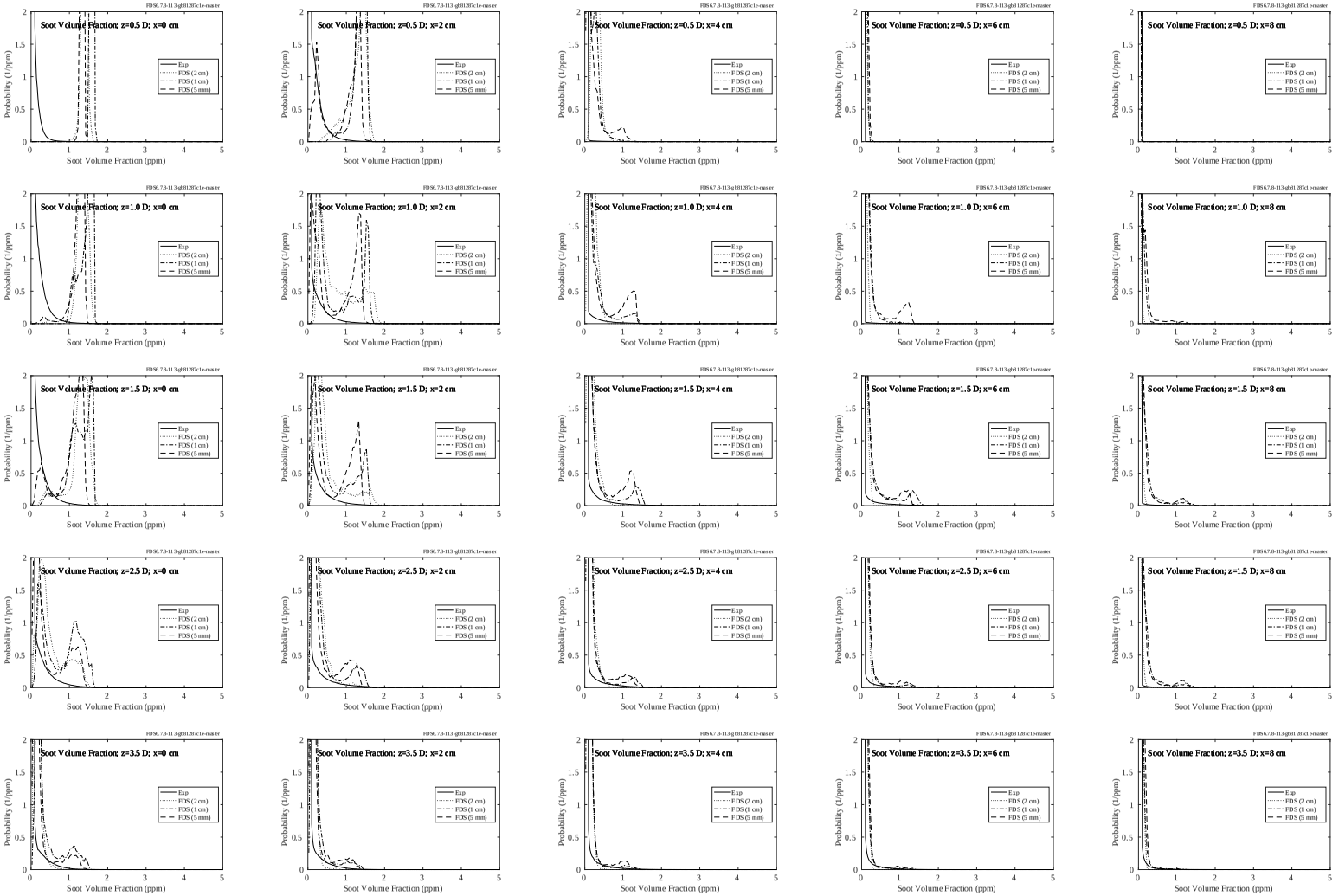

Figure 9.45: FM Burner experiments, soot volume fraction PDFs, 15.2 % O_2.

9.2.2 FM/FPRF Data Center Experiments

Results of the low exhaust rate (78 ACH) and high exhaust rate (265 ACH) tests for propylene and cables is shown in the figure below. Each test had three measurement locations (subfloor, ceiling, and ceiling plenum); however, not all locations for all tests had a measurement above background noise in the laser signal.

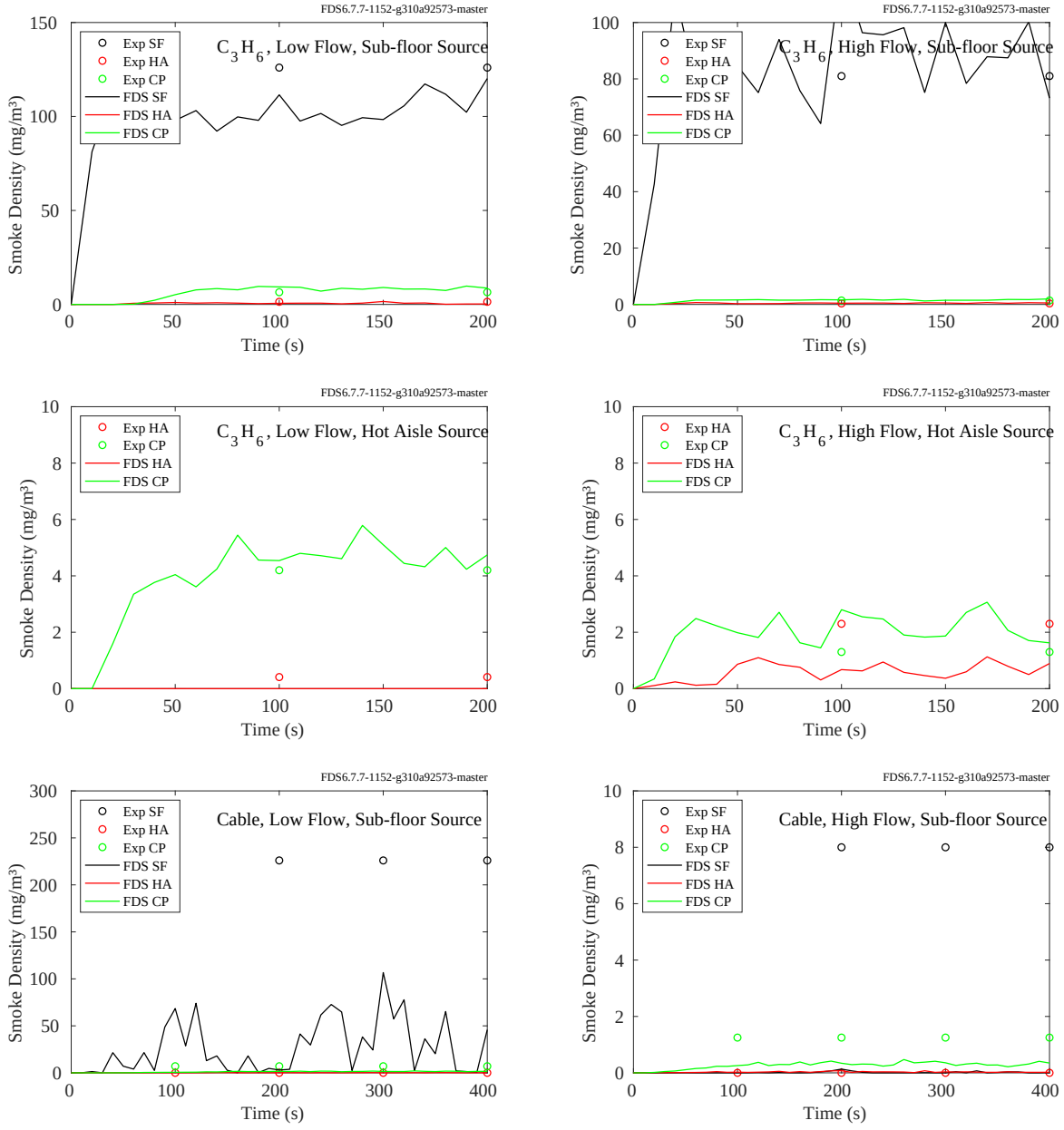

Figure 9.46: FM/FPRF Data Center, smoke concentration, low and high exhaust rate, propylene and cable sources.

9.2.3 NIST/NRC Experiments

For the simulations of the NIST/NRC tests, the smoke yield is specified as one of the test parameters. The figures on the following pages contain comparisons of measured and predicted smoke concentration at one measuring station in the upper layer.

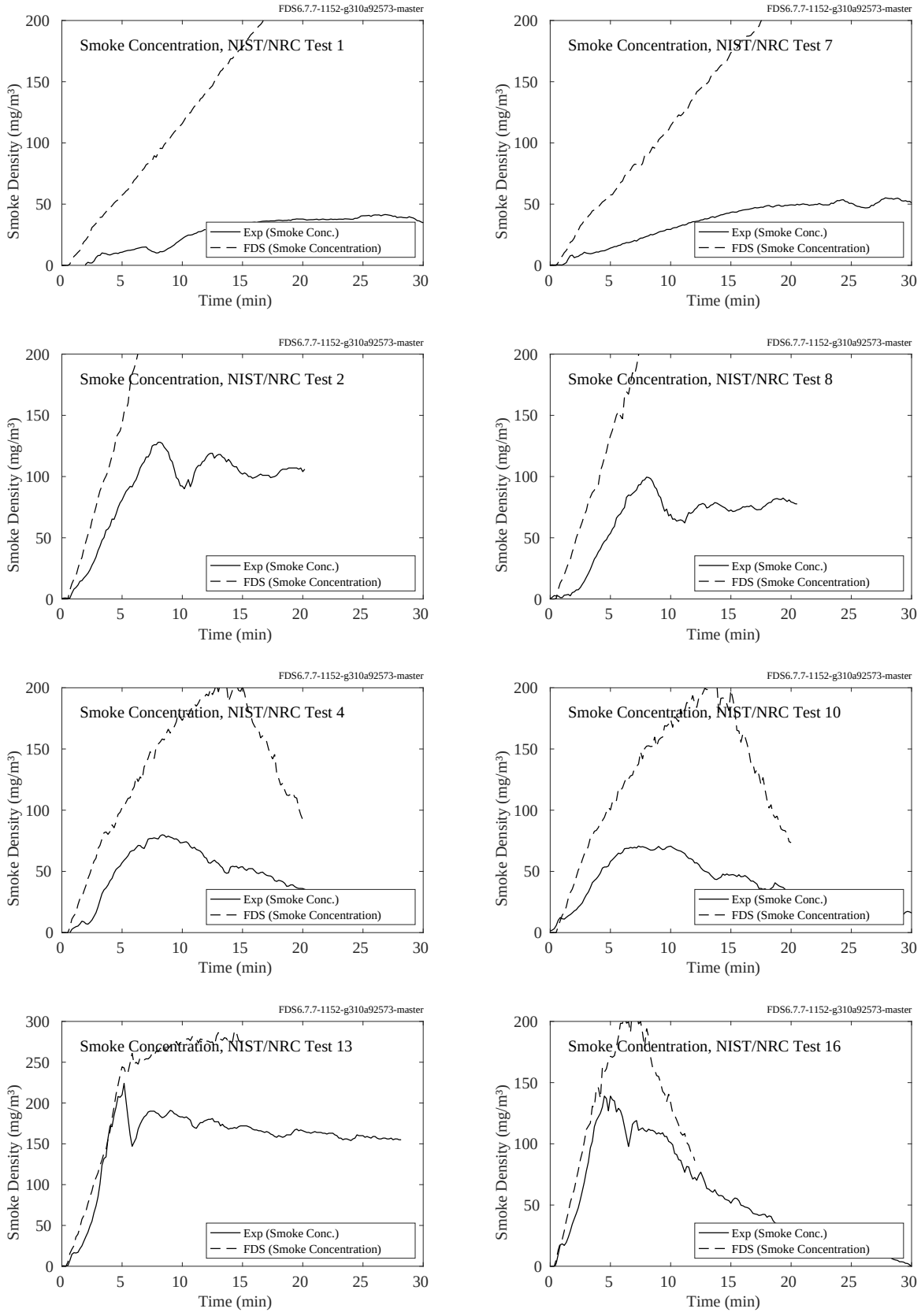

Figure 9.47: NIST/NRC experiments, smoke concentration, Tests 1, 2, 4, 7, 8, 10, 13, 16.

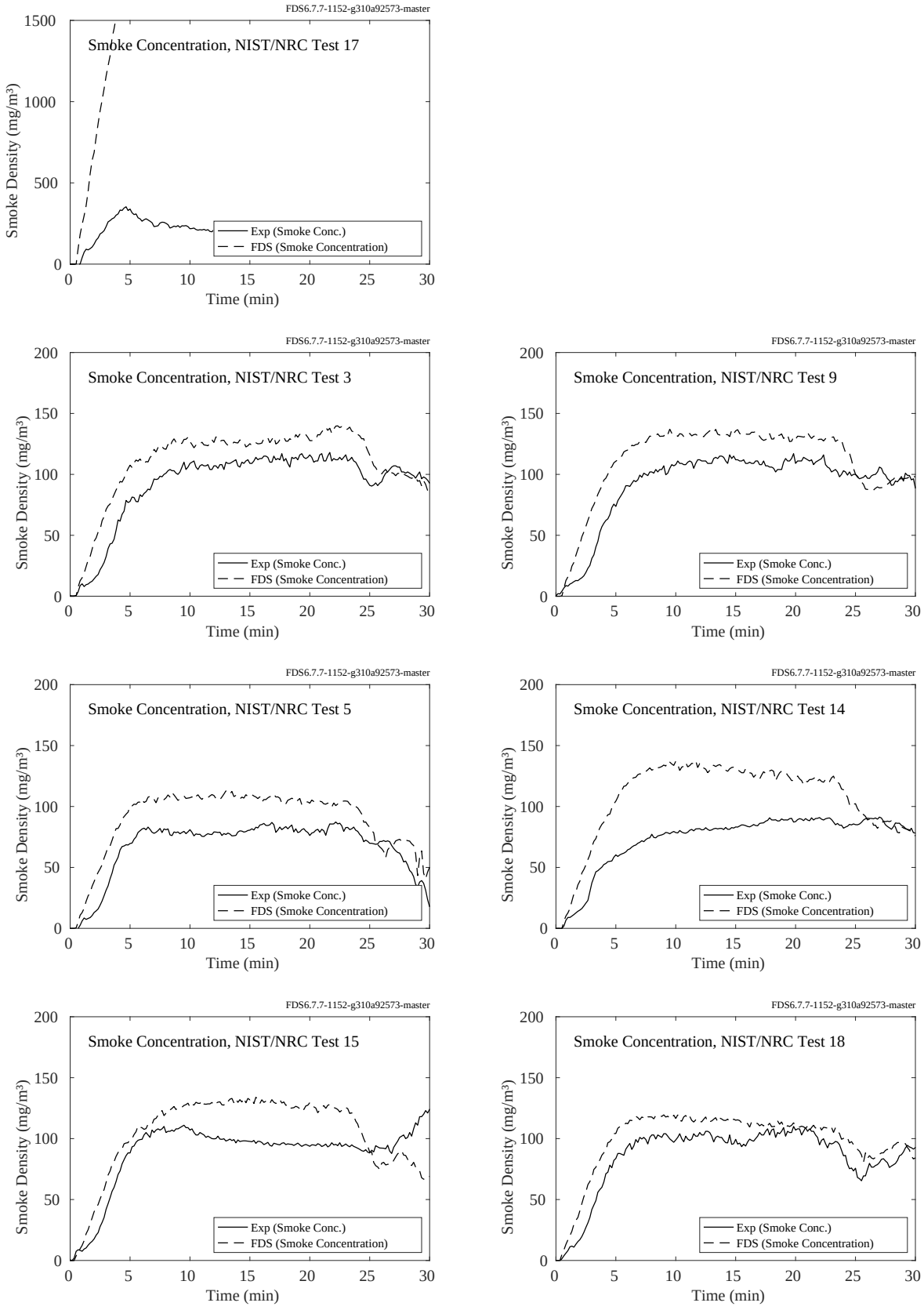

Figure 9.48: NIST/NRC experiments, smoke concentration, Tests 3, 5, 9, 14, 15, 17, 18.

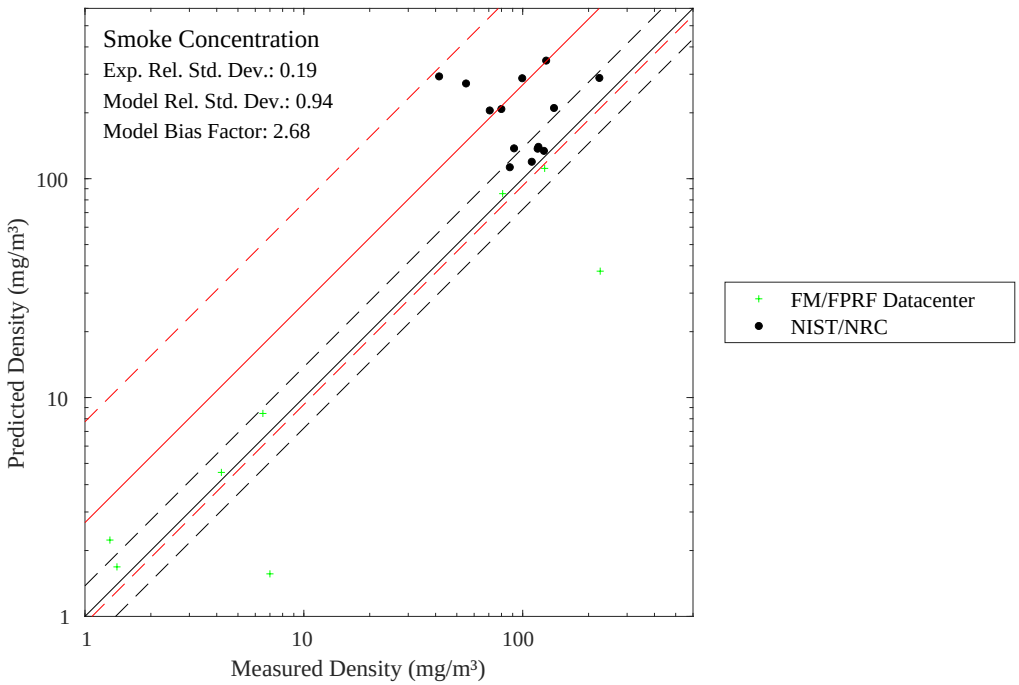

Figure 9.49: Summary of smoke concentration predictions.

9.2.4 FAA Cargo Compartments

Beam obscuration measurements were made at different locations within the compartment (see Fig. 7.10). The data is presented below in terms of percent transmission per meter, $100(I/I_0)^{1/L}$, where I is the light intensity and L is the beam pathlength in units of meters.

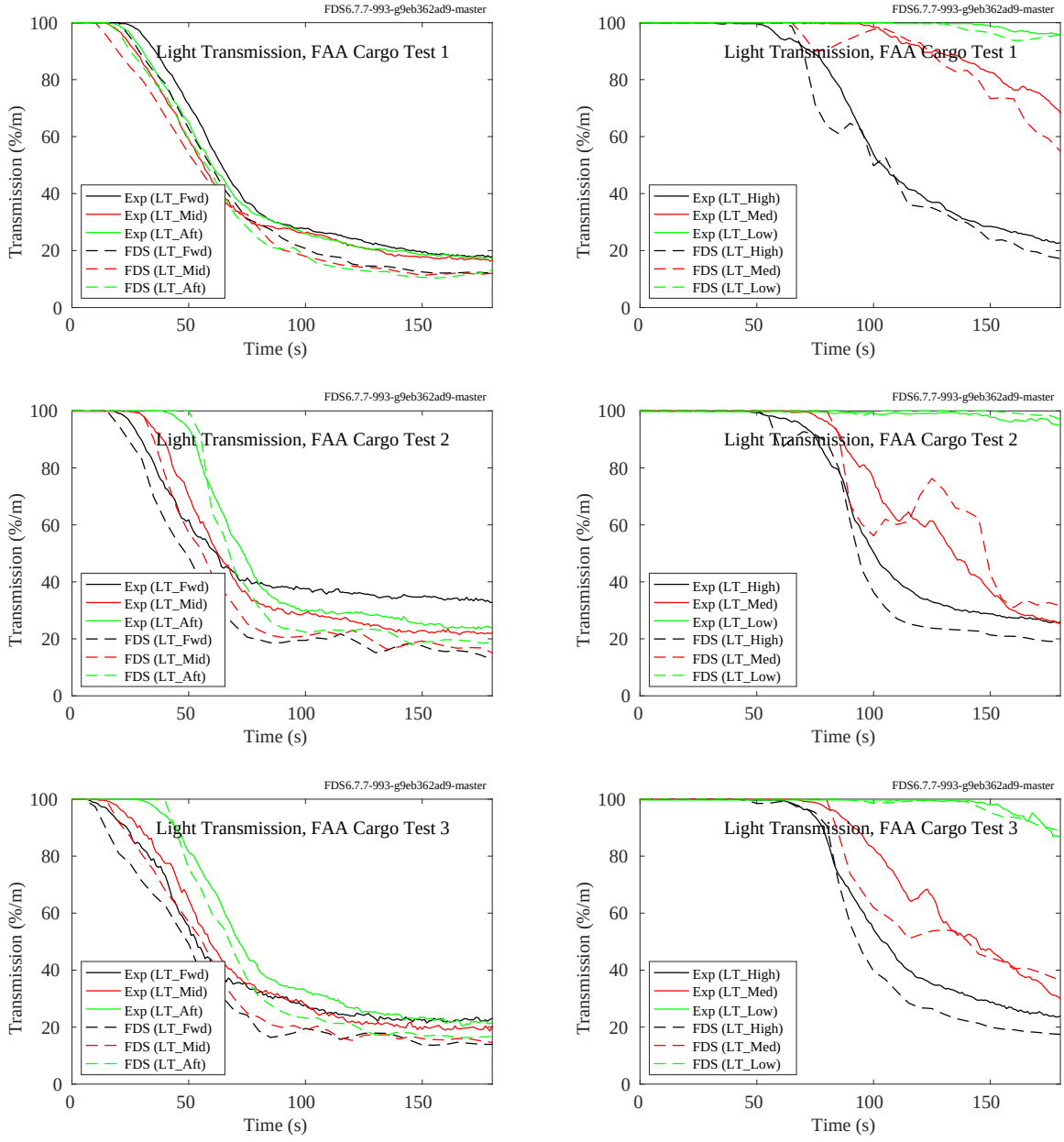

Figure 9.50: FAA Cargo Compartments experiments, smoke obscuration.

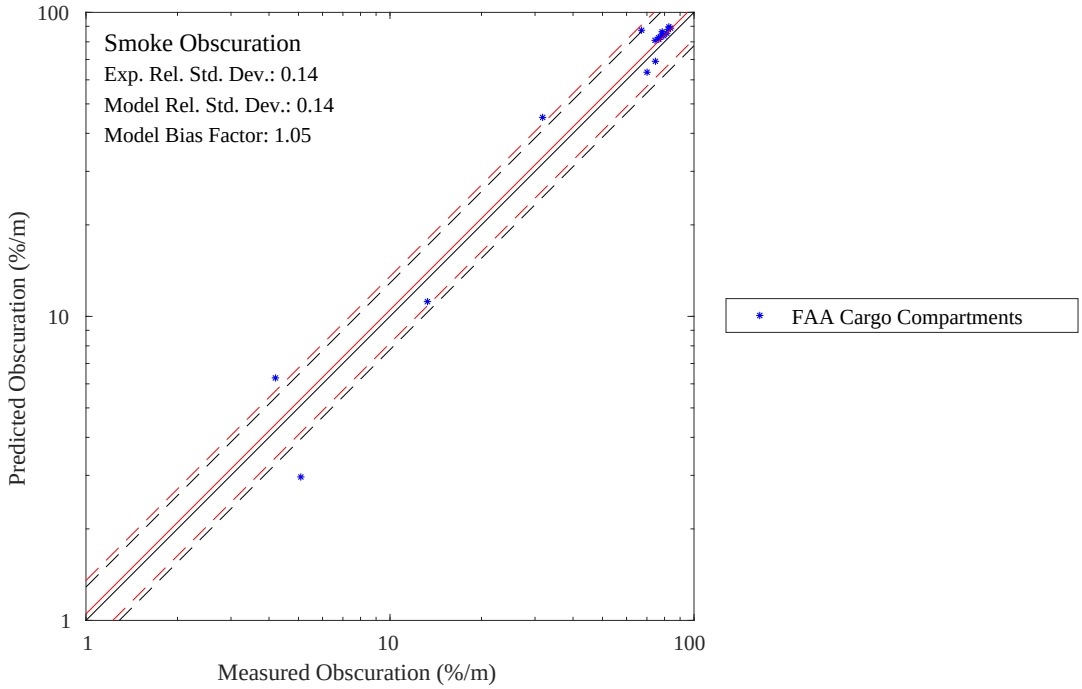

Figure 9.51: Summary of smoke obscuration predictions.

9.3 Aerosols

9.3.1 Sippola Aerosol Deposition Experiments

Figure 9.52 compares the measured and predicted aerosol deposition velocities in the Sippola experiments, and Figure 9.53 shows a summary of the results. Details of the experiment and simulation are found in Section 3.68

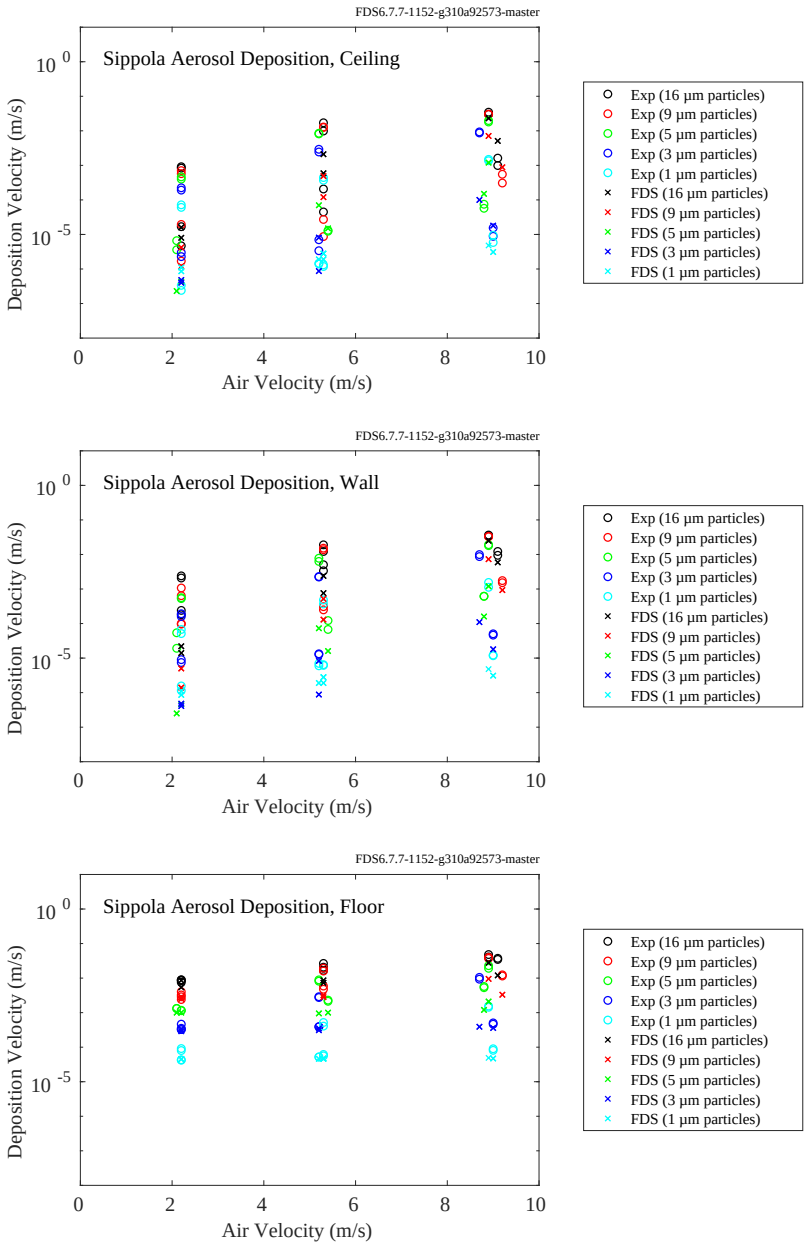

Figure 9.52: Predicted and measured aerosol deposition velocities, Sippola experiments.

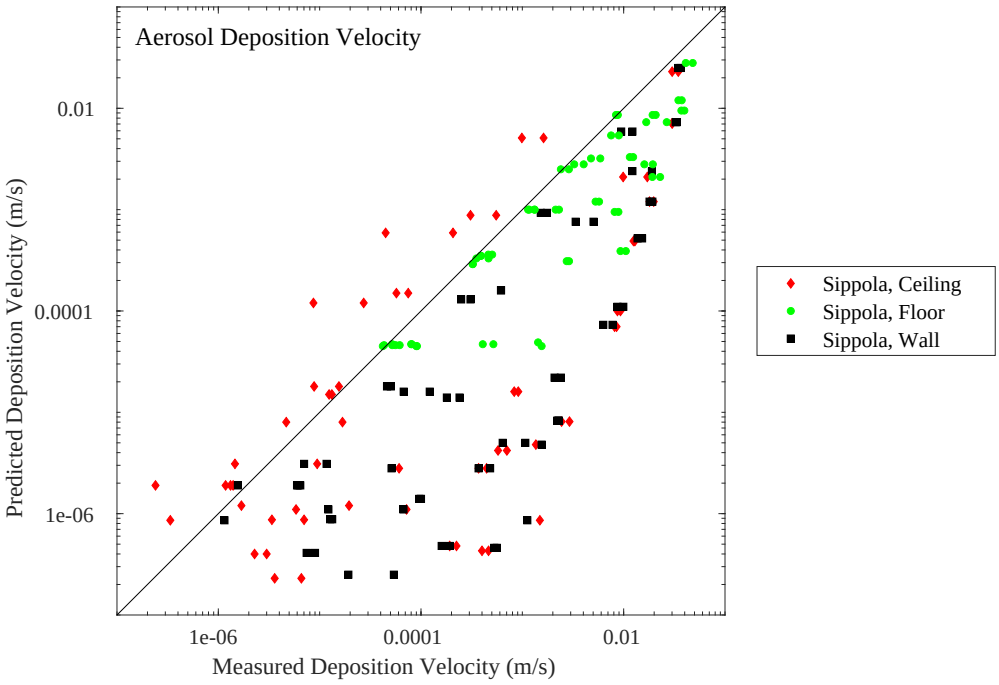

Figure 9.53: Summary of aerosol deposition velocity predictions.

9.3.2 NIST Soot Deposition Gauge Experiments

Figure 9.54 compares the measured and predicted aerosol mass deposition velocities in the NIST Soot Deposition Gauge experiments, and Figure 9.55 shows a summary of the results. Details of the experiment and simulation are found in Section 3.53

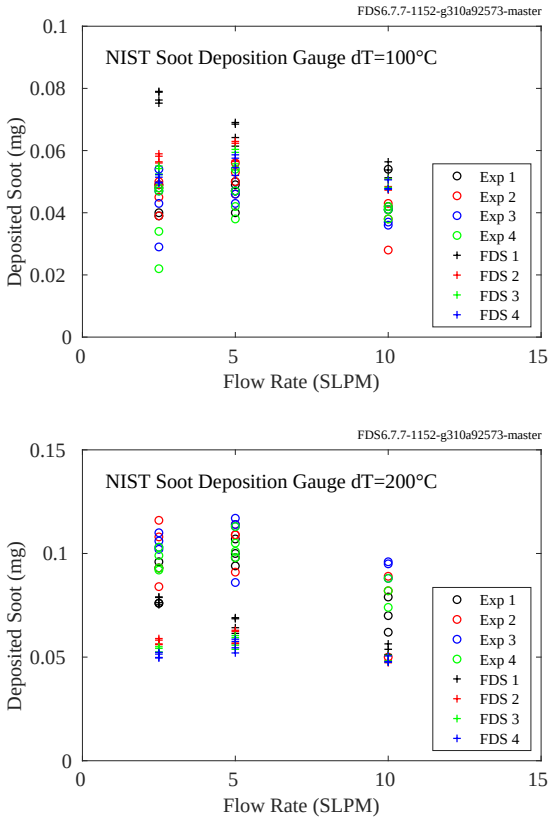

Figure 9.54: Predicted and measured aerosol deposited mass, NIST Soot Deposition Gauge experiments.

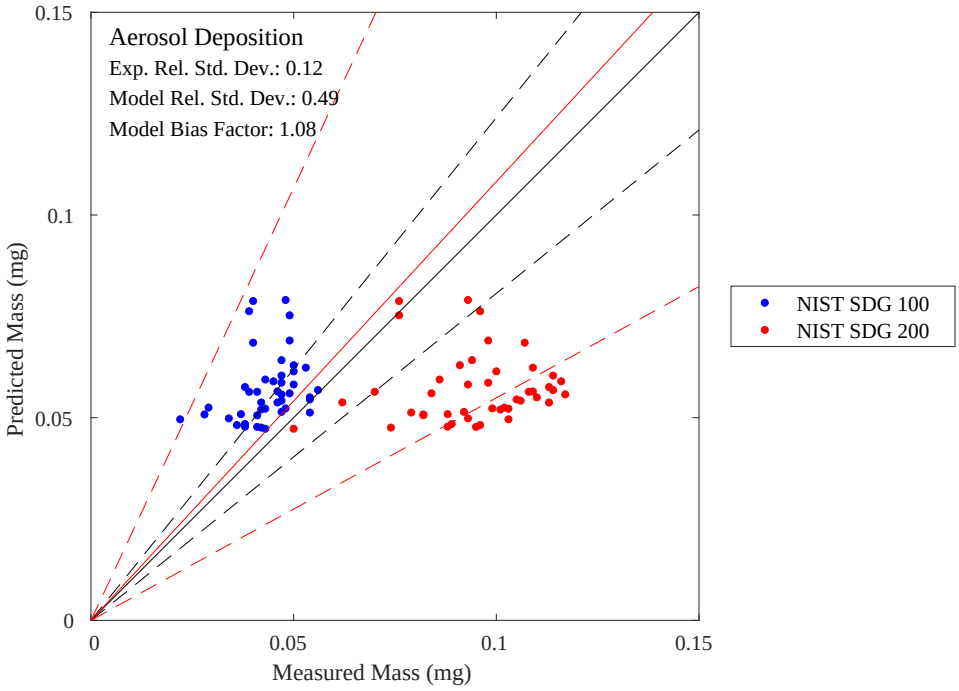

Figure 9.55: Summary of aerosol deposited mass predictions.

9.4 Droplet Evaporation

This section presents the results of simulations of liquid droplet evaporation experiments. The titles of the sections below are named for the experimentalists.

9.4.1 Ranz and Marshall

A description of the experiments is included in Sec. 3.62. Figure 9.56 shows the results of predicting the drop diameter of a single droplet evaporating in dry air.

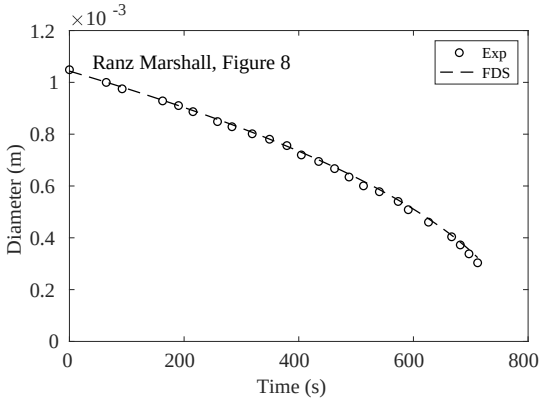

Figure 9.56: Measured and predicted droplet diameter for the Ranz and Marshall experiment shown in Fig. 8 of [268].

Figure 9.57 compares the measured and predicted evaporation rates for Table 1 through Table 4 in [268]. The Table 1 experiments were water droplets in ambient air, the Table 2 experiments were water droplets at in warm air (less than boiling), the Table 3 experiments were water droplets in hot air (greater than boiling), and the Table 4 experiments were benzene droplets in ambient air. A summary of the results is shown in Fig. 9.58.

9.4.2 Fujita et al.

A description of the experiments is included in Sec. 3.19. Figure 9.59 shows the droplet area normalized by its initial area, and Fig. 9.60 shows the droplet temperature change.

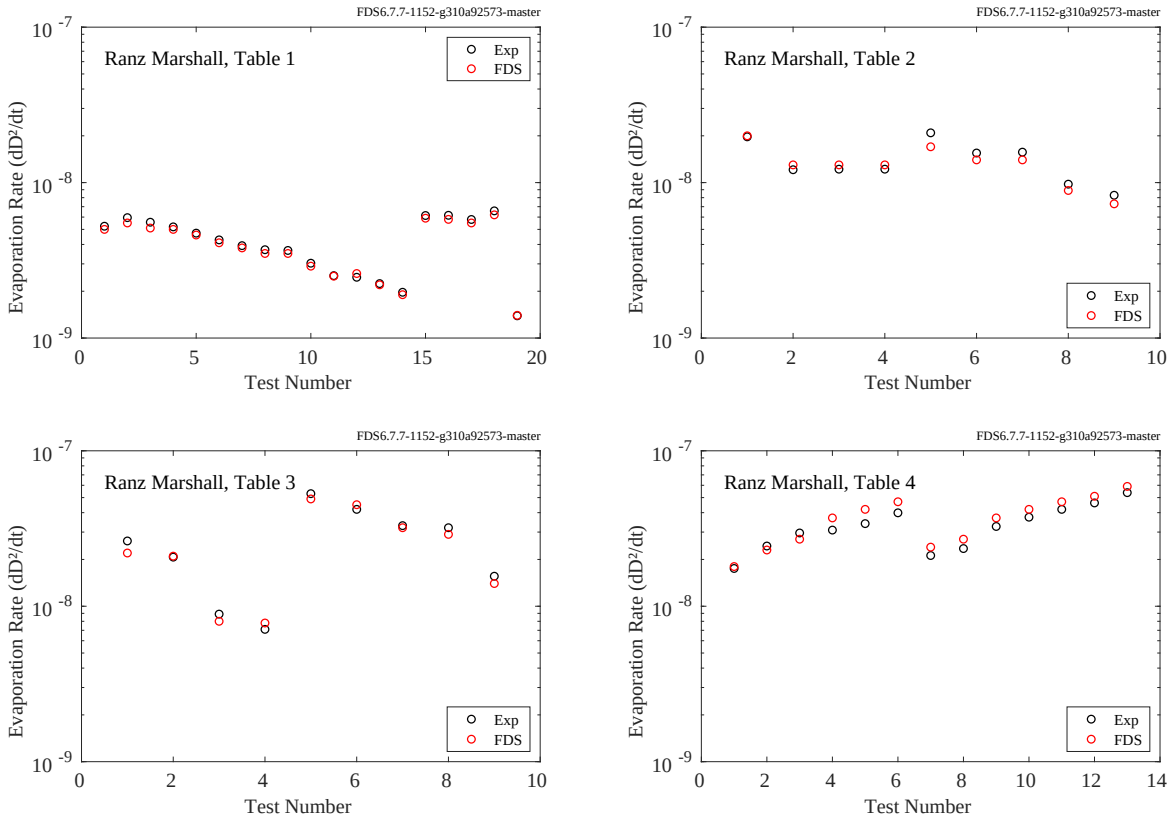

Figure 9.57: Evaporation rates for the Ranz and Marshall experiments [268].

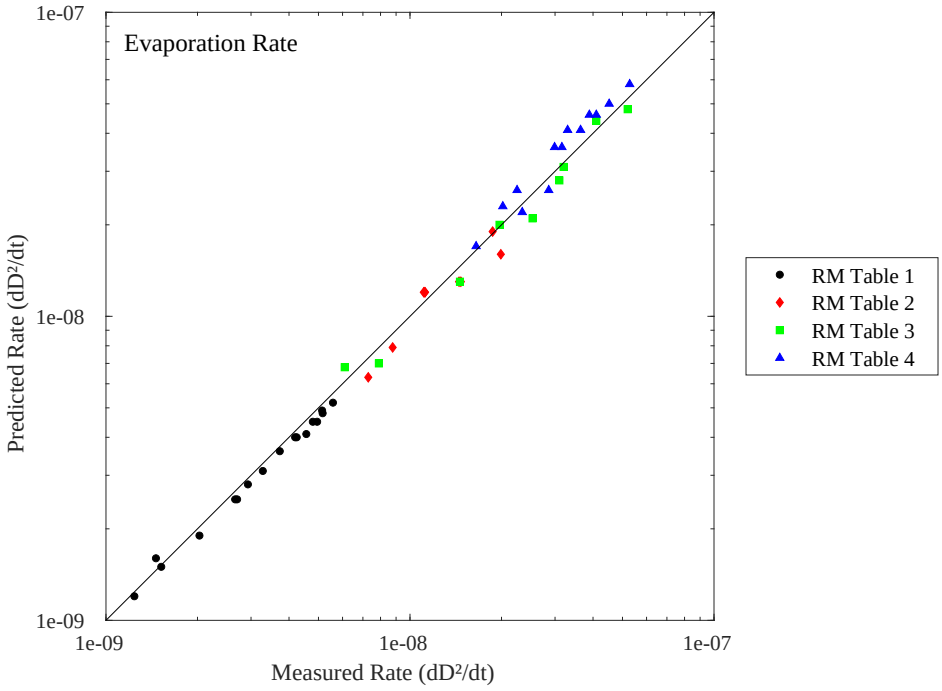

Figure 9.58: Summary of evaporation rates for the Ranz and Marshall experiments [268].

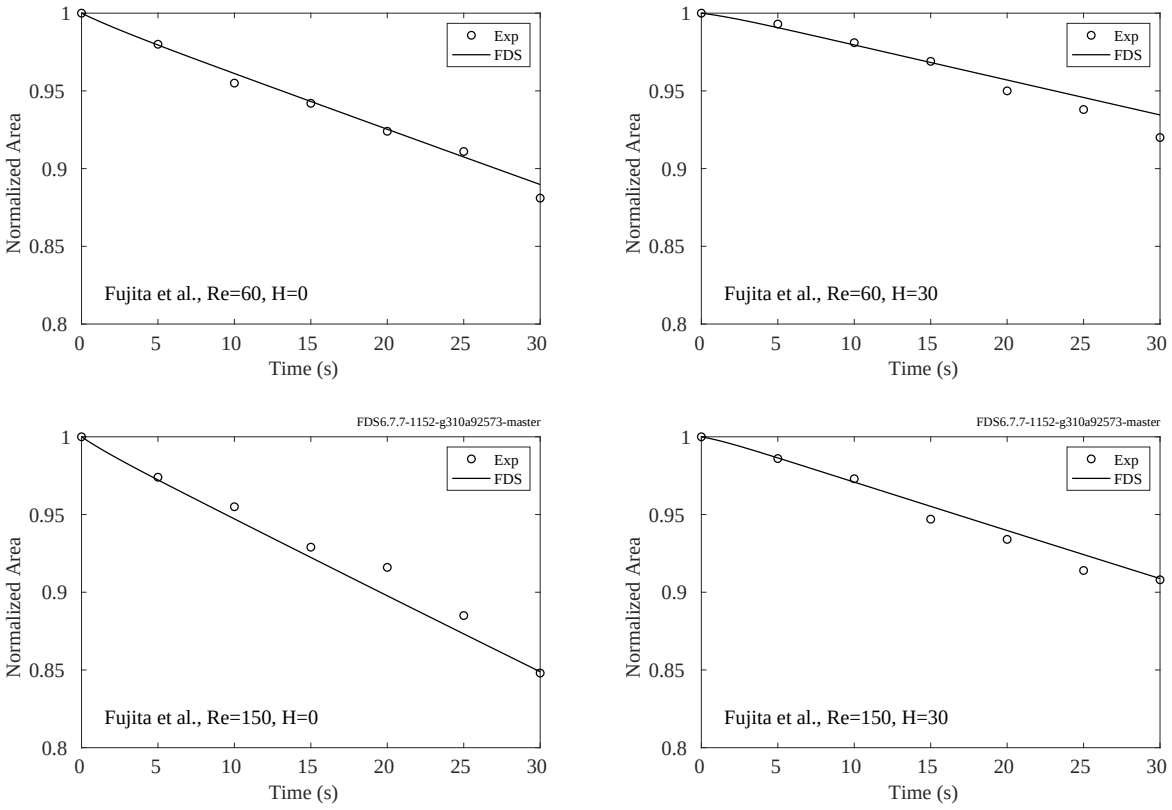

Figure 9.59: Normalized droplet area for the Fujita experiments for varying Reynolds number (Re) and Humidty (H)

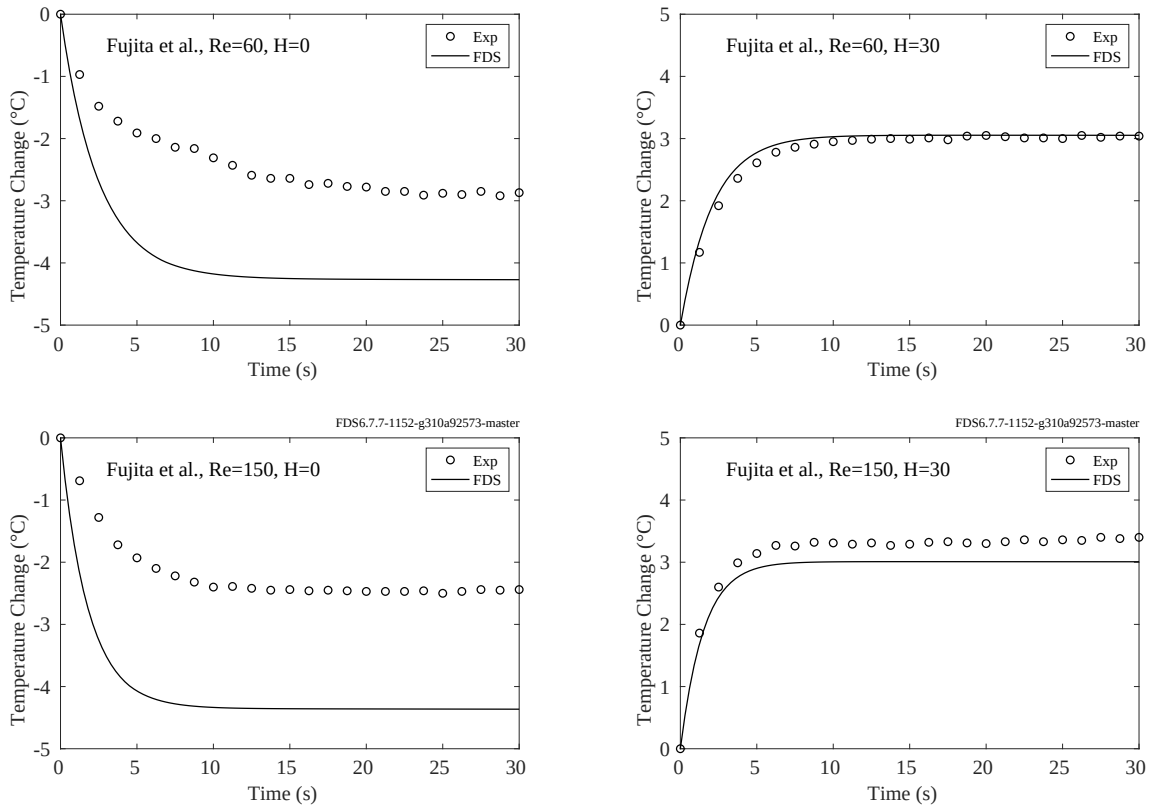

Figure 9.60: Droplet temperature change for the Fujita experiments for varying Reynolds number (Re) and Humidity (H).

9.4.3 Gavin

A description of the experiments is included in Sec. 3.19. Figure 9.61 shows the simulation results for the droplet terminal velocity.

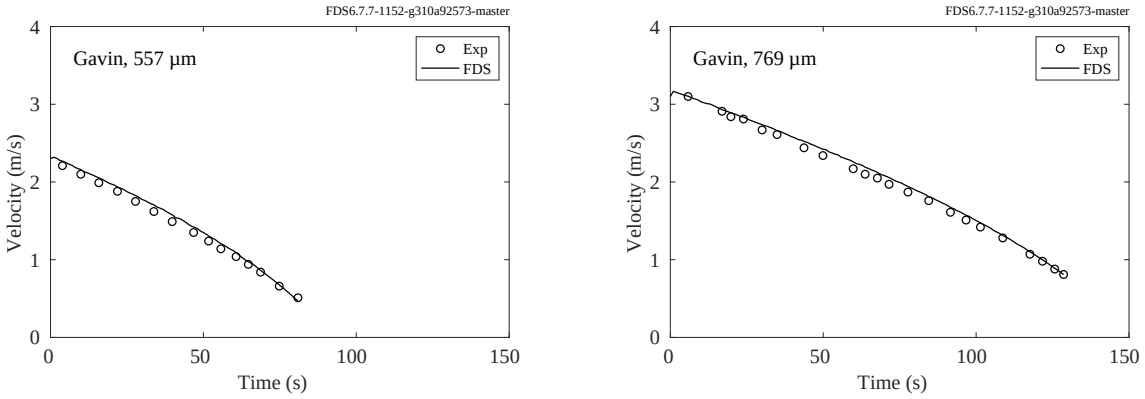

Figure 9.61: Droplet terminal velocity for the Gavin experiments.

9.4.4 Kolaitis and Founti

A description of the experiments is included in Sec. 3.19. Figure 9.62 shows the simulation results for the squared droplet diameter. Figure 9.63 shows the simulation results for the droplet surface temperature.

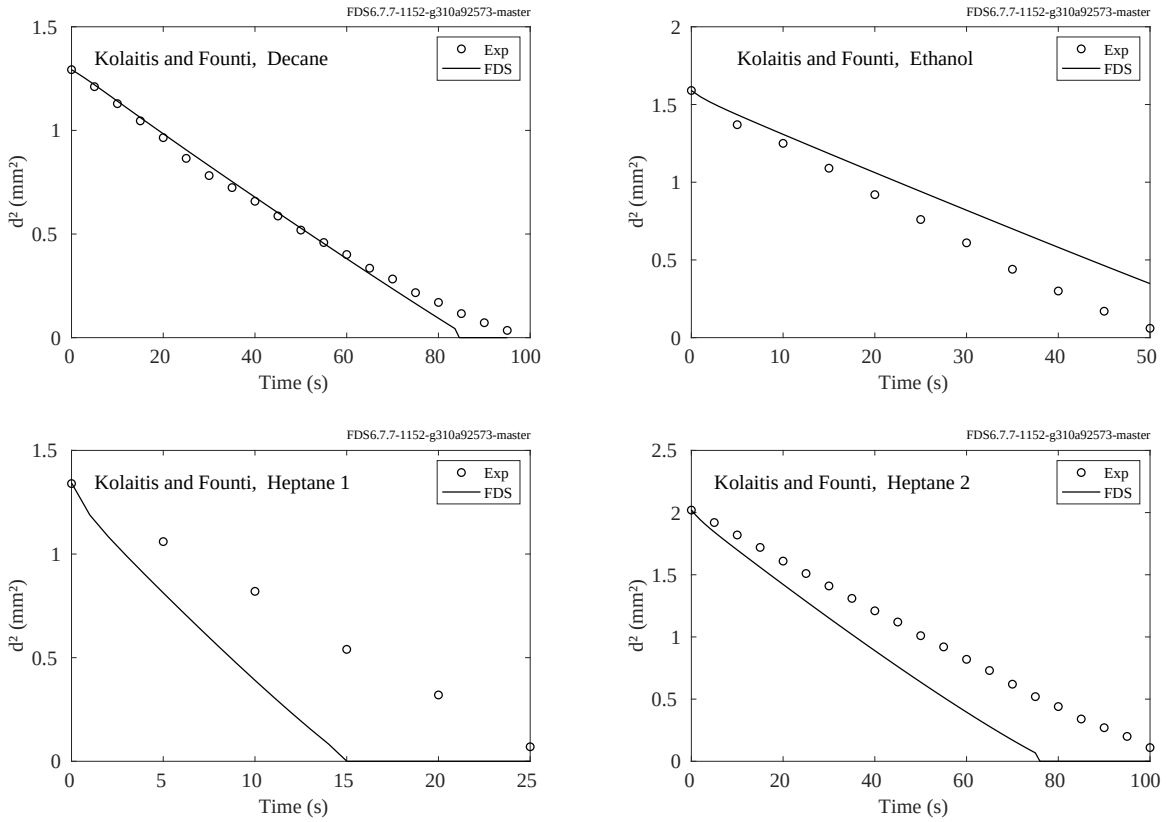

Figure 9.62: Square of the droplet diameter, Kolaitis and Founti.

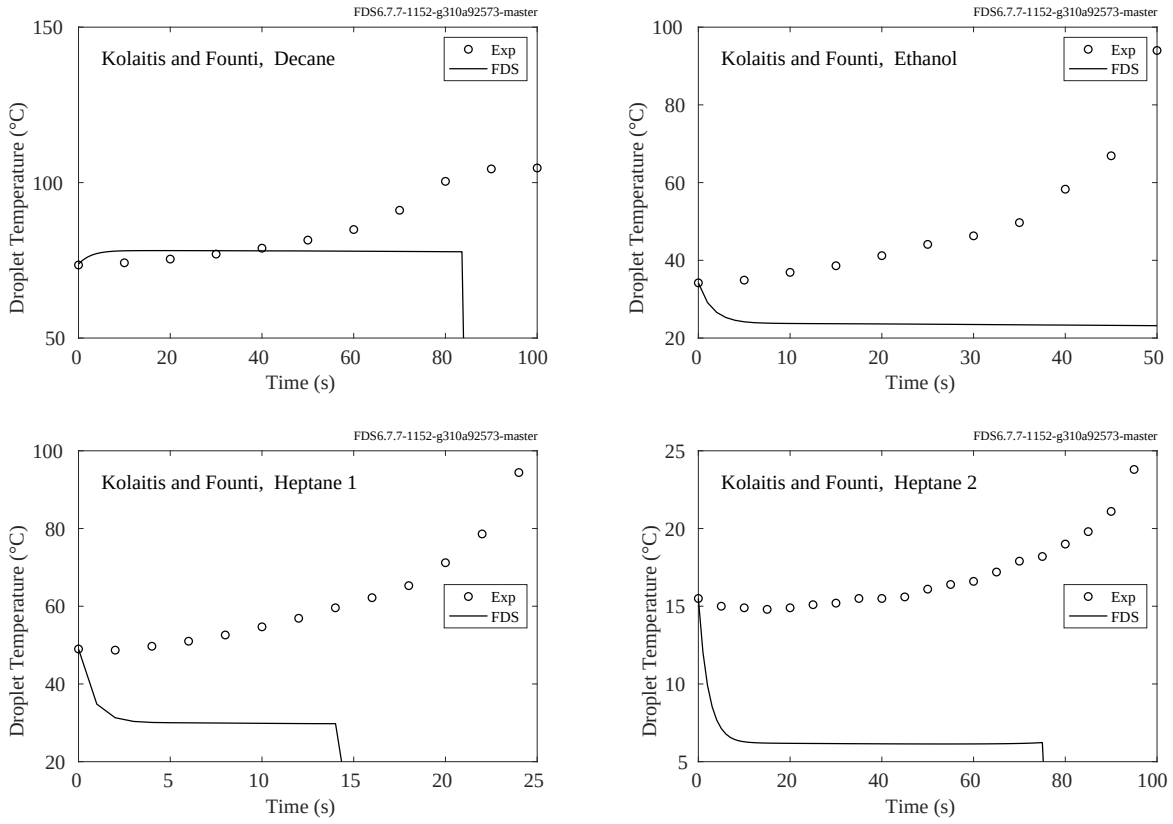

Figure 9.63: Droplet surface temperature, Kolaitis and Founti.

9.4.5 Maqua et al.

A description of the experiments is included in Sec. 3.19. Figure 9.64 shows the droplet surface temperature for the two experiments.

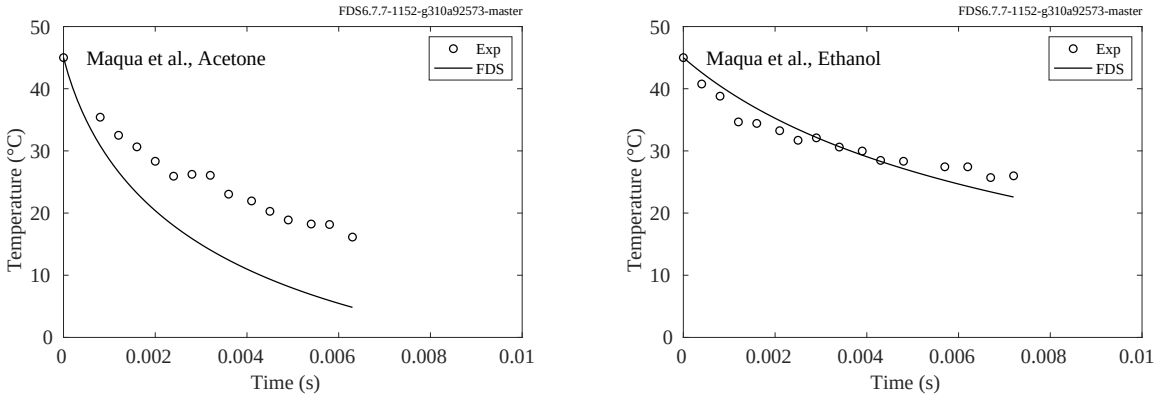

Figure 9.64: Droplet surface temperature for the Maqua et al. experiments.

9.4.6 Taflin Experiments

A description of the experiments is included in Sec. 3.19. Figure 9.65 shows the droplet diameter for the two Taflin experiments.

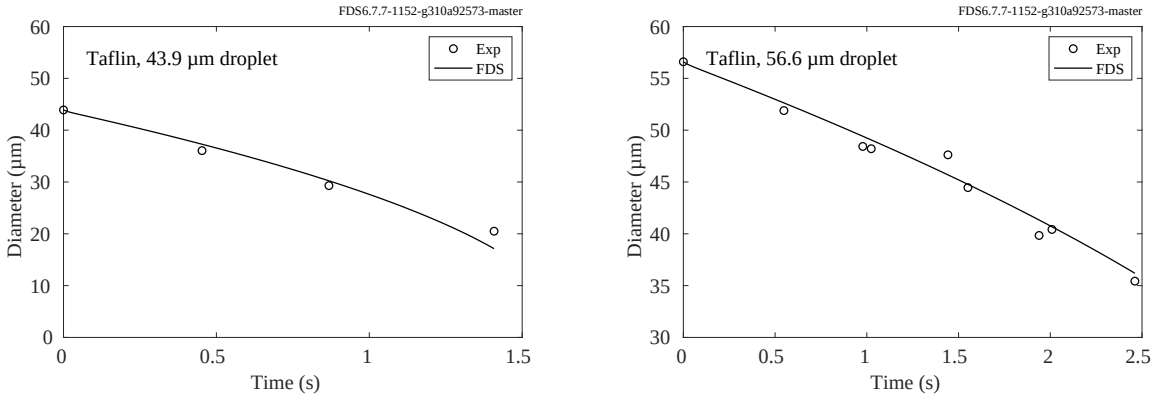

Figure 9.65: Droplet diameter for the Taflin experiments.

9.5 Products of Incomplete Combustion

Predicting the concentration of products of incomplete combustion is challenging because it requires information about the chemical composition of the fuel and the multiple reactions that convert fuel to products. FDS contains a fairly general framework by which users can specify the reaction mechanism, and the examples in the following subsections highlight some of the more commonly used schemes.

9.5.1 Smyth Slot Burner Experiment

Figure 9.66 shows predicted and measured temperatures at three elevations above the Smyth slot burner (see Section 3.69 for details). Figures 9.67 through 9.69 show predicted and measured concentrations of CH_4, O_2, CO, CO_2, H_2O and H_2 at the same three elevations. The reported uncertainty in the species concentration measurements ranges from 10 % to 20 %. The abbreviation "FR" in the labels means that the conversion of CO to CO_2 is modeled using a finite-rate, reversible reaction. The word "Fast" implies that this reaction is infinitely fast, but occurs following the first reaction, also infinitely fast.

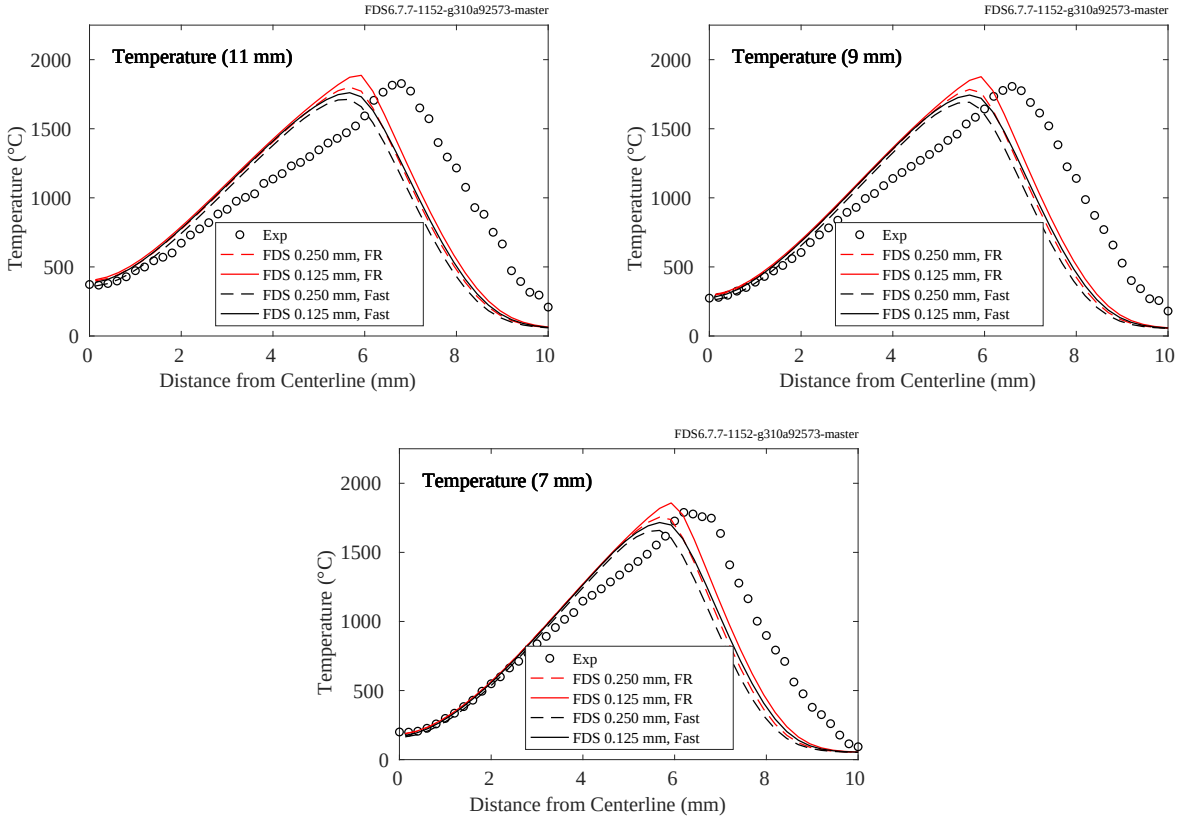

Figure 9.66: Predicted and measured temperature at 7 mm, 9 mm, and 11 mm above a methane-air slot burner.

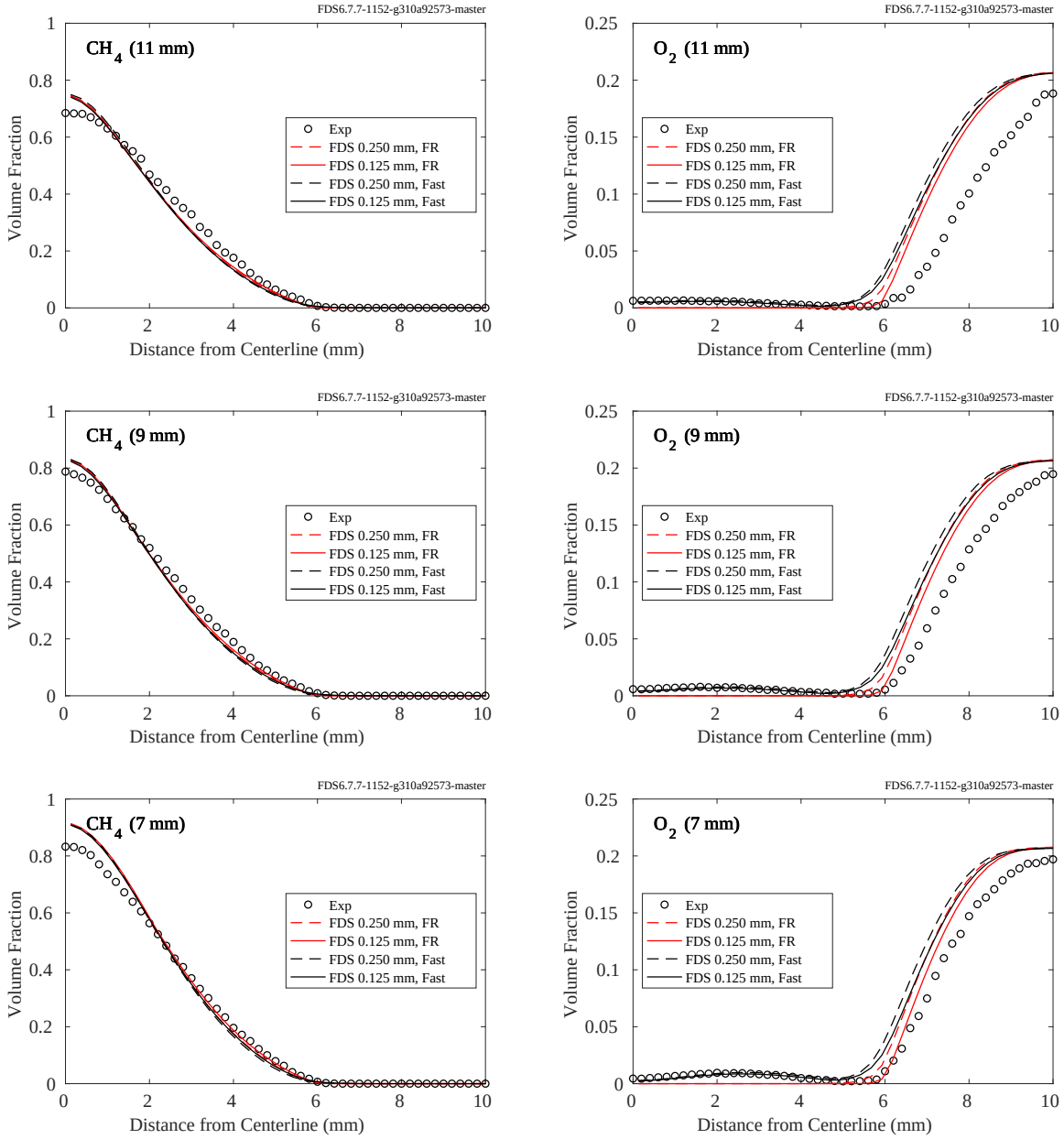

Figure 9.67: Predicted and measured CH_4 and O_2 volume fractions at 11 mm, 9 mm, and 7 mm above a methane-air slot burner.

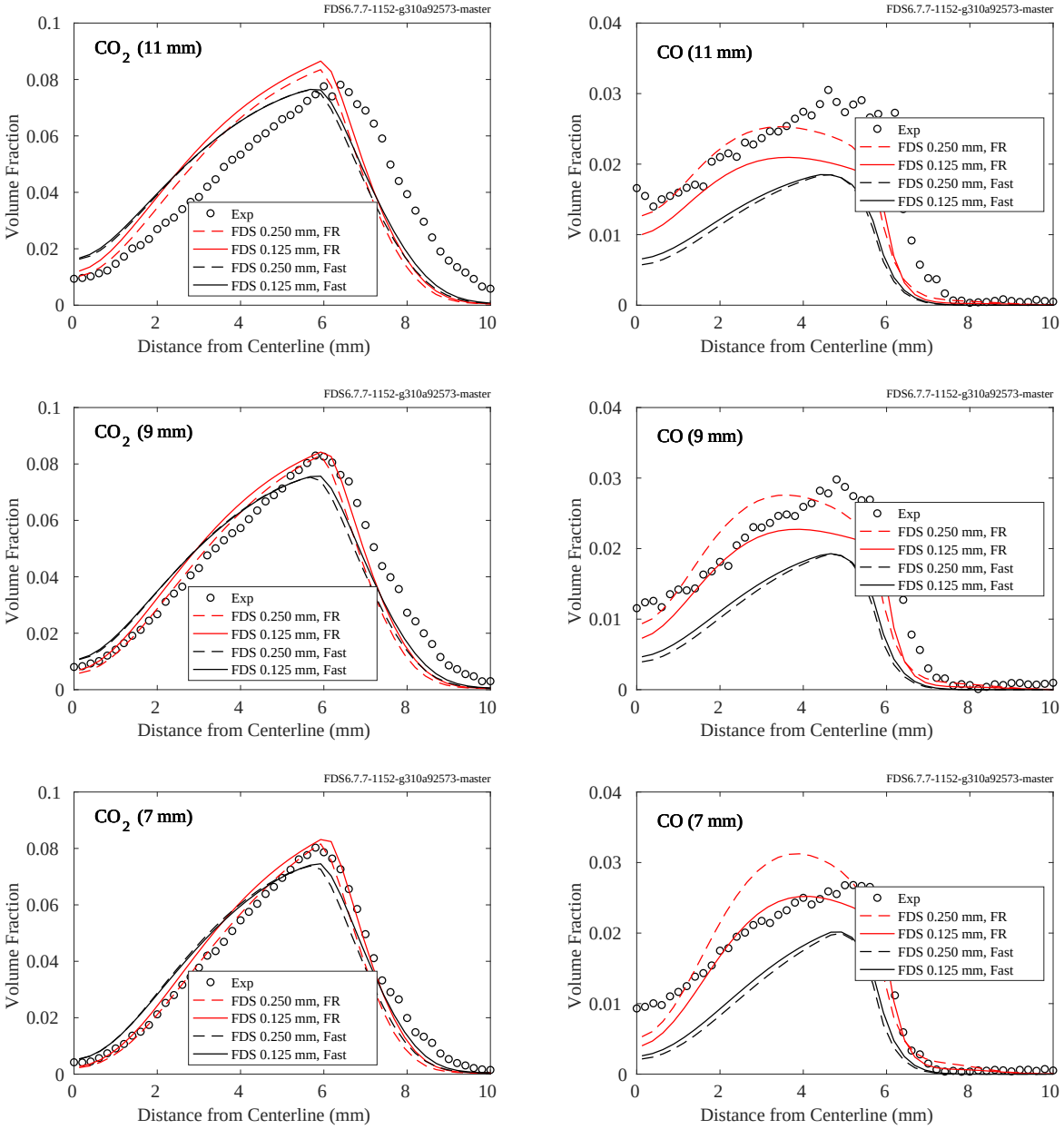

Figure 9.68: Predicted and measured CO_2 and CO volume fractions at 11 mm, 9 mm, and 7 mm above a methane-air slot burner.

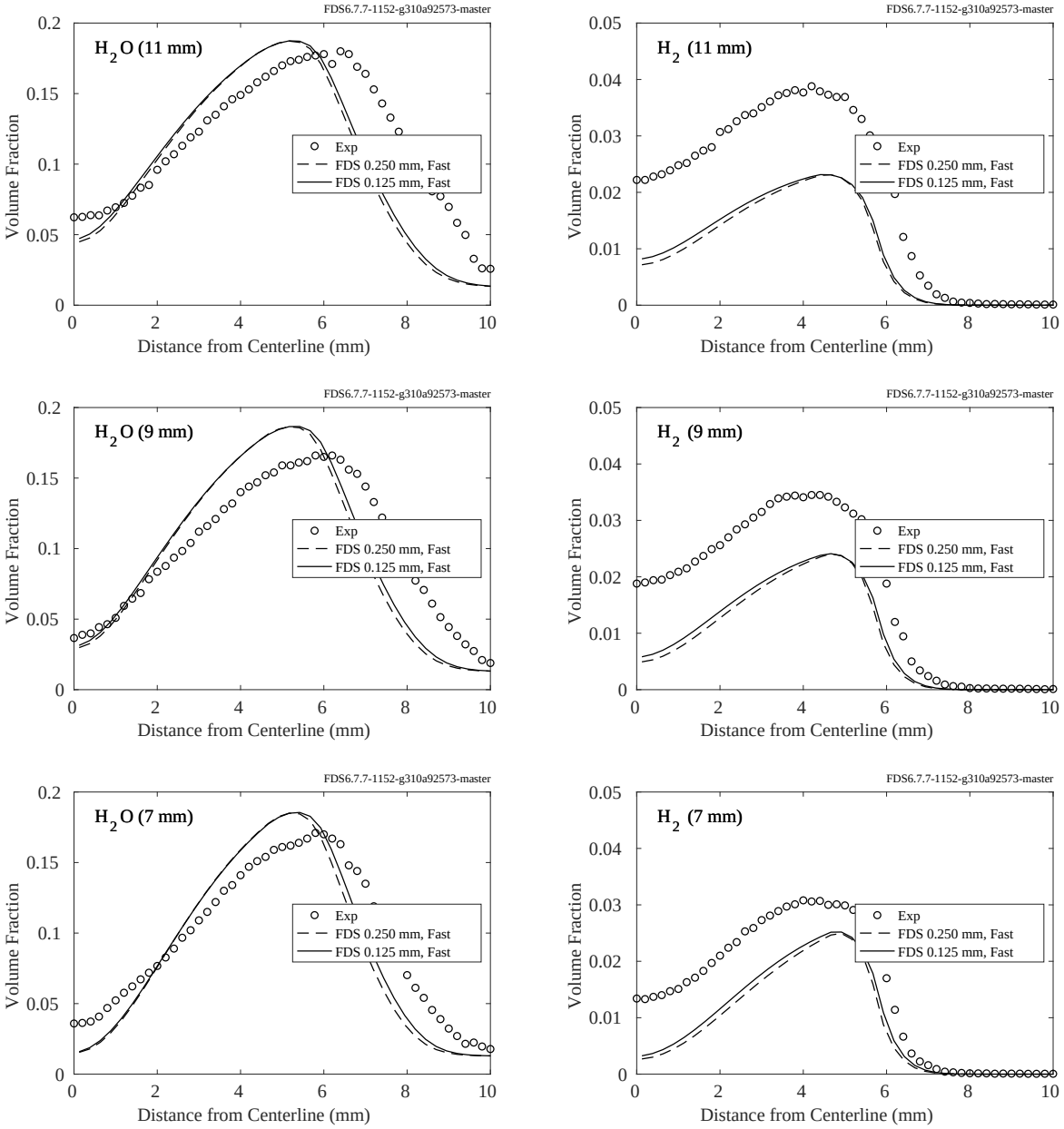

Figure 9.69: Predicted and measured H_2O and H_2 volume fractions at 11 mm, 9 mm, and 7 mm above a methane-air slot burner.

9.5.2 Beyler Hood Experiments

Fig. 9.70 compares measured and predicted species mass fractions in the Beyler Hood experiments. Both measured and predicted values are time-averaged. The FDS results are taken at the extraction vent, whereas the measurements were made downstream of the vent. Details of the experiments can be found in Section 3.5.

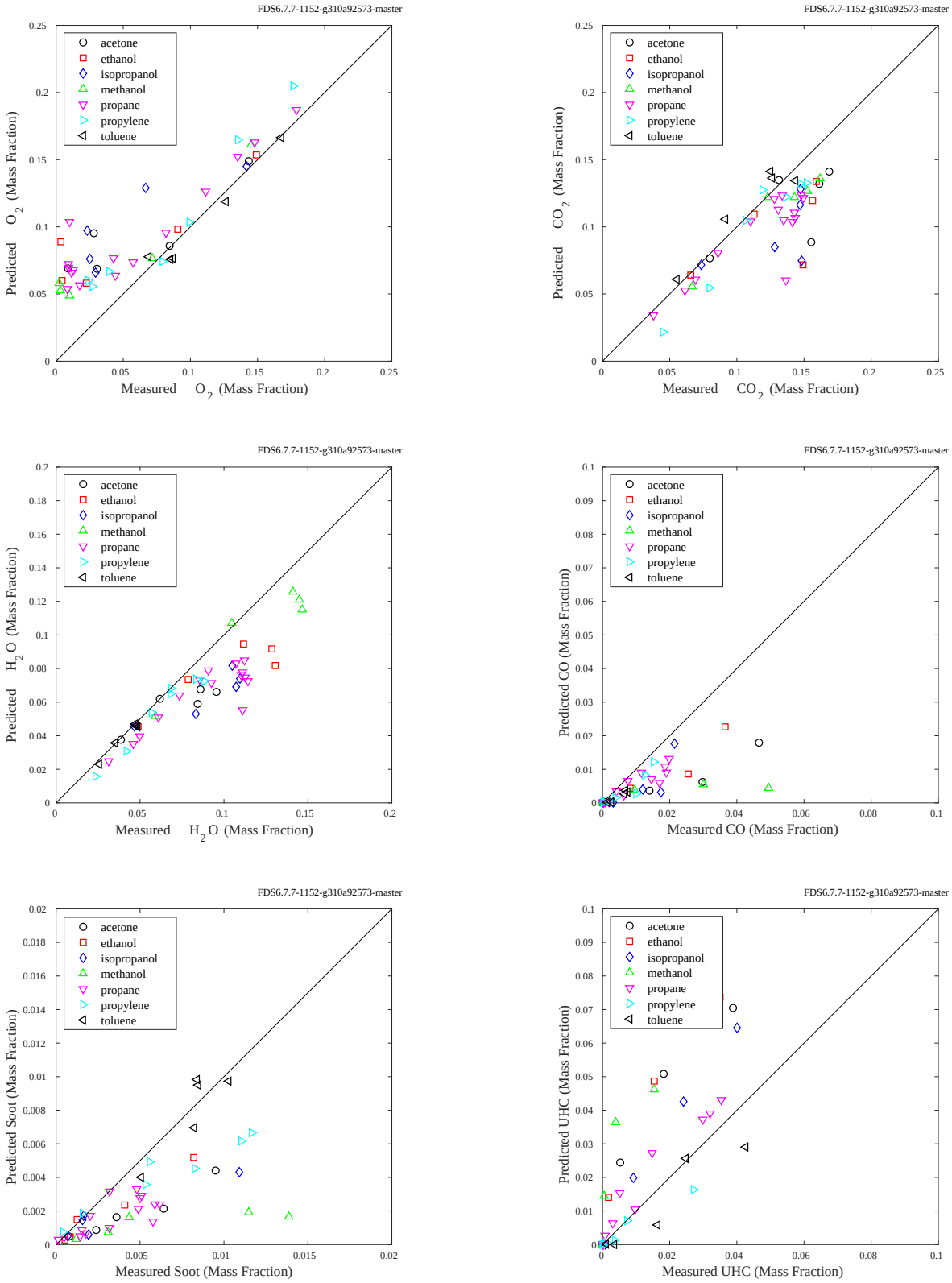

Figure 9.70: Comparison of measured and predicted species concentrations in the Beyler hood experiments

9.5.3 NIST Reduced Scale Enclosure (RSE) Experiments, 1994

Figures 9.71 through 9.74 show the measured and predicted CO, CO_2 and O_2, and H_2O concentrations. Figure 9.75 shows the measured and predicted thermocouple temperatures in the front and rear of the compartment. The measurements were made 10 cm below the ceiling and 30 cm from the left side wall. The front position was 10 cm from the wall with the door; the back position was 30 cm from the rear wall. Details of the experiments are found in Section 3.44.1.

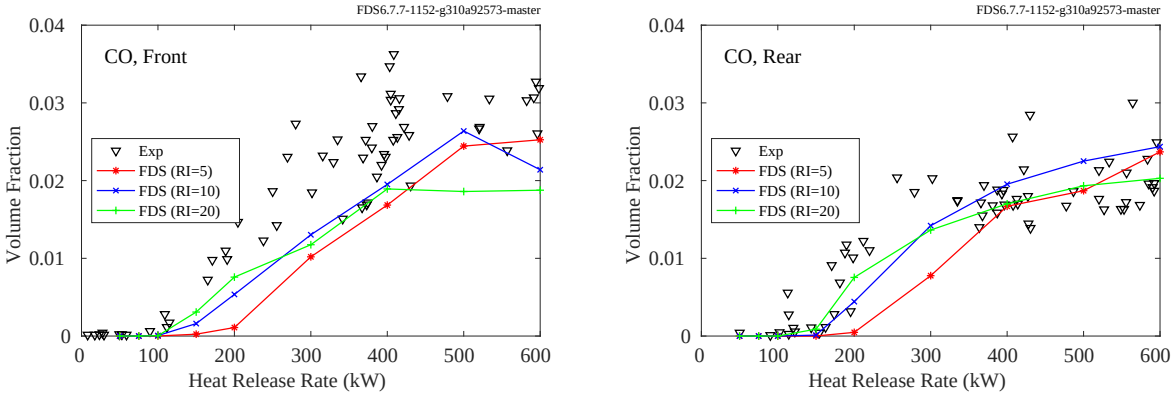

Figure 9.71: Comparison of measured and predicted CO concentration, NIST RSE experiments.

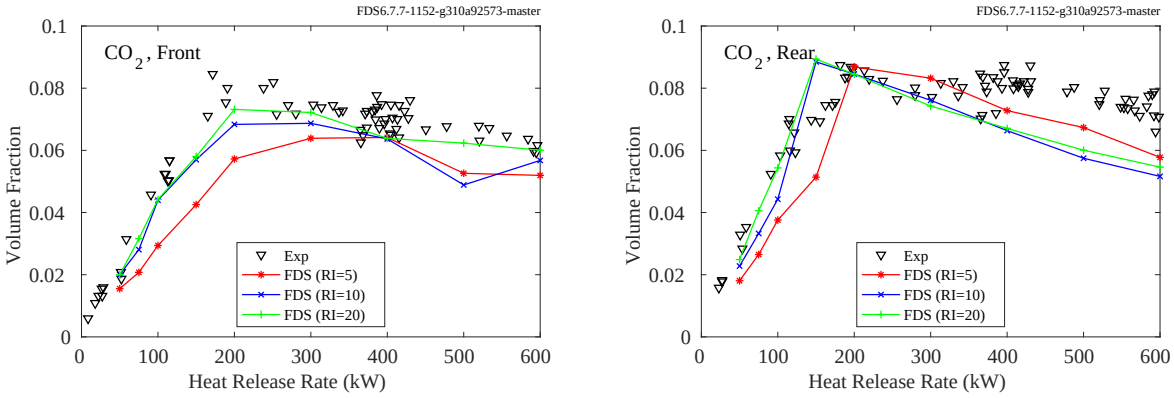

Figure 9.72: Comparison of measured and predicted CO_2 concentration, NIST RSE experiments.

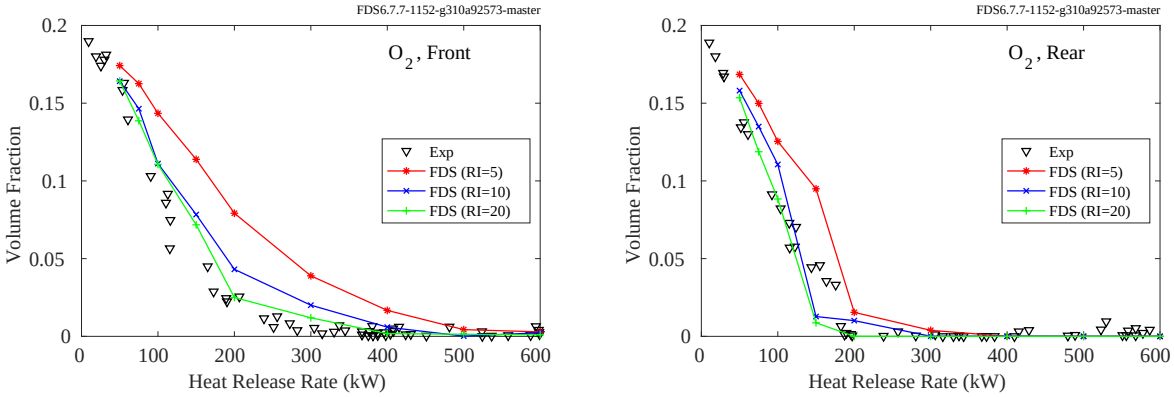

Figure 9.73: Comparison of measured and predicted O_2 concentration, NIST RSE experiments.

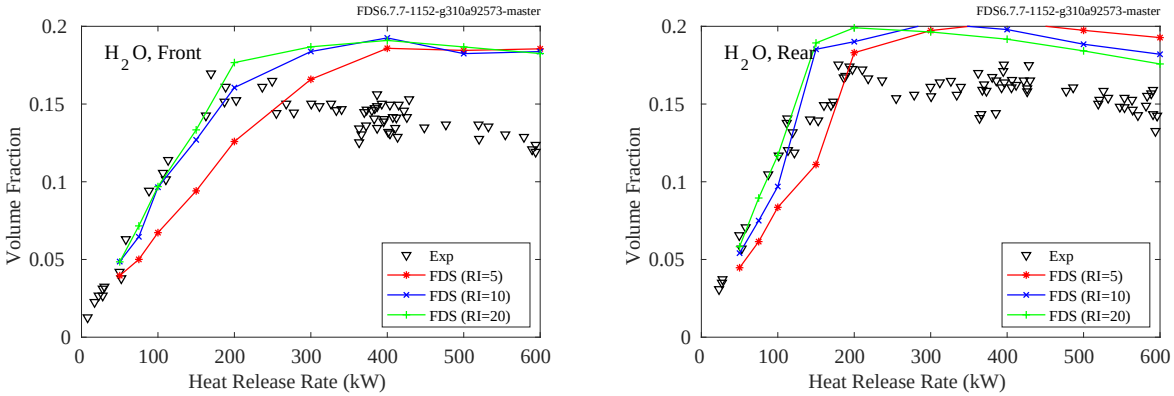

Figure 9.74: Comparison of measured and predicted H_2O concentration, NIST RSE experiments.

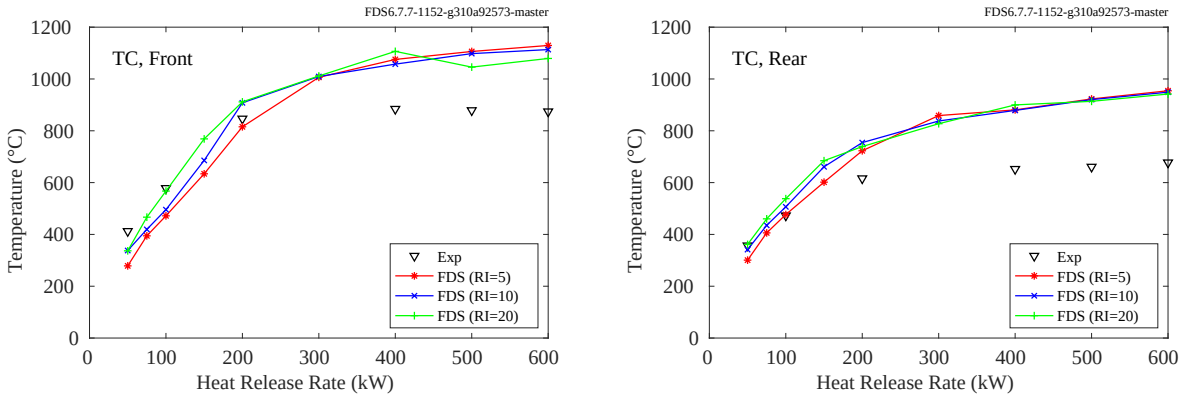

Figure 9.75: Comparison of measured and predicted temperature, NIST RSE experiments.

9.5.4 NIST Reduced-Scale Enclosure (RSE) Experiments, 2007

Species and temperature measurements were made in the front and rear of the compartment, 10 cm below the ceiling, 29 cm from the right wall (looking into the compartment), and 10 cm from the front wall or 29 cm from the rear wall. The compartment was 0.95 m wide by 1.42 m deep by 0.98 m tall with a door 0.48 m wide by 0.81 m tall centered on one of the short walls. Measurements of temperature, O_2, CO_2, CO, and unburned hydrocarbon concentration were made near the ceiling in the front and back of the compartment. Details of the experiments are found in Section 3.44.2.

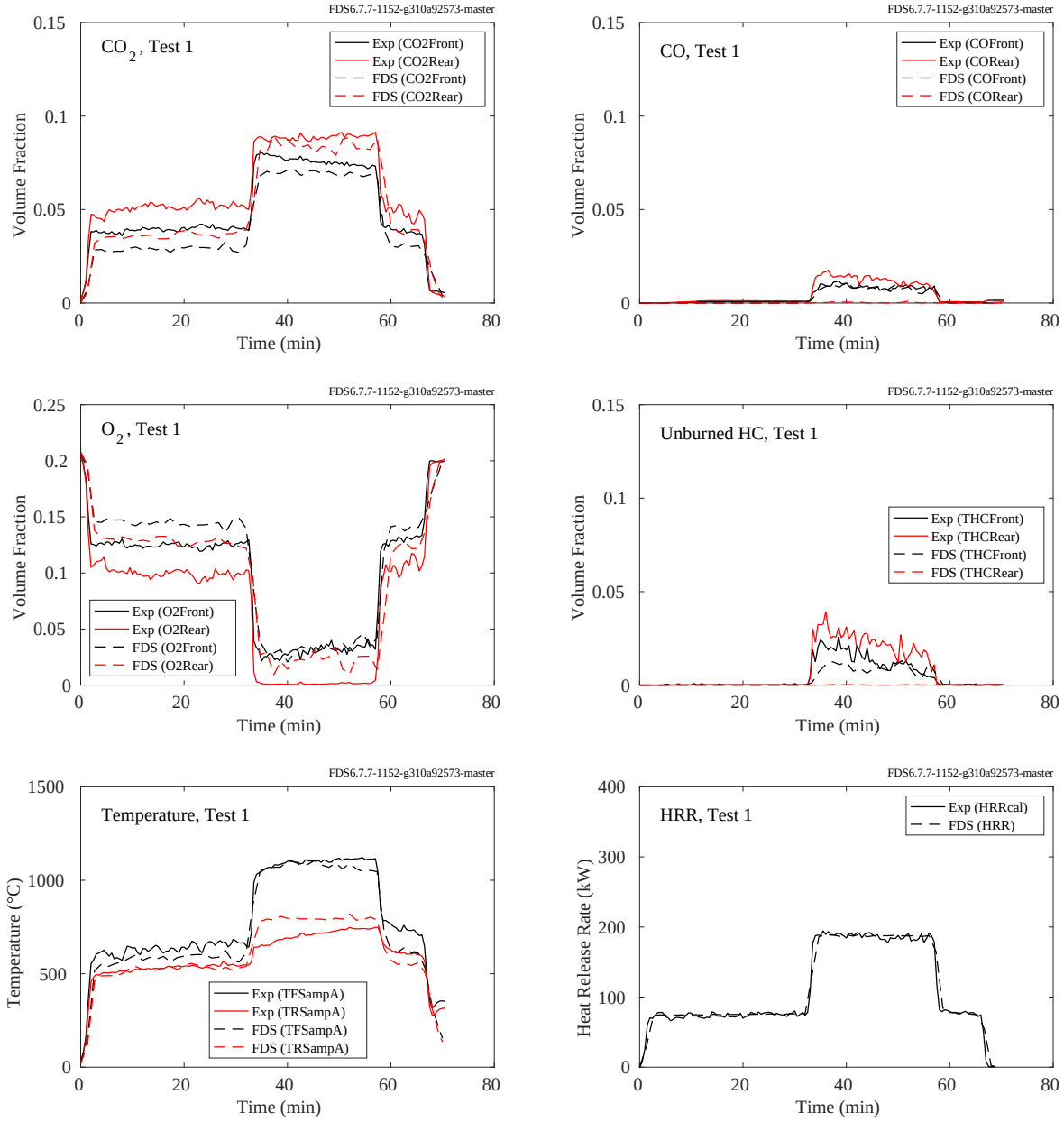

Figure 9.76: Summary of Test 1, NIST RSE 2007.

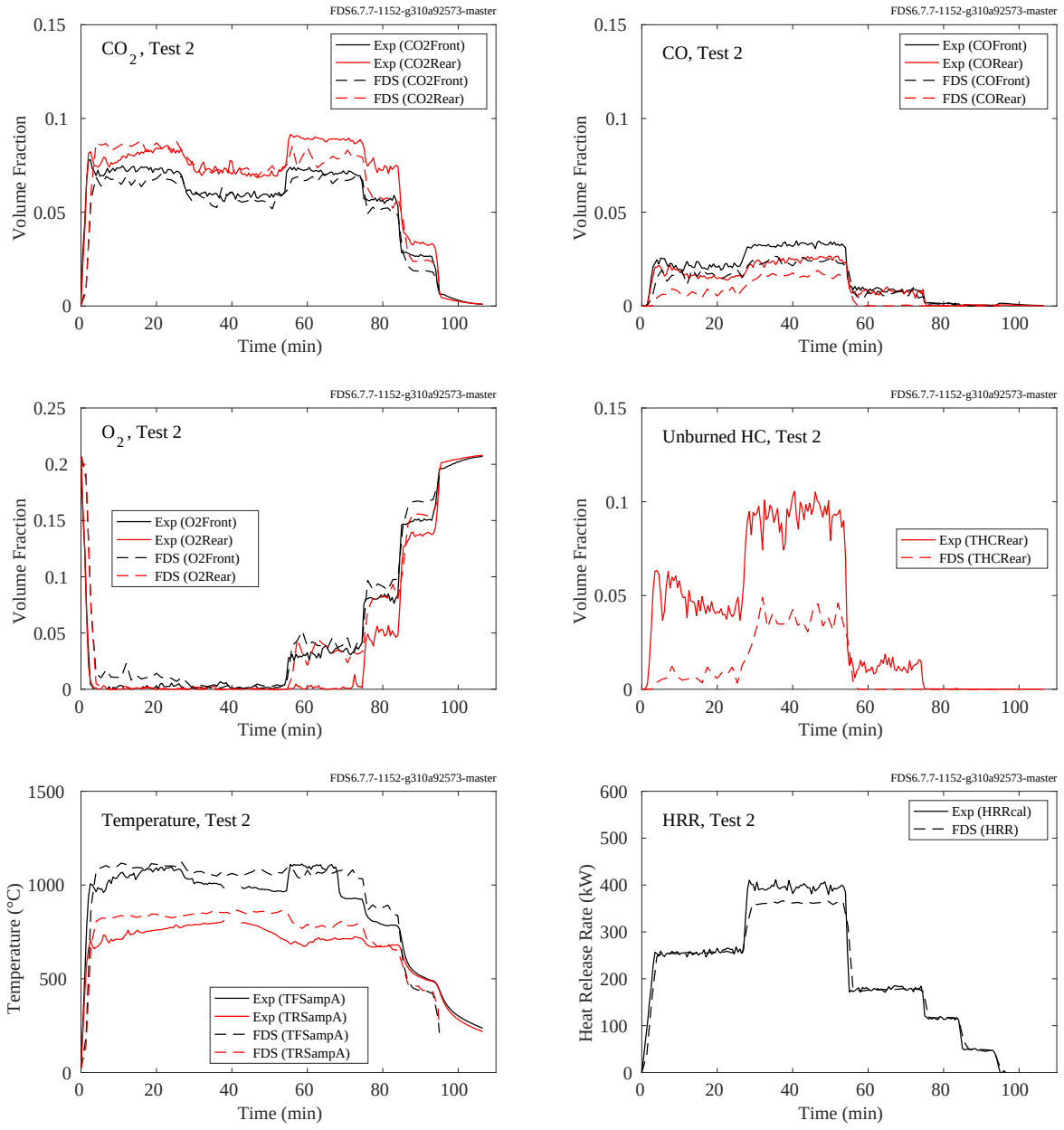

Figure 9.77: Summary of Test 2, NIST RSE 2007.

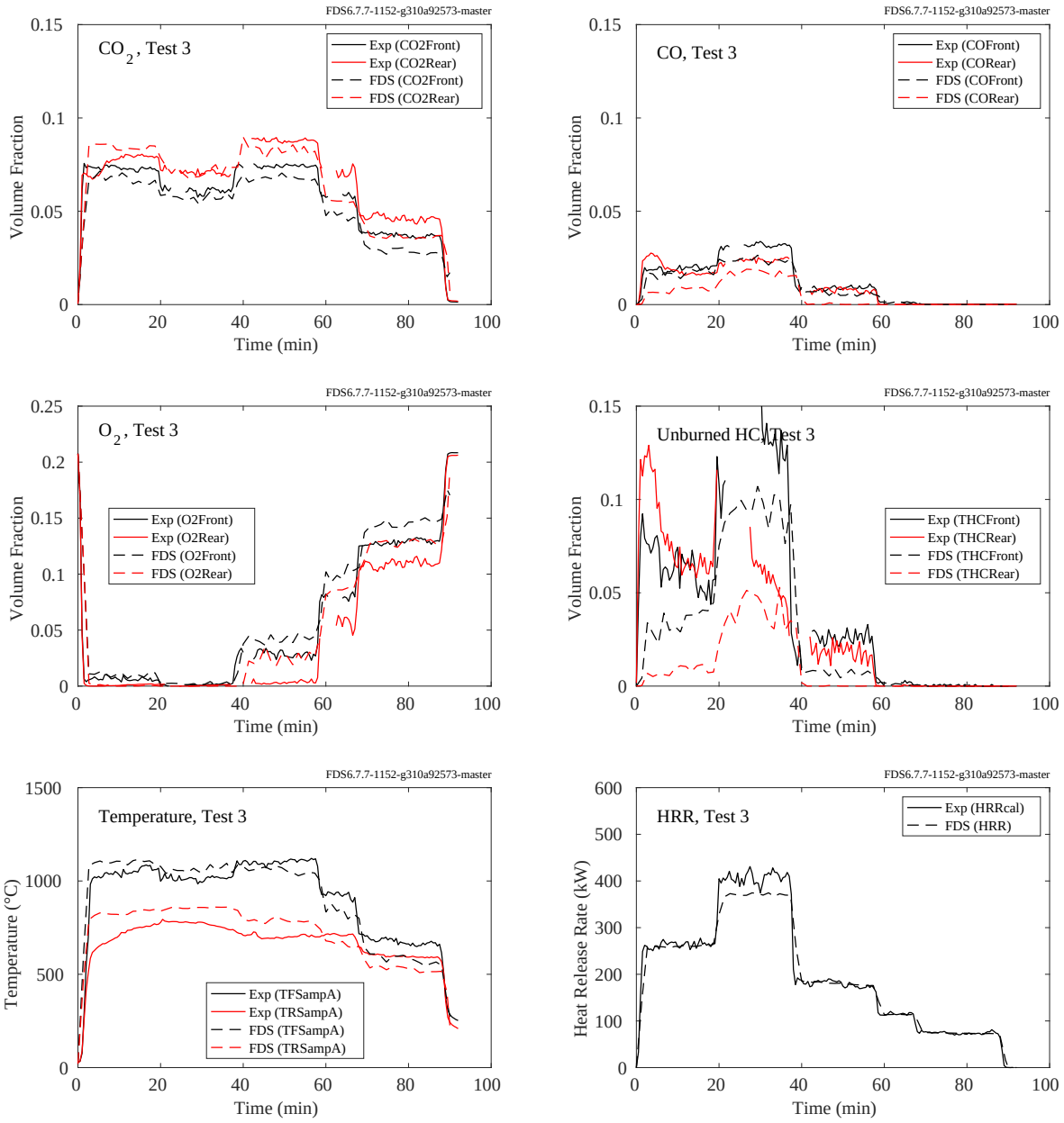

Figure 9.78: Summary of Test 3, NIST RSE 2007.

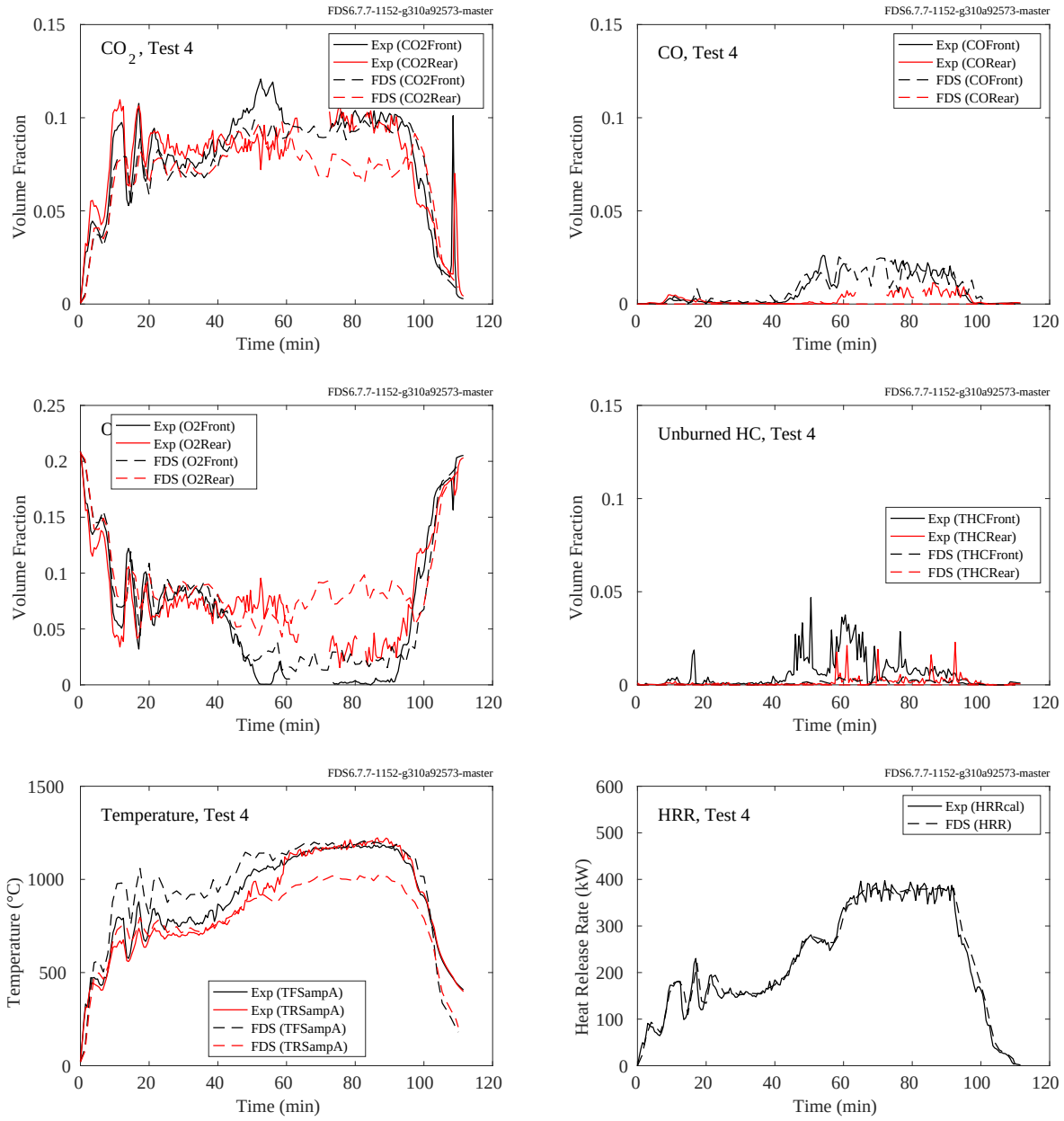

Figure 9.79: Summary of Test 4, NIST RSE 2007.

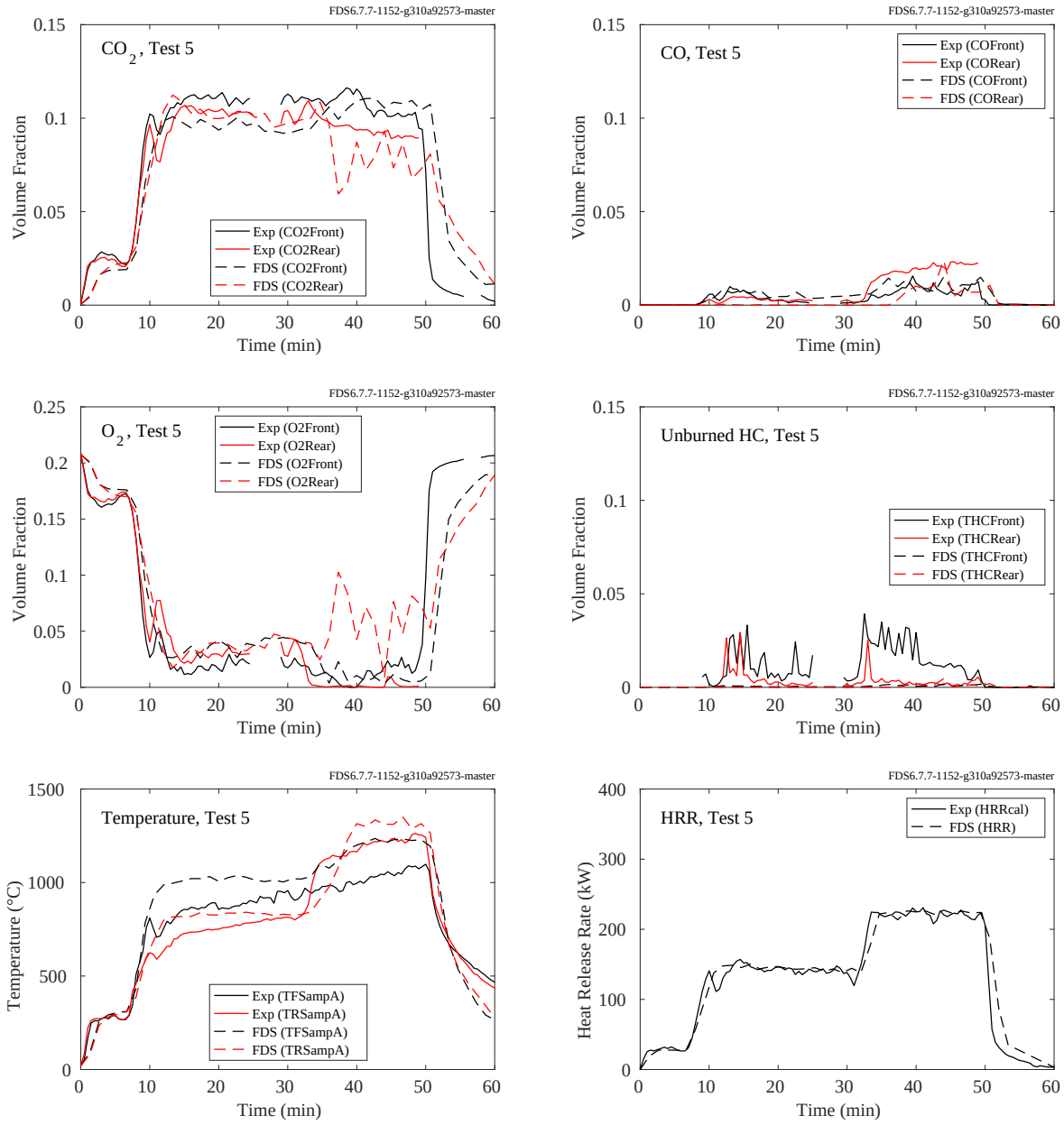

Figure 9.80: Summary of Test 5, NIST RSE 2007.

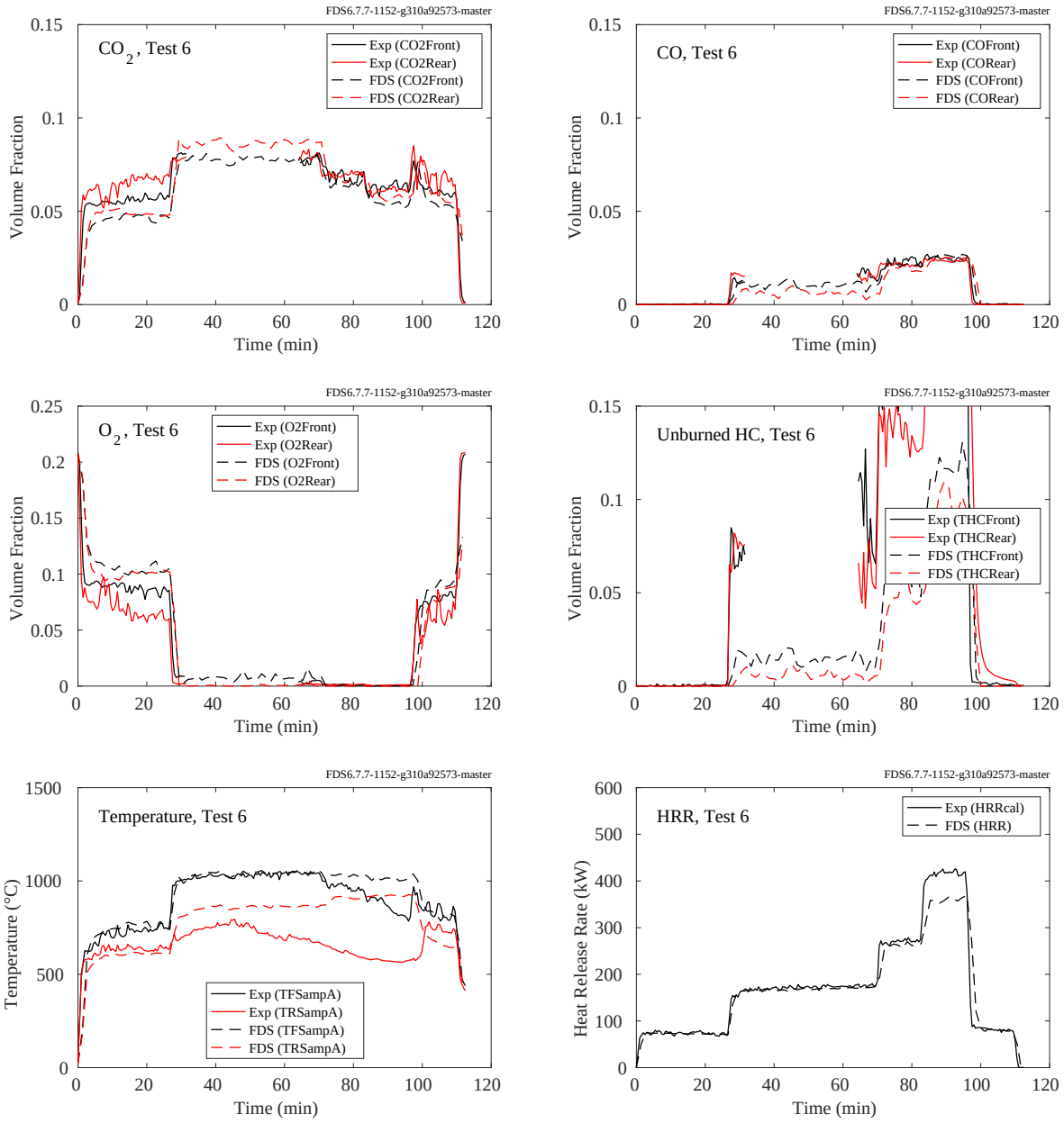

Figure 9.81: Summary of Test 6, NIST RSE 2007.

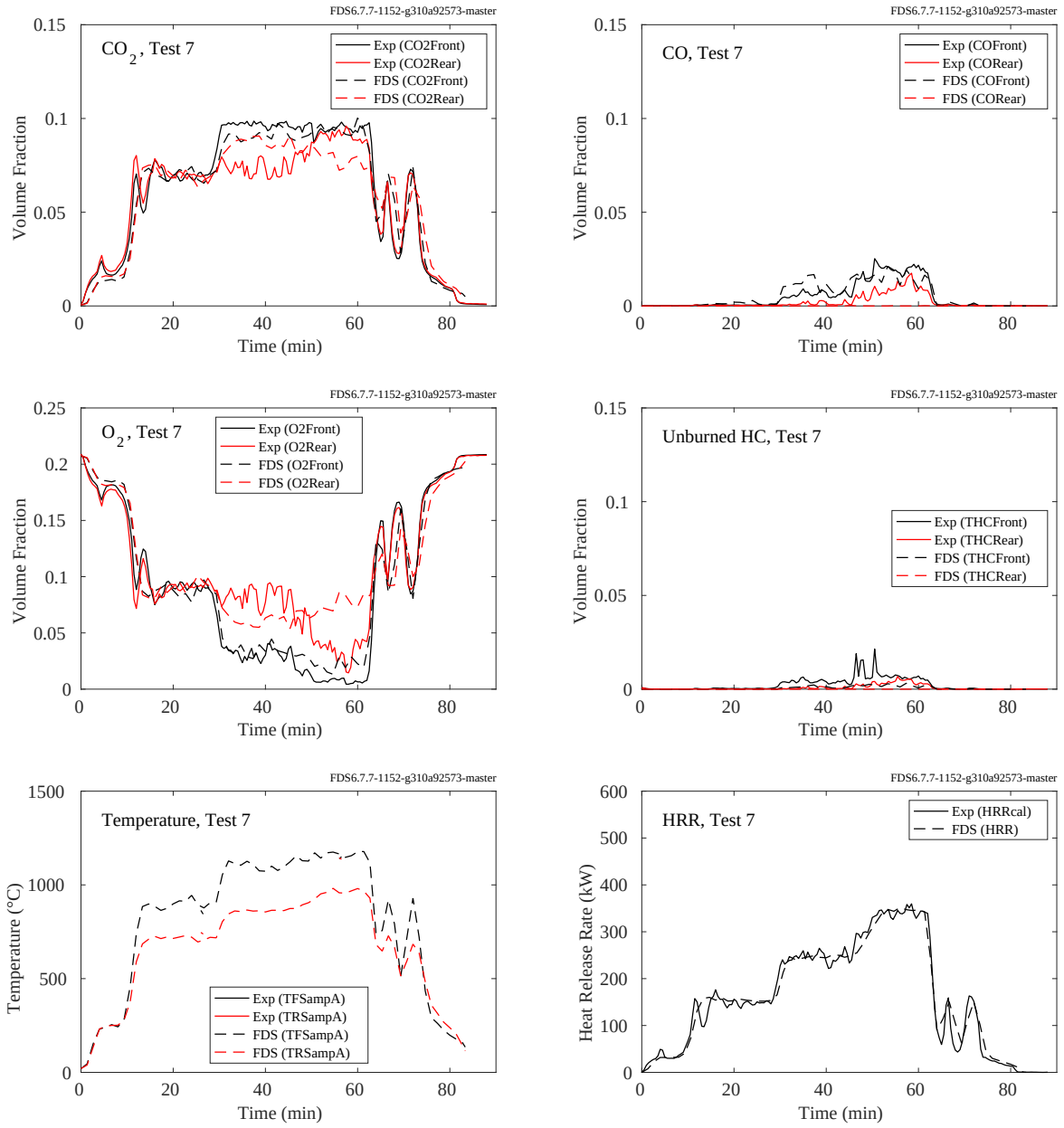

Figure 9.82: Summary of Test 7, NIST RSE 2007.

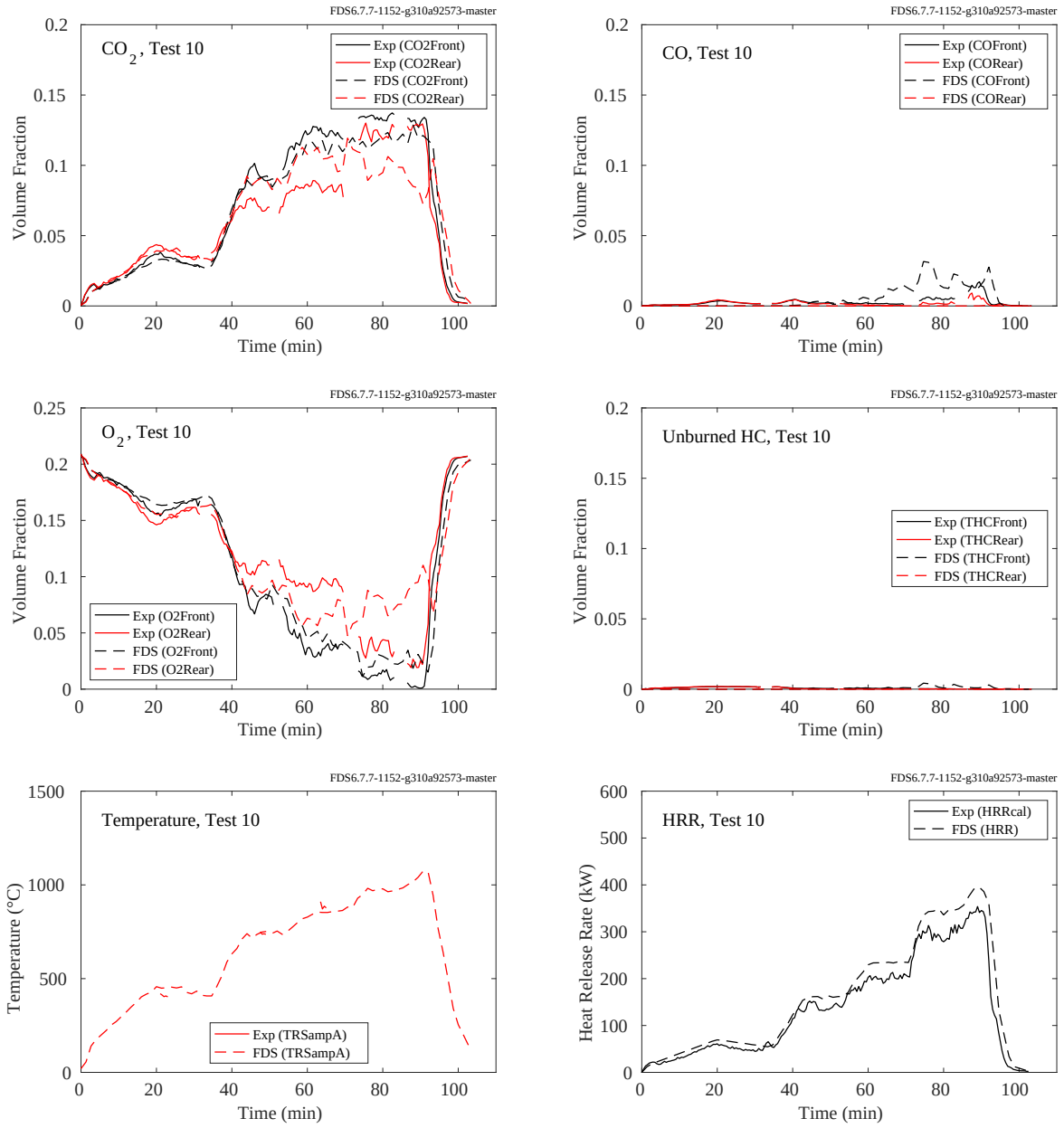

Figure 9.83: Summary of Test 10, NIST RSE 2007.

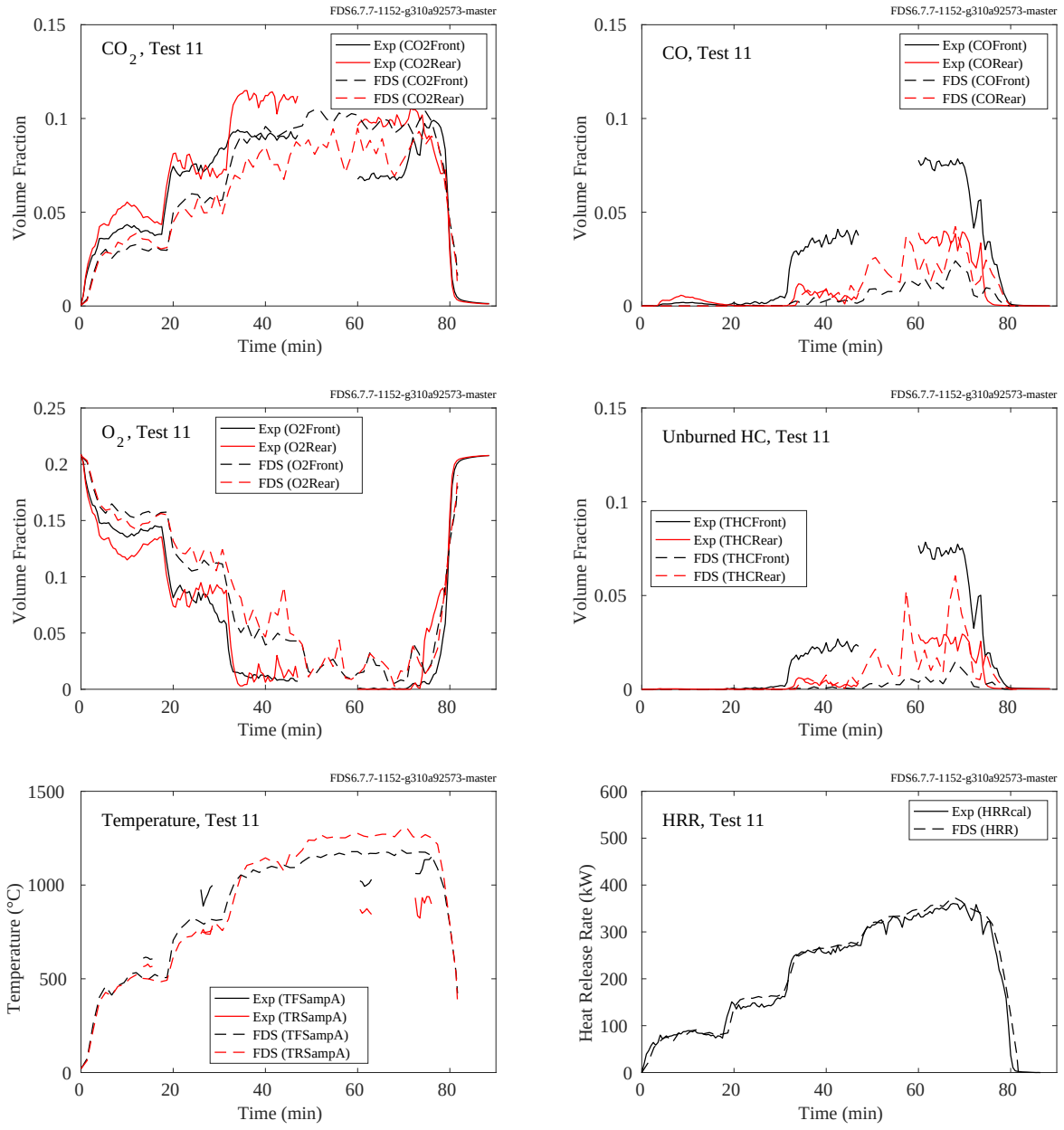

Figure 9.84: Summary of Test 11, NIST RSE 2007.

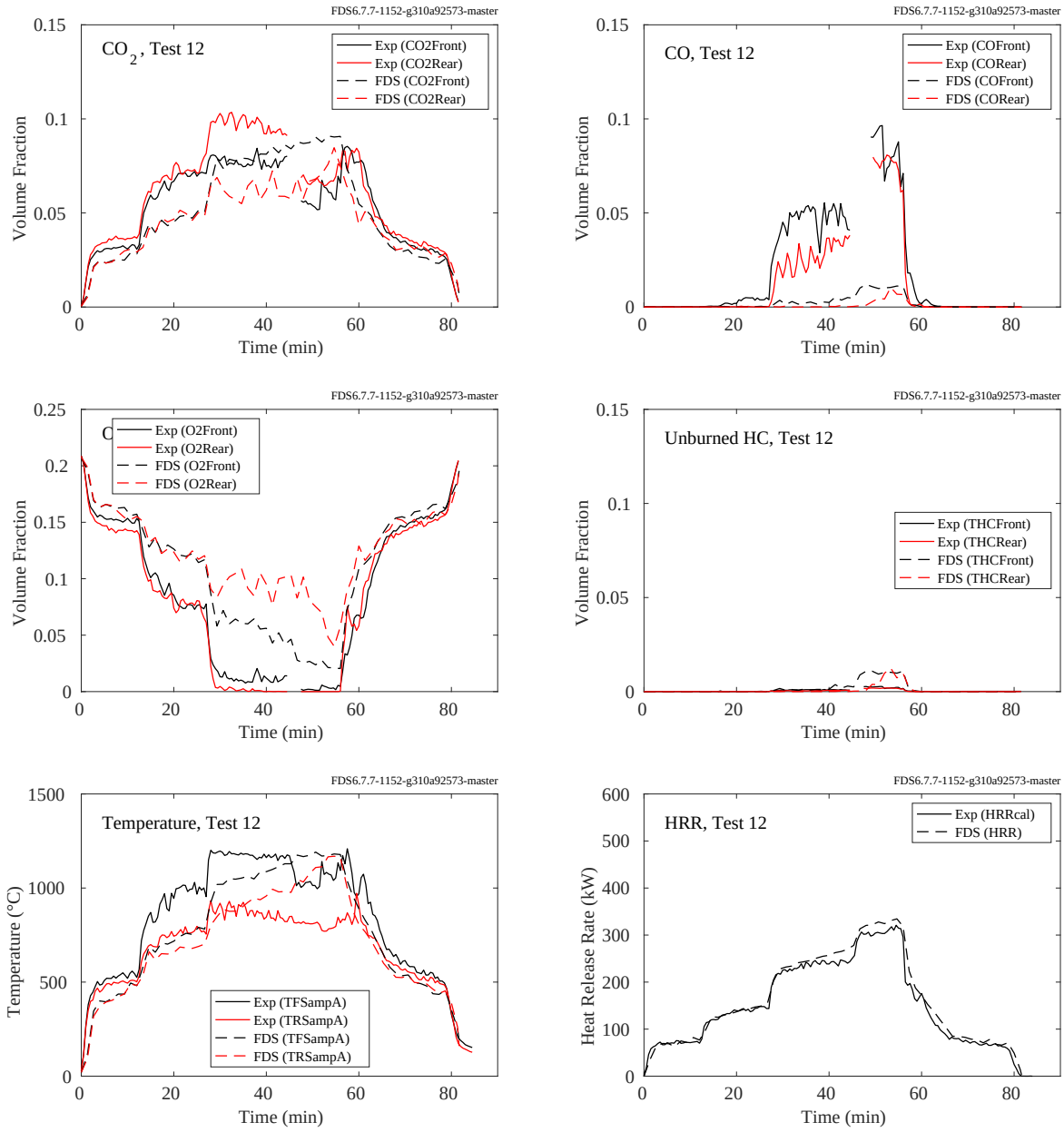

Figure 9.85: Summary of Test 12, NIST RSE 2007.

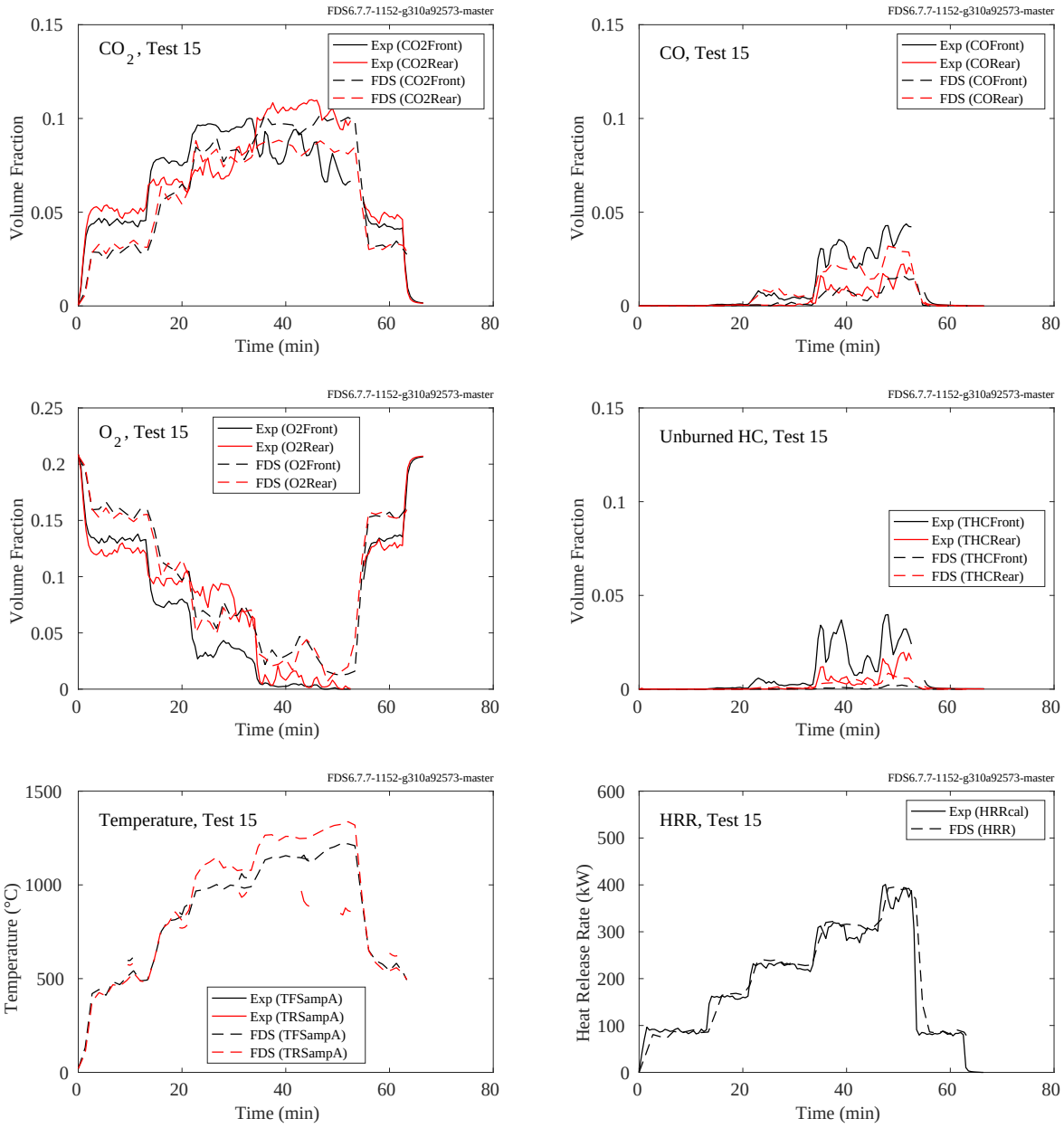

Figure 9.86: Summary of Test 15, NIST RSE 2007.

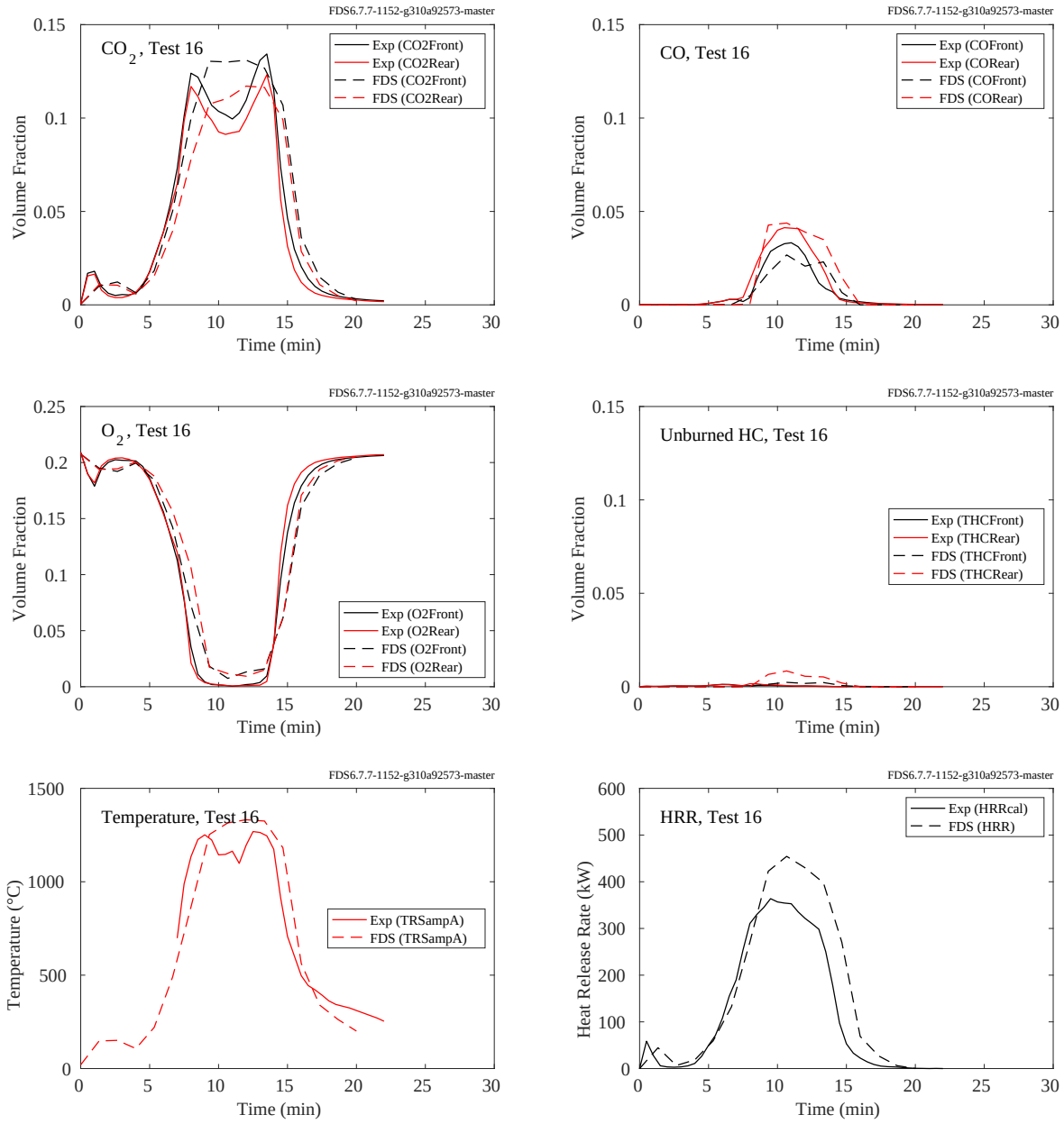

Figure 9.87: Summary of Test 16, NIST RSE 2007.

9.5.5 NIST Full-Scale Enclosure (FSE) Experiments, 2008

Species concentrations and temperature measurements were made at the front and rear of the compartment. Details of the experiments are found in Section 3.44.3.

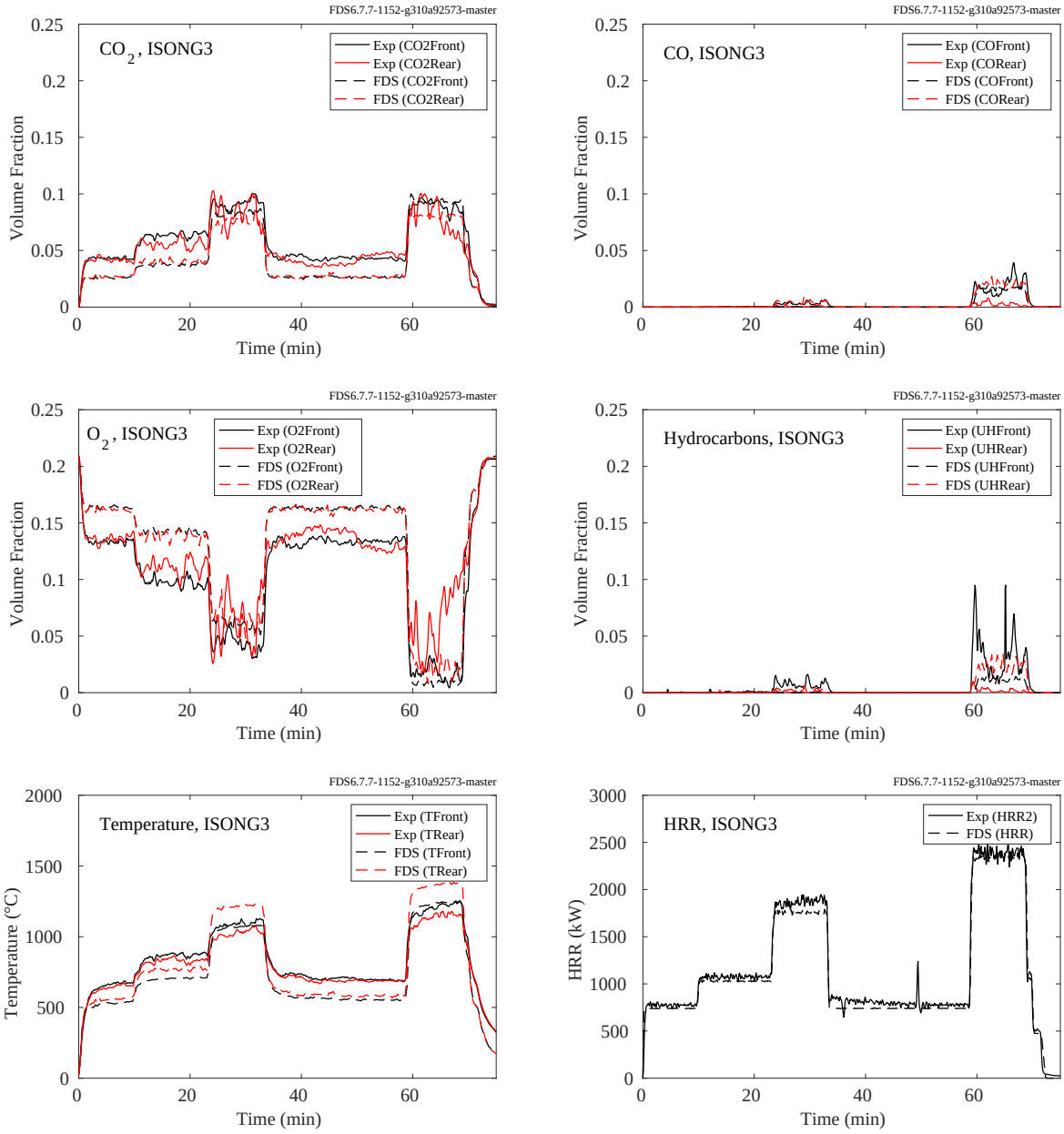

Figure 9.88: Summary of ISONG3, NIST FSE 2008.

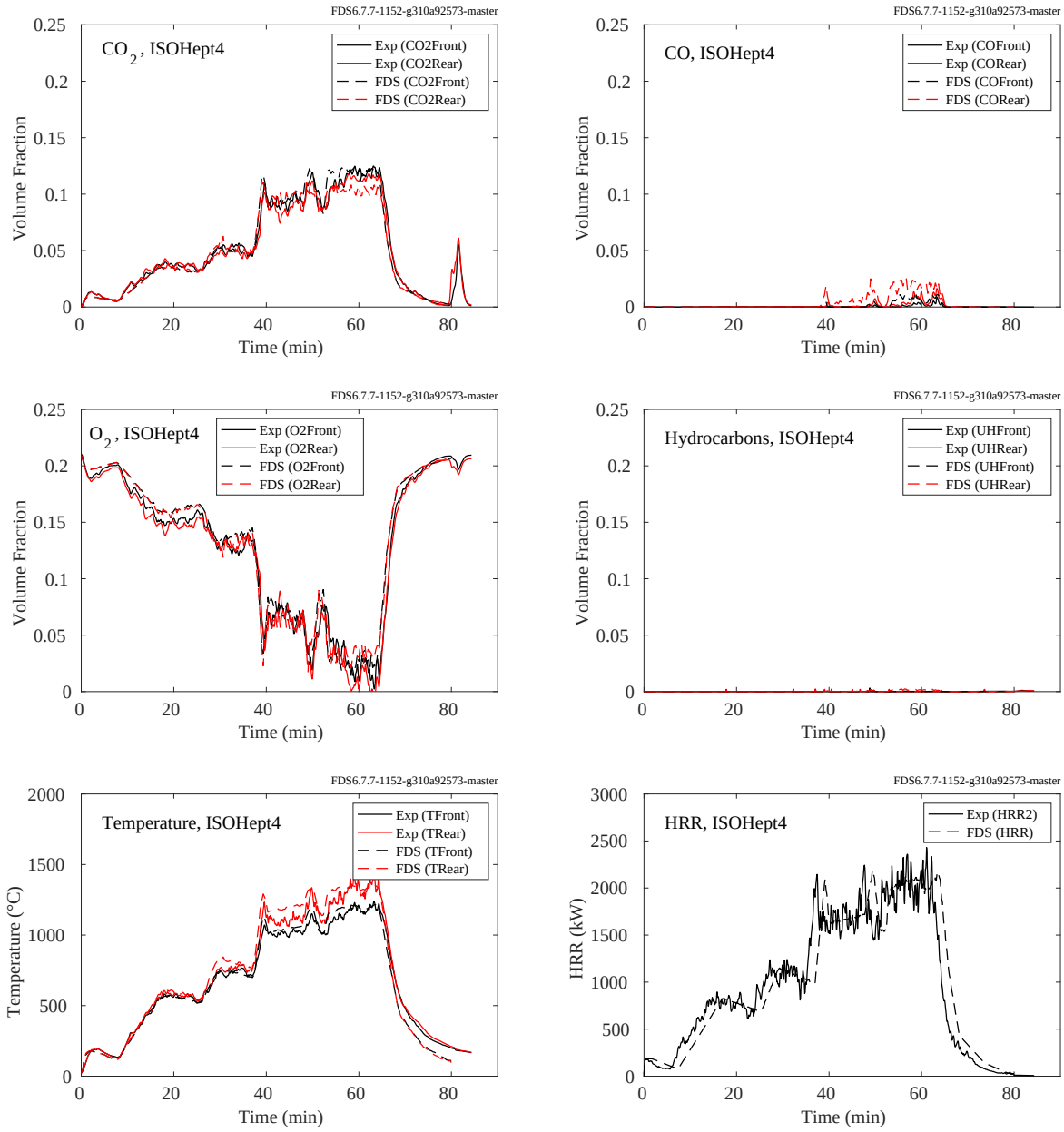

Figure 9.89: Summary of ISOHept4, NIST FSE 2008.

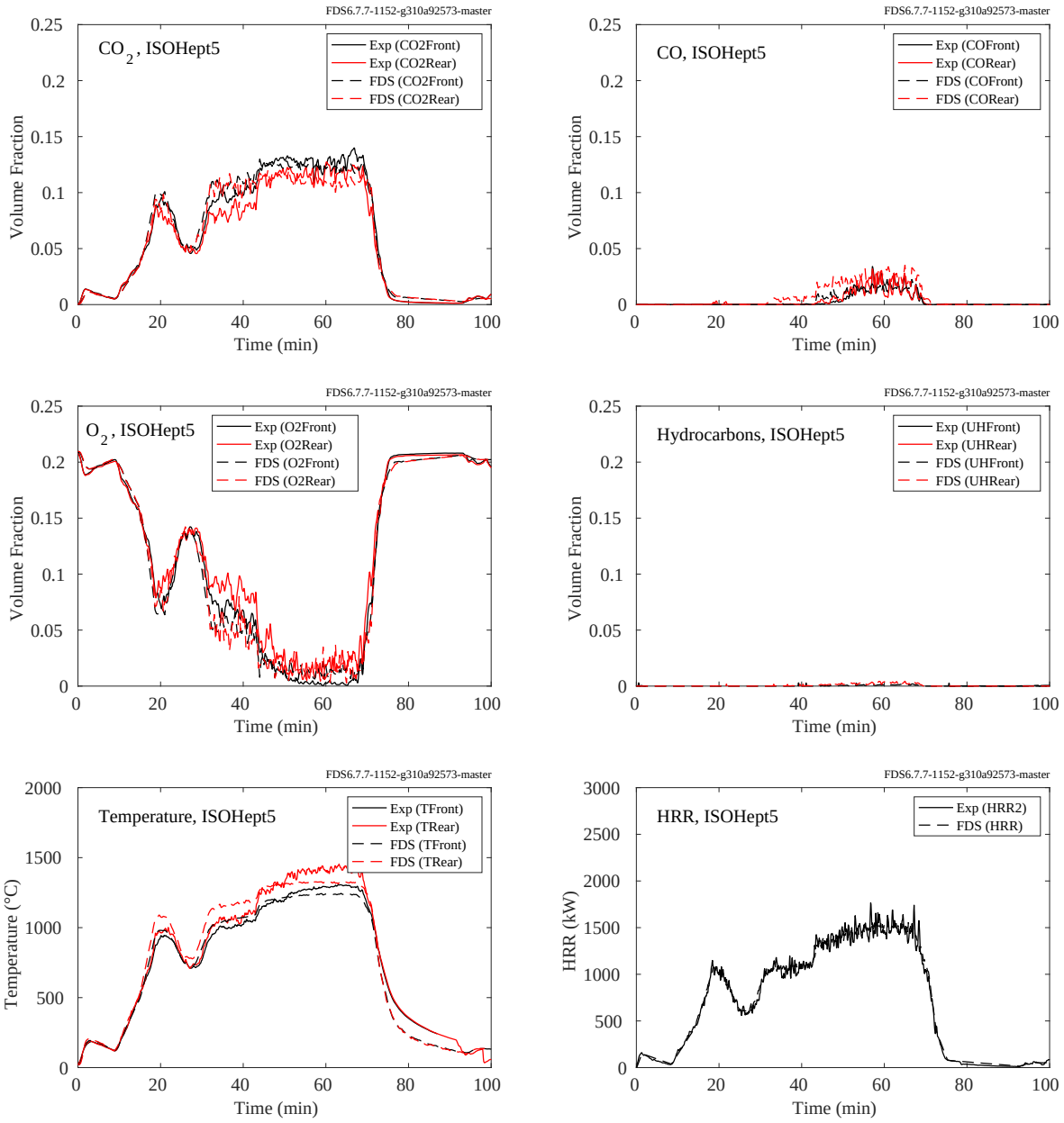

Figure 9.90: Summary of ISOHept5, NIST FSE 2008.

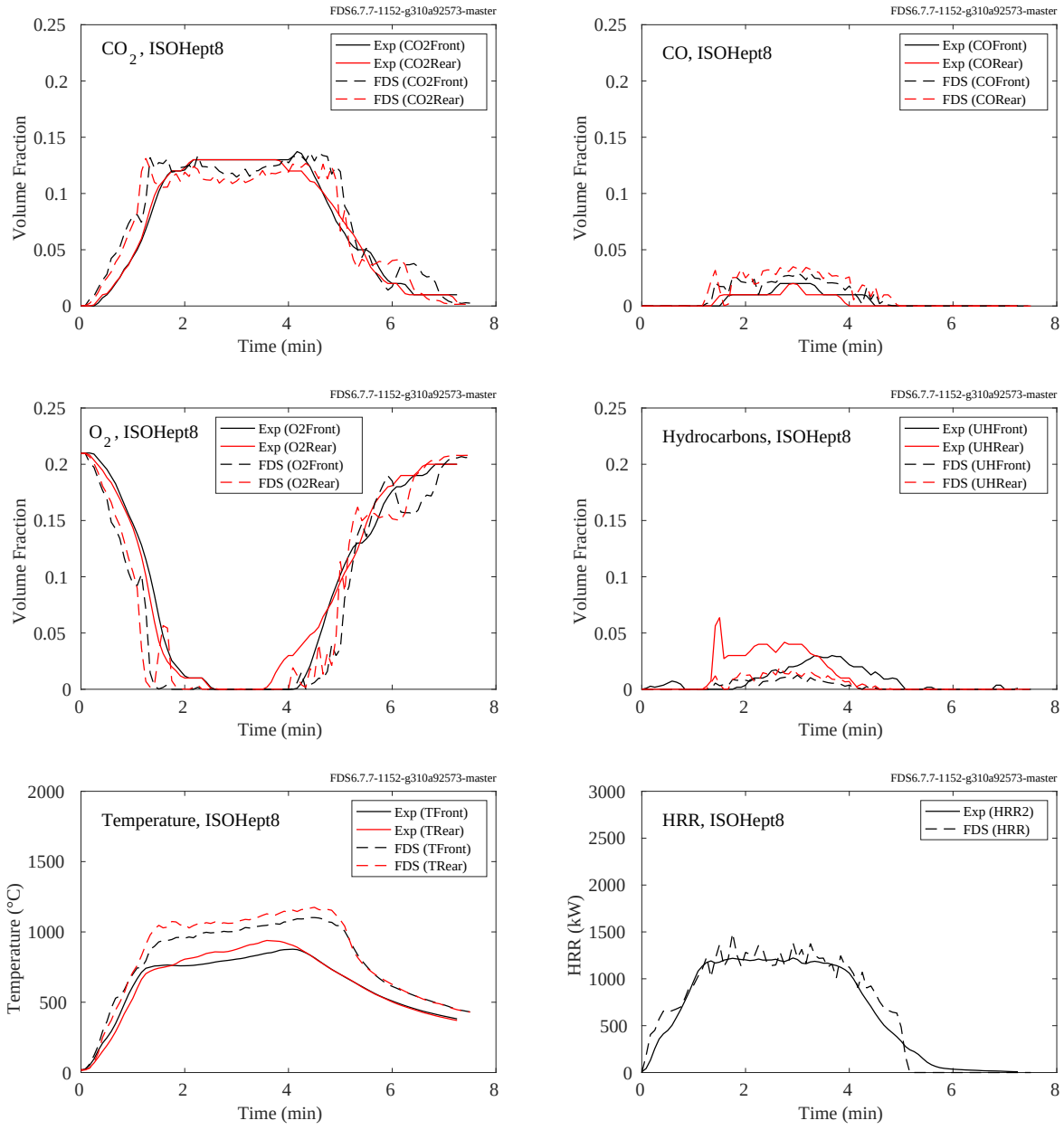

Figure 9.91: Summary of ISOHept8, NIST FSE 2008.

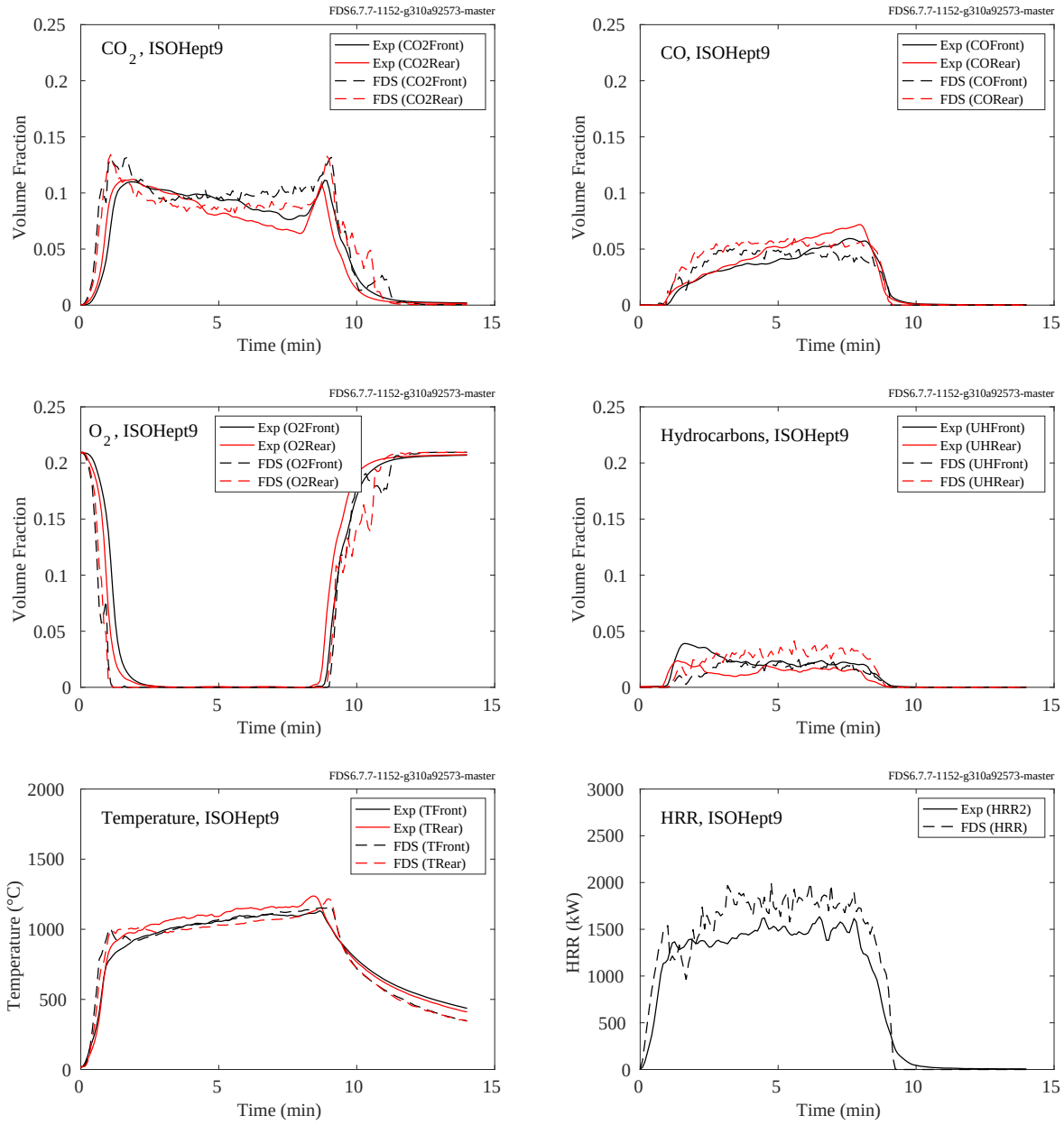

Figure 9.92: Summary of ISOHept9, NIST FSE 2008.

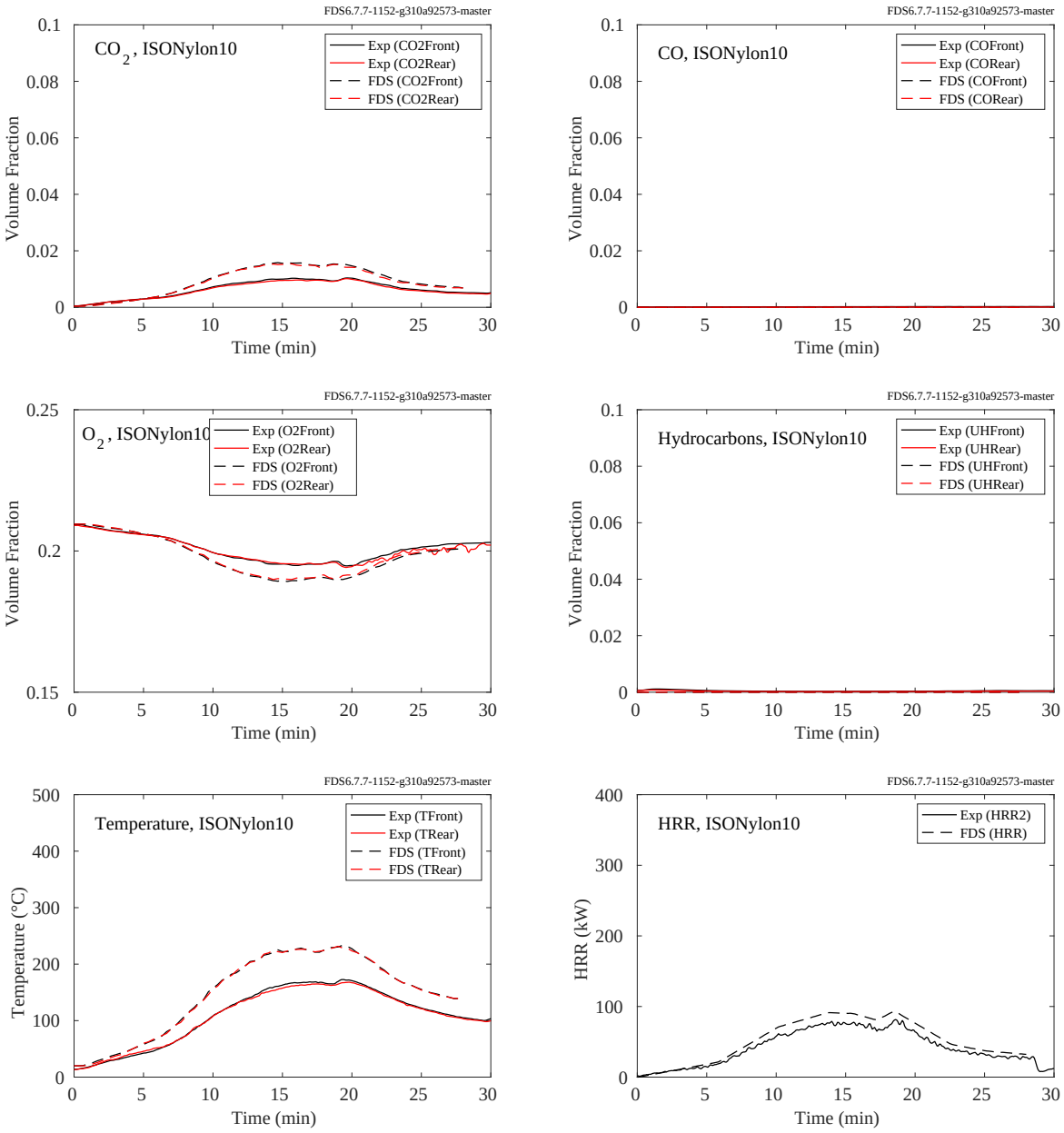

Figure 9.93: Summary of ISONylon10, NIST FSE 2008.

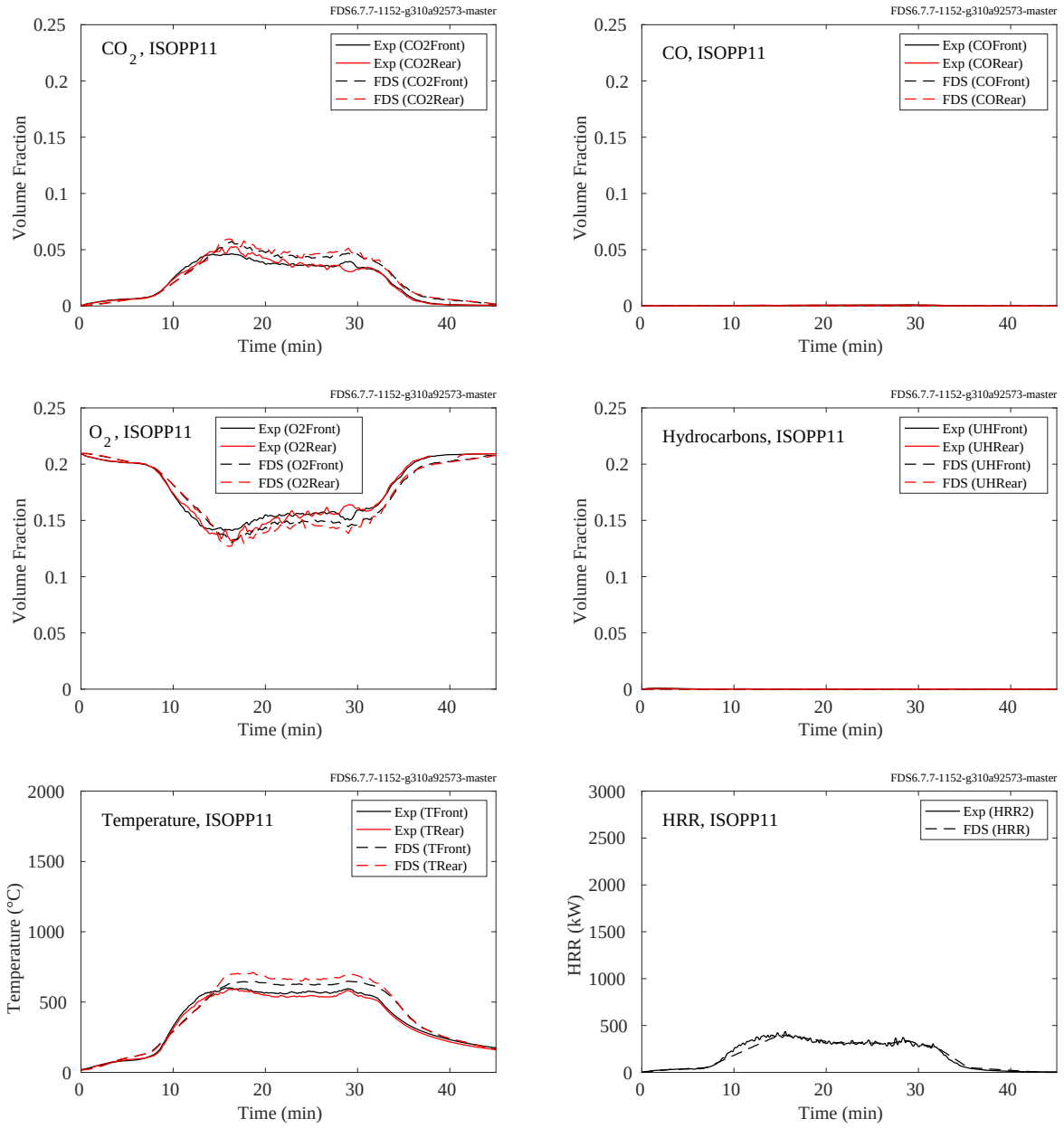

Figure 9.94: Summary of ISOPP11, NIST FSE 2008.

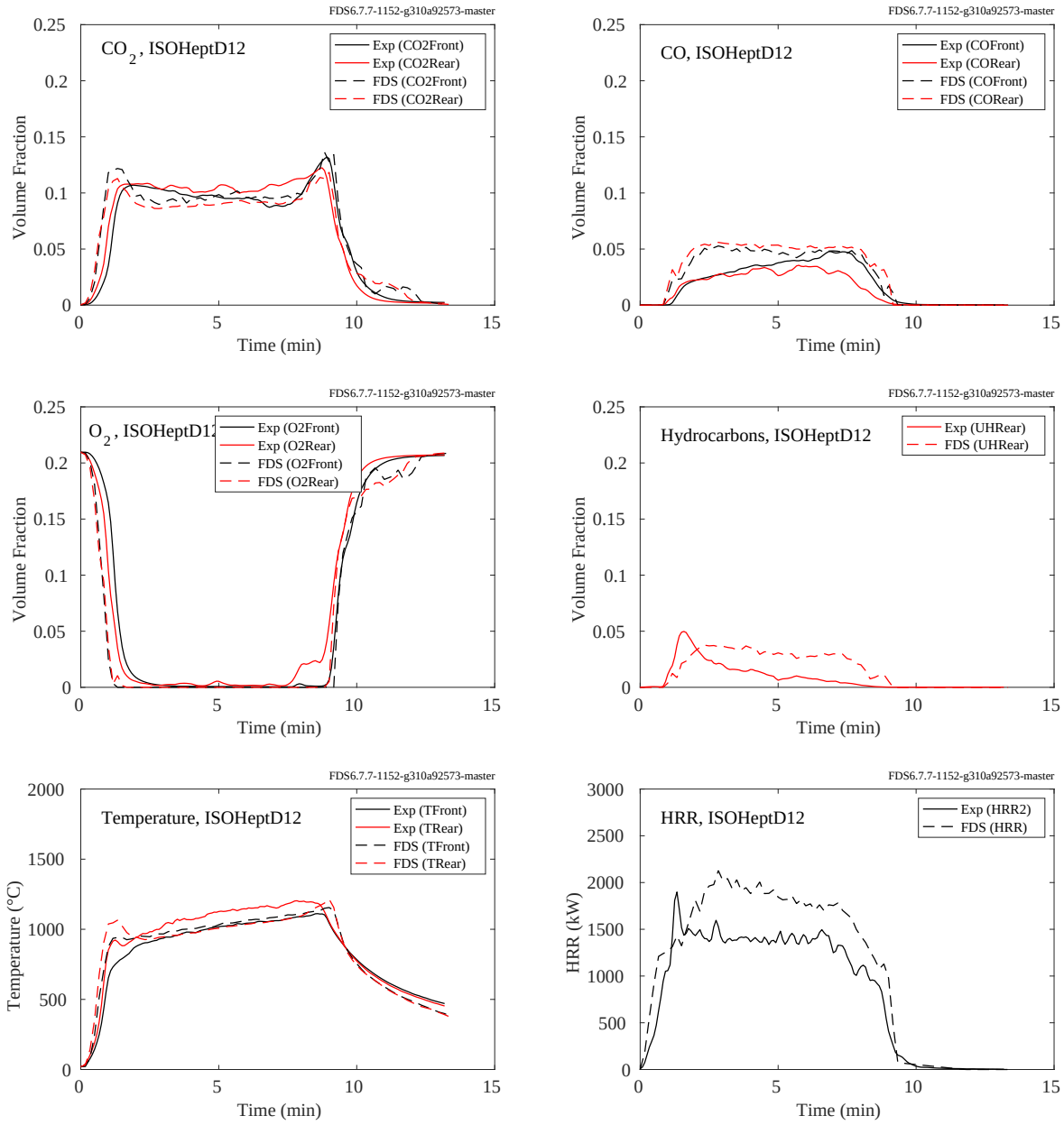

Figure 9.95: Summary of ISOHeptD12, NIST FSE 2008.

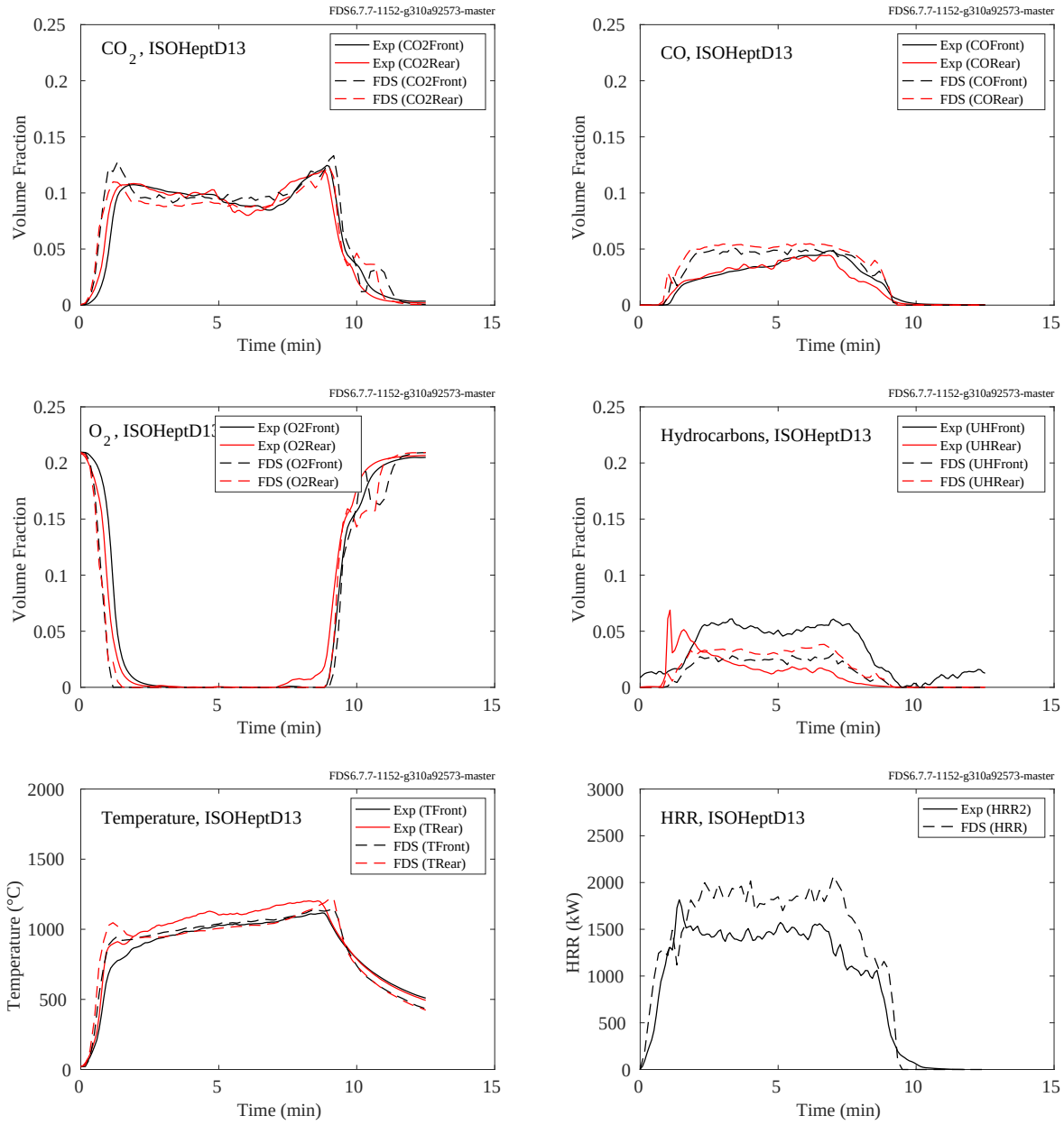

Figure 9.96: Summary of ISOHeptD13, NIST FSE 2008.

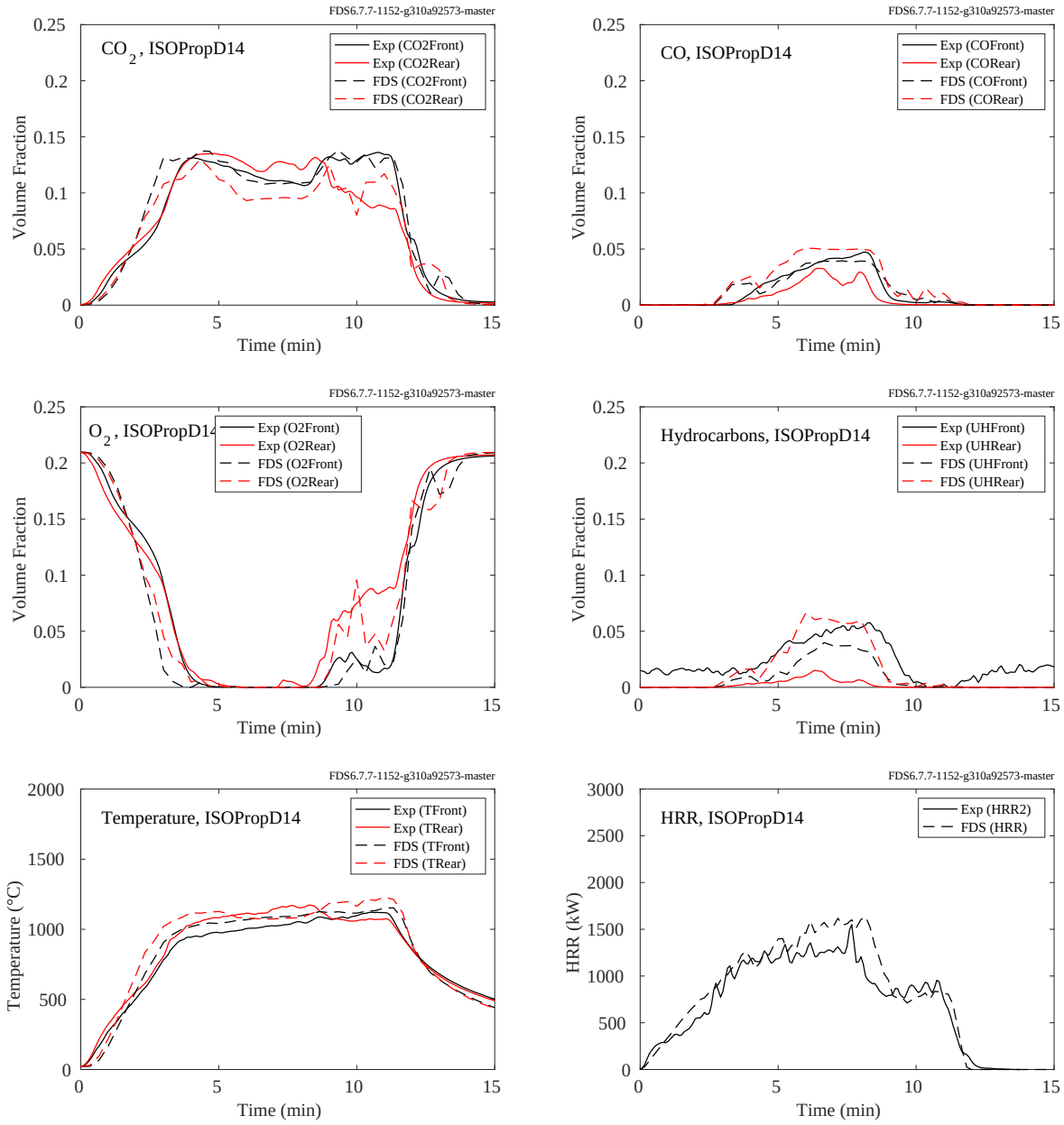

Figure 9.97: Summary of ISOPropD14, NIST FSE 2008.

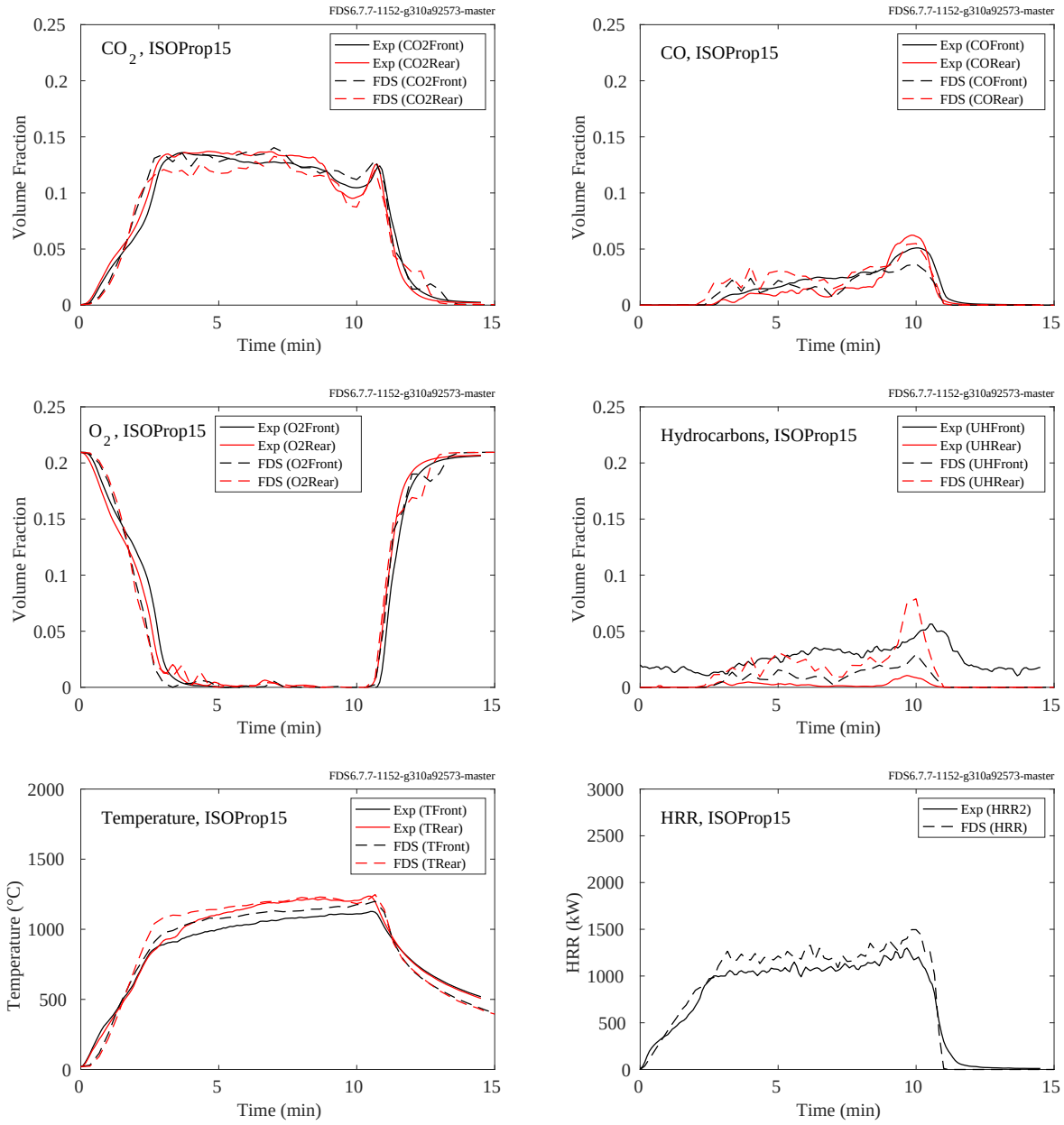

Figure 9.98: Summary of ISOProp15, NIST FSE 2008.

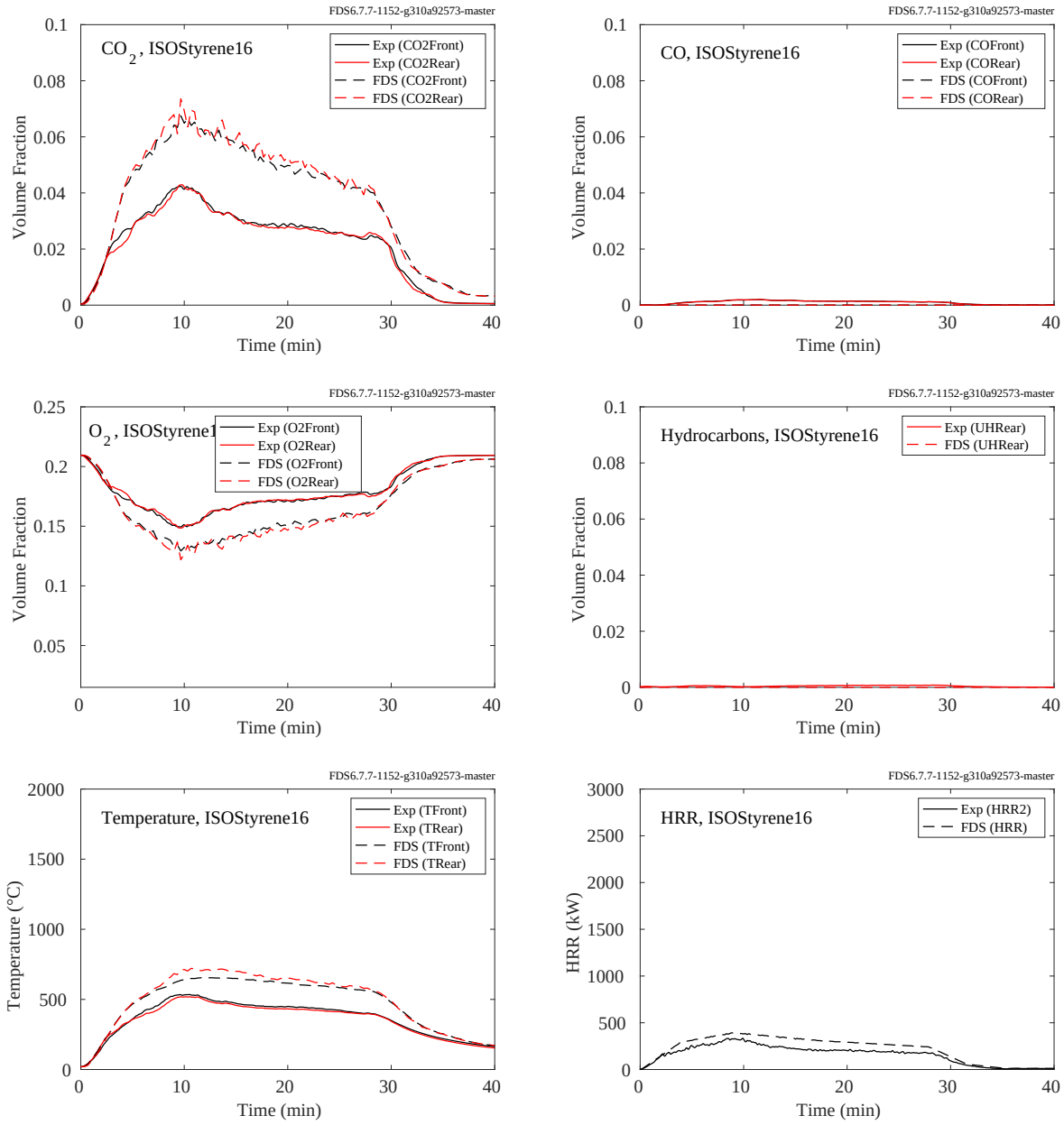

Figure 9.99: Summary of ISOStyrene16, NIST FSE 2008.

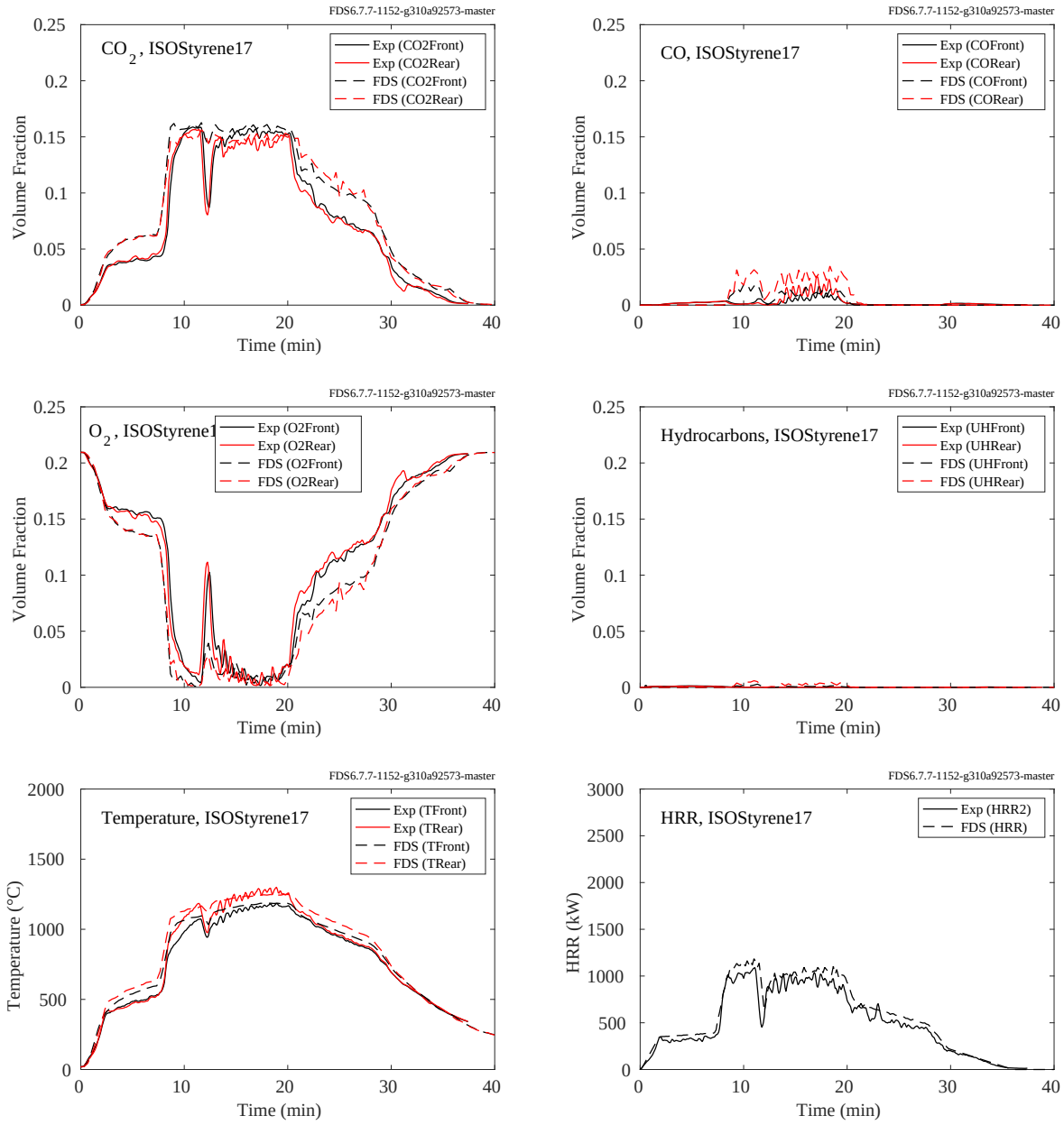

Figure 9.100: Summary of ISOStyrene17, NIST FSE 2008.

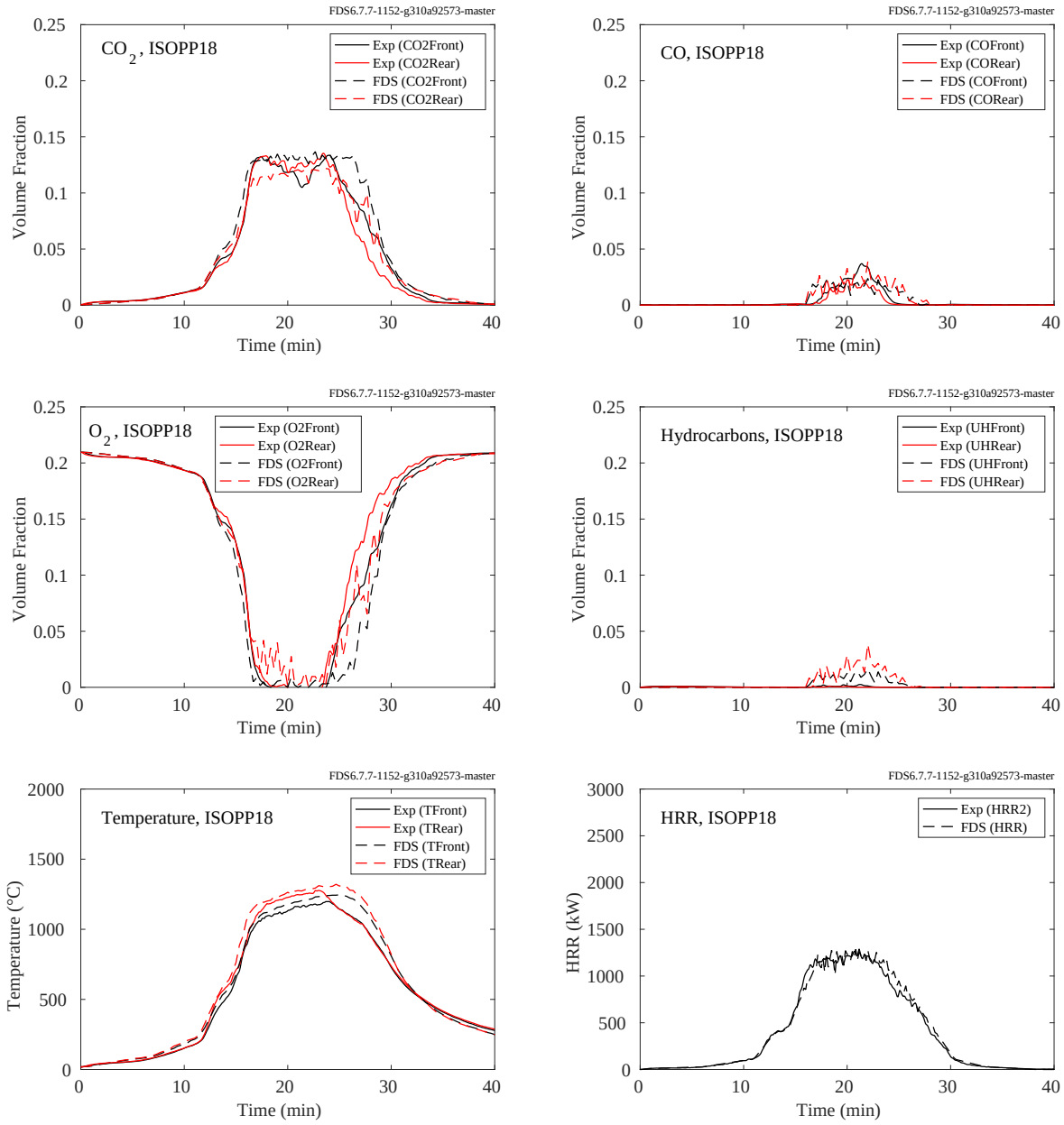

Figure 9.101: Summary of ISOPP18, NIST FSE 2008.

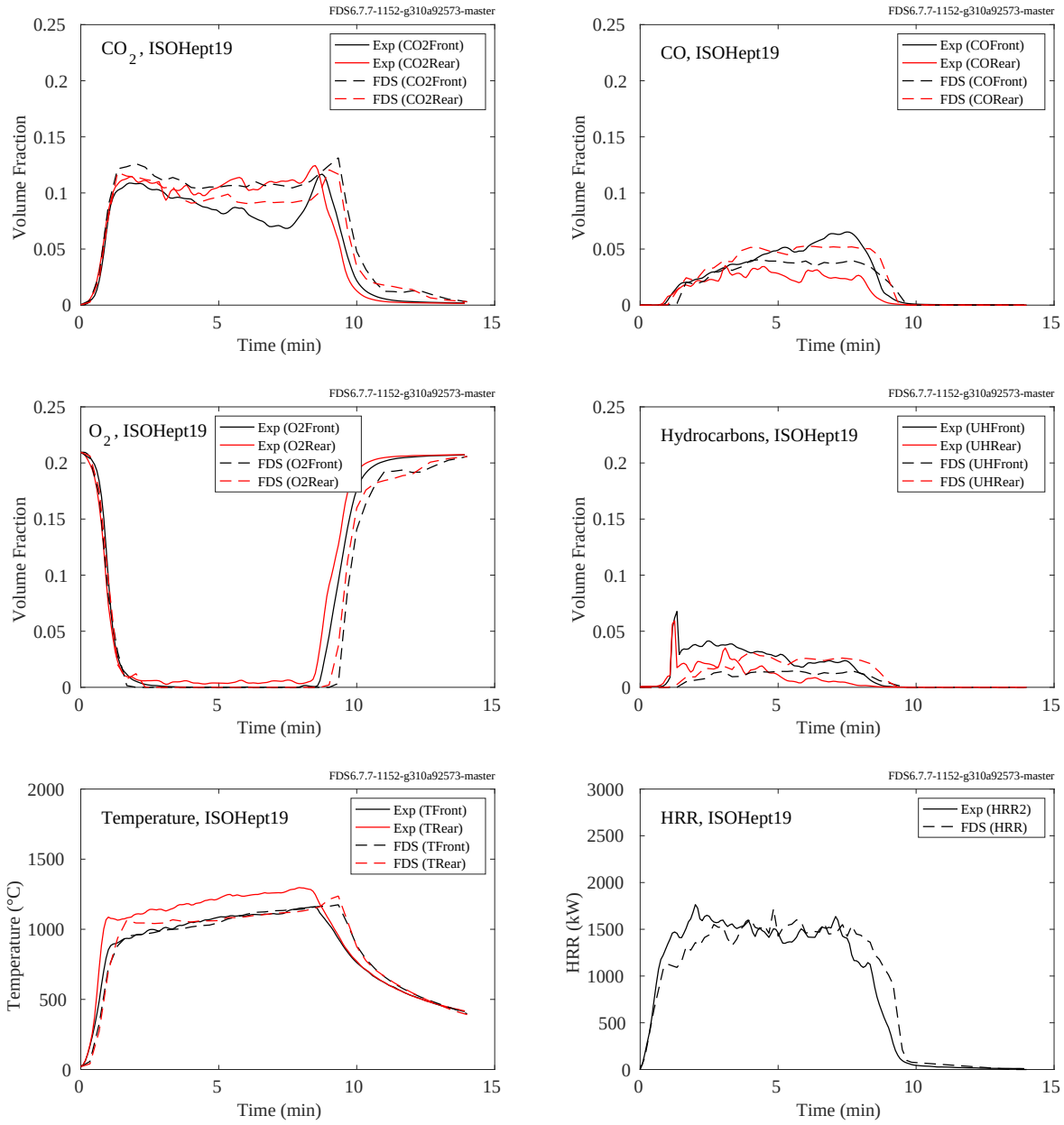

Figure 9.102: Summary of ISOHept19, NIST FSE 2008.

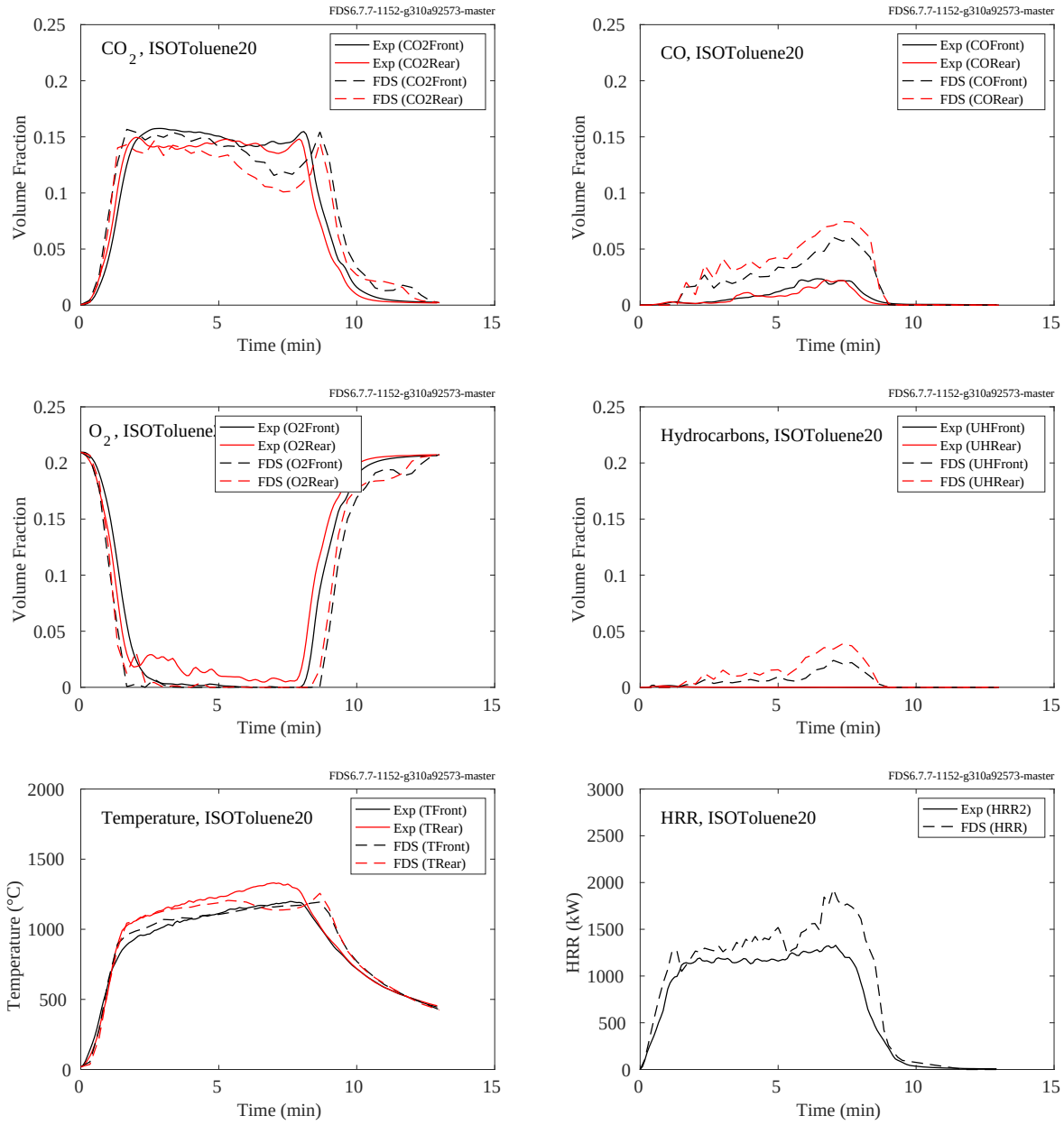

Figure 9.103: Summary of ISOToluene20, NIST FSE 2008.

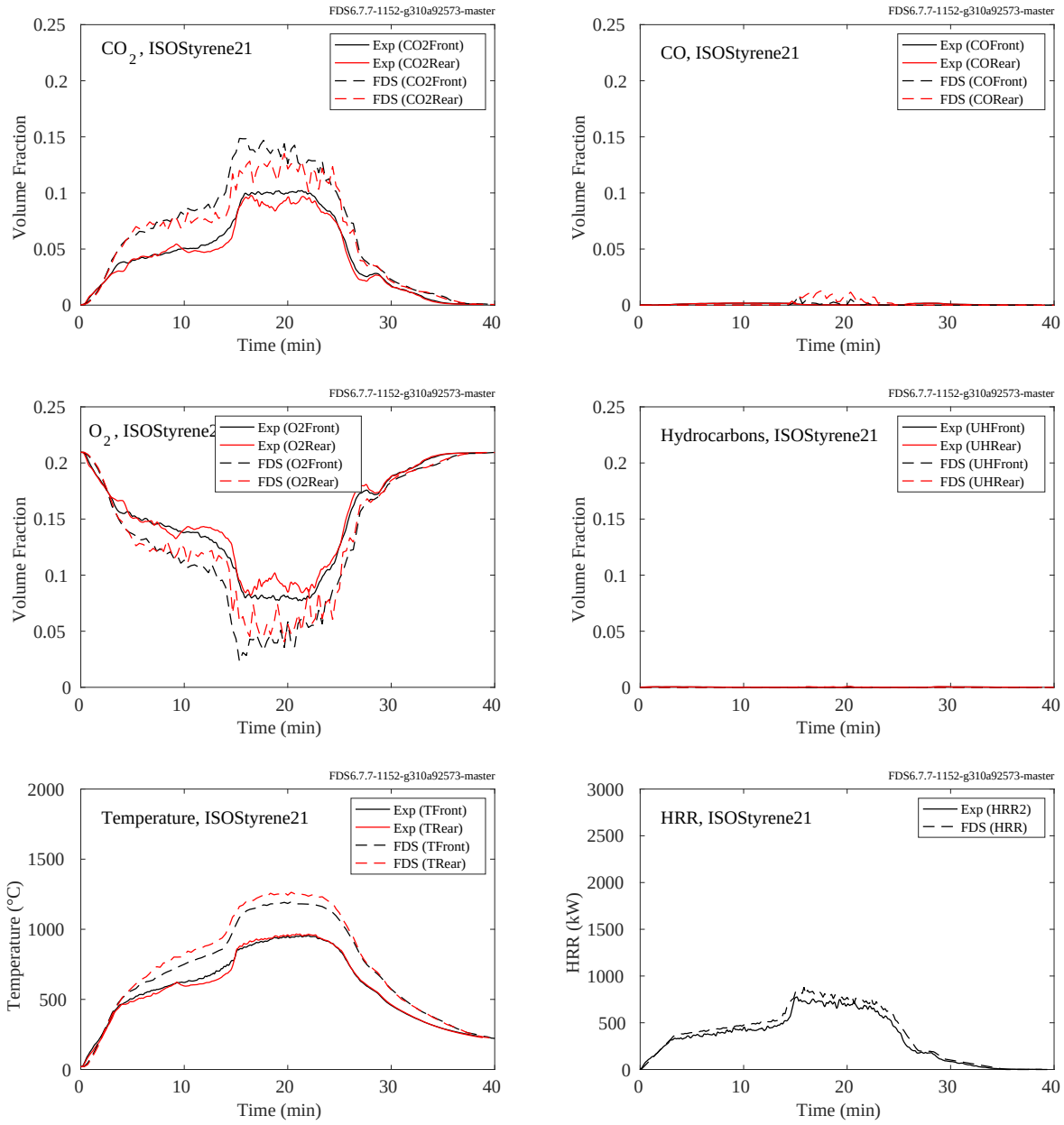

Figure 9.104: Summary of ISOStyrene21, NIST FSE 2008.

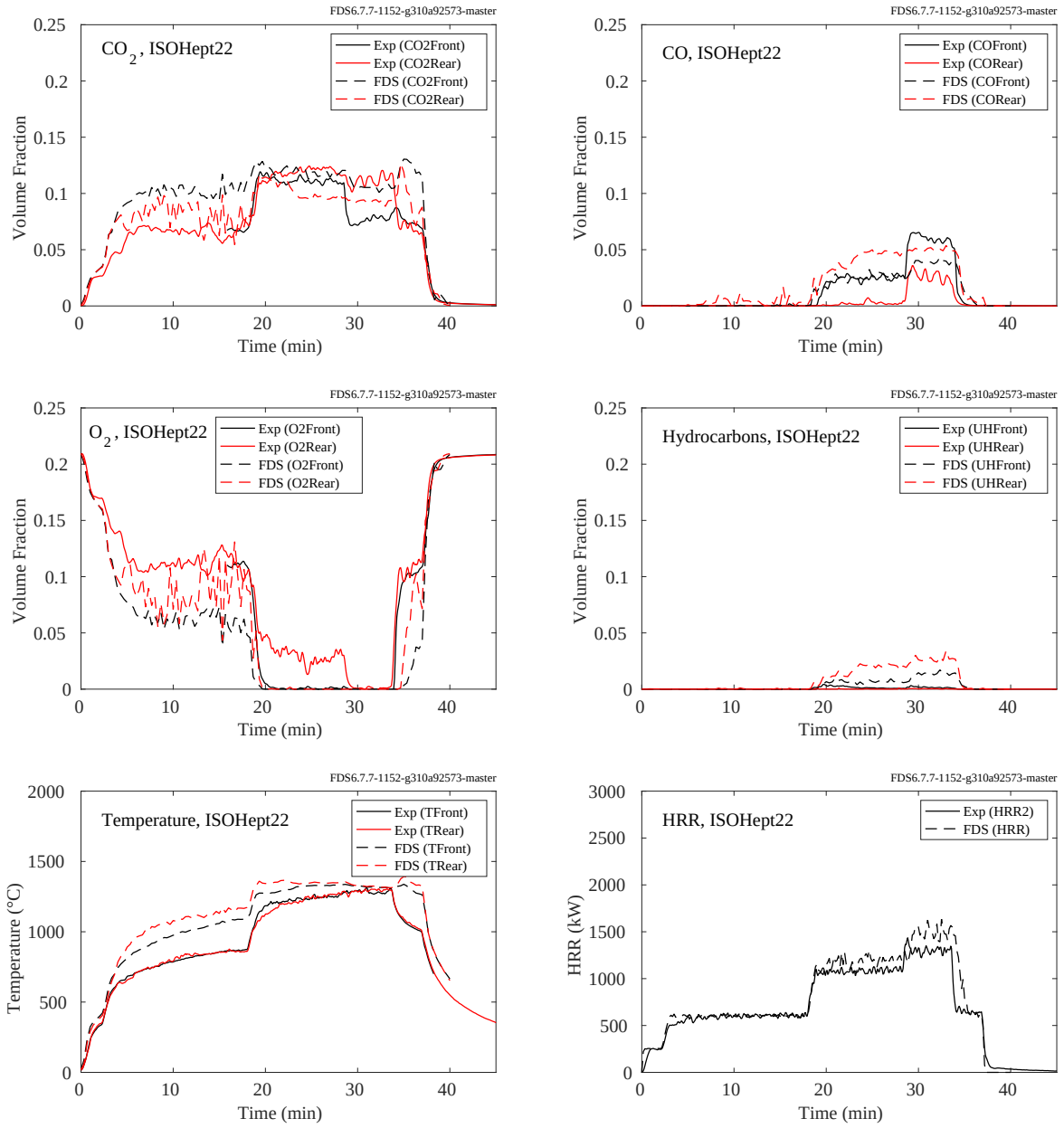

Figure 9.105: Summary of ISOHept22, NIST FSE 2008.

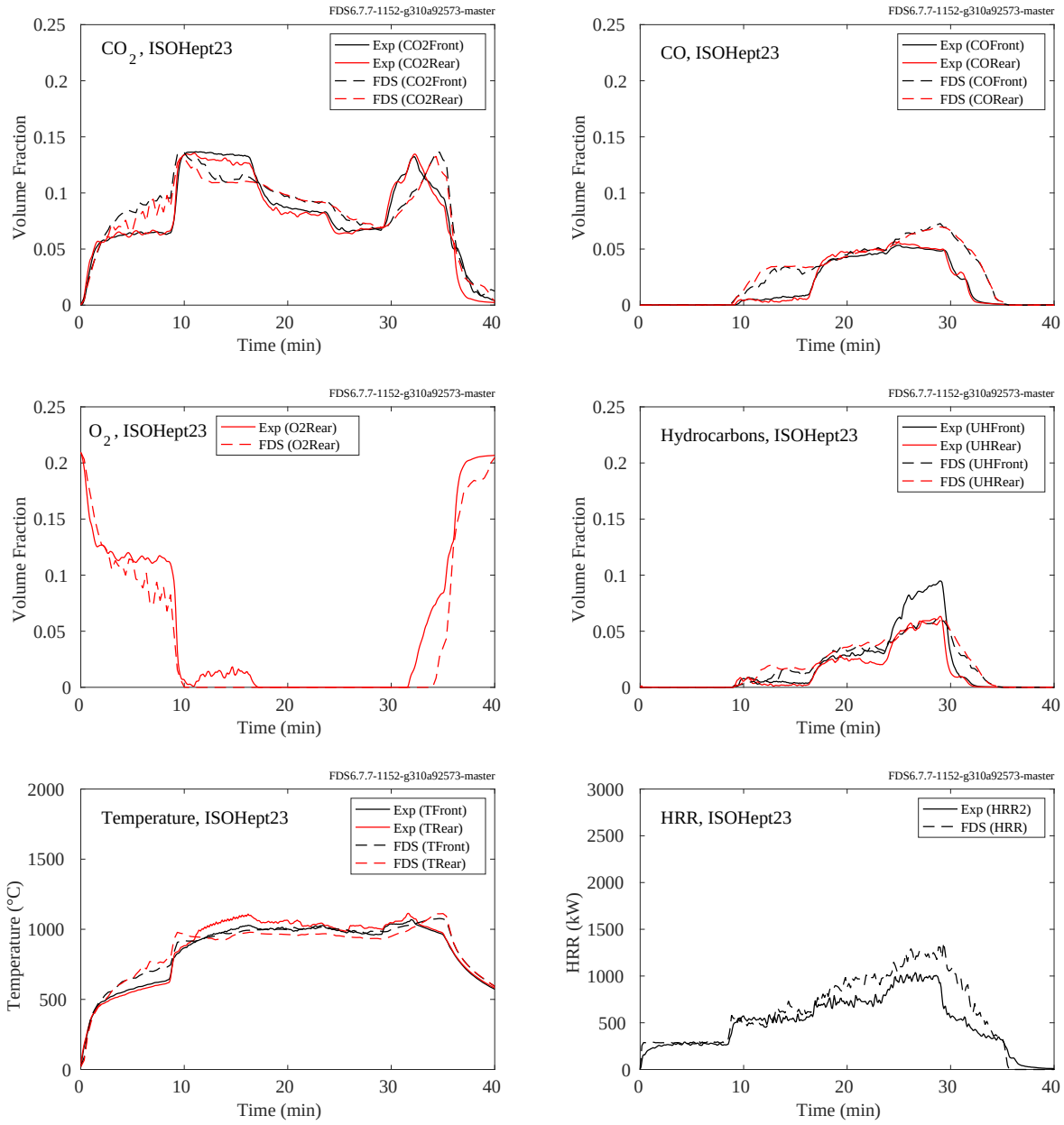

Figure 9.106: Summary of ISOHept23, NIST FSE 2008.

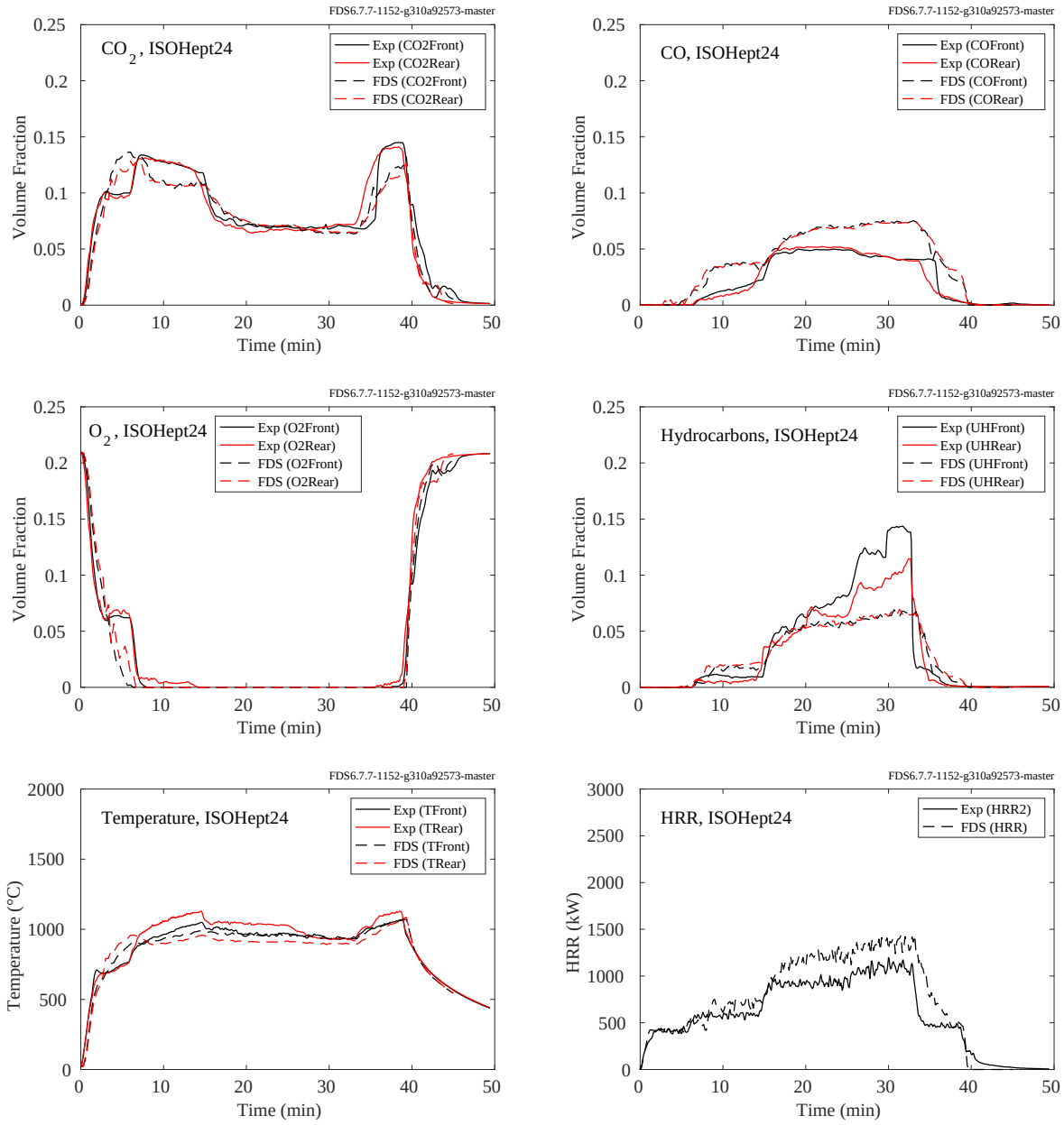

Figure 9.107: Summary of ISOHept24, NIST FSE 2008.

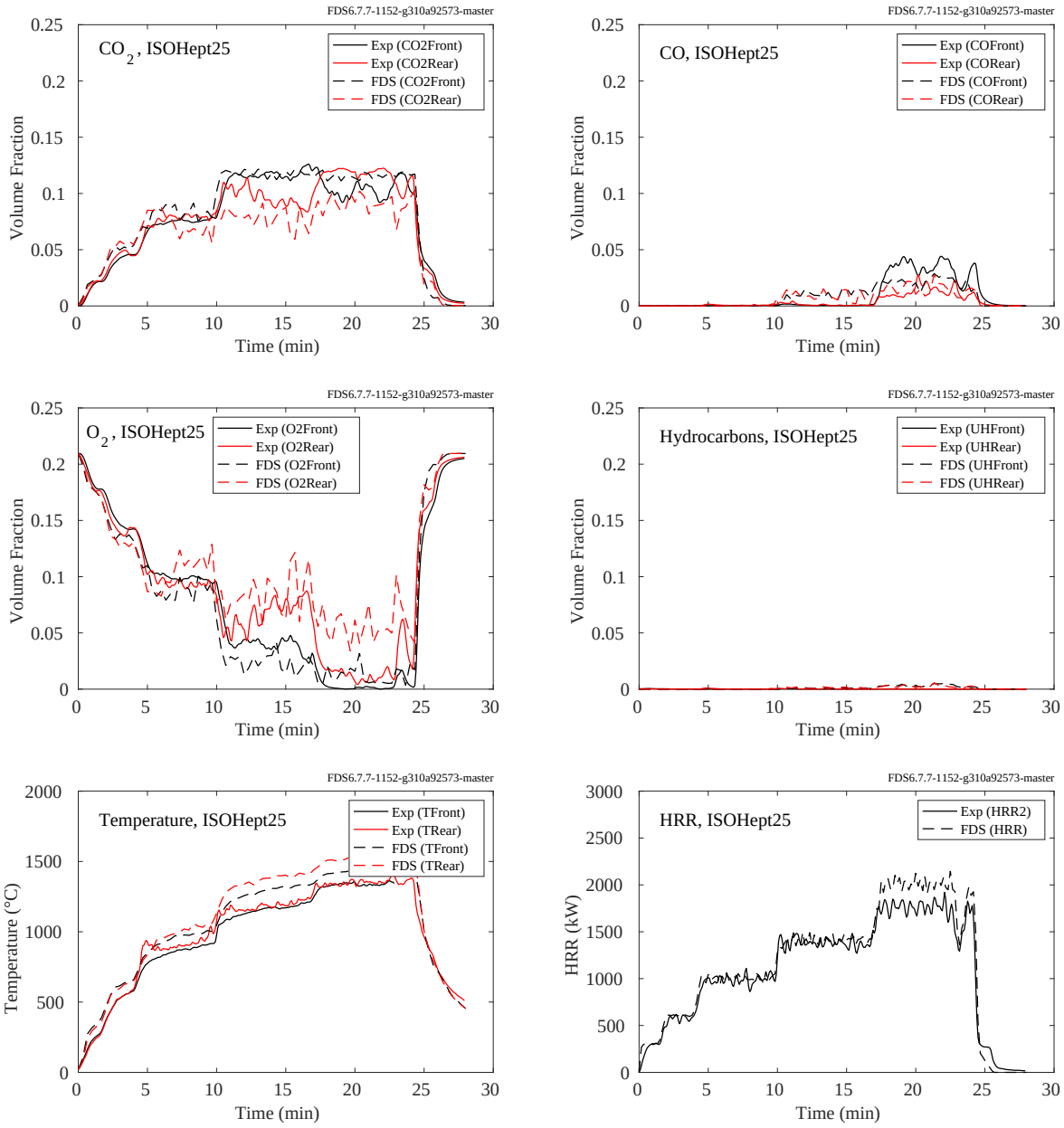

Figure 9.108: Summary of ISOHept25, NIST FSE 2008.

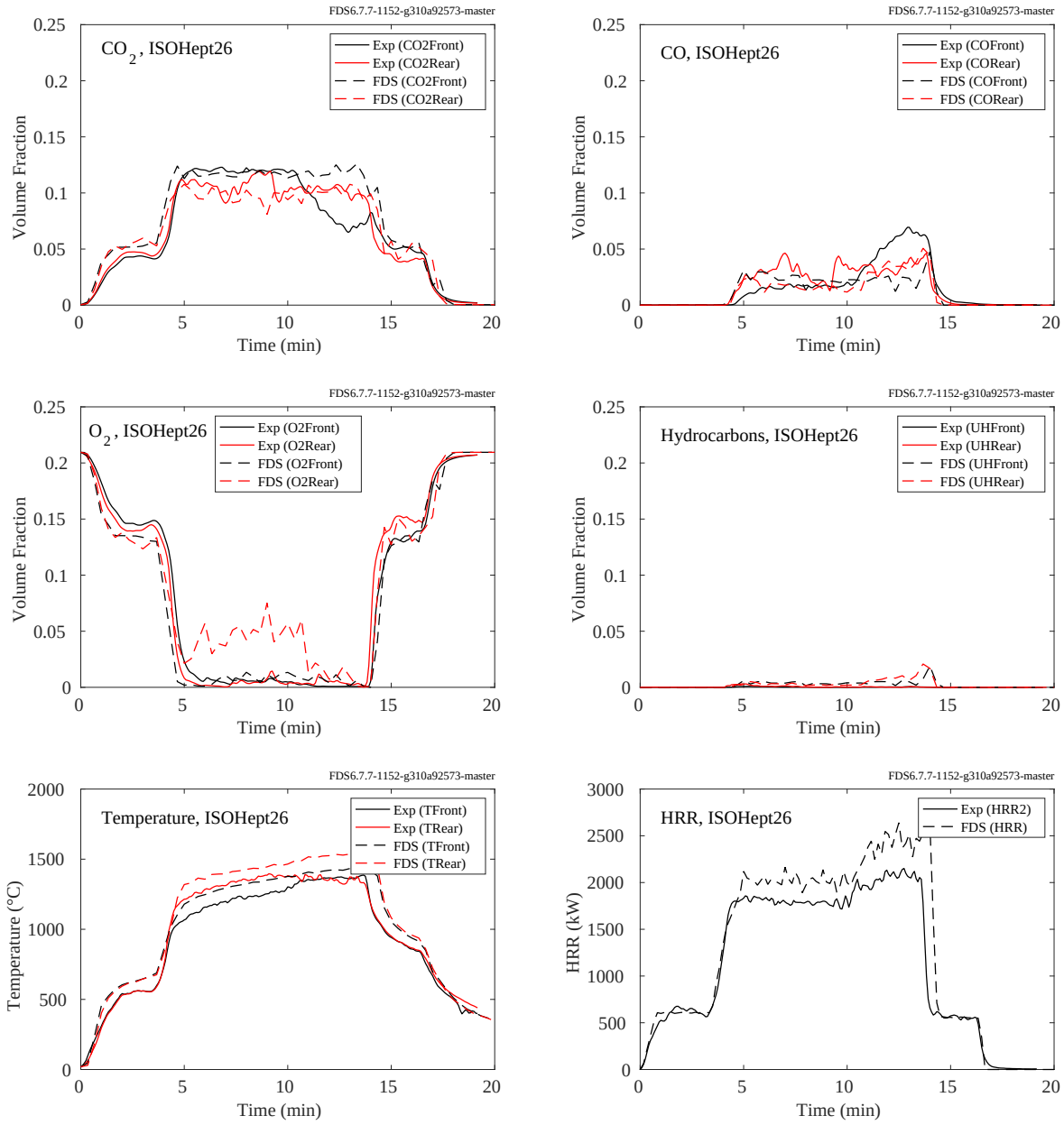

Figure 9.109: Summary of ISOHept26, NIST FSE 2008.

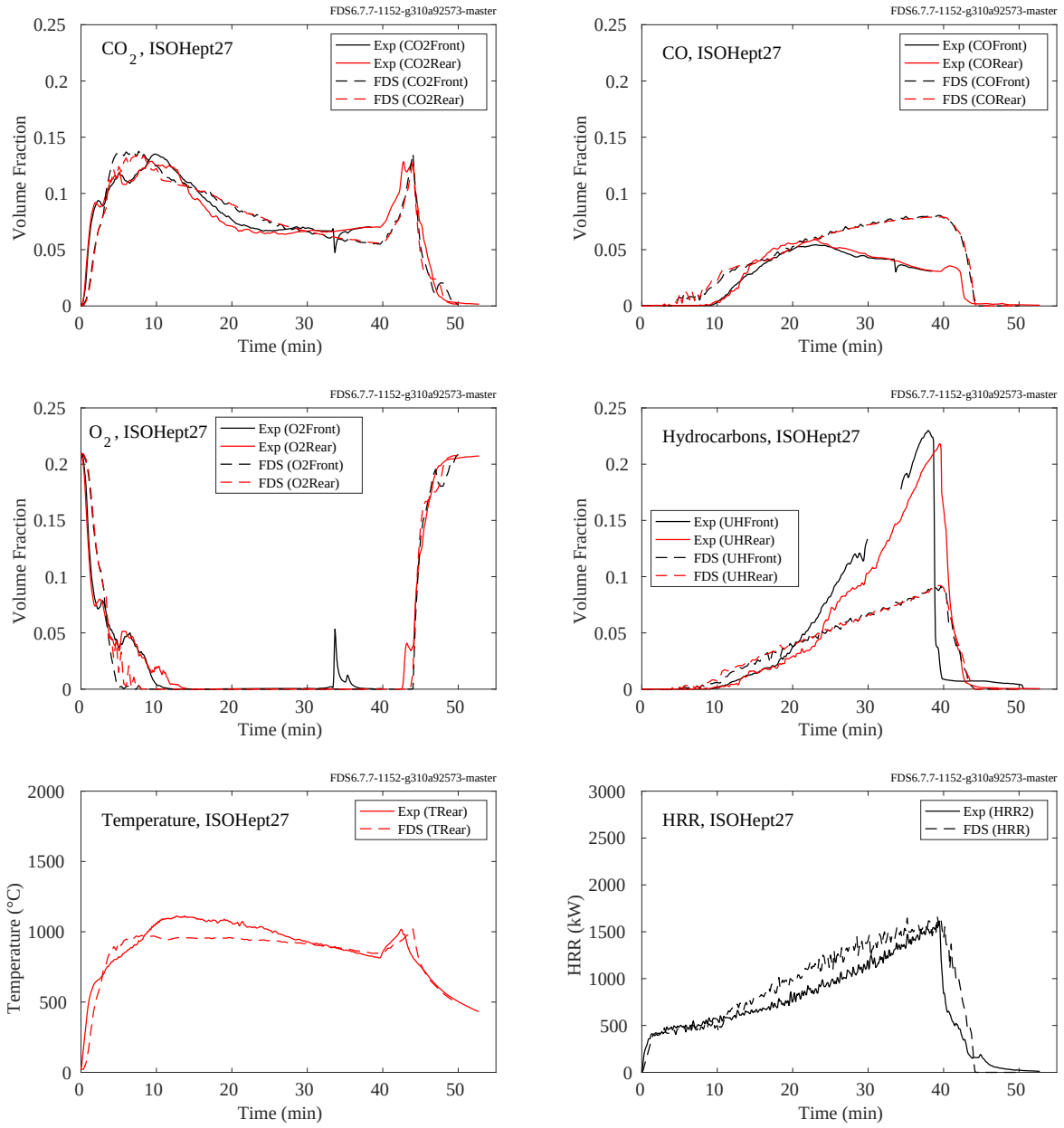

Figure 9.110: Summary of ISOHept27, NIST FSE 2008.

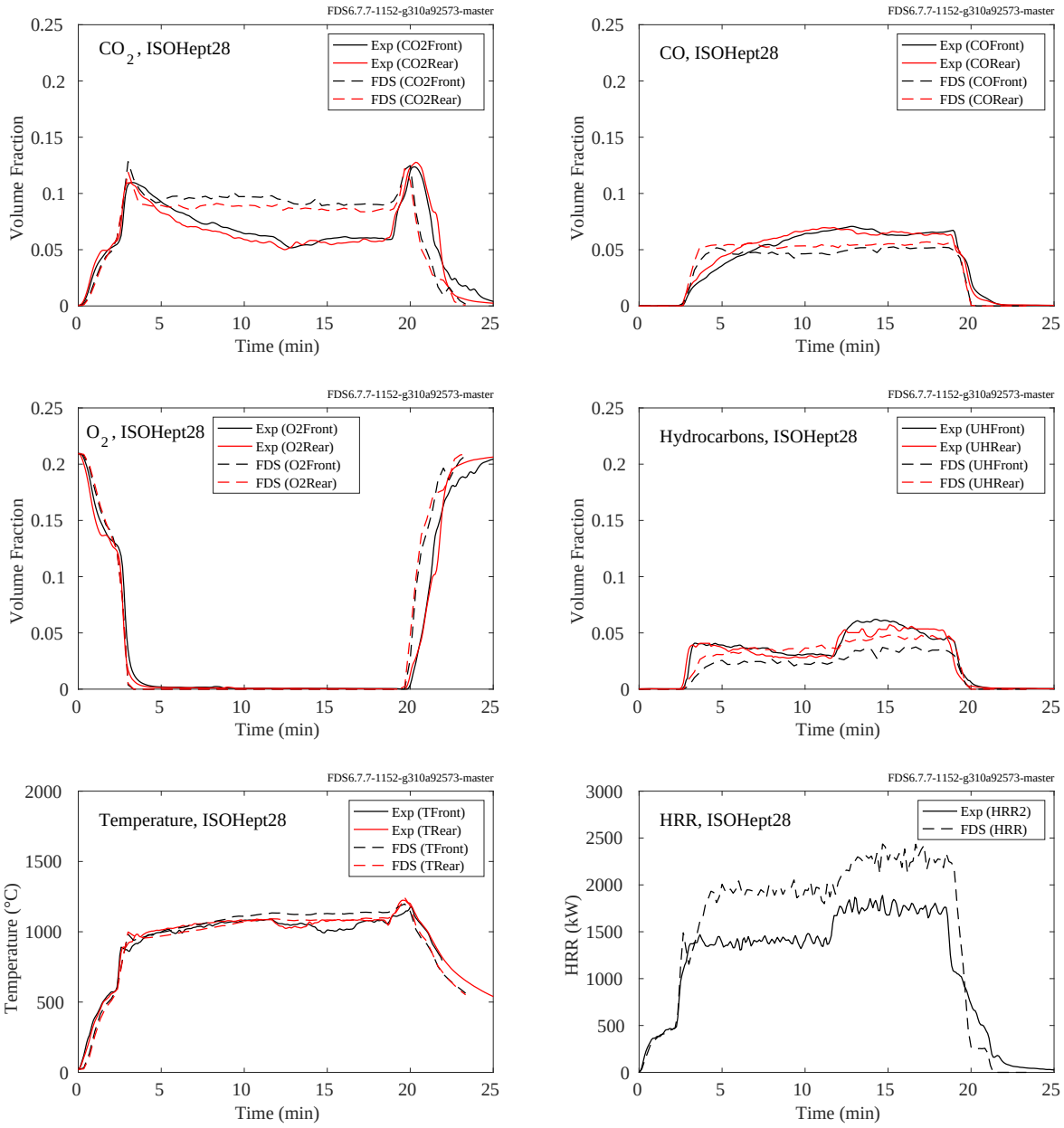

Figure 9.111: Summary of ISOHept28, NIST FSE 2008.

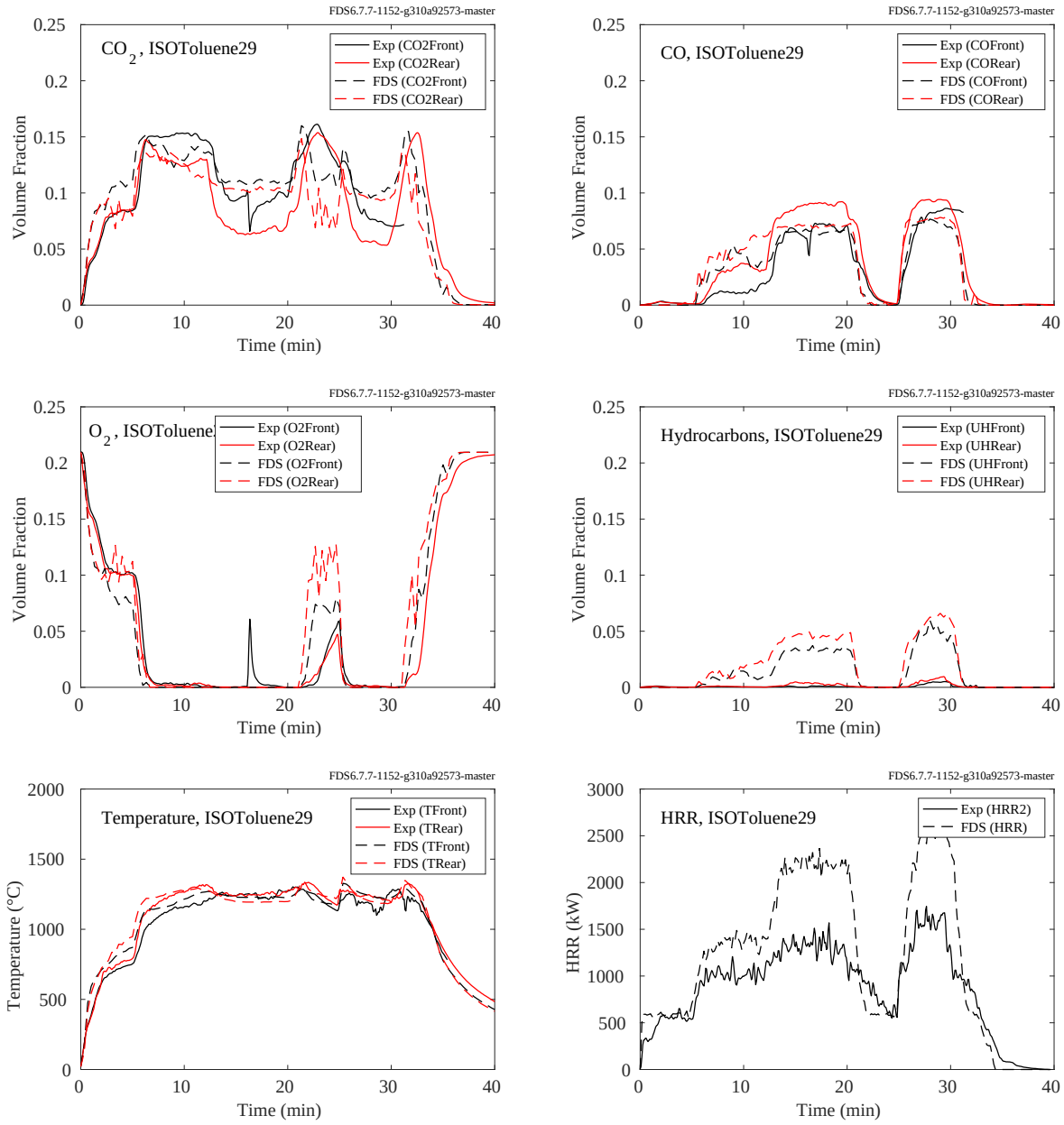

Figure 9.112: Summary of ISOToluene29, NIST FSE 2008.

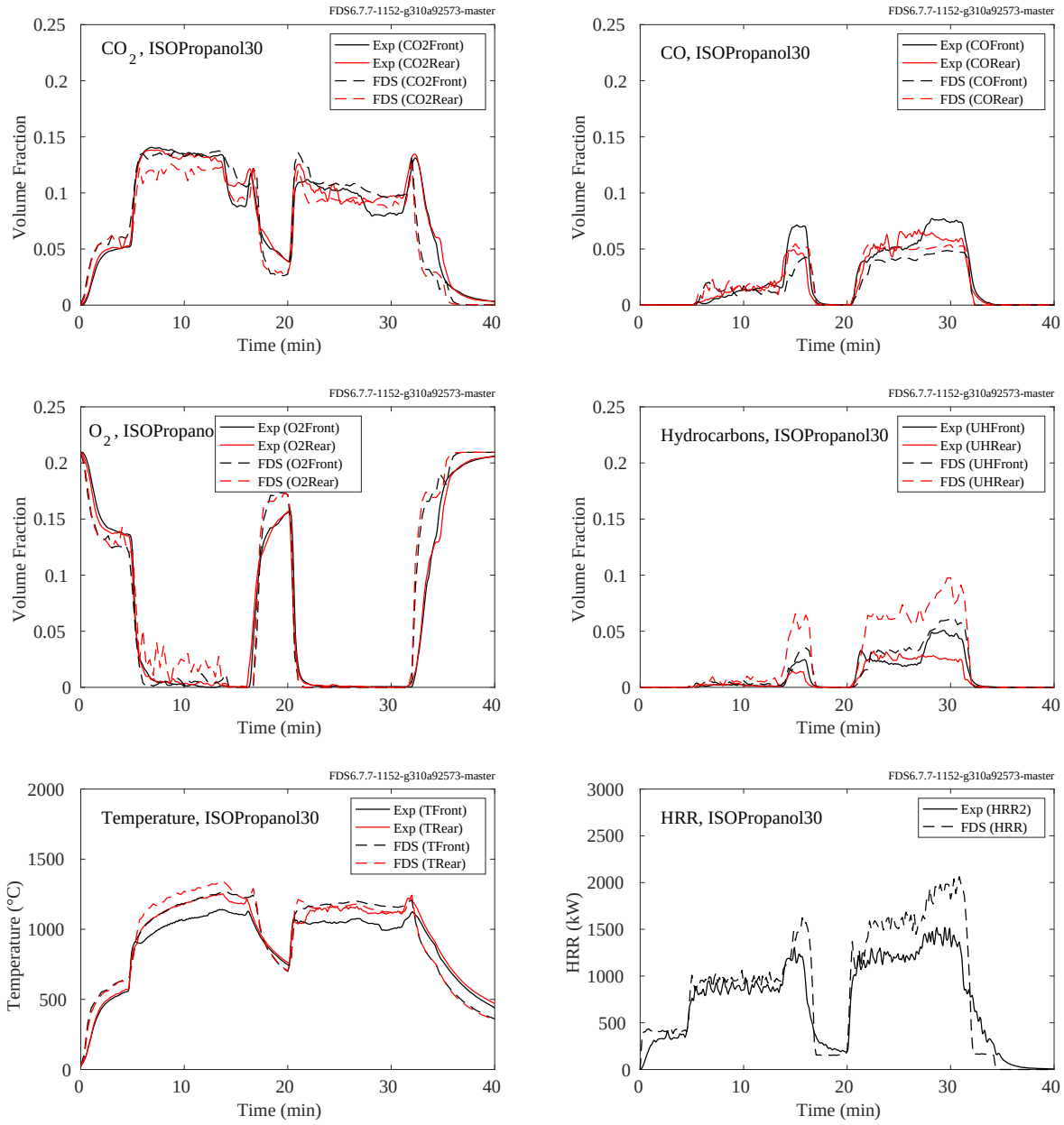

Figure 9.113: Summary of ISOPropanol30, NIST FSE 2008.

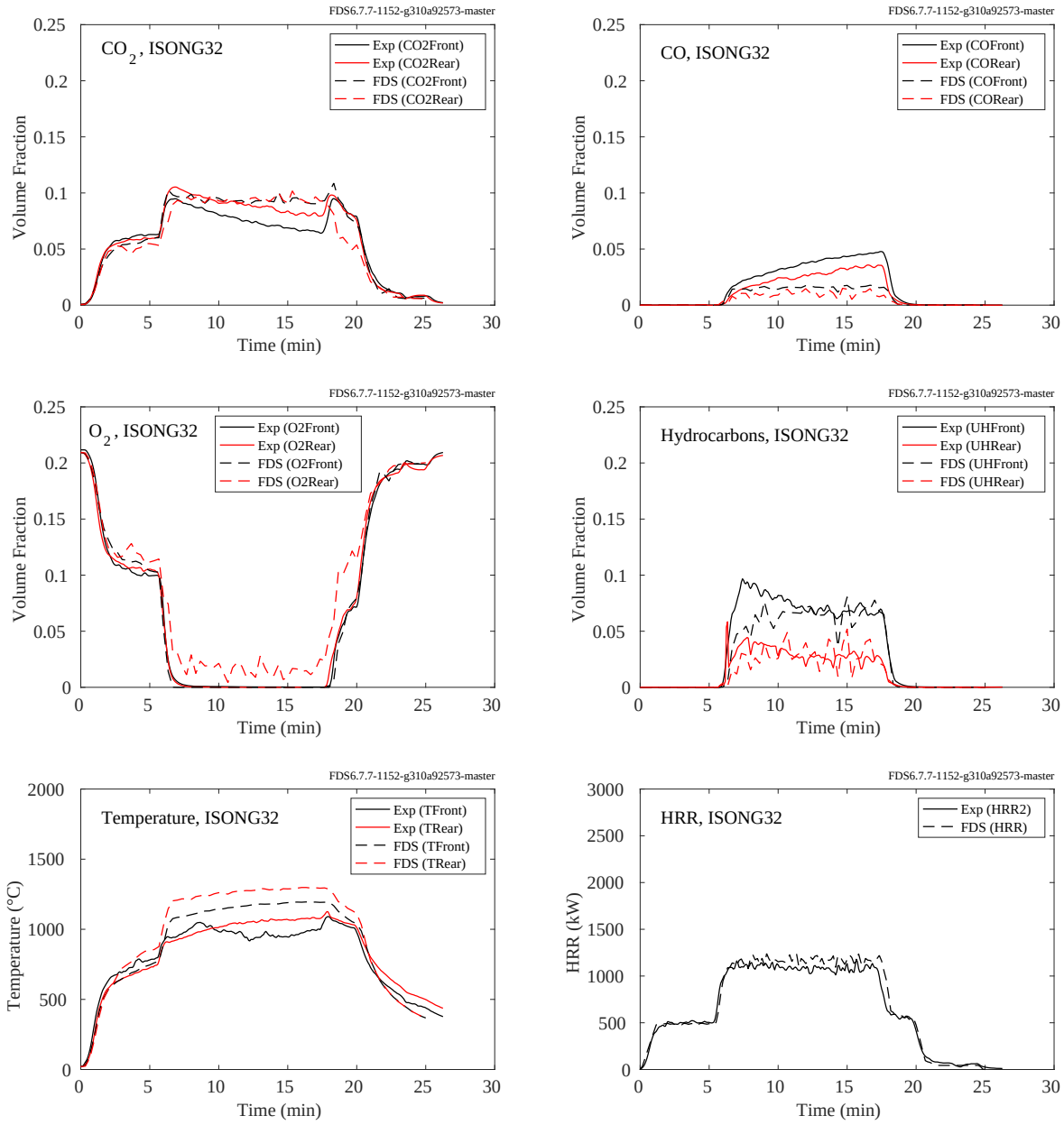

Figure 9.114: Summary of ISONG32, NIST FSE 2008.

9.5.6 NIST Pool Fires

Falkenstein-Smith et al. [328] made mean temperature and product species concentration measurements along the centerline above 30.5 cm diameter liquid pool fires of acetone, ethanol, and methanol; and a 37.0 cm diameter burner of methane and propane. The measurements were made using a gas chromatograph/mass spectrometer system (GC/MSD). The volume fraction of each species was calculated via the number of moles identified by the GC/MSD at each centerline point. Soot mass fractions were measured during the gas sampling process. Note that the species measurements include the vapor form of the primary fuel molecule, in addition to intermediate fuel species. FDS does not model the decomposition of the fuel molecule into intermediate hydrocarbon species except for CO and H_2.

The mean centerline temperature profiles are found in Section 6.1.5. The species concentrations are found in Figs. 9.115 through 9.120 on the following pages.

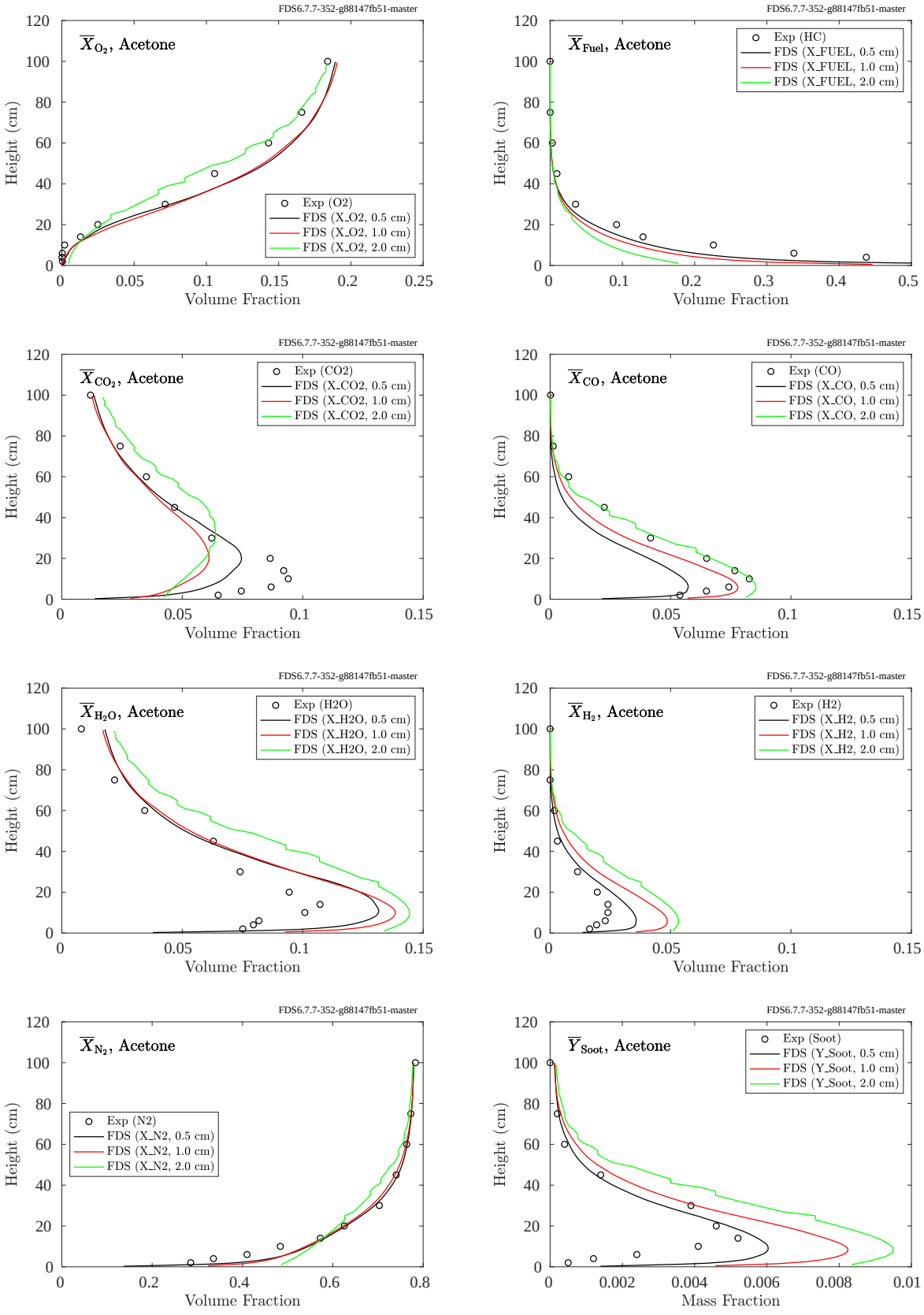

Figure 9.115: NIST Pool Fires, centerline product species, acetone.

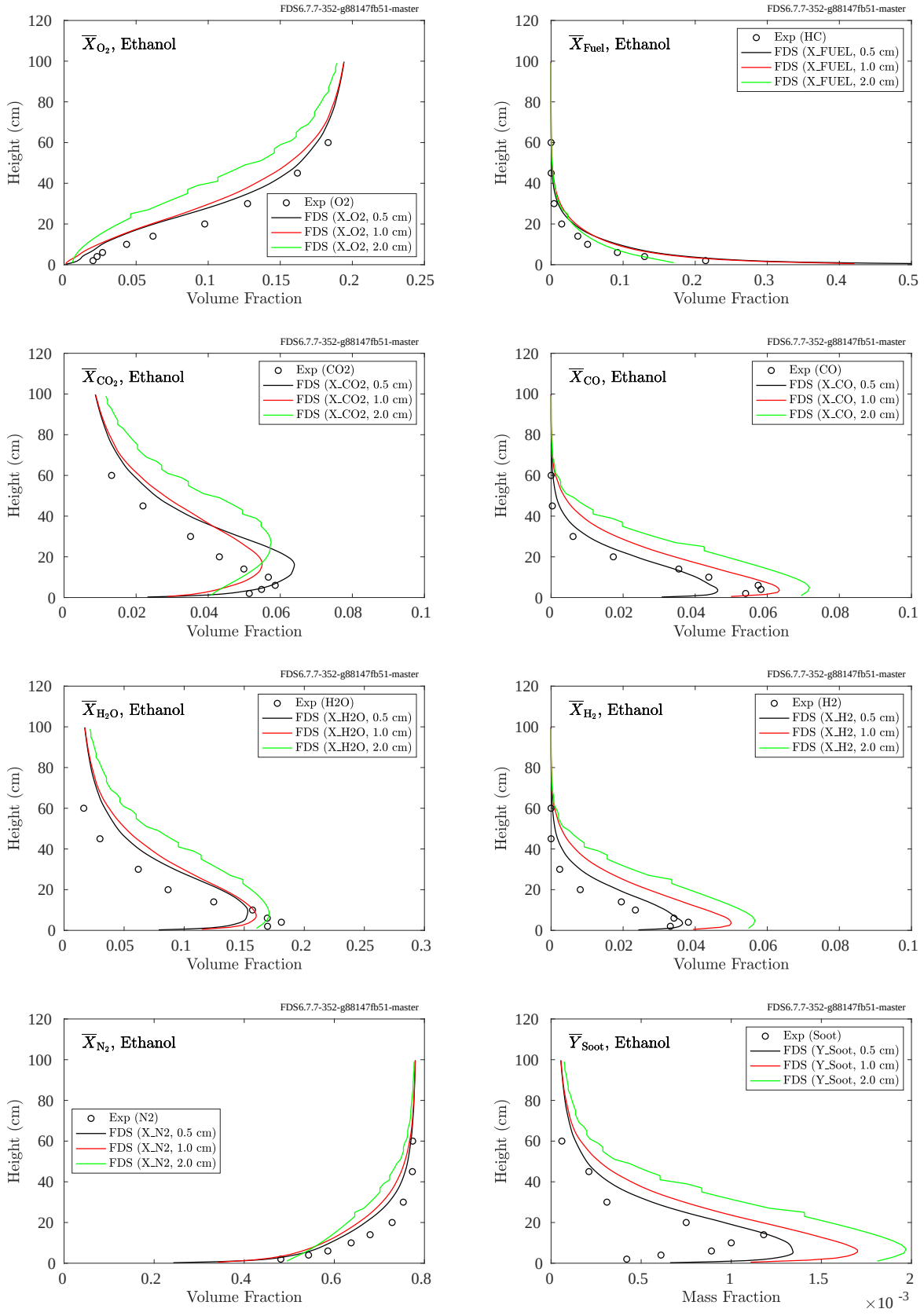

Figure 9.116: NIST Pool Fires, centerline product species, ethanol.

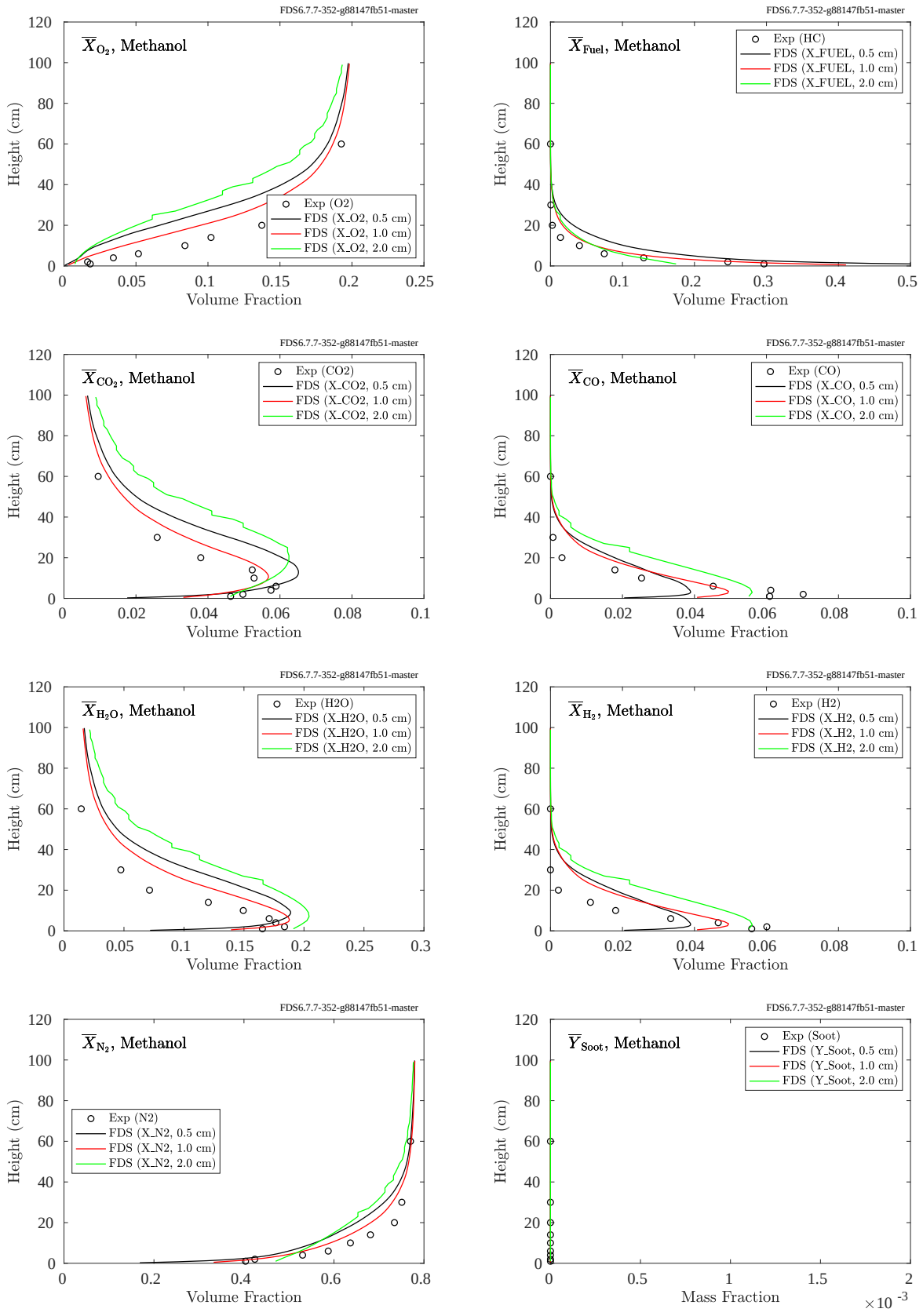

Figure 9.117: NIST Pool Fires, centerline product species, methanol.

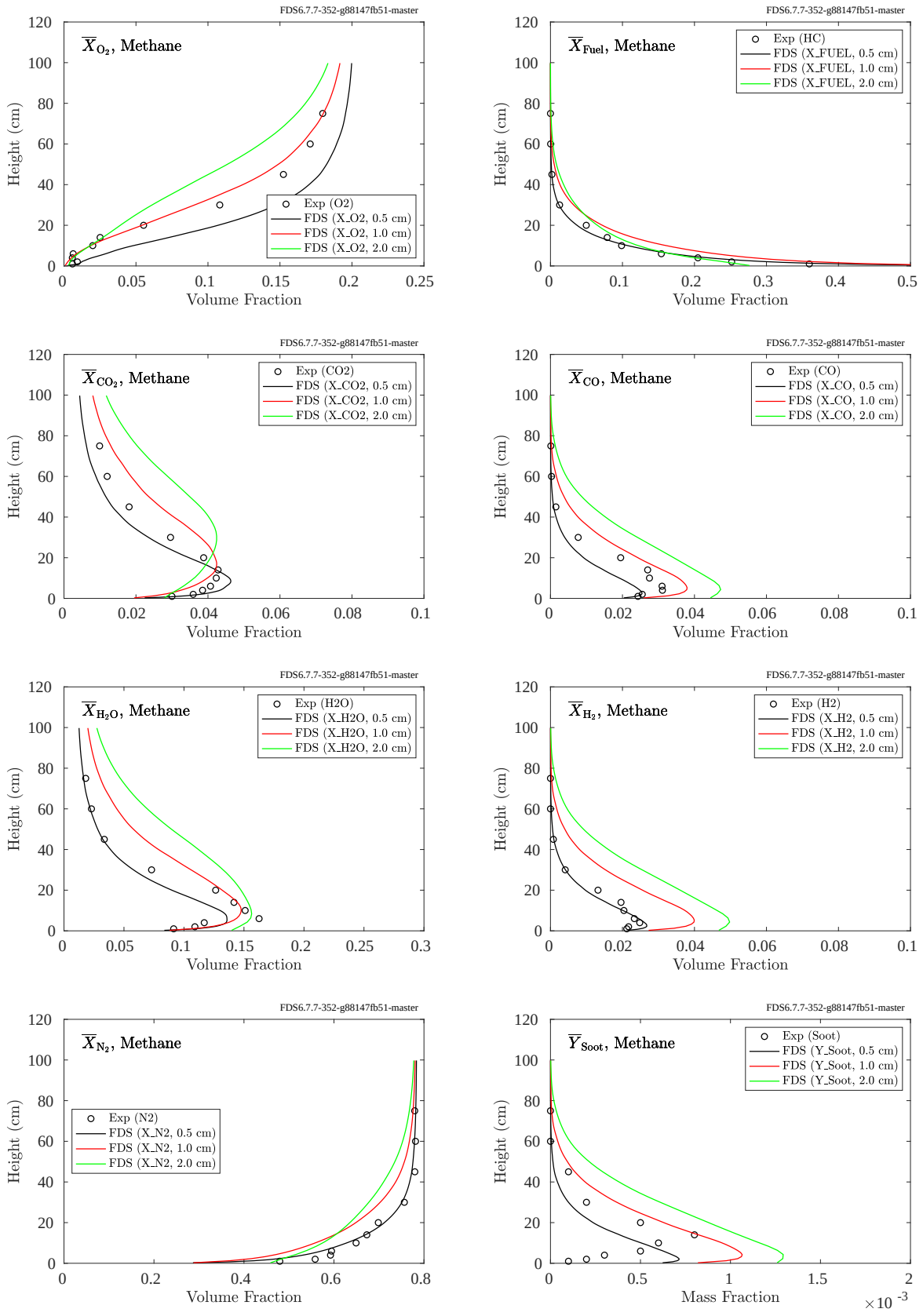

Figure 9.118: NIST Pool Fires, centerline product species, methane.

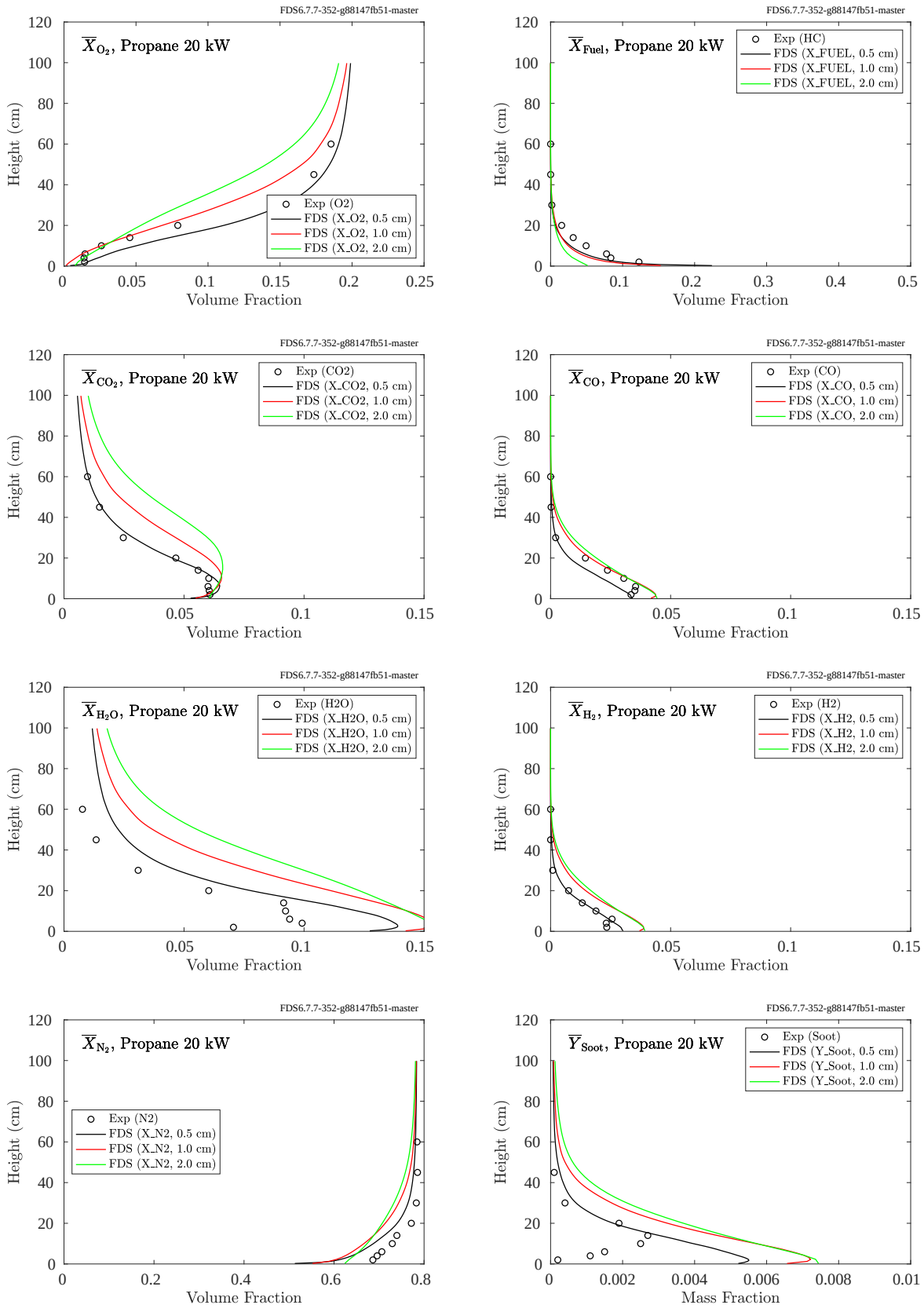

Figure 9.119: NIST Pool Fires, centerline product species, propane, 20 kW.

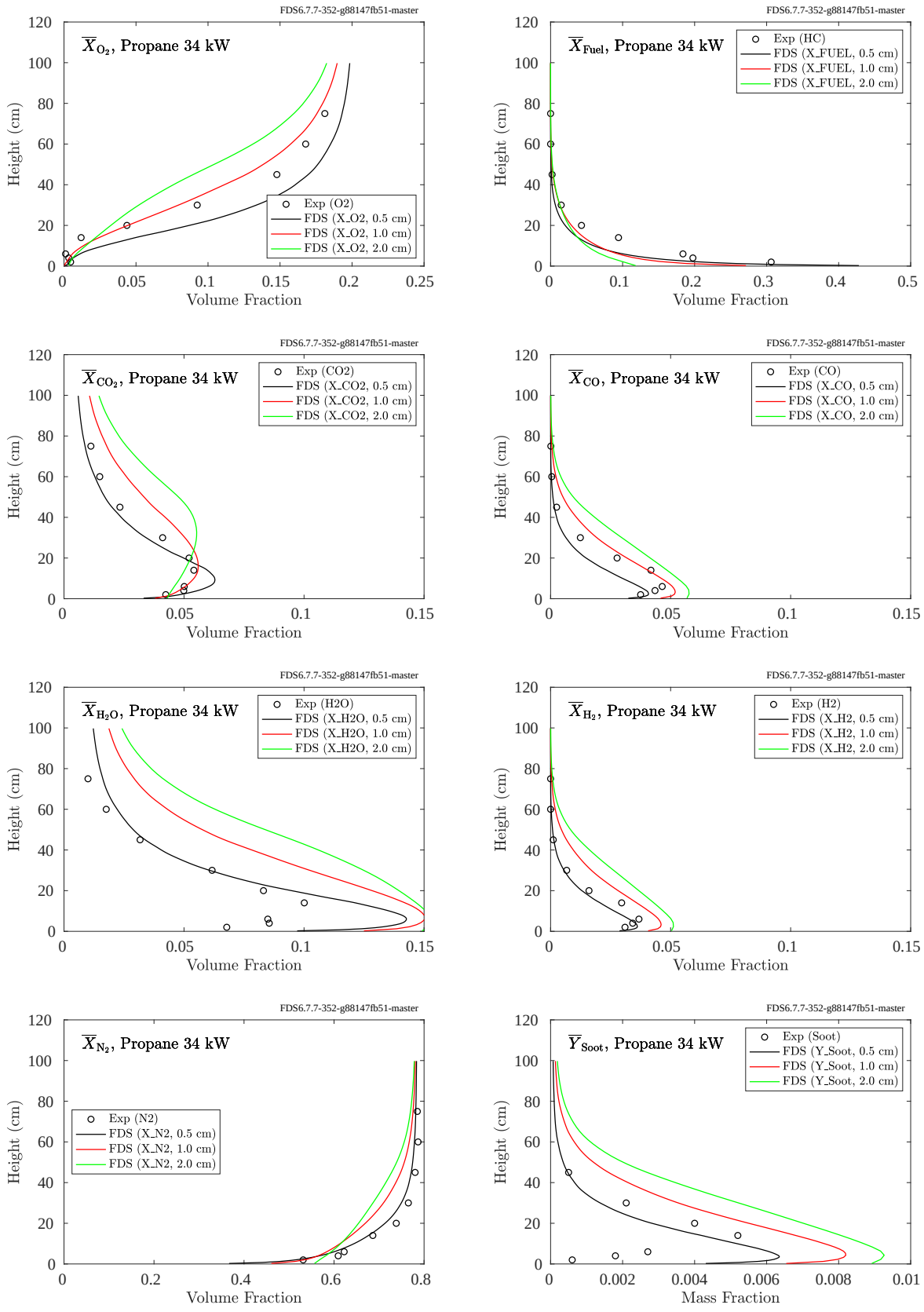

Figure 9.120: NIST Pool Fires, centerline product species, propane, 34 kW.

9.5.7 Summary, Products of Incomplete Combustion

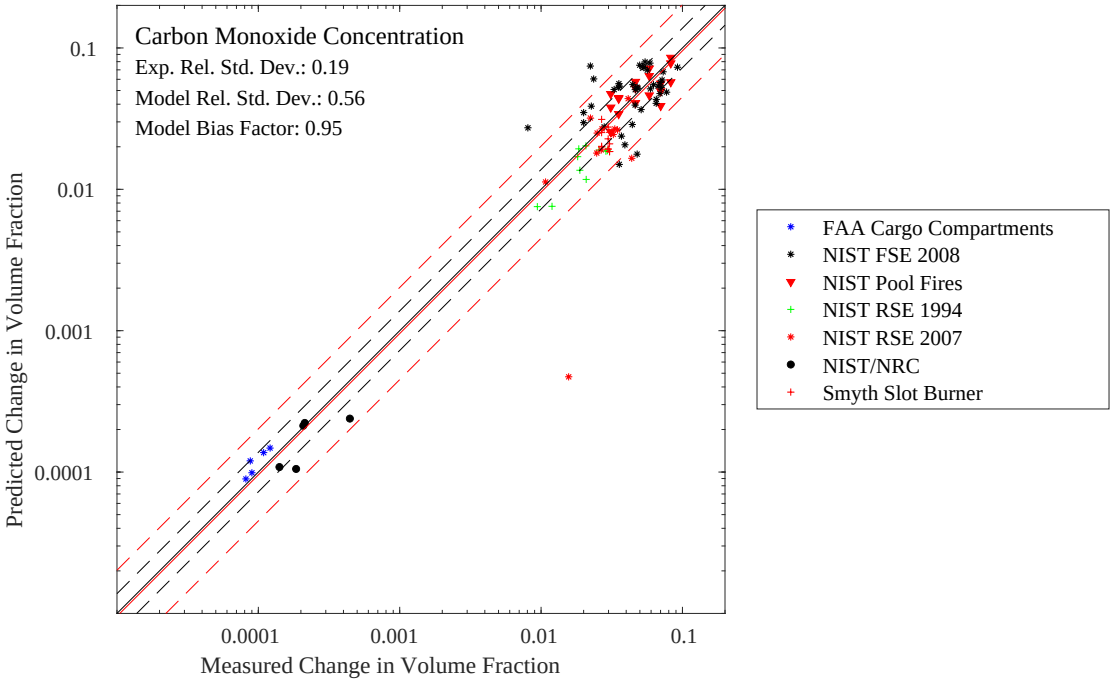

Figure 9.121: Summary of carbon monoxide predictions.

9.6 Helium Release in a Reduced Scale Garage Geometry

FDS simulations were performed to predict the helium release and dispersion in a reduced scale garage geometry. The figures on the following pages show the comparison between the FDS predictions and the measured values for the eighteen experiments. Table 9.1 lists the experimental parameters, including the release duration, release location (21 cm off the floor at the center of the compartment, 21 cm off the floor and 5 cm from the center of the rear wall, and 2.5 cm below the ceiling at the center of the compartment), and the leak area (single small vent, 2.4 cm by 2.4 cm, at the center of the front wall, single large vent, 3.05 cm by 3.05 cm, at the center of the front wall, and a pair of vents, 2.15 cm by 2.15 cm, centered on the front wall, 2.5 cm from the floor and ceiling, respectively). The seven sensors were located 37.5 cm from the front and side walls, at heights of 9 cm, 19 cm, 28 cm, 37 cm, 47 cm, 56 cm, and 65 cm off the floor. In the figures on the following pages, the highest concentrations correspond to the highest measurement locations.

Table 9.1: Test parameters of the NIST_He_2009 experiments.

Test Label	Release Duration (h)	Release Location	Leak Configuration
3600-LC-SSV	1	Lower Center	Single Small Vent
3600-LC-SLV	1	Lower Center	Single Large Vent
3600-LC-ULV	1	Lower Center	Dual Vents
3600-LR-SSV	1	Lower Rear	Single Small Vent
3600-LR-SLV	1	Lower Rear	Single Large Vent
3600-LR-ULV	1	Lower Rear	Dual Vents
3600-UC-SSV	1	Upper Center	Single Small Vent
3600-UC-SLV	1	Upper Center	Single Large Vent
3600-UC-ULV	1	Upper Center	Dual Vents
14400-LC-SSV	4	Lower Center	Single Small Vent
14400-LC-SLV	4	Lower Center	Single Large Vent
14400-LC-ULV	4	Lower Center	Dual Vents
14400-LR-SSV	4	Lower Rear	Single Small Vent
14400-LR-SLV	4	Lower Rear	Single Large Vent
14400-LR-ULV	4	Lower Rear	Dual Vents
14400-UC-SSV	4	Upper Center	Single Small Vent
14400-UC-SLV	4	Upper Center	Single Large Vent
14400-UC-ULV	4	Upper Center	Dual Vents

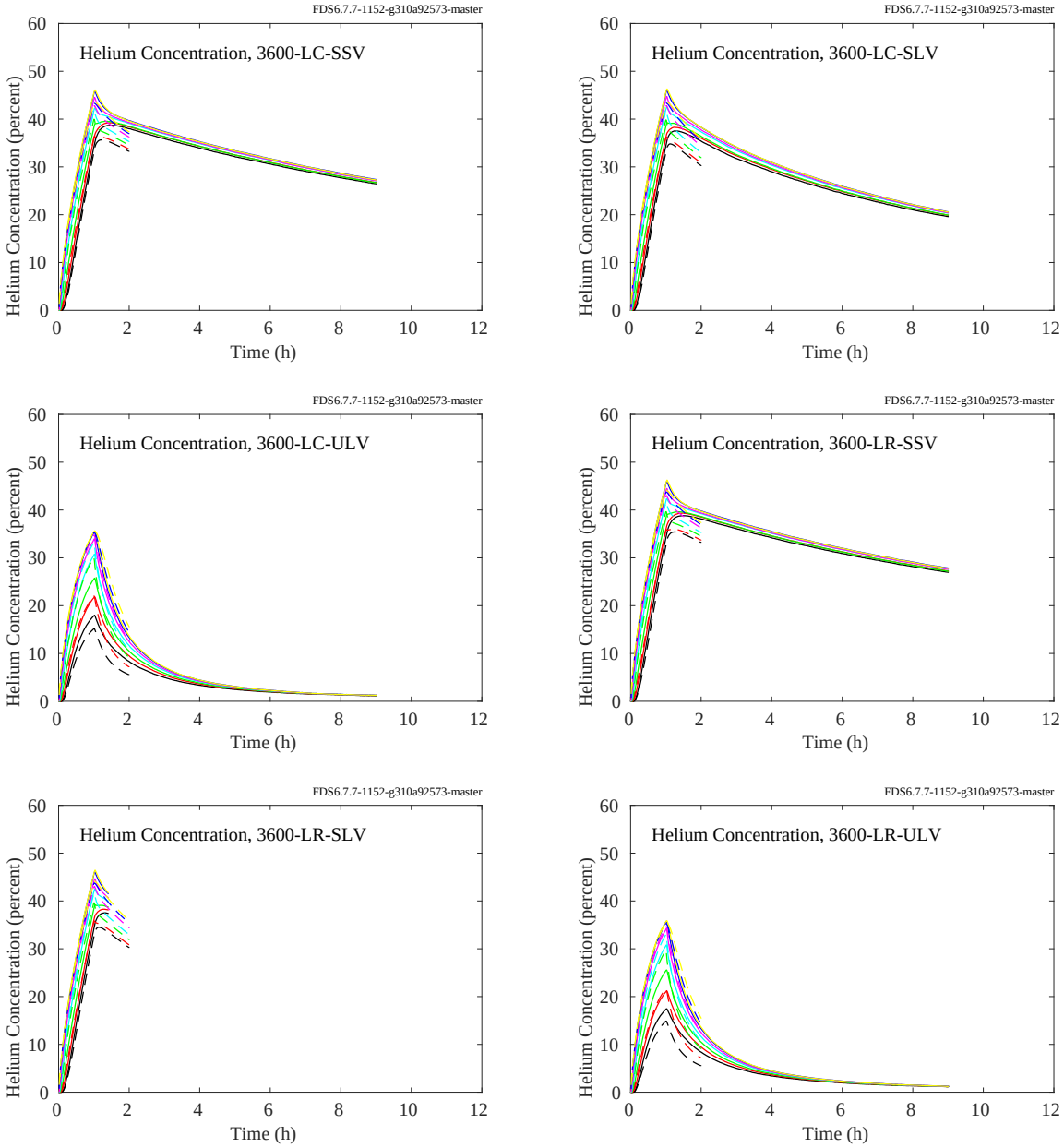

Figure 9.122: Comparison of measured (solid lines) and predicted (dashed lines) helium concentrations in the NIST_He_2009 experiments.

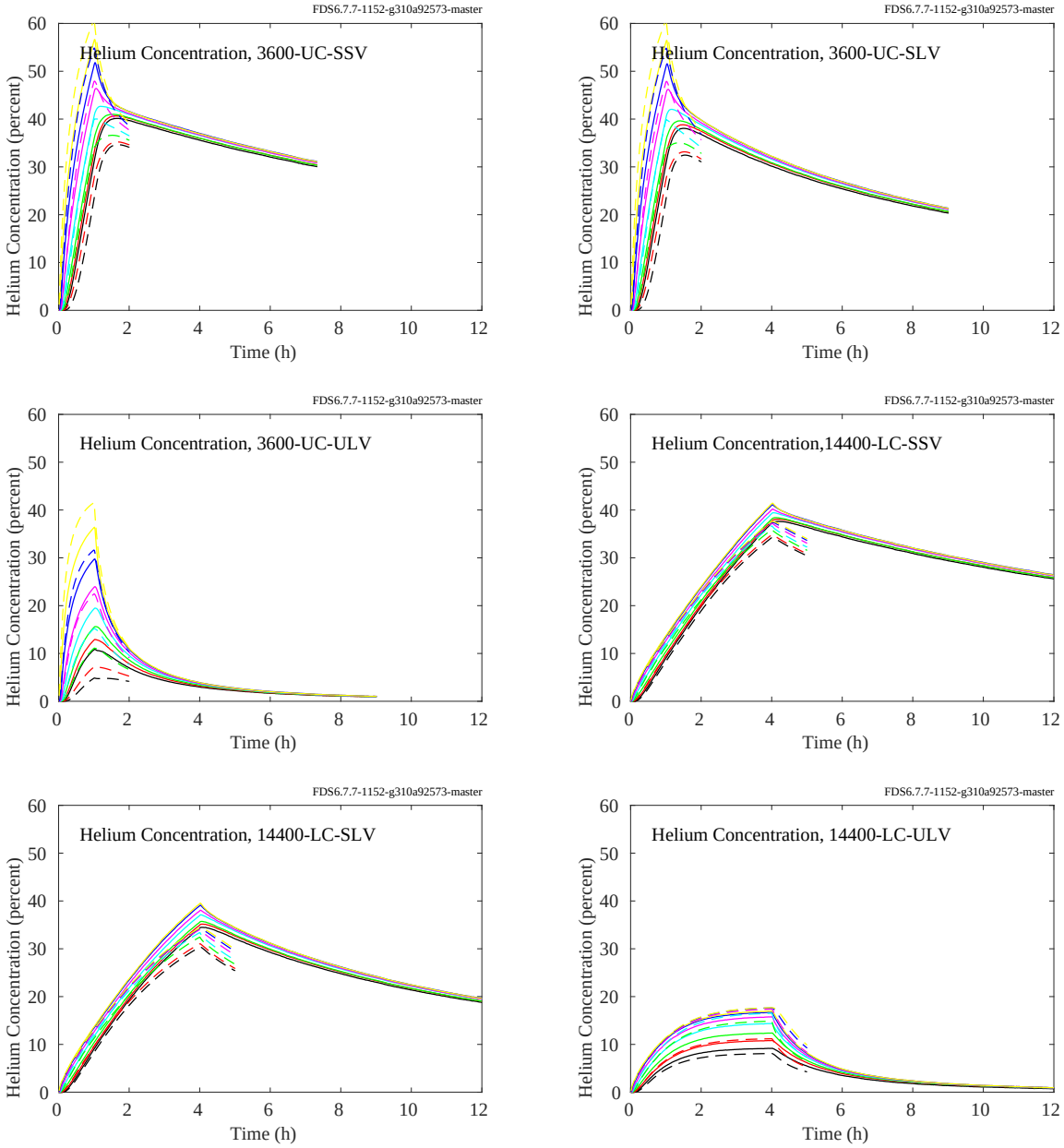

Figure 9.123: Comparison of measured (solid lines) and predicted (dashed lines) helium concentrations in the NIST_He_2009 experiments.

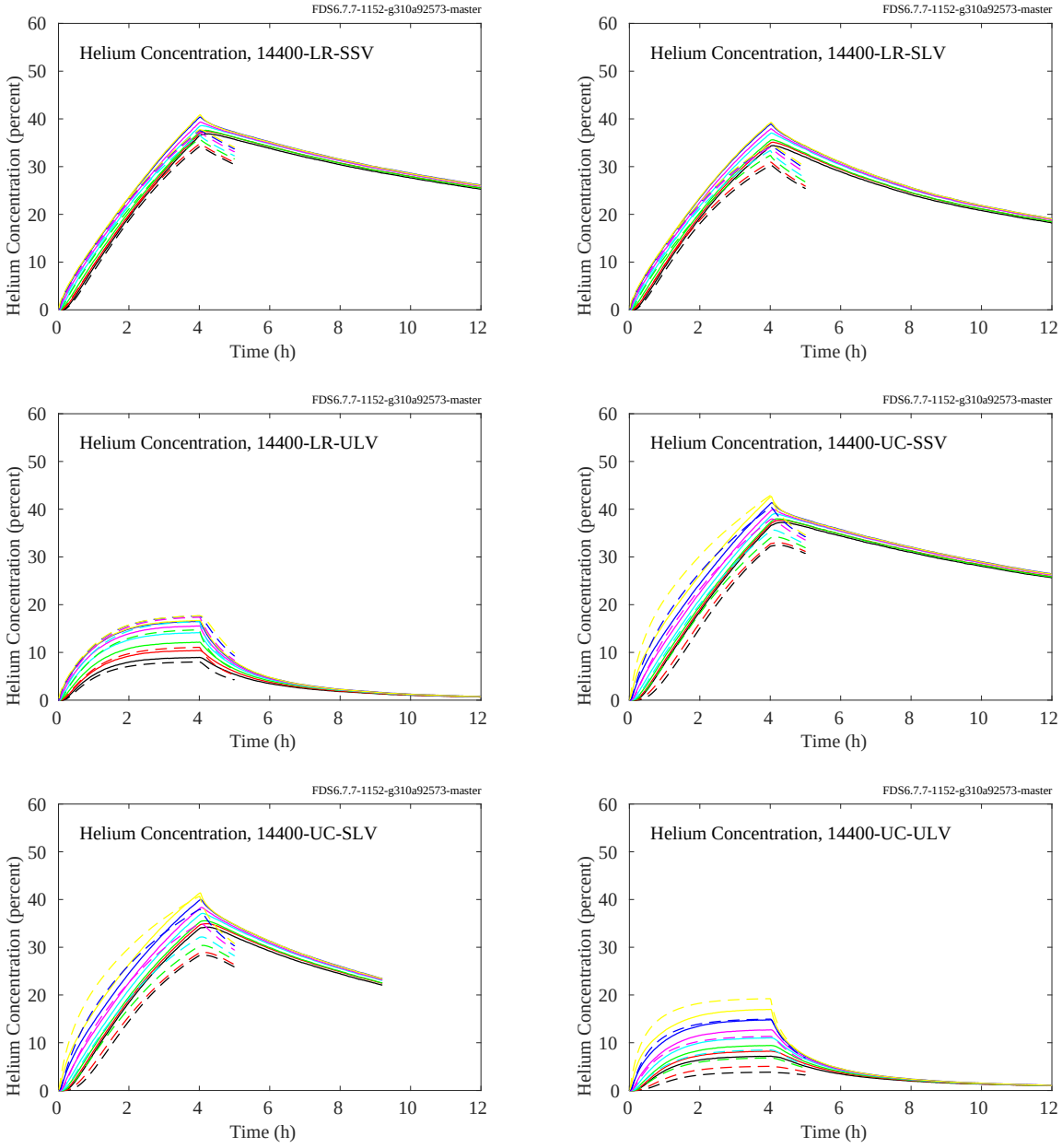

Figure 9.124: Comparison of measured (solid lines) and predicted (dashed lines) helium concentrations in the NIST_He_2009 experiments.

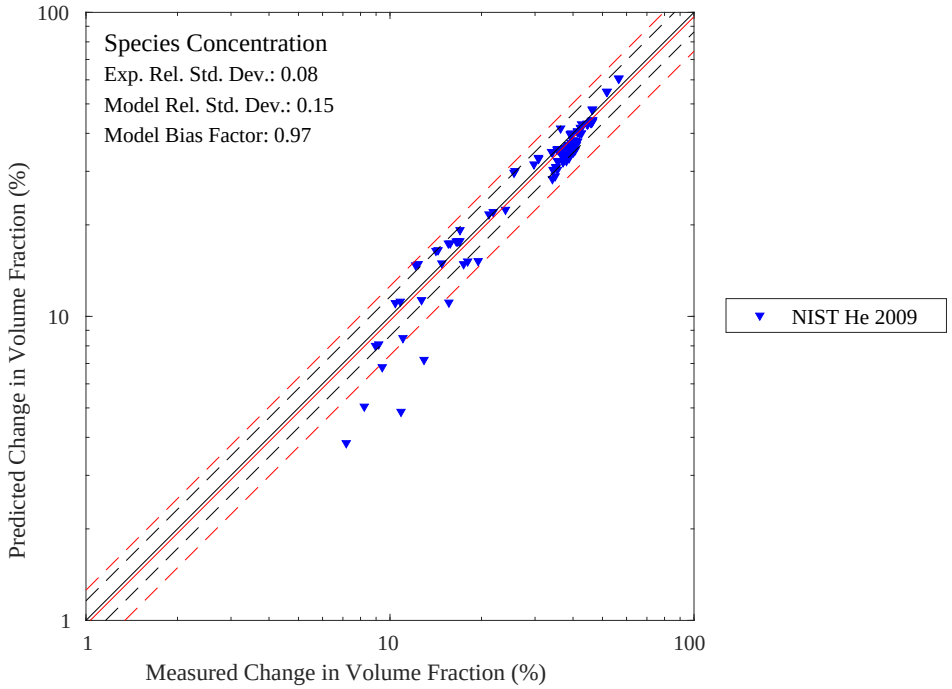

Figure 9.125: Summary of species concentration predictions.

Chapter 10

Pressure

In FDS, the pressure is decomposed into a temporally-varying background pressure plus a temporally and spatially-varying perturbation that drives the flow. The former can be thought of as the "over-pressure" which increases if heat is introduced into a closed compartment. In real buildings, leakage and ventilation affect the compartment "over-pressure" along with the fire.

10.1 FM/FPRF Datacenter Experiments

Measurements made during flow mapping in the FM datacenter mockup included two pairs of differential pressure transmitters. One pair measured the pressure difference between the subfloor (SF) and the cold aisle (CA). The other pair measured the pressure difference between the hot aisle (HA) and the ceiling plenum (CP). A comparison of measured and predicted pressures for the exhaust rate (78 ACH) and high exhaust rate (265 ACH) tests is shown in the figure below.

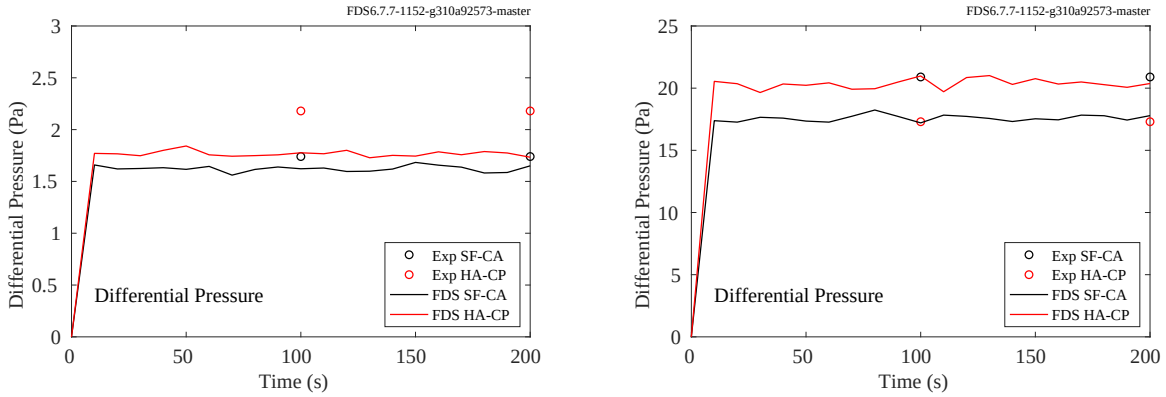

Figure 10.1: FM/FPRF Data Center, differential pressure (Left - low exahust rate, Right - high exhaust rate)

10.2 NIST/NRC Experiments

Comparisons between measured and predicted pressures for the NIST/NRC series are shown on the following pages. For those tests in which the door to the compartment was open, the over-pressures were only a few Pascals, whereas when the door was closed, the over-pressures were several hundred Pascals. The pressure within the compartment was measured at a single point, near the floor. For the simulations of the closed door tests, the compartment is assumed to leak via a small uniform flow distributed over the walls and ceiling. The flow rate is calculated based on the assumption that the leakage rate is proportional to the measured leakage area times the square root of compartment over-pressure.

Note that for the closed door tests, there is often a dramatic drop in the predicted compartment pressure. This is the result of the assumption in FDS that the heat release rate is decreased to zero in one second at the time in the experiment when the fuel flow was stopped for safety reasons. In reality, the fire did not extinguish immediately because there was an excess of fuel in the pan following the flow stoppage. For the purpose of model comparison, the peak over-pressures are compared in the closed door tests, and the peak (albeit small) under-pressures are compared in the open door tests.

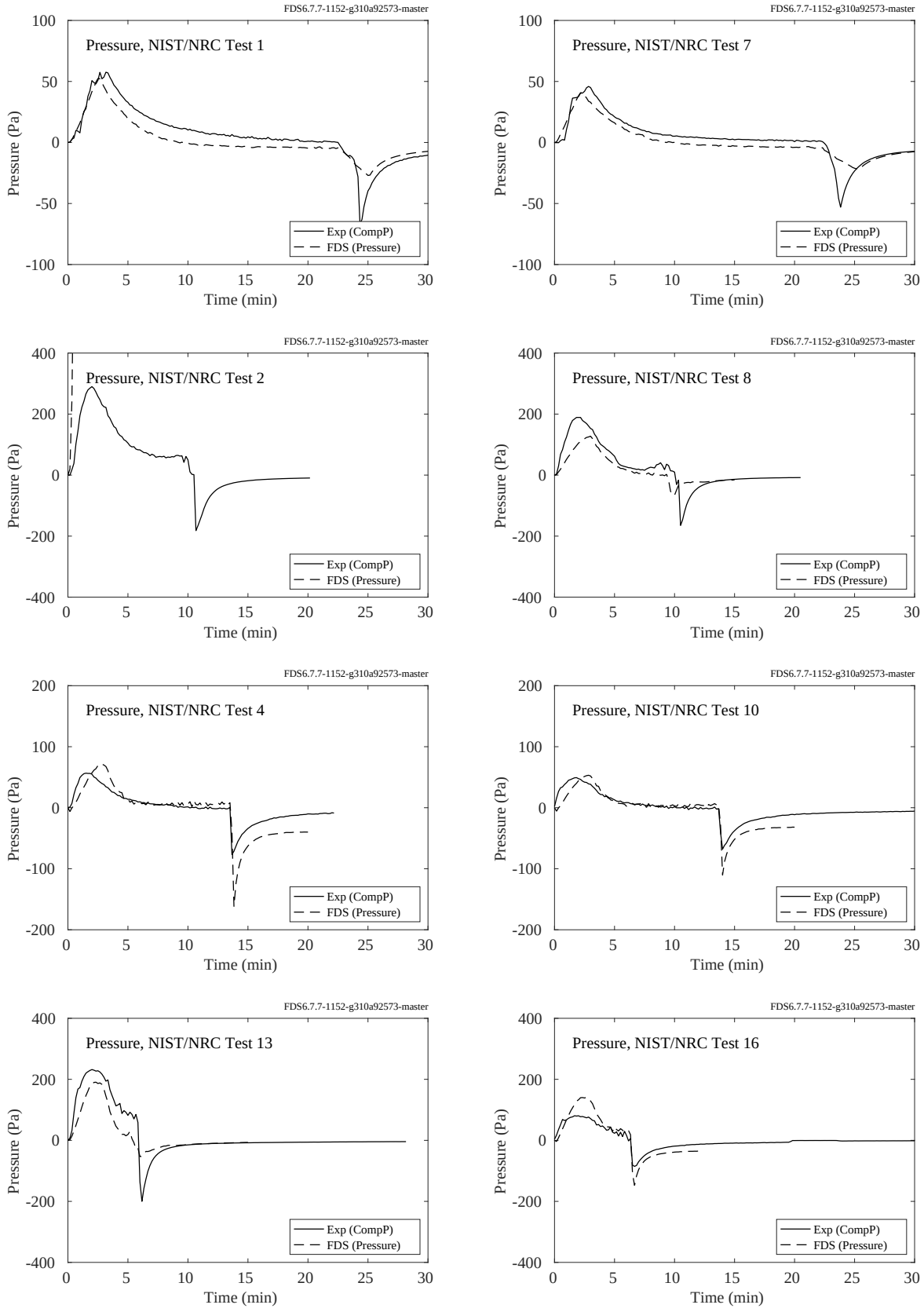

Figure 10.2: NIST/NRC experiments, compartment pressure, Tests 1, 2, 4, 7, 8, 10, 13, 16.

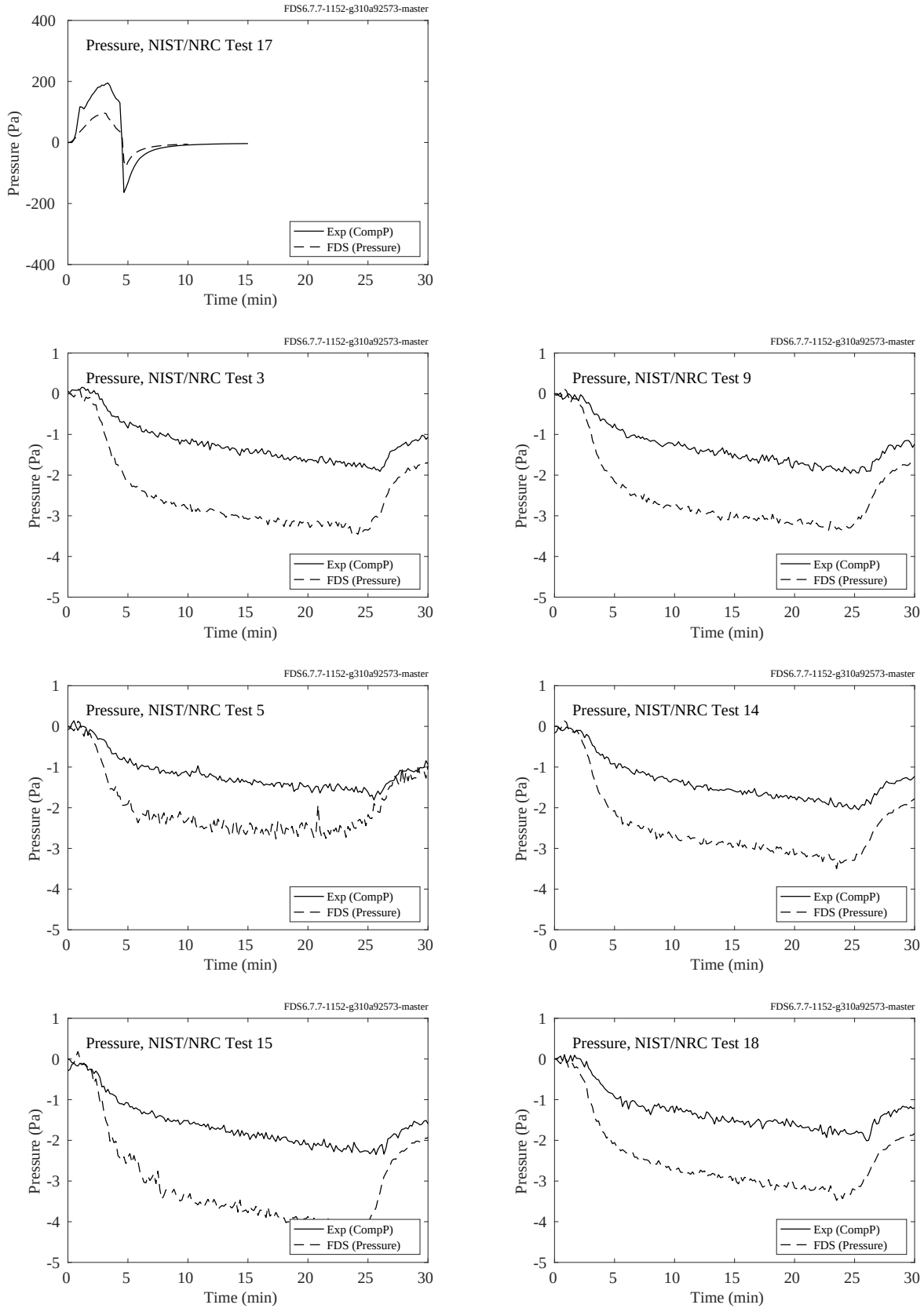

Figure 10.3: NIST/NRC experiments, compartment pressure, Tests 3, 5, 9, 14, 15, 17, 18.

10.3 LLNL Enclosure Experiments

The reported compartment pressure in the LLNL Enclosure experiments was taken near the ceiling of the compartment, 0.6 m from the wall including the exhaust duct, and 0.6 m from the wall opposite the wall with the door. Further details of the experiments can be found in Section 3.35.

In the figures on the following pages, the open circles represent the measured pressure; the solid line represents the predicted pressure. The predicted pressures are time-averaged over a time interval of 30 s, whereas the measurements appear to be instantaneous values separated by hundreds or thousands of seconds. Because of this, the short-duration pressure spike that is typical of fires within relatively tight compartments is seen in the model prediction but not necessarily the measured data. The comparison of measurement and prediction is based on the final few pressure points, not the initial spike.

The results of all 64 experiments are plotted for completeness, but a few of the results were excluded from the computation of the summary statistics because the fire self-extinguished near the time of the last pressure measurement, sometimes leading to a reported final pressure being less than the initial pressure, typical when there is a sudden decrease in the heat release rate. In other cases, the difference between initial and final measured pressure was too small to make a meaningful comparison.

For cases where the door to the compartment was open, the measured gauge pressures at the start of the experiment ranged from 0 Pa to 10 Pa. There is not enough information in the test report to explain why the starting pressures were not 0 Pa; thus, the measured pressures were adjusted so that the starting pressure is 0 Pa.

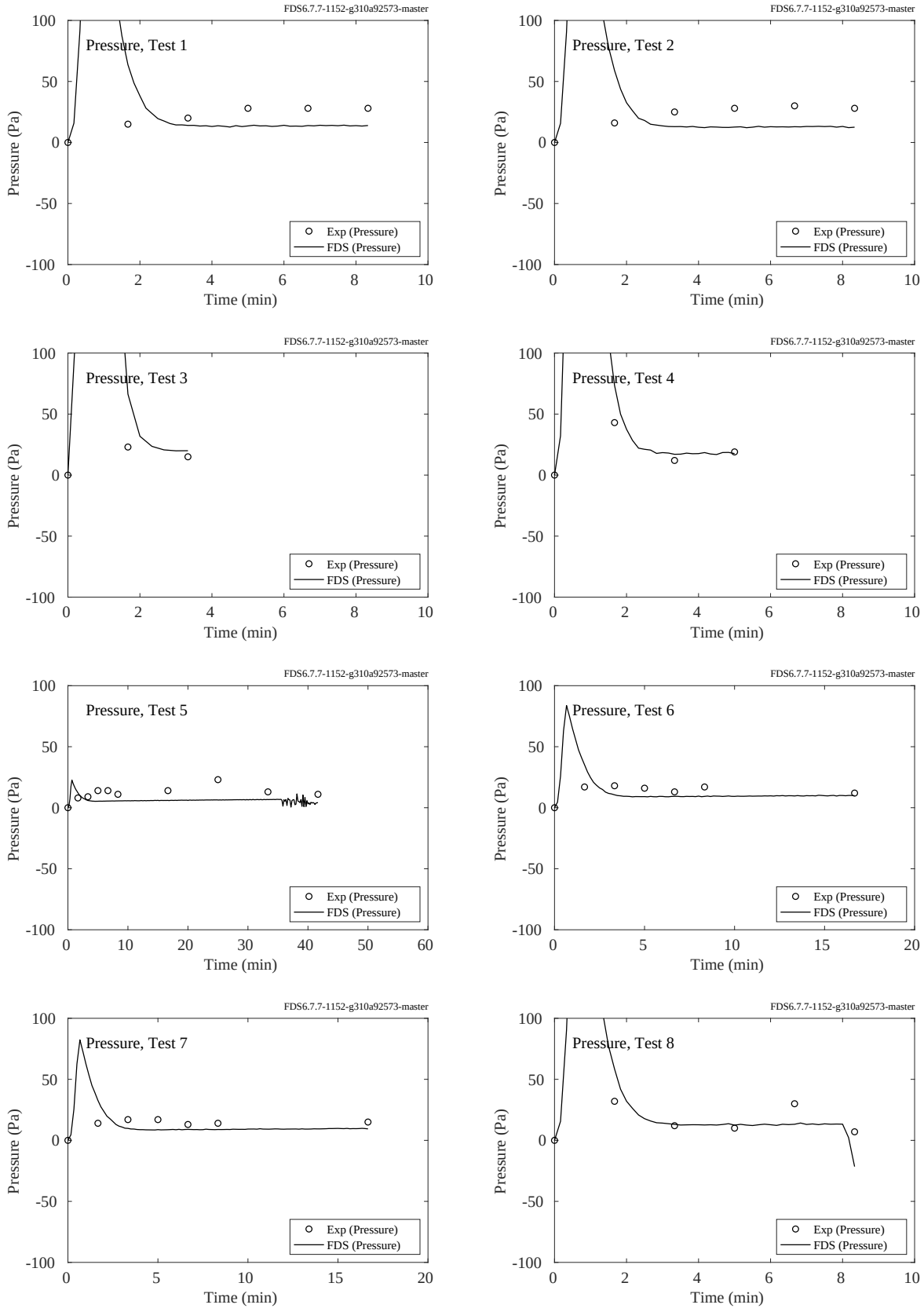

Figure 10.4: LLNL Enclosure experiments, compartment pressure, Tests 1-8.

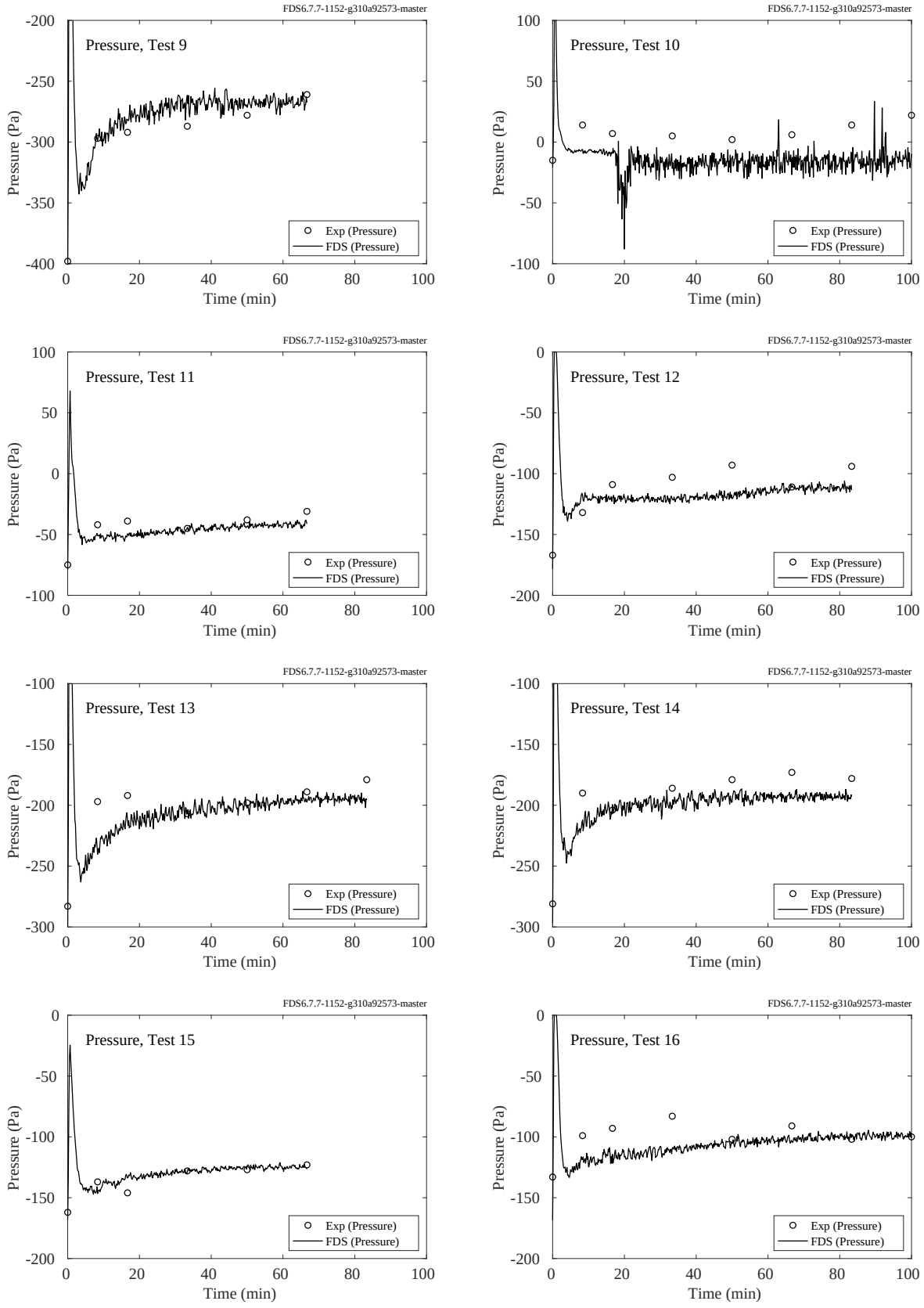

Figure 10.5: LLNL Enclosure experiments, compartment pressure, Tests 9-16.

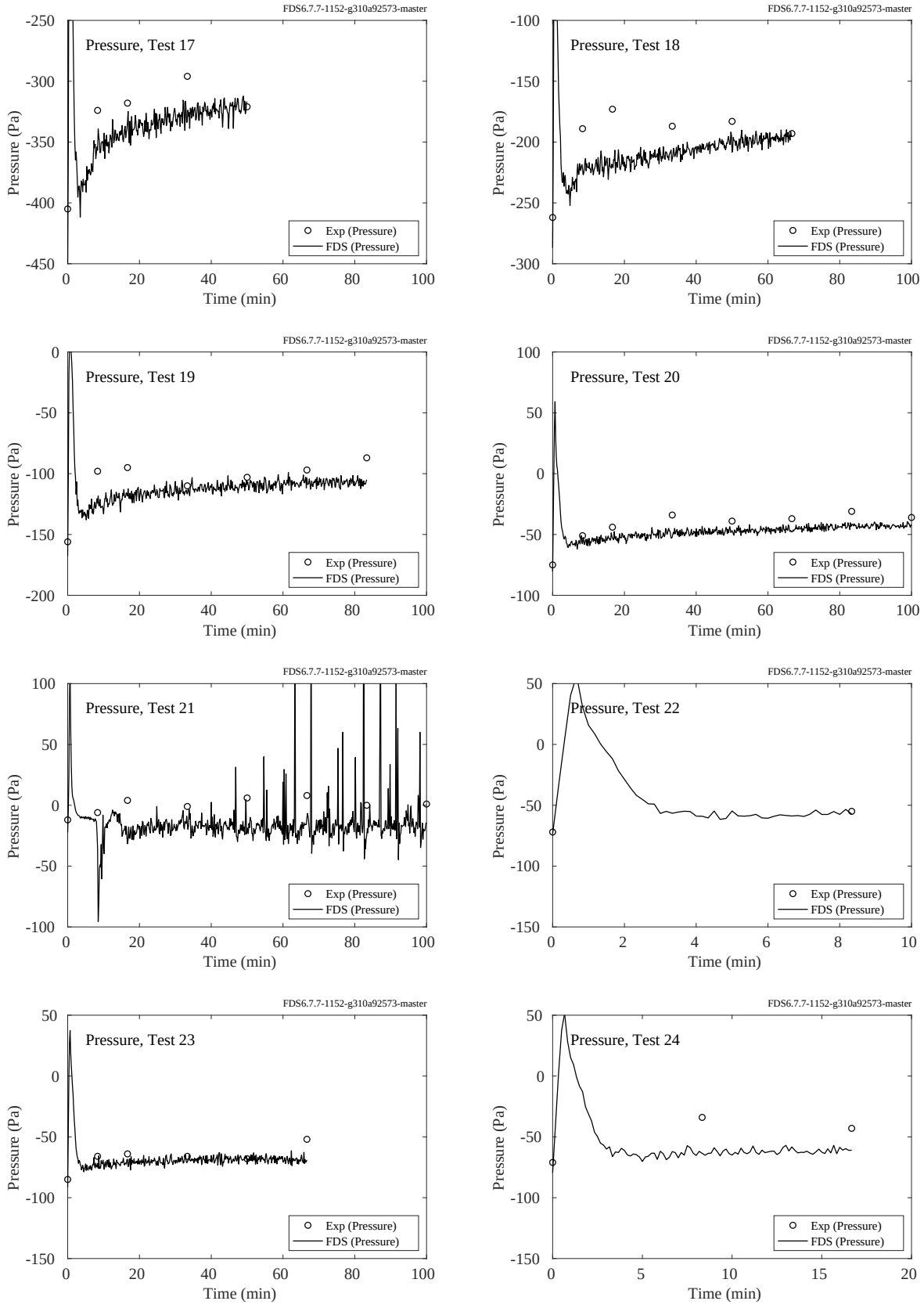

Figure 10.6: LLNL Enclosure experiments, compartment pressure, Tests 17-24.

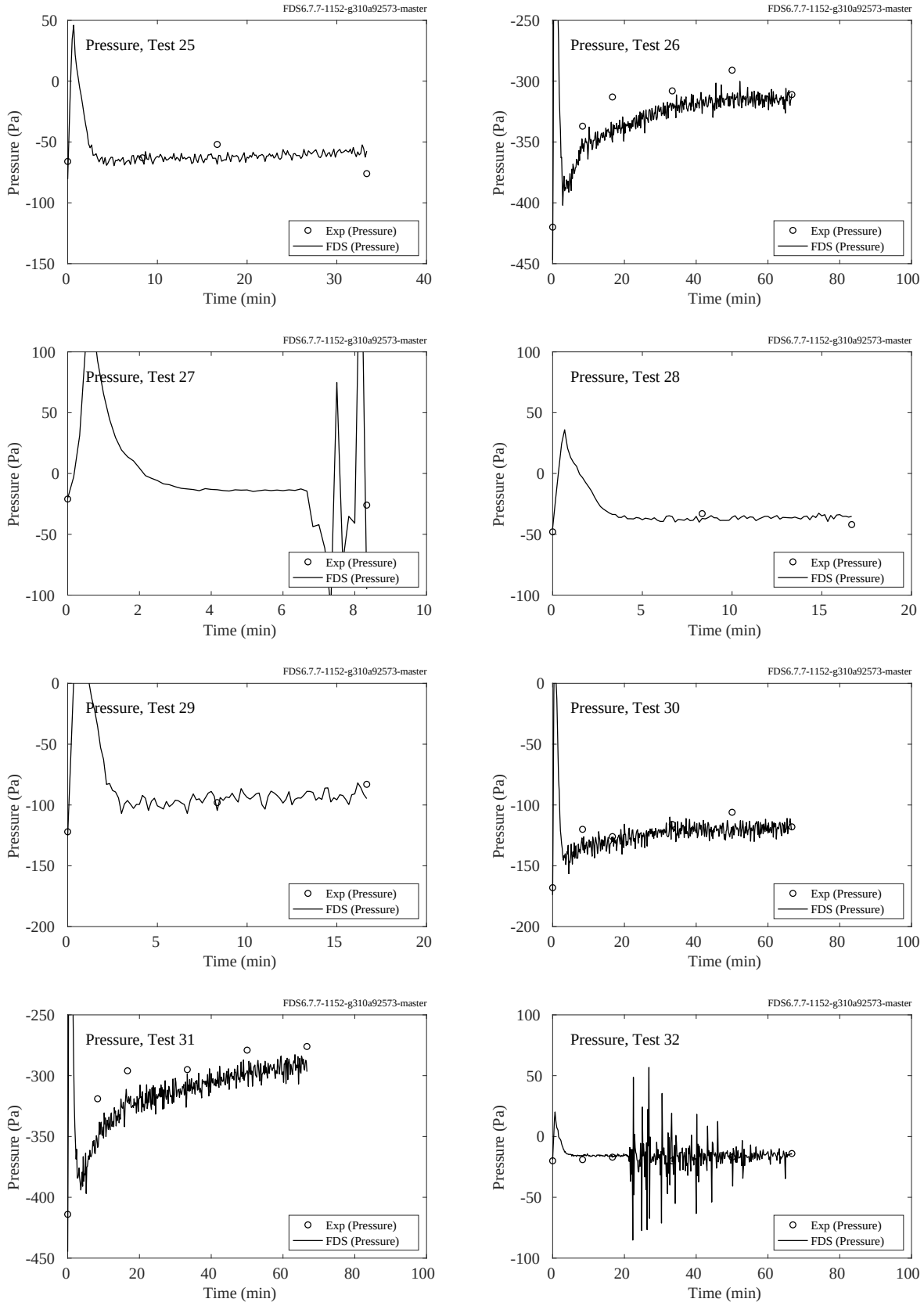

Figure 10.7: LLNL Enclosure experiments, compartment pressure, Tests 25-32.

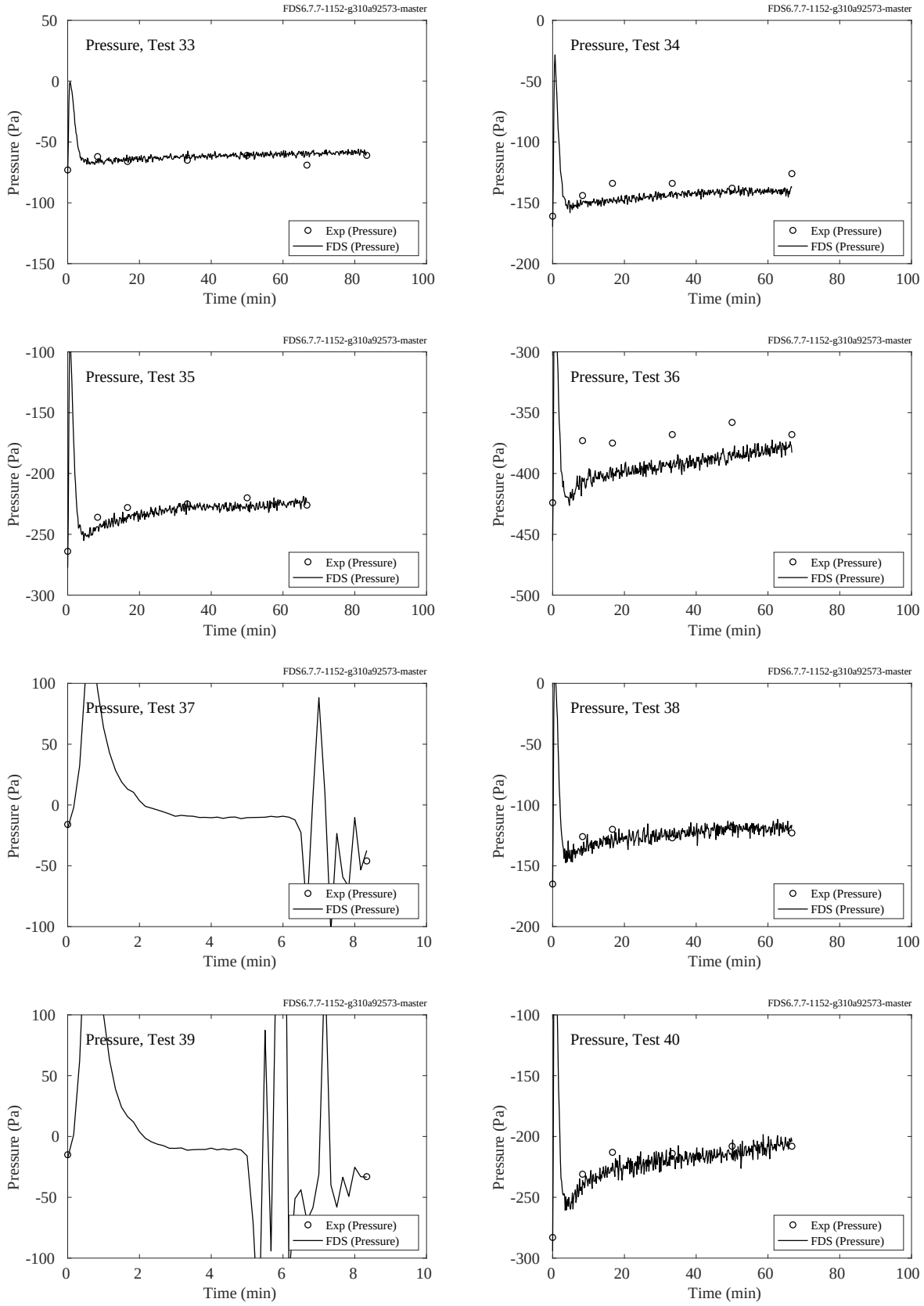

Figure 10.8: LLNL Enclosure experiments, compartment pressure, Tests 33-40.

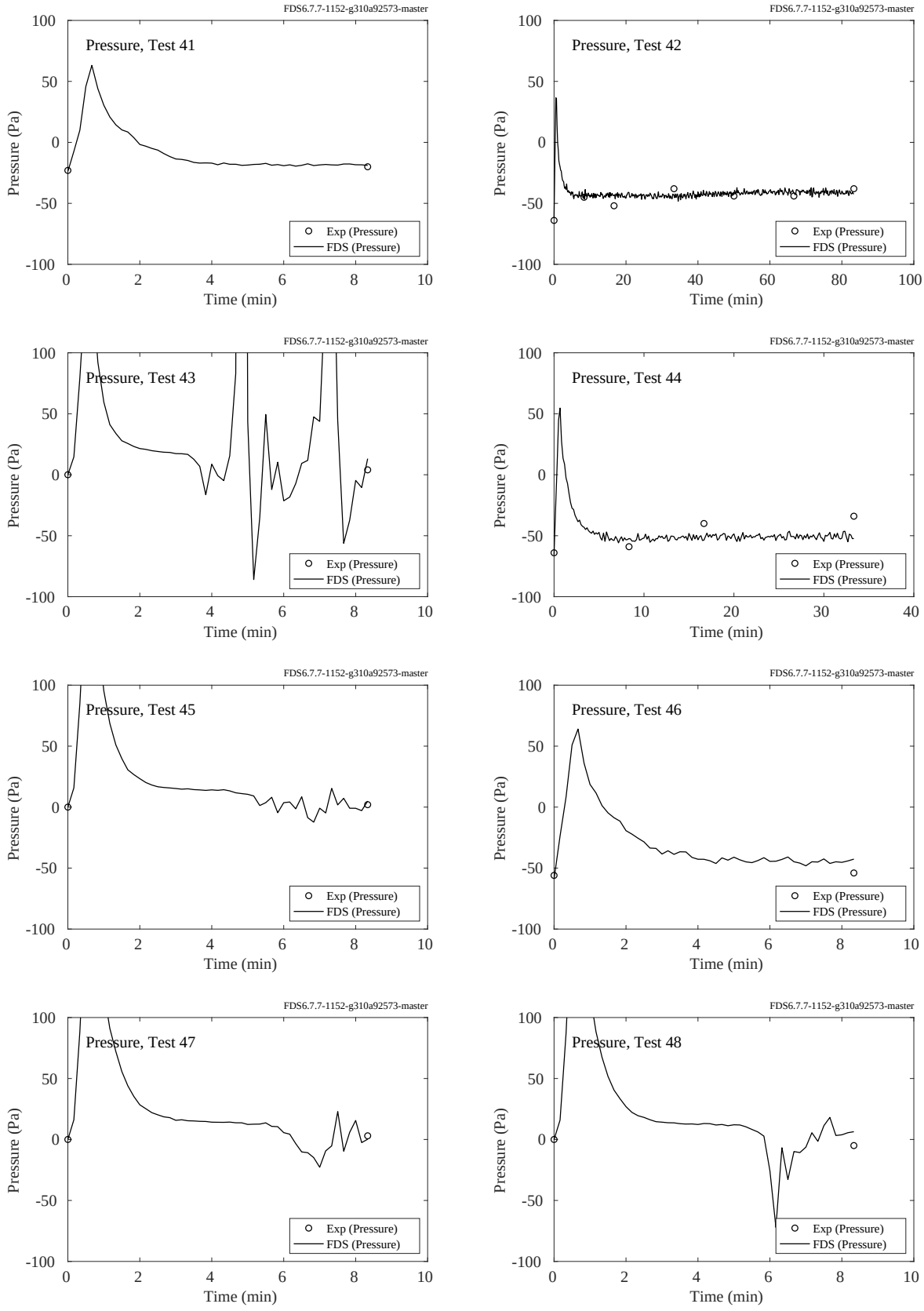

Figure 10.9: LLNL Enclosure experiments, compartment pressure, Tests 41-48.

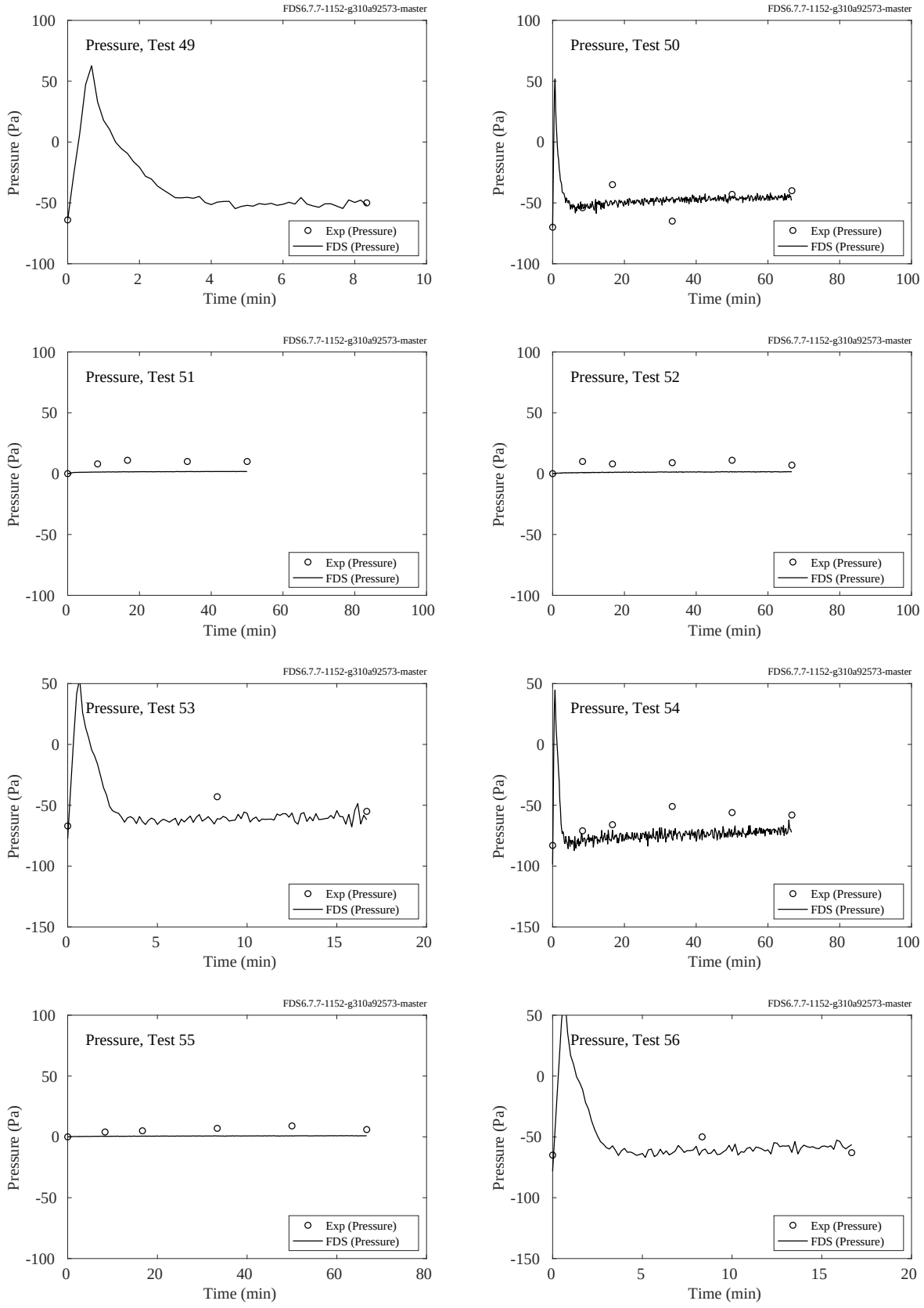

Figure 10.10: LLNL Enclosure experiments, compartment pressure, Tests 49-56.

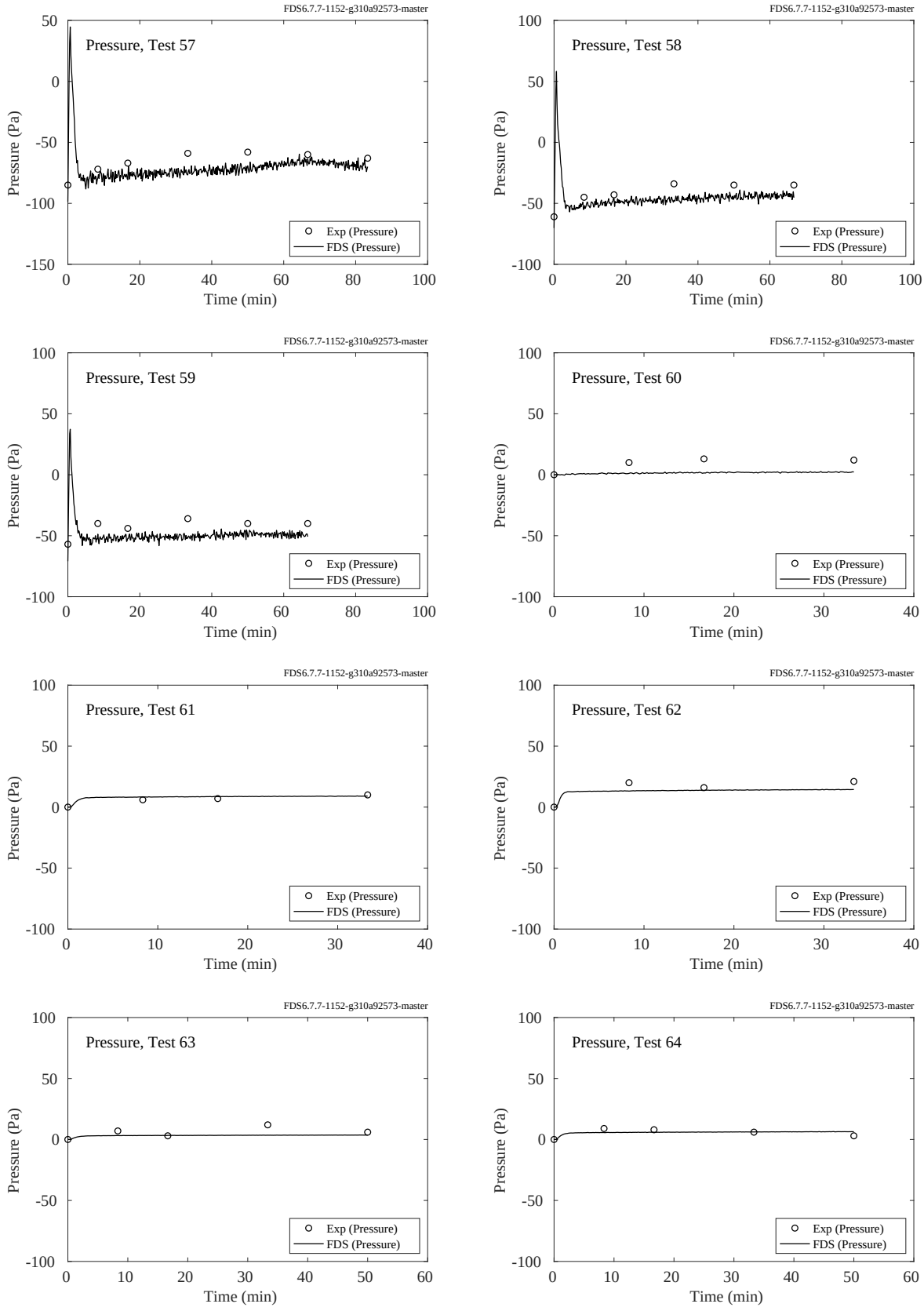

Figure 10.11: LLNL Enclosure experiments, compartment pressure, Tests 57-64.

10.4 PRISME DOOR Experiments

The PRISME experiments were conducted in a relatively well-sealed set of compartments with a well-controlled ventilation system. Supply air was forced into and exhaust products extracted from the test compartments via two fans and a fairly extensive ventilation network. The air flow rates and nodal pressures were measured throughout the system. The FDS simulations included the ventilation system, and for each segment of the network a loss coefficient was calculated so as to match the initial conditions of the experiments. The plots to follow show the predicted and measured compartment pressures and supply and exhaust flows. These air flows were predicted by the model, based on the initial specification of the ventilation system.

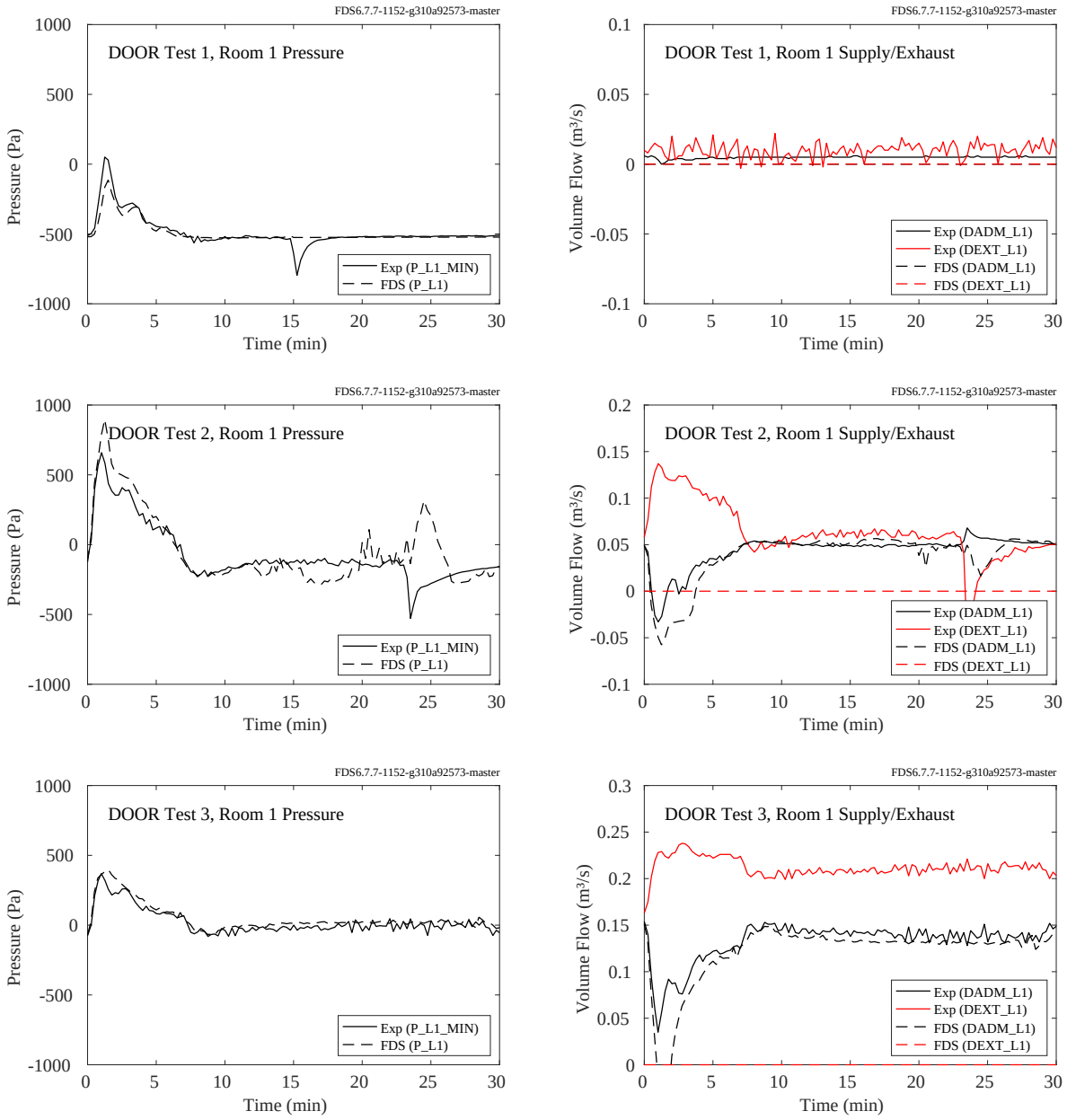

Figure 10.12: PRISME DOOR, compartment pressure and supply/exhaust, Room 1, Tests 1-3.

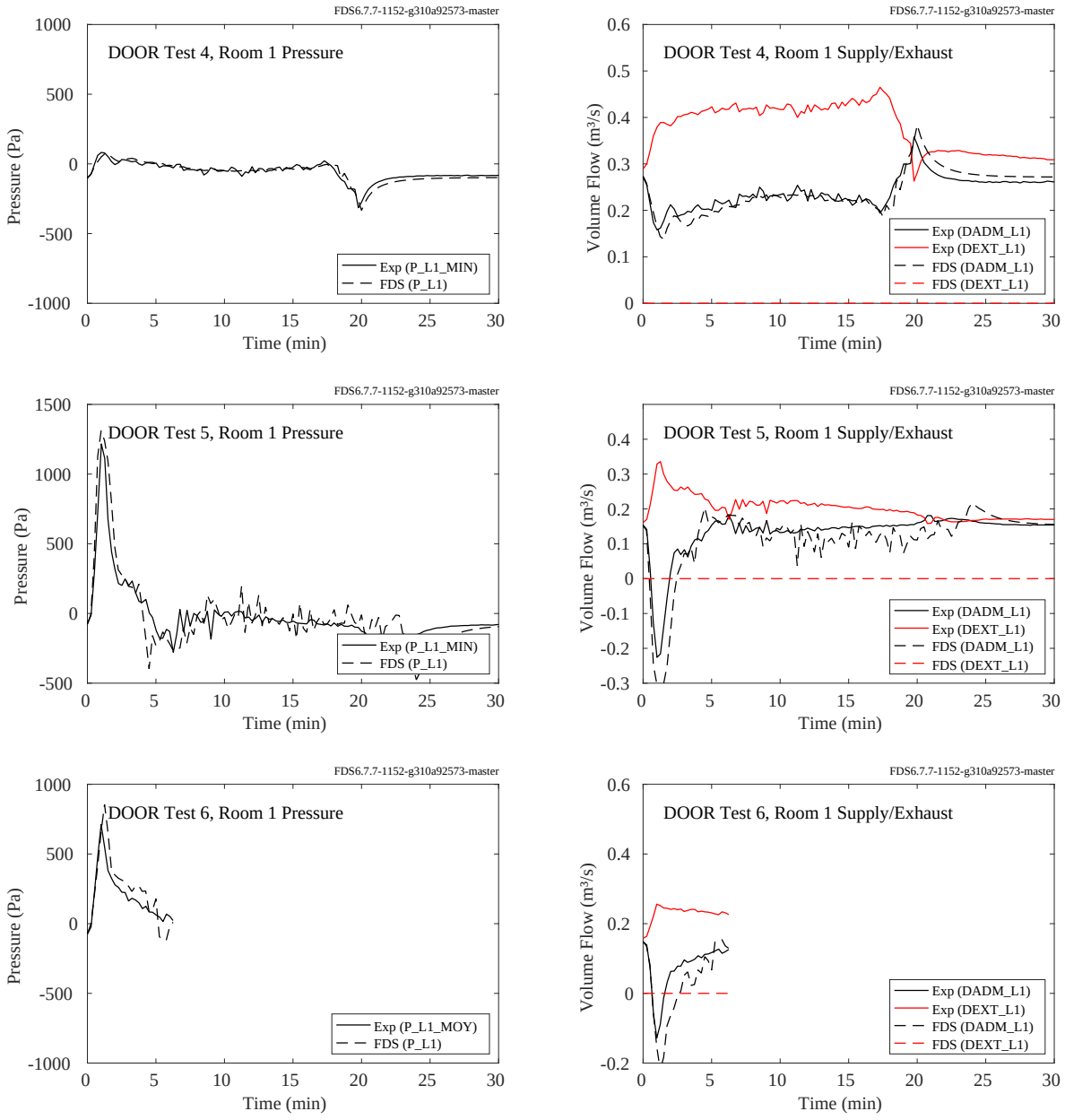

Figure 10.13: PRISME DOOR, compartment pressure and supply/exhaust, Room 1, Tests 4-6.

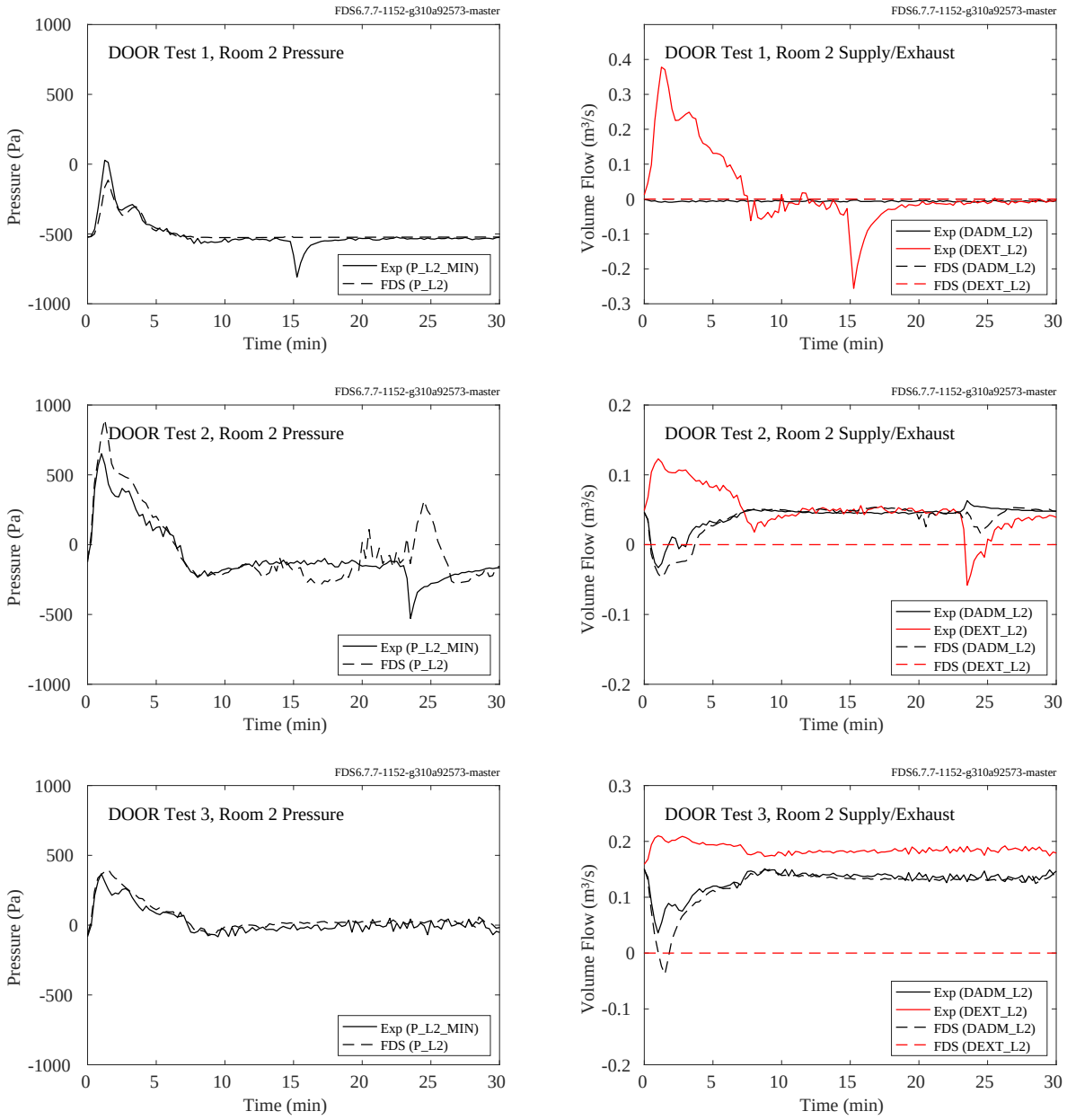

Figure 10.14: PRISME DOOR, compartment pressure and supply/exhaust, Room 2, Tests 1-3.

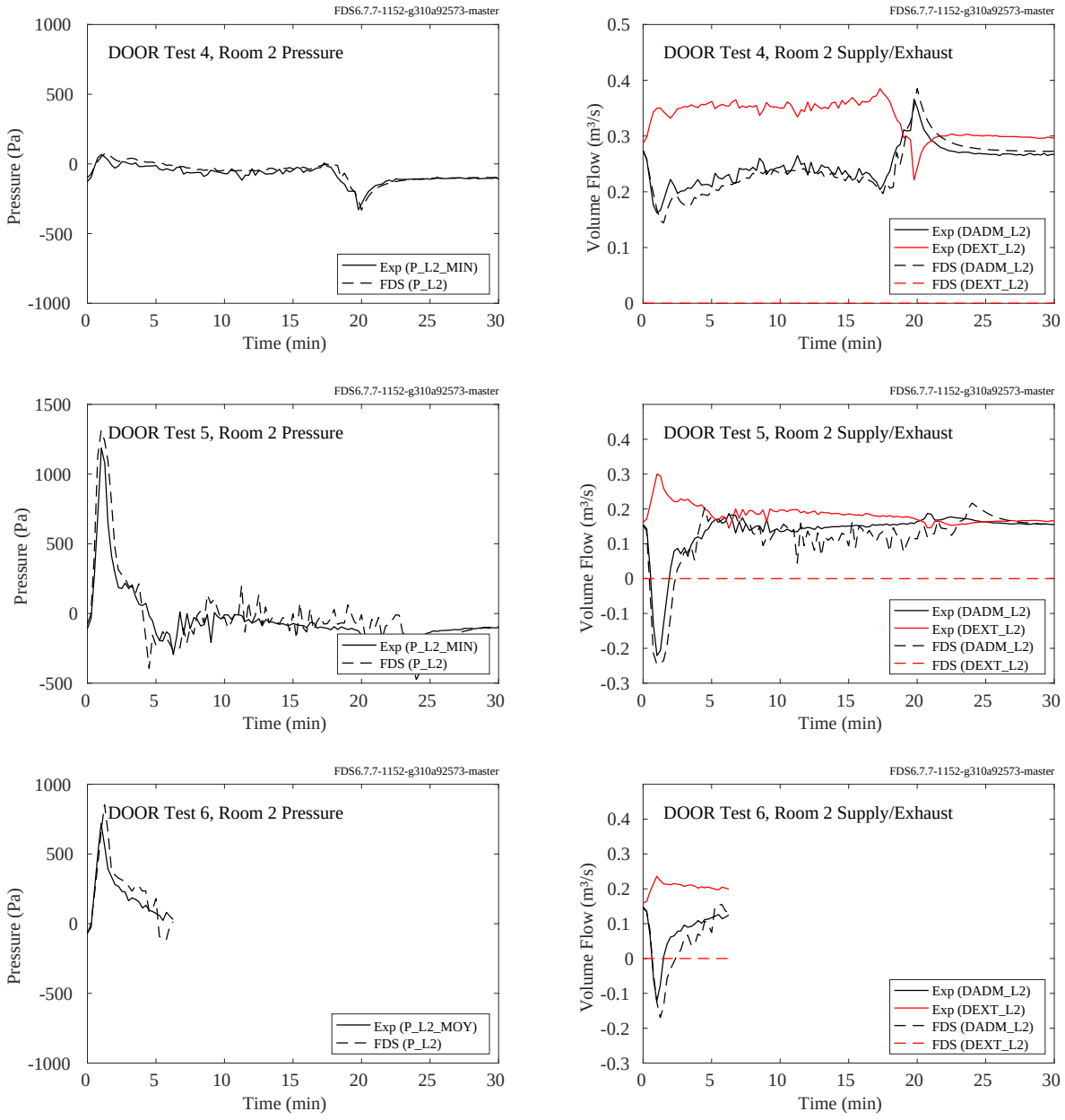

Figure 10.15: PRISME DOOR, compartment pressure and supply/exhaust, Room 2, Tests 4-6.

10.5 PRISME SOURCE Experiments

The PRISME SOURCE experiments were conducted in a single compartment with a well-controlled ventilation system. Supply air was forced into and exhaust products extracted from the test compartment via two fans and a fairly extensive ventilation network. The air flow rates and nodal pressures were measured throughout the system. The FDS simulations included the ventilation system, and for each segment of the network a loss coefficient was calculated so as to match the initial conditions of the experiments. The plots to follow show the predicted and measured compartment pressures and supply and exhaust flows. These air flows were predicted by the model, based on the initial specification of the ventilation system.

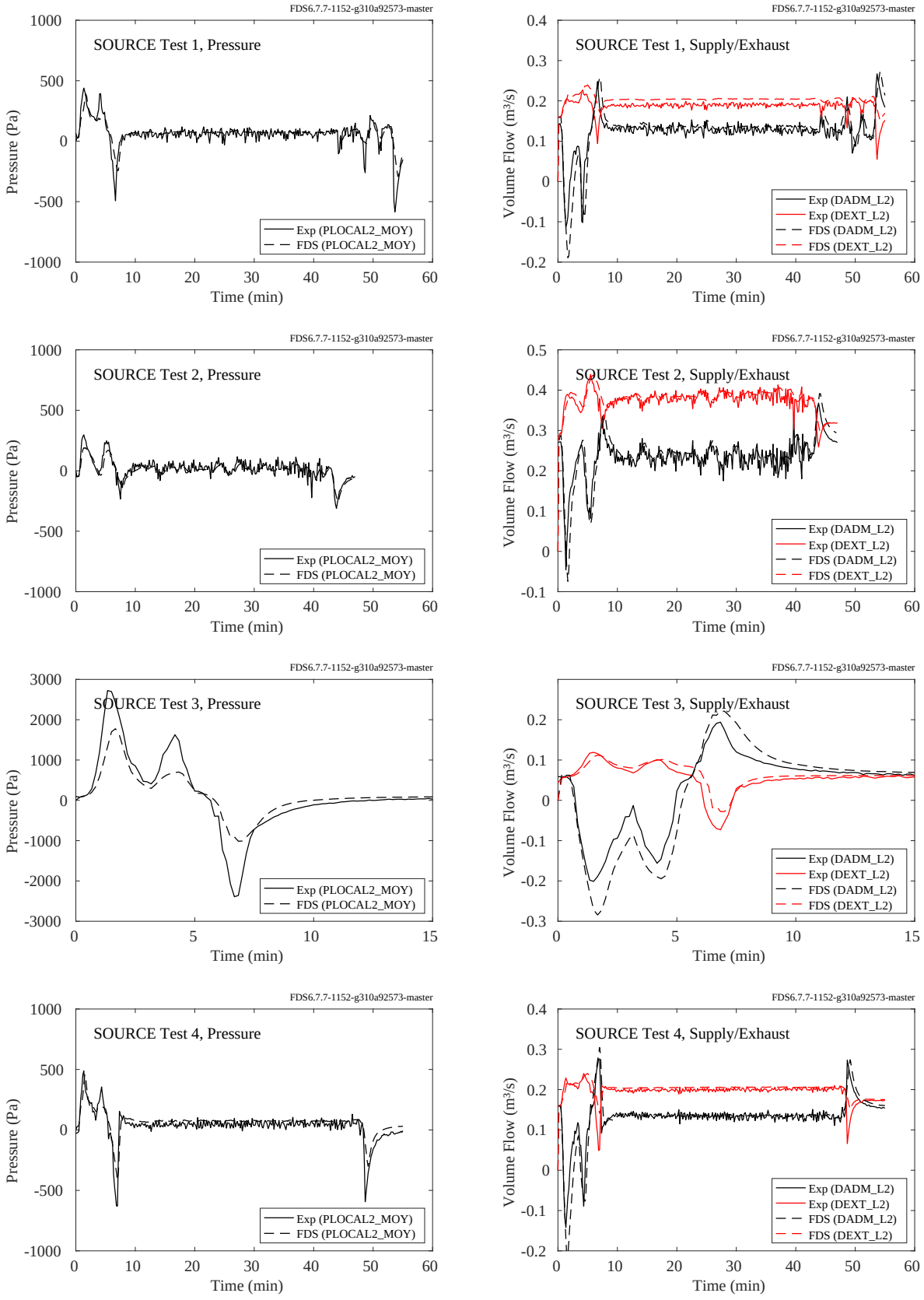

Figure 10.16: PRISME SOURCE, pressure and supply/exhaust flow rates, Tests 1, 2, 3 and 4.

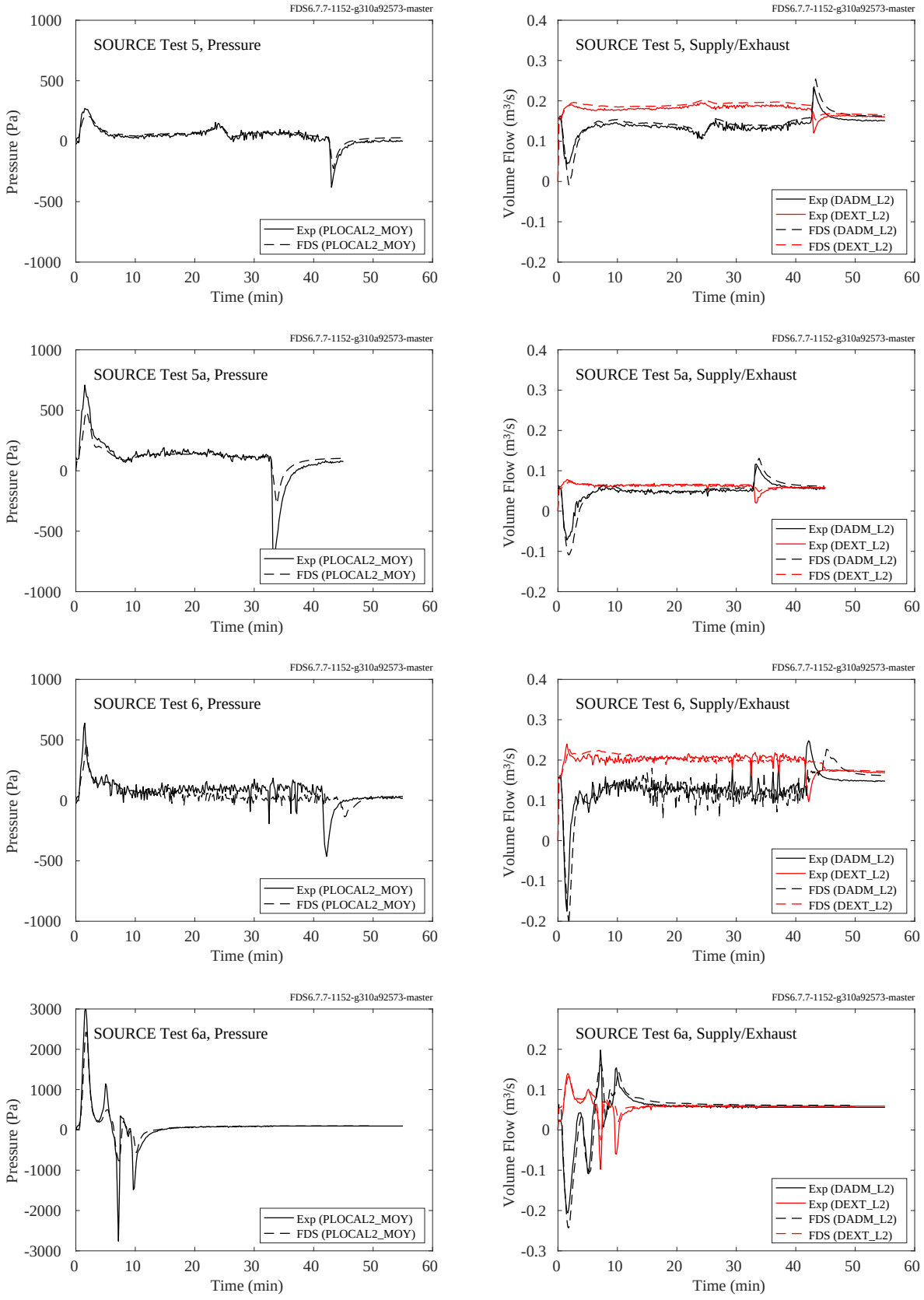

Figure 10.17: PRISME SOURCE, pressure and supply/exhaust flow rates, Tests 5, 5a, 6 and 6a.

10.6 UL/NIJ House Experiments

A description and drawings from these experiments are included in Section 3.77

For both the one and two-story house experiments, pressures were measured at three elevations in various locations. All pressure taps were installed within 0.3 m of a wall. In the single-story house, the taps were located 0.3 m (1 ft), 1.2 m (4 ft), and 2.1 m (7 ft) below the ceiling. In the two-story house, the taps were located 0.3 m (1 ft), 2.4 m (8 ft), and 4.6 m (15 ft) below the ceiling in the family room atrium (9PT), and 0.3 m (1 ft), 1.2 m (4 ft), and 2.1 m (7 ft) below the ceiling in all other rooms. Note that for the two-story house, Test 6, the den was closed and no pressure measurements are reported for this room.

The plots on the following pages compare the measured pressures with corresponding model predictions. Note that the pressures are reported relative to the ambient pressure at the given elevation. That is, all reported pressures are zero at the time of ignition.

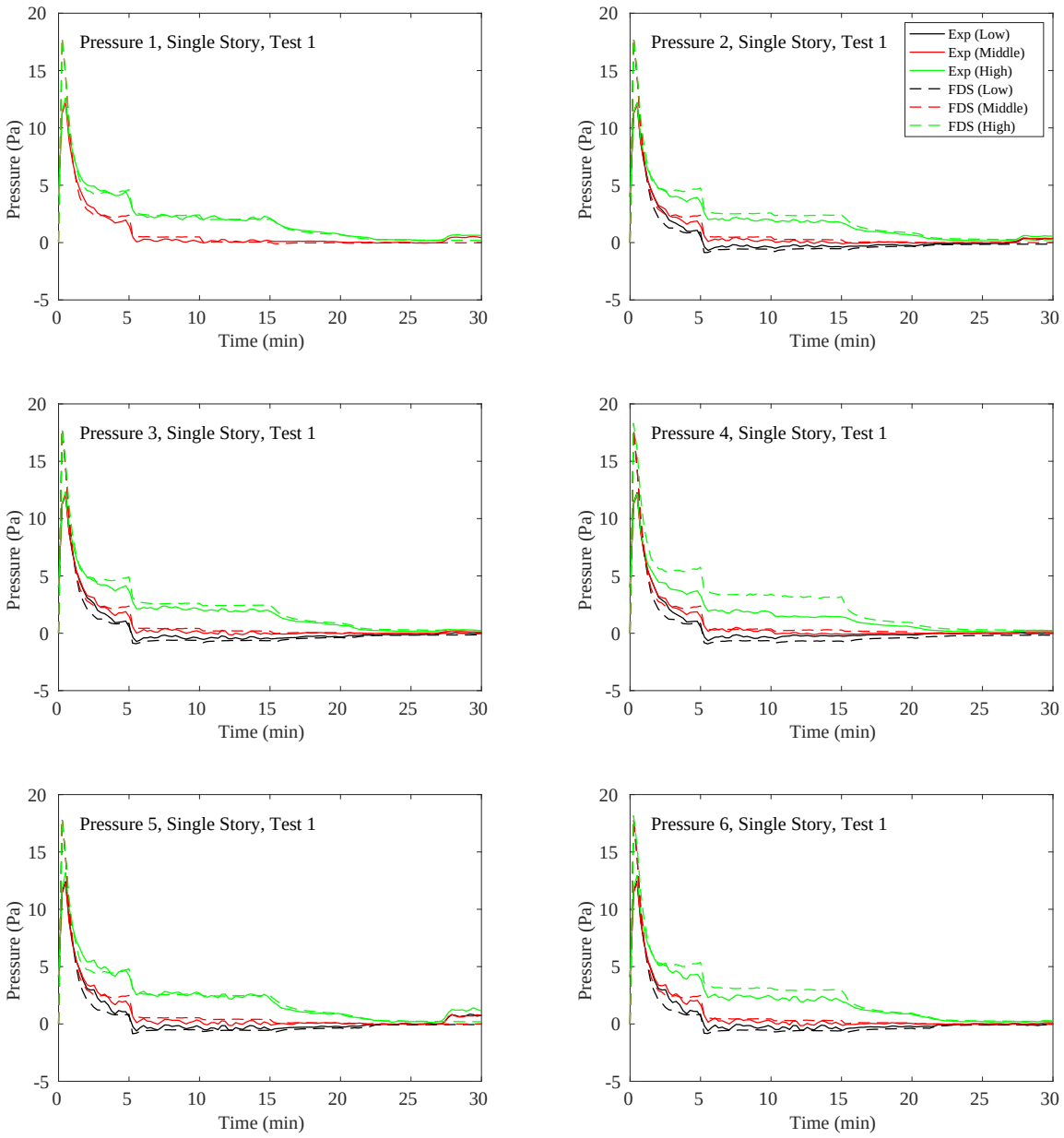

Figure 10.18: UL/NIJ Experiments, Pressure, Single-Story (Ranch) House, Test 1.

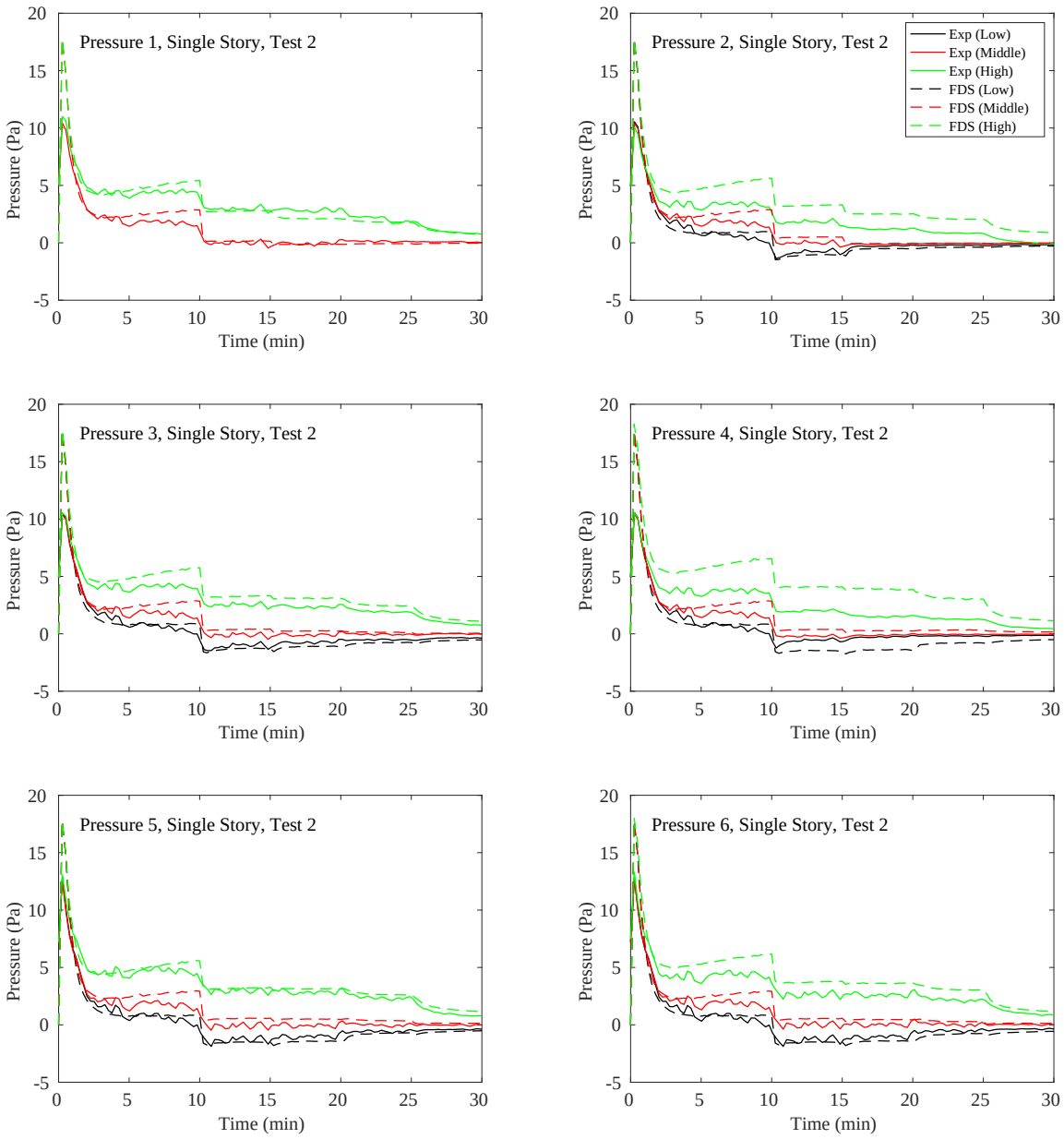

Figure 10.19: UL/NIJ Experiments, Pressure, Single-Story (Ranch) House, Test 2.

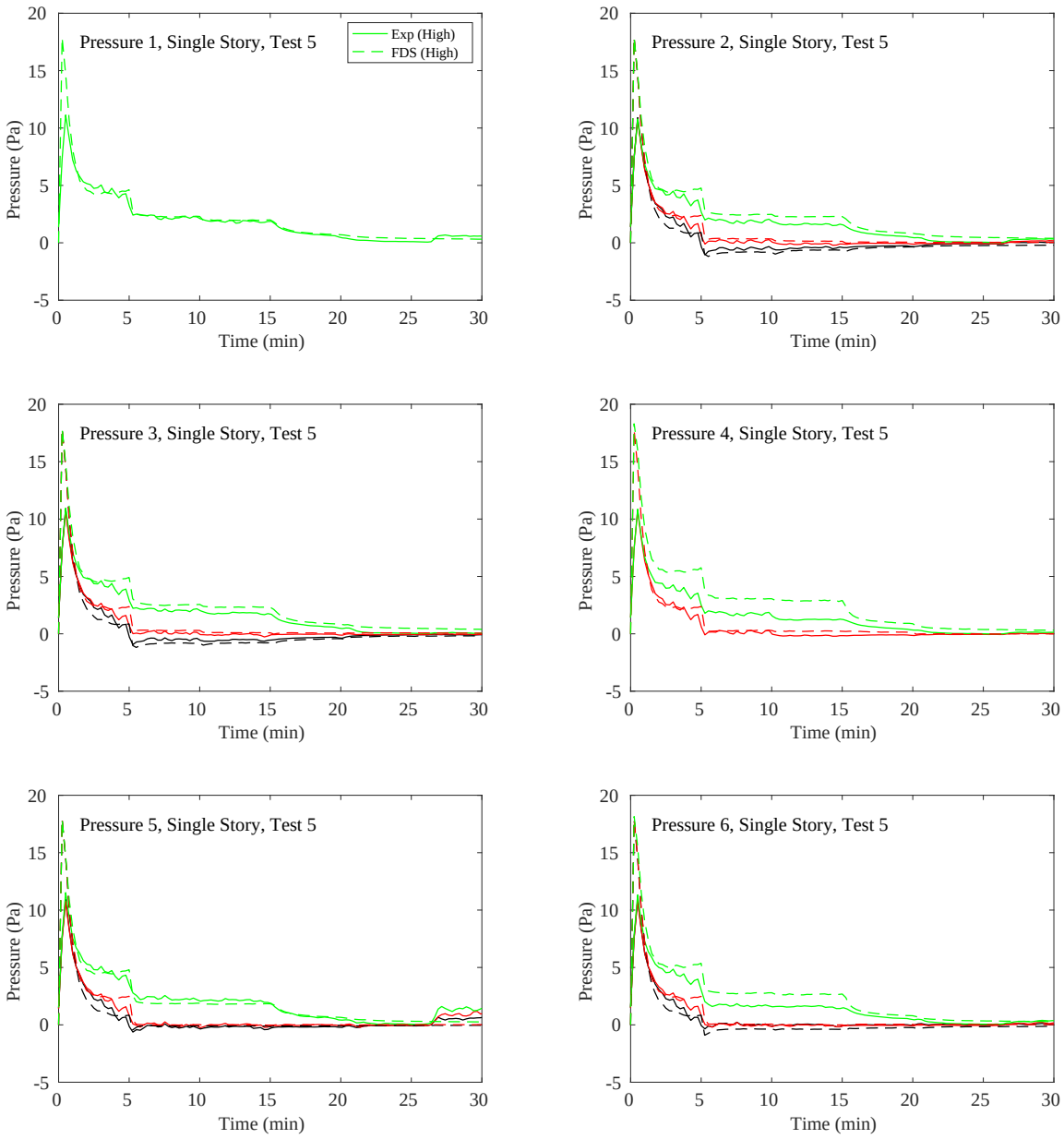

Figure 10.20: UL/NIJ Experiments, Pressure, Single-Story (Ranch) House, Test 5.

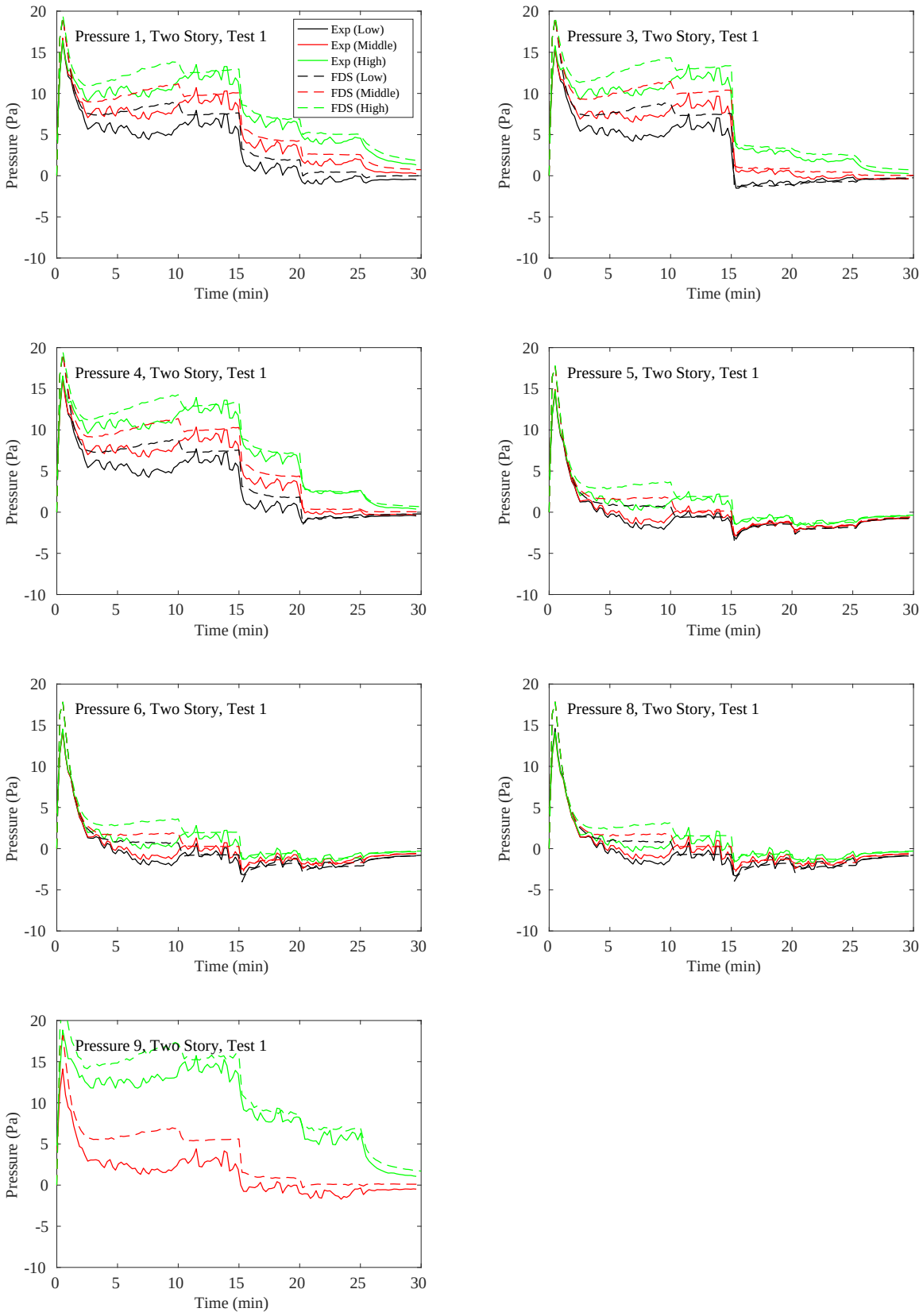

Figure 10.21: UL/NIJ Experiments, Pressure, Two-Story (Colonial) House, Test 1.

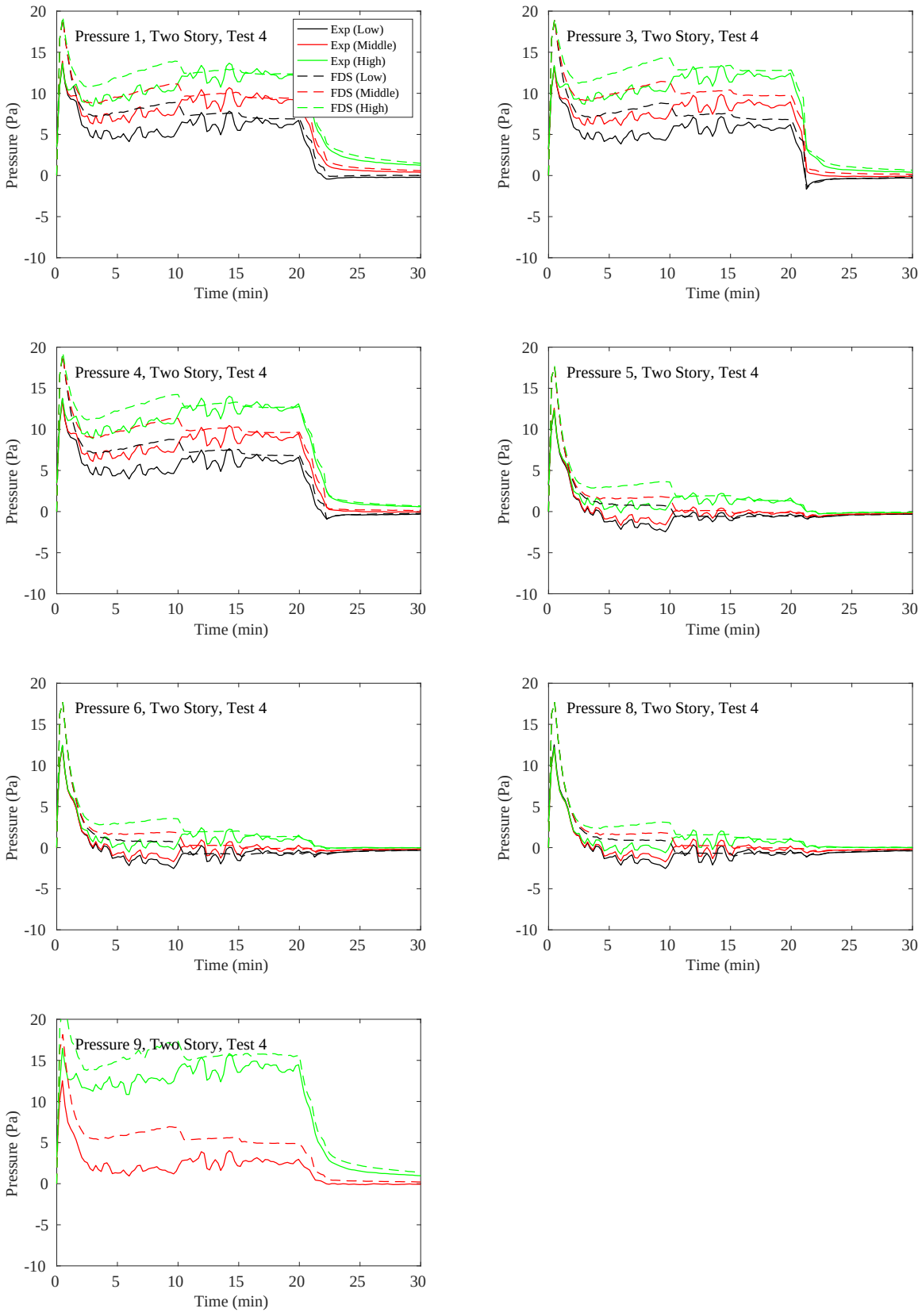

Figure 10.22: UL/NIJ Experiments, Pressure, Two-Story (Colonial) House, Test 4.

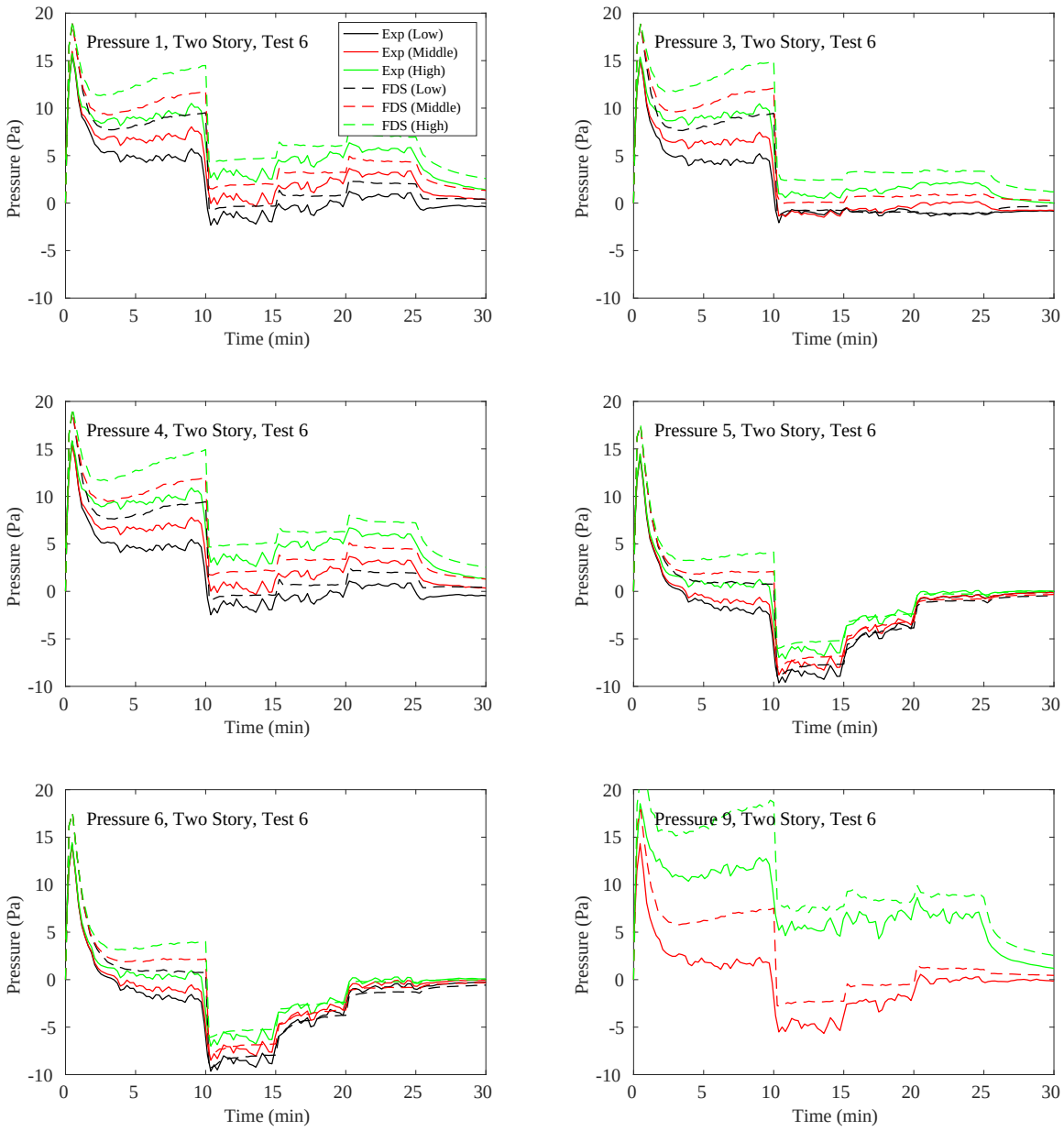

Figure 10.23: UL/NIJ Experiments, Pressure, Two-Story (Colonial) House, Test 6.

10.7 Summary of Pressure Predictions

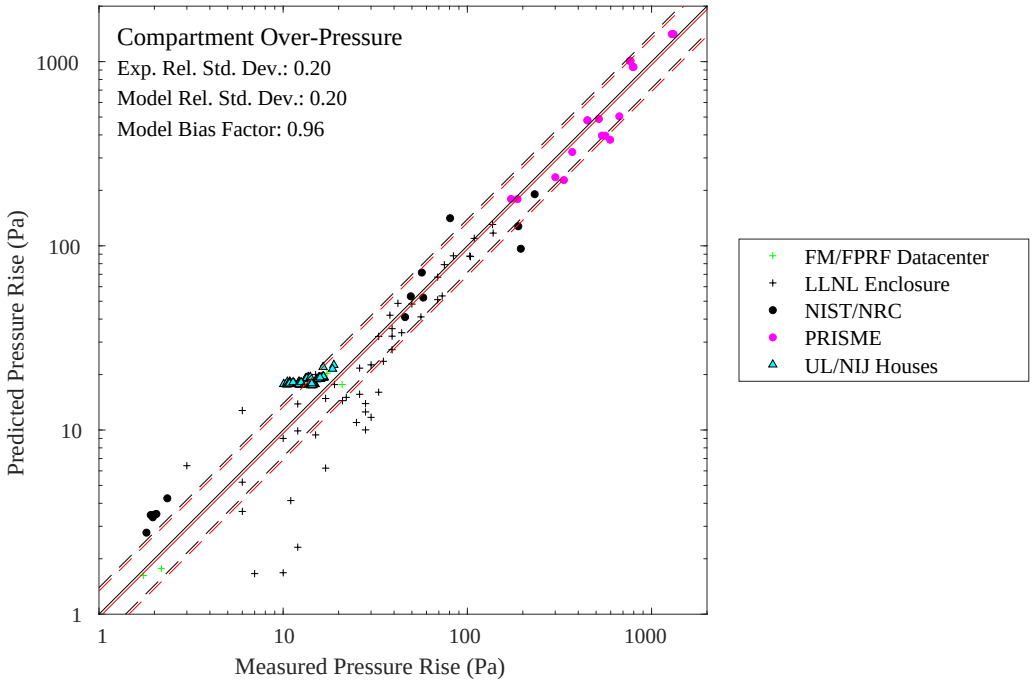

Figure 10.24: Summary of pressure predictions for open and closed compartments.

Chapter 11

Surface Temperature

All solid surfaces in an FDS model are assigned thermal boundary conditions. Heat and mass transfer to and from surfaces is usually handled with empirical correlations, although it is possible to compute directly the heat and mass transfer when performing a Direct Numerical Simulation (DNS). Heat conduction into a solid surface is calculated via a one-dimensional solution of the heat equation in cartesian, cylindrical, or spherical coordinates. The latter two are useful for predicting the thermal response of so-called "targets," which include structural steel, electrical cables, sensitive equipment, or any type of intervening combustible.

This chapter divides solid surfaces into two major categories – compartment linings (i.e., walls, ceiling, floor) and targets (i.e., anything that is not a wall, ceiling, or floor). The reason for this distinction is that some models treat the two categories differently. In general, FDS does not.

11.1 Wall, Ceiling and Floor Temperatures

11.1.1 FAA Cargo Compartments

Measurements of surface temperature were made at two ceiling locations (denoted A and B in Fig. 7.10). The surface temperature measurements are shown below.

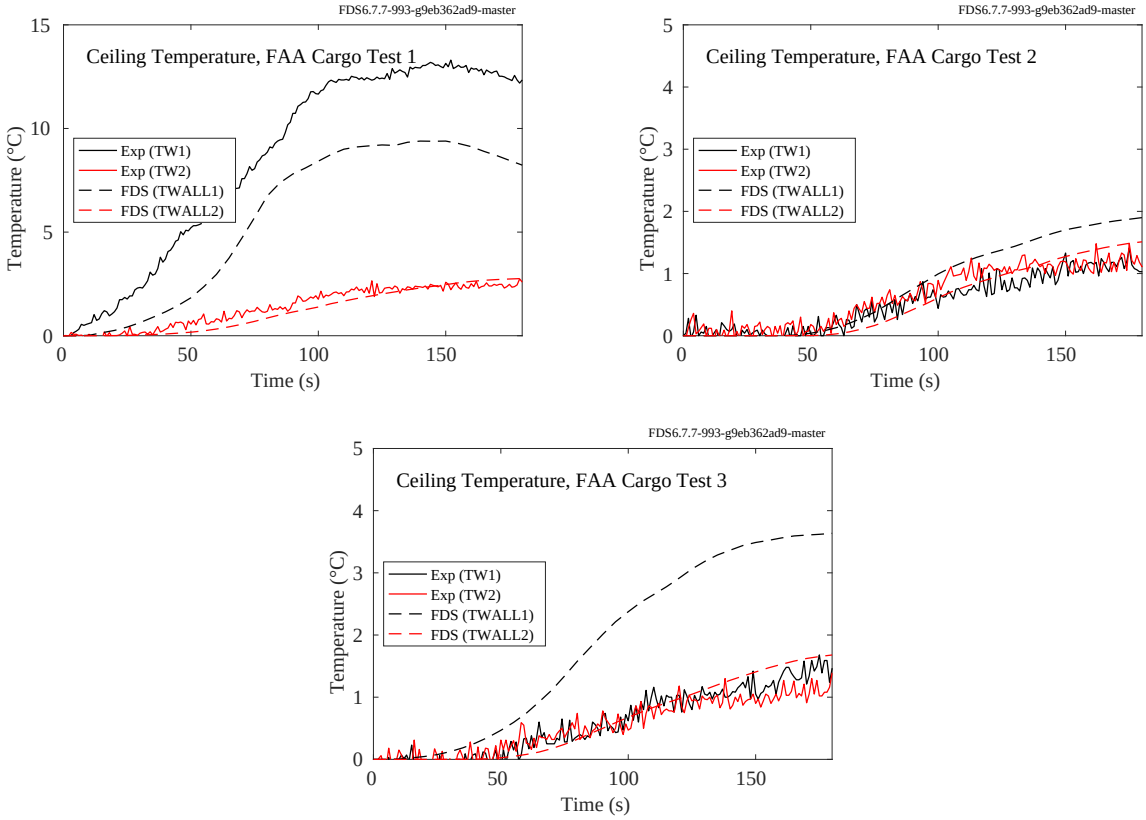

Figure 11.1: FAA Cargo Compartment experiments, ceiling surface temperatures.

11.1.2 NIST Composite Beam

A brief description of the experiments is given in Section 3.41. The compartment interior dimensions are 12.4 m long, running east-west, 1.9 m wide, and 3.77 m high. Four experiments with fires were performed, labeled as Tests 2-5. Test 1 did not include a fire.

Figures 11.2 through 11.3 display the under-surface temperature of the steel deck at Sections 3-6. Figures 11.4 through 11.7 display the temperatures of the concrete slab between the concrete and steel deck at Sections 1-8.

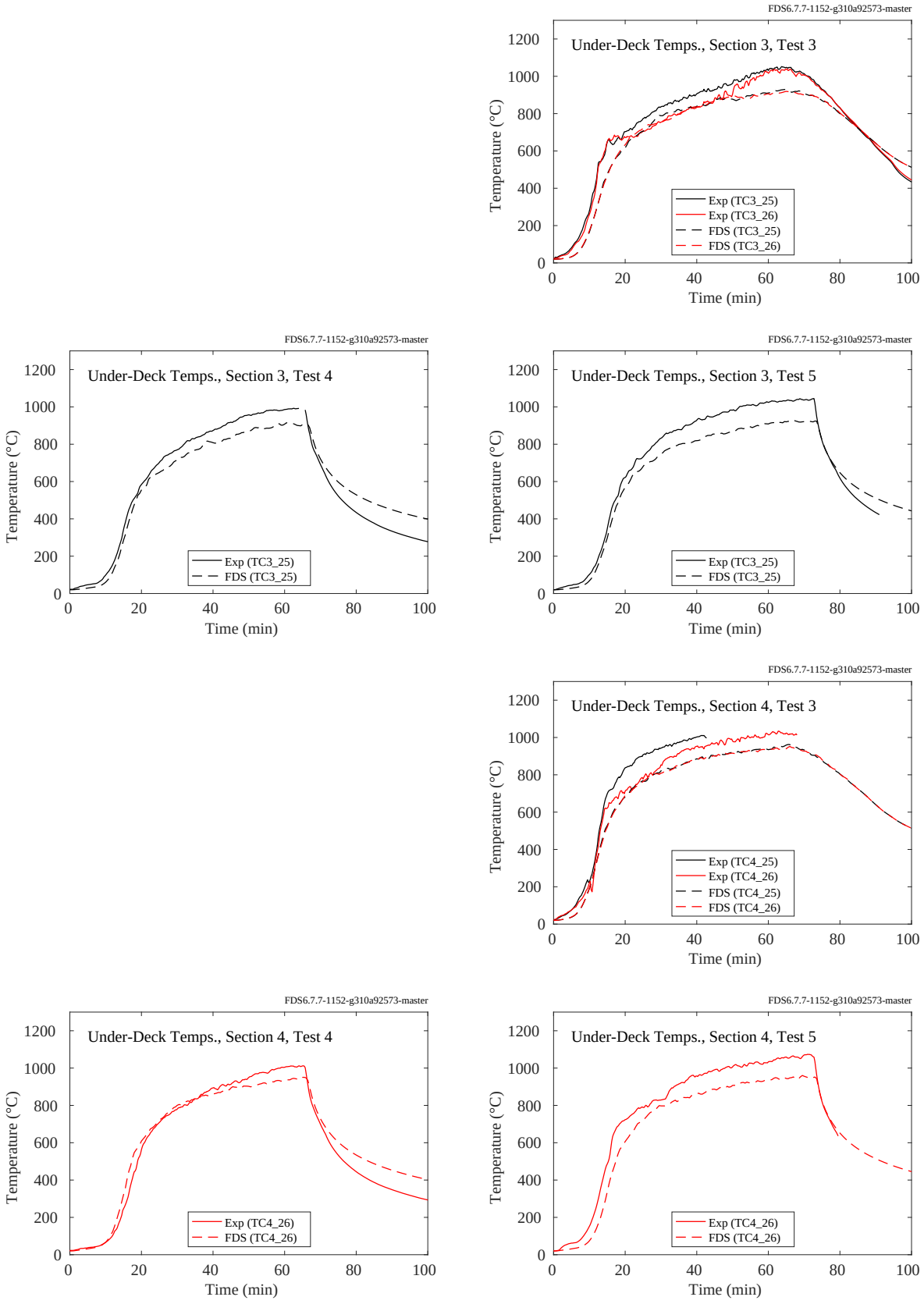

Figure 11.2: NIST Composite Beam, under-deck temperatures, Sections 3 and 4.

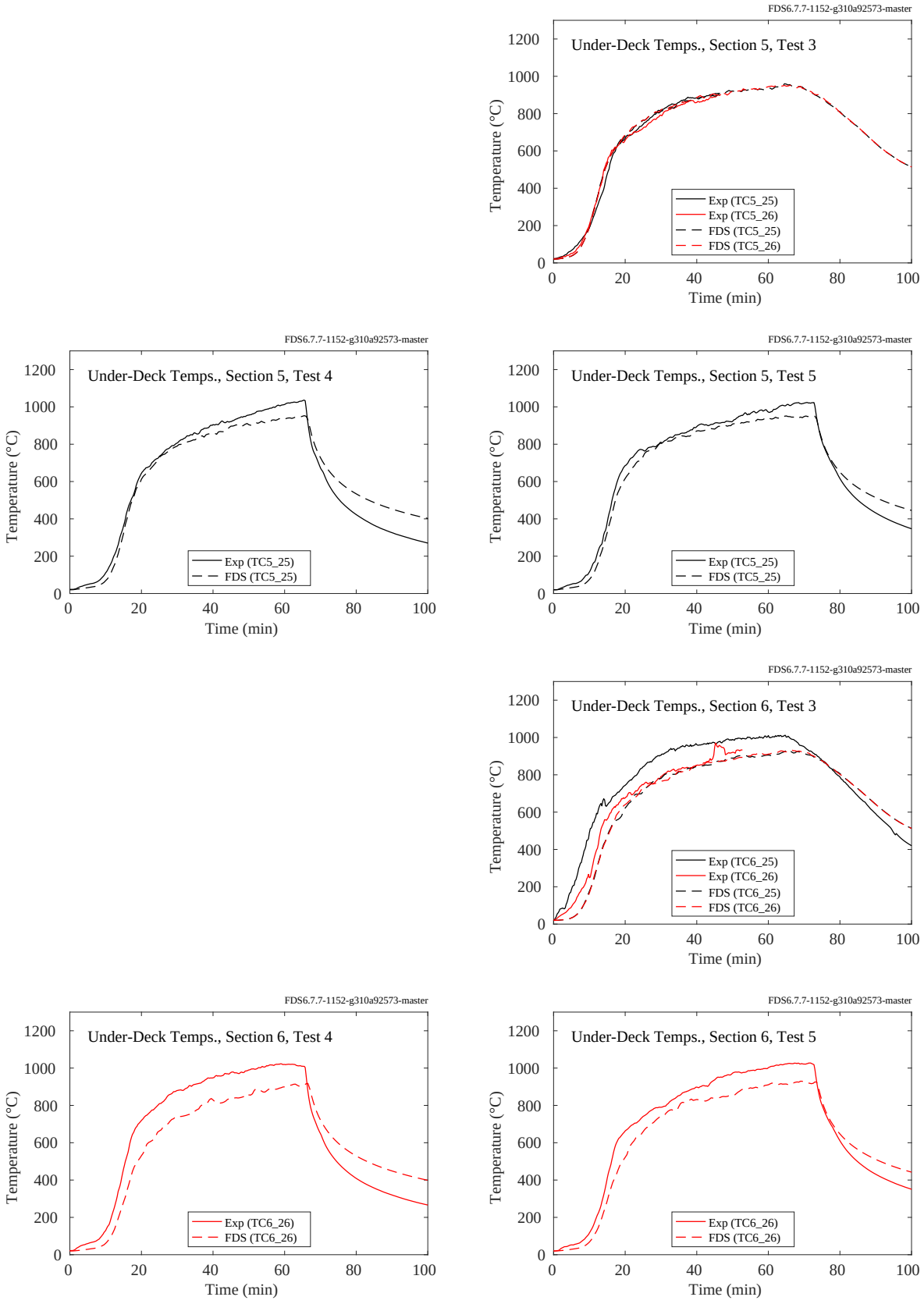

Figure 11.3: NIST Composite Beam, under-deck temperatures, Sections 5 and 6.

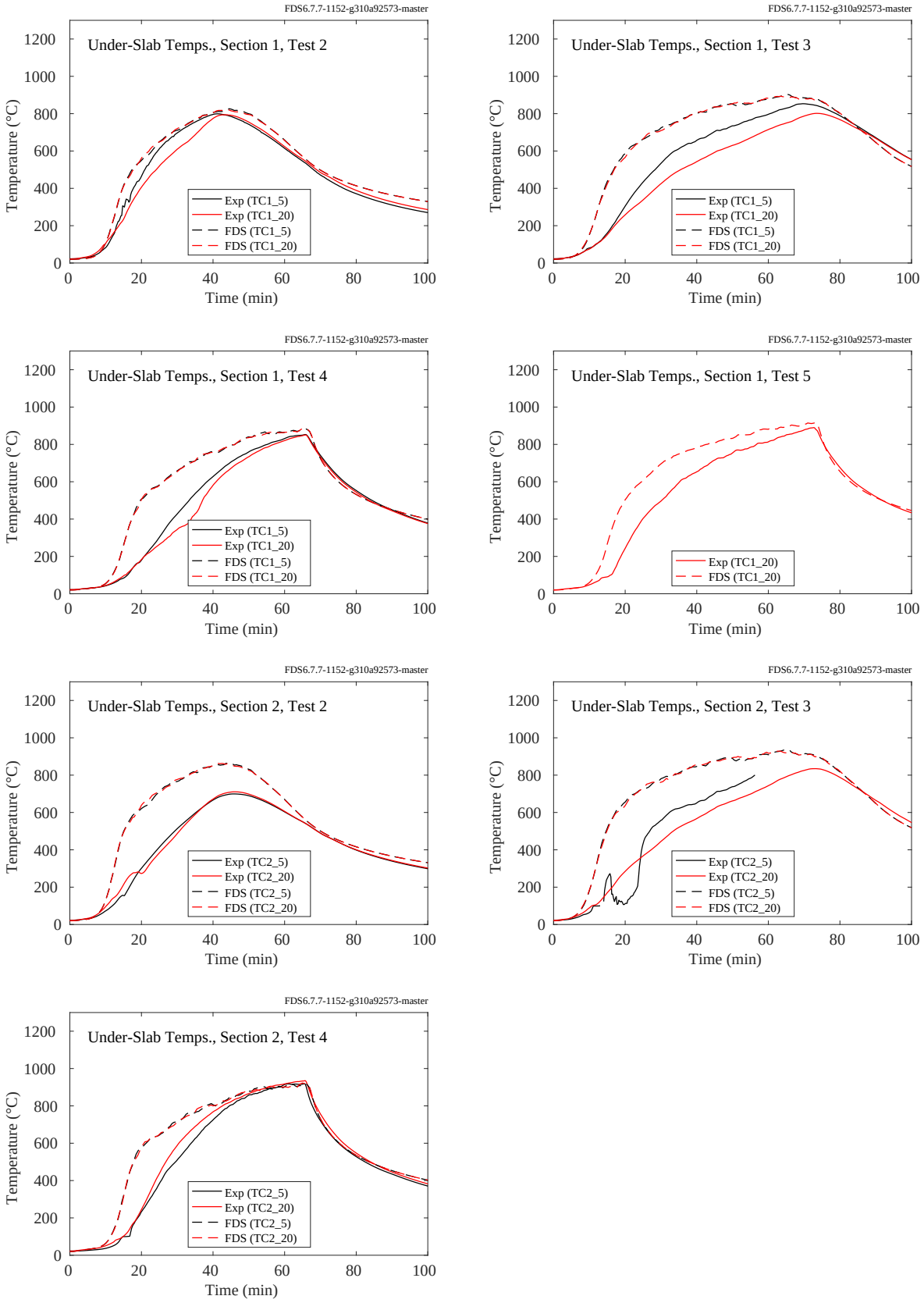

Figure 11.4: NIST Composite Beam, inside-deck temperatures, Sections 1 and 2.

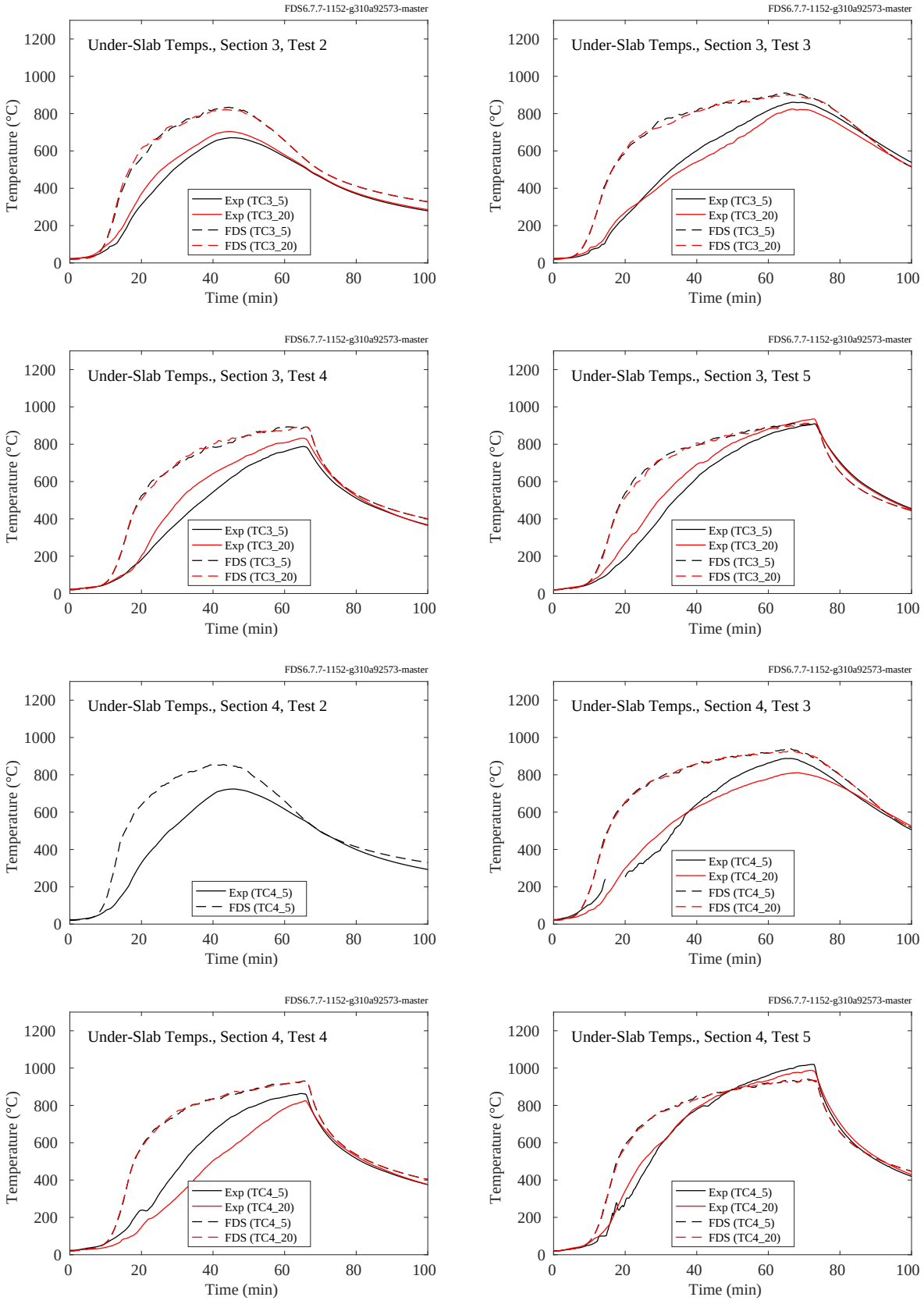

Figure 11.5: NIST Composite Beam, inside-deck temperatures, Sections 3 and 4.

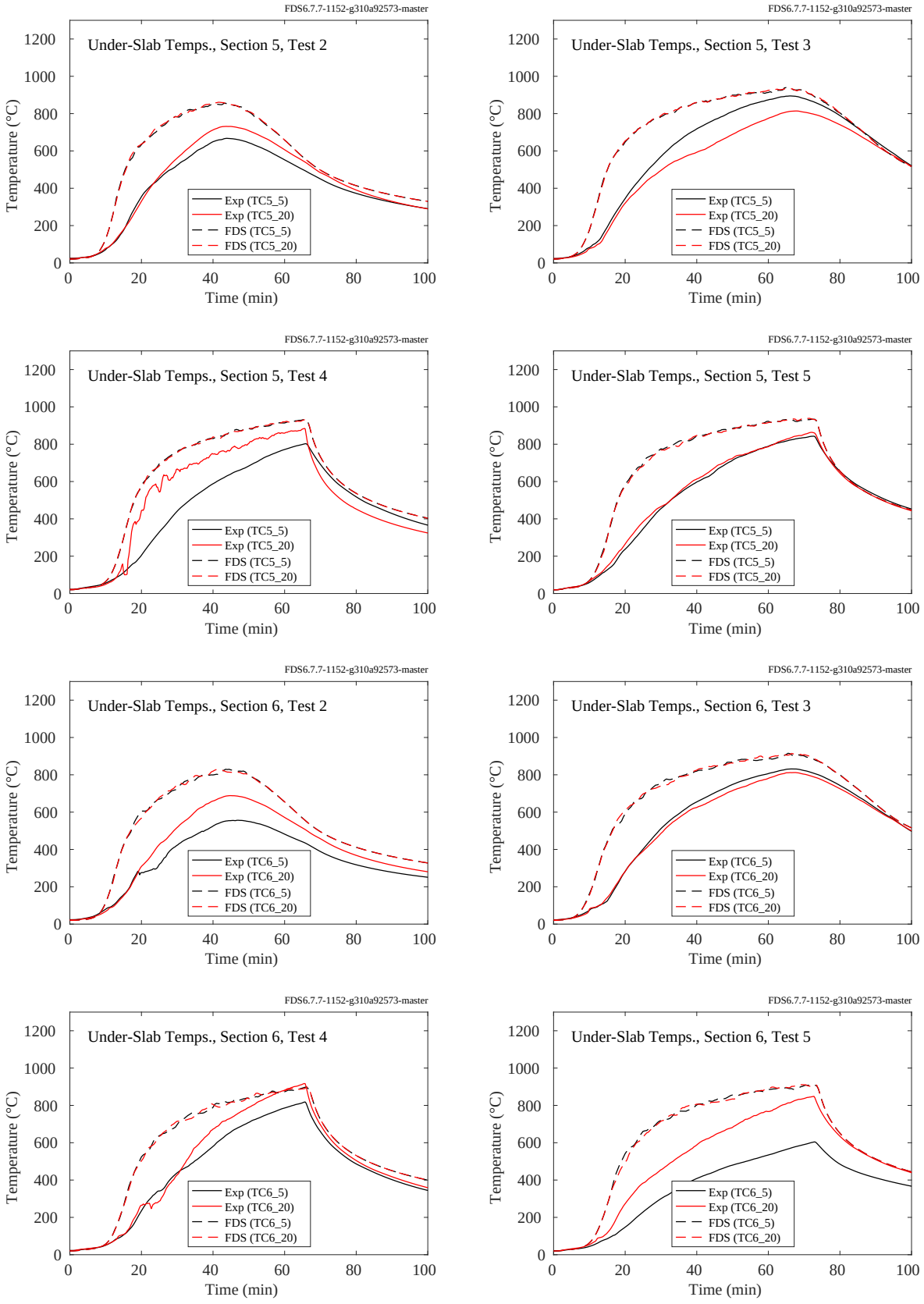

Figure 11.6: NIST Composite Beam, inside-deck temperatures, Sections 5 and 6.

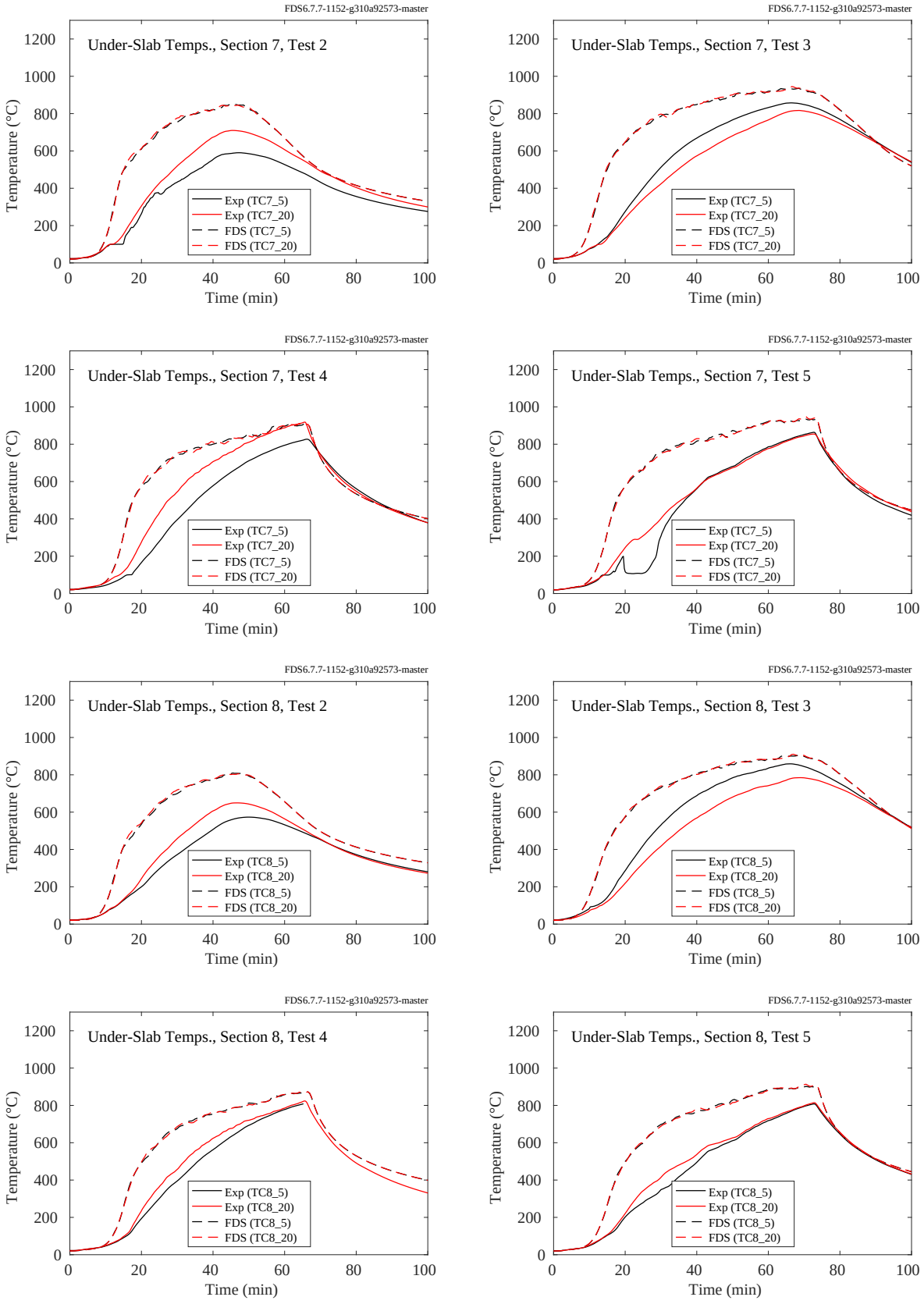

Figure 11.7: NIST Composite Beam, inside-deck temperatures, Sections 7 and 8.

11.1.3 NIST Full-Scale Enclosure (FSE), 2008

Measurements of surface temperature were made at three ceiling and three floor locations in a standard ISO 9705 compartment. In the plots on the following the pages, the ceiling measurements at the rear, center and front of the compartment are denoted by TSHFRCE, TSHFCCE, and TSHFFCE, respectively (Temperature Surface Heat Flux Rear CEiling, etc.). The floor measurements at the rear and front are denoted TSHFRFL and TSHFFFL. The surface temperatures measurements that were made just outside the door were faulty and are not used. All of the floor measurements for the experiment labeled ISOHept8 were faulty.

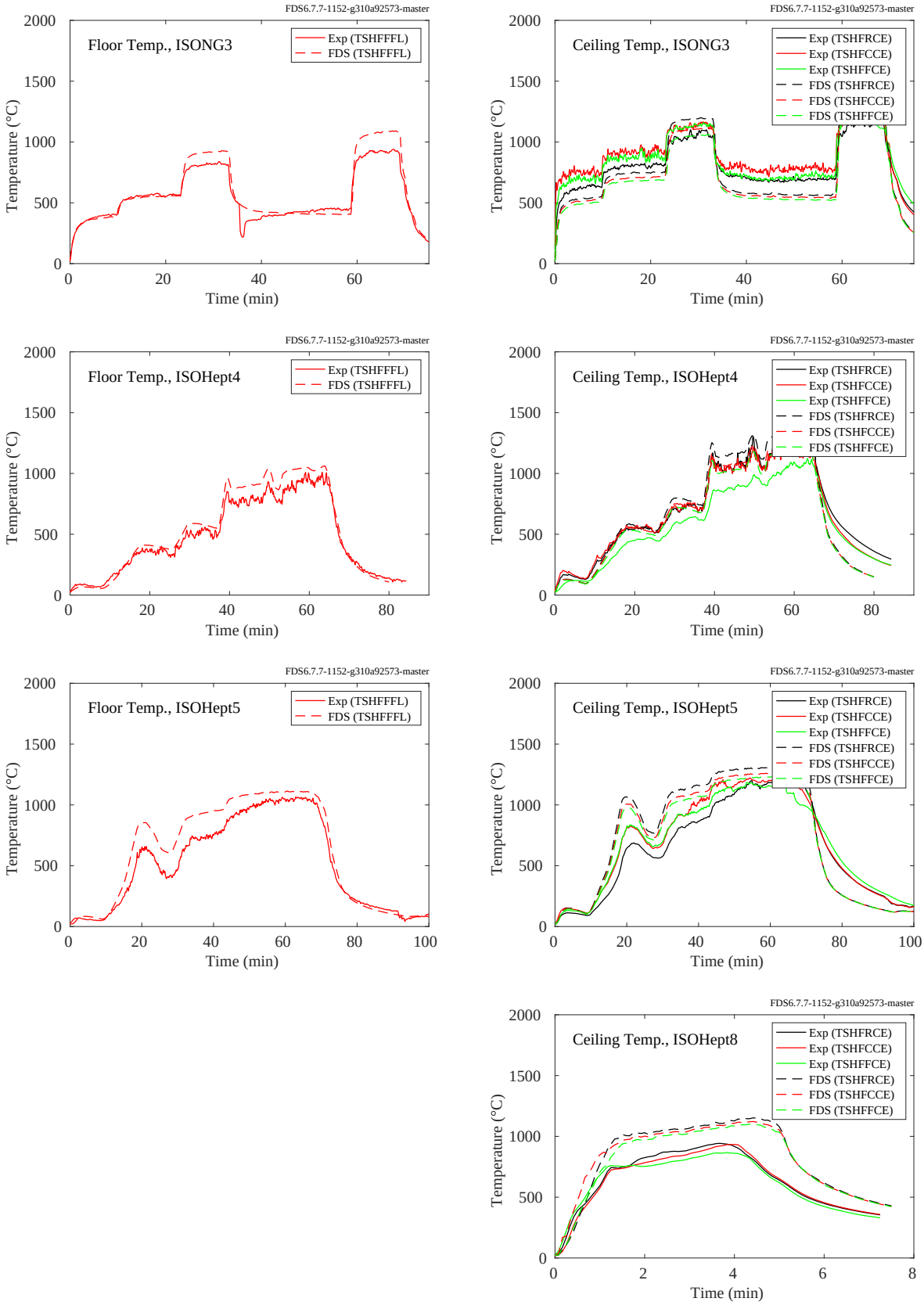

Figure 11.8: NIST FSE experiments, floor and ceiling temperatures, Tests 3-4, 8.

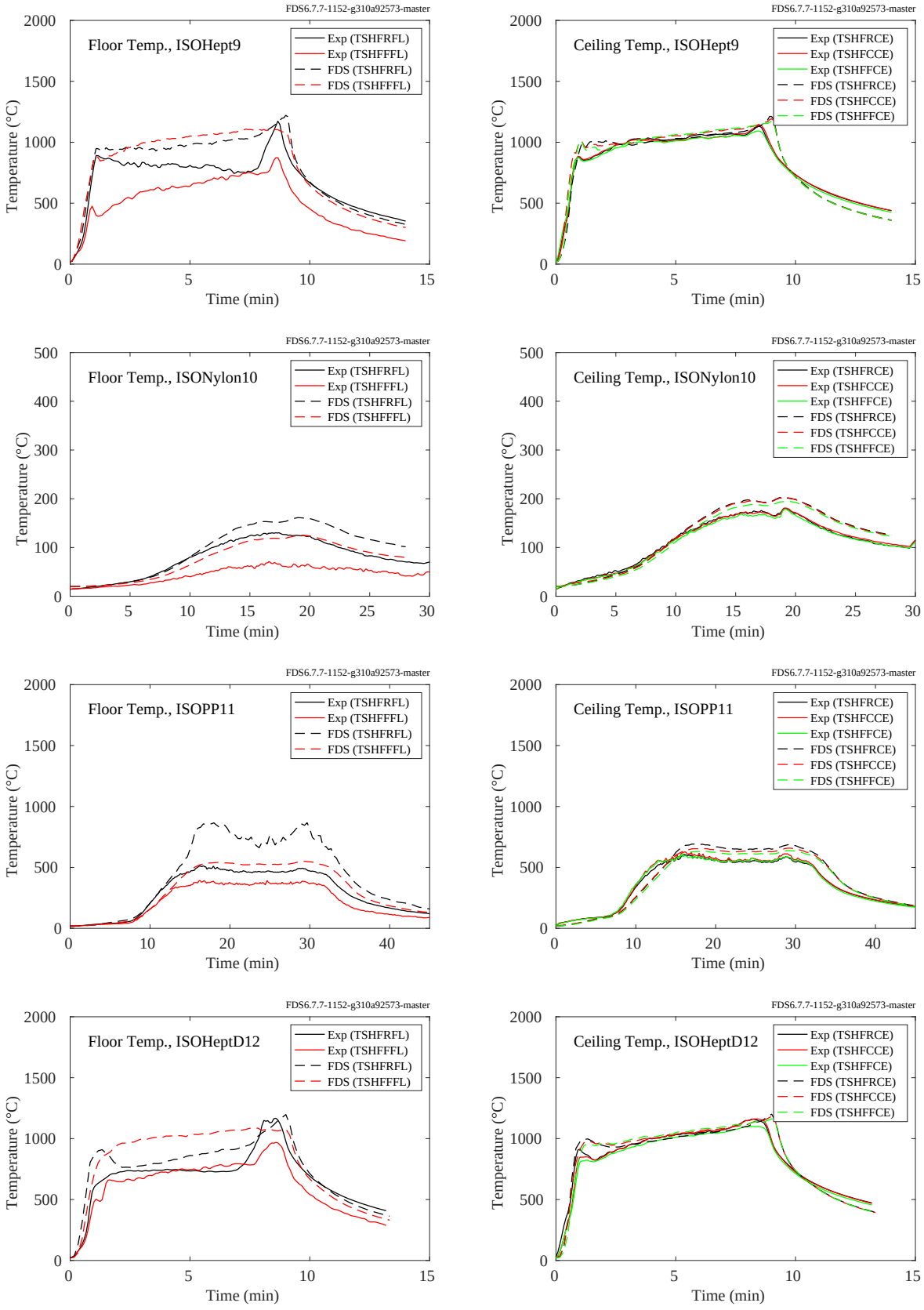

Figure 11.9: NIST FSE experiments, floor and ceiling temperatures, Tests 9-12.

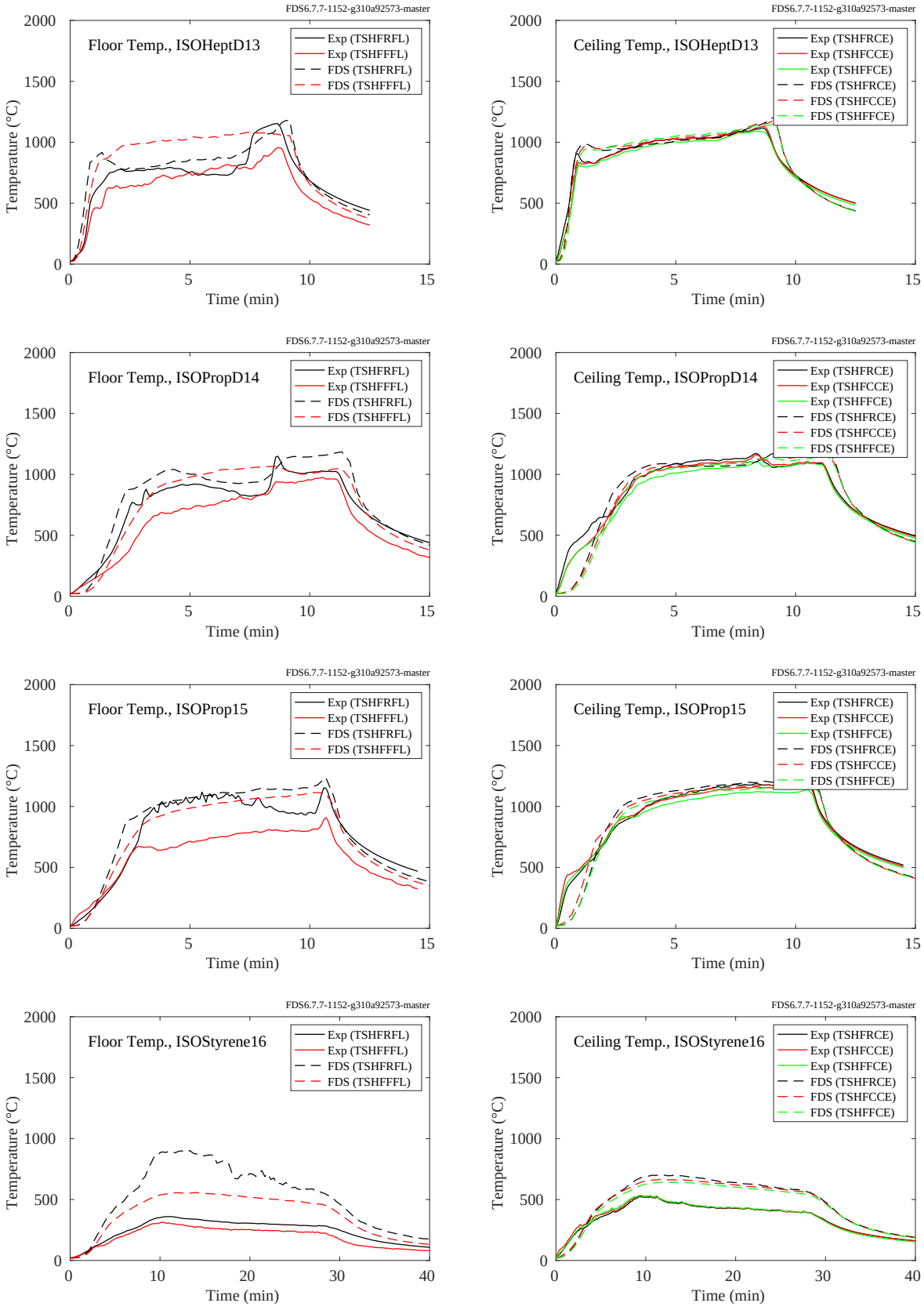

Figure 11.10: NIST FSE experiments, floor and ceiling temperatures, Tests 13-16.

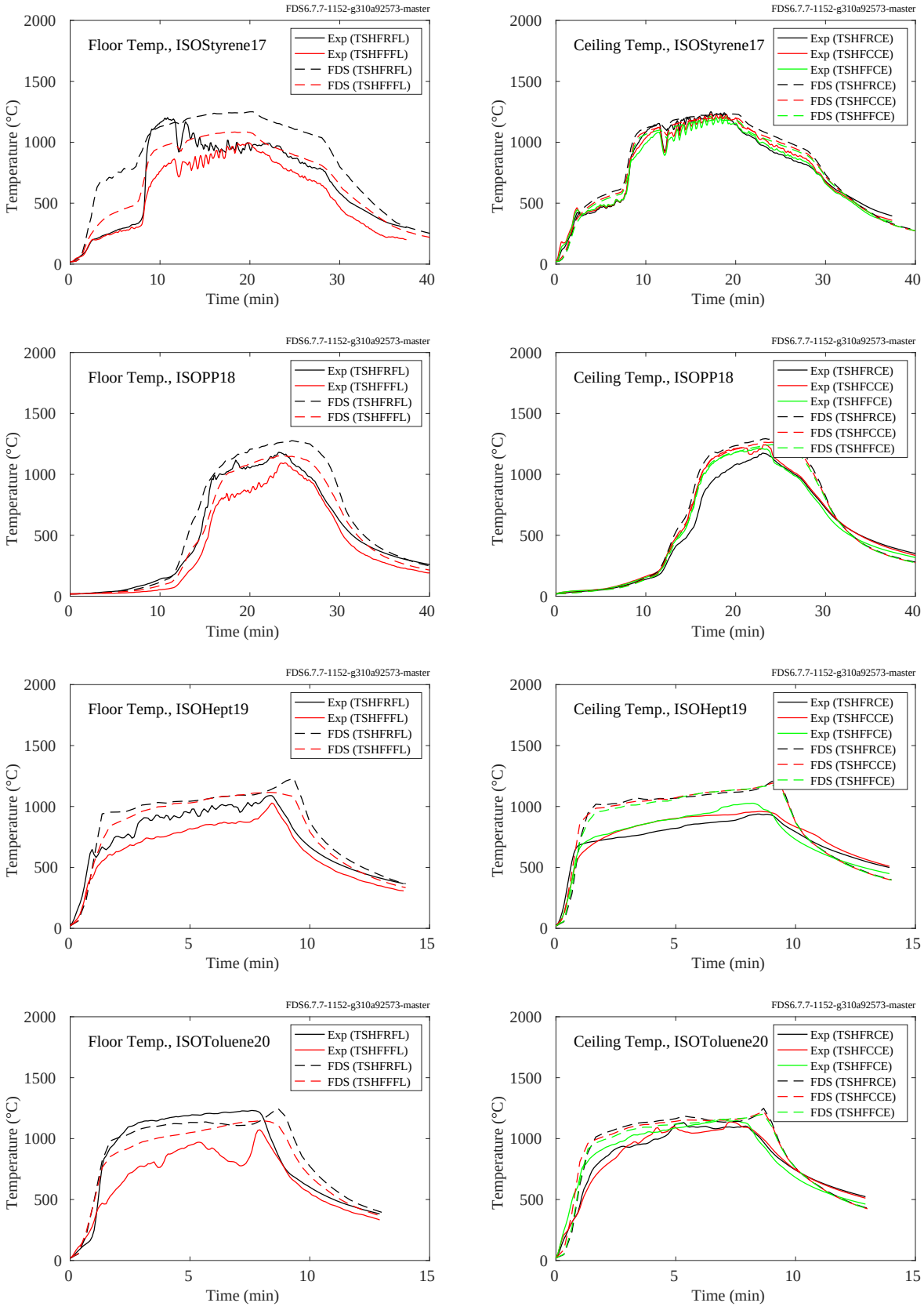

Figure 11.11: NIST FSE experiments, floor and ceiling temperatures, Tests 17-20.

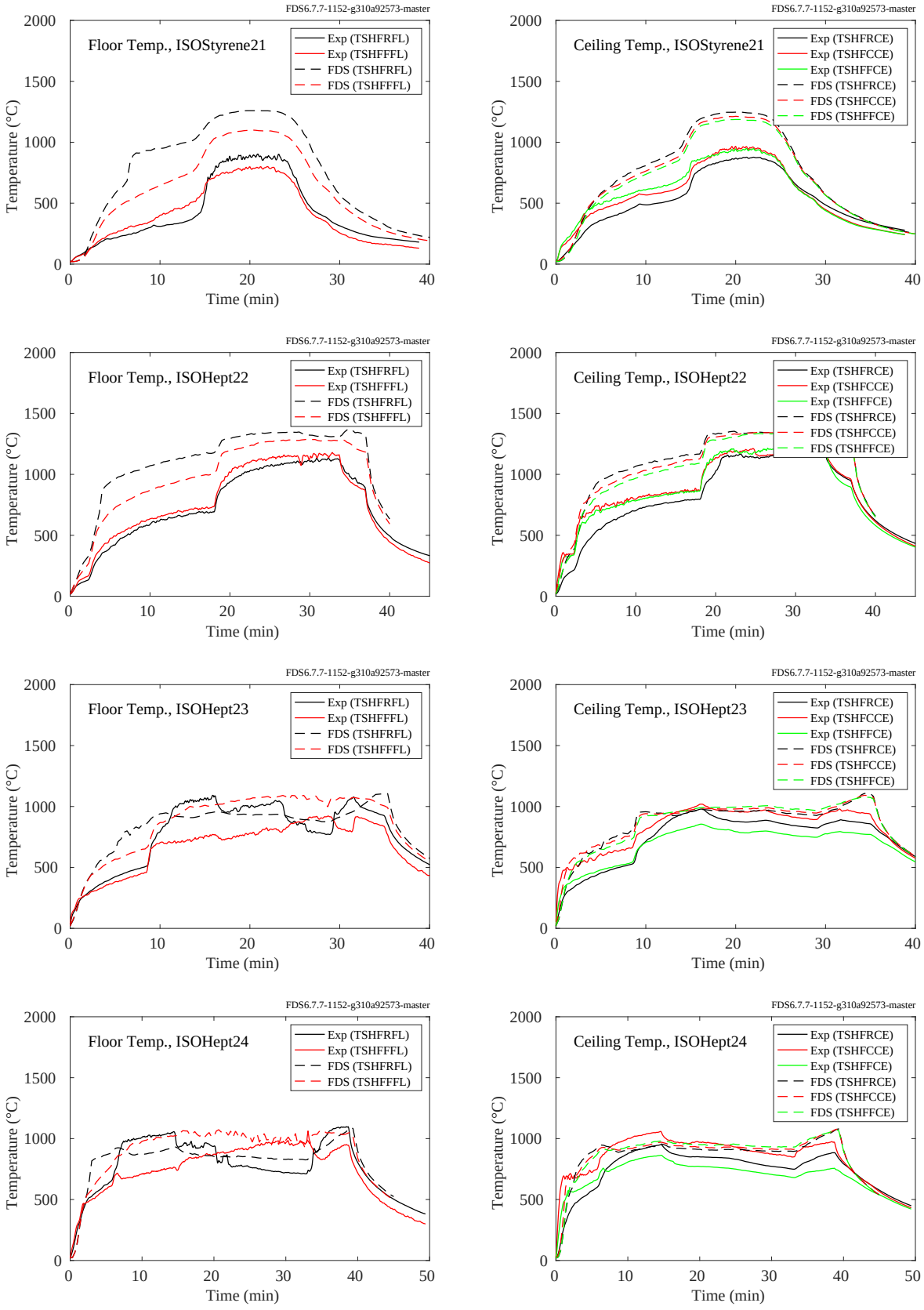

Figure 11.12: NIST FSE experiments, floor and ceiling temperatures, Tests 21-24.

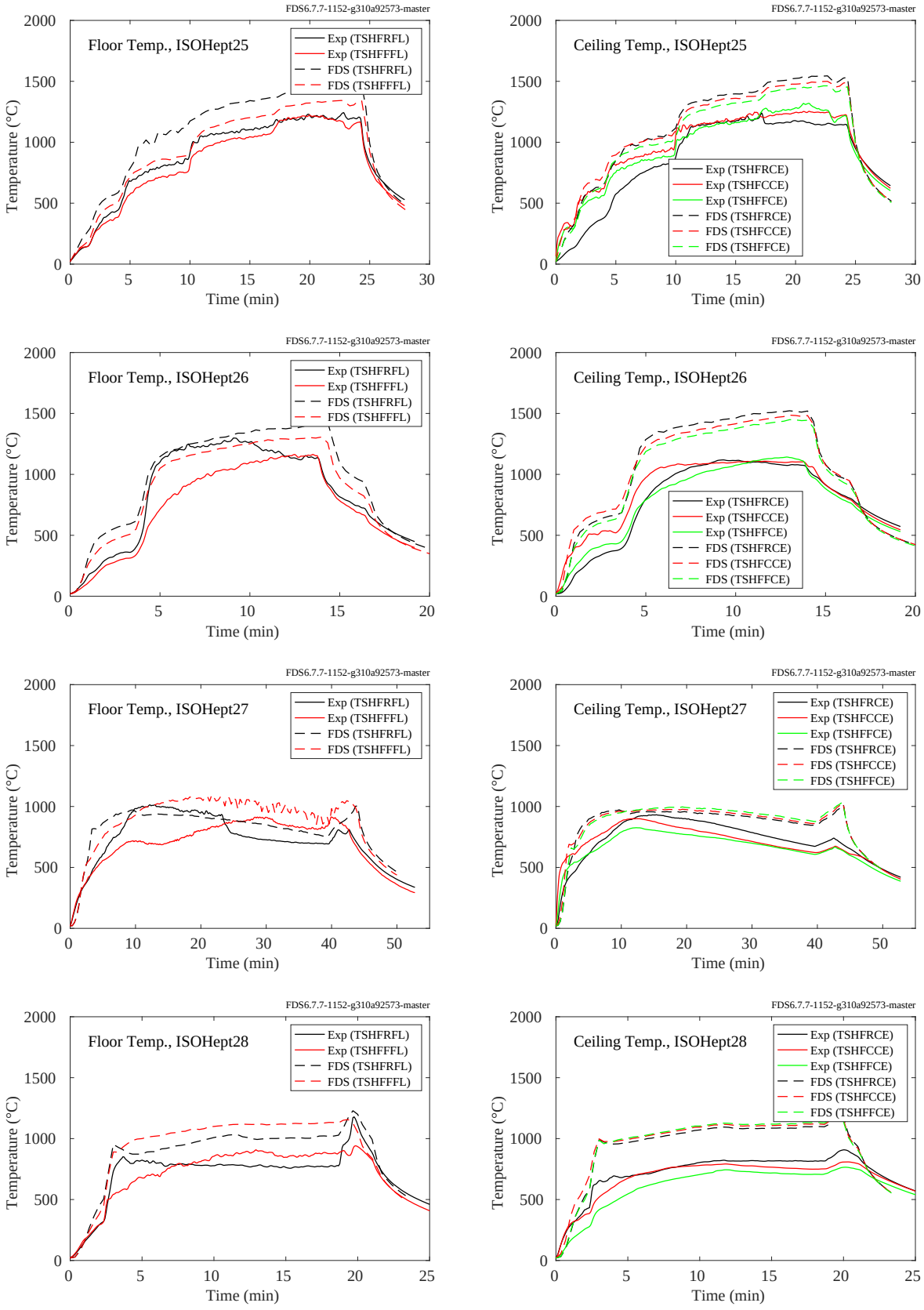

Figure 11.13: NIST FSE experiments, floor and ceiling temperatures, Tests 25-28.

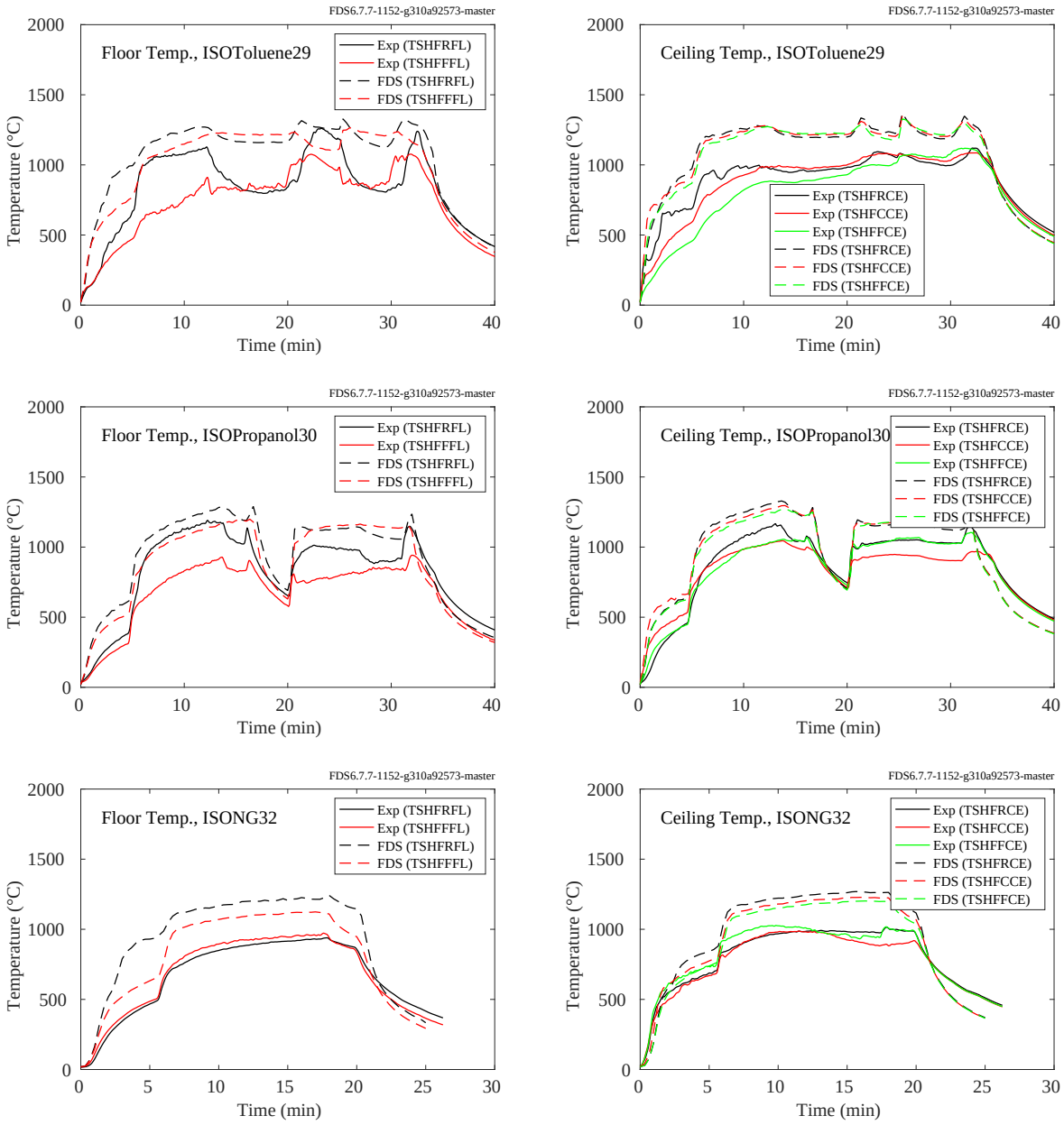

Figure 11.14: NIST FSE experiments, floor and ceiling temperatures, Tests 29, 30, 32.

11.1.4 NIST/NRC Experiments

Thermocouples and heat flux gauges were positioned at various locations on all four walls of the test compartment, plus the ceiling and floor. Comparisons between measured and predicted surface temperatures are shown on the following pages. Over the course of 15 experiments, a number of the thermocouples and gauges failed, but because over half of the measurement points were in roughly the same relative location to the fire, the faulty data was discarded based on examining replicate experiments or locations on the opposite wall. Note that Position 8 for the floor and ceiling is not used, simply because the plotting routine is limited to 7 distinct colors and Position 8 is on the opposite side of the compartment to Position 1. Table 11.1 lists the locations for each test.

Table 11.1: Wall thermocouple and heat flux gauge positions for the NIST/NRC series. The origin of the coordinate system lies on the floor in the southwest corner of the compartment. The designation "U" and "C" is irrelevant, and the last digit "2" indicates that the thermocouple is measuring the wall temperature rather than the heat flux gauge temperature.

Name	x	y	z	Name	x	y	z
TC North U-1-2	3.85	7.04	1.49	TC South U-1-2	3.86	0	1.49
TC North U-2-2	3.86	7.04	3.71	TC South U-2-2	3.86	0	3.82
TC North U-3-2	9.48	7.04	1.86	TC South U-3-2	9.54	0	1.86
TC North U-4-2	12.07	7.04	1.88	TC South U-4-2	12.08	0	1.86
TC North U-5-2	17.69	7.04	1.49	TC South U-5-2	17.69	0	1.50
TC North U-6-2	17.69	7.04	3.69	TC South U-6-2	17.74	0	3.70
TC East U-1-2	21.66	1.52	1.12	TC West U-1-2	0	1.59	1.12
TC East U-2-2	21.66	1.52	2.40	TC West U-2-2	0	1.59	2.42
TC East U-3-2	21.66	5.68	1.13	TC West U-3-2	0	5.70	1.12
TC East U-4-2	21.66	5.70	2.42	TC West U-4-2	0	5.70	2.42
TC Floor U-1-2	3.08	3.51	0	TC Ceiling U-1-2	3.04	3.60	3.82
TC Floor U-2-2	9.08	1.94	0	TC Ceiling C-2-2	8.99	2.00	3.82
TC Floor U-3-2	9.06	5.97	0	TC Ceiling C-3-2	9.03	5.97	3.82
TC Floor U-4-2	10.86	2.38	0	TC Ceiling C-4-2	10.79	2.38	3.82
TC Floor C-5-2	10.93	5.20	0	TC Ceiling C-5-2	10.79	5.20	3.82
TC Floor U-6-2	13.13	1.99	0	TC Ceiling C-6-2	13.00	2.07	3.82
TC Floor U-7-2	13.00	5.92	0	TC Ceiling C-7-2	12.84	5.98	3.82
TC Floor U-8-2	18.63	3.54	0	TC Ceiling U-8-2	18.71	3.54	3.82

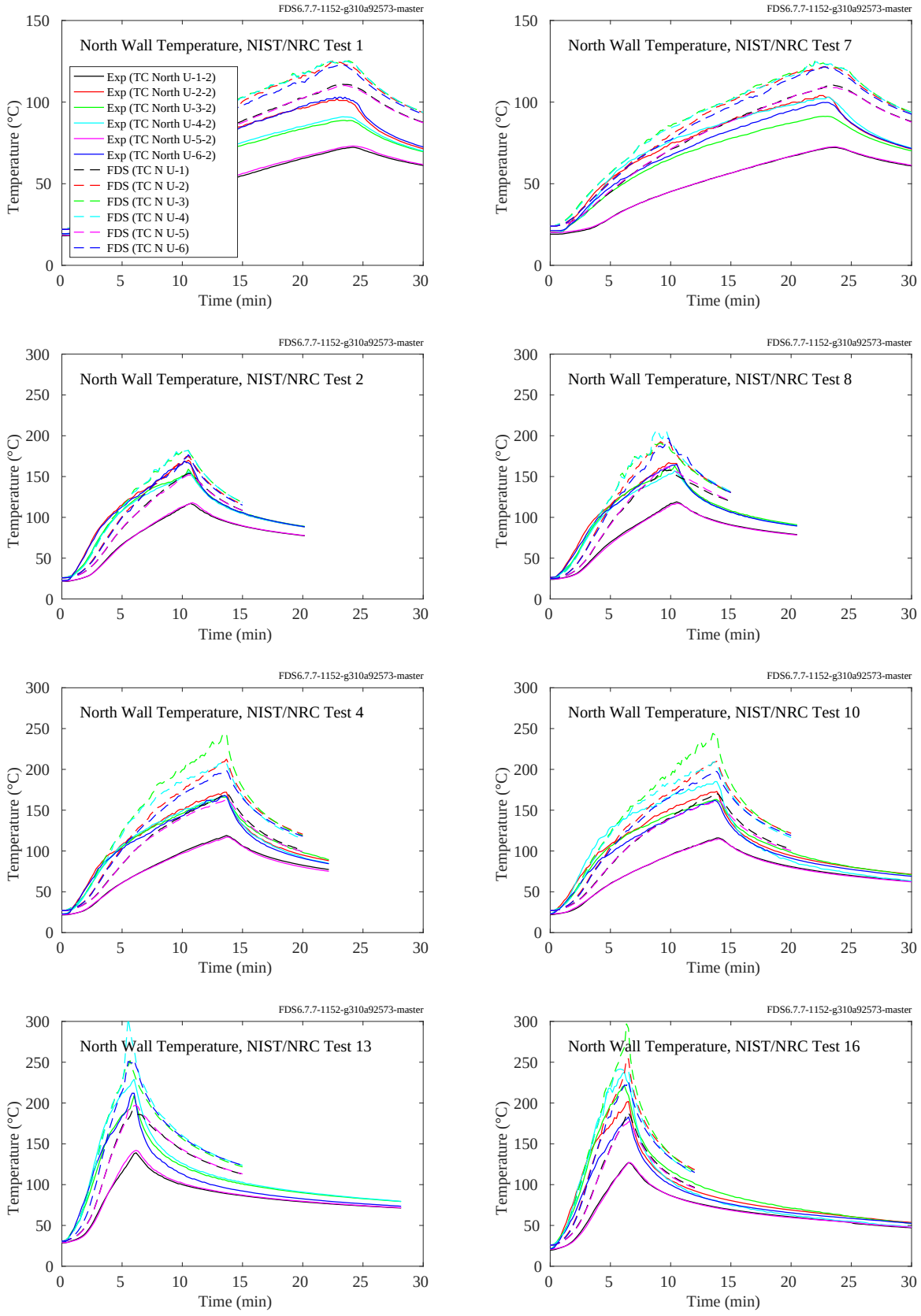

Figure 11.15: NIST/NRC experiments, north wall temperatures, Tests 1, 2, 4, 7, 8, 10, 13, 16.

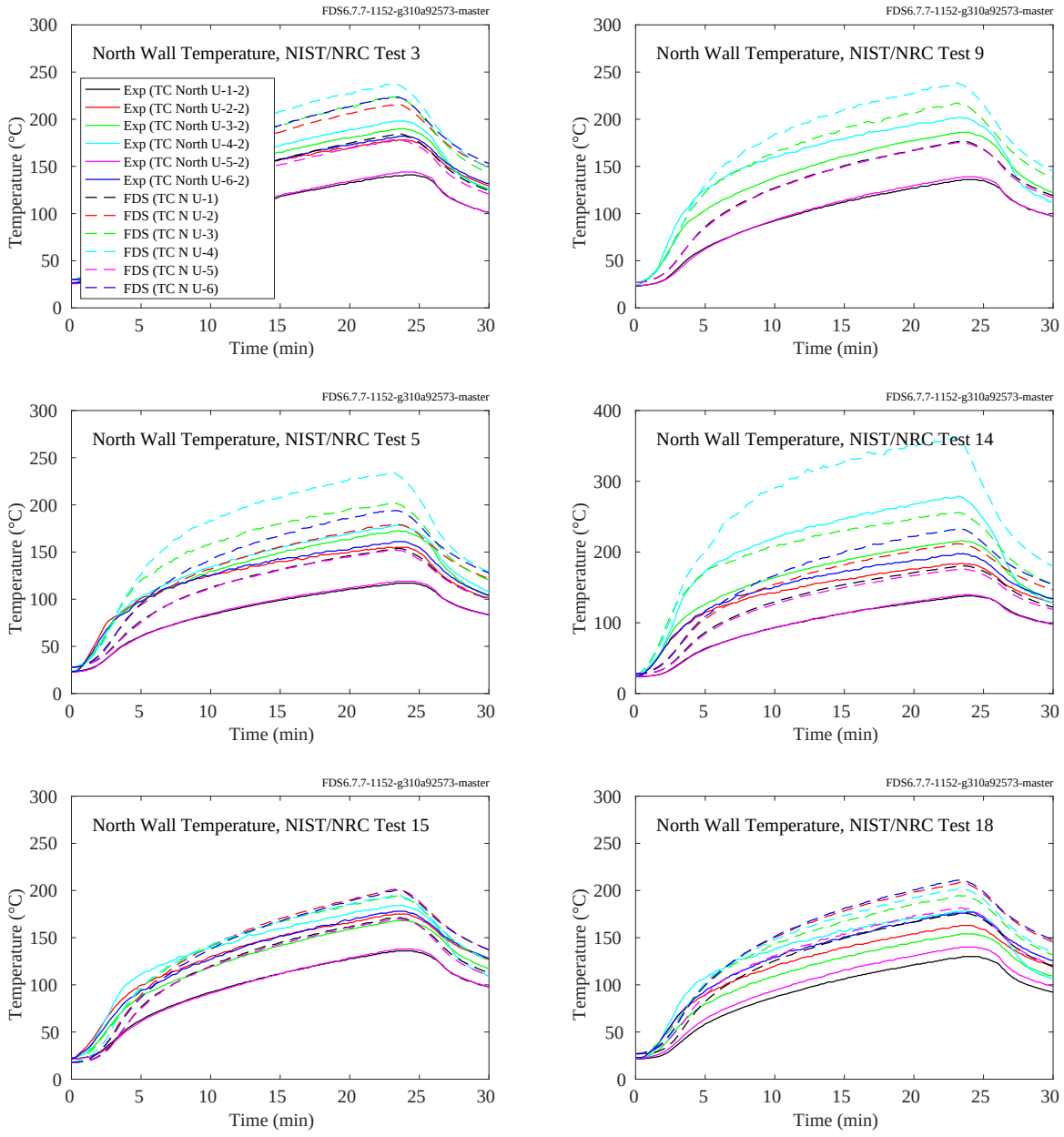

Figure 11.16: NIST/NRC experiments, north wall temperatures, Tests 3, 5, 9, 14, 15, 18.

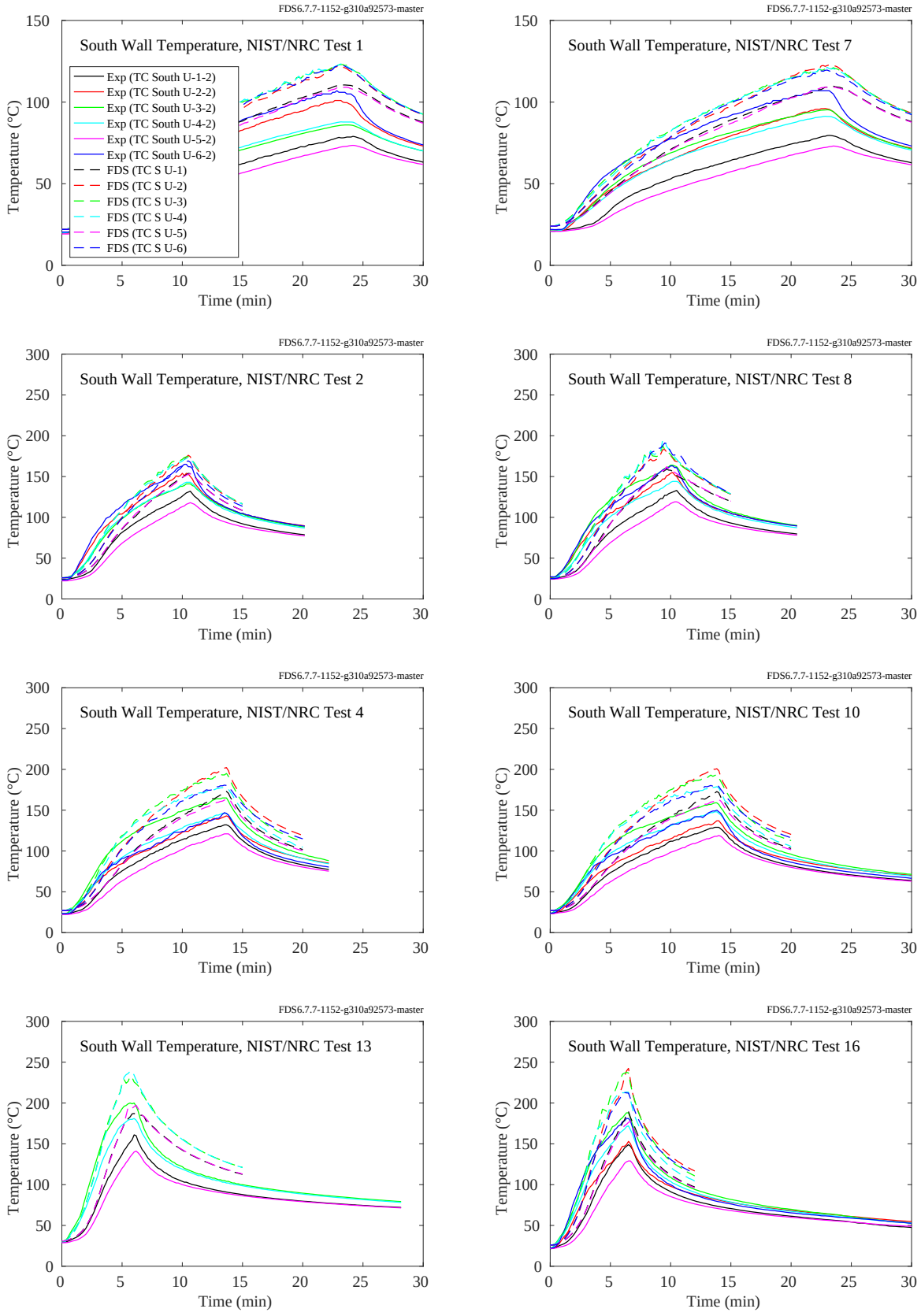

Figure 11.17: NIST/NRC experiments, south wall temperatures, Tests 1, 2, 4, 7, 8, 10, 13, 16.

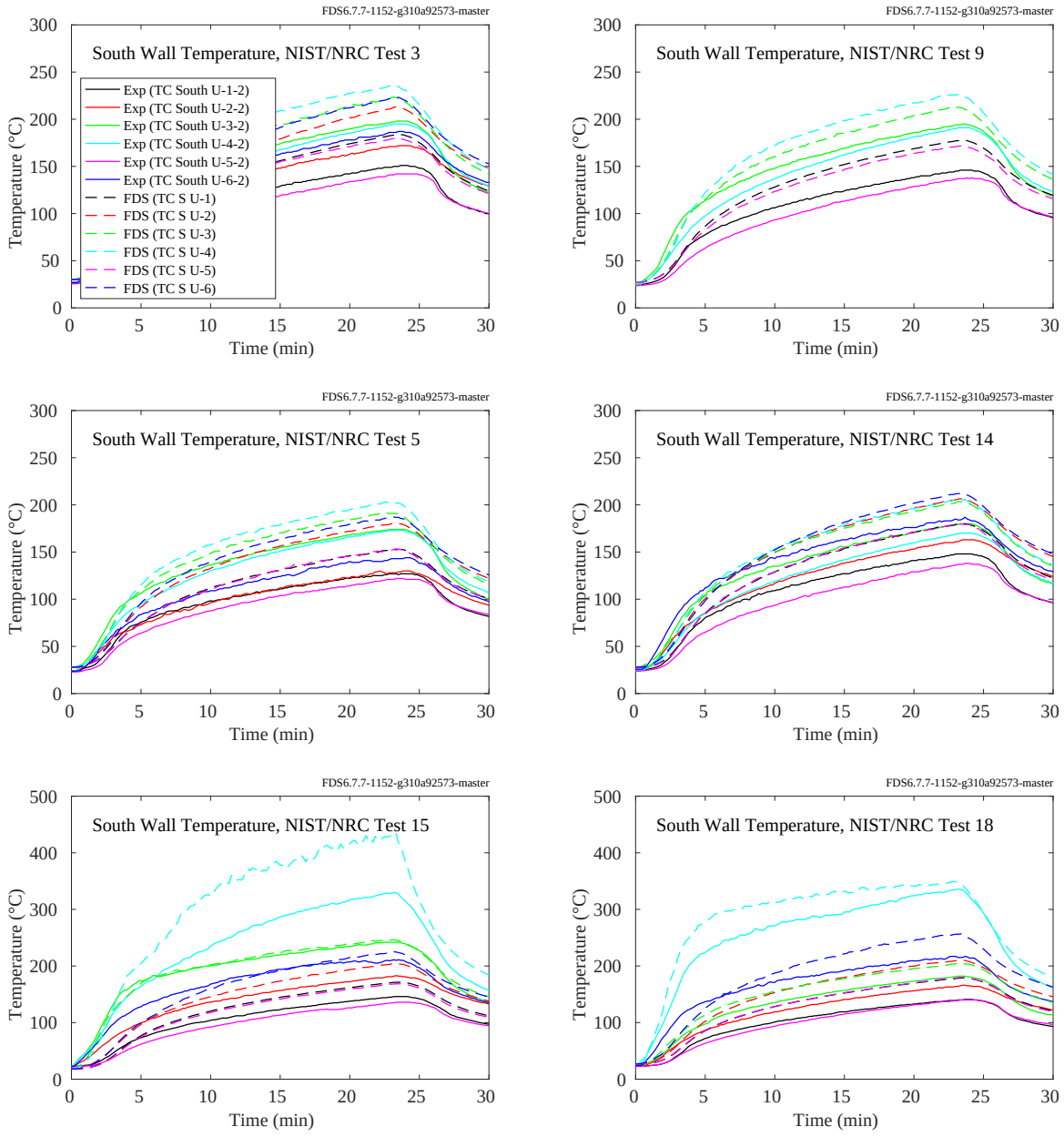

Figure 11.18: NIST/NRC experiments, south wall temperatures, Tests 3, 5, 9, 14, 15, 18.

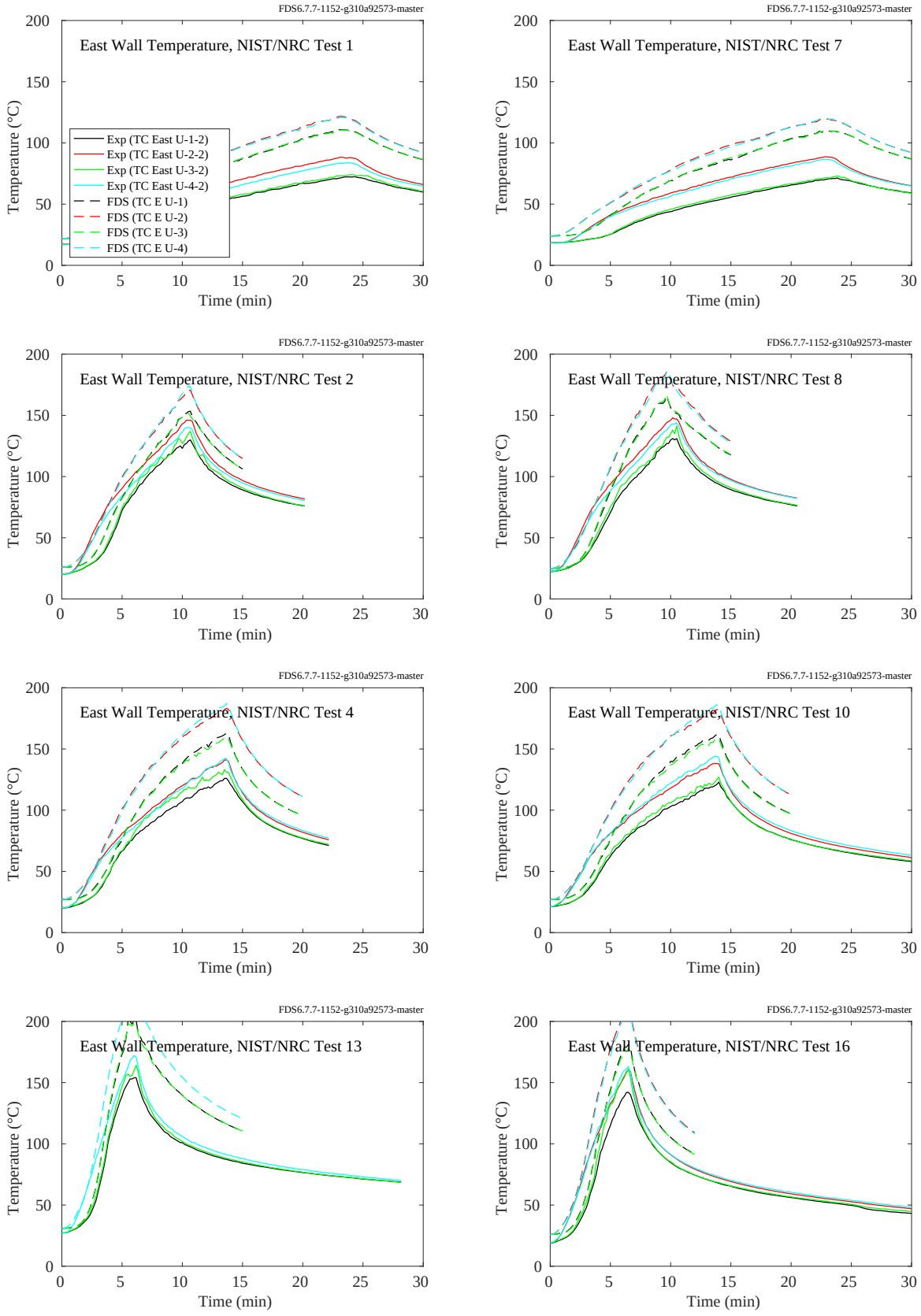

Figure 11.19: NIST/NRC experiments, east wall temperatures, Tests 1, 2, 4, 7, 8, 10, 13, 16.

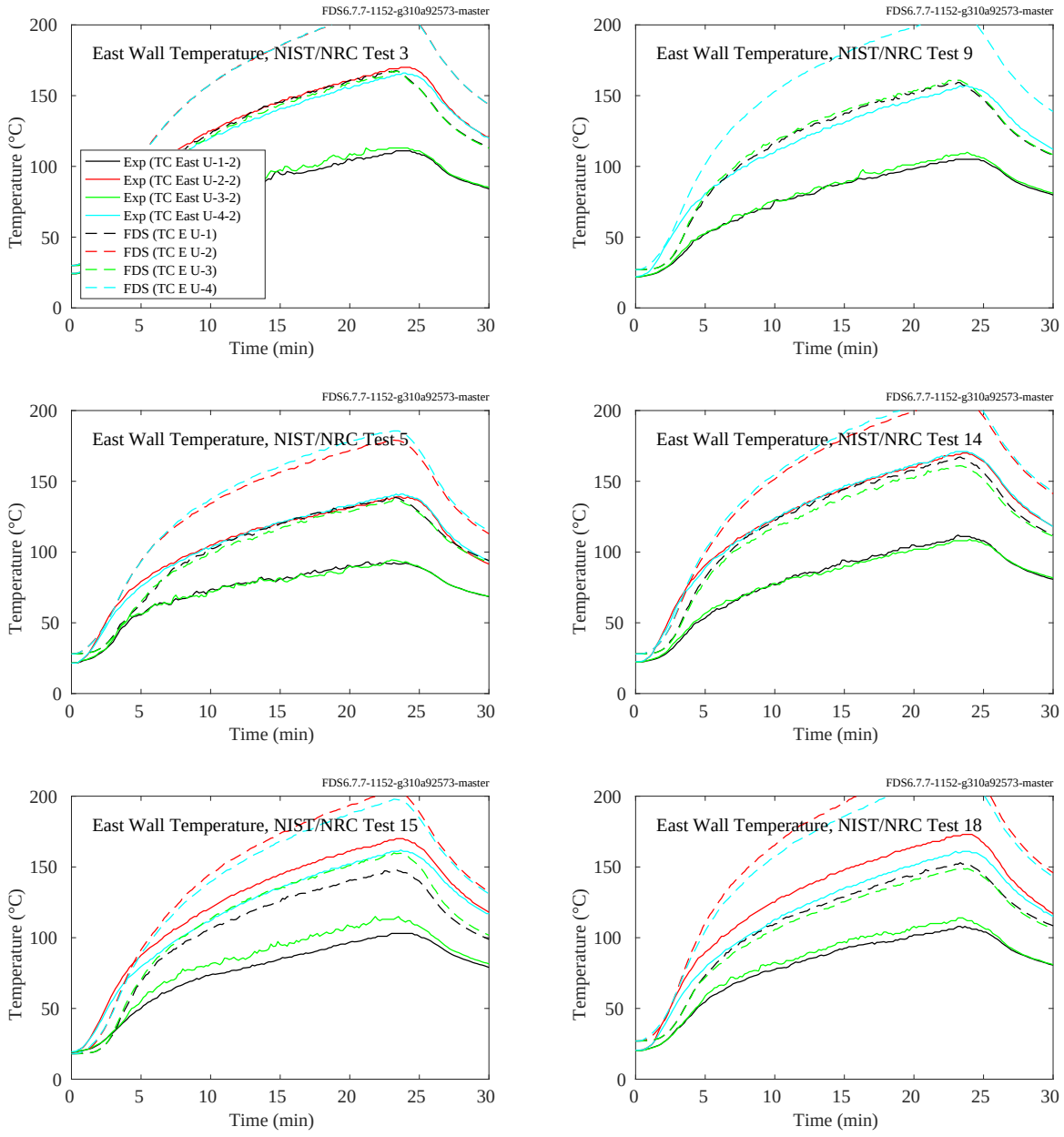

Figure 11.20: NIST/NRC experiments, east wall temperatures, Tests 3, 5, 9, 14, 15, 18.

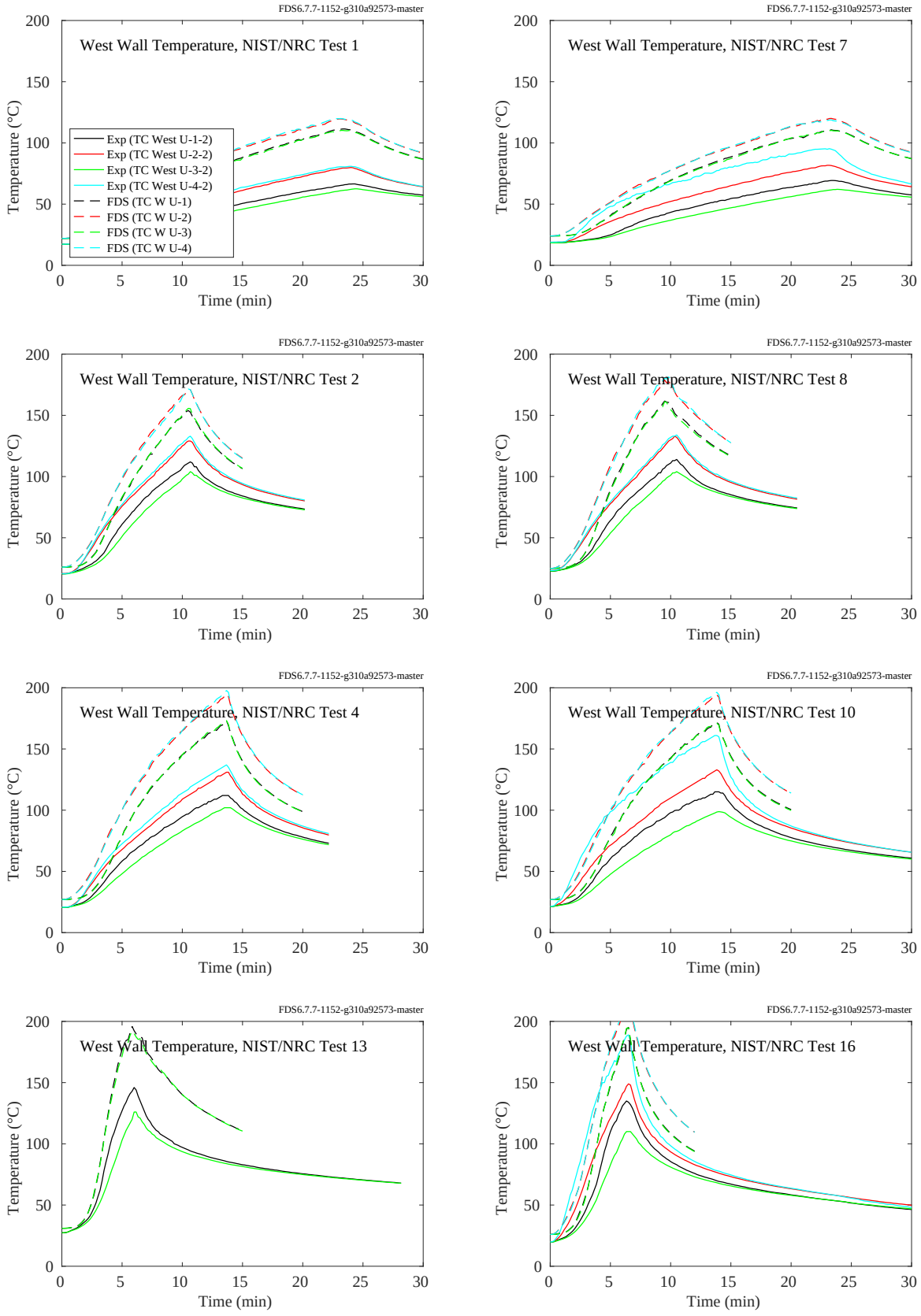

Figure 11.21: NIST/NRC experiments, west wall temperatures, Tests 1, 2, 4, 7, 8, 10, 13, 16.

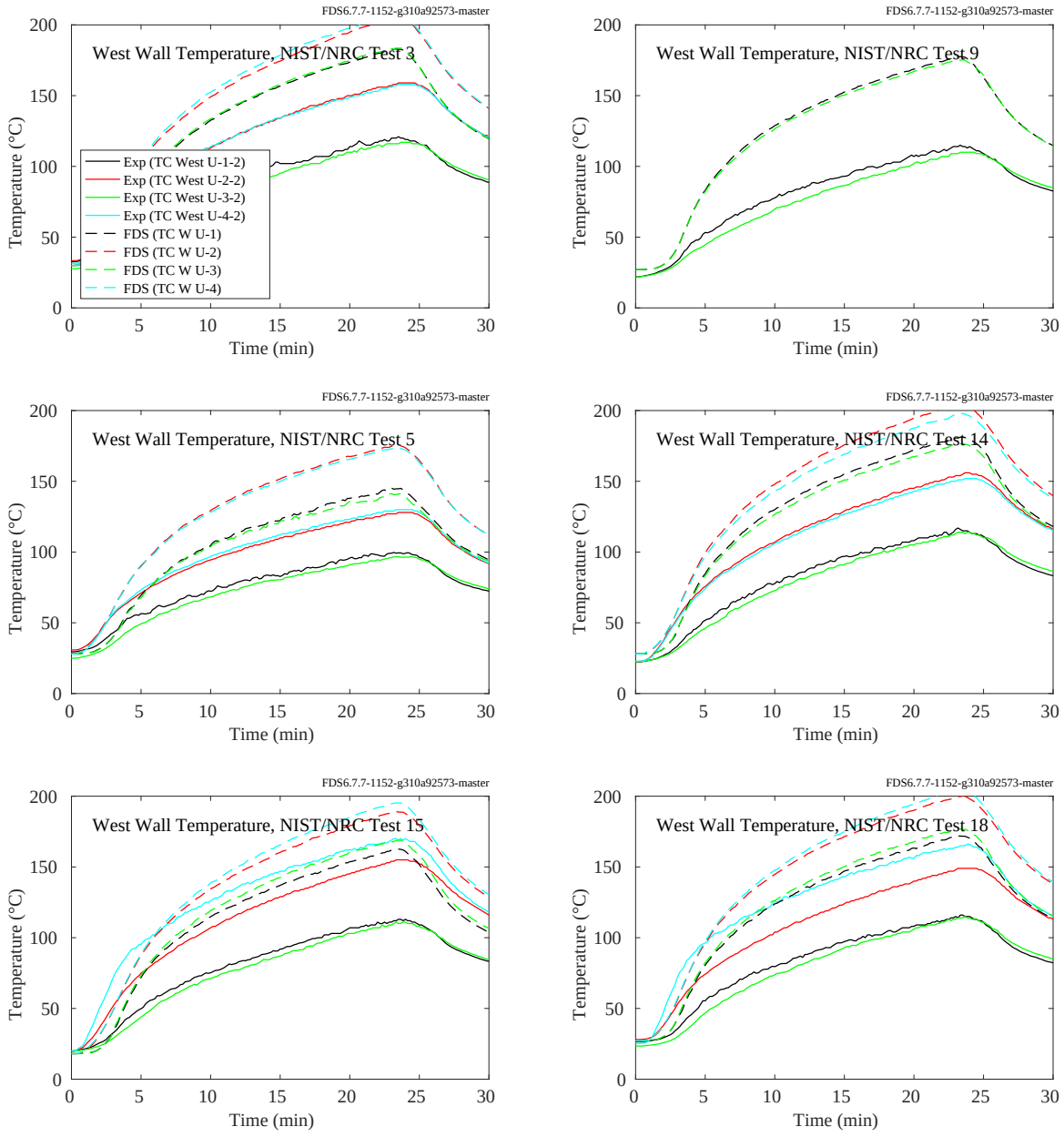

Figure 11.22: NIST/NRC experiments, west wall temperatures, Tests 3, 5, 9, 14, 15, 18.

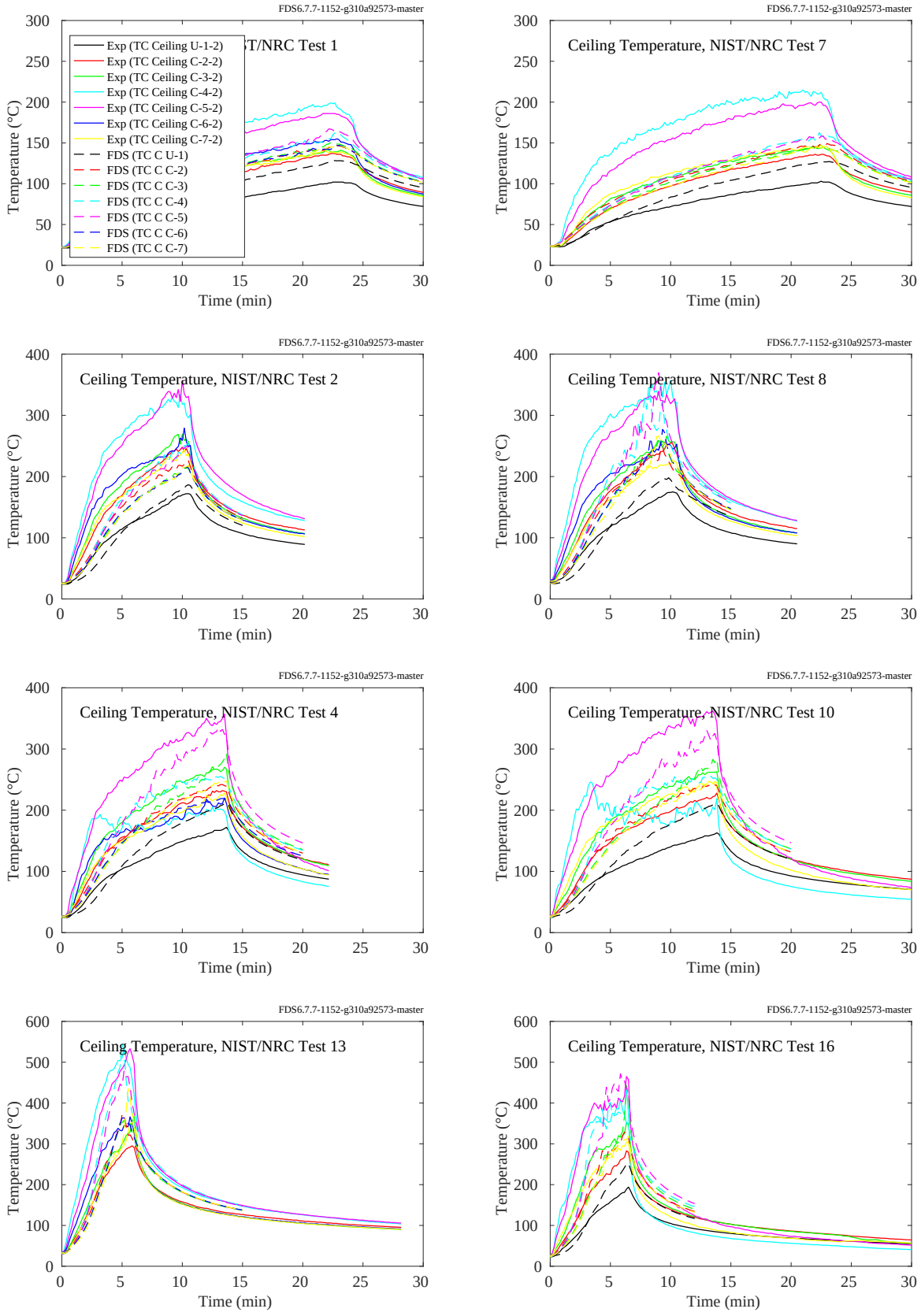

Figure 11.23: NIST/NRC experiments, ceiling temperatures, Tests 1, 2, 4, 7, 8, 10, 13, 16.

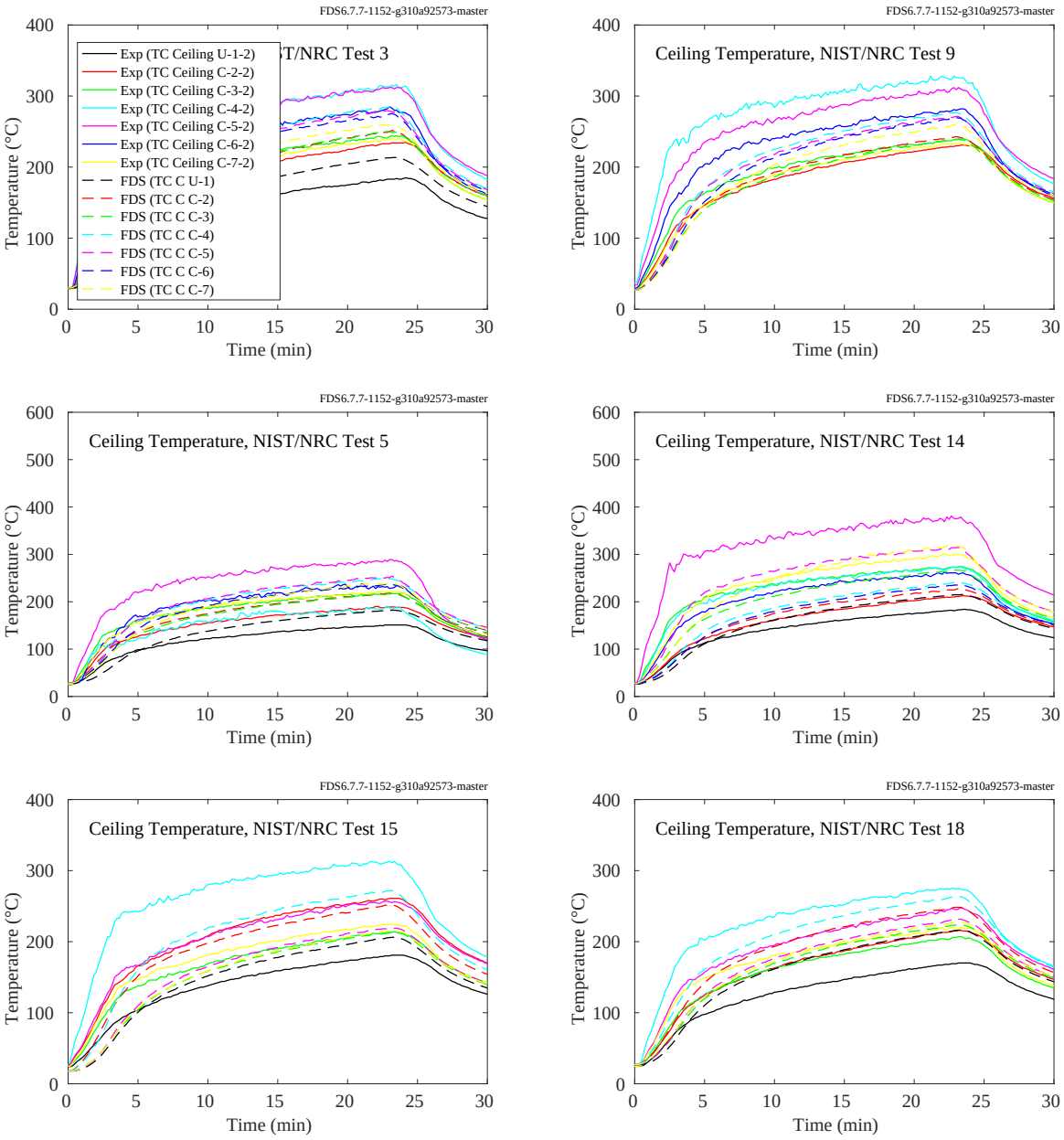

Figure 11.24: NIST/NRC experiments, ceiling temperatures, Tests 3, 5, 9, 14, 15, 18.

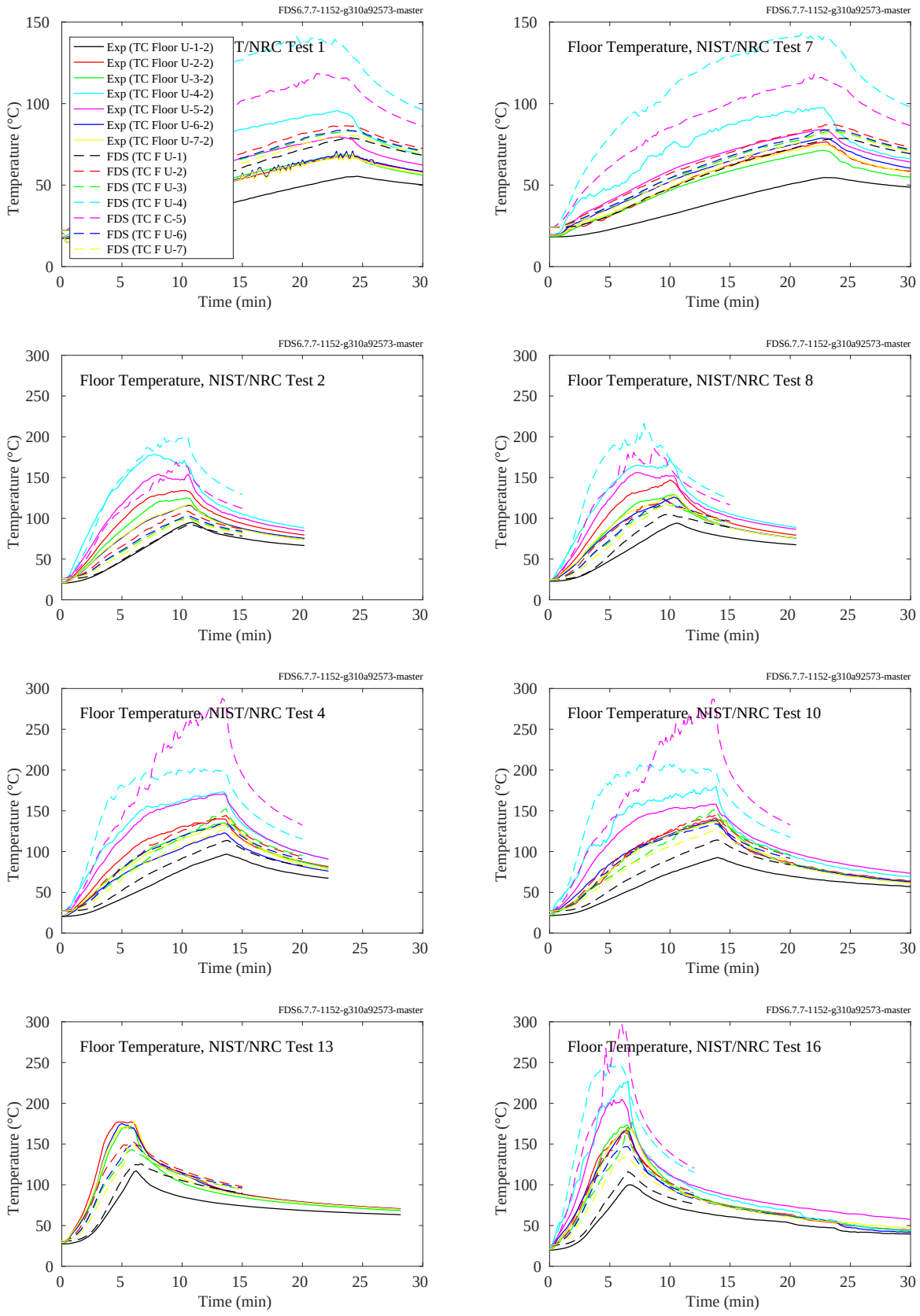

Figure 11.25: NIST/NRC experiments, floor wall temperatures, Tests 1, 2, 4, 7, 8, 10, 13, 16.

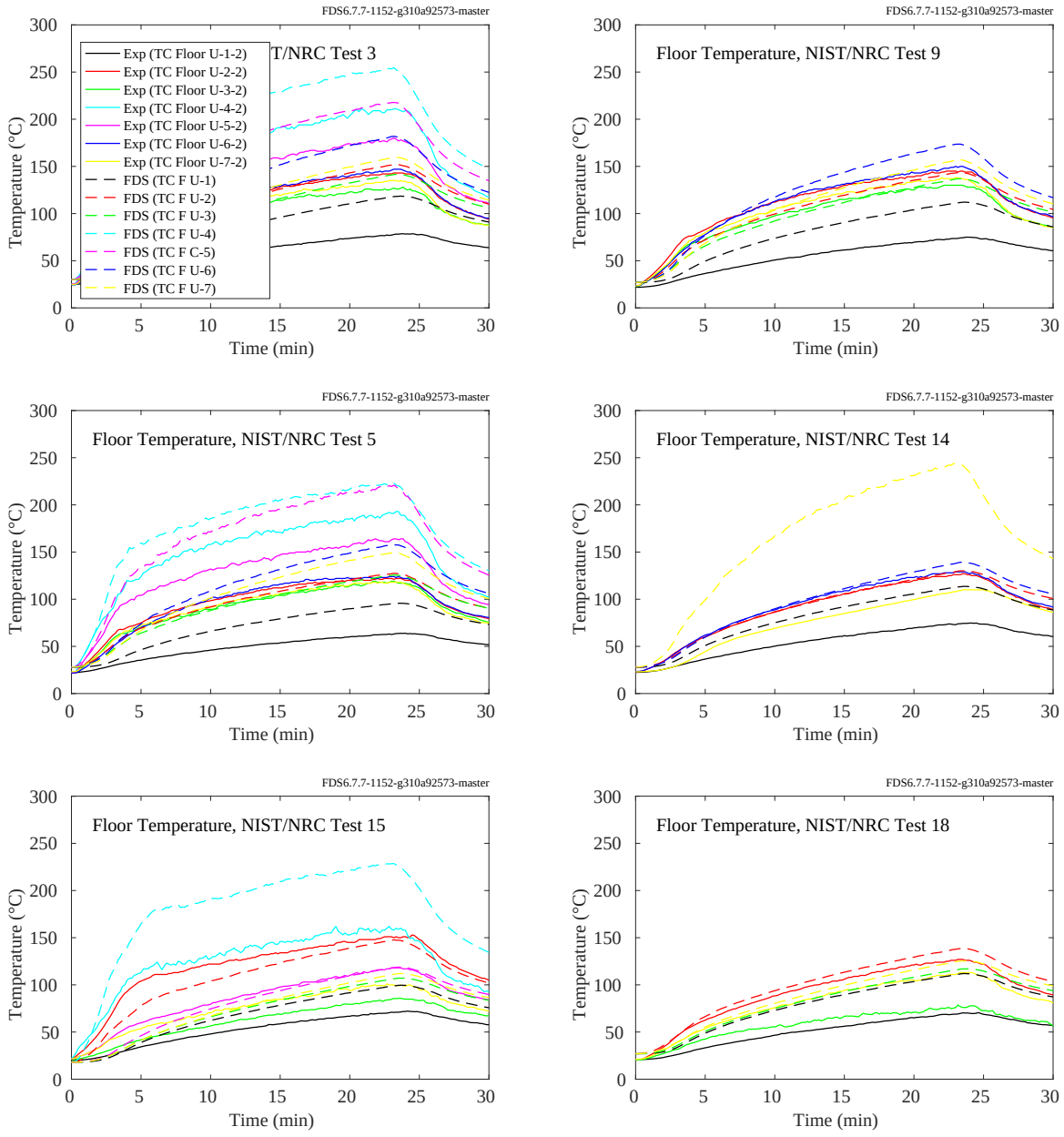

Figure 11.26: NIST/NRC experiments, floor temperatures, Tests 3, 5, 9, 14, 15, 18.

11.1.5 PRISME DOOR Experiments

Thermocouples were positioned at various points on the walls. Each room contained a vertical array labeled, for example, TP_L1_NE265. The TP indicates a surface temperature measurement, L1 indicates compartment 1, which is where the fire was located, NE indicates northeast corner of the room, and 265 indicates the number of centimeters above the floor. In addition, each room contained four measurement points centered on each wall at a height of approximately 260 cm. These points are labeled, for example, TP_L2_SC265, compartment 2, center of south wall, 265 cm high.

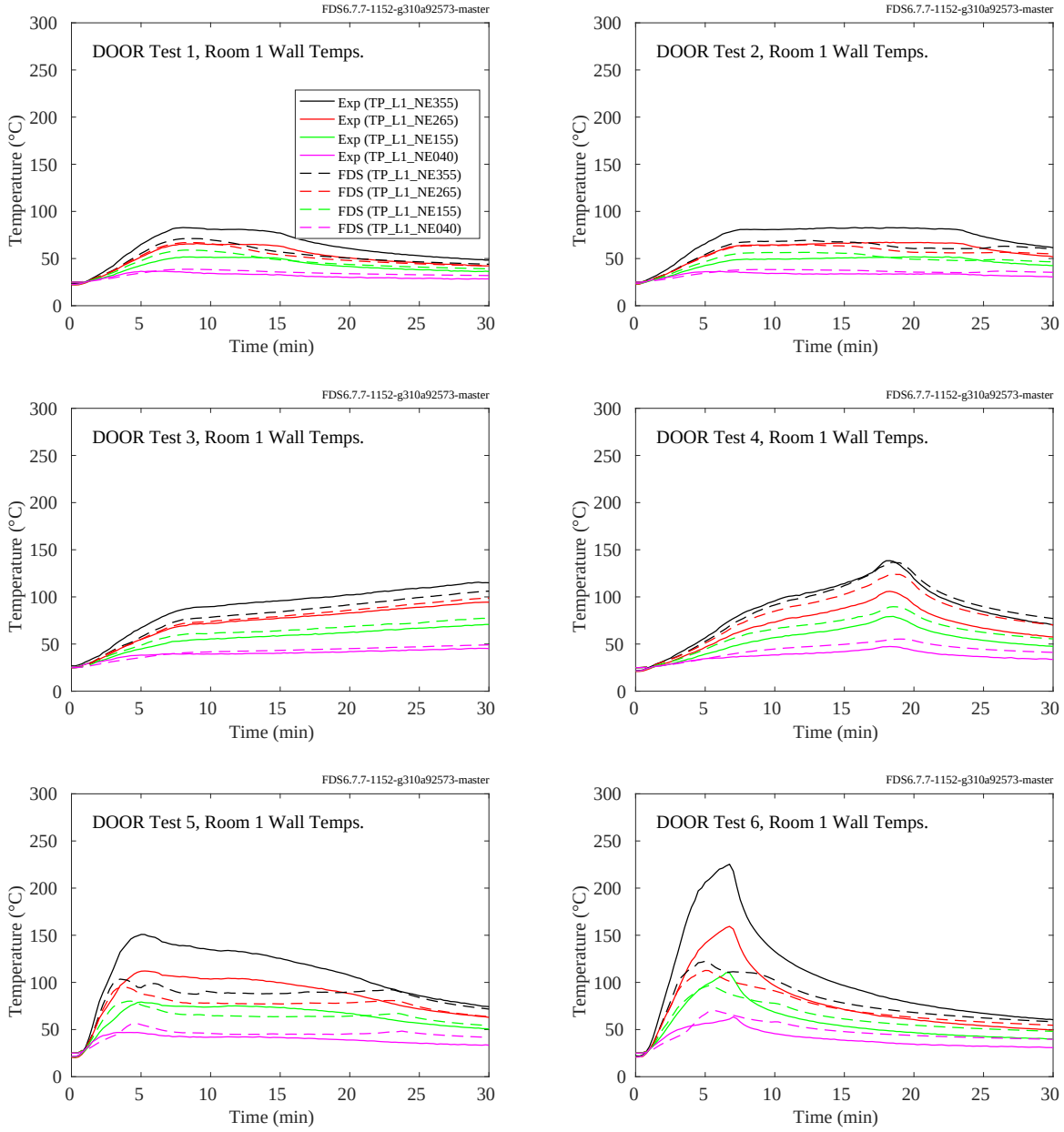

Figure 11.27: PRISME DOOR experiments, wall temperatures, vertical array, Room 1.

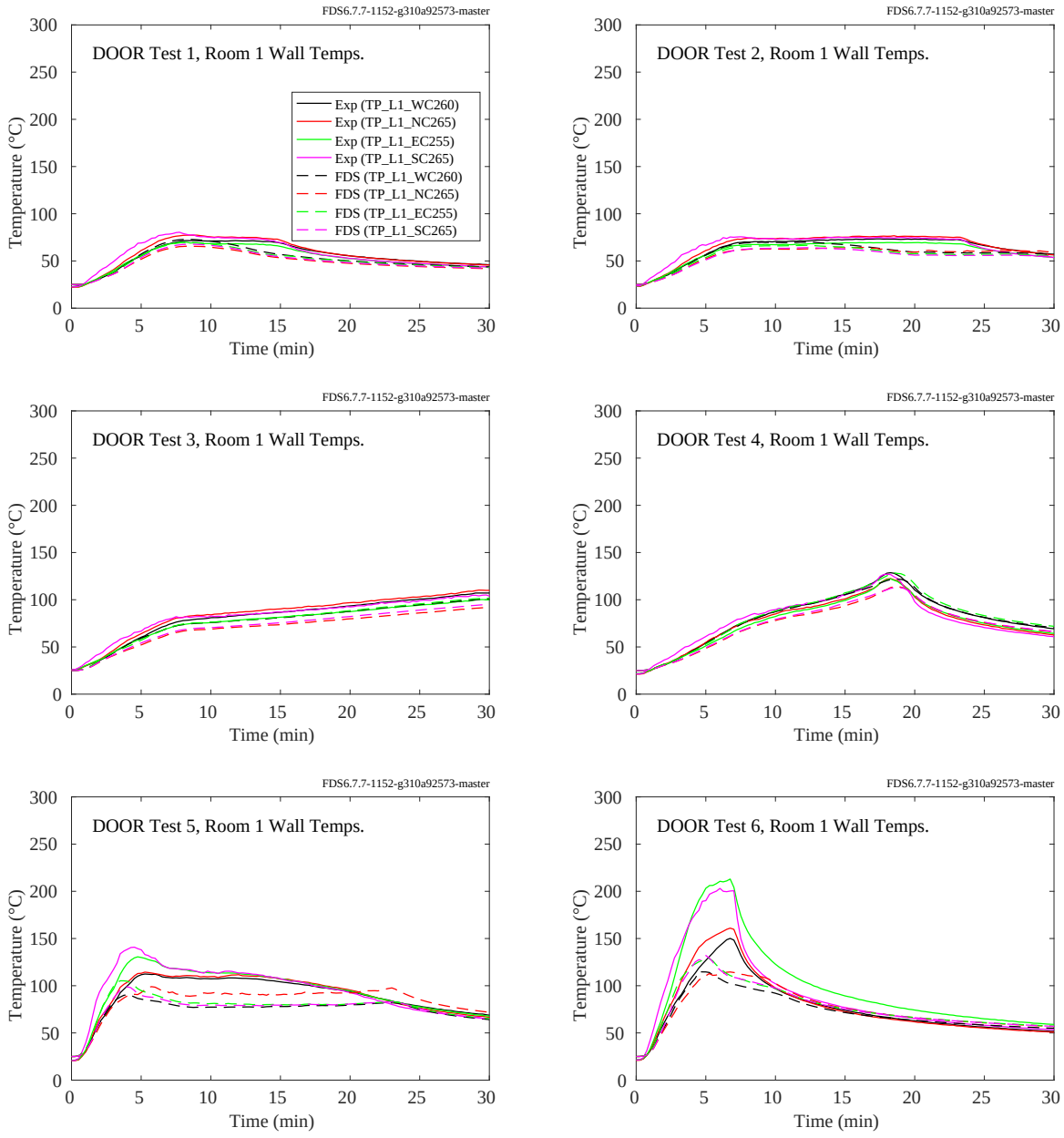

Figure 11.28: PRISME DOOR experiments, wall temperatures, four sides, Room 1.

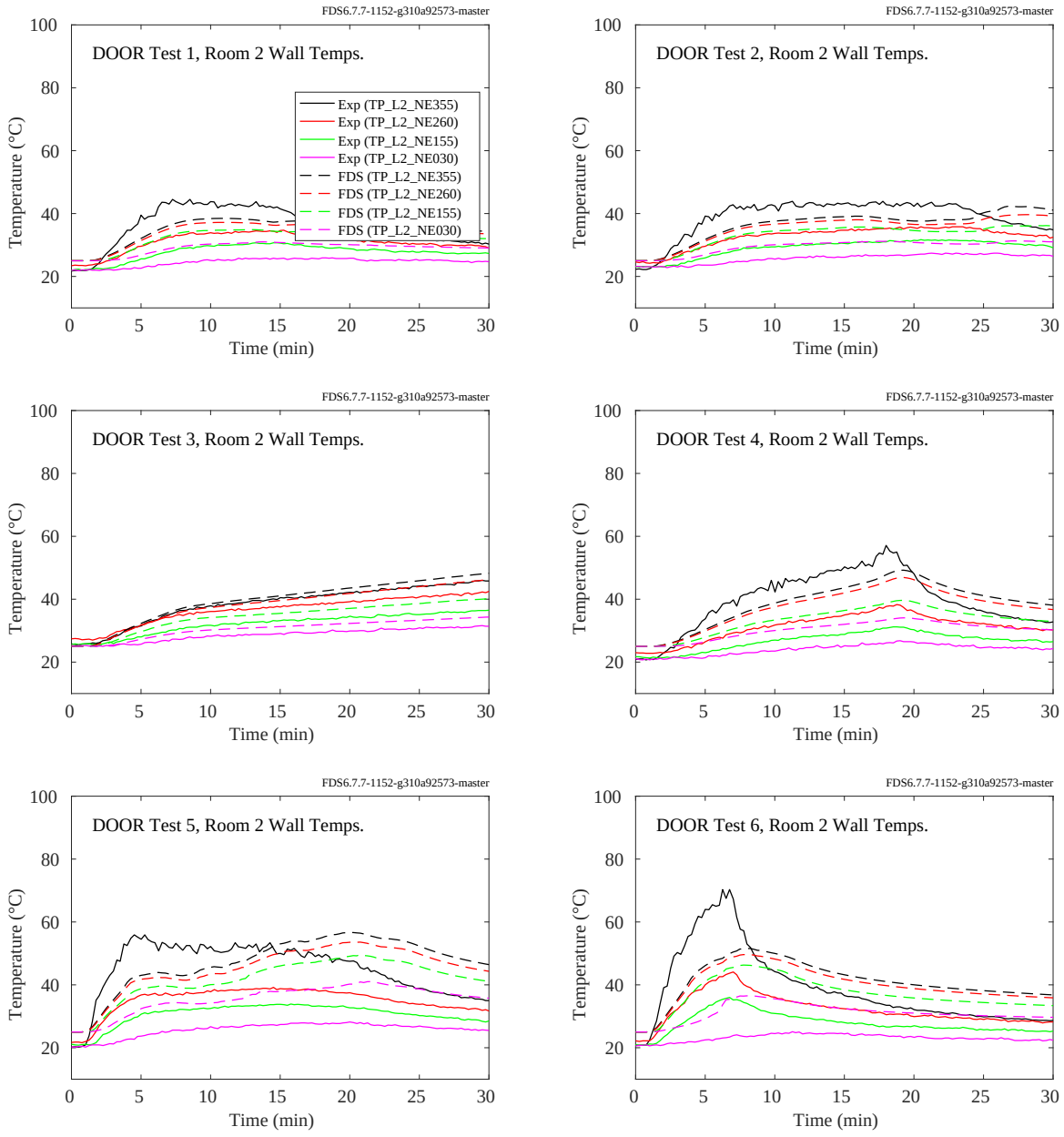

Figure 11.29: PRISME DOOR experiments, wall temperatures, vertical array, Room 2.

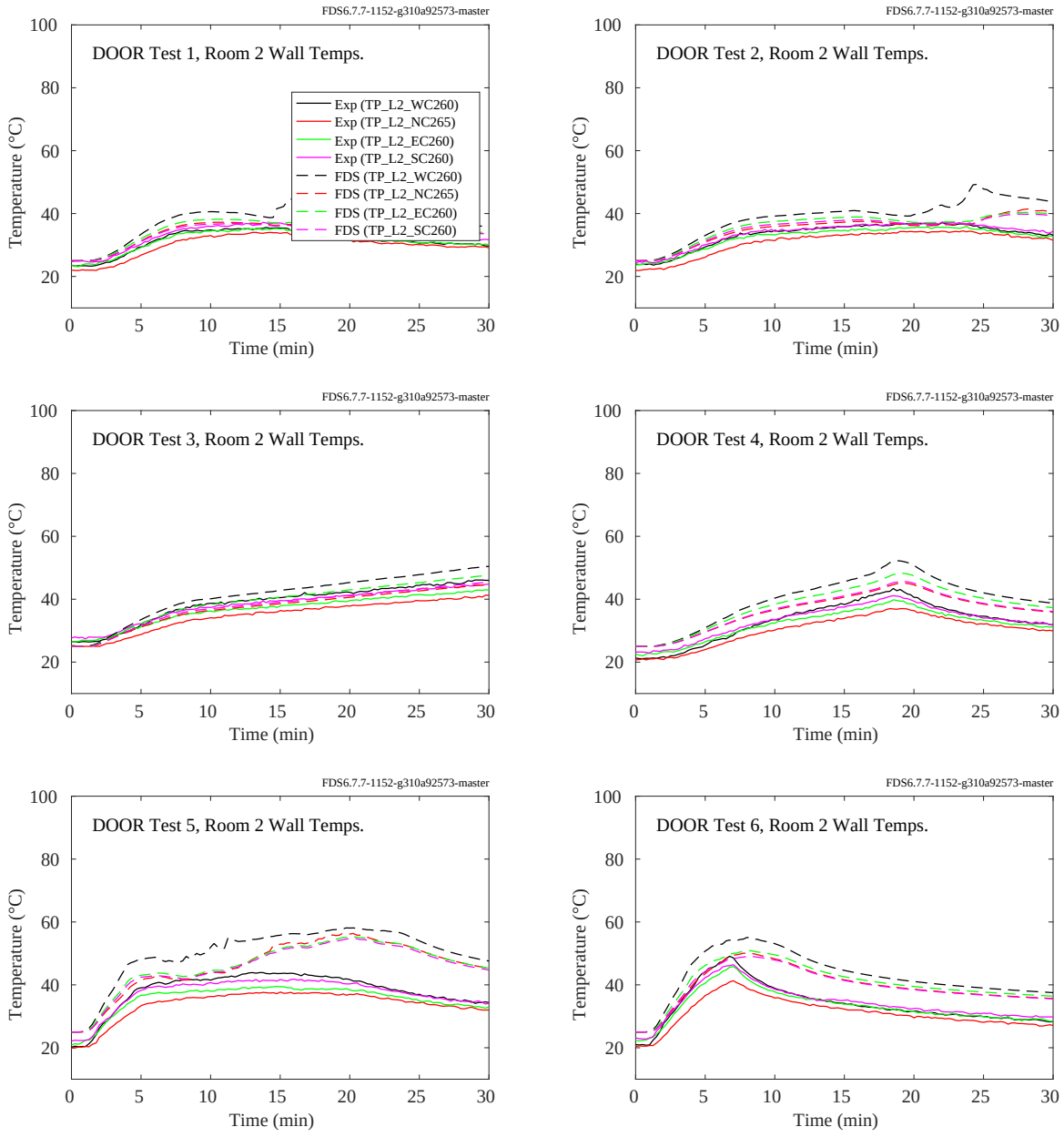

Figure 11.30: PRISME DOOR experiments, wall temperatures, four sides, Room 2.

11.1.6 PRISME SOURCE Experiments

Thermocouples were positioned at various points on the walls. The room contained a vertical array labeled, for example, TP_L2_NE265. The TP indicates a surface temperature measurement, L2 indicates compartment 2, which is where the fire was located, NE indicates northeast corner of the room, and 265 indicates the number of centimeters above the floor. In addition, each room contained four measurement points centered on each wall at a height of approximately 260 cm.

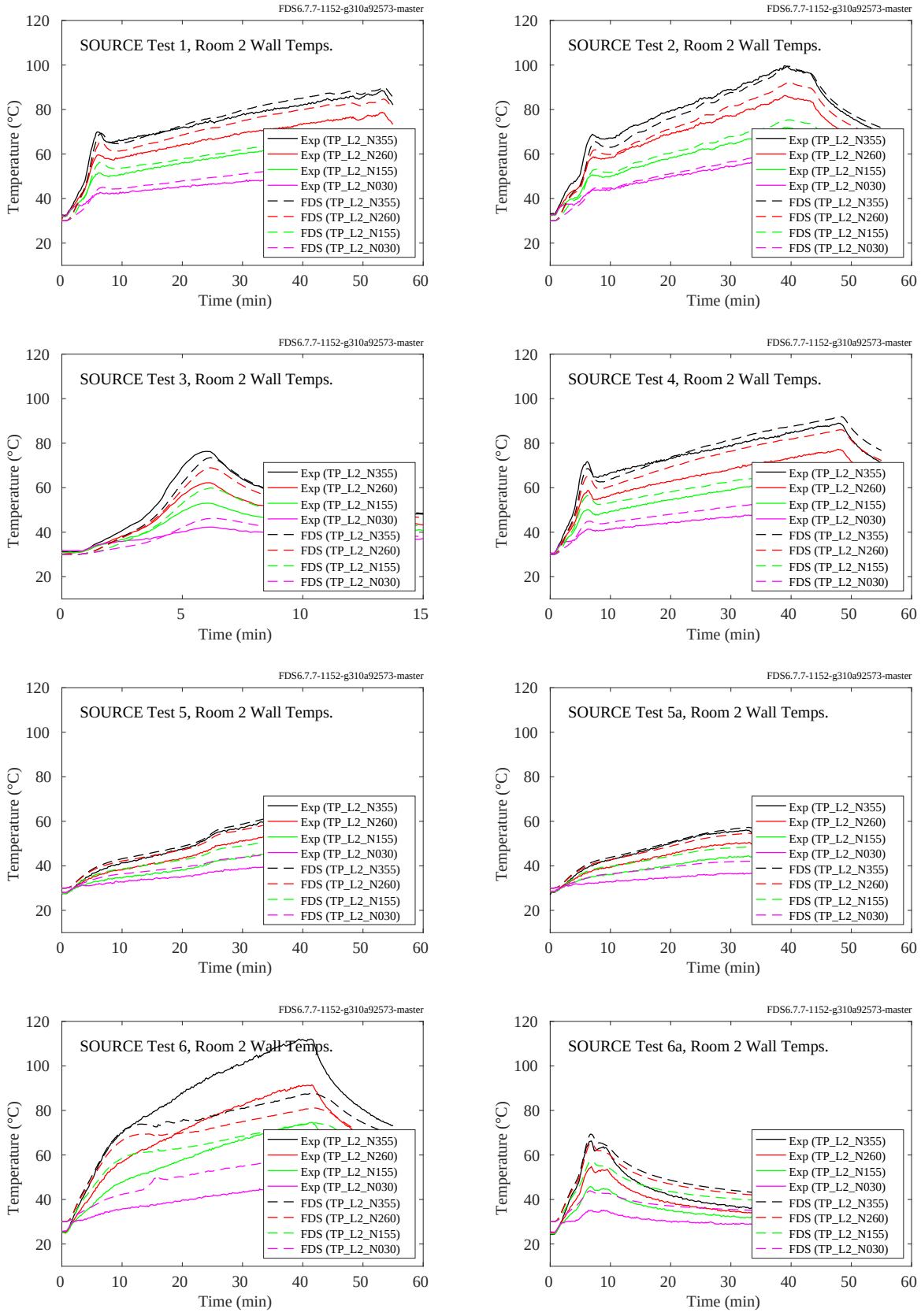

Figure 11.31: PRISME SOURCE experiments, wall temperatures, vertical array, Room 2.

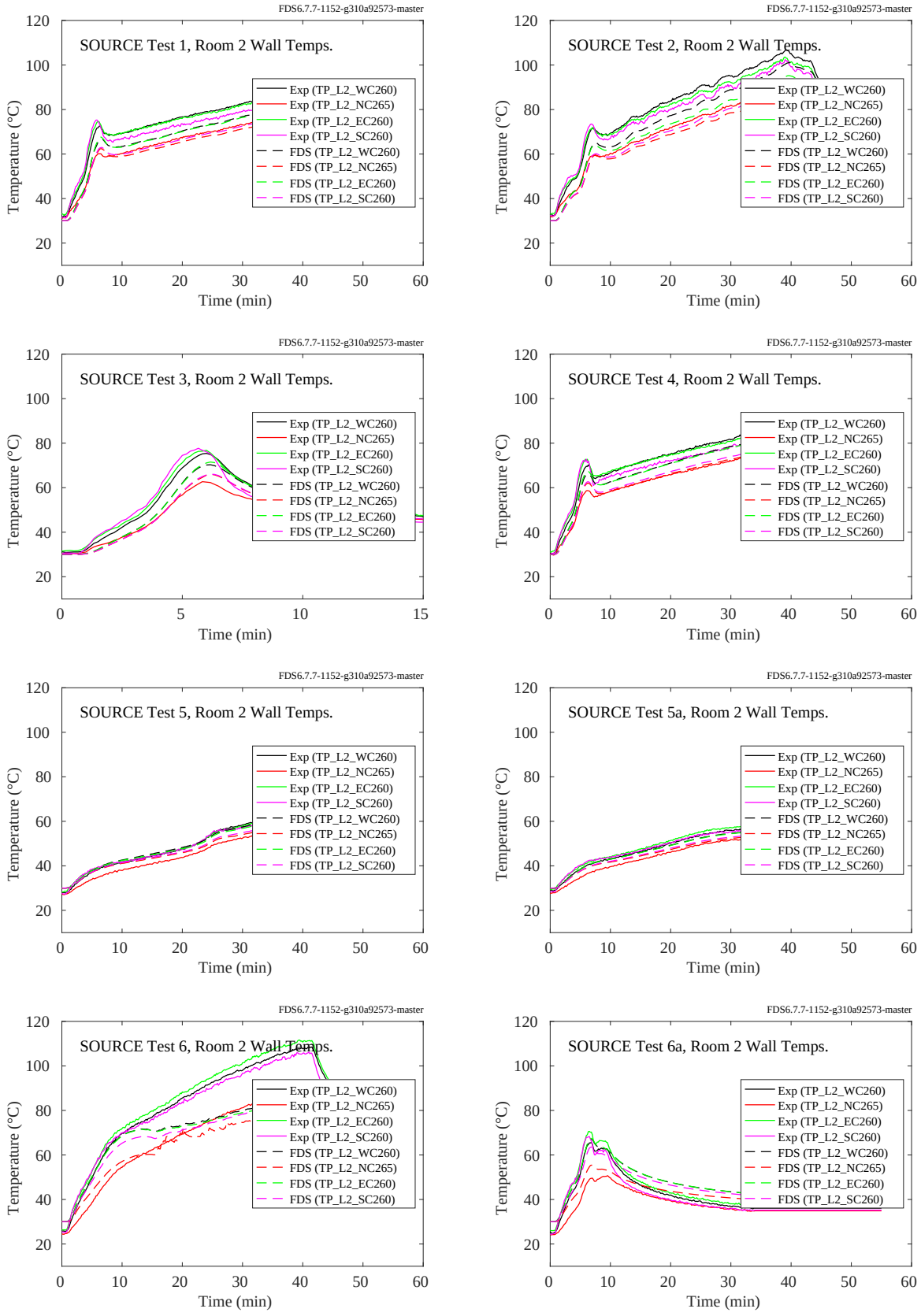

Figure 11.32: PRISME SOURCE experiments, wall temperatures, four sides, Room 2.

11.1.7 WTC Experiments

The following pages contain comparisons of predicted and measured ceiling temperatures, both at the surface and beneath a layer of marinite board. Table 11.2 below lists the coordinates of the measurement locations relative to the center of the fire pan. Names with "IN" appended are measurements made under the marinite board.

Table 11.2: Locations of ceiling surface temperature measurements relative to the fire pan in the WTC series.

Name	x (m)	y (m)	z (m)
TCC	0.62	0.07	3.82
TCN3	0.62	0.67	3.82
TCS3	0.62	-0.53	3.82
TCE7	2.18	0.07	3.82
TCW7	-1.15	0.07	3.82
TCCIN	0.62	0.07	3.83
TCN3IN	0.62	0.67	3.83
TCS3IN	0.62	-0.53	3.83
TCE4IN	1.28	0.07	3.83
TCW4IN	0.05	0.07	3.83

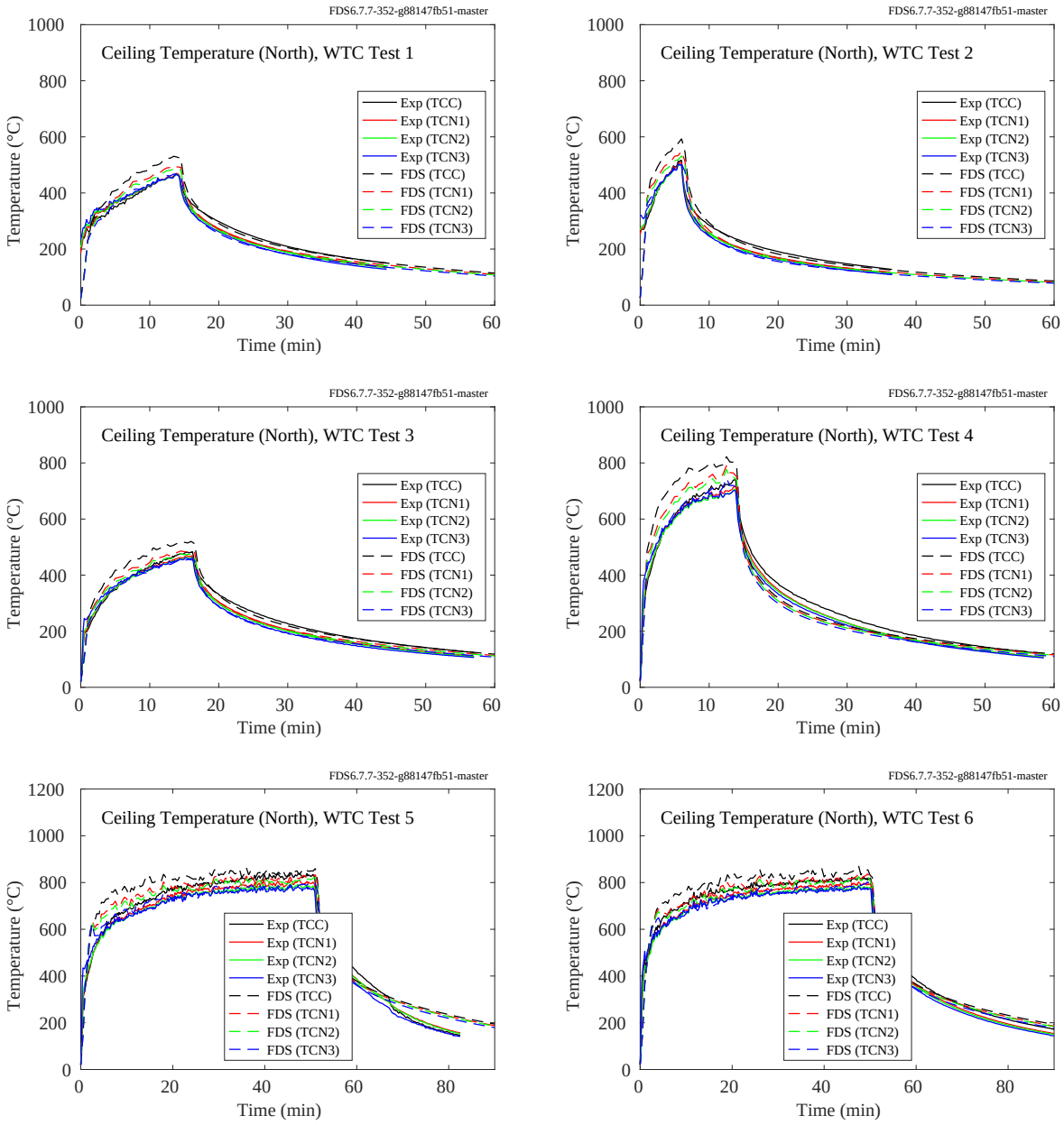

Figure 11.33: WTC experiments, ceiling temperatures, north array.

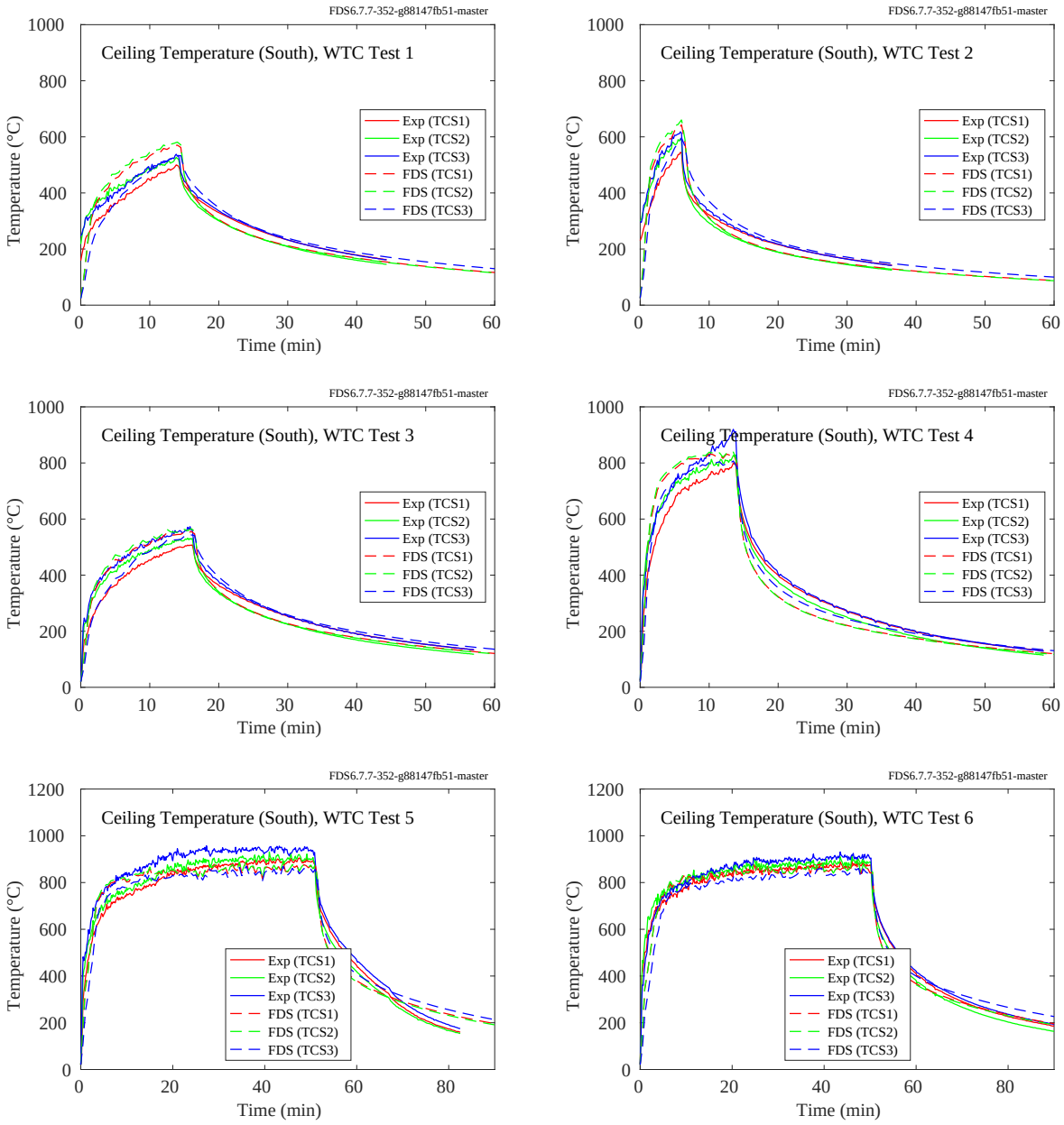

Figure 11.34: WTC experiments, ceiling temperatures, south array.

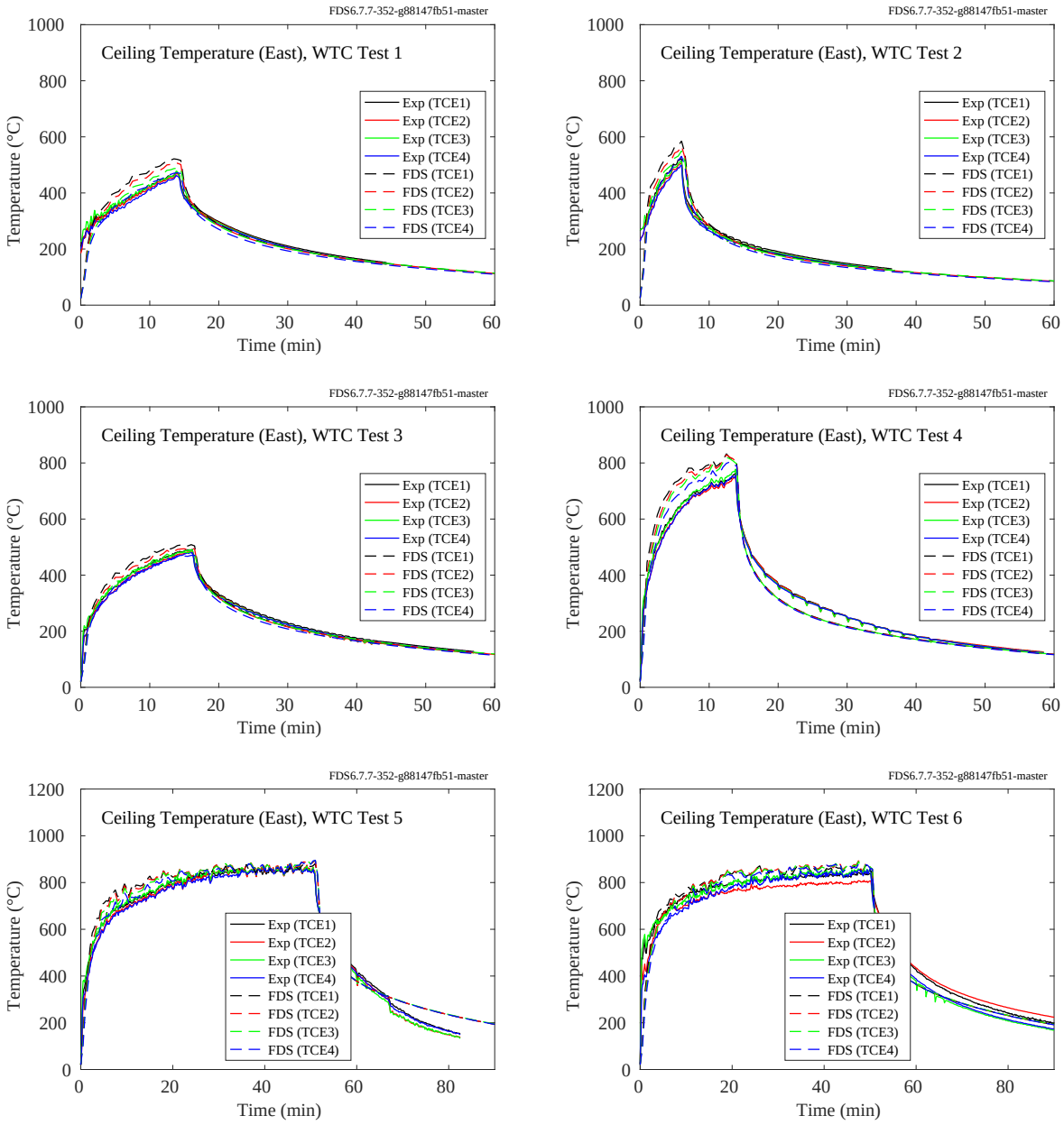

Figure 11.35: WTC experiments, ceiling temperatures, east array, Points 1-4.

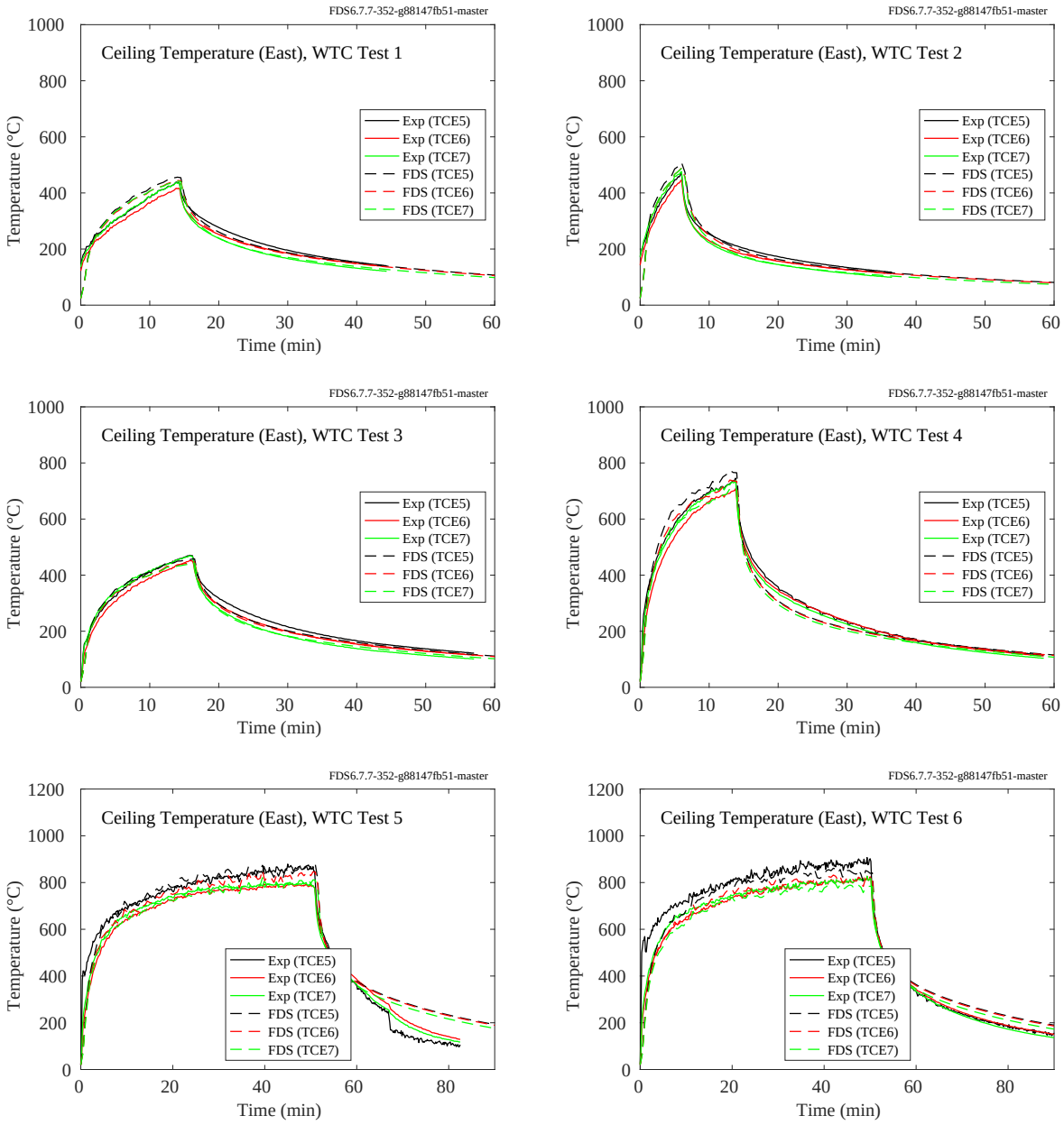

Figure 11.36: WTC experiments, ceiling temperatures, east array, Points 5-7.

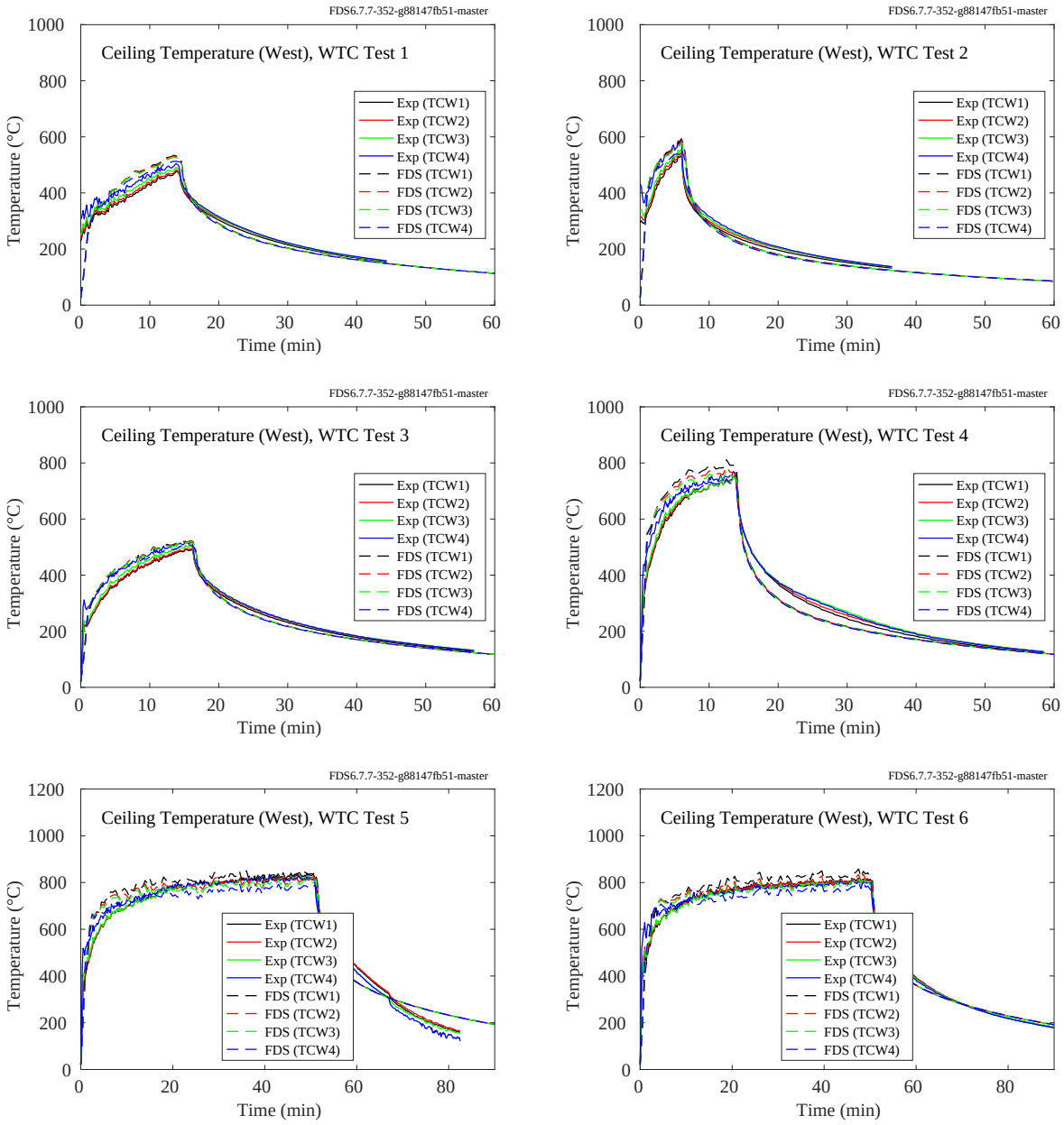

Figure 11.37: WTC experiments, ceiling temperatures, west array, Points 1-4.

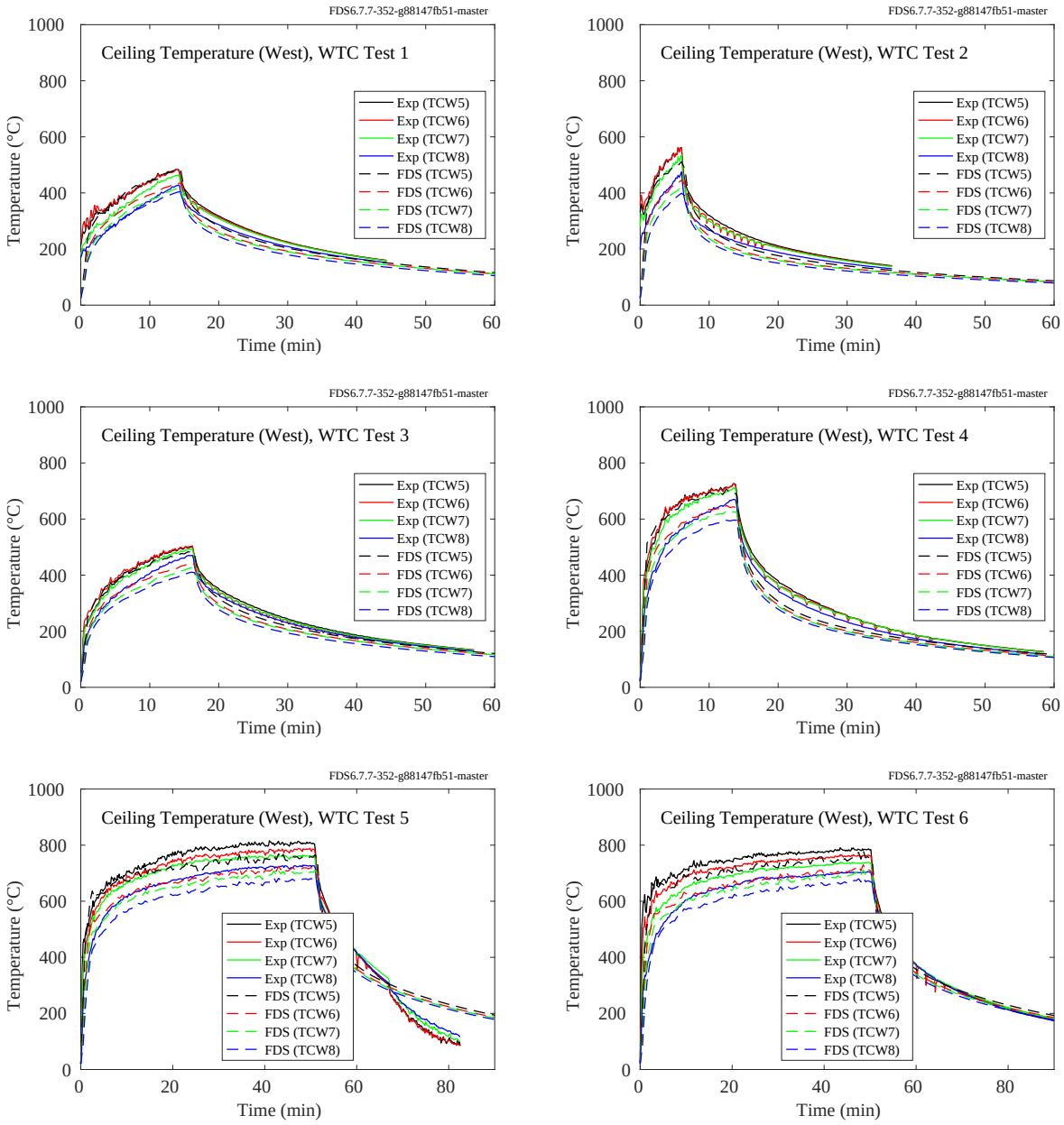

Figure 11.38: WTC experiments, ceiling temperatures, west array, Points 5-8.

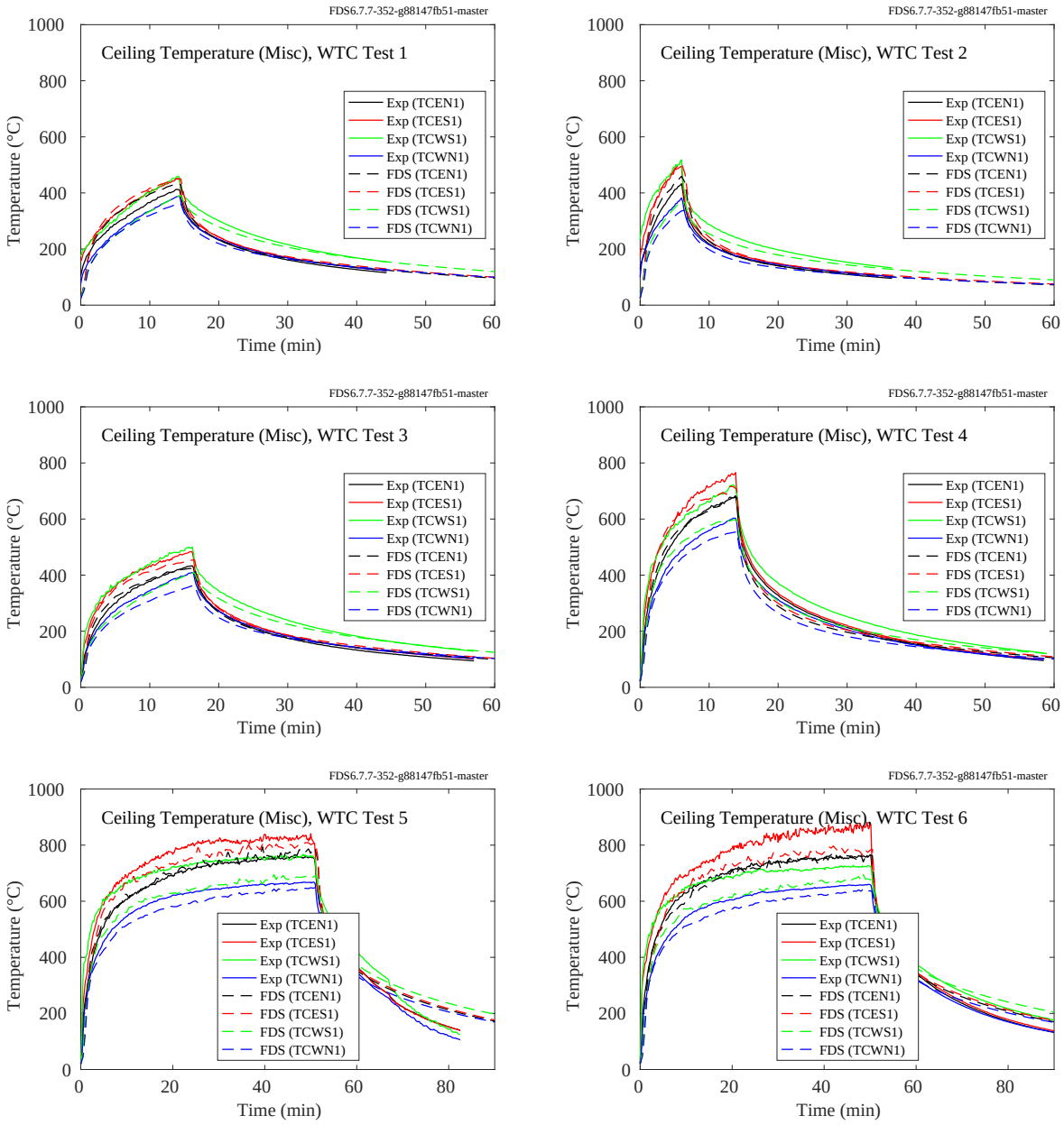

Figure 11.39: WTC experiments, ceiling temperatures, diagonal array.

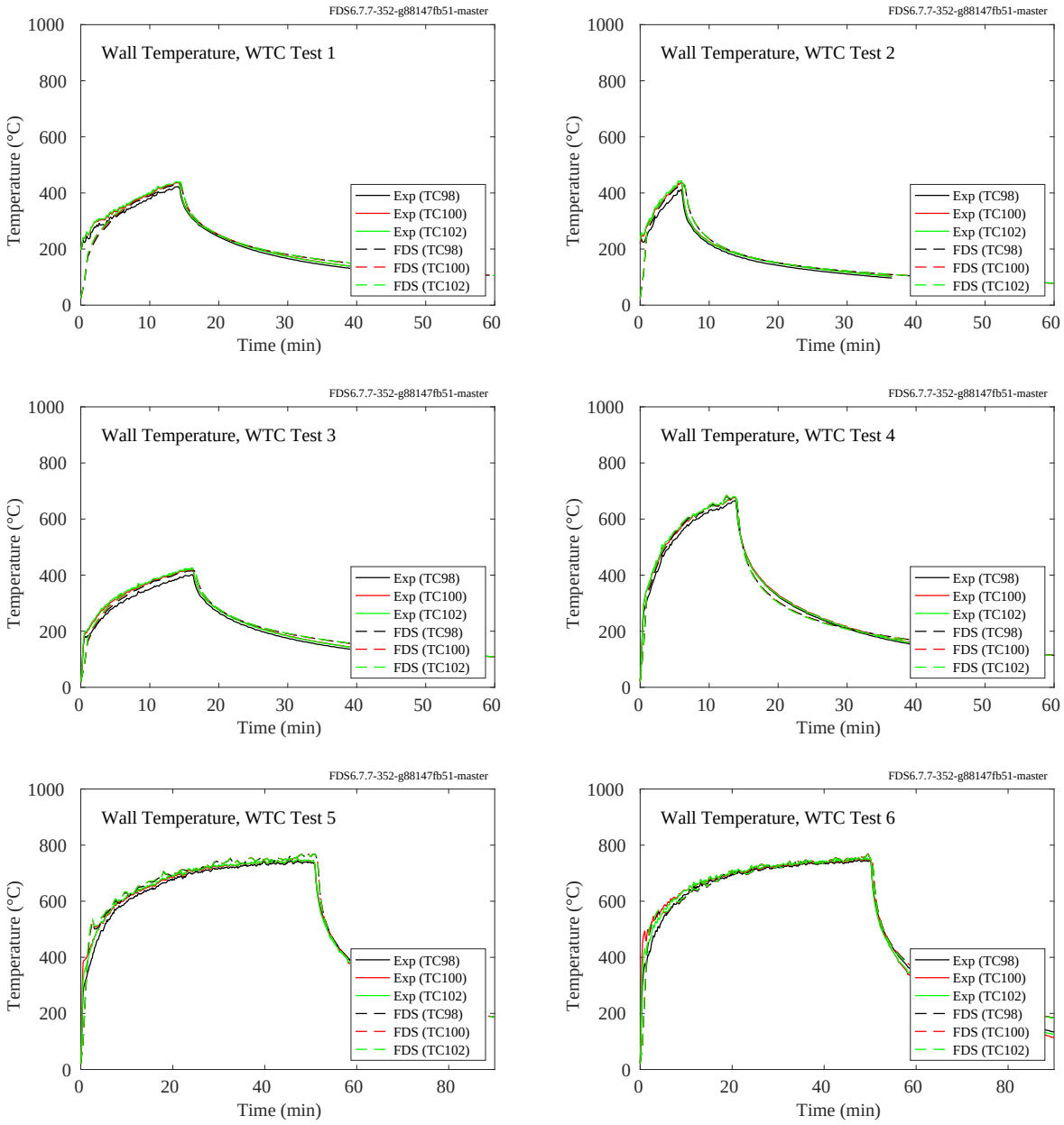

Figure 11.40: WTC experiments, wall temperatures, Points 98, 100, 102.

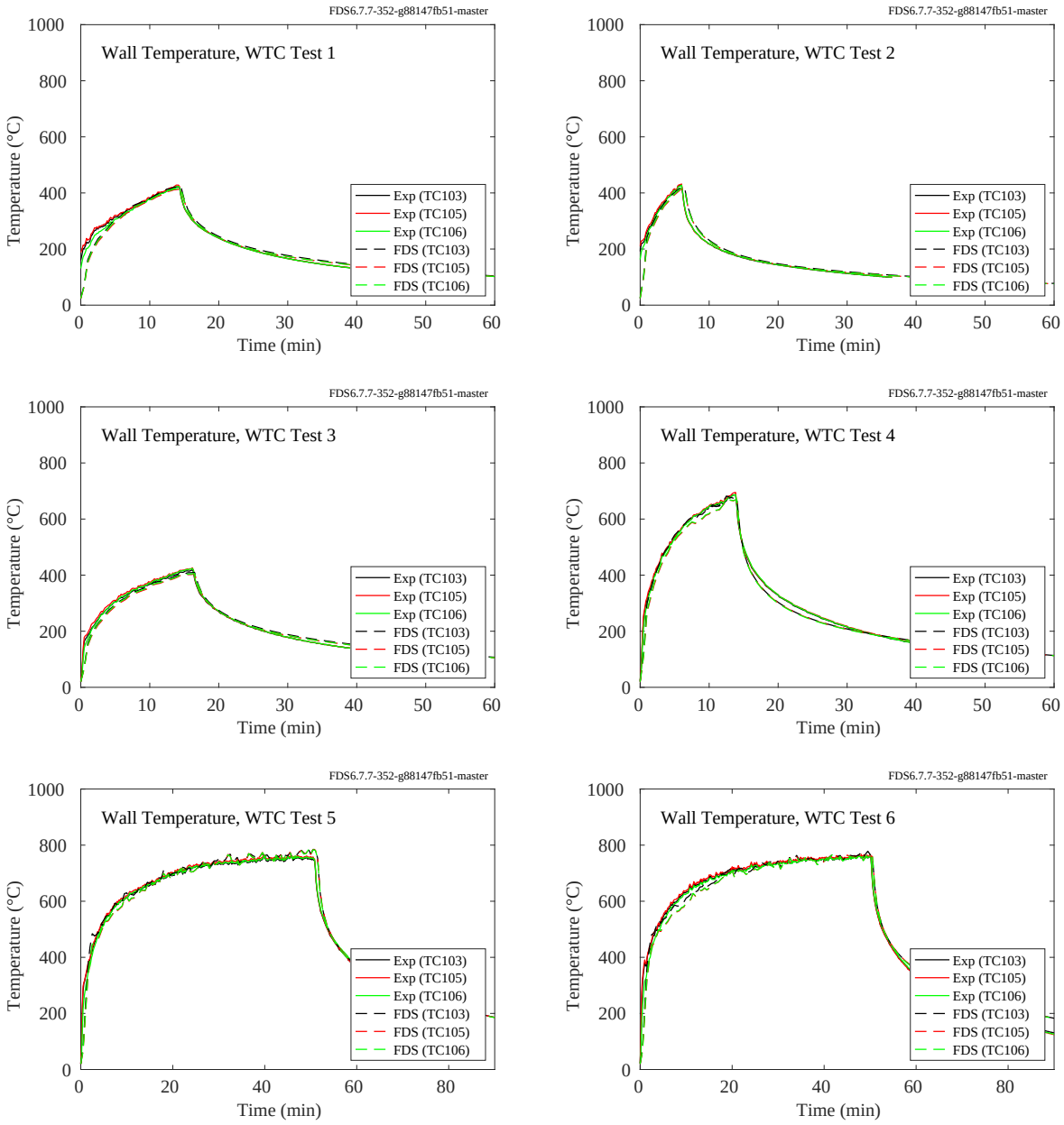

Figure 11.41: WTC experiments, wall temperatures, Points 103, 105, 106.

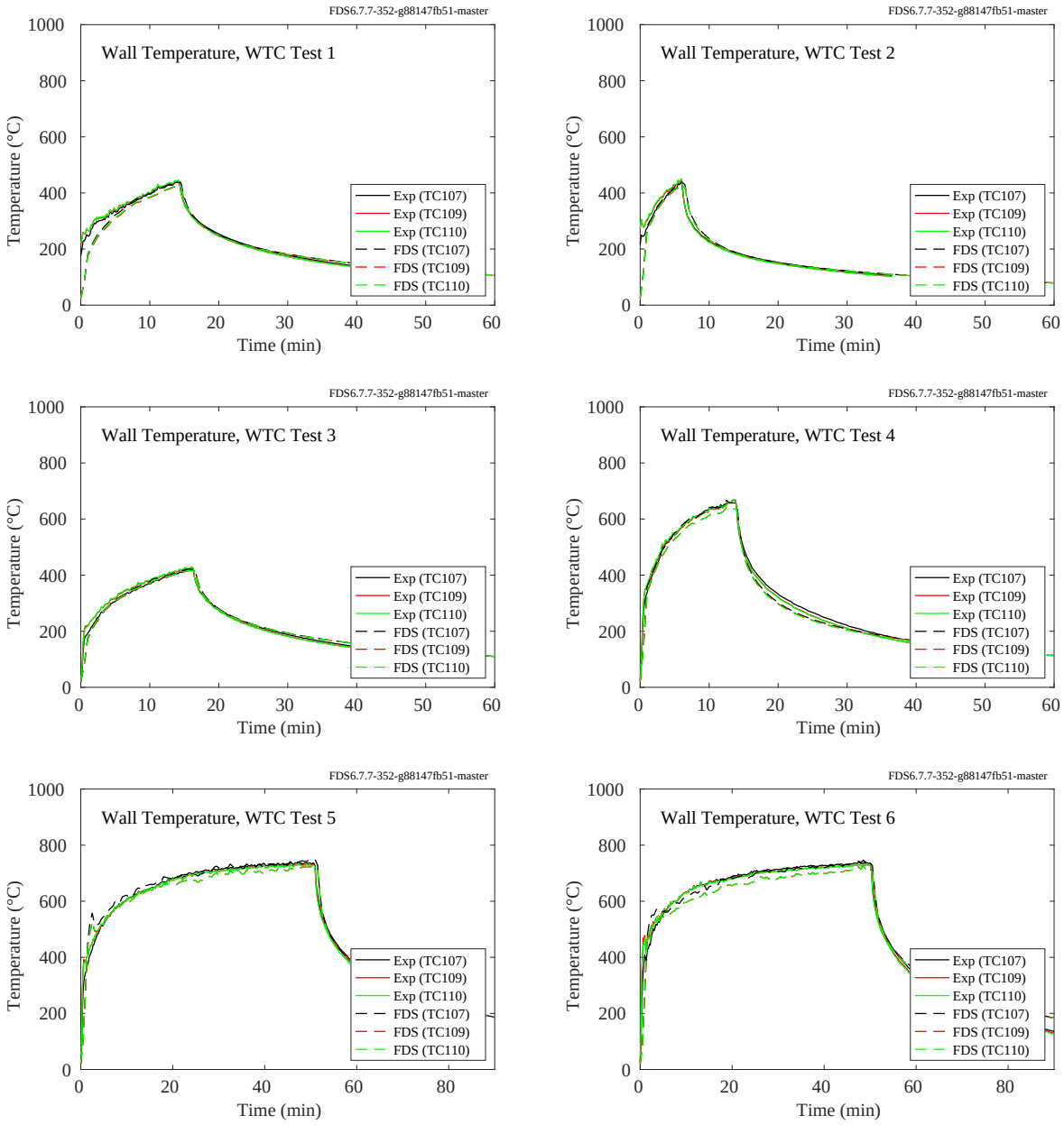

Figure 11.42: WTC experiments, wall temperatures, Points 107, 109, 110.

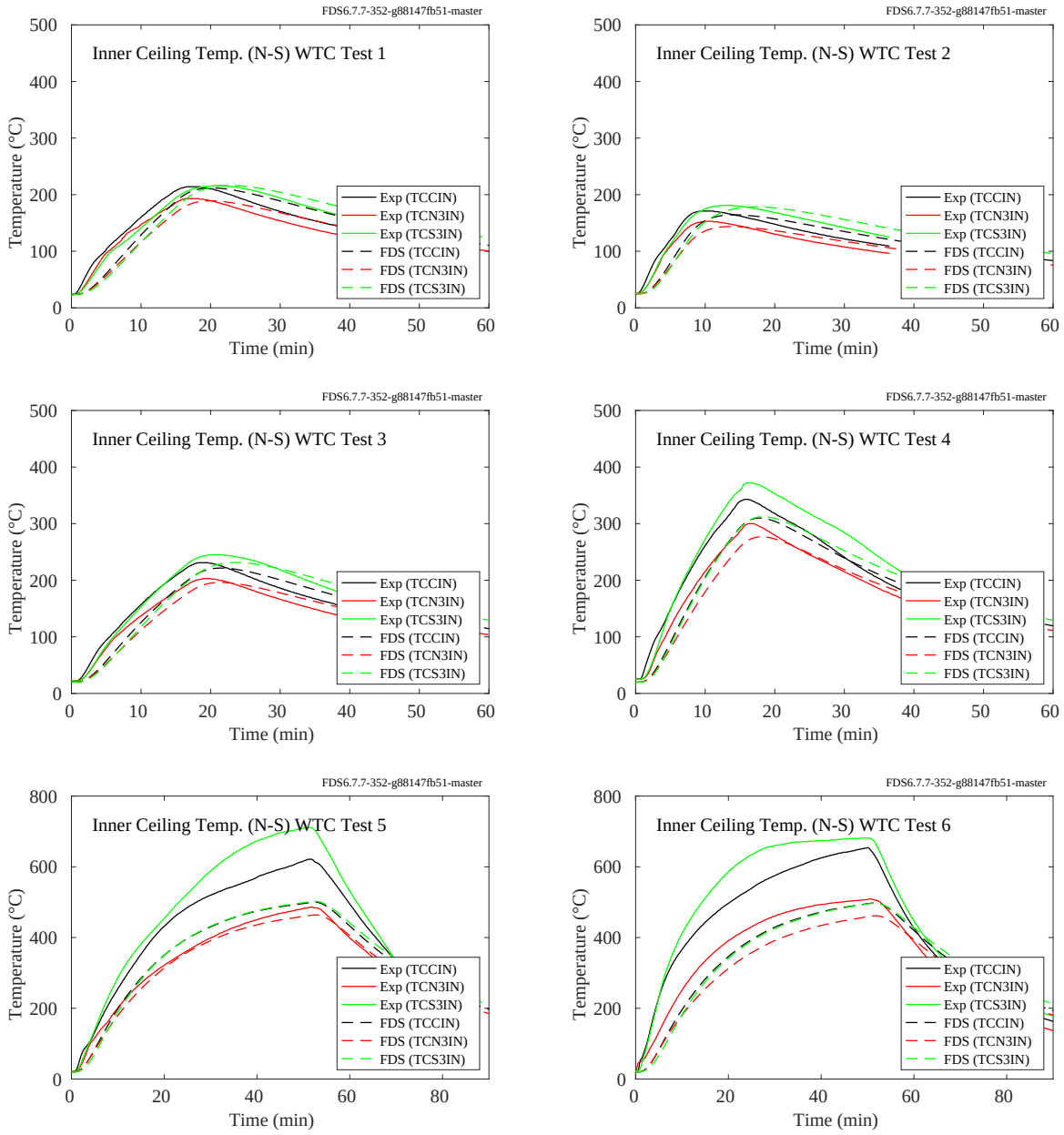

Figure 11.43: WTC experiments, inner ceiling temperatures, north-south axis.

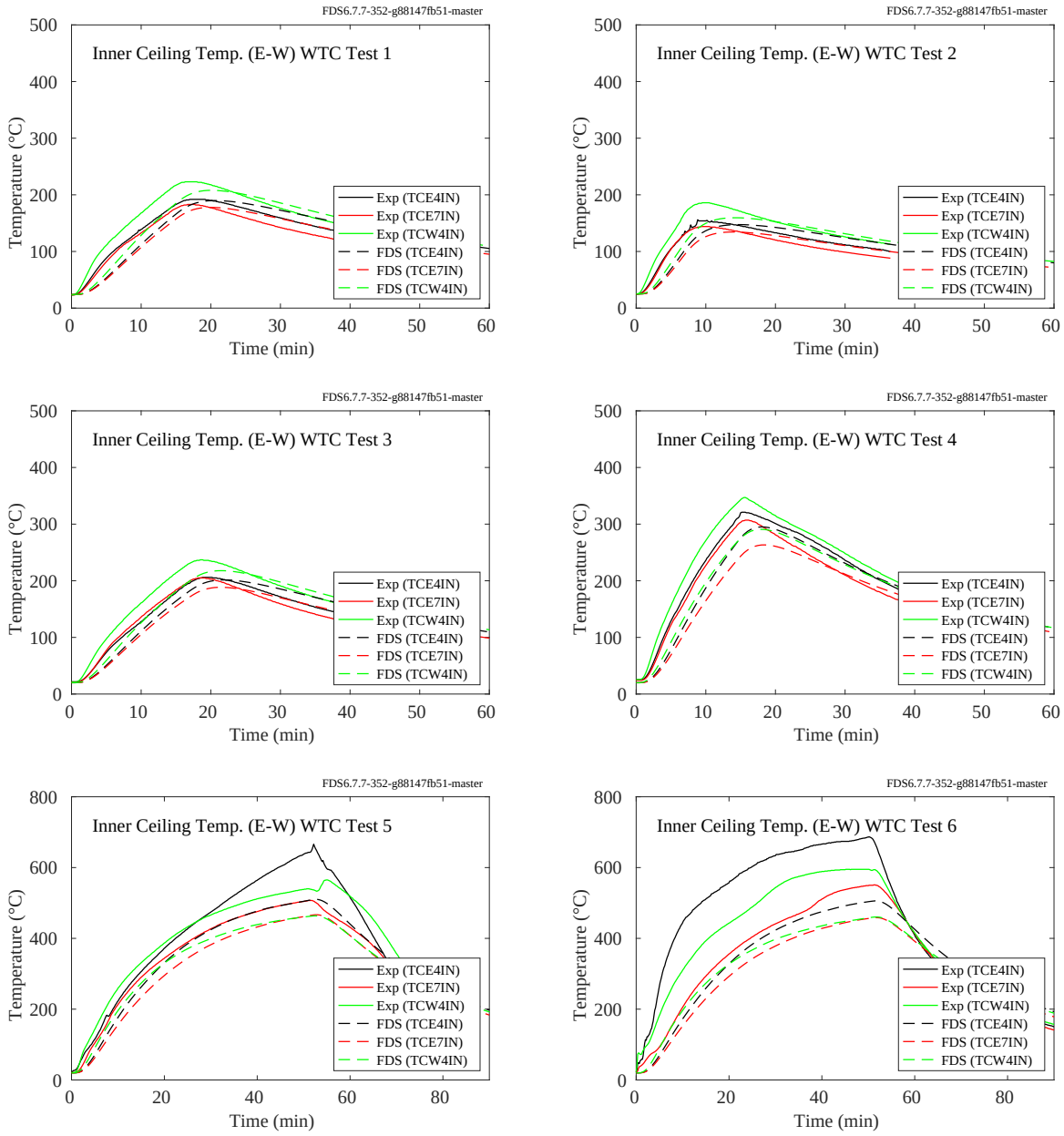

Figure 11.44: WTC experiments, inner ceiling temperatures, east-west axis.

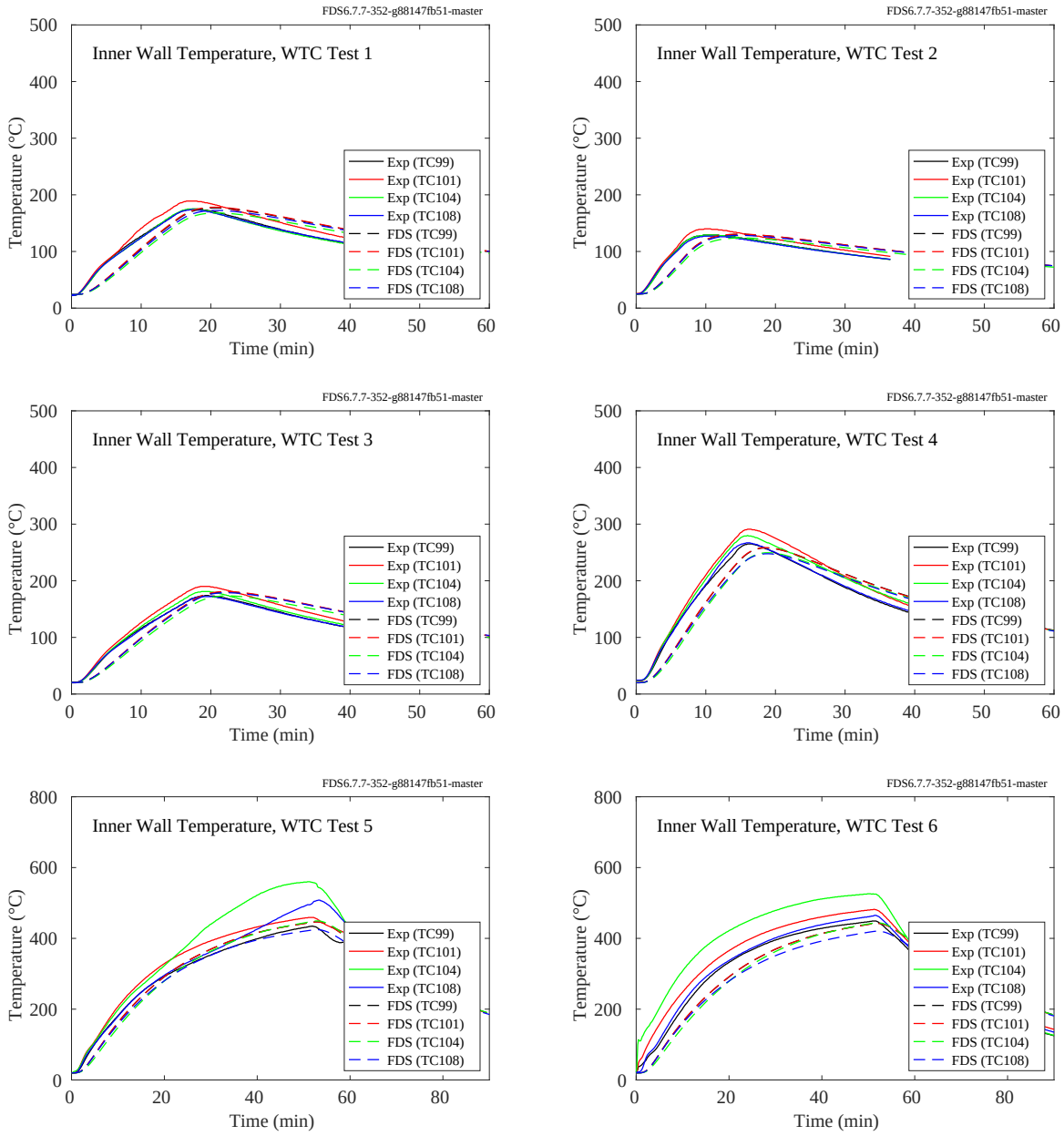

Figure 11.45: WTC experiments, inner wall temperatures.

11.1.8 Insulation Materials Fire Resistance Tests

Figures 11.46 through 11.49 contain comparisons of predicted and measured cold side temperatures of stone wool insulation samples in small-scale fire resistance tests. The measured temperatures are the average of 8 thermocouples. The physical properties of the materials are given in Table 11.3. Further details on the experiments and modeling can be found in Section 3.33.

Table 11.3: Physical properties of stone wool insulation materials [211].

Test No.	Thickness (mm)	Density (kg/m^3)	Loss (%)
1	61.9	101.4	1.5
2	62.4	100.5	1.3
3	60.0	97.2	1.4
4	63.2	95.3	1.2
5	61.7	100.7	1.2
6	60.5	100.2	1.1
7	60.0	99.6	1.1
8	61.8	90.2	1.3
9	61.1	69.8	1.3
10	61.7	79.3	1.5
11	60.1	90.3	1.3
12	60.1	90.3	1.4
13	61.4	100.0	1.4
14	60.3	100.9	1.5
15	61.0	138.8	2.1
16	41.2	107.2	1.3
17	72.7	78.9	1.6
18	61.3	141.2	1.9
19	61.9	147.7	1.5
20	52.0	38.3	0.7
21	60.5	147.3	1.3
22	75.7	66.3	6.9
23	75.2	71.1	9.0
24	76.2	51.4	9.8
25	71.5	63.9	1.1
26	72.8	75.1	1.2
27	60.4	85.0	1.3
28	75.0	68.5	4.7
29	75.7	48.7	6.7
30	75.3	48.2	4.8

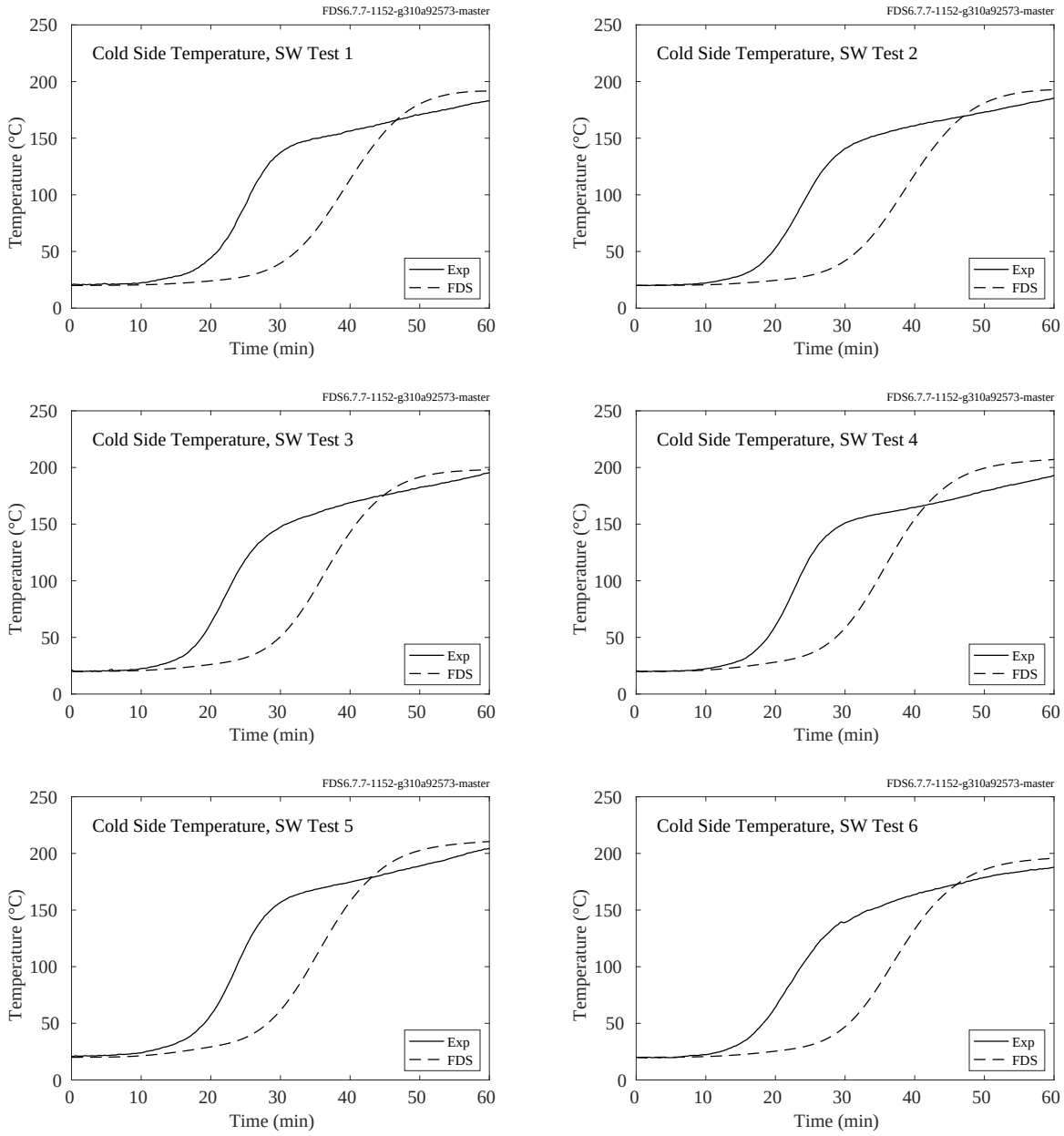

Figure 11.46: Insulation material cold side temperatures, Tests 1-6.

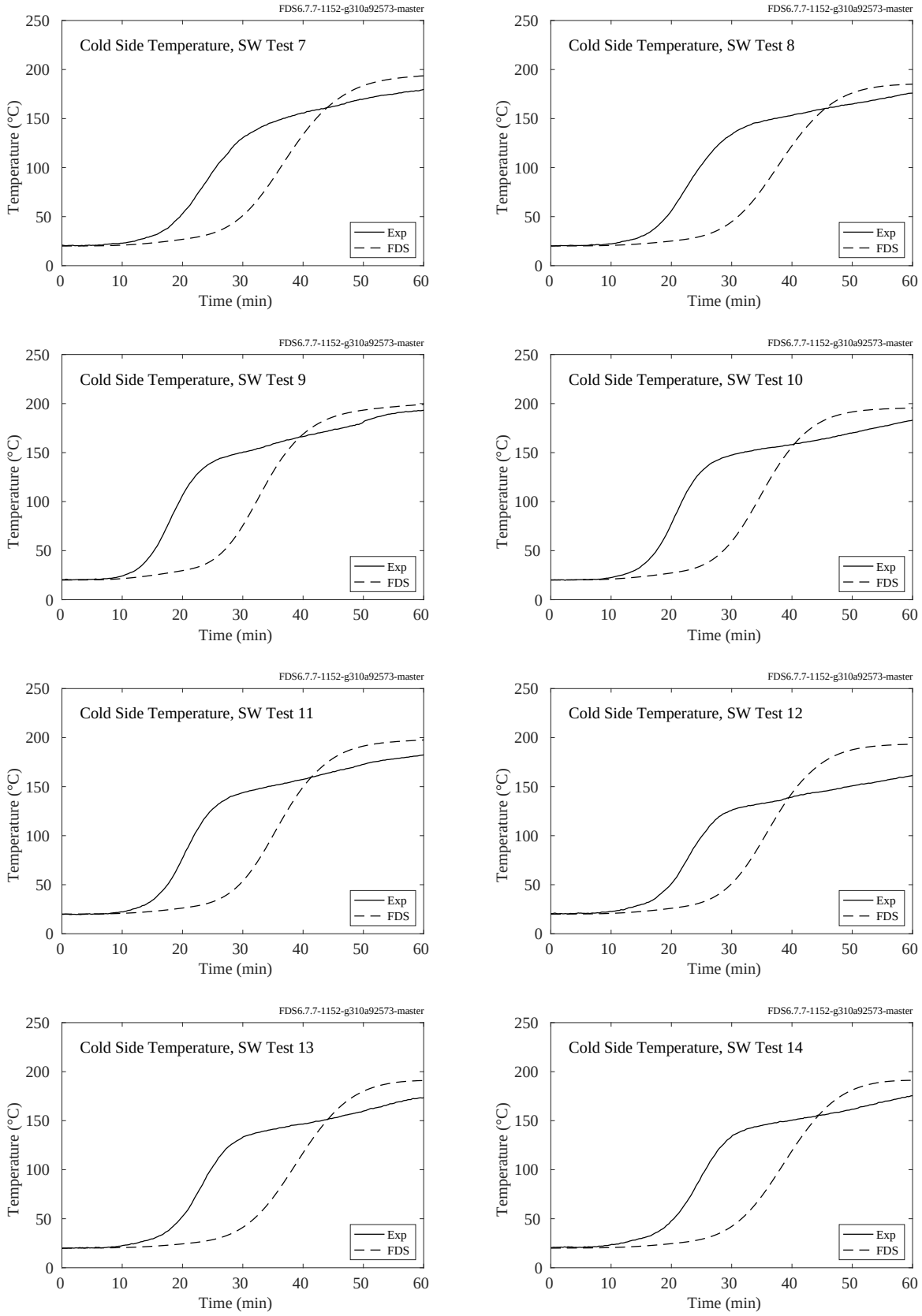

Figure 11.47: Insulation material cold side temperatures, Tests 7-14.

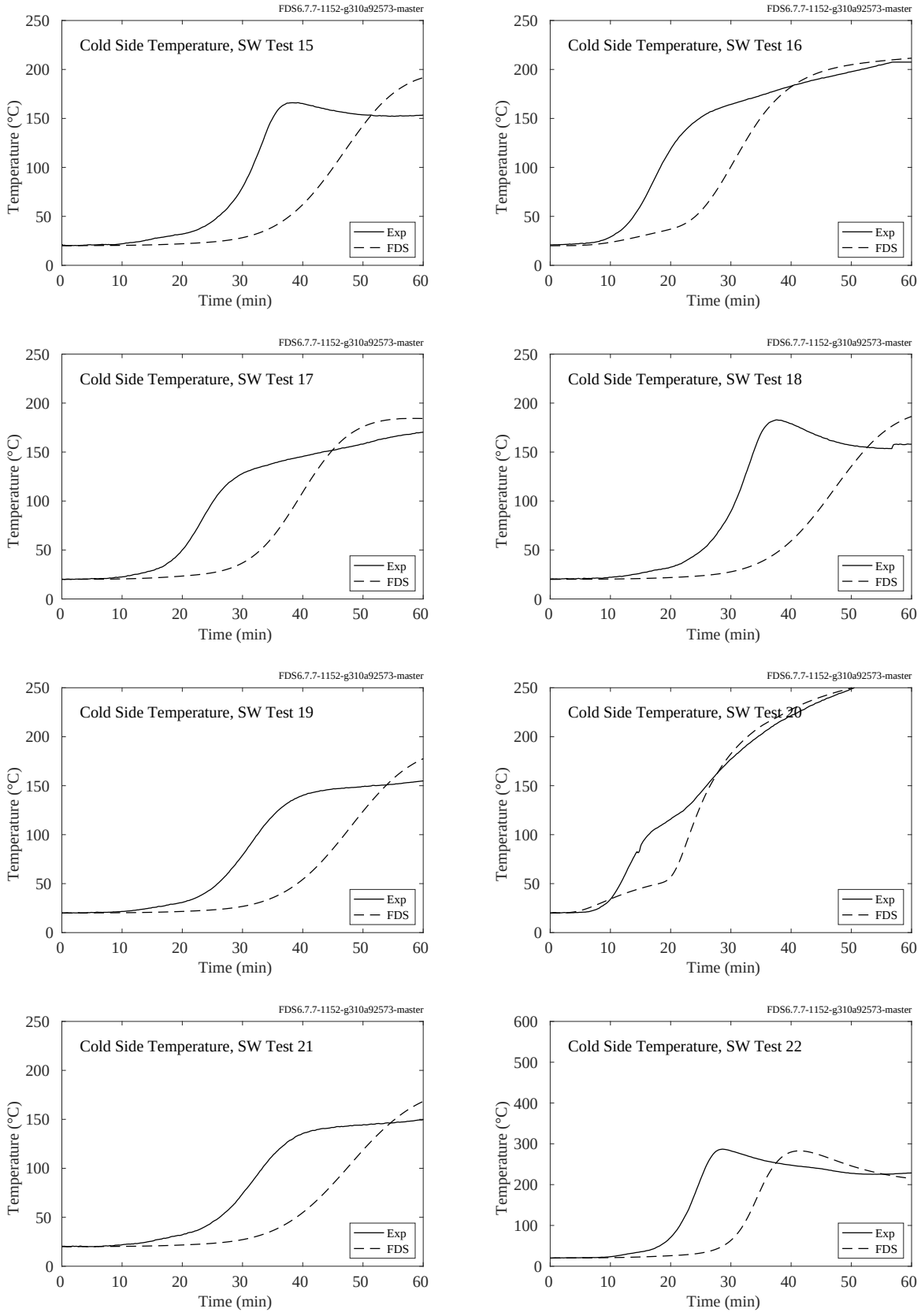

Figure 11.48: Insulation material cold side temperatures, Tests 15-22.

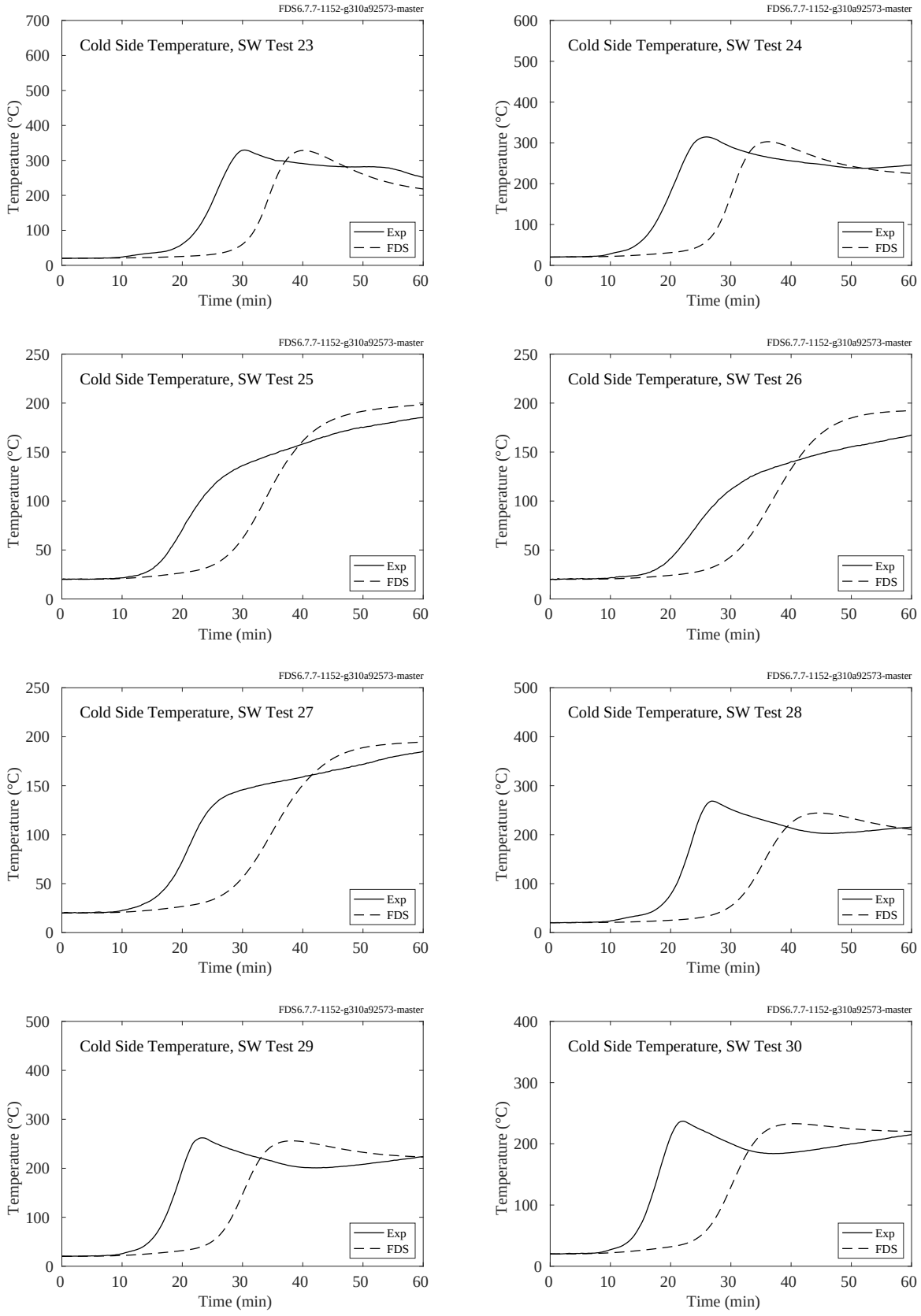

Figure 11.49: Insulation material cold side temperatures, Tests 23-30.

11.1.9 Summary of Wall, Ceiling, and Floor Temperature Predictions

Figure 11.50 summarizes the temperature predictions for walls, ceilings, and floors.

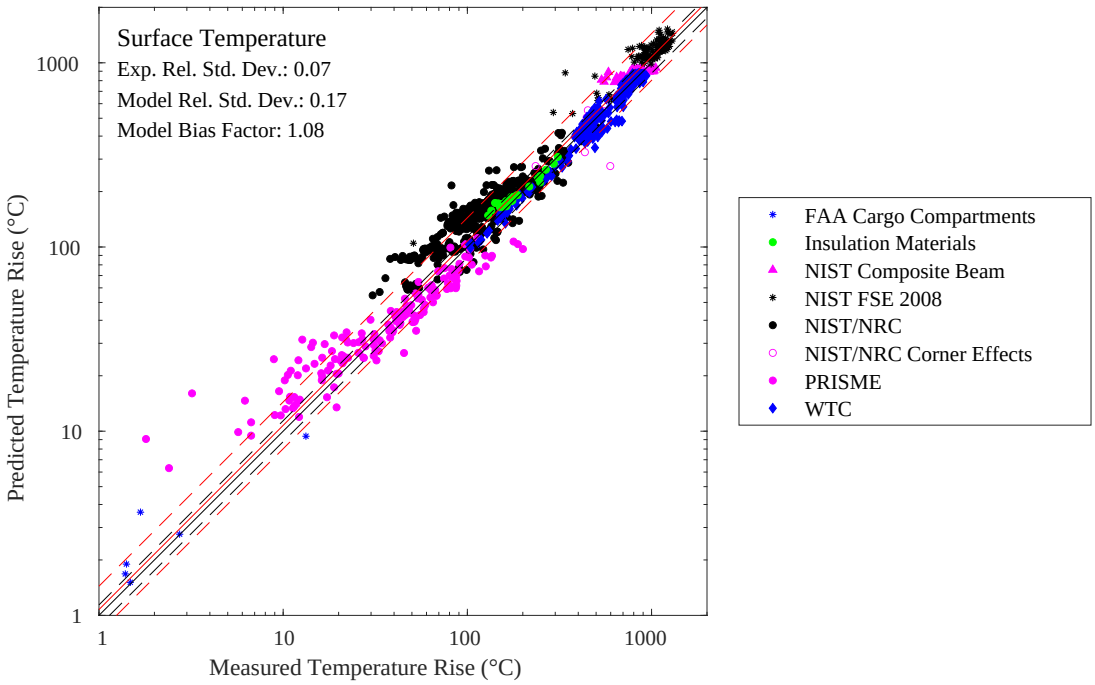

Figure 11.50: Summary of compartment surface temperature predictions.

11.2 Target Temperature

A "target" refers to any object that is not a wall, ceiling, or floor. In the sections to follow, the targets consist of structural steel members, electrical cables, and various other objects.

11.2.1 NIST Composite Beam

A brief description of the experiments is given in Section 3.41. The compartment interior dimensions are 12.4 m long, running east-west, 1.9 m wide, and 3.77 m high. Four experiments with fires were performed, labeled as Tests 2-5. Test 1 did not include a fire.

Figure 11.51 displays the plate thermometer temperatures at three locations. PT1 is mounted on the east wall facing west. PT2 is mounted just north of the beam at mid-span, pointing north. PT3 is also mounted at mid-span, just below the beam and facing downward.

Figure 11.52 displays the steel temperature at Sections 1, 3-8 for Test 5 only. TCC11 is the upper flange temperature. TCC12, TCC13, and TCC14 are the web temperatures, and TCC15 is the lower flange temperature.

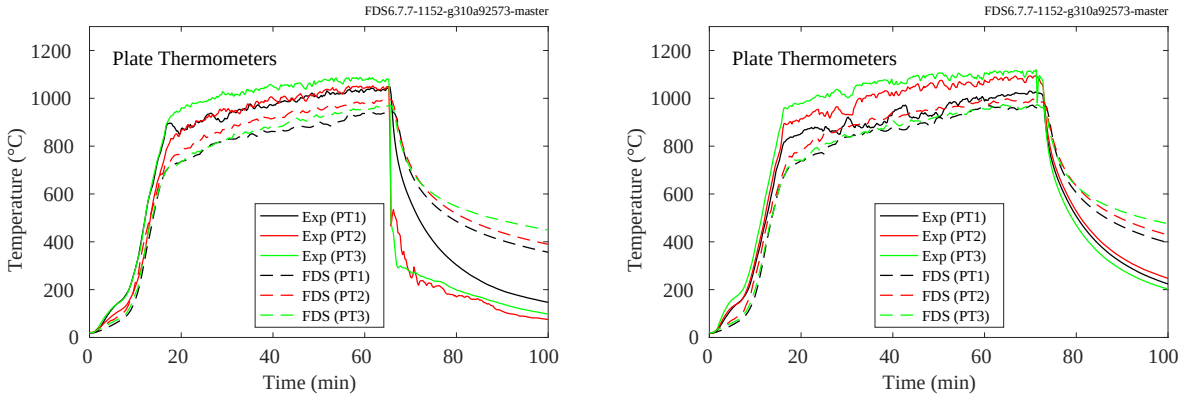

Figure 11.51: NIST Composite Beam, beam temperatures.

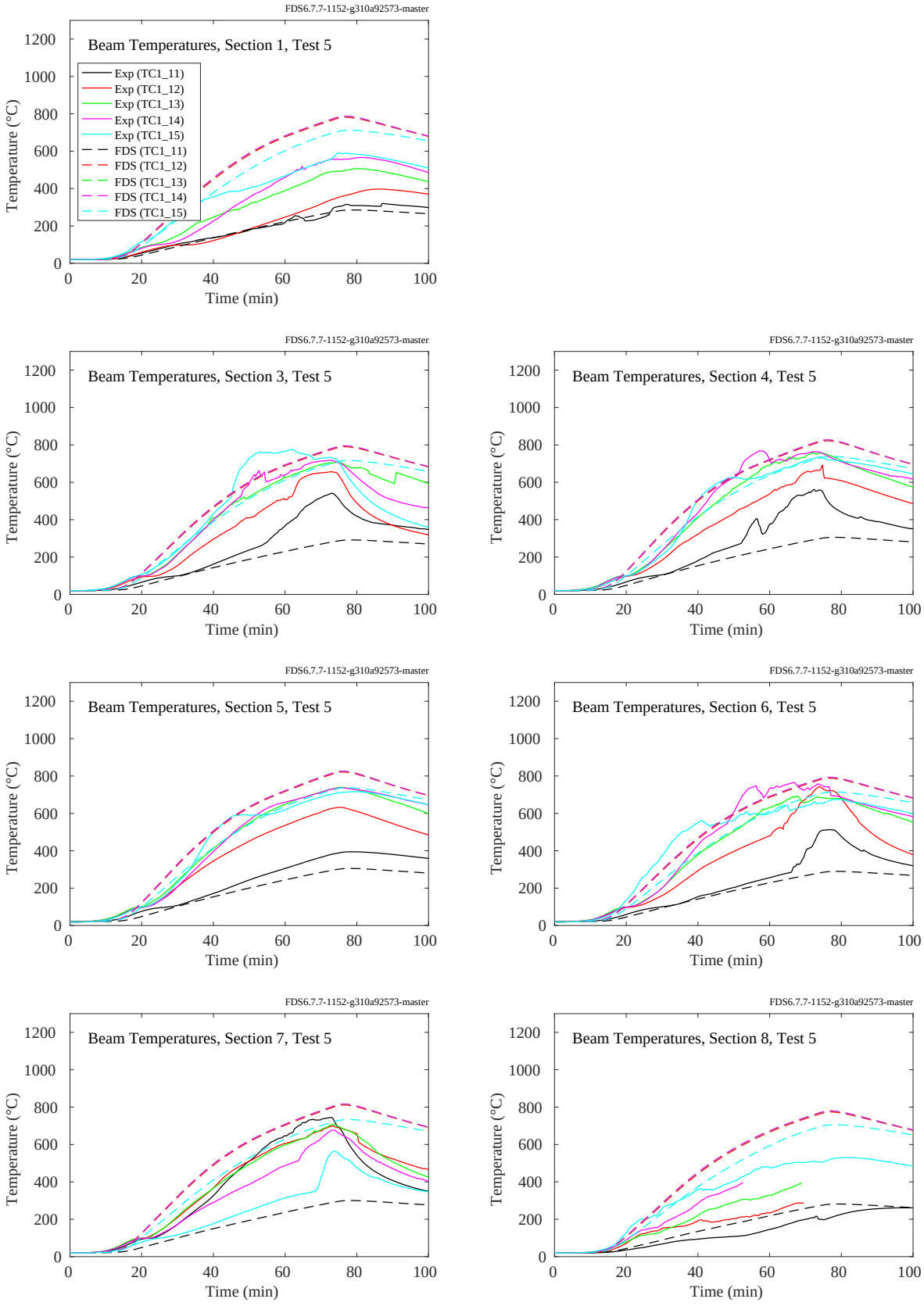

Figure 11.52: NIST Composite Beam, beam temperatures.

11.2.2 NIST E119 Compartment

A brief description of the experiments is given in Section 3.42. The compartment interior dimensions are 10.8 m long, running east-west, 7.0 m wide, and 3.8 m high. Three fire experiments were performed, labeled as Tests 1-3.

Figure 11.53 displays the plate thermometer temperatures at three locations. Locations of PT1 through PT3 were shown in Fig. 3.22.

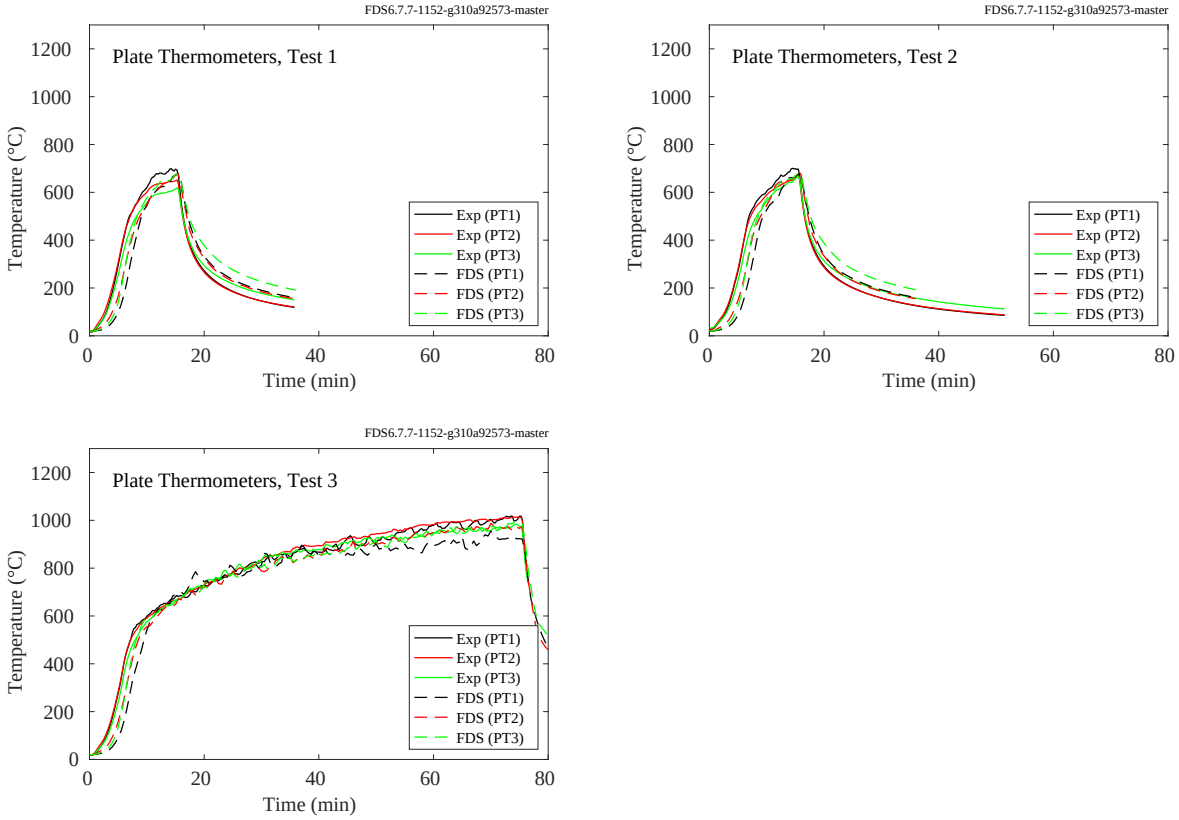

Figure 11.53: NIST E119 Compartment, Plate temperatures.

11.2.3 NIST/NRC Experiments

Electrical cables of various types (power and control), and configurations (horizontal or vertical; in tray or free-hanging), were installed in the test compartment. For each of the four cable targets considered, measurements of the local gas temperature, surface temperature, radiative heat flux, and total heat flux are available. The following pages display comparisons of surface temperature for Control Cable B, Horizontal Cable Tray D, Power Cable F, and Vertical Cable Tray G. For the bundled cables within horizontal and vertical trays (Targets D and G), FDS assumes them to be rectangular slabs of thickness comparable to the diameter of the individual cables. For the free-hanging cables B and F, FDS assumes them to be cylinders of uniform composition.

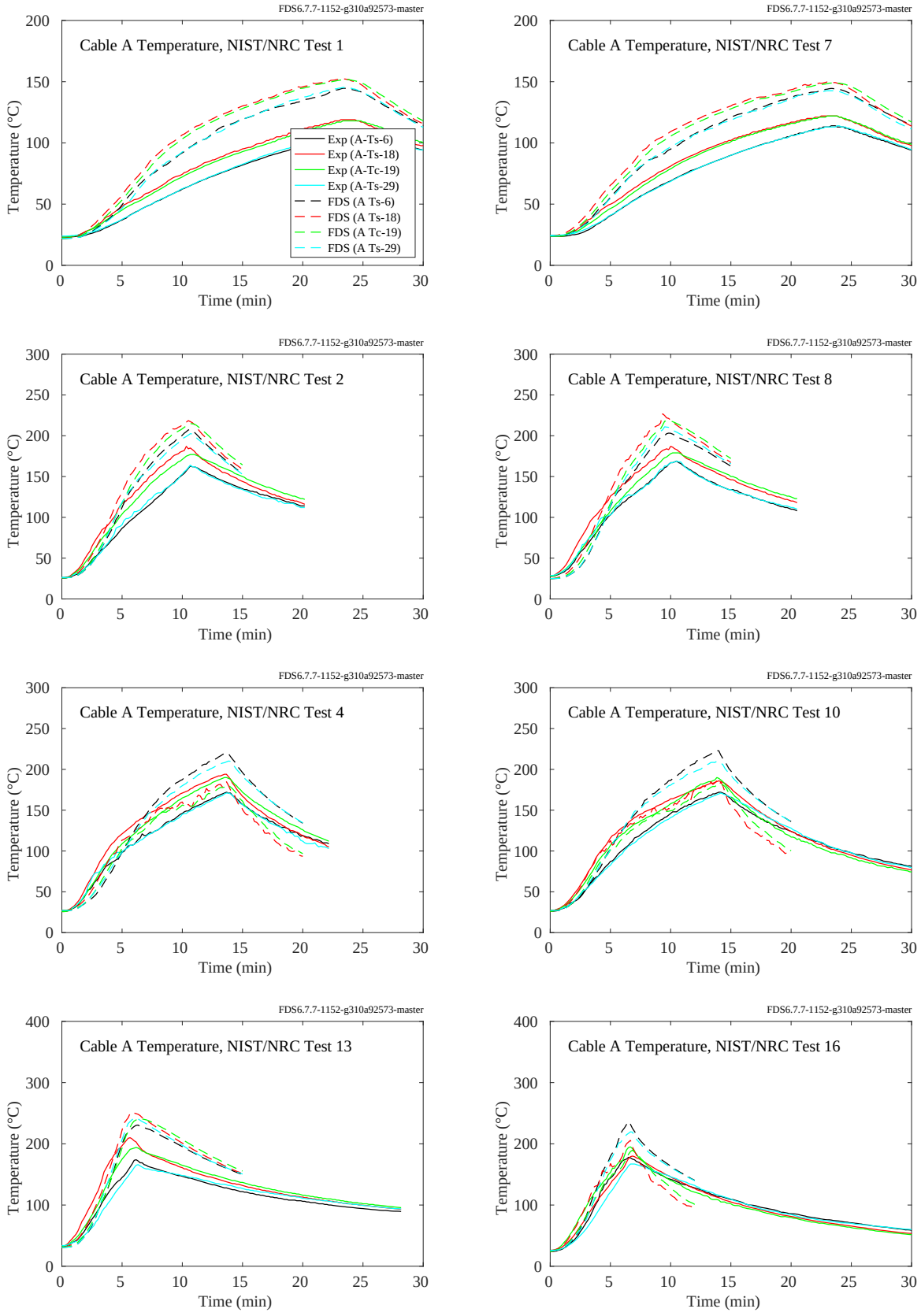

Figure 11.54: NIST/NRC experiments, Cable A temperatures, Tests 1, 2, 4, 7, 8, 10, 13, 16.

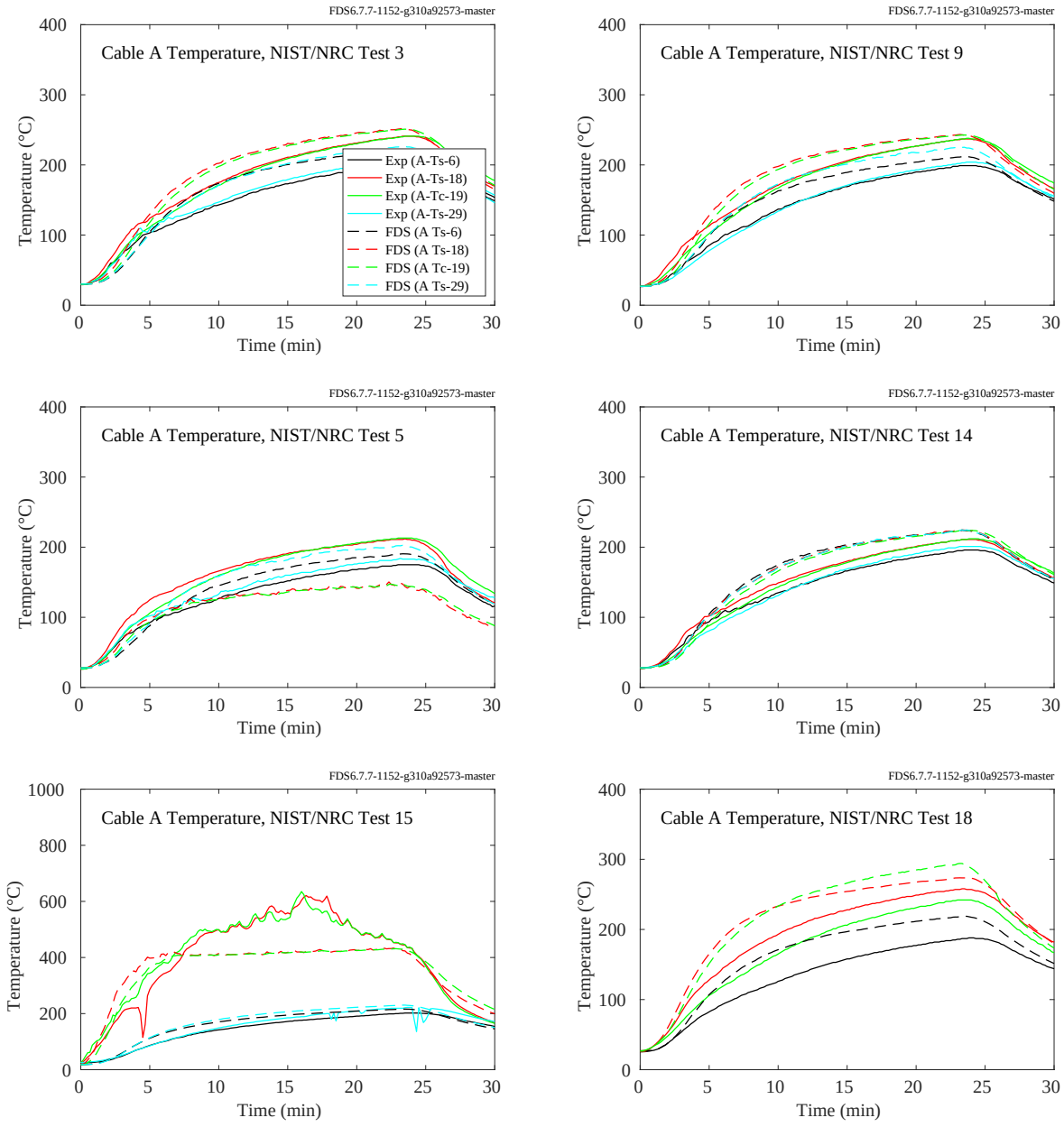

Figure 11.55: NIST/NRC experiments, Cable A temperatures, Tests 3, 5, 9, 14, 15, 18.

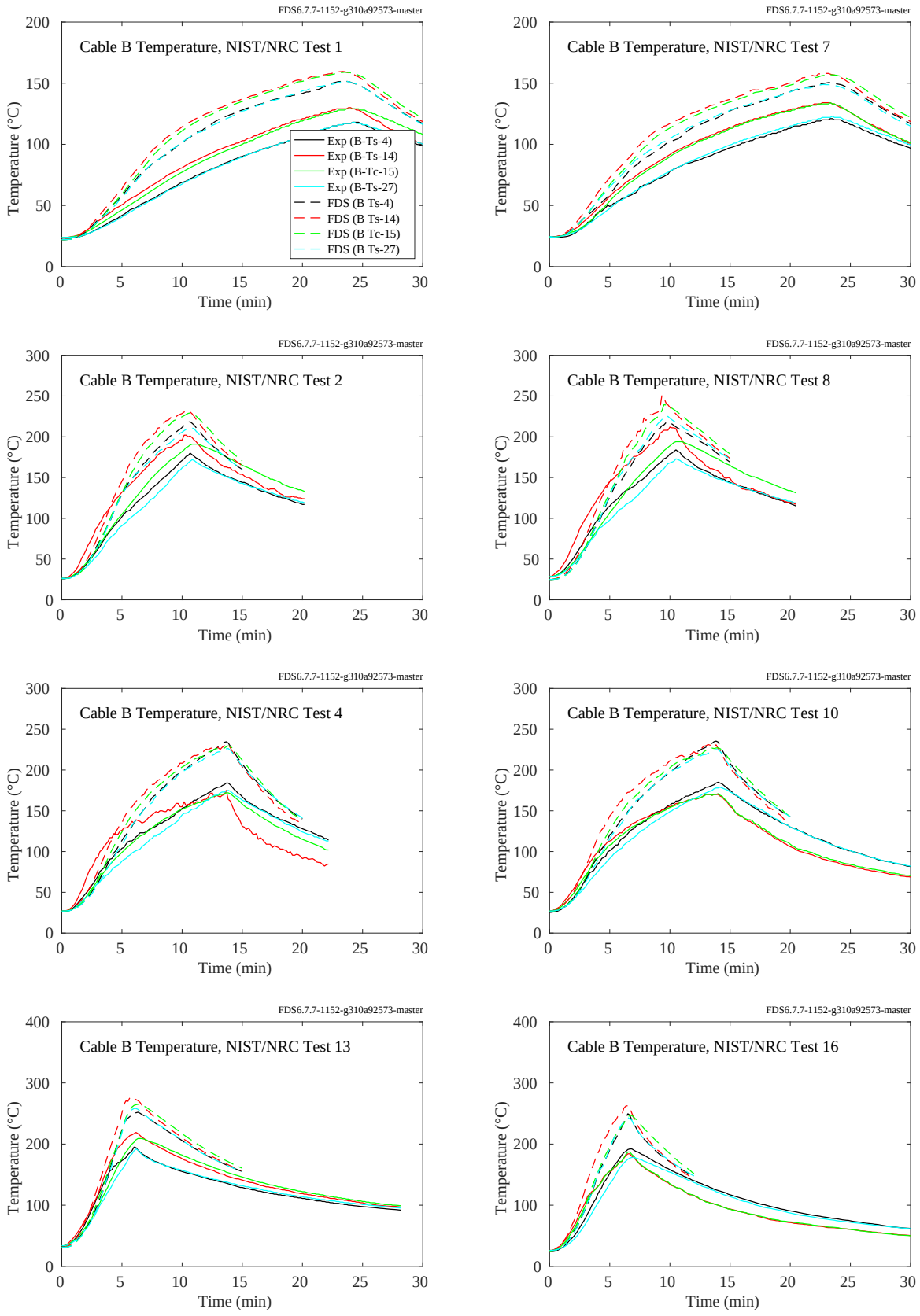

Figure 11.56: NIST/NRC experiments, Cable B temperatures, Tests 1, 2, 4, 7, 8, 10, 13, 16.

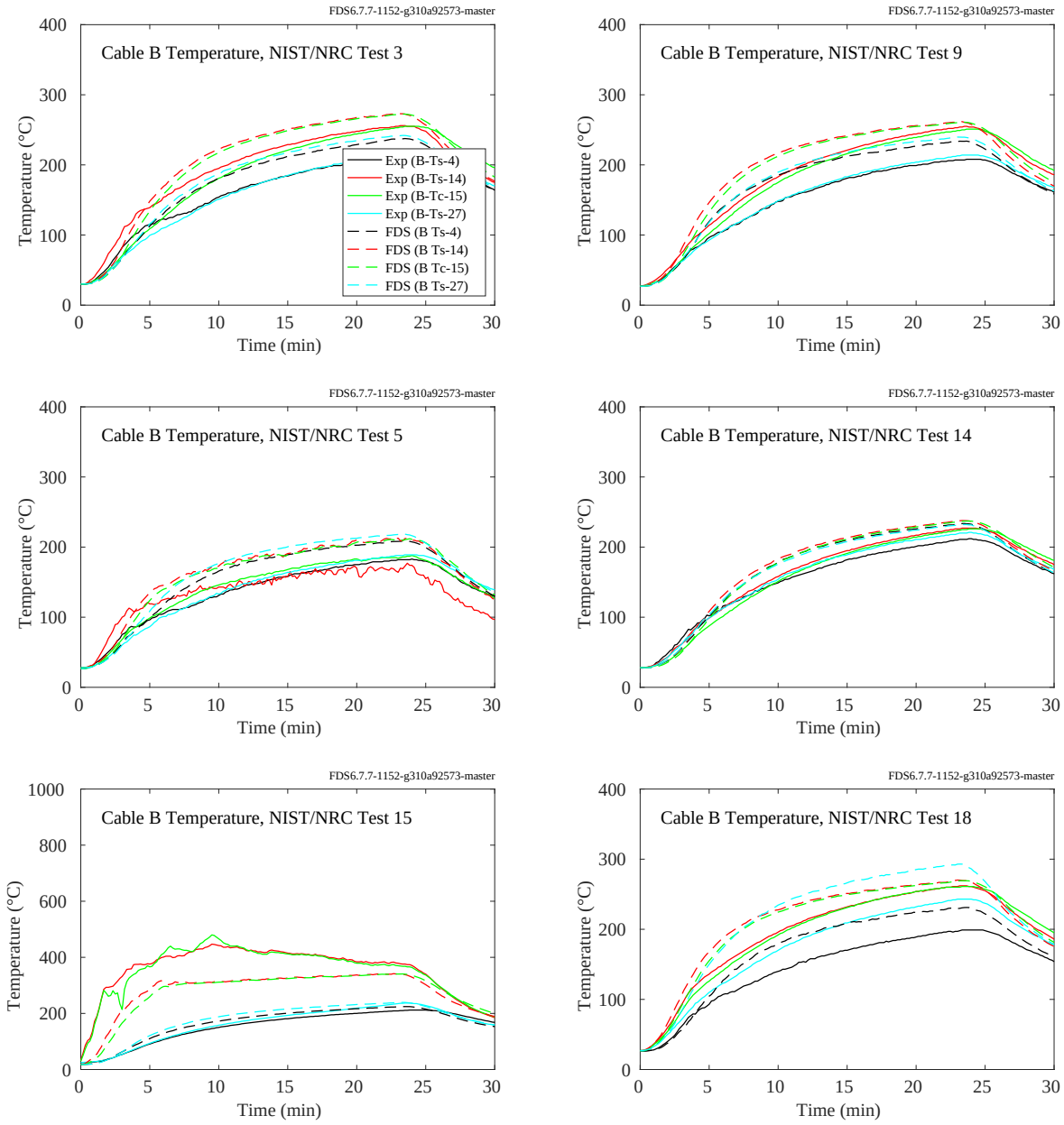

Figure 11.57: NIST/NRC experiments, Cable B temperatures, Tests 3, 5, 9, 14, 15, 18.

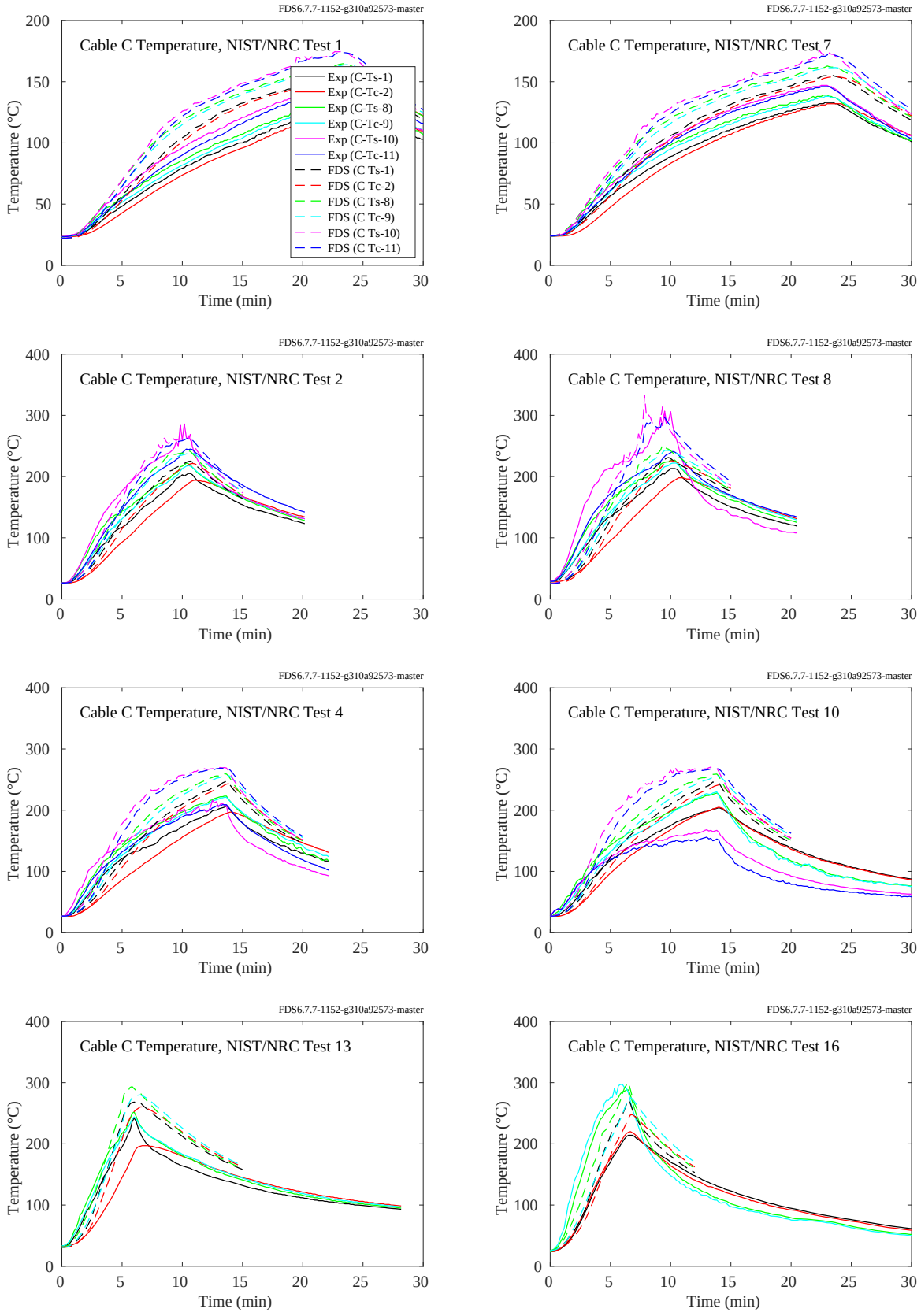

Figure 11.58: NIST/NRC experiments, Cable Ca temperatures, Tests 1, 2, 4, 7, 8, 10, 13, 16.

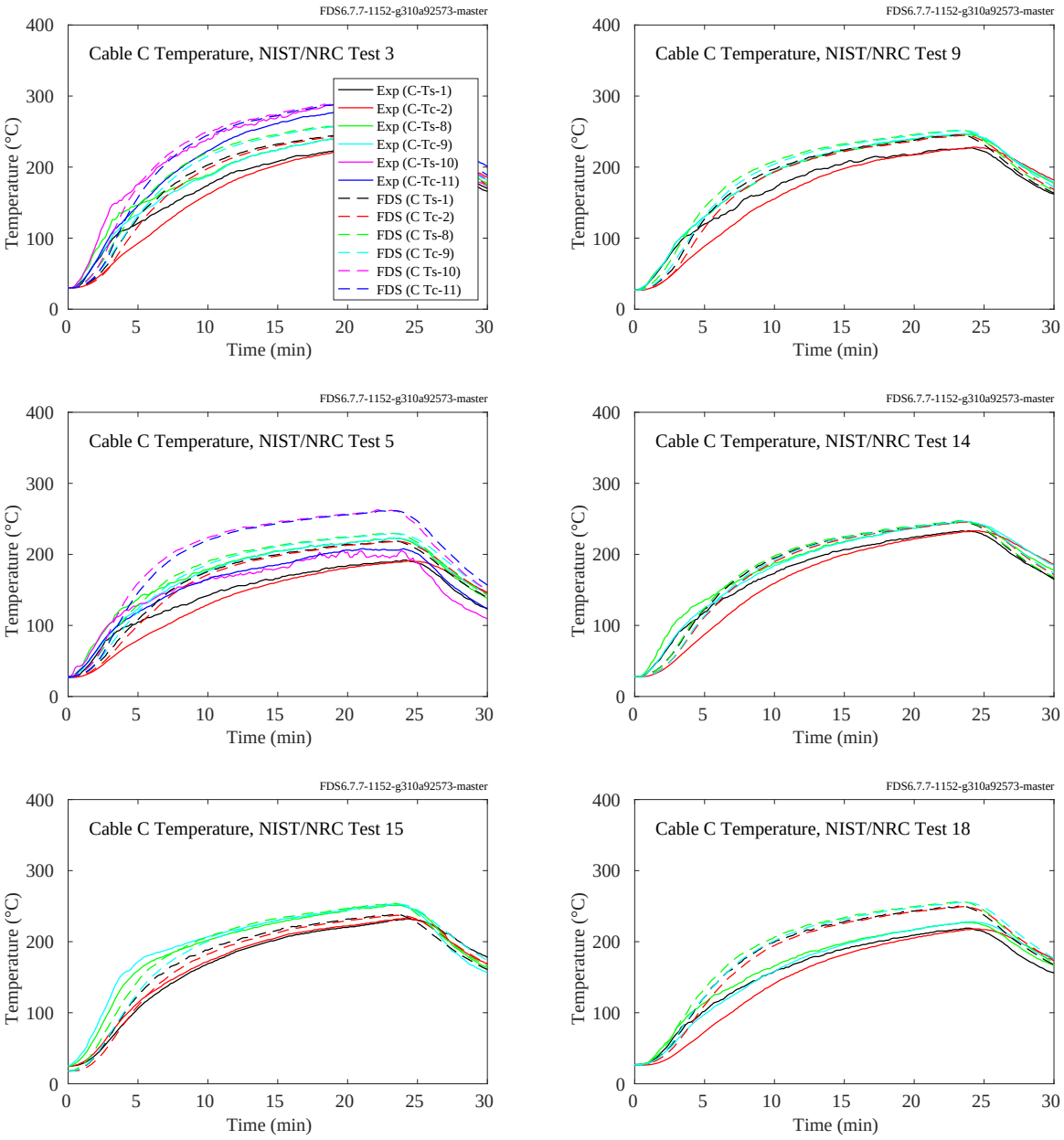

Figure 11.59: NIST/NRC experiments, Cable Ca temperatures, Tests 3, 5, 9, 14, 15, 18.

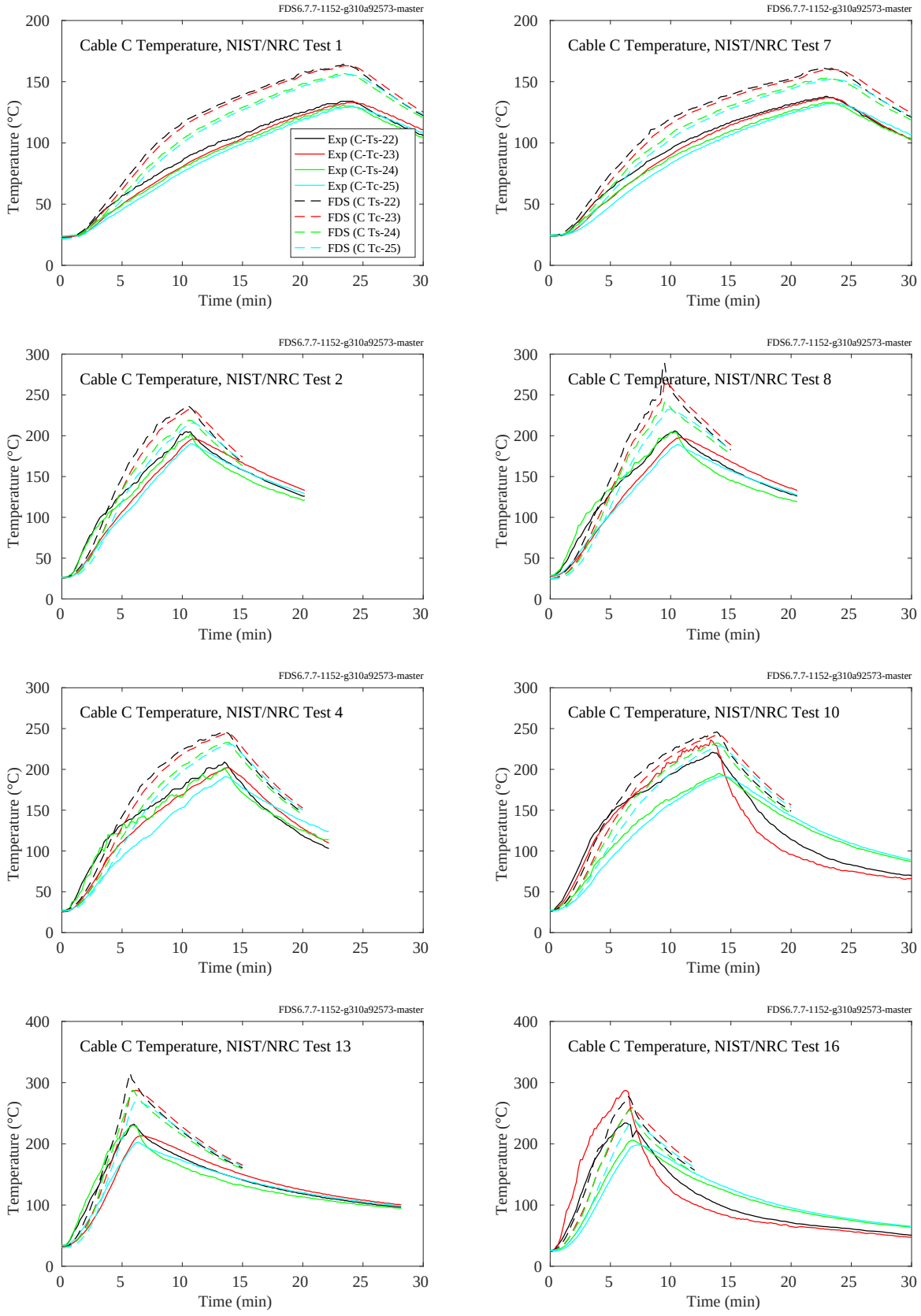

Figure 11.60: NIST/NRC experiments, Cable Cb temperatures, Tests 1, 2, 4, 7, 8, 10, 13, 16.

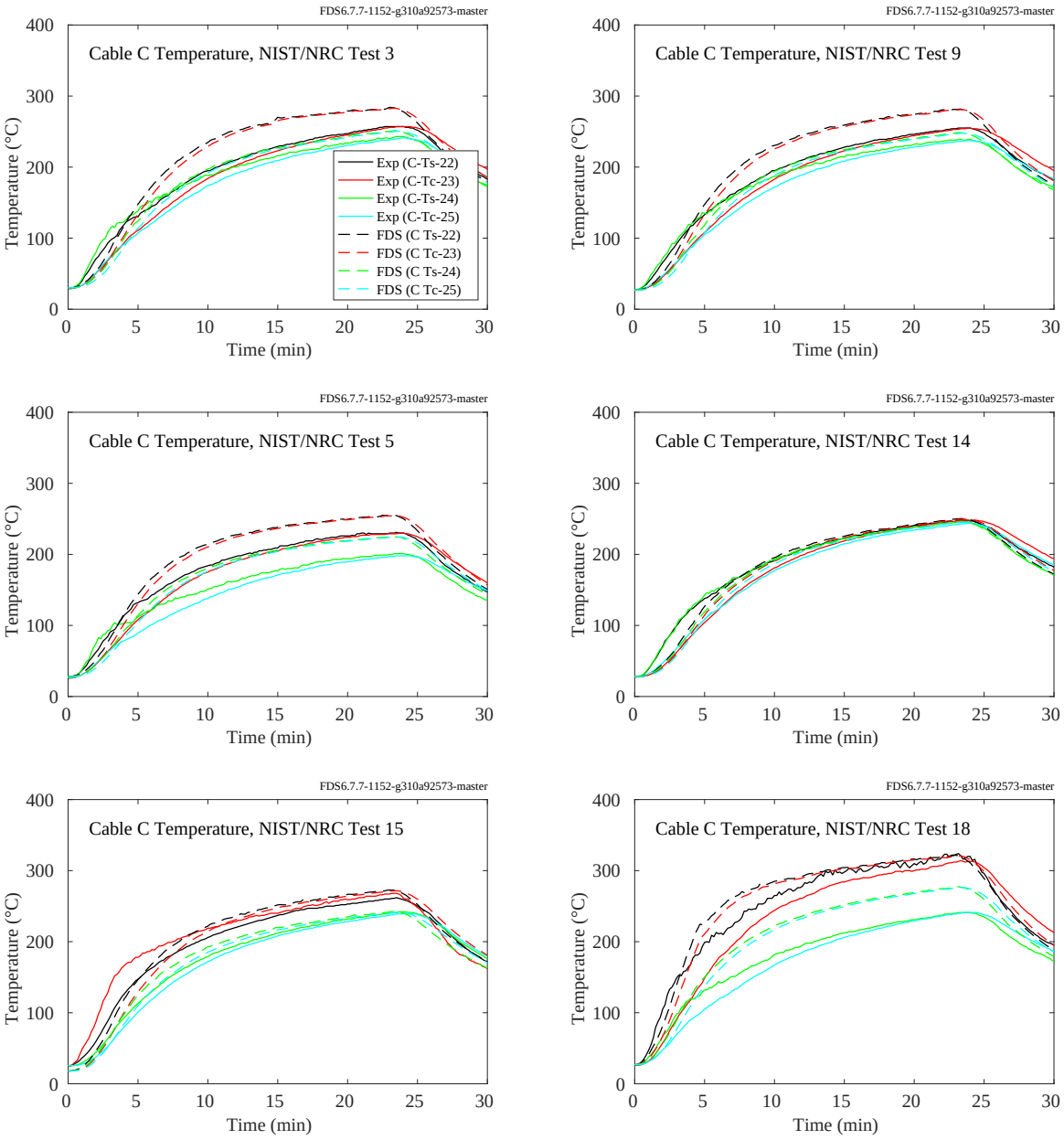

Figure 11.61: NIST/NRC experiments, Cable Cb temperatures, Tests 3, 5, 9, 14, 15, 18.

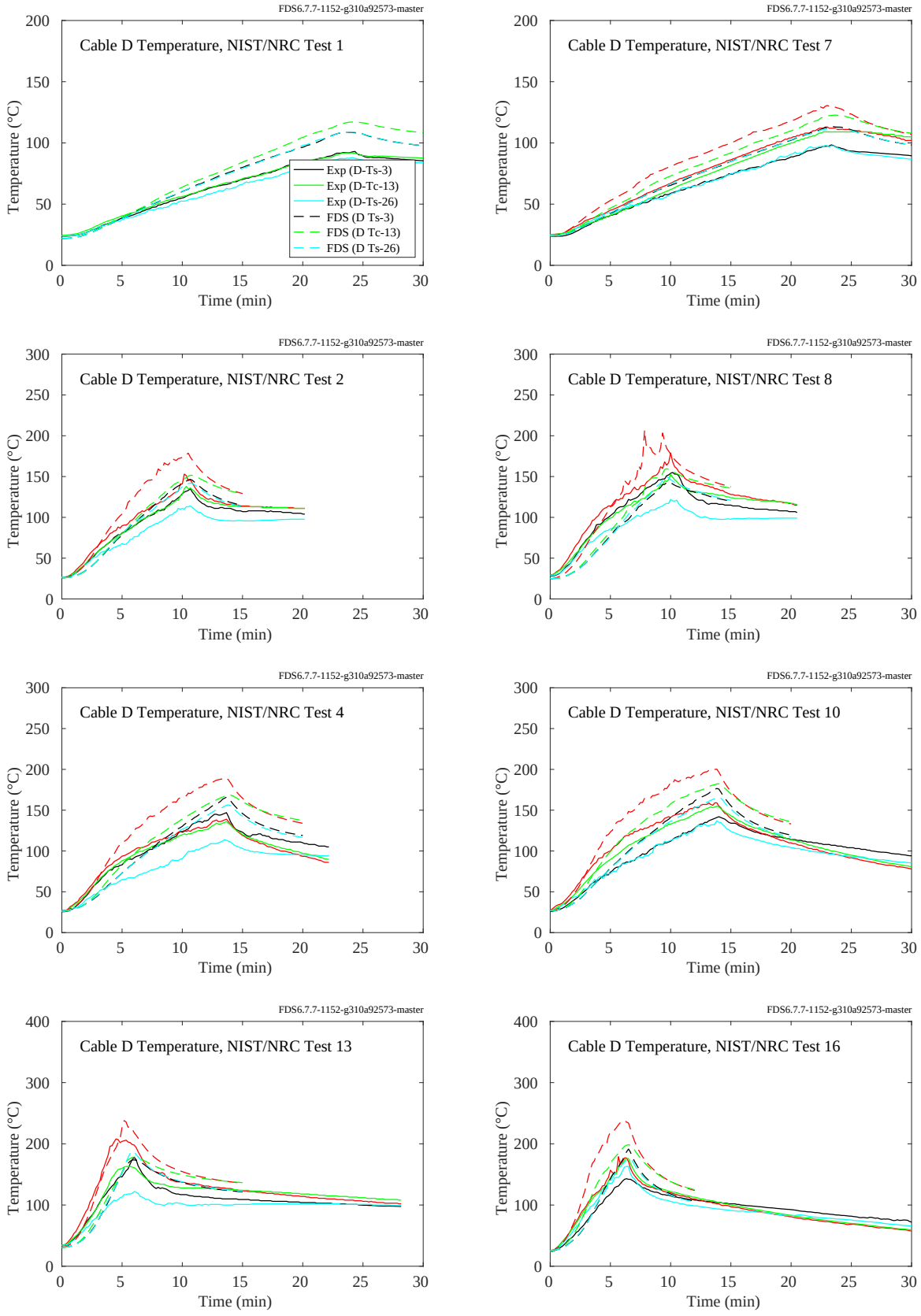

Figure 11.62: NIST/NRC experiments, Cable D temperatures, Tests 1, 2, 4, 7, 8, 10, 13, 16.

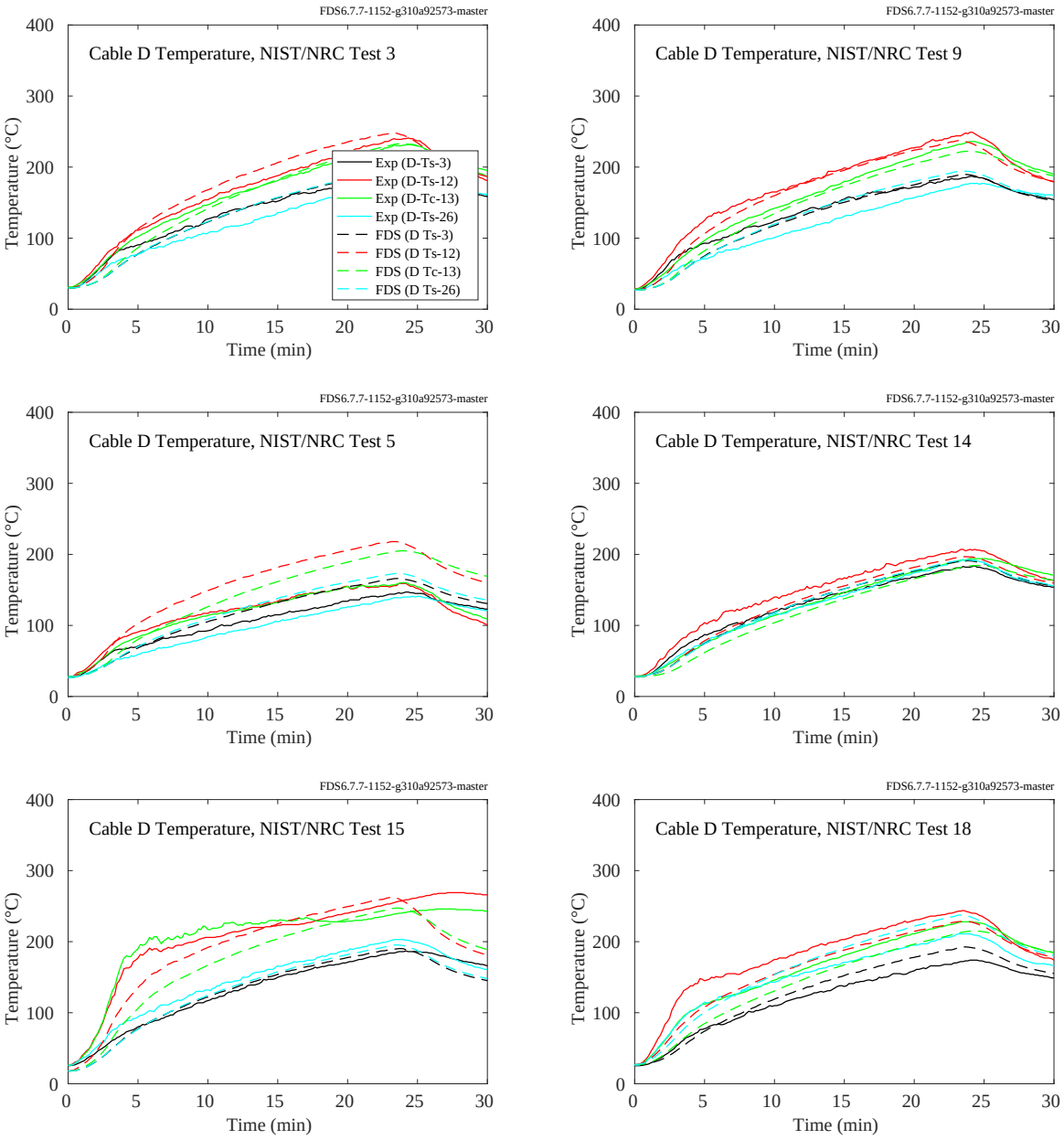

Figure 11.63: NIST/NRC experiments, Cable D temperatures, Tests 3, 5, 9, 14, 15, 18.

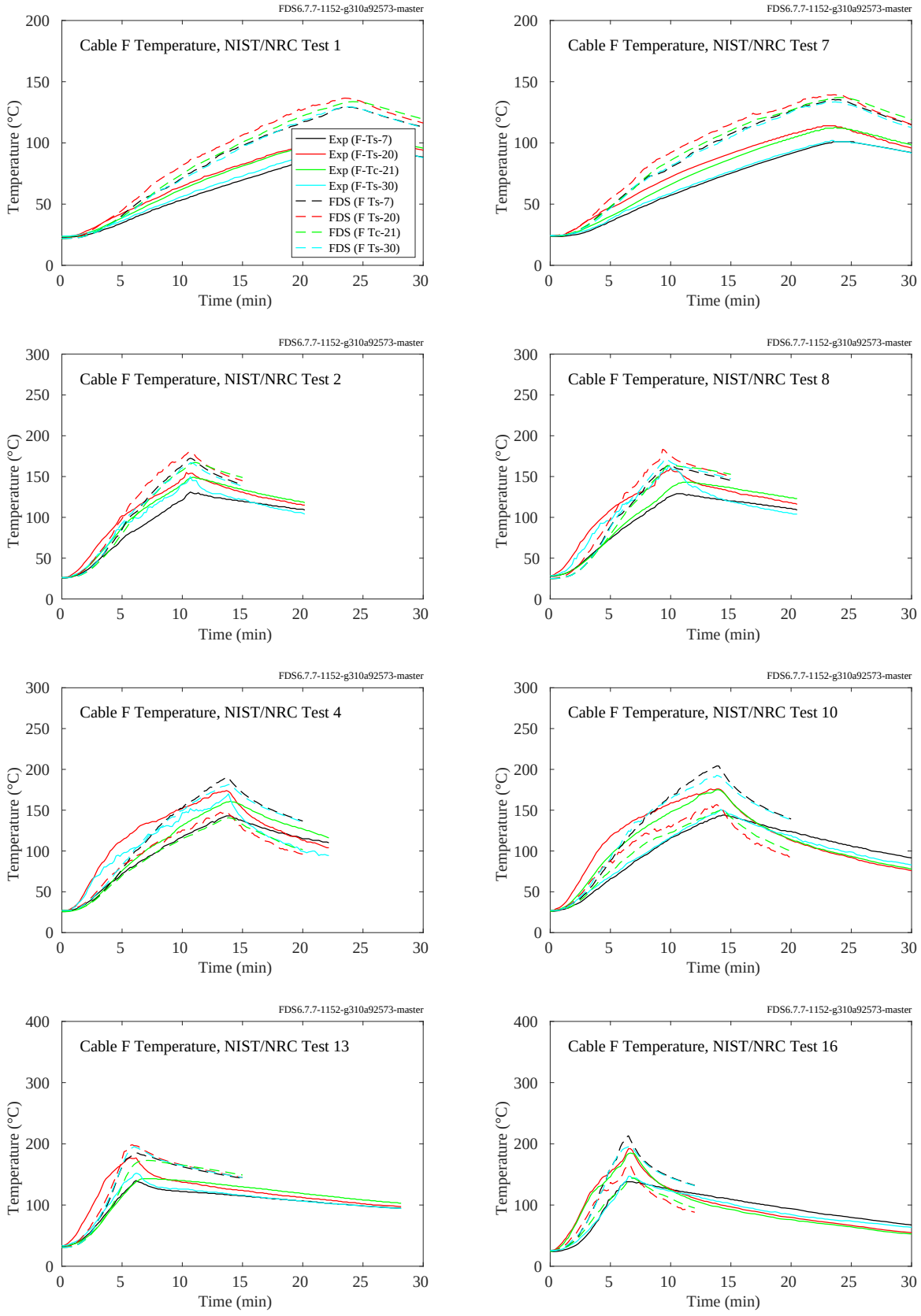

Figure 11.64: NIST/NRC experiments, Cable F temperatures, Tests 1, 2, 4, 7, 8, 10, 13, 16.

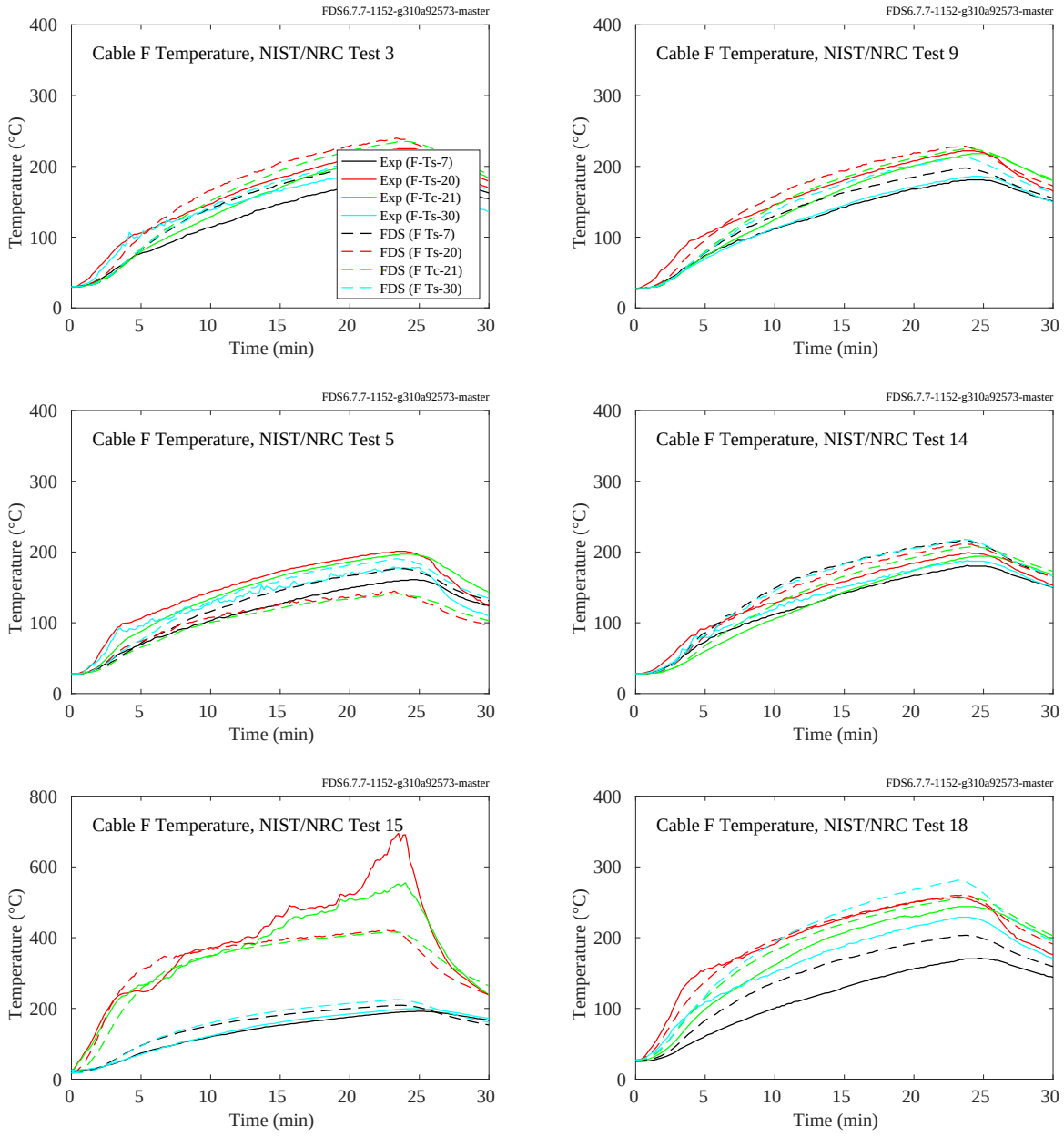

Figure 11.65: NIST/NRC experiments, Cable F temperatures, Tests 3, 5, 9, 14, 15, 18.

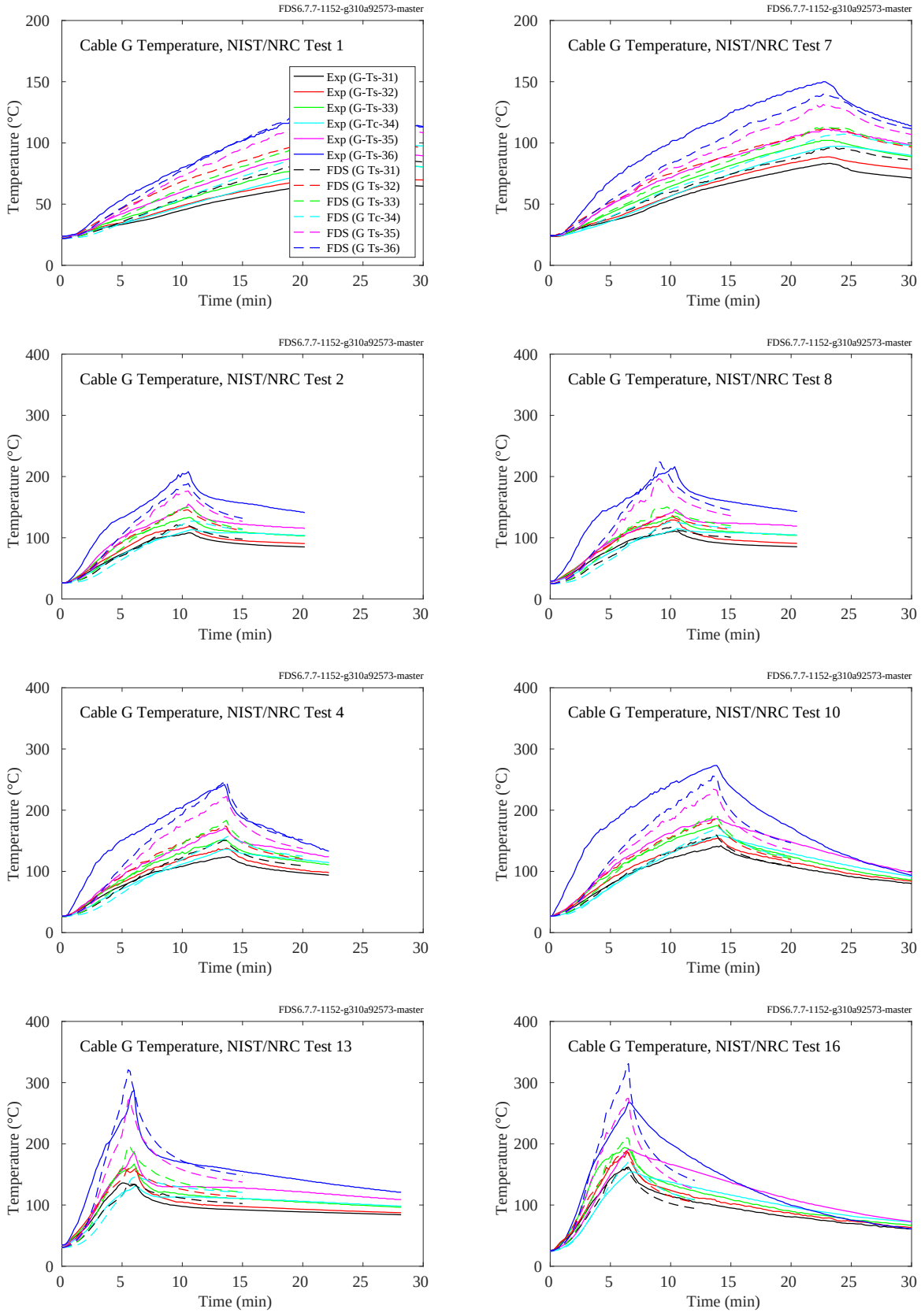

Figure 11.66: NIST/NRC experiments, Cable G temperatures, Tests 1, 2, 4, 7, 8, 10, 13, 16.

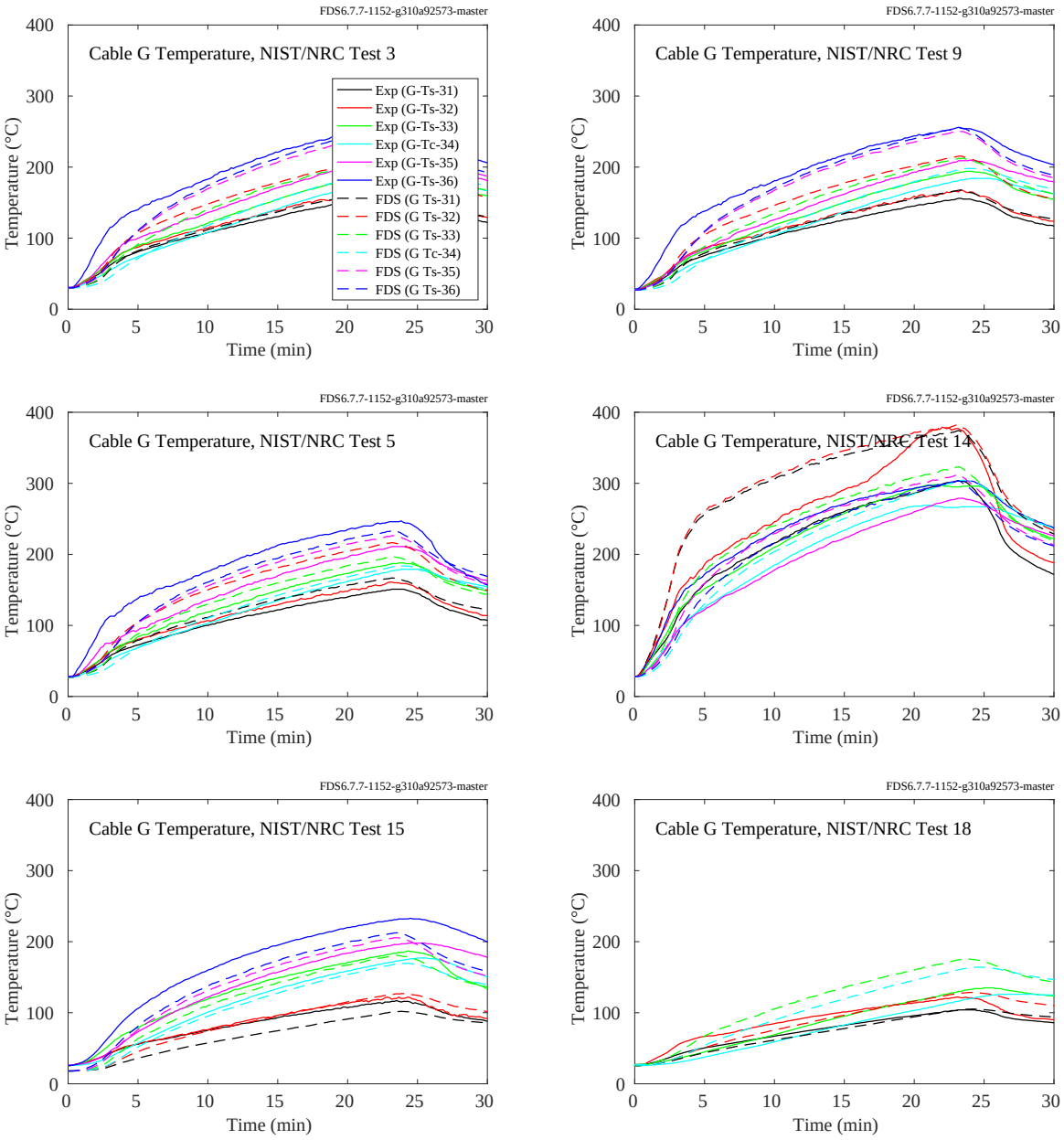

Figure 11.67: NIST/NRC experiments, Cable G temperatures, Tests 3, 5, 9, 14, 15, 18.

11.2.4 NIST/NRC Corner Effects Experiments

The plots on the following pages display comparisons of plate thermometer (PT) temperatures for the cabinet experiments. Two PTs were positioned facing each side of the cabinets, at a distance of 60 cm and heights of 76 cm and 137 cm, on center. In addition, a Type K thermocouple (TC) was welded to the back of the cabinet, centered both horizontally and vertically.

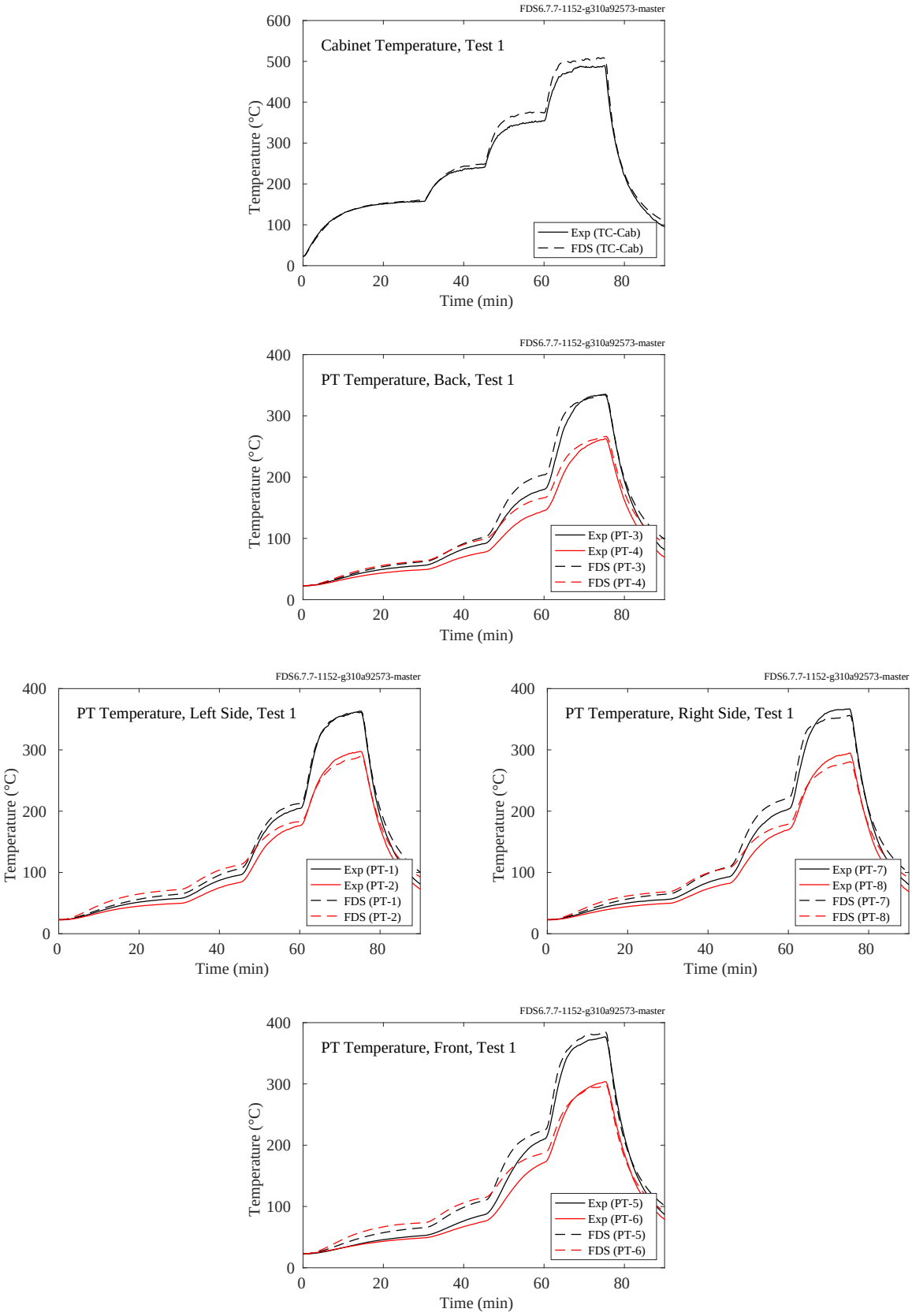

Figure 11.68: NIST/NRC Corner Effects, plate and cabinet temperatures, Test 1.

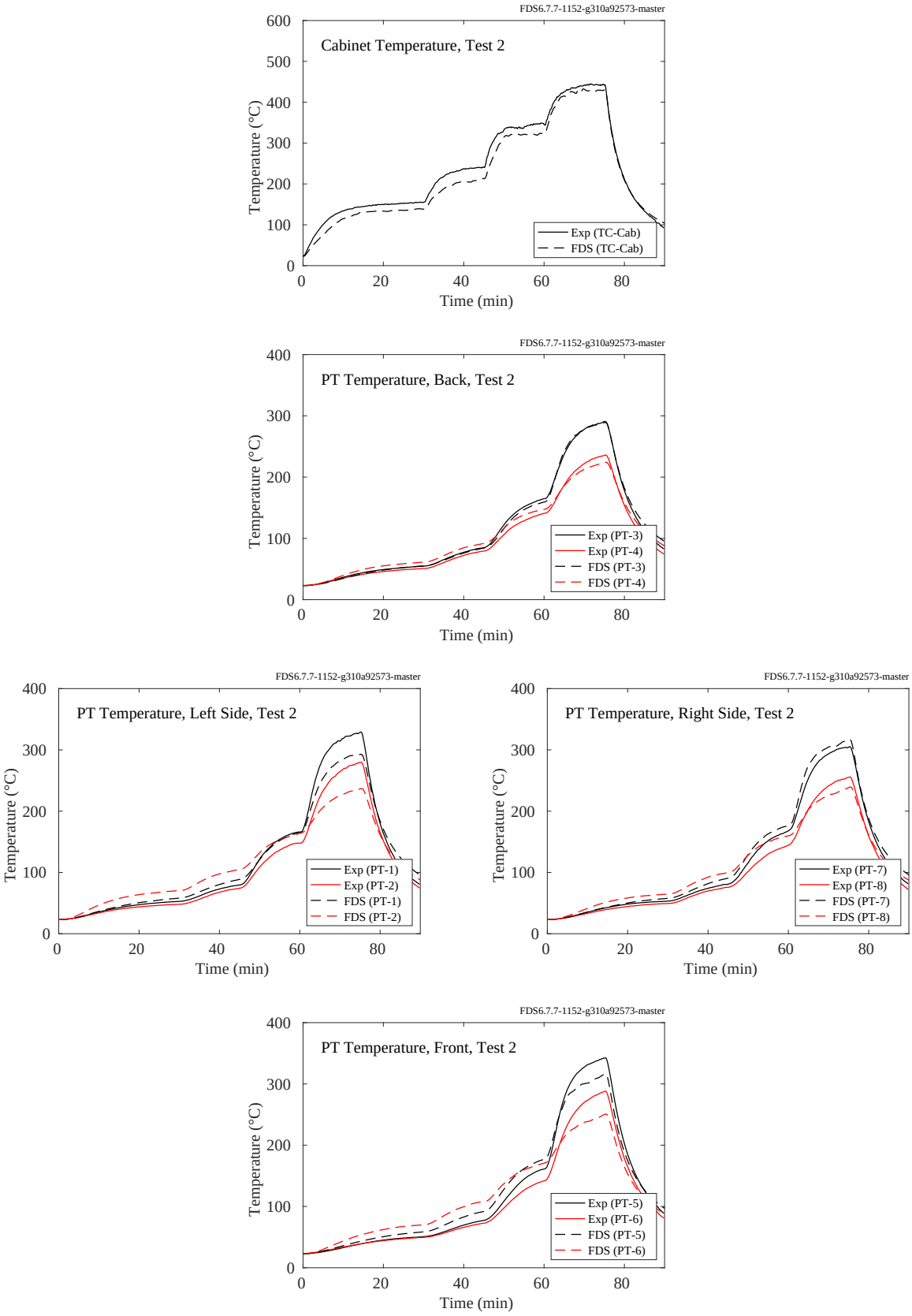

Figure 11.69: NIST/NRC Corner Effects, plate and cabinet temperatures, Test 2.

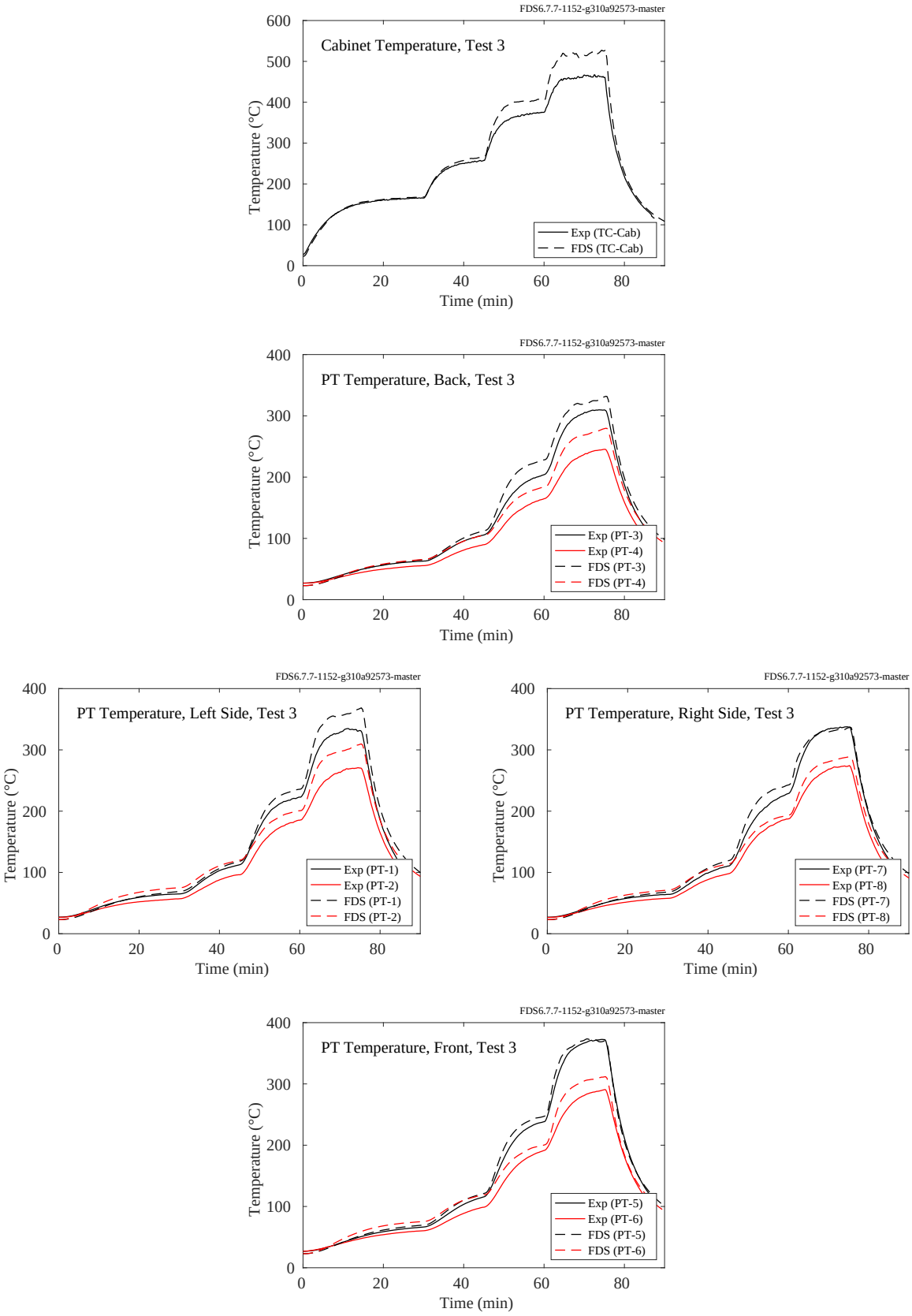

Figure 11.70: NIST/NRC Corner Effects, plate and cabinet temperatures, Test 3.

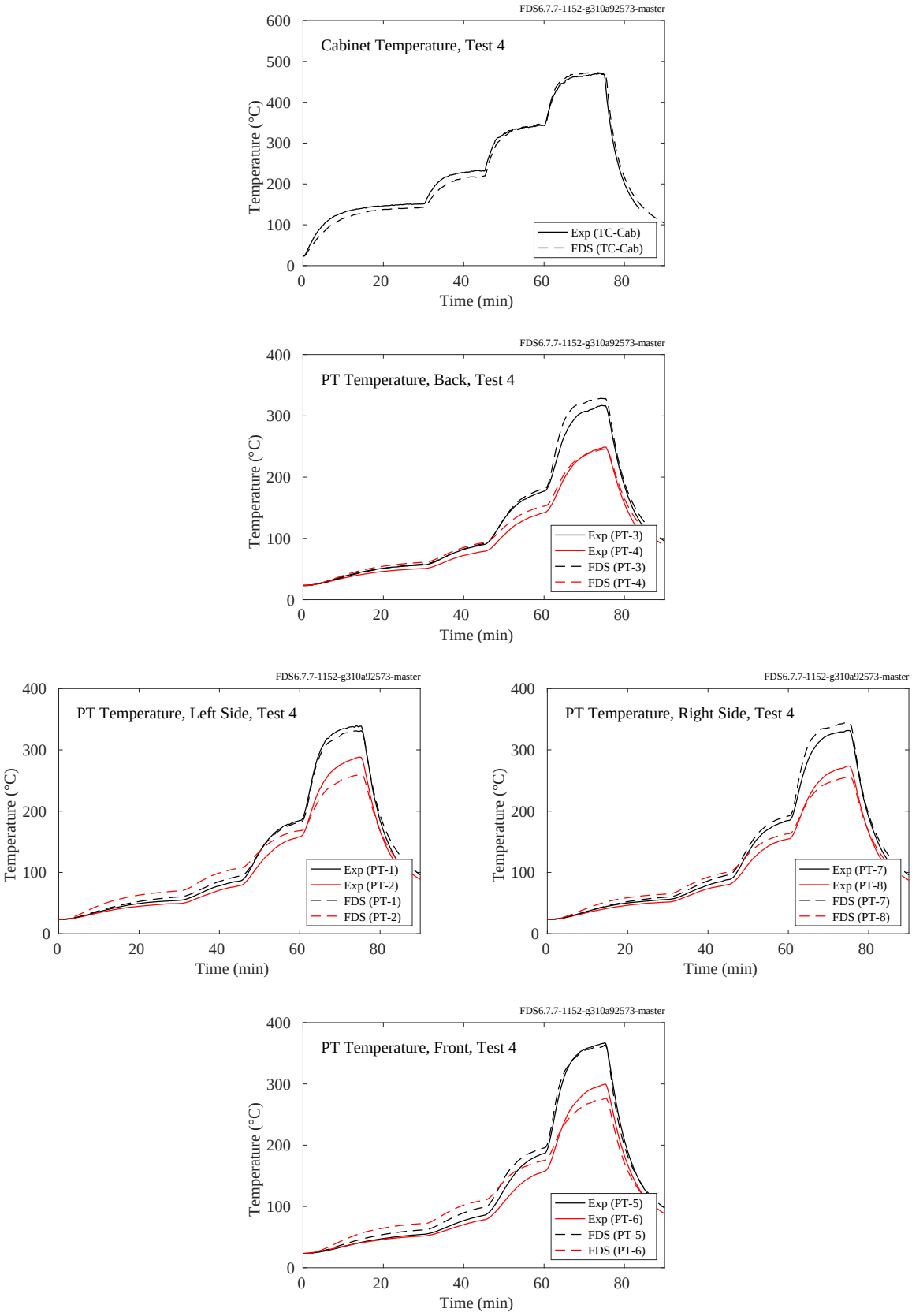

Figure 11.71: NIST/NRC Corner Effects, plate and cabinet temperatures, Test 4.

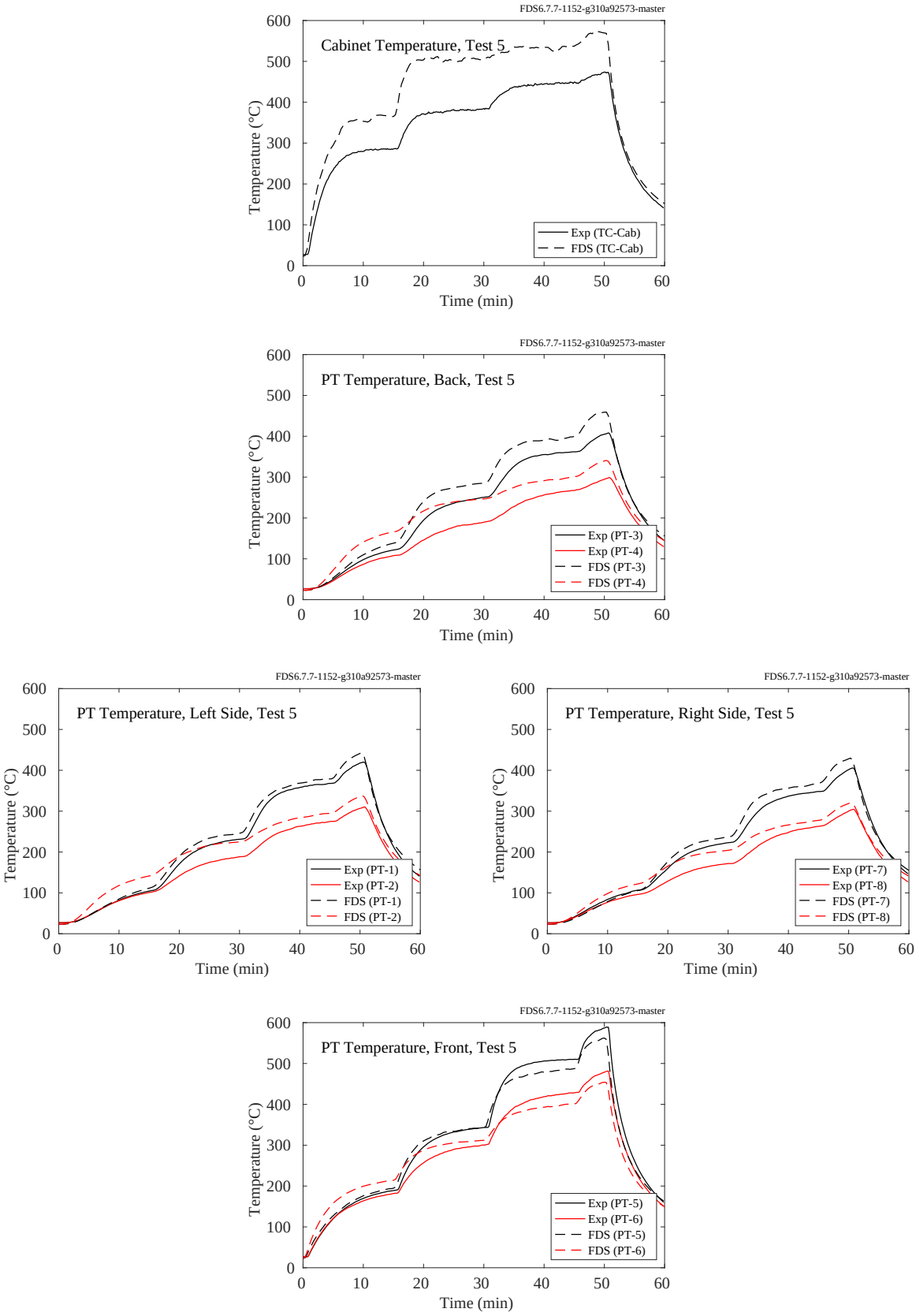

Figure 11.72: NIST/NRC Corner Effects, plate and cabinet temperatures, Test 5.

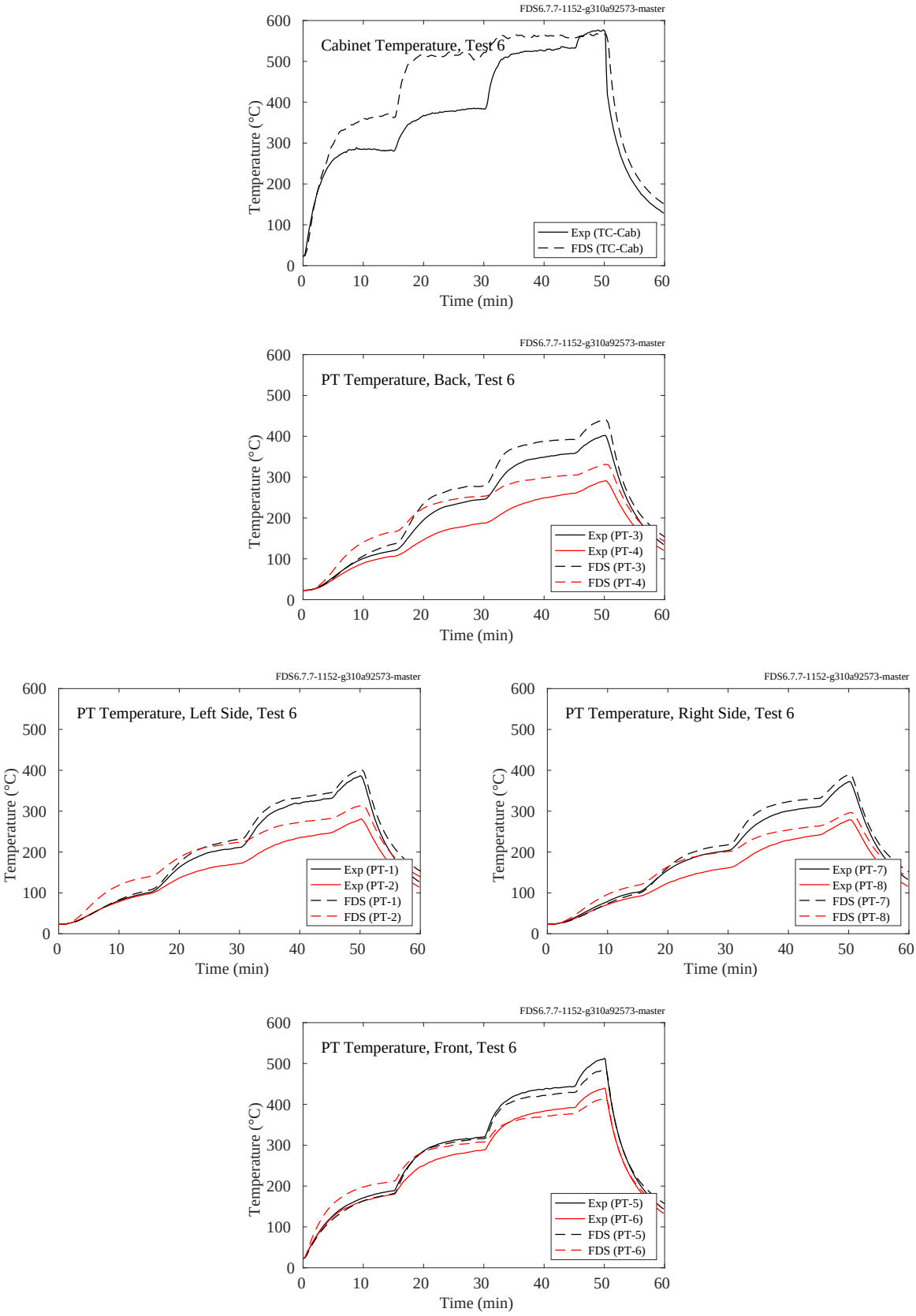

Figure 11.73: NIST/NRC Corner Effects, plate and cabinet temperatures, Test 6.

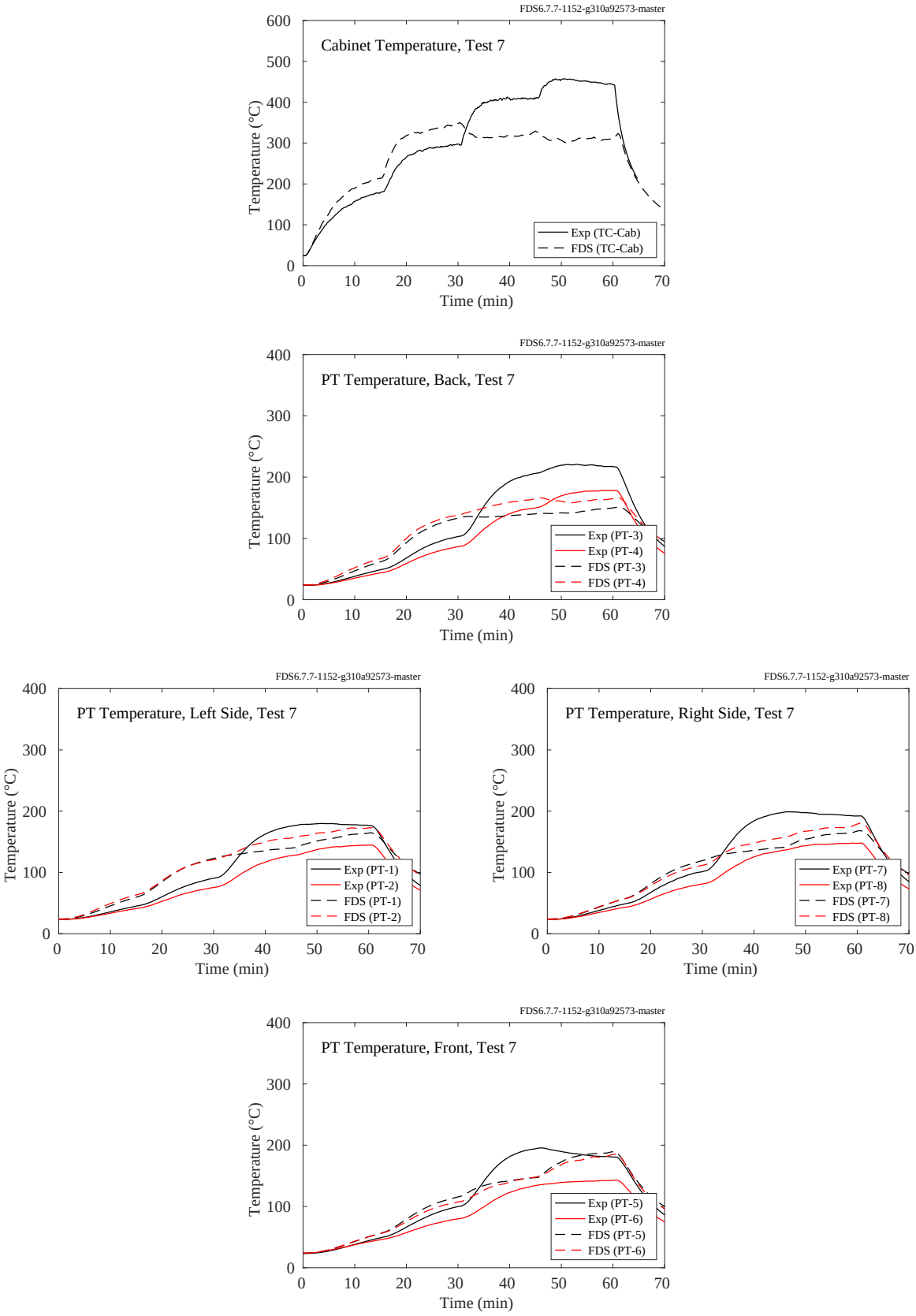

Figure 11.74: NIST/NRC Corner Effects, plate and cabinet temperatures, Test 7.

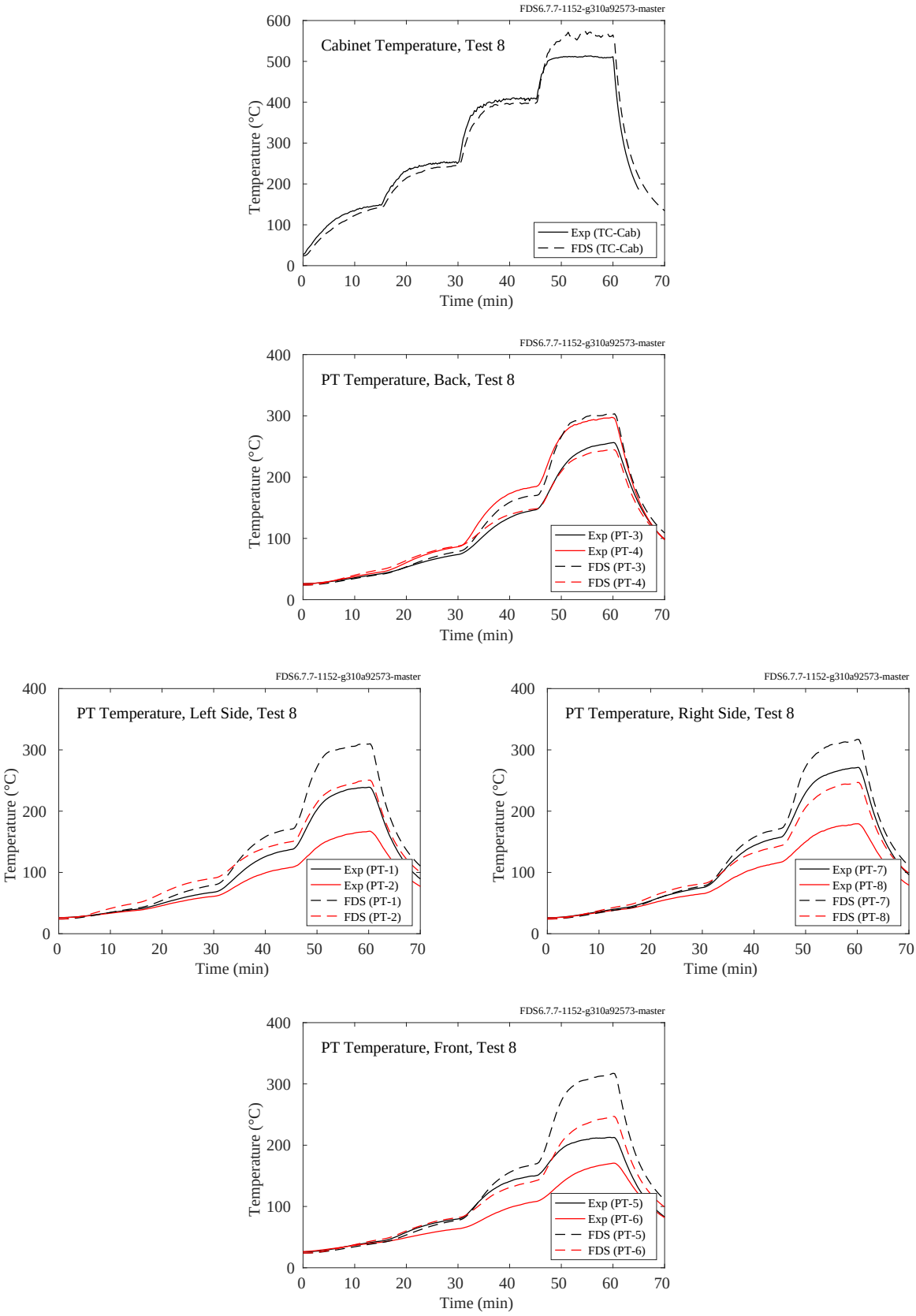

Figure 11.75: NIST/NRC Corner Effects, plate and cabinet temperatures, Test 8.

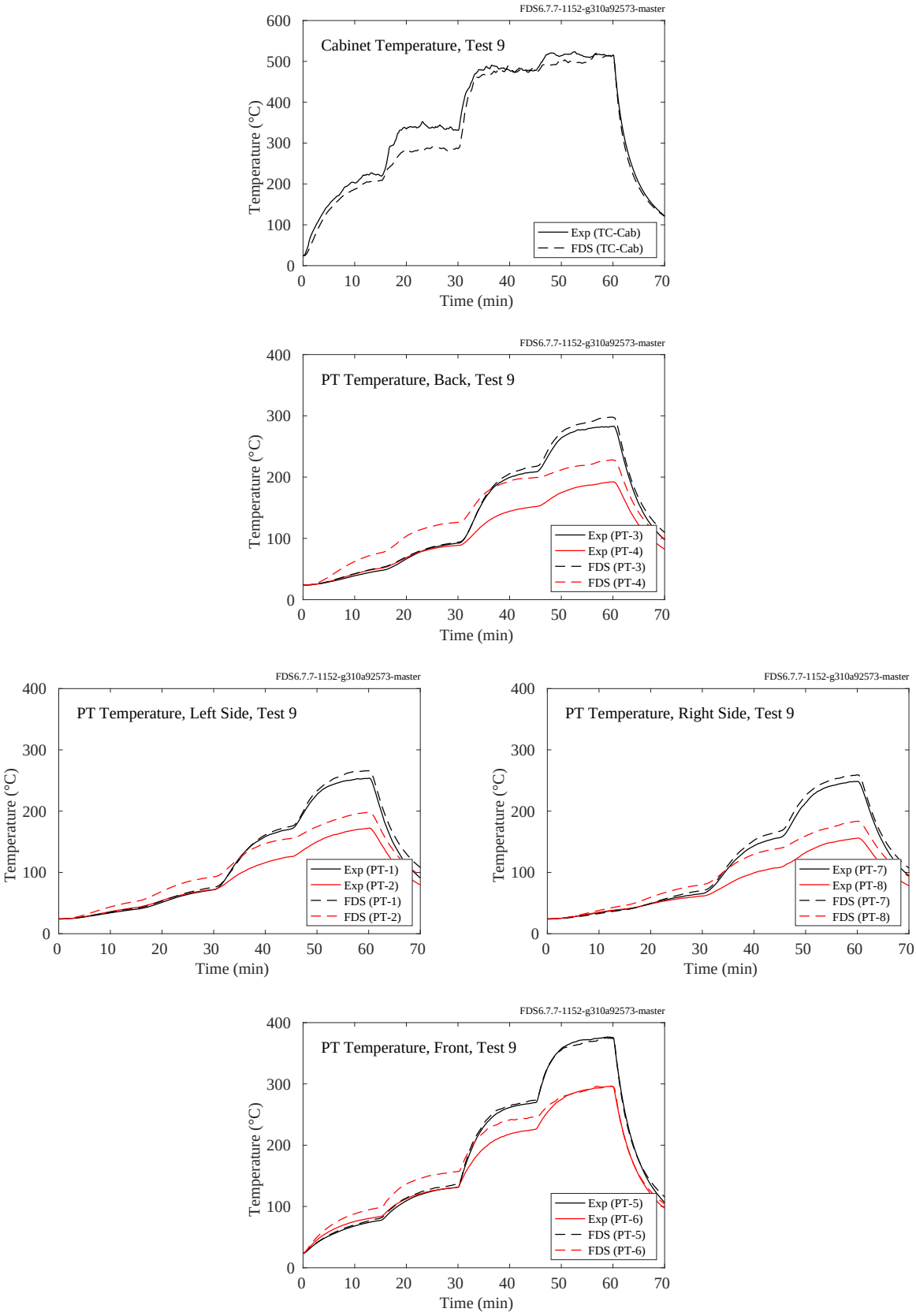

Figure 11.76: NIST/NRC Corner Effects, plate and cabinet temperatures, Test 9.

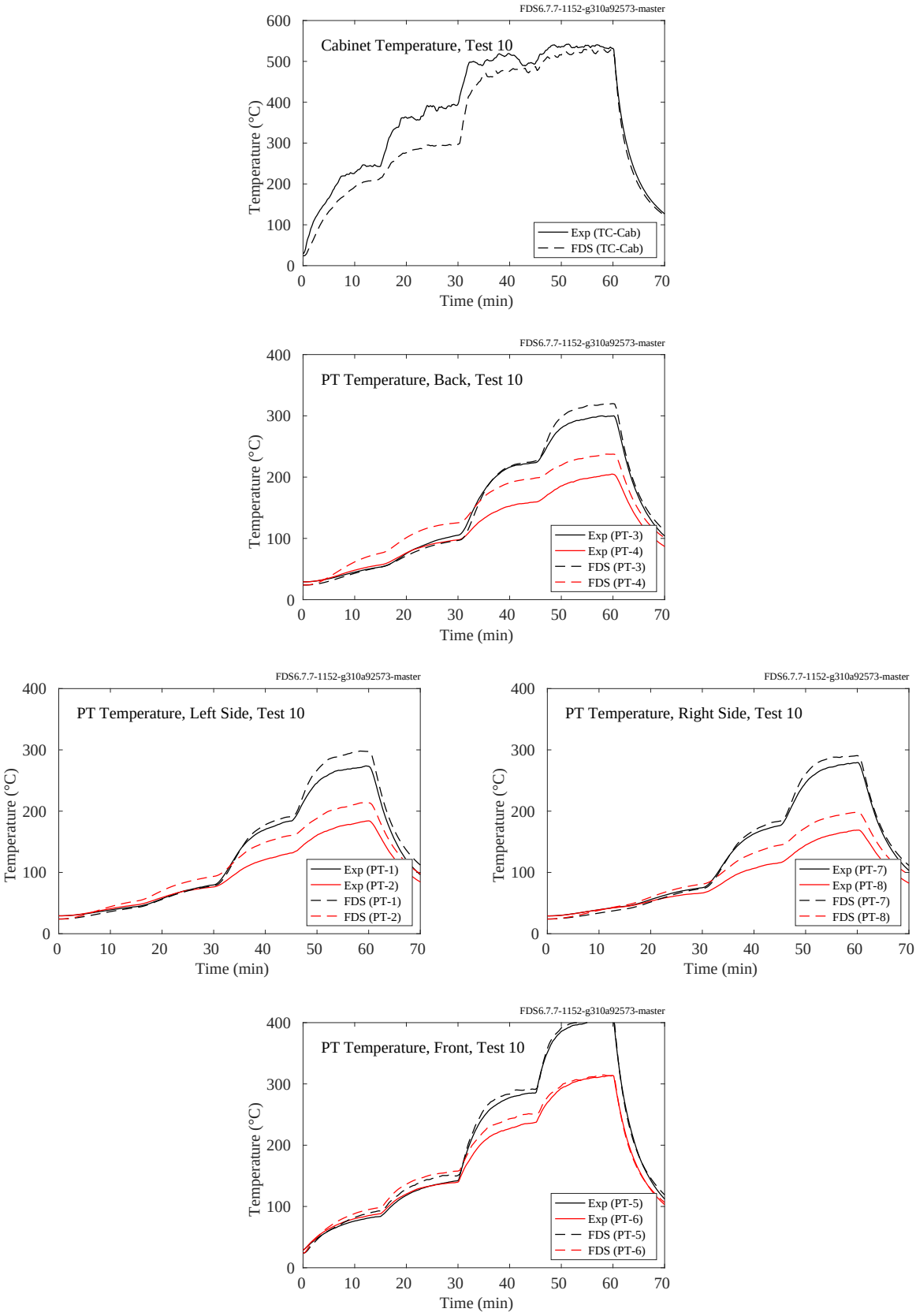

Figure 11.77: NIST/NRC Corner Effects, plate and cabinet temperatures, Test 10.

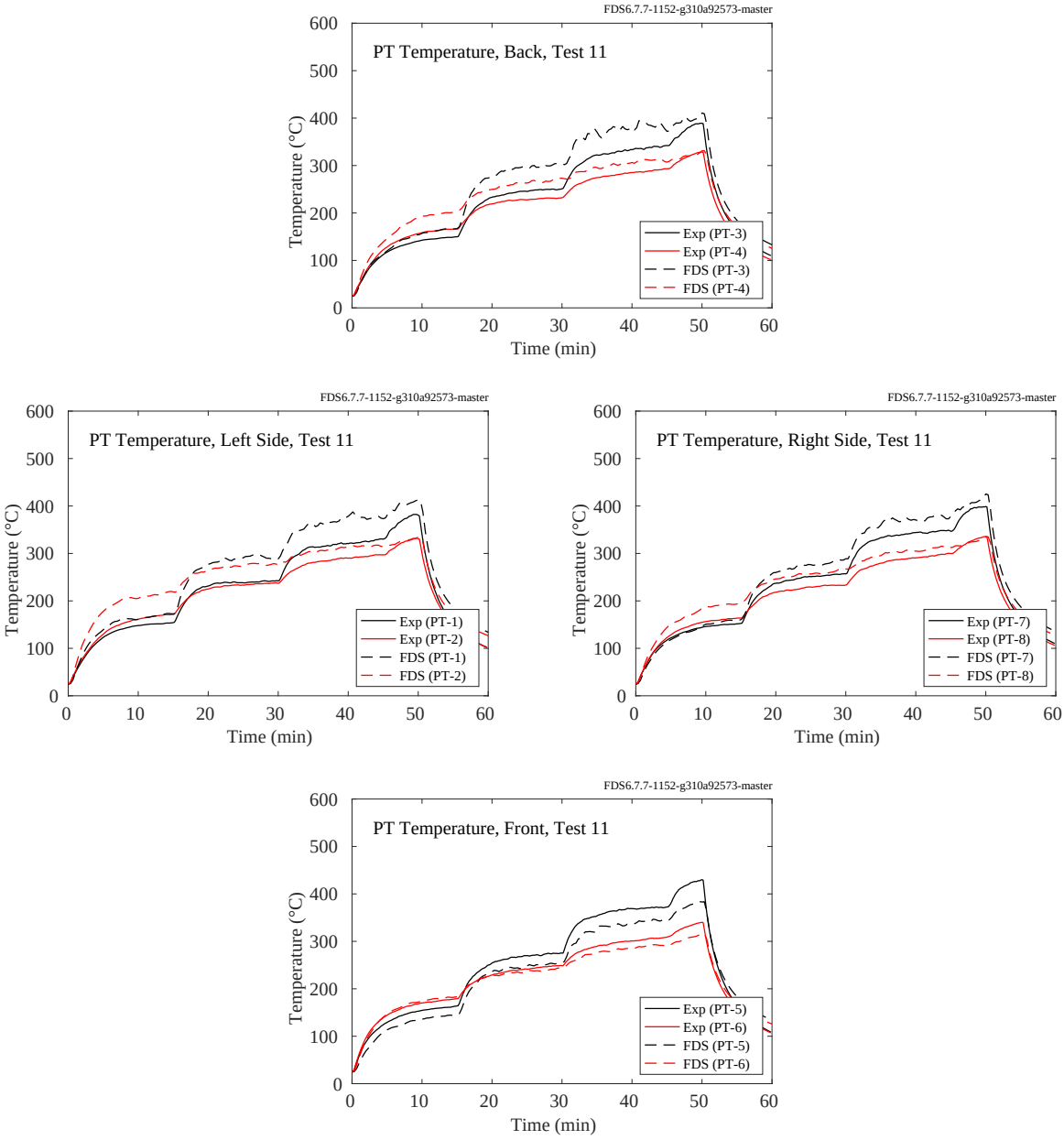

Figure 11.78: NIST/NRC Corner Effects, plate and cabinet temperatures, Test 11.

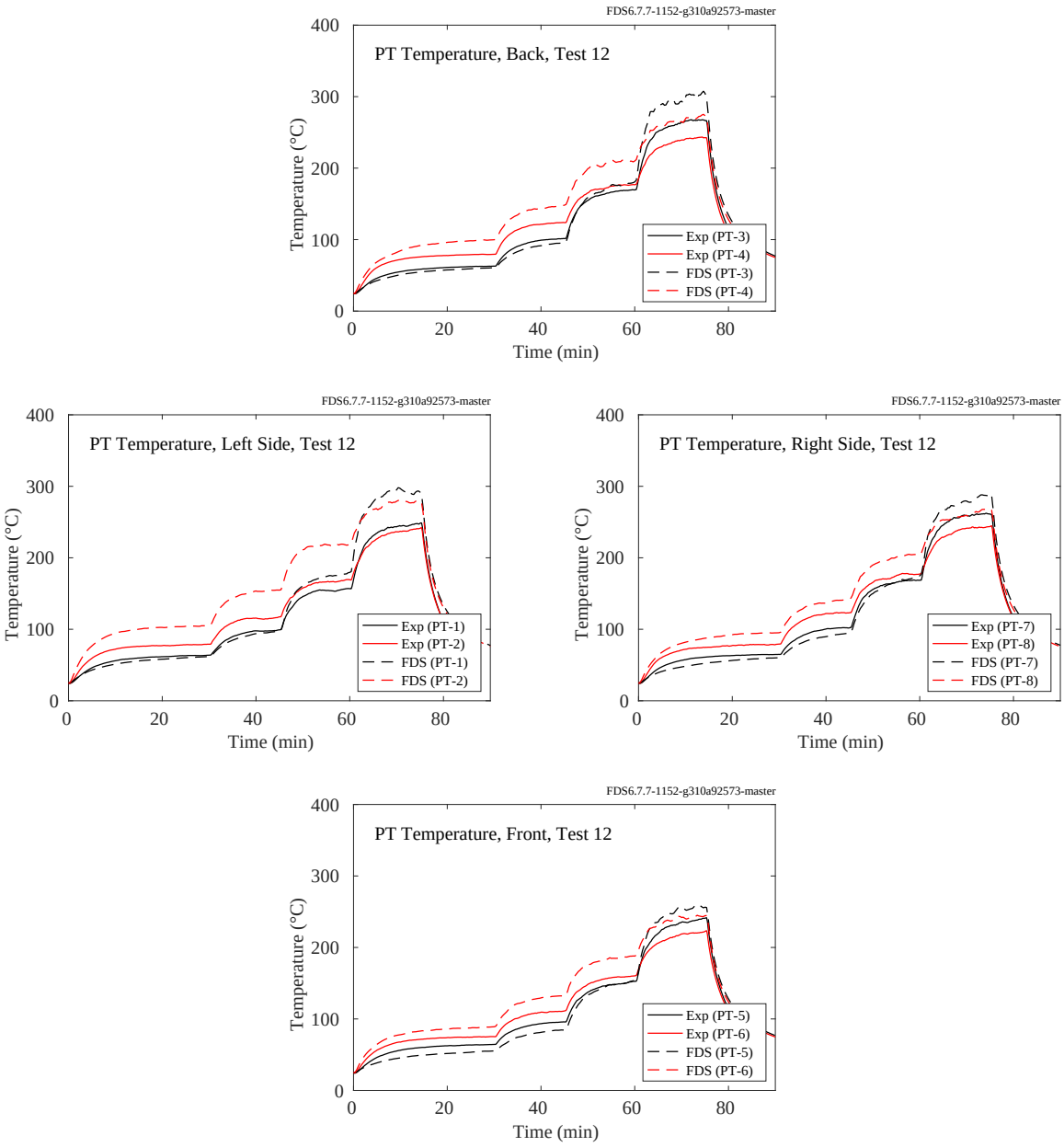

Figure 11.79: NIST/NRC Corner Effects, plate and cabinet temperatures, Test 12.

11.2.5 SP Adiabatic Surface Temperature Experiments

Comparisons of FDS predictions of gas, plate thermometer, and steel temperatures for compartment and pool fire experiments conducted at SP, Sweden, are presented on the following pages.

Compartment Fire Experiments

Three experiments were conducted in a standard compartment, 3.6 m long by 2.4 m wide by 2.4 m high, with a 0.8 m wide by 2.0 m high door centered on the narrow wall. Each experiment used a constant 450 kW propane burner and a single beam suspended 20 cm below the ceiling along the centerline of the compartment. There were three measurement stations along the beam at lengths of 0.9 m (Position A), 1.8 m (Position B), and 2.7 m (Position C) from the far wall where the fire was either positioned in the corner (Tests 1 and 2), or the center (Test 3). The beam in Test 1 was a rectangular steel tube filled with an insulation material. The beam in Tests 2 and 3 was an I-beam. Details can be found in the test report [283].

Each page to follow contains the results for a single experiment and measuring station. There are nine in all. In addition to predictions plate thermometer and steel temperatures, there are predictions of the adiabatic surface temperature (AST) for the locations and orientations of the plate thermometers. The AST is a useful quantity that serves as a boundary condition for thermal resistance calculations of structures. The basic idea is as follows. The *net* heat flux to the solid surface is given as the sum of radiative and convective components:

$$\dot{q}''_r + \dot{q}''_c = \varepsilon \left(\dot{q}''_{r,inc} - \sigma T_s^4 \right) + h(T_g - T_s) \tag{11.1}$$

where $\dot{q}''_{r,inc}$ is the incident radiative flux, T_s the surface temperature, T_g the gas temperature near the surface, and h the convective heat transfer coefficient. Following the idea proposed by Wickström [339], the AST is defined as the surface temperature of a perfectly insulated solid. This is equivalent to saying that the net heat flux to this (hypothetical) surface is zero:

$$0 = \varepsilon \left(\dot{q}''_{r,inc} - \sigma T_{\rm AST}^4 \right) + h(T_g - T_{\rm AST}) \tag{11.2}$$

This definition of the AST forms the theory behind the plate thermometer, a 10 cm by 10 cm thin metal plate with an insulated backing that is designed to measure the AST, albeit with a slight time lag due to the fact that it is not a perfect insulator.

FDS calculates the AST by solving the following equation implicitly for $T_{\rm AST}$:

$$\dot{q}''_r + \dot{q}''_c = \varepsilon \left(\sigma T_{\rm AST}^4 - \sigma T_s^4 \right) + h(T_{\rm AST} - T_s) \tag{11.3}$$

Equation (11.3) is simply Eq. (11.1) minus Eq. (11.2). As such, it shows that the AST can be regarded as an *effective* gas temperature for the purpose of providing boundary conditions for a detailed heat conduction calculation within the solid.

FDS calculates the AST using Eq. (11.3) and the plate thermometer temperature via its standard one-dimensional heat conduction calculation for a two layer solid of metal and insulating material. In the experiments, the plate thermometer temperature was obtained from a thermocouple attached to the back side of the thin metal plate, and the AST was derived from the measured plate thermometer temperature by a back calculation involving only the thermal lag due to the plate, not the insulation material.

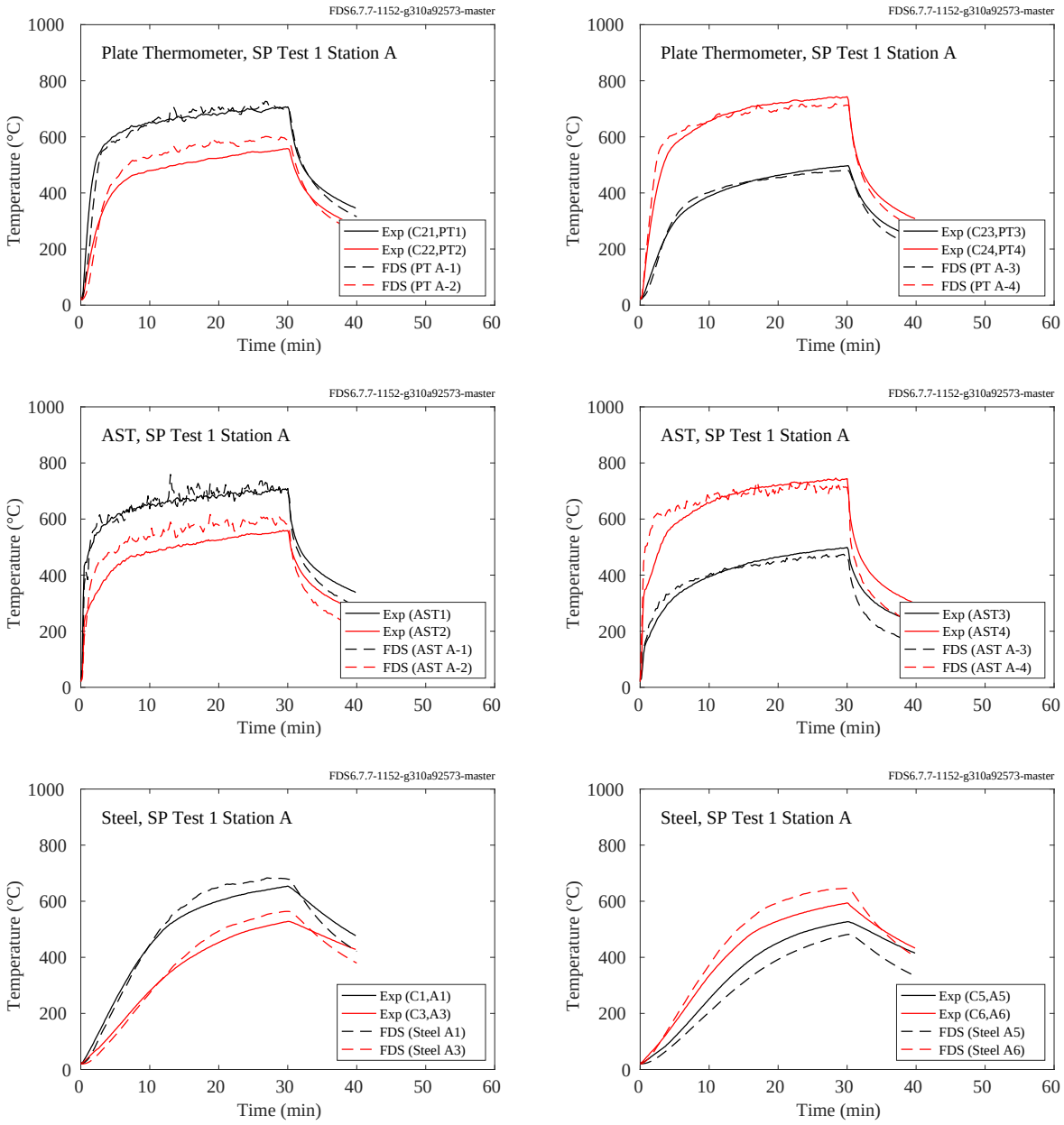

Figure 11.80: SP AST experiments, Station A plate, adiabatic surface, and steel temperatures, Test 1.

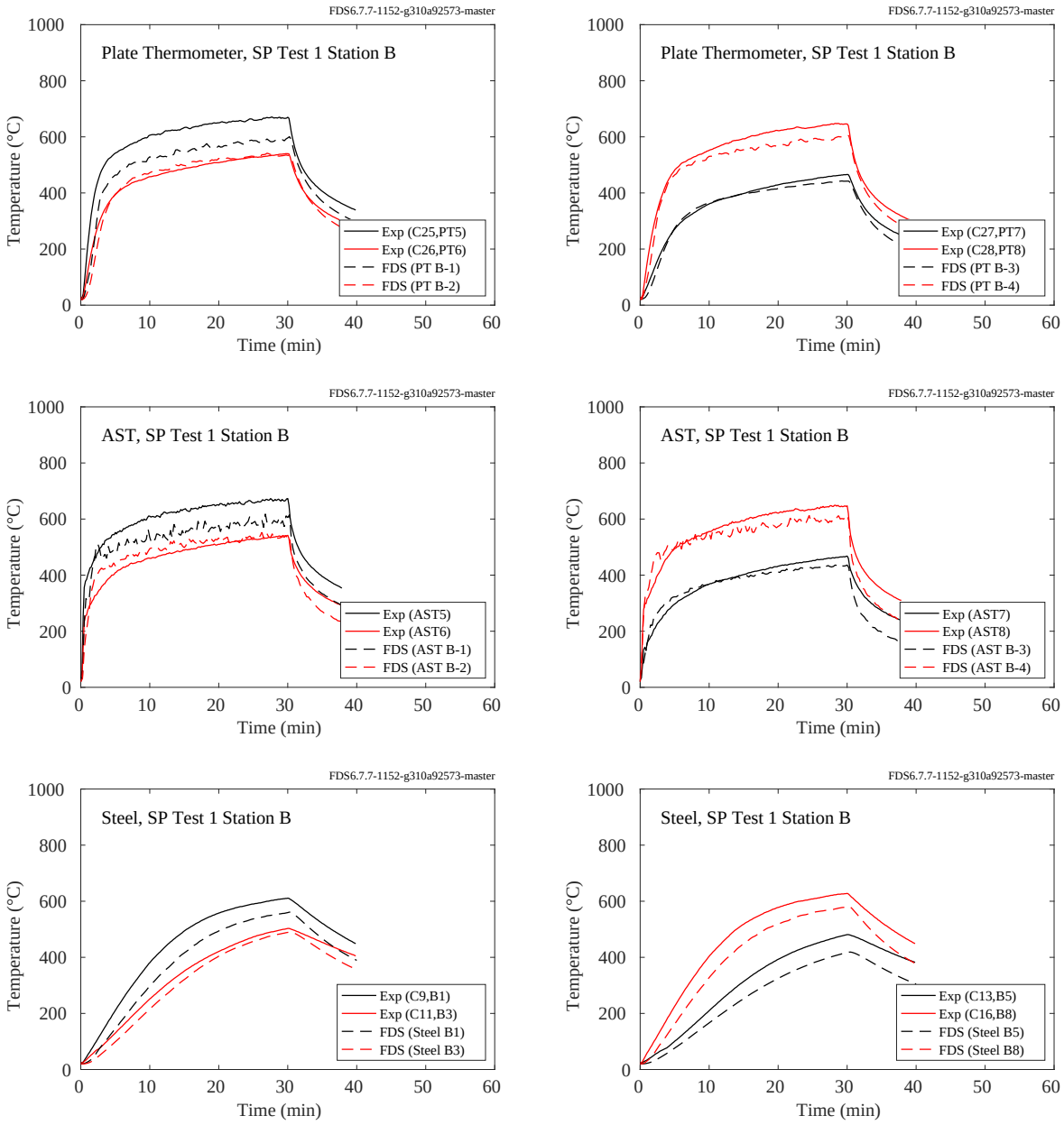

Figure 11.81: SP AST experiments, Station B plate, adiabatic surface, and steel temperatures, Test 1.

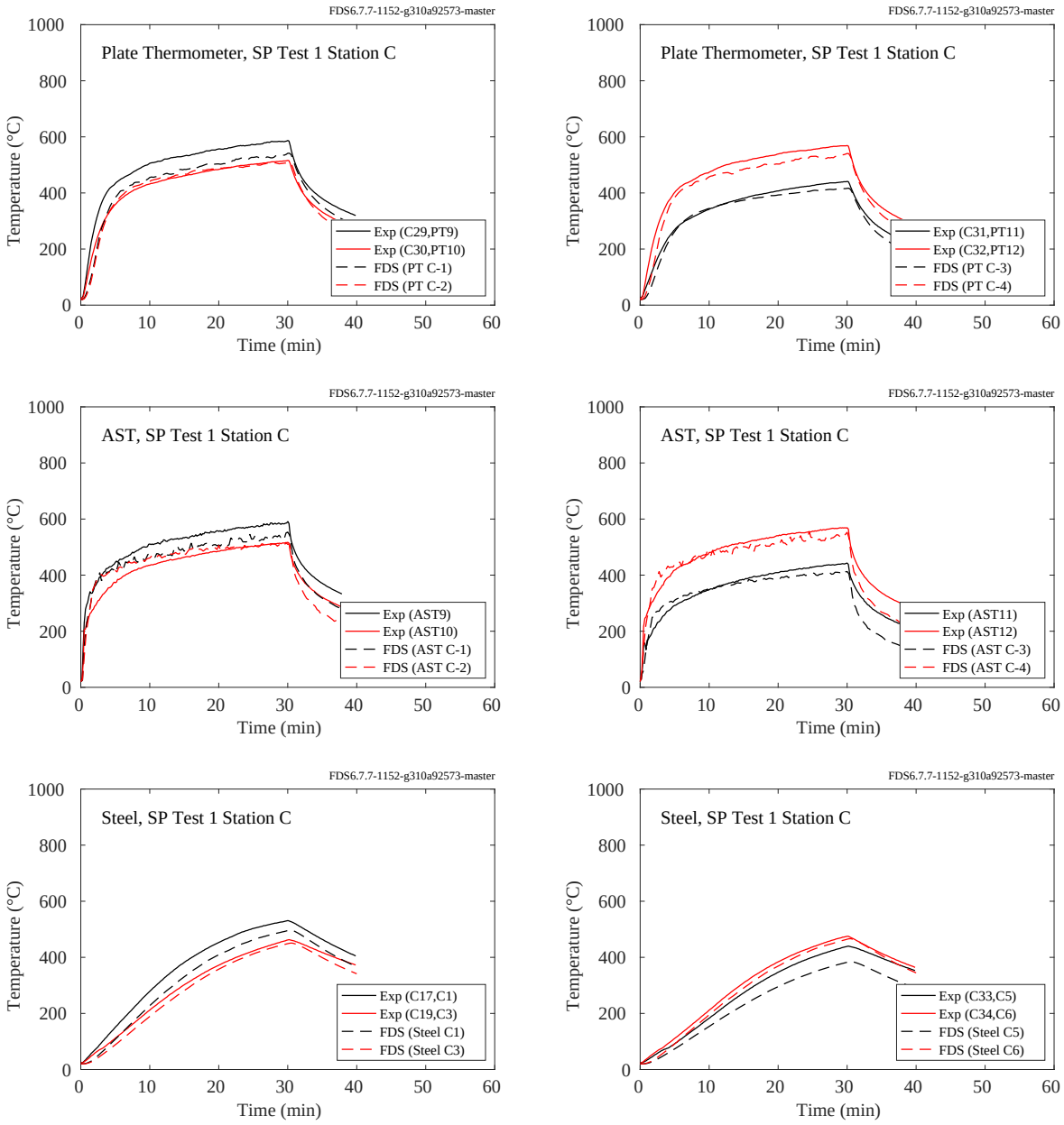

Figure 11.82: SP AST experiments, Station C plate, adiabatic surface, and steel temperatures, Test 1.

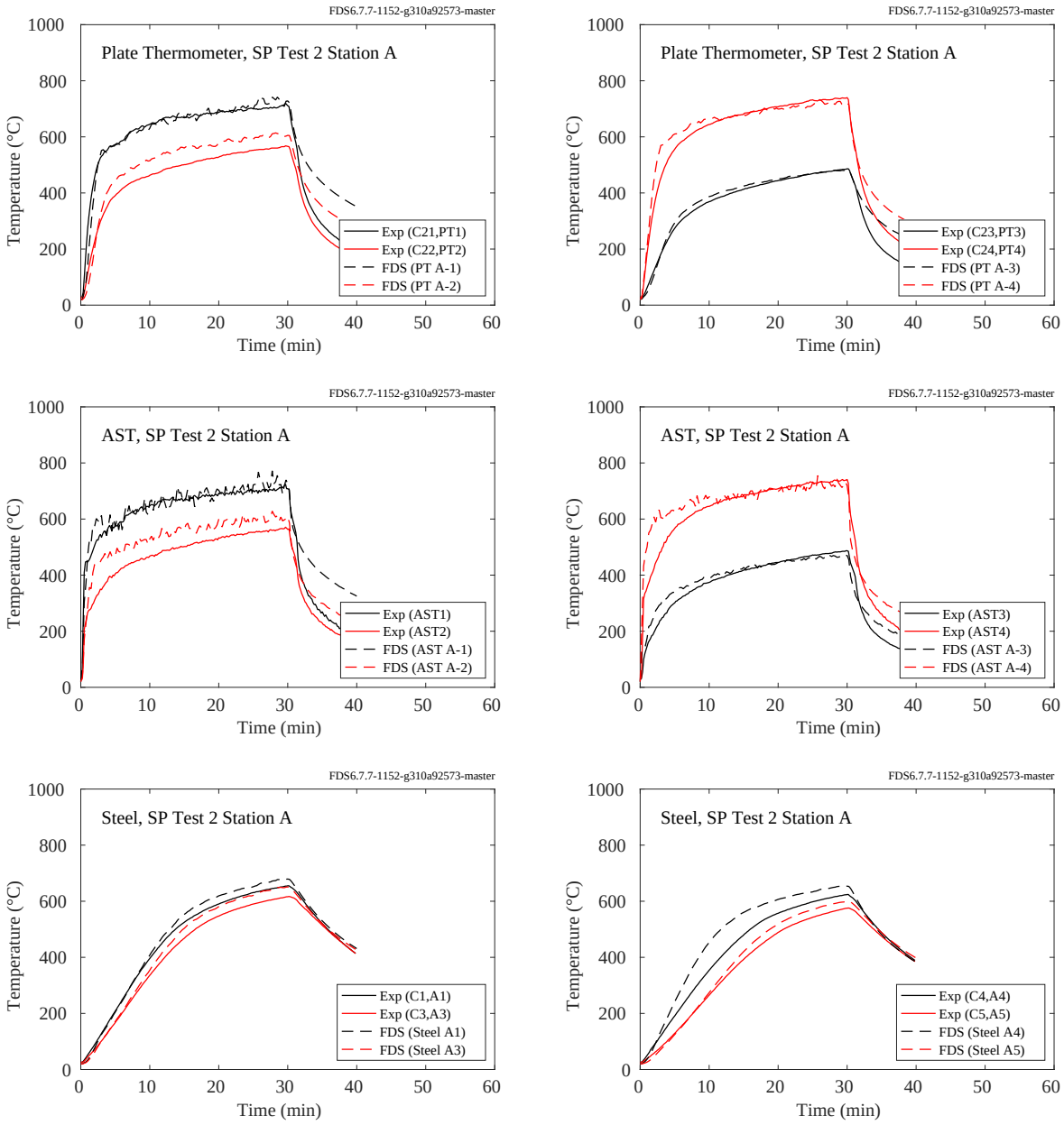

Figure 11.83: SP AST experiments, Station A plate, adiabatic surface, and steel temperatures, Test 2.

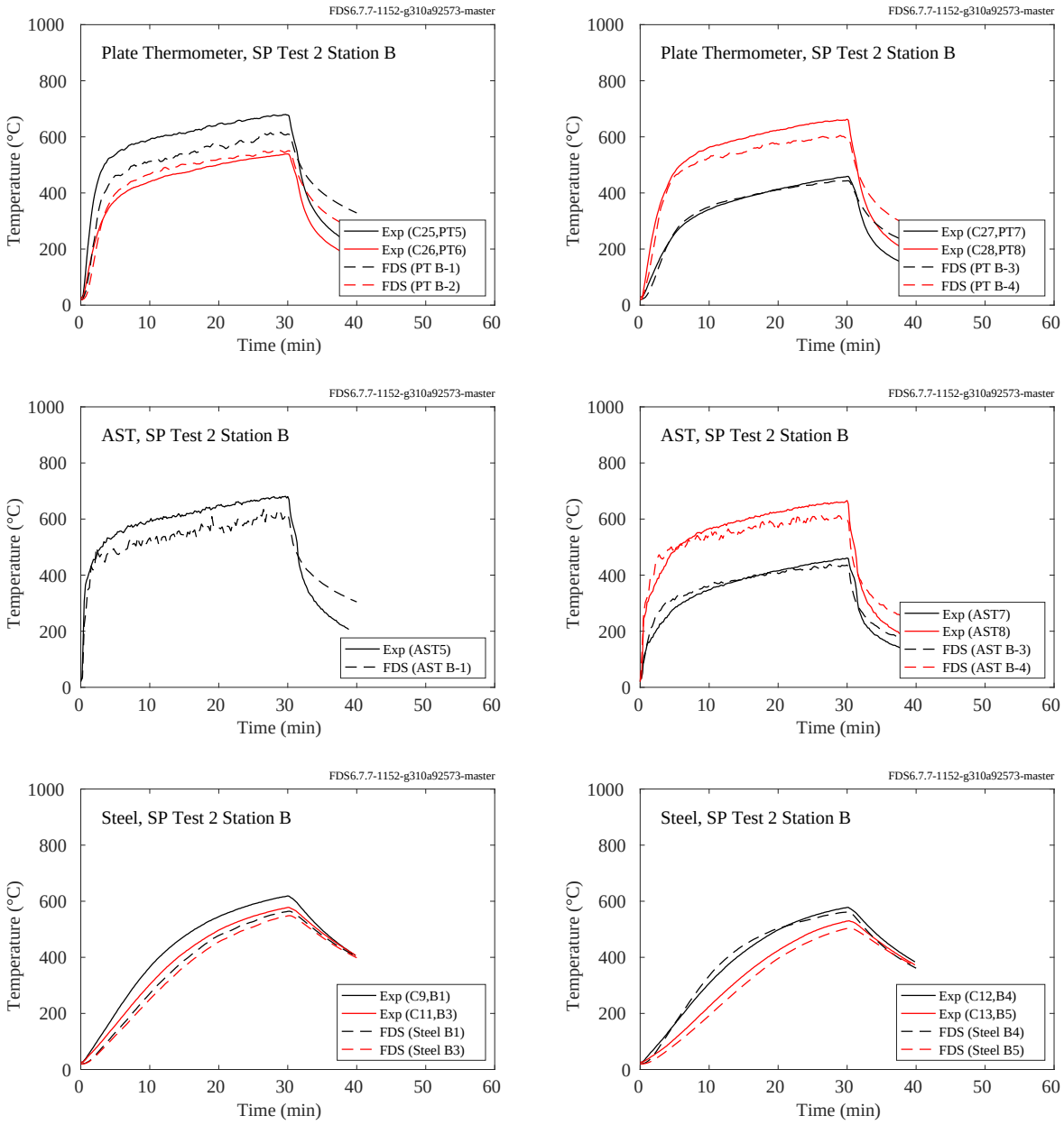

Figure 11.84: SP AST experiments, Station B plate, adiabatic surface, and steel temperatures, Test 2.

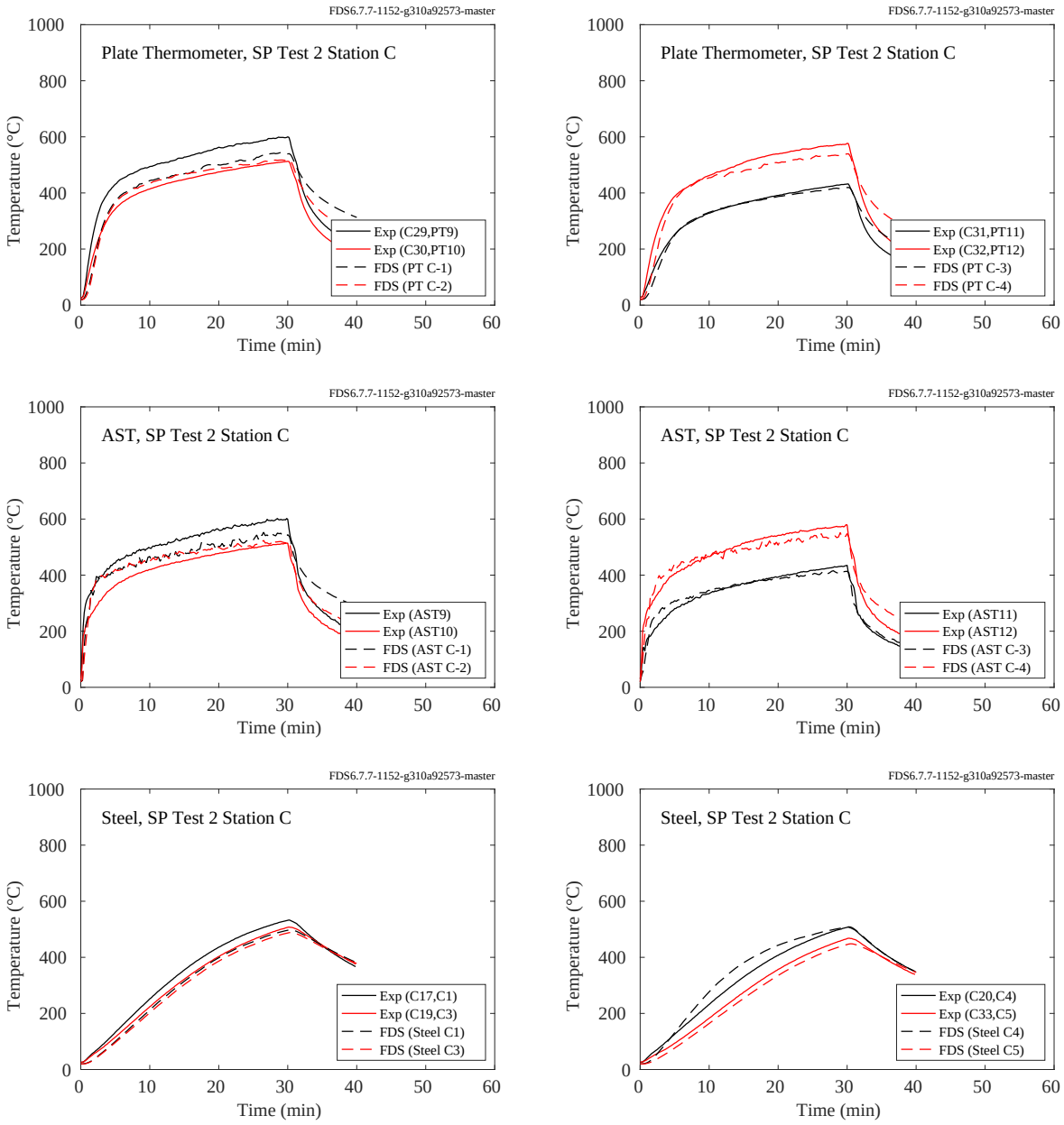

Figure 11.85: SP AST experiments, Station C plate, adiabatic surface, and steel temperatures, Test 2.

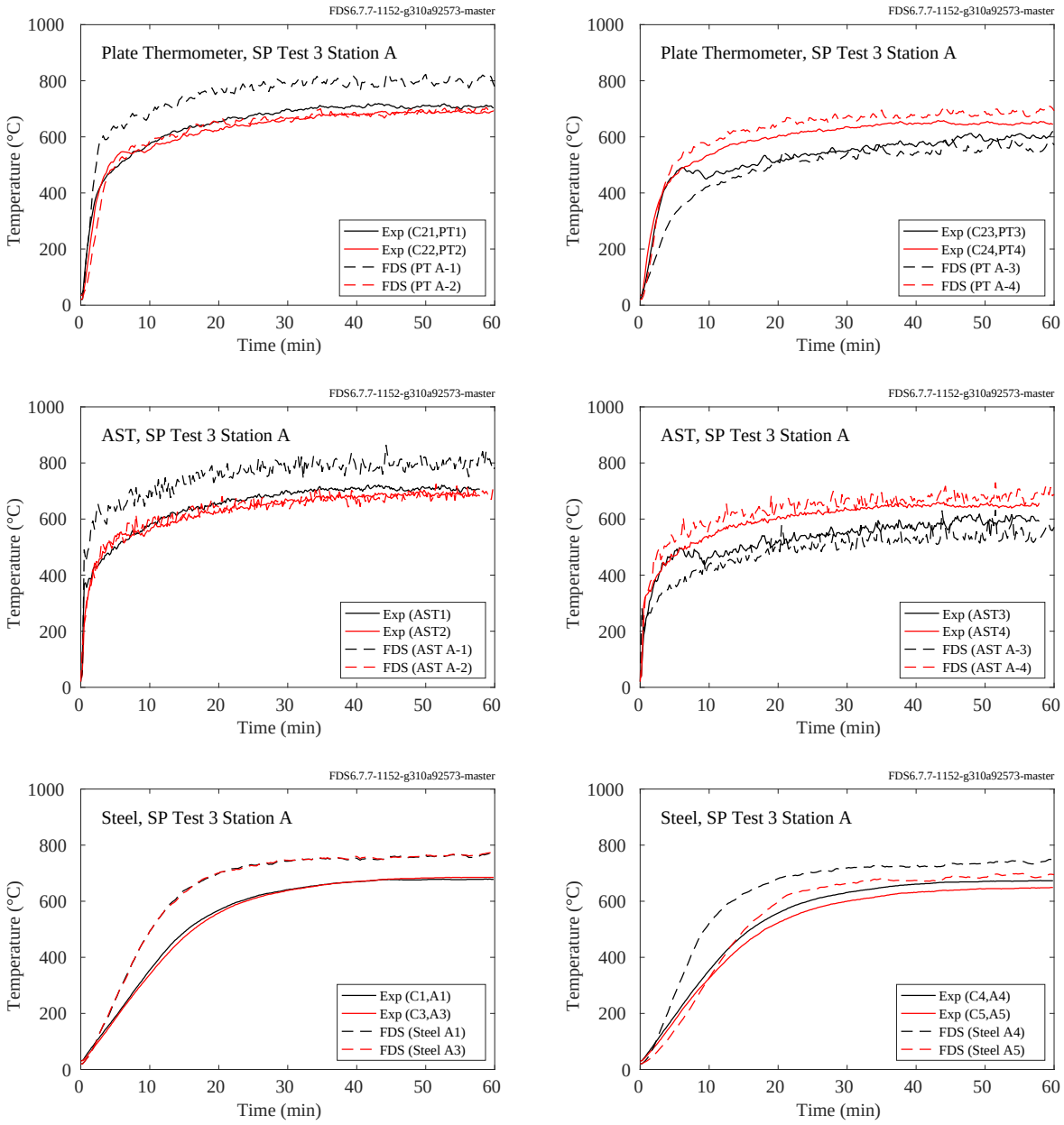

Figure 11.86: SP AST experiments, Station A plate, adiabatic surface, and steel temperatures, Test 3.

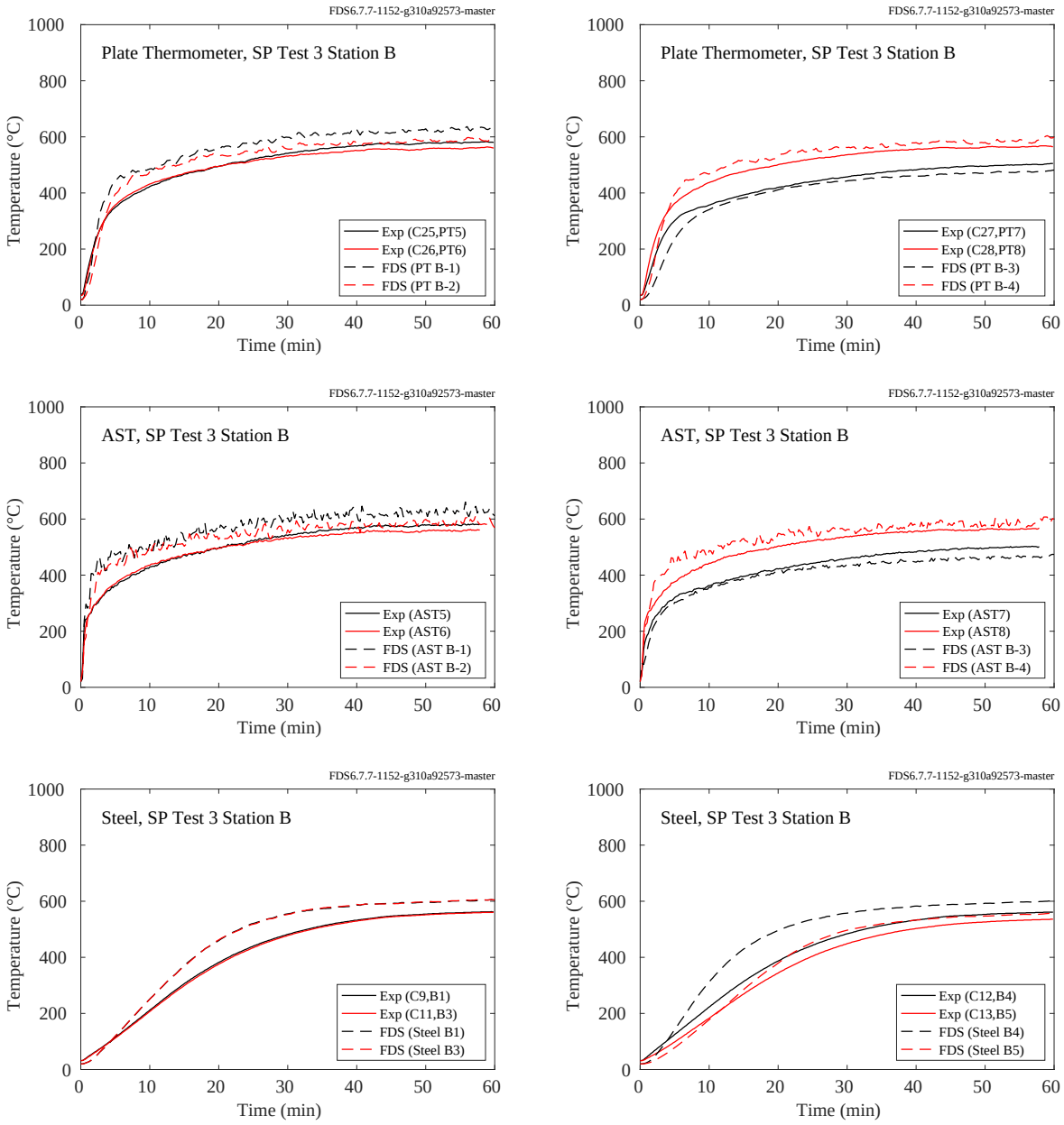

Figure 11.87: SP AST experiments, Station B plate, adiabatic surface, and steel temperatures, Test 3.

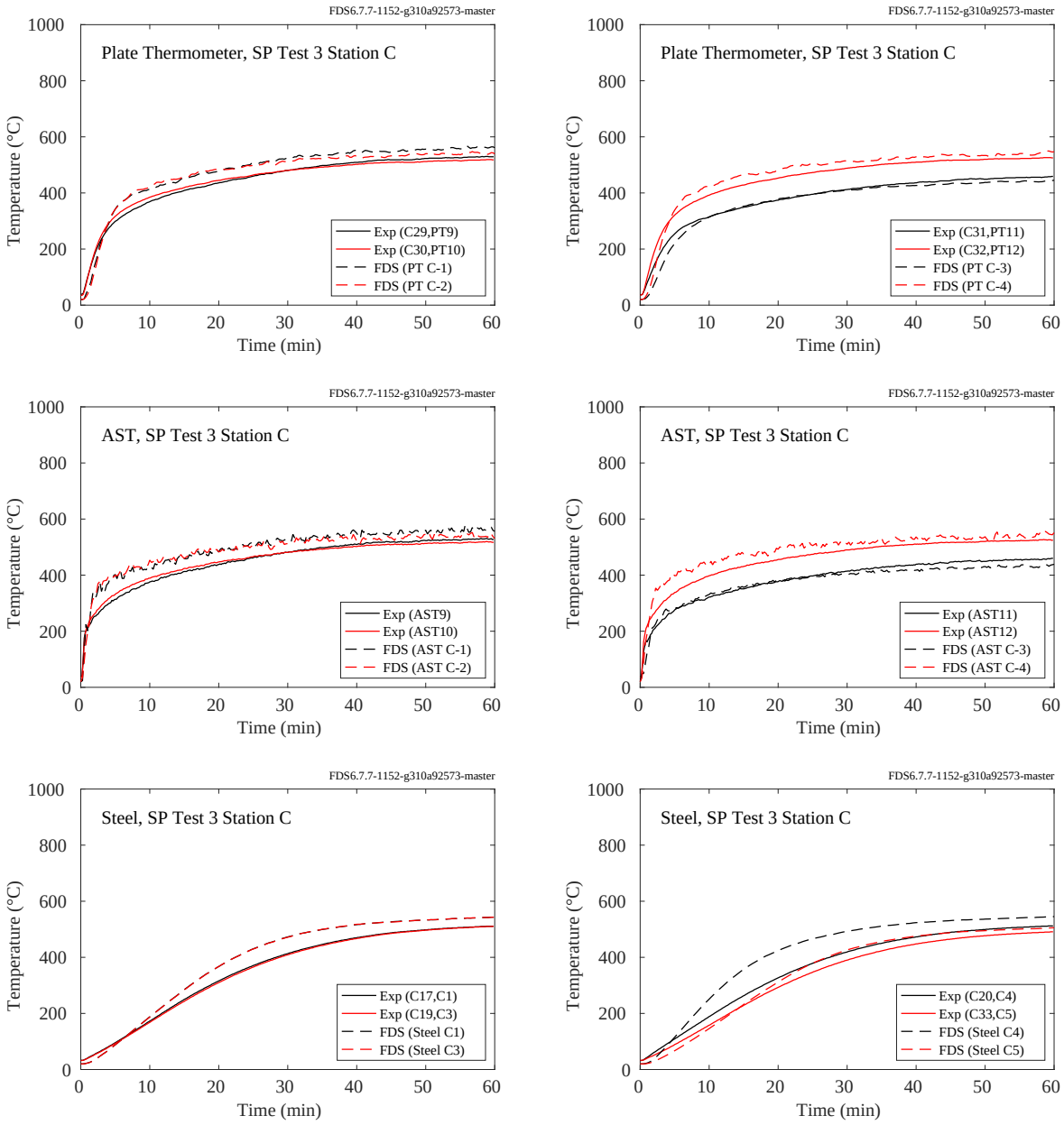

Figure 11.88: SP AST experiments, Station C plate, adiabatic surface, and steel temperatures, Test 3.

Pool Fire Experiments

Three experiments were conducted at SP, Sweden, in 2011, in which a 6 m long, 20 cm diameter vertical column was positioned in the middle of 1.1 m and 1.9 m diesel and 1.1 m heptane pool fires [284]. Gas, plate, and steel surface temperature measurements were made at heights of 1 m, 2 m, 3 m, 4 m, and 5 m above the pool surface. At heights of 1 m, 3 m, and 5 m, these measurements were made at only one angular position. However, at 2 m and 4 m, the measurements were made at four positions. At these heights, two conventional plates thermometers were positioned approximately 10 cm from the column surface, along with two special plate thermometers (SPT) that were installed flush with the column surface. At each height, comparable predictions were made with FDS, but at only one angular position because there is no predominant direction of leaning in the simulation. In the experiments, the fire was reported to lean in the direction of Position 1. The lean was significant for the 1.9 m diesel fuel fires, in which case only data from 1 m and 2 m above the pool are used. Also, FDS assumes the column to be square in cross section (20 cm by 20 cm), rather than circular. The grid spacing is 10 cm.

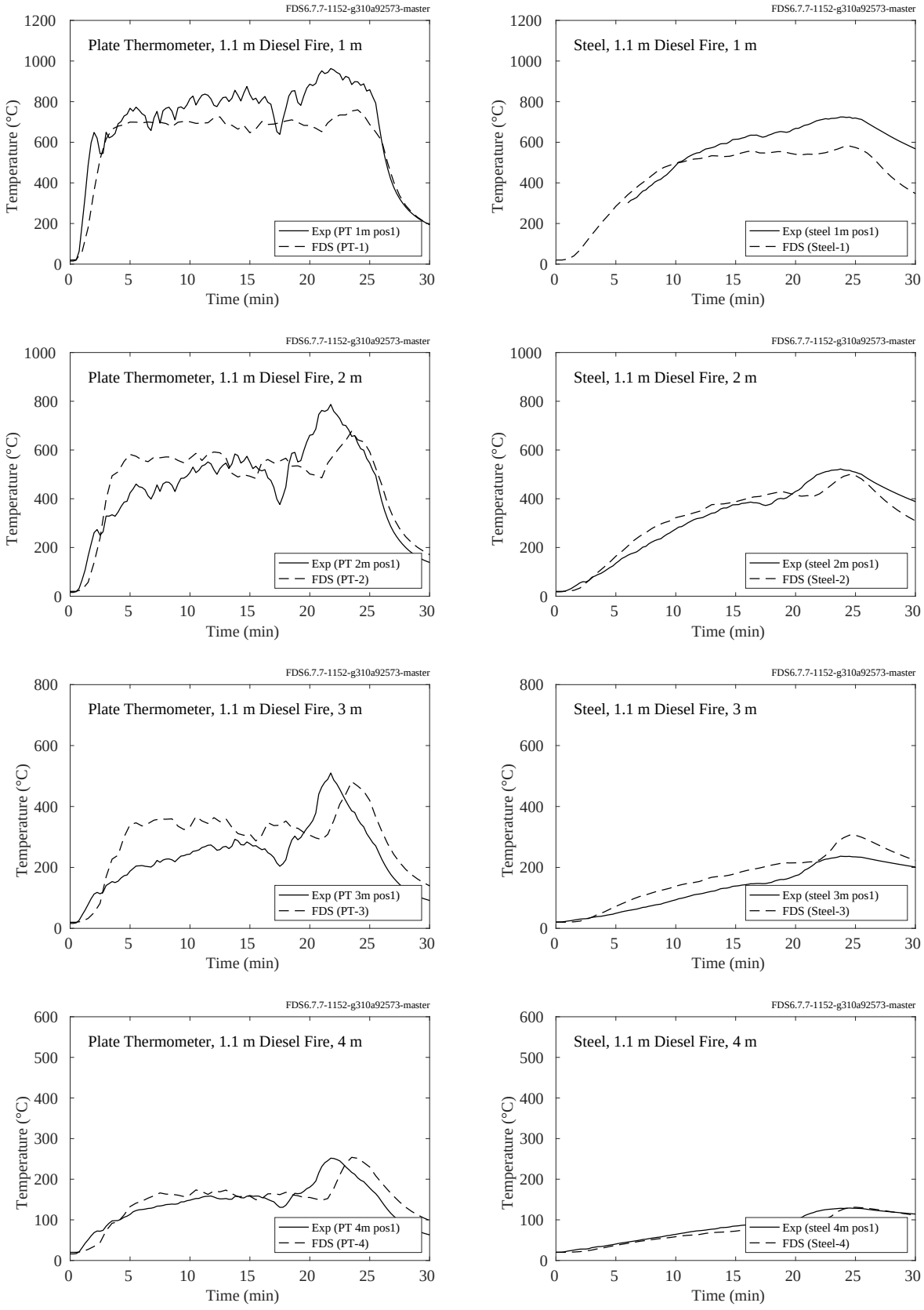

Figure 11.89: SP AST experiments, steel temperatures, 1.1 m diesel fire.

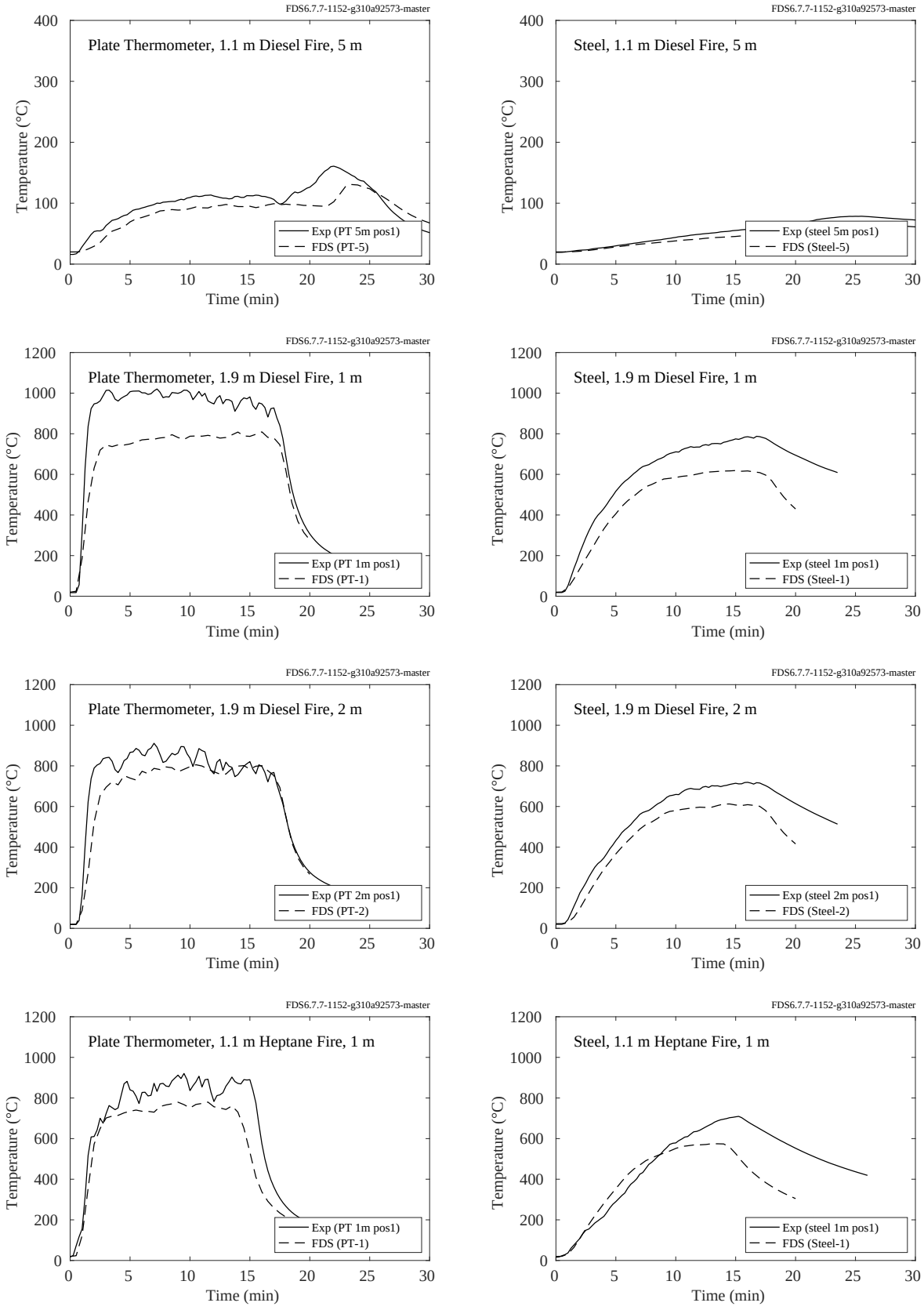

Figure 11.90: SP AST experiments, steel temperatures, 1.1 m and 1.9 m diesel, 1.1 m heptane fires.

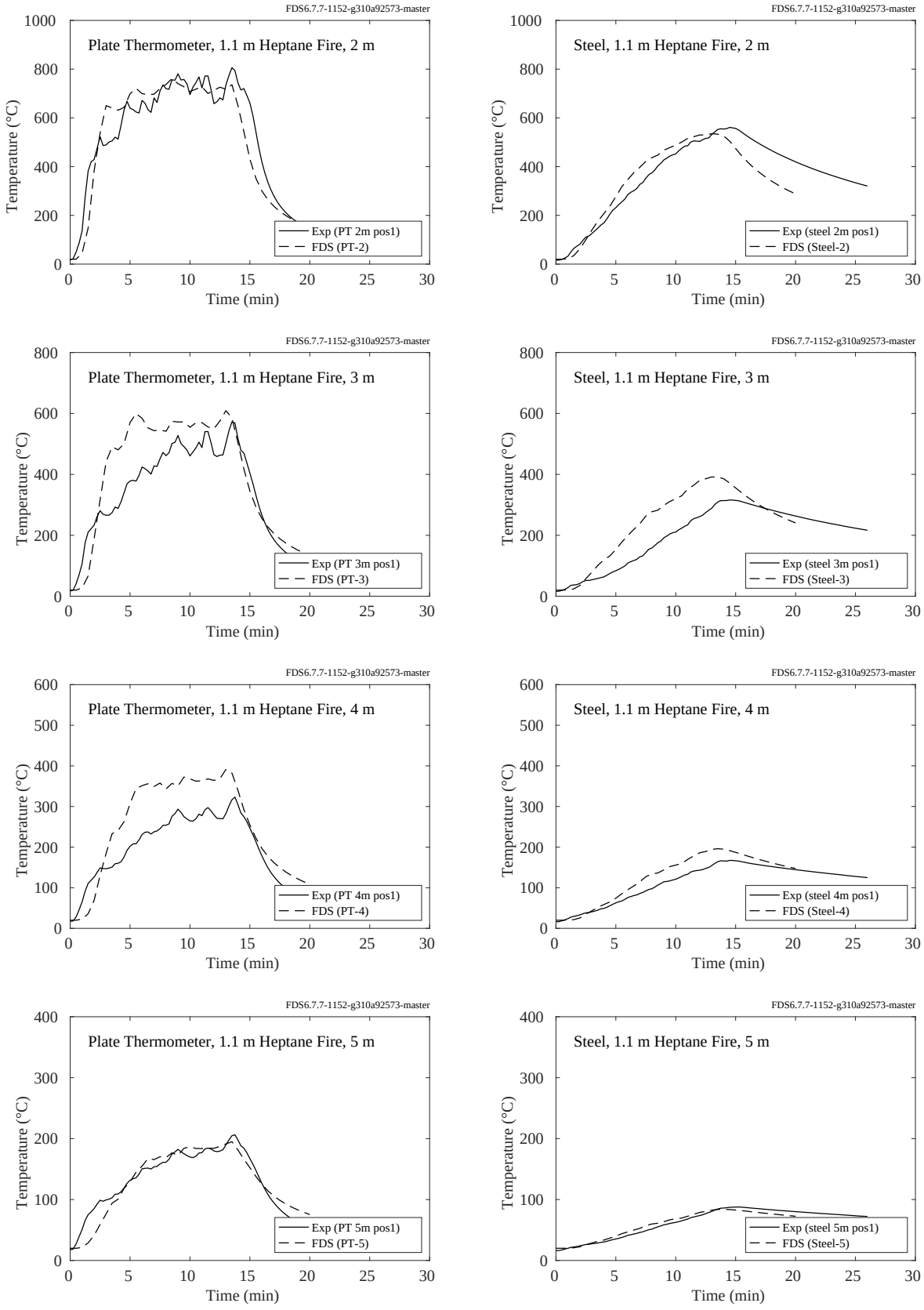

Figure 11.91: SP AST experiments, steel temperatures, 1.1 m heptane fire.

Insulated Room Experiments

The plots on the following pages display measured and predicted plate thermometer (PT) temperatures for a series of single compartment experiments conducted by SP, Sweden [285]. The compartment was 2.7 m long, 1.8 m wide, and 1.8 m tall, with a 0.6 m by 1.5 m door centered on one of the short walls. The PTs were affixed to the walls. The designations of right and left wall are from the perspective of a person looking into the room. The back wall is the short wall without the door; the front wall is opposite. When referring to a given PT, the terms left/right, upper/lower, front/back refer to the quadrant where the PT is located. The PTs are centered within each quadrant, and are thus located at one-fourth or three-fourths of the wall's length, width or height. The term "center" refers to the center point of the entire wall. The designation "back wall upper" refers to the upper left quadrant of the back wall, and "back wall lower" refers to the lower right quadrant of the back wall.

The 12 experiments were conducted with four different wall linings. In Series A, the compartment was lined with a 10 cm thick light concrete block. In Series B, the compartment was lined with a 5 cm thick layer of insulation backed by a 3 mm thick plate of steel. In Series C, the compartment was lined with an uninsulated 3 mm thick steel plate. In Series D, the compartment was lined with a 3 mm thick steel plate backed by a 5 cm thick layer of insulation (the opposite of Series B).

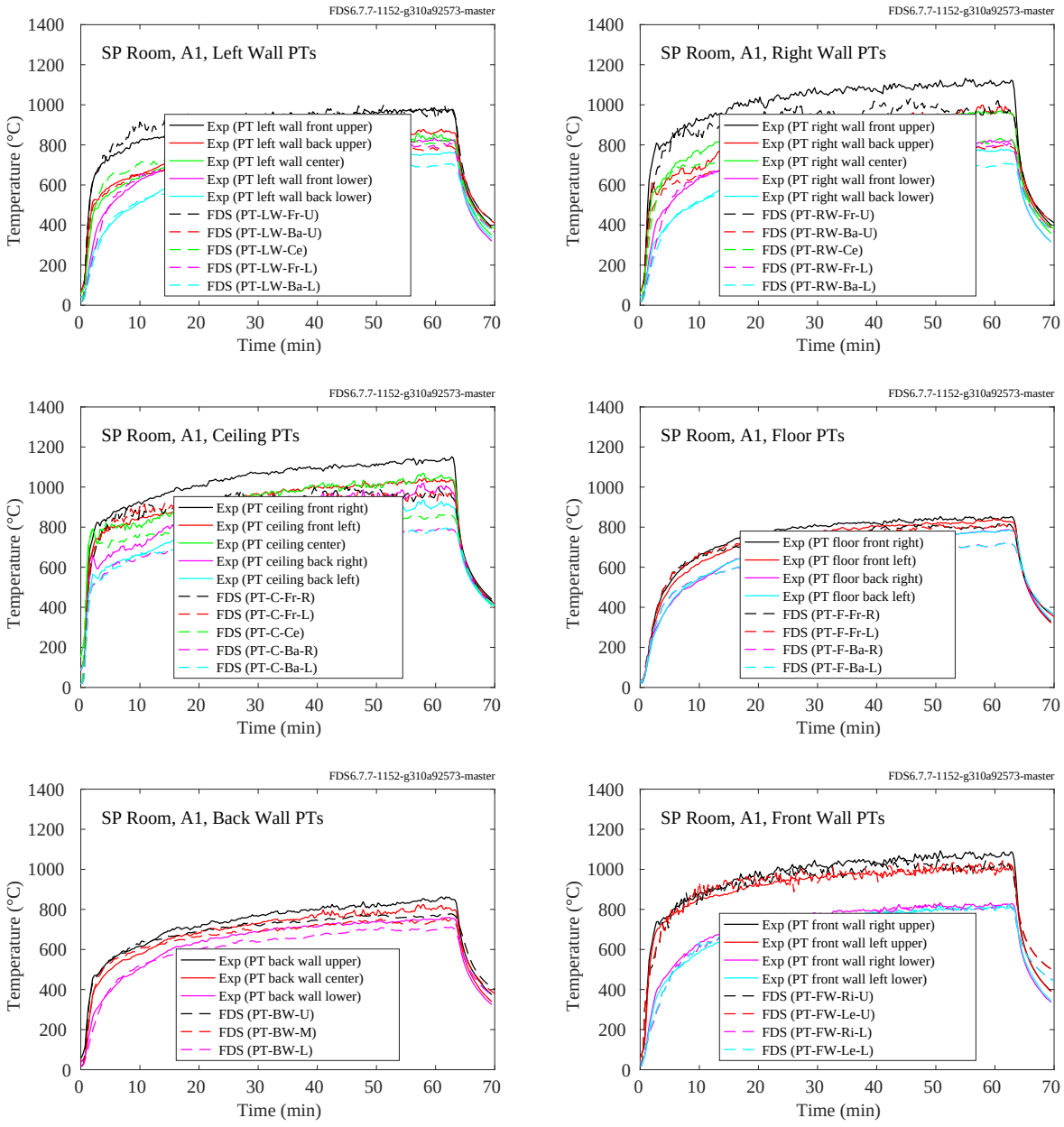

Figure 11.92: SP AST experiments, Insulated Room, Test A1.

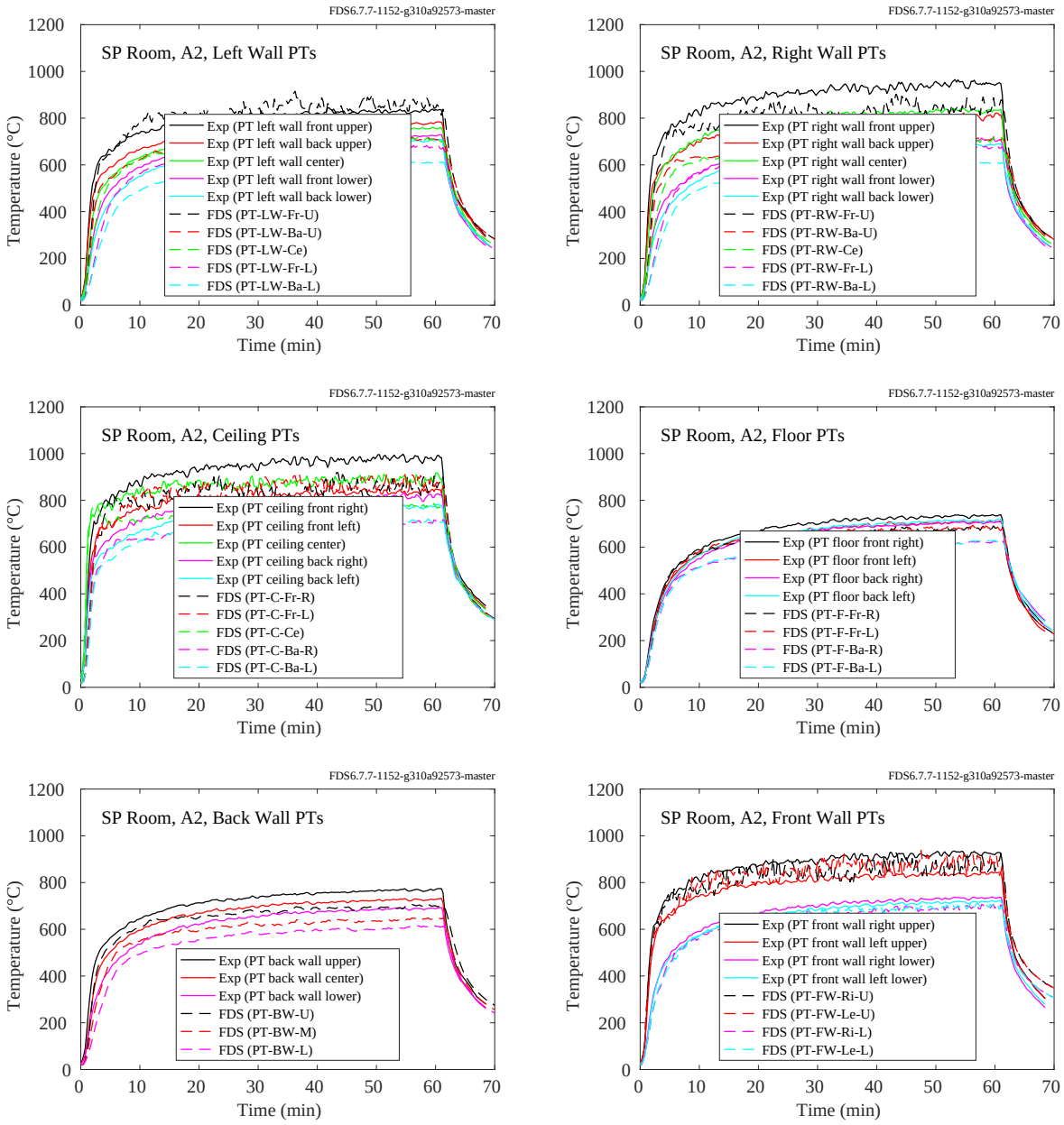

Figure 11.93: SP AST experiments, Insulated Room, Test A2.

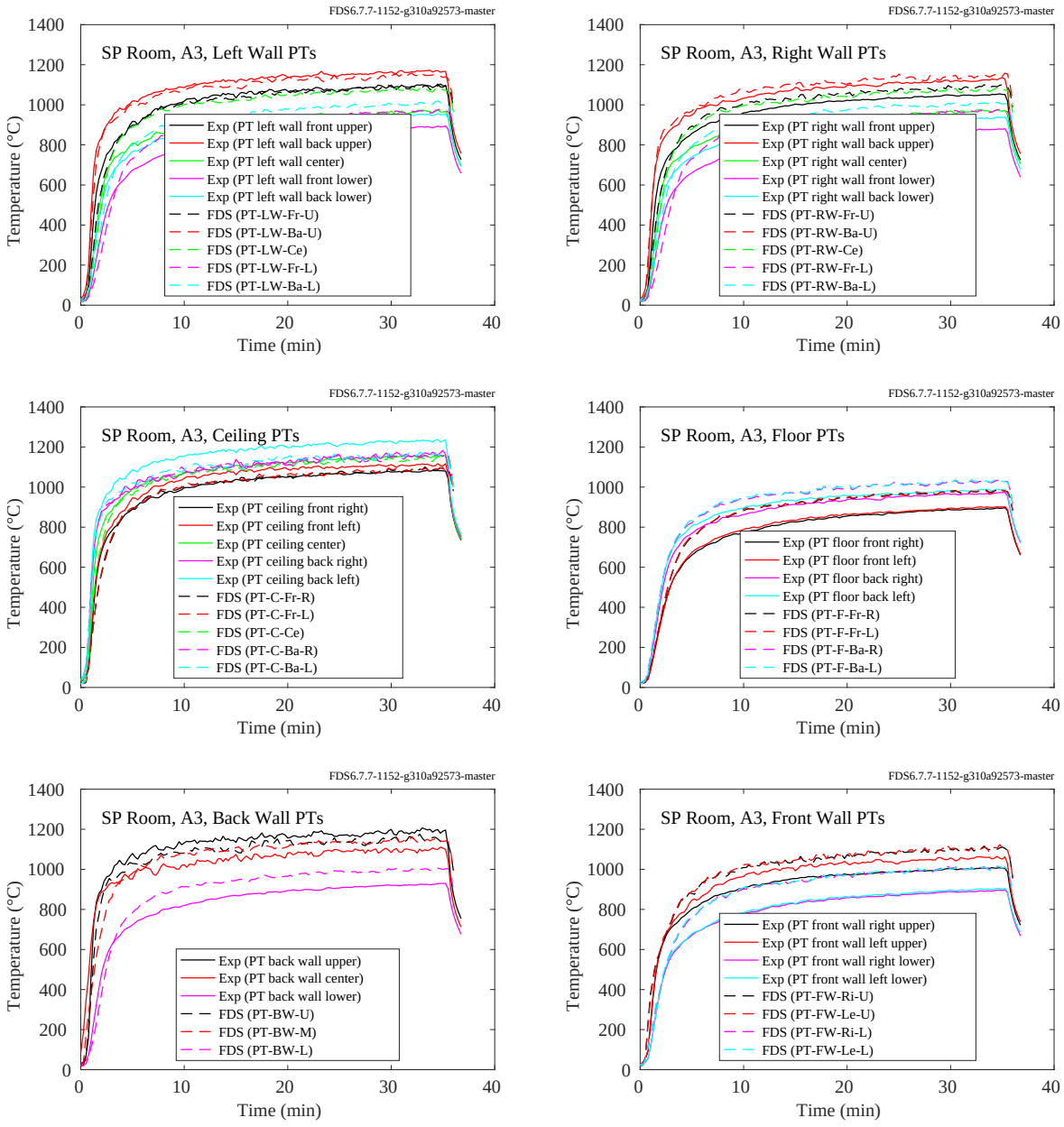

Figure 11.94: SP AST experiments, Insulated Room, Test A3.

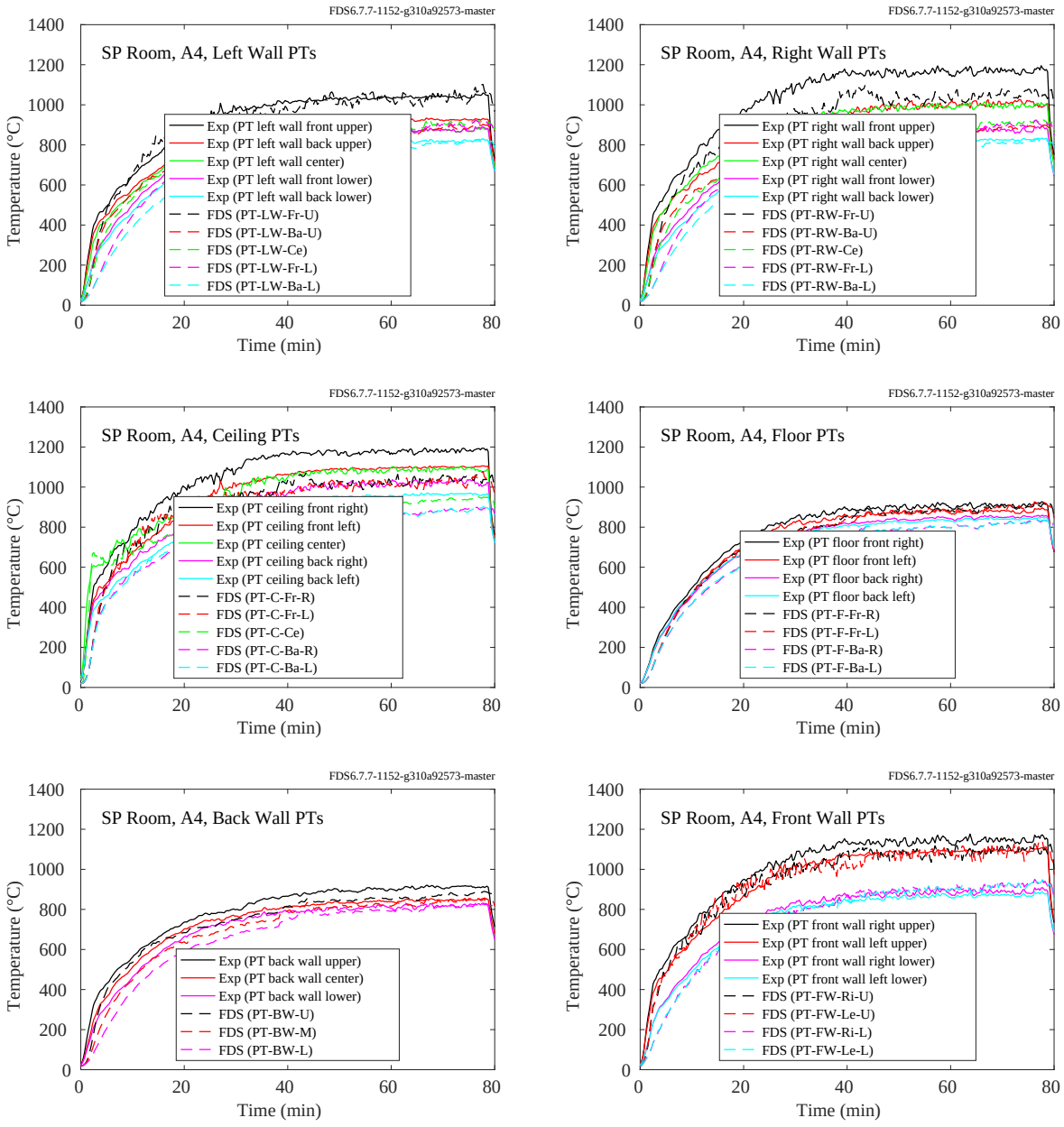

Figure 11.95: SP AST experiments, Insulated Room, Test A4.

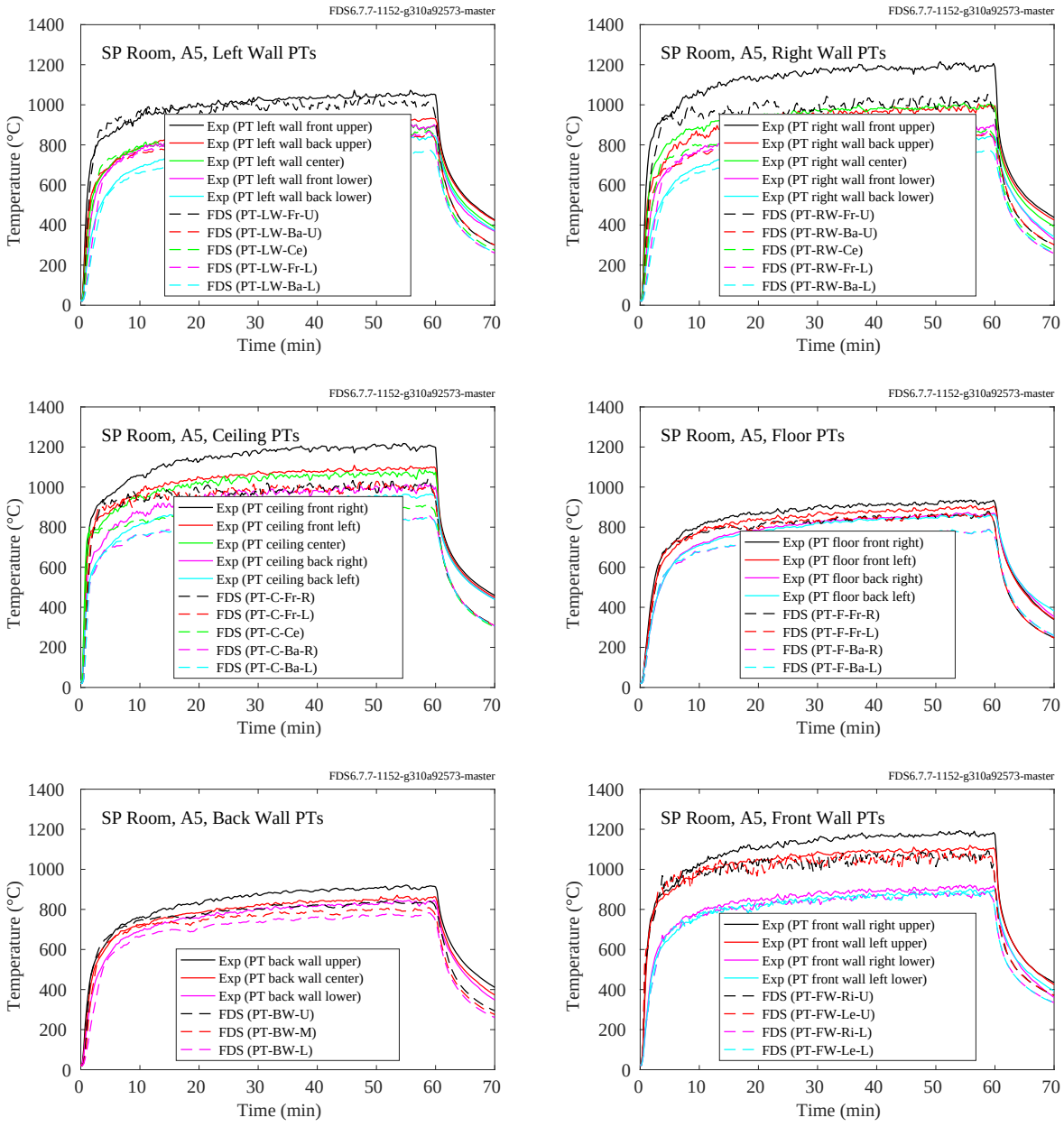

Figure 11.96: SP AST experiments, Insulated Room, Test A5.

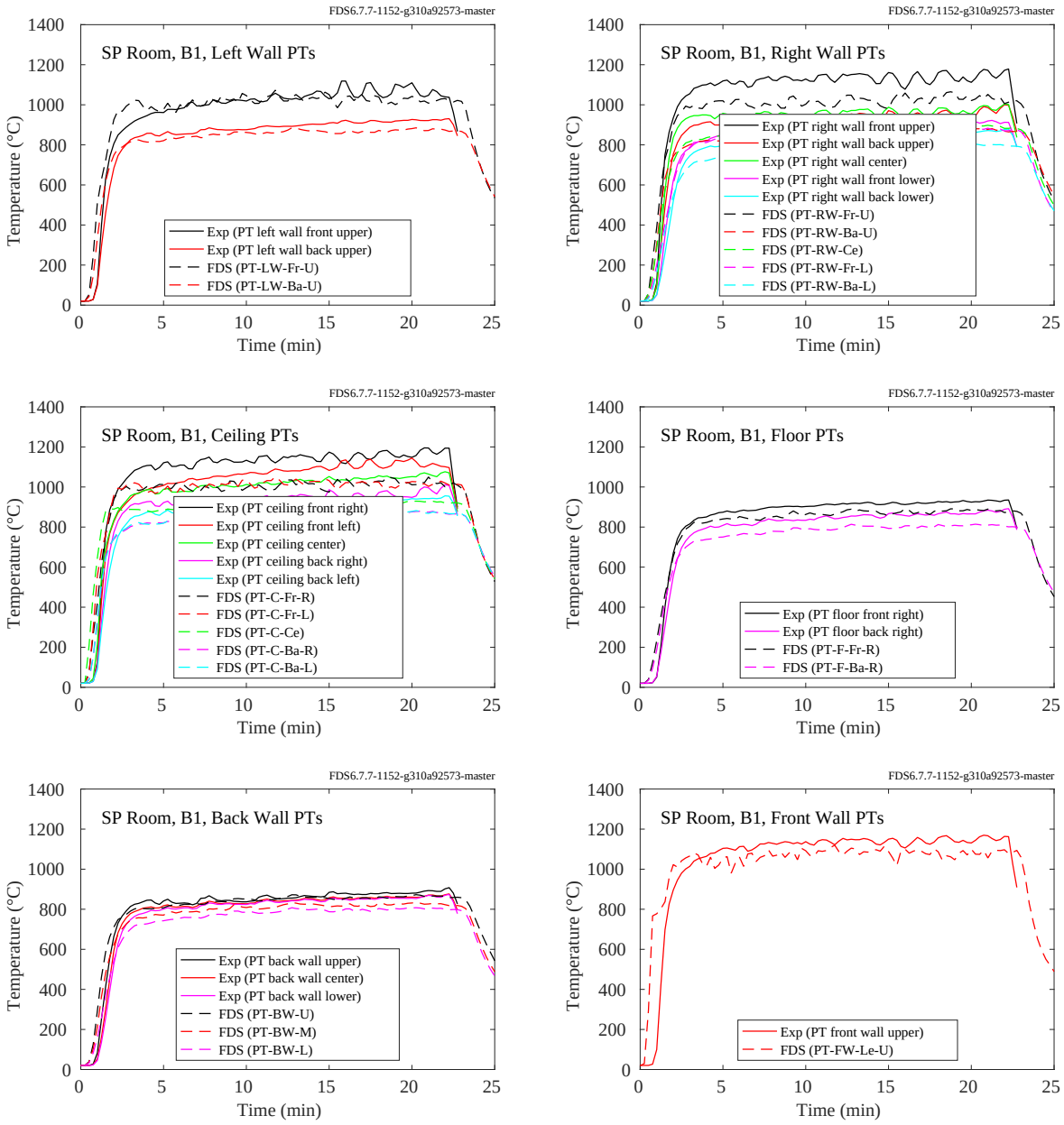

Figure 11.97: SP AST experiments, Insulated Room, Test B1.

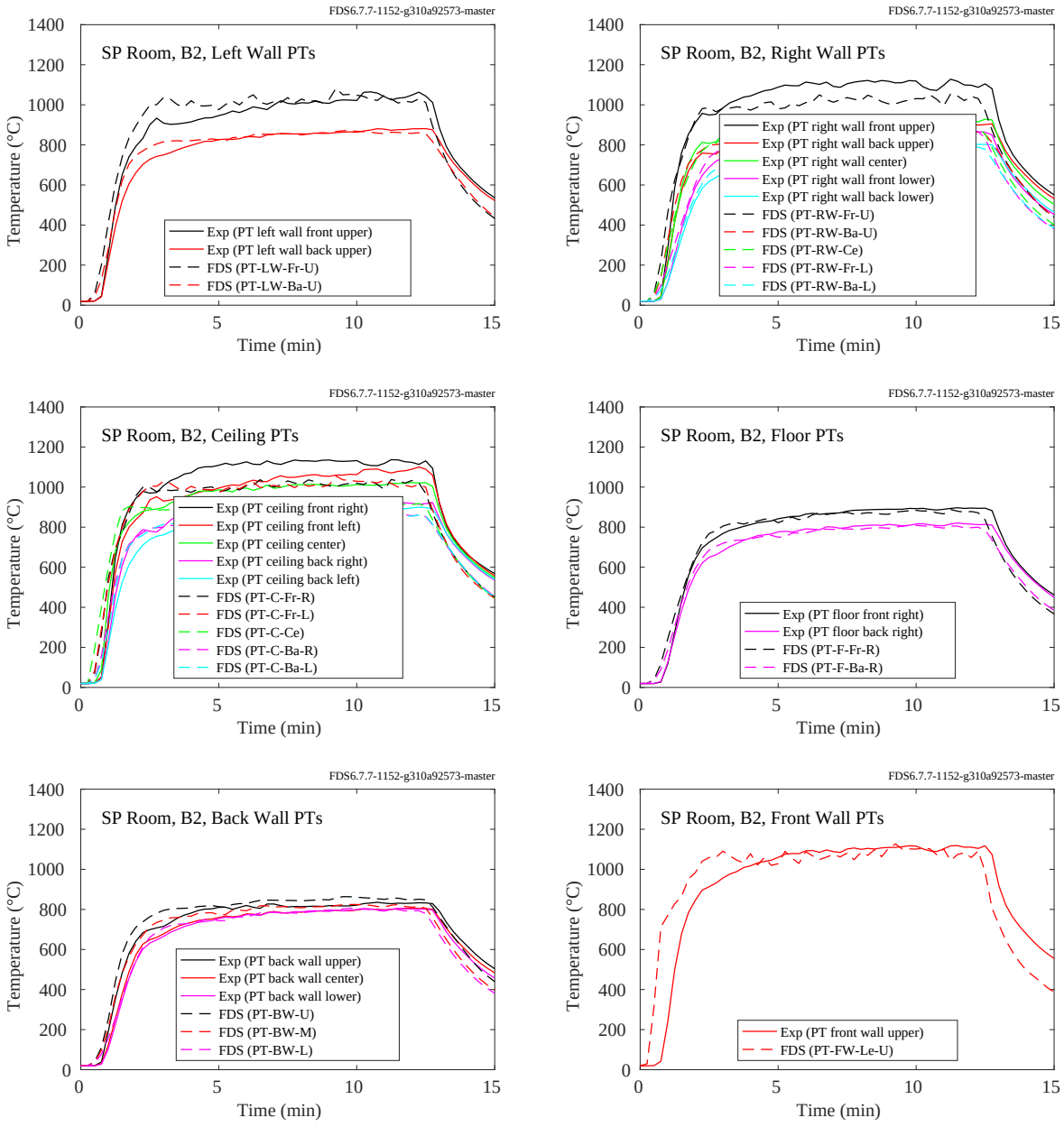

Figure 11.98: SP AST experiments, Insulated Room, Test B2.

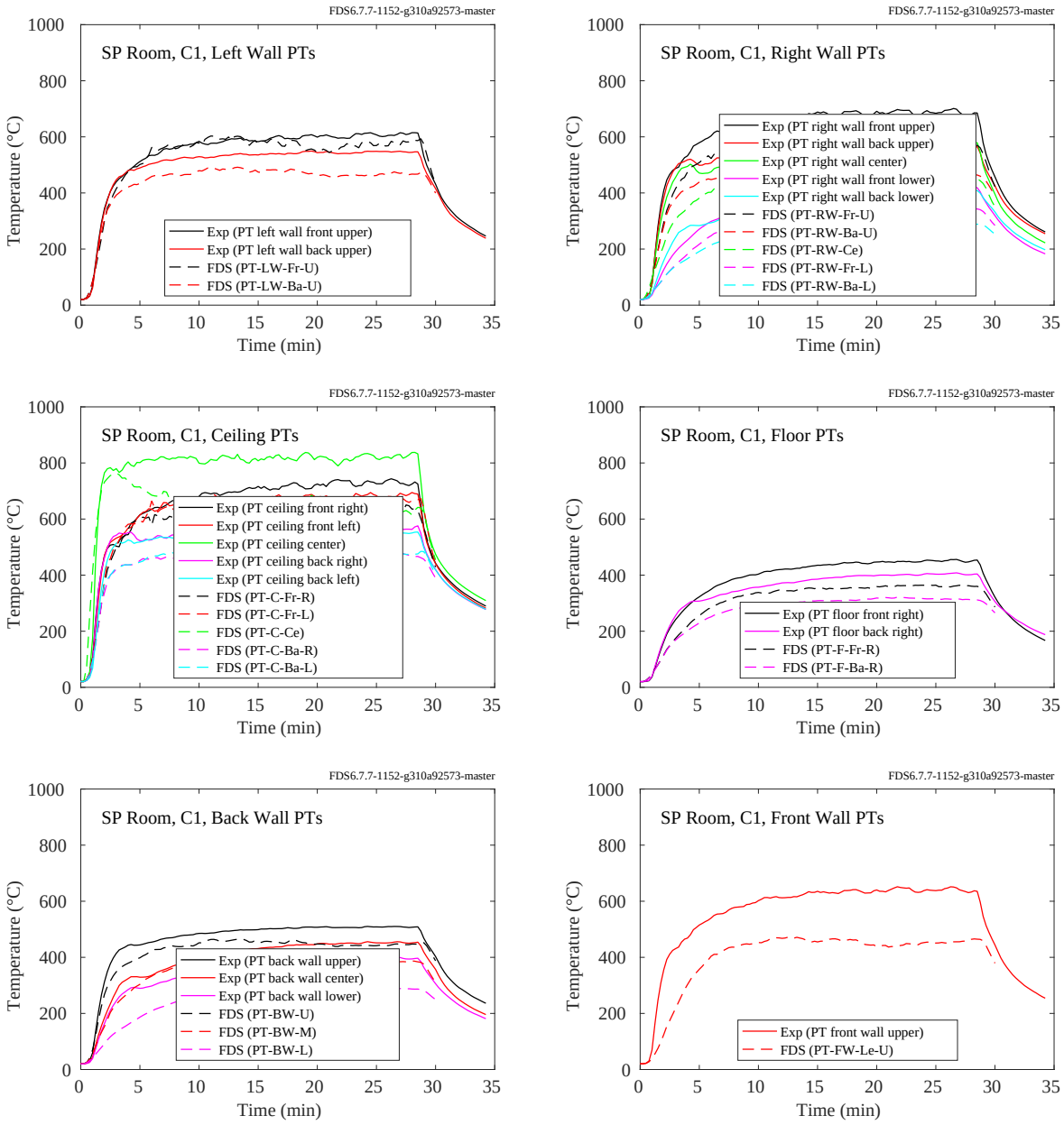

Figure 11.99: SP AST experiments, Insulated Room, Test C1.

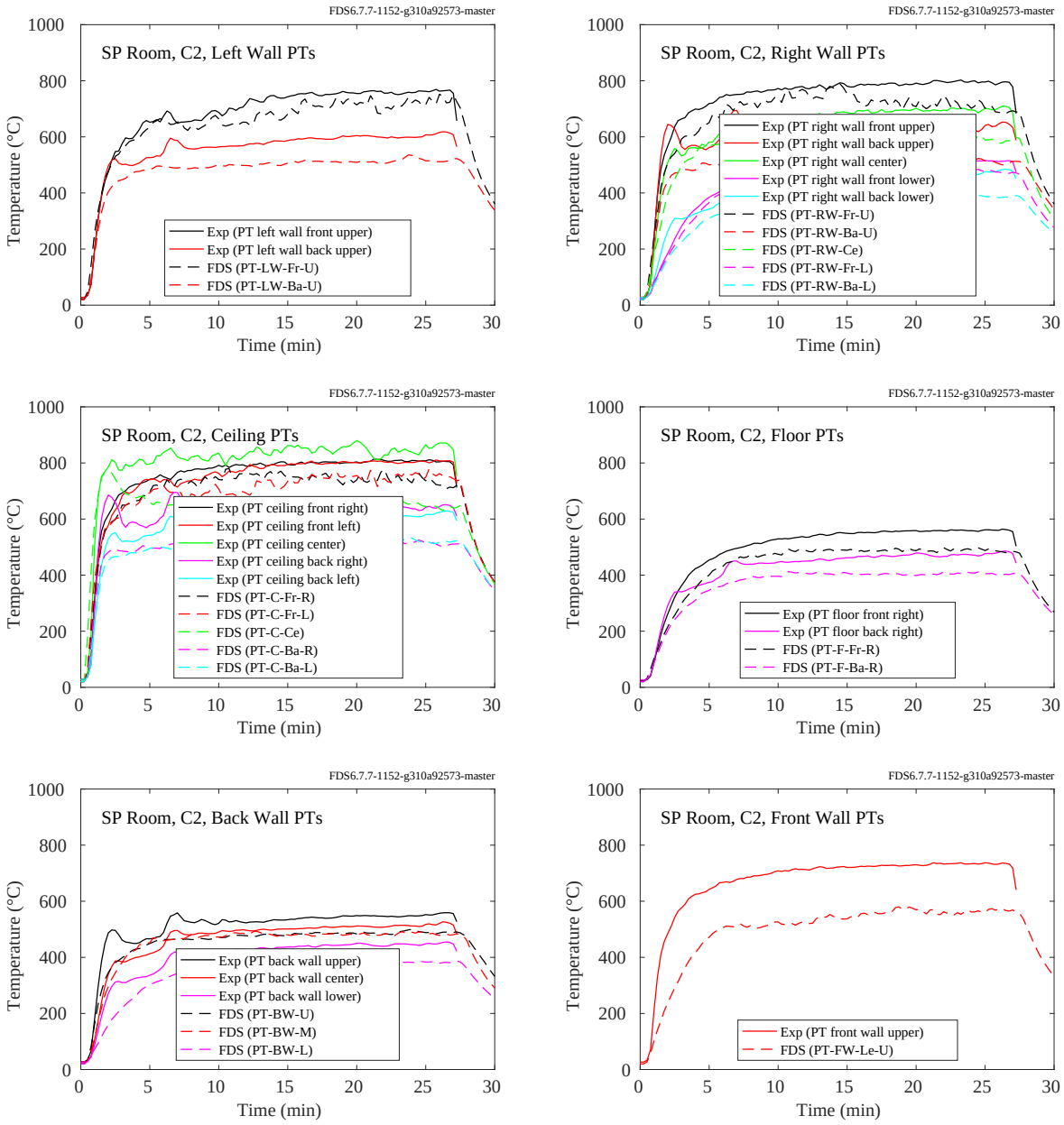

Figure 11.100: SP AST experiments, Insulated Room, Test C2.

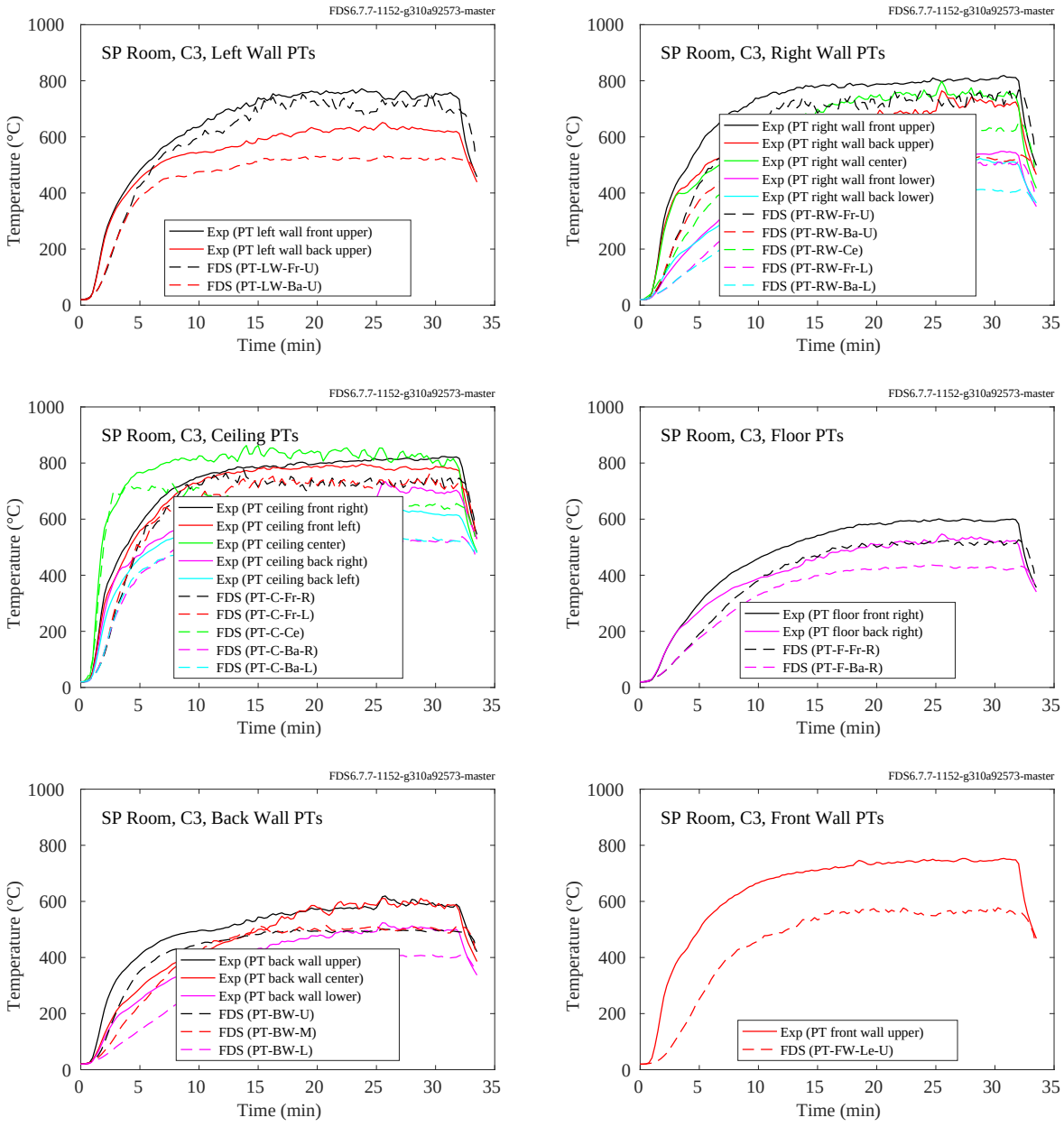

Figure 11.101: SP AST experiments, Insulated Room, Test C3.

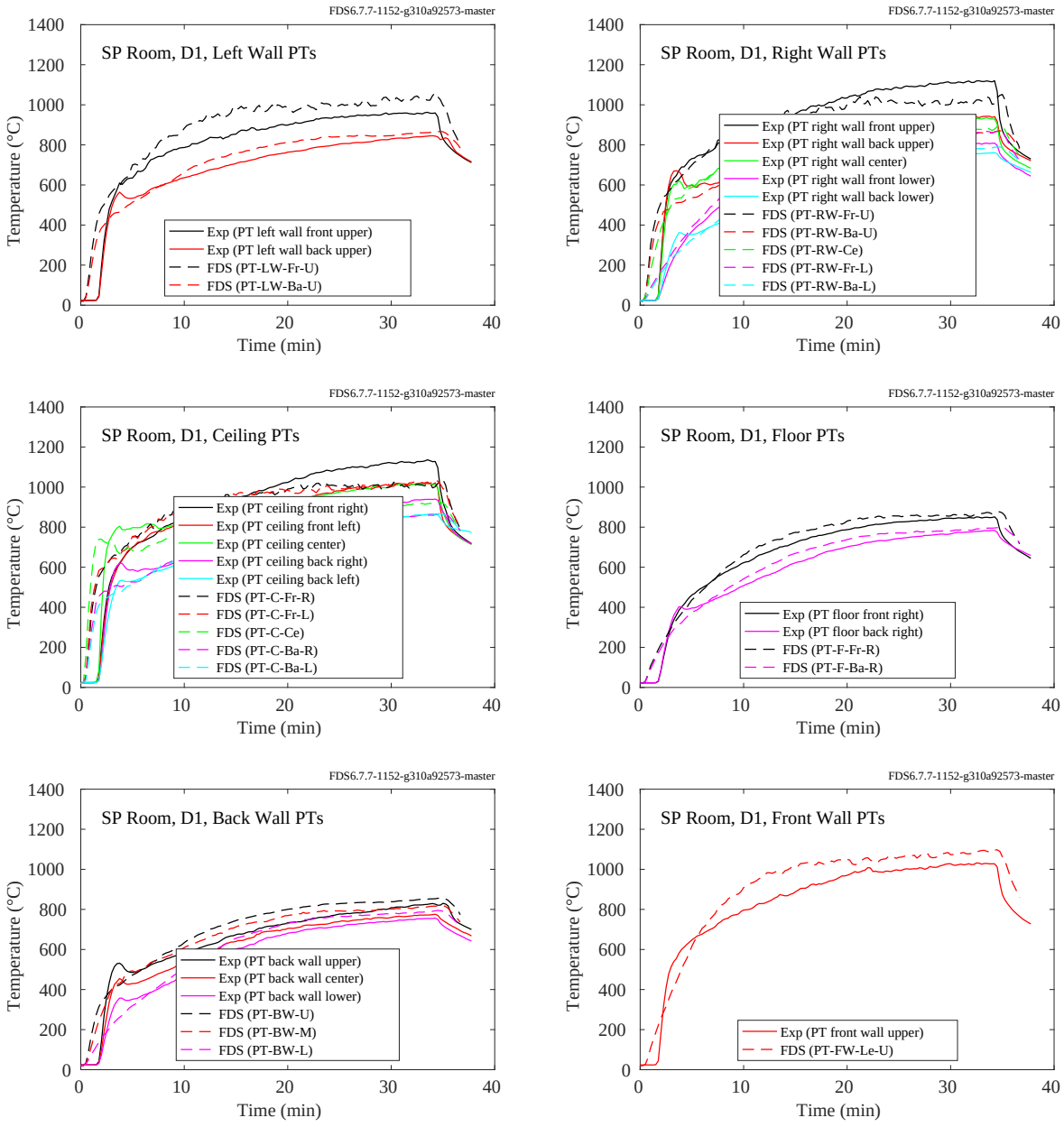

Figure 11.102: SP AST experiments, Insulated Room, Test D1.

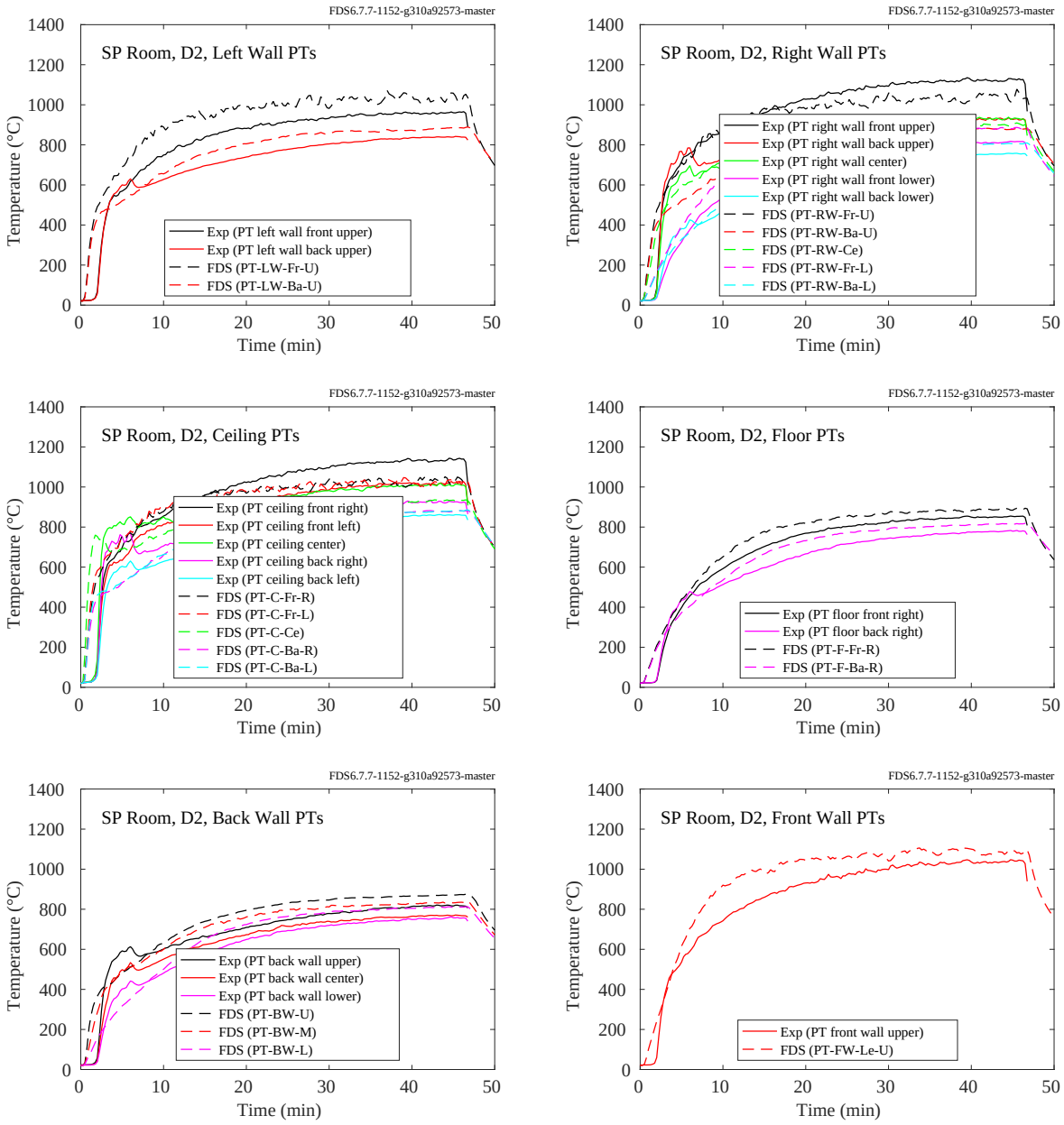

Figure 11.103: SP AST experiments, Insulated Room, Test D2.

Plate Thermometer Validation

The simulations of the SP Adiabatic Surface Temperature experiments include a 1-D model of a plate thermometer (PT), a temperature measurement device constructed of a thin, 10 cm square sheet of Inconel with a single thermocouple attached and backed by a layer of insulation material. To test the FDS PT model, a PT designed by Anthony Putorti at NIST, shown in Fig. 11.104 and described in detail in Ref. [340], was placed in a cone calorimeter and exposed to nominal heat fluxes of 25 kW/m^2 and 75 kW/m^2. The measured and predicted temperatures are shown in Fig. 11.105.

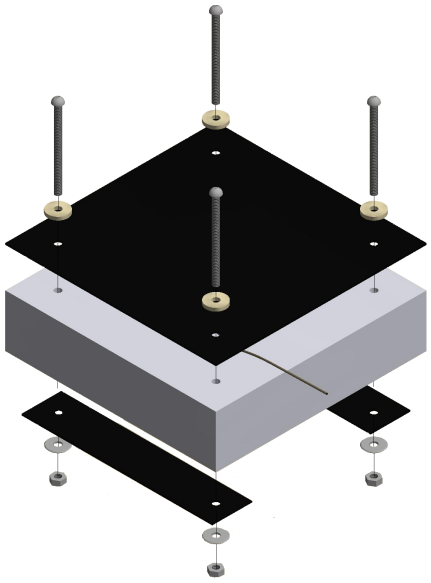

Figure 11.104: Exploded view of a plate thermometer.

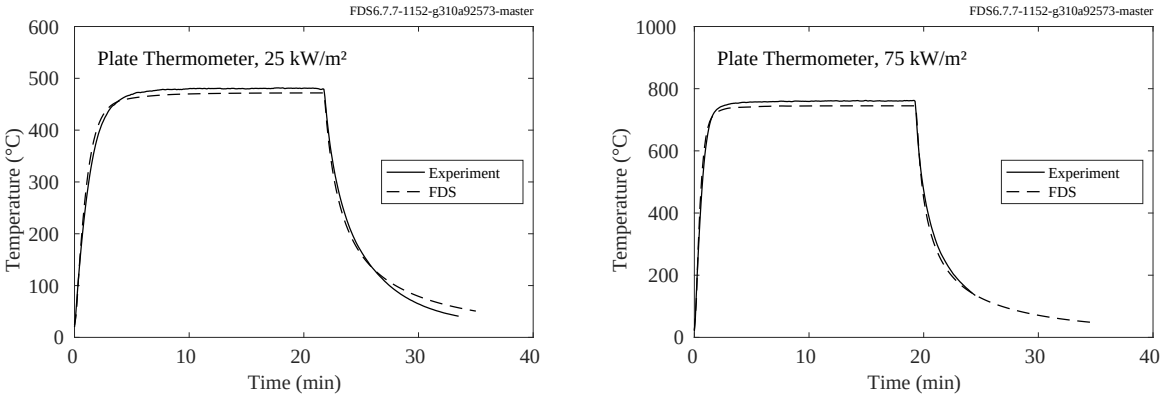

Figure 11.105: Predictions of plate thermometer temperatures in a cone calorimeter.

11.2.6 WTC Experiments

The compartment for the WTC experiments contained a hollow box column roughly 0.5 m from the fire pan, two trusses over the top of the pan, and one or two steel bars resting on the lower truss flanges. In Tests 1, 2 and 3, the steel was bare, and in Tests 4, 5 and 6, the steel was coated with various thicknesses of sprayed fire-resistive materials. The column was instrumented near its base (about 0.5 m from the floor, middle (1.5 m), and upper (2.5 m). Four measurements of steel (and insulation) temperatures were made at each location, for each of its four sides. These elements were modeled using thin sheet obstructions with a resolution of 10 cm.

In addition to the steel structural elements, five cylinders ("slugs") of nickel 200 ($\geq$ 99 % nickel), 25.4 cm long and 10.2 cm in diameter, were positioned 50 cm north of the centerline in the WTC experiments. Slugs 1 through 5 were 2.92 m, 1.82 m, 0.57 m, 0.05 m, and 1.56 m, respectively, from the longitudinal axis of the fire pan. All the slugs were 50 cm north of the lateral axis. The fire pan measured 2 m by 1 m. Four thermocouples were inserted into each slug at various locations. All four temperatures for each slug were virtually indistinguishable. Rectangular obstructions were used to model the slugs, but the one-dimensional heat conduction calculation was performed using cylindrical coordinates.

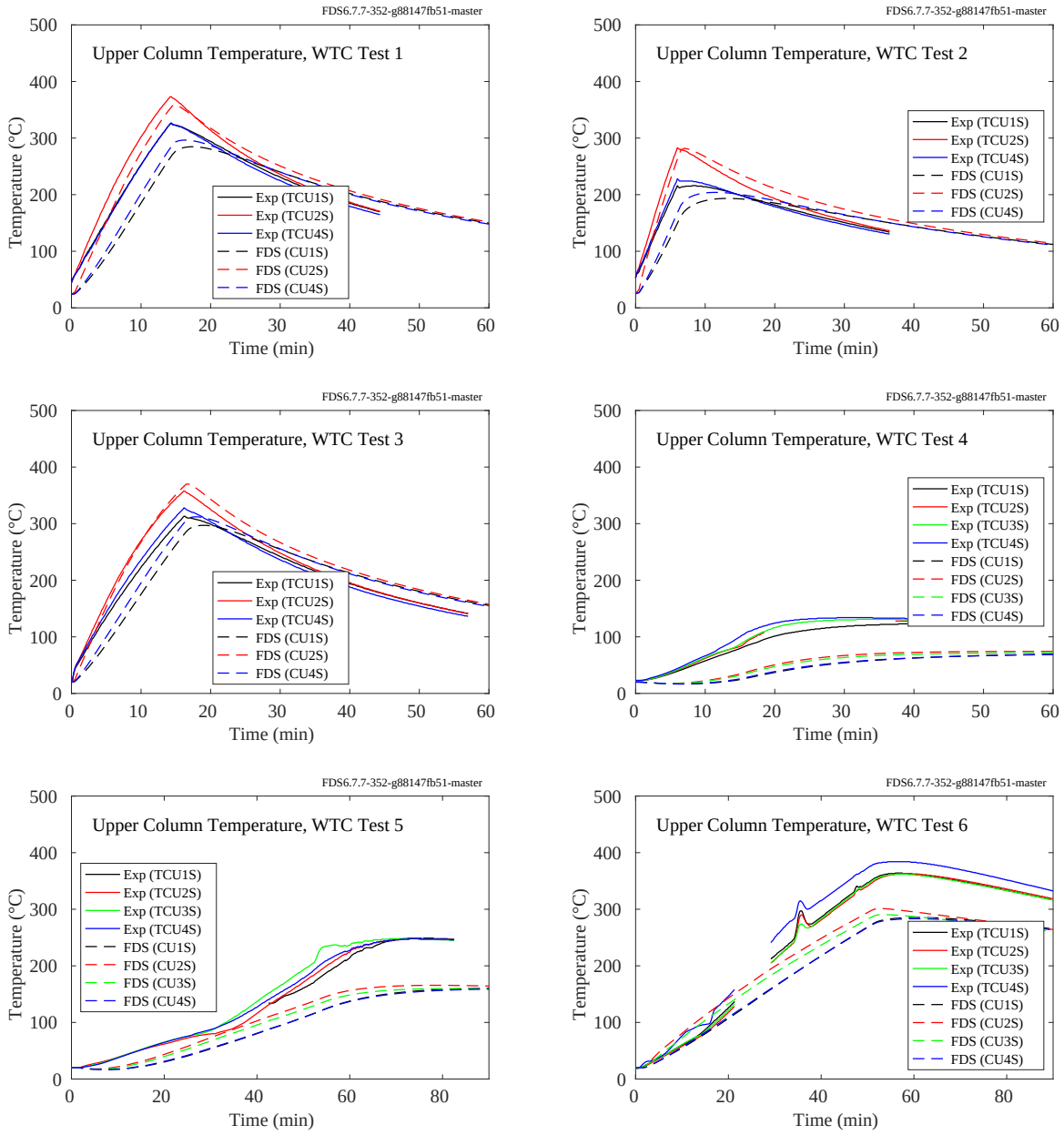

Figure 11.106: WTC experiments, steel temperatures, upper column.

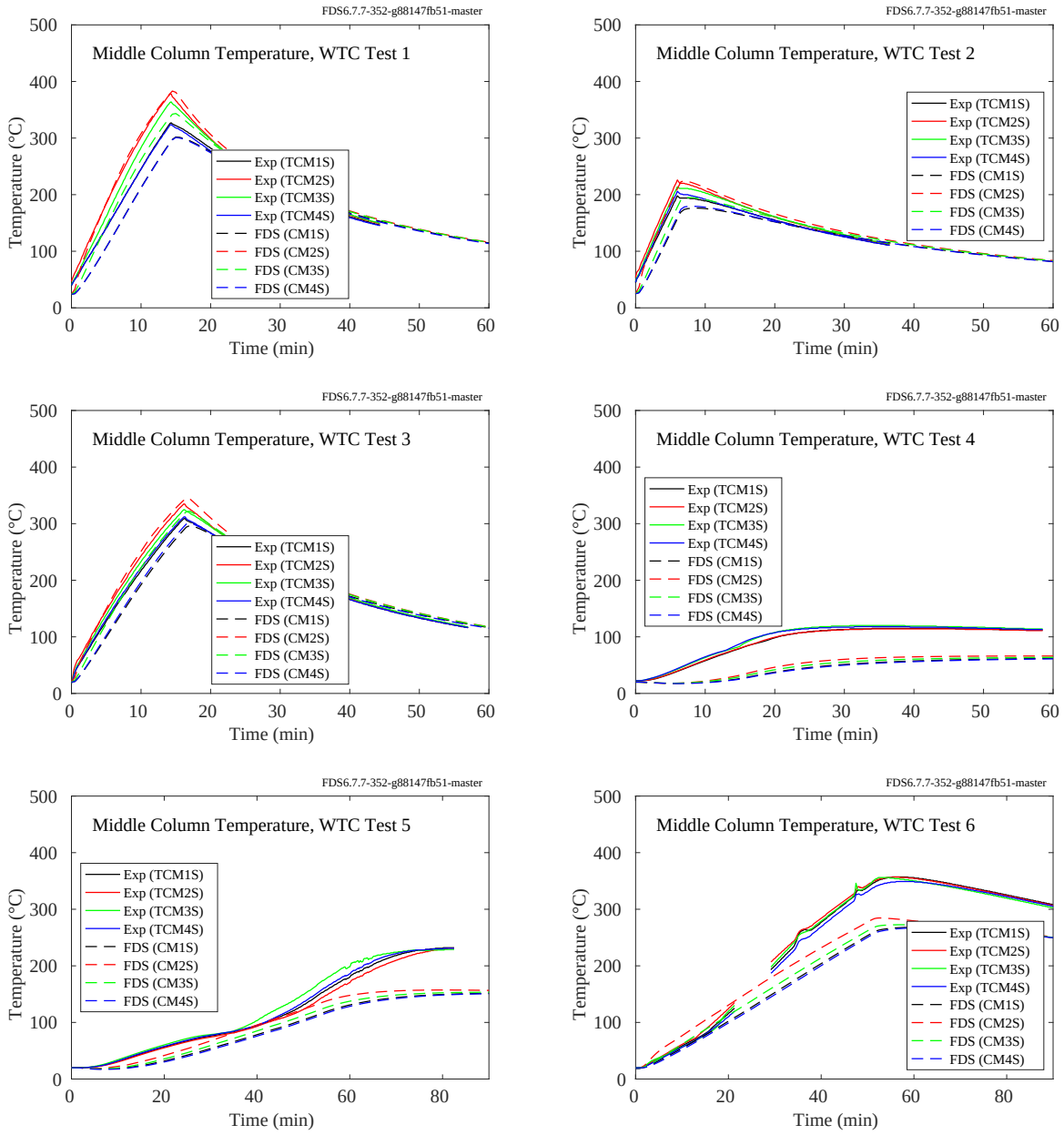

Figure 11.107: WTC experiments, steel temperatures, middle column.

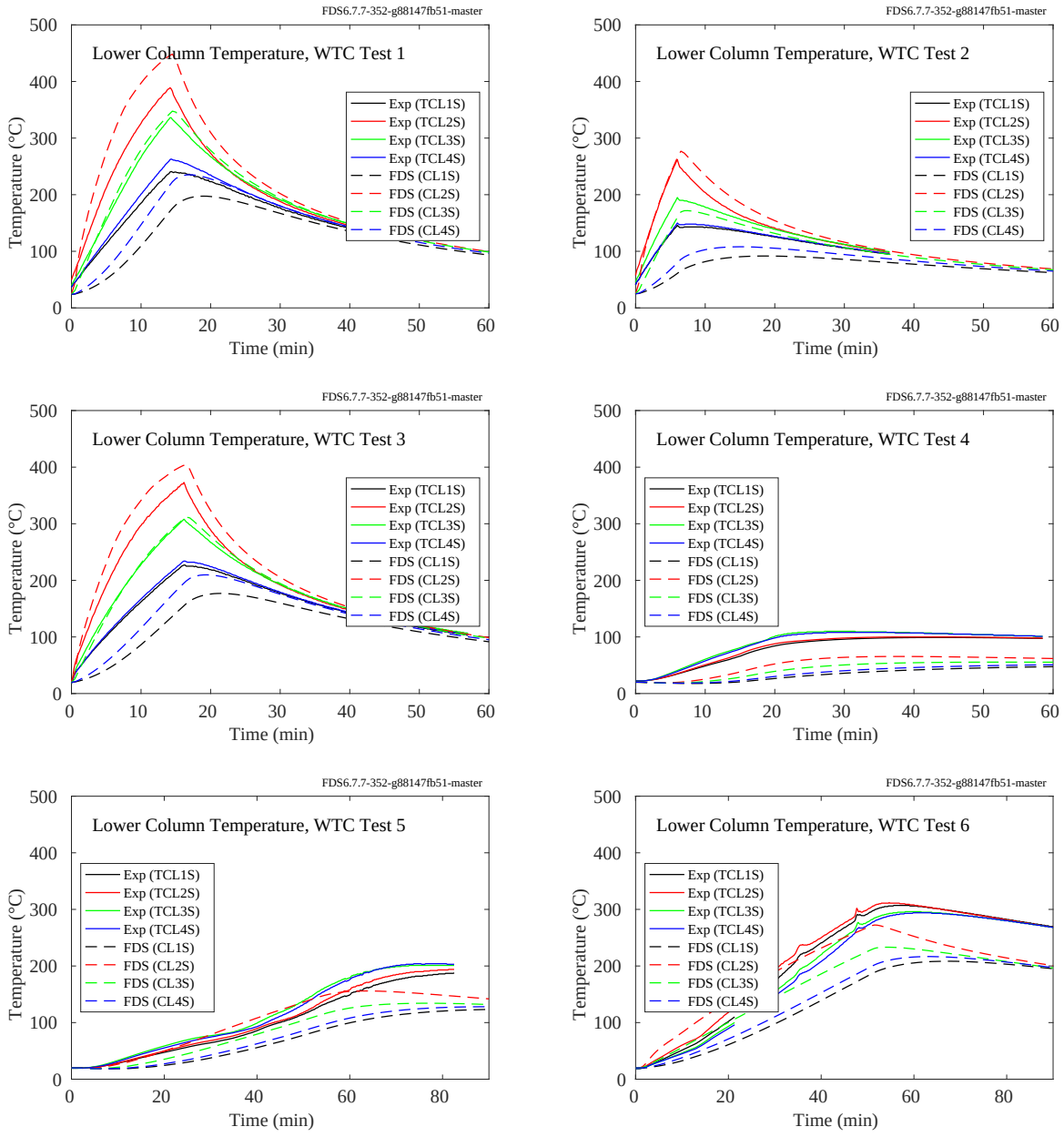

Figure 11.108: WTC experiments, steel temperatures, lower column.

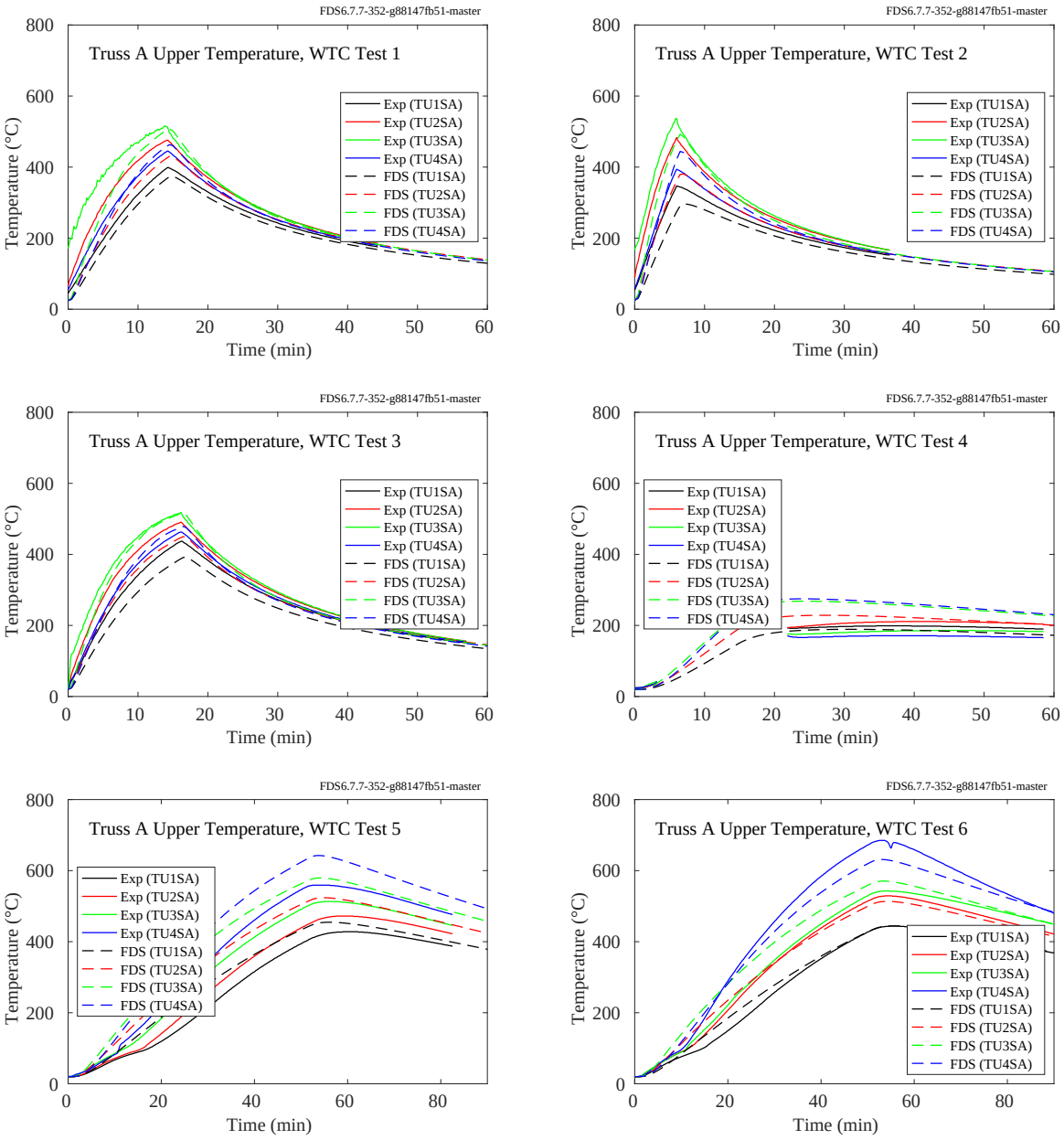

Figure 11.109: WTC experiments, steel temperatures, upper Truss A.

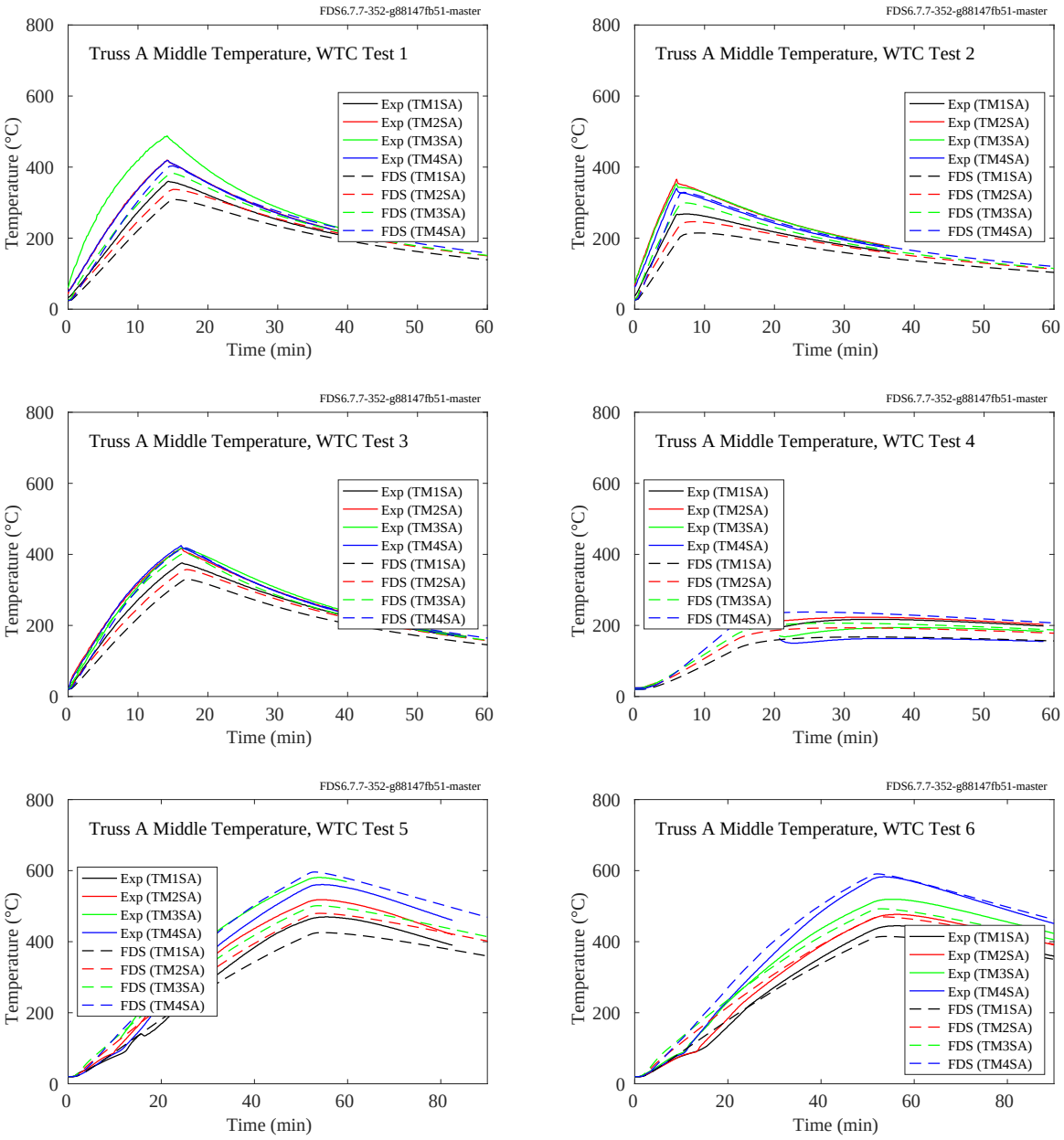

Figure 11.110: WTC experiments, steel temperatures, middle Truss A.

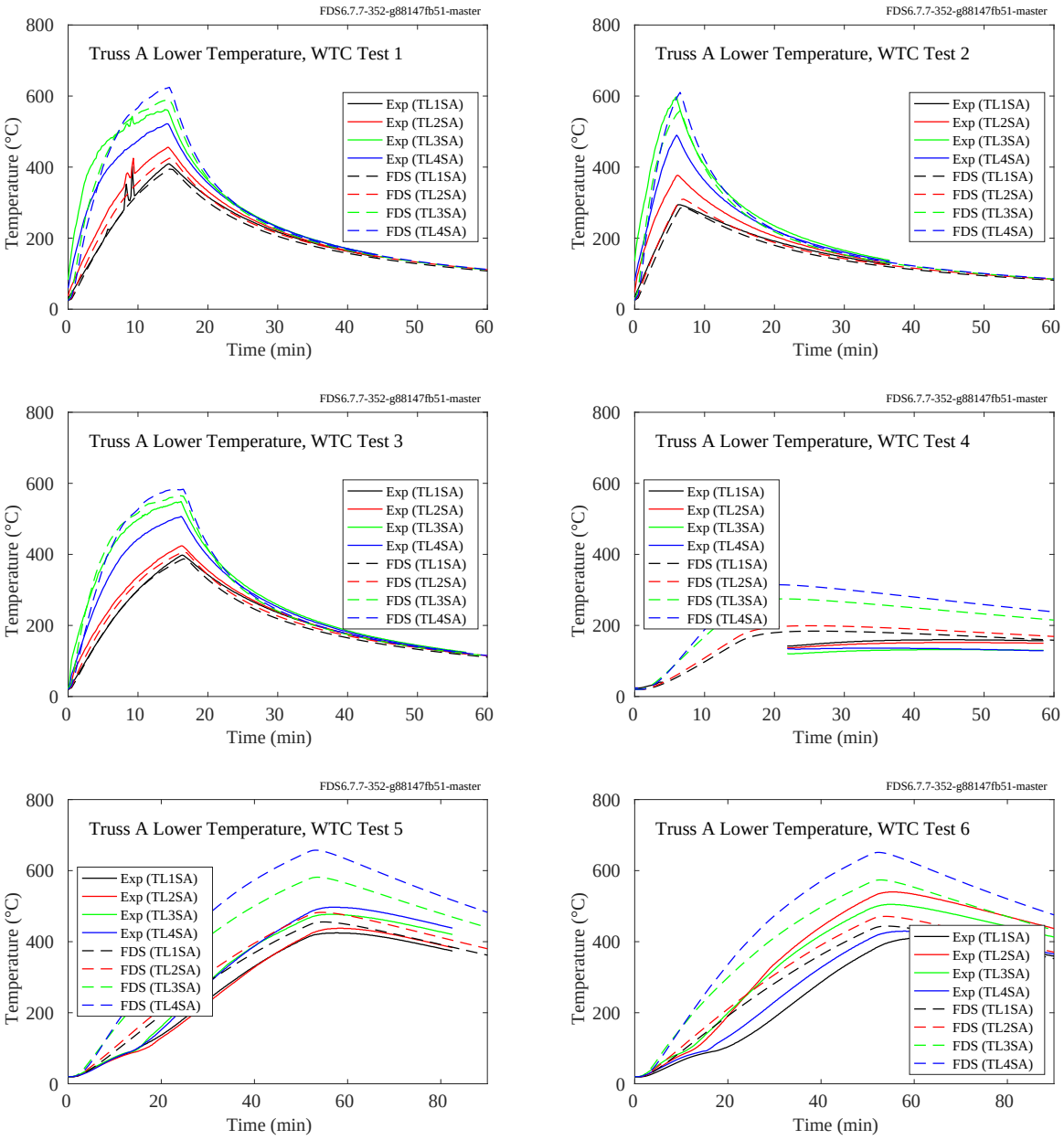

Figure 11.111: WTC experiments, steel temperatures, lower Truss A.

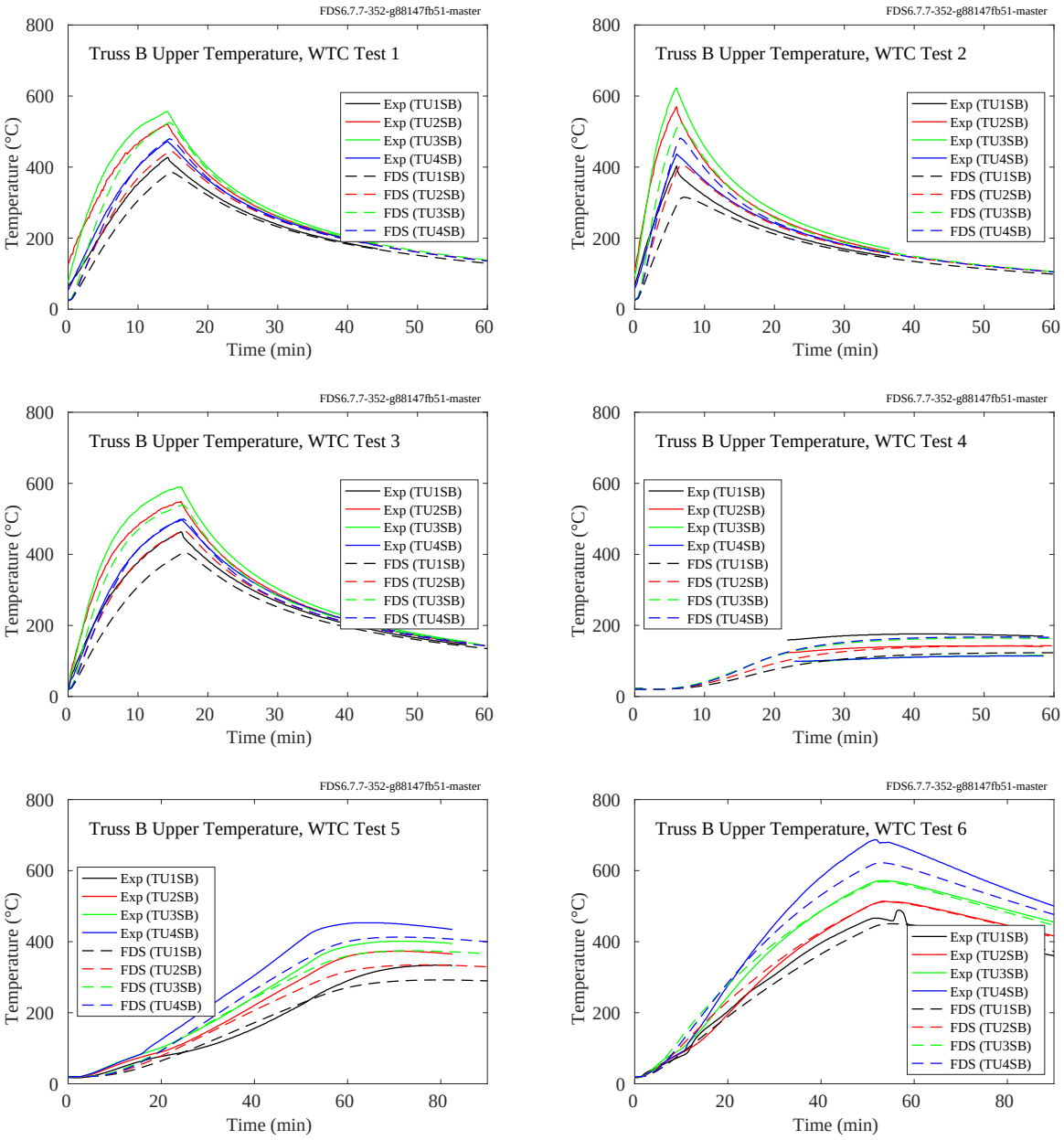

Figure 11.112: WTC experiments, steel temperatures, upper Truss B.

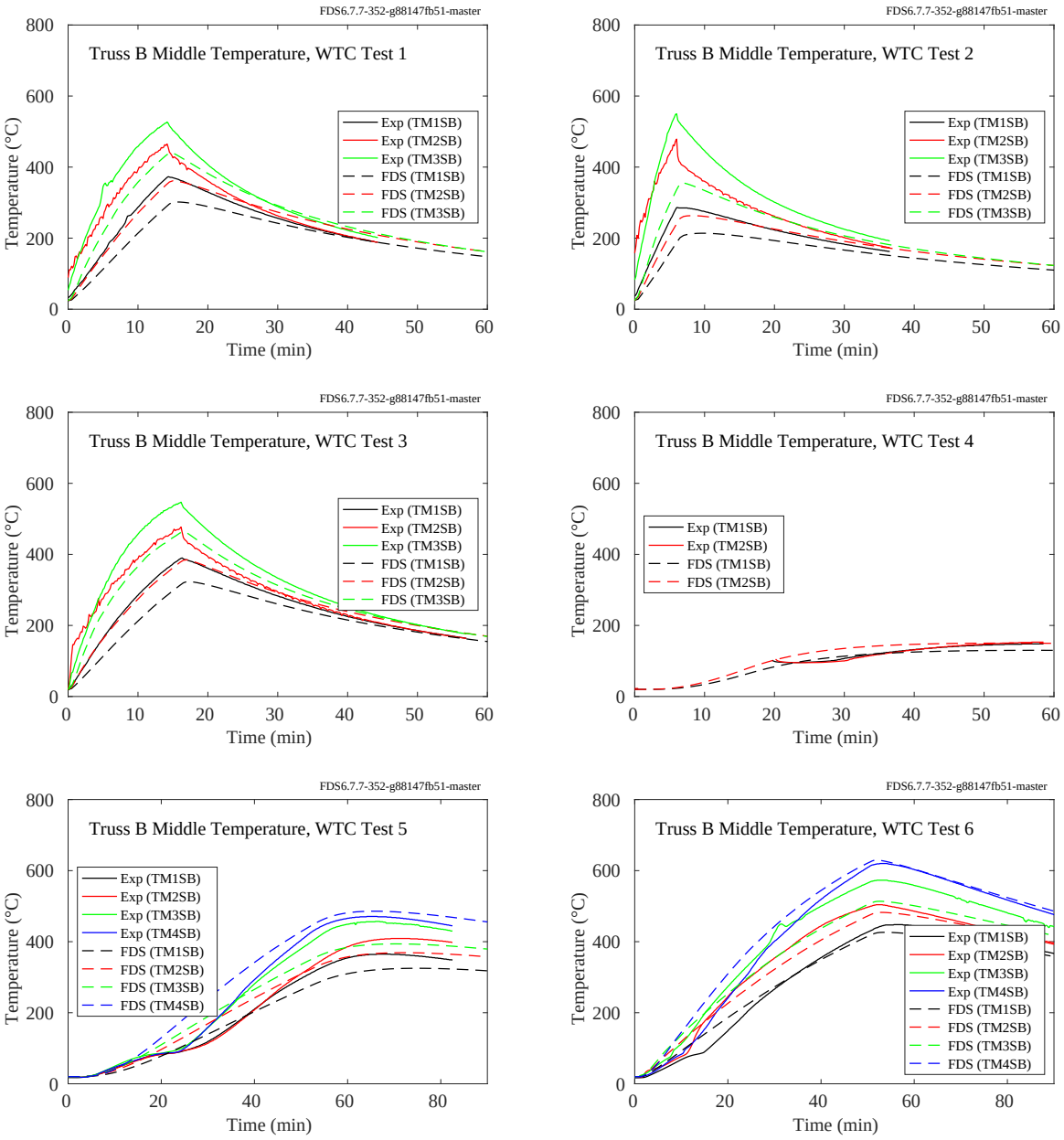

Figure 11.113: WTC experiments, steel temperatures, middle Truss B.

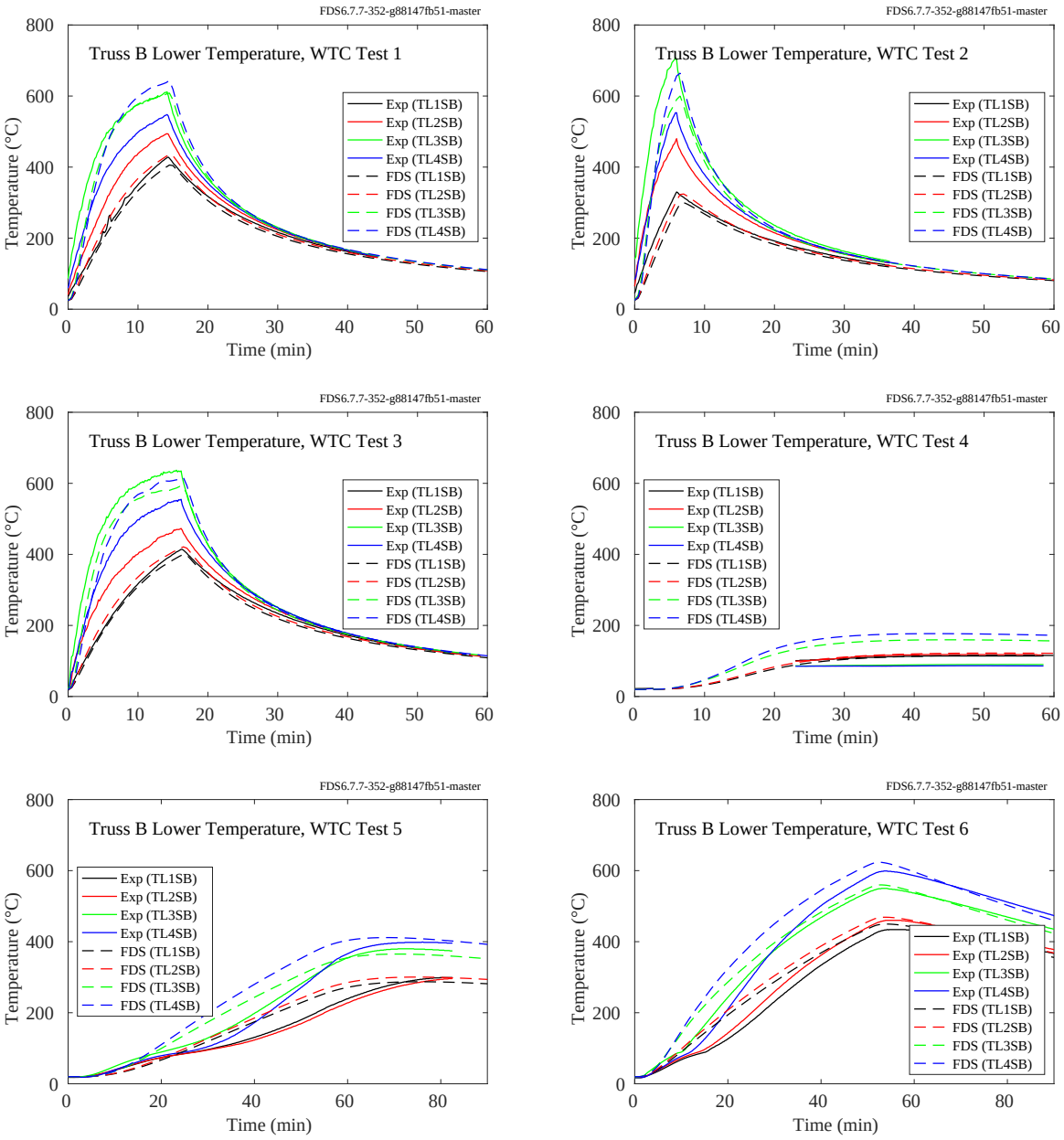

Figure 11.114: WTC experiments, steel temperatures, lower Truss B.

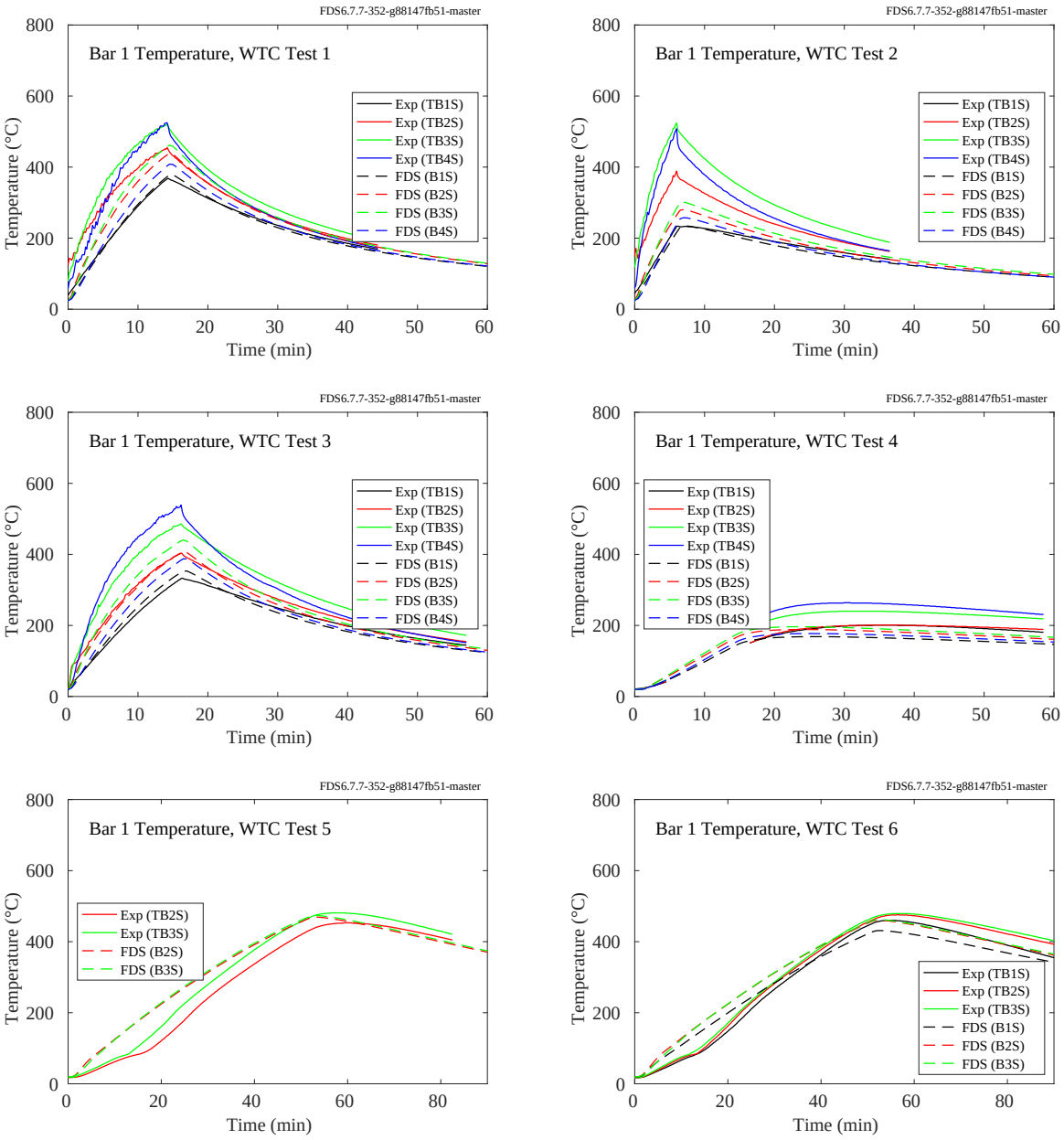

Figure 11.115: WTC experiments, steel temperatures, Bar 1.

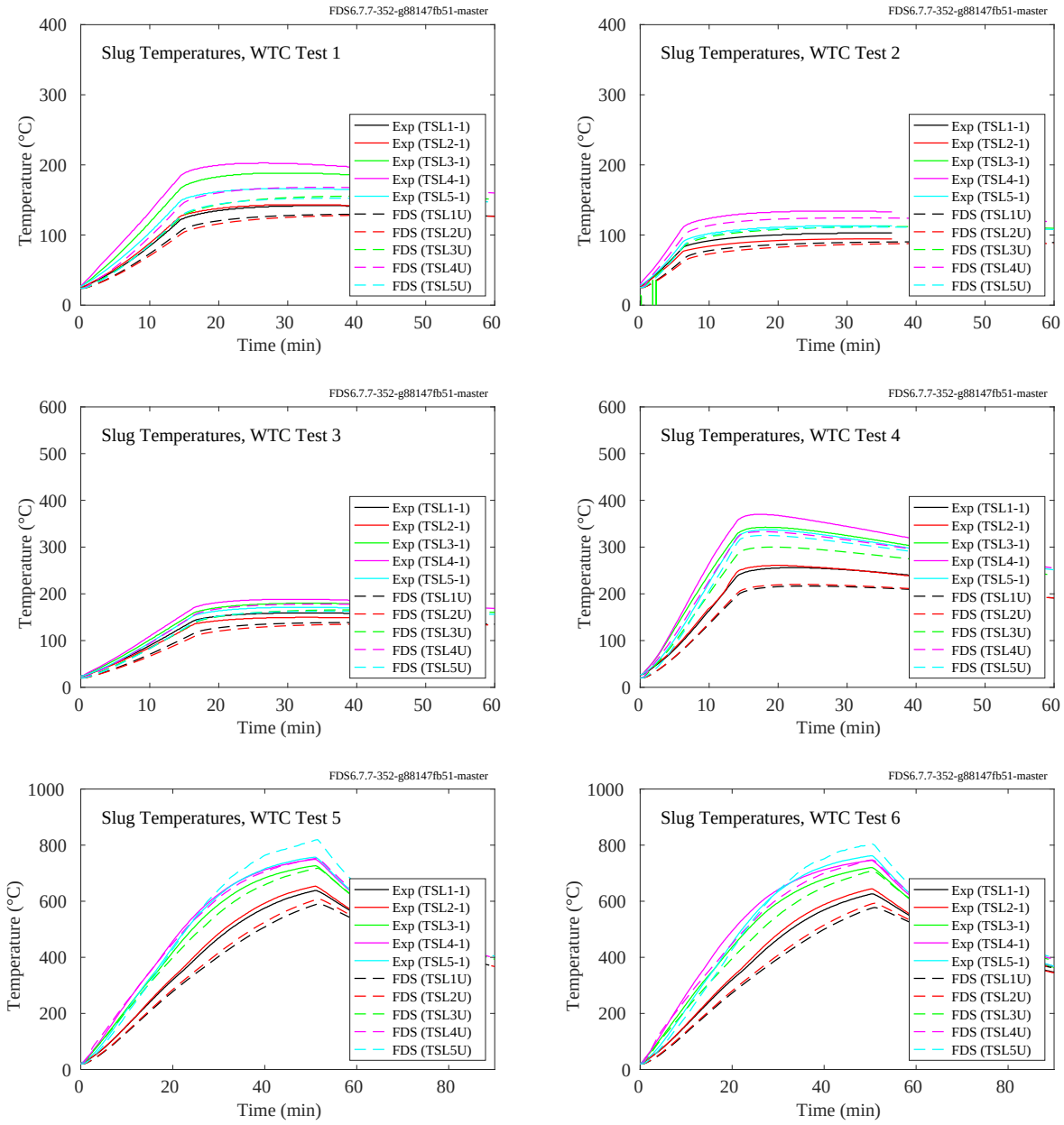

Figure 11.116: WTC experiments, slug temperatures.

11.2.7 CAROLFIRE Experiments

On the following pages are predictions of the THIEF (thermally-induced electrical failure) model compared to 35 experiments conducted at Sandia National Laboratory [148]. In these experiments, an instrumented electrical cable was run through a heated cylindrical "shroud." The shroud temperature is an input for the model, and the cable temperature (and in some cases that of the steel conduit enclosing the cable) is predicted. Note that the cables generally fall into two categories – thermoset and thermoplastic. Thermoset cables form a char layer when burned and typically fail electrically at temperatures near 400 °C. Thermoplastic cables typically melt and then burn, leaving little residue behind except the conductors. These cables typically fail between 200 °C and 250 °C. Some cables, as in Tests 18 and 31, do not fall into either category. The thermoset cables were exposed to temperatures in the neighborhood of 480 °C, and the thermoplastics were exposed to temperatures near 300 °C.

Note in the plots to follow that the objective of the calculation is to predict the cable temperature just inside of the jacket until the cable fails electrically. In some experiments, the short-circuiting of the cable led to ignition of the pyrolyzates. This behavior is not captured in the model, which is why some of the experimental data shows a rapid rise in temperature at a certain point in the test. In many cases, electrical failure occurred very shortly, or at about the same time, as ignition.

Figure 11.131 compares the measured versus predicted time to a "threshold" temperature. The threshold temperature is 400 °C for thermoset cables and 200 °C for thermoplastics.

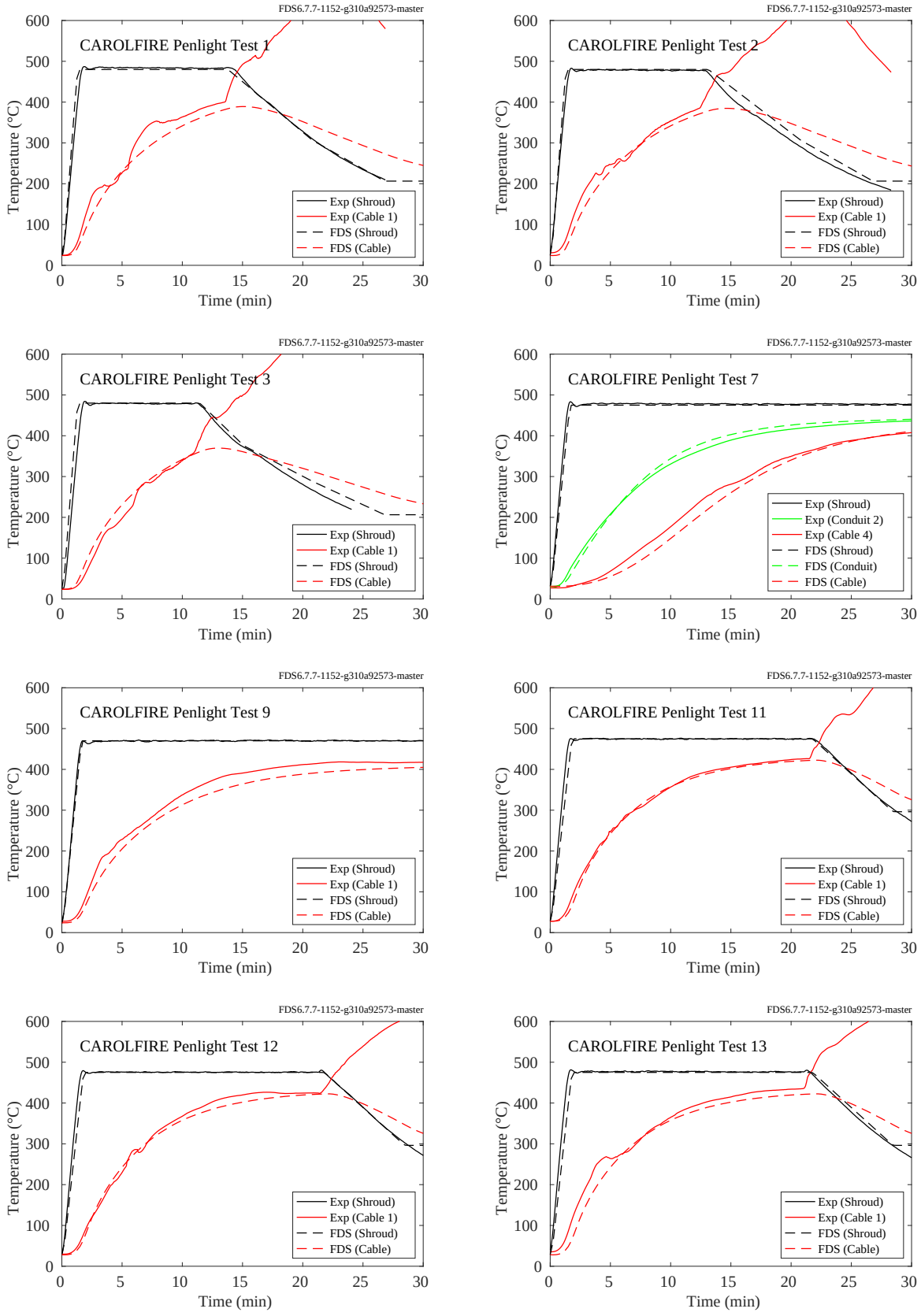

Figure 11.117: CAROLFIRE, electrical cable temperatures, Penlight Tests 1, 2, 3, 7, 9, 11-13.

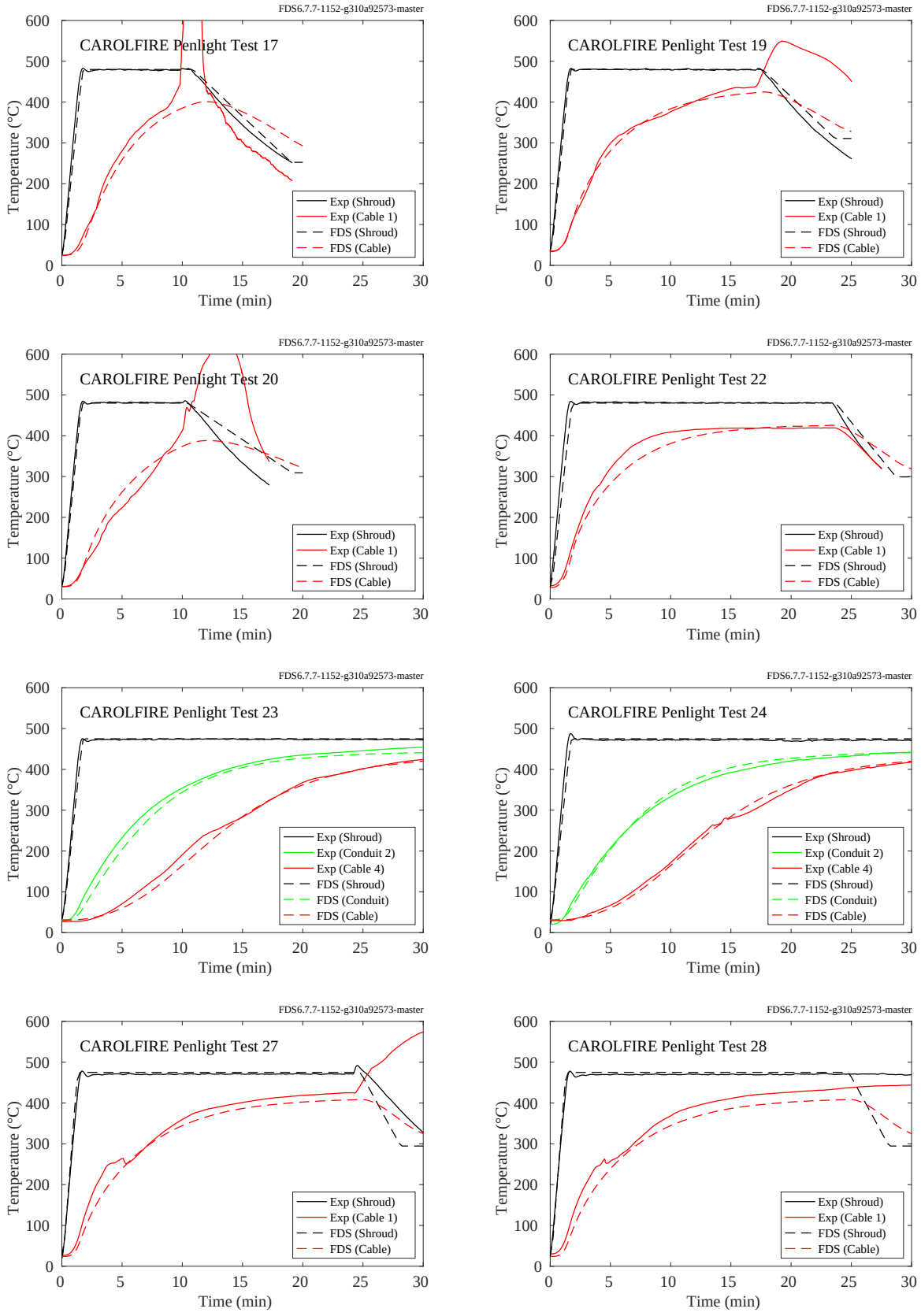

Figure 11.118: CAROLFIRE, electrical cable temperatures, Penlight Tests 17, 19-20, 22-24, 27-28.

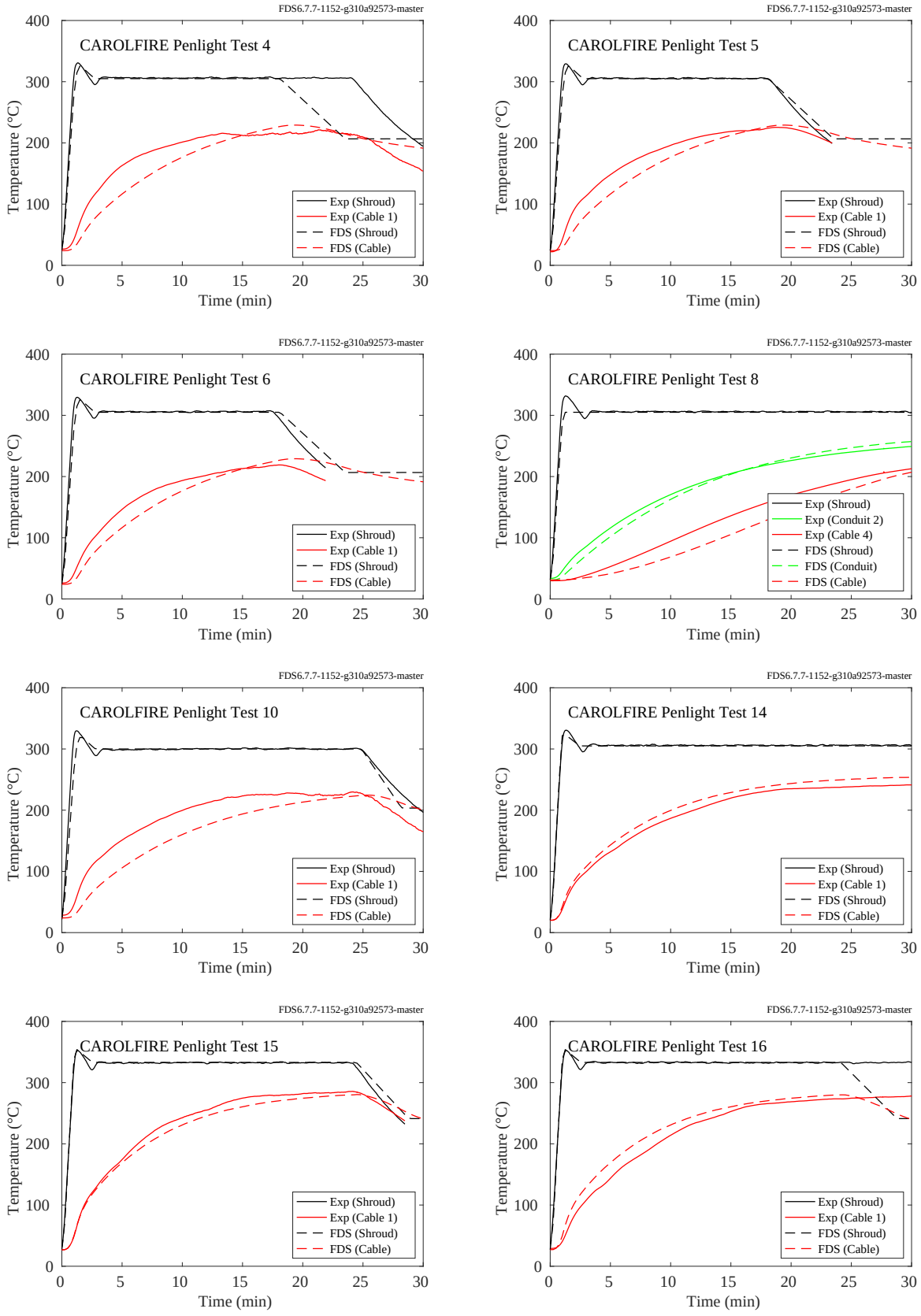

Figure 11.119: CAROLFIRE, electrical cable temperatures, Penlight Tests 4-6, 8, 10, 14-16.

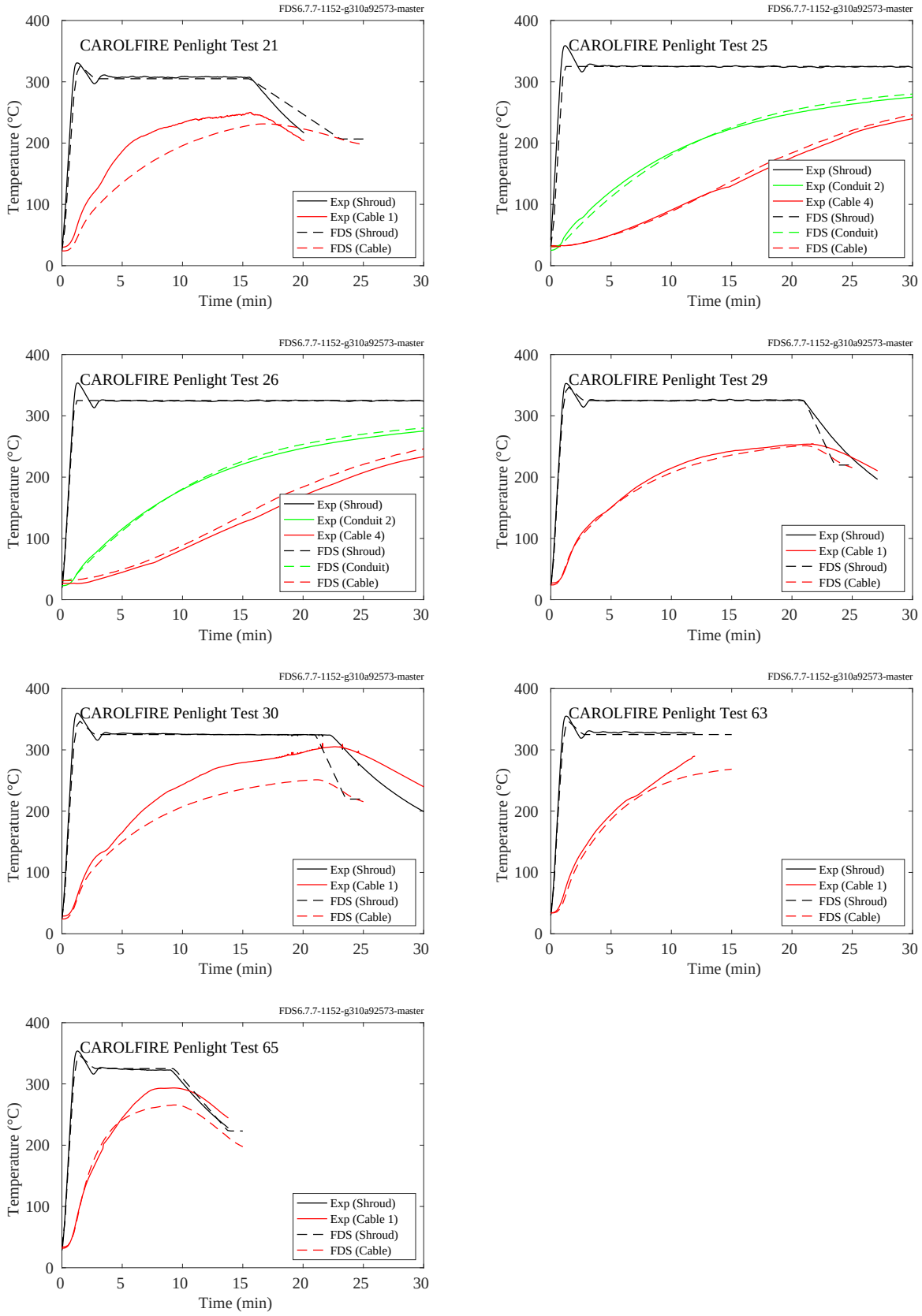

Figure 11.120: CAROLFIRE, electrical cable temperatures, Penlight Tests 21, 25-26, 29-30, 63, 65.

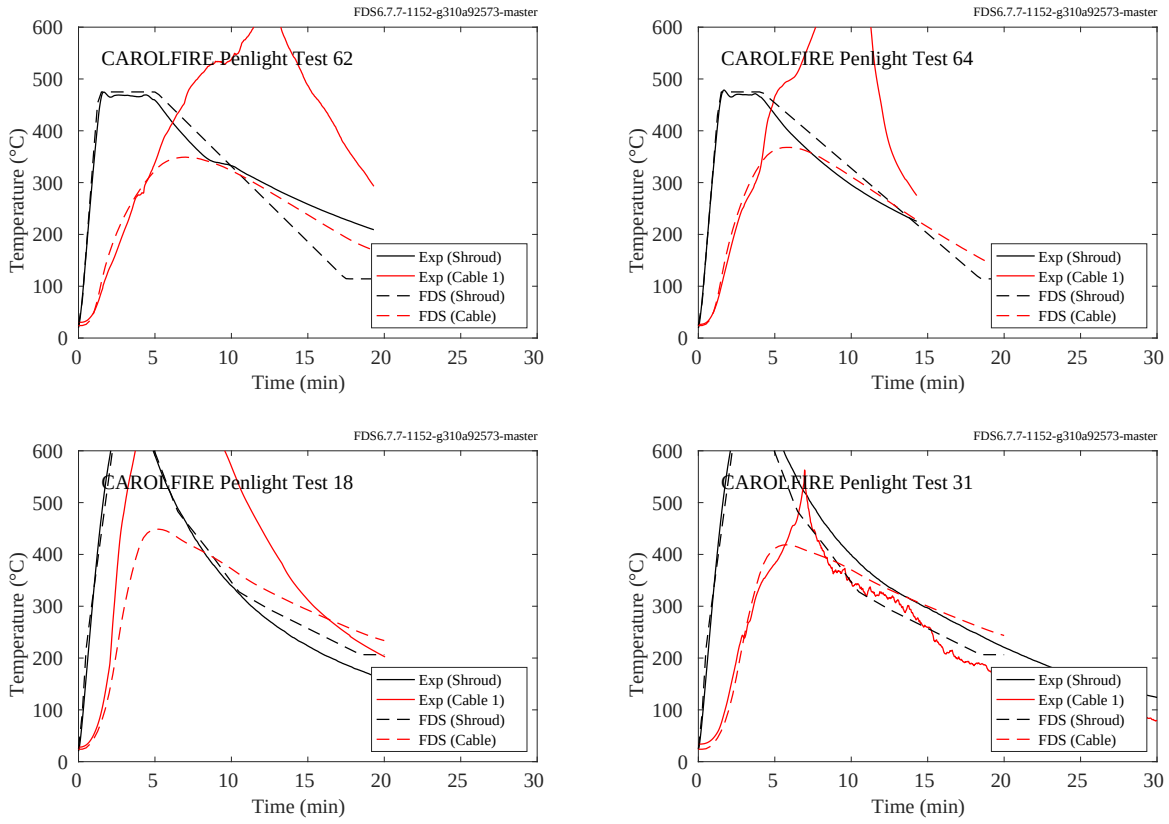

Figure 11.121: CAROLFIRE, electrical cable temperatures, Penlight Tests 18, 31, 62, 64.

11.2.8 Frankman Vegetation Experiments

Results of the Frankman vegetation experiments are shown in Fig. 11.122. Each plot represents a particular fuel sample. “SmEx15”, for example, is the small excelsior at 15 cm from the burner. Details and references can be found in Section 3.29.

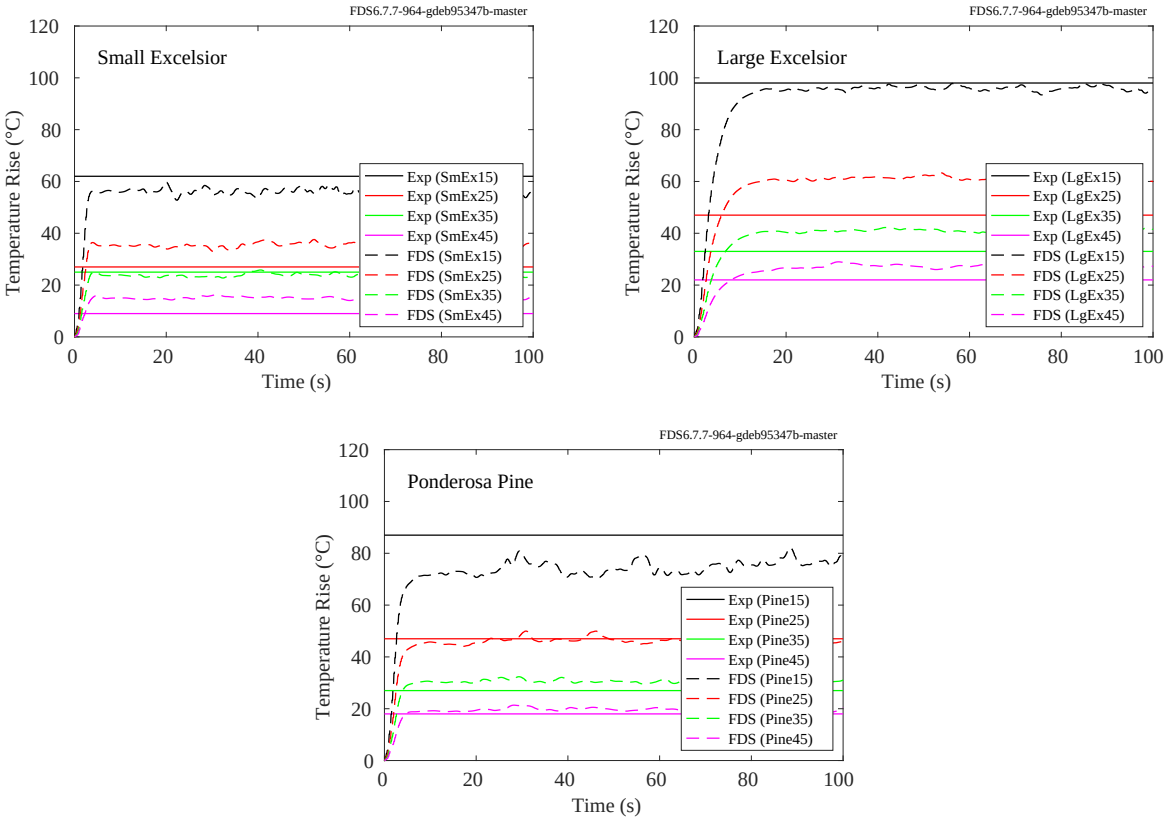

Figure 11.122: Frankman vegetation experiments, fuel temperatures.

11.2.9 PRISME Experiments

In most of the PRISME experiments, instrumented electrical cables were laid within trays at various heights in the test compartment. For the PRISME LEAK series of experiments (Figs. 11.123 and 11.124), the gas temperature in the vicinity of the cables was measured and served as the exposing heat source for calculations using the THIEF (Thermally-Induced Electrical Failure) model [265].

For the PRISME Door experiments, the temperatures of surrogate cables were predicted directly from the predicted thermal environment of the entire compartment. The measurement points in these experiments were labeled, for example, TCA_L2_HE_SURF, meaning thermocouple of the "analytical" cable, compartment 2, *haut* (high), east, surface. BW means *bas* (low) west, for example. Thermocouples were positioned on the cable surface (SURF), halfway towards center (INTER), and center (CENTRE).

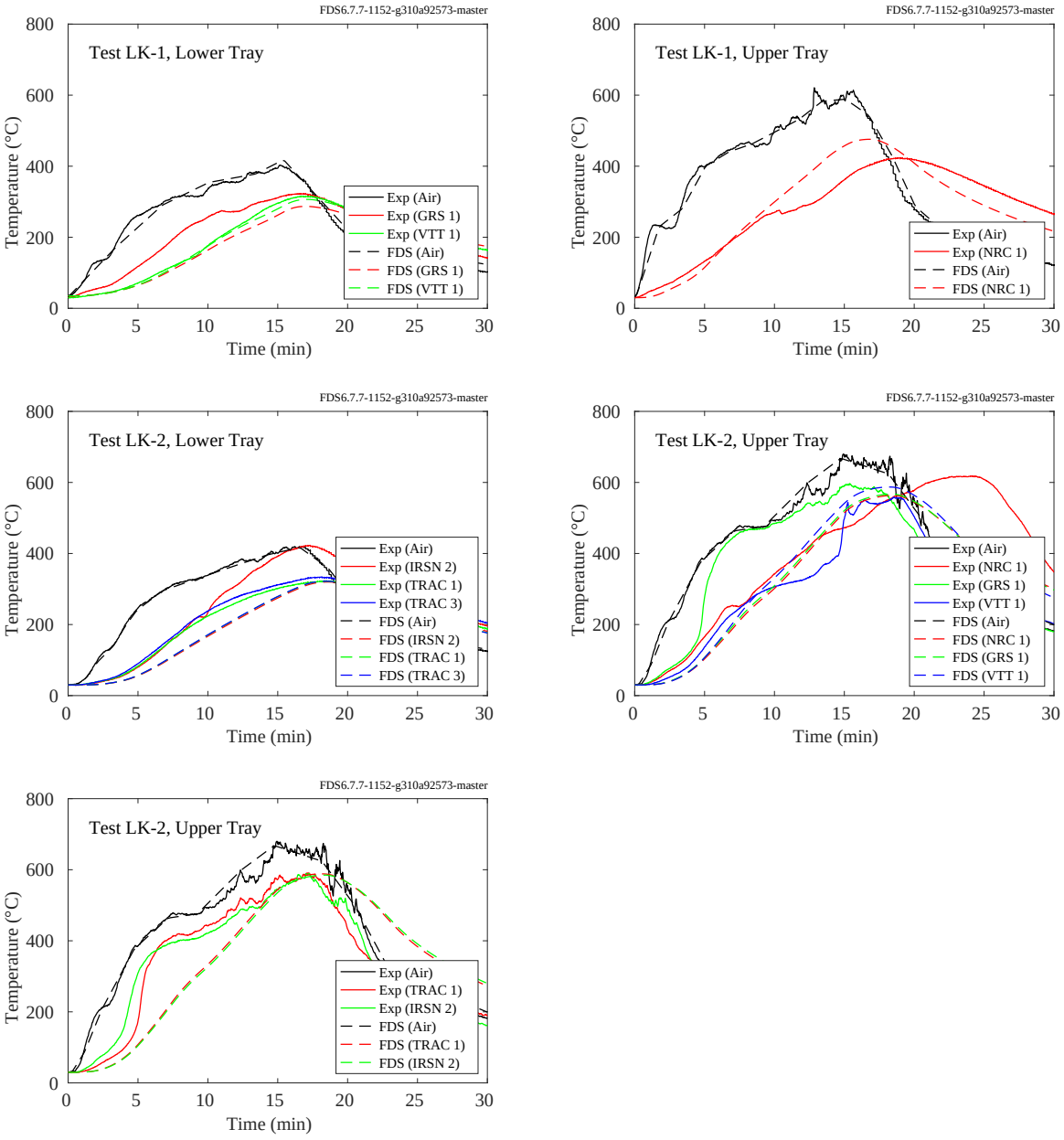

Figure 11.123: PRISME LEAK experiments, cable temperature, Tests 1 and 2.

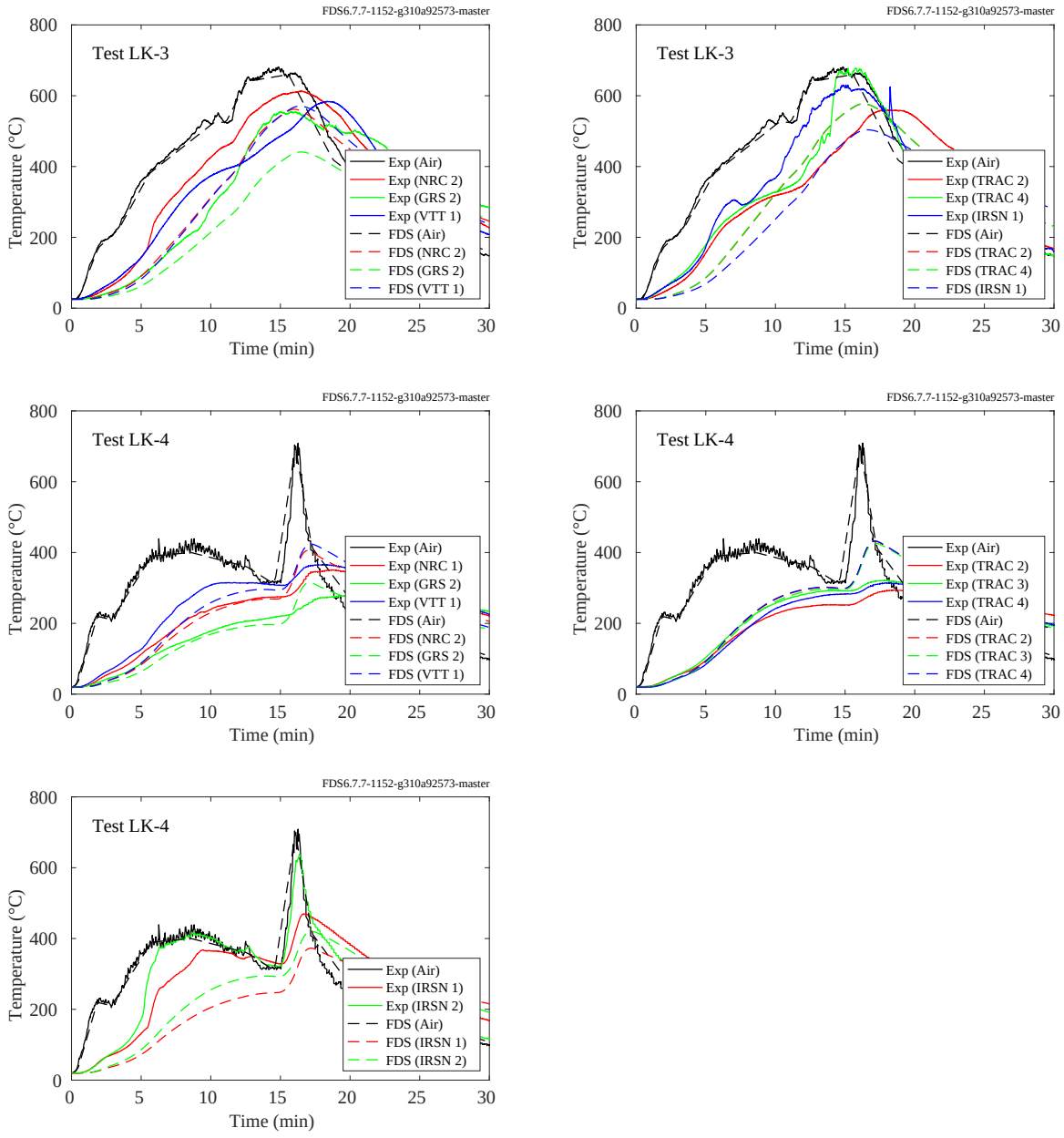

Figure 11.124: PRISME LEAK experiments, cable temperature, Tests 3 and 4.

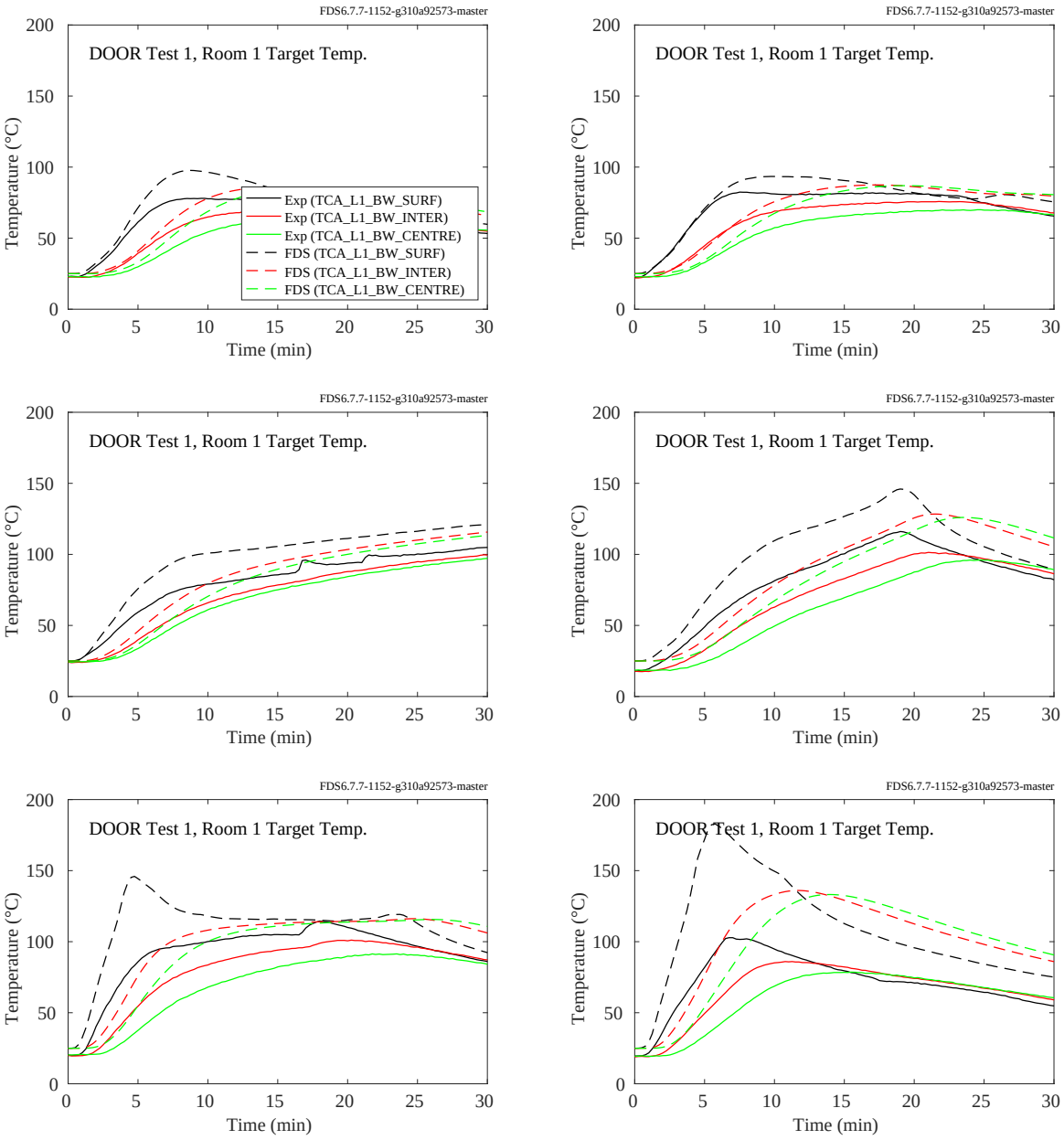

Figure 11.125: PRISME DOOR experiments, cable temperature, Room 1, Cable BW.

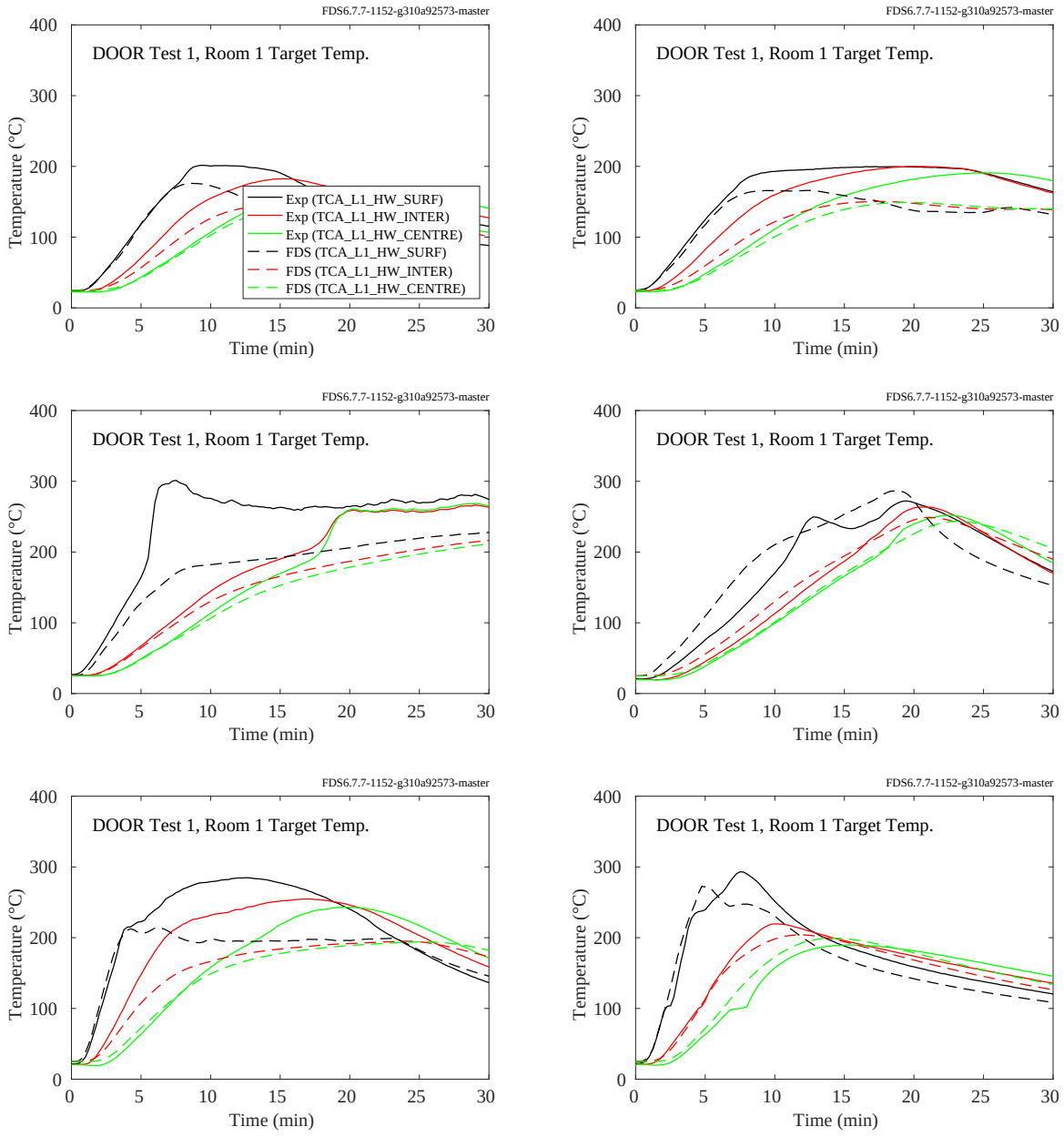

Figure 11.126: PRISME DOOR experiments, cable temperature, Room 1, Cable HW.

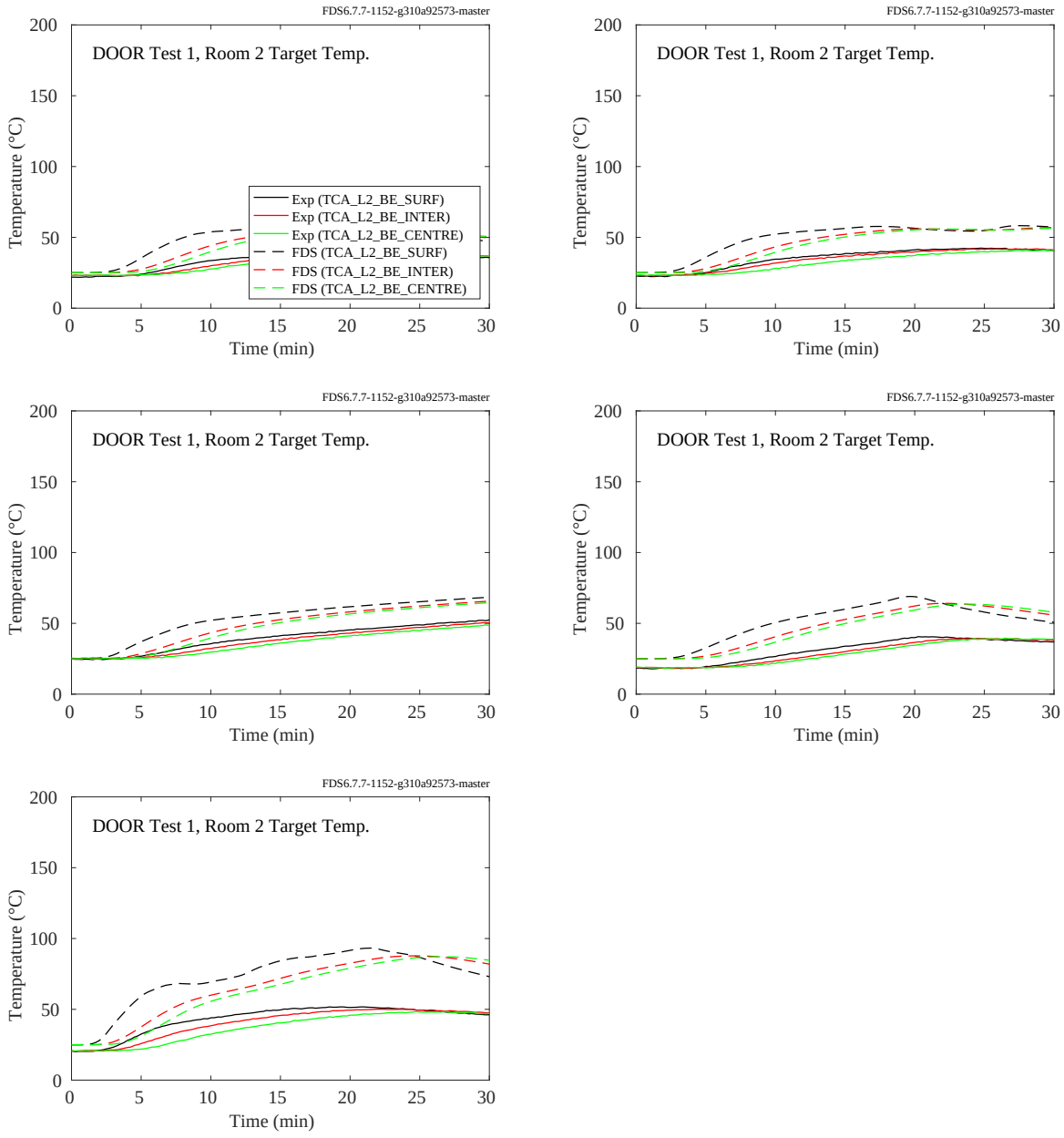

Figure 11.127: PRISME DOOR experiments, cable temperature, Room 2, Cable BE.

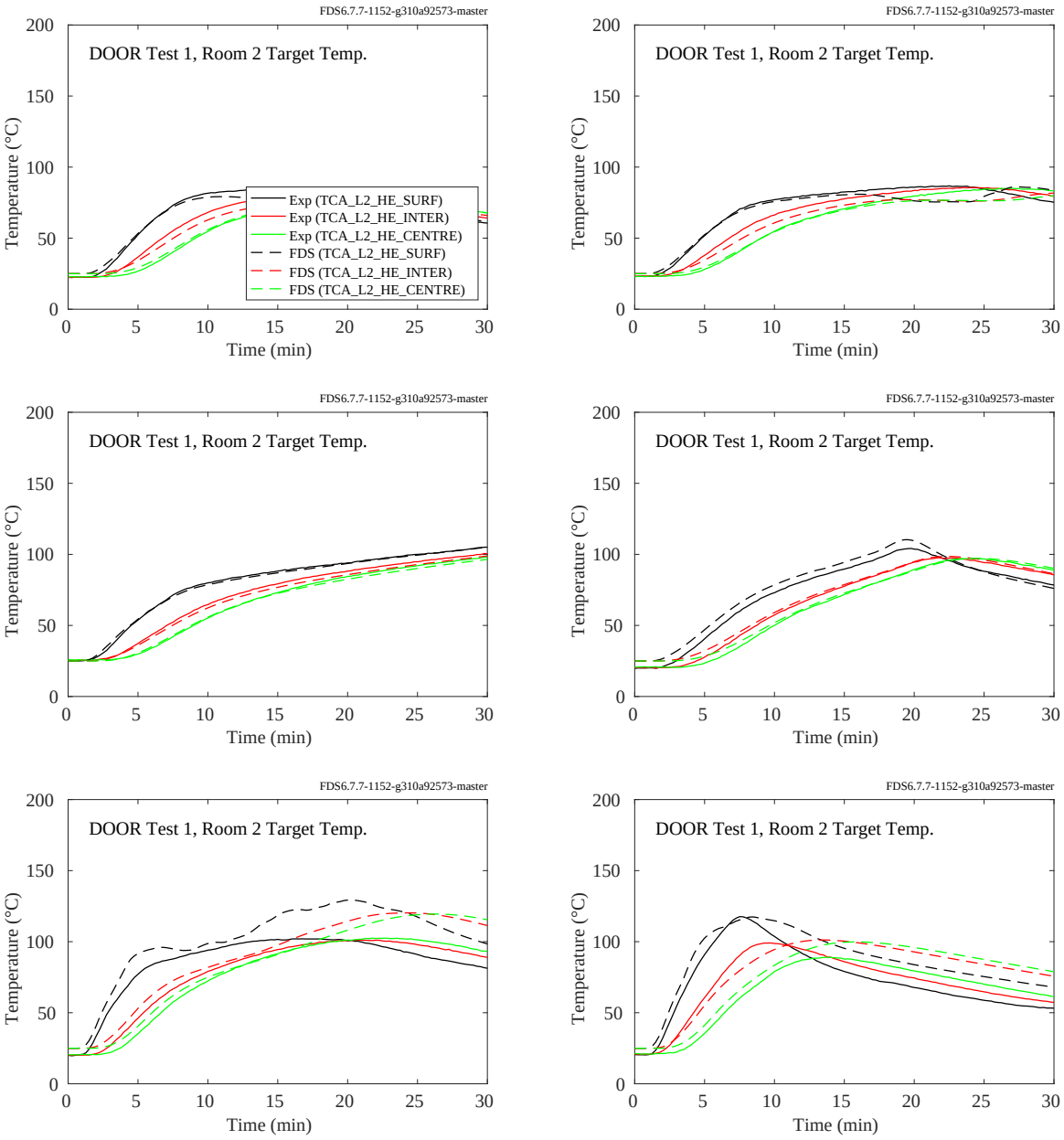

Figure 11.128: PRISME DOOR experiments, cable temperature, Room 2, Cable HE.

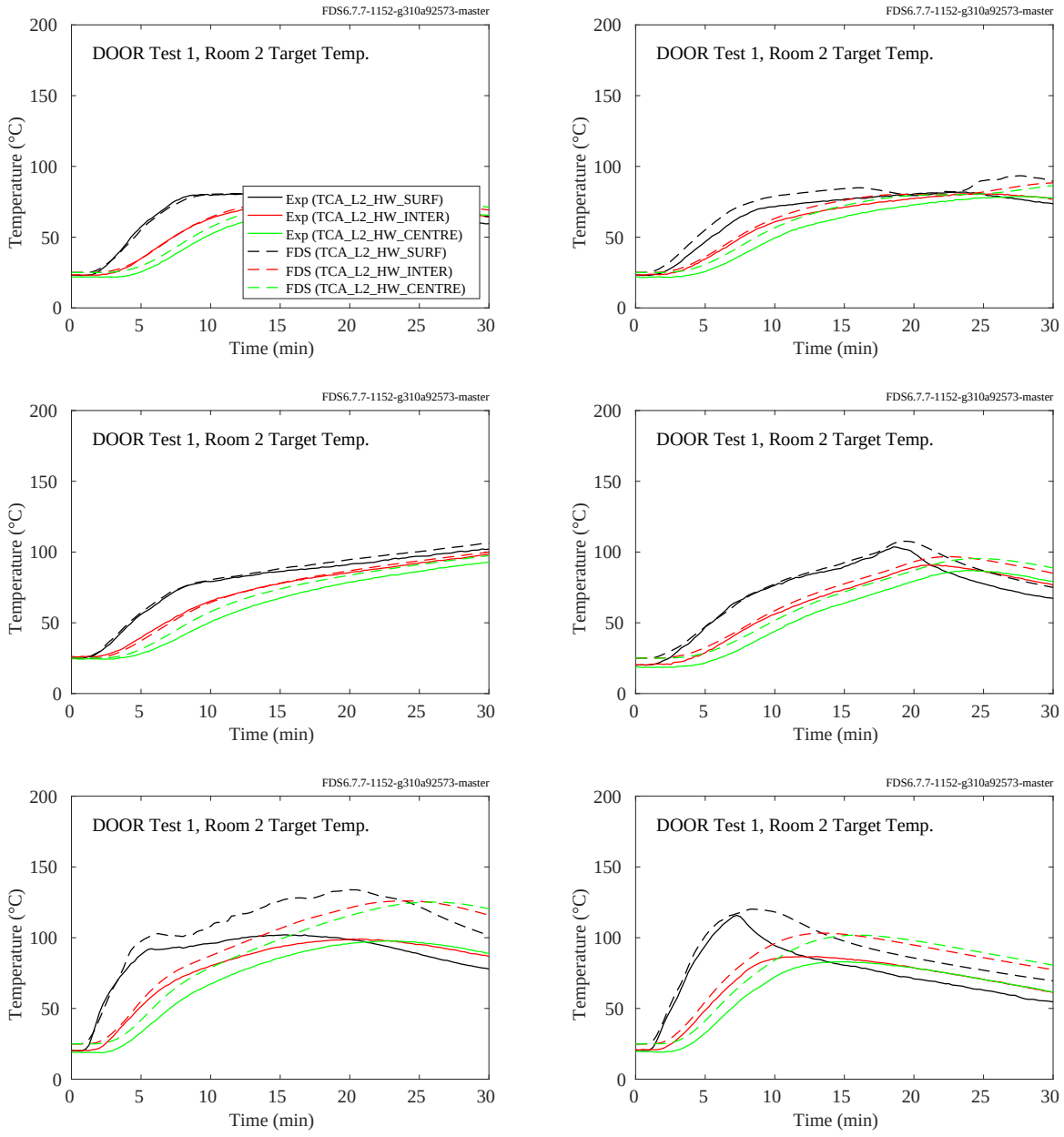

Figure 11.129: PRISME DOOR experiments, cable temperature, Room 2, Cable HW.

11.2.10 Summary of Target Temperature Predictions

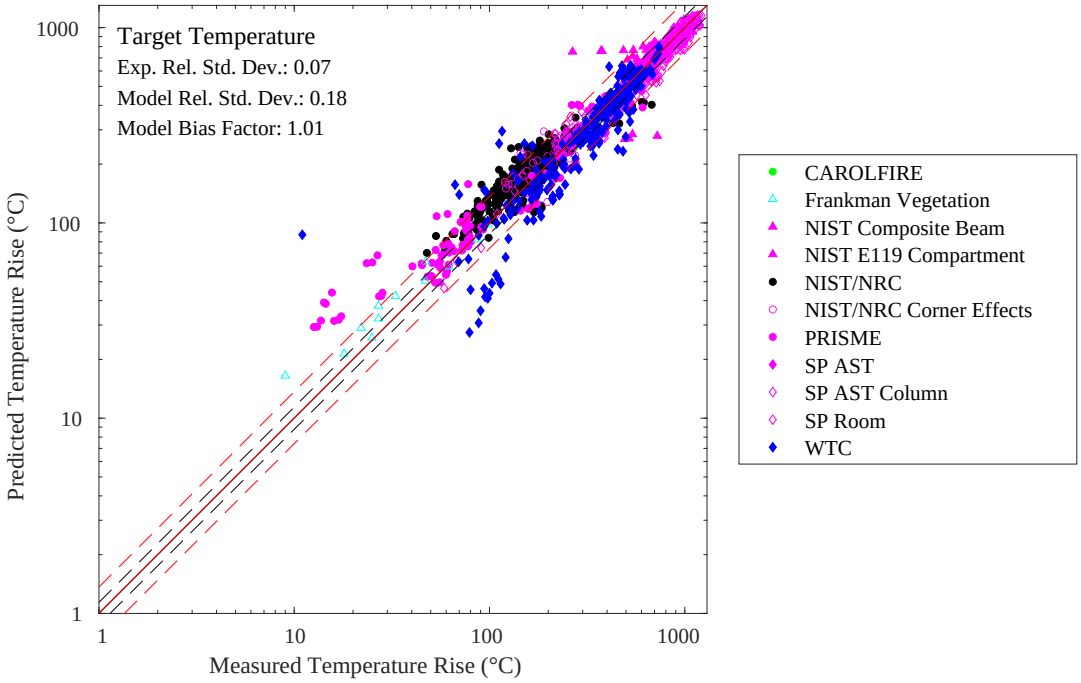

Figure 11.130: Summary of target temperature predictions.

11.2.11 Time to Failure

In addition to comparing the peak temperature predictions and measurements for electrical cables, it is also useful to consider the uncertainty in predicting the time to cable failure. Obviously, the two quantities are related, but from a practical standpoint, it is the time to failure that is of interest in these types of analyses. Figure 11.131 displays results for the CAROLFIRE experiments.

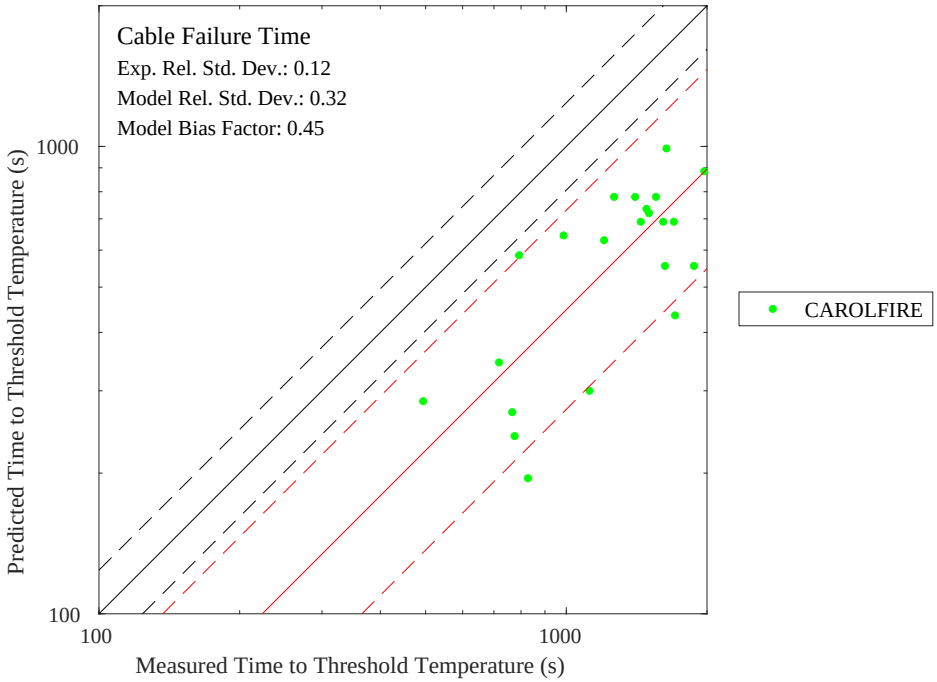

Figure 11.131: Summary of time to failure predictions for electrical cables.

11.3 Liquid Pool Surface Temperature

This section presents predicted liquid pool fire surface temperatures compared with the respective liquid boiling temperatures. Mass loss rate comparisons are shown in Section 14.5.

11.3.1 Pool Fires

Figure 11.132 displays the surface temperature of a pan of boiling water. Figure 11.133 displays the surface temperature of 1 m^2 and 2 m^2 heptane pool fires. Figure 11.134 displays the surface temperature of various other liquid pool fires.

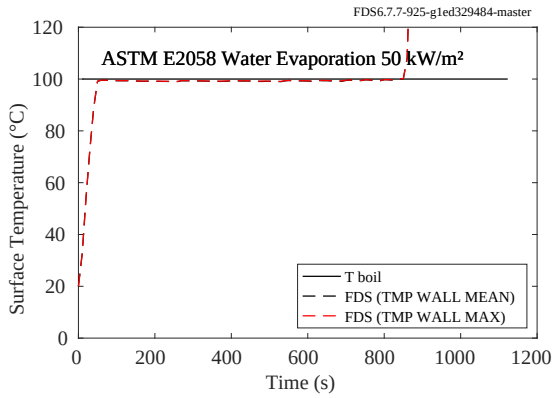

Figure 11.132: ASTM E2058 water evaporation 50 kW/m^2, surface temperature.

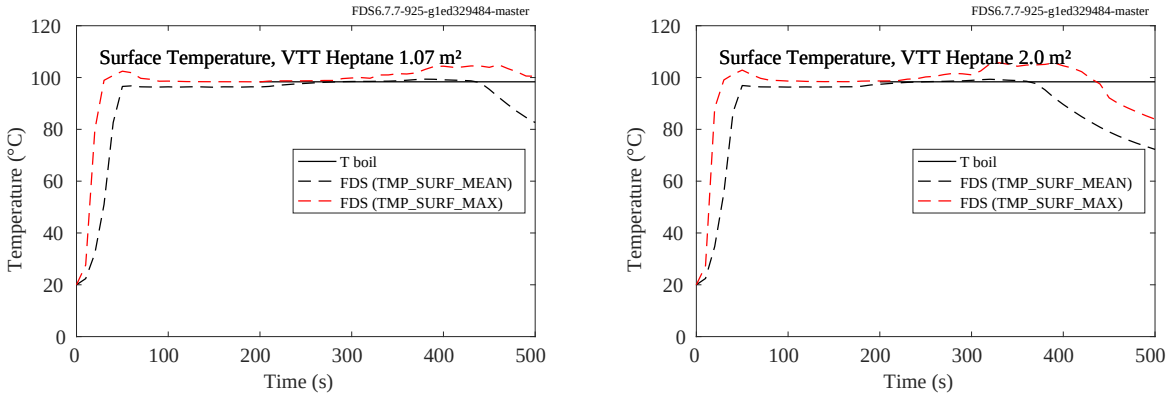

Figure 11.133: VTT heptane pool fire surface temperatures.

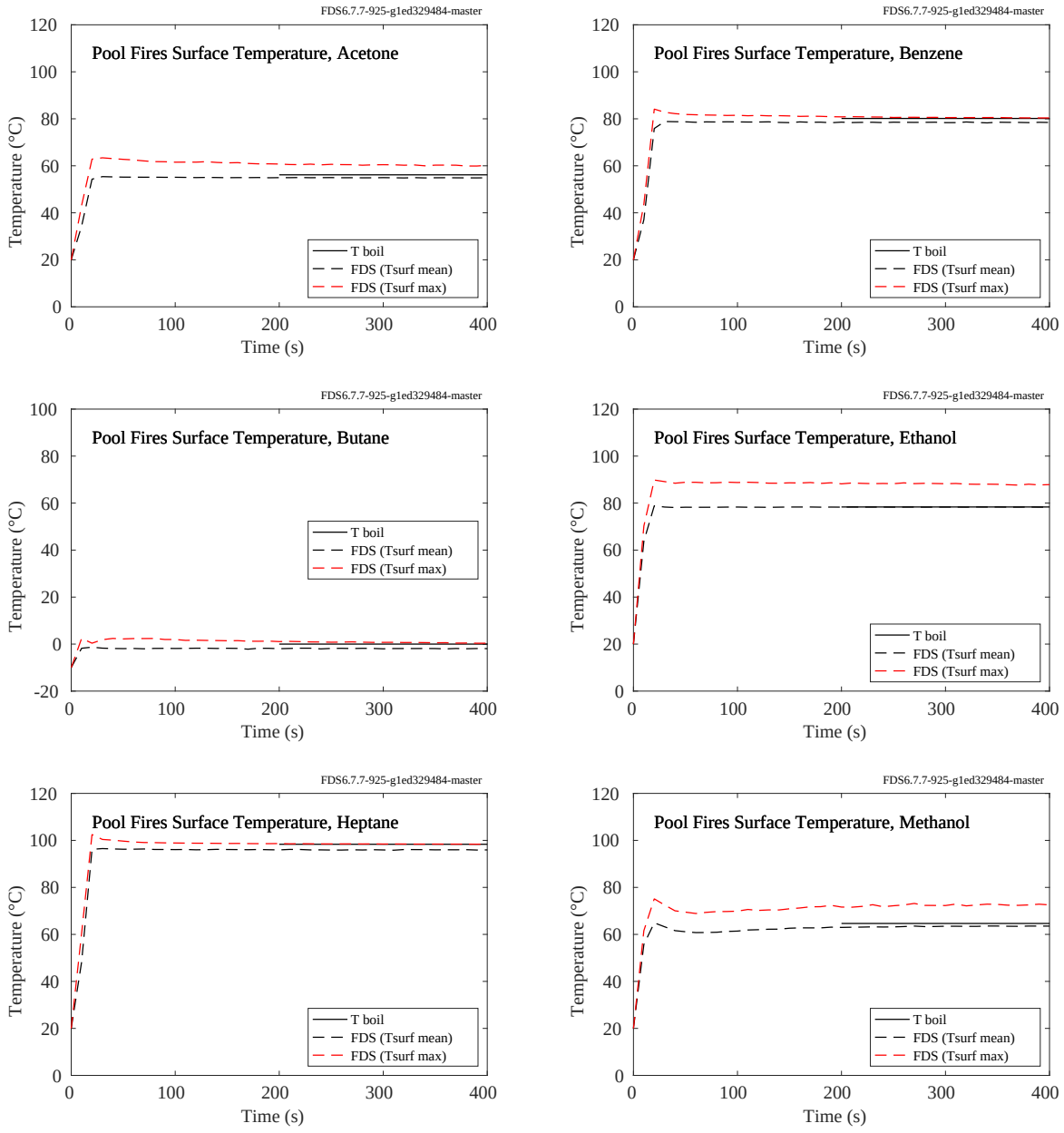

Figure 11.134: Pool fire experiments, surface temperatures.

11.3.2 NIST Pool Fires and Waterloo Methanol

Figure 11.135 displays the mean surface temperature for the 1 m NIST methanol pool fire [330] and the 30 cm Waterloo methanol pool fire [310]. The predicted surface temperatures are compared to the boiling temperature of methanol, 64.7 °C.

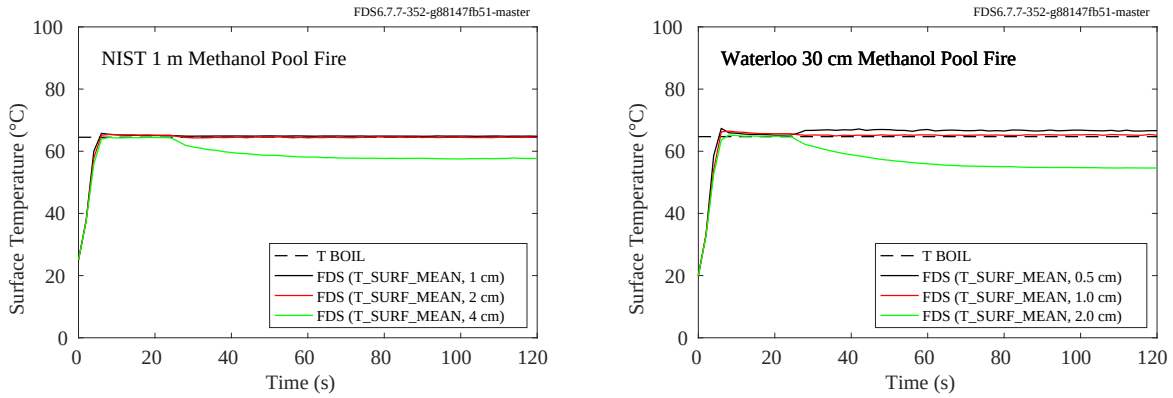

Figure 11.135: NIST 1 m (left) and Waterloo 30 cm (right) methanol pool fires, surface temperature.

11.3.3 Summary of Liquid Pool Surface Temperature Predictions

Figure 11.136 summarizes the temperature predictions for liquid pool surface temperatures under high heat flux conditions such as pool fires.

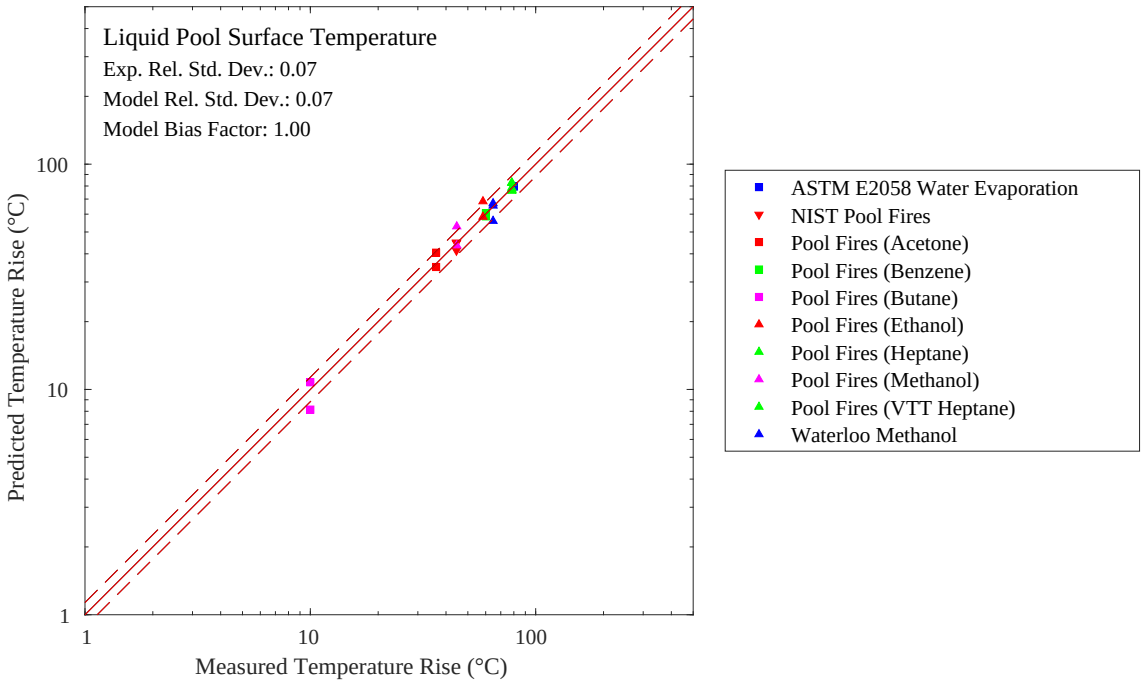

Figure 11.136: Summary of liquid pool surface temperature predictions.

Chapter 12

Heat Flux

This chapter contains a wide variety of heat flux measurements, ranging from less than a kW/m^2 from very small methane gas burners up to about 150 kW/m^2 in full-scale compartment fires. The results are broken up into two broad categories—heat flux to compartment walls, ceiling, and floor, and heat flux to "targets". A target is any object of interest in a fire simulation, like a steel beam or electrical cable.

There are also sections that look at special cases, like the heat flux measured at a liquid fuel surface, attenuation of thermal radiation by water sprays, and convective heat flux.

12.1 Heat Flux to Walls, Ceiling, and Floor

12.1.1 FAA Cargo Compartments

Measurements of heat flux and surface temperature were made at two ceiling locations (denoted A and B in Fig. 7.10). The heat flux measurements are shown below.

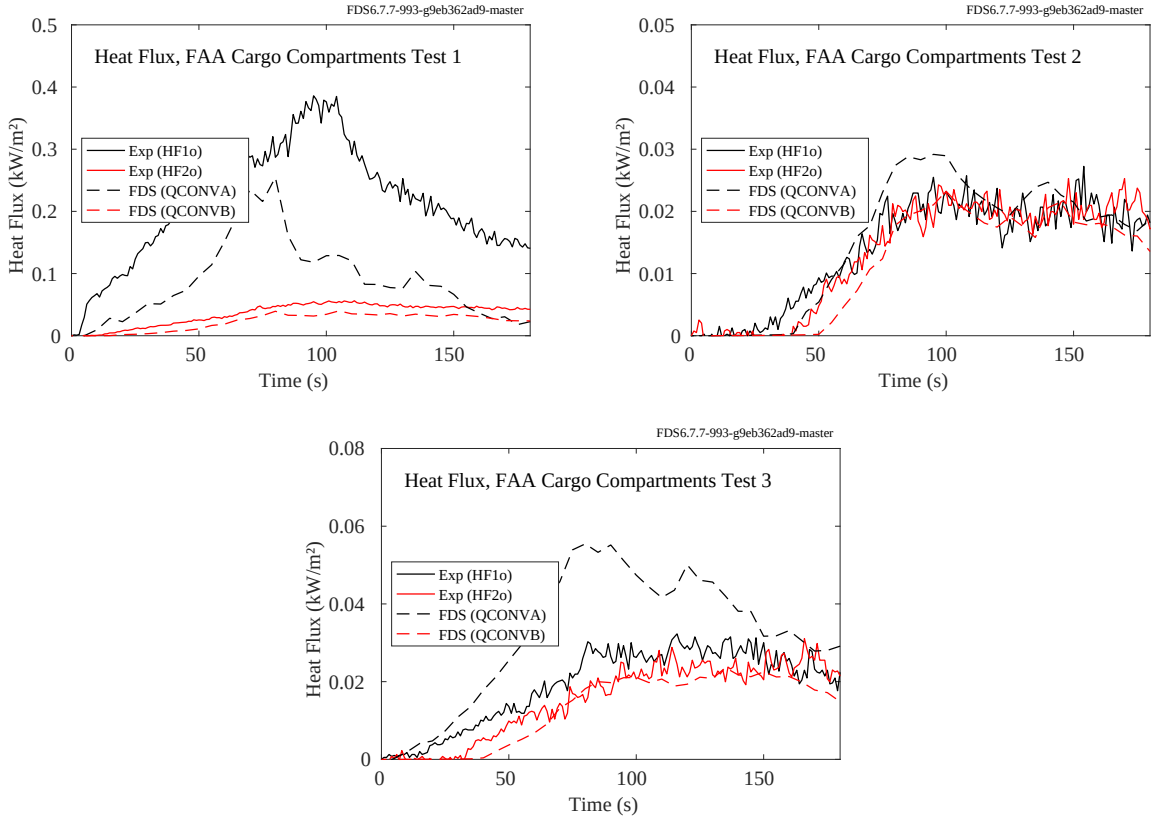

Figure 12.1: FAA Cargo Compartment experiments, heat flux to ceiling.

12.1.2 FM Parallel Panel Experiments

Predicted and measured vertical heat flux profiles for three propane and three propylene fires (30 kW, 60 kW, and 100 kW) sandwiched between two 2.4 m high, 0.6 m wide panels are presented below.

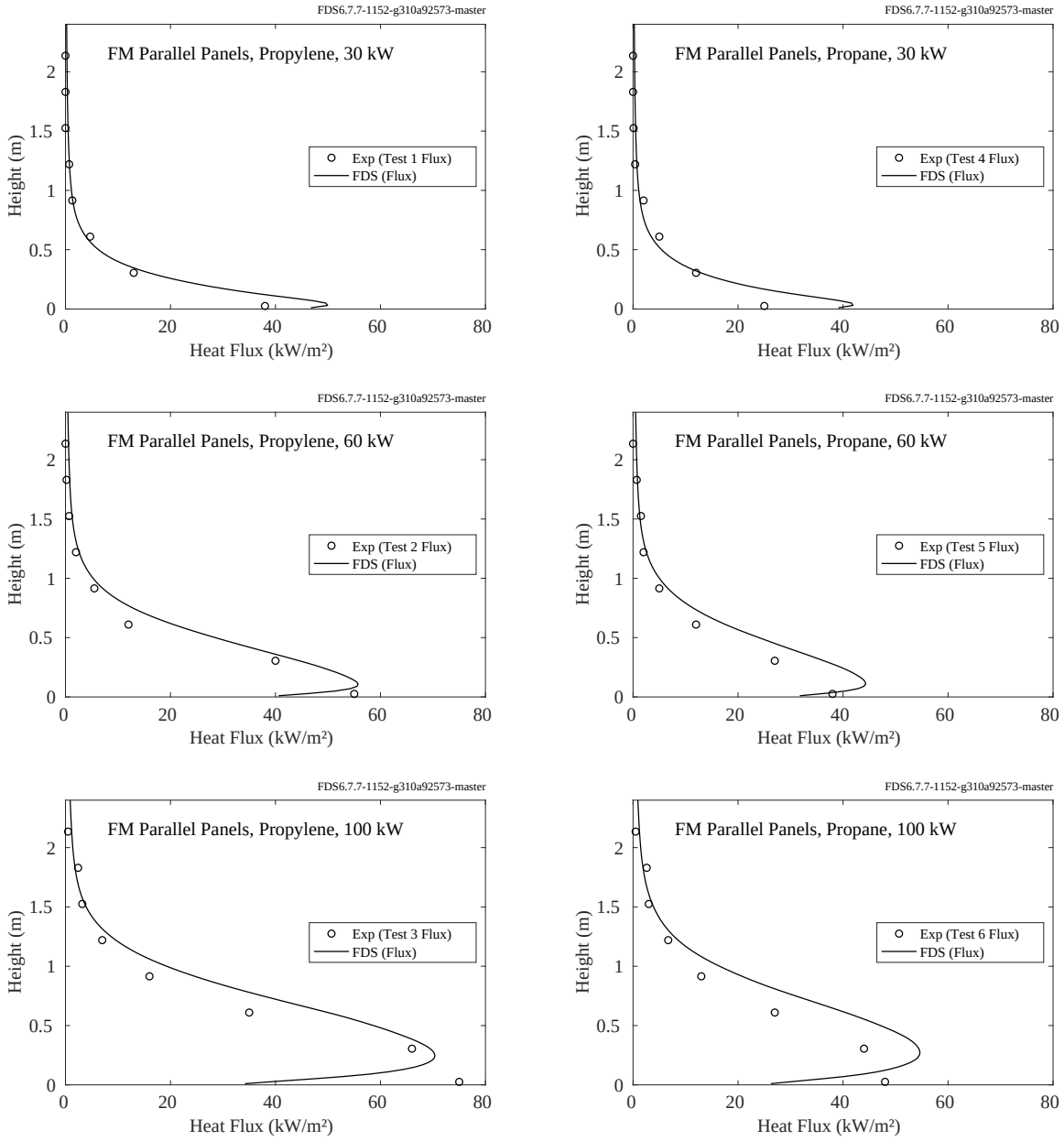

Figure 12.2: FM Parallel Panel experiments, side wall heat flux.

12.1.3 FM Vertical Wall Flame Experiments

Figure 12.3 displays the measured and predicted outward flame radiance at heights of 66, 330, 594, and 990 mm above the base of the burner, for a range of burning rates. The radiance is defined as the radiant flux per unit solid angle in the outward normal direction. The radiance of an ideal black body at temperature T is $\sigma T^4/\pi$.

Figure 12.4 displays the measured and predicted heat flux from propylene, ethane, ethylene, and methane wall fires. The fuel flow rates for propylene are 12.68, 17.05, and 22.37 g/m^2/s.

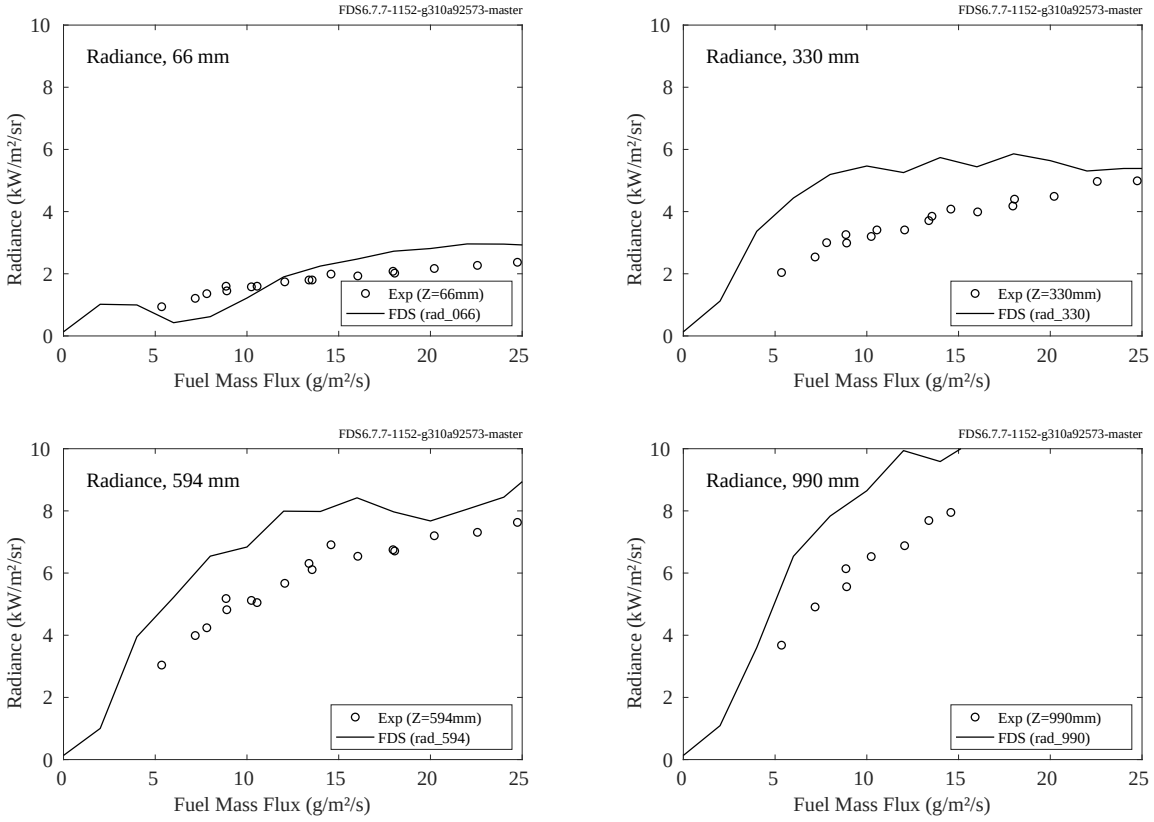

Figure 12.3: Flame radiance as a function of fuel flow rate at heights of 66, 330, 594, and 990 mm.

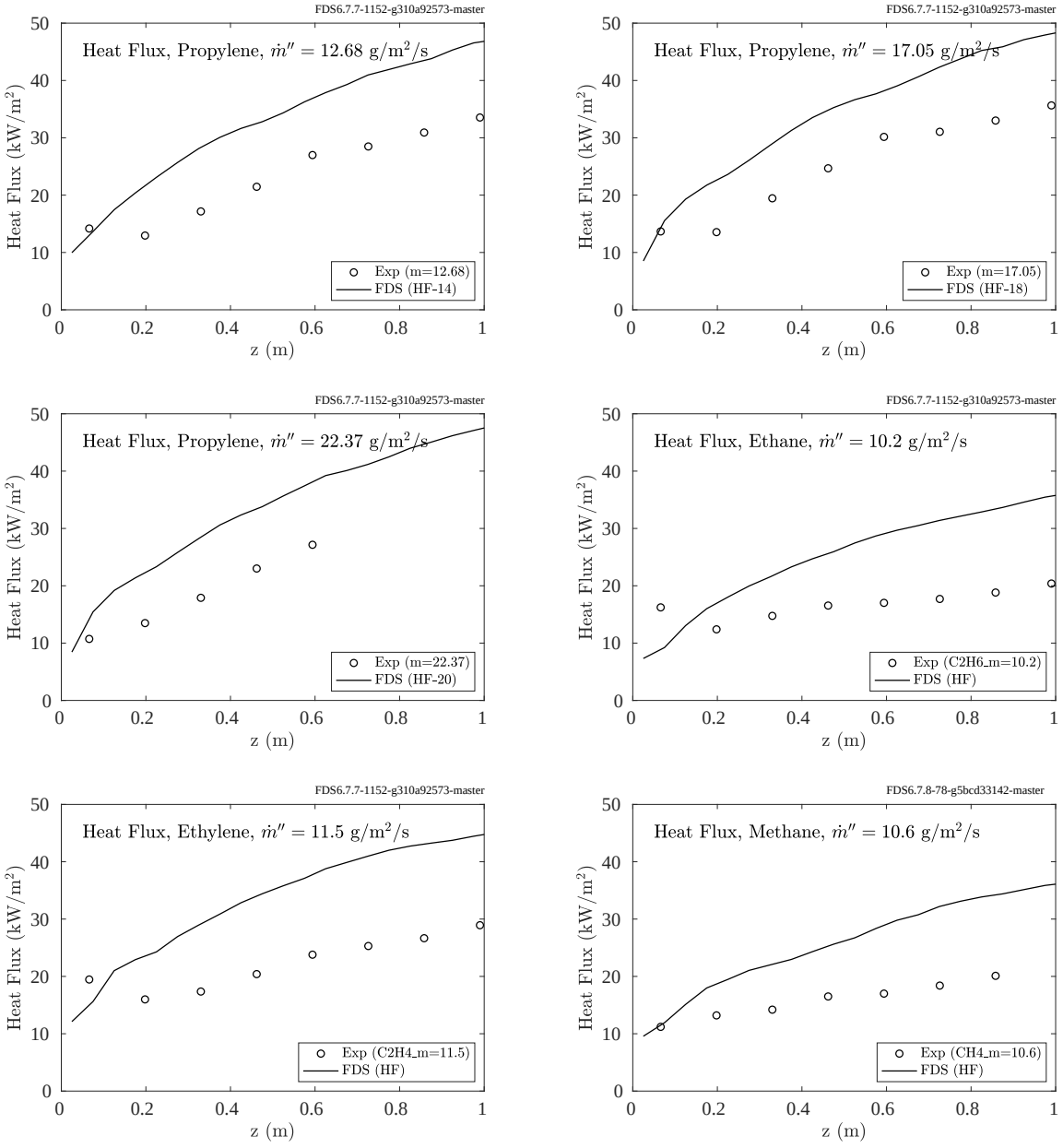

Figure 12.4: Vertical profiles of heat flux to the burner surface for fuel flow rates of 12.68, 17.05, and 22.37 g/m^2/s.

12.1.4 NIST E119 Compartment

Heat flux gauges (Gardon, Model 64-20-18) were placed at three locations in the compartment, in water-cooled steel pipes of 25 mm inside diameter. Results are shown in Fig. 12.5. Gauge locations are shown in Fig. 3.22.

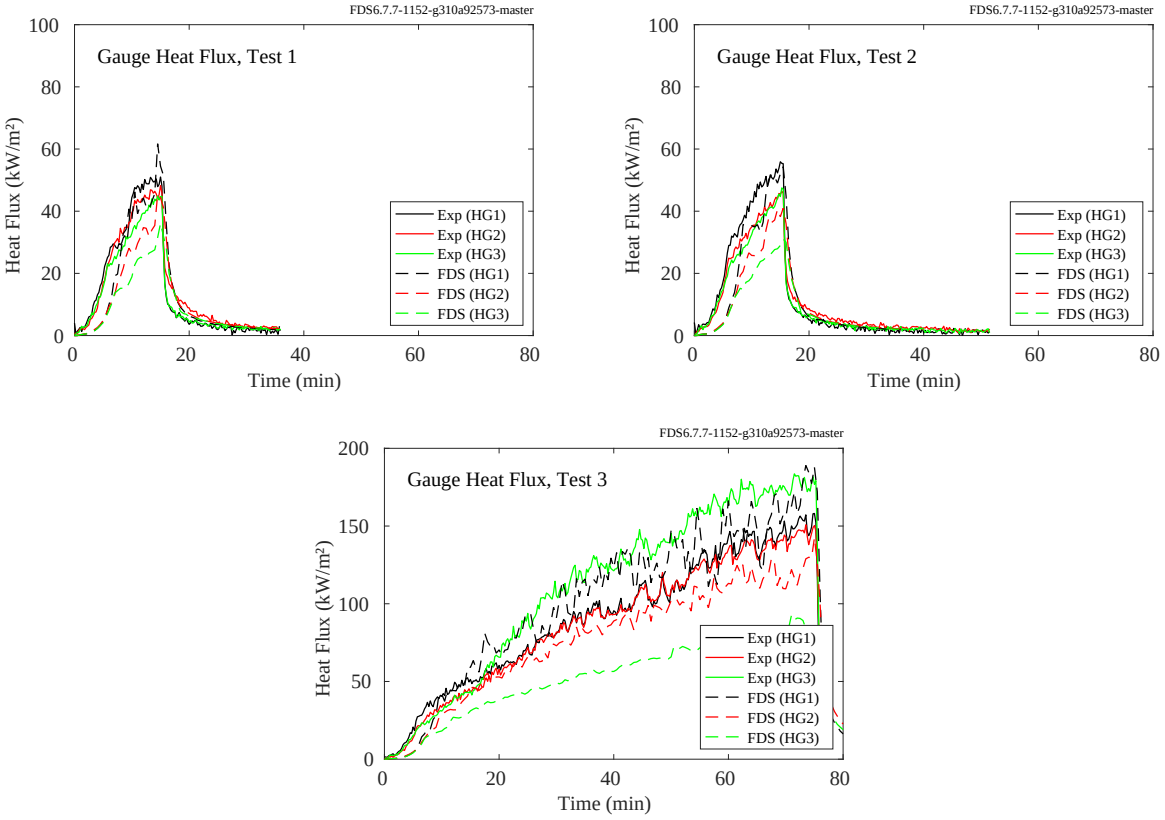

Figure 12.5: NIST E119 Compartment, wall heat fluxes.

12.1.5 NIST/NRC Experiments

Heat flux gauges and thermocouples were positioned at various locations on the walls, floor, and ceiling of the compartment. The locations are given in Table 11.1. The heat flux gauges were not water cooled; thus, they measured the *net* rather than the *gauge* heat flux. However, the net heat flux is a function of the temperature of the heat flux gauge itself, which is not something that is modeled. To better compare model and measurement, the measured net heat flux is converted into a gauge heat flux using the following formula:

$$\dot{q}''_{\text{gauge}} = \dot{q}''_{\text{net}} + \sigma\left(T^4_{\text{gauge}} - T^4_{\infty}\right) + h\left(T_{\text{gauge}} - T_{\infty}\right) \quad \text{kW/m}^2 \tag{12.1}$$

where $\sigma = 5.67 \times 10^{-11}$ kW/m^2/K^4 and $h = 0.005$ kW/m^2/K.

Also, over the course of 15 experiments, numerous heat flux gauges failed, most often due to loss of contact with the wall or faulty thermocouples. All of the measurements from Test 13 and 16 were found to be flawed.

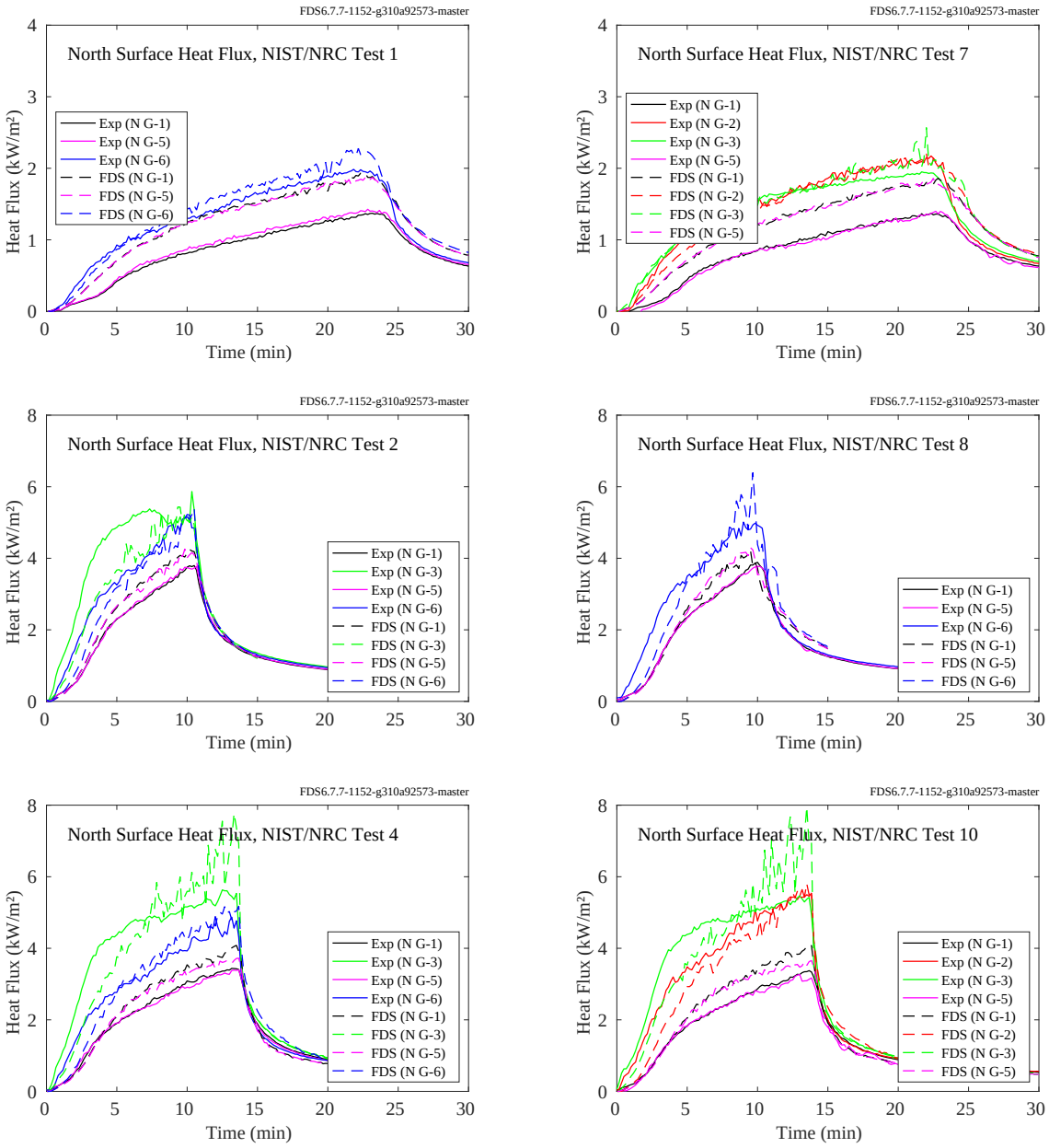

Figure 12.6: NIST/NRC experiments, heat flux to north wall, Tests 1, 2, 4, 7, 8, 10.

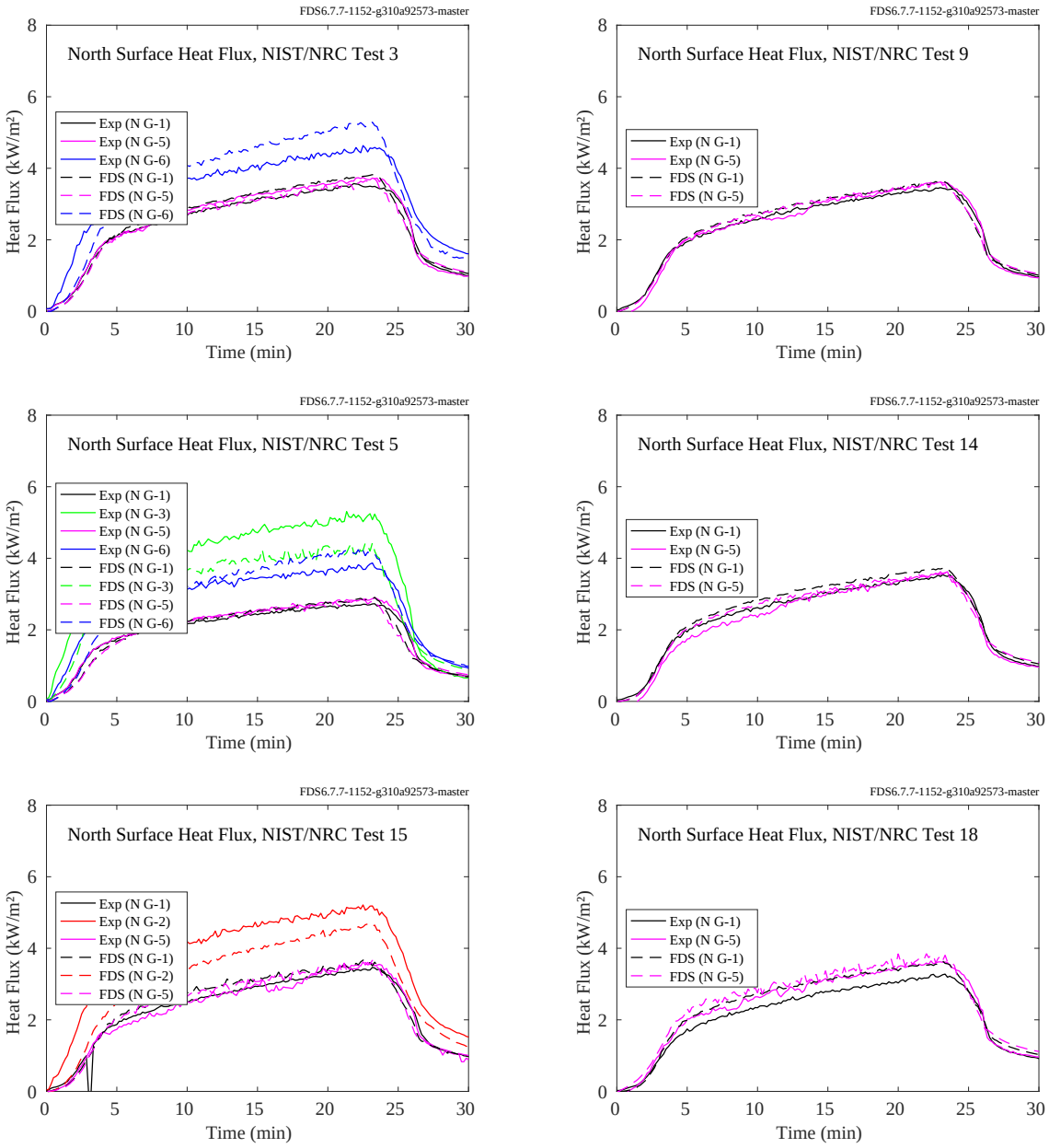

Figure 12.7: NIST/NRC experiments, heat flux to north wall, Tests 3, 5, 9, 14, 15, 18.

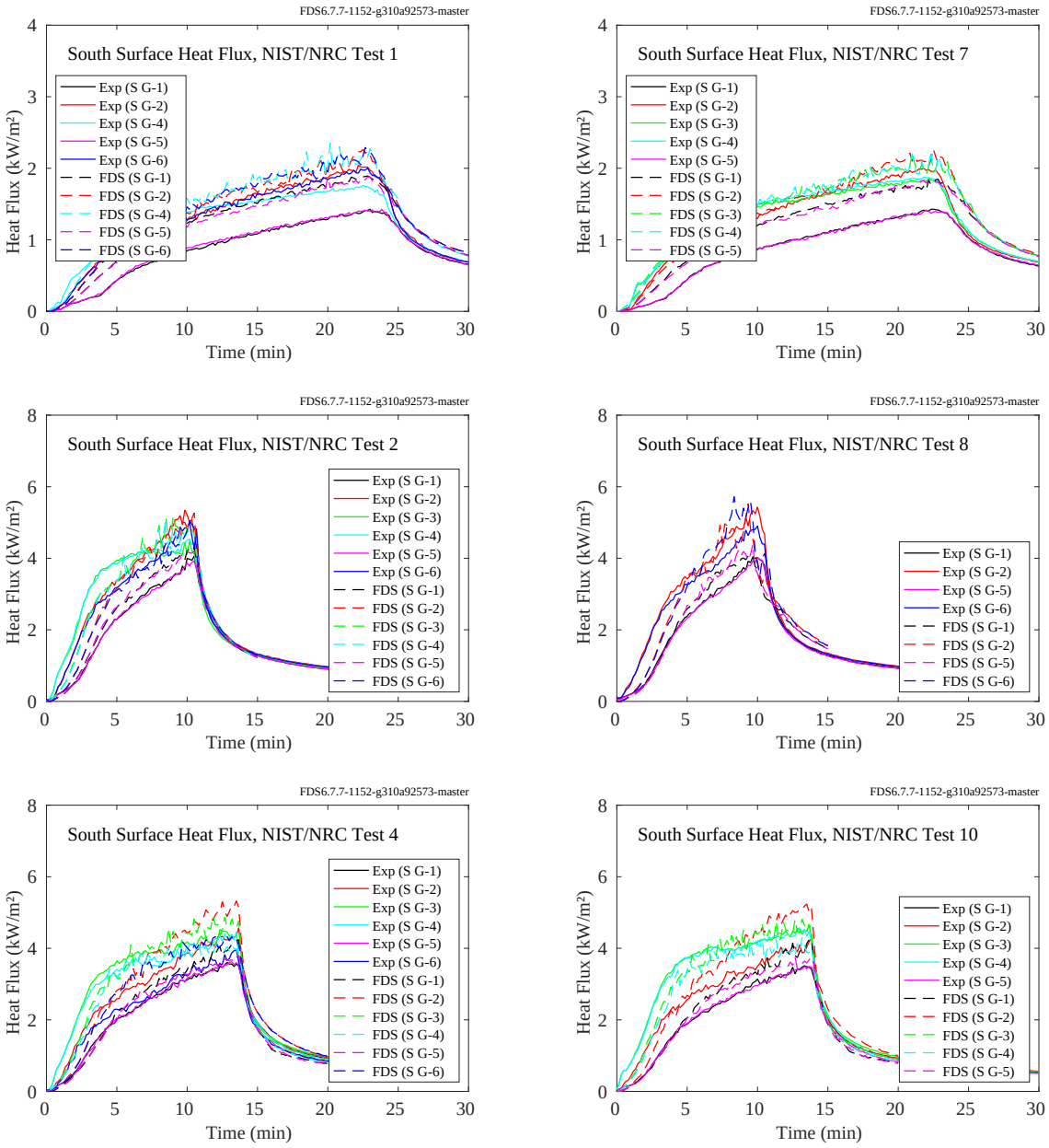

Figure 12.8: NIST/NRC experiments, heat flux to south wall, Tests 1, 2, 4, 7, 8, 10.

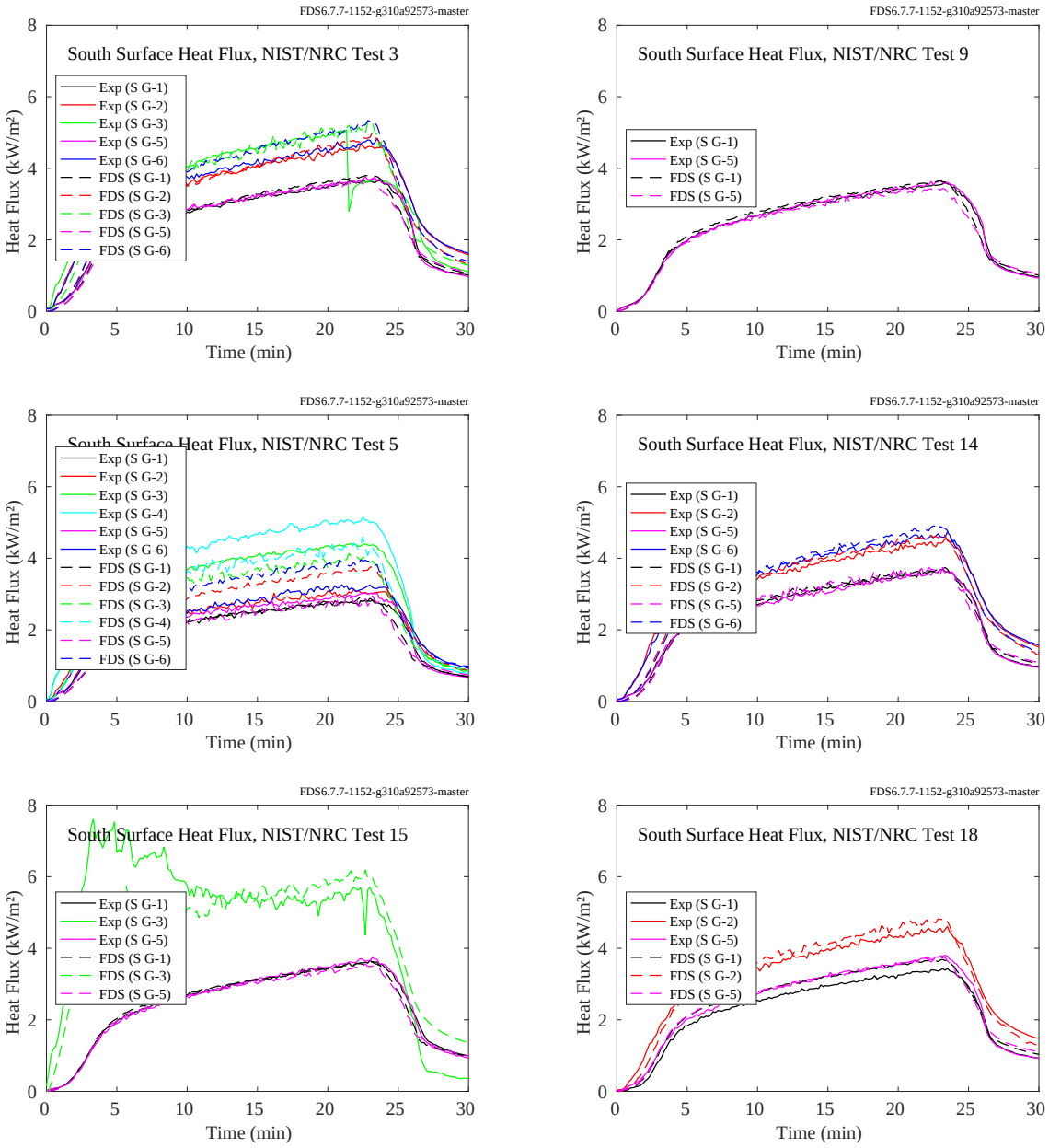

Figure 12.9: NIST/NRC experiments, heat flux to south wall, Tests 3, 5, 9, 14, 15, 18.

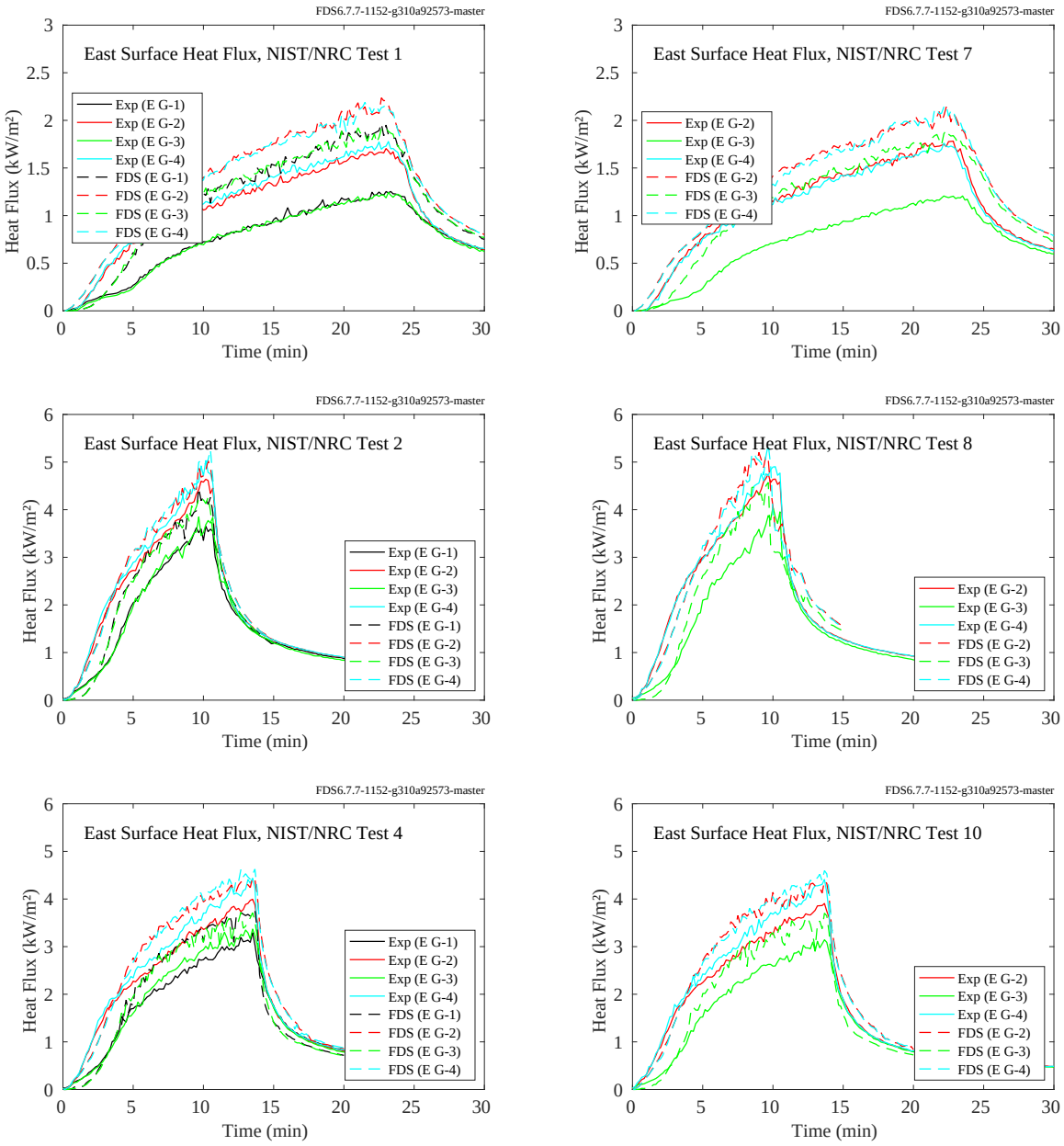

Figure 12.10: NIST/NRC experiments, heat flux to east wall, Tests 1, 2, 4, 7, 8, 10.

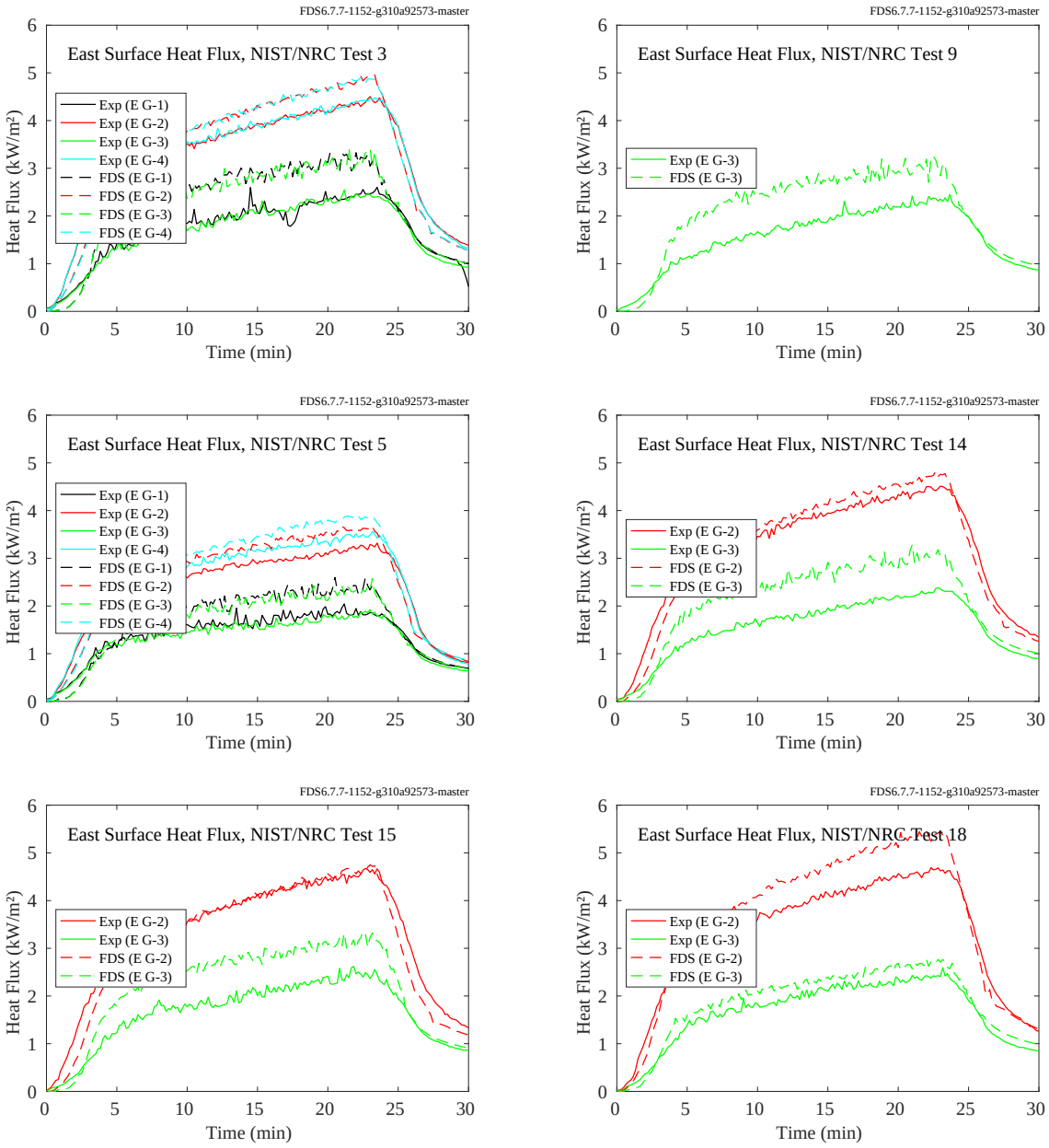

Figure 12.11: NIST/NRC experiments, heat flux to east wall, Tests 3, 5, 9, 14, 15, 18.

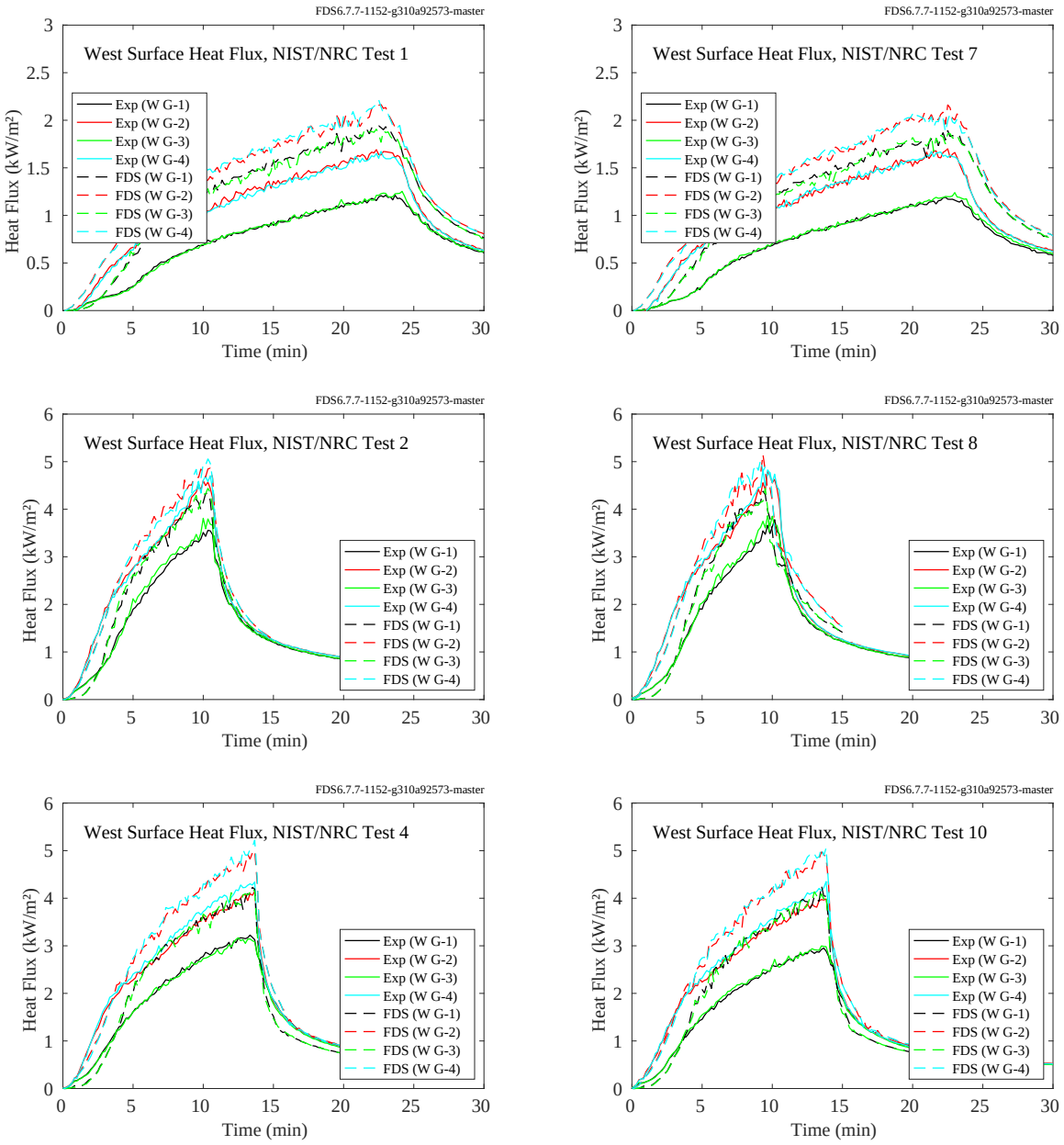

Figure 12.12: NIST/NRC experiments, heat flux to west wall, Tests 1, 2, 4, 7, 8, 10.

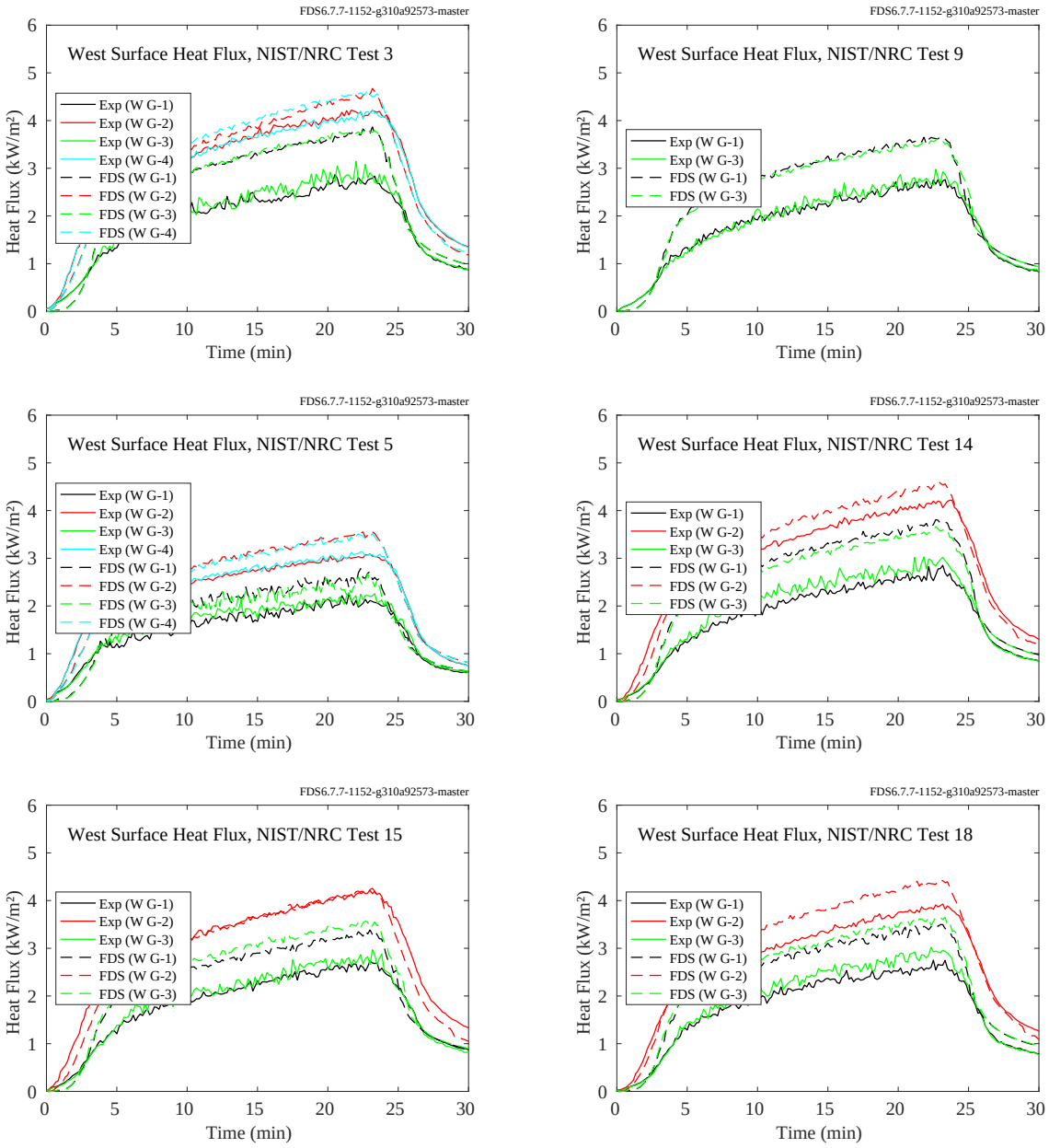

Figure 12.13: NIST/NRC experiments, heat flux to west wall, Tests 3, 5, 9, 14, 15, 18.

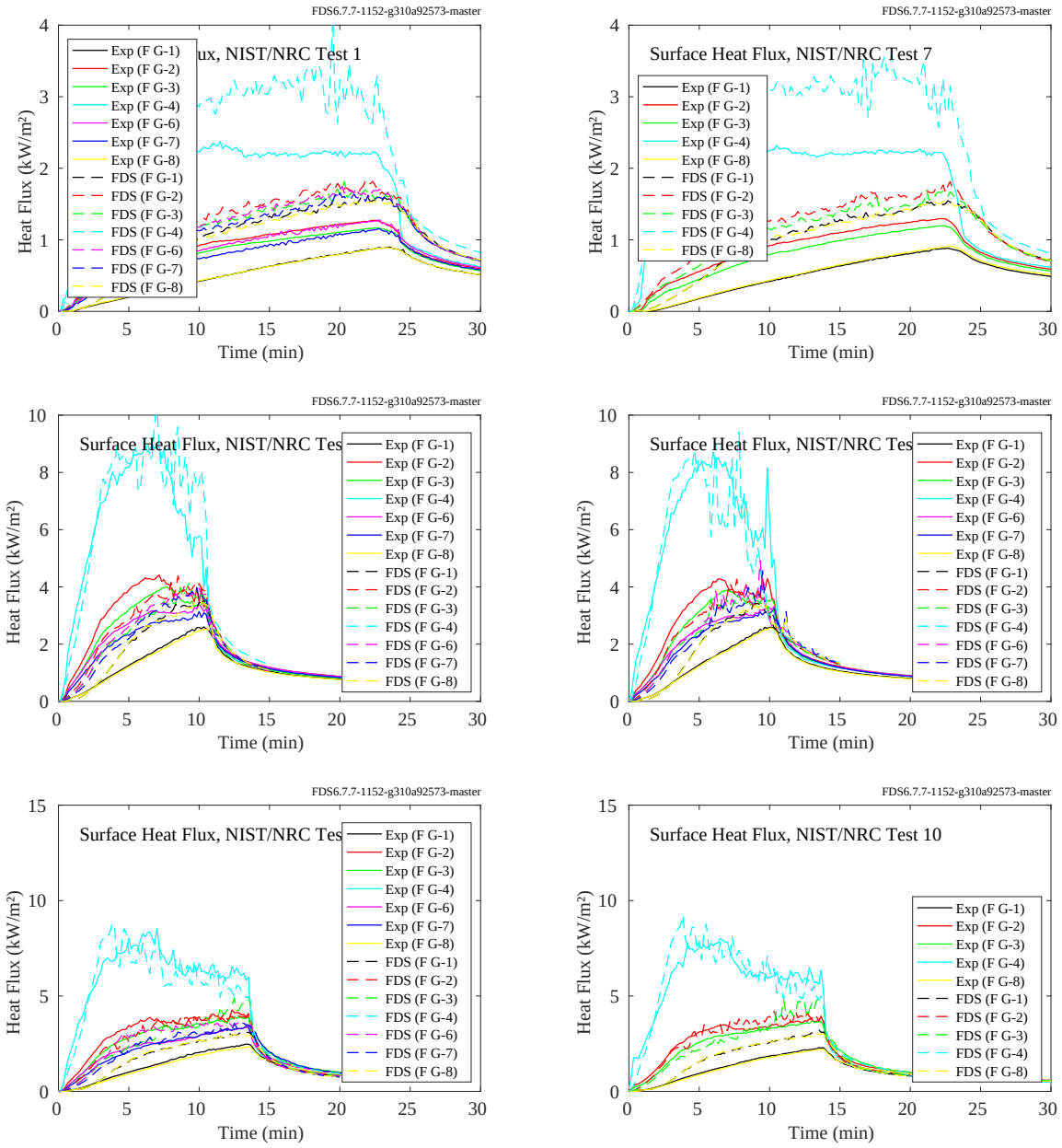

Figure 12.14: NIST/NRC experiments, heat flux to the floor, Tests 1, 2, 4, 7, 8, 10.

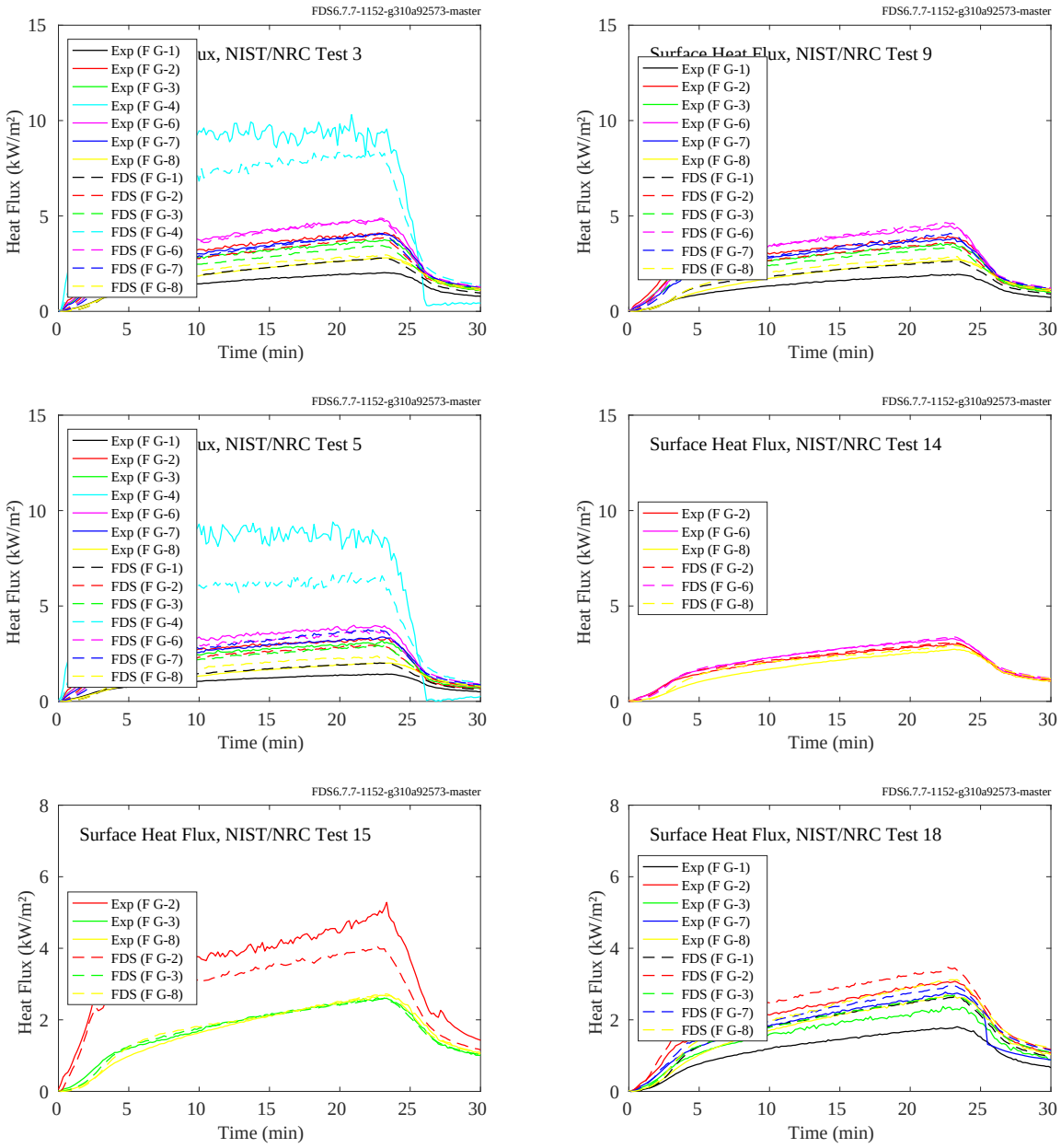

Figure 12.15: NIST/NRC experiments, heat flux to the floor, Tests 3, 5, 9, 14, 15, 18.

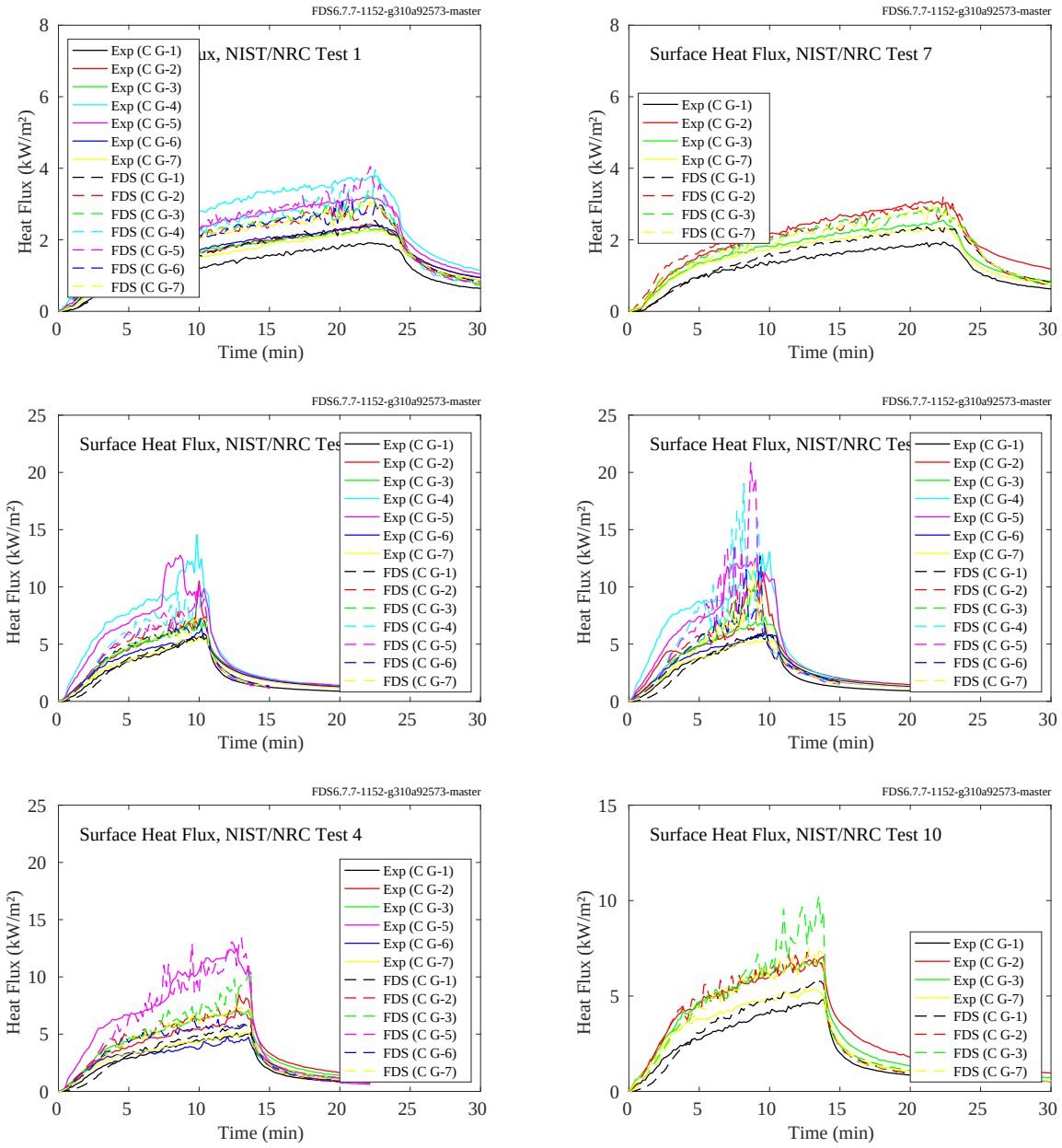

Figure 12.16: NIST/NRC experiments, heat flux to the ceiling, Tests 1, 2, 4, 7, 8, 10.

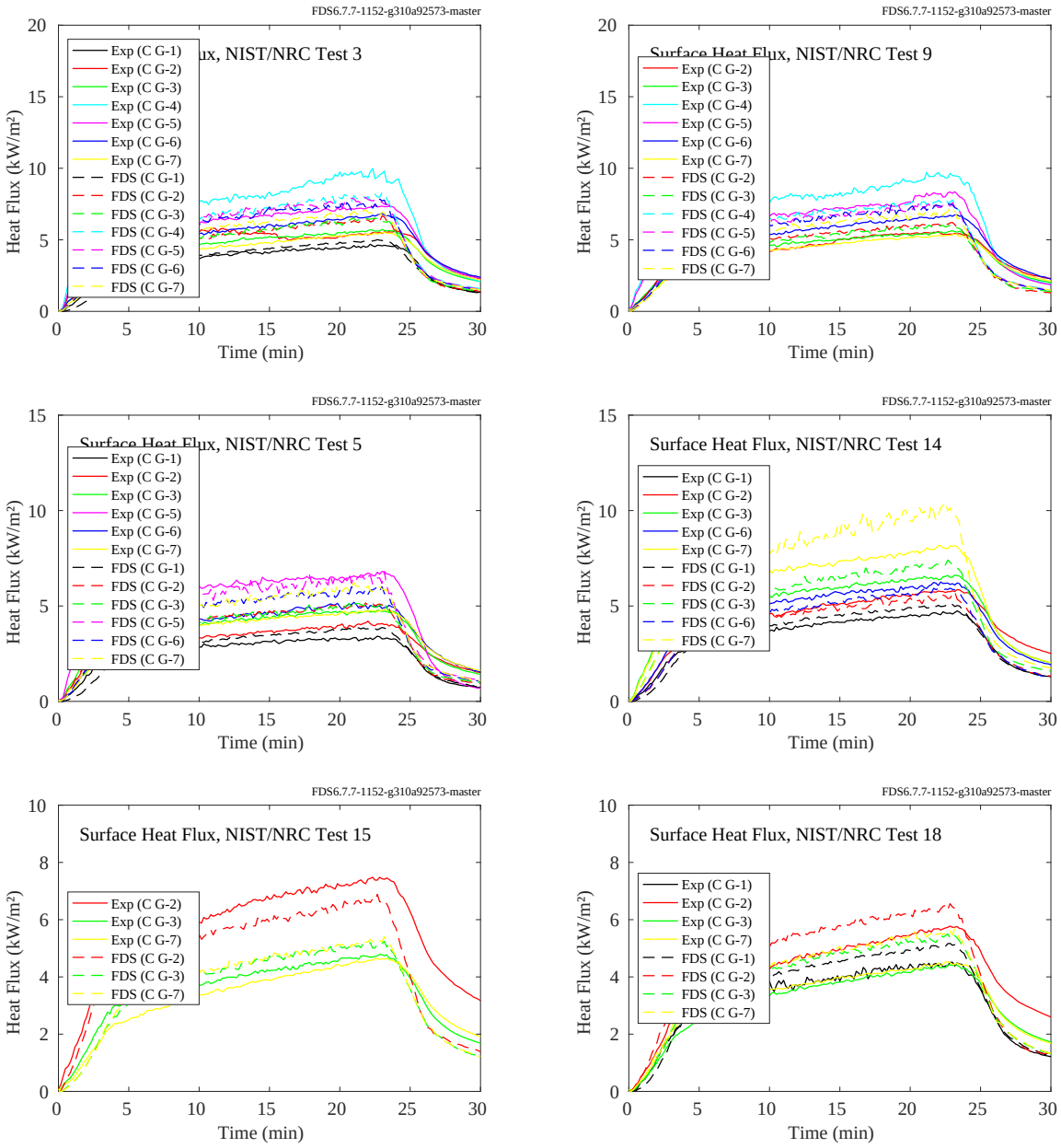

Figure 12.17: NIST/NRC experiments, heat flux to the ceiling, Tests 3, 5, 9, 14, 15, 18.

12.1.6 NRCC Facade Experiments

Figure 12.18 displays the simulation of a 10.3 MW fire inside and outside of a small enclosure. The purpose of the experiment was to measure the heat flux to the exterior facade. The FDS heat flux predictions are made at the location of the green points.

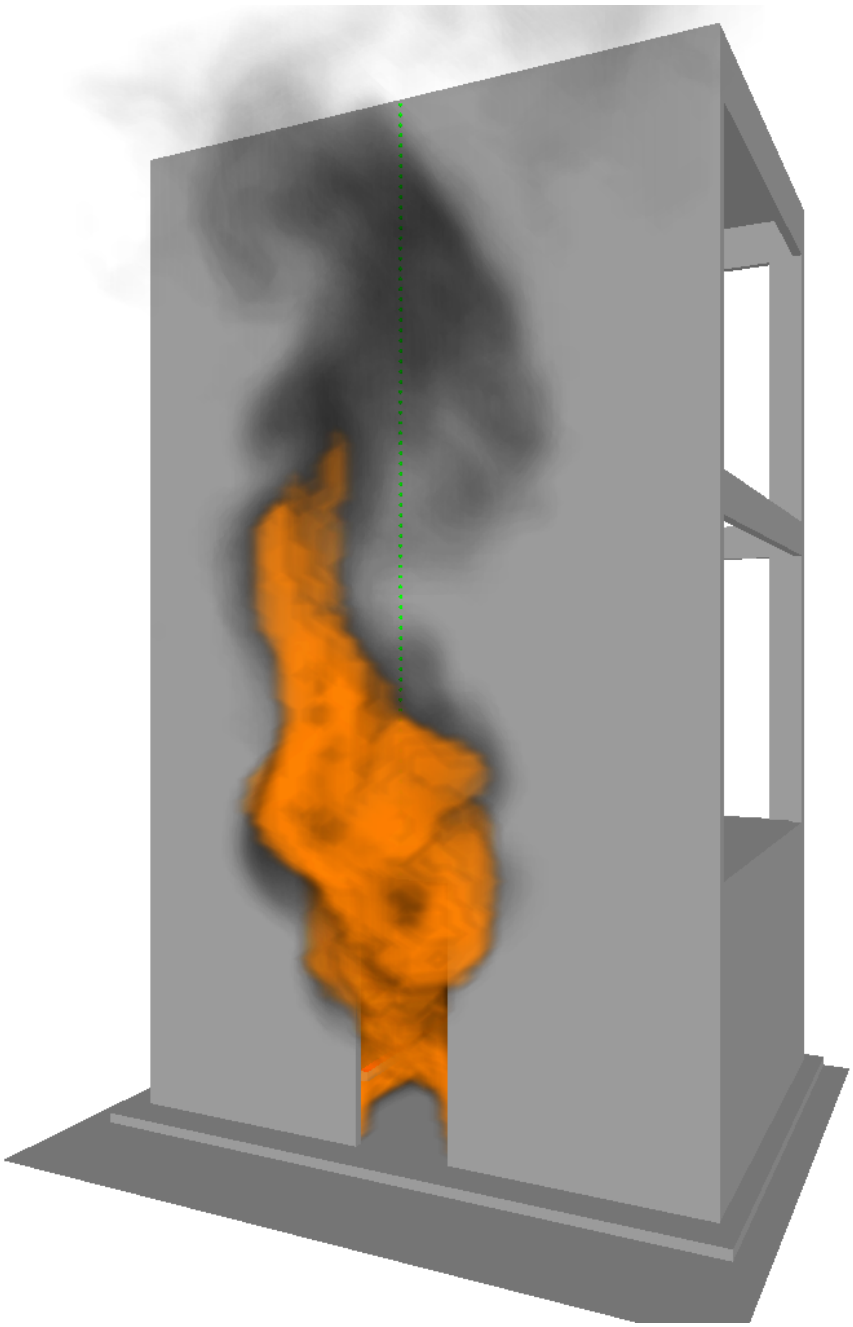

Figure 12.18: Smokeview rendering of one of the NRCC Facade experiments. The door is 0.94 m by 2.70 m tall (referred to as "Window 2" in the comparison plots). The fire is 10.3 MW.

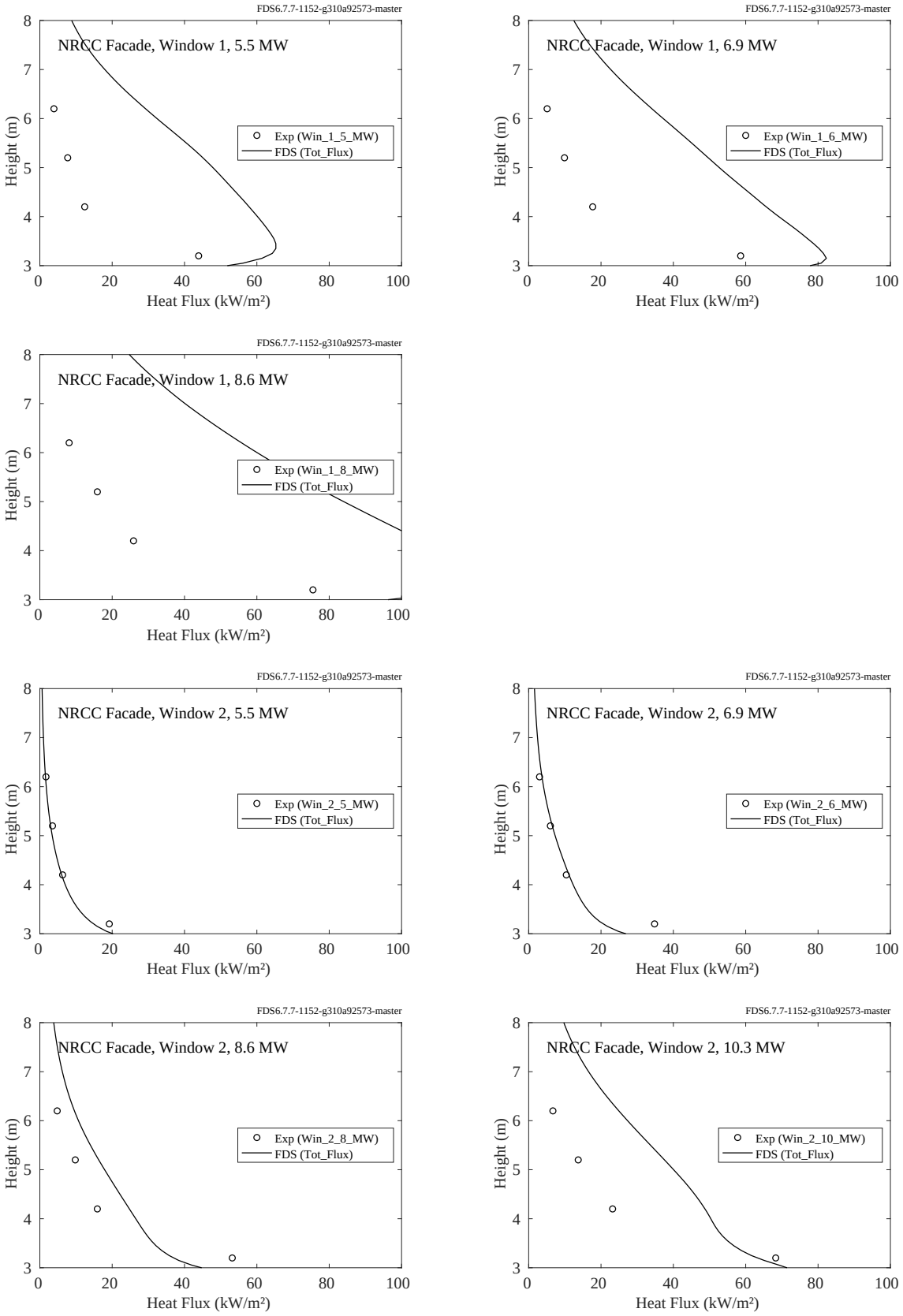

Figure 12.19: NRCC Facade experiments, heat flux, window configuration 1 and 2.

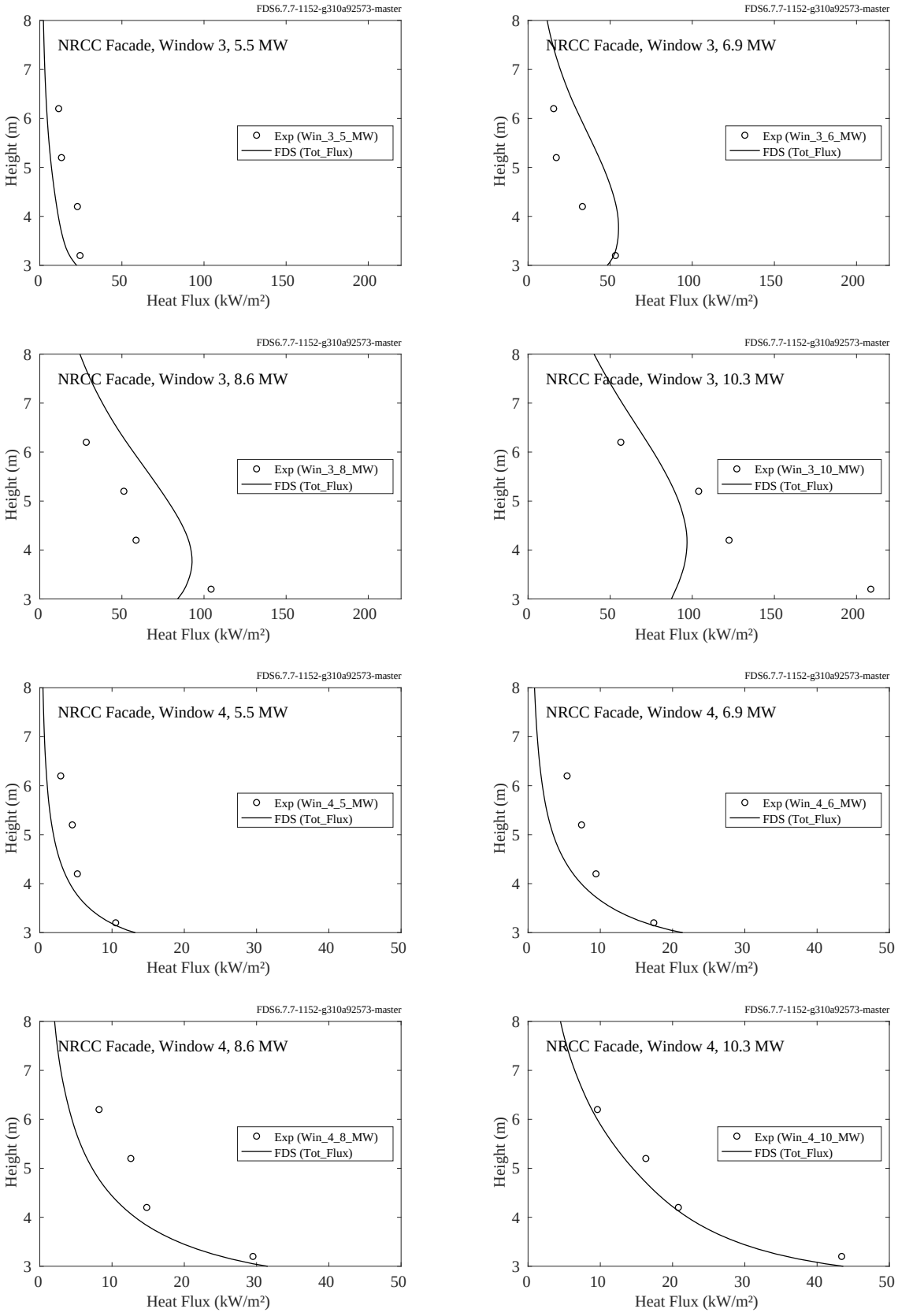

Figure 12.20: NRCC Facade experiments, heat flux, window configuration 3 and 4.

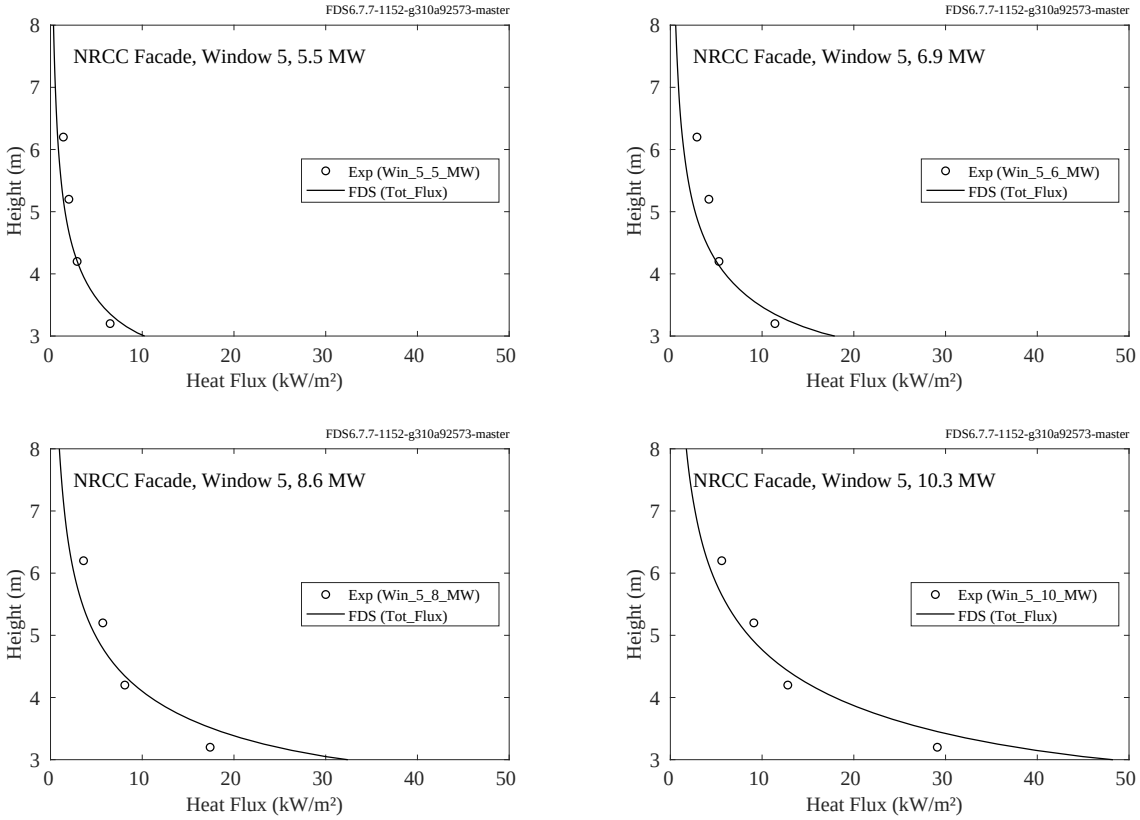

Figure 12.21: NRCC Facade experiments, heat flux, window configuration 5.

12.1.7 NRL/HAI Experiments

Predicted and measured vertical heat flux profiles from 9 propane sand burner fires are shown on the following pages. The parameters for each experiment are listed in Table 12.1 below. Note that all the FDS simulations were performed with a grid resolution such that $D^*/\delta x = 10$.

Table 12.1: Summary of the NRL/HAI Wall Heat Flux Measurements.

Test Number	D (m)	D^* (m)	$\dot{Q}$ (kW)	Q^*	Observed Flame Height (m)
1	0.28	0.30	53	0.85	0.79
2	0.70	0.30	56	0.09	0.36
3	0.48	0.33	68	0.28	0.60
4	0.37	0.39	106	0.84	1.00
5	0.48	0.43	136	0.57	0.87
6	0.48	0.51	204	0.85	1.45
7	0.70	0.52	220	0.36	1.20
8	0.57	0.60	313	0.85	2.20
9	0.70	0.74	523	0.85	2.9 (based on 500 °C)

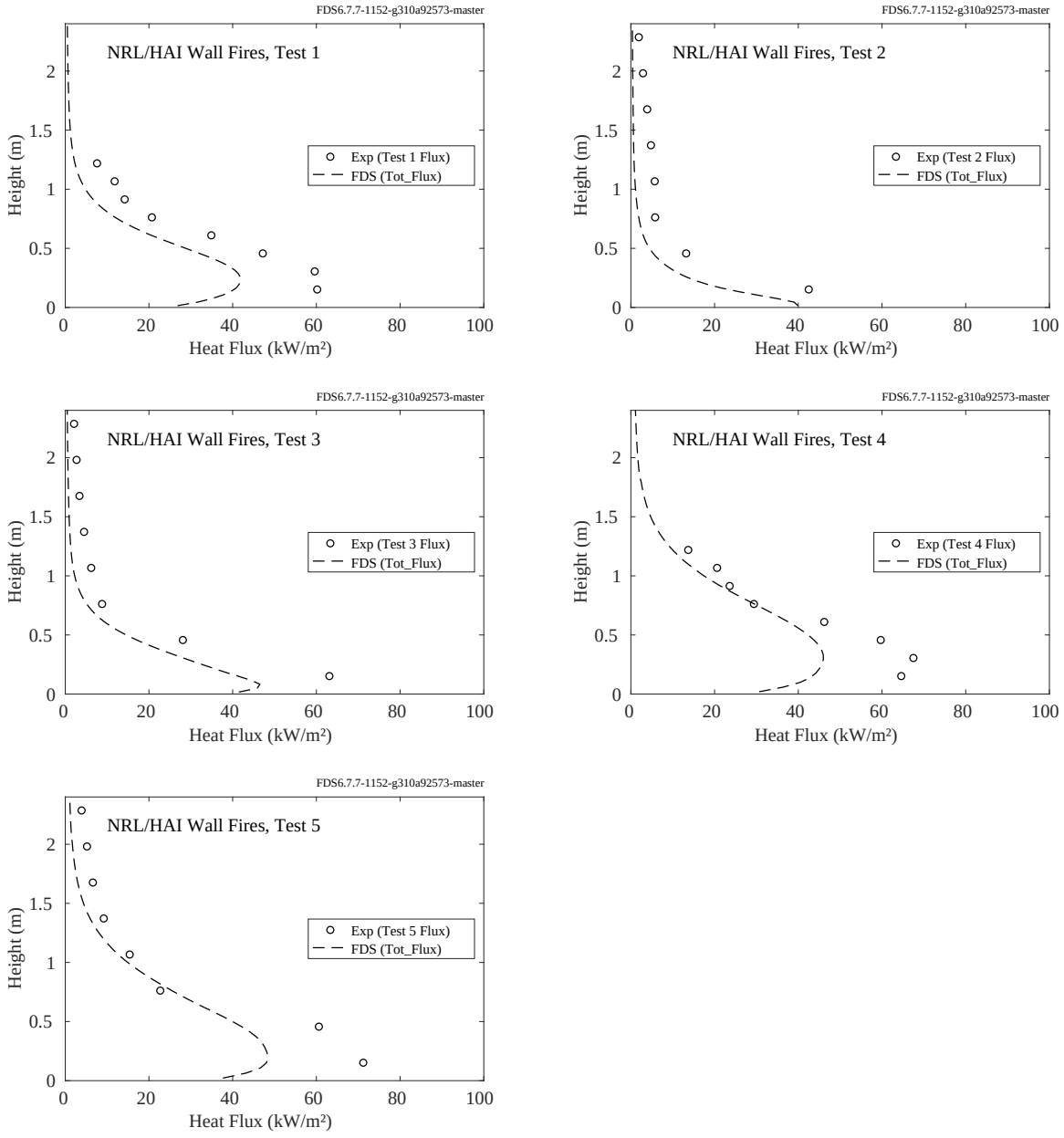

Figure 12.22: NRL/HAI experiments, heat flux to the wall, Tests 1-5.

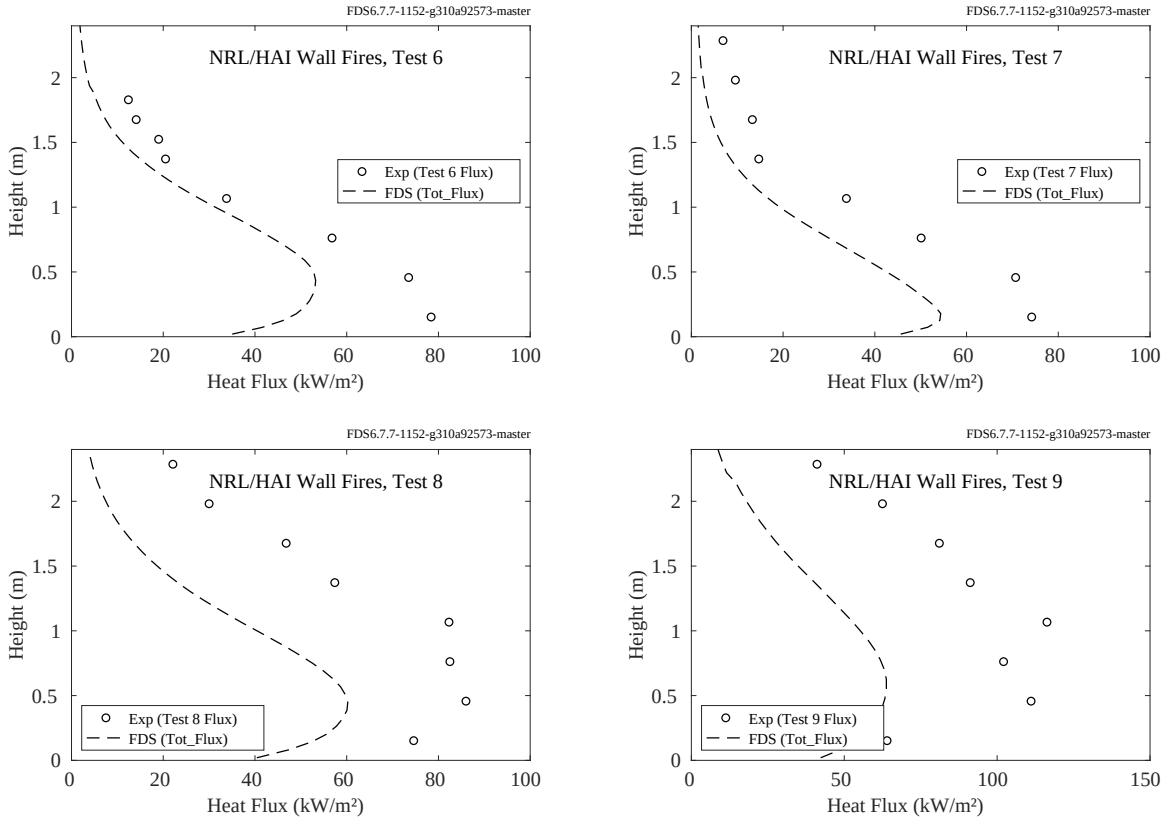

Figure 12.23: NRL/HAI experiments, heat flux to the wall, Tests 6-9.

12.1.8 PRISME DOOR Experiments

Total and radiative heat flux gauges were positioned at various points on the walls. Each room contained a vertical array labeled, for example, FLT_L1_NC265. The FLT indicates a surface total heat flux measurement, L1 indicates compartment 1, which is where the fire was located, NC indicates north wall center, and 265 indicates the number of centimeters above the floor. In addition, each room contained four measurement points centered on each wall at a height of approximately 260 cm. These points are labeled, for example, FLT_L2_SC265, compartment 2, center of south wall, 265 cm high.

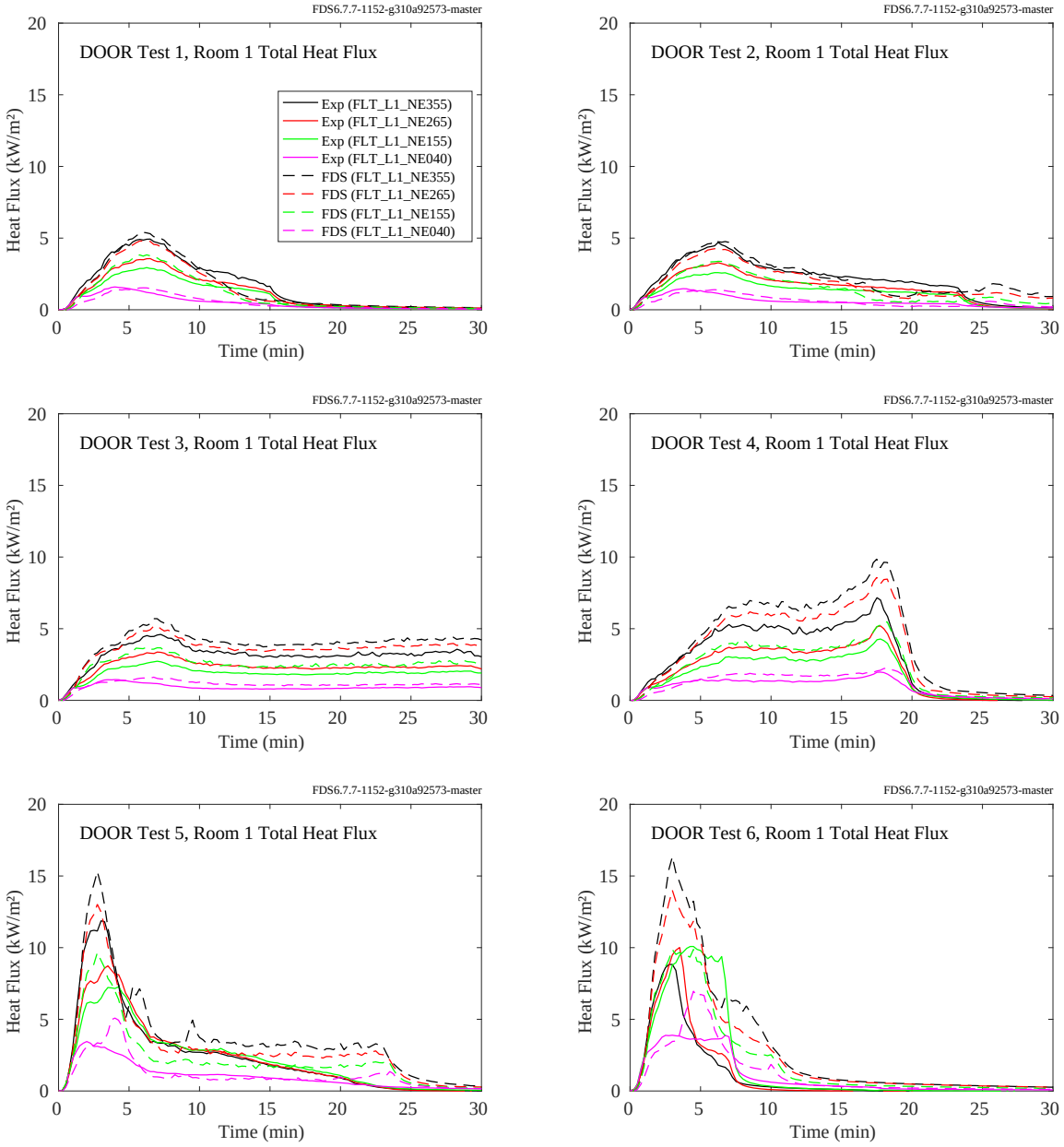

Figure 12.24: PRISME DOOR experiments, total heat flux, vertical array, Room 1.

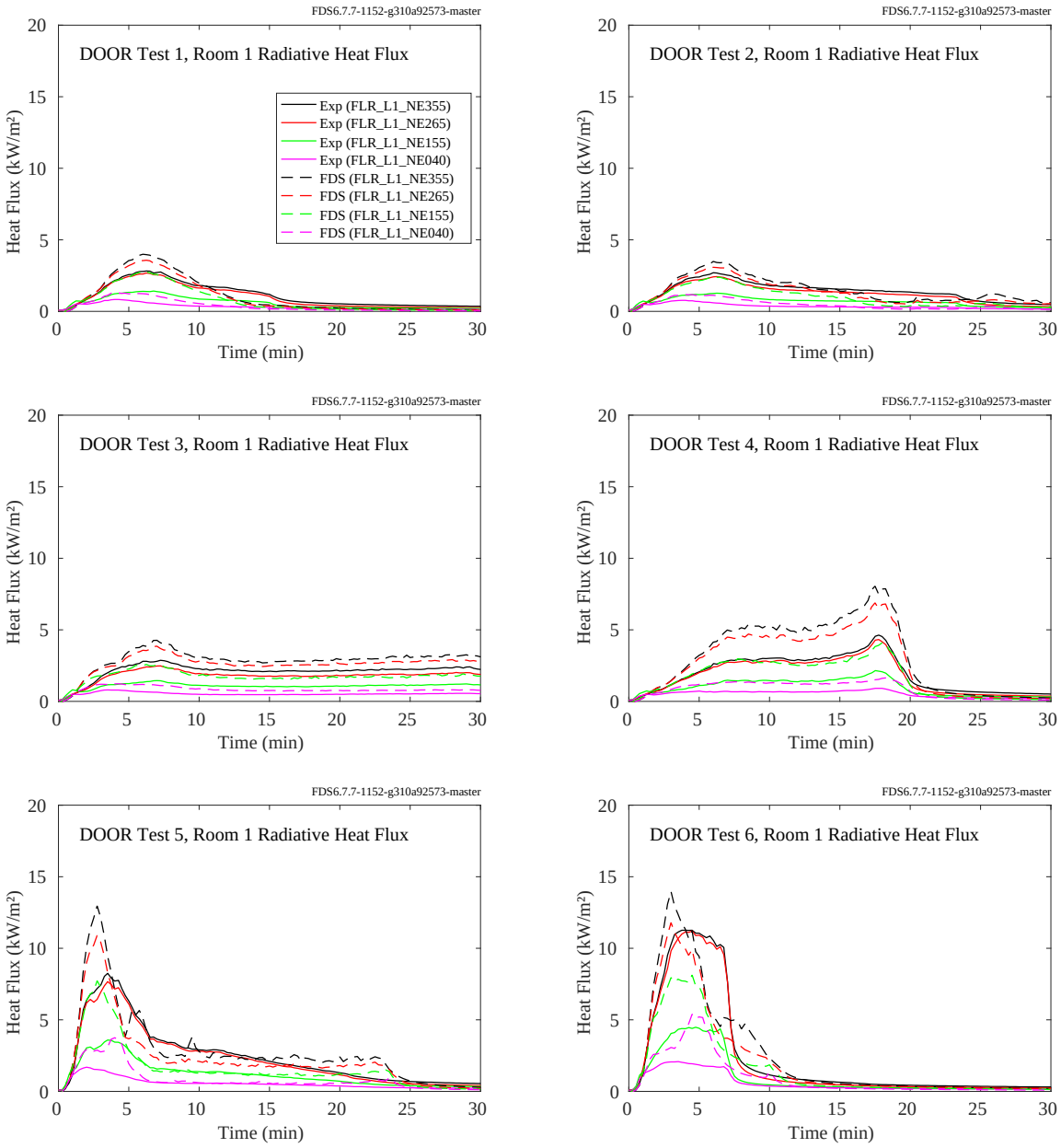

Figure 12.25: PRISME DOOR experiments, radiative heat flux, vertical array, Room 1.

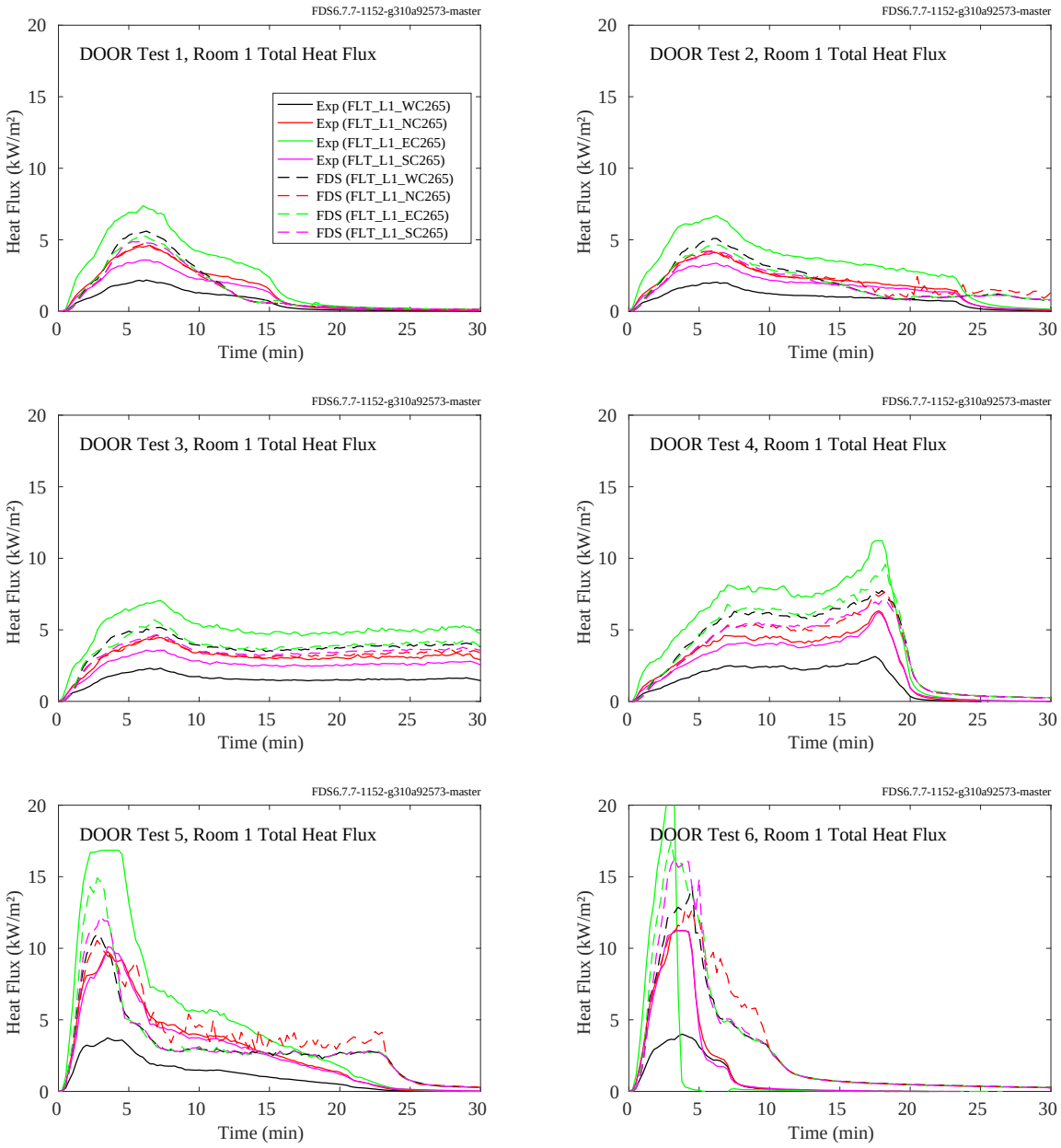

Figure 12.26: PRISME DOOR experiments, total heat flux, four walls, Room 1.

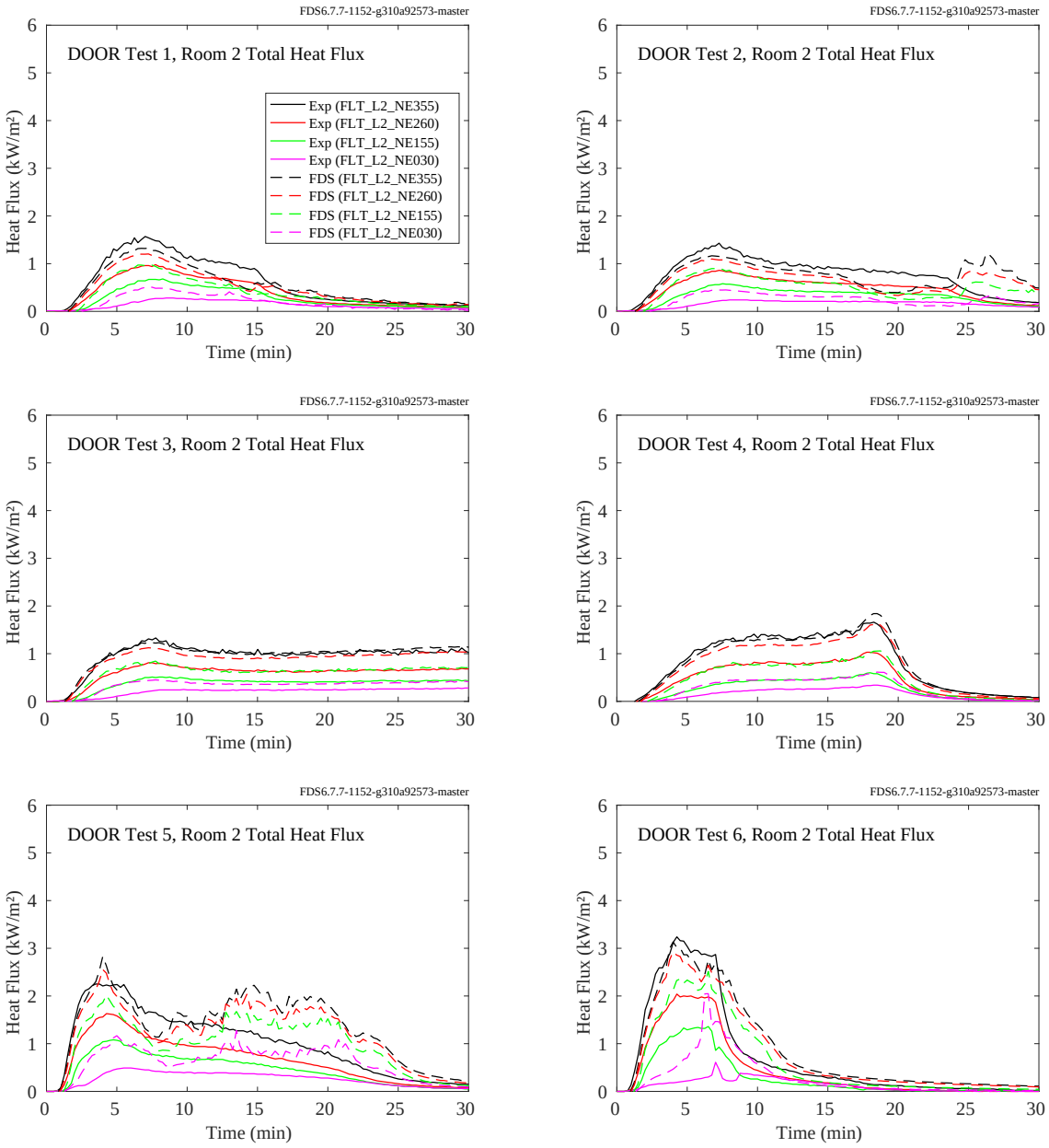

Figure 12.27: PRISME DOOR experiments, total heat flux, vertical array, Room 2.

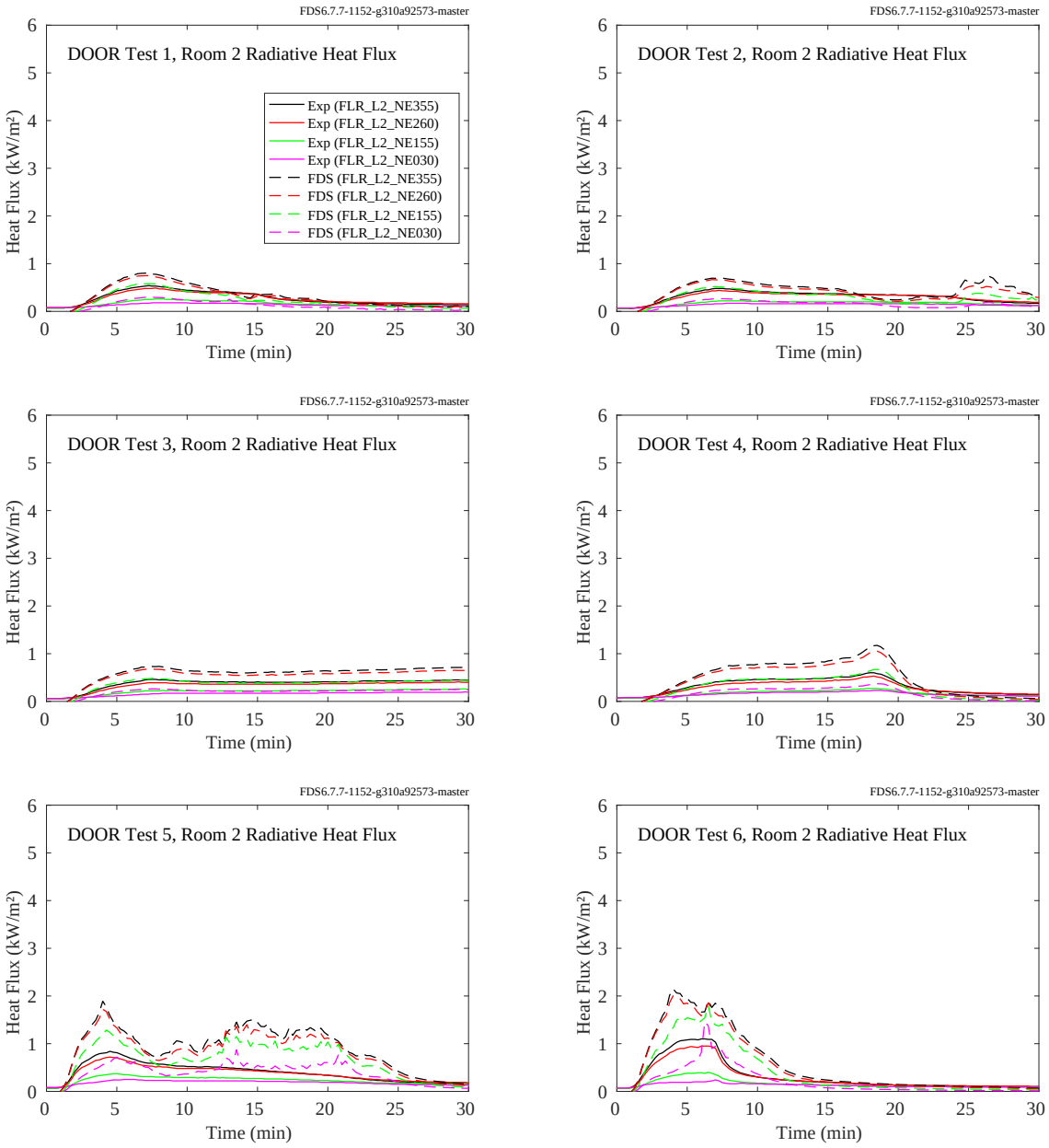

Figure 12.28: PRISME DOOR experiments, radiative heat flux, vertical array, Room 2.

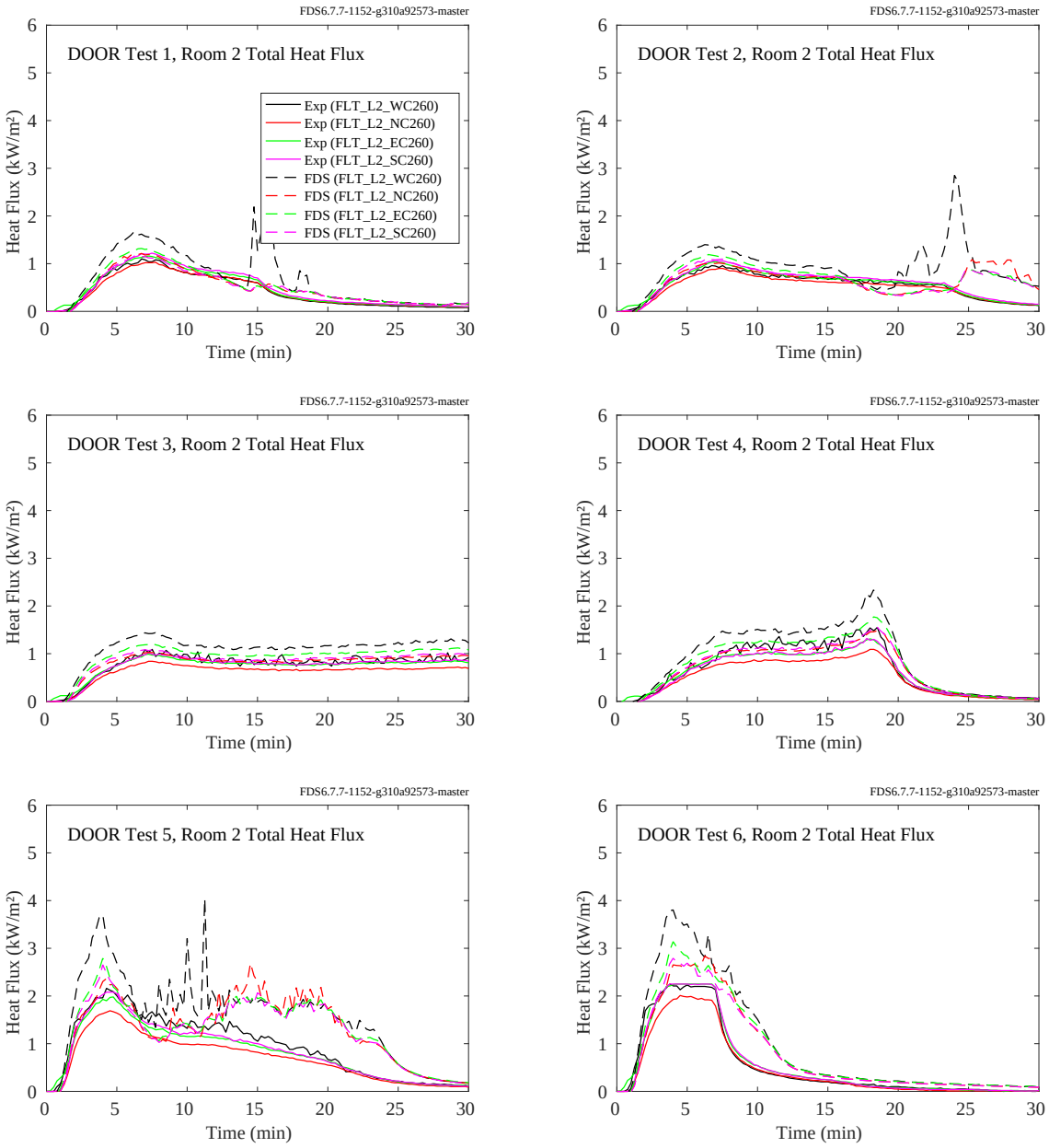

Figure 12.29: PRISME DOOR experiments, total heat flux, four walls, Room 2.

12.1.9 PRISME SOURCE Experiments

Total and radiative heat flux gauges were positioned at various points on the walls. Each room contained a vertical array labeled, for example, FLT_L1_NC265. The FLT indicates a surface total heat flux measurement, L1 indicates compartment 1, which is where the fire was located, NC indicates north wall center, and 265 indicates the number of centimeters above the floor. In addition, each room contained four measurement points centered on each wall at a height of approximately 260 cm. These points are labeled, for example, FLT_L2_SC265, compartment 2, center of south wall, 265 cm high.

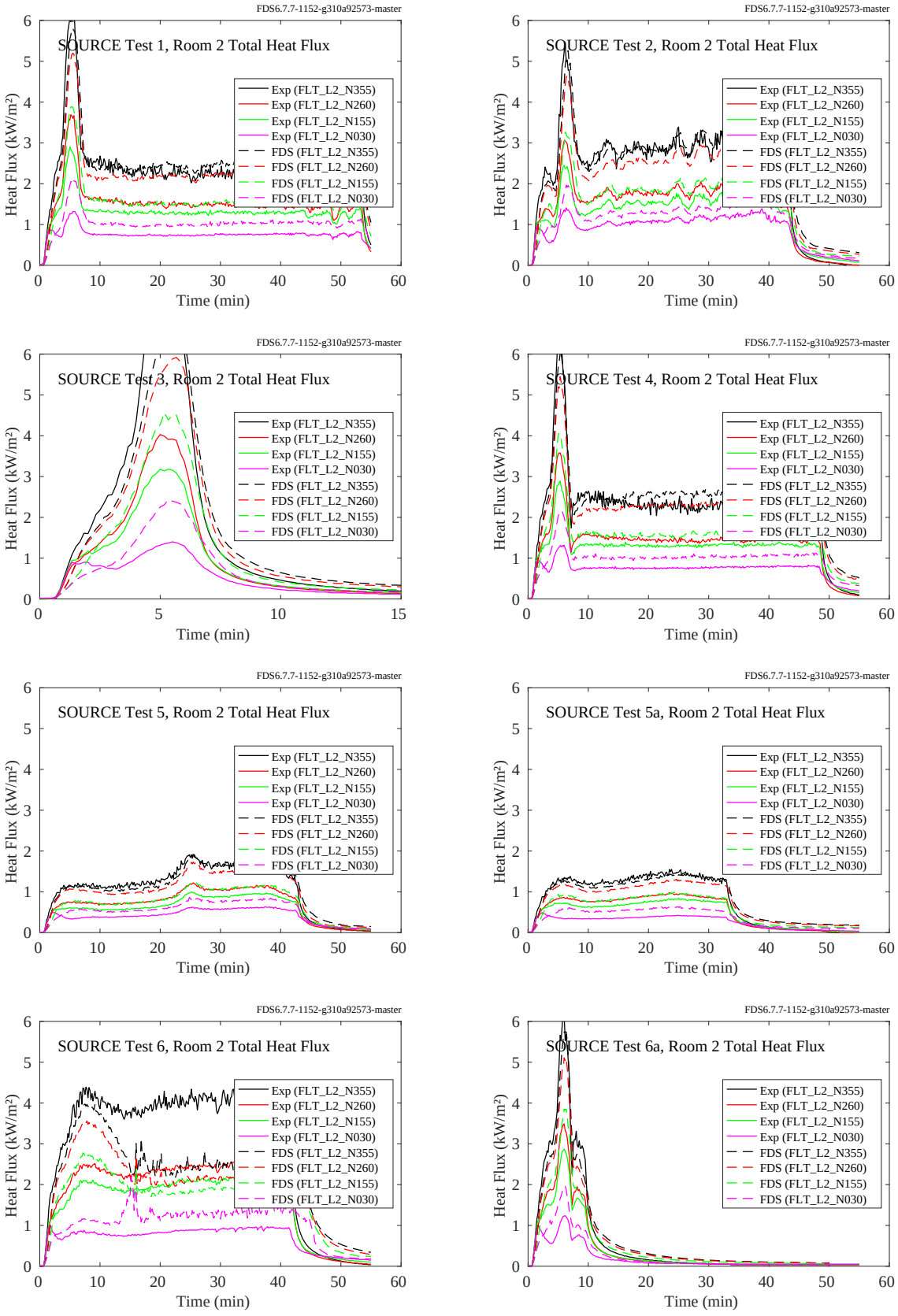

Figure 12.30: PRISME SOURCE experiments, total heat flux, vertical array, Room 2.

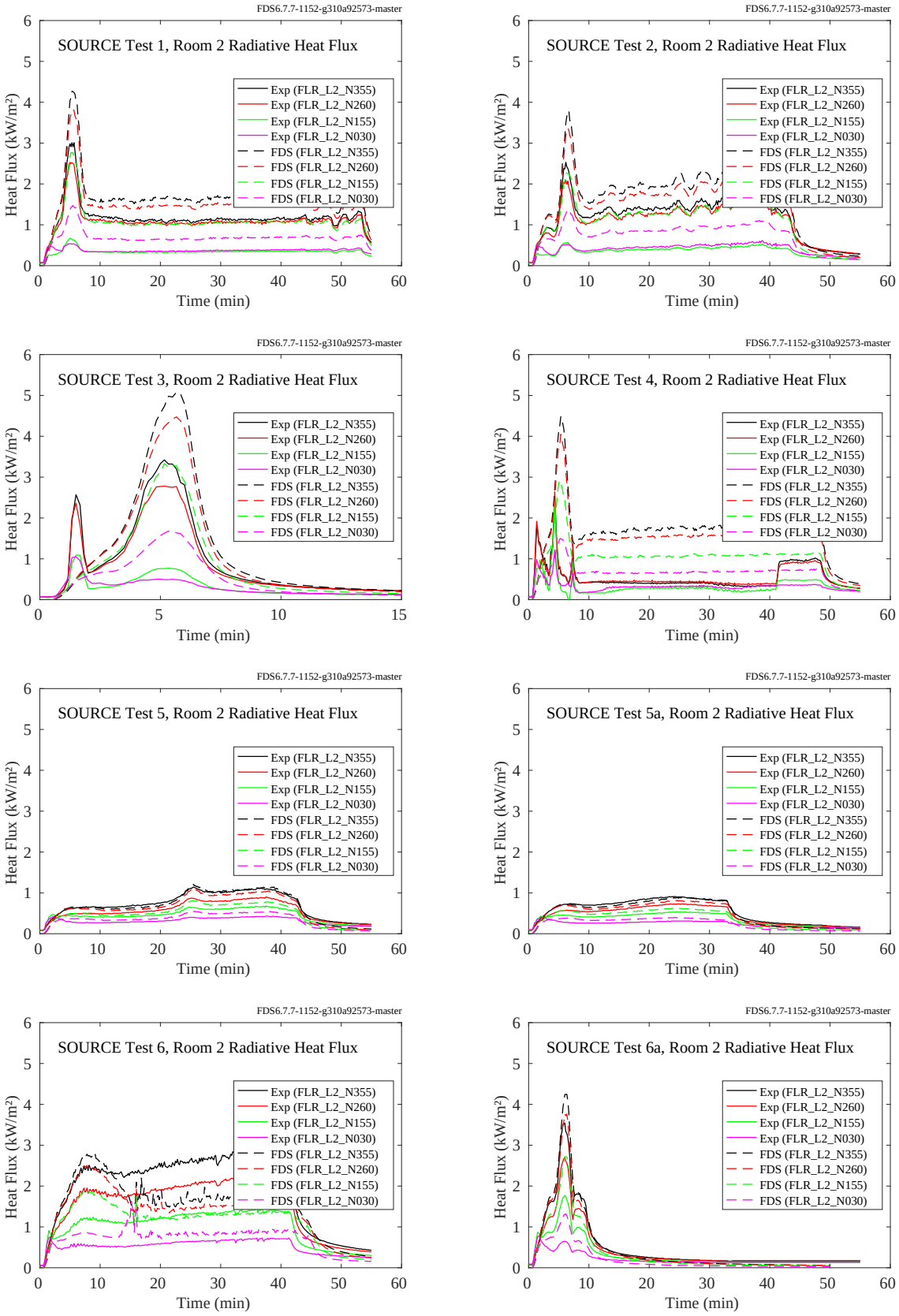

Figure 12.31: PRISME SOURCE experiments, radiative heat flux, vertical array, Room 2.

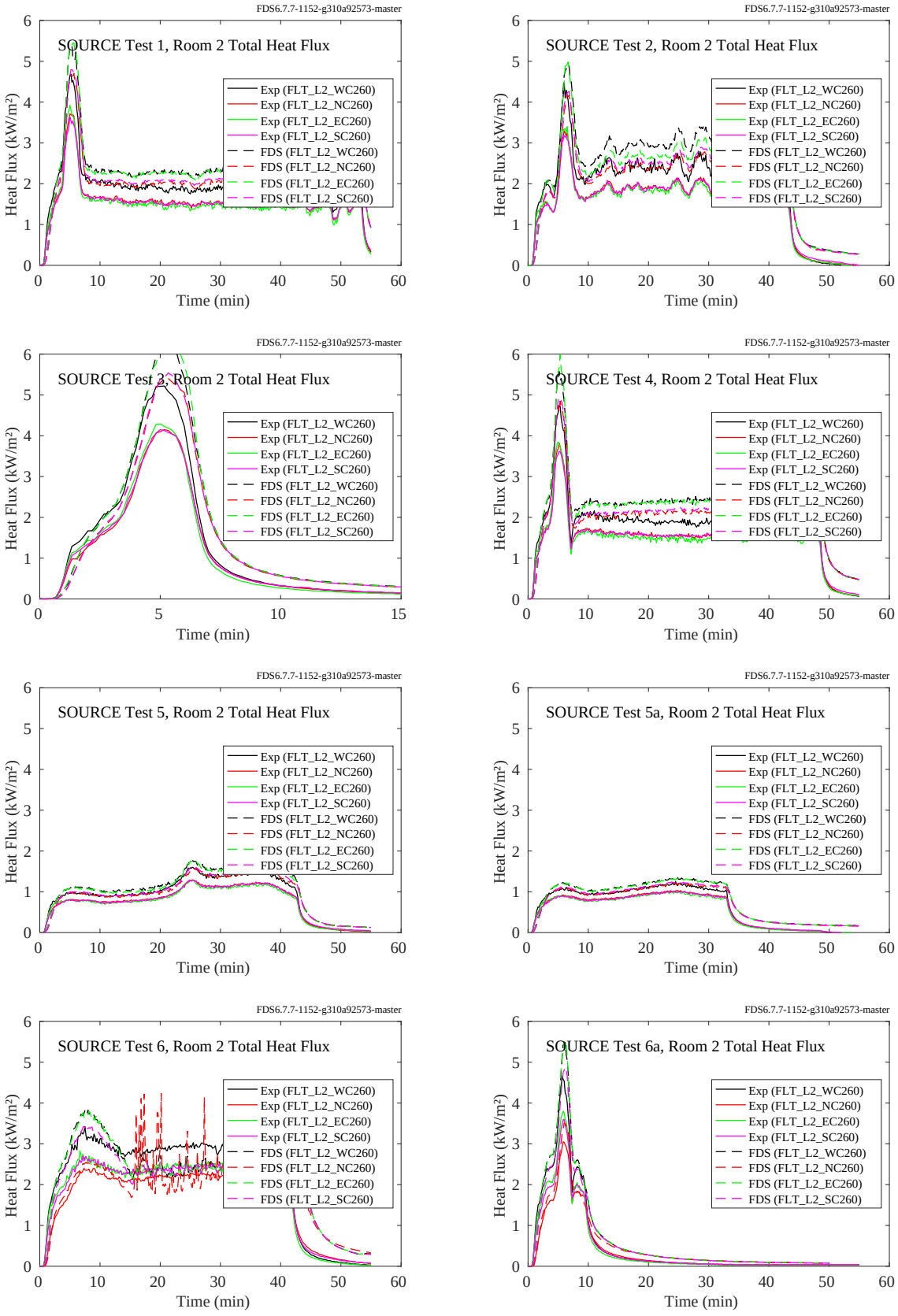

Figure 12.32: PRISME SOURCE experiments, total heat flux, four walls, Room 2.

12.1.10 Ulster SBI Experiments

Predicted and measured vertical heat flux profiles for three propane fire sizes in the single burning item (SBI) enclosure at the University of Ulster are shown on the following page. Measurements were made on two vertical panels that form a corner, at the base of which was a triangular-shaped burner with sides of length 25 cm. Three vertical profiles were measured on each panel at distances of 3.25 cm, 16.5 cm, and 29 cm from the corner.

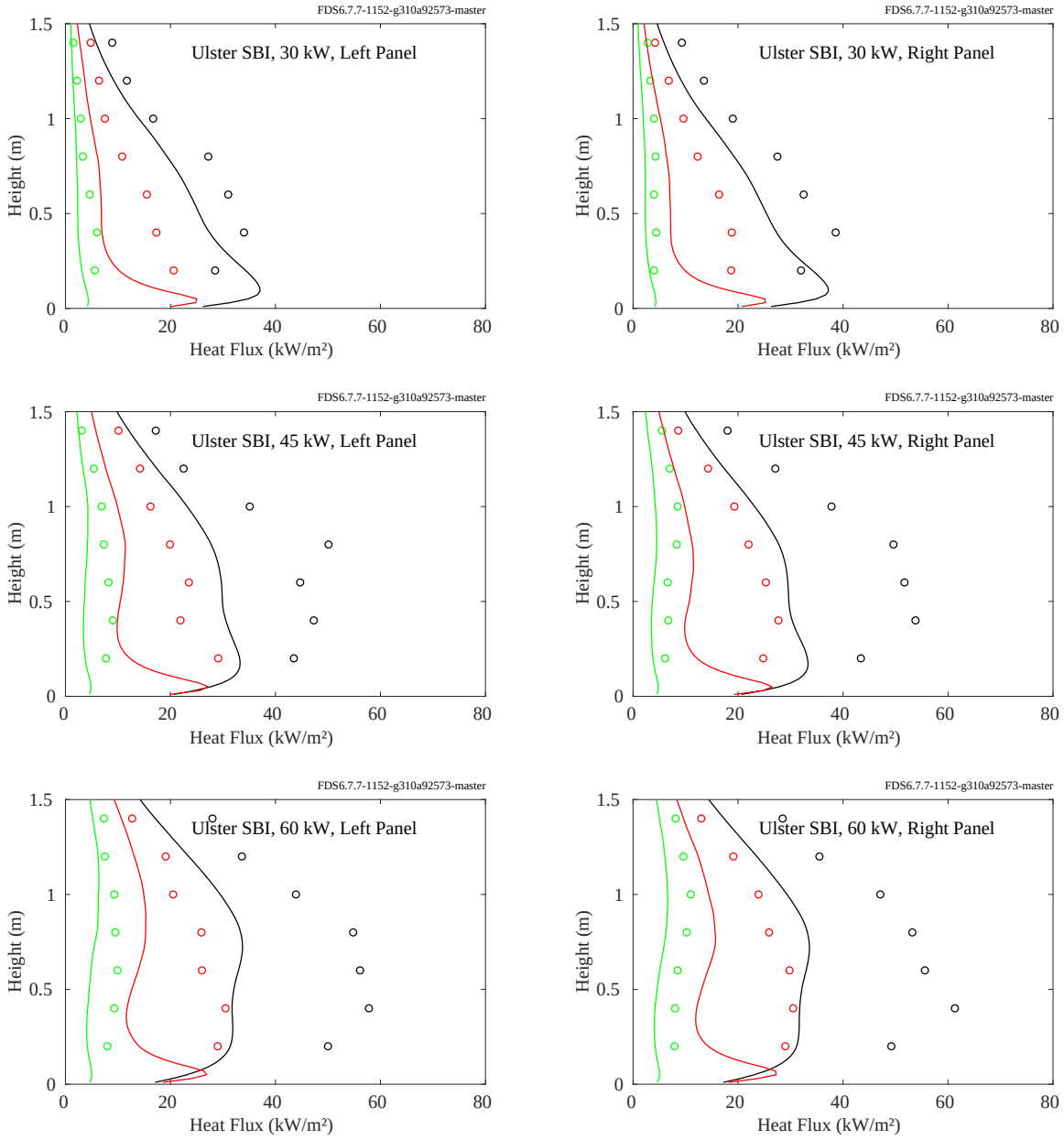

Figure 12.33: Comparison of predicted (lines) and measured (circles) heat fluxes to adjacent panels forming a corner in the single burning item (SBI) apparatus at the University of Ulster.

12.1.11 WTC Experiments

There were a variety of heat flux gauges installed in the test compartment. Most were within 2 m of the fire. Their locations and orientations are listed in Table 12.2. This section contains the measurements at the floor and ceiling.

Table 12.2: Heat flux gauge positions relative to the center of the fire pan in the WTC series.

Name	x (m)	y (m)	z (m)	Orientation	Location
H2FU	0.64	0.63	3.30	$+z$	Truss Support
H2RU	0.64	0.51	3.30	$+z$	Truss Support
H2FD	0.64	0.30	3.15	$-z$	Truss Support
H2RD	0.64	0.42	3.15	$-z$	Truss Support
HCoHF	-0.90	0.84	3.46	$+x$	Column, facing fire
HCoHW	-0.97	0.92	3.27	$+y$	Column, facing north
HCoLF	-0.90	0.84	0.92	$+x$	Column, facing fire
HCoLW	-0.97	0.92	1.02	$+y$	Column, facing north
HF1	1.06	0.13	0.13	$+z$	Floor
HF2	1.56	0.10	0.13	$+z$	Floor
HCe1	-0.45	0.35	3.82	$-z$	Ceiling
HCe2	0.05	0.35	3.82	$-z$	Ceiling
HCe3	0.80	0.35	3.82	$-z$	Ceiling
HCe4	2.56	0.35	3.82	$-z$	Ceiling

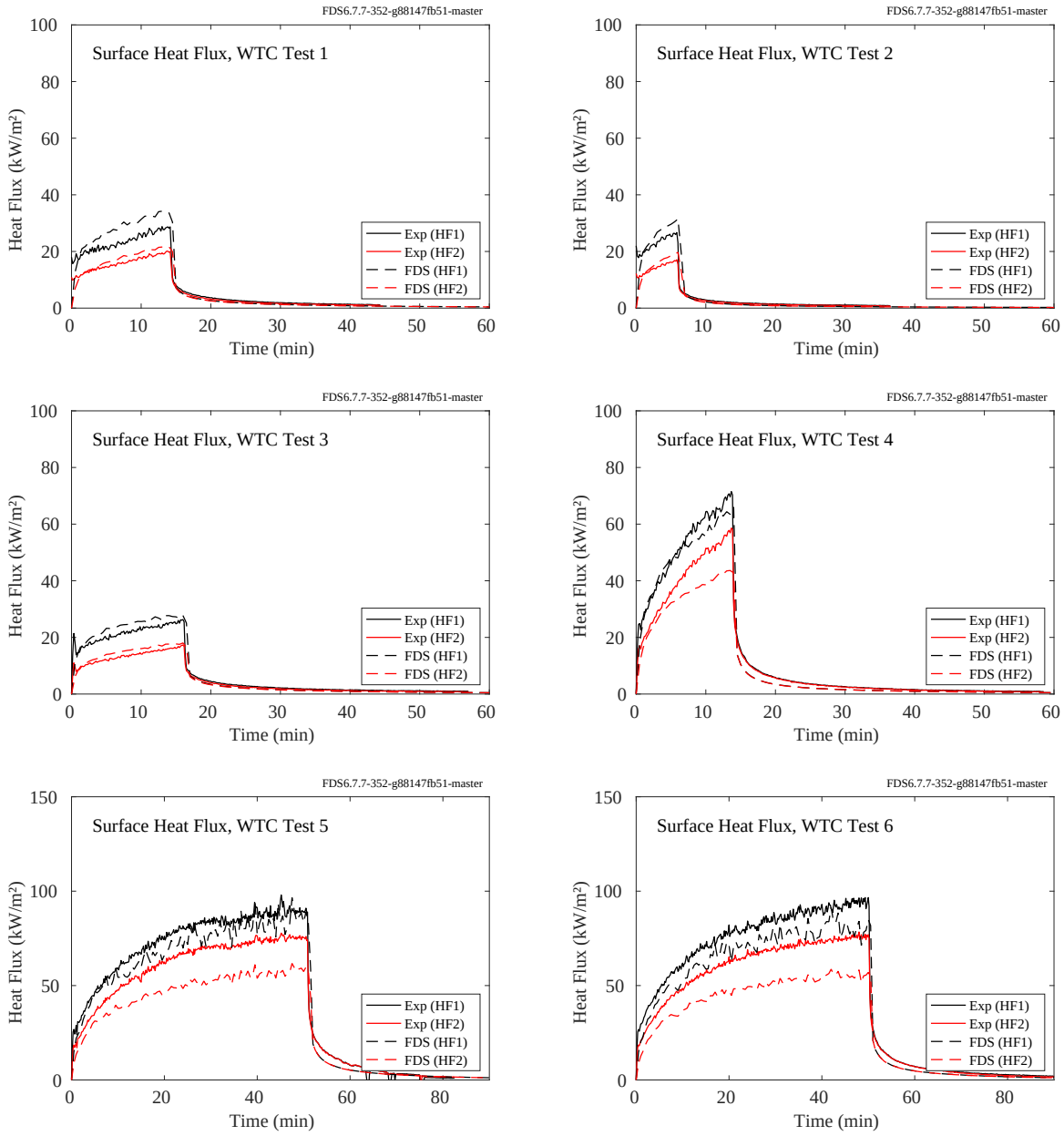

Figure 12.34: WTC experiments, heat flux to the floor.

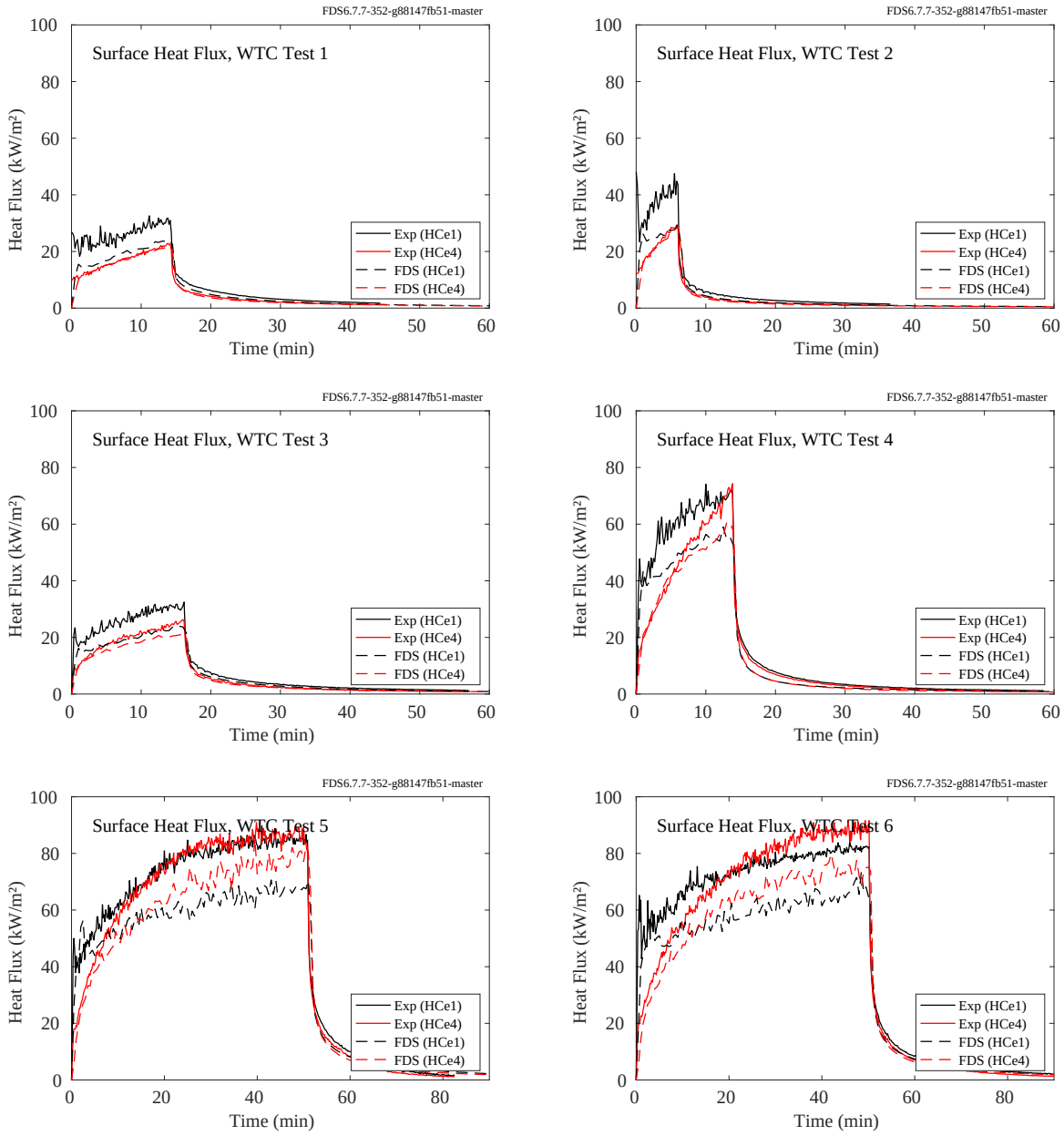

Figure 12.35: WTC experiments, heat flux to the ceiling.

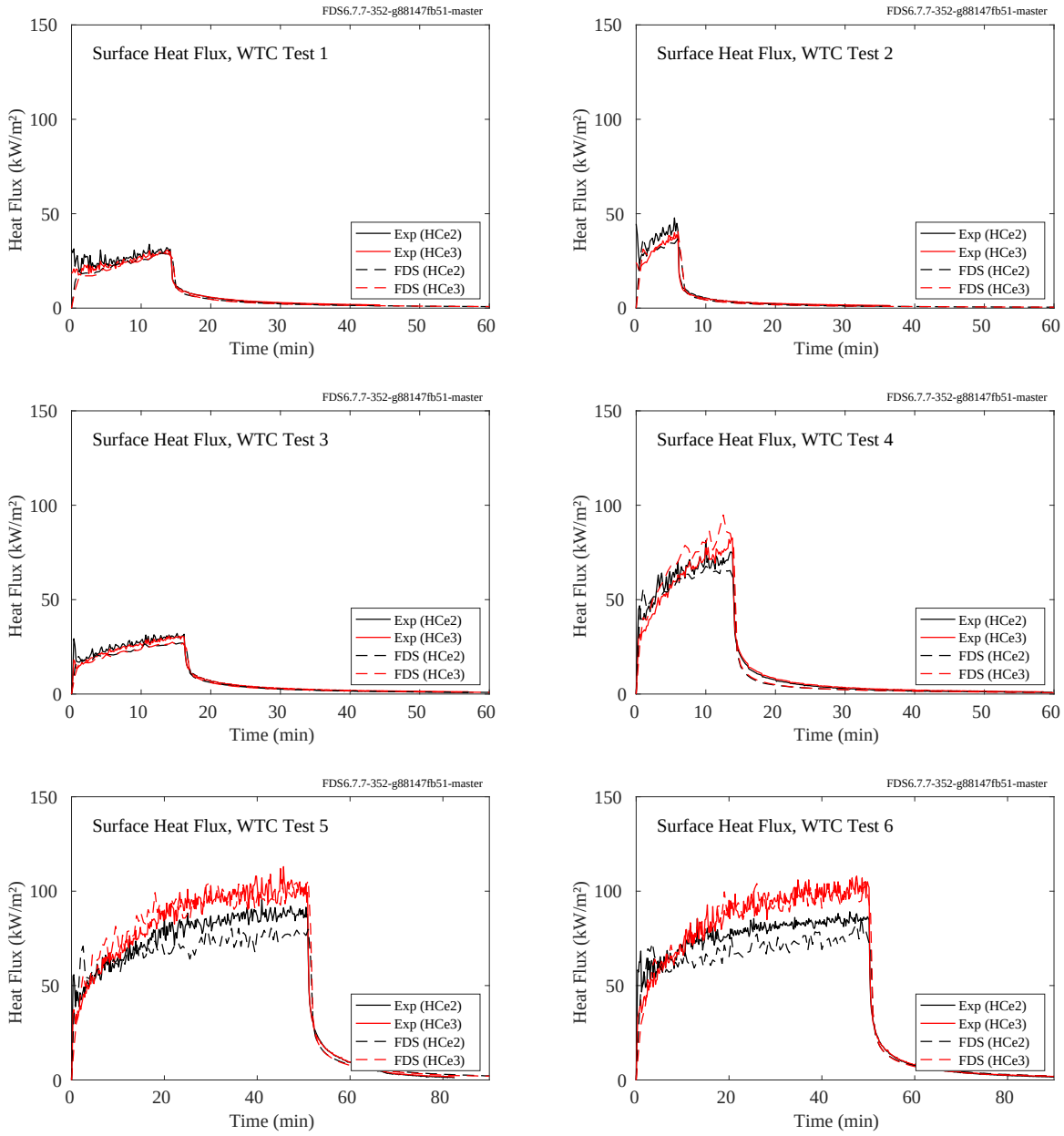

Figure 12.36: WTC experiments, heat flux to the ceiling.

12.1.12 Summary of Wall, Ceiling and Floor Heat Flux Predictions

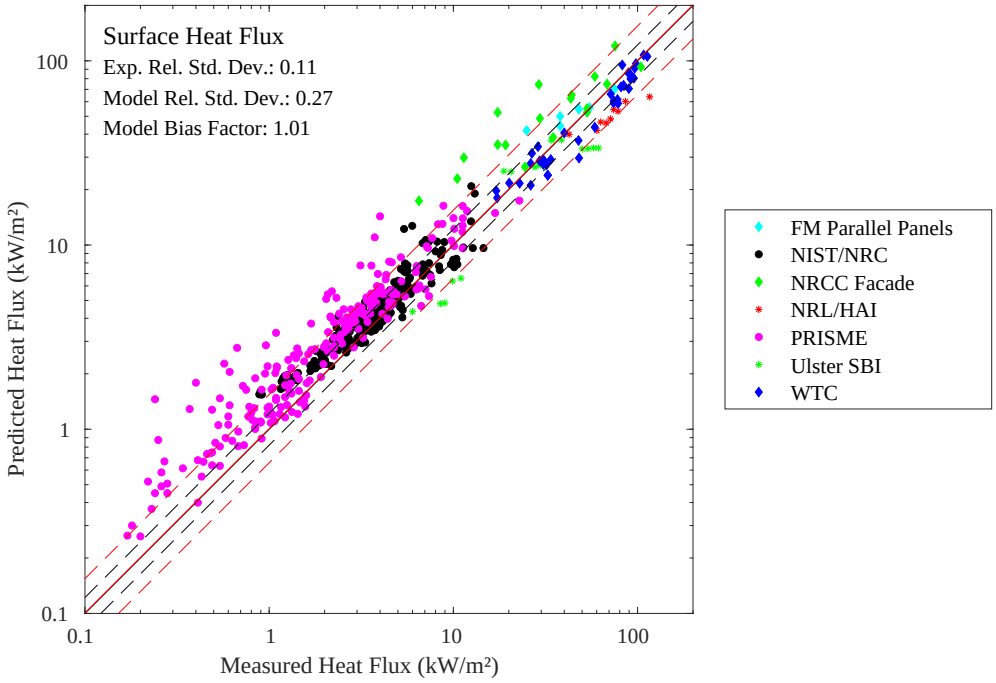

Figure 12.37: Summary of surface heat flux predictions.

12.2 Heat Flux to Targets

The heat flux measurements are broken up into two broad categories—heat flux to walls, floors, and ceiling, and heat flux to "targets". A target is any object of interest in a fire, like a steel beam or electrical cable. The following subsections consider heat flux to targets.

12.2.1 Fleury Experiments

The plots on the following pages contain comparisons of predicted and measured heat fluxes from a series of propane burner fires. Heat flux gauges were mounted on moveable dollies that were placed in front of, and to the side of, burners with dimensions of 0.3 m by 0.3 m (1:1 burner), 0.6 m by 0.3 m (2:1 burner), and 0.9 m by 0.3 m (3:1 burner). The heat release rates were set to 100 kW, 150 kW, 200 kW, 250 kW, and 300 kW. The gauges were mounted at heights of 0 m, 0.5 m, 1.0 m, and 1.5 m relative to the top edge of the burner. Each page contains the results for a given HRR.

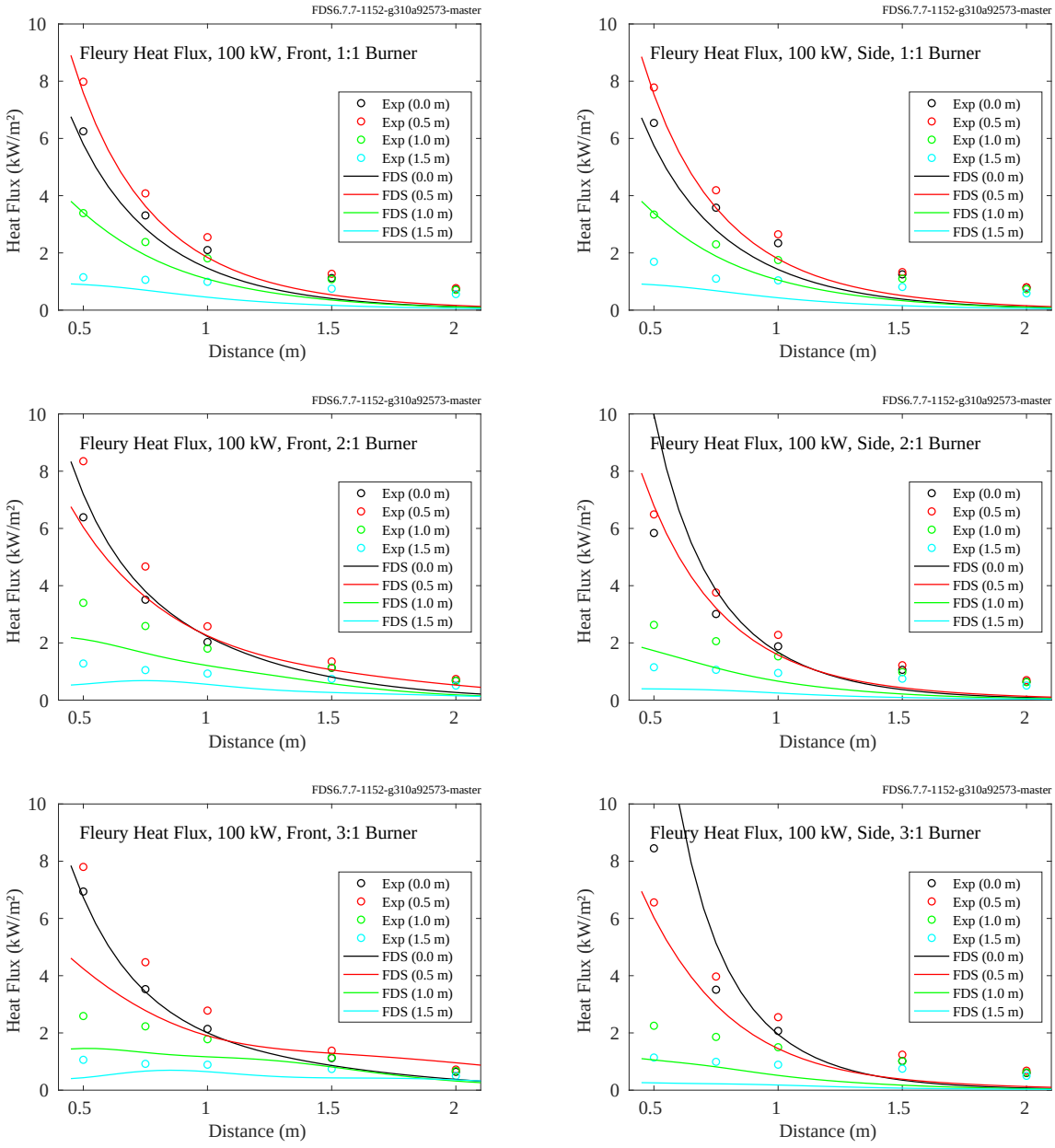

Figure 12.38: Comparison of predicted (lines) and measured (circles) heat flux for the 100 kW Fleury fires.

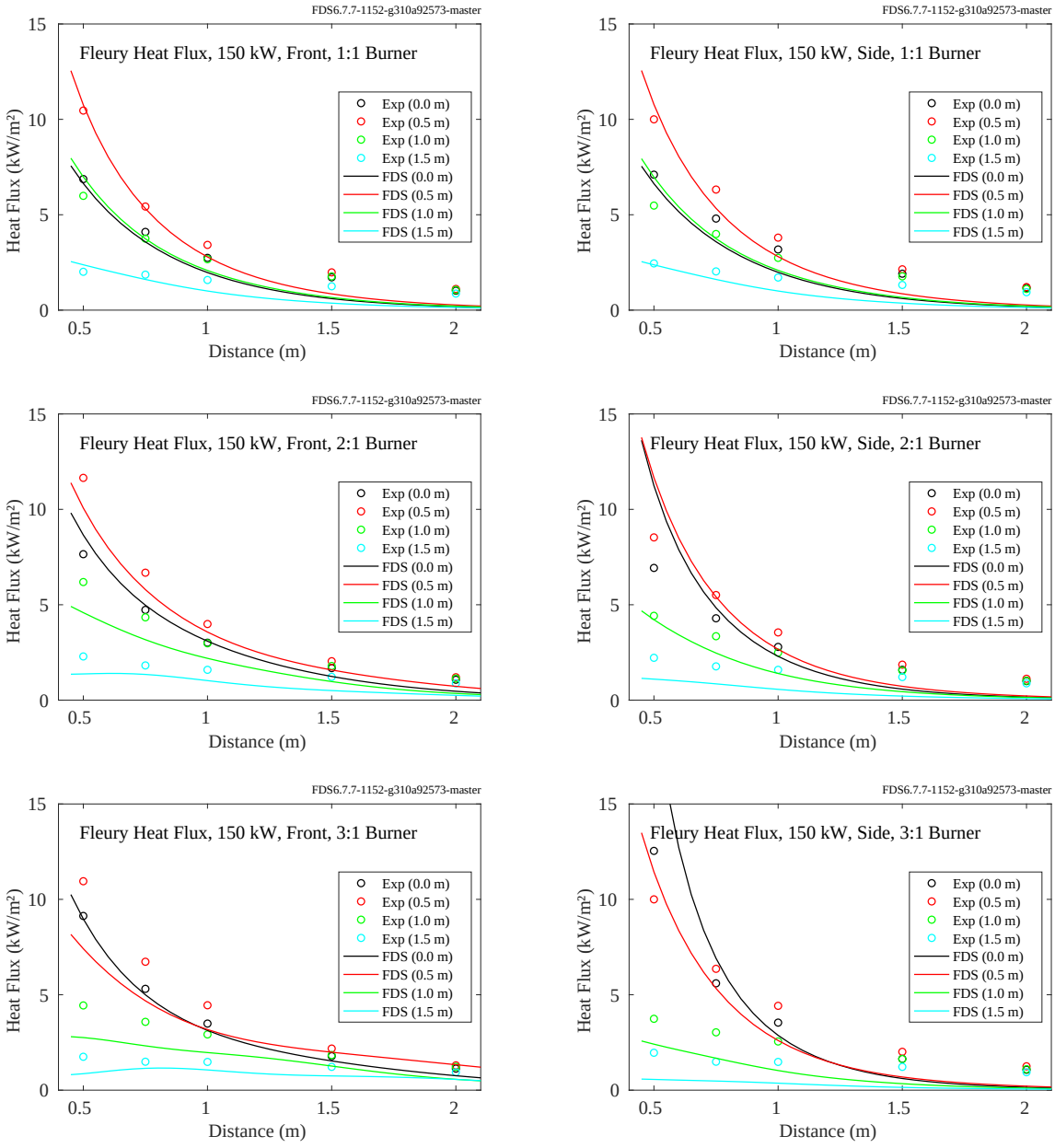

Figure 12.39: Comparison of predicted (lines) and measured (circles) heat flux for the 150 kW Fleury fires.

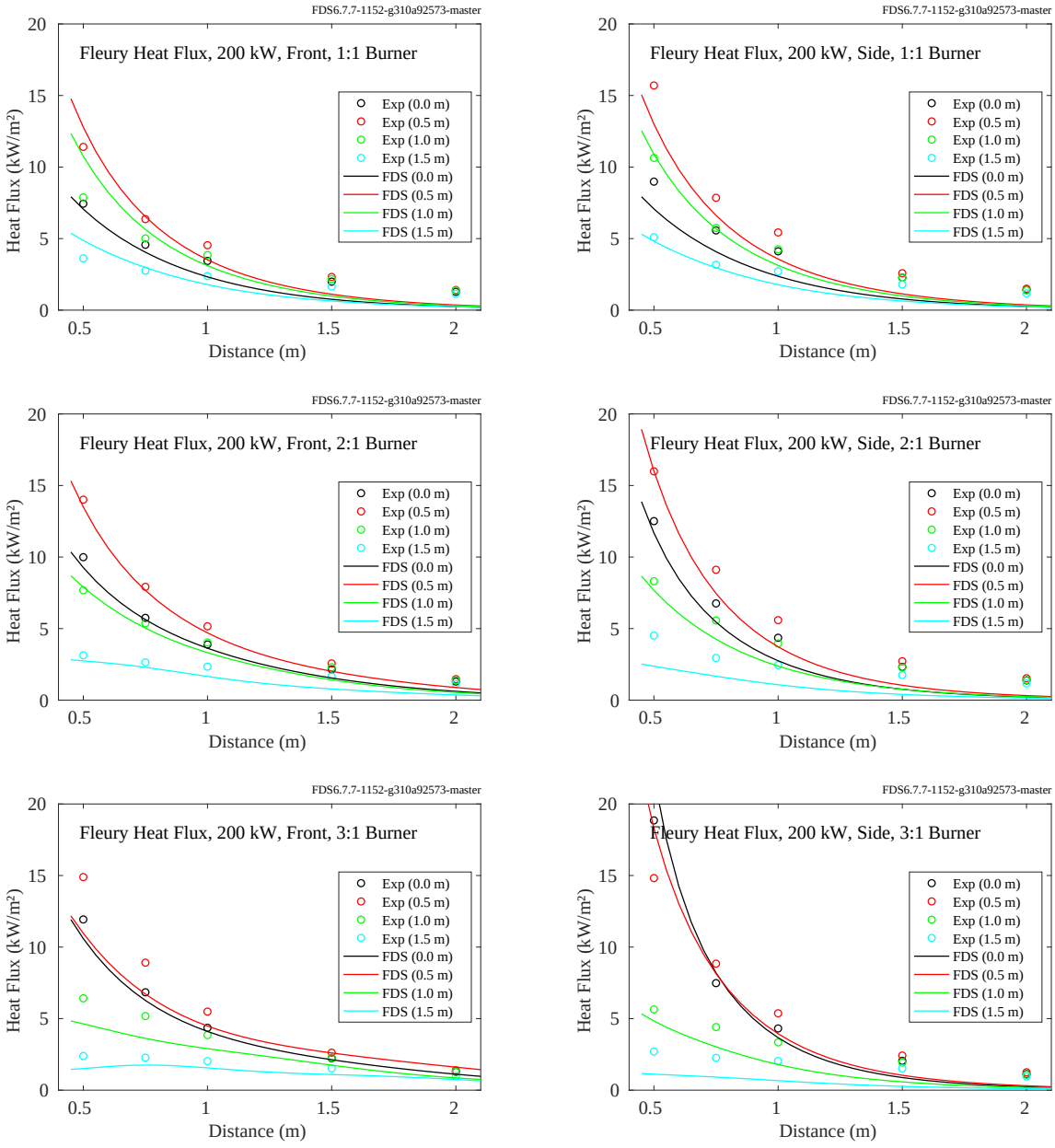

Figure 12.40: Comparison of predicted (lines) and measured (circles) heat flux for the 200 kW Fleury fires.

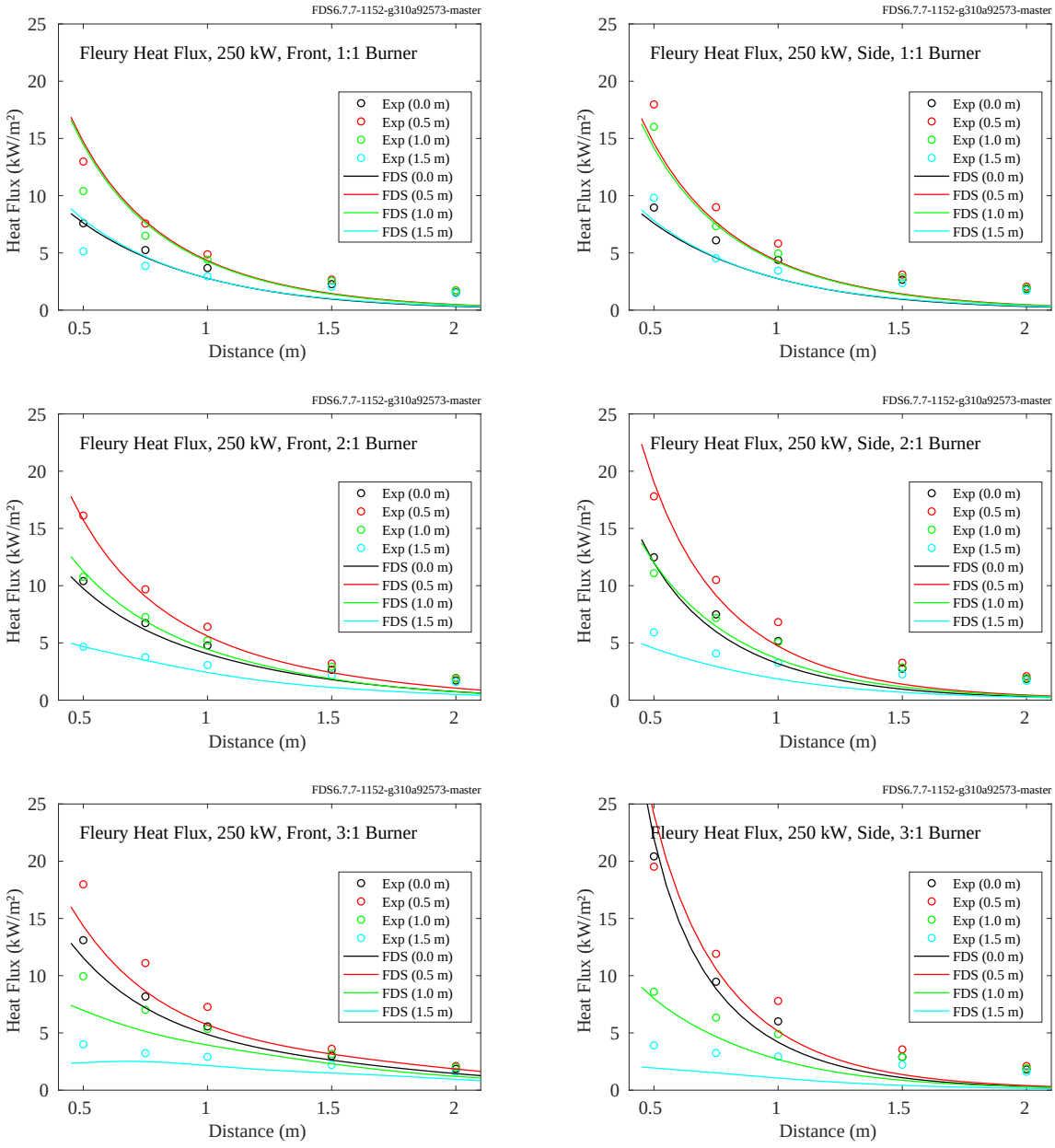

Figure 12.41: Comparison of predicted (lines) and measured (circles) heat flux for the 250 kW Fleury fires.

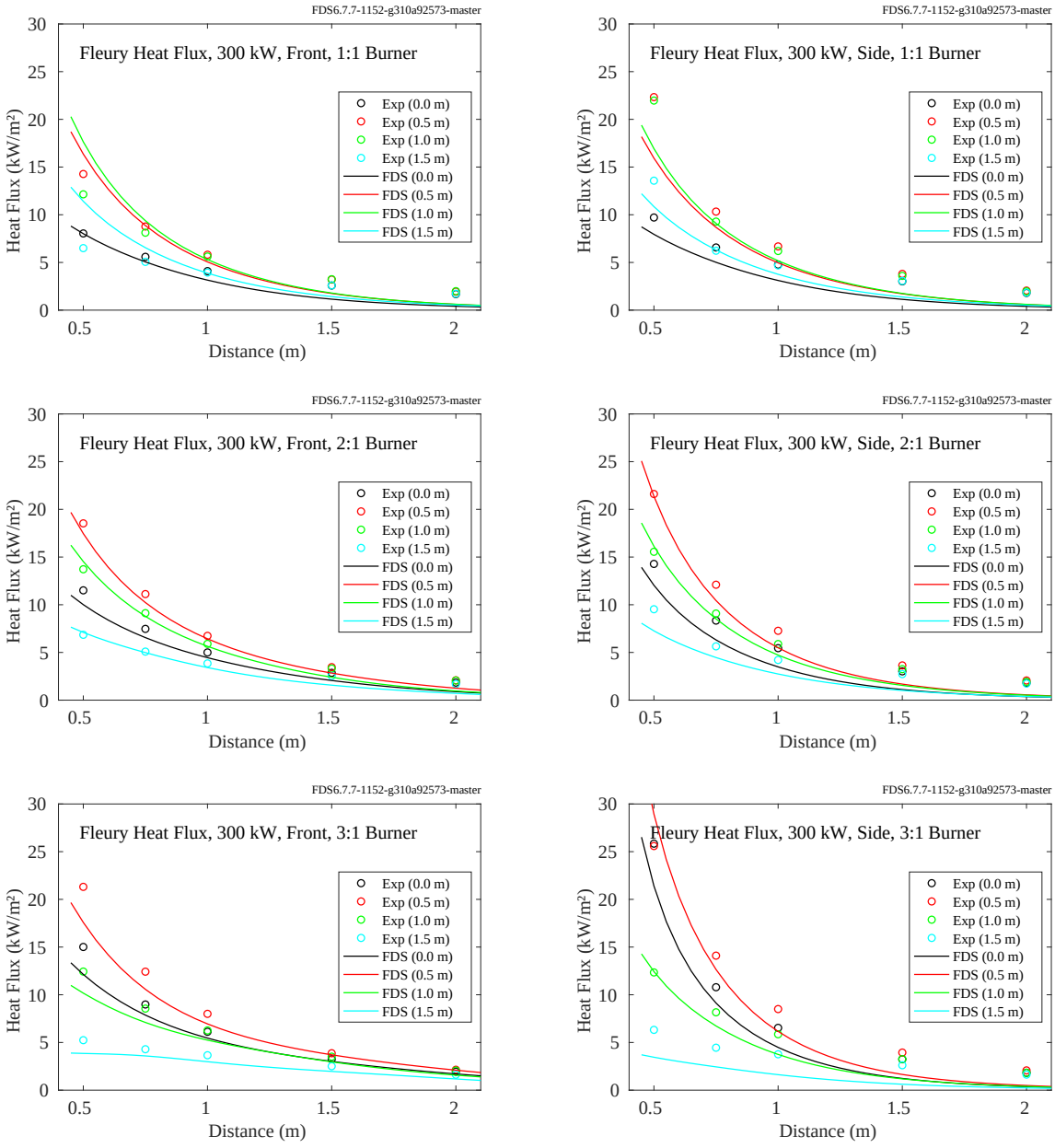

Figure 12.42: Comparison of predicted (lines) and measured (circles) heat flux for the 300 kW Fleury fires.

12.2.2 Hamins Gas Burner Experiments

Predicted and measured radial and vertical heat flux profiles from 30 methane, 34 propane, and 16 acetylene gas burner fire experiments conducted by Anthony Hamins [341] are displayed in this section. The relevant information about the fires is included in Tables 12.3, 12.4, and 12.5. In each table, D is the diameter of the burner and R_0 is the radial distance from the burner centerline to the position of the vertical heat flux measurements. $\dot{Q}$ is the product of the mass loss rate, $\dot{m}$, and the heat of combustion. The heat of combustion of acetylene is 48.2 kJ/g; and for propane, 46.4 kJ/g. For the methane experiments, either methane (50.03 kJ/g) or natural gas (49.4 kJ/g) was used. $\dot{Q}''$ is the heat release rate per unit area, and

$$\dot{Q}^* = \frac{\dot{Q}}{\rho_\infty T_\infty c_p \sqrt{gD} D^2} \quad ; \quad D^* = \left(\frac{\dot{Q}}{\rho_\infty T_\infty c_p \sqrt{g}} \right)^{2/5} \tag{12.2}$$

Note that in the test matrices, the values to the right of the double lines indicate parameters used in the simulations. The values for radiative fraction, χ_{rad}, are suggested by Hamins [341]. The quantity $D^*/\delta x$ is an indicator of grid resolution, where D^* is the characteristic burner dimension and δx is the grid cell size.

Methane Experiments

Table 12.3: Parameters of the Hamins methane burner experiments. The asterisk after the Test No. indicates that natural gas was used as fuel. The soot and CO yields were assumed to be zero.

Test No.	D (m)	R_0 (m)	$\dot{Q}$ (kW)	$\dot{m}$ (g/s)	$\dot{Q}''$ (kW/m^2)	$\dot{Q}^*$	$\chi_{\rm rad}$	$D^*/\delta x$
1	0.1	0.13	0.42	0.0085	53.5	0.12	0.13	8.6
2	0.1	0.13	0.61	0.0122	77.7	0.18	0.13	10.0
3	0.1	0.13	0.78	0.0155	99.3	0.22	0.13	11.0
4	0.1	0.13	1.11	0.0222	141.3	0.32	0.16	12.7
5	0.1	0.13	1.89	0.0378	240.6	0.54	0.16	15.7
6*	0.35	0.40	11.2	0.226	115.9	0.14	0.08	6.4
7*	0.35	0.40	15.3	0.310	159.0	0.19	0.10	7.2
8*	0.35	0.40	10.5	0.212	109.0	0.13	0.08	6.2
9*	0.35	0.40	6.67	0.135	69.3	0.08	0.07	5.2
10*	0.35	0.64	19.3	0.391	200.7	0.24	0.12	7.9
11*	0.35	0.63	27.0	0.546	280.3	0.34	0.15	9.1
12*	0.35	0.81	40.6	0.822	422.2	0.51	0.18	10.7
13*	0.35	0.92	63.5	1.285	659.9	0.80	0.21	12.8
14*	0.35	0.92	90.3	1.828	938.7	1.13	0.22	14.7
15	0.35	0.92	178	3.567	1854.6	2.24	0.20	19.3
16	0.35	0.92	210	4.194	2180.8	2.63	0.20	20.6
17	0.35	0.92	34.0	0.679	353.2	0.43	0.16	9.9
18	0.35	0.90	145	2.904	1510.0	1.82	0.28	17.8
19	0.35	0.90	125	2.495	1297.7	1.56	0.23	16.7
20*	1.0	1.00	49.0	0.997	62.4	0.04	0.14	5.8
21*	1.0	1.00	81.0	1.648	103.1	0.07	0.15	7.0
22*	1.0	1.00	112	2.282	142.8	0.10	0.17	8.0
23*	1.0	1.00	129	2.635	164.8	0.12	0.18	8.5
24*	1.0	0.79	52.7	1.069	67.1	0.05	0.12	5.9
25*	1.0	0.79	69.7	1.414	88.8	0.06	0.12	6.6
26*	1.0	0.79	87.3	1.771	111.2	0.08	0.13	7.3
27*	1.0	0.79	102	2.081	130.6	0.09	0.13	7.7
28*	1.0	0.79	121	2.462	154.5	0.11	0.14	8.3
29*	1.0	0.79	138	2.793	175.3	0.12	0.16	8.7
30*	1.0	0.79	172	3.482	218.5	0.16	0.18	9.5

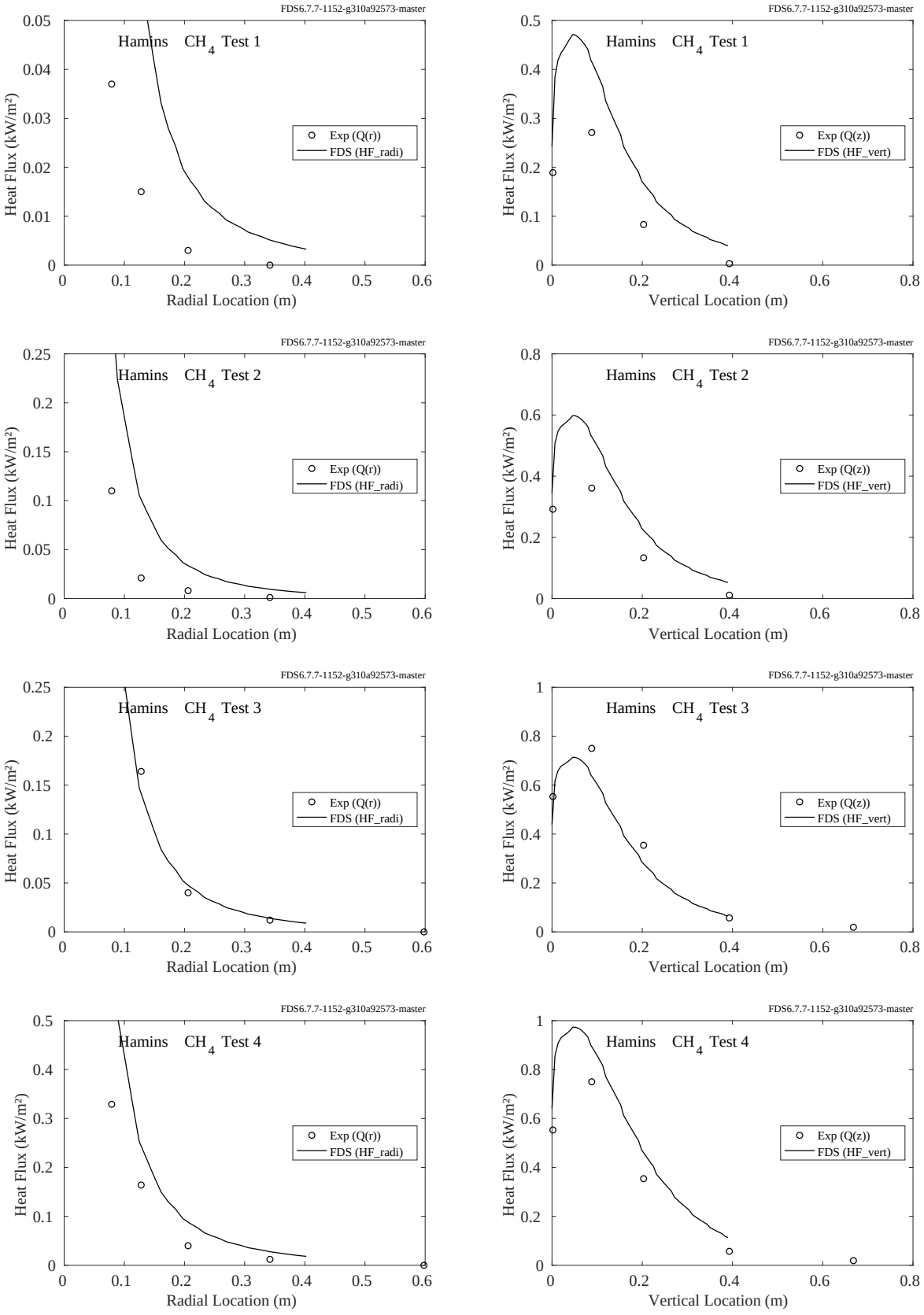

Figure 12.43: Comparison of predicted and measured heat fluxes, Hamins Methane Tests 1-4.

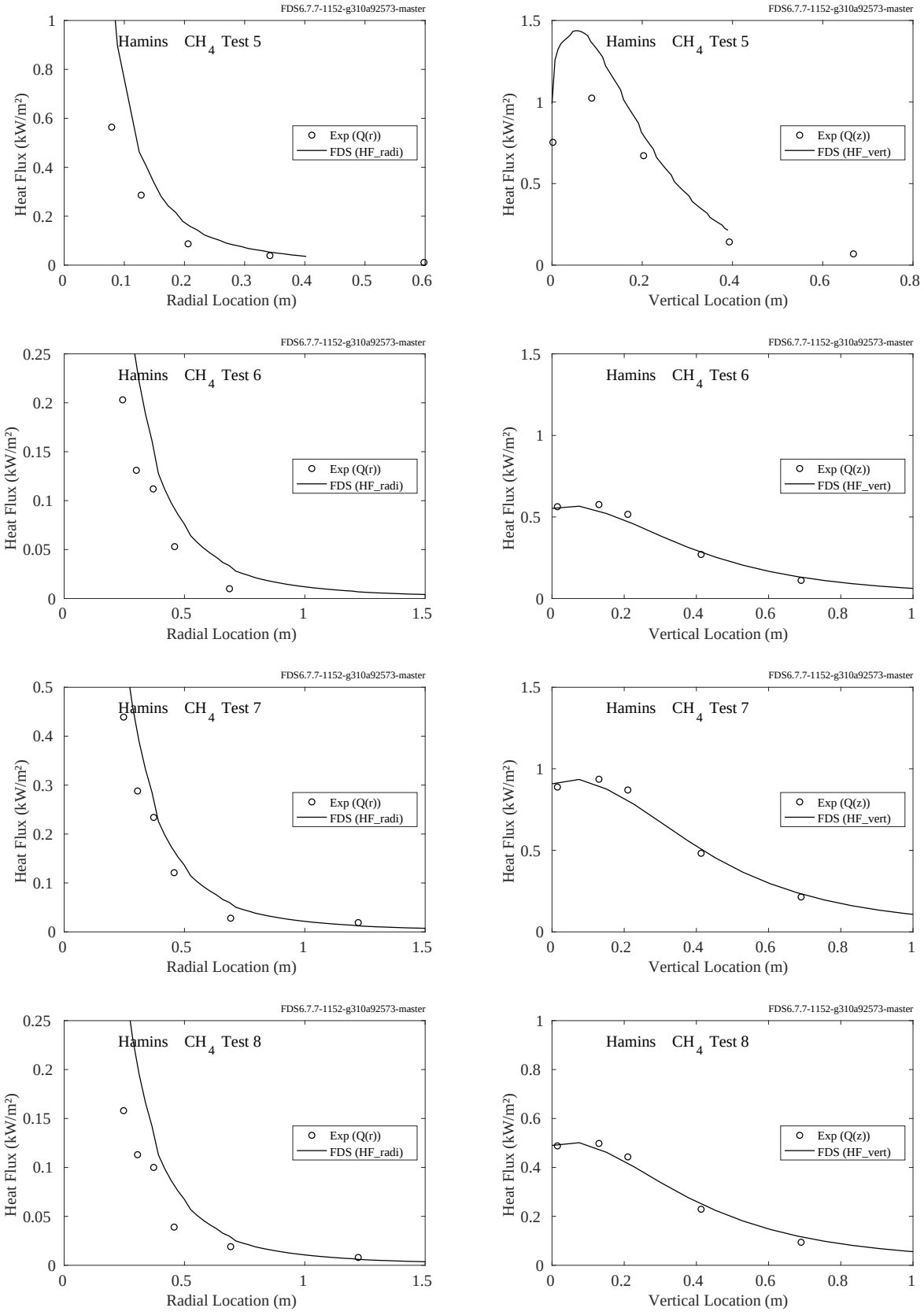

Figure 12.44: Comparison of predicted and measured heat fluxes, Hamins Methane Tests 5-8.

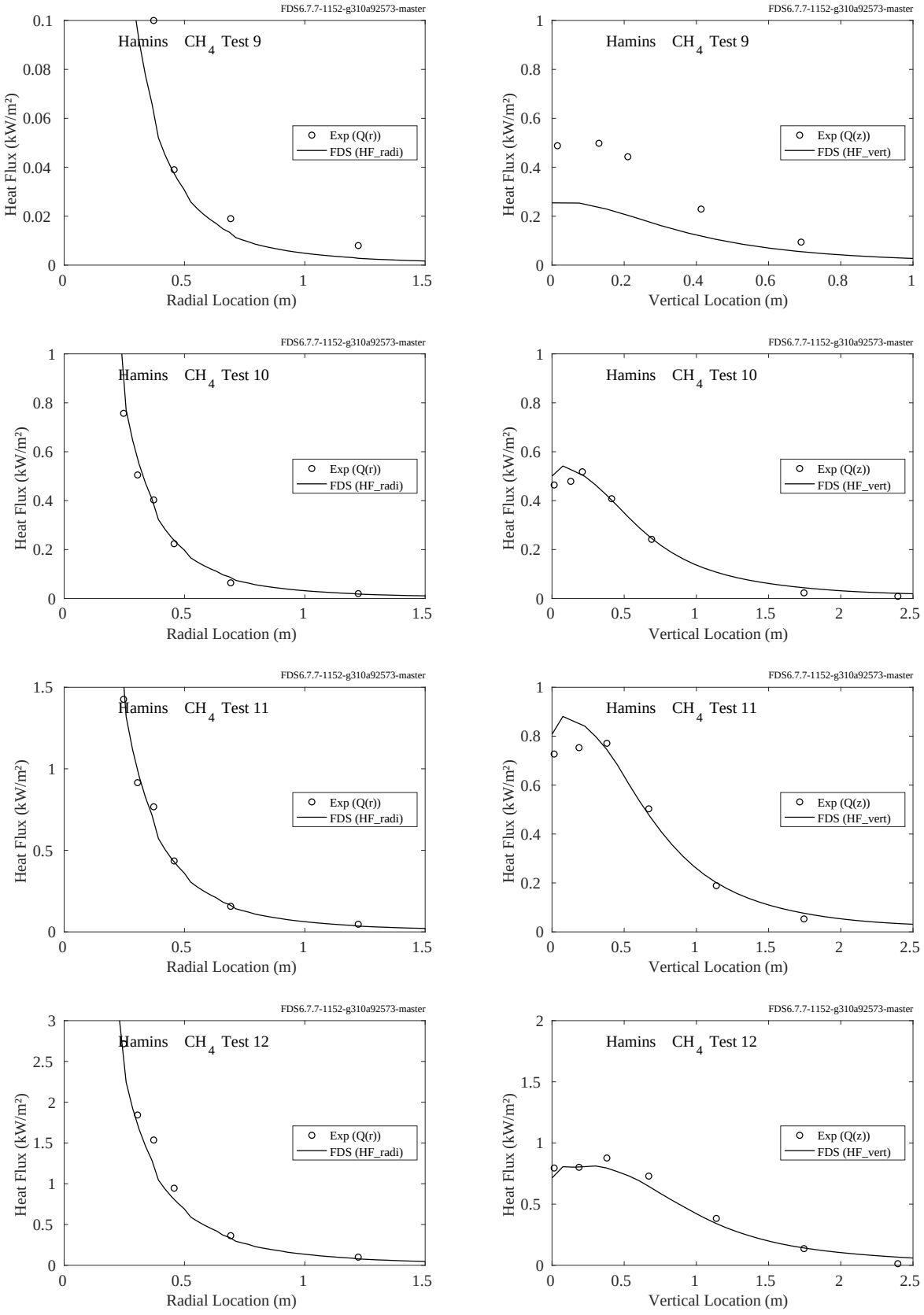

Figure 12.45: Comparison of predicted and measured heat fluxes, Hamins Methane Tests 9-12.

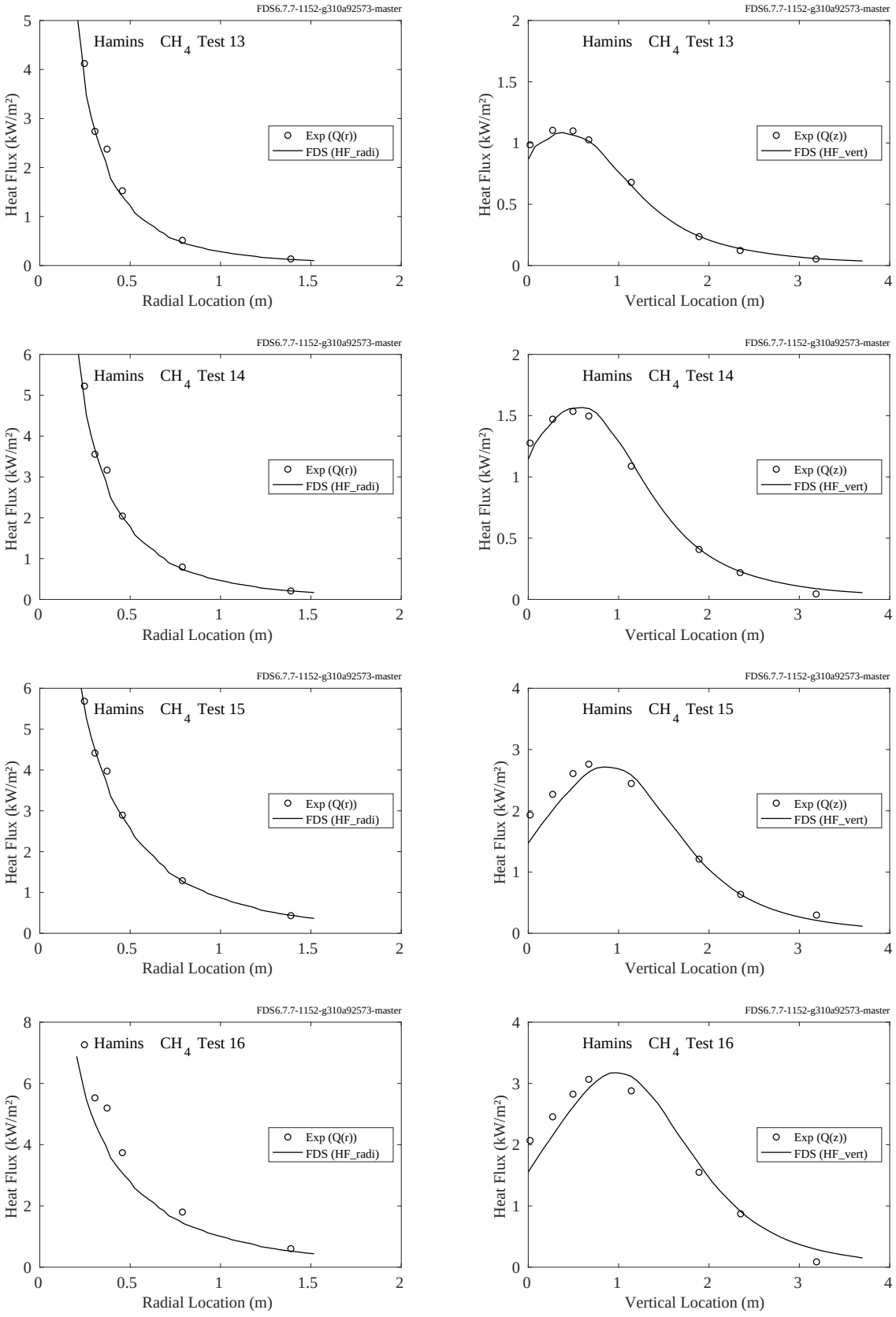

Figure 12.46: Comparison of predicted and measured heat fluxes, Hamins Methane Tests 13-16.

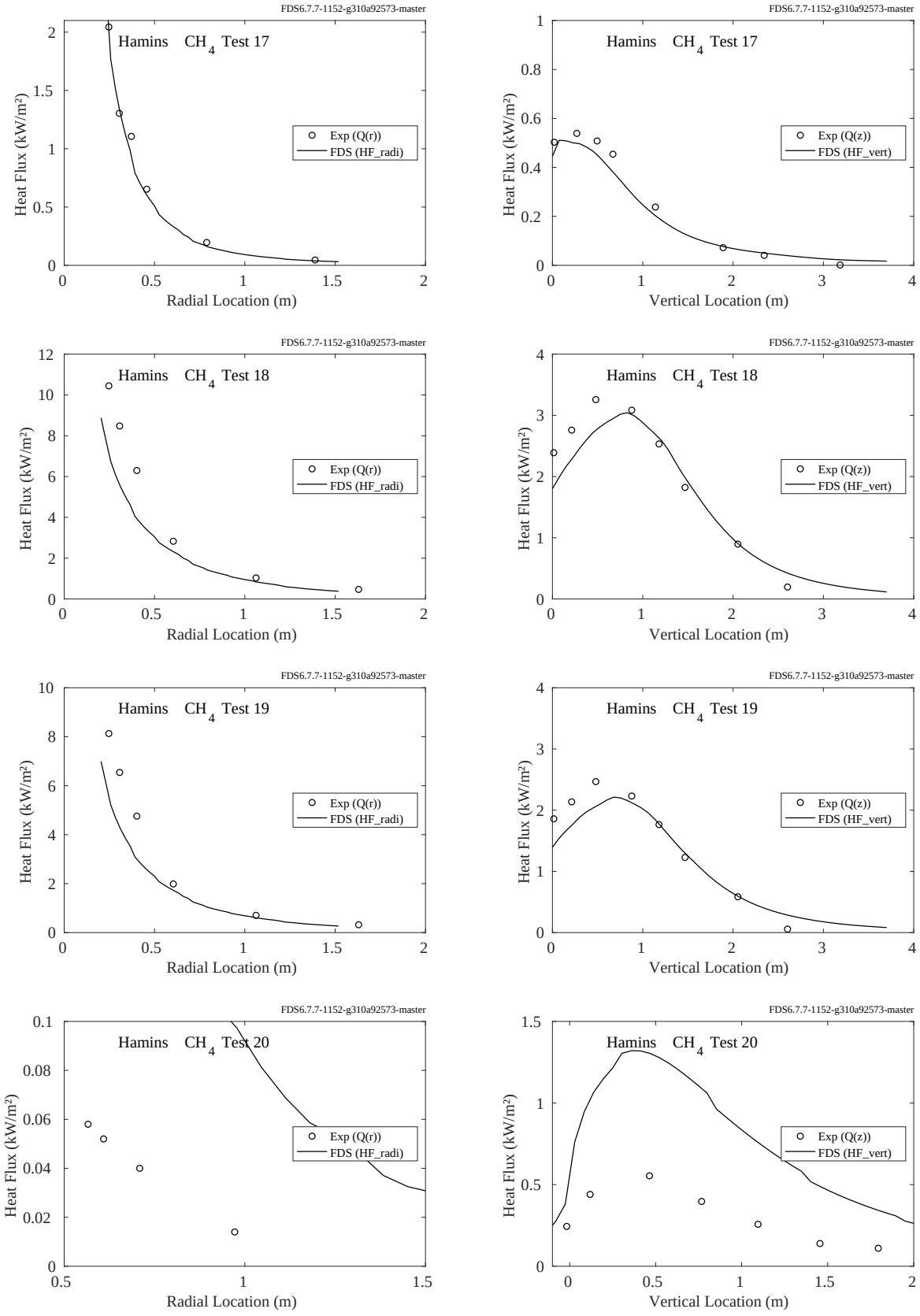

Figure 12.47: Comparison of predicted and measured heat fluxes, Hamins Methane Tests 17-20.

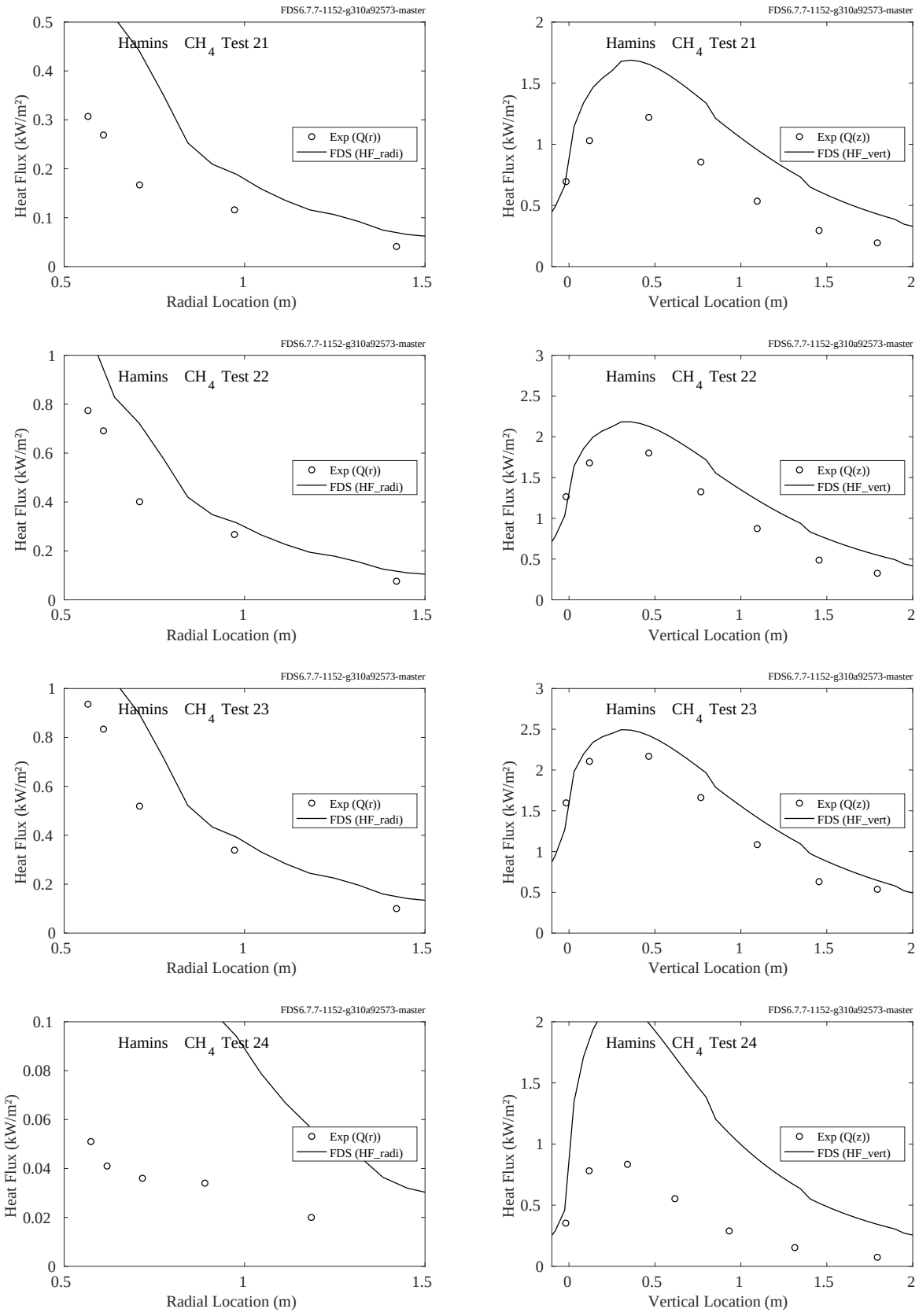

Figure 12.48: Comparison of predicted and measured heat fluxes, Hamins Methane Tests 21-24.

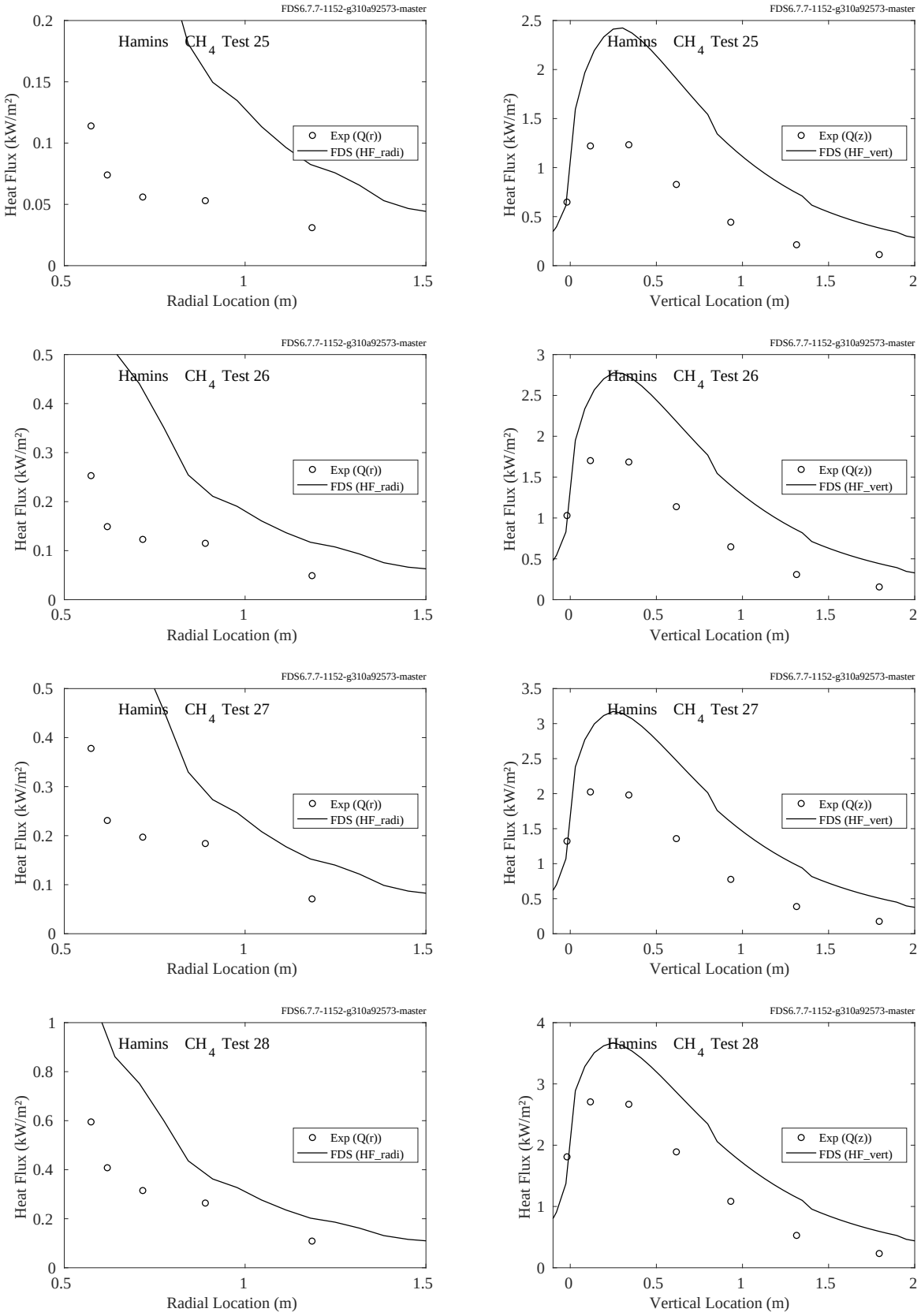

Figure 12.49: Comparison of predicted and measured heat fluxes, Hamins Methane Tests 25-28.

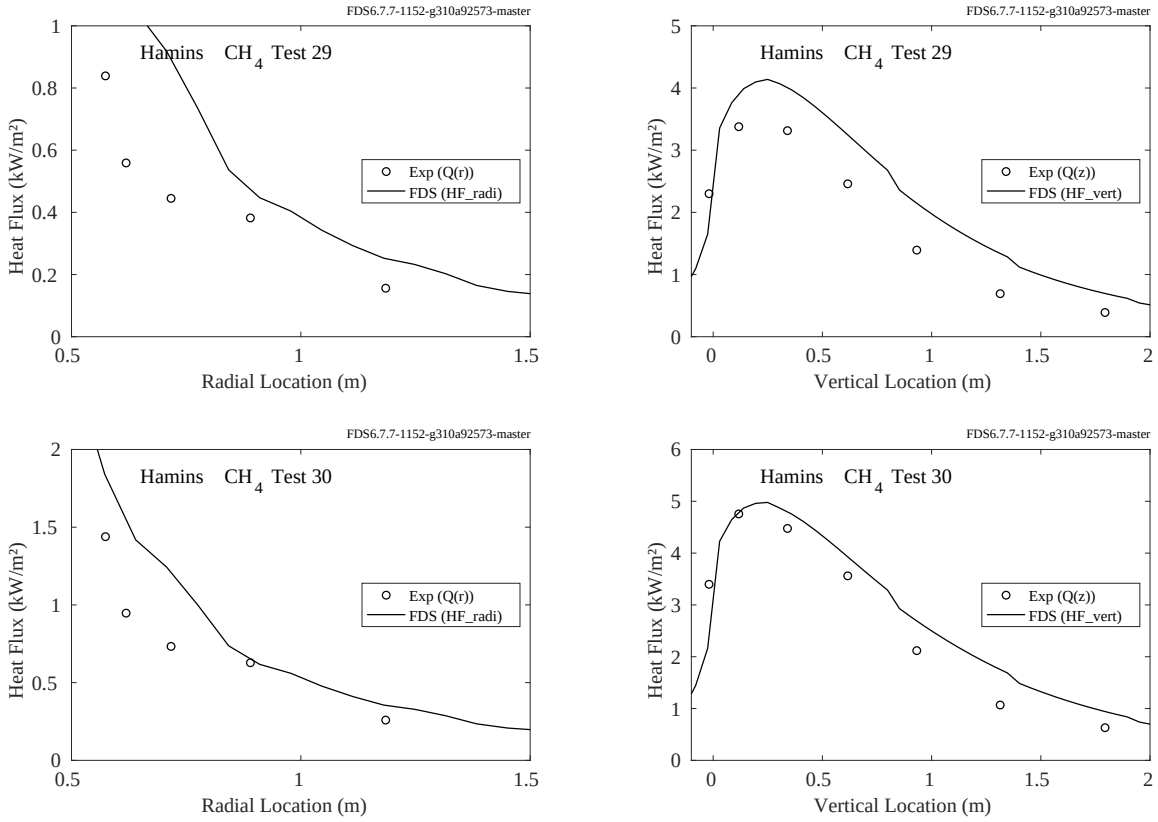

Figure 12.50: Comparison of predicted and measured heat fluxes, Hamins Methane Tests 29-30.

Propane Experiments

Table 12.4: Parameters of the Hamins propane burner experiments. Note that in all cases, the soot and CO yields were taken to be 0.024 and 0.005, respectively, based on the measurements of Tewarson [135].

Test No.	D (m)	R_0 (m)	$\dot{Q}$ (kW)	$\dot{m}$ (kg/s)	$\dot{Q}''$ (kW/m^2)	$\dot{Q}^*$	$\chi_{\rm rad}$	$D^*/\delta x$
1	0.1	0.26	2.7	0.058	343.8	0.78	0.22	9.0
2	0.1	0.26	6.8	0.148	870.9	1.96	0.27	13.1
3	0.1	0.26	11.8	0.254	1499.9	3.38	0.29	16.3
4	0.1	0.37	17.9	0.386	2277.8	5.14	0.29	19.2
5	0.1	0.37	25.2	0.543	3203.5	7.22	0.30	22.1
6	0.1	0.49	36.9	0.796	4698.3	10.6	0.30	25.7
7	0.1	0.13	0.4	0.010	56.0	0.13	0.12	4.4
8	0.1	0.13	0.8	0.017	99.3	0.22	0.12	5.5
9	0.1	0.13	0.6	0.013	76.4	0.17	0.12	4.9
10	0.1	0.13	1.0	0.021	123.5	0.28	0.15	6.0
11	0.1	0.13	1.4	0.031	183.3	0.41	0.18	7.0
12	0.1	0.13	2.2	0.046	273.7	0.62	0.23	8.2
13	0.1	0.19	3.4	0.074	434.2	0.98	0.24	9.9
14	0.1	0.19	5.6	0.122	718.1	1.62	0.26	12.1
15	0.1	0.28	11.9	0.257	1513.9	3.41	0.26	16.3
16	0.1	0.28	24.8	0.535	3156.4	7.12	0.29	21.9
17	0.35	0.92	33.9	0.732	352.8	0.43	0.25	9.9
18	0.35	0.92	124.9	2.694	1298.1	1.56	0.30	16.7
19	0.35	0.57	20.0	0.431	207.9	0.25	0.18	8.0
20	0.35	0.57	15.6	0.336	162.0	0.20	0.14	7.3
21	0.35	0.39	19.0	0.409	197.3	0.24	0.13	7.9
22	0.35	0.39	14.6	0.316	152.2	0.18	0.10	7.1
23	0.35	0.68	108.2	2.334	1124.5	1.36	0.29	15.8
24	0.35	0.68	102.3	2.207	1063.7	1.28	0.31	15.5
25	0.35	0.68	79.7	1.719	828.4	1.00	0.28	14.0
26	0.35	0.51	12.0	0.258	124.5	0.15	0.08	6.6
27	1.0	0.81	55.2	1.190	70.2	0.05	0.11	6.0
28	1.0	0.81	81.7	1.761	104.0	0.07	0.15	7.1
29	1.0	0.81	107.3	2.315	136.7	0.10	0.18	7.9
30	1.0	1.00	136.4	2.943	173.7	0.12	0.22	8.7
31	1.0	0.97	55.6	1.199	70.8	0.05	0.12	6.1
32	1.0	0.97	82.5	1.779	105.0	0.07	0.14	7.1
33	1.0	0.97	107.9	2.326	137.3	0.10	0.17	7.9
34	1.0	0.97	137.3	2.963	174.9	0.12	0.23	8.7

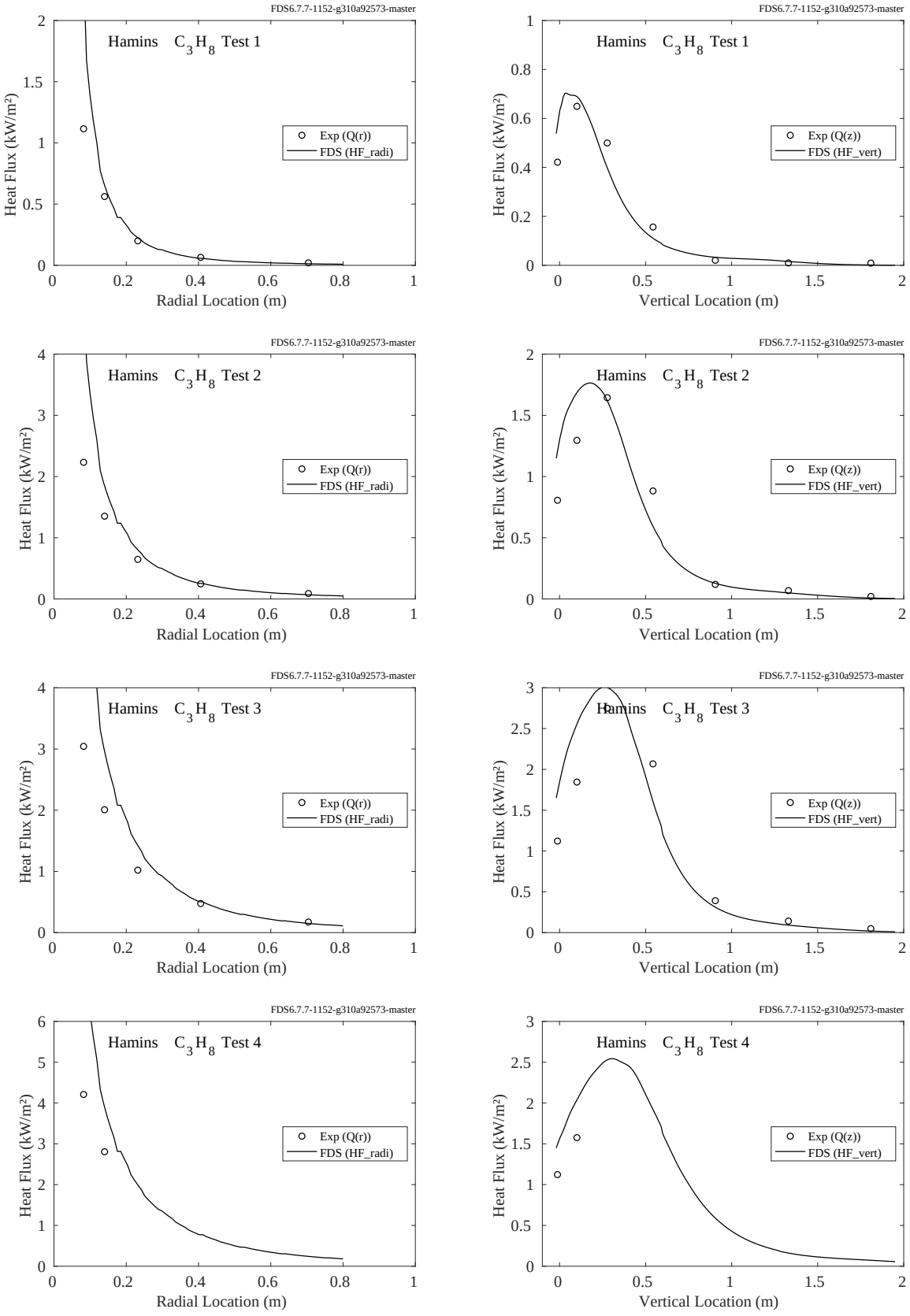

Figure 12.51: Comparison of predicted and measured heat fluxes, Hamins Propane Tests 1-4.

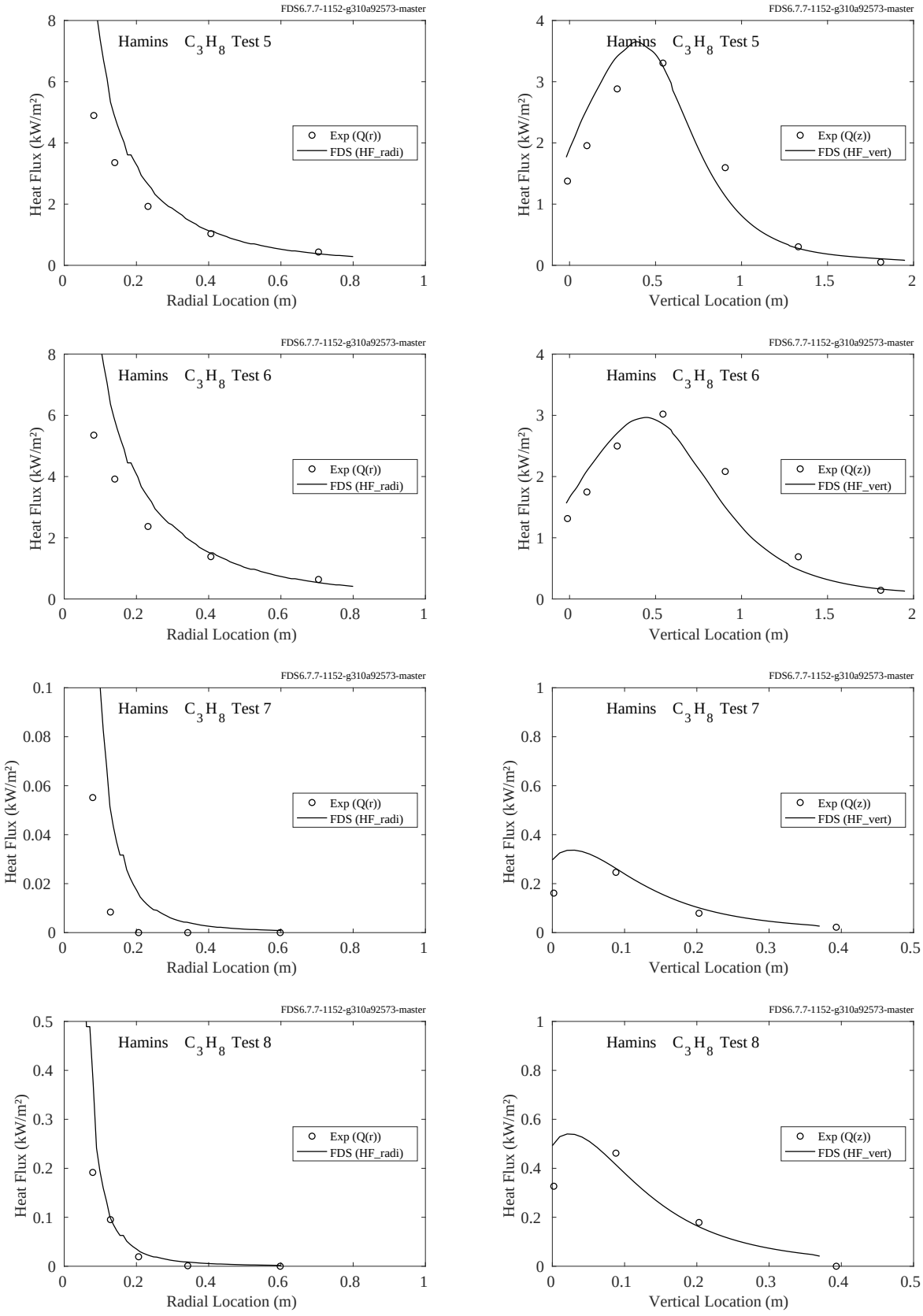

Figure 12.52: Comparison of predicted and measured heat fluxes, Hamins Propane Tests 5-8.

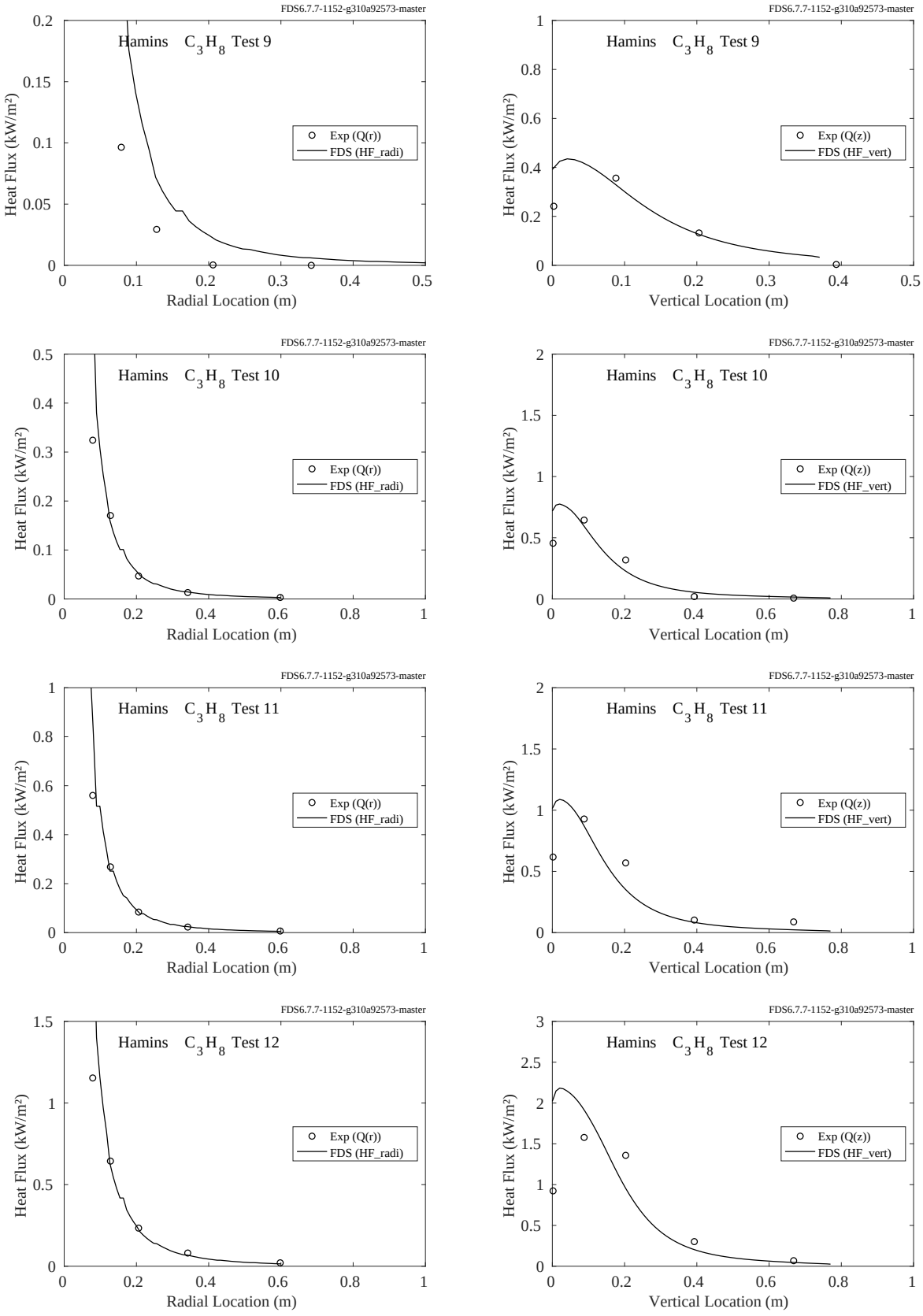

Figure 12.53: Comparison of predicted and measured heat fluxes, Hamins Propane Tests 9-12.

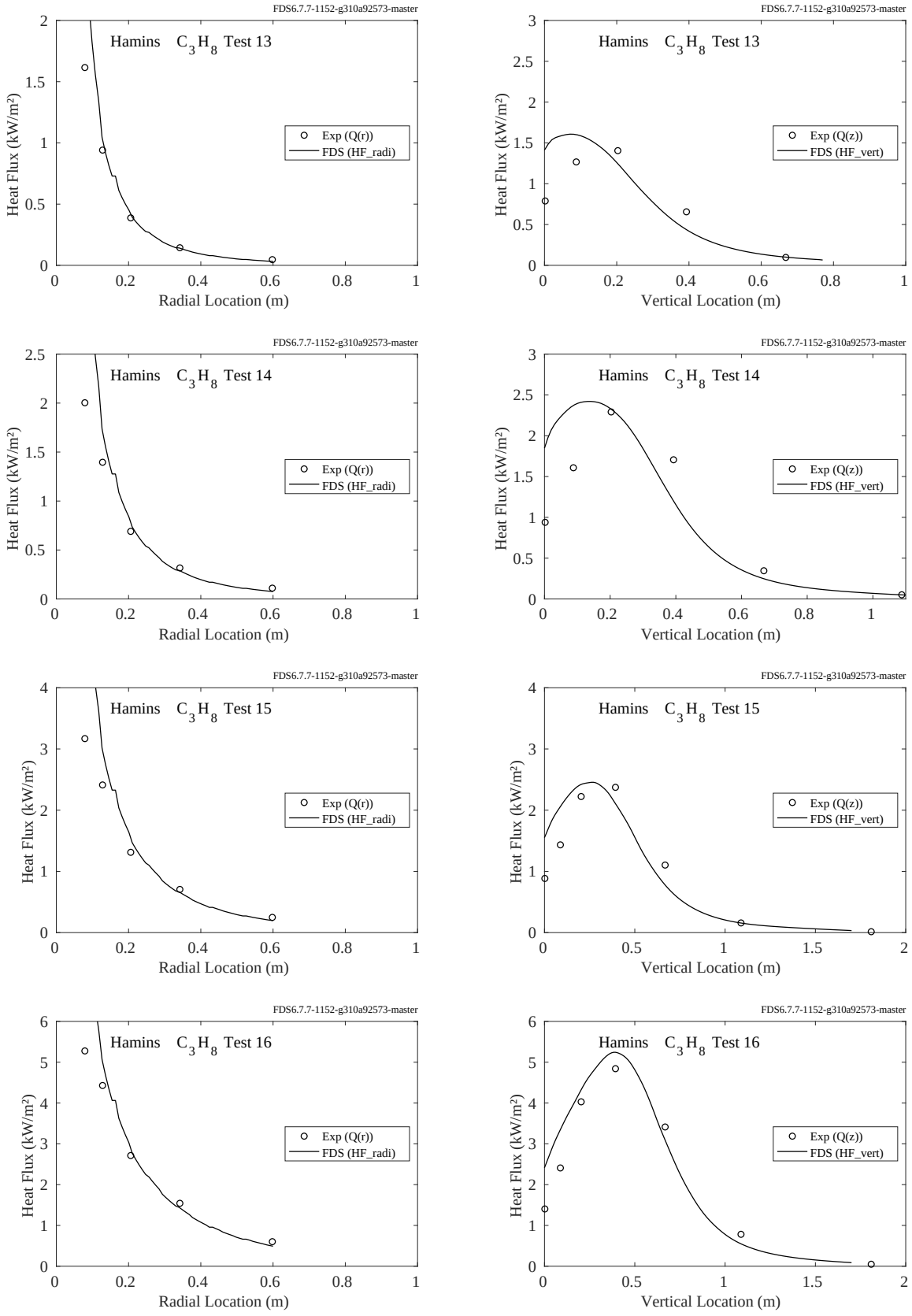

Figure 12.54: Comparison of predicted and measured heat fluxes, Hamins Propane Tests 13-16.

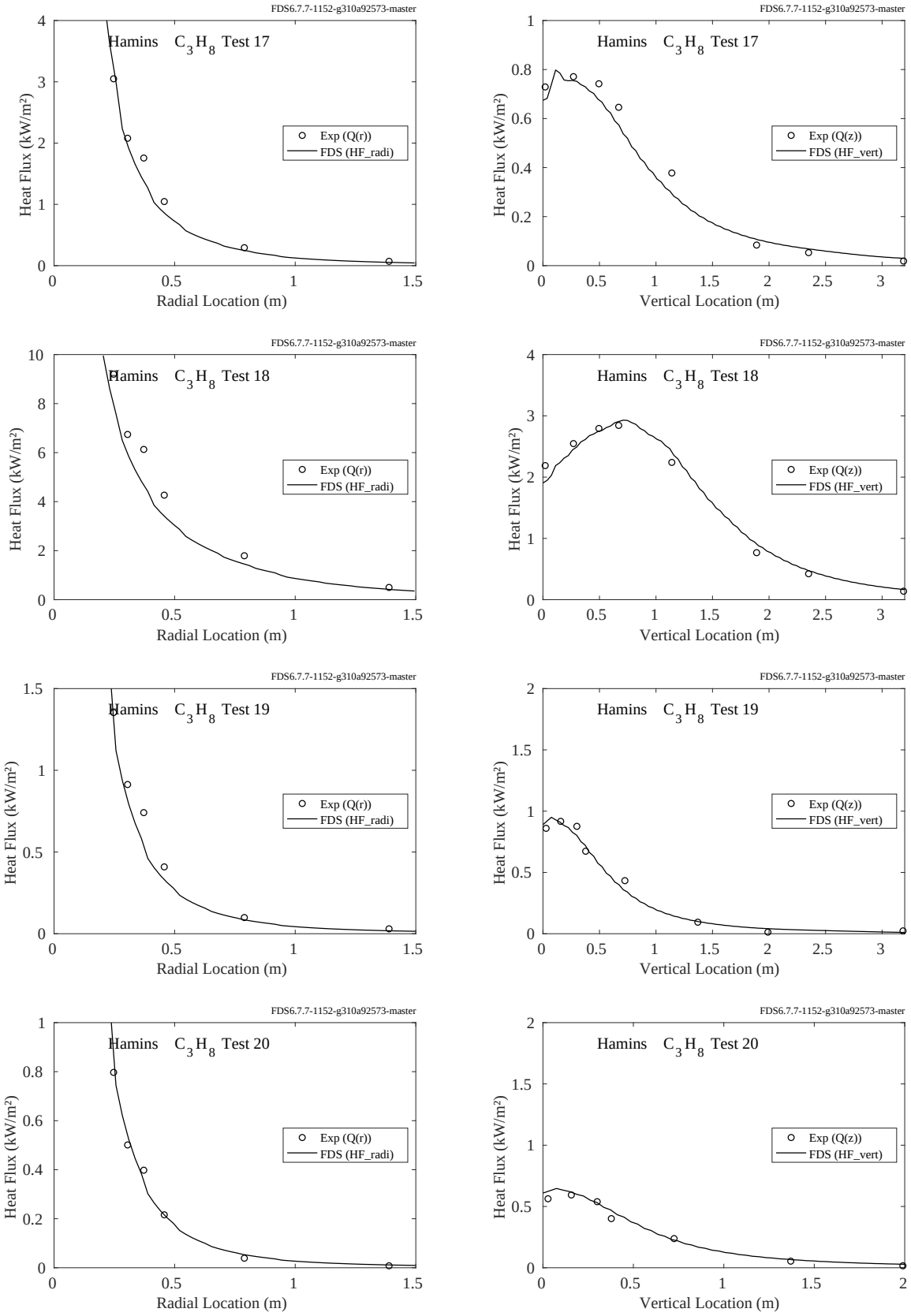

Figure 12.55: Comparison of predicted and measured heat fluxes, Hamins Propane Tests 17-20.

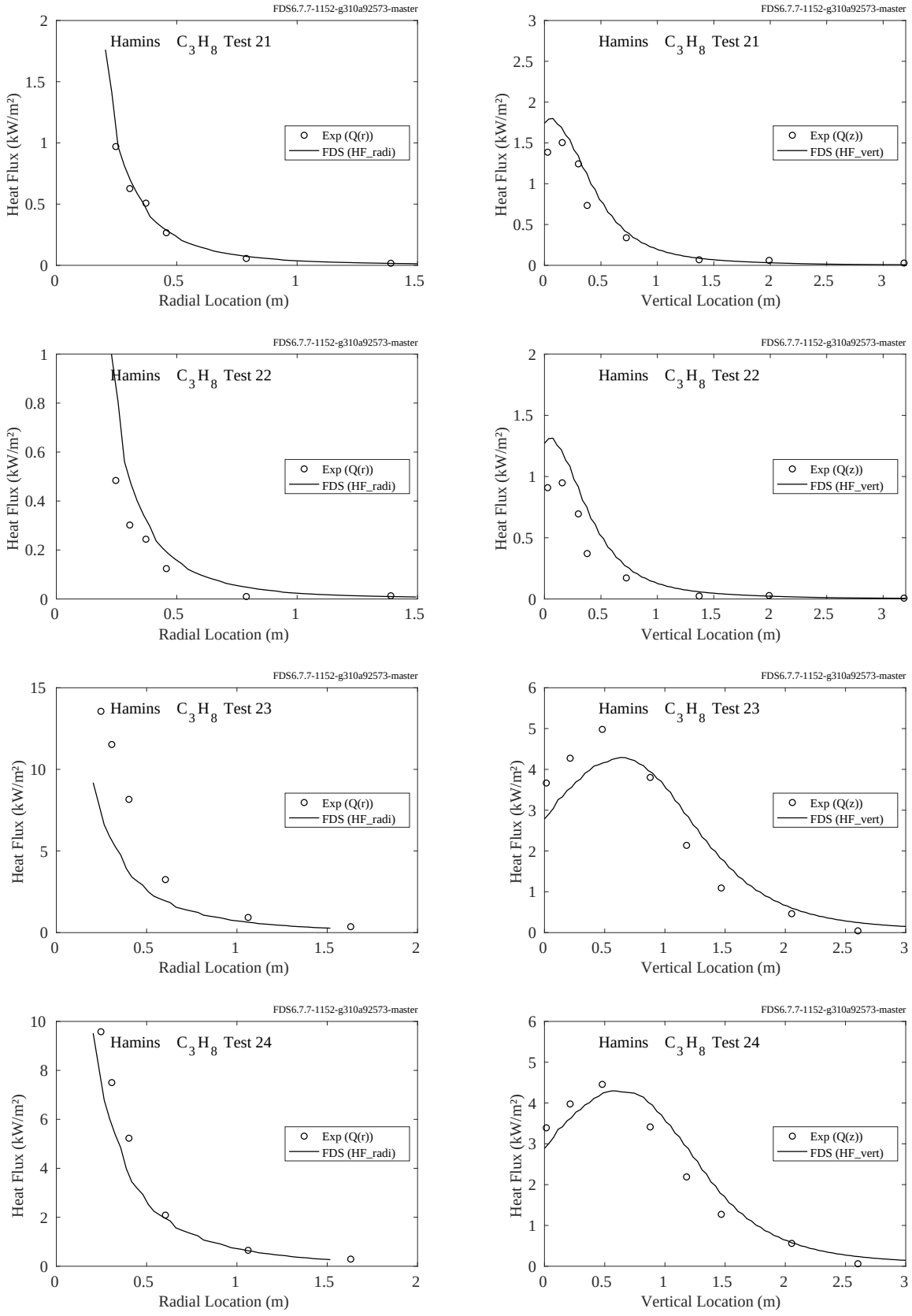

Figure 12.56: Comparison of predicted and measured heat fluxes, Hamins Propane Tests 21-24.

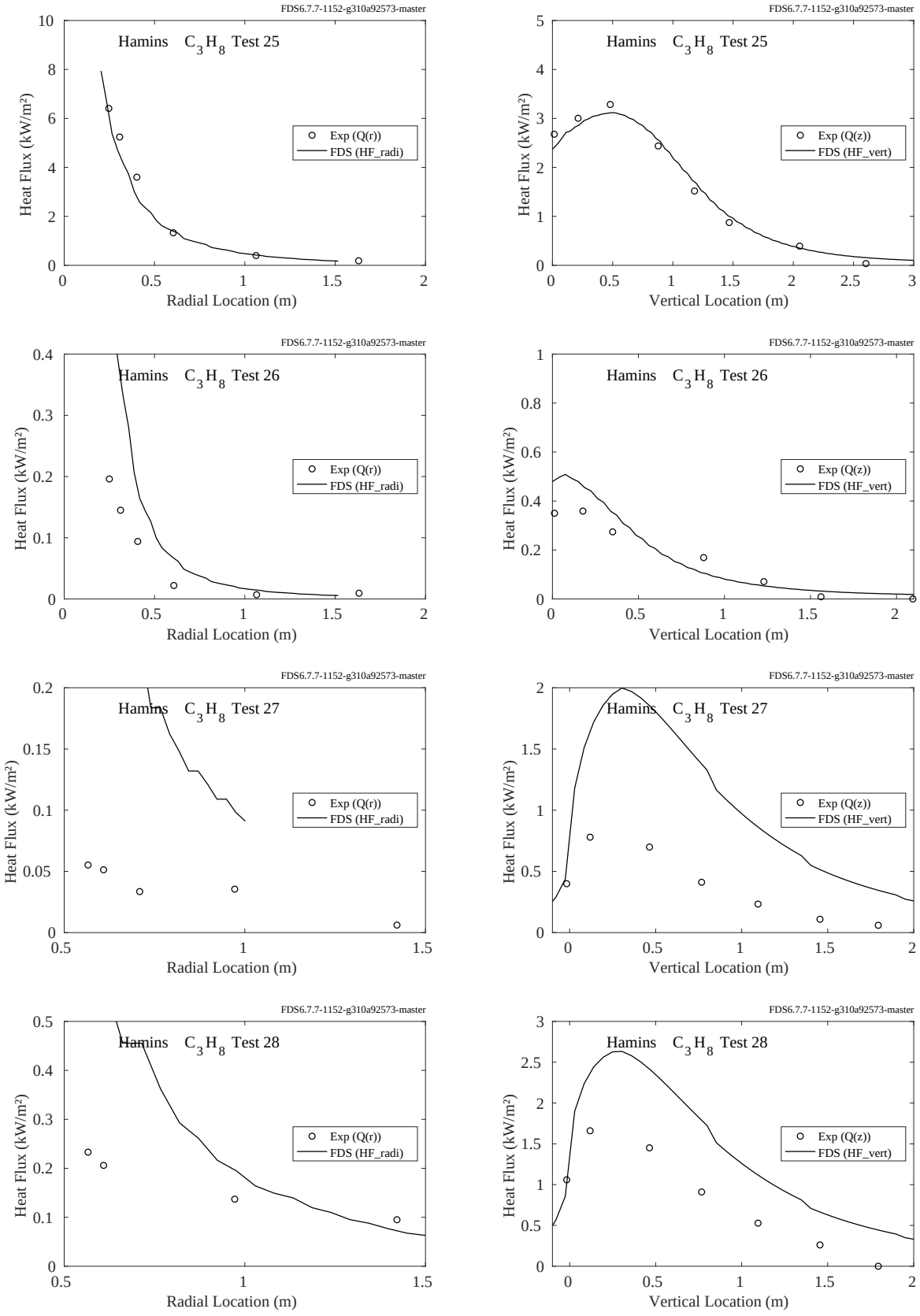

Figure 12.57: Comparison of predicted and measured heat fluxes, Hamins Propane Tests 25-28.

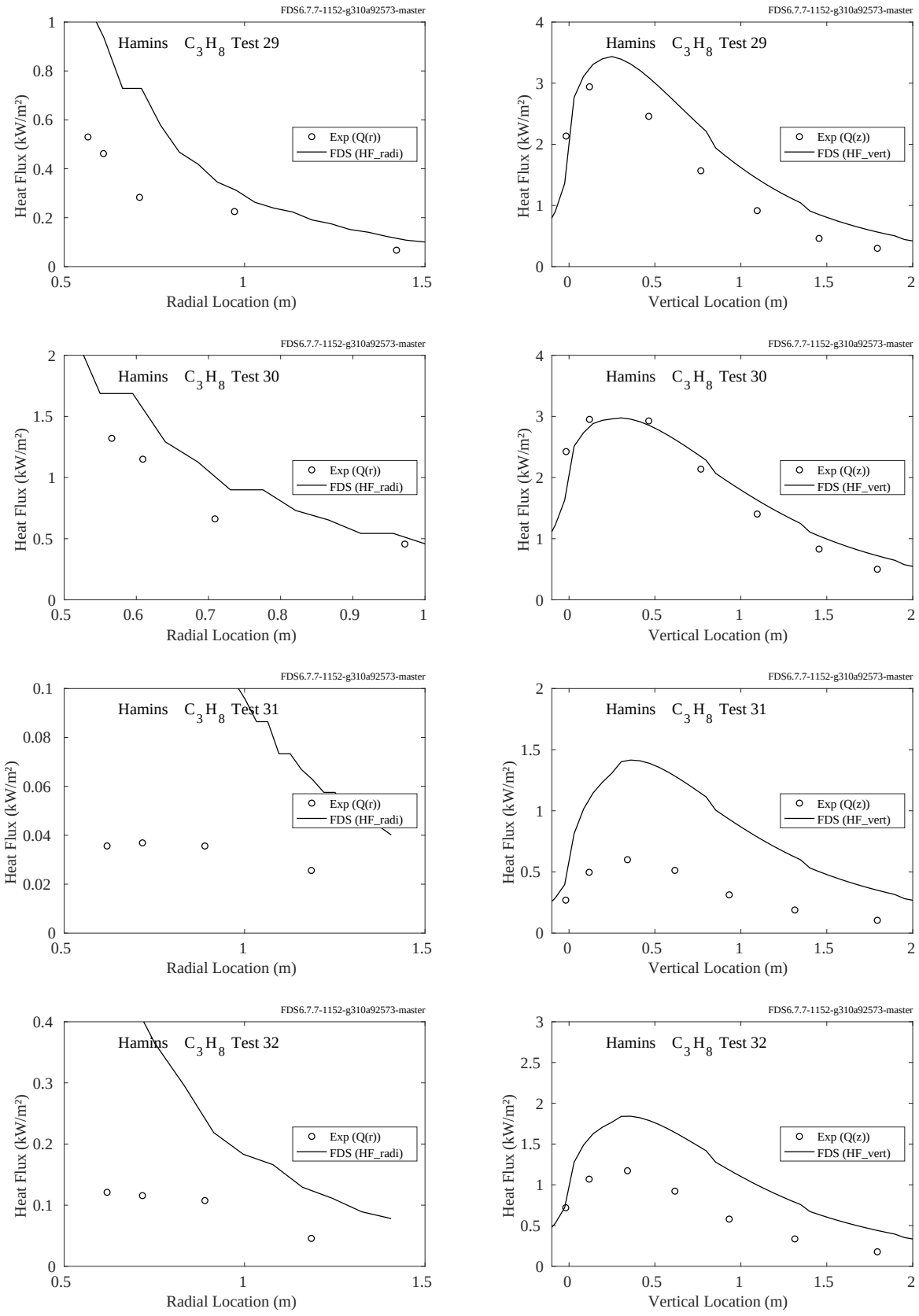

Figure 12.58: Comparison of predicted and measured heat fluxes, Hamins Propane Tests 29-32.

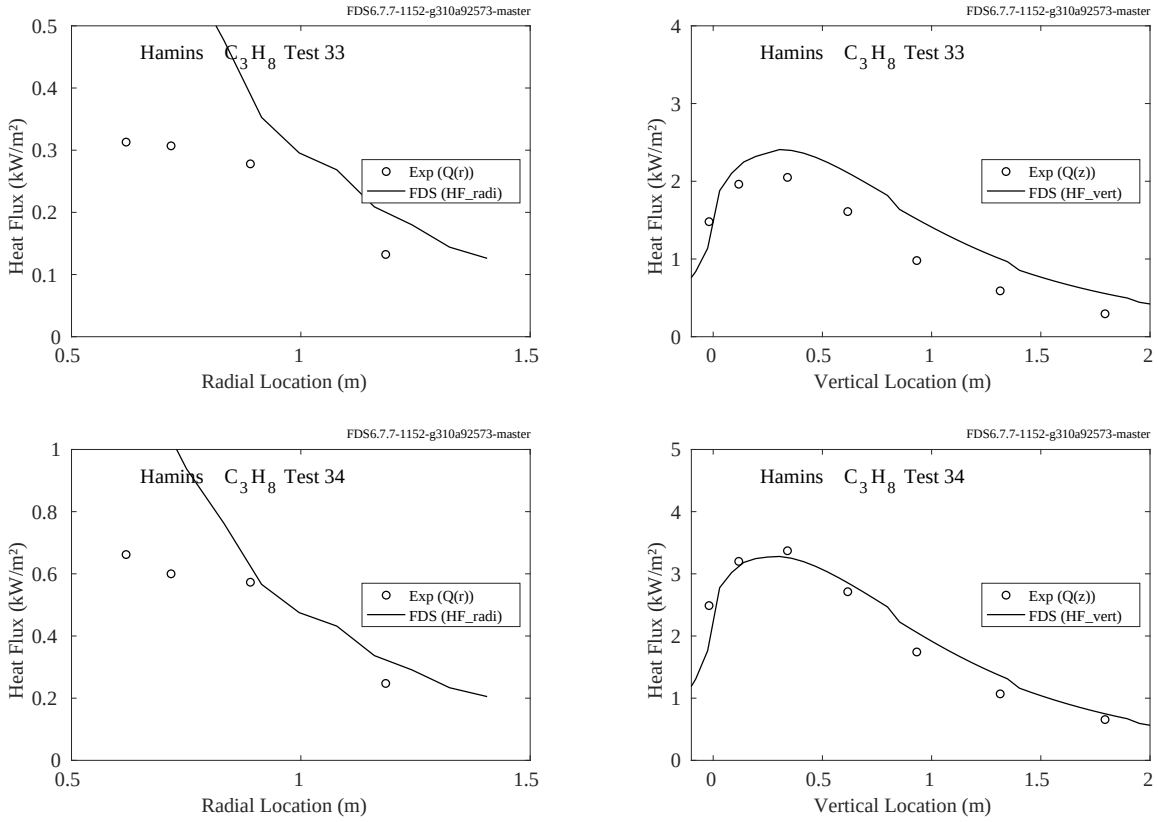

Figure 12.59: Comparison of predicted and measured heat fluxes, Hamins Propane Tests 33-34.

Acetylene Experiments

Table 12.5: Parameters of the Hamins acetylene burner experiments. Note that in all cases, the soot and CO yields were taken to be 0.096 and 0.042, respectively, based on the measurements of Tewarson [135].

Test No.	D (m)	R_0 (m)	$\dot{Q}$ (kW)	$\dot{m}$ (kg/s)	$\dot{Q}''$ (kW/m^2)	$\dot{Q}^*$	$\chi_{\rm rad}$	$D^*/\delta x$
1	0.10	0.13	0.45	0.009	57.3	0.13	0.12	4.4
2	0.10	0.13	0.56	0.012	71.3	0.16	0.15	4.8
3	0.10	0.13	0.90	0.019	114.6	0.26	0.18	5.8
4	0.10	0.13	1.29	0.027	164.2	0.37	0.27	6.7
5	0.10	0.13	1.54	0.032	196.1	0.44	0.31	7.2
6	0.35	0.39	12.5	0.259	129.9	0.16	0.13	6.7
7	0.35	0.51	11.0	0.229	114.3	0.14	0.09	6.3
8	0.35	0.51	20.4	0.424	212.0	0.26	0.22	8.1
9	0.35	0.51	31.3	0.648	325.3	0.39	0.33	9.6
10	0.35	0.69	38.2	0.793	397.0	0.48	0.38	10.4
11	0.35	0.69	48.0	1.000	498.9	0.60	0.41	11.4
12	0.35	0.69	62.4	1.290	648.6	0.78	0.42	12.7
13	0.35	0.69	76.3	1.580	793.0	0.96	0.43	13.8
14	0.35	0.69	109.2	2.270	1135.0	1.37	0.44	15.9
15	0.35	0.69	117.2	2.430	1218.2	1.47	0.43	16.3
16	0.35	0.69	134.7	2.790	1400.0	1.69	0.46	17.3

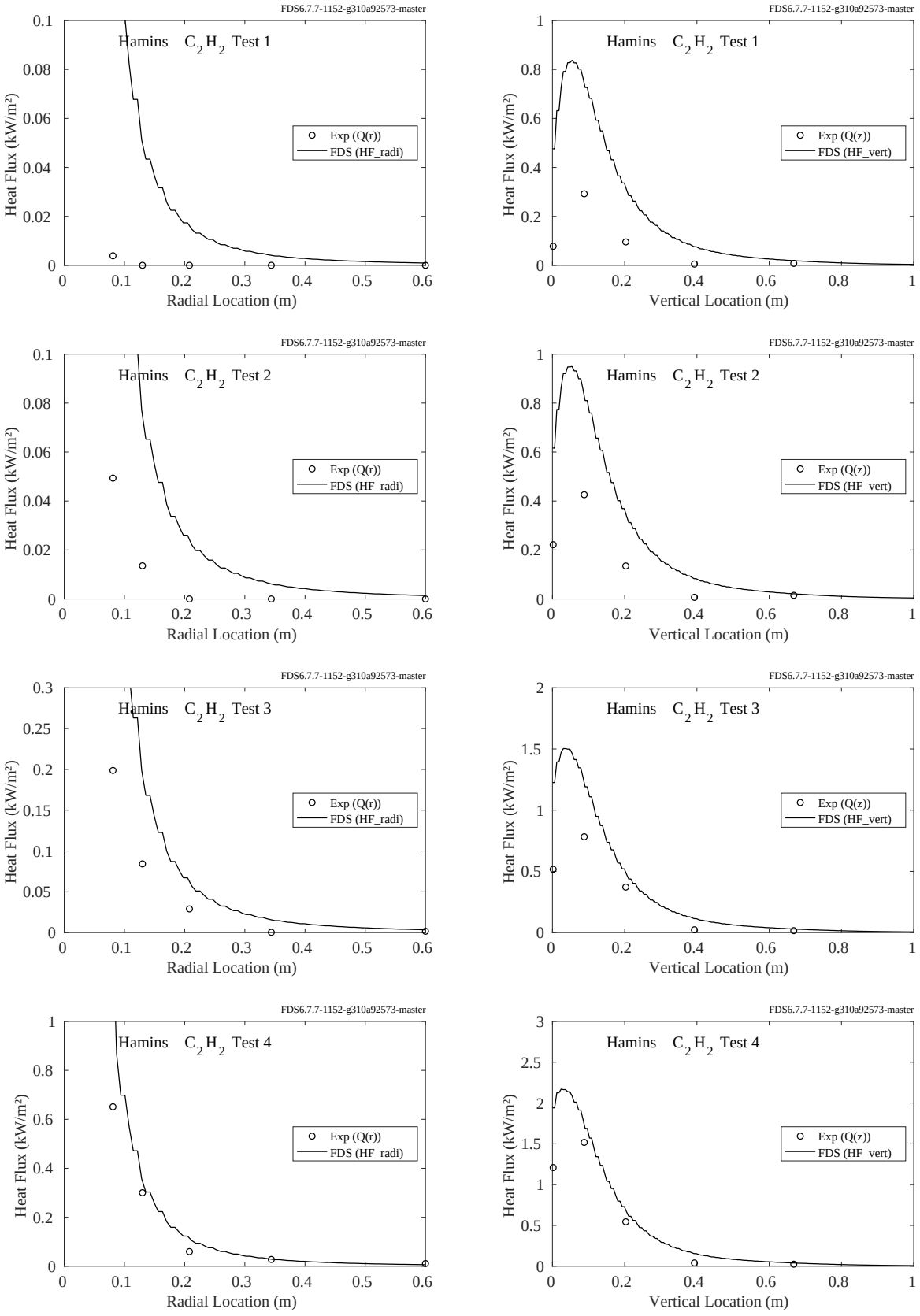

Figure 12.60: Comparison of predicted and measured heat fluxes, Hamins Acetylene Tests 1-4.

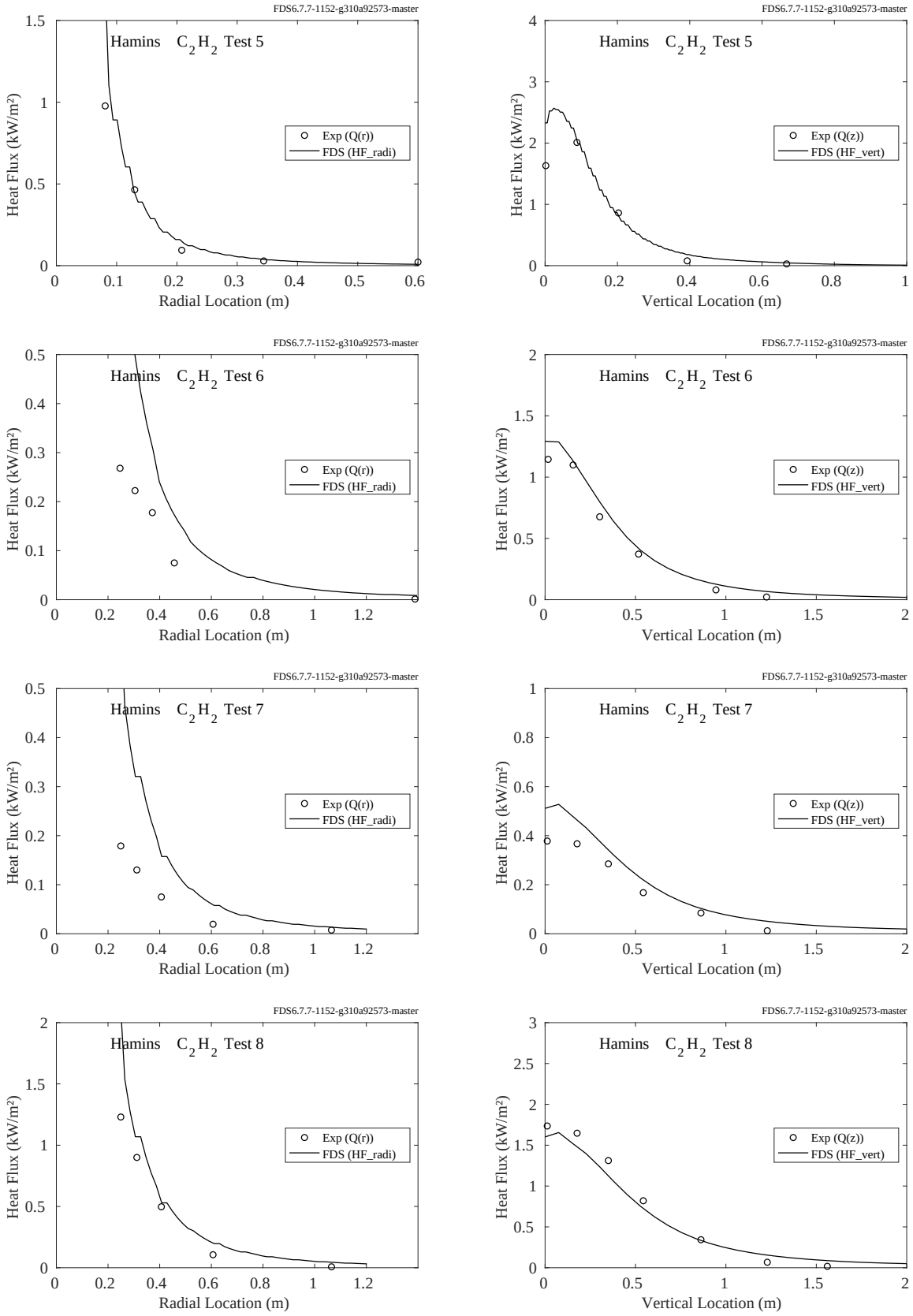

Figure 12.61: Comparison of predicted and measured heat fluxes, Hamins Acetylene Tests 5-8.

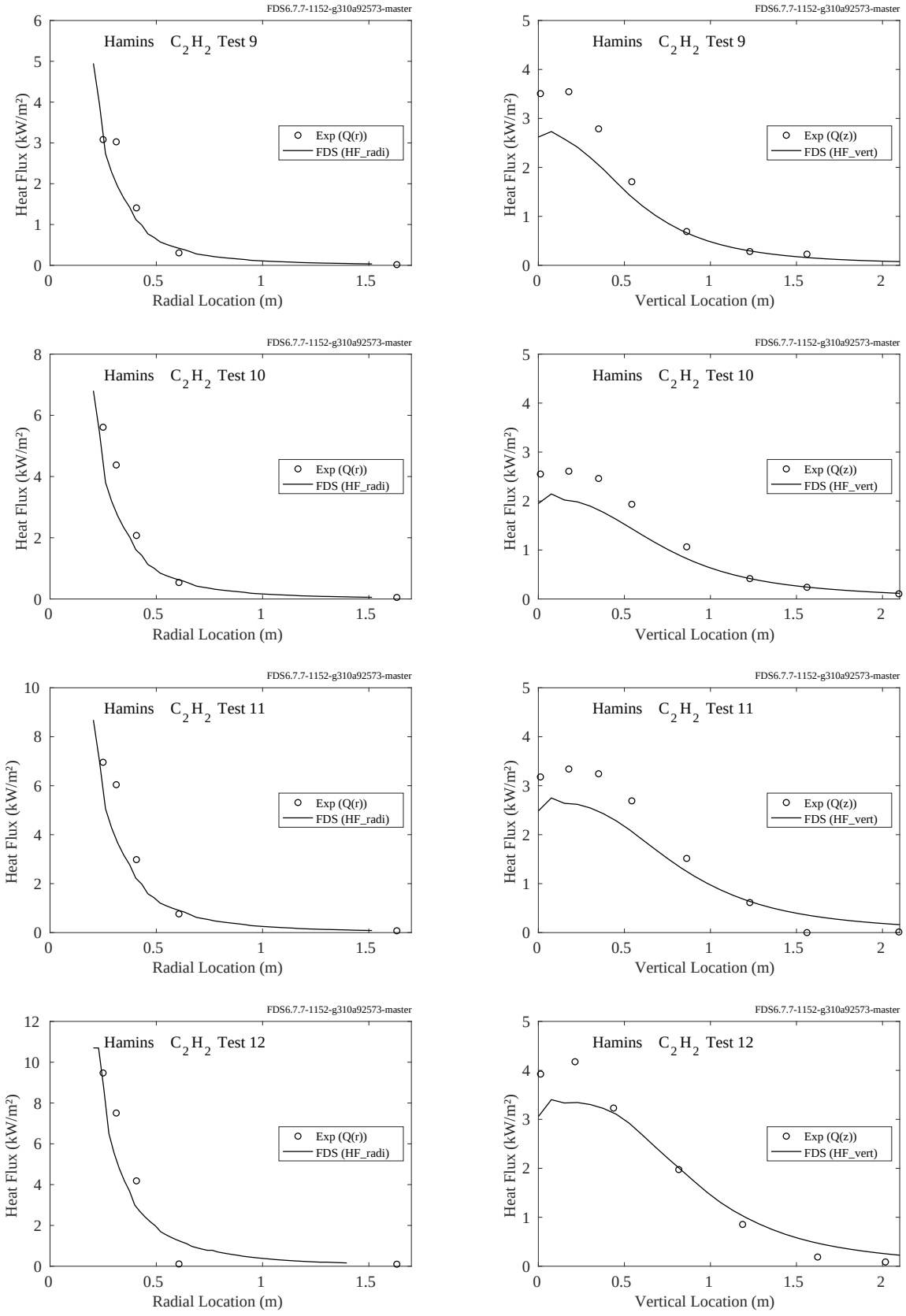

Figure 12.62: Comparison of predicted and measured heat fluxes, Hamins Acetylene Tests 9-12.

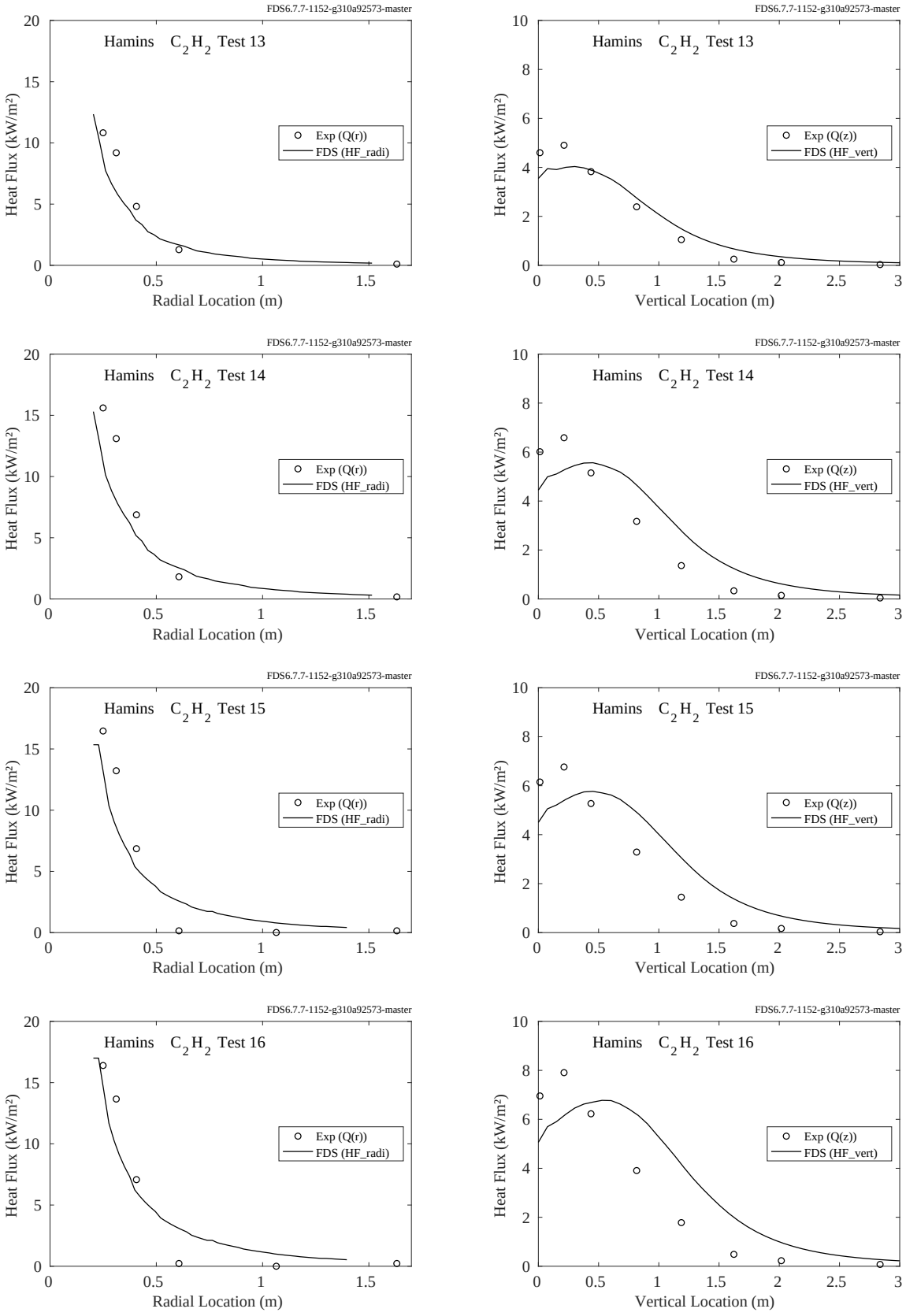

Figure 12.63: Comparison of predicted and measured heat fluxes, Hamins Acetylene Tests 13-16.

12.2.3 BGC/GRI LNG Fires

A description of the 13 LNG trench fire experiments is given in Section 3.6.

Figures 12.65 and 12.66 compare predicted and measured heat fluxes to radiometers at various distances from the LNG trench fire. The general layout of the facility is shown in Fig. 12.64. The radiometers were positioned approximately 1.2 m off the ground along the axis lines shown in the figure. The wind direction was typically perpendicular to the longer dimension of the trench.

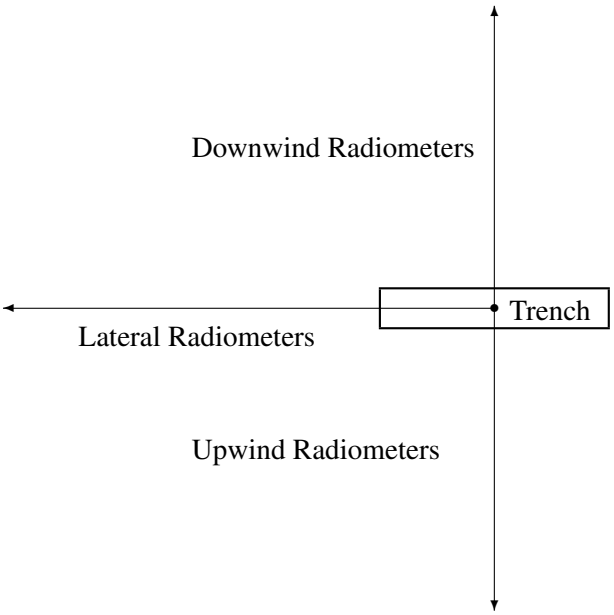

Trench Dimensions		
Test	Length (m)	Width (m)
1	23.53	1.81
2	15.52	1.81
3	9.23	1.83
4	23.50	1.83
5	9.05	1.82
6	23.45	3.94
7	23.45	0.82
8	11.82	0.82
9	9.10	0.82
10	52.05	3.89
11	4.37	0.81
12	52.15	1.82
13	23.10	0.77

Figure 12.64: Schematic diagram of BGC/GRI test facility.

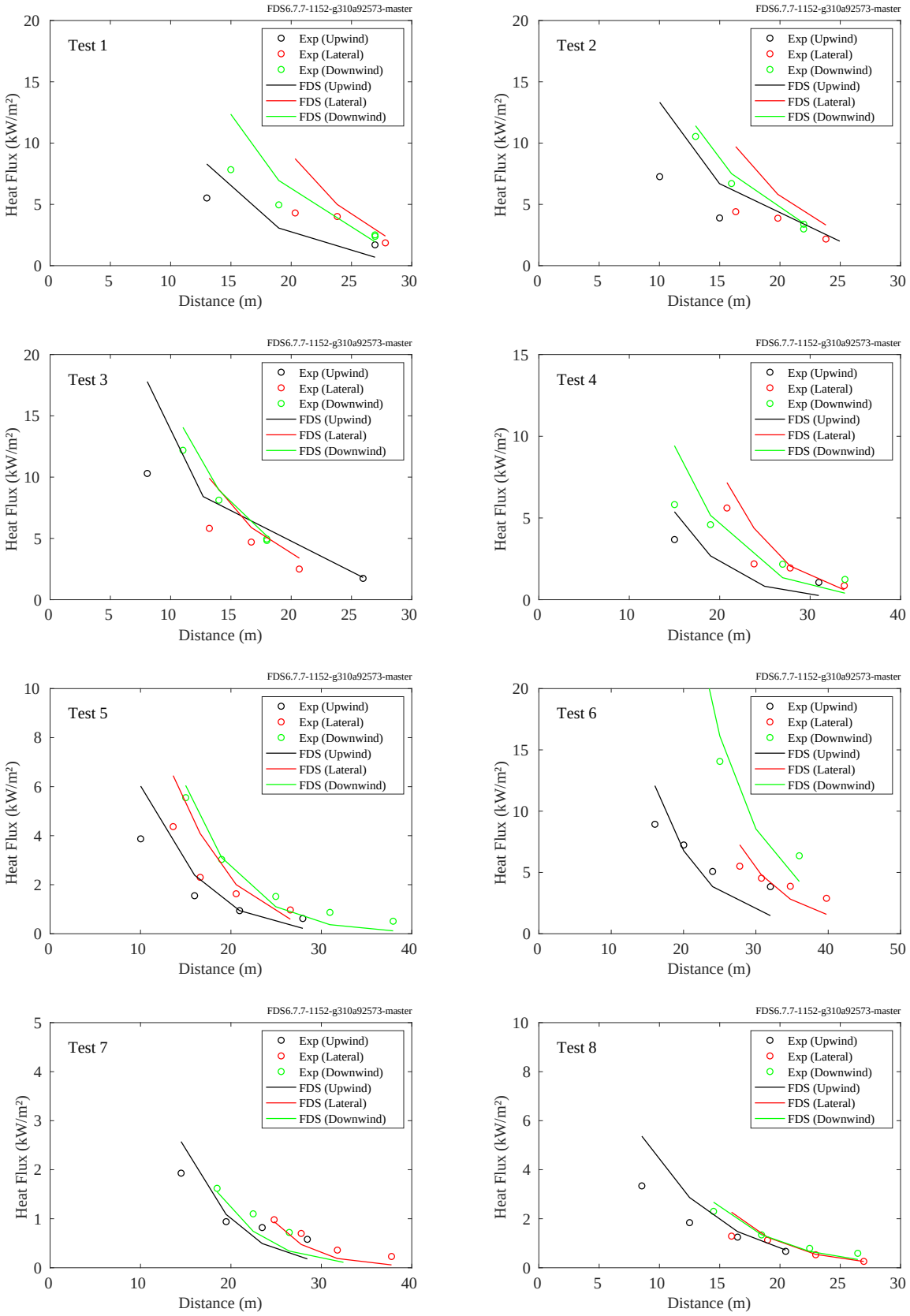

Figure 12.65: BGC/GRI LNG Fires, heat flux profiles for Tests 1-8.

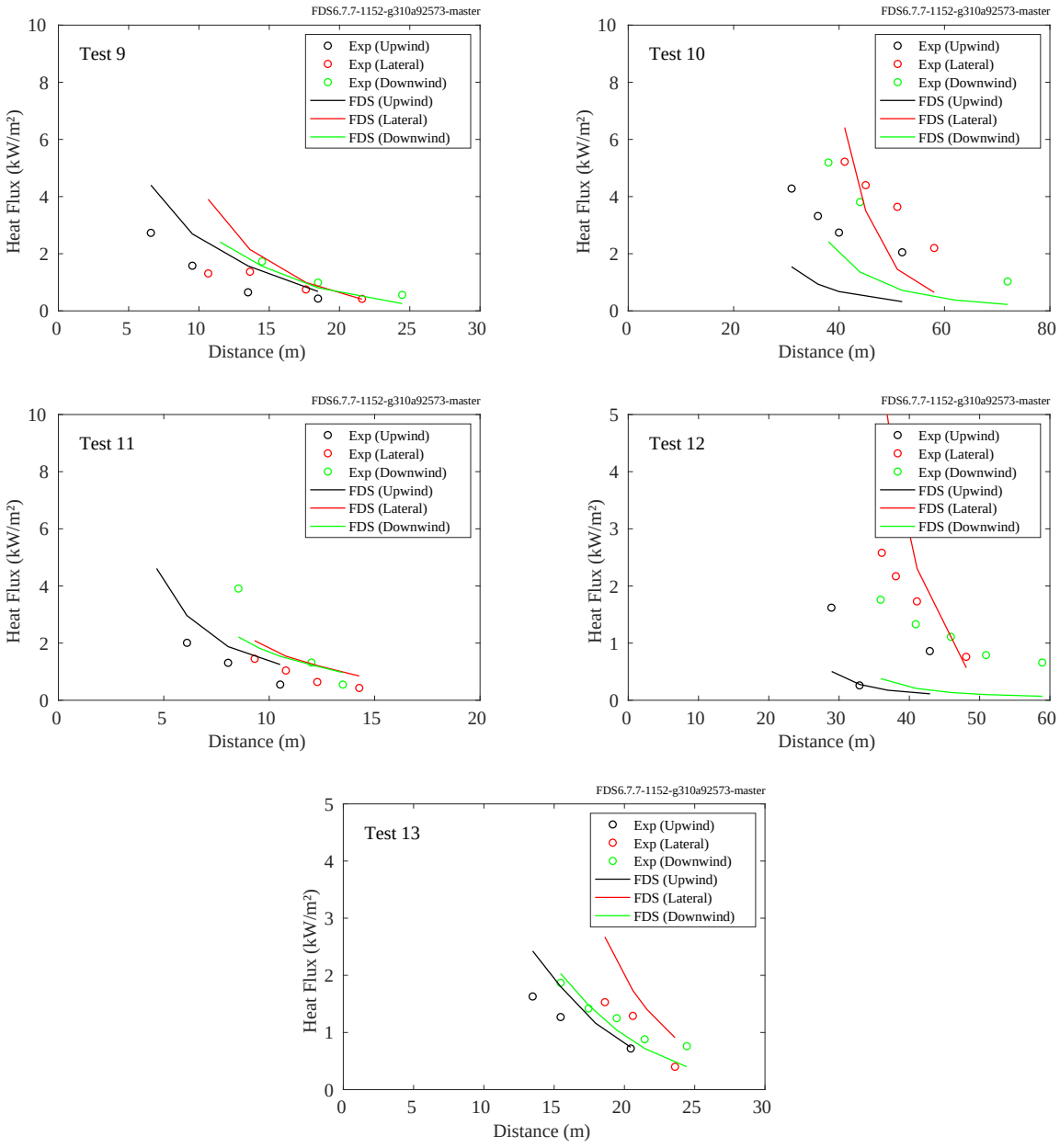

Figure 12.66: BGC/GRI LNG Fires, heat flux profiles for Tests 9-13.

12.2.4 Loughborough Jet Fire Experiments

A brief description of the experiments and modeling is found in Section 3.37.

The plots on the following pages present near-field and far-field heat flux measurements of natural gas jet fires. Figures 12.68 through 12.70 compare measured and predicted heat fluxes to a 0.9 m diameter, 16 m long pipe segment engulfed in the fire. The locations of the gauges are shown in Fig. 12.67.

Figure 12.71 presents the far-field radiometer predictions and measurements. Table 12.6 lists the radiometer coordinates relative to the center of the target pipe.

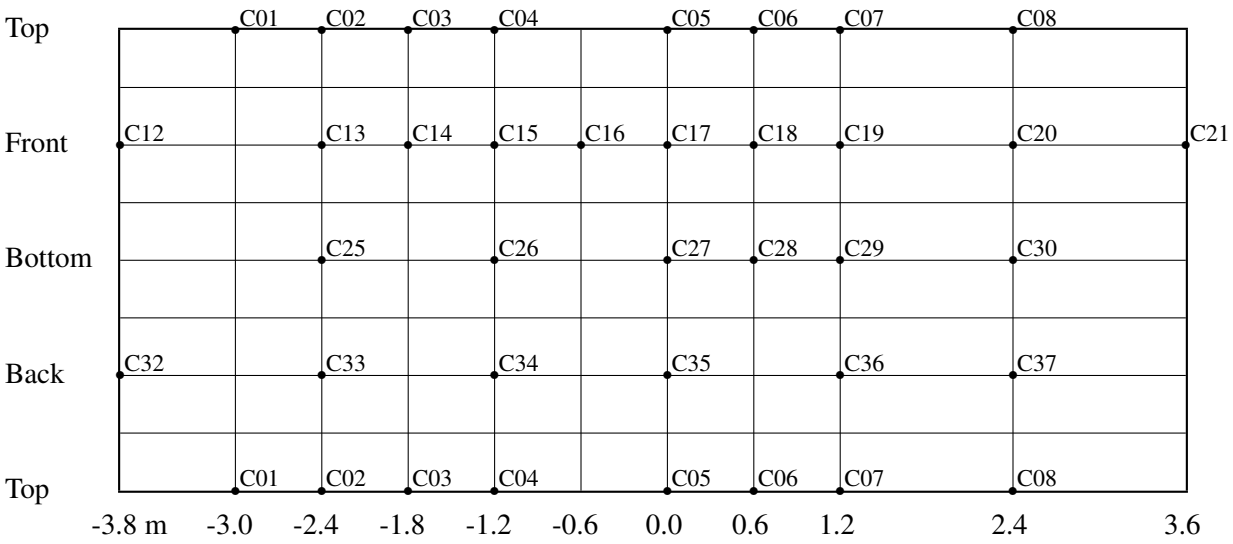

Figure 12.67: Location of the heat flux gauges mounted on the target pipe segment for the Loughborough Jet Fires. The pipe is oriented in the north-south direction, with the negative positions to the north. The "Front" of the pipe faces the jet.

Table 12.6: Radiometer positions (m) relative to the center of the target pipe, Loughborough Jet Fires.

Test No.	Rad 1 (N,W)	Rad 2 (N,W)	Rad 3 (N,W)	Rad 4 (S,W)	Rad 5 (S,W)	Rad 6 (S,W)	Rad 7 (S,W)	Rad 8 (S,W)	Rad 9 (S,W)
1	(20,5)	(15,0)	(15,5)	(15,0)	(15,5)	(20,0)	(20,5)	(25,0)	(30,0)
2	(30,0)	(20,0)	(20,5)	(15,0)	(20,0)	(20,5)	(30,0)	(30,5)	(40,0)
3	(35,0)	(25,0)	(25,5)	(20,0)	(25,0)	(25,5)	(35,0)	(35,5)	(52,0)

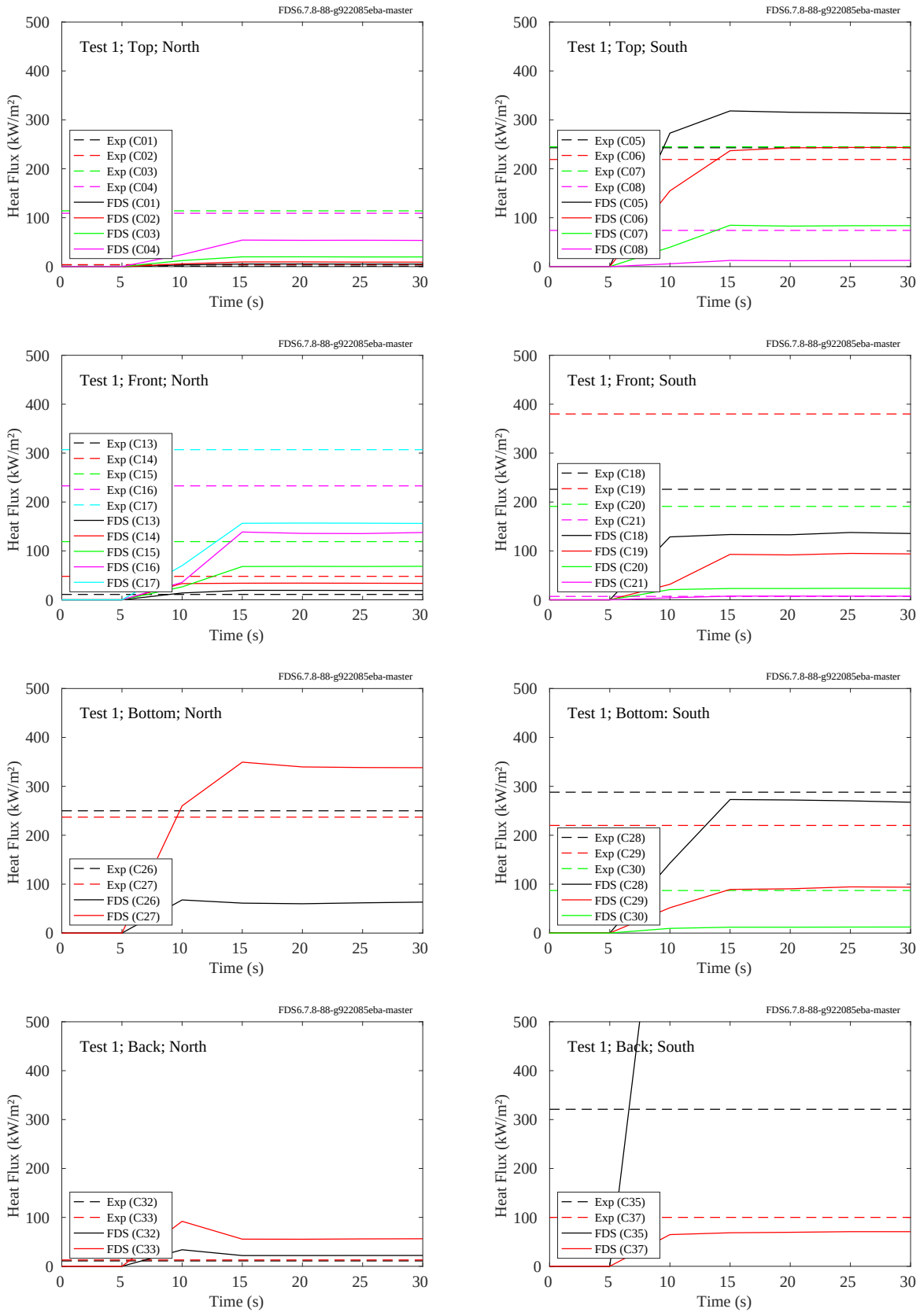

Figure 12.68: Loughborough Jet Fires, heat flux to pipe, Test 1.

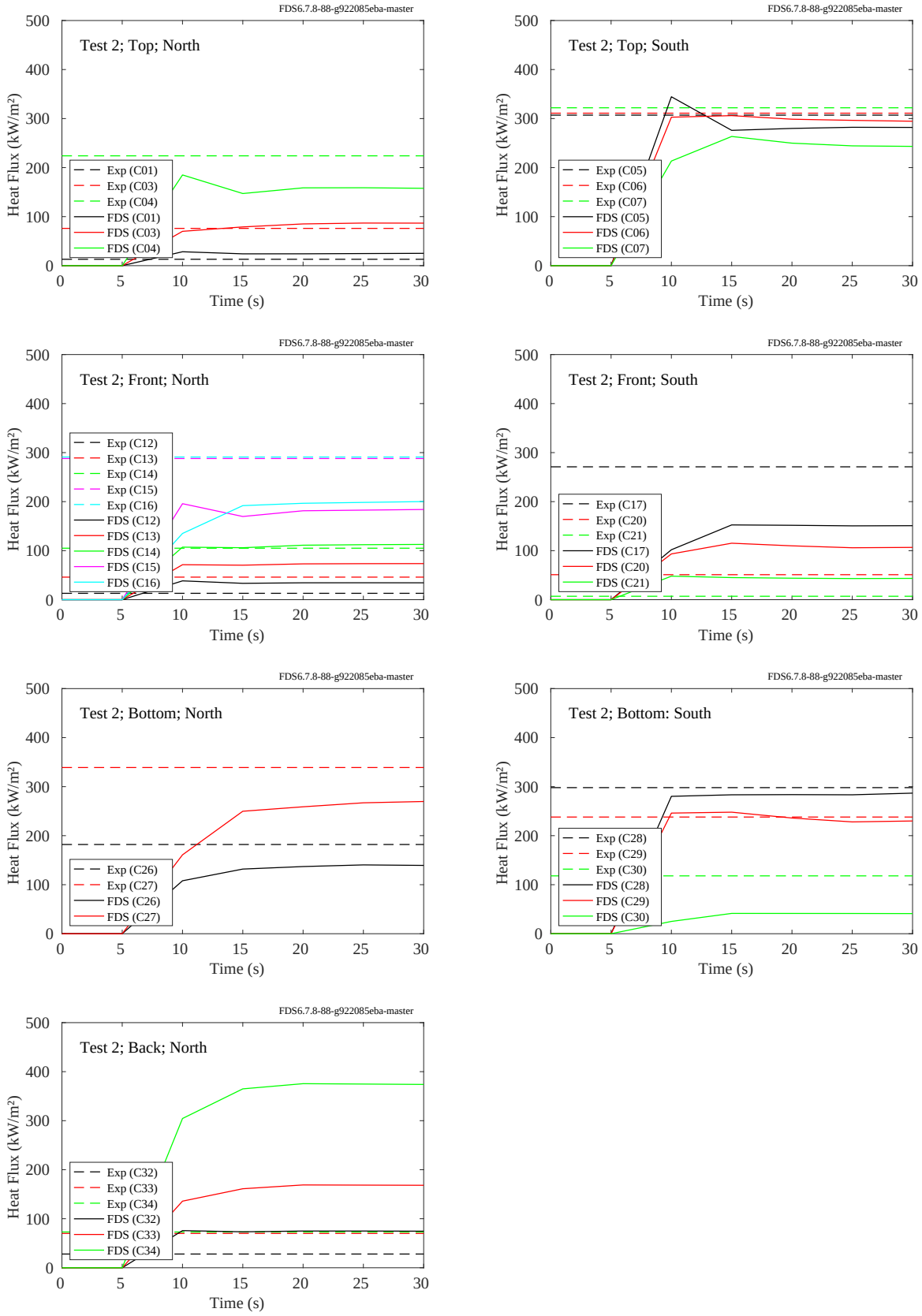

Figure 12.69: Loughborough Jet Fires, heat flux to pipe, Test 2.

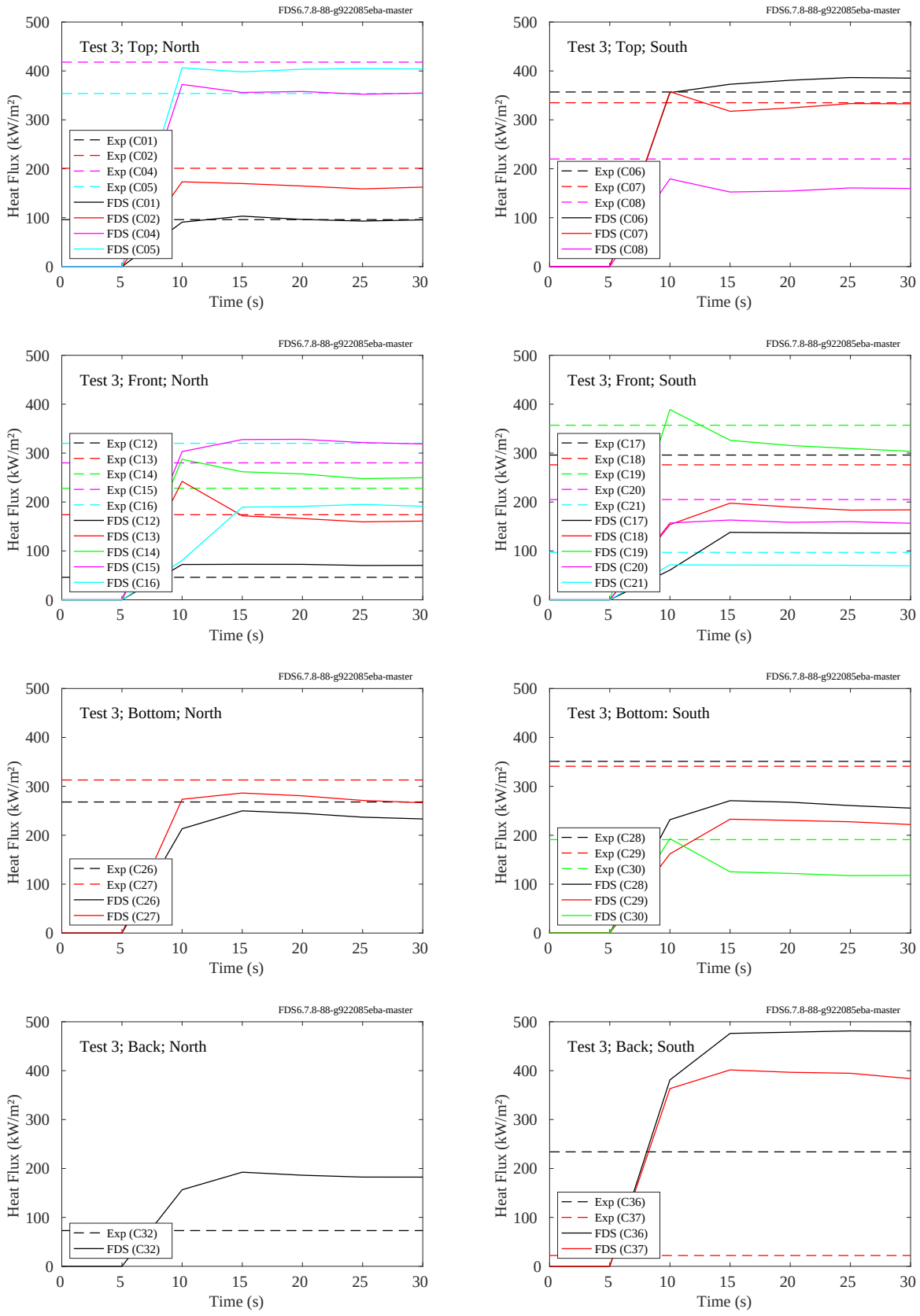

Figure 12.70: Loughborough Jet Fires, heat flux to pipe, Test 3.

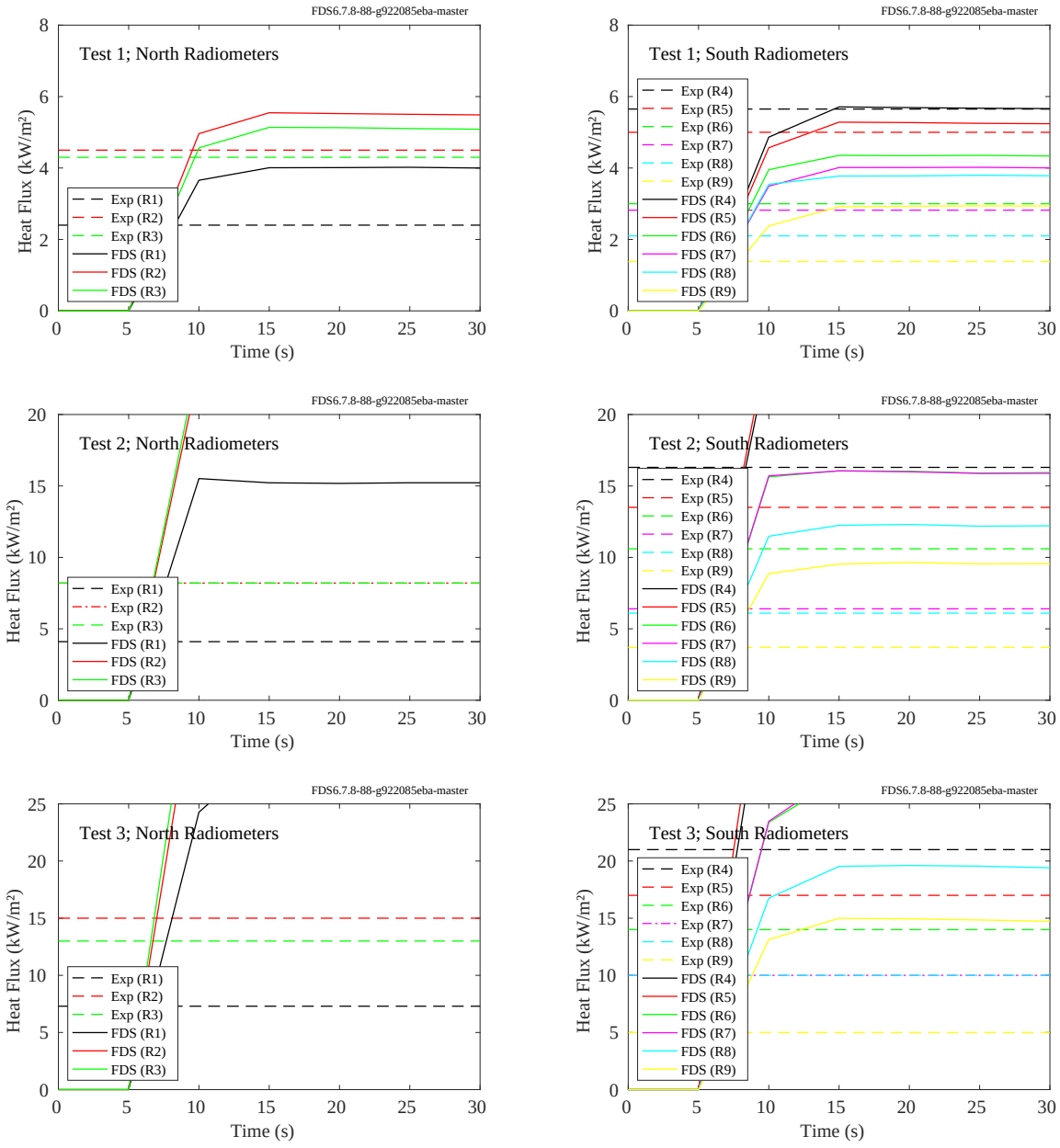

Figure 12.71: Loughborough Jet Fires, far-field radiometers.

12.2.5 Montoir LNG Fires

A brief description of these experiments can be found in Section 3.39. Figure 12.72 indicates the radial lines emanating outwards from the 35 m pool along which the radiometers were positioned. Figures 12.73 through 12.75 display the results of measured and predicted heat fluxes along the radial lines.

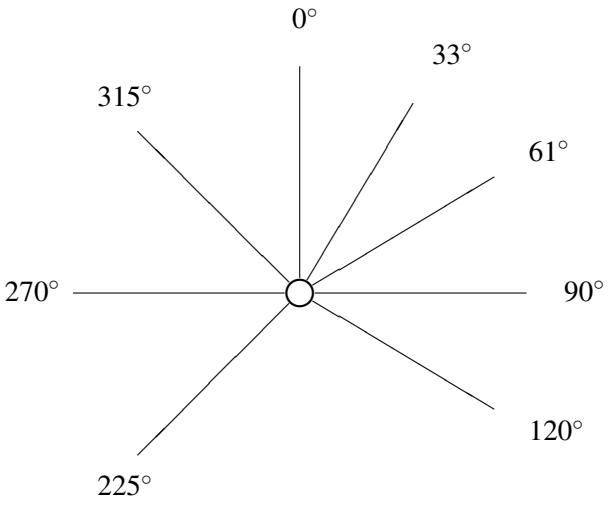

Figure 12.72: Layout of the Montoir LNG Fires.

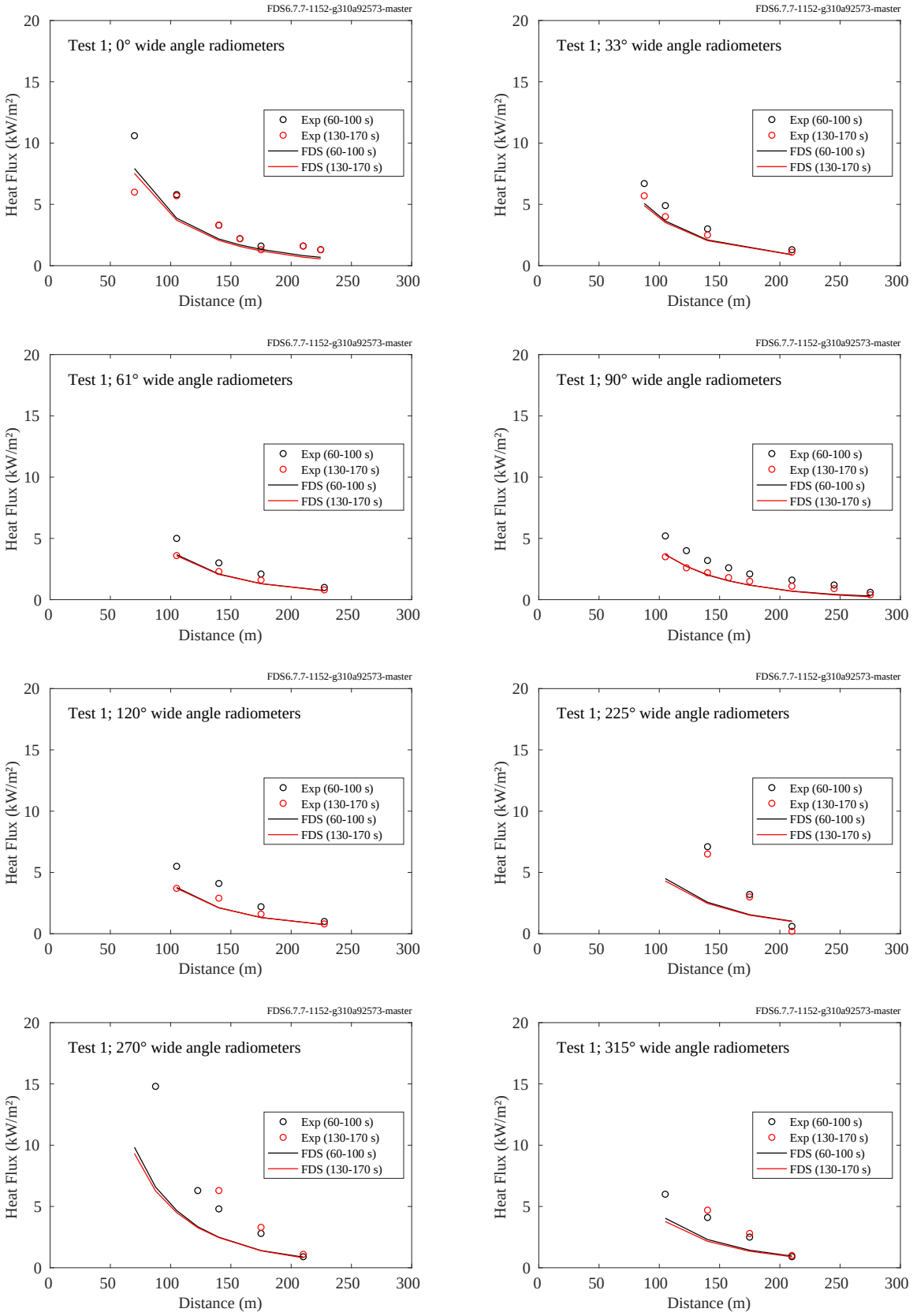

Figure 12.73: Montoir LNG Fires, far-field radiometers, Test 1.

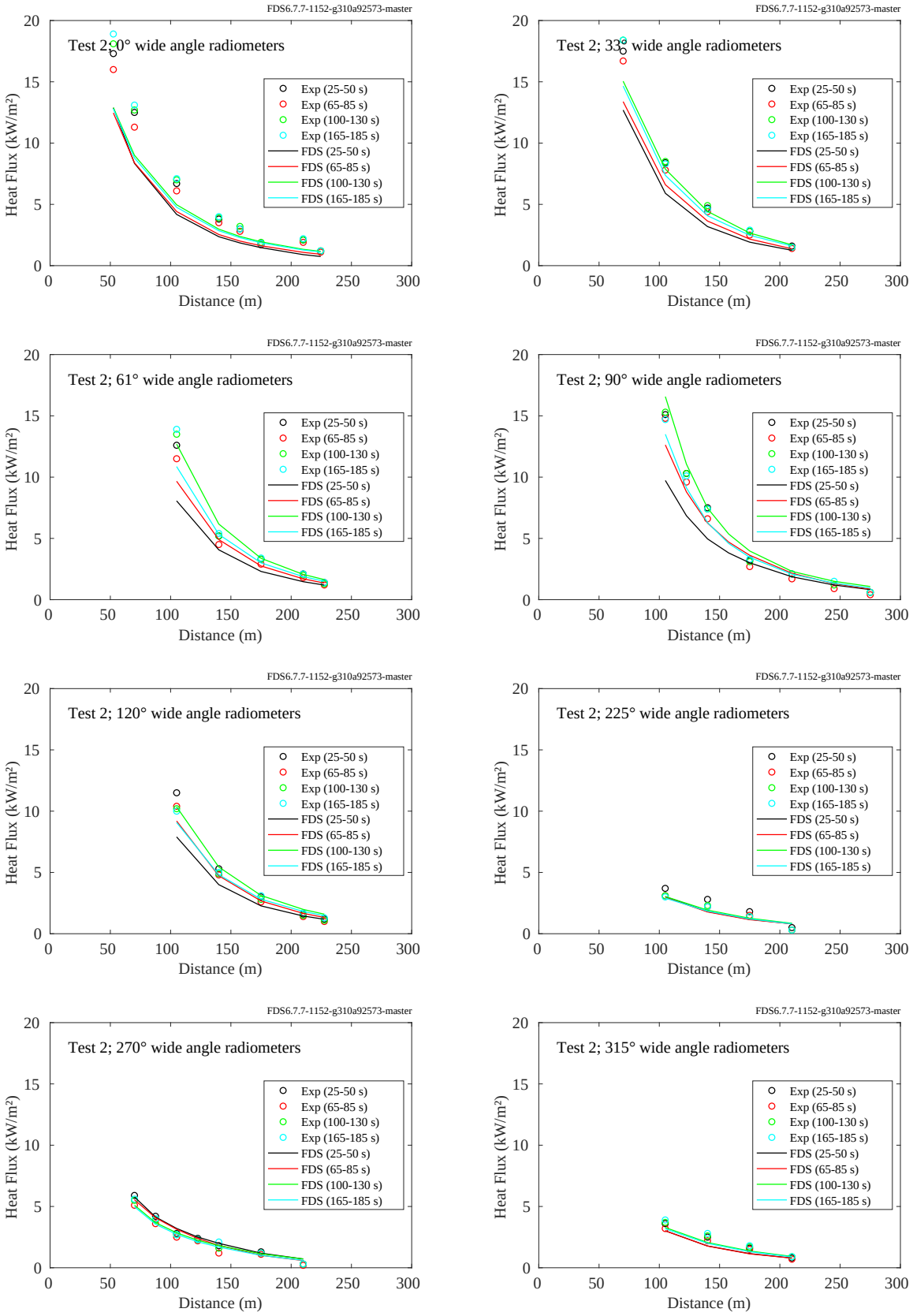

Figure 12.74: Montoir LNG Fires, far-field radiometers, Test 2.

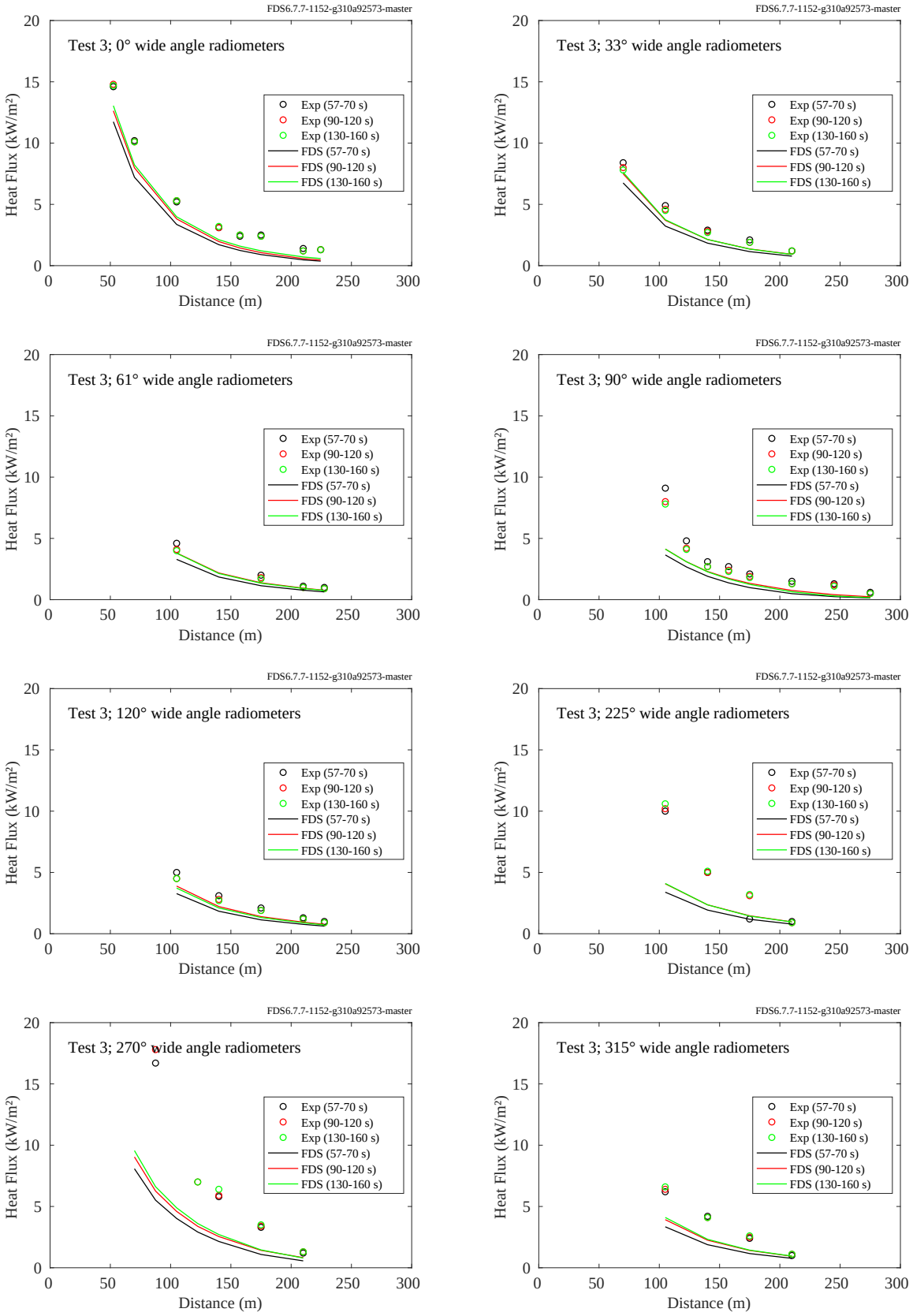

Figure 12.75: Montoir LNG Fires, far-field radiometers, Test 3.

12.2.6 NIST Douglas Firs

A description of the experiments and modeling assumptions are given in Section 3.43. Heat flux gauges were positioned on two vertical arrays, a distance of 2 m and 3 m from the burning trees. Average experimental values for test condition are shown below.

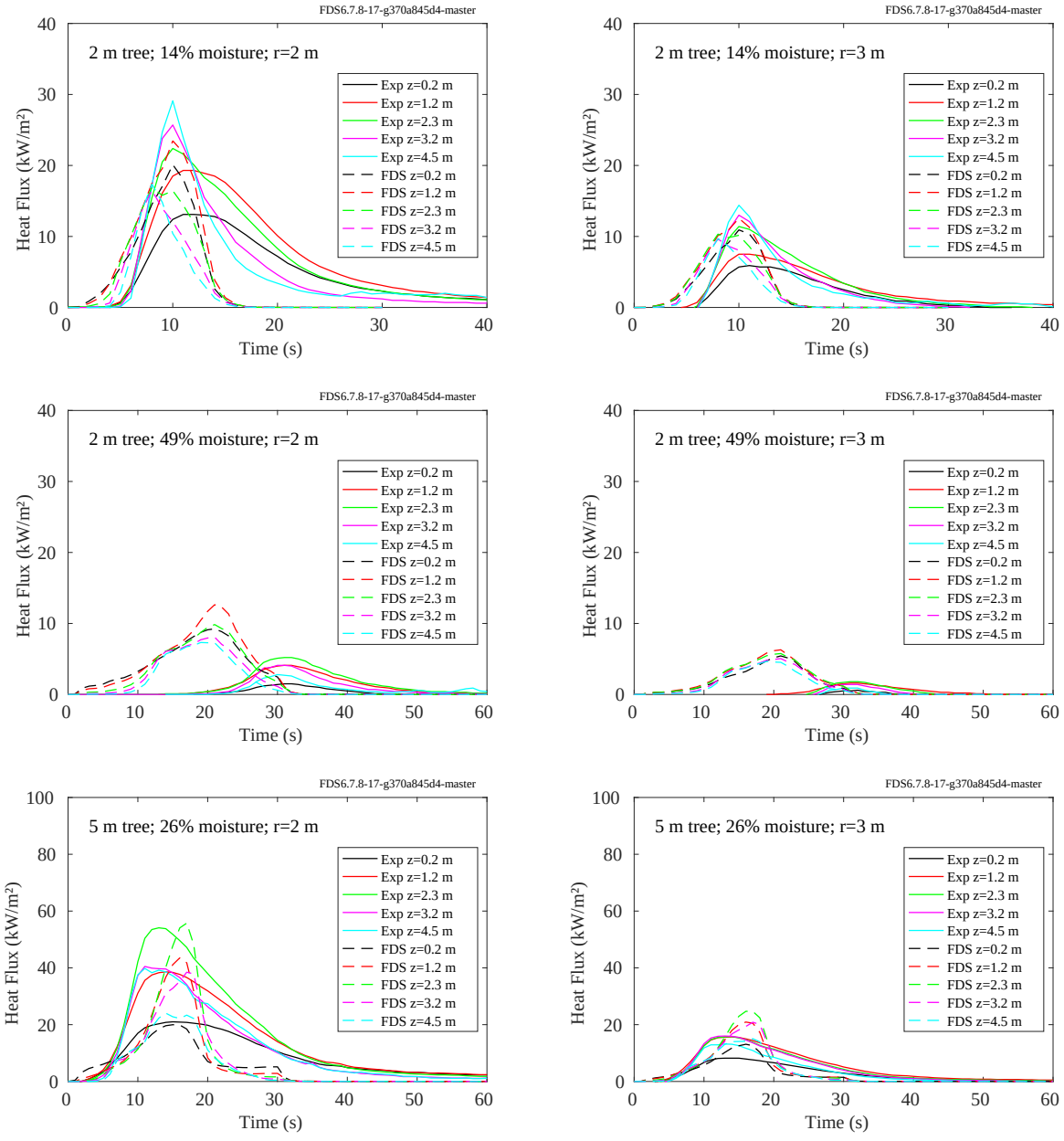

Figure 12.76: NIST Douglas Firs, heat flux at a distance of $x = 2$ m and $x = 3$ m

12.2.7 NIST/NRC Experiments

Cables of various types (power and control), and configurations (horizontal, vertical, in trays or free-hanging), were installed in the test compartment. For each of the four cable targets considered, measurements of the radiative and total heat flux were made with gauges positioned near the cables themselves. The following pages display comparisons of these heat flux predictions and measurements for Control Cable B, Horizontal Cable Tray D, Power Cable F and Vertical Cable Tray G.

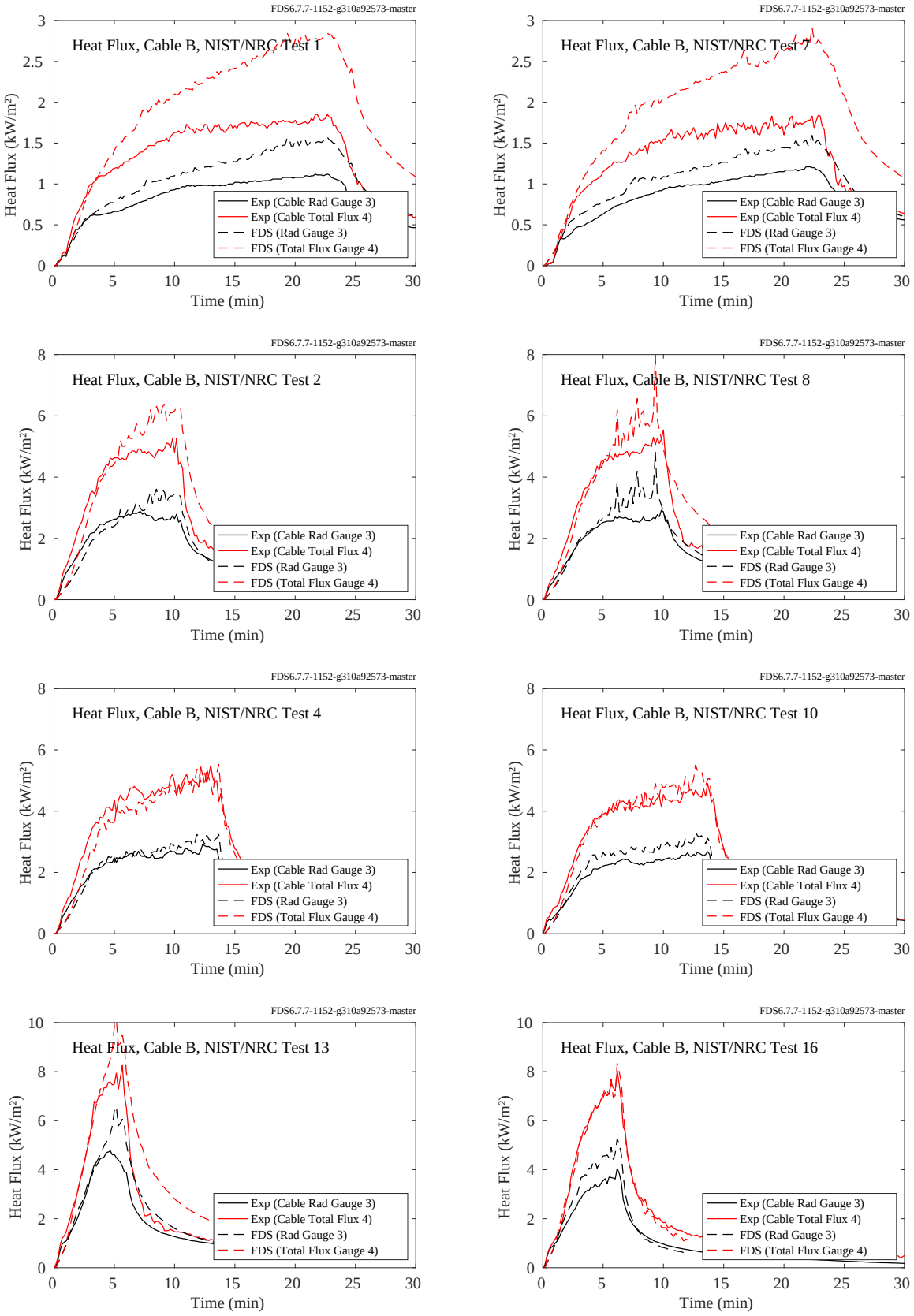

Figure 12.77: NIST/NRC experiments, heat flux to Cable B, Tests 1, 2, 4, 7, 8, 10, 13, 16.

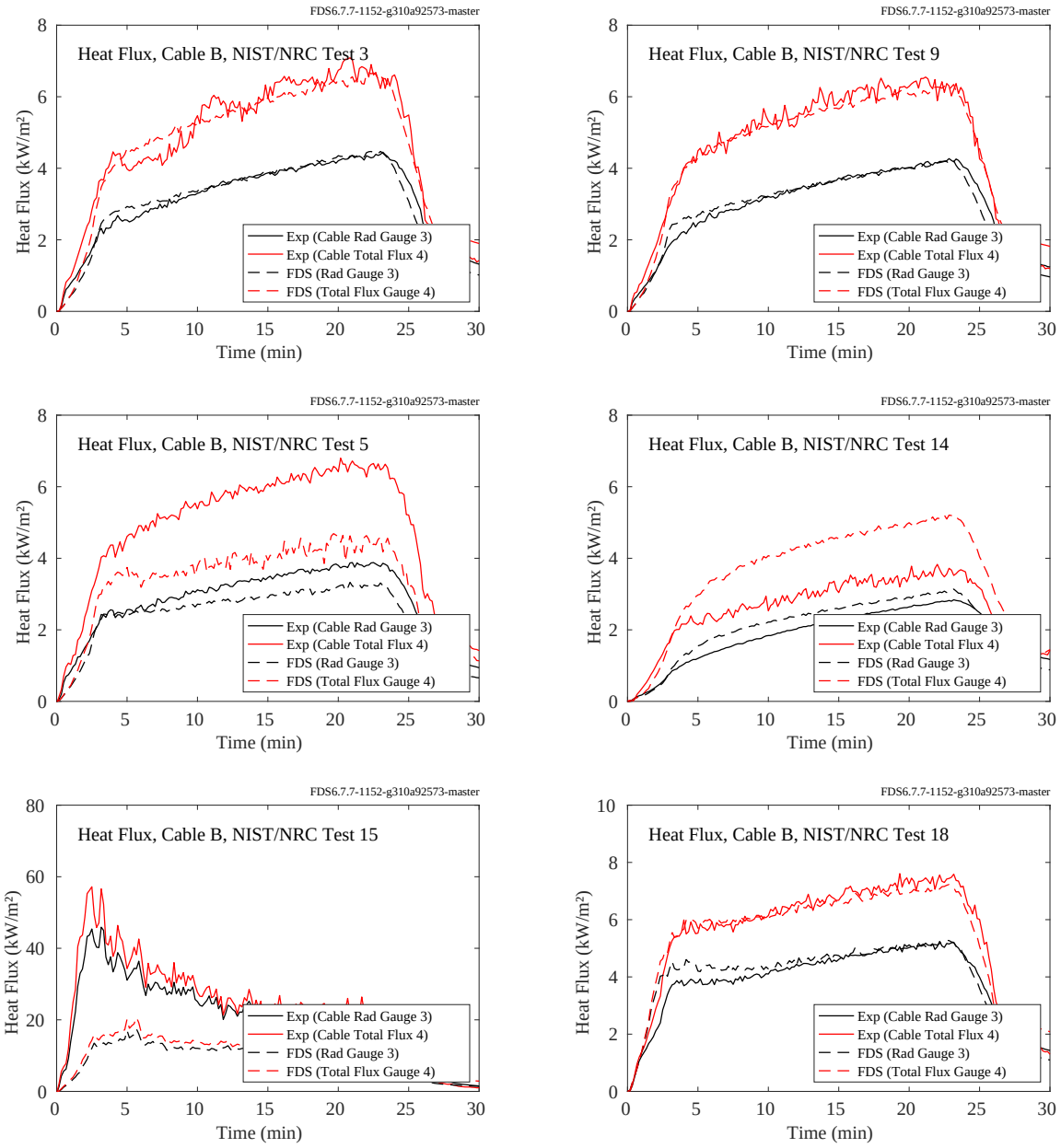

Figure 12.78: NIST/NRC experiments, heat flux to Cable B, Tests 3, 5, 9, 14, 15, 18.

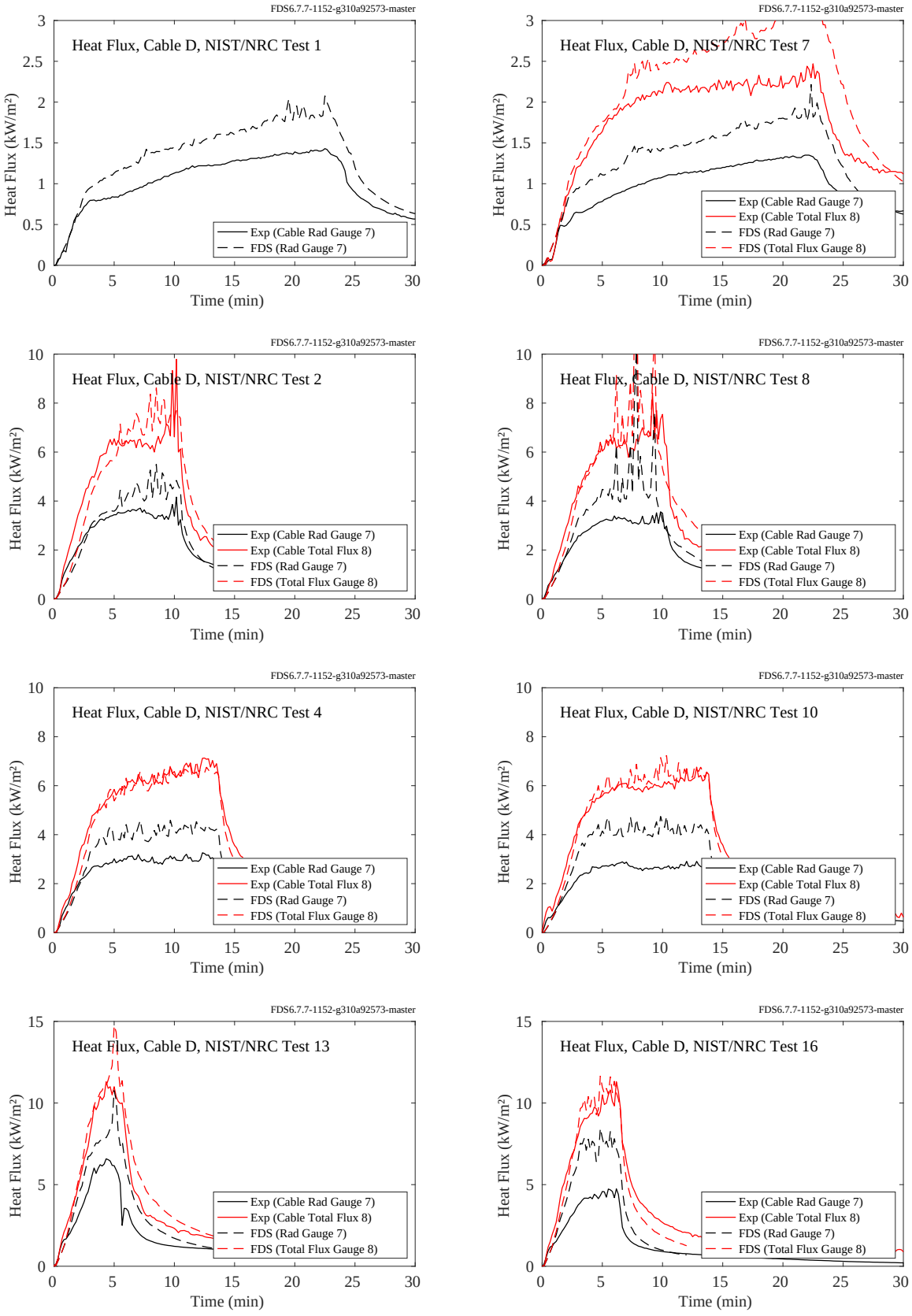

Figure 12.79: NIST/NRC experiments, heat flux to Cable D, Tests 1, 2, 4, 7, 8, 10, 13, 16.

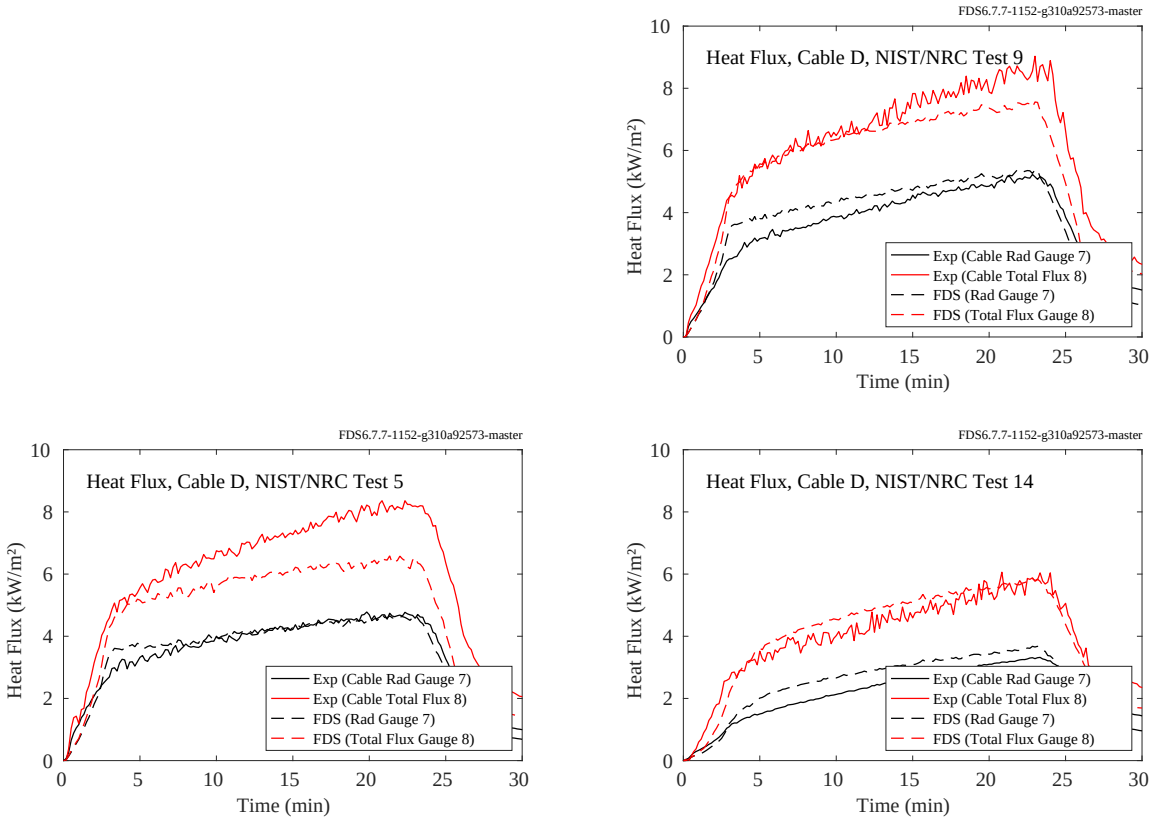

Figure 12.80: NIST/NRC experiments, heat flux to Cable D, Tests 5, 9, 14.

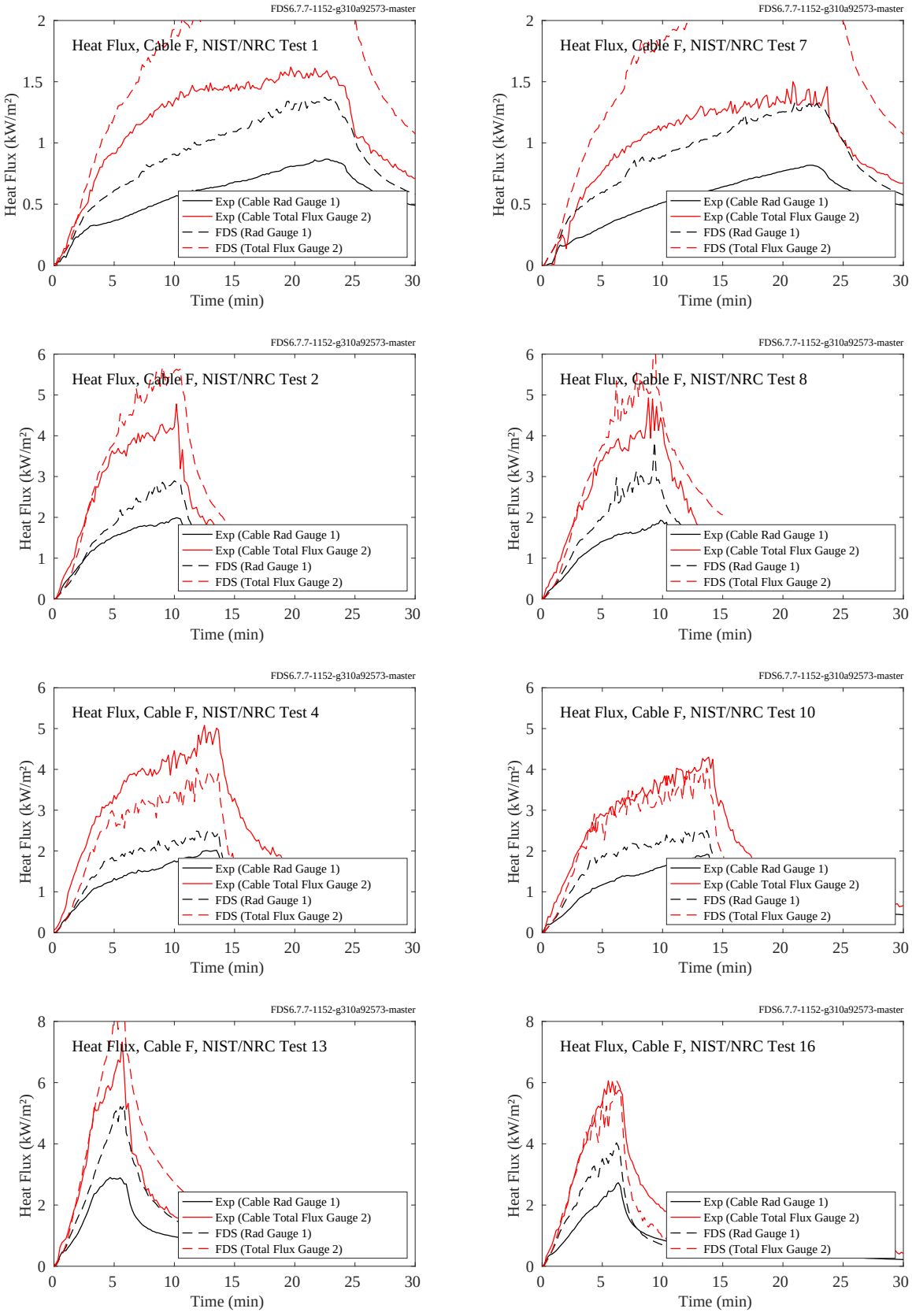

Figure 12.81: NIST/NRC experiments, heat flux to Cable F, Tests 1, 2, 4, 7, 8, 10, 13, 16.

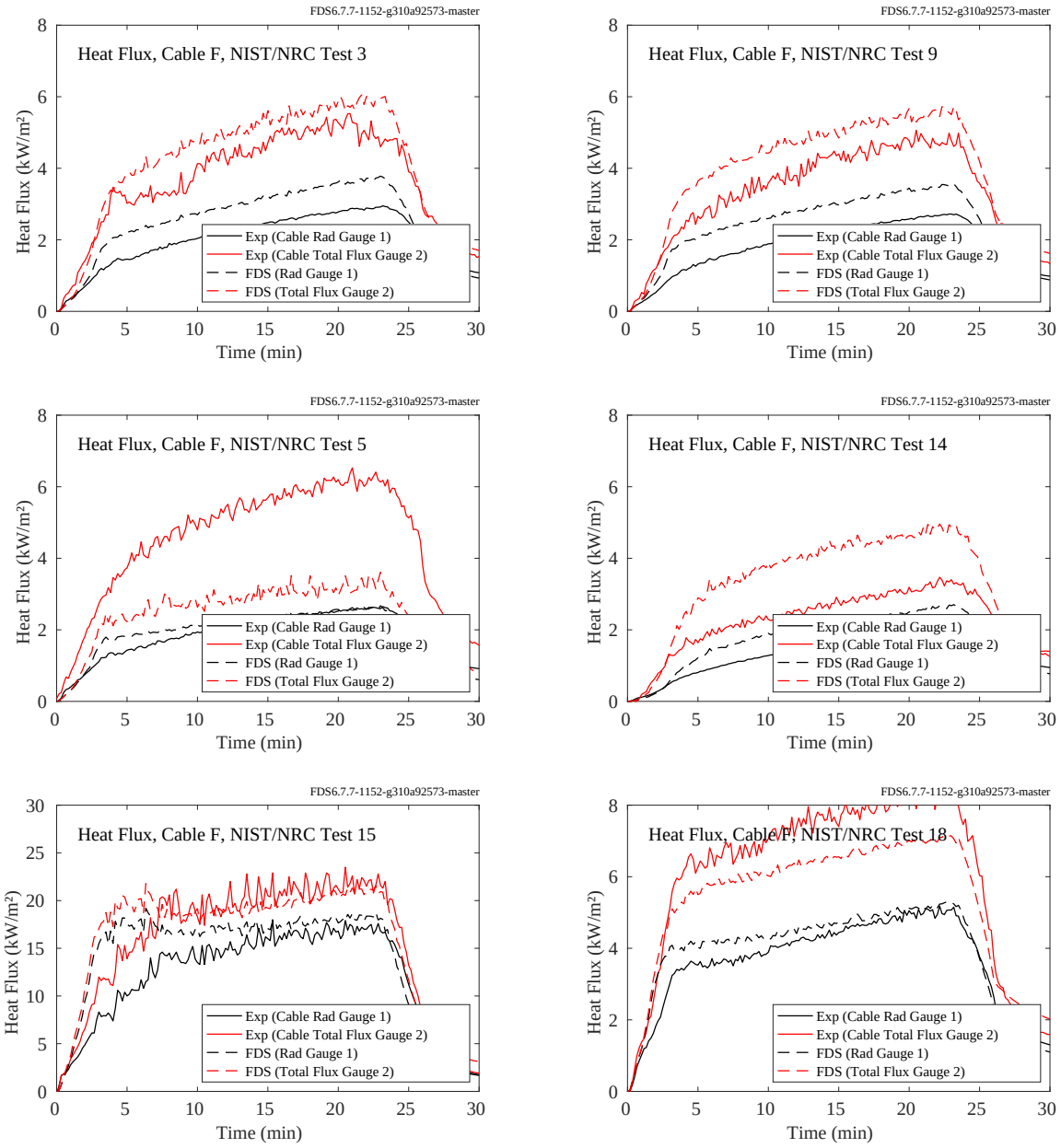

Figure 12.82: NIST/NRC experiments, heat flux to Cable F, Tests 3, 5, 9, 14, 15, 18.

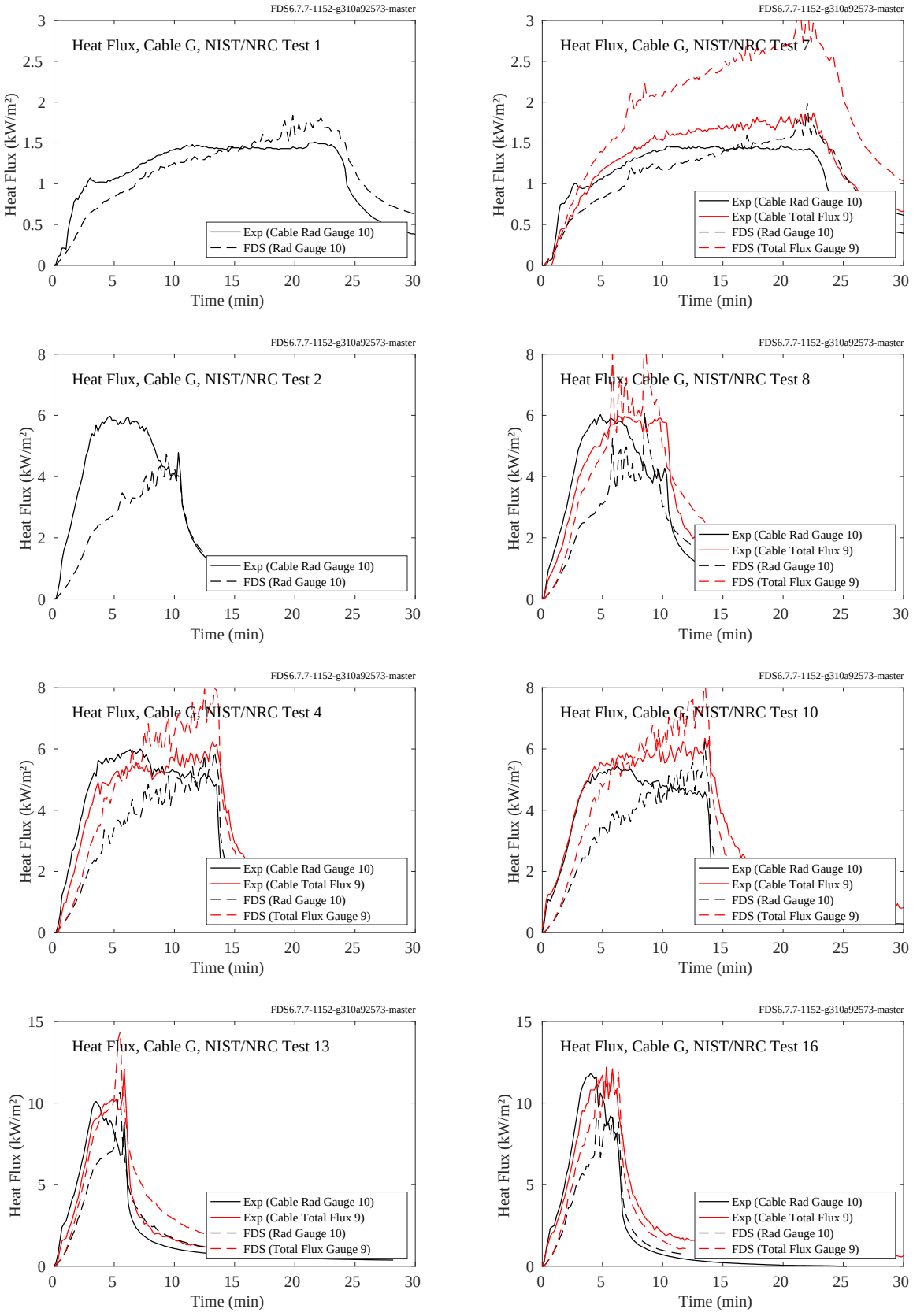

Figure 12.83: NIST/NRC experiments, heat flux to Cable G, Tests 1, 2, 4, 7, 8, 10, 13, 16.

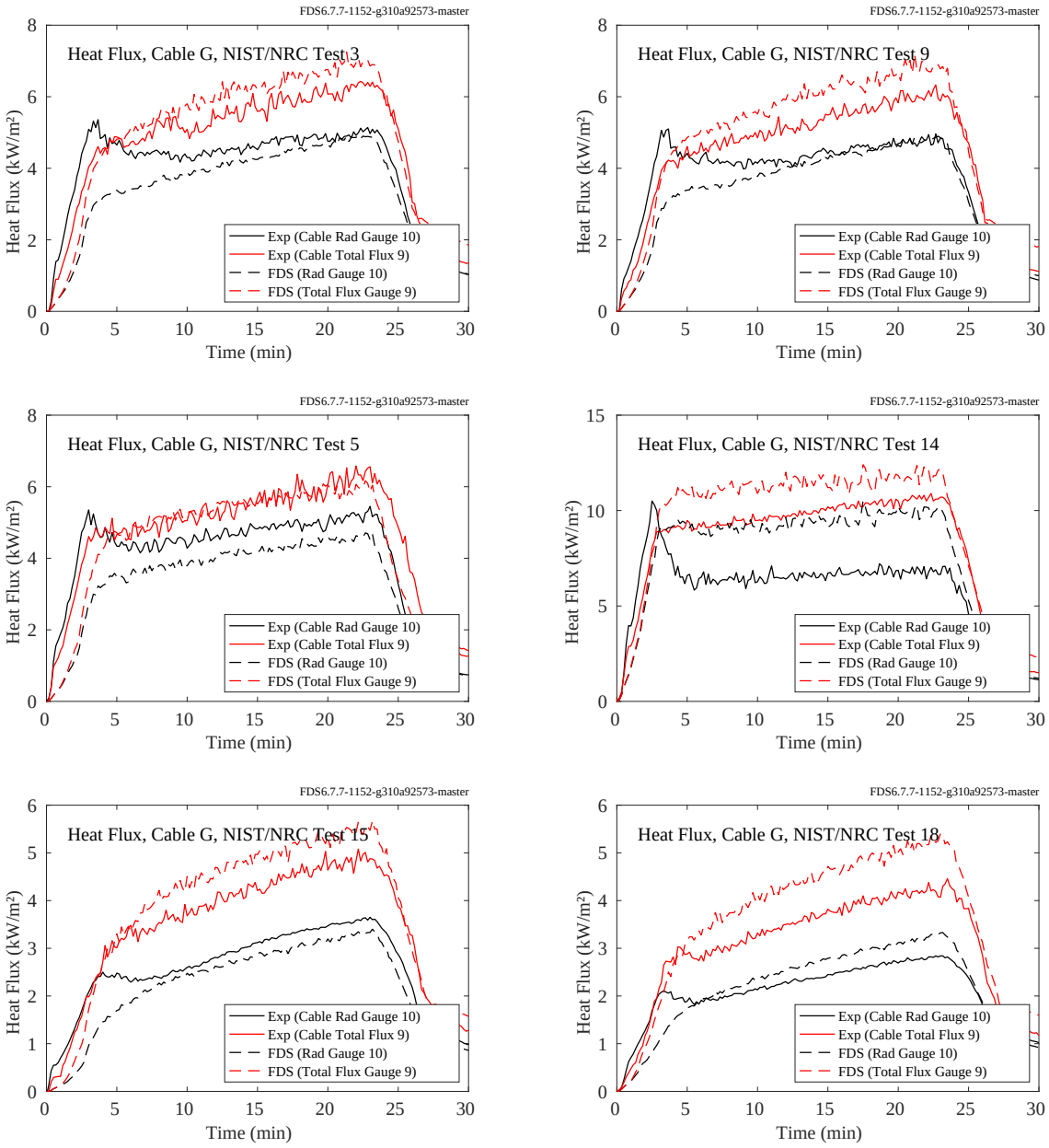

Figure 12.84: NIST/NRC experiments, heat flux to Cable G, Tests 3, 5, 9, 14, 15, 18.

12.2.8 NIST Pool Fires

A description of the NIST Pool Fire experiments and modeling is given in Section 3.51. On the following pages are comparisons of heat flux measurements and predictions at various locations and orientations.

- Figure 12.85 displays downward radiative and total heat flux near the liquid pool surface of a 30 cm methanol fire. The radiative heat flux measurements were made by Hamins et al. [311] and the *total* heat flux measurements were made by Kim et al. [342].
- Figure 12.86 displays radial and vertical profiles of *total* heat flux for a 30 cm methanol fire extending beyond the outer rim of the pan [342]. The vertical profile was made at $r = 60$ cm. Additional radial measurements were made by Klassen et al. [343].
- Figure 12.87 displays a radial profile of the total heat flux in the downward direction for a 100 cm pan methanl fire. The radial distance ranges from the burner edge ($r = 50$ cm) to $r = 200$ cm. The positions of the heat flux gauges were located $z = 1$ cm above the fuel surface and oriented in the upward direction [330].
- Figure 12.88 displays radial profiles of the total heat flux emitted radially away from the fire at heights of $z = 41$ cm, $z = 61$ cm, and $z = 81$ cm above the fuel surface. The heat flux guages were oriented in the horizontal direction towards the fire centerline [330].

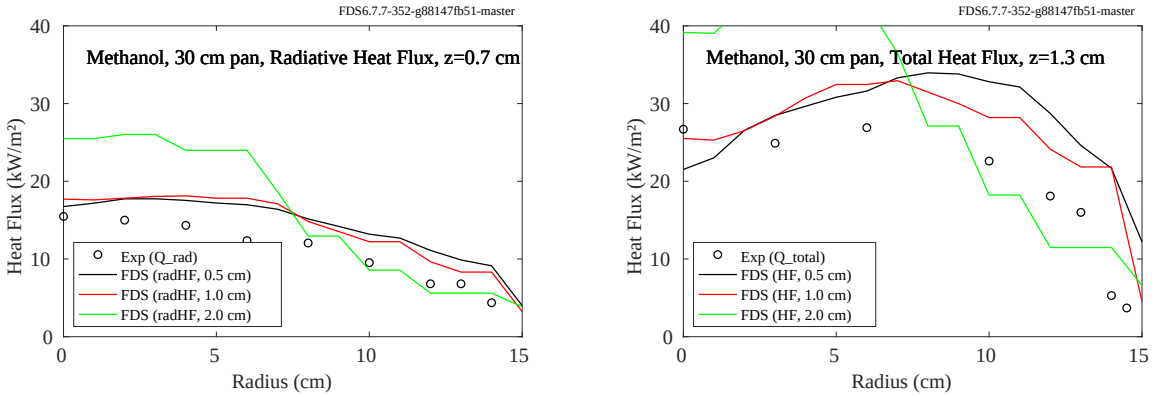

Figure 12.85: NIST Pool Fires, 30 cm methanol fire, radial profiles of downward radiative and total heat flux, respectively, at $z = 0.7$ cm (left) and $z = 1.3$ cm (right).

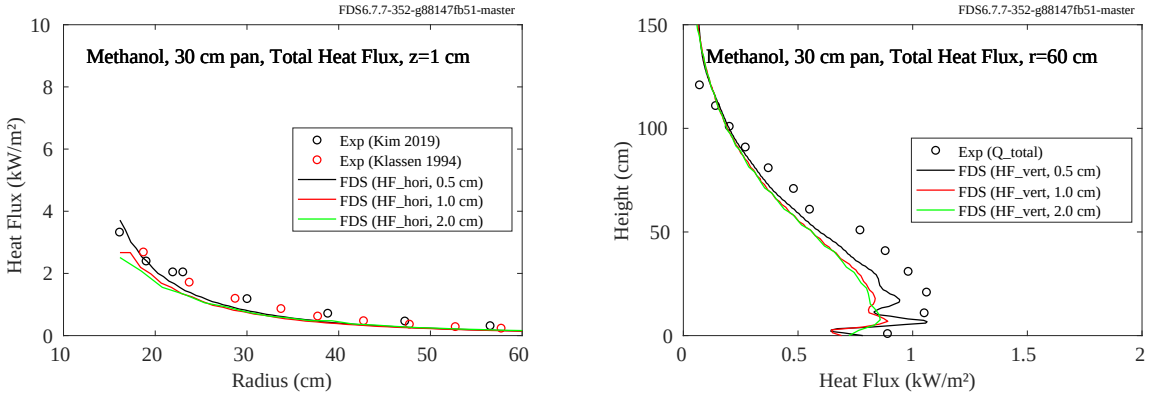

Figure 12.86: NIST Pool Fires, 30 cm methanol fire, radial and vertical profiles of total heat flux from a 30 cm methanol fire.

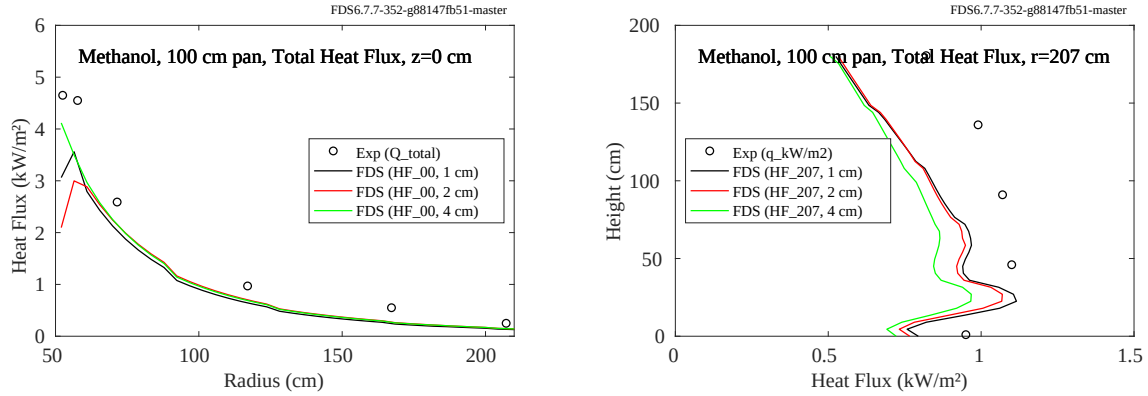

Figure 12.87: NIST Pool Fires, 100 cm methanol fire, total heat flux downward at $z = 0$ cm (left) and outward at $r = 207$ cm (right).

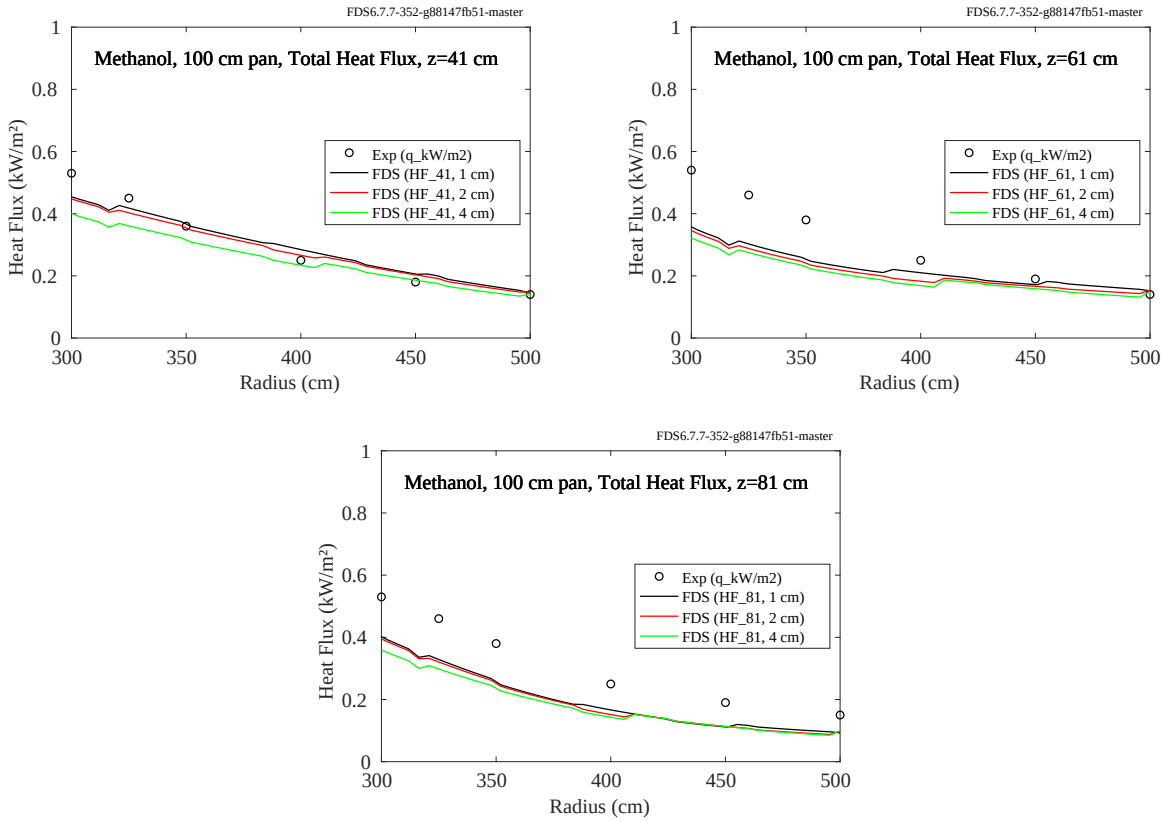

Figure 12.88: NIST Pool Fires, 100 cm methanol fire, total heat flux outward at $z = 41$ cm, $z = 61$ cm, and $z = 61$ cm.

12.2.9 Phoenix LNG Fires

A description of the two LNG pool fire experiments is given in Section 3.58.

The general layout of the facility is shown in Fig. 12.89. Wide-angle and narrow-angle radiometers were positioned at various heights off the ground and at various inclination angles along the axes shown in the figure.

Figure 12.90 compares predicted and measured heat fluxes for the wide-angle radiometers as a function of distance from the LNG pool fires. These radiometers were positioned along all four directional axes. Figure 12.91 compares predicted and measured heat flux for the narrow-angle radiometers along the north and south axes. There were three measurement towers along each axis. The nearest tower contained five narrow-angle radiometers at various inclination angles. The further two towers contained one narrow-angle radiometer each, along with one wide-angle radiometer. The vertical axes of the plots in Fig. 12.90 represent the "spot height" of the radiometers; that is, the height of the fire plume at which the radiometers were aimed. The "spot diameter" of the various radiometers ranged from 5 m to 15 m.

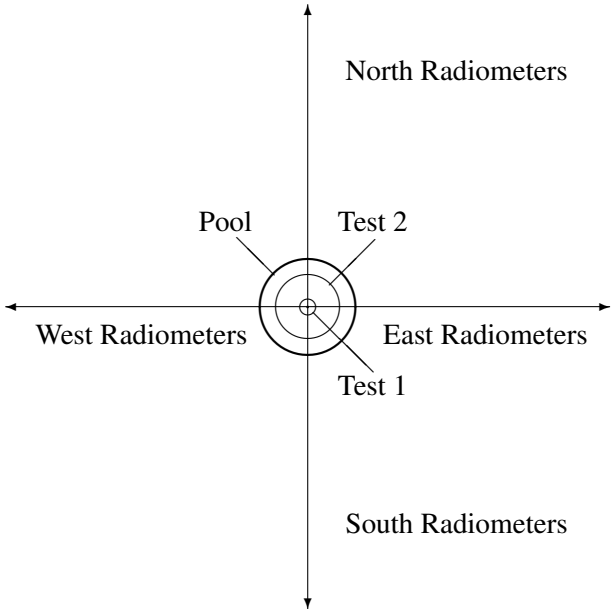

Figure 12.89: Layout of the Phoenix LNG Fires.

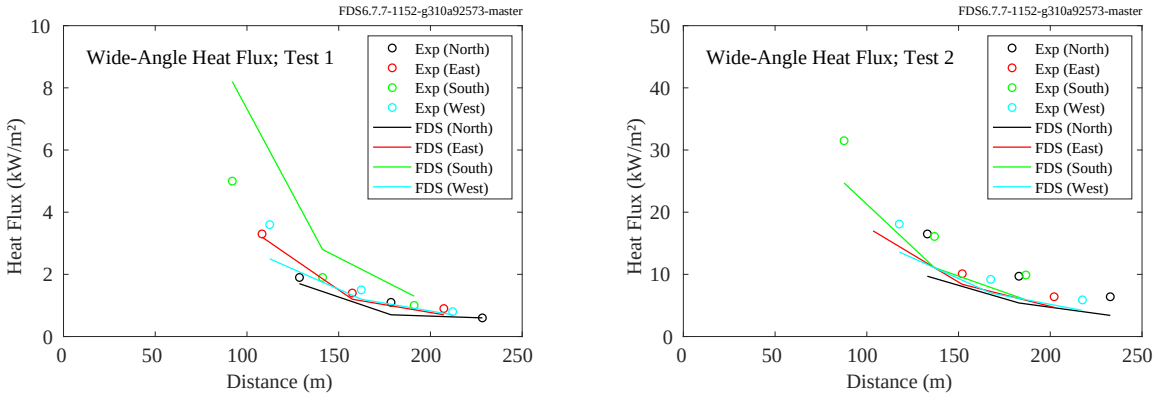

Figure 12.90: Phoenix LNG Fires, radial profiles of wide-angle heat flux.

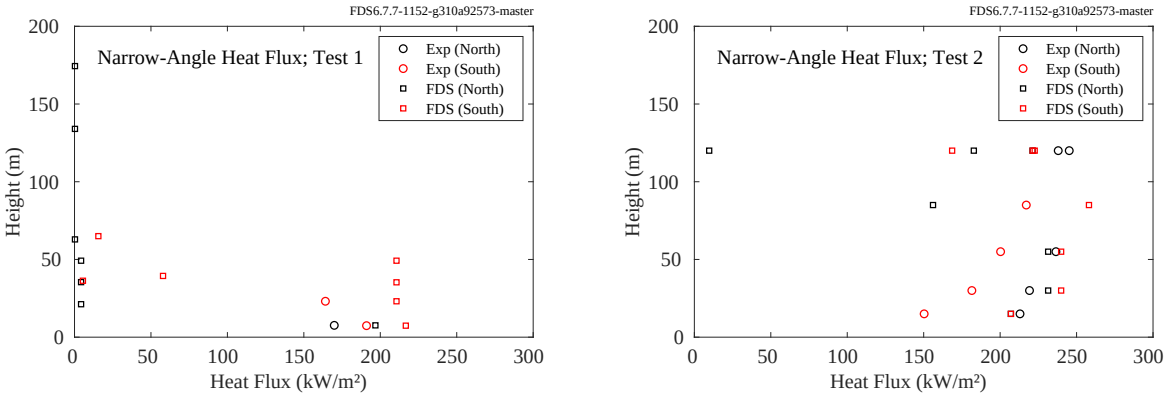

Figure 12.91: Phoenix LNG Fires, vertical profiles of narrow-angle heat flux.

12.2.10 Sandia Methane Burner Experiments

A brief summary of these experiments and the modeling strategy is found in Section 3.64.

On the following pages are comparisons of vertical profiles of the measured and predicted heat flux approximately 9 m from the centerline of a 3 m diameter methane burner of various heat release rates. There were two types of gauges used in the experiments—a conventional wide-angle heat flux gauge and a narrow-angle radiometer designed to measure the surface emissive power (SEP) of the fire. The narrow-angle radiometer had a view angle of 5° which was focused on a circular patch of flame of diameter approximately 0.8 m. This narrow-angle heat flux is modeled in FDS as the radiance (kW/m^2/sr) of a single ray multiplied by π sr. The unit sphere is discretized into approximately 600 solid angles, and the angle closest to the radiometer direction vector is used.

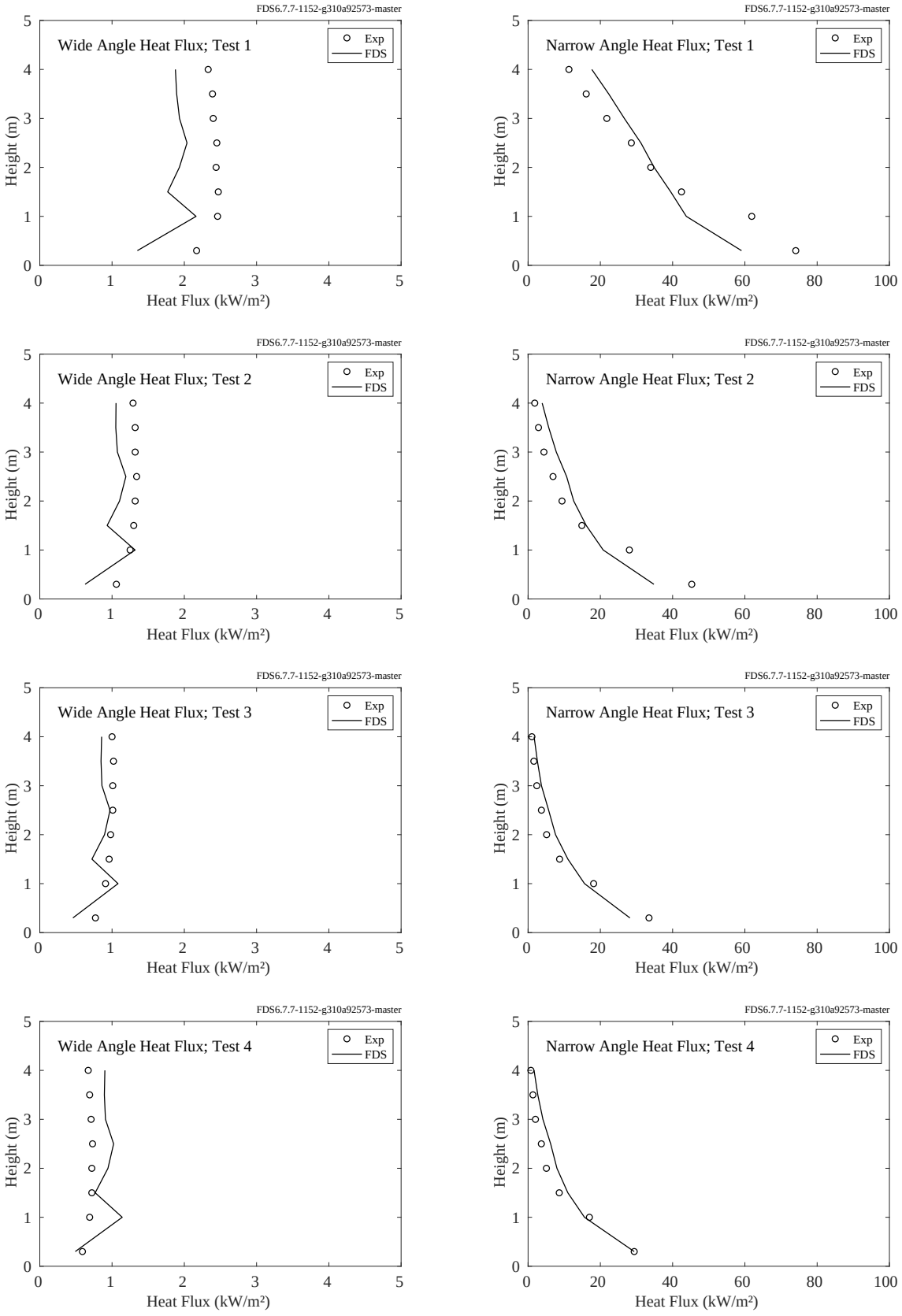

Figure 12.92: Sandia Methane Burner, heat flux, Tests 1-4.

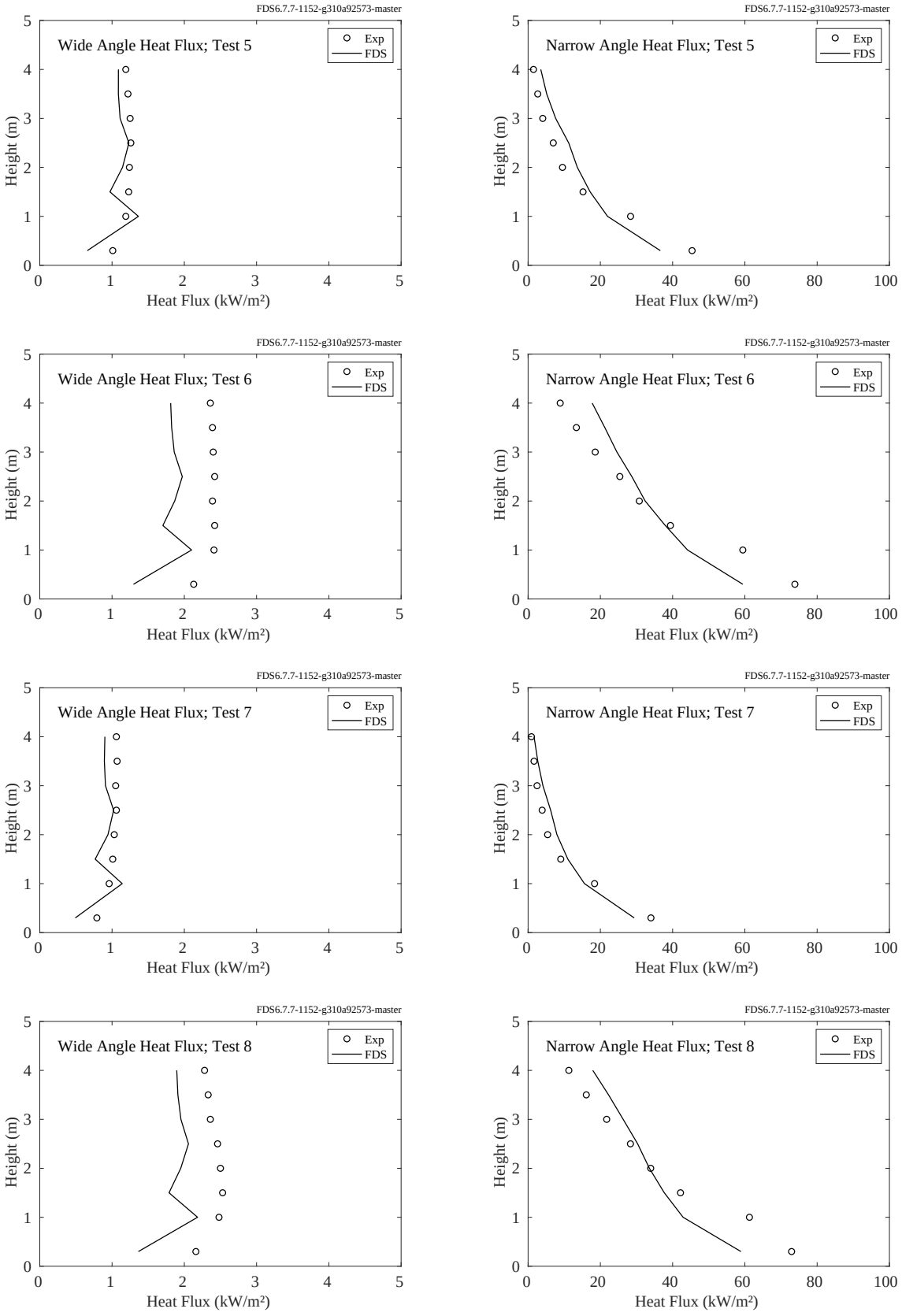

Figure 12.93: Sandia Methane Burner, heat flux, Tests 5-8.

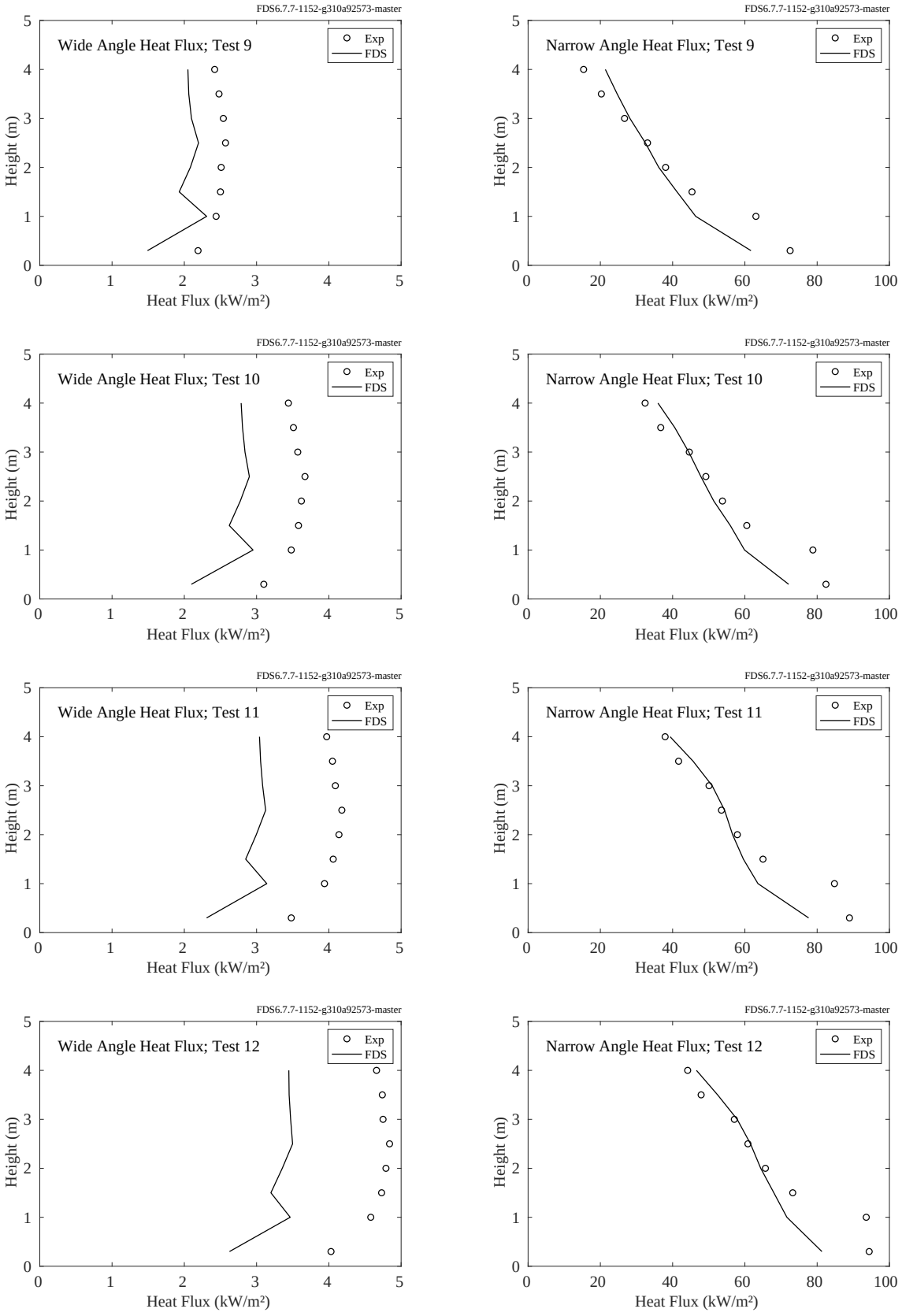

Figure 12.94: Sandia Methane Burner, heat flux, Tests 9-12.

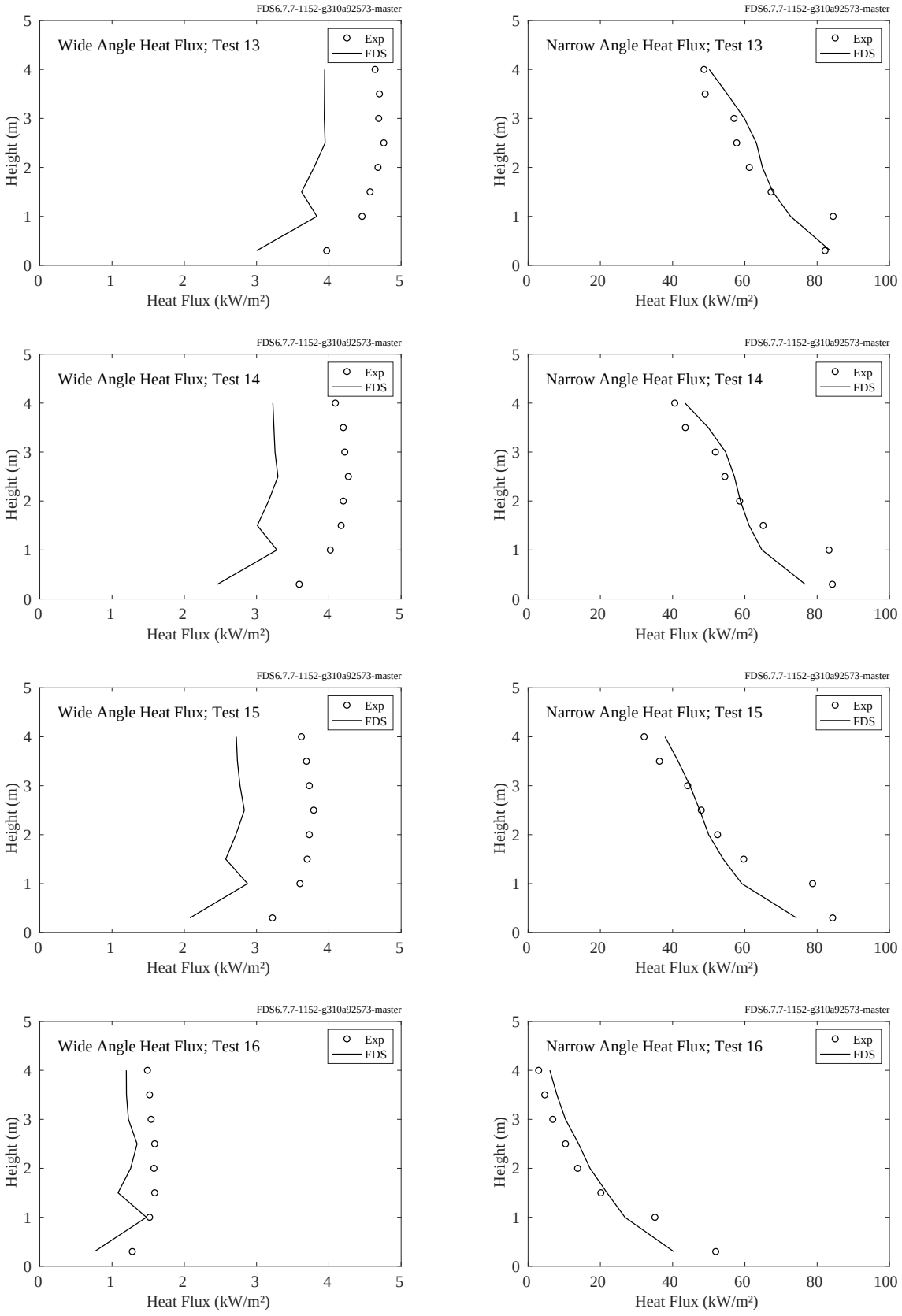

Figure 12.95: Sandia Methane Burner, heat flux, Tests 13-16.

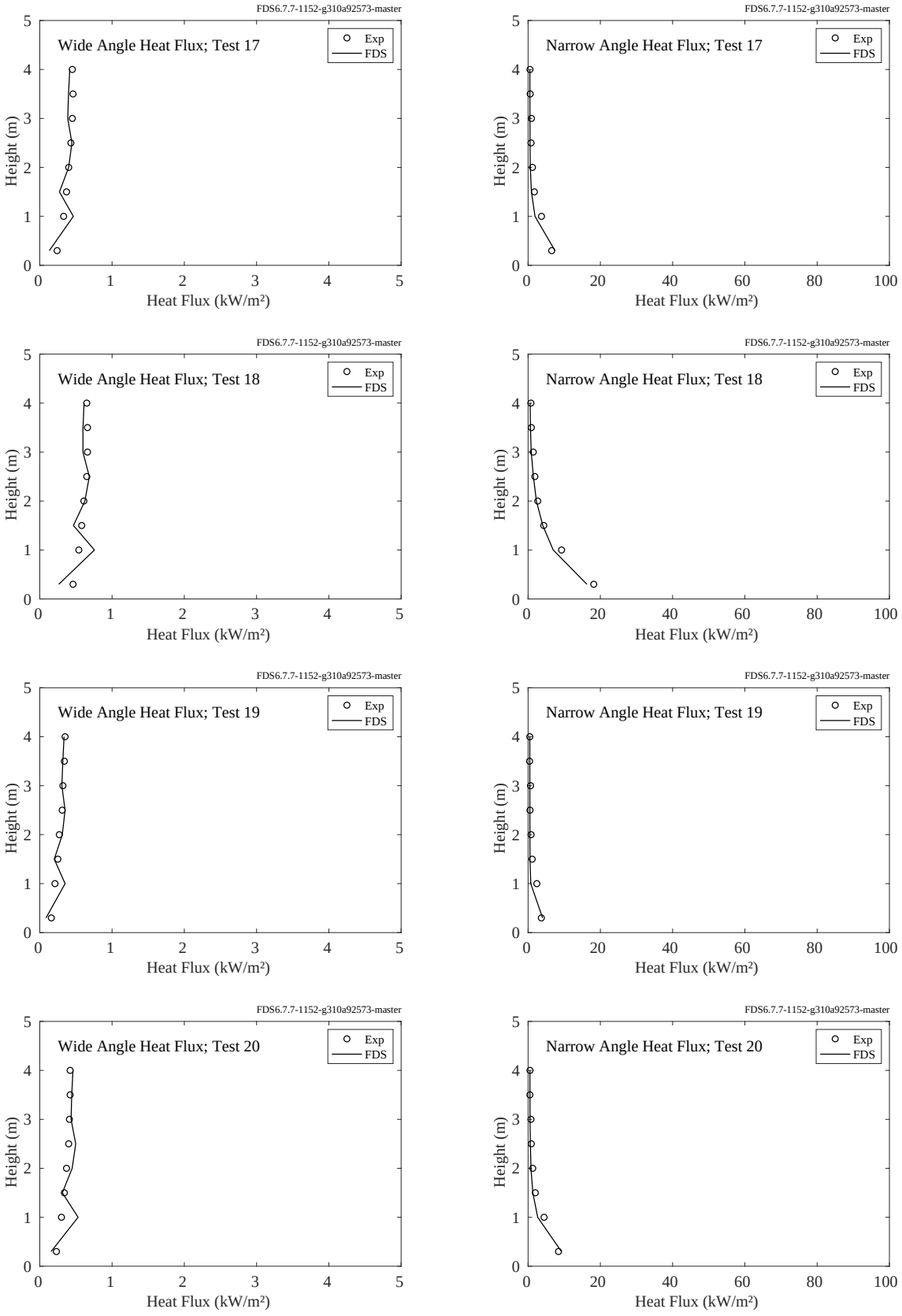

Figure 12.96: Sandia Methane Burner, heat flux, Tests 17-20.

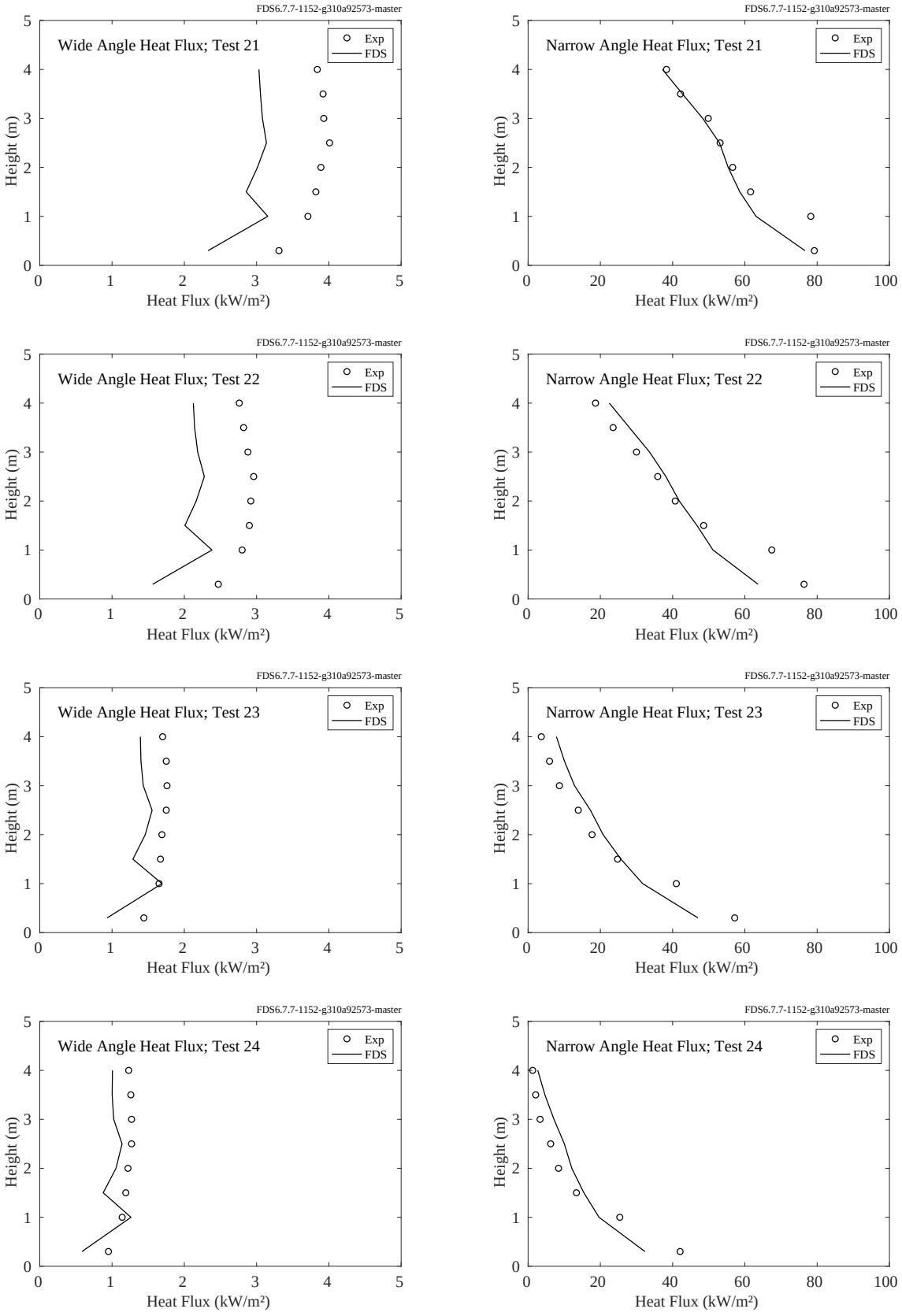

Figure 12.97: Sandia Methane Burner, heat flux, Tests 21-24.

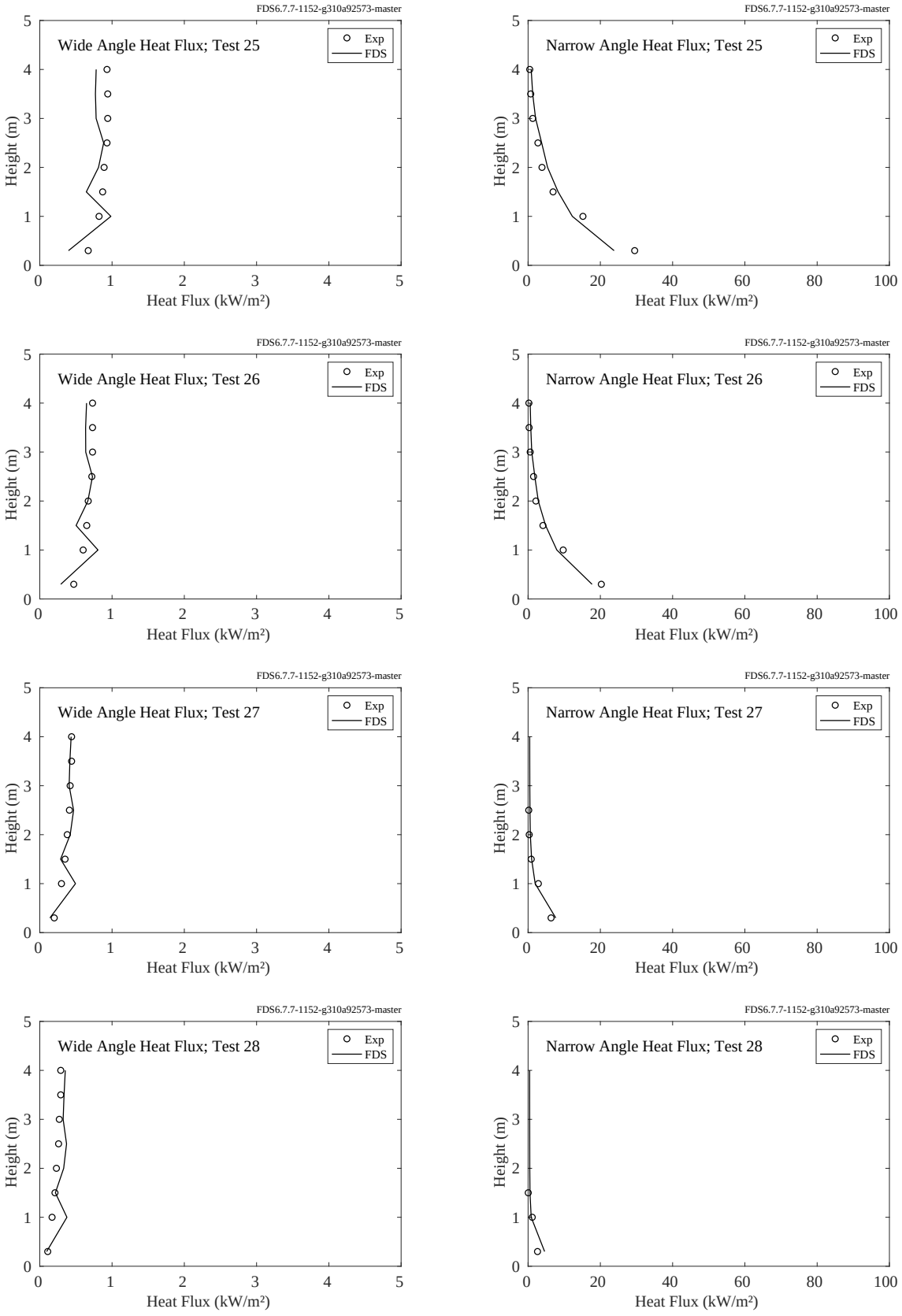

Figure 12.98: Sandia Methane Burner, heat flux, Tests 25-28.

12.2.11 Shell LNG Fireballs

A brief description of the experiments and modeling assumptions is given in Section 3.67.

Figure 12.99 compares the measured and predicted heat flux from three large fireballs at a distance of 100 m from the test vessel. Experiment 4 also includes measurements at distances of 40 m and 70 m.

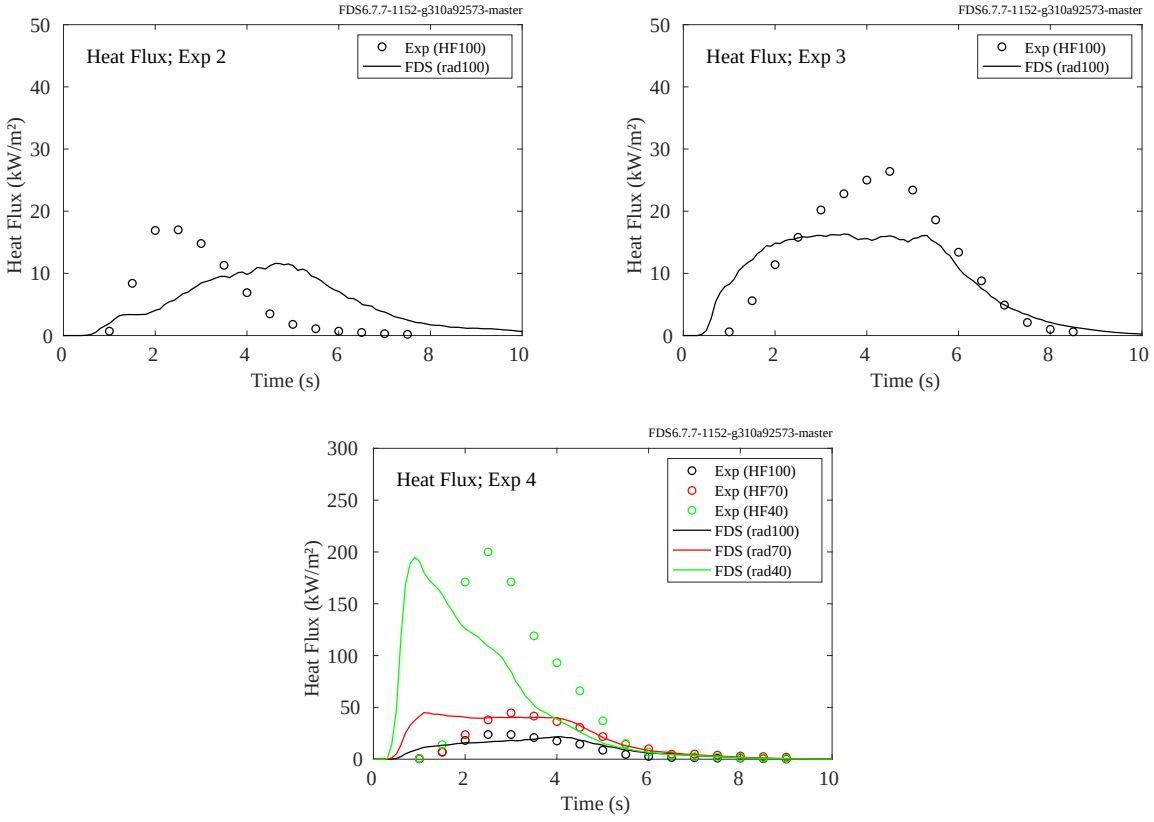

Figure 12.99: Heat flux for the Shell LNG Fireball experiments.

12.2.12 WTC Experiments

There were a variety of heat flux gauges installed in the test compartment. Most were within 2 m of the fire. Their locations and orientations are listed in Table 12.2.

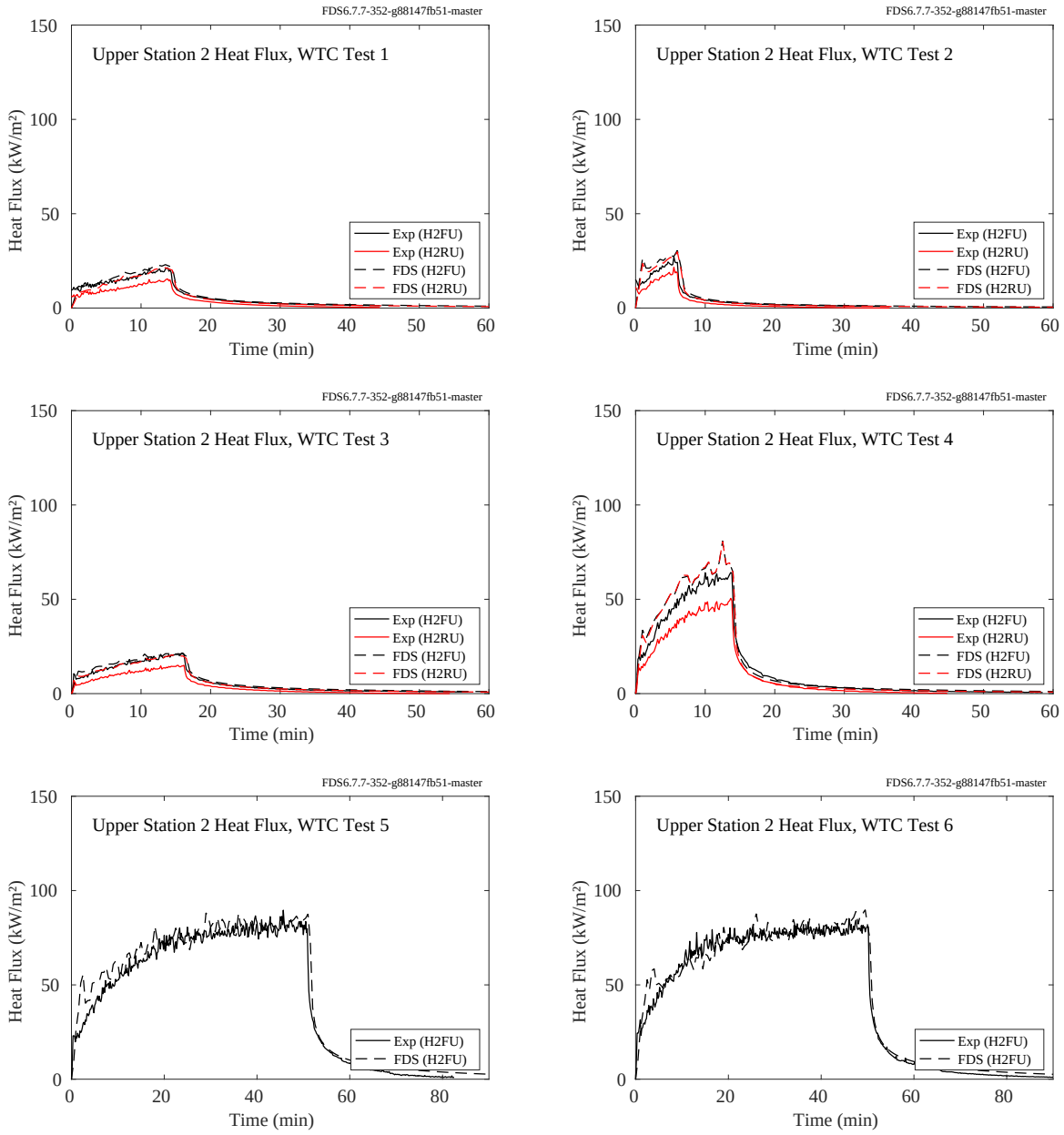

Figure 12.100: WTC experiments, heat flux at Station 2, high position.

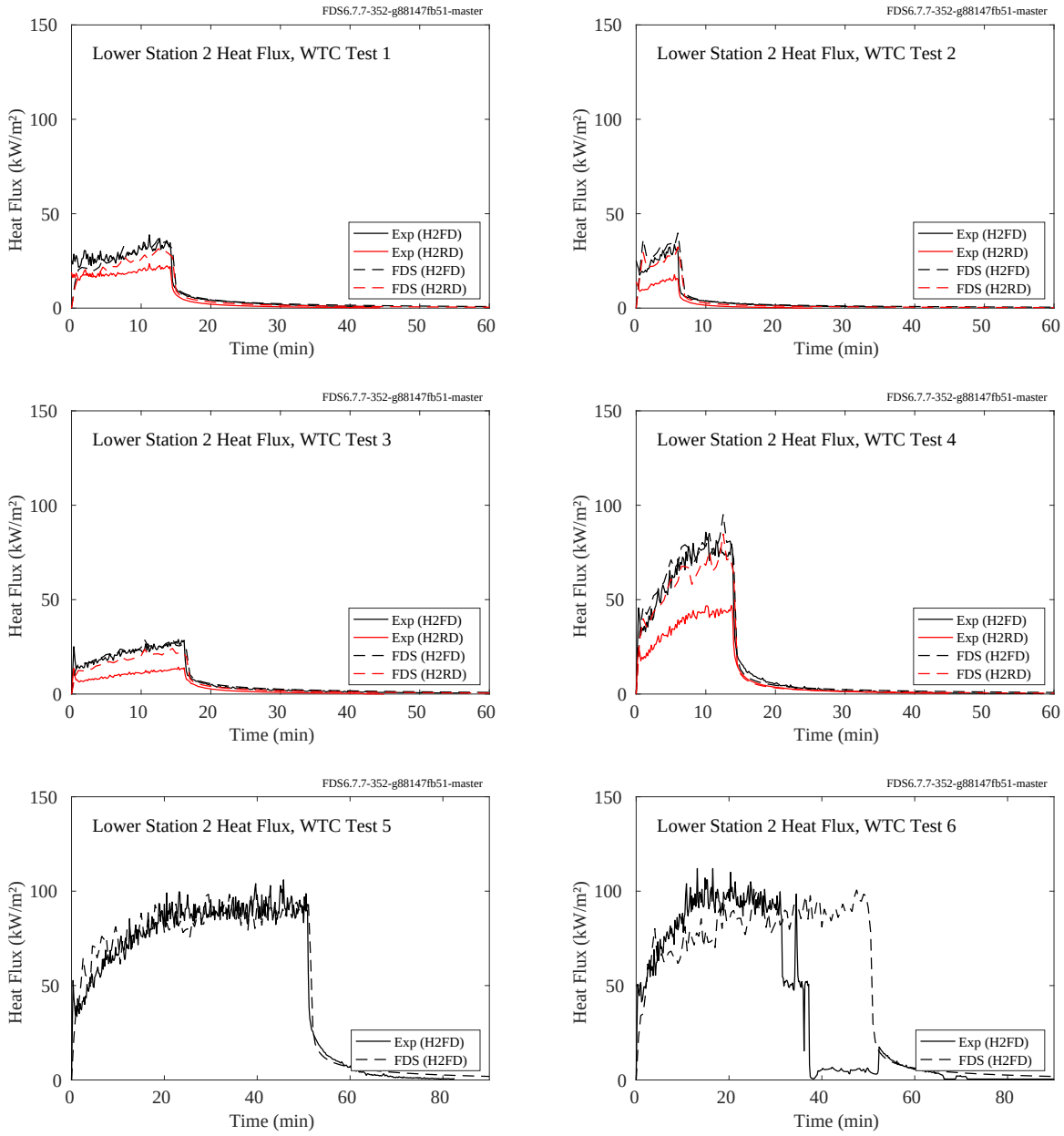

Figure 12.101: WTC experiments, heat flux at Station 2, low position.

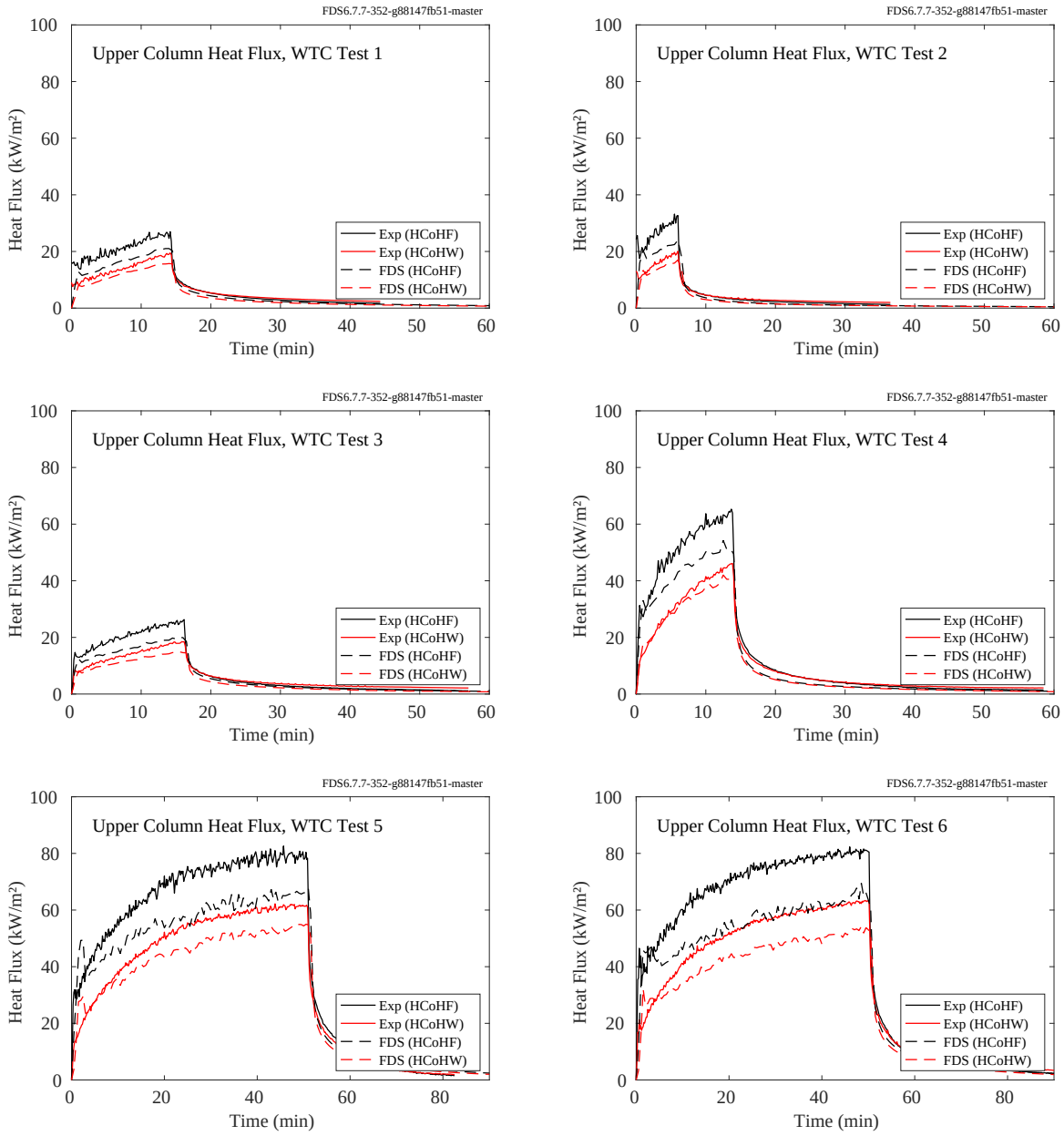

Figure 12.102: WTC experiments, heat flux to upper column.

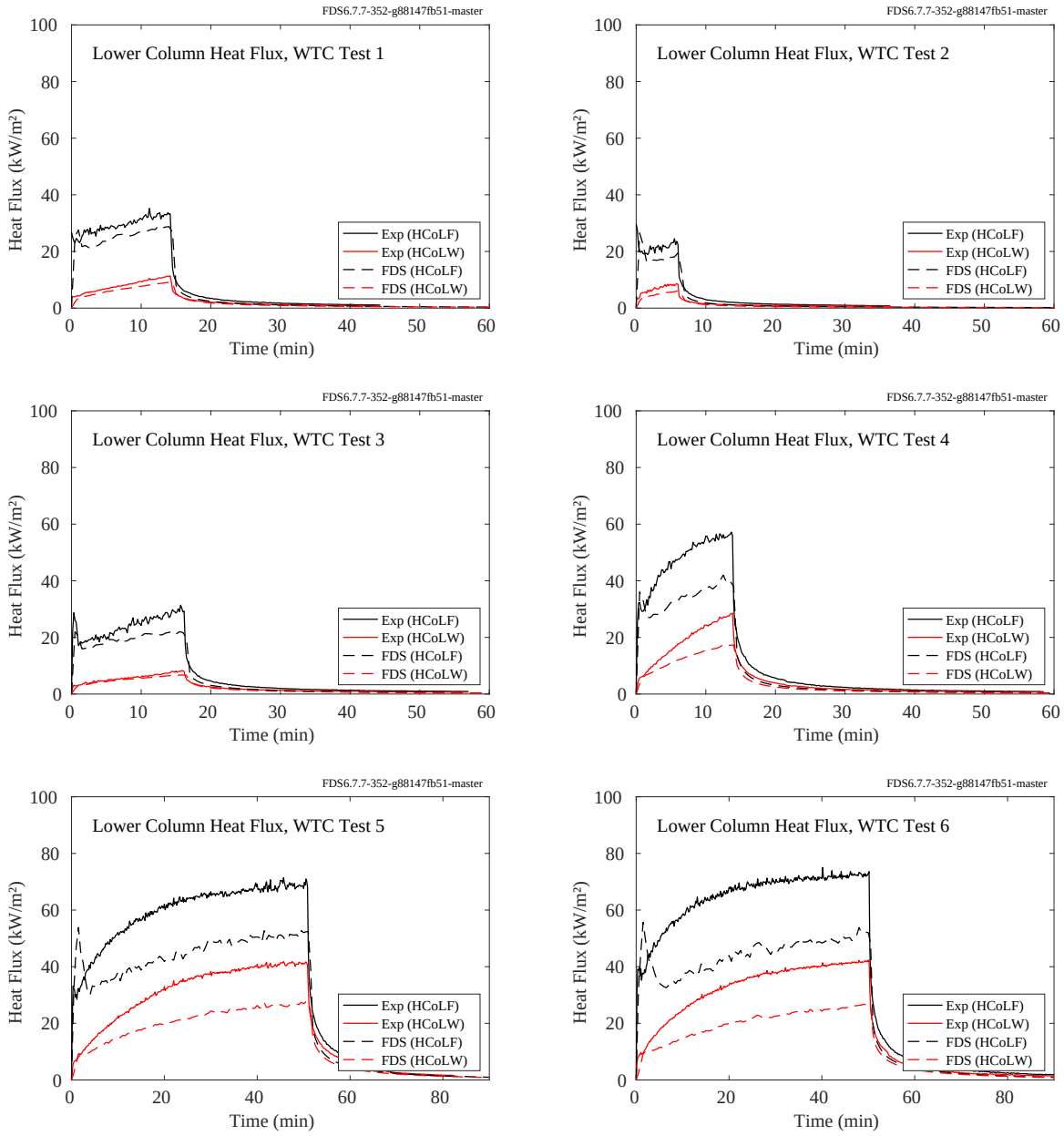

Figure 12.103: WTC experiments, heat flux to lower column.

12.2.13 UMD Line Burner

In the UMD line burner experiments, radiative heat flux was measured at a distance of 1 m normal to the flame sheet. In the FDS calculations the domain is extended to encompass the heat flux measurement location; two devices are placed at the 1 m distance on either side of the flame as shown in Fig. 12.104. This figure also shows a slice contour of integrated radiation intensity to confirm the pattern is smooth.

The radiative fraction and radiative heat flux as functions of oxygen volume fraction in the coflow have been measured by White et al. [302]. FDS does not employ a specified radiative fraction in these simulations. Rather it uses a three step reaction mechanism that produces CO and soot in the first step and the oxidation of these species in the second and third. The source of thermal radiation is the CO, CO_2, water vapor, and soot in the flame, as calculated by RadCal. Figure 12.105 displays the measured and predicted global radiative fraction and heat flux.

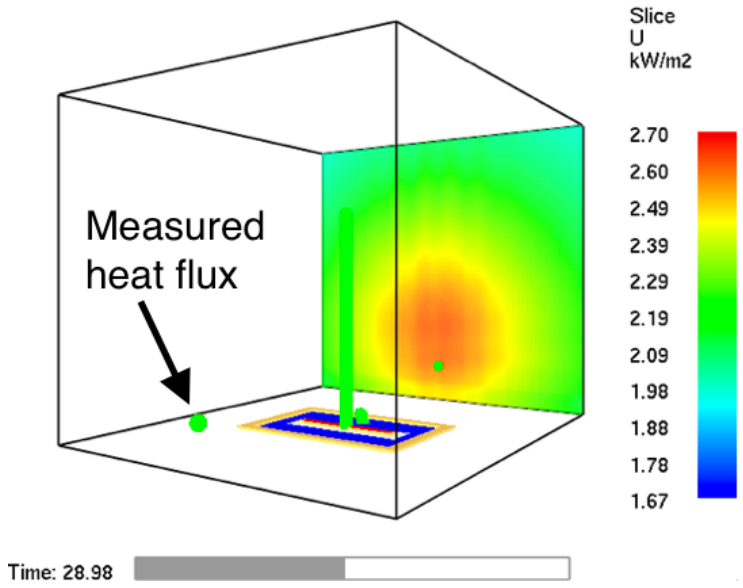

Figure 12.104: UMD Line Burner contour of integrated radiation intensity.

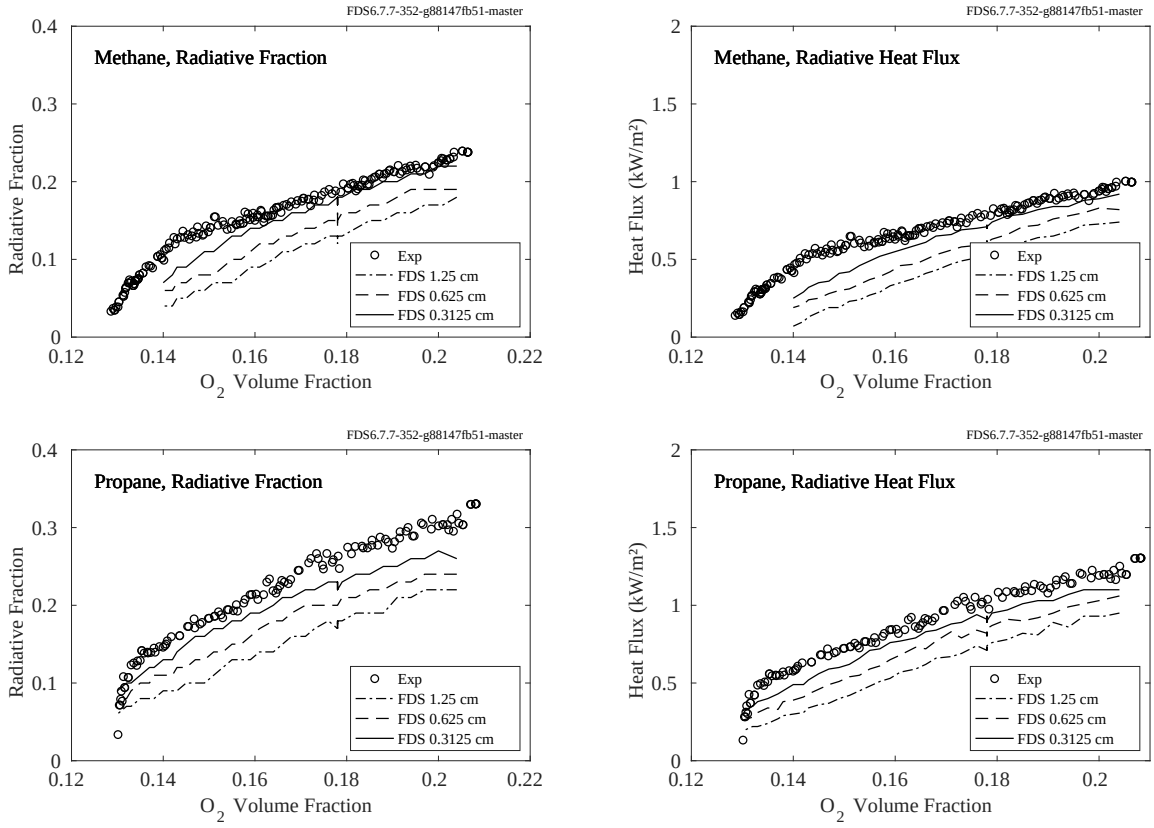

Figure 12.105: The plots on the left compare measured and predicted radiative fraction, and the plots on the right compare measured and predicted heat flux to a target 1 m away from the flame.

12.2.14 Summary of Target Heat Flux Predictions

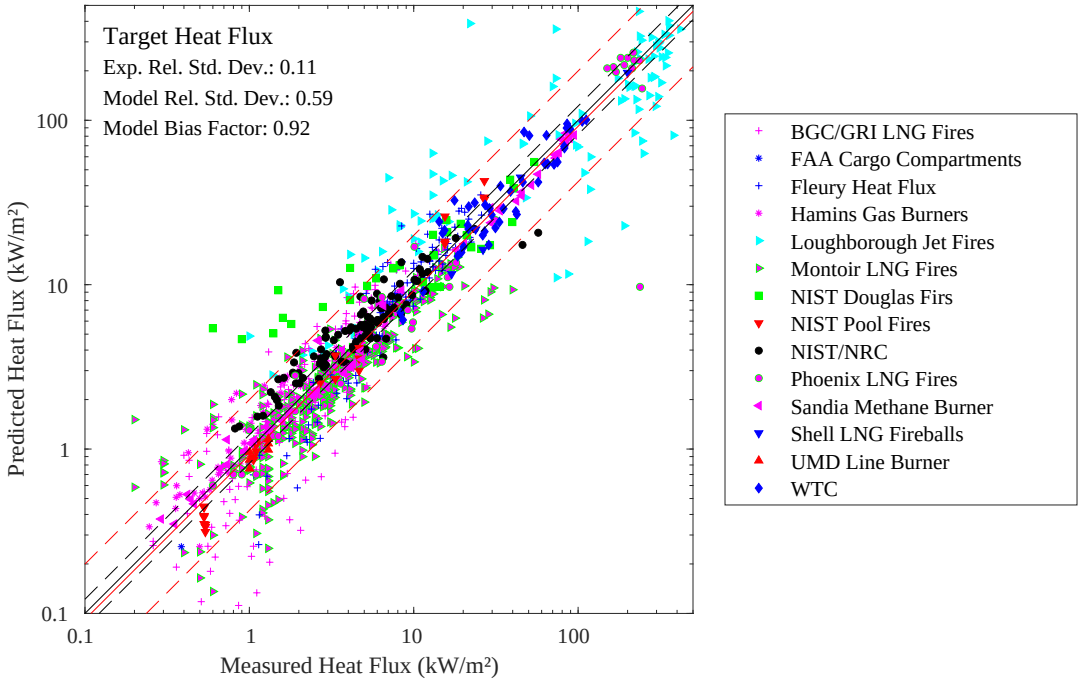

Figure 12.106: Summary of target heat flux predictions.

12.3 Attenuation of Thermal Radiation in Water Spray

This section presents the results of simulations of spray experiments where the reduction of thermal radiation by a fine water spray was measured.

12.3.1 BRE Spray Experiments

Attenuation of thermal radiation by a water spray was measured using three full-cone type hydraulic nozzles at eight different pressures. The initial droplet speeds were determined using a simple hydraulic relation, $v = 0.9\sqrt{2P/\rho}$. The median drop size distributions were determined by assuming $d_m \propto p^{-1/3}$ and finding the constant of proportionality by fitting to the experimental PDPA measurement 1 m below the nozzles. Measured median diameters, d_{v50}, are compared against mean diameters, d_{43}. The arithmetic mean of the droplets is used for vertical velocity. The comparison of predicted and measured attenuation, Fig. 12.108, is made at a distance of 4 m from the heat source.

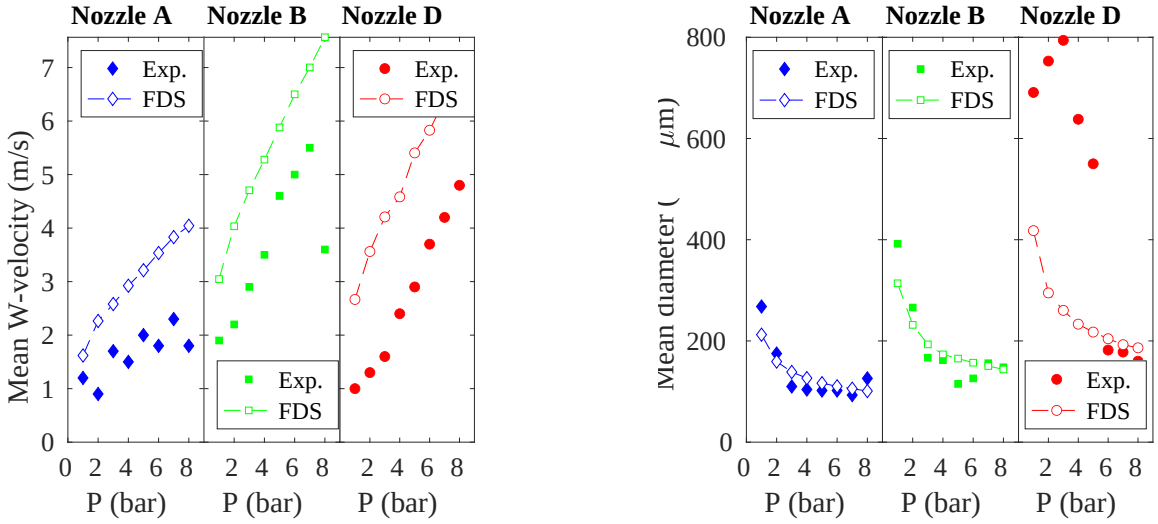

Figure 12.107: Comparison of experimental and predicted droplet speeds and mean diameters for the three nozzles and different pressures.

12.3.2 LEMTA Spray Experiments

The attenuation of thermal radiation was measured at five heights in water sprays produced by seven full-elliptic type hydraulic nozzles. The operating pressure was 4 bar. The initial speed was deduced from the water flow rate and the orifice diameter. The droplet size at the injection point was determined by comparing the predicted and measured results at the PDPA measurement location 0.2 m below the nozzles. The comparison of predicted and measured attenuations, Fig. 12.108, is made at five locations.

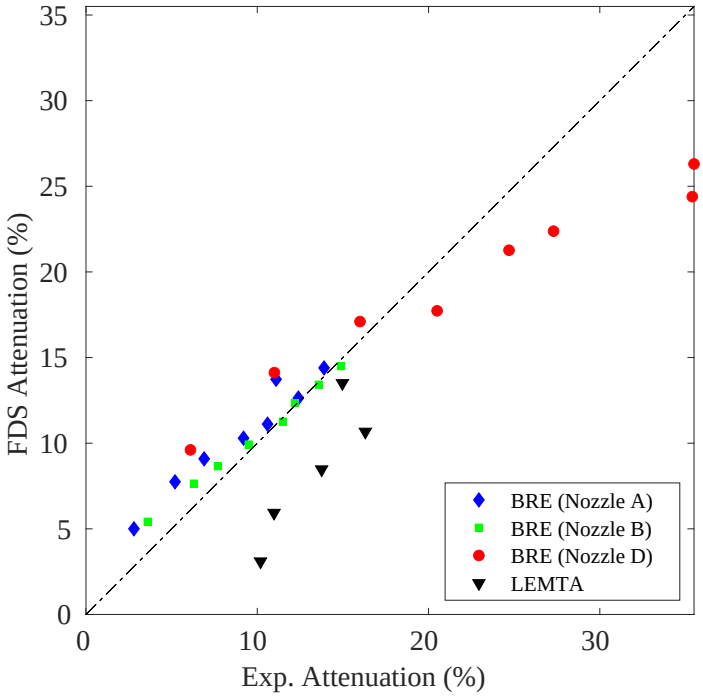

Figure 12.108: Comparison of predicted and measured radiation attenuation in the spray experiments at BRE and at LEMTA.

12.4 Convective Heat Flux

This section focuses specifically on experiments that primarily involved convective heat transfer.

12.4.1 Bouchair Solar Chimney

The plots on the following pages compare the predicted air mass flow rates through the test apparatus shown in Fig. 3.5. The measurements were made at both the inlet and outlet of the thermal cavity. Note that in Bouchair's thesis [140], the measurements were presented as mass flow rates per unit length of the inlet slot, 1.4 m. In the plots on the following pages, the measurements and simulation results are presented simply as a total mass flux, kg/s.

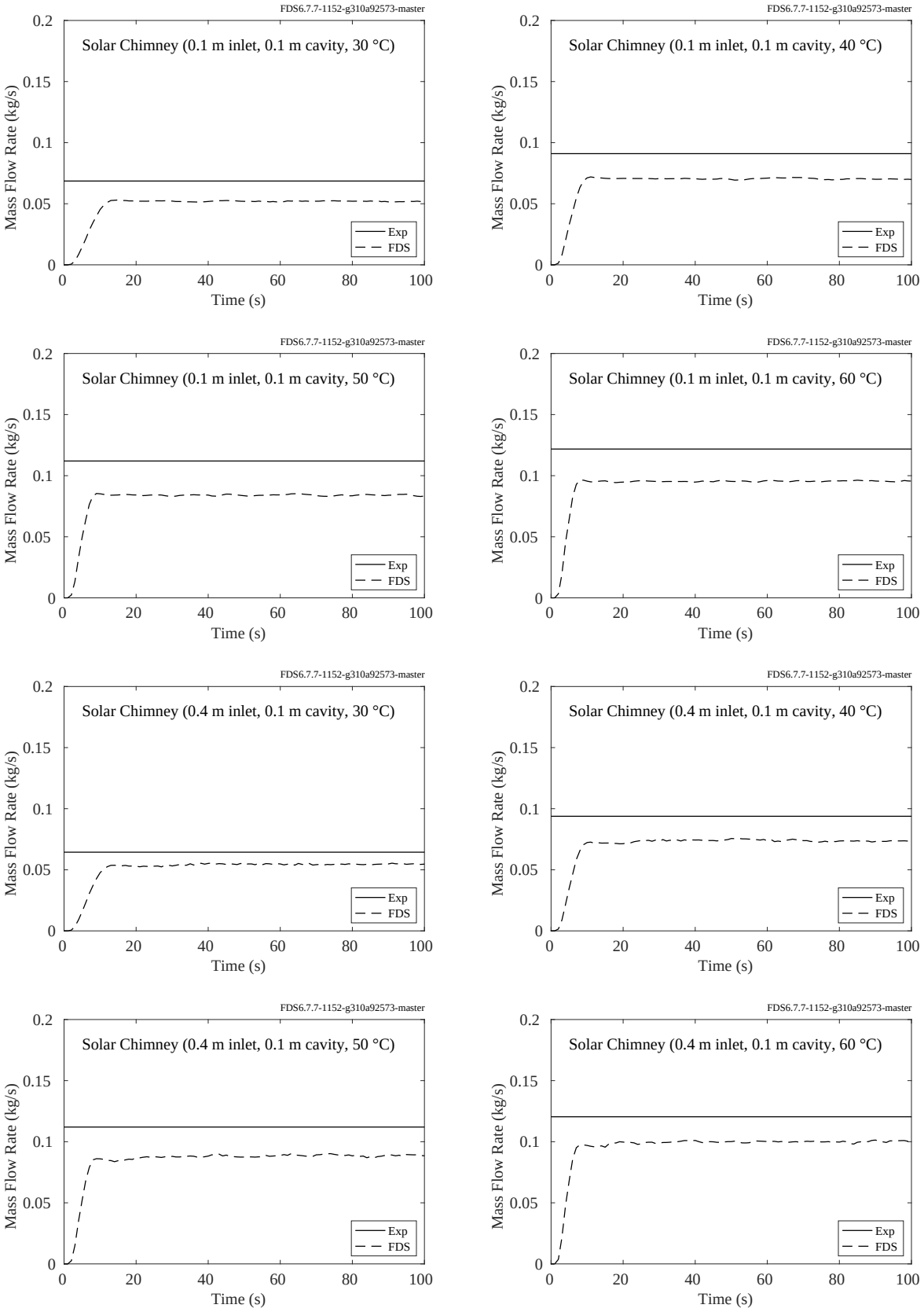

Figure 12.109: Bouchair Solar Chimney, 0.1 m thermal cavity.

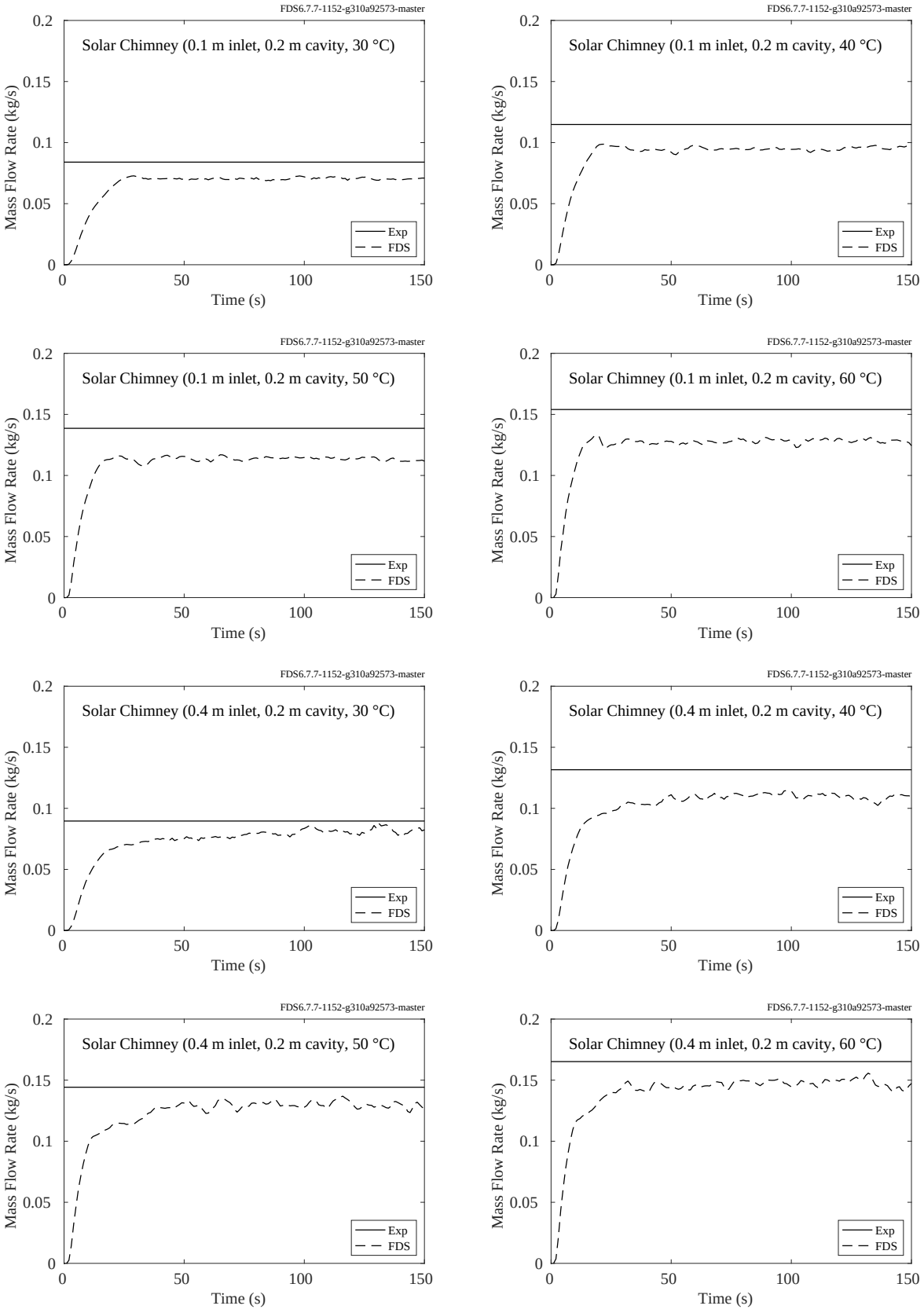

Figure 12.110: Bouchair Solar Chimney, 0.2 m thermal cavity.

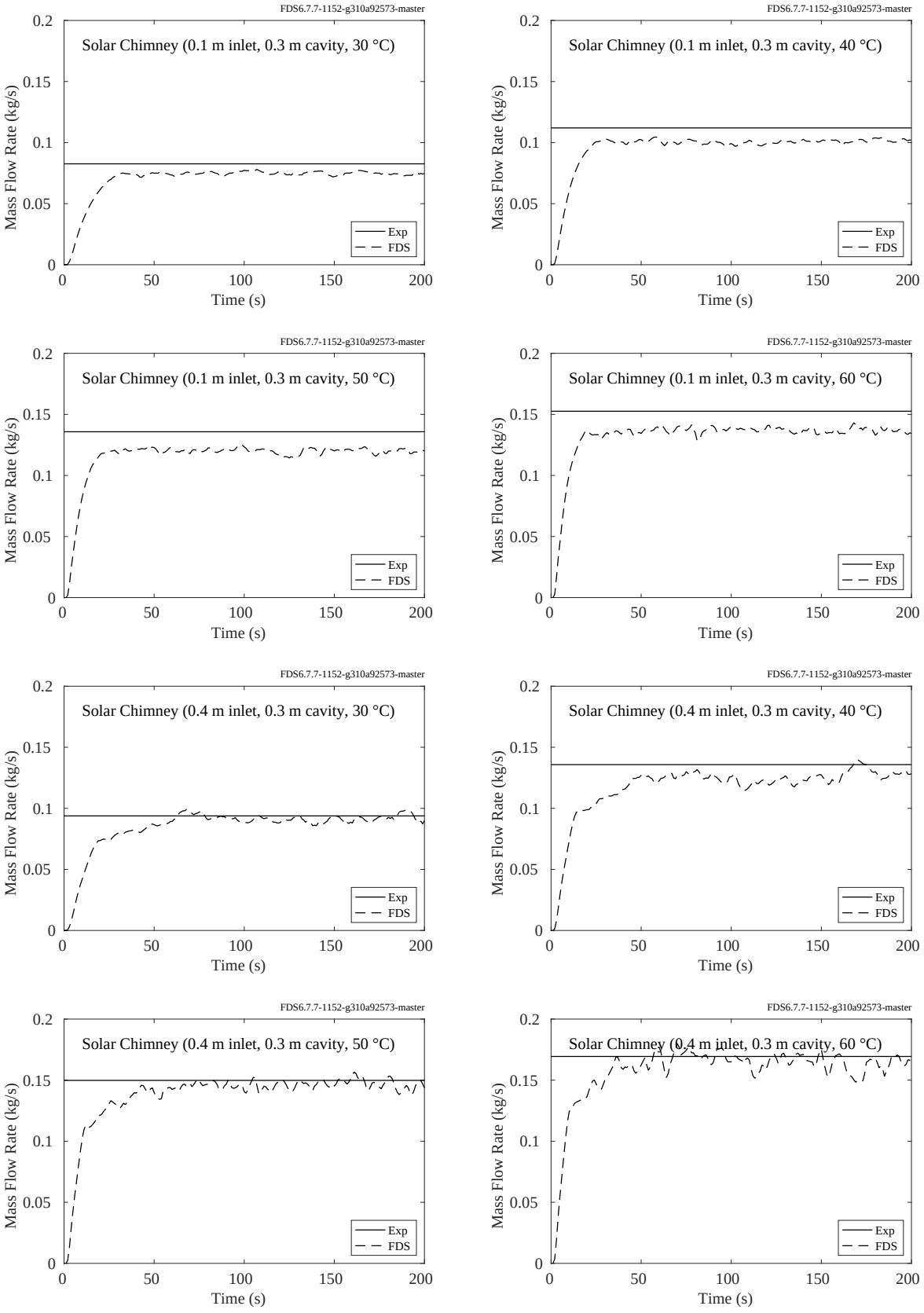

Figure 12.111: Bouchair Solar Chimney, 0.3 m thermal cavity.

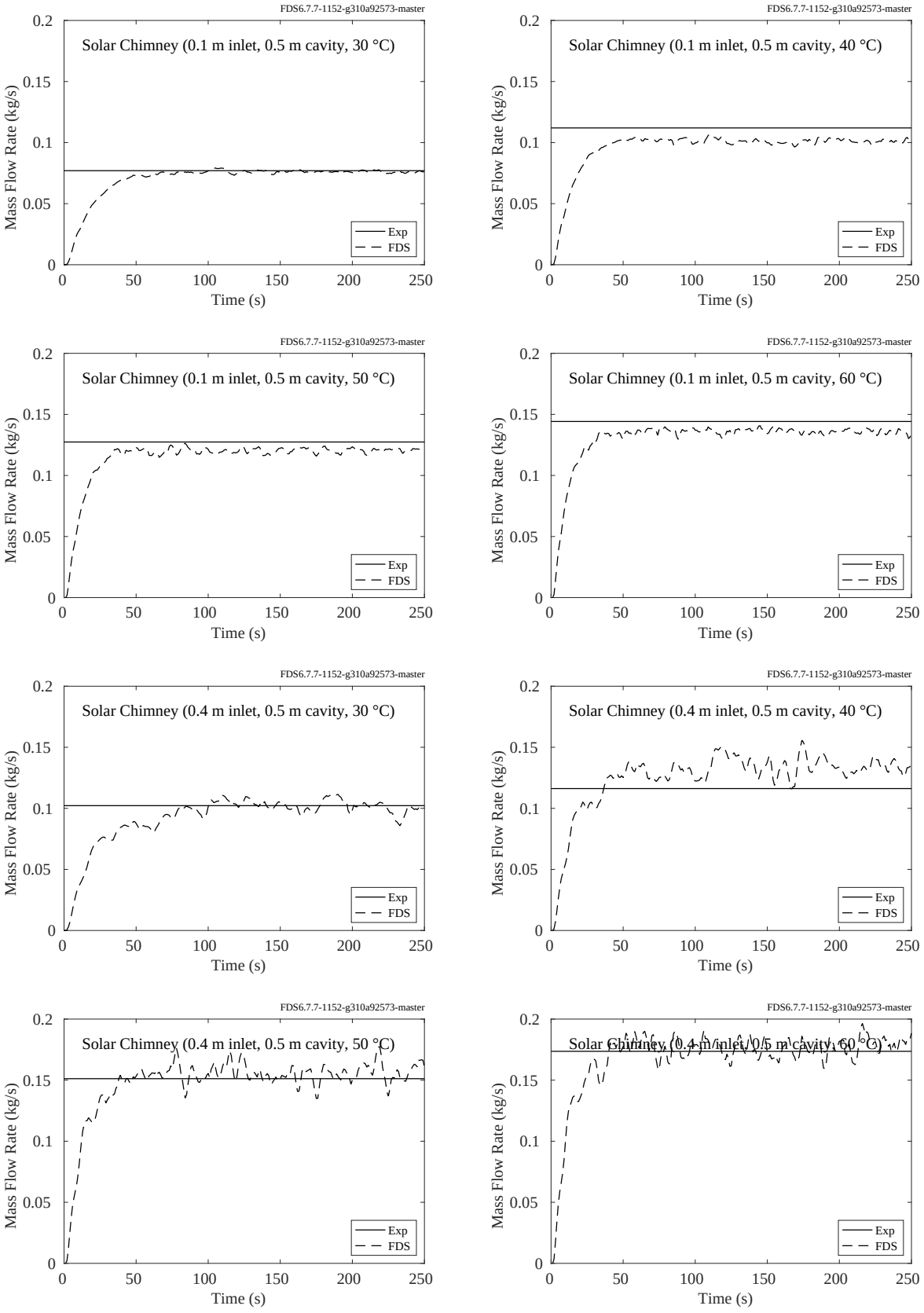

Figure 12.112: Bouchair Solar Chimney, 0.5 m thermal cavity.

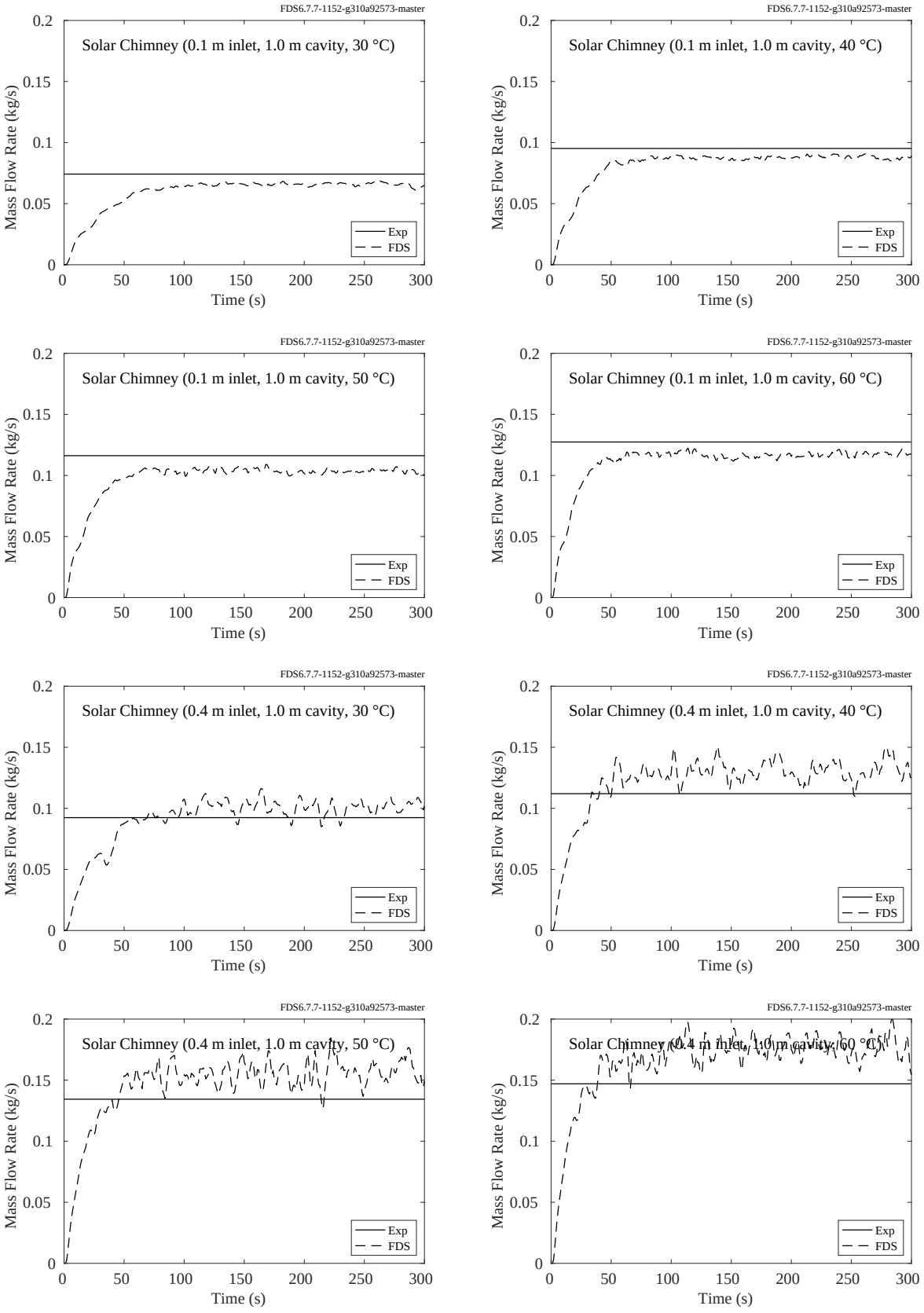

Figure 12.113: Bouchair Solar Chimney, 1.0 m thermal cavity.

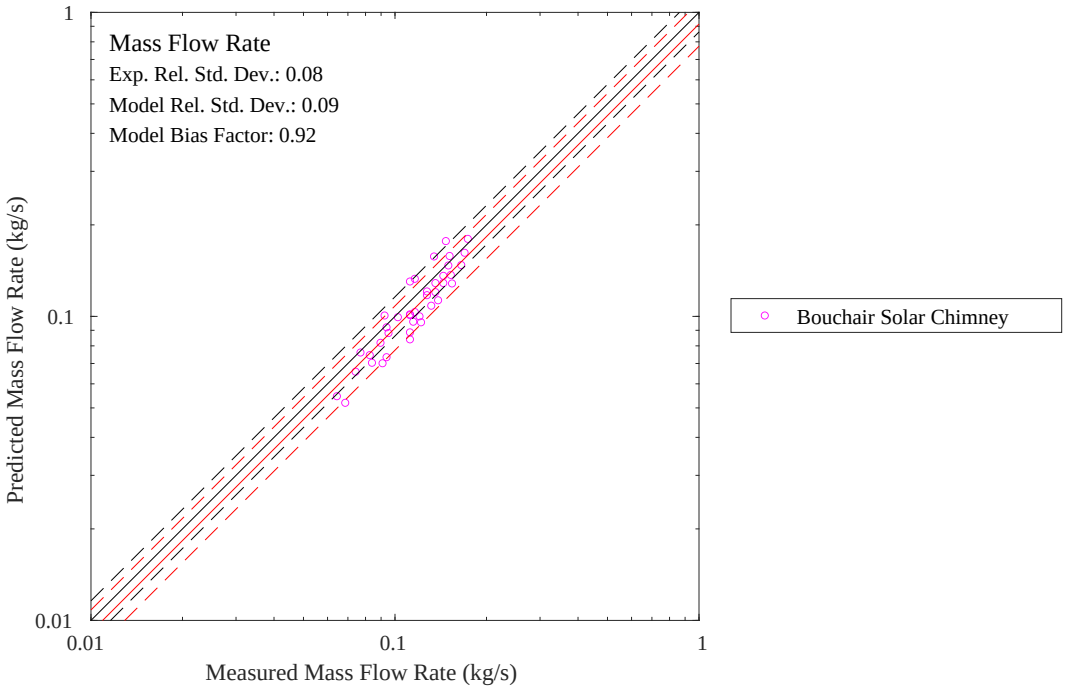

Figure 12.114: Summary of Bouchair Solar Chimney results.

12.5 Radiation Source Term

12.5.1 FM Burner Experiments

Figure 12.115 displays mean and rms vertical profiles of the radiation emission, in units of kW/m, from a 15 kW, 13.7 cm (inner) diameter ethylene burner at ambient oxygen concentrations of 21 %, 19 %, 17 %, and 15 %. Figure 12.116 displays the predicted total radiant fraction for the four ambient oxygen levels.

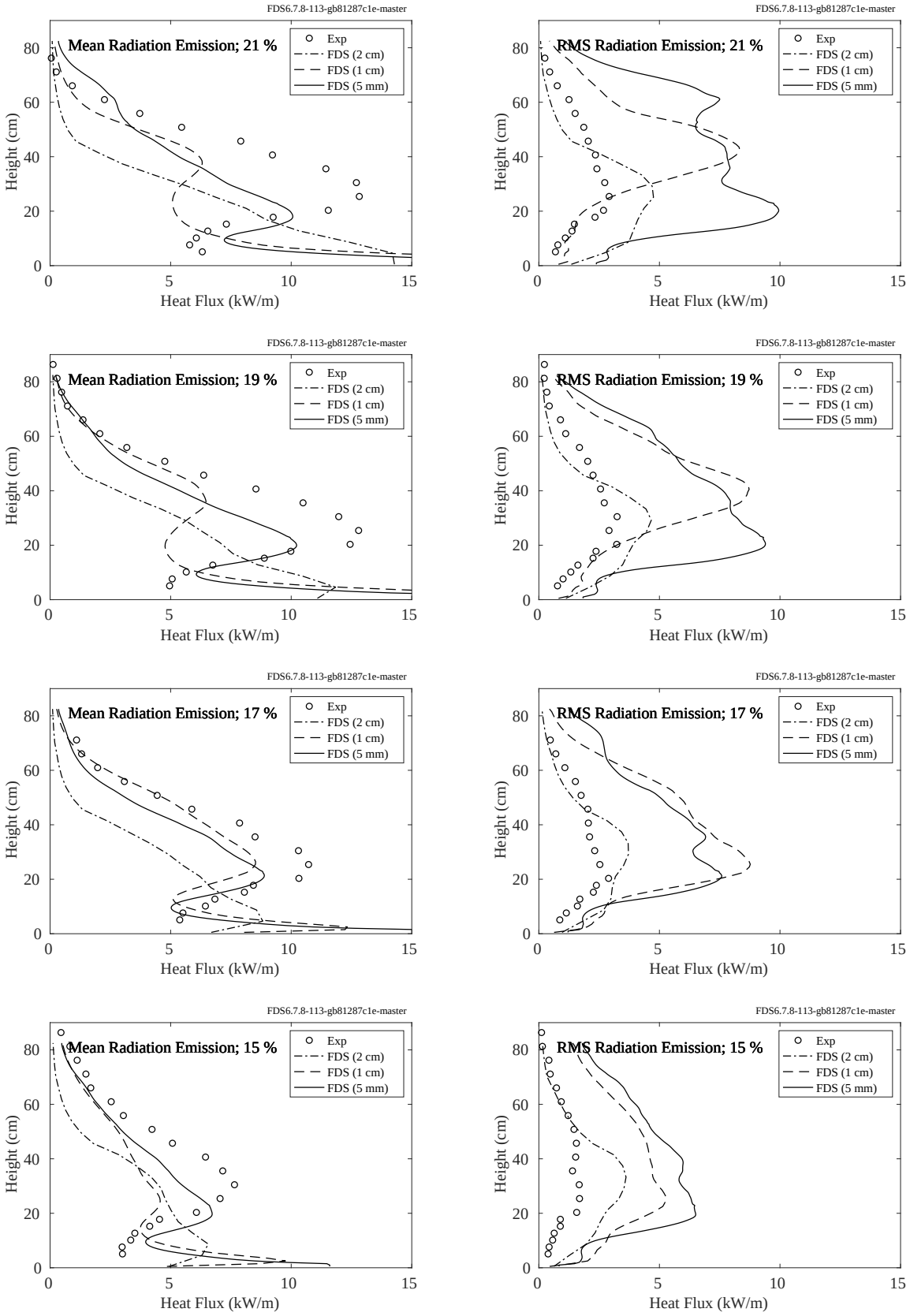

Figure 12.115: FM Burner experiments, mean and rms vertical heat flux profiles.

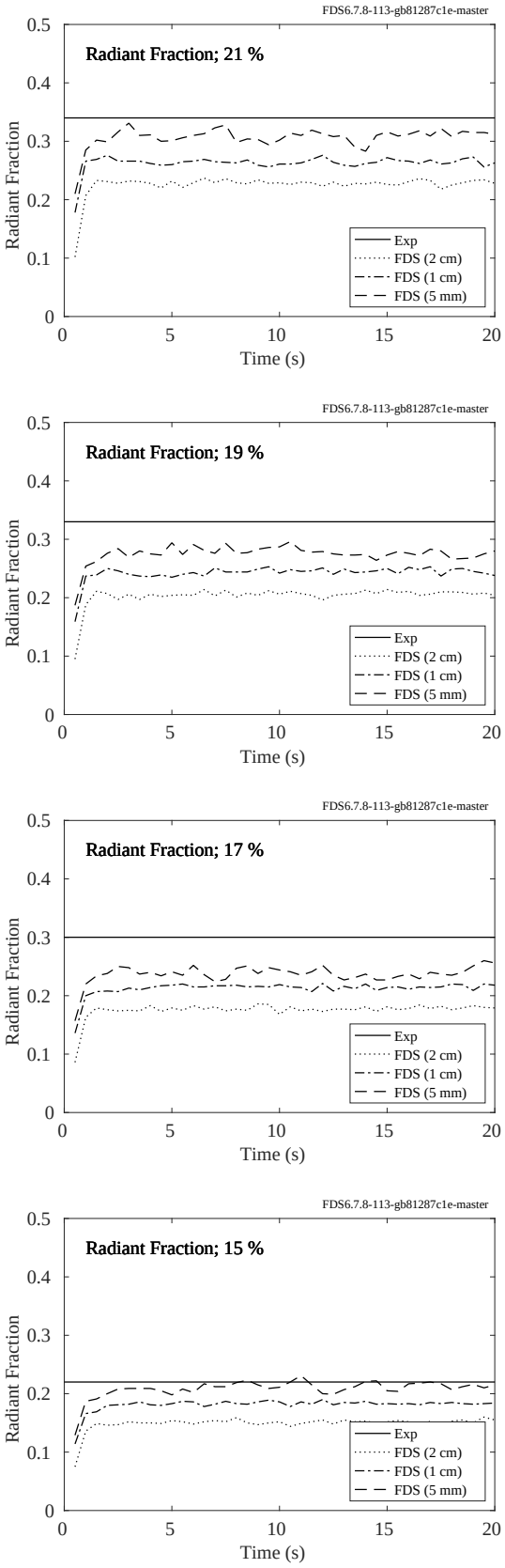

Figure 12.116: FM Burner experiments, radiant fraction for four oxygen levels.

12.6 Condensation Heat Flux

This section focuses on experiments involving condensation onto surfaces.

12.6.1 SETCOM Experiments

The following plot shows the results of modeling the SETCOM experiments.

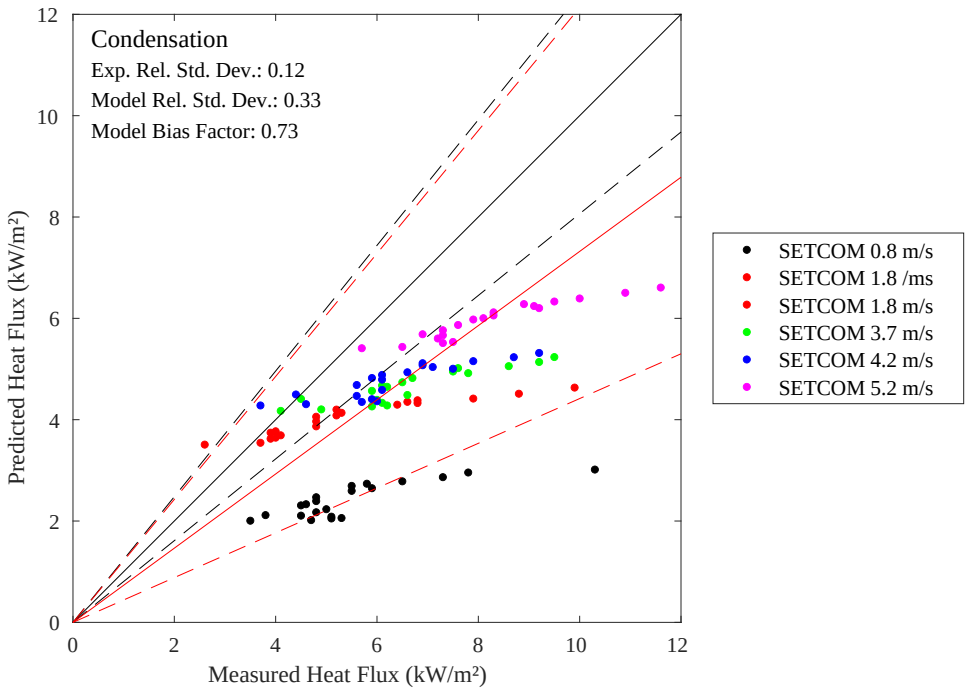

Figure 12.117: Summary of SETCOM results.

Chapter 13

Suppression

This chapter looks at validation exercises where the aim is to predict the extinguishment of a fire.

13.1 Minimum Agent Concentration Experiments

In the following sections, results of experiments are presented in which relatively small flames are extinguished due to the introduction of an inerting agent in the oxidizer stream.

13.1.1 Cup Burner Experiments

A cup burner is an apparatus used to determine the minimum extinguishing concentration (MEC) for combinations of fuels and suppression agents. Sixteen fuels (acetone, acetylene, benzene, butane, dodecane, ethanol, ethylene, heptane, hexane, hydrogen, methane, methanol, octane, propane, propanol, and toluene) and five suppression agents (argon, carbon dioxide, helium, nitrogen, and sulfur hexaflouride) are considered. For the simulations, the MEC is found when the post-ignition HRR remains below 1×10^{-10} kW. The critical flame temperatures specified for the fuel reactions are shown in Table 3.8. The extinguishing agent concentration is measured at the outer edge of the cup burner tube at a level slightly below the cup rim. Results are shown in Fig. 13.1 where color indicates the fuel and shape indicates the extinguishing agent.

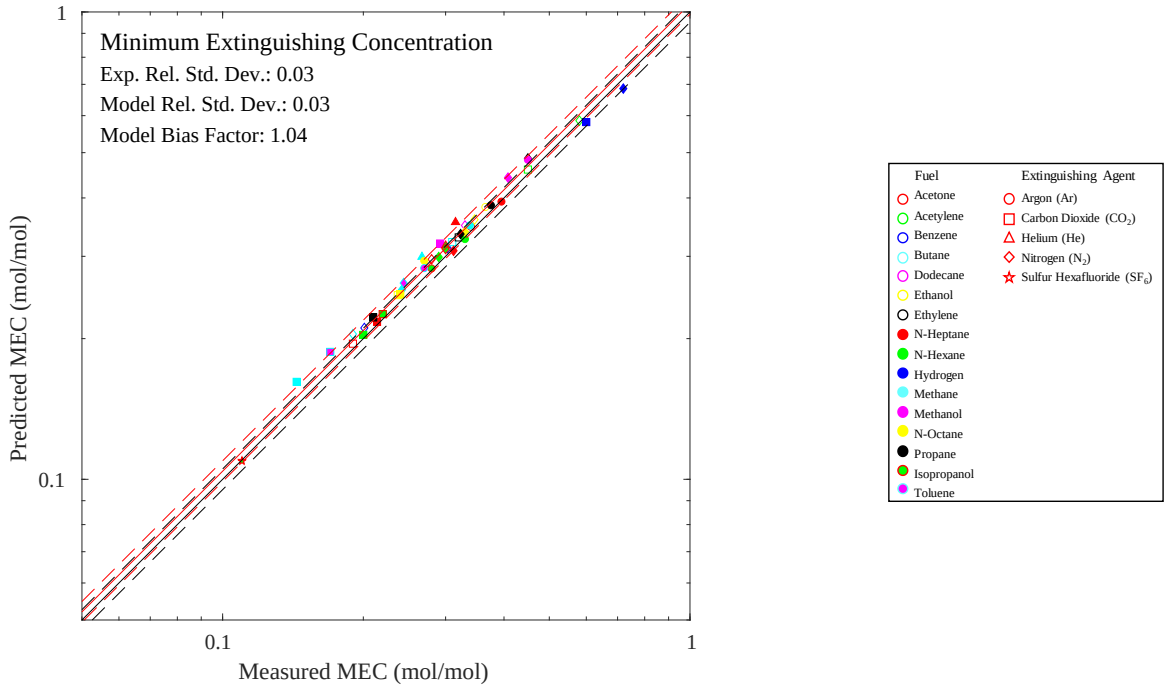

Figure 13.1: Comparison of measured and predicted minimum extinguishing volume fractions for the cup burner tests. Fuel type is indicated by color, and extinguishing agent is indicated by shape.

13.1.2 FM Burner Experiments

A description of the FM Burner experiments can be found in Section 3.24. Briefly, a 15.2 cm round steel burner generating a 10 kW fire was supplied with oxygen by an air stream from below that was slowly diluted with nitrogen until the flame extinguished. In the FDS simulations, nitrogen is added to the air stream supplied through the floor of the enclosure, linearly decreasing the oxygen volume fraction over one minute of simulated time. In Fig. 13.2, the combustion efficiency, η, is plotted as a function of oxygen volume fraction for all four fuels tested and compared with the measurements of Zeng and Wang [196]. The auto-ignition temperature (AIT) threshold for each fuel is set according to the Beyler's chapter in the SFPE Handbook [136]. The modeled burner is piloted using a ring of 36 hot (2000 °C) particles ejecting enough fuel to produce 1 kW (to match the experimental pilot).

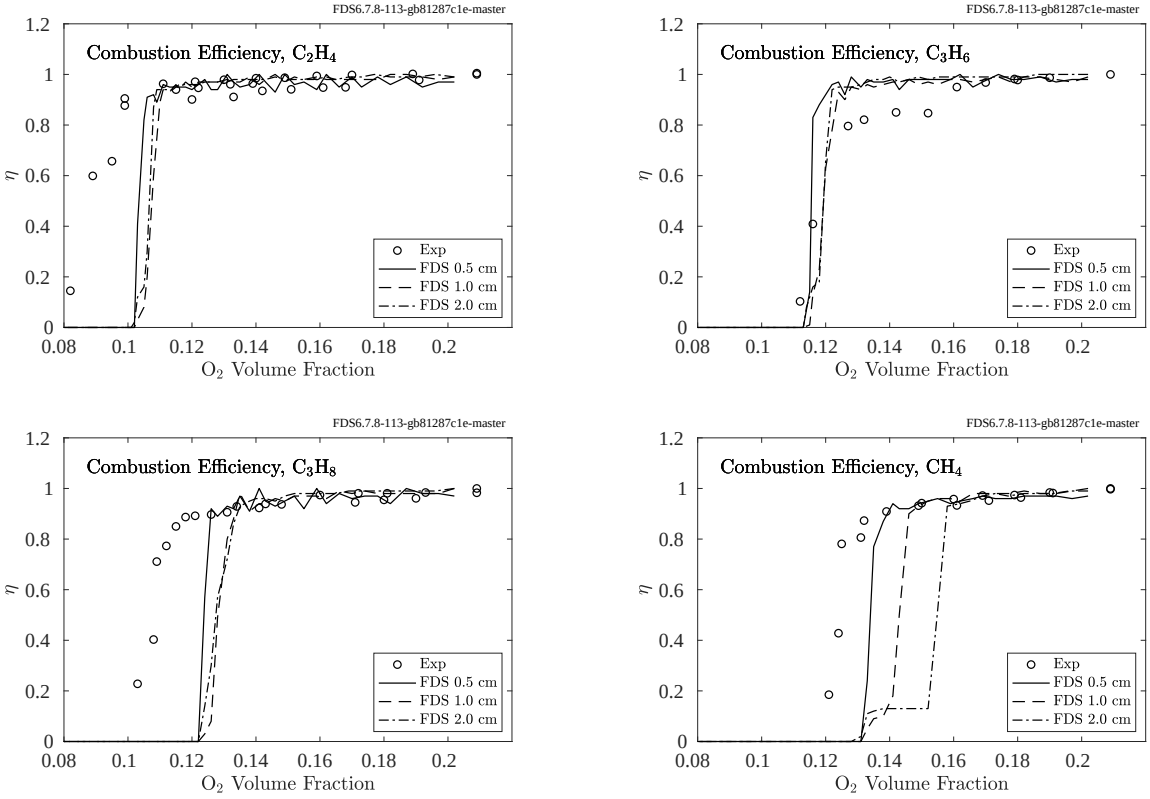

Figure 13.2: FM Burner combustion efficiency.

13.1.3 UMD Line Burner

A description of UMD Line Burner experiments can be found in Section 3.80. In the experiments, the oxygen co-flow was slowly diluted with nitrogen until the flame weakened and eventually extinguished. In the FDS simulations, the nitrogen co-flow is setup with a ramp in time to achieve a linear decrease in the co-flow oxygen volume fraction over one minute of real time. In Fig. 13.3, we plot the combustion efficiency as a function of oxygen volume fraction for both methane and propane and compare with the measurements of White et al. [302]. Note that the FDS results are presented for three different grid resolutions corresponding to $W/\delta x$ = 4, 8, and 16 (δx = 1.25 cm, 0.625 cm, and 0.3125 cm, respectively), where $W = 5$ cm is the width of the burner. A simple re-ignition model with an ignition temperature threshold set to the SFPE Handbook [238] value of the Auto-Ignition Temperature (AIT) for methane and propane is used. A piloted ignition region (AIT = 0 K) is set just within the near field of the line burner. Details of the re-ignition model and pilot region as well as parameter sensitivity studies are provided in White et al. [344].

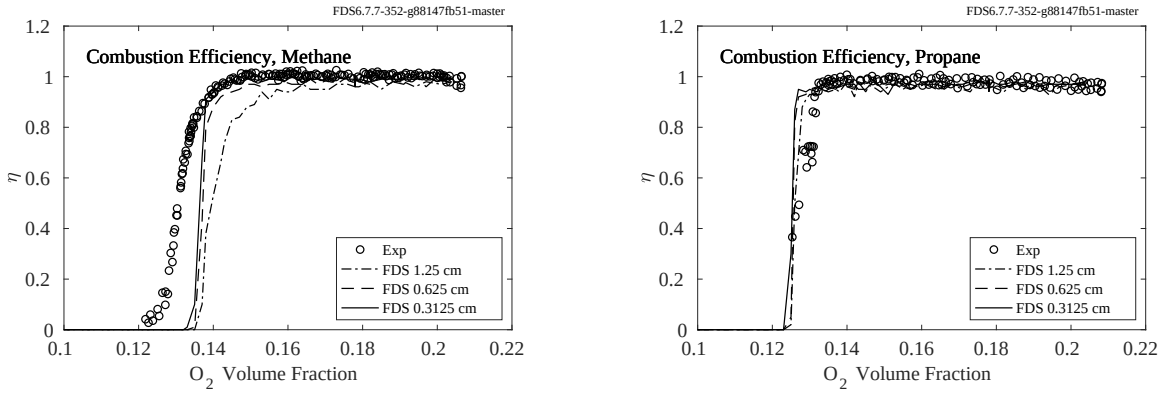

Figure 13.3: UMD Line Burner combustion efficiency.

13.2 Compartment Fire Extinction

The following sections present results for experiments in which fires within forced ventilation compartments either self-extinguish due to lack of oxygen, or extinguish due to a water mist system.

13.2.1 LLNL Enclosure Experiments

The figures on the following pages contain plots of the heat release rate in both the experiments and the simulation. The experimental curve is just the value reported in the test report, which drops to zero instantly at the reported extinguishment time. In cases where the model does not predict extinction, the extinction time data is not used in the summary scatter plot, Fig. 13.17.

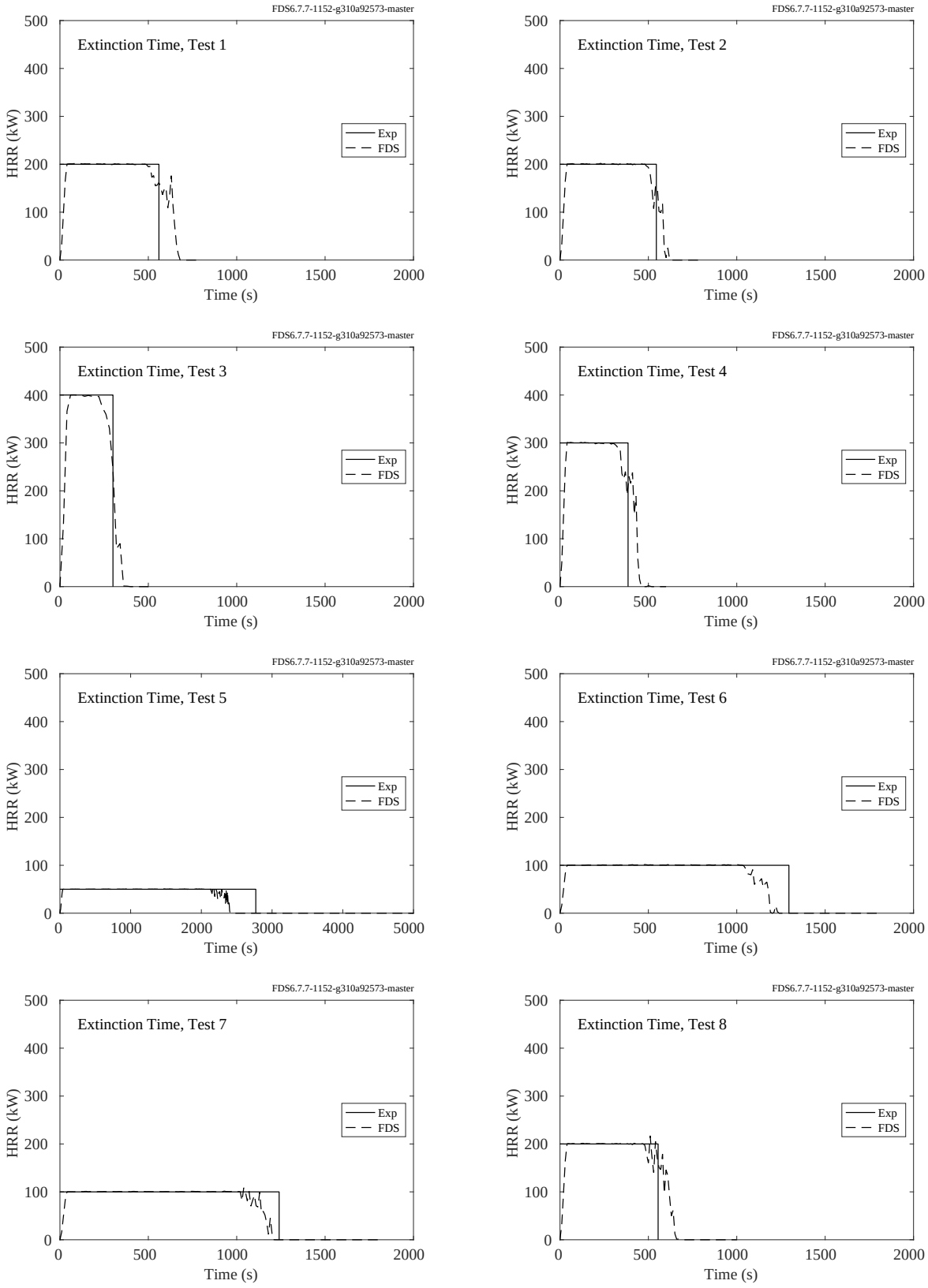

Figure 13.4: LLNL Extinction Time, Tests 1-8.

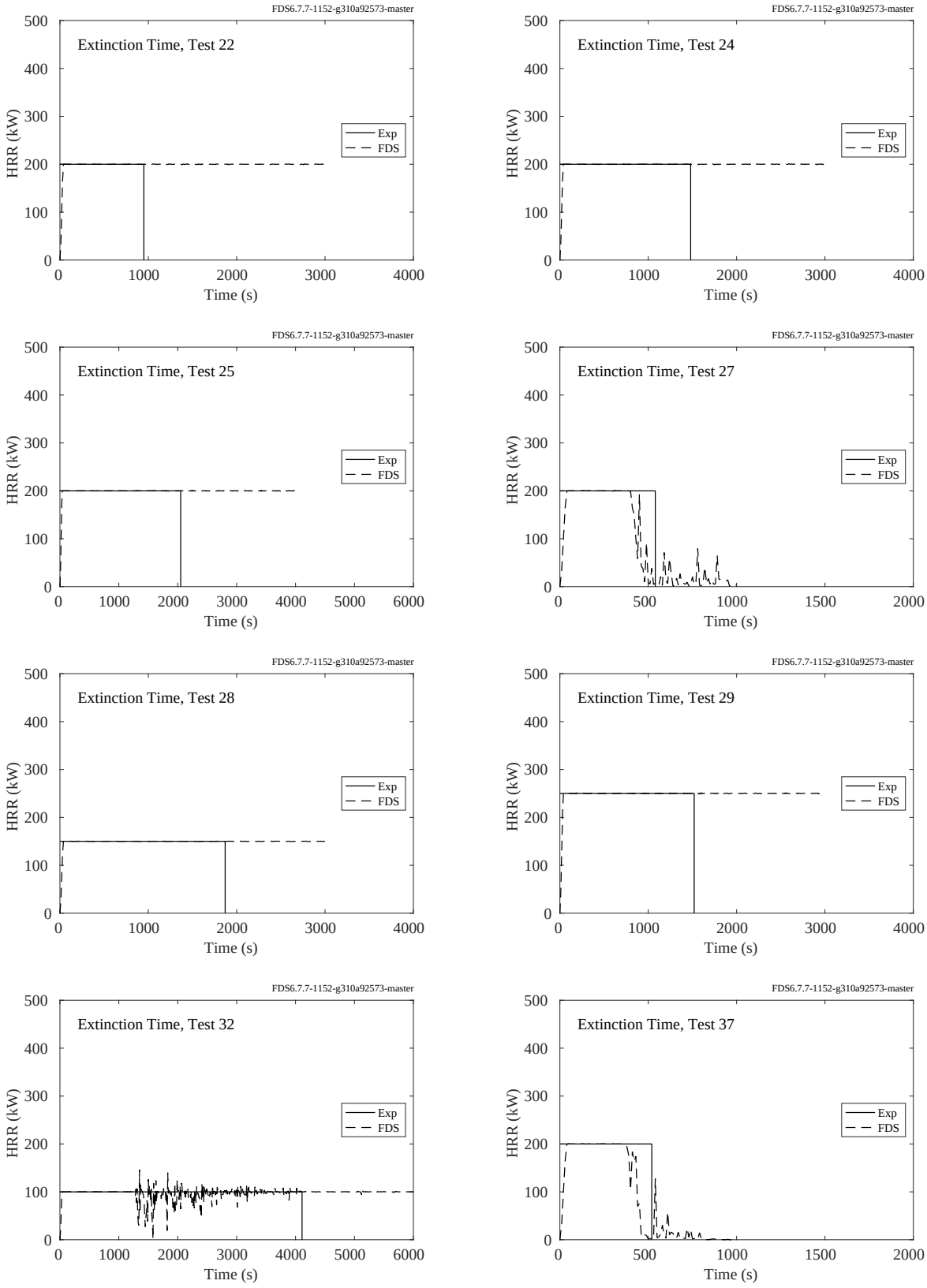

Figure 13.5: LLNL Extinction Time, Tests 22, 24, 25, 27, 28, 29, 32, 37.

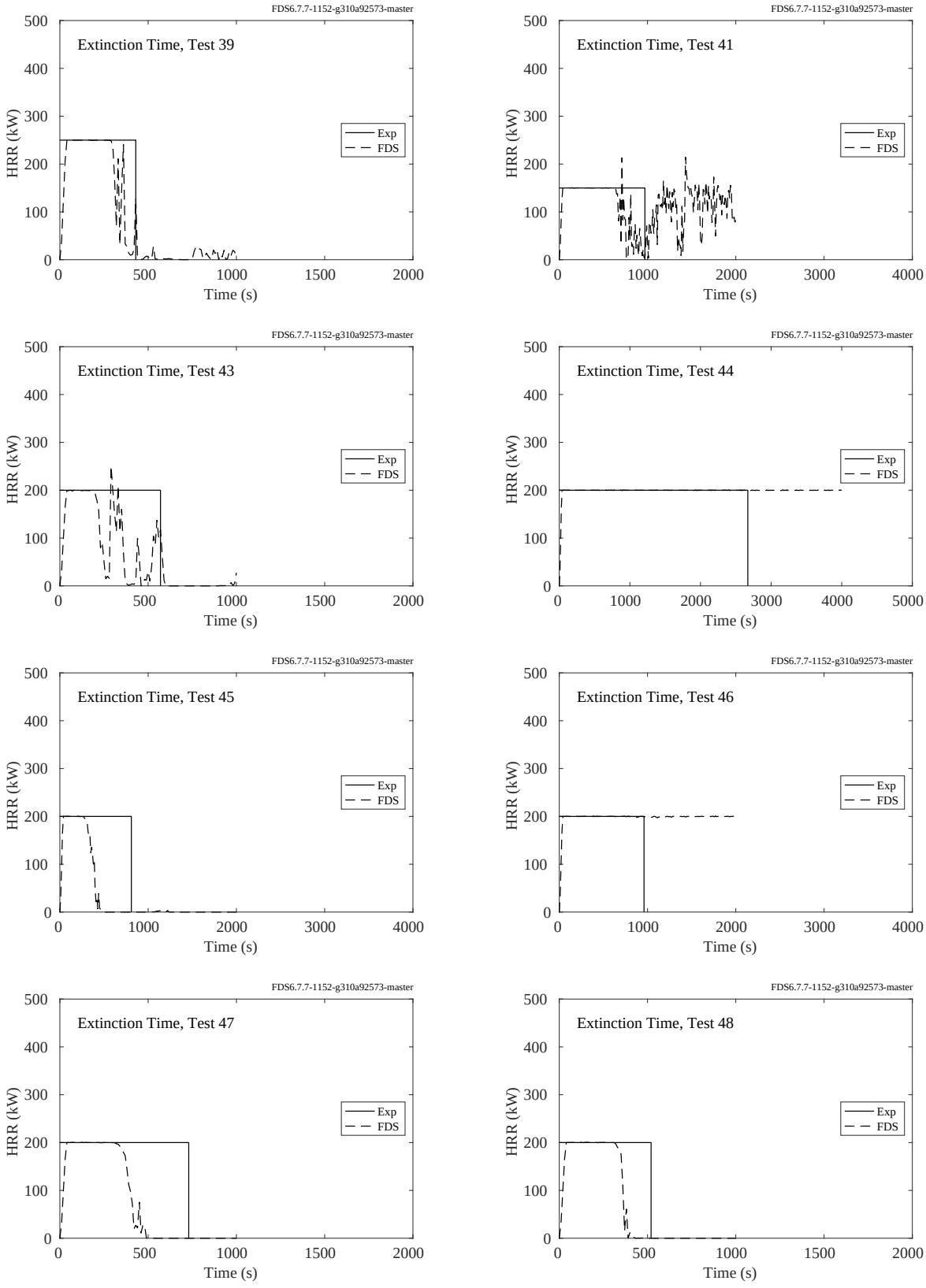

Figure 13.6: LLNL Extinction Time, Tests 39, 41, 43-48.

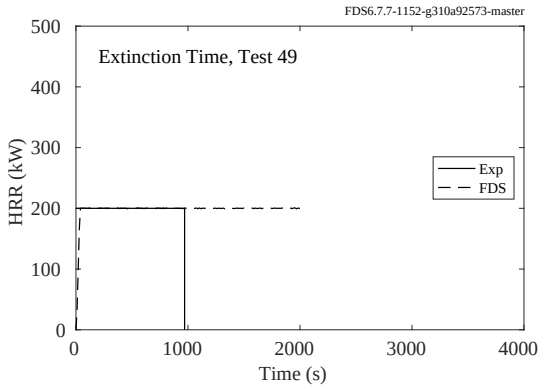

Figure 13.7: LLNL Extinction Time, Test 49.

13.2.2 NIST/NRC OLIVE-Fire Experiments

These experiments involve fires within large, steel electrical enclosures. A brief description of the experiments and photographs of the enclosures are found in Section 3.48. Table 13.1 lists the leakage and vent areas of the enclosures, along with the measured maximum heat release rate (HRR).

Figures 13.8 through 13.10 compare predicted versus measured heat release rates. Each plot contains two sets of curves. The black curves represent the nominal HRR based solely on the metered natural gas flow. The gas flow was ramped up in increments of 25 kW, 50 kW, or 100 kW until the HRR determined via oxygen consumption calorimetry (red curves) diverged, at which point the maximum achievable HRR within the enclosure had been reached.

Table 13.1: Summary of NIST/NRC OLIVE-Fire Experiments.

Exp. No.	Encl. No.	Leak Area (m^2)	Vent Area (m^2)	Total Area (m^2)	Max HRR (kW)
3	5	0.060	0.032	0.092	160
4	5	0.060	0	0.060	105
8	5	0.060	0.108	0.168	230
9	6	0.017	0	0.017	45
12	2	0.170	0.164	0.334	580
13	2	0.170	0	0.170	270
15	3	0.039	0	0.039	70
16	3	0.039	0.016	0.055	100
17	3	0.039	0.032	0.071	130
19	8	0.079	0	0.079	165
22	7	0.036	0.008	0.044	65
23	7	0.033	0.008	0.041	60
24	7	0.058	0.008	0.066	180
26	4	0.043	0.030	0.073	120
27	4	0.043	0.030	0.073	125
29	1	0.110	0	0.110	240
30	1	0.110	0.070	0.180	250
31	1	0.110	0.070	0.180	400

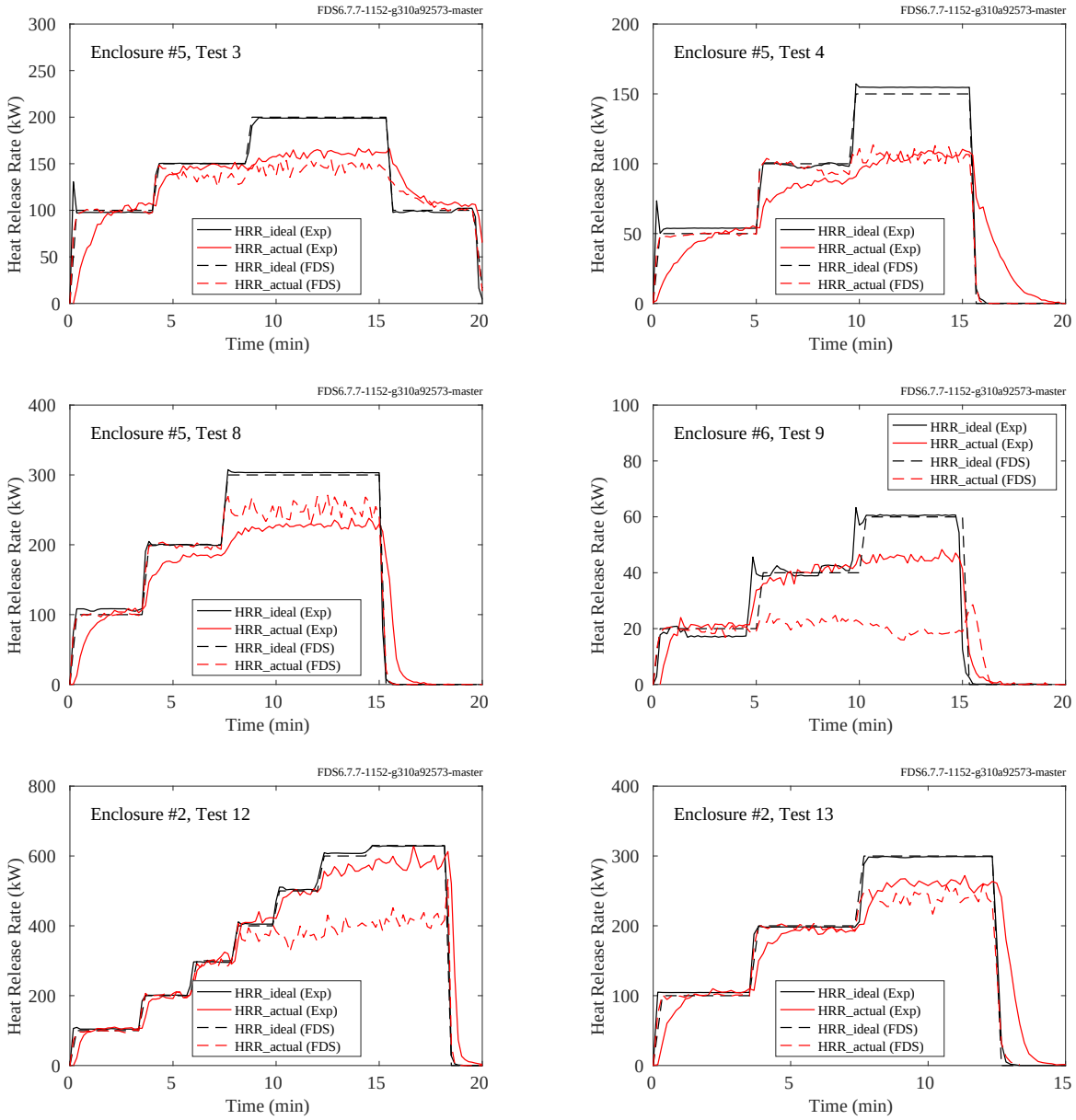

Figure 13.8: NIST/NRC OLIVE-Fire maximum HRR, Tests 3, 4, 8, 9, 12, 13.

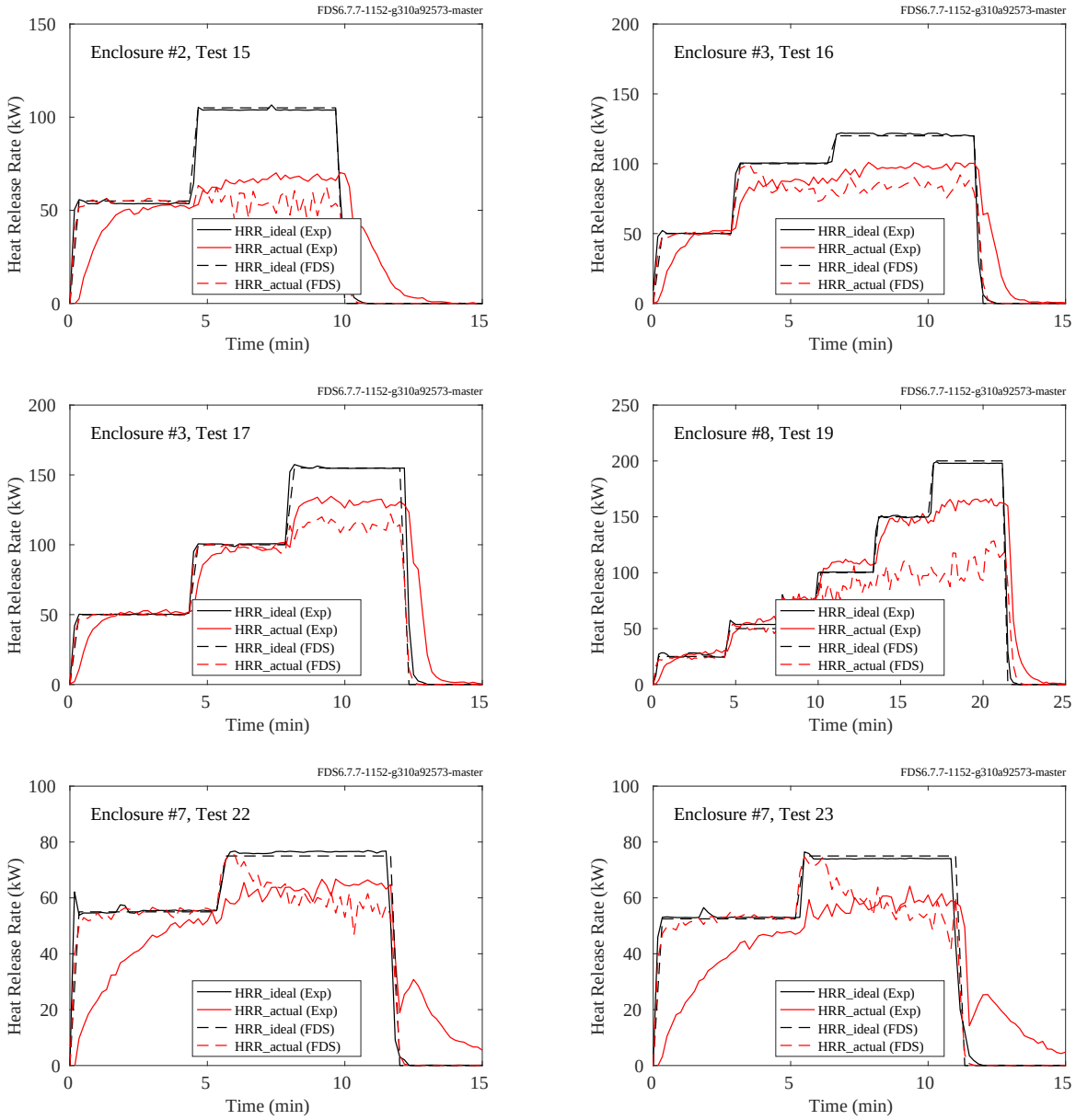

Figure 13.9: NIST/NRC OLIVE-Fire maximum HRR, Tests 15, 16, 17, 19, 22, 23.

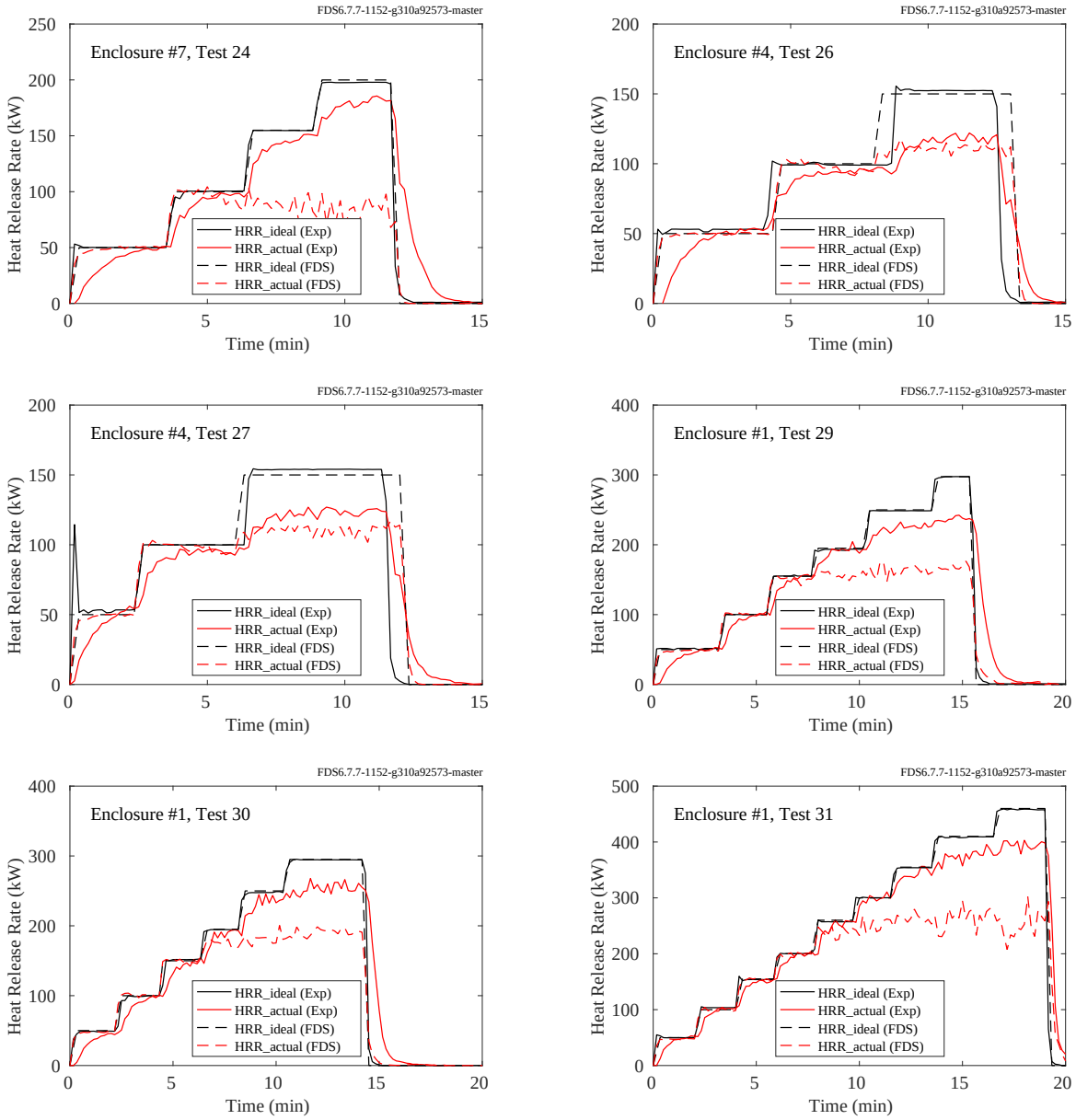

Figure 13.10: NIST/NRC OLIVE-Fire maximum HRR, Tests 24, 26, 27, 29, 30, 31.

13.2.3 SWJTU Tunnel Experiments

The figures below display the heat release rate as a function of time for the SWJTU Tunnel experiments.

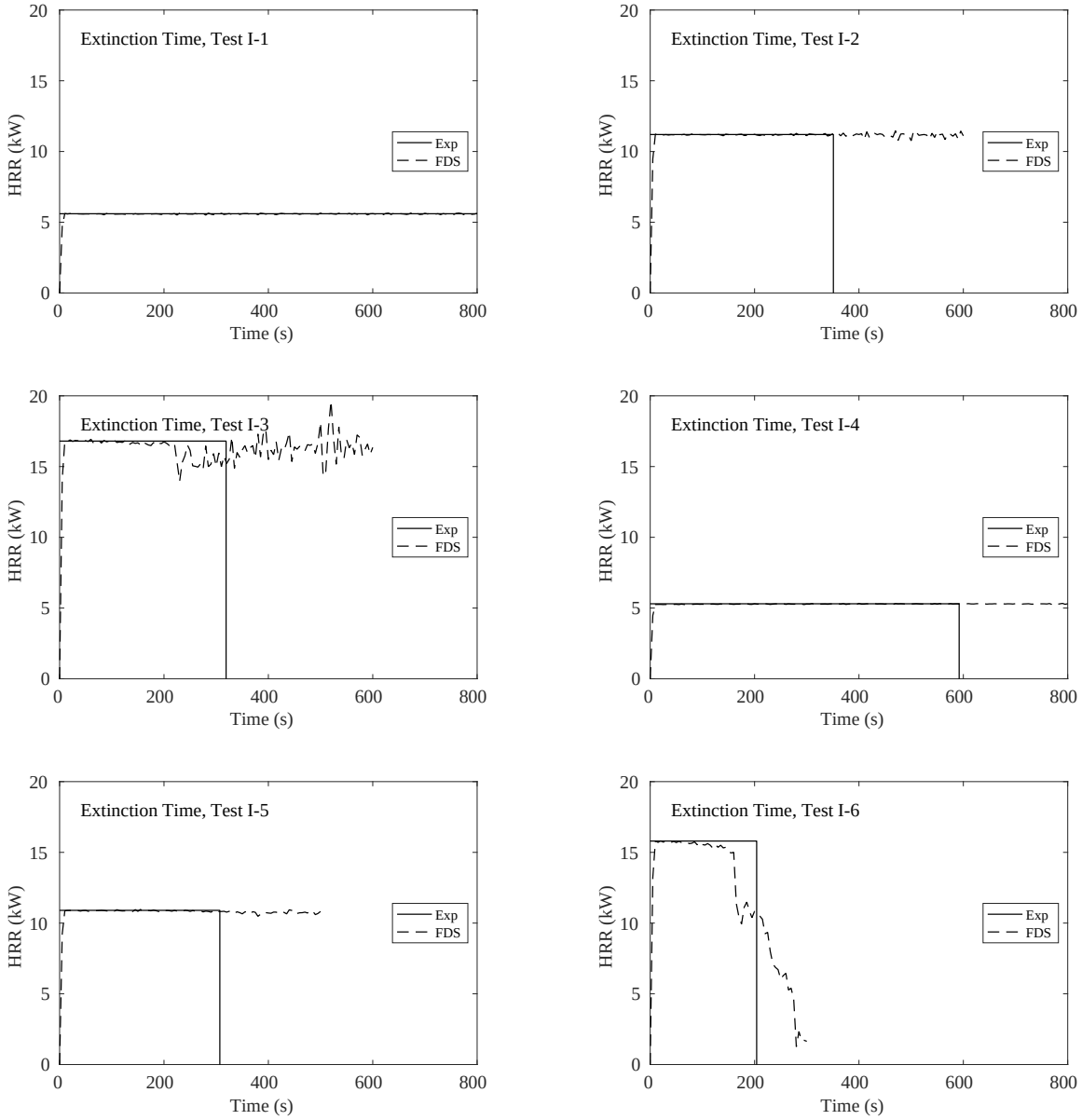

Figure 13.11: SWJTU Tunnel experiments, extinction time.

13.2.4 USCG/HAI Water Mist Suppression Tests

The following pages contain comparisons of the predicted heat release rates for fires that are suppressed with a water mist system. In all cases, the flow rate of liquid fuel is specified in the model, but the decrease in HRR due to the extinguishing system is predicted by the model. Table 13.2 reports the observed extinguishment times. Figure 13.17 compares the measured versus predicted extinguishment times. For the simulations, the extinguishment time is taken to be when the HRR drops to half of its specified value.

In cases where there is no reported fire extinction or the model does not predict extinction, the extinction time data is not used in the summary scatter plot, Fig. 13.17.

Table 13.2: Recorded extinguishment times for the USCG/HAI water mist suppression tests in a small shipboard machinery space. "No" means that the fire was not extinguished within 600 s of nozzle activation.

System		Navy	Grinnell	Fogtec	Chemetron	Fike
Number of Nozzles		6	6	6	15	6
Operating Pressure (bar)		70	13	100	12	21
Flow Rate (L/min)		68	75	22	70	48
Assumed Median Drop Size (μm)		175	225	100		200
Assumed Initial Velocity (m/s)		75	32	90		41
Assumed Spray Angle (deg.)		120	90	120		90
Fire Scenario	Ventilation	Extinguishment Time (s)				
1.0 MW Spray	Closed	15	26	21	27	21
1.0 MW Spray	Natural	15	40	32	43	35
1.0 MW Spray	Forced	17	55	76	357	133
0.5 MW Spray	Closed	34	70	39	53	56
0.5 MW Spray	Natural	41	117	67	158	140
0.5 MW Spray	Forced	124	No	No	No	No
0.25 MW Spray	Closed	157	360	169	314	277
0.25 MW Spray	Natural	206	No	290	525	566
0.25 MW Spray	Forced	No	No	No	No	No

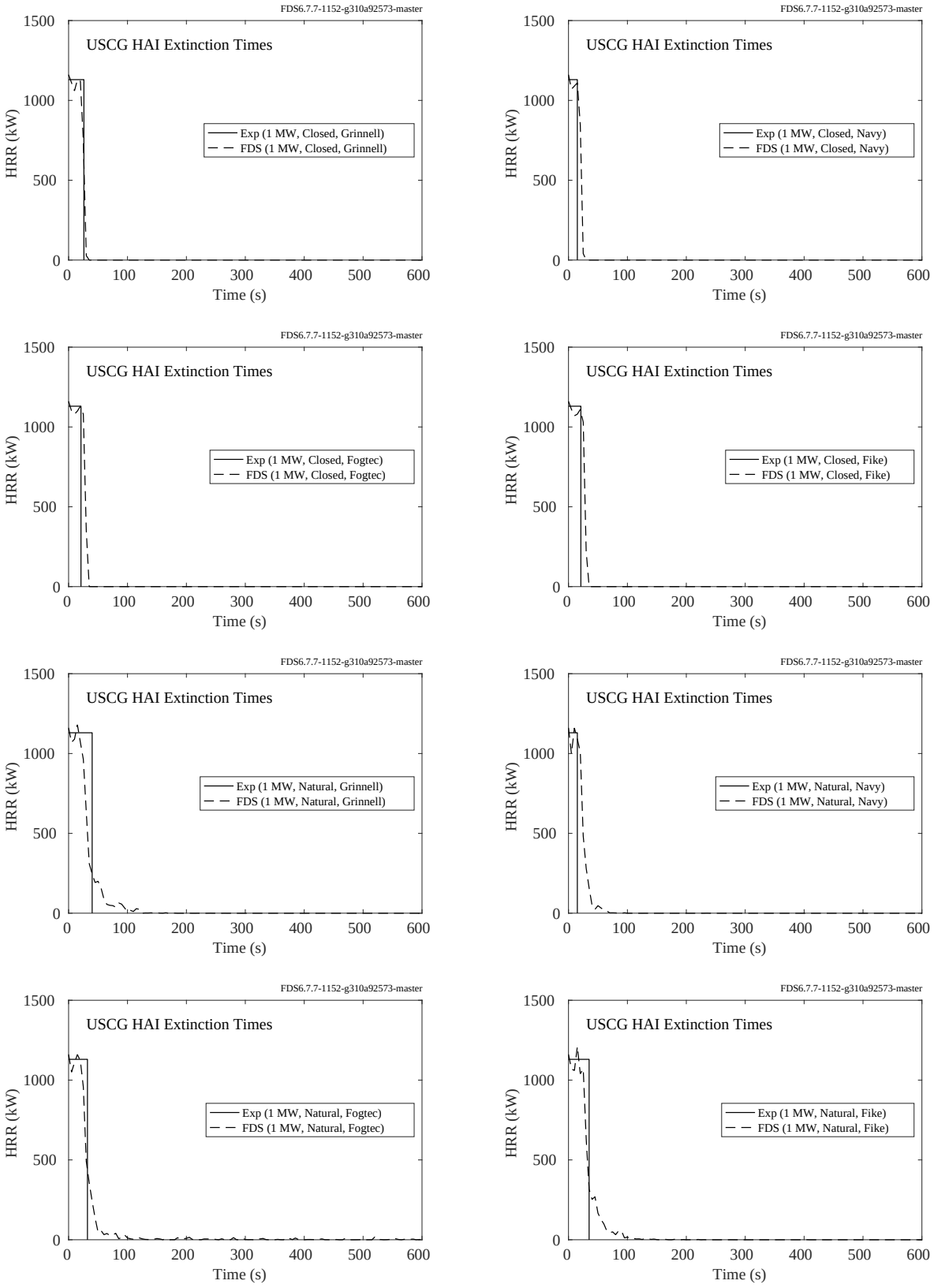

Figure 13.12: USCG/HAI experiments, extinction time.

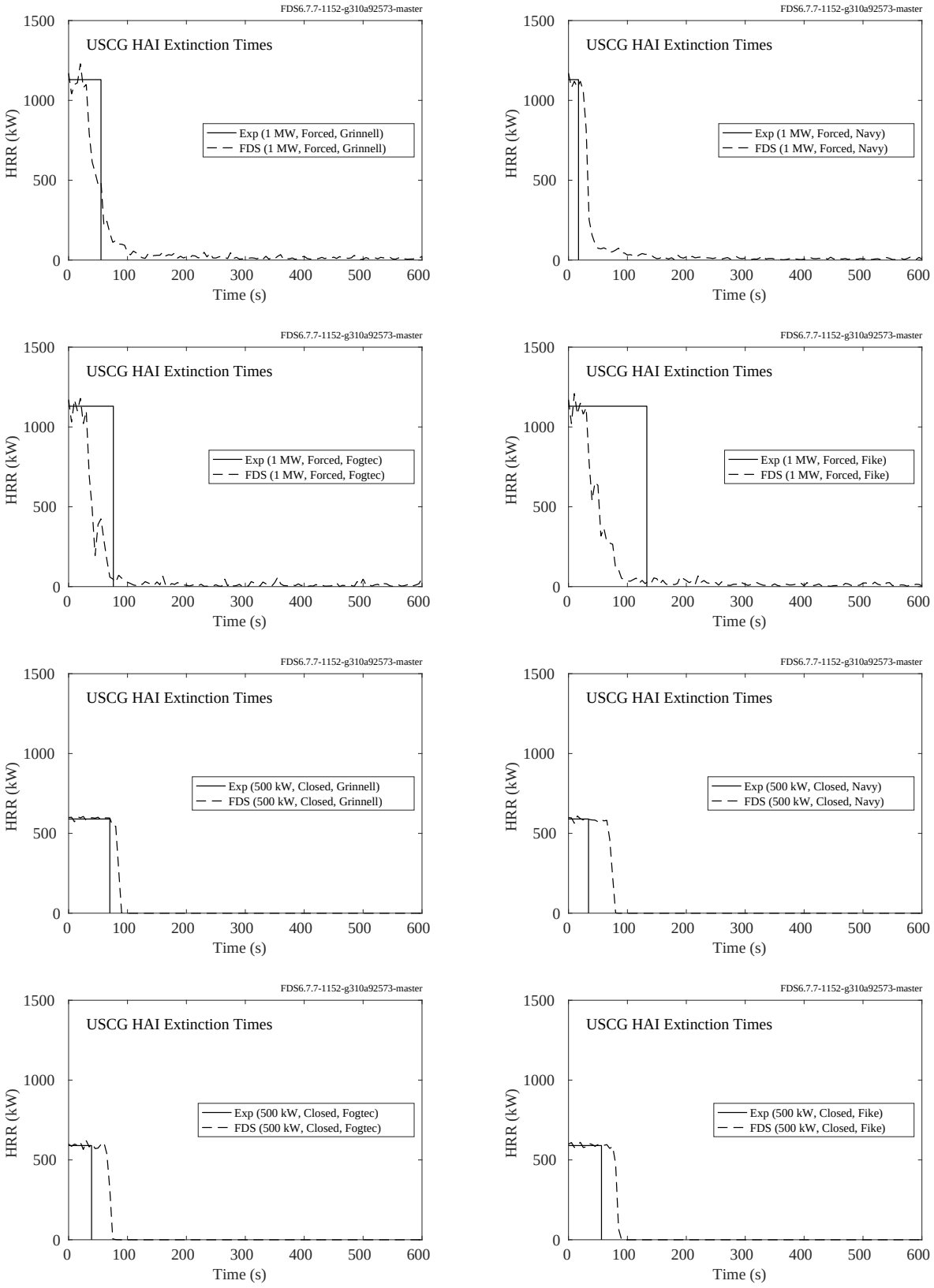

Figure 13.13: USCG/HAI experiments, extinction time.

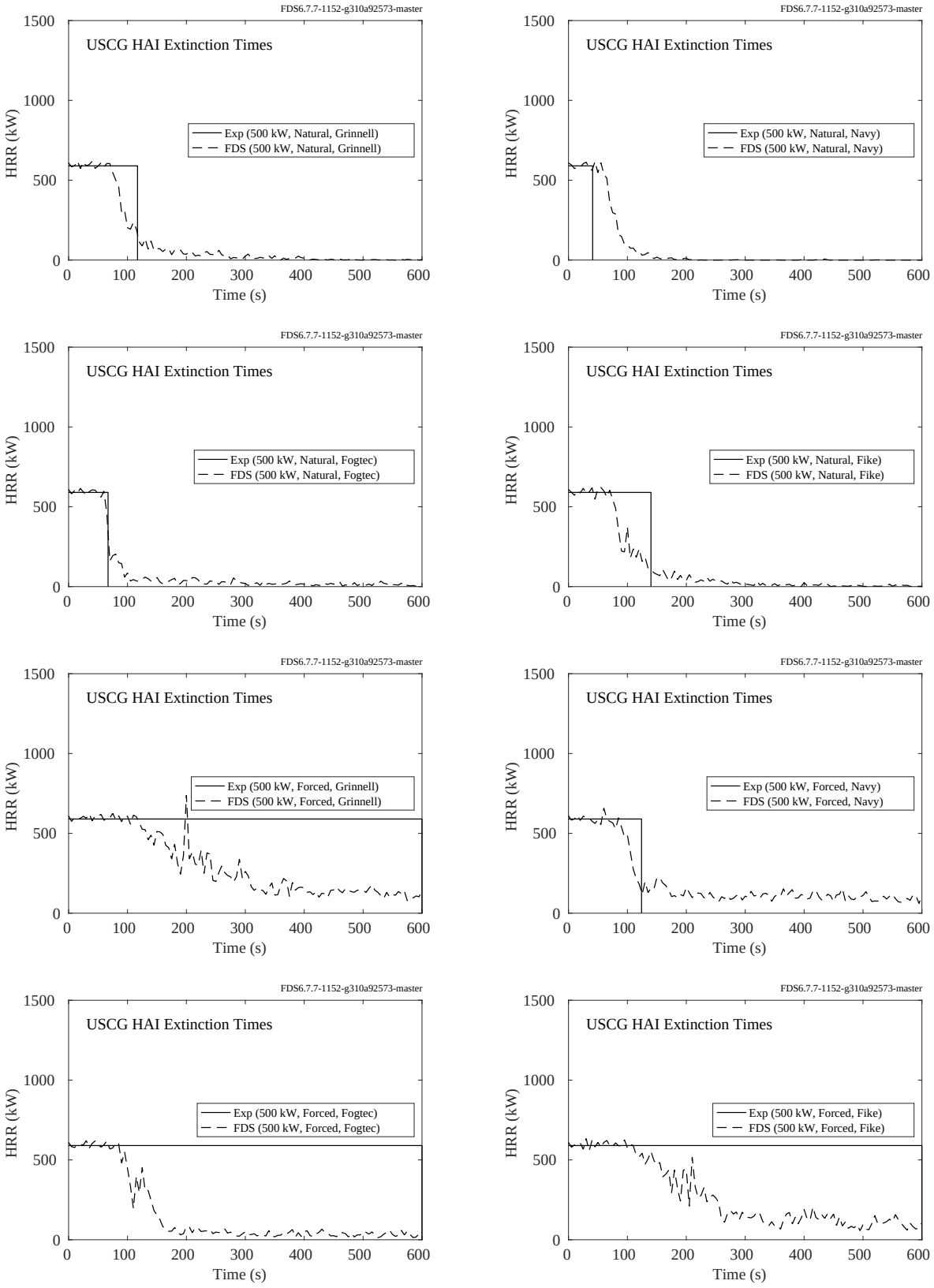

Figure 13.14: USCG/HAI experiments, extinction time.

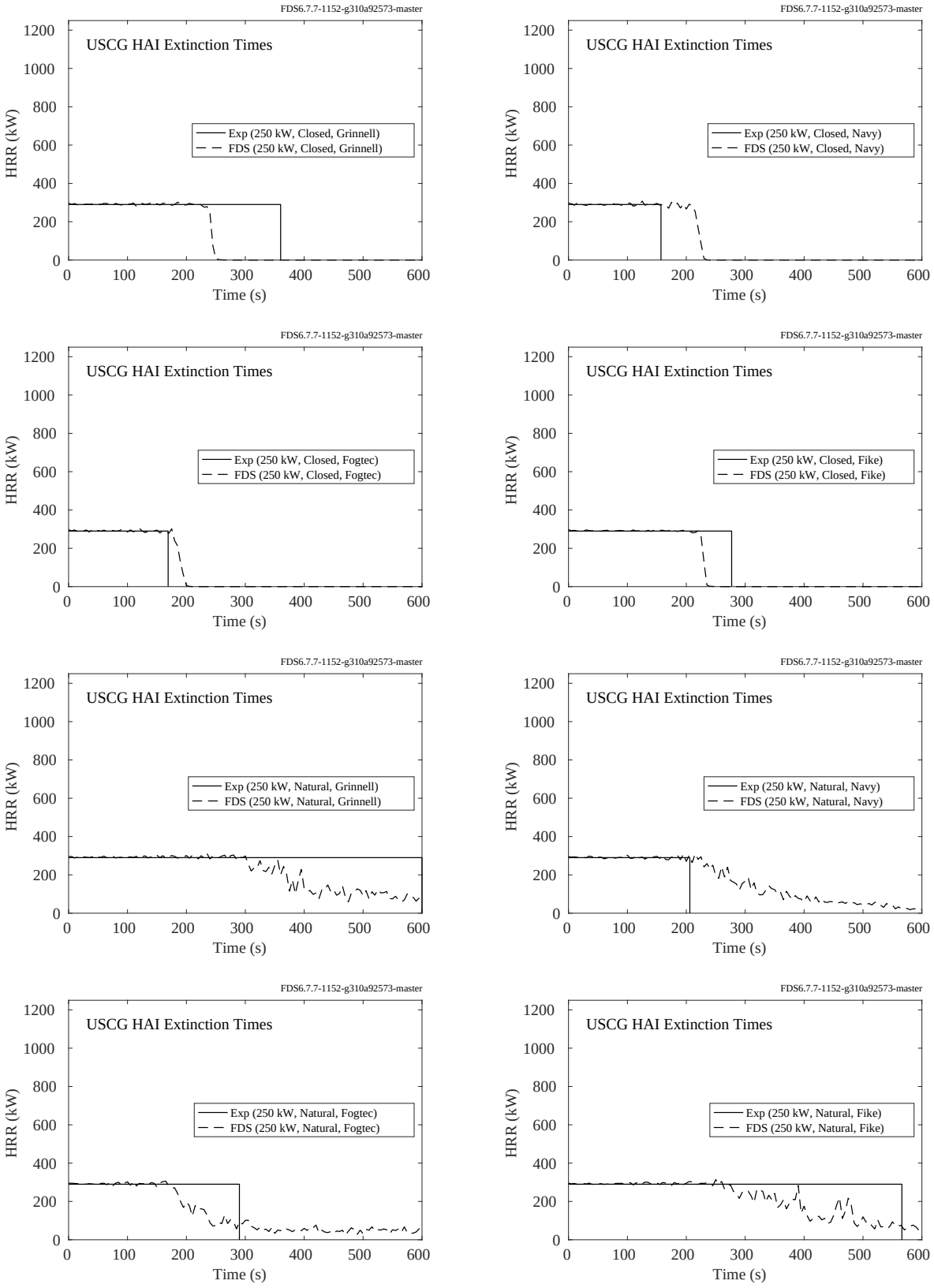

Figure 13.15: USCG/HAI experiments, extinction time.

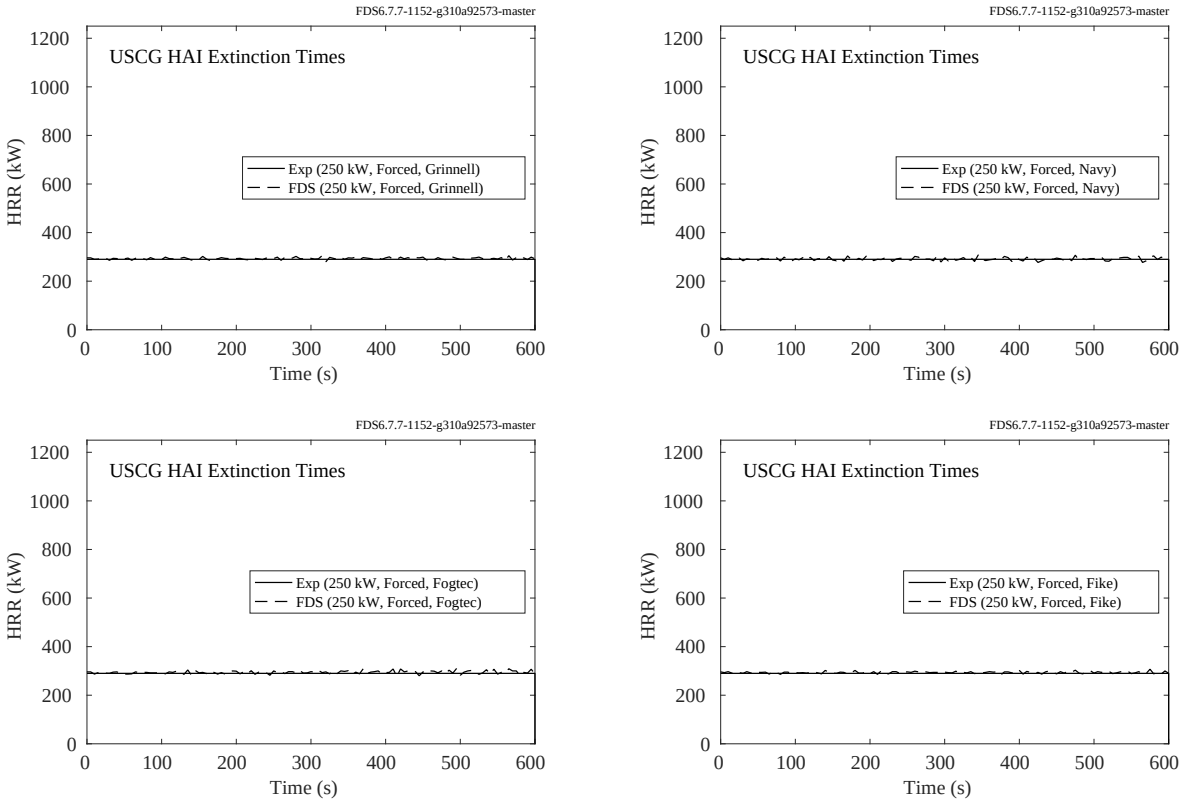

Figure 13.16: USCG/HAI experiments, extinction time.

13.2.5 Summary, Flame Extinction Time

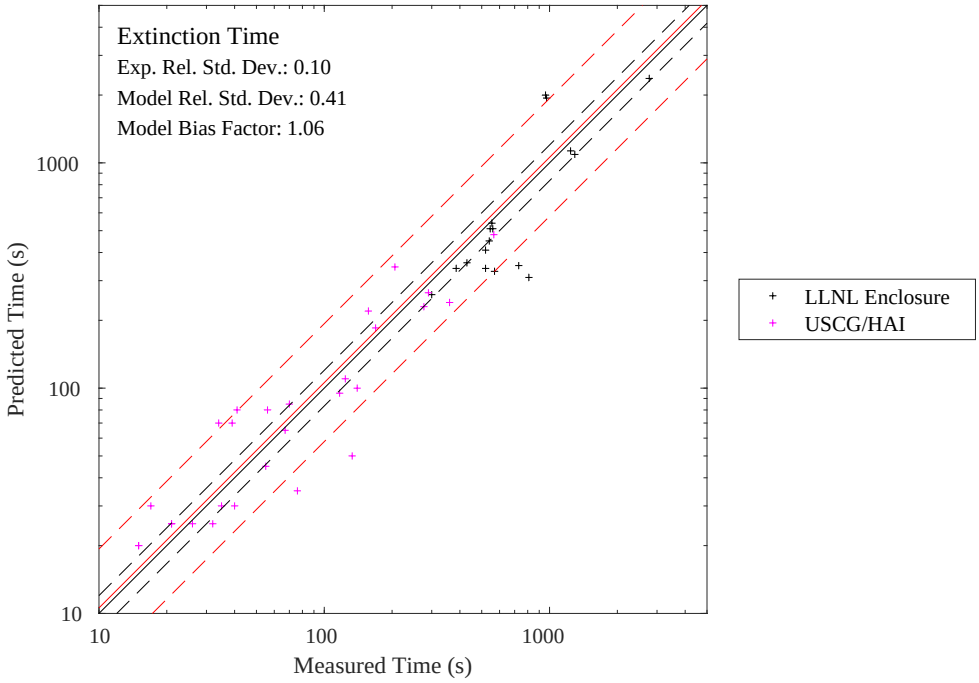

Figure 13.17: Comparison of measured and predicted extinguishment times for the USCG/HAI water mist suppression tests.

13.3 VTT Water Spray Experiments

Figure 13.18 presents profiles of mean droplet diameter, mean velocity, and droplet flux below a single 74° hollow-cone water mist nozzle. The pressure behind the nozzle was 2 MPa, and the flow constant was 0.077 L/min/bar$^{1/2}$. The The experimental data represents average values at each distance calculated over the four measuring points at that distance (except for the point at the spray axis). A comparison of droplet speed, mist flux and Sauter mean diameter (D_{32}) profiles are shown in Fig. 13.18. Comparisons are shown at 40 cm and 62 cm vertical distances from the nozzle. Simulation results are reported for three spatial resolutions: 1 cm, 2 cm, and 4 cm.

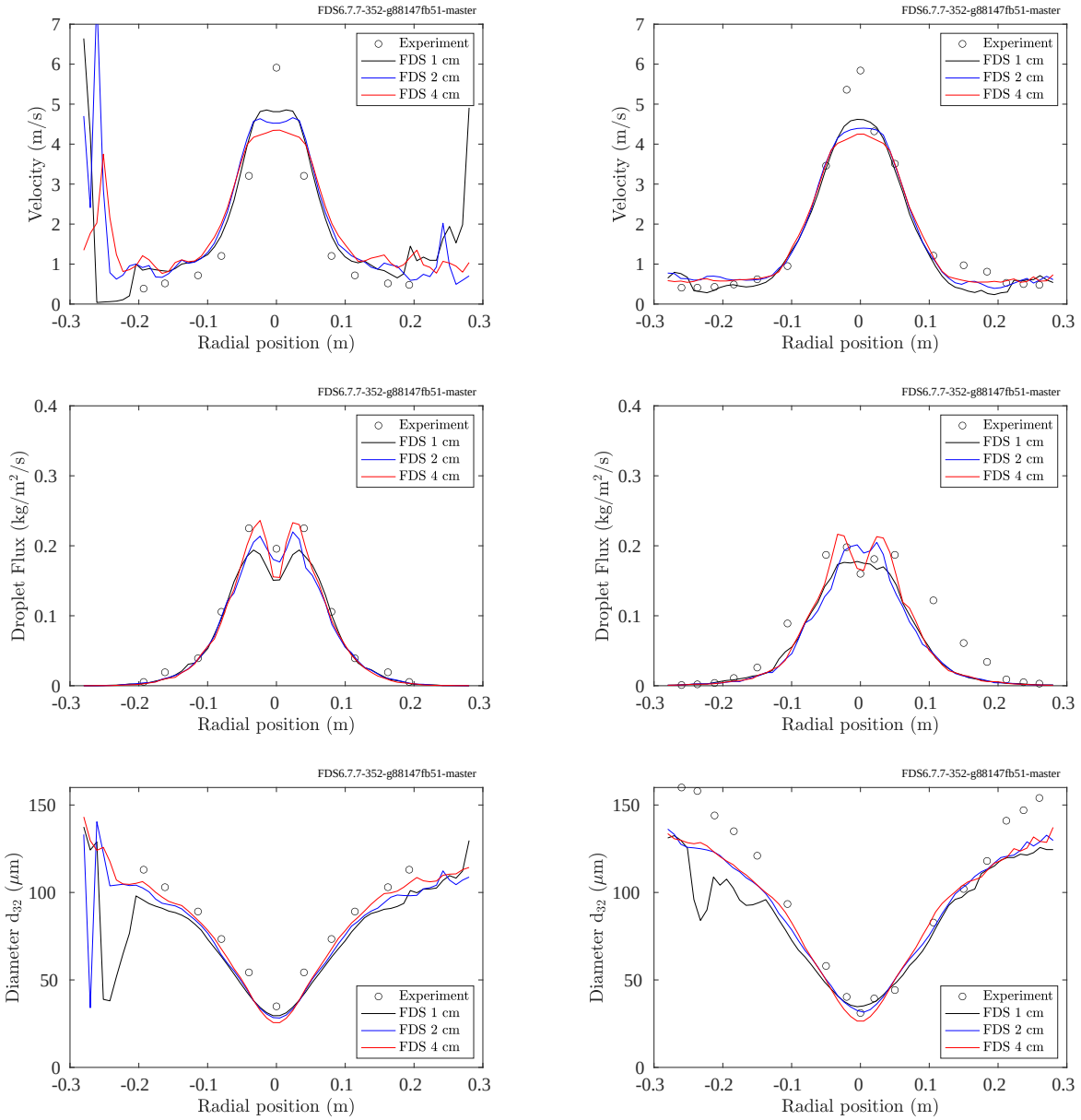

Figure 13.18: Comparison of predicted and experimental droplet speed (top), droplet flux (middle) and mean diameter (bottom) profiles of the LN-2 nozzle. The left column corresponds to measurements made 40 cm from the nozzle, while the right column corresponds to measurements made 62 cm from the nozzle.

Chapter 14

Burning Rate and Fire Spread

This chapter contains a series of validation exercises where the aim is to *predict* the burning and spread rate of the fire. Most of the simulations included in the previous chapters involved a *specified* burning or heat release rate. Here, the objective is to apply measured thermophysical properties of the material and predict its burning rate, either with a specified heat flux or as a free burn.

14.1 FAA Polymers

The U.S. Federal Aviation Administration (FAA) has studied various plastics that are commonly used aboard commercial aircraft.

This section presents measured properties of various polymers and the numerical predictions of their mass loss and/or burning rates under constant heat heating. Two types of experiments are considered. First, the NIST Gasification Apparatus is used to measure the mass loss rate of non-burning samples in a nitrogen atmosphere. Second, the standard Cone Calorimeter [345] is used to measure the heat release rate of materials in a normal atmosphere. When just the mass loss rate of a non-burning sample has been measured, FDS is run in "solid phase only" mode; that is, a 1-D heat conduction calculation is performed in a single grid cell. The result is the predicted mass loss rate as a function of time. To simulate a cone calorimeter experiment, FDS simulates the burning of a 10 cm by 10 cm sample with a specified heat flux to represent the effect of the cone heater. The cone itself is not included in the simulation. As the sample burns, FDS predicts the additional radiative and convective heating of the sample as a result of the fire.

In general, the burning/gasification rate of a charring polymer is more difficult to predict than a non-charring one because there are more parameters that need to be measured and more complicated behavior, like intumescence, need to be considered.

14.1.1 Glossary of Terms

Assumption: Characteristics were assumed from known properties in similar materials.

Cone Calorimeter (ASTM E 1354 [345]) The Cone Calorimeter exposes a small sample to a constant external radiant heat flux simulating exposure of the sample to a large scale fire. The device records mass loss data along with heat release data through oxygen consumption calorimetry. From this a variety of heat release related properties can be found including heat of combustion.

Constant Volume: The material is assumed to maintain a constant volume during the solid phase reactions.

Direct: Direct measurement of densities is performed by measuring the dimensions and mass of the sample.

DSC: (ASTM E 2070 [346]) A Differential Scanning Calorimeter precisely raises the temperature of a small sample of material at a constant rate. This coupled with knowledge of heat absorbed by the sample allows for the calculation of the specific heat function of a material as well as heats of reaction and phase change.

Estimated: Characteristics were approximated based on known properties in similar materials.

FTIR: Fourier Transform Infrared Spectroscopy uses a spectrometer to simultaneously characterize the absorption of all frequencies of infrared light. In testing a sample is exposed to infrared light and a detector records light that has passed through the sample. A Fourier transform of detector measurement is then translated into absorption information.

Gasification Apparatus: Similar to the Cone Calorimeter however flaming is prevented. This is done typically through the introduction of inert purge gases.

Inherited: The properties of the product or component are assumed to be the same as the original material.

Inverse Analysis: Property was established by fitting a model to measured temperatures from the Cone Calorimeter or Gasification Apparatus.

IS: (ASTM E 1175 [347]) An Integrating Sphere, or an Ulbricht Sphere, is a hollow cavity whose interior has a high diffuse reflectivity. A sample placed inside the sphere is exposed to incident radiation and reflectivity measured. Emissivity can be determined from this information. The standard above is for measurement of Solar reflectivity, and was not necessarily precisely followed.

Laser Flash: (ASTM E1461 [348]) In the Laser Flash Method one surface of a sample is rapidly heated using a single pulse from a laser. Heat sensors on the opposite side of the sample record the arrival of the resulting temperature disturbance. From this thermal diffusivity/thermal conductivity can be calculated.

Literature: Results were found within previously published literature.

MCC: (ASTM D 7309 [349]) The Microscale Combustion Calorimeter (MCC) rapidly pyrolyzes a milligram size sample in an inert atmosphere. The pyrolyzate is then exposed to an abundance of oxygen. Heat release history is obtained from oxygen consumption. Similar to TGA with heat release recorded rather than mass loss rate.

Pulsed Current: Can refer to different types of tests. Generally, a sample is positioned between two electrodes in a sealed chamber with an inert atmosphere. The sample is heated through pulses of current. Measurements of the sample and the chamber can give information regarding specific heat, emissivity, or other material properties.

TGA: (ASTM E 1131 [350]) In Thermal Gravimetric Analysis (TGA) a small sample is heated at uniform rate, generally in a Nitrogen (N_2) atmosphere. The percentage weight loss of the sample is recorded relative to the sample's temperature. Rate constants can then be fitted to the data. Similar to MCC with mass loss recorded instead of heat release.

TLS: (ASTM D 5930 [351]) The Transient Line Source method records temperature of a single point at a fixed distance in a sample over time using a probe. Given knowledge of the heat exposure of the sample the thermal conductivity can be found from the slope of the recorded data.

14.1.2 Non-Charring Polymers, HDPE, HIPS, and PMMA

A non-charring polymer is considered one of the easiest solids to model because it typically involves only a single, first order reaction that converts solid plastic to fuel vapor. No residue is formed and the plastic is completely pyrolyzed. Table 14.1 lists nine parameters for each polymer studied. These values have been input directly into FDS, and the predicted mass loss rates are compared with measured values from the NIST Gasification Apparatus, a device that pyrolyzes the solid in a nitrogen environment to prevent combustion of fuel gases. The results are shown in Fig. 14.1. The exposing heat flux was 52 kW/m^2. A 1 cm layer of insulation was placed under the sample. Its properties are given in Ref. [193].

Table 14.1: Input parameters for FAA Polymers non-charring samples. Courtesy S. Stoliarov, M. McKinnon and J. Li, University of Maryland. See Section 14.1.1 for an explanation of terms.

Property	Units	HDPE	HIPS	PMMA	Unc. (%)	Method	Ref.
Density	kg/m^3	860	950	1100	5	Direct	[193]
Conductivity	W/m/K	0.29	0.22	0.20	15	TLC	[193]
Specific Heat	kJ/kg/K	3.5	2.0	2.2	15	DSC	[352]
Emissivity		0.92	0.86	0.85	20	IS	[353]
Absorption Coef.	m^{-1}	1300	2700	2700	50	FTIR	[354]
Pre-Exp. Factor	s^{-1}	4.8×10^{22}	1.2×10^{16}	8.5×10^{12}	50	TGA	[193]
Activation Energy	J/mol	3.49×10^5	2.47×10^5	1.88×10^5	3	TGA	[193]
Heat of Reaction	kJ/kg	920	1000	870	15	DSC	[352]

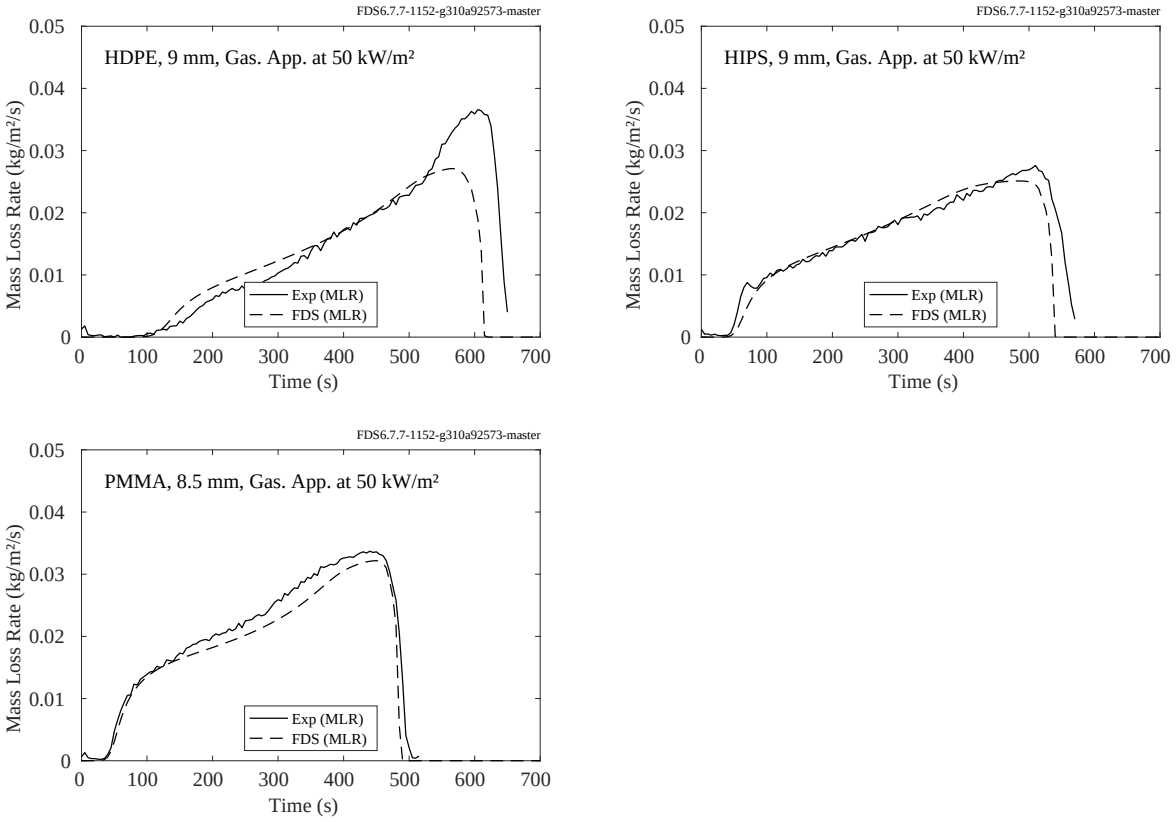

Figure 14.1: Comparison of predicted and measured mass loss rates for three non-charring polymers exposed to a heat flux of 52 kW/m^2 in a nitrogen environment.

14.1.3 Complex Non-Charring Polymers: PP, PA66, POM, and PET

The polymers described in this section exhibit slightly more complex behavior than those in the previous section because they exhibit foaming and bubbling as they degrade. Table 14.2 lists the properties of each polymer. In the model, the polymers melt to form a liquid with identical properties as the solid. The melting is characterized by a relatively fast reaction that occurs near the melting temperature with a heat of reaction equivalent to a heat of melting. The predicted mass loss rates are compared with measured values from the NIST Gasification Apparatus, a device that pyrolyzes the solid in a nitrogen environment to prevent combustion of fuel gases. The results are shown in Fig. 14.2. The exposing heat flux is 50 kW/m^2. A thin sheet of aluminum foil and a 2.5 cm layer of Foamglas insulation underlies the sample. Its properties are given in Ref. [355].

Table 14.2: Input parameters for FAA Polymers complex non-charring samples [355]. Courtesy S. Stoliarov, G. Linteris and R.E. Lyon. See Section 14.1.1 for an explanation of terms.

Property	Units	PP	PA66	POM	PET	Unc. (%)	Method
Density	kg/m^3	910	1150	1425	1380	5	Direct
Conductivity	W/m/K	0.24	0.34	0.28	0.29	15	TLC
Specific Heat	kJ/kg/K	2.68	2.54	1.88	2.01	15	DSC
Emissivity		0.96	0.95	0.95	0.903	20	IS
Absorption Coef.	m^{-1}	966	3920	3550	2937	50	FTIR
Pre-Exp. Factor	s^{-1}	1.6×10^{23}	5.7×10^{17}	3.7×10^{10}	4.50×10^{18}	50	TGA
Activation Energy	J/mol	3.52×10^5	2.74×10^5	1.57×10^5	2.81×10^5	3	TGA
Heat of Reaction	kJ/kg	1310	1390	1570	1800	15	DSC
Heat of Melting	kJ/kg	80	55	141	37	15	DSC
Melting Temperature	K	158	262	165	253	15	DSC

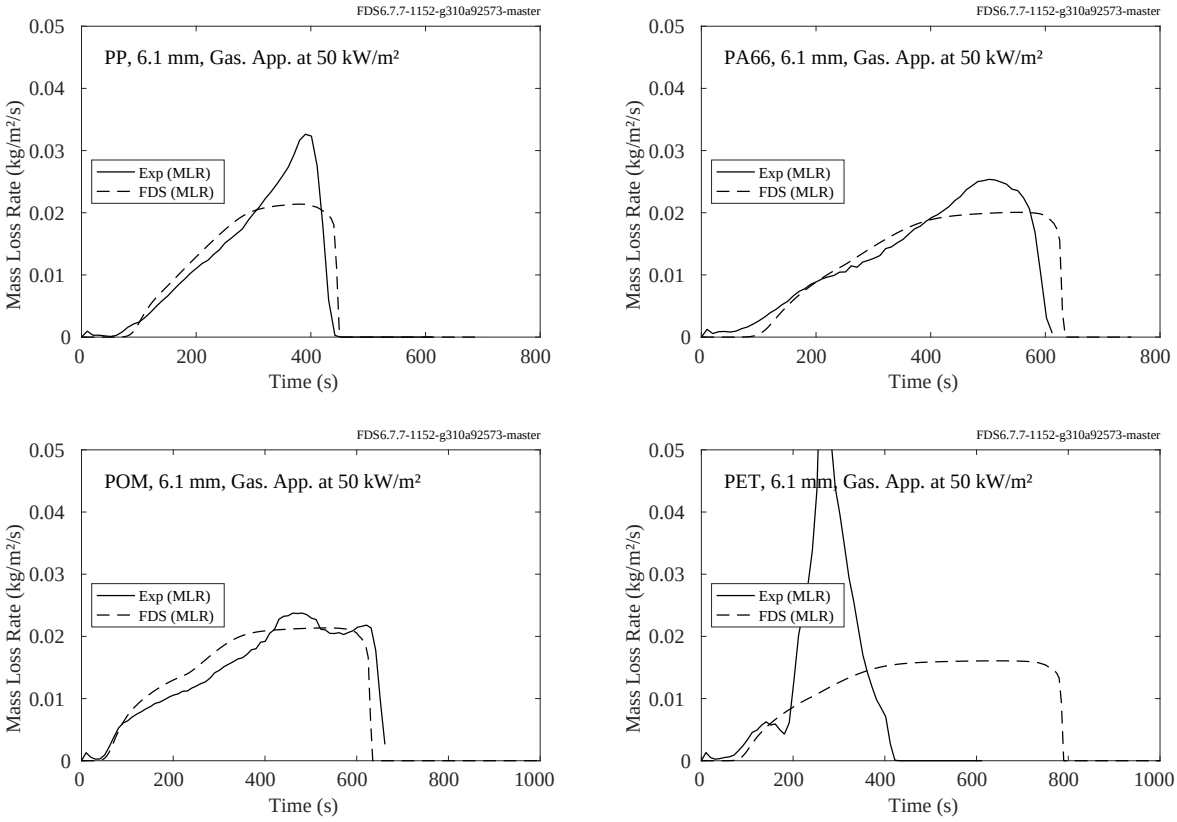

Figure 14.2: Comparison of predicted and measured mass loss rates for four complex non-charring polymers exposed to a heat flux of 50 kW/m^2 in a nitrogen environment.

14.1.4 Polycarbonate (PC)

Table 14.3 lists the measured properties of polycarbonate. These values have been input directly into FDS, and the predicted heat release rates are compared with measured values from the Cone Calorimeter. The results for samples of various thicknesses and imposed heat fluxes are shown in Fig. 14.3. A 1 cm layer of Kaowool insulation was placed under the sample. Its properties are given in Ref. [194]. It is assumed that the polymer undergoes a single step reaction that forms fuel gas and char.

$$\mathrm{PC} \rightarrow 0.21\,\mathrm{Char} + 0.79\,\mathrm{Gas} \tag{14.1}$$

Table 14.3: Properties of polycarbonate (PC). Courtesy S. Stoliarov, University of Maryland. See Section 14.1.1 for an explanation of terms.

Property	Units	Value	Method	Reference
Polymer Density	kg/m^3	1180 ± 60	Direct	[194]
Polymer Conductivity	W/m/K	0.22 ± 0.03	Literature	[194]
Polymer Specific Heat	kJ/kg/K	1.9 ± 0.3	DSC	[352]
Polymer Emissivity		0.90 ± 0.05	IS	[353]
Polymer Absorption Coef.	m^{-1}	1770 ± 590	FTIR	[354]
Char Density	kg/m^3	248	Cone Calorimeter	[194]
Char Conductivity	W/m/K	0.37	Cone Calorimeter	[194]
Char Specific Heat	kJ/kg/K	1.72 ± 0.17	Pulsed Current	[194, 356]
Char Emissivity		0.85 ± 0.05	Pulsed Current	[194, 356]
Char Absorption Coef.	m^{-1}	Opaque	Assumption	[194]
Pre-Exp. Factor	s^{-1}	$(1.9 \pm 1.1) \times 10^{18}$	TGA	[194]
Activation Energy	J/mol	$(2.95 \pm 0.06) \times 10^5$	TGA	[194]
Heat of Reaction	kJ/kg	830 ± 140	DSC	[352]
Heat of Combustion	kJ/kg	25600 ± 130	MCC	[194]
Combustion Efficiency		0.84 ± 0.03	Cone Calorimeter	[194]

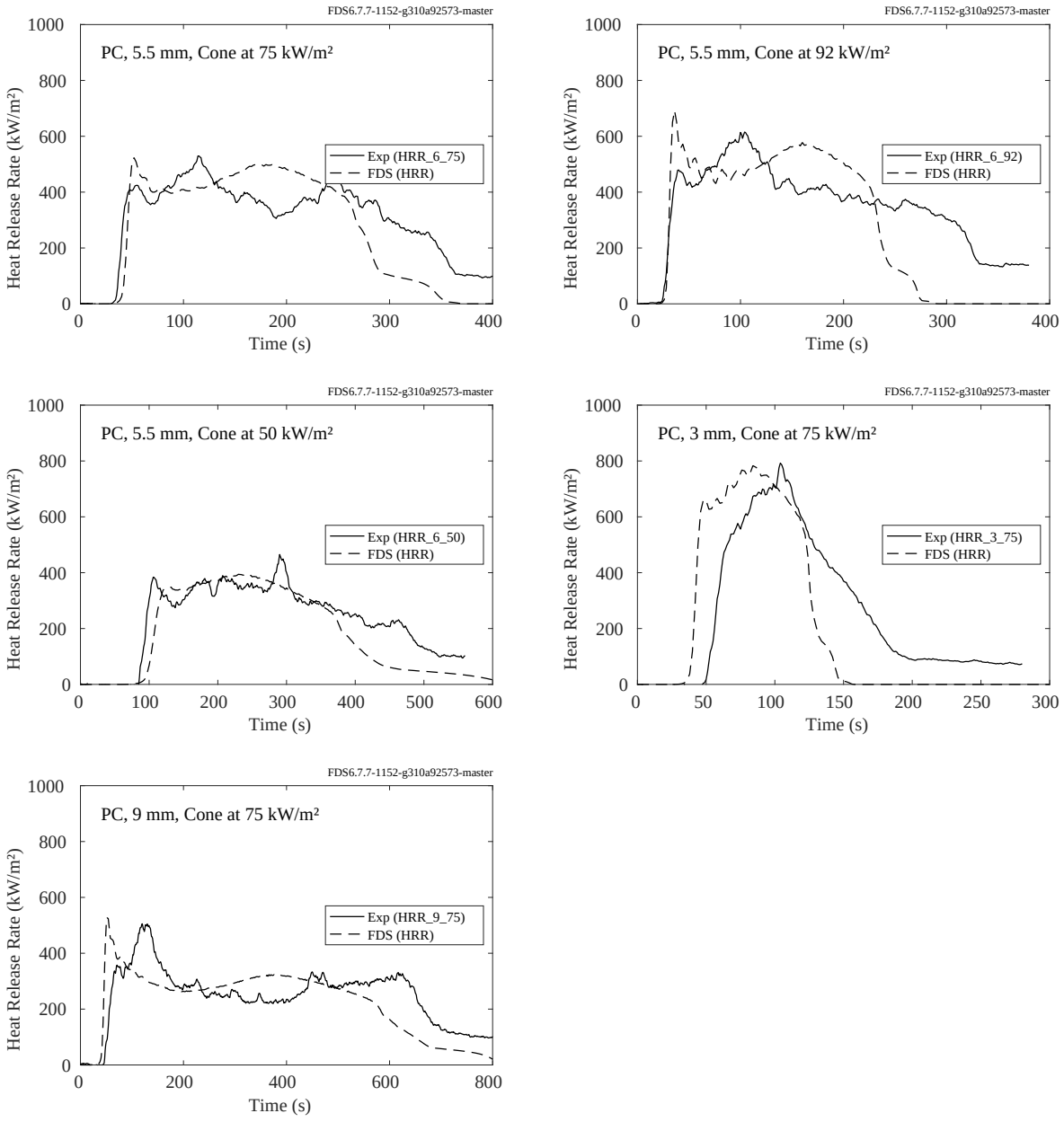

Figure 14.3: Comparison of predicted and measured heat release rates for polycarbonate (PC).

14.1.5 Poly(vinyl chloride) (PVC)

Table 14.4 lists the measured properties of poly(vinyl chloride). These values have been input directly into FDS, and the predicted heat release rates are compared with measured values from the Cone Calorimeter. The results for samples of various thicknesses and imposed heat fluxes are shown in Fig. 14.4. A 1 cm layer of Kaowool insulation was placed under the sample. Its properties are given in Ref. [194].

It is assumed that the polymer decomposes via a two-step reaction:

$$\text{Polymer} \rightarrow 0.44\,\text{Char 1} + 0.56\,\text{Gas 1} \tag{14.2}$$

$$\text{Char 1} \rightarrow 0.47\,\text{Char 2} + 0.53\,\text{Gas 2} \tag{14.3}$$

Table 14.4: Properties of poly(vinyl chloride) (PVC). Courtesy S. Stoliarov, University of Maryland. See Section 14.1.1 for an explanation of terms.

Property	Units	Value	Method	Reference
Polymer Density	kg/m^3	1430 ± 70	Direct	[194]
Polymer Conductivity	W/m/K	0.17 ± 0.01	Literature	[194]
Polymer Specific Heat	kJ/kg/K	1.55 ± 0.25	DSC	[352]
Polymer Emissivity		0.90 ± 0.05	IS	[353]
Polymer Absorption Coef.	m^{-1}	2145 ± 715	FTIR	[354]
Char 1 Density	kg/m^3	629	Constant Volume	[194]
Char 1 Conductivity	W/m/K	0.17	Inherited	[194]
Char 1 Specific Heat	kJ/kg/K	1.55 ± 0.25	Inherited	[194]
Char 1 Emissivity		0.90 ± 0.05	Inherited	[194]
Char 1 Absorption Coef.	m^{-1}	2453	Inverse Analysis	[194]
Char 2 Density	kg/m^3	296	Constant Volume	[194]
Char 2 Conductivity	W/m/K	0.26	Inverse Analysis	[194]
Char 2 Specific Heat	kJ/kg/K	1.72 ± 0.17	Pulsed Current	[194, 356]
Char 2 Emissivity		0.85 ± 0.05	Pulsed Current	[194, 356]
Char 2 Absorption Coef.	m^{-1}	Opaque	Assumption	[194]
Reac 1 Pre-Exp. Factor	s^{-1}	$(1.4 \pm 0.8) \times 10^{33}$	TGA	[194]
Reac 1 Activation Energy	J/mol	$(3.67 \pm 0.07) \times 10^5$	TGA	[194]
Reac 1 Char Yield		0.44 ± 0.01	TGA	[194]
Reac 1 Heat of Reaction	kJ/kg	170 ± 17	DSC	[352]
Gas 1 Heat of Combustion	kJ/kg	2700 ± 300	MCC	[194]
Gas 1 Combustion Efficiency		0.75 ± 0.03	Cone Calorimeter	[194]
Reac 2 Pre-Exp. Factor	s^{-1}	$(3.5 \pm 2.1) \times 10^{12}$	TGA	[194]
Reac 2 Activation Energy	J/mol	$(2.07 \pm 0.04) \times 10^5$	TGA	[194]
Reac 2 Char Yield		0.47 ± 0.01	TGA	[194]
Reac 2 Heat of Reaction	kJ/kg	1200 ± 900	DSC	[352]
Gas 2 Heat of Combustion	kJ/kg	36500 ± 1800	MCC	[194]
Gas 2 Combustion Efficiency		0.75 ± 0.03	Cone Calorimeter	[194]

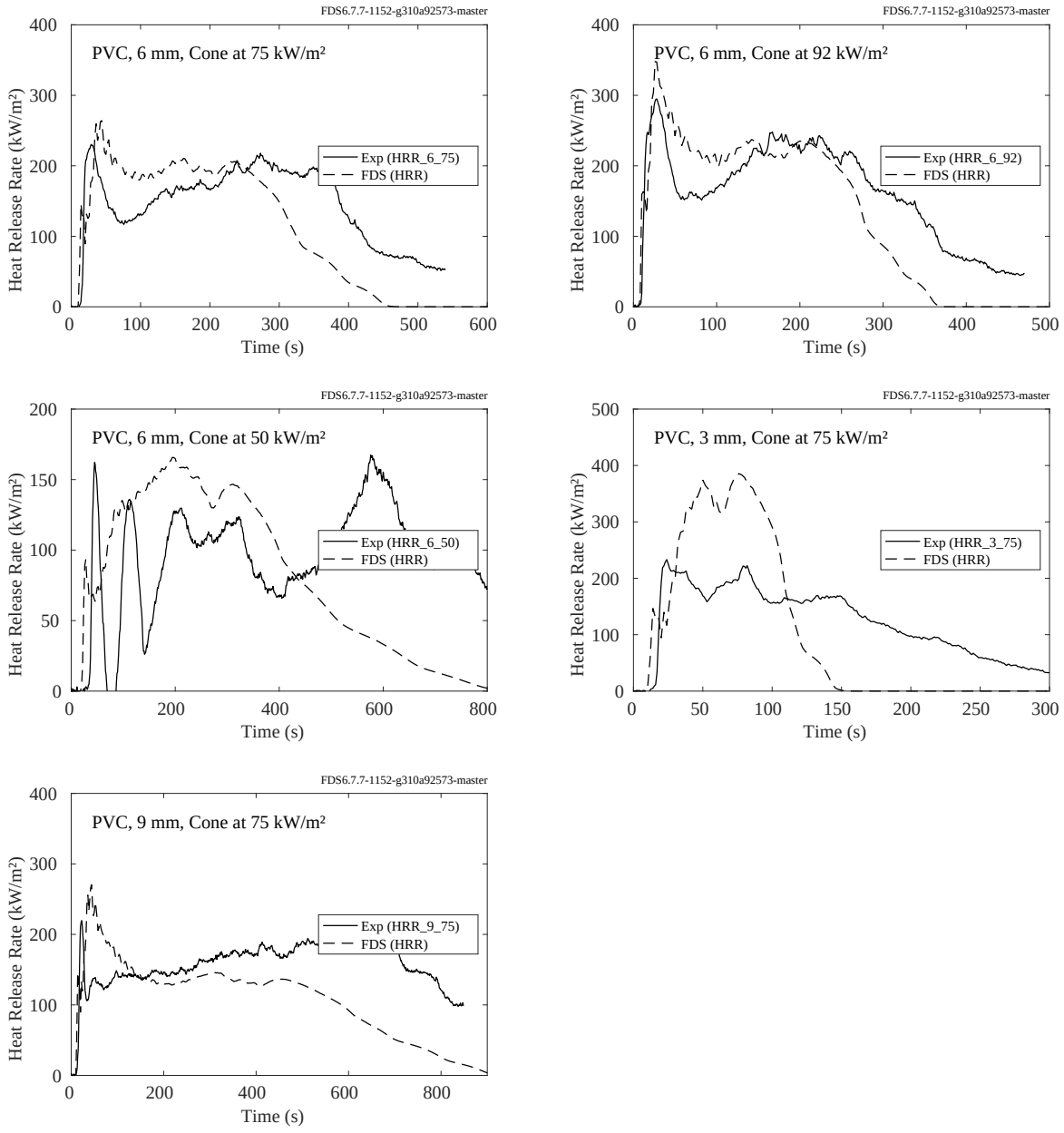

Figure 14.4: Comparison of predicted and measured heat release rates for poly(vinyl chloride) (PVC).

14.1.6 Poly(aryl ether ether ketone)) (PEEK)

Table 14.5 lists the measured properties of poly(aryl ether ether ketone)[1]. Its property values have been input directly into FDS, and the predicted heat release rates are compared with measured values from the Cone Calorimeter. It is assumed that the polymer decomposes via a four-step reaction:

$$\text{Polymer} \rightarrow 0.62\,\text{Char 1} + 0.38\,\text{Gas 1} \tag{14.4}$$

$$\text{Char 1} \rightarrow 0.88\,\text{Char 2} + 0.12\,\text{Gas 2} \tag{14.5}$$

$$\text{Char 2} \rightarrow 0.88\,\text{Char 3} + 0.12\,\text{Gas 2} \tag{14.6}$$

$$\text{Char 3} \rightarrow \text{Gas 2} \tag{14.7}$$

It is also assumed that the gaseous fuel molecule is $C_{19}H_{12}O_3$. A 1 cm layer of Kaowool insulation was placed under the sample. Its properties are given in Ref. [194].

The results for 3.9 mm samples at imposed heat fluxes of 50 kW/m^2, 70 kW/m^2, and 90 kW/m^2 are shown in Fig. 14.5. Note that the plots on the left are the results of simulations of the solid phase only, where the heat feedback from the fire is assumed to be 15 kW/m^2 and it is applied at the time of ignition. The plots on the right are from 3-D simulations of the solid sample and the fire. In these cases, the radiative feedback is not specified but rather calculated.

[1] Trade name VICTREX PEEK 450G. The sample has been thoroughly dried.

Table 14.5: Properties of poly(aryl ether ether ketone) (PEEK). Courtesy E. Oztekin, U.S. FAA and S. Stoliarov, University of Maryland. See Section 14.1.1 for an explanation of terms.

Property	Units	Value	Method	Reference
Polymer Density	kg/m^3	1300	Direct	[357]
Polymer Conductivity	W/m/K	0.28	Inverse Analysis	[357]
Polymer Specific Heat	kJ/kg/K	2.05	Inverse Analysis	[357]
Polymer Emissivity		0.90	Inverse Analysis	[357]
Polymer Absorption Coef.	m^{-1}	1690	Inverse Analysis	[357]
Char 1 Density	kg/m^3	810	Constant Volume	[357]
Char 1 Conductivity	W/m/K	0.37	Inverse Analysis	[357]
Char 1 Specific Heat	kJ/kg/K	0.24	Assumed	[357]
Char 1 Emissivity		1	Assumed	[357]
Char 1 Absorption Coef.	m^{-1}	81000	Assumed opaque	[357]
Char 2 Density	kg/m^3	710	Constant Volume	[357]
Char 2 Conductivity	W/m/K	0.37	Inverse Analysis	[357]
Char 2 Specific Heat	kJ/kg/K	0.27	Assumed	[357]
Char 2 Emissivity		1	Assumed	[357]
Char 2 Absorption Coef.	m^{-1}	71000	Assumed opaque	[357]
Reac 1 Pre-Exp. Factor	s^{-1}	1.0×10^{32}	TGA	[357]
Reac 1 Activation Energy	J/mol	5.57×10^5	TGA	[357]
Reac 1 Char Yield		0.62	TGA	[357]
Reac 1 Heat of Reaction	kJ/kg	350	Inverse Analysis	[357]
Gas 1 Heat of Combustion	kJ/kg	16000	Cone calorimetry	[357]
Gas 1 Combustion Efficiency		1	Assumed	[357]
Reac 2 Pre-Exp. Factor	s^{-1}	1.0×10^3	TGA	[357]
Reac 2 Activation Energy	J/mol	8.9×10^4	TGA	[357]
Reac 2 Char Yield		0.88	TGA	[357]
Reac 2 Heat of Reaction	kJ/kg	0	Assumed	[357]
Gas 2 Heat of Combustion	kJ/kg	27000	Cone Calorimetry	[357]
Gas 2 Combustion Efficiency		1	Assumed	[357]
Reac 3 Pre-Exp. Factor	s^{-1}	1.0×10^5	TGA	[357]
Reac 3 Activation Energy	J/mol	1.47×10^5	TGA	[357]
Reac 3 Char Yield		0.88	TGA	[357]
Reac 3 Heat of Reaction	kJ/kg	0	Assumed	[357]
Reac 4 Pre-Exp. Factor	s^{-1}	1.0×10^3	TGA	[357]
Reac 4 Activation Energy	J/mol	1.29×10^5	TGA	[357]
Reac 4 Char Yield		0	TGA	[357]
Reac 4 Heat of Reaction	kJ/kg	0	Assumed	[357]

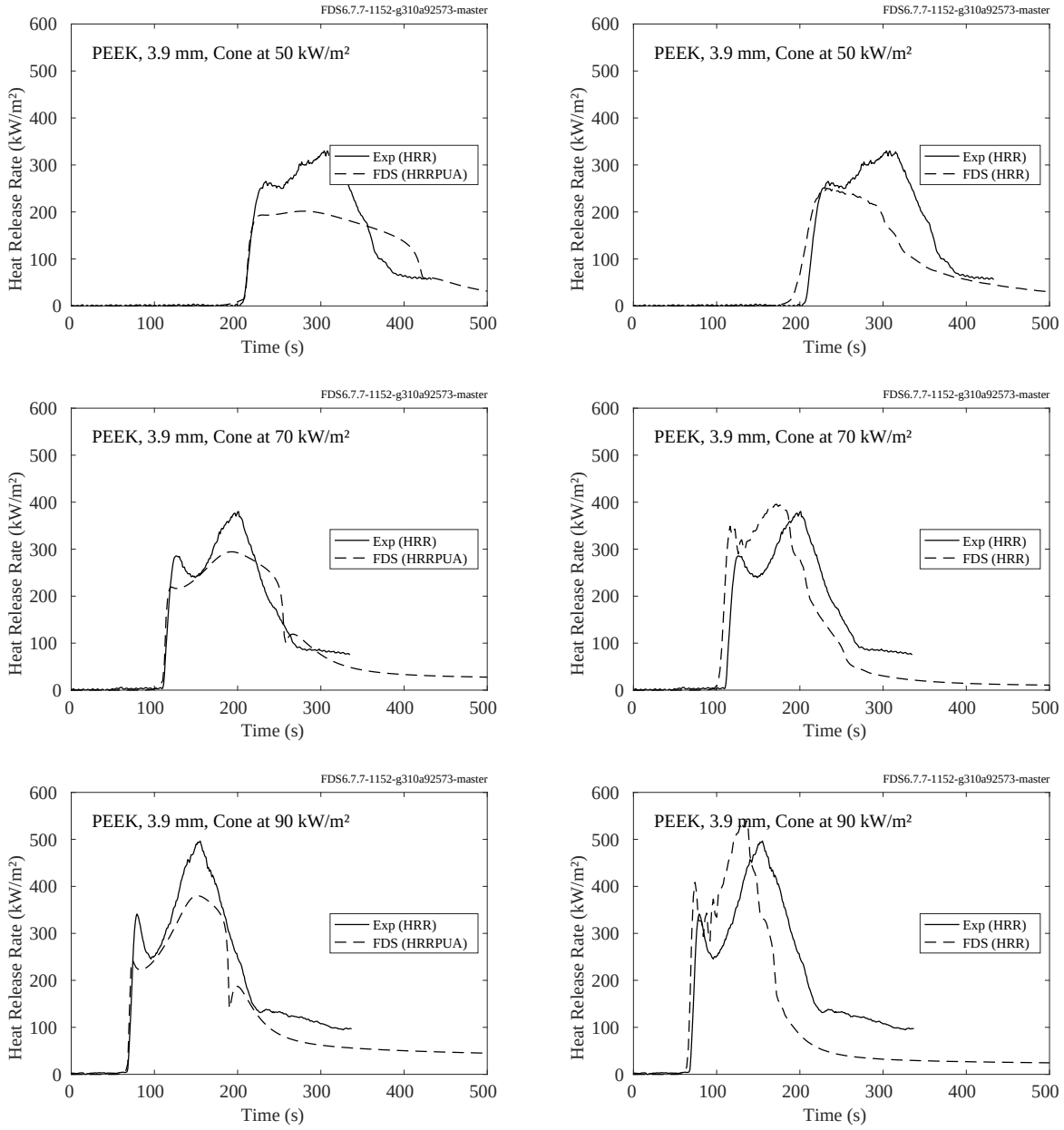

Figure 14.5: Comparison of predicted and measured heat release rates for poly(aryl ether ether ketone) (PEEK). The plots on the left include only a simulation of the solid phase with an added heat flux of 15 kW/m^2 to account for the radiative feedback from the flame. The plots on the right are 3-D simulations of the solid sample and the fire.

14.1.7 Poly(butylene terephtalate) (PBT)

Samples of poly(butylene terephtalate) (PBT)[2] have been burned without oxygen in the Gasification Apparatus and with oxygen in the Cone Calorimeter. The properties of PBT are listed in Table 14.6. It is assumed that the polymer undergoes a single step reaction that forms fuel gas and no char.

The results of the simulations are shown in Fig. 14.6. Note that the effect of the flame radiation heat feedback to the sample surface is accounted for by increasing the imposed heat fluxes of 35 kW/m^2 by 39 %, 50 kW/m^2 by 22 %, and 70 kW/m^2 by 6 % [358].

Table 14.6: Properties of poly(butylene terephtalate) (PBT). Courtesy S. Stoliarov, University of Maryland, and Florian Kempel. See Section 14.1.1 for an explanation of terms. Note that the Specific Heat and Conductivity result from averaging the reported temperature dependent properties over the room to decomposition temperature range (300 K – 650 K). The heat capacity value is increased by 0.13 kJ/kg/K to account for the heat of melting (-46 kJ/kg), which takes place at 493 K.

Property	Units	Value	Method	Reference
Density	kg/m^3	1300 ± 70	Direct	[358]
Specific Heat	kJ/kg/K	2.23 ± 0.34	DSC	[358]
Conductivity	W/m/K	0.29 ± 0.05	TLS	[358]
Emissivity		0.88 ± 0.05	FTIR	[359]
Absorption Coefficient	m^{-1}	2561 ± 140	FTIR	[359]
Pre-Exp. Factor	s^{-1}	$(2.49 \pm 0.62) \times 10^{14}$	TGA	[358]
Activation Energy	J/mol	$(2.12 \pm 0.53) \times 10^5$	TGA	[358]
Heat of Reaction	kJ/kg	507	DSC, Literature	[358, 360]
Heat of Combustion	kJ/kg	19500	Cone Calorimeter	[358]
Combustion Efficiency		1	Assumption	[358]

[2] Tradename Arnite T06-200, DSM Engineering Plastics

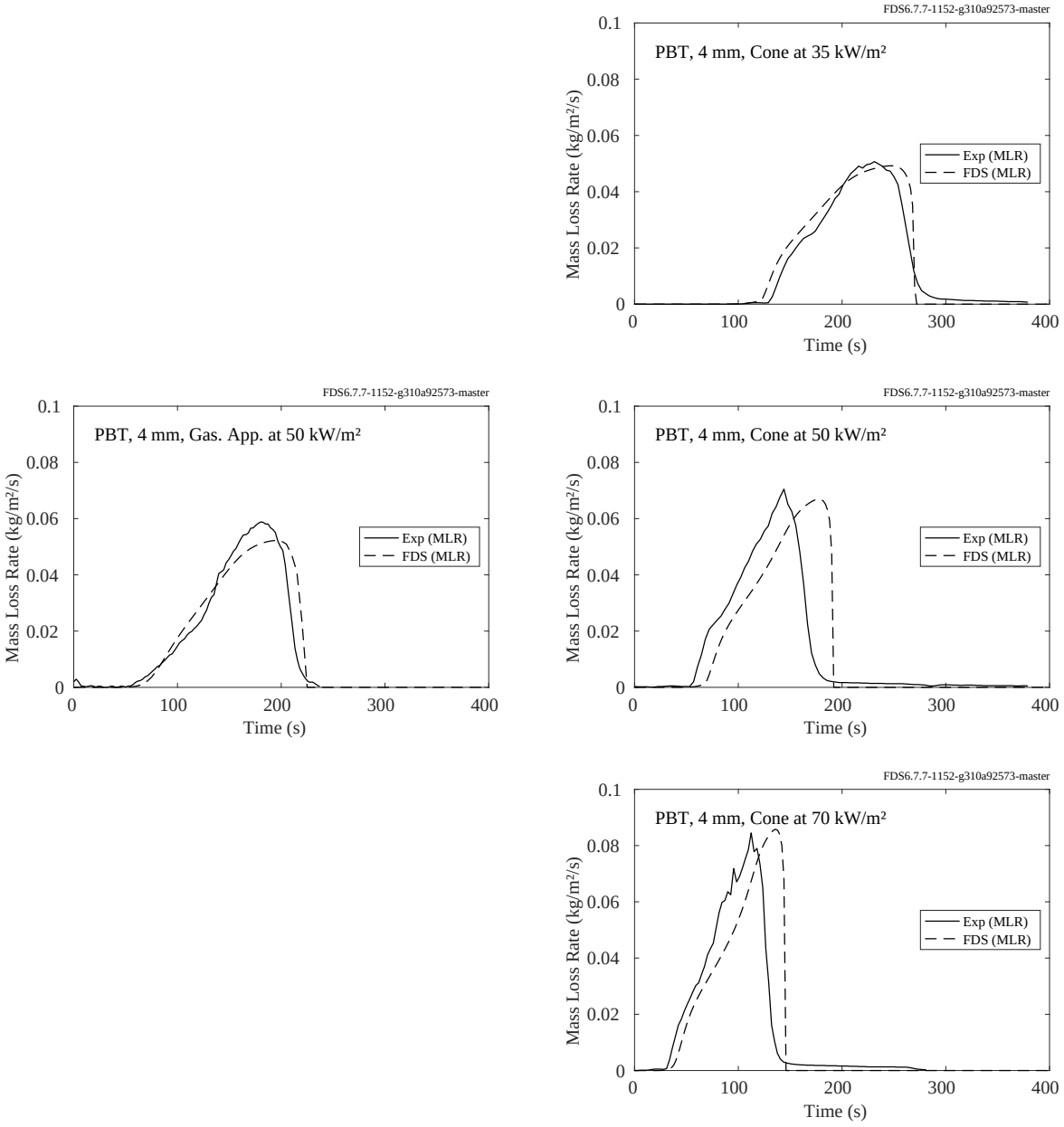

Figure 14.6: Comparison of predicted and measured mass loss rates for poly(butylene terephtalate) (PBT) in both the Gasification Apparatus and Cone Calorimeter.

14.1.8 PBT with Glass Fibers (PBT-GF)

Samples of poly(butylene terephtalate) (PBT), blended with 30 % by mass glass fibers[3], have been burned without oxygen in the Gasification Apparatus and with oxygen in the Cone Calorimeter. The properties of PBT-GF are listed in Table 14.7. It is assumed that the polymer undergoes a single step reaction that forms fuel gas and char.

$$\text{PBT-GF} \rightarrow 0.32\,\text{Char} + 0.68\,\text{Gas} \tag{14.8}$$

The results of the simulations are shown in Fig. 14.7. Note that the effect of the flame radiation heat feedback to the sample surface is accounted for by increasing the imposed heat fluxes of 35 kW/m^2 by 33 %, 50 kW/m^2 by 16 %, and 70 kW/m^2 by 5 % [358].

Table 14.7: Properties of poly(butylene terephtalate) with glass fibers (PBT-GF). Courtesy S. Stoliarov, University of Maryland. See Section 14.1.1 for an explanation of terms. Note that the Polymer Specific Heat and Polymer Conductivity are the result of averaging the reported temperature dependent properties over the room to decomposition temperature range (300 K – 650 K). The heat capacity value is increased by 0.09 kJ/kg/K to account for the heat of melting (-32 kJ/kg), which takes place at 493 K.

Property	Units	Value	Method	Reference
Polymer Density	kg/m^3	1520 ± 80	Direct	[358]
Polymer Specific Heat	kJ/kg/K	1.68 ± 0.26	DSC	[358]
Polymer Conductivity	W/m/K	0.36 ± 0.06	TLS	[358]
Polymer Emissivity		0.87 ± 0.05	FTIR	[359]
Polymer Absorption Coef.	m^{-1}	2860 ± 150	FTIR	[359]
Char Density	kg/m^3	482	Constant Volume	[358]
Char Specific Heat	kJ/kg/K	0.85	Literature	[361]
Char Conductivity	W/m/K	0.07 ± 0.02	Laser Flash	[358]
Char Emissivity		0.85	Literature	[362]
Char Absorption Coef.	m^{-1}	10000	Estimated	[358]
Pre-Exp. Factor	s^{-1}	$(2.49 \pm 0.63) \times 10^{14}$	TGA	[358]
Activation Energy	J/mol	$(2.12 \pm 0.53) \times 10^5$	TGA	[358]
Heat of Reaction	kJ/kg	355	DSC, Literature	[358, 360]
Heat of Combustion	kJ/kg	19500	Cone Calorimeter	[358]
Char Yield		0.32 ± 0.05	Gasification Device	[358]
Combustion Efficiency		1	Assumption	[358]

[3]Tradename Arnite TV4-261, DSM Engineering Plastics

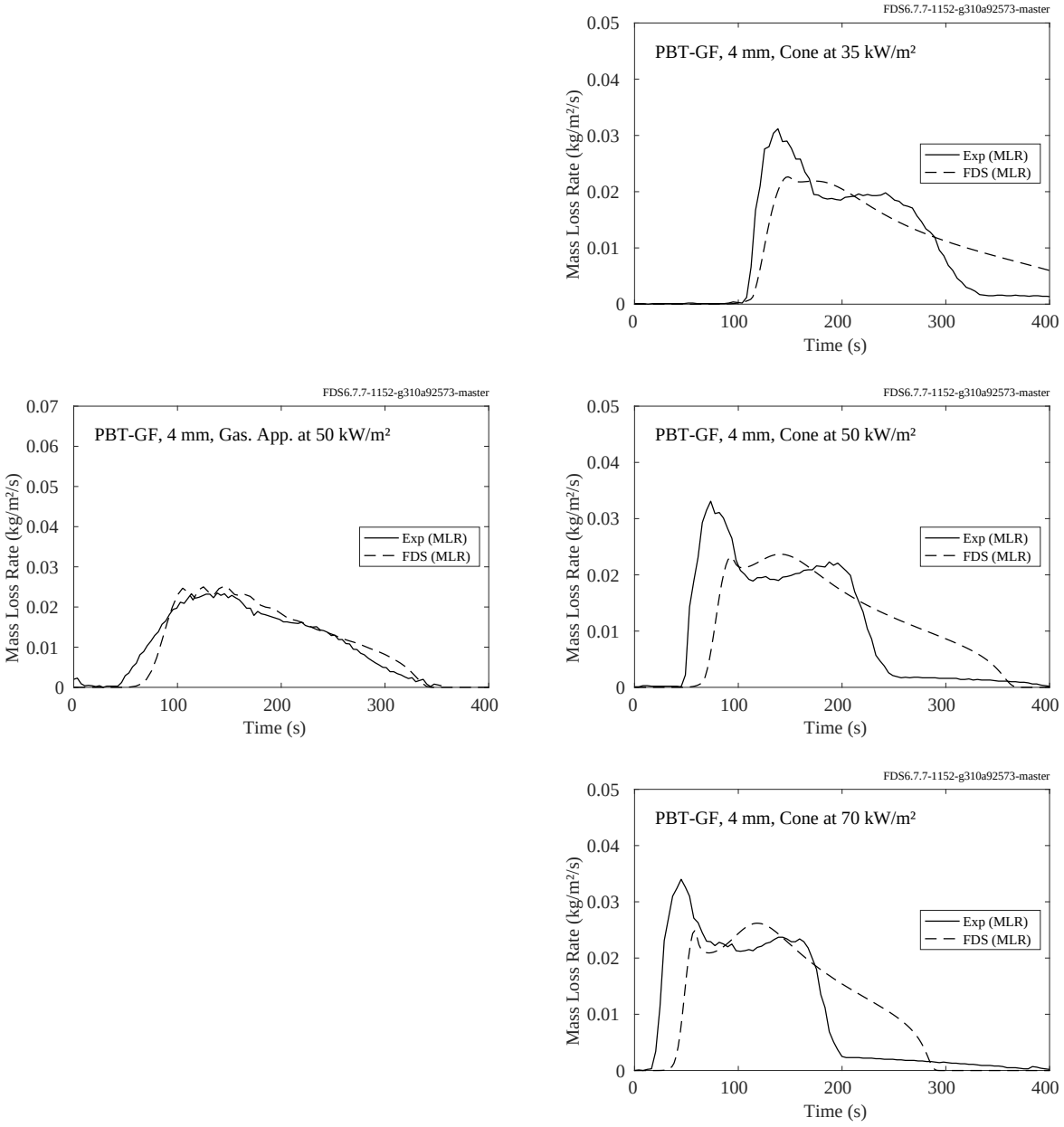

Figure 14.7: Comparison of predicted and measured mass loss rates for poly(butylene terephtalate) with glass fibers (PBT-GF) in both the Gasification Apparatus and Cone Calorimeter.

14.2 UMD Polymers

This section contains a description of seven polymers analyzed by J. Li for his doctoral thesis at the University of Maryland [363]. In addition to the thesis itself, details of the measurement techniques can be found in Refs. [298, 299, 359, 300, 301].

In the experiments, samples of seven different polymers were exposed to several different heat flux levels in the controlled atmosphere pyrolysis apparatus (CAPA) developed at the University of Maryland. This apparatus is similar to a cone calorimeter, but with a nitrogen environment. Thus, it is similar in function to the Gasification Apparatus. In each experiment, a roughly 6 mm sample was placed upon a wire mesh with no insulated backing. The top side of the sample was exposed to a specified heat flux, while the bottom remained exposed to ambient conditions. The mass loss rate of the sample was measured, and in the sections to follow the measured values are compared to FDS predictions. The seven polymers are organized into groups with one, two, or three degradation steps.

14.2.1 One-Step Degradation: ABS, HIPS, and PMMA

These three polymers are assumed to pyrolyze according to the following single step process:

$$\text{Polymer} \rightarrow \nu_r \,\text{Char} + (1-\nu_r)\,\text{Gas} \tag{14.9}$$

The properties of the virgin polymer, the char, and the reaction kinetics are listed in Table 14.8.

Table 14.8: Properties of ABS, HIPS, and PMMA. Note that the temperature dependence of the thermal conductivity is assumed to be linear, unlike some of those reported in Ref. [363].

Property	Units	ABS	HIPS	PMMA
Polymer Density	kg/m^3	1050	1060	1160
Polymer Cond.	W/m/K	$0.30-0.00028\,T$	$0.10+0.0001\,T$	$0.45-0.00038\,T,\ T<378$ K $0.27-0.00024\,T,\ T\geq 378$ K
Polymer Spec. Heat	kJ/kg/K	$1.58+0.0013\,T$	$0.59+0.0034\,T$	$0.60+0.0036\,T$
Polymer Emissivity		0.95	0.95	0.95
Polymer Abs. Coef.	m^{-1}	1800	2250	2240
Char Density	kg/m^3	80	Same as Polymer	Same as Polymer
Char Conductivity	W/m/K	$0.13-0.00054\,T$	Same as Polymer	Same as Polymer
Char Specific Heat	kJ/kg/K	$0.82+0.00011\,T$	Same as Polymer	Same as Polymer
Char Emissivity		0.86	Same as Polymer	Same as Polymer
Char Abs. Coef.	m^{-1}	2500	Opaque	Same as Polymer
Pre-Exp. Factor	s^{-1}	1.00×10^{14}	1.70×10^{20}	8.60×10^{12}
Activation Energy	J/mol	2.19×10^{5}	3.01×10^{5}	1.88×10^{5}
Heat of Reaction	kJ/kg	460	689	846
Heat of Combustion	kJ/kg	28750	29900	24450
Residue Fraction		0.023	0.043	0.015

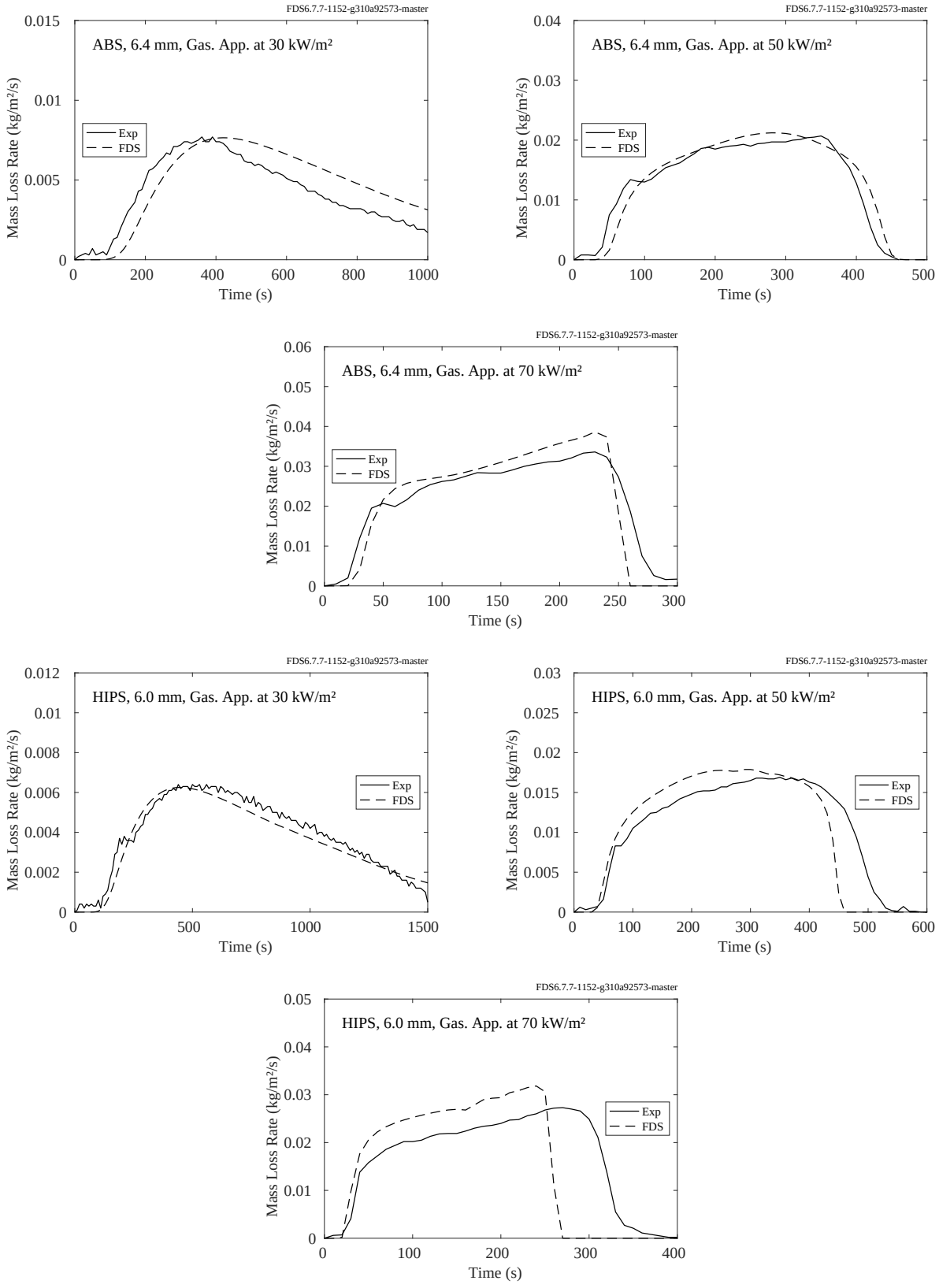

Figure 14.8: Comparison of predicted and measured mass loss rates for ABS and HIPS.

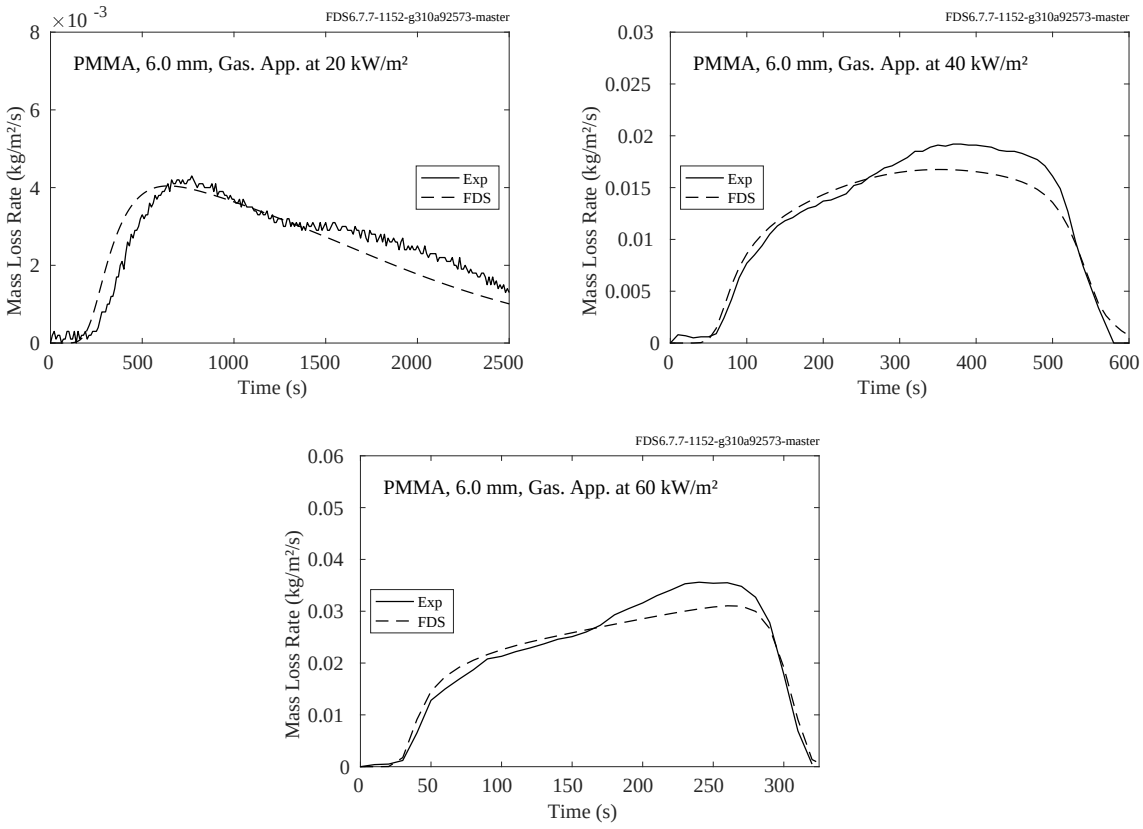

Figure 14.9: Comparison of predicted and measured mass loss rates for PMMA.

14.2.2 Two-Step Degradation: Kydex

This polymer is assumed to pyrolyze according to the following two step process:

$$\text{Polymer} \rightarrow 0.45\,\text{Intermediate} + 0.55\,\text{Gas} \tag{14.10}$$

$$\text{Intermediate} \rightarrow 0.31\,\text{Char} + 0.69\,\text{Gas} \tag{14.11}$$

The properties of the polymer and the reaction kinetics are listed in Table 14.9 and the mass loss rate comparisons are shown on the following page. Note that nominal exposing heat flux values of 30 kW/m^2, 50 kW/m^2, and 70 kW/m^2 were changed slightly in the simulations to account for the fact that the intumescing material surface moved closer to the heater during the course of the experiment [301].

Table 14.9: Properties of Kydex. Note that the temperature dependence of the thermal conductivity is assumed to be linear, unlike some of those reported in Ref. [363].

Property	Units	Kydex
Polymer Density	kg/m^3	1350
Polymer Cond.	W/m/K	$0.28 - 0.00029\,T$
Polymer Spec. Heat	kJ/kg/K	$-0.62 + 0.00593\,T$
Polymer, Int. Emissivity		0.95
Polymer Abs. Coef.	m^{-1}	2135
Int. Density	kg/m^3	Same as Char
Int. Cond.	W/m/K	$0.55 + 0.00003\,T$
Int. Spec. Heat	kJ/kg/K	$0.27 + 0.00301\,T$
Int. Abs. Coef.	m^{-1}	3000
Char Density	kg/m^3	100
Char Conductivity	W/m/K	$0.21 + 0.00034\,T$
Char Specific Heat	kJ/kg/K	$1.15 + 0.00010\,T$
Char Emissivity		0.86
Char Abs. Coef.	m^{-1}	10000
Reac. 14.10 Pre-Exp. Factor	s^{-1}	6.03×10^{10}
Reac. 14.10 Act. Energy	J/mol	1.41×10^5
Reac. 14.10 Heat of Reac.	kJ/kg	180
Reac. 14.10 Residue Frac.		0.45
Reac. 14.11 Pre-Exp. Factor	s^{-1}	1.36×10^{10}
Reac. 14.11 Act. Energy	J/mol	1.74×10^5
Reac. 14.11 Heat of Reac.	kJ/kg	125
Reac. 14.11 Residue Frac.		0.31
Gas Heat of Combustion	kJ/kg	12650

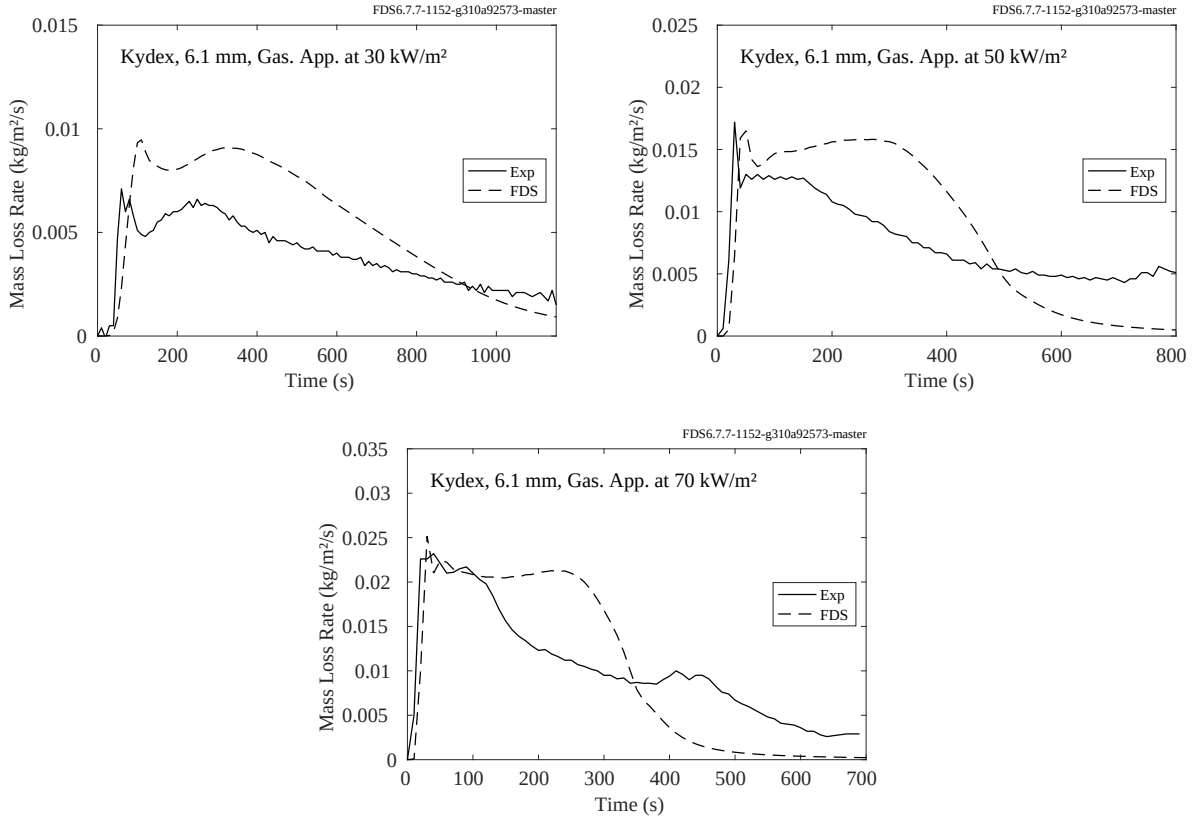

Figure 14.10: Comparison of predicted and measured mass loss rates for Kydex.

14.2.3 Three-Step Degradation: PEI, PET, and POM

These three polymers are assumed to pyrolyze following the three-step process:

$$\text{Polymer} \rightarrow \text{Melt} \tag{14.12}$$

$$\text{Melt} \rightarrow \nu_{r,2}\,\text{Intermediate} + (1-\nu_{r,2})\,\text{Gas} \tag{14.13}$$

$$\text{Intermediate} \rightarrow \nu_{r,3}\,\text{Char} + (1-\nu_{r,3})\,\text{Gas} \tag{14.14}$$

The property data is listed in Table 14.10 and the mass loss rate comparisons are shown on the subsequent pages.

Table 14.10: Properties of PEI, PET, and POM. Note that the temperature dependence of the thermal conductivity is assumed to be linear, unlike some of those reported in Ref. [363].

Property	Units	PEI	PET	POM
Polymer, Melt Density	kg/m^3	1285	1385	1424
Polymer Cond.	W/m/K	$0.40-0.00040\,T$	$0.34-0.00046\,T$	$0.25+0.00002\,T$
Polymer Spec. Heat	kJ/kg/K	$-0.04+0.00410\,T$	$-0.27+0.00464\,T$	$-1.86+0.0099\,T$
Polymer, Melt, Int. Emiss.		0.95	0.95	0.95
Polymer Abs. Coef.	m^{-1}	1745	1940	3050
Melt Cond.	W/m/K	$0.32-0.00033\,T$	$0.33-0.00002\,T$	$0.21+0.00001\,T$
Melt Spec. Heat	kJ/kg/K	$1.88+0.00057\,T$	$2.05-0.00021\,T$	$1.65+0.00120\,T$
Melt Abs. Coef.	m^{-1}	128500	Same as Polymer	Same as Polymer
Int. Density	kg/m^3	Same as Char	730	Same as Polymer
Int. Cond.	W/m/K	$0.45+0.00019\,T$	$0.45+0.00020\,T$	$0.19-0.00006\,T$
Int. Spec. Heat	kJ/kg/K	$1.59+0.00031\,T$	$1.44-0.00005\,T$	Same as Melt
Int. Abs. Coef.	m^{-1}	8000	1025	Same as Polymer
Char Density	kg/m^3	80	80	Same as Int.
Char Conductivity	W/m/K	$0.45+0.00013\,T$	$0.34+0.00046\,T$	Same as Polymer
Char Specific Heat	kJ/kg/K	$1.30+0.00004\,T$	$0.82+0.00011\,T$	Same as Int.
Char Emissivity		0.86	0.86	Same as Polymer
Char Abs. Coef.	m^{-1}	Same as Int.	8000	Same as Polymer
Reac. 14.12 Pre-Exp. Factor	s^{-1}	1	1.50×10^{36}	2.69×10^{42}
Reac. 14.12 Act. Energy	J/mol	0	3.80×10^{5}	3.82×10^{5}
Reac. 14.12 Heat of Reac.	kJ/kg	1	30	192
Reac. 14.12 Residue Frac.		1	1	1
Reac. 14.13 Pre-Exp. Factor	s^{-1}	7.66×10^{27}	1.60×10^{15}	3.84×10^{14}
Reac. 14.13 Act. Energy	J/mol	4.65×10^{5}	2.35×10^{5}	2.00×10^{5}
Reac. 14.13 Heat of Reac.	kJ/kg	-80	220	1192
Reac. 14.13 Residue Frac.		0.65	0.18	0.4
Reac. 14.14 Pre-Exp. Factor	s^{-1}	6.50×10^{2}	3.53×10^{4}	4.76×10^{44}
Reac. 14.14 Act. Energy	J/mol	0.88×10^{5}	0.96×10^{5}	5.90×10^{5}
Reac. 14.14 Heat of Reac.	kJ/kg	-5	250	1352
Reac. 14.14 Residue Frac.		0.77	0.72	0.018
Gas Heat of Combustion	kJ/kg	18050	15950	14350

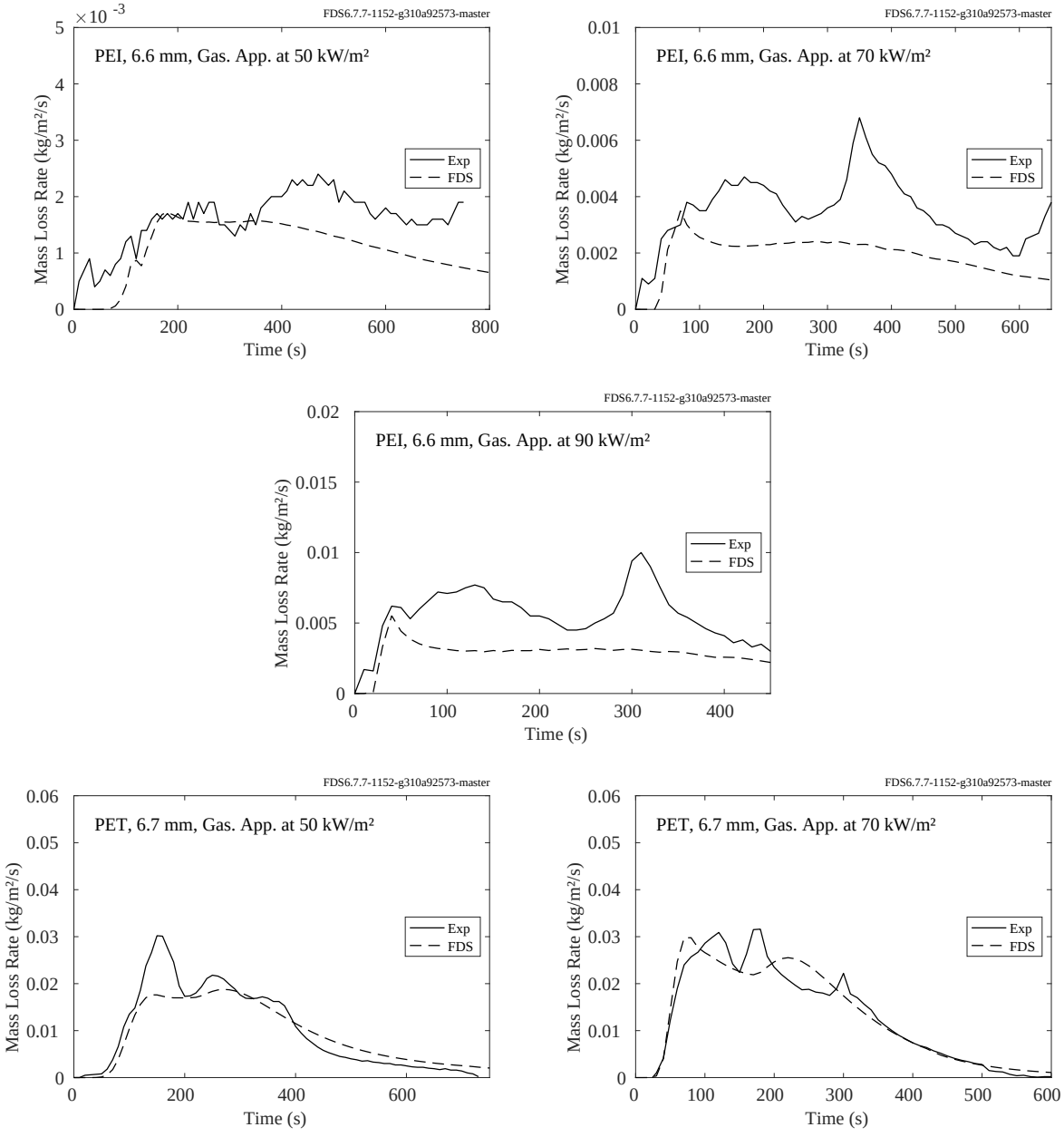

Figure 14.11: Comparison of predicted and measured mass loss rates for PEI and PET.

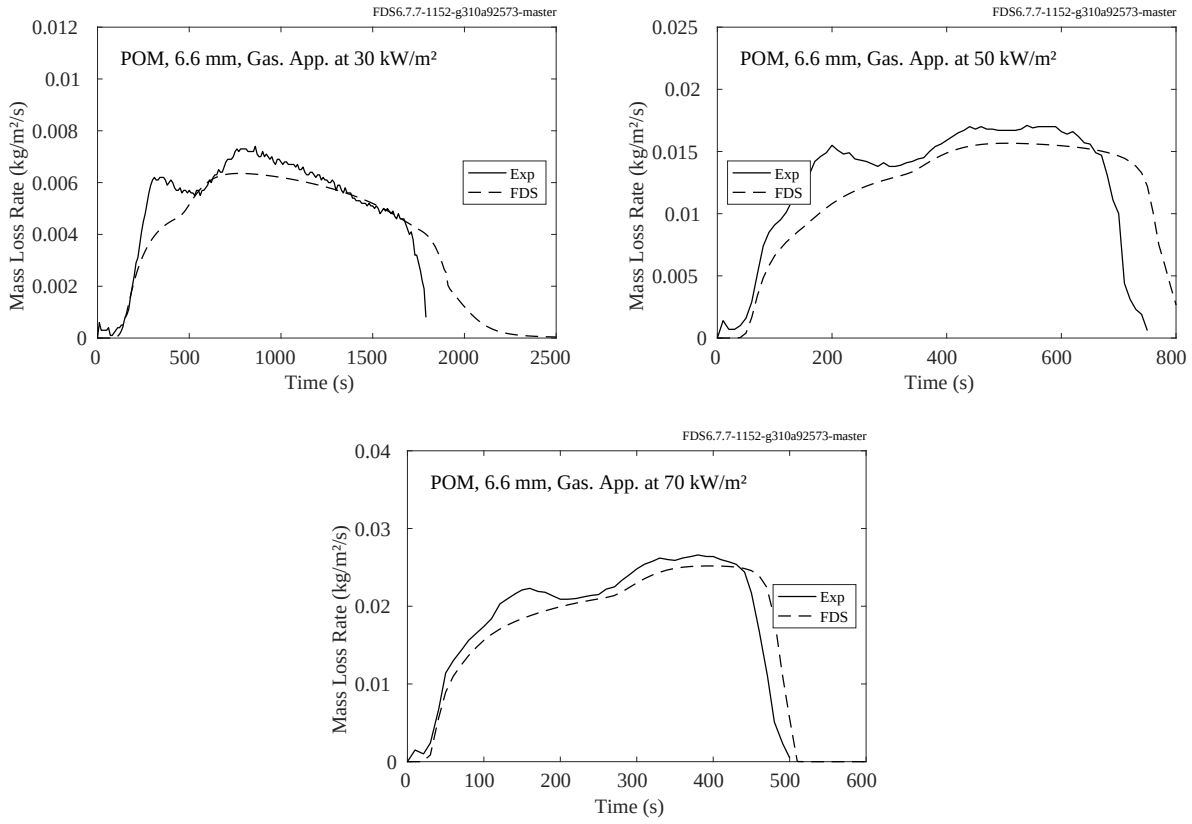

Figure 14.12: Comparison of predicted and measured mass loss rates for POM.

14.3 Corrugated Cardboard

Table 14.11 lists the measured properties of a double-wall corrugated cardboard with the conventional U.S. designation 69-23B-69-23C-69. Corrugated cardboard is characterized by alternating layers of homogeneous, planar liner boards and corrugated sections made up of periodic flutes. The numbers in the specification indicate the areal density in lb/(1000 ft^2) and the letters indicate the flute designation (B indicates a range of 45 to 52 flutes per foot and C indicates a range of 39 to 43 flutes per foot). It is assumed that each layer consists of the same lingo-cellulosic, charring material with the density defined as the mass of the solid material divided by the volume of the layer. This representation requires slightly different definitions for the properties of each unique layer – liner board (LB), C-flute layer (CFL), and B-flute layer (BFL).

The reaction mechanism for the cardboard material includes one reaction to describe the release of residual moisture and three sequential reactions to describe the thermal degradation of the virgin material to a final residual char. Each of the initial solid components (LB, CFL, and BFL) undergoes the same four-step mechanism.

$$\text{Moisture} \rightarrow \text{Water Vapor} \tag{14.15}$$

$$\text{Virgin Cardboard} \rightarrow 0.90\,\text{Intermediary Solid} + 0.10\,\text{Fuel Gas 2} \tag{14.16}$$

$$\text{Intermediary Solid} \rightarrow 0.37\,\text{Char 1} + 0.63\,\text{Fuel Gas 3} \tag{14.17}$$

$$\text{Char 1} \rightarrow 0.59\,\text{Char 2} + 0.41\,\text{Fuel Gas 4} \tag{14.18}$$

Table 14.11: Properties of corrugated cardboard. Courtesy M. McKinnon, University of Maryland. See Section 14.1.1 for an explanation of terms.

Property	Units	Value	Method	Reference
Moisture Density	kg/m^3	1000	Direct	[364]
Moisture Conductivity	W/m/K	0.1	Inherited	[364]
Moisture Specific Heat	kJ/kg/K	4.19	Literature	[365]
Moisture Emissivity		0.7	Inherited	[364]
LB Density	kg/m^3	520	Direct	[364]
LB Conductivity	W/m/K	0.1	Inverse Analysis	[364]
LB Specific Heat	kJ/kg/K	1.8	DSC	[364]
LB Emissivity		0.7	Inverse Analysis	[364]
LB Intermediary Density	kg/m^3	468	Constant Volume	[364]
LB Intermediary Conductivity	W/m/K	$0.05 + 7.5 \times 10^{-11} \times T^3$	Inverse Analysis	[364]
LB Intermediary Specific Heat	kJ/kg/K	1.55	DSC	[364]
LB Intermediary Emissivity		0.775	Inverse Analysis	[364]
LB Char 1 Density	kg/m^3	173	Constant Volume	[364]
LB Char 1 Conductivity	W/m/K	$1.5 \times 10^{-10} \times T^3$	Inverse Analysis	[364]
LB Char 1 Specific Heat	kJ/kg/K	1.3	DSC	[364]
LB Char 1 Emissivity		0.85	Literature	[366]
LB Char 2 Density	kg/m^3	102	Constant Volume	[364]
LB Char 2 Conductivity	W/m/K	$1.5 \times 10^{-10} \times T^3$	Inverse Analysis	[364]
LB Char 2 Specific Heat	kJ/kg/K	1.3	DSC	[364]
LB Char 2 Emissivity		0.85	Literature	[366]
CFL Density	kg/m^3	49	Constant Volume	[364]
CFL Conductivity	W/m/K	0.1	Inverse Analysis	[364]

Table 14.11: Continued

CFL Specific Heat	kJ/kg/K	1.8	DSC	[364]
CFL Emissivity		0.7	Inverse Analysis	[364]
CFL Intermediary Density	kg/m^3	44	Constant Volume	[364]
CFL Intermediary Conductivity	W/m/K	$0.05 + 7.5 \times 10^{-10} \times T^3$	Inverse Analysis	[364]
CFL Intermediary Specific Heat	kJ/kg/K	1.55	DSC	[364]
CFL Intermediary Emissivity		0.775	Inverse Analysis	[364]
CFL Char 1 Density	kg/m^3	16	Constant Volume	[364]
CFL Char 1 Conductivity	W/m/K	$1.5 \times 10^{-9} \times T^3$	Inverse Analysis	[364]
CFL Char 1 Specific Heat	kJ/kg/K	1.3	DSC	[364]
CFL Char 1 Emissivity		0.85	Literature	[366]
CFL Char 2 Density	kg/m^3	9.4	Constant Volume	[364]
CFL Char 2 Conductivity	W/m/K	$1.5 \times 10^{-9} \times T^3$	Inverse Analysis	[364]
CFL Char 2 Specific Heat	kJ/kg/K	1.3	DSC	[364]
CFL Char 2 Emissivity		0.85	Literature	[366]
BFL Density	kg/m^3	74	Constant Volume	[364]
BFL Conductivity	W/m/K	0.1	Inverse Analysis	[364]
BFL Specific Heat	kJ/kg/K	1.8	DSC	[364]
BFL Emissivity		0.7	Inverse Analysis	[364]
BFL Intermediary Density	kg/m^3	67	Constant Volume	[364]
BFL Intermediary Conductivity	W/m/K	$0.05 + 7.5 \times 10^{-10} \times T^3$	Inverse Analysis	[364]
BFL Intermediary Specific Heat	kJ/kg/K	1.55	DSC	[364]
BFL Intermediary Emissivity		0.775	Inverse Analysis	[364]
BFL Char 1 Density	kg/m^3	25	Constant Volume	[364]
BFL Char 1 Conductivity	W/m/K	$1.5 \times 10^{-9} \times T^3$	Inverse Analysis	[364]
BFL Char 1 Specific Heat	kJ/kg/K	1.3	DSC	[364]
BFL Char 1 Emissivity		0.85	Literature	[366]
BFL Char 2 Density	kg/m^3	15	Constant Volume	[364]
BFL Char 2 Conductivity	W/m/K	$1.5 \times 10^{-9} \times T^3$	Inverse Analysis	[364]
BFL Char 2 Specific Heat	kJ/kg/K	1.3	DSC	[364]
BFL Char 2 Emissivity		0.85	Literature	[366]
Reaction 1 Pre-Exp. Factor	s^{-1}	6.14	TGA	[364]
Reaction 1 Activation Energy	J/mol	23500	TGA	[364]
Reaction 1 Heat of Reaction	kJ/kg	2445	Literature	[365]
Reaction 1 Char Yield		0	TGA	[364]
Reaction 2 Pre-Exp. Factor	s^{-1}	7.95×10^9	TGA	[364]
Reaction 2 Activation Energy	J/mol	1.30×10^5	TGA	[364]
Reaction 2 Char Yield		0.9	TGA	[364]
Reaction 2 Heat of Reaction	kJ/kg	0	DSC	[364]
Fuel Gas 2 Heat of Combustion	kJ/kg	18500	MCC	[364]
Reaction 3 Pre-Exp. Factor	s^{-1}	2×10^{11}	TGA	[364]
Reaction 3 Activation Energy	J/mol	1.60×10^5	TGA	[364]
Reaction 3 Char Yield		0.37	TGA	[364]
Reaction 3 Heat of Reaction	kJ/kg	126	DSC	[364]
Fuel Gas 3 Heat of Combustion	kJ/kg	13600	MCC	[364]

Table 14.11: Continued

Reaction 4 Pre-Exp. Factor	s^{-1}	0.0261	TGA	[364]
Reaction 4 Activation Energy	J/mol	17000	TGA	[364]
Reaction 4 Char Yield		0.59	TGA	[364]
Reaction 4 Heat of Reaction	kJ/kg	0	DSC	[364]
Fuel Gas 4 Heat of Combustion	kJ/kg	14000	MCC	[364]

Table 14.12 lists the composition and thickness of each of the layers. The sample is insulated with 28 mm of Kaowool PM board, manufactured by ThermalCeramics (www.thermalceramics.com). The gasification

Table 14.12: Cardboard composition and dimensions.

Layer	Composition	Thickness (mm)
1	Liner Board	0.64
2	C Flute Layer	3.2
3	Liner Board	0.64
4	B Flute Layer	2.1
5	Liner Board	0.64
6	Kaowool	28

experiments were conducted in a modified cone calorimeter referred to as the controlled atmosphere pyrolysis apparatus (CAPA) [367], in which the sample is surrounded by nitrogen to prevent ignition. Measured and predicted mass loss rates at imposed heat fluxes of 20 kW/m^2, 40 kW/m^2, and 60 kW/m^2 are shown in Fig. 14.13.

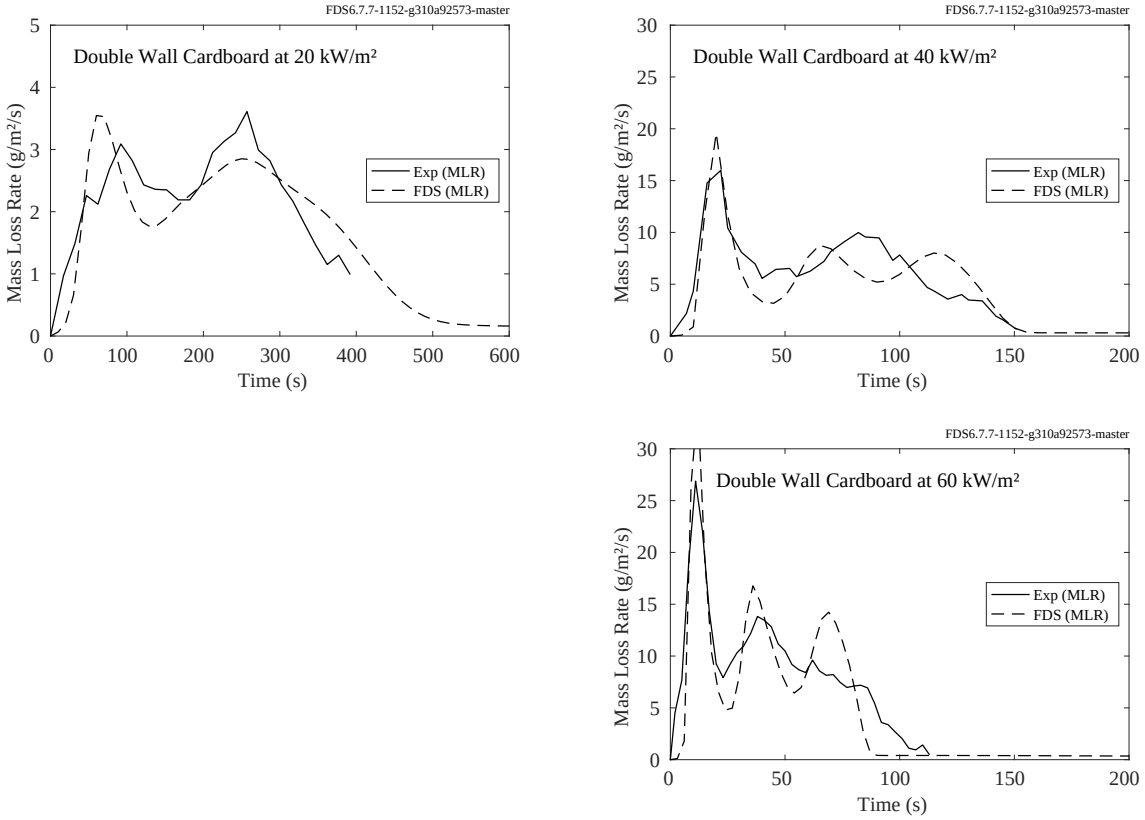

Figure 14.13: Mass loss rate of corrugated cardboard.

14.4 Wood Cribs and Similar Wood/Paper Combustibles

A common combustible used in fire research and testing is a wood crib; that is, a uniform array of wooden dowels of nearly square cross section. However, a stack of wooden pallets can be viewed as a wood crib as well. Whatever its form, these cribs tend to burn at a consistent and predictable rate, making them ideal for fire testing.

14.4.1 BST/FRS Wood Crib Experiments

Figures 14.14 through 14.16 display comparisons of the measured and predicted gas temperatures along three "crib lines" within a long compartment filled with 33 wooden cribs. The experiments are described in Section 3.11. The crib lines are located at row 2 (back), 6 (middle) and 10 (front). Each measurement is an average of three thermocouples at the same distance.

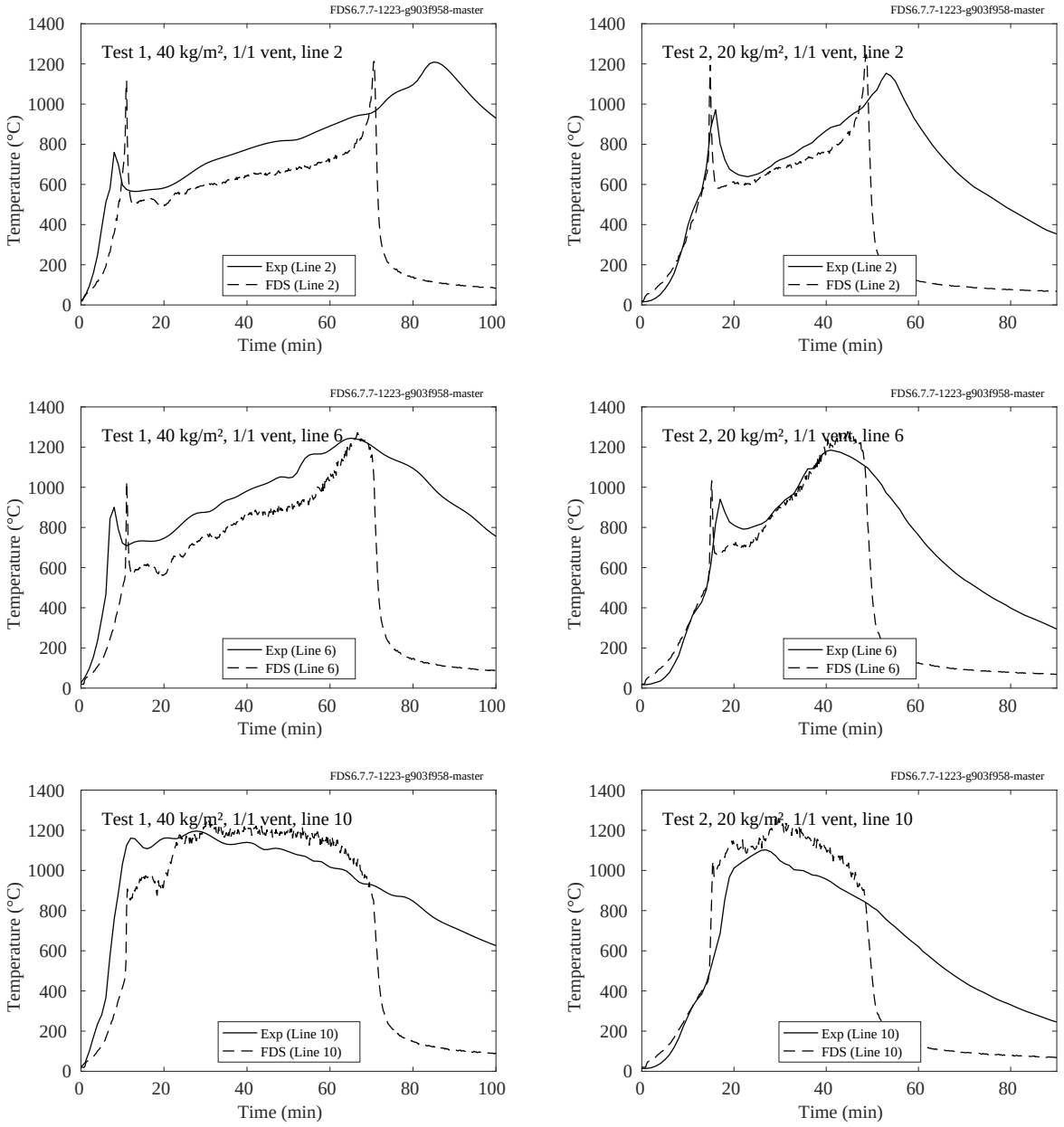

Figure 14.14: BST/FRS Wood Cribs temperatures, Tests 1 (left) and 2 (right).

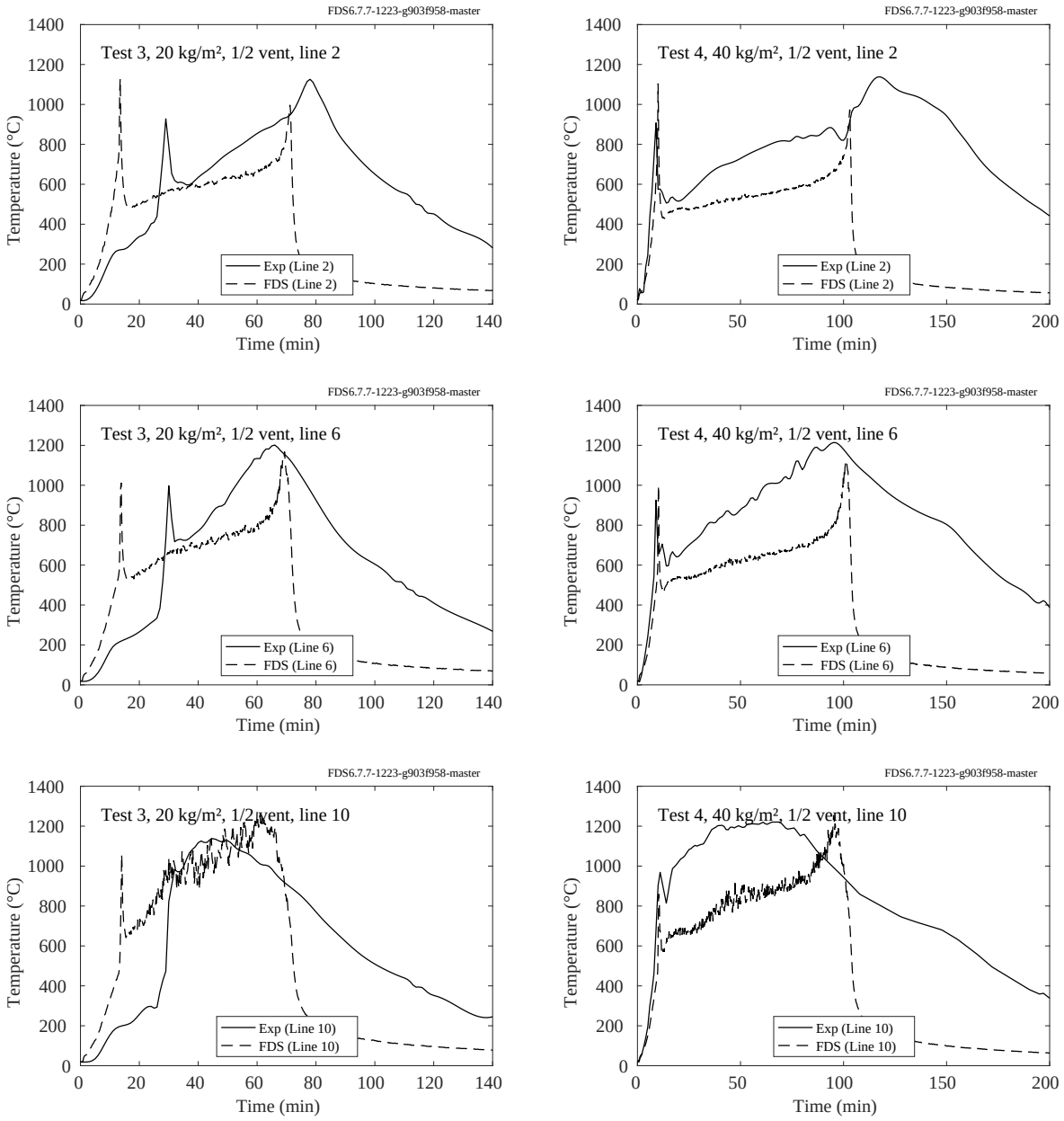

Figure 14.15: BST/FRS Wood Cribs temperatures, Tests 3 (left) and 4 (right).

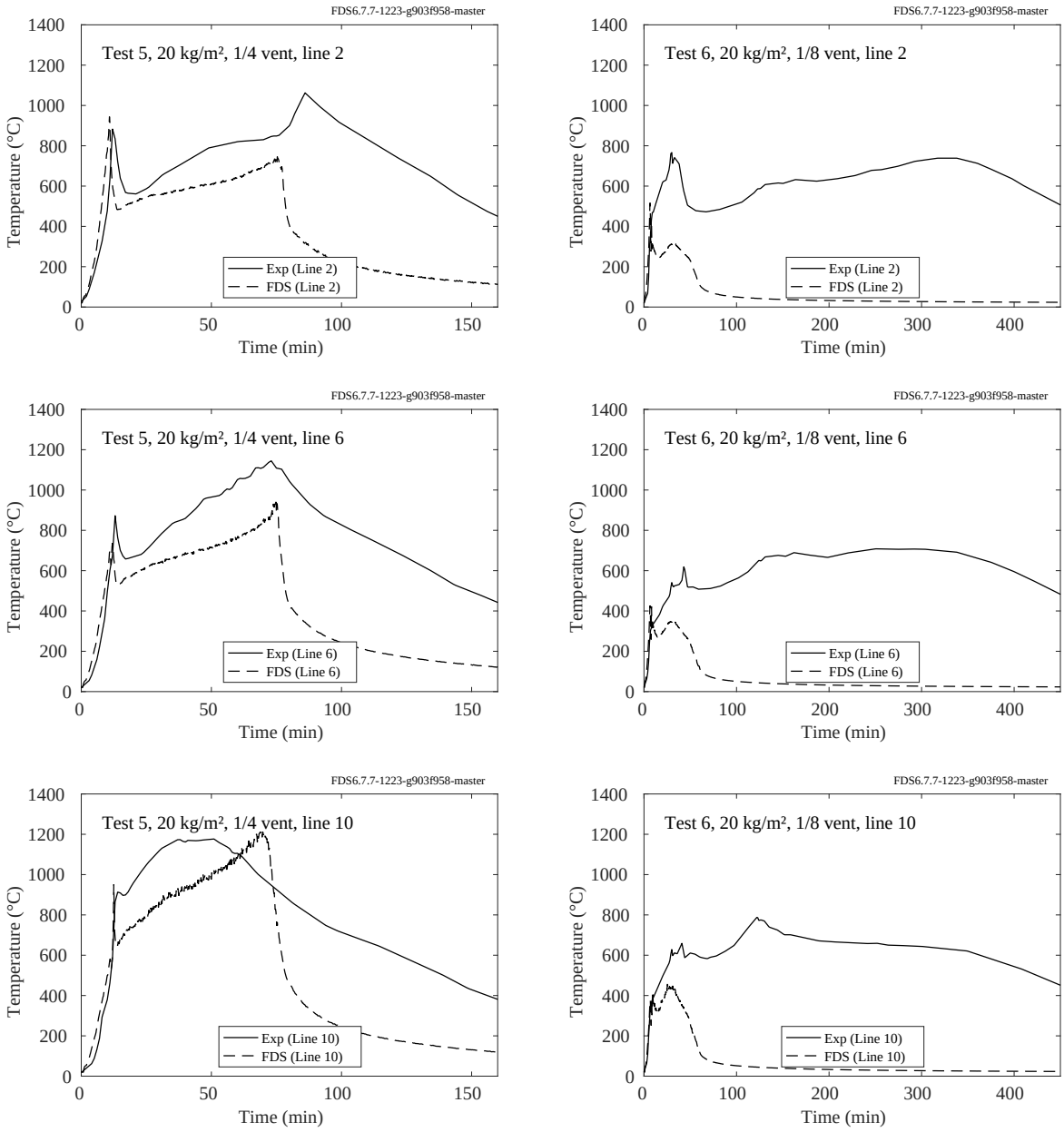

Figure 14.16: BST/FRS Wood Cribs temperatures, Tests 5 (left) and 6 (right).

14.4.2 NIST/NRC Transient Combustibles

Figure 14.17 compares measured and predicted heat release rates for a single wood crib and arrays of multiple cribs. The simulations are all performed using Lagrangian particles as surrogates for the 56 cm long, 3.8 cm square pine sticks. The grid resolution in all cases is 8 cm, with additional simulations performed with 4 cm and 2 cm resolution for the single crib.

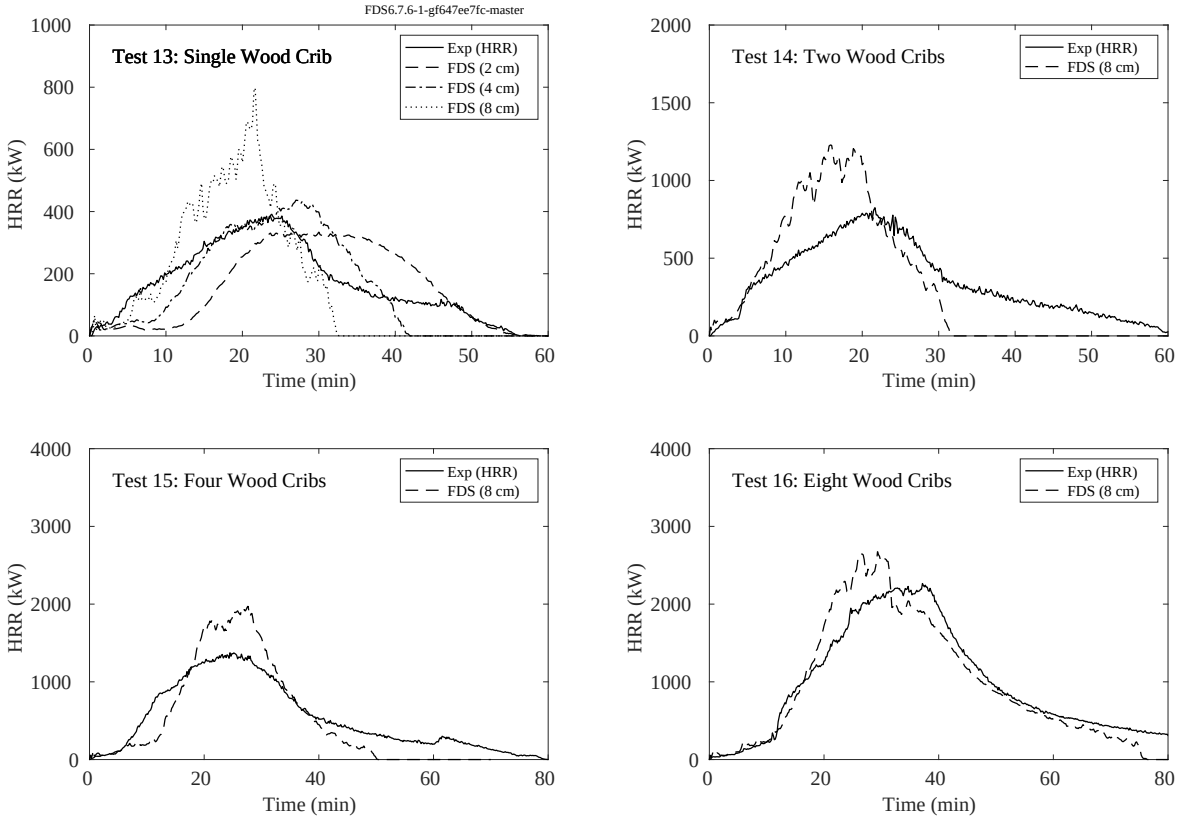

Figure 14.17: NIST/NRC Transient Combustibles: wood cribs.

Figure 14.18 compares measured and predicted heat release rates for a single cardbard box filled with shredded craft paper and arrays of multiple boxes. The simulations are all performed using Lagrangian particles as surrogates for the small paper strips. The grid resolution in all cases is 5 cm.

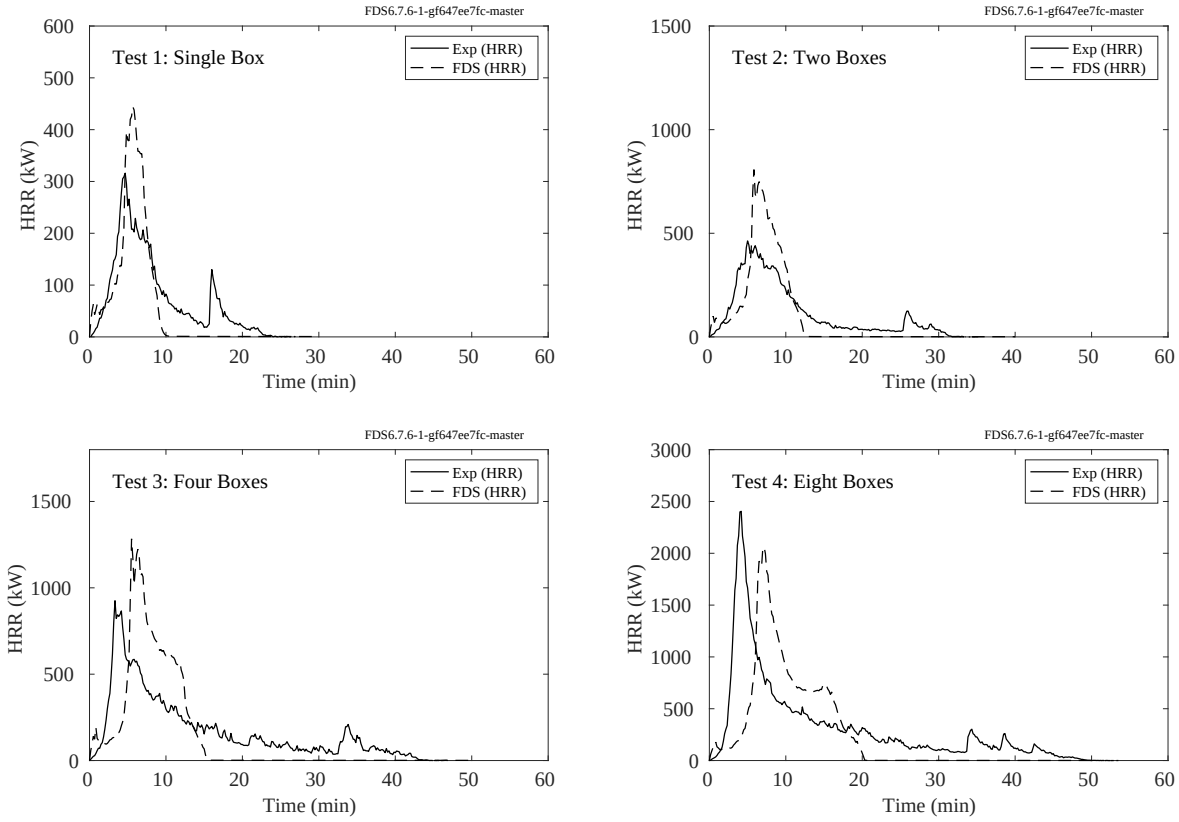

Figure 14.18: NIST/NRC Transient Combustibles: boxes.

Figure 14.19 compares measured and predicted heat release rates for a stack of two, four and eight wood pallets. The simulations are all performed using Lagrangian particles as surrogates for the wooden planks. The grid resolution in all cases is 6 cm.

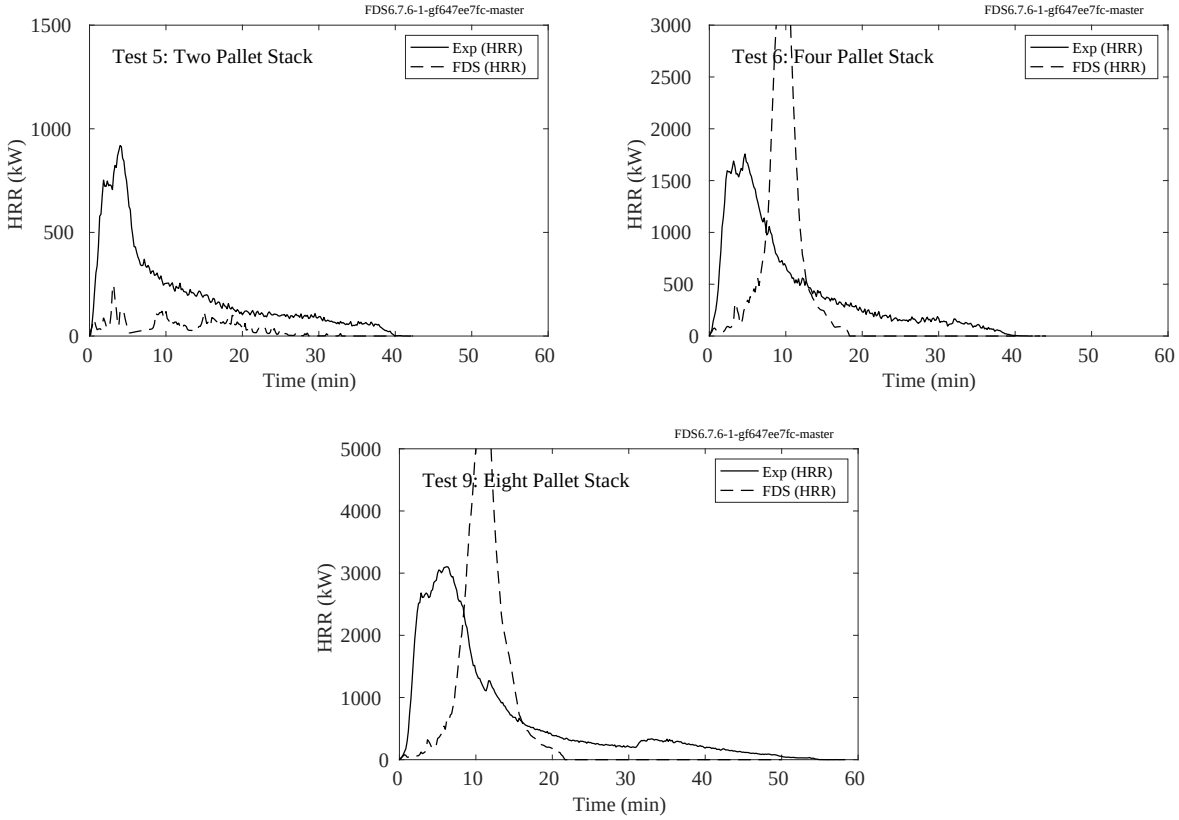

Figure 14.19: NIST/NRC Transient Combustibles: pallets.

14.4.3 SP Wood Crib Experiments

These experiments and the modeling strategy are described in Section 3.71. Briefly, four piles of 1:4 scale wood pallets are positioned in a wind tunnel with various separation distances. The upwind pile is ignited and the fire spreads from pile to pile. The wind velocity for Test 1 is 0.3 m/s; and for Test 12 it is 0.9 m/s. For all others, it is 0.6 m/s. Tests 1, 4, and 12 have only a single pile; the rest have four.

Figures 14.20 and 14.21 display the measured and predicted HRR for 11 of the 12 SP Wood Crib experiments. Test 2 was set up differently than the other experiments and was not used in the analysis.

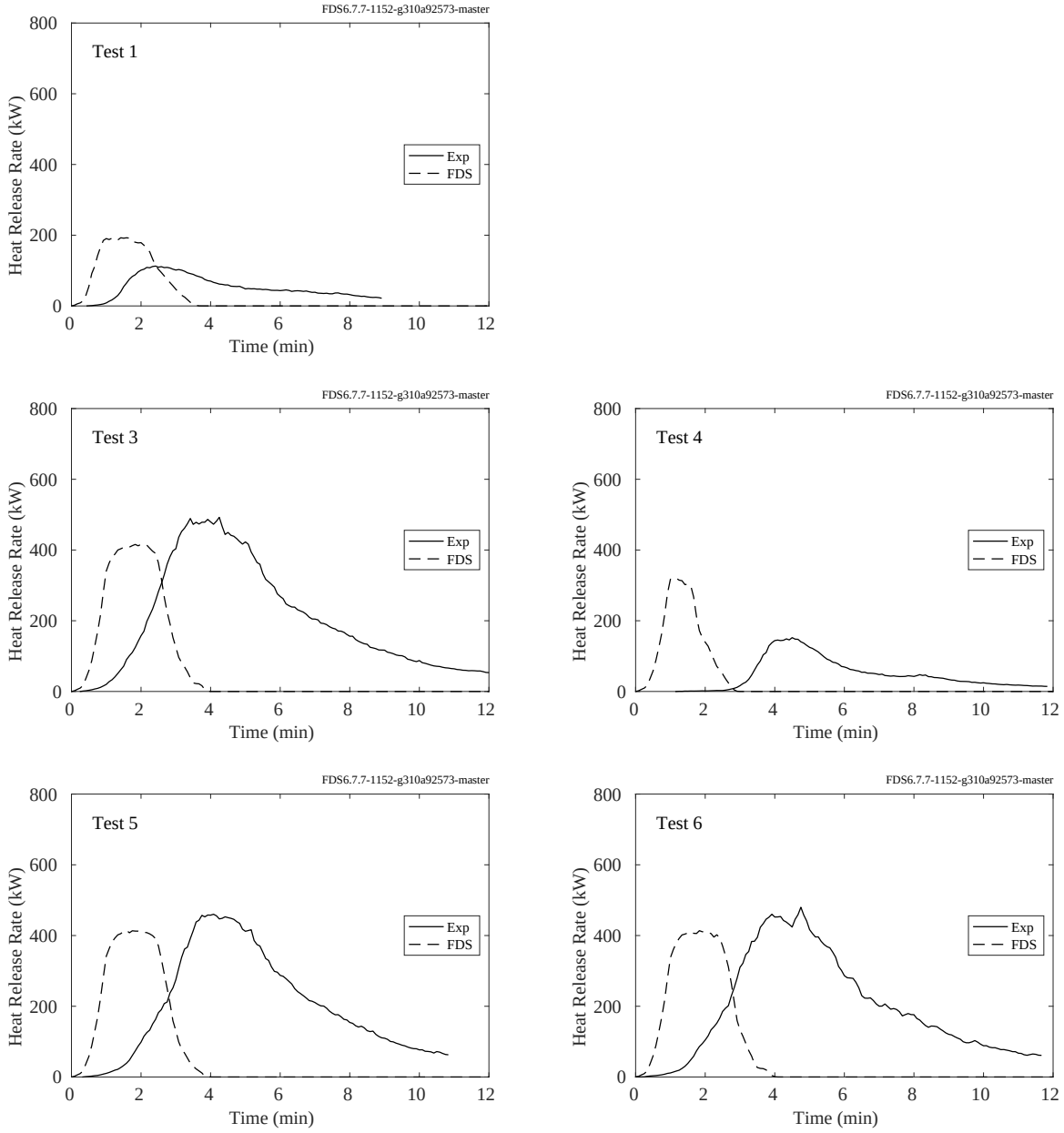

Figure 14.20: SP Wood Cribs heat release rates, Tests 1-6.

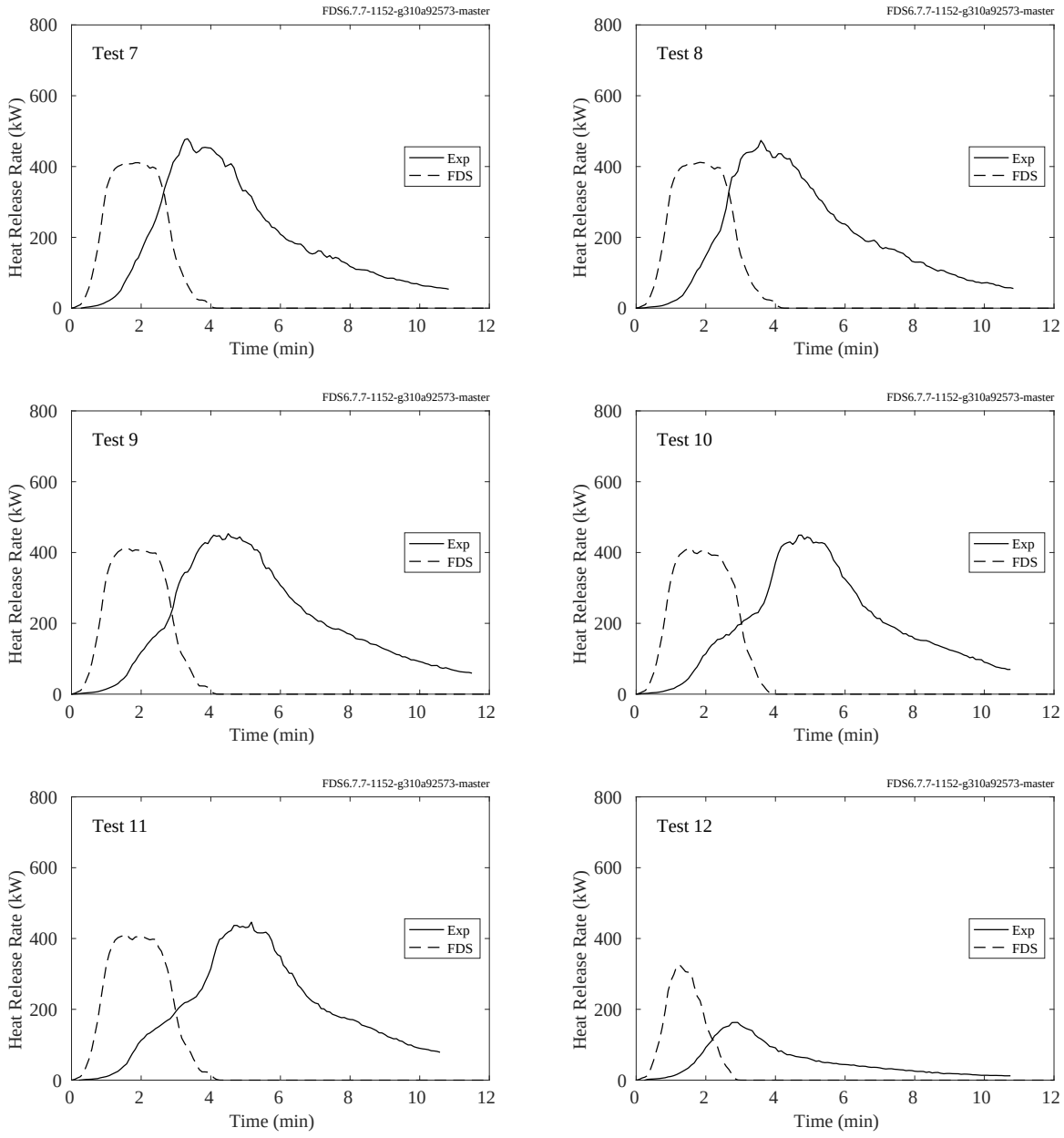

Figure 14.21: SP Wood Cribs heat release rates, Tests 7-12.

14.5 Liquid Pool Fires

14.5.1 DoJ/HAI Pool Fires

Table 14.13 lists the relevant parameters for a series of gasolene and kerosene pool fire experiments.

Figures 14.22 through 14.27 display measured and predicted burning rate of a variety of gasoline and kerosene pool fires in 0.3 m, 0.6 m, and 1.2 m square pans of various depths and two substrates—concrete and vinyl.

Table 14.13: Summary of DoJ/HAI Diked Fire Tests.

Test ID	Pan Side Length (m)	Fuel	Depth (mm)	Substrate
DSF1-C-CC-G-1-0.093	0.31	Gasoline	1	Coated Concrete
DSF2-C-CC-G-5-0.093	0.31	Gasoline	5	Coated Concrete
DSF3-C-CC-G-10-0.093	0.31	Gasoline	10	Coated Concrete
DSF4-C-CC-G-20-0.093	0.31	Gasoline	20	Coated Concrete
DSF5-C-CC-K-1-0.093	0.31	Kerosene	1	Coated Concrete
DSF6-C-CC-K-5-0.093	0.31	Kerosene	5	Coated Concrete
DSF7-C-CC-K-10-0.093	0.31	Kerosene	10	Coated Concrete
DSF8-C-CC-K-20-0.093	0.31	Kerosene	20	Coated Concrete
DSF9-C-CC-G-1-0.372	0.61	Gasoline	1	Coated Concrete
DSF10-C-CC-G-5-0.372	0.61	Gasoline	5	Coated Concrete
DSF11-C-CC-G-10-0.372	0.61	Gasoline	10	Coated Concrete
DSF12-C-CC-G-20-0.372	0.61	Gasoline	20	Coated Concrete
DSF13-C-CC-K-1-0.372	0.61	Kerosene	1	Coated Concrete
DSF14-C-CC-K-5-0.372	0.61	Kerosene	5	Coated Concrete
DSF15-C-CC-K-10-0.372	0.61	Kerosene	10	Coated Concrete
DSF16-C-CC-K-20-0.372	0.61	Kerosene	20	Coated Concrete
DSF17-C-CC-G-1-1.488	1.22	Gasoline	1	Coated Concrete
DSF18-C-CC-G-2-1.488	1.22	Gasoline	2	Coated Concrete
DSF19-C-CC-G-3-1.488	1.22	Gasoline	3	Coated Concrete
DSF20-C-CC-G-4-1.488	1.22	Gasoline	4	Coated Concrete
DSF21-C-CC-G-5-1.488	1.22	Gasoline	5	Coated Concrete
DSF22-C-CC-G-20-1.488	1.22	Gasoline	20	Coated Concrete
DSF25-C-V-G-1-0.093	0.31	Gasoline	1	Vinyl
DSF26-C-V-G-5-0.093	0.31	Gasoline	5	Vinyl
DSF27-C-V-G-10-0.093	0.31	Gasoline	10	Vinyl
DSF28-C-V-G-20-0.093	0.31	Gasoline	20	Vinyl
DSF29-C-V-K-1-0.093	0.31	Kerosene	1	Vinyl
DSF30-C-V-K-5-0.093	0.31	Kerosene	5	Vinyl
DSF31-C-V-K-10-0.093	0.31	Kerosene	10	Vinyl
DSF32-C-V-K-20-0.093	0.31	Kerosene	20	Vinyl
DSF33-C-V-G-1-0.372	0.61	Gasoline	1	Vinyl
DSF34-C-V-G-5-0.372	0.61	Gasoline	5	Vinyl
DSF35-C-V-G-10-0.372	0.61	Gasoline	10	Vinyl
DSF36-C-V-G-20-0.372	0.61	Gasoline	20	Vinyl
DSF37-C-V-K-1-0.372	0.61	Kerosene	1	Vinyl
DSF38-C-V-K-5-0.372	0.61	Kerosene	5	Vinyl
DSF39-C-V-K-10-0.372	0.61	Kerosene	10	Vinyl
DSF40-C-V-K-20-0.372	0.61	Kerosene	20	Vinyl
DSF41-C-V-G-1-1.488	1.22	Gasoline	1	Vinyl
DSF42-C-V-G-2-1.488	1.22	Gasoline	2	Vinyl
DSF43-C-V-G-3-1.488	1.22	Gasoline	3	Vinyl
DSF44-C-V-G-4-1.488	1.22	Gasoline	4	Vinyl
DSF45-C-V-G-5-1.488	1.22	Gasoline	5	Vinyl
DSF46-C-V-G-15-1.488	1.22	Gasoline	15	Vinyl

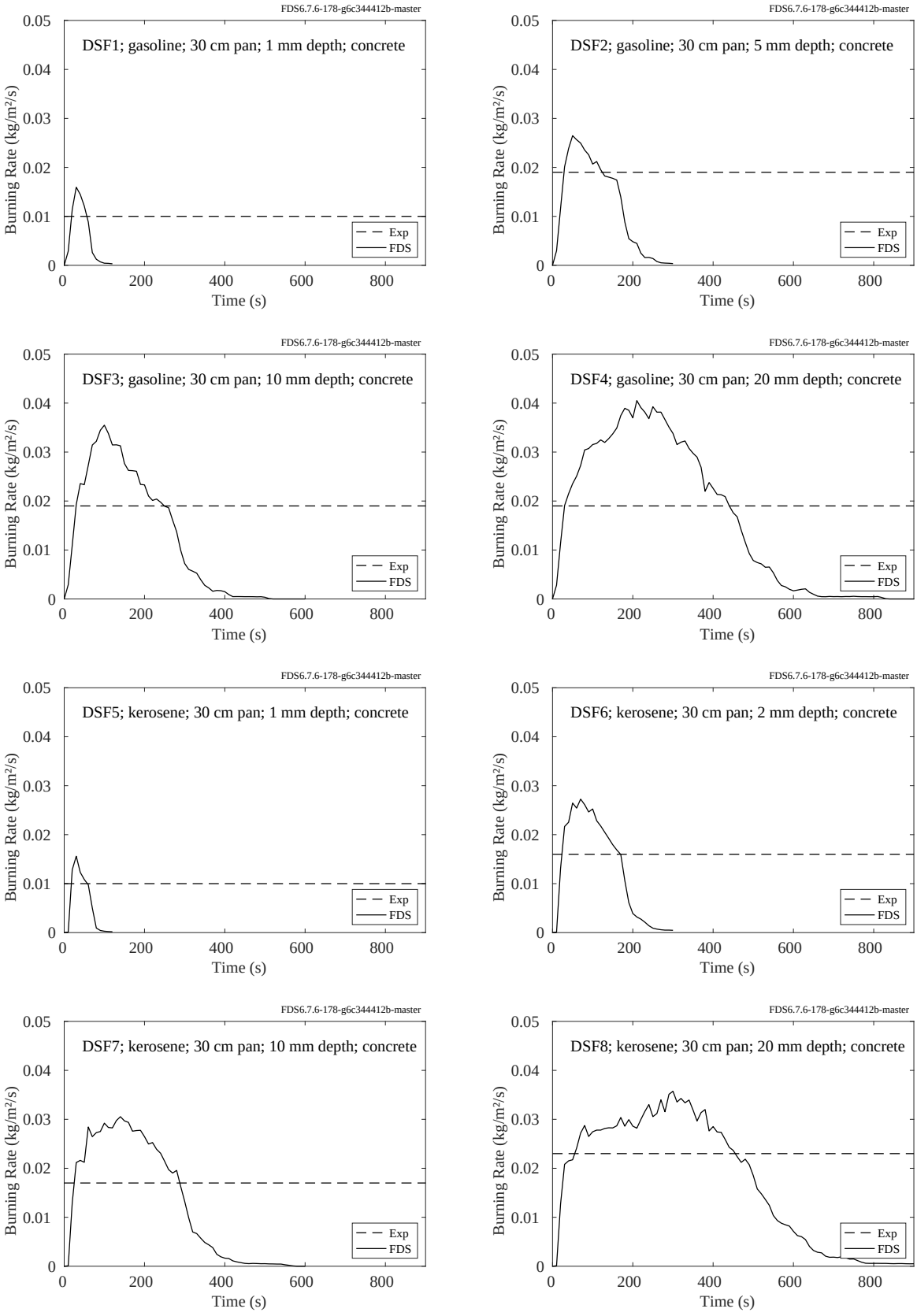

Figure 14.22: DoJ/HAI Pool Fires, Tests 1-8.

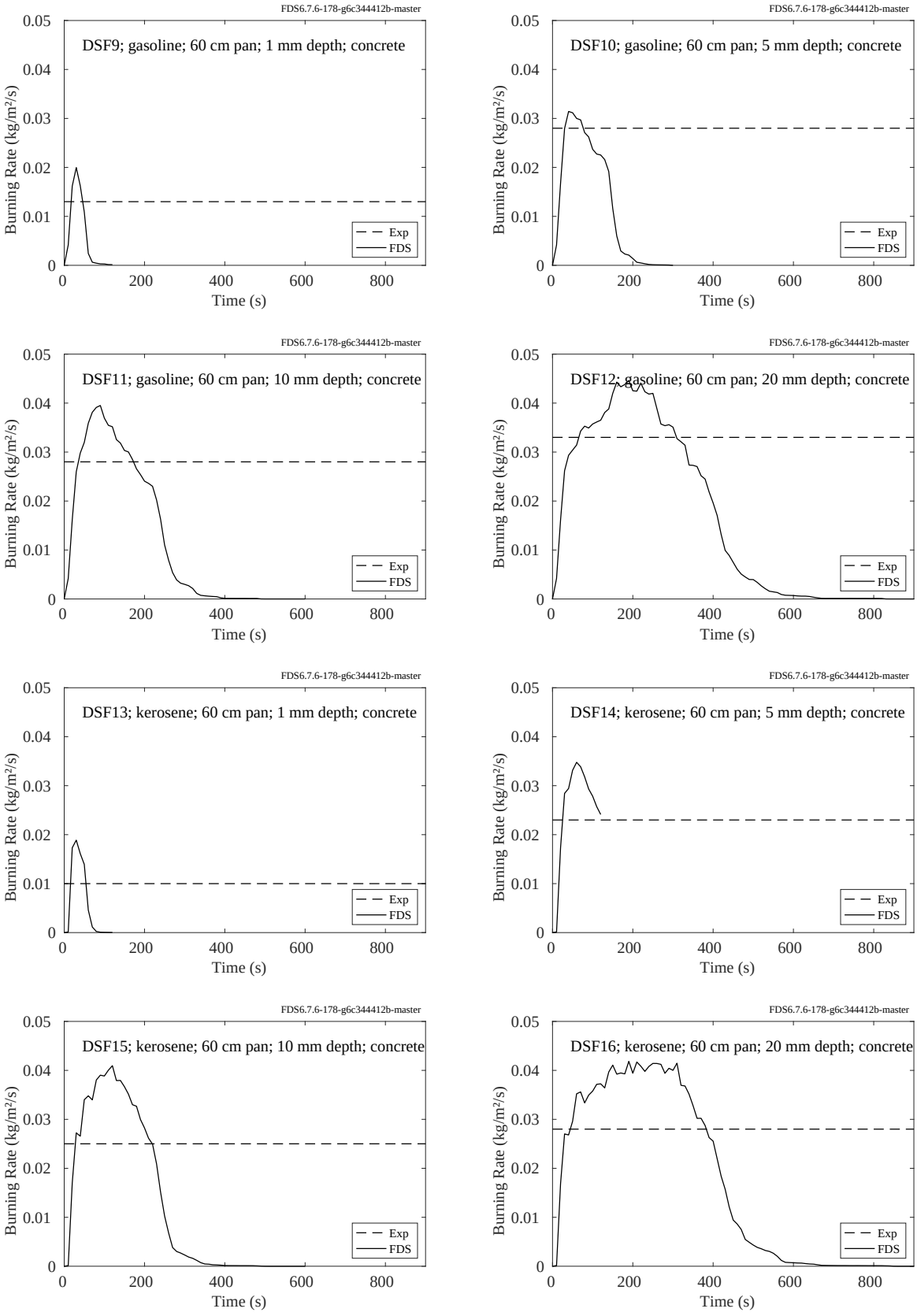

Figure 14.23: DoJ/HAI Pool Fires, Tests 9-16.

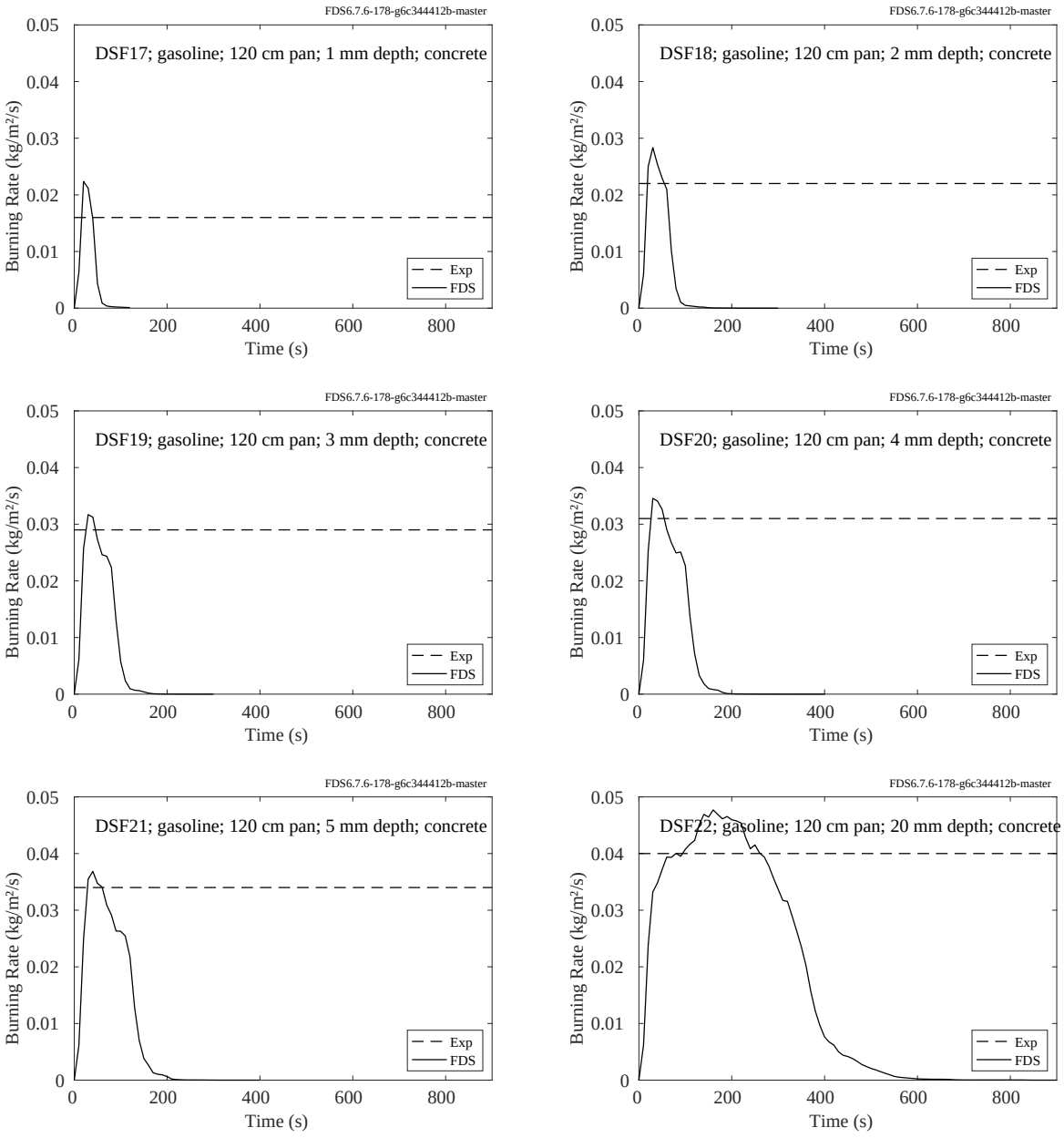

Figure 14.24: DoJ/HAI Pool Fires, Tests 17-22.

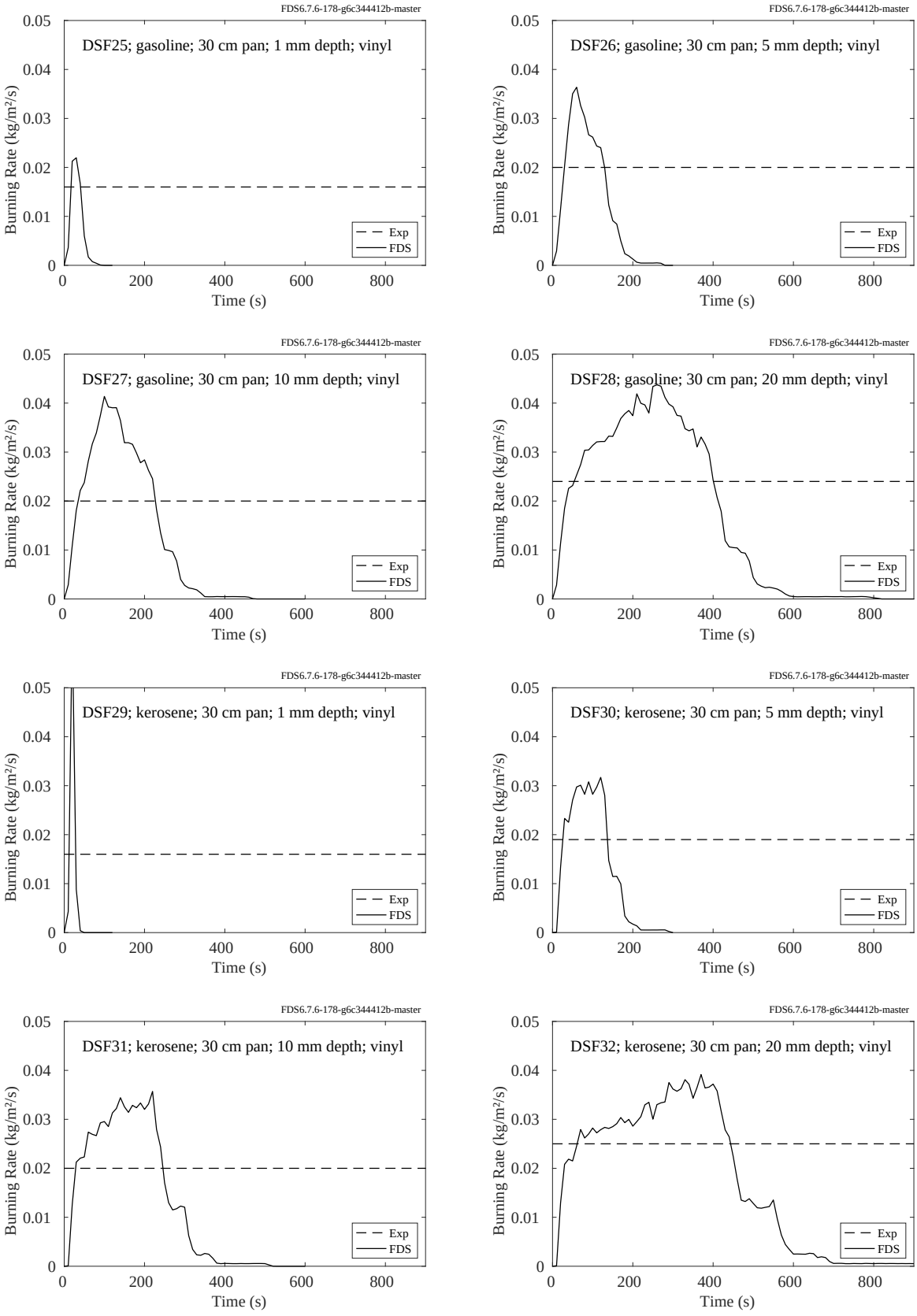

Figure 14.25: DoJ/HAI Pool Fires, Tests 25-32.

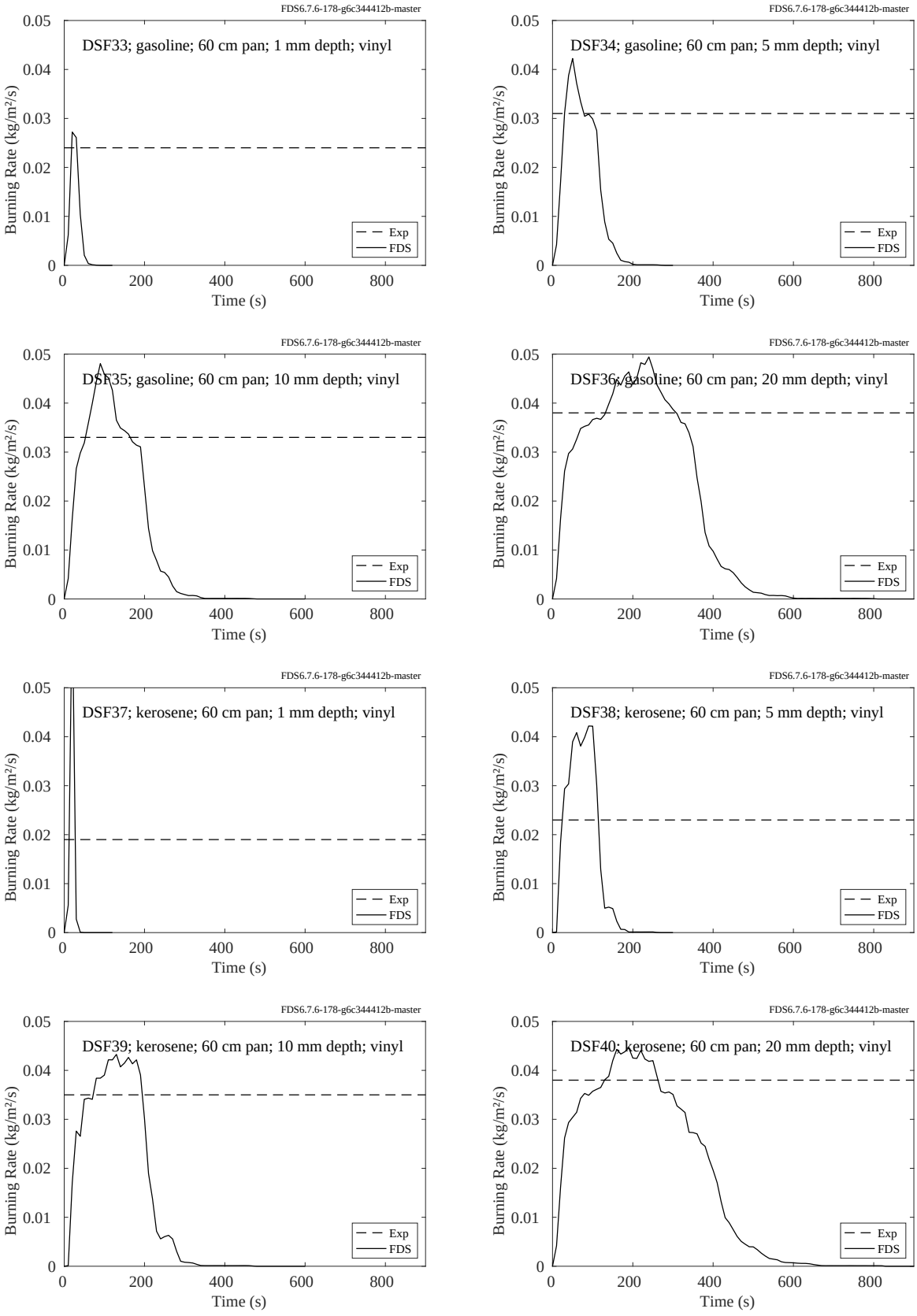

Figure 14.26: DoJ/HAI Pool Fires, Tests 33-40.

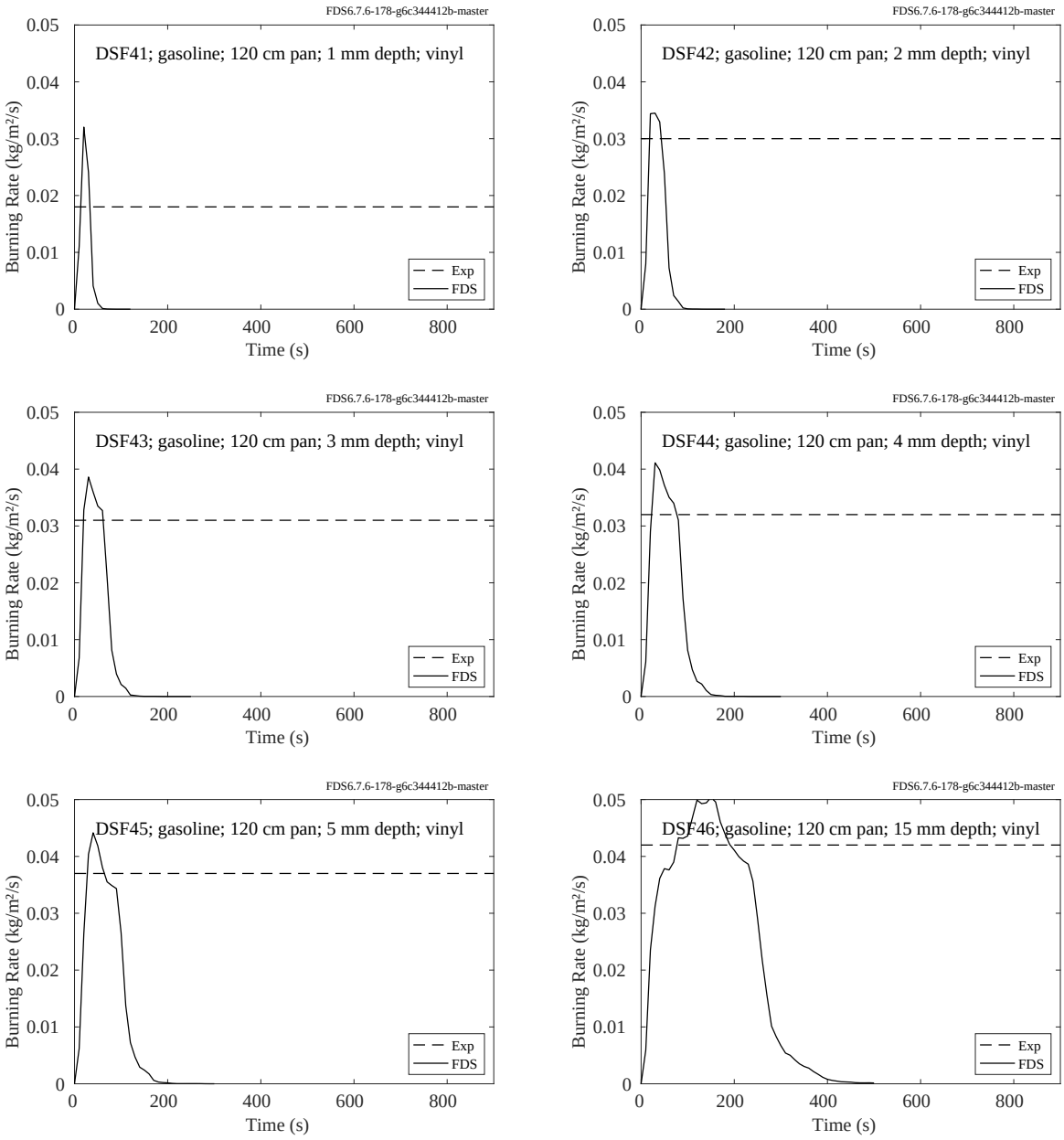

Figure 14.27: DoJ/HAI Pool Fires, Tests 41-46.

14.5.2 Pool Fire Measurements

Shown below are comparisons of measured and predicted evaporation/burning rates of various liquid pools. Surface temperature comparisons of these same experiments are shown in Section 11.3.

Figure 14.28 compares the measured and predicted evaporation rate of water subjected to a 50 kW/m^2 heat flux.

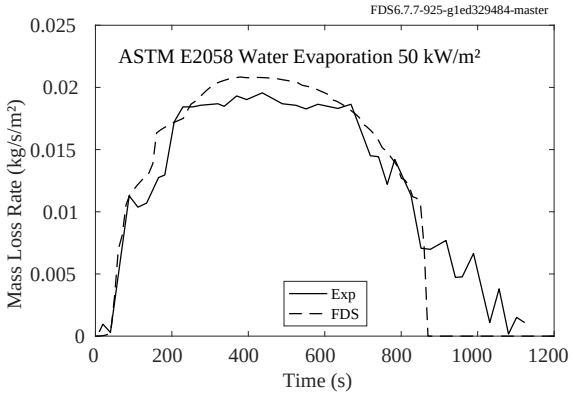

Figure 14.28: ASTM E2058 fire propagation apparatus water evaporation at 50 kW/m^2 heat flux.

Figure 14.29 shows the measured and predicted mass loss rates of 1.17 m (1.07 m^2) and 1.6 m (2.0 m^2) diameter heptane pool fires. The measured mass loss rates are averages of two or three individual experiments.

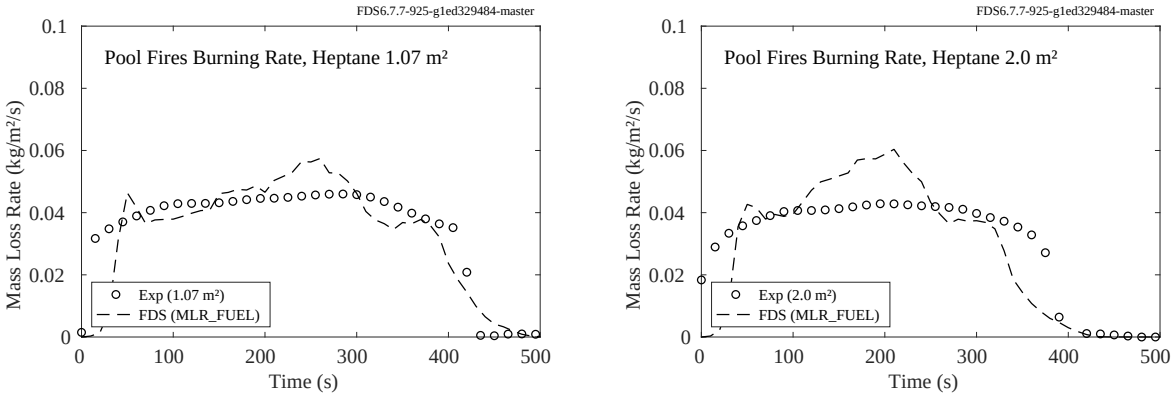

Figure 14.29: VTT Large Hall Test burning rate.

Figure 14.30 compares predicted and measured burning rates of a variety of liquid fuels.

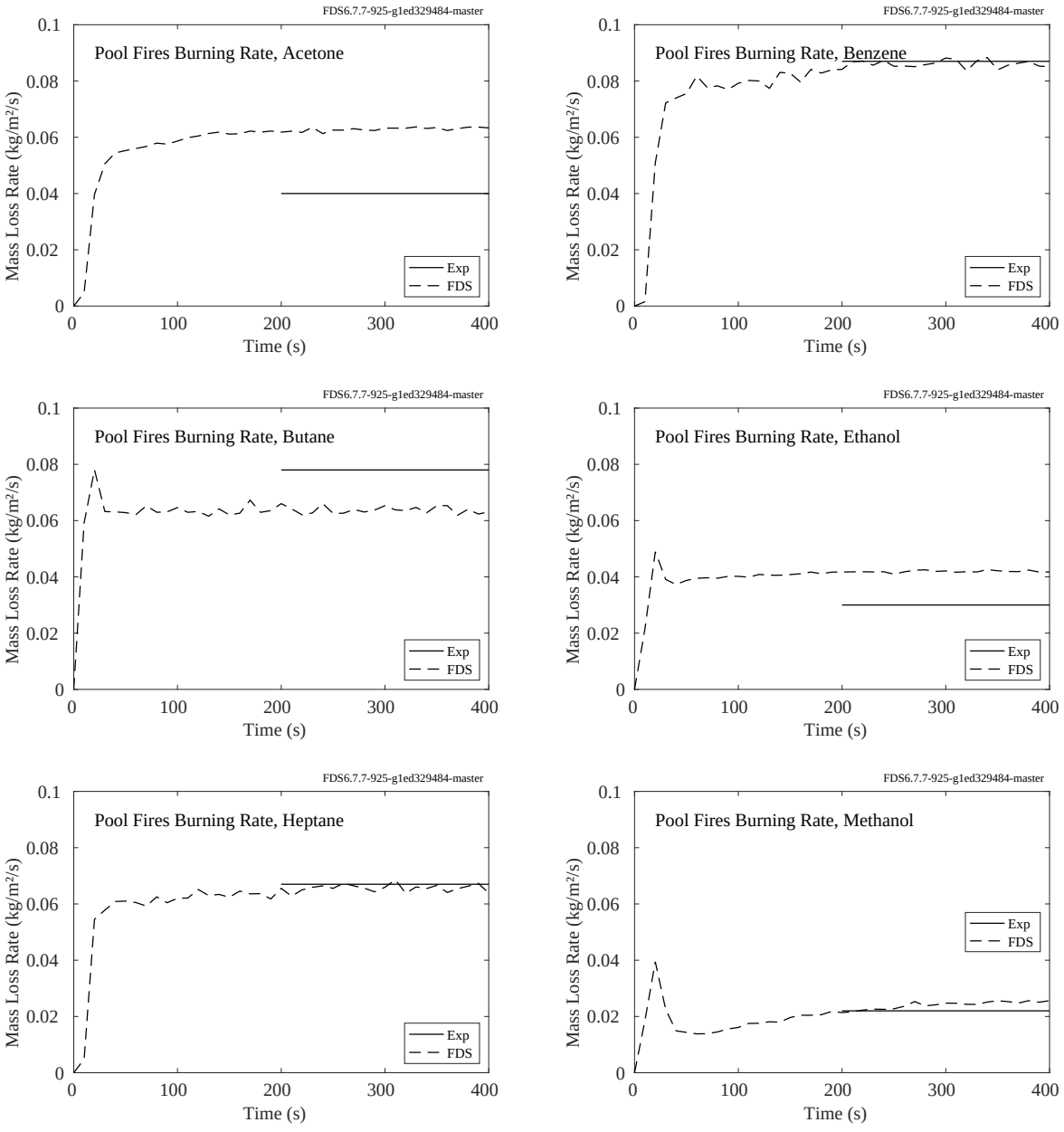

Figure 14.30: Comparison of burning rates for various liquid pool fires.

14.5.3 NIST Pool Fires

Figure 14.31 displays the measured and predicted burning rate of a 100 cm diameter methanol pool fire experiment conducted by Sung et al. at NIST [330].

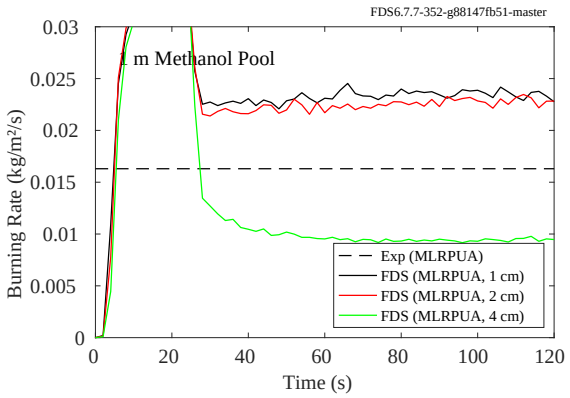

Figure 14.31: Burning rate of a 1 m methanol pool fire.

14.5.4 Waterloo Methanol Pool Fire

Figure 14.32 displays the measured and predicted burning rate for a 30 cm diameter methanol pool fire experiment conducted by Weckman at the University of Waterloo [310]. The experimental result came after at least 10 min of burning, whereas the model is only run for 2 min.

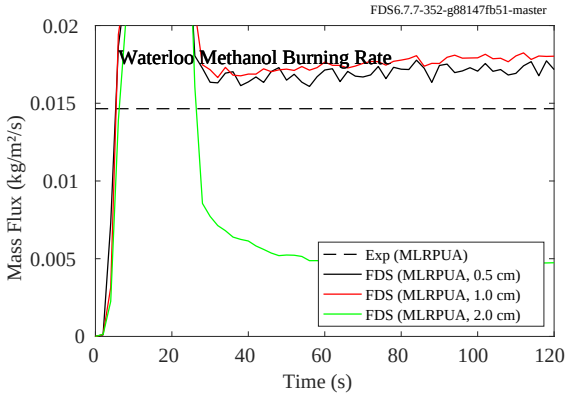

Figure 14.32: Waterloo Methanol mass loss rate.

14.6 Vertical Flame Spread

14.6.1 NIST/NRC Parallel Panel Experiments

The figures below contain predictions of the burning rate of various plastics in a parallel panel apparatus described in Section 3.49.

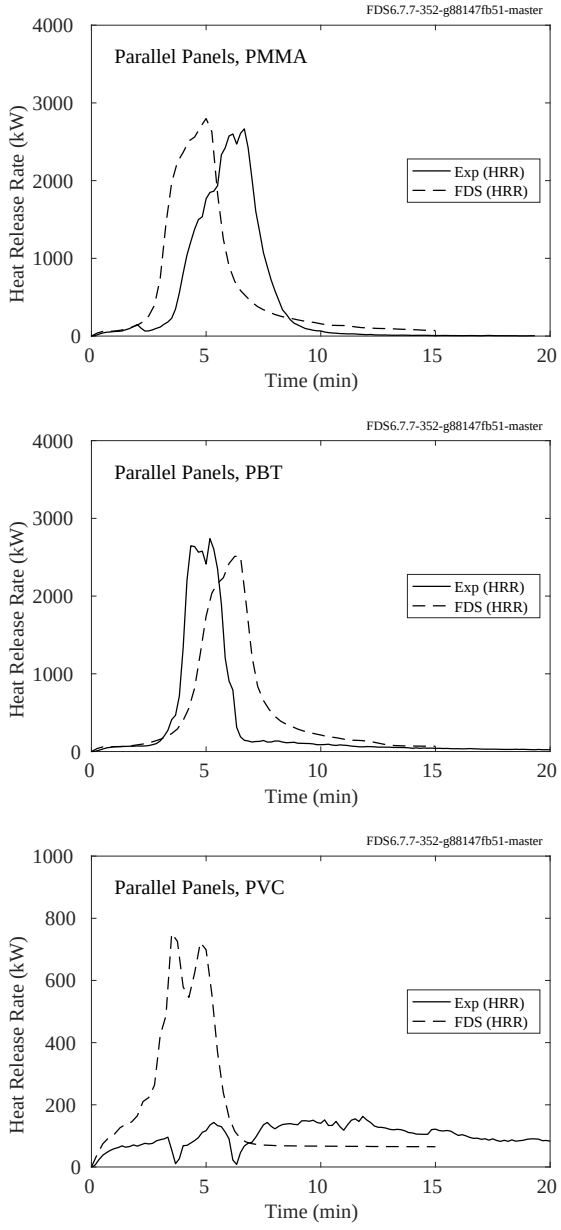

Figure 14.33: NIST/NRC Parallel Panels experiments.

14.7 Wildland Fire Burning and Spread Rates

The following sections present examples of fire spread through vegetation, both small and full-scale. Summary plots of burning and spread rates are presented in Figs. 14.86 and 14.88.

14.7.1 Crown Fires

This section presents the rate of spread for simulations of crown fires. For a description of the experiments and simulations, see Section 3.13. The experimental data consists of 57 observed crown fires. The simulations are performed with comparable conditions, but not all input parameters can be gleaned from the experimental reports. Thus, the comparison is largely qualitative, and has not been quantified in any way other than the comparison plot in Fig. 14.34.

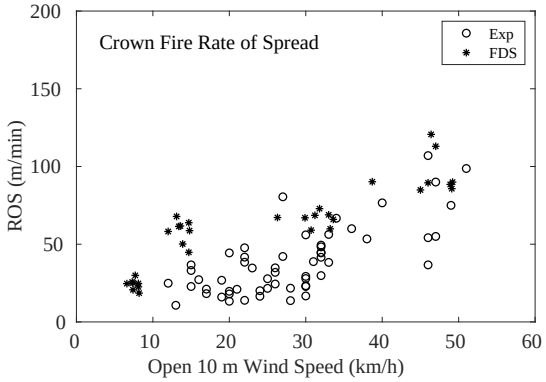

Figure 14.34: Comparison observed and predicted rates of spread for a variety of crown fires.

14.7.2 CSIRO Grassland Fires

This section presents the rate of spread for simulations of two of the CSIRO Grassland Fire experiments. For details of the experiments and simulations, see Section 3.14. The first experiment, C064, was conducted on a 100 m by 100 m plot; the second, F19, was conducted on a 200 m by 200 m plot. The results of the simulations are shown in Fig. 14.35. The fire front in the FDS simulations is defined as the location of the maximum gas temperature in a 1 m wide, 1 m tall strip along the centerline of the grass field. The experimental points were determined from aerial photography.

For each case, three simulations are performed—one using Lagrangian particles to represent the vegetation, one using the Boundary Fuel Model (BFM), and the other using Rothermel-Albini fuel models in a level set fire spread simulation.

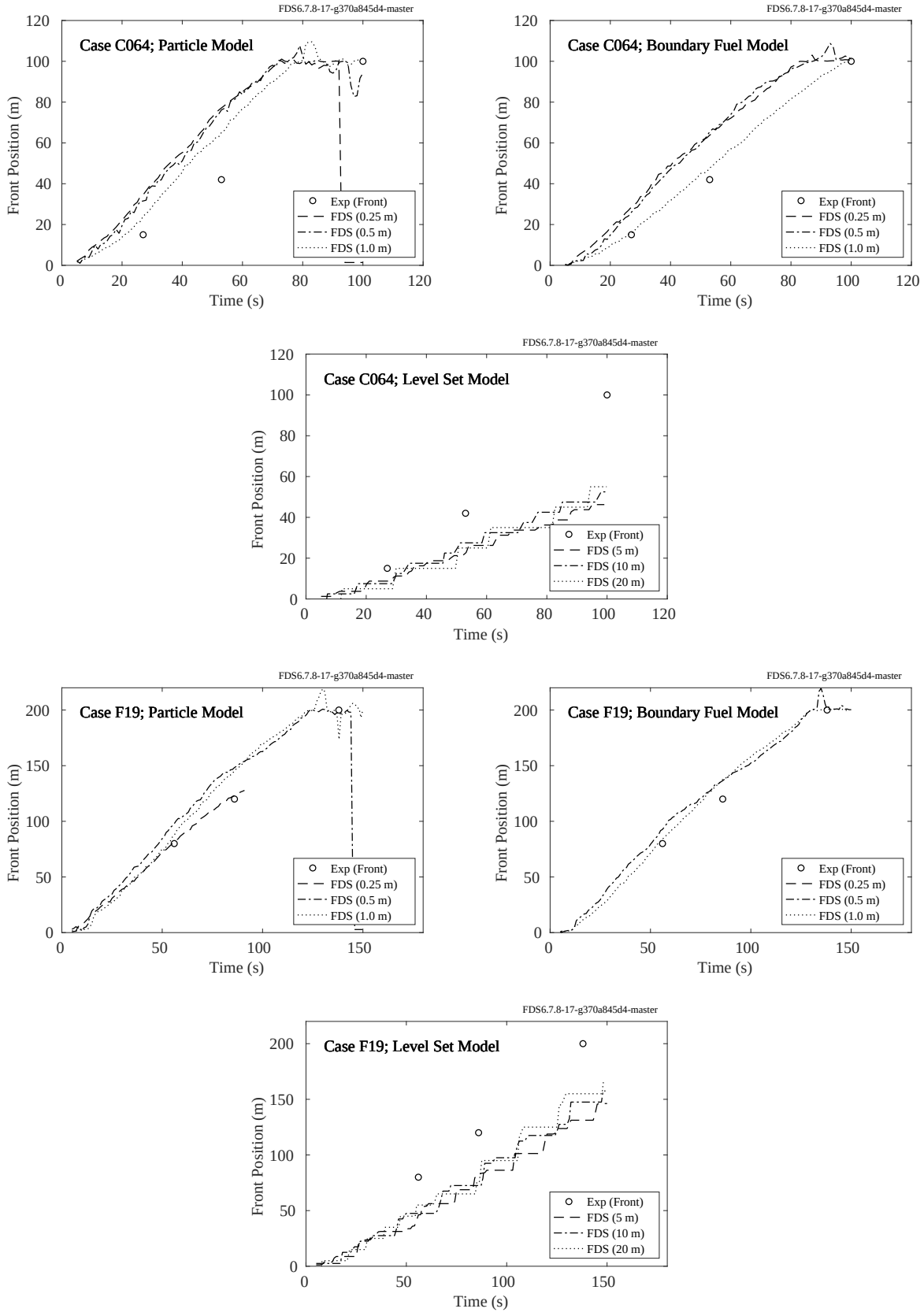

Figure 14.35: Comparison of the measured and predicted fire front position for the CSIRO Grassland Fires using three different methods of fire spread.

14.7.3 USFS/Catchpole Experiments

Figures 14.36 through 14.80 present the results of 354 simulations of the USFS/Catchpole experiments. A brief description is given in Section 3.82. The paper by Catchpole et al. [304] reports a single rate of spread for each experiment, which is depicted in the figures as a straight black line. The rate of spread of the simulations was calculated by fitting the best line through the data points over a time interval between 10 % and 90 % of the observed transit time of the real fire over the 8 m fuel bed. The red dashed line is the best fit line from which the rate of spread is taken.

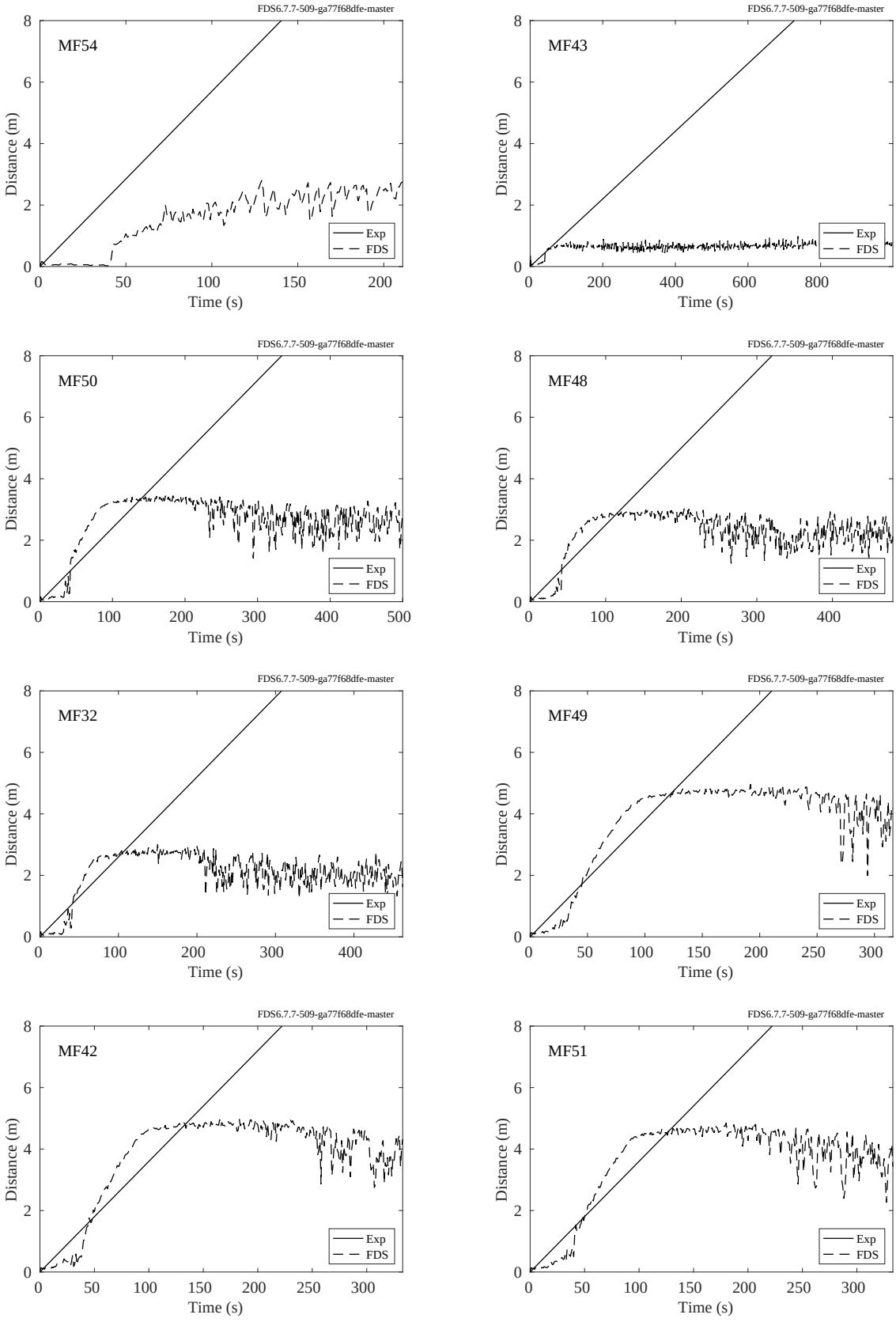

Figure 14.36: Flame front, USFS/Catchpole experiments

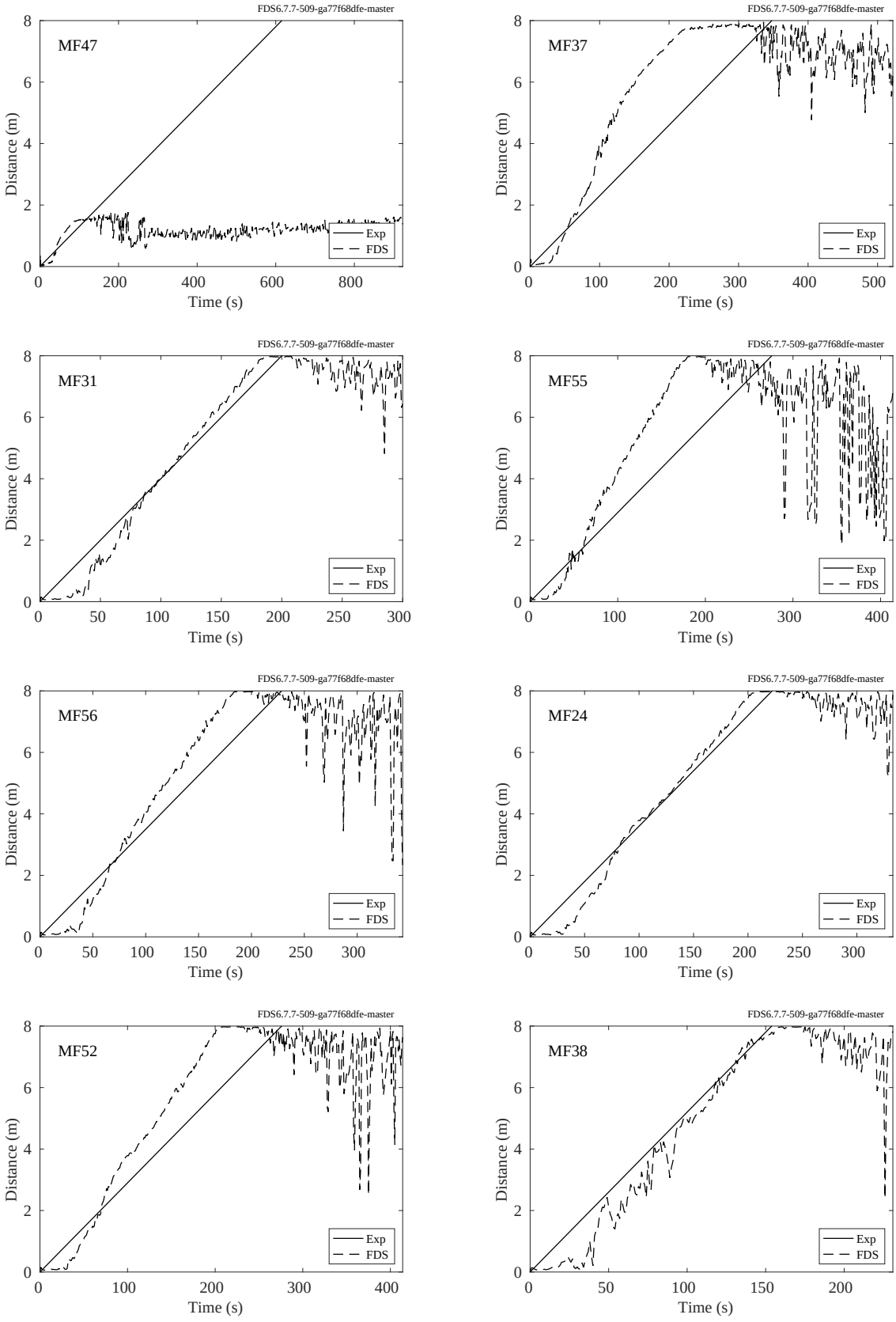

Figure 14.37: Flame front, USFS/Catchpole experiments

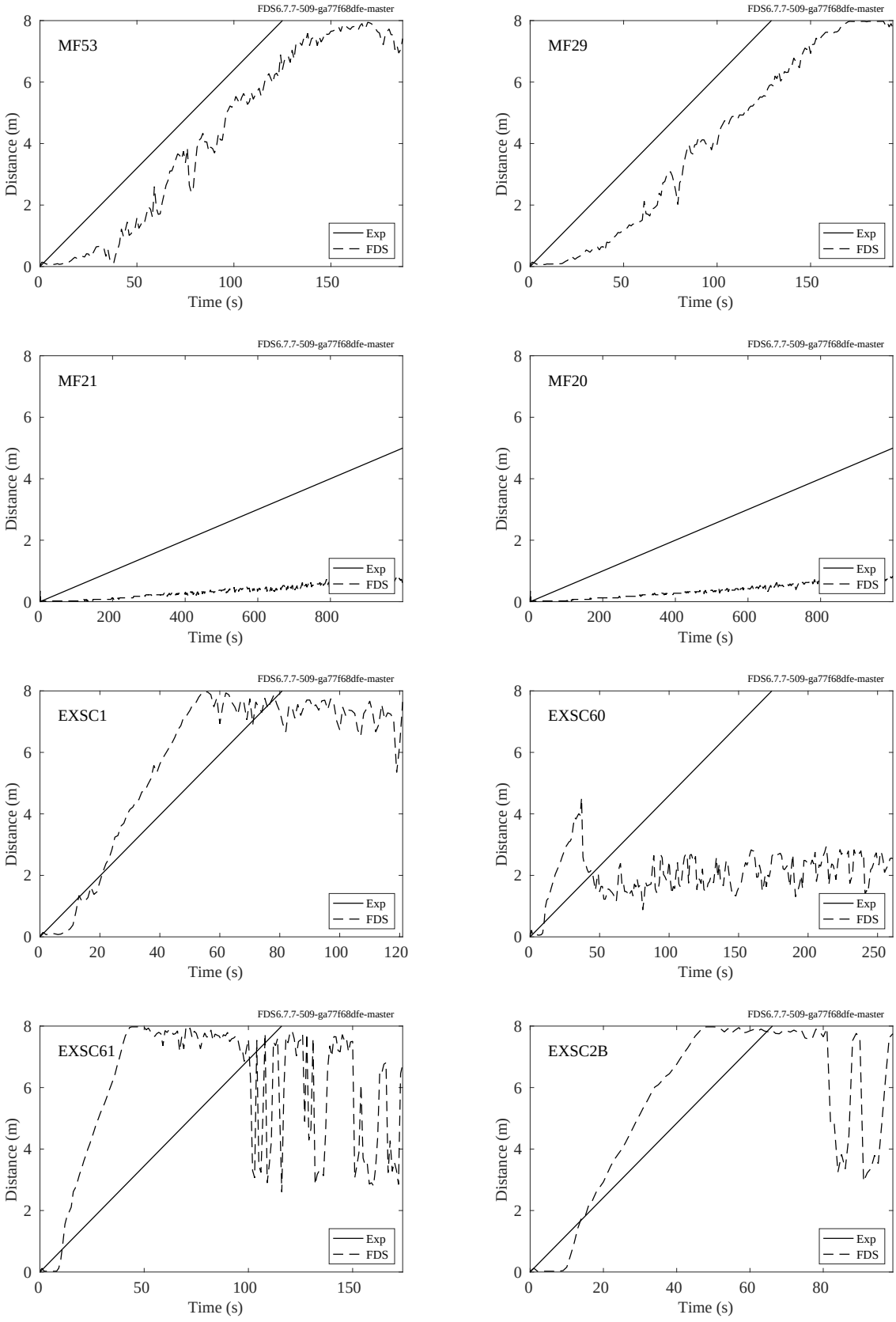

Figure 14.38: Flame front, USFS/Catchpole experiments

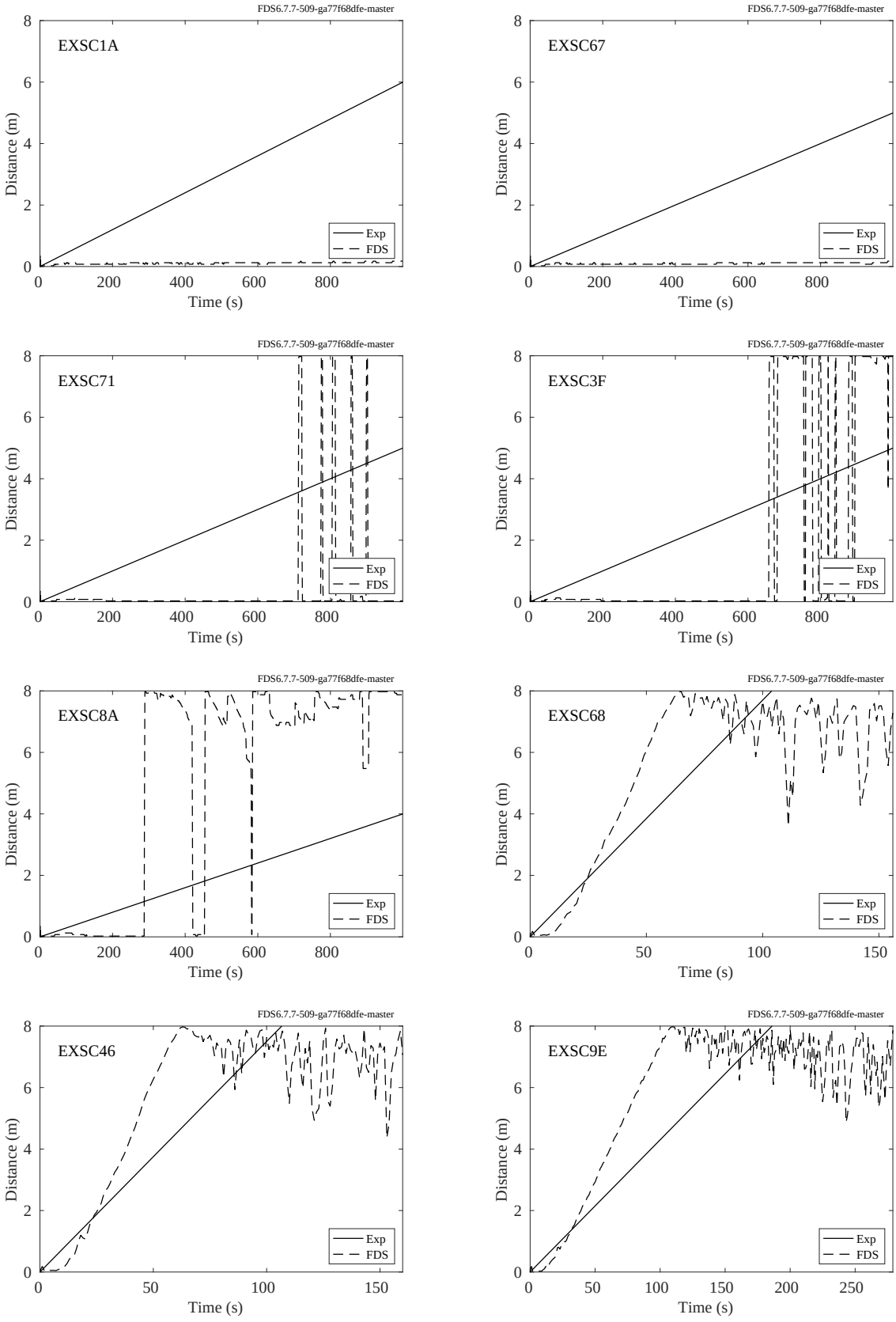

Figure 14.39: Flame front, USFS/Catchpole experiments

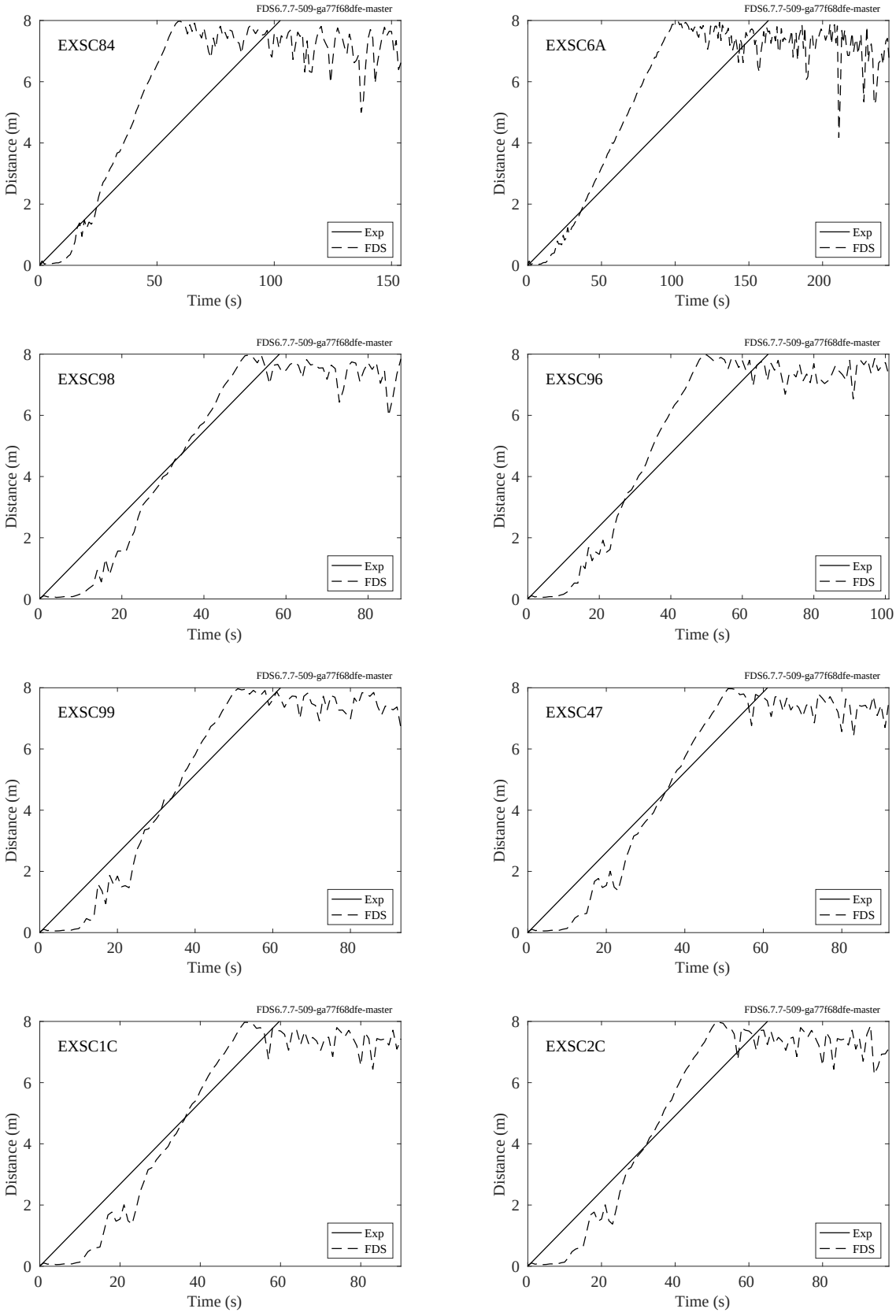

Figure 14.40: Flame front, USFS/Catchpole experiments

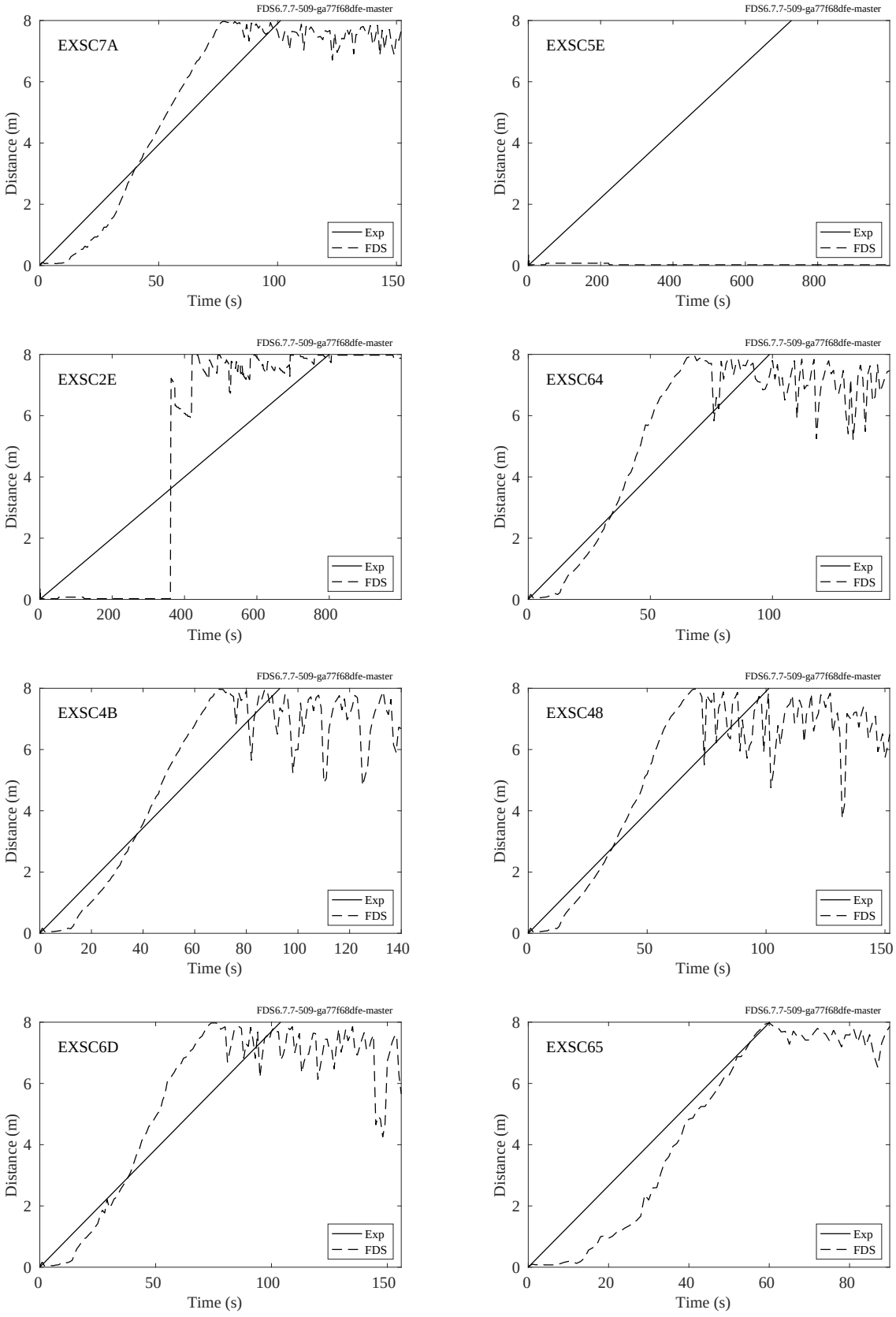

Figure 14.41: Flame front, USFS/Catchpole experiments

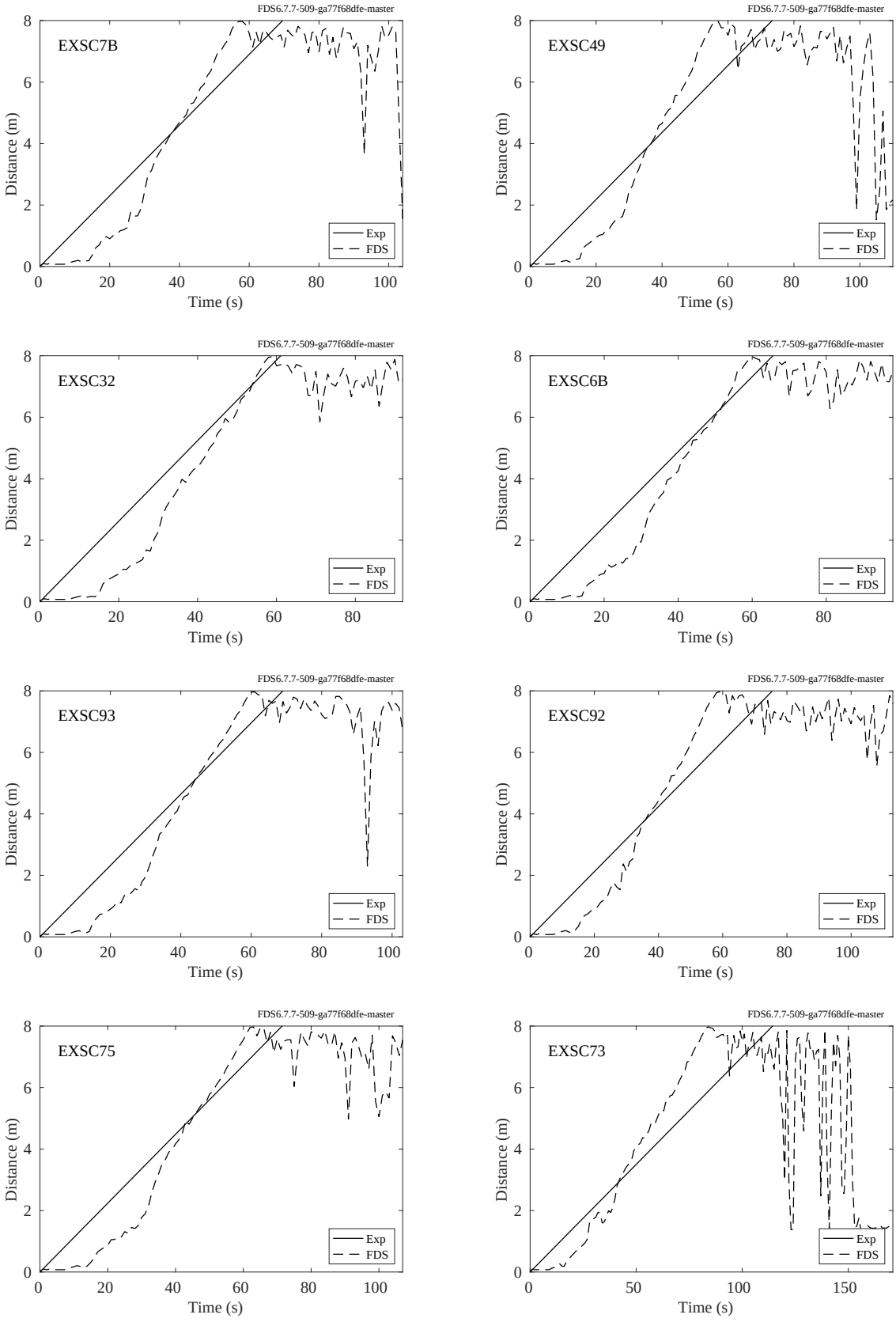

Figure 14.42: Flame front, USFS/Catchpole experiments

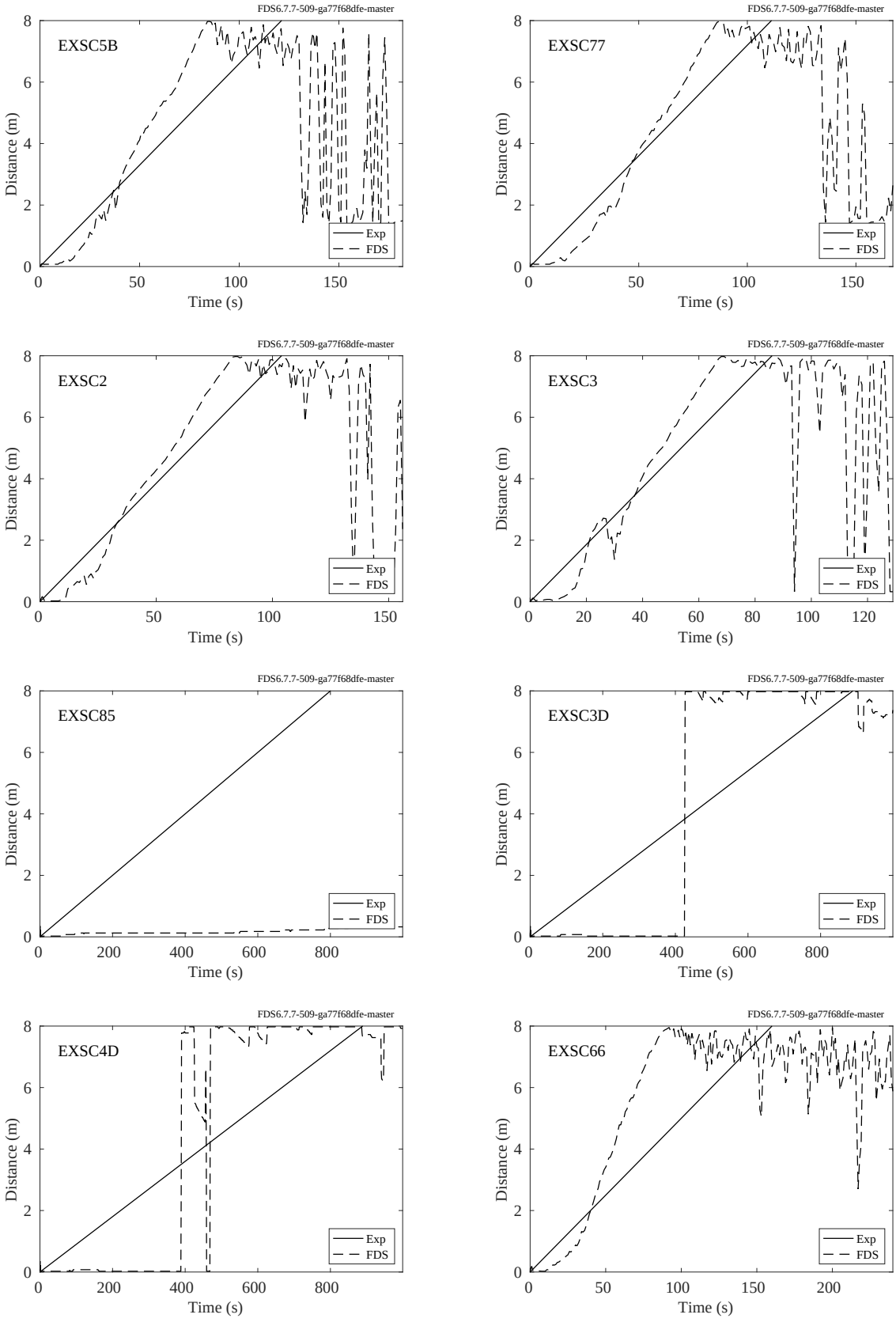

Figure 14.43: Flame front, USFS/Catchpole experiments

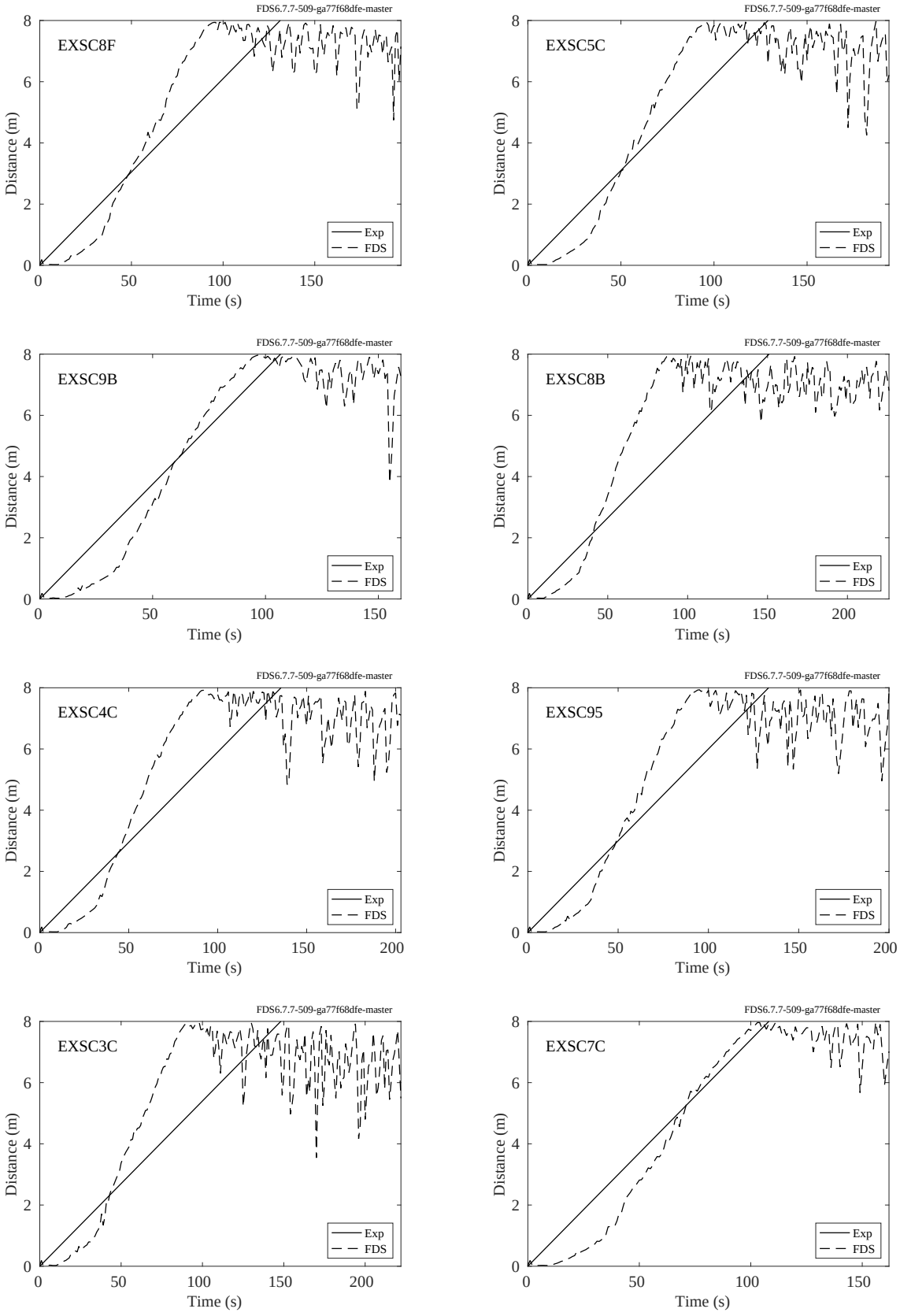

Figure 14.44: Flame front, USFS/Catchpole experiments

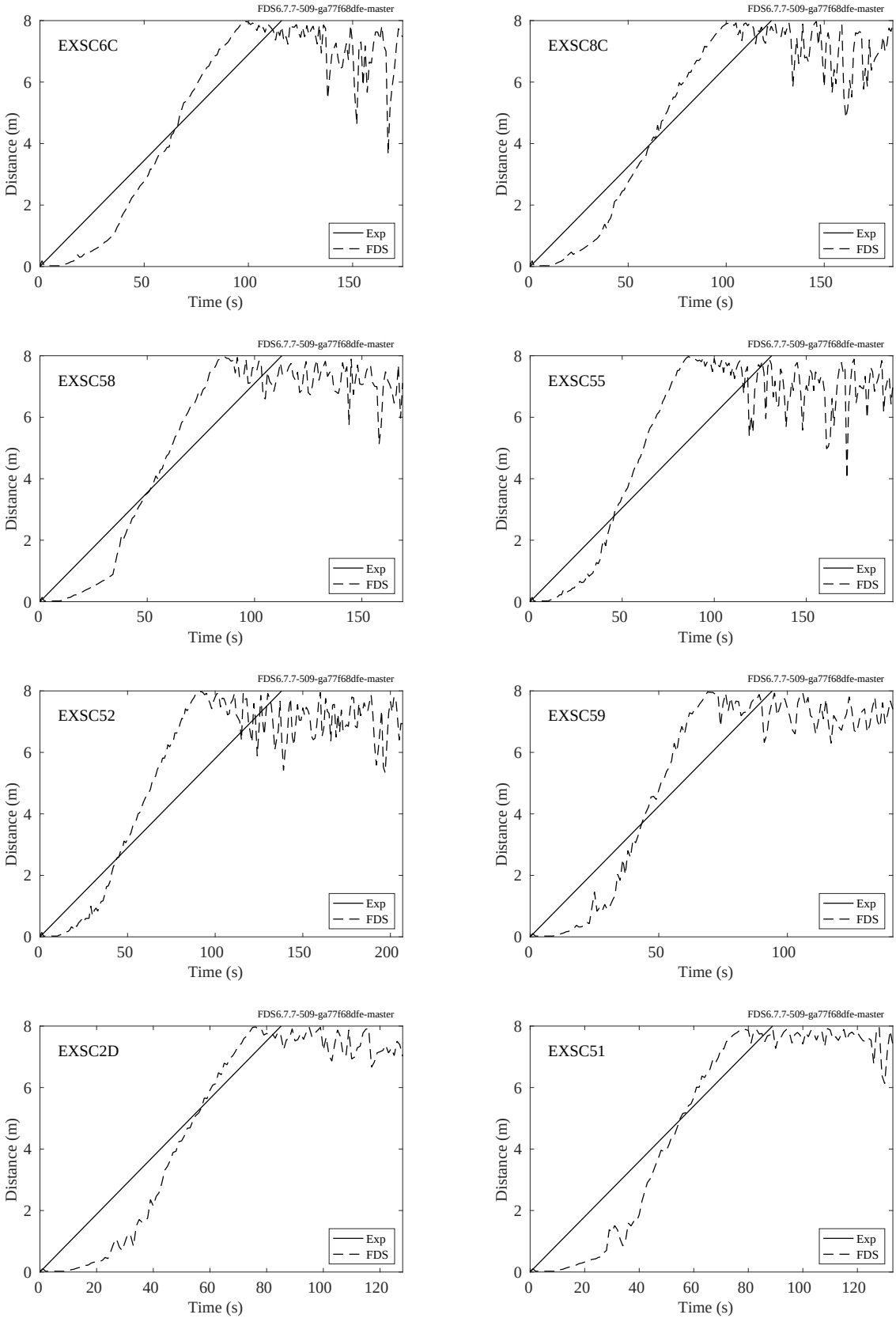

Figure 14.45: Flame front, USFS/Catchpole experiments

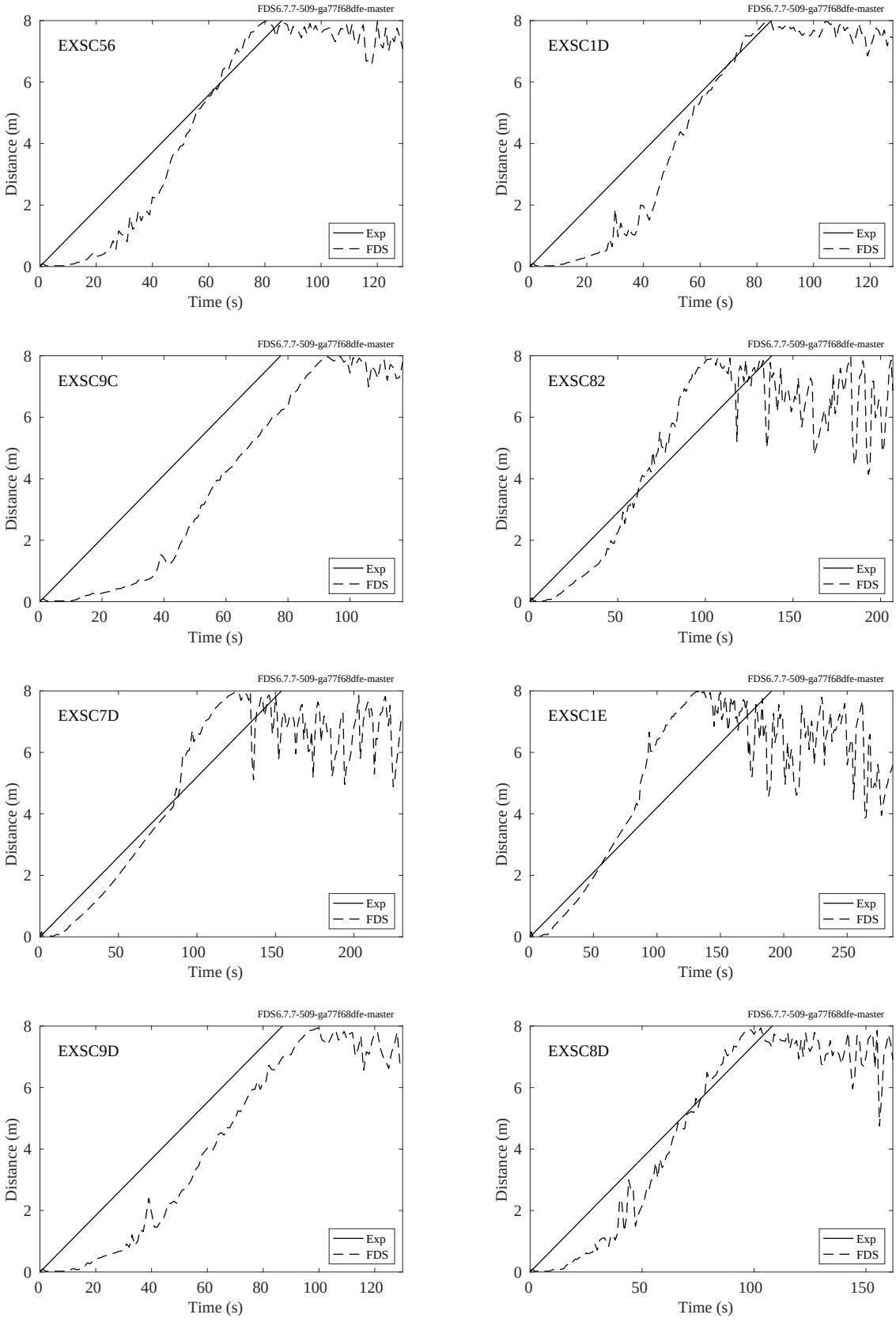

Figure 14.46: Flame front, USFS/Catchpole experiments

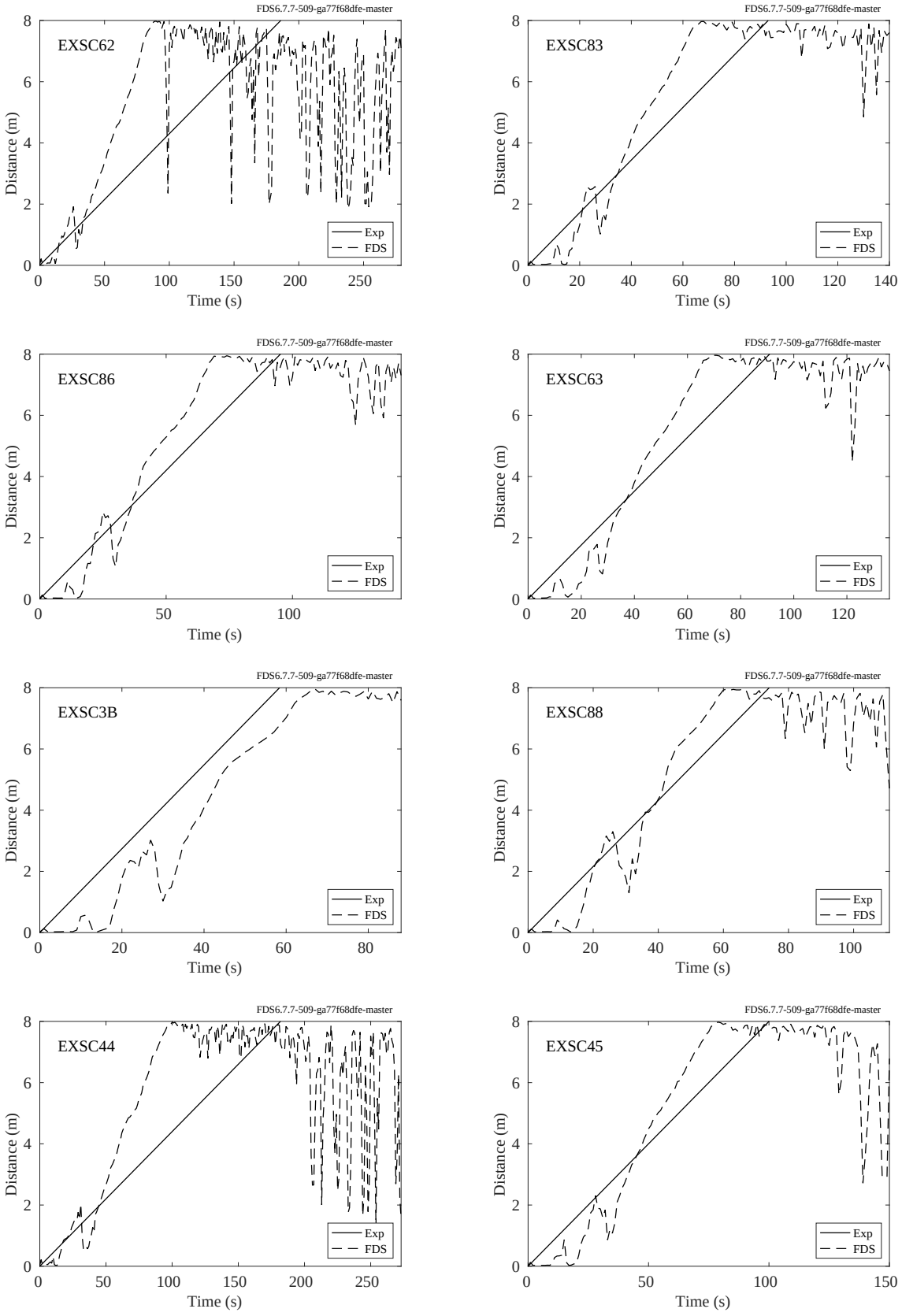

Figure 14.47: Flame front, USFS/Catchpole experiments

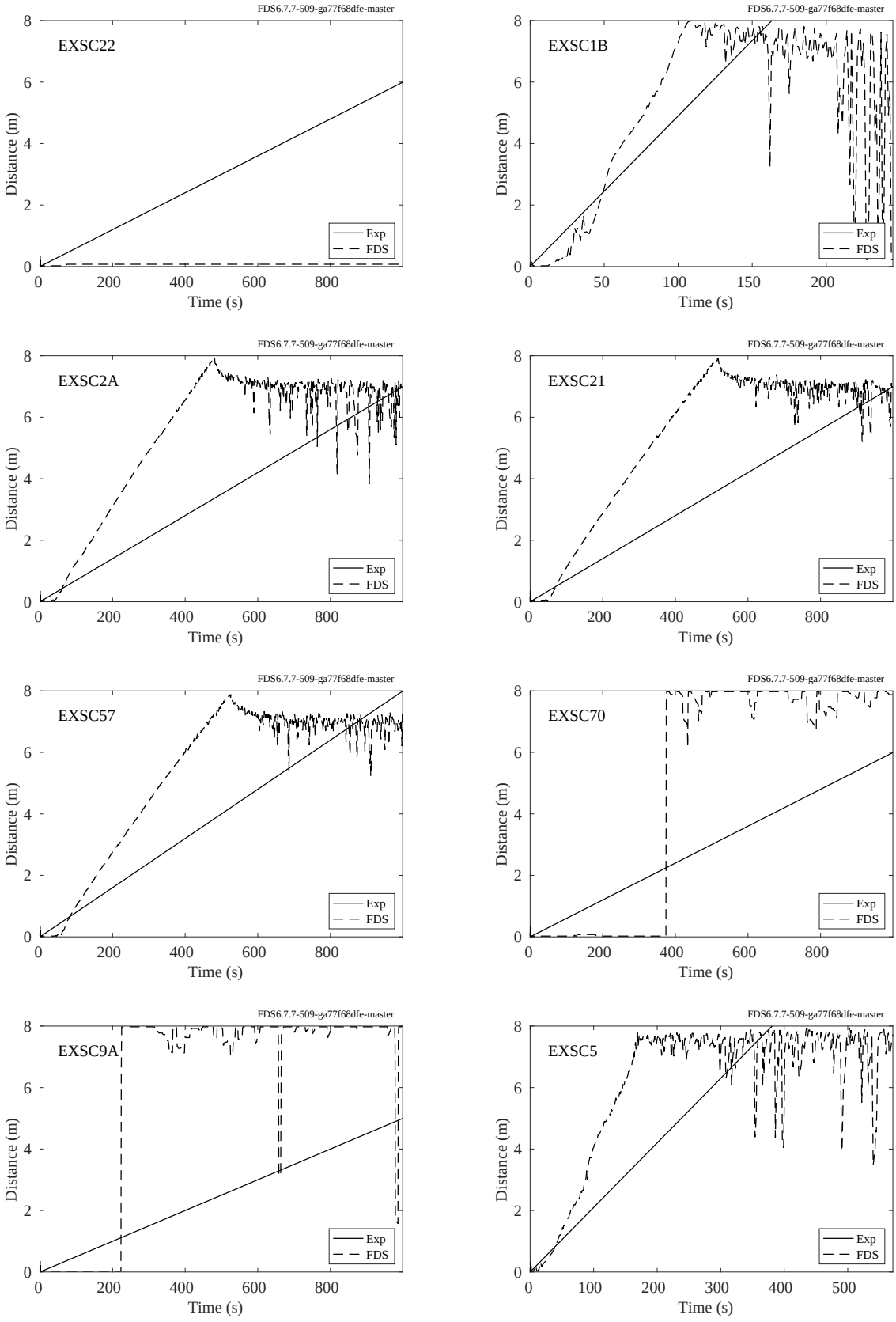

Figure 14.48: Flame front, USFS/Catchpole experiments

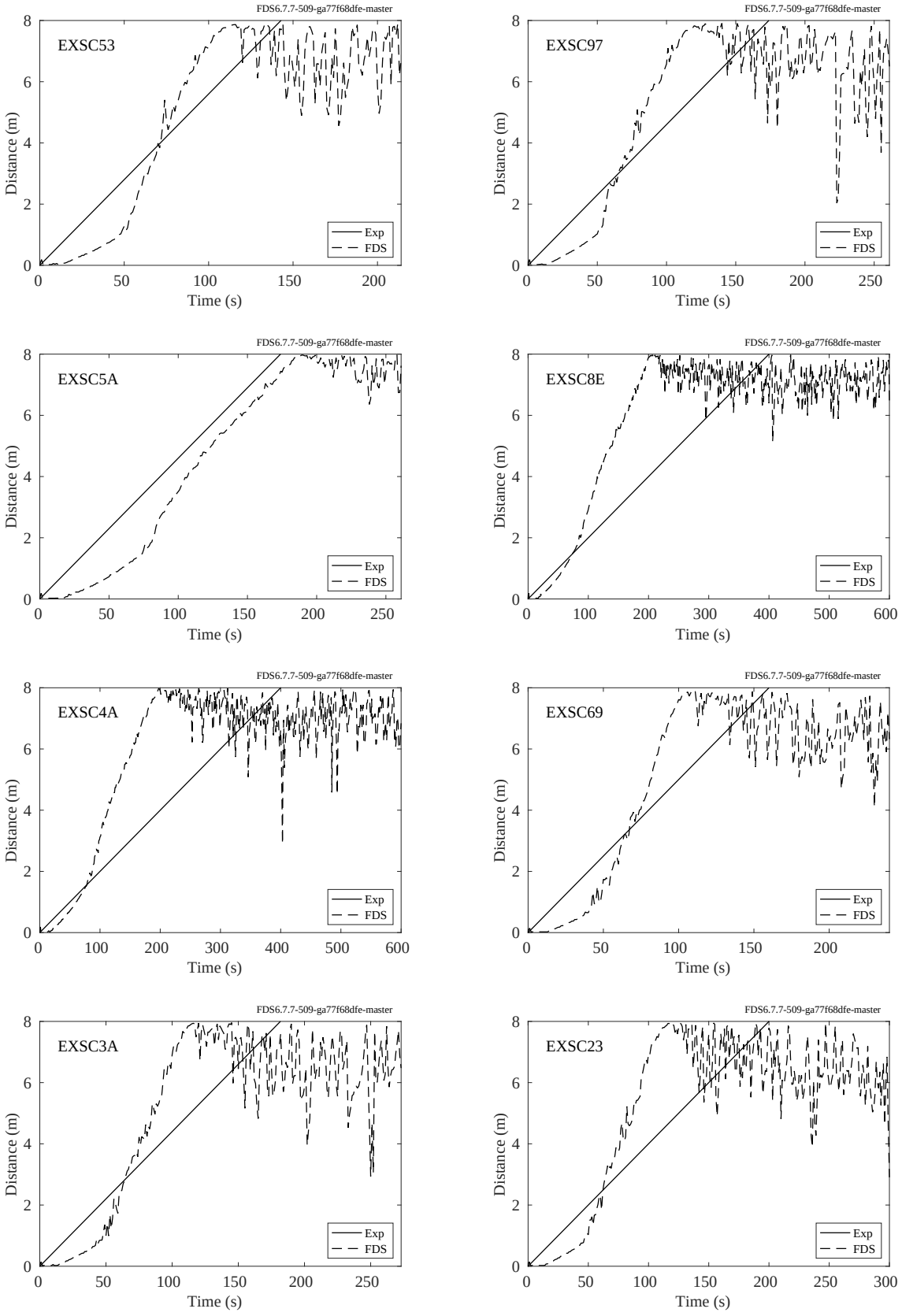

Figure 14.49: Flame front, USFS/Catchpole experiments

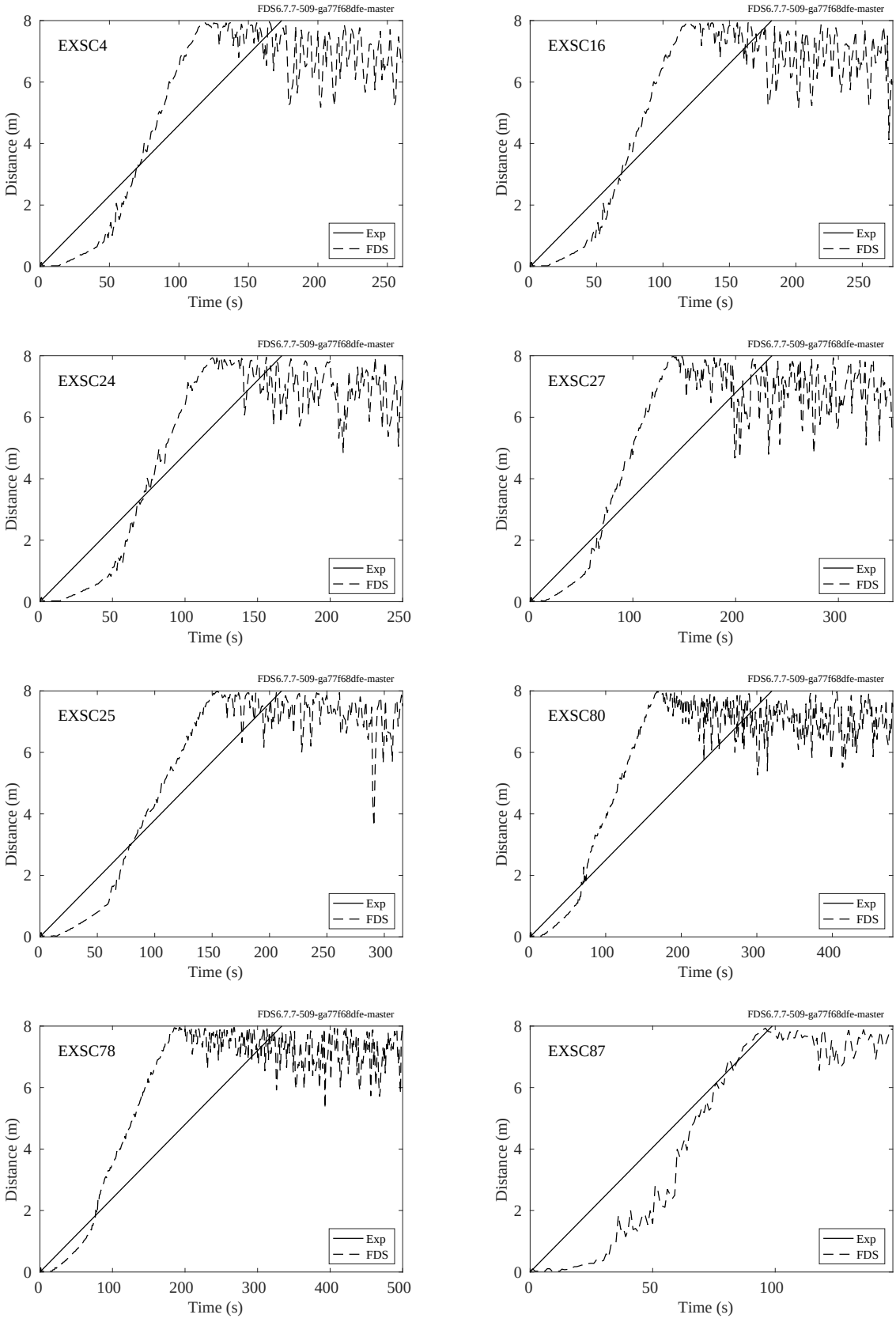

Figure 14.50: Flame front, USFS/Catchpole experiments

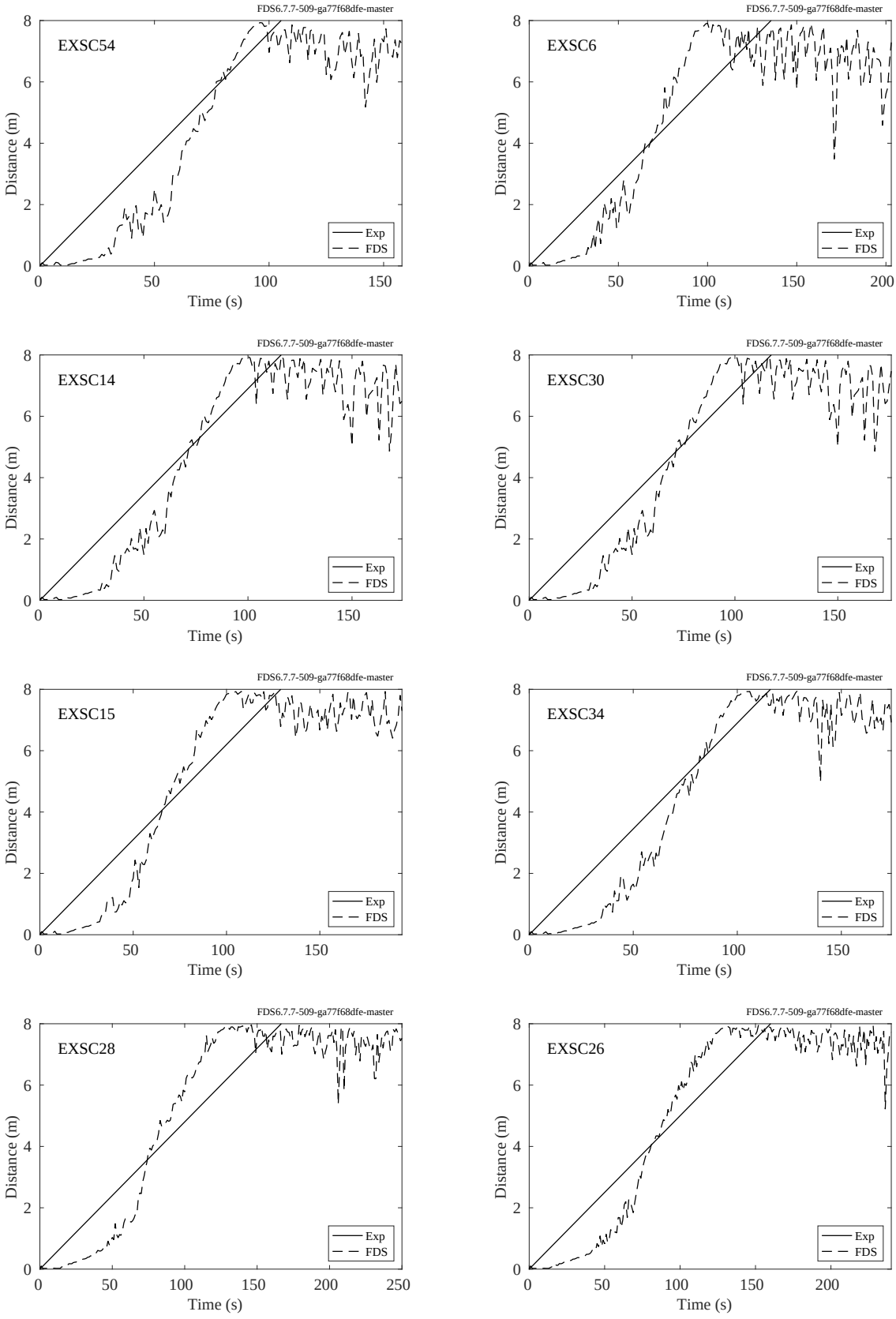

Figure 14.51: Flame front, USFS/Catchpole experiments

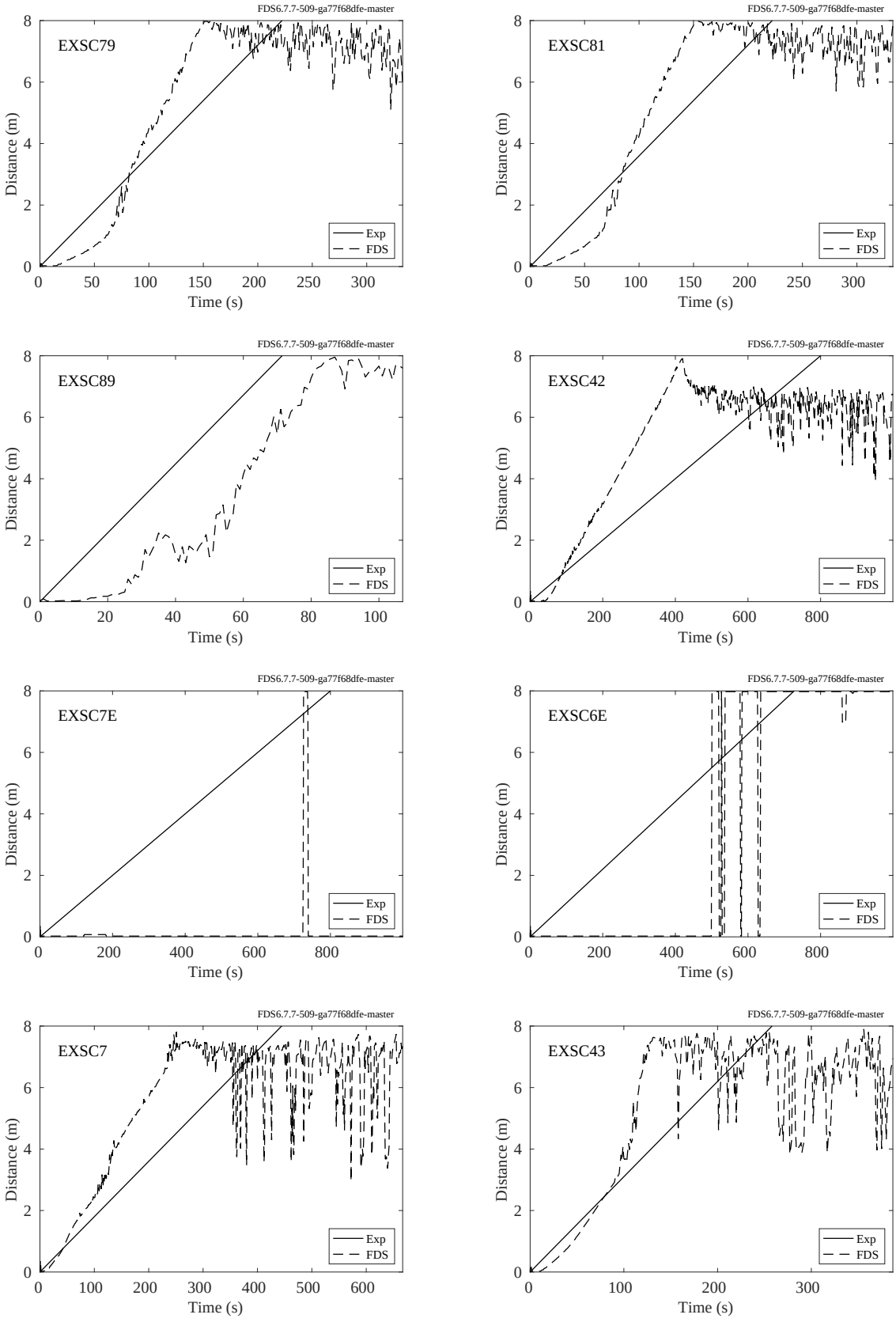

Figure 14.52: Flame front, USFS/Catchpole experiments

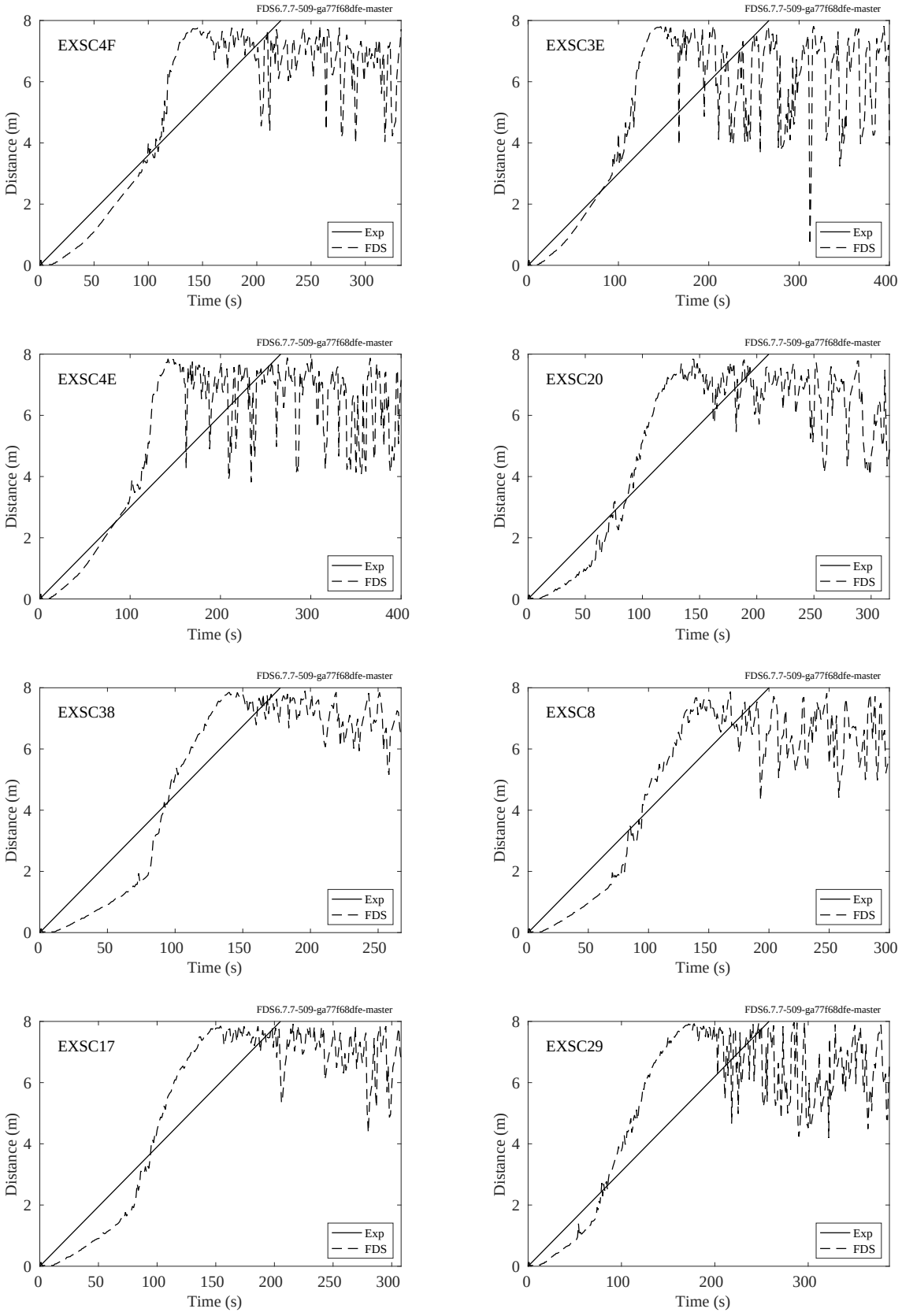

Figure 14.53: Flame front, USFS/Catchpole experiments

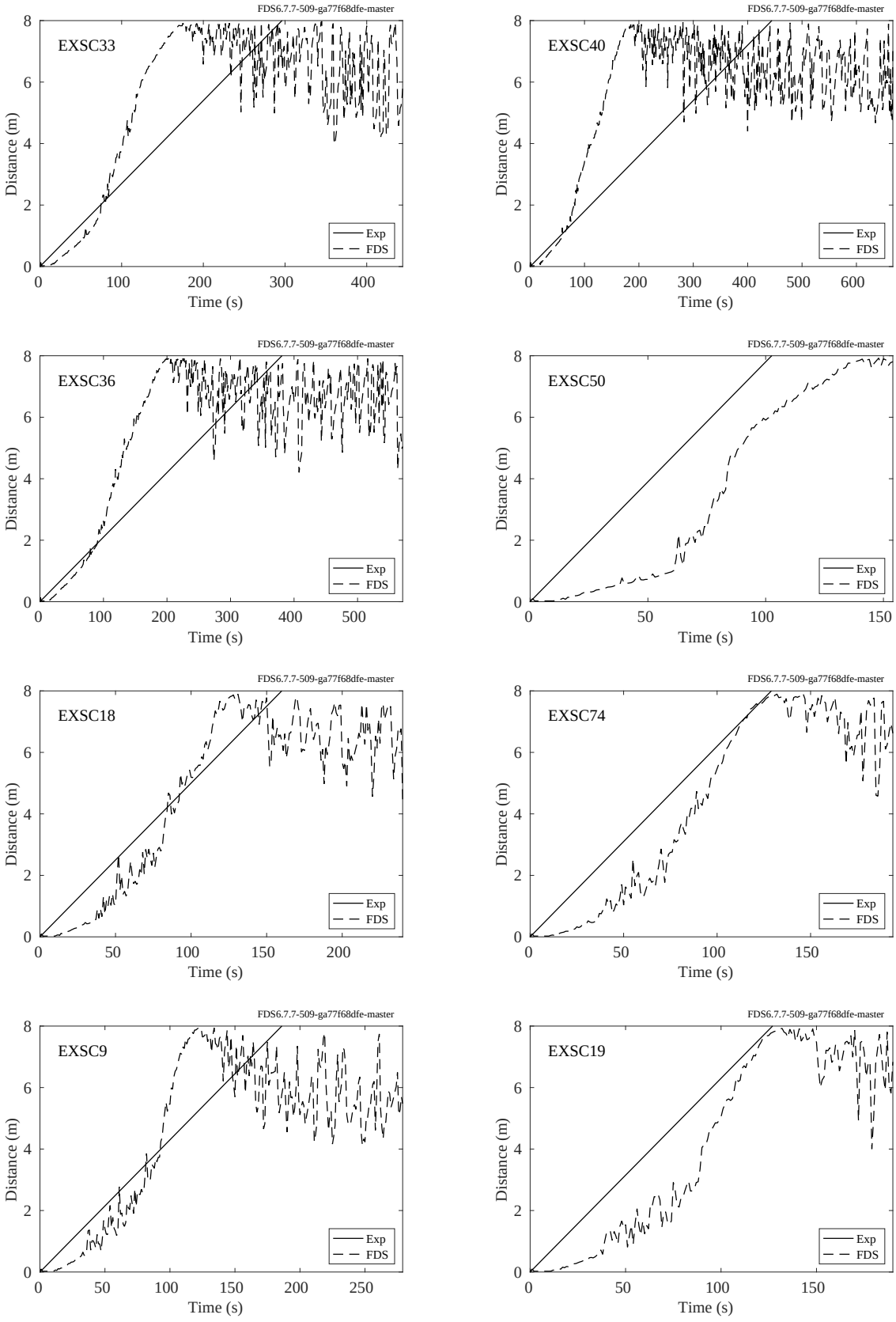

Figure 14.54: Flame front, USFS/Catchpole experiments

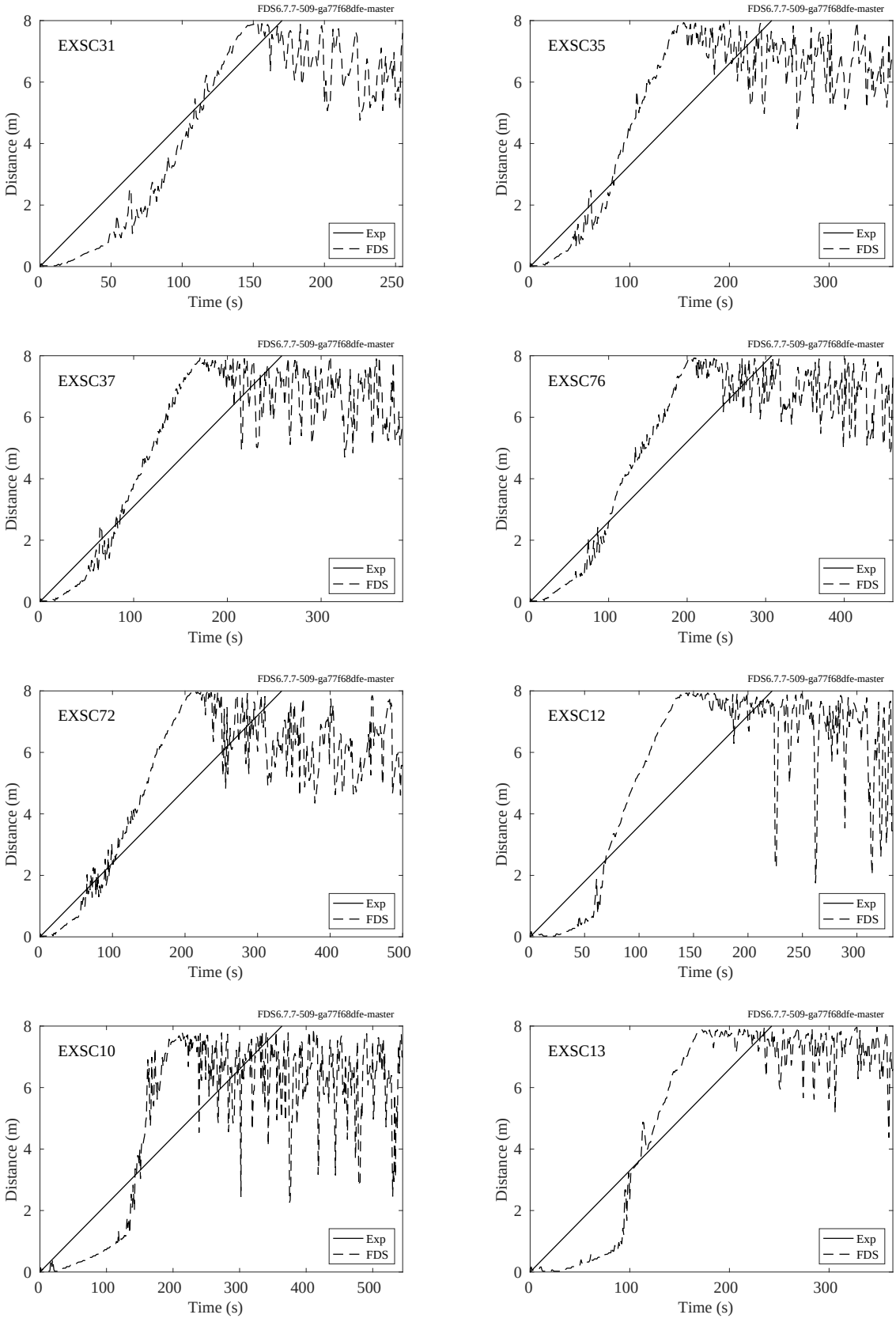

Figure 14.55: Flame front, USFS/Catchpole experiments

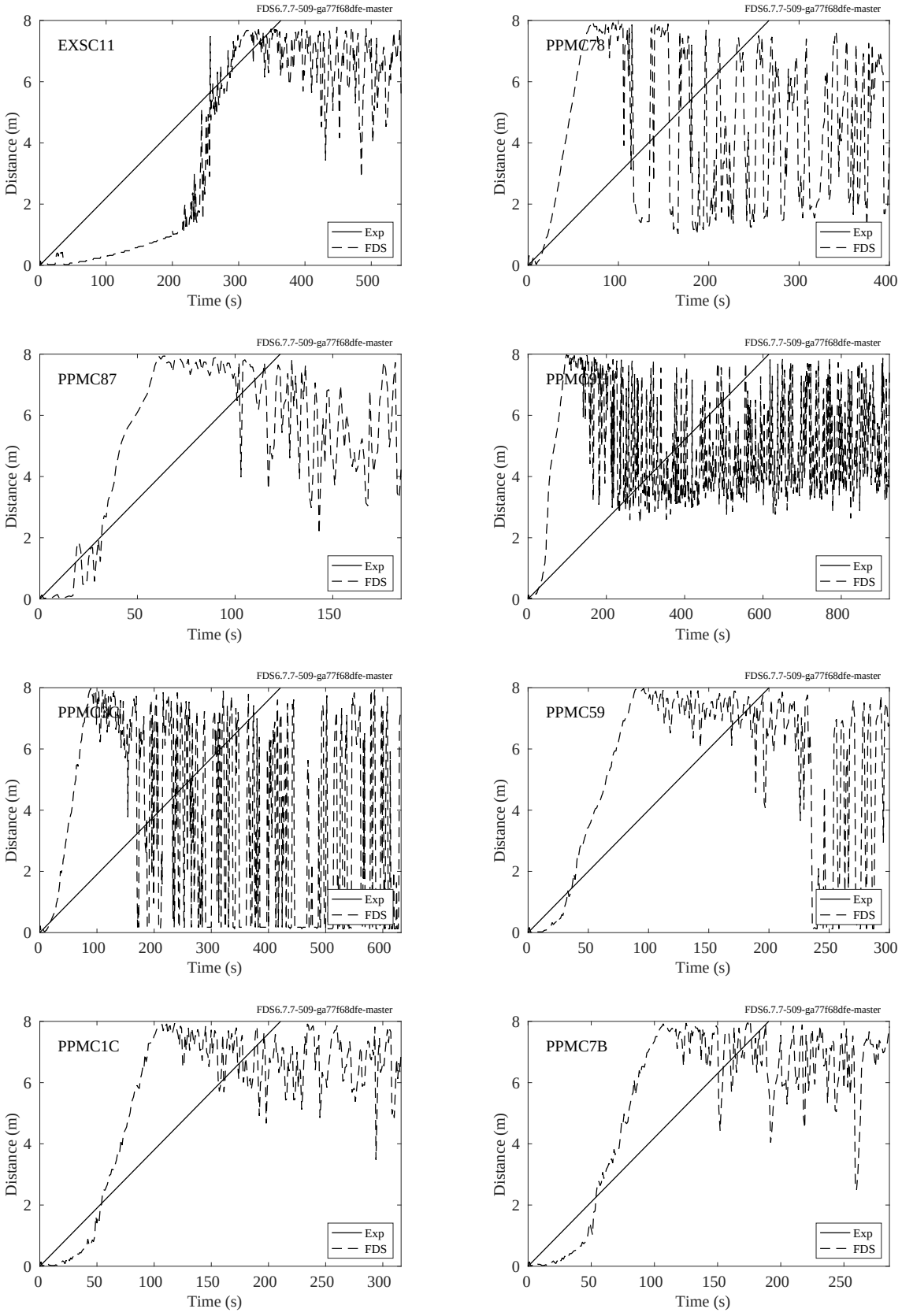

Figure 14.56: Flame front, USFS/Catchpole experiments

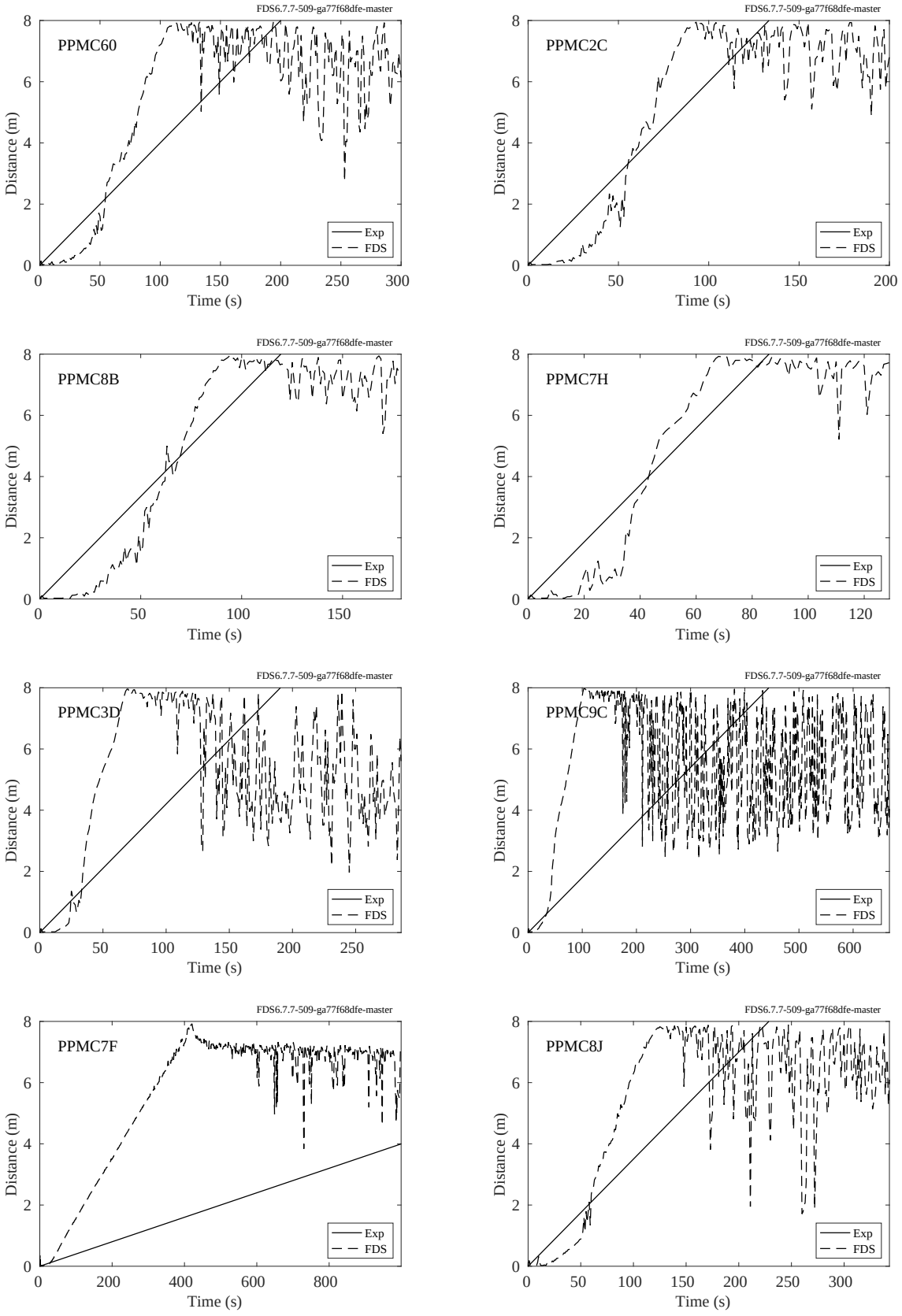

Figure 14.57: Flame front, USFS/Catchpole experiments

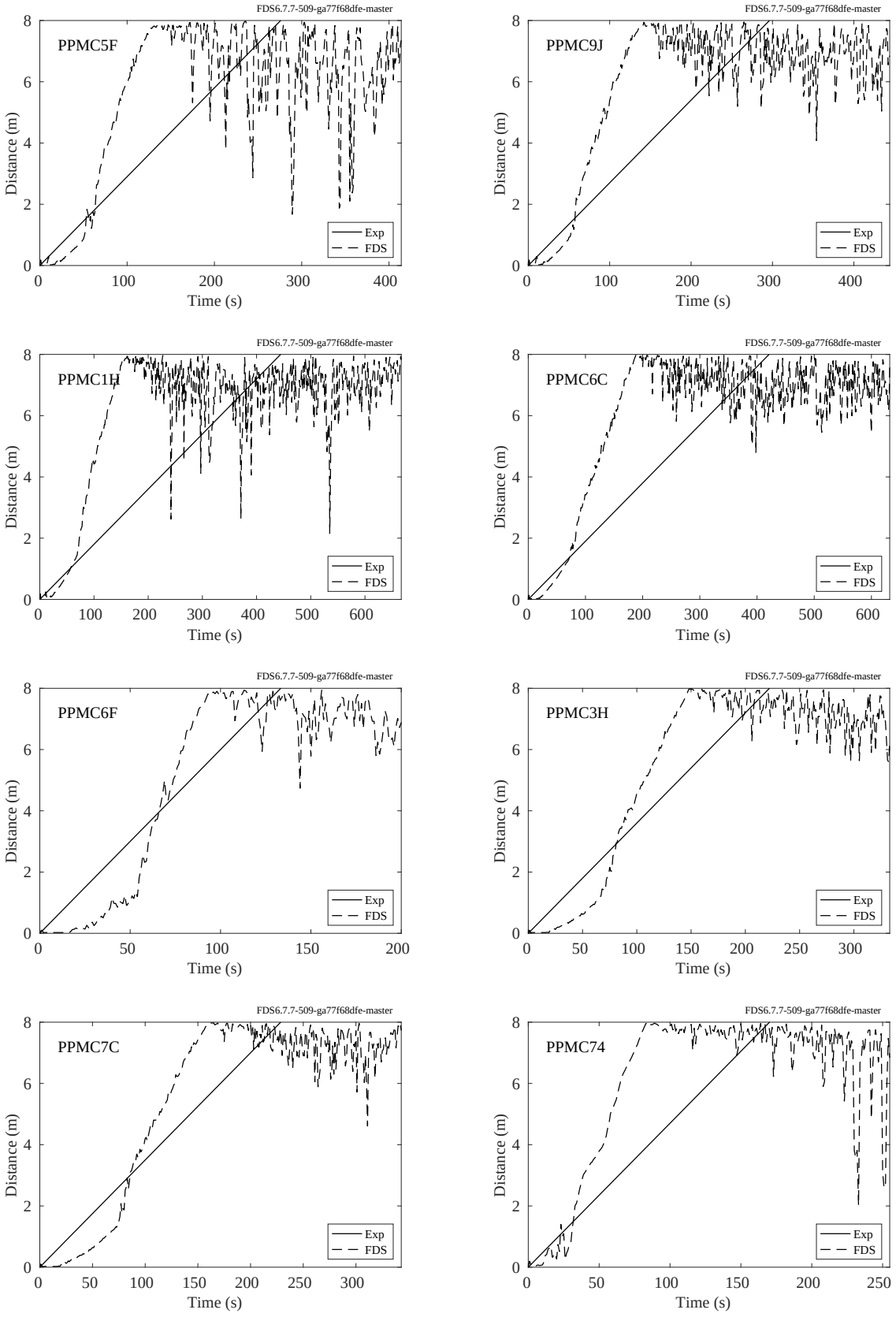

Figure 14.58: Flame front, USFS/Catchpole experiments

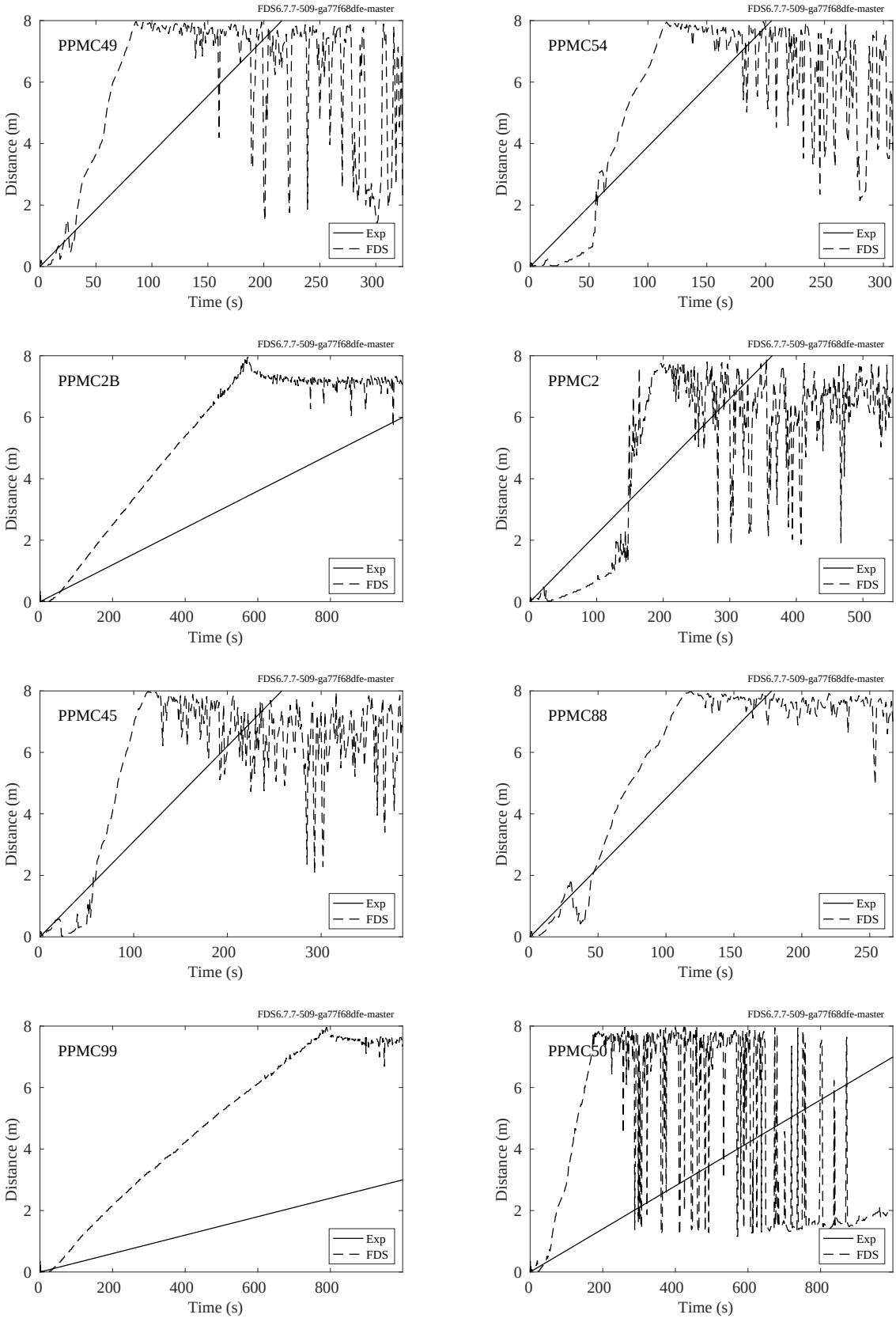

Figure 14.59: Flame front, USFS/Catchpole experiments

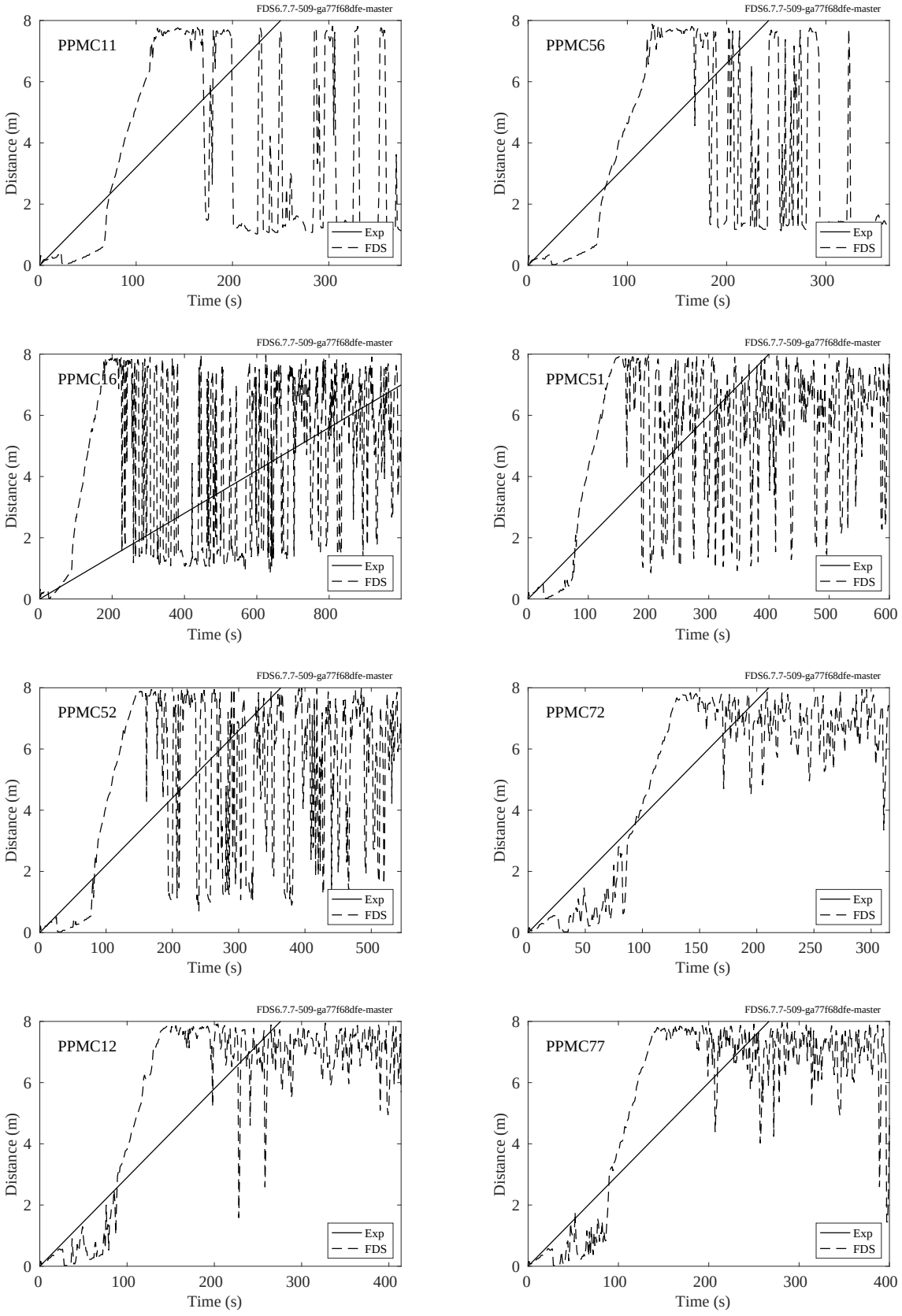

Figure 14.60: Flame front, USFS/Catchpole experiments

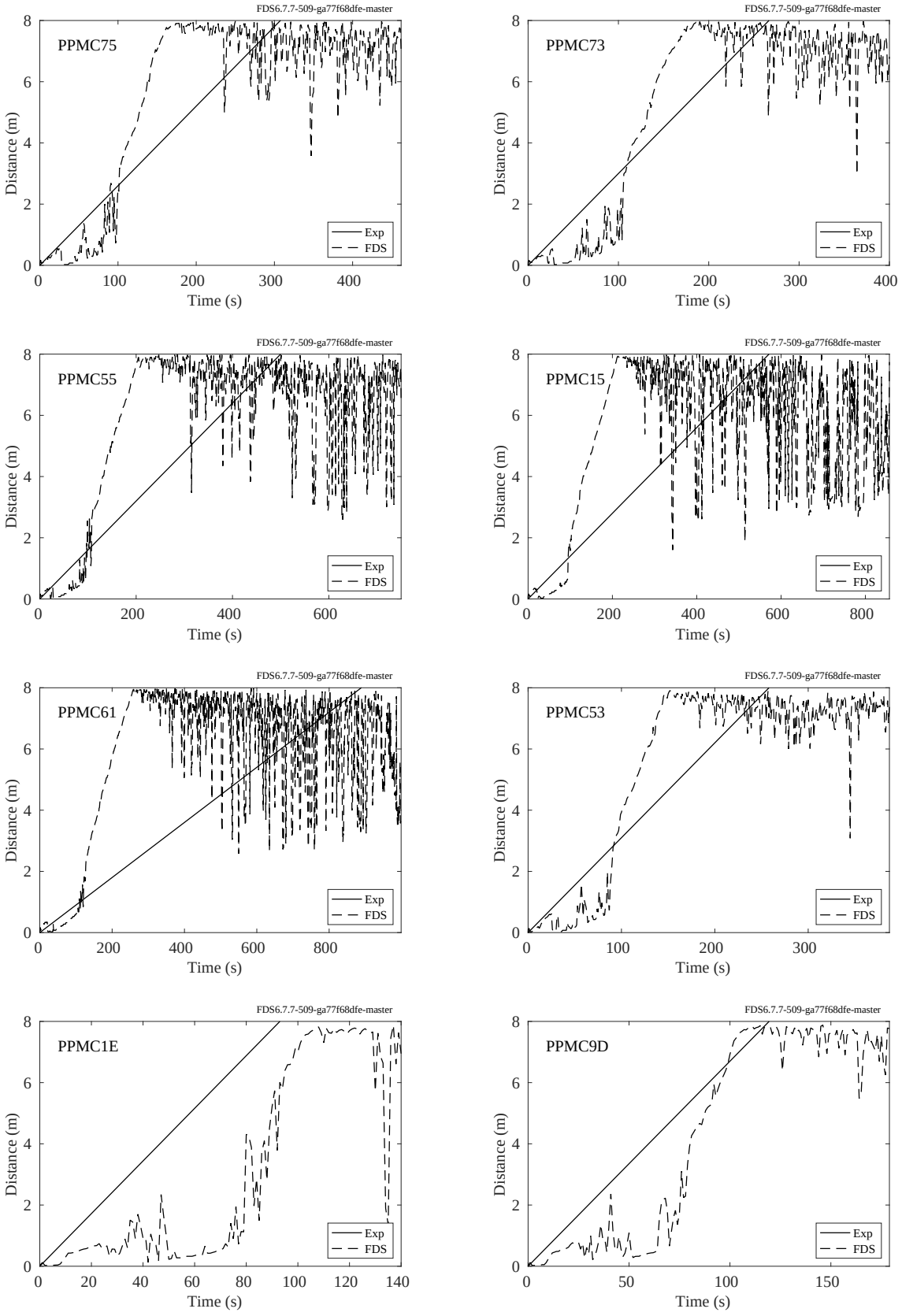

Figure 14.61: Flame front, USFS/Catchpole experiments

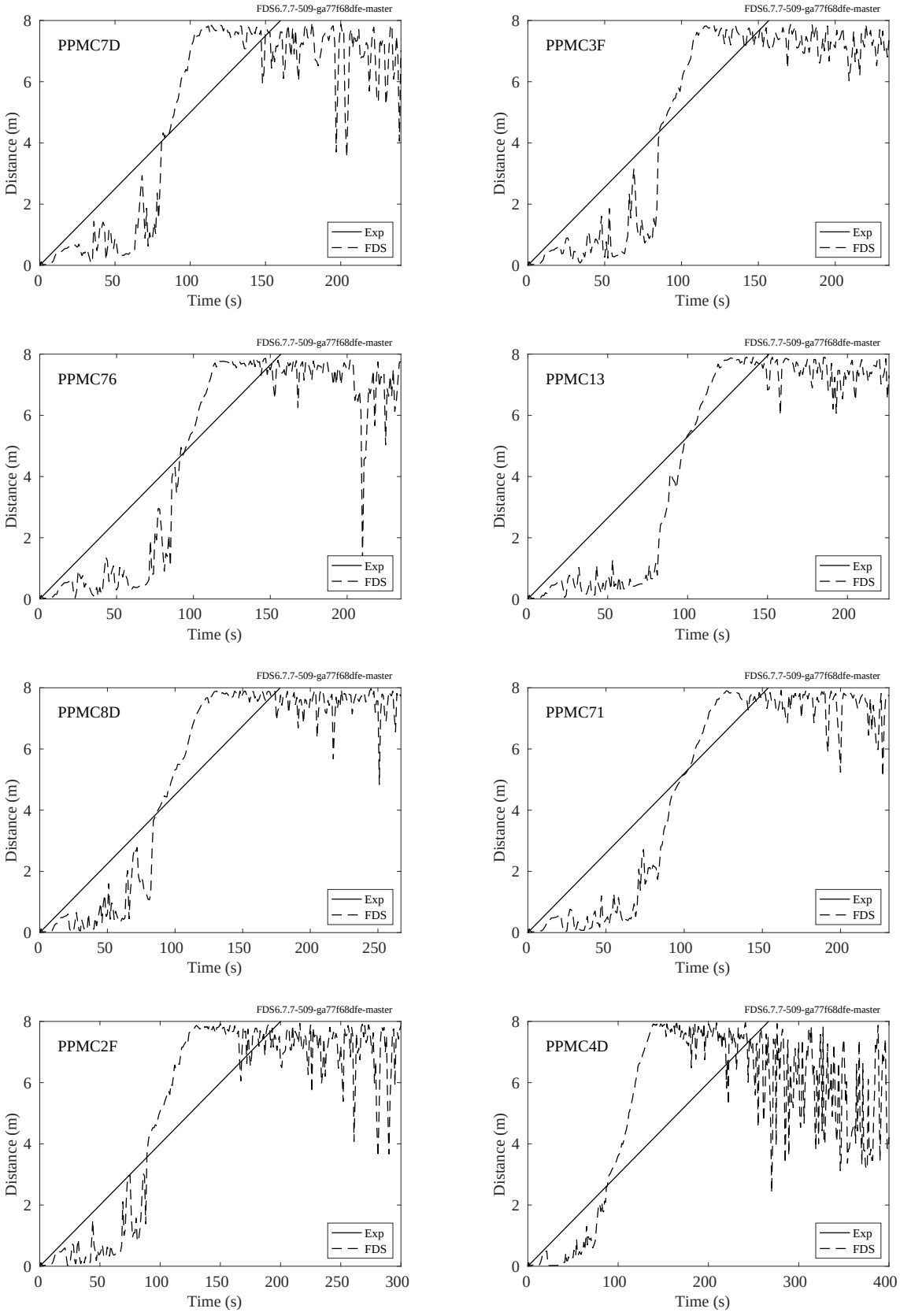

Figure 14.62: Flame front, USFS/Catchpole experiments

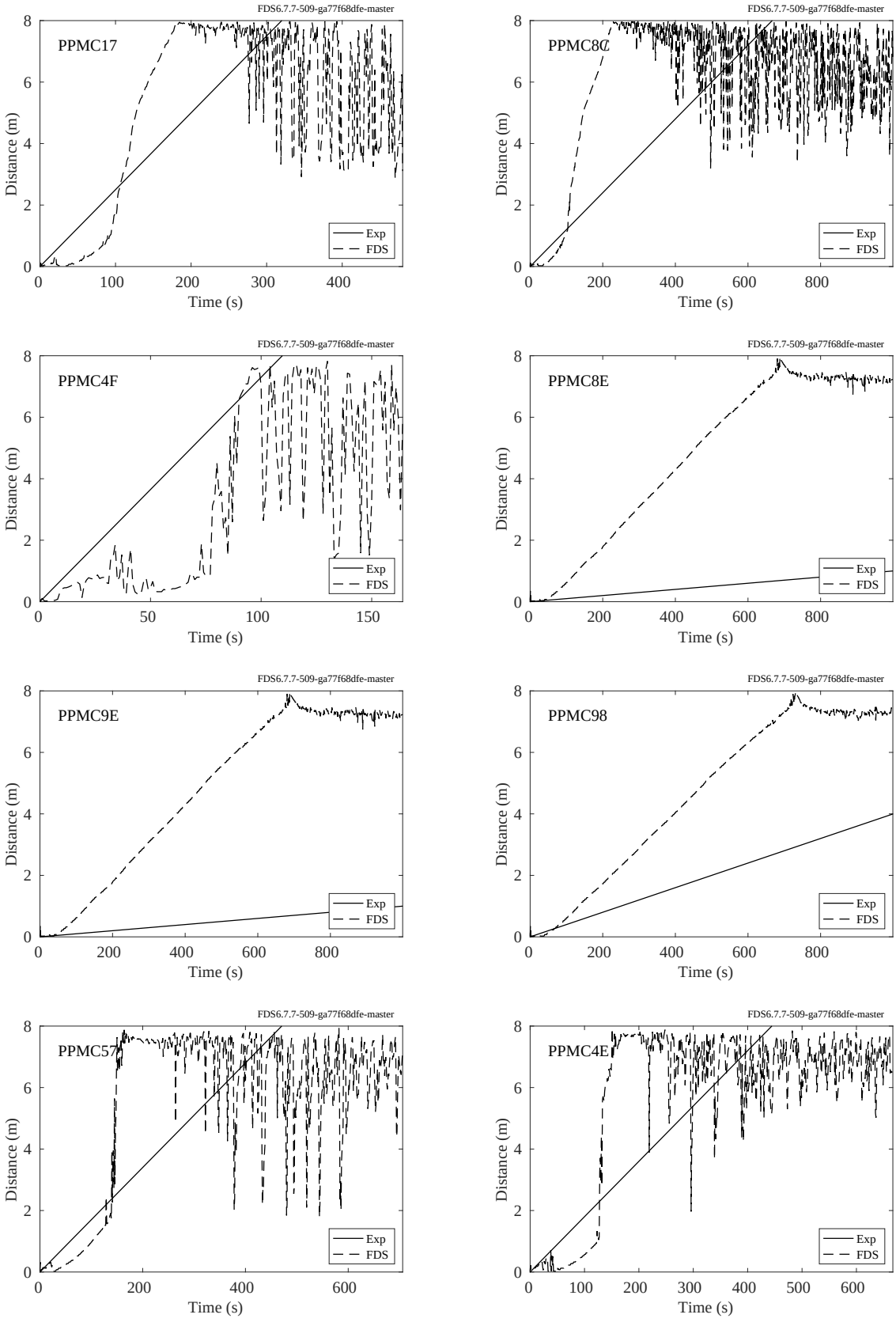

Figure 14.63: Flame front, USFS/Catchpole experiments

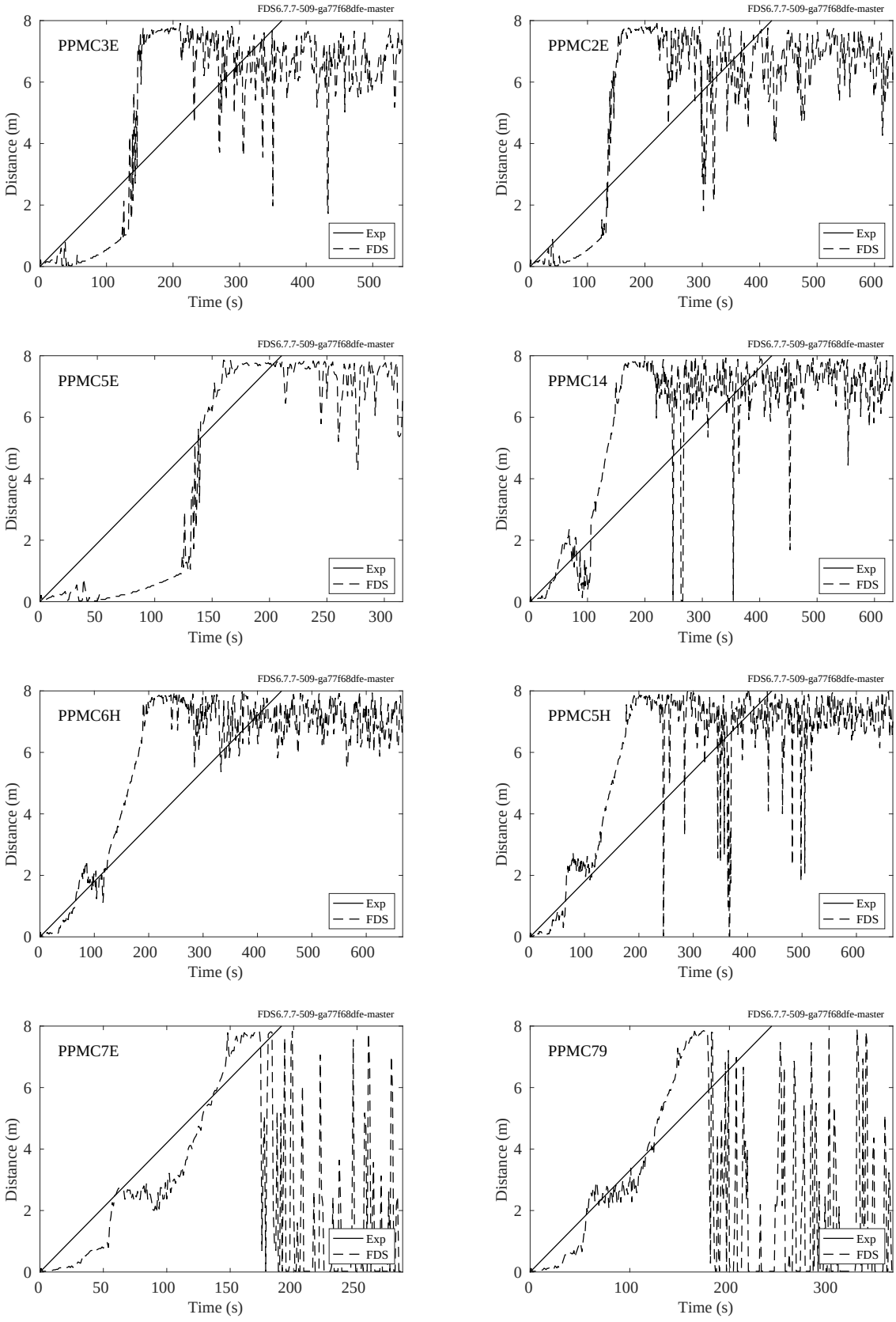

Figure 14.64: Flame front, USFS/Catchpole experiments

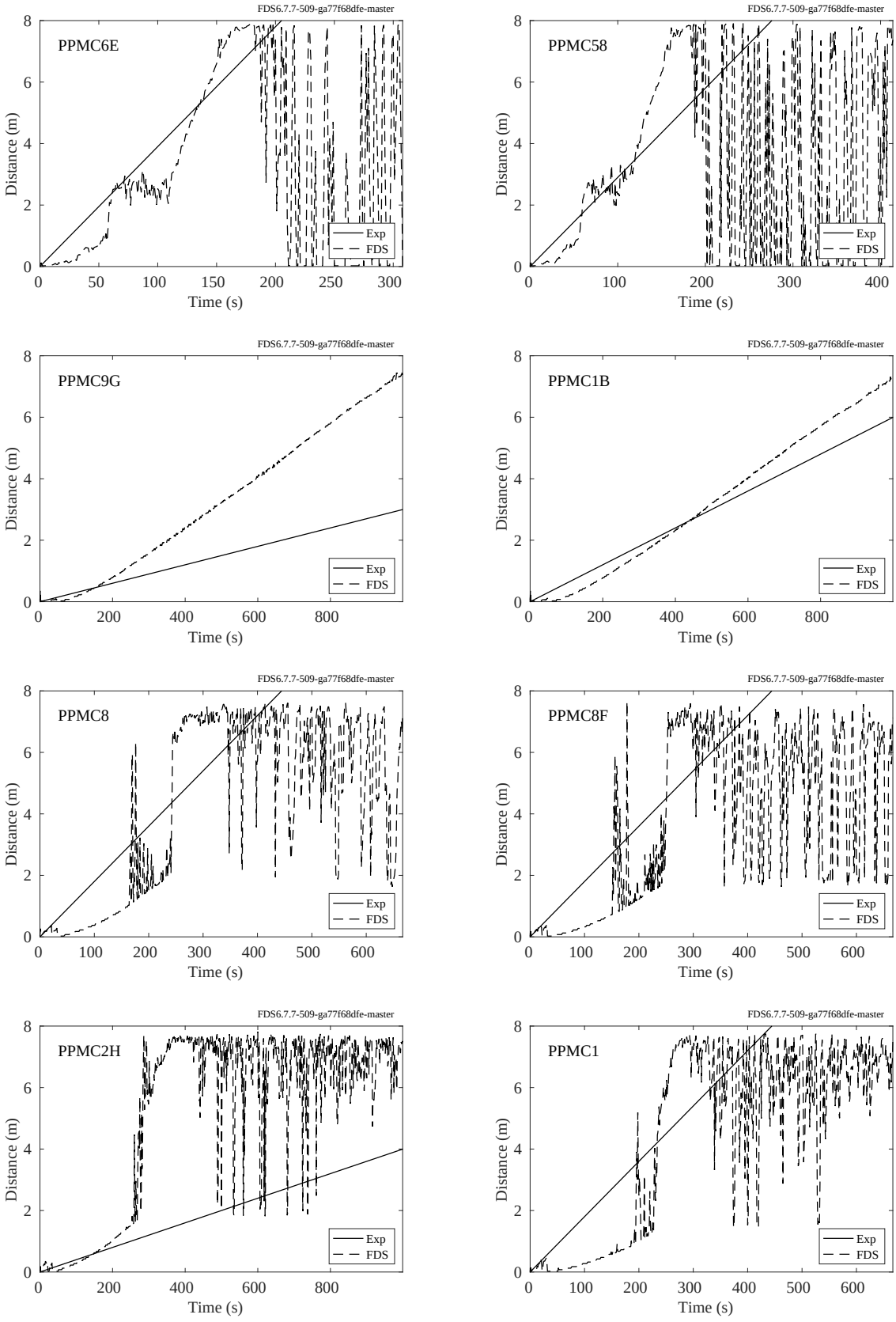

Figure 14.65: Flame front, USFS/Catchpole experiments

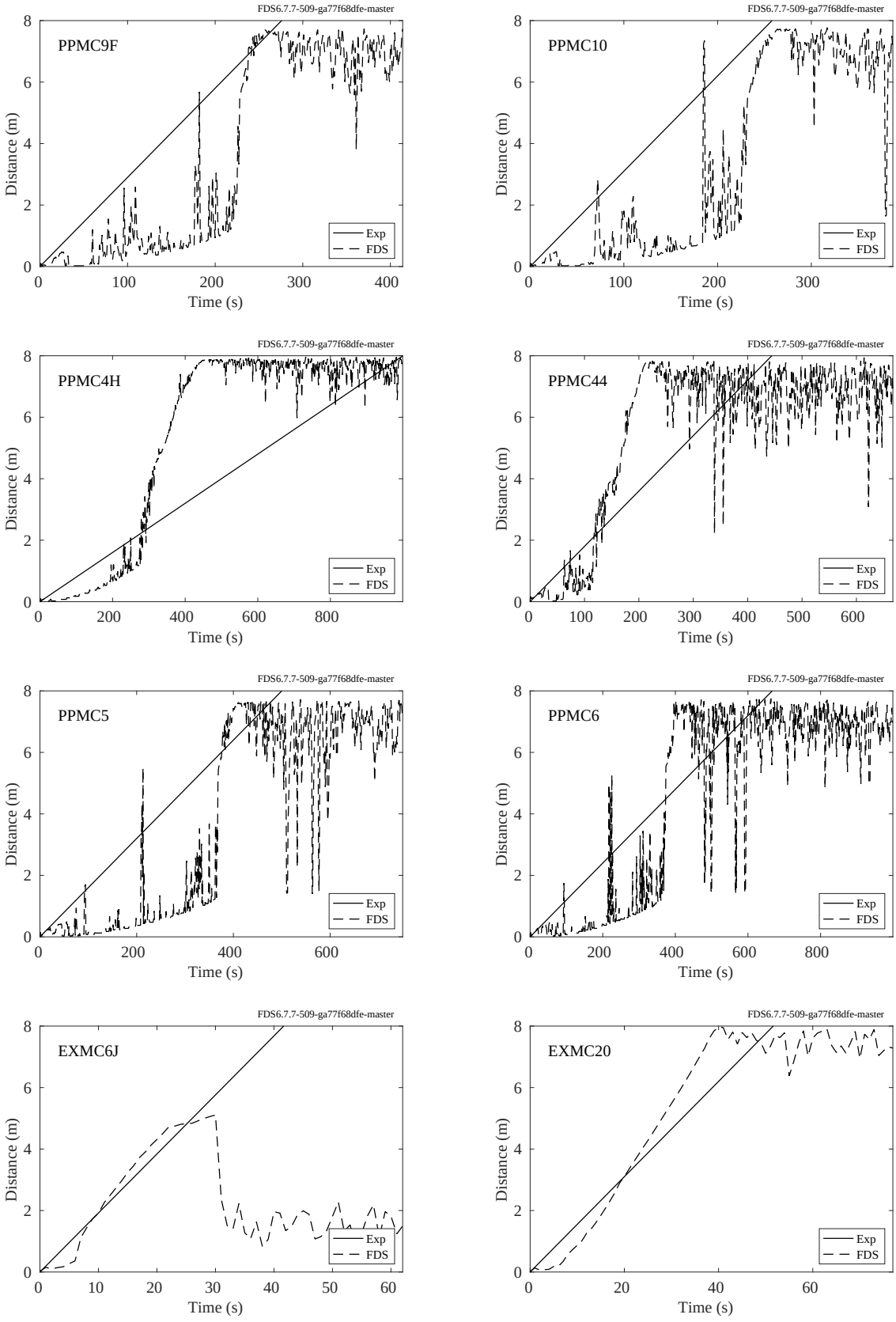

Figure 14.66: Flame front, USFS/Catchpole experiments

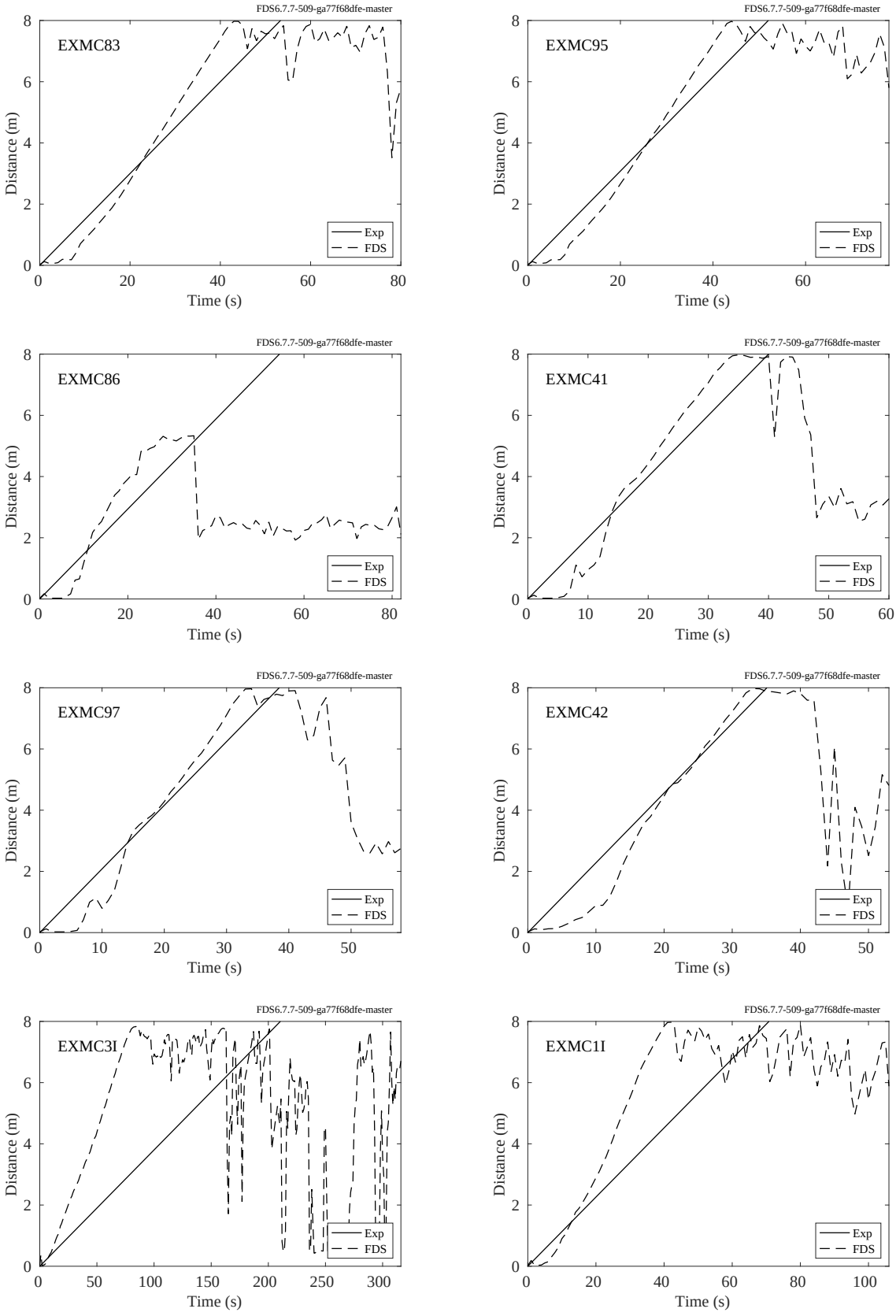

Figure 14.67: Flame front, USFS/Catchpole experiments

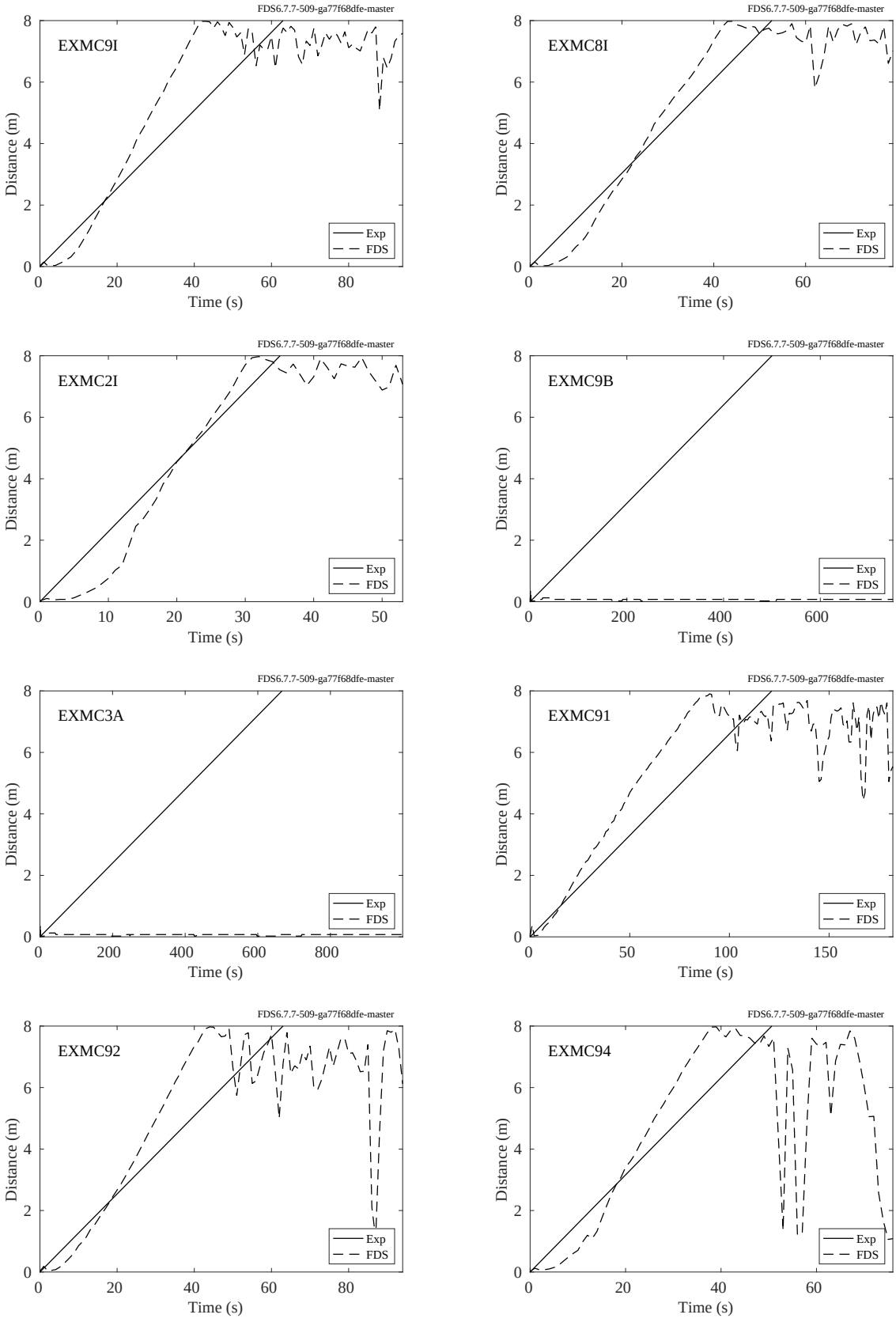

Figure 14.68: Flame front, USFS/Catchpole experiments

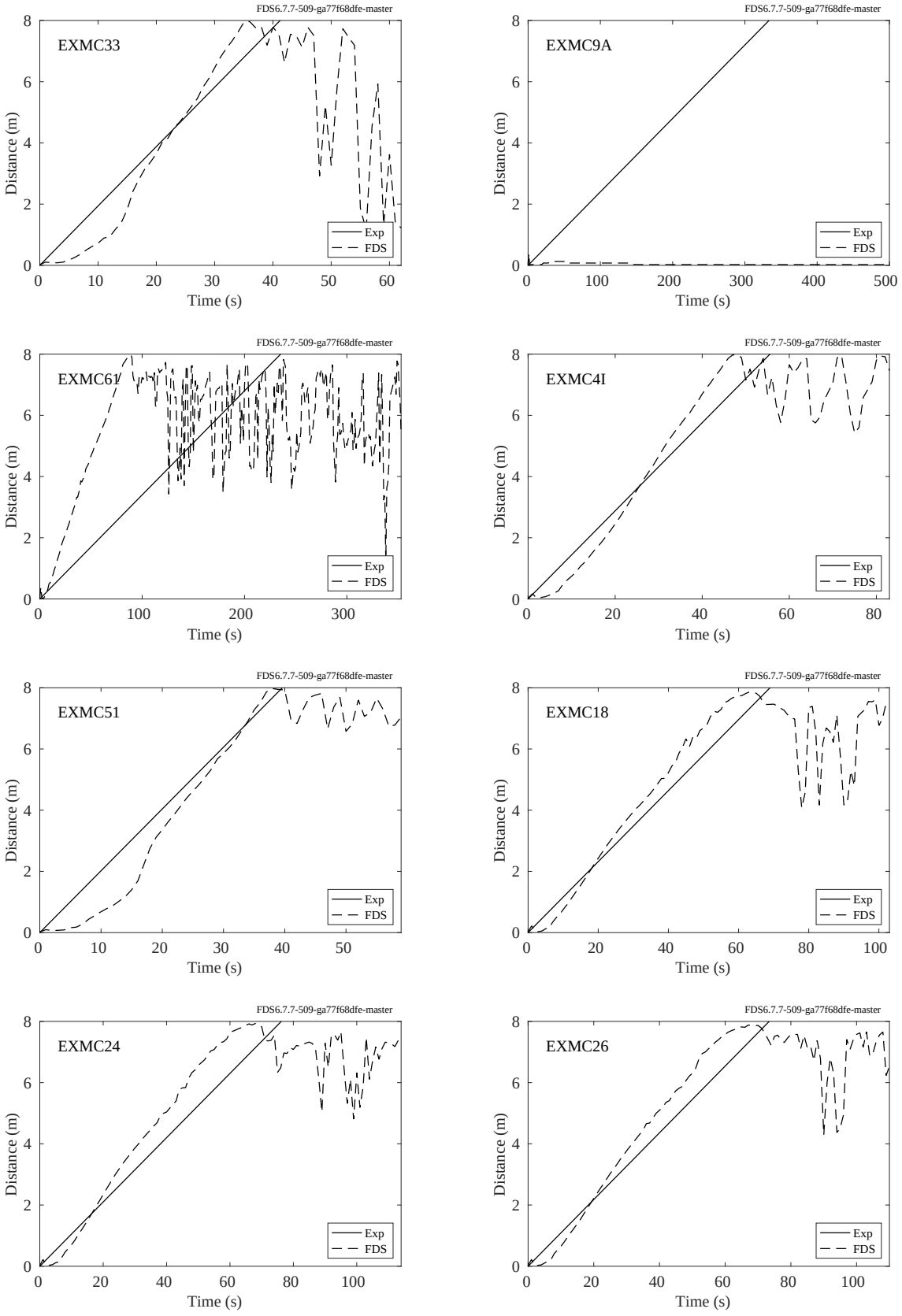

Figure 14.69: Flame front, USFS/Catchpole experiments

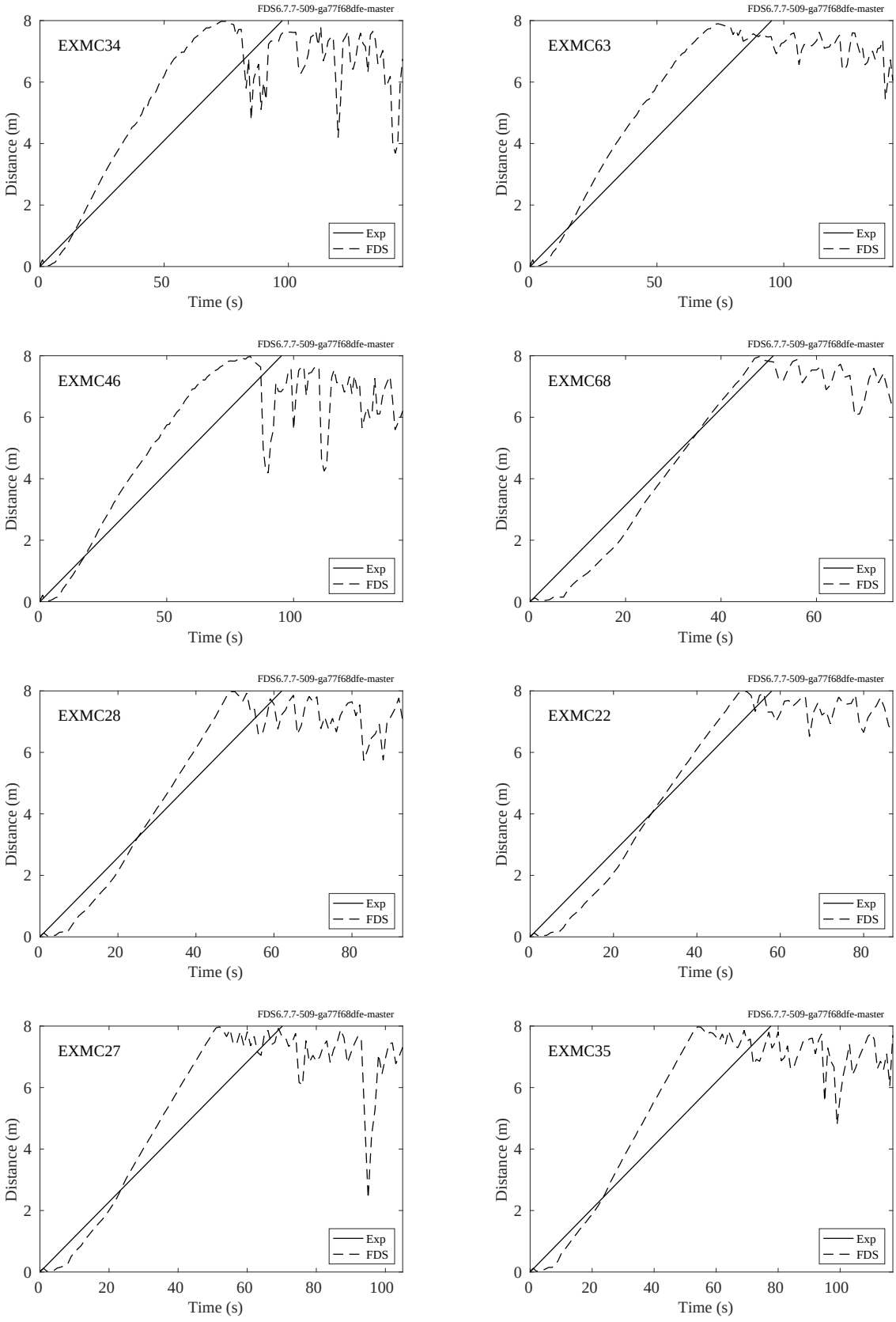

Figure 14.70: Flame front, USFS/Catchpole experiments

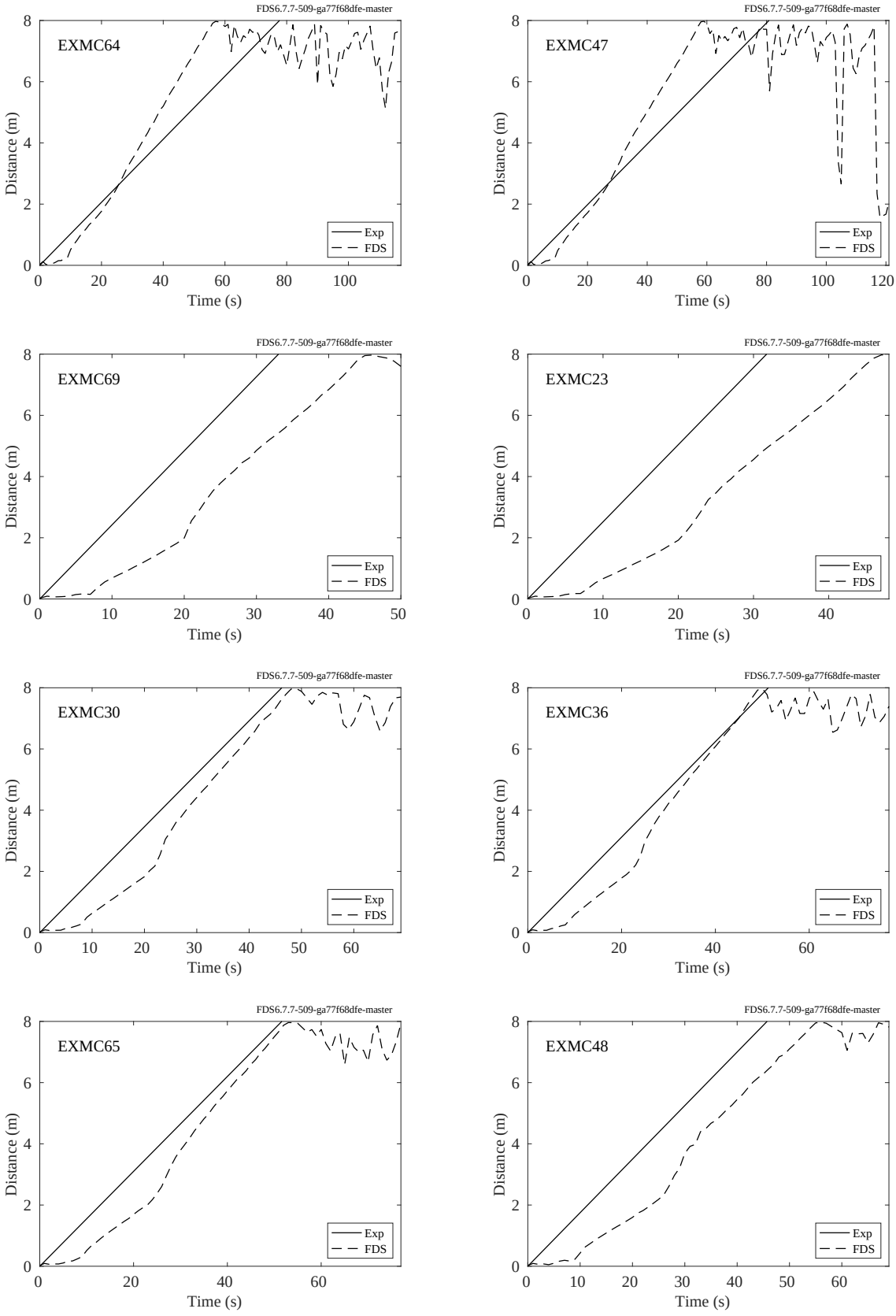

Figure 14.71: Flame front, USFS/Catchpole experiments

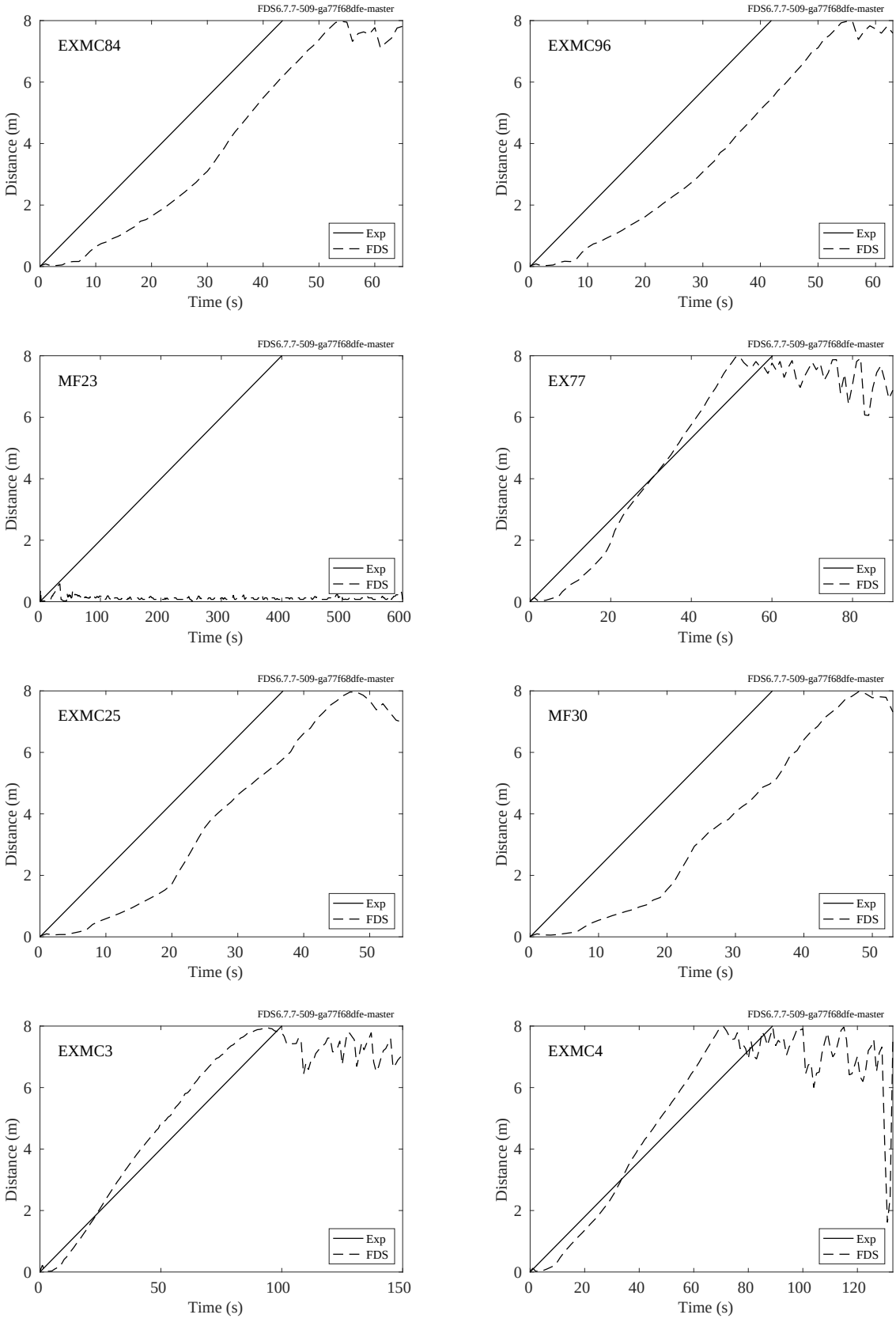

Figure 14.72: Flame front, USFS/Catchpole experiments

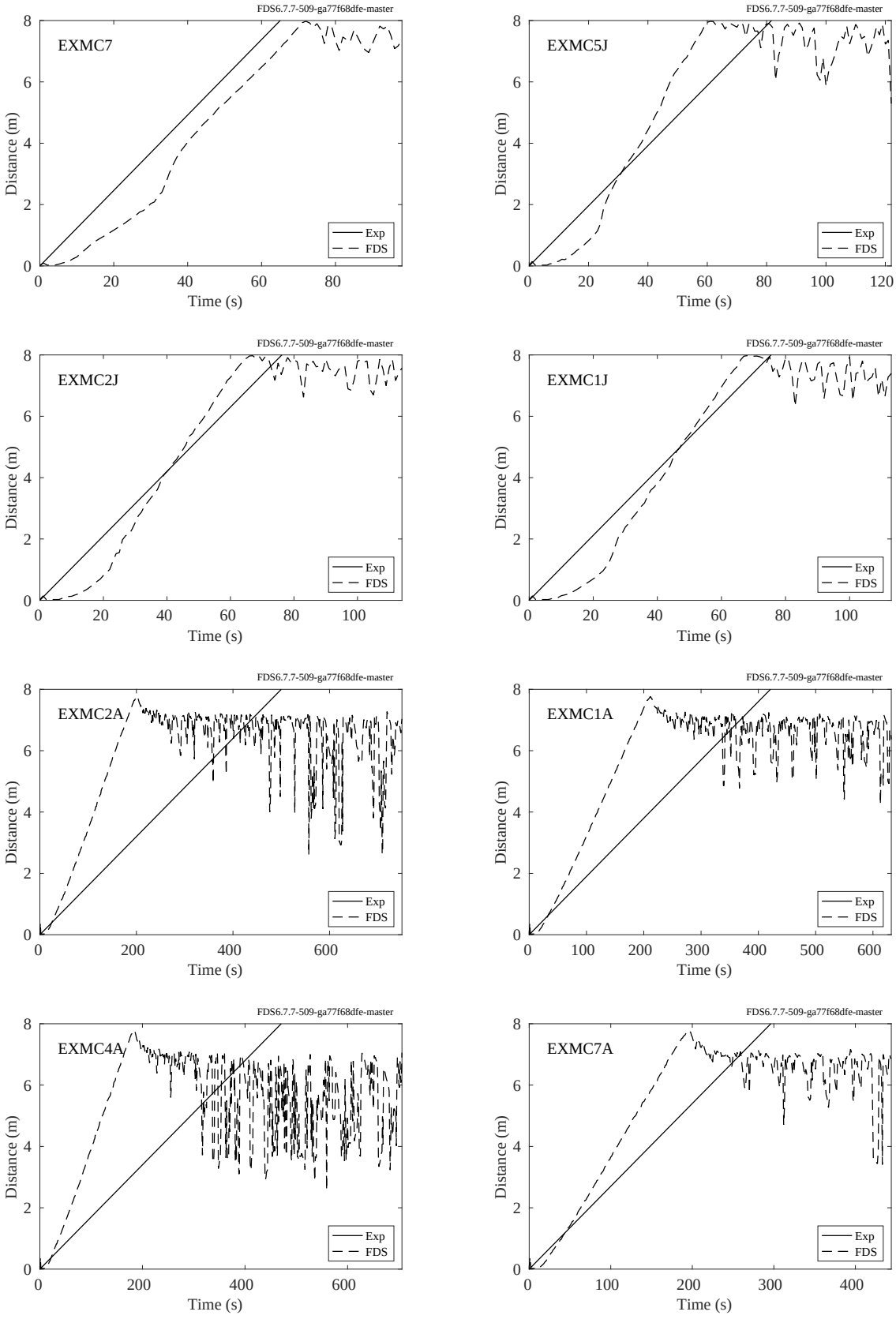

Figure 14.73: Flame front, USFS/Catchpole experiments

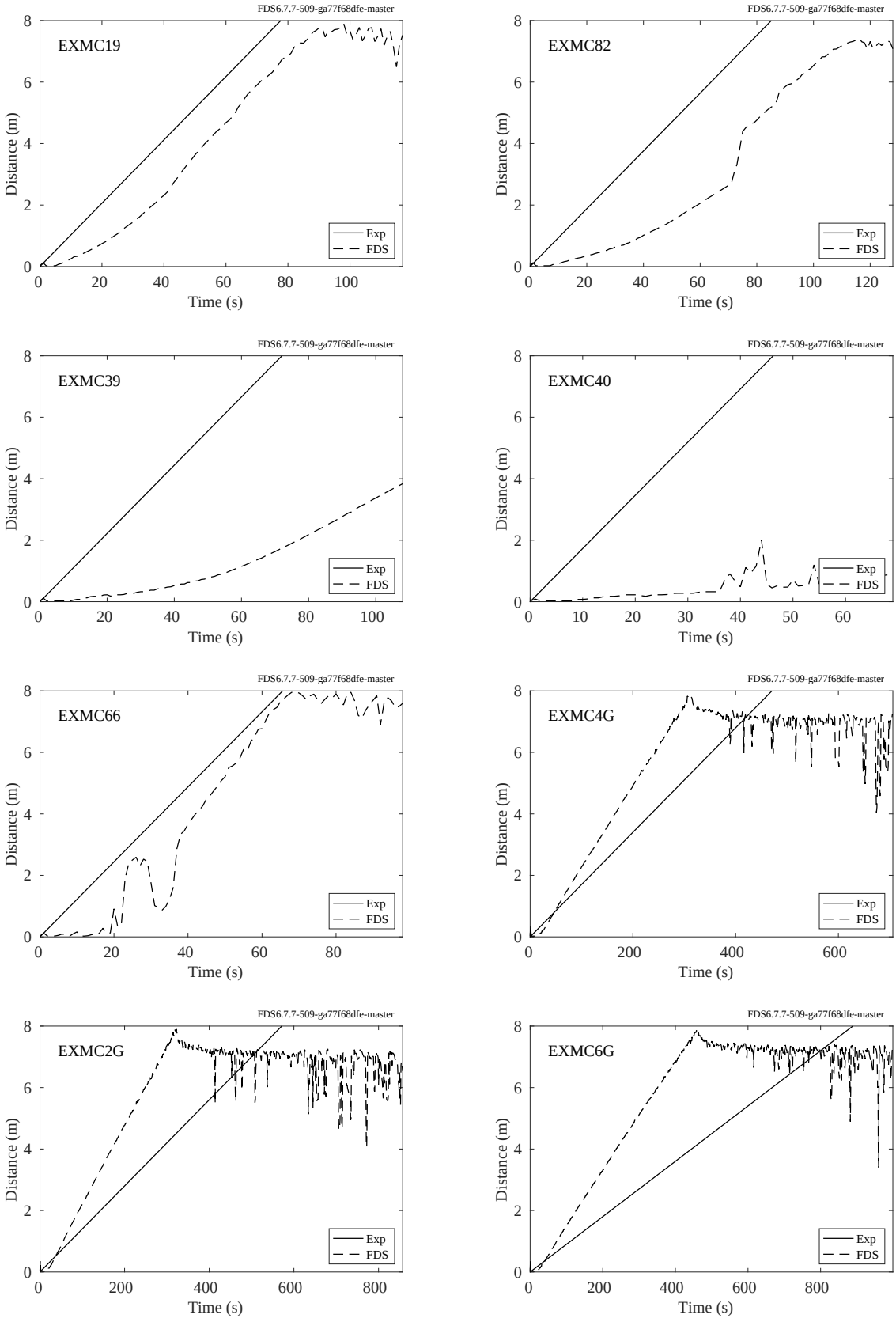

Figure 14.74: Flame front, USFS/Catchpole experiments

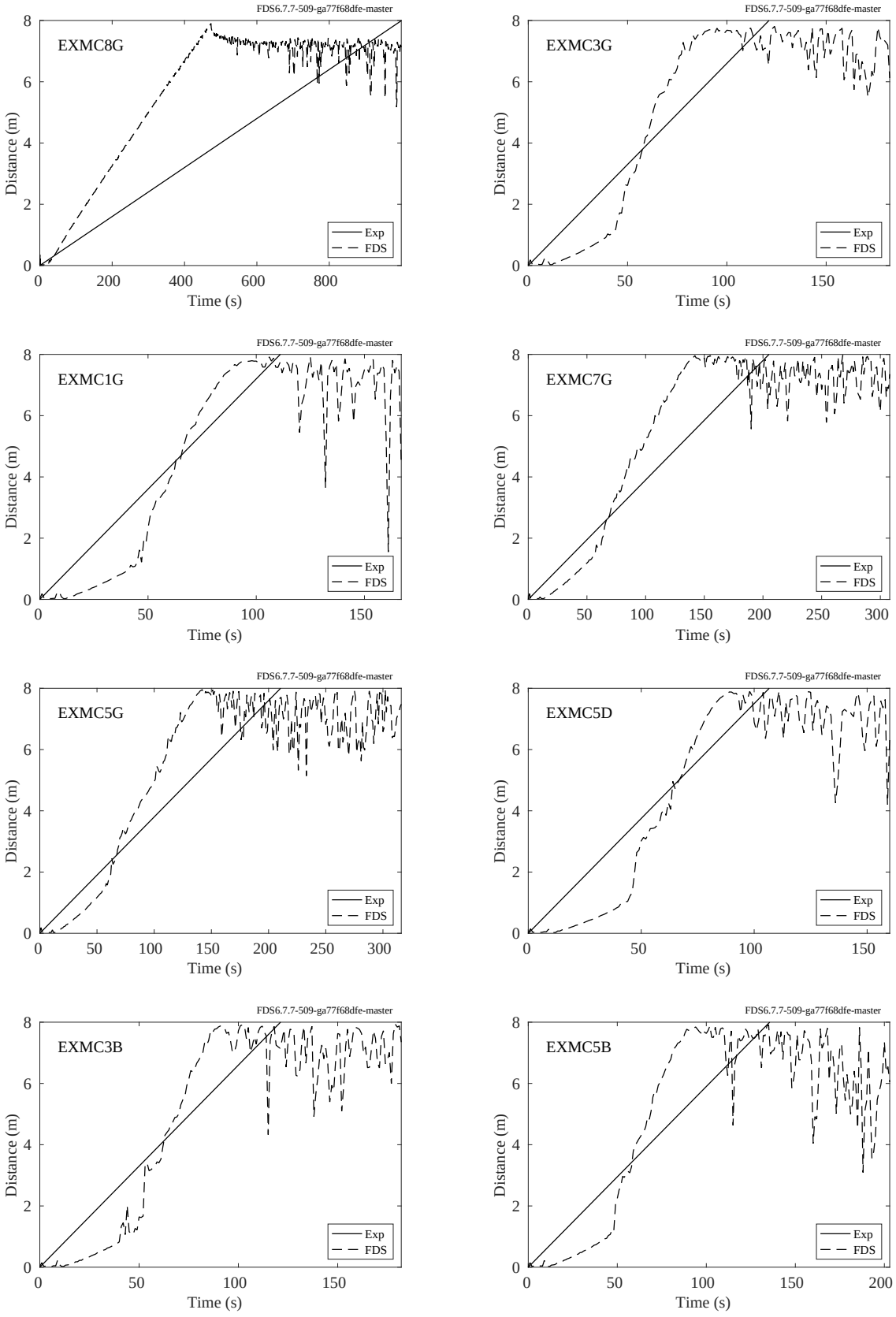

Figure 14.75: Flame front, USFS/Catchpole experiments

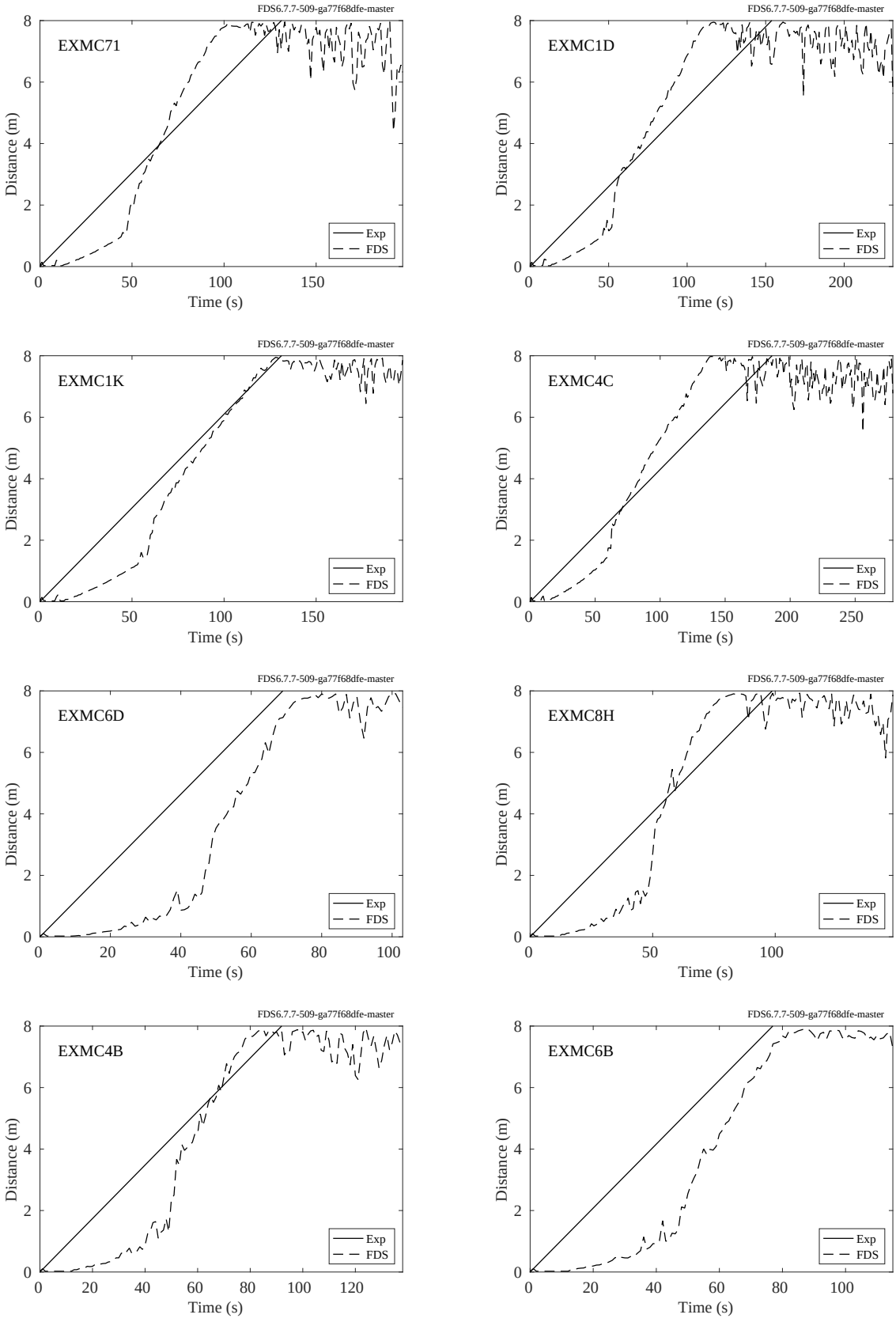

Figure 14.76: Flame front, USFS/Catchpole experiments

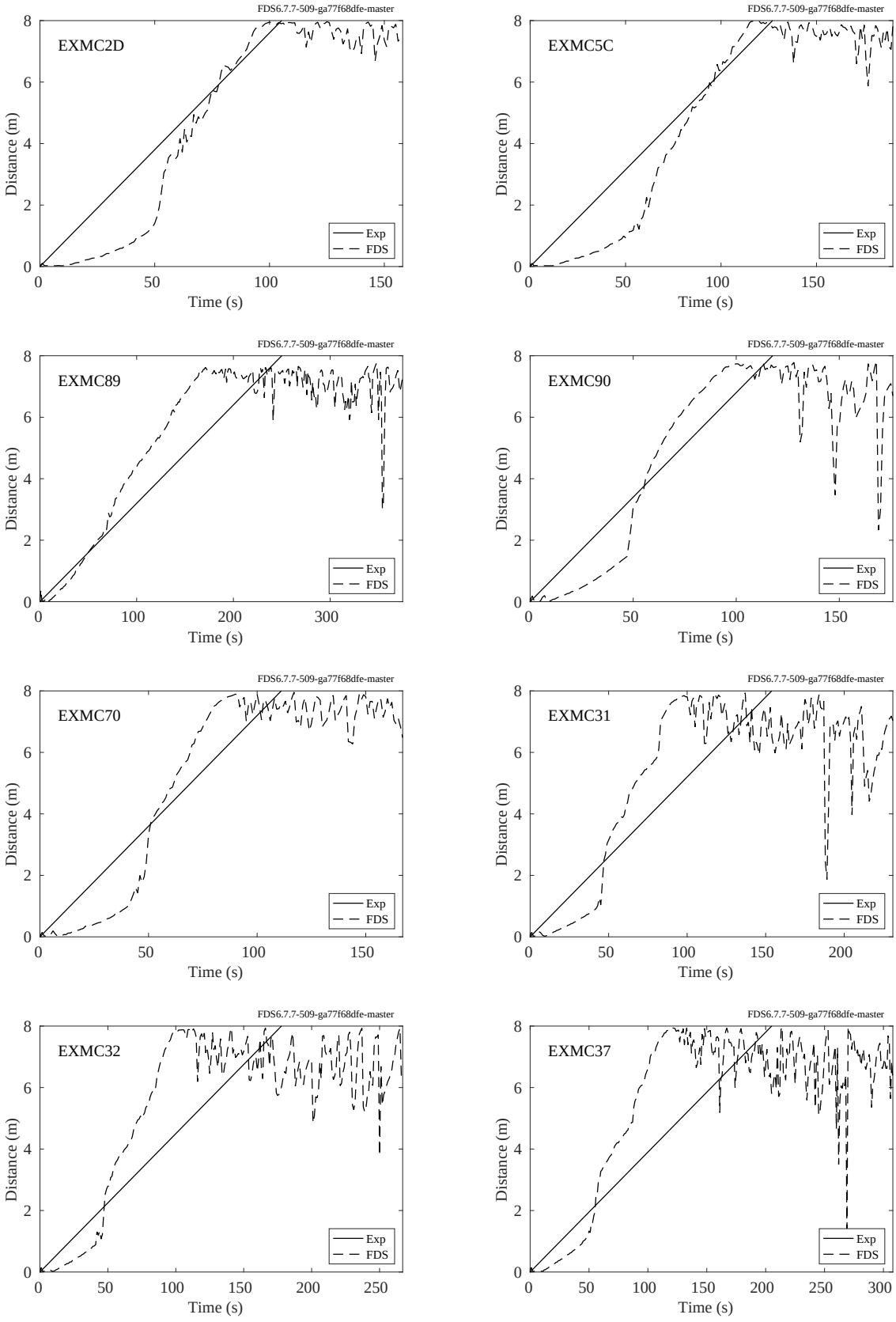

Figure 14.77: Flame front, USFS/Catchpole experiments

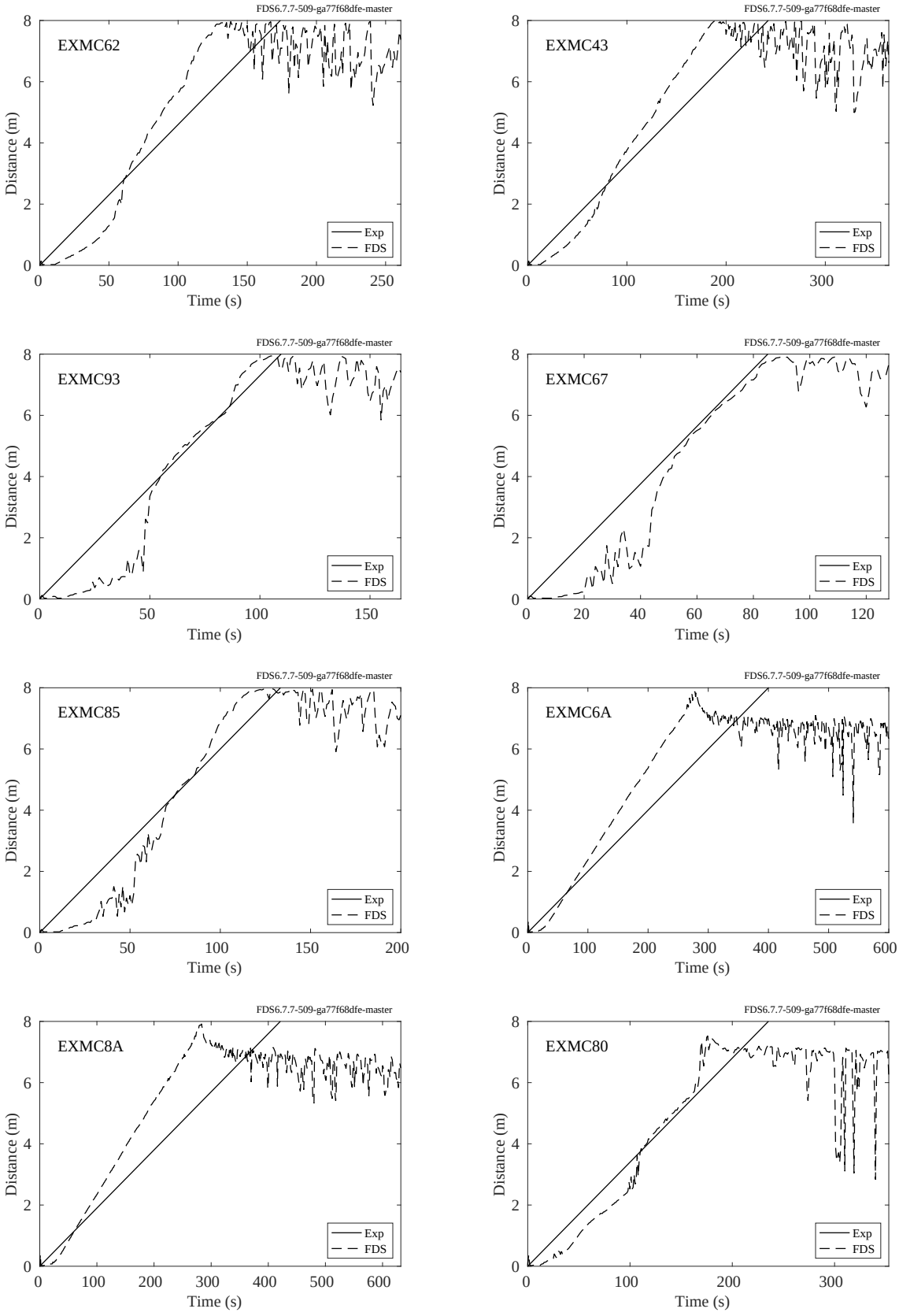

Figure 14.78: Flame front, USFS/Catchpole experiments

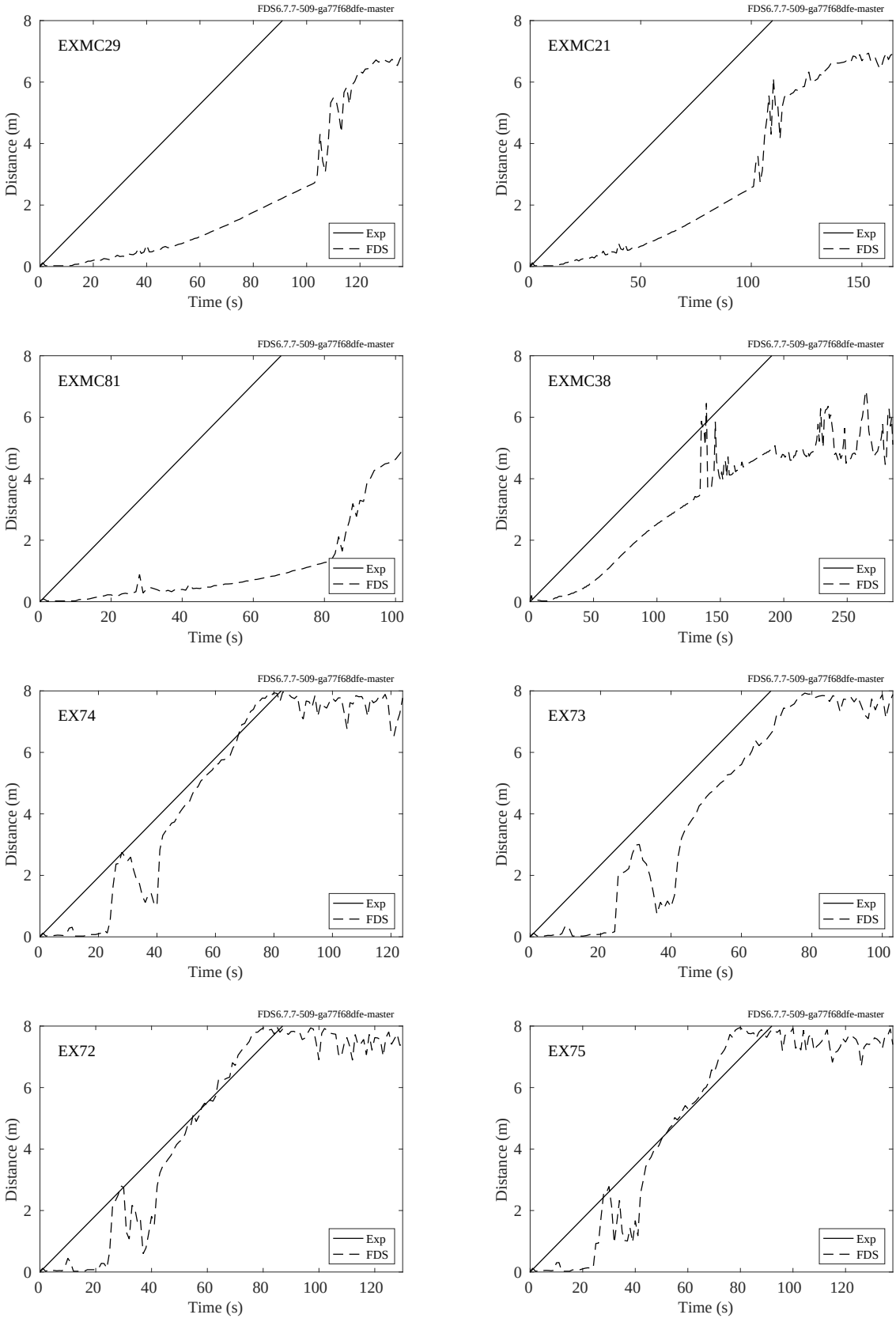

Figure 14.79: Flame front, USFS/Catchpole experiments

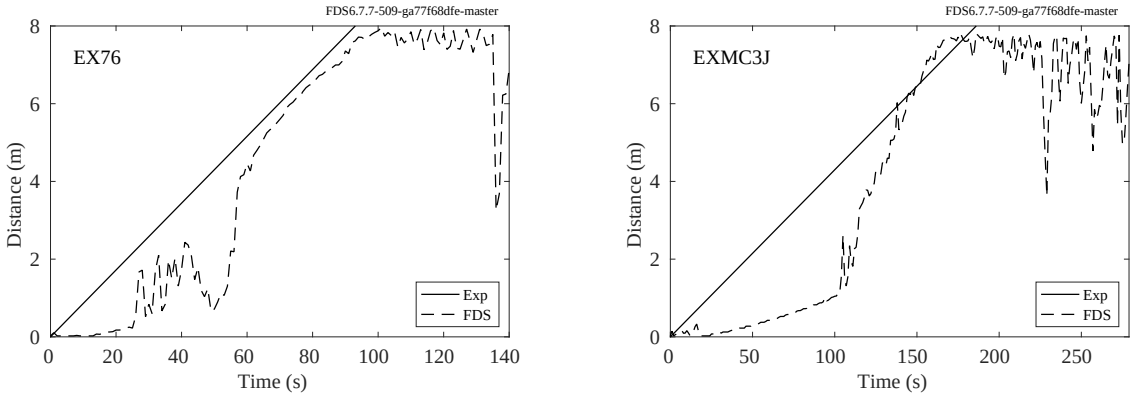

Figure 14.80: Flame front, USFS/Catchpole experiments

14.7.4 USFS/Corsica Fire Spread Experiments

A description of the experiments and modeling strategy can be found in Section 3.83. Comparisons of the measured and predicted heat release rates for six bench-scale (1 m by 2 m) fires spreading over pine needles are shown in Fig. 14.81 below. Front trajectory plots are shown in Fig. 14.82.

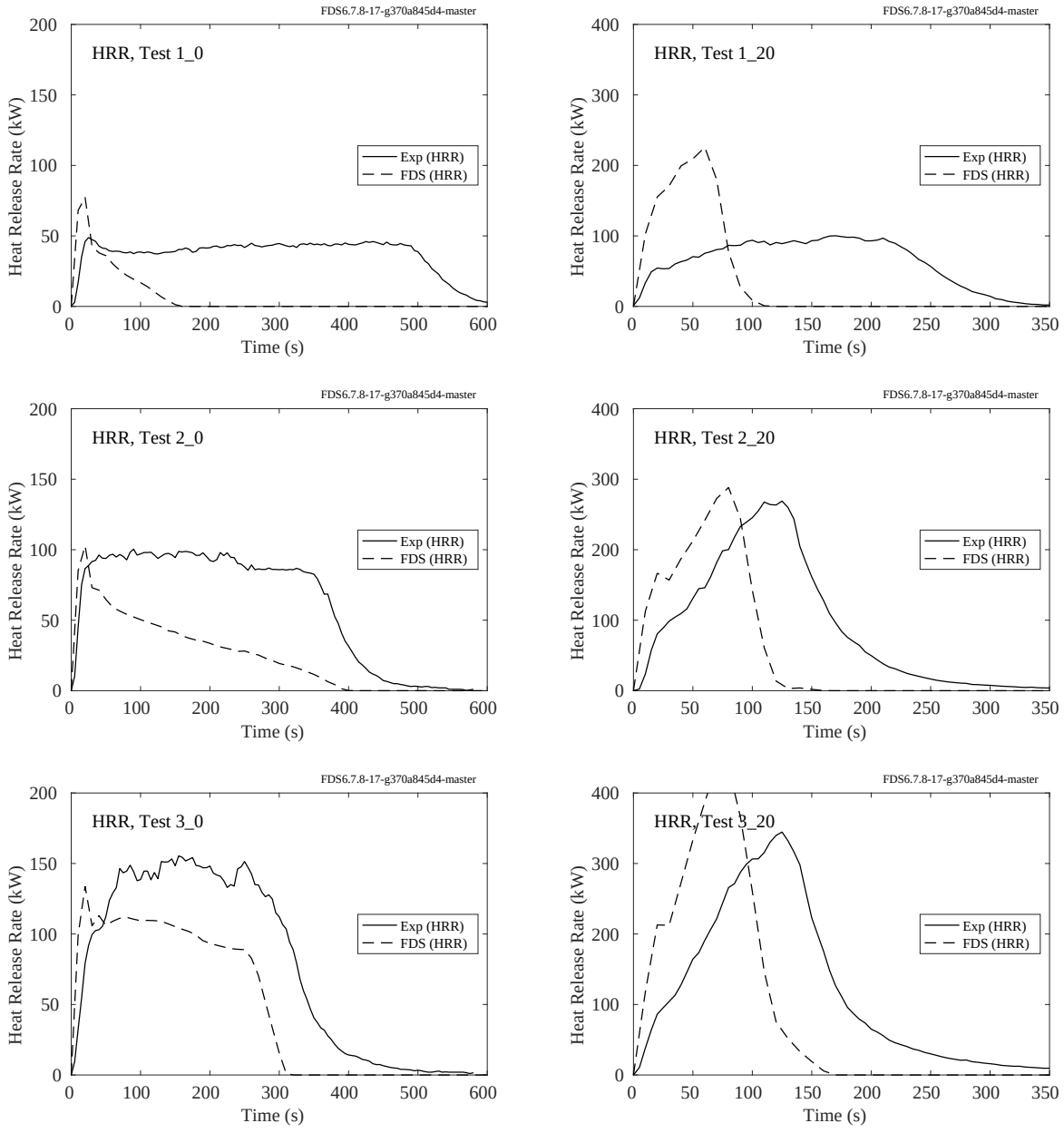

Figure 14.81: HRR, USFS/Corsica experiments.

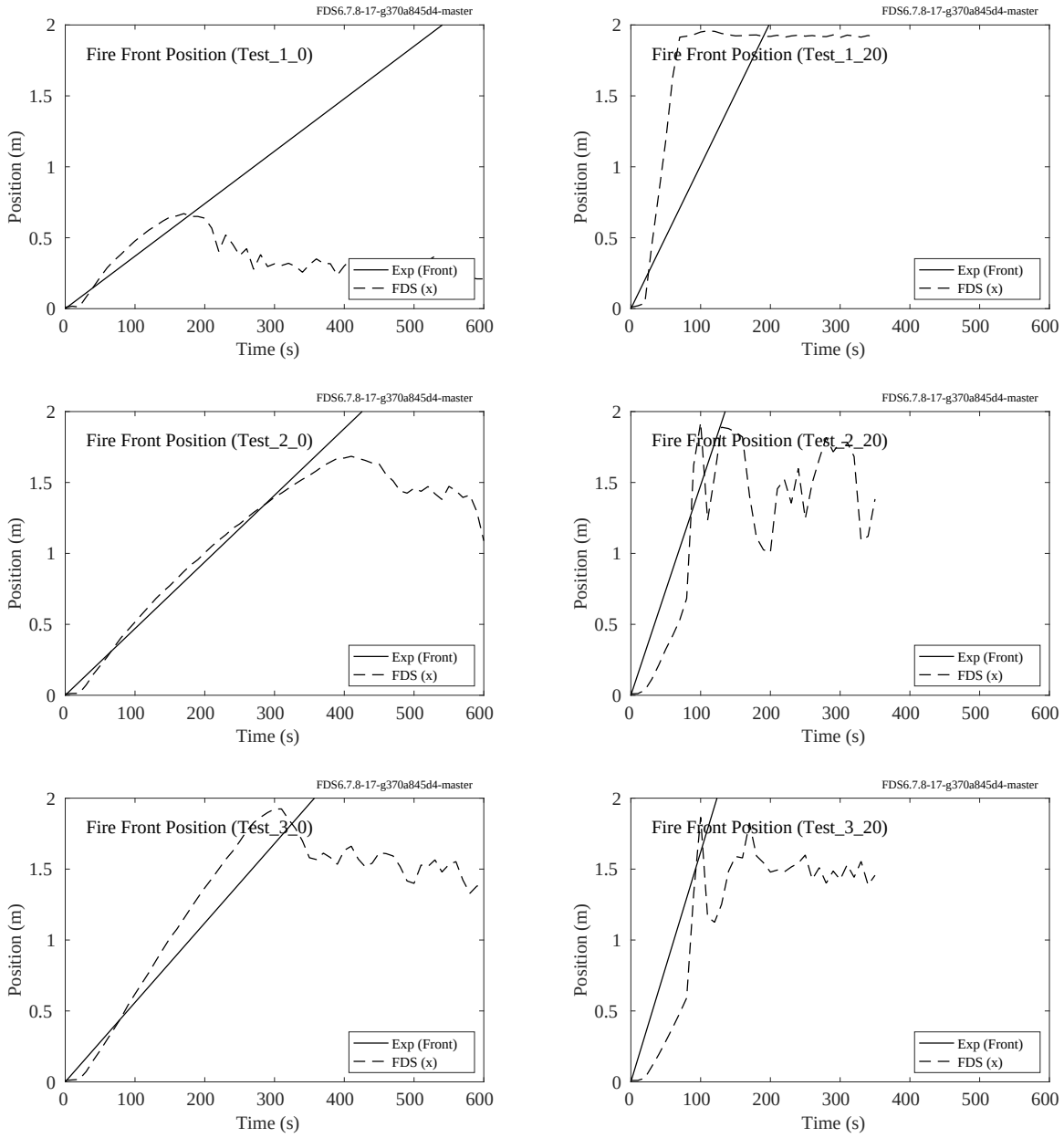

Figure 14.82: Rate of Spread, USFS/Corsica experiments.

14.7.5 Burning Trees (NIST Douglas Firs)

A description of the experiments and modeling assumptions are given in Section 3.43.

Snapshots of the simulation of the 2 m tall, 14 % moisture tree are shown in Fig. 14.83. The computational domain in this case is 2 m by 2 m by 4 m. The grid cells are 5 cm cubes. The pine needles are represented by 130,000 Lagrangian particles with a cylindrical geometry, or about 25 simulated needles per grid cell. The radius of the cylinder is derived from the measured surface area to volume ratio. Each simulated pine needle or segment of roundwood represents many more actual needles or segments. The weighting factor is determined from the estimated bulk mass per unit volume. The results of the simulations are shown in Fig. 14.84.

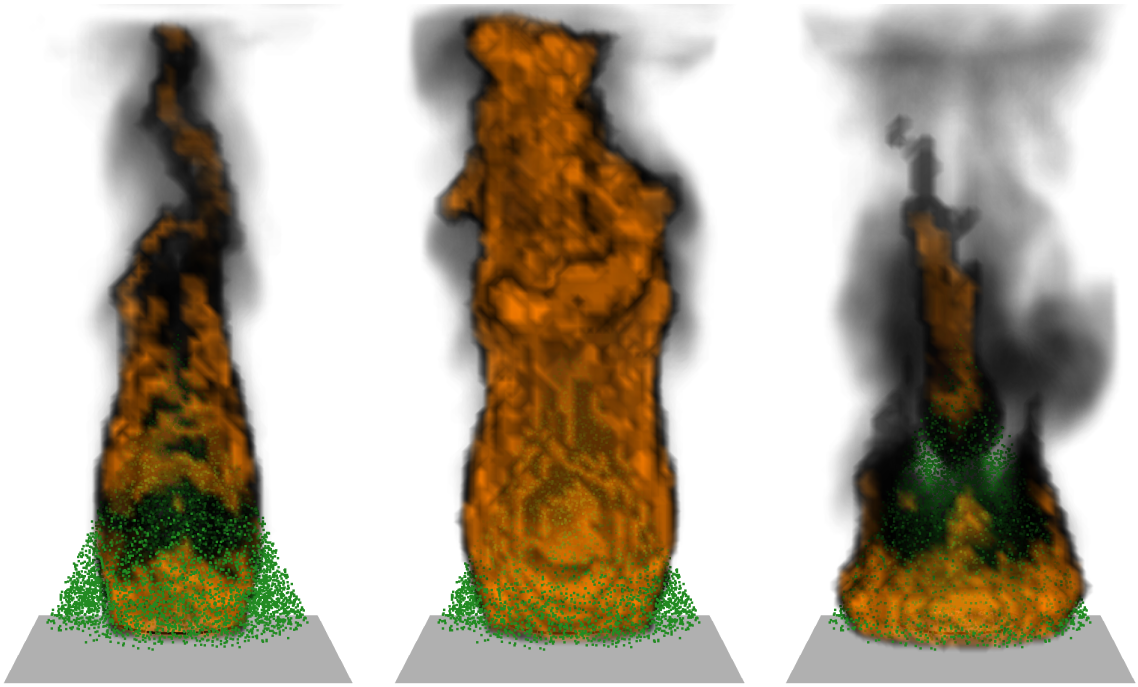

Figure 14.83: Snapshots of the simulation of the 2 m tall Douglas fir tree, 14 % moisture.

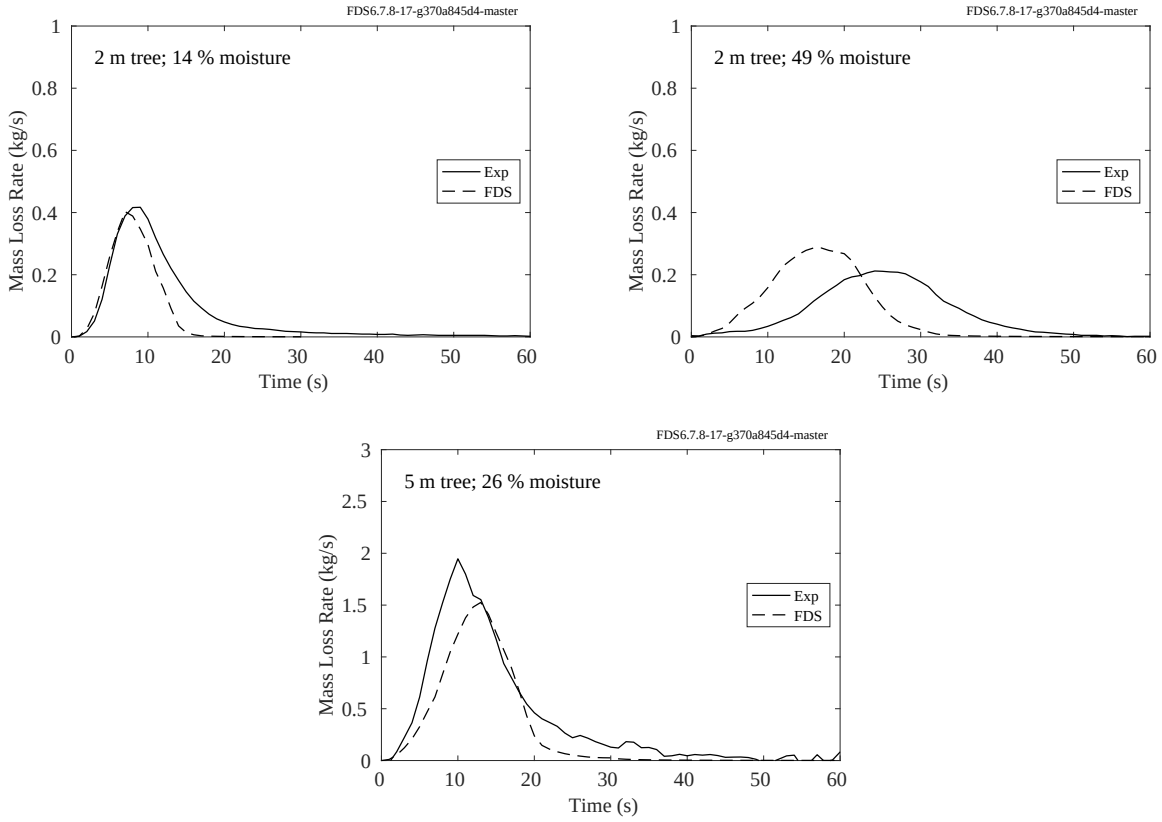

Figure 14.84: Comparison measured and predicted mass loss rate for the Douglas fir tree experiments.

14.8 Summary of Burning and Spread Rates

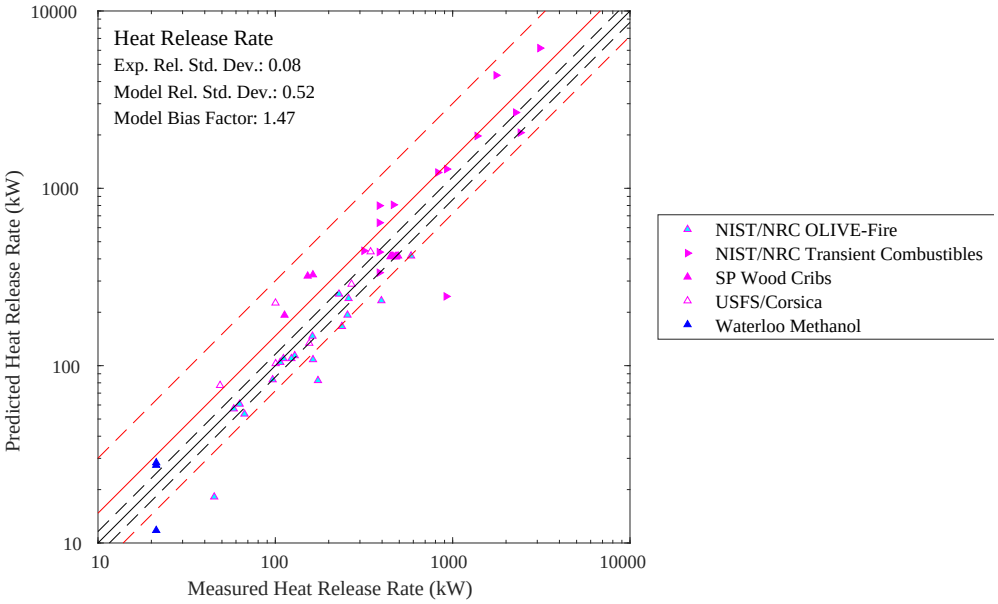

Figure 14.85: Summary of heat release rate predictions.

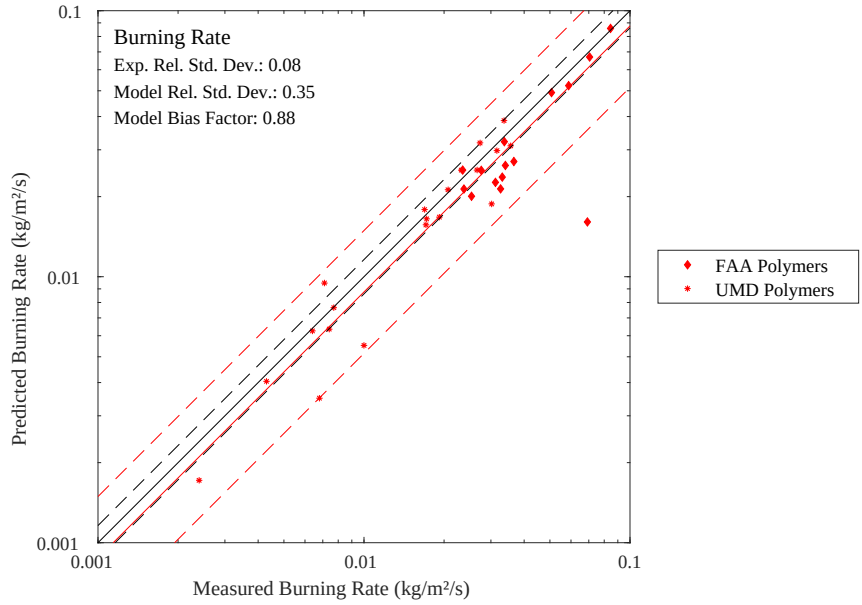

Figure 14.86: Summary of burning rate predictions.

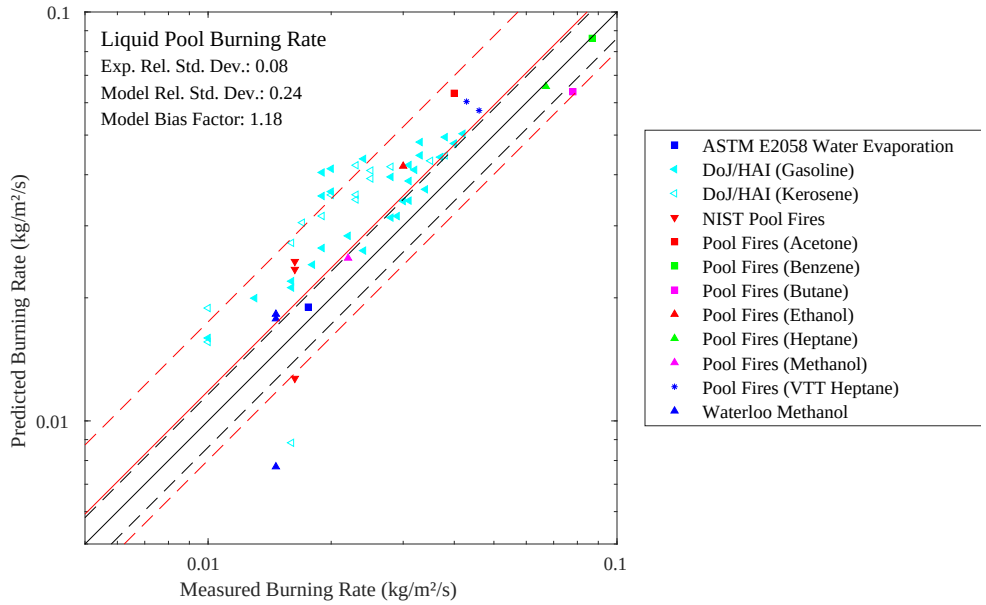

Figure 14.87: Summary of liquid pool burning rate predictions.

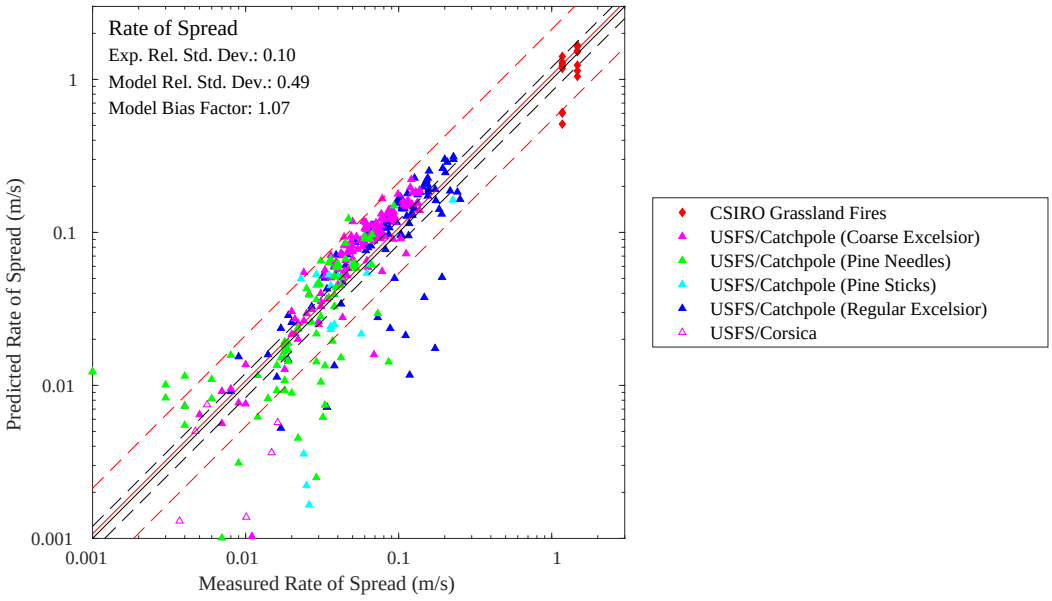

Figure 14.88: Summary, Wildfire Rate of Spread.

Chapter 15

Wind Engineering and Atmospheric Dispersion

This chapter presents results of simulations of wind over structures and atmospheric dispersion, all involving a simplified atmospheric boundary layer model in FDS.

15.1 UWO Wind Tunnel Experiments

A description of the UWO Wind Tunnel experiments is included in Section 3.85. Schematic drawings of the wind tunnel models are shown in Fig. 15.1.

Figures 15.2 through 15.5 show comparisons of measured and predicted mean, rms, minimum and maximum values of the pressure coefficients on the surface of a 1:100 scale model of a building in a wind tunnel. The model building is shown at the top of Fig. 15.1. Figures 15.6 through 15.9 show similar results for the model shown at the bottom of Fig. 15.1. The comparisons are made for two wind directions for each model. For SS20-Test 7, the 180° wind direction is perpendicular to the model's shorter side. The 270° wind direction is perpendicular to the model's longer side. For the SS21-Test 6 model, the wind directions are 0° (perpendicular to short side) and 45°.

The diagrams in Fig. 15.1 indicate the location of the "lines" where the data is compared. The discontinuities in the lines represent the transition from the windward side, to the roof, to the leeward side. The side plots do not include windward or leeward side data.

The simulations are run for approximately one-tenth the time as that of the experiments, which were run for 100 s. The minimum and maximum values for the simulations are extrapolated so that they may be compared to the measured min and max for the 100 s experiment. The procedure is described in the FDS User's Guide [1], in the section describing the `TEMPORAL_STATISTIC 'MIN'` and `'MAX'`.

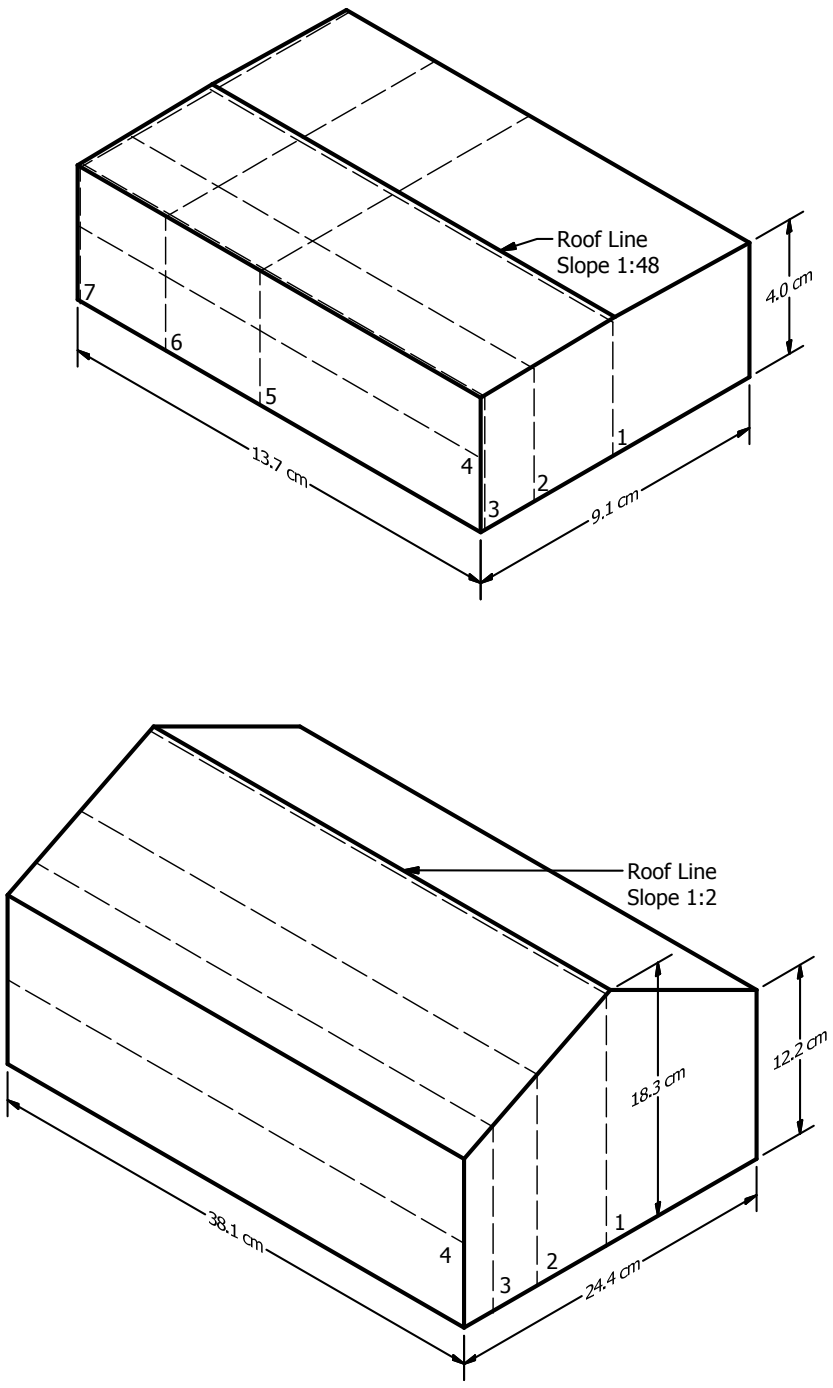

Figure 15.1: UWO Wind Tunnel schematic drawings. (Top) SS20-Test 7. (Bottom) SS21-Test 6. The numbers at the base of the models denote the starting points of the lines over which the measurements and predictions are compared.

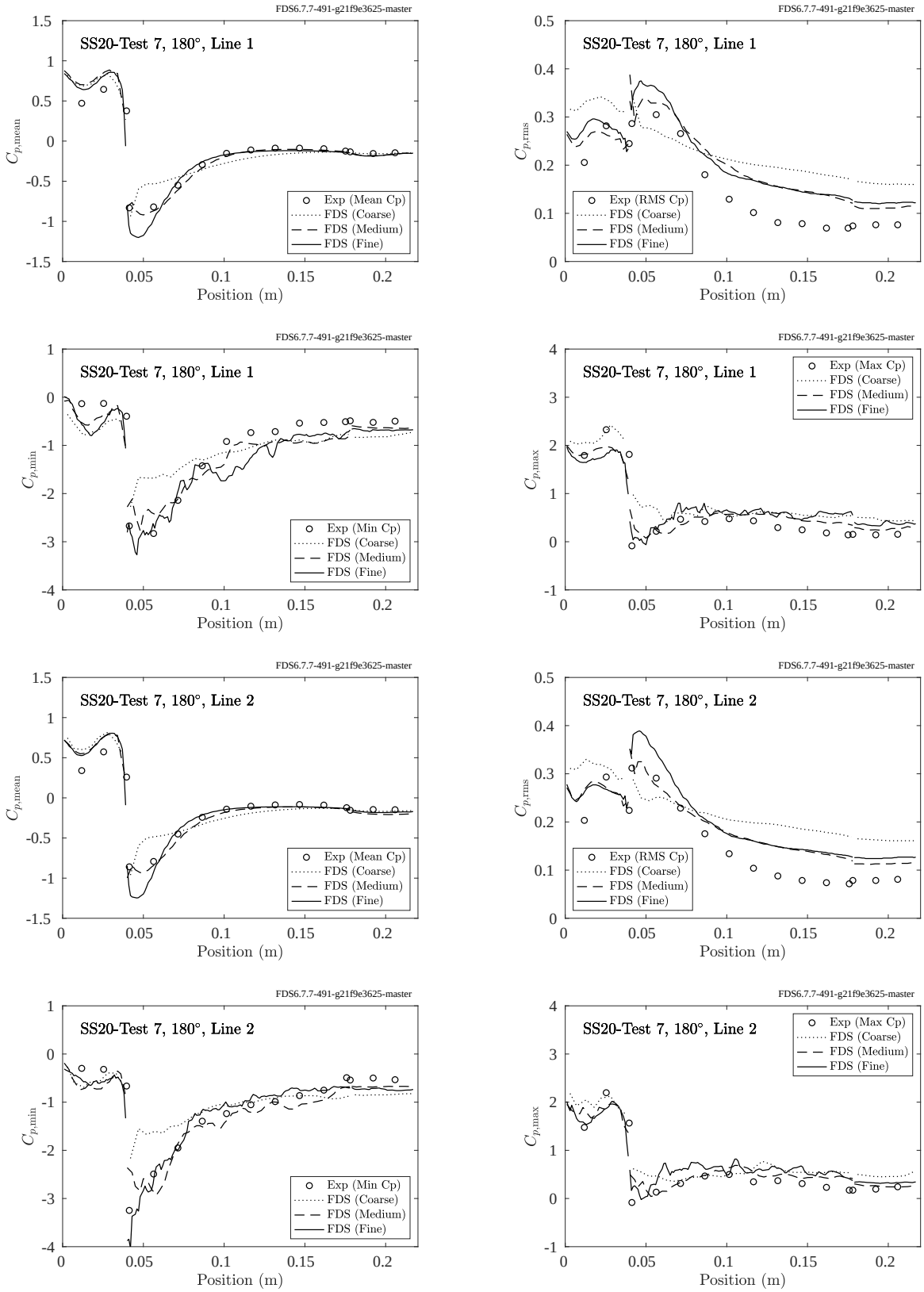

Figure 15.2: UWO Wind Tunnel, SS20-Test 7 pressure coefficients, 180° wind direction.

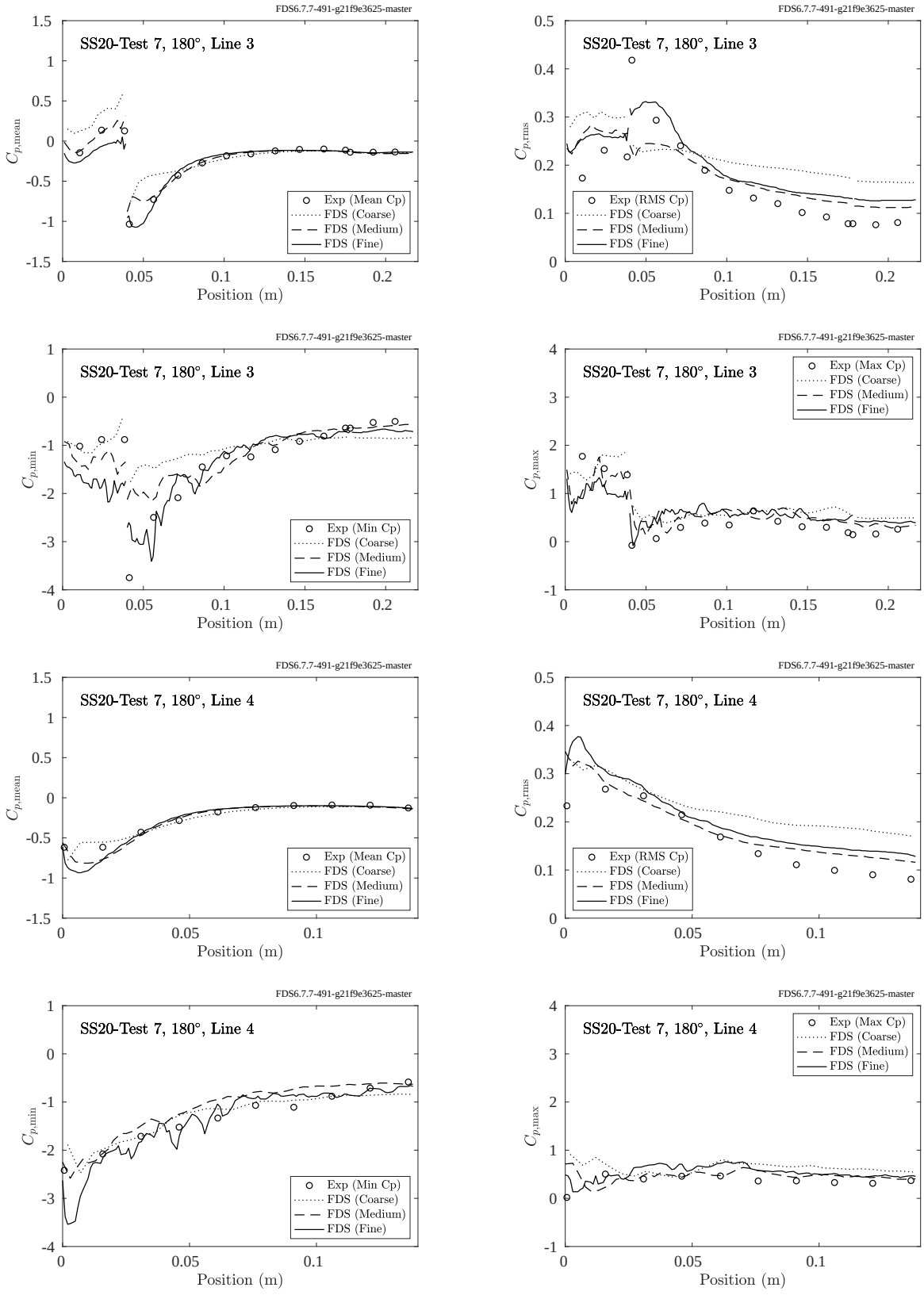

Figure 15.3: UWO Wind Tunnel, SS20-Test 7 pressure coefficients, 180° wind direction.

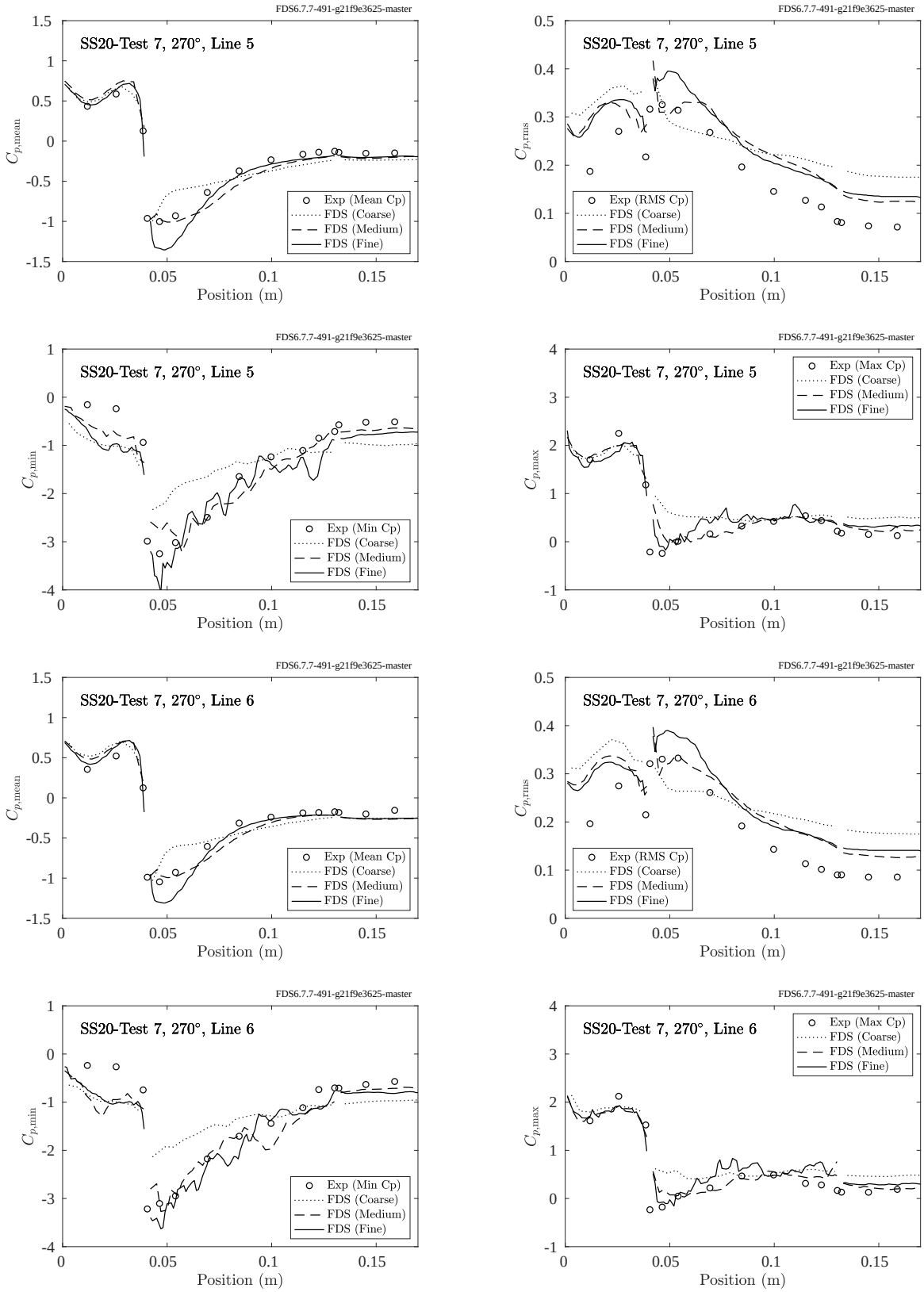

Figure 15.4: UWO Wind Tunnel, SS20-Test 7 pressure coefficients, 270° wind direction.

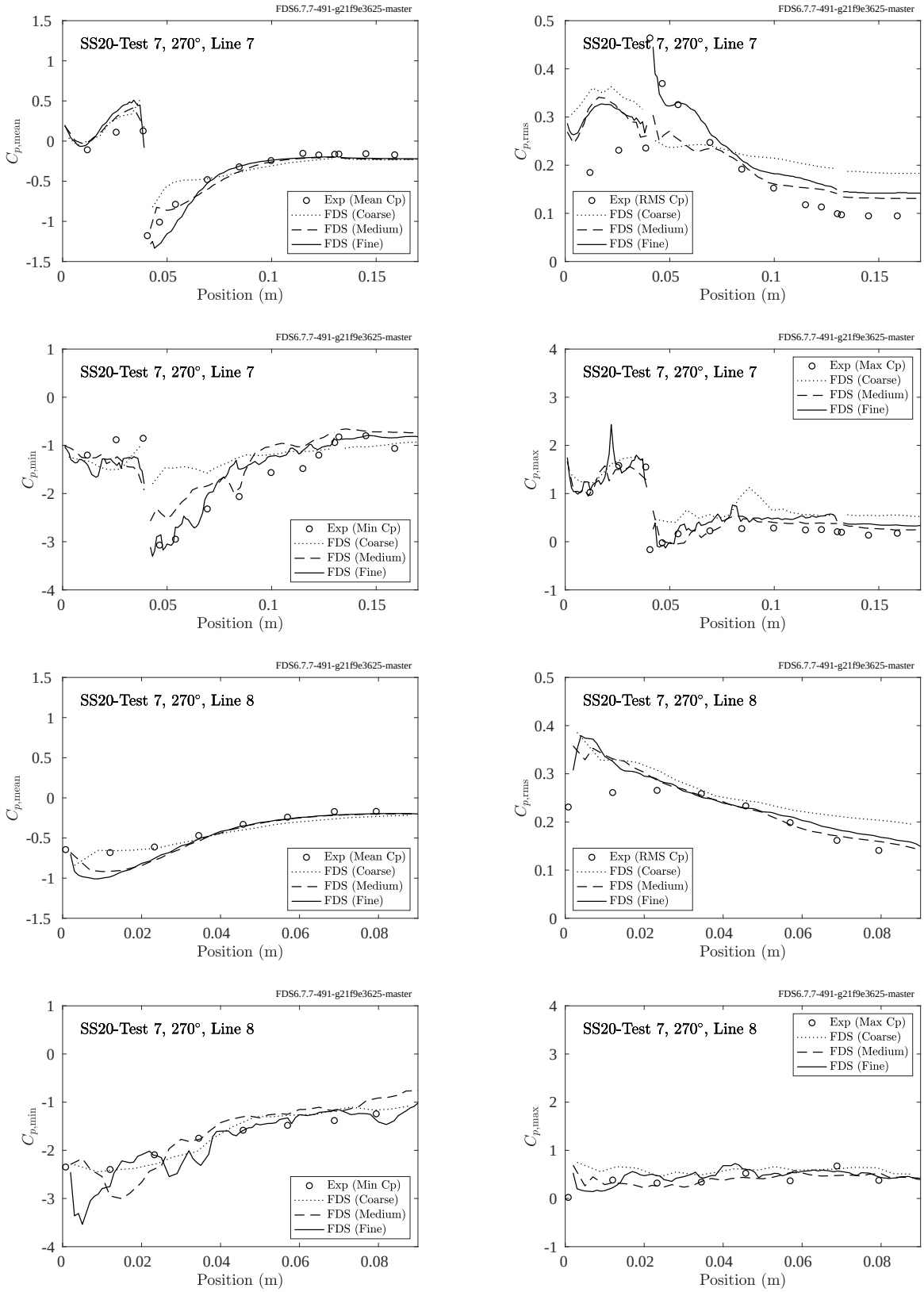

Figure 15.5: UWO Wind Tunnel, SS20-Test 7 pressure coefficients, 270° wind direction.

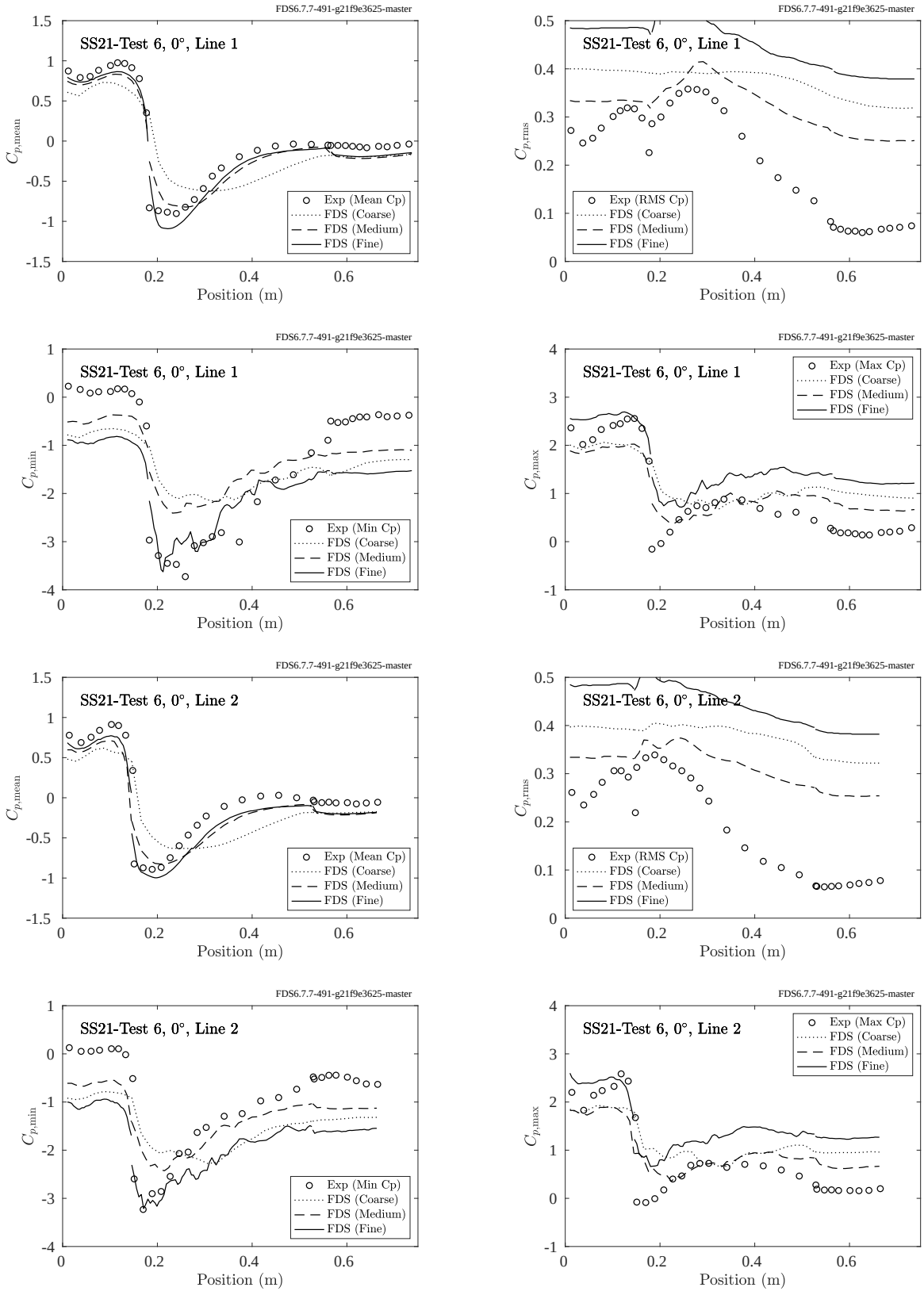

Figure 15.6: UWO Wind Tunnel, SS21-Test 6 pressure coefficients, 0° wind direction.

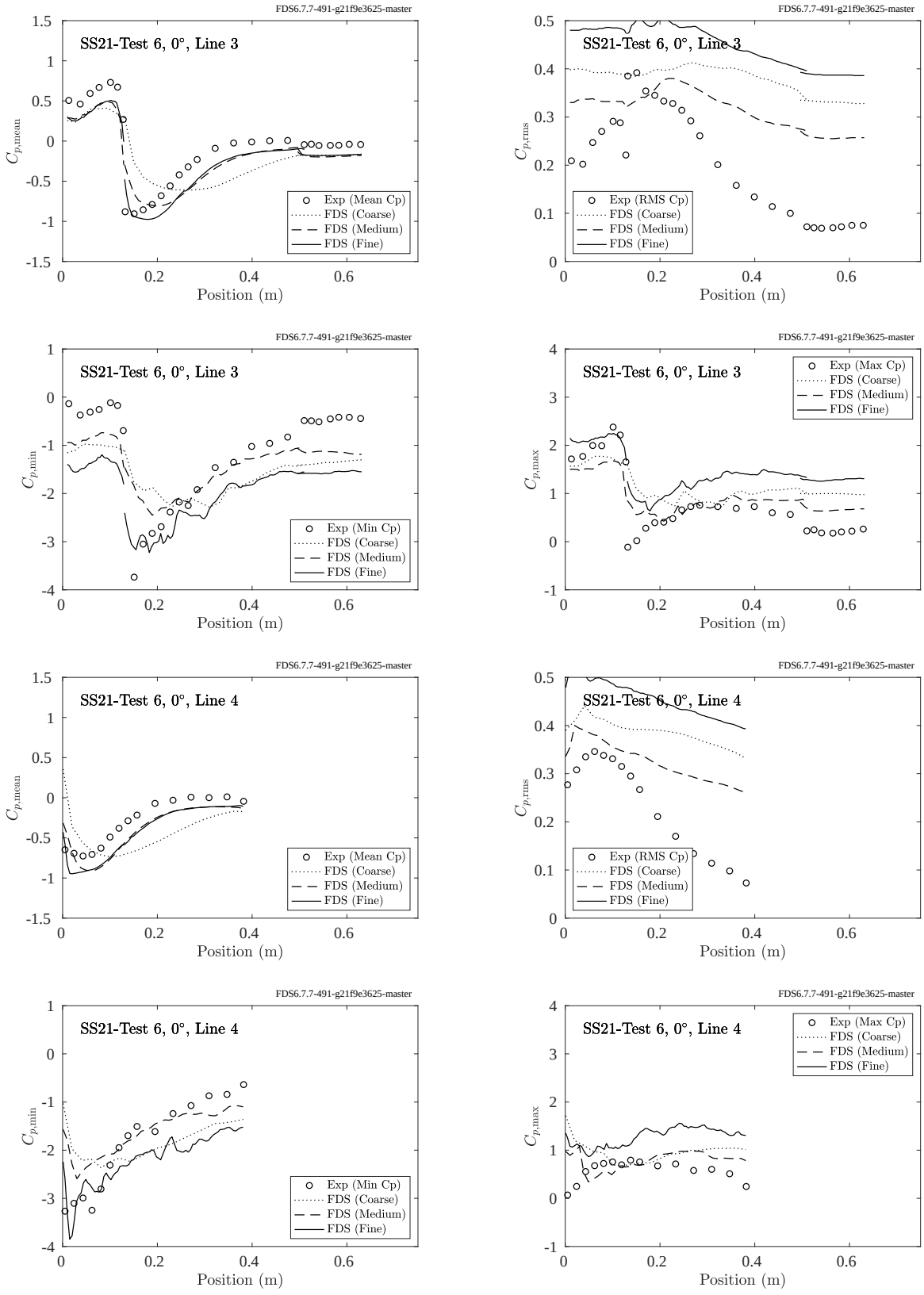

Figure 15.7: UWO Wind Tunnel, SS21-Test 6 pressure coefficients, 0° wind direction.

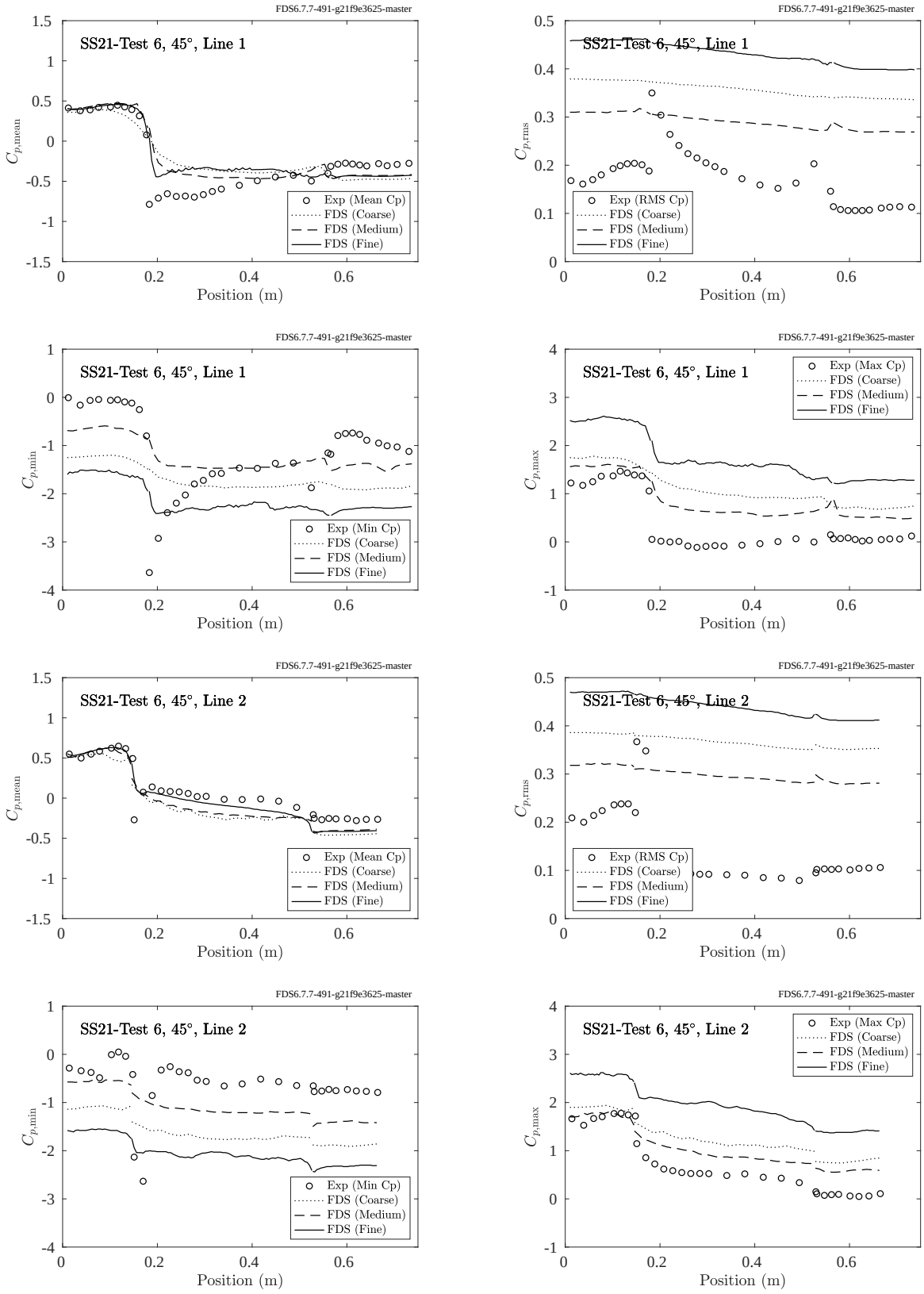

Figure 15.8: UWO Wind Tunnel, SS21-Test 6 pressure coefficients, 45° wind direction.

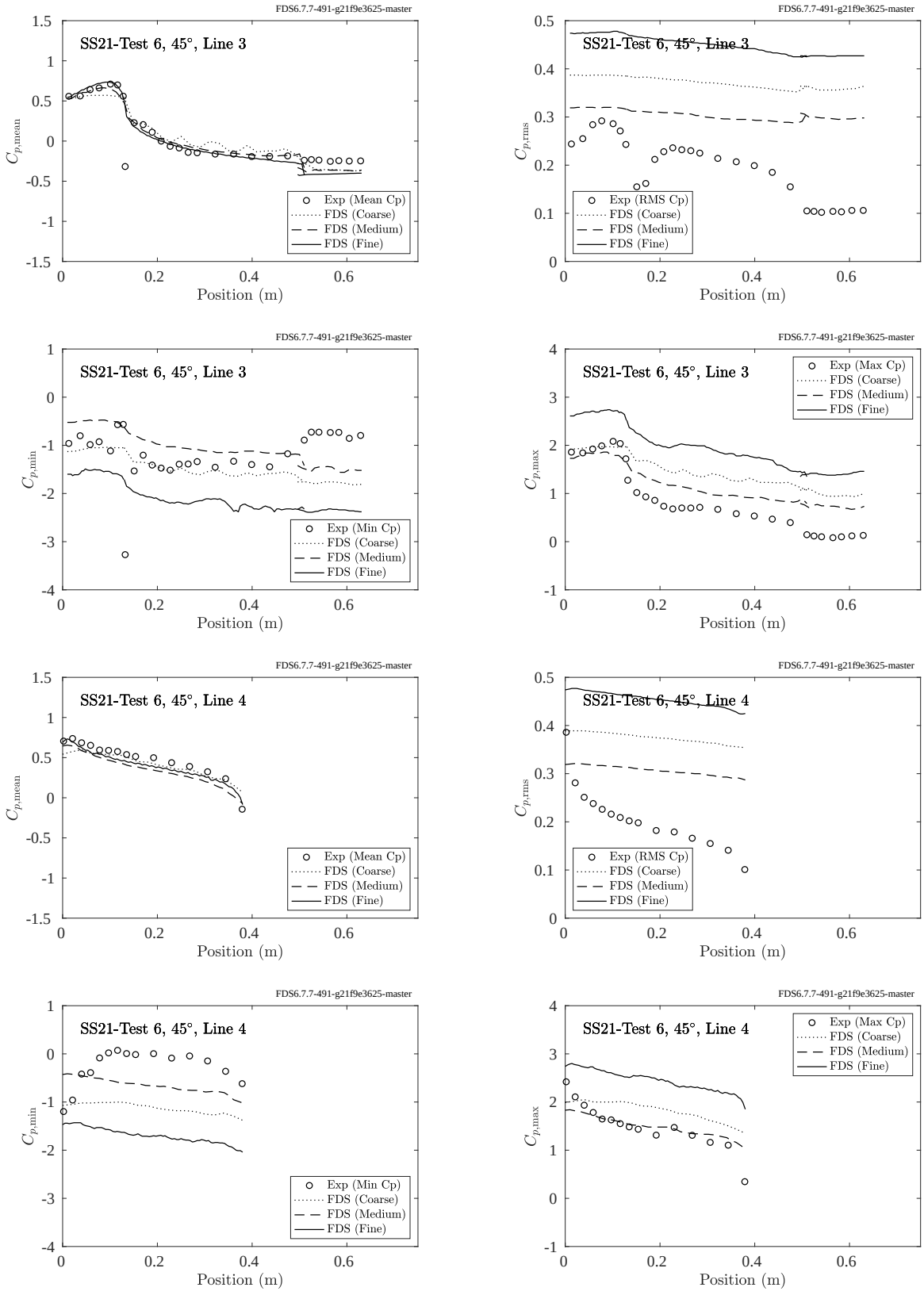

Figure 15.9: UWO Wind Tunnel, SS21-Test 6 pressure coefficients, 45° wind direction.

15.2 LNG Dispersion Experiments

Details of the numerical modeling of these experiments is found in Section 3.36.

Figure 15.10 through Fig. 15.13 display the measured velocity and temperature profiles, the corresponding Monin-Obukhov profiles that serve as initial and boundary conditions for FDS, and the resulting time-averaged profiles from the FDS simulations.

Figures 15.14–15.15 compare measured and predicted downwind concentrations of natural gas originating from spills of liquefied natural gas (LNG) on water. In each case, the measured values are short-time (1 s to 3 s) averages of sensors positioned in arcs at discrete distances downwind of the spill site. For each arc, the maximum value is chosen. The processing of the FDS results follows the same procedure. The sensors were generally located a few meters off the relatively dry, flat terrain.

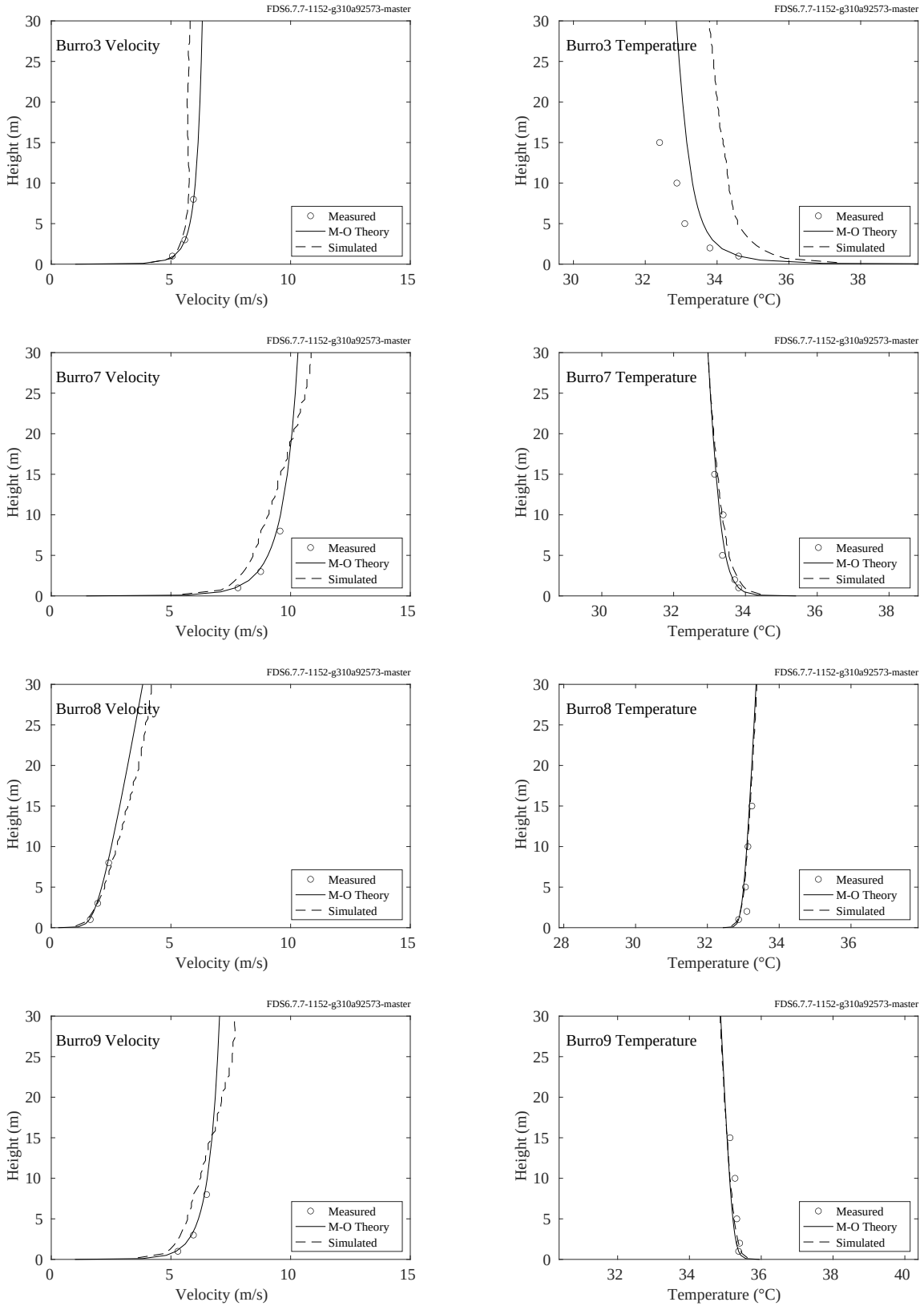

Figure 15.10: LNG Dispersion experiments, Burro velocity and temperature profiles.

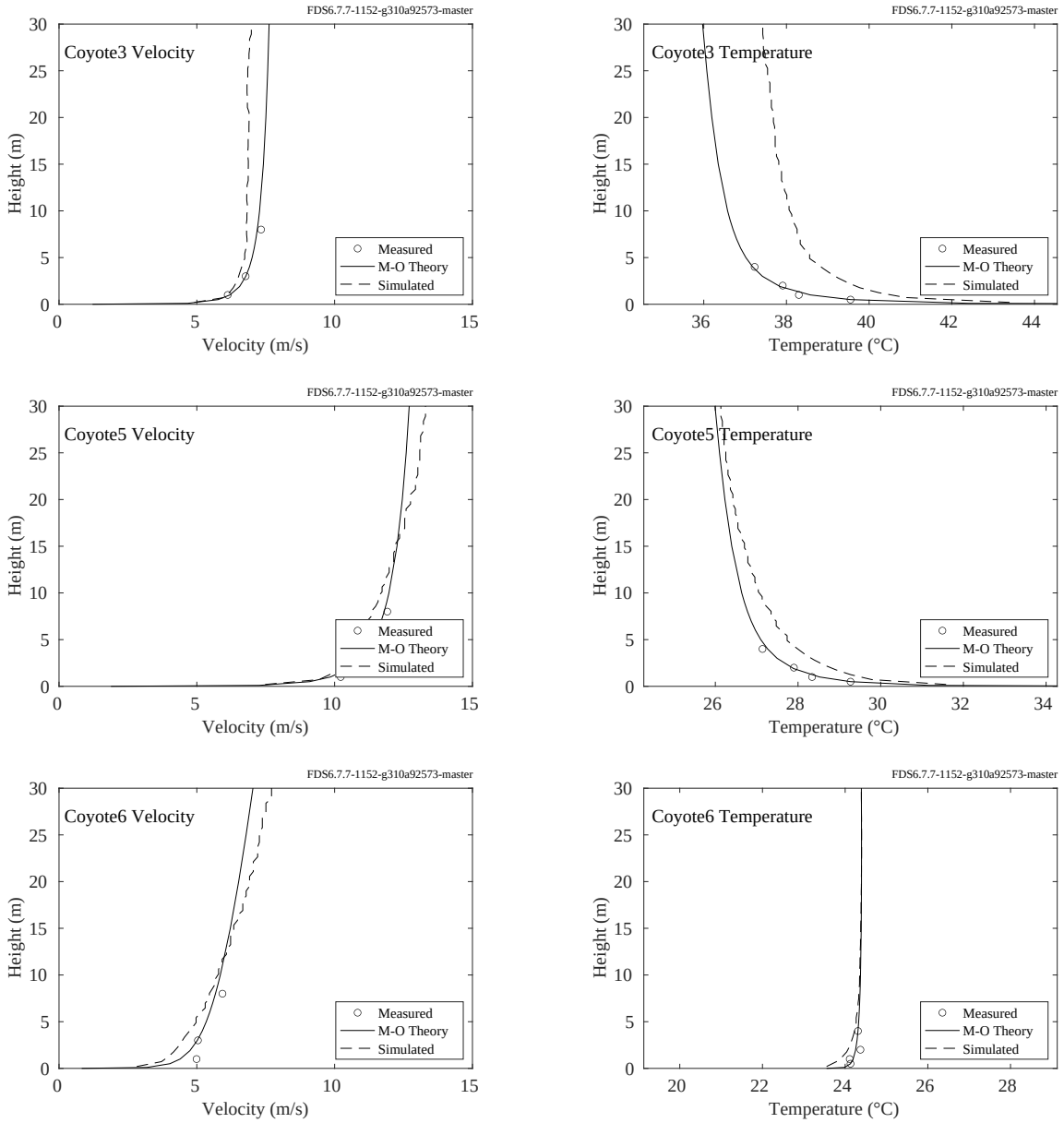

Figure 15.11: LNG Dispersion experiments, Coyote velocity and temperature profiles.

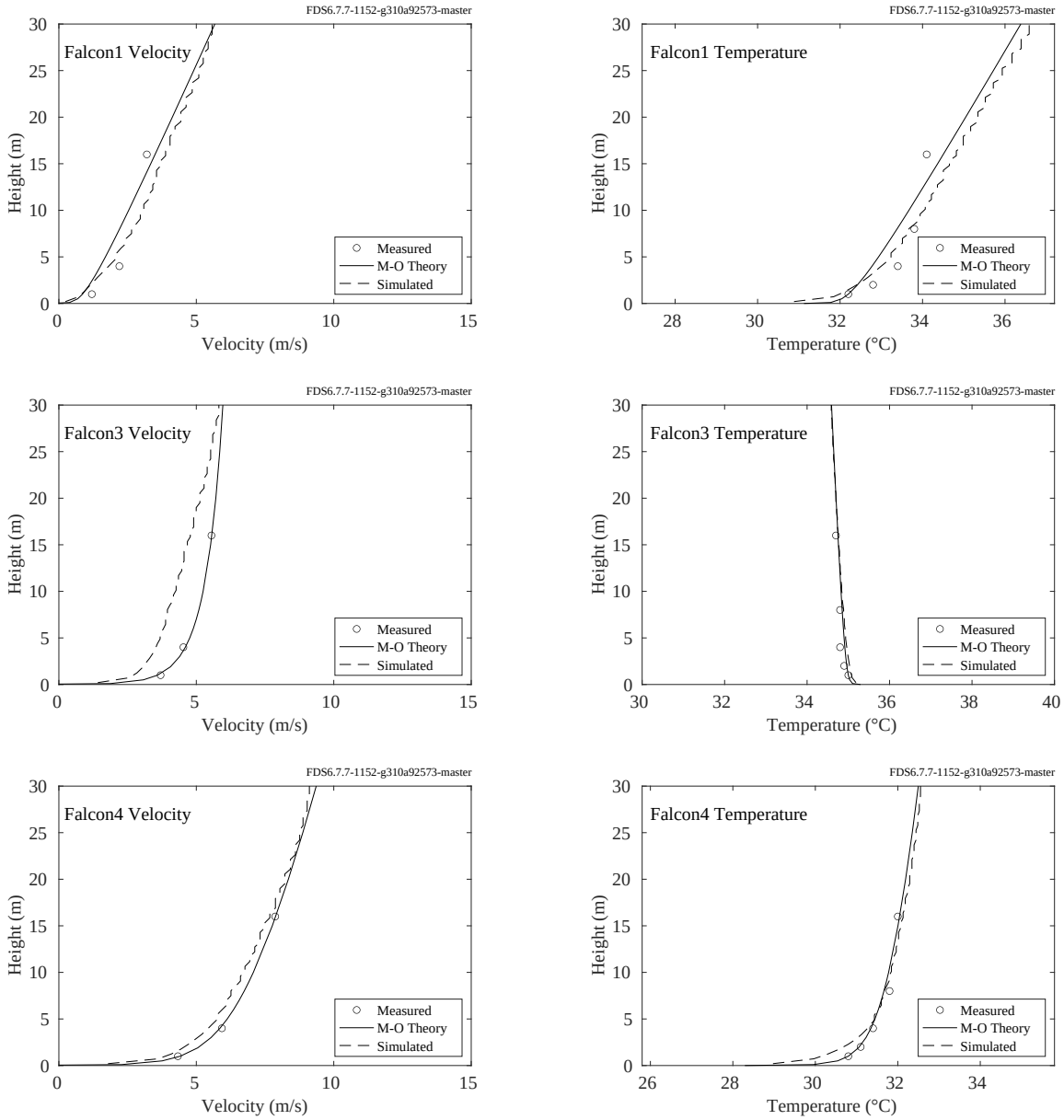

Figure 15.12: LNG Dispersion experiments, Falcon velocity and temperature profiles.

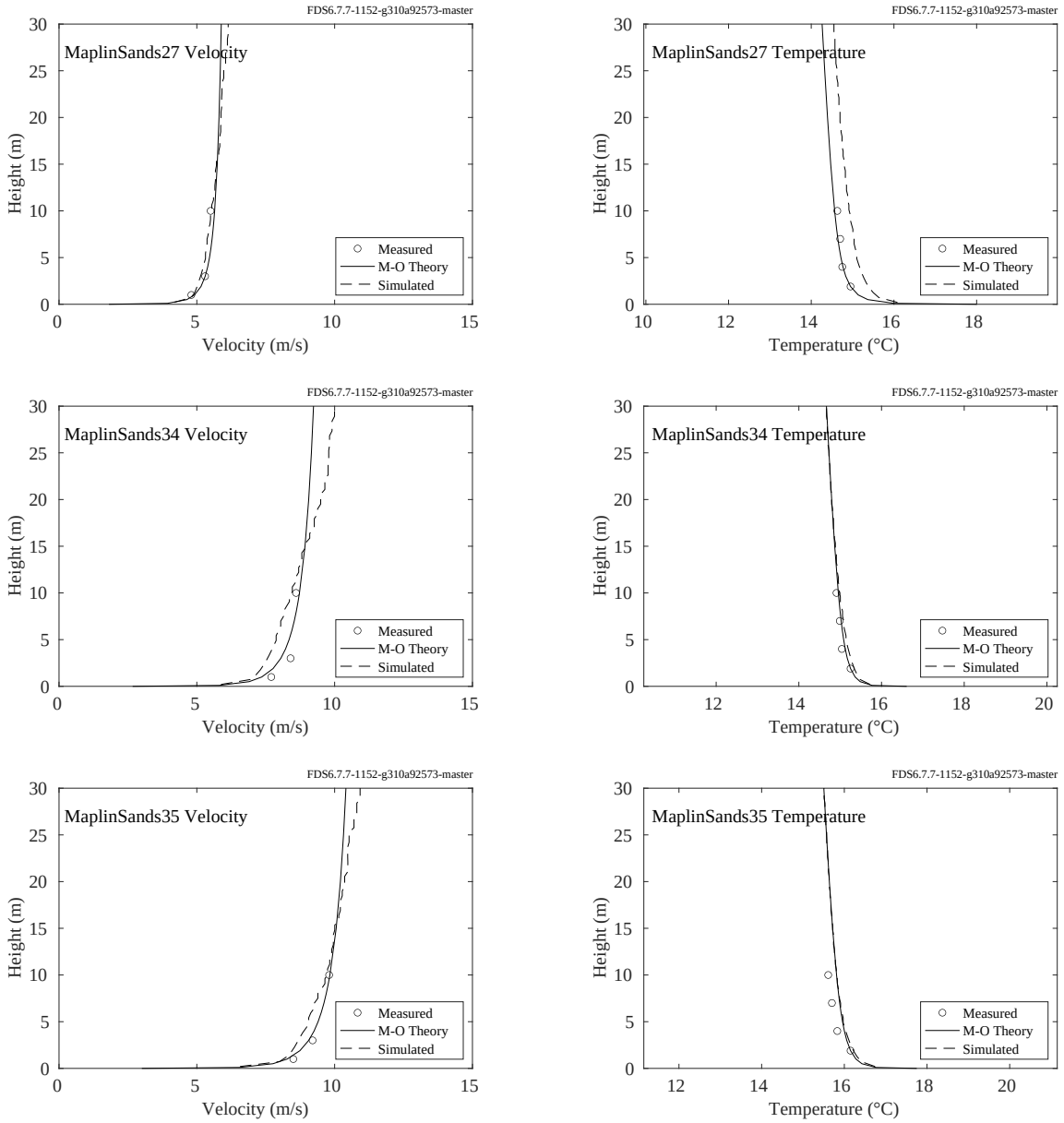

Figure 15.13: LNG Dispersion experiments, Maplin Sands velocity and temperature profiles.

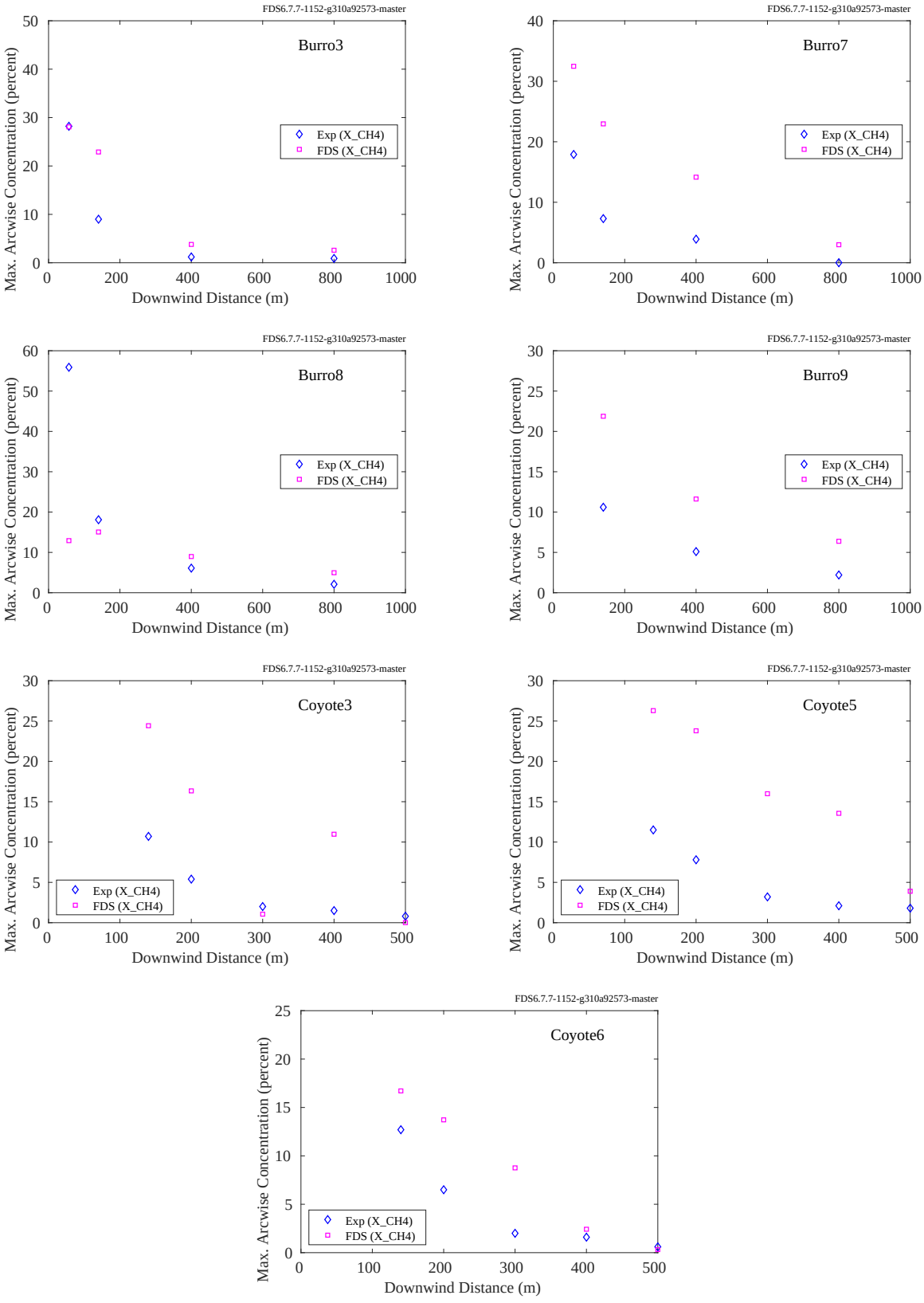

Figure 15.14: LNG Dispersion experiments, Burro and Coyote.

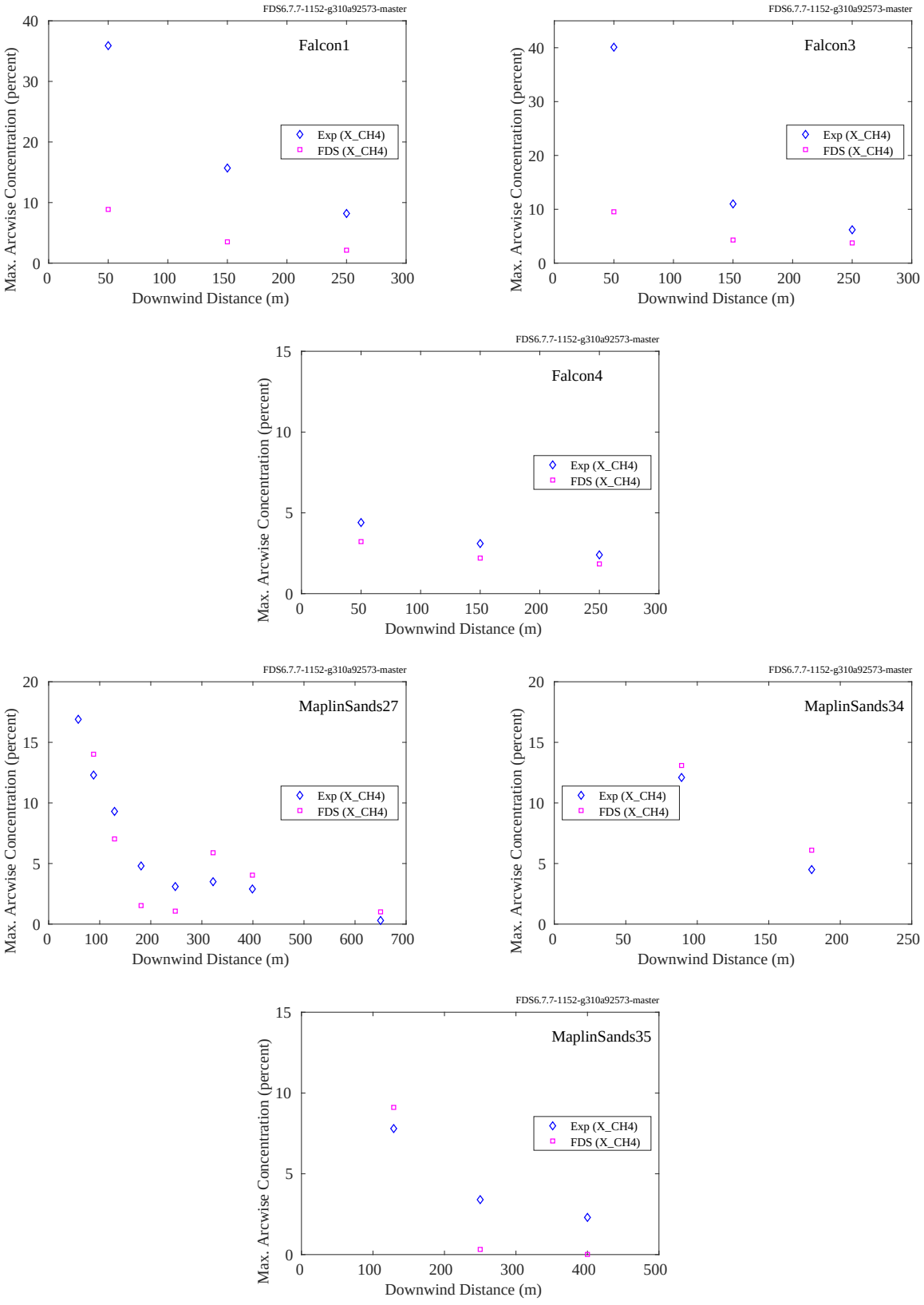

Figure 15.15: LNG Dispersion experiments, Falcon and Maplin Sands.

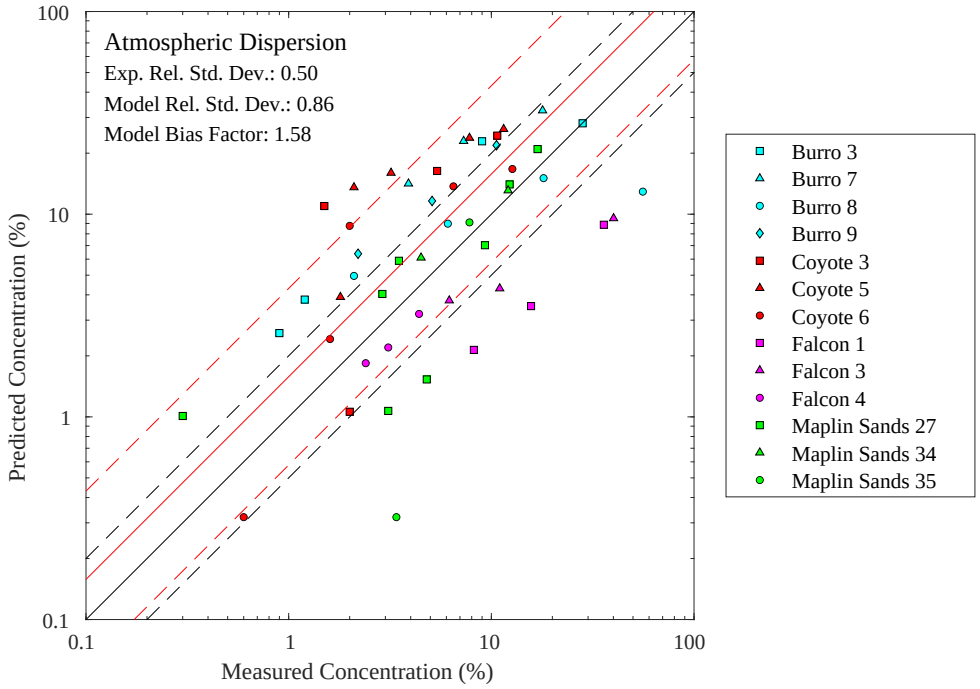

Figure 15.16: Summary of LNG Dispersion predictions. Note that the dashed black lines denote plus/minus a factor of two from the measured values. The red dashed lines represent two relative standard deviations about the solid red line, the model average.

15.3 Stack Emission Plume Rise

A common exercise in atmospheric dispersion modeling is predicting the plume rise height of stack emissions. In an example given by Stull [133], a $z_s = 75$ m stack emits SO_2 at a rate of 250 g/s with an exit velocity of $W_0 = 20$ m/s and temperature of $\Delta T = 180$ K above ambient ($T_0 = 293$ K) through an orifice with radius $R_0 = 2$ m. The wind speed is $U = 5$ m/s. Three cases are considered where the atmosphere is stably stratified with temperature gradients, $\mathrm{d}T/\mathrm{d}z$, of -4.8, -8.8 and 5.2 K/km. The expected equilibrium height is given by the empirical expression:

$$z_c = z_s + 2.6\left(\frac{I_b U^2}{N_{BV}^2}\right)^{1/3} \approx \begin{cases} 290\text{ m} & \text{Case 1} \\ 443\text{ m} & \text{Case 2} \\ 224\text{ m} & \text{Case 3} \end{cases} \tag{15.1}$$

where I_b is a buoyancy length scale given by

$$I_b = \frac{W_0 R_0^2 g}{U^3}\frac{\Delta T}{T_0} \approx 3.85\text{ m} \quad \text{(all cases)} \tag{15.2}$$

and the Brunt-Väisälä frequency is given by:

$$N_{BV}^2 = \frac{g}{T_0}\left(\frac{\mathrm{d}T}{\mathrm{d}z} + \Gamma_d\right) \approx \begin{cases} 1.67\times10^{-4}\text{ s}^{-2} & \text{Case 1} \\ 0.334\times10^{-4}\text{ s}^{-2} & \text{Case 2} \\ 5.02\times10^{-4}\text{ s}^{-2} & \text{Case 3} \end{cases} \qquad \Gamma_d = 9.8\times10^{-3}\text{ K/m} \tag{15.3}$$

Notice that the exhaust rate of SO_2 has no role in the calculation of plume height because it is greatly diluted by hot air (or other exhaust products) exiting the stack at 20 m/s.

Figure 15.17 displays snapshots of the simulations, and Fig. 15.18 displays the comparison of FDS simulations with the empirical correlation. In the simulations, the plume height was taken as the location of the peak concentration of the SO_2 far downwind of the stack. The stack is approximated as a rectangular solid measuring 4 m by 4 m by 76 m. The grid surrounding stack is composed of 2 m cubes. The next grid to the right is 4 m, and the next is 8 m. The wind speed is fixed at 5 m/s, and the temperature is linearly stratified.

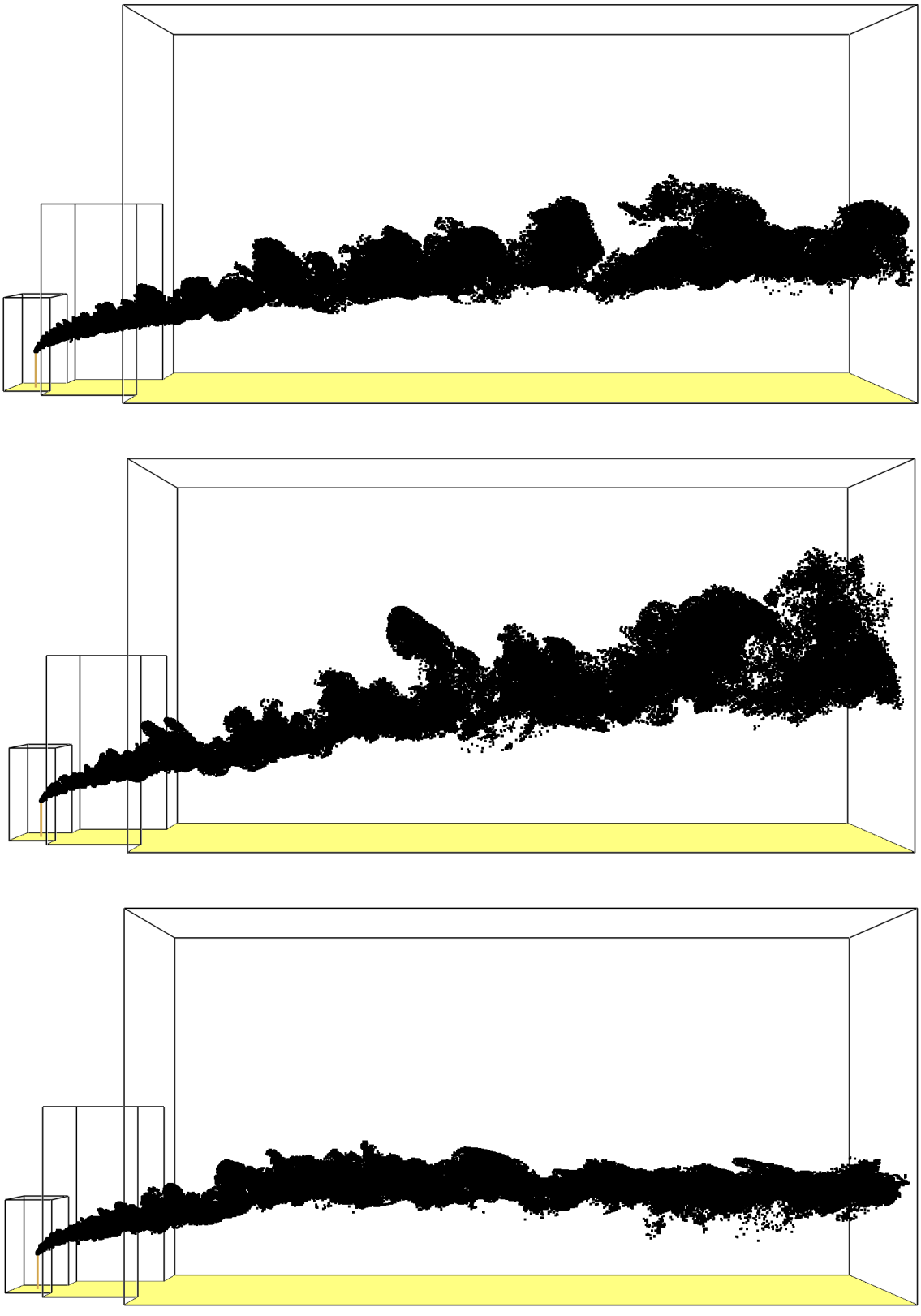

Figure 15.17: Snapshots of the simulations of plume rise. The largest computational domain is 800 m high and 1600 m long. The stack at left is 75 m high.

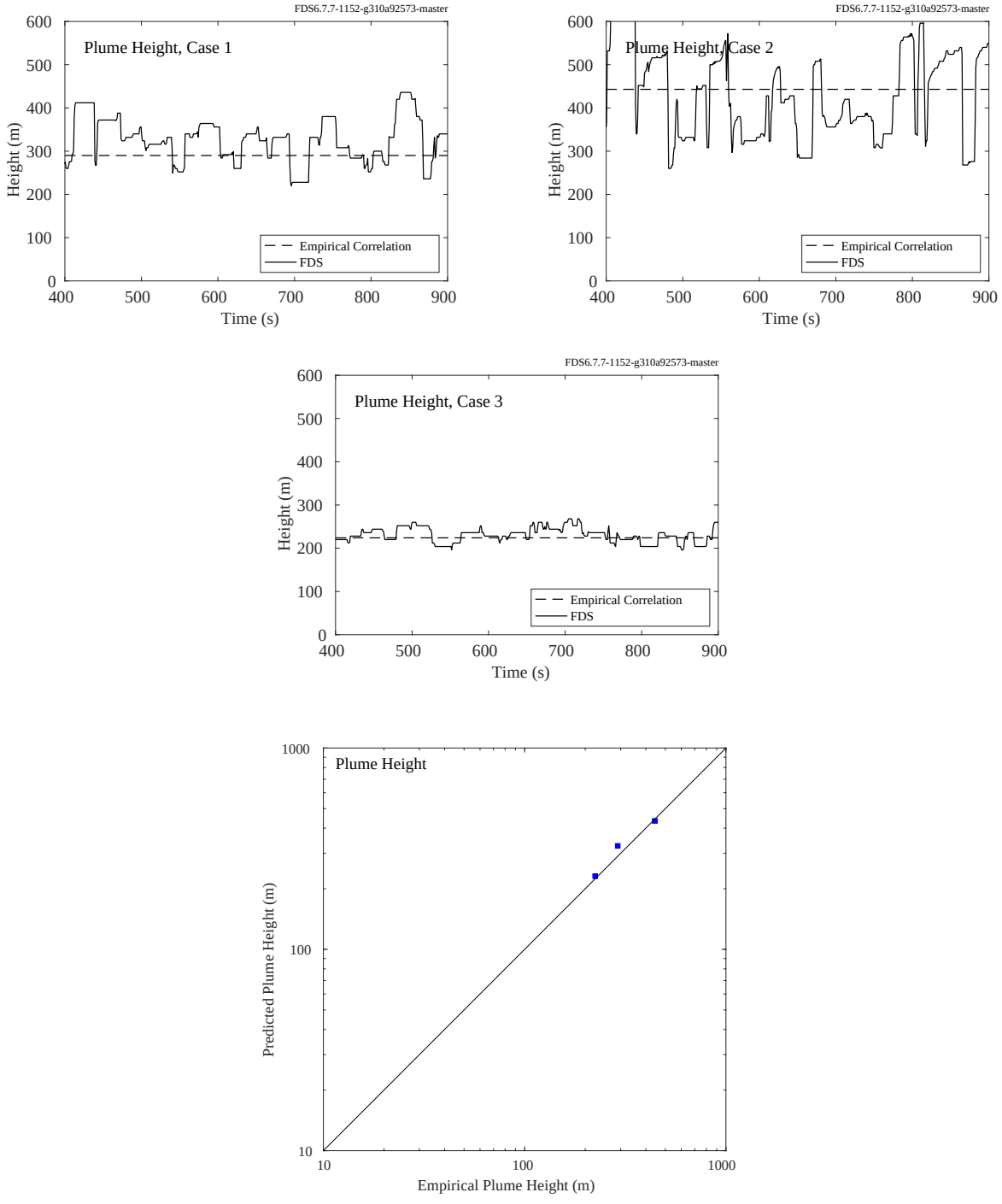

Figure 15.18: Atmospheric Dispersion, Plume Height results.

Chapter 16

Conclusion

16.1 Summary of FDS Model Uncertainty Statistics

Table 16.1 lists the summary statistics for the different quantities examined in this Guide. This is, for each quantity of interest, Table 16.1 lists the bias and relative standard deviation of the predicted values. It also lists the total number of experimental data sets on which these statistics are based, as well as the total number of point to point comparisons. Obviously, the more data sets and the more points, the more reliable the statistics.

For further details about model uncertainty and the meaning of these statistics, see Chapter 4.

Table 16.1: Summary statistics for all quantities of interest

Quantity	Section	Datasets	Points	$\widetilde{\sigma}_E$	$\widetilde{\sigma}_M$	Bias
HGL Temperature, Forced Ventilation	5.22	6	158	0.07	0.15	1.14
HGL Temperature, Natural Ventilation	5.22	16	307	0.07	0.10	1.02
HGL Temperature, No Ventilation	5.22	3	32	0.07	0.10	1.09
HGL Depth	5.22	14	269	0.05	0.08	1.06
Ceiling Jet Temperature	7.1.21	22	1060	0.07	0.12	1.03
Plume Temperature	6.1.13	14	292	0.07	0.23	1.06
Oxygen Concentration	9.1.10	13	279	0.08	0.16	0.98
Carbon Dioxide Concentration	9.1.10	13	272	0.08	0.15	1.01
Smoke Concentration	9.2.3	2	22	0.19	0.94	2.68
Compartment Over-Pressure	10.7	5	189	0.20	0.20	0.96
Target Temperature	11.2.10	11	1391	0.07	0.18	1.01
Surface Temperature	11.1.9	8	1127	0.07	0.17	1.08
Liquid Pool Surface Temperature	11.3.3	10	24	0.07	0.07	1.00
Target Heat Flux	12.2.14	14	1136	0.11	0.59	0.92
Surface Heat Flux	12.1.12	7	633	0.11	0.27	1.01
Velocity	8.14	11	301	0.08	0.08	1.02
Sprinkler Activation Time	7.2.1	6	273	0.06	0.16	1.04
Smoke Detector Activation Time	7.3	1	142	0.27	0.27	0.61
Smoke Detector Activation Time, Temp. Rise	7.3	1	142	0.33	0.33	1.21
Cable Failure Time	11.2.11	1	22	0.12	0.32	0.45
Sprinkler Actuations	7.2.2	3	38	0.15	0.46	1.08
Heat Release Rate	14.8	5	52	0.08	0.52	1.47

Quantity	Section	Datasets	Points	$\widetilde{\sigma}_E$	$\widetilde{\sigma}_M$	Bias
Burning Rate	14.8	2	35	0.08	0.35	0.88
Liquid Pool Burning Rate	14.8	12	58	0.08	0.24	1.18
Carbon Monoxide Concentration	9.5.7	7	102	0.19	0.56	0.95
Entrainment	6.4	2	87	0.06	0.06	1.15
Extinction Time	13.2.5	2	45	0.10	0.41	1.06
Species Concentration	9.6	1	126	0.08	0.15	0.97
Smoke Obscuration	9.2.4	1	18	0.14	0.14	1.05
Mass Flow Rate	12.114	1	40	0.08	0.09	0.92
Atmospheric Dispersion	15.2	13	49	0.50	0.86	1.58
Minimum Extinguishing Concentration	13.1.1	46	46	0.03	0.03	1.04
Flame Height	6.2.3	6	100	0.10	0.33	1.18
Flame Tilt	6.3	3	24	0.10	0.69	0.86
Rate of Spread	14.8	6	353	0.10	0.49	1.07
Condensation	12.6	6	101	0.12	0.33	0.73
Aerosol Deposition	9.3.2	2	88	0.12	0.49	1.08

16.2 Normality Tests

The histograms on the following pages display the distribution of the quantity $\ln(M/E)$, where M is a random variable representing the Model prediction and E is a random variable representing the Experimental measurement. Recall from Chapter 4 that $\ln(M/E)$ is assumed to be normally distributed. To test this assumption for each of the quantities of interest listed in Table 16.1, Spiegelhalter's normality test has been applied [368]. This test examines a set of values, $x_1, ..., x_n$ whose mean and standard deviation are computed as follows:

$$\bar{x} = \sum_{i=1}^{n} x_i \quad ; \quad \sigma^2 = \frac{1}{n-1} \sum_{i=1}^{n} (x_i - \bar{x})^2 \tag{16.1}$$

Spiegelhalter tests the null hypothesis that the sample x_i is taken from a normally distributed population. The test statistic, S, is defined:

$$S = \frac{N - 0.73n}{0.9\sqrt{n}} \quad ; \quad N = \sum_{i=1}^{n} Z_i^2 \ln Z_i^2 \quad ; \quad Z_i = \frac{x_i - \bar{x}}{\sigma} \tag{16.2}$$

Under the null hypothesis, the test statistic is normally distributed with mean 0 and standard deviation of 1. If the p-value

$$p = 1 - \left| \text{erf}\left(\frac{S}{\sqrt{2}} \right) \right| \tag{16.3}$$

is less than 0.05, the null hypothesis is rejected.

The flaw in most normality tests is that they tend to reject the assumption of normality when the number of samples is relatively large. As can be seen in some of the histograms on the following pages, some fairly "normal" looking distributions fail while decidedly non-normal distributions pass. For this reason, the p-value is less important than the qualitative appearance of the histogram. If the histogram exhibits the typical bell-shaped curve, this adds confidence to the statistical treatment of the data. If the histogram is not bell-shaped, this might cast doubt on the statistical treatment for that particular quantity.

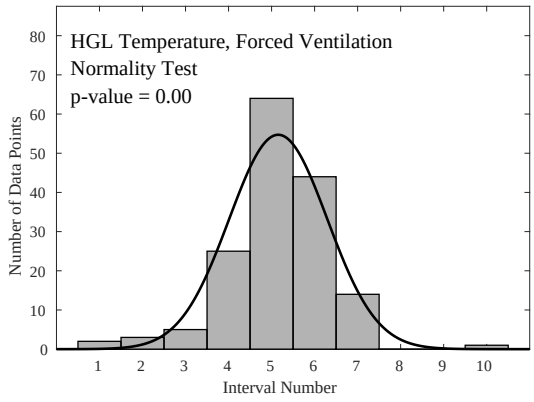
HGL Temperature, Forced Ventilation
Normality Test
p-value = 0.00
Number of Data Points
Interval Number

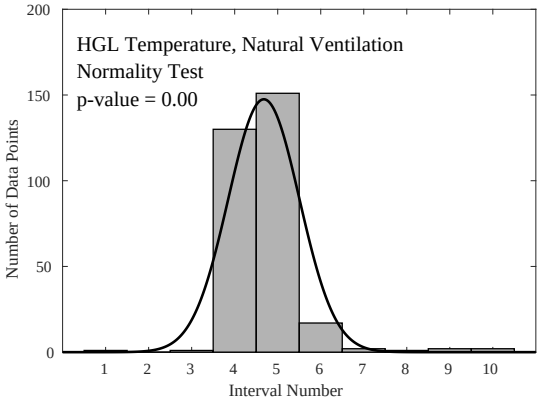
HGL Temperature, Natural Ventilation
Normality Test
p-value = 0.00
Number of Data Points
Interval Number

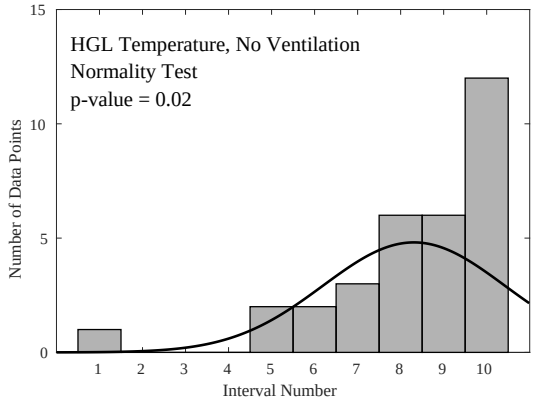
HGL Temperature, No Ventilation
Normality Test
p-value = 0.02
Number of Data Points
Interval Number

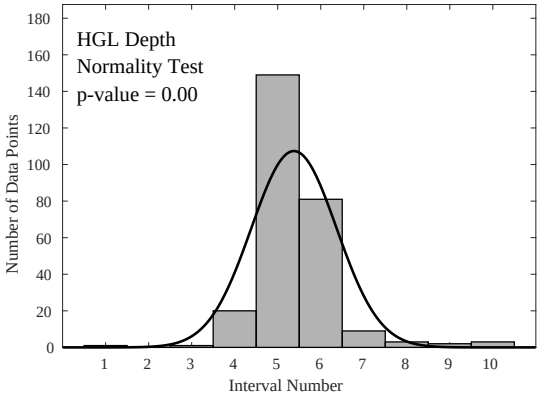
HGL Depth
Normality Test
p-value = 0.00
Number of Data Points
Interval Number

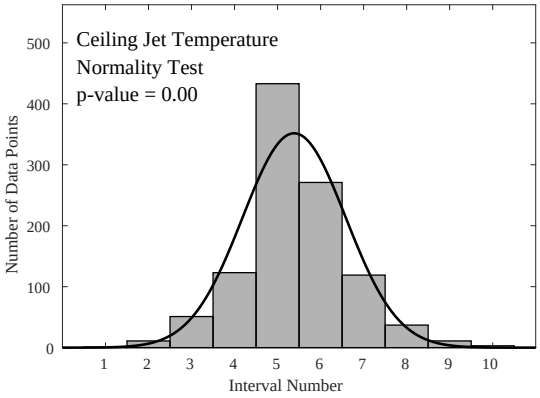
Ceiling Jet Temperature
Normality Test
p-value = 0.00
Number of Data Points
Interval Number

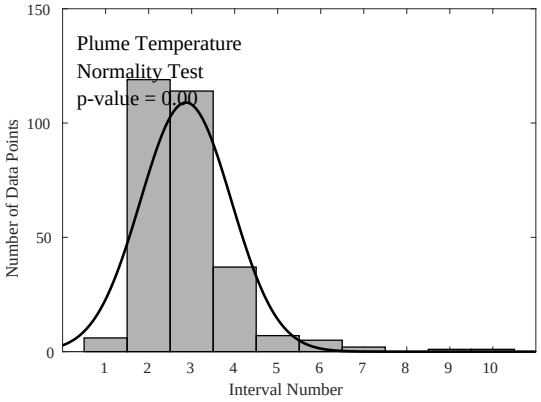
Plume Temperature
Normality Test
p-value = 0.00
Number of Data Points
Interval Number

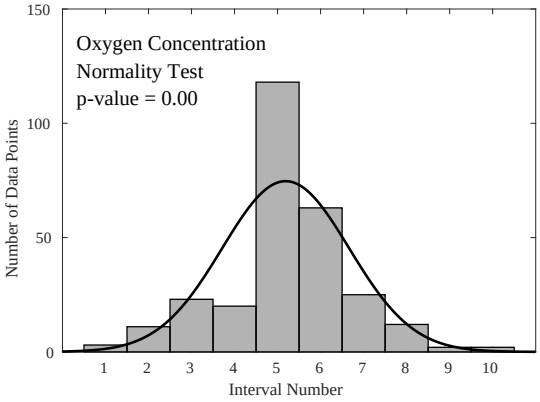
Oxygen Concentration
Normality Test
p-value = 0.00
Number of Data Points
Interval Number

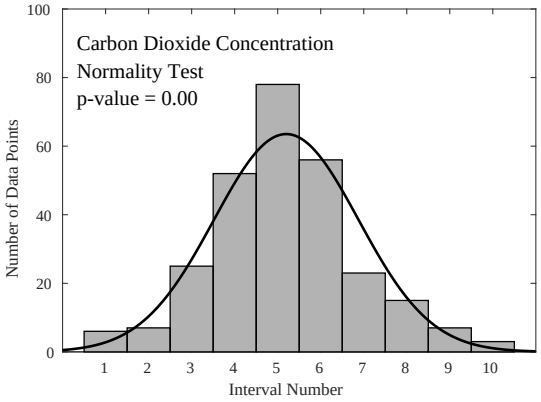
Carbon Dioxide Concentration
Normality Test
p-value = 0.00
Number of Data Points
Interval Number

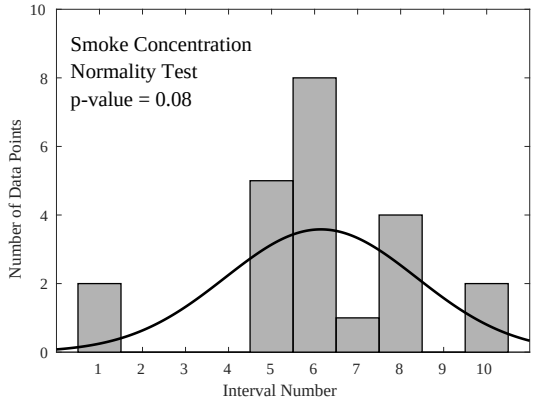
Smoke Concentration
Normality Test
p-value = 0.08
Number of Data Points
Interval Number

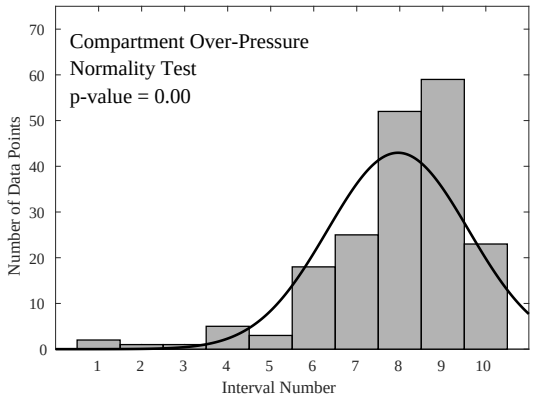
Compartment Over-Pressure
Normality Test
p-value = 0.00
Number of Data Points
Interval Number

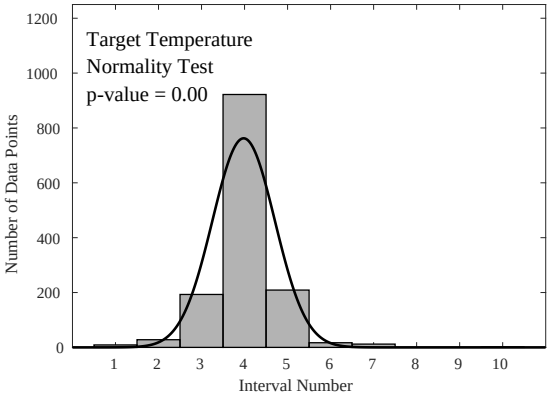
Target Temperature
Normality Test
p-value = 0.00
Number of Data Points
Interval Number

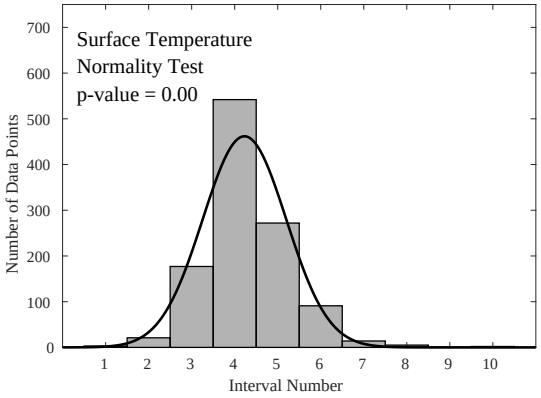
Surface Temperature
Normality Test
p-value = 0.00
Number of Data Points
Interval Number

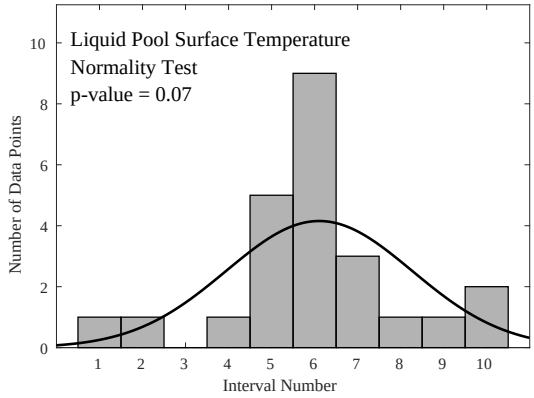
Liquid Pool Surface Temperature
Normality Test
p-value = 0.07
Number of Data Points
Interval Number

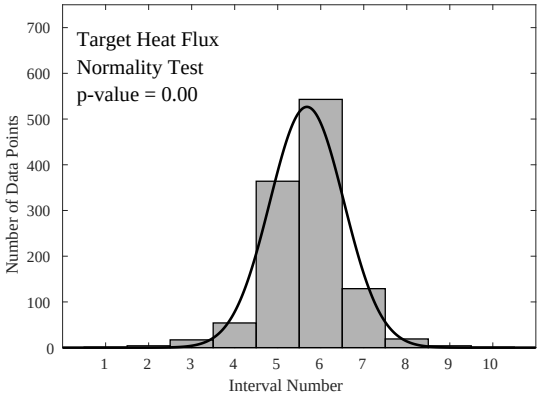
Target Heat Flux
Normality Test
p-value = 0.00
Number of Data Points
Interval Number

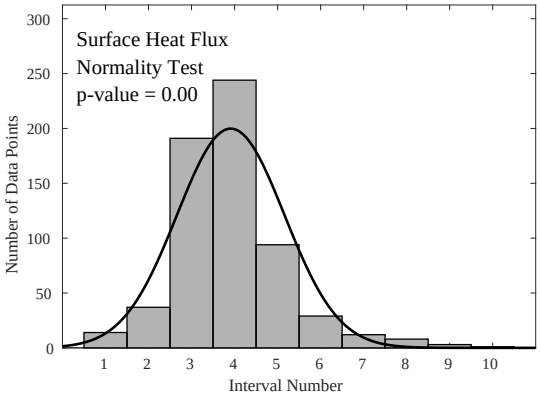
Surface Heat Flux
Normality Test
p-value = 0.00
Number of Data Points
Interval Number

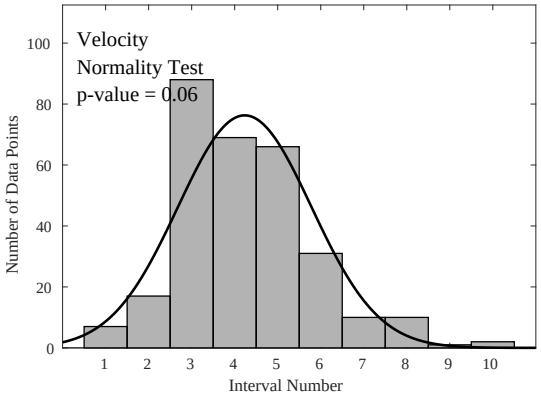
Velocity
Normality Test
p-value = 0.06
Number of Data Points
Interval Number

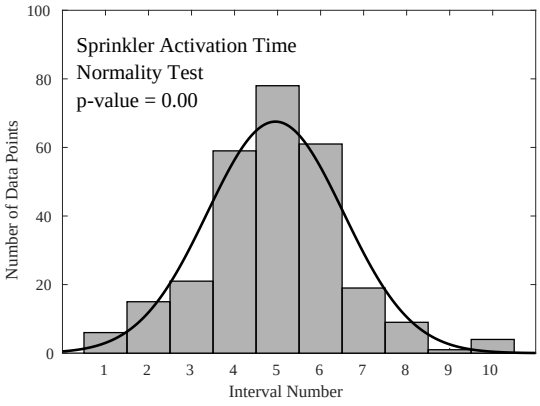
Sprinkler Activation Time
Normality Test
p-value = 0.00
Number of Data Points
Interval Number

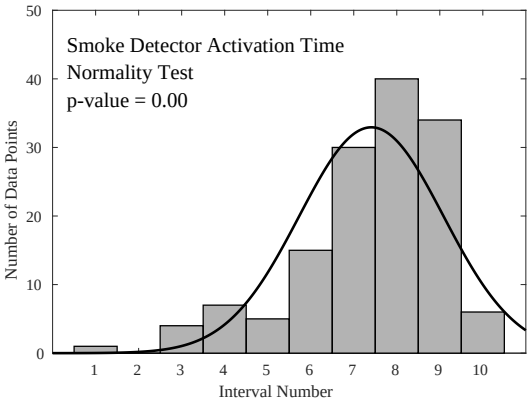
Smoke Detector Activation Time
Normality Test
p-value = 0.00
Number of Data Points
Interval Number

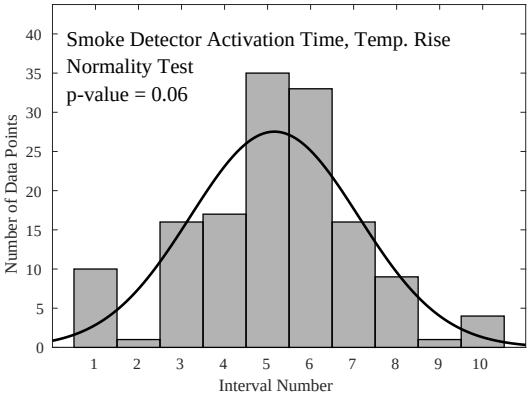
Smoke Detector Activation Time, Temp. Rise
Normality Test
p-value = 0.06
Number of Data Points
Interval Number

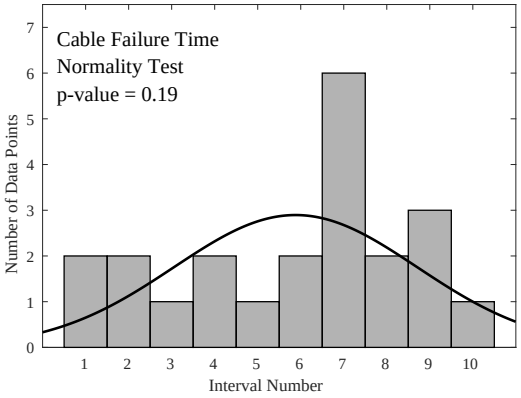
Cable Failure Time
Normality Test
p-value = 0.19
Number of Data Points
Interval Number

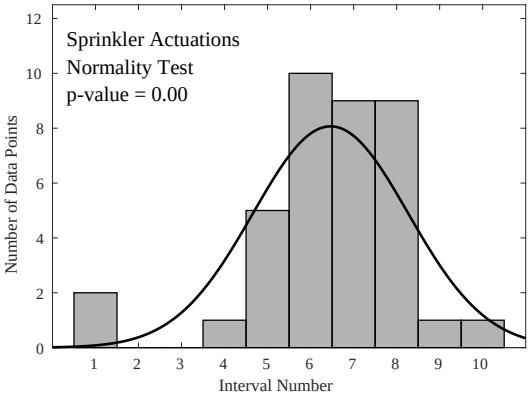
Sprinkler Actuations
Normality Test
p-value = 0.00
Number of Data Points
Interval Number

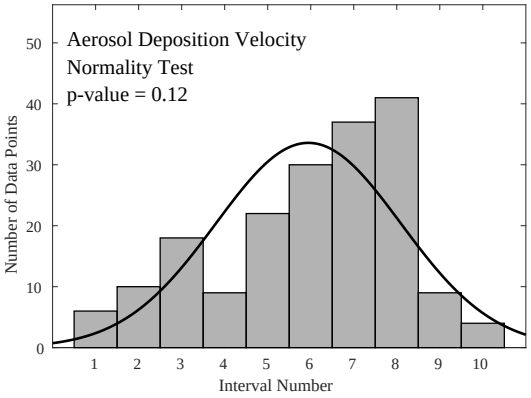
Aerosol Deposition Velocity
Normality Test
p-value = 0.12
Number of Data Points
Interval Number

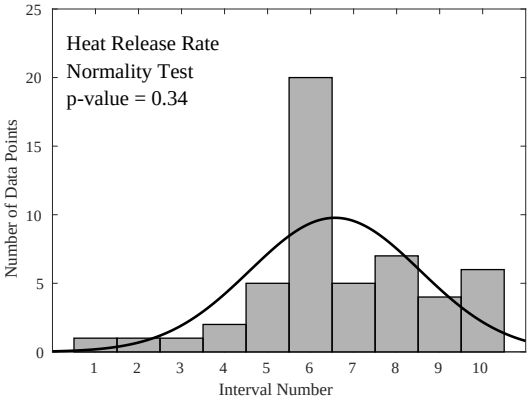
Heat Release Rate
Normality Test
p-value = 0.34
Number of Data Points
Interval Number

16.3 Summary of FDS Validation Git Statistics

Table 16.2 shows the Git repository statistics for all of the validation datasets. For each dataset, the corresponding last changed date and Git revision string are shown. This indicates the Git revision string and date for which the most recent validation results for a given dataset were committed to the repository.

Table 16.2: Validation Git statistics for all data sets

Dataset	FDS Revision Date	FDS Revision String
NIST_NRC_Parallel_Panels	Dec 22, 2021	FDS6.7.7-352-g88147fb51-master
NIST_Pool_Fires	Dec 22, 2021	FDS6.7.7-352-g88147fb51-master
SWJTU_Tunnels	Dec 22, 2021	FDS6.7.7-352-g88147fb51-master
UMD_Line_Burner	Dec 22, 2021	FDS6.7.7-352-g88147fb51-master
Vettori_Flat_Ceiling	Dec 22, 2021	FDS6.7.7-352-g88147fb51-master
Vettori_Sloped_Ceiling	Dec 22, 2021	FDS6.7.7-352-g88147fb51-master
VTT_Sprays	Dec 22, 2021	FDS6.7.7-352-g88147fb51-master
Waterloo_Methanol	Dec 22, 2021	FDS6.7.7-352-g88147fb51-master
WTC	Dec 22, 2021	FDS6.7.7-352-g88147fb51-master
Casara_Arts_Ribbed_Channel	Jan 6, 2022	FDS6.7.7-401-g748d75ebc-master
UWO_Wind_Tunnel	Jan 13, 2022	FDS6.7.7-491-g21f9e3625-master
USFS_Catchpole	Jan 20, 2022	FDS6.7.7-509-ga77f68dfe-master
MPI_Scaling_Tests	Feb 4, 2022	FDS6.7.7-609-g3c7638d7d-master
Pool_Fires	Apr 21, 2022	FDS6.7.7-925-g1ed329484-master
FAA_Cargo_Compartments	Apr 27, 2022	FDS6.7.7-993-g9eb362ad9-master
Arup_Tunnel	May 13, 2022	FDS6.7.7-1152-g310a92573-master
ATF_Corridors	May 13, 2022	FDS6.7.7-1152-g310a92573-master
Atmospheric_Dispersion	May 13, 2022	FDS6.7.7-1152-g310a92573-master
Backward_Facing_Step	May 13, 2022	FDS6.7.7-1152-g310a92573-master
Beyler_Hood	May 13, 2022	FDS6.7.7-1152-g310a92573-master
BGC_GRI_LNG_Fires	May 13, 2022	FDS6.7.7-1152-g310a92573-master
Bittern_Sprinkler_Experiments	May 13, 2022	FDS6.7.7-1152-g310a92573-master
Bouchair_Solar_Chimney	May 13, 2022	FDS6.7.7-1152-g310a92573-master
BRE_Spray	May 13, 2022	FDS6.7.7-1152-g310a92573-master
Bryant_Doorway	May 13, 2022	FDS6.7.7-1152-g310a92573-master
CAROLFIRE	May 13, 2022	FDS6.7.7-1152-g310a92573-master
CSTB_Tunnel	May 13, 2022	FDS6.7.7-1152-g310a92573-master
Cup_Burner	May 13, 2022	FDS6.7.7-1152-g310a92573-master
DelCo_Trainers	May 13, 2022	FDS6.7.7-1152-g310a92573-master
Droplet_Evaporation	May 13, 2022	FDS6.7.7-1152-g310a92573-master
Edinburgh_Vegetation_Drag	May 13, 2022	FDS6.7.7-1152-g310a92573-master
FAA_Polymers	May 13, 2022	FDS6.7.7-1152-g310a92573-master
Fleury_Heat_Flux	May 13, 2022	FDS6.7.7-1152-g310a92573-master
FM_FPRF_Datacenter	May 13, 2022	FDS6.7.7-1152-g310a92573-master
FM_Parallel_Panels	May 13, 2022	FDS6.7.7-1152-g310a92573-master
FM_SNL	May 13, 2022	FDS6.7.7-1152-g310a92573-master
FM_Vertical_Wall_Flames	May 13, 2022	FDS6.7.7-1152-g310a92573-master
Hamins_Gas_Burners	May 13, 2022	FDS6.7.7-1152-g310a92573-master

Dataset	FDS Revision Date	FDS Revision String
Harrison_Spill_Plumes	May 13, 2022	FDS6.7.7-1152-g310a92573-master
Heated_Channel_Flow	May 13, 2022	FDS6.7.7-1152-g310a92573-master
Heskestad_Flame_Height	May 13, 2022	FDS6.7.7-1152-g310a92573-master
Insulation_Materials	May 13, 2022	FDS6.7.7-1152-g310a92573-master
Juelich_SETCOM	May 13, 2022	FDS6.7.7-1152-g310a92573-master
LEMTA_Spray	May 13, 2022	FDS6.7.7-1152-g310a92573-master
LLNL_Enclosure	May 13, 2022	FDS6.7.7-1152-g310a92573-master
LNG_Dispersion	May 13, 2022	FDS6.7.7-1152-g310a92573-master
McCaffrey_Plume	May 13, 2022	FDS6.7.7-1152-g310a92573-master
Montoir_LNG_Fires	May 13, 2022	FDS6.7.7-1152-g310a92573-master
Moody_Chart	May 13, 2022	FDS6.7.7-1152-g310a92573-master
NBS_Multi-Room	May 13, 2022	FDS6.7.7-1152-g310a92573-master
NIST_Composite_Beam	May 13, 2022	FDS6.7.7-1152-g310a92573-master
NIST_Deposition_Gauge	May 13, 2022	FDS6.7.7-1152-g310a92573-master
NIST_E119_Compartment	May 13, 2022	FDS6.7.7-1152-g310a92573-master
NIST_FSE_2008	May 13, 2022	FDS6.7.7-1152-g310a92573-master
NIST_He_2009	May 13, 2022	FDS6.7.7-1152-g310a92573-master
NIST_NRC_Corner_Effects	May 13, 2022	FDS6.7.7-1152-g310a92573-master
NIST_NRC	May 13, 2022	FDS6.7.7-1152-g310a92573-master
NIST_NRC_OLIVE-Fire	May 13, 2022	FDS6.7.7-1152-g310a92573-master
NIST_RSE_1994	May 13, 2022	FDS6.7.7-1152-g310a92573-master
NIST_RSE_2007	May 13, 2022	FDS6.7.7-1152-g310a92573-master
NIST_Smoke_Alarms	May 13, 2022	FDS6.7.7-1152-g310a92573-master
NIST_Vent_Study	May 13, 2022	FDS6.7.7-1152-g310a92573-master
NRCC_Facade	May 13, 2022	FDS6.7.7-1152-g310a92573-master
NRCC_Smoke_Tower	May 13, 2022	FDS6.7.7-1152-g310a92573-master
NRL_HAI	May 13, 2022	FDS6.7.7-1152-g310a92573-master
Phoenix_LNG_Fires	May 13, 2022	FDS6.7.7-1152-g310a92573-master
PRISME	May 13, 2022	FDS6.7.7-1152-g310a92573-master
Ranz_Marshall	May 13, 2022	FDS6.7.7-1152-g310a92573-master
Restivo_Experiment	May 13, 2022	FDS6.7.7-1152-g310a92573-master
Sandia_Methane_Burner	May 13, 2022	FDS6.7.7-1152-g310a92573-master
Sandia_Plumes	May 13, 2022	FDS6.7.7-1152-g310a92573-master
Shell_LNG_Fireballs	May 13, 2022	FDS6.7.7-1152-g310a92573-master
Sippola_Aerosol_Deposition	May 13, 2022	FDS6.7.7-1152-g310a92573-master
Smyth_Slot_Burner	May 13, 2022	FDS6.7.7-1152-g310a92573-master
SP_AST	May 13, 2022	FDS6.7.7-1152-g310a92573-master
SP_Wood_Cribs	May 13, 2022	FDS6.7.7-1152-g310a92573-master
Steckler_Compartment	May 13, 2022	FDS6.7.7-1152-g310a92573-master
Turbulent_Jet	May 13, 2022	FDS6.7.7-1152-g310a92573-master
UL_NFPRF	May 13, 2022	FDS6.7.7-1152-g310a92573-master
UL_NIJ_Houses	May 13, 2022	FDS6.7.7-1152-g310a92573-master
UL_NIST_Vents	May 13, 2022	FDS6.7.7-1152-g310a92573-master
Ulster_SBI	May 13, 2022	FDS6.7.7-1152-g310a92573-master
UMD_Polymers	May 13, 2022	FDS6.7.7-1152-g310a92573-master

Dataset	FDS Revision Date	FDS Revision String
USCG_HAI	May 13, 2022	FDS6.7.7-1152-g310a92573-master
USN_Hangars	May 13, 2022	FDS6.7.7-1152-g310a92573-master
VTT	May 13, 2022	FDS6.7.7-1152-g310a92573-master
Wu_Bakar_Tunnels	May 13, 2022	FDS6.7.7-1152-g310a92573-master
Crown_Fires	Jun 2, 2022	FDS6.7.8-17-g370a845d4-master
CSIRO_Grassland_Fires	Jun 2, 2022	FDS6.7.8-17-g370a845d4-master
NIST_Douglas_Firs	Jun 2, 2022	FDS6.7.8-17-g370a845d4-master
USFS_Corsica	Jun 2, 2022	FDS6.7.8-17-g370a845d4-master
Loughborough_Jet_Fires	Jun 16, 2022	FDS6.7.8-88-g922085eba-master
Purdue_Flames	Jun 16, 2022	FDS6.7.8-88-g922085eba-master
FM_Burner	Jun 22, 2022	FDS6.7.8-113-gb81287c1e-master

Bibliography

[1] K. McGrattan, S. Hostikka, R. McDermott, J. Floyd, C. Weinschenk, and K. Overholt. *Fire Dynamics Simulator, User's Guide*. National Institute of Standards and Technology, Gaithersburg, Maryland, USA, and VTT Technical Research Centre of Finland, Espoo, Finland, sixth edition, September 2013. vii, 30, 132, 133, 1027

[2] American Society for Testing and Materials, West Conshohocken, Pennsylvania. *ASTM E1355-12, Standard Guide for Evaluating the Predictive Capabilities of Deterministic Fire Models*, 2012. vii, 1

[3] R.G. Rehm and H.R. Baum. The Equations of Motion for Thermally Driven, Buoyant Flows. *Journal of Research of the NBS*, 83:297–308, 1978. 6

[4] H.R. Baum, R.G. Rehm, P.D. Barnett, and D.M. Corley. Finite Difference Calculations of Buoyant Convection in an Enclosure, Part I: The Basic Algorithm. *SIAM Journal of Scientific and Statistical Computing*, 4(1):117–135, March 1983. 6

[5] R.G. Rehm, P.D. Barnett, H.R. Baum, and D.M. Corley. Finite Difference Calculations of Buoyant Convection in an Enclosure: Verification of the Nonlinear Algorithm. *Applied Numerical Mathematics*, 1:515–529, 1985. 6

[6] R.G. Rehm, H.R. Baum, D.W. Lozier, H. Tang, and J. Sims. Buoyant Convection in an Inclined Enclosure. In *Fire Safety Science – Proceedings of the Third International Symposium*, pages 313–323. International Association for Fire Safety Science, 1991. 6

[7] H.R. Baum, O.A. Ezekoye, K.B. McGrattan, and R.G. Rehm. Mathematical Modeling and Computer Simulation of Fire Phenomenon. *Theoretical and Computational Fluid Dynamics*, 6:125–139, 1994. 6

[8] K.B. McGrattan, R.G. Rehm, and H.R. Baum. Fire-Driven Flows in Enclosures. *Journal of Computational Physics*, 110(2):285–291, 1994. 6

[9] R.G. Rehm, K.B. McGrattan, H.R. Baum, and K.W. Cassel. Transport by Gravity Currents in Building Fires. In *Fire Safety Science – Proceedings of the Fifth International Symposium*, pages 391–402. International Association for Fire Safety Science, 1997. 6

[10] H.R. Baum, K.B. McGrattan, and R.G. Rehm. Three Dimensional Simulations of Fire Plume Dynamics. In *Fire Safety Science – Proceedings of the Fifth International Symposium*, pages 511–522. International Association for Fire Safety Science, 1997. 6

[11] H.R. Baum, K.B. McGrattan, and R.G. Rehm. Large Eddy Simulations of Smoke Movement in Three Dimensions. In *Proceedings of the Seventh International Interflam Conference*, pages 189–198. Interscience Communications, London, 1996. 6

[12] H.R. Baum and B.J. McCaffrey. Fire Induced Flow Field – Theory and Experiment. In *Fire Safety Science – Proceedings of the Second International Symposium*, pages 129–148. International Association for Fire Safety Science, 1989. 6

[13] H.R. Baum, K.B. McGrattan, and R.G. Rehm. Three Dimensional Simulations of Fire Plume Dynamics. *Journal of the Heat Transfer Society of Japan*, 35(139):45–52, 1997. 6

[14] J.M. Clement and C.M. Fleischmann. Experimental Verification of the Fire Dynamics Simulator Hydrodynamic Model. In *Fire Safety Science – Proceedings of the Seventh International Symposium*, pages 839–862. International Association for Fire Safety Science, 2002. 6

[15] K.B. McGrattan, H.R. Baum, and R.G. Rehm. Large Eddy Simulations of Smoke Movement. *Fire Safety Journal*, 30:161–178, 1998. 6

[16] W. Mell, K.B. McGrattan, and H. Baum. Numerical Simulation of Combustion in Fire Plumes. In *Twenty-Sixth Symposium (International) on Combustion*, pages 1523–1530. Combustion Institute, Pittsburgh, Pennsylvania, 1996. 6

[17] T. Cleary, M. Anderson, J. Averill, and W. Grosshandler. Evaluating Multi-Sensor Fire Detectors in the Fire Emulator/Detector Evaluator. In *Proceedings of the Eighth International Interflam Conference*, pages 453–464. Interscience Communications, June 1999. 6

[18] W. Davis, K Notarianni, and K. McGrattan. Comparison of Fire Model Predictions with Experiments Conducted in a Hangar with a 15 Meter Ceiling. NISTIR 5927, National Institute of Standards and Technology, Gaithersburg, Maryland, December 1996. 6

[19] S.J. Emmerich and K.B. McGrattan. Application of a Large Eddy Simulation Model to Study Room Airflow. *ASHRAE Transactions*, 104(1):1–9, 1998. 6, 103

[20] S.J. Emmerich. Use of Computational Fluid Dynamics to Analyze Indoor Air Quality Issues. NISTIR 5997, National Institute of Standards and Technology, Gaithersburg, Maryland, April 1997. 6, 103

[21] W.K. Chow and R. Yin. Discussion on Two Plume Formulae with Computational Fluid Dynamics. *Journal of Fire Sciences*, 20:179–201, May 2002. 7

[22] F. Battaglia, K. McGrattan, R. Rehm, and H. Baum. Simulating Fire Whirls. *Combustion Theory and Modeling*, 4:123–138, 2000. 7

[23] K.M. Liang, T. Ma, J.G. Quintiere, and D. Rouson. Application of CFD Modeling to Room Fire Growth on Walls. NIST GCR 03-849, National Institute of Standards and Technology, Gaithersburg, Maryland, April 2003. 7, 10

[24] T. Ma and J. Quintiere. Numerical Simulation of Axi-Symmetric Fire Plumes: Accuracy and Limitations. *Fire Safety Journal*, 38:467–492, 2003. 7, 10

[25] G. Heskestad. *SFPE Handbook of Fire Protection Engineering*, chapter Fire Plumes, Flame Height and Air Entrainment. Springer, New York, 5th edition, 2016. 7, 48, 301, 303

[26] C. Gutiérrez-Montes, E. Sanmiguel-Rojas, A. Viedma, and G. Rein. Experimental data and numerical modelling of 1.3 and 2.3 MW fires in a 20 m cubic atrium. *Building and Environment*, 44:1827–1839, 2009. http://hdl.handle.net/1842/2761. 7

[27] M. Hurley and A. Munguia. Analysis of FDS Thermal Detector Response Prediction Capability. NIST GCR 09-921, National Institute of Standards and Technology, Gaithersburg, Maryland, 2009. 7

[28] M. Hurley and A. Munguia. Analysis of FDS Thermal Detector Response Prediction Capability. *J. Fire Protection Engineering*, 20, 2009. 7

[29] Y. Xin. Baroclinic Effects on Fire Flow Field. In *Proceedings of the Fourth Joint Meeting of the U.S. Sections of the Combustion Institute*. Combustion Institute, Pittsburgh, Pennsylvania, March 2005. 8

[30] Y. Xin, J.P. Gore, K.B. McGrattan, R.G. Rehm, and H.R. Baum. Fire dynamics simulation of a turbulent buoyant flame using a mixture-fraction-based combustion model. *Combustion and Flame*, 141:329–335, 2005. 8, 101, 323, 324

[31] Y. Xin, J.P. Gore, K.B. McGrattan, R.G. Rehm, and H.R. Baum. Large Eddy Simulation of Buoyant Turbulent Pool Fires. In *Twenty-Ninth Symposium (International) on Combustion*, pages 259–266. Combustion Institute, Pittsburgh, Pennsylvania, 2002. 8

[32] X.C. Zhou and J.P. Gore. Experimental estimation of thermal expansion and vorticity distribution in a buoyant diffusion flame. In *Twenty-Seventh Symposium (International) on Combustion*. Combustion Institute, Pittsburgh, Pennsylvania, 2001. 8, 101, 323, 325

[33] Y. Xin, J.P. Gore, K.B. McGrattan, R.G. Rehm, and H.R. Baum. Large Eddy Simulation of Buoyant Turbulent Pool Fires. In *Proceedings of the 2002 Spring Technical Meeting, Central States Section*. Combustion Institute, Pittsburgh, Pennsylvania, April 2002. 8

[34] Y. Xin and J.P. Gore. Two-dimensional soot distributions in buoyant turbulent fires. In *Thirtieth Symposium (International) on Combustion*. Combustion Institute, Pittsburgh, Pennsylvania, 2005. 8

[35] Y. Biswas, Y. Zheng, C.H. Kim, and J.P. Gore. Stochastic time series analysis of pulsating buoyant pool fires. In *Thirty First Symposium (International) on Combustion*. Combustion Institute, Pittsburgh, Pennsylvania, 2007. 8

[36] S. Hostikka, K.B. McGrattan, and A. Hamins. Numerical Modeling of Pool Fires using Large Eddy Simulation and Finite Volume Method for Radiation. In *Fire Safety Science – Proceedings of the Seventh International Symposium*, pages 383–394. International Association for Fire Safety Science, 2002. 8, 46

[37] J. Hietaniemi, S. Hostikka, and J. Vaari. FDS Simulation of Fire Spread – Comparison of Model Results with Experimental Data. VTT Working Papers 4, VTT Building and Transport, Espoo, Finland, 2004. 8, 10

[38] A. Musser, K. B. McGrattan, and J. Palmer. Evaluation of a Fast, Simplified Computational Fluid Dynamics Model for Solving Room Airflow Problems. NISTIR 6760, National Institute of Standards and Technology, Gaithersburg, Maryland, June 2001. 8, 103, 426

[39] X. Yuan, Q. Chen, L.R. Glicksman, Y. Hu, and X. Yang. Measurements and Computations of Room Airflow with Displacement Ventilation. Technical Report RP-949, American Society of Heating, Refrigerating, Air-Conditioning Engineers, 1999. 8

[40] A. Musser and L. Tan. Control of Diesel Exhaust Fumes in Enclosed Locomotive Facilities. Technical Report RP-1191, American Society of Heating, Refrigerating, Air-Conditioning Engineers, 2003. 8

[41] K. Mniszewski. The Use of FDS for Estimation of Flammable Gas/Vapor Concentrations. In *Proceedings of the 3rd Technical Symposium on Computer Applications in Fire Protection Engineering*, pages 143–155. Society for Fire Protection Engineers, Bethesda, Maryland, September 2001. 8

[42] S. Kerber and W. Walton. Characterizing Positive Pressure Ventilation using Computational Fluid Dynamics. NISTIR 7065, National Institute of Standards and Technology, Gaithersburg, Maryland, February 2003. 8

[43] R. Rehm, K. McGrattan, H. Baum, and E. Simiu. An Efficient Large Eddy Simulation Algorithm for Computational Wind Engineering: Application to Surface Pressure Computations on a Single Building. NISTIR 6371, National Institute of Standards and Technology, August 1999. 9

[44] R.G. Rehm, K.B. McGrattan, and H.R. Baum. Large Eddy Simulation of Flow over a Wooded Building Complex. *Wind & Structures*, 5(2):291–300, 2002. 9

[45] H.Y. Wang and P. Joulain. Numerical Simulation of Wind-Aided Turbulent Fires in a Ventilated Model Tunnel. In *Fire Safety Science – Proceedings of the Seventh International Symposium*, pages 161–172. International Association for Fire Safety Science, 2002. 9

[46] B.F. Magnussen and B.H. Hjertager. On Mathematical Modeling of Turbulent Combustion with Special Emphasis on Soot Formation and Combustion. In *Proceedings of the Sixteenth Symposium (International) on Combustion*, pages 719–729. Combustion Institute, Pittsburgh, Pennsylvania, 1977. 9

[47] C.H. Chang and R.N. Meroney. Concentration and flow distributions in urban street canyons: wind tunnel and computational data. *Journal of Wind Engineering and Industrial Aerodynamics*, 91:1141–1154, 2003. 9

[48] K. Moon, J. M. Hwang, B. G. Kim, C. Lee, and J. Choi. Large-eddy simulation of turbulent flow and dispersion over a complex urban street canyon. *Environmental Fluid Mechanics (on-line)*, January 2014. 9

[49] H. Le, P. Moin, and J. Kim. Direct numerical simulation of turbulent flow over a backward-facing step. *Journal of Fluid Mechanics*, 330:349–374, 1997. 9

[50] S. Jovic and D. M. Driver. Backward-facing step measurements at low Reynolds number, Re_h=5000. *NASA Technical Memorandum*, 108807, February 1994. 9, 19, 412

[51] M. Sarwar, K. A. M. Moinuddin, and G. R. Thorpe. Large eddy simulation of flow over a backward facing step using Fire Dynamics Simulator (FDS). *Fourteenth Asian Congress of Fluid Mechanics*, pages 469–474, October 2013. 9

[52] K.B. McGrattan, H.R. Baum, and R.G. Rehm. Numerical Simulation of Smoke Plumes from Large Oil Fires. *Atmospheric Environment*, 30(24):4125–4136, 1996. 9

[53] T. Yamada. Smoke Plume Trajectory from In-Situ Burning of Crude Oil in Tomakomai. Technical report, National Research Institute of Fire and Disaster, Japan, November 1998. 9

[54] Y. Mouilleau and A. Champassith. CFD simulations of atmospheric gas dispersion using the Fire Dynamics Simulator (FDS). *Journal of Loss Prevention in the Process Industries*, 22:316–323, 2009. published by Elsevier. 9

[55] J. Floyd. Comparison of CFAST and FDS for Fire Simulation with the HDR T51 and T52 Tests. NISTIR 6866, National Institute of Standards and Technology, Gaithersburg, Maryland, March 2002. 10

[56] J.E. Floyd, K.B. McGrattan, S. Hostikka, and H.R. Baum. CFD Fire Simulation Using Mixture Fraction Combustion and Finite Volume Radiative Heat Transfer. *Journal of Fire Protection Engineering*, 13:11–26, February 2003. 10, 14

[57] A. Kashef, N. Benichou, G.D. Lougheed, and C. McCartney. A Computational and Experimental Study of Fire Growth and Smoke Movement in Large Spaces. Technical Report NRCC-45201, National Research Council Canada, 2002. 10

[58] K.B. McGrattan, T. Kashiwagi, H.R. Baum, and S.L. Olson. Effects of Ignition and Wind on the Transition to Flame Spread in a Microgravity Environment. *Combustion and Flame*, 106:377–391, 1996. 10

[59] T. Kashiwagi, K.B. McGrattan, S.L. Olson, O. Fujita, M. Kikuchi, and K. Ito. Effects of Slow Wind on Localized Radiative Ignition and Transition to Flame Spread in Microgravity. In *Twenty-Sixth Symposium (International) on Combustion*, pages 1345–1352. Combustion Institute, Pittsburgh, Pennsylvania, 1996. 10

[60] W. Mell and T. Kashiwagi. Dimensional Effects on the Transition from Ignition to Flame Spread in Microgravity. In *Twenty-Seventh Symposium (International) on Combustion*, pages 2635–2641. Combustion Institute, Pittsburgh, Pennsylvania, 1998. 10

[61] W. Mell, S.L. Olson, and T. Kashiwagi. Flame Spread Along Free Edges of Thermally-Thin Samples in Microgravity. In *Twenty-Eighth Symposium (International) on Combustion*, pages 2843–2849. Combustion Institute, Pittsburgh, Pennsylvania, 2000. 10

[62] K. Prasad, Y. Nakamura, S.L. Olson, O. Fujita, K. Nishizawa, K. Ito, and T. Kashiwagi. Effect of Wind Velocity on Flame Spread in Microgravity. In *Twenty-Ninth Symposium (International) on Combustion*, pages 2553–2560. Combustion Institute, Pittsburgh, Pennsylvania, 2002. 10

[63] Y. Nakamura, T. Kashiwagi, K.B. McGrattan, and H.R. Baum. Enclosure Effects on Flame Spread over Solid Fuels in Microgravity. *Combustion and Flame*, 130:307–321, 2002. 10

[64] W.E. Mell, K.B. McGrattan, and H.R. Baum. g-Jitter Effects on Spherical Diffusion Flames. *Microgravity Science and Technology*, 15(4):12–30, 2004. 10

[65] S. Hostikka and K.B. McGrattan. Large Eddy Simulations of Wood Combustion. In *Proceedings of the Ninth International Interflam Conference*, pages 755–762. Interscience Communications, London, 2001. 10

[66] S.J. Ritchie, K.D. Steckler, A. Hamins, T.G. Cleary, J.C. Yang, and T. Kashiwagi. The Effect of Sample Size on the Heat Release Rate of Charring Materials. In *Fire Safety Science - Proceedings of the 5th International Symposium*, pages 177–188. International Association For Fire Safety Science, 1997. 10, 70, 112

[67] J.W. Kwon, N.A. Dembsey, and C.W. Lautenberger. Evaluation of FDS V.4: Upward Flame Spread. *Fire Technology*, 43:255–284, 2007. 10

[68] J. Mangs and S. Hostikka. Experiments and Numerical Simulations of Vertical Flame Spread on Charring Materials at Different Ambient Temperatures. In *Fire Safety Science 10 – Proceedings of the 10th International Symposium*, pages 499–512, University of Maryland, College Park, Maryland, USA, 2011. 11

[69] A. Hamins, A. Maranghides, K.B. McGrattan, E. Johnsson, T. Ohlemiller, M. Donnelly, J. Yang, G. Mulholland, K. Prasad, S. Kukuck, R. Anleitner, and T. McAllister. Federal Building and Fire Safety Investigation of the World Trade Center Disaster: Experiments and Modeling of Structural Steel Elements Exposed to Fire. NIST NCSTAR 1-5B, National Institute of Standards and Technology, Gaithersburg, Maryland, September 2005. 11, 141, 449

[70] A. Hamins, A. Maranghides, K.B. McGrattan, Ohlemiller, and R. Anletiner. Federal Building and Fire Safety Investigation of the World Trade Center Disaster: Experiments and Modeling of Multiple Workstations Burning in a Compartment. NIST NCSTAR 1-5E, National Institute of Standards and Technology, Gaithersburg, Maryland, September 2005. 11

[71] K. McGrattan, C. Bouldin, and G. Forney. Federal Building and Fire Safety Investigation of the World Trade Center Disaster: Computer Simulation of the Fires in the WTC Towers. NIST NCSTAR 1-5F, National Institute of Standards and Technology, Gaithersburg, Maryland, September 2005. 11, 15

[72] G. Rein, C. Abecassis Empis, and R. Carvel, editors. *The Dalmarnock Fire Tests: Experiments and Modelling*. University of Edinburgh, 2007. 11

[73] G. Rein, J.L. Torero, W. Jahn, J. Stern-Gottfried, N.L. Ryder, S. Desanghere, M. Läzaro, F. Mowrer, A. Coles, D. Joyeux, D. Alvear, J.A. Capote, A. Jowsey, C. Abecassis-Empis, and P. Reszka. Round-Robin Study of a priori Modelling Predictions of The Dalmarnock Fire Test One. *Fire Safety Journal*, 44(4):590–602, 2009. http://hdl.handle.net/1842/2704. 11

[74] W. Jahn, G. Rein, and J.L. Torero. The Effect of Model Parameters on the Simulation of Fire Dynamics. In *Proceedings of the Ninth Symposium on Fire Safety Science*, Karlsruhe, Germany, September 2008. http://hdl.handle.net/1842/2696. 11

[75] B.M. Storm and M.R. Pantesjö. The use of simulation in fire investigation. Bachelors thesis, Stord/Haugesund University College, Norway, 2009. 11

[76] V. Drean, R. Schillinger, H. Leborgne, G. Auguin, and E. Guillaume. Numerical Simulation of Fire Exposed Façades Using LEPIR II Testing Facility. *Fire Technology*, March 2018. https:doi.org/10.1007/s10694-018-0718-y. 11

[77] R. Vettori. Effect of an Obstructed Ceiling on the Activation Time of a Residential Sprinkler. NISTIR 6253, National Institute of Standards and Technology, Gaithersburg, Maryland, November 1998. 12, 134, 158

[78] R. Vettori. Effect of a Beamed, Sloped, and Sloped Beamed Ceilings on the Activation Time of a Residential Sprinkler. NISTIR 7079, National Institute of Standards and Technology, Gaithersburg, Maryland, December 2003. 12, 137

[79] K.B. McGrattan, A. Hamins, and D. Stroup. Sprinkler, Smoke & Heat Vent, Draft Curtain Interaction — Large Scale Experiments and Model Development. NISTIR 6196-1, National Institute of Standards and Technology, Gaithersburg, Maryland, September 1998. 12, 118

[80] A. Hamins and K.B. McGrattan. Reduced-Scale Experiments to Characterize the Suppression of Rack Storage Commodity Fires. NISTIR 6439, National Institute of Standards and Technology, Gaithersburg, Maryland, 1999. 12

[81] A. Hamins and K.B. McGrattan. Reduced-Scale Experiments on the Water Suppression of a Rack-Storage Commodity Fire for Calibration of a CFD Fire Model. In *Fire Safety Science – Proceedings of the Seventh International Symposium*, pages 457–468. International Association for Fire Safety Science, 2002. 12

[82] S. Olenick, M. Klassen, and R.J. Roby. Validation Study for FDS for a High Rack Storage Fire Involving Pool Chemicals. In *Proceedings of the 3rd Technical Symposium on Computer Applications in Fire Protection Engineering*. Society of Fire Protection Engineers, Bethesda, Maryland, September 2001. 12

[83] S.C. Kim and H.S. Ryou. An Experimental and Numerical Study on Fire Suppression using a Water Mist in an Enclosure. *Building and Environment*, 38:1309–1316, 2003. 12

[84] S.C. Kim and H.S. Ryou. The Effects of Water Mist on the Compartment Fire. *International Journal of Air-Conditioning and Refrigeration*, 12(1):30–36, 2004. 12

[85] B.P. Hume. Water Mist Suppression in Conjunction with Displacement Ventilation. Master's thesis, University of Canterbury, Christchurch, New Zealand, February 2003. Fire Engineering Research Report 03/4. 12

[86] S. Hostikka and K.B. McGrattan. Numerical modeling of radiative heat transfer in water sprays. *Fire Safety Journal*, 41:76–86, 2006. 12

[87] N. O'Grady and V. Novozhilov. Large Eddy Simulation of Sprinkler Interaction with a Fire Ceiling Jet. *Combustion Science and Technology*, 181(7):984–1006, 2009. 12

[88] H. Ingason and S. Olsson. Interaction between Sprinklers and Fire Vents. Technical report, Swedish National Testing and Research Institute (SP), 1992. SP Report 1992:11. 12

[89] B. Xiao. Comparison of Numerical and Experimental Results of Fire Induced Doorway Flows. *Fire Technology*, 48:595–614, 2012. 13

[90] P. Friday and F. W. Mowrer. Comparison of FDS Model Predictions with FM/SNL Fire Test Data. NIST GCR 01-810, National Institute of Standards and Technology, Gaithersburg, Maryland, April 2001. 13

[91] W. Zhang, A. Hamer, M. Klassen, D. Carpenter, and R. Roby. Turbulence Statistics in a Fire Room Model by Large Eddy Simulation. *Fire Safety Journal*, 37:721–752, 2002. 13

[92] S. Cochard. Validation of Fire Dynamics Simulator (Version 2.0) Freeware. *Tunnel Management International Journal*, 6(4), December 2003. 13

[93] K. B. McGrattan and A. Hamins. Numerical Simulation of the Howard Street Tunnel Fire, Baltimore, Maryland, July 2001. NISTIR 6902, National Institute of Standards and Technology, Gaithersburg, Maryland, January 2003. Joint Publication of NIST and the US Nuclear Regulatory Commission (NUREG/CR-6793). 13

[94] A. Piergiorgio, D. Giuseppe, F. Dino, G. Zappellini, and A. Ferrari. CFD Simulations of a Truck Fire in the Underground Gran Sasso National Laboratory. In *Proceedings of the 5th Italian Conference on Chemical and Process Engineering*, volume 5 of *AIDIC Conference Series*. Associazione Italiana Di Ingegneria Chimica (AIDIC), Elsevier, May 2002. Papers presented at ICeaP-5, Florence, Italy, May 20-23, 2001. 13

[95] J.C. Edwards, R.A. Franks, G.F. Friel, and L. Yuan. Experimental and Modeling Investigation of the Effect of Ventilation on Smoke Rollback in a Mine Entry. In *Proceedings of the SME Annual Meeting*, pages 1–6. Society for Mining, Metallurgy and Exploration, 2005. 13

[96] C.C. Hwang and J.C. Edwards. The critical ventilation velocity in tunnel fires – a computer simulation. *Fire Safety Journal*, 40:213–244, 2005. 13

[97] J.C. Edwards and C.C. Hwang. CFD Modeling of Fire Spread Along Combustibles in a Mine Entry. In *Proceedings of the SME Annual Meeting*, pages 1–5. Society for Mining, Metallurgy and Exploration, 2006. 13

[98] M. Bilson, A. Purchase, and C. Stacey. Deluge System Operating Effectiveness in Road Tunnels and Impacts on Operating Policy. In *Proceedings 13th Australian Tunnelling Conference, Melbourne, Victoria, Australia*, May 2008. The Australasian Institute of Mining and Metallurgy. 13

[99] K.J. Harris. Water Application Rates for Fixed Fire Fighting Systems in Road Tunnels. In *Proceedings of the Fourth International Symposium on Tunnel Safety and Security*, pages 351–362, 2010. 13

[100] M. Arvidson. Large-Scale Water Spray and Water Mist Fire Suppression System Tests. In *Proceedings of the Fourth International Symposium on Tunnel Safety and Security*, pages 283–296, 2010. 13

[101] J. Trelles and J.R. Mawhinney. CFD Investigation of Large Scale Pallet Stack Fires in Tunnels Protected by Water Mist Systems. *Journal of Fire Protection Engineering*, 20(3):149–198, August 2010. 13

[102] J.R. Mawhinney and J. Trelles. Testing Water Mist Systems Against Large Fires in Tunnels: Integrating Test Data with CFD Simulations. *Fire Technology*, 48:565–594, 2012. 13

[103] V. D'Souza, J.A. Sutula, S.M. Olenick, W. Zhang, and R.J. Roby. Use of Fire Dynamics Simulator to Predict Smoke Detector Activation. In *Proceedings of the 2001 Fall Technical Meeting, Eastern States Section*, pages 175–178. Combustion Institute, Pittsburgh, Pennsylvania, December 2001. 14

[104] R.J. Roby, S.J. Olenick, W. Zhang, D.J. Carpenter, M.S. Klassen, and J.L. Torero. A Smoke Detector Algorithm for Large Eddy Simulation Modeling. NIST GCR 07-911, National Institute of Standards and Technology, Gaithersburg, Maryland, 2007. 14

[105] W. Zhang, S.M. Olenick, M.S. Klassen, D.J. Carpenter, R.J. Roby, and J.L. Torero. A smoke detector activation algorithm for large eddy simulation fire modeling. *Fire Safety Journal*, 43:96–107, 2008. 14

[106] D.R. Brammer. A Comparison between Predicted and Actual Behaviour of Domestic Smoke Detectors in a Realistic House Fire. Master's thesis, University of Canterbury, Christchurch, New Zealand, 2002. 14

[107] T. Cleary, M. Donnelly, G. Mulholland, and B. Farouk. Fire Detector Performance Predictions in a Simulated Multi-Room Configuration. In *Proceedings of the 12th International Conference on Automatic Fire Detection (AUBE '01)*. National Institute of Standards and Technology, Gaithersburg, Maryland, March 2001. NIST SP 965. 14

[108] A. Mukhopadhyay and I.K. Puri. An Assessment of Stretch Effects on Flame Tip Using the Thin Flame and Thick Formulations. *Combustion and Flame*, 133:499–502, 2003. 14

[109] A. Hamins, M. Bundy, I.K. Puri, K.B. McGrattan, and W.C. Park. Suppression of Low Strain Rate Non-Premixed Flames by an Agent. In *Proceedings of the 6th International Microgravity Combustion Workshop, NASA/CP-2001-210826*, pages 101–104. National Aeronautics and Space Administration, Lewis Research Center, Cleveland, Ohio, May 2001. 14

[110] S. Dillon and A. Hamins. Ignition Propensity and Heat Flux Profiles of Candle Flames for Fire Investigation. In Vytenis Babrauskas, editor, *Fire Science Applications to Fire Investigations*, pages 363–376. Interscience Communications, London, 2003. 14

[111] A. Hamins, M. Bundy, and S.E. Dillon. Characterization of Candle Flames. *Journal of Fire Protection Engineering*, 15(4):265–285, 2005. 14

[112] J.E. Floyd, C. Wieczorek, and U. Vandsburger. Simulations of the Virginia Tech Fire Research Laboratory Using Large Eddy Simulation with Mixture Fraction Chemistry and Finite Volume Radiative Heat Transfer. In *Proceedings of the Ninth International Interflam Conference*. Interscience Communications, London, 2001. 14

[113] Y. Xin and J.P. Gore. Measurements and Calculations of Spectral Radiation Intensities in Buoyant Turbulent Flames. In *Proceedings of the Third Joint Meeting of the U.S. Sections of the Combustion Institute*. Combustion Institute, Pittsburgh, Pennsylvania, 2003. 14

[114] W. Zhang, N. Ryder, R.J. Roby, and D. Carpenter. Modeling of the Combustion in Compartment Fires Using Large Eddy Simulation Approach. In *Proceedings of the 2001 Fall Technical Meeting, Eastern States Section*. Combustion Institute, Pittsburgh, Pennsylvania, December 2001. 14

[115] D. Gottuk, C. Mealy, and J. Floyd. Smoke Transport and FDS Validation. In *Fire Safety Science – Proceedings of the Ninth International Symposium*, pages 129–140. International Association for Fire Safety Science, 2008. 15

[116] A. Hamins, A. Maranghides, R. Johnsson, M. Donnelly, G. Yang, G. Mulholland, and R.L. Anleitner. Report of Experimental Results for the International Fire Model Benchmarking and Validation Exercise 3. NIST Special Publication 1013-1, National Institute of Standards and Technology, Gaithersburg, Maryland, May 2006. Joint Publication of NIST and the US Nuclear Regulatory Commission (NUREG/CR-6905). 15, 74, 153, 154, 156, 157

[117] J. Floyd and R. McDermott. Modeling Soot Deposition Using Large Eddy Simulation with a Mixture Fraction Based Framework. In *Proceedings of the Twelfth International Interflam Conference*. Interscience Communications, London, 2010. 15

[118] S. Riahi. *New Tools for Smoke Residue and Deposition Analysis*. PhD thesis, The George Washington University, Washington, DC, 2011. 15

[119] B.D. Cohan. Verification And Validation Of A Candidate Soot Deposition Model In Fire Dynamics Simulator Version 5.5.1. Master's thesis, University of Maryland, 2010. 15

[120] K.J. Overholt and O.A. Ezekoye. An Inverse Fire Modeling Methodology for the Determination of Fire Size, Fire Location, and Soot Deposition in a Compartment. In *Proceedings of 2012 ASME International Mechanical Engineering Congress and Exposition*. American Society of Mechanical Engineering, November 2012. IMECE2012-88924. 15

[121] W.L. Grosshandler, N. Bryner, D. Madrzykowski, and K. Kuntz. Report of the Technical Investigation of The Station Nightclub Fire. NIST NCSTAR 2, National Institute of Standards and Technology, Gaithersburg, MD, June 2005. 15

[122] D. Madrzykowski and R.L. Vettori. Simulation of the Dynamics of the Fire at 3146 Cherry Road NE Washington D.C., May 30, 1999. NISTIR 6510, National Institute of Standards and Technology, Gaithersburg, Maryland, April 2000. 15

[123] R.L. Vettori, D. Madrzykowski, and W.D. Walton. Simulation of the Dynamics of a Fire in a One-Story Restaurant – Texas, February 14, 2000. NISTIR 6923, National Institute of Standards and Technology, Gaithersburg, Maryland, October 2002. 15

[124] D. Madrzykowski, G.P. Forney, and W.D. Walton. Simulation of the Dynamics of a Fire in a Two-Story Duplex, Iowa, December 22, 1999. NISTIR 6854, National Institute of Standards and Technology, Gaithersburg, Maryland, January 2002. 15

[125] D. Madrzykowski and W.D. Walton. Cook County Administration Building Fire, 69 West Washington, Chicago, Illinois, October 17, 2003: Heat Release Rate Experiments and FDS Simulations. NIST Special Publication SP-1021, National Institute of Standards and Technology, Gaithersburg, Maryland, July 2004. 15

[126] N. Bryner, S.P. Fuss, B.W. Klein, and A.D. Putorti. Technical Study of the Sofa Super Store Fire, South Carolina, June 18, 2007. NIST Special Publication 1118, National Institute of Standards and Technology, Gaithersburg, MD, March 2011. 15

[127] P. Camp and N. Townsend. Computer Modelling vs Reality – Can We Predict the Behaviour of Fires? In *Proceedings of the Ninth International Interflam Conference*, pages 195–202. Interscience Communications, London, 2001. 16

[128] G. Rein, A. Bar-Ilan, N. Alvares, and A.C. Fernandez-Pello. Estimating the Performance of Enclosure Fire Models by Correlating Forensic Evidence of Accidental Fires. In *Proceedings of the Tenth International Interflam Conference*, pages 1183–1194. Interscience Communications, London, 2004. 16

[129] M. Spearpoint, F.W. Mowrer, and K. McGrattan. Simulation of a Compartment Flashover Fire Using Hand Calculations, Zone Models and a Field Model. In *Proceedings of the Third International Conference on Fire Research and Engineering (ICFRE3)*, pages 3–14. Society of Fire Protection Engineers, Bethesda, Maryland, 1999. 16

[130] D.J. Carpenter and C.B. Wood, editors. *Proceedings of the 3rd Technical Symposium on Computer Applications in Fire Protection Engineering*. Society for Fire Protection Engineers, Bethesda, Maryland, September 2001. 16

[131] A.M. Christensen and D.J. Icove. The Application of NIST's Fire Dynamics Simulator to the Investigation of Carbon Monoxide Exposure in the Deaths of Three Pittsburgh Fire Fighters. *Journal of Forensic Sciences*, 49(1):1–4, 2004. 16

[132] D.T. Sheppard and B.W. Klein. Burn Tests in Two Story Structure with Hallways. Technical report, ATF Laboratories, Ammendale, Maryland, 2009. 17

[133] R.B. Stull. *Meteorology for Scientists and Engineers*. Brooks/Cole, Pacific Grove, California, 2nd edition, 2000. 19, 1045

[134] C. Belyer. Major Species Production by Diffusion Flames in a Two-Layer Compartment Fire Environment. *Fire Safety Journal*, 10:47–56, 1986. 19

[135] M.M. Khan, A. Tewarson, and M. Chaos. *SFPE Handbook of Fire Protection Engineering*, chapter Combustion Characteristics of Materials and Generation of Fire Products. Springer, New York, 5th edition, 2016. 20, 32, 41, 71, 100, 101, 138, 825, 835

[136] C. Beyler. *SFPE Handbook of Fire Protection Engineering*, chapter Flammability Limits of Premixed and Diffusion Flames. Springer, New York, 5th edition, 2016. 20, 49, 132, 899

[137] P.A. Croce, K.S. Mudan, and J. Moorhouse. Thermal Radiation from LNG Trench Fires. Technical Report 88682, Gas Research Institute (GRI), September 1984. 21

[138] A. Bittern. Analysis of FDS Predicted Sprinkler Activation Times with Experiments. Master's thesis, University of Canterbury, Christchurch, New Zealand, 2004. 22, 23

[139] C. Wade, M.J. Spearpoint, A. Bittern, and K. Tsai. Assessing the sprinkler activation predictive capability of the BRANZFIRE fire model. *Fire Technology*, 43(3):175–193, 2007. doi: 10.1007/s10694-007-0009-5. 22, 23

[140] A. Bouchair. *Solar Induced Ventilation in the Algerian and Similar Climates*. PhD thesis, University of Leeds, Leeds, West Yorkshire, England, 1989. 24, 885

[141] L. Shi and G. Zhang. An empirical model to predict the performance of typical solar chimneys considering both room and cavity configurations. *Building and Environment*, 103:250–261, 2016. 25

[142] J.V. Murrel, D. Crowhurst, and P. Rock. Experimental Study of The Thermal Radiation Attenuation of Sprays from Selected Hydraulic Nozzles. In *Proceedings of Halon Options Technical Working Conference 1995*, pages 369–378. The University of New Mexico, Albuquerque, 1995. 25

[143] R.A. Bryant. A comparison of gas velocity measurements in a full-scale enclosure fire. *Fire Safety Journal*, 44:793–800, 2009. 26, 154, 415

[144] R.A. Bryant. The application of stereoscopic particle image velocimetry to measure the flow of air into an enclosure containing fire. *Experiments in Fluids*, 47:295–308, 2009. 26

[145] R.A. Bryant. Evaluating practical measurements of fire-induced vent flows with stereoscopic PIV. In *Proceedings of the Combustion Institute*. Elsevier, 2010. 26

[146] B.R. Kirby, D.E. Wainman, L.N. Tomlinson, T.R. Kay, and B.N. Peacock. Natural Fires in Large Scale Compartments—A British Steel Technical, Fire Research Station Collaborative Project. Technical report, British Steel Technical, Swinden Laboratories, Moorgate, Rotherham S60 3AR, England, UK, June 1994. 27, 28

[147] R.Kallada Janardhan and S. Hostikka. When is the fire spreading and when it travels? – Numerical simulations of compartments with wood crib fire loads. *Fire Safety Journal*, 126, December 2021. https://doi.org/10.1016/j.firesaf.2021.103485. 28, 112, 113

[148] S.P. Nowlen, F.J. Wyant, and K.B. McGrattan. Cable Response to Live Fire (CAROLFIRE). NUREG/CR 6931, United States Nuclear Regulatory Commission, Washington, DC, April 2008. 28, 745

[149] P. Andersson and P. Van Hees. Performance of Cables Subjected to Elevated Temperatures. In *Fire Safety Science – Proceedings of the Eighth International Symposium*, pages 1121–1132. International Association of Fire Safety Science, 2005. 28

[150] M.E. Alexander and M.G. Cruz. Evaluating a model for predicting active crown fire rate of spread using wildfire observations. *Canadian Journal of Forest Research*, 36:3015–3028, 2006. http://dx.doi.org/10.1139/X06-174. 29

[151] J. Ziegler. *Impacts of Treatments on Forest Structure and Fire Behavior in Dry Western Forests*. PhD thesis, Colorado State University, Fort Collins, Colorado, 2014. 29

[152] J.P. Ziegler, C.M. Hoffman, M.A. Battaglia, and W. Mell. Spatially explicit measurements of forest structure and fire behavior following restoration treatments in dry forests. *Forest Ecology and Management*, 386, 2017. http://dx.doi.org/10.1016/j.foreco.2016.12.002. 29

[153] J.P. Ziegler, C.M. Hoffman, M.A. Battaglia, and W. Mell. Stem-Maps of Forest Restoration Cuttings in *Pinus ponderosa*-Dominated Forests in the Interior West, USA. *Data*, 4(68), 2019. http://dx.doi.org/10.3390/data4020068. 29

[154] C.M. Hoffman, J. Ziegler, J. Canfield, R.R. Linn, W. Mell, C.H. Sieg, and F. Pimont. Evaluating Crown Fire Rate of Spread Predictions from Physics-Based Models. *Fire Technology*, 52:221–237, 2016. 29

[155] N.P. Cheney, J.S. Gould, and W.R. Catchpole. The Influence of Fuel, Weather and Fire Shape Variables on Fire-Spread in Grasslands. *International Journal of Wildland Fire*, 3(1):31–44, 1993. 29, 30

[156] W. Mell, M.A. Jenkins, J. Gould, and P. Cheney. A physics-based approach to modelling grassland fires. *International Journal of Wildland Fire*, 16(1):1–22, 2007. 29

[157] Y. Perez-Ramirez, P.A. Santoni, J.B. Tramoni, F. Bosseur, and W.E. Mell. Examination of WFDS in Modeling Spreading Fires in a Furniture Calorimeter. *Fire Technology*, 53:1795–1832, 2017. 30, 132

[158] R.C. Rothermel. A Mathematical Model for Predicting Fire Spread in Wildland Fuels. Research Paper INT-115, Intermountain Forest and Range Experiment Station, USDA Forest Service, Ogden, Utah, January 1972. http://www.treesearch.fs.fed.us/pubs/32533. 30, 32, 70

[159] F.A. Albini. Estimating Wildfire Behavior and Effects. Research Paper INT-30, Intermountain Forest and Range Experiment Station, USDA Forest Service, Ogden, Utah, 1976. https://www.fs.fed.us/rm/pubs_int/int_gtr030.pdf. 30

[160] D. Morvan and J.L. Dupuy. Modeling the propagation of a wildfire through a Mediterranean shrub using a multiphase formulation. *Combustion and Flame*, 138(3):199–210, 2004. 32, 70

[161] R.A. Susott. Characterization of the thermal properties of forest fuels by combustible gas analysis. *Forest Science*, 2:404–420, 1982. 32, 70

[162] R. Falkenstein-Smith, K. McGrattan, B. Toman, and M. Fernandez. Measurement of the Flow Resistance of Vegetation. NIST Technical Note 2039, National Institute of Standards and Technology, Gaithersburg, Maryland, March 2019. https://doi.org/10.6028/NIST.TN.2039. 32, 112

[163] O.T. Farouki. Thermal properties of soils. CRREL Monograph 81-1, U.S. Army Corps of Engineers, Cold Regions Research and Engineering Laboratory, Hanover, New Hampshire, December 1981. 32

[164] R. Meyrand. *Étude sur l'usage de brouillards d'eau en milieu tunnel - Travail en réduction d'échelle*. PhD thesis, École Nationale Supérieure de Mécanique et d'Aérotechnique, Poitiers, France, 2009. 32

[165] E. Blanchard, P. Fromy, P. Carlotti, P. Boulet, S. Desanghere, J.P. Vantelon, and J.P. Garo. Experimental and Numerical Study of the Interaction Between Water Mist and Fire in an Intermediate Test Tunnel. *Fire Technology*, 50:565–587, 2014. 32

[166] R. E. Tapscott. "Best Values" of Cup-Burner Extinguishing Concentrations. In *Halon Options Technical Working Conference*, pages 265–274, 1996. 34

[167] T. E. Moore, C. A. Weitz, and R. E. Tapscott. An Update and NMERI Cup-Burner Test Results. In *Halon Options Technical Working Conference*, pages 551–564, 1996. 34

[168] I. Yamamoto and K. Saitor and. S. Yamashika. Flame Extinguishing Concentration by Cup Burner Method. *Report of Fire Research Institute of Japan*, 57, 1984. 34

[169] R. Sakei, N. Saito, Y. Saso, and Y. Ogawa. Flame Extinguishing Concentrations of Halon Replacements for Flammable Liquids. *Report of Fire Research Institute of Japan*, 90, 1995. 34

[170] B. Z. Dlugogorski, E. M. Kennedy, and K. A. Morris. Thermal Behavior of Cup Burners. In *Proceedings of the Seventh International Interflam Conference*, pages 445–457. Interscience Communications, London, 1996. 34

[171] R. S. Sheinson, J. E. Penner-Hahn, and D. Indritz. The physical and chemical action of fire suppressants. *Fire Safety Journal*, 15:437–450, 1989. 34

[172] W. L. Grosshandler, R. G. Gann, and W. M. Pitts. Evaluation of alternative in-flight fire suppressants for full-scale testing in simulated aircraft engine nacelles and dry bays. NIST SP 861, National Institute of Standards and Technology, 1994. 34

[173] N. Saito, Y. Ogawa, Y. Saso, C. Laio, and R. Sakei. Flame-extinguishing concentrations and peak concentrations of N_2, Ar, CO_2 and their mixtures for hydrocarbon fuels. *Fire Safety Journal*, 27:185–200, 1996. 34

[174] National Fire Protection Association, Quincy, Massachusetts. *NFPA 2001, Standard on Clean Agent Fire Extinguising Systems*, 2015. 34

[175] International Organization for Standardization, Geneva, Switzerland. *ISO 14520, Gaseous fire-extinguishing systems - Physical properties and system design*, 2006. 34

[176] J. A. Senecal. Flame extingsuishment in the cup-burner by inert gases. *Fire Safety Journal*, 40:579–591, 2005. 34

[177] A. Hamins. Flame extinction by sodium bicarbonate powder in a cup burner. In *Twenty-seventh Symposium (International) on Combustion*, pages 2857–2864. Combustion Institute, Pittsburgh, Pennsylvania, 1998. 34

[178] R. Hirst and K. Booth. Measurement of Flame-Extinguishing Concentrations. *Fire Technology*, 13:296–315, 1977. 34

[179] F. Takahashi, G. Linteris, and V. Katta. Extinguishment mechanisms of coflow diffusion flames in cup-burner apparatus. In *Thirty First Symposium (International) on Combustion*, pages 2721–2729. Combustion Institute, Pittsburgh, Pennsylvania, 2007. 34

[180] E. A. Ural. Measurement of the Extinguishing Concentration of Gaseous Fuels Using the Cup-Burner Apparatus. In *Halon Options Technical Working Conference*, pages 278–283, 2007. 34

[181] J.M. Willi. Propane Gas Fire Experiments in Residential Scale Structures. NIST Technical Note 1953, National Institute of Standards and Technology, Gaithersburg, Maryland, 2016. 35

[182] C.L. Mealy, M.E. Benfer, and D.T. Gottuk. Fire Dynamics and Forensic Analysis of Liquid Fuel Fires. U.S. Department of Justice Document Number 238704, Hughes Associates, Inc., 3610 Commerce Drive, Suite 817, Baltimore, Maryland, 21227, May 2012. Grant No. 2008-DN-BX-K168. 37

[183] J.R. Rumble, editor. *CRC Handbook of Chemistry and Physics*, chapter Enthalpy of Vaporization. CRC Press/Taylor and Francis, Boca Raton, Florida, 101st edition, (Internet Version 2020). 37

[184] A. Fujita, R. Kurose, and S. Komori. Experimental study on effect of relative humidty on heat transfer of an evaporating water droplet in air flow. *International Journal of Multiphase Flow*, 36:244–247, 2010. 38

[185] P.M. Gavin. PROGRAM DROP: A Computer Program for Prediction of Evaporation from Freely Falling Multicomponent Drops. SAND 96-2878, Sandia National Laboratories, Albuquerque, NM, December 1996. 38

[186] D. Kolaitis and M. Founti. Comparing Evaporation Rates of Single Suspended Droplets. In *10th Workshop on Two-Phase Flow Predictions*. European Research Community on Flow, Turbulence, and Combustion, 2002. 38

[187] C. Maqua, G. Castanet, and F. Lempoine. Bicomponent droplets evaporation: Temperature measurements and modelling. *Fuel*, 87:2932–2942, 2008. 38

[188] A. Snegirev, V. Talavov, I. Sheinman, and S. Sazhin. An enhanced spray model for flame suppression simulations. In *Proceedings of the European Combustion Meeting*. Combustion Institute, 2011. 38

[189] Eric V. Mueller, Michael R. Gallagher, Nicholas Skowronski, and Rory M. Hadden. Approaches to Modeling Bed Drag in Pine Forest Litter for Wildland Fire Applications. *Transport in Porous Media*, 138(3):637–660, 2021. https://doi.org/10.1007/s11242-021-01637-8. 38

[190] J. Suo-Anttila, W. Gill, C. Gallegos, and J. Nelsen. Computational Fluid Dynamics Code for Smoke Transport During an Aircraft Cargo Compartment Fire: Transport Solver, Graphical User Interface, and Preliminary Baseline Validation. Report DOT/FAA/AR-03/49, Federal Aviation Administration, Office of Aviation Research, Washington, DC 20591, October 2003. 39

[191] J. Suo-Anttila, W. Gill, A. Luketa-Hanlin, and C. Gallegos. Cargo Compartment Smoke Transport Computational Fluid Dynamics Code Validation. Report DOT/FAA/AR-07/27, Federal Aviation Administration, Office of Aviation Research and Development, Washington, DC 20591, July 2007. 39

[192] D. Blake. Development of a Standardized Fire Source for Aircraft Cargo Compartment Fire Detection Systems. Report DOT/FAA/AR-06/21, Federal Aviation Administration, Office of Aviation Research and Development, Washington, DC 20591, May 2006. 39

[193] S.I. Stoliarov, S. Crowley, R.E. Lyon, and G.T. Linteris. Prediction of the burning rates of non-charring polymers. *Combustion and Flame*, 156:1068–1083, 2009. 39, 923

[194] S.I. Stoliarov, S. Crowley, R.N. Walters, and R.E. Lyon. Prediction of the burning rates of charring polymers. *Combustion and Flame*, 157:2024–2034, 2010. 39, 927, 929, 931

[195] R. Fleury. Evaluation of Thermal Radiation Models for Fire Spread Between Objects. Master's thesis, University of Canterbury, Christchurch, New Zealand, 2010. 40

[196] D. Zeng and Y. Wang. Dependence of Limiting Oxygen Index of Buoyant Turbulent non-premixed Flame on Fuel. In *Proceedings of the 26th International Colloquium on the Dynamics of Explosions and Reactive Systems*, Boston, Massachusetts, 2017. 40, 899

[197] N. Ren, D. Zeng, K.V. Meredith, Y. Wang, and S.B. Dorofeev. Modeling of flame extinction/re-ignition in oxygen-reduced environments. In *Proceedings of the Combustion Institute*, 2018. https://doi.org/10.1016/j.proci.2018.06.076. 40

[198] X. Ren, D. Zeng, Y. Wang, G. Xiong, G. Agarwal, and M. Gollner. Temperature measurement of a turbulent buoyant ethylene diffusion flame using a dual-thermocouple technique. In *Proceedings of the 13th Symposium on Fire Safety Science*. International Association of Fire Safety Science, 2020. 40

[199] S. Thumuluru, B. Ditch, P. Chatterjee, and M. Chaos. Experimental Data for Modeling Validaton of Smoke Transport in Data Centers. Technical report, FM Global, Norwood, Massachusetts, 2014. 41

[200] J. Floyd, H. Boehmer, and D. Gottuk. Validation of Modeling Tools for Detection Design in High Air flow Environments: Phase II – Task 4b and 4c: Full Scale Model Verification and Validation. Technical report, Fire Protection Research Foundation, Quincy, Massachusetts, 2014. 41

[201] P.A. Beaulieu. Parallel Panel Experiments of FRP Composites. Technical Report 0003024286, FM Global, Norwood, Massachusetts, December 2007. 42

[202] S.P. Nowlen. Enclosure Environment Characterization Testing for the Baseline Validation of Computer Fire Simulation Codes. NUREG/CR-4681 (SAND86-1296), Sandia National Laboratory, Albuqueque, New Mexico, March 1987. Work performed under contract to the US Nuclear Regulatory Agency, Washington DC. 42

[203] J.M. Chavez and S.P. Nowlen. An Experimental Investigation of Internally Ignited Fires in Nuclear Power Plant Control Cabinets, Part II: Room Effects Tests. NUREG/CR-4527 (SAND86-0336), Sandia National Laboratory, Albuqueque, New Mexico, November 1988. Work performed under contract to the US Nuclear Regulatory Agency, Washington DC. 42

[204] J.L. de Ris, G.H. Markstein, L. Orloff, and P.A. Beaulieu. Similarity of Turbulent Wall Fires. In *Fire Safety Science – Proceedings of the Seventh International Symposium*, pages 259–270. International Association for Fire Safety Science, 2002. 45

[205] D. Frankman, B.W. Webb, B.W. Butler, and D.J. Latham. Fine Fuel Heating by Radiant Flux. *Combustion Science and Technology*, 182:215–230, 2010. 45

[206] R. Harrison. *Entrainment of air into thermal spill plumes*. PhD thesis, University of Canterbury, Christchurch, New Zealand, 2009. 46, 308

[207] R. Harrison and M. Spearpoint. Characterization of Balcony Spill Plume Entrainment using Physical Scale Modeling. In *Fire Safety Science – Proceedings of the Ninth International Symposium*, pages 727–738. International Association for Fire Safety Science, 2008. 46

[208] R. Harrison and M. Spearpoint. The balcony spill plume: entrainment of air into a flow from a compartment opening to a higher projecting balcony. *Fire Technology*, 43(4):301–317, 2007. 46

[209] R. Harrison and M. Spearpoint. Physical scale modeling of adhered spill plume entrainment. *Fire Safety Journal*, 45:149–158, 2010. 46

[210] G. Heskestad. Luminous Heights of Turbulent Diffusion Flames. *Fire Safety Journal*, 5:103–108, 1983. 48

[211] D. Paudel, A. Rinta-Paavola, H.P. Mattila, and S. Hostikka. Multiphysics modelling of stone wool fire resistance. *Fire Technology*, 2020. Under review. 48, 668

[212] S. Lechêne. *Étude expérimentale et numérique des rideaux d'eau pour la protection contre le rayonnement thermique*. PhD thesis, Université Henri Poincaré, Nancy, France, 2010. 48

[213] K.L. Foote. 1986 LLNL Enclosure Fire Tests Data Report. Technical Report UCID-21236, Lawrence Livermore National Laboratory, August 1987. 49, 462

[214] K.L. Foote, P.J. Pagni, and N.J. Alvares. Temperature Correlations for Forced-Ventilation Compartment Fires. In *Fire Safety Science – Proceedings of the First International Symposium*, pages 139–148. International Association for Fire Safety Science, 1986. 49

[215] M.J. Ivings, S.E. Gant, S.F. Jagger, C.J. Lea, J.R. Stewart, and D.M. Webber. Evaluating vapor dispersion models for safety analysis of LNG facilities. Report Number MSU/2016/17, Health and Safety Laboratory, Buxton, Derbyshire, United Kingdom, September 2016. 52

[216] J.R. Stewart, S. Coldrick, C.J. Lea, S.E. Gant, and M.J. Ivings. Validation Database for Evaluating Vapor Dispersion Models for Safety Analysis of LNG Facilities: Guide to the LNG Model Validation Database Version 12. Report Number MSU/2016/12, Health and Safety Laboratory, Buxton, Derbyshire, United Kingdom, September 2016. 52

[217] A.J. Dyer. A review of flux profile relationships. *Boundary-Layer Meteorology*, 7:363–372, 1974. 52

[218] T.C. Brown, R.T. Cederwall, S.T. Chan, D.L. Ermak, R.P. Koopman, K.C. Lamson, J.W. McClure, and L.K. Morris. Falcon Series Data Report: 1987 LNG Vapor Barrier Verification Field Trials. Data Report GRI-89/0138, Lawrence Livermore National Laboratory, June 1990. 52

[219] B.J. Lowesmith and G. Hankinson. Large scale high pressure jet fires involving natural gas and natural gas/hydrogen mixtures. *Process Safety and Environmental Protection*, 90:108–120, 2012. 54

[220] T.L. Bergman, A.S. Lavine, F.P. Incropera, and D.P. DeWitt. *Fundamentals of Heat and Mass Transfer*. John Wiley and Sons, New York, 7th edition, 2011. 55

[221] B.J. McCaffrey. Purely Buoyant Diffusion Flames: Some Experimental Results. NBSIR 79-1910, National Bureau of Standards (now NIST), Gaithersburg, Maryland, October 1979. 55

[222] B.J. McCaffrey. Some Measurements of the Radiative Power Output of Diffusion Flames. In *Proceedings of the Western States Section of the Combustion Institute*, 1981. Paper WSS/CI 81-15. 55

[223] D. Nedelka, J. Moorhouse, and R.F. Tucker. The Montoir 35 m Diameter LNG Pool Fire Experiments. In *Proceedings of 9th International Congress and Exposition of Liquified Natural Gas, LNG9, Vol. 2*, pages 1–23. Institute of Gas Technology, Chicago, 1990. 58

[224] R.D. Peacock, S. Davis, and W.T. Lee. An Experimental Data Set for the Accuracy Assessment of Room Fire Models. NBSIR 88-3752, National Bureau of Standards (now NIST), Gaithersburg, Maryland, April 1988. 59

[225] S. Ramesh, L. Choe, M. Seif, M. Hoehler, A. Sauca, W. Grosshandler, M. Bundy, Y. Bao, M. Klegseth, G. Chen, J. Reilly, and B. Glisic. Compartment Fire Experiments of Long-Span Composite-Beams with Simple Shear Connections, Part I: Experiment Design and Behavior at Ambient Temperature. NIST Technical Note XXXX, National Institute of Standards and Technology, Gaithersburg, Maryland, June 2019. 61

[226] A. Sauca, C. Zhang, W. Grosshandler, L. Choe, and M. Bundy. ASTM E119 fire experiment in a large compartment using NFRL natural gas fuel delivery system. NIST Technical Note XXXX, National Institute of Standards and Technology, Gaithersburg, Maryland, June 2019. 65

[227] American Society for Testing and Materials, West Conshohocken, Pennsylvania. *ASTM E 119, Standard Test Methods for Fire Tests of Building Construction and Materials*, 2002. 65

[228] W. Mell, A. Maranghides, R. McDermott, and S. Manzello. Numerical simulation and experiments of burning Douglas fir trees. *Combustion and Flame*, 156:2023–2041, 2009. 69, 70

[229] K. McGrattan, S. Hostikka, R. McDermott, J. Floyd, C. Weinschenk, and K. Overholt. *Fire Dynamics Simulator, Technical Reference Guide, Volume 2: Verification*. National Institute of Standards and Technology, Gaithersburg, Maryland, USA, and VTT Technical Research Centre of Finland, Espoo, Finland, sixth edition, September 2013. 69

[230] W.J. Parker. Prediction of the Heat Release Rate of Douglas Fir. In *Fire Safety Science, Proceedings of the Second International Symposium*. International Association of Fire Safety Science, 1989. 70

[231] N. Bryner, E. Johnsson, and W. Pitts. Carbon Monoxide Production in Compartment Fires - Reduced-Scale Test Facility. NISTIR 5568, National Institute of Standards and Technology, Gaithersburg, MD, 1994. 70

[232] M. Bundy, A. Hamins, E.L. Johnsson, S.C. Kim, G.H. Ko, and D.B. Lenhert. Measurements of Heat and Combustion Products in Reduced-Scale Ventilation-Limited Compartment Fires. NIST Technical Note 1483, National Institute of Standards and Technology, Gaithersburg, Maryland, 2007. 70

[233] A. Lock, M. Bundy, E.L. Johnsson, A. Hamins, G.H. Ko, C. Hwang, P. Fuss, and R. Harris. Experimental Study of the Effects of Fuel Type, Fuel Distribution, and Vent Size on Full-Scale Underventilated Compartment Fires in an ISO 9705 Room . NIST Technical Note 1603, National Institute of Standards and Technology, Gaithersburg, Maryland, 2008. 70

[234] W.M. Pitts, J.C. Yang, and M.G. Fernandez. Experimental Characterization of Helium Dispersion in a 1/4-Scale Two-Car Residential Garage. NIST Technical Note 1694, National Institute of Standards and Technology, Gaithersburg, Maryland, March 2011. 73

[235] K.B. McGrattan, M.J. Selepak, and E.J. Hnetkovsky. The Influence of Walls, Corners and Enclosures on Fire Plumes. NIST Technical Note 1984, National Institute of Standards and Technology, Gaithersburg, Maryland, March 2018. 76

[236] K. McGrattan and I. Leventon. Oxygen-Limited Fires Inside Under-Ventilated Enclosures (OLIVE-Fire). NIST Technical Note XXXX, National Institute of Standards and Technology, Gaithersburg, Maryland, April 2022. 81

[237] K. McGrattan. Heat Release Rates of Multiple Transient Combustibles. NIST Technical Note 2102, National Institute of Standards and Technology, Gaithersburg, Maryland, July 2020. 84

[238] M.J. Hurley, editor. *SFPE Handbook of Fire Protection Engineering*. Springer, New York, 5th edition, 2016. 84, 900

[239] L.G. Fraga, J. Silva, S. Teixeira, D. Soares, M. Ferreira, and J. Teixeira. Thermal Conversion of Pine Wood and Kinetic Analysis under Oxidative and Non-Oxidative Environments at Low Heating Rate. *Proceedings*, 58(23), 2020. https://www.mdpi.com/2504-3900/58/1/23. 86

[240] D. Morvan and J.L. Dupuy. Modeling of fire spread through a forest fuel bed using a multiphase formulation. *Combustion and Flame*, 127(1):1981–1994, 2001. 86

[241] R.W. Bukowski, R.D. Peacock, J.D. Averill, T.G. Cleary, N.P. Bryner, W.D. Walton, P.A. Reneke, and E.D. Kuligowski. Performance of Home Smoke Alarms Analysis of the Response of Several Available Technologies in Residential Fire Settings. NIST Technical Note 1455-1, National Institute of Standards and Technology, Gaithersburg, Maryland, February 2008. 87, 158, 405

[242] A. Mencsh and T. Cleary. A Soot Deposition Gauge for Fire Measurements. NIST TN 1985, National Institute of Standards and Technology, Gaithersburg, MD, March 2018. . 90

[243] S.L. Manzello, S.H. Park, T. Mizukami, and D.P. Benz. Measurement of Thermal Properties of Gypsum Board at Elevated Temperatures. In *Proceedings of the Fifth International Conference on Structures in Fire (SiF'08)*, pages 656–665, Nanyang Technological University, Singapore, 2008. 91

[244] I. Oleszkiewicz. Heat Transfer from a Window Fire Plume to a Building Facade. In *HTD – Collected Papers in Heat Transfer*, volume 123, pages 163–170. American Society of Mechanical Engineers, 1989. Book No. H00526. 93

[245] I. Oleszkiewicz. Fire Exposure to Exterior Walls and Flame Spread on Combustible Cladding. *Fire Technology*, 26(4):357–375, 1990. 93

[246] Y. Wang. A Study of Smoke Movement in Multi-storey Buildings Using Experiments and Computer Modelling. Master's thesis, Carleton University, Ottawa, Ontario, Canada, 2008. 96

[247] Y. Wang, E. Zalok, and G. Hadjisophocleous. An Experimental Study of Smoke Movement in Multi-Storey Buildings. *Fire Technology*, 47:1141–1169, 2011. 96

[248] G. Hadjisophocleous and Q. Jia. Comparison of FDS Prediction of Smoke Movement in a 10-Storey Building with Experimental Data. *Fire Technology*, 45:163–177, 2009. 96

[249] P.J. Tyson. Validation of Fire Dynamics Simulator (FDS) v6.2 for Smoke and Heat Transport in Multi-Storey Multi-Compartment Buildings. Master's thesis, Ulster University, Londonderry, Northern Ireland, United Kingdom, 2015. 96

[250] G.Y. Achakji. NRCC Experimental Fire Tower for Studies on Smoke Movement and Smoke Control in Tall Buildings. Internal Report No. 512, National Research Council Canada, 1987. 96

[251] National Fire Protection Association, Quincy, Massachusetts. *NFPA 92, Standard for Smoke Control Systems*, 2012. 96

[252] G. Back, C. Beyler, P. DiNenno, and P. Tatem. Wall Incident Heat Flux Distributions Resulting from an Adjacent Fire. In *Fire Safety Science – Proceedings of the Fourth International Symposium*, pages 241–252. International Association of Fire Safety Science, 1994. 98

[253] T. Blanchat, P. Helmick, R. Jensen, A. Luketa, R. Deola, J. Suo-Anttila, J. Mercier, T. Miller, A. Ricks, R. Simpson, B. Demosthenous, S. Tieszen, and M. Hightower. The Phoenix Series Large Scale LNG Pool Fire Experiments. Technical Report SAND2010-8676, Sandia National Laboratory, Albuquerque, New Mexico, 2011. 98, 99, 104

[254] D.T. Gottuk and D.A. White. *SFPE Handbook of Fire Protection Engineering*, chapter Liquid Fuel Fires. Springer, New York, 5th edition, 2016. 100

[255] K.S. Mudan. Thermal Radiation Hazards from Hydrocarbon Pool Fires. *Progress in Energy and Combustion Science*, 10:59–80, 1984. 100

[256] T. Sikanen and S. Hostikka. Modeling and simulation of liquid pool fires with in-depth radiation absorption and heat transfer. *Fire Safety Journal*, 80:95–109, 2016. 100

[257] W.M. Haynes, editor. *CRC Handbook of Chemistry and Physics*, chapter Thermal Conductivity of Liquids. CRC Press/Taylor and Francis, Boca Raton, Florida, 95th edition, (Internet Version 2015). 100, 101

[258] E.W. Lemmon, M.O. McLinden, and D.G. Friend. *NIST Chemistry WebBook, NIST Standard Reference Database Number 69*, chapter Thermophysical Properties of Fluid Systems. National Institute of Standards and Technology. http://webbook.nist.gov, (retrieved May 23, 2014). 100, 101

[259] M.W. Chase. *NIST-JANAF Thermochemical Tables*. Journal of Physical and Chemical Reference Data, Monograph No. 9. American Chemical Society, Woodbury, New York, 4th edition, 1998. 100

[260] V. Babrauskas. *SFPE Handbook of Fire Protection Engineering*, chapter Heat Release Rates. Springer, New York, 5th edition, 2016. 101

[261] E.S. Domalski and E.D. Hearing. *NIST Chemistry WebBook, NIST Standard Reference Database Number 69*, chapter Condensed Phase Heat Capacity Data. National Institute of Standards and Technology. http://webbook.nist.gov, (retrieved May 23, 2014). 101

[262] R.L. Brown and S.E. Stein. *NIST Chemistry WebBook, NIST Standard Reference Database Number 69*, chapter Boiling Point Data. National Institute of Standards and Technology. http://webbook.nist.gov, (retrieved May 23, 2014). 101

[263] L. Audouin, L. Rigollet, H. Prétrel, W. LeSaux, and M. Röwekamp. OECD PRISME project: Fires in confined and ventilated nuclear-type multi-compartments–Overview and main experimental results. *Fire Safety Journal*, 62:80–101, 2013. 101

[264] J. Wahlqvist and P. van Hees. Validation of FDS for large-scale well-confined mechanically ventilated fire scenarios with emphasis on predicting ventilation system behavior. *Fire Safety Journal*, 62:102–114, 2013. 101

[265] J. Dreisbach, S. Nowlen, K. McGrattan, and S. Hostikka. Electrical Cable Failure – Experiments and Simulation. In *Interflam 2010: Proceedings of the Twelfth International Symposium*, pages 1857–1866. Interscience Communications, London, 2010. 101, 752

[266] Y. Xin. *A theoretical and experimental study of buoyant turbulent flames with emphasis on soot and radiation*. PhD thesis, Purdue University, West Lafayette, USA, 2002. 101

[267] X.C. Zhou. *An experimental and theoretical investigation of flows induced by buoyant diffusion flames*. PhD thesis, Purdue University, West Lafayette, USA, 1999. 101

[268] W. E. Ranz and W. R. Marshall. Evaporation from drops - Part II. *Chemical Engineering Progress*, 48:173–180, March 1952. 102, 516, 517, 518

[269] A. Restivo. Turbulent Flow in Ventilated Rooms. Technical report, University of London, Department of Mechanical Engineering, 1979. 103

[270] T. J. O'Hern, E. J. Weckman, A. L. Gerhart, S. R. Tieszen, and R. W. Schefer. Experimental study of a turbulent buoyant helium plume. *J. Fluid Mech.*, 544:143–171, 2005. 105, 309

[271] T. K. Blanchat. Characterization of the Air Source and Plume Source at FLAME. Technical Report SAND01-2227, Sandia National Laboratory, Albuquerque, New Mexico, 2001. 105, 309

[272] P. E. DesJardin, T. J. O'Hern, and S. R. Tieszen. Large eddy simulation and experimental measurements of the near-field of a large turbulent helium plume. *Physics of Fluids*, 16(6):1866–1883, 2004. 105, 309

[273] S. R. Tieszen, T. J. O'Hern, E. J. Weckman, and R. W. Schefer. Experimental study of the effect of fuel mass flux on a 1-m-diameter methane fire and comparison with a hydrogen fire. *Combustion and Flame*, 139:126–141, 2004. 105, 314, 320

[274] S. R. Tieszen, T. J. O'Hern, R. W. Schefer, E. J. Weckman, and T. K. Blanchat. Experimental study of the flow field in and around a one meter diameter methane fire. *Combustion and Flame*, 129:378–391, 2002. 105, 314, 319

[275] H. Müller, J. Lehmkuhl, A. Hundhausen, A. Belt, and H.-J. Allelein. Development of a wall condensation model for coarse mesh containment scale applications. In *CFD for Nuclear Reactor Safety Applications (CFD4NRS-6)*, cambridge, Massachusetts, 2016. 106

[276] S. Betteridge and L. Phillips. Large scale pressurized LNG BLEVE experiments. In *Proceedings of the 2015 AIChE Annual Meeting*, Symposium Series No. 160, New York, 2015. American Institute of Chemical Engineers. 106, 107

[277] M. Sippola. *Particle Deposition in Ventilation Ducts*. PhD thesis, University of California, Berkeley, Berkeley, California, 2002. 108

[278] M. Sippola and W.W. Nazaroff. Experiments Measuring Particle Deposition from Fully Developed Turbulent Flow in Ventilation Ducts. *Aerosol Science and Technology*, 38:914–925, 2010. 108

[279] T.S. Norton, K.C. Smyth, J.H. Miller, and M.D. Smooke. Comparison of Experimental and Computed Species Concentration and Temperature Profiles in Laminar, Two-Dimensional Methane/Air Diffusion Flames. *Combustion Science and Technology*, 90:1–34, 1993. 110

[280] K.C. Smyth. NO Production and Destruction in a Methane/Air Diffusion Flame. *Combustion Science and Technology*, 115:151–176, 1996. 110

[281] J. Andersen, C.L. Rasmussen, T. Giselsson, and P. Glarborg. Global Combustion Mechanisms for Use in CFD Modeling Under Oxy-Fuel Conditions. *Energy & Fuels*, 23(3):1379–1389, 2009. 110

[282] C.K. Westbrook and F.L. Dryer. Simplified Reaction Mechanisms for the Oxidation of Hydrocarbon Fuels in Flames. *Combustion Science and Technology*, 27:31–43, 1981. 110

[283] U. Wickström, R. Jansson, and H. Tuovinen. Verification fire tests on using the adiabatic surface temperature for predicting heat transfer. Technical Report 2009:19, SP Technical Research Institute of Sweden, Bŏras, Sweden, 2009. 110, 705

[284] J. Sjöström, A. Byström, and U. Wickström. Large scale test on thermal exposure to steel column exposed to pool fires. Technical Report 2012:04, SP Technical Research Institute of Sweden, Bŏras, Sweden, 2012. ISBN: 978-91-87017-21-6. 111, 282, 715

[285] J. Sjöström, U. Wickström, and A. Byström. Validation data for room fire models: Experimental background. Technical Report 2016:54, SP Technical Research Institute of Sweden, Bŏras, Sweden, 2016. ISBN: 978-91-88349-56-9. 111, 719

[286] R. Hansen and H. Ingason. Model scale fire experiments in a model tunnel with wooden pallets at varying distances. Technical report, Mälardalen University, Sweden, August 2010. 112

[287] R. Hansen and H. Ingason. Heat release rates of multiple objects at varying distances. *Fire Safety Journal*, 52:1–10, 2012. 112

[288] R.Kallada Janardhan and S. Hostikka. Predictive Computational Fluid Dynamics Simulation of Fire Spread on Wood Cribs. *Fire Technology*, 55:2245–2268, 2019. 112

[289] K.D. Steckler, J.G. Quintiere, and W.J. Rinkinen. Flow Induced By Fire in A Compartment. NBSIR 82-2520, National Bureau of Standards (now NIST), Gaithersburg, Maryland, September 1982. 113, 240, 427

[290] K.H. Wang, J.M. Chen, Z.K. Wang, D.L. Gao, G.Y. Wang, and P. Lin. An experimental study on self-extinction of tunnel fire under natural ventilation condition. *Tunnelling and Underground Space Technology*, 84:177–188, 2019. 116

[291] Y. Wu and M.Z.A. Bakar. Control of smoke flow in tunnel fires using longitudinal ventilation systems—a study of the critical velocity. *Fire Safety Journal*, 35:363–390, 2000. 116, 456

[292] K.M. Opert. Assessment of Natural Vertical Ventilation for Smoke and Hot Gas Layer Control in a Residential Scale Structure. Master's thesis, University of Maryland, College Park, Maryland, 2012. 116

[293] D.T. Sheppard and D.R. Steppan. Sprinkler, Heat & Smoke Vent, Draft Curtain Project – Phase 1 Scoping Tests. Technical report, Underwriters Laboratories, Northbrook, Illinois, May 1997. 118, 122

[294] J.M.A Troup. Large-Scale Fire Tests of Rack Stored Group A Plastics in Retail Operation Scenarios Protected by Extra Large Orifice (ELO) Sprinklers. Technical Report FMRC J.I. 0X1R0.RR, Factory Mutual Research Corporation, Norwood, Massachusetts, November 1994. Prepared for Group A Plastics Committee, Lansdale, Pennsylvania. 123

[295] D. Madrzykowski and C. Weinschenk. Impact of Fixed Ventilation on Fire Damage Patterns in Full-Scale Structures. Technical report, Underwriters Laboratories Firefighter Safety Research Institute, Columbia, MD, April 2019. 124

[296] M.B. McKinnon and C. Weinschenk. Validation of cfd fire model pressure predictions for modern residential style structures. *Fire Safety Journal*, 126:103466, 2021. 124

[297] J.P. Zhang, M. Delichatsios, M. Colobert, J. Hereid, M. Hagen, and D. Bakirtzis. Experimental and Numerical Investigations of Heat Impact and Flame Heights from Fires in SBI Tests. In *Proceedings of the Ninth Symposium on Fire Safety Science*, September 2008. Karlsruhe, Germany. 129

[298] J. Li, J. Gong, and S.I. Stoliarov. Gasification Experiments for Pyrolysis Model Parameterization and Validation. *International Journal of Heat and Mass Transfer*, 77:738–744, 2014. 129, 938

[299] J. Li and S.I. Stoliarov. Measurement of kinetics and thermodynamics of the thermal degradation for non-charring polymers. *Combustion and Flame*, 160:1287–1297, 2013. 129, 938

[300] J. Li and S.I. Stoliarov. Measurement of kinetics and thermodynamics of the thermal degradation for charring polymers. *Polymer Degradation and Stability*, 106:2–15, 2014. 129, 938

[301] J. Li, J. Gong, and S.I. Stoliarov. Development of pyrolysis models for charring polymers. *Polymer Degradation and Stability*, 115:138–152, 2015. 129, 938, 941

[302] J. P. White, E. D. Link, A. C. Trouvé, P. B. Sunderland, A. W. Marshall, J. A. Sheffel, M. L. Corn, M. B. Colket, M. Chaos, and H.-Z. Yu. Radiative emissions measurements from a buoyant, turbulent line flame under oxidizer-dilution quenching conditions. *Fire Safety Journal*, 76:74–84, 2015. 129, 130, 285, 494, 880, 900

[303] G. Back, B. Lattimer, C. Beyler, P. DiNenno, and R. Hansen. Full-Scale Testing of Water Mist Fire Suppression Systems for Small Machinery Spaces and Spaces with Combustible Boundaries, Volume I. Report CG-D-21-99, I, U.S. Coast Guard Research and Development Center, 1082 Shennecossett Road, Groton, Connecticut, 06340, October 1999. 132

[304] W.R. Catchpole, E.A. Catchpole, B.W. Butler, R.C. Rothermel, G.A. Morris, and D.J. Latham. Rate of Spread of Free-Burning Fires in Woody Fuels in a Wind Tunnel. *Combustion Science and Technology*, 131:1–37, 1998. 132, 974

[305] J.E. Gott, D.L. Lowe, K.A. Notarianni, and W.D. Davis. Analysis of High Bay Hangar Facilities for Fire Detector Sensitivity and Placement. NIST Technical Note 1423, National Institute of Standards and Technology, Gaithersburg, Maryland, February 1997. 133

[306] T.C.E. Ho, D. Surry, and D. Morrish. NIST/TTU Cooperative Agreement—Windstorm Mitigation Initiative: Wind Tunnel Experiments on Generic Low Buildings. Technical Report BLWT-SS20-2003, The Boundary Layer Wind Tunnel Laboratory, University of Western Ontario, London, Ontario, Canada, May 2003. 133

[307] N. Jarrin. *Synthetic Inflow Boundary Conditions for the Numerical Simulation of Turbulence*. PhD thesis, The University of Manchester, Manchester M60 1QD, United Kingdom, 2008. 134, 412

[308] S. Hostikka, M. Kokkala, and J. Vaari. Experimental Study of the Localized Room Fires. VTT Research Notes 2104, VTT Technical Research Centre of Finland, Espoo, Finland, 2001. 137

[309] J. Vaari, S. Hostikka, T. Sikanen, and A. Paajanen. Numerical simulations on the performance of water-based fire suppression systems. VTT Technology Report 54, VTT Technical Research Centre of Finland, Espoo, Finland, 2012. 140

[310] E.J. Weckman and A.B. Strong. Experimental Investigation of the Turbulence Structure of Medium-Scale Methanol Pool Fires. *Combustion and Flame*, 105:245–266, 1996. 140, 292, 764, 969

[311] A. Hamins, S.J. Fischer, T. Kashiwagi, M.E. Klassen, and J.P. Gore. Heat Feedback to the Fuel Surface in Pool Fires. *Combustion Science and Technology*, 97:37–62, 1994. 140, 862

[312] A. Hamins and A. Lock. The Structure of a Moderate-Scale Methanol Pool Fire. NIST Technical Note 1928, National Institute of Standards and Technology, Gaithersburg, Maryland, November 2016. https://doi.org/10.6028/NIST.TN.1928. 140, 270, 292, 295, 296

[313] Methanol Institute. *Physical Properties of Pure Methanol*. http://www.methanol.org/wp-content/uploads/2016/06/Physical-Properties-of-Pure-Methanol.pdf. 140

[314] K.A. Notarianni and G.W. Parry. *SFPE Handbook of Fire Protection Engineering*, chapter Uncertainty. Springer, New York, 5th edition, 2016. 149

[315] N.O. Siu and G.E. Apostolakis. Probabilistic Models for Cable Tray Fires. *Reliability Engineering*, 3:213–227, 1982. 150

[316] D. Stroup and A. Lindeman. Verification and Validation of Selected Fire Models for Nuclear Power Plant Applications. NUREG-1824, Supplement 1, United States Nuclear Regulatory Commission, Washington, DC, 2013. 151, 163

[317] B.N. Taylor and C.E. Kuyatt. Guidelines for Evaluating and Expressing the Uncertainty of NIST Measurement Results. NIST Technical Note 1297, National Institute of Standards and Technology, Gaithersburg, Maryland, 1994. 153

[318] G.W. Mulholland and C. Croarkin. Specific Extinction Coefficient of Flame Generated Smoke. *Fire and Materials*, 24:227–230, 2000. 154

[319] R.L. Alpert. *SFPE Handbook of Fire Protection Engineering*, chapter Ceiling Jet Flows. Springer, New York, 5th edition, 2016. 156, 157, 158

[320] R.W. Bukowski and J.D. Averill. Methods for Predicting Smoke Detector Activation. In *Proceedings of the Fire Suppression and Detection Research Application Symposium, Orlando, Florida*. National Fire Protection Association, Quincy, Massachusetts, 1998. 159, 405

[321] K. McGrattan and B. Toman. Quantifying the predictive uncertainty of complex numerical models. *Metrologia*, 48:173–180, 2011. 159

[322] R.D. Peacock, P.A. Reneke, W.D. Davis, and W.W. Jones. Quantifying fire model evaluation using functional analysis. *Fire Safety Journal*, 33:167–184, 1999. 160

[323] G. Oehlert. A Note on the Delta Method. *The American Statistician*, 46(1):27–29, 1992. 160

[324] A. Gelman, J.B. Carlin, H.S. Stein, and D.B. Rubin. *Bayesian Data Analysis*. Chapman and Hall/CRC Press, Boca Raton, Florida, 2nd edition, 2004. 161

[325] J.W. Tukey. Curves as Parameters, and Touch Estimation. In *Proc. Fourth Berkeley Symp. on Math. Statist. and Prob.*, volume 1, pages 681–694. (Univ. of Calif. Press, 1961. 162

[326] M.L. Janssens and H.C. Tran. Data Reduction of Room Tests for Zone Model Validation. *Journal of Fire Science*, 10:528–555, 1992. 165

[327] Y.P. He, A. Fernando, and M.C. Luo. Determination of interface height from measured parameter profile in enclosure fire experiment. *Fire Safety Journal*, 31:19–38, 1998. 165

[328] R. Falkenstein-Smith, K. Sung, J. Chen, K. Harris, and A. Hamins. The Structure of Medium-Scale Pool Fires. NIST Technical Note 2082, National Institute of Standards and Technology, Gaithersburg, Maryland, February 2020. https://doi.org/10.6028/NIST.TN.2082. 270, 573

[329] K. Sung and A. Hamins. Velocity and Temperature Structure of Medium-Scale Pool Fires. NIST Technical Note in preparation, National Institute of Standards and Technology, Gaithersburg, Maryland, 2021. 270, 424

[330] K. Sung, J. Chen, M. Bundy, M. Fernandez, and A. Hamins. The Characteristics of a 1 m Methanol Pool Fire. NIST Technical Note in preparation, National Institute of Standards and Technology, Gaithersburg, Maryland, September 2019. 270, 764, 862, 969

[331] F.R. Steward. Prediction of the height of buoyant diffusion flames. *Combustion Science and Technology*, 2(4):203–212, 1970. 301, 303

[332] H. Becker and D. Liang. Visible length of vertical free turbulent diffusion flames. *Combustion and Flame*, 32:115–137, 1978. 301, 303

[333] G. Cox and R. Chitty. Some source-dependent effects of unbounded fires. *Combustion and Flame*, 60:219–232, 1985. 301, 303

[334] Y. Hasemi and T. Tokunaga. Some experimental aspects of turbulent diffusion flames and buoyant plumes from fire sources against a wall and in corners. *Combustion Science and Technology*, 40:1–17, 1984. 301, 303

[335] B.M. Cetegen, E.E. Zukoski, and T. Kubota. Entrainment in the near and far field of fire plumes. *Combustion Science and Technology*, 39(1):305–331, 1984. 301, 303

[336] M.A. Delichatsios. Flame heights in turbulent wall fires with significant flame radiation. *Combustion Science and Technology*, 39:195–214, 1984. 301, 303

[337] F. Tamanini. Direct Measurement of the Longitudinal Variation of Burning Rate and Product Yield in Turbulent Diffusion Flames. *Combustion and Flame*, 51:231–243, 1983. 301

[338] Y.Z. Li, B. Lei, and H. Ingason. Study of critical velocity and backlayering length in longitudinally ventilated tunnel fires. *Fire Safety Journal*, 45:361–370, 2010. 455

[339] U. Wickström, D. Duthinh, and K.B. McGrattan. Adiabatic Surface Temperature for Calculating Heat Transfer to Fire Exposed Structures. In *Proceedings of the Eleventh International Interflam Conference*. Interscience Communications, London, 2007. 705

[340] A. Putorti, N. Melly, S. Bareham, and J. Praydis. Characterizing the Thermal Effects of High Energy Arc Faults. In M. R owekamp, editor, *23rd International Conference on Structural Mechanics in Reactor Technology (SMiRT 23)-—14th International Post-Conference Seminar on Fire Safety in Nuclear Power Plants and Installations*, number GRS-A-3845, pages 125–137. Gesellschaft f ur Anlagen-und Reaktorsicherheit (GRS), December 2015. http://www.grs.de/en/publications/grs-a-3845. 732

[341] A. Hamins. Energetics of Small and Moderate-Scale Gaseous Pool Fires. NIST Technical Note 1926, National Institute of Standards and Technology, Gaithersburg, Maryland, 2016. 815

[342] S.C. Kim, K.Y. Lee, and A. Hamins. Energy Balance in Medium-Scale Methanol, Ethanol, and Acetone Pool Fires. *Fire Safety Journal*, 107:44–53, 2019. 862

[343] M. Klassen and J.P. Gore. Structure and Radiation Properties of Pool Fires. NIST GCR 94-651, National Institute of Standards and Technology, Gaithersburg, Maryland, June 1994. 862

[344] J. P. White, S. Vilfayeau, A. W. Marshall, A. C. Trouvé, and R. J. McDermott. Modeling flame extinction and reignition in large eddy simulations with fast chemistry. *Fire Safety Journal*, 90:72–85, 2017. 900

[345] American Society for Testing and Materials, West Conshohocken, Pennsylvania. *ASTM E 1354-04a, Standard Test Method for Heat and Visible Smoke Release Rates for Materials and Products Using an Oxygen Combustion Calorimeter*, 2007. 921

[346] American Society for Testing and Materials, West Conshohocken, Pennsylvania. *ASTM E 2070-08, Standard Test Method for Kinetic Parameters by Differential Scanning Calorimetry Using Isothermal Methods*, 2008. 922

[347] American Society for Testing and Materials, West Conshohocken, Pennsylvania. *ASTM E 1175-87(2009), Standard Test Method for Determining Solar or Photopic Reference, Transmittance, and Absorptance of Materials Using a Large Diameter Integrating Sphere*, 2009. 922

[348] American Society for Testing and Materials, West Conshohocken, Pennsylvania. *ASTM E 1461-07, Standard Test Method for Thermal Diffusivity by the Flash Method*, 2007. 922

[349] American Society for Testing and Materials, West Conshohocken, Pennsylvania. *ASTM D 7309-11, Standard Test Method for Determining Flammability Characteristics of Plastics and Other Solid Materials Using Microscale Combustion Calorimetry*, 2011. 922

[350] American Society for Testing and Materials, West Conshohocken, Pennsylvania. *ASTM E 1131-08, Standard Test Method for Compositional Analysis by Thermogravimetry*, 2008. 922

[351] American Society for Testing and Materials, West Conshohocken, Pennsylvania. *ASTM D 5930-09, Standard Test Method for Thermal Conductivity of Plastics by Means of a Transient Line-Source Technique*, 2009. 922

[352] S.I. Stoliarov and R.N. Walters. Determination of the heats of gasification of polymers using differential scanning calorimetry. *Polymer Degradation and Stability*, 93:422–427, 2008. 923, 927, 929

[353] J.R. Hallman. Polymer surface reflectance-absorptance characteristics. *Polymer Engineering and Science*, 14:717–723, 1974. 923, 927, 929

[354] P.T. Tsilingiris. Comparative evaluation of the infrared transmission of polymer films. *Energy Conversion and Management*, 44:2839–2856, 2003. 923, 927, 929

[355] S.I. Stoliarov, R.E. Lyon, and G.T. Linteris. Prediction of the Gasification Rate of POM, PP, PA66 and PET in Fire-Like Environments. *Fire and Materials*, 2012. 925

[356] T. Matsumoto, A. Ono, Y. Noumaru, and F. Takeda. Measurements of Specific Heat Capacity and Emissivity of Graphite Samples using Pulse Current Heating at High Temperatures (III). In *Proceedings of the Seventeenth Japan Symposium on Thermophysical Properties*, pages 183–186, 1996. 927, 929

[357] E.S. Oztekin, S.B. Crowley S.B., R.E. Lyon, S.I. Stoliarov, P. Patel, and T.R. Hull. Sources of Variability in Fire Test Data: A Case Study on Poly(aryl ether ether ketone) (PEEK). *Combustion and Flame*, 159(4):1720–1731, 2012. 932

[358] F. Kempel, B. Schartel, G. T. Linteris, S.I. Stoliarov, R.E. Lyon, R.N. Walters, and A. Hofmann. Prediction of the Mass Loss Rate of Polymer Materials: Impact of Residue Formation. *Combustion and Flame*, 159:2974–2984, 2012. 934, 936

[359] G. Linteris, M. Zammarano, B. Wilthan, and L. Hanssen. Absorption and reflection of infrared radiation by polymers in fire-like environments. *Fire and Materials*, 36(7):537–553, 2012. 934, 936, 938

[360] R.E. Lyon and M.L. Janssens. *Encyclopedia of Polymer Science & Engineering*, chapter Polymer Flammability. Wiley, New York, 2005. 934, 936

[361] TIE-31: Mechanical and Thermal Properties of Optical Glass. Technical Information, Advanced Optics, SCHOTT AG, July 2004. 936

[362] G. Braeuer. Large Area Glass Coating. *Surface and Coatings Technology*, 112:358–365, 1999. 936

[363] J. Li. *A Multi-Scale Approach to Parameterization of Burning Models for Polymeric Materials*. PhD thesis, University of Maryland, College Park, Maryland, 2014. 938, 941, 943

[364] M.B. McKinnon, S.I. Stoliarov, and A. Witkowski. Development of a pyrolysis model for corrugated cardboard. *Combustion and Flame*, 160:2595–2607, 2013. 946, 947, 948

[365] P.J. Linstrom and W.G. Mallard. Evaluated Infrared Reference Spectra. WebBook. NIST Chemistry WebBook, NIST Standard Reference Database Number 69. 946, 947

[366] T. Matsumoto and A. Ono. Specific Heat Capacity and Emissivity Measurements of Ribbon-Shaped Graphite Using Pulse Current Heating. *International Journal of Thermophysics*, 16:267–275, 1995. 946, 947

[367] M.R. Semmes, X. Liu, M.B. McKinnon, S.I. Stoliarov, and A. Witkowski. A Model for Oxidataive Pyrolysis of Corrugated Cardboard. In *Fire Safety Science – Proceedings of the 11th International Symposium*, University of Canterbury, Christchurch, New Zealand, 2014. Accepted. 948

[368] D.J. Spiegelhalter. Diagnostic tests of distributional shape. *Biometrika*, 70(2):401–409, 1983. 1050